QC
1
P47

JOURNAL
OF THE
PHYSICAL SOCIETY
OF JAPAN

Volume 12
1957

Published by the
PHYSICAL SOCIETY OF JAPAN

Digitized by the Internet Archive
in 2024

https://archive.org/details/physical-society-of-japan-journal_january-december-1957_12_1-12

JOURNAL OF THE PHYSICAL SOCIETY OF JAPAN Vol. 12, No. 1, JANUARY, 1957

Group-Theoretical Treatment of the Energy Bands in Metal Borides MeB_6

By Masatoshi YAMAZAKI

Faculty of Liberal Arts and Science, Yamagata University, Yamagata

(Received August 8, 1956)

The tight-binding approximation is applied to a study of electronic energy bands in metal borides MeB_6. The 25×25 determinantal secular equation for the energy is reduced by a group-theoretical treatment of the spatial symmetry at certain special values of the wave vector $\boldsymbol{K}$. The results are that if metal atoms have two valence electrons the valence bands are all filled and the conduction bands are all empty, and in the case of calcium boride CaB_6 the narrowest gap between valence- and conduction-bands is at edges of the first Brillouin zone, the simple cube in the reciprocal space and its width is about 1.5 eV, in good agreement with empirical results that there exist only borides of elements having two valence *s* electrons in this type of structure.

§ 1. Introduction

According to the results of Kiessling's X-ray analysis[1)], structures of metal boride crystals MeB_6 are that six boron atoms *en bloc* make one octahedron the center of which makes a simple cube, and metal atoms which are at interstices of boron octahedra and enclosed by twenty-four boron atoms make another simple cube, and thus six boron atoms B_6 *en bloc* and metal atoms Me make a structure of cesium chloride type. Every boron atom has five other adjacent boron atoms at equal distances. The shortest boron-boron distances of MeB_6 are almost independent of the participating metals, as seen in Table I. It is significant that metals with a higher ionization potential than yttrium (8.71 eV) cannot form MeB_6 crystals. Thus in MeB_6 crystals parts of electrons are considered to be transferred to boron atoms, so the high stability of MeB_6 crystal very likely depends on the ionization of Me. After the results of another X-ray analysis of several boron hydrides by Lipscomb[2)], five boron atoms in B_5H_9 occupy almost five vertex sites of a octahedron (B–B (base) 1.80 and B–B (slant) 1.69 A), and five boron atoms in B_5H_{11} imperfectly occupy five vertex sites of a distorted octahedron (average B–B 1.74 A). It is thought to be characteristic that boron atoms make structures of octahedron type. Longuet-Higgins and de V. Roberts[3)] and Flodmark[4)] performed theoretical analysis of MeB_6 and reached the conclusions fairly agreeing with experimental results. It is the purpose of this paper to calculate more quantitatively the variation of energy with the wave vector in the reciprocal space for

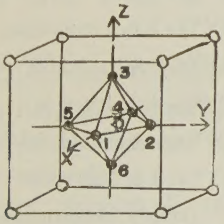

Fig. 1. Structure of the MeB_6 crystal. Six B atoms make one octahedron, whose center is situated at the body center of simple cube made by Me atoms. Every B atom has five nearest B atoms at equal distance, one of which belongs to the next octahedron. The coordination number of Me atom is 24.

Table I. Distance between adjacent atoms in MeB_6 due to Kiessling[1)] (in angstrom units)

	B-B	Me–B	Me–Me
Ca	1.72	3.06	4.15
Ba	1.78	3.16	4.29
Sr	1.74	3.09	4.20
Yb	1.71	3.05	4.14
La	1.72	3.06	4.15
Ce	1.71	3.05	4.14
Nd	1.71	3.04	4.13
Pr	1.71	3.04	4.13
Gd	1.71	3.04	4.13
Th	1.72	3.07	4.16
Y	1.69	3.01	4.08
Er	1.70	3.03	4.11

M55/63 20 mar

MeB_6.

In this paper the energies of Bloch orbitals which are based on the four atomic orbitals 2*s*, 2*px*, 2*py*, and 2*pz* of the boron atom and one *ns* of the metal atom are calculated under the simplified periodic field at certain special values of the wave vector $\boldsymbol{K}$. Since there are six B atoms and one Me atom per unit cell, there are twenty-five basis atomic orbitals to be considered. The 25×25 determinantal secular equation for the energy based on twenty-five Bloch sums is factorized with respects to sets of basis of different irreducible representations for the subgroup of the rotation group of the lattice and the group of the wave vector, so leaving us with seculor equations of lower degree to solve. Because MeB_6 lattice is polyatomic, the cubic harmonics of von der Lage and Bethe⁵⁾ developed about different points in the lattice must be matched over the surface of subcells, resulting from the division of the unit cell and one surrounding each site, by the condition that the Bloch orbital is smooth throughout the crystal⁶⁾. Here we regard six boron atoms *en bloc* making one octahedron as to constitute one lattice site, and MeB_6 crystals are considered to have the structure of cesium chloride type, Me atoms making simple cube and B_6 atoms occupying its body centers. The twenty-four AO's of B_6 atoms are combined to form bases of different irreducible representations of the crystal symmetry, the octahedral group $\boldsymbol{O}_h$. In the following the band structure of calcium boride is calculated at certain points in the Brillouin zone.

§2. Method and Calculation

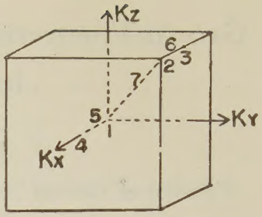

Fig. 2. The first Brillouin zone of the MeB_6 crystal (CsCl type) 1), 2), 3), 4), 5), 6) and 7) are the special points in the zone cited in the text.

The direct lattice vectors $\boldsymbol{a}_i$ and the reciprocal lattice vectors $\boldsymbol{b}_j$ are

$$\boldsymbol{a}_1=a(1,0,0)\,; \qquad \boldsymbol{b}_1=2\pi/a(1,0,0)\,;$$
$$\boldsymbol{a}_2=a(0,1,0)\,; \qquad \boldsymbol{b}_2=2\pi/a(0,1,0)\,;$$
$$\boldsymbol{a}_3=a(0,0,1)\,; \qquad \boldsymbol{b}_3=2\pi/a(0,0,1)\,.$$

Thus, the unit lattice cell is a cube of side *a* and the first Brillouin zone a cube of side $2\pi/a$. The MeB_6 lattice is *so-called diatomic*, made up of two interpenetrating simple cubic lattices of B_6 atoms and Me atoms based on the points (0, 0, 0) and $a/2(1,1,1)$, respectively, such that the potential has full cubic symmetry about each site. The *x*-, *y*-, and *z*-axes and the numbering of six boron atoms making one octahedron are taken as shown in Fig. 1. The coordinates of six boron atoms are with the center of octahedron as zero;

$$1,\ (a/(2+\sqrt{2}),0,0); \qquad 2,\ (0,a/(2+\sqrt{2}),0);$$
$$3,\ (0,0,a/(2+\sqrt{2})); \qquad 4,\ (-a/(2+\sqrt{2}),0,0);$$
$$5,\ (0,-a/(2+\sqrt{2}),0); \quad 6,\ (0,0,-a/(2+\sqrt{2})).$$

The twenty-four AO's, four on each atom, are combined to form bases of the crystal symmetry $\boldsymbol{O}_h$ as:

$$a_{1g}\ :\quad (1/6)^{1/2}(s_1+s_2+s_3+s_4+s_5+s_6)\,,$$
$$(1/6)^{1/2}(x_1-x_4+y_2-y_5+z_3-z_6);$$
$$e_g(1):\quad (1/12)^{1/2}(2s_1-s_2-s_3+2s_4-s_5-s_6)\,,$$
$$(1/12)^{1/2}(2x_1-y_2-z_3-2x_4+y_5+z_6);$$
$$e_g(2):\quad (1/4)^{1/2}(s_2-s_3+s_5-s_6)\,,$$
$$(1/4)^{1/2}(y_2-z_3-y_5+z_6)$$

(doubly degenerate):

$$f_{1u}(x):\quad (1/2)^{1/2}(s_1-s_4)\,,\quad (1/2)^{1/2}(x_1+x_4)\,,$$
$$(1/4)^{1/2}(x_2+x_3+x_5+x_6);$$
$$f_{1u}(y):\quad (1/2)^{1/2}(s_2-s_5)\,,\quad (1/2)^{1/2}(y_2+y_5)\,,$$
$$(1/4)^{1/2}(y_3+y_4+y_6+y_1);$$
$$f_{1u}(z):\quad (1/2)^{1/2}(s_3-s_6)\,,\quad (1/2)^{1/2}(z_3+z_6)\,,$$
$$(1/4)^{1/2}(z_1+z_2+z_4+z_5)$$

(triply degenerate):

$$f_{1g}(x):\quad (1/4)^{1/2}(z_2-y_3-z_5+y_6);$$
$$f_{1g}(y):\quad (1/4)^{1/2}(x_3+z_4-x_6-z_1);$$
$$f_{1g}(z):\quad (1/4)^{1/2}(y_1-x_2-y_4+x_5)$$

(triply degenerate):

$$f_{2g}(x):\quad (1/4)^{1/2}(z_2+y_3-z_5-y_6);$$
$$f_{2g}(y):\quad (1/4)^{1/2}(x_3-z_4-x_6+z_1);$$
$$f_{2g}(z):\quad (1/4)^{1/2}(y_1+x_2-y_4-x_5)$$

(triply degenerate):

$$f_{2u}(x):\quad (1/4)^{1/2}(x_2-x_3+x_5-x_6);$$
$$f_{2u}(y):\quad (1/4)^{1/2}(y_3-y_4+y_6-y_1);$$
$$f_{2u}(z):\quad (1/4)^{1/2}(z_1-z_2+z_4-z_5)$$

(triply degenerate):

here s_i, x_i, y_i, and z_i means $2s$, $2px$, $2py$, and $2pz$ AO's of B atom i, respectively. The overlapping of atomic orbitals are all neglected.

For AO's of Me atoms we consider only valence s orbitals which belong to a_{1g} representation of $\boldsymbol{O}_h$ group. These Me orbitals match the boron AO's at special values of the wave vector as:

1) $\boldsymbol{K}=(0, 0, 0)$ Γ_1

2) $K=\pi/a(1, 1, 1)$ R_2',

so there is none in our treatment

3) $K=\pi/a(0, 1, 1)$ M_3

4) $K=\pi/a(1, 0, 0)$ X_4'

5) $K=\pi/a(\alpha, 0, 0)$, $0<\alpha<1$ Δ_1

6) $K=\pi/a(\alpha, 1, 1)$, $0<\alpha<1$ T_2'

7) $K=\pi/a(\alpha, \alpha, \alpha)$, $0<\alpha<1$ Λ_1

8) $K=\pi/a(0, \alpha, \alpha)$, $0<\alpha<1$ Σ_1

9) $K=\pi/a(1, \alpha, \alpha)$, $0<\alpha<1$ S_3

10) $K=\pi/a(\alpha, 0, 1)$, $0<\alpha<1$ Z_4.

Following Bloch's method, the one electron wave functions in the periodic potential field are written as

$$\Psi_N(\boldsymbol{K})=\sum(\boldsymbol{R}_i)\exp(i\boldsymbol{K}\boldsymbol{R}_i)\bar{\chi}_N(\boldsymbol{r}-\boldsymbol{R}_i),$$

where $\boldsymbol{R}_i$ is the position vector of the crystal lattice site, $\boldsymbol{K}$ is the wave vector, and $\bar{\chi}_N$'s are linear combinations of several AO's χ_n of one lattice site. ($\bar{\chi}_N(\boldsymbol{K})=\sum(n)\lambda_{Nn}(\boldsymbol{K})\chi_n$; λ_{Nn}'s are functions of $\boldsymbol{K}$). We make Bloch sums φ_n for every same kinds of AO's on each same lattice site as

$$\varphi_n=\sum(\boldsymbol{R}_i)\exp(i\boldsymbol{K}\boldsymbol{R}_i)\chi_n(\boldsymbol{r}-\boldsymbol{R}_i),$$

so we obtain $\Psi_N(\boldsymbol{K})=\sum(n)\lambda_{Nn}(\boldsymbol{K})\varphi_n$. For simplification we assume the Bloch sums are orthogonal to each other.

In the case of general K values we have secular equations for the energy as

$$|H_{nm}-E\delta_{nm}|=0,$$

where $\boldsymbol{H}$ is the one electron hamiltonian operator in the crystal and

$$H_{nm}=\int\varphi_n^*\boldsymbol{H}\varphi_m d\tau.$$

Factorizations of secular equations at special points in the first Brillouin zone are tabulated in the appendix.

The matrix elements H_{nm}'s are expressed as (Bloch sums are normalized over the cyclic domain, and N is the number of atoms in the cyclic domain):

$$\begin{aligned}H_{nm}&=\int\varphi_n^*\boldsymbol{H}\varphi_m d\tau\\&=N^{-1}\sum(\boldsymbol{R}_i)\sum(\boldsymbol{R}_j)\exp(i\boldsymbol{K}(\boldsymbol{R}_j-\boldsymbol{R}_i))\\&\quad\times\int\chi_n^*(\boldsymbol{r}-\boldsymbol{R}_i)\boldsymbol{H}\chi_m(\boldsymbol{r}-\boldsymbol{R}_j)d\tau\\&=\sum(\boldsymbol{R}_j)\exp(i\boldsymbol{K}(\boldsymbol{R}_j-\boldsymbol{R}_i))\\&\quad\times\int\chi_n^*(\boldsymbol{r}-\boldsymbol{R}_i)\boldsymbol{H}\chi_m(\boldsymbol{r}-\boldsymbol{R}_j)d\tau.\end{aligned}$$

For arbitrary B atoms interactions with five atoms within that octahedron and shortest distance one within next one are considered and for B–Me, Me–Me only the nearest neighbour interactions are taken into account. Coulomb energies

$$\int\chi_n^*(\boldsymbol{r}-\boldsymbol{R}_i)\boldsymbol{H}\chi_n(\boldsymbol{r}-\boldsymbol{R}_i)d\tau$$

are approximated by one-electron orbital energies of the free atom given by Slater[7], i.e., -14.01, -5.71, and -6.12 eV for $2s$, $2p$ of B, and $4s$ of Ca, respectively, and resonance energies are approximated to be proportional to the corresponding overlap integrals[8] of Slater atomic orbitals[9], the proportional constant being taken as -10.153 eV determined from the ratio of the resonance energy for carbon-carbon neighbour in benzene, -2.39 eV, the value suggested by Pariser and Parr[10], to the corresponding overlap integral, 0.2354, calculated from formulas by Mulliken et al.[8]*. The effective nuclear charge of boron $2s$, $2p$ AO's is first taken as $2\delta=2.60$ (5 electrons per atom), but after preliminary calculations it is decided to be $2\delta=2.482$ ($5+\frac{1}{3}$ electrons per atom). The calculated energy bands are shown in Fig. 3.

If the metal atom has two valence s electrons, the valence bands are completely filled and the conduction bands are completely empty. The shortest gap between valence-

---

* The overlap integrals for B atoms are:

$$\begin{aligned}&S_{s1s2}=0.452, \quad S_{s1\sigma2}=0.442,\\&\qquad\qquad\qquad\quad S_{\sigma1\sigma2}=0.322, \quad S_{\pi1\pi2}=0.282,\\&S_{s1s4}=0.216, \quad S_{s1\sigma4}=0.257,\\&\qquad\qquad\qquad\quad S_{\sigma1\sigma4}=0.274, \quad S_{\pi1\pi4}=0.105;\end{aligned}$$

with effective nuclear charge $2\delta=2.482$.

The overlap integral for Ca atoms is approximated to be $S_{ss}=0.395$ with effective nuclear charge $3.7\delta=3.2$, and those between nearest Ca–B neighbours are approximated to be $S_{ss}=0.275$ and $S_{s\sigma}=0.165$.

and conduction-bands is at edges of the first Brillouin zone, the simple cube in the reciprocal space and its width is proved to be about 1.5 eV.

The assumptions we have used are undoubtedly crude by quantitative standards, but we feel fairly confident of our obtained results qualitatively.

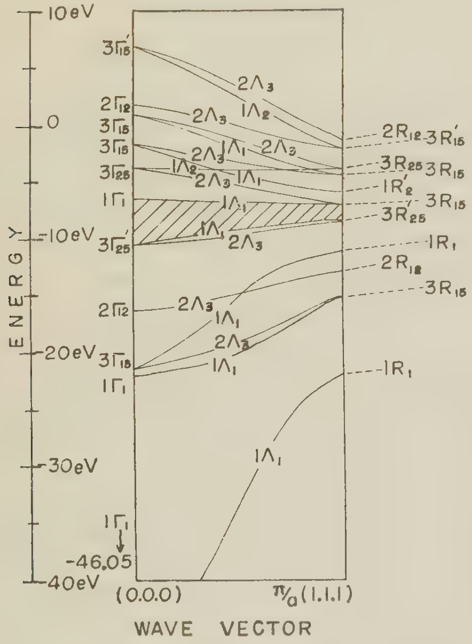

Fig. 3. a

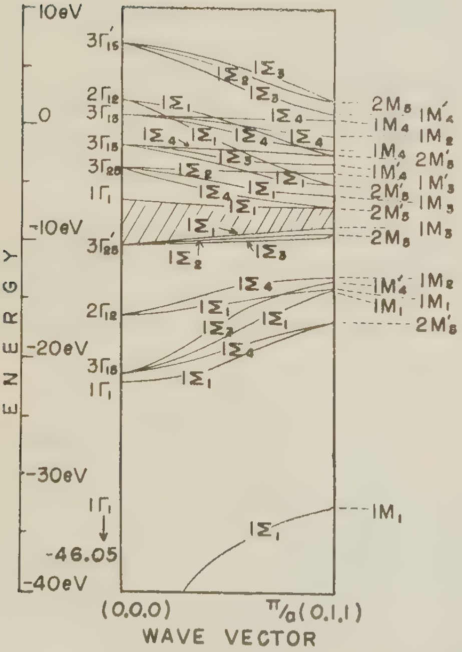

Fig. 3. b

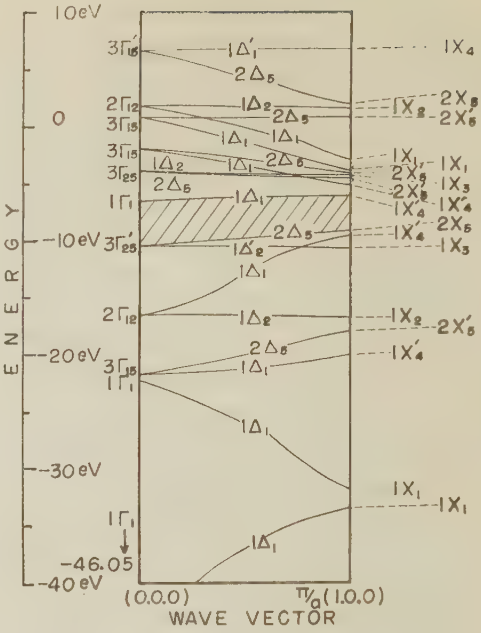

Fig. 3. c

Fig. 3. Variation of energy with wave vector in reciprocal space for CaB_6. The figures "2" and "3" denote the degree of degeneracy of energy-versus-wave vector curves.

Appendix

The factorizations of secular equations for the energy at certain special points in the first Brillouin zone:

S_i, X_i, Y_i, Z_i, and S_M means the Bloch sum constructed from the atomic orbital $2s$, $2px$, $2py$, and $2pz$ of the i-site of B atom, and the $4s$ atomic orbital of the metal-site of Ca atom. Unnormalized forms of Bloch sums and notations of different irreducible representations about the B-site are described.

1) $K=(0, 0, 0)$ and 2) $K=\pi/a(1, 1, 1)$ (symmetry type: O_h)

In case 1) three 1st order-(each triply degenerated), one second order-(doubly degenerated), and two third order-secular equations (one of which is triply degenerated) are obtained.

In case 2) four 1st order-(three of which are triply degenerated), two second order-(one of which is doubly degenerated), and one third order-(triply degenerated) secular equations are obtained.

Γ_1 : $(S_1+S_2+S_3+S_4+S_5+S_6)$, $(X_1-X_4+Y_2-Y_5+Z_3-Z_6)$, S_M(for case 1));
$\Gamma_{12}(1)$: $(2S_1-S_2-S_3+2S_4-S_5-S_6)$, $(2X_1-Y_2-Z_3-2X_4+Y_5+Z_6)$;
$\Gamma_{12}(2)$: $(S_2-S_3+S_5-S_6)$, $(Y_2-Z_3-Y_5+Z_6)$;
$\Gamma_{15}(x)$: (S_1-S_4), (X_1+X_4), $(X_2+X_3+X_5+X_6)$;
$\Gamma_{15}(y)$: (S_2-S_5), (Y_2+Y_5), $(Y_3+Y_4+Y_6+Y_1)$;
$\Gamma_{15}(z)$: (S_3-S_6), (Z_3+Z_6), $(Z_1+Z_2+Z_4+Z_5)$;
$\Gamma_{15}'(x)$: $(Z_2-Y_3-Z_5+Y_6)$; $\Gamma_{25}'(x)$: $(Z_2+Y_3-Z_5-Y_6)$;
$\Gamma_{15}'(y)$: $(X_3+Z_4-X_6-Z_1)$; $\Gamma_{25}'(y)$: $(X_3-Z_4-X_6+Z_1)$;
$\Gamma_{15}'(z)$: $(Y_1-X_2-Y_4+X_5)$; $\Gamma_{25}'(z)$: $(Y_1+X_2-Y_4-X_5)$;
$\Gamma_{25}(x)$: $(X_2-X_3+X_5-X_6)$; Γ_2' : S_M(for case 2)).
$\Gamma_{25}(y)$: $(Y_3-Y_4+Y_6-Y_1)$;
$\Gamma_{25}(z)$: $(Z_1-Z_2+Z_4-Z_5)$;

3) $\boldsymbol{K}=\pi/a(0, 1, 1)$ and 4) $\boldsymbol{K}=\pi/a(1, 0, 0)$ (symmetry type: $\boldsymbol{D}_{4h}$)

In case 3) two first order-, three second order-(one of which is doubly degenerated), one third order-, and two fourth order-(one of which is doubly degenerated) secular equations are obtained.

In case 4) three 1st order-, two 2nd order-(one of which is doubly degenerated), and three fourth order-(one of which is doubly degenerated) sec. equ. are obtained.

X_1 : $(S_1+S_2+S_3+S_4+S_5+S_6)$, $(X_1-X_4+Y_2-Y_5+Z_3-Z_6)$, $(2S_1-S_2-S_3+2S_4-S_5-S_6)$,
$(2X_1-Y_2-Z_3-2X_4+Y_5+Z_6)$;
X_4 : $(Z_2-Y_3-Z_5+Y_6)$;
X_2 : $(S_2-S_3+S_5-S_6)$, $(Y_2-Z_3-Y_5+Z_6)$;
X_3 : $(Z_2+Y_3-Z_5-Y_6)$, S_M(for case 3));
$X_5(1)$: $(X_3-Z_4-X_6+Z_1)$, $(X_3+Z_4-X_6-Z_1)$;
$X_5(2)$: $(Y_1+X_2-Y_4-X_5)$, $(-(Y_1-X_2-Y_4+X_5))$;
X_4' : (S_1-S_4), (X_1+X_4), $(X_2+X_3+X_5+X_6)$, S_M(for case 4));
X_3' : $(X_2-X_3+X_5-X_6)$;
$X_5'(1)$: (S_2-S_5), (Y_2+Y_5), $(Y_3+Y_4+Y_6+Y_1)$, $(Y_3-Y_4+Y_6-Y_1)$;
$X_5'(2)$: (S_3-S_6), (Z_3+Z_6), $(Z_1+Z_2+Z_4+Z_5)$, $(-(Z_1-Z_2+Z_4-Z_5))$.

5) $\boldsymbol{K}=\pi/a(\alpha, 0, 0)$ and 6) $\boldsymbol{K}=\pi/a(\alpha, 1, 1)$, $0<\alpha<1$ (symmetry type: $\boldsymbol{C}_{4v}$)

In case 5) two 1st order-, one third order-, one sixth order-(doubly degenerated), and one eighth order secular equations are obtained.

In case 6) one first order-, one second order-, one third order-, one sixth order-(doubly degenerated), and one seventh order-secular equations are obtained.

Δ_1 : $(S_1+S_2+S_3+S_4+S_5+S_6)$, $(X_1-X_4+Y_2-Y_5+Z_3-Z_6)$, $(2S_1-S_2-S_3+2S_4-S_5-S_6)$,
$(2X_1-Y_2-Z_3-2X_4+Y_5+Z_6)$, (S_1-S_4), (X_1+X_4), $(X_2+X_3+X_5+X_6)$,
S_M(for case 5));
Δ_1' : $(Z_2-Y_3-Z_5+Y_6)$;
Δ_2 : $(S_2-S_3+S_5-S_6)$, $(Y_2-Z_3-Y_5+Z_6)$, $(X_2-X_3+X_5-X_6)$;
Δ_2' : $(Z_2+Y_3-Z_5-Y_6)$, S_M(for case 6));
$\Delta_5(1)$: (S_2-S_5), (Y_2+Y_5), $(Y_3+Y_4+Y_6+Y_1)$, $(Y_3-Y_4+Y_6-Y_1)$, $(Y_1+X_2-Y_4-X_5)$,
$(-(Y_1-X_2-Y_4+X_5))$;
$\Delta_5(2)$: (S_3-S_6), (Z_3+Z_6), $(Z_1+Z_2+Z_4+Z_5)$, $(-(Z_1-Z_2+Z_4-Z_5))$, $(X_3-Z_4-X_6+Z_1)$,
$(X_3+Z_4-X_6-Z_1)$;

7) $\boldsymbol{K}=\pi/a(\alpha, \alpha, \alpha)$ $0<\alpha<1$ (symmetry type: $\boldsymbol{C}_{3v}$)

One second order-, one seventh order-, and one eighth order-(doubly degenerated) secular equations are obtained.

Λ_1 : $(S_1+S_2+S_3+S_4+S_5+S_6)$, $(X_1-X_4+Y_2-Y_5+Z_3-Z_6)$, $(Z_2+Y_3-Z_5-Y_6+X_3-Z_4-X_6+Z_1+Y_1+X_2-Y_4-X_5)$, $(S_1+S_2+S_3-S_4-S_5-S_6)$, $(X_1+Y_2+Z_3+X_4+Y_5+Z_6)$, $(X_2+X_3+X_5+X_6+Y_3+Y_4+Y_6+Y_1+Z_1+Z_2+Z_4+Z_5)$, (S_M);

Λ_2 : $(X_2-X_3+X_5-X_6+Y_3-Y_4+Y_6-Y_1+Z_1-Z_2+Z_4-Z_5)$, $(Z_2-Y_3-Z_5+Y_6+X_3+Z_4-X_6-Z_1+Y_1-X_2-Y_4+X_5)$;

$\Lambda_3(1)$: $(2S_1-2S_4-S_2+S_5-S_3+S_6)$, $(2X_1+2X_4-Y_2-Y_5-Z_3-Z_6)$, $(2X_2+2X_3+2X_5+2X_6-Y_3-Y_4-Y_6-Y_1-Z_1-Z_2-Z_4-Z_5)$, $(Z_1-Z_2+Z_4-Z_5-Y_3+Y_4-Y_6+Y_1)$, $(2S_1-S_2-S_3+2S_4-S_5-S_6)$, $(2X_1-Y_2-Z_3-2X_4+Y_5+Z_6)$, $(2Z_2+2Y_3-2Z_5-2Y_6-X_3+Z_4+X_6-Z_1-Y_1-X_2+Y_4+X_5)$, $(Y_1-X_2-Y_4+X_5-X_3-Z_4+X_6+Z_1)$;

$\Lambda_3(2)$: $(S_2-S_5-S_3+S_6)$, $(Y_2+Y_5-Z_3-Z_6)$, $(Y_3+Y_4+Y_6+Y_1-Z_1-Z_2-Z_4-Z_5)$, $(2X_2-2X_3+2X_5-2X_6-Y_3+Y_4-Y_6+Y_1-Z_1+Z_2-Z_4+Z_5)$, $(X_3-Z_4-X_6+Z_1-Y_1-X_2+Y_4+X_5)$, $(S_2-S_3+S_5-S_6)$, $(Y_2-Z_3-Y_5+Z_6)$, $(2Z_2-2Y_3-2Z_5+2Y_6-X_3-Z_4-X_6+Z_1-Y_1+X_2+Y_4-X_5)$.

References

1) R. Kiessling: Acta Chem. Scand. **4** (1950) 209.
2) W. N. Lipscomb: J. Chem. Phys. **22** (1954) 985.
3) H. C. Longuet-Higgins and M. de V. Roberts: Proc. Roy. Soc. **A 224** (1954) 336.
4) S. Flodmark: Ark. for Fysik 9 paper **24** (1955) 357.
5) F. C. von der Lage and H. Bethe: Phys. Rev. **71** (1947) 612.
6) D. G. Bell: Rev. Moder. Phys. **26** (1954) 311.
7) J. C. Slater: Phys. Rev. **98** (1955) 1039.
8) R. S. Mulliken, C. A. Rieke, D. Orloff and H. Orloff: J. Chem. Phys. **17** (1949) 1248.
9) J. C. Slater: Phys. Rev. **36** (1930) 57.
10) R. Pariser and R. G. Parr: J. Chem. Phys. **21** (1953) 767.

JOURNAL OF THE PHYSICAL SOCIETY OF JAPAN Vol. 12, No. 1, JANUARY 1957

On the Period of Out-of-step of Ordered Alloys with Anti-phase Domain Structure

By Kunio FUJIWARA

The Research Institute for Iron, Steel and Other Metals,
Tohoku University, Sendai, Japan

(Received September 13, 1956)

The period of out-of-step of ordered alloys with anti-phase domain structure, measured in atomic distance, is generally not an integer, in spite of sharp splits of superlattice reflections. This fractional property of the period has theoretically been examined. The general treatment of this problem has shown that a regular and uniform arrangement of the different periods of anti-phase domains can explain the fractional value of the period, M. The results of numerical calculations in some models of arrangement have suggested, however, that complete regularity in arrangement is not always necessary but only uniformity is essential for the interpretation of the diffraction patterns.

§1. Introduction

Recently, many X-ray and electron diffraction studies[1] have been made on the ordered alloys with anti-phase domain structure, such as CuAu, Cu_3Pd, etc., and even a fairly complex type of anti-phase domain has been discovered[2]. The writer has also studied the anti-phase domain structure of Ag_3Mg in single crystal as well as polycrystal[3]. The diffraction patterns of such alloys show sharp splits of superlattice reflections, due to anti-phase domains, and the period of out-of-step or the length of anti-phase domain, measured in atomic distance, M, can be calculated from the separation of split spots. The value of M is, however, generally not an integer* in spite of sharpness of the splitting. This curious property may be interpreted, if M means a mean length of anti-phase domains. Namely, we consider that a crystal contains several sorts of anti-phase domains whose lengths correspond to different integers respectively and that these domains are mixed in such a manner that M is given as a mean length. The type of arrangement of anti-phase domains can be classified as follows:

i) Regular arrangement with uniform mixing,
ii) Regular arrangement with not uniform mixing,
iii) Irregular arrangement with almost uniform mixing,
iv) Irregular arrangement with not uniform mixing.

To explain the sharpness of split diffraction spots, it seems to be necessary that some regularities are contained in the arrangements. Models of regular arrangement which correspond to the same value of M are, however, innumerable and it is difficult to decide which model is realized in a real crystal. Such a problem will much more complicate the image of the anti-phase domain structure. On the other hand, the idea that no regularity is contained in the arrangements seems to be attractive for its simplicity. In this case, however, it should be examined whether this model can explain the sharpness of splitting of spots or not. Some calculations have been made in the present work, in order to interpret the fractional values of M, and the results are believed to give a fairly clear conclusion on the period of out-of-step.

§2. The Regular Arrangements of the Anti-phase Domains

Let us now deal with an ordered crystal lattice of Cu_3Au type as shown in Fig. 1. Its dimensions parallel to the x, y, z-axes are N_1a_1, N_2a_2 and N_3a_3 respectively, where a_1, a_2 and a_3 are the lattice constants and N_1, N_2 and N_3 the numbers of the unit cells. An

---

* For example,

Cu_3Pd(2)—	$M_1=5.5$,	$M_2=3.7$	(25 at. % Pd)
	$M_1=3.5$,	$M_2=3.2$	(28 at. % Pd)
Ag_3Mg(3)—	$M=1.77$		(25 at. % Mg)
	$M=1.83$		(24. 3 at. % Mg)

anti-phase domain structure is assumed to occur along the z-direction in this lattice. The arrows in the figure show the positions of anti-phase domain boundaries, where a displacement $(\vec{a}_1+\vec{a}_2)/2$ takes place. This type of anti-phase domain structure can be observed in Cu_3Pd, Ag_3Mg[1),3)], an incompletely ordered lattice of Cu_3Au and so on. In such a crystal the unit cell* in terms of a disordered lattice is considered in two ways, as shown in Fig. 2. If the structure factor of the left cell in the figure is given by Φ, that of the right cell becomes $\Phi\cdot\exp\{\pi i(h+k)\}$, if h, k and l represent the coordinates in reciprocal space. It can easily be shown that only superlattice reflections with odd $h+k$ split along the l-direction. As we are mainly interested in the split reflections, we shall restrict our calculations only to the case of odd $h+k$. Thus, the structure factors of two unit cells become Φ and $-\Phi$ respectively, and the intensity distribution in reciprocal space is given by

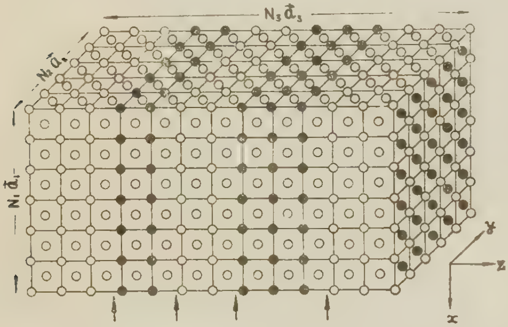

Fig. 1. An ordered lattice of Cu_3Au type with anti-phase domains along the z-direction.

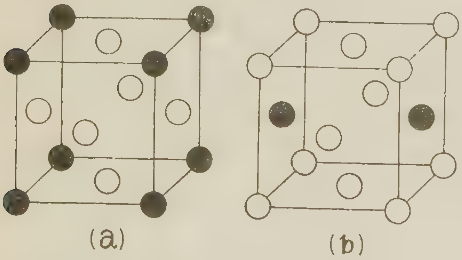

Fig. 2. (a) unit cell of positive type
(b) unit cell of negative type

$$I(hkl)=\left|\sum_{n_1=0}^{N_1-1}\sum_{n_2=0}^{N_2-1}\sum_{n_3=0}^{N_3-1}\Phi\cdot f(n_3)\cdot\exp\{2\pi i(n_1h+n_2k+n_3l)\}\right|^2$$
$$=\Phi^*\Phi\cdot\frac{\sin^2 N_1\pi h}{\sin^2 \pi h}\cdot\frac{\sin^2 N_2\pi k}{\sin^2 \pi k}\cdot\left|\sum_{n_3=0}^{N_3-1} f(n_3)\cdot\exp(2\pi i n_3 l)\right|^2, \qquad (1)$$

where a set of (n_1, n_2, n_3) represents the number of a unit cell contained in this crystal. $f(n)$ is a factor which takes either value, $+1$ or -1, according as the type of the n-th unit cell along the z-axis is positive or negative, and so it will be called 'anti-phase factor.' It is the factor

$$F\equiv\sum_{n=0}^{N-1} f(n)\cdot\exp(2\pi inl) \qquad (2)$$

that gives splitting of spots in the l-direction, and in the following calculations, therefore, we shall concern ourselves only with this factor. If a functional form of $f(n)$ is given, then the corresponding arrangement of anti-phase domains in crystal will be determined, and the factor F can be calculated at once.

a) *Regular arrangements with uniform mixing*

If it could be proved that several models of regular arrangement give acceptable intensity distributions, a complete solution of the problem would not be obtained unless the general law could be found which give an acceptable regular arrangement corresponding to a given value of M. Thus, the present problem is to find the general form of $f(n)$ corresponding to a regular arrangement with uniform mixing. If n is replaced, for convenience, by a continuous variable, ξ, the following periodic function $f_M(\xi)$ with the period $2M$ can be obtained as a solution:

$$f_M(\xi)=\begin{cases}1 & \text{for}\quad 2kM\leq\xi<(2k+1)M\\ -1 & \text{for}\quad (2k+1)M\leq\xi<(2k+2)M\end{cases}$$
$$(k=0,\,1,\,2,\,\cdots)\,. \qquad (3)$$

Fig. 3-(a) shows the form of $f_{1.70}(\xi)$ as an examale. Of course, $f_M(\xi)$ has a physical meaning only when $\xi=n$, and, hereafter, such functions as $f_M(\xi)$ will be called 'anti-phase function.' When $M=1.80$, for example, $f_{1.80}(\xi)$ gives the arrangement

$$(2\bar{2}2\bar{2}1\bar{2}2\bar{2}2\bar{1}\cdots)$$

and when $M=1.70$, $f_{1.70}(\xi)$ gives the arrange-

---

* If there is a complete regularity in the arrangement of anti-phase domains, a larger unit cell should be adopted as an actual one, as described later,

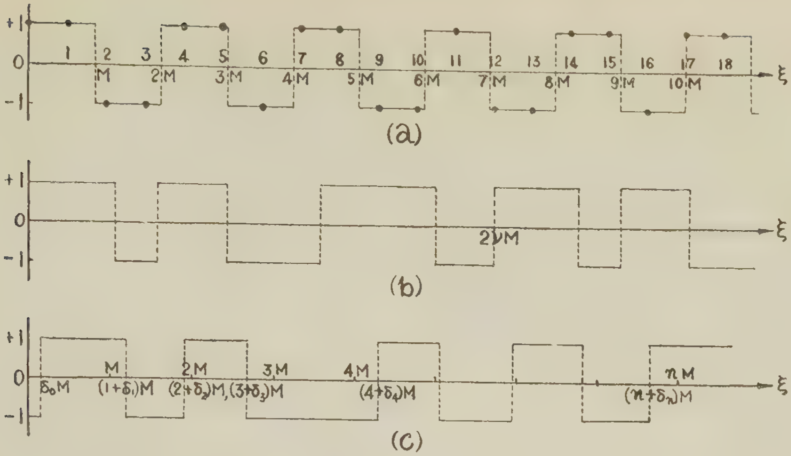

Fig. 3. Anti-phase functions in various cases.
(a) $f_{1.70}(\xi)$ (b) An example of $\varphi_M(\xi)$ (c) An example of $\psi_M(\xi)$

ment

$$(2\bar{2}2\bar{1}2\bar{2}1\bar{2}2\bar{1}\cdots),$$

where each number represents the length of an anti-phase domain in the z-direction, measured in atomic distance, and upper bars mean the domains of negative type. As to the regular arrangements with $M=1.80$, other models may be considered;

$$(2\bar{2}2\bar{1}2\bar{2}2\bar{2}2\bar{1}\cdots),$$

$$(2\bar{2}2\bar{2}2\bar{2}2\bar{2}1\bar{1}\cdots),$$

$$(2\bar{2}2\bar{2}2\bar{1}2\bar{2}2\bar{1}2\bar{2}2\bar{1}2\bar{2}2\bar{2}2\bar{1}\cdots)$$

and so on. None of them, however, can be more uniform than the arrangement

$$(2\bar{2}2\bar{2}1\bar{2}2\bar{2}2\bar{1}\cdots)$$

corresponding to $f_{1.80}(\xi)$. It should be noticed that the arrangement arising from $f_M(\xi)$ is periodically repeated every m_0 unit cells, where m_0 is a minimum value of the integer, m, which satisfies the next condition,

$$2\nu M=m \qquad (\nu,\ m\text{: positive integers}). \tag{4}$$

For example, when $M=1.80$ and 1.83, $m_0=18$ and 183 respectively. In other words, the lattice has a large unit cell whose dimensions along the three axes are a_1, a_2 and m_0a_3 respectively. To calculate the factor F in a general way, $f_M(\xi)$ is expanded in Fourier series:

$$f_M(\xi)=\frac{4}{\pi}\sum_{m=0}^{\infty}\frac{1}{2m+1}\sin\frac{(2m+1)\pi}{M}\xi. \tag{5}$$

Thus, the following expression is obtained as the intensity distribution in reciprocal space:

$$\begin{aligned}F^*F&=\left|\sum_{n=0}^{N-1}f_M(n)\exp(2\pi inl)\right|^2\\&=\frac{4}{\pi^2}\left|\sum_{m=0}^{\infty}\frac{1}{2m+1}\left[\exp\left\{i\pi\left(l+\frac{2m+1}{2M}\right)(N-1)\right\}\cdot\frac{\sin N\pi(l+(2m+1)/2M)}{\sin\pi(l+(2m+1)/2M)}\right.\right.\\&\qquad\left.\left.-\exp\left\{i\pi\left(l-\frac{2m+1}{2M}\right)(N-1)\right\}\cdot\frac{\sin N\pi(l-(2m+1)/2M)}{\sin\pi(l-(2m+1)/2M)}\right]\right|^2.\end{aligned}\tag{6}$$

The right hand side of formula (6) shows that the intensity distribution in reciprocal space has sharp maxima only when $l=n\pm(2m+1)/2M$ (n, $m=0$ or integers). It can be said, therefore, that the regular arrangement with uniform mixing corresponding to $f_M(\xi)$ explains the diffraction patterns quite well.

b) *Regular arrangements with not uniform mixing*

The anti-phase function, $\varphi_M(\xi)$, leading to a regular arrangement with not uniform mixing is illustrated in Fig. 3-(b). In this case, the period of $\varphi_M(\xi)$ is not $2M$ but $2\nu M$ which satisfies the condition (4), and so its Fourier expansion takes the following form:

$$\varphi_M(\xi)=\sum_{k=-\infty}^{\infty}A_k(M)\exp(i\pi k\xi/\nu M), \tag{7}$$

where $A_k(M)=A_{-k}^*(M)$.

Thus we obtain

$$F^*F=\left|\sum_{k=-\infty}^{\infty} A_k(M)\exp\left\{i\pi\left(l+\frac{k}{2\nu M}\right)(N-1)\right\}\times\frac{\sin N\pi(l+k/2\nu M)}{\sin \pi(l+k/2\nu M)}\right|^2. \tag{8}$$

Now, it follows that appreciable peaks take place not only at $l=n\pm(2m+1)/2M$ but also at $l=n\pm k/2\nu M$ $(k=0, 1, 2, \cdots)$ unless the modulus of Fourier coefficient, $|A_k(M)|$, is negligibly small. Such a situation is well illustrated in Fig. 4. Here, the results of numerical calculations on two models of regular arrangement corresponding to $M=1.80$ and $N=72$,

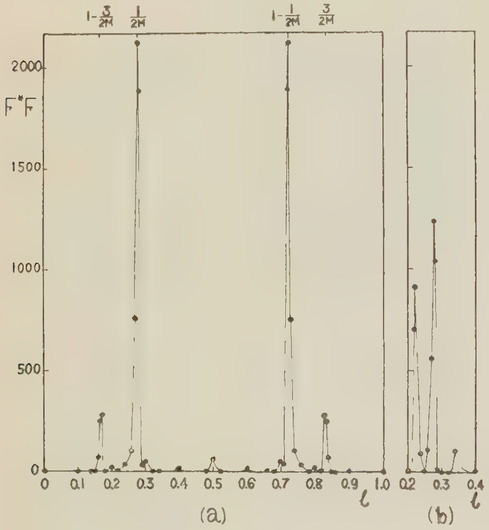

Fig. 4. The intensity distribution along the l-direction, given by numerical calculation.
(a) Uniform regular arrangement $M=1.80$, $N=72$
(b) Not uniform regular arrangement $M=1.80$, $N=72$

$$(2\bar{2}2\bar{2}1\bar{2}2\bar{2}2\bar{1}2\bar{2}2\bar{2}1\bar{2}2\bar{2}2\bar{1}2\bar{2}2\bar{2}1\bar{2}2\bar{2}2\bar{1}2\bar{2}2\bar{2}1\bar{2}2\bar{2}2\bar{1})$$

and

$$(2\bar{2}2\bar{2}2\bar{2}2\bar{2}1\bar{1}2\bar{2}2\bar{2}2\bar{2}2\bar{2}1\bar{1}2\bar{2}2\bar{2}2\bar{2}2\bar{2}1\bar{1}2\bar{2}2\bar{2}2\bar{2}2\bar{2}1\bar{1})$$

are shown. The former model is uniform, while the latter not uniform. It should be noticed that the latter gives an excessive peak at $l=k/2\nu M=4/18$. Since such an excessive peak has never been observed, the regular arrangements with not uniform mixing is hardly realized in the actual alloys.

§ 3. The Irregular Arrangements and Their Statistical Assembly

So far as anti-phase domains are almost uniformly mixed, irregularities in their arrangement may be allowed to some extent. To exemplify this conjecture, the results of numerical calculations are shown in Fig. 5, three models of irregular arrangement being adopted.

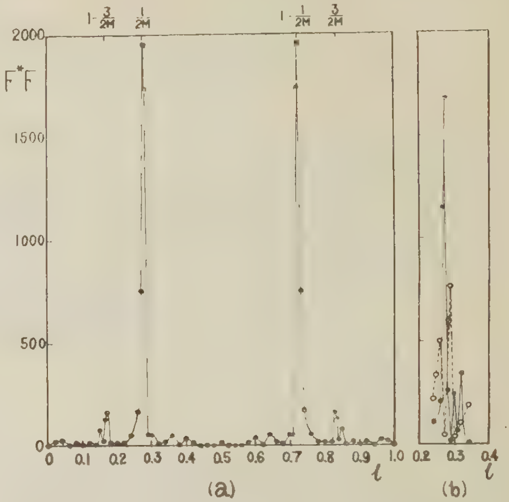

Fig. 5 The intensity distribution along the l-direction, given by numerical calculation.
(a) uniform irregular arrangement $M=1.80$, $N=72$
(b) not uniform irregular arrangements
1) $M=1.85$, $N=72$ —●——●—
2) $M=1.76$, $N=72$ ----○-------○---

It is really wonderful that an irregular arrangement such as

$$(2\bar{2}2\bar{1}2\bar{2}2\bar{2}1\bar{2}2\bar{2}2\bar{2}1\bar{2}2\bar{2}2\bar{1}2\bar{2}1\bar{2}2\bar{2}2\bar{2}1\bar{2}2\bar{2}2\bar{1}2\bar{2}2\bar{2}1\bar{2})$$

$$\cdots M=1.80,\ N=72$$

can still give the intensity distribution which fits well in actual diffraction patterns. On the other hand, two models of irregular arrangement with not uniform mixing,

$$(2\bar{2}2\bar{1}2\bar{2}2\bar{2}1\bar{2}2\bar{2}2\bar{2}1\bar{2}2\bar{2}3\bar{1}2\bar{2}2\bar{1}2\bar{1}2\bar{2}1\bar{2}2\bar{4}1\bar{2}2\bar{2}2\bar{1}2)$$

$$\cdots M=1.85,\ N=72$$

and

$$(2\bar{2}2\bar{1}2\bar{2}1\bar{1}2\bar{1}2\bar{2}2\bar{2}2\bar{1}2\bar{2}2\bar{2}2\bar{1}2\bar{2}2\bar{2}2\bar{1}1\bar{2}2\bar{1}2\bar{2}2\bar{2}2\bar{1}2\bar{2}2)$$

$$\cdots M=1.76,\ N=72$$

give many excessive peaks and, therefore, are not acceptable. Then, the question arises to what extent irregularity and non-uniformity can be allowed. The general treatment of this problem is considered to require some 'short range theory' instead of 'long range theory' based on the concept of anti-phase function. But the construction of such theory seems fairly troublesome, and the larger M becomes, the more complexity will arise. For simplicity, therefore, only 'long range theory' will be developed, and the problem mentioned above will thus be treated in terms of statistics applied to the anti-phase function.

It was considered at the beginning that a single crystal forms a coherent region for superlattice reflections as well as mainlattice reflections. But such a view is not correct in real crystals. For, from the aspects of diffraction photographs, it is evident that a single crystal itself is divided into many small coherent regions in which the directions of anti-phase are different from one another, as shown in Fig. 6. Therefore, as to superlattice reflections, a single crystal behaves as if it were polycrystalline[†]. Here an assumption is made, for convenience, that each region has the same form and dimensions and that the number of regions in which anti-phase occurs along the z-directions is W. In this case, the total intensity distribution corresponding to formula (1) is given by

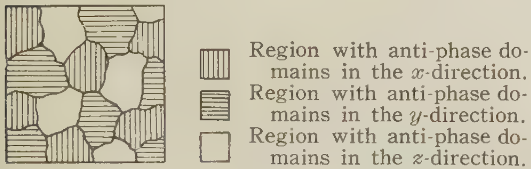
▥ Region with anti-phase domains in the x-direction.
▤ Region with anti-phase domains in the y-direction.
□ Region with anti-phase domains in the z-direction.

Fig. 6. A model of an ordered single crystal of Cu_3Au type.

$$I(hkl)=\Phi^*\Phi\,\frac{\sin^2 N_1\pi h}{\sin^2 \pi h}\cdot\frac{\sin^2 N_2\pi k}{\sin^2 \pi k}\cdot\sum_{j=1}^{W}F_j{}^*F_j\,, \tag{9}$$

where F_j is the F-factor of j-th region, and the summation must be taken over whole regions in which anti-phase occurs along the z-direction. Thus, the new object of calculation is to evaluate

$$I(l)=\sum_{j=1}^{W}F_j{}^*F_j\,. \tag{10}$$

When the regular arrangement corresponding to $f_M(\xi)$ takes place in each region, $I(l)$ becomes

$$I(l)=W\cdot\frac{4}{\pi^2}\left|\sum_{m=0}^{\infty}\frac{1}{2m+1}\left[\exp\left\{i\pi\left(l+\frac{2m+1}{2M}\right)(N-1)\right\}\cdot\frac{\sin N\pi(l+(2m+1)/2M)}{\sin\pi(l+(2m+1)/2M)}\right.\right.$$
$$\left.\left.-\exp\left\{i\pi\left(l-\frac{2m+1}{2M}\right)(N-1)\right\}\cdot\frac{\sin N\pi(l-(2m+1)/2M)}{\sin\pi(l-(2m+1)/2M)}\right]\right|^2. \tag{11}$$

When some irregular arrangement with almost uniform mixing takes place in each region, on the other hand, it is shown, using statistics, that the total intensity distribution also coincides with actual diffraction patterns. That is,

$$\begin{aligned}I(l)&=\sum_{j=1}^{W}F_j{}^*F_j\\&=\sum_{j=1}^{W}\sum_{m=0}^{N-1}f^{(j)*}(m)\exp(-2\pi iml)\sum_{n=0}^{N-1}f^{(j)}(n)\exp(2\pi inl)\\&=\sum_{m=0}^{N-1}\sum_{n=0}^{N-1}\exp\{2\pi il(n-m)\}\sum_{j=1}^{W}f^{(j)}(m)f^{(j)}(n)\\&=W\cdot\sum_{m=0}^{N-1}\sum_{n=0}^{N-1}\exp\{2\pi il(n-m)\}\cdot\langle f^{(j)}(m)\rangle\cdot\langle f^{(j)}(n)\rangle\\&\quad+W\sum_{m=0}^{N-1}\sum_{n=0}^{N-1}\exp\{2\pi il(n-m)\}\cdot(\langle f^{(j)}(m)\cdot f^{(j)}(n)\rangle-\langle f^{(j)}(m)\rangle\cdot\langle f^{(j)}(n)\rangle)\,,\end{aligned}$$

where $f^{(j)}(n)$ is the anti-phase factor of j-th region and $\langle\ \rangle$ represents the mean value. By putting $s\equiv n-m$, we obtain

$$I(l)=W\cdot\left|\sum_{n=0}^{N-1}\langle f^{(j)}(n)\rangle\exp(2\pi inl)\right|^2+W\cdot\sum_{n=0}^{N-1}(1-\langle f^{(j)}(n)\rangle^2)$$

---

[*] In most ordered alloys with anti-phase domains, such as CuAu, Cu_3Pd, Ag_3Mg, etc., the crystal lattice distorts more or less as the anti-phase domain structure is completed, e.g., the maximum tetragonality, c/a, amounts to 1.006 in Ag_3Mg. The crystal, therefore, is not single even in a true sense.

$$+2W\sum_{s=1}^{N-1}\cos 2\pi sl\cdot\sum_{n=0}^{N-1-s}(\langle f^{(j)}(n)\cdot f^{(j)}(n+s)\rangle-\langle f^{(j)}(n)\rangle\langle f^{(j)}(n+s)\rangle)\,. \tag{12}$$

To calculate $I(l)$ further, the following assumptions are made:

1. Anti-phase function of $f^{(j)}(n)$, $\psi_M^{(j)}(\xi)$, is of the form

$$\psi_M^{(j)}(\xi)=\begin{cases}+1 & \text{for}\quad (2k+\delta_{2k}^{(j)})M\le\xi<(2k+1+\delta_{2k+1}^{(j)})M\\ -1 & \text{for}\quad (2k+1+\delta_{2k+1}^{(j)})M\le\xi<(2k+2+\delta_{2k+2}^{(j)})M\end{cases}\qquad (k=0,\,1,\,2,\,\cdots)\,. \tag{13}$$

as shown in Fig. 3-(c).

2. In each $\psi_M^{(j)}(\xi)$, $\delta_m^{(j)}$ is independent of all other $\delta_n^{(j)}$'s $(n\neq m)$.
3. Each set of $\delta_m^{(j)}$'s with the same m and different j has a normal distribution, $N(0,\sigma^2)$†, as its 'population distribution.' Therefore, a standard distribution, σ, represents the degree of disturbance in a regular arrangement.

Thus the following expression is obtained as a final result:

$$\begin{aligned}I(l)=W\cdot\frac{4}{M^2}\Bigg|\sum_{m=0}^{\infty}&\left\{\int_0^{M/2}\operatorname{erf}\,(\eta/\sqrt{2}\,\sigma M)\cdot\sin\frac{(2m+1)\pi\eta}{M}\,d\eta\right\}\\&\times\left[\exp\left\{i\pi\left(l+\frac{2m+1}{2M}\right)(N-1)\right\}\cdot\frac{\sin N\pi(l+(2m+1)/2M)}{\sin\pi(l+(2m+1)/2M)}\right.\\&\left.-\exp\left\{i\pi\left(l-\frac{2m+1}{2M}\right)(N-1)\right\}\frac{\sin N\pi(l-(2m+1)/2M)}{\sin\pi(l-(2m+1)/2M)}\right]\Bigg|^2\\&+W\cdot K_0+2W\sum_{s=1}^{[M]}K_s\cos 2\pi sl\,,\end{aligned} \tag{14}$$

where $[M]$ is the maximum integer smaller than M, and

$$K_0=\sum_{n=0}^{N-1}(1-\langle f^{(j)}(n)\rangle^2)$$

$$K_s=\sum_{n=0}^{N-1-s}(\langle f^{(j)}(n)\cdot f^{(j)}(n+s)\rangle-\langle f^{(j)}(n)\rangle\cdot\langle f^{(j)}(n+s)\rangle)\,.$$

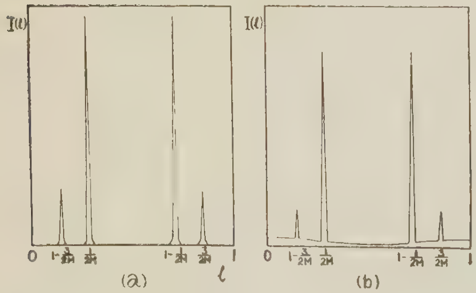

Fig. 7. Intensity distribution along the l-direction in reciprocal space. $(M<2)$
(a) regular arrangement
(b) statistical arrangement

These are constants independent of l. The first term of (14) gives sharp peaks only for $l=n\pm(2m+1)/2M$, but their heights decrease as σ grows larger, or as the arrangement in each region becomes more irregular. The second and third terms of (14) do not make any peaks. So far as σ is small, these terms are much smaller than the first. Even if they give very weak streaks in diffraction patterns, we can hardly observe them. Schematic diagrams of (11) and (14) are illustrated in Fig. 7. As σ grows larger, the said terms increase more and more, and, finally, they will become comparable with the first term of (14). Such irregular, not uniform arrangements corresponding to large σ, however, seem not to have been observed.

§ 4. Discussion

From the above calculations two acceptable types of arrangement of anti-phase domains can be concluded. They are

1. regular arrangements with uniform mixing

and

2. incomplete, or disturbed, regular arrangements with uniform mixing.

It should be noticed that the essential condition consists not in regularity but in uniformity. The reason why uniformity is re-

---

† The normal distribution $N(0,\sigma^2)$ is defined by the following probability density function:

$$g(\delta)=\exp(-\delta^2/2\sigma^2)/\sqrt{2\pi}\cdot\sigma\,.$$

quired in actual arrangements of anti-phase domains is not clear at the present stage. There seems to be not any conclusive answer to the question whether a complete regularity exists or not in atomic arrangements of real alloys. For, an exceedingly exact observation of diffraction intensity will be required to examine the problem and it is very difficult according to the present experimental technique.

Acknowledgement

The author wishes to express his sincere thanks to Prof. Shiro Ogawa and Mr. Makoto Hirabayashi for their kind guidance and useful discussions throughout the present work.

References

1) For example,
K. Schubert, B. Kiefer, M. Wilkens and R. Haufler: Z. Metallkde. **46** (1955) 692.
S. Ogawa and D. Watanabe: J. Phys. Soc. Japan **9** (1954) 475.
2) D. Watanabe, M. Hirabayashi and S. Ogawa: Acta Cryst. **8** (1955) 510.
D. Watanabe and S. Ogawa: J. Phys. Soc. Japan **11** (1956) 226.
3) K. Fujiwara, M. Hirabayashi, D. Watanabe and S. Ogawa: to be published.

JOURNAL OF THE PHYCICAL SOCIETY OF JAPAN Vol. 12, No. 1, JANUARY, 1957

Study of Simultaneous Reflexion in Electron Diffraction by Crystals

I. Theoretical Treatment*

By Kyozaburo KAMBE**

Tokyo Institute of Technology, Oh-Okayama, Meguro-ku, Tokyo

(Received September 22, 1956)

The simultaneous reflexion by two lattice planes (with indices h and h') in electron diffraction has been treated by the dynamical theory in order to investigate how it is influenced by the phases of structure amplitudes. For convenience of treatment, a modified formulation of the theory has been developed using particular cross sections of the dispersion surface in reciprocal space. Applying the theory to a lamellar crystal, it was proved that the intensities of transmitted and diffracted waves depend in a relatively simple way on the value of $|\Phi_{hh'}|=|\varphi_h-\varphi_{h'}+\varphi_{h'-h}|$, where φ_h, $\varphi_{h'}$, and $\varphi_{h'-h}$ are the phase angles of structure amplitudes for the indices h, h', and $h'-h$. It was shown that the phase effect can be most easily demonstrated by observing fine structures of reflexion spectra which are obtained by rotating the crystal in a specified manner. The determination of the value of $|\Phi_{hh'}|$ is most simple when the coupling reflexion $h'-h$ is strong compared with the reflexions h and h', and the crystal is centrosymmetric.

§ 1. Introduction

The simultaneous reflexion of X-ray, electron, or neutron waves by a crystal takes place when the orientation of the crystal relative to the direction of incident beam satisfies Bragg conditions for two or more lattice planes at the same time. The simultaneous reflexion is usually accompanied by intensity anomalies, such as the phenomenon of *Aufhellung*,2) *Umweganregung* (Renninger effect),3) and peculiar structures of Kossel lines or Kikuchi lines at their cross points.4)5)6)7) Some anomalous effects due to simultaneous reflexion have been also found in reflexion patterns7)8)9) and convergent-beam patterns10)11)12) in electron diffraction.

---

* Cf. previous short notes of this paper.1)

** Now at Electrotechnical Laboratory, Nagata-cho, Chiyoda-ku, Tokyo.

In the present paper we treat the simultaneous reflexion by the dynamical theory to study how the intensity anomaly is related to the phases of structure amplitudes. The existence of this relation was previously pointed out by Lipscomb[13)] by the consideration as follows.

When two reflexions with indices $h(h_1h_2h_3)$ and $h'(h_1'h_2'h_3')$ occur simultaneously, the wave-number vectors of the primary and the two reflected waves, denoted by $\boldsymbol{k}_0$, $\boldsymbol{k}_h$, and $\boldsymbol{k}_h'$ respectively, satisfy the conditions

$$\boldsymbol{k}_h=\boldsymbol{k}_0+\boldsymbol{b}_h\,,\qquad \boldsymbol{k}_{h'}=\boldsymbol{k}_0+\boldsymbol{b}_{h'}\,,$$

where $\boldsymbol{b}_h$ and $\boldsymbol{b}_{h'}$ are the reciprocal lattice vectors. We have immediately a relation

$$\boldsymbol{k}_{h'}=\boldsymbol{k}_h-\boldsymbol{b}_h+\boldsymbol{b}_{h'}=\boldsymbol{k}_h+\boldsymbol{b}_{h'-h}\,,$$

which shows that the two reflected waves mutually satisfy the Bragg condition for the lattice plane $h-h'$.

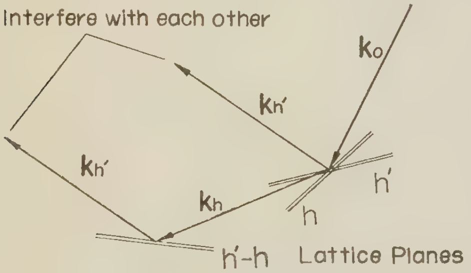

Fig. 1. Interference between singly and doubly reflected waves.

Thus the reflected wave having the wave-number vector $\boldsymbol{k}_{h'}$ is obtained not only through the direct reflexion of the primary wave by the lattice plane h', but also through the successive reflexions first by the lattice plane h and then by the lattice plane $h'-h$ (Fig. 1). As is well known, the wave reflected by a lattice plane is accompanied by a phase depending on the phase of the associated structure amplitude. Accordingly, the component obtained through the direct reflexion has a phase determined by $\varphi_{h'}$, and the component obtained through the successive reflexions has a phase determined by φ_h and $\varphi_{h'-h}$, where φ_h, $\varphi_{h'}$, $\varphi_{h'-h}$ are the phase angles of the structure amplitudes with indices h, h', $h'-h$ respectively. As the result of superposition of the above two components, the intensity of the wave with the wave-number vector $\boldsymbol{k}_{h'}$ depends on the phase angles φ_h, $\varphi_{h'}$, and $\varphi_{h'-h}$.

Although the above consideration is not rigorous, the same conclusion is obtained, as shown in this paper, by a more exact treatment on the basis of dynamical theory.

Lipscomb[13)] and others[14)] have tried to detect experimentally the phase effect in X-ray diffraction, but so far the successful results have not been obtained. It is perhaps on account of severe requirements for the parallelity and monochromatism of the incident beam and for the perfectness of crystals.* It is expected however, that the phase effect can be detected more readily in the case of electron diffraction by virtue of stronger coupling between the reflected waves. Actually, Fues[16)] and Hoerni[12)] have shown a few examples of the phase effect in convergent-beam patterns.

In this paper (Part I) we first develope the dynamical theory of electron diffraction in a particular form which is convenient to treat the phase problem. Then, applying the theory to the case of a lamellar crystal, the effect of the phases of structure amplitudes on the intensities of the diffracted waves is discussed. An experimental verification of the theory by means of the convergent-beam electron diffraction using graphite crystal is described in Part II.

§ 2. The Dynamical Theory of the Simultaneous Reflexion by Two Lattice Planes

The Schrödinger equation for an electron in a crystal is given by

$$\Delta\psi+\frac{8\pi^2me}{h^2}(E+V)\psi=0\,. \tag{1}$$

In (1) eE is the total energy, and V is the periodic potential of the crystal which is expressed by

$$V=\sum_h V_h\exp(-2\pi i\boldsymbol{b}_h\boldsymbol{r})\,, \tag{2}$$

$$V_h=V_{-h}{}^*\,, \tag{2a}$$

where the index h represents the triple indices $(h_1h_2h_3)$.

The solution of (1) is given by Bloch function

---

* Recent work of Renninger[15)] which obtained angular aperture of 2″ using triple-crystal method seems to make promising the phase-effect investigations by X-rays.

$$\psi=\sum_h u_h\psi_h\,, \tag{3}$$

where

$$\psi_h=\exp(-2\pi i\boldsymbol{k}_h\boldsymbol{r})\,, \tag{3a}$$

$$\boldsymbol{k}_h=\boldsymbol{k}_0+\boldsymbol{b}_h\,. \tag{3b}$$

ψ_h is a plane wave having unit amplitude.

The simultaneous reflexion by two lattice planes with indices h and h' occurs provided

$$|\boldsymbol{k}_0|\approx|\boldsymbol{k}_h|\approx|\boldsymbol{k}_{h'}|\,. \tag{4}$$

Let us assume that only three amplitudes u_0, u_h, $u_{h'}$ are appreciable. Then, (3) is reduced to a combination of three plane waves

$$\psi=u_0\psi_0+u_h\psi_h+u_{h'}\psi_{h'}\,. \tag{5}$$

Substituting (5) into (1), multiplying $\psi_0{}^*$, $\psi_h{}^*$, and $\psi_{h'}{}^*$, and finally integrating over the whole crystal, we get a set of equations

$$\left.\begin{aligned}
&(\kappa^2-|\boldsymbol{k}_0|^2)u_0+\frac{2me}{h^2}V_{-h}u_h+\frac{2me}{h^2}V_{-h'}u_{h'}=0\,,\\
&\frac{2me}{h^2}V_hu_0+(\kappa^2-|\boldsymbol{k}_h|^2)u_h+\frac{2me}{h^2}V_{h-h'}u_{h'}=0\,,\\
&\frac{2me}{h^2}V_{h'}u_0+\frac{2me}{h^2}V_{h'-h}u_h+(\kappa^2-|\boldsymbol{k}_{h'}|^2)u_{h'}=0\,,
\end{aligned}\right\} \tag{6}$$

where

$$\kappa^2=\frac{2me}{h^2}(E+V_0)\,. \tag{6a}$$

Let us define the quantities x_0, x_h and $x_{h'}$ by

$$x_0=\kappa-|\boldsymbol{k}_0|\,,\quad x_h=\kappa-|\boldsymbol{k}_h|\,,\quad x_{h'}=\kappa-|\boldsymbol{k}_{h'}|\,. \tag{7}$$

Then, with the conditions (4) and $V\ll E$, (6) can be rewritten as

$$\left.\begin{aligned}
&x_0u_0+\alpha V_{-h}u_h+\alpha V_{-h'}u_{h'}=0\,,\\
&\alpha V_hu_0+x_hu_h+\alpha V_{h-h'}u_{h'}=0\,,\\
&\alpha V_{h'}u_0+\alpha V_{h'-h}u_h+x_{h'}u_{h'}=0\,,
\end{aligned}\right\} \tag{8}$$

where

$$\alpha=\frac{1}{2\kappa}\,\frac{2me}{h^2}\,. \tag{8a}$$

We get a secular equation

$$\begin{vmatrix} x_0 & \alpha V_{-h} & \alpha V_{-h'}\\ \alpha V_h & x_h & \alpha V_{h-h'}\\ \alpha V_{h'} & \alpha V_{h'-h} & x_{h'}\end{vmatrix}=0\,. \tag{9}$$

(9) determines the dispersion surface[6)12)17)] in reciprocal space. In Fig. 2, O is the origin of reciprocal space, and H and H' are the reciprocal lattice points corresponding to the indices h and h'. A point P lying on the dispersion surface is the wave point associated with a set of wave-number vectors $\boldsymbol{k}_0=\overrightarrow{PO}$, $\boldsymbol{k}_h=\overrightarrow{PH}$, $\boldsymbol{k}_{h'}=\overrightarrow{PH'}$. The values of x_0, x_h, $x_{h'}$ obtained from these vectors using (7) satisfy (9). By their definition, x_0, x_h, $x_{h'}$ are the distances from P to the spheres Σ_0, Σ_h, $\Sigma_{h'}$ of radius κ having the centers at O, H, H' respectively. As $\alpha V_h\ll\kappa$ (from $V\ll E$ in (1)), the dispersion surface deviates appreciably from the spheres only near the intersections of the spheres.

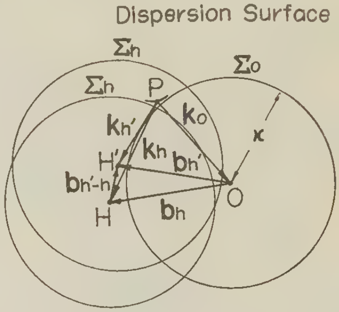

Fig. 2. Geometrical construction of wave vectors in reciprocal space.

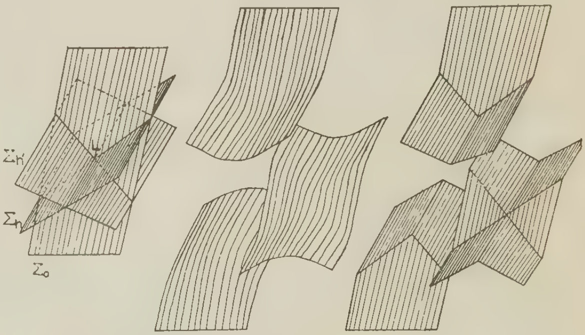

(a) (b) (c)

Fig. 3. (a) Three spheres meeting at the point L.
(b) Three sheets of dispersion surface.
(c) Three component surfaces of (a), roughly approximating the components in (b).

Fig. 3 (a) shows the three spheres meeting at the point L by approximating them by planes. As was studied in detail by Fues,[6)17)] the dispersion surface determined by (9) is made up of three curved sheets as shown in Fig. 3 (b). They approach asymptotically to the three surfaces shown in Fig. 3 (c) which are divided components of the combination of the spheres shown in Fig. 3 (a).

To investigate the shape of the dispersion surface it is useful to examine first a special case where $V_h = V_{h'} = 0$ and $V_{h'-h} \neq 0$. This case is of course trivial because the amplitudes of the reflected waves are zero, but it serves as a convenient basis for later considerations. In this case (8) becomes

$$x_0 u_0 = 0\,, \tag{10a}$$

$$\left.\begin{aligned} x_h u_h + \alpha V_{h-h'} u_{h'} &= 0\,, \\ \alpha V_{h'-h} u_h + x_{h'} u_{h'} &= 0\,, \end{aligned}\right\} \tag{10b}$$

and (9) becomes

$$x_0 = 0\,, \tag{11a}$$

$$\begin{vmatrix} x_h & \alpha V_{h-h'} \\ \alpha V_{h'-h} & x_{h'} \end{vmatrix} = 0\,. \tag{11b}$$

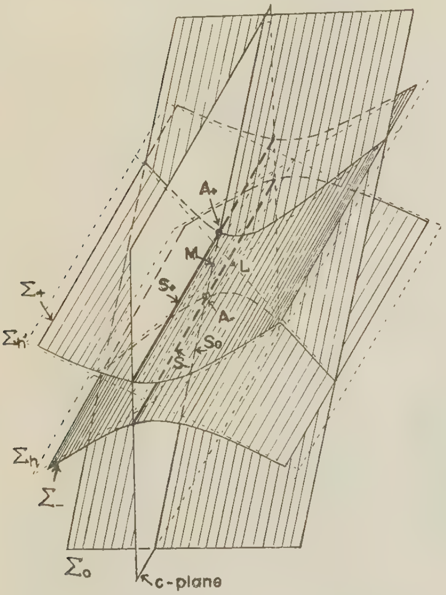

Fig. 4. Surfaces Σ_0, Σ_+, Σ_- and c-plane, with lines of intersection S_0, S_+, and S_-.

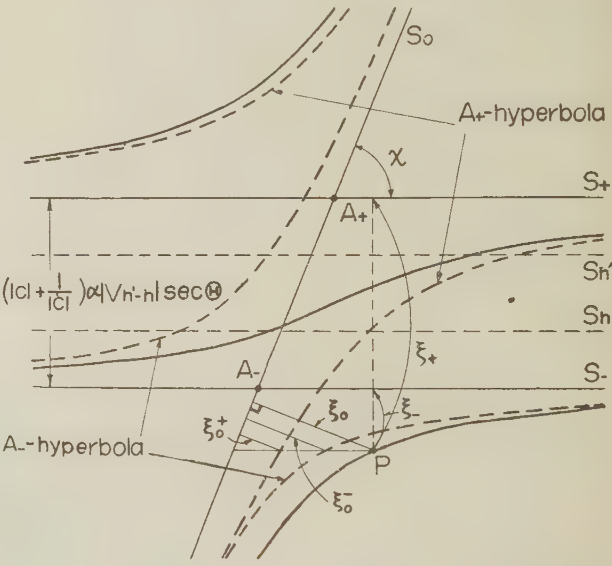

Fig. 5. Dispersion curve, a cross section of dispersion surface, obtained by combining two hyperbolae. ($|c|>1$)

We have a dispersion surface which is made up of Σ_0, in accordance with (11a), and two surfaces Σ_+ and Σ_-, in accordance with (11b) (Fig. 4). The latter two surfaces are cylindrical surfaces having a hyperbolic section; Σ_h and $\Sigma_{h'}$ are their asymptotic surfaces. Σ_+ and Σ_- lie respectively outside and inside of the two spheres Σ_h and $\Sigma_{h'}$, therefore x_h and $x_{h'}$ are negative on Σ_+ and positive on Σ_-. The combination of the surfaces Σ_0, Σ_+, and Σ_- is obviously the limiting form to which the dispersion surface of the general case shown in Fig. 3 (b) approaches when V_h and $V_{h'}$ approach zero from finite values.

Let us next consider the general case where V_h, $V_{h'}$, and $V_{h'-h}$ are all finite. To investigate the shape of the dispersion surface we make use of its cross section by a plane which is perpendicular to the line HH', i.e., parallel to the lattice plane $h'-h$. We call this plane hereafter the 'c-plane' (Fig. 4). Since in what follows we are concerned only with the region of reciprocal space near the intersection of Σ_h and $\Sigma_{h'}$, the c-plane can be expressed by an equation

$$x_{h'} - x_h = \delta\,, \tag{12}$$

where δ is a constant determining the position of the c-plane; for instance, the c-plane for $\delta=0$ contains the intersection of Σ_h and $\Sigma_{h'}$, and bisects the line HH' (Fig. 2).

Fig. 5 shows the cross section of the dispersion surface made by a c-plane. S_0, S_h, and $S_{h'}$ are the cross sections of the spheres Σ_0, Σ_h, and $\Sigma_{h'}$ respectively, and S_+ and S_- are the cross sections of the surfaces Σ_+ and Σ_- respectively. The four lines S_h, $S_{h'}$, S_+, and S_- are parallel to each other. The 'dispersion curve,' or the cross section of the dispersion surface, is composed of three branches corresponding to the three sheets shown in Fig. 3 (b). As shown in Fig. 5 the asymptotes of these curves are not S_0, S_h, and $S_{h'}$, but S_0, S_+, and S_-. This can be proved by putting (12) into (9).

§ 3. A Modified Treatment of the Simultaneous Reflexion

In (9) the dispersion surface is expressed in terms of the variables x_0, x_h, and $x_{h'}$. As mentioned before, these variables are defined with reference to the spheres Σ_0, Σ_h, and $\Sigma_{h'}$. On the other hand, in the end of the preceding section we have seen that the asymptotes for the dispersion curve on a c-plane are S_+ and S_-, instead of S_h and $S_{h'}$. This indicates the fact that Σ_+ and Σ_- are closer asymptotic surfaces of the dispersion surface than Σ_h and $\Sigma_{h'}$. Hence, a more convenient expression of the dispersion surface (or curve) may be obtained when the surface is expressed in terms of some new variables which are defined with reference to the surfaces Σ_0, Σ_+, and Σ_-. We can introduce such variables by the following modified theory.

Let us define the functions ψ_+ and ψ_- as follows:

$$\psi_+=\frac{1}{N}(\psi_h+c\psi_{h'})\,, \quad \psi_-=\frac{1}{N}(c^*\psi_h-\psi_{h'})\,, \tag{13}$$

where ψ_h and $\psi_{h'}$ are given by (3a), c a constant, and N the normalizing factor given by

$$N=\sqrt{1+cc^*}\,. \tag{13a}$$

Then, (5) is rewritten as

$$\psi=u_0\psi_0+u_+\psi_++u_-\psi_-\,, \tag{14}$$

with

$$u_+=\frac{1}{N}(u_h+c^*u_{h'})\,, \qquad u_-=\frac{1}{N}(cu_h-u_{h'})\,. \tag*{(15)*}$$

Since ψ_+ and ψ_- are orthogonal to each other and normalized, we get from (1) and (14), by applying the same procedure as adopted to give (6), the relations

$$\left.\begin{aligned}
&x_0u_0 \qquad\qquad +\frac{\alpha}{N}(V_{-h}+cV_{-h'})u_+ \\
&\qquad\qquad\qquad\qquad\qquad +\frac{\alpha}{N}(c^*V_{-h}-V_{-h'})u_- \;=0\,, \\
&\frac{\alpha}{N}(V_h+c^*V_{h'})u_0+\frac{1}{N^2}[x_h+cc^{**}x_{h'}+\alpha(cV_{h-h'}+c^*V_{h'-h})]u_+ \\
&\qquad\qquad\qquad +\frac{1}{N^2}[c^*(x_h-x_{h'})-\alpha(V_{h-h'}-c^{*2}V_{h'-h})]u_-=0\,, \\
&\frac{\alpha}{N}(cV_h-V_{h'})u_0+\frac{1}{N^2}[c(x_h-x_{h'})+\alpha(c^2V_{h-h'}-V_{h'-h})]u_+ \\
&\qquad\qquad\qquad +\frac{1}{N^2}[cc^*x_h+x_{h'}-\alpha(cV_{h-h'}+c^*V_{h'-h})]u_-=0\,.
\end{aligned}\right\} \tag{16}$$

The secular equation of (16) is equivalent to (9), being nothing but another form of expression for the dispersion surface.

In order to obtain the expression for the dispersion curve on a c-plane, we must take account of the relation (12) between x_h and $x_{h'}$. Let us now rewrite (12) in the form

$$\delta=x_{h'}-x_h=\left(|c|-\frac{1}{|c|}\right)\alpha|V_{h'-h}|\,, \tag{17}$$

defining thus the absolute value of the parameter c which has been an arbitrary number up to here. Let us further assume that c has the same phase angle $\varphi_{h'-h}$ with $V_{h'-h}$,

$$c=|c|\exp i\varphi_{h'-h}\,. \tag{18}$$

Then, by (17) and (18) the third term in the second equation and the second term in the third equation in (16) vanish, and (16) becomes

$$\left.\begin{aligned}
x_0u_0 &+\alpha V_+^*u_+ + \alpha V_-^*u_-=0\,, \\
\alpha V_+u_0 &+ \quad x_+u_+ \qquad\qquad\;\; =0\,, \\
\alpha V_-u_0 & \qquad\qquad\qquad + x_-u_-=0\,,
\end{aligned}\right\} \tag{19}$$

where

$$V_+=\frac{1}{N}(V_h+c^*V_{h'})\,, \quad V_-=\frac{1}{N}(cV_h-V_{h'})\,, \tag{20}$$

and

$$\left.\begin{aligned}
x_+&=x_h+|c|\alpha|V_{h'-h}|=x_{h'}+\frac{1}{|c|}\alpha|V_{h'-h}|\,, \\
x_-&=x_h-\frac{1}{|c|}\alpha|V_{h'-h}|=x_{h'}-|c|\alpha|V_{h'-h}|\,.
\end{aligned}\right\} \tag{21}$$

The secular equation for (19) can thus be written in a quite simple form

---

[*] In a previous note[1] $1/N$ was erroneously replaced by N.

$$x_0=\frac{|\alpha V_+|^2}{x_+}+\frac{|\alpha V_-|^2}{x_-}. \tag{22}$$

Since this equation is derived under the condition (17), it represents the dispersion curve on the c-plane. It should be noted that (22) has only two independent variables, because from (21) x_+ and x_- are related by

$$x_+-x_-=\left(|c|+\frac{1}{|c|}\right)\alpha|V_{h'-h}|. \tag{23}$$

The geometrical meaning of the newly introduced variables x_+ and x_- is illustrated in Fig. 6, which shows the cross section of reciprocal space by a plane containing the three points H, H', and P. The cross sections of the spheres Σ_h and $\Sigma_{h'}$ are approximated by the two straight lines, which make the angle $2\Theta=2\sin^{-1}(|\boldsymbol{b}_{h'-h}|/2\kappa)$. In accordance with (11b), the cross sections of Σ_+ and Σ_- make a hyperbola with the inter-vertex distance between their branches equal to $2\alpha|V_{h'-h}|\sec\Theta$. The vertical line $c-c$ is the cross section of the c-plane. The points S_h, $S_{h'}$, S_+, and S_- are the cross points of the corresponding lines shown in Fig. 5.

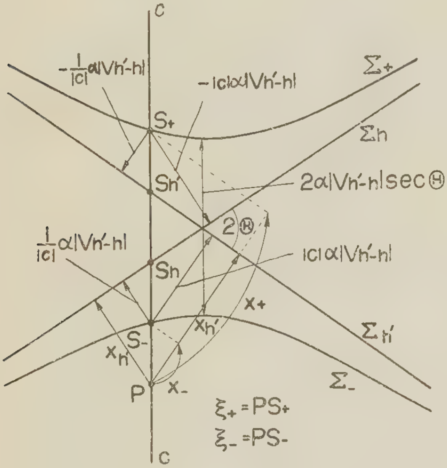

Fig. 6. Cross section by a plane which contains the points H, H', and P, showing the geometrical meaning of x_+ and x_-. ($|c|>1$)

Since the surfaces Σ_+ and Σ_- are derived from (11b), the values of x_h and $x_{h'}$ appropriate for the points S_+ and S_- are obtained from (11b) and (17) as follows:

$$\left.\begin{aligned}
&x_h=-|c|\alpha|V_{h'-h}|, \quad x_{h'}=-\frac{1}{|c|}\alpha|V_{h'-h}| && \text{for } S_+,\\
&x_h=\frac{1}{|c|}\alpha|V_{h'-h}|, \quad x_{h'}=|c|\alpha|V_{h'-h}| && \text{for } S_-.
\end{aligned}\right\} \tag{24}$$

These are the distances from the points S_+ and S_- to Σ_h and $\Sigma_{h'}$. From (21) and (24) we have

$$x_+=\xi_+\cos\Theta, \quad x_-=\xi_-\cos\Theta, \tag{25}$$

where $\xi_+=PS_+$ and $\xi_-=PS_-$ (Fig. 6). Since S_+ and S_- lie on Σ_+ and Σ_- respectively, x_+ and x_- can be regarded as the variables defined with respect to Σ_+ and Σ_-, as expected in the beginning of this section.

When the values of x_+ and x_- for a specified point on the dispersion curve are found, the values of u_+/u_0 and u_-/u_0 are determined from (19) as

$$\frac{u_+}{u_0}=-\frac{\alpha V_+}{x_+}, \quad \frac{u_-}{u_0}=-\frac{\alpha V_-}{x_-}. \tag{26}$$

The values of u_h/u_0 and $u_{h'}/u_0$ are obtained from (15) and (26) as

$$\left.\begin{aligned}
\frac{u_h}{u_0}&=-\frac{1}{N}\left(\frac{\alpha V_+}{x_+}+c^*\frac{\alpha V_-}{x_-}\right),\\
\frac{u_{h'}}{u_0}&=-\frac{1}{N}\left(c\frac{\alpha V_+}{x_+}-\frac{\alpha V_-}{x_-}\right).
\end{aligned}\right\} \tag{27}$$

In passing, it is to be noted here that the functions ψ_+ and ψ_- are intimately related to the surfaces Σ_+ and Σ_- respectively. In the limiting problem treated in § 2, in which it is assumed that $V_h=V_{h'}=0$, and $V_{h'-h}\neq 0$, the dispersion surface is composed of Σ_0, Σ_+, and Σ_-. When the wave point lies on the surface Σ_+ or Σ_- the wave function (the Bloch function) has the form

$$\psi=u_h\psi_h+u_{h'}\psi_{h'}, \tag{28}$$

because we have $u_0=0$ from (10a). The ratio between u_h and $u_{h'}$ in (28) is obtained from (10b) as

$$\frac{u_{h'}}{u_h}=-\frac{x_h}{\alpha V_{h-h'}}=-\frac{\alpha V_{h'-h}}{x_{h'}}. \tag{28a}$$

When the wave point lies particularly on the lines S_+ and S_- the values of x_h and $x_{h'}$ are given by (24). Hence, we have

$$\left.\begin{aligned}
\frac{u_{h'}}{u_h}&=c && \text{for } S_+,\\
&=-\frac{1}{c^*} && \text{for } S_-.
\end{aligned}\right\} \tag{29}$$

We can see from (13), (28), and (29) that ψ_+ and ψ_- are the normalized wave functions associated respectively with the surfaces Σ_+ and Σ_-, or more accurately, with the lines S_+ and S_-. This circumstance is just like ψ_0, ψ_h, and $\psi_{h'}$ are the functions associated with the spheres Σ_0, Σ_h, and $\Sigma_{h'}$ in the case $V_h=V_{h'}=V_{h'-h}=0$.

§ 4. The Form of Dispersion Curve on the *c*-plane

With the aid of the expression (22) we explain briefly the main features of the dispersion curve on the *c*-plane (Fig. 5). The distances ξ_+ and ξ_- from a wave point P on the *c*-plane to the lines S_+ and S_- are given by (25). The distance ξ_0 from P to the line S_0 is given by

$$\xi_0=x_0 \operatorname{cosec} \Phi\,, \tag{30}$$

where Φ is the angle between the sphere Σ_0 and the *c*-plane which is given by

$$\Phi=\cos^{-1}[||\boldsymbol{b}_h|^2-|\boldsymbol{b}_{h'}|^2|/2\kappa|\boldsymbol{b}_{h'-h}|]\,.$$

Thus (22) is written in the form

$$\xi_0=\frac{\beta|\alpha V_+|^2}{\xi_+}+\frac{\beta|\alpha V_-|^2}{\xi_-}\,, \tag{31}$$

where

$$\beta=\sec\Theta \operatorname{cosec}\Phi\,. \tag{31a}^*$$

On the basis of the expression (31) the dispersion curve can be drawn in the following way. Writing (31) in the form

$$\xi_0=\xi_0{}^+ + \xi_0{}^-\,, \tag{32a}$$

$$\xi_0{}^+=\frac{\beta|\alpha V_+|^2}{\xi_+}\,,\quad \xi_0{}^-=\frac{\beta|\alpha V_-|^2}{\xi_-}\,, \tag{32b}$$

we draw first the two hyperbolae defined by (32b), which are called hereafter the A_+ and A_--hyperbola respectively. The asymptotic lines of these hyperbolae are the lines S_0 and S_+, and the lines S_0 and S_-, respectively (Fig. 5). The inter-vertex distances are $2\sqrt{\beta}\,\alpha|V_+|\sec\chi$ and $2\sqrt{\beta}\,\alpha|V_-|\sec\chi$ respectively, where χ is the angle between S_0 and S_+ or S_- (Fig. 5). From (32a) the dispersion curve can be drawn quite easily by graphical procedure as illustrated in Fig. 5.

From this procedure it is clear that the shape of the dispersion curve has more or less the characteristics of the combination of the two hyperbolae. When, especially, $|V_{h'-h}|$ is much larger than $|V_h|$ and $|V_{h'}|$, the distance between S_+ and S_- given by

$$\xi_+-\xi_-=(x_+-x_-)\sec\Theta$$
$$=\left(|c|+\frac{1}{|c|}\right)\alpha|V_{h'-h}|\sec\Theta \tag{33}$$

becomes much larger than the inter-vertex distances of the hyperbolae. In this case, the dispersion curve can be approximated satisfactorily by the combination of the two independent hyperbolae (Fig. 9).

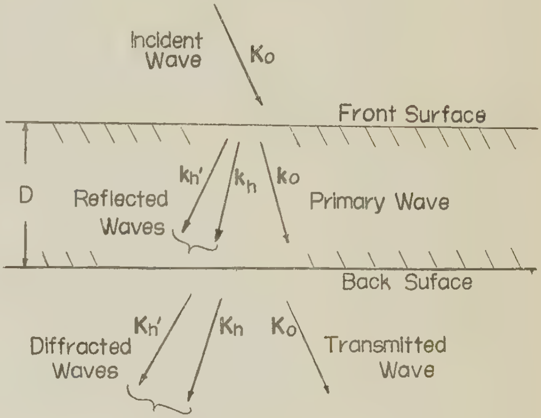

Fig. 7. Arrangement of wave-number vectors in Laue case.

§ 5. Application of the Theory to a Lamellar Crystal

(a) General consideration

In this section we apply the above theory to the electron diffraction by a parallel crystal slab. Fig. 7 shows schematically the waves inside and outside the crystal, representing them by wave-number vectors. The incident wave and the transmitted wave have the same vector $\boldsymbol{K}_0$. We assume that the simultaneously diffracted waves $\boldsymbol{K}_h$ and $\boldsymbol{K}_{h'}$ emerge from the back surface of the crystal, corresponding to the so-called 'Laue case.'

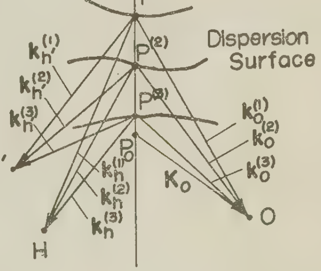

Fig. 8. Three sets of wave-number vectors inside the crystal determined by the boundary condition.

---

* In usual conditions of electron diffraction, $\kappa\approx 20$ Å^{-1}, $|\boldsymbol{b}_h|\approx 1$ Å^{-1}, hence $\sec\Theta\approx 1$, $\operatorname{cosec}\Phi\approx 1$. Thus (31) may be replaced by (22).

The wave number vectors of the waves inside and outside the crystal should satisfy the continuity of tangential components on the crystal surface. In accordance with this requirement, the three wave points $P^{(1)}$, $P^{(2)}$, and $P^{(3)}$ for the waves inside the crystal are obtained as the intersecting points of the dispersion surface with the line (the ν-normal) which is drawn perpendicular to the surface of the crystal through the point P_0 for which $\overrightarrow{P_0O}=\boldsymbol{K}_0$ (Fig. 8). Corresponding to each of the three wave points the wave-number vectors $\boldsymbol{k}_0$, $\boldsymbol{k}_h$, and $\boldsymbol{k}_{h'}$ are determined as

$$\left.\begin{aligned} &\boldsymbol{k}_0^{(i)}=\overrightarrow{P^{(i)}O}\,, \qquad \boldsymbol{k}_h^{(i)}=\overrightarrow{P^{(i)}H}\,, \\ &\boldsymbol{k}_{h'}^{(i)}=\overrightarrow{P^{(i)}H'} \qquad (i=1,2,3)\,. \end{aligned}\right\} \tag{34}$$

The wave function ψ in the crystal is given by a superposition of three Bloch functions relating to these wave points,

$$\psi=\psi^{(1)}+\psi^{(2)}+\psi^{(3)}\,, \tag{35}$$

where $\psi^{(i)}(i=1, 2, 3)$, the Bloch function corresponding to the i-th wave point, is given by

$$\begin{aligned} \psi^{(i)}&=u_0^{(i)}\psi_0^{(i)}+u_h^{(i)}\psi_h^{(i)}+u_{h'}^{(i)}\psi_{h'}^{(i)} \\ &=u_0^{(i)}\exp(-2\pi i\boldsymbol{k}_0^{(i)}\boldsymbol{r}) \\ &\quad+u_h^{(i)}\exp(-2\pi i\boldsymbol{k}_h^{(i)}\boldsymbol{r}) \\ &\quad+u_{h'}^{(i)}\exp(-2\pi i\boldsymbol{k}_{h'}^{(i)}\boldsymbol{r})\,. \\ &(i=1, 2, 3) \end{aligned} \tag{36}$$

Since the ratios $u_0^{(i)}$: $u_h^{(i)}$: $u_{h'}^{(i)}$ $(i=1, 2, 3)$ are determined by (8) or (27), ψ is obtained when the values of $u_0^{(1)}$, $u_0^{(2)}$, $u_0^{(3)}$ are determined by the boundary condition, or the conditions requiring the continuity of ψ and of its normal derivative on the crystal surfaces. Under the condition $V\ll E$, however, the continuity of normal derivative can be discarded because it is equivalent to the continuity of ψ, provided the wave-number vectors shown in Fig. 7 do not make too small angles with the crystal surfaces.

When the origin of coordinates is taken on the front surface and the amplitude of the incident wave is taken to be unity, the boundary condition on the front surface is given by

$$1=u_0^{(1)}+u_0^{(2)}+u_0^{(3)} \tag{37a}$$

$$\left.\begin{aligned} 0&=u_h^{(1)}+u_h^{(2)}+u_h^{(3)}\,, \\ 0&=u_{h'}^{(1)}+u_{h'}^{(2)}+u_{h'}^{(3)}\,, \end{aligned}\right\} \tag{37b}$$

and on the back surface by

$$\left.\begin{aligned} U_0\exp(-2\pi i\Gamma_0 D)&=u_0^{(1)}\exp(-2\pi i\gamma_0^{(1)}D)+u_0^{(2)}\exp(-2\pi i\gamma_0^{(2)}D)+u_0^{(3)}\exp(-2\pi i\gamma_0^{(3)}D)\,, \\ U_h\exp(-2\pi i\Gamma_h D)&=u_h^{(1)}\exp(-2\pi i\gamma_h^{(1)}D)+u_h^{(2)}\exp(-2\pi i\gamma_h^{(2)}D)+u_h^{(3)}\exp(-2\pi i\gamma_h^{(3)}D)\,, \\ U_{h'}\exp(-2\pi i\Gamma'_{h'} D)&=u_{h'}^{(1)}\exp(-2\pi i\gamma_{h'}^{(1)}D)+u_{h'}^{(2)}\exp(-2\pi i\gamma_{h'}^{(2)}D)+u_{h'}^{(3)}\exp(-2\pi i\gamma_{h'}^{(3)}D)\,, \end{aligned}\right\} \tag{38}$$

where D is the thickness of the crystal, and U_0, U_h, $U_{h'}$ are the amplitudes of the waves leaving the crystal with the wave-number vectors $\boldsymbol{K}_0$, $\boldsymbol{K}_h$, $\boldsymbol{K}_{h'}$ respectively. Γ'_0, $\gamma_0^{(1)}$ etc. are the normal components of $\boldsymbol{K}_0$, $\boldsymbol{k}_0^{(1)}$ etc..

Using (27) the ratios $u_0^{(1)}$: $u_0^{(2)}$: $u_0^{(3)}$ are determined from (37b) as

$$\begin{aligned} u_0^{(1)}:u_0^{(2)}:u_0^{(3)}&=\frac{1}{x_+^{(2)}x_-^{(3)}}-\frac{1}{x_+^{(3)}x_-^{(2)}}:\frac{1}{x_+^{(3)}x_-^{(1)}}-\frac{1}{x_+^{(1)}x_-^{(3)}}:\frac{1}{x_+^{(1)}x_-^{(2)}}-\frac{1}{x_+^{(2)}x_-^{(1)}} \\ &=\frac{1}{\xi_+^{(2)}\xi_-^{(3)}}-\frac{1}{\xi_+^{(3)}\xi_-^{(2)}}:\frac{1}{\xi_+^{(3)}\xi_-^{(1)}}-\frac{1}{\xi_+^{(1)}\xi_-^{(3)}}:\frac{1}{\xi_+^{(1)}\xi_-^{(2)}}-\frac{1}{\xi_+^{(2)}\xi_-^{(1)}}\,. \end{aligned} \tag{39}$$

The values of $u_0^{(1)}$, $u_0^{(2)}$, $u_0^{(3)}$ are determined by (37a) and (39). Finally, the intensities of the transmitted and diffracted waves are obtained from (38) as

$$|U_g|^2=\sum_{i=1,2,3}|u_g^{(i)}|^2+2\sum_{i\neq j}|u_g^{(i)}||u_g^{(j)}|\cos\{2\pi(\gamma_g^{(i)}-\gamma_g^{(j)})D-(\theta_g^{(i)}-\theta_g^{(j)})\}\,, \tag{40}$$

$$(g=0, h, h')$$

where $\theta_g^{(i)}$ is the phase angle of $u_g^{(i)}$, that is,

$$u_g^{(i)}=|u_g^{(i)}|\exp i\theta_g^{(i)}\,. \tag{40a}$$

(b) The case where $|V_{h'-h}|\gg|V_h|, |V_{h'}|$, and the lattice plane $h'-h$ is perpendicular to the crystal surface

We investigate first the case where $|V_{h'-h}|$ is much larger than $|V_h|$ and $|V_{h'}|$. The dispersion curve coincides in this case almost exactly with the two hyperbolae (Fig. 9). We assume further that the lattice plane $h'-h$ is perpdicular to the crystal surface. Then, since the c-plane is parallel to the lattice plane $h'-h$, the ν-normal and accordingly the three wave points on it are contained in a c-plane.

When the ν-normal passes through the central region of the A_+-hyperbola, as shown in Fig. 9, the values of $\xi_+^{(1)}$, $\xi_+^{(2)}$, and $\xi_-^{(3)}$ (for the wave points $P^{(1)}$, $P^{(2)}$, and $P^{(3)}$, respectively) are small compared with $\xi_-^{(1)}$, $\xi_-^{(2)}$, and $\xi_+^{(3)}$, so that $u_0^{(3)}$ in (39) may be negligible compared with $u_0^{(1)}$ and $u_0^{(2)}$. From (26) and (27) it can be shown that $u_+^{(3)}$, $u_-^{(3)}$, $u_h^{(3)}$, and $u_{h'}^{(3)}$ are also negligible. This means that the wave point $P^{(3)}$ can be entirely neglected.* In this case we say after Hoerni⁽²⁾ that only the two branches belonging to the A_+-hyperbola are the 'effective' branches.

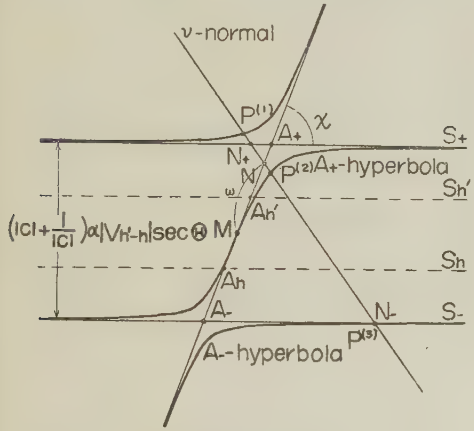

Fig. 9. Dispersion curve in the case $|V_{h'-h}| \gg |V_h|, |V_{h'}|$.

The fact that the dispersion curve can be approximated by the A_+-hyperbola implies that $\xi_+^{(1)}$ and $\xi_+^{(2)}$ are so small compared with $\xi_-^{(1)}$ and $\xi_-^{(2)}$ that the second term of (31) can be neglected. For the same reason we can neglect $u_-^{(1)}$ and $u_-^{(2)}$ considering (25) and (26). As the result, only the four amplitudes $u_0^{(1)}$, $u_0^{(2)}$, $u_+^{(1)}$, and $u_+^{(2)}$ are regarded as appreciable, and the wave function in the crystal is given by

$$\psi = \psi^{(1)} + \psi^{(2)}, \tag{41}$$

where

$$\psi^{(i)} = u_0^{(i)}\psi_0^{(i)} + u_+^{(i)}\psi_+^{(i)}. \quad (i=1,2) \tag{42}$$

The amplitudes $u_0^{(i)}$ and $u_+^{(i)}$ $(i=1,2)$ satisfy the relation

$$\left.\begin{aligned} x_0^{(i)}u_0^{(i)} + \alpha V_+^* u_+^{(i)} &= 0, \\ \alpha V_+ u_0^{(i)} + x_+^{(i)}u_+^{(i)} &= 0, \end{aligned}\right\} \tag{43}$$

which is the reduced form of (19). From (43) we have

$$x_0^{(i)} = \frac{|\alpha V_+|^2}{x_+^{(i)}}, \tag{44}$$

and

$$\frac{u_+^{(i)}}{u_0^{(i)}} = -\frac{\alpha V_+}{x_+^{(i)}} = -\frac{x_0^{(i)}}{\alpha V_+^*}. \tag{45}$$

The equations from (41) to (45) are analogous to the relations found in the ordinary problem of single reflexion with the Fourier amplitude V_+, although the excited wave ψ_+ in the present case is not a single plane wave, but a superposition of two plane waves ψ_h and $\psi_{h'}$ in the ratio $u_{h'}/u_h = c$ (Cf. (13) or (29)).

When the ν-normal passes through the central region of the A_--hyperbola, their two branches are the effective ones, and the same relations (41) to (45) hold when we replace the symbol $+$ by $-$, and the superfices $i=1, 2$ by $i=2, 3$. The excited wave ψ_- is a superposition of ψ_h and $\psi_{h'}$ in the ratio $u_{h'}/u_h = -1/c^*$ from (13) or (29).

The position of the ν-normal in a c-plane is conveniently represented by the distance $\omega = NM$ as shown in Fig. 9, where N is the intersecting point of the ν-normal with S_0, and M is the middle point of A_+A_-; A_+ and A_- are the intersecting points of S_0 with S_+ and S_- respectively. We take as the positive direction of ω the direction pointing from M to A_-. In the example of Fig. 9 ω is negative.

The amplitudes of the waves as functions of ω can be calculated using the equations (41) to (45) in an analogous way to the problem of single reflexion.¹²⁾,¹⁸⁾,¹⁹⁾ Using (27) and (40) the intensities of the waves leaving the crystal can be obtained as:

(i) In the region of ω near $\omega_+ \equiv A_+M$ (the central region of the A_+-hyperbola),

$$\left.\begin{aligned} &|U_0|^2 = 1-(|U_h|^2+|U_{h'}|^2) = 1-|U_+|^2, \\ &|U_h|^2 = \frac{1}{N^2}|U_+|^2, \qquad |U_{h'}|^2 = \frac{|c|^2}{N^2}|U_+|^2; \end{aligned}\right\} \tag{46}$$

(ii) In the region of ω near $\omega_- \equiv A_-M$ (the central region of the A_--hyperbola),

$$\left.\begin{aligned} &|U_0|^2 = 1-|U_-|^2, \\ &|U_h|^2 = \frac{|c|^2}{N^2}|U_-|^2, \qquad |U_{h'}|^2 = \frac{1}{N^2}|U_-|^2, \end{aligned}\right\} \tag{47}$$

---

* The possibility of similar cases has been discussed by Niehrs (H. Niehrs: Zeit. f. Phys. 139 (1954) 88).

where

$$|U_\pm|^2 = \frac{1}{1+W_\pm{}^2}\sin^2\left[2\pi D\alpha|V_\pm|\sqrt{1+W_\pm{}^2}/\cos\theta\right], \tag{48}$$

$$W_\pm = \frac{b(\omega-\omega_\pm)}{\alpha|V_\pm|}. \tag{48a}$$

θ is the angle between $\boldsymbol{K}_0$ and the ν-normal, which is nearly constant in the range of ω concerned. b is defined by $b=NN_\pm/NA_\pm$ (Cf. Fig. 9),* being a geometrical parameter determined by the direction of the ν-normal and the angle χ between the lines S_0 and S_+ (or S_-). $W_\pm$ corresponds to the parameter W used by Bethe.[20] (Cf. Thomson-Cochrane,[18] p. 292).

Fig. 10 shows schematically the intensities of the transmitted wave and the two diffracted waves as functions of ω, where the values in the range of ω near ω_+ is obtained from (46) and those near ω_- from (47). Rapid oscillations due to the so-called 'Pendellösung' are smoothed out; that is, we consider here only the factor $1/(1+W_\pm{}^2)$ in (48), neglecting the squared sine factor. The values in the middle range is obtained by interpolation taking account of the fact that we have obviously $|U_0|^2=1$, $|U_h|^2=0$, $|U_{h'}|^2=0$ except in the narrow ranges near $\omega=\omega_+$ and $\omega=\omega_-$.

The intensity variations as shown in Fig. 10 may be followed experimentally if the direction of the incident wave is changed keeping the ν-normal in the c-plane concerned. This corresponds to the movement of $\boldsymbol{K}_0$ keeping the angle between $\boldsymbol{K}_0$ and the lattice plane $h'-h$ constant.

In Fig. 10 we note that the intensities $|U_h|^2$ and $|U_{h'}|^2$ have double peaks, each made up of A_+ and A_--peaks located at ω_+ and ω_- respectively. From (46) and (47) we can consider that the intensities $|U_h|^2$ and $|U_{h'}|^2$ are divided components of $|U_+|^2$ or $|U_-|^2$ in the ratios $1:|c|^2$ or $|c|^2:1$, respectively. The distance between the A_+-peak and the A_--peak is given by $\left(|c|+\frac{1}{|c|}\right)\alpha|V_{h'-h}|\sec\Theta\sec\chi$, and is minimum for $|c|=1$.

If the reflexion takes place solely by the lattice plane h, $|U_h|^2$ would have only a single peak at the position $\omega=\omega_h\equiv A_hM$ as indicated by a broken line in Fig. 10 (Cf. Fig. 9). Similarly, the single reflexion h' would give a single peak of $|U_{h'}|^2$ at $\omega=\omega_{h'}\equiv A_{h'}M$.

It is to be noted in Fig. 10 that ω_+ is always negative, and ω_- is always positive for any value of $|c|$ (Cf. Fig. 4). It means that both the angles between $\boldsymbol{K}_0$ and the lattice planes h and h' are always smaller for A_+-peak than for A_--peak. In other words, the angle between $\boldsymbol{K}_h$ and the lattice plane h and also the angle between $\boldsymbol{K}_{h'}$ and the lattice plane h' are both always larger for A_+-peak than for A_--peak. This is an important criterion to distinguish A_+ and A_--peaks from each other in experiment.

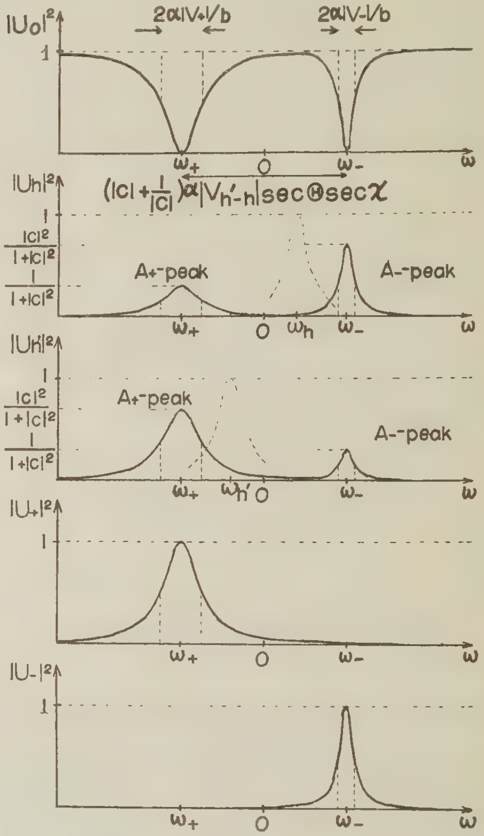

Fig. 10. Intensity curves of transmitted and diffracted waves shown with the curves of $|U_+|^2$ and $|U_-|^2$. Peaks shown by broken lines indicate diffracted intensities in the case of single reflexion.

(c) General Cases

When $|V_{h'-h}|$ is not particularly large compared with $|V_h|$ and $|V_{h'}|$, the treatment becomes more complicated, not only because the dispersion curve cannot well be approximated by the combination of the A_+ and A_--hyperbolae, but also because all three branches become effective so that the primary and reflected waves should be treated as superpositions of three waves. We do not discuss this case in further detail. It may be worth noting, however, that use of the cross sections by c-planes and of the functions ψ_+ and ψ_- is highly profitable also in this case. For instance, simple form of (31) enables us to work out a graphical solution in obtaining the wave points instead of carrying out troublesome numerical solution of third-order argebraic equations.

---

* In Fig. 9, N_- incidentally coincides with $P^{(3)}$.

When the lattice plane with the index $h'-h$ is not perpendicular to the crystal surface, the ν-normal does not lie in the c-plane. Therefore, the procedure to obtain wave points is not so simple as that described above. However, the difficulty is not so serious when the smallness of the curvature of the dispersion surface is taken into account. Let us consider the projection of the ν-normal onto the c-plane passing through the cross point of the ν-normal with the sphere Σ_0. Then, when the curvature of the dispersion surface in the direction perpendicular to the c-plane is neglected, the three cross points of the projection of the ν-normal with the dispersion curve coincide with the projections of the wave points lying on the ν-normal.* From the wave points obtained in this way, the intensities as functions of ω can be calculated by the similar procedure as before.

§ 6. Effect of the Phases of Structure Amplitudes

On the basis of the above results we investigate how the intensities of the transmitted and diffracted waves are related to the phases of structure amplitudes in Laue case.

Let us study first the relation between the quantities contained in the expression (40) and the phase angles $\varphi_g (g=h,\ h',\ h'-h)$ of the structure amplitudes. Since $\gamma_g^{(i)}$ is determined by the position of the wave point $P^{(i)}$, it depends on $|V_+|$ and $|V_-|$ through (31).

By (20) and (18) $|V_+|$ and $|V_-|$ are written as

$$\left.\begin{aligned} |V_+| &= \frac{1}{N}(|V_h|^2+|c|^2|V_{h'}|^2 \\ &\qquad +2|c||V_h||V_{h'}|\cos\Phi_{hh'})^{1/2}, \\ |V_-| &= \frac{1}{N}(|c|^2|V_h|^2+|V_{h'}|^2 \\ &\qquad -2|c||V_h||V_{h'}|\cos\Phi_{hh'})^{1/2}, \end{aligned}\right\} \tag{49}$$

where

$$\Phi_{hh'}=\varphi_h-\varphi_{h'}+\varphi_{h'-h}\,. \tag{49a}$$

It can be proved easily that $\Phi_{hh'}$ is an invariant quantity, while φ_h, $\varphi_{h'}$, and $\varphi_{h'-h}$ vary when the origin of coordinates in crystal is displaced. We see that $|V_+|$ and $|V_-|$, and hence, $\gamma_g^{(i)}$ in (40) depend on the phases of the structure amplitudes only through the absolute value $|\Phi_{hh'}|$. Similarly, we can prove from (39) and (37a) that $u_0^{(i)}$ $(i=1, 2, 3)$ depends on the absolute value $|\Phi_{hh'}|$. Since $x_+^{(i)}$ and $x_-^{(i)}$ are all real in Laue case, $u_0^{(i)}$ is real, thus $\theta_0^{(i)}$ is equal to 0 or π. Concerning the amplitudes $u_h^{(i)}$ and $u_{h'}^{(i)}$, we can prove similarly from (18), (20) and (27) that $|u_h^{(i)}|$ and $|u_{h'}^{(i)}|$ depend on $|\Phi_{hh'}|$ while $\theta_h^{(i)}$ and $\theta_{h'}^{(i)}$ depend on $\Phi_{hh'}$. Thus, it is concluded that the intensities given by (40) depend on the phases of structure amplitudes through the value of $\Phi_{hh'}$.

The result of the theory developed in the preceding sections indicates that the value of $\Phi_{hh'}$ can be determined by experiments most conveniently by observing the intensity curves as studied in § 5. These curves are obtained by varying the direction of $\boldsymbol{K}_0$ keeping the angle between $\boldsymbol{K}_0$ and the lattice plane $h'-h$ constant. Though the intensities depend on the value of $\Phi_{hh'}$ as mentioned above, it may be difficult to determine the sign of $\Phi_{hh'}$ from these curves,* because it requires detailed observation of rapid intensity oscillation due to the second term of (40). On the other hand, the absolute value $|\Phi_{hh'}|$ can be relatively easily determined from the smoothed-out-curves as those shown in Fig. 10.

It is instructive to consider again the case where $|V_{h'-h}|$ is very large compared with $|V_h|$ and $|V_{h'}|$. We see in the equations from (46) to (48a) that the intensities of waves depend only on $|V_+|$ and $|V_-|$. If the intensity curves as shown in Fig. 10 are obtained experimentally, the values of $|V_+|$ and $|V_-|$ can be found from the half-value widths of the A_+ and A_--peaks, or, when the value of $|c|$ is known, from the integrated intensities. The half-value widths $\varDelta\omega_\pm$ determined from (48a) by the condition $W_\pm{}^2=1$ are given by

---

* This approximation is generally quite satisfactory. An essentially similar approximation is included in the analytical procedure to obtain (48) in the single-reflexion problem.

* When the polarity of a non-centrosymmetric crystal is reversed, the sign of $\Phi_{hh'}$ is changed, thus, the intensities may change. This means that Friedel's law fails.[21]

$$\varDelta\omega_\pm=\frac{2}{b}\alpha|V_\pm|\,. \tag{50}$$

The integrated intensities $I_\pm$ are given by

$$\begin{aligned} I_\pm &= I_\pm{}^m\int_{-\infty}^{\infty}\frac{1}{1+W_\pm{}^2}d\omega \\ &= I_\pm{}^m\int_{-\infty}^{\infty}\frac{1}{1+W_\pm{}^2}\frac{\alpha|V_\pm|}{b}dW \\ &= I_\pm{}^m\frac{\pi\alpha|V_\pm|}{b}\,, \end{aligned} \tag{51}$$

where $I_\pm{}^m$ is the peak intensities depending on the value of $|c|$. These characteristic values are both proportional to $|V_+|$ and $|V_-|$.

When the crystal has a centre of symmetry, $\varPhi_{hh'}$ is either equal to 0 or π, accordingly $\cos\varPhi_{hh'}$ is either equal to 1 or -1. The two possibilities can be discriminated simply by comparing the widths of the A_+ and A_--peaks. Let us assume for simplicity that $|c|=1$, then

(i) if the A_+-peak is wider than the A_--peak, we have $|V_+|>|V_-|$, namely $\cos\varPhi_{hh'}=1$ from (49);

(ii) if the A_+-peak is narrower than the A_--peak, we have $|V_+|<|V_-|$, namely $\cos\varPhi_{hh'}=-1$.

When the origin of coordinates is chosen at the symmetry center, all structure amplitudes become real, being positive or negative. If $V_{h'-h}$ is positive, V_+ and V_- for the case $|c|=1$ becomes respectively equal to the sum and difference of V_h and $V_{h'}$. Hence, the case (i) tells us that V_h and $V_{h'}$ have the same sign, and the case (ii) tells V_h and $V_{h'}$ have opposite signs. This relation is reversed when $V_{h'-h}$ is negative.

Also in the case of non-centrosymmetric crystals we can find by a simple comparison of the peak widths the sign of $\cos\varPhi_{hh'}$, that is, we can find whether $|\varPhi_{hh'}|$ is larger or smaller than $\pi/2$.* The value of $|\varPhi_{hh'}|$ are determined more exactly when the ratio between $|V_+|$ and $|V_-|$ for a given value of $|c|$ is determined by measuring the half-value width or integrated intensities of the peaks.

When $|V_{h'-h}|$ is not very large compared with $|V_h|$ and $|V_{h'}|$, the two peaks in Fig. 10 approach and overlap each other. In this case, the value of $|\varPhi_{hh'}|$ may not be so easily determined as in the former cases, since a more accurate measurement of intensity variation is required to obtain the value of $|V_+|$ and $|V_-|$. Difficulties may come from the fact that the intensity variations occur usually in very small angular ranges and, moreover, often the value of $|c|$ cannot be experimentally determined with a sufficient accuracy.

For centrosymmetric crystals, however, we have only two possibilities for the value of $\varPhi_{hh'}$, namely 0 or π. Therefore, a simple qualitative observation may be sometimes sufficient to discriminate the two cases even when $|V_{h'-h}|$ is not particularly large.

References

1) K. Kambe and S. Miyake: Acta Cryst. **7** (1954) 218.
S. Miyake and K. Kambe: Ibid. **7** (1954) 220.
K. Kambe: Ibid. **7** (1954) 777.
2) E. Wagner: Phys. Zeit. **21** (1920) 632.
Y. Cauchois, H. Hulubei, and J. Weigle: Helv. Phys. Acta **10** (1937) 218.
3) (In X-ray)
M. Renninger: Zeit. f. Phys. **106** (1937) 141. Zeit. f. Krist. **97** (1937) 107.
J. Weigle and H. Mühsam: Helv. Phys. Acta **10** (1937) 139.
M. Blanc and J. Weigle: Ibid **10** (1937) 495.
(In electron diffraction)
H. Raether: Zeit. f. Phys. **78** (1932) 527.
R. D. Heidenreich: Phys. Rev. **77** (1950) 271.
4) K. Shinohara: Sci. Pap. Inst. Phys. Cem. Res. **20** (1932) 39.
5) E. Lamla: Ann. d. Phys. (5) **32** (1938) 178, 225.
6) E. Fues: Ann. d. Phys. (5) **36** (1939) 209.
7) S. Kikuchi and S. Nakagawa: Sci. Pap. Inst. Phys. Chem. Res. **21** (1933) 256.
8) S. Miyake and R. Uyeda: Acta Cryst. **3** (1950) 461.
K. Kohra, R. Uyeda and S. Miyake: Ibid. **3** (1950) 479.
K. Kohra: J. Phys. Soc. Jap. **9** (1954) 690.
9) S. Miyake, K. Kohra, and M. Takagi: Acta. Cryst. **7** (1954) 393.
10) W. Kossel and G. Möllenstedt: Ann. d. Phys. (5) **36** (1939) 113.
G. Möllenstedt: Ibid. (5) **40** (1941) 39.

---

* $\varPhi_{hh'}$ is considered always in the range $-\pi<\varPhi_{hh'}\leqq\pi$.

W. Kossel and G. Möllenstedt: Ibid. (5) **42** (1942) 287.
I. Ackermann: Ibid. (6) **2** (1948) 19.
C. Menzel-Kopp: Ibid. (6) **9** (1951) 259. Zeit. f. Naturforsch. **8a** (1953) 28.
H. Pfister: Ann. d. Phys. (6) **11** (1953) 239.
11) E. Fues: Ann. d. Phys. (5) **43** (1943) 538. Zeit. f. Phys. **125** (1949) 531.
E. Fues and E. W. Wagner: Zeit. f. Naturforsch. **6a** (1951) 1, 79.
E. W. Wagner: Ibid. **6a** (1951) 133.
12) J. Hoerni: Helv. Phys. Acta **23** (1950) 587.
13) W. N. Lipscomb: Acat Cryst. **2** (1949) 193.
14) I. Fankuchen and H. Ekstein: Private Communication.
15) M. Renninger: Acta Cryst. **8** (1955) 597.
16) E. Fues: Ann. d. Phys. (5) **43** (1949) 531.
17) E. Fues: Zeit. f. Phys. **109** (1938) 14, 236.
18) G. P. Thomson and W. Cochrane: Theory and Practice of Electron Diffraction (1939) London, Macmillian and Co.
19) C. H. MacGillavry: Physica **7** (1940) 329.
20) H. Bethe: Ann. d. Phys. (4) **85** (1928) 55.
21) S. Miyake and R. Uyeda: Acta Cryst. **8** (1955) 335.
H. Niehrs: Zeit. f. Phys. **140** (1955) 106.

JOURNAL OF THE PHYSICAL SOCIETY OF JAPAN Vol. 12., No. 1, JONUARY, 1957

Study of Simultaneous Reflexion in Electron Diffraction by Crystals

II. Experimental Confirmation

By Kyozaburo KAMBE*

Tokyo Institute of Technology, Oh-Okayama, Meguro-ku, Tokyo

(Received September 22, 1956)

The effect of the phases of structure amplitudes appearing in the simultaneous reflexion in electron diffraction as predicted by the dynamical theory has been examined experimentally in convergent-beam electron-diffraction patterns of graphite. Anomalous structures of Kossel-Möllenstedt lines at their cross points have been satisfactorily explained by the theory. Thus, it has been proved that the experimental determination of the phases of structure amplitudes is feasible by the observation of simultaneous reflexion. The phase effects have been found also at the intersecting points of Kikuchi lines.

§ 1. Introduction

In a preceding paper[1] (Part I) it has been shown theoretically that observations on the simultaneous reflexion in electron diffraction give information on the phases of structure amplitudes. When the simultaneous reflexion by the lattice planes with indices h and h' takes place, the intensities of the reflected waves depend on the value of $\Phi_{hh'}=\varphi_h-\varphi_{h'}+\varphi_{h'-h}$, where φ_h, $\varphi_{h'}$, and $\varphi_{h'-h}$ are the phase angles of Fourier coefficients V_h, $V_{h'}$, and $V_{h'-h}$ of the crystal inner potential V, respectively. Calculations developed for the case of electron diffraction by a lamellar crystal has revealed that in some cases the value of $|\Phi_{hh'}|$ may be easily found from the fine structure of reflexion peaks.

In the present paper an experimental verification of the theoretical result is described. The experiment has been performed by the so called convergent-beam method originated by Kossel and Möllenstedt[2].

§ 2. Convergent-beam Method

The fundamental scheme of the convergent-beam method is illustrated in Fig. 1. The electron beam passed through a slit is coverged on the specimen by an electron lens. The angular aperture of the beam is generally from 1/100 to 1/40 rad, and the diameter of the focus on the specimen is usually smaller than 10 μ. The wave transmitted the crystal produces a circular spot on the fluorescent screen. When a Bragg reflexion takes place, the reflected beam also produces a circular spot (the reflexion spot) on the screen. A diffraction pattern thus obtained is called Kossel-Möllenstedt pattern or briefly 'K-M pattern'.

---

* Now at Electrotechnical Laboratory, Nagata-cho, Chiyoda-ku, Tokyo.

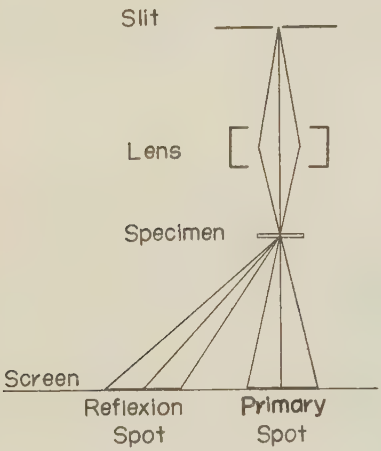

Fig. 1. Diagram of convergent-beam method.

A point in the primary spot corresponds to a certain direction of the primary wave. Similarly, a point in the reflexion spot corresponds to a certain direction of the reflected wave. The two points related by a Bragg reflexion, one in the primary spot and the other in the reflexion spot, can be easily found geometrically on the photograph by noting the relation

$$\boldsymbol{K}_{ht}=\boldsymbol{K}_{ot}+\boldsymbol{b}_{ht}\ , \qquad (1)$$

where $\boldsymbol{K}_{ot}$ and $\boldsymbol{K}_{ht}$ are the tangential components of the wave number vectors of the primary and diffracted waves, and $\boldsymbol{b}_{ht}$ the tangential component of the reciprocal lattice vector concerned.

The primary and reflected spots contain respectively extinction lines and bright lines (K-M lines) at the positions where the Bragg condition is exactly satisfied. These lines are accompanied by subsidiary maxima and minima due to the finite thickness of the crystal.

A K-M pattern is always accompanied by a number of Kikuchi lines in its diffuse background. K-M lines are similar to Kikuchi lines since the both are due to the diffraction of the wave diverging in the crystal, though in the former the wave comes from outside while in the latter the wave is produced inside the crystal by the incoherent scattering of the incident wave.

When the incident wave satisfies the Bragg condition for a certain lattice plane, one in a parallel pair of Kikuchi lines passes through the primary spot, and the other passes through the corresponding reflexion spot. Geometrically, the Kikuchi lines outside the spots are extensions of the K-M lines inside the spots.

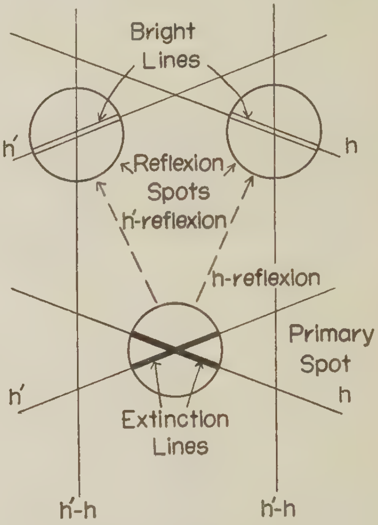

Fig. 2. Simultaneous reflexion in K-M pattern. Pairs of lines marked h, h', and $h'-h$ are Kikuchi lines.

Fig. 2 shows the case where the reflxions h and h' occur simultaneously. The pairs of Kikuchi lines for these indices pass through the primary and reflexion spots. Another pair of Kikuchi lines with the index $h'-h$ passes through the two reflexion spots, showing that the reflected waves satisfy mutually the Bragg condition for the lattice plane $h'-h$. By the coupling between the reflected waves due to this reflexion, intensity anomalies appear at the cross point of extinction lines in the primary spot and at the corresponding points on the bright lines in the reflexion spots.

The convergent-beam method is particularly suitable for the investigation of simultaneous reflexion owing to the following advantages.

1) By virture of a fine focus on the specimen, we can pick up a perfect portion of the crystal.

2) Since the angular aperture of the incident wave is finite, the intensity variation near the

condition of simultaneous reflexion can be observed at once without rotating the crystal.

3) With the aid of Kikuchi lines, the condition of simultaneous reflexion can be realized very easily by rotating the crystal so as to put an intersecting point of the Kikuchi lines, associated with the wanted reflexions, into the primary spot.

It must be noted that K-M lines and Kikuchi lines are superposed in the spots. Thus, when we want to investigate K-M lines in detail, we have to use sufficiently thin crystals for which the intensities of Kikuchi lines are reasonably weak compared with K-M lines.

§3. Experimental

We used an electron diffraction apparatus of so called 'high resolution' type. A slit 0.01∼0.1 mm in diameter was used as the point source. Using two-stage electron-microscope lenses a reduced image of about 5 μ in diameter was obtained with the beam having the angular aperture 1/100∼1/40 rad.

We have chosen graphite crystal as the sample, because 1) it has a simple crystal structure, 2) it is easily cleavable to get a thin lamellar crystal, 3) owing to small scattering power of carbon atom we can avoid undesirable dynamical effects. A disadvantage of graphite is its tendency of containing stacking faults and rhombehedral phases within the layers. However, these faults or extraordinary phases are readily detected by characteristic variations of the pattern, so that it is easy to choose crystals free from the imperfections.

It was necessary to use crystal flakes thinner than 1000 Å, to get a clear K-M pattern free from excessive incoherent scattering with the electron acceleration 40–50 kV. We used graphite crystals from Mongoria and Korea. Crystal flakes having the area about 3 mm ×3 mm were cloven with a sharp needle and a pincet. The obtained cloven flakes were in general smaller than 1 mm×1 mm. Small areas (usually smaller than 10 μ×10 μ) thinner than 1000 Å could be sometimes found at edges of the cloven flakes.

These thin crystals were always more or less curved. Therefore, with the focus of electron beam larger than 5 μ in diameter, only very limited number of specimens were sufficiently flat to give satisfactory K-M patterns. The Kikuchi pattern could be used as a convenient criterion of the flatness of the crystal. As pointed out by Uyeda, Fukano, and Ichinokawa[3)], Kikuchi lines can be observed distinctly even from very thin crystals provided the crystal is not curved. As a rule, Kikuchi patterns are more sensitively disturbed by the curving of the crystal than K-M patterns.

§4. Theoretical Predictions

Fig. 3 illustrates the primary spot in the case where the reflexions h and h' occur simultaneously. As mentioned before the position of a point in the primary spot corresponds to a direction of the incident wave. Points on the lines $h\cdots h$ and $h'\cdots h'$ represent the directions of the primary wave for which the Bragg condition is exactly satisfied. Thus, these lines correspond to the positions of the Kikuchi lines.

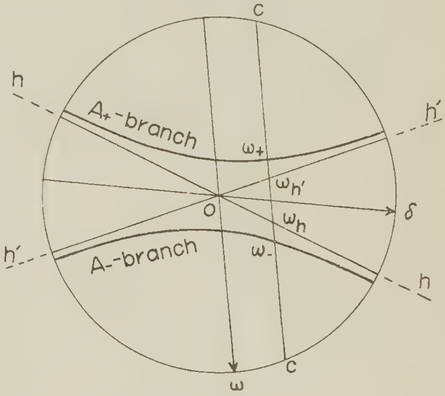

Fig. 3. The primary spot in the case of simultaneous reflexion.

In Part I the direction of the incident wave has been specified by the quantities δ (or $|c|$) and ω*. Therefore, these quantities can be used as coordinates for points in the primary spot. The origin of coordinates lies at the intersecting point of the lines $h\cdots h$ and $h'\cdots h'$. We can show easily from the definition of δ and ω in Part I that the ω-axis is parallel to the Kikuchi line with the index $h'-h$.

In Part I the intensity variation of the transmitted wave $|U_0|^2$ was calculated for a fixed value of δ (that is, for a fixed c-plane,

---

* In Part I direction of the incident wave is specified in reciprocal space by the position of the ν-normal on a c-plane, namely by the value of δ or $|c|$ (Eq. (17), Part I) and by the value of ω specifing the position of the point N (Fig. 9, Part I).

Cf. (17) in Part I). It gives the intensity distribution of the primary spot along a line $c\cdots c$ parallel to the ω-axis. Fig. 10 in Part I shows that when $|V_{h'-h}|$ is particularly large compared with $|V_h|$ and $|V_{h'}|$, we have two intensity dips at ω_+ and ω_- on the line $c\cdots c$. With the variation of δ, the line $c\cdots c$ moves in parallel. The loci of the dips make a hyperbola having $h\cdots h$ and $h'\cdots h'$ as its asymptotes. The intervertex distance between the branches of this hyperbola is proportional to $|V_{h'-h}|$.

We call the locus of ω_+ the A_+-branch, and that of ω_- the A_--branch. In accordance with the consideration in § 5 (b) in Part I, the distinction between the two branches can be easily made in the observed pattern by discriminating which branch lies between the Kikuchi-line pairs concerned, and which one lies outside. This relation is reversed in the reflexion spots.

As shown in Fig. 10 in Part I, the dips located at ω_+ and ω_- in the intensity curve for the transmitted wave $|U_0|^2$ have the half-value widths $2\alpha|V_+|/b$ and $2\alpha|V_-|/b$ respectively. The values of $|V_+|$ and $|V_-|$ which vary with the value of δ (or $|c|$) are given, according to (49) in Part I, by

$$\left.\begin{aligned} |V_+| &= \frac{1}{\sqrt{1+|c|^2}}(|V_h|^2+|c|^2|V_{h'}|^2 \\ &\qquad +2|c||V_h||V_{h'}|\cos\Phi_{hh'})^{1/2} \\ |V_-| &= \frac{1}{\sqrt{1+|c|^2}}(|c|^2|V_h|^2+|V_{h'}|^2 \\ &\qquad -2|c||V_h||V_{h'}|\cos\Phi_{hh'})^{1/2} \end{aligned}\right\} \qquad (2)$$

where $|c|$ is related to δ by (17) in Part I, namely,

$$\delta=\left(|c|-\frac{1}{|c|}\right)\alpha|V_{h'-h}| \qquad (3)$$

Accordingly, the extinction lines making a hyperbola in the primary spot show variations in their widths with the value of δ or $|c|$, as shown in Fig. 4. It should be noted that the depth of the dips do not vary in the primary spot.

From (2) we see that the branches in the primary spot should have following features according to the value of $\cos\Phi_{hh'}$.

1) When $\cos\Phi_{hh'}>0$, the A_+-branch is wider than A_--branch (Fig(5 (a)).

2) When $\cos\Phi_{hh'}<0$, the A_+-branch is narrower than A_--branch (Fig. 5 (b)).

3) When $\cos\Phi_{hh'}=0$, the two branches are symmetric with respect to the origin in the primary spot (Fig. 5 (c)).

Particularly, when the crystal has a center of symmetry, $\cos\Phi_{hh'}$ is either equal to 1 or -1, so we have only the cases 1) and 2). In this case we have further:

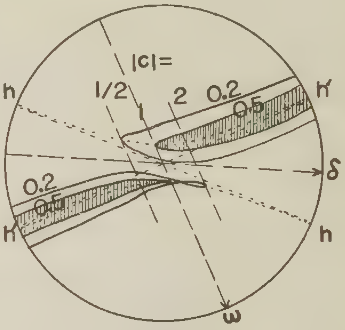

h' Reflexion Spot

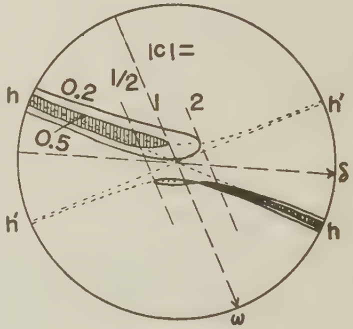

h Reflexion Spot

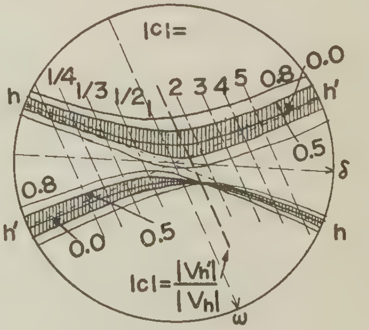

Primary Spot

Fig. 4. Intensity variation calculated for the case $|V_{h'-h}|\gg|V_h|,|V_{h'}|$ assuming $|V_{h'}|/|V_h|=3/2$, and $\cos\Phi_{hh'}=1$. The numbers attached to the contour indicate intensity values assuming that the intensity of the incident wave is unity. In the shadowed area the intensity is smaller than 0.5 for the primary spot, and larger than 0.5 for the reflexion spots.

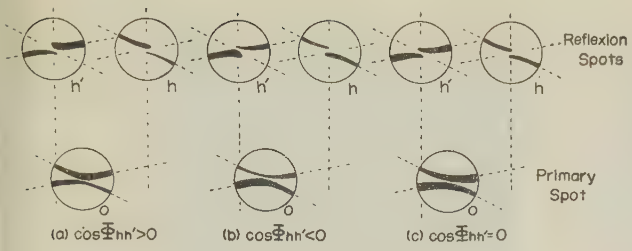

(a) $\cos\Phi_{hh'}>0$ (b) $\cos\Phi_{hh'}<0$ (c) $\cos\Phi_{hh'}=0$

Fig. 5. Intensity variations predicted by the theory, showing different characters depending on the value of $\cos\Phi_{hh'}$.

1′) When $\cos\Phi_{hh'}=1$, the A_+-branch has maximum width $2\alpha\sqrt{|V_h|^2+|V_{h'}|^2}/b$ and the A_--branch has zero width at $|c|=|V_{h'}|/|V_h|$ (Fig. 4).

2′) When $\cos\Phi_{hh'}=-1$, the A_+-branch has zero width and the A_--branch has maximum width $2\alpha\sqrt{|V_h|^2+|V_{h'}|^2}/b$ at $1/|c|=|V_{h'}|/|V_h|$.

By the similar treatment it can be shown that characteristic intensity variations appear at the corresponding positions of bright lines in the reflexion spots, as illustrated in Fig. 4 and Fig. 5.

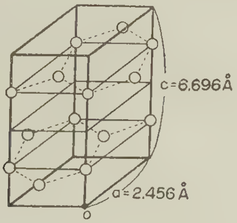

Fig. 6. Unit cell of graphite.

§ 5. Results

Graphite has a well known crystal structure, being piling up of hexagonal nets in alternating sequences $ABAB\cdots$. It belongs to a hexagonal space group $C_{6v}{}^4(C6mc)$. In order to make all the structure amplitudes real, we have chosen the origin of unit cell at a symmetry center lying halfway between the layears (Fig. 6). The unit cell contains four atoms located at

$$0\,0\,\frac{1}{4},\ 0\,0\,\frac{3}{4},\ \frac{2}{3}\,\frac{1}{3}\,\frac{1}{4},\ \frac{1}{3}\,\frac{2}{3}\,\frac{3}{4}.$$

The sings of structure amplitudes are determined by the factor

$$\sum\exp 2\pi i(hx+ky+lz)$$

The values of this factor for various combinations of reflexion indices are shown in Table I.

Table I. Values of $\sum\exp 2\pi i(hx+ky+lz)$ for hexagonal graphite.

	$h-k=3m$	$3m+1$	$3m+2$
$l=4n+0$	4	1	1
1	0	$\sqrt{3}$	$\sqrt{3}$
2	-4	-1	-1
3	0	$-\sqrt{3}$	$-\sqrt{3}$

In our experiment two sets of the *h*

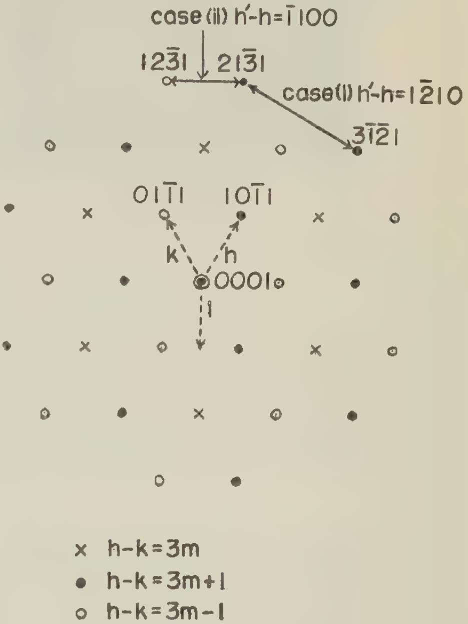

Fig. 7. The reciprocal lattice plane specified by $l=1$.

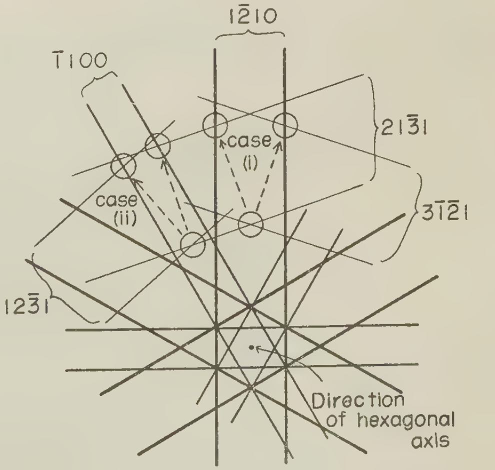

Fig. 8. Kikuchi pattern of graphite illustrating the positions of simultaneous reflexion used in the observation.

and h' reflexions were chosen from the group {211} as tabulated in Table II. Fig. 7 shows the reciprocal lattice plane specified by $l=1$ which contains the reciprocal lattice points concerned. Fig. 8 shows the Kikuchi pattern for graphite. To realize the two cases of simultaneous reflexion, the orientation of the crystal was adjusted so as to put the primary spot at the positions as shown in Fig. 8. In each case, two reflected spots appear at the positions as indicated.

We see in Table II that the value of $|V_{h'-h}|$ is large compared with $|V_h|$ and $|V_{h'}|$ in the both cases. The value of $\cos\Phi_{hh'}$ is 1 for Case (i), -1 for Case (ii). In other words, V_h and $V_{h'}$ have the same sign for (i), opposite signs for (ii), since $V_{h'-h}$ is positive for the present choice of the origin (Cf. Part I, 6). The cases (i) and (ii) correspond respectively to the cases 1′) and 2′) in the preceding section.

Table II. Two combinations of simultaneously excited reflexions used in the present observation.

	$hkil$			
Case (i)	$h=(21\bar{3}1)$	$\lvert V_h\rvert=0.63$ volt	$\varphi_h=0$	$\cos\Phi_{hh'}=1$
	$h'=(\bar{3}1\bar{2}1)$	$\lvert V_{h'}\rvert=0.63$	$\varphi_{h'}=0$	
	$h'-h=(1\bar{2}10)$	$\lvert V_{h'-h}\rvert=3.29$	$\varphi_{h'-h}=0$	
Case (ii)	$h=(21\bar{3}1)$	$\lvert V_h\rvert=0.63$	$\varphi_h=0$	$\cos\Phi_{hh'}=-1$
	$h'=(12\bar{3}1)$	$\lvert V_{h'}\rvert=0.63$	$\varphi_{h'}=\pi$	
	$h'-h=(\bar{1}100)$	$\lvert V_{h'-h}\rvert=1.47$	$\varphi_{h'-h}=0$	

Since $|\boldsymbol{b}_h|=|\boldsymbol{b}_{h'}|$ and $|V_h|=|V_{h'}|$ for the both cases, the patterns in the primary spot are symmetrical with respect to the ω-axis. When $|c|=|V_{h'}|/|V_h|=1$ ($\delta=0$), the line $c\cdots c$ in Fig. 3 passes the vertices of the hyperbola, and we have in Case (i)

$$|V_+|=\sqrt{2}\,|V_h|, \quad |V_-|=0\,,$$

so that the A_--branch vanishes at its vertex, while in Case (ii)

$$|V_+|=0\,, \quad |V_-|=\sqrt{2}\,|V_h|\,,$$

so that the A_+-branch vanishes at its vertex.

Fig. 9 shows the photographs obtained for these cases. We see that the observation verifies the theoretical predictions quite satisfactorily. At the vertices the A_+-branch has a maximum width and A_--branch vanishes in Case (i), while in Case (ii) the A_+-branch vanishes and A_--branch has a maximum width. It is seen also that the bright lines in the reflexion spots show corresponding intensity variations. Although in Case (ii) the value of $|V_{h'-h}|$ is only about twice the values of $|V_h|$ and $|V_{h'}|$, the photograph shows that this is sufficient to discriminate the value of $\cos\Phi_{hh'}$ from the observation.

§ 6. Discussion

The result obtained above shows that the phase determination is practically feasible by the present method. However, since our observation is limited to most favourable cases, it is desired that the method is applied to more general cases of phase determination in crystal analysis. As the convergent-beam method requires a very thin plate of perfect single crystal, it can be applied to very limited kind of crystals. However, also some other experimental methods can be used for the study of simultaneous reflexion; for example, observation of Kikuchi lines, and observation of extinction lines due to Bragg reflexion in electron-micrographs may be applied for this purpose.

Fig. 10 shows the Kikuchi pattern obtained from a relatively thick crystal. This corresponds to the part indicated in Fig. 8 as Case (i). The phase effect similar to the case of K-M line can be observed for the intersecting points of Kikuchi lines appearing at the positions corresponding to the reflexion spots in Fig. 9. This result can be proved theoretically by applying our method described in Part I to Kikuchi lines. Thus, the range of practical application of our method is considerably extended, since the observation of Kikuchi lines is comparatively easier than K-M lines. Particularly, we may utilize Kikuchi patterns obtained by reflexion from natural or cloven

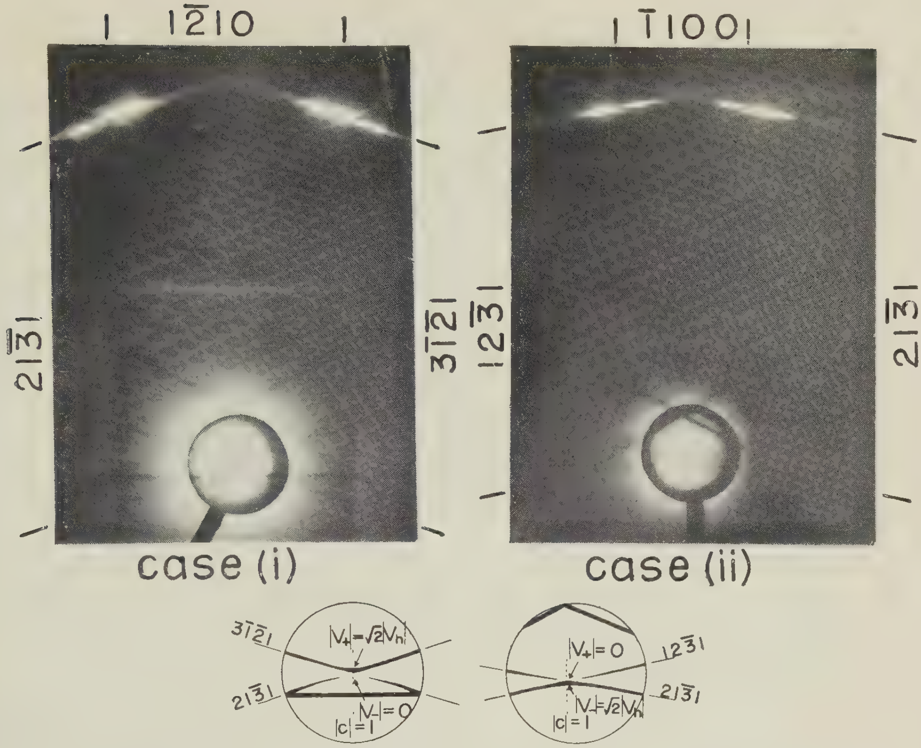

Fig. 9. Convergent-beam electron-diffraction photographs of graphite, showing the phase effect in simultaneous reflexion. (Accelerating voltage 41 kV, crystal thickness $\sim$1000 Å.) The exposure of the primary spot is diminished by covering it with a disc. Sketches illustrate the intensity variation in the primary spot.

faces of block single crystals. We have actually found examples of Kikuchi lines in reflexion patterns revealing the phase effect. A more detailed analysis of Kikuchi lines will be reported in another paper.

When we observe thin crystal plates by an electron microscope, extinction lines due to Bragg reflexion appear frequently in the image. The phase effect may appear at the cross point of two extinction lines; dark-field micrographs obtained by using reflected rays may be utilized for indexing the extinction lines[4][5].

The author expresses his sincere thanks to Prof. S. Miyake for his guidance throughout the work.

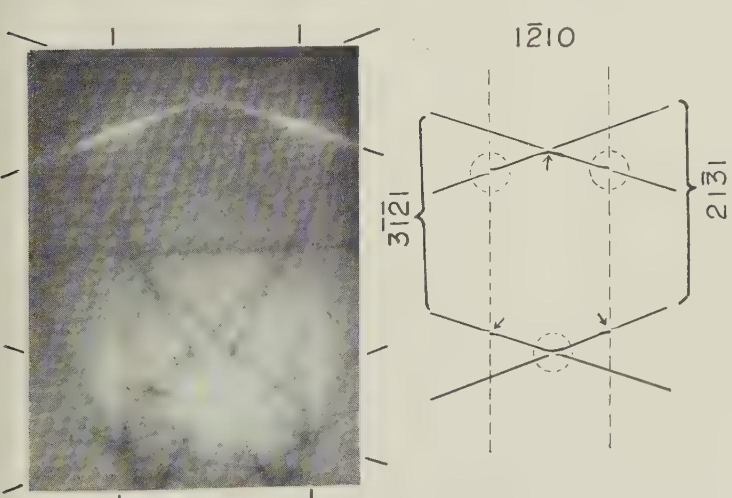

Fig. 10. Kikuchi pattern corresponding to Case (i) in Fig. 9, obtained by using a relatively thick crystal. At the cross points surrounded by circles in the sketch the same intensity variations as in the spots in Fig. 9 are observed. Also the points indicated by arrows show similar intensity variations, though white and black relation is reversed.

References

1) K. Kambe: Journ. Phys. Soc. Japan **12** (1957) 13.
2) W. Kossel and G. Möllenstedt: Ann. d. Phys. (5) **36** (1939) 113.
3) R. Uyeda, Y. Fukano, and T. Ichinokawa: Acta Cryst. **7** (1954) 217.
4) O. Rang and H. Schluge: Optik **9** (1952) 463.
5) K. Ito and T. Ito: Journ. of Electronmicroscopy **1** (1953) 18.

JOURNAL OF THE PHYSICAL SOCIETY OF JAPAN Vol. 12, No. 1, JANUARY, 1957

Intermolecular Potential between Large Molecules

By Akira ISIHARA*

Department of Physics, University of Maryland, College Park, Maryland

and Ryuzo KOYAMA

The Electrical Communication Laboratory, Musashino, Tokyo, Japan

(Received August 28, 1956)

The intermolecular potential between spherical polyatomic molecules is calculated, assuming the Lennard-Jones potential between atoms of polyatomic molecules. Owing to the distribution of atoms in polyatomic molecules the degree of infinit of potential is lowered when two polyatomic molecules approach each other. In the case of uniform distribution of atoms in polyatomic molecules, the degree is lowered by 5 orders and the minimum value of the potential is proportional to the radius of polyatomic molecule and to the square of the density of the atoms. At large intermolecular distance, the result of calculation of this case coincides with the results of Atoji and Lipscomb and of Hamaker. Calculation for a parabolic distribution of atoms is also given. The temperature and molecular weight dependence of the second virial coefficient of high polymer solutions are explained by the aid of calculated potential function.

§ 1. Introduction

In 1937, following the calculation of de Boer¹⁾, Hamaker¹⁾ calculated the potential energy between two spheres composed of particles which are uniformly distributed within each sphere, assumping Van der Waals-London forces between the particles in one sphere and those in the other. Hamaker showed that various colloidal phenomena can be explained with the aid of total potential curves, obtained by superposing these Van der Waals-London attractive forces and a repulsive force, conforming to a very simple and crude approximation. Since then, many calculation have been made, using the repulsive potential arising from electric double layer interactions¹⁾.

Recently, Atoji and Lipscomb²⁾ calculated the potential energy between polyatomic molecules composed of randomly distributed atoms, but they used a series expansion which is only applicable to molecular distances which are sufficiently large in comparison with the radius of the molecules.

In this paper, we shall first calculate the potential energy between two polyatomic molecules having spherical symmetry. The calculation is general and can be applied even if the density of the polyatomic molecules is not constant. It can be used when the distance between the polyatomic molecules is very small.

Theoretical investigations on high polymers, particularly those on high polymer solutions³⁾, make remarkable strides in recent years. However, with respect to the interaction potential between polymer molecules we do not have sufficient knowledge. Although most of important properties of polymers are determined by the molecular weight, specific properties of polymers should depend on the interaction potential between high polymer molecules.

We have shown in a previous paper⁴⁾ that the temperature and molecular weight dependence of the second virial coefficient can be interpreted if we take all the interactions between segments of polymer molecules into consideration. Particularly, our theoretical predictions about the behavior of second virial coefficient near the Flory point—the temperature at which the second virial coefficient vanishes—fit the experimental data of Krigbaum and Flory on polyisobutyrene in benzene⁵⁾ and of Krigbaum on polystyrene in cyclohexane⁶⁾.

The second virial coefficient is determined by the radial distribution function of two polymer molecules in solutions and the function is determined by the interaction potential between chain polymers. We can consider that the interaction potential is a function of the molecular weight and, as a result, the second virial coefficient become dependent on the molecular weight.

---

* On leave from Department of Physics, Faculty of Science, University of Tokyo, Japan.

Polymer molecules takes various configurations, and the potential function between two polymer molecules is a function of such configurations. However, the average value should be a function of the distance between centers of gravity of two polymer molecules and also of the degree of polymerization and the distribution of segments in polymer molecules. We are concerned here in calculating such average potential functions.

§ 2. Potential Energy between Polyatomic Molecules

We wish to calculate the potential energy between two spherical polyatomic molecules as a function of their distance, each polyatmic molecule being composed of atoms whose interaction is assumed to be known. The object of the calculation is to see the relation between the interactions of atoms and that of polyatomic molecules. Let the distance between the centers of gravity O and O′ of two polyatomic molecules be S, and consider the differential volumes $d\boldsymbol{r}$ and $d\boldsymbol{r}'$ located respectively at the distances $\boldsymbol{r}$ and $\boldsymbol{r}'$ from O and O′. If $\rho \boldsymbol{r} d\boldsymbol{r}$ or $\rho(\boldsymbol{r}')\,d\boldsymbol{r}'$ atoms are included in each differential volume, then the average potential energy between the two polyatomic molecules is given by

$$\varPhi(s)=\iint \rho(\boldsymbol{r})\varphi(s)\rho(\boldsymbol{r}')d\boldsymbol{r}d\boldsymbol{r}' , \qquad (2.1)$$

where $\varphi(s)$ is the potential between the atoms of different polyatomic molecules and s is the distance between $\boldsymbol{r}$ and $\boldsymbol{r}'$ (Fig. 1). The integration is over the volumes of two polyatomic molecules.

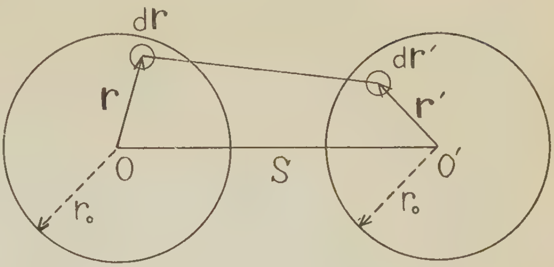

Fig. 1. The spherical polyatomic molecules at distance S.

In Eq. (1), it is assumed that deformation of polyatomic molecules does not occur even when the two polyatomic molecules approach each other closely and the potential energy between atoms is additive. Some kinds of potential function will make the value of Eq. (1) infinite for S below a certain value. In such a case, we consider that the polyatomic molecules interact there with a rigid body potential and cannot get nearer to each other. For convenience sake, we assume that the polyatomic molecules have spherical symmetry around their center of gravity and that the distribution functions $\rho(\boldsymbol{r})$ and $\rho(\boldsymbol{r}')$ depend only on the magnitude r and r' of the vector-arguments.

For the potential $\varphi(s)$, we adopt the Lennard-Jones potentials:

$$\varphi(s)=\varphi_0\{(s_0/s)^{12}-2(s_0/s)^6\} , \qquad (2.2)$$

where s_0 is the position of the minimum of $\varphi(s)$ and φ_0 is the corresponding value $\varphi(s_0)$. Let the radius of polyatomic molecules as rigid bodies be r_0, than Eq. (1) can be reformed as follows

$$\varPhi(S)=4\pi^2N^2\varphi_0(s_0/r_0)^6[(s_0/r_0)^6\psi_{12}(S')-2\psi_6(S')] ,$$
$$\psi^{12}(S')=\frac{1}{90}\frac{1}{S'}\int_{-1}^{1}\int_{-1}^{1}\frac{xy\sigma(x)\sigma(y)}{(S'+x+y)^9}dxdy ,$$
$$\psi^{6}(S')=\frac{1}{12}\frac{1}{S'}\int_{-1}^{1}\int_{-1}^{1}\frac{xy\sigma(x)\sigma(y)}{(S'+x+y)^3}dxdy ,$$
$$S'=S/r_0 , \qquad (2.3)$$

by a straight-forward calculation.

Here N represents the total number of atoms in one polyatomic molecule and the function $\sigma(x)$ is a reformed distribution function normalized to unity:

$$r^2\rho(r)\,dr=Nx^2\sigma(x)\,dx ,$$
$$\int_0^\infty 4\pi x^2\sigma(x)dx=1 ,$$
$$r=r_0x . \qquad (2.4)$$

The first and the second terms in the bracket of $\varPhi(S)$ of Eq. (2.3) come respectively from the first and the second terms of the Lennard-Jones potential and are respectively the repulsive and the attractive parts of the potential $\varPhi(S)$. The repulsive part of $\varPhi(S)$ has a factor $(s_0/r_0)^{12}$ which is very small in the case of large molecules so that the repulsive part becomes effective only when the polyatomic molecules are near to each other. At $S'=2$ or $S=2r_0$, where the polyatomic molecules will contact with each other, $\Phi(S)$ becomes infinite.

To obtain the potential function explicitly, we must know the distribution function $\rho(r)$. For this, we can think of several functional forms. If polyatomic molecules are chain like polymer molecules, and if we assume the random flight model for these polymers, we may use the results of the calculation for $\rho(r)$ of Isihara, Debye-Bueche, Benoit-Goldstein[7]. However, this adoption makes the result of the integration of Eq. (2.3) very annoying, particularly at small values of $S'-2$, also there arises the problem of how to normalize the distribution function in accordance with the rigid body radius r_0. Thus, in the following sections we shall calculate $\Phi(S)$ for much simpler forms of $\rho(r)$.

§ 3. Uniform distribution of Atoms

As the simplest example, we shall treat first the case of a uniform distribution of atoms:

$$\begin{aligned}\rho(r)&=q=\text{const.}, \quad r\leq r_0\,,\\ &=0 \qquad\quad\;\;, \quad r>r_0\,.\end{aligned}\tag{3.1}$$

In terms of the reduced distribution function:

$$\begin{aligned}\sigma(x)&=\frac{3}{4\pi}\,, \quad x\leq 1\,,\\ &=0\;\;, \quad x>1\,.\end{aligned}\tag{3.2}$$

Inserting this into Eq. (2.3), we obtain

$$\begin{aligned}\Phi(S)=&\frac{2}{3}\pi^2q^2\varphi_0 s_0{}^6\\ &\times\left[\frac{1}{15}\left(\frac{s_0}{r_0}\right)^6\left\{\frac{1}{56}\frac{1}{S'}\left(\frac{1}{(S'-2)^7}+\frac{1}{(S'+2)^7}+\frac{2}{S'^7}\right)-\right.\right.\\ &-\frac{1}{168}\frac{1}{S'}\left(\frac{1}{(S'-2)^6}-\frac{1}{(S'+2)^6}\right)+\\ &\left.+\frac{1}{1680}\left(\frac{1}{(S'-2)^5}+\frac{1}{(S'+2)^5}+\frac{1}{S'^5}\right)\right\}-\\ &\left.-\left\{\frac{1}{S'^2-4}+\frac{1}{S'^2}+\frac{1}{2}\log\frac{S'^2-4}{S'}\right\}\right].\end{aligned}\tag{3.3}$$

The first and the second terms in the braces represent respectively the repulsive and attractive parts of the potential. The latter can be easily shown to coincide with the result obtained by Hamaker.

When two polyatomic molecules are close to each others, Eq. (3.3) is approximated by the following formula:

$$\begin{aligned}\Phi(S)=&\frac{2}{3}\pi^2q^2\varphi_0 s_0{}^6\\ &\times\left[\frac{1}{15}\left(\frac{s_0}{r_0}\right)^6\frac{1}{112}\left\{\frac{1}{x^7}-\frac{5}{6}\frac{1}{x^6}+\frac{9}{20}\frac{1}{x^5}-\cdots\cdots\right\}-\right.\\ &\left.-\frac{1}{4}\left\{\frac{1}{x}+2\log x+\frac{3}{4}-\frac{39}{16}x+\cdots\right\}\right],\end{aligned}\tag{3.4}$$

where

$$x=S'-2\,.\tag{3.5}$$

From this equation, the minimum point S_0 $\Phi(S)$ can be calculated as follows:

$$x_0=60^{-1/6}\left(\frac{s_0}{r_0}\right)\left\{1+\frac{3}{14}60^{-1/6}\left(\frac{s_0}{r_0}\right)+\cdots\cdots\right\},\tag{3.6}$$

that is

$$S_0=2r_0+60^{-1/6}s_0\left\{1+\frac{3}{14}60^{-1/6}\left(\frac{s_0}{r_0}\right)+\cdots\cdots\right\}.\tag{3.7}$$

In deriving this, it was assumed that the ratio (s_0/r_0) is very small compared with 1. Accordingly, the minimum value of $\Phi(S)$ is given

$$\begin{aligned}\Phi(S_0)=&-\frac{1}{7}60^{1/6}\pi^2\varphi_0 s_0{}^5q^2r_0\\ &\times\left\{1+\frac{7}{3}60^{-1/6}\left(\frac{s_0}{r_0}\right)\log\left(\frac{s_0}{r_0}\right)-\right.\\ &\left.-0.5884\cdot 60^{-1/6}\left(\frac{s_0}{r_0}\right)+\cdots\cdots\right\}.\end{aligned}\tag{3.8}$$

From Eq. (3.8) the minimum value of the potential seems to be proportional to the radius and to the square of the density q of the atoms of the polyatomic molecule.

When the intermolecular distance S becomes much larger than the radius of the polyatomic molecule, $\Phi(S)$ can be expanded[2)] in the power series of $r_0/s_0=1/S'$:

$$\begin{aligned}\Phi(S)=N^2\varphi_0&\left[\left(\frac{r_0}{S}\right)^{12}\left\{1+\frac{132}{5}\left(\frac{r_0}{S}\right)^2+\right.\right.\\ &\left.+\frac{10296}{25}\left(\frac{r_0}{S}\right)^4+\cdots\cdots\right\}-2\left(\frac{s_0}{S}\right)^6\left\{1+\right.\\ &\left.\left.+6\left(\frac{r_0}{S}\right)^2+\frac{144}{5}\left(\frac{r_0}{S}\right)^4+\cdots\cdots\right\}\right].\end{aligned}\tag{3.9}$$

In the limit when S/r_0 is sufficiently large compared to 1, $\Phi(S)$ approaches the Lennard-Jones type function:

$$\Phi(S)\approx N^2\varphi_0\left\{\left(\frac{s_0}{S}\right)^{12}-2\left(\frac{s_0}{S}\right)^6\right\}.\tag{3.10}$$

Eq. (3.4) shows that the repulsive and the attractive parts of the potential begin respectively from the terms $(1/x)^7$ and $(1/x)$, these powers being just greater by 5 than those in the corresponding terms of the original Lennard-Jones potential. Accordingly, $\Phi(S)$ becomes infinite when S approaches $2r_0$ by 5 orders lower than the degree of infinity of the Lennard-Jones potential.

§ 4. Parabolic Distribution of Atoms

Next, we shall apply the general formula (2.3) to the case of a parabolic distribution of atoms about the center of gravity:

$$\begin{aligned}\rho(r)&=\frac{15}{8\pi}\frac{1}{r_0^3}N\left(1-\frac{r^2}{r_0^2}\right), && r\le r_0\,,\\ &=0 && ,\ r>r_0\,,\\ \sigma(x)&=\frac{15}{8\pi}(1-x^2) && ,\ x\le 1\,,\\ &=0 && ,\ x>1\,, \qquad (4.1)\end{aligned}$$

and shall compare the result with the former case. The calculation of the potenial $\Phi(S)$ in the present case is more complicated but since it is straight-forward we shall only give the result:

$$\begin{aligned}\Phi(S)=\frac{75}{32}\pi^2N^2\varphi_0(s_0/r_0)^6\Bigg[&\frac{1}{15}\left(\frac{s_0}{r_0}\right)^6\Bigg\{\frac{1}{420}\frac{1}{S'}\left(\frac{1}{(S'-2)^5}+\frac{1}{(S'+2)^5}-\frac{1}{2}\frac{1}{S'^5}\right)-\\ &-\frac{1}{280}\frac{1}{S'}\left(\frac{1}{(S'+2)^4}-\frac{1}{(S'+2)^4}\right)+\frac{1}{336}\frac{1}{S'}\left(\frac{1}{(S'-2)^3}-\frac{1}{(S'+2)^3}+\frac{2}{5}\frac{1}{S'^3}\right)-\\ &-\frac{1}{560}\frac{1}{S'}\left(\frac{1}{(S'-2)^2}-\frac{1}{(S'+2)^2}\right)+\frac{1}{1120}\frac{1}{S'}\left(\frac{1}{S'-2}+\frac{1}{S'+2}-\frac{2}{S'}\right)\Bigg\}-\\ &-\left\{\left(\frac{3}{20}S'^4-S'^2+2\right)\log\frac{S'^2-4}{S'^2}-\frac{4}{5}\frac{1}{S'}\log\frac{S'-2}{S'+2}+\frac{3}{5}S'^2-\frac{4}{15}\right\}\Bigg]. \qquad (4.2)\end{aligned}$$

If an intermolecular separation is small, it is convenient to use x, equal to $S'-2$, and to reform Eq. (4.2) as follows:

$$\begin{aligned}\Phi(S)=\frac{75}{32}\pi^2N^2\varphi^0\left(\frac{s_0}{r_0}\right)^6\Bigg[&\frac{1}{1260}\left(\frac{s_0}{r_0}\right)^6\left\{\frac{1}{x^5}-\frac{2}{x^4}+\frac{9}{4}\frac{1}{x^3}-\cdots\cdots\right\}-\\ &-\left\{\left(x+\frac{5}{2}x^2\right)\log x+\frac{4}{5}\left(\log 2-\frac{1}{2}\right)-\frac{2}{5}\left(\log 2-\frac{11}{2}\right)x+\frac{1}{5}\left(\log 2+\frac{1}{8}\right)x^2+\cdots\right\}\Bigg].\end{aligned}$$

(4.3)

When x approaches zero, the attractive part approaches a constant value $4/5\cdot(\log 2-\frac{1}{2})$. The repulsive parts has a power 7 orders higher than that of the original Lennard-Jones potential and starts at $1/x^5$. The power in the attractive part is diminished similarly.

Thus, the degree of infiniteness in the present case is lower than the uniform distribution of segments. The difference comes particularly from the distribution of atoms in the neighborhood of the polyatomic molecule. The minimum point of the potential function just calculated is given by the following equation when s_0/r_0 is very small compared to 1.

$$(s_0/r_0)^6\approx 2520x^6\left\{-\log x-\frac{2}{5}(8-\log 2)\right\}. \qquad (4.4)$$

§ 5. The Potential Curves

Fig. 2 and Fig. 3 illustrate the potential function given by Eq. (3.3) or (3.4) between polyatomic molecules with uniform distribution of atoms. As shown in Eqs. (3.3) and (3.4), the absolute value of the potential $\Phi(S)$ is depend on the molecular radius r_0 as well as on the density of atoms $q=3N/4\pi r_0^3$ even if φ_0 and s_0 are constant. For convenience, we designate that part of the potential function of Eq. (3.4) which is dependent upon the distance S by $\Psi(S)$ and express the potential function in the following form:

$$\Phi(S)=\frac{60^{1/6}}{42}\pi^2q^2\varphi_0 s_0^5 r_0\Psi(S)\,, \qquad (5.1)$$

where $\Psi(S)$ depends on s_0/r_0 as well as on S. The three curves in Fig. 2 and Fig. 3 correspond to the following values of s_0/r_0:

curve 1. $s_0/r_0=1/10$,
curve 2. $s_0/r_0=1/100$,
curve 3, $s_0/r_0=1/1000$.

Fig. 2 shows the function $\Psi(S)$ plotted against the intermolecular distance. The abscissa is the intermolecular distance divided by the molecular radius r_0. Fig. 2 is useful to see how the potential curves depend on the molecular diameters. It also shows that how the potentials are different from the rigid body potential at various molecular diameters.

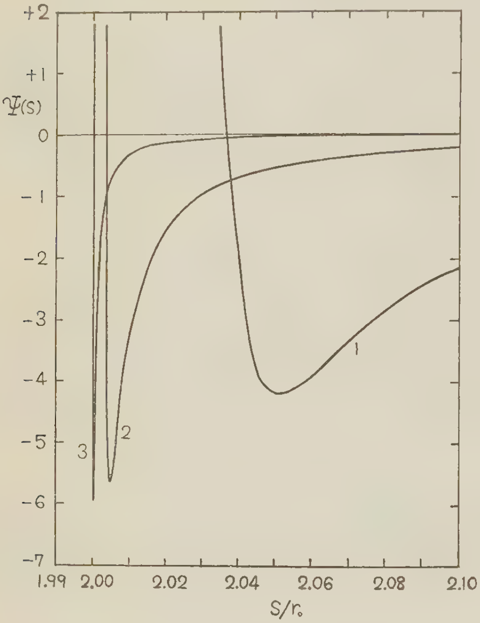

Fig. 2. Potential between polyatomic molecules composed of atoms distributed uniformly as a function of molecular distances S.

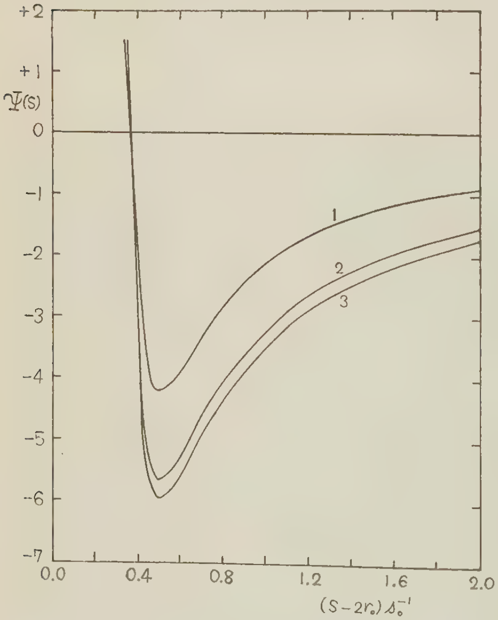

Fig. 3. Potential between polyatomic molecules composed of atoms distributed uniformly as a function of molecular separation $S-2r_0$.

Fig. 3 represents the function $\Psi(S)$ for the intermolecular separation $S-2r_0$. The unit of the abscissa is s_0, which is the minimum point of the original Lennard-Jones potential. From Fig. 3, we can infer that the minimum position of potential function of polyatomic molecules appear, as they should, at positions corresponding to the intermolecular separation of about $1/2\cdot s_0$, nearly independent of molecular sizes when the diameters of molecules become large.

When the polyatomic molecules are randomly kinked chain molecules which are spherical, and if we use the result of the random flight model, we can put

$$r_0=\lambda(Nb^2)^{1/2}, \tag{5.2}$$

where b is the length of one segment and λ is a constant independent of the degree of polymerization N.

§ 6. Application to High Polymer Molecules

The potentials we have calculated are functions of the total number of atoms in a molecule, and thus it is expected that if we use such potentials to calculate the second virial coefficient A_2, in the expansion of osmotic pressure π as a power series of concentration c:

$$\frac{\pi}{RTc}=\frac{1}{M}+A_2c+A_2c^2+\cdots, \tag{6.1}$$

π becomes a function of molecular weight. Here, R is the gas constant and T the absolute temperature. Accoding to the theories of McMillan and Mayer[8] and Kirwood and Buff[9], A_2 assume the form:

$$A_2=-\frac{2\pi N_0}{M^2}\int_0^\infty (g_2(S)-1)\,S^2\,dS, \tag{6.2}$$

where N_0 is Avogadro's number of $g_2(S)$ is the radial distribution function at infinite dilution of two polymer molecules separated by a distance S.

For the distribution function $g_2(S)$, we shall adopt the form:

$$g_2(S)=e^{-\Phi(S)/kT}, \tag{6.3}$$

where $\Phi(S)$ is an average potential given by Eq. (3.3) or Eq. (4.2). If we use Eq. (3.3) in Eq. (6.3), we arrive at the following expression for the second virial coefficient:

$$A_2=\frac{16}{3}\pi N_0 r_0^3 M^{-2}\{1+(s_0/r_0)f(-\Phi(S_0)/kT)\}, \tag{6.4}$$

where $-\Phi(S_0)$ is the potential minimum given by Eq. (3.8). For small values of x, $f(x)$ is estimated as follows:

$$f(x)=\frac{1}{2}\sqrt{\frac{\pi}{2}}\left\{6^{6/7}e^{-1}x^{1/7}-\sqrt{7}\,e^{-1/7}x\right\}. \tag{6.5}$$

Whereas for large values of x, $f(x)$ is approximately proportional to $\sqrt{x}\,e^x$.

If we neglect the possible temperature dependence of r_0 or q, the temperature variation of the second virial coefficient A_2 is given by

$$\frac{\partial A_2}{\partial(1/T)}=\frac{16}{3}\pi N_0 r_0^3 M^{-2}\cdot(-\Phi(S_0)/kT)\cdot(s_0/r_0)\cdot\times$$
$$\times f'(-\Phi(S_0)/kT)\,. \tag{6.6}$$

On the other hand, in dilute solution the partial heat of dilution is calculated as follows:

$$\Delta H_1=\frac{16}{3}\pi R N_0 V_S s_0 r_0^2 M^{-2}c^2\Phi(S_0)/k\cdot f'(-\Phi(S_0)/kT), \tag{6.7}$$

where V_S is the molar volume of solvent. The function $f(x)$ increases according to whether the argument x is small or large. Since x is small when T is large or when $-\Phi(S_0)$ is small, we see from Eqs. (6.6) and (6.7) that the temperature derivative of the second virial coefficient is positive in poor solvents where the heat of solution of negative. This is in line with experiments.

In the theory of high polymer solution, Huggins' parameter μ is often used. To explain the temperature dependence of A_2, a semi empirical temperature dependent form of μ is assumed. From our theory, μ is calculated as a function of temperature:

$$\mu=\frac{1}{2}-\frac{16}{3}\pi N_0 r_0^3 V_S \rho^2 M^{-2}$$
$$\times\{1+(s_0/r_0)\cdot f(-\Phi(S_0)/kT)\},$$
$$r_0=\lambda N^{1/2}b\,. \tag{6.8}$$

where ρ is the density of high polymer.

In the region where $f(-\Phi(S_0)/kT)$ is small A_2 is expressed by the equation:

$$A_2\approx\frac{16}{3}\pi N_0 \lambda^3 b^3 M_0^{-3/2} M^{-1/2}, \tag{6.9}$$

from which we can see the molecular weight dependence of A_2 easily. Here we introduce λ which is a proportional constant connecting the radius of polymer molecule r_0 and the end-to-end distance and is defined by Eq. (5.2). In Eq. (6.9), we have neglected the second term in the bracket of Eq. (6.4). If we insert the experiment data of Outer, Carr, and Zimm[10] into Eq. (6.9), using the Eq. (5.2), the following values for λ are obtained:

polystyrene–butanone	0.264 ,
polystyrene–dichlorethane	0.296 .

The theory of random flight predicts the value 0.408, because if we consider the radius r_0 to be the average square root distance of segments from the center of gravity, r_0 is given by $(1/6\cdot Nb^2)^{1/2}$. Both values of λ are of the same order of magnitude. This is a reasonable correspondence.

In turn, if we consider that λ is related to a volume exclusion effect which varies with the molecular weight, Eq. (6.9) can be expressed as

$$A_2=CM^{-\alpha}, \tag{6.10}$$

which is an empirical formula. Here α is a constant and assumes numerical values between about 0.2 and 0.5.

In the region where $f(-\Phi(S_0)/kT)$ is not small we can not predict easily the molecular weight dependence of A_2.

We shall now discuss the second virial coefficient near the Flory point. If only the neighborhood of the Flory point is concerned, we can deduce from Eq. (6.4) following approximate expression for the second virial coefficient:

$$A_2\approx\frac{16}{3}\pi N_0 r_0^3 M^{-2}$$
$$\times\left[1-\exp\left\{-\left(-\frac{\Phi(S_0)}{k\Theta}+\frac{1}{2}\right)\left(1-\frac{\Theta}{T}\right)\right\}\right], \tag{6.11}$$

where Θ means the Flory point. This expression shows that when $T-\Theta$ is small, A_2 versus temperature curve is a straight line which has a positive slope, determined by $r_0^3M^{-2}\left(-\frac{\Phi(S_0)}{k\Theta}+\frac{1}{2}\right)\frac{1}{\Theta}$. At larger values of $T-\Theta$, the curve bends towards the abscissa.

This is determined by the magnitude of $r_0{}^3M^{-2}\left(-\frac{\Phi(S_0)}{k\Theta}+\frac{1}{2}\right)\left(-\frac{\Phi(S_0)}{k\Theta}+\frac{5}{2}\right)\frac{1}{\Theta^2}$.

All these behaviors coincide with the data of Krigbaum⁶⁾ on polystyrene in cyclohexane and the data of Krigbaum and Flory⁵⁾ on polyisobutylene in benzen. By comparing Eq. (6.11) with these data we can determine r_0 and $\Phi(S_0)$ separately. The values we thus obtained from the data of Krigbaum⁶⁾ for polystyrene in cyclohexane systems are illustrated in Table I. In this table R means the root of the average of squre distances of segments from the center of gravity of the polymer molecule. This quantity was calculated by using the relations:

$$R=(1/6\cdot Nb^2)^{1/2},$$

$$(Nb^2/M)^{1/2}=735\times10^{-11}\ \mathrm{cm}.$$

The numerical value of the right hand side of the second equation is calculated from the data of Krigbaum, Mandelkern and Flory, and Schults¹¹⁾. r_0 is the radius of polymer molecule as a rigid sphere and is considerep to be nearly equal to R. Table I shows this is actually true. In the last column of Table I the minimum values of the potential between polymer molecules are indicated. Similar to r_0 these depend on the molecular weight. In Fig. 4 we illustrated the dependence. As can see from Fig. 4., r_0 and $-\Phi(S_0)$ are nearly proportional to $M^{0.56}$ and $M^{0.23}$ respectively. This is a very natural dependence.

Table I

M	r_0	R	$-\Phi(S_0)/k\Theta$
50,500	49 Å	67 Å	6.1
125,000	80	107	8.2
359,000	148	180	9.4
566,000	188	226	11.2

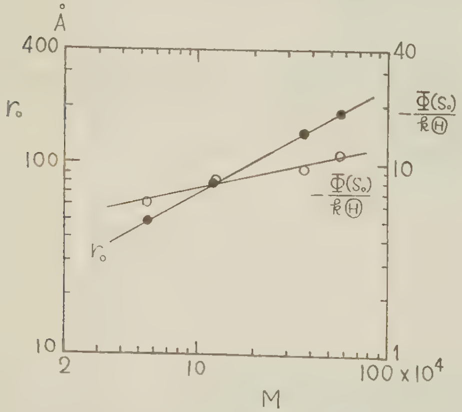

Fig. 4. Molecular radius r_0 and minimum values of intermolecular potentials $-\Phi(S_0)/k\Theta$ of polystyrene molecules in cyclohexane as a function of the molecular weight, calculated from the experimental data of Krigbaum⁶⁾.

According to the theories of Flory and Krigbaum³⁾, Grimley³⁾, and the previous one of ourselves⁴⁾, the Flory point does not depend on the molecular weight or degree of polymerization of polymers. However, from our present theory there is a possibility that the point depend on the molecular weight or degree of polymerization. The data of Krigbaum⁶⁾ show the possibility. We hope that this point will be elucidated in the near future.

So far we have only treated high polymer solutions. Overbeek and Sparnaay¹²⁾ reported that such type of attractive forces as calculated by de Boer and Hamaker¹⁾ and ourselves was found experimentally. Further applications of the potentials we have calculated will be given in a subsequent paper.

Acknowledgement

The authors wish to express their thanks to Professor E. W. Montroll for his valuable suggestions.

References

1) J. H. de Boer: Trans. Fraday Soc. **32** (1936) 21; H. C. Hamaker: Physica **4** (1937) 1058; Verway and Overbeek, Theory of the Stability of Lypophobic Colloids, (Elsevier Pub. Comp. Inc. 1948).
2) M. Atoji and W. N. Lipscomb, J. Chem. Phys. **21** (1953) 1480.
3) P. J. Flory and W. R. Krigbaum: J. Chem. Phys. **18** (1950) 1086; **20** (1952) 873; A. Isihara: J. Chem. Phys. **18** (1950) 1946; **19** (1951) 1142; **19** (1951) 397; J. Polymer Sci. **7** (1951) 277; B. H. Zimm: J. Chem. **21** (1953) 934; T. B. Grimley: Proc. Roy. Soc. **A 212** (1952) 339; E. A. Guggenheim: Discussion Faraday Soc. No. **15** (1953) 67; G. S. Rushbroke, H. I. Scoins and A. J. Wakefield: Discussion Faraday Soc. No. **15** (1953) 57; I. Prigogin et al: J. Chem. Phys. **20** (1952) 49; **21** (1953) 559, 560, 561; Discussion Faraday Soc. No. **15** (1953) 80; V. Mathot and Desmyter: J. Chem. Phys. **21** (1953) 782; M. Kurata, M. Tamura and T. Watari: J. Chem.

Phys. **23** (1955) 991; W. H. Stockmayer and E. F. Casassa: J. Chem. Phys. **20** (1952) 1560; M. L. Huggins: J. Polymer Sci. **16** (1955) 209.
4) A. Isihara and Koyama: J. Chem. Phys. to be published.
5) W. R. Krigbaum and P. J. Flory: J. Am. Chem. Soc. **75** (1953) 1775, 5254.
6) W. R. Krigbaum: J. Am. Chem. Soc. **76** (1954) 3785.
7) A. Isihara: J. Phys. Soc. Japan **5** (1950) 201; J. Polymer Sci. **8** (1952) 574; P. Debye and F. Bueche: J. Chem. Phys. **20** (1952) 1337; H. Benoit and M. Goldstein: J. Chem. Phys. **21** (1953) 947; R. Ullman and J. J. Hermans: J. Polymer Sci. **10** (1953) 559.
8) W. G. McMillan and J. E. Mayer: J. Chem. Phys. **13** (1954) 276.
9) J. G. Kirkwood and F. P. Buff: J. Chem. Phys. **19** (1951) 774.
10) P. Outer, C. J. Carr and B. H. Zimm: J. Chem. Phys. **18** (1950) 830.
11) A. R Schultz: thesis, Corhell University, (1953); W. R. Krigbaum, L. Mandelkern and P. J. Flory: J. Polymer Sci. **9** (1952) 381.
12) J. Th. G. Overbeek and M. J. Sparnaay: Proceedings Koninkhjke Nederl. Akad. Van Wetenschappen, Series B. **54** (1951) 387.

JOURNAL OF THE PHYSICAL SOCIETY OF JAPAN Vol. 12, No. 1, JANUARY, 1957

Dependence of Quadrupole Coupling Constant on the Vibrational State in ICN Molecule

By Takeshi OKA, Hiromasa HIRAKAWA and Akira MIYAHARA*

Department of Physics, Faculty of Science,
University of Tokyo, Tokyo, Japan

(Received September 20, 1956)

The microware spectrum of the hyperfine components of the $J=1\leftarrow 0$ and $J=2\leftarrow 1$ rotational transitions of ICN molecule has been measured and the dependence of quadrupole coupling constant on the vibrational state was found. The values of $(eqQ)_I$ for each vibrational state are as follows:

Vibrational States	$(eqQ)_I$ in Mc/sec from the frequencies of the $J=1\leftarrow 0$ transition	 from the frequencies of the $J=2\leftarrow 1$ transition
(0, 0, 0)	-2418.8 ± 0.5	-2420.1 ± 0.3
(1, 0, 0)	-2426.8 ± 0.7	-2425.1 ± 0.5
(0, 2, 0)	-2403.3 ± 0.8	-2403.1 ± 0.5

The difference in the $(eqQ)_I$ value for the (0, 2, 0) state from that for the (0, 0, 0) state, previously explained by Javan for the (0, 1, 0) state, was confirmed, thuogh the numerical values are slightly different from his. The change of $(eqQ)_I$ due to the excitation of the stretching vibration was also found and was explained in terms of the change of the double bond character of I–C bond.

§ 1. Introduction

The dependence of quadrupole coupling constant on the vibrational states of the molecule has been described by several authors.[1)–5)] Tetenbaum pointed out the change of $(eqQ)_{Br}$ of BrCN molecule when the bending viration was excited.[2)] Javan remeasured the lines of the $J=4\leftarrow 3$ rotational transition of ICN molecule and confirmed the change of $(eqQ)_I$ [5)]. He explained it taking into account the change of q, the gradient of the electric field along the nuclear axis produced by the electrons.

Though both of them did not refer to the change of the quadrupole coupling constant due to the excitation of the stretching vibration, this change seems to be possible, because the stretching vibration tends to elongate the bond and thus decreases the double bond character of I–C bond, which results in the increase of $(eqQ)_{\mathrm{I}}$. This work has been carried out with the aim of investigating these changes.

---

* Now at Institute for Nuclear Study, University of Tokyo.

§ 2. Experiments and Results

The hyperfine components of the $J=1\leftarrow 0$ and $J=2\leftarrow 1$ rotational transitions of ICN molecule have been measured with the Stark modulation spectrometer of four meters in length. The frequencies have been obtained by extrapolating the observed frequencies at various Stark fields to those at zero field. The measured frequencies with the calculated ones are shown in Table I a and II a. For almost all lines, probable errors were less than 0.05 Mc/sec. The largest probable error amounted to 0.5 Mc/sec for the weakest lines.

Table I a.
Frequencies of the hyperfine components of the $J=1\leftarrow 0$ rotational transition for $IC^{12}N$ in Mc/sec.

		(0, 0, 0) lines	
F_i	F_f	observed	calculated
5/2	7/2	6577.06 6577.95	6577.81
5/2	5/2	6070.66 6071.61	6071.33
5/2	3/2	6799.79	6799.77
		(1, 0, 0) lines	
F_i	F_f	observed	calculated
5/2	7/2	6559.63	6559.56
5/2	5/2	6051.36	6051.41
5/2	3/2	6782.16	6782.28
		(0, 2, 0) lines	
F_i	F_f	observed	calculated
5/2	7/2	6610.24	6610.00
5/2	5/2	6106.71	6106.75
5/2	3/2	6830.47	6830.50

Table I b.
Values of $(eqQ)_{\mathrm{I}}$ and rotational constant B for $IC^{12}N$ derived from the frequencies of the $J=1\leftarrow 0$ transition

Vibrational state	$(eqQ)_{\mathrm{I}}$ in Mc/sec	B in Mc/sec
(0, 0, 0)	-2418.8 ± 0.5	3225.77 ± 0.1
(1, 0, 0)	-2426.8 ± 0.7	3216.42 ± 0.1
(0, 2, 0)	-2403.3 ± 0.8	3242.30 ± 0.1

I. Hyperfine components of the $J=1\rightarrow 0$ rotational transition.

Three hyperfine components due to the nuclear quadrupole moment of I^{127} were observed for each vibrational state, (0, 0, 0), (1, 0, 0), and (0, 2, 0). Since the initial state is $l=0$, (0, 1, 0) lines are not allowed. Because of the nuclear quadrupole moment of N^{14}, the lines are further split. This effect was taken into consideration in the analysis of the frequencies using the method proposed by Bardeen and Townes with -3.8 Mc/sec for $(eqQ)_{\mathrm{N}}$ of ICN molecule.⁷⁾ The lines of the excited vibrational states were so weak that the splitting due to the nitrogen quadrupole moment could not be measured. The values of $(eqQ)_{\mathrm{I}}$ and the rotational constants B derived from the measured frequencies and used in the calculation are listed in Table I b.

II. Hyperfine components of the $J=2\leftarrow 1$ rotational transition.

According to the selection rule $\Delta F=\pm1, 0,$

Table II a.
Frequencies of the hyperfine components of the $J=2\leftarrow 1$ rotational transition for $IC^{12}N$ in Mc/sec

		(0, 0, 0) lines	
F_i	F_f	observed	calculated
7/2	9/2	12956.38	12956.08
7/2	7/2	12489.27 12489.88	12489.35
7/2	5/2	12622.19	12622.62
5/2	7/2	12996.93 12996.50 12994.98	12996.09
5/2	5/2	13129.36 13129.68	13129.35
5/2	3/2	13465.77	13465.73
3/2	5/2	12400.35 12401.33	12400.54
3/2	3/2	12737.22	12736.92
3/2	1/2	13048.33	13048.42
		(1, 0, 0) lines	
F_i	F_f	observed	calculated
7/2	7/2	12451.36	12451.37
5/2	7/2	12959.17	12959.17
5/2	3/2	13429.80	13429.80
3/2	3/2	12699.69	12699.46
3/2	1/2	13011.34	13011.63
		(0, 2, 0) lines	
F_i	F_f	observed	calculated
7/2	9/2	13021.92	13021.88
7/2	7/2	12558.38	12558.42
5/2	5/2	13193.32	13193.80
5/2	3/2	13527.88	13527.95

Table II b.
Values of $(eqQ)_{\mathrm{I}}$ and rotational constant B for $\mathrm{IC^{12}N}$ derived from the frequencies of the $J=2\leftarrow1$ transition

Vibrational state	$(eqQ)_{\mathrm{I}}$ in Mc sec	B in Mc sec
(0, 0, 0)	-2420.1 ± 0.3	3225.56 ± 0.05
(1, 0, 0)	-2425.1 ± 0.5	3216.28 ± 0.04
(0, 2, 0)	-2403.1 ± 0.5	3242.11 ± 0.05

nine hyperfine components should be observed for each vibrational state, (0, 0, 0), (1, 0, 0), (0, 2, 0), (0, 1, 0), and (1, 1, 0), where the last two allow l-doublets. Because of complexity of the Stark pattern of these l-doublets and their inadequacy for the purpose of this work, only strong lines belonging to the (0, 0, 0), (1, 0, 0), and (0, 2, 0) vibrational states have been measured. Many strong l-doublets with large Stark shift made it very difficult to measure accurately the lines which overlap with them, and some lines were abandoned for this reason. The values of $(eqQ)_{\mathrm{I}}$ and rotational constants B derived from these frequencies and used in the calculation are listed in Table II b.

§ 3. Discussions

The changes of $(eqQ)_{\mathrm{I}}$ due to the excitation of the bending vibration were 15.5 Mc/sec and 17.0 Mc/sec for the $J=1\leftarrow0$ and $J=2\leftarrow1$ transitions, respectively. Javan5) measured (0, 1, 0) lines and obtained 9.45 Mc/sec for the change, which corresponds to 18.90 Mc/sec of our case, because of the fact that the mean sequare amplitude is proportional to the vibrational quantum number. The gradient of the electric field when the bending vibration is excited is given by the formula, $q=(1-3/2\,\overline{\theta^2})q_0$5) where q_0 is the value of q for the ground vibrational state and $\overline{\theta^2}$ is the mean square amplitude of the deflection angle of I–C bond from its equilibrium direction when the bending vibration is excited. Using the above formula with the mean square amplitude calculated from the vibrational spectrum, the change of $(eqQ)_{\mathrm{I}}$ is calculated to be 12.6 Mc/sec. The rest of the change seems to be due to the fact that the valence electrons do not follow the motion of I and C nuclei.

The changes of $(eqQ)_{\mathrm{I}}$ due to the excitation of the stretching vibration are 8.0 Mc/sec and 5.0 Mc/sec for the $J=1\leftarrow0$ and $J=2\leftarrow1$ transitions, respectively. Though there is rather large discrepancy between these values, the change of $(eqQ)_{\mathrm{I}}$ is beyond the experimental error. This change may be explained by considering the change of the weight of the two resonating structures,6) $\mathrm{I{-}C{\equiv}N}$ and $\mathrm{I^+{=}C{=}N^-}$. The magnitude of q of the double bond structure is half as large as that of the single bond structure. When the stretching vibration is excited, the bond is elongated owing to the anharmonicity of the potential energy and thus the double bond character of I–C bond is decreased. This consideration explains the increase in the magnitude of $(eqQ)_{\mathrm{I}}$ in agreement with the experiment. The order of magnitude of this kind of change is estimated using Pauling's relation between the bond length and the double bond character. The change of the rotational constant B due to the excitation of the stretching vibration is assumed to be due to the proportional stretching of I–C bond and C–N bond, approximating the bond length of I–C bond in (1, 0, 0) state as $r_v=r_0\,(B_0/B_v)^{1/2}$, where r_0 is the bond length of I–C bond in the ground vibrational state and B_0 and B_v are rotational constants of the ground and excited vibrational states, respectively. Substituting the values in Table I b and II b with $r_0=1.995$ A8), it gives $r_v=1.998$ A. The double bond character x of I–C bond for ICN molecule calculated from the observed value of $(eqQ)_{\mathrm{I}}$ is 0.136). From Pauling's relation,9)

$$R=[R_1(1-x)+3R_2x]/[(1-x)+3x]\ ,$$

the variation of x due to the change of the bond length δR is calculated to be

$$\delta x=x(2x+1)\delta R/(R-R_1)\ ,$$

where R_1 is the I–C bond length when pure single bond is assumed. Substituting $x=0.13$, $R=1.995$ A, $R_1=2.10$ A, and $\delta R=r_v-r_0=0.003$ A, this formula gives the change of the double bond character due to the stretching of the I–C bond as $\delta x=-0.0047$. Though the value of 2.10 A for R_1 is not quite definite, the difference as large as 0.01 A in R_1 does not affect the first figure of δx. The gradient of the electric field is given by the formula,

$$q(x)=[-(1-s+d)(1-x)\\ -(1/2-s+d)(1+\mathcal{E})x]\,q_{510}\ ,$$ 10)

where q_{510} is the value of q for iodine atom, and s and d indicate the fraction of s and d

hybridization, respectively. Because of the positive ionization of the I atom in the $I^{+}=C=N^{-}$ structure, which pulls the electron closer to the nuleus, the factor $1+\mathcal{E}$ is multiplied to the second term. This is differentiated to give the variation of q due to the change of the double bond character x as

$$\delta q=[1/2-\mathcal{E}(1/2-s+d)]q_{510}\delta x\ .$$

For the case of I–C bond $s-d$ and $\mathcal{E}$ can safely be estimated to be 0.15 and 0.15, respectively. With these values and the above mentioned value of δx, it is shown that

$$q(1,0,0)/q(0,0,0)=1.0026$$

which is in fair agreement with the following experimental values

$$q(1,0,0)/q(0,0,0)=\begin{cases}1.0033 & (J=1\leftarrow 0)\\ 1.0021 & (J=2\leftarrow 1).\end{cases}$$

Major part of the discrepancy between the two values seems to be due to the experimental error, which arises chiefly from the weakness of the lines and the splittings due to the nuclear quadrupole moment of N^{14}. The value derived from the lines of the $J=2\leftarrow 1$ transition seems to be more reliable than that from the $J=1\leftarrow 0$ transition, because more appropriate lines could be adopted for analysis in the former case than the latter.

§ 4. Isotope Lines

The spectrum of the hyperfine components of the $J=1\leftarrow 0$ rotational transition for $IC^{13}N$ molecule in the (0, 0, 0) state was observed. The measured frequencies are shown in Table III. The hyperfine components of the $J=2\leftarrow 1$ transition of $IC^{13}N$ molecule could not be measured, being hidden by the complicated l-doubling lines of $IC^{12}N$.

Table III.

Frequencies of the hyperfine components of the $J=1\leftarrow 0$ rotational transition for $IC^{13}N$ in Mc/sec

(0, 0, 0) lines		
F_i	F_f	
5/2	7/2	6480.72
5/2	5/2	5974.43
5/2	3/2	6703.25

§ 5. Acknowledgement

The authors are indebted to Prof. K. Shimoda for his encouragement during the course of this investigation. They are also grateful to Prof. C. H. Townes for valuable suggestions, and to Prof. Y. Morino, Dr. I. Miyagawa, and Mr. T. Chiba of Department of Chemistry for many helpful discussions.

References

1) J. Duchesne: J. Chem. Phys. **20** (1952) 1804.
2) S. J. Tetenbaum: Phys. Rev. **86** (1952) 440.
3) B. P. Fabricand, R. O. Carlson, C. A. Lee and I. I. Rabi: Phys. Rev. **91** (1953) 1403.
4) J. A. Kraitchman and B. P. Dailey: J. Chem. Phys. **22** (1954) 1477.
5) A. Javan: Phys. Rev. **99** (1955) 1302.
6) C. H. Townes and B. P. Dailey: J. Chem. Phys. **17** (1949) 782.
7) J. Bardeen and C. H. Townes: Phys. Rev. **73** (1948) 97.
8) C. H. Townes, A. N. Holden and F. R. Merrit: Phys. Rev. **74** (1948) 1113.
9) L. Pauling: *Nature of the Chemical Bond* (Cornell University Press, (1939), p. 164.
10) C. H. Townes and A. L. Schawlow: *Microwave Spectroscopy* (McGraw-Hill Book Company, Ltd. (1955), p. 240.

JOURNAL OF THE PHYSICAL SOCIETY OF JAPAN Vol. 12, No. 1, JANUARY, 1957

Microwave Spectrum of Vinylidene Chloride

By Shōzō SEKINO* and Tetsuji NISHIKAWA**

Department of Physics, Faculty of Science,
University of Tokyo, Tokyo, Japan

(Received September 22, 1956)

The microwave spectrum of vinylindene chloride has been observed and analyzed. The molecular parameters have been determined to be $d_{CCl}=1.727$A and $\angle$Cl C C$=123°10'$ on the assumption of $d_{CC}=1.32$A, $d_{CH}=1.07$A and $\angle$H C C$=120°$. The quadrupole coupling constant along the bond direction has been found to be -78.7 Mc together with the asymmetry parameter $\eta=0.12$, for Cl^{35}. The five percent double bond character of C Cl bond estimated from the quadrupole data is consistent with the value of six percent estimated from the bond length.

§ 1. Introduction

It is known that the bond length, d_{CCl}, in carbone-chlorine compounds decreases as the electronic structure around the carbon atom tends to have more s character than sp_3 hybridization. For example, the bond length was determined to be 1.781 A in methyl chloride, whereas 1.632 A in chloroacetylene[1),2)].

These values are compared with the values of C H bond distance in methane 1.094 A and in acetylene, 1.059 A. Since the change in C Cl bond length, 0.150 A, is larger than that in C H bond, 0.035 A, some other effects besides the increase of s character in bonding electron of carbon atom have to be considered. The double-bond character of C Cl bond would take a considerable part in this change, while Duchesne[3)] presented an effect of the hybridization of chlorine atom which would change in a way as to increase the overlap integral between carbon and chlorine orbitals.

In these respects, it is interesting to examine the C Cl bond in chloroethylenes, in which the bonding electron around the carbon has sp_2 hybridization. The vinylidene chloride is such a typical molecule with a permanent dipole moment and a two-fold symmetry axis. The molecular structure was obtained by Brockway and others[4)] by an electron diffraction method. The bond length, d_{CCl}, and the bond angle, $\angle$Cl C Cl, were reported to be 1.69 ± 0.02 A and $116°\pm2°$, respectively, on the assumption of the bond length, d_{CC}, of 1.38 A. Theoretical discussion of the structure was given by Pauling, Brockway, and Beach[5)] on the line of Pauling's resonance method. However, their assumed value of C=C bond length seems to be too large compared with the recent value, ~1.32 A, in ethylene-like molecule determined by Karl and Karl[6)] and others.

The microwave investigation of this molecule can give informations of its structure and the quadrupole coupling constant of the C Cl bond which is another clue to examine the bond structure. Recently, Goldstein[7)] gave a method to estimate the double-bond structure from the asymmetry parameter of quadrupole coupling constant in a planar asymmetric molecule such as the chloroethylene.

§ 2. Experiment

The sample of vinylidene chloride was obtained from the Asahi Dow Chemical Company by courtecy of Dr. Y. Tsunoda. The boiling point is about 31°C. Though the pure one is coloreless, the sample used was colored with very little stabilizer (less than 1%) in order to prevent polimerization.

An ordinary Stark-modulation microwave spectrometer with sine-wave modulation at 120 kc superposed on a dc voltage was used. A three meter X-band absorption cell with teflon seals similar to that reported by Hardy and others[8)] was constructed. The vacuum system was composed of metals, glass, and teflon without using any other organic compound, since the sample is an active solvent.

Table I and II show the observed frequencies of nearly 90 lines in the frequency range

---

[*] Present address: Technical Laboratory of Yahata Iron and Steel Company, Yahata, Fukuoka-ken, Japan.

[**] Present address: Institute for Nuclear Study, University of Tokyo, Tanashi-machi, Tokyo, Japan.

Table I. Assigned Lines

Assignment	Obs. Freq. (Mc)	Intensity	Calc. Freq. (Mc)
$Cl^{35}_2C_2H_2$			
$3_{13}\rightarrow 2_{02}$	18703.9	W	18704.0
$4_{14}\leftarrow 3_{03}$	22701.2	MW	22701.2
$5_{05}\leftarrow 4_{14}$	24739.8	W	24739.7
$4_{32}\leftarrow 4_{23}$	23530.7	W	23529.9
$5_{24}\leftarrow 5_{15}$	22318 22314	W	22315.4
$5_{32}\leftarrow 5_{23}$	19747.0	W	19748.5
$6_{33}\leftarrow 6_{24}$	18281.0	W	18281.0
$6_{34}\leftarrow 6_{25}$	25771.6	MS	25770.7
$9_{36}\leftarrow 9_{27}$	18657.3	MW	18657.4
$9_{45}\leftarrow 9_{36}$	24962.72 24961.40 24960.08	MS	24960.1
$10_{37}\leftarrow 10_{28}$	21494.8 21492.3 21490.1	MS	21491.3
$10_{46}\leftarrow 10_{37}$	23303.7	M	23303.5
$11_{38}\leftarrow 11_{29}$	25785.7	MW	25786.1
$11_{47}\leftarrow 11_{38}$	22650.6	MS	22650.9
$12_{48}\leftarrow 12_{39}$	23428.5	MS	23428.1
$13_{49}\leftarrow 13_{310}$	25859.5 25861.5 25863.3	S	25864.8
$Cl^{35}Cl^{37}C_2H_2$			
$4_{14}\leftarrow 3_{03}$	22351.3	MW	22351.4
$5_{15}\leftarrow 4_{04}$	26287 3	MS	26287.7
$5_{05}\leftarrow 4_{14}$	24131.4	W	24131.2
$6_{34}\leftarrow 6_{25}$	25692.5	W	25692.3
$9_{27}\leftarrow 9_{18}$	25497.8	W	25498.5
$9_{36}\leftarrow 9_{27}$	18367.5	MW	18367.1
$9_{45}\leftarrow 9_{36}$	25573.4	W	25572.7
$10_{37}\leftarrow 10_{28}$	20804.2 20801.9 20799.9	MW	20802.5
$10_{46}\leftarrow 10_{37}$	23796.8	M	23797.8
$11_{38}\leftarrow 11_{29}$	24672.6	W	24669.3
$11_{47}\leftarrow 11_{38}$	22858.7	M	22861.2
$12_{48}\leftarrow 12_{39}$	23203.8	M	23204.8
$13_{49}\leftarrow 13_{310}$	25093.7	M	25093.8

Table II. Unassigned Lines

Obs. Freq. (Mc)	Intensity	Obs. Freq. (Mc)	Intensity
26236.0	W	23400.0	WW
26011.8	W	23386.5	WW
25991.1	MW	23380.3	W
25918.4	W	23350.2	WW
25783.1	WW	23326.2	WW
25766.9	W	23315.1	MW
25740.9	WW	23262.7	WW
25736.1	WW	23240.0	WW
25734.8	W	23153.9	W
25328.2	WW	23103.8	W
25215.5	MW	22958.7	W
25075.0	W	22874.0	W
25063.5	WW	22782.8	W
24661.2	W	22752.7	W
24607.2	WW	22727.2	WW
24563.5	MW	22631	WW
24491.2	MW	22597	WW
24469.0	WW	22578.6	MW
24403.2	W	22526.9	WW
24366.5	W	22311.8	WW
23896.5	WW	22234.1	W
23754.6	WW	21601.5	WW
23660.0	WW	21564	W
23643.3	W	21562.5	
23618.6	WW	21560.3	
23558.5	WW	21483.0	WW
23539.4	MW	21461.5	W
23418.5	WW	21428.5	W

between 18 and 26 kMc/sec. Having two chlorine atoms in one molecule, the spectrum of vinylidene chloride shows very complicated quadrupole hyperfine structures which have been generally observed as unresolved broad lines. Therefore, rather large errors in frequencies are estimated as ±1.5 Mc/sec for very weak lines (*WW*), ±1 Mc/sec for weak lines (*W*), and ±0.5 Mc/sec for stronger lines.

§ 3. Analysis of the Observed Spectrum

Vinylidene chloride is a planar asymmetric top molecule, principal axes of which are shown in Fig. 1. The dipole moment (~1.3 D[9]) lies along b axis.

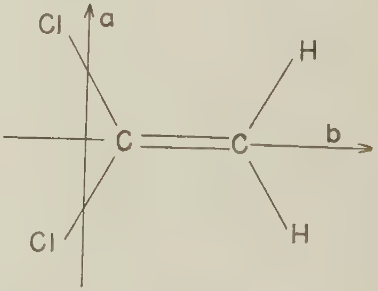

Fig. 1.

The rigid rotor model can be used in a good approximation for this molecule. The rotational energy was calculated by the method of King, Hainer, and Cross[10] using the Table of Turner, Hicks, and Reitwiener[11], and the Table of Erlandsson[12]. First, the molecular structure by Brockway and others was assumed in calculating frequencies. Comparing the calculated frequencies with the experimental data, the Q-branch lines could be assigned easily, and more accurate values of asymmetry parameter, $\kappa=\{2B-(A+C)\}/(A-C)$, as well as $(A-C)/2$, was determined. Secondly, using a relation $1/C=1/A+1/B$, $(A+C)/2$ could be estimated, so that the *R*-branch lines were assigned definitely. The assignments of lines with their calculated frequencies are shown in Table I both for $Cl_2{}^{35}C_2H_2$ and $Cl^{35}Cl^{37}C_2H_2$, while the lines of $Cl_2{}^{37}C_2H_2$ were so weak that they could not be assigned. Table III gives the rotational constants used in the calculation. The assignments of some *Q*-branch lines have been confirmed by their characteristic triplet patterns of their quadrupole hyperfine structures. The Stark effect study was also used to check the assignment of low *J* *R*-branch lines.

Table III. Rotational Constants of Vinylidene Chloride

	$Cl^{35}Cl^{35}C_2H_2$	$Cl^{35}Cl^{37}C_2H_2$
$\frac{A+C}{2}$ (Mc)	4902.9	4857.6
$\frac{A-C}{2}$ (Mc)	2563.9	2566.2
κ	−0.58178	−0.59948
A (Mc)	7466.8	7423.8
B (Mc)	3411.3	3319.2
C (Mc)	2339.0	2291.4
I_a (amu.A)	67.697	68.088
I_b (amu.A)	148.18	152.29
I_c (amu.A)	216.11	220.60
Δ (amu.A)	0.23	0.22

Calculated frequencies contain errors due to the centrifugal distorsion which are smaller than 1 Mc/sec even for $J=10$. Since the rotational constants in a vibrational state $v_1,\cdots,v_{12}$ are expressed as

$$A(v_1,\cdots,v_{12})=A_e+\sum_i \alpha_i\left(v_i+\frac{1}{2}\right)$$

$$B(v_1,\cdots,v_{12})=B_e+\sum_i \beta_i\left(v_i+\frac{1}{2}\right)$$

$$C(v_1,\cdots,v_{12})=C_e+\sum_i \gamma_i\left(v_i+\frac{1}{2}\right),$$

the equilibrium rotational constants, A_e, B_e, and C_e, can not be obtained, unless thirty six vibrational coupling constants, α_i, β_i, and γ_i are determined. Many vibrationally excited lines have been found for each rotational transition, but the complete analysis could not be done. Therefore, the calculated rotational constants in Table III include the error due to the zero-point vibration, the order of which can also be estimated from the quantum defect $\Delta=I_c-(I_a+I_b)$. The magnitude of quantum defect of vinylidene chloride is compared with those of related molecules as shown in Table IV.

§ 4. Molecular Structure

Five parameters are necessary in describing the molecular structure of vinylidene chloride. Two of them, d_{CCl} and $\angle$Cl C C can be calculated from the rotational constants A and B of $(Cl^{35})_2C_2H_2$, assuming d_{CC}, d_{CH} and $\angle$H C C. The rotational constants of $Cl^{35}Cl^{37}C_2H_2$ could also be used to determine the molecular parameters, but, actually, they give no further knowledge on account of the error due to zero-point vibration.

Because d_{CH} and $\angle$H C C would not be very different from those of ethylene values, and also because of the lightness of the hydrogen atom, it is safe to assume them equall to the ethylene values. The C C bond length of the ethylene molecule was determined to be 1.353 A from the infrared spectroscopic method by Gallaway and Barker[13]), while that of tetrachloroethylene was obtained to be 1.30 A from the electron diffraction method by Karle and Karle[6]). In any case, the values of $d_{CC}=1.38$ A assumed by Brockway and others appeared to be too large*. We have assumed the C C bond length of vinylidene chloride to be 1.32 A, and obtain the C Cl bond length of 1.727A ± 0.01A and the Cl C C bond angle of 123°10′ ± 1°30′, which are compared with the values of tetrachloroethylene, $d_{CCl}=1.72$ A and $\angle$Cl C C $=123°$. The probable errors of these values correspond to the change of assumed C C bond length by ±0.02 A.

§ 5. Quadrupole Coupling Constants

The quadrupole hyperfine structure of vinylidene chloride is very much complicated, since two chlorine atoms are in one molecule. The theory for this case was worked out by Robinson and Cornwell[14]). The perturbation energy described by the quantum numbers J and F, and a pseudoquantum number ε is written by

$$E_{\varepsilon JF}=X^{+}\lambda_{\varepsilon JF}\,, \qquad (1)$$

---

* It is also noticed that the C C bond length of 1.38A is nearly equal to that in benzene (1.39A), in which one must assume about 50 percent single bond structure in C C bond.

where

$$X^{+}=eQ\left(\frac{\partial^2 V}{\partial Z^2}\right)_{av}=\frac{eQ}{J(J+1)(2J+3)}$$
$$\times\left\{\frac{\partial^2 V}{\partial a^2}\left[J(J+1)+E(\kappa)-(\kappa+1)\frac{\partial E(\kappa)}{\partial\kappa}\right]\right.$$
$$+2\frac{\partial^2 V}{\partial b^2}\frac{\partial E(\kappa)}{\partial\kappa}+\frac{\partial^2 V}{\partial c^2}$$
$$\left.\times\left[J(J+1)-E(\kappa)+(\kappa-1)\frac{\partial E(\kappa)}{\partial\kappa}\right]\right\},$$

and Z is the axis along the direction of J. The values of $\lambda_{\varepsilon JF}$ were given in a table$^{14)}$. The coupling scheme is chiefly written by

$$\boldsymbol{I}_1+\boldsymbol{I}_2=\boldsymbol{I}\,,\quad \boldsymbol{I}+\boldsymbol{J}=\boldsymbol{F} \tag{2}$$

while a little contribution from another scheme,

$$\boldsymbol{I}_1+\boldsymbol{J}=\boldsymbol{F}_1\,,\quad \boldsymbol{I}_2+\boldsymbol{F}_1=\boldsymbol{F}\,, \tag{3}$$

have to be taken into account. $\boldsymbol{I}_1$ and $\boldsymbol{I}_2$ are the nuclear spin angular momentum vectors of two chlorine nucleus. The pseudo-quantum number, $\varepsilon=0, 1, 2, 3$, becomes equal to $\boldsymbol{I}$ when J becomes large. With the selection rules, $\Delta F=0, \pm1$ and $\Delta\varepsilon=0$, each rotational line splits into many hyperfine component lines.

Since the total wave function of vinylidene chloride is symmetric with respect to 180° rotation about the two-fold symmetry axis, b, a symmetric rotational wave function must be paired with a symmetric total spin function. The total spin function is composed of the spin function of chlorine nucleus and that of hydrogen nucleus; an odd ε line corresponds to a symmetric spin function of chlorine nucleus, whereas an even ε line corcesponds to the antisymmetric chlorine spin function. Therefore, if the rotational wave function is symmetric, the statistical weight due to proton spin is 3 for $\varepsilon=3$ and 1, and 1 for $\varepsilon=0$ and 2; the relation is revered for an antisymmetric rotational level. The lines corresponding to the transitions, $\Delta F=\pm1$ are negligibly weak and only the $\Delta F=0$ lines should be considered. The relative intensity of each $\Delta F=0$ line is approximately given by

$$(2F+1)\frac{\{F(F+1)-I(I+1)+J(J+1)\}^2}{F(F+1)}\times g_{IH} \tag{4}$$

$g_{IH}=3$ when $\varepsilon=3$, 1 for a symmetric rotational level.
when $\varepsilon=0$, 2 for an antisymmetric rotational level.
$g_{IH}=1$ for other lines.

For a Q-branch line, these component lines can be grouped into three, being observed as a triplet. The separation can be calculated from equation (1) taking the weighted means of unresolved components. These quadrupole triplets have been measured for $9_{45}\leftarrow9_{36}$, $10_{37}\leftarrow10_{28}$, and $13_{49}\leftarrow13_{310}$ lines. A typical Stark effect pattern of the triplet line is shown in Fig. 2.

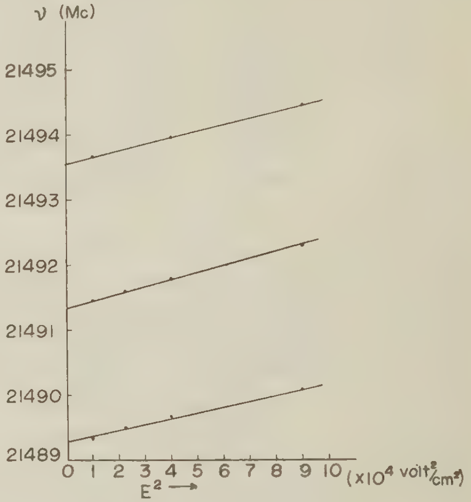

Fig. 2. Stark pattern of $10_{37}\leftarrow10_{28}$ line, showing quadrupole triplet.

From the observed separations of these triplet lines, the quadrupole coupling coefficient, $eq_{zb}Q$ (direction of C Cl bond), has been determined to be -78.7 ± 1.0 Mc/sec and the asymmetry parameter to be

$$\eta=\frac{q_{xb}-q_{yb}}{q_{zb}}=0.12\pm0.01 \text{ for Cl}^{35}.$$

§6. Discussion

The C Cl bond length and quadrupole coupling constant for various carbon-chlorine compounds are listed in Table *V*. It is noted that the bond length decreases systematically and the quadrupole coupling constant increases, as the *s* character of carbon bonding orbital increases. Following effects will be considered in addition to the change of *s* character of carbon orbital:

1) ionic structure with Cl^-,
2) double-bond character with Cl^+,
and 3) other effects concerning the charge distribution around the chlorine nucleus, such as hybridization of *s* character in the chlorine bonding orbitals.

Taking account these effects, the quadrupole coupling constant along the bond direction can approximately be written as[15]

$$eQ\approx\left[(-1+s)(1-i-k)-\left(\frac{1}{2}-s\right)(1+\xi)k\right]\times eq_{310}Q\ , \qquad (5)$$

where s, i, and k are the importance of s character in the chlorine bonding orbital, of ionic structure, and of double-bond character, respectively. ξ is a correction factor for the change in screening caused by positive ionizaton of chlorine atom, and it was estimated to be 0.15[16]. In this expression, the double-bond character with Cl^+ atom is assumed to be a p_σ bond of the same hybridized one as the single bond plus a pure p_π bond perpendicular to the bond direction.

In such an asymmetric planar molecule as vinylidene chloride, we can take the p_π bond perpendicular to the molecular plane or in the x_b direction. Then the double bond importance, k, is given by[7],

$$k=\frac{2}{3}\,\frac{\delta}{109.6(1+\xi)}\ , \qquad (6)$$

where $\delta\,(\mathrm{Mc})=eq_{yb}Q-eq_{xb}Q=-\eta eq_{zb}Q$. The importance of double-bond character has been calculated to be 5% for vinylidene chloride from the observed values. This value is compared with the double-bond character of 6% for vlnyl chloride determined by Goldstein[7]. He pointed out too, that these values appeared to be considerably smaller than the value of 18% estimated from the bond length of 1.69 A by Pauling and others[5]. However, if we take the C Cl bond length of 1.72~1.73 A (See also Appendix for vinyl chloride), the importance of double-bond character is now calculated to be 5~8% using Pauling's method. The consideration on the dipole moment also imparted the importance of about 7%[17].

On the other hand, the importance of ionic structure, i, is not uniquely determined from the observed quadrupole coupling constant until the bond hybridization is determined. It seems unfavourable, however, to suppose as Duchesne[3] that the change of s character would play considerable role in the carbon-chlorine bonds. We can rather assume that the hybridization of chlorine atom is constant for C Cl bonds in various molecules, and to be 15% for p_σ bond and 0% for p_π bond[18]. Based upon this assumption, we have obtained he ionic character from the observed $eq_{zb}Q$ to be about 15% for vinylidene chloride and vinyl chloride.

Accordingly, the importance of double-bond character and ionic structure for various carbon-chlorine compounds are shown in Table VI. In this table, the double-bond character and the ionic structure were determined in order to give the observed quadrupole coupling constant when the s character of 15% was assumed for p_σ bonds. As is known, the double-bond character of 17% for Cl C N and Cl C C H is rather small to explain the shorteness of their C Cl bond length, whereas it is too large to explain the C N or C C bond length of these molecules. This interal inconsistency needs further discussion on the nature of C Cl bond.

Table IV. Quantum Defects

Molecule	Δ(amu.A)
$C_2H_2F_2$	0.143
$C_2H_2Cl^{35}F$	0.191
$C_2H_2Cl^{37}F$	0.190
$C_2H_2Cl^{35}Cl^{35}$	0.23
$C_2H_2Cl^{35}Cl^{37}$	0.22
$C\,Cl^{35}Cl^{35}O$	0.251
$C\,Cl^{35}Cl^{37}O$	0.252
$C\,H_2O$	0.057

On the other molecules than vinylidene chloride, the above values were taken from reference 1).

Table V. C Cl bond length and quadrupole coupling constant of various carbon-chlorine compounds.

Molecule	Hybridization of carbon	$d_{C\,Cl}$ (A)	$eQ(Cl^{35})$ (Mc)	η (Cl^{35})
$C\,H_3Cl$*	sp_3	1.781	−74.74	—
C_2H_5Cl*	sp_3	(1.78)	−69.1	0.46
C_2H_3Cl	sp_2	1.724	−77.8	0.20
$C_2H_2Cl_2$	sp_2	1.727	−78.7	0.12
C_2Cl_4	sp_2	1.72	—	—
C_2HCl*	sp	1.632	−79.7	—
$C\,Cl\,N$	sp	1.629	−83.2	—

* See reference 1)

Acknowledgement

The authors express their hearty thanks to Professor K. Shimoda for his continuous encouragement and valuable discussion on this work. They also thank to Dr. Y. Tsunoda for the preparation of the sample.

Appendix: The Structure of Vinyl Chloride

The microwave spectrum of vinyl chloride

was studied by Goldstein and Bragg.[19] Goldstein[7] calculated the bond angle, $\angle$Cl C C, to be about 123° on the assumption of Brockway's value;
$d_{CC}=1.38$ A, $d_{CCl}=1.69$ A, $d_{CH}=1.08$ A and $\angle$C C H$=120°$.

We have, however, reexamined the structure on our assumption of $d_{CC}=1.34\pm0.02$ A, and the results are $d_{CCl}=1.724\pm0.015$ A and $\angle$Cl C C$=120°3'\pm30'$. This value of C Cl bond length also agrees with the C Cl bond length of vinylidene chloride and that of tetrachloroethylene. The assumed bond length d_{CC} of 1.34 A has been chosen by interpolating the values of those in ethylene, vinylidene chloride, and tetrachloroethylene.

Table VI. Double-bond character and ionic structure of various carbon-chlorine compounds.

Molecule	Importance of double-bond character (%)	Importance of ionic structure (%)
CH_3Cl*	0	20
C_2H_3Cl	7	16
$C_2H_2Cl_2$	5	15
C_2HCl*	18	0
CClN*	17	0

* See reference 1)

The quadrupole coupling constant along the bond direction, $eq_{zb}Q(Cl^{35})$, and the asymmetry parameter, η, have also been calculated to be -77.8 Mc and 0.20, respectively. These values give the importance of double-bond character of 7% and that of ionic structure of 16% as shown in Table VI.

References

1) C. H. Townes and A. L. Shawlow: Microwave Spectroscopy, Mc Graw-Hill, (1955).
2) W. Gordy, W. V. Smith, and R. F. Trambarulo: Microwave Spectroscopy, Wiley, (1953).
3) J. Duchesne: J. Chem. Phys. **19** (1951) 246.
4) L. O. Brockway, J. Y. Beach, and L. Pauling: J. Am. Chem. Soc. **57** (1935) 2693.
5) L. Pauling, L. O. Brockway, and J. Y. Beach: J. Am. Chem. Soc. **57** (1935) 2705.
6) I. L. Karle and J. Karle: J. Chem. Phys. **20** (1952) 63
7) J. H. Goldstein: J. Chem. Phys. **24** (1956) 106
8) W. A. Hardy, P. Fletcher and V. Suarez: Rev. Sci. Instr. **25** (1954) 1135
9) M. T. Rogers: J. Am. Chem. Soc. **69** (1947) 1243
10) G. W. King, R. M. Hainer and P. C. Cross: J. Chem. Phys. **11** (1943) 27
11) cited in reference 1).
12) G. Erlandsson: Ark. För Fysik **10** (1955) 65 The authors express their thanks to Dr. Erlandsson for his kind sending a copy of his table.
13) W. S. Gallaway and E. F. Barker: J. Chem. Phys. **10** (1942) 88
14) G. W. Robinson and C. D. Cornwell: J. Chem. Phys. **21** (1953) 1436
15) C. H. Townes and B. P. Dailey: J. Chem. Phys. **17** (1949) 782; See also reference 1).
16) Reference 1) P. 239
17) J. A. C. Hugill, I. E. Coop and L. E. Sutton: Trans. Faraday Soc. **34** (1938) 1518
18) B. P. Dailey and C. H. Townes: J. Chem. Phys. **23** (1955) 118; See also reperence 1).
19) J. H. Goldstein and J. K. Bragg: Phys. Rev. **75** (1949) 1453

JOURNAL OF THE PHYSICAL SOCIETY OF JAPAN Vol. 12, No. 1, JANUARY, 1957

Line Width of the Pure Quadrupole Resonance of Bromine in $NaBrO_3$

By Yoshitaka Kôi

Faculty of Technology, Tokushima University, Tokushima

(Received September 27, 1956)

Using a regenerative spectrometer the line widths of the two bromine isotopes in $NaBrO_3$ were measured at melting ice and liquid oxygen temperatures. The full width at half-maximum intensity of Br^{79} is 3.85 ± 0.1 kc and that of Br^{81} is 4.09 ± 1 kc. No observable dependence of the line width on temperature was found. From the ratio of the line widths it is concluded that the main cause of the line width in $NaBrO_3$ is the magnetic dipole interaction, and the contribution from the relaxation is of the order of 0.1 kc.

§ 1. Introduction

The pure quadrupole resonance of bromine in solid state has been investigated for a good many compounds by many workers. The positions of the resonance lines and the problems relating to the positions are their main concerns, the origin of the line width, however, is also an interesting problem. The possible causes of the line broadening are spin-lattice relaxation, magnetic dipole interaction, and field fluctuation due to the crystal strain. The electron-coupled spin-spin interaction found by Kojima and Tsukada[1] in iodine crystals will be important provided that the atom bonded covalently to bromine has a nuclear magnetic moment. However, this condition is met only in a few compounds such as Br_2. Therefore, in most compounds the above three are the possible causes. Their contributions to the observed line width are, however, not yet fully understood. Fortunately, since the two equally abundant bromine isotopes Br^{79} and Br^{81} have the same spin number 3/2 and the isotope with the larger magnetic moment has the smaller quadrupole moment, comparison of the widths of the two isotopes in one and the same chemical compound should give much information about this problem. From this point of view, measurements of the line width were made on the bromine isotopes in $NaBrO_3$ at melting ice and liquid oxygen temperature.

$NaBrO_3$ gives the sharpest resonance of all the bromine compounds. The resonant frequency of Br^{79} is about 180 Mc at 0°C, and that of Br^{81} is 150 Mc[2]. The ratio of the quadrupole couping constant of Br^{79} to that of Br^{81} is 1.2. By the way, the magnetic moment of Br^{79} and Br^{81} is 2.1058 and 2.2296 nuclear magnetons respectively; the ratio between them is 0.928.

A brief report of a regenerative spectrometer and the result of measurement made on one sample has already been reported[3]. In this article are given the details of the experimental method and the results of later measurements made on several samples with more precision. A conclusion different from the previous one was drawn from the results of later measurements.

§ 2. Regenerative Spectrometer and Experimental Procedure

The resonant frequency of bromine is in the range of 140–350 Mc, and for the detection of the resonance super-regenerative spectrometers with Lecher's lines are usually used

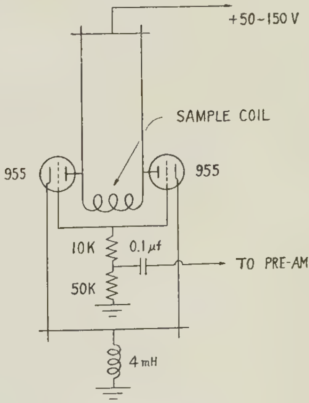

Fig. 1. Regenerative spectrometer. When a quenching voltage is applied to the top of the choke, this can be used as a super-regenerative one.

because of their simplicity and high sensitivity[4][2]. However, super-regenerative scheme seems not to be suitable for the study of line shape and line width, because the line shape depends upon the amplitude and frequency of the quenching voltage. Therefore, in order to get reliable results, it is necessary to use a regenerative spectrometer. The circuit shown in Fig. 1 has proved to be usable for this purpose.

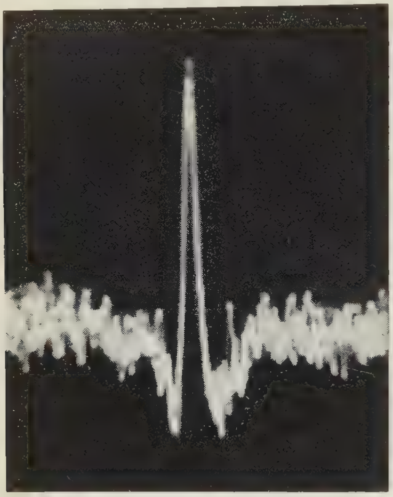

Fig. 2. Oscilloscope trace of the pure quadrupole resonance of Br^{81} in $NaBrO_3$ at melting ice temperature.

It is similar to the one used by Dehmelt[4] as a super-regenerative spectrometer, but with an important alteration that a choke is used in place of the cathode resistance. This choke is characteristic of the circuit and has the role of preventing the self-quenching oscillation. The detection principle is obvious and needs no account. Fig. 2 shows the absorption line of Br^{81} at melting ice temperature displayed on a cathode ray oscilloscope. From the oscilloscope trace, rough measurement of the line width is possible, but very precise one is impossible.

Accordingly, the derivative of the absorption line was recorded by means of conventional narrow-band and phase-sensitive detection technique, the spectrometer being frequency modulated at 210 cps.

Fig. 3 shows the schematical side view of the spectrometer and the block diagram of the whole measuring system. The frequency modulator is a metal foil attached to a $6\frac{1}{2}''$ dynamic speaker and placed near the plate Lecher's lines as shown in Fig. 3. The frequency sweeper is another metal foil placed also near the plate Lecher's lines and rotated slowly with a clock motor suitably reduced. The level of oscillation was kept sufficiently weak, though there seemed to be no tendency for the line to saturate. The spurious 210 cps voltage due to the frequency modulation was cancelled by applying a suitable voltage to the suppressor grid of the pre-amplifier from the 210 cps oscillator.

As is well known, in order to obtain the faithful derivative of the line, the modulation amplitude must be sufficiently small with respect to hte line width. However, the signal-to-noise ratio decreases with the amplitude. As a compromise between these two conside-

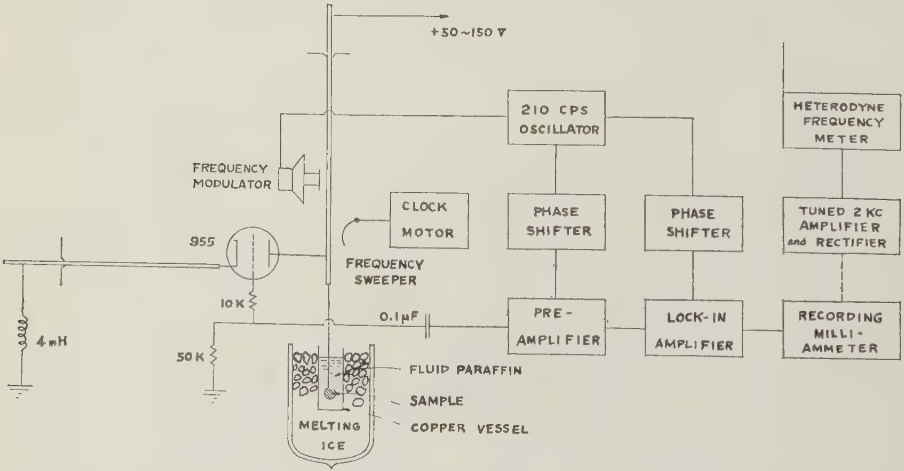

Fig. 3. The schematical side view of the spectrometer and the block diagram of the whole measuring system.

rations, amplitudes used were about one-tenth of the line width. When they were of this order of magnitude, there was no effect of modulation on the line width. They were measured by the following way.

The electromagnetic wave from the spectrometer was received with a heterodyne frequency meter, whose dial was fixed at a suitable position. Then the mean frequency of the spectrometer was swept slowly. The beat-output produced between the spectrometer and the frequency meter was amplified with a tuned 2 kc amplifier and rectified with a diod. The rectified output was recorded with the recording meter. In Fig. 4 are shown the records of the 2 kc beat. From these records the modulation amplitude and also the sweep rate of the mean frequency were able to be measured easily. The sweep rates used were 0.2–0.3 kc per second, and the times required to sweep over the absorption lines were 1–2 minutes. The time constant of the phase-sensitive detector and the associated circuit was 0.25–0.5 sec.

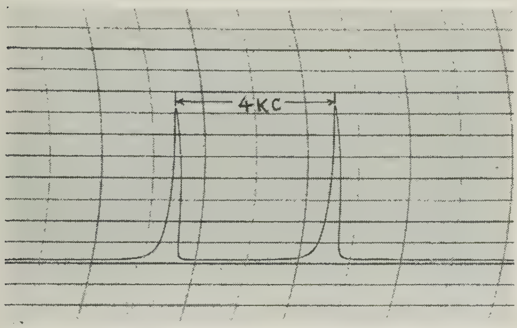

(a) Medulation amplitude = 0

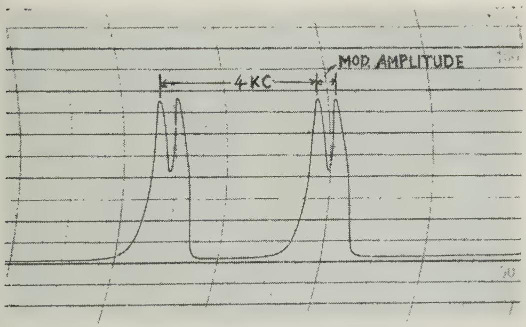

(b) Modulation amplitude = 0.5 kc

Fig. 4. Records of the 2 kc beat.

Since the resonant frequency has a temperature coefficient of the order of 100 parts per million per degree C[5,2], even a temperature inhomogeneity of the order of 0.01°C in the sample may cause a considerable broadening of the line width. Therefore, for precise measurement of the line width, it is essential to keep the sample at a constant temperature. Accordingly, the sample was immersed in a fluid paraffin whose temperature was kept at 0°C by means of melting ice as shown in Fig. 3. For the observations at liquid oxygen temperature the sample was immersed directly in a liquid oxygen. In this case the sample coil and the plate Lecher's lines were connected through condencers in order to prevent heat conduction.

The terrestrial magnetic field also gives rise to a broadening of the line width[6]. Therefore, its horizontal and vertical components were concelled separately by two small permanent magnets placed about 35 cm apart from the sample.

The samples used were assemblages of small crystal grains prepared by means of recrystallization from aqueous solutions of $NaBrO_3$ which was purified by repeated recrystallizations. The sample No. 1 was recrystallized with slowest rate, each grain of which is transparent and about 10 mm^3 in volume. No. 3 was rather rapidly recrystallized and may well be said to be a powder. No. 2 is intermediate between No. 1 and No. 3 with respect to both the speed of recrystallization and the size of the grain.

§ 3. Results and Discussions

The results of measurements are tabulated in Table I. The experimental derivative of Br^{81} and its integration are also shown for No. 1 in Fig. 5. The line shape is symmetric and has an intermediate character between a Lorentzian and a Gaussian shape, but it is rather close to the latter. Measurements at liquid oxygen temperature were made only on the sample No. 1. No measurable dependence of the line width on temperature was found. It is seen from the Table I that there

Table I. Width at half-maximum intensity (kc).

Sample	Br^{79}	Br^{81}
No. 1	3.85±0.1	4.09±0.1
No. 2	4.80±0.2	4.85±0.2
No. 3	6.55±0.2	6.25±0.2

is a considerable change of the line width with the samples, that is, the width and the ratio of the line width of Br^{79} to that of Br^{81} increase with the speed of recrystallization. Since, however, this is obviously to be attributable to the crystal strain, only the result on the sample No. 1, which gave the sharpest resonance and can be considered to be an assemblage of perfect crystal grain, will be discussed in the following.

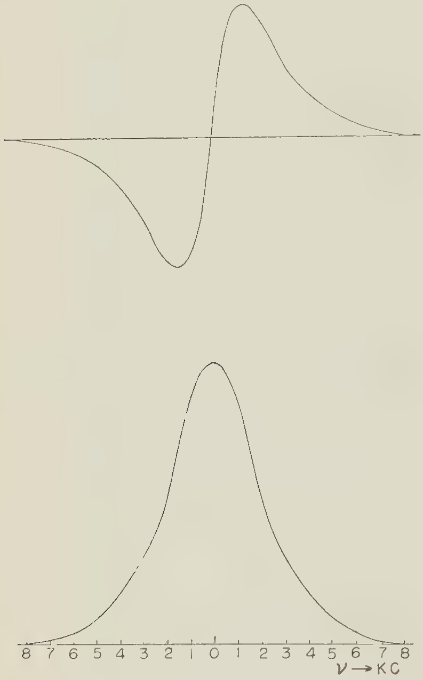

Fig. 5. Line shape of Br^{81} in $NaBrO_3$. The upper curve is the experimental derivative, and the lower is its integration.

As mentioned already, the possible mechanisms of the line broadening are the following: quadrupole spin-lattice relaxation, magnetic dipole interaction, and field fluctuation due to the crystal strain. If the first mechanism predominates, the ratio of the line widths for the isotopes Br^{79} and Br^{81} will be equal to the ratio of the squares of their quadrupole coupling constants, i.e. 1.44⁷⁾. If the second predominates, it will be equal to the ratio of their magnetic moments, i.e. 0.928, and if the third predominates, the ratio of their quadrupole coupling constants, i.e. 1.2. Of the line widths due to these mechanisms, only that due to the relaxation will depend on and decrease with temperature⁸⁾. As to the line shape, the first mechanism will give the Lorentzian shape, and the second, if there are many interacting neighbours as in the case of bromine in $NaBrO_3$, the Gaussian⁹⁾. The line shape due to the strain would depend on its nature.

Now the observed ratio is 0.94, a value which is almost equal to the ratio of the magnetic moments. Therefore, it can be concluded that the main cause of the line width of perfect $NaBrO_3$ crystal is the magnetic dipole interaction (between bromine nuclei themselves and between bromine and sodium nuclei), and the contribution from the relaxation to the line width is very small. This conclusion is in accordance with the facts that there was no observable dependence of the line width on temperature and that the line shape is rather close to the Gaussian. Abragam and Kambe¹⁰⁾ have given formulas for the contribution from the dipolar broadening to the second moment of the resonance line. Unfortunately, their formulas can not be adapted to the case of $NaBrO_3$, because there are four different directions of the electric field gradient in this substances, so that it is not possible at present to evaluate exactly the dipolar broadening. The observed values are, however, of the right order of magnitude as dipolar width.

If it is assumed somewhat arbitrarily that the width due to the strain is negligible, and those due to the dipole interaction and the relaxation are additive, the last one can be estimated to be of the order of 0.1 kc from the ratio of the line widths. Further, using the formula $\Delta\nu=1/2\pi T_1$¹¹⁾, the relaxation time T_1 of Br^{81} can be estimated to be of the order of 0.001 sec from the width due to the relaxation. Although the T_1 of Cl^{35} in $NaClO_3$, which has the same crystal structure as $NaBrO_3$, is known to be 0.4 sec¹²⁾, that of Br^{81} in $NaBrO_3$ is not yet measured. If the foregoing argument is extended to Cl^{35}, the latter is estimated to be 0.002 sec, because the quadrupole coupling constant of Br^{81} in $NaBrO_3$ is five times that of Cl^{35} in $NaClO_3$. The value is in substantial argeement with the order of magnitude estimation from the ratio of the line widths.

The author would like to express his sincere thanks to Dr. T. Kushida for valuable suggestions and kind reading of the manuscript. He also wishes to thank Messrs. A.

Tsujimura and T. Fuke for the cooperation in the earlier stage of this experiment. This work was partially supported by the Scientific Research Expenditure of the Ministry of Education.

References

1) S. Kojima and K. Tsukada: J. Phys. Soc. Japan **10** (1955) 591.
S. Kojima et al: J. Phys. Soc. Japan **11** (1956) 964.
2) A. L. Schawlow: J. Chem. Phys. **22** (1954) 1211.
3) Y. Kôi, A. Tsujimura and T. Fuke: J. Chem. Phys. **23** (1955) 1346.
4) H. G. Dehmelt: Z. Physik **130** (1951) 356.
5) H. G. Dehmelt and H. Krüger: Z. Physik **129** (1951) 401.
6) H. Krüger and U. Meyer-Berkhout: Z. Physik **132** (1952) 221.
7) R. V. Pound: Phys. Rev. **79** (1950) 685.
8) H. Bayer: Z. Physik **130** (1951) 227.
9) G. E. Pake and E. M. Purcell: Phys. Rev. **74** (1948) 894.
10) A. Abragam and K. Kambe: Phys. Rev. **91** (1953) 1184.
11) N. Bloembergen, E. M. Purcell and R. V. Pound: Phys. Rev. **91** (1948) 1168.
12) M. Bloom, E. L. Hahn and B. Herzog: Phys. Rev. **97** (1955) 1699.
T. C. Wang: Phys. Rev. **99** (1955) 566.

JOURNAL OF THE PHYSICAL SOCIETY OF JAPAN Vol. 12, No. 1, JANUARY, 1957

Gloss of Machine Glazed Papers

By Jien NISHIWAKI

Department of Physics, Faculty of Science,
Tokyo Metropolitan University

(Received August 23, 1956)

The flux I_0 reflected at specular angles 45°–45° from the surface of glossy paper and the assumed value of its diffuse component I_2 defined experimentally are measured with a goniophotometer. The ratio of I_0 to I_2 is taken as a measure of gloss, and denoted by G_{NF} according to an earlier paper of E. Fukushima.[1]

For a series of machine glazed papers differing considerably in colour, the values of C_{NF} are compared with the visual gradings of 36 Japanese observers, and a linear correlation of the logarithm of G_{NF} with the visual gloss is found with a correlation coefficient +0.986 except for two papers. The method of determining the value of I_2 is also introduced and the voting distributions of the observers for the gloss of the papers are discussed.

§ 1. Introduction

If the illuminator and receptor axes of a goniophotometer are fixed with any given angle ϕ between them (this is kept 90° throughout the experiment), and the glossy surface of specimen is so rotated that its normal approaches the receptor axis from the initial position of specular reflection, the reflected flux I generally decreases rapidly first and slowly then as the angle of rotation θ increases. For many papers, the slowly decreasing part of I–θ curve has been found to be expressed approximately by $I_2 \exp(-\beta\theta^n)$, where the two constants I_2 and β depend on the sample and the other constant n on the optical geometry of goniophotometer. The value of n is equal to 2 for the photometer[2] used here which has the geometry to measure the relative brightness. A typical form of I–θ curve obtained with this photometer is shown in Figs. 1 and 2. In Fig. 1 I is plotted against θ, and in Fig. 2 $\log I$ against θ^2. From Fig. 2, I_2 can be estimated and is assumed to be the diffuse component of I_0 which is the value of I at $\theta=0$, the position of specular reflection. Thus the ratio of I_0 to I_2 may be supposed to be one kind of contrast gloss and is denoted by G_{NF}. This notation was originally adopted by E. Fukushima. In his photometer which had different geometry, above constant n was 1, whereas in the present photometer of higher resolving power and a wider available range of θ, n is 2.

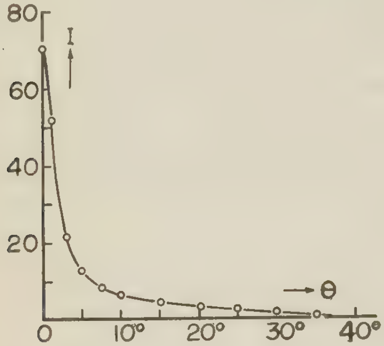

Fig. 1. A typical I–θ curve.

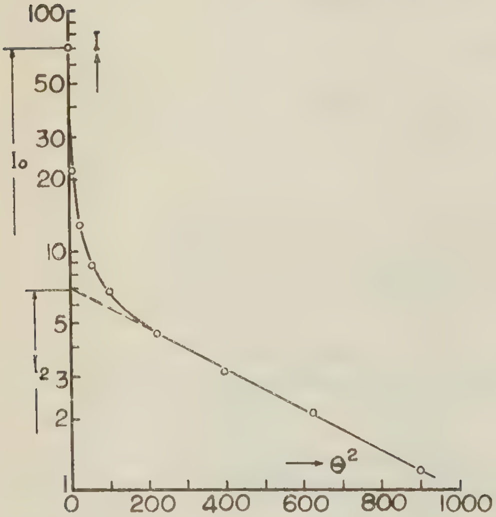

Fig. 2. log I–θ^2 curve corresponding to Fig. 1.

The author has been supplied through Professor E. Fukushima with a series of samples of machine glazed papers differing considerably in colour which he had received from Dr. V. G. W. Harrison of Printing, Packaging and Allied Trades Research Association, Leatherhead, Surrey, England.

The object of the present work is to compare the value of G_{NF} with the visual gloss for these papers. The colours of the papers evaluated by Harrison[3)] are recorded in Table I. The papers may be divided into two groups with respect to the excitation purity. Six papers A, B, D, E, L and M have the values smaller than 10%, and the others larger than 30%.

Table I. Colours of papers for C. I. E. Illuminant A evaluated by Harison[3)]. The values of chromatic coodinates are not quoted here.

Paper	Dominant wave-length (mμ)	Excitation purity (%)	Luminance factor (%)
A	490	0.4	63.0
B	508	8.7	32.3
C	587	40.5	22.3
D	603	4.1	46.7
E	589	2.0	58.8
F	588	49.1	30.2
G	591	43.5	23.6
H	590	37.2	30.2
I	595	48.3	25.7
K	589	42.2	30.0
L	499	1.2	4.2
M	430	5.7	15.5

§ 2. Experimental

With the method described above the specularly reflected flux I_0 and its diffuse component I_2 for each paper were measured. Their values in terms of scale reading and the logarithms of $G_{NF}=I_0/I_2$ are shown in Table II. The samples were backed with black matt papers througout the whole experiments.

Table II. The values of I_0, I_2 and log G_{NF}.

Paper	I_0	I_0	$\log_{10}G_{NF}$ $=\log_{10}I_0/I_2$
A	40.0	15.0	0.426
B	38.0	11.0	0.539
C	52.0	7.7	0.830
D	40.2	12.0	0.524
E	46.1	15.0	0.487
F	36.0	8.6	0.622
G	49.2	7.2	0.834
H	31.5	9.5	0.526
I	44.4	9.0	0.694
K	47.5	10.2	0.668
L	28.0	1.53	0.767
M	43.5	6.9	0.800

According to the records obtained in other experiments[2)], the value of log G_{NF} for a craped kraft paper, extremely matt, was 0.055. It was also of the same order for non-glazed ceramic surfaces or plaster surfaces. And that of a high glossy red flint paper was 1.77. The present papers had the intermediate values of 0.43 to 0.83.

In order to obtain the visual gradings for these papers, 36 Japanese observers were asked to arrange the samples visually in ascending order of gloss. The assessment of individual observer was generally carried out under uniform diffuse daylight through a winder facing south in a light room of his laboratory or home. He was also asked to be so situated that he could catch the specularly reflected light from the sample under about 45°-45° conditions of illuminating and viewing on the average.

Table III. Voting Distributions of 36 Japanese Observers.

Paper	Least Glossy					Rank						Most Glossy
	1	2	3	4	5	6	7	8	9	10	11	12
A	23	6	1	1	0	3	0	0	0	1	0	1
B	0	5	2	3	3	7	4	4	4	3	1	0
C	0	0	1	1	2	0	0	0	6	7	12	7
D	2	7	4	10	4	4	3	2	0	0	0	0
E	0	3	6	3	2	4	11	2	3	1	1	0
F	2	4	4	5	6	5	2	6	1	1	0	0
G	0	0	0	1	1	2	1	0	3	7	10	11
H	4	9	9	4	2	1	3	2	1	0	1	0
I	1	1	3	2	3	4	2	7	6	5	1	1
K	0	1	5	5	7	1	4	6	4	1	0	2
L	2	0	0	1	5	4	4	6	6	2	4	2
M	2	0	1	0	1	1	2	1	2	8	6	12

The actual voting of all the observers is summarized in Table III, where the figures relate to the number of votes for each of the possible rankings from 1 to 12. The means (μ) of these voting distributions are shown in the 2nd column of Table IV. But the forms of those distributions in Table III are not well defined. For some papers, particularly for papers E and K, they have two peaks neither of which can be ignored. This is supposed to be due to the systematic difference in the rankings given by the two groups into which the observers are divided.

The first group consists of 18 observers who had not so far participated in any similar test, and the second consists of the other 18 observers who had the experience several times in the past. The former group is denoted by Group I, and the second by Group II. The means of the voting distributions of each group are shown in the 3rd and 4th columns of Table IV.

Table IV. Means μ of voting distributions.

Paper	All observers	Group I	Group II	All Observers	
					Reduced value
A	2.3	3.1	1.5	2.1	2.3
B	6.2	7.2	5.2	exc.	—
C	9.9	9.9	9.9	8.1	9.8
D	4.1	4.9	3.4	3.6	4.2
E	5.9	7.1	4.7	exc.	—
F	5.1	4.8	5.3	4.4	5.2
G	10.2	9.6	10.8	8.4	10.2
H	3.8	3.4	4.3	3.4	3.9
I	7.1	5.9	8.3	5.8	6.9
K	6.2	5.4	7.1	5.3	6.3
L	7.6	6.8	8.4	6.2	7.4
M	9.6	10.1	9.1	7.7	9.3

For two papers B and E, the means given by Group I are considerably higher than the means given by Group II. Similar differences can also be found for papers A, D and M though they are not appreciably large. The values of excitation purity for these five papers are all smaller than the other papers except a black paper L, as shown in Table I. Thus it seems that many observers in Group I evaluate the gloss of so-called " more white " papers higher than those in Group II. The similar ambiguous effect of colour in relation to whether the observer is experienced or not has been found too in another experiment[2] where a different series of papers were graded. But this will be a subject of further study.

It is only indicated here that the exclusion of two papers B and E from the rankings of every observer was found to give fairly normal or moderate skew distributions for the rest of the papers. The means of those distributions are shown in the 5th column of Table IV. If the values of the means of the least and most glossy papers A and G are raised to those in the 2nd column and re-arrange the scale accordingly, it enables the relative positions of the other eight papers to be compared with those given by the means in the 2nd column. The reduced values for the means in the 5th column to this scale are easily calculated by the expression

$$\mu' = 2.3 + (\mu - 2.1)(10.2 - 2.3)/(8.4 - 2.1)$$

where μ represents the original value of the means for any paper. The results are shown in the last column of Table IV. Each of these values is almost equal to the corresponding one in the 2nd column. It may be then concluded that, the irregular forms of distributions in Table III originate mainly from the disagreement of the two groups for the gloss of papers B and E. Though the means for these two papers are not acceptable, the means for the other papers can be taken as the gloss value judged by all the observers, in spite of such indeterminate forms of distributions.

In Fig. 3 the values of log G_{NF} in Table II are plotted against the means of the voting distributions of all the observers in the 2nd column of Table IV. Except the doubtful points for papers B and E, all the points lie close to a straight line and the correlation coefficient is +0.986.

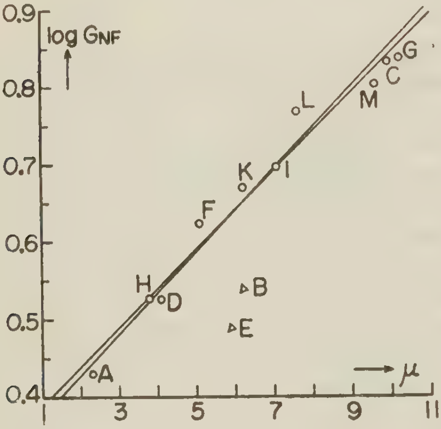

Fig. 3. Correlation between log G_{NF} & μ. (all observers)

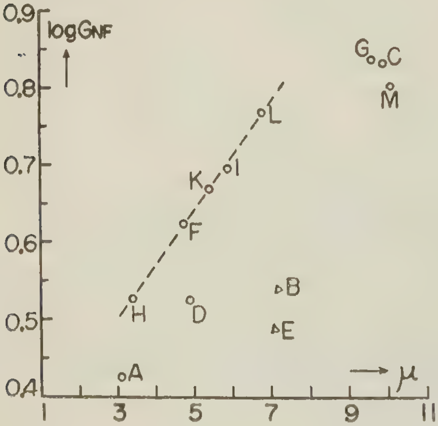

Fig. 4. Correlation between log G_{NF} & μ (Group I).

The result of plotting the values of log G_{NF} against the means given by Group I is shown in Fig. 4. The points for five papers—H, F, K, I and L—lie almost on a straight line and the points for parers B and E deviate far from this line to the higher end of the scale. If these two papers are properly down-graded, points for them will be placed more to the left and this will shift the above five points to the right. Thus the correlation will become linear. This is nearly the case in Fig. 5, where the values of log G_{NF} are shown against the means given by Group II. In this case, the correlation coefficient is +0.971 without exception.

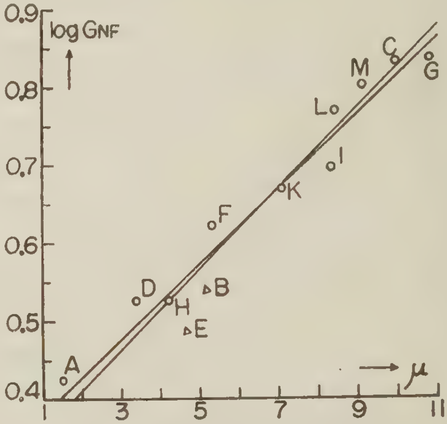

Fig. 5. Correlation between log G_{NF} & μ (Group II).

§ 3. Discussions of Disagreement with Other Visual Gradings

For the papers given above the visual gradings of 476 Swedish observers have been obtained by Steenberg[3] and many series of gradings of British observers under various viewing conditions by Harrison[3]. No good correlation of G_{NF} with any of these series of gradings could be found. This means that there is a considerable disagreedent between Swedish or British and Japanese observers. It may be due partly to the somewhat different viewing conditions and partly to the small alterations of surface or colour undergone by the samples. It must be also taken into account that the same samples have not been used for grading by all the groups of observers. The viewing conditions of Japanese observers are more or less similar to those of five British observers where the samples are illuminated at 45° with a uniformly diffused light through an opaque rectangular frame. Table V shows the rankings nearest the judgements of these five observers on the 2nd row and those nearest the values of log G_{NF} on the 3rd row. Except for the pale green paper B which might have faded appreciably, the difference between rankings for each paper is not so large.

If the rank for B on the 3rd row is raised from 5 to 8, the differences will become 1 or less except 1.5 for one paper H. The resulting rankings are shown on the 4th row of this table. The remaining minor differences will probably be attributed to the various factors mentioned above. In any case, it is likely that the illuminating and viewing conditions are the most important factors.

Table V. Rankings nearest the judgements of 5 British observers and the values of $\log G_{NF}$.

	A	B	C	D	E	F	G	H	I	K	L	M
5 British observers	1	8	11	4	3	6	12	2	7	5	$9\frac{1}{2}$	$9\frac{1}{2}$
$\log G_{NF}$	1	5	11	$3\frac{1}{2}$	2	6	12	$3\frac{1}{2}$	8	7	9	10
$\log G_{NF}$ (modified)	1	8	11	$3\frac{1}{2}$	2	5	12	$3\frac{1}{2}$	7	6	9	10

§ 4. Conclusions

The value of $\log G_{NF}$ may be supposed to be the diffuse component, expressed in logarithmic scale, of the reflected flux I_0 at given specular angles, since

$$\log G_{NF} = \log I_0/I_2$$
$$= \log I_0 - \log I_2$$

where I_2 is the diffuse component of I_0. For an extremely matt surface such as mentioned § 5, this value becomes approximately zero. Accordingly, the experimental results, though accompanied by a few doubtful exceptions, suggest that this value is practically proportional to the visual gloss estimated under the viewing conditions similar to that of the photometer with which G_{NF} is measured. But no claim is made to finalty.

The author's sincere thanks are due to Professor E. Fukushima for his advice and also to Dr. V. G. W. Harrison for his valuable suggestion as told to Prof. Fukushima.

References

1) E. Fukushima: Japan J. Appl. Phys. **23** (1954) 218.
2) J. Nishiwaki: Japan J. Appl. Phys. **25** (1956) 370.
3) V. G. W. Harrison and S. R. C. Poulter: Research **7** (1954) 128.

JOURNAL OF THE PHYSICAL SOCIETY OF JAPAN Vol. 12, No. 1, JANUARY, 1957

Application of the M^2-Expansion Method to Compressible Flow past Isolated and Lattice Aerofoils

By Isao IMAI

*Institute for Fluid Dynamics and Applied Mathematics, University of Maryland, U.S.A.**

(Received September 12, 1956)

In this paper two-dimensional compressible flow past an arbitrary aerofoil in unlimited fluid or past a straight lattice of aerofoils is considered on the basis of the M^2-expansion method, which consists in expanding various quantities in powers of M^2, M being the Mach number.

The general expressions for the velocity components at any point in the field of flow are obtained, which are correct to M^4 for an isolated aerofoil and to M^2 for a wing lattice respectively. In particular, the formulae giving the velocity distribution on the surface of the aerofoil are of such a simple form that the numerical calculation for any arbitrary aerofoil or lattice of aerofoils is no longer a prohibitive work as generally believed.

As an interesting special case, the flow past a symmetrical aerofoil placed symmetrically in a channel is also considered, which was previously dealt with by Goldstein and Lighthill by means of a different method.

§ 1. Introduction

For the calculation of subsonic flow of a compressible fluid past an arbitrarily given aerofoil there are at present two methods of successive approximation, that is, the M^2-expansion method and the thin-wing-expansion method. As is well known, the former is preferable to the latter for moderately thick profiles.

After Janzen and Rayleigh's original work, a number of variants of their method have been put forward. The most famous among them is perhaps the method of Poggi16),17), which has been employed successfully by Kaplan11),12), Tomotika and Tamada20) and Tomotika and Umemoto22) for the investigation of flow past elliptic cylinders and Joukowski aerofoils. Also, Kaplan13) and Tomotika and Tamada (unpublished) have used the theory of residues to improve on the Poggi method.

On the other hand, the present author has simplified the original method of Janzen and Rayleigh by the use of complex variables4),9) and later by introducing complex velocity potential just as in the theory of incompressible flow, developing a systematic procedure of successive approximation5). Further, on the basis of this procedure the author7) has obtained general formulae which enable us to calculate the velocity distribution on the surface of any arbitrary aerofoil exact to M^4, M being the Mach number. As examples of application of the method, a circular cylinder with arbitrary circulation and a circular arc aerofoil set parallel to the uniform flow have been dealt with correctly to M^4 7). Flow past an elliptic cylinder with its major axis parallel to the undisturbed flow was also dealt with to the order M^2 by the author8), and later to M^4 by Kawaguti14) with the aid of the formulae. Also, in order to test the practicability of the method, purely numerical calculations have been carried out for flow past elliptic cylinders and Joukowski aerofoils by the author with the cooperation of Kawata10) and Sindi (unpublished) respectively.

Similar treatment based on the use of complex variables has been independently made by Goldstein and Lighthill2); their analysis is more general than ours in one respect that it covers the case of a solid body symmetrically placed in a channel as well as a single body in unlimited fluid, but it is confined to the first approximation (i.e. correct to M^2) only. Moreover, their final formulae are apparently more complicated than ours. In fact, as yet no effort seems to have been made to carry out numerical calculation based on their method.

---

* On leave of absence from the University of Tokyo.

Part I of the present paper is concerned with the refinement of the author's previous formulae concerning the velocity distribution on the surface of any arbitrary aerofoil, such that the number of necessary numerical integration involved is reduced. Moreover the formulae for the calculation of velocity components at any point in the field of flow will be explicitly given in this paper, while the procedure to be taken for such a purpose has already been given implicitly in the previous paper⁶⁾.

In part II is considered the compressible flow past an arbitrary straight lattice of aerofoils, and various formulae, exact to M^2, analogous to those for an isolated aerofoil are derived. The case of a symmetrical body symmetrically placed in a channel, which has been treated by Goldstein and Lighthill²⁾, is included as a special case. Our formulae obtained in this paper are apparently much simpler than their formulae. As an example, the case of a nearly circular cylinder placed in a channel is briefly considered, which was previously dealt with by Hasimoto³⁾.

It may be mentioned that Takami¹⁸⁾,¹⁹⁾ has recently successfully applied our formulae to two special cases of much theoretical interest: one is that of a special profile for which Cherry¹⁾ calculated the exact velocity distribution on the basis of the hodograph method, and the other is that of a family of aerofoils for which Tomotika and Tamada²¹⁾ have obtained exact solution of continuous transonic flow on the assumption of a hypothetical but very realistic pressure-density relation. Thus we may say that owing to our formulae the labour required to obtain the velocity distribution over any arbitrary aerofoil correct to M^4 is no longer prohibitive, contrary to the general opinion.

Finally, it may be of interest to remark that the results of calculation by the M^2-expansion method can be utilized as a basis for further powerful approximation. Thus, the results which could be obtained by the thin-wing-expansion method, that is the method of successive approximation starting from Prandtl-Glauert's linear theory, or by Meksyn's new procedure for treating transonic flows¹⁵⁾ are also obtainable by appropriate interpretation of the results of the M^2-expansion method. These points will be reported elsewhere.

§ 2. Fundamental Equations

Consider the steady two-dimensional irrotational flow of a compressible fluid in the (x, y) plane. Then the velocity potential Φ and the stream function Ψ can be defined by the equations:

$$u=\frac{\partial\Phi}{\partial x}=\frac{\rho_\infty}{\rho}\frac{\partial\Psi}{\partial y}\,, \tag{2.1}$$

$$v=\frac{\partial\Phi}{\partial y}=-\frac{\rho_\infty}{\rho}\frac{\partial\Psi}{\partial x}\,, \tag{2.2}$$

where (u, v) are the component velocities, ρ is the density at any point and ρ_∞ is the density in the undisturbed stream. If we introduce the complex variables z, $\bar{z}$ and F defined by

$$z=x+iy\,,\qquad \bar{z}=x-iy\,, \tag{2.3}$$

$$F=\Phi+i\Psi\,, \tag{2.4}$$

then (2.1) and (2.2) can be combined to give

$$\frac{\partial F}{\partial z}=\frac{1}{2}\left(1+\frac{\rho}{\rho_\infty}\right)(u-iv)\,, \tag{2.5}$$

$$\frac{\partial F}{\partial \bar{z}}=\left(1-\frac{\rho}{\rho_\infty}\right)\frac{\partial\Phi}{\partial\bar{z}}\,. \tag{2.6}$$

For adiabatic flow, we have

$$\frac{\rho}{\rho_\infty}=\left\{1-\frac{\gamma-1}{2}M^2\left(\frac{q^2}{U^2}-1\right)\right\}^{1/(\gamma-1)}, \tag{2.7}$$

where q is the resultant fluid velocity, U and M are the velocity and Mach number of the undisturbed flow, and γ is the ratio of specific heats.

If we suppose F to be expanded in powers of M^2,

$$F=F_0+M^2F_1+M^4F_2+\cdots\,, \tag{2.8}$$

where

$$F_N=\Phi_N+i\Psi_N\,,\quad N=0,\,1,\,2,\,\cdots\,, \tag{2.9}$$

and write

$$q^2=q_0^2+M^2q_1^2+M^4q_2^2+\cdots\,, \tag{2.10}$$

$$1-\frac{\rho}{\rho_\infty}=M^2\rho_1+M^4\rho_2+\cdots\,, \tag{2.11}$$

then

$$\left.\begin{aligned}\rho_1&=\frac{1}{2}\left(\frac{q_0^2}{U^2}-1\right),\\ \rho_2&=\frac{1}{2}\frac{q_1^2}{U^2}-\frac{2-\gamma}{8}\left(\frac{q_0^2}{U^2}-1\right)^2,\\ &\cdots\cdots\end{aligned}\right\} \tag{2.12}$$

$$q_N^2=4\left(\frac{\partial\Phi_0}{\partial z}\frac{\partial\Phi_N}{\partial\bar{z}}+\frac{\partial\Phi_1}{\partial z}\frac{\partial\Phi_{N-1}}{\partial\bar{z}}+\cdots+\frac{\partial\Phi_N}{\partial z}\frac{\partial\Phi_0}{\partial\bar{z}}\right),$$
$$N=0,\,1,\,2,\,\cdots\,. \tag{2.13}$$

Substituting these in (2.6), comparing terms of the same powers of M^2, and integrating, we find

$$F_0 = G_0(z)\ , \tag{2.14}$$

$$F_N = \int\left(\rho_1 \frac{\partial \Phi_{N-1}}{\partial \bar{z}} + \rho_2 \frac{\partial \Phi_{N-2}}{\partial \bar{z}} + \cdots + \rho_N \frac{\partial \Phi_0}{\partial \bar{z}}\right) d\bar{z} + G_N(z)\ , \tag{2.15}$$

where $G_N(z)$ are arbitrary analytic functions of z, which should be determined by appropriate boundary conditions in each particular case.

It is obvious that F_0 is the complex velocity potential for incompressible flow. Starting from F_0 we should be able to determine F_N successively by means of (2.15) together with (2.12) and (2.13).

PART I. COMPRESSIBLE FLOW PAST A SOLID BODY IN UNLIMITED FLUID

§ 3. General Expressions for the Velocity at Any Point

For a uniform flow past a solid body in unlimited fluid, the following conditions are to be satisfied:

$\partial F/\partial z$ is one-valued and continuous, (3.1)

at infinity: $z \to \infty\ , \quad \partial F/\partial z \to U e^{-i\alpha}\ ,$ (3.2)

on the boundary, $\Psi = \operatorname{Im} F = 0\ ,$ (3.3)

where α is the angle between the x-axis and the direction of the undisturbed flow. The conditions (3.1) and (3.2) are obvious from eqns. (2.5).

As is well known the zeroth approximation, which corresponds to the incompressible flow, is given by

$$F_0 = f(z) \equiv \lambda\{e^{i(\delta-\alpha)} Z + e^{-i(\delta-\alpha)} Z^{-1}\} + i\kappa \log Z\ . \tag{3.4}$$

Here it is assumed that the profile in the z-plane is conformally mapped on to a unit circle with its centre at the origin in the Z-plane by the transformation function

$$z = c_{-1} Z + c_0 + \frac{c_1}{Z} + \cdots\ , \qquad c_{-1} = \lambda e^{i\delta}\ . \tag{3.5}$$

Also, for simplicity, we have put $U=1$, and $2\pi\kappa$ is the circulation around the profile, which may be determined by Joukowski's assumption.

Now, starting from $F_0 = f(z)$ and substituting the expressions already obtained for $F_1, F_2, \cdots$ successively in (2.15), we shall find

$$F_N = H_N(z, \bar{z}) + g_N(z)\ , \qquad N = 1, 2, \cdots\ , \tag{3.6}$$

where $H_N(z, \bar{z})$ is a known function of $z, \bar{z}$ such that $\partial H_N/\partial z$ satisfies the conditions imposed on $\partial F_N/\partial z$ given by (3.1) and (3.2). Therefore

$$\frac{dg_N}{dZ} = \frac{dg_N}{dz}\frac{dz}{dZ} = \left(\frac{\partial F_N}{\partial z} - \frac{\partial H_N}{\partial z}\right)\frac{dz}{dZ}$$

is one-valued and continuous, and hence regular, outside the unit circle in the Z-plane, so that

$$g_N = i\kappa_N \log Z + a_0^{(N)} + a_1^{(N)} Z^{-1} + \cdots\ . \tag{3.7}$$

We may conveniently absorb κ_N in the zeroth approximation κ, so that κ in (3.4) becomes

$$\kappa = \kappa_0 + M^2\kappa_1 + M^4\kappa_2 + \cdots\ , \tag{3.8}$$

and then we may write (3.7) in a simpler form:

$$g_N = a_0^{(N)} + a_1^{(N)} Z^{-1} + a_2^{(N)} Z^{-2} + \cdots\ . \tag{3.9}$$

The complementary function $g_N(Z)$ can be determined by the Poisson-Schwarz formula in the following way.

For simplicity, we shall drop the suffix N in the following analysis. On the unit circle, $Z = e^{i\theta}$, which corresponds to the profile $z = z_P$ in the physical plane, let us write

$$g(e^{i\theta}) = R(\theta) + iI(\theta)\ , \tag{3.10}$$

$$H(z_P, \bar{z}_P) = P(\theta) + iQ(\theta) \equiv H(e^{i\theta})\ . \tag{3.11}$$

Then, from (2.9) and (3.6),

$$\Phi(\theta) = P(\theta) + R(\theta)\ , \qquad \Psi(\theta) = Q(\theta) + I(\theta)\ . \tag{3.12}$$

But the boundary condition (3.3) requires that $\Psi = 0$. Hence

$$I(\theta) = -Q(\theta) = -\frac{1}{2i}[H(\zeta) - \bar{H}(\bar{\zeta})]\ , \tag{3.13}$$

where $\zeta = e^{i\theta}$. By the application of the Poisson-Schwarz formula to the analytic function $g(Z)$, we have

$$\begin{aligned} g(Z) &= a_0 + \frac{1}{2\pi}\oint_C I(\theta)\frac{Z+\zeta}{Z-\zeta}\frac{d\zeta}{\zeta} \\ &= \frac{1}{\pi}\oint_C I(\theta)\frac{d\zeta}{Z-\zeta} + \text{const} \\ &= \frac{1}{2\pi i}\oint_C [H(\zeta) - \bar{H}(\zeta^{-1})]\frac{d\zeta}{\zeta - Z} + \text{const}\ , \end{aligned} \tag{3.14}$$

where the path of integration C is the unit circle $\zeta = e^{i\theta}$. In many cases where the transformation function $z = z(Z)$ is given in an explicit analytic form (e.g. elliptic cylinders and Joukowski aerofoils), the integral (3.14) may be conveniently evaluated by means of the theory of residues. It may be remarked that the constant term in (3.14) has no physical significance and so can be safely neglected.

Now that the complex velocity potential F has been found, the velocity at any point can be easily obtained. Thus we have

$$\left.\begin{aligned} u&=u_0+M^2u_1+M^4u_2+\cdots\,,\\ v&=v_0+M^2v_1+M^4v_2+\cdots\,,\end{aligned}\right\} \tag{3.15}$$

where

$$u_0-iv_0=\frac{df}{dz}\,, \tag{3.16}$$

$$\begin{aligned} u_N-iv_N=\Bigg\{&\frac{\partial H_N}{\partial Z}+\frac{\partial \overline{H}_N}{\partial Z}+\frac{1}{2\pi i}\oint_C [H_N(\zeta)\\ &-\overline{H}_N(\zeta^{-1})]\frac{d\zeta}{(\zeta-Z)^2}\Bigg\}\left(\frac{dz}{dZ}\right)^{-1}\,. \end{aligned} \tag{3.17}$$

According to the previous paper[16) the explicit form of H_N in terms of f can be given as follows:

$$H_1=\frac{1}{4}w\overline{B}-\frac{1}{4}\overline{A}\,, \tag{3.18}$$

$$\begin{aligned} H_2=&\frac{1}{16}(w\overline{w}-1)\overline{w}B+\frac{1}{32}w'\overline{B}^2\\ &+\frac{1}{16}\left\{4g_1'-i\kappa(2e^{i\alpha}w-1)\frac{Z'}{Z}\right\}\overline{B}\\ &+\frac{1}{8}w\left[\int_{z_0}^{z}\left\{4g_1'-i\kappa(e^{i\alpha}w-1)\frac{Z'}{Z}\right\}w\,dz\right]^*\\ &-\frac{1}{16}(4g_1+i\kappa\log Z\overline{Z})^*+\frac{1}{2}H_1\\ &-\frac{\gamma+1}{16}(8H_1+\overline{A}-w^2\overline{C})\,, \end{aligned} \tag{3.19}$$

with

$$w=f'=df/dz\,, \tag{3.20}$$

$$A=f+i\kappa\log\overline{Z}\,, \tag{3.21}$$

$$B=\int w^2dz+2i\kappa e^{-i\alpha}\log\overline{Z}\,, \tag{3.22}$$

$$C=\int w^3dz+3i\kappa e^{-2i\alpha}\log\overline{Z}\,. \tag{3.23}$$

Here asterisks as well as bars denote complex conjugate and dashes denote differentiation with respect to z.

§ 4. Velocity Distribution on the Surface of a Cylinder of Any Shape

The general expressions, correct to M^4, for the complex velocity potential F and for the velocity components u, v are given by (3.6), (3.14), and (3.17) together with (3.18) and (3.19). The author believes, however, that the true merit of these formulae should be found in the fact that they enable us to calculate velocity distributions over any arbitrary profile whose transformation function to a unit circle cannot be given in an explicit analytic form. In fact, the previous papers[6),7),8),14) were exclusively concerned with the velocity distribution on the surface of the obstacle.

It is well known that there exists a functional relation between the real and imaginary parts of an analytic function; thus in (3.10) we have

$$R(\theta)=I^*(\theta)+\mathrm{Re}\,(a_0)\,. \tag{4.1}$$

Here $I^*(\theta)$ is the conjugate Fourier series associated with $I(\theta)$, so that if

$$I(\theta)=a_0+\sum_{n=1}^{\infty}(a_n\cos n\theta+b_n\sin n\theta)\,, \tag{4.2}$$

then

$$I^*(\theta)=\sum_{n=1}^{\infty}(a_n\sin n\theta-b_n\cos n\theta)\,. \tag{4.3}$$

It is also known that the conjugate Fourier series can be expressed in an integral form:

$$I^*(\theta)=-\frac{1}{2\pi}\int_0^{2\pi}[I(\varphi+\theta)-I(\theta)]\cot\frac{\varphi}{2}\,d\varphi\,. \tag{4.4}$$

On account of (3.13) and (4.1), we can rewrite (3.10) and (3.12) as

$$g(e^{i\theta})=-[Q^*(\theta)+iQ(\theta)]+\text{const}\,, \tag{4.5}$$

$$\Phi(\theta)=P(\theta)-Q^*(\theta)+\text{const}\,, \tag{4.6}$$

where, by (3.11), $P(\theta)$ and $Q(\theta)$ are given as the real and imaginary parts of the known function $H(e^{i\theta})$.

From (3.4), we have, on the profile,

$$f=\Phi_0(\theta)=2\lambda\cos(\theta-\alpha+\delta)-\kappa\theta\,. \tag{4.7}$$

Also we can write

$$dz=ds\,e^{i\omega}\,, \tag{4.8}$$

where ds is the line element along the profile and ω is the angle which the line element makes with the x-axis. Substituting (4.7) and (4.8) into (3.20), (3.21), and (3.22) gives

$$w=-qe^{-i\omega}\,, \tag{4.9}$$

$$A=2\lambda\cos(\theta-\alpha+\delta)\,, \tag{4.10}$$

$$B=\int q^2e^{-i\omega}ds+2\kappa e^{-i\alpha}\theta\,, \tag{4.11}$$

where

$$q=-\frac{d\Phi_0}{d\theta}\frac{d\theta}{ds} \tag{4.12}$$

is the zeroth approximation to the velocity (incompressible fluid velocity). Inserting these in (3.18) and separating real and imaginary parts, we obtain

$$P_1 = -\frac{1}{4} q (C \cos \omega + S \sin \omega) - \frac{\lambda}{2} \cos (\theta - \alpha + \delta) , \tag{4.13}$$

$$Q_1 = -\frac{1}{4} q (S \cos \omega - C \sin \omega) , \tag{4.14}$$

where

$$C = \int q^2 \cos \omega \, ds + 2\kappa\theta \cos \alpha , \tag{4.15}$$

$$S = \int q^2 \sin \omega \, ds + 2\kappa\theta \sin \alpha . \tag{4.16}$$

These are essentially the same as the results obtained in the previous paper[6].

Purely numerical calculations based on the above formulae were carried out for the cases of elliptic cylinders[10] and symmetrical Joukowski aerofoils at zero angle of attack, obtaining quite satisfactory agreement with known analytical results.

Recently, however, it has been discovered that a modification of the formulae is possible that brings about a considerable reduction of numerical work. In the next sections such modified formulae suitable for the numerical calculation will be presented.

§ 5. Simplified Formula for the Velocity Potential along the Profile to the Order M^2

The function $H(e^{i\theta})$ defined in (3.1) can be expressed in the form

$$P(\theta) + iQ(\theta) \equiv H(e^{i\theta}) = \sum_{n=-\infty}^{\infty} C_n e^{ni\theta} . \tag{5.1}$$

Then, remembering (4.3) we have

$$P(\theta) - Q^*(\theta) = 2 \operatorname{Re} \sum_{n=0}^{\infty} C_n e^{ni\theta} + \text{const} . \qquad (5.2)^*$$

Thus, in order to obtain the velocity potential on the profile, we have only to take positive power terms in the Laurent series of $H(\zeta)$ where $\zeta = e^{i\theta}$. This is just the principle on which following modification of the expressions for the velocity potential is based. Thus we attempt to simplify the above obtained expressions for P_1 and Q_1 by adding to $H_1(Z)$ some appropriate analytic function which is regular outside the profile and so is expressible as an ascending power series in Z^{-1}.

By (3.4) and (3.5) we have

$$w = \frac{df}{dz} = e^{-i\alpha} + i\kappa \frac{1}{z} + O\left(\frac{1}{z^2}\right) , \tag{5.3}$$

and

$$\int w^2 dz = e^{-2i\alpha} z + 2i\kappa e^{-i\alpha} \log Z + \text{const} + O(z^{-1}) . \tag{5.4}$$

Consequently, on the profile, that is for $Z = e^{i\theta}$, (3.21) and (3.22) become

$$A = e^{-i\alpha} z + O(Z^{-1}) , \tag{5.5}$$

$$B = e^{-2i\alpha} z + \text{const} + O(Z^{-1}) . \tag{5.6}$$

Therefore we can express (3.18) in the form

$$\begin{aligned} 4H_1 &= w(\bar{B} - B) - (\bar{A} - A) + wB - A \\ &= -2iw \operatorname{Im} (B) + 2i \operatorname{Im} (A) \\ &\quad + \lambda e^{-i(\alpha - \delta)} (e^{-2i\alpha} - 1) Z + \boldsymbol{P}(Z^{-1}) , \end{aligned} \tag{5.7}$$

where, and hereafter, $\boldsymbol{P}(z)$ denotes a certain power series in z. As mentioned above $\boldsymbol{P}(Z^{-1})$ contributes nothing to $\Phi_1(\theta)$, so that we can simply drop it for the calculation of $\Phi_1(\theta)$. Thus substituting w, A, B from (4.9), (4.10) and (4.11) into (5.7) and separating real and imaginary parts, we get for the "modified" functions

$$P_{1m}(\theta) = -\frac{1}{2} qS \sin \omega + \lambda \sin \alpha \sin (\theta - 2\alpha + \delta) , \tag{5.8}$$

$$Q_{1m}(\theta) = -\frac{1}{2} qS \cos \omega . \tag{5.9}$$

It will be seen that the formulae (5.8) and (5.9) are more convenient than those previously given (4.13) and (4.14). Indeed, we can dispense with the numerical evaluation of C defined by (4.15); this is of particular significance in view of the fact that S can in general be calculated more accurately than C since $\sin \omega$ is usually of very small magnitude for ordinary thin aerofoils.

Further, (5.8) and (5.9) can be brought into

---

* It can be shown that

$$\sum_{n=0}^{\infty} C_n e^{ni\theta} = \frac{1}{2\pi i} \oint_C \frac{H(Z)}{Z - e^{i\theta}} dZ ,$$

where the path of integration C is a simple closed curve lying in the regularity region of the analytic function $H(Z)$ and enclosing the point $Z = e^{i\theta}$. Hence, by (4.6) and (5.2), we have

$$\Phi(\theta) = \frac{1}{\pi} \operatorname{Im} \oint_C \frac{H(Z)}{Z - e^{i\theta}} dZ ,$$

where H is given by (3.18) or (3.19). This formula is very convenient for the analytical calculation of velocity potential when the profile is given by a simple transformation function (such as the Joukowski transformation)[8),14].

more symmetric forms in the following way. For the case of vanishing angle of attack,

$$P_{1m}(\theta)=-\frac{1}{2}\,q\sin\omega\int q^2\sin\omega ds\,,$$

$$Q_{1m}(\theta)=-\frac{1}{2}\,q\cos\omega\int q^2\sin\omega ds\,.$$

These can be immediately generalized to cover the case of non-vanishing angle of attack by means of a simple geometrical consideration:

$$P_{1m}(\theta)=-\frac{1}{2}\,q\sin(\omega-\alpha)\int q^2\sin(\omega-\alpha)ds\,, \tag{5.10}$$

$$Q_{1m}(\theta)=-\frac{1}{2}\,q\cos(\omega-\alpha)\int q^2\sin(\omega-\alpha)ds\,. \tag{5.11}$$

It will be interesting to note that the circulation constant κ does not appear explicitly in these formulae; though, of course, it is involved in the expression for q.

§ 6. Simplified Formulae for the Velocity along the Profile to the Order M^4

Similar modification can be carried out for $\Phi_2(\theta)$, the second order correction to the velocity potential. Here, care must be taken of the fact that the circulation constant is usually determined by Joukowski's assumption so that $\partial\Phi/\partial\theta=0$ at the trailing edge, and hence κ is in general expressed in the form

$$\kappa=\kappa_0+M^2\kappa_1+M^4\kappa_2+\cdots\,.$$

Since, however, we have absorbed the total circulation in the zeroth approximation, q as given by (4.12) and (4.7) really contains terms dependent on κ_1, κ_2, $\cdots$. Accordingly P_{1m} and Q_{1m} given by (5.10) and (5.11) contribute a term involving κ_1 to the second approximation.

For the sake of brevity, only the final results will be given here. The velocity along the surface of an arbitrary cylinder is given by

$$q=q_0+M^2q_1+M^4q_2+\cdots\,, \tag{5.12}$$

where

$$q_0=\{2\lambda\sin(\theta-\alpha+\delta)+\kappa_0\}\frac{d\theta}{ds}\,, \tag{5.13}$$

$$q_N=\{-P_{Nm}'(\theta)+Q_{Nm}{}^{*\prime}(\theta)+\kappa_N\}\frac{d\theta}{ds}\,,\qquad N=1,\,2 \tag{5.14}$$

$$\left.\begin{aligned}P_{1m}&=-\frac{1}{2}\,Sq_0\sin(\omega-\alpha)\,,\\ Q_{1m}&=-\frac{1}{2}\,Sq_0\cos(\omega-\alpha)\,,\end{aligned}\right\} \tag{5.15}$$

$$\begin{aligned}P_{2m}+iQ_{2m}&\\ =-\frac{1}{16}&(q_0^2-1)q_0e^{i(\omega-\alpha)}(C-iS)\\ &-\frac{i}{8}\,e^{-i(\omega-\alpha)}\frac{d}{ds}(q_0e^{-i(\omega-\alpha)})CS\\ &-\frac{i}{8}\,e^{-i(\omega-\alpha)}[4(Q_1{}^{*\prime}+iQ_1{}')\\ &\qquad+\kappa_0(2q_0e^{-i(\omega-\alpha)}+1)]\frac{d\theta}{ds}S\\ &-\frac{i}{4}\,q_0e^{-i(\omega-\alpha)}\int[(4Q_1{}^{*\prime}+\kappa_0)q_0\sin(\omega-\alpha)\\ &\qquad-4Q_1{}'q_0\cos(\omega-\alpha)\\ &\qquad+\kappa_0q_0^2\sin2(\omega-\alpha)]d\theta+\frac{1}{2}P_1\\ &-(\gamma+1)\Big[\frac{i}{8}\,q_0^2e^{-2i(\omega-\alpha)}\int q_0^3\sin2(\omega-\alpha)ds\\ &\qquad+\frac{1}{2}(P_{1m}+iQ_{1m})\Big]\\ &-\frac{i}{2}\,\kappa_1e^{-i(\omega-\alpha)}\Big\{\frac{d\theta}{ds}S\\ &\qquad+2q_0\int q_0\sin(\omega-\alpha)\,d\theta\Big\}\,,\end{aligned} \tag{5.16}$$

where

$$C=\int q^2\cos(\omega-\alpha)ds+2\kappa_0\theta\,, \tag{5.17}$$

$$S=\int q_0^2\sin(\omega-\alpha)ds\,, \tag{5.18}$$

$$P_1=\frac{1}{2}P_{1m}-\frac{1}{4}Cq_0\cos(\omega-\alpha)-\frac{\lambda}{2}\cos(\theta-\alpha+\delta)\,, \tag{5.19}$$

$$Q_1=\frac{1}{2}Q_{1m}+\frac{1}{4}Cq_0\sin(\omega-\alpha)\,, \tag{5.20}$$

$$Q_1{}^*=P_1-\Phi_1\,. \tag{5.21}$$

PART II. COMPRESSIBLE FLOW PAST A LATTICE OF AEROFOILS

§ 7. Incompressible Flow past a Lattice of Aerofoils

As is well known, an arbitrary wing lattice in the z-plane can be mapped conformally on to the unit circle in the Z-plane by means of a transformation function of the form

$$z=\frac{h}{2\pi}\log\frac{(Z+a^{-1})(Z+a)}{(Z-a^{-1})(Z-a)}+C(Z)\,,\qquad 0<a<1\,, \tag{7.1}$$

where $C(Z)$ is regular outside the unit circle: $|Z|>1$, so that

$$C(Z)=C_0+C_1Z^{-1}+C_2Z^{-2}+\cdots\,; \tag{7.2}$$

$Z=-a^{-1}$, a^{-1} correspond to infinity up- and downstream respectively, and h denotes the spacing of the wing lattice.

Consider a complex velocity potential

$$f=\frac{h}{2\pi}\{U_1e^{-i\alpha_1}\log(Z+a^{-1})+U_1e^{i\alpha_1}\log(Z+a)$$
$$-U_2e^{-i\alpha_2}\log(Z-a^{-1})-U_2e^{i\alpha_2}\log(Z-a)\}\,. \tag{7.3}$$

In the z-plane it represents the incompressible flow past the above mentioned lattice of aerofoils such that the inflow and outflow angles and velocities are α_1, α_2 and U_1, U_2 respectively. This can be seen from (7.1) and (7.3) in the following way.

When $Z\to-a^{-1}$,

$$f\to\frac{h}{2\pi}U_1e^{-i\alpha_1}\log(Z+a^{-1})\sim U_1e^{-i\alpha_1}z\,,$$

and when $Z\to a^{-1}$,

$$f\to-\frac{h}{2\pi}U_2e^{-i\alpha_2}\log(Z-a^{-1})\sim U_2e^{-i\alpha_2}z\,.$$

This shows the behaviour of flow at infinity up- and downstream.

Next we consider the condition at the surface of the aerofoil, that is, on the unit circle in the Z-plane: $Z=e^{i\theta}$. Putting $Z=e^{i\theta}$ in (7.3) and taking the imaginary part, we have $\Psi_0=$ constant, provided that the condition holds:

$$U_1\cos\alpha_1=U_2\cos\alpha_2\,. \tag{7.4}$$

Thus the complex velocity potential f represents flow along the aerofoil. The condition (7.4) is readily recognized to be one of continuity of mass flow past the lattice.

§ 8. Complex Velocity Potential for the Compressible Flow past Lattice of Aerofoils

For simplicity we shall consider only a first approximation (that is correct to the order of M^2).

In the following, quantities pertaining to points at infinity up- and downstream will be indicated by suffixes 1 and 2 respectively. Thus (2.5) can be written as

$$\frac{\partial F}{\partial z}=\frac{1}{2}\left(1+\frac{\rho}{\rho_1}\right)(u-iv)\,. \tag{8.1}$$

Hence the boundary conditions at infinity are expressed as

$$\frac{\partial F}{\partial z}\sim U_1e^{-i\alpha_1}\qquad\text{as } Z\to-a^{-1}, \tag{8.2}$$

$$\frac{\partial F}{\partial z}\sim\frac{1}{2}\left(1+\frac{\rho_2}{\rho_1}\right)U_2e^{-i\alpha_2}\quad\text{as } Z\to a^{-1}\,. \tag{8.3}$$

But, from (2.7) we have

$$\frac{\rho}{\rho_1}=1-\frac{1}{2}M_1^2\left(\frac{q^2}{U_1^2}-1\right)+O(M_1^4)\,. \tag{8.4}$$

Hence (8.3) can be rewritten as

$$\frac{\partial F}{\partial z}\sim\left\{1-\frac{1}{4}M_1^2\left(\frac{U_2^2}{U_1^2}-1\right)\right\}U_2e^{-i\alpha_2}$$
$$\text{as}\quad Z\to a^{-1}\,. \tag{8.5}$$

It should be noted that U_1, U_2, α_1 and α_2 are not independent from each other but subject to the condition of continuity

$$\rho_1U_1\cos\alpha_1=\rho_2U_2\cos\alpha_2\,, \tag{8.6}$$

of which the limiting case for $M_1\to0$ has already been met with in (7.4). Accordingly, if α_1, α_2 and U_1 are fixed, U_2 will in general vary with the Mach number M_1. Therefore we put

$$U_2=U_{20}+M_1^2U_{21}+\cdots\,. \tag{8.7}$$

Substituting from (8.4) and (8.7) in (8.6) and expanding in powers of M_1^2, we obtain

$$\cos\alpha_1=U_{20}\cos\alpha_2\,, \tag{8.8}$$

$$U_{21}=\tfrac{1}{2}(U_{20}^2-1)U_{20}\,, \tag{8.9}$$

where we have put for brevity $U_1=1$. The condition (8.8) is nothing other than (7.4).

Now, (8.2) and (8.5) can also be expanded in powers of M_1^2; thus, for the zeroth approximation

$$\frac{df}{dz}\sim\begin{cases}e^{-i\alpha_1}\\ U_{20}e^{-i\alpha_2}\end{cases}\quad\text{as}\quad Z\to\begin{cases}-a^{-1}\\ a^{-1}\end{cases} \tag{8.10}$$

and for the first approximation

$$\frac{\partial F}{\partial z}\sim\begin{cases}0\\ \tfrac{1}{2}U_{21}e^{-i\alpha_2}\end{cases}\quad\text{as}\quad Z\to\begin{cases}-a^{-1}\\ a^{-1}\end{cases}. \tag{8.11}$$

The zeroth approximation f has already been given by (7.3), which can be rewritten as $(U_1=1)$

$$f=\frac{h}{2\pi}[e^{-i\alpha_1}\log(Z+a^{-1})+e^{i\alpha_1}\log(Z+a)$$
$$-U_{20}\{e^{-i\alpha_2}\log(Z-a^{-1})+e^{i\alpha_2}\log(Z-a)\}]\,. \tag{8.12}$$

The general formula (2.15) gives for $N=1$

$$F_1=\frac{1}{4}\frac{df}{dz}\int\left(\frac{d\bar{f}}{d\bar{z}}\right)^2d\bar{z}-\frac{1}{4}\bar{f}+G_1(z)\,. \tag{8.13}$$

Considering the asymptotic behaviour at infinity of f as given by (8.10), we introduce a pair of new functions defined by

$$f_1=\frac{h}{2\pi}\,[e^{i\alpha_1}\log(Z+a^{-1})+e^{-i\alpha_1}\log(Z+a)$$
$$-U_{20}\{e^{i\alpha_2}\log(Z-a^{-1})+e^{-i\alpha_2}\log(Z-a)\}]\,, \tag{8.14}$$

$$f_2=\frac{h}{2\pi}\,[e^{2i\alpha_1}\log(1+a^{-1}Z^{-1})$$
$$+e^{-2i\alpha_1}\log(1+aZ^{-1})$$
$$-U_{20}^2\{e^{2i\alpha_2}\log(1-a^{-1}Z^{-1})$$
$$+e^{-2i\alpha_2}\log(1-aZ^{-1})\}]\,. \tag{8.15}$$

Then it is readily seen that

$$\bar{f}+f_1=\text{o.v.f.}\,,\qquad \int\left(\frac{d\bar{f}}{d\bar{z}}\right)^2 d\bar{z}+f_2=\text{o.v.f.}\,,$$

where o.v.f. stands for "one-valued function."

Now (8.13) can be written as

$$F_1=H_1(Z,\bar{Z})+g_1(Z)\,, \tag{8.16}$$

where

$$H_1(Z,\bar{Z})=\frac{1}{4}\frac{df}{dz}\left\{\int\left(\frac{d\bar{f}}{d\bar{z}}\right)^2 d\bar{z}+f_2(Z)\right\}$$
$$-\frac{1}{4}\{\bar{f}(\bar{Z})+f_1(Z)\}\,, \tag{8.17}$$

and $g_1(Z)$ is a certain analytic function of Z. Now it can easily be shown that $dg_1/dZ=\partial F_1/\partial Z-\partial H_1/\partial Z$ is one-valued outside the unit circle in the Z-plane, and that

$$\frac{dg_1}{dZ}\to\begin{cases}0\\ -iU_{21}\sin\alpha_2\end{cases}\qquad\text{as}\qquad Z\to\begin{cases}-a^{-1}\\ a^{-1}\end{cases}.$$

Therefore, taking account of (7.1), we can conclude that the function

$$g=g_1-iU_{21}\sin\alpha_2\frac{h}{2\pi}\log\frac{1-a^{-1}Z^{-1}}{1-aZ^{-1}}$$

is one-valued and analytic outside the unit circle. Hence, employing the formula (3.14) and making an analysis similar to that for an isolated aerofoil, we finally arrive at

$$g_1=iU_{21}\sin\alpha_2\frac{h}{2\pi}\log\frac{1-a^{-1}Z^{-1}}{1-aZ^{-1}}$$
$$+\frac{1}{4\pi^2}\oint_{\mathrm{C}}\mathrm{Im}\left[\frac{df}{dz}\left\{\int\left(\frac{d\bar{f}}{d\bar{z}}\right)^2 d\bar{z}+f_2\right\}\right]\frac{d\zeta}{\zeta-Z}, \tag{8.18}$$

where the path of integration C is the unit circle in the Z-plane and f and f_2 are given by (8.12) and (8.15) respectively. Substitution of (8.17) and (8.18) in (8.16) yields the required first approximation to the complex velocity potential. The velocity at any point in the field of flow can then be calculated by means of (3.16) and (3.17).

§ 9. Velocity Distribution on the Aerofoil

In this case the velocity potential on the aerofoil is shown to be given by

$$\Phi_1(\theta)=P(\theta)-Q^*(\theta)$$
$$+\frac{h}{2\pi}U_{21}\sin\alpha_2\left(2\tan^{-1}\frac{a\sin\theta}{1-a\cos\theta}+\theta\right), \tag{9.1}$$

where $P_1+iQ_1=H_1(e^{i\theta},e^{-i\theta})$. But the formula can be simplified in the same way as for an isolated aerofoil. For this purpose, we introduce another new function defined as

$$f_3=\frac{h}{\pi}\left\{\cos 2\alpha_1\log\frac{1+a^{-1}Z^{-1}}{1+a^{-1}Z}\right.$$
$$-U_{20}^2\cos 2\alpha_2\log\frac{1-a^{-1}Z^{-1}}{1-a^{-1}Z}$$
$$\left.+(\cos 2\alpha_1-U_{20}^2\cos 2\alpha_2)\log Z\right\}, \tag{9.2}$$

and write (8.17) in the form

$$H_1=\frac{1}{4}w\left\{\int\bar{w}^2 d\bar{z}-\int w^2 dz+f_3\right\}$$
$$+\frac{1}{4}w\left\{f_2+\int w^2 dz-f_3\right\}-\frac{1}{4}(\bar{f}+f_1)\,, \tag{9.3}$$

with $w=df/dz$. Then the second term on the right-hand side can be shown to be regular outside the unit circle and of the form $\boldsymbol{P}(Z^{-1})$, so that it contributes nothing to $\Phi_1(\theta)$. Thus after some calculation we can find the explicit form of $\Phi_1(\theta)$.

Summarizing, the velocity distribution on the surface of the aerofoil is given by

$$q=q_0(\theta)+M_1^2q_1(\theta)+\cdots\,, \tag{9.4}$$

with

$$q_N(\theta)=-\frac{d\Phi_N}{d\theta}\frac{d\theta}{ds}\,,\qquad N=0,1,\cdots\,, \tag{9.5}$$

where

$$\Phi_0(\theta)=\frac{h}{2\pi}\left\{\sin\alpha_1(\theta-2\psi)+U_{20}\sin\alpha_2(2\varphi-\theta)\right.$$
$$\left.+\cos\alpha_1\log\frac{1+a^2+2a\cos\theta}{1+a^2-2a\cos\theta}\right\}, \tag{9.6}$$

$$\Phi_1(\theta)=-\frac{h}{4\pi}\left\{\cos\alpha_1\log\frac{1+a^2+2a\cos\theta}{1+a^2-2a\cos\theta}\right.$$
$$\left.+2U_{21}\sin\alpha_2(\theta-2\varphi)\right\}$$
$$-\frac{1}{2}T(\theta)q_0\sin\omega+\frac{1}{2}[T(\theta)q_0\cos\omega]^*\,, \tag{9.7}$$

and

$$T(\theta)=\int q_0{}^2 \sin\omega\, ds-\frac{h}{2\pi}\{\cos 2\alpha_1(2\psi-\theta)$$
$$+U_{20}^2 \cos 2\alpha_2(\theta-2\varphi)\}\,, \tag{9.8}$$

$$\varphi=\tan^{-1}\frac{\sin\theta}{\cos\theta-a}\,,\qquad \psi=\tan^{-1}\frac{\sin\theta}{\cos\theta+a}\,. \tag{9.9}$$

Here $d\theta/ds$ should be regarded as already known for the case of incompressible flow.

In this connection it may be worthwhile to remark that the correspondence between θ and s can in principle be found if the velocity distribution on the aerofoil is already known for incompressible flow either theoretically (e.g. by means of the method of singularities) or experimentally; indeed, the relation

$$\Phi_0=-\int q_0 ds$$

in conjunction with (9.6) gives the functional relation between θ and s.

Finally, it may be mentioned that the various formulae for a single aerofoil in unlimited fluid, given in Part I, can be deduced by a limiting process from those for a wing lattice, as should naturally be expected.

§ 10. Symmetrical Body Symmetrically Placed in a Channel

In this case we have to put

$$U_1=U_2=1\,,\qquad \alpha_1=\alpha_2=0\,, \tag{10.1}$$

so that by (8.7)

$$U_{20}=1\,,\qquad U_{21}=0\,. \tag{10.2}$$

Hence f, f_1, f_2 as given by (8.12), (8.14) and (8.15) reduce to one and the same function:

$$f=f_1=f_2=\frac{h}{2\pi}\log\frac{(Z+a^{-1})(Z+a)}{(Z-a^{-1})(Z-a)}\,. \tag{10.3}$$

Hence (8.17) becomes

$$H_1(Z,\overline{Z})=\frac{1}{4}\,w\left\{\int\overline{w}^2\,d\overline{z}+f\right\}-\frac{1}{4}\,(f+\overline{f})\,. \tag{10.4}$$

Also (8.18) is simplified to

$$g_1=\frac{1}{4\pi^2}\oint_C \operatorname{Im}\left[w\left\{\int\overline{w}^2\,d\overline{z}+f\right\}\right]\frac{d\zeta}{\zeta-Z}\,. \tag{10.5}$$

Next, the velocity potential along the aerofoil is given by (9.8) and (9.5) in the form

$$\Phi_1(\theta)=-\frac{h}{4\pi}\log\frac{1+a^2+2a\cos\theta}{1+a^2-2a\cos\theta}$$
$$-\frac{1}{2}\,T(\theta)q_0\sin\omega+\frac{1}{2}\,[T(\theta)q_0\cos\omega]^*\,, \tag{10.6}$$

where

$$T(\theta)=\int q_0{}^2\sin\omega\, ds+\frac{h}{\pi}\tan^{-1}\left(\frac{2a}{1-a^2}\sin\theta\right). \tag{10.7}$$

This case has been treated by Goldstein and Lighthill[2] by quite a different method obtaining more complicated expressions.

§ 11. Compressible Flow past a Nearly Circular Cylinder Symmetrically Placed in a Channel

By the use of the author's formula (2.15) ($N=1$), Hasimoto[3] investigated the compressible flow past a nearly circular cylinder which is placed symmetrically between two parallel walls. For the determination of the complementary function $G_1(z)$ he was obliged to have recourse to a more or less intuitive argument. In effect, he considered a profile in the ζ-plane which is derived from a circle of radius σ in the z-plane by means of the transformation function

$$\zeta=\frac{D}{2\pi}\log\frac{(z+1)(z-\mu^2)}{(z-1)(z+\mu^2)}+\frac{i}{2}D\,,$$
$$0<\mu<\sigma<1\,. \tag{11.1}$$

To express this in terms of our notation in the present paper, we have only to make the substitution

$$z\to\sigma Z\,,\qquad \zeta\to z\,,$$
$$D\to h\,,\quad \sigma\to a\,,\quad \sigma^{-1}\mu^2\to b\quad (0<b<a<1)\,.$$

Thus we obtain

$$z=\frac{h}{2\pi}\log\frac{(Z+a^{-1})(Z-b)}{(Z-a^{-1})(Z+b)}+\frac{i}{2}h\,, \tag{11.2}$$

which can be further put in the form of (7.1):

$$z=\frac{h}{2\pi}\log\frac{(Z+a^{-1})(Z+a)}{(Z-a^{-1})(Z-a)}+C(Z)\,, \tag{11.3}$$

if we take

$$C(Z)=\frac{i}{2}h+\frac{h}{2\pi}\log\frac{(Z-a)(Z-b)}{(Z+a)(Z+b)}\,, \tag{11.4}$$

which is clearly analytic in the region outside the unit circle: $|Z|>1$.

The first approximation to the complex velocity potential can now be obtained as

$$F_1=H_1(Z,\overline{Z})+g_1(Z)\,,$$

where H_1 and g_1 are to be calculated by (10.4) and (10.5). Such a calculation employing (10.3) is straightforward, without any special consideration about the boundary conditions. For the detail of the numerical result reference should be made to Hasimoto's original paper[3].

The author wishes to thank Mr. Hideo Takami for checking some of the results in Part I and Mr. Eiji Kasahara for helpful discussions concerning the material of Part II.

The author also wishes to express his appreciation for the hospitality of the Institute for Fluid Dynamics and Applied Mathematics.

Appendix

As an illustration of the application of the formulae obtained in this paper, let us consider the flow past a circular cylinder with circulation. For a circular cylinder of radius unity, we have

$$f=z+z^{-1}+i\kappa\log z\,, \tag{A1}$$

which, on substitution in (3.18), gives

$$\begin{aligned}H_1=&\frac{1}{4}(1+i\kappa z^{-1}-z^{-2})\Big\{\bar{z}(\kappa^2+2)\bar{z}^{-1}\\&-i\kappa\bar{z}^{-2}-\frac{1}{3}\bar{z}^{-3}-2i\kappa\log z\bar{z}\Big\}\\&-\frac{1}{4}(\bar{z}+\bar{z}^{-1}-i\kappa\log z\bar{z})\,.\end{aligned} \tag{A2}$$

On the circle we can put

$$z=\zeta\,,\qquad \bar{z}=\zeta^{-1}\,,\qquad \zeta=e^{i\theta}\,,$$

and hence

$$\begin{aligned}H_1=&\frac{1}{4}\Big\{-\zeta^{-3}+i\kappa\zeta^{-2}-(\kappa^2+2)\zeta^{-1}+i\kappa(\kappa^2+3)\\&+\Big(2\kappa^2+\frac{4}{3}\Big)\zeta-\frac{4}{3}i\kappa\zeta^2-\frac{1}{3}\zeta^3\Big\}\,,\end{aligned} \tag{A3}$$

$$\begin{aligned}H_1-\overline{H}_1=&\frac{1}{4}\Big\{-\frac{2}{3}\zeta^{-3}-\frac{1}{3}i\kappa\zeta^{-2}\\&-\Big(3\kappa^2+\frac{10}{3}\Big)\zeta^{-1}+2i\kappa(\kappa^2+3)\\&+\Big(3\kappa^2+\frac{10}{3}\Big)\zeta-\frac{1}{3}i\kappa\zeta^2+\frac{2}{3}\zeta^3\Big\}\,.\end{aligned} \tag{A4}$$

Now (3.14) gives

$$g_1=\frac{1}{2\pi i}\oint_C(H_1-\overline{H}_1)\frac{d\zeta}{\zeta-z}=\mathrm{Res}_{\zeta=0}\left[\frac{H_1-\overline{H}_1}{\zeta-z}\right],$$

since the integrand is regular in the unit circle except at $\zeta=0$. Thus, calculating the residue we find

$$g_1=\frac{1}{6z^3}+\frac{1}{12}i\kappa\frac{1}{z^2}+\Big(\frac{5}{6}+\frac{3}{4}\kappa^2\Big)\frac{1}{z}\,. \tag{A5}$$

Substituting (A2) and (A5) in $\Phi_1+i\Psi_1=F_1=H_1+g_1$, we have the first order correction to the complex velocity potential.

If only the value of the velocity potential at the surface of the cylinder is required, we can more conveniently use the formulae (4.6) and (5.2). Thus, taking the real part of the positive power terms of (A3), we immediately find

$$\Phi_1(\theta)=\Big(\kappa^2+\frac{2}{3}\Big)\cos\theta+\frac{2}{3}\kappa\sin 2\theta-\frac{1}{6}\cos 3\theta\,. \tag{A6}$$

References

1) T. M. Cherry: Proc. Roy. Soc. London **A 196** (1949) 32.
2) S. Goldstein and M. J. Lighthill: Phil. Mag. **35** (1944) 549.
3) Z. Hasimoto: Proc. Phys.-Math. Soc. Japan **25** (1943) 563.
4) I. Imai: Rep. Aeron. Res. Inst. Tokyo Imp. Univ. No. 216 (1941).
5) I. Imai: Proc. Phys.-Math. Soc. Japan **24** (1942) 120.
6) I. Imai: Rep. Aeron. Res. Inst. Tokyo Imp. Univ. No. 275 (1943).
7) I. Imai: Rep. Aeron. Res. Inst. Tokyo Imp. Univ. No. 290 (1944).
8) I. Imai: Proc. Phys.-Math. Soc. Japan **26** (1944) 71.
9) I. Imai and T. Aihara: Rep. Aeron. Res. Inst. Tokyo Imp. Univ. No. 194 (1940).
10) I. Imai and D. Kawata: Rep. Aeron. Res. Inst. Tokyo Imp. Univ. No. 325 (1945).
11) C. Kaplan: NACA Rep. No. 621 (1938).
12) C. Kaplan: NACA Rep. No. 624 (1938).
13) C. Kaplan: NACA Rep. No. 728 (1942).
14) M. Kawaguti: J. Phys. Soc. Japan **6** (1951) 168.
15) D. Meksyn: Proc. Roy. Soc. London **A 220** (1953) 239.
16) L. Poggi: Aerotecnica **12** (1932) 1579.
17) L. Poggi: Aerotecnica **14** (1934) 532.
18) H. Takami: J. Phys. Soc. Japan **11** (1956) 145.
19) H. Takami: J. Phys. Soc. Japan **11** (1956) 446.
20) S. Tomotika and K. Tamada: Rep. Aeron. Res. Inst. Tokyo Imp. Univ. No. 201 (1940).
21) S. Tomotika and K. Tamada: Quart. Appl. Math. **9** (1951) 129.
22) S. Tomotika and H. Umemoto: Rep. Aeron. Res. Inst. Tokyo Imp. Univ. No. 205 (1941).

JOURNAL OF THE PHYSICAL SOCIETY OF JAPAN Vol. 12, No. 1, JANUARY, 1957

Boundary Layer Growth on a Flat Plate with Suction or Injection

By Hidenori HASIMOTO

*Department of Physics, Faculty of Science,**
University of Tokyo

(Received September 22, 1956)

Exact solutions of the Navier-Stokes equations are obtained for the boundary layer growth on an infinite flat plate with uniform suction or injection (with velocity V normal to its plane) which is started at time $t=0$ (with velocity U along its plane), for the two cases: i) $U=$arbitrary, $V=$const and ii) $U\propto t^{\alpha}$, $V\propto t^{-1/2}$.

i) gives simple relations between the cases of suction and injection and ii) gives similar velocity profiles.

Rayleigh's problem ($U=$const) is investigated in detail, and the resulting solutions show the same qualitative natures as the corresponding steady flow solutions for an semi-infinite flat plate so far obtained.

§1. Introduction

The problem of boundary layer control has become very important in the field of aerodynamics. Among several methods[1] the application of suction is widely used in recent times, in order to prevent separation and to delay transition to turbulence, by means of which we get much larger maximum lift and reduced drag.

On the other hand, we know the possibility of using injection at the wall to cool the body in a high-temperature gas.

Many authors have made mathematical studies on these problems, especially in the case of steady flow. In this paper we want to study the problem of boundary layer growth on an infinite flat plate started at time $t=0$, with uniform suction or injection. Exact solutions of the Navier-Stokes equations of motion are derived for the case of uniform suction (and injection) which is steady or proportional to $t^{-1/2}$. They have very simple forms and may give a clear insight into the corresponding steady boundary layer problem, as Rayleigh's problem for the impulsive motion which was considered initially by Rayleigh[2] for a flat plate without suction (classical Rayleigh's problem) and has been extended to general cylinder by many authors[3,4,5]. The fundamental equations of our problem were those given by Stuart[6], but his detailed study is confined to the case of periodic motion of the plate with constant suction. In §3 we treat the case when suction or injection is constant. It is found that there are very simple relation between the cases of suction and injection. In §4 we treat the case when suction or injection varies as $t^{-1/2}$ and the velocity of the plate is proportional to t^{α}. This is the case which allows similar solutions.

Numerical calculations are made for the case of impulsive motion of the plate in §3 and §4. In the case of injection, velocity profiles have inflection points. The qualitative natures of the flow are the same as the results of the corresponding studies on the steady boundary layer, so far obtained.

§2. Fundamental Equations

Let us consider the unsteady motion of an infinite flat plate $y=0$ parallel to the x-axis, starting at time $t=0$ in a viscous incompressible fluid. Uniform normal velocity of the fluid V from the surface of the plate represents suction or injection according as $V<0$ or $V>0$. In this case the Navier-Stokes equations of motion of the fluid and a equation of continuity reduce to

$$\frac{\partial u}{\partial t}+v\frac{\partial u}{\partial y}=\nu\frac{\partial^2 u}{\partial y^2}, \tag{2.1}$$

$$\frac{\partial v}{\partial t}+v\frac{\partial v}{\partial y}=\nu\frac{\partial^2 v}{\partial y^2}-\frac{1}{\rho}\frac{\partial p}{\partial y}, \tag{2.2}$$

$$\frac{\partial v}{\partial y}=0 \tag{2.3}$$

taking into account independence of the flow field on x, where $u(y, t)$ and $v(y, t)$ are velocity components, p is the pressure, and ν is the kinematic viscosity.

---

* Now at Depertment of Aeronautics University of Kyoto.

(2.1)–(2.3) are subject to the boundary conditions

$$u(0, t)=U(t)\ , \qquad u(\infty, t)=0\ , \tag{2.4}$$

$$v(0, t)=V(t) \tag{2.5}$$

and an initial condition

$$u(y, 0)=0\ . \tag{2.6}$$

(2.3) and (2.5) show that

$$v(y, t)=V(t)\ . \tag{2.7}$$

Introducing (2.7) into (2.2) and (2.1) we get equations for p and u respectively

$$p=p_0-\rho y\frac{dV}{dt}\ , \tag{2.8}$$

$$\frac{\partial u}{\partial t}+V\frac{\partial u}{\partial y}=\nu\frac{\partial^2 u}{\partial y^2}\ . \tag{2.9}$$

where p_0 is the value of p at $y=0$, ρ is the density of the fluid.

(2.9) is an equation already given by Stuart. The exact solution of it, however, is not simple for the general functional form of $V(t)$ except the cases I) $V=V_0=$const. and II) $V=V_0t^{-1/2}$ which will be studied in detail in the following sections.

§ 3. The Case $V=V_0=$Constant

In this section we consider the case of constant suction or injection; $V=V_0$.

Multiplying (2.9) and (2.4) by $\exp(-pt)$ and integrating with respect to t from 0 to ∞, we obtain

$$\frac{d^2u^*}{dy^2}-2\kappa\frac{du^*}{dy}-\frac{p}{\nu}u^*=0 \tag{3.1}$$

subject to

$$u^*(0.\ p)=U^*(p)\ , \qquad u^*(\infty, p)=0\ , \tag{3.2}$$

for the Laplace transform of $u(y, t)$:

$$u^*(y, p)=\int_0^\infty e^{-pt}u(y, t)dt \tag{3.3}$$

where

$$\kappa=V/(2\nu)\ , \tag{3.4}$$

and we used an initial condition (2.6).

These can be solved easily and yield

$$u^*=U^*\exp\left[\kappa y-\sqrt{\kappa^2+p/\nu}\,y\right]\ . \tag{3.5}$$

We want to calculate the inverse transform of $\exp(-\sqrt{\kappa^2+p/\nu}\,y)$:

$$L^{-1}\left[e^{-\sqrt{\kappa^2+p/\nu}\,y}\right]=\frac{1}{2\pi i}\int_{c-i\infty}^{c+i\infty}e^{pt-\sqrt{\kappa^2+p/\nu}\,y}dp\ .$$

$$c>0\ . \tag{3.6}$$

Putting $\kappa^2+p/\nu=q/\nu$, (3.6) reduces to[7]

$$\frac{1}{2\pi i}e^{-\kappa^2\nu t}\int_{c+\nu\kappa^2-i\infty}^{c+\nu\kappa^2+i\infty}e^{-\sqrt{q/\nu}\,y+qt}+dq$$

$$=e^{-\kappa^2\nu t}L^{-1}\left[e^{-\sqrt{p/\nu}\,y}\right]$$

$$=\frac{y}{2\sqrt{\pi\nu t^3}}\exp\left[-\frac{y^2}{4\nu t}-\kappa^2\nu t\right]. \tag{3.7}$$

Making use of the convolution theorem we obtain from (3.5) and (3.7)

$$u=e^{\kappa y}\int_0^t U(t-\tau)\frac{y}{2\sqrt{\pi\nu\tau^3}}\exp\left[-\frac{y^2}{4\nu\tau}-\kappa^2\nu\tau\right]d\tau\ . \tag{3.8}$$

This has a very compact form but is inconvenient for studying the behaviour near the plate $y\sim 0$. In this case the solution $E(y, t)$ for the case of the impulsive motion ($U=1$, $U^*=1/p$) is suitable. Making use of a formula 19 in Appendix V of Carslaw and Jaeger[7] we obtain for $E(y, t)$:

$$e^{-\kappa y}E(y, t)=L^{-1}\left[p^{-1}e^{-\sqrt{\kappa^2+p/\nu}\,y}\right]$$

$$=e^{-\kappa^2\nu t}L^{-1}\left[(p-\nu\kappa^2)^{-1}e^{-\sqrt{p/\nu}\,y}\right]$$

$$=\frac{1}{2}\{e^{-|\kappa|y}\operatorname{erfc}[\eta-\sqrt{\kappa^2\nu t}]$$

$$+e^{|\kappa|y}\operatorname{erfc}[\eta+\sqrt{\kappa^2\nu t}]\}\ , \tag{3.9}$$

where

$$\eta=\frac{y}{2\sqrt{\nu t}}\ , \tag{3.10}$$

and

$$\operatorname{erfc}\xi=\frac{2}{\sqrt{\pi}}\int_\xi^\infty e^{-\xi^2}d\xi\ . \tag{3.11}$$

$E(y, t)$ can be expanded into a series form in powers of t, using a formula V–11 of 7):

$$E(y, t)=e^{\kappa y-\kappa^2\nu t}L^{-1}\left[\frac{1}{p}\sum_{n=0}^\infty\left(\frac{\nu\kappa^2}{p}\right)^n e^{-\sqrt{p/\nu}\,y}\right]$$

$$=e^{\kappa y-\kappa^2\nu t}\sum_{n=0}^\infty(4\kappa^2\nu t)^n \mathrm{i}^{2n}\operatorname{erfc}\eta\ , \tag{3.12}$$

where

$$\mathrm{i}^n\operatorname{erfc}x=\int_x^\infty \mathrm{i}^{n-1}\operatorname{erfc}\xi d\xi\ ,$$

$$\mathrm{i}^0\operatorname{erfc}x=\operatorname{erfc}x\ . \tag{3.13}$$

For general $U(t)$ we get from the convolution theorem

$$u=\int_0^t U'(t-\tau)E(y, \tau)d\tau\ . \quad U'(t)=\frac{dU}{dt}\ , \tag{3.14}$$

which is equivalent to (3.8).

The frictional drag D per unit area of the plate is given by

$$D=-\mu\left(\frac{\partial u}{\partial y}\right)_{y=0}=\int_0^t U'(t-\tau)D_E(\tau)d\tau\ , \qquad (3.15)$$

where

$$D_E(\tau)=-\mu\left(\frac{\partial E}{\partial y}\right)_{y=0}$$

$$=\mu\left[\frac{1}{\sqrt{\pi\nu t}}e^{-\kappa^2\nu t}-\kappa\ \mathrm{erfc}\,(\kappa\sqrt{\nu t})\right], \qquad (3.16)$$

and μ is the viscosity: $\mu=\rho\nu$.

Here we note very interesting relations between the values for the cases of suction and injection: If the absolute value of κ or V_0 is the some, the following formulae are found,

$$\frac{u_{\kappa>0}}{u_{\kappa<0}}=e^{2|\kappa|y}\ , \qquad (3.17)$$

$$D_{\kappa<0}-D_{\kappa>0}=2\mu|\kappa|\int_0^t U'(t-\tau)d\tau=\rho|V_0|U(t)\ . \qquad (3.18)$$

where the suffix $\kappa>0$ denotes the value for the case of $\kappa>0$ and *vice versa*. It is rather interesting that (3.18) is different from $2\rho|V_0|U$ which may be supposed simply by the naive momentum consideration.

The most interesting case is that corresponding to Rayleigh's problem $U=U_0=$constant, when u and D are given respectively by

$$\frac{u}{U_0}=E(y,\ t)\ , \qquad \frac{D}{V_0}=D_E(t)\ . \qquad (3.19)$$

Fig. 1 shows the velocity profiles $E(y,\ t)$ for some values of $\xi=\kappa\sqrt{\nu t}=V_0\sqrt{t}/(2\sqrt{\nu})$. They are not similar among themselves, and have inflection points for the case of injection $V_0>0$. If $\kappa^2\nu t$ is sufficiently large they tend to $\exp(\kappa y-|\kappa|y)=\exp\frac{1}{2\nu}(V_0-|V_0|)y$ rapidly, of which profile $u/U_0=\exp(-|V_0|y/\nu)$ for $V_0<0$ is a well known suction profile for the steady flow obtained by Meredith and Grifith1).

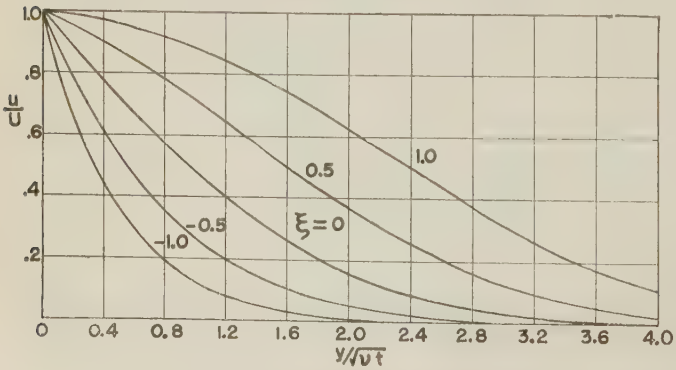

Fig. 1. The Velocity Profiles: $U=U_0$, $V=V_0$, $\xi\ \ V_0\sqrt{t}/(2\sqrt{\nu})$.

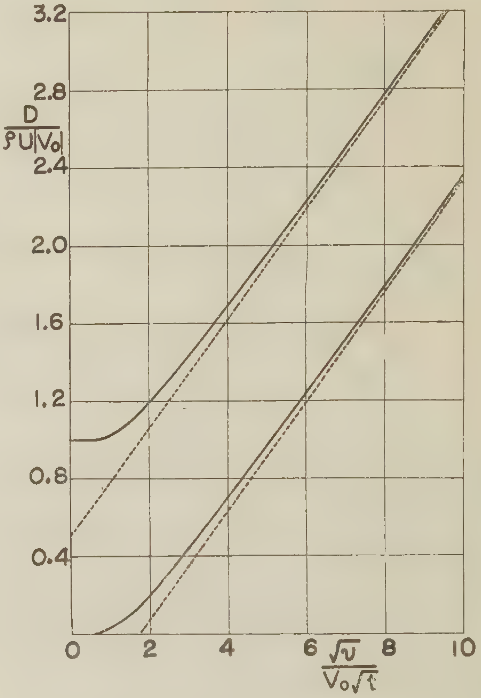

Fig. 2. Frictional Drag: $U=U_0$, $V=V_0$.

Fig. 2 shows the skin frictional drag D for the plate. If we use $|\xi|$ as an independent variable $D_E/(2\mu|\kappa|)=D/(\rho U_0|V_0|)$ is represented by two single curves:

$$\frac{D}{\rho U|V_0|}=\frac{1}{2}\left[\frac{e^{-|\xi|^2}}{\sqrt{\pi}\ |\xi|}+\mathrm{erf}\ |\xi|\mp 1\right] \qquad \xi\gtrless 0 \qquad (3.16')$$

If $\xi^2=\kappa^2\nu t$ is small D is practically identical with the classical Raylgith's value $\mu U/\sqrt{\pi\nu t}$, then it tends to 0 or $\rho U|V_0|$ according as $V_0>0$ or $V_0<0$, in the limit of $\kappa^2\nu t\to\infty$.

§ 4. The Case of Similar Profile

As the most simple case of variable V, we want to investigate the case when (2.9) gives similar solutions, which must have the following form.

$$u=U(t)G(\eta)\ , \qquad \eta=y/g(t)\ . \qquad (4.1)$$

Introducting (4.1) into (2.9) and dividing by U/g^2 we obtain

$$-[gg']\eta G'+[g^2U'/U]G+[gV]G'=\nu G'' \quad (4.2)$$

In order that (4.2) reduces to an ordinary differential equation for G the three terms in the square brackets must be equal to constants:

$$2gg'=A\,, \quad g^2U'/U=B\,, \quad gV=C\,, \quad (4.3)$$

which determine g, U and V as follows if $A \neq 0$:

$$g=\sqrt{At+k}\,,\ U\infty(At+k)^{B/A}\,,\ V=C/\sqrt{At+k}\,. \quad (4.4)$$

The case corresponding to $A=0$:

$$g=\sqrt{k}\,, \quad U\infty e^{Bt/k}\,, \quad V=C/\sqrt{k} \quad (4.5)$$

is a special case of constant V, which has been studied already in § 3 and 6). In either case (4.2) reduces to

$$G''+\frac{1}{\nu}\left[\frac{A}{2}\eta-C\right]G'-\frac{B}{\nu}G=0\,. \quad (4.6)$$

We can take in (4.4)

$$\left.\begin{aligned} U=U_0t^{\alpha}\,, \quad V=V_0t^{-1/2}\,,\\ g=2\sqrt{\nu t} \end{aligned}\right\} \quad (4.4')$$

without loss of generality (i.e. $A=4\nu$, $C=2\sqrt{\nu}V_0$, $B=4\nu\alpha$).

Then (4.6) gives for the solution $G(\eta)=G_\alpha(\eta)$

$$G_\alpha''+2(\eta-\eta_0)G_\alpha'-4\alpha G_\alpha=0\,, \quad (4.6')$$

where

$$\eta=2\frac{y}{\sqrt{\nu t}}\,, \qquad \eta_0=\frac{V_0}{\sqrt{\nu}}\,, \quad (4.7)$$

which must be solved under the boundary conditions derived from (2.4) and (2.6):

$$G_\alpha(0)=1\,, \quad G_\alpha(\infty)=0\,. \quad (4.8)$$

The solution of (4.6′) satisfying (4.8) is found to be

$$G_\alpha(\eta)=\frac{F_\alpha(\eta-\eta_0)}{F_\alpha(-\eta_0)}\,, \quad (4.9)$$

where

$$F_\alpha(\xi)=e^{-\xi^2/2}D_{-2\alpha-1}(\sqrt{2}\,\xi)\,. \quad (4.10)$$

$D_\beta(z)$ is a parabolic cylinder function which satisfies the equation

$$\frac{d^2}{dz^2}D_\beta+\left(\beta+\frac{1}{2}-\frac{1}{4}z^2\right)D_\beta=0\,. \quad (4.11)$$

When $\eta_0=0$ G_α reduces to the solution obtained by Watson[8].

Corresponding steady boundary layer on a semi-infinite flat plate has been investigated by Schlichting, Bussmann and Schaefer[1]. They have shown the existence of similar solutions for the case $U(x)\infty x^m$ and $V(x)\infty x^{(m-1)/2}$. Their x corresponds to our t.

Rayleigh's case is given by taking $\alpha=0$ ($U=U_0$). Taking into account

$$D_{-1}(x)=\sqrt{\frac{\pi}{2}}e^{x^2/4}\operatorname{erfc}\left(\frac{x}{\sqrt{2}}\right) \quad (4.12)$$

we obtain

$$\frac{u}{U_0}=\frac{\operatorname{erfc}(\eta-\eta_0)}{\operatorname{erfc}(-\eta_0)}=\frac{\operatorname{erfc}[y/(2\sqrt{\nu t})-V_0/\sqrt{\nu}\,]}{\operatorname{erfc}(-V_0/\sqrt{\nu}\,)} \quad (4.13)$$

The frictional drag D per unit area is given by

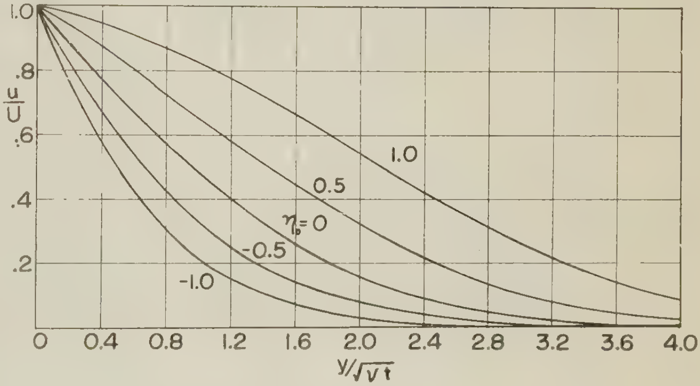

Fig. 3. The Velocity Profiles: $U=U_0$, $V=V_0t^{-1/2}$, $\eta_0=V_0/\sqrt{\nu}=V\sqrt{t}/\sqrt{\nu}$.

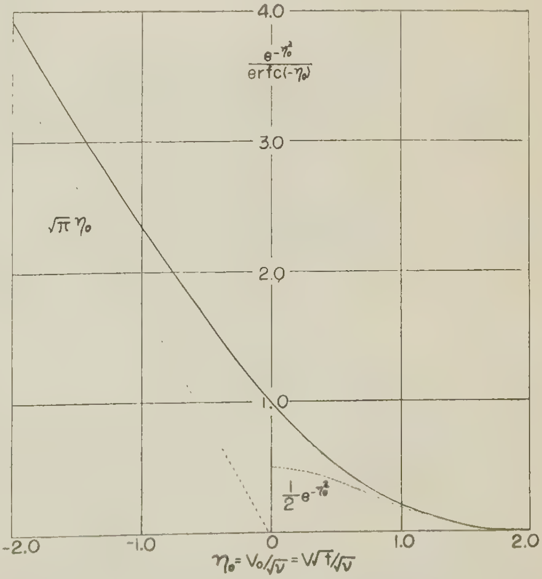

Fig. 4. $D_{\eta=\eta_0}/D_{\eta=0}$: $U=U_0$, $V=V_0t^{-1/2}$.

$$\frac{D}{\mu U_0}=\frac{1}{\sqrt{\pi\nu t}}\frac{e^{-\eta_0^2}}{\operatorname{erfc}(-\eta_0)}. \tag{4.14}$$

Fig. 3 shows the velocity profiles for some values of $\eta_0=V_0/\sqrt{\nu}$. They have inflection points at $\eta=\eta_0$, for the case of injection $V_0>0$.

Fig. 4 gives $D_{\eta=\eta_0}/D_{\eta=0}=e^{-\eta_0^2}/\operatorname{erfc}(-\eta_0)$, the factor which represents the effect of injection or suction compared with the classical Rayleigh's value $D_{\eta=0}=1/\sqrt{\pi\nu t}$. If $|\eta_0|$ is sufficiently large it is approximated by $e^{-\eta_0^2/2}$ or $\sqrt{\pi}\,|\eta_0|$ according as $V_0>0$ or $V_0<0$. These behaviours are qualitatively the same as what have been found for the corresponding steady boundary layer solution[1].

In conclusion the author expresses his cordial thanks to Professor Isao Imai for the continual guidance and encouragement throughout this work. This work was supported by the Scientific Research Fund of the Ministry of Education of Japan.

References

1) H. Schlichting: Boundary Layer Theory, Pergamon press. London (1955) 226.
2) Lord Rayleigh: Phil. Mag. (6) **21** (1911) 697.
3) G. K. Batchelor: Quart. J. Mech. and Appl. Math. **7** (1954) 179.
4) H. Hasimoto: J. Phys. Soc. Japan **9** (1954) 611, **10** (1955) 397.
5) J. C. Cooke: J. Phys. Soc. Japan **11** (1956).
6) J. T. Stuart: Proc. Roy. Soc. **231** (1955) 116.
7) H. S. C. Carslaw and J. C. Jaeger: Conduction of Heat in Solids (1947) 380.
8) E. J. Watson: Proc. Roy. Soc. **231** (1955) 103.

JOURNAL OF THE PHYSICAL SOCIETY OF JAPAN Vol. 12, No. 1, JANUARY, 1957

Application of the Thin-Wing-Expansion Method to the Compressible Flow past an Elliptic Cylinder, with Special Reference to its Fourth Approximation

By Yaso'o MATUNOBU

Department of Physics, Faculty of Science,
University of Tokyo

(Received September 22, 1956)

Both the complete and transonic thin-wing-expansion methods are utilized to obtain the steady irrotational flow of a compressible fluid past an elliptic cylinder. The velocity distribution over the surface is calculated up to the fourth powers in thickness ratio t. Then it is found that the fourth order perturbations include not only terms of $O(t^4)$ but also those of $O(t^4\log t)$, and that the latter group becomes negatively predominant over the former in the transonic range. In calculating the fluid velocity near the stagnation point there still remains insurmountable difficulty even for moderate subsonic flow. The resulting expressions for an elliptic cylinder prove to be transformed into those for a parabolic cylinder.

§1. Introduction and Summary

The steady irrotational flow of a compressible fluid past an elliptic cylinder at zero incidence has been studied by a number of authors by means of various methods; especially Hasimoto[1], having recourse to the (complete) thin-wing-expansion method, calculated velocity distribution over the surface exactly up to the third order of approximation. Later Imai[2,3] proposed a new method called transonic thin-wing-expansion method, showing that the velocity distribution could be obtained more easily up to the same order by the introduction of the transonic similarity hypothesis. As a continuation of these two works the fourth order of approximation will be considered in this paper.

The thin-wing-expansion method has often been proved to give a most suitable approach for such problems as chosen here. It is true, however, that the method could be successfully applied to the flow past a sharp-edged aerofoil such as Kaplan bumps[4),5)] and symmetrical circular arc aerofoils[6),7)], but it is not necessarily the case for the elliptic cylinder owing to its rounded edges which cause enormous change of the flow speed. In fact, it cannot be predicted qualitatively what happens near the stagnation point, even from the exact results including the fourth order perturbation. This fact has been corroborated by recent studies[8),9)] with regard to the flow past aparabolic cylinder with its axis parallel to the oncoming flow which can be looked upon as a magnified picture of the stagnation region of the elliptic cylinder; i.e., the small disturbance theory yields no reliable information concerning the flow pattern around such blunt-nosed bodies.

Furthermore, the resulting expressions for the velocity distribution show that the fourth order perturbation includes terms of order $t^4 \log \sqrt{1-M^2}\,t$ (t: thickness ratio, M: free stream Mach number) which did not appear in the calculation of the flow field around the sharp-edged aerofoils cited above*. Undoubtedly, these terms play such a dominant role in the high subsonic range that it becomes impossible to apply the transonic similarity approximation to the resulting expressions. It can be shown that when t is sufficiently small the fourth order perturbation as a whole proves negative even for the moderate subsonic free stream.

In the following sections calculations on the basis of the transonic thin-wing-expansion method are chiefly developed; in particular, more detailed account is given of the fourth approximation, since the analytical expressions up to the third order have already been obtained. As for the complete thin-wing-expansion method, only final results are summarized in § **6** and the basic formulae utilized are brought in the appendix in forms ready for practical use.

§ 2. Transonic Thin-Wing-Expansion Method

Suppose a uniform flow directed along x-axis blows against an aerofoil fixed in x-y plane, with velocity U and Mach number M. On the assumption that the disturbance velocities due to the presence of the obstacle are everywhere small and of the same order as the thickness ratio t, the velocity potential Φ and the stream function Ψ can be written in the forms

$$\Phi = x + \varepsilon\phi\,, \qquad \Psi = y + \varepsilon\psi\,, \tag{2.1}$$

where $\varepsilon = O(t)$ and U has been taken as unit of velocity. Further, defining the following complex quantities:

$$\begin{aligned}&\zeta = x + i\mu y, \quad \bar{\zeta} = x - i\mu y,\\ &G = \phi + i\psi/\mu, \quad \bar{G} = \phi - i\psi/\mu; \quad \mu = \sqrt{1-M^2}\end{aligned} \tag{2.2}$$

and assuming that M is nearly unity, we obtain the following equation, upon which the transonic thin-wing-expansion method is based, from the equation of motion for the two-dimensional steady irrotational flow of an inviscid fluid (cf. Ref. 4); namely,

$$\frac{\partial G}{\partial \bar{\zeta}} = \frac{\varepsilon}{16}\nu\left(\frac{\partial G}{\partial \zeta} + \frac{\partial G}{\partial \bar{\zeta}} + \frac{\partial \bar{G}}{\partial \zeta} + \frac{\partial \bar{G}}{\partial \bar{\zeta}}\right)^2, \tag{2.3}$$

where

$$\nu = 4M^2\left(1 + \frac{\gamma+1}{4}\frac{M^2}{1-M^2}\right), \tag{2.4}$$

γ being the ratio of specific heats.

On the assumption that $\beta(=\varepsilon\nu/16)$ is small, the solution of Eq. (2.3) may be expanded as

$$G = G_1 + \beta G_2 + \beta^2 G_3 + \beta^3 G_4 + \cdots\,. \tag{2.5}$$

Then G_n can be expressed in explicit forms after successive integrations, but they are omitted here since they have already appeared in Ref. 4.

The boundary conditions are

(i) $\partial G/\partial\zeta$ is one-valued and continuous throughout the flow field,

(ii) $\partial G/\partial\zeta$ vanishes at infinity,

(iii) $\mathrm{Im}\,(\zeta + \varepsilon\mu^2 G) = 0$ at the boundary surface.

§ 3. Calculations up to the Third Approximation

Now we consider the flow past an elliptic cylinder with its major axis parallel to the uniform flow. Let the ellipse be given by

---

* For symmetrical circular arc aerofoils this fact has been inferred from the results up to $O(t^3)$, whereas it is actually proved in the case of Kaplan bumps. Moreover, it is well known that such terms are required from the outset in the axially symmetrical flow past a slender body (for example, cf. Ref. 10).

$$x=a\cos\theta,\quad y=b\sin\theta;\quad b/a=t. \tag{3.1}$$

Then, by means of the transformation

$$\zeta=Z+\frac{\sigma^2}{Z};\quad \sigma^2=\frac{1-\mu t}{1+\mu t}, \tag{3.2}$$

the flow field in the ζ-plane is conformally mapped onto the region outside the unit circle $(Z=e^{i\theta})$ in the Z-plane. The boundary conditions (i) to (iii) are entirely satisfied by assuming that

$$G_1=f(\zeta)=\frac{k}{Z},\quad k=(1+\sigma^2)\frac{t}{\varepsilon\mu}. \tag{3.3}$$

The perturbation velocity potentials of higher order than the first can be obtained successively by determining the arbitrary functions $g_n(\zeta)$ corresponding to $G_n(\zeta,\bar{\zeta})$ so as to satisfy the following conditions:

(i′) $\partial G_n/\partial\zeta$ is one-valued and continuous throughout the flow field,

(ii′) $\partial G_n/\partial\zeta$ vanishes at infinity,

(iii′) $\operatorname{Im} G_n=0$ at the boundary surface $(n=2, 3, 4, \cdots)$.

Thus, we obtain

$$G_2=\frac{k^2}{\sigma^2}\left(\frac{1}{Z}+J\right)+c.c., \tag{3.4}$$

$$G_3=k^3\left\{\frac{16}{3\sigma^4}\frac{1}{Z}+\left(\frac{8+3\sigma^2}{3\sigma^4}-\frac{14}{\sigma^2}L\right)\frac{Z}{V}+\frac{8+\sigma^2}{\sigma^4}J-\frac{14}{\sigma^2}\frac{1}{V}J\right\}+c.c., \tag{3.5}$$

$$g_2=k^2\left\{2\frac{Z}{V}+\frac{1}{\sigma^2}\left(\frac{1}{Z}+J\right)\right\}, \tag{3.6}$$

$$g_3=k^3\left\{\frac{16}{3\sigma^4}\frac{1}{Z}+\frac{22+\sigma^2}{\sigma^4}J+\left(\frac{15}{\sigma^2}+\frac{8}{3\sigma^4}-\frac{14}{\sigma^2}L\right)\frac{Z}{V}-4(3-\sigma^2)\frac{Z}{V^2}+4\sigma^4\frac{Z}{V^3}-\frac{14}{\sigma^2}S\right\}, \tag{3.7}$$

where

$$\left.\begin{aligned}&J=\frac{1}{2\sigma}\log\frac{Z-\sigma}{Z+\sigma},\quad V=Z^2-\sigma^2,\\&S=\left(LZ+\frac{1}{\sigma^2}J\right)\Big/(1-\sigma^2Z^2),\end{aligned}\right\} \tag{3.8}$$

$$L=\frac{1}{2\sigma^2}\log\frac{1+\sigma^2}{1-\sigma^2}=-\frac{1}{2\sigma^2}\log\mu t, \tag{3.9}$$

and $c.c.$ denotes the complex conjugate of the preceding term. It must be noted that (3.4) and (3.5) express G_2 and G_3 at the surface and substitution $Z=e^{i\theta}$ there gives immediately the expressions for the perturbation velocity potentials $\phi_2(\theta)$ and $\phi_3(\theta)$ respectively.

§ 4. Calculation of the Fourth Approximation

In this section the practical procedure of finding the fourth order perturbation will be outlined. Calculations involved are quite analogous to, but more lengthy than, the foregoing ones.

First, substituting (3.3), (3.6), and (3.7) into the integrated form for G_4, we determine $G_4(\zeta,\bar{\zeta})$ exclusive of the arbitrary function $g_4(\zeta)$. Then, we rearrange the resulting expression appropriately with the aid of the relation $Z\bar{Z}=1$ at the surface. Further, it is necessary to choose the complementary function for each of the derived terms, i.e., the function which, in conjunction with the derived ones, satisfies the conditions (i′) to (iii′). Collecting all the sums of the derived and the complementary functions, we thus obtain G_4 at the surface. These procedures are exhibited term by term in the following scheme:

Coefficient	Derived Function	Complementary Function	Sum
$-\frac{280}{3\sigma^4}+\frac{28}{\sigma^2}L$	$\frac{Z}{V}$	$-\frac{Z}{V}$	0
$\frac{182}{\sigma^2}-36+\left(\frac{28}{\sigma^2}+84\right)L$	$\frac{Z}{V^2}$	$-\frac{Z}{V^2}$	0
$-\frac{292}{3}+52\sigma^2-16\sigma^4+56\sigma^2L$	$\frac{Z}{V^3}$	$-\frac{Z}{V^3}$	0
$88\sigma^4-32\sigma^6$	$\frac{Z}{V^4}$	$-\frac{Z}{V^4}$	0
$-48\sigma^6+32\sigma^8$	$\frac{Z}{V^5}$	$-\frac{Z}{V^5}$	0

$-\frac{28}{\sigma^2}$	$\frac{Z^3}{V}\frac{dS}{dZ}$	$-\frac{Z^3}{V}\frac{dS}{dZ}$	0
$-\frac{182}{\sigma^4}+\frac{14}{\sigma^2}$	$\frac{1}{V}\bar{J}$	$-\frac{1}{\sigma^2}J+S+L\frac{Z}{V}$	$\left(\frac{\bar{J}}{V}+L\frac{Z}{V}\right)+c.c.$
$\frac{168}{\sigma^2}+28$	$\frac{1}{V^2}\bar{J}$	$\frac{1}{\sigma^4}J+\frac{1}{\sigma^2}T+L\frac{Z}{V^2}$ $+\frac{1}{2\sigma^2}\left(\frac{1}{1-\sigma^4}-L\right)\frac{Z}{V}$	$\Big[\frac{\bar{J}}{V^2}+L\frac{Z}{V^2}+\frac{1}{2\sigma^2}$ $\times\left(\frac{1}{1-\sigma^4}-L\right)\frac{Z}{V}\Big]+c.c.$
$\frac{14}{\sigma^2}$	$\frac{1}{V^2}\bar{J}+J\frac{1}{\bar{V}^2}$	0	$\frac{1}{V^2}\bar{J}+J\frac{1}{\bar{V}^2}$
$\frac{84}{\sigma^6}+\frac{35}{2\sigma^4}-\frac{1}{2\sigma^2}-\frac{7}{\sigma^4}L$	$\bar{J}$	J	$J+\bar{J}$
$\frac{140}{3\sigma^6}+\frac{35}{2\sigma^4}-\frac{1}{2\sigma^2}-\frac{7}{\sigma^4}L$	$\frac{\bar{Z}}{\bar{V}}$	$\frac{Z}{V}$	$\frac{Z}{V}+\frac{\bar{Z}}{\bar{V}}$
$\frac{112}{3\sigma^6}$	$\frac{1}{\bar{Z}}$	$\frac{1}{Z}$	$\frac{1}{Z}+\frac{1}{\bar{Z}}$
$-\frac{182}{3\sigma^4}-\frac{14}{\sigma^2}+\frac{28}{\sigma^2}L$	$\frac{1}{V}\frac{\bar{Z}}{\bar{V}}$	$-\frac{1}{1+\sigma^2}\frac{Z}{V}$	$\frac{\sigma^2}{1-\sigma^4}\left(\frac{Z}{V}+\frac{\bar{Z}}{\bar{V}}\right)$
$-\frac{28}{3\sigma^4}-\frac{7}{\sigma^2}-1+\frac{14}{\sigma^2}L$	$\frac{\bar{Z}}{\bar{V}^2}$	$\frac{Z}{V^2}$	$\frac{Z}{V^2}+\frac{\bar{Z}}{\bar{V}^2}$
$\frac{28}{\sigma^2}$	$\bar{I}$	I	$I+\bar{I}$
$\frac{28}{\sigma^2}$	$\frac{J}{V}\frac{1}{\bar{V}}$	$-\frac{\sigma^2}{1-\sigma^4}\left(\frac{J}{V}+S+L\frac{Z}{V}\right)$	$-\frac{\sigma^2L}{1-\sigma^4}\left(\frac{Z}{V}+\frac{\bar{Z}}{\bar{V}}\right)$

where

$$T=\frac{1}{1-\sigma^2Z^2}\left\{S-\frac{2}{\sigma^2}J-LZ+\frac{1}{2}\left(\frac{1}{1-\sigma^4}-L\right)\right\}, \qquad I=\int\frac{dS}{dZ}\frac{dZ}{V}. \tag{4.1)*$$

Hence, from the first and fourth columns, we can build up G_4 at the surface; namely,

$$\begin{aligned}G_4=k^4\Big[&\frac{112}{3\sigma^6}\frac{1}{Z}+\left\{\frac{140}{3\sigma^4}+\frac{35}{2\sigma^4}-\frac{1}{2\sigma^2}+\frac{14}{1-\sigma^4}\left(\frac{6}{\sigma^4}-\frac{1}{3\sigma^2}-1\right)-\frac{273}{\sigma^4}L\right\}\frac{Z}{V}\\&+\left(\frac{84}{\sigma^6}+\frac{35}{2\sigma^4}-\frac{1}{2\sigma^2}-\frac{7}{\sigma^4}L\right)J-\left\{\frac{28}{3\sigma^4}+\frac{7}{\sigma^2}+1-\left(\frac{182}{\sigma^2}+28\right)L\right\}\frac{Z}{V^2}\\&+\left(-\frac{182}{\sigma^4}+\frac{14}{\sigma^2}\right)\frac{1}{V}\bar{J}+\left(\frac{182}{\sigma^2}+28\right)\frac{1}{V^2}\bar{J}+\frac{28}{\sigma^2}I\Big]+c.c.\end{aligned} \tag{4.2}$$

§ 5. Velocity Distribution

Let *ds* denote the line element of the profile contour measured in the positive sense. Then, from (3.1)

$$ds=(1+\sigma^2)\sin\theta\sqrt{1+t^2\cot^2\theta}\;d\theta\,. \tag{5.1}$$

Therefore, the velocity at the upper surface is given by

$$q=-\frac{d\Phi}{ds}=\frac{1}{(1+\sigma^2)\sqrt{1+t^2\cot^2\theta}}\frac{d}{d(\cos\theta)}\{\cos\theta+\mathcal{E}(\phi_1+\phi_2+\phi_3+\phi_4)\}. \tag{5.2}$$

Substituting (3.3), (3.4), (3.5), and (4.2) into (5.2) with the aid of the relation

---

* The functions T and I, as well as S given (by 3.8), can be verified to be one-valued and regular functions of Z even at the point $Z=\pm 1/\sigma$.

$$\frac{d\phi_n}{d(\cos\theta)}=\left[\frac{2}{Z-\overline{Z}}\left(Z\frac{\partial G_n}{\partial Z}-\overline{Z}\frac{\partial \overline{G}_n}{\partial \overline{Z}}\right)\right]_{Z=e^{i\theta}}, \tag{5.3}$$

we arrive at the expression for the velocity distribution over the surface:

$$q(\sigma,\,\theta)=(1+t^2\cot^2\theta)^{-1/2}[1+(t/\mu)\{1+\beta k q_2+(\beta k)^2 q_3+(\beta k)^3 q_4\}], \tag{5.4}$$

where

$$q_2=\frac{2}{\sigma^2}\left(1-\frac{1+\sigma^2}{\Theta}\right), \tag{5.5}$$

$$\begin{aligned}q_3=&\frac{32}{3\sigma^4}-\left\{\frac{64}{3\sigma^4}(1+2\sigma^2)-28\left(\frac{1}{\sigma^2}-1\right)L\right\}\frac{1}{\Theta}+4(1+\sigma^2)^2(1-\sigma^2)\\&\times\left(\frac{8+3\sigma^2}{3\sigma^4}-\frac{14}{\sigma^2}L\right)\frac{1}{\Theta^2}+\frac{28(1-\sigma^4)}{\sigma^3}\frac{\lambda}{\Theta^2}+\frac{14}{\sigma^5}\left\{\frac{1+\sigma^4}{\Theta}-\frac{(1-\sigma^4)^2}{\Theta^2}\right\}\tau,\end{aligned} \tag{5.6}$$

$$\begin{aligned}q_4=&\frac{224}{3\sigma^6}-2\left\{\frac{112}{\sigma^6}+\frac{1330}{3\sigma^4}+\frac{14}{\sigma^2}+\frac{14}{1+\sigma^2}\left(\frac{6}{\sigma^4}-\frac{10}{3\sigma^2}-1\right)-14\left(\frac{33}{\sigma^4}-\frac{19}{\sigma^2}\right)L\right\}\frac{1}{\Theta}\\&+2(1+\sigma^2)\left\{\frac{112}{\sigma^6}+\frac{1148}{3\sigma^4}-\frac{464}{3\sigma^2}-46+4\sigma^2-28\left(\frac{52}{\sigma^4}-\frac{21}{\sigma^2}-6+3\sigma^2\right)L\right\}\frac{1}{\Theta^2}\\&-\frac{8}{\sigma^2}(1+\sigma^2)^3(1-\sigma^2)^2\left\{\frac{28}{3\sigma^4}+\frac{7}{\sigma^2}+1-\left(\frac{182}{\sigma^2}+28\right)L\right\}\frac{1}{\Theta^3}+\frac{28}{\sigma}\left\{\left(\frac{39}{\sigma^4}+\frac{3}{\sigma^2}-15+\sigma^2\right)\frac{1}{\Theta^2}\right.\\&\left.-2\left(\frac{13}{\sigma^4}+\frac{2}{\sigma^2}\right)(1-\sigma^4)^2\frac{1}{\Theta^3}\right\}\lambda+\frac{14}{\sigma}\left\{\left(\frac{39}{\sigma^6}+\frac{3}{\sigma^4}+\frac{15}{\sigma^2}-1\right)\frac{1}{\Theta}\right.\\&\left.-(1-\sigma^4)\left(\frac{65}{\sigma^6}+\frac{7}{\sigma^4}+\frac{11}{\sigma^2}+5\right)\frac{1}{\Theta^2}+\left(\frac{26}{\sigma^6}+\frac{4}{\sigma^4}\right)(1-\sigma^4)^3\frac{1}{\Theta^3}\right\}\tau,\end{aligned} \tag{5.7}$$

where

$$\beta k=\frac{1+\sigma^2}{16}\frac{\nu t}{\mu},$$

$$\left.\begin{aligned}&\Theta=1-2\sigma^2\cos 2\theta+\sigma^4,\quad \lambda=\cos\theta\log\frac{1+2\sigma\cos\theta+\sigma^2}{1-2\sigma\cos\theta+\sigma^2},\\&\tau=\frac{1}{\sin\theta}\tan^{-1}\frac{2\sigma\sin\theta}{1-\sigma^2}.\end{aligned}\right\} \tag{5.8}$$

Substitution $\theta=\pi/2$ in the above expressions leads to

$$\begin{aligned}q\left(\sigma,\,\frac{\pi}{2}\right)=1+\frac{t}{\mu}\Bigg[&1+\frac{1}{8}\frac{\nu t}{\mu}+\frac{1}{64}\left(\frac{\nu t}{\mu}\right)^2\left\{\frac{14}{\sigma^3}\tan^{-1}\sigma-7\left(\frac{1}{\sigma^2}-1\right)L-\frac{7}{\sigma^2}+\frac{5}{3}\right\}\\&-\frac{1}{1024}\left(\frac{\nu t}{\mu}\right)^3\left\{\frac{49}{\sigma^4}+\frac{658}{3\sigma^2}+\frac{43}{3}+7\left(\frac{19}{\sigma^4}+\frac{40}{\sigma^2}-29-2\sigma^2\right)L\right.\\&\left.-\frac{14}{\sigma}\left(\frac{1}{\sigma^2}+3\right)\left(\frac{13}{\sigma^2}+1\right)\tan^{-1}\sigma\right\}\Bigg].\end{aligned} \tag{5.9}$$

Further, it is permissible to put $\sigma^2=1$, or $\mu t=0$, in these results, because from the beginning the terms multiplied by factors $(\overline{\zeta}-\zeta)^n$ have been neglected, $\overline{\zeta}-\zeta$ being of $O(\mu t)$ at the boundary surface (cf. Ref. 4). Thus, from (5.5), (5.6), and (5.7),

$$\left.\begin{aligned}&q_2=2-\frac{1}{\sin^2\theta},\quad q_3=\frac{32}{3}-\frac{16}{\sin^2\theta}+\frac{7\pi}{2\sin^3\theta},\\&q_4\to\frac{224}{3}-\frac{581}{2\sin^2\theta}+\frac{98\pi}{\sin^3\theta}+\frac{149}{2\sin^4\theta}+\frac{98}{\sin^4\theta}\cos\theta\log\cot\frac{\theta}{2}\\&\quad+\left(\frac{98}{\sin^4\theta}-\frac{49}{\sin^2\theta}\right)\log\mu t,\end{aligned}\right\} \tag{5.10}$$

and from (5.9),

$$q\left(1,\ \frac{\pi}{2}\right)=1+\frac{t}{\mu}\left[1+\frac{1}{8}\frac{\nu t}{\mu}+\frac{1}{64}\left(\frac{\nu t}{\mu}\right)^2\left(\frac{7}{2}\pi-\frac{16}{3}\right)-\frac{1}{1024}\left(\frac{\nu t}{\mu}\right)^3\left(\frac{848}{3}-196\pi+98\log\frac{1}{\mu t}\right)\right]. \tag{5.11}$$

These expressions are nothing other than the results based upon the transonic similarity law extended by Imai. It should be noticed, however, that q_4 has logarithmic singularity for $\sigma=\pm 1$, and consequently (5.10) and (5.11) seem to be inconsistent with the results expected from the transonic similarity law.

§ 6. Results due to the Complete Thin-Wing-Expansion Method

The exact treatment of the two-dimensional compressible flow by means of the complete thin-wing-expansion method is, in general, much more tedious than by means of the transonic thin-wing-expansion method. For comparison, however, it is worth while to reinvestigate the the same problem by the complete method. In this section, instead of following the course of the calculation, only the results corresponding to equations (5.9), (5.10), and (5.11) will be given in the following (see Appendix II):

Velocity at the mid-chord point ($\theta=\pi/2$)——

$$\begin{aligned}Q\left(\frac{\pi}{2}\right)=1&+\frac{t}{\mu}+\frac{t^2}{\mu^2}D+2\frac{t^3}{\mu^3}\left[B'+\left(C'+\frac{D^2}{2}\right)\left\{\frac{2}{\sigma^3}\tan^{-1}\sigma-\frac{1}{\sigma^2}-\left(\frac{1}{\sigma^2}-1\right)L\right\}\right]\\&-\frac{t^4}{\mu^4}\Bigg[\frac{1}{\sigma^4}\left(\frac{K_1}{2}+3K_2\right)+\frac{1}{\sigma^2}(K_1+14K_2)+(3K_1-2K_3+2K_4-D^3)\\&+\left\{\frac{1}{\sigma^4}\left(9K_2-\frac{K_1}{2}\right)+\frac{1}{\sigma^2}(K_1+18K_2)-\left(15K_2-\frac{7}{2}K_1\right)-2\sigma^2K_1\right\}L\\&-\frac{2}{\sigma}\tan^{-1}\sigma\left\{\frac{6}{\sigma^4}K_2+\frac{1}{\sigma^2}(K_1+18K_2)+3K_1\right\}\\&-\frac{1}{2}M^2\kappa\left(C'+\frac{1}{2}D^2\right)\Bigg\{\left(\frac{7}{8\sigma^6}-\frac{1}{3\sigma^4}-\frac{11}{24\sigma^2}-\frac{2}{3}\right)+(1-\sigma^2)\Bigg(\frac{13}{8\sigma^6}+\frac{13}{8\sigma^4}\\&+\frac{11}{8\sigma^2}-\frac{5}{8}\Bigg)L-(1-\sigma^2)\left(\frac{5}{2\sigma^6}+\frac{3}{\sigma^4}+\frac{5}{2\sigma^2}\right)\frac{\tan^{-1}\sigma}{\sigma}\Bigg\}\Bigg].\end{aligned} \tag{6.1}$$

Full expression expanded in powers of t——

$$\begin{aligned}Q_t(\theta)=1&+\frac{t}{\mu}+t^2\left\{2\frac{D}{\mu^2}\left(1-\frac{1}{2\sin^2\theta}\right)-\frac{1}{2}\cot^2\theta\right\}+t^3\Bigg[\frac{4}{\mu^3}\Bigg\{2B'\left(1-\frac{3}{4\sin^2\theta}\right)\\&-D^2\cot^2\theta+2\left(C'+\frac{D^2}{2}\right)\left(-\frac{1}{4\sin^2\theta}+\frac{\pi}{8\sin^3\theta}\right)\Bigg\}-\frac{1}{\mu}\left(\frac{1}{2}+2D\right)\cot^2\theta\Bigg]\\&+t^4\Bigg[\frac{1}{\mu^4}\Bigg\{16K_3-\left(\frac{7}{2}K_1+25K_2+16K_3+4K_4\right)\frac{1}{\sin^2\theta}+(-K_1+8K_2+2K_3\\&+2K_4+D^3)\frac{1}{\sin^4\theta}+(K_1+6K_2)\left(\frac{2\pi}{\sin^3\theta}+\frac{2\cos\theta}{\sin^4\theta}\log\cot\frac{\theta}{2}\right)\\&+\frac{7}{24}M^2\kappa\left(C'+\frac{1}{2}D^2\right)\left(\frac{1}{\sin^2\theta}-\frac{2}{\sin^4\theta}\right)\Bigg\}+\frac{4}{\mu^2}\Bigg\{-4B'\cot^2\theta\left(1-\frac{1}{4\sin^2\theta}\right)\\&-D^2\cot^2\theta\left(2-\frac{1}{\sin^2\theta}\right)+\left(C'+\frac{D^2}{2}\right)\Bigg(-\frac{1}{\sin^2\theta}-\frac{1}{2\sin^4\theta}+\frac{3\pi}{4\sin^3\theta}\\&+\frac{\cos\theta}{\sin^4\theta}\log\cot\frac{\theta}{2}\Bigg)+\frac{D}{2}\left(\frac{3}{2}-M^2\right)\left(\frac{1}{2\sin^2\theta}-1\right)\cot^2\theta\\&+\frac{1}{3}M^2\kappa D\left(1-\frac{1}{4\sin^2\theta}\right)\cot^2\theta\Bigg\}+\frac{3}{8}\cot^4\theta\Bigg]\\&+t^4\log\mu t\left\{\frac{1}{\mu^4}(\mathrm{K}_1+6K_2)+\frac{2}{\mu^2}\left(C'+\frac{D^2}{2}\right)\right\}\left(\frac{2}{\sin^4\theta}-\frac{1}{\sin^2\theta}\right),\end{aligned} \tag{6.2}$$

whence, putting $\theta=\pi/2$, we have

$$Q_t\left(\frac{\pi}{2}\right)=1+\frac{t}{\mu}+\frac{t^2}{\mu^2}D+2\frac{t^3}{\mu^3}\left\{B'+\left(C'+\frac{D^2}{2}\right)\left(\frac{\pi}{2}-1\right)\right\}$$
$$-\frac{t^4}{\mu^4}\left[\left\{K_1+6K_2+2\mu^2\left(C'+\frac{D^2}{2}\right)\right\}\log\frac{1}{\mu t}-6\mu^2\left(C'+\frac{D^2}{2}\right)\left(\frac{\pi}{2}-1\right)\right.$$
$$\left.-\left(2\pi-\frac{9}{2}\right)K_1-(12\pi-17)K_2-2K_3+2K_4-D^3+\frac{7}{24}M^2\kappa\left(C'+\frac{D^2}{2}\right)\right], \tag{6.3}$$

where

$$\left.\begin{aligned}&K_1=D\left(C'+\frac{D^2}{2}\right), \quad K_2=\frac{1}{3}F'+\frac{1}{2}B'D+\frac{1}{2}C'D-\frac{1}{4}D^3,\\&K_3=\frac{1}{4}E'+\frac{5}{2}B'D+\frac{1}{2}D^3, \quad K_4=3B'D+D^3.\end{aligned}\right\} \tag{6.4}$$

The other constants B', C', D, E', F', and κ involved in the above expressions are given in Appendix I. Table V lists these values in the case of high subsonic air flow ($\gamma=1.4$).

If only the highest powers of $1/\mu$ are retained in each of the third and the fourth order perturbations, equations (6.1), (6.2), and (6.3) are respectively in accord with equations (5.9), (5.10), and (5.11), as was discussed for the flow past a Kaplan bump (cf. Ref. 4). The full expression in terms of σ, which corresponds to (5.4), is shown in Appendix II. It should be mentioned that (II-1) proves to be transformed into the expression for the velocity distribution of a parabolic cylinder by suitable limiting process[8].

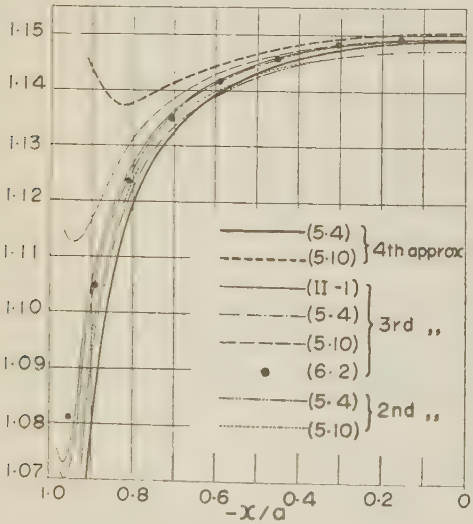

Fig. 1. The chordwise velocity distribution for an elliptic cylinder of thickness ratio 0.1, when free stream Mach number $M=0.7$.

§7. Numerical Discussions

Numerical calculations are now made for the velocity distributions (5.4) and (5.10); in particular, the results for $M=0.7$ and 0.8 with $t=0.1$ are shown in Fig. 1 and 2 respectively, and the corresponding values in Table I. In order to assess the accuracy of the transonic thin-wing-expansion method and of the derivable similarity approximation, the third approximations that were calculated from equations (II-1) and (6.2) by Hasimoto are also plotted in these figures. Then it is found that the exact equation (5.4) obtained from equation (2.3) yields satisfactory results over

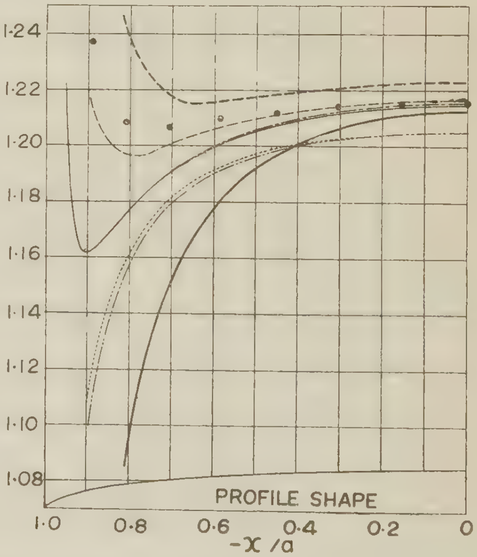

Fig. 2. The chordwise velocity distribution for an elliptic cylinder of thickness ratio 0.1, when free stream Mach number $M=0.8$.

Table I. The velocity distribution at the surface of an elliptic cylinder of $t=0.1$ for $M=0.7$ (*top*) and 0.8 (*bottom*).

θ (deg.)	2nd approx.		3rd approx.			4th approx.	
	(5.4)	(5.10)	(II−1)*	(5.4)	(5.10)	(5.4)	(5.10)
0	0.0000	$-\infty$	0.0000	0.0000	$+\infty$	0.0000	$+\infty$
4.5	0.2337	——	1.9431	1.9953	——	−5.2012	——
9	0.7268	0.7151	1.1484	1.1528	1.4871	0.1649	——
18	1.0218	1.0283	1.0749	1.0711	1.1127	0.9340	1.2707
27	1.0939	1.0975	1.1067	1.1047	1.1178	1.0837	1.1435
36	1.1207	1.1227	1.1254	1.1244	1.1302	1.1167	1.1374
45	1.1333	1.1344	1.1359	1.1354	1.1384	1.1318	1.1412
54	1.1400	1.1406	1.1420	1.1418	1.1435	1.1400	1.1450
63	1.1439	1.1442	1.1458	1.1457	1.1466	1.1448	1.1477
72	1.1461	1.1462	1.1480	1.1480	1.1486	1.1475	1.1495
81	1.1472	1.1473	1.1492	1.1492	1.1496	1.1490	1.1504
90	1.1476	1.1476	1.1495	1.1496	1.1499	1.1494	1.1507
0	0.0000	$-\infty$	0.0000	0.0000	$+\infty$	0.0000	$+\infty$
4.5	−0.5705	——	9.0849	9.6868	——	−79.636	——
9	0.3936	0.3828	2.4505	2.6006	4.1993	−8.6545	——
18	0.9519	0.9663	1.1946	1.2044	1.3838	0.1851	2.5950
27	1.0859	1.0934	1.1423	1.1424	1.1939	0.8977	1.3735
36	1.1355	1.1395	1.1556	1.1552	1.1766	1.0657	1.2230
45	1.1587	1.1609	1.1699	1.1698	1.1806	1.1292	1.1982
54	1.1711	1.1723	1.1801	1.1804	1.1864	1.1599	1.1961
63	1.1782	1.1787	1.1869	1.1875	1.1910	1.1766	1.1983
72	1.1822	1.1825	1.1912	1.1920	1.1941	1.1860	1.2008
81	1.1844	1.1844	1.1935	1.1944	1.1959	1.1908	1.2024
90	1.1850	1.1850	1.1943	1.1952	1.1965	1.1924	1.2029

* The values listed in this column are not in accord with Hasimoto's[1]), perhaps owing to his coarse calculation.

Table II. The velocity at the mid-chord point as a function of M, for an elliptic cylinder of $t=0.1$.

M	1st approx.	2nd approx.	3rd approx.			4th approx.		
			(6.1)	(5.9)	(6.3)	(6.1)	(5.9)	(6.3)
0.50	1.1155	1.1175	1.1177	1.1176	1.1177	1.1177	1.1176	1.1177
0.55	1.1197	1.1225	1.1228	1.1228	1.1229	1.1228	1.1228	1.1229
0.60	1.1250	1.1288	1.1293	1.1293	1.1295	1.1293	1.1293	1.1295
0.65	1.1316	1.1369	1.1379	1.1379	1.1381	1.1378	1.1378	1.1382
0.70	1.1400	1.1476	1.1495	1.1496	1.1498	1.1493	1.1494	1.1503
0.75	1.1512	1.1626	1.1665	1.1668	1.1671	1.1658	1.1662	1.1684
0.80	1.1667	1.1850	1.1943	1.1952	1.1955	1.1915	1.1924	1.1996
0.85	1.1898	1.2232	1.2502	1.2529	1.2535	1.2293	1.2363	1.2685
0.90	1.2294	1.3053	1.4238	1.4337	1.4365	1.2583	1.2587	1.5049

the greater part of the surface, whereas the calculated values for equation (5.10) obtained by assuming $\mu t=0$ deviate seriously from those for equation (II–1) near the end of the profile, rather having the tendency analogous to equation (6.2). Further, in the fourth ap-

Table III. The velocity at the mid-chord point, as a function of M, for an elliptic cylinder of $t=0.05$, calculated by use of equation (6.3).

M	1st approx.	2nd approx.	3rd approx.	4th approx.
0.50	1.0577	1.0582	1.0583	1.0583
0.55	1.0599	1.0606	1.0606	1.0606
0.60	1.0625	1.0634	1.0635	1.0635
0.65	1.0658	1.0671	1.0673	1.0673
0.70	1.0700	1.0719	1.0722	1.0722
0.75	1.0756	1.0784	1.0790	1.0790
0.80	1.0833	1.0879	1.0892	1.0891
0.85	1.0949	1.1033	1.1070	1.1060
0.90	1.1147	1.1337	1.1501	1.1386

Table IV. The coefficients of t, t^2, t^3, t^4, and $t^4 \log t$ in equation (6.3); $Q_t(\pi/2)=1+a_1t+a_2t^2+a_3t^3+(a_4+a_4' \log t)t^4$.

M	a_1	a_2	a_3	a_4	a_4'
0.50	1.154701	0.200000	0.254991	1.6788	0.6907
0.55	1.197369	0.273272	0.413380	3.1932	1.2657
0.60	1.250000	0.376172	0.690182	6.3778	2.4497
0.65	1.315903	0.526373	1.203032	13.6158	5.1038
0.70	1.400280	0.757324	2.230315	31.8485	11.7497
0.75	1.511858	1.138776	4.521341	84.7268	31.0835
0.80	1.666667	1.837037	10.48827	272.621	100.775
0.85	1.898316	3.335427	30.28249	1189.276	451.193
0.90	2.294157	7.583934	131.2595	9071.91	3642.992

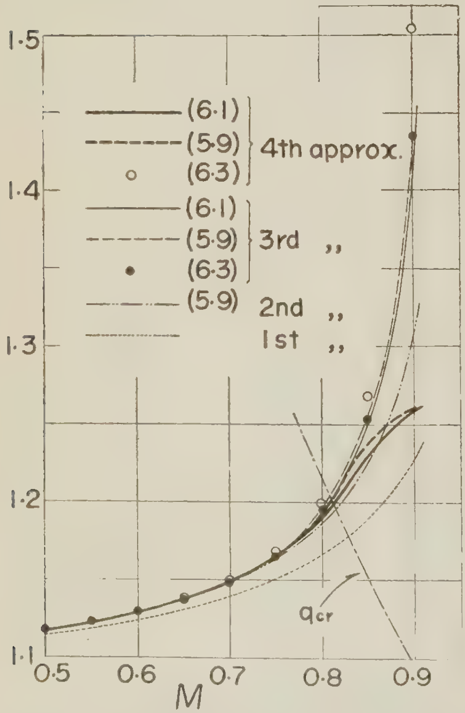

Fig. 3. The mid-chord velocity for an elliptic cylinder of thickness ratio 0.1.

proximation this deviation becomes more conspicuous, and the fourth order perturbation proves negative for equation (5.4), but positive for equation (5.10).

The situation can be more clarified if we examine the velocity at the mid-chord point as a function of the free stream Mach number. Fig. 3 and Table II give this relation for $t=0.1$; then it can be concluded that the results due to the transonic thin-wing-expansion method well approximate those due to the complete thin-wing-expansion method provided that the expressions in terms of σ are used, and that the results obtained as a series expansion of t seem inadequate in the fourth approximation owing to too large a value of t. In addition Fig. 4 and Table III show the variation of the mid-chord velocity $Q_t(\pi/2)$ calculated by means of Table IV for $t=0.05$; the fourth approximation now appears below the third approximation.

At any rate, neither of our results enables us to obtain the flow velocity near the stagnation point, since the series expansion based upon the assumption of small perturbation

Table V. The main constants used in the complete thin-wing-expansion method.

M	κ	D	A'	B'	C'	E'	F'
0.50	0.200000	0.150000	0.003333	0.013958	0.109375	0.016688	0.064453
0.55	0.260215	0.190608	0.006529	0.022755	0.152906	0.034875	0.116830
0.60	0.337500	0.240750	0.012416	0.036731	0.216213	0.071872	0.213445
0.65	0.438961	0.303981	0.023236	0.059408	0.312200	0.148708	0.399111
0.70	0.576471	0.386235	0.043423	0.097621	0.465943	0.315437	0.778278
0.75	0.771429	0.498214	0.082524	0.166016	0.731142	0.705264	1.624350
0.80	1.066667	0.661333	0.163840	0.300525	1.239296	1.733659	3.778785
0.85	1.562162	0.925581	0.356304	0.608716	2.382923	5.048871	10.542962
0.90	2.557895	1.440947	0.942167	1.538164	5.789546	20.49906	41.45739

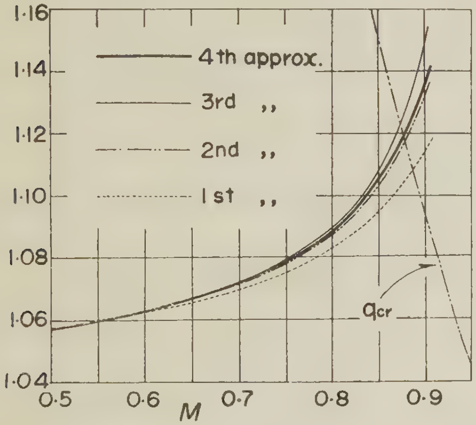

Fig. 4. The mid-chord velocity for an elliptic cylinder of thickness ratio 0.05, calculated by the use of equation (6.3).

diverges there even before sonic speed is reached at the mid-chord point. To investigate stagnation condition we must call for quite different approaches.

Acknowledgements

The author would like to express his sincere thanks to Professor Isao Imai for his continual guidance and encouragement throughout the the present work. The author's thanks are also due to Professor Saburô Asaka, Dr. M. Kawaguti, Dr. H. Hasimoto, and Mr. H. Takami for their advice and discussions in the course of the calculation and during the preparation of this paper.

References

1) H. Hasimoto: Jour. Phys. Soc. Japan **7** (1952) 322.
2) I. Imai: Read at the 8th International Congress on Theoretical and Applied Mechanics.
3) I. Imai: Jour. Phys. Soc. Japan **9** (1954) 103.
4) Y. Matunobu: Jour. Phys. Soc. Japan **11** (1956) 452.
5) Y. Matunobu: Jour. Phys. Soc. Japan **10** (1955) 814.
6) S. Asaka: Natural Science Report, Ochanomizu Univ. **4** (1953) 213, and **5** (1954) 59.
7) S. Asaka: Jour. Phys. Soc. Japan **10** (1955) 482.
8) Y. Matunobu: Read at the 9th annual meeting of the Phys. Soc. Japan, Ôsaka (1954).
9) C. Kaplan: N.A.C.A. Tech. Note. No. 3318 (1955).
10) G. N. Ward: Linearized Theory of Steady High-Speed Flow. Cambridge Univ. Press, (1955) 17.
11) I. Imai & S. Ôyama: Rep. Inst. Sci. & Tech. Univ. Tokyo **2** (1948) 37.

Appendix I

Formulae of the Complete Thin-Wing-Expansion Method

The complete thin-wing-expansion method has already been formulated up to the third approximation by Imai in collaboration with Ôyama[11]. The expressions discribed in §6, however, have been derived from slightly different formulation in that solutions can be obtained in an expansion series in powers of $\bar{\zeta}-\zeta$. In the following the formulae including the fourth order correction will be given in a form ready for general application.

Now the $G_n(\zeta, \bar{\zeta})$ are differently defined as (cf. §2)

$$\left.\begin{aligned} \Phi &= x+\phi_1+\phi_2+\cdots, \\ \Psi &= y+\psi_1+\psi_2+\cdots, \\ G_n &= \phi_n+i\psi_n/\mu, \end{aligned}\right\} \qquad \text{(I-1)}$$

where the suffixes n denote the order of magnitude ε^n, ε being a constant of $O(t)$. Then it follows that

$$G_1=f(\zeta)\,, \tag{I-2}$$

$$G_2=\frac{M^2}{4}\left\{\kappa(\bar\zeta-\zeta)f'^2+(1+\kappa)\left(2f'\bar f+\int\bar f'^2d\bar\zeta\right)\right\}+g_2(\zeta)\,, \tag{I-3}$$

$$\begin{aligned}G_3=&\frac{M^4}{8}\kappa^2(\bar\zeta-\zeta)^2f'^2f''+(\bar\zeta-\zeta)\left\{A'f'^3+\frac{M^2}{2}\kappa f'g_2'+\frac{M^2}{12}\kappa D(6f'f''\bar f\right.\\&\left.-3f'\bar f'^2-2\bar f'^3)\right\}+3B'f'^2\bar f+\frac{D^2}{2}(2ff'\bar f'+f''\bar f^2+f\bar f'^2)+C'f'\int\bar f'^2d\bar\zeta\\&+B'\int\bar f'^3d\bar\zeta+D\left(f'\bar g_2+g_2'\bar f+\int\bar f'\bar g_2'\,d\bar\zeta\right)+g_3(\zeta)\,,\end{aligned} \tag{I-4}$$

$$\begin{aligned}G_4=&\frac{M^6}{48}\kappa^3(\bar\zeta-\zeta)^3(f'^3f'')'+(\bar\zeta-\zeta)^2\left[\frac{M^4}{8}\kappa^2D\{(f'^2f'')'\bar f-f'f''\bar f'^2+f'\bar f'^2\bar f''+\bar f'^3\bar f''\}\right.\\&\left.+\frac{3}{2}M^2\kappa A'f'^3f''+\frac{M^4}{8}\kappa^2(f'^2g_2')'\right]+(\bar\zeta-\zeta)\left[H'f'^4+3A'f'^2g_2'+\frac{M^2}{4}\kappa(g_2'^2+2f'g_3')\right.\\&+3(DA'+M^2\kappa B')f'^2f''\bar f+\frac{M^2}{2}\kappa D\{(f'g_2')'\bar f+f'f''\bar g_2-\frac{1}{2}g_2'\bar f'^2-f'\bar f'\bar g_2'-\bar f'^2\bar g_2'\}\\&+\frac{M^2}{4}\kappa D^2\{(ff'^2)'\bar f'+(f'f'')'\bar f^2-2ff'\bar f'\bar f''-f''\bar f\bar f'^2-2f\bar f'^2\bar f''\}+\frac{M^2}{2}\kappa C'f'f''\int\bar f'^2d\bar\zeta\\&\left.-\frac{M^2}{8}\kappa(6B'-D^2)f'^2\bar f'^2-\left(DA'+\frac{M^2}{3}\kappa C'\right)f'\bar f'^3-\frac{3}{8}(2DA'+M^2\kappa B')\bar f'^4\right]\\&+(E'f'^3+6B'f'g_2'+Dg_3')\bar f+D\left\{3B'ff'^2+C'f'\int f'^2d\zeta+D(fg_2)'\right\}\bar f'+\frac{D^3}{2}f^2f'\bar f''\\&+D\left(6B'f'f''+\frac{D}{2}g_2''\right)\bar f^2+(F'f'^2+C'g_2')\int\bar f'^2d\bar\zeta+D^3(ff')'\bar f\bar f'+(3B'f'^2+Dg_2')\bar g_2\\&+D\left\{(3B'+C')ff'+\frac{C'}{2}\int f'^2d\zeta+\frac{D}{2}g_2\right\}\bar f'^2+D^2(ff'\bar g_2'+f''\bar f\bar g_2+f\bar f'\bar g_2')\\&+\frac{D^3}{2}\left(f^2\bar f'\bar f''+\frac{1}{3}f'''\bar f^3+f\bar f\bar f'^2\right)+C'Df''\bar f\int\bar f'^2d\bar\zeta+\frac{2}{3}F'f'\int\bar f'^3d\bar\zeta\\&-2C'f'\int\bar f'\bar g_2'd\bar\zeta+3B'Df\bar f'^3+\frac{1}{8}(2E'-D^3)\int\bar f'^4d\bar\zeta+3B'\int\bar f'^2\bar g_2'd\bar\zeta\\&+D\left(f'\bar g_3+\frac{1}{2}\int\bar g_2'^2d\bar\zeta+\int\bar f'\bar g_3'd\bar\zeta\right)+g_4(\zeta)\,.\end{aligned} \tag{I-5}$$

where

$$\left.\begin{aligned}&\kappa=\frac{\gamma+1}{4}\frac{M^2}{\mu^2}\,, && D=\frac{M^2}{2}(1+\kappa)=\frac{\nu}{8}\,;\\&A'=A+\frac{M^4}{8}\kappa(2+\kappa)\,, && A=-\frac{M^6}{96\mu^2}(1+\gamma)(3-2\gamma)\,;\\&B'=B+\frac{M^4}{24}(1+\kappa)(3+5\kappa)\,, && B=\frac{M^4}{96\mu^2}\{6(\gamma-1)-(2\gamma-1)(3-\gamma)M^2\}\,;\\&C'=C+\frac{M^4}{8}(5+10\kappa+6\kappa^2)\,, && C=\frac{M^2}{32\mu^2}\{8-8(3-\gamma)M^2+(13-9\gamma+2\gamma^2)M^4\}\,;\\&E'=E+3DA+\frac{M^2}{2}(10+7\kappa)B+M^2\kappa C+\frac{M^6}{48}(18+89\kappa+118\kappa^2+50\kappa^3)\,,\\&E=-\frac{M^6}{192\mu^2}(2-\gamma)\{16\gamma-(3+13\gamma-6\gamma^2)M^2\}\,;\end{aligned}\right\} \tag{I-6*}$$

---

* The unprimed constants A, B, C, and D were used as such in Ref. 11.

$$\left.\begin{aligned}
F' &= F+\frac{3}{4}M^2\kappa A+\frac{3}{4}M^2(7+10\kappa)B+\frac{M^2}{4}(9+8\kappa)C+\frac{M^6}{32}(39+130\kappa+157\kappa^2+65\kappa^3)\,,\\
F &= -\frac{3M^4}{128\mu^2}(2-\gamma)\{8-8(2-\gamma)M^2+(7-7\gamma+2\gamma^2)M^4\};\\
H' &= H+\frac{5}{4}M^2A+\frac{5}{4}M^2\kappa B+\frac{M^6\kappa}{192}(53+61\kappa+23\kappa^2)\,,\\
H &= -\frac{M^8}{256\mu^2}(2-\gamma)(1+\gamma)(2\gamma-1)\,;
\end{aligned}\right|$$

(f' and g_n' denote differentation with respect to ζ, and over-bars complex conjugate).

The arbitrary analytic functions f and g_n should be determined in compliance with the conditions that $\partial G/\partial\zeta$ be one-valued and regular in the flow field and that at the boundary surface $\mathrm{Im}\,(\mu^2 G+\zeta)=0$.

It is noticed that if we substitute 10/3, 12, 2, 200/3, and 130 for B', C', D, E', and F' respectively in the above expressions, we obtain the basic formula for the transonic thin-wing-expansion method (cf. Ref. 4).

Appendix II.

Full Expression in Terms of σ, Derived from the Complete Thin-Wing-Expansion Method

$$Q(\theta)=(1+t^2\cos^2\theta)^{-1/2}\left\{1+\frac{t}{\mu}+Q_2(\theta)+Q_3(\theta)+Q_4(\theta)\right\} \tag{II–1}$$

with

$$\begin{aligned}
Q_2(\theta) &= \frac{t^2}{\mu^2}D\left(\frac{1}{\sigma^2}+1\right)\left(1-\frac{1+\sigma^2}{\Theta}\right),\\
Q_3(\theta) &= \frac{t^3}{\mu^3}(1+\sigma^2)^2\Bigg[2B'\left\{\frac{1}{\sigma^4}-\left(\frac{2}{\sigma^4}+\frac{1}{\sigma^2}\right)\frac{1}{\Theta}+\frac{1}{\sigma^4}(1-\sigma^2)(1+\sigma^2)^2\frac{1}{\Theta^2}\right\}\\
&\quad+D^2\left\{\frac{1}{\sigma^4}-\frac{2}{\sigma^4}(1+\sigma^2)\frac{1}{\Theta}+\frac{1}{\sigma^4}(1-\sigma^2)(1+\sigma^2)^3\frac{1}{\Theta^2}\right\}+2\left(C'+\frac{D^2}{2}\right)\Bigg\{\frac{(1-\sigma^2)L-1}{\sigma^2}\frac{1}{\Theta}\\
&\quad-\frac{2L}{\sigma^2}(1-\sigma^2)(1+\sigma^2)^2\frac{1}{\Theta^2}+\frac{1}{2\sigma^5}\left[\frac{1+\sigma^4}{\Theta}-\frac{(1-\sigma^4)^2}{\Theta^2}\right]\tau+\frac{1}{\sigma^3}(1-\sigma^4)\frac{\lambda}{\Theta^2}\Bigg\}\Bigg]\\
&\quad-\frac{t^3}{\mu^3}\frac{(1+\sigma^2)^2(1-\sigma^2)}{6\sigma^6}M^2\kappa D\left\{1-\frac{3+2\sigma^2}{\Theta}+\frac{(1+\sigma^2)^2(3-2\sigma^2)}{\Theta^2}-\frac{(1+\sigma^2)^4(1-\sigma^2)^2}{\Theta^3}\right\},\\
Q_4(\theta) &= \frac{t^4}{\mu^4}(1+\sigma^2)^3\Bigg\{\alpha_0+\frac{\alpha_1}{\Theta}+\frac{\alpha_2}{\Theta^2}+\frac{\alpha_3}{\Theta^3}+\frac{\alpha_4}{\Theta^4}+\frac{\alpha_5}{\Theta^5}\\
&\quad+\left(\frac{\beta_1}{\Theta}+\frac{\beta_2}{\Theta^2}+\frac{\beta_3}{\Theta^3}+\frac{\beta_4}{\Theta^4}\right)\tau(\theta)+\left(\frac{\gamma_2}{\Theta^2}+\frac{\gamma_3}{\Theta^3}+\frac{\gamma_4}{\Theta^4}\right)\lambda(\theta)\Bigg\},
\end{aligned}$$

where

$$\begin{aligned}
\alpha_0 &= \frac{2}{\sigma^6}K_3-\frac{1-\sigma^2}{2\sigma^8}N_2+\frac{(1-\sigma^2)^2}{\sigma^{10}}N_4\,,\\
\alpha_1 &= -\frac{6}{\sigma^6}K_3-\frac{1}{\sigma^4}(K_1+12K_2+2K_3+2K_4)-\frac{K_1}{\sigma^2}+\left\{\frac{1}{\sigma^4}\left(\frac{K_1}{2}+15K_2\right)-\frac{1}{\sigma^2}\left(9K_2-\frac{K_1}{2}\right)\right\}L\\
&\quad-\frac{1}{1+\sigma^2}\left\{\frac{1}{\sigma^4}\left(3K_2-\frac{1}{2}K_1\right)-\frac{1}{\sigma^2}(2K_2-K_1)-K_1\right\}+(1-\sigma^2)\Bigg[\frac{2}{\sigma^8}N_2+\frac{1}{\sigma^2}\left(\frac{N_1}{2}+N_2\right)\\
&\quad+\left\{-\left(\frac{25}{8\sigma^6}-\frac{1}{\sigma^4}-\frac{1}{8\sigma^2}\right)L+\frac{1}{1-\sigma^4}\left(\frac{25}{8\sigma^6}-\frac{1}{3\sigma^4}-\frac{53}{24\sigma^2}\right)\right\}N_3\Bigg]-\frac{1}{\sigma^{10}}(1-\sigma^2)^2(5+3\sigma^2)N_4\,,\\
\alpha_2 &= 2(1+\sigma^2)\Bigg[\frac{3}{\sigma^6}K_3+\frac{1}{\sigma^4}(6K_2-K_3+2K_1)-\frac{1}{\sigma^2}\left(-K_1+2K_2+K_3+K_4-\frac{D^3}{2}\right)-\left(\frac{3}{2}K_1+\frac{D^3}{2}\right)
\end{aligned}$$

$$+\frac{\sigma^2}{2}D^3+\left\{-\frac{24}{\sigma^4}K_2+\frac{1}{\sigma^2}(12K_2-5K_1)+6K_1-3\sigma^2K_1\right\}L\Bigg]$$

$$-(1-\sigma^4)\left[\frac{3}{\sigma^8}N_2+\frac{3}{2\sigma^6}N_1-\frac{1}{\sigma^4}\left(\frac{N_1}{2}+N_2\right)-\left\{\frac{1}{4}\left(\frac{55}{\sigma^6}-\frac{13}{\sigma^4}-\frac{3}{\sigma^2}-7\right)L\right.\right.$$

$$\left.\left.-\frac{1}{1-\sigma^2}\left(\frac{21}{4\sigma^6}-\frac{20}{3\sigma^4}+\frac{31}{12\sigma^2}\right)\right\}N_3\right]+\frac{1}{\sigma^{10}}(1+\sigma^2)(1-\sigma^2)^2(10+2\sigma^2-3\sigma^4)N_4\,,$$

$$\alpha_3=(1+\sigma^2)^3(1-\sigma^2)^2\left[-\frac{2}{\sigma^6}K_3-\frac{2}{\sigma^4}K_4-\frac{D^3}{\sigma^2}+8\left(\frac{3}{\sigma^4}K_2+\frac{K_1}{\sigma^2}\right)L+\frac{2}{\sigma^8}N_2\right.$$

$$+\frac{1}{\sigma^6}\left(\frac{3}{2}N_1-N_2\right)-\left(\frac{1}{\sigma^4}-\frac{1}{2\sigma^2}\right)N_1+\left\{-\left(\frac{15}{\sigma^6}-\frac{10}{\sigma^4}+\frac{7}{\sigma^2}\right)L+\frac{3}{\sigma^6}-\frac{2}{3\sigma^4}\right\}N_3$$

$$\left.-\frac{1}{\sigma^{10}}(10-12\sigma^2+3\sigma^4)N_4\right],$$

$$\alpha_4=(1+\sigma^2)^5(1-\sigma^2)^4\left[-\frac{1}{2}\left(\frac{N_2}{\sigma^8}+\frac{N_1}{\sigma^8}\right)+\frac{6}{\sigma^6}LN_3+\frac{1}{\sigma^{10}}(5-3\sigma^2+\sigma^4)N_4\right],$$

$$\alpha_5=-\frac{1}{\sigma^{10}}(1+\sigma^2)^7(1-\sigma^2)^6N_4\,,$$

$$\beta_1=\frac{1}{\sigma}\left\{\frac{9}{\sigma^6}K_2+\frac{3}{2\sigma^4}K_1+\frac{1}{\sigma^2}(K_1+3K_2)-\frac{K_1}{2}\right\}-\frac{1-\sigma^2}{8\sigma}\left(\frac{17}{\sigma^8}+\frac{5}{\sigma^6}+\frac{5}{\sigma^4}+\frac{1}{\sigma^2}\right)N_3\,,$$

$$\beta_2=-\frac{1-\sigma^4}{\sigma}\left\{\frac{15}{\sigma^6}K_2+\frac{7}{2\sigma^4}K_1+\frac{1}{\sigma^2}(3K_2-K_1)+\frac{5}{2}K_1-\left(\frac{41}{8\sigma^8}-\frac{5}{2\sigma^6}-\frac{1}{4\sigma^4}-\frac{1}{2\sigma^2}+\frac{9}{8}\right)N_3\right\},$$

$$\beta_3=\frac{(1-\sigma^4)^3}{\sigma^5}\left\{\frac{6}{\sigma^2}K_2+2K_1-\left(\frac{9}{2\sigma^4}-\frac{1}{\sigma^2}+\frac{5}{2}\right)N_3\right\},$$

$$\beta_4=\frac{3}{2\sigma^9}(1-\sigma^4)^5N_3\,,$$

$$\gamma_2=\frac{2}{\sigma}\left\{\frac{9}{\sigma^4}K_2+\frac{3}{2\sigma^2}K_1-(K_1+3K_2)+\frac{\sigma^2}{2}K_1\right\}-\frac{1-\sigma^2}{4\sigma}\left(\frac{17}{\sigma^6}+\frac{5}{\sigma^4}-\frac{5}{\sigma^2}-1\right)N_3\,,$$

$$\gamma_3=-\frac{4}{\sigma^3}(1-\sigma^4)^2\left(\frac{3}{\sigma^2}K_2+K_2\right)+\frac{2(1-\sigma^4)^2}{\sigma^3}\left(\frac{3}{\sigma^4}-\frac{1}{\sigma^2}+1\right)N_3\,,$$

$$\gamma_4=-\frac{3}{\sigma^7}(1-\sigma^4)^4N_3;$$

$$N_1=M^2\kappa D^2\,,\qquad N_2=\frac{5}{6}N_1+A'D+\frac{3}{2}M^2\kappa B'\,,\qquad N_3=\frac{1}{2}M^2\kappa\left(C'+\frac{1}{2}D^2\right),$$

$$N_4=\frac{1}{16}M^4\kappa^2D\,.$$

Erratum

Application of Imai's Transonic Approximation Method to the Compressible Flow past a Kaplan Bump

By Yaso'o MATUNOBU

J. Phys. Soc. Japan **11** (1956) 458

Eq. (2.15) $4ff'^2\bar{f}''$ should be read $4f^2f'\bar{f}''$

JOURNAL OF THE PHYSICAL SOCIETY OF JAPAN Vol. 12, No. 1, JANUARY, 1957

Phenomenological Theory of the Molecular Absorption and Dispersion of Sound in Fluids and the Relation between the Relaxation Time of the Internal Energy and the Relaxation Time of the Internal Specific Heat*

By Otohiko NOMOTO

Kobayasi Institute of Physical Research,
Kokubunzi Tokyo

(Received March 7, 1956; Received in
amended from on September 3, 1956)

Molecular absorption and dispersion formulas applicable for both liquids and gases have been derived in a phenomenological manner. It was pointed out that the relaxation time of the molecular internal energy τ must be distinguished from the relaxation time of the internal specific heat β and the relation between these two quantities was discussed in detail. The relaxation time τ has the advantage of making the dispersion formula simpler and directly comparable with the dispersion formulas in other cases, such as the relaxation of shear viscosity. The relaxation time β on the other hand, is more closely related with the collision excitation probability of the molecules than τ.

§1. Introduction

Theoretical treatment of the phenomenon of the molecular absorption and dispersion of sound has been performed by Herzfeld and Rice¹⁾, Kneser²⁾, Bourgin³⁾ and many others. (cf. the books and monographs of Bergmann⁴⁾, Vigoureux⁵⁾, Richardson⁶⁾, Kudrijawzew⁷⁾, Hiedemann⁸⁾ and Nomoto⁹⁾, and the review articles of Kneser¹⁰⁾, Markham, Beyer and Lindsay¹¹⁾, Karim and Rosenhead¹²⁾, Petralia¹³⁾, Dubois¹⁴⁾, Sette¹⁵⁾ and Richardson¹⁶⁾ for detailed references.)

In the first place, we intend to perform a simple, phenomenological derivation of the absorption and dispersion formulas applicable for both gases and liquids. The method is similar to the one used by the present author¹⁷⁾ for deriving the absorption and dispersion formulas in gases (§2, 3). Also the second approximation formulas are derived (§6).

Secondly, we intend to clarify the relation between the relaxation time of the internal energy τ to be introduced in our derivation and the relaxation time of the internal specific heat β, more commonly used for describing the relaxation phenomenon in gases (§4). Recently, the apparent relaxation time β is being distinguished from the relaxation time β_1 of the lowest normal mode vibration for organic vapours (cf. Fogg, Hanks, Lambert²⁶⁾; Fogg and Lambert²⁷⁾). If the mechanism of vibrational activation is for the mode of lowest frequency to be activated directly with relaxation time β_1, and for the energy to spread very rapidly to the other modes, the whole dispersion phenomenon takes place with a single, apparent relaxation time $\beta=\beta_1(C_s/C_1)$, where C_s means the total vibrational specific heat, and C_1 the vibrational specific heat due to the lowest normal mode.

In these circumstances, however, the difference between β and τ cannot be also disregarded, and we have to consider the meanings of β and τ more closely. It becomes all the more important, because both β and τ are being used in liquids, and sometimes indiscriminately. The difference in magnitude of these two relaxation times is trivial as long as the simple gases are concerned. It becomes, however, of importance for gases and vapours consisting of more complex molecules, or for gases at high temperatures.

First we will consider of the present status of the research in this field and the relation of our theory to the existing ones briefly. Markham, Beyer and Lindsay¹¹⁾ have made an excellent analysis of the existing theories on acoustic relaxation phenomena and classified them into four groups: (a) the method of *kinetic theory* originating from the work of Jeans in 1904 and including the papers of Bourgin2) and Saxton, (b) the method of *irreversible thermodynamics* originating from the work of Herzfeld and Rice1) and including the works of Henry18), Eucken and Becker19), Hoff Lu20), Mandelstam and Leontovich, Damköhler21), Meixner22) and Eckart's unpublished lecture, (c) the method of *statistical thermodynamics* including the works of Kneser2),10), Markham, and Landau and Teller, this method also being applied to the systems in chemical equilibrium by Einstein, Luck, Kneser and Gauler, Hall, Ghosh and liebermann, and (d) the *phenomenological approach* as performed by Frenkel and Obrastzov. The equivalence of these various approaches is not always demonstrated, although many papers assume that the methods are essentially equivalent. For gases, however, it is known that the formulation based on statistical thermodynamics gives the same result as the one based on irreversible thermodynamics. Also the kinetic theory approach and the phenomenological approach leads to the same acoustical behaviour (cf. Markham, Beyer and Lindsay11)).

---

* The text in Japanese of this paper will be published in "Bulletin of the Kobayasi Institute of Physical Research".

A considerable number of theories on these subjects are summarized in Table I, classified into groups and indicating the main scopes or contents. The table is not complete, of course. Many of the earlier papers have been omitted and some of the more recent ones must have been missed. Also the classification may not be quite adequate in some cases; especially it seems difficult to classify some of the papers on reaction kinetics into one of these four groups because they use both the relaxation equation (=equation of irreversibility) and the reaction equation at the same time. In this case they have been included in group (I)–(c)–(ii), although they are also related to the group (I)–(b)–(ii). Other theories of rather general nature were classified as (II), while the above four groups (a), (b), (c) and (d) were classified as (I). Some papers of the group (I)–(a), those on translational dispersion, are strictly speaking not the relaxation theories, although they give dispersion and absorption of sound. They deal with the transport phenomena. These theories, however, are closely related with the relaxation theories. This may be said also of the hydrodynamical theory of translational dispersion included in group (I)–(d).

It is of course beyond the scope of this paper to discuss these points in any detail. It may suffice here to notice that our theory belongs to the method of the irreversible thermodynamics together with the previous ones17),24), although the thermodynamics enters into our relaxation equation not explicitly. This is also the case in many of the theories of this group, while there are also attempts to establish the relaxation theory on irreversible thermodynamics (Damköhler21), Meixner22), Eckart, etc.). Another attempt of more direct nature, to calculate the sound absorption directly from the amount of irreversible entropy production, have been described elsewhere25).

The present theory is a phenomenological one. In this form, however, it enables a more close comparison with the results of the phenomenological approach (group (I)–(d)) as well as with those of the method of statistical thermodynamics.

As the present paper is more closely related with the theory of Herzfeld and Rice1) and that of Henry18), we will begin with the comparison with these theories. Herzfeld and Rice derived the molecular absorption and dispersion formulas for the first time by the method of irreversible thermodynamics.

For an irreversible process the entropy increases with time, even for an isolated system, and we require a statement of its increase, the equation of irreversibility (named after Markham, Beyer and Lindsay11)). In general, however, this equation needs not contain the entropy explictly. The equation of irreversibility in Herzfeld-Rice's theory is

$$\frac{dT}{dt}=-\frac{1}{\tau_H}(T-T_i)\,, \tag{1.1}$$

where T_i means the temperature of the internal degrees of freedom of the molecules (=internal temperature) and T that of the external degrees of freedom (=external temperature), and τ_H (=τ, in Herzfeld's notation) the relaxation time. As the change in external temperature and that in internal temperature are related with

$$dE=C_{v\infty}dT=-C_i dT_i=-dE_i \tag{1.2}$$

in an adiabatic system, where $C_{v\infty}$ means the

Table I. Classification of acoustic relaxation theories

Authors	Main scopes or contents	References
(I)		
(a) **Kinetic theory**		
Jeans (1904)	rigid sphere molecules, rotational relaxation	"Dynamical theory of gases," 1st. ed. 302
Bourgin (1929–36)	molecular absorption and dispersion, gages	cf. Reference (3)
Saxton (1938)	molecular absorption and dispersion, gases, effect of heat conduction and viscosity	J. Chem. Phys. **6** 30, 168
Tsien and Schamberg (1946)	helium, translational dispersion	J. Acous. Soc. Amer. **18** 334
Wang Chang (1948)	helium, translational dispersion	Applied Physics Lab. Johns Hopkins Univ. Rep. CM–467, UMH–3–F
Truesdell (1952)	viscosity according to kinetic theory	Zeits. Phys. **131** 273
(b) **Irreversible thermodynamics theory**		
(i) *Molecular absorption*		
Herzfeld-Rice (1928)	low frequency absorption, dispersion, thermal relaxation, viscosity, heat conduction	Phys. Rev. **31** 691
Henry (1932)	absorption, dispersion, gases	Proc. Camb. Phil. Soc. **28** 77
Eucken-Becker (1934)	dispersion, gases, relaxation of internal specific heat	Zeits. Phys. Chem. **27B** 235
Nomoto (1940)	phenomenological theory, gases, mechanism of phase difference between pressure and density-wave	Proc.-Phys. Math. Soc. Japan **22** 77
Nomoto (1951)	non-ideal gas, phenomenological theory	Bull. Kobayasi Inst. Phys. Res. **1** 162
Beyer (1952)	Van der Weals gas, relaxation of the internal specific heat	J. Acous. Soc. Amer. **24** 714
Herzfeld (1941)	liquids, relaxation of internal specific heat	J. Acous. Soc. Amer. **13** 33
Herzfeld (1952)		J. Chem. Phys. **20** 288
Hoff Lu (1951)	liquids, relaxation of volume compression	J. Acous. Soc. Amer. **23** 12
Bauer (1949)	liquids,	Proc. Phys. Soc. **62A** 141
Nomoto (1957)	liquids and gases, relation between various relaxation times, phenomenological theory	present paper
Mandelstem-Leontovich (1937)	thermodynamical foundation	*J. exp. theor. phys. USSR **7** 438
Meixner (1948)	concept of the internal temperature	Zeits. Phys. **124** 129
Meixner (1952)	gases and liquids, with consideration of transport phenomena	Acustica **2** 101
De Groot (1952)	treatment based on irreversible thermodynamics	"Thermodynamics of irreversible processes" p. 51
Nomoto (1956)	irreversible entropy production	J. Phys. Soc. Japan, **11** 818
(ii) *Chemical systems*		
Damköhler (1942)	dissociating gases, connection with irreversible thermodynamics	Zeits. Elektrochem. **48** 62, 116
Meixner (1943)	chemical reaction, molecular absorption	Ann. Phys. **43** 470
Eckart	irreversible thermodynamics treatments	unpublished lecture (cited in (11))
Meixner (1952)	heat conduction in reactive mixtures	Zeits. Naturforsch. **7a** 553
Leontovich (1938)	ionic relaxation	J. exp. theor. phys. USSR **8** 40
Hall (1952)	ionic relaxation	J. Acous. Soc. Amer. **24** 704; **25** 799 (errata)

Table I. (continued)

Authors	Main scopes or contents	References
(iii) *Thermodynamic theory of the elastic relaxation*		
Sugita (1942)	thermodynamical foundation of Maxwell's equation	Proc. Phys..Math. Soc. Japan **25** 396
Sugita (1947)	thermodynamical foundation of Maxwell's equation	Kagaku **18** 173, 219
Sugita (1953)	ibid. effect of Brownian motion, generalization of Maxwell's equation	Busseiron Kenkyu, No. 66, p. 31; Bull. Kobayasi Inst. Phys. Res. **3** 93
Meixner (1951)	thermodynamic consideration of bulk viscosity	Colloquium over ultrasonore trillingen, Brussels. 107
Meixner (1954)	elastic relaxation	Zeits. Naturforsch. **9a** 654
Meixner (1954)	elastic after effect theory	Zeits. Phys. **139** 30
Meixner (1954)	after effect theory of elastic relaxation	Zeits. angew. Phys. **6** 215
Takizawa (1953)	thermal stresses in liquids	Mem. Fac. Engng. Nagoya Univ. **5** 1
Takizawa (1953)	heat transfer in supersonic fields	Mem. Fac. Engng. Nagoya Univ. **5** 27
Davies (1954)	second viscosity	Proc. Roy. Soc. **226A** 24
Oldroyd (1954)	hydrodynamic and thermodynamic pressure	Proc. Roy. Soc. **226A** 57
Davies-Jones (1953)	glasses, thermodynamic and kinetic properties	Phil. Mag. Supplement **2** 370-410
Davies-Jones (1953)	glasses, irreversible approach	Proc. Roy. Soc. **217A** 26
(c) **Statistical thermodynamics theory**		
(i) *Molecular absorption*		
Kneser (1931)	gases, dispersion	Ann. Phys. **11** 777; **12** 1015
Rutgers (1933)	gases, absorption	Ann. Phys. **16** 350
Kneser (1933)	gases, absorption, dispersion	Ann. Phys. **16** 337
Sakadi (1941)	gases, effect of heat conduction and viscosity on molecular absorption	Proc. Phys.-Math. Soc. Japan **23** 208
Richards (1933)	several energy levels, gases	J. Chem. Phys. **1** 863
Rose (1934)	three energy levels, gases	J. Chem. Phys. **2** 260
Landau-Teller (1936)	higher energy levels, harmonic oscillator	Phys. Zeits. Sowjet. **10** 34
Scaäfer (1940)	several energy levels, gases & mixtures	Zeifs. Phys. Chem. **46** 212
Tabuchi (1952, 1954)	several energy levels, gases	J. Chem. Soc. Japan **73** 5, 382 (1952); Mem. Sci. & Industr. Res. Osaka Univ. **9** 65 (1952); **11** 47 (1954)
Kneser (1938)	liquids, absorption and dispersion	Ann. Phys. **32** 277
Kneser (1949)	liquids and gases	Erg. Exakt. Naturw. **22** 121
Markham (1950)	liquids and gases	J. Acous. Soc. Amer. **22** 628 (cf. also (11))
Andreae-Lamb (1951)	liquids	Proc. Phys. Soc. **64B** 1021
Gierer-Wirtz (1950)	liquids, structural relaxation, "exchange of positions"	Zeits. Naturforsch. **5a** 270
(ii) *Chemical systems*		
Einstein (1920)	gases, dissociation equilibrium, dispersion	Sitzungsber. Berliner Akad. **19** 380
Luck (1932)	gases, dissociation equilibrium absorption	Phys. Rev. **40** 440
Kneser-Gauler (1936)	gases, absorption and dispersion	Phys. Zeits. **37** 380

Table I. (continued)

Authors	Main scopes or contents	References
Tabuchi (1950, 1951)	gases	J. Chem. Soc. Japan **71** (1950) 167, 329; Mem. Res. Inst Acous. Sci. Osaka Univ. **2** 50
Tabuchi (1950, 1953)	gases, combined case of chemical reaction and molecular absorption	J. Chem. Soc. Japan **73** 597; Mem. Inst. Sci. Industr. Res. Osaka Univ. **10** 117
Tabuchi (1955)	imperfect gases, general chemical equilibrium	J. Chem. Phys. **23** 2033
Hall (1948)	water, association equilibrium	Phys. Rev. **73** 775
Ghosh (1950)	water	*Indian J. Phys. **24** 1
Nomoto (1956)	aqueous solutions	J. Phys. Soc. Japan **11** 827
Liebermann (1949)	chemically active media	J. Acous. Soc. Amer. **24** 1791
Lamb-Pinkerton (1949)	acetic acid	Proc. Roy. Soc. **199A** 114
Barthel (1952)	magnesium sulfate solution	J. Acous. Soc. Amer. **24** 1791
Manes (1953)	reaction kinetics	J. Chem. Phys. **21** 1791
Freedman (1953)	reaction rates, carboxylic acid	J. Chem. Phys. **21** 1784
Bies (1955)	chemical kinetics, magnesium sulfate	J. Chem. Phys. **23** 428
(d) **Phenomenological theory**		
Issakovich (1939)	relaxation of shear and bulk viscosity	C. R. (Doklady) USSR **23** 789
Osida (1945)	relaxation of shear and bulk viscosity	Proc. Phys.-Math. Soc. Japan **25** 406
Frenkel-Obrastzov (1940)	relaxation, three kinds of viscosity	J. of Phys. (USSR) **2** 406
Osida (1950)	any number of relaxation times	Mem. Fac. Engng. Nagoya Univ. **2** 29
Tisza (1942)	relation between bulk viscosity and molecular absorption, gases	Phys. Rev. **61** 531
Truesdell (1950)	Stokesian fluid	J. de Mathématiques **29** 215
Truesdell (1952)	pure fluids	J. Washington Acad. Sci. **42** 33
Truesdell (1952, 1953)	mechanical foundation of elasticity and fluid dynamics	J. Rational Mechanics and Analysis **1** (1951) 125; **2** (1953) 593
Truesdell (1953)	Navier-Stokes equation, absorption & dispersion	J. Rat. Mech. & Anal. **2** 643
Truesdell (1954)	controversy regarding the bulk viscosity	Proc. Roy. Soc. **226A** 59
Truesdell (1955)	hypoelasticity	J. Rat. Mech. Analysis **4** 83
G. I. Taylor (1954)	water containing bubbles, two coefficients of viscosity	Proc. Roy. Soc. **226A** 34, 38
Davies (1954)		Proc. Roy. Soc. **226A** 39
(II) **General theory**		
Kneser (1951)	classification of theories after equation of state and relaxation eq.	Colloquium over ultrasonore trillingen, Brusssels. 130
Kneser (1953)	classification of relaxation phenomena	Kolloid-Zeits. **134** 20
Kneser (1954)	transport and relaxation phenomena	Proc. Roy. Soc. **226A** 40
Lindsay (1951)	spatial and temporal attenuation, fluids	Colloquium over ultrasonore trillingen, Brussels. 100
Hiedemann-Spence (1952)	general theory of relaxation phenomena, elastic relaxation, treatment by the theory of functions	Zeits. Phys. **133** 109

molar specific heat at constant volume at sufficiently high frequency (=for instantaneous change), and C_i the molar specific heat of the internal system (=internal degrees of freedom)

$$\frac{dT_i}{dt}=-\frac{C_{v\infty}}{C_i\tau_H}(T_i-T)=-\frac{1}{\tau_{H'}}(T_i-T)\,. \tag{1.3}$$

We will show later that the relaxation time in this latter case $\tau_{H'}$ is equal to β, the relaxation time of the internal specific heat (cf. § 5).

After De Groot[23], the equation of irreversibility of the type (1.1) or (1.2) corresponds to the expression

$$\frac{dE_i}{dt}=L\frac{T-T_i}{T_m^2}\,, \tag{1.4}$$

representing the proportionality of the "flow" dE_i/dt to the "force" $T-T_i$, where $L=C_iT_m^2/\tau_{H'}$, and T_m means the equilibrium temperature. This conclusion is to be obtained from the fact that the entropy production in this case is

$$\frac{dS}{dt}=\frac{1}{T}\frac{dE}{dt}+\frac{1}{T_1}\frac{dE_i}{dt}=\frac{dE}{dt}\frac{T_i-T}{T_m^2}\,. \tag{1.5}$$

Henry used the relaxation equation (equation of irreversibility)

$$\frac{d(E_x-E_0)}{dt}=\frac{1}{\beta}(E_T-E_0)\,, \tag{1.6}$$

where E_T means the total equiribrium energy, E_0 the total energy without vibration (or rotation) and E_x the actual energy of system at time t. This is equivalent to our equation (3.2) if β means the relaxation time of the vibrational energy. Henry, however, thinks this to be equal to the "*mean life of energy quantum*" of Kneser[2], and so he confuses the "relaxation time of the vibrational energy" with "rilaxation time of the vibrational specific heat." Thus he solves the relaxation equation (1.6) by assuming

$$T=T_0+T_1e^{i\omega t} \tag{1.7a}$$

and

$$E_T=E_0+C_xT_1e^{i\omega t}\,, \tag{1.7b}$$

and gives

$$E_x=E_0+\frac{C_xT_1}{1+i\omega\beta}e^{i\omega t}\,. \tag{1.8}$$

And he *regards* the specific heat as

$$C_v'=C_a+\frac{C_x}{1+i\omega\beta}\,, \tag{1.9}$$

where C_a means the molar specific heat (at constant volume) of the external system. This, however, is not correct, because we have to regard T defined by (1.7a) as the equilibrium temperature when the quantity C_x is the equilibrium value of the intermal specific heat, and because the actual temperature becomes no longer T when the internal energy of the molecules undergoes a change as given by (1.8).

In liquids, the circumstance is more complicated than in gases. In a paper by Hoff Lu[20], the equation of irreversibility takes the form:

$$\frac{d(s-s_\infty)}{dt}=\frac{1}{\tau}(s_0-s)\,, \tag{1.10}$$

where s_0 means the static value of the compression ($=-\Delta v/v$, v=volume), s_∞ the instantaneous compression, and s the compression at any instant. The assumption is made that the equation holds true for liquids and gases. In general, however, the relation (1.10) depends on the thermodynamic path selected.

Equations of this form, however, is also used in group (I)–(d) theories, which is obtainable from the Navier-Stokes equation and the Maxwell's equation of stress relaxation. The group (I)–(d) theories, however, contains assumptions on the relation between the thermodynamic and the hydrodynamic pressure. Attempts to explain the phenomenological theories of bulk viscosity and elastic relaxation (I)–(d) from thermodynamic standpoint are being performed (I)–(b)–(iii), especially by Sugita, Takizawa and Meixner (cf. Table I for references).

The equation of irreversibility in Herzfeld-Rice's theory is somewhat more closely related to the thermodynamics than that in the present paper. Our relaxation equation is more phenomenological than that of Herzfeld. Herzfeld uses energy relation in sound wave together with the relaxation equation. In the present treatment, the energy relation is not employed. It is replaced by the instantaneous variation of pressure accompanying the density change in the sound wave to be superposed on the relaxational pressure qariation due to the equation of irreversibility (cf. (3.11)). Our relaxation equation (3.2), however, is equivalent to that of Herzfeld, as is to be shown in § 5.

§2. General Theory of the Absorption of Sound*

We will treat of the case when there is no classical mechanism of sound absorption as viscosity, heat conduction and heat radiation. Then the equation of sound propagation is given by

$$\frac{\partial^2}{\partial t^2}(\varDelta\rho)=\nabla^2(\varDelta p)\,, \tag{2.1}$$

where $\varDelta p$ means the excess pressure and $\varDelta\rho$ the excess density. When there is sound absorption, there is produced in general a phase shift between the pressure wave and the density wave. A plane wave of sound propagating in x-direction, therefore, can be written as

$$\left.\begin{aligned}\varDelta p&=\varDelta p_0\exp i\left\{\omega t-\left(\frac{\omega}{V}-i\alpha\right)x+\psi\right\},\\ \varDelta\rho&=\varDelta\rho_0\exp i\left\{\omega t-\left(\frac{\omega}{V}-i\alpha\right)x\right\}\end{aligned}\right\} \tag{2.2}$$

where $\omega\,(=2\pi\nu;\ \nu=\text{frequency})$ means the circular frequency, V the sound velocity and α the absorption coefficient (amplitude absorption coefficient per unit length). Substituting (2.2) into (2.1) we get

$$\frac{\varDelta p_0}{\varDelta\rho_0}e^{i\psi}=\frac{V^2}{\left(1-i\dfrac{\alpha V}{\omega}\right)^2}\,. \tag{2.3}$$

This gives

$$\exp\left(-\frac{1}{2}i\psi\right)=\sqrt{\frac{\varDelta p_0}{\varDelta\rho_0}}\,\frac{1}{V}\left(1-i\frac{\alpha V}{\omega}\right),$$

and by equating the real and imaginary parts on both sides of the equation we have

$$V=\sqrt{\frac{\varDelta p_0}{\varDelta\rho_0}}\sec\frac{\psi}{2}=\sqrt{\frac{\varDelta p_0}{\varDelta\rho_0}\left(1+\frac{\alpha^2V^2}{\omega^2}\right)} \tag{2.4}$$

and

$$\alpha=\frac{\omega}{V}\tan\frac{\psi}{2}=\frac{2\pi}{\lambda}\tan\frac{\psi}{2}\,, \tag{2.5}$$

where λ means the wavelength. These become, approximately

$$V=\sqrt{\frac{\varDelta p_0}{\varDelta\rho_0}} \tag{2.6}$$

and

$$\alpha=\frac{\pi}{\lambda}\tan\psi\,. \tag{2.7}$$

If we define the complex velocity $\boldsymbol{V}$ by

$$\boldsymbol{V}=\sqrt{\frac{\varDelta p}{\varDelta\rho}}=\sqrt{\frac{\varDelta p_0}{\varDelta\rho_0}e^{i\psi}} \tag{2.8}$$

we have from (2.3) the relation

$$\boldsymbol{V}^2=\frac{V^2}{1+(\alpha^2V^2/\omega^2)^2}\left[\left(1-\frac{\alpha^2V^2}{\omega^2}\right)+2i\frac{\alpha V}{\omega}\right],$$

and the velocity and absorption are given by

$$V^2=\frac{(1+\alpha^2V^2/\omega^2)^2}{1-\alpha^2V^2/\omega^2}\Re(\boldsymbol{V}^2)=\sec\psi\cdot\sec^2\frac{\psi}{2}\Re(\boldsymbol{V}^2) \tag{2.9}$$

and

$$\begin{aligned}\alpha&=\frac{1}{2}\frac{\omega}{V}\frac{\Im(\boldsymbol{V}^2)}{\Re(\boldsymbol{V}^2)}\left(1-\frac{\alpha^2V^2}{\omega^2}\right)\\&=\frac{1}{2}\frac{\omega}{V}\frac{\Im(\boldsymbol{V}^2)}{\Re(\boldsymbol{V}^2)}\left(1-\tan^2\frac{\psi}{2}\right)\end{aligned} \tag{2.10}$$

respectively. Here $\Re(\boldsymbol{V}^2)$ and $\Im(\boldsymbol{V}^2)$ represent the real and imaginary parts of $\boldsymbol{V}^2$ respectively. In approximations up to the order of $(\alpha V/\omega)^2$ we have for the sound velocity (in second approximation)

$$V^2=\left\{1+3\frac{\alpha^2V^2}{\omega^2}\right\}\Re(\boldsymbol{V}^2)=\left\{1+\frac{3}{4}\frac{\Im(\boldsymbol{V}^2)}{\Re(\boldsymbol{V}^2)}\right\}\Re(\boldsymbol{V}^2), \tag{2.11}$$

and for the absorption coefficient (in third approximation)

$$\alpha=\frac{1}{2}\frac{\omega}{V}\frac{\Im(\boldsymbol{V}^2)}{\Re(\boldsymbol{V}^2)}\left\{1-\frac{1}{4}\frac{\Im(\boldsymbol{V}^2)}{\Re(\boldsymbol{V}^2)}\right\}. \tag{2.12}$$

The zero order approximation formula for sound velocity is

$$V^2=\Re(\boldsymbol{V}^2) \tag{2.13}$$

and the first order approximation formula for sound absorption

$$\alpha=\frac{1}{2}\frac{\omega}{V}\frac{\Im(\boldsymbol{V}^2)}{\Re(\boldsymbol{V}^2)}\,. \tag{2.14}$$

§3. Relaxation Phenomenon of the Internal Energy

When a gas or liquid contained in a vessel is instantaneously compressed, the volume experiences a sudden decrease (cf. Fig. 1, (a)) energy E_i of the internal degrees of freedoms of the molecules, however, does not change at this moment, but slowly approaches the new equilibrium value $E_i+\varDelta E_i^0$ with a relaxation time τ, after ending of the instantaneous compression (cf. Fig. 1 (b)). The value at time t is given by

---

* The treatment here presented is essentially the same as described in a former paper Nomoto[24]), §3), except the use of the complex velocity. The procedure for obtaining dispersion and absorption formulas, and especially the second approximation formulas, becomes more simple by this method.

$$\Delta E_i = \Delta E_i^0 (1 - e^{-t/\tau}) \,. \tag{3.1}$$

The external work of compression is transformed into the translational energy of the molecules at first and then into the rotational and vibrational energies of the molecules with respective relaxation times. Here we consider the case when one of the internal energies (vibrational or rotational) fail to accompany the sudden volume change, and we assume single relaxation time for simplicity's sake. (Rotational energy is known to establish equilibrium with the translational energy more rapidly than the vibrational energy, and it is the problem of time-scale of the experiment whether the rotational energy can be regarded as external energy of the molecules or not.)

The translational energy, on the other hand, increases by an amount ΔE_t^∞ in a sudden compression. This is somewhat too large as compared with the increment ΔE_t^0 corresponding to the equilibrium state, because the external work of compression is not shared to the internal degrees of freedom as yet. The increment of the translational energy approaches the new equilibrium value according to the exponential law

$$\begin{aligned} \Delta E_t &= \Delta E_t^\infty + (\Delta E_t^0 - \Delta E_t^\infty)(1 - e^{-t/\tau}) \\ &= \Delta E_t^0 + (\Delta E_t^\infty - \Delta E_t^0) e^{-t/\tau} \end{aligned} \tag{3.2}$$

with the same relaxation time τ as in (3.1) (cf. Fig. 1 (c)). The pressure, however, is a quantity proportional to the translational energy of the molecules. For example, we have in case of gases the relation

$$p = \frac{2}{3} \frac{E_t}{v} \tag{3.3}$$

where v means the molar volume. So the pressure change after an instantaneous compression is given by

$$\begin{aligned} \Delta p &= \Delta p^\infty + (\Delta p^0 - \Delta p^\infty)(1 - e^{-t/\tau}) \\ &= \Delta p^0 + (\Delta p^\infty - \Delta p^0) e^{-t/\tau} \,, \end{aligned} \tag{3.4}$$

where Δp^∞ and Δp^0 mean the instantaneous and the equilibrium increment of pressure respectively.

Differentiating this equation with time, we obtain the rate of change of pressure after an instantaneous volume change:

$$\begin{aligned} \frac{\partial(\Delta p)}{\partial t} &= -\frac{1}{\tau} (\Delta p^\infty - \Delta p^0) e^{-t/\tau} \\ &= -\frac{1}{\tau} (\Delta p - \Delta p^0) \,. \end{aligned} \tag{3.5}$$

Assuming a sinusoidal change of density at a fixed point in space, traversed by a sound beam

$$\rho = \rho_0 + \Delta\rho = \rho_0 + \Delta\rho_0 e^{i\omega t} \,, \tag{3.6}$$

the pressure will be given by

$$p^0 = p_0 + \Delta p^0 = p_0 + \Delta p_0{}^0 e^{i\omega t} \,, \tag{3.7}$$

if the change is sufficiently slow so that the pressure and density are in equilibrium, and by

$$p^\infty = p_0 + \Delta p^\infty = p_0 + \Delta p_0{}^\infty e^{i\omega t} \,, \tag{3.8}$$

if the change is sufficiently fast. The actual pressure

$$p = p_0 + \Delta p \,, \tag{3.9}$$

however, is generally different from these two extreme values. So the excess pressure Δp always tends to approach the equilibrium value

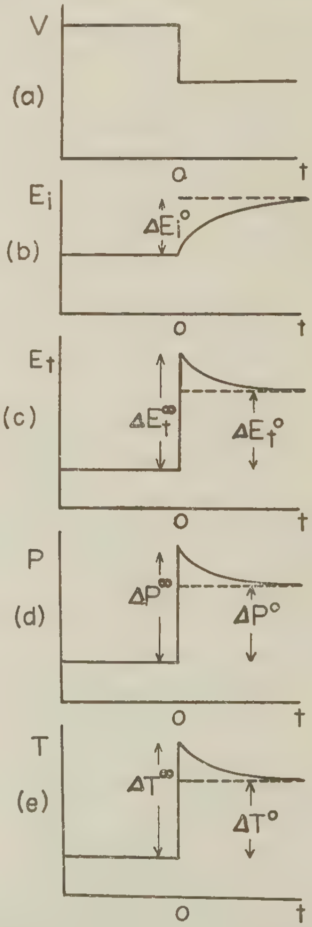

Fig. 1. The time variation of (a) volume, (b) internal energy of the molecules, (c) translational energy of the molecules, (d) pressure, and (e) temperature after an instantaneous compression.

Δp^0 after (3.5). At the same time the pressure experiences an instantaneous change accompanying the sinusoidal change of density in the sound wave (cf. (3.6)), this change being given by

$$\frac{\partial(\Delta p)}{\partial(\Delta \rho)}\cdot\frac{\partial(\Delta \rho)}{\partial t}=\left(\frac{\partial p}{\partial \rho}\right)_\infty\cdot i\omega\cdot\Delta\rho_0 e^{i\omega t}\,. \qquad (3.10)$$

The total rate of change of pressure at a fixed point in a sound beam, therefore, is given by

$$\begin{aligned}\frac{d(\Delta p)}{dt}&=\frac{\partial(\Delta p)}{\partial t}+\frac{\partial(\Delta p)}{\partial(\Delta \rho)}\cdot\frac{\partial(\Delta \rho)}{\partial t}\\&=-\frac{1}{\tau}(\Delta p-\Delta p^0)+\left(\frac{\partial p}{\partial \rho}\right)_\infty\cdot i\omega\cdot\Delta\rho_0\cdot e^{i\omega t}\,.\end{aligned} \qquad (3.11)$$

Substituting further the relation

$$\Delta p^0=\left(\frac{\partial p}{\partial \rho}\right)_0\Delta\rho=\left(\frac{\partial p}{\partial \rho}\right)_0\cdot\Delta\rho_0\cdot e^{i\omega t} \qquad (3.12)$$

in (3.11), we have

$$\begin{aligned}\frac{d(\Delta p)}{dt}=-\frac{1}{\tau}\Delta p+\Bigg\{&\frac{1}{\tau}\left(\frac{\partial p}{\partial \rho}\right)_0\\&+i\omega\left(\frac{\partial p}{\partial \rho}\right)_\infty\Bigg\}\Delta\rho\cdot e^{i\omega t}\,.\end{aligned} \qquad (3.13)$$

As we have $d(\Delta p)/dt=i\omega\cdot\Delta p$ in a sound wave, we have as the solution of (3.13)

$$\Delta p=\frac{\left(\frac{\partial p}{\partial \rho}\right)_0+i\omega\tau\left(\frac{\partial p}{\partial \rho}\right)_\infty}{1+i\omega\tau}\cdot\Delta\rho_0\cdot e^{i\omega t} \qquad (3.14)$$

or

$$\Delta p=\frac{\left\{\left(\frac{\partial p}{\partial \rho}\right)_0+\omega^2\tau^2\left(\frac{\partial p}{\partial \rho}\right)_\infty\right\}+i\omega\tau\left\{\left(\frac{\partial p}{\partial \rho}\right)_\infty-\left(\frac{\partial p}{\partial \rho}\right)_0\right\}}{1+\omega^2\tau^2}\times\Delta\rho_0 e^{i\omega t}\,. \qquad (3.15)$$

If we write this as

$$\Delta p=\Delta p_0^\omega\cdot e^{i\omega t+\psi}=\Delta p_0^\omega(\cos\psi+i\sin\psi)e^{i\omega t}\,, \qquad (3.16)$$

according to (2.2), we have the relations:

$$\Delta p_0^\omega=\frac{\left(\frac{\partial p}{\partial \rho}\right)_0+\omega^2\tau^2\left(\frac{\partial p}{\partial \rho}\right)_\infty}{1+\omega^2\tau^2}\Delta\rho_0\sec\psi \qquad (3.17)$$

and

$$\tan\psi=\frac{\omega\tau\left\{\left(\frac{\partial p}{\partial \rho}\right)_\infty-\left(\frac{\partial p}{\partial \rho}\right)_0\right\}}{\left(\frac{\partial p}{\partial \rho}\right)_0+\omega^2\tau^2\left(\frac{\partial p}{\partial \rho}\right)_\infty}\,. \qquad (3.18)$$

So the complex velocity (cf. (2.8)) is given by

$$V^2=\frac{\left(\frac{\partial p}{\partial \rho}\right)_0+\omega^2\tau^2\left(\frac{\partial p}{\partial \rho}\right)_\infty}{1+\omega^2\tau^2}(1+i\tan\psi)\,, \qquad (3.19)$$

and we have as the approximate expression of sound velocity by (2.13)

$$V^2=\mathfrak{R}(V^2)=\frac{V_0^2+\omega^2\tau^2V_\infty^2}{1+\omega^2\tau^2}\,, \qquad (3.20)$$

where

$$V_0=\sqrt{\left(\frac{\partial p}{\partial \rho}\right)_0}=\sqrt{\left(\frac{\partial p}{\partial \rho}\right)_T\frac{C_{p0}}{C_{v0}}} \qquad (3.21)$$

and

$$V_\infty=\sqrt{\left(\frac{\partial p}{\partial \rho}\right)_\infty}=\sqrt{\left(\frac{\partial p}{\partial \rho}\right)_T\frac{C_{p\infty}}{C_{v\infty}}} \qquad (3.22)$$

mean the sound velocity at sufficiently low frequency and at sufficiently high frequency respectively. In these relations, C_{p0} and $C_{p\infty}$ mean the molar specific heats at constant pressure at sufficiently low frequency and at sufficiently high frequency respectively, and C_{v0} and $C_{v\infty}$ the molar specific heats at constant volume at the respective frequencies. The absorption coefficient per wavelength becomes by (2.7) and (3.18) as

$$\alpha_\lambda=\alpha\lambda=\pi\tan\psi=\pi\frac{(V_\infty^2-V_0^2)\omega\tau}{V_0^2+V_\infty^2\omega^2\tau^2}\,. \qquad (3.23)$$

The dispersion formula (3.20) and the absorption formula (3.23) can be expressed also in terms of the specific heats by substituting (3.21) and (3.22) and using the symbols

$$D=C_{p0}-C_{v0}=C_{p\infty}-C_{v\infty} \qquad (3.24)$$

and

$$C_i=C_{v0}-C_{v\infty}(=C_{p0}-C_{p\infty})\,, \qquad (3.25)$$

where C_i means the static value of the internal specific heat (per mole) exhibiting thermal relaxation. We have the dispersion formula

$$V^2=\left(\frac{\partial p}{\partial \rho}\right)_T\left[1+D\frac{C_{v\infty}+C_{v0}\omega^2\tau^2}{C_{v0}C_{v\infty}(1+\omega^2\tau^2)}\right] \qquad (3.26)$$

or,

$$V^2=\left(\frac{\partial p}{\partial \rho}\right)_T\left[1+\frac{D}{C_{v0}}+\frac{DC_i\omega^2\tau^2}{C_{v0}C_{v\infty}(1+\omega^2\tau^2)}\right] \qquad (3.26a)$$

and the absorption formula

$$\alpha_\lambda=\alpha\lambda=\pi\frac{DC_i\omega\tau}{C_{p0}C_{v\infty}+C_{v0}C_{p\infty}\omega^2\tau^2}\,. \qquad (3.27)$$

The relations (3.26) and (3.27) are general formulas applicable both for gases and liquids. The dispersion formula (3.26) can be also written as

$$V^2=V_0^2\left[1+\frac{DC_i\omega^2\tau^2}{C_{p0}C_{v\infty}(1+\omega^2\tau^2)}\right] \qquad (3.28)$$

by employing (3.21). The form of (3.20), i.e.,

$$V^2=V_0{}^2+(V_\infty{}^2-V_0{}^2)\frac{\omega^2\tau^2}{1+\omega^2\tau^2} \tag{3.29}$$

is also often used for liquids. This simple formula, naturally, is also valid in case of gases, though hitherto not in use. This formula (3.29) has further the advantage that in this form it coincides with the relaxation formula in other cases, as for example, in case of the relaxation of shear viscosity (group (I)-(d) theories).

§ 4. Relation between the Two Relaxation Times τ and β

Although the formula (3.29) with relaxation time τ is sometimes employed for liquids, the formulas of general use in gases (Kneser's dispersion and absorption formulas) employ another relaxation time β, also called the "*period of adjustment* (*Einstelldauer*)" of the internal energy. τ was introduced in our previous paper[17] and first denoted by β'. It was called the "relaxation time of the internal energy" by Hubbard, while β was called the "relaxation time of the internal specific heat." Kneser's formulas are to be obtained from our result by employing a relaxation time β given by

$$\beta=\tau\frac{C_{v0}}{C_{v\infty}}=\tau\frac{C_{v\infty}+C_i}{C_{v\infty}} \tag{4.1}$$

in place of τ, i.e., by substituting

$$\tau=\beta\frac{C_{v\infty}}{C_{v0}} \tag{4.2}$$

in our equations. For example, the dispersion formula (3.26) transforms into

$$V^2=\left(\frac{\partial p}{\partial\rho}\right)_T\left[1+D\frac{C_{v0}+C_{v\infty}\omega^2\beta^2}{C_{v0}{}^2+C_{v\infty}{}^2\omega^2\beta^2}\right] \tag{4.3}$$

by this substitution, and the absorption formula (3.27) becomes

$$\alpha_\lambda=\pi\frac{DC_i\omega\beta}{C_{p0}C_{v0}+C_{p\infty}C_{v\infty}\omega^2\beta^2}\,. \tag{4.4}$$

As we have further

$$D=R \tag{4.5}$$

(R=universal gas constant) and

$$\left(\frac{\partial p}{\partial\rho}\right)_T=\frac{p_0}{\rho_0} \tag{4.6}$$

for an ideal gas, (4.3) and (4.4) becomes in this case as

$$V^2=\frac{p_0}{\rho_0}\left[1+R\frac{C_{v0}+C_{v\infty}\omega^2\beta^2}{C_{v0}{}^2+C_{v\infty}{}^2\omega^2\beta^2}\right] \tag{4.7}$$

and

$$\alpha_\lambda=\pi\frac{RC_i\omega\beta}{C_{p0}C_{v0}+C_{p\infty}C_{v\infty}\omega^2\beta^2} \tag{4.8}$$

in accordance with Kneser's formulas.

Kneser's formulas are to be obtained most simply by assuming a relaxation phenomenon of internal specific heat C_i with relaxation time β and formally putting

$$C_i(\omega)=\frac{C_i}{1+\omega\beta} \tag{4.9}$$

in the expression of the sound velocity (cf. Eucken-Becker[19])

$$V^2=\left(\frac{\partial p}{\partial\rho}\right)_T\frac{C_p}{C_v}=\left(\frac{\partial p}{\partial\rho}\right)_T\left[1+\frac{D}{C_{v\infty}+C_i(\omega)}\right]. \tag{4.10}$$

The sound velocity becomes complex in this case, the real part giving the approximate sound velocity and the imaginary part the effect of absorption. Thus we have

$$\begin{aligned}V^2&=\left(\frac{\partial p}{\partial\rho}\right)_T\left[1+\frac{D}{C_{v\infty}+C_i/(1+i\omega\beta)}\right]\\&=\left(\frac{\partial p}{\partial\rho}\right)_T\left[1+\frac{D(C_{v0}+C_{v\infty}\omega^2\beta^2)+iDCi\omega\beta}{C_{v0}{}^2+C_{v\infty}{}^2\omega^2\beta^2}\right].\end{aligned} \tag{4.11}$$

This immediately gives the dispersion formula (4.3) by (2.13) and the absorption formula (4.4) by (2.14).

The fact that the formulas (4.3) and (4.4) are obtained from (3.28) and (3.27) by the substitution of (4.2) means that the internal specific heat shows a relaxation phenomenon with a relaxation time β and that this relaxation time is related with the relaxation time of internal energy τ by (4.2). This is to be shown more directly from (3.14). By substituting

$$\begin{aligned}\Delta p&=\left(\frac{\partial p}{\partial\rho}\right)\Delta\rho=\left(\frac{\partial p}{\partial\rho}\right)_T\frac{C_p}{C_v}\Delta\rho\\&=\gamma\left(\frac{\partial p}{\partial\rho}\right)_T\Delta\rho_0e^{i\omega t}\end{aligned} \tag{4.12}$$

and

$$\left.\begin{aligned}\left(\frac{\partial p}{\partial\rho}\right)_0&=\frac{C_{p0}}{C_{v0}}\left(\frac{\partial p}{\partial\rho}\right)_T=\gamma_0\left(\frac{\partial p}{\partial\rho}\right)_T,\\\left(\frac{\partial p}{\partial\rho}\right)_\infty&=\frac{C_{p\infty}}{C_{v\infty}}\left(\frac{\partial p}{\partial\rho}\right)_T=\gamma_\infty\left(\frac{\partial p}{\partial\rho}\right)_T\end{aligned}\right\} \tag{4.13}$$

in (3.14), we have the relation

$$\gamma=\frac{\gamma_0+\gamma_\infty\cdot i\omega\tau}{1+i\omega\tau}\,. \tag{4.14}$$

And by putting

$$\gamma = 1 + \frac{D}{C_{v\infty}+C_i(\omega)} \tag{4.15}$$

in this equation, we have

$$\frac{1}{C_{v\infty}+C_i(\omega)} = \frac{1}{C_{v0}} \frac{C_{v\infty}+C_{v0}\cdot i\omega\tau}{C_{v\infty}(1+i\omega\tau)} ,$$

or,

$$C_i(\omega) = \frac{C_{v\infty}C_i}{C_{v\infty}+C_{v0}\cdot i\omega\tau} , \tag{4.16}$$

a relation, which coincides with (4.9) by (4.2).

It is, however, desirable to deduce the relation between the two relaxation times more directly from the relation

$$C_i = \frac{\Delta E_i}{\Delta T} . \tag{4.17}$$

For this purpose, we have first to consider the meaning of the temperature T in a sound wave. The directly observable quantities in this case are V and α; first we deduce $\partial p/\partial \rho$ from these quantities, then γ, and finally C_i. The temperature T in (4.17) means therefore, the temperature to be deduce from the pressure p, i.e., the temperature as indicated in the translational energy of the molecules. This is called the external temperature, i.e., the temperature of the external degrees of freedoms of the molecules. As E_i is not in equilibrium with E_t in this case, the temperature of the internal degrees of freedom (T_i) is naturally different from T and the internal specific heat (under infinitesimal amplitude) must be constant if we use the internal temperature as the temperature.

First we will consider of the instantaneous static compression as indicated in Fig. 1. Here the time dependence of the internal energy of the molecules E_i follows (3.1) and is represented in Fig. 1 (b). Now the temperature T of the external degrees of freedom is a quantity proportional to the translational energy E_t of the molecules, the proportionality factor being

$$\frac{\Delta E_t}{\Delta T} = 3R \tag{4.18}$$

by the law of equipartition of energy. So the time dependence of ΔT must be the same as that of ΔE_t (cf. Fig. 1 (e)) and is to be given by an equation analogous to (3.2), i.e., by

$$\begin{aligned}\Delta T &= \Delta T^\infty + (\Delta T^0 - \Delta T^\infty)(1-e^{-t/\tau}) \\ &= \Delta T^0 + (\Delta T^\infty - \Delta T^0)e^{-t/\tau} .\end{aligned} \tag{4.19}$$

Thus the time dependence of the internal specific heat after an instantaneous compression is given by

$$C_i = \frac{\Delta E_i}{\Delta T} = \frac{\Delta E_{i0}(1-e^{-t/\tau})}{\Delta T^0 + (\Delta T^\infty - \Delta T^0)e^{-t/\tau}} . \tag{4.20}$$

Denoting the static value of the internal molar specific heat by $C_i{}^0$, we have

$$C_i{}^0 = \frac{\Delta E_i{}^0}{\Delta T^0} \tag{4.21}$$

and we have by the law of conservation of energy the relation

$$C_v{}^\infty \Delta T^\infty = C_{v0}\Delta T^0 . \tag{4.22}$$

Substituting (4.21), (4.22) and (3.25) in (4.20) we have

$$C_i(t) = \frac{C_i{}^0 C_{v\infty}(1-e^{-t/\tau})}{C_{v\infty}+C_i e^{-t/\tau}} . \tag{4.23}$$

This gives by differentiation the relation

$$\frac{\partial C_i(t)}{\partial t} = \frac{1}{\tau} \frac{C_{v\infty}+C_i(t)}{C_{v0}} \{C_i{}^0 - C_i(t)\} . \tag{4.24}$$

The relations (4.23) and (4.24) are of course to be deduced more simply from (3.4) and (3.5). By substituting (4.12) and (4.13) in these relations, (3.4) gives

$$\gamma = \gamma^0 + (\gamma^\infty - \gamma^0)e^{-t/\tau} \tag{4.25}$$

and we have from (3.5)

$$\frac{\partial \gamma}{\partial t} = -\frac{1}{\tau}(\gamma - \gamma_0) . \tag{4.26}$$

As

$$\gamma = \frac{C_p}{C_v} = 1 + \frac{D}{C_{v\infty}+C_i(t)} , \tag{4.27}$$

in this case, we have (4.23) from (4.25) and (4.24) from (4.27).

At any rate, it is to be seen from (4.23) and (4.24) that the time change of C_i after an instantaneous static compression does not correspond to a simple exponential approach to the equilibrium value with a single relaxation time. Thus by writing (4.24) as

$$\frac{\partial C_i}{\partial t} = -\frac{1}{\beta'}(C_i - C_i{}^0) \tag{4.28}$$

we find that the apparent relaxation time

$$\beta' = \tau \frac{C_{v0}}{C_{v\infty}+C_i(t)} \tag{4.29}$$

changes with time from

$$\left.\begin{aligned} &\beta' = \tau\frac{C_{v0}}{C_{v\infty}} = \beta \quad \text{at} \quad t=0 \\ &\text{to} \\ &\beta' = \tau \qquad\qquad \text{at} \quad t=\infty . \end{aligned}\right\} \tag{4.30}$$

The reason of the discrepancy of this result from the case of sound wave is due to the fact that in the sound wave $\varDelta T$ has also a component which instantaneously accompanies the density change. $\varDelta E_i$, on the other hand, has no such component.

Now we will consider the case of a sound wave. (4.17) is also valid in this case. $\varDelta E_i$ satisfies the differential equation

$$\frac{\partial(\varDelta E_i)}{\partial t}=\frac{1}{\tau}(\varDelta E_i{}^9-\varDelta E_i) \tag{4.31}$$

by (3.1), after an instantaneous volume change. The time variation of $\varDelta E_i$ becomes

$$\frac{d(\varDelta E_i)}{\partial t}=\frac{\partial(\varDelta E_i)}{\partial t}+\frac{\partial(\varDelta E_i)}{\partial(\varDelta\rho)}\frac{d(\varDelta\rho)}{dt}$$

at a fixed point in a sound wave. As $\varDelta E_i$ does not change in phase with the density change, as above mentioned, we have

$$\left(\frac{\partial(\varDelta E_i)}{\partial(\varDelta\rho)}\right)_\infty=0\,. \tag{4.23}$$

So we have

$$\frac{d(\varDelta E_i)}{dt}=\frac{\partial(\varDelta E_i)}{\partial t}$$

and accordingly

$$\frac{d(\varDelta E_i)}{\partial t}=\frac{1}{\tau}(\varDelta E_i{}^0-\varDelta E_i) \tag{4.33}$$

at a fixed point in a sound wave. If $\varDelta E_i$ and $\varDelta E_i{}^0$ make sinusoidal changes with circular frequency ω, we have as the solution of (4.33)

$$\varDelta E_i=\frac{\varDelta E_i{}^0}{1+i\omega\tau}\,. \tag{4.34}$$

Now the quantity $\varDelta T$ in the denominator of (4.17) satisfies

$$\frac{\partial(\varDelta T)}{\partial t}=-\frac{1}{\tau}(\varDelta T-\varDelta T^0) \tag{4.35}$$

by (4.19) after an instantaneous static volume change. In a sound wave we have

$$\frac{d(\varDelta T)}{dt}=\frac{\partial(\varDelta T)}{\partial t}+\left(\frac{\partial(\varDelta T)}{\partial(\varDelta\rho)}\right)_\infty\frac{d(\varDelta\rho)}{dt}\,. \tag{4.36}$$

If we think, for simplicity's sake, the ideal gas, we have for sufficiently rapid adiabatic changes

$$T=c\rho^{\gamma_\infty-1}\,;\qquad c=\text{const.} \tag{4.37}$$

This gives

$$\left(\frac{\partial(\varDelta T)}{\partial(\varDelta\rho)}\right)_\infty=\left(\frac{\partial T}{\partial\rho}\right)_\infty=\frac{T}{\rho}(\gamma_\infty-1)=\frac{T}{\rho}\frac{R}{C_{v\infty}}\,. \tag{4.38*}$$

On the other hand, we have for sufficiently slow adiabatic change of an ideal gas

$$T=c'\rho^{\gamma_0-1}\,;\qquad c'=\text{const.} \tag{4.39}$$

This gives

$$\left(\frac{\partial T}{\partial\rho}\right)_0=\frac{T}{\rho}(\gamma_0-1)=\frac{TR}{\rho C_{v0}} \tag{4.40}$$

and we have from this

$$\varDelta T^0=\left(\frac{\partial T}{\partial\rho}\right)_0\varDelta\rho=\frac{TR}{\rho C_{v0}}\varDelta\rho\,. \tag{4.41}$$

Substituting (4.35), (4.38) and (4.41) into (4.36) we have as the differential equation

$$\frac{d(\varDelta T)}{dt}=-\frac{1}{\tau}\left(\varDelta T-\frac{TR}{\rho C_{v0}}\varDelta\rho\right)+\frac{TR}{\rho C_{v\infty}}\frac{d(\varDelta\rho)}{dt}\,. \tag{4.42}$$

Assuming sinusoidal changes with circular frequency ω for $\varDelta T$ and $\varDelta\rho$, we obtain as the solution of (4.42)

$$\varDelta T=\frac{TR(C_{v\infty}+C_{v0}i\omega\tau)}{\rho C_{v0}C_{v\infty}(1+i\omega\tau)}\varDelta\rho\,, \tag{4.43}$$

or, expressed in terms of $\varDelta T^0$ by (4.1),

$$\varDelta T=\varDelta T^0\frac{(C_{v\infty}+C_{v0}\cdot i\omega\tau)}{C_{v\infty}(1+i\omega\tau)}\,. \tag{4.44}$$

Substituting (4.34) and (4.44) into (4.17) we have

$$C_i=\frac{\varDelta E_i}{\varDelta T}=\frac{\varDelta E_i{}^0}{\varDelta T^0}\frac{C_{v\infty}}{C_{v\infty}+C_{v0}\cdot i\omega\tau}\,, \tag{4.45}$$

or,

$$C_i=\frac{C_i{}^0}{1+i\omega\beta}\,, \tag{4.46}$$

where

$$\beta=\tau\frac{C_{v0}}{C_{v\infty}}\,. \tag{4.47}$$

These are the required relations (4.9) and (4.1).

Non-phenomenological deductions of the relationship between β and τ has been given in a previous paper[17)].

§ 5. Relation of τ and β with the Relaxation Times of Herzfeld and Rice's Theory

The relaxation equations of Herzfeld and Rice, (1.1) and (1.3), have the form of Newton's law of cooling, the rate of temperature change being proportional to the temperature difference. The relaxation equation of pressure

---

[*] In general, we have for any fluid (liquid or gas), $\left(\frac{\partial(\varDelta T)}{\partial(\varDelta\rho)}\right)_\infty=\frac{C_{p0}-C_{v0}}{\alpha\rho C_{v\infty}}$, where α means the expansion coefficient, (cf. Nomoto (25), eq. (3.16)). Eq. (4.44) holds true also in this case.

used in the present theory, (3.5), on the other hand, is based on the phenomenological relaxation equations of energy (3.1) and (3.2). These equations, however, leads to the Herzfeld's relaxation equations. As the Herzfeld's relaxation equations are thermodynamically founded by De Groot, the phenomenological equations here employed also gain the thermodynamical supports. At the same time, the relation between the relaxation times τ_H' $(=C_i\tau/C_{v\infty}$ by Herzfeld's notation) and τ and β can be obtained.

As the increment of the internal temperature $\varDelta T_i$ is proportional to the increment of the molecular internal energy $\varDelta E_i$ by

$$\varDelta E_i = C_i \varDelta T_i\ , \tag{5.1}$$

the time change of T_i after an instantaneous compression of Fig. 1 is similar to that of E_i and is given by

$$\varDelta T_i = \varDelta T_i^0 (1-e^{-t/\tau})\ , \tag{5.2}$$

(cf. (3.1)), where $\varDelta T_i^0$ is the value of $\varDelta T_i$ corresponding to the new equilibrium state, while the external temperature is given by (4.19), i.e.,

$$\varDelta T = \varDelta T^\infty - (\varDelta T^\infty - \varDelta T^0)(1-e^{-t/\tau})\ . \tag{5.3}$$

As the energy obtained by the internal system $C_i\varDelta T_i^0$ till the equilibrium is established, is equal to the energy lost by the external system $C_{v\infty}(\varDelta T^\infty - \varDelta T^0)$, we have

$$\varDelta T - \varDelta T^0 = (C_i/C_{v\infty})\varDelta T_i^0\ . \tag{5.4}$$

Accordingly, (5.3) becomes as

$$\varDelta T = \varDelta T^\infty - \varDelta T_i^0 (C_i/C_{v\infty})(1-e^{-t/\tau})\ . \tag{5.5}$$

Then we have from (5.5) and (5.2)

$$\varDelta T - \varDelta T_i = \varDelta T^\infty - \varDelta T_i^0 (C_{v0}/C_{v\infty})(1-e^{-t/\tau})\ . \tag{5.6}$$

Differentiating (5.5) with respect to time, we have

$$\frac{\partial(\varDelta T)}{\partial t} = -\frac{1}{\tau}\varDelta T_i^0 (C_i/C_{v\infty})e^{-t/\tau}\ . \tag{5.7}$$

As the equilibrium temperature is common for the internal system and the external system, we have

$$\varDelta T_i^0 = \varDelta T^0\ , \tag{5.8}$$

and (5.7) becomes

$$\partial(\varDelta T)/\partial t = -(1/\tau)(C_i/C_{v\infty})\varDelta T^0 e^{-t/\tau}\ . \tag{5.9}$$

Moreover, there is the energy relation

$$C_{v\infty}\varDelta T^\infty = C_{v0}\varDelta T^0\ . \tag{5.10}$$

So we have from (5.6) by substituting (5.8) and (5.10)

$$\varDelta T - \varDelta T_i = (C_{v0}/C_{v\infty})\varDelta T^0 e^{-t/\tau}\ . \tag{5.11}$$

Substituting this into (5.9) we have

$$\frac{\partial(\varDelta T)}{\partial t} = -\frac{1}{\tau}\frac{C_i}{C_{v0}}(\varDelta T - \varDelta T_i)\ , \tag{5.12}$$

which corresponds to Herzfeld's relaxation equation (1.1). So we see that the relaxation time τ_H in (1.1) is related to τ and β by

$$\tau_H = \tau\frac{C_{v0}}{C_i} = \beta\frac{C_{v\infty}}{C_i}\ . \tag{5.13}$$

Similarly, we obtain from (5.2)

$$\frac{\partial(\varDelta T_i)}{\partial t} = \frac{1}{\tau}\frac{C_{v\infty}}{C_{v0}}(\varDelta T - \varDelta T_i)\ . \tag{5.14}$$

This corresponds to Herzfeld's equation (1.3), and we have accordingly the relation*

$$\tau_{H'} = \tau\frac{C_{v0}}{C_{v\infty}} = \beta\ . \tag{5.15}$$

It is known that Kneser's "period of adjustment of vibrational energy" β has the meaning of the "mean lifetime of the energy quantum" and related to the "collision probability of desactivation" f_{10} by

$$\beta = 1/(2\kappa N f_{10})\ , \tag{5.16}$$

where κ means the number of collisions taking place per each second if the molecular density is one per cm³, and N the number of molecules per cm³. It seems at first strange that the relaxation time of the internal specific heat β is more closely related to the collision probability than does the relaxation time of the internal energy τ. The Herzfeld's equation (1.3), however, explains this together with the relation (5.15). It means that the internal energy increases only at the expense of the external energy, and that the relaxation time for this process is β, instead of τ.

---

* It was erroneously stated in one[24] of our previous papers: "τ is the relaxation time to follow the change of thermal equilibrium at constant volume, i.e., after ending of an instantaneous volume change, whereas β is the relaxation time to follow the *change of thermal equilibrium* in a sinusoidal volume change, i.e., accompanying a sinusoidal change of the equilibrium state in a sound wave."

We have to correct this as follows: "τ is the relaxation time *of the internal energy* to follow the change of thermal equilibrium at constant volume, while β is the relaxation time to follow the *difference of temperature between the external and the internal degrees of freedom* in a sinusoidal volume change." (Cf. Nomoto[25], Fig. 3 as regards the relation between the various temperatures $\varDelta T$, $\varDelta T_i$ and the equilibrium value $\varDelta T^\circ (=\varDelta T_i^\circ)$).

Thus we see that the relaxation time of the internal specific heat β is physically a more significant quantity than the relaxation time of the internal energy τ.

§ 6. Second Approximation Formulas

More precisely, the sound velocity is given by (2.11). By correcting the zero approximation velocity equation (3.26) by this equation, employing the absorption value of (3.27), we have

$$V^2=\left(\frac{\partial p}{\partial \rho}\right)_T\left[1+\frac{D}{C_{v0}}+\frac{DC_i\omega^2\tau^2}{C_{v0}C_{v\infty}(1+\omega^2\tau^2)}\right]\cdot\left[1+\frac{3}{4}\frac{D^2C_i^2\omega^2\tau^2}{(C_{p0}C_{v\infty}+C_{v0}C_{p\infty}\omega^2\tau^2)}\right].$$

And by retaining terms up to $(DC_i/C_{p0}C_{v\infty})^2$, we have the second approximation velocity formula

$$V^2=\left(\frac{\partial p}{\partial \rho}\right)_T\left[1+D\frac{C_{v\infty}+C_{v0}\omega^2\tau^2}{C_{v0}C_{v\infty}(1+\omega^2\tau^2)}+\frac{3}{4}\frac{C_{p0}D^2C_i^2\omega^2\tau^2}{C_{v0}(C_{p0}C_{v\infty}+C_{v0}C_{p\infty}\omega^2\tau^2)^2}\right], \qquad (6.1)$$

or,

$$V^2=\left(\frac{\partial p}{\partial \rho}\right)_T\left[1+\frac{D}{C_{v0}}+\frac{DC_i\omega^2\tau^2}{C_{v0}C_{v\infty}(1+\omega^2\tau^2)}+\frac{3}{4}\frac{C_{p0}D^2C_i^2\omega^2\tau^2}{C_{v0}(C_{p0}C_{v\infty}+C_{v0}C_{p\infty}\omega^2\tau^2)^2}\right]. \qquad (6.2)$$

This may also be written as

$$V^2=V_0^2+(V_\infty^2-V_0)\frac{\omega^2\tau^2}{1+\omega^2\tau^2}+\frac{3}{4}\frac{(V_\infty^2-V_0^2)^2V_0^2\omega^2\tau^2}{(V_0^2+V_\infty^2\omega^2\tau^2)^2}. \qquad (6.3)$$

In terms of the relaxation time β, we have by (4.2) in place of (6.1) the expression

$$V^2=\left(\frac{\partial p}{\partial \rho}\right)_T\left[1+D\frac{C_{v0}+C_{v\infty}\omega^2\beta^2}{C_{v0}^2+C_{v\infty}^2\omega^2\beta^2}+\frac{3}{4}\frac{C_{p0}D^2C_i\omega^2\beta^2}{C_{v0}(C_{v0}C_{p0}+C_{v\infty}C_{p\infty}C^2\beta^2)^2}\right]. \qquad (6.4)$$

The second approximation absorption formula is obtained from (2.12) as

$$\alpha_\lambda=\pi\frac{DC_i\omega\tau}{C_{p0}C_{v\infty}+C_{v0}\omega_{p\infty}\omega^2\tau^2}\times\left[1-\frac{1}{4}\frac{D^2C_i^2\omega^2\tau^2}{(C_{p0}C_{v\infty}+C_{v0}C_{p\infty}\omega^2\tau^2)^2}\right], \qquad (6.5)$$

or, in terms of the relaxation time β, as

$$\alpha_\lambda=\pi\frac{DC_i\omega\beta}{C_{p0}C_{v0}+C_{p\infty}C_{v\infty}\omega^2\beta^2}\times\left[1-\frac{1}{4}\frac{D^2C_i^2\omega^2\beta^2}{(C_{p0}C_{v0}+C_{p\infty}C_{v\infty}\omega^2\beta^2)^2}\right]. \qquad (6.6)$$

The second approximation dispersion formulas (6.2) and (6.3) nearly coincides with the previously obtained ones (Nomoto[16], eq. (3.21) and (3.22)) in case of an ideal gas, up to a minor difference in the second order term in $\omega^2\tau^2$ (or $\omega^2\beta^2$) coming from the difference in methods of expansion. The second approximation formulas become indispensable in obtaining the dispersion formula for non-ideal gas or in calculating deviations of velocity for any real equation of state from an ideal gas. No such formulas applicable to both gases and liquids have been obtained before.

References

(cf. Table I for further references)

1) K. F. Herzfeld and F. O. Rice: Phys. Rev. **31** (1928) 691.

2) H. O. Kneser: Ann. Phys. **11** (1931) 761.

3) D. G. Bourgin: Nature **122** (1928) 133; Phil. Mag. **7** (1929) 821; Phys. Rev. **34** (1929, 521; Phys. Rev. **42** (1932) 721; J. Acous. Soc. Amer. **4** (1932) 108; **5** (1933) 57; Phys. Rev. **50** (1936) 355.

4) L. Bergmann: "Ultraschall," 6. Aufl. S Hirzel (1954).

5) P. Vigoureux: "Ultrasonics," Wiley (1951).

6) E. G. Richardson: "Ultrasonic Physics," Elsevier (1952).

7) B. B. Kudrjawzew: "Anwendung von Ultraschallverfahren bei physikalisch-chemischen Untersuchungen." D. V. W. (1955) (original russian 1952).

8) E. Hiedemann: "Ultraschallforschung" (1939).

9) O. Nomoto: "Ultrasonics—Velocity and absorption of sound." (in Japanese) (1948); "Molecular acoustics" (in Japanese) (1940).

10) H. O. Kneser: Molekulare Schallabsorption und -dispersion. Ergebnisse der Exakt. Naturwiss. **22** (1949) 121.

11) J. J. Markham: R. T. Beyer and R. B. Lindsay: Absorption of sound in fluids. Rev. Modern Phys. **23** (1951) 353.

12) S. M. Karim and L. Rosenhead: The second coefficient of viscosity of liquids and gases. Rev. Modorn Phys. **24** (1952) 108.

13) S. Petralia: Velocita e assorbimento di ultrasuoni nei gas. Nuuvo Cimento **9** Supplemento (1952) 1–58.

14) Maurice Dubois: L'absorption des sons et ultrasons dans les gaz. J. de physique **12**

(1951) 876.
15) D. Sette: L'assorbimento delle onde ultrasonore nei liquidi. Nuovo Cimento, **6** Supplemento (1949) 1–145.
16) E. G. Richardson: Absorption and velocity of sound in vapors. Rev. Modern Phys. **27** (1955) 12.
17) O. Nomoto: Proc. Phys.-Math. Soc. Japan **22** (1940) 77.
18) P. S. H. Henry: Proc. Cambr. Phil. Soc. **28** (1932) 249.
19) A. Eucken und R. Becker: Zeits. Phys. Chem. **27B** (1934) 235.
20) Hoff Lu: J. Acous. Soc. Amer. **23** (1951) 12.
21) G. Damköhler: Zeits. Elektrochem. **48** (1942) 62, 116.
22) J. Meixner: Ann. Phys. **43** (1943) 470.
23) S. R. De Groot: "Thermodynamics of irreversible processes." Amsterdam (1952) 51.
24) O. Nomoto: Bull. Kobayasi Inst. Phys. Res. **1** (1951) 162.
25) O. Nomoto: Irreversible production of entropy and the absorption of sound. J. Phys. Soc. Japan **11** (1956) 818.
26) P. G. T. Fogg, P. A. Hanks and J. D. Lambert: Proc. Roy. Soc. **A219** (1953) 490.
27) P. G. T. Fogg and J. D. Lambert: Proc. Roy. Soc. **A232** (1955) 537.

Short Notes

This section is intended to secure prompt publication of important discoveries in physics. The reports should not exceed 800 words in length. A figure of size 7 cm × 7 cm will be counted as 150 words.

J. Phys. Soc. Japan **12** (1957) 100

Electrical Properties of GeTe

By Yoshiro Moriguchi and Yutaka Koga
Kurume University

(Received October 20, 1956)

The electrical properties of the compounds, SnSe[1], GeSe[2] and SnTe[3], whose component elements belonging to the IV and VI groups of the periodic table have recently been reported. According to these reports, the first two compounds behave like an ordinary semiconductor, while, on the contrary the last shows rather a semi-metallic property. The measurements for GeTe, whose component elements also belong to the same groups as above, have been performed to compare with them.

The samples of the stoichiometric composition were made from Ge (from Eagle Picher Co., a few Ω cm) and Te (from Nihon Kogyo KK., 99.998%) by heating up to the melting point in an evacuated silica tube, and some of them were made into single crystals by zone-melting. The measured Hall coefficient R, resistivity ρ and thermoelectric power Q of the typical samples are shown in Fig. 1, and the Hall mobility R/ρ in Fig. 2. The signs of the Hall coefficient and thermoelectric power are positive through the whole temperature range.

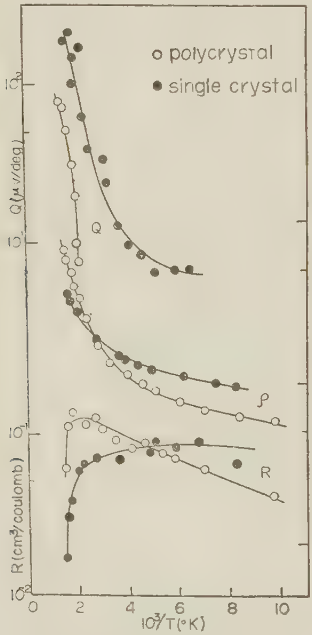

Fig. 1. The Hall coefficient R, resistivity ρ and thermoelectric power Q.

As shown in Fig. 1, the resistivity is comparatively small and its temperature coefficient is positive. In addition, the carrier concentrations obtained from the Hall coefficient have large value of about $10^{20}\sim10^{21}$ per cm³. It is to be noticed that these characteristics seem to be scarcely influenced by zone-refining. The large value of the carrier concentration and the positive temperature coefficient of the resistivity in the whole temperature range indicate that the ordinary theory for semiconductors, both homopolar and ionic, may be not able to be assumed for GeTe. These behaviours closely resemble those of SnTe, except that the Hall coefficient of GeTe decreases suddenly in high temperature range. The fact that the value of the carrier concentration is very large and do not decrease by zone-refining seems to suggest that the source of the charge carriers may be neither impurity atoms, nor the excess of one of the components as are usual in many ordinary semiconductors.

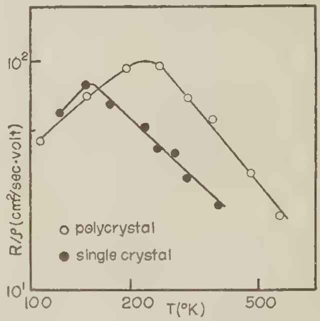

Fig. 2. The Hall mobility R/ρ.

The Hall coefficient and resistivity of GeTe are rather semi-metallic as mentioned above, but we have no preparations for the explanation of such electrical properties of GeTe at present.

We wish to express our gratitudes to Prof. Atuyosi Okazaki, Assist. Prof. Toshihiro Okada and the members of their laboratory for their kind guidances and for placing research facilities at our disposal.

References

1) Y. Matukura, T. Yamamoto and A. Okazaki: Memoirs of the Faculty of Science, Kyusyu University Ser. B, **1** (1953) 98
2) A. Okazaki, K. Hashimoto and S. Asanabe: reported at the annual meeting of the Physical Society of Japan in 1956.
3) K. Hashimoto and K. Hirakawa: J. Phys. Soc. Japan **11** (1956) 716

J. PHYS. SOC. JAPAN **12** (1957) 101

Electronic Structure of a Moving Exciton in Alkali Halides

By Toshinosuke MUTO and Sei-ichi OYAMA
Institute of Science and Technology, University of Tokyo

(Received November 2, 1956)

The solutions of Wannier-Slater equation, which have been actually obtained in the previous work¹⁾, can be made use of as one-electron orbitals in our new approach of a moving exciton problem. As is well-known, the theoretical treatment of a moving exciton is considered to become essentially many electron problem in which the configuration interaction plays decisive role. As for the one-electron orbitals from which determinantal functions can be constructed, the solutions of Wannier-Slater equation corresponding to the conduction continuum and the localized exciton states just below the mentioned continuum have been used for one-electron orbitals of the excited states. The normal state of valence electrons is supposed to be approximately represented by that of the band theory since the majority of valence electrons of the crystal is expected to be in the continuum region of the energy states and a few of them is considered to be brought into the localized states below the valence continuum.

As for the electron configuration, we shall confine ourselves to the configurations with one electron excited to the ground state of a localized exciton state below the conduction continuum from any one level of the valence band. Different configurations will be specified by different hole state of the valence band and different location of the localized exciton state. The other possible configurations in which an electron is raised into the excited states of a localized exciton or to the conduction continuum, and two or more electrons are raised into the similar excited states, will be entirely disregarded for the sake of simplicity*.

Then, we can set up the determinantal functions corresponding to each electron configuration mentioned above, a suitable linear combination of which is shown to be expressed by the determinantal functions constructed directly from the corresponding Wannier functions and a wave function of a localized exciton at, say $\vec{R}_l$. The latter determinantal function, specified by the location $\vec{R}_l$ of a localized exciton and by a hole in the n-th branch of the valence band, shall be denoted by $\Psi^{(s)}(\vec{R}_l;n)$ in which $s=1$ and 3 correspond to a singlet and triplet configuration, respectively. Since the valence band of the chlorides is seen to become the Cl 3p band, it has been shown to split into three branches ($n=1, 2, 3$) according to the method of tight-binding approximation by Bethe²⁾.

The correct linear combination of the above determinantal functions and the corresponding secular equation can be worked out along the usual method of procedure.

Then, we have, for the wave function of a moving exciton in the j-th branch of the exciton band.

$$\Psi_j^{(s)}=\sum_{\vec{R}_l}e^{i\vec{K}\vec{R}_l}\sum_{n=1}^{3}A_{j,n}^{(s)}\Psi^{(s)}(\vec{R}_l;n)$$

and, for the secular equation from which $A_{j,n}^{(s)}$ and the corresponding energy E_j of the exciton band are solved,

$$\sum_{n'=1}^{3}\Big\{\sum_{\vec{R}_l\neq\vec{R}_l'}e^{i\vec{K}(\vec{R}_l-\vec{R}'_l)}(\vec{R}'_l;n'',s|H|\vec{R}_l;n',s)$$
$$+(\vec{R}'_l;n'',s|H|\vec{R}'_l;n'',s)-E\delta_{n'',n'}\Big\}A_{j,n'}^{(s)}=0,$$

in which $\vec{K}$ denotes a wave number vector in the reciprocal lattice of the crystal and

$$(\vec{R}_l';n'',s|H|\vec{R}_l;n',s)$$
$$=\int\Psi^{(s)*}(\vec{R}_l';n'')H\Psi^{(s)}(\vec{R}_l;n')\,dV,$$
$$H=-\frac{h^2}{2m}\sum_{i=1}^{N}\Delta_i+\sum_{i=1}^{N}V_0(\vec{r}_i)+\sum_{i<j}^{N}e^2/r_{ij}.$$

The propagation of our localized exciton through the lattice can be observed in the first summation factor of the wave function mentioned above. Since the secular determinant will become of a cubic as mentioned above, we have, for the lowest exciton band, at least three branches, i.e., $E=E_j(\vec{K})$, $j=1, 2, 3$ as far as the spin-orbit coupling is neglected. The spin-orbit coupling which can mix triplet and singlet states of the exciton band and higher order configuration interaction can give rise to still more multiplet structure of the exciton band, the corresponding secular equation being set up in a straightforward way.

The details of the mentioned calculation together with the numerial evaluation of the energy values of the exciton multiplet shall be reported in this journal in near future.

References

1) T. Muto and H. Okuno: J. Phys. Soc. Japan **11** (1956) 633.
2) H. Bethe: Handbuch der Physik **24**/II (1933) 404.

---

* In this connection, we should like to note that two excitons problem is now being worked by Miyagawa, one of our graduate students.

J. PHYS. SOC. JAPAN **12** (1957) 102

Asymptotic Behaviour of the Laminar Compressible Boundary Layer over a Circular Cylinder with Uniform Suction*

By Michiru YASUHARA

Institute of Science and Technology, University of Tokyo

(Received August 15, 1956)

The Solution of the incompressible boundary layer equations for the flow over a circular cylinder with uniform suction has already been presented by Wuest¹⁾ and Lew²⁾ in a simple closed form. This note treats the compressible case. If the cylinderical coordinates (x, r) is chosen, and the asymptotic state in which all quantities are independent of x is considered, the boundary layer equations become

$$\rho v \frac{du}{dr} = \frac{1}{r}\frac{d}{dr}\left(\mu r \frac{du}{dr}\right), \tag{1}$$

$$C_p \rho v \frac{dT}{dr} = \frac{1}{r}\frac{d}{dr}\left(\frac{C_p \mu}{P_r} r \frac{dT}{dr}\right) + \mu\left(\frac{du}{dr}\right)^2, \tag{2}$$

where (u, v) are the velocity components and P, ρ, T, μ, C_p, and P_r show the pressure, the density, the temperature, the coefficient of viscosity, the specific heat at constant pressure, and the Prandtl number respectively, and further suffix ∞ and w express quantities at infinity and on the cylinder. Eqs. (1) and (2) can be integrated as follows.

$$\frac{T}{T_\infty} = 1 - \left(1 - \frac{u}{u_\infty}\right)^{P_r}\left(1 - \frac{T_w}{T_\infty} + \frac{\gamma-1}{2}M_\infty^2\right) - \frac{(\gamma-1)P_r}{2(2-P_r)}M_\infty^2\left\{\left(1-\frac{u}{u_\infty}\right)^2 - \frac{2}{P_r}\left(1-\frac{u}{u_\infty}\right)^{P_r}\right\}, \tag{3}$$

$$\rho_w v_w \varepsilon \log \frac{r}{\varepsilon} = -\int_0^u \frac{\mu}{(u_\infty - u)}du, \tag{4}$$

where ε is the radius of the cylinder. μ is a function of temperature as given by Sutherland, and is known as a function of u from (3). If μ is approximated by a linear function of the temperature used by Chapman and Rubesin³⁾, (4) is integrated as follows.

$$\frac{\rho_\infty V r}{C\mu_\infty} = \left\{R_{e\varepsilon} \Big/ \left(1 - \frac{u}{u_\infty}\right)^{T_w/T_\infty R_{e\varepsilon}}\right\} \times \exp\left[\frac{T_w}{T_\infty R_{e\varepsilon}}\left[\frac{(\gamma-1)P_r}{4(2-P_r)}M_\infty^2\left\{\left(1-\frac{u}{u_\infty}\right)^2 - 1\right\} + \frac{1}{P_r}\left\{1 - \frac{T_w}{T_\infty} - \frac{(\gamma-1)M_\infty^2}{2(2-P_r)}\right\}\left\{\left(1-\frac{u}{u_\infty}\right)^{P_r} - 1\right\}\right]\right], \tag{5}$$

where C is the Chapman-Rubesin constant, and

$$V \equiv -v_\omega, \qquad R_{e\varepsilon} \equiv \frac{\rho_\infty V \varepsilon}{C\mu_\infty}, \tag{6}$$

The shear stress on the cylinder τ_w and the temperature gradient on the cylinder are given by

$$\tau_w = \left(\mu \frac{du}{dr}\right)_w = \rho_w u_\infty V, \tag{7}$$

$$\left\{\frac{d(T/T_\infty)}{d(\rho_\infty V r / C\mu_\infty)}\right\}_w = P_r\left(\frac{T_\infty}{T_w}\right)^2\left(1 - \frac{T_w}{T_\infty} + \frac{\gamma-1}{2}M_\infty^2\right), \tag{8}$$

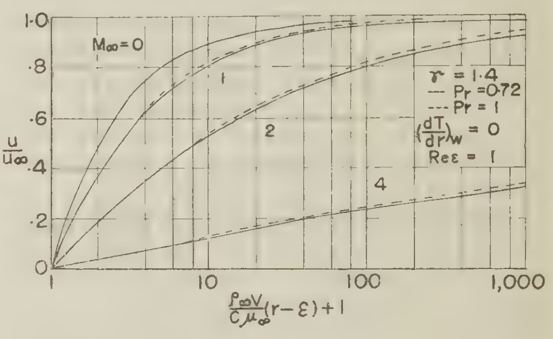

Fig. 1

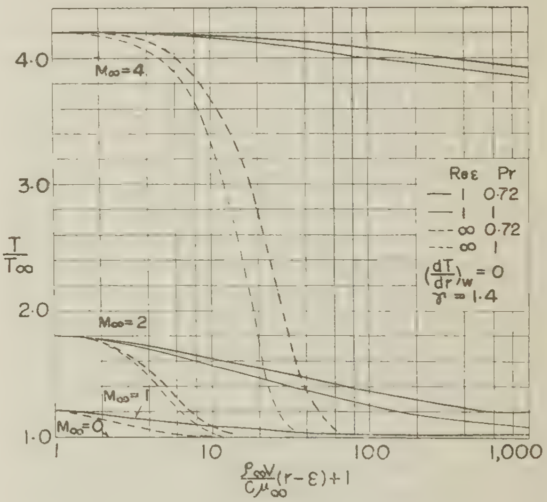

Fig. 2

Fig. 1 and Fig. 2 are several numerical examples which show qualitative natures of the flow.

Last, it should be noticed that, the condition to keep the displacement thickness finite is expressed as follows.

$$R_{e\varepsilon} > 2\frac{T_w}{T_\infty} \tag{9}$$

References

1) W. Wuest: Ing. Arch. **23** (1955) 198–208.
2) H. G. Lew: J. Aero. Sci. **23** (1956) 276–277.
3) D. Chapman and M. Rubesin: J. Aero. Sci. **16** (1949) 550–551.

---

* Note added in proof. It is interesting to note that, Prof. Lew has presented the same result independently, for the compressible case in "J. Aero. Sci. **23** (1956) 895–897".

J. Phys. Soc. Japan **12** (1957) 103~104

Carrier Concentration Changes in p-Si Induced by Heat Treatment

By Yasuo MATUKURA
Electrotechnical Laboratory, Tokyo, Japan

(Received August 14, 1956)

C. S. Fuller et al[1] has reported the changes in the resistivity of Si induced by heat treatment. We have observed the changes of carrier concentration in p-Si caused by heating at temperatures between 400° and 1000°C.

A p-Si single crystal of resistivity about 18 Ω cm was grown from the melt by the pulling technique. The room temperature-resistivity and Hall coefficient of bridge shaped specimens with Ni plated electrodes were measured before and after the heat treatment. After removing the Ni plating, the specimen were cleaned in HNO_3 and HF, then heated in H_2, air, or vacuum. The variation of the number of thermally induced electrons and holes with the temperature of treatment is shown in Fig. 1. Here the specimens were heated for 50 minutes in purified H_2 gas and quenched. The effect of the rate of cooling is shown in Table I, where specimens were heated in H_2 gas for 50 minutes. The slowest cooling (the last column) from 700°C gives an increase in electron content, which may be expected from the fact that the specimen is cooled through the region of 400° to 600°C at slow cooling rate. On the other hand, thermally induced carriers seem to influenced by the ambient gas. The heat treatment at 500°C in vacuum of 1×10^{-5} mm Hg has induced the smaller electron density than in H_2 or air, and the largest effect has been obtained in air as ambient. At 700°C, we could see no influence of the ambient. The relation between carrier concentration and heat treatment time, as shown in Fig. 2, was obtained by heating in vacuum and quenching. When specimens which showed an increase in hole concentration by heating at 700°C were heated at 500°C, they turned to n-type by the induced electrons. They were again turned to p-type by heating at 700°C. These cycles were reversible provided to heating times were successively prolonged.

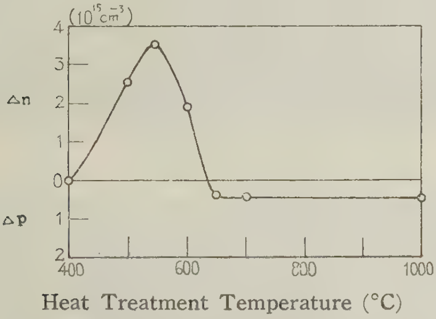

Fig. 1. Relation between the heat treatment temperature and induced electron concentration (Δn) or hole's (Δp).

Table I. Thermally induced carrier concentrations of silicon cooled at various rates after heating for 50 minutes in hydrogen gas. Minus signs represent the increase in holes.

Heating temperature (°C)	500			700		
Cooling rate (°C/min.)	quench	23	5	quench	50	6
Change of carrier density (10^{15} cm^{-3})	2.57	4.35	4.59	−0.41	−0.25	0.89

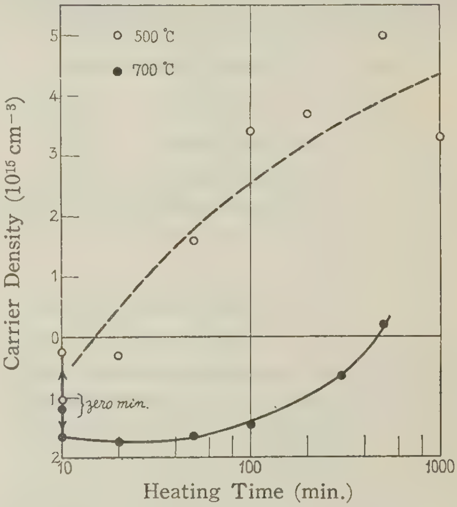

Fig. 2. Changes of carrier density by the heat treatment time in vacuum.

In order to interpret the complicated changes mentioned above, it seems better to consider that the phenomena observed in the case of low temperature treatment (under 650°C) are different in their origin to that observed in the case of high temperature treatment (above 650°C). In the former case, some kinds of surface impurities such as copper[2-3] in germanium may play a part of roles in the mechanisms. In the latter case, the lattice defcts of Schottky or Frenkel type would take part in the generation of holes[4].

These phenomena depend also on the conditions of preparing the sample. At the present situation it is proper to reserve the decisive conclusions on the mechanism of these phenomena.

The author wished to express his gratitude to Dr. G. M. Hatoyama, the members of his laboratory, and Mr. M. Kikuchi for various inspiring discussions, and Dr. T. Momota and Mr. T. Suzuki for their encouragements.

References

1) C. S. Fuller, J. A. Ditzenberger, N. B. Hannay and E. Buehler: Phys. Rev. **96** (1954) 833, and Acta Metallurgica **3** (1955) 97.
2) W. P. Slichter and E. D. Kolb: Phys. Rev. **87** (1952) 527.
3) R. J. Hodgkinson: Physica **20** (1951) 1001.
4) S. Mayburg and L. Rotondi: Phys. Rev. **91** (1953) 1015.

J. Phys. Soc. Japan **12** (1957) 104

On the Hall Effect in Bismuth at Low Temperature

By Hirosi HASEGAWA, Sigeru NAKANO
Department of Physics, Tokyo University
and Natsuki HASHITSUME
Department of Physics, Ochanomizu University

(Received October 29, 1956)

The galvano- and thermomagnetic properties of several metals show oscillatory behavior against magnetic field at liquid helium temperatures[1], which is similar to the de Haas-van Alphen oscillation. One of the characteristics of the field variation of these transport phenomena is, however, that these also have the monotonic part of the field dependence relatively steep in comparison with the susceptibility curves. The measurements of the Hall voltage in bismuth by J. M. Reynolds et al[2] show that the envelope is proportional to H^δ, where δ takes values between 2 and 3 under magnetic field up to 8 kilogauss. In their analysis of data, this dependence has not been accounted for, and the oscillatory part has been attributed to the periodic change in the number of conduction electrons versus reciprocal field intensity according to Landau-Dingle's formula[3]. We present here an interpretation of the monotonic part and also a remark on the oscillation of the Hall effect against field.

The galvanomagnetic effects of semi-metals are analyzed usually on the basis of the two band model[4], where very large magnetoresistance of these metals is interpreted as a result of the compensation of electrons and holes in contributing to the Hall field and also of their long mean free paths. In liquid helium temperatures and under strong magnetic field where the circular frequency ω_c of carriers is much larger than collision frequency $1/\tau$, the slight difference in number of electrons and holes alters the field dependence of Hall effect qualitatively from that expected under the condition $\omega_c\tau<1$[4].

In the case of bismuth it turns out that the excess of electrons less than 1% is sufficient to cause a rapid increase of the Hall voltage, what is actually observed by experiment. Reynolds' data were reanalyzed on this model, and we obtained an estimation of the difference as follows;

$$\Delta n=(3.7\pm0.3)\times10^{15}\,\mathrm{cm}^{-3}\ \text{at}\ 4.2°\mathrm{K}.$$

Assuming the concentration of conduction electrons to be $n=10^{18}\,\mathrm{cm}^{-3}$, we can estimate another parameter

$$\mu_1\mu_2/\mu_1+\mu_2=(2.8\pm0.3)\times10^6\,\mathrm{cm}^2/\text{volt sec}.$$

where μ_1 and μ_2 are the mobilities of an electron and a hole respectively which correspond to the respective maximum mass in the direction perpendicular to the principal axis, whereas the mobility estimated from residual resistance at vanishing field corresponds to the minimum mass.

The above-mentioned excess of electrons Δn would arise presumably from the ionization, say, of impurities. In the range of magnetic field used in experiments the distribution of charge carriers is determined almost always between the upper and the lower band themselves, because the ionization energy would not be affected appreciably by the increase of field intensity. If, for instance, some electrons fall into the lower band, the number of electrons in the upper band changes, but the difference Δn should not change. Therefore, even if the distribution of carriers is changed periodically with increasing field, the condition

$$\Delta n=\text{independent of } H$$

should be satisfied. This means that the oscillation of a conductivity tensor versus $1/H$ should occur at least through the second order terms which relate to the relaxation processes. If the oscillation is attributed to Δn in the expression of the Hall coefficient, we shall obtain a too rapid increase of the amplitude of oscillation, which contradicts with experimental data[6]. Similar remark has been made by M. C. Steele[1] in connection with the analysis of his experimental data in antimony.

Detailed calculations and discussions of the more basic problem of the transport theory under strong magnetic field will be presented later. The authors would like to express our thanks to Professor R. Kubo for his suggestions on this problem.

References

1) M. C. Steele: Phys. Rev. **99** (1955) 1751.
2) J. M. Reynolds, H. W. Hemstreet, T. E. Leinhardt, and D. D. Triantos: Phys. Rev. **96** (1954) 1203.
3) B. Abeles, and S. Meiboom: Phys. Rev. **101** (1956) 544.
4) T. Okada: J. Phys. Soc. Japan **11** (1956) 89.
5) W. C. Overton, and T. G. Berlincourt: Phys. Rev. **99** (1955) 1165.

J. Phys. Soc. Japan **12** (1957) 105

Spiral Etch Pits on Germanium Surface

By Makoto Kikuchi and Seiichi Denda
Electrotechnical Laboratory, Tokyo, Japan

(Received October 27, 1956)

Spiral etch pits have been formed on (111) germanium surface. It is already reported by Ellis[1] that this type of etch pits can be formed by using special kind of etching solution, i.e., bubbling Cl_2 in the mixture of KOH and H_2O at 0°C. We have succeeded, however, to form this kind of etch pits using rather usual solutions, i.e., the combination of HNO_3, HF, HCl, and H_2O_2.

Figs. 1 and 2 are the photographs of the spiral pits of left-hand and right-hand screw type, respectively. It has been confirmed that the density of this type of etch pits is at least two or three orders of magnitude smaller than the other kinds which are formed by ordinary etching.

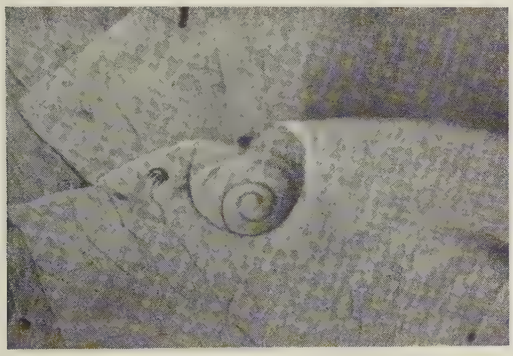

Fig. 1. Left-hand type spiral etch pit.

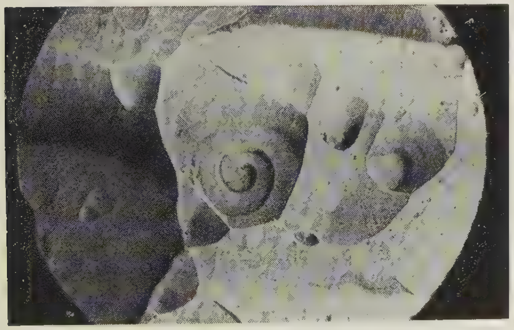

Fig. 2. Right-hand type spiral etch pit.

It must also be noticed that the etches which are effective in forming the pits of closed terraces[2] is quite useless to form the spiral pits.

Fig. 3 shows a pair of spiral etch pits, one is left-hand and the other is right-hand screw type.

It has been experienced that the number and the structure of etch pits critically depend on the relative amounts and combination of etching solutions, temperature, the treatment of the germanium surface before the etching, and on some important but unknown factors. The details are now being investigated.

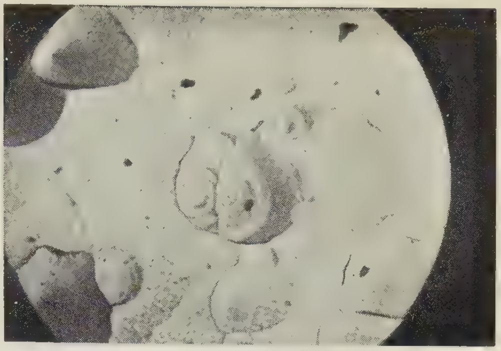

Fig. 3. A pair of spiral etch pits.

References

1) Ellis: J. A. P. **26** (1955) 1140.
2) M. Kikuchi and S. Denda: J. Phys. Soc. Jap. **11** (1956) 1127.

J. Phys. Soc. Japan **12** (1957) 105~106

On the Release of Alkaline Earth Metals by the Electron Dissociation of Oxide Films Evaporated from the Oxide Coated Cathodes

By Tetsuji Imai and Isao Mitsufuji
Electrical Communication Laboratory, Nippon Telegraph & Telephone Public Corporation, Tokyo, Japan

(Received October 23, 1956)

It was pointed out by Sproull[1] that a large quantity of condensable gas which is enough to cause a glow discharge is present in the anode-cathode space of the oxide-coated cathode magnetrons.

The author observed a quite similar phenomenon in the ordinary oxide-coated cathode vacuum tubes in which a electrode contaminated with cathode materials is utilized as the anode. In Fig. 1, variations of gas pressure measured by the external ionization gauge and of anode current are shown together with the schematic indication of the intensity of the glow observed in the anode-cathode space. The glow is analyzed spectroscopically and the several spectral lines of Ba, Sr and a trace of Ca are observed but other lines are not found as shown in Fig. 2.

In Fig. 1, it is noted that though in the first stage (small anode loss) increase of gas pressure measured by the gauge is as large as that of the second stage (large anode loss), glow between the anode and the cathode is observed only in the second stage. This fact implies that the increase of gas pressure observed by the gauge is not the direct cause of the glow. The latter may be attributed to the localized atomic and ionic Ba, Sr and Ca vapours which are left at first on the electron bombarded anode by the preferential removal of oxygen of the deposited oxide materials such as BaO, SrO and CaO and then released from the anode by sublimation.

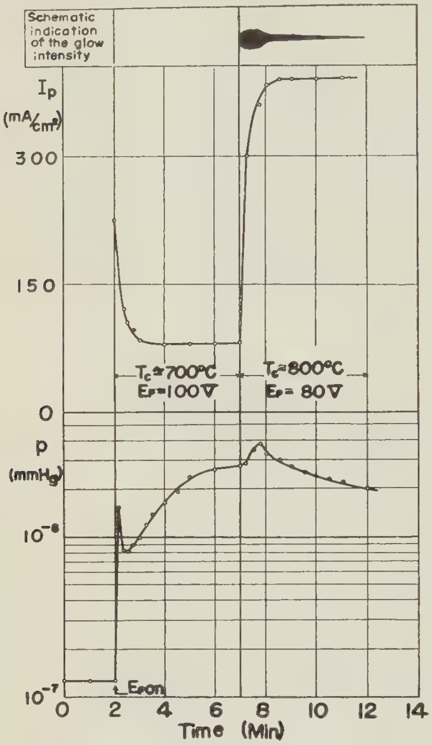

Fig. 1. Variations of anode current and gas pressure caused by electron bombardment of the open caovered with deposited oxide materials.

The releasing energy of Ba at the electron dissociation of the BaO cathodes is obtained by S. Yoshida and others²⁾ by the use of radioactive isotope. In this method, the electron bombardment is undertaken at various cathode temperatures and the quantities of Ba deposited on the outer electrodes are counted for each case. Therefore, the releasing energy obtained by this temperature dependency may be attributed reasonably to the sublimation energy of the Ba atoms or ions dissociated from BaO.

It is pointed out further that not only BaO but also considerably large quantity of SrO evaporate from the oxide coated cathode in contradiction to the previous supposition of the preferential evaporation of BaO only³⁾.

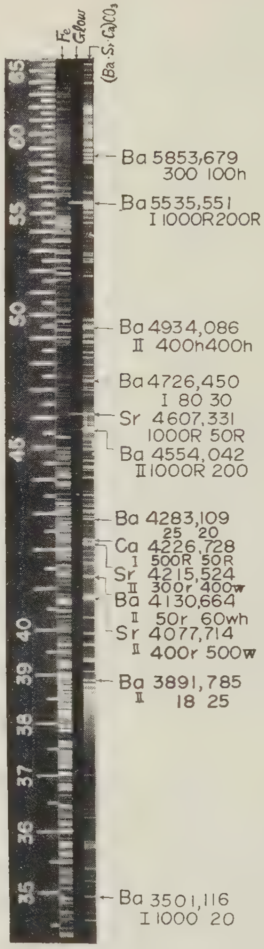

Fig. 2. Spectroscopical analysis of the glow.

References

1) R. L. Sproull: J. App. Phys. **18** (1947) 314.
2) S. Yoshida, N. Shibata, Y. Igarashi and H. Arata: J. App. Phys. **27** (1956) 497.
3) T. Imai: J. Phys. Soc. Japan **9** (1954) 28.

J. Phys. Soc. Japan **12** (1957) 107

Temperature Dependence of Electron Spin Resonance Absorption of Thiophenol in Sulfuric Acid

By Yasaburo YOKOZAWA and Isao MIYASHITA

Research Institute of Applied Electricity, Hokkaido University

(Received October 13, 1956)

Electron spin resonance absorption has been observed in free radicals embracing unpaired electrons. The resonance frequency ν in the static magnetic field H is given by

$$h\nu = g\beta H. \tag{1}$$

As the intensity of resonance absorption is proportional to the magnetic susceptibility χ,

$$\chi = \frac{Ng^2\beta^2 S(S+1)}{3kT}, \tag{2}$$

where S is the electronic spin quantum number and N the density of the unpaired electrons, it is important to examine the temperature dependence of the resonance absorption intensity.

The present writers have examined the temperature dependence of the absorption intensity of thiophenol (C_6H_5SH) in sulfuric acid. This absorption has been reported to consist of two parts, the g values being 2.015 and 2.008, respectively.[1]

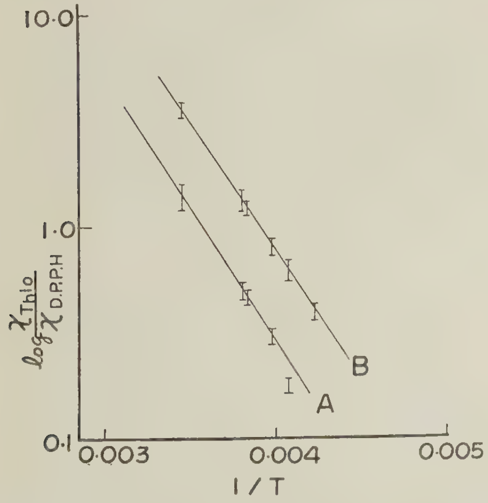

Fig. 1. The temperature dependency of resonance intensity of thiophenol in sulfuric acid. Ordinate: the logarithm of the ratio of the absorption intensity of the sample to that of D.P.P.H.. Abscissa: the reciprocal of absolute temperature.

The measurements were carried out at a frequency about 9000 mc/sec, covering the range from room temperature to liquid-nitrogen temperature. The absorptions were detected by the method of magnetic field modulation and the derivative of absorption curves were recorded using a lock-in amplifier. The absorption intensities were determined comparing the absorption area of the sample with that of diphenyl-picryl hydrazyl, inserted into the cavity together with the sample.[2]

The spectroscopic g factros do not change with temperature. The line widths are nearly independent of temperature, while the absorption intensities decrease with decreasing temperature and become too small to be detected under -55°C. One may infer from this that N in Eq. (2) is not constant in this case but dependent upon temperature. The intensity varies with temperature as shown in Fig. 1. In this figure the ratio of absorption intensity of the sample to that of D.P.P.H. is plotted against the reciprocal of absolute temperature. As the absorption intensity of D.P.P.H. is inversely proportional to the absolute temperature[3], this ratio is directly proportional to the density of unpaired electron, *viz* N in Eq. (2).

The two straight lines A and B of almost the same slope within experimental errors are obtained. A and B correspond to the absorptions of two g values, 2.015 and 2.008, respectively. Hence, the activation energies determined from these two slopes result in the same value 5.8 kcal/mol.

In this laboratory similar dependence on temperature was found in the case of perylen in sulfuric acid and it was concluded then that the absorption was arising from the triplet state.[2] In this case of thiophenol it is anticipated that the resonance absorption is also due to the triplet state. But further discussion on this problem will be given in a subsequent paper.

The present writers wish to present our sincere thanks to Professor K. Higasi for his kind interest and encouragement. A part of the expense has been defrayed from a grant by the Ministry of Education.

References

1) J. E. Wertz and J. L. Vivo: J. Chem. Phys. **23** (1955) 2193.
2) Y. Yokozawa and I. Miyashita: J. Chem. Phys. **25** (1956) 796.
3) H. J. Gerritsen, R. Okkes, H. M. Gijsman and J. van den Handel: Physica **20** (1954) 13.

J. PHYS. SOC. JAPAN **12** (1957) 108

On the Electronic Structure of Localized Exciton in Alkali Chlorides

By Toshinosuke MUTO and Hiroshi OKUNO

Institute of Science and Technology, University of Tokyo

(Received October 25, 1956)

As a continuation of the previous work[1] on KCl, our method of procedure based on Wannier-Slater equation for perturbed lattice has been extended to all chlorides which have been actually observed experimentally. Our numerical results are shown in the following table.

	κ	m^*/m	$-E'_{\text{cal.}}$	$-E'_{\text{obs.}}$
LiCl	2.75	0.6	0.89 ev	0.86 ev
NaCl	2.25	1.0	1.81	1.83
KCl	2.13	0.85	1.83	1.80
RbCl	2.19	0.7	1.53	1.50
CsCl	2.60	0.9	1.33	1.39

According to our experience in the best-fit procedure of the previous report[1], the effective dielectric constants κ have been tentatively assumed to be the high frequency values. The assigned values of the effective m^* in our procedure are observed to be of the order of magnitude ranging 0.5 m to m in accordance with the available experimental data. Generally speaking, therefore, the comparison shown in the Table seems to be good as far as the approximation in our method of procedure is allowed for. In order to avoid the misunderstanding, however, a few words should be added on our definition of a localized exciton. In fact our localized exciton does concern the exciton state localized around a lattice point only for the short duration of light absorption process but not for a still longer time. For a still longer time, the displacement of surrounding ions, i.e., lattice distortion will give rise to an essential influence on the exciton state.

In this connection, we should like to point out another example of the applicability of the Wannier-Slater equation for perturbed lattice. Pringsheim[2] and others discovered the so-called Greek bands in the longer wave length side of the usual exciton band of KI at low temperatures and such new absorption bands were ascribed to the localized exciton around a negative ion vacancy or a F-center, respectively. For an exciton trapped around a negative ion vacancy, the perturbation potential in the Wannier-Slater equation will become negative of the potential energy due to a Cl^- ion $V_{\text{cl}}(\vec{r}-\vec{n}a)$ in addition to that of a usual exciton $V(r)$.

Then, we have

$$-\frac{h^2}{2m^*}\Delta\psi(\vec{r})+\{V(r)+V_{\text{cl}}(\vec{r}-\vec{n}a)\}\psi(\vec{r})=E'\psi(\vec{r}).$$

The solution of the above equation can be obtained by the ordinary perturbation theory or through a similar method to that in the hydrogen molecule iron problem. The numerical evaluation is now in progress.

References

1) T. Muto and H. Okuno: J. Phys. Soc. Japan **11** (1956) 633.
2) C. J. Delbecq, P. Pringsheim and P. Yuster: J. Chem. Phys. **19** (1951) 574; **20** (1952) 746.

JOURNAL OF THE PHYSICAL SOCIETY OF JAPAN Vol. 12, No. 2, FEBRUARY, 1957

The Multipolarity of γ-ray Absorption in ^{12}C(γ, 3α) Reaction produced by (Li, p)γ-rays

By J. MUTO, E. TAKEKOSHI, T. NAKAMURA, A. IMAMURA
and Y. TSUNEOKA

Department of Physics, Faculty of Science, University of Kyoto

(Received September 6, 1956)

The mechanism of the ^{12}C(γ, 3α) reaction for (Li, p)γ-rays has been estimated from a study of 576 stars in nuclear emulsions. By the analysis of the angular distributions and correlation of the α-particles, the multipolarity of the absorption process of (Li, p)γ-rays by the ^{12}C nucleus can be explained by the mixture of two sorts of interaction $E1$ and $E2$. This result is consistent with Goward and Wilkins' conclusion, but our experimental data of the angular distribution of the first α-particles show significant forward asymmetry contrary to their backward asymmetry.

§ 1. Introduction

The reaction ^{12}C(γ, 3α) has been studied by many authors (Hänni, Telegdi & Zünti$^{1)}$, 1948; Nabholz, Stoll & Wäffler$^{2)}$, 1950; Telegdi & Zünti$^{3)}$, 1950; Telegdi$^{4)}$, 1951; Chastel$^{5)}$, 1954) by using the (Li, p)γ-rays, and by others (Eder & Telegdi$^{6)}$, 1952; Goward & Wilkins$^{7)8)}$, 1953, 1955; Liversey & Smith$^{9)}$, 1953; Dawson & Bigham$^{10)}$, 1953; Havliček & Dobovišek$^{11)}$, 1955) with the bremsstrahlung up to several ten MeV.

These experimental studies have shown that the reaction is expressed by the cascade form: ^{12}C(γ, α_1)^{8}Be(α_2)α_3, and demonstrated the general predominance of transitions to the 3 MeV level of ^{8}Be for γ-ray energy below 20 MeV. For the multipole character of the initial γ-ray interaction, Telegdi$^{4)}$ determined, by the energy analysis of carbon star α-particles produced by (Li, p)γ-rays, that it is the mixture of M1 and E2. On the other hand, Goward and Wilkins$^{8)}$ concluded that the γ-ray interaction is the mixture of E1 and E2, by analysing the angular distributions and correlation of cascade α-prongs of the star produced by the bremsstrahlung whose energy interval is from 17.0 MeV to 17.8 MeV.

We have analysed the angular distributions and correlation of carbon star α-prongs in the emulsion produced by (Li, p)γ-rays under the good geometrical condition, arriving at the conclusion that the multipolarity of γ-ray interaction is the mixture of E1 and E2.

§ 2. Procedure

Nuclear emulsions were irradiated for about 10 hours with γ-rays produced by proton bombardment of lithium. The proton beam was accelerated to 500 KV by an accelerator of the Cockcroft-Walton type, and the intensity of magnetically analysed beam was 500 μA. The diameter of thick Li-target was 8 mm. 1.5″×1″ Ilford C2 plates (200 μ thickness) were used. Each plate was arranged in such a manner that a 1 in. edge was 12 cm apart from the target and the 1.5 in. edges parallel to the γ-rays, giving glancing incidence.

Emulsions were processed by low pH amidol developer$^{12)}$, with the purpose of obtaining good discrimination between α-particles and protons, combined with a sufficiently low background, and then located with 2 precent glycerine solution.

The processed emulsions were scanned using "Tiyoda" microscope and "Nippon Kogaku" microscope at a magnification of 600. Detected tracks were measured at a magnification of 1350 or 1500. Each depth measurement (the mean of three readings) was subject to about $\pm 0.3\,\mu$ standard deviation. Errors in horizontal projections were $\pm 0.5\,\mu$.

The shrinkage factor was obtained by measuring the horizontal and vertical components of the lengths of Polonium α-tracks$^{13)}$.

The range-enery relation in C2 plate used was obtained from the range-energy curve corrected with P_0 α.

By momentum-balance analysis[7] 769 stars (momentum unbalance vector $|\Delta P| \leq 1.4$ in (a. m. u. MeV)$^{1/2}$) among the measured 957 stars were treated as ^{12}C(γ, 3α). Fig. 1 shows the histogram of values of the energy-release (E_T) for 769 stars. Then 606 stars, whose energies are $16.0 \text{ MeV} \leq E_T + Q \leq 18.6$ MeV (Q=7.28 MeV), were selected as ^{12}C(γ, 3α) stars produced by 17.6 MeV γ-ray.

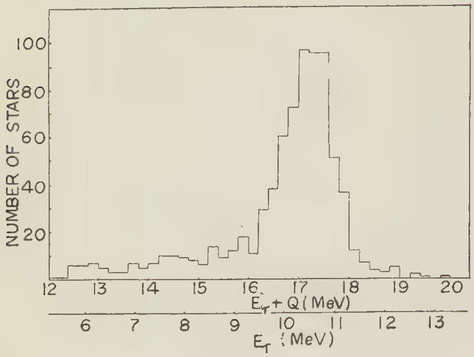

Fig. 1. Energy-release histogram for ^{12}C(γ, 3α).

Values of E^*_{ij} defined by the equation:

$$E^*_{ij} = \frac{1}{8}(P_i - P_j)^2$$

were calculated for 606 stars, where P_i and P_j are the observed vector momenta of α_i and α_j (i, j=1, 2, 3; $i \neq j$). E^*_{23} is the energy released when the unstable ^{8}Be nucleus breaks up into α_2 and α_3. Fig. 2 shows the histogram of E^* values. The histogram of E^* exhibits a pronounced peak at $E^* \simeq 3$ MeV with half-width $\Gamma \sim 1.0$ MeV. In order to assign the three α prongs of a star to α_0, α_2 and α_3, the significant E^* value, E^*_{23}, was taken to be the value nearest to (2.95+0.09) MeV, or the energy of α_1 was taken to be the value

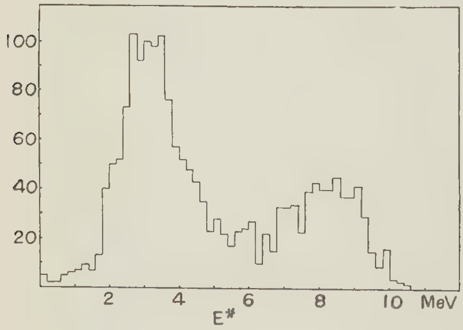

Fig. 2. E^* histograms (three values for each star).

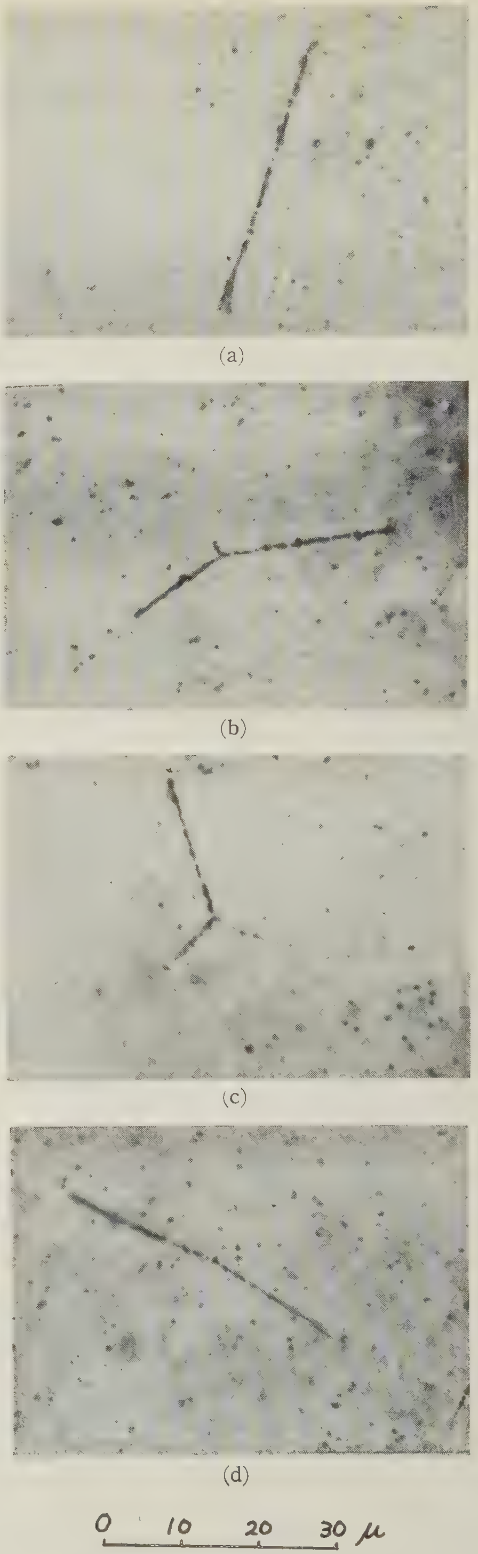

Fig. 3. Microphotographs of carbon star involving the transition to ^{8}B ground state (a) and the first excited state (b) (c) (d).

JOURNAL OF THE PHYSICAL SOCIETY OF JAPAN Vol. 12, No. 2, FEBRUARY, 1957

The Multipolarity of γ-ray Absorption in $^{12}C(\gamma, 3\alpha)$ Reaction produced by (Li, p)γ-rays

By J. MUTO, E. TAKEKOSHI, T. NAKAMURA, A. IMAMURA and Y. TSUNEOKA

Department of Physics, Faculty of Science, University of Kyoto

(Received September 6, 1956)

The mechanism of the $^{12}C(\gamma, 3\alpha)$ reaction for (Li, p)γ-rays has been estimated from a study of 576 stars in nuclear emulsions. By the analysis of the angular distributions and correlation of the α-particles, the multipolarity of the absorption process of (Li, p)γ-rays by the ^{12}C nucleus can be explained by the mixture of two sorts of interaction $E1$ and $E2$. This result is consistent with Goward and Wilkins' conclusion, but our experimental data of the angular distribution of the first α-particles show significant forward asymmetry contrary to their backward asymmetry.

§ 1. Introduction

The reaction $^{12}C(\gamma, 3\alpha)$ has been studied by many authors (Hänni, Telegdi & Zünti1), 1948; Nabholz, Stoll & Wäffler2), 1950; Telegdi & Zünti3), 1950; Telegdi4), 1951; Chastel5), 1954) by using the (Li, p)γ-rays, and by others (Eder & Telegdi6), 1952; Goward & Wilkins7)8), 1953, 1955; Liversey & Smith9), 1953; Dawson & Bigham10), 1953; Havliček & Dobovišek11), 1955) with the bremsstrahlung up to several ten MeV.

These experimental studies have shown that the reaction is expressed by the cascade form: $^{12}C(\gamma, \alpha_1)^8Be(\alpha_2)\alpha_3$, and demonstrated the general predominance of transitions to the 3 MeV level of ^8Be for γ-ray energy below 20 MeV. For the multipole character of the initial γ-ray interaction, Telegdi4) determined, by the energy analysis of carbon star α-particles produced by (Li, p)γ-rays, that it is the mixture of M1 and E2. On the other hand, Goward and Wilkins8) concluded that the γ-ray interaction is the mixture of E1 and E2, by analysing the angular distributions and correlation of cascade α-prongs of the star produced by the bremsstrahlung whose energy interval is from 17.0 MeV to 17.8 MeV.

We have analysed the angular distributions and correlation of carbon star α-prongs in the emulsion produced by (Li, p)γ-rays under the good geometrical condition, arriving at the conclusion that the multipolarity of γ-ray interaction is the mixture of E1 and E2.

§ 2. Procedure

Nuclear emulsions were irradiated for about 10 hours with γ-rays produced by proton bombardment of lithium. The proton beam was accelerated to 500 KV by an accelerator of the Cockcroft-Walton type, and the intensity of magnetically analysed beam was 500 μA. The diameter of thick Li-target was 8 mm. $1.5'' \times 1''$ Ilford C2 plates (200 μ thickness) were used. Each plate was arranged in such a manner that a 1 in. edge was 12 cm apart from the target and the 1.5 in. edges parallel to the γ-rays, giving glancing incidence.

Emulsions were processed by low pH amidol developer12), with the purpose of obtaining good discrimination between α-particles and protons, combined with a sufficiently low background, and then located with 2 precent glycerine solution.

The processed emulsions were scanned using "Tiyoda" microscope and "Nippon Kogaku" microscope at a magnification of 600. Detected tracks were measured at a magnification of 1350 or 1500. Each depth measurement (the mean of three readings) was subject to about $\pm 0.3\,\mu$ standard deviation. Errors in horizontal projections were $\pm 0.5\,\mu$.

The shrinkage factor was obtained by measuring the horizontal and vertical components of the lengths of Polonium α-tracks13).

The range-enery relation in C2 plate used was obtained from the range-energy curve corrected with P_0 α.

By momentum-balance analysis[7] 769 stars (momentum unbalance vector $|\Delta P| \leq 1.4$ in (a. m. u. MeV)$^{1/2}$) among the measured 957 stars were treated as $^{12}\mathrm{C}(\gamma, 3\alpha)$. Fig. 1 shows the histogram of values of the energy-release (E_T) for 769 stars. Then 606 stars, whose energies are 16.0 MeV$\leq E_T + Q \leq$18.6 MeV (Q=7.28 MeV), were selected as $^{12}\mathrm{C}(\gamma, 3\alpha)$ stars produced by 17.6 MeV γ-ray.

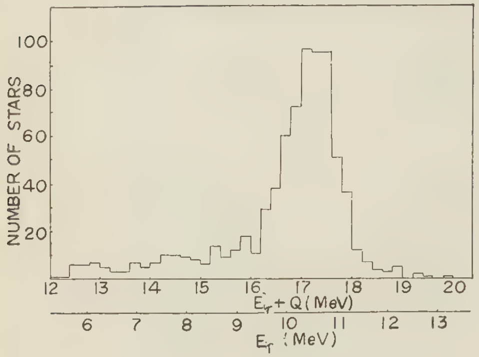

Fig. 1. Energy-release histogram for $^{12}\mathrm{C}(\gamma, 3\alpha)$.

Values of E^*_{ij} defined by the equation:

$$E^*_{ij} = \frac{1}{8}(P_i - P_j)^2$$

were calculated for 606 stars, where P_i and P_j are the observed vector momenta of α_i and α_j ($i, j = 1, 2, 3$; $i \neq j$). E^*_{23} is the energy released when the unstable ^{8}Be nucleus breaks up into α_2 and α_3. Fig. 2 shows the histogram of E^* values. The histogram of E^* exhibits a pronounced peak at $E^* \simeq 3$ MeV with half-width $\Gamma \sim 1.0$ MeV. In order to assign the three α prongs of a star to α_0, α_2 and α_3, the significant E^* value, E^*_{23}, was taken to be the value nearest to (2.95+0.09) MeV, or the energy of α_1 was taken to be the value

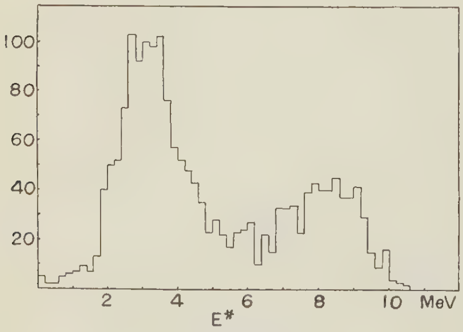

Fig. 2. E^* histograms (three values for each star).

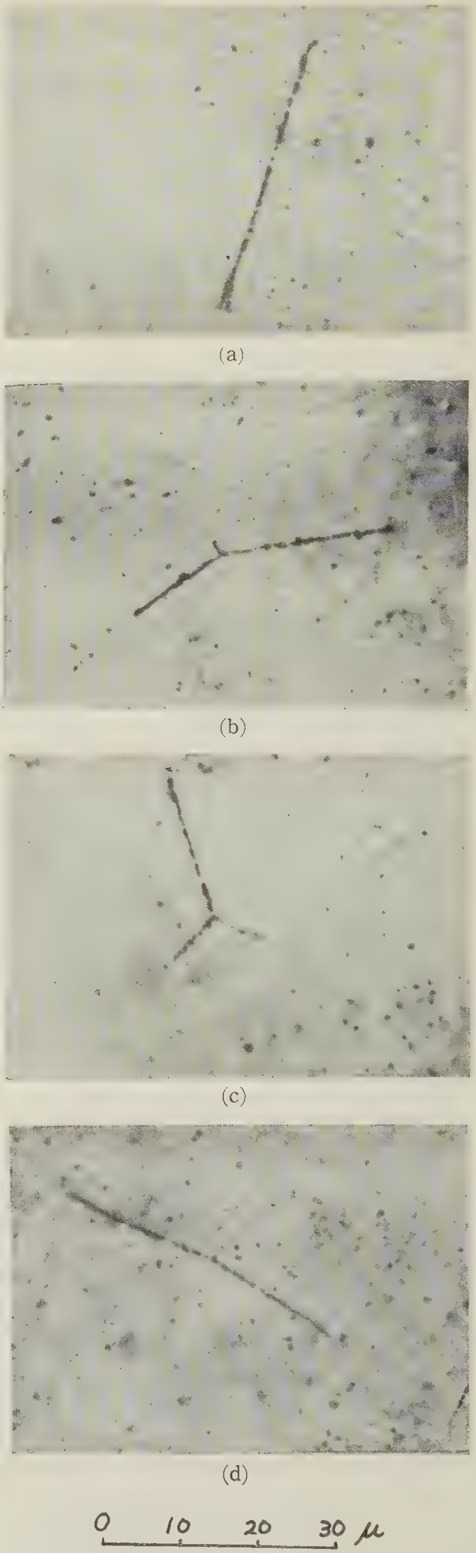

Fig. 3. Microphotographs of carbon star involving the transition to ^{8}B ground state (a) and the first excited state (b) (c) (d).

nearest to $\frac{2}{3}\{17.6-(7.28+3.04)\}$ MeV. Then 576 stars were selected as stars involving the first excited state of ^{8}Be. While 19 stars in the interval $E^* \leq 0.9$ MeV were selected as stars involving the ground state of ^{8}Be. The microphotographs of representative types of carbon star are shown in Fig. 3.

The angle θ_1 of emission of the α_1-particle relative to the direction of the incident γ-ray, as observed in the rest system of the ^{12}C nucleus, the correlation angle θ_C between the direction of break-up of the recoiling ^{8}Be nucleus and the direction of α_1 in the ^{12}C system, and the angle θ_{23} between the direction of break-up of the ^{8}Be nucleus and γ-ray direction are given by the following equations respectively:

$$\theta_1=\psi_1+\tan^{-1}\left[\frac{P_\gamma \sin\psi_1}{3P_1-P_\gamma\cos\psi_1}\right],$$

$$\cos^2\theta_C=\frac{(E^*_{12}-E^*_{13})^2}{E^*_{23}(2E^*_{12}+2E^*_{13}-E^*_{23})},$$

$$\cos^2\theta_{23}=\frac{(P_2\cos\psi_2-P_3\cos\psi_3)^2}{8E^*_{23}},$$

where P_i ($i=1, 2, 3$) is the momentum vector of α_i, P_γ is the momentum of γ-ray and ψ_i ($i=1, 2, 3$) is the observed angle between α_i and the γ-ray. These are shown in Fig. 4.

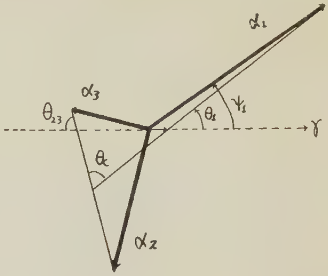

Fig. 4. Velocity vectors of $^{12}C(\gamma\alpha_1)^8Be^*(\alpha_2)\alpha_3$.

θ_0, θ_C and θ_{23} were calculated for 507 stars involving the first excited level of ^{8}Be.

§3. Results and Discussion

The α-particle angular distributions and correlation associated with the first excited state transitions are presented in Fig. 5. These corrected distributions of I (θ_1, θ_C or θ_{23}) values are presented in the form:

$$I(\theta)=N(\theta)\ \mathrm{cosec}\ \theta\ ,$$

where $N(\theta)$ is the number of stars having $\theta(\theta_1, \theta_C$ or $\theta_{23})$ values within the interval 20°. The fraction of randomly oriented $^{12}C(\gamma, 3\alpha)$ stars which escape from an emulsion of 200 μ thickness is 10 percent at $\theta=90°$. In Fig. 5 the vertical lines indicate the purely statistical standard deviations.

In order to compare the experimental results with theory, it was assumed that the 2.95 MeV level of ^{8}Be has spin-parity 2^+, and the $E1$, $M1$ and $E2$ γ-ray interaction were considered. The general theoretical expressions for $I(\theta_1)$, $I(\theta_C)$ and $I(\theta_{23})$ are given in Appendix. It is worth noticing that for mixed $E1+E2$ interactions interference terms $P_1(\cos\theta_1)$, $P_3(\cos\theta_1)$ may be present in $I(\theta_1)$, but $E1+M1$ or $M1+E2$ mixtures have no such interference

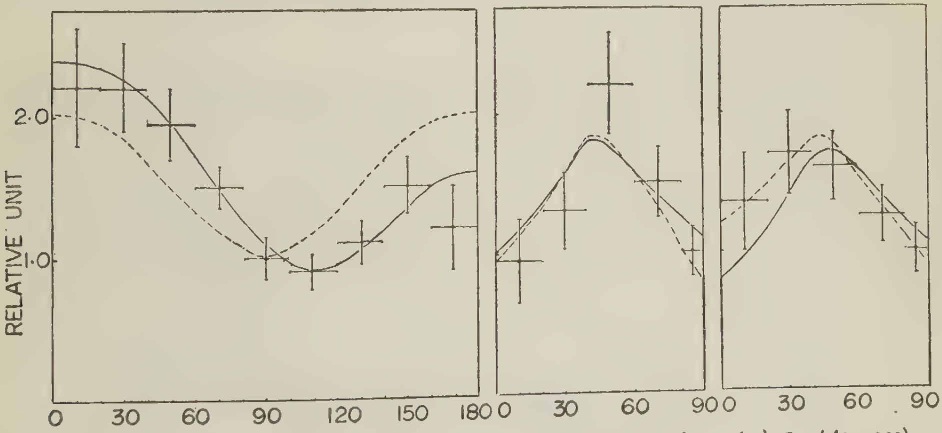

(a) θ₁ (degrees) (b) θc (degrees) (c) θ23 (degrees)

Fig. 5. Angular distributions and correlation in the 2.95 MeV transitions. The curves indicate possible theoretical results for a $J=2$ level, and $E1+E2$ (full lines) of $M1+E2$ (dotted lines) γ-ray interactions.

Table I. Transition to 2.95 MeV level of ^{8}Be: Angular Distributions and Correlation Analysis.

γ-ray interaction	ratio to $E2$	unknown parameter	$I(\theta_1)$	$I(\theta\ )$	$I(\theta_{23})$
$E1+E2$	1/2	$\sigma_1=\sigma_3=0.25$ $\sigma_0=\sigma_2=\sigma_4=0.3$ $\cos\eta_{02}=2/3$, $\cos\eta_{13}=1$ $\cos\eta_{04}=-2/3$ $\cos\eta_{24}=-1/3$	$1.4+0.60P_1+0.67P_2$ $-0.20P_3-0.06P_4$	$1.4+0.39P_2-0.78P_4$	$1.4+0.07P_2-0.66P_4$
$M1+E2$	1/2	$\sigma_{M1}=0.5$ $\sigma_0=\sigma_2=\sigma_4=0.3$ $\cos\eta_{02}=2/3$ $\cos\eta_{04}=-2/3$ $\cos\eta_{24}=-1/3$	$1.4+0.68P_2-0.06P_4$	$1.4+0.39P_2-0.84P_4$	$1.4+0.48P_2-0.66P_4$

terms.

The three experimental curves $I(\theta_1)$, $I(\theta_C)$ and $I(\theta_{23})$ could not be consistently explained by each pure interaction $E1$, $M1$ or $E2$ only. Therefore, it was considered that the 17.6 MeV γ-ray is absorbed by mixed levels but not by pure level of ^{12}C. Then the experimental data were approximated, as far as possible, by $E1+M1$, $E1+E2$ and $M1+E2$ interaction mixtures. It was found, however, that $E1+M1$ mixtures are unsatisfactory. Each particular set of parameter values of the $E1+E2$ and $M1+E2$ mixtures are given in Table I. The percentage given in this table should be unreliable, since the assumed values for σ and η may be considerably in error (see Appendix). Fig. 5 illustrates that in $I(\theta_C)$ and $I(\theta_{23})$ the agreement between theory and experiment is good for two mixtures $E1+E2$ and $M1+E2$, but in $I(\theta_1)$ a good agreement is found only for the $E1+E2$ mixture. The strong experimental evidence of asymmetry in $I(\theta_1)$ about $\theta_1=90°$ suggests at least a predominant $E1+E2$ mixture. This result is in agreement with that of Goward and Wilkins$^{8)}$, but our $I(\theta_1)$ distribution shows significant asymmetry contrary to their distribution which shows backward asymmetry in the region 17.0 MeV $\leq E_\gamma \leq$ 17.8 MeV.

Acknowledgments

The authors wish to thank Professor K. Kimura, Professor Y. Fujimoto and members of our laboratory for helpful advices. Their thanks are also due to Mr. J. Iwadare for valuable theoretical discussions, and to Miss N. Shiomi, Miss M. Arisada and Miss K. Ikeda for scanning many plates.

Appendix

The general theoretical expressions for angular distributions and correlation in a three-stage nuclear reaction have been derived by Brinkworth$^{14)}$. This general theory was applied to following special cases.

When the intermediate ^{8}Be state is 2$^+$ in ^{12}C(γ, α_1)^{8}Be(α_2)α_3 reaction, then, for $E1$ γ-ray interaction, we have

$$I(\theta_1)=(\sigma_1+\sigma_3)+[-0.10\sigma_1-0.40\sigma_3+1.47(\sigma_1\sigma_3)^{1/2}\cos\eta_{13}]P_2(\cos\theta_1)\ ,$$

$$\begin{aligned}I(\theta_c)=(\sigma_1+\sigma_3)&+[\sigma_1+1.14\sigma_3-0.71(\sigma_1\sigma_3)^{1/2}\cos\eta_{13}]P_2(\cos\theta_c)\ ,\\&+[0.86\sigma_3-4.22(\sigma_1\sigma_3)^{1/2}\cos\eta_{13}]P_4(\cos\theta_c)\ ,\end{aligned}$$

$$I(\theta_{23})=(\sigma_1+\sigma_3)-[0.50\sigma_1+0.14\sigma_3]P_2(\cos\theta_{23})\ ,$$

where σ_1 and σ_3 are proportional to the intensity of the angular momentum of the $l=1$ and $l=3$ waves respectively, and η_{13} is an arbitrary (unknown) phase angle.

For $M1$ interaction and 2$^+$ ^{8}Be we have

$$I(\theta_1)=\sigma_{M1}+0.50\sigma_{M1}P_2(\cos\theta_1)\ ,$$

$$I(\theta_c)=\sigma_{M1}+0.71\sigma_{M1}P_2(\cos\theta_c)-1.71P_4(\cos\theta_c)\ ,$$

$$I(\theta_{23})=\sigma_{M1}+0.50\sigma_{M1}P_2(\cos\theta_{23})\ .$$

For $E2$ interaction and 2$^+$ ^{8}Be we have

$$\begin{aligned}I(\theta_1)=&(\sigma_0+\sigma_2+\sigma_4)\\&+[0.16\sigma_2+1.90\sigma_4-1.20(\sigma_0\sigma_2)^{1/2}\cos\eta_{02}-0.01(\sigma_0\sigma_4)^{1/2}\cos\eta_{04}-0.54(\sigma_2\sigma_4)^{1/2}\cos\eta_{24}]P_2(\cos\theta_1)\end{aligned}$$

$$
\begin{aligned}
&\quad -[2.14\sigma_2+1.61\sigma_4+9.34(\sigma_0\sigma_4)^{1/2}\cos\eta_{04}-7.98(\sigma_2\sigma_4)^{1/2}\cos\eta_{24}]P_4(\cos\theta_1)\,,\\
I(\theta_c)&=(\sigma_0+\sigma_2+\sigma_4)\\
&\quad +[0.31\sigma_2+1.02\sigma_4-2.43(\sigma_0\sigma_2)^{1/2}\cos\eta_{02}-1.10(\sigma_2\sigma_4)^{1/2}\cos\eta_{24}]P_2(\cos\theta_c)\\
&\quad +[0.80\sigma_2+0.60\sigma_4+3.52(\sigma_0\sigma_4)^{1/2}\cos\eta_{04}-3.00(\sigma_2\sigma_4)^{1/2}\cos\eta_{24}]P_4(\cos\theta_c)\,,\\
I(\theta_{23})&=(\sigma_0+\sigma_2+\sigma_4)\\
&\quad +[0.71\sigma_0-0.15\sigma_2+0.20\sigma_4]P_2(\cos\theta_{23})\\
&\quad -[1.71\sigma_0+0.49\sigma_2+0.01\sigma_4]P_4(\cos\theta_{23})\,.
\end{aligned}
$$

References

1) H. Hänni, V. L. Telegdi and W. Zünti: Helv. Phys. Acta **21** (1948) 203.
2) H. Nabholz, P. Stoll and H. Wäffler: Helv. Phys. Acta **23** (1950) 858.
3) V. L. Telegdi and W. Zünti: Helv. Phys. Acta **23** (1950) 745.
4) V. L. Telegdi: Phys. Rev. **84** (1951) 600.
5) R. Chastel: J. Phys. Radium **15** (1954) 240.
6) M. Eder and V. L. Telegdi: Helv. Phys. Acta **25** (1952) 55.
7) F. K. Goward and J. J. Wilkins: Proc. Roy. Soc. **A217** (1953) 357.
8) F. K. Goward and J. J. Wilkins: Proc. Roy. Soc. **A228** (1955) 376.
9) D. L. Liversey and C. L. Smith: Proc. Phys. Soc. **A66** (1953) 689.
10) W. K. Dawson and C. B. Bigham: Canad. J. Phys. **31** (1953) 167.
11) F. I. Havliček and B. Dobovišek: Phys. Rev. **100** (1955) 1355.
12) J. Rotblat and C. T. Tai: *Fundamental Mechanism of Photographic Sensitivity* (1951) 331.
13) R. Chastel and A. Bernet: *Science and Application of Photography*. (Proceedings of the R. P. S. Centenary Conference, London, 1953) 441.
14) M. J. Brinkworth: A. E. R. E. Rep. GP/R (1954) 1364.

JOURNAL OF THE PHYSICAL SOCIETY OF JAPAN Vol. 12, No. 2, FEBRUARY, 1957

Intensity and Energy Spectrum of Fast Neutrons in Cosmic Radiation

By Saburo MIYAKE, Kensaku HINOTANI and Kan-ichi NUNOGAKI

Institute of Polytechnics, Osaka City University, Osaka

(Received July 9, 1956)

The intensity and the energy spectrum of low energy neutrons at Mt. Norikura (2740 m above sea level and 25°N geomagnetic latitude) were obtained by observing recoil protons with the randomly operated high pressure cloud chamber filled with hydrogen gas at the pressure of 92 atm. The differential energy spectrum for neutrons in the energy range from 1 Mev to 15 Mev was found to be expressed by

$$(1.2\pm40\%)\times10^{-3}\times E^{-1.25\pm0.10}\,\mathrm{cm^{-2}\,sec^{-1}\,sterad^{-1}\,Mev^{-1}}\,.$$

The neutron flux is in conformity with what one would expect from the density of thermal neutrons. Connecting the present data with the others which were obtained by many investigations in different energy ranges, the energy spectrum of neutrons ranging from 1 ev to 10 Bev are discussed.

§ 1. Introduction

The intensity of fast neutrons in cosmic radiation is related to the intensity of the primary radiation and the process of nucleon cascade of the N-component in the atmosphere. It should be noticed that as the low energy neutron component has the largest latitude effect among all others,[1] it is a good indicater for the primary radiations of such energies as to be influenced by the terrestrial magnetic field. On the other hand, one can obtain some information for nucleon cascade in the atmosphere from energy spectrum of greater than 10 Mev.

The absolute intensity of the nucleon component has been derived from the data using a variety of detecting method2). Data of cosmic ray hard showers obtained in multiplate cloud chamber or counter trays, and a positive excess of penetrating particles observed in magnetic could chamber allow an estimation of the intensity of the nucleonic component which has the energy larger than serveral Bev. The data on stars observed in photographic emulsion3) also give an estimation of the nucleon component for the energy larger than about 200 Mev, and the observation by proportional counter gives the proton flux of this energy region4).

The density of the thermal neutrons which have the energy lower than 0.4 ev in the atmosphere has been measured by means of difference method between two geometrically identical BF_3 counters one of which was shielded with cadmium sheet and the other with tin sheet5). Concerning the absolute intensity of the neutrons, however, it is very difficult to show the energy spectrum over the whole energy range because the measurement has been done for the energy range from about 1 ev to 200 Mev, and some of the methods above mentioned are indirect for obtaining the absolute intensity.

In this report, the observation of the neutrons of 1 Mev to 15 Mev at Mt. Norikura (2740 m above sea level and 25°N geomagnetic latitude) will be described and the absolute intensity of the neutron will be discussed making use of other energy ranges which were obtained already by many investigations, considering latitude and altitude effects.

§ 2. Experimental Apparatus and Procedure

A cloud chamber6) filled with high pressure hydrogen gas is suitable for measuring the intensity and the energy distribution of neutrons ranging from 1 to 10 Mev, because it has adequate stopping power and comparatively long sensitive time. The proton tracks observed in our investigation were analysed as recoil protons by neutrons, because other processes, for example, Compton scattering of protons by gamma rays or single prong stars of impurity nuclei are negligible. The experimental conditions of the instrument used are as follows:

1) *Effective volume*

The size of the high pressure cloud chamber which was used is 50 cm in dia, and 20 cm in depth, but the whole volume was not used in our experiment. From the stereoscopic analysis, the positions of the tracks were determined and the distribution map of the positions were obtained. From the map, the volume in which the tracks were distributed uniformly, was determined. The volume was corrected considering the sweeped distance by electric field and the expansion ratio of the chamber. The effective volume was 15.1 ±2.5 liter.

2) *Range-energy relation for proton*

The pressure of inner gas was 92±3 atm, this value was estimated from the range of *mu*-meson of *pi-mu-e* decay and the stopping power of the hydrogen gas. The range energy relation in hydrogen gas was obtained from the range energy relation in air7) and the atomic stopping power ratio8) of hydrogen to air, and is shown in Fig. 1, in which an experimental point of *mu*-meson is also shown.

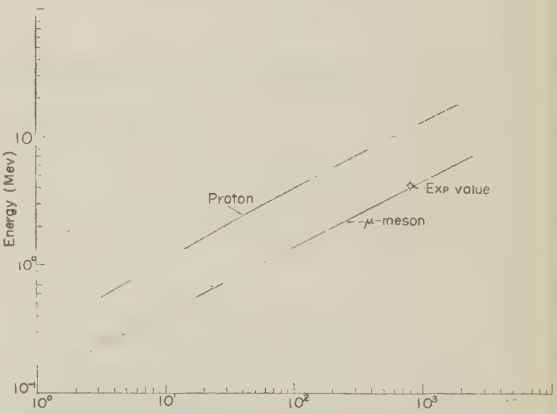

Fig. 1. The range-energy relations for proton and μ-meson in hydrogen gas in NTP. The experimental value of μ-meson range is obtained from the range of 4.1 Mev μ-meson in $\pi-\mu-e$ decay observed in the high pressure cloud chamber.

3) *Sensitive time*

The sensitive time of the chamber depends upon the pressure, the kind of gas contained, the intensity of electric field and the ionization density of the tracks. In the present work, since the recoil proton tracks are heavily ionizing, the sensitive time could be determined easily from the measurement of the track width. If N_0 is the number of ions per unit length produced along a track, the ionization density $I(x)$ at distance x from the track center after the time elapse of time t from the beginning of the diffusion is given by:

$$I(x)=(4\pi Dt)^{-1/2}N_0\exp(-x^2/4Dt) \qquad (1)$$

The 90% width of image, X, is given by:

$$X=4.68(Dt)^{1/2}\,\text{cm} \qquad (2)$$

The width X_0 of the oldest track was estimated from the relation between the integrated number of tracks and their width as shown in Fig. 2. It can be seen from the curve, that the track width is proportional to the square root of t, because the frequency of the recoil protons is assumed to be equal in each time interval. From the track width at the saturation point of the curve, the value of X_0 was determined to be 3.2±0.3 mm, and using $D=1.2\times10^{-3}\,\text{cm}^2\,\text{sec}^{-1}$ (for hydrogen at 92 atm.)[9] the sensitive time was obtained as 3.4±0.6 sec. from Eq. (2).

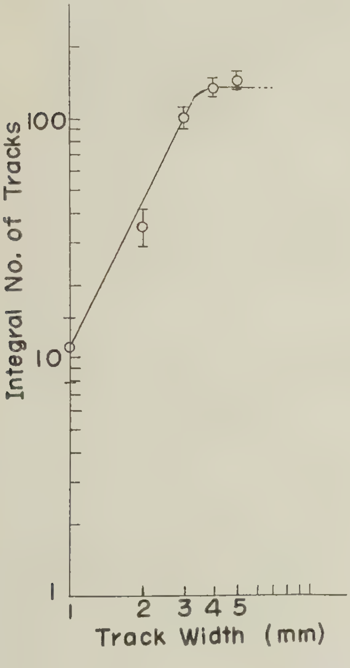

Fig. 2. Integral track width distribution of recoil protons. From the saturated width in this curve, the sensitive time of the chamber was determined.

4) *Effect of surrounding materials*

The observed neutron intensity is affected by the surrounding materials, which consisted of an iron wall of about 8 cm thickness, and water and oil in fore and back section of the chamber, respectively[6]. It was difficult to perform an exact correction owing to the complex geometry of the chamber. So an approximate procedure was taken by assuming the chamber to be a cylinder of average wall thickness, and assuming that the fast neutron in cosmic ray decrease with the absorption path of the geometrical path through the material as in the case of air nuclei[10]. To obtain the intensity of neutron in the air, the correction of 80, 10 and 10% of the total flux for the absorption in the iron wall, water and oil respectively must be applied. Thus, the correction factor of the neutron flux in the chamber to that of outside was estimated to be 1.25. Even if 2.5 times of the geometrical path is assumed for the absorption path, the factor decreases only about 5%.

The effect of the materials on the energy spectrum must also be considered. Little is known concerning this problem and only two facts are known. One is that[11] the difference of rates of production of low energy neutrons in carbon and in the iron by air shower is only 30% per unit weight, while the difference amounts to 130% for carbon and lead, and the other is that there is no process which can be considered to cause a large change of the energy spectrum by iron of such thickness. Thus the observed spectrum can be considered to be nearly equal to that in the atmosphere. (This is acertained by comparing the spectrum with that of nitrogen stars[14].)

§ 3. Experimental Data

1) *Frequency of recoil protons*

252 pairs of the high pressure cloud chamber photographs were scanned and 375 tracks and 532 " point tracks " (this means the tracks shorter than 0.5 cm) of recoil protons which have both ends within the sensitive region of the chamber.

The observed frequency of the tracks must be duely corrected, since the detection efficiency varies according to the track length.

Considering four sections of the cylindrical volume as shown in Fig. 3, the density distribution of the centers of the tracks, whose length is $2l$ and both ends are observed in the measurable volume, $F(r, x, l)$, for each section is easily shown as follows:

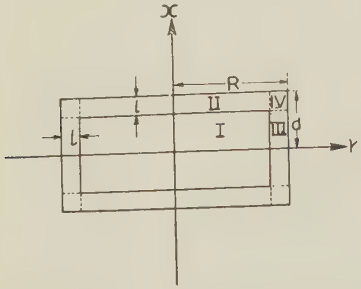

Fig. 3. Cross section of the chamber. The cross section is devided into four sections by track length $2l$. The correction function is determined in each section. x and r axes represents axial and radial directions respectively.

$$F(r, x, l)_1=1 \qquad \text{for section 1}$$

$$F(r, x, l)_2=\frac{d-x}{l} \qquad \text{for section 2}$$

$$F(r, x, l)_3=\frac{R-r}{l} \qquad \text{for section 3}$$

$$F(r, x, l)_4=\frac{(d-x)(R-r)}{l^2} \qquad \text{for section 4}$$

where r and x are radial and axial distances from the center of the chamber, and R and d are radius and half depth of the volume respectively. It was assumed that the angular distribution of the tracks was spherically symmetric, and the diameter of the cylinder was large enough compared to the track length. Error caused by this approximation is about 4% for 10 cm long tracks.

Table I. The observed and corrected No. of the recoil proton tracks.

Energy (Mev.)	Obs. No.	Corrected No.
3.0– 4.0	94	97
4.0– 5.0	86	93
5.0– 6.0	48	54.6
6.0– 7.0	32	39
7.0– 8.0	21	27.7
8.0– 9.0	18	26.7
9.0–10.0	9	14.8
10.0–11.0	11	19.8
11.0–12.0	9	18
12.0–13.0	4	8.8

Use of these functions leads to the correction factor $K(l)$ as follows:

$$\frac{1}{K(l)}=\frac{1}{V}\iint F(r, x, l)\,2\pi r dr\,dx$$

where V is the total volume.

The observed and corrected number of the recoil proton tracks are given in Table I.

2) *Energy distribution of recoil protons*

The differential energy distridution of recoil protons is shown in Fig. 4 and can be expressed by the empirical formula $kE^{-2.0\pm0.1}$. In this figure, it must be noted that the statistical error is small in the energy range lower than 3 Mev but the observed number may not be accurate because of the missing the tracks, as these are very short.

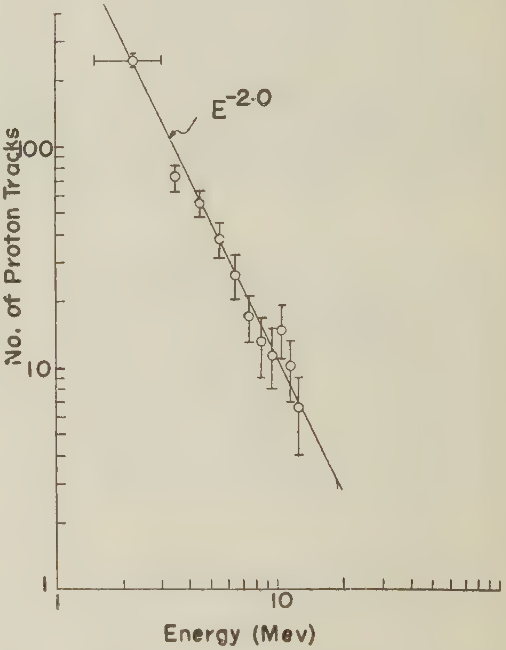

Fig. 4. Differential energy distribution of recoil proton tracks. The solid line is $E^{-2.0}$ obtained by means of the least square.

3) *Angular distribution*

As shown in Fig. 5 the zenith angle distribution of recoil proton tracks seems to be isotropic.

The direction of the motion of a particle can not be determined, unless the recoil protons collide further with hydrogen nuclei in the chamber. The ratio of having the upward and downward directions is estimated to be about 1/4 from the observation of 14

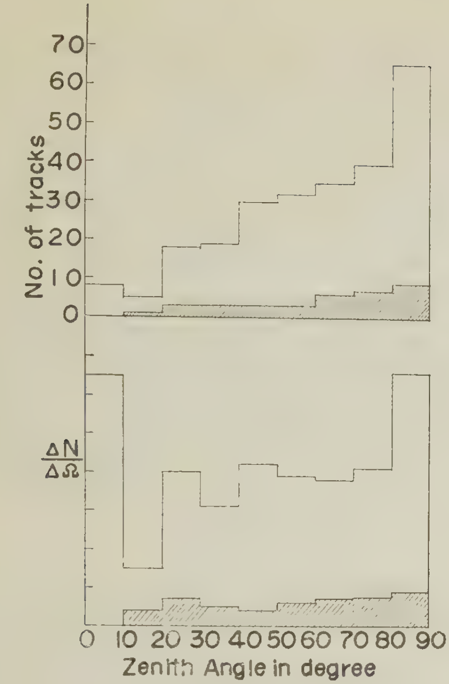

Fig. 5. Zenith angle distribution of the recoil proton tracks. The lower figure shows zenith angle distribution per steradian.

tracks (the tracks of order of 10 Mev).

The angular distribution of primary neutron cannot be determined in detail, but it seems to be isotropic at least in low energy region.

§ 4. Intensity and Spectrum of Neutrons

The intensity and energy distribution of the neutrons were derived from the data of recoil protons as follows.

When the velocity of the neutron is small, the energy, E_p', of the secondary proton in the laboratory system is related to the scattering angle, θ^*, of the neutron in the center of mass system by the equation:

$$E_p' = E_n \frac{1-\cos\theta^*}{2} \qquad (3)$$

On the other hand the differential scattering cross section $\sigma_{np}(E_n)\psi(\theta^*)$, where $\sigma_{np}(E_n)$ is the total cross section and $\psi(\theta^*)d\omega^*$ represents the probability that the neutron is scattered into the solid angle $d\omega^*$ at an angle θ^* to the original direction of its motion, is nerely constant for the neutron energies below about 20 Mev[12]. If this circumstance is combined with Eq. (3), it can be shown that the probability $\sigma(E_n, E_p')dE_p'$ that the energy of the recoil proton lies between E_p' and $E_p'+dE_p'$, is related to the total cross section $\sigma_{np}(E_n)$ by the equation:

$$\sigma(E_n, E_p') = \frac{\sigma_{np}(E_n)}{E_n} \qquad (4)$$

If the cosmic ray neutrons, whose energy spectrum is represented by $N_n(E_n)$, are scattered by protons, the energy spectrum $N_p(E_p')$ of the recoil protons is

$$N_p(E_p') = \int_{E_p'}^{\infty} N_n(E_n)\sigma(E_n, E_p')dE_n\,. \qquad (5)$$

Assuming that the energy spectrum of the cosmic ray neutrons can be expressed in the form of kE_n^{-m}, Eq. (5) is transformed into:

$$N_p(E_p') = k\int_{E_p'}^{\infty} E_n^{-m-1}\sigma_{np}dE_n\,. \qquad (6)$$

The quantum mechanical treatment of neutron proton scattering was given by Wigner[13], who show that the cross section as a function of neutron kinetic energy E_n is given (in the limit of neutron wave length large compared to the range of the neutron proton force) by the expression:

$$\sigma_{np} = \frac{4\pi\hbar^2}{M(1/2E_n + |\mathcal{E}|)}\,, \qquad (7)$$

where $\mathcal{E}$ is the binding energy of the neutron proton system. The above expression was found to agree with the observed cross sections for neutrons of 1 Mev and greater.

In the present work, since $N_p(E_p')$, was the observed as $E_p'^{-2}$ for the energy ranging from 1 Mev to 15 Mev, the energy spectrum of the incident cosmic ray neutrons $N_n(E_n)$ is expressed in the form of

$$E_n^{-1} + \frac{|\mathcal{E}|}{2}E_n^{-2}$$

from Eq. (4) and (5).

To simplify the expression, the cross section σ_{np} is approximated to the form of $E_n^{-1.25}$ which is determined from the experimental data for the energy range 1 Mev to 15 Mev. And therefore, $N_n(E_n)$ is given by the expression $k'E_n^{-1.25}$ which is nearly equal to the above result.

In the practical computation, following value were used

$$N_p(E_p') = kE_p'^{-2}$$
$$= 1.48\times10^{-4}E_p'^{-2}\,\mathrm{cm}^{-3}\,\mathrm{Mev}^{-1}\,\mathrm{sec}^{-1} \qquad (8)$$

$$\sigma_{np} = 10^{-23}E_n^{-0.75}\,\mathrm{cm}^2 \qquad (9)$$

$$\sigma(E_n, E_p') = k'E_n^{-1.75}$$

$$=4.94\times10^{-2}\,E_n^{-1.75}\,\mathrm{cm}^2 \qquad (10)$$

and from Eq. (5) and (8), we obtained;

$$N_n(E_n)=\frac{2k}{k'}\fallingdotseq E^{-1\cdot25}$$

$$=6.0\times10^{-3}\times E^{-1\cdot25}\,\mathrm{cm}^{-2}\,\mathrm{sec}^{-1}\,\mathrm{sterad}^{-1}$$

Assuming that the angular distribution is isotropic, vertical intensity was computed as;

$$9.5\times10^{-4}\times E^{-1\cdot25}\,\mathrm{cm}^{-2}\,\mathrm{sec}^{-1}\,\mathrm{sterad}^{-1}\,\mathrm{Mev}^{-1}.$$

After the correction for the surrounding materials (described in § 2. (4)), the vertical intensity of the neutron at 2740 m above sea level and 25°N is obtained as $1.2\times10^{-3}\times E^{-1\cdot25\pm0\cdot1}\pm40\%$ cm^{-2} sterad^{-1} sec^{-1} Mev^{-1}.

If the energy distribution is expressed in the form of $E/T^2\exp(-E/T)$, as well as in the case of evaporated neutrons from nuclear disintegrations, the mean temperature can be estimated to be about 2.6 Mev at 5 Mev to 10 Mev as shown in Fig. 6. As described in a later section this mean temperature shows that of the original stars of neutrons, and it agrees with the data of nitrogen stars[14] in the same energy region.

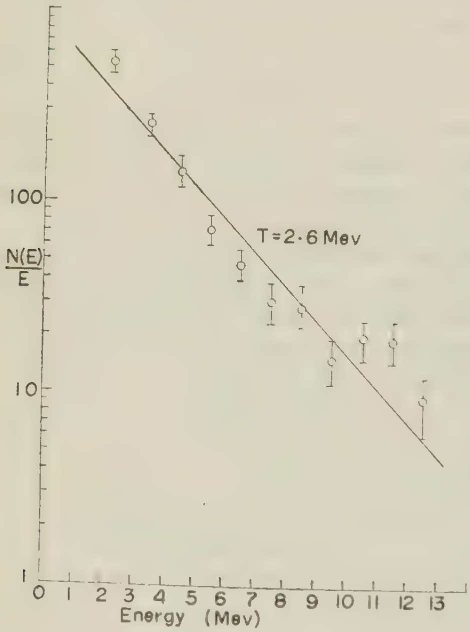

Fig. 6. Energy distribution in the expression of $N(E)\sim E\exp(-E/T)$.
Ordinate: $\log N(E)/E$ in arbitrary scale
Abscissa: E in Mev
The solid line is $T=2.6$ Mev.

§ 5. Discussion

1) *Relation to the data in higher energy region*

There are, unifortunately, no direct observation of the spectrum of neutrons in the energy range from 100 Mev to a few Bev, though the spectrum for the energy region higher than several Bev is considered to be equal to that of protons. So we computed the neutron intensity in the following way. First, the data of the proton spectrum obtained at sea level and at mountain altitude at about 50°N were translated to our altitude (760 g/cm^2) using the absorption path of 140 g/cm^2 to 125 g/cm^2 for 100 Mev to 10 Bev. Secondly the intensity ratio of the neutron to the protons is known to have the form

$$U^2/U^2-(Mc^2)^2$$

where U is the total energy and Mc^2 is a rest energy of nucleon. The form has been derived from emulsion experiments[15] and was used to obtain the neutron intensity. Finally, the latitude effect was considered and 20% decrease was assumed at 1 Bev and about 50% decrease at several hundred Mev was assumed to translate the 50°N values to those at 25°N.

Even though the intensity of a few hundred Mev neutrons by means of the above procedure is not reliable, the spectral curve

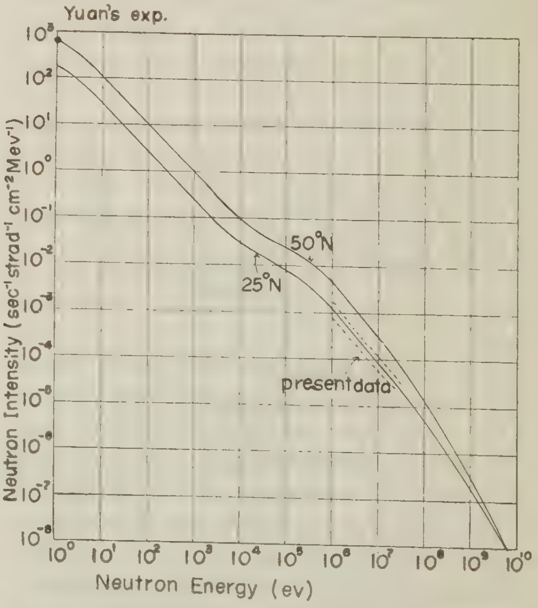

Fig. 7. Differential energy spectrum of neutrons at geomagnetic latitude 50°N and 25°N atmospheric depth 760 g/cm^2, and energy of 1 ev–10^{10} ev.

from 1 Mev to 10 Bev can be obtained by connecting our data to the above values with smooth curve as shown in Fig. 7.

Rossi[16] has calculated the energy spectrum of cosmic ray neutron flux for the energy range from 50 Mev to 1 Bev, and obtained the function

$$N_n(E_n,\ x)=\frac{Ax}{(50+E_n)^2}\exp\left(-x/L\right) \tag{11}$$

It explains the energy dependence of the neutrons of 100 Mev to 1 Bev substantially, but it does not fit to the lower data than about 50 Mev. And the same tendency is shown by the well known expression of the similar type[17];

$$A\exp\left(-x/L\right)(a+b+E)^{-\alpha-1}$$

where a and b are the constants which give the values of proton neutron difference and latitude effect respectively and α is an numerical constant equal to 1.8.

A detailed discussion about the energy spectrum may be difficult because the experimental data on the nuclear interactions in these energy region are very few and the conclusions that one may derive from these data are of a crude and tentative character.

Since the angular distribution varies rapidly in this energy region, total intensity is suitable for discussion rather than the vertical intensity. It is proportional to $E^{-1.6\sim1.8}$ assuming that the angular distribution changes gradually from the isotropic one to the one proportional to $\cos^5\theta$ as the energy changes from several Mev to 1 Bev. For the wide energy range from 1 Mev to 10 Bev the total intensity is approximated as;

$$kE^{-a-b\log E}\ \mathrm{cm}^{-2}\ \mathrm{sec}^{-1}\ \mathrm{Mev}^{-1} \tag{12}$$

where K, a and b are constants 4.8×10^{-3}, 1 and 0.17 respectively.

The energy spectrum at the depth x g/cm², $F(E,\ x)$, is represented by $f(E)\exp(-x/L)$ from the fact that the absorption path is not so sensitive to energy, and $F(E,\ x)$ must be a solution of the equation;

$$\frac{dF(E,\ x)}{dx}=\frac{-1}{\lambda}F(E,\ x)+\frac{1}{\lambda}\int_E^\infty F(E,\ x')g(E',\ E)dE' \tag{13}$$

where λ is a mean free path for inelastic collision, and is thought to be a constant for the energy region. In this equation, proton flux is neglected considering that it does not contribute so much to neutron flux unless the energy is higher than several hundred Mev.

As the generation function $g(E',E)$ is approximately proportional to E^{-1} for given E'[18], Eq. (13) is satisfied by $f(E)=AE^n$. From the initial condition of this equation (there is a data on the secondary protons from high energy stars at 50 g/cm²), $f(E)$ is determined as $AE^{-1\cdot6}$ which is in accord with the present data.

For the detailed expression, Eq. (12), the generating function is of the form $E^{-1}\log E'$ and it explains the tendency of prong number and energy dependence of high energy stars.

Concerning the latitude effect in the energy region of stars, the values of 6–7 obtained by Yagoda et al[19] and by Kaneko et al[20] do not agree with the values 2–3 which were used here and are also shown to be in the low energy region. It is difficult to imagine a mechanism of such large latitude effect, and if we admit such large values we cannot smoothly connect the intensity curves from the present data to high energy data.

2) *Diffusion of neutron in atmosphere*

In the energy region of more than several Mev, in which inelastic collision occurs frequently, the neutron are created from high energy nuclear disintegrations, $(\gamma,\ n)$, $(p,\ n)$, $(n,\ 2n)$, and so on, and some of them are absorbed by the processes of $(n,\ \gamma)$, $(n,\ p)$, $(n,\ \alpha)$ and so on. Fermi's theory of neutron slowing down[21] will be used as the first approximation if we considered the following circumstances. When the energy transfer is small in an inelastic collision $(n,\ n)$, it may be treated as an elastic collision, and when energy transfer is fairly large compared with elastic collision, the process can be considered to be the one which the neutron is absorbed and a slow energy neutron is created.

One dimentional age equation with absorption is written as;

$$\frac{d^2q(x,\ \tau)}{dx^2}-\frac{1}{L'^2}q(x,\ \tau)=\frac{dq(x,\ \tau)}{d\tau} \tag{14}$$

where x is the atmospheric depth, τ the age parameter in Fermi's theory, $L'^2=L_1L_2/3$, (L_2 is absorption mean free path and L_1 a collision mean free path), and finally q is the slowing down density.

Under following initial condition

$$q(x,\ 0)=A(E_0)\exp(-x/L_0) \qquad (15)$$

where $A(E_0)$ is a neutron energy spectrum from the source, and L_0 is the absorption length of the neutron producing radiation. The solution of Eq. (14) is;

$$q(x,\ \tau)=A(E_0)\exp(-x/L_0-(1/L'^2-1/L_0^2)) \qquad (16)$$

where

$$\tau=\frac{7L_1^2}{24\xi}\ln\frac{E_0}{E}$$

and ξ is a energy reduction rate per collision. Then the equation can be written in the following form;

$$q(x,\ E)=A(E_0)\left(\frac{E}{E_0}\right)^n\exp(-x/L_0) \qquad (17)$$

Assuming that $A(E_0)=aE_0^{-m}$ for E_0 ranging from 5 to 10 Mev, we can obtain the expression of neutron flux by integrating Eq. (17) over E_0 larger than E. As the flux is given by;

$$\text{Flux } p(x,\ E)=\text{density } (x,\ E)\times\text{velocity}$$
$$=q(x,\tau)\frac{L_1}{\xi E}, \qquad (18)$$

and since $n+m>1$, we have;

$$p(x,\ E)=\exp(-x/L_0)aE^n\int_E^\infty\frac{dE_0}{E_0^{-n-m+1}}$$
$$=a'E^{-m}\exp(-x/L_0) \qquad (19)$$

where ξ is 0.14 for air nuclei and L_1 is about 18 g.

Thus the observed spectrum is approximately equal to the production spectrum from the source in the energy region which satisfy the assumption and the mean temperature described in the last of Section § 4., may have such meaning.

3) *Relation to the intensity of low energy neutrons*

The absolute absorption rate of slow neutron in air per unit time and mass has been determined in several experiments[5]. From the difference of the density of neutrons whose energies are lower than about 0.4 ev observed by BF_3 counters which are shielded by cadmium and tin respectively, we can estimate the absolute neutron flux, assuming the spectrum given by Placzek[22] which states that the density of low energy neutrons which suffer scattering and absorption by air nuclei is approximately expressed by the following equation;

$$\text{const. } E^{-3/2}\exp\left(-15.5\sqrt{\frac{E_c}{E}}\right) \qquad (20)$$

where E_c is the energy which is $L_1=L_2$ and its value is 6.25×10^{-4} ev in this case.

The intensity at 1 ev shown in Fig. 7 is computed from this spectrum and from Yuan's data, and the points of the curve (25°N) continued to the present data are obtained from Equation (18);

$$A_0\exp(1/L^2\tau)\frac{L_1dE}{\xi E}\exp\left(-15.5\sqrt{\frac{E_c}{E}}\right) \qquad (21)$$

assuming that the source of low energy neutron is given as the intensity at 1 Mev in the present data and that there is no absorption except for the absorption of $1/v$ low in the low energy region.

The curves for 55° and 25°N in Fig. 7 shows good agreement with the latitude effect of 2.9 obtained by Staker[23] for thermal neutrons and of about 3 by Simpson[1] for fast neutrons.

Concerning the source of the thermal neutrons, it may be said that most of them are produced with energies ranging from 1 Mev to 4 Mev because the neutron slowing down density at 1 Mev agrees with that of slow neutrons through it is about one half of the value at 4 Mev. (most of the neutrons from stars have the energy of about 10 Mev, but they will collide with air nuclei about 12 times during the process of slowing down to the energy of 1 Mev and most of them will be absorbed by $(n,\ p)$ and $(n,\ \alpha)$ reactions)

§ 6. Conclusion

The energy spectrum of the neutrons were obtained over the energy range from that of the thermal neutrons to the neutrons of energies of about 10 Bev, and the absolute intensity of the different energy regions was discussed.

It might be considered that the origin of the thermal neutrons is the stars as they are seen in photographic emulsion, but low energy nuclear events as $(\gamma,\ n)$ reaction etc. must also be considered, since the contributions may be comparable to those from the stars.

The spectrum is smooth, and there is no rapid increase for about 10 Mev, that was expected from the data of stars.

The calculation[16] and empirical formula[17] for the intensity of cosmic ray neutrons were checked, and it was found that they were not applicable for wide range of energy, and an expression of the form of $kE^{-a-b\log E}$, was found for the total intensity in the energy range from 1 Mev to 10 Bev.

The integrated value of fast neutrons which originate in the air column of 1 cm² is estimated to be about 5 at 25°N and it was thought to be one half of the value from the data of thermal neutrons.

The authers express their sincere thanks to Prof. Y. Watase for his continual interest and encouragement. This study has been supported in part by a Grant in Aid for Fundamental Scientific Research from the Ministry of Education and from Cosmic Ray Observatory of the University of Tokyo.

References

1) J. A. Simpson: Phys. Rev. **83** (1951) 1175.
2) W. E. Hazen, C. A. Randall and O. L. Tiffany: Phys. Rev. **75** (1949) 694.
T. G. Walsh and O. Piccioni: Phys. Rev. **80** (1950) 619.
B. Rossi: Rev. Mod. Phys. **20** (1948) 537.
M. G. Mylroi and J. G. Wilson: Proc. Phys. Soc., Lond. **A64** (1951) 404.
W. L. Whittemore and R. P. Shutt: Phys. Rev. **86** (1952) 940.
M. Conversi: Phys. Rev. **79** (1950) 749.
3) E. P. George and J. Evans: Proc. Phys. Soc. Lond. **A63** (1950) 1248.
G. Bernardini, G. Cortini and A. Manfredini: Phys. Rev. **79** (1950) 952.
S. Lattimore: Phil. Mag. **40** (1949) 394.
M. Addario and S. Tamburino: Phys. Rev. **80** (1950) 749.
E. O. Salant, J. Hornbostel, C. B. Fisk and J. E. Smith: Phys. Rev. **79** (1950) 184.
4) H. Filthuth: Z. Naturforschung **10a**, (1955) 219.
5) W. O. Davis: Phys. Rev. **80** (1950) 150.
C. L. Yuan: Phys. Rev. **81** (1951) 175.
M. J. Swetnick: Phys. Rev. **95** (1954) 793.
6) S. Miyake: Jour. Phys Soc. Japan **11** (1956) 195.
7) B. Rossi "*High Energy Particles*" Prentice Hall, New York, p. 40 (1952).
8) S. C. Curran and J. D. Craggs "*Counting Tubes*" p. 20 (1949).
9) B. Rossi and H. H. Staub "*Ionization chamber and counters*" Mcgraw Hill (1949) p. 18.
10) G. Puppi and N. Dallaporta "*Progress in Cosmic Ray Physics*" edited by J. G. Wilson, North Holland Publishing Co. Amsterdam, p. 354 (1952).
11) V. C. Tongiorgi: Phys. Rev. **75** (1949) 1532.
12) B. Rossi "*High Energy Particles*" Prentice Hall, New York p. 347 (1952).
13) E. P. Wigner: Z. Physik **83** (1933) 253.
14) S. Miyake, et al: to be published.
15) G. Puppi and N. Dallaporta "*Progress in Cosmic Ray Physics*" edited by J. G. Wilson, North Holland Publishing Co. Amsterdam p. 359 (1952).
16) B. Rossi "*High Energy Particles*" Prentice Hall Incorporated. New York p. 486 (1952).
17) S. Hayakawa "*Uchusen*" Iwanami Tokyo (in Japanese) p. 103 (1955).
18) G. Bernardini, E. T. Booth and S. J. Lindenbaum: Phys. Rev. **85** (1952) 826.
19) H. Yagoda and N. Kaplan: Phys. Rev. **75** (1949) 339.
20) S. Kaneko, T. Kubozoe and M. Takahata: Jour. Phys. Soc. Japan **10** (1955) 915.
21) E. Fermi "Nuclear Physics" Notes compiled by J. Orear, A. H. Rosenfeld and R. A. Schluter p. 191 (1949).
22) G. Placzek: Phys. Rev. **69** (1946) 423.
23) W. P. Staker: Phys. Rev. **80** (1950) 52.
24) Y. Fujimoto and T. Tamura: Prog. Theo. Phys. **8** (1952) 221.

JOURNAL OF THE PHYSICAL SOCIETY OF JAPAN Vol. 12, No. 2, FEBRUARY, 1957

Observation of Cosmic-Ray Neutron Intensity at Geomagnetic Latitude 25°N

Part I. Atmospheric Effects

By Masahiro KODAMA*, Kazuaki MURAKAMI* and Yataro SEKIDO

Physical Institute, Nagoya University, Nagoya

(Received August 15, 1956)

The intensity of cosmic-ray neutrons has been continuously observed at sea level and mountain.

The value of absorption mean free path of neutron in the atmosphere, deduced from the barometer effect observed at each station, is 139±5 gr/cm^2, while 136±2 gr/cm^2 was obtained from the intensity difference between two stations at different altitude.

§1. Introduction

Continuous observations of cosmic-ray neutrons were already carried out by Simpson$^{1)}$, Elliot$^{2)}$ and other authors$^{3)}$. The intensity of cosmic-ray neutrons was observed at Nagoya (geomagnetic latitude 25°N, sea level) from September, 1954 to July, 1955 and is being observed at Mt. Norikura (25°N, 2840 m) since August, 1955.

It is plausible that the atmospheric effects on cosmic-ray neutrons are chiefly due to mass absorption. Therefore, in order to confirm this idea, it is important to investigate the atmospheric pressure and temperature effects and altitude dependence.

§2. Instruments

To measure cosmic-ray neutrons, four proportional BF$_3$-counters (filled with normal BF$_3$) were located in a paraffin and lead pile of Simpson's type$^{4)}$, as shown in Fig. 1.

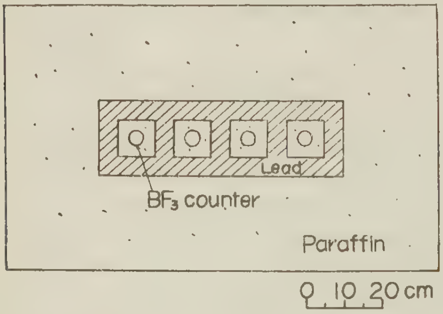

Fig. 1. Structure of lead and paraffin pile.

At the beginning, several kinds of external cathode and internal cathode counters were made, whose walls were made of glass. Using these counters, the following special features$^{5)}$ concerning neutrons were confirmed, namely, gas multiplication for BF_3, the effect of Cd, CH$_2$ and Pb surrounding a counter and the relation between intensities and distances from a neutron source.

The counters used for continuous observation of cosmic-ray neutrons have the size and the characteristics shown in Fig. 2, where the plateau slope is less than 1% per 100 volts.

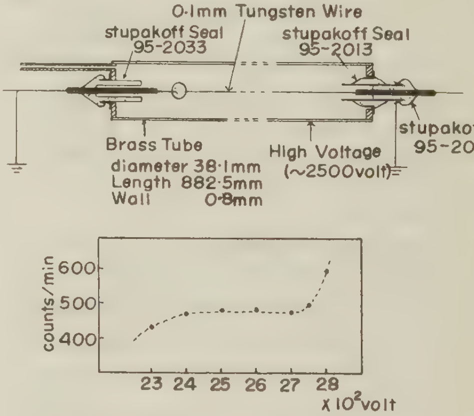

Fig. 2. Construction and characteristics of neutron counter.

The characteristics of our pulse amplifier are as follows. Gain: ~10^5, rise time: 0.2~0.4 μsec, clipping time: 2~3 μsec. The variation of gain is less than 0.3% per 1 volt of line voltage, but this variation has no effect upon the actual observation because of the flatness of the plateau of our counters.

Before starting continuous observation of neutron intensity, it is necessary to measure disturbances from outer noise sources and those due to spurious noise inside. No disturbance was observed in a continuous measurement during about half a year at Nagoya. But about 3 counts per hour of disturbances were recorded at Mt. Norikura, where instantaneous heavy current was being used in some other experiments.

---

* Now at Scientific Research Institute, Tokyo.

Moreover, it is essential to use counters with constant, low background counting rates. The background rate measured at sea level with the counter surrounded by 2 mm thick cadmium is about 2.5%.

§ 3. Atmospheric Effects

(A) Barometric Pressure Effect

In Fig. 3, the variations of cosmic-ray neutron intensity and barometric pressure P during a certain period are shown. To confirm the barometric pressure effect, the data before September, 1954 are added to the data mentioned in § 1. The pressure coefficients for each period are shown in Table I.

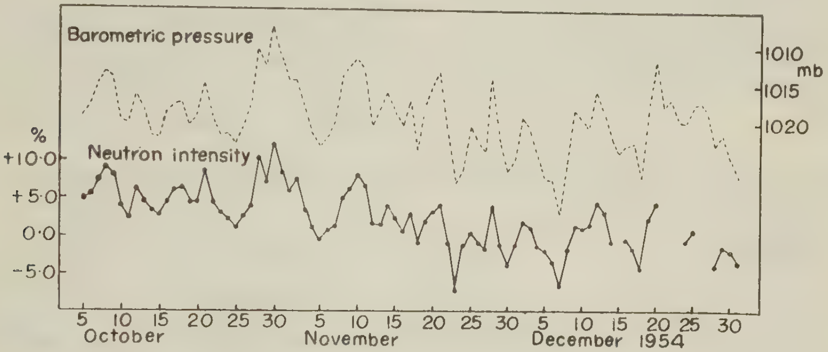

Fig. 3. Daily variations of neutron intensity and barometric pressure.

Table I. Barometric pressure coefficients of cosmic-ray neutron intensity.

Period	Location	Correlation coefficients	Pressure coefficients
June 5—June 7, 1954	Sea level	−0.87	−0.61 (%/mb)
June 8—July 14, 1954	,,	−0.95	−0.65
Aug. 16—Aug. 20, 1954	,,	−0.84	−0.65
Aug. 22—Aug. 24, 1954	,,	−0.99	−0.71
Sep. 3—Sep. 20, 1954	,,	−0.94	−0.66
Sep. 24—Sep. 29, 1954	,,	−0.91	−0.59
Oct. 5—Oct. 31, 1954	,,	−0.97	−0.64
Nov. 1—Nov. 30, 1954	,,	−0.96	−0.73
Dec. 1—Dec. 31, 1954	,,	−0.91	−0.58
Aug. 8—Aug. 31, 1955	Mountain	−0.99	−0.69
Sep. 1—Sep. 30, 1955	,,	−0.97	−0.66
Oct. 1—Oct. 9, 1955	,,	−0.90	−0.56

Since these coefficients were calculated as a simple correlation between the neutron intensity and the barometric pressure, it is possible that these values may contain an error due to other effects than the barometric pressure, for example, the variation of primary cosmic-ray intensity. In such a case, the obtained value $|\beta|$ may be smaller than the true value of the coefficient.

To obtain the true barometer coefficient, an empirical line was determined by the method of least squares between the correlation coefficients r and β obtained for various periods, and the true value was assumed to be the limiting value corresponding to $r \rightarrow 1$. The results are as follows:

$$\beta = -0.72 \pm 0.03\%/\text{mb} ,$$

$$L_p = 139 \pm 5\ \text{gr/cm}^2 ,$$

where L_p is the absorption mean free path estimated from the barometer effect.

(B) Temperature effect

Any atmospheric temperature effect on neutron intensity can hardly be expected theoretically. This was confirmed from our data. The following quantities were used for the indicator of the temperature,

H_{30}: difference of height between 300 mb and 100 mb isobar levels,
H_{13}: difference of height between 1000 mb and 300 mb isobar levels.

The results of the multiple correlation among I_n, P, H_{30} and H_{13} are shown in Table II, where I_n is the neutron intensity not corrected for the barometric pressure P. This result seems to show that there is no significant correlation between neutron intensity and temperature.

Next, the meson intensity I_m was added as an indicator of the variation of primary cosmic-ray intensity. The results of the multiple correlation between I_m, H_{30}, H_{13} and $I_n(P)$ are shown in Table III, where $I_n(P)$ is the neutron intensity corrected for the barometric pressure. The results show that there is no significant correlation between neutron intensities and atmospheric temperatures.

The same conclusion was obtained from the multiple correlation among I_n, P, H_{30}, H_{13} and I_m.

(C) Absorption mean free path

Table II. Partial correlation ceofficients between cosmic-ray neutron intensities and atmospheric temperatures.

Coefficients	Oct. 1954	Nov. 1954	Dec. 1954
$r_{I_n H_{30} P H_{13}}$	$+0.04^{+0.20}_{-0.21}$	$-0.04^{+0.20}_{-0.21}$	$-0.00^{+0.23}_{-0.25}$
$r_{I_n H_{13} P H_{30}}$	$+0.03^{+0.20}_{-0.21}$	$-0.33^{+0.20}_{-0.17}$	$-0.08^{+0.23}_{-0.22}$

Table III. Correlation between neutron and temperature using meson as an indicator of the primary cosmic-ray intensity (Nov.–Dec., 1954)

Coefficients	N	±85°
$r_{I_n H_{30} \cdot I_m H_{13}}$	−0.09	−0.11
$r_{I_n H_{13} \cdot I_m H_{30}}$	−0.08	−0.06

N: Nishina type ion chamber (Tokyo).
±85°: Counter telescope, no absorber, aperture ±85° (Tokyo)

By another method, the absorption mean free path L_{al} can be obtained from the altitude dependence comparing the intensities at Nagoya and Mt. Norikura. The mean values of barometric pressure and neutron intensity $\overline{P}$, $\overline{I_n}$, respectively, and L_{al} are as follows:

	Nagoya	Mt. Norikura
$\overline{I_n}$	1508/hr	10560/hr
$\overline{P}$	1010.4 mb	745.4 mb

$L_{al} = 136 \pm 2$ gr/cm²,

where the counts at both stations are in good agreement with the counts at Climax, considering several factors which may affect the counts, i.e., the latitude dependence of neutron intensity, number of counters, content of B^{10} in BF_3 and altitude dependence.

Because of the good agreement between L_p and L_{al}, we may conclude that the barometer effect on neutron intensity is due exclusively to the mass absorption in the atmosphere.

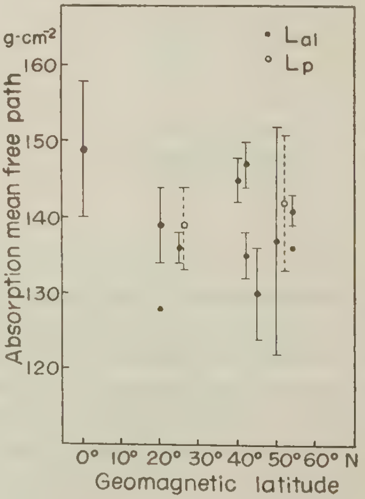

Fig. 4. Latitude dependence of absorption mean free path of cosmic-ray neutron in the atmosphere, where the range of atmospheric depth is 600 ∼ 1000 gr/cm².

Formerly, Simpson[1] concluded that L_{al} has no latitude dependence at the depth more than 700 gr/cm². Similarly we can conclude that there is no latitude dependence of L_p by comparing the values of L_p obtained by him and by us respectively (see Fig. 4).

§ 4. Acknowledgements

We greatly thank to Prof. Hayakawa for his many suggestions about BF_3-counters. And we are grateful to the people of Scientific Research Institute for their co-operation with our observation and for supplying us with meson intensities. In performing the experiment at Mt. Norikura, we are indebted to The Cosmic-Ray Observatory of The University of Tokyo.

References

1) J. A. Simpson: Phys. Rev. **83** (1951) 1175.
2) H. Elliot: Bagneres Meeting (1953).
3) V. Cocconi Tongiorgi: Phys. Rev. **76** (1949) 517.
N. Adams and H. J. J. Braddick: Z. Naturforschg. **6a** (1951) 592.
4) J. A. Simpson, W. Fonger and S. B. Treiman: Phys. Rev. **90** (1953) 934.
5) V. Cocconi Tongiorgi, S. Hayakawa and M. Widgoff: Rev. Sci. Instr. **22** (1951) 899. B. Rossi and H. Staub: Ionization Chamber and Counters (McGrow-Hill Book Company Inc. New York, 1949, Chapter 4). Bracci, Facchini, Germagnali and Zimmer: Nuovo Ciment **7** (1950) 512.

JOURNAL OF THE PHYSICAL SOCIETY OF JAPAN Vol. 12, No. 2, FEBRUARY, 1957

Electrical Properties of Nickel Doped Germanium at Low Temperatures*

By Yasuo KANAI and Riro NII
The Electrical Communication Laboratory, Musashinoshi, Tokyo

(Received September 25, 1956)

To study the anomalous phenomena of so-called impurity band conduction in semiconductors, the electrical properties of nickel doped p- and n-type germanium have been measured from room temperature to liquid air temperature. The energy differences between nickel levels and the edges of conduction and valence bands are so large that the anomalous behaviour was found in the temperature range of liquid air. A systematic study was made for the samples with different carrier concentration in nickel levels, and it was concluded that Hung's model was succesful to explain qualitatively the systematic change of the electrical properties of these samples. But to understand the experimental facts quantitatively, it seems to be necessary to develop further theoretical and experimental investigations on this problem.

§ 1. Introduction

a) Survey of the previous investigations on the so-called impurity band conduction.

In 1946, Busch and Labhart¹⁾ discovered anomalous electrical properties on the n-type single crystals of black SiC. They found that the Hall coefficient of their samples did not increase indefinitely as the temperature was lowered, but reached a maximum value at about 200°K and decreased thereafter by orders of magnitude. In the log resistivity versus 1/T curve, they also found a larger slope in the higher temperature range, before the Hall maximum was reached, and a much smaller slope at still lower temperatures. To explain these anomalous behaviours, they assumed that there was a simultaneous conduction in two bands, one was the ordinary conduction band and the other the acceptor band in n-type crystals. Unfortunately, informations about the nature of the impurities in their samples were insufficient to confirm their assumption.

---

* A part of this article has been reported as a short note in the Jour. Phys. Soc. Japan **11** (1956) 83.

In 1950, Hung and Gliessman[2] observed similar anomalies on Sb doped n-type and slow neutron bombarded p-type germanium at the temperature range of liquid helium. To explain their anomalies, Hung[3] also assumed a simultaneous conduction in two bands, and in his case the second band was a donor band in n-type crystals or acceptor band in p-type crystals. Furthermore, assuming that the impurity band was formed at the ground states of the impurity atoms, and the carriers in donor (or acceptor) band were electrons (or holes), he was successful to explain the systematic change of the electrical anomalies at low temperatures in the various specimens, containing different amount of impurities.

Thereafter, Fritzsche and Lark-Horovitz[4] carried out very careful and systematic studies on n- and p-type germanium single crystals doped with Sb, In, or Ga to temperatures as low as 1.5°K. In this case, they observed that the magnetoresistance decreased sharply as the Hall coefficient went through its maximum. In their investigations, the general behaviour of the low temperature anomalies was explainable by Hung's model, although they found a more complicated behaviour of samples with impurity concentrations between about 1×10^{16} and 1×10^{17}/cc.

Anomalies similar to those discovered on SiC and Ge samples have been found recently on p-type indium antimonide[5] at the temperature ranges of liquid helium. In this material, further anomalous behaviour, i.e. negative magnetoresistance (magnetoconductance) effect has been observed in the low temperature ranges[6]. Unfortunately, imformations about the nature of the acceptor center in this material are also insufficient. More recently, similar anomalies were also found on the n-type single crystals of Cd, Cl or Ga doped CdS at about 50°K.[7]

Although the conduction properties of an impurity band have been discussed by several authors[8], a detailed theory has not yet been worked out. In the case of Ge, the anomalous effect has been observed at impurity concentrations below 10^{15}/c.c. As the average distance between impurity atoms is much larger than the estimated orbit radius of the impurity states at such low concentrations, it would be difficult to explain conduction in the impurity states. Atempts have been made to take into account exited impurity states[9] or random distribution of impurity atoms[10]. But a theory which can be applied to the interpretation of experimental results mentioned above with complete satisfaction has not been worked out so far.

b) Objects of this work.

As mentioned above, the mechanism of the so-called impurity band conduction is not clear. Under these circumstances, it seems worth while carrying out some experimental investigations on the low temperature anomalies of semiconductors. There are two main aims of our work; The first one is as follows: The conventional idea about an impurity band conduction tells us that the electrical anomalies are found when the current carriers are trapped to the impurity states as the temperature is lowered. Following this idea, if we use a semiconductor in which the impurity level is so far from the edges of the conduction and valence bands, the anomalies will be found at rather high temperatures. As is well known, Au[11], Fe, Co, Ni and Mn[12] have deep lying acceptor levels in Ge. It may be expected, therefore, that the Ge crystals containing such materials as impurities will exhibit the anomalous electrical properties at higher temperature than the case of previous investigators.

The second aim is as follows: In the previous investigations, there were systematic studies on many samples with different *impurity concentrations* but systematic study on the samples containing different *carrier concentrations* in impurity state has not been worked out so far. As it is seen easily, the conduction properties in an impurity band would depend strongly on the population of carriers in the impurity band, and one would expect that in some cases the carrier in donor state will be holes and that in acceptor state electrons. On the other hand, the reversal of the sign of Hall coefficient has never been observed in any experiments. Hence systematic investigation of samples with different carrier concentrations in impurity state would be worthwhile to understand the conduction properties in impurity band.

§ 2. Experimental Procedures

a) Preparation of the samples.

As mentioned in the previous section, Au, Fe, Co, Ni and Mn have deep lying acceptor levels in Ge. Unfortunately, however, the solubility limit of these elements in Ge is so small[13] that it is not easy to prepare Ge samples containing such an amount of these impurities as to expect the impurity band conduction. Especially, the concentrations of these impurities would be very small in the samples prepared by the usual Czochralski method, because of the annealing process which would occur after the growth of single crystals. Hence, to get the samples in which sufficient amounts of any of these impurities are contained, we must use the method of diffusion of these elements at high temperatures. To obtain a uniform sample by this diffusion method, it is desirable to use an impurity element having large diffusion constant in Ge. Fortunately, the diffusion constant of Ni in Ge is quite large[14], so we decided to use Ni as the impurity element.

The details of the preparation of our samples were as follows: An ingot of As doped n-type Ge (about 50 g weight), whose resistivity was approximately $1\sim0.05\,\Omega$-cm at room temperature, was melted together with a high purity Ni plate (about 50 mg weight), and a single crystal was pulled out from the melt by the Czochralski method. As mentioned above, the crystal prepared by the above procedures contained rather small amounts of Ni, so the major part of the crystal was n-type. After cutting out the end part of the crystal, a thin plate whose thickness was approximately 2 mm was cut with its longitudinal direction parallel to the direction of crystal growth. This thin plate was etched by CP-4 and KCN solutions and then Ni plated by evaporation in vacuum. After heat treatment at 880°C for about several hours in vacuum, this plate was quenched as rapidly as possible. As the result of such treatment, sufficient amounts of Ni diffused into Ge, and converted the major part of the crystal to p-type. As it is seen in Figs. 1 and 2, there were four distinct parts in the crystal. In part I, the concentration of thermal acceptors (N_T), produced in the course of the thermal treatment (whose nature was not clear), was larger than the concentration of donor element As, N_D, so a part of thermal acceptor level was empty, hence this part was p-type and the low temperature resistivity was small. In part II, N_D was larger than N_T but N_D-N_T was smaller than the concentration of Ni, N_N, so a part of the lower Ni level was empty, hence this part was p-type and low tempera-

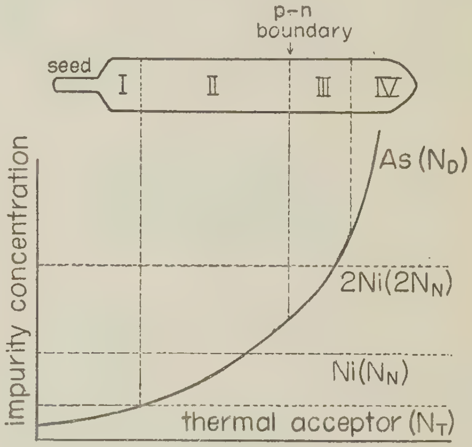

Fig. 1. Schematic representation of the impurity distributions in Ni doped Ge.

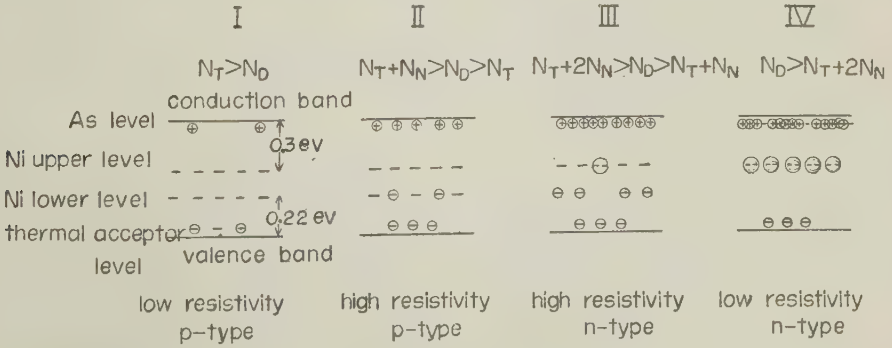

Fig. 2. Schematic representations of energy levels in Ni doped Ge at 0°K.

ture resistivity was high. In part III, N_D-N_T was larger than N_N but smaller than $2N_N$, so a part of the upper Ni level was filled, hence this part was n-type and the low temperature resistivity was high. In part IV, N_D-N_T was larger than $2N_N$, so a part of the donor level was filled, hence this part was n-type and the low temperature resistivity was small.

Then we cut the plate into many rectangular bars in shape approximately $10\times2\times1$ mm³, with its longitudinal axis perpendicular to the direction of crystal growth, and these bars were numbered as shown in Fig. 3. Following the previous considerations, we could expect that the samples cut from parts II and III of the crystal may show the low temperature anomalies, and the concentration of electrons in the Ni levels will gradually increase from the sample 12–1 to 15–2.

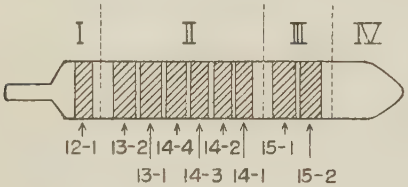

Fig. 3. Numbering of the samples.

b) Measurements

After the surfaces of the samples were ground by No. 180 corundum paper, the both ends of them were electro-plated with Ni, and then current leads were soldered there. The resistivity and Hall probes were made of 0.2 mm diameter Pt wires and pressure contact was made. The measuring equipment consisted of a dc potentiometer, suitable current sources and standard resistances, etc. The temperature was measured by a chromel-alumel thermocouple soldered at one end of the specimen. The magnetic field strength was measured by a flux-meter which was calibrated by the method of radio frequency magnetic resonance of protons. Since the samples were photo sensitive, precaution was taken to keep them in the dark for all measurements.

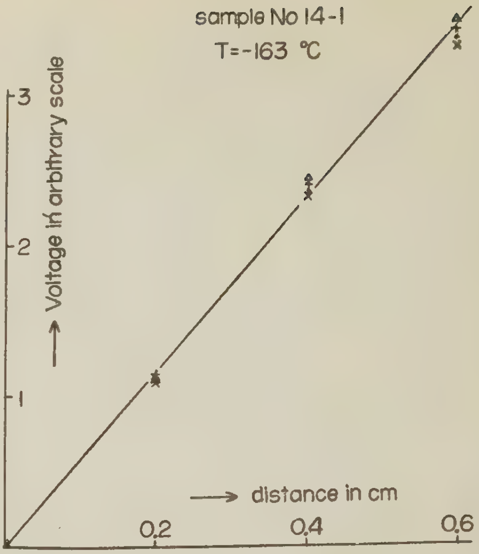

Fig. 4. Voltage drop versus distance in a sample. The sign × · + △ indicate the different cases of measurement.

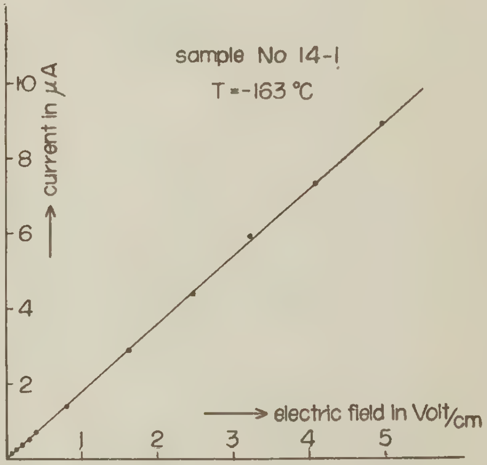

Fig. 5. Current versus voltage characteristics of a sample.

c) Preliminary check of the samples.

Since the inhomogeneity of a sample would make very serious errors in our experiments, we paid our attention as much as possible to this point. Fig. 4 shows an example of the voltage drop along the long axis of a sample at low temperature, and from it one can expect that this sample is homogeneous. In Fig. 5, there is a typical example of current-voltage characteristics of a sample at low temperature, and this shows that there is no breakdown phenomena in this sample.

§ 3. Experimental Results and Discussion

a) Resistivity and Hall effect

The resistivity, ρ, and Hall coefficient, R, versus 1/T curves are shown in Figs. 6 and 7. In Fig. 8, Hall mobility, $\mu=R/\rho$, versus T curves of these samples are shown. These figures show that the anomalous electric behaviours is found at about 170∼120°K in our

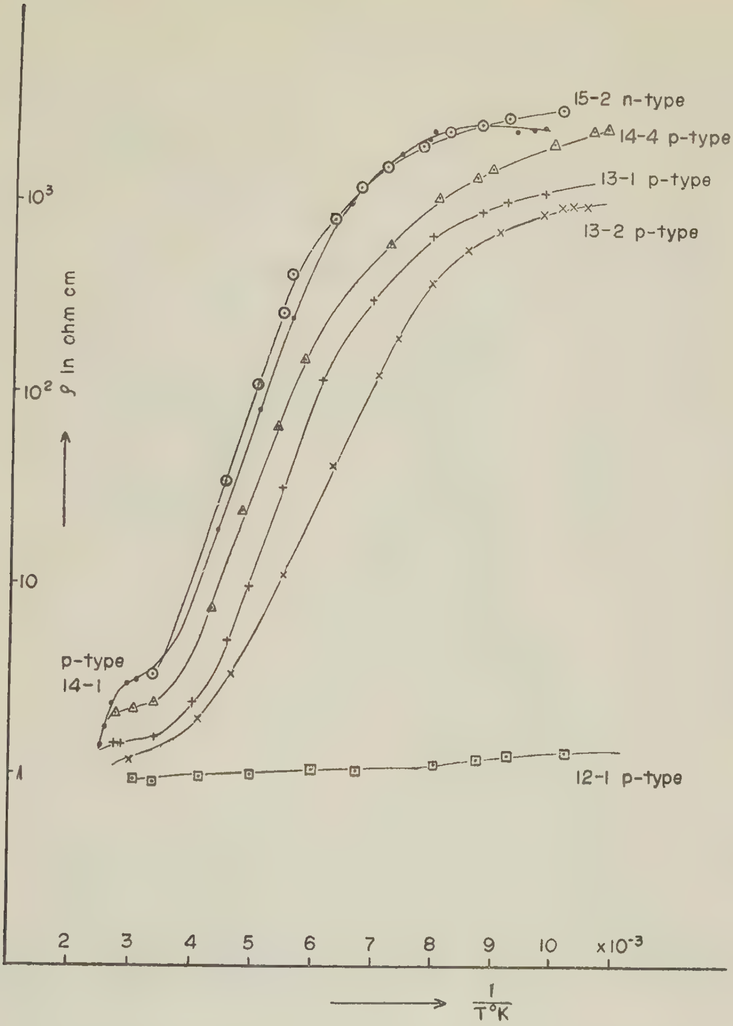

Fig. 6. The resistivity, ρ, versus $1/T$ curves.

samples as we expected above. Furthermore, as the upper Ni level is more apart (about 0.3 ev.) from the conduction band than the lower Ni level (about 0.22 ev.) from the valence band, the anomaly in n-type sample is found at higher temperature than the case of p-type samples. Hence these data suggest that our prediction done in section 1—*b*) is correct, and the first aim of our work was satisfied.

Turning now to our second aim, it can be recognised, at a glance, that there is a systematic change of the slope in the log R versus 1/T curves of p-type samples in the normal behaviour ranges. These behaviours are well understood by considering the different carrier concentrations in the impurity state in these samples, as Dunlap did¹¹⁾ in the analysis of the characteristics of Au doped Ge crystals. Then we shall determine the Ni density from these curves as follows; Consider the Hall curves of a series of p-type samples, ...13–1, 13–2, 12–1..., in which the concentration of electrons (or holes) in lower Ni level is gradually decreasing (or increasing). Then, as one can see in Figs. 6 and 7, the sample 13–2 is high resistivity at low temperature, while 12–1 is low resistivity. Hence we can expect that the density of Ni atoms is nearly equal to the hole density of the sample 13–2 at the exhaustion range (2.7×10^{15}/cc.). This value is consistent with the value obtained by another method¹⁴⁾ (about 2.0×10^{15}/cc.).

We shall next determine the electron (or hole) concentrations in the upper (or lower)

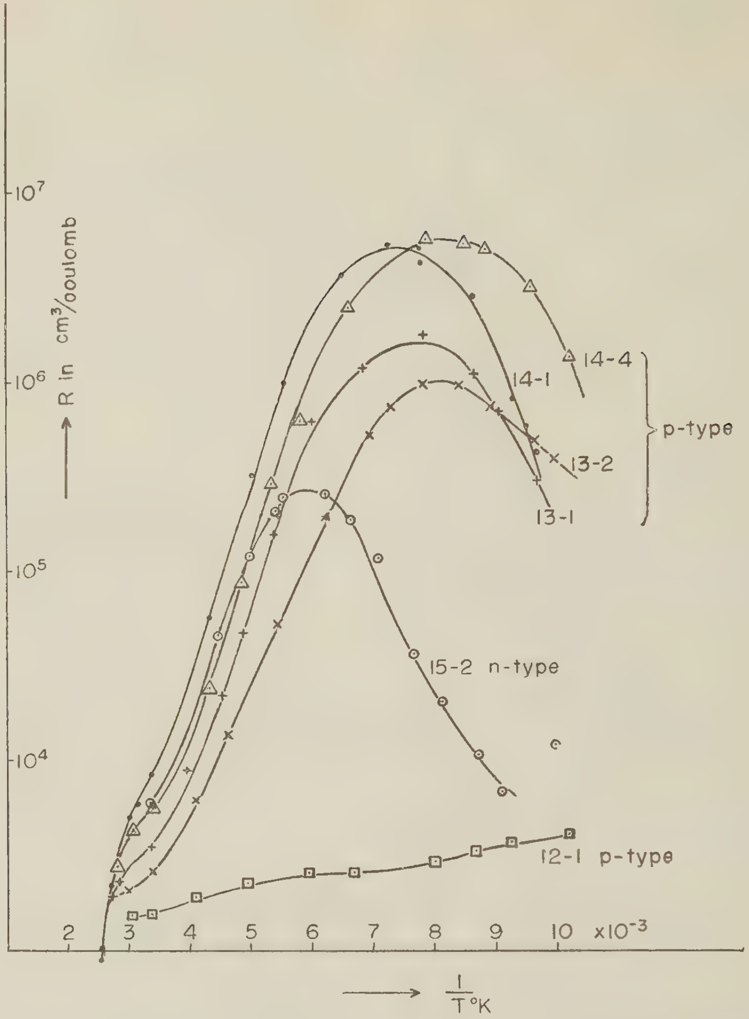

Fig. 7. Hall coefficient, R, versus $1/T$ curves. The applied magnetic field was about 5700 gauss.

Ni level at 0°K, n_0 (or p_0), by the next formula

$$n_0(\text{or } p_0)=3\pi/8ceR_{ex} \tag{3.1}$$

where R_{ex} is the Hall coefficient of the high resistivity sample at the exhaustion range. These values are listed in Table I.

Following Hung's model, ρ and R are given by the next formula;

$$\rho=1/e(n_b\mu_b+n_i\mu_i)$$

$$R=(r_bn_b\mu_b^2+r_in_i\mu_i^2)/e(n_b\mu_b+n_i\mu_i)^2 \tag{3.2}$$

where the suffices b and i refer to the normal and impurity band respectively. In the above expression r is a numerical factor depending upon the statistics and the scattering mechanism of the carriers. Unfortunately, imformation about r_i is quite insufficient, we have assumed $r_b=r_i=3\pi/8$. Furthermore, if we consider the fact that $n_b+n_i=n_0$, then after simple calculations, we can see that the maximum value of R, R_m, occurs at the condition $n_i\mu_i=n_b\mu_b$. Assuming $\mu_i \ll \mu_b$, the following simple relations are obtained at this temperature;

$$\mu_b\simeq 1.7R_m/\rho_m$$

$$\mu_i\simeq 0.85R_{ex}/\rho$$

$$n_i\simeq 7.4\times 10^{18}/R_{ex}$$

$$n_b\simeq 1.85\times 10^{18}/R_m \tag{3.3}$$

where the units of ρ, R, μ and n are ohm-cm, cm³/coulomb, cm²/volt. sec and no./cc. respectively. The numerical values of these quantities for our samples are listed in Table I. The values R_{ex}/ρ of our samples at 100°K,

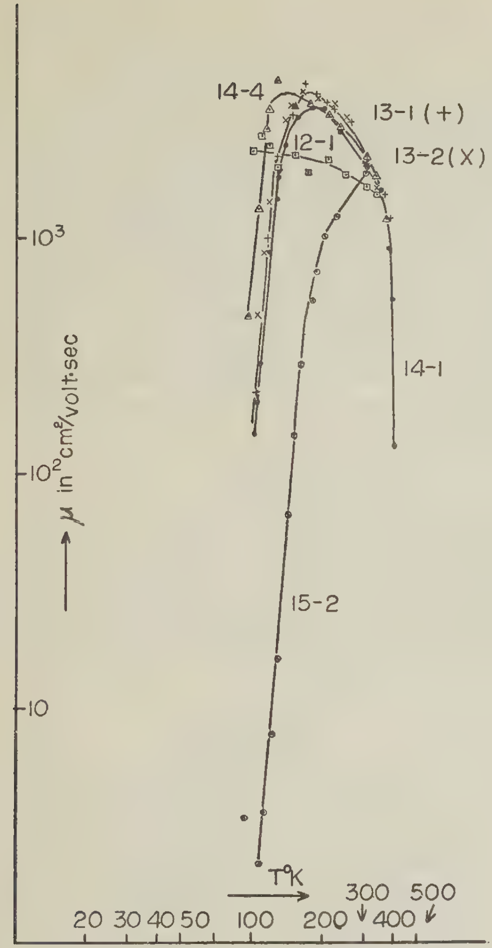

Fig.8. Hall mobility $\mu=R/\rho$ versus T curves.

which are approximately equal to μ_i at 100°K, are also listed there. In this table we can see that the carrier mobility in the impurity band is scarcely affected by the carrier concentrations, and the temperature dependency of it is also small.

Now we notice the shifts of temperature, T_m, at which the Hall maximum occurs, to lower temperature and R_m to lower value as n_0 increases. This tendency can be explained by Hung's model as follows. As we mentioned above, T_m occurs at the condition, $n_i/n_b=\mu_b/\mu_i$, namely, $n_b/n_0 \simeq \mu_i/\mu_b$. Since Table I shows that μ_i/μ_b has a nearly constant value independent of T and n_0, so n_b/n_0 should have a nearly constant value at T_m. On the other hand, as we can see in Fig. 7, the larger n_0, the smaller is the slope of log R versus $1/T$ curve before Hall maximum. Hence we can expect that the larger n_0, the lower temperature is needed to fulfil the condition of $n_b/n_0 \simeq \mu_i/\mu_b$, and in this case n_b is also larger, R_m has a lower value according to the last equation of (3.3).

b) Magnetoresistance

Transverse magnetoresistance $\Delta\rho_t/\rho(0)=\rho(H)_t/\rho(0)-1$ versus $1/T$ curve of sample 14−1 is shown in Fig. 9. As Fritzsche and Lark-Horovitz have pointed out[4)], Hung's model tells us that the next relation must hold in the temperature range of $r_b n_b \mu_b^2 \gg r_i n_i \mu_i^2$;

$$\Delta\rho_t/\rho(0) \simeq BH^2\rho/\rho_b \qquad (3.4)$$

where ρ_b is the value of ρ extrapolated to the low temperature region, and B is a numerical constant. In Fig. 9, this relation is checked for the sample 14-1, and it shows that Hung's model is self-consistent.

In Fig. 10, the angular dependency of magnetoresistance of sample 14-1 at low temperature is shown. One can see that the magnetoresistance is essentially constant for all directions, and this fact indicates that the energy surface in the impurity band is not of spherically symmetric form.

Table I.

Sample No.	type	N_N n_o/c.c.	n_o or p_o n_o/c.c.	T_m °K	at T_m μ_b cm²/v.sec.	μ_i cm²/v.sec.	n_i n_o/c.c.	n_b n_o/c.c.	at 100°K $R_{ex}/\rho_{100°K}$ cm²/v.sec.
12−1	p	2.7×10^{15}	—	—	—	—	—	—	—
13−2	p	〃	2.7×10^{15}	125	3.6×10^3	2.6	2.7×10^{15}	1.9×10^{12}	2.6
13−1	p	〃	2.0 〃	130	4.7 〃	2.5	2.0 〃	1.1. 〃	2.8
14−4	p	〃	1.3 〃	125	8.5 〃	2.1	1.3 〃	0.33 〃	2.4
14−1	p	〃	0.88 〃	135	4.2 〃	1.8	0.88 〃	0.37 〃	3.1
15−2	n	〃	1.3 〃	167	0.36 〃	2.0	1.3 〃	6.7 〃	1.7

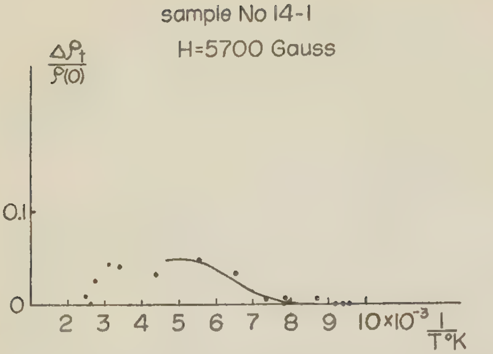

Fig. 9. Transverse magnetoresistance $\Delta\rho_t/\rho(0)$ versus $1/T$ curve. The solid curve is calculated by the Eq. (3.4).

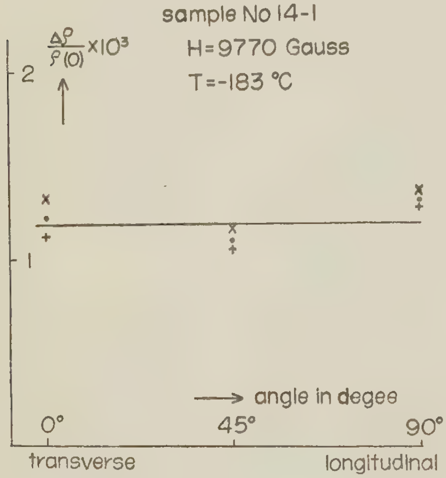

Fig. 10. Angular dependency of magnetoresistance of a sample. The sign × · + indicate the different cases of measurement.

§ 4. Conclusion

As discussed above, our work were carried out as follows: Firstly, as expected from the energy gaps of the Ni levels lying apart from conduction or valence band edges, the low temperature anomalies are found at rather high temperatures. This fact indicates that the carriers in impurity state play an essential role in the anomalous behaviours of semiconductors at low temperatures[15]. Secondly, in spite of the variety of carrier concentrations in impurity state of our samples, we find no great differences in the character of low temperature amomalies. It seems to us that this fact implies that the impurity band is much narrower than KT, so the carriers populate randomly in the energy state of impurity. Hence, contrary to the case of usual wide band, carrier concentration in impurity state may not affect strongly the anomalous electrical properties of the samples. However, even the above consideration does not answer the question why the carriers in donor state behave as electrons and those in acceptor state as holes. We have to conclude, therefore, that the carrier in impurity state plays an essential role in the phenomena of low temperature anomalies in semiconductors, but more detailed imformations than Hung's model about the electronic state of these carriers would be necessary to understand these phenomena completely.

§ 5. Acknowledgement

The authors thank heartily to Dr. Y. Takeda, the chief of the semiconductors research section and to Dr. T. Shindo, the leader of the semiconductor physics group in our laboratory, for the encouragements in the course of this work.

References

1) G. Busch: Helv. Phys. Acta **19** (1946) 167; G. Busch and H. Labhart: Helv. Phys. Acta **19** (1946) 463.
2) C. S. Hung and J. R. Gliessman: Phys. Rev. **79** (1950) 726 and **96** (1954) 1226.
3) C. S. Hung: Phys. Rev. **79** (1950) 727.
4) H. Fritzsche and K. Lark-Horovitz: Physica **20** (1954) 834; H. Fritzsche: Phys. Rev. **99** (1955) 406.
5) J. Hatton and B. V. Rollin: Proc. Phys. Soc. **A67** (1954) 385; B. V. Rollin and A. D. Petford: Jour. Electronics **1** (1955) 171; H. Fritzsche and K. Lark-Horovitz: Phys. Rev. **99** (1955) 400; H. J. Hrostowski, F. J. Morin, T. H. Geballe and G. H. Geballe and G. H. Wheatley: Phys. Rev. **100** (1955) 1672.
6) Recently, similar magnetoconductive effect has been also found in Sb doped n-type Ge at liquid helium temperatures. W. Sasaki and Y. Kanai: J. Phys. Soc. Japan **11** (1956) 894.
7) F. A. Kroeger, H. J. Vink and J. Volger: Physica **20** (1954) 1095 and Philips Res. Rep. **10** (1955) 39.
8) B. Gudden and W. Schottky: Z. tech. Phys. **16** (1935) 323; W. Schottky: Z. Electrochem. **45** (1939) 33.
9) C. Erginsoy: Phys. Rev. **80** (1950) 1104 and **88** (1952) 893; X. Baltensperger: Phil. Mag. **44** (1953) 1355; S. Koshino: J. Phys. Soc. Japan **11** (1956) 608.
10) H. M. James and A. S. Ginsbarg: J. Phys.

Chem. **57** (1953) 840; P. Aigrain: Physica **20** (1954) 978.

11) W. C. Dunlap Jr.: Phys. Rev. **97** (1955) 614

12) W. W. Tyler and H. H. Woodbury: Phys. Rev. **96** (1954) 874; W. W. Tyler, R. Newman and H. H. Woodbury: Phys. Rev. **97** (1955) 669 and **98** (1955) 461; H. H. Woodburg and W. W. Tyler: Phys. Rev. **100** (1955) 659.

13) J. A. Burton: Physica **20** (1954) 845.

14) F. van der Maesen and J. A. Brenkman: Philips Res. Rep. **9** (1954) 225.

15) Recently, Frederikse et al (Phys. Rev. **103** (1956) 67) concluded that the low temperature anomalies in Mg_2Sn were due to the surface conductance. But in our experiment, we could not find any anomalies of the samples containing smaller amounts of Ni than that described in this paper. Hence we can conclude that the anomalies in our samples are due to the conduction of carriers in Ni state.

JOURNAL OF THE PHYSICAL SOCIETY OF JAPAN Vol. 12, No. 2, FEBRUARY, 1957

Peripheral Inhomogeneties of the Alloyed Germanium p-n Junction

By Makoto KIKUCHI

Electrotechnical Laboratory, Tokyo, Japan

(Received October 12, 1956)

It has been found out that the local photocurrent is not homogeneous on the periphery of an alloyed germanium p-n junction, but there appear peaks at some positions. These peaks appear even for relatively lower reverse bias voltages and some of them disappear when the voltage is increased. When the bias voltage exceeds certain value, there appears another peak at a new position. There is a remarkable difference among these peaks in the voltage dependency of local photocurrent.

Experimental results on these peaks of photocurrent and other related phenomena are given. In the last section, the results are discussed and a physical picture for the understanding of the actual alloyed junctions is suggested.

§ 1. Introduction

In the course of recent development of power diodes and power transisters, it has become an important problem to make alloyed *p–n* junctions as perfect as possible in their characteristics, i.e., to make their electrical characteristics coincide with the theoretically ideal ones. But unfortunately, it turned out to be quite difficult to do it. For instance, the reverse characteristic of an alloyed germanium *p–n* junction does not saturate perfectly as the theory predicts, but it shows ohmic current component, and moreover, it breaks down at much lower voltage than the theoretical breakdown voltage estimated from the bulk resistivity.

Several reasons might be considered to be responsible for these discrepancies, e.g., lattice imperfections, inhomogeneities in the recrystallized regions, etc. Among them, the surface inperfections which occur on and near the periphery of the alloyed In dot may be one of the most important factors. It is the main purpose of this work to observe such peripheral inhomogeneities and discuss their effects on the electrical characteristics of the actual *p–n* junctions.

Recently, Garrett and Brattain[1] observed local photocurrent, and measured its dependence on the position of the small light spot on the germanium surface. In the case of their work, the local photocurrent was measured by scanning the light spot in two dimensions on the surface. We have adopted an improved method for doing this, as follows.

§ 2. Experimental Procedures

To measure the dependence of the local photocurrent i_p on the position of light spot, the light spot was moved along on the peripheral circle of the alloyed In dot as shown in Fig. 1. Practically, the light spot was fixed and the specimen was rotated about the vertical axis through the center of the dot. The position of the light spot was read by the angle of rotation as scaled in Fig. 1 (b).

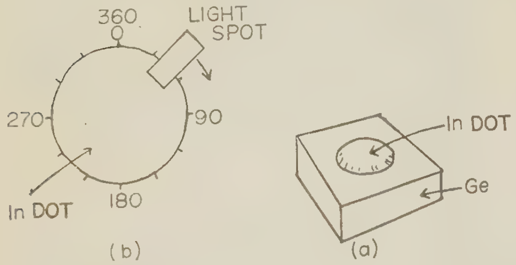

Fig. 1. Movement of light spot. Its position is read by the angle of rotation.

The light spot should have been made as small as possible, but the size of the spot was practically limited by the accuracy in the opitical system and the signal to noise ratio of the detecting circuit. The In electrodes of about 1.5–2 mm in diameter were alloyed on n-type (pulled) germanium single crystals. The diode characteristics of these specimens were not necessarily good, but they served satisfactorily for the purpose of our experiments.

Measuring apparatus is shown schematically in Fig. 2. Light is chopped at 200 cps by a rotating disc, and focused on the periphery. Local photocurrent is read by amplifying a.c. voltage drops across the series resistor.

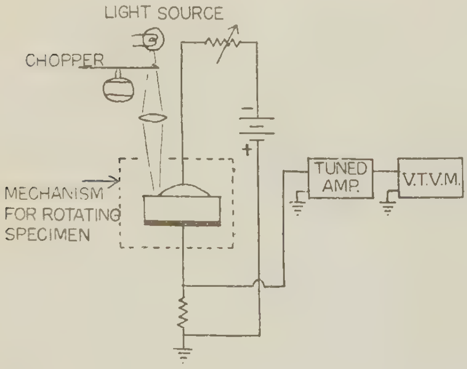

Fig. 2. Schematic representation of experimental apparatus.

§ 3. Experimental Results

A. *Distribution of local photocurrent on the periphery.*

Interesting experimental result which came out first is the fact that the local photocurrent i_p is not constant on the peripheral circle of the In electrode, but it shows some peaks at some positions. Typical result of this effect on the sample No. 0 with etched surface is shown in Fig. 3. It must be noticed that the value of i_p is in arbitary unit and has important meaning only in relative magnitude.

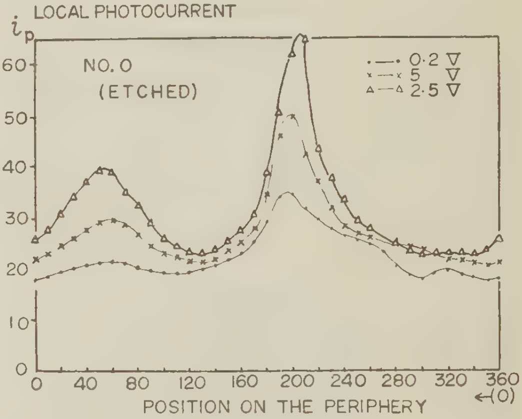

Fig. 3. Peripheral distribution of the local photocurrent i_p.

As is shown in Fig. 3, i_p depends on the bias voltage only at the peaks, and it remains almost constant in the regions between the peaks. Since the measured values of i_p is quite accurate and the curves are also quite reproducible, the experimental results will be shown by curves only, without plotting each points. When the surface is slightly etched and rinsed in de-ionized water, some of these peaks disappear, but some of them remain at the same position.

B. *Making peaks by surface treatments*

It has been found out that the above mentioned peaks of i_p can be made to occur by certain surface treatments. First, a small drop of impure water was put on a position, where there was no peak before the treatment. Typical result is shown in Fig. 4. In this case, a drop of impure water is put on the position "270". The peak appears there (as shown by the broken line), and it remains after the water is dried (dotted line). It must be noticed that in any case, the sharpness of peak is softened by the finite size of the light spot and the wetted area, and the diffusion of holes.

In the experiment of Fig. 4, the reverse characteristic of the junction varies as shown in Fig. 5, where the curves I, II and III correspond to the original, wet, and after dried conditions, respectively.

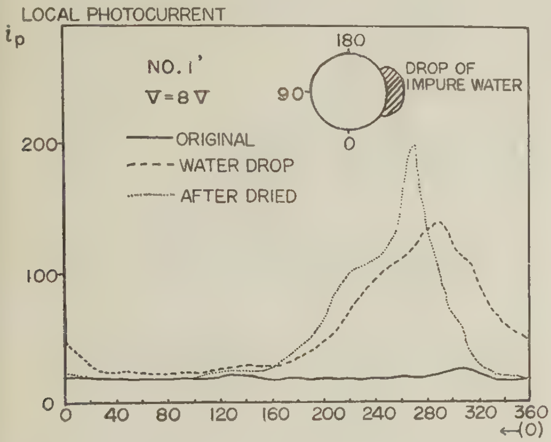

Fig. 4. Appearance of a peak of i_p by a drop of impure water on the periphery.

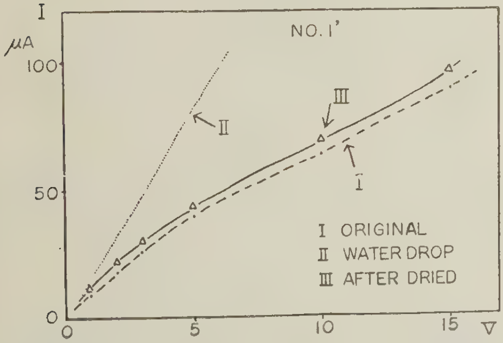

Fig. 5. Diode characteristis corresponding to the conditions of Fig. 4.

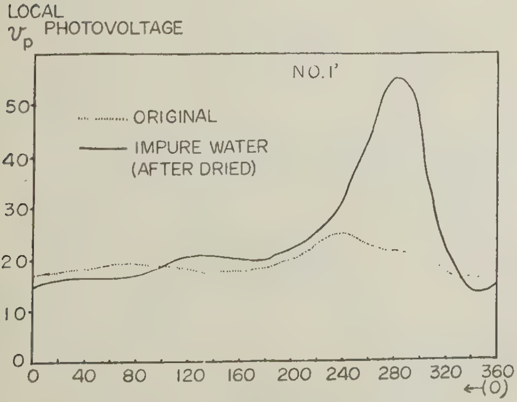

Fig. 6. Peripheral distribution of local photovoltage v_p before and after the water drop treatment of Fig. 4 and Fig. 5.

Fig. 6 is the distribution of local photovoltage v_p before and after the surface treatment mentioned above, where the paek appears at the treated position. In the case of such surface treatments, the peak of v_p appeared at the treated position. But we could not find out definite correlation between the distribution of the photocurrent i_p and the photovoltage v_p *in general*.

Other surface treatments were tried. The same results could be obtained by the copper nitrate solution, but it was impossible to make peaks appear by using de-ionized water. Anyhow, these peaks made by above-mentioned surface treatments could easily be put off by rinsing with pure water.

C. *Variation of i_p distribution with bias voltage*

The distribution of local photocurrent i_p on the periphery has been found to be dependent on the bias voltage. The experimental results are shown in Figs. 7 and 8. In the case of sample No. 1 whose characteristic is as shown in Fig. 7, the distribution of i_p is varied by the bias voltage as shown in Fig. 8. When the voltage reaches 25 volts, two peaks disappear and a sharp peak appears at a new positions. This phenomenon is reproducible and these peaks appear at definite positions.

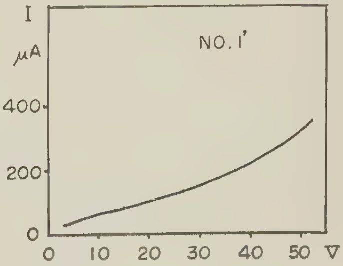

Fig. 7. Reverse characteristic of sample No. 1'.

It must be emphasized here, that the peaks in i_p distribution curve can be clearly classified into two groups. These two types of peaks are different in the voltage dependence of i_p on the bias voltage.

One of them is shown in Fig. 9, where i_p varies almost linearly with the voltage. This

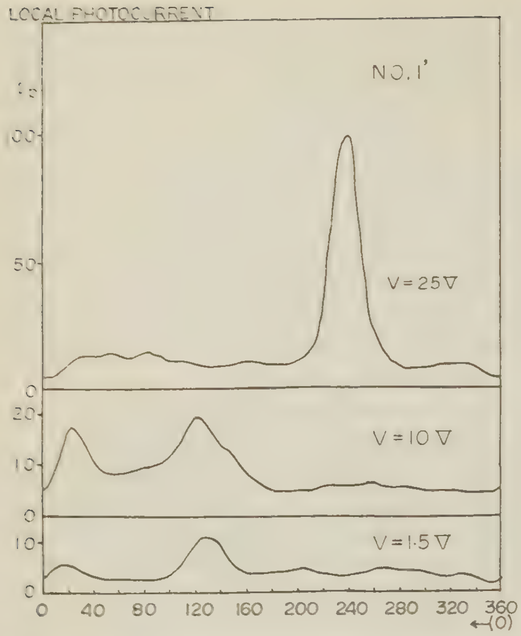

Fig. 8. Variation of i_p distribution with the bias voltage.

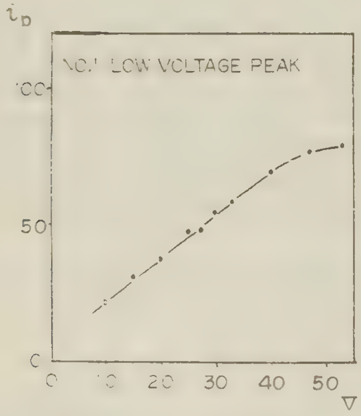

Fig. 9. Dependence of i_p on bias voltage at the "ohmic peak", or "low-voltage peak".

type of peaks are called "ohmic peaks", or "low-voltage peaks", since they appear for relatively low bias voltages. The peaks in Fig. 8 for bias voltages of 1.5 V and 10 V belong to this group. As is shown in Fig. 9, i_p tends to saturate above 45 V.

The other type of peaks are called "avalanche peaks" or "high-voltage peaks", and a typical example is shown in Fig. 10. i_p remains almost constant below 25 V, but it increases at about 30 V quite sharply, the curve being strictly distinguished from the former type. It tends to saturate above 40 V.

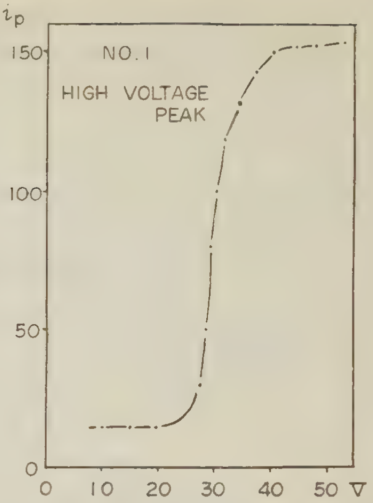

Fig. 10. Dependence of i_p on bias voltage at the "avalanche peak", or "high-voltage peak".

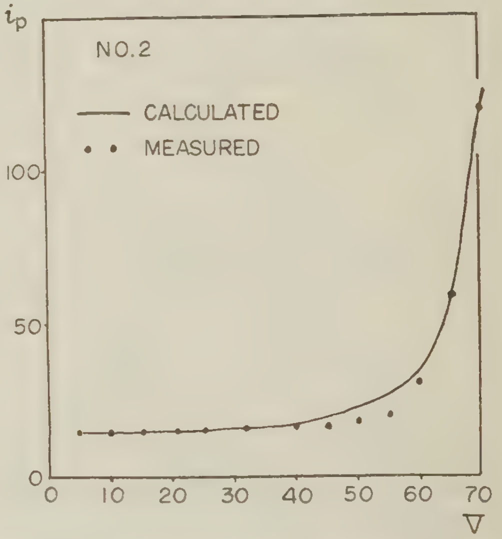

Fig. 11. Lower voltage part of the i_p-V curve of the avalanche type. Solid line represents calculated curve from Eq. (1).

The rapidly rising part of the curve of this type for sample No. 2 is shown in Fig. 11, where the solid line is a theoretical curve based on the avalanche mechanism, i.e.,

$$i_p=\frac{A}{1-(V/V_B)^n}. \tag{1}$$

A is a constant, V_B is a critical voltage, and n can be put to be equal to 3 for n-type germanium[2].

D. *"Creep" phenomenon*

In actual diodes and transistors, it is often observed that the current under the constant reverse voltage varies with time. This phenomenon is called " creep " or " drift ". In our samples, some of them showed considerable creep as shown in Fig. 12 (a). This is the result of creep under the reverse bias of 45 V for about 7 minutes. It has been observed that the i_p distribution varies during the creep is going on. Fig. 12 (b) and (c) correspond to the condition of before and after the creep, respectively. As is shown, the peak appears at different positions for two conditions.

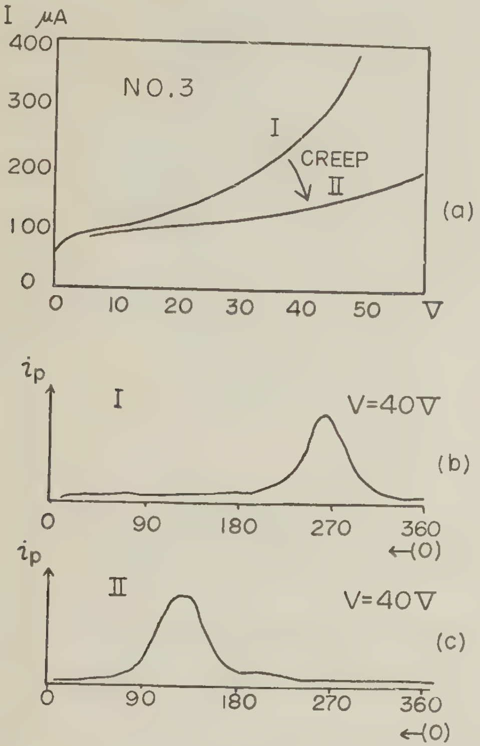

Fig. 12. (a) Creep phenomenon in the reverse characteristic. (b) i_p distribution for the condition I, before the creep. (c) i_p distribution for the condition II, after the creep.

Fig. 13 shows other experimental results of creep phenomenon. In this case, 40 V of reverse bias is applied to the diode, and the diode current I and the local photocurrent i_p are measured for 4 minutes. i_p measured here (at position 105) corresponds to the " ohmic peak " and it increases, while the diode current I decreases with time. After switching off the voltage, local photovoltage is observed at the same position for 40 seconds. The result is shown by the solid line in Fig. 13. The broken line (A) in the same figure represents the photovoltage v_p at the position 220, which corresponds to the " avalanche peak ". In some cases, v_p decreases with time also for the " avalanche peak ".

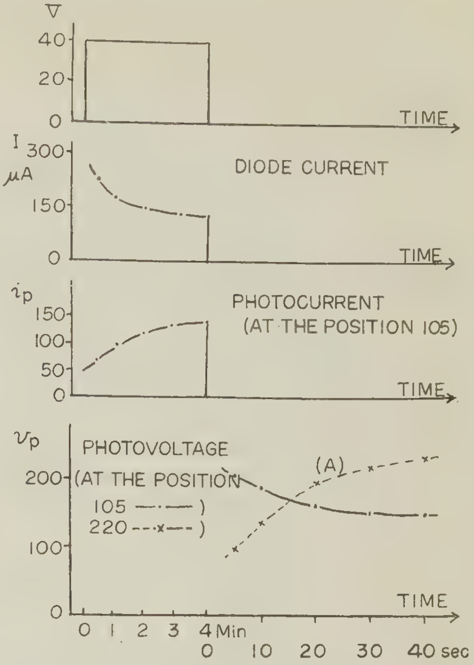

Fig. 13. Creep phenomenon, variation of the diode current I and i_p during the creep, and the recovery of local photovoltage v_p.

E. *Effect of castor oil*

When the surface of the diode is covered with caster oil, the distribution of i_p varies as shown in Fig. 14. One of two peaks in the original disappears in the oil, and the i_p becomes several times larger than the

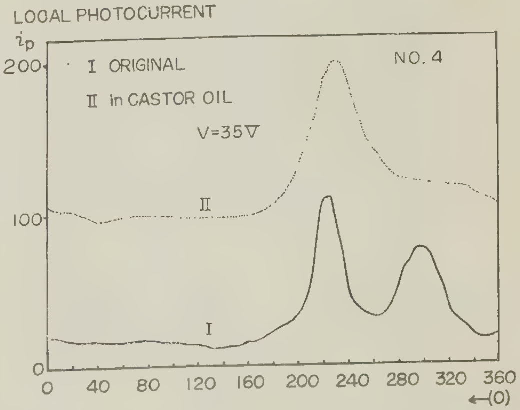

Fig. 14. Distribution of i_p before and after the castor oil is put on the surface.

orignal at every point on the periphery. These results are in agreement with the results of Garrett et al[2].

§ 4. Discussion

It has been confirmed that there exist some inhomogeneities on the periphery of alloyed In dot of germanium *p-n* junction. They are observed as the peaks of local photocurrent, and can be classified into two types, i.e., the "ohmic" peaks and the "avalanche" peaks.

In general, the reverse characteristic of actual diode differs from the theoretical one, and the reverse current seems to contain ohmic current component and rapidly rising current component. Hence, above mentioned experimental results will give some information to solve these discrepancies.

First, we may consider that the dependence of i_p on the bias voltage is the replica of the dependence of the local current flowing through that small spot on the periphery. "Ohmic" peak of i_p, therefore, arises from the ohmic charactor of that spot. These ohmic spots will contribute ohmic current components to the total diode current.

In the same way, the spot of "avalanche" peak of i_p contributes local current whose characteristic is just like shown in Fig. 10. The breakdown voltage V_B of these spots are dependent on the local conditions of the bulk resistivity, surface energy scheme, some kinds of imperfections on the surface and in the bulk, etc..

One of the most important factors affecting these conditions may be the ions on and in the vicinity of the periphery of In dot, which are influenced or controlled by the surface treatments and ambients. As a matter of fact, we have observed "avalanche" peak, whose V_B was varied from less than 10 V to above 75 V by the surface and ambient conditions. Moreover, it may be considered that most of the deterioration of the junction devices occur in the same way as shown in Fig. 4 and 5.

The results of Fig. 8 may be explained on the above mentioned physical picture. As the voltage is increased, one of the "avalanche" spots will break down at first, causing the readjustment of the distribution of the local currents.

In the same way, the "creep" may also be explained taking such inhomogeneities into account. Under certain constant bias voltage, the distribution of ions on the periphery will be varied gradually, which in turn tends to change the distribution of local currents.

In general, our physical picture will be modellized as shown in Fig. 15, where "avalanche" spot A and "ohmic" spots B_1, and B_2 are in parallel with ideal diode spots. The characteristic of these spots are shown in Fig. 16. Hence the total current I may be expresed in the form;

$$I=\sum_j \lambda_{Aj} j_{Aj}(V_{Bj})+\sum_j \lambda_{Bj} j_{Bj}+\sum_j \lambda_{Cj} j_{Cj}, \quad (2)$$

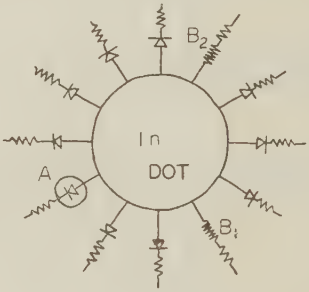

Fig. 15. Physical model of the actual junction.

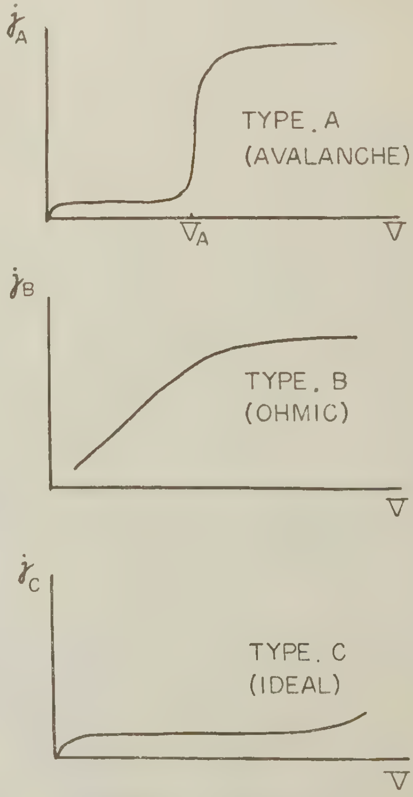

Fig. 16. Characteristic of local current at avalanche, ohmic, and ideal spots, respectively.

where λ_{Aj}'s are fractional area of the spots, V_B is the breakdown voltage of the spots, and j_{Aj}, j_{Bj} and j_{Cj} respresent the current densities of the avalanche, ohmic, and ideal diode components, respectively. Thus the problems of the discrepancies between actual and ideal diode characteristics may be reduced to the relative importance of the coefficients λ's in Eq. (2).

The inhomogeneities which were observed in our experiments on the periphery of the In dot, may also exist in the junction area in the bulk. It was, however, not checked in this work. The discussions on the detailed mechanisms of the influence of surface ions on the characteristics of the alloyed germanium *p–n* junction are also kept untouched in this report.

§ 5. Conclusion

Employing a measuring technique of the local photocurrent, it has been confirmed that there exist two kinds of inhomogeneities on the periphery of the alloyed In dot which cause the diode characteristic to be worse than the ideal one.

§ 6. Acknowledgment

The author wishes to express his thanks to Mr. N. Narukami for the preparation of measuring circuits, and to the members of his group for interesting discussions.

References

1) Garrett and Brattain: J. of Appl. Phys. **27** (1956) 299.
2) Miller and Ebers: B.S.T.J. **34** (1955) 883.

JOURNAL OF THE PHYSICAL SOCIETY OF JAPAN Vol. 12, No. 2, FEBRUARY, 1957

Observation of the Grain Boundary in Soap Bubble Raft.
Part III. The Grain Boundary in Vibrating State

By Einosuke FUKUSHIMA
Department of Physics, Tokyo Metropolitan University, Tokyo
and Akiya OOKAWA*
Department of Physics and Chemistry, Gakushuin University.
Mejiro, Tokyo

(Read October 30, 1955; Received November 5, 1956)

It was reported previously that the bubble raft model under mechanical vibration shows characteristics corresponding to the thermal agitation in the real crystals. With the same device, observations are made on the static as well as the dynamical features of the grain boundary in bubble raft under vibration. In the process of increasing the reduced temperature, the diffused hole (*B*-type) boundary transforms itself to the dislocation (*A*-type or *C*-type) boundary, and vice versa. The transformation temperature varies depending on the angle of misorientation between the grains. In relation to these observations, it is suggested that the marked correspondence between the dislocation theory and the experiment as to the grain boundary energy is but a natural consequence. Preliminary discussions are tried on the molecular mechanism of the transformation between the incoherent and the coherent boundaries, and on the probable causes of the hysteresis effect observed.

§ 1. Introduction

The grain boundary in the metal crystals has a structure depending on the angle of misorientation between the neighbouring two grains and the orientation of the dividing boundary.

The symmetrical tilt boundary of small misorientation angle is constituted of parallel edge dislocations, the seperation L between the constituent dislocations being given by

---

* Research member of the Kobayashi Institute of Physical Research, Kokubunji, Tokyo.

$$L=a/2\sin(\theta/2)\,, \qquad (1)$$

a being the distance between the net planes. The angle of misorientation θ is shown in Table I for some integer values of L/a. As was suggested by Burgers[1] at first, this type of the grain boundary displaces itself in normal direction to the boundary under shearing stress. Between the amount of boundary displacement D and the relative displacement S between the two grains parallel to the boundary, we have the relation

$$S/D=2\tan(\theta/2) \qquad (2)$$

due to Shockley and Read[2]. This relation is verified quantitatively by the experiment of Washburn and Parker[3] on zinc crystal.

With increasing the misorientation angle θ the separation L between the dislocations decreases as shown in Table I, and the increased interference between the dislocations results in the degeneration of the dislocation structure for the grain boundary of the angle of misorientation larger than about 20°. For the larger angle grain boundary, other types of the boundary structure are proposed, such as the diffused hole boundary[4] or the island boundary[5] constituted of regions in good-fit and those in bad-fit.

Table I.

θ	9°34′	11°30′	14°28′	19°14′	29°	60°
L/a	6	5	4	3	2	1

The grain boundary in the soap bubble raft has been studied by Lomer and Nye[6] and the present authors[7]. Summing up the observations of the latter, the grain boundary is classified as shown in Table II. It can be seen that the small angle symmetrical boundary (type A) is constituted of parallel dislocations, but that the larger angle grain boundary (type B) is constituted of diffused holes and that the unsymmetrical boundary of small angle of misorientation (type C) is constituted of regions in good-fit and those in bad-fit. Thus we have, in spite of the apparent defects of the two-dimensional bubble raft model devoid of the thermal agitation, the much expectation of good correspondence between the boundaries in real crystal and those in the soap bubble raft.

The bubble raft model, hithertofore used, is to correspond to a state of the real crystal at very low temperature, as the model lacks the mode corresponding to the thermal vibration in real crystals. On our recent observations on the bubble raft in a vibrating state[8], however, we could detect that the bubble raft under vibration proximates to the real crystal with thermal vibration. It was reported that the bubble raft under vibration expands itself and each type of the lattice imperfections, such as the vacant site, the interstitial bubble and the dislocation, takes more diffused structure than in static state. Here, it is reported on the characteristics of the grain boundary in the bubble raft in vibrating state.

§ 2. Experimental Method

The iron base plate of 1.5 *mm* thickness is excited by an electromagnet by *a. c.* of 90 *cps*. The raft is set in vibration through the sustaining soap solution. The diameter of the bubble used is about 1 *mm*, the behaviour of raft of such a bubble size being said to correspond to the real crystal copper. We could set, by means of the thermal expanions of the raft, an experimental formula[8]

$$T=1356\exp[-3.96(1-W/W_m)] \qquad (3)$$

between the reduced temperature T°K of the raft under vibration at an input power W, W_m being the critical input power where the raft melts. Accordingly, the bubble raft excited by an input power W is to correspond to the real crystal copper at the reduced temperature T by formula (3).

To obtain the neighbouring grains at desired relative angle of misorientation, two frames were used, each holding each raft grains. It is feared with the device if these frames, through constraints on the grain, might have unfavourable effects on the observed boundary structure and on the effect due to vibration. Repeating the observations, the one with frames and the other without the frames, however, we could check the effect of the frames negligible. In the respect, the usage of the frames is but for experimental convenience.

The sustaining liquid is kept at constant real temperature as possible. The critical input power W_m is read before and after each set of observations and the mean value of these is used in Eq. (3) to derive the reduced temperature for each input power W in each set of observations.

§ 3. Results Obtained

(1) *Transformation of boundary structure at elevated temperature*

The grain boundary shows the characteristic structure depending on the angle of misorientation θ and the reduced temperature T. For each angle of misorientation, comparative description is made between the structure at low temperature without vibration and the structure at elevated temperature of about 800°C under vibration.

For the angle of misorientation θ smaller than 15°, the boundary is of A-type, constituted of parallel dislocations $(01\bar{1})' \perp (01\bar{1})$*, both at low temperature and at high temperature. The grain boundary of misorientation angle between 15°∼20° is constituted of dislocations and diffused holes at low temperature, but, increasing the temperature, the diffused holes transform themselves soon to the dislocations and we have the boundary of type A, constituted of parallel dislocations only. In the case of the boundary with θ exceeding 20°, the *B*-type boundary at low temperature transforms itself to the *A*-type boundary at high temperature. Fig. 1 (a) and (b) show respectively the boundary at low temperature and that at high temperature for $\theta=25°$. The separation between the constituent dislocations in (b) is two to three bubbles, in accord with Table I. Fig. 2 shows the *A*-type boundary for $\theta=32°$ constituted of dislocations of two bubbles separation at $T=800°C$.

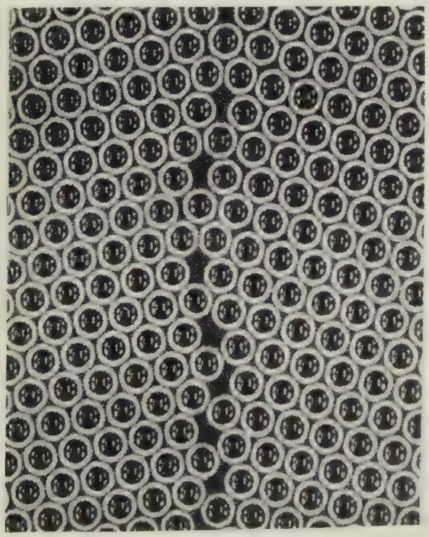

(a)

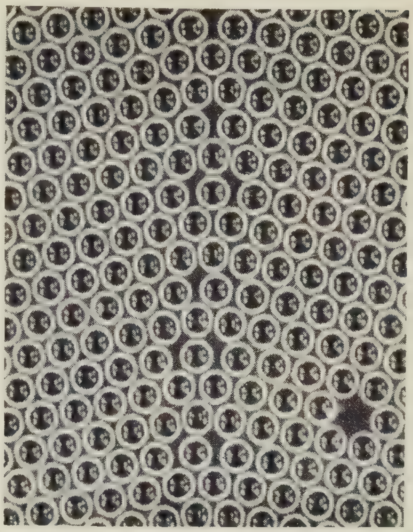

(b)

Fig. 1. Grain boundary with misorientation angle $\theta=25°$ (a) at low temperature without vibration, showing *B*-type and (b) at about 800°C under vibration, showing *A*-type ($d=1.0$ mm). d is the diameter of the bubble.

For θ exceeding 32°, the dislocation boundary at elevated temperature includes not only the parallel dislocations $(01\bar{1})' \perp (0\bar{1}\bar{1})$ but also the non-parallel dislocations $(01\bar{1})' \perp (1\bar{1}0)$ and

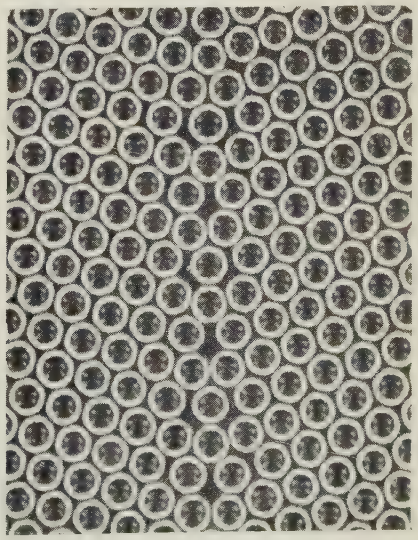

Fig. 2. Parallel dislocation boundary with $\theta=32°$ at about 800°C.

---

* About the notation, refer to the reference cited 7).

$(1\bar{1}0)' \perp (01\bar{1})$, and for θ exceeding 38°, the dislocation boundary has no $(10\bar{1})' \perp (01\bar{1})$ dislocations, thus forming the *C*-type boundary. Fig. 3 shows the dislocation boundory for $\theta = 37°30'$ at $T = 800°C$, the constituent dislocations marked at one side.

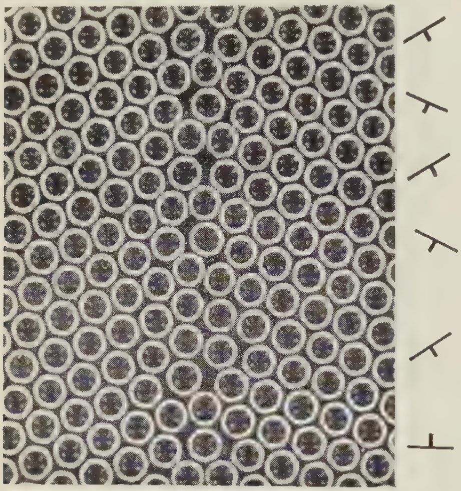

Fig. 3. Non parallel dislocation boundary with $\theta = 37°30'$ at about 800°C. Marks at the right side show the sort of dislocations.

For θ exceeding 45°, the boundary is of type *C* at low temperature as well as at high temperature. It is note-worthy, however, that, when kept for a long time at elevated temperature, in place of the alternating sort of constituent dislocations in linear alignment characteristic to the *C*-type boundary at low temperature, the constituent dislocations of the same sort each tend to coagulate to form a local symmetrical tilt boundaries, thus resulting to a zig-zag boundary in total.

(2) *Dynamical feature*

Under applied shearing stress to displace one grain relative to the other along the boundary, each type of the grain boundary responses specifically, as shown in Table II. Now, the transformation of the boundary structure from the *B*-type to the *A*-type or the *C*-type in the heating process and the inverse transformation

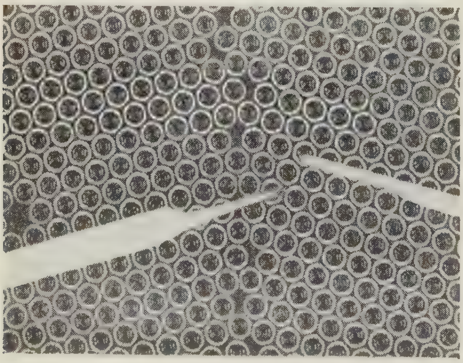

(a)

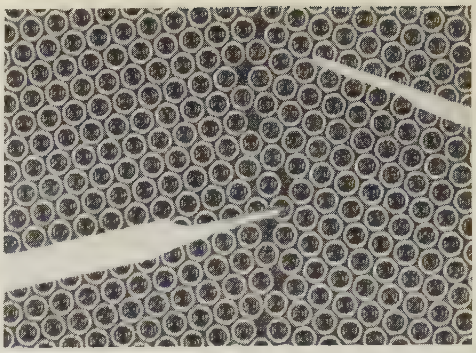

(b)

Fig. 4. Diffused hole boundary with $\theta = 32°$ at low temperature; (a) before and (b) after upward displacement of the right grain, showing that the boundary remain stationary. The white bars are the standard to indicate the relative displacement between the grains.

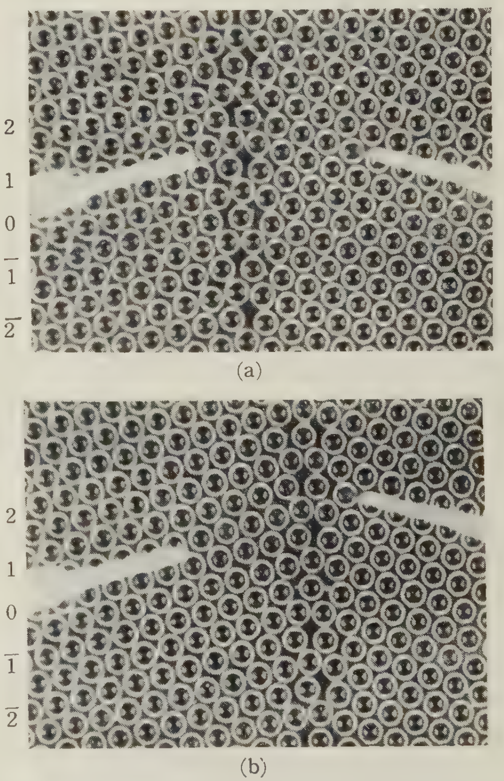

Fig. 5. Dislocation boundary with $\theta = 32°$ at about 750°C; (a) before and (b) after upward displacement of the right grain, showing the displacement of the grain boundary.

in the cooling precess are expected detectable in the specific response of the observed boundary to an applied shear stress.

Table II.

range of mis-orientation	nomenclature	constitution	behaviour under shearing stress
0°~15°	A	parallel dislocations	parallel displacement, normal to boundary
15°~45°	B	diffused hole	viscous flow along boundary
45°~60°	C	non-parallel dislocations	slip along boundary, with dislocation reaction

Fig. 4 shows the boundary for $\theta=32°$ at low temperature. (a) is the initial state and (b) is the state after upwards motion of the right grain relative to the left one by five bubbles. The white bars are the standards to indicate the relative displacement between the grains. It is apparent that the grain boundary stays stationary and the two grains flow viscously along the boundary, typically to the *B*-type boundary. Fig. 5 shows, in contrast, the same boundary at elevated temperature (*ca.* 750°C). Starting from the initial state (a), the right grain in the state (b) is displaced upwards relative to the left one by 1.8 bubbles. In this case, the grain boundary moves in normal direction to the boundary orientation rightwards by 3.2 bubbles, typically to the *A*-type boundary. That each of the constituent dislocations move conservatively along the respective slip lines can be seen with reference to the slip lines marked $\bar{2}$, $\bar{1}$, 0, 1 and 2 in the figure. Quantitatively, we have $S/D=0.56$ for $S=1.8$ bubbles and $D=3.2$ bubbles and $2\tan(\theta/2)=0.572$, thus in comformity with Eq. (2). The boundary for θ not exceeding 38° behaves substantially as the *A*-type boundary.

The boundary for θ exceeding 38° behaves typically to the *C*-type boundary, where the grains flow relatively along the boundary, while the constituent dislocations change their sorts repeatedly, thus reflecting the underlying reactions between the constituent and the transient dislocations. The boundary for θ between 32° and 38° shows combined characteristics for the *A*-type and the *C*-type boundaries, where the relation (2) is no more satisfied quantitatively.

(3) *Relation between the transformation temperature and the angle of misorientation*

The boundary for $\theta=0°\sim15°$ is of *A*-type and that for $\theta=45°\sim60°$ is of *C*-type already without the vibration, that is, at low temperature. The transformation between the types of the boundary is characteristic for the boundary of $\theta=15°\sim45°$. The reduced temperature of transformation, however, depends on the angle of misorientations between the neighbouring grains.

The *B*-type boundary of θ near 20° and that of θ near 45° transform to the *A*-type boundary and the *C*-type boundary, respectively, at moderate temperature. But the *B*-type boundary of θ near 30° does not transform to the

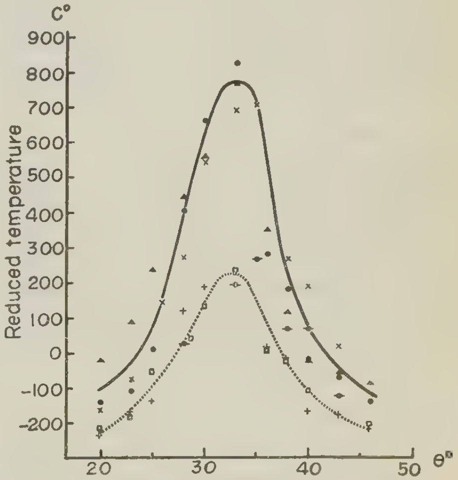

Fig. 6. The transformation temperature of the boundary for each angle of misorientation, full line showing the process from *B*-type to *A* or *C*-type and dotted line that from *A* or *C*-type to *B*-type. × ◆ 1st, ● + 2nd and ▲ □ 3rd observation.

A-type boundary before an elevated temperature is reached. The transformation temperature of the boundary for each angle of misorientation is shown in Fig. 6, where the full line marks the point where the diffused hole (B-type) boundary transforms to the dislocation (A-type or C-type) boundary in the process of increasing the input power or the reduced temperature. The curve has a maximum of about 750°C for $\theta=32°$. Thus we have, at temperatures exceeding *ca.* 800°C, the tilt grain boundary constituted of the dislocations, irrespective of the angle of misorientation and the orientation of the boundary itself.

That the range of θ between 15° and 20°, and the range between 40° and 45° are excluded from Fig. 6 is merely because of the undetermined ambiguity in the initial stage. In realizing the diffused hole boundary or the dislocation boundary to start, an effect similar to a kind of local heating is unavoidable in process of forming the initial boundary by hand-manipulation with fine needle.

In the process of decreasing the input power or the reduced temperature, the dislocation boundary transforms to the B-type boundary at temperatures lower than the transformation temperatures marked in the heating process. The dotted line in Fig. 6 marks the transformation temperatures in the cooling process. The amount of this hysteresis effect is most prominent for θ near 32°. At lower temperature attained after a cycle of heating and cooling, the boundaries for $\theta=15°\sim20°$ and those for $\theta=40°\sim45°$ are of A-type and of C-type, respectively.

Speaking in general, in spite of the relatively large scattering of the experimental points in Fig. 6, the transformation temperature between the diffused hole boundary and the dislocation boundary varies descriminatively with the angle of misorientation between the neighbouring grains.

(4) *Discussions*

(*a*) *On the transformation between the hole boundary and the dislocation boundary*

The transformation between the diffused hole boundary and the dislocation boundary in the processes of increasing and decreasing the input power of exciting the vibration may be likened to a sort of phase transformation in the heating and cooling processes in common sense. On the abnormal hysteresis nature of the transformation, it will be discussed later.

It was shown in a previous article[8] that the mechanical vibration given to the bubble model has some resemblances to the thermal agitation of the real crystal, and that the expansion of the raft and the increasing diffuseness of local imperfection characteristic to each type of the lattice imperfections are qualitatively in accord with the presumption of the characteristic frequency modified by the raft expansion and the degree of local imperfection, respectively. In thermodynamical language, the bubble raft in the vibrating state is realized in the state of minimum free energy.

The boundary in a raft without vibration has its stable form as shown in Table II for each range of the angle of misorientation, which corresponds respectively to the state of minimum potential energy. But in a raft under vibration, as is apparent from Fig. 6, the stable range of the misorientation angle for each specy of the boundary types is different from that in a static raft, thus reflecting the predominance of the state of minimum free energy.

If we approximate a bubble along the boundary with a linear harmonic oscillator of characteristic frequency ν at potential energy ε, the free energy per bubble at a temperature T°K is given, with the high temperature approximation $h\nu \ll kT$, by

$$f=\varepsilon-kT\log(kT/h\nu)\,, \tag{4}$$

k and h being the Boltzmann's and the Planck's constants, respectively. Specifying the quantities for the incoherent (B-type) boundary by the suffix i and those for the coherent (A-type or C-type) boundary by the suffix c, we have

$$\left.\begin{array}{l} f_i(T)=\varepsilon_i-kT\log(kT/h\nu_i) \\ f_c(T)=\varepsilon_c-kT\log(kT/h\nu_c) \end{array}\right\}. \tag{5}$$

To these approximations, the transformation temperature T_t between the incoherent and the coherent boundaries is determined by the thermodynamical condition

$$f_i(T_t)=f_c(T_t)\,, \tag{6}$$

from which it follows

$$T_t=\frac{\varepsilon_c-\varepsilon_i}{k}\Big/\log\frac{\nu_i}{\nu_c}\,. \tag{7}$$

As to the potential energies ε_i and ε_c, it is natural with reference to Table II to expect $\varepsilon_i < \varepsilon_c$ for the range $15° < \theta < 45°$ of the angle of misorientation. As to the characteristic frequencies ν_i and ν_c, however, our insight is too poor to estimate the ratio between them. To the effect of having the coherent boundary stable at higher temperature, it is required to presume $\nu_i > \nu_c$.

It goes without saying that the above treatment is too elementary to represent the real boundary system. While the relative sharpness of the incoherent boundary provides the convenience of marking the bubbles on surface of the boundary, the intrinsic breadth of the coherent boundary constituted of dislocations prohibits such conveniences, and we can not dispense with calculations of the characteristic frequency spectrum of such an imperfect crystals. In the present stage in short of such a knowledge on the frequency spectrum, however, we are far from understanding the molecular mechanism of transformation between the boundary types.

That the transformation temperature depends on the angle of misorientation as shown in Fig. 6 is due to variance with the angle of both the potential energies ε_i, ε_c and the characteristic frequencies ν_i, ν_c, but the relative predominance between them is hardly to predict in the present stage.

(b) *On the observation of the grain boundary energy*

The grain boundary in general has an excess boundary energy over the perfect crystal, due to misfit of atoms along the boundary. As the interfacial excess free energy is equivalent to a kind of surface tension, we have the convenience of measuring the relative value of the excess boundary energies of each set of three interfaces by the procedure of observing the angles between them in equilibrium⁹⁾. Thus we can determine experimentaly the excess boundary energy γ per unit area varying with the angle of misorientation θ. For a given angle of misorientation, the boundary energy varies in general but negligibly with the orientation of the boundary itself, except for such special θ's as corresponding to the case of two grains in twin relation to each other.

On the other hand, on the supposition of the dislocation boundary, the boundary energy γ per unit area of a symmetrical tilt boundary is to vary²⁾,¹⁰⁾ for small angle of misorientation θ, according to

$$\gamma = \gamma_0 \theta (A - \log \theta) , \qquad (8)$$

where the term $\gamma_0 A \theta$ corresponds to the misfit energy in the cores of the constituent dislocations, and the term $-\gamma_0 \theta$ long θ to the strain energy in short range.

The theoretical formula (8) is shown in Fig. 7 with the experimental points on lead⁹⁾,

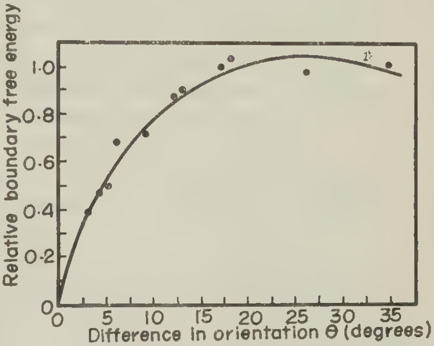

Fig. 7. The relation between boundary free energy and misorientation angle; 1. theoretical curve; ● experimental value of Aust and Chalmers on lead.

where it is to be noted that the formula is in good accord with the experimental data throughout the whole range of the angle of misorientation.

Now, the seperation L between the dislocations constituting the dislocation boundary decreases with the angle of misorientation as shown in Table I, and the increasing interference between the constituent dislocations unstabilizes the dislocation structure, to have in effect the hole boundary stable for the range $15° < \theta < 45°$ (see Table II). Accordingly, from the viewpoint of the previous classification of the boundary type (Table II). stable for each range of the angle of misorientation, the good correspondense between the dislocation theory and the experiment throughout the whole range of the angle as shown in Fig. 7 seems rather fortuitous.

The present observation with the grain boundary in the bubble raft under vibration, however, reveals that, at the higher temperature, the dislocation boundary is the more favoured to the hole boundary (see Fig. 6). The circumstances suggest that the experimental condition in the process of determining the grain boundary energies was in favour to the dislocation boundary than to the hole boundary.

Recalling on the experimental procedure, we notice the annealing processes of specimen with grain boundaries at elevated temperature, that is to the purpose of setting the relative orientation between the grain boundaries in equilibrium under the relevant surface tensions. It is then of high probability that the grain boundary energy estimated from the measured angles in equilibrium at such a high temperature corresponds rather to the dislocation boundaries stable at the high temperature. Thus the good correspondence between the dislocation theory and the experiment as shown in Fig. 7 is but natural consequence of the grain boundary constituted of dislocations, stabilized thermodynamically at the higher temperature.

(*c*) *On the hysteresis of the transformation*

The hysteresis effect as to the transformation temperature in the heating and the cooling processes is hardly avoidable in the present stage of our experimentation. It is of much interest to know if such a hysteresis effect might be characteristic for the real metal crystals too.

In the respect, however, we must be modest to stress on the correspondence between the present model and the real crystals. We can indeed enumerate some factors as to the undesired defects of our present model, such as the viscous resistance between neighbouring bubbles in the process of relative rearrangement, the minute inhomogeneity in the bubble size issueing to the impurity effect, and the monochromaticity of the exciting vibration replacing the thermal vibration in real crystal. Among these possibilities, it can not yet be decided on the predominant origin of the hysteresis effect and accordingly on the correspondence between the raft model and the real crystal as to this effect.

The authors are indebted to Mr. T. Zempô for the earnest experimental assistance throughout the present work. This work was supported by the Scientific Research Fund granted by the Ministry of Education.

References

1) J. M. Burgers: Proc. Kon. Ned. Acad. Wet. **42** (1939) 293.
2) W. Shockley, W. T. Read: Phys. Rev. **78** (1950) 275.
4) R. Smoluchowski: Phys. Rev. **87** (1952) 482.
5) N. F. Mott: Proc. Phys. Soc. **60** (1948) 391.
6) W. M. Lomer, J. F. Nye: Proc. Roy. Soc. **A212** (1952) 576.
7) E. Fukushima, A. Ookawa: J. Phys. Soc. Japan **8** (1953) 609; **9** (1954) 44.
8) E. Fukushima, A. Ookawa: J. Phys. Soc. Japan **10** (1955) 970.
9) A. H Cottrell: Dislocations and Plastic flow in crystals. 96, Oxford (1953).
10) J. H. van der Merwe: Proc. Phys. Soc. **A63** (1950) 616.

JOURNAL OF THE PHYSICAL SOCIETY OF JAPAN Vol. 12, No. 2, FEBRUARY, 1957

An X-Ray Tube with a Rotating Anode and an Earthed Cathode

Shozo SAWADA, Ine TAKOO and Shin'ichi FUJII

Institute of Science and Technology, University of Tokyo

(Received July 23, 1956)

An x-ray tube with a rotating anode and an electro-static lens was constructed, in which the cathode instead of the anode was earthed. Each of the Cu and Fe characteristic rays is obtained without breaking vacuum. An adjustment of position of a camera can be made with quite security, since the total area on the side of a window emitting x-rays is earthed. By this tube, photographs of metals and oxides can be taken in 10 sec and 1 min respectively, using Cu radiation filtered by a nickel foil, the voltage and the current being 50 kV and 30 mA respectively, when the electron beam is focussed in an area of 0.25 mm × 0.75 mm by a biasing voltage of about 600 V.

§1. Introduction

Recently the necessity of intense source of x-rays is increasing more and more in the research work of chemical physics, i.e., in the determination of crystal structure of organic compounds, that of inorganic ones at high or low temperatures, the quantitative measurement of diffuse scattering by crystals, etc.

Hitherto, we have had three methods of obtaining an intense source of x-rays[1),2),3)]. In the first one, the power input to the unit area of anticathode is increased by its movement; in the second one, the specific load on the anticathode is increased by focussing the electron beam attacking it and thus the effective flux of x-rays passing through the slit s further increased[7),8)]; and the movement of anticathode and the focussing of electron beam are combined in the third one. Each of these three methods has merits and demerits respectively and especially the second one has its utility not only in increasing the intensity of a source of x-rays but also in investigating the structure of grain boundaries in metals, the inhomogeneity in crystals of high polymers, etc.

The brightness of a source of x-rays is determined not by the total load but by the pecific load on the anticathode. The first method increases the specific load by increasng the total load itself and the second one by reducing the size of focus. Although in he first one we can increase the total load rbitrarily, at least in principle, by increasing he dimension of anticathode, then the apparatus must become very enormous. In the second one there is a defect that we can only supply extremely small total load on the anticathode if we reduce the size of focus too much. Thus the third method in which the merits of both of the first and second ones are utilized seems the most profitoble in obtaining a high brightness by a relatively small apparatus.

Electro-static or electro-magnetic lenses are usually used for the focussing of electron beam and Ehrenberg and Spear[7)] showed that a high brightness was obtained in a small x-ray tube with an electro-static lens when its cathode instead of its anode was earthed—that is, they could take a photograph of ZnO in one minute by Cu radiation filtered by a nickel foil, using a Seemann-Bohlin type camera, when the focus was reduced down to 40μ by a biasing voltage of about 50 V, the tube voltage and the electron current being 50 kV and 300–500 μA (the maximum specific load being 11 kW/mm^2)*. We can easily understand why the focussing is more easy in an earthed cathode type tube than in an earthed anode type one, if we compare the potential distribution in both cases.

In all of the moving anode type x-ray tubes which have already been reported, the anticathode was always earthed, since it was rather troublesome to insulate the moving part from earth. Considering the above mentioned situation, however, it is expected that an enough intense source of x-ray would be obtained by a relatively small apparatus with a rotating anode in which the electron beam is focussed only by an electro-static lens and the electron current is about 30 mA, when not the anode but the cathode is earthed. We have constructed such type of x-ray tube and it has become clear that this tube has the expected ability.

---

* The specific load is generally less than this in moving anode type tubes.

§ 2. Structure

Fig. 1, 2 and 3 show an elevation, a plan and a side view in the direction of emission of x-ray, of our apparatus, where *AA′*, BB′ and *CC′* are 500 mm, 230 mm and 320 mm respectively. ① is a compound cylindrical anticathode of 60 mm diameter and 22 mm breadth. The fixed right half is made of copper and the left half is attached to the right one by a screw through a rubber packing and accordingly it can easily be substituted by another one, especially of different metal. Now we have one made of iron at this position. ② is a brass tube supportin the anticathode, ③ are bearings*, ④ are stop of thrust, ⑤ is a thrust bearing and the anod is rotated by a d.c. motor (1/4 H and a pulley ⑥ through doub belts** which are long enoug for insulation. Cooling wate flows in from ⑦, goes throug a pipe ⑧ concentric with ②, i jetted upon the inner surface o the lateral part of anticathod from a narrow gap between tw parallel discs ⑨, goes bac between ② and ⑧ and flow out from ⑩. Cooling water i circulated through a tank an a gear pump which are mounte on an insulated table. Or w can use water works by the ai of vinyl tubes long enough fo insulation. ⑪ and ⑫ are Wilso seals stopping leakage of water

⑬ is a lid of vacuum and ha a two stage Wilson seal ⑭. flange ⑮ adapting to ⑬ is fixe to a plank ⑰ which stands on fou

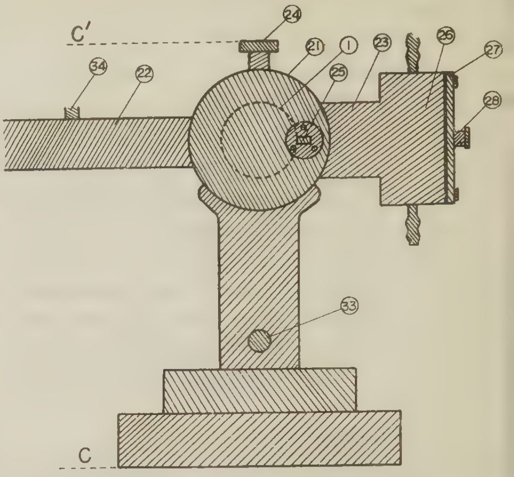

Fig. 3. A side view in the direction of emission of x-ray.

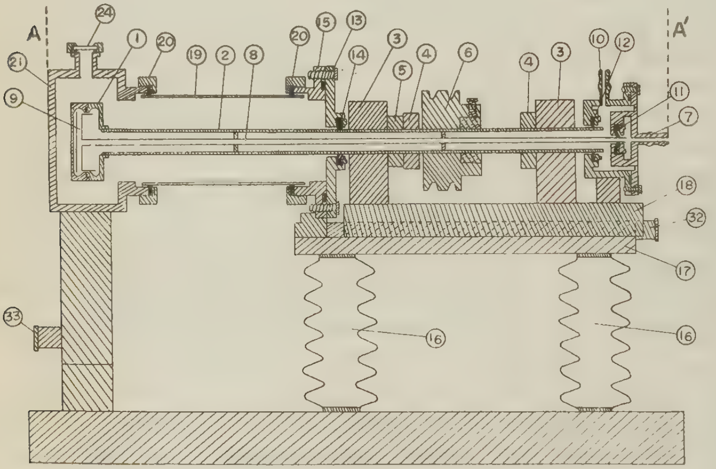

Fig. 1. An elevation.

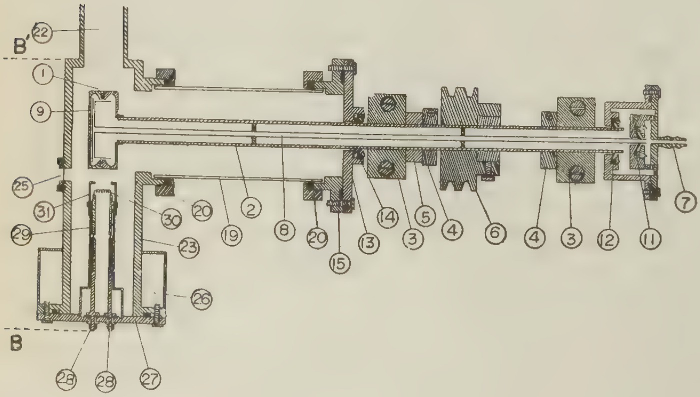

Fig. 2. A Plan.

---

* Plane bearing are used in orde to avoid vibrations. The amplitud of a vibration of the anticathod is kept less than 0.008 mm.

** Since the anticathode is damaged during a stop of rotation of onl several seconds, double belts ar used to avoid an accident due to break of one belt.

insulators. A plate ⑱ bearing the anode upon it can move back and forth along a rail engraved on the lateral sides of ⑰. We can put the anode out of the tube, if we release three bolts on ⑬ and let ⑱ go back.

⑲ is a hard glass tube for insulation and is fixed by rings ⑳. ㉑ is a body of tube surrounding the anticathode ① and has a leading pipe ㉒ to a vacuum pump, a cathode part ㉓, a viewing window ㉔ and a window ㉕ ejecting x-rays. ㉕ is covered by a cellophane film. ㉖ is a water-cooling pipe, ㉗ is a lid of vacuum and two bars ㉘ holding a horizontal fiilament ㉚ and a pipe ㉙ holding a grid ㉛ are fixed to ㉗, the former insulatedly and the latter directly. The distance between the filament and anticathode can be changed by adjusting each plug at the middle of each ㉘ and also the grid can be slided along ㉙. ㉜ is a high tension terminal, ㉝ is an earth terminal and ㉞ is a leading pipe a to vacuum gauge.

§ 3. Characteristics and Abilities

By this apparatus each of Cu and Fe characteristic rays are obtained by a displacement of ⑱, without breaking vacuum. The position of anticathode can be determined by a scale engraved on ⑰ and further we can see it directly through ㉔. ㉔ is also useful in supervising the damage of anticathode.

The other merit of this apparatus is that the total area on the side of the window ㉕ is earthed and accordingly an adjustment of position of a camera can be made with quite security.

The distance between the anticathode and the filament is 11 mm and that between the filament and an aderture (3 mm × 9 mm) of the grid is 1 mm. These values, determined by taking account of published data until now[5),7)], seem to be adequate.

The filament is a coil of W wire of 0.20mm diameter, the diameter and the length of which are 1 mm and 3 mm respectively.

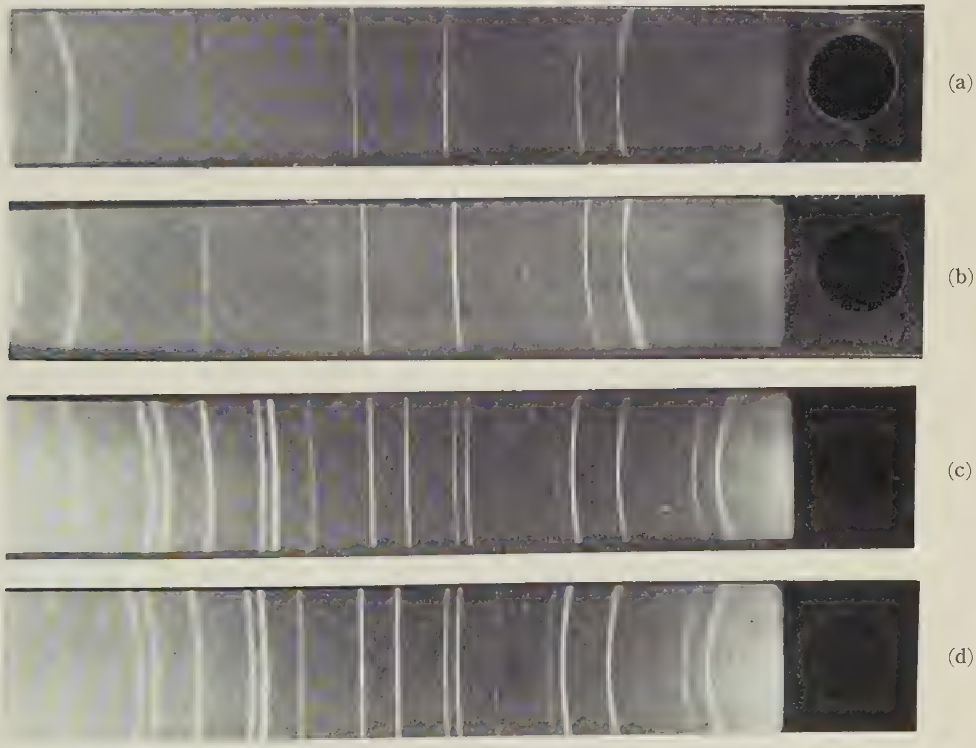

Fig. 4. Photographs taken by CuK radiation filtered by a nickel foil using a camera of 80 mm diameter. (50 kV, 30 mA).

(a)	Ni	10 sec.
(b)	Ni	20 sec.
(c)	PbTho$_3$	1 min.
(d)	PbTho$_3$	2 min.

Electrons emitted from this filament is focussed on the lateral surface of the anticathode in an area of about 0.25 mm × 0.75 mm by a biasing voltage of about 600 V and hence the dimension of x-ray source is about 0.25 mm × 0.25 mm, when the axis of camera makes about 20° to the lateral surface of the anticathode in a horizontal plane.

Although the adequate number of revolution of the anode has not yet been studied thoroughly, the usually adopted value is 1000 rev/min.

In Figs. 4 (a), (b), (c) and (d), we show photographs of Ni and $PbThO_3$ taken by Cu characteristic ray filtered by a nickel foil, using an ordinary powder camera of 80 mm diameter, the voltage and the current being 50 kV and 30 mA respectively. The time of exposure were 10 sec, 20 sec, 1 min and 2 min respectively and no damage was observed on the anticathode. The present value of specific load is 6 kW/mm² and is not so high. The result that the necessary time of exposure is very short, regardless the relatively low value of specific load, seems to show us that the increase of total load rather than the extreme decrease of focus size (less than 0.2 mm) is effective to the shortening of exposure time, as far as the diameter of slit is about 0.5 mm.

It is expected that we would have a more intense source of x-rays if we increase the electron current up to about 100 mA by using a more large anticathode and oscillate it in the direction of its axis in addition to the ordinary rotation of it. Such type of apparatus is now under construction at our laboratory.

References

1) British Journ. Appl. Phys. **1** (1950) 305.
2) R. Ueda and S. Hoshino: Appl. Phys. **21** (1952) 105; 149.
3) S. Goldsztaub: Acta Cryst. **9** (1956) 118.
4) A. Taylor: Journ. Sci. Inst. **26** (1949) 225.
5) P. Gay, P. B. Hirsch, J. S. Thorp and J. N. Keller: Proc. Phys. Soc. **B 64** (1951) 374.
6) S. Miyake and S. Hoshino: X-Ray **8** (1954) 45.
7) W. Ehrenberg and W. F. Spear: Proc. Phys. Soc. **64**. (1951) 67.
8) B. Ya. Pines: Izvest. Akad. Nauk S.S.S.R. Ser. Fiz. **16** (1952) 333

JOURNAL OF THE PHYSICAL SOCIETY OF JAPAN Vol. 12, No. 2, FEBRUARY, 1957

Electron Diffraction Study on Polish Layers of Gold I

By Masao KURIYAMA, Kazutake KOHRA* and Satio TAKAGI
Institute of Physics, College of General Education,
University of Tokyo,
Komaba, Meguroku, Tokyo

(Received September 22, 1956)

Polish layers of gold were examined by means of the transmission method of electron diffraction. Line breadths were measured at various stages of polishing. The mean grain size and the mean strain were determined using Hall's method (Proc. Phys. Soc A **62** (1949), 741) for medium polish layers which produce broad ring patterns. The grain size was also determined from the electron micrograph and from the number of spots on a spotty diffraction ring obtained from a minute region of the specimen. The values obtained from those different methods agree in order of magnitude with each other.

Even at medium stages of polishing, the specimen is polished so heavily as to gain grain size 80 Å and strain 3.6%. The grain size rapidly decreases as polishing proceeds. At the final stage of polishing broad ring patterns change into the halo pattern composed of three haloes. The Bragg spacing corresponding to the most inner halo is 4.08 Å, agreeing with the results obtained by Nonaka and Kohra by the reflexion method (J. Phys. Soc. **9** (1954), 512).

§1. Introduction

When polished metallic surfaces are examined by electron diffraction at successive stages of polishing, normal sharp Debye-Scherrer rings initially given by an unpolished surface gradually become broader and finally change into a few haloes[1]. The broadening of rings is usually observed in *X*-ray diffraction patterns from cold worked metals and is attributed to small sizes of crystal grains and to inhomogeneous strains[2]-[8]. The halo pattern, on the other hand, is not obtained from cold worked metals, but only from heavily polished layers of metal. This layer, called the "Beilby layer", was supposed to be amorphous by Beilby before the discovery of electron diffraction[9]. Many investigations have been done on the structure of the Beilby layer by the reflexion method of electron diffraction[1],[10]. Most workers have obtained diffraction patterns consisting of two haloes and have deduced some kind of amorphous structure for the polish layer on metals.

Cochrane[11] first obtained transmission patterns from polish layer of gold and observed another halo *outside* the two haloes mentioned above. Afterwards, Raether and his collabolator[12][13] carried out extensive studies by means of the transmission method. They suggested that crystal size in the upper most layer of heavily polished metals is as small as one or two unit cells in dimension and pointed out from the line broadening that the distortion takes no appreciable role.

It seems unlikely, however, to the present authors that crystallites subjected to heavy polishing are not appreciably distorted. In order to determine the distortion in crystallites, it is necessary to measure exactly the breadth of several Debye-Scherrer rings and particularly to examine their dependence on the scattering angle. This study cannot be performed on the Beilby layer obtained at the final stage, but on specimens at medium stages of polishing where at least several inner rings are clearly resolved. Nevertheless, this study will throw some light on the structure of the Beilby layer. For this purpose, the transmission method is adopted, since it is not only more appropriate for the quantitative analysis than the reflexion method, but also convenient for obtaining direct electron micrographs and selected area microdiffraction.

In the present work, the grain size and the magnitude of strain in the crystallites are obtained, and the values of the grain size are compared with those obtained directly from electron micrograph and from the number of spots on a spotty ring of the microdiffraction pattern.

---

* Now at Fritz-Haber Institut der Max-Planck Gesellschaft.

Recently, Nonaka and one of the authors (K.K.)[14] pointed out the occurence of another halo *inside* the two haloes by the reflexion method. This point is confirmed in the present work by the transmission method.

A more direct method to study the structure of the Beilby layer is to determine the radial distribution function of atoms from measured intensities of halo patterns. In the second part of this work, the results of the study will be given and the structure of Beilby layer will be discussed in more detail.

§ 2. Experimental

Gold was chosen as specimen because of its chemical stability especially against oxidation. Thin polycrystalline films were made on zinc plates by the electro-deposition method following Kranert and Raether[12]. Thin single-crystal-like films were also made by the electro-deposition on single-crystal copper. The thickness of films was about 500 Å. In order to prevent specimens from oxidation and recrystallization by the temperature rise during polishing, the film was polished under benzene by chamois leather without any polishing materials. Polishing was performed in the same manner as was done by Nonaka and Kohra[14]. During the polishing the whole area of the specimen was pushed onto the surface of the rotating disk with a uniform pressure 5 or 200 g/cm². The polishing speed varied from 5 to 250 cm/sec.

At various stages of polishing, films were examined by means of the transmission method of electron diffraction. The electron diffraction camera is of a usual type with a focusing lens and the specimen-to-plate distance of 15 cm. Two slits were used before the specimen which was supported on a fine platinum or brass gauze. The first slit which was 0.1 mm in diameter was used for reducing the aperture of the incident beam and the second which was 0.5 mm in diameter, for getting rid of the irregular scattering from the periphery of the first.

The photometry was performed using a series of diffraction photographs of the same specimen which were taken successively with different exposures. Intensity distribution curves were obtained from microphotometer traces by the method employed by Karle and Karle[15].

Some of the specimens were also examined after various heat treatments. The specimens on platinum gauze were heated *in vacuo* in the diffraction camera or in air in another furnace. Electron micrographs of some specimens were taken, and a selected area ($\sim 1\mu \times 1\mu$) microdiffraction of each was obtained.

§ 3. Result

Upon slight polishing, sharp spots initially given by single-crystal-like films are replaced by Debye-Scherrer rings with arcings showing preferred orientations. On further polishing preferred orientations rapidly weaken and rings become broader. Breadths of the rings are measured for lightly polished single-crystal-like films showing only slight preferred orientations and for polycrystalline films polished to a medium extent. The results are given in § 4.

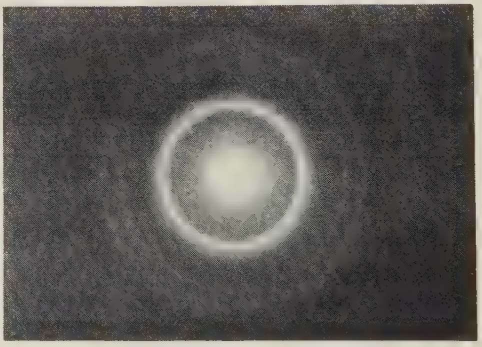

Fig. 1. a. Broad ring pattern from the polish layer of gold. The polishing pressure is 200 g/cm², and the polishing time, 8 hours.

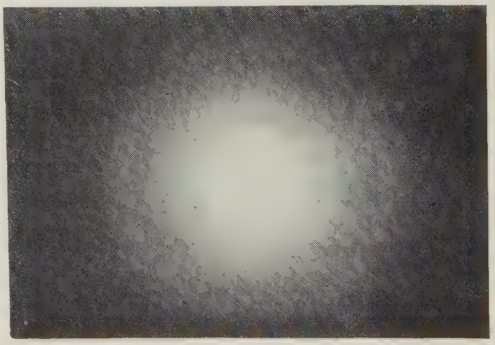

Fig. 1. b. Halo pattern from the polish layer of gold. The polishing pressure is 200 g/cm², and the time, more than 15 hours.

At the final stage of polishing the film yields the characteristic halo pattern of polish layer. The Bragg spacing corresponding to each halo is listed in Table I together with the results obtained by Cochrane[11] and by Nonaka and Kohra[14] and with the spacings of crystalline gold. As was already described, a new halo is observed inside the usually known two haloes. In addition to these three haloes, the innermost halo whose spacing was about 10 Å sometimes appeared around the incident spot. This halo was especially visible during the process of annealing. It may be due to the small angle scattering from severely distorted crystals. A similar hump was observed in the intensity distribution of the pattern from a foil of supercooled gold by Suzuki[16].

Table I. Bragg spacings of halo pattern

Beilby layer			Crystalline gold	
Present results	Nonaka Kohra (reflexion)	Cochrane		
4.08 Å	4.1 Å	.... Å	(4.07) Å	(100)
			2.35	(111)
2.22	2.25	2.10		
			2.04	(200)
			1.44	(220)
1.24	1.24	1.30		
			1.23	(311)
		0.96	1.18	(222)

Five specimens giving halo patterns were annealed in the diffraction camera at temperatures 250°, 325° and 400°C. At 325°C, for instance, annealing for more than twenty minutes began to barely reveal broad Debye-Scherrer rings in the obscure halo pattern. After about an hour the pattern became the broad Deye-Scherrer rings. The broadening of the rings implies the existence of crystal grains of about 100 Å in size with appreciable distortions. The rings became sharper as annealing proceeded. The Bragg spacings of these rings were confirmed to agree with those of gold within the experimental error.

§4. Line Broadening

Intensity curves of broad ring patterns were divided into individual peaks corresponding to each of the reflexions, assuming a symmetrical profile for each peak (Fig. 2). We shall not concern with the line profiles of peaks, but with half value breadths of these peaks. The true breadth was obtained simply by subtracting the geometrical broadening from the observed one; the former being determined experimentally from sharp Debye-Scherrer rings given by the same specimen after prolonged annealing[17),18)].

Breadths of lines thus obtained correspond to grain size of about 15–20 Å, if only the size effect is assumed to be responsible for the line broadening. However, this conclusion is not correct as is shown in the following. When line breadths are plotted against radii of the rings (Fig. 3), the points corresponding to each of the diffraction rings are scattered along a straight line intersecting the vertical axis at a point apart from the origin. This is due to the fact that both the particle size and the strain are effective to the line broadening.

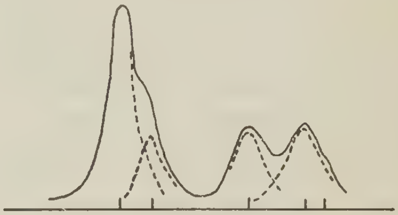

Fig. 2. Intensity distribution curve and line profiles obtained from the broad ring pattern. (Specimen no. 3)

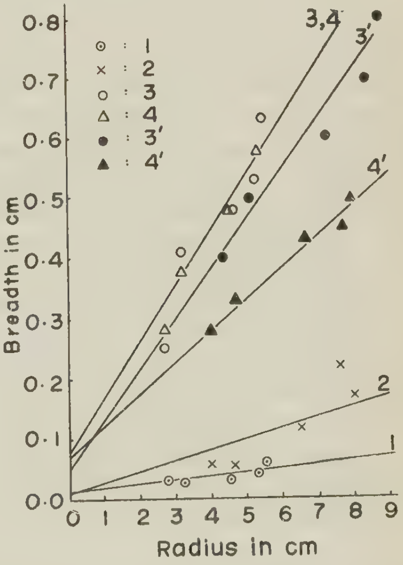

Fig. 3. Variation of line breadth with radius. Numerals in the figure are specimen numbers. (The breadth and the radius are expressed in a magnified scale.)

Hall [19] pointed out that if both causes of broadening were operative, the individual contributions to breadths could be added for a commonly occuring line shape*, thus

$$\frac{\beta\cos\theta}{\lambda}=\frac{1}{t}+2\eta\frac{\sin\theta}{\lambda} \qquad (1)$$

where θ is Bragg angle of a reflexion; λ, the wave length of the radiation; t, the apparent particle size and η, a coefficient relating to the strain distribution. In the case of electron diffraction, θ is usually small and (1) becomes

$$B=\frac{\lambda L}{t}+\eta r \qquad (2)$$

where B is the line breadth on the photographic plate, L, the specimen-to-plate distanc and r, the radius of the ring. If the strai distribution is isotropic, η is independent o the indices of reflexion, and is given by

$$\eta=(2\pi\overline{e^2_{xx}})^{1/2} \qquad (3$$

where e_{xx} is the tensile strain and the ba means the mean value. Straight lines in Fig 3 imply that the strain rather than the stres distribution is isotropic in this case. If th stress distribution were isotropic, a straigh line would be obtained by plotting the breadth against r/E_{hkl} where E_{hkl} is Young's modulu in (hkl) direction. This plotting was tried. The points did not lie even on a smooth curve.

Table II. Mean size and strain in polished gold films

Specimen number	Polishing pressure	Polishing time	Time of observation	Mean size		Strain from (2)
				from (2)	form electron micrographs	
1	5 g/cm²	2 hours	Immediately after polishing	....	....	0.3%
2	5	3		....	....	0.7
3	200	8		80 Å	....	3.6
4	200	8		80	....	3.6
3′	200	8	About two weeks after polishing	150	200 Å	3.3
4′	200	8		130	100 and 300 Å	2.1

The values of particle size and the root mean square of the strain obtained from Fig. 3 for different specimens are tabulated in Table II. At early stages of polishing (specimens 1 and 2) the grain size is too large to be determined from line breadths and the mean strain is of the order of 0.1%. At a more advanced stage (specimens 3 and 4), the grain size is reduced to about 100 Å and the mean strain increased to 2–3%. After being left at the room temperature for about two weeks (specimens 3′ and 4′) the films recrystallize to varying extent.

§ 5. Electron Micrographs

Some of the specimens giving broad rings were observed by an electron microscope. A typical micrograph is shown in Fig. 4a. Most of the grains appearing in a micrograph are of the same degree in size except specimen 4′. Selecting many grains at random, we directly obtained their mean size which is shown i Table II. Specimen 4′ is composed of two kind of grains (Table II).

At the same time, microdiffraction pattern were obtained from minute portions, abou $1\mu\times1\mu$ in size, of specimens. An example i shown in Fig. 4b. It is seen that the ring are composed of many spots. The mean siz of grains can be obtained[21] also from th number of spots on a ring. The estimate value is 200–300 Å, assuming the spherica shape and the uniform distortion.

§ 6. Discussion and Conclusion

Hall's formula (2) is derived under the assumption that the size broadening β_p and th strain broadening β_s can be directly added t make the total broadening β. This assumption is proved to be valid when broadenin functions are of the Cauchy form $1/(1+k^2x^2)$ If these are of Gaussian form, the square o total broadening is expressed as $\beta_p^2+\beta_s^2$. A accurate determination, however, of the lin profile is difficult in the present experimen The results in §§ 4 and 5 have inferred tha the linear relation holds between the breadt

---

* We have tacitly made use of this additivity assumption in deriving the true breadth from the observed one.

Fig. 4. a. Electron micrograph. (Specimen no. 4′)

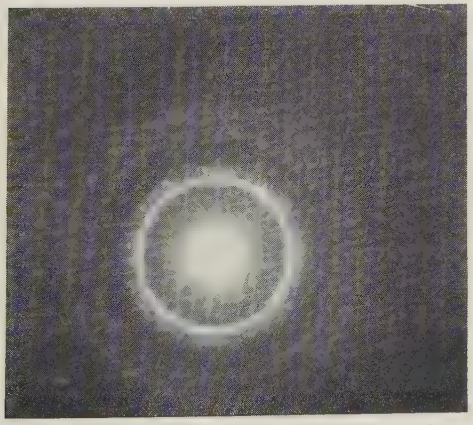

Fig. 4. b. Electron diffraction patterns from a minute portion ($1 \times 1\ \mu^2$) in the above micrograph.

and the radius of rings and the values of the grain size obtained by three different methods do not show significant difference. On the other hand, the trial based on the assumption of Gaussian form showed that the grain size differs from the values obtained by the two other methods. It can be said, accordingly, that Hall's method is reliable as the first approximation in the present case and the value of the strain obtained by this method may be understood to be reliable as much as the value of the grain size.

From the observation given in §§ 4 and 5, the following conclusions on polish layers can be deduced. Even at the medium stage of polishing, the grain size can attain the value of 80 Å, and the strain, that of 3.6%. The value of size and that of strain are ten or hundred times smaller, and about five times larger, respectively than the values usually obtained from cold worked metals. Williamson and Hall⁽⁷⁾, for example, have observed from the line broadening of Al that the value of the grain size is 0.2 μ and that of the strain breadth is 0.6%. This value of strain roughly corresponds to yield stress and may be regarded as the limit value in the usual cold work. The value 3.6% of the strain in polished films corresponds to the stress several times larger than the yield stress. Such a large strain can exist in a crystallite as small as are examined in the present experiment[22)].

The present result that the line breadth varies with radii so that a considerable amount of strain remains in crystallites at least in the medium stage of polishing differs to that of Kranert and Raether[12)]. This point will be discussed further in Part II of this study.

It is possible that the line broadening of the type similar to the strain broadening is caused by the presence of impurities making a solid solution with gold with varying local content. If this is the case, the position of the peaks will be shifted by approximately equal amount to the half breadth of the line. Such a shift was not found in any of the broad ring patterns, nor in the extremely sharp rings obtained from the specimen after prolonged annealing at 450°C.

The authors thanks are due to Mr. T. Suzuki for his suggestions concerning experimental techniques, to Mr. K. Suzuki of the Tokyo Institute of Technology for the use of the microphotometer, and to the Hitachi Central Research Laboratory for obtaining the electron micrographs.

References

1) G. P. Thomson and W. Cochrane: "Theory and Practice of Electron Diffraction" Ch. XIII (1939)

2) G. B. Greenough: Progress in Metal Physics **3** (1952) 176.

3) P. B. Hirsch and J. N. Kellar: Acta Cryst. **5** (1952) 162.

4) P. B. Hirsch: ibid **5** (1952) 172.

5) P. Gay and A. Kelly: ibid **6** (1953) 165, 172.

6) A. Kelly: ibid **7** (1954) 554.

7) G. K. Williamson and W. H. Hall: Acta Metall. **1** (1953) 22.

8) G. K. Williamson and R. E. Smallman: Acta Cryst. **7** (1954) 574.

9) G. T. Beilby: Rep. Brit. Ass. (1901) 604, "Aggregation and flow of Solid" London, (1921)

10) H. Raether: Ergb. d. exakten Naturwiss. XXIV (1951) 54.

11) W. Cochrane: Proc. Roy. Soc. **A 166** (1938) 228.

12) W. Kranert and H. Raether: Ann. d. Physik **43** (1943) 520.

13) H. Raether: Zeits. f. Phys. **124** (1948) 286

14) K. Nonaka and K. Kohra: J. Phys. Soc. Japan **9** (1954) 512.

15) J. Karle and I. L. Karle: J. Chem. Phys. **18** (1950) 957.

16) T. Suzuki: J. Phys. Soc. Japan **10** (1955) 1026.

17) W. A. Wood and W. A. Rachinger: J. Inst. Metals **75** (1949) 571.

18) F. W. Jones: Proc. Roy. Soc. **A 166** (1938) 16.

19) W. H. Hall: Proc. Phys. Soc. **A 62** (1949) 741.

20) A. R. Stokes and A.J.C. Wilson: Proc. Camb. Phil. Soc. **38** (1942) 313, ibid **40** (1944) 197, Proc. Phys. Soc. **56** (1944) 174.

21) P. B. Hirsch, A. Kelly and J. W. Menter: Proc. Phys. Soc. **B 68** (1955) 1132.

22) W. T. Read, Jr.: "Dislocations in Crystals" p. 7 (1953)

JOURNAL OF THE PHYSICAL SOCIETY OF JAPAN Vol. 12, No. 2, FEBRUARY, 1957

On the Magnetic Properties of Nickel-Arsenide Type Crystals[*]

By Tokutaro HIRONE and Kengo ADACHI

The Research Institute for Iron, Steel and Other Metals
Tohoku University, Sendai

(Received October 20, 1956)

The formation of the ordered arrangement of the magnetic moments of cations (spin ordering or spin arrangement) in the crystal lattice of the nickel-arsenide type is studied theoretically with the molecular field approximation, taking into account interaction between pairs of cations, which form the first, second or third neighbours in the crystal lattice. Various types of spin arrangement in this structure with two kinds of cations are derived. Based on the results obtained the magnetic properties of the compounds are discussed. The theory is applied as a typical example to the interpretation of the magnetism of the ternary solid solution of manganese-chromium-antimony system.

§1. Introduction

It has been known that a number of compounds formed from transition metals and the elements of V_a or VI_a group in the periodic table have nickel-arsenide type crystal structure at or near the stoichiometric composition (1:1), and that many of them show interesting magnetic behaviours. As shown in Fig. 1, the crystal lattice of the nickel-arsenide type is composed of a simple hexagonal lattice of metallic ions and of a close-packed hexagonal lattice of metalloid ions, both lattices interpenetrating into each other. The magnetism in such a crystal structure may be considered to be attributed to the moments of metallic ions; in this case it may be necessary to take account of the exchange coupling between the third neighbouring cations as well as the first and the second. (cf. the positions of metalloid ions as illustrated in Fig. 1) The relative magnitude of these interactions will be considered to be the leading factor determining the magnetic properties of the compounds. In the present paper, we shall discuss the spin ordering in the case of a stoichiometric nickel-arsenide type compound with two different kinds of cations, and apply the results to the interpretation of the anomalous behaviours of magnetism which were observed in some nickel-arsenide compounds.

---

[*] This investigation was supported in part by the Grant-in-Aid of the Ministry of Education (Ferromagnetism of Metals and Alloys, 1955).

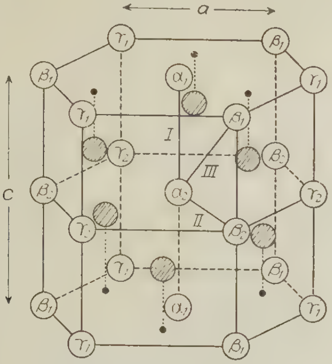

○ Ni (metal)...simple hexagonal
▨ As (metalloid)...close-packed hexagonal
$\alpha_1, \beta_1, \cdots, \gamma_2$. ...sublattices of metal lattice
I, II, and III. ...the 1st, 2nd and 3rd neighbours ($c/a < 2$)

Fig. 1. NiAs type crystal structure and its sublattices.

§ 2. Types of Spin Ordering in the Compounds with the Nickel-Arsenide Structure

In order to discuss the spin ordering (the ordered arrangement of the magnetic moments of cations) in the crystal lattice of the nickel-arsenide structure, we divide the metallic lattice into six sublattices, $\alpha_1, \beta_1, \cdots \gamma_2$ as shown in Fig. 1, because here we have three kinds of interactions mentioned in the introduction and the hexagonal symmetry of the structure.

According to Van Vleck's and Smart's[1)] theory based upon the molecular field approximation, the most stable type of spin ordering is determined by the relative magnitude of the three different interactions mentioned above. In the case of just one kind of cation, we have four types of spin ordering as shown in Fig. 2. If the crystalline magnetic anisotropy is neglected, the ferromagnetic or antiferromagnetic Curie points for these types are given as follows.

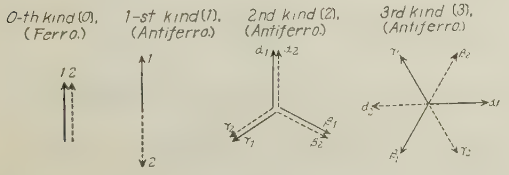

Fig. 2. The stable spin orderings.

$$\left.\begin{array}{lll} \text{0-th} & \text{kind} & T_{c0}=c(\Gamma^1+\Gamma^2+\Gamma^3) \\ \text{1st} & \text{kind} & T_{c1}=c(-\Gamma^1+\Gamma^2-\Gamma^3) \\ \text{2nd} & \text{kind} & T_{c2}=c\left(\Gamma^1-\dfrac{\Gamma^2}{2}-\dfrac{\Gamma^3}{2}\right) \\ \text{3rd} & \text{kind} & T_{c3}=c\left(-\Gamma^1-\dfrac{\Gamma^2}{2}+\dfrac{\Gamma^3}{2}\right) \end{array}\right\} \quad (1)$$

In these expressions $\Gamma^\nu=2z^\nu J^\nu(g\beta)^{-1}$ ($\nu=1, 2$ and 3) means the molecular field coefficients due to the pair of ν-th neighbour ions, z^ν and J^ν are the coordination number and the exchange interactions due to ν-th neighbour respectively and $c=\frac{g\beta}{3k}s(s+1)$ is the ionic Curie constant. The stable types of ordering are specified by the values of different interaction coefficients between neighbouring cations. In Fig. 3 the stable ranges of these types of ordering are illustrated with respect to the values of these exchange integrals between neighbouring pair of ions. The ratio θ/T_{ci} is also shown in the same figure, where $\theta=c(\Gamma^1+\Gamma^2+\Gamma^3)$ means the paramagnetic (asymptotic) Curie point. The transition between different ordering types observed in the compounds such as MnAs and MnBi[1)] (ferromagnetic⇄antiferromagnetic) should be considered from the results indicated in Fig. 3.

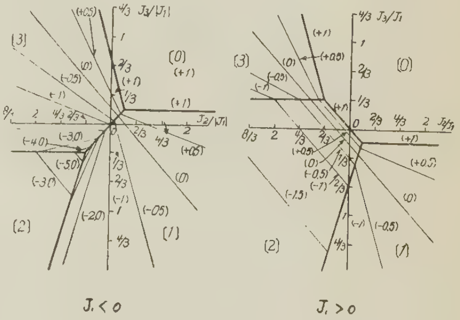

Fig. 3. The types of stable spin ordering and (θ/T_{ci}) values for the magnitude of each exchange integral for neighbouring pair of cations.

§ 3. Triangular Spin Arrangement Due to Mixing of Different Kinds of Cation

In the compounds of nickel-arsenide type, it will occur that several kinds of metallic ions are found in the same cation lattice. For instance, the manganese atom in the compound MnSb can be substituted by chromium atom in any desired composition ($Mn_{1-x}Cr_xSb$)2). Also the binary compound of nickel-arsenide type is not always composed at the stoichiometric concentration (1:1) of metal and metalloid element, but the compounds with off-stoichiometric concentrations are frequently found. In such cases, we may assume without introducing any serious error, that each anion has the same valence; thus it might be presumed that the mixed states of the two kinds of cation valence are present in the off-stoichiometric cases. In the case of pyrrhotite3), $FeS_{1+\delta}$, for example, both the ferrous and ferric ions will occupy the cation lattice.

In the case of the substitutional type above mentioned, it will be shown that the resultant spin moments of cations on different sublattices are not necessarily parallel or antiparallel but they will sometimes form an angular coupling depending on the presence of the various kinds of exchange interactions. Assuming such angular arrangements of spins, Yafet-Kittel4), Kishi5) and Lotgering6) explained the magnetism of ferrites, manganites*) and some sulphides and oxides. We shall now discuss the magnetic behaviour of the compound with nickel-arsenide structure above mentioned from the same point of view.

For simplicity, it will be assumed that the two kinds of ions occupy the cation sites completely at random and further that no vacant sites are present in the lattice. If the mean magnetic moment of the a-ion on α_1-sublattice is denoted by $s_a^{\alpha_1}$ and so forth, then the molecular field acting on an a-ion on α_1-sublattice, $\boldsymbol{H}_a^{\alpha_1}$, etc. are expressed by

$$\begin{aligned}\boldsymbol{H}_a^{\alpha_1}=&\Gamma_{aa}^1\boldsymbol{s}_a^{\alpha_2}+\frac{\Gamma_{aa}^2}{2}(\boldsymbol{s}_a^{\beta_1}+\boldsymbol{s}_a^{\gamma_1})\\&+\frac{\Gamma_{aa}^3}{2}(\boldsymbol{s}_a^{\beta_2}+\boldsymbol{s}_a^{\gamma_2})+\Gamma_{ab}^1\boldsymbol{s}_b^{\alpha_2}\\&+\frac{\Gamma_{ab}^2}{2}(\boldsymbol{s}_b^{\beta_1}+\boldsymbol{s}_b^{\gamma_1})\frac{\Gamma_{ab}^3}{2}(\boldsymbol{s}_b^{\beta_2}+\boldsymbol{s}_b^{\gamma_2}),\ \text{etc.,}\end{aligned}\tag{2}$$

and

$$\boldsymbol{s}_a^{\alpha_1}=x_a s_a^0 B_{s_a^0}\left[\frac{g\beta}{kT}s_a^0(\boldsymbol{H}_a^{\alpha_1}+\boldsymbol{H})\right],\ \text{etc.}\tag{3}$$

In these expressions x_a, x_b and s_a^0, s_b^0 are the concentrations and spin quantum numbers of a and b-ions respectively, and $B_{s^0}[\ \ ]$ means the Brillouin function.

To obtain the coupling energy on the basis of equations (2) and (3), the orientations of $s_a^{\alpha_1}$ etc. must be expressed explicitly. If the orientation of the resultant magnetic moment of the a-ions on the α_1-sublattice is expressed by polar coordinates θ_a, φ_a and that of b-ions by θ_b, φ_b respectively, then the orientations of other moments are expressed as given in Table I. The direction of the polar axis is taken arbitrary owing to the isotropic nature of the exchange coupling, although it is actually determined by the crystalline magnetic anisotropy. Neglecting the terms of the magnetic anisotropy energy, the magnetic coupling energy can be obtained as follows:

$$\begin{aligned}E(\theta_a,\theta_b,\varphi_a,\varphi_b)=&-\frac{1}{2}\frac{1}{6}\sum_{ab}\sum_{\alpha_1\cdots\gamma_2}\boldsymbol{s}_a^{\alpha_1}\boldsymbol{H}_a^{\alpha_1}\\=&-\frac{1}{2}\Bigg[s_a^2x_a^2\Big\{[\mathcal{E}_a(\Gamma_{aa}^1+\Gamma_{aa}^3)+\Gamma_{aa}^2]\cos^2\theta_a\\&+\Big[\Big(\Gamma_{aa}^1-\frac{\Gamma_{aa}^3}{2}\Big)\cos^2\varphi_a-\frac{\Gamma_{aa}^2}{2}\Big]\sin^2\theta_a\Big\}\\&+s_b^2x_b^2\Big\{[\mathcal{E}_b(\Gamma_{bb}^1+\Gamma_{bb}^3)+\Gamma_{bb}^2]\cos^2\theta_b\\&+\Big[\Big(\Gamma_{bb}^1-\frac{\Gamma_{bb}^3}{2}\Big)\cos^2\varphi_b-\frac{\Gamma_{bb}^2}{2}\Big]\sin^2\theta_b\Big\}\\&+2s_as_bx_ax_b\Big\{[\mathcal{E}_c(\Gamma_{ab}^1+\Gamma_{ab}^3)+\mathcal{E}_c'\Gamma_{ab}^2]\cos\theta_a\cos\theta,\\&+\Big[\Big(\Gamma_{ab}^1-\frac{\Gamma_{ab}^3}{2}\Big)\cos(\varphi_a+\varphi_b)\\&-\frac{\Gamma_{ab}^2}{2}\cos(\varphi_a-\varphi_b)\Big]\sin\theta_a\sin\theta_b\Big\}\Bigg],\end{aligned}\tag{4}$$

where $\mathcal{E}$'s take the values ±1 depending on the types of spin arrangement.

The stable positions of θ and φ are determined by the minimum point of the coupling

---

*) Dr. Kishi applied with success the concept of the triangular arrangement to the explanations of the magnetic properties of the compounds with perovskite structure, La-Ca manganite and La-Sr cobaltite. His results for the manganite system however disagree with the results of neutron diffraction study of this system recently observed by Wollan and Koehler [Phys. Rev. **100** (1955) 545].

Table I. The orientation scheme of the spins of a and b ions on sublattices.

Sublattice	a-ion		b-ion	
α_1	θ_a	φ_a,	θ_b,	φ_b,
β_1	θ_a,	$\frac{2}{3}\pi+\varphi_a$,	θ_b,	$\frac{2}{3}\pi+\varphi_b$,
γ_1	θ_a,	$\frac{4}{3}\pi+\varphi_a$,	θ_b,	$\frac{4}{3}\pi+\varphi_b$,
α_2	θ_a or $\pi-\theta_a$,	$-\varphi_a$,	θ_b or $\pi-\theta_b$,	$-\varphi_b$,
β_2	θ_a or $\pi-\theta_a$,	$\frac{2}{3}\pi-\varphi_a$,	θ_b or $\pi-\theta_b$,	$\frac{2}{3}\pi-\varphi_b$,
γ_2	θ_a or $\pi-\theta_a$,	$\frac{4}{3}\pi-\varphi_a$,	θ_b or $\pi-\theta_b$,	$\frac{4}{3}\pi-\varphi_b$.

energy (4). A short calculation will show that the values of θ's and φ's for the minimum energy occur when

$$\left.\begin{aligned} &\varphi_a=\varphi_b=0 \quad \text{or} \quad \pm\pi \quad \text{or} \quad \pm\frac{\pi}{2}: \\ \text{and} \\ &0<\theta_a \quad \text{and} \quad \theta_b<\pi\,, \end{aligned}\right\}$$

or

$$\left.\begin{aligned} &\theta_a=\theta_b=0 \quad \text{or} \quad \pm\pi \quad \text{or} \quad \pm\frac{\pi}{2}: \\ \text{and} \\ &0<\varphi_a \quad \text{and} \quad \varphi_b<\pi\,. \end{aligned}\right\}$$

In the former case the angular arrangement above mentioned occurs from the difference between θ_a and θ_b, while in the latter case, it is caused by φ's. Now the case of the triangular arrangement in θ will be considered first. Using the following abbreviations

$$\left.\begin{aligned} A&=\mathcal{E}_a(\Gamma_{aa}{}^1+\Gamma_{aa}{}^3)-\delta_a\left(\Gamma_{aa}{}^1-\frac{\Gamma_{aa}{}^3}{2}\right)+\frac{3}{2}\Gamma_{aa}{}^2, \\ B&=\mathcal{E}_b(\Gamma_{bb}{}^1+\Gamma_{bb}{}^3)-\delta_b\left(\Gamma_{bb}{}^1-\frac{\Gamma_{bb}{}^3}{2}\right)+\frac{3}{2}\Gamma_{bb}{}^2, \\ C_1&=\mathcal{E}_c(\Gamma_{ab}{}^1+\Gamma_{ab}{}^3)+\mathcal{E}_c'\Gamma_{ab}{}^2\,, \\ C_2&=\delta_c\left(\Gamma_{ab1}-\frac{\Gamma_{ab}{}^3}{2}\right)-\delta_c'\frac{\Gamma_{ab}{}^2}{2}\,, \end{aligned}\right\} \tag{5}$$

and denoting $s_b x_b/s_a x_a$ by y, the energy formula (4) can be rewritten as the following equation,

$$\begin{aligned} E(\theta_a,\theta_b)=-\frac{1}{2}s_a{}^2x_a{}^2[&A\cos^2\theta_a+By^2\cos^2\theta_b \\ &+2y(C_1\cos\theta_a\cos\theta_b+C_2\sin\theta_a\sin\theta_b)]+\text{const.}, \end{aligned} \tag{6}$$

where δ's can take either of the values ± 1. The added constant does not depend on θ and φ. Then the extremum condition for the energy, $\partial E/\partial\theta_a=\partial E/\partial\theta_b=0$, lead to the following simultaneous equations for θ_a and θ_b,

$$\left.\begin{aligned} &(A\cos\theta_a+yC_1\cos\theta_b)\sin\theta_a \\ &\quad -yC_2\cos\theta_a\sin\theta_b=0\,, \\ &-C_2\cos\theta_b\sin\theta_a \\ &\quad +(yB\cos\theta_b+C_1\cos\theta_a)\sin\theta_b=0\,. \end{aligned}\right\} \tag{7}$$

Of course these equations have the solutions $\theta_a=\theta_b=0$ or $\pm\pi$ or $\pm\frac{\pi}{2}$, but they have besides these another solution satisfying the following equation,

$$\begin{aligned} &AC_1\cos^2\theta_a+y^2BC_1\cos^2\theta_b \\ &\quad +y(AB+C_1{}^2-C_2{}^2)\cos\theta_a\cos\theta_b=0\,. \end{aligned} \tag{8}$$

From equations (7) and (8), θ_a and θ_b are obtained as follows;

$$\left.\begin{aligned} \cos^2\theta_a&=\frac{y^2-Q^2}{P^2-Q^2}\,, \\ \cos^2\theta_b&=\frac{P}{y^2}\cos^2\theta_a\,, \end{aligned}\right\} \tag{9}$$

where

$$\left.\begin{aligned} P&=\frac{1}{2BC_1}[-(AB+C_1{}^2-C_2{}^2) \\ &\qquad \pm\sqrt{(AB+C_1{}^2-C_2{}^2)^2-4ABC_1{}^2}], \\ Q&=\frac{A}{C_2}+\frac{C_1}{C_2}P\,. \end{aligned}\right\} \tag{10}$$

In equation (9), $y=P$ and $y=Q$ gives $\theta_a=\theta_b=0$ or $\pm\pi$ and $\theta_a=\theta_b=\pm\frac{\pi}{2}$ respectively. For the occurrence of the triangular arrangement in θ the signs of A and B should be different from each other, and also $P \lesseqgtr y \lesseqgtr Q$ $(P, Q > 0)$ should hold. In the ranges of $y \gtrless P, Q$ usual ferrimagnetic theory as developed by Néel[7] can be applied.

In Fig. 4 the types of spin angular arrangement and the values of ε's and φ's for each type are illustrated. In the case of F_1 all the resultant moments are parallel to each other (ferromagnetic), which in F_2 the resultant moments of a-ions are antiparallel to those of b-ions (ferrimagnetic). In the cases of A_1 and A_2, the moments of a-ions on the sublattices $1(\alpha_1, \beta_1, \gamma_1)$ are antiparallel to those of the same ions on the sublattices $2(\alpha_2, \beta_2, \gamma_2)$, and the same is said for those of b-ions, so that the system as a whole has no resultant moment (antiferromagnetic). TF_1, TF_2 and TA_1, TA_2 are the ferrimagnetic and antiferromagnetic triangular arrangements respectively, which are derived from F_1, F_2 and A_1 A_2 states. The cone in the figure means three resultant moments with the same θ value on the triad of the sublattices $(\alpha_1, \beta_1, \gamma_1)$ of $(\alpha_2, \beta_2, \gamma_2)$. The same can be said for the configurations f_1, f_2, a_1, a_2 and their T-states of triangular arrangement in φ (antiferromagnetic).

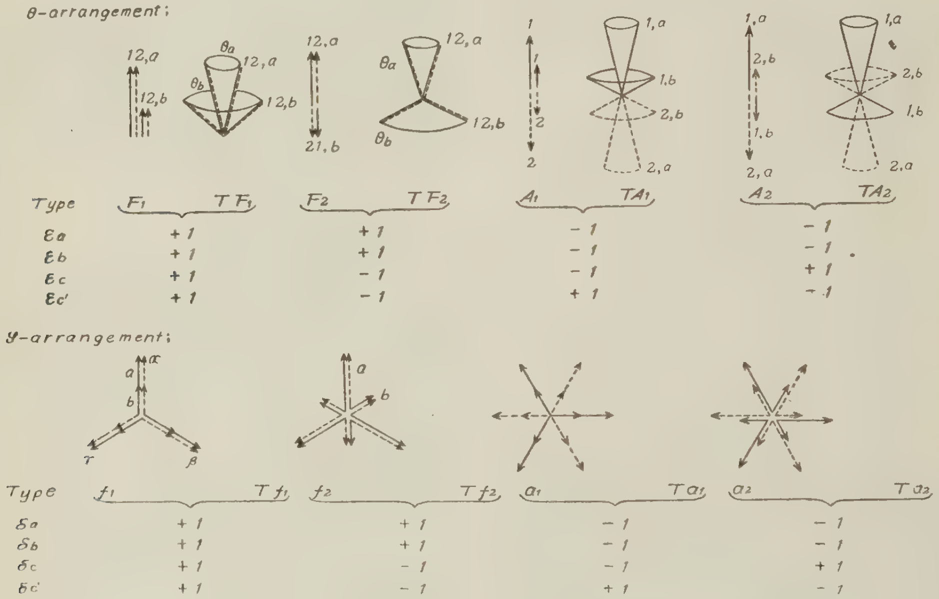

Fig. 4. Types of triangular spin arrangements.

It is to be noted that in such a case as the nickel arsenide structure here discussed, discontinuous transitions between each type of arrangement can occur with the change of the temperature or of the composition of the system, and the compound undergoes thereby discontinuous changes of magnetic properties.

§ 4. The Magnetic Properties of Compounds with Triangular Spin Arrangement

The change of magnetic properties caused by the rise of temperature and the change of cation concentration in the crystal lattice now in consideration (§ 3) can be derived from the minimum condition of the energy due to spin angular arrangement as mentioned above. Neglecting the terms of the crystalline magnetic anisotropy, we will proceed to work out expressions for some magnetic properties in the case of the triangular arrangement in θ.

a) Magnetization *vs* concentration relation at absolute zero.

The spontaneous magnetization $\sigma_0(x)$ at absolute zero of temperature in the case of the triangular arrangement, is given by

$$\sigma_0 = s_a{}^0 x_a \cos\theta_a \pm s_b{}^0 x_b \cos\theta_b$$
$$= (1 \pm P)\sqrt{\frac{(s_b{}^0 x_b)^2 - (s_a{}^0 x_a)^2 Q^2}{P^2 - Q^2}}, \qquad (11)$$

where + and − signs correspond to TF_1 and TF_2 respectively.

b) Magnetization *vs* temperature relation.

Based on the equations (2) and (3) the molecular fields acting on a- and b-ion can be written as follows,

$$\left.\begin{aligned} H_a&=(A\cos^2\theta_a+a)s_a x_a \\ &\quad+(C_1\cos\theta_a\cos\theta_b+C_2\sin\theta_a\sin\theta_b)s_b x_b\,, \\ H_b&=(C_1\cos\theta_a\cos\theta_b+C_2\sin\theta_a\sin\theta_b)s_a x_a \\ &\quad+(B\cos^2\theta_b+b)s_b x_b\,. \end{aligned}\right\} \tag{12}$$

In these equations a and b represent the following expressions,

$$\left.\begin{aligned} a&=\delta_a\left(\Gamma_{aa}{}^1-\frac{\Gamma_{aa}{}^3}{2}\right)-\frac{\Gamma_{aa}{}^2}{2}\,, \\ b&=\delta_b\left(\Gamma_{bb}{}^1-\frac{\Gamma_{bb}{}^3}{2}\right)-\frac{\Gamma_{bb}{}^2}{2}\,, \end{aligned}\right\} \tag{13}$$

Then (12) can be put in the following form by using the definition of y and (9),

$$\left.\begin{aligned} H_a&=s_a x_a(\alpha_1 y^2+\alpha_2)\,, \\ H_b&=s_b x_b(\beta_1 y^{-2}+\beta_2)\,, \end{aligned}\right\} \tag{14}$$

where α_1, α_2, β_1 and β_2 are given by

$$\left.\begin{aligned} \alpha_1&=(A+PC_1-QC_2)(P^2-Q^2)^{-1} \\ \alpha_2&=a+QC_2-Q^2(A+PC_1-QC_2)(P^2-Q^2)^{-1}\,, \\ \beta_1&=-Q^2(B+P^{-1}C_1-Q^{-1}C_2)(P^2-Q^2)^{-1}\,, \\ \beta_2&=b+Q^{-1}C_2 \\ &\quad+P^2(B+P^{-1}C_1-Q^{-1}C_2)(P^2-Q^2)^{-1}. \end{aligned}\right\} \tag{15}$$

Then the mean spin moments of a- and b-ions, $s_a(T)$ and $s_b(T)$, are expressed by

$$\left.\begin{aligned} s_a(T)&=s_a{}^0 B_{s_a^0}\left[\frac{g\beta}{kT}\{(\alpha_1 y^2+\alpha_2)x_a s_a+H\}\right], \\ s_b(T)&=s_b{}^0 B_{s_b^0}\left[\frac{g\beta}{kT}\{(\beta_1 y^{-2}+\beta_2)x_b s_b+H\}\right], \end{aligned}\right\} \tag{16}$$

respectively. Hence by putting $H=0$ and eliminating y, s_a and s_b can be determined as functions of temperature. The magnetization for TF type can then be written as

$$\sigma(T)=s_a(T)x_a\cos\theta_a(T)\pm s_b(T)x_b\cos\theta_b(T)\,. \tag{17}$$

The magnetic susceptibility above the Curie point is obtained by the usual procedure. For the antiferromagnetic case the susceptibility below the Néel point will not be treated here, since the calculation requires the knowledge of magnetic anisotropy, for which we have not at present enough experimental data as far as the antiferromagnetic compounds with nickel arsenide structure are concerned.

c) Curie point *vs* concentration.

The Curie temperature T_c of this system can be obtained by the high temperature expansion of the right hand side of equation (16) and by elimination of y. Thus it is determined by solving the following equation for T_c;

$$\Theta_a\Theta_b-\alpha_2 x_a\Theta_b-\beta_2 x_b\Theta_a-(\alpha_1\beta_1-\alpha_2\beta_2)x_a x_b=0 \tag{18}$$

where Θ_a and Θ_b means $3kT_c\{s_a{}^0(s_a{}^0+1)g\beta\}^{-1}$ and $3kT_c\{s_b{}^0(s_b{}^0+1)g\beta\}^{-1}$ respectively.

d) Specific heat.

In this theory it is shown that the change of spin directions at the transition point does not introduce any entropy change of the system, hence the discontinuous transformation between each type of angular arrangement does not accompany any latent heat.

§ 5. Applications

As a typical example of triangular spin arrangement in nickel arsenide structure, the magnetism of $Mn_{1-x}Cr_xSb$ system will at first be discussed. According to the experimental results hitherto presented MnSb is a ferromagnetic substance with the Curie point at 587°K, while CrSb is an antiferromagnetic one with the Néel point at 713°K. It has been known that their type of spin ordering are of 0-th kind and of 1st kind respectively and that their easy axis of magnetization is the c-axis[8),9)] for both compounds. According to the recent investigation[2)], both compounds form a homogeneous solid solution over all ranges of concentration. X-ray analysis shows that no superstructure of vacant sites in the crystal lattice are formed in these compounds. In this system the ferro-, ferri- and antiferromagnetic phases have been found in the proper concentration and temperature rangs respectively. It has been reported that the ferromagnetism of manganese antimonide transforms into ferrimagnetic type when the manganese atom is substituted by chromium. With further increase of chromium content, however, an antiferromagnetic temperature range appears above the ferrimagnetic Curie temperature. With further addition of chromium the range of antiferromagnetic ordering becomes remarkably wider.

The magnetic properties of this system above mentioned cannot be explained by the ferrimagnetic theory based exclusively on the antiparallel orientation of spins. Now such a behaviour above mentioned will be reproduced theoretically by the results obtained in § 4. It might be reasonable to assume the spin arrangement of the following type with reference to some experimental evidence: In this case the interactions between a pair of Mn ions and that between a Mn–Cr pair may be assumed to be both ferromagnetic and that of Cr–Cr antiferromagnetic. Hence it is to be expected that at the Mn rich side the triangular spin arrangement of TF$_1$ type (ferrimagnetic) appears and also at the Cr rich side, antiferromagnetic triangular arrangement, e.g. of TA$_2$ type, will occur. On the basis of the theory developed in the previous section, assuming the ionic states of mangnese and chromium in this system to be $Mn^{3+}(s^0=0)$ and $Cr^{3+}(s^0=3/2)$ respectively, some magnetic behaviours, such as the change of saturation moment with concentration, thermomagnetic curves and the magnetic phase diagram can be derived by the use of the above equations with suitable choice of the values of exchange interactions between neighbouring ions. In Fig. 3 the relation between the saturation moment and concentration is shown. The curves for TF$_1$ state in this figure is obtained by taking the values, $P=1/12(x=0.1)$ and $Q=3(x=0.8)$ in equation (11). Also the magnetic phase diagram as illustrated in Fig. 6 is obtained on the basis of equations (16) and (18). In the antiferromagnetic region of this figure the types of spin arrangement TA$_2$ are assumed, and the values of constants in equation (18) are taken as $\alpha_2=0.97$, $\beta_2=0.68$ and $\alpha_1\beta_1=1.61$ in the TF$_1$-state and $\alpha_2=25.0$, $\beta_2=2.0$ and $\alpha_1\beta_1=7.1$ in the TA$_2$-state in the unit of $3kT_c\{2(2+1)g\beta\}^{-1}$ (i.e. T_c of MnSb). The normal ferrimagnetic theory holds for the F$_1$- and A$_2$-states in both figures. In these figures experimental data for the compounds Mn$_{1-x}$Cr$_x$Sb are shown. As they shows these points show satisfactory agreement with the theoretical curves.

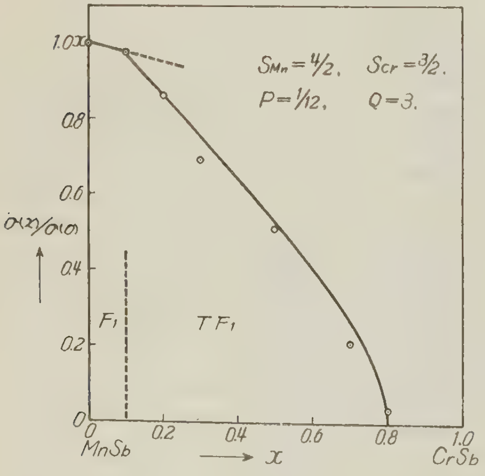

Fig. 5. The saturation moments of Mn$_{1-x}$Cr$_x$Sb system.

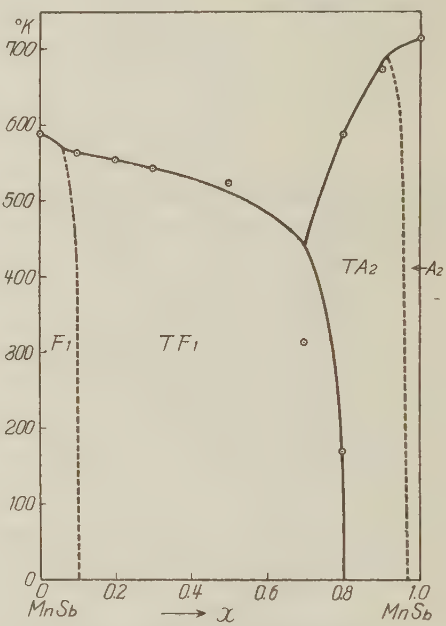

Fig. 6. The magnetic phase diagram of Mn$_{1-x}$Cr$_x$Sb system.

It is to be noted here that, as discussed in § 4, by the theoretical result above mentioned the discontinuous transition between different types of spin arrangement is also expected. As mentioned in § 3, three stable or metastable orientation in φ_a and φ_b, namely 0, $\pi/2$, π are obtained. With the rise of temperature (or concentration change), the transition between different orientation will occur. In such a case the values of θ_a and θ_b corresponding to the value of φ's will change discontinuously. Thus the discontinuous change of magnetism will follow. Such a discontinuous change may explain the abrupt appearance of spontaneous magnetization as found during heating the compound $CrS_{1.17}$[10] (for example TA$\rightleftarrows$TF type transition) though a more detailed study is required before to be conclusive.

Thus it is possible to explain various magnetic behaviours of the compounds with nickel arsenide structure from the present theory. However, in the actual cases, several factors, which are not taken into account in the present discussion, will affect the magnetic behaviours of the compounds. The order-disorder change in the arrangement of vacant sites and ions has been confirmed to be present in some compounds of nickel arsenide type with off-stoichiometric compositions and such a change will affect the molecular field distribution. The magnetic anisotropy energy will also specify the direction of spin arrangement with respect to the crystallographic axes and will give an influence on the magnetic susceptibility as well as parasitic ferromagnetism of compounds. Recently, Goodenough11) has proposed an explanation of the magnetism of La–Ca manganite by using the concept of covalent bonding. This might be to be considered also in our problem. Full studies of neutron diffraction analysis of spin arrangement of nickel arsenide type magnetic substances are most desirable.

References

1) J. H. Van Vleck: J. Phys. Radium **12** (1951) 262.
J. S. Smart: Phys. Rev. **86** (1952) 968 and Rev. Modern Phys. **25** (1953) 327.
2) T. Hirone, S. Maeda, I. Tsubokawa and N. Tsuya: J. Phys. Soc. Japan **11** (1956) 1083.
3) H. Haraldsen: Z. anorg. Chem. **231** (1937) 78; **246** (1941) 169.
F. Bertaut: J. Phys. Radium **15** (1954) 77.
4) Y. Yafet and C. Kittel: Phys. Rev. **87** (1952) 290.
5) T. Kishi: Memoirs of the Defence Academy **1** (1956) 41.
6) F. K. Lotgering: "*On the Ferrimagnetism of Some Sulphides and Oxides*" (Thesis).
7) L. Neel: Ann. Phys. **3** (1948) 137.
8) A. I. Snow: Rev. Modern Phys. **25** (1953) 127.
9) R. M. Bozorth: "*Ferromagnetism*" (1951) 576.
10) H. Haraldsen and A. Neuber: Z. anorg. allg. Chem. **234** (1937) 337.
11) J. B. Goodenough: Phys. Rev. **100** (1955) 564.

JOURNAL OF THE PHYSICAL SOCIETY OF JAPAN Vol. 12, No. 2, FEBRUARY, 1957

Theory of the Para-Ortho Conversion in Solid Deuterium

By Kazuko MOTIZUKI
Department of Physics, Ōsaka University

(Received November 10, 1956)

The rate of para-ortho conversion in solid deuterium (D_2) is calculated taking two types of interactions, i.e., the magnetic dipole-dipole interaction between D_2 molecules and the coupling between the nuclear quadrupole moments of one D_2 molecule and the total quadrupole moment of the other molecule. It is found that both interactions make about the same contributions to the para-ortho conversion if only the interactions among para molecules are taken into account. However, the ortho molecules with $I=2$ also interact magnetically with para molecules and convert them into ortho molecules. The calculated conversion rate due to the para-para interactions is found to be 0.01 % per hour times c^2, where c is the para concentration, while that due to the para-ortho interactions to be 0.01 % per hour times $c(1-c)$, so that the c^2 termes eventually cancel each other, leaving a total conversion rate which is proportional to c.

§1. Introduction

In a preceding paper1) (quoted as (I)) the rate of ortho-para conversion in solid hydrogen (H_2) was calculated taking magnetic dipole-dipole interactions between ortho-molecules into consideration. When an ortho-molecule converts into a para-molecule, the rotational state of this molecule changes from $J=1$ to $J=0$, and the difference of the energies of these states is taken up by the lattice vibrations. The Debye approximation was made for the lattice vibrations and it was found that the two phonon emission process was dominant. The result obtained (2 % per hour) was in good agreement with the experiment.*

In this paper a similar calculation of the rate of conversion in solid deuterium (D_2) will be given. One point of difference between H_2 and D_2 is the difference in their statistical characters. In the case of hydrogen molecule, the nuclei have spins of magnitude 1/2 and obey the Fermi-Dirac statistics. The ground state of the hydrogen molecule is para state (both the rotational and total spin quantum numbers are zero) and the first excited state is ortho state (rotational and total spin quantum numbers are both 1). On the other hand, in the case of deuterium, the nuclei have spins of magnitude 1 and obey the Bose statistics. The ground state of deuterium has zero rotational quantum number and its resultant spin quantum number is either zero or two. The energy splitting between these spin states ($I=0$ and $I=2$) is negligible compared with the energy splitting of the rotational states. The first excited state of D_2 has $J=1$ and $I=1$. The former states are called ortho and the latter state para.

There are two types of interactions causing the transition between para and ortho states. The first type is the magnetic dipole-dipole interaction between D_2 molecules and consists of two kinds of interaction as in the case of H_2: interaction between nuclear spins of one molecule and those of the other molecule and interaction between the rotational magnetic moment of one molecule and the nuclear spins of the other molecule. The second is the coupling between the nuclear quadrupole moment and the total quadrupole moment of the other molecule. Both are present in the interactions among para-molecules, while there is evidently only the first kind of interaction between para-molecules and the ortho-molecules with $I=2$. Therefore, the para-concentration, c, should change with time as

$$\frac{dc}{dt}=-kc^2-k'c(1-c)\ . \tag{1.1}$$

The result of the present calculation shows that the both interactions make about the same contributions to k and the value of it is 0.01 % per hour, which is much smaller than the corresponding value for H_2 (2 % per hour). The value of k' is found to be almost the same as that of k, so that we have practically $dc/dt=-kc$.

Furthermore, the effect of a small amount of dissolved oxygen molecules is studied. As in the case of H_2, the conversion rate is greatly enhanced by the magnetic dipole interaction between the oxygen molecules and the nuclei of the hydrogen molecules.

§ 2. Wave Functions and Interactions

The lowest rotational state of D_2 is a state in which the wave function of the nuclear spins is symmetrical and the total spin angular momentum I is either zero or two. In the next higher rotational state, $J=1$, the wave function of the nuclear spins is antisymmetrical, the total spin angular momentum I being 1. The former states, $J=0$, $I=0$ and $J=0$, $I=2$, belong to ortho-D_2 and the latter state, $J=1$, $I=1$, to para-D_2. The abundance ratio of ortho to para in normal deuterium gas is 6:3.

The nuclear spin functions of a D nucleus will be denoted as ϕ_{+1}, ϕ_0 and ϕ_{-1}. The total wave functions φ_0, $\varphi_{1,\pm M}$ ($M=0, 1$) and $\varphi_{2,\pm M}$ ($M=0, 1, 2$) of the states of total spin 0, 1 and 2 are then given by

$$\varphi_0=\frac{1}{\sqrt{3}}[\phi_{+1}(1)\phi_{-1}(2)-\phi_0(1)\phi_0(2)+\phi_{-1}(1)\phi_{+1}(2)] \qquad (I=0) \tag{2.1}$$

$$\varphi_{1,\pm1}=\frac{1}{\sqrt{2}}[\phi_0(1)\phi_{\pm1}(2)-\phi_{\pm1}(1)\phi_0(2)] \tag{2.2}$$

$$\varphi_{1,0}=\frac{1}{\sqrt{2}}[\phi_{-1}(1)\phi_{+1}(2)-\phi_{+1}(1)\phi_{-1}(2)] \qquad (I=1)$$

$$\varphi_{2,\pm2}=\phi_{\pm1}(1)\phi_{\pm1}(2)$$

$$\varphi_{2,\pm1}=\frac{1}{\sqrt{2}}[\phi_0(1)\phi_{\pm1}(2)+\phi_{\pm1}(1)\phi_0(2)] \tag{2.3}$$

$$\varphi_{2,0}=\frac{1}{\sqrt{6}}[\phi_{+1}(1)\phi_{-1}(2)+2\phi_0(1)\phi_0(2)$$

---

* The conversion rate of 0.9 % per hour observed by Hill is for normal hydrogen, not for the reaction constant k, as was misquoted in paper (I). Thus, k is $(3/2)^2$ times 0.9 % per hour, i.e. 2.0 % per hour. This comes in close agreement with Polanyi and Cremer's value (1.75 %) and our theoretical value (1.94 %). The writer is indebted to Dr. R. Hill for calling attention to this fact.

$$+\phi_{-1}(1)\phi_{+1}(2)] \qquad (I=2)$$

Rotational wave functions are

for the state $J=0$

$$\psi_0=1/2 \qquad (2.4)$$

for the state $J=1$

$$\psi_{1,1}=-\frac{1}{2}\left(\frac{3}{2\pi}\right)^{1/2}\sin\theta e^{i\varphi}$$

$$\psi_{1,0}=\left(\frac{3}{4\pi}\right)^{1/2}\cos\theta \qquad (2.5)$$

$$\psi_{1,-1}=\frac{1}{2}\left(\frac{3}{2\pi}\right)^{1/2}\sin\theta e^{-i\varphi}$$

where θ, φ denote the polar and azimuthal angles of the molecular axis. The polar axis can be taken arbitrarily in the space.

In the case of H_2, the interactions which cause the ortho-para conversion are the spin-spin and spin-rotational magnetic dipole-dipole interactions between ortho-molecules. In paper (I), we denoted these two interactions by H_{ss} and H_{rs}, respectively, and their expressions were given by (2.5), (2.7) of the paper. In the case of D_2, the nuclei have nuclear quadrupole moment, so the quadrupole interaction also contributes to the conversion. This quadrupole interaction is the coupling between the nuclear quadrupole moments of one D_2 molecule and the electric field gradients at these nuclei produced by the total quadrupole momet of another D_2 molecule.

The electric coulomb potential V at the nucleus 1 of the b-molecule due to the charge distribution of the a-molecule is

$$V=\sum_i \frac{e_i}{R_i}$$

where $\sum_i$ represents the sum over the charges belonging to the a-molecule and R_i denotes the distance between that charge i and nucleus 1 of the b-molecule. The potential V can be expanded as follows:

$$V=\frac{1}{R_{a,b1}}\sum_i e_i+\frac{1}{R^2_{a,b1}}\sum_i e_i\rho_i P_1(\cos\Theta_i)$$
$$+\frac{1}{R^3_{a,b1}}\sum_i e_i\rho_i^2 P_2(\cos\Theta_i)\ldots \quad (2.6)$$

For the notation, see Fig. 1. The first and second terms represent the potential due to the total charge and electric dipole of the a-molecule, which must vanish since D_2 molecule is neutral and has no electric dipole moment. The third term represents the potential due to the quadrupole moment of the a-molecule and this is what we need. We write this as V_Q. With the use of the angle Θ defined in

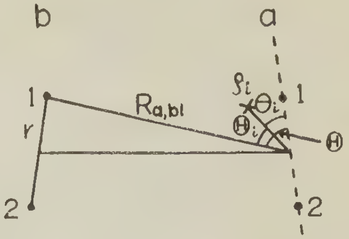

Fig. 1.

Fig. 1, V_Q can be written simply as

$$V_Q=\frac{1}{4}eQ_{D_2}(3\cos^2\Theta-1)\frac{1}{R^3_{a,b1}}, \qquad (2.7)$$

where Q_{D_2} represents the quadrupole moment of a D_2 molecule. The angle changes with the rotations of the a-and b-molecules. So, using the rotational coordinates of the a and b molecules, V_Q is rewritten as

$$V_O=\frac{1}{4}eQ_{D_2}\frac{1}{R^5_{a,b1}}[3(X_{a,b1}\sin\theta_a\cos\varphi_a$$
$$+Y_{a,b1}\sin\theta_a\cos\varphi_a+Z_{a,b1}\cos\theta_a)^2-R^2_{a,b1}], \quad (2.8)$$

where

$$X_{a,b1}=R\sin\theta\cos\varphi+r\sin\theta_b\cos\varphi_b$$
$$Y_{a,b1}=R\sin\theta\sin\varphi+r\sin\theta_b\sin\varphi_b$$
$$Z_{a,b1}=R\cos\theta+r\cos\theta_b$$
$$R_{a,b1}=(X^2_{a,b1}+Y^2_{a,b1}+Z^2_{a,b1})^{1/2}$$

R, θ and φ denote the polar coordinates of the vector joining the centres of the two molecules and (θ_a, φ_a), (θ_b, φ_b) the polar and azimuthal angles of the molecular axes of the a-and b-molecules.

Thus the quadrupole interaction can be written

$$H_Q=H_Q(a, b1)+H_Q(a, b2) \qquad (2.9)$$

where for instance $H_Q(a, b1)$ represents the interaction between the quadrupole moment of nucleus 1 in the b-molecule and the electric field gradient at this molecules due to the a-molecule. Each term can be represented as follows:

$$H_Q(a, bi)=\sum_\mu Q_\mu(bi)\nabla E_{-\mu}(a, bi) \quad (i=1, 2) \quad (2.12)$$

where Q_μ is the nuclear quadrupole moment operator and consists of the following five components:

$$Q_0(b1)=\left[\frac{eQ_D}{2i(i-1)}\right][3i_{b1,z}^2-i(i+1)]$$

$$Q_{\pm1}(b1)=\mp\frac{\sqrt{6}}{2}\left[\frac{eQ_D}{2i(i-1)}\right][(i_{b1,X}\pm ii_{b1,Y})i_{b1,Z}$$

$$+i_{b1,Z}(i_{b1,X}\pm ii_{b1,Y})] \qquad (2.11)$$

$$Q_{\pm2}(b1)=\frac{\sqrt{6}}{2}\left[\frac{eQ_D}{2i(i-1)}\right](i_{b1,X}\pm ii_{b1,Y})^2$$

In these expressions Q_D is the nuclear quadrupole moment of D and i the nuclear spin vector ($i=1$), ∇E_μ is the electric field gradient and is a function of the rotational coordinates of molecules a and b, i.e.,

$$E_0=\frac{eQ_{D_2}}{8}(3A_0+6B_0-60C_0-15D_0)$$

$$E_{\pm1}=\mp\frac{\sqrt{6}}{24}eQ_{D_2}(-15A_{\pm1}+6B_{\pm1}$$

$$-30C_{\pm1}+105D_{\pm1}) \qquad (2.12)$$

$$E_{\pm2}=\frac{\sqrt{6}}{24}eQ_{D_2}(-15A_{\pm2}+6B_{\pm2}$$

$$-60C_{\pm2}+105D_{\pm2})$$

where

$$A_0=(R_{a,b1})^{-7}(R_{a,b1}^2-5Z_{a,b1}^2)$$

$$B_0=(R_{a,b1})^{-5}\cos^2\theta_a$$

$$C_0=(R_{a,b1})^{-7}(X_{a,b1}\sin\theta_a\cos\varphi_a+Y_{a,b1}\sin\theta_a\sin\varphi_a+Z_{a,b1}\cos\theta_a)Z_{a,b1}\cos\theta_a$$

$$D_0=(R_{a,b1})^{-9}(X_{a,b1}\sin\theta_a\cos\varphi_a+Y_{a,b1}\sin\theta_a\sin\varphi_a+Z_{a,b1}\cos\theta_a)^2(R_{a,b1}^2-7Z_{a,b1}^2)$$

$$A_{\pm1}=(R_{a,b1})^{-7}Z_{a,b1}(X_{a,b1}\pm iY_{a,b1})$$

$$B_{\pm1}=(R_{a,b1})^{-5}\cos\theta_a(\sin\theta_a\cos\varphi_a\pm i\sin\theta_a\sin\varphi_a)$$

$$C_{\pm1}=(R_{a,b1})^{-7}(X_{a,b1}\sin\theta_a\cos\varphi_a+Y_{a,b1}\sin\theta_a\sin\varphi_a+Z_{a,b1}\cos\theta_a)$$

$$\times[(X_{a,b1}\pm iY_{a,b1})\cos\theta_a+Z_{a,b1}(\sin\theta_a\cos\varphi_a\pm i\sin\theta_a\sin\varphi_a)]$$

$$D_{\pm1}=(R_{a,b1})^{-9}(X_{a,b1}\sin\theta\cos\varphi_a+Y_{a,b1}\sin\theta_a\sin\varphi_a+Z_{a,b1}\cos\theta_a)^2Z_{a,b1}(X_{a,b1}\pm iY_{a,b1})$$

$$A_{\pm2}=(R_{a,b1})^{-7}(X_{a,b1}\pm iY_{a,b1})^2$$

$$B_{\pm2}=(R_{a,b1})^{-5}(\sin\theta_a\cos\varphi_a\pm i\sin\theta_a\sin\varphi_a)^2$$

$$C_{\pm2}=(R_{a,b1})^{-7}(X_{a,b1}\pm iY_{a,b1})(X_{a,b1}\sin\theta_a\cos\varphi_a+Y_{a,b1}\sin\theta_a\sin\varphi_a+Z_{a,b1}\cos\theta_a)$$

$$\times(\sin\theta_a\cos\varphi_a\pm i\sin\theta_a\sin\varphi_a)$$

$$D_{\pm2}=(R_{a,b1})^{-9}(X_{a,b1}\pm iY_{a,b1})^2(X_{a,b1}\sin\theta_a\cos\varphi_a+Y_{a,b1}\sin\theta_a\sin\varphi_a+Z_{a,b1}\cos\theta_a)^2 \qquad (2.13)$$

We expand each of (2.13) in powers of r/R, where r is half the inter-nuclear distance in a D_2 molecule and R the distance between the centres of the two molecules; $r/R=10\ll1$ if we take for R the mean distance in the actual crystal.

Since H_Q is the sum of $H_Q(a,b1)$ and $H_Q(a,b2)$ and invariant against the inversion of molecule b with respect to its centre, and since the matrix elements of i_{b1} have opposite signs to those of i_{b2}, as seen from (A. 4), we have only to retain those terms of the expansion which change sign under the inversion of molecule b. The first terms of expansion can be discarded for this reason, the second terms adopted and the higher order terms will be neglected.

§ 3. Result and Discussion

We seek the matrix elements of H_d+H_Q (H_d: the dipolar interaction) between the state a=para and b=para and the state a=para and b=ortho. The details of the calculation of such matrix elements with respect to the rotational states and spin states will be given in Appendices. The change of energy of the rotational state of molecule b, which converts into ortho from para, must be balanced by an emission of phonons. If we denote by ψ_T and ψ_T' the wave functions of the initial and final vibrational states of the lattice, the para-ortho transition probability is proportional to

$$\frac{1}{81}\sum|\langle a=\text{para},\ b=\text{para},\ T|$$

$$H_d+H_Q|a=\text{para},\ b=\text{ortho},\ T'\rangle|^2. \qquad (3.1)$$

The summation in (3.1) runs over the initial 81 and final 54 states. After calculating the matrix elements with respect to the rotational and spin states, the term due to the dipole interaction can be expressed as

$$\frac{1}{81}\sum_{i=0}^{9}C_i|\langle T|f_i|T'\rangle|^2 \qquad (3.2)$$

where f_i's are functions of the relative coordinates of the centres of molecules a and b and are given by eq. (A. 4) of paper (I) and

C_i's are

$$\begin{aligned} C_0 &= 102\,\mu_D^4[1+(\mu_R/\mu_D)^2] \\ C_1+C_2 &= 378\,\mu_D^4[1+(\mu_R/\mu_D)^2] \\ C_3+C_4 &= 4110\,\mu_D^4[1+(\mu_R/\mu_D)^2] \\ C_5 &= 648\,\mu_D^4[1+(\mu_R/\mu_D)^2] \\ C_6+C_7 &= 675\,\mu_D^4[1+(\mu_R/\mu_D)^2] \\ C_8+C_9 &= 648\,\mu_D^4[1+(\mu_R/\mu_D)^2] \end{aligned} \tag{3.3}$$

The other term due to the quadrupole interaction can be expressed as

$$\frac{1}{81}\sum_{i,\pm} d_i^{\pm} |<T|g_i^{\pm}|T'>|^2 \tag{3.4}$$

where g_i's are given in (B. 3) and d_i's are

$$\begin{aligned} d_0 &= \frac{27\times 9}{4}\left[\frac{e^2 Q_D Q_{D_2}}{2i(i-1)}\right]^2 \\ d_1^+ + d_1^- &= \frac{27^2\times 43}{32}\left[\frac{e^2 Q_D Q_{D_2}}{2i(i-1)}\right]^2 \\ d_2^+ + d_2^- &= \frac{63^2\times 135}{16}\left[\frac{e^2 Q_D Q_{D_2}}{2i(i-1)}\right]^2 \\ d_3^+ + d_3^- &= \frac{63^2\times 15}{32}\left[\frac{e^2 Q_D Q_{D_2}}{2i(i-1)}\right]^2 \\ d_4^+ + d_4^- &= \frac{189^2\times 21}{16}\left[\frac{e^2 Q_D Q_{D_2}}{2i(i-1)}\right]^2 \\ d_5^+ + d_5^- &= \frac{189^2\times 3}{16}\left[\frac{e^2 Q_D Q_{D_2}}{2i(i-1)}\right]^2 \end{aligned} \tag{3.5}$$

We express f_i and $g_i^{\pm}$ in terms of the lattice vibration coordinates by the same methods as that described in Appendix *B* of paper (I) taking the Debye approximation. We calculate the transition probability due to two phonons emission processes. The lattice constant of solid D_2 is a little smaller than that of solid H_2. Assuming the same value for the lattice constant for D_2 as that of H_2, the Debye temperature is found to be 64.4°K ($1/\sqrt{2}$ times of H_2), while the energy difference between the rotational states $J=1$ and $J=0$ is found to be 86°K (half that of H_2). Therefore, the one phonon emission process is impossible. The processes involving more than two phonons might be much less important than the two phonons emission processes, as they were in paper (I), and will be neglected. Necessary data for the calculation of the two phonons emission processes are as follows:

Difference in rotational energy between $J=1$ and $J=0$ (in temperature scale): $E_r=86°\mathrm{K}$

Debye temperature: $\Theta_D=64.4°\mathrm{K}$

Sound velocity: $v=0.722\times 10^5$ cm/sec

Density: $\rho=0.179$ gr/cm^3

Internuclear distance: $2r=0.74$ Å

Deuteron magnetic moment:

$\mu_D=4.329\times 10^{-24}$ (erg/gauss)[2)]

Rotational magnetic moment:

$\mu_R=0.517\times\mu_D$ (erg/gauss)[2)]

Nuclear quadrupole moment of D:

$Q_D=2.738\times 10^{-27}$ cm^2 [2)]

Quadrupole moment of D_2 molecule:

$Q_{D_2}=0.232\times 10^{-16}$ cm^2 [3)]

We denote the transition probabilities due to the dipole and the quadrupole interactions by $W_d(2)$ and $W_Q(2)$, respectively. The theoreticel results for the respective conversion rates are:

$$\begin{aligned} 12\,W_d(2) &= 0.502\times 10^{-4} \text{ per hour} \\ 12\,W_Q(2) &= 0.622\times 10^{-4} \text{ per hour} \\ \text{total:} &\quad 1.124\times 10^{-4} \text{ per hour} \end{aligned} \tag{3.6}$$

Thus, in deuterium, magnetic dipole-dipole interaction and the quadrupole interaction contribute nearly equally to the conversion rate, when only the change of para-para pairs into para-ortho pairs is considered. The total conversion rate is about 0.01 % per hour which is very small compared with the corresponding value in solid H_2 (2 % per hour). This difference is mainly due to the following. The magnetic moment of deuteron is about one third of that of hydrogen. The magnetic dipole interaction between two molecules is proportional to the second power of this ratio, and the conversion rate due to the magnetic interactions is proportional to its fourth power, i.e. 10^{-2}.

Next we calculate the conversion rate due to the interaction between the para-molecules and the ortho-molecules with $I=2$. We have to seek the matrix elements of H_d between the states a=ortho b=para and a=ortho b=ortho with respect to the rotational and spin states. The result can be expressed by the same formula as eq. (3.2) except that C_i's are now replaced by

$$\begin{aligned} C_0 &= 270\,\mu_D^4 \\ C_1+C_2 &= 630\,\mu_D^4 \\ C_3+C_4 &= 6750\,\mu_D^4 \\ C_5 &= 1080\,\mu_D^4 \\ C_6+C_7 &= 1125\,\mu_D^4 \\ C_8+C_9 &= 1080\,\mu_D^4 \end{aligned}$$

We denote the corresponding transition probability by $W_d'(2)$. The conversion rate is found to be

$$12W_d'(2)=1.106\times10^{-4} \text{ per hour.} \tag{3.8}$$

The above calculations show that the para-concentration c changes with time according to the equation

$$\frac{dc}{dt}=-kc^2-k'c(1-c) \tag{3.9}$$

where, according to (3.6) and (3.8) $k=1.124\times10^{-4}$ per hour and $k'=1.106\times10^{-4}$ per hour. Since k and k' are nearly equal each other, we find that c is determined by

$$\frac{dc}{dt}=-kc\,, \qquad c=c_0e^{-kt}\,. \tag{3.10}$$

In all the above calculations, we neglected, as in paper (I), the interferences of the twelve interactions between one molecule and its twelve neighbours. This is, however, valid since the rotational substate of each molecule changes very frequently during the life time of a para D_2 molecule (ortho-molecule in the case of H_2), so that the phase of the rotational substate of any one molecule becomes uncorrelated with the phases of the rotational substates of other molecules.*

§ 4. Effect of Oxygen Molecules Dissolved in Solid Deuterium

The oxygen molecule has a magnetic moment of two Bohr magnetons in its ground state, so that the ortho-para conversion rate is greatly enhanced by oxygen molecules contaminated in the solid hydrogen. Already, in paper (I), this effect was treated assuming the oxygen spins to be at rest and self-diffusion of the hydrogen molecules to be negligible. In another paper[4)] the effect of self-diffusion was discussed. We obtained the result that the rate of conversion of a hydrogen molecule at a distance R from each oxygen molecule is $250\times(R_0/R)^{12}$ per hour, so that the ortho-molecules in the neighbourhood of each oxygen molecule change to para in a relatively short time. This initial increase of para-concentration reasonably explained experiments.

In D_2 molecule, a similar phenomenon will occur. The coupling between the nuclear quadrupole moments of D_2 and the total quadrupole moment of O_2 molecule may be negligible compared with the effect of the magnetic dipole-dipole interactions, as the quadrupole moment of O_2 may be of the same order of magnitude as that of D_2. The transition probability for a D_2 molecule at a distance R from an oxygen molecule is calculated by the same method as that used in paper (I). Here, instead of previous C_i's given by (4.1) in paper (I), the following C_i's appear:

$$\begin{aligned} C_0&=18\,\mu_D^2\mu_{0_2}^2\\ C_1+C_2&=36\,\mu_D^2\mu_{0_2}^2\\ C_3+C_4&=225\,\mu_D^2\mu_{0_2}^2\\ C_5&=54\,\mu_D^2\mu_{0_2}^2 \end{aligned} \tag{4.1}$$

The result of the calculation is:

$$W_{oxy.}(2)=35.9\times(R_0/R)^{12} \text{ per hour} \tag{4.2}$$

This value is 1/7 times that for H_2. Comparing this result with (3.6), we find that at $R=3.54R_0$ the effect of an oxygen molecule and the effect of the mutual interaction of D_2 molecules become comparable.

The writer would like to express her sincere thanks to Professor T. Nagamiya for encouragement and helpful discussions. She is also indebted to Mr J. Kanamori for valuable comments and to Miss H. Kobayashi of Tōhoku University for kind communications of her experimental results prior to publication.

Appendix A. The matrix elements of the dipole and quadrupole interactions with respect to the spin states.

(a) The matrix elements of the dipole interaction.

The non-vanishing matrix elements of the spin operators, of molecule b with respect to states $I=1$ and $I=0$ of molecule b are as follows:

$$\begin{aligned} &\langle 1,0|i_{b1,z}|0\rangle=-2/\sqrt{6}\\ &\langle 1,1|i_{b1,x}+ii_{b1,y}|0\rangle=2/\sqrt{3}\\ &\langle 1,-1|i_{b1,x}-ii_{b1,y}|0\rangle=2/\sqrt{3} \end{aligned} \tag{A.1}$$

The matrix elements with respect to states $I=1$ and $I=2$ are:

$$\begin{aligned} &\langle 1,\pm1|i_{b1,z}|2,\pm1\rangle=\mp1/2\\ &\langle 1,0|i_{b1,z}|2,0\rangle=-1/\sqrt{3}\\ &\langle 1,\pm1|i_{b1,x}\pm ii_{b1,y}|2,0\rangle=-1/\sqrt{6}\\ &\langle 1,0|i_{b1,x}\pm ii_{b1,y}|2,\mp1\rangle=\mp1/\sqrt{2}\\ &\langle 1,\mp1|i_{b1,x}\pm ii_{b1,y}|2,\mp2\rangle=1 \end{aligned} \tag{A.2}$$

The matrix elements of i_{b2} have opposite signs to those of i_{b1}.

---

* The writer is indebted to Dr. M. Bloom of the University of Vancouver for this interpretation.

The non-vanishing matrix elements of the spin operators of molecule a with respect to substates of $I=2$ and $I=1$, respectively, are as follows:

$$\begin{aligned}
&\langle 2, \pm 2 | i_{aj,z} | 2, \pm 2\rangle = \pm 1 \\
&\langle 2, 1 | i_{aj,z} | 2, \pm 1\rangle = \pm 1/2 \\
&\langle 2, \pm 2 | i_{aj,x} \pm i i_{aj,y} | 2, \pm 1\rangle = 1 \\
&\langle 2, \pm 1 | i_{aj,x} \pm i i_{aj,y} | 2, 0\rangle = 3/\sqrt{6} \\
&\langle 2, 0 | i_{aj,x} \pm i i_{aj,y} | 2, \mp 1\rangle = 3/\sqrt{6} \qquad \text{(A.3)} \\
&\langle 2, \mp 1 | i_{aj,x} \pm i i_{aj,y} | 2, \mp 2\rangle = 1 \\
&\langle 1, \pm 1 | i_{aj,z} | 1, \pm 1\rangle = \pm 1/2 \\
&\langle 1, \pm 1 | i_{aj,x} \pm i i_{aj,y} | 1, 0\rangle = \pm 1/\sqrt{2} \\
&\langle 1, 0 | i_{aj,x} \pm i i_{aj,y} | 1, \mp 1\rangle = \mp 1/\sqrt{2} \\
&\qquad\qquad\qquad\qquad (j=1,\ 2)
\end{aligned}$$

(b) The matrix elements of the quadrupole interaction.

This interaction has no matrix elements between states of $I=1$ and $I=0$. The non-vanishing matrix elements between $I=1$ and $I=2$ of b-molecule are as follows:

$$\begin{aligned}
&\langle 1, \pm 1 | 3 i_{b1,z}^2 - i(i+1) | 2, \pm 1\rangle = -3/2 \\
&\langle 1, \pm 1 | (i_{b1,x} \pm i i_{b1,y}) i_{b1,z} \\
&\quad + i_{b1z}(i_{b1,x} \pm i i_{b1,y}) | 2, 0\rangle = \mp \sqrt{3}/\sqrt{2} \\
&\langle 1, 0 | (i_{b1,x} \pm i i_{b1,y}) i_{b1,z} \\
&\quad + i_{b1,z}(i_{b1,x} \pm i i_{b1,y}) | 2, \mp 1\rangle = -1/\sqrt{2} \qquad \text{(A.4)} \\
&\langle 1, \mp 1 | (i_{b1,x} \pm i i_{b1,y}) i_{b1,z} \\
&\quad + i_{b1,z}(i_{b1,x} \pm i i_{b1,y}) | 2, \mp 2\rangle = \mp 1 \\
&\langle 1, \pm 1 | (i_{b1,x} \pm i i_{b1,y})^2 | 2, \mp 1\rangle = -1 \\
&\langle 1, 0 | (i_{b1,x} \pm i i_{b1,y})^2 | 2, \mp 2\rangle = \mp \sqrt{2}
\end{aligned}$$

The matrix elements of i_{b2} have opposite sign to those of i_{b1}.

Appendix B. The matrix elements of the dipole and the quadrupole interactions with respect to the rotational states.

The matrix elements of the dipole interaction was given in (A.2) and (A.3) of paper (I).

The non-vanishing matrix elements of the quadrupole interaction between the states $J=1$ and $J=0$ of the b-molecule: Expanding eq. (2.13) in powers of r/R, the second terms are the function of the rotational coordinates of the b-molecule and contain the terms $\cos\theta_b$, $\sin\theta_b \cos\varphi_b$ and $\sin\theta_b \sin\varphi_b$. The matrix elements of these functions are:

$$\begin{aligned}
&\langle 1, 0 | \cos\theta_b | 0\rangle = 1/\sqrt{3} \\
&\langle 1, \pm 1 | \sin\theta_b \cos\varphi_b | 0\rangle = \pm 1/\sqrt{6} \qquad \text{(B.1)} \\
&\langle 1, \pm 1 | \sin\theta_b \sin\varphi_b | 0\rangle = -i/\sqrt{6}
\end{aligned}$$

Using these relations the matrix elements of each of A, B, C and D in (2.13) with respect to the rotational states of the b-molecule can be calculated.

The non-vanishing matrix elements of the quadrupole interaction between the sub-states of $J=1$ of the a-molecule: The second terms of (2.13), expanded in power of r/R, contain the several types of the function of the rotational coordinates of the a-molecule. The non-vanishing matrix elements of these functions are:

$$\begin{aligned}
&\langle \pm 1 | \zeta_a^2 | \pm 1\rangle = \frac{1}{5} \\
&\langle 0 | \zeta_a^2 | 0\rangle = \frac{3}{5} \\
&\langle \pm 1 | \zeta_a(\xi_a \pm i\eta_a) | 0\rangle = \mp \frac{\sqrt{2}}{5} \\
&\langle 0 | \zeta_a(\xi_a \pm i\eta_a) | \mp 1\rangle = \pm \frac{\sqrt{2}}{5} \\
&\langle \pm 1 | (\xi_a \pm i\eta_a)^2 | \mp 1\rangle = -\frac{4}{5} \\
&\langle \pm 1 | \xi_a^2 + \eta_a^2 | \pm 1\rangle = \frac{4}{5} \\
&\langle 0 | \xi_a^2 + \eta_a^2 | 0\rangle = \frac{2}{5} \\
&\langle \pm 1 | \zeta_a(\xi\xi_a + \eta\eta_a + \zeta\zeta_a) | \pm 1\rangle = \frac{1}{5}\zeta \\
&\langle \pm 1 | \zeta_a(\xi\xi_a + \eta\eta_a + \zeta\zeta_a) | 0\rangle = \mp \frac{1}{5\sqrt{2}}(\xi \mp i\eta) \\
&\langle 0 | \zeta_a(\xi\xi_a + \eta\eta_a + \zeta\zeta_a) | \pm 1\rangle = \mp \frac{1}{5\sqrt{2}}(\xi \pm i\eta) \\
&\langle 0 | \zeta_a(\xi\xi_a + \eta\eta_a + \zeta\zeta_a) | 0\rangle = \frac{3}{5}\zeta \qquad \text{(B.2)} \\
&\langle \pm 1 | (\xi_a \pm i\eta_a)(\xi\xi_a + \eta\eta_a + \zeta\zeta_a) | \pm 1\rangle \\
&\quad = \langle \mp 1 | (\xi_a \pm i\eta_a)(\xi\xi_a + \eta\eta_a + \zeta\zeta_a) | \mp 1\rangle \\
&\quad = \frac{2}{5}(\xi \pm i\eta) \\
&\langle \pm 1 | (\xi_a \pm i\eta_a)(\xi\xi_a + \eta\eta_a + \zeta\zeta_a) | 0\rangle \\
&\quad = \langle 0 | (\xi_a \pm i\eta_a)(\xi\xi_a + \eta\eta_a + \zeta\zeta_a) | \pm 1\rangle \\
&\quad = \mp \frac{\sqrt{2}}{5}\zeta \\
&\langle \pm 1 | (\xi_a \pm i\eta_a)(\xi\xi_a + \eta\eta_a + \zeta\zeta_a) | \mp 1\rangle \\
&\quad = -\frac{2}{5}(\xi \mp i\eta) \\
&\langle 0 | (\xi_a \pm i\eta_a)(\xi\xi_a + \eta\eta_a + \zeta\zeta_a) | 0\rangle = \frac{1}{5}(\xi \pm i\eta)
\end{aligned}$$

$$\langle \pm 1|(\xi\xi_a+\eta\eta_a+\zeta\zeta_a)^2|\pm 1\rangle=\frac{1}{5}(2-\zeta^2)$$

$$\langle \pm 1|(\xi\xi_a+\eta\eta_a+\zeta\zeta_a)^2|0\rangle=\mp\frac{\sqrt{2}}{5}\zeta(\xi\mp i\eta)$$

$$\langle \pm 1|(\xi\xi_a+\eta\eta_a+\zeta\zeta_a)^2|\mp 1=-\frac{1}{5}(\xi\mp i\eta)^2$$

$$\langle 0|(\xi\xi_a+\eta\eta_a+\zeta\zeta_a)^2|\pm 1\rangle=\pm\frac{\sqrt{2}}{5}\zeta(\xi\pm i\eta)$$

$$\langle 0|(\xi\xi_a+\eta\eta_a+\zeta\zeta_a)^2|0\rangle=\frac{1}{5}(1+2\zeta^2)$$

where $\zeta_a=\cos\theta_a$, $\xi_a=\sin\theta_a\cos\varphi_a$ and $\eta_a=\sin\theta_a\sin\varphi_a$.

Using (B.1) and (B.2), the matrix elements with respect to the rotational states of a and b molecules can be obtained. The results are functions of the relative coordinates X, Y, and Z of the centres of molecules a and b which we will not reproduce here. The functions g_i are given as follows:

$$\begin{aligned}
g_0&=Z(15R^4-70R^2Z^2+63Z^4)r/R^{11}\\
g_1^\pm&=(X\pm iY)(R^4-12R^2Z^2+21Z^4)r/R^{11}\\
g_2^\pm&=(X\pm iY)^2Z(R^2-3Z^2)r/R^{11}\\
g_3^\pm&=(X\pm iY)^3(R^2-9Z^2)r/R^{11}\\
g_4^\pm&=(X\pm iY)^4Zr/R^{11}\\
g_5^\pm&=(X\pm iY)^5r/R^{11}
\end{aligned}\qquad\text{(B.3)}$$

References

1) K. Motizuki and T. Nagamiya: J. Phys. Soc. Japan **11** (1956) 93.
2) N. F. Ramsey: *Molecular Beams*, Oxford at the Clarendon Press, (1956) 168, 172.
3) J. O. Hirschfelder, C. F. Curtiss and R. B. Bird: *Molecular Theory of Gasses and Liquids*, John Wiley Sons, Inc., New York (1956) 1028.
4) K. Motizuki and T. Nagamiya: J. Phys. Soc. Japan **11** (1956) 654.

JOURNAL OF THE PHYSICAL SOCIETY OF JAPAN Vol. 12., No. 2, FEBRUARY, 1957

Electromagnetic Fields due to Current Flowing Parallel to Interface of Two Different Media

By Kazuo HORIUCHI

Department of Electrical Communication Engineering, School of Science and Engineering, Waseda University

(Received September 12, 1956)

The electromagnetic fields due to the line and surface current flowing in one direction parallel to an interface of two different media are theoretically investigated. Whole problems are dealt with by integral equations of Wiener-Hopf type, and described from a relatively general point of view. Particularly, illustrative cases of a plane wave incident upon a conducting half-plane and a uniform line-current parallel to its rim are studied in detail, and the solutions are given in integral forms. The results may be applied to practical problems.

§ 1. Introduction

Exact solutions in diffraction theory are seldom given, apart from the representation by an infinite series of suitable orthogonal functions. The most classical exact solution in closed form has been obtained by Sommerfeld[1] for diffraction from a half-plane sheet. His basic concept lay in a multi-valued solution of the wave equation, which was naturally adapted to the wedge problem where the physical discontinuities are in inclined planes, as formulated by MacDonald[2]; and its generalization has recently been completed by Nomura[3].

Since integral equations were introduced into the diffraction theory[4], they have formed the basis of many modern investigations. Exact solutions can be obtained from these integral equations only when they are susceptible to the method of Wiener-Hopf5). Copson6) published a solution for a half-plane problem based on this procedure for the first time, and its generality was appreciated by Schwinger7). He pointed out that any diffraction problem might be formulated in the form of inhomogeneous Wiener-Hopf integral equations, in case where waves are incident upon a structure of parallel conducting plates or cylinders. On the basis of his suggestion, Carlson and Heins8) solved the problem of scattering of waves by an infinite set of staggered semi-infinite plates, Heins9) solved a similar problem with a pair of semi-infinite parallel plates, and Levine10) solved the scalar problem of radiation from the open end of a circular cylinder. After that, Schwinger himself11) made an effort for the extention of the Levine's problem to the vector field, and Iijima12) gave independently a more detailed solution.

The series of these investigations also forms a generalization of Sommerfeld's problem, although it is different from MacDonald's work. It is the special feature of this system that the physical discontinuities are in parallel planes.

Moreover, there are several other similar but more complicated problems; namely, problems of reflection, refraction and diffraction which occur from a half-plane in the interface of two different media. They are important in the theoretical treatment of radio propagation over an inhomogeneous earth. Clemmow13) suggested that for this problem appeal will have to be made to the general theory of Wiener-Hopf, although he could not solve it exactly himself.* His idea was concerned only with the plane wave incidence, but in this paper we shall investigate these problems from the most general point of view. If we consider the case that a half-plane conductor or a current distribution lies parallel to the interface of two media, then the problem has the same property as those described at the beginning, and, therefore, is susceptible to Schwinger's method in its current form. In this case, however, it is necessary to extend the Sommerfeld's representation of the field due to a horizontal antenna over the earth15), for reasons of the inhomogeneity of medium. Under these circumstances the solutions are greatly complicated.

§ 2. Formulation of Problems

Let us first consider a uniform horizontal line current in the x-direction above the earth, at $y=y_0$, $z=h$ as shown in Fig. 1. Then the fields are represented by the following formulas by the Hertzian vectors in x-direction Π_x and Π_{xe} for the two media, respectively.

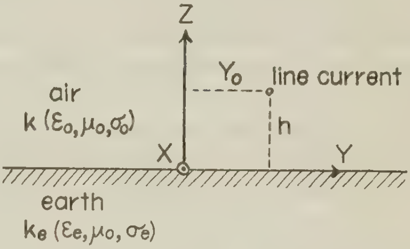

Fig. 1. A line current above the earth.

$$E_x=k^2\Pi_x\,,\qquad E_{xe}=k_e^2\Pi_{xe}\,,$$
$$H_y=\frac{k^2}{i\mu_0\omega}\frac{\partial\Pi_x}{\partial z}\,,\qquad H_{ye}=\frac{k_e^2}{i\mu_0\omega}\frac{\partial\Pi_{xe}}{\partial z}\,,\tag{1}$$

where

$$k^2=\mu_0\varepsilon_0\omega^2+i\omega\mu_0\sigma_0\,,\quad k_e^2=\mu_0\varepsilon_e\omega^2+i\omega\mu_0\sigma_e\,,$$

and it is assumed that the field-quantities have the harmonic time factor $\exp(-i\omega t)$ which is suppressed throughout. These Hertzian vectors are obtained by extending the Sommerfeld's solution for the horizontal antenna over the earth15), as follows:

$$\Pi_x(y,\,z;\,y_0,\,h)=\int_0^\infty\frac{d\lambda}{\mu}\cos\{\lambda(y-y_0)\}$$
$$\cdot\left\{e^{\mp(z-h)\mu}+\frac{\mu-\mu_e}{\mu+\mu_e}e^{-(z+h)\mu}\right\},\quad 0<z\gtrless h\tag{2}$$

$$\Pi_{xe}(y,\,z;\,y_0,\,h)$$
$$=\frac{2}{n^2}\int_0^\infty\frac{d\lambda}{\mu+\mu_e}e^{z\mu_e-h\mu}\cos\{\lambda(y-y_0)\}\,,\quad z<0\,,\tag{3}$$

where

---

*In reference 13) Clemmow gave relatively elegant solutions for the above series of problems by the method of the angular spectrum of plane waves, but only this problem he did not because of its complexity. Afterwards he investigated the same problem by his own method, but his theory is as yet incomplete in the sense that he excepted the difficult factorization of some important functions from his work14). Concerning this problem we will present a more complete theory in a separate paper.

$$\mu(\lambda)=\sqrt{\lambda^2-k^2}\,,\quad \mu_e(\lambda)=\sqrt{\lambda^2-k_e^2}$$

and

$$n=k_e/k\,.$$

The first term of Eq. (2) corresponds to the Hertzian vector for the line current located at $y=y_0$, $z=h$ in free space, and, therefore, may also be represented in the form of the zero order Hankel function:

$$(\pi i/2)H_0^{(1)}\{k\sqrt{(z-h)^2+(y-y_0)^2}\}\,.$$

If we use the above representations of the Hertzian vectors, the fields (1) automatically satisfy the boundary condition $E_x=E_{xe}$, $H_y=H_{ye}$ on the surface $z=0$.

When we wish to solve some problems of insertion of a third body into the system of two different media, *e.g.* air and earth, it is very convenient to consider an equivalent current distribution in place of the body. Particularly, if this current flows only in the x-direction, the aforementioned representations of the fields are very useful.

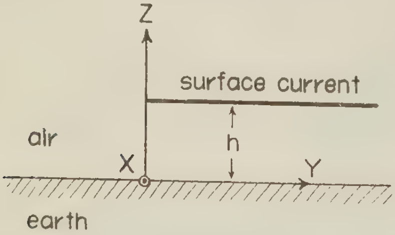

Fig. 2. A conducting half-plane above the earth.

Let us consider, as an illustrative case, a surface current flowing only in the x-direction, whose distribution is subject to a function $I(y)$ of the variable y, on the half-plane $z=h$, $y>0$, as in Fig. 2. Then, the fields due to such a current distribution are easily derived from the Hertzian vectors in the form:

$$\Pi_{\substack{x,\\xe}}(y,\,z)=\int_0^\infty I(y')\,\Pi_{\substack{x,\\xe}}(y,\,z;\,y',\,h)dy'\,, \quad (4)$$

where $\Pi_{\substack{x,\\xe}}$ under the integration are the same with the formulas of Eqs. (2) and (3). These fields also naturally satisfy the boundary conditions at $z=0$ and $z=h$, but the discontinuity of H_y occurs at the half-plane $z=h$, $y>0$ because of the surface current distribution in the x-direction. Since the density $J_x(y)$ of this surface current is measured by the discontinuity of H_y as follows

$$J_x(y)=\frac{2k^2}{i\mu_0\omega}\int_0^\infty dy'I(y')\int_0^\infty d\lambda\cos\{\lambda(y-y')\}\,, \quad (5)$$

$I(y)$ is related to the current density $J_x(y)$ by the formula

$$I(y)=\frac{i\mu_0\omega}{2\pi k^2}J_x(y)\,. \quad (6)$$

Such a current distribution is immeadiately and conveniently applied for the problem of plane wave incident upon a conducting half-plane on the earth, and for the problem of the similar conducting half-plane and a uniform line current parallel to its rim, and so on. We will investigate these problems in the following sections, in turn.

§3. A Plane Wave Incident upon A Conducting Half-Plane on the Earth

Let the half-plane $z=h$, $y>0$ on the earth be occupied by an infinitely thin, parfectly conducting sheet. Consider an incident plane wave E-polarized in which the electric field has only one component E_x^i in the x-direction given by

$$E_x^i=\exp\,[ikr\cos(\theta+\alpha)] \quad (7)$$

as in Fig. 3. Then on the conducting sheet a surface current in the x-direction is induced, which is subject to an unknown function $I(y)$. This conducting sheet, therefore, may be replaced by the surface current distribution as described in the preceding section.

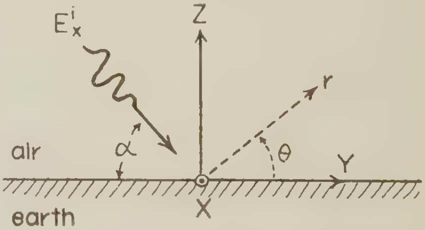

Fig. 3. An incident plane wave upon the earth.

In this case the fields consist of two parts. The first is the primary fields incident on, reflected from and transmitted through the boundary surface $z=0$, and always satisfies the boundary conditions at $z=0$. The second is the secondary fields produced by the surface current distribution on the conducting sheet. The latter also independently satisfies the condition of continuity at $z=0$ and $z=h$, provided the representations (4) are used. Thus, it is only necessary that the total electric field vanishes on the conducting sheet $z=h$, $y>0$. This condition leads to the next integral equation:

$$k^2\int_0^\infty dy'\, I(y')\int_0^\infty \frac{d\lambda}{\mu}\cos\{\lambda(y-y')\}$$
$$\cdot\left\{1+\frac{\mu-\mu_0}{\mu+\mu_e}e^{-2h\mu}\right\}+e^{iky\cos\alpha}$$
$$\cdot\{e^{-ikh\sin\alpha}-(1-T)e^{ikh\sin\alpha}\}=0 \qquad (8)$$

at $z=h$, $y>0$, where T is the transmission coefficient for the primary wave. Particularly, in the case $h=0$ the above equation is reduced to

$$k^2\int_0^\infty dy'\, I(y')\int_0^\infty \frac{2d\lambda}{\mu+\mu_e}\cos\{\lambda(y-y')\}$$
$$=-Te^{iky\cos\alpha}, \quad y>0. \qquad (9)$$

These equations are inhomogeneous integral equations of Wiener-Hopf type:

$$\int_0^\infty I(y')K(y-y')dy'=F(y), \quad y>0, \qquad (10)$$

and, therefore, our problems are converted into one of solving these integral equations with respect to the unknown function $I(y)$.

Now we confine ourselves to the case of $h=0$. Then the functions F and K in Eq. (10) have the following forms, respectively:

$$F(y)=-\frac{T}{k^2}e^{iky\cos\alpha},$$
$$K(y)=\int_0^\infty \frac{2d\lambda}{\mu+\mu_e}\cos(\lambda y), \qquad (11)$$

for $y>0$. If we define the following functions,

$$I(y)=\begin{cases} I(y), & y>0,\\ 0, & y<0;\end{cases}$$
$$F(y)=\begin{cases} F(y), & y>0,\\ 0, & y<0;\end{cases} \qquad (12)$$
$$G(y)=\begin{cases} 0, & y>0,\\ \int_0^\infty I(y')K(y-y')\,dy' & y<0;\end{cases}$$

then Eq. (10) is replaced by

$$\int_{-\infty}^\infty I(y')K(y-y')dy'=F(y)+G(y) \qquad (13)$$

for $-\infty<y<+\infty$. Let $\mathfrak{K}(\zeta)$, $\mathfrak{I}(\zeta)$, $\mathfrak{F}(\zeta)$ and $\mathfrak{G}(\zeta)$ be the Fourier transforms of $K(y)$, $I(y)$ $F(y)$ and $G(y)$, respectively. Then the Fourier transform of Eq. (13) formally becomes to

$$\mathfrak{I}(\zeta)\cdot\mathfrak{K}(\zeta)=\mathfrak{F}(\zeta)+\mathfrak{G}(\zeta). \qquad (14)$$

Now we easily find that

$$\mathfrak{K}(\zeta)=2\pi/\{\mu(\zeta)+\mu_e(\zeta)\} \qquad (15)$$

which is regular in the strip region

$$S:\quad |\mathscr{I}_m(\zeta)|<|\mathscr{I}_m(k)|, \qquad (16)$$

provided we assume

$$|\mathscr{I}_m(k)|\leq|\mathscr{I}_m(k_e)|,$$

and

$$\mathfrak{F}(\zeta)=\frac{T}{ik^2}\Big/(\zeta-k\cos\alpha) \qquad (17)$$

which is regular in the lower half-plane: $\mathscr{I}_m(\zeta)<\mathscr{I}_m(k\cos\alpha)$. The unknown function $\mathfrak{I}(\zeta)$ also is regular in the similar half-plane; *i.e.*, since we may assume for $I(y)$, a behavior like $\exp(i\kappa y)$ for large y, where $\mathscr{I}_m(\kappa)>0$, and then from the formula

$$\mathfrak{I}(\zeta)=\int_0^\infty I(y)e^{-i\zeta y}\,dy,$$

we find that $\mathfrak{I}(\zeta)$ will be regular in the lower half-plane $\mathscr{I}_m(\zeta)<\mathscr{I}_m(\kappa)$, which starts above the real axis in the ζ-plane. The other unknown function $\mathfrak{G}(\zeta)$, on the one hand, is regular in an upper half-plane starting below the real axis.

Next, let us consider a new function

$$\tau(\zeta)=\frac{2\mu(\zeta)}{\mu(\zeta)+\mu_e(\zeta)} \qquad (18)$$

which is regular in the strip S. Since $\tau(\zeta)\sim 1+O(1/\zeta)$ in S as $|\zeta|\to+\infty$, $\ln\tau(\zeta)\sim O(1/\zeta)$ in S as $|\zeta|\to+\infty$ on an appropriate branch of the ζ-plane. Thus $\ln\tau(\zeta)$ is regular in the whole strip-region S, and there we may apply the Cauchy's integral formula as follows

$$\ln\tau(\zeta)=\oint_C\frac{\ln\tau(t)}{t-\zeta}\,dt$$
$$=\int_{C_{(+)}}\frac{\ln\tau(t)}{t-\zeta}\,dt-\int_{C_{(-)}}\frac{\ln\tau(t)}{t-\zeta}\,dt, \qquad (19)$$

where ζ is an internal point of the contour C, and $C_{(+)}$, $C_{(-)}$ designate infinite straight

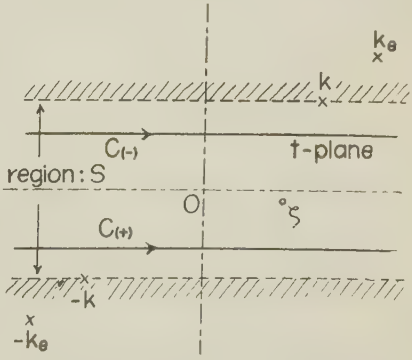

Fig. 4. Integration paths of Eq. (19).

line contours in the strip S as in Fig. 4. Let $\chi_{(+)}(\zeta)$, $\chi_{(-)}(\zeta)$ be the first and second integrals of Eq. (19), respectively, then $\exp\{\chi_{(+)}(\zeta)\}$, $\exp\{\chi_{(-)}(\zeta)\}$ may be analytically continued over the all ζ-plane, and the former is regular and different from zero in the upper half-plane of ζ above the line $C_{(+)}$ and the latter in the lower half-plane below $C_{(-)}$. Thus, we can represent $\mathfrak{K}(\zeta)$ as a quotient of functions $\mathfrak{K}_{(+)}(\zeta)$ and $\mathfrak{K}_{(-)}(\zeta)$, which are regular and not zero in the upper and lower half-planes, respectively:

$$\mathfrak{K}(\zeta)=\mathfrak{K}_{(+)}(\zeta)/\mathfrak{K}_{(-)}(\zeta)\,, \tag{20}$$

$$\left.\begin{aligned} \mathfrak{K}_{(+)}(\zeta)&=\pi^{1/2}\exp\{\chi_{(+)}(\zeta)\}\cdot/\sqrt{\zeta+k}\,,\\ \mathfrak{K}_{(-)}(\zeta)&=\pi^{-1/2}\exp\{\chi_{(-)}(\zeta)\}\cdot\sqrt{\zeta-k}\,. \end{aligned}\right\} \tag{21}$$

It is easily shown that these new functions behave in the following manner.

$$\begin{aligned} &\mathfrak{K}_{(+)}(\zeta)\sim O(\zeta^{-1/2}) \text{ as } |\zeta|\to+\infty,\\ &\qquad\qquad \mathscr{Im}(\zeta)>\mathscr{Im}(-k)\\ &\mathfrak{K}_{(-)}(\zeta)\sim O(\zeta^{1/2}) \text{ as } |\zeta|\to+\infty,\\ &\qquad\qquad \mathscr{Im}(\zeta)<\mathscr{Im}(k). \end{aligned}, \tag{22}$$

If Eq. (20) is inserted in Eq. (14) and suitable manipulations are applied, it follows that

$$\frac{\mathfrak{G}(\zeta)}{\mathfrak{K}_{(+)}(\zeta)}+\frac{(iT/k^2)}{\zeta-k\cos\alpha}\left\{\frac{1}{\mathfrak{K}_{(+)}(\zeta)}-\frac{1}{\mathfrak{K}_{(+)}(k\cos\alpha)}\right\}$$
$$=\frac{\mathfrak{J}(\zeta)}{\mathfrak{K}_{(-)}(\zeta)}-\frac{iT}{k^2}\cdot\frac{1}{(\zeta-k\cos\alpha)\cdot\mathfrak{K}_{(+)}(k\cos\alpha)}\,. \tag{23}$$

The left-hand side of Eq. (23) is regular in the upper half-plane and the right-hand side in the lower half-plane. Since these half-planes overlap each other, both sides may be considered as analytic continuations of each other and together they define an integral function throughout the ζ-plane. For absolute convergence of $I(y)$ and $G(y)$ in the interval including the point $y=0$, one may assume that

$$\begin{aligned} &\mathfrak{J}(\zeta)\sim O(\zeta^{\alpha-1})\,,\quad \alpha<1\,,\\ &\qquad\qquad \mathscr{Im}(\zeta)<\mathscr{Im}(k)\,,\\ &\mathfrak{G}(\zeta)\sim O(\zeta^{\beta-1})\,,\quad \beta<1\,,\\ &\qquad\qquad \mathscr{Im}(\zeta)>-\mathscr{Im}(-k)\,, \end{aligned} \tag{24}$$

as $|\zeta|\to+\infty$. Thus it turns out that both sides have algebraic behavior of negative fractional degree at infinity, and the integral function above defined is zero by a modification of *Liouville*'s theorem. Hence the left- and right-hand sides of Eq. (23) are identically zero, and this determines $\mathfrak{J}(\zeta)$ and $\mathfrak{G}(\zeta)$ simultaneously; for instance

$$\mathfrak{J}(\zeta)=\frac{iT}{k^2}\cdot\frac{\mathfrak{K}_{(-)}(\zeta)}{\mathfrak{K}_{(+)}(k\cos\alpha)}\cdot\frac{1}{\zeta-k\cos\alpha}\,, \tag{25}$$

and, moreover, by the inverse transformation,

$$I(y)=-\frac{T}{2\pi ik^2}\int_{i\eta-\infty}^{i\eta+\infty}\frac{\mathfrak{K}_{(-)}(\zeta)}{\mathfrak{K}_{(+)}(k\cos\alpha)}\cdot\frac{e^{i\zeta y}}{\zeta-k\cos\alpha}d\zeta\,, \tag{26}$$

where $\eta<\mathscr{Im}(k)$. It is easy to obtain formally the secondary fields produced by this current distribution $I(y)$ from these formulas.

In addition, since the function $\mathfrak{J}(\zeta)$ vanishes to the order $\zeta^{-1/2}$ as $|\zeta|\to+\infty$, it is to be noted that the density of the surface current behaves in the vicinity of its rim as follows

$$J_x(y)\sim O(y^{-1/2})\,,\ \text{as } y\to+0\,. \tag{27}$$

§ 4. A Conducting Half-Plane in Interface of Two Different Media and A Uniform Line-Current Parallel to Its Rim

In this section we consider the case that a uniform line-current parallel to the x-axis is located at $y=y_0$, $z=h$ and the half-plane $z=0$, $y>0$ is occupied by a conducting sheet, as in Fig. 5. In this case, too, the fields are represented by the primary fields due to the line-current and the secondary fields due to an unknown surface current $I(y)$ in the x-direction on the conducting sheet, just as in the preceding section.

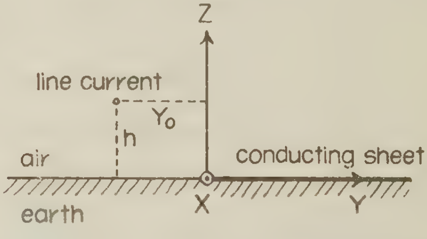

Fig. 5. A line current and a conducting half-plane on the earth.

Applying the representations in § 2, we can obtain the function $I(y)$ from the next equation

$$\int_0^\infty dy'\,I(y')\int_0^\infty\frac{2d\lambda}{\mu+\mu_e}\cos\{\lambda(y-y')\}$$
$$+\int_0^\infty\frac{2d\lambda}{\mu+\mu_e}e^{-h\mu}\cos\{\lambda(y-y_0)\}=0,\ y>0; \tag{28}$$

which follows from the boundary condition at the conducting surface $z=0$, $y>0$. Let $K(y)$ be the same as in Eq. (11) and $F(y)$ be

$$F(y)=-\int_0^\infty \frac{2d\lambda}{\mu+\mu_e} e^{-h\mu}\cos\{\lambda(y-y_0)\}, \tag{29}$$

then it is found that the above equation (28) has the same form as Eq. (10), which is the integral equation of Wiener-Hopf. If we consider that $I(y)$ vanishes for $y<0$, whereas $F(y)$ has the bounded values throughout $-\infty<y<+\infty$, and if we define a new function

$$G(y)=\begin{cases}\int_0^\infty I(y')K(y-y')dy'-F(y), & y<0,\\ 0, & y>0,\end{cases} \tag{30}$$

then the integral equation above described is rewritten into the same form as Eq. (13). Therefore, its Fourier transform becomes equal to Eq. (14), provided the same notations are adopted. In this case, $\mathfrak{K}(\zeta)$ is given by Eq. (15) and has the same behavior as in the preceding section, but

$$\mathfrak{F}(\zeta)=-\frac{2\pi}{\mu(\zeta)+\mu_e(\zeta)}e^{-i\zeta y_0-h\mu(\zeta)} \tag{31}$$

is regular in the strip region S as same as $\mathfrak{K}(\zeta)$. On the other hand, we may assume

$$\begin{aligned} I(y) &\sim \frac{1}{\sqrt{y}}e^{iky}, \quad \text{as} \quad y\to+\infty,\\ G(y) &\sim \frac{1}{\sqrt{-y}}e^{-iky}, \quad \text{as} \quad y\to-\infty; \end{aligned} \tag{32}$$

hence it is easily shown that $\mathfrak{J}(\zeta)$ and $\mathfrak{G}(\zeta)$ are regular in the lower half-plane $\mathscr{I}_m(\zeta)<\mathscr{I}_m(k)$ and the upper half-plane $\mathscr{I}_m(\zeta)>-\mathscr{I}_m(k)$, respectively.

Since $\mathfrak{K}(\zeta)$ is now factorized in the form of Eq. (20), we have, from Eq. (14),

$$\frac{1}{\mathfrak{K}_{(-)}(\zeta)}\exp[-i\zeta y_0-h\mu]=\frac{\mathfrak{G}(\zeta)}{\mathfrak{K}_{(+)}(\zeta)}-\frac{\mathfrak{J}(\zeta)}{\mathfrak{K}_{(-)}(\zeta)}, \tag{33}$$

an equation whose left-hand side is regular in the strip S, while the first and second terms of the right-hand side are regular in upper and lower half-planes, respectively. For absolute convergence of $I(y)$ and $G(y)$ in the interval including the vicinity of $y=0$, we may assume the same behavior of $\mathfrak{J}(\zeta)$ and $\mathfrak{G}(\zeta)$ at infinity as Eq. (24); hence the right-hand side of Eq. (33) has algebraic behavior of negative fractional degree at infinity. Thus, from transform theory, the inverse of the first term of the right-hand side of Eq. (33) vanishes for $y>0$, and the inverse of the second term vanishes for $y<0$. The inverse transform of the left-hand side exists over all y. Consequently, the inverse transform of the whole Eq. (33) becomes to

$$\int_{-\infty}^{+\infty}\frac{e^{-i\zeta y0-h\mu}}{\mathfrak{K}_{(-)}(\zeta)}\cdot e^{i\zeta y}d\zeta=j(y)+g(y), \qquad -\infty<y<+\infty, \tag{34}$$

where

$$\begin{aligned} j(y)&=0, \text{ for } y<0; =\int_{-\infty}^{+\infty}\frac{\mathfrak{J}(\zeta)}{\mathfrak{K}_{(-)}(\zeta)}e^{i\zeta y}d\zeta, \quad y>0;\\ g(y)&=\int_{-\infty}^{+\infty}\frac{\mathfrak{G}(\zeta)}{\mathfrak{K}_{(+)}(\zeta)}e^{i\zeta y}d\zeta, \text{ for } y<0;\\ &=0, \quad \text{for } y>0. \end{aligned} \tag{35}$$

Multiplying Eq. (34) by e^{-izy} and integrating over positive values of y, we have

$$\frac{\mathfrak{J}(z)}{\mathfrak{K}_{(-)}(z)}=\frac{1}{2\pi i}\int_{-\infty}^{+\infty}\frac{e^{-i\zeta y_0-h\mu(\zeta)}}{(\zeta-z)\cdot\mathfrak{K}_{(-)}(\zeta)}d\zeta, \tag{36}$$

which is regular in the lower half-plane $\mathscr{I}_m(\zeta)>\mathscr{I}_m(z)$. Hence the current distribution $I(y)$ is calculated from this formula by the inverse transformation as follows

$$I(y)=\frac{1}{2\pi}\int_{-\infty}^{+\infty}dz\,e^{izy}\cdot\frac{\mathfrak{K}_{(-)}(z)}{2\pi i}\int_{-\infty}^{+\infty}d\zeta \cdot\frac{e^{-i\zeta y_0-h\mu(\zeta)}}{(\zeta-z)\cdot\mathfrak{K}_{(-)}(\zeta)}, \tag{37}$$

where

$$|\mathscr{I}_m(\zeta)|<|\mathscr{I}_m(k)|, \ \mathscr{I}_m(\zeta)>\mathscr{I}_m(z), \ y>0.$$

It is the final expression for the current distribution.

§ 5. Final Representations of Fields

In our cases, the secondary fields are formulated in the form

$$f(y,z)=\int_0^{+\infty}dy'I(y')\int_0^{+\infty}d\lambda g\{\lambda;z\}\cos\{\lambda(y-y')\}, \tag{38}$$

where $g\{\lambda;z\}$ is always an even function with respect to λ, as shown in § 2, $I(y)$ is the inverse transform of $\mathfrak{J}(\zeta)$ and also the integration

$$G(y,z)=\int_0^{+\infty}d\lambda\, g\{\lambda;z\}\cos(\lambda y) \tag{39}$$

is the inverse transform of $g\{\lambda;z\}$ multiplied by π. Hence we easily find, by the *convolution* theorem of Fourier transforms, that

$$\begin{aligned} f(y,z)&=\int_0^{+\infty}dy'I(y')G(y-y';z)\\ &=\frac{1}{2}\int_{-\infty}^{+\infty}d\lambda\,\mathfrak{J}(\lambda)\cdot g\{\lambda;z\}e^{i\lambda y}. \end{aligned} \tag{40}$$

Thus, we can directly obtain the secondary fields from the transform $\mathfrak{J}(\zeta)$ of $I(y)$ rather than from $I(y)$ itself, calculating the integrals as Eq. (40).

§ 6. Conclusion

We have rigorously investigated, in this paper, the problems of the line and surface current flowing in one direction parallel to an interface of two different media. Whole problems have been dealt with by the integral equations of Wiener-Hopf type, and described from the relatively general point of view.

They are problems having a theoretical interest, but the results here obtained may be applied to several practical problems: wave propagations over the inhomogeneous earth, effects of snow in microwave transmission systems and diffraction of waves by a mountain-chain which divides the atmosphere into two parts whose meteorological properties are different, and so on. It is necessary, however, to give more detailed or rather numerical solutions, which we shall investigate in other paper.

Particularly, the solution of § 3 is important because it leads to the analysis of the problems of reflection, refraction and diffraction due to a screen which lies in an interface of of two different media.

In conclusion, it is a pleasure for the author to express his sincere gratitude to Professor T. Hirota and Assistant Professor T. Soejima who have given kind encouragements and helpful advices.

References

1) Sommerfeld: *Math. Ann.* **47** (1896), 317.
2) MacDonald: *Elastic Waves*, Cambridge, 1902.
3) Nomura: *Sci. Rep. Res. Inst. Tohoku Univ.* B **4** (1952), 29.
4) King: *Proc. Roy. Soe.* A **153** (1936), 1.
5) Titchmarsh: *Introduction to the Theory of Fourier Iutegrals*, Oxford (1937) 339.
6) Copson: *Quart. J. Math.* **17** (1946) 19
7) Schwinger: *Seminor on the Theory of Guided Waves*, M. I. T. Rad. Lab. 1944.
8) Carlson & Heins: *Quart. Appl. Math.* **4** (1947) 313; **5** (1947), 82.
9) Heins: *ibid.* **6** (1948), 157.
10) Levine & Schwinger: *Phys. Rev.* **73** (1948) 383.
11) Marcuvitz: *Waveguide Handbook* M. I. T.-Ser. (1951) 196.
12) Iijima: *Res. Electrotechnical Laboratory* (1952) 531.
13) Clemmow: *Proc. Roy. Soc.* A **205** (1951) 286.
14) Clemmow: *Phil. Trans.* A **246** (1953) 1.
15) Sommerfeld: *Part. Diff. Eqs. in Phys.* New York (1949) 236.

JOURNAL OF THE PHYSICAL SOCIETY OF JAPAN Vol. 12, No. 2, FEBRUARY, 1957

On the Hypersonic Viscous Flow past a Flat Plate with Suction or Injection

By Michiru YASUHARA

Institute of Science and Technology, University of Tokyo

(Received June 28, 1956)

The hypersonic viscous flow past a flat plate with suction or injection is dealt with by Kármán-Pohlhausen's method in special cases when suction or injection velocity proportional to $p_B^{1/2}$ or $x^{-1/4}$, especially for the region of strong interaction between the shock wave and the boundary layer, were p_B is the pressure on the plate and x is the distance measured along the plate from its leading edge.

Several numerical examples are given, which shows similar effects of injection to those in the case of incompressible flow that the injection makes all the height of the shock wave, the thickness of the boundary layer and the pressure on the plate larger than those in the case of no injection. On the contrary, in the case of suction no remarkable change both in the height of the shock wave and the pressure on the plate can be seen and only the velocity profile in the boundary layer is affected by the suction.

§ 1. Introduction

Recently various investigations have been made on the hypersonic viscous flow over slender bodies, and the results have led us to expect that the thickness of the boundary layer becomes larger and larger with increasing Mach number and at the same time the temperature on the body becomes higher and higher. Therefore it may be expected that strong suction will be necessary to keep the thickness of the boundary layer within a small amount, while the surface cooling or injection will be required to avoid the extremely high temperature on the body.

The purpose of the present paper is to estimate the effects of suction or injection on the region of strong interaction between the shock wave and the boundary layer. Either suction or injection may be used for the boundary-layer control and the surface cooling etc. in high-speed flights.

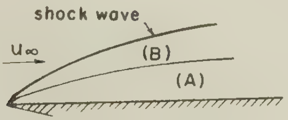

Fig. 1. Flow model on a flat plate.

As a preliminary, we first consider the hypersonic viscous flow past a plate without suction as shown in Fig. 1. As suggested by various previous writers, a shock wave emanates from the leading edge of the plate and the boundary layer is also formed on the plate. In this case, the flow field between the shock wave and the plate can be divided into two regions: In region (A) extending from the plate part of the way to the shock wave, viscous effects are important but the pressure change across it is so small that boundary layer theory may be used to describe the flow within it. Between the shock wave and the region (A), which is nothing but the boundary layer, there is a region (B) in which the effects of viscosity are small, but large entropy gradients occur near the junction with the region (A). This region (B) is called the "inviscid layer."

A region far behind the leading edge of the plate was investigated by Lees and Probstein$^{1)}$. Shen, Li and Nagamatsu$^{2)}$ investigated a region in which the interaction between the shock wave and the boundary layer is strong, assuming that the shock wave coincides with the outer edge of the region (A), and they found that there exists a similar solution throughout the region (A). Recently, Stewartson$^{3)}$ also discussed the problem more accurately by considering the existence of the region (B) and showed that there exists a similar solution in the region (B), too, which may be joined up to that in the region (A) without inconsistency.

Similar argument may be assumed to be valid also in cases when there is suction or injection on the plate, provided that the suction or injection is of moderate strength not to violate the boundary-layer approximation, and the object of the present paper is to discuss the effects of such a suction or injection on the height of the shock wave, the thickness of the boundary layer and the pressure on the plate.

§2. Equations of Motion and their Solutions

2.1 General Equations of Motion

Taking a flat plate occupying the positive half of the x-axis, we assume that the fluid flows along it with uniform velocity u_∞ at infinity and that a shock wave emanates from the leading edge of the plate (Fig. 2).

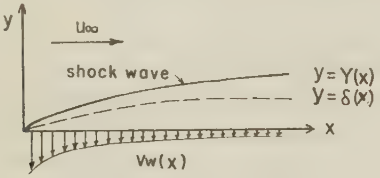

Fig. 2. Flow model on a flat plate with suction.

We denote by p the pressure, ρ the density, μ the coefficient of viscosity, T the temperature, y the distance normal to the plate, u, v the components of the fluid velocity in the x, y directions, respectively, and c_p the specific heat at constant pressure of the fluid. Also, let the equation of the shock wave be

$$Y=Y(x)\,, \tag{1}$$

where Y is for the present unknown.

Throughout this paper, subscripts ∞, s, and w represent quantities at infinity, those just behind the shock wave, and those on the wall, respectively.

We now assume that the flow behind the shock wave either inviscid or of the boundary-layer type in which the pressure is a function of x only, and then we consider the following system of equations:

$$\frac{\partial(\rho u)}{\partial x}+\frac{\partial(\rho v)}{\partial y}=0\,, \tag{2}$$

$$\rho u\frac{\partial u}{\partial x}+\rho v\frac{\partial u}{\partial y}=-\frac{\partial p}{\partial x}+\frac{\partial}{\partial y}\left(\mu\frac{\partial u}{\partial y}\right), \tag{3}$$

$$\rho u\frac{\partial v}{\partial x}+\rho v\frac{\partial v}{\partial y}=-\frac{\partial p}{\partial y}\,, \tag{4}$$

$$\rho u\frac{\partial(C_pT)}{\partial x}+\rho v\frac{\partial(C_pT)}{\partial y}-u\frac{\partial p}{\partial x}-v\frac{\partial p}{\partial y}=\mu\left(\frac{\partial u}{\partial y}\right)^2+\frac{\partial}{\partial y}\left\{\frac{\mu}{P_r}\frac{\partial(C_pT)}{\partial y}\right\}, \tag{5}$$

$$p/p_\infty=\rho T/\rho_\infty T_\infty\,, \tag{6}$$

where P_r is the Prandtl number. Equation (2) is the equation of continuity valid everywhere. Equation (3) is from the x-component of the momentum equation valid in the boundary layer regime and in the inviscid regime. Equation (4) is from the y-component of the momentum equation valid in the inviscid layer. In the boundary layer its effect on p must be negligible. Equation (5) is the energy equation valid in both regions, and Equation (6) is the equation of state valid everywhere. There are many terms neglected in these equations, but as shown by Stewartson, their effect is negligible if $Y\ll x$, and u can be replaced by u_∞ in the inviscid layer[3)].

Throughout this paper it is assumed that the fluid possesses the properties

$$P_r=1\,,\qquad \mu/\mu_\infty=CT/T_\infty\,, \tag{7}$$

where

$$C=\left(\frac{T_w}{T_\infty}\right)^{1/2}\frac{(T_\infty+S)}{(T_w+S)}\,,$$

and S denotes Sutherland's constant.

Now, on the plate $y=0$, $x>0$,

$$u=0,\quad v=v_w,\quad \partial T/\partial y=0,$$

taking it to be thermally insulated and with suction or injection velocity on the plate, where $v_w{}^2\ll u_\infty{}^2$. Then, the equations of motion have a simple integral

$$\frac{T}{T_\infty}=1+\frac{\gamma-1}{2a^2_\infty}(u^2_\infty-u^2-v^2)\,, \tag{8}$$

where a_∞ represents the velocity of sound in the undisturbed flow, and v is neglected in comparison with u_∞ in the boundary layer.

2.2 Inviscid Layer

Under above fundamentals, Stewarton discussed the solution in the inviscid layer using a stream function ψ defined by

$$\left.\begin{aligned}\rho_\infty\frac{\partial\psi}{\partial y}&=\rho u\,,\\ \rho_\infty\frac{\partial\psi}{\partial x}&=-\rho v\,.\end{aligned}\right\} \tag{9}$$

The results are as follows. If the equation of the shock wave is assumed to be

$$Y=\vartheta x^{3/4}(1+\alpha x^{1/2}+\cdots\cdot), \tag{10}$$

where the reason that $x^{3/4}$ is chosen as the leading term will be discussed in 2.3, and, if the following expressions are used,

$$\begin{aligned}
\eta&=\psi/u_\infty Y\ ,\\
v&=\{2u_\infty/(\gamma+1)\}(dY/dx)\,V(\eta,x)\ ,\\
p/p_\infty&=\{2\gamma M^2_\infty/(\gamma+1)\}(dY/dx)^2\,P(\eta,x)\ ,\\
V&=V_0(\eta)-x^{1/2}[4\alpha V_1(\eta)/3\\
&\qquad+16V_2(\eta)/9M^2_\infty\vartheta^2]+\cdots\ ,\\
P&=P_0(\eta)-x^{1/2}[4\alpha P_1(\eta)/3\\
&\qquad+16P_2(\eta)/9M^2_\infty\vartheta^2]+\cdots\ ,
\end{aligned} \tag{11}$$

the ordinary differential equations for P_0, V_0, P_1, V_1, $\cdots$ are obtained, which were integrated by Stewarton numerically, and it was found at $\eta=0$ that

$$\left.\begin{aligned}P_0&=0.599\ , & P_1&=-1.64\ , & P_2&=1.285\ ,\\ V_0&=0.711\ , & V_1&=-2.04\ , & V_2&=2.49\ ,\end{aligned}\right\} \tag{12}$$

taking $\gamma=1.4$ for air. Since ψ is a measure of the mass of fluid confined between the shock wave and the plate, almost mass of fluid is contained between $\eta=1$ and $\eta=0$, that is, in the inviscid layer. Lastly, it is convenient to give the value of y instead of v at the end of the inviscid layer. From the definition of ψ in Eq. (9), we find

$$v_E\equiv v_{\eta=0}=\left\{u\left(\frac{\partial y}{\partial x}\right)_\psi\right\}_{\eta=0}=u_\infty\frac{dy_E}{dx}\ ,$$

and therefore

$$y_E=\int_0^\infty\frac{v_B}{u_E}\,dx\ , \tag{13}$$

where suffix E denotes quantities at $\eta=0$ in the inviscid layer. As v at $\eta=0$ is obtained from Eqs. (11) and (12) when $\gamma=1.4$, y_E can be calculated by using Eq. (13), and the result is given by

$$y_E=\frac{2Y(x)}{\gamma+1}\left[V_0(0)-\frac{3}{5}\left\{\frac{4}{3}\alpha V_1(0)+\frac{16}{9M^2_\infty\vartheta^2}V_0(0)\right\}x^{1/2}+\cdots\cdot\right]. \tag{14}$$

2.3 *Boundary Layer*

The dominant equations of motion in the boundary layer are Eqs. (2) and (3), with boundary conditions $u=0$, $v=v_w$ at $y=0$ and $u=u_B$ outside the boundary layer, and Eq. (4) is reduced to $\partial p/\partial y=0$, that is, $p=p(x)$, where suffix B represents quantities outside the boundary layer. This boundary condition can be replaced by $u\to u_\infty$ as $y\to y_B$, where y_B is the thickness of the boundary layer and corresponds to y at $\eta=0$ in the inviscid layer. The adoptability of the latter condition is shown as follows.

$\eta=0$ corresponds to a stream line $\psi=0$ of the inviscid layer as seen from Eq. (11). While from Eqs. (2), (3) and (9) with the aid of Eq. (8) in which v must be neglected in this layer, the value of v at the boundary layer is reduced to

$$\begin{aligned}
v_B&=\left[u\frac{\partial}{\partial x}\int_{\psi_w}^{\psi}\frac{\rho_\infty}{\rho u}\,d\psi\right]_B\\
&=\left[u\frac{\partial}{\partial x}\int_{\psi_w}^{\psi}\frac{p_\infty}{pu}\left\{1+\frac{\gamma-1}{2a^2_\infty}(u^2_\infty-u^2)\right\}d\psi\right]_B,
\end{aligned}$$

where ψ_w respresents the value of ψ at the wall and is a function of x. The term unity in the bracket of the above equation can be neglected, since in the boundary layer

$$1\ll\{(\gamma-1)/2a^2_\infty\}(u^2_\infty-u^2)\ .$$

Futher, the upper limit of the integration can be replaced by ∞, since when ψ is large on the scale of the boundary layer, $u-u_\infty$ is exponentially small as shown by Stewartson. At the edge of the boundary layer therefore

$$v_B=\frac{\gamma-1}{2}M^2_\infty u_\infty\frac{d}{dx}\left\{\frac{p_\infty}{p_B}\int_{\psi_w}^\infty\left(\frac{u_\infty}{u}-\frac{u}{u_\infty}\right)d\psi\right\}, \tag{15}$$

since $p=p(x)=p_w=p_B$ and $u=u_\infty$ there. In the boundary layer, the pressure will be represented by p_B. In the same way, from Eq. (9), y_B is reduced to

$$y_B=y_{\psi\to\infty}=\frac{\gamma-1}{2}M^2_\infty\frac{p_\infty}{p_B}\int_{\psi_w}^\infty\left(\frac{u_\infty}{u}-\frac{u}{u_\infty}\right)d\psi.$$

Comparing the above equation with Eq. (15), the following relation is deduced:

$$v_B=u_\infty\frac{dy_B}{dx}\ , \tag{16}$$

which shows that the outer edge of the boundary layer also corresponds to a stream line. From Eqs. (13) and (16), if a match of v between the inviscid solution at $\psi=0$ and the boundary-layer solution for $\psi=\infty$ is effected, the value of y between both layers is done smoothly.

In the present paper, Kármán-Pohlhausen's approximation is used to discuss the boundary layer. Integrating Eqs. (2) and (3) over the boundary layer, and combining these, the following momentum integral relation is obtained:

$$\frac{\tau_w}{\rho_\infty u^2_\infty} \equiv \frac{(\mu \partial u/\partial y)_w}{\rho_\infty u^2_\infty}$$
$$= \frac{2}{(\gamma-1)M^2_\infty} \frac{d}{dx} \left\{ \frac{p_B}{p_\infty} \int_0^\delta \frac{u/u_\infty}{1+(u/u_\infty)} dy \right\}$$
$$- \frac{\delta}{\gamma M^2_\infty} \frac{d}{dx} \left(\frac{p_B}{p_\infty} \right) - \frac{\rho_w v_w}{\rho_\infty u_\infty} , \tag{17}$$

where δ corresponds to y_B approximated in Kármán-Pohlhausen's sense. The above relation have been used by Shen, Li and Nagamatsu[2)] in their treatment of the hypersonic Shock wave boundary layer interaction problems in case when $v_w=0$.

As in the case of incompressible boundary layer, we now put

$$u/u_\infty = f(\xi) , \quad \xi = y/\delta , \tag{18}$$

where $f(\xi)$ is a polynomial of ξ of any degree. It is well known that in the case of imcompressible boundary layer, the quartic form of $f(\xi)$, i.e. a polynomial of degree four, gives plausible results and that no more accuracy can be gained by considering a polynomial of higher degree. However, it is not certain whether the situation is similar in the present problem or not.

In the present paper, the quadratic form of $f(\xi)$, i.e. a polynomial of degree two, is used for reason described later on. Thus,

$$f(\xi) = \xi + \frac{\Lambda}{2} \xi (1-\xi) . \tag{19}$$

Then, Eq. (2) is reduced to

$$\rho_w v_w u_\infty \delta \left(1 + \frac{\Lambda}{2} \right) = - \delta^2 \frac{dp_B}{dx} - \mu_w u_\infty \Lambda , \tag{20}$$

at the wall, taking the plate to be thermally insulated, i.e. $(\partial T/\partial y)_w = 0$.

Further, if we introduce a function $F(\Lambda)$ defined by

$$F(\Lambda) \equiv \int_0^1 \frac{d\xi}{1+f(\xi)} , \tag{21}$$

Eq. (17) is reduced to

$$\frac{\mu_w \left(1 + \frac{\Lambda}{2} \right)}{\rho_\infty u_\infty} = \frac{2\delta}{(\gamma-1)M^2_\infty} \frac{d}{dx} \left[\frac{p_B}{p_w} \delta \{ 1 - F(\Lambda) \} \right]$$
$$- \frac{\delta^2}{\gamma M^2_\infty} \frac{d}{dx} \left(\frac{p_B}{p_\infty} \right) - \frac{\rho_w v_w}{\rho_\infty u_\infty} \cdot \delta , \tag{22}$$

Now, we shall here confirm that the form of the shock wave as assumed in Eq. (10) is consistent. If $Y \sim x^n$, we have from Eqs. (11) and (14) $p_B \sim x^{2(n-1)}$ and $y_B \sim x^n$ when x is small, since V_0 and P_0 are functions of η only. While we see from Eqs. (20) and (22) that if $p_B \sim x^{2(n-1)}$

$$\delta \sim 1/\sqrt{\ } dp_B/dx \sim x^{3/2-n} ,$$

in order to make the expanded form of Λ in power series of x begin with a constant term, when $v_w=0$. Therefore for consistency of y_B and δ, we must have $n=3/2-n$, whence $n=3/4$. The existence of such n in the boundary layer was first demonstrated by Li, Nagamatsu, and Stewartson showed that such n also exists in the inviscid layer. Referring to Eqs. (20) and (22), it is easily known that if $\rho_w v_w \sim x^{-3/4}$, the similar solution exists also in case when $v_w \not\fallingdotseq 0$.

Next, the evaluation of the term $\rho_w v_w$ will be discussed. From Eq. (8) we have on the wall

$$\frac{\rho_w}{\rho_\infty} \doteq \frac{2}{(\gamma-1)M^2_\infty} \frac{p_B}{p_\infty} \sim x^{-1/2} ,$$

and therefore if $v_w \sim x^m$, then $\rho_w v_w \sim x^{-1/2+m}$ and the similar solution exists when $-1/2+m = -3/4$ or $m=-1/4$. Whence $v_w \sim {}^{-1/4} \sim p_B{}^{1/2}$ garantees the existence of the similar solution. Recently, porous wall methods have been used as a transonic wind tunnel technique with great interest, which suggest that the flow velocity v_w passing through the wall is proportional to $(p_w - p_a)$ near the transonic range where p_a represents the pressure in the plenum chamber, and $v_w \sim (p_w - p_a)^{1/1.3}$ at slightly higher Mach number range. Though these experimental relations have not yet been investigated in the high supersonic range, it seems to be plausible to consider the case when the power is equal to 1/2 as a model. This model just corresponds to $v_w \sim p_B{}^{1/2}$.

Based upon the above discussions, it is assumed that there exists the following relation:

$$\frac{\rho_w v_w}{\rho_\infty u_\infty} = \frac{2}{(\gamma-1)M^2_\infty} \frac{p_B}{p_\infty} \alpha \left(\frac{p_B}{p_\infty} \right)^{1/2}$$
$$= \frac{2}{(\gamma-1)M^2_\infty} \left(\frac{p_B}{p_\infty} \right)^{3/2} , \tag{23}$$

where α denotes a proportionality factor. In the case of suction $\alpha < 0$.

In the case of injection $(\alpha > 0)$ we assume also that the injection velocity along the wall is proportional to $p_w{}^{1/2}$, or more directly to $x^{-1/4}$. Although its physical meaning is not clear, yet numerical calculations for this case have also been carried out for the purpose of estimating the injection effect.

2.4 Matching Procedure

Now, a match between the inviscid solution at $\psi=0$ and the boundary layer solution for $\psi\to\infty$ will be effected. For the discussion about such conditions reference should be made to Stewarton's paper. It was shown in 2.2 that if the equation of the shock wave is given by Eq. (10), p_E/p_∞ and y_E at the inner edge of the inviscid layer are obtained by setting $\eta=0$ in Eqs. (11) and (14). On the other hand, p_B/p_∞ and δ must be satisfied by Eqs. (20) and (22), and therefore solutions matching at the boundary of both layers can be obtained by making $p_E/p_\infty=p_B/p_\infty$ and $y_E=\delta$. By introducing the following relations

$$\delta \doteq y_B = \frac{2}{(\gamma+1)} V_0(0)\,\vartheta\, x^{3/4}+\cdots ,$$

$$\frac{p_B}{p_\infty}=\frac{p_E}{p_\infty}=\frac{9\gamma M^2_\infty}{8(\gamma+1)}P_0(0)\vartheta^2 x^{-1/2}+\cdots , \tag{24}$$

into Eqs. (20) and (22), equations for determining ϑ and Λ can be obtained. From these equations together with Eqs. (19) and (21), Λ and ϑ are determined, where ϑ is of the form

$$\vartheta=\theta\left(\frac{M^2_\infty C\mu_\infty}{\rho_\infty u_\infty}\right)^{1/4}\equiv\theta L^{1/4}, \tag{25}$$

and Y, δ, v_B/u_∞, P_B/P_∞ and $\tau_w/\rho_\infty u^2_\infty$ are obtained as follows:

$$Y=\theta\left(\frac{L}{x}\right)^{1/4}x+0\,(x^{5/4})\equiv R_S\left(\frac{L}{x}\right)^{1/4}x+\cdots ,$$

$$\delta=\frac{2V_0(0)\theta}{(\gamma+1)}\cdot\left(\frac{L}{x}\right)^{1/4}x+0(x^{5/4})\equiv\Lambda\cdot\left(\frac{L}{x}\right)^{1/4}x+\cdots ,$$

$$\frac{v_B}{u_\infty}=\frac{3V_0(0)\theta}{2(\gamma+1)}\left(\frac{L}{x}\right)^{1/4}+0(x^{1/4})\equiv V_B\left(\frac{L}{x}\right)^{1/4}x+\cdots ,$$

$$\frac{p_w}{p_\infty}=\frac{p_B}{p_\infty}=\frac{9\gamma P_0(0)\theta^2}{8(\gamma+1)}\left(\frac{LM^4_\infty}{x}\right)^{1/2}+0(1)$$
$$\equiv P_w\left(\frac{LM^2_\infty}{x}\right)^{1/2}+\cdots .$$

$$\frac{\tau_w}{\rho_\infty u^2_\infty}=\frac{(\gamma^2-1)\left(1+\frac{\Lambda}{2}\right)}{2V_0(0)\,\theta}\left(\frac{L}{x}\right)^{3/4}+0(x^{-1/4})$$
$$\equiv S_w\left(\frac{L}{x}\right)^{3/4}+\cdots . \tag{26}$$

It is required to determine the region of validity of Eqs. (2) to (6) and of the division of the flow field into a boundary layer and an inviscid layer. Stewartson found that the region of validity is restricted by the condition $(Y/x)^2\ll 1$, and further that the flow field may be divided into inviscid and viscous fields if, in terms of ψ, the thickness of the viscous layer is much thinner than that of inviscid field. The situation is the same in the present problem, too. For the detail of the reduction procedure, the reader may be referred to Stewartson's paper. Combining above results and the condition of convergency of the power series, it is known that the results of the present paper should be taken to be valid in the range

$$\frac{M^2_\infty C\mu_\infty}{\rho_\infty u_\infty}\ll x\ll\frac{M^2_\infty C\mu_\infty}{\rho_\infty u_\infty},$$
$$\alpha=0\,(1/M^2_\infty)\ , \tag{27}$$

The lower bound is also the lower bound for the validity of the assumption of a continuum. Further, errors caused by Kármán-Pohlhausen's approximation should be estimated, these are not discussed exactly in the present paper, but concerning the values of Y, δ, and p_B/p_∞ when $\alpha=0$, comparison with Stewartson's results as shown in Table I may be of use for the present purpose.

Table I. Comparison of numerical values for the flat plate without suction

	R_S	Λ	P_w
Stewartson's result	1.188	0.704	0.555
Kármán-Pohlhausen's approximation			
Quadratic	1.245	0.738	0.602
Quartic	1.387	0.822	0.756
Sextic	1.505	0.892	0.890

§ 3. Numerical Results and Discussions

Numerical values for the present problem are compared with Stewartson's ones in Table I in case when $v_w=0$. From the table, it will be seen that polynomials of lower degree give more plausible values than polynomials of higher degree. Thus, our calculations have been confined only to the quadratic form of $f(\xi)$.

It is known from Eq. (26) that effects of suction or injection can be characterized by the term θ and Λ which are functions of γ and αM^2_∞. Fig. 3 shows the values of $z\equiv\theta/\theta_{\alpha=0}$ and z^2 for several values of αM^2_∞ when $\gamma=1.4$. Y, δ, and v_B are proportional to z, and p_B is proportional to z^2. Fig. 4 shows the coefficient S_w of the shear stress.

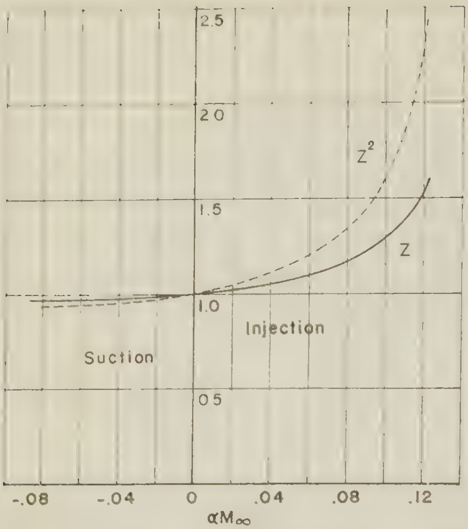

Fig. 3. Relation between αM_∞ and z or z^2.

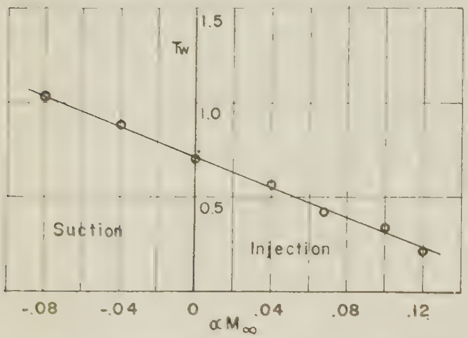

Fig. 4. Relation between αM_∞ and S_w.

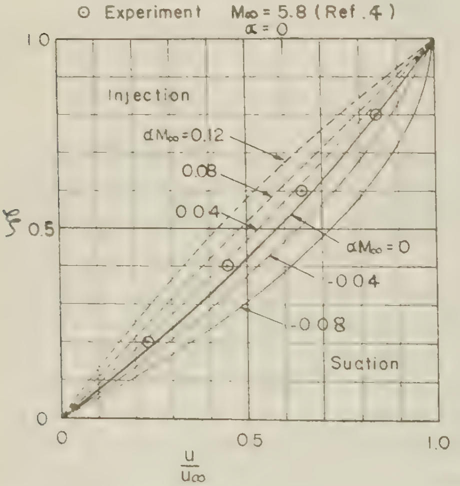

Fig. 5. Velocity profiles in the boundary layer.

Fig. 5 shows the velocity profiles for several values of αM^2_∞. Fig. 3 shows that z does not diminish sensibly with increasing $-\alpha M^2_\infty$, the suction parameter, and therefore also Y, δ, v_B, and $p_w = p_B$ are not affected sensibly by the suction in contrast to the ordinary boundary-layer theory, while visible effects can be seen in the velocity profile and the shear stress as shown in Figs. 4 and 5. On the contrary, z increases with increasing αM^2_∞, the injection parameter, and therefore Y, δ, v_B and p_B are also increased, while the shear stress decreased as expected from the ordinary boundary-layer theory. It should be remarked, however that these results are concerned with the leading term of each quantity, and further that our results are only valid in cases when $v_w \sim p_B^{1/2} \sim x^{-1/4}$.

§ 4. Conclusion

The hypersonic viscous flow past a flat plate with suction or injection is dealt with by Kármán-Pohlhausen's method in special cases when suction or injection velocity is proportional to $p_B^{1/2}$ or $x^{-1/4}$, especially for the region of strong interaction between the shock wave and the boundary layer, where p_B is the pressure on the plate and x is the distance measured along the plate from its leading edge. Several numerical examples are given, which show similar effects of injection to those in the case of incompressible flow that the injection makes all the height of the shock wave, the thickness of the boundary layer and the pressure on the plate larger than those in the case of no injection. On the contrary, in the case of suction no remarkable changes both in the shock wave and the pressure on the plate can be seen, and only the velocity profile in the boundary layer is affected by the suction. These results are deduced by calculating only the leading term of each quantity. In addition, the results of the present paper are restricted by assumptions that the plate is thermally insulated, $P_r = 1$, and $C_p = \text{const}$.

In conclusion, the author would like to express his gratitude to Prof. S. Uchida for his kind suggestion and valuable discussions during the course of the present investigation.

References

1) L. Lees, and R. F. Probstein, Princeton Univ. Aero. Engi. Labo. Rep. 195, 1952.
2) T. Y. Li, and H. T. Nagamatsu, Contract No. PA-04-495-Ord 19, Memo. No. 1314, 1930, GALCIT Pasadena, California, 1955.
3) K. Stewartson, Proc. Cambridge Phil. Soc. **51** (1955) 202; J. Aero. Sci. **22** (1955) 303.
4) R. H. Korkegi, J. Aero. Sci. **23** (1956) 97.

JOURNAL OF THE PHYSICAL SOCIETY OF JAPAN Vol. 12, No. 2, FEBRUARY, 1957

Experimental Studies on Laminar Sub-layer in Turbulent Boundary Layer involving Separation

By Yutaka SHIGEMITSU

Transportation Technical Research Institute, Tokyo

(Received July 30, 1956)

Observations were made on the mean and fluctuational velocities of the flow near a wall in turbulent boundary layer with non-zero pressure gradient. The edge of the sub-layer was defined as the maximum-point of the u-distribution curve. Important results obtained are as follows (suffixes 1 and 0 denoting here the values at the edge of the sub-layer and just outside the boundary layer): (i) In the field with constant pressure the curves of $\overline{U}/\overline{U}_1$ versus y/δ_1 are similar to those in the field with a fixed value of $\overline{U}_1\delta_1/\nu$ equal to about 165, indicating that the well-known relation between $\overline{U}/U_\tau$ and yU_τ/ν holds near the wall, U_τ being the frictional velocity; (ii) The curve of $\overline{U}/\overline{U}_1$ varies in such a manner that $\partial^2(\overline{U}/\overline{U}_1)/\partial(y/\delta_1)^2$ increases with dP_0/dx near the wall; (iii) The laminar sub-layer persists until the boundary layer separates and the separation of the sub-layer seems to be equivalent to turbulent separation phenomenon.

§ 1. Introduction

One of the important purposes of the investigation of turbulent boundary layer is to search for either theoretically or experimentally, the relation between the mean velocity distribution across the layer and the effect of pressure gradient of main stream. As is well known, the logarithmic law describes the mean velocity distribution approximately in the case of no pressure gradient. Observation of the mean velocity distribution in many cases in which there exists pressure gradient shows that the effect of pressure gradient seems to be conspicuous in the flow remote from a wall. As pointed out by Ludieg and Tillmann,[1] however, the effect of a wall is large in its vicinity and the logarithmic law can well be applied there even in the case of non-zero pressure gradient.

On the other hand, since the pioneer work by T. E. Stanton[2] it has been widely believed that in the immediate vicinity of a wall in turbulent boundary layer there exists a region where the effect of molecular viscosity is very strong, and such a region has been called generally laminar sub-layer. The above descriptions are concerned with the turbulent region of the turbulent boundary layer above the laminar sub-layer. It is known that in the laminar sub-layer with constant pressure, the velocity distribution is linear and the logarithmic law in turbulent region cannot be extended either logically or experimentally into the laminar sub-layer. As for the mechanism of this sub-layer, K. Suyehiro[3] proposed an important suggestion, based upon the conception of stability of Couette flow, that the Reynolds number at the edge of sub-layer $\overline{U}_1\delta_1/\nu$ is constant (suffix 1 denoting the value at the edge of the laminar sub-layer). Althouth this characteristic feature has been ascertained experimentally, yet it leads to a troublesome result that the logarithmic and linear velocity distributions in the two regions develop independently, and therefore the whole velocity distribution in the boundary layer has no similarity character even in the case of constant pressure. We consider that this is a significant character which should not be overlooked when we study the turbulent boundary layer in general case. To search for the similarity character in turbulent region in the case of flow with non-zero pressure gradient, F. H. Clauser[4] has made an important investigation. However, the mechanism of flow in the laminar sublayer is different from that in turbulent region, and it is quite questionable whether the linear velocity distribution in the laminar sub-layer may not be affected by pressure gradient as in the case of flow just above the sub-layer, or whether there may be another similarity law prescribing its effect apart from that in turbulent region.

In connexion with this problem the writer has attempted[5], a few years ago, to develop Suyehiro's supposition into the general case of turbulent boundary layer with non-zero pressure gradient and to formulate it mathematically. According to these interpretations the laminar sub-layer is one type of viscous flow under its lower critical condition of stability being affected by the Reynolds stress outside the layer, and to characterize the effect of pressure gradient in the laminar sub-layer we have introduced such a parameter $\lambda=\frac{-1}{\rho\nu}\frac{dP_0}{dx}\frac{\delta_1^2}{\bar{U}_1}$ where suffix 0 means the value in the main flow. Important results obtained from this formulation are enumerated as follows: (i) In the case of constant pressure the mean velocity distribution in the sub-layer has approximately a similar curve of $\bar{U}/\bar{U}_1$ plotted against y/δ_1 for a constant Reynolds number $\bar{U}_1\delta_1/\nu$; (ii) In case when there exists non-zero pressure gradient both the value of $\bar{U}_1\delta_1/\nu$ and the functional form of $(\bar{U}/\bar{U}_1)(y/\delta_1\}$ vary as the parameter λ; (iii) The function $(\bar{U}/\bar{U}_1)(y/\delta_1)$ has such a character that $\partial^2(\bar{U}/\bar{U}_1)/\partial(y/\delta_1)^2$ has negative, zero or positive value near $y/\delta_1=0$ according as the value of λ is positive, zero or negative; (iv) There is a negative critical value λ_c at which the value of $\partial\bar{U}/\partial y$ vanishes at the wall. Based upon these interpretations we can also develop[6] the decaying similarity law of isotropic turbulence or of turbulent wake into non-decaying form in turbulent boundary layer.

In order to assert the validity of these results, however, more experimental verifications are needed. So far, there have been only few measurements on the laminar sub-layer, especially for the case of pressure gradient. As will be mentioned later, the thickness δ_1 of the sub-layer becomes too small for usual Reynolds numbers, and the previous observations concerning the turbulent boundary layer have been carried out for such cases. Unless the undisturbed velocity is sufficiently low it becomes very difficult to survey the state of flow in the laminar sub-layer. From this point of view, we have carried out observations on the mean and fluctuational velocities in the laminar sub-layer with non-zero pressure gradient, by making δ_1 to be about 0.4~1.0 mm for undisturbed velocities of 3~12 m/sec. In this paper, some observed results will be presented for the purpose of understanding the fundamental character of the laminar sub-layer in general case and checking, at the same time, the above-mentioned theoretical results.

§ 2. Preliminary Measurements

The experiment was conducted in a small-scale low-turbulence wind tunnel with the test section of 20 cm × 30 cm × 200 cm in our laboratory. Turbulence level $u_0/\bar{U}_0$ in the main flow is 0.01~0.05 per cent according as the mean speed $\bar{U}_0=1\sim30$ m/sec. A lacquered iron plate was placed horizontally near the floor, and a tripping wire of diameter of about 1 mm was stretched on the plate 30 cm downstream the leading edge so as to produce fully developed turbulent flow in the boundary layer. Measurements were made along the centre line of the plate. If necessary, pressure gradient was given along the plate by placing a curved wall on the ceiling, and in order to make the boundary layer separate steadily, a curved bluff body was placed at the end of the plate. The pressure distribution was measured by a small static-tube of diameter of about 1.5 mm which was slided on the plate. An example of the arrangements is shown in Fig. 1.

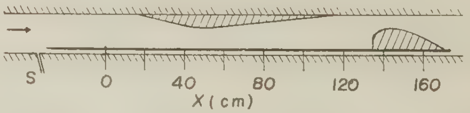

Fig. 1. Schematic diagram of arrangement of the equipments. S is a slit which serves to draw out the boundary layer upstream of the plate.

Measurements of the mean speed $\bar{U}$ and fluctuational velocity u near the plate in turbulent boundary layer were made by a hot-wire anemometer for various undisturbed velocities as well as for various pressure gradients. In the measurements of velocity distribution, the constant-temperature method was employed. The moved distance of the position of the hot-wire was found by the micro-screw reading, and the absolute value of its nearest location to the plate was measured by an optical height gauge which determined the distance between the tip of the hot-wire prong and its image on the lacquered plate.

It is well known that when a hot-wire anemometer is used near a solid wall, the heat loss at a given speed is probably affected by the presence of the wall. To avoid this effect as far as possible, the hot-wire temperature used was made not so high. In still air the said effect became perceptible at a distance of about 0.5 mm from the plate, but in moving air it became very small. At positions near the plate where the mean velocity was larger than 1 m/sec, the conspicuous effect was not found in the measurements, and any correction has not been made to the determination of the mean and fluctuational velocity distributions. Near the separation-point, however, this become remarkable owing to low mean speed, but these uncorrected values were rejected from the data. As an example of these measurements, that for the laminar boundary layer, the velocity distribution of which is known theoretically, is shown in Fig. 2.

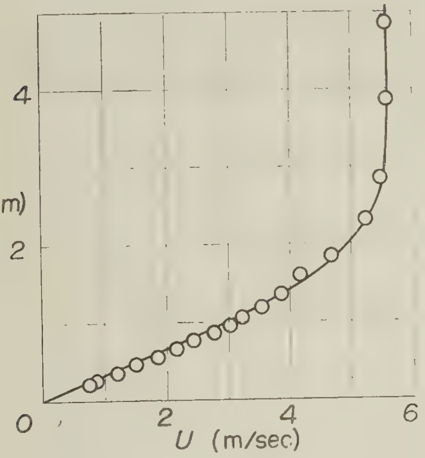

Fig. 2. Comparison of observed velocity distribution in the laminar boundary layer along a flat plate with the Blasius curve. The data were obtained upstream of the tripping wire in the case of no pressure gradient.

§ 3. Similarity Character in the Case of Flow along a Flat Plate

For the purpose of surveying general aspects of flow near a wall in turbulent boundary layer, a field of zero pressure gradient was first made along the plate by taking away curved obstacles from the test section. Fig. 3 shows an example of observed distributions of $\bar{U}$ and u near the plate. They both tend smoothly to zero at the wall. But, was widely observed in turbulent boundary layer flow or in turbulent pipe flow (non-decaying turbulence) it is significant that the fluctuational velocity u tends to zero rapidly through the maximum point very near the wall, while the mean velocity becomes zero gradually. Such a character has never been found in turbulent wake or free jet (decaying turbulence). We consider this maximum-point as an evidence of the appearance of the edge of the laminar sub-layer, where the stability of viscous flow begins to break down and small vortices are produced incessantly. Thus, it is supposed that the region of flow outside this point (near the mark D in Fig. 3) has a feature of complicated vortex chaos motion caused by these vortices. In the laminar sub-layer, however, the fluctuational velocity does not indicate vortex chaos motion, being only affected by vortex motions outside the sub-layer. The principal character of the sub-layer is determined by molecular viscosity even if effects of fluctuational velocity cannot be neglected near the edge. Fig. 4 shows variations of the fluctuational velocity u outside and inside the same laminar sub-layer as shown in Fig. 3. High-frequency harmonics outside the sub-layer tend to vanish in the layer by molecular viscosity, and the fluctuation becomes like

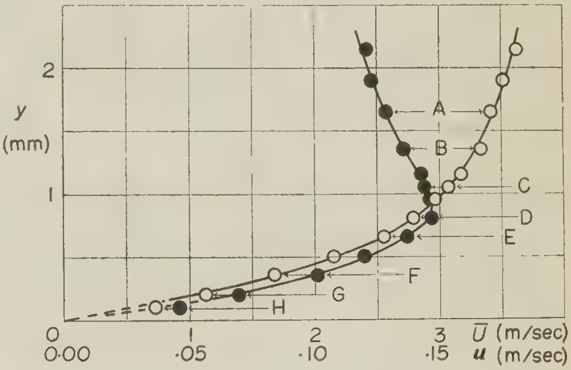

Fig. 3. Distributions of the mean velocity $\bar{U}$ indicated by the mark ○ and the fluctuational velocity u indicated by the mark ● near the flat plate in case when the main-stream velocity $\bar{U}_0$ is 5.30 m/sec.

the laminar-boundary-layer oscillation in case when the main flow has a moderate degree of turbulence. According to the above discussions, the thickness of the sub-layer can be defined as the distance of the maximum-point of **u**-distribution curve from the wall, and therefore other outer boundary conditions are easily surveyed experimentally.

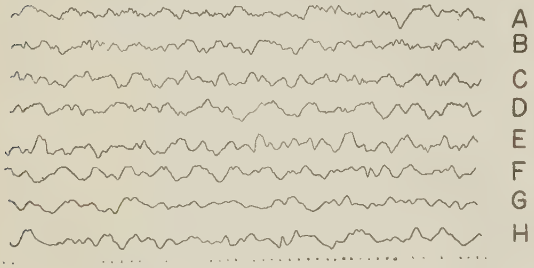

Fig. 4. Oscillograph records of u-fluctuation near the plate. States of flow are the same as in Fig. 3, marks A, B, $\cdots$ indicating the corresponding positions of hot-wire and time-marks being 0.01 second apart.

As mentioned in §1, $\overline{U}_1\delta_1/\nu$ is considered to be constant in the case of zero pressure gradient under consideration. Through several series of measurements for various undisturbed velocities ranging from 3 to 12 m/sec, this constant value was ascertained to be about 165, and no systematic variation of the value due to Reynolds number could be detected. These values are indicated in Fig. 5 with corresponding values of δ_1. As another boundary condition prescribing the effect of Reynolds shearing stress outside the sub-layer,

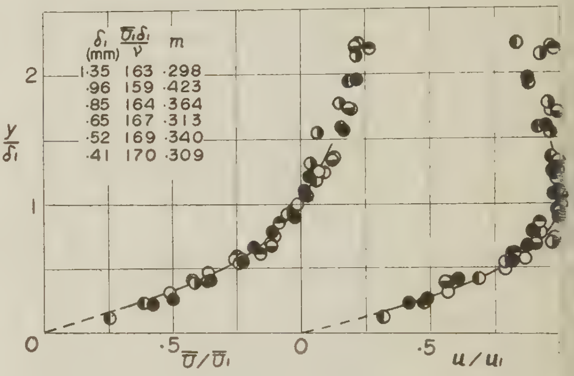

Fig. 5. Constancy of the Reynolds number $\overline{U}_1\delta_1/\nu$ at the edge of the laminar sub-layer and similarity character in $\overline{U}$- and **u**-distributions in the case of flow along a flat slate. Marks ●, ○, ◕, ◑, ⊖ and ◓ show respectively the observed values in cases when the thickness δ_1 of the sub-layer was 1.35, 0.96, 0.85, 0.65, 0.52 and 0.41mm respectively.

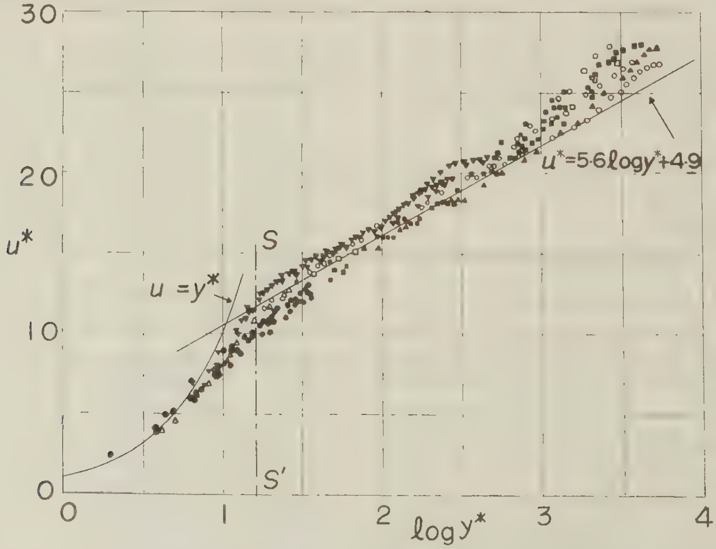

Fig. 6. Universal velocity distribution in turbulent boundary layer along a flat plate. The mark ● shows evaluated values from the data in Fig. 5. Other marks correspond to the observed values by several investigators:

○ Ludwieg-Tillmann, ■ Schultz-Grunow, □ Freemann,
▲ Klevanoff-Diehl, △ Klevanoff, ▼ Tani-Hama.

SS′ indicates the position of the maximum-point in **u**-distribution curve in our data corresponding to $\overline{U}_1\delta_1/\nu=165$.

variation of the value of the quantity $(\partial\overline{U}/\partial y)_1(\delta_1/\overline{U}_1)(=m)$ is important. Some of the observed values of this quantity are shown in Fig. 5. Theoretical estimation of the value of this quantity seems to be very difficult.

As mentioned in § 1, the laminar sub-layer in the present case of zero pressure gradient is considered to have a similarity character approximately. To survey it experimentally, the values of $\overline{U}/\overline{U}_1$ and $\boldsymbol{u}/\boldsymbol{u}_1$ were plotted against y/δ_1 in Fig. 5. It will be seen from this figure that no deviation from the similitude in $\overline{U}$- and $\boldsymbol{u}$-distributions can be detected experimentally. It is well known that when u^* and y^* are taken respectively as $\overline{U}/U_\tau$ and yU_τ/ν where $U_\tau=\sqrt{\nu(\partial\overline{U}/\partial y)_{y=0}}$, there exists a universal relation between them in the turbulent boundary layer with a constant pressure. In our notations they can be written as:

$$u^*=\sqrt{\frac{c}{\alpha}}\frac{\overline{U}}{\overline{U}_1}\,,\qquad y^*=\sqrt{c\alpha}\,\frac{y}{\delta_1}\,,\qquad (3.1)$$

where $c=\overline{U}_1\delta_1/\nu$ and $\alpha=(\partial\overline{U}/\partial y)_{y=0}(\delta_1/\overline{U}_1)$. Then, the similarity character of the curve of $\overline{U}/\overline{U}_1$ versus y/δ_1 subject to $\overline{U}_1\delta_1/\nu=c$ gives rise to the universal velocity distribution $u^*(y^*)$ in the laminar sub-layer. In our data the values of U_τ are estimated by tangents at the wall in $\overline{U}$-distribution curves, and these representations are shown in Fig. 6 compared with other observed values in the laminar sub-layer and in the turbulent region.

§ 4. Variation of Similitude with a Pressure Gradient

It is important that in the case of constant pressure, the observed similarity character of the curve $\overline{U}/\overline{U}_1$ versus y/δ_1 subject to $\overline{U}_1\delta_1/\nu=c$ gives rise to the universal $u^*\sim y^*$ relation in the laminar sub-layer and at the same time it belongs to the special case of $\lambda=0$ in our similarity character mentioned in § 1 (ii). In the case of non-zero pressure gradient the interrelation between dP_0/dx and the form of $u^*(y^*)$-curve has not been clarified in the whole turbulent region, besides the fact that just outside the sub-layer the logarithmic law is not affected by dP_0/dx. Then, in the laminar sub-layer the effects of dP_0/dx will be surveyed experimentally in the extended form of our similarity character, by which the form of $\overline{U}/\overline{U}_1$ versus y/δ_1 and the value of $\overline{U}_1\delta_1/\nu$ are determined uniquely by the parameter λ.

Experimental equipments to produce non-zero pressure gradient along the plate are as mentioned in § 2. Two sets of curved walls on the ceiling were used under several undisturbed velocities. For instance, when the

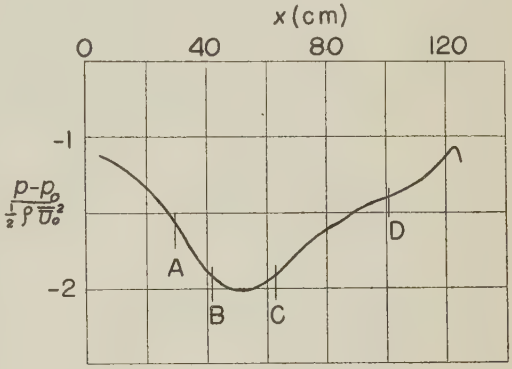

Fig. 7. Pressure distribution along the centre line on the flat plate in the same arrangement of equipments as shown in Fig. 1, with undisturbed velocity $\overline{U}_0=11.51$ m/sec upstream of the slit S. The values of abscissa are the same as in Fig. 1.

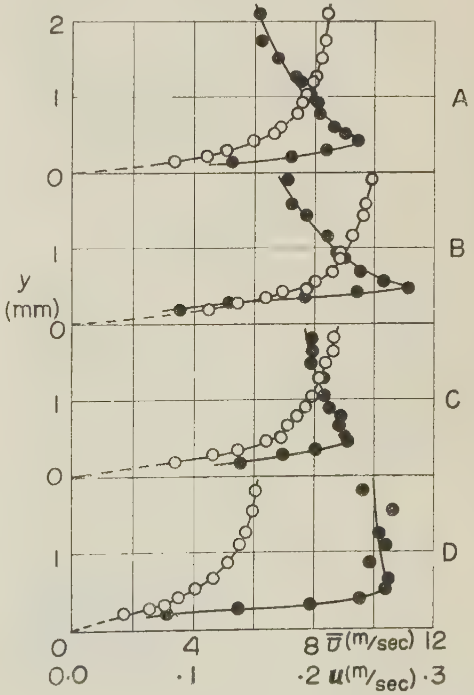

Fig. 8. Distributions of the mean velocity indicated by the mark ○ and the fluctuational velocity $\boldsymbol{u}$ indicated by the mark ● near the plate for various pressure gradients. The states of flow and positions of observation are the same as shown in Fig. 7.

velocity $\overline{U}_0$ was made to be 11.51 m/sec in the arrangement as shown in Fig. 1, the pressure distribution became as shown in Fig. 7. To get a general view of the effect of pressure gradient on the state of the sub-layer, $\overline{U}$- and u-distributions were observed at four sections A, B, C, D. They are shown in Fig. 8. It is seen that the curvature at the maximum-point of the u-distribution curve increases or decreases respectively according as the pressure gradient is negative or positive. Such a tendency has been partly observed previously[7]. This character is considered to be an evidence of the accumulation or diffusion of vortices, which are produced at the up-stream edge of laminar sub-layer and are carried respectively with approaching or detaching mean direction of the flow to the wall. At any rate, the thickness δ_1 of the layer can be determined by the measured u-distribution.

Since it is difficult to realize experimentally a pressure gradient with constant λ along the x-direction, the state of the sub-layer was surveyed with local values of λ under several undisturbed velocities and pressure gradients. Fig. 9 shows the distributions of observed values of $\overline{U}_1\delta_1/\nu$ and m plotted against λ. The observed points are fairly scattered because of the difficulty of experimental measurement, but general view of these empirical results may be understood. The scattering of the observed points of m may be caused to some extent by the character that it cannot be expressed essentially by the single parameter λ.

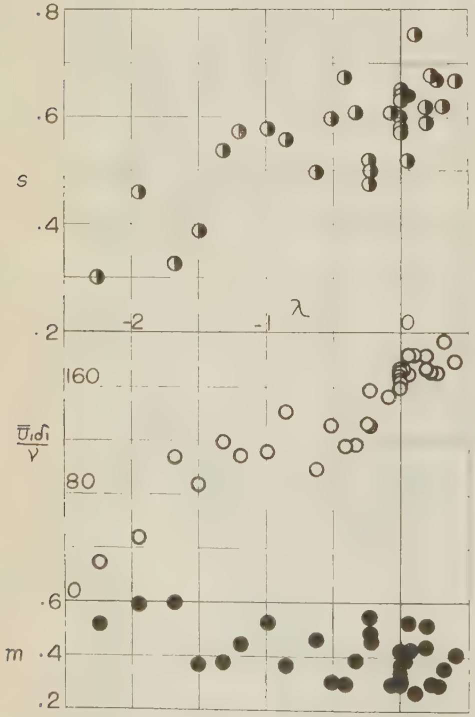

Fig. 9. Empirical results of the distributions of $\overline{U}_1\delta_1/\nu$ and $(\partial\overline{U}/\partial y)_1(\delta_1/\overline{U}_1)$ $(=m)$ plotted against the parameter λ, and an appearance of the effect of pressure gradient on the mean velocity distribution in the laminar sub-layer expressed in the parameter in (4.1).

Concerning the mean velocity distribution in the laminar sub-layer, any conspicuous variation did not appear as in the case of the u-distribution curve. But, observed precisely, the variation of the form of the curve of $\overline{U}/\overline{U}_1$ versus y/δ_1 with a pressure gradient was found. As a method to examine this effect quantitatively, a parameter s defined as:

$$s=\overline{U}(y')/\overline{U}_1\,,\qquad y'/\delta_1=0.4 \tag{4.1}$$

was introduced. Experimentally evaluated values of s are plotted against λ in Fig. 9. These data are still scattered, but a tendency that s decreases with a negative value of λ can be ascertained. In the immediate vicinity of the wall, the inertia force and Reynolds stress may be neglected, and the essential feature of the equations of motion is written as:

$$-\lambda \doteqdot \partial^2(\overline{U}/\overline{U}_1)/\partial(y/\delta_1)^2\,. \tag{4.2}$$

The above-observed character is important as the effect of pressure gradient in the laminar sub-layer subject to the theoretical relation (4.2). But, by the above measurements it cannot be proved whether the similarity character of the curve of $\overline{U}/\overline{U}_1$ versus y/δ_1 under a constant $\overline{U}_1\delta_1/\nu$ may exist in the case of constant λ, as observed in the case of constant pressure.

§ 5. States of Flow near the Turbulent Separation-point

It is important to investigate the mechanism of turbulent separation phenomena experimentally, but because of experimental difficulties many observed results have not been presented. In the arrangement of equipments as shown in Fig. 1, we can make the flow separate from the wall stationarily by keeping the vortex motion produced after the separation fixed in the corner of the plate and the bluff body. The picture in Fig. 10 shows an example of the flow pattern near the turbulent separation-point, where the pressure distribution along the centre line of the plate is also indicated. It is well recognized by these observations that the boundary layer separated clearly at a certain line on the plate. But, near this separation-line, it was very difficult to retain two-dimentionality of the mean flow because of the small scale of the test section, and the data are not necessarily reliable to be compared quantitatively with the two-dimentional theoretical results concerning the sub-layer.

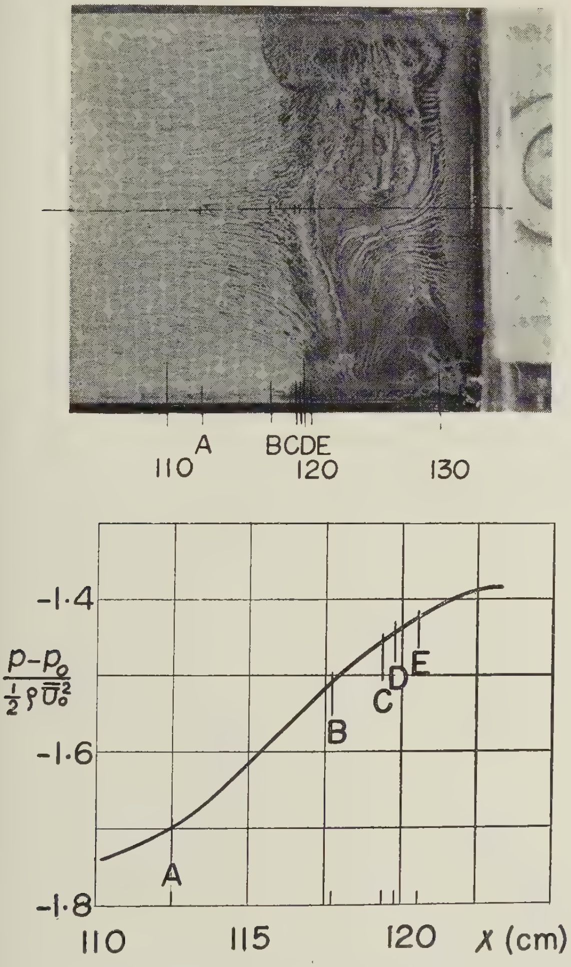

Fig. 10. States of flow near the turbulent separation-point. The flow pattern was obtained by kerosene-lampblack method in the flow with $\overline{U}_0=7.35$ m/sec upstream of the slit S, using an arrangement of equipments other than that is shown in Fig. 1. The pressure-distribution curve was measured in this state of flow where the abscissa x is measured in cm from the tripping wire.

Distributions of the mean and fluctuational velocities are shown in Fig. 11, which shows that the flow separates near the position D and the distributions at E are those of the back flow. From $\boldsymbol{u}$- and $\overline{U}$-distribution curves near the wall at A, B, C, it may be said that the laminar sub-layer exists until the boundary layer separates and the separation of the laminar sub-layer itself tells turbulent separation phenomenon. It is an important qualitative result of the present observations, but owing to the lack of two-dimentionality we could not determine the critical value λ_c at which the laminar sub-layer separates from the wall.

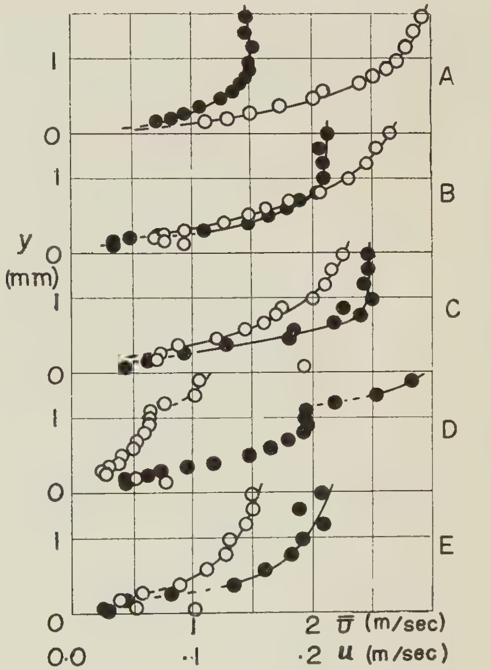

Fig. 11. Distributions of the mean velocity indicated by the mark ○ and the fluctuational velocity $\boldsymbol{u}$ indicated by the mark ● near the separation-line. The states of flow and positions of observation are the same as shown in Fig. 10. In this case the effect of heat loss by the wall appears clearly owing to the very low mean speed. Data in the cases D and E are not inserted in Fig. 9.

In conclusion, the author wishes to express

his sincere gratitude to Professor I. Tani for his valuable advice and also to members of the Turbulence Research Group in Japan for helpful discussions.

References

1) H. Ludwieg and W. Tillmann: NACA Tech. Memo. 1285 (1950).
2) T. E. Stanton, D. Marshall and C. N. Bryant: Proc. Roy. Soc. A **97** (1920) 413.
3) K. Suyehiro: J. Soc. Naval Architects, Japan **36** (1925) 87.
4) F. H. Clauser: J. Aero. Sci. **21** (1954) 91.
5) Y. Shigemitsu: J. Phys. Soc. Japan **4** (1949) 61, 123, 129.
6) Y. Shigemitsu: J. Phys. Soc. Japan **10** (1955) 890, §§ 15–18.
7) V. A. Sandborn and R. J. Slogar: NACA Tech. Note 3264 (1955).

JOURNAL OF THE PHYSICAL SOCIETY OF JAPAN Vol. 12, No. 2, FEBRUARY, 1957

Diffraction of Electromagnetic Waves by Ribbon and Slit. I

By Yûkichi NOMURA and Shigetoshi KATSURA
Department of Applied Science, Tôhoku University

(Received September 26, 1956)

Rigorous solutions are presented of the problem of diffraction of plane electromagnetic waves by an infinitely thin, perfectly conducting infinitely long ribbon and by an infinitely long slit in a plane conducting screen, where the plane of incidence is perpendicular to the edge of the ribbon or slit but arbitrary angle of incidence and polarization. The unique solution satisfying the edge condition is obtained from the electric and magnetic type Hertz vectors, each of which has one scalar component, by the method of expansion in the hypergeometric polynomial. The expressions of the scattering coefficient, transmission coefficient, electric current on the ribbon, electric field in the slit, electric field at the distant place are obtained as a function of $ka=2\pi a/\lambda$.

§ 1. Introduction

The diffraction of electromagnetic waves by an infinitely long ribbon and slit are solved by Mathieu functions by McLachlan[1], and by integral equation method by Bouwkamp[2], Hönl and others[14),15)] Müller and Westpfahl[16] and de Hoop[17]. Most of their results, however, are restricted to normal incidence, and still far from numerical computation. Here we want to solve this problem in case where the plane of incidence is perpendicular to the edge of the ribbon or slit but arbitrary angle of incidence and polarization, by the expansion in hypergeometric polynomial. This method succeeds in many cases for problems of potential, vibration, and of wave propagation[3)–13)]. Particularly the former papers "Acoustic field by a vibrating source arbitrarily distributed on a plane circular disk[10]" and "Diffraction of electromagnetic waves by circular plate and circular hole[13]" are referred to I and II respectively.

In case of diffraction of electromagnetic field by circular plate and hole, the field is assumed to be derived by the electric type Hertz vector Π which has two scalar components Π_x and Π_y. In the present case the field is assumed to be derived by two Hertz vectors Π and Π^*, of electric type and magnetic type, each of which has one scalar component. Then the diffracted field is described in terms of Weber-Schafheitlin integrals with unknown coefficients, which are determined with the aid of hypergeometric polynomial expansion. In this method the expression of scattering cross section, transmission coefficient, electric current on the ribbon, electric field in the slit, electric field at the distant place are obtained. The numerical results and discussions will be reported in the subsequent papre.

In case of normal incidence our results agree to the work of Bouwkamp[2] and others[16],[17]. Our method, however, has advantage to be able to solve other kind of problems which cannot be solved by other method[3]-[9].

The theory of ribbon and slit corresponds each other by Babinet principle, so the formula for a ribbon and a slit are listed in the left and right side respectively.

§ 2. General Solutions

We consider an infinitesimally thin perfectly conducting ribbon or infinitesimally thin perfectly conducting screen of infinite extent with a slit. A rectangular coordinate system is chosen so that the ribbon or screen lies in the xy-plane and their edge is given by $y=\pm a$. We consider a plane wave incident from the negative half space, with its plane of incidence yz plane, angle of incidence α. The electromagnetic field of the incident wave (i) and the reflected wave (r) is described by

Case of ribbon

$$E^{(i)}=(E_2,\ -E_1\cos\alpha,\ E_1\sin\alpha)\times\exp(-ikz\cos\alpha-iky\sin\alpha)\ ,$$

$$H^{(i)}=\frac{k}{\mu\omega}(E_1,\ E_2\cos\alpha,\ -E_2\sin\alpha)\times\exp(-ikz\cos\alpha-iky\sin\alpha)\ ,$$

for all space.

Case of slit

$$\left.\begin{aligned}E^{(i)}&=(E_1,\ -E_2\cos\alpha,\ E_2\sin\alpha)\times\exp(-ikz\cos\alpha-iky\sin\alpha)\ ,\\ H^{(i)}&=\frac{k}{\mu\omega}(E_2,\ E_1\cos\alpha,\ -E_1\sin\alpha)\times\exp(-ikz\cos\alpha-iky\sin\alpha)\ ,\\ E^{(r)}&=(-E_1,\ E_2\cos\alpha,\ E_2\sin\alpha)\times\exp(ikz\cos\alpha-iky\sin\alpha)\ ,\\ H^{(r)}&=\frac{k}{\mu\omega}(E_2,\ E_1\cos\alpha,\ E_1\sin\alpha)\times\exp(ikz\cos\alpha-iky\sin\alpha)\ .\end{aligned}\right\}\quad(2.1)$$

for negative half space.

Here $k=2\pi/\lambda$ is the wave number, the harmonic time dependence $\exp i\omega t$ being omitted throughout. The electromagnetic field is assumed to be derived in terms of the electric type Hertz vector and magnetic type Hertz vector both of which has only x-component.

$$E=\text{rot rot}\ \Pi-i\mu\omega\ \text{rot}\ \Pi^*\ ,\qquad H=i\varepsilon\omega\ \text{rot}\ \Pi+\text{rot rot}\ \Pi^*\ ,$$

$$\left.\begin{aligned}E&=-i\mu\omega\ \text{rot}\ \Pi+\text{rot rot}\ \Pi^*\ ,\\ H&=\text{rot rot}\ \Pi+i\varepsilon\omega\ \text{rot}\ \Pi^*\ ,\end{aligned}\right\}\quad(2.2)$$

$$\Pi=(f^{(i)}+f,\ 0,\ 0)\ ,\qquad \Pi^*=\sqrt{\varepsilon/\mu}\,(f^{*(i)}\mp f^*,\ 0,\ 0)\ .$$

where the upper and lower sign refers to positive and negative z respectively.

$$\left.\begin{aligned}\Pi&=\sqrt{\varepsilon/\mu}\,(-f,\ 0,\ 0) && (z>0)\\ &=\sqrt{\varepsilon/\mu}\,(f^{(i)}+f^{(r)}+f,\ 0,\ 0) && (z<0)\ ,\\ \Pi^*&=(f^*,\ 0,\ 0) && (z>0)\\ &=(f^{*(i)}+f^{*(r)}+f^*,\ 0,\ 0) && (z<0)\ .\end{aligned}\right\}\quad(2.3)$$

The Hertz vectors of the incident and reflected waves are given by

$$f^{(i)}=\frac{E_2}{k^2}e^{-ikz\cos\alpha-iky\sin\alpha}\ ,\qquad f^{*(i)}=\frac{E_1}{k^2}e^{-ikz\cos\alpha-iky\sin\alpha}\ .$$

$$\left.\begin{aligned}f^{(i)}&=\frac{E_2}{k^2}e^{-ikz\cos\alpha-iky\sin\alpha}\ ,\\ f^{*(r)}&=\frac{E_2}{k^2}e^{ikz\cos\alpha-iky\sin\alpha}\ ,\\ f^{*(i)}&=\frac{E_1}{k^2}e^{-ikz\cos\alpha-iky\sin\alpha}\ ,\\ f^{*(r)}&=-\frac{E_1}{k^2}e^{ikz\cos\alpha-iky\sin\alpha}\ ,\end{aligned}\right\}\quad(2.4)$$

The Hertz vector of the diffracted field is assumed to be given by

$$\left.\begin{aligned} f&=\frac{E_2}{k^2}\left(\sum_{n=0}^{\infty}A_nS_n^{-1/2}(y,z)+\sum_{n=0}^{\infty}B_nS_n^{1/2}(y,z)\right)\cdot\\ f^*&=\frac{E_1}{k^2}\cos\alpha\left(\sum_{n=0}^{\infty}A_n^*S_n^{*-1/2}(y,z)+\sum_{n=0}^{\infty}B_n^*S_n^{*1/2}(y,z)\right),\end{aligned}\right\}\tag{2.5}$$

where

$$\left.\begin{aligned} S_n^{m}(y,z)&=\sqrt{\frac{y}{a}}\int_0^{\infty}\frac{\sqrt{\xi}\,J_m(y\xi/a)\,J_{2n+m+1/2}(\xi)}{\sqrt{\xi^2-\gamma^2}}\exp\left(\mp(\xi^2-\gamma^2)^{1/2}\frac{z}{a}\right)d\xi\,,\\ S_n^{*m}(y,z)&=\sqrt{\frac{y}{a}}\int_0^{\infty}\frac{J_m(y\xi/a)\,J_{2n+m+3/2}(\xi)}{\sqrt{\xi}}\exp\left(\mp(\xi^2-\gamma^2)^{1/2}\frac{z}{a}\right)d\xi\,,\end{aligned}\right\}\tag{2.6}$$

where

$$\gamma=ka\,,\qquad m=\pm\tfrac{1}{2}\,.$$

Here each of $S_n^{\pm1/2}(y,z)$ and $S_n^{*\pm1/2}(y,z)$ is a solution of the two-dimensional wave equation $\partial^2\phi/\partial y^2+\partial^2\phi/\partial z^2+k^2\phi=0$. The solution with superscript $m=-\frac{1}{2}$ is an even solution and that with $m=\frac{1}{2}$ is an odd solution of y respectively. $\mp$ sign in the exponential corresponds to $z\gtrless0$ respectively.

Let z derivative of f and f^* be $\mp g$ and $\mp g^*$, then

$$\left.\begin{aligned} g&=\frac{E_2}{k^2a}\left(\sum_{n=0}^{\infty}A_nT_n^{-1/2}(y,z)+\sum_{n=0}^{\infty}B_nT_n^{1/2}(y,z)\right),\\ g^*&=\frac{E_1\cos\alpha}{k^2a}\left(\sum_{n=0}^{\infty}A_n^*T_n^{*-1/2}(y,z)+\sum_{n=0}^{\infty}B_n^*T_n^{*1/2}(y,z)\right),\end{aligned}\right\}\tag{2.7}$$

where

$$\left.\begin{aligned} T_n^{m}(y,z)&=\sqrt{\frac{y}{a}}\int_0^{\infty}\sqrt{\xi}\,J_m(y\xi/a)\,J_{2n+m+1/2}(\xi)\exp\left(\mp(\xi^2-\gamma^2)^{1/2}\frac{z}{a}\right)d\xi\,,\\ T_n^{*m}(y,z)&=\sqrt{\frac{y}{a}}\int_0^{\infty}\frac{\sqrt{\xi^2-\gamma^2}\,J_m(y\xi/a)\,J_{2n+m+3/2}(\xi)}{\sqrt{\xi}}\exp\left(\mp(\xi^2-\gamma^2)^{1/2}\frac{z}{a}\right)d\xi\,.\end{aligned}\right\}\tag{2.8}$$

$S_n^{*\mp1/2}(y,0)$ and $T_n^{\pm1/2}(y,0)$ are Weber-Schafheitlin's integrals, and have the property to become zero for $y\geq a$. By the use of this property several problems of potentials, vibrations, and wave equations have been solved[3)–13)]. Then it is found that on the plane $z=0$:

the electric and magnetic field of the diffracted wave for $y>a$, are continuous	the tangential component of the resultant electric field and the normal component of the resultant magnetic field are zero for $y>a$ (perfectly conducting screen). The tangential component of the resultant electric field and the normal component of the resultant magnetic field are continuous for $y<a$.
The condition for the conducting plate, that the resultant tangential component of electric field and the resultant normal component of the magnetic field are zero for $y<a$, is expressed by	The other condition for the slit, that the tangential component of the resultant magnetic field and the normal component of the resultant electric field† are continuous for $y<a$ is expressed by

$$f+f^{(i)}=0\tag{2.9}$$

---

† p. 287 in II, the second and the fourth lines from the bottom in the right hand side part, electric should be read magnetic, and magnetic should be read electric.

and

$$g^*+\partial f^{*(i)}/\partial z=0 \tag{2.10}$$

for $y<a$, $z=0$. (2.9) and (2.10) are rewritten by

$$\left.\begin{aligned} &\sum_{n=0}^{\infty} A_n S_n^{-1/2}(y,\,0)=-\cos(ky\sin\alpha)\,, \\ &\sum_{n=0}^{\infty} B_n S_n^{1/2}(y,\,0)=i\sin(ky\sin\alpha) \end{aligned}\right\} \tag{2.11}$$

and

$$\left.\begin{aligned} &\sum_{n=0}^{\infty} A_n^* T_n^{*-1/2}(y,\,0)=ika\cos(ky\sin\alpha)\,, \\ &\sum_{n=0}^{\infty} B_n^* T_n^{*1/2}(y,\,0)=ka\sin(ky\sin\alpha)\,. \end{aligned}\right\} \tag{2.12}$$

Now we expand the both hand sides of (2.11) and (2.12) by the hypergeometric polynomials. By Appendix in II and by similar calculations,

$$J_m(p\sqrt{x})=x^{m/2}\sum_{\nu=0}^{\infty}(2m+4\nu+1)\frac{J_{m+2\nu+1/2}(p)}{\sqrt{p}}u_\nu{}^m(x) \tag{2.13}$$

$$=x^{m/2}\sum_{\nu=0}^{\infty}(2m+4\nu+3)\frac{J_{m+2\nu+3/2}(p)}{p^{3/2}}v_\nu{}^m(x)\,, \tag{2.14}$$

where

$$u_\nu{}^m(x)=x^{-m/2}\int_0^\infty\frac{J_m(\sqrt{x}\,\xi)J_{m+2\nu+1/2}(\xi)}{\sqrt{\xi}}d\xi$$

$$=\frac{\Gamma(m+\nu+\frac{1}{2})}{\sqrt{2}\,\nu!\,\Gamma(\nu+m+1)}x^{-m}(1-x)^{1/2}\frac{d^\nu}{dx^\nu}\{x^{m+\nu}(1-x)^{\nu-1/2}\} \tag{2.15}$$

and

$$v_\nu{}^m(x)=x^{-m/2}\int_0^\infty\sqrt{\xi}\,J_m(\sqrt{x}\,\xi)J_{m+2\nu+3/2}(\xi)d\xi$$

$$=\frac{\sqrt{2}\,\Gamma(m+\nu+3/2)}{\nu!\,\Gamma(m+\nu+1)}x^{-m}(1-x)^{-1/2}\frac{d^\nu}{dx^\nu}\{x^{m+\nu}(1-x)^{\nu+1/2}\} \tag{2.16}$$

and $x=(y/a)^2$. Thus the right hand sides of (2.11) and (2.12) are expanded.

Let

$$S_n^m(y,\,0)=\sum_{\nu=0}^{\infty}(2m+4\nu+1)G_{n\nu}^m u_\nu^m(x) \tag{2.17}$$

and

$$T_n^{*m}(y,\,0)=\sum_{\nu=0}^{\infty}(2m+4\nu+3)\,G_{n\nu}^{*m}v_\nu^m(x)\,, \tag{2.18}$$

then

$$G_{n\nu}^m=\int_\gamma^\infty\frac{J_{2n+m+1/2}(\xi)J_{2\nu+m+1/2}(\xi)}{(\xi^2-\gamma^2)^{1/2}}d\xi$$

$$-i\int_0^\gamma\frac{J_{2n+m+1/2}(\xi)J_{2\nu+m+1/2}(\xi)}{(\gamma^2-\xi^2)^{1/2}}d\xi\,, \tag{2.19}$$

$$G_{n\nu}^{*m}=\int_\gamma^\infty\frac{(\xi^2-\gamma^2)^{1/2}J_{2n+m+3/2}(\xi)J_{2\nu+m+3/2}(\xi)}{\xi^2}d\xi$$

$$+i\int_0^\gamma\frac{(\gamma^2-\xi^2)^{1/2}J_{2n+m+3/2}(\xi)J_{2\nu+m+3/2}(\xi)}{\xi^2}d\xi\,. \tag{2.20}$$

Substitution of (2.13) (2.14) (2.17) (2.18) with (2.19) and (2.20) into (2.11) and (2.12) gives

$$\left.\begin{aligned} A_n &= -\sqrt{\pi/2}\sum_{\nu=0}^{\infty} X_{n\nu} J_{2\nu}(\gamma\sin\alpha)\,, \\ B_n &= i\sqrt{\pi/2}\sum_{\nu=0}^{\infty} Y_{n\nu} J_{2\nu+1}(\gamma\sin\alpha)\,, \\ A_n^* &= i\gamma\sqrt{\pi/2}\sum_{\nu=0}^{\infty} X_{n\nu}^* \frac{J_{2\nu+1}(\gamma\sin\alpha)}{\gamma\sin\alpha}\,, \\ B_n^* &= \gamma\sqrt{\pi/2}\sum_{\nu=0}^{\infty} Y_{n\nu}^* \frac{J_{2\nu+2}(\gamma\sin\alpha)}{\gamma\sin\alpha}\,. \end{aligned}\right\} \tag{2.21}$$

where $X_{n\nu}$, $Y_{n\nu}$, $X_{n\nu}^*$ and $Y_{n\nu}^*$ are inverse matrices of $G_{n\nu}^{-1/2}$, $G_{n\nu}^{1/2}$, $G_{n\nu}^{-*1/2}$ and $G_{n\nu}^{*1/2}$ respectively, that is

$$\left.\begin{aligned} &\sum_{\nu=0}^{\infty} G_{\nu n}^{-1/2} X_{\nu s} = \delta_{sn}\,, && \sum_{\nu=0}^{\infty} G_{\nu n}^{1/2} Y_{\nu s} = \delta_{sn}\,, \\ &\sum_{\nu=0}^{\infty} G_{\nu n}^{*-1/2} X_{\nu s}^* = \delta_{sn}\,, && \sum_{\nu=0}^{\infty} G_{\nu n}^{*1/2} Y_{\nu s}^* = \delta_{sn}\,. \end{aligned}\right\} \tag{2.22}$$

where δ_{sn} is Kronecker's symbol.

In case of normal incidence,

$$\left.\begin{aligned} A_n &= -\sqrt{\pi/2}\,X_{n0}\,, & B_n &= 0\,, \\ A_n^* &= \frac{i\gamma}{2}\sqrt{\pi/2}\,X_{n0}^*\,, & B_n^* &= 0\,. \end{aligned}\right\} \tag{2.23}$$

The solutions (2.5) with coefficients (2.21) by (2.22) thus determined, satisfies the edge condition (Cf. § 5).

§ 3. Calculation of $G_{n\nu}^m$ and $G_{n\nu}^{*m}$

Imaginary part of $G_{n\nu}^m$ and $G_{n\nu}^{*m}$ are given by I (15) and II (32). Results for the real part of $G_{n\nu}^m$ in the former papers are not valid for half integer of m. Here we calculate the real part of $G_{n\nu}^{\mp 1/2}$.

Write $2\nu+m+\frac{1}{2}=\alpha$, $2n+m+\frac{1}{2}=\beta$. The integral representation of the product of the Bessel functions is substituted and the integral representation by Γ-function is used, then

$$\mathscr{R}\,G_{n\nu}^m = \int_\gamma^\infty \frac{J_\alpha(\xi)J_\beta(\xi)}{(\xi^2-\gamma^2)^{1/2}}\,d\xi \tag{3.1}$$

$$= \frac{2}{\pi}\int_0^{\pi/2} d\theta\,\cos(\alpha-\beta)\theta\,\frac{1}{2\pi i}\int_{-1/3-i\infty}^{-1/3+i\infty} ds\,\frac{\Gamma(-s)\cos^{\alpha+\beta+2s}\theta}{\Gamma(\alpha+\beta+s+1)}\int_\gamma^\infty d\xi\,\frac{\xi^{\alpha+\beta+2s}}{(\xi^2-\gamma^2)^{1/2}}\,. \tag{3.2}$$

The contour in s plane is shifted to the straightline from $-(\alpha+\beta)/2-1/3-i\infty$ to $-(\alpha+\beta)/2-1/3+i\infty$, and the integration over ξ and θ are carried out, then

$$= \sqrt{\pi/2}\,\frac{1}{2\pi i}\int_C \frac{\Gamma(-s)\Gamma(\alpha+\beta+2s+1)\Gamma(-(\alpha+\beta)/2-s)(\gamma/2)^{\alpha+\beta+2s}ds}{\Gamma(\alpha+\beta+s+1)\Gamma(\alpha+s+1)\Gamma(\beta+s+1)\Gamma(-(\alpha+\beta)/2-s+\frac{1}{2})}\,, \tag{3.3}$$

where C is the contour consisted of the circumference in the right half plane and the straight line parallel to the imaginary axis at $s=-(\alpha+\beta)/2-1/3$ in the clock-wise direction. The poles of the integrand are simple poles at $s=-(\alpha+\beta)/2$, $-(\alpha+\beta)/2+1$, $\cdots$ -2, -1, and double poles at $s=0, 1, 2, \cdots$ The sum of the residues of the former is denoted by I_1, and the latter by I_2 respectively. As the residue of $\Gamma(-s)$ at $s=n$ is $-(-)^n/n!$ we have

$$I_1 = \frac{\sqrt{\pi}}{2}\sum_{\mu=0}^{(\alpha+\beta)/2-1}\frac{(-)^\mu}{\mu!}\,\frac{\Gamma((\alpha+\beta)/2-\mu)\Gamma(2\mu+1)(\gamma/2)^{2\mu}}{\Gamma((\alpha+\beta)/2+\mu+1)\Gamma((\alpha-\beta)/2+\mu+1)\Gamma((\beta-\alpha)/2+\mu+1)\Gamma(\frac{1}{2}-\mu)}\,, \tag{3.4}$$

$$I_2=\frac{\sqrt{\pi}}{2}\frac{1}{2\pi i}\int_C\frac{\pi}{\sin\pi s}\frac{\pi}{\sin\pi((\alpha+\beta)/2+s)}$$

$$\times\frac{\Gamma(\alpha+\beta+2s+1)(\gamma/2)^{\alpha+\beta+2s}}{\Gamma(1+s)\Gamma((\alpha+\beta)/2+s+1)\Gamma(\alpha+\beta+s+1)\Gamma(\alpha+\beta+1)\Gamma(\beta+s+1)\Gamma(-(\alpha+\beta)/2-s+\frac{1}{2})}$$

$$=(-)^{(\alpha+\beta)/2+1}\frac{\sqrt{\pi}}{2}\sum_{\mu=0}^{\infty}\left[\frac{d}{ds}\right.$$

$$\left.\times\frac{\Gamma(\alpha+\beta+2s+1)(\gamma/2)^{\alpha+\beta+2s}}{\Gamma(1+s)\Gamma((\alpha+\beta)/2+s+1)\Gamma(\alpha+\beta+s+1)\Gamma(\alpha+s+1)\Gamma(\beta+s+1)\Gamma(-(\alpha+\beta)/2-s+\frac{1}{2})}\right]_{s=\mu}$$

$$=(-)^{(\alpha+\beta)/2+1}\frac{\sqrt{\pi}}{2}\sum_{\mu=0}^{\infty}$$

$$\times\frac{\Gamma(\alpha+\beta+2\mu+1)(\gamma/2)^{\alpha+\beta+2\mu}}{\Gamma(1+\mu)\Gamma((\alpha+\beta)/2+\mu+1)\Gamma(\alpha+\beta+\mu+1)\Gamma(\alpha+\mu+1)\Gamma(\beta+\mu+1)\Gamma(-(\alpha+\beta)/2-\mu+\frac{1}{2})}$$

$$\times\left\{2\log\frac{\gamma}{2}+2\psi(\alpha+\beta+2\mu+1)-\psi(1+\mu)-\psi\left(\frac{\alpha+\beta}{2}+\mu+1\right)-\psi(\alpha+\beta+\mu+1)\right.$$

$$\left.-\psi(\alpha+\mu+1)-\psi(\beta+\mu+1)+\psi\left(-\frac{\alpha+\beta}{2}-\mu+\frac{1}{2}\right)\right\}. \tag{3.5}$$

where $\psi(z)=d\log\Gamma(z)/dz$.

Real part of $G_{n\nu}^{*m}$ can be calculated similary and the result is $(2\nu+m+3/2=\alpha,\ 2n+m+3/2=\beta)$

$$\mathscr{R}G_{n\nu}^{*m}=\int_{\gamma}^{\infty}\frac{(\xi^2-\gamma^2)^{1/2}J_\alpha(\xi)J_\beta(\xi)}{\xi^2}d\xi=I_1{}^*+I_2{}^*, \tag{3.6}$$

$$I_1{}^*=\frac{\sqrt{\pi}}{4}\sum_{\mu=0}^{(\alpha+\beta)/2-1}\frac{(-)^\mu}{\mu!}\frac{\Gamma((\alpha+\beta)/2-\mu)\Gamma(2\mu+1)(\gamma/2)^{2\mu}}{\Gamma(\mu+1+(\alpha-\beta)/2)\Gamma(\mu+1+(\beta-\alpha)/2)\Gamma(\mu+1+(\alpha+\beta)/2)\Gamma(-\mu+3/2)}, \tag{3.7}$$

$$I_2{}^*=(-)^{(\alpha+\beta)/2+1}\frac{\sqrt{\pi}}{4}\sum_{\mu=0}^{\infty}$$

$$\times\frac{\Gamma(\alpha+\beta+2\mu+1)(\gamma/2)^{\alpha+\beta+2\mu}}{\Gamma(\mu+1)\Gamma((\alpha+\beta)/2+\mu+1)\Gamma(\alpha+\mu+1)\Gamma(\beta+\mu+1)\Gamma(\alpha+\beta+\mu+1)\Gamma(-(\alpha+\beta)/2-\mu+3/2)}$$

$$\times\left\{2\log\frac{\gamma}{2}+2\psi(\alpha+\beta+2\mu+1)-\psi(\mu+1)-\psi\left(\frac{\alpha+\beta}{2}+\mu+1\right)\right.$$

$$\left.-\psi(\alpha+\mu+1)-\psi(\beta+\mu+1)-\psi(\alpha+\beta+\mu+1)+\psi\left(-\frac{\alpha+\beta}{2}-\mu+\frac{3}{2}\right)\right\}. \tag{3.8}$$

The first a few terms of $G_{n\nu}^{-1/2}$ and $G_{n\nu}^{*-1/2}$ are shown as follows.

$$G_{00}^{-1/2}=-\frac{1}{2}\left\{2\log\frac{\gamma}{2}-3\psi(1)+\psi\left(\frac{1}{2}\right)\right\}+\frac{1}{2}\left(\frac{\gamma}{2}\right)^2\left\{2\log\frac{\gamma}{2}+2\psi(3)-5\psi(2)+\psi\left(-\frac{1}{2}\right)\right\}$$

$$-\frac{9}{32}\left(\frac{\gamma}{2}\right)^4\left\{2\log\frac{\gamma}{2}+2\psi(5)-5\psi(3)+\psi\left(-\frac{3}{2}\right)\right\}+\cdots$$

$$-i\frac{\pi}{2}\left[1-4\left(\frac{\gamma}{2}\right)^2+9\left(\frac{\gamma}{2}\right)^4+\cdots\right],$$

$$G_{10}^{-1/2}=G_{01}^{-1/2}=-\frac{1}{8}\left(\frac{\gamma}{2}\right)^2\left\{2\log\frac{\gamma}{2}-2\psi(1)-\psi(2)+\psi\left(-\frac{1}{2}\right)\right\}$$

$$+\frac{1}{8}\left(\frac{\gamma}{2}\right)^4\left\{2\log\frac{\gamma}{2}+2\psi(5)-2\psi(4)-\psi(3)-2\psi(2)+\psi\left(-\frac{3}{2}\right)\right\}+\cdots$$

$$-i\frac{\pi}{2}\left[\frac{1}{4}\left(\frac{\gamma}{2}\right)^2-\frac{1}{4}\left(\frac{\gamma}{2}\right)^4+\cdots\right],$$

$$G_{11}^{-1/2}=\frac{1}{4}+\frac{1}{12}\left(\frac{\gamma}{2}\right)^2$$
$$-\frac{3}{64}\left(\frac{\gamma}{2}\right)^4\left\{2\log\frac{\gamma}{2}+\psi(5)-\psi(1)-3\psi(3)+\psi\left(-\frac{3}{2}\right)\right\}+\cdots$$
$$-i\frac{\pi}{2}\left[\frac{3}{32}\left(\frac{\gamma}{2}\right)^4+\cdots\right. \tag{3.9}$$

$$G_{00}^{*-1/2}=\frac{1}{2}+\frac{1}{4}\left(\frac{\gamma}{2}\right)^2\left\{2\log\frac{\gamma}{2}+\psi(3)-3\psi(2)+\psi\left(\frac{1}{2}\right)-\psi(1)\right\}$$
$$-\frac{1}{16}\left(\frac{\gamma}{2}\right)^4\left\{2\log\frac{\gamma}{2}+2\psi(5)-\psi(4)-3\psi(3)+\psi\left(-\frac{1}{2}\right)-\psi(2)\right\}+\cdots$$
$$+i\frac{\pi}{2}\left[\frac{1}{2}\left(\frac{\gamma}{2}\right)^2-\frac{1}{24}\left(\frac{\gamma}{2}\right)^4+\cdots\right],$$

$$G_{10}^{*-1/2}=G_{01}^{*-1/2}=-\frac{1}{24}\left(\frac{\gamma}{2}\right)^2$$
$$+\frac{1}{96}\left(\frac{\gamma}{2}\right)^4\left\{2\log\frac{\gamma}{2}+\psi(5)-\psi(4)-\psi(2)+\psi\left(-\frac{1}{2}\right)-\psi(1)-\psi(3)\right\}+\cdots$$
$$+i\frac{\pi}{2}\left[\frac{1}{48}\left(\frac{\gamma}{2}\right)^4+\cdots\right],$$

$$G_{11}^{*-1/2}=\frac{1}{6}-\frac{1}{48}\left(\frac{\gamma}{2}\right)^2-\frac{1}{320}\left(\frac{\gamma}{2}\right)^4+O(\gamma^6,\log\gamma)+iO(\gamma^6)\,. \tag{3.10}$$

The inversion of $G_{n\nu}^{-1/2}$ and $G_{n\nu}^{*-1/2}$ gives the series representation of $X_{n\nu}$, and $X_{n\nu}^*$. The first a few terms are given by

$$X_{00}=\frac{2}{-2\log\gamma/2-a_1-\pi i}+\cdots,$$
$$a_1=-3\psi(1)+\psi(1/2)=2C-2\log 2=-0.23188\,. \tag{3.11}$$

$$X_{00}^*=2-\left(\frac{\gamma}{2}\right)^2\left(2\log\frac{\gamma}{2}+a_2+\pi i\right)+\left(\frac{\gamma}{2}\right)^4\left[\frac{19}{240}+\frac{a_3}{4}+\frac{\pi^2}{2}+\frac{1}{2}\log\frac{\gamma}{2}\right.$$
$$\left.+\frac{1}{2}\left(2\log\frac{\gamma}{2}+a_2\right)^2+i\left\{\frac{\pi}{4}+2\pi\log\frac{\gamma}{2}+\pi a_2\right\}\right]+O(\gamma^6)\,,$$
$$X_{01}^*=X_{10}^*=\frac{1}{2}\left(\frac{\gamma}{2}\right)^2-\left(\frac{\gamma}{2}\right)^4\left\{\frac{3}{8}\log\frac{\gamma}{2}+\frac{a_4}{8}-\frac{1}{16}+\frac{a_2}{4}+\frac{3\pi i}{8}\right\}+O(\gamma^6)\,,$$
$$a_2=\psi(3)-3\psi(2)+\psi(1/2)-\psi(1)=2C-3/2-2\log 2=-1.73186\,,$$
$$a_3=2\psi(5)-\psi(4)-3\psi(3)+\psi(-1/2)-\psi(2)\,,$$
$$a_4=\psi(5)-\psi(4)-\psi(2)+\psi(-1/2)-\psi(1)-\psi(3)\,. \tag{3.12}$$

§ 4. Diffracted Field at Large Distances from the Ribbon

Each of Π and Π^* determined in § 2 satisfies the two-dimensional wave equation. We express Π and Π^* at a distant point by Green's function in two dimensions and values of Π and $\partial\Pi/\partial z$ on the ribbon,

$$\Pi=-\frac{i}{4}\int\left\{H_0^{(2)}(kR')\frac{\partial\Pi}{\partial n}-\Pi\frac{\partial}{\partial n}H_0^{(2)}(kR')\right\}dS'\,. \tag{4.1}$$

The same equation holds for Π^*. Here R' is the distance between the point $Q(y)$ on the ribbon and P at the distant point. The integration dS' is carried out on both sides of the ribbon, S_+ and S_-. Evidently

$$(\Pi)_{S_+}=(\Pi)_{S_-}=f\ , \qquad \left(\frac{\partial \Pi}{\partial n}\right)_{S_+}=\left(\frac{\partial \Pi}{\partial n}\right)_{S_-}=-g\ ,$$

$$\frac{\partial}{\partial n}H_0^{(2)}(kR')=-k\cos\theta H_1^{(2)}(kR')\ ,$$

hence

$$\Pi=-\frac{i}{2}\int_{-a}^{a}\frac{\partial \Pi}{\partial n}H_0^{(2)}(kR')dy\ , \tag{4.2}$$

$$\Pi^*=-\frac{ik}{2}\cos\theta\int_{-a}^{a}\Pi^* H_1^{(2)}(kR')dy\ , \tag{4.3}$$

where θ is the angle between z axis and the semi-straight line joining the origin and P. When $PQ=R$ is large enough,

$$\Pi=e^{3\pi i/4}\sqrt{\frac{2}{\pi}}\frac{E_2}{k^2a}\frac{e^{-ikR}}{\sqrt{kR}}\int_0^a e^{iky\sin\theta}\left\{\sum_{n=0}^{\infty}A_nT_n^{-1/2}(y,0)+\sum_{n=0}^{\infty}B_nT_n^{1/2}(y,\,0)\right\}dy\ . \tag{4.4}$$

Integration of y yields[†]

$$=e^{-\pi i/4}\sqrt{\frac{\pi}{2}}\frac{E_2}{k^2}\frac{e^{-ikR}}{\sqrt{kR}}A(\alpha,\,\theta)\ ,$$

where $A(\alpha,\,\theta)$ is a scattering amplitude of incident direction α and observation direction θ, and is given by

$$A(\alpha,\,\theta)=\sum_{n=0}^{\infty}\sum_{\nu=0}^{\infty}\{X_{n\nu}J_{2\nu}(\gamma\sin\alpha)J_{2n}(\gamma\sin\theta)+Y_{n\nu}J_{2\nu+1}(\gamma\sin\alpha)J_{2n+1}(\gamma\sin\theta)\}\ . \tag{4.5}$$

Similarly for Π^*,

$$\left.\begin{aligned}&-(\Pi^*)_{S_+}=(\Pi^*)_{S_-}=\sqrt{\varepsilon/\mu}\,f^*\ , \qquad \left(\frac{\partial \Pi^*}{\partial n}\right)_{S_+}=-\left(\frac{\partial \Pi^*}{\partial n}\right)_{S_-}\ ,\\ &\Pi^*=\sqrt{\frac{\varepsilon}{\mu}}e^{-\pi i/4}\sqrt{\frac{\pi}{2}}\frac{E_1}{k^2}\frac{e^{-ikR}}{\sqrt{kR}}A^*(\alpha,\,\theta)\ ,\end{aligned}\right\} \tag{4.6}$$

where

$$\begin{aligned}A^*(\alpha,\,\theta)=\gamma\cos\alpha\cdot\gamma\cos\theta\sum_{n=0}^{\infty}\sum_{\nu=0}^{\infty}\Bigg\{&X^*_{n\nu}\frac{J_{2\nu+1}(\gamma\sin\alpha)}{\gamma\sin\alpha}\frac{J_{2n+1}(\gamma\sin\theta)}{\gamma\sin\theta}\\ &+Y^*_{n\nu}\frac{J_{2\nu+2}(\gamma\sin\alpha)}{\gamma\sin\alpha}\frac{J_{2n+2}(\gamma\sin\theta)}{\gamma\sin\theta}\Bigg\}\ .\end{aligned} \tag{4.7}$$

When we neglect the smaller term, the electromagnetic field of the diffracted wave at distant point is given by

$$\left.\begin{aligned}&E_x=k^2\Pi_x\ , \qquad E_\theta=-k^2\sqrt{\mu/\varepsilon}\,\Pi_x^*\ , \qquad E_R=0\ ,\\ &H_x=k^2\Pi_x^*\ , \qquad H_\theta=k^2\sqrt{\varepsilon/\mu}\,\Pi_x\ , \qquad H_R=0\ ,\end{aligned}\right\} \tag{4.8}$$

[†] $\int_0^1 d\rho\int_0^\infty d\xi\cos(\rho\gamma\sin\alpha)\sqrt{\rho}\,\xi^{-1/2}J_{-1/2}(\xi)J_{2n+1}(\xi)=\sqrt{\frac{2}{\pi}}\frac{J_{2n+1}(\gamma\sin\alpha)}{\gamma\sin\alpha}$,

$\int_0^1 d\rho\int_0^\infty d\xi\cos(\rho\gamma\sin\alpha)\sqrt{\rho}\,\xi^{1/2}J_{-1/2}(\xi)J_{2n}(\xi)=\sqrt{\frac{2}{\pi}}J_{2n}(\gamma\sin\alpha)$,

$\int_0^1 d\rho\int_0^\infty d\xi\sin(\rho\gamma\sin\alpha)\sqrt{\rho}\,\xi^{-1/2}J_{1/2}(\xi)J_{2n+2}(\xi)=\sqrt{\frac{2}{\pi}}\frac{J_{2n+2}(\gamma\sin\alpha)}{\gamma\sin\alpha}$,

$\int_0^1 d\rho\int_0^\infty d\xi\sin(\rho\gamma\sin\alpha)\sqrt{\rho}\,\xi^{1/2}J_{1/2}(\xi)J_{2n+1}(\xi)=\sqrt{\frac{2}{\pi}}J_{2n+1}(\gamma\sin\alpha)$.

$|A(\alpha, \theta)|$ and $|A^*(\alpha, \theta)|$ give the relative field intensity at the distant point.

The energy flow from the surface of semi-cylinder of radius R is

$$W=\frac{\pi}{4}\sqrt{\frac{\varepsilon}{\mu}}\frac{1}{k}\mathscr{R}\{E_2^2|A(\alpha, \theta)|^2+E_1^2|A^*(\alpha, \theta)|^2\}\,. \tag{4.9}$$

The half of the scattering coefficient σ of the ribbon, which is equal to the transmission coefficient t of the slit, is given by

$$t=\frac{\sigma}{2}=\frac{\pi}{2}\frac{1}{\gamma\cos\alpha}\int_0^{\pi/2}\{\sin^2\psi|A(\alpha, \theta)|^2+\cos^2\psi|A^*(\alpha, \theta)|^2\}d\theta\,, \tag{4.10}$$

where $E_2=E\sin\psi$, $E_1=E\cos\psi$.

In case of electric type normal incidence ($\psi=\pi/2$, $\alpha=\pi/2$),

$$\begin{aligned}\frac{\sigma_2}{2}=t_2=\frac{\pi^2}{2\gamma}\Big[&\frac{1}{2}|X_{00}|^2+\Big\{-\frac{1}{2}|X_{00}|^2+\frac{1}{4}|X_{00}X_{10}|\Big\}\Big(\frac{\gamma}{2}\Big)^2\\&+3\Big\{\frac{1}{32}|X_{00}|^2-\frac{1}{12}|X_{00}X_{10}|+\frac{1}{192}|X_{00}X_{20}|+\frac{1}{64}|X_{20}|^2\Big\}\Big(\frac{\gamma}{2}\Big)^4+O(\gamma^6)\Big]\end{aligned} \tag{4.11}$$

$$=\frac{\pi^2}{\gamma}\frac{1}{(2\log(\gamma/2)+a_1)^2+\pi^2}+\cdots\,, \tag{4.12}$$

It is noted that t_2 tend to infinity when γ tend to zero.

In case of magnetic type normal incidence ($\psi=0$, $\alpha=\pi/2$),

$$\begin{aligned}\frac{\sigma_1}{2}=t_1=\frac{\pi^2\gamma^3}{32}\Big[&\frac{1}{4}|X_{00}^*|^2+\Big\{-\frac{1}{16}|X_{00}^*|^2+\frac{1}{48}|X_{00}^*X_{10}^*|\Big\}\Big(\frac{\gamma}{2}\Big)^2\\&+\Big\{\frac{5}{384}|X_{00}^*|^2-\frac{1}{96}|X_{00}^*X_{10}^*|+\frac{1}{1920}|X_{00}^*X_{20}^*|+\frac{1}{1152}|X_{10}^*|^2\Big\}\Big(\frac{\gamma}{2}\Big)^4+O(\gamma^6)\Big]\end{aligned} \tag{4.13}$$

$$=\frac{\pi^2\gamma^3}{32}\Big[1+\Big(\frac{\gamma}{2}\Big)^2\Big(-2\log\frac{\gamma}{2}-a_2-\frac{1}{4}\Big)+O(\gamma^4)\Big], \tag{4.14}$$

(4.14) is qualitatively similar to the transmission coefficient of circular plate or hole. (4.14) agrees with those obtained by Bouwkamp2) and others16)-17).

§ 5. Electromagnetic Field on the Ribbon and Slit

The electromagnetic field caused by the diffracted field on the ribbon and slit is given by

$$\left.\begin{array}{l|l}
E_x=k^2\Pi_x\,, & E_x=k^2\Pi_x^*\,,\\
E_y=-ik\sqrt{\dfrac{\mu}{\varepsilon}}\dfrac{\partial\Pi_x^*}{\partial z}\,, & E_y=-ik\sqrt{\dfrac{\mu}{\varepsilon}}\dfrac{\partial\Pi_x}{\partial z}\,,\\
E_z=ik\sqrt{\dfrac{\mu}{\varepsilon}}\dfrac{\partial\Pi_x^*}{\partial y}\,, & E_z=ik\sqrt{\dfrac{\mu}{\varepsilon}}\dfrac{\partial\Pi_x}{\partial y}\,,\\
H_x=\pm J_y=k^2\Pi_x^*\,, & H_x=k^2\Pi_x\,,\\
H_y=\mp J_z=ik\sqrt{\dfrac{\varepsilon}{\mu}}\dfrac{\partial\Pi_x}{\partial z}\,, & H_y=ik\sqrt{\dfrac{\varepsilon}{\mu}}\dfrac{\partial\Pi_x^*}{\partial z}\,,\\
H_z=-ik\sqrt{\dfrac{\varepsilon}{\mu}}\dfrac{\partial\Pi_x}{\partial y}\,. & H_z=-ik\sqrt{\dfrac{\varepsilon}{\mu}}\dfrac{\partial\Pi_x^*}{\partial y}\,.
\end{array}\right\} \tag{5.1}$$

Here the terms $\partial^2\Pi/\partial y^2$ and $\partial^2\Pi/\partial y\partial z$ do not appear and hence it is evident that the edge conditions are satisfied.

The surface current density due to the diffracted field and the incident field is

$$J_y=\sqrt{\frac{\varepsilon}{\mu}}E_1\Bigg[\mp e^{-iky\sin\alpha}-\sqrt{\frac{\pi}{2}}\cos\alpha$$
$$\times\left\{i\gamma\sum_{n=0}^{\infty}\sum_{\nu=0}^{\infty}X_{n\nu}^{*}\frac{J_{2\nu+1}(\gamma\sin\alpha)}{\gamma\sin\alpha}S_n^{*-1/2}(y,0)\right.$$
$$\left.+\gamma\sum_{n=0}^{\infty}\sum_{\nu=0}^{\infty}Y_{n\nu}^{*}\frac{J_{2\nu+2}(\gamma\sin\alpha)}{\gamma\sin\alpha}S_n^{*1/2}(y,0)\right\}\Bigg],$$

$$J_x=\sqrt{\frac{\varepsilon}{\mu}}E_2\Bigg[\mp\cos\alpha\, e^{-iky\sin\alpha}+\frac{i}{\gamma}\sqrt{\frac{\pi}{2}}$$
$$\times\left\{-\sum_{n=0}^{\infty}\sum_{\nu=0}^{\infty}X_{n\nu}J_{2\nu}(\gamma\sin\alpha)T_n^{-1/2}(y,0)\right.$$
$$\left.+i\sum_{n=0}^{\infty}\sum_{\nu=0}^{\infty}Y_{n\nu}J_{2\nu+1}(\gamma\sin\alpha)T_n^{1/2}(y,0)\right\}\Bigg],$$

Here the upper sign indicates the current density of the back surface of the ribbon and the lower sign indicates that of the front surface.

The electric field in the slit is

$$\left.\begin{aligned}
E_x&=E_1\cos\alpha\sqrt{\frac{\pi}{2}}\\
&\quad\times\left\{i\gamma\sum_{n=0}^{\infty}\sum_{\nu=0}^{\infty}X_{n\nu}^{*}\frac{J_{2\nu+1}(\gamma\sin\alpha)}{\gamma\sin\alpha}S_n^{*-1/2}(y,0)\right.\\
&\quad\left.+\gamma\sum_{n=0}^{\infty}\sum_{\nu=0}^{\infty}Y_{n\nu}^{*}\frac{I_{2\nu+2}(\gamma\sin\alpha)}{\gamma\sin\alpha}S_n^{*1/2}(y,0)\right\},\\
E_y&=-E_2\frac{i}{\gamma}\sqrt{\frac{\pi}{2}}\\
&\quad\times\left\{-\sum_{n=0}^{\infty}\sum_{\nu=0}^{\infty}X_{n\nu}J_{2\nu}(\gamma\sin\alpha)T_n^{-1/2}(y,0)\right.\\
&\quad\left.+i\sum_{n=0}^{\infty}\sum_{\nu=0}^{\infty}Y_{n\nu}J_{2\nu+1}(\gamma\sin\alpha)T_n^{1/2}(y,0)\right\},
\end{aligned}\right\}\tag{5.2}$$

where

$$\left.\begin{aligned}
S_n^{*-1/2}(y,0)&=\sqrt{\frac{2}{\pi}}\frac{1}{(2n+1)}(1-\rho^2)^{1/2}F\left(-n,\,n+1;\,\frac{1}{2};\,\rho^2\right),\\
S_n^{*1/2}(y,0)&=\sqrt{\frac{2}{\pi}}\rho(1-\rho^2)^{1/2}F\left(-n,\,n+2;\,\frac{3}{2};\,\rho^2\right),\\
T_n^{-1/2}(y,0)&=\sqrt{\frac{2}{\pi}}(1-\rho^2)^{-1/2}F\left(-n,\,n;\,\frac{1}{2};\,\rho^2\right),\\
T_n^{1/2}(y,0)&=\sqrt{\frac{2}{\pi}}(2n+1)\rho(1-\rho^2)^{-1/2}F\left(-n,\,n+1;\,\frac{3}{2};\,\rho^2\right)\qquad \rho=y/a\,.
\end{aligned}\right\}\tag{5.3}$$

When the incident electric wave is parallel to the ribbon, $J_y=0$ and $J_x\propto(1-\rho^2)^{-1/2}f_1(\rho)$ and when it is perpendicular to it, $J_x=0$ and $J_y\propto(1-\rho^2)^{1/2}f_2(\rho)$,

When the incident electric wave is perpendicular to the slit, $E_x=0$ and $E_y\propto(1-\rho^2)^{-1/2}f_1(\rho)$ and when it is parallel to it, $E_y=0$ and $E_x\propto(1-\rho^2)^{1/2}f_2(\rho)$,

where $f_1(\rho)$ and $f_2(\rho)$ are regular function of ρ in $-1\leqq\rho\leqq1$.

The total amount of the diffracted energy flow on the upper surface of the slit is equal to the scattered energy for $z>0$.

$$\begin{aligned}
S_z&=\frac{1}{2}\mathscr{R}(E_x\tilde{H}_y-E_y\tilde{H}_x)\\
&=\frac{1}{2}\mathscr{R}\Bigg[\Bigg\{E_1^2\cos^2\alpha\left(\sum_{n=0}^{\infty}A_n^{*}S_n^{*-1/2}(y,0)+\sum_{n=0}^{\infty}B_n^{*}S_n^{*1/2}(y,0)\right)\\
&\quad+i\frac{E_2^2}{\gamma}\left(\sum_{n=0}^{\infty}A_nT_n^{-1/2}(y,0)+\sum_{n=0}^{\infty}B_nT_n^{1/2}(y,0)\right)\Bigg\}e^{-iky\sin\alpha}\Bigg],
\end{aligned}$$

where ~ denotes the complex conjugate quantity. The transmission coefficient is

$$t=\frac{\pi}{2\gamma\cos\alpha}\mathscr{I}\{\sin^2\psi A(\alpha,\alpha)-\cos^2\psi A^*(\alpha,\alpha)\}\,.\tag{5.4†}$$

---

† de Hoop's scattering amplitude $A_2(\theta,\theta_0)$ refers to f (not to Π). Hence

$$2\pi\tilde{A}(\alpha,\theta)=A_2(\theta,\theta_0)\,,\qquad -2\pi\tilde{A}^*(\alpha,\theta)=A_1(\theta,\theta_0)\,.$$

In case of normal incidence, the current density, field intensity, and the transmission coefficient are given by

$$\left.\begin{array}{ll} J_x=\sqrt{\dfrac{\varepsilon}{\mu}}E_2\Big[\mp 1-\dfrac{i}{\gamma}\sum\limits_{n=0}^{\infty}X_{n0}(1-\rho^2)^{-1/2} & E_y=E_2\dfrac{i}{\gamma}\sum\limits_{n=0}^{\infty}X_{n0}(1-\rho^2)^{-1/2} \\ \qquad\times F\left(-n,n;\dfrac{1}{2};\rho^2\right)\Big], & \qquad\times F\left(-n,n;\dfrac{1}{2};\rho^2\right), \\ J_y=\sqrt{\dfrac{\varepsilon}{\mu}}E_1\Big[\mp 1-\dfrac{i\gamma}{2}\sum\limits_{n=0}^{\infty}X_{n0}^*\dfrac{1}{(2n+1)} & E_x=E_1\dfrac{i\gamma}{2}\sum\limits_{n=0}^{\infty}X_{n0}^*\dfrac{1}{2n+1}(1-\rho^2)^{1/2} \\ \qquad\times(1-\rho^2)^{1/2}F\left(-n,n+1;\dfrac{1}{2};\rho^2\right)\Big]. & \qquad\times F\left(-n,n+1;\dfrac{1}{2};\rho^2\right). \end{array}\right\} \tag{5.5}$$

$|J_x|$ and $|J_y|$ in (5.5) are qualitatively similar to Fig. 6 and Fig. 7 in II respectively. $|E_y|$ and $|E_x|$ are qualitatively similar to Fig. 8 and Fig. 9 in II respectively. [r/a in Fig. 6, 7, 8 and 9 in II should be read $(r/a)^2$.]

$$t=\frac{\pi}{2}\mathscr{I}\left\{\sin^2\psi\frac{X_{00}}{\gamma}-\cos^2\psi\frac{\gamma X_{00}^*}{4}\right\}. \tag{5.6}$$

Substitution of series representation of X_{00} and X_{00}^* into (5.6) gives the same results with (4.12) and (4.13).

The numerical calculation of the results and discussions will be published in the subsequent paper.

§ 6. Summary

The authors have solved the problem of the diffraction of electromagnetic waves by an infinitely long ribbon or slit in case where the plane of incidence is perpendicular to the edge of the ribbon or slit and the angle of incidence and polarizations are arbitrary. The diffracted field is assumed to be derived by electric type and magnetic type Hertz vectors, both of which have only one scalar component and which are expressed in terms of Weber-Schafheitlin's integrals with unknown coefficients. These coefficients are determined by hypergeometric polynomial expansion. The expressions for scattering cross section, transmission coefficients, electric current density of the ribbon, electric field intensity in the slit, electric field intensity at the distant point are obtained. Numerical results and discussions will be reported in the subsequent paper.

References

1) N. W. McLachlan: *Theory and Applications of Mathieu functions*, p. 358 (Oxford: 1947).

2) Cf. C. J. Bouwkamp: Diffraction Theory, Report on Progress in Physics **17** (1954) 35.

3) I. Kobayashi: Sci. Rep. Tôhoku Imp. Univ. (I) **27** (1939), 365. Das elektrostatische Potential um zwei auf derselben Ebene liegende und sich nicht schneidende gleichgrosse Kreisscheiben.

4) Y. Nomura: ibid. (I) **28** (1940) 304. The forces on two parallel coaxial circular discs placed in uniform flow.

5) Y. Nomura: ibid. (I) **29** (1940) 22. The forces on two parallel infinitely long plates placed in uniform flow.

6) Y. Nomura: ibid. (I) **29** (1940) 268. On the wave resistance of a plane plate.

7) Y. Nomura: Proc. Phys-Math. Soc. Japan, **28** (1941) 168. The electrostatic problems of two equal parallel circular plates.

8) Y. Nomura: Sci. Rep. Tôhoku Imp. Univ. (I) **30** (1941) 363. Current flow in a parallel plane conductor with circular electrodes.

9) Y. Nomura: ibid. (I) **31** (1943) 133. The theory of two plane wings.

10) Y. Nomura and N. Kawai: ibid. (I) **33** (1949) 197. On the acoustic field by a vibrating source arbitrarily distributed on a plane circular plate.

11) Y. Nomura and N. Kawai: ibid. (I) **33** (1949) 208. On the radiation of sound wave from a vibrating plane circular plate with a fixed circular baffle.

12) N. Kawai: ibid. (I) **35** (1952) 210. On the theory of Rayleigh disc.

13) Y. Nomura and S. Katsura: Jour. Phys. Soc. Japan, **10** (1955) 285. Diffraction of electromagnetic waves by circular plate and circular hole.

14) E. Groschwitz und H. Hönl: Zeits. f. Phys. **131** (1952) 305.

15) H. Hönl und Eva Zimmer: Zeits. f. Phys. **135** (1953) 196.

16) R. Müller und K. Westpfahl: Zeits. f. Phys. **134** (1953) 245.

17) A. T. de Hoop: Proc. Koninkl. Nederl. Akademie van Wetensschappen, B. **58** (1955) 401.

JOURNAL OF THE PHYSICAL SOCIETY OF JAPAN Vol. 12, No. 2 FEBRUARY, 1957

Application of Variational Method to the Thomas-Fermi Equation

By Teruo IKEBE and Tosio KATO

Department of Physics, Faculty of Science, University of Tokyo

(Received October 22, 1956)

Variational method is applied to derive two inequalities giving rigorous upper and lower bounds for the initial slope $B_0=-\varphi'(0)$ of the ordinary Thomas-Fermi function $\varphi(x)$, the solution of the non-linear equation

$$\varphi''=x^{-1/2}\varphi^{3/2}$$

with the boundary conditions

$$\varphi(0)=1\,,\qquad \varphi(\infty)=0\,.$$

Application of these formulas using simple trial functions leads to the estimate

$$1.5865\leq B_0\leq 1.5883\,.$$

§1. Introduction

In the Thomas-Fermi statistical model of a free neutral atom, we are to solve the following non-linear differential equation of second order[2] over the interval $(0, \infty)$

$$\varphi''=x^{-1/2}\varphi^{3/2} \tag{1.1}$$

with the boundary conditions

$$\varphi(0)=1\,,\qquad \varphi(\infty)=0\,. \tag{1.2}$$

The unique solution of the above problem, the so-called ordinary Thomas-Fermi function, can be shown to exist[5]. Practically, however, as has been done by a number of authors, it can be solved with the aid of numerical integration method. Since the behavior of a solution of (1.1) subject to the condition $\varphi(0)=1$ alone depends very sensitively upon the initial value of its derivative, it is important in numerical solution to determine the initial slope $B_0=-\varphi'(0)$ as precisely as possible.

It is noted that solution of (1.1) and (1.2) could be reduced to the variational problem of minimizing the functional

$$J[u]=\int_0^\infty\left(u'^2+\frac{4}{5}\,x^{-1/2}u^{5/2}\right)dx\,, \tag{1.3}$$

where the trial function $u(x)$ is positive and subject to the same conditions as (1.2). Eq. (1.1) is nothing but the Euler's equation of $J[u]$. On the other hand, the initial slope can be written in the following form:

$$B_0=-\varphi'(0)=\int_0^\infty(\varphi'^2+x^{-1/2}\varphi^{5/2})dx\,, \tag{1.4}$$

for

$$\int_0^\infty\varphi'^2dx=\varphi\varphi'\Big|_0^\infty-\int_0^\infty\varphi\varphi''dx=-\varphi'(0)$$
$$-\int_0^\infty x^{-1/2}\varphi^{5/2}dx$$

using (1.1) and (1.2). In case of linear differential equations, such quantities B_0 as required above often turn out to be the extremal values themselves of the corresponding functionals $J[u]$, but in our case it cannot be expected on account of non-linearity.

By variational observation, however, we shall derive in §2 the relation

$$\frac{6}{7}\,B_0=J[\varphi]\,, \tag{1.5}$$

which E. A. Milne deduced by partial integration already in 1927[4].

In order to carry out the estimation of B_0, we shall transform the functional $J[u]$ into its reciprocal form

$$I[v]=-2v(0)-\int_0^\infty\left(v^2+\frac{6}{5}\,x^{1/3}v'^{5/3}\right)dx \tag{1.6}$$

by means of the Friedrichs transformation[1], and make use of the relation $I[v]\leq J[u]$ (see §2). Then with (1.5) we are led to the inequalities

$$\frac{7}{6}\,I[v]\leq B_0\leq\frac{7}{6}\,J[u]\,, \tag{1.7}$$

estimating the initial slope.

§2. Derivation of the Inequalities

We shall denote by $\varphi(x)$ the ordinary Thomas-Fermi function, which is also the extremal function of $J[u]$, and consider an admissible trial function defined by $\varphi_\lambda(x)=\varphi(\lambda x)$ with λ sufficiently near to 1. Then the stationary value of

$$J[\varphi_\lambda]=\int_0^\infty\left[\lambda^2\varphi'(\lambda x)^2+\frac{4}{5}\,x^{-1/2}\varphi(\lambda x)^{5/2}\right]dx$$
$$=\int_0^\infty\left[\lambda\varphi'(x')^2+\frac{4}{5}\,\lambda^{-1/2}x'^{-1/2}\varphi(x')^{5/2}\right]dx'$$
$$(\lambda x=x')$$

should be attained at $\lambda=1$; in other words $(\partial J[\varphi_\lambda]/\partial\lambda)_{\lambda=1}=0$. This immediately leads to

$$5\int_0^\infty \varphi'^2 dx = 2\int_0^\infty x^{-1/2}\varphi^{5/2}dx \,.$$

In view of (1.4), therefore, we have the result (1.5).

Now we shall perform the Friedrichs or involutory transformation[1)] on the functional $J[u]$ as follows: Put

$$F(x,\, u,\, u') = u'^2 + \frac{4}{5}\,x^{-1/2}u^{5/2}\,, \tag{2.1}$$

x, u, u' being independent variables, and

$$F_{u'} = 2v\,, \qquad F_u = 2v'\,, \tag{2.2}$$

$$2vu' + 2v'u - F(x,\, u,\, u') = \Phi(x,\, v,\, v')\,, \tag{2.3}$$

where u, u' solved from Eqs. (2.2) as functions of x, v, v' should be substituted in (2.1) and (2.3). This is known as the Legendre transformation in the theory of differential equations. The condition that this transformation could be carried out is

$$\frac{\partial(F_u,\, F_{u'})}{\partial(u,\, u')} = F_{uu}F_{u'u'} - F_{uu'}{}^2 \neq 0\,, \tag{2.4}$$

which in our case can be easily proved to hold, for

$$F_{uu}F_{u'u'} - F_{uu'}{}^2 = 6x^{-1/2}u^{1/2} > 0\,. \tag{2.5}$$

Thus we arrive at the following reciprocal functional form to $J[u]$:

$$\begin{aligned} I[v] &= 2v(\infty)u(\infty) - 2v(0)u(0) - \int_0^\infty \Phi(x,\, v,\, v')dx \\ &= -2v(0) - \int_0^\infty \left(v^2 + \frac{6}{5}\,x^{1/3}v'^{5/3}\right)dx \end{aligned} \tag{2.6}$$

with

$$v' = \frac{dv}{dx}\,,$$

where no boundary conditions are assumed on $v(x)$. A sufficient condition that

$$I[v] \leq J[u] \tag{2.7}$$

is[1)]

$$F_{uu}F_{u'u'} - F_{uu'}{}^2 > 0\,, \qquad F_{u'u'} > 0\,,$$

which is seen to be satisfied by (2.5) and $F_{u'u'}=2$. The equality sign in (2.7) holds for $u=\varphi$ and $v=\psi=\varphi'$, so that we have

$$I[v] \leq J[\varphi] = I[\psi] \leq J[u]\,.$$

This is noting but the inequalities (1.7) except for a numerical factor.

In order to simplify further calculation we shall carry out some transformations on (1.3) and (2.6). First in (1.3) let us replace the integration variable x by μx, and find the optimum value of μ, which minimizes $J[u]$ for the given $u(x)$. Then we obtain

$$J[u] = 3\left(\frac{2}{5}\right)^{2/3}\left(\int_0^\infty u'^2dx\right)^{1/3}\left(\int_0^\infty x^{-1/2}u^{5/2}dx\right)^{2/3}.$$

If we want to remove the condition $u(0)=1$, $u(x)$ should be replaced by $u(x)/u(0)$, which results in multiplying the factor $u(0)^{-7/3}$ on the above expression. A similar procedure can be applied to (2.6) with another transformation which replaces $v(x)$ by $\nu v(\mu x)$. The result is

$$I[v] = \frac{15}{7}\left(\frac{2}{7}\right)^{4/3}(-v(0))^{7/3} \times\left(\int_0^\infty v^2dx\right)^{-1/3}\left(\int_0^\infty x^{1/3}v'^{5/3}dx\right)^{-1}.$$

By use of the above expressions and (1.5), we now obtain for B_0 the following inequalities:

$$\begin{aligned} &\frac{5}{2}\left(\frac{2}{7}\right)^{4/3}(-v(0))^{7/3} \\ &\qquad\times\left(\int_0^\infty v^2dx\right)^{-1/3}\left(\int_0^\infty x^{1/3}v'^{5/3}dx\right)^{-1} \leq B_0 \\ &\leq \frac{7}{2}\left(\frac{2}{5}\right)^{2/3}u(0)^{-7/3} \\ &\qquad\times\left(\int_0^\infty u'^2dx\right)^{1/3}\left(\int_0^\infty x^{-1/2}u^{5/2}dx\right)^{2/3}, \end{aligned} \tag{2.8}$$

where u, v are any smooth functions such that $u(x)\geq 0$, $v'(x)\geq 0$.

§ 3. Numerical Results

Let us compute the bounds of B_0 using some simple functions for u and v. Before entering into calculation, however, we remark that linear trial functions containing some variational parameters will not do so well in our case as in linear problems, for the calculation will be, in general, more complicated than in linear cases. Therefore we shall choose our trial functions so that the desired integrals in (2.8) may be obtained analytically, and that, if possible, $u(x)$ and $v(x)$ may approximate $\varphi(x)$ respectively $\psi(x)=\varphi'(x)$ fairly well.

If we adopt for $u(x)$ the function

$$u(x) = (1+x^{1/\alpha})^{-\beta} \qquad (0<x<\infty)\,,$$

where α, β are variational parameters to be determined, then both the integrals $\int_0^\infty u'^2dx$

and $\int_0^\infty x^{-1/2}u^{5/2}dx$ can be expressed in terms of beta functions and we have

$$\frac{7}{6}J[u]=\frac{7}{2}\left(\frac{2}{5}\right)^{2/3}\alpha^{1/3}\beta^{2/3}$$
$$\times B(2-\alpha,\ 2\beta+\alpha)^{1/3}B\left(\frac{\alpha}{2},\ \frac{5\beta-\alpha}{2}\right)^{2/3}.$$

Thus any pair of positive numbers α, β furnishes us with an upper bound of B_0. The pair of suitable values of α, β are determined from the simultaneous equations

$$\frac{\partial J[u]}{\partial\alpha}=0 \quad\text{and}\quad \frac{\partial J[u]}{\partial\beta}=0\,.$$

But these values and also the corresponding value of the functional $J[u]$ have been computed by K. Umeda and S. Kobayashi as follows:⁶⁾

$$\alpha=1.08252\,,\quad \beta=2.0892\,,\quad J[u]=1.3614\,.$$

So we have

$$B_0\leq 1.5883\,.$$

Next let us take for $v(x)$ the function

$$v(x)=\begin{cases}-(1-x^{1/\alpha})^{\beta} & (0<x\leq 1)\\ 0 & (1<x<\infty)\end{cases}$$

(α, β: variational parameters).

The integrals $\int_0^\infty v^2dx$ and $\int_0^\infty x^{1/3}v'^{5/3}dx$ are again obtained in terms of beta functions;

$$\frac{7}{6}I[v]=\frac{5}{2}\left(\frac{2}{7}\right)^{4/3}\alpha^{1/3}\beta^{-5/3}$$
$$\times B(\alpha,\ 2\beta+1)^{-1/3}B\left(\frac{5-\alpha}{3},\ \frac{5\beta-2}{3}\right)^{-1}.$$

Again, any pair of positive numbers α, β substituted in the expression gives a lower bound of B_0. Determining α, β from the equations

$$\frac{\partial I[v]}{\partial\alpha}=0 \quad\text{and}\quad \frac{\partial I[v]}{\partial\beta}=0\,,$$

we find $\alpha=1.831$ and $\beta=18$. With these values we obtain for a lower bound of B_0

$$B_0\geq 1.5865\,.$$

Thus we have estimated the initial slope B_0 as

$$1.5865\leq B_0\leq 1.5883 \qquad (3.1)$$

with an error less than 0.1 percent.

Though (3.1) is a rigorous estimate of B_0, it is not sharp enough compared with the values obtained by other authors, especially those by Umeda and his collaborators³⁾. However, it should be remarked that a more detailed calculation by use of existing tables of the ordinary Thomas-Fermi function²⁾,³⁾ will lead to a much sharper and still rigorous estimate of B_0.

References

1) R. Courant and D. Hilbert: Methods of Mathematical Physics, New York, 1953, Volume I, Chapter IV § 9.
2) P. Gombás: Die statistische Theorie des Atoms, Wien, 1949, §§ 3, 4.
3) S. Kobayashi, T. Matsukuma, S. Nagai and K. Umeda: J. Phys. Soc. Japan **10** (1955) 759.
4) E. A. Milne: Proc. Cambridge Phil. Soc. **23** (1927) 794.
5) A. Sommerfeld: Zs. f. Phys. **78** (1932) 283.
6) K. Umeda and S. Kobayashi: J. Phys. Soc. Japan **10** (1955) 749.

JOURNAL OF THE PHYSICAL SOCIETY OF JAPAN Vol. 12, No. 2 FEBRUARY, 1957

A New Method of Electro-Machining of Hard Metals

By Tasaburô YAMAGUTI

Physical Institute, College of Arts and Sciences, Chiba University

(Received October 18, 1955)

In the customary method of electro-machining of hard metals, it is necessary to initiate some condenced discharges or quenched sparks between the metal to the machined and the tool by incomplete contracts or repeated contacts, where the tool must be kept as the cathode in the circuit of direct current.

In the present method, an ordinary alternating current is used, superposed with some adequate high frequency electric oscillations. The metal and the tool are dipped in water and they are adjusted to keep a certain small separation. Thus, we can initiate favorable quenched discharges in every half cycle, in which the metal is in positive potential.

A merit of the present method is that the developments of any cracks in the machined surface are perfectly prevented even for hard metals, such as tungsten. The time required for drilling a tungsten plate of 3 mm in thickness by a tungsten rod, 1.54 mm in dia., is 4 minutes resulting a hole 1.75 mm in diameter. Screw cutting through a quenched steel plate is proved successful by choosing a brass external thread as a tooling electrode. The mechanism of electro-mechanical machining due to quenched discharges is explained qualitatively; the drilling effect being ascribed to electric attraction working on the melt of the plate, and the consumption of the electrode to a bluster effect of positive ions.

§ 1. Introduction

In the usual electro-machining method, a plate to be machined and the tool are connected to a direct current circuit with a condencer parallel to it[1]. The drilling performed by condenced discharge or quenched spark maintained by incomplete contacts or by repeated contacts of the plate and the electrode. There are, however, some difficulties in this usual method. Deformation of the electrode often caused by machanical contacts with the plate and by stickings of the molten metal drops reduces the accuracy of the machining. Further, when the electrode is drawn back from the contact, very minute cracks are apt to be formed on the surface which was liquified and softened by heating action of large current flowing through the contact point. Furthermore, as the repeated contacts of the electrode are required in this method, feed and rotation of the electrode necessary for the cutting of screw threads cannot be done with simple mechanisms.

The objects of the present experiment are to avoid these difficulties and to perform the machining with the supply from commercial alternating current source. Discharges between the tool and the plate connected in the alternating current circuit are initiated by superposition of high frequency oscillations. The superposition, however, is limited to every half cycle, when the plate is in positive potential[2]. To get a quenched discharge, a condenser connected with a helical wire of small inductance in series is inserted parallel to the electrodes.

§ 2. Experimental Method and Apparatus

The electric circuit of the experimental arrangement is shown in Fig. 1, where E is a

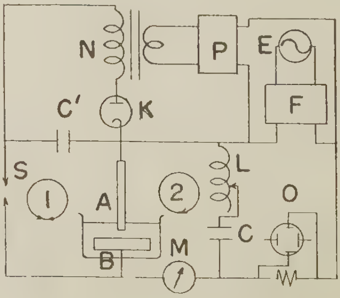

Fig. 1. Electrical circuit of the apparatus.

110 vlot, 50 cycle, single phase alternating current source. The electrode A and the plate B to be drilled are immersed in water and are connected to E through a wave filter F. A condenser C and an inductance L made of herical copper wire, arranged in series, are connected to A and B. Drilling of B is done by quenched discharges of C. One of the secondary terminals of a neon-transformer N is connected to the electrode A passing through a kenotron K, and another to the plate B through a park gap S. A condenser C' 2000 pF in capacity is inserted between one terminal of spark gap and the filament of K. By the rectifying action of K, C' is charged up in every other half cycle and is discharged through the gap, causing high frequency oscillations in the circuit 1. These oscillations initiate quenched discharges of the condenser C in the space between A and B, when these are brought approach. The number of the initiations can be counted by the use of a cathode ray oscillograph inserted in the position O. Furthermore, the initiation of quenched discharges is limited only when the plate is in positive potential by adjustment of a phase shifter P inserted in the primary circuit of the neon-transformer N. The spark gap is made of two tungsten discs about 10 mm in diameter facing each other at a distance 0.25 mm. The secondary potential of N is about 2.3 kv. Capacities of C are varied by several different combinations of condensers of 8 μF. Inductance L of the helical wire is also variable from 0 to 5 μH. Inductance of the lead wire in the circuit 2, excluding the helical wire, is about 2 μH, and this inductance increases with the capacity in the present experiment. M is a dc ammeter to measure discharge current.

In the present experiment, time needed for drilling, loss of the electrode A and diameter of holes drilled in B are measured for several values of C and L, and thus favourable optimum conditions for the drilling are obtained. Thicknesss of the tungsten plates is from 2.82 to 2.97 mm and the diameter of the tool of tungsten rod is 1.54 mm.

Preliminary experiments on the electromechanical cutting of internal screw threads in steel and tungsten carbide plate are carried out. A brass screw, 8 mm in diameter and 1.25 mm in pitch, is used as the cathode and is made to approach to the plate to be drilled guided by a screw of the same pitch.

§ 3. Experimental Results

The observed time interval to finish the drilling and loss of the rod are reduced to values for 3 mm plate for the sake of comparison of the results. The values are shown in Figs. 2 a and b, where the absissa is capacity of condenser C and the ordinate is the reduced time t for drilling. The marks given in the figure represent values of inductance L inserted in the circuit 2. The time t excluding the case for large C decreases with increase of C. The relation between t and C is discussed in the later section. When the capacity is kept constant, the time varies with L having a minimum at a certain value of L as can be seen from the distribution of the marks along vertical lines in the figure. The discharge current measur-

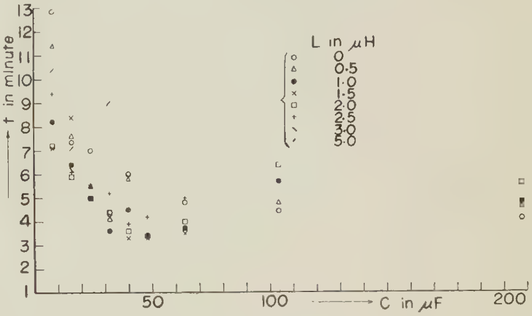

Fig. 2a. Effect of capacity and inductance inserted in the circuit on the working time for the electric discharge drilling of a tungsten plate 3 mm in thickness. Diameter of a tungsten electrode used as cathode is 1.54 mm. Marks representing values of the inductance are illustrated in the figure.

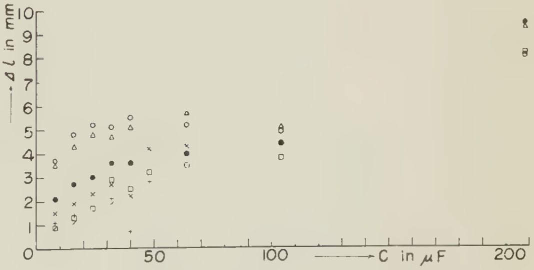

Fig. 2b. Effect of capacity and inductance on the loss of the tungsten electrode for the drilling. Marks representing the inductance are the same as in Fig. 2a.

ed by the dc ammeter M increases with C and L: from 1 ampere at $8\,\mu F$, $2.5\,\mu H$ to 3.2 ampere at $100\,\mu F$, $2.5\,\mu H$. The optimum conditions for drilling speed are $L=1.5\,\mu H$ and $C=40\,\mu F$.

Loss of the electrode also varies with C and L, as is shown in Fig. 2b. The absissa represents the capacity C in μF and the ordinate the loss Δl in mm, which increases with C. At constant C, the loss decreases with the increase of L and reaches nearly to a definite value for L larger than $2\,\mu H$. The conditions for the least loss are $C=8\,\mu F$ and $L=2\,\mu H$.

Diameter of the drilled holes varies with width of the spark gap S, and depends also upon C and L. In Fig. 3, the ordinate represents the diameter ϕ of holes drilled keeping the spark gap in 0.25 mm and using a tungsten electrode 1.54 mm in diameter, and the absissa capacity C. Values of L are represented with the same marks as illustrated in Fig. 2a. As will be seen from the figure the diameter increases with C and L. When C is small, difference between the diameter of the holes and of electrode are about 0.2 mm, and even when C is increased up to comparatively large value such as $64\,\mu F$ the difference is only 0.32 mm for small L. For $C=40\,\mu F$ and $L=1.5\,\mu H$, which are the optimum conditions for the shortest time of drilling and for the least loss of the electrode, the difference is 0.30 mm. Roughness of the electro-machined surface is determined by magnitudes of minute hemispherical droplets of tungsten formed on the surface. Magnitude of these droplets is about 0.02 mm for small values of C and 0.05 mm for large values.

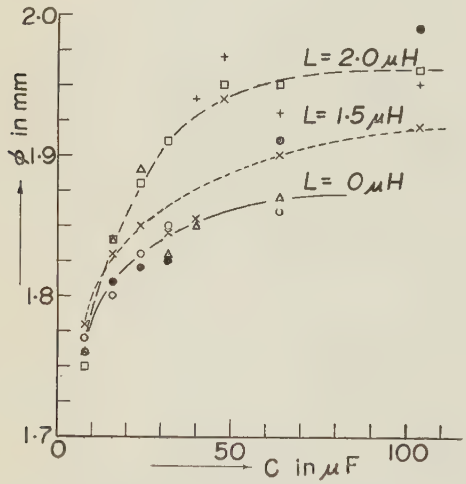

Fig. 3. Variation of diameter ϕ of drilled holes wilh the capacity and the inductance. The marks are the same as in Fig. 2a.

If the plate is kept as cathode, contrary to the experimental conditions mensioned above, the drilling speed becomes slow, and roughness of the machined surface and the difference between the diameter of the hole and of the electrode become increased. As the machining is still possible even in this inefficient case, it is attempted to shorten the working time by the use of alternating current discharges, which can be initiated by elimination of the kenotron K in Fig. 1. Experiments show, however, that the time, the loss and taper of the hole increase remarkably compared with ones obtained by the above method. Thus alternating current discharges are not suitable for machining.

To count the number of quenched discharges starting within one half cycle, a cathode ray oscillograph is inserted in the position O in Fig. 1. Oscillograms show numerous peaks, the number which are about 15 to 30 depending upon values of C and L. These number can be considered as ones of quenched discharges started during the half cycle.

Cutting of screw threads by the present method is done in quenched steel (files) and tungsten carbide plates using brass external threads as the electrode. Fig. 4 shows a photograph of a section of a screw cut in a quenched steel plate 4.4 mm in thickness. Diameter in crest and root of the internal thread cut are 6.90 and 8.19 mm respectively,

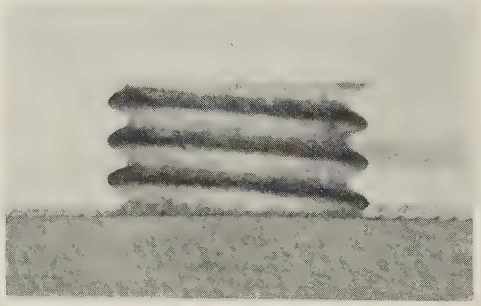

Fig. 4. A section (magnification: 4.1) of an internal thread cut in a file with the use of a brass external thread, 8 mm in diameter of the crest, 6.38 mm in the root and 1.25 mm in the pitch.

and the values of the external ones used as cathode being 8.00 and 6.38 mm. Thus gaps between the two threads are 0.10 and 0.26 mm at root and crest of the internal thread.

§ 4. Interpretation of the Experimental Results

As will be seen from Fig. 2a, time of drilling decreases gradually with the increase of *C* in a range from 8 to 64 μF. Time for large *C*, however, seems to deviate from this mode of decrease. To interpret this fact we must notic that inductance of the leading wire and of condensers, hence the total inductance of the circuit 2, are increased in experiments with the use of large *C* even if inductance *L* inserted is the same. Furthermore, time for a definite *C* reaches minimum at a certain L. Thus it will be reasonable to consider that if we are able to shorten the leading wire in experiments with Large *C*, time for large *C* may be diminished more than that determined experimentally, and minimum time to be obtained at certain *L* will decrease regularly with increase of *C*. This decrease of time with increase of *C* merely means that the electric charge carried by the quenched discharge and thereby mass of the melt of the positive plate increases with *C*. The fact that the time shows a minimum at a certain *L*, however, is explained as due to superposition of two effects. Before proceeding this explanation, the reason must be clarified why the drilling efficiency of the quenched discharges surpasses that by arcing.

In our experiments on the initiation of arc, which will be reported in a short time, it is observed that, when the arc is initiated in methane gas (to diminish the oxidation of the electrodes), melt formed on a top of positive electrode is attracted towards cathode, sometimes being elongated like a needle, and melt on negative electrode becomes flat on the top as if it is pressed by swift gas flow of positive charges. As such phenomena can be expected to occur also in the present quenched discharges, the following explanation on the mechanism of the drilling may be considered to be reasonable. By a quenched discharge of the condenser *C* a minute portion of the anode is heated to a liquid state having a small round surface. The melt thus formed is further elongated towards the cathode by attraction of electric force, until it is formed into a droplet and is blown off. These processes are repeated from 15 to 30 times in each half cycle as is shown by the cathode ray oscillograph above mentioned, and the drilling progresses efficiently. Whereas, if the discharge is the kind of arcing, which starts when *L* is large or *C* is small, the arc current continues to flow during one half cycle. Melting due to such arcing is not localzed upon a small region by conduction of heat, which is supplied slowly and continuously. As the mass and surface area of such melt are considerablly large, rounding of the melt is not remarkable and the attraction towards the cathode will not be large enough to produce a droplet to be sputtered.

By the same consideration as the above, one of the two effects, which minimize the work time at a certain value of *L*, can be explained. Namely, as duration time of the quenched discharge increases with increase of *L*, local melting suitable for formation of droplets to be blown off is hindered by slow supply of heat and by conduction of heat. Thus the time *t* increases with the increase of *L*. On the contrary of this, another second effect of *L* diminishes the time. When *L* is small, the high frequency current flows mainly through the branch circuit *CL* and feebly through the branch *AB*. Therefore, in these *L* ranges the initiation of the quenched discharge becomes uncertain and the working time increases with the decrease of *L*. By combination of these two effects, when *C* is kept constant, the time may be diminished at first and then increased with the increase of *L* passing through a minimum value at a certain value of *L*.

As the mode of loss of the electrode is quite different from that of the plate in the point that no maximum loss is observed with variation of *L*, we must consider that mechanisms of the two losses are different. The following explanation may be allowed for the electrode loss. When the working is done with insertion of large *L*, the surface of the electrode is liquified in a large area and simply becomes flat and is blown off scarcely by pressure of positive ions and of small particles imprining on the electrode. The loss in these states can be considered as being chiefly due to the evaporation, which is proportional to the discharge current. When L is small on the contrary, although initiations of the quenched discharge may be not always certain, materials of the electrode can be sputtered in forms of minute solid and melted particles by collisin of positive ions produced by quenched discharges of large current density, as like some materials can be graved by a sand bluster. Thus, by the considerations stated above it may be said that the loss of anode plate is due to electric attraction acting on droplets of the melt formed on the plate and the loss of cathodic electrode is due to a bluster effect of positive particles produced by the quenched discharge.

In conclusion the author's thanks are due to the Ministry of Education for financial support, and to Mr. N. Kobayashi and Mr. Y. Sasada for their assistance.

References

1) I. Weber: The Iron Age, May (1952) 88, J. S. Roller: Machinery, Feb. (1952) 322.
2) T. Yamaguti: Jap. Gov. patent No. 218716.

JOURNAL OF THE PHYSICAL SOCIETY OF JAPAN Vol. 12, No. 2 FEBRUARY, 1957

On the Ricochet Motion of a Projectile Striking a Water Surface

By Tikao HUZITA
Faculty of Fisheries, Kagoshima University

(Received October 13, 1956)

Analysing the photographs of the ricochet motion, the following results were obtained. (1) The mean hydrodynamical impulsive force is practically independent of the incident angle except for the blunt head projectile. (2) The horizontal component of the force becomes smaller as the incident angle increases and the projectile becomes hard to ricochet as the component nears zero. (3) The point of application of the force recedes as the incident angle increases. (4) The vertical velocity component of the projectile after the ricochet is generally greater than that before.

Furthermore a coefficient of retardation, a coefficient of ricochet, and a coefficient of slip were newly introduced in order to compare the ricochet motion with the motion of repulsing upon a solid wall.

§1. Introduction

The experiments on the motion of a projectile striking a water surface were formerly carried out by Isobe[1], by Hirata[2], and by the writer[3][4] on a bullet, on a harpoon and on a projectile with tailplane respectively. The writer recently made an indoor experiment[5] in which the head shape and the incident angle were changed systematically.

Four kinds of projectile used in this experiment are shown in Fig. 1 and each number of the projectile indicates the apex angle of the head cone. The symbol 60 b indicates Proj. 60 with a resistance ring[5]. Each projectile is 15 mm in diameter, about 62 mm in length and about 28 g in weight.

The arrangement of the apparatus is shown in Fig. 2. The water tank T, 35 cm deep, 23 cm wide, and 140 cm long, has a glass wall GW on one side. On the left side of the tank there is a spring gun G, its spring force being about 10 kg and the projectiles being shot

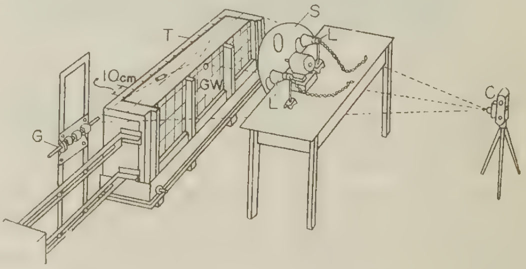

Fig. 2. Arrangement of the apparatus.

horizontally with the initial velocity of 6∼11 m/s. The trajectory of the projectile is photographed on a film and at the same time observed by naked eye through the finder of a reflex camera *C*. Furthermore, in order to illuminate the projectile, two spot light lamps *L* are placed obliquely upwards before the tank. Before the lamps, there is a rotating shutter *S* by which the light is intercepted 115 times per second, and so the image of the projectile is intermittently photographed on the film and the posture of the projectile is clearly observed on the film. An example of the photograph of the trajectory of a projectile is shown in Fig. 3. According to the change in the height of the gun which was 2.5, 5.0, 10.0, 20.0 and 30.0 cm from the water level, incident angle of the projectile varied between 3.6° and 21.5°.

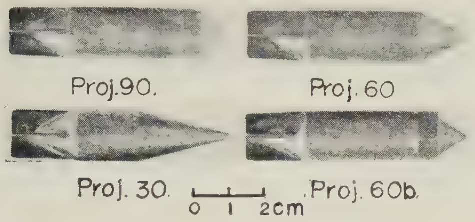

Fig. 1. Models used in the experiment.

As the results of this experiment, the motion of the projectile was classified into four groups, namely, ricochet, swimming, straight forwards and reverse turn, each trajectory being indicated schematically in Fig. 4. Proj. 180 goes always straight forwards into the water independently of its incident angle. Other projectiles make the above mentioned four kinds of motion according as their incident angles. The ranges of the incident angle corresponding to the various kinds of motion of each projectile are tabulated in Table I.

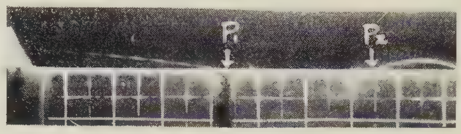

Fig. 3. Photograph of the ricochet motion.

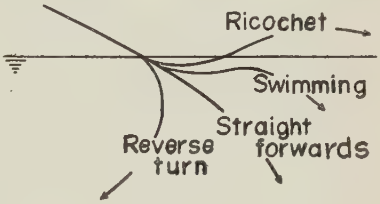

Fig. 4. Classification of the trajectory.

Here in the present study, the writer, analysing the photographs which correspond to the ricochet motion, intends to make clear the ricochet motion observed in the indoor experiment.

Table I. Behavior diagram

Proj.	Incident angle ($\alpha_1{}^0$)												
	2	4	6	8	10	12	14	16	18	20	22	24	26
180	Straight forwards												
90	Ricochet				Swimming			Straight forwards		Reverse turn			
60	Ricochet					Swimming			Straight forwards	Reverse turn			
30	Ricochet					Reverse turn							
60b	Ricochet				Straight forwards								

§ 2. Treatment of the Experimental Results

In Figs. 5 and 6, let the path of the projectile be in the xy-plane, x-axis the water surface, $P_0P_1QP_2P_3$ the path of the projectile and ABC the cross section of the projectile head. $h_1, h_3, s_1, s_2, s_3, \alpha_1$ and α_2 are measured from the photographs. The velocities of the projectile v_1 and v_2 are calculated by the equation of a projectile. Then non-dimensional coefficients:

coefficient of retardation

$$e_x = 1-(v_2 \cos \alpha_2 / v_1 \cos \alpha_1)\,, \qquad (1)$$

coefficient of ricochet

$$e_y = v_2 \sin \alpha_2 / v_1 \sin \alpha_1 \, , \qquad (2)$$

coefficient of slip

$$e_s = s_2/d \, .$$

are newly introduced analogously with the coefficient of restitution $e(=e_y)$ and the coefficient of friction $\mu(=\cot \alpha_1 \cdot e_x/(1+e_y)$. The third coefficient e_s is necessary in order to obtain the mean force instead of the impulse.

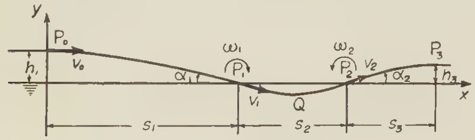

Fig. 5. Schematic diagram of the ricochet motion.

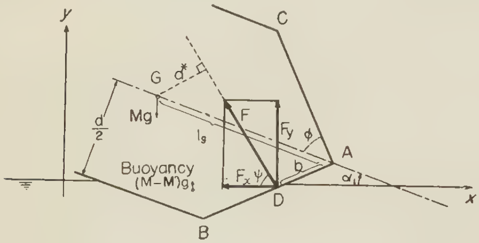

Fig. 6. Forces acting on the projectile.

In Fig. 6 let the mass of the projectile be M, the moment of inertia about the center of gravity (G) be I $(=Mk^2)$, the rotational velocity about the center of gravity be ω, the force exerted by water be F, the point of application of F on AB be D, the gravity force minus the buoyancy be $M'g$, the resultant force of F and $M'g$ be F', the arm length of F and F' about the center of gravity be a^* and $a^{*\prime}$ and the time interval during which the projectile passes through the water be $\varDelta t$. The suffixes and the other symbols are used as indicated in Figs. 5 and 6. Then we obtain

$$M(v_2 \cos \alpha_2 - v_1 \cos \alpha_1) = -\overline{F}_x \cdot \varDelta t \, , \qquad (4)$$

$$M(v_2 \sin \alpha_2 + v_1 \sin \alpha_1) = (\overline{F}_y - \overline{M}'g) \cdot \varDelta t \, , \qquad (5)$$

$$I(\omega_2 - \omega_1) = \overline{F' a^{*\prime}} \cdot \varDelta t \, , \qquad (6)$$

$$\varDelta t = 2s_2/(v_1 \cos \alpha_1 + v_2 \cos \alpha_2) \, , \qquad (7)$$

in which — is used to indicate the time-average value during $\varDelta t$.

In the case of a projectile with tailplane, ω_1 and ω_2 are nearly equal to zero (ω_1 or ω_2 × length of the projectile is always less than 4% of v_1 or v_2 respectively) though the direction of the projectile changes, therefore in the equation (6) $\overline{F'a^{*\prime}} = 0$ but $a^{*\prime} \neq 0$. For convenience sake, if we put $F'a^{*\prime} = \overline{F'}a'$, the simplest form of a' which satisfies these conditions is as follows:

$$a' = a_0'(1 - 2t/\varDelta t) \, . \qquad (8)$$

Then, integrating the equation (6) by using the boundary conditions, we get

$$a_0' = 6I(\alpha_1 + \alpha_2)/\{\overline{F'} \cdot (\varDelta t)^2\}. \qquad (9)$$

From these equations $\overline{F'}$, $\overline{\psi}'$, $\varDelta t$ and a_0' are obtained. The manner in which the arm of the moment about the center of gravity changes can be conjectured from a_0'. The non-dimensional expressions of these quantities are represented by e_x, e_y and e_s as follows:

$$\begin{aligned} \overline{C'} &= 2\overline{F'}/(\rho v_1{}^2 d^2) \\ &= \{\cos^2\alpha_1 \cdot e_x{}^2 + \sin^2\alpha_1 \cdot (1+e_y)^2\}^{1/2} \\ &\quad \times (\varDelta t \cdot v_1/d)^{-1} \cdot (2M/\rho d^3) \, , \qquad (10) \end{aligned}$$

$$\tan \psi' = \overline{\tan} \, \alpha_1 \cdot (1+e_y)/e_x \, , \qquad (11)$$

$$\begin{aligned} a_0'/d &= 12(M/\rho d^3) \cdot (k/d)^2 \cdot (\varDelta t \cdot v_1/d)^{-2} \\ &\quad \times (\alpha_1 + \alpha_2)/\overline{C'} \, , \qquad (12) \end{aligned}$$

$$\varDelta t \cdot v_1/d = 2(s_2/d)/\{\cos \alpha_1 \cdot (2 - e_x)\} \, . \qquad (13)$$

Let the intersecting point of the line of mean force with the surface of the projectile be $\overline{D'}$ and let us denote the length of $A\overline{D'}$ by $\overline{b'}$ and that of AG by l_g. Then

$$\overline{b'}/l_g = \sin(\overline{\psi'} - \alpha_1)/\sin(\overline{\psi'} - \alpha_1 + \phi) \, . \qquad (14)$$

In the case of the restitution upon a solid wall, static forces are usually negligible to the impulsive force and $\overline{F}$ may be put equal to $\overline{F'}$. But in this case, as they amount to about 20% of $\overline{F}$, we must substitute $\sin \alpha_1 \cdot (1+e_y) + (\overline{M}'/M) \cdot (dg/v_{12}) \cdot (\varDelta t \cdot v_1/d)$ for $\sin \alpha_1 \cdot (1+e_y)$ in the formulas (10), (11), (12) and (14), in order to obtain the pure impulsive quantities $\overline{C}$, $\tan \overline{\psi}$, a_0/d and $\overline{b}/l_g$. If Mg is used instead of $M'g$, the error due to this substitution is about 30% of Mg and therefore 6% of $\overline{F}$.

Now, we shall assume the relation between α_1 and each non-dimentional quantity to be a linear functional form. Then, the regression line and the correlation coefficient γ are obtained by treating the results acquired from the above indoor experiment, and as for the significancy of the correlation γ it is tested. These results are shown in Table II, and some of the plotted figures from which the results were obtained are shown in Figs. 7∼12. Each

Table II. Experimental formula and its correlation coefficient r.

Proj.	$\overline{C}$	r	Proj.	e_x	r
90	$0.72-0.073\alpha_1$	-0.73*	90	$0.97-0.121\alpha_1$	-0.78*
60	$0.51-0.012\alpha_1$	-0.41	60	$0.70-0.047\alpha_1$	-0.70*
30	$0.53-0.010\alpha_1$	-0.24	30	$0.71-0.062\alpha_1$	-0.89**
60b	$0.45-0.007\alpha_1$	-0.15	60b	$0.71-0.044\alpha_1$	-0.62**

Proj.	$\overline{\psi}$ (deg.)	r	Proj.	e_y	r
90	$-26.6+12.64\alpha_1$	0.88**	90	$2.00-0.147\alpha_1$	-0.70
60	$-\ 4.0+\ 6.80\alpha_1$	0.83**	60	$2.12-0.100\alpha_1$	-0.64
30	$-11.9+\ 8.81\alpha_1$	0.96**	30	$1.65-0.066\alpha_1$	-0.81**
60b	$-\ 5.1+\ 6.58\alpha_1$	0.88**	60b	$1.43-0.041\alpha_1$	-0.67**

Proj.	$\overline{b}/lg$	r	Proj.	α_2 (deg.)	r
90	$-0.25+0.156\alpha_1$	0.66	90	$15.75-1.147\alpha_1$	-0.74*
60	$0.16+0.068\alpha_1$	0.86**	60	$12.01+0.486\alpha_1$	0.28
30	$0.25+0.074\alpha_1$	0.94**	30	$10.36+0.141\alpha_1$	0.17
60b	$0.12+0.069\alpha_1$	0.86**	60b	$9.18+0.601\alpha_1$	0.38

Proj.	a_0/d	r	Proj.	s_2/d	r
90	$0.12+0.017\alpha_1$	0.51	90	$5.9+2.39\alpha_1$	0.66
60	$0.08+0.025\alpha_1$	0.28	60	$13.3+0.55\alpha_1$	0.33
30	$0.04+0.017\alpha_1$	0.77**	30	$12.7+0.15\alpha_1$	0.14
60b	$0.06+0.021\alpha_1$	0.49*	60b	$14.3+0.55\alpha_1$	0.30

The mark * denotes that r is significant and ** definitely significant.

number distinguishing the kind of projectile indicates the head angle in degrees and Projectile 60 b has a resistance ring[5]).

Taking d (diameter 15 mm) as a standard length, Reynolds' number is $0.9\sim 2.0\times 10^5$, Froude's number is $16\sim 36$, the ratio $\rho v_1^2 d$ to the surface tension (Weber's number) is $0.7\sim 3.9\times 10^4$ and $\{(M-M')/M\}_{max.}$ is 0.3.

§ 3. Discussion of Results

Now, considering the above results, the writer will discuss the nature of the ricochet motion.

a) *Impulsive force*

$\overline{C}$ is shown in Fig. 7 and is about $0.4\sim 0.5$ at a small incident angle. For each projectile except Proj. 90, $\overline{C}$ decreases gradually as α_1 increases, and for Proj. 90, $\overline{C}$ decreases rapidly. Therefore $\overline{C}$ is practically independent of α_1 except for the blunt head projectile.

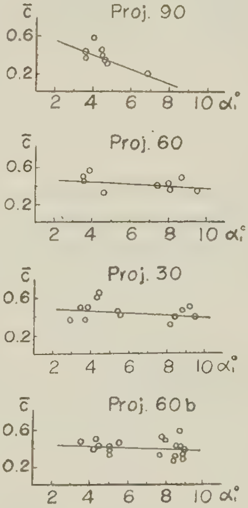

Fig. 7. $\overline{C}$ versus α_1 for Projs. 90, 60, 30 and 60b.

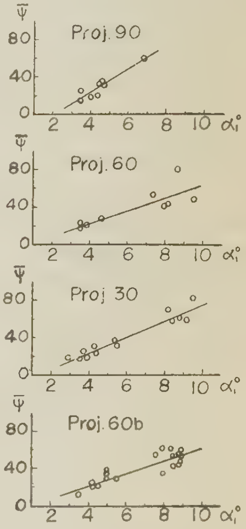

Fig. 8. $\overline{\psi}$ versus α_1 for Projs. 90, 60, 30 and 60b.

$\overline{\psi}$ is shown in Fig. 8 and increases with α_1 and approaches to 90°. Therefore $\overline{F}_x$ becomes smaller as α_1 increases and the projectile becomes easy to slip or difficult to ricochet. Though $\overline{\psi}$ is thought to be smaller than 90°, the incident angles obtained by extrapolating the regression line up to $\bar{\phi}=90°$ are tabulated in the first line, Table III.

a_0/d is shown in Fig. 9 and increases with α_1, and the correlation is small except Projs. 30 and 60 b.

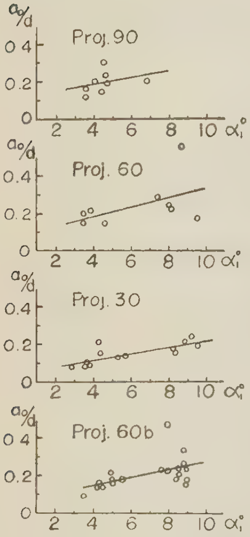

Fig. 9. a_0/d versus α_1 for Projs. 90, 60, 30 and 60b.

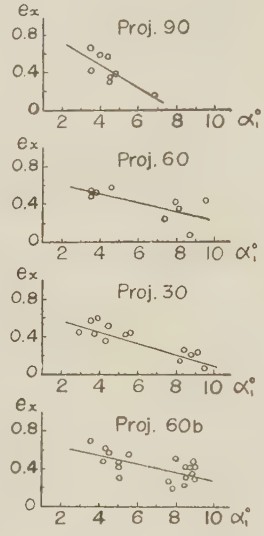

Fig. 10. e_x versus α_1 for Projs. 90, 60, 30 and 60b.

$\bar{b}/l_g$ increases with α_1 and this shows that the point of application of the mean impulsive force recedes from the top of the head cone towards the rear part of the projectile as α_1 increases and this tendency is seen markedly in Proj. 90.

b) *Comparison with a restitution upon a solid wall*

e_x is shown in Fig. 10 and decreases up to zero as α_1 increases, and the slope is steepest for Proj 90. This means that the projectile is apt to slip as α_1 or the head angle ϕ increases. The incident angles corresponding to the limiting condition $e_x=0$ are obtained by extrapolation and tabulated in the second line, Table III.

e_y is shown in Fig. 11 and decreases as α_1 increases and approaches to 1. Contrary to the restitution coefficient and also to the usual conjecture, the ricochet coefficient e_y is, generally, greater than 1. It approaches to 1 and sometimes it is smaller than 1 but within the experimental error. As $e_y=1$ seems to be the boundary between ricochet and restitution, the incident angles corresponding to $e_y=1$ are obtained and tabulated in the third line, Table III.

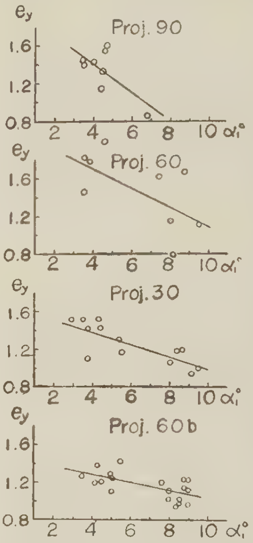

Fig. 11. e_y versus α_1 for Projs. 90, 60, 30 and 60b.

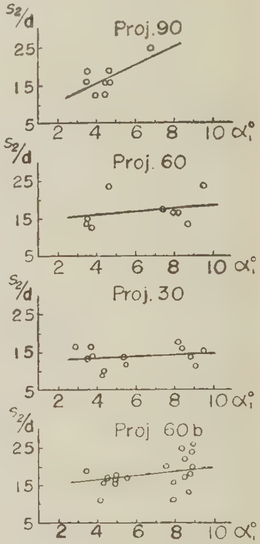

Fig. 12. s_2/d versus α_1 for Projs. 90, 60, 30 and 60b.

s_2/d is shown in Fig. 12 and increases with α_1, and the slop becomes steeper as the head angle increases. This tendency to slip shows the same physical meaning as the tendency

Table III. Critical incident angles obtained by extrapolation or interpolation.

Line	Critical condition	Projectile			
		90	60	30	60b
1	$\bar{\phi}=90°$	9.3°	13.8°	11.6°	14.5°
2	$e_x=0$	8.0°	14.9°	11.6°	16.2°
3	$e_y=1$	6.8°	11.3°	9.8°	10.6°
4	$e_y=0$	13.7°	21.3°	24.9°	35.2°
5	$\alpha_{r.sw.}$	about 9°	about 11°	about 12°	about 9°

of e_x.

α_2 increases with α_1 for Projs. 60, 30 and 60 b, while for Proj. 90 it decreases as α_1 increases.

c) *Critical incident angle between ricochet and swimming*

The critical incident angles between ricochet and swimming ($\alpha_{r.sw.}$) obtained from the above indoor experiments are tabulated in the fifth line, Table III.

The most intuitive condition for this critical angle $\alpha_{r.sw.}$ is $e_y=0$, but as is shown in the fourth line, Table III this is far from the critical condition. The incident angles corresponding to $\bar{\psi}=90°$, $e_x=0$ and $e_y=1$ are close to the critical angle. Accordingly, it may be said that for Projs. 90 and 30 the conditions $\bar{\psi}=90°$ and $e_x=0$, and for Projs. 60 and 60 b the condition $e_y=1$, are more suitable in this experiment.

The conditions of $\bar{\psi}=90°$ and $e_x=0$ mean that the projectile ceases to ricochet when it receives no horizontal force, i. e. when slips. In the case of a solid wall, this corresponds to the fact that the wall is perfectly smooth. Therefore it seems to be extremely interesting to carry out an experiment of restitution upon a perfectly smooth wall. In short, as for the critical condition, there seems to be much to be done.

The regression lines of various coefficients of Proj. 90 are steeper than those of the other projectiles and the regression line of α_2 differs in sign from the others. These facts seem to indicate that the blunt head is disadvantageous for ricochet. From this fact it may be conjectured that a projectile with resistance ring or Proj. 180 (flattened head) is advantageous to be driven into the water, the fact of which has already been verified by the writer[3)5)] and by Hirata[2)].

Acknowledgements

The writer wishes to express his sincerest thanks to Prof. T. Fujiwara of Hiroshima University who has enabled the writer to conduct this research for his useful suggestions and kind encouragement, and also to Prof. T. Maekawa of Hiroshima University for his hearty guidance and valuable discussion through the progress of this subject.

References

1) T. Isobe: Jour. Ordn. Soc. Japan **36** (1942) 237, **36** (1943) 387, in Japanese.
2) M. Hirata: Scientific Reports of Whales Research Institute No. 6 (1951) 199.
3) T. Huzita: Report of Air Ordnance Technical Laboratory No. 04398, (1944) in Japanese.
4) J. Okamura and the others: The Whole Aspect of Air Ordnance Technology **2** (1955) 102, 115, in Japanese.
5) T. Huzita: Jour. Sci. Hiroshima Univ. **19** (1955) 137, 151.

Short Notes

This section is intended to secure prompt publication of important discoveries in physics. The reports should not exceed 800 words in length. A figure of size 7 cm × 7 cm will be counted as 150 words.

J. Phys. Soc. Japan **12** (1957) 214

Effect of Plastic Deformation on the Dielectric Breakdown of Silver Chloride Crystals

By Noriaki Itoh and Tokuo Suita

Department of Electrical Engineering, College of Engineering, Osaka University

(Received November 29, 1956)

Effects of plastic deformation on the dielectric breakdown have been observed with alkali halide crystals by several authors and it has been shown that the breakdown strength was affected by plastic deformation to a considerable degree in some cases[1][2]. We investigated these effects with locally deformed silver chloride which is more plastic than alkali halide and seems to be convenient for the study of these effects.

To obtain locally deformed specimens we pressed them in the [110] direction by adding weight through a thin cover glass of thickness 0.15 mm. This method is similar to the prismatic punching developed by Smakula and Klein[3]. Although the punching figure was not clearly observed in our AgCl specimens, it seemed to be evident that the stress under the puncher was larger than that in the other part of the specimen at the beginning of the application of stress. The strain would spread over the whole specimen with the application time, which is known as creep.

The specimens we used were cut from a large block of single crystal grown by Kyropoulos method, their form and dimensions being as shown in Fig. 1. The puncher was applied just upon the edge of the hollow electrode and the breakdown voltage under the stress was measured in both cases where the strained part was at the positive electrode and at the negative electrode. The applied voltage was rectangular pulse repeated 10 cycles/sec, which was raised at the rate of about 3 kv/min until the breakdown occured.

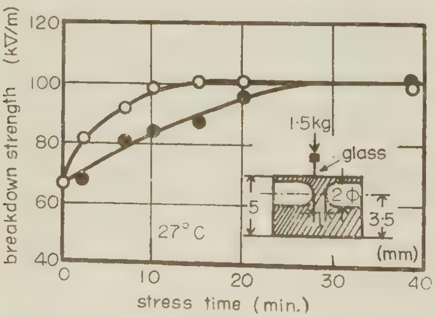

Fig. 1. Dependence of the dielectric breakdown strength of AgCl on the stress time.
○: Stressed on the negative side,
●: Stressed on the positive side.

The dependence of the breakdown voltage on the stress time in the both configurations at room temperature is shown in Fig. 1. The weight of the load was 1.5 kg and the shear stress was 250 kg/cm². It is clearly seen that the breakdown strength increases with the stress time and reaches to a same saturation value in the both cases. The increase of the breakdown voltage is more rapid when the shear stress is applied near the negative electrode. Therefore the strain seems to be more effective to the breakdown when it is applied near the cathode.

If the applied voltage was raised much more rapidly (about 20 kv/min) the effects of the stress were almost negligible, that is, the increase of the breakdnown strength due to mechanical stress occured only when the applied pulse voltage increased slowly. As we have already shown the deposit of silver atoms seemed to play an important role in the dielectric breakdown even in pulse field[4]. Therefore we can conclude that a great deal of silver atoms deposited in the deformed region near the cathode mainly raise the dielectric strength in silver chloride.

We wish to thank to Dr. E. Mizuki and other staffs of Fuji Photofilm Co. for supplying silver halide materials and for their valuable discussions. We also thank to Mr. C. Okazaki for investigating the crystallographic orientation of our crystal blocks by Laue's method.

References

1) J. H. Calderwood, R. Cooper and A. Wallace: Proc. I. E. E. Part II A **100** (1953) 105.

2) Y. Inuishi and T. Suita: Proc. Phys. Soc. Japan **10** (1955) 589, 590.

3) A. Smakula and M. W. Klein: Phys. Rev. **84** (1951) 1043.

4) T. Suita and N. Itoh: Proc. Phys. Soc. Japan **11** (1956) 474.

J. Phys. Soc. Japan **12** (1957) 215

The Energy Spectrum of Nucleons in the Air Shower

By Y. Tanaka*, K. Suga* and S. Mitani†
Institute for Nuclear Study, University of Tokyo, Tanashi-machi, Kitatama-gun, Tokyo
†*Faculty of Science, Osaka University, Nakanoshima, Kita-ku, Osaka*

(Received November 16, 1956)

A preliminary experiment on the energy spectrum of nucleons in the air shower was carried out at Mt. Norikura Cosmic-Ray Laboratory, University of Tokyo, (2840 m altitude). Two piles of G-M counter trays, E and H, shielded by lead layers were set as shown in Fig. 1. Hodoscope records of both counter piles for the coincidences $(A\geqq 3)+(E_1\geqq 3)$ were obtained. Of these records the events satisfying the condition $(B\geqq 3)+(C\geqq 1)$ were regarded as high-energy nuclear interactions inside the lead layer above Tray B caused by nucleons in air showers. Because the most part of the electronic component of the air shower may be absorbed by 20 cm thickness of lead and the contribution of μ-mesons in these records is expected to be very small in this experiment. These were subdivided into two groups: (I) those with three or more struck counters in Tray E_3, and (II) those with less than three struck counters in the same tray. Average densities of air showers were estimated to be several hundreds per square meter for (I) and several tens per square meter for (II) respectively.

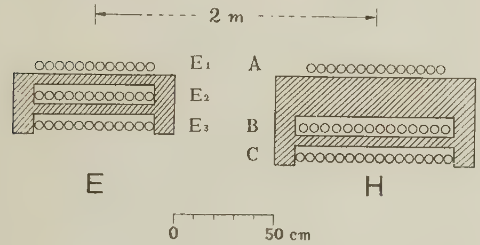

Fig. 1. The arrangement of counter piles.

Supposing that discharges of counters in Tray E_3 were caused by high-energy electrons in the air shower, one may expect that the core of the air shower hit the ground as close as 10 m for (I) and within the range extending from 10 m to 100 m for (II), respectively, in comparison with the results of Cocconi et al1). And if one takes the events originated by single nucleons $(A\leqq 1)+(E_1, E_2 \text{ and } E_3=0)+(B\geqq 3)+(C\geqq 1)$ as group (III) which were observed separately by the same apparatus, these might be more than 100 m apart from the core.

The integral multiplicity-distributions of struck counters in Tray C for these groups are shown in three curves in Fig. 2. There might be cases in which more than one nucleon struck counter-pile (H) simultaneously so that apparently higher multiplicities were observed in Tray C. This effect is important only for showers of very high density in this experiment, and the correction was applied in Fig. 2. These curves can be considered as showing indirectly the energy distributions of nucleons, because the multiplicity in Tray C is the function of the energy of the nucleon on the average. If it is assumed that Curve (III) shows the energy spectrum of single nucleon, i.e. $E^{-1.5\sim 1.8}$ 2), the energy spectra $E^{-0.7\sim 1.1}$ and $E^{-0.9\sim 1.4}$ are obtained for (I) and (II) respectively. The energy of nucleons in this analysis may extend from 10 Bev to 100 Bev3).

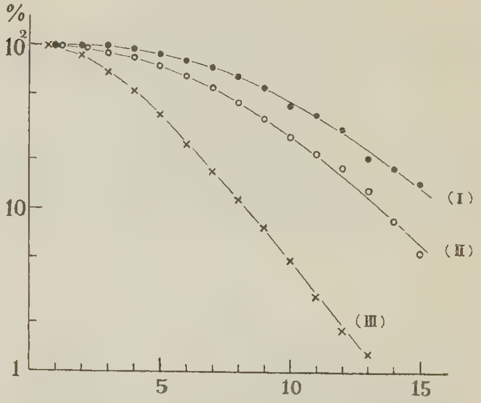

Fig. 2. Integral multiplicity-distributions of struck counters in Tray C for groups (I), (II) and (III). The abscissa is the number of struck counters in Tray C, and the ordinate shows the integral number of events in percentage of the total number in each group.

Of course, the above-mentioned assumption includes several problems and further study should be necessary. However, Fig. 2 seems to show that the energy spectrum of nucleons in the air shower is flatter and, hence, the proportion of high-energy nucleon is larger at the point which is closer to the core than that apart from the core.

In the end, the authors wish to express their heartfelt thanks to Prof. Y. Watase for his very helpful discussions and advice.

References

1) G. Cocconi, V. Cocconi Tongiorgi and K. Greisen: Phys. Rev. **76** (1949) 1020.

2) J. G. Wilson: Progress in Cosmic-Ray Physics I. (1952).

3) Y. Watase, K. Suga, Y. Tanaka and S. Mitani: Nuovo Cimento **X-2** (1955) 1183.

J. PHYS. SOC. JAPAN **12** (1957) 216

Effects of Shock Wave upon Gaseous Discharge

By Shigeo NAGAO
Engineering Faculty, Tohoku University, Sendai

(Received November 27, 1956)

In order to investigate the effects of shock wave upon gaseous discharge we constructed a shock wave-discharge tube as is shown in Fig. 1

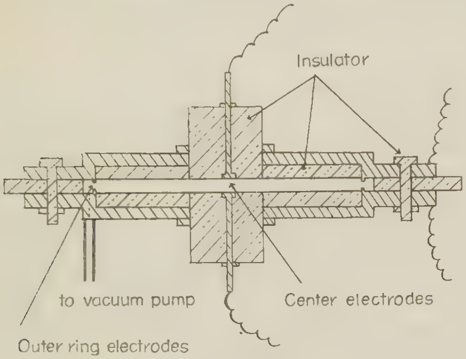

Fig. 1. Shock wave-discharge tube. Gap length of center electrodes: 1 cm.

and measured the lowering of sparking voltages of gap attacked by shock wave. When the tube is evacuated enough, spark discharge induced by the application of impulse voltage upon the outer ring electrodes covers their whole surface and then the cylindrically converging shock wave generated thereby propagates towards the center electrodes, increasing rapidly its strength, i.e. its pressure and temperature[1)2)]. Thus if a voltage well below the sparking value of the gap in normal state had been applied upon the center electrodes, sparking will follow suddenly at the gap when the shock front arrived at the center electrodes.

Fig. 2 shows the circuit used for the measurement of sparking voltage mentioned above and the results are shown in Fig. 3. It may be clear that the greater the capacity and voltage of the condensor used for the initiation of shock wave, the more intense will become the shock wave generated by the sparking between the outer electrodes. In Fig. 3 it is worth noting that even very weak shock wave lowers the sparking voltage of center electrodes upto about the minimum sparking voltage in Paschen's law. This fact may be due to the instantaneous increase of pressure at the center of tube by shock wave, since the product of initial pressure times gap length is slightly below the value which corresponds to the minimum sparking voltage. Oscilloscopic observation of discharging current gives the estimation of time lag of center sparking and shock velocity can be calculated assuming that Mach number of cylindrically coverging shock increases with inverse proportionality of one fifth power of the distance from converging center[2)] and rough estimation of temperature rise near the center electrodes will be possible therefrom. An example of the calculation is shown in Table I. Thus we may conclude that arc discharge without sparking follows immediately after the arrival of an intense shock wave.

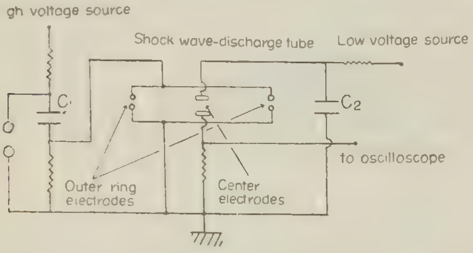

Fig. 2. Circuit used for the measurement of sparking voltage of center electrodes.

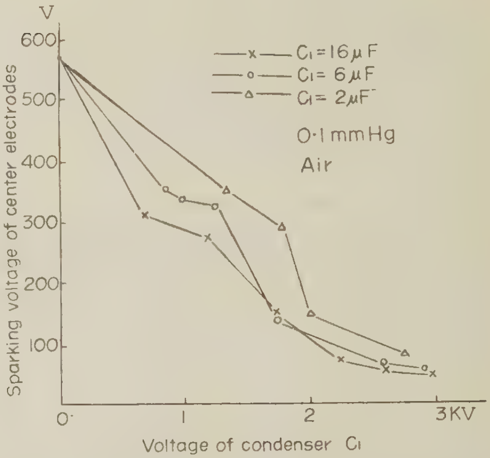

Fig. 3. Sparking voltage of center electrodes.

Table I

Capacity of condensor C_1	16 μF
Capacity of condensor C_2	4000 μF
Voltage of C_1	3 KV.
Voltage of C_2	400 V
Mean discharging current of C_2	1000 A.
Mean shock velocity	2.0 Km/sec.
Temperature at the center electrodes (calculated)	4500° K.

References

1) R. G. Fowler et al.: Phys. Rev. **88** (1952) 137.
2) R. W. Perry and A. Kantrowitz: J. A. P. **22** (1951) 261.

J. PHYS. SOC. JAPAN **12** (1957) 217

On the Electrical Properties of Degenerate Semiconductors

By Eijirô HAGA

Department of Physics, Faculty of Science, Niigata University

(Received November 14, 1956)

In his recent theoretical work[1] on the electrical conductivity, the writer has succeeded in derving Grüneisen's formula for simple metals and the corresponding one for highly degenerate polar crystals by an elementary method, assuming that the high degeneracy criterion $df_0/d\varepsilon=-\delta(\varepsilon-\zeta)$ is valid. Once this assumption is admitted, then we can easily deduce the so called Mattiessen's rule for the cases where more than one kinds of the sources for the scattering of conduction electrons are present. On the other hand, Kohler[2] has given a general proof that the total resistivity should be in general larger than the simple sum of resistivities due to a single kind of scattering sources. It will, then, be worth while to investigate how the deviations from the Mattiessen's rule take place when the conduction electrons are not perfectly degenerate. In this connection we will also see the relation between the Hall coefficient and the degree of degeneracy.

In this note we treat, as an example, non polar semiconductors in which lattice vibrations and ionized impurities are predominant as the scattering sources. Then, with the same assumptions as done by JL[3], we calculate the two ratios, $F=(\rho_L+\rho_I)/\rho$ and $r=R/(1/nec)=\mu_H/\mu_a$, which are in this case expressible as

$$F=(1+\xi)[1-\xi A(\mu)F_2(\mu)\times\int_0^\infty e^t/(e^t+e^\mu)^2\cdot t/(\xi B(\mu)+t^2)\,dt\,,$$

$$r=(1+\xi)^2A(\mu)F_{1/2}(\mu)/2F^2\times\int_0^\infty e^t/(e^t+e^\mu)^2\cdot t^{9/2}/(\xi B(\mu)+t^2)^2\,dt\,,$$

where

$$\mu=\zeta/kT,\quad \xi=x/(1-x),\quad x=\rho_I/(\rho_L+\rho_I),$$

$$A(\mu)=3e^\mu/[\ln(e^\mu+1)]^2,\quad B(\mu)=3F_2(\mu)/\ln(e^\mu+1).$$

The calculation was carried out numerically using the numerical tables[4] of $F_2(\mu)$ and $F_{1/2}(\mu)$. The results are shown in Figs. 1 and 2 as the functions of x for several μ values. We see that the Mattiessen's rule becomes a good approximation and the Hall mobility approaches to the drift mobility as the degree of degeneracy becomes high enough. We see also that minima of F and r occur at the x values nearly independent on μ.

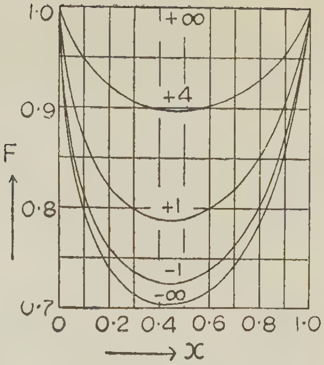

Fig. 1. The dependence of F upon x for several μ values.

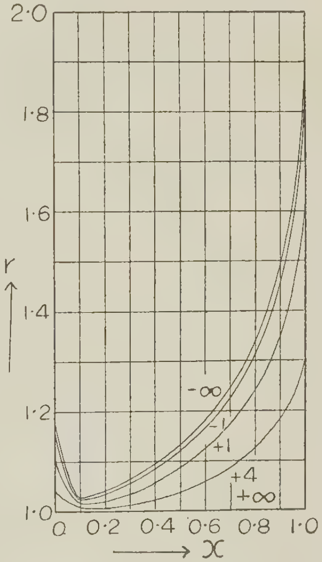

Fig. 2. The dependence of F upon x for several μ values.

The case $\mu=-\infty$ corresponds to the classical statistics previously treated by JL[3].

This work was supported by the Scientific Research Fund of the Ministry of Education.

References

1) E. Haga: Busseiron Kenkyû **92** (1956) 64.
2) M. Kohler: Z. f. Phys. **126** (1949) 495.
3) V. A. Johnson and K. Lark-Horovitz: Phys. Rev. **82** (1951) 977.
4) P. Rhodes: Proc. Roy. Soc. **A 204** (1950) 396.
J. McDougall and E. C. Stoner: Philos. Trans. **A 237** (1938) 67.

J. Phys. Soc. Japan **12** (1957) 218

Preparation of $BaTiO_3$ Single Crystals in Coal Gas Atmosphere

By Kazuo Kawabe
Department of Physics, Osaka University
and Shozo Sawada
Institute of Science and Technology, University of Tokyo

(Received November 13, 1956)

Several investigators have reported on methods of growing barium titanate single crystals using sodium carbonate as a flux.(1)-(4) Sawada, Nomura and Fujii(4) prepared their samples in a nickel crucible put in a kryptol furnace which had reductive atmosphere. We have modified their method by using a resistance furnance (the main constituent of the heater is SiC) and a nickel crucible put in the stream of coal gas to avoid the oxidation. The nickel crucible used in the coal gas stream was hardly oxidized and had almost completely metallic appearance after operation. In air or nitrogen atmosphere nickel reacted with carbonate solution to become black, yielding black crystals which were not ferroelectric.

The solute is the stoichiometrical mixture of TiO_2 and $BaCO_3$ of high purity. The molar ratio of the solute to the flux (Na_2CO_3, c.p.) is about 1 to 4. The composition in volume of the coal gas used is as follows: H_2 about 30 %, N_2 30 %, CH_4 20 %, CO 15 % and the rests 5 %. The furnace is heated up to about 1200°C and is held at this temperature for several hours. A cooling rate of about 25°C/hr seems to be suitable, until a temperature of 1050°C is reached, where the furnace is held for about twelve hours and then cooled again at a rate of about 20°C/hr down to 900°C. At this temperature the still-liquid flux is sucked up through a nickel pipe by a rotary pump and the crystals are annealed by slow cooling down to the room temperature. The crystal plates can be separated from the flux by soaking the crucible in hot water which dissolves the carbonate rapidly.

The thin platelike crystals produced in this way are all tetragonal ones, having a Curie temperature of about 118°C. The size is about several mm on an edge and some one reaches 1 cm and the thickness is $20\sim30\,\mu$. They have *a*- and *c*-domains mixed showing strip patterns under a polarizing microscope. Single *c*-domain crystals are scarcely obtained by this method.

The nickel crucibles employed were commercial ones of about 30 cc in volume. Larger crystals might be expected by using larger crucibles and giving some favorable temperature gradient to the crucible.

We have tried to use KF as a flux in this method. Potassium fluoride was successfully used with platinum crucibles by J.P. Remeika.(5) We have got some large crystals after the same manner as above except the flux, all of them, however, being found to be dark colored. On heating them in air at about 1000°C for about 30~40 hr, they become light brown and have a Curie temperature of 122°C according to the measurement of the dielectric constant. In air atmosphere the nickel crucible was heavily attacked.

This work was done during one of the author's (K.K.) stay at Institute of Science and Technology, University of Tokyo as a fellow of the Yukawa Foundation of Osaka University. He wishes to express his thanks to Dr. S. Nomura of this Institute for valuable discussions, and to Prof. I. Nitta, Dean of the Faculty of Science of Osaka University and Prof. T. Horie for giving him this opportunity all through the 1955 school year.

References

1) H. Blattner, H. Gränicher, W. Känzig and W. Merz: Helv. Phys. Acta **21** (1948) 341.
2) H. Blattner, W. Känzing and W. Merz: Helv. Phys. Acta **22** (1949) 35.
3) H. F. Kay: Acta Cryst. **1** (1948) 229.
4) S. Sawada, S. Nomura and S. Fujii: Rept. Inst. Sci. Tech., Univ. Tokyo **5** (1951) 7.
5) J. P. Remeika: J. Am. Chem. Soc. **76** (1954) 940.

JOURNAL OF THE PHYSICAL SOCIETY OF JAPAN Vol. 12, No. 3, MARCH, 1957

A Cascade Shower in Nuclear Emulsions

By Senzo TOKUNAGA
Department of Physics, Saikyo University, Kyoto
Kiyoshi NISHIKAWA
Department of Physics, Wakayama University, Wakayama
and Taka ISHII
Department of Physics, Saikyo University, Kyoto

(Received November 20, 1956)

A good example of a cascade shower in nuclear emulsions was analysed, and its energy was determined from its lateral distribution at successive stages of its development comparing with cascade theory, and was found to be 2.5×10^{11} eV. It is possible to measure the energy of high energy γ-rays or electrons with an accuracy of a factor two.

§ 1. Introduction

For high energy events observed in nuclear emulsions in which it is impossible to measure the energy of particle by scattering method, it is very important to decide the energy by any other method. One method is to make use of the phenomena of cascade shower. Here, we described the method to determine the energy of the cascade from its lateral distribution at successive stages of its development through several radiation lengths comparing with cascade theory.

§ 2. Experimental

Our stack, consisting of 48 4-inch by 6-inch Ilford G5 600 micron pellicles, was flown with the emulsion surfaces vertical for 6 hours up to the maximum altitude of 8 mb by a polyethylene balloon in Japan in 1955. The emulsions were processed by the usual temperature development. Cascade showers were sought in the stack. For this purpose the emulsions were line scanned along the horizontal direction at the time of exposure in the lower part of the stack. Several cascades were found, but many of them had great dips and did not develop so much, except the one which had a total length of 4.5 radiation lengths (a length of 1 cm per plate), and was suitable for analysis. We looked for the nuclear event from which neutral π meson, the origin of the primary photon of our cascade, would be emitted, but we could not find such an event.

The electron tracks of the cascade were identified when they had the blob density of plateau value, ran nearly parallel to the core

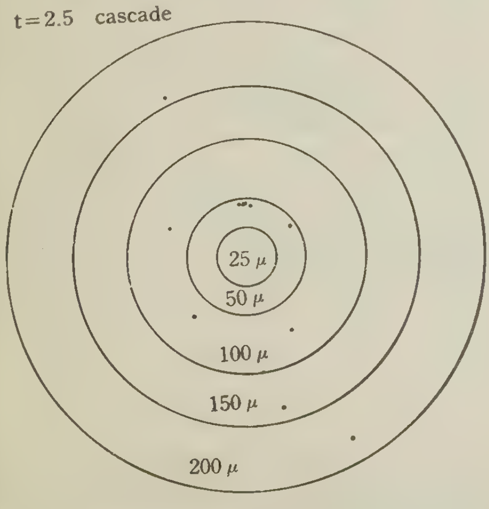

Fig. 1. Target diagram for the cascade shower at 2.5 radiation lengths from the origin.

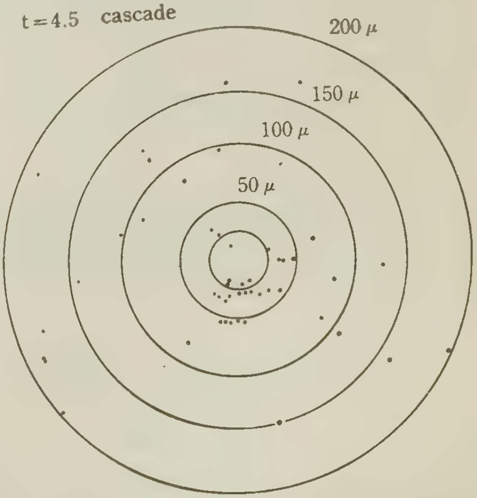

Fig. 2. Target diagram for the cascade shower at 4.5 radiation lengths from the origin.

and had almost the same track lengths.

For this cascade shower target diagrams were obtained at successive stages of its development. In Fig. 1 and 2 two of them were shown. In the figures the points represent electron tracks projected onto a plane perpendicular to the shower axis, and the circles centered on the shower axis are of 50, 100 and 200 microns radius, respectively. The shower axis was determined as the center of mass of particles. In Fig. 4 were shown the observed numbers of electrons within several values of radius r as a function of the distance t in emulsion.

§ 3. Theoretical

In order to compare with the cascade theory the Nishimura-Kamata's function[1), 2)] was used as the normalised structure function $f(r/r_1, s)$, where r denotes the distance from the shower axis on the plane perpendicular to the shower axis and s the shower age.

$$\int_0^\infty f(r/r_1, s)2\pi r dr = 1 \tag{1}$$

$$f(r/r_1, s) = \frac{c(s)}{r_1^2(r/r_1)^{2-s}}\left(1+\frac{4}{s}\frac{r}{r_1}\right)e^{-a(r/r_1)b}$$
$$\simeq \frac{c(s)}{\left(\frac{k}{\mathcal{E}}\right)^2\left(\frac{\mathcal{E}r}{k}\right)^{2-s}} = c(s)\left(\frac{\mathcal{E}r}{k}\right)^{s-2}\left(\frac{\mathcal{E}}{k}\right)^2 \tag{2}$$

where $r_1 = k/\mathcal{E}$, $k = 21$ MeV, $\mathcal{E}$ the critical energy, and $c(s)$ is the function given in ref. 1).

The number of electrons with all energies at a depth t from the point at which a photon of energy E_0 is incident in the stack is given by one dimensional cascade function[3)] (approximation B of ref. 3))

$$\Pi(E_0, 0, t) = \frac{1}{2\pi i}\int\left(\frac{E_0}{\mathcal{E}}\right)^s \frac{M(s)}{s^{1/2}} k(s, -s)e^{\lambda_1(s)t}ds \tag{3}$$

Then the number of electrons lying within an annular ring between radii r and $r+dr$ centered on the shower axis $\Pi(E_0, r, 0, t)2\pi r dr$ is given by the equation

$$\Pi(E_0, r, 0, t)2\pi r dr$$
$$= \frac{1}{2\pi i}\int\left(\frac{E_0}{\mathcal{E}}\right)^s\left(\frac{\mathcal{E}}{k}\right)^2\left(\frac{\mathcal{E}r}{k}\right)^{s-2} c(s)\frac{M(s)}{s^{1/2}}$$
$$\times k(s, -s)e^{\lambda_1(s)t}ds 2\pi r dr \tag{4}$$

Integrating with respect to r, we get the number of electrons Π which are contained within the circle of radius r and

$$\Pi = \int_0^r \Pi(E_0, r, 0, t)2\pi r dr$$
$$= \frac{1}{2\pi i}\int 2\pi\frac{c(s)}{s^{3/2}}\left(\frac{E_0 r}{k}\right)^s M(s)k(s, -s)e^{\lambda_1(s)t}ds \tag{5}$$

The integration with respect to s is calculated by the usual saddle point method, and

$$\Pi = \frac{\sqrt{2\pi}c(\bar{s})(E_0 r/k)^{\bar{s}}M(\bar{s})k(\bar{s}, -\bar{s})e^{\lambda_1(\bar{s})t}}{\bar{s}^{3/2}(\lambda_1''(\bar{s})t + 3/2\bar{s}^2 + (c'/c)')} \tag{6}$$

where $\bar{s}$ is given by

$$-\frac{3}{2s} + \frac{c'}{c} + \lambda_1'(s)t + \ln\frac{E_0 r}{k} = 0 \tag{7}$$

§ 4. Results and Discussion

In Fig. 3, 4, 5, and 6 were shown the results of the calculation using equation (6) for several values of the energies of the incident primary

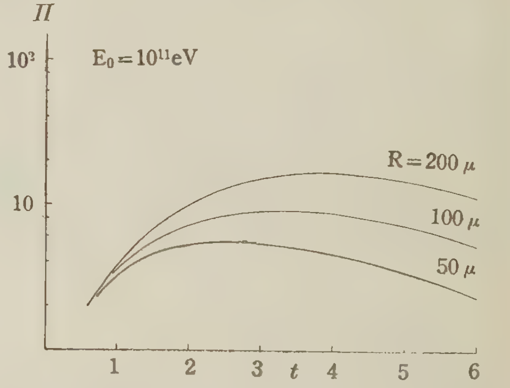

Fig. 3. The radial distribution function for the cascade shower when the energy of the primary photon is 10^{11} eV.

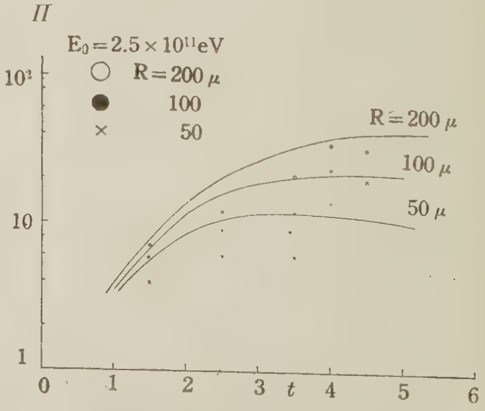

Fig. 4. The radial distribution function for the cascade shower when the energy of the primary photon is 2.5×10^{11} eV, together with the observed radial electron distributions.

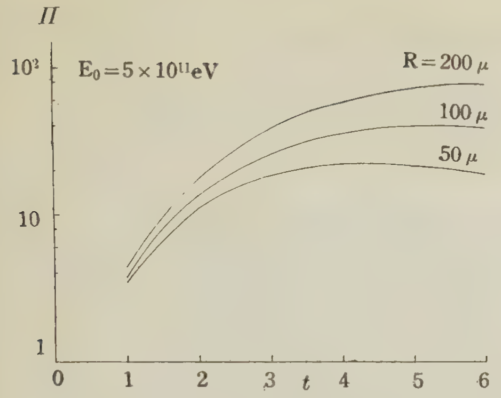

Fig. 5. The radial distribution function for the cascade shower when the energy of the primary photon is 5×10^{11}eV.

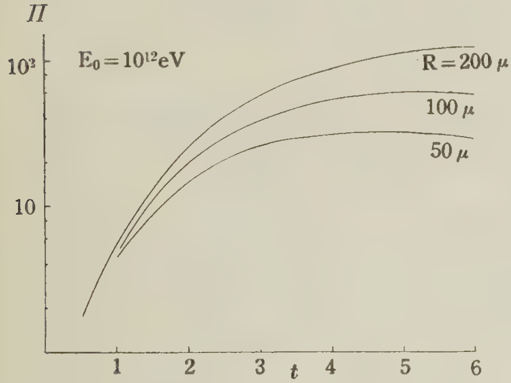

Fig. 6. The radial distribution function for the cascade shower when the energy of the primary photon is 10^{12} eV.

photon. Comparing with our experimental results, the energy of the primary photon of our cascade is estimated to be 2.5×10^{11} eV, the tendency of the development of the cascade differing clearly if the energy is assumed to be 10^{11} eV or 5×10^{11} eV.

From the above result the energy of the cascade shower can be determined with an accuracy of a factor two. It would be significant that we can estimate the energy of particle in the very high energy region with such an accuracy, where it is impossible to determine the energy by the oridinary scattering method.

It will be possible to justify the theory if we find the cascade showers developed by two photons which have their origin in $\pi^\circ\rightarrow2\gamma$ event, in which we can estimate the energy of π°-meson more accurately from the opening angle between the two γ-rays. In our case such a case has not been found. But as the studies with emulsion cloud chambers are now going on, it must soon be found.

Making use of the approximation A of Rossi and Greisen applying the theory by Fernbach and Erges[4], Kaplon and Ritson[5] also estimated the energies of cascade showers in their emulsion cloud chambers. Their results agree with ours within the fluctuations. Recently, Pinkau[6] has also reported the analysis of cascade shower in nuclear emulsions in which he obtained the energy of γ-ray by measuring the energy of each electron track by scattering method. His results are well in accord with ours.

The authors wish to express their gratitude to Prof. O. Minakawa and J. Nishimura for their comments and suggestions. To the members of the Kansai Balloon Group go our sincere appreciation and thanks for making possible the balloon flight.

This work was financially supported by the Grant for Scientific Research of the Ministry of Education for the 1955 fiscal year.

References

1) J. Nishimura: Ultra High Energy Phenomena (1955) 117.
2) J. Nishimura and K. Kamata: Prog. Theor. Phys. **5** (1950) 899. Prog. Theor. Phys. **7** (1952) 185.
3) B. Rossi and K. Greisen: Rev. Mod. Phys. **13** (1941) 288.
4) L. L. Eyges and S. Fernbach: Phys. Rev. **82** (1951) 288.
5) M. F. Kaplon and D. M. Ritson: Phys. Rev. **88** (1952) 386.
6) K. Pinkau: Nuovo Cimento **3** (1956) 1285.

JOURNAL OF THE PHYSICAL SOCIETY OF JAPAN Vol. 12, No. 3, MARCH, 1957

Layer Structures of Magnetic Oxides

By Shūichi IIDA

Department of Physics, Faculty of Science, University of Tokyo

(Received November 24, 1955)

In most of the ferromagnetic oxides, the anion lattices are constructed by piling up two dimentional trigonal lattice layers in succession. Metallic ions locate on the proper interstices of these anion layers, forming themselves also several kinds of layers. It has been shown that the crystal lattices of these oxides can be constructed uniquely by assuming 1) the layer structures outlined above, 2) requirement of minimizing the sum of electrostatic energy and interionic repulsive energy and, 3) the numbers of cations locating between two neighbouring anion layers are all the same, e. g. equal to that corresponding to the molecular ratio notwithstanding that there may be several kinds of cation structures as such inter-layer cation arragements. From this consideration, 13 M−O−M configurations are derived as possible configurations acting for the superexchange interaction in magnetic oxides. It is shown that the magnetic lattices also have layer structures.

§1. Introduction

The most of the crystal structures of magnetic oxides are so complex that it seems difficult to understand these structures physically; for instance the spinel structure contains fifty-six ions in a unit cell. However, it has been shown by the carefull analysis based upon certain assumptions, that each of these structures is a unique one which can be constructed from the constituent ions having definite ratio of anions to cations. Since these assumptions are so simple and reasonable, by using these ideas, we can understand the crystal structures of various magnetic oxides more deeply than by the usual crystallographic representation. It would become easier to consider possible imperfect structures in these crystals (lattice defect, dislocation, stacking fault, etc.). These ideas can also be applied to many other compounds to elucidiate their crystal structures.

An application of these ideas to the problem of superexchange interaction will be given in the last sections.

§2. Assumptions

Oxides of iron group elements are generally discussed in this paper. It is well known that in almost all of these crystals anions make approximately close packed lattices (face centered cubic lattice or hexagonal close packed lattice). The fact will be mainly due to the large difference in ionic radii between the oxygen ion ($O^{--}=1.32$ A) and the metal ions of iron group elements ($Mn^{++}=0.91$, $Fe^{++}=0.83$, $Fe^{+++}=0.67$, $Co^{++}=0.82$, $Ni^{++}=0.78$, etc.)[1]. It is also well known that the close packed lattices can be constructed by piling up plane trigonal lattices. The plane trigonal lattice has two kinds of interstices, each of which forms itself a plane trigonal lattice. These are shown in Fig. 1. We shall specify each one of these with its phase A, B or C. Then a layer structure ABCABC··· forms a face centered cubic lattice and ABABAB··· forms a hexagonal close packed lattice.

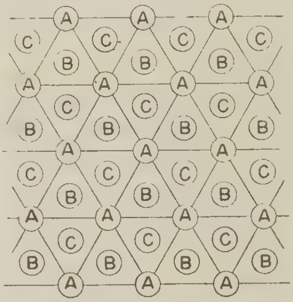

Fig. 1. Mutual configuration of three plane trigonal lattices with phases A, B, and C.

It is our standpoint throughout this paper that every crystal is considered as having a layer structure. Thus the following three assumptions can be derived semi-empirically as the guiding principles.

Assumption I.

In these crystals, oxygen ions form close packed lattices. Therefore, the lattices can be considered as layer structures composed of plane trigonal lattices of oxygen ions*.

Assumption II.

In these crystals, cations locate on proper interstices of their close packed oxygen lattices. The arrangement of cations on various interstices are so determined as to minimize the sum of the interionic repulsive energy and the electrostatic Coulomb energy. The phase selection of the successive oxygen layers (ABC··· or ABA··· etc.) are also ruled by the same principle.

Assumption III.

Cations distribute equally in number to each interspace region present between every two nearest oxygen layers. Therefore, the ionic ratio of cations to anions is maintained as constant at between every two neighbouring oxygen layers; it is equal to the molecular ratio of the crystal.

It seems at this stage that Assumption II requires quantitative calculations of the Madelung constant. However, it will be shown later that in almost all cases only qualitative considerations of this sort are enough to understand the actual arrangements of anions and cations. Assumption III might be supported by the requirements for the balance of electrostatic charge or by that for the maximum entropy. However, this assumption is derived here mainly from empirical facts.

§ 3. Subdivisions "S" and "T"

Before entering into the analysis of the actual crystals, several geometrical relations existing in the plane trigonal lattices A, B and C are studied.

Now we consider first the possible ways of subdivision of a plane trigonal lattice. If we postulate that the sublattices after the subdivision should be all equivalent and be all nearest neighbours with each other, it is possible to find three ways of such subdivision. These are shown in Fig. 2. The unit length of these sublattices are $\sqrt{3}a$, $2a$ and $\sqrt{7}a$ respectively, where a is an unit length of the original lattice. These subdivisions subdivide the original trigonal lattice into 3, 4 and 7 equivalent trigonal sublattices. We shall call these, subdivisions "S", "T" and "U" respectively.

"S" subdivision

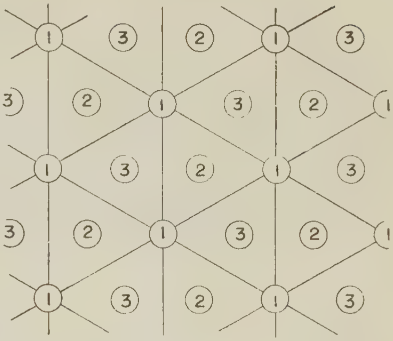

(a), Subdivision "S" (with three sublattices).

"T" subdivision

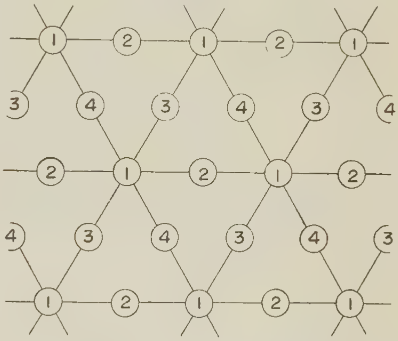

(b), Subdivision "T" (with four sublattices).

"U" subdivision

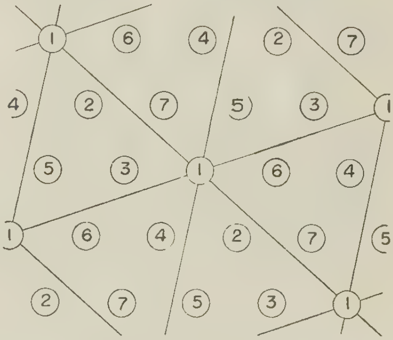

(c), Subdivision "U" (with seven sublattices).

Fig. 2. Three ways of subdivision for a plane trigonal lattice.

---

* In this stage, we disregard entirely the deviations from the geometrical lattice points that exist often in actual crystals.

We concern ourselves with "S" and "T" subdivisions in this paper. "U" subdivision is rather artificial. It should be noticed that if one sublattice in "S" subdivision is removed from the original lattice, then the remaining lattice forms a honey-comb lattice, and on the other hand in "T" subdivision, the remaining lattice forms a "kagome" lattice as shown in Fig. 3. For the sake of the later analysis we define the individual sublattices on the three plane trigonal lattices A, B and C as

SA1 SA2 SA3 TA1 TA2 TA3 TA4
SB1 SB2 SB3 or TB1 TB2 TB3 TB4
SC1 SC2 SC3 TC1 TC2 TC3 TC4 .

The mutual relation of these sublattices are shown in Fig. 4(a) or (b). In "T" subdivision, TA1+TB1+TC1 forms also a trigonal lattice and TA1, TB1 and TC1 form "S" subdivision in this trigonal lattice. TA2+TB2+TC2, TA3+TB3+TC3, and TA4+TB4+TC4 also have the same relation.

"S1+S2"

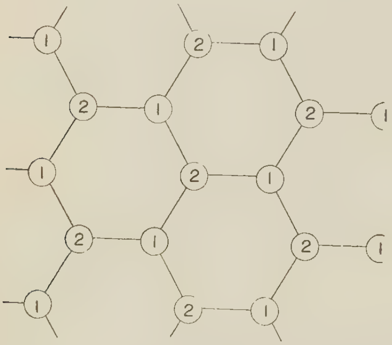

(a), honey-comb lattice as composed of two sublattices in "S" subdivision.

"T1+T2+T3"

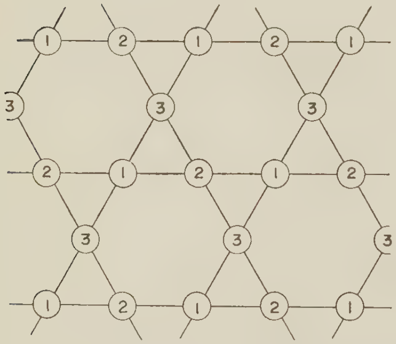

(b), "kagome" lattice as composed of three sublattices in "T" subdivision.

Fig. 3. Plane trigonal lattices with vacant sublattice.

"S" subdivision

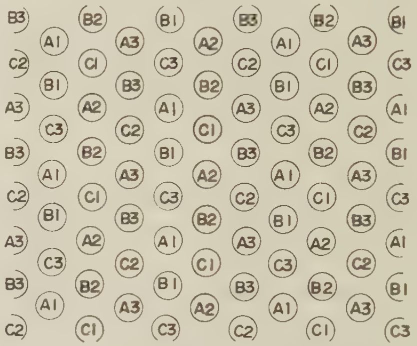

(a), in "S" subdivision

"T" subdivision

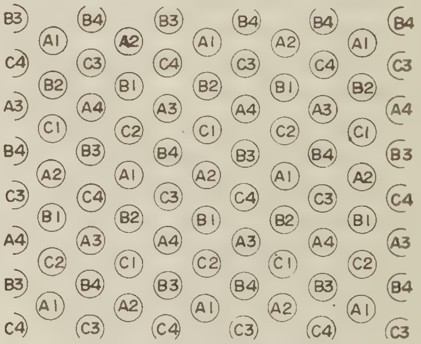

(b), in "T" subdivision

Fig. 4. Notation of individual sublattices on three plane trigonal lattices A, B, and C.

It should be noticed here that subdivisions "S" and "T" subdivide the trigonal lattices by completely different ways and there is no simple correlation between them. It has been found actually that the whole crystals in which some ions form close packed lattices can be classified into three groups, namely, 1) having no subdivision (NaCl, NiAs, ZnO, ZnS, CdI_2, $CdCl_2$ types etc.), 2) obeying "S" subdivision (Cr_2O_3, $TiFeO_3$, Ni_3S_2 types etc.), and 3) obeying "T" subdivision ($MgAl_2O_4$, $BaFe_{12}O_{19}$, Fe_7S_8, $LaMnO_3$, $HFeO_2$ types etc.)[2]. If two crystal structures belong to "S" and "T" group respectively, there is no habit plane of good registry. At low temperatures, Fe_3O_4 transforms into γFe_2O_3 by further oxidation, and not into αFe_2O_3, in spite of the fact that the true equilibrium state is αFe_2O_3. The phenomenon will be explained by the fact that both Fe_3O_4 and γFe_2O_3 belong to "T" group and can transform continuously from one to another, while αFe_2O_3 belongs to "S" group.

§ 4. Iron-Oxygen Crystals

Now the analysis of the actual crystal structures will be given. For convenience, we explain first iron-oxides in detail. These are wüstite (FeO, NaCl type), magnetite (Fe_3O_4, $MgAl_2O_4$ type) and α hematite (Fe_2O_3, Cr_2O_3 type).

1) FeO[2].

According to Assumption I, a plane trigonal lattice of O^{--} ions is taken as the first layer. Let the phase of the layer be A (Diagram 1). Then Assumptions II and III promise that the phase of next Fe^{++} layer should be B or C, and Fe^{++} ions should occupy the whole lattice points of the same layer. If we assume the layer is B, then we must conclude the next O^{--} layer is C according to Assumption II. The diagram thus constructed is shown in Diagram 1. In the diagram, z means vertical distances of the layers. It will be easy to understand why wüstite has NaCl type structure.

4	O		C		
	Fe			B	←
3	O	—	A		
	Fe	↑		C	→
2	O		B		
	Fe	Unit Cell		A	←
1	O		C		
	Fe	↓		B	→
0	O	—	A		
z			O^{++}	Fe^{++}	Spin

FeO

Diagram 1. Structure of FeO.

2) αFe_2O_3[2].

Like the previous case, we first set an O^{--} ion layer of phase A (Diagram 2). By Assumption III, the next Fe^{+++} ion layer must occupy two thirds of the lattice points of a plane trigonal lattice of phase B. Then, it will be required by assumption II, that the lattice should be subdivided by subdivision "S" and two of the three sublattices be occupied. Let them be SB2 and SB3. They form an honey-comb lattice. The next O^{--} ion layer must be C. The configuration thus obtained is shown in Fig. 5.

2			O^{--}	Fe^{+++}	Fe^{+++}	Fe^{+++}		
7	O		C					
	Fe					SB3	→	←
	Fe				SB2		→	→
6	O	—	A					
	Fe	↑		SB1			←	←
	Fe					SB3	←	→
5	O		C					
	Fe				SB2		→	←
	Fe			SB1			→	→
4	O		A					
	Fe					SB3	←	←
	Fe				SB2		←	→
3	O	Unit Cell	C					
	Fe			SB1			→	←
	Fe						→	→
2	O		A			SB3		
	Fe				SB2		←	←
	Fe			SB1			←	→
1	O		C					
	Fe					SB3	→	←
	Fe				SB2		→	→
0	O	↓ —	A					
z			O^{--}	Fe^{+++}	Fe^{+++}	Fe^{+++}	Spin	Spin in Cr_2O_3

αFe_2O_3

Diagram 2. Structure of αFe_2O_3.

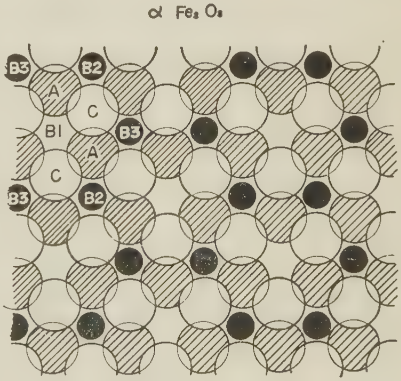

Fig. 5. Projection of α Fe_2O_3 crystal as seen from <111> asis. It corresponds to a cross section at $z=1$ in Diagram 2.

It will be clear that the positions SB1 become the positions with minimum energy for the next Fe^{+++} ions. Consequently, the next Fe^{+++} ion layer is SB1 as shown in Diagram 2. But according to Assumption III, one more layer is necessary and the sublattice SB2 or SB3 seems most probable for this. In this case, the existence of Fe^{+++} ion layer on SB1 sublattice denies the possibility of occupation of A positions for the next Fe^{+++} ions. Let it be SB2, the next layer should be an A layer of O^{--} ions. Repeating these procedures, Diagram 2 is easily constructed, which shows that the structure is a hexagonal one. It should be noticed that the initial SB2+SB3 layer of Fe^{+++} ions must separate into two layers SB2 and SB3 by the influence of underlying SB3 layer of Fe^{+++} ions. Diagram 2 is drawn after the consideration of this effect. Oxygen ions also have small displacements from the geometrical positions. These are discussed in section 6.

3) Fe_3O_4[2].

In this case there are two kinds of iron ion: Fe^{++} and Fe^{+++}. But here we disregard the difference of the two ions[3]. By a similar way to that of the preceding case, we can construct Diagram 3. Let the first O^{--} ion layer be of phase A. It is uniquely determined by Assumption III that the next $Fe^{(+)}$ ion layer should follow subdivision "T" and one sublattice becomes vacant. Let it be TB1+TB2+TB3. Then the next O^{--} ion layer must be C. The configuration constructed in this way is shown in Fig. 6, as seen from z axis. With the aid of the figure, it will be clear that the next $Fe^{(+)}$ ion layer is in TB4. However, because of Assumption III, more $Fe^{(+)}$ ion layers must be present. These are TA4 and TC4. The occupation of $Fe^{(+)}$ ions on TC4 sublattice is caused by the electrostatic energy requirement from $Fe^{(+)}$ ions in TB4 and TA4 sublattices. The next O^{--} ion layer must be B. Repeating these precedures we can construct Diagram 3. It represents the spinel structure. It should be noticed that in this case, the $Fe^{(+)}$ ions occupy two different interstices of the oxygen lattice; one is the tetrahedral position and the other is the octahedral position. They correspond to 8(a) and 16(d) sites of the spinel crystal respectively[4].

7	O		C			
	Fe			B–TB4	16d	→
6	O	——	A			
	Fe	↑		TB4	8a	←
	Fe			TC4	16d	→
	Fe			TA4	8a	←
5	O		B			
	Fe			A–TA4	16d	→
4	O		C			
	Fe			TA4	8a	←
	Fe			TB4	16d	→
	Fe	Unit Cell		TC4	8a	←
3	O		A			
	Fe			C–TC4	16d	→
2	O		B			
	Fe			TC4	8a	←
	Fe			TA4	16d	→
	Fe			TB4	8a	←
1	O		C			
	Fe	↓		B–TB4	16d	→
0	O	——	A			
z			O^{--}	$Fe^{(+)}$		Spin

Fe_3O_4

Diagram 3. Structure of Fe_3O_4.

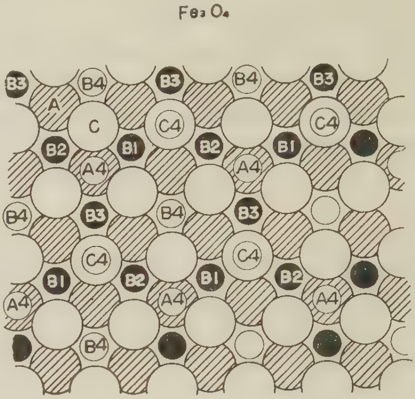

Fig. 6. Projection of Fe_3O_4 crystal as seen from <111> axis. It corresponds to a cross section at $z=7/4$ in Diagram 3.

§ 5. Other Examples

By the explanation of the previous section, it will be understood that each one of the crystal structures of iron-oxygen system can be constructed uniquely by the assumptions I, II and III. The reason why these assumptions are varid so simply for these crystals may be due to the fact that the cohesive energy of the crystals is of purely ionic nature and the oxygen ion has a larger ionic radious than that of the iron ion. The theory can be applied to almost all oxides of iron group elements.

It can be applied also to almost all magnetic compounds. Although some deviations from our theory appear often in these crystals, it will be interpreted as showing the difference in the binding nature in these crystals from the simple theory; it can be ascribed partly to the variety in ionic radii of the component ions and partly to the covalent nature of their binding force. Several examples will be introduced hereafter.

4) FeS[2].

The structure before the α transformation (T > 140°C)* is shown in Diagram 4 and is generally called NiAs type structure. The difference from the structure of FeO is that the two nearest iron ion layers do not elude overlapping in this crystal. This will be due to the homopolar binding tendency of S^{--} ions. Many of the magnetic compounds consisting of iron group elements and metalloid elements (S, Se, Te, As, Sb, Bi, etc.) have the same crystal structure[2]. Various properties of these compounds would be influenced by the mentioned homopolar binding tendency of this structure[6].

z		S^{--}	Fe^{++}	
3		C		
			B	→
2	——	A		
	↑		B	←
1	Unit Cell	C		
	↓		B	→
0	——	A		

FeS

Diagram 4. Structure of FeS.

5) Fe_7S_8[7].

Bertaut has found by a X-ray study that a superstructure Fe_7S_8 exists. The structure is shown in Diagram 5. In this case, it is obvious that "T" subdivision should be used and it becomes also easy by using the same scheme to understand the structures of

z	$S^{(-)}$	$Fe^{(+)}$	$Fe^{(+)}$	$Fe^{(+)}$	$Fe^{(+)}$	Spin
5	C					
					TB4	→
		TB1				→
			TB2			→
4	A					
				TB3		←
					TB4	←
		TB1				←
			TB2			←
3	C					
				TB3		→
					TB4	→
		TB1				→
2	A					
			TB2			←
				TB3		←
					TB4	←
		TB1				←
1	C					
			TB2			→
				TB3		→
					TB4	→
0	A					

Fe_7S_8

Diagram 5. Structure of Fe_7S_8.

z				O^{--}	Ba^{++}	$Fe^{++}+Fe^{+++}$		Spin
12	O			A				
	Fe						C-TC4	→
11	O			B				
	Fe						TC4	←
10	O	BaFe	——	A-TA4	TA4	TB4		→
	Fe		↑				TC4	←
9	O			B				
	Fe						C-TC4	→
8	O			A				
	Fe						TC4	←
	Fe						TB4	→
	Fe						TA4	←
7	O			C				
	Fe						A-TA4	→
6	O			B				
	Fe						TA4	←
5	O	BaFe	Unit Cell	C-TC4	TC4	TB4		→
	Fe						TA4	←
4	O			B				
	Fe						A-TA4	→
3	O			C				
	Fe						TA4	←
	Fe						TB4	→
	Fe						TC4	←
2	O			A				
	Fe						C-TC4	→
1	O			B				
	Fe		↓				TC4	←
0	O	BaFe	——	A-TA4	TA4	TB4		→

$BaO\cdot 6Fe_2O_3$

Diagram 6. Structure of $BaO\cdot 6Fe_2O_3$.

---

* After the α transformation, the structure deforms slightly[5].

various polysynthetic twin crystals present.

6) $BaO\cdot 6Fe_2O_3$[8].

The structure is called magnetoplumbite structure and is shown in Diagram 6. The structure can easily be understood by approving the existence of close packed layers consisting of O^{--}, Ba^{++} and Fe^{+++} ions. In this layer, Ba^{++} ions occupy the special positions which are usually occupied by O^{--} ions. This fact will be due to the large ionic radius of Ba^{++} ion (1.38 A). The layer lies between two spinel units and "T" subdivision is used.

	Mn					TB4		
3	O	La	——	A-TA4	TA4			
	Mn		↑			TC4	→	→
2	O	La		B-TB4	TB4			
	Mn		Unit Cell			TA4	←	→
1	O	La		C-TC4	TC4			
	Mn		↓			TB4	→	→
0	O	La	——	A-TA4	TA4			
z				O^{--}	La^{+++}	Mn^{+++}	Spin Anti	Spin Ferro

$LaMnO_3$

Diagram 7. Structure of $LaMnO_3$.

	Fe					
11	O		B			
	Fe				TA4	→
10	O	K	TA4	TC4		
	Fe				TA4	←
9	O		B			
	Fe				A-TA4	→
8	O		C			
	Fe				TA4	←
	Fe				TB4	→
	Fe				TC4	←
7	O		A			
	Fe				C-TC4	→
6	O		B			
	Fe				TC4	←
5	O	K	TC4	TA4		
	Fe				TC4	→
4	O		B			
	Fe				C-TC4	←
3	O		A			
	Fe				TC4	→
	Fe				TB4	←
	Fe				TA4	→
2	O		C			
	Fe				A-TA4	←
1	O		B			
	Fe				TA4	→
0	O	K	TA4	TC4		
z			O^{--}	K^{+}	Fe^{+++}	Spin

$KFe_{11}O_{17}$

Diagram 8. Structure of $KFe_{11}O_{17}$.

7) $LaMnO_3$[9].

The structure is called perovskite structure and is shown in Diagram 7. In this case also, the ionic radius of La^{+++} ion is so large that O^{--} ions and La^{+++} ions construct together a face centered cubic structure. Mn^{+++} ions locate on all the octahedral interstices which are surrounded only by O^{--} ions in this close packed lattice. "T" subdivision is used.

8) $KFe_{11}O_{17}$[8].

The structure is shown in Diagram 8. In this case the ionic radius of K^{+} ion is so large that a K^{+} ion in TC4 position is considered to play the same role as three O^{--} ions at TA1+TA2+TA3 positions.

§ 6. Discussion

It should be remarked here that in the actual crystals there are often some deviations from the geometrical lattice points which are mentioned above. These deviations are induced usually by the lack of certain symmetry existing occasionally in the original geometrical lattices, and the deviations occure so as to reduce the total cohesive energy, which are easily comprehensibe. Therefore, for instance, the presence of parameter u in the spinel structure[2], and u, v in the rhombohedral sesquioxide (αFe_2O_3)[2] can be expected *a priori* from the original structures. These deviations occur normally so as to equate approximately all the contact distances between cation and oxygen ion for these cases.

As an example, in Fig. 7, the atomic arrangement of αFe_2O_3 are shown in the actual proportions. (a=5.427 A[10], α=55°16′, u=0.105, v=0.295[11], $r(O^{--})$=1.32 A, $r(Fe^{+++})$=0.67 A). The projection to (110) plane is shown in (a), and that to (001) plane, in (b) (hexagonal coordination). The induced displacement of each ion from the geometrical position are illustrated in the figure. In the left side of Fig. 7(a), the original position of each layer is shown. As illustrated already in Diagram 2, each Fe^{+++} ion layer splits into two in order to increase Fe–Fe distances, resulting in the simple displacements of Fe^{+++} ions along ⟨001⟩ or ⟨00$\bar{1}$⟩ direction. The displacements of oxygen ions are understood easily as the consequence of these cation displacements. The displacements of oxygen ions are shown in Fig. 7(b) by short lines. It will be also clear that the direction of each displacement is unique. In the figure, oxygen ions in C layer changes their positions such that they approach to the nearest SB2 positions in the same (001) plane. The contact distances between oxygen ion and iron ion become 2.07 A or 1.97 A in αFe_2O_3[12].

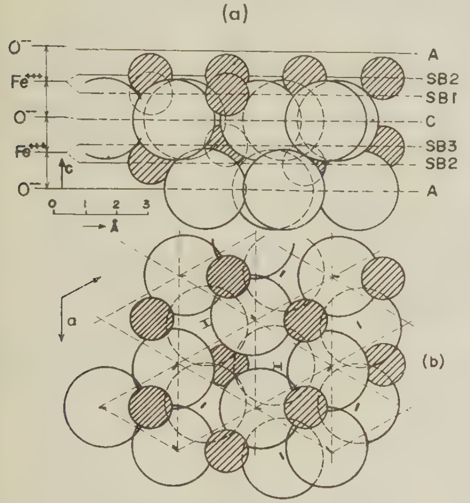

Fig. 7. Atomic arrangement in αFe_2O_3. (a), as projected to (110) plane; (b), as projected to (001) plane. Short lines indicate the induced displacements of oxygen ions from the geometrical positions. All configurations are written in actual proportion.

But there are several crystals in which the deformation occurs unusually which can not be expected from the symmetry of the original lattice. Tetragonal deformation of spinel structure (Mn_3O_4, $ZnMn_2O_4$[1], $CuFe_2O_4$[13]), deformation to MnP structure from NiAs structure (MnAs,[14], FeAs[12]), etc. are such cases. In these cases it will be necessary to make clear the driving force for such deformation. It will be necessary in such cases to introduce the consideration of covalency. However[13], we do not concern ourselves with such topics in the present paper.

It is well known that in the actual crystal growth from the melt or the solution, each crystal grows layer by layer probably with the aid of screw dislocations in the center[15]. At these circumstances each ion might sought its favouroble position on the surface of the mother crystal, in obedience to the law similar to the assumptions which we postulated in section 2. In the compound like as treated in the present paper, the growing surface coincide frequently with the layer surface being considered now. This fact might indicate that there are some relationships between the idea developed in the present paper and the mechanism of the actual crystal growth.

§ 7. Possible Types of Super Exchange Interaction

In the arrangement of ions discussed above, we can find thirteen kinds of super exchange interactions[16] with different cation-anion-cation configurations. These are shown in Table I. In the table, the first column indicates the interaction angle $\angle M_1OM_2$, (M_1, M_2 mean interacting cations, O means intermediate oxygen), and the second column, the M_1–O, M_2–O distances. The configurations in which M_1–O and M_2–O are contact distances are only listed. There are two contact distances p and q corresponding to tetrahedral and octahedral positions respectively. The third column indicates the corresponding configurations expressed by our notations with the relevant oxygen ion layer having A phase, and the fourth and fifth columns indicate the possibility of each configuration in cubic and hexagonal sequence of oxygen. The last two columns indicate whether the interaction connects the cations at different side (upper or lower) of the intermediate oxygen layer or not. As is shown, most of the strong coupling (having large interaction angle) are of inter layer nature. Therefore, it can be supposed from this table that magnetic coupling also have often layer like structure. As will be shown in the next section, in the actual crystals this expectation is realized in almost all cases; their dominant interactions are those of inter-layer nature. However, it should be noticed that this does not mean that all the spin magnetic moments present between two adjacent oxygen ion layers are parrallel. The last line of the table indicates the special super exchange configuration appearing in $BaFe_{12}O_{19}$[8]. It should be remarked that the interaction angles or the M–O distances shown in the

Table I. Possible M_1-O-M_2 configurations in magnetic oxides.

The tabulated configurations can be responsible for superexchange interaction. The interaction angles $\angle M_1OM_2$ and the oxygen ion-metal ion distances M_1-O, M_2-O are those for the ideal geometrical arrangements in which oxygen ions make regular close packed arrangements.

$p=\sqrt{3/8}\ a=0.612a$, and $q=\sqrt{1/2}\ a=0.707a$, where a means nearest O-O distance.

The third column indicates the individual configurations. For instance, $T^{B}_{C}\mathrm{i}(1/4)-\mathrm{A}(0)-T^{C}_{B}\mathrm{i}(+1/4)$ means two configurations, in which one is the configuration from M_1 at TBi position (Fig. 4(b)) with $z=-1/4$ (z means the vertical coordinate of each ion measured by the interlayer distance of oxygen layers, i.e. $\sqrt{2/3}a$, to M_2 at TCi position with $z=+1/4$ intermediated by an oxygen ion at A position with $z=0$. The relevant oxygen ion layer is constantly assumed to be A phase at $z=0$.

Cubic or Hexa. mean that the configuration may appear in the cubic or hexagonal sequence of oxygen layers (BAC and CAB, or BAB and CAC).

Inter or Intra layer means the configuration in which M_1 and M_2 belong to the different side or the same side of the intermediate oxygen ion layer.

	$\angle M_1OM_2$	M_1-O, M_2-O	$M_1(z)-O(z)-M_2(z)$	Cubic	Hexa	Inter layer	Intra layer
I	180°	pp	$\mathrm{Ai}(-3/4)-\mathrm{Ai}(0)-\mathrm{Ai}(+3/4)$	○	○	○	×
		pp	$T^{B}_{C}\mathrm{i}(-1/4)-\mathrm{TAj}(0)-T^{C}_{B}\mathrm{i}(+1/4)$	○	×	○	×
II	180°	qq	$T^{B}_{C}\mathrm{i}(-1/2)-\mathrm{TAj}(0)-T^{C}_{B}\mathrm{i}(+1/2)$	○	×	○	×
III	165°13′	pq	$T^{B}_{C}\mathrm{i}(-1/4)-\mathrm{TAj}(0)-T^{C}_{B}\mathrm{i}(+1/2)$	×	○	○	×
		qp	$T^{B}_{C}\mathrm{i}(-1/2)-\mathrm{TAj}(0)-T^{C}_{B}\mathrm{i}(+1/4)$	×	○	○	×
IV	131°49′	qq	${}^{B}_{C}\mathrm{i}(-1/2)-\mathrm{A}(0)-{}^{B}_{C}\mathrm{j}(+1/2)$	×	○	○	×
V	125°16′	pq	$\mathrm{TAi}(-3/4)-\mathrm{TAi}(0)-T^{B}_{C}\mathrm{j}(+1/2)$	○	○	○	×
		qp	$T^{B}_{C}\mathrm{i}(-1/2)-\mathrm{TAj}(0)-\mathrm{TAj}(+3/4)$	○	○	○	×
		pq	${}^{B}_{C}\mathrm{i}(-1/4)-\mathrm{A}(0)-{}^{B}_{C}\mathrm{j}(+1/2)$	○	×	○	×
		qp	${}^{B}_{C}\mathrm{i}(-1/2)-\mathrm{A}(0)-{}^{B}_{C}\mathrm{j}(+1/4)$	○	×	○	×
		pq	$T^{B}_{C}\mathrm{i}(\mp1/4)-\mathrm{TAj}(0)-T^{C}_{B}\mathrm{i}(\mp1/2)$	○	○	×	○
VI	123°45′	pp	${}^{B}_{C}\mathrm{i}(-1/4)-\mathrm{A}(0)-{}^{B}_{C}\mathrm{j}(+1/4)$	×	○	○	×
VII	109°28′	pp	$\mathrm{TAi}(-3/4)-\mathrm{TAi}(0)-T^{B}_{C}\mathrm{j}(+1/4)$	○	○	○	×
		pp	$T^{B}_{C}\mathrm{i}(-1/4)-\mathrm{TAj}(0)-\mathrm{TAj}(+3/4)$	○	○	○	×
		pp	${}^{B}_{C}\mathrm{i}(\mp1/4)-\mathrm{A}(0)-{}^{B}_{C}\mathrm{j}(\mp1/4)$	○	○	×	○
VIII	90°	qq	$T^{B}_{C}\mathrm{i}(-1/2)-\mathrm{TAk}(0)-T^{C}_{B}\mathrm{j}(+1/2)$	○	×	○	×
		qq	${}^{B}_{C}\mathrm{i}(\mp1/2)-\mathrm{A}(0)-{}^{B}_{C}\mathrm{j}(\mp1/2)$	○	○	×	○

Table I. (Continued)

	$\angle M_1OM_2$	M_1-O, M_2-O	$M_1(z)-O(z)-M_2(z)$	Cubic	Hexa	Inter layer	Intra layer
IX	73°10′	pq	$T^{B}_{C}i(-1/4)-TAk(0)-T^{C}_{B}j(+1/2)$	×	○	○	×
		qp	$T^{B}_{C}i(-1/2)-TAk(0)-T^{C}_{B}j(+1/4)$	×	○	○	×
X	70°32′	pp	$TAi(\mp 3/4)-TAi(0)-T^{B}_{C}j(\mp 1/4)$	○	○	×	○
			$T^{B}_{C}i(-1/4)-TAk(0)-T^{C}_{B}j(+1/4)$	○	×	○	×
XI	70°32′	qq	$T^{B}_{C}i(-1/2)-TAj(0)-T^{B}_{C}i(+1/2)$	×	○	○	×
XII	54°44′	pq	${}^{B}_{C}i(-1/4)-A(0)-{}^{B}_{C}i(+1/2)$	○	×	○	×
		qp	${}^{B}_{C}i(-1/2)-A(0)-{}^{B}_{C}i(+1/4)$	○	×	○	×
		pq	$TAi(\mp 3/4)-TAi(0)-T^{B}_{C}j(\mp 1/2)$	○	○	×	○
		pq	$T^{B}_{C}i(\mp 1/4)-TAk(0)-T^{C}_{B}j(\mp 1/2)$	○	○	×	○
XIII	38°57′	pp	${}^{B}_{C}i(-1/4)-A(0)-{}^{B}_{C}i(+1/4)$	×	○	○	×
IV′	144°44′	$q-\sqrt{2/3}q$	$T^{B}_{C}i(\mp 1/2)-TAj(0)-T^{C}_{B}i(0)$	in $BaFe_{12}O_{19}$			

table do not correspond accurately to the actual angles or distances in many cases. The fact is due to the presence of the induced displacement of each ion from each geometrical position, as we mentioned in the foregoing section.

§ 8. Interpretation of Magnetic Coupling in Actual Crystals

By using the result of the crystal structure analysis (Figs. 4(a), (b), and Diagrams 1, 2, $\cdots$, 8) and Table I, we shall give the interpretation of the structures of magnetic coupling in several actual crystals. It should be noticed that all these magnetic lattices also have layer structures in which the ions in such layer have the same spin orientation.

1) FeO.

In this case, all cations are on octahedral positions and accordingly, all z in Table I are $\pm 1/2$. Therefore configurations II and VIII are only responsible for super exchange interaction. Interaction II should be dominant, having certainly negative sign. This interaction is of interlayer nature. Thus cations at TAi, TBi and TCi positions construct an antiferromagnetic lattice of spins. There are four such sublattices TA1+TB1+TC1, TA2+TB2+TC2, TA3+TB3+TC3, and TA4+TB4+TC4. There are two ways for the mutual spin relations among these four lattices effectively. One is cubic (Néel type) and the other is rhombohedral[17]. It should be noticed that the VIII type interactions are cancelled out in both cases and it does not contribute to select one from the two. Actually, rhombohedral structure is realized. Therefore, it has a layer structure as shown in Diagram 1.

2) αFe_2O_3*[11].

In this case also, all cations are on octahedral positions and configurations IV, VIII, and XI should be responsible for superexchange interaction. It will be most reasonable to assume the interaction IV is dominant and negative. This interaction is also of interlayer nature and it predicts perfect antiparrallelism of successive cation layers as shown in Diagram 2. Here, it should be remarked in this case that the induced deformation of crystal lattice from the geometrical arrangement changes the configuration IV into two slightly different configurations. Therefore, we consider the interaction IV as consisting of two different configurations: One, IV_1 has the equal M–O distances and the other, IV_2 has two M–O distances in which one is slightly different (longer) from that in the former. They correspond to SB3–C–SB1 and SB2–C–SB1 at $z=1$ in Diagram 2.

---

* Note added in proof—Quite recently Y. Y. Li[1] has pointed out that the interaction XI is important in αFe_2O_3 and Cr_2O_3. However, Li has missed the presence of IV_2 interaction. We have given a detailed discussion in J. Phys. Soc. Japan. **11** (1956) 1300[12].

The spin arrangement in Cr_2O_3 are also shown in Diagram 2. Though there are two cation layers between two neighbouring oxygen layers, it has also a layer structure. The structure can be understood by assuming that the interaction IV_1 has negative sign, whereas the interaction IV_2 has positive sign.

3) Fe_3O_4.

In this case cations are on both octahedral positions and tetrahedral positions. This case was treated already by Gorter[18, 4] considering the higher order interactions. In our consideration, the configurations present are V and VIII. It should be expected that V interaction is dominant and has negative sign. The interaction V covers all the magnetic lattice and results in the well-known ferrimagnetism[19, 4] in spinels as shown in Diagram 3. It will be clear that in this case also the magnetic lattice has a layer structure.

In this case also oxygen ions displace slightly from their geometrical positions[2]. Though these displacements distorts the configurations V slightly, the distortion is similar to every configuration V and, contrary to the preceding case, all configurations V are equivalent after the deformation.

4) $BaO \cdot 6Fe_2O_3$[8].

In this compound the oxygen layers which contain barium ions contain also iron ions and a new type of interaction is present which is named as IV′ in Table I. The interaction IV′ may be considered to be fairly strong. This interaction bind the spinel units present at both sides of the layer so as to result in ferrimagnetism.

6) $LaMnO_3$[9, 20].

In this compound configuration II is only responsible for exchange interaction. Normally it operates as super exchange interaction and antiferro-magnetism is realized The manganese ions in this case are all in trivalency state. But, when lanthanum ions are substituted partly by alkaline-earths ions (Ca, Sr, etc.), the tetravalency state of manganese ions appears associated with the participation of double exchange interaction In this case the situation is very complex and the actual magnetic structures become beyond the scope of our scheme.

7) FeS.

In this case also all cations are on octahedral positions. Therefore, configurations IV, VIII, and XI are present. It is doubtful whether we can extend Anderson's theory of directional super exchange interaction of magnetic oxides to sulphides. However, if we assume it can be applied to sulphide, the dominant interaction should be the interaction IV, and perfect antiparrallelism of successive cation layers are expected. According to the Bertaut's analysis[5], it is expected that the configuration IV splits into six different configurations after α transformation (T < 140°C).

If NiAs structure deforms to MnP structure as has been suggested also in MnAs[14], the configuration IV splits into two different configurations.

§ 9. Conclusion

By the analysis of this paper, it will become clear that the crystal structure of magnetic oxides are comprehensible by the model of layer structures on a purely ionic base, and the magnetic superstructure are also comprehensive by the same model. Generally, the magnetic oxides often contain vacancies of cation or interstitial cations. It will be hoped to apply our theory further to the study of these point imperfections in crystal lattices. We hope also to extend our theory to the study of one dimentional or two dimentional imperfections in these crystals (dislocations, or stacking faults).

Acknowledgement

The writer expresses his sincere thanks to Professor Seiji Kaya for his constant encouragement.

References

1) F. C Romeijn: Philips Res. Rep. **8** (1953) 304.
2) R. W. G. Wyckoff: Crystal structures I (1948) New York.
3) L. R. Bickford, Jr.: Rev. Mod. Phys. **25** (1953) 75; S. C. Abrahams and B. A. Calhoun: M. I. T. Prog. Rep. No. 15 (1954) 23.
4) E. W. Gorter: Proc. IRE, **43**, No 12 (1955) 245.
5) E. F. Bertaut: J. de Phys. Rad. **15** (1954) 776.
6) T. Hirone, S. Maeda, and N. Tsuya: J. Phys. Soc. Japan **9** (1954) 500, 503, 736; C. Guillaud: J. de Phys. Rad. **12** (1951) 223; B. T. M. Willis and H. P. Rooksby: Proc. Phys. Soc. (London) B. **67** (1954) 296.
7) E. F. Bertaut: Acta Cryst. **6** (1953) 557.
8) J. J. Went. G. W. Rathenau, E. W. Gorter and G. W. Van Oosterhout: Philips Tech. Rep. **13** (1952) 194.
9) G. H. Jonker and J. H. Van Santan: Physica **16** (1950) 337.
10) B. T. M. Willis and H. P. Rooksby: Proc. Phys. Soc. (London) B. **65** (1952) 950.
11) Y. Y. Li: Phys. Rev. **102** (1956) 1015.
12) S. Iida: J. Phys. Soc. Japan, **11** (1956) 1300.
13) L. Weil, F. Bertaut, et L. Bochirol: J. de Phys. Rad. **11** (1950) 208; J. B. Goodenough and A. L. Loeb: Phys. Rev. **98** (1955) 391.
14) S. Nagasaki: Private communications.
15) F. C. Frank: Advance in Physics 1 (1952) 91; A. R. Verma: Phil. Mag. **42** (1951) 1005.
16) P. W. Anderson: Phys. Rev. **79** (1950) 350; T. Nagamiya, K. Yoshida and R. Kubo: Phil. Mag. Suppl. **4** (1955) 1.
17) C. G. Shull, W. A. Strauser and E. O. Wollan: Phys. Rev. **83** (1951) 333.
18) E. W. Gorter: Philips Res. Rep. **9** (1955) 321.
19) L. Néel: Ann. Physique **3** (1948) 137.
20) E. O. Wollan and W. C. Koehler: Phys. Rev. **100** (1955) 545; J. B. Goodenough: Phys. Rev. **100** (1955) 564.

JOURNAL OF THE PHYSICAL SOCIETY OF JAPAN Vol. 12, No. 3, MARCH, 1957

Anisotropy in Polarized Barium Titanate Ceramics[†]

By Masakazu MARUTAKE and Takuro IKEDA

Kobayasi Institute of Physical Research, Kokubunji, Tokyo

(Received October 18, 1956)

Dielectric constants ε_1^T and ε_3^T (perpendicular and parallel to the direction of the polarization) and elastic compliance coefficients s_{11}^E, s_{33}^E and s_{44}^E of fully prepolarized $BaTiO_3$ ceramics are measured, and are compared with the dielectric constant ε^0 and the elastic compliance coefficients s_{11}^0 and s_{44}^0 of the unpolarized ceramics.

Anisotropy is small (a few percent). By semi-quantitative calculations, it is shown that the 180°-reversals of domains mainly remain after the poling process, and that anisotropy is due to the piezoelectric interactions among single crystals which constitute the ceramic.

§1. Introduction

In piezoelectric applications, $BaTiO_3$ ceramics are used usually after they are polarized in a d.c. electric field of about 20 kV/cm. In this poling process, domain orientations are altered and there remains the remanent polarization. Meanwhile, $BaTiO_3$ single crystal is highly anisotropic in the tetragonal phase; for instance, $\varepsilon_1^T=4500$ and $\varepsilon_3^T=200$ for the dielectric constants[1)], and $s_{11}^E=1.1\times10^{-12}\,\mathrm{cm^2/dyne}$ and $s_{33}^E=2.3\times10^{-12}\,\mathrm{cm^2/dyne}$ for the elastic compliance coefficients[2)] at room temperature. Therefore, if 90°-rotations of domains remain after the poling process, the dielectric and elastic constants of the polarized ceramics are expected to be very different from those of the unpolarized ones. From this point of view, the anisotropy of the polarized $BaTiO_3$ ceramics was studied in the tetragonal phase.

The unpolarized ceramic is isotropic, and has one dielectric constant ε^{*0}, two elastic compliance coefficients s_{11}^{*0} and s_{44}^{*0}, and does not show the piezoelectric effects. (Superscript * denotes the constant of the ceramic to distinguish it from that of the single crystal[3], and 0 denotes the constant of the unpolarized ceramic.) The polarized ceramic, on the other hand, has the symmetry of $C_n(n=\infty)$[4], and has the following matrix elements for the dielectric, the piezoelectric and the elastic constants.

[†] Main part of this paper was read at the meeting of the Acoustical Society of Japan, held on May 14, 1953.

$$\begin{pmatrix} \varepsilon_1^* & 0 & 0 \\ 0 & \varepsilon_1^* & 0 \\ 0 & 0 & \varepsilon_3^* \end{pmatrix} \qquad (1)$$

$$\begin{pmatrix} 0 & 0 & 0 & 0 & d_{15}^* & 0 \\ 0 & 0 & 0 & d_{15}^* & 0 & 0 \\ d_{31}^* & d_{31}^* & d_{33}^* & 0 & 0 & 0 \end{pmatrix} \qquad (2)$$

$$\begin{pmatrix} s_{11}^* & s_{12}^* & s_{13}^* & 0 & 0 & 0 \\ s_{12}^* & s_{11}^* & s_{13}^* & 0 & 0 & 0 \\ s_{13}^* & s_{13}^* & s_{33}^* & 0 & 0 & 0 \\ 0 & 0 & 0 & s_{44}^* & 0 & 0 \\ 0 & 0 & 0 & 0 & s_{44}^* & 0 \\ 0 & 0 & 0 & 0 & 0 & 2(s_{11}^*-s_{12}^*) \end{pmatrix} \qquad (3)$$

In this study, ε_1^{*T}, ε_3^{*T}; d_{31}^*, d_{33}^*; s_{11}^{*E}, s_{33}^{*E}, s_{44}^{*E} were measured at the temperatures between 10°C and 80°C, and were compared with ε^{*0}, s_{11}^{*0} and s_{44}^{*0}.

Furthermore, for comparison, the dielectric constant ε_3^{*T} and the elastic compliance coefficient s_{11}^{*E} were measured under a biasing d.c. electric field. Though these measurements were reported by many authors[5][6][7], we repeated here especially to make clear the behaviors in a weak biasing field.

§2. Experimental Procedures and Results

BaTiO$_3$ ceramics were sintered at about 1400°C from the mixtures of BaCO$_3$ and TiO$_2$ (reagent-grade) in an ordinary way. These specimens have the Curie temperature at 115°C, and the density of about 5.5.

(1) *Dielectric Measurements*

The dielectric constants were measured with a Q-meter at 50 kc (far below the mechanical resonant frequency of the specimen).

The specimen was polarized, first, along the z-axis (*cf.* Fig. 1) in a d.c. field of 20 kV/cm, and ε_3^{*T} was measured after the specimen was aged for 2 days at 75°C. Then, ε_1^{*T} along the x-axis was measured, by applying air-drying silver electrodes (P$_2$) after old electrodes (P$_1$) were removed. Finally, ε^{*0} was measured, after the specimen was depolarized by heating above the Curie temperature and was aged again. ε^{*0}, ε_1^{*T} and ε_3^{*T} are shown in Fig. 2, and it is found that at room temperature ε_1^{*T} and ε_3^{*T} are larger than ε^{*0} (*e.g.* $(\varepsilon_1^{*T}-\varepsilon^{*0})/\varepsilon^{*0}=3\%$ and $(\varepsilon_3^{*T}-\varepsilon^{*0})/\varepsilon^{*0}=12\%$ at 20°C), but that ε_3^{*T} is smaller than ε^{*0} at the temperatures above 60°C.

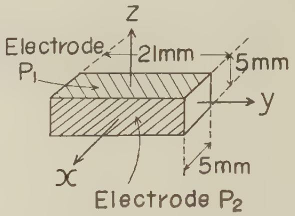

Fig. 1. Specimen for dielectric measurements.

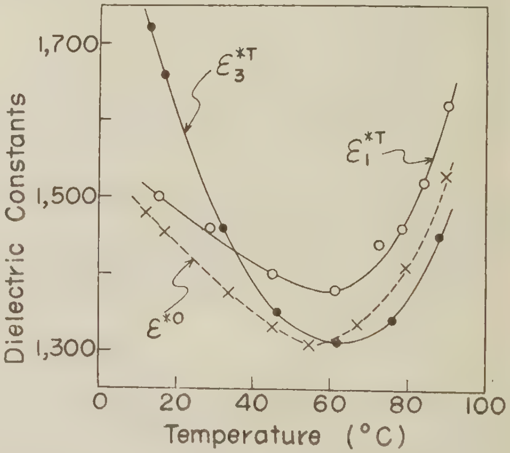

Fig. 2. Dielectric constants of the polarized and the unpolarized ceramic.

Generally, the dielectric constant of ferroelectric materials is reduced by a biasing electric field. We also measured the dielectric constant ε_3^{*T} by applying various d.c. voltage at 27°C and 78°C. A rectangular plate of $10\times8.1\times0.6\,\mathrm{mm}^3$ was used as specimen. The results are shown in Fig. 3 and Fig. 4.

On the virgin curve (ABC), it will be seen, ε_3^{*T} increases at first with the biasing field (AB), and then decreases rapidly (BC). Next, returning to the zero bias (CDE), ε_3^{*T} increases smoothly with the decreasing field; and when the biasing field is reversed, ε_3^{*T} decreases, first very rapidly (EF), and then slowly (FG). These cycles can be repeated in the same way, and at the zero bias (E) ε_3^{*T} is larger than at the starting point (A).

Unsymmetrical curves like Fig. 3 and Fig. 4 were previously obtained by Roberts[5] and recently by Mesnard and Eyraud[7], and we shall conclude later (§ 3) that these phenomena are mainly due to the piezoelectric interactions among single crystallites. These phenomena, however, are relaxation processes, and the time during which the biasing voltages are applied changes the shape of the curve. Sakudo[8] has obtained a symmetrical butterfly-type curve (Fig. 5) when the biasing field is changed at the period of 1/50 sec., while in our measurements ε_3^{*T} was measured after the biasing voltage was applied for about 5 minutes.

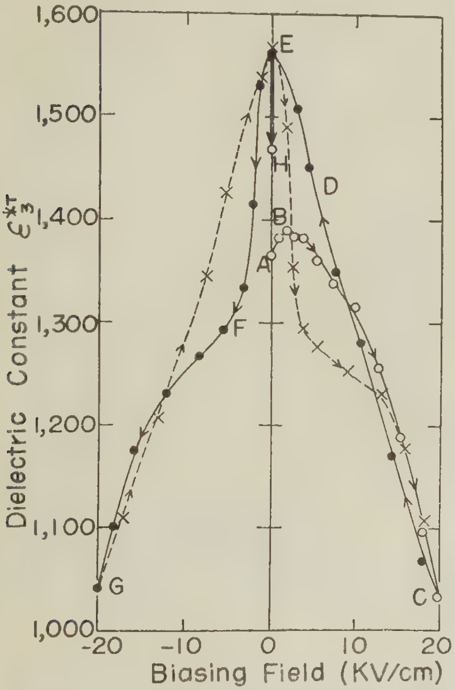

Fig. 3. Effects of the biasing field on ε_3^{*T} (27°C).

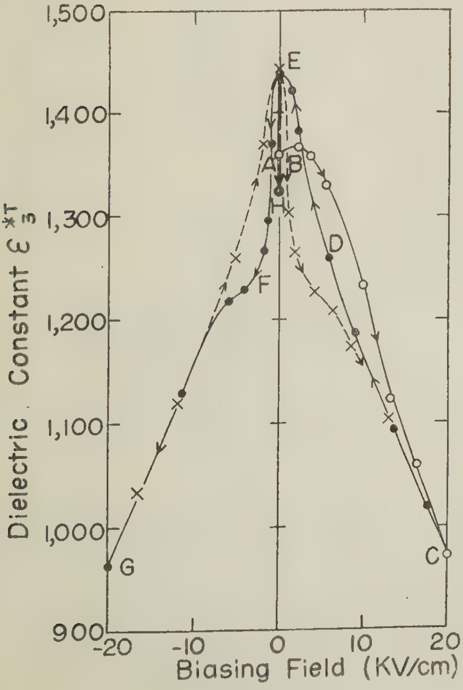

Fig. 4. Effects of the biasing field on ε_3^{T} (78°C).

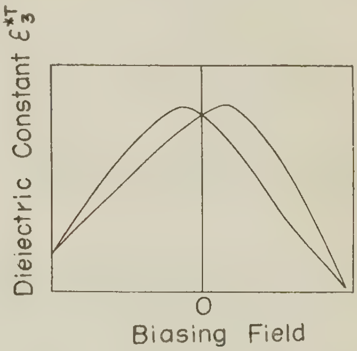

Fig. 5. Effects of the biasing field (short duration) on ε_3^{*T} (after Sakudo[8]).

It is also noted that the aging process (in a larger scale of time) plays a great rôle, and that the value at the starting point (A) is that measured after being aged for a day at 80°C, while the value at the zero bias (E) is that of unaged state, so that the latter decreases considerably (from E to H) at the fully aged state.

(2) *Elastic Measurements*

The elastic compliance coefficients s_{11}^{*E}, s_{33}^{*E}, s_{44}^{*E}; s_{11}^{*0}, s_{44}^{*0} were measured at the temperatures between 10°C and 90°C, and s_{11}^{*E} was also measured in the various biasing electric field at 23°C. The elastic constants were obtained from the resonant frequencies of bars (with rectangular or circular sections), which were measured either by the self-resonance method (s_{11}^{*E} and s_{33}^{*E}) or by the composite-bar method (s_{11}^{*E}, s_{44}^{*E}, s_{11}^{*0}, s_{44}^{*0} and the measurements under the biasing field).

(i) s_{11}^{*E} and d_{31}^{*}

Resonant and antiresonant frequencies f_R and f_A of the lengthwise compressional vibrations of the bar were measured (Fig. 6) after the specimen was polarized at 18 kV/cm at room temperature and was aged for a day at 80°C.

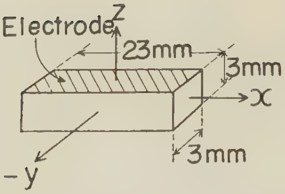

Fig. 6. Measurements of s_{11}^{*E} and d_{31}^{*}.

s_{11}^{*E} and d_{31}^{*} are calculated from the following equations:

$$\left.\begin{aligned} f_R &= \frac{1}{2l}\sqrt{\frac{1}{\rho s_{11}^{*E}}}\,, \\ \frac{f_A - f_R}{f_R} &= \frac{4}{\pi^2} k_{31}^2\,, \\ k_{31}^2 &= \frac{4\pi d_{31}^{*2}}{s_{11}^{*E}\varepsilon_3^{*T}}\,; \end{aligned}\right\} \quad (4)$$

where ρ is the density and l is the length of the specimen. The results are shown in Fig. 8 and Fig. 9.

(ii) s_{33}^{*E} and d_{33}^{*}

Resonant and antiresonant frequencies f_R and f_A of the lengthwise compressional vibration of the bar were measured by applying the electric field along the direction of the length (*cf.* Fig. 7), after the specimen was polarized at 15 kV/cm at room temperature and was aged for a day at 80°C.

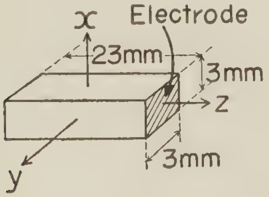

Fig. 7. Measurements of s_{33}^{*E} and d_{33}^{*}.

s_{33}^{*E} and d_{33}^{*} are calculated from the following equations:

$$\left.\begin{aligned} f_R &= \frac{1}{2l}\sqrt{\frac{1}{\rho s_{33}^{*E}\{1-(1-8/\pi^2)k_{33}^2\}}}\,, \\ \frac{f_A - f_R}{f_R} &= \frac{4}{\pi^2} k_{33}^2\,, \\ k_{33}^2 &= \frac{4\pi d_{33}^{*2}}{s_{33}^{*E}\varepsilon_3^{*T}}\,. \end{aligned}\right\} \quad (5)^{\dagger}$$

In these measurement, the capacity of the sample was small (about 5 $\mu\mu F$), and accordingly, the errors due to the stray capacity (2 $\mu\mu F$) were corrected in determining the antiresonant frequency f_A. The results are shown in Fig. 8 and Fig. 9.

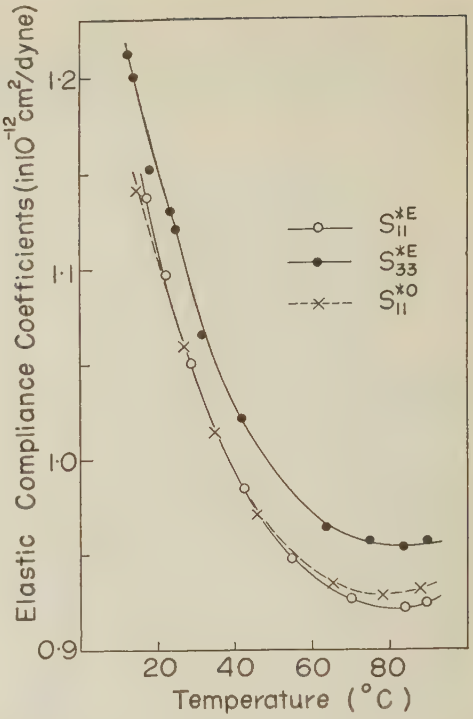

Fig. 8. Elastic compliance coefficients s_{11}^{*E} s_{33}^{*E} and s_{11}^{*0}.

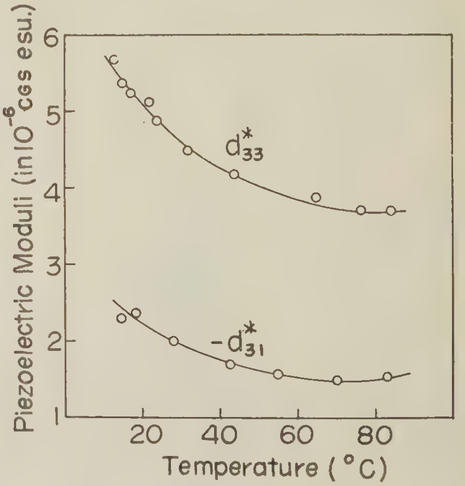

Fig. 9. Piezoelectric moduli d_{31}^{*} and d_{33}^{*}.

(iii) s_{11}^{*0} and s_{11}^{*E} in a biasing electric field.

The elastic compliance coefficient s_{11}^{*0} of the unpolarized ceramic was measured by the composite-bar method (*v.* ref. 10), and is shown in Fig. 8. By the same method, s_{11}^{*E} was measured by applying the various biasing voltage, and the results are shown in Fig. 10.

---

† *v.* notes added in proof (1) at the end of the paper.

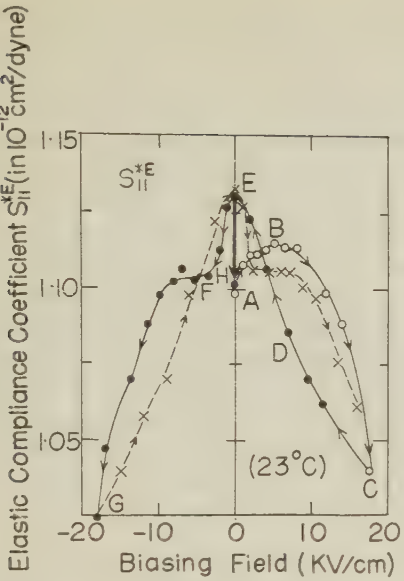

Fig. 10. Effects of the biasing electric field on s_{11}^{*E} (23°C).

(iv) s_{44}^{*0} and s_{44}^{*E}.

s_{44}^{*0} and s_{44}^{*E} were measured also by the composite-bar method (*v.* ref. 10), and the results are shown in Fig. 11.

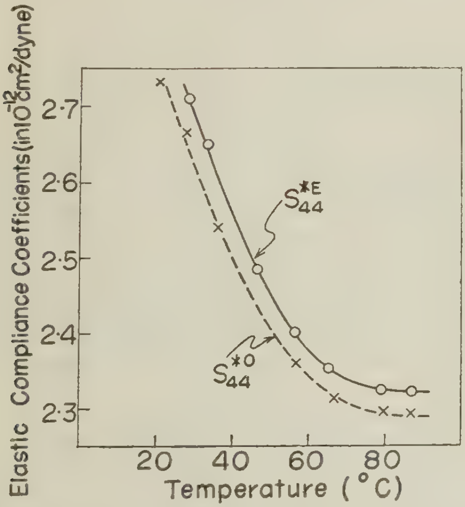

Fig. 11. Elastic compliance coefficients s_{44}° and s_{44}^{*E}.

(v) Results.

In these measurements of elastic constants, following results were obtained.

(a) At room temperature, s_{33}^{*E} and s_{44}^{*E} are larger, respectively, by a few per cent than s_{11}^{*0} and s_{44}^{*0} (*e.g.* $(s_{33}^{*E}-s_{11}^{*0})/s_{11}^{*0}=3.5\%$ and $(s_{44}^{*E}-s_{44}^{*0})/s_{44}^{*0}=4\%$ at 20°C). s_{11}^{*E}, however, does not differ from s_{11}^{*0} within experimental errors at room temperature, and the former is smaller than the latter at the temperatures above 60°C; these behaviors are similar to those of the dielectric constant ε_3^{*T}.

(b) s_{11}^{*E} shows the similar behaviors to those of ε_3^{*T} when the biasing voltage was applied along the *z*-axis. (A, B, C, ···, H in Fig. 10 corresponds, respectively, to those points in Fig. 3 and Fig. 4.)

§ 3. Discussions

Physical contants of the BaTiO$_3$ ceramics are certainly mean values of those of the single crystals which constitute the ceramic, but the evaluation of the mean values is very comlicated, because (1) each single crystal is composed of domains, (2) each domain shows piezoelectric effects, and (3) internal strains in the single crystal may change its physical constants. We shall consider thses effects in the following.

In the tetragonal phase, the unit cell of the single domain deforms from the cube and the length of the unit cell is larger along the *z*-axis by about 1% than along the *x*-axes. Accordingly, when the ceramic passes through the Curie point, very large internal stresses will be produced in the single crystals the axes of which are uniformly distributed, if there exist no internal stresses in the cubic phase. These stresses are minimized when each single crystal splits up into three kinds of domains (the *z*-axis of each kind is perpendicular to those of other kinds) and the total volume of each kind of domains is 1/3 of that of whole the crystal. The existence of the *herringbone* type domains (Fig. 12), as observed recently by Kulcsar[11] and Cook[12], may support these considerations, because herringbone type domains will appear at the place where

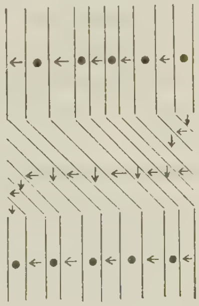

Fig. 12. Herringbone type domains (after Kulcsar[11] and Cook [12]).

three kinds of domains coexist. Hence, in the tetragonal phase, the internal stresses may be reduced and may not play a great rôle.

When the electric field is applied, 90°–rotations of domains will take place as well as 180°–reversals in favor of the poling field, and the dielectric constant $\varepsilon_3{}^{*T}$ and the elastic compliance coefficient $s_{11}{}^{*E}$ of the ceramic are reduced very much as was shown in Fig. 3 and Fig. 10.

In the non-biased prepolarized ceramic, however, the remanent polarization is considered mainly due to the 180°–reversals of domains, because 90°–rotations are accompanied with mechanical strains and will not remain after the poling field is removed. If only 180°–reversals of domains remain in the prepolarized ceramic, the anisotropy is caused by the piezoelectric interactions among the single crystals (or single domains) which constitute the ceramic. Piezoelectric interactions are very important in determining the dielectric and elastic constants in unpolarized ceramics, as was shown by one of the authors[3], and they contribute also to the change of the dielectric and elastic properties in polarized ceramics. Namely, the dielectric constant of the unpolarized ceramic is a mean of those values which are intermediate between the free and the clamped dielectric constants of the single crystal. In the polarized ceramic, which is piezoelectric as a whole, the "freedom", so to speak, of the single crystal is restored to a certain extent, and the dielectric constant of the prepolarized ceramic is raised because the dielectric constants of each single crystal approach to the free dielectric constants. (In the case of the multi-domain single crystal, Drougard and Young[13] discussed such effects on the dielectric constant.) On the elastic compliance coefficients s^*'s the situations are similar—namely, the constant s's of the single crystal approach to s^E's when the ceramic is polarized, while they are intermediate between s^E's and s^D's when the ceramic is unpolarized; and the constants s^{*E}'s of the ceramic become larger when polarized than when unpolarized.

The unsymmetrical curves shown in Fig. 3, Fig. 4 and Fig. 10 are also explained in the same way. Namely, at the points F's on these curves, the ceramics are depolarized and are non-piezoelectric, though 90°–rotations of the domains occur to some extent by the biasing field. Accordingly, the curves show minima at the points F's (also see the point F in Fig. 13).

Furthermore, to confirm above discussions, the dielectric and elastic constants of the polarized ceramic were calculated on the assumption that the ceramic is made up of spherical single domain crystallites, in the same way as the constants of unpolarized ceramic were calculated[3].

When the ceramic is perfectly polarized, all the 90°–rotations and 180°–reversals occur and the z-axes of the crystallites are assumed to be distributed uniformly within the angle of $\pi/4$ around the direction of the polarizing field (Strictly speaking, this distribution is not correct[14][15].), and the calculated values in this case at 20°C are as follows.

$$\left.\begin{aligned}\varepsilon_1{}^{*T}/\varepsilon^{*0}&=1.40\,,\\ \varepsilon_3{}^{*T}/\varepsilon^{*0}&=0.58\,;\\ s_{11}{}^{*E}/s_{11}{}^{*0}&=0.74\,,\\ s_{33}{}^{*E}/s_{11}{}^{*0}&=1.38\,.\end{aligned}\right\}\qquad(6)$$

The observed values at 20 kV/cm are (Fig. 3 and Fig. 10):

$$\left.\begin{aligned}\varepsilon_3{}^{*T}/\varepsilon^{*0}&=0.76\,,\\ s_{11}{}^{*E}/s_{11}{}^{*0}&=0.93\,.\end{aligned}\right\}\qquad(7)$$

As will be seen from Eq. (6), the elastic compliance coefficient $s_{33}{}^{*E}$ is expected to increase with the biasing field. From this point of view, the resonant frequency of the thickness compressional vibration of a circular plate (diameter: 30 mm, thikness: 2.8 mm) was measured by the self-resonance method, and the results are shown in Fig. 13. The prepolarized and aged specimen is biased firstly at the positive (favored) direction (ABCDE), and then the field is reversed (EFG); the point

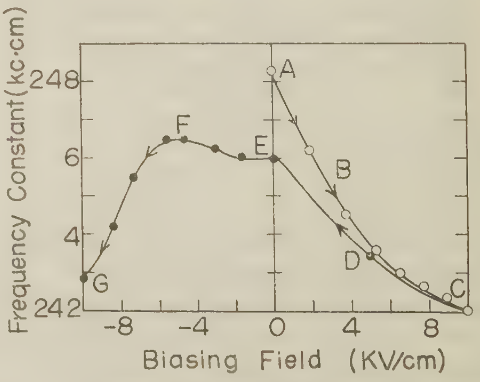

Fig. 13. Resonant frequency for the thickness compressional vibrations (24°C).

F shows the depolarized state. Although the frequency constant in this case does not give the value of $s_{33}{}^{*E}$ directly, we may conclude that $s_{33}{}^{*E}$ increases with the biasing field.

If we can measure the dielectric constant $\varepsilon_1{}^{*T}$, it will also increase with the biasing field, and it is to be noted that these effects should not be confused with the saturation phenomena as observed above the Curie temperature.

Now let us continue the calculation. When only the 180°-reversals are perfect and any 90°-rotations do not remain, the z-axes of the single crystals are distributed uniformly within the right angle around the direction of the polarizing field, and the calculations in this case show

$$\left.\begin{aligned}&(\varepsilon_1{}^{*T}-\varepsilon^{*0})/\varepsilon^{*0}=4\%\,,\\&(\varepsilon_3{}^{*T}-\varepsilon^{*0})/\varepsilon^{*0}=10\%\,,\\&(s_{11}{}^{*E}-s_{11}{}^{*0})/s_{11}{}^{*0}=0.7\%\,,\\&(s_{33}{}^{*E}-s_{11}{}^{*0})/s_{11}{}^{*0}=5\%\,,\\&(s_{44}{}^{*E}-s_{44}{}^{*0})/s_{44}{}^{*0}=3\%\,.\end{aligned}\right\}\qquad(8)$$

Observed values of non-biased prepolarized ceramics are (Fig. 2, Fig. 8 and Fig. 11):

$$\left.\begin{aligned}&(\varepsilon_1{}^{*T}-\varepsilon^{*0})/\varepsilon^{*0}=3\%\,,\\&(\varepsilon_3{}^{*T}-\varepsilon^{*0})/\varepsilon^{*0}=12\%\,;\\&(s_{11}{}^{*T}-s_{11}{}^{*0})/s_{11}{}^{*0}=0\%\,,\\&(s_{33}{}^{*E}-s_{11}{}^{*0})/s_{11}{}^{*0}=3.5\%\,,\\&(s_{44}{}^{*E}-s_{44}{}^{*0})/s_{44}{}^{*0}=4\%\,.\end{aligned}\right\}\qquad(9)$$

These experiments are also in agreement with the measurement by Moseley[16]) who measured $s_{11}{}^{*E}$, $s_{33}{}^{*E}$ and $s_{11}{}^{*0}$ at room temperature, and with the measurements by Bechmann[17]) who measured all dielectric, piezoelectric and elastic constants shown in (1), (2) and (3) also at room temperature.

From above considerations, we can conclude that in the poling process 180°-reversals of domains remain mainly and that anisotropy is mainly due to the piezoelectric interactions (*cf.* (8) and (9)). Some proportions of 90°-rotations of domains may also remain in the polarized ceramic, and it explains why $\varepsilon_3{}^{*T}$ and $s_{11}{}^{*E}$ are smaller, respectively, than ε^{*0} and $s_{11}{}^{*0}$ at the temperatures above 60°C (Fig. 2 and Fig. 8).

Finally, we shall consider the aging effects studied by Mason[9]). He showed that the piezoelectric moduli in the polarized ceramic diminish gradually after the ceramic is polarized, and that the dielectric constant and the elastic compliance coefficients also diminish at the same time. The cause of these aging effects is considered to be the same as that of the anisotropy in the polarized ceramic which has just been discussed; namely the changes of the piezoelectric interactions among the crystallites cause the changes of the dielectric and elastic constants, as some part of the domains returns to the more stable orientations and the piezoelectric effects, hence, diminish as a whole. Mason also showed that the decrease of the piezoelectric effects reduces the dielectric constant and the elastic compliance coefficients in his phenomenological treatments[9]), and our conclusion is that it is mainly piezoelectric interactions that causes the changes of the dielectric and elastic constants in Mason's theory.

Also we shall point out here that the effects of the change of the orientation of domains due to 90°-rotation are considered to be smaller, because the dielectric constant $\varepsilon_3{}^{*T}$ and the elastic compliance coefficient $s_{11}{}^{*E}$ of the polarized ceramic are smaller at the aged state than at the unaged one (*cf.* E and H in Fig. 3, Fig. 4 and Fig. 10), while the reverse is the case if the orientations of domains are predominant in determining the dielectric and elastic constants.

Piezoelectric interactions discussed above, however, do not explain all of the aging effects, because aging effects appear also in the unpolarized ceramics, which show no piezoelectric effects, when the temperature is reduced through the Curie temperature. There may be an unstable state, so to speak, when the crystal structure changes suddenly from cubic to tetragonal and the crystat splits up into multi-domains, and the dielectric constant, for instance, may be raised because the domain boundaries are movable even in a weak field in such an unstable state, as Mason suggested in his paper. We cannot, however, discuss in more detail here, because further informations will be necessary about the nature of the behaviors of domains as studied by Little[18]).

§4. Summary and Acknowledgements

In this study, following results were obtained.

(1) In the prepolarized ceramic (in the tetragonal phase), the change of domain structures is, in the greater part, due to the 180°-reversals, and most of 90°-rotations of domains do not remain after the poling field is removed.

(2) The anisotropy in the prepolarized ceramic is within several per cent, and is mainly due to the piezoelectric interactions among the single crystals which constitute the ceramic. The piezoelectric interactions also make the dielectric and elastic constants unsymmetrical as functions of biasing field.

(3) The aging effects are also due to the piezoelectric interactions in some part, but other causes must be considered to explain the aging of the unpolarized ceramic.

In conclusion, the authors wish to express their hearty thanks to Mr. A. Takeda for helpful discussions and to Mr. K. Utino for the aid of the preparation of the specimens. Their thanks are also due Mr. T. Sakudo of the Electrotechnical Laboratory who showed them his unpublished data. This work was supported by the Scientific Research Expenditure of the Ministry of Education.

Notes added in proof: (1) The derivation of Eq. (5) is shown in detail in C. V. Stephenson's paper (J. Acoust. Soc. Amer. **28** (1956) 1192). (2) In the previous paper10), we calculated the elastic constants of the porous materials, and were not aware of J. K. MacKenzie's work (Proc. Phys. Soc. (London) **63B** (1950) 2). Our results are identical with his formulae, though the derivation and the expressions are different. For this carelessness, one of the authors (M. M.) is responsible.

References

1) W. J. Merz: Phys. Rev. **76** (1949) 1221.
2) A. F. Devonshire: Phil. Mag. **40** (1949) 1040; **42** (1951) 1065.
3) M. Marutake: J. Phys. Soc. Jap. **11** (1956) 807.
4) W. P. Mason: *Piezoelectric Crystals and their Application to Ultrasonics* (1950).
5) S. Roberts; Phys. Rev. **71** (1947) 890.
6) L. A. Pipes: J. Appl. Phys. **23** (1952) 818.
7) G. Mesnard et L. Eyraud: J. de Phys. et Rad. **17** (1956) 62A.
8) T. Sakudo: Private Communication.
9) W. P. Mason: J. Acoust. Soc. Amer. **27** (1955) 73.
10) M. Marutake and T. Ikeda: J. Phys. Soc. Jap. **11** (1956) 814.
11) F. Kulcsar: J. Amer. Cer. Soc. **39** (1956) 13.
12) W. R. Cook: J. Amer. Cer. Soc. **39** (1956) 17.
13) M. E. Drougard and D. R. Young: Phys. Rev. **94** (1954) 1561.
14) R. Becker u. W. Döring: *Ferromagnetismus* (1939) p. 287.
15) M. Marutake: Bull. Kobayasi Inst. Phys. Res. **6** (1956) 115 (in Japanese).
16) D. S. Moseley: J. Acoust. Soc. Amer. **27** (1955) 947.
17) R. Bechmann: J. Acoust. Soc. Amer. **28** (1956) 347.
18) E. A. Little: Phys. Rev. **98** (1955) 978.

JOURNAL OF THE PHYSICAL SOCIETY OF JAPAN Vol. 12, No. 3, MARCH, 1957

Lattice Energies and Other Properties of Crystals of Alkaline Earth Chalcogenides*

By Maurice L. HUGGINS** and Yosio SAKAMOTO***

Research Laboratories, Eastman Kodak Co., Rochester, N.Y., U.S.A.

and

Department of Chemistry, Faculty of Science, Hirosima University

(Received October 23, 1956)

The lattice energies of the 20 binary compounds composed of Be^{++}, Mg^{++}, Ca^{++}, Sr^{++}, Ba^{++}, O^{--}, S^{--}, Se^{--} and Te^{--} have been computed by previously well-tested procedures. Because of lack of sufficiently reliable compressibility data, the computations have been made with two different assumptions regarding the magnitude of the constant a in the exponent of the repulsion energy term. These two assumptions yield lattice energies which differ, in most cases, by about 20 kcal.

In general, a single value of the "constant energy radius" suffices for each type of ion. For the beryllium compounds, however, it was necessary to use different radii for the Be^{++} ion for each compound. In MgTe also, a slightly different Mg^{++} radius from that deduced for the other magnesium compounds was required. These irregularities may be related to the fact that these crystals have "tetrahedral" structures, unlike the others, with significant but unknown amounts of covalent bonding.

The characteristic constants deduced should be useful in the theoretical treatment of many properties dependent on interactions between ions, both in these crystals and in other systems. For these crystals, the interionic distances, compressibilities and maximum infrared lattice-vibration frequencies have been computed.

By combining the computed lattice energies with thermochemical data, electron affinities (for the addition of *two* electrons to each of the electronegative atoms) have been computed and compared. Based on these results, the authors' best estimates, in kcal/mole, are as follows: O, -162 ± 15; S, -99 ± 15; Se, -117 ± 15; Te, -97 ± 20.

§ 1. Introduction

This paper reports the results of calculations of lattice energies and several related properties for the alkaline earth chalcogenides[1], i.e., the oxides, sulfides, selenides and tellurides of beryllium, magnesium, calcium, strontium and barium. These results are more extensive and presumably more accurate than those previously published for some of these substances by Mayer and Maltbie[2], de Boer and Verwey[3], van Arkel and de Boer[4], Fowler[5], Kapustinskiĭ and Yatsimirskiĭ[6] and others.

The theory underlying the calculations is that of Born and Mayer[7]. The general procedure followed that of Huggins and Mayer[8] and Huggins[9] for the alkali halogenides[1]. As an important step in the work, a set of "constant energy radii"[10], characteristic of the ions concerned, was calculated. Using these, lattice energies, equilibrium distances between the centers of closest ions, compressibilities, characteristic maximum infrared lattice-vibration frequencies, and electron affinities were computed.

It may be noted that Brauer[11], from a consideration of elastic constant and dielectric constant data for MgO, has concluded that in that crystal there are noncentrosymmetric, hence noncoulombic, forces of considerable magnitude, the coulombic forces being reduced to those corresponding to effective charges of ±1.83 electron charge units per ion. Since the significance of this is not clear and since the data needed for similar calculations for the other crystals with which we are concerned are lacking, the previous treatment, in which centrosymmetric forces were assumed, has been adopted in the present work.

---

* Communication from the Faculties of Science of Osaka and Hirosima Universities and from the Research Laboratories of the Eastman Kodak Company (Comm. No. 1857). Presented at the Kyoto Meeting of the Chemical Society of Japan, April 4, 1956. A preliminary report was presented by M.L.H. at the Rochester Meeting of the American Chemical Society in September, 1937.

** Fulbright Visiting Professor, Osaka University and Kyoto University, 1955–1956; on leave from the Eastman Kodak Company, Rochester, New York, U.S.A.

*** Lecturer, Hirosima University.

§ 2. The Lattice Energy Equation

The lattice energy at 0°K was assumed to be given by the following equations:

$$E_{\mathrm{L}} = -10^{-10}\left(\frac{N_{\mathrm{Av}}}{J}\right)(\Phi+\Psi)\,, \qquad (1)^{7),9),12)}$$

$$\Phi = -\frac{4\alpha_{\mathrm{Mad}}e^2}{r_0} - \frac{C_{\mathrm{AB}}}{r_0{}^6} - \frac{D_{\mathrm{AB}}}{r_0{}^8} + bc_{+-}M\exp\left[a(r_{\mathrm{A}}+r_{\mathrm{B}}-r_0)\right] + \frac{bc_{--}M'}{2}\exp\left[a(2r_{\mathrm{B}}-k_2r_0)\right] + \frac{bc_{++}M'}{2}\exp\left[a(2r_{\mathrm{A}}-k_2r_0)\right]\,. \qquad (2)^{7),9)}$$

The symbols in these equations have the following significance:

E_{L} = lattice energy per mole, in kilocalories.
N_{Av} = Avogadro's number = 6.02283×10^{23}.
J = joule equivalent = 4.1840 abs. joule/cal. (defined).
Φ = average potential energy per "molecule", in ergs.
Ψ = zero-point energy per "molecule", in ergs. This is7) approximately equal to $9h\nu_{\max}/4$, where
h = Planck's constant = 6.6242×10^{-27} erg sec., and
$\nu_{\max}$ = maximum infrared frequency, for oscillation of the lattice of positive ions relative to the lattice of negative ions.
α_{Mad} = Madelung's constant, referred to r_0, for univalent ions. (The value given for the $B4$ type in Table I is for the ideal values of the axial ratio and atomic parameter, corresponding to close-packing of spheres. Use of the experimental axial ratios and parameters leads to results which are only slightly (0.0001 to 0.0005) larger.)
e = electron charge = 4.8024×10^{-10} e.s.u.
r_0 = equilibrium distance between closest ions. (r_0 chosen for the $B4$ type: r_0 (eff.) = $(9a^2c)^{1/3}/4$, where a and c are the lattice constants.)
C_{AB}, D_{AB} = van der Waals constants, calculated as described below.
$b = 10^{-12}$ erg.
M = number of closest unlike neighbor ions (Table I).
M' = number of closest like neighbor ions (Table I).
a = repulsion constant, equal to the reciprocal of Born and Mayer's7) ρ.
r_{A} = constant energy radius for a positive ion (Table III).
r_{B} = constant energy radius for a negative ion (Table III).
c_{+-}, c_{++} and c_{--} are factors to allow roughly for the dependence of the overlap repulsion energy between two ions on their charges and the numbers of electrons in their outermost shells. They are taken, respectively, as 1.75, 3.00 and 0.50 for the beryllium compounds and 1.00, 1.50 and 0·50 for the others. These values were obtained by substituting into an approximate equation given by Pauling13). They may be very inaccurate, especially for the beryllium compounds. Trial calculations showed, however, that, although the assumption of quite different values (even putting them all equal to unity) led to slightly different values of the constant energy radii, approximately the same interionic distances and lattice energies were obtained.
k_2 = ratio of the shortest distance between like neighbors to that between unlike neighbors (Table I).

Table I. Constants Pertaining to Structure Type.

Structure type	Compounds	α_{Mad}	M	M'	k_2	S_6'	S_6''	S_8'	S_8''	k_1
$B3$ ZnS(cubic)	BeS, BeSe, BeTe	1.6381	4	12	$2\sqrt{2}/\sqrt{3}$	4.354	0.762	4.104	0.253	3.079
$B4$ ZnO	BeO, MgTe	1.6413	4	12	$2\sqrt{2}/\sqrt{3}$	4.354	0.762	4.104	0.253	3.079
$B1$ NaCl	All others	1.7476	6	12	$\sqrt{2}$	6.5952	1.8067	6.146	0.800	2

§ 3. The Repulsion Constant "a"

Experimental compressibility data have been reported by Bridgman[14-17] for 11 of the substances dealt with; Durand[18] has published a value for MgO; and Parodi[19] has quoted, without reference, experimental values for CaO and BaO. It was hoped that these data could be used, as by Born and Mayer[7] for the alkali halogenides, to determine what value of the repulsion constant a to employ. However, the experimental values are quite inaccurate. Bridgman[16] writes: "The nine compounds of calcium, strontium and barium are probably the least satisfactory [of the substances measured]. The compressibility of the sulfides of these is probably too high because of the presence of a comparatively large amount of amorphous material, and the selenides and tellurides had a tendency to chemical instability." Moreover, the measurements were all made with powdered samples, except that in the case of MgO a single crystal was also studied. The experimental compressibility of the crystal powder was 67% larger than that for the single crystal. Because of this very large discrepancy, it seems unwise to trust any a values deduced from the experimental compressibilities.

The calculations reported here were made with two values of a: 3.00 and $2.50\times10^8\,\text{cm}^{-1}$. The differences between the two sets of results indicate the magnitude of the errors which would be produced by an incorrect choice of this constant. The first value is the same as that used by Huggins[9] for the alkali halogenides; the constant energy radii in the two series of compounds are therefore strictly comparable and should be applicable, for example, to crystals such as CaF_2, containing ions from both series. The second choice of a is close to that (2.55×10^8) deduced from Bridgman's[17] compressibility measurements on the MgO single crystal.

Since this paper was essentially completed, new compressibility measurements of the powdered oxides have been reported by Weir[20] The results are included in Table IV. With the aid of approximations which should not introduce much error, he has computed values of Born and Mayer's repulsion constant ρ for all but BeO. The reciprocals, a, are as follows: MgO, 2.4; CaO, 2.5; SrO, 3.0; BaO, 1.9 (in units of $10^8\,\text{cm}^{-1}$)*. The barium oxide data are of doubtful value since the specimen used was not very pure.

§ 4. Van der Waals Attraction Constants

The van der Waals attraction terms contribute relatively little to the lattice energies, but, in the calculation of other properties dealt with here, they are far from negligible. The constants C_{AB} and D_{AB} for the crystals are related[21] to the constants (c_{AA}, d_{AA}, etc.) for the interaction between pairs of ions by the equations

$$C_{AB}=S_6'c_{AB}+S_6''(c_{AA}+c_{BB})/2 \qquad (3)$$

and

$$D_{AB}=S_8'd_{AB}+S_8''(d_{AA}+d_{BB})/2\,. \qquad (4)$$

The magnitudes of the S constants for the $B1$ and $B3$ structures, as given by Mayer[21),22)], are listed in Table I. For the $B4$ structures, the same values as for $B3$ have been assumed. This should be a close approximation.

Theoretically[23),24)], for ions having the same effective number of polarizable electrons, the van der Waals c constants should be proportional to the 3/2 power of the polarizability and, hence, to the 3/2 power of the atomic or ionic refraction, R. For an isoelectronic sequence, such as O^{--}, F^-, Ne, Na^+, Mg^{++}, it seems reasonable to assume a rectilinear change of the ratio $c/R^{3/2}$. Thus, the constant c_{MgMg} has been computed from the relation

$$\frac{c_{MgMg}}{R_{Mg}^{3/2}}=\frac{3}{2}\frac{c_{NaNa}}{R_{Na}^{3/2}}-\frac{1}{2}\frac{c_{FF}(\text{in NaF})}{R_F^{3/2}(\text{in NaF})}\,, \qquad (5)$$

and likewise the constant c_{OO}, for the interaction between two oxide ions in MgO, has been computed from the relation

$$\frac{c_{OO}(\text{in MgO})}{R_O^{3/2}(\text{in MgO})}=\frac{3}{2}\frac{c_{FF}(\text{in NaF})}{R_F^{3/2}(\text{in NaF})}-\frac{1}{2}\frac{c_{NaNa}}{R_{Na}^{3/2}}\,. \qquad (6)$$

The values of c_{MM} and c_{XX}, for the alkali and halogenide ions, have been taken from Mayer[21]. The R_M and R_A values, for the alkali and alkaline earth ions, have been taken from Pauling[25]. Each is assumed to have the same magnitude in all crystals containing

[*] Our recalculated values, with $F_{T,P}$ (in Eq. 19) ±1, are 2.6; 2.4; 3.0; 1.9 (with $r_{Ba}=1.7_2$ A and $r_O=1.1_7$ A), resp.; and BeO, 3.4 (with $r_{Be}=0.34$ A and $r_O=1.41$ A) (The use of "3.4" leads to the electron affinity value of -245 units, which, however, is hardly probable).

the ion in question. The values of R_X and R_B have been obtained by subtracting the appropriate R_M and R_A from the R_{MX} and R_{AB} refractions published by Spangenberg[26] and Haase[27].

For the interaction between unlike ions, Kirkwood[28] has deduced the relationship

$$c_{AB}=K\alpha_A\alpha_B\Big/\left[\left(\frac{\alpha_A}{n_A}\right)^{1/2}+\left(\frac{\alpha_B}{n_B}\right)^{1/2}\right], \quad (7)$$

where α_A and α_B are the polarizabilities, n_A and n_B are the effective numbers of polarizable electrons in the two species, and K is a constant. From the relationship

$$\alpha_A \text{ or } \alpha_B=\frac{3R}{4\pi N_{Av}}, \quad (8)$$

one then obtains the equation

$$\frac{2}{c_{AB}}=\frac{R_A}{R_Bc_{AA}}+\frac{R_B}{R_Ac_{BB}}\,. \quad (9)$$

From equations for the c and d constants given by Mayer[21], with Eq. (8), the following relations are readily derived:

$$d_{AA}=\frac{8\pi N_{Av}}{n_Ae^2}\cdot\frac{c_{AA}^2}{R_A}, \quad (10)$$

$$d_{BB}=\frac{8\pi N_{Av}}{n_Be^2}\cdot\frac{c_{BB}^2}{R_B}, \quad (11)$$

$$d_{AB}=\frac{4\pi N_{Av}}{e^2}\left(\frac{c_{AA}}{n_AR_A}+\frac{c_{BB}}{n_BR_B}\right)c_{AB}\,. \quad (12)$$

Although there are 8 electrons in the outermost shell of each of the ions, except Be^{++}, with which we are concerned, Mayer[21] has computed 3.2 as the *effective* number for chloride ion in NaCl and KCl, and 4.0 for iodide ion in KI. Herzfeld and Wolf[29] have computed 4.6 for argon and 5.6 for xenon. In the present work, a value of 5.5 has been taken for all the ions. Then

$$d_{AA}=0.1\ \times10^{44}c_{AA}^2/R_A\,, \quad (13)$$

$$d_{BB}=0.1\ \times10^{44}c_{BB}^2/R_B\,, \quad (14)$$

$$d_{AB}=0.05\times10^{44}\left(\frac{c_{AA}}{R_A}+\frac{c_{BB}}{R_B}\right)c_{AB}\,. \quad (15)$$

The isoelectronic sequence procedure, described above, is inapplicable to the beryllium compounds. For these, c_{BeBe}, c_{BeB}, d_{BeBe} and d_{BeB} were taken as zero, and c_{OO}, d_{OO}, c_{SS}, d_{SS}, etc. were estimated by extrapolation from the values of these constants in the series BaO, SrO, CaO, MgO, etc.

The C_{AB} and D_{AB} values, computed with the aid of the relationships just given, are listed in Table II.

Table II. Van der Waals Constants, Expansion Coefficients, and Zero-point and Thermal Energy Factors.

AB	c_{AA}	c_{BB}	c_{AB}	C_{AB}	d_{AA}	d_{BB}	d_{AB}	D_{AB}	α	θ
	10^{-60} erg cm^6				10^{-76} erg cm^8				10^{-5} deg^{-1}	
BeO	0	24	0	9	0	17	0	2	1.6[30),31)]	2.92
BeS	0	120	0	46	0	150	0	19	3	2.06
BeSe	0	180	0	69	0	250	0	32	4	1.63
BeTe	0	290	0	110	0	470	0	59	5	1.41
MgO	0.7	30	2.9	47	0.2	21	1.4	17	3.1[32),33)]	1.76
MgS	0.7	140	5.4	163	0.2	173	4.2	95	4	1.46
MgSe	0.7	203	6.0	224	0.2	277	5.0	142	4	1.29
MgTe	0.7	302	7.1	146	0.2	483	28	89	4	1.28
CaO	12	39	13	135	13	25	11	83	3.5[34)]	1.38
CaS	12	160	26	327	13	193	29	261	4	1.18
CaSe	12	222	29	400	13	289	33	325	4	1.12
CaTe	12	313	32	507	13	461	40	437	5	1.10
SrO	34	43	24	231	54	26	27	197	4	1.21
SrS	34	177	48	505	54	221	67	524	4	1.13
SrSe	34	258	56	631	54	357	82	671	4	1.07
SrTe	34	373	63	780	54	599	100	874	5	1.05
BaO	97	48	40	394	237	27	60	477	4.0[35),36)]	1.12
BaS	97	198	83	725	237	227	150	1109	4	1.07
BaSe	97	261	87	897	237	317	160	1207	4	1.04
BaTe	97	359	100	1071	237	495	192	1475	5	1.03

§ 5. Interionic Distances and Constant Energy Radii

For each of the two assumed values of a, sets of values of r_A and r_B were computed by successive approximations from the experimental r_0 values and the equation

$$a[r_0-(r_A+r_B)]=-\ln\frac{\tau}{r_0}+\ln(bc_{+-}Ma)+\ln\{1+S\exp[(1-k_2)ar_0]\}\,, \tag{16}$$

with

$$\tau=\frac{4\alpha_{\rm Mad}e^2}{r_0}+\frac{6C_{\rm AB}}{r_0^6}+\frac{8D_{\rm AB}}{r_0^8}-3T\theta k_1\frac{\alpha}{\beta}r_0^3 \tag{17}$$

and

$$S=\frac{k_2M'}{2Mc_{+-}}\{c_{--}\exp[a(r_B-r_A)]+c_{++}\exp[a(r_A-r_B)]\}\,. \tag{18}$$

These equations are like those previously used for the alkali halogenides[8], except for the introduction of the factor θ in the relatively small last term of Eq. (17). This factor, designated as $(1+c-f)\upsilon$ by Sakamoto (Ref. 12, Eq. 22), results from a more precise theoretical analysis of the variations of the zero-point energy (Ψ) and the thermal energy with temperature[37),38)]. Estimated values are given in Table II.

This table also lists the values used for the expansion coefficient, $\alpha=(\partial V/\partial T)_P/V$, entering into the last term of Eq. (17). Except for the cases for which references are given, these are estimated values.

For the compressibility, $\beta=-(\partial V/\partial P)_T/V$, estimates, based in part on the experimental values listed in Table IV, were used until the final approximation, when the computed values were employed. T was taken as 298°K. The constant k_1, defined as $V/N_{\rm Av}r_0^3$, has the values given in Table I.

The r_A and r_B values obtained are collected in Table III.

These radii and Eqs. (16), (17) and (18) were then used to compute the calculated interionic distances given in Table IV. These are seen to be in substantial agreement with the best experimental values. It should be noted that this agreement is but little affected by uniformly increasing (or decreasing) all the positive ion radii by a few hundredths of an ångström unit, and simultaneously decreasing (or increasing) the negative ion radii by the same amount and making a few minor adjustments.

It was impossible to obtain good agreement for the beryllium compounds with a constant value of $r_{\rm Be}$. This may be attributed to various causes. It may result primarily from the (probably incorrect) assumption that the same value of the repulsion constant a is applicable to all the compounds. The neglect of covalent bond contributions in these "tetrahedral" crystals may also be important. Incorrectness of the Pauling c_{+-}, c_{++} and c_{--} factors may cause some error, and inaccuracies in other approximations may contribute.

Table III. Constant Energy Radii.

A or B	r_A or r_B in 10^{-8} cm $a=2.5$ $\times 10^8\,{\rm cm}^{-1}$	$a=3.0$ $\times 10^8\,{\rm cm}^{-1}$
Be^{++} in BeO	0.75	0.52
BeS	0.66	0.44
BeSe	0.64	0.42
BeTe	0.62	0.40
Mg^{++} in MgO	1.10	0.93
MgS	1.10	0.93
MgSe	1.10	0.93
MgTe	1.15	0.97
Ca^{++}	1.31	1.17
Sr^{++}	1.44	1.31
Ba^{++}	1.58	1.46
O^{--}	1.27	1.35
S^{--}	1.62	1.69
Se^{--}	1.71	1.78
Te^{--}	1.86	1.93

In the case of MgTe also, the calculated and experimental values of r_0 differ considerably (by 0.04 to 0.05 A), if $r_{\rm Mg}$ is taken to be the same as in the other magnesium compounds.

Pending better knowledge of the true magnitudes of a in these crystals and of the other factors just mentioned, a has been assumed to be the same for the beryllium compounds and MgTe as for the others, and values of $r_{\rm Be}$ and $r_{\rm Mg}$ have been computed which lead to agreement between the experimental and calculated interionic distances. These have been used in the calculation of the lattice energies and other properties.

Constant energy radii are given in Table III to two decimal places only. Although

Table IV. Interionic Distances, Compressibilities and Lattice Frequencies.

	r_0 (in 10^{-8} cm)			$\frac{10^4\Delta r_0}{r_0}$	β (in 10^{-12} barye^{-1})				ν_{max} (in 10^{12} sec^{-1})			
$10^{-8}a$	calcd. 2.50	calcd. 3.0	exptl.	estd.	calcd. 2.5	calcd. 3.0	calcd.	exptl.	calcd. 2.5	calcd. 3.0	exptl.	estd.
BeO	1.643	1.648	1.649[39],[40]	6	0.53	0.37		0.27[20]				23
BeS	2.104	2.109	2.105[41]	13	0.94	0.66	0.73[47]					18
BeSe	2.223	2.228	2.225[42]	19	1.07	0.75						15
BeTe	2.436	2.435	2.436[42]	27	1.35	0.94						12
MgO	2.102	2.107	2.106[39]	14	0.61	0.48	0.42[48]	0.60[17] 0.65[18] 0.59[20]	15	18	17.1[49]	16
MgS	2.601	2.603	2.602[43],[44]	21	1.07	0.82	0.69[48] 0.83[47]		11	12		13
MgSe	2.729	2.730	2.731[42]	23	1.20	0.91	0.75[48]		9	10		10
MgTe	2.770	2.768	2.770[45],[46]	23	2.10	1.62						10
CaO	2.399	2.396	2.405[39],[43]	19	0.86	0.69	0.71[43]	4.7[15] 0.88[20]	13	15	11.1[19]	12
CaS	2.848	2.848	2.846[43],[44]	27	1.39	1.09	0.98[48]	2.8[15]	10	11		8
CaSe	2.969	2.969	2.962[42]	27	1.55	1.21	1.04[48]	2.2[15]	8	9		7
CaTe	3.180	3.175	3.179[42]	35	1.87	1.46		2.4[15]	7	7		6
SrO	2.586	2.575	2.580[39]	25	1.03	0.84		0.83[20]	11	13	6.4[19]	9
SrS	3.009	3.007	3.010[43],[44]	27	1.61	1.28		3.8[15]	8	9		7
SrSe	3.123	3.121	3.122[43]	30	1.78	1.40		2.5[15]	6	7		5
SrTe	3.328	3.322	3.331[42]	38	2.14	1.68		3.1[15]	5	6		4
BaO	2.786	2.767	2.770[36]	27	1.24	1.00		1.74[20]	10	13	5.7[19]	7
BaS	3.188	3.186	3.194[44]	29	1.88	1.50		2.9[15]	7	8		5
BaSe	3.299	3.298	3.302[42]	31	2.07	1.65		2.9[15]	5	6		4
BaTe	3.497	3.493	3.500[42]	40	2.46	1.96		3.3[15]	4	5		4

slightly better agreement between calculated and experimental r_0 values could be obtained by using some radii to three decimal places, this was considered to be without significance. The probable error of many of the experimental values is not much less than 0.01 A.

§6. Compressibilities and Lattice Frequencies

By using the constant energy radii of Table III and the calculated interionic distances of Table IV, compressibilities have been computed by means of the equation[7],[9]

$$\beta=\frac{9k_1 r_0^3 F_{T,P}}{r_0^2\left(\frac{\mathrm{d}^2\Phi}{\mathrm{d}r_0^2}\right)}, \tag{19}$$

where $F_{T,P}$ is a complex function involving α, β, the variation of β with temperature and pressure, and the heat capacity. As for the alkali halogenides, $F_{T,P}$ has been taken as unity. In further justification, its value for MgO, for which the requisite experimental data are available, was computed to be 1.0_2 using the equation given by Huggins[9], or 1.01 ± 0.04 using the refinements introduced by Sakamoto (Ref. 12, Eq. 23).

The compressibilities calculated for MgO (especially that obtained with the smaller value of a) are in good agreement with the experimental single-crystal data. There is also good agreement with the new experimental data of Weir for the oxides, except in the case of BeO, for which our calculated values were expected to be too large, because its $F_{T,P}$ might be smaller than unity like LiF's (0.85) or covalency contributions were ignored and the magnitude of a might have been underestimated for the tetrahedral crystals, and in the case of BaO, for which his result is of dubious accuracy, because the material used was not of high purity. As was to be expected, the computed compressibilities are somewhat smaller than the other experimental values obtained from crystal powders.

The calculated compressibilities agree reasonably well with those deduced quantum-mechanically for six compounds by Brück[48] and for two compounds by Ždanow, *et al.*[47] There is rough agreement also with the results of calculations by Fowler[5], using methods similar to those used here, but less refined.

Characteristic maximum lattice frequencies for the $B1$ (sodium chloride) type crystals were computed from the relationship[9]

$$\nu_{\max}=\left\{\frac{ba^2\left(1-\dfrac{2}{ar_0}\right)\exp\left[a(r_A+r_B-r_0)\right]-\dfrac{30c_{AB}}{r_0^8}-\dfrac{56d_{AB}}{r_0^{10}}}{2\pi^2\mu}\right\}^{1/2}, \qquad (20)$$

where

$$\mu=\frac{M_AM_B}{N_{Av}(M_A+M_B)} \qquad (21)$$

and M_A and M_B are the atomic weights of A and B.

Very few experimental values have been published for the lattice frequencies for these crystals, and they are rather contradictory. Those which appear to be most reliable are listed in Table IV.

The calculated values of β and $\nu_{\max}$ in this table, are for room temperature. Estimates have been made for the change of $\nu_{\max}$ on cooling to 0°K, by using the derivative of Eq. (20) with respect to temperature. This change is negligible, in comparison with other errors.

§ 7. Lattice Energies

Lattice energies at 0°K have been calculated, using Eqs. (1) and (2). Ψ was computed from the characteristic frequencies of Table IV, Col. 13. These were estimated from the directly measured values (Col. 12), specific

Table V. Lattice Energies at 0°K (in kcal).

	Coulomb Energy	Van der Waals Attraction	Overlap Repulsion $10^{-8}a=$ 2.5	Overlap Repulsion $10^{-8}a=$ 3.0	Zero-point Energy	Total Lattice Energy $10^{-8}a=$ 2.5	Total Lattice Energy $10^{-8}a=$ 3.0	Ref. (2)	Ref. (3,4)	Ref. (5)	Ref. (6)	Ref. (47)
BeO	−1323	−7	298	242	5	1026	1082		1080			
BeS	−1035	−8	185	146	4	854	893					907
BeSe	−980	−9	166	130	3	820	855					
BeTe	−895	−8	138	106	3	763	795					
MgO	−1104	−8	202	170	4	907	938	939	936	976	934	
MgS	−894	−8	135	111	3	764	788	800	790	766	807	801
MgSe	−852	−9	124	101	2	734	757			743		
MgTe	−789	−5	113	93	2	678	699					
CaO	−967	−11	159	134	3	816	841	831	830	876	845	
CaS	−818	−10	119	99	2	707	726	737	710	714	740	
CaSe	−786	−9	111	93	2	683	701			700	704	
CaTe	−733	−8	94	77	1	644	662			648		
SrO	−902	−13	144	121	2	769	792	766	784	829	789	
SrS	−773	−11	108	90	2	675	692	686	680	688	696	
SrSe	−746	−11	101	85	1	654	671			675	664	
SrTe	−699	−9	88	72	1	620	635			626		
BaO	−840	−15	129	107	2	724	746	727	740	780	751	
BaS	−729	−12	96	80	1	643	659	647	640	662	666	
BaSe	−705	−11	91	76	1	624	639			652	638	
BaTe	−666	−10	81	67	1	594	608			609		

heat data, and the trends shown by the data for the alkali halogenides[9] and by the calculated frequencies (Cols. 10 and 11). Correction was made for the difference between r_0 at room temperature and at the absolute zero, by means of an equation given by Sakamoto (Ref. 12, Eq. 54). See Table IV, Col. 5. This correction makes no difference larger than 3 kcal in any of the computed energy contributions (Cols. 2–6 of Table V), nor larger than 0.3 kcal in their sum (Cols. 7 and 8).

Table V shows the negatives of the computed contributions of the different kinds of energy to the total lattice energy, together with the algebraic sum of these contributions. For comparison, the best of the previously published values are included. There is general agreement, but, in view of the more precise treatment of various pertinent factors, the present results are believed to be more reliable than the earlier ones.

The molal lattice energies computed on the basis of $a = 3.0 \times 10^8\,\mathrm{cm}^{-1}$, like the corresponding repulsion energies, are generally about 20 kcal higher than those computed using the smaller *a*. The probable error of the average of these calculated lattice energies can reasonably be assumed to be of about half this magnitude, except for the "tetrahedral" crystals. Covalent bond energy contributions in the latter may be far from negligible[50]. The neglect here of such contributions may thus result in considerable error.

§ 8. Electron Affinities

The heat content increments for the reaction

$$AB_{cr} \longrightarrow A_{gas}^{++} + B_{gas} + 2e_{gas}^{-} \qquad (22)$$

at 298°K and 1 atmosphere have been computed (Table VI, Col. 2). The heats of formation of AB_{cr} used for this, except for CaS, are those considered best by Kubaschewski and Evans[52]. In most instances, they are based directly on experimental measurements and are identical with, or very close to, the values adopted by Rossini, *et al.*[53], of the U. S. National Bureau of Standards. For MgSe, CaTe, SrTe and BaTe, however, the

Table VI. Calculation of Electron Affinities at 0°K (in kcal).

AB	ΔH_{298} for Eq. (22)	Prob. Error of $\Delta H_f°$ for AB_{cr}	$\int_0^{298} C_P dT$ for AB_{cr}	ΔH_0 for Eq. (22)	Electron Affinity $10^{-8}a=$ 2.5	Electron Affinity $10^{-8}a=$ 3.0	Electron Affinity Average	Supplementary Lattice Energy (± Inacc.)
BeO	916.7[51-53]	3	0.69[54]	911.4	−115	−171	−143	20
MgO	764.6[52],[53]	0.2	1.23[55]	760.0	−147	−178	−162	0*
CaO	674.7[52],[53]	0.5	1.67[55]	670.4	−146	−171	−158	4
SrO	627.9[52],[53]	1.5	2.04[56]	624.0	−145	−168	−156	6
BaO	587.9[52],[53]	2.5	2.37[56]	584.3	−140	−161	−151	12
BeS	823.5[52],[53]	2	1.1	818.7	− 35	− 74	− 55	44
MgS	698.0[52],[53]	2	1.6	693.7	− 70	− 94	− 82	17
CaS	632.2[53]		2.15[57]	628.4	− 78	− 98	− 88	11
SrS	589.1[52],[53]	8	2.3	585.5	− 89	−107	− 98	1
BaS	555.0[52],[53]	5	2.6	551.6	− 91	−107	− 99	0*
MgSe	675.4[53],[52]	4	1.9	671.3	− 63	− 86	− 74	42
CaSe	586.7[52],[53]	6	2.4	583.3	− 99	−118	−108	8
SrSe	554.9[52],[53]	4	2.6	551.6	−102	−119	−111	6
BaSe	518.3[52],[53]	5	2.8	515.1	−109	−124	−117	0*
MgTe	659.4[52],[53]	5	1.9	655.4	− 23	− 43	− 33	64
CaTe	576.2[53],[52]	8	2.5	572.8	− 72	− 89	− 80	17
SrTe	536.8[53],[52]	8	2.7	533.7	− 86	−102	− 94	3
BaTe	506.8[53],[52]	8	2.9	503.8	− 90	−104	− 97	0*

* Assumed.

heats of formation given are merely estimates, based on assumptions regarding series regularities. In the case of CaS, the experimental value has been used here, in preference to Kubaschewski and Evans's estimate, which is 5.3 kcal lower. The probable errors of the heats of formation, estimated by these authors, are given in Col. 3. For the heats of formation of A_{gas}^{++} and B_{gas}, on the other hand, the values selected by Rossini, *et al.* have been used exclusively. The probable errors of these values are a few kilocalories.

From the figures in Col. 2, by subtraction of 10 RT and addition of the heat capacity integral, $\int_0^{298} C_P \mathrm{d}T$, for the crystal, one obtains (Col. 5) the corresponding heat change at 0°K. Experimental data are available for the evaluation of the heat capacity integral for six of the compounds. For the others, estimates have been made, with the aid of the (estimated) $\nu_{\max}$ values and an equation given by Sakamoto (Ref. 12, Eq. 57).

The lattice energy is the increase in heat content for the reaction

$$AB_{cr} \longrightarrow A_{gas}^{++} + B_{gas}^{--} . \qquad (23)$$

The electron affinity (for the addition of *two* electrons to the B atom) is the decrease in heat content for the reaction

$$B_{gas} + 2e_{gas}^{-} \longrightarrow B_{gas}^{--} . \qquad (24)$$

It is thus the difference between the ΔH values for reactions (22) and (23).

The electron affinities so calculated for the chalcogens are all negative. For each of the two assumed values of a, they are reasonably consistent, at least for the $B1$ type compounds, but show definite trends. The two sets of electron affinities, like the two sets of lattice energies and the two sets of repulsion energies, differ by about 20 kcal, in most cases.

To estimate the most probable true values of the electron affinities, several factors must be considered. In the first place, the probable errors of the heat of formation data, on which they depend directly, are, in most instances, rather large, as mentioned above.

A second factor is the neglect of overlap repulsion energies between like ions, other than those which are closest together. This factor might be appreciable for crystals containing small ions.

A third factor is the error introduced by assuming the constant a to have the same value for all the compounds.

In the fourth place, the lattice energies computed for the tetrahedral compounds are doubtless too low, by unknown amounts, because of the neglect of covalent bond contributions. This neglect tends to make the values of the electron affinity, calculated from BeO, BeS and MgTe too negative.

Finally, there may be errors due to polarization (departure from spherical shape) of the larger, more deformable ions, when combined with much smaller ions of the other kind. (This is the "primary polarization", previously discussed by Sakamoto (Ref. 12, Note 13)). From this consideration, the lattice energies and electron affinities computed for compounds (MgO, CaO, SrO, BaO, SrS, BaS, SrSe, BaSe and BaTe), composed of ions having radii which do not differ much, would be expected to be somewhat more reliable, other things being equal, than those computed for compounds of ions with very different radii.

On the basis of these ideas and the computed electron affinities in Table VI, the authors propose the following, as their best estimates of the true electron affinities:

O: -162 ± 15 S: -99 ± 15
Se: -117 ± 15 Te: -97 ± 20 .

The differences between the electron affinities are believed to be somewhat more precisely known than the individual values, since the differences do not change much with a change in the assumed value of a, nor with mutually consistent changes in the assumed values of the constant energy radii.

The irregularity in the series is thus believed to be real. It was also shown by the earlier calculations[5),6),58)].

In the final column of Table VI are the differences between the calculated electron affinities (Col. 8) for the individual compounds and the authors' best estimates, just given. The large values of this difference for BeO, BeS and MgTe can probably be attributed to neglect of the covalent bond energy. It seems unlikely, however, that this is of importance in MgSe, which has the NaCl type structure, with coordination number 6. The large value of the "supplementary lattice energy" for this compound and the fact that the trend in the series MgO⟶BaO is opposite to that in the other series (MgS⟶BaS, MgSe⟶BaSe, MgTe⟶BaTe) suggest that these differences are due largely to the energy of polarization deformation of the larger ions by the smaller ones (primary polarization energy).

There seem to be no experimental data with which the calculated electron affinities can be directly compared[59].

The *first* electron affinities of oxygen and sulfur (for addition of *one* electron) have been studied by many experimental and theoretical methods, but different investigators still do not agree, even approximately[59-63]. Further discussion and comparison with the present results do not seem profitable at this time.

§ 9. Acknowledgments

The senior author (M.L.H.) wishes to express his appreciation to Osaka and Kyoto Universities for inviting him to join their faculties and to his Japanese colleagues for their warm hospitality. The financial aid of a Fulbright grant is also gratefully acknowledged.

Note added Feb. 7, 1957

In the foregoing calculations, as in former calculations[2,3,7-9] of this sort, noncoulombic repulsion energies between pairs of ions other than those closest together (unlike ions) and those which are next closest (like ions) were neglected. To determine whether this is justifiable, we have computed the effect of including terms for repulsions between third nearest neighbors—for the $B1$ type, for example, those between unlike ions which are at diagonally opposite corners of each eighth-unit cube.

Better agreement with the experimental interionic distances is now obtained, if the following new constant energy radii are used (r in 10^{-8} cm; a in 10^{8} cm^{-1}):

For $a=2.5$:

$r_{\rm Be}=0.72$, 0.64, 0.63 and 0.61, in BeO, BeS, BeSe and BeTe, resp.

$r_{\rm O}=1.26$ (Note the new r_0 (calcd., BaO): 2.781.)

For $a=3.0$:

$r_{\rm Be}=0.50$, 0.43 and 0.41, in BeO, BeS and BeSe, resp.

N.B. $r_0(\text{new})-r_0(\text{old})=9$ to -5×10^{-11} cm.

The only new values of compressibility, β, overlap repulsion energy, ORE, total lattice energy, TLE, electron affinity, EA, and supplementary lattice energy, SLE, which differ from those previously listed (in Tables IV–VI) by more than one unit in the last place, are those given below *in italics* (in the same units as before).

	β		ORE		TLE		$-$EA			SLE
a:	2.5	3.0	2.5	3.0	2.5	3.0	2.5	3.0	Av.	Av.
BeO	*0.47*	*0.35*	*286*	*237*	*1038*	*1088*	*127*	*176*	*152*	*10*
BeS	*0.90*	0.65	*181*	*144*	*858*	*895*	*39*	*76*	*58*	*41*
BeSe	*1.05*	0.74	*165*	*128*		*857*				
BeTe	*1.32*		*136*		*765*					
MgO	0.60	0.47		*172*		*936*		*176*		
MgS			*137*	112	*762*		69		81	18
CaO	*0.84*	0.68	158	135	*818*	840	147	170		3
SrO	1.02	0.83	*142*		*771*		*147*		157	*4*
BaO	*1.22*		*127*	108	*726*		*142*		152	*10*

The changes from the previous results are thus very minor ones. They are certainly negligible, relative to other inaccuracies, except possibly for the case of BeO. Our best estimates of the (two-electron) electron affinities remain as before, except that for Se we now prefer the value: -116 ± 15 kcal/mole.

The values in the footnote in § 3 now become, resp.: 2.5, 2.3,···1.15,···0.32, 1.40,··· and -251.

References

1) W. P. Jorissen, H. Bassett, A. Damiens, F. Fichter and H. Remy: Ber. **73A** (1940) 53; J. Chem. Soc. **1940**, 1404; J. Am. Chem. Soc. **63** (1941) 889.
2) J. E. Mayer and M. McC. Maltbie: Z. Physik **75** (1932) 748.
3) J. H. de Boer and E. J. W. Verwey: Rec. trav. chim. **55** (1936) 443.
4) A. E. van Arkel and J. H. de Boer: "Chemische Bindung als elektrostatische Erscheinung" (Hirzel, Leipzig, 1931).
5) R. H. Fowler: "Statistical Mechanics", Second Edition (Cambridge Univ. Press, 1936), page 330.
6) A. F. Kapustinskiĭ and K. B. Yatsimirskiĭ: Zhur. Obshchei Khim. **26** (1956) 941.
7) M. Born and J. E. Mayer: Z. Physik **75** (1932) 1.
8) M. L. Huggins and J. E. Mayer: J. Chem. Phys. **1** (1933) 643.
9) M. L. Huggins: J. Chem. Phys. **5** (1937) 143; **15** (1947) 212.
10) M. L. Huggins: J. Am. Chem. Soc. **75** (1953) 4126.
11) P. Brauer: Z. Naturforsch. **6a** (1951) 255.
12) Y. Sakamoto: J. Sci. Hiroshima Univ., Ser. A, **17** (1954) 387,

13) L. Pauling: Z. Krist. **67** (1928) 377; Eq. (7).
14) P. W. Bridgman: Proc. Am. Acad. Arts Sci. **67** (1932) 345.
15) P. W. Bridgman: Proc. Am. Acad. Arts Sci. **74** (1940) 21.
16) P. W. Bridgman: Phys. Rev. **57** (1940) 237.
17) P. W. Bridgman: Proc. Am. Acad. Arts Sci. **77** (1949) 187.
18) M. A. Durand: Phys. Rev. **50** (1936) 449.
19) M. Parodi: Compt. rend. **204** (1937) 1636.
20) C. E. Weir: J. Research Natl. Bur. Standards **56** (1956) 187.
21) J. E. Mayer: J. Chem. Phys. **1** (1933) 270.
22) J. E. Mayer: J. Chem. Phys. **1** (1933) 327.
23) J. C. Slater and J. G. Kirkwood: Phys. Rev. **37** (1931) 682.
24) R. A. Buckingham: Proc. Roy. Soc. (London) **A160** (1937) 113.
25) L. Pauling: Proc. Roy. Soc. (London) **A114** (1927) 181.
26) K. Spangenberg: Z. Krist. **57** (1922) 494.
27) M. Haase: Z. Krist. **65** (1927) 509; **66** (1928) 236.
28) J. G. Kirkwood: Physik. Z. **33** (1932) 57.
29) K. F. Herzfeld and K. L. Wolf: Ann. Physik [4] **76** (1925) 71.
30) H. Nitka: Naturwiss. **29** (1941) 336.
31) G. E. Bacon and S. A. Wilson: Acta Cryst. **8** (1955) 844.
32) M. A. Durand: Physics **7** (1936) 297.
33) S. S. Sharma: Proc. Indian Acad. Sci. **32A** (1950) 268.
34) G. R. Rigby and A. T. Green: Trans. Brit. Ceram. Soc. **41** (1942) 123.
35) A. Eisenstein: J. Appl. Phys. **17** (1946) 434.
36) R. J. Zollweg: Phys. Rev. **100** (1955) 671.
37) K. Huang: Phil. Mag. [7] **42** (1951) 202.
38) R. O. Davis: Phil. Mag. [7] **43** (1952) 473.
39) H. E. Swanson, *et al.*: "Standard X-ray Diffraction Powder Patterns", Natl. Bur. Standards Circular 539, Vols. 1 and 5 (U. S. Govt. Printing Office, Washington, D. C., 1953 and 1955).
40) G. E. Bacon: Acta Cryst. **1** (1948) 337.
41) E. Staritzky: Anal. Chem. **28** (1956) 915.
42) Landolt-Börnstein: "Zahlenwerte und Funktionen", 6. Aufl., Bd. I, Tl. 4 (J. Springer, Berlin, 1955), Ziff. 15021.
43) W. Primak, H. Kaufman and R. Ward: J. Am. Chem. Soc. **70** (1948) 2043.
44) O. J. Güntert and A. Faessler: Z. Krist. **107** (1956) 357.
45) W. Klemm and K. Wahl: Z. anorg. u. allgem. Chem. **266** (1951) 289.
46) W. Zachariasen: Z. physik. Chem. **A128** (1927) 417.
47) V. Ždanow, A. Erschow and G. Galachow: Z. Physik **94** (1935) 241.
38) H. Brück: Z. Physik **51** (1928) 707.
49) J. C. Willmott: Proc. Phys. Soc. (London) **63A** (1950) 389; single crystal.
50) S. Asano and Y. Tomishima: J. Phys. Soc. Japan **11** (1956) 644.
51) L. A. Cosgrove and P. E. Snyder: J. Am. Chem. Soc. **75** (1953) 3102.
52) O. Kabaschewski and E. L. Evans: "Metallurgical Thermochemistry", Second Edition (Pergamon Press Ltd., London, 1956).
53) F. D. Rossini, D. D. Wagman, W. H. Evans, S. Levine and I. Jaffe: "Selected Values of Chemical Thermodynamic Properties", Circular of the Natl. Bur. Standards 500 (U. S. Govt. Printing Office, Washington, D. C., 1952).
54) K. K. Kelley: J. Am. Chem. Soc. **61** (1939) 1217.
55) G. S. Parks and K. K. Kelley: J. Phys. Chem. **30** (1926) 47.
56) C. T. Anderson: J. Am. Chem. Soc. **57** (1935) 429.
57) C. T. Anderson: J. Am. Chem. Soc. **53** (1931) 476.
58) J. Sherman: Chem. Revs. **11** (1932) 93.
59) H. O. Pritchard: Chem. Revs. **52** (1953) 529.
60) H. Schüler and W. Bingel: Z. Naturforsch. **10a** (1955) 250.
61) S. J. Smith and L. M. Branscomb: J. Research Natl. Bur. Standards **55** (1955) 165.
62) L. M. Branscomb and S. J. Smith: J. Chem. Phys. **25** (1956) 598.
63) S. Geltman: J. Chem. Phys. **25** (1956) 782.

JOURNAL OF THE PHYSICAL SOCIETY OF JAPAN Vol. 12, No. 3, MARCH, 1957

On Electrical Resistivity and Hall Coefficient of PbTe Crystals

By Kisaburo SHOGENJI and Susumu UCHIYAMA

Department of Electrical Engineering, Faculty of Engineering, Nagoya University, Nagoya

(Received November 19, 1956)

The electrical resistivity and Hall coefficient of p-type synthetic PbTe crystals and those after heat treatment in the air were measured at various temperatures down to liquid air temperature. By heat treatment at moderate temperature in the air the resistivity and Hall coefficient of the crystals increased. An analysis of the data on Hall coefficient shows that the intrinsic energy gap is about 0.3 ev. and the mobility ratio $b=\mu_e/\mu_n$ is about 2.5 at 300°～400°K. The activation energy of the acceptor levels is very small. The mobility of the hole is approximately proportional to $T^{-5/2}$. Discussions concerning this question are presented.

§ 1. Introduction

PbTe crystal is similar to PbS and PbSe cristals. This group of semiconductors has been investigated recently by many authors1)-9). These materials are known to have the following properties. They become n-type or p-type according not only to the condition during preparation but also to the heat treatments. This change in type depends upon what atmosphere arrounds the crystal during the heat treatment. Even if the heat treatment does not change the type of conduction it is often the case that it changes the numbers of denors and/or acceptors. Accordingly it has happened frequently that the crystal undergoes an irreversible change during the measurements at higher temperatures, and the results obtained have some uncertainties. The discrepancy between the intrinsic energy gap reported earlier8) and that reported later1)2)6) is considered to be attributed to this phenomenon9).

The resistivity and Hall coefficient of p-type PbTe crystals and their changes introduced by heat treatments are reported in this paper. The measurements were made in the temperature range from 450°K to liquid air temperature. An anomalous reversal of the sign of Hall coefficient, which was reported by Putley1) to have taken place in the extrinsic temperature range, was carefully looked for during the heat treatments, but we could not observe it. The matter relating to the sign reversal will be described in a separate paper. By heat treatment in air at about 400°K, the resistivity and the Hall coefficient increased. The experimental results are analyzed and some characteristic values are obtained.

§ 2. Experimental Procedures

Preparation of Crystals. The crystals used were synthetic single crystals. The method of preparation is similar to that of Lawson10). The lead was zone-refined in vacuum several times and the tellurium was distilled in vaccum. The resultant materials were mixed in the proportion of atomic equivalents. They were put into a fused silica tube crucible, which had a conical bottom in order that the crystal began to solidify at the bottom. Then the crucible was evacuated and sealed off. After being heated at about 1000°C for 8 hours in a furnace, the crucible was lowered slowly through the region of high temperature gradient in the furnace, the speed of lowering being about 1 mm/3 min.

Measurements. The crystal obtained by the above procedure was shaped to a rectangular parallele piped of 10× 4 × 1 mm³ in size. Platinum wires of 0.3 mm in diameter were attached to the both ends of the specimen as the current leads. The platinum wire was bent to form a sharp edge and heated by passing a current through it, then the edge was pressed to the end of the specimen to be welded. The ends of the specimen to be welded were covered by paraffin wax before welding11). The potential probes were platinum wires of 0.1 mm in diameter whose tips were sharpened. They were attached to the specimen by condenser discharge through their contacts[12]. The specimen was held in a cage by the current leads and potential probes as shown in Fig. 1. The diameter of the cage was 15 mm.

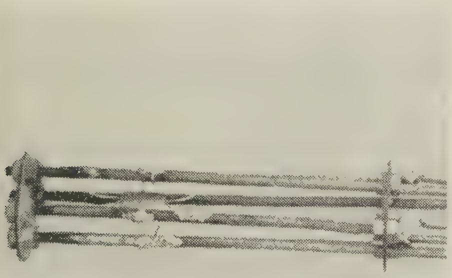

Fig. 1. Photograph of specimen and cage for measurement.

The measurements were made by usual *d. c.* method. In determining the Hall coefficient sets of four measurements were made in order to avoid associated electromotive forces such as due to IR drop and thermoelectromotive force: the four measurements were done by reversing the directions of both *d. c.* currents flowing the specimen and the coil of the magnet separately. In measuring the resistivity the average values for both directions of the current were used, although the values obtained in the two directions were practically the same.

The specimen was placed in a furnace which had non-ferromagnetic wire as a heater, when the measurements at higher temperatures were made. In measuring at low temperatures a Dewar vessel and a furnace within it were used and liquid air was used for lowering the temperature. The temperature was measured by copper-constantan thermocouple put closely to the specimen.

§ 3. Experimental Results

The resistivity ρ and the Hall coefficient R measured are shown as a function of temperature in Figs. 2∼5. Figs. 2 and 3 show the curves for various specimens. The curves labelled *Cu* are for the specimens cut from the same ingot which was doped with 0.01% copper. The curves *Cu*-132 and *Cu*-133 are those for the specimen *Cu*-131 after being heat treated in air at about 440°K for 5 hours and 10 hours respectively. Figs. 4 and 5 are for a series of measurements carried out on a specimen, and show the change of the electrical properties of the specimen produced by heat treatment in air at 400°K. Table I indicates the total time duration of heat treatment, which the specimen was subjected to before each measurement.

Table I.

Curve	P11	P12	P13	P14	P15
Time duration of heat treatment		0.5 days	3.5 days	9.5 days	24.5 days
N_A-N_D calculated from R_{exh}	2.5×10^{18}	1.2×10^{18}	7.8×10^{17}	5.9×10^{17}	4.8×10^{17}

The Hall coefficient in the extrinsic temperature range is almost constant as shown in Figs. 3 and 5. For impure specimens the Hall coefficient increases slightly at temperatures a little below the transition temperature to the intrinsic range. For copper-doped specimens with higher Hall coefficient which are considered to have so-called compensated impurities, the Hall coefficient begins to decrease at a lower temperature and continues to decrease, without kink (*Knick*), to the intrinsic values with increasing temperature. These figures show that the activation energy of acceptor levels is very small. The transition temperature to the intrinsic range is about 500°K. As the temperature rises the Hall coefficient inverts its sign before the temperature reaches the intrinsic range, though Figs. 3 and 5 do not show the whole of their behaviours. This indicates that the mobility of electron is larger than that of hole, at least in this temperature range. As the heat treatment proceeds, the extrinsic Hall coefficient becomes gradually larger.

The temperature coefficient of the resistivity at the extrinsic range is positive, as expected from the constant Hall coefficient independent of temperature in this range. The variation of the resistivity with temperature is pretty large, especially at higher temperatures. The mobility μ_h of the hole calculated from R/ρ is plotted as a function of the temperature in Figs. 6 and 7. From these figures it is seen that the relation $\mu_h \propto T^{-5/2}$ holds almost for the whole temperature range of our experiments. As easily seen, this strong temperature dependence corresponds to the fact that the temperature dependence of the resistivity is large as shown in Figs. 2 and 4.

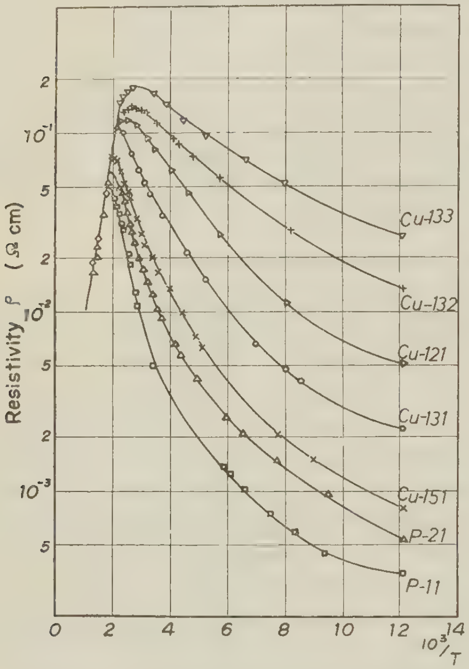

Fig. 2. Resistivity of various specimens.

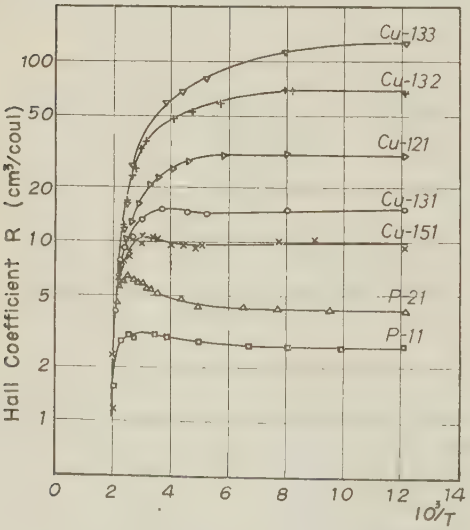

Fig. 3. Hall coefficient of various specimens.

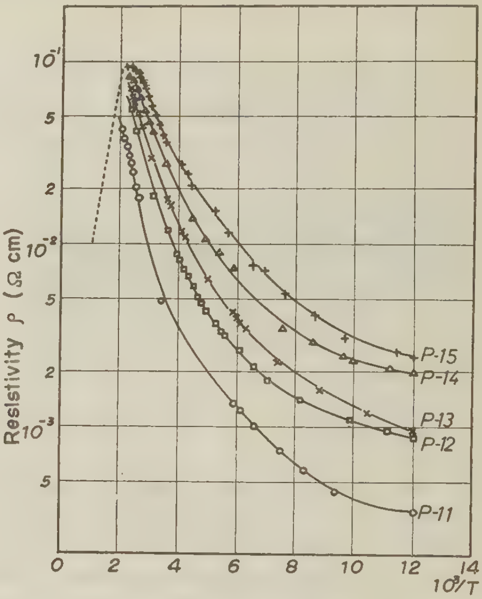

Fig. 4. Variation of resistivity of a certain specimen induced by heat treatment.

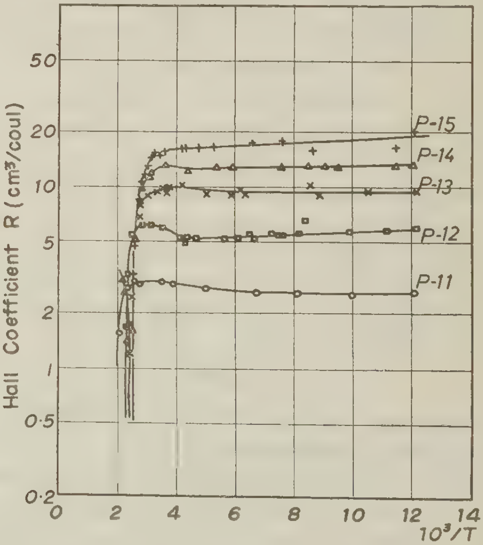

Fig. 5. Variation of Hall coefficient of a certain specimen induced by heat treatment.

§ 4. Analysis of the Hall Coefficient Data

In this experiment the data in the intrinsic

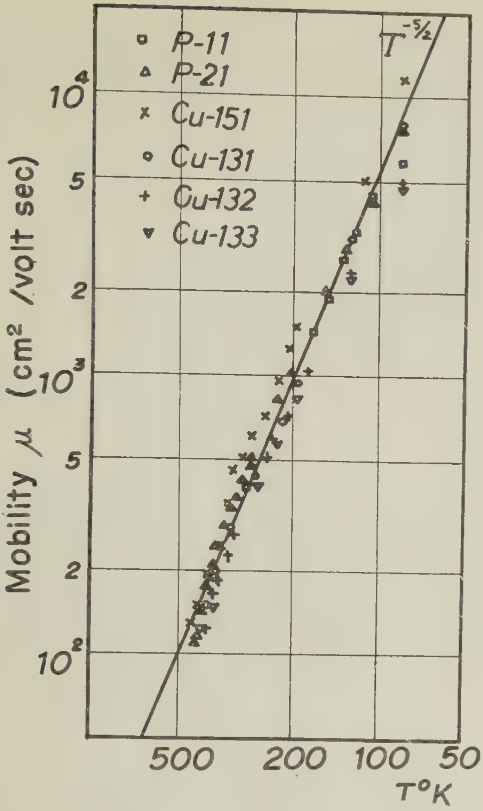

Fig. 6. Mobility (I), corresponding to Figs. 2 and 3.

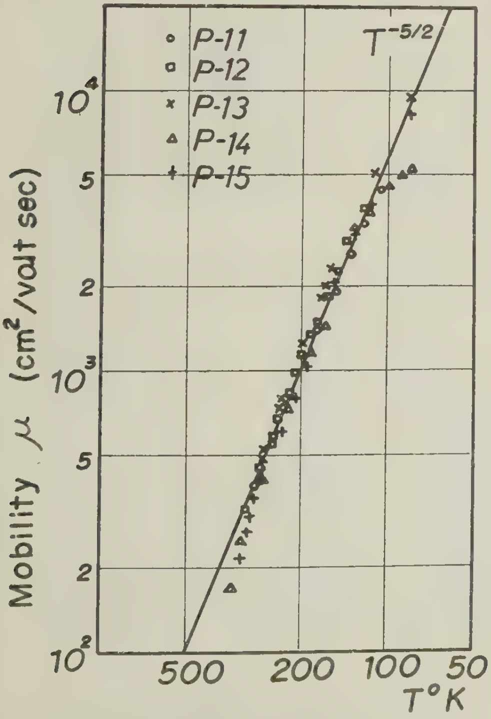

Fig. 7. Mobility (II), corresponding to Figs. 4 and 5.

temperature range could not be obtained, because in the measurements at higher temperatures there was a fear that the properties of the specimen might change irreversibly and consequently the measurements of the change of the properties introduced by heat treatments would be disturbed. The intrinsic energy gap, therefore, cannot be obtained from the slope of the intrinsic curves. The resistivity curves are especially steep at the temperatures slightly below the intrinsic range, and it should be noticed that the resistivity becomes larger at these temperatures than those expected from the Hall coefficient and the temperature dependence of the mobility. This is, perhaps, due to the fact that the mobility becomes abnormally small. Therefore we shall content ourselves, in this section, only with analyzing the data of Hall coefficient putting aside those of resistivity.

We assume that acceptor levels, whose number is N_A per unit volume, exist within the forbidden band. The activation energy of the levels is very small, as is deduced from the variation of Hall coefficient with temperature. It is assumed that the number p of the holes in the full band and the number n of the electrons in the conduction band are related by the equation

$$p=n+N_A\,. \tag{1}$$

The mobility ratio $b=\mu_e/\mu_h$ is assumed to be constant in our temperature range, where μ_e and μ_h are the mobilities of the electron and the hole respectively. The Hall coefficient is generally expressed by

$$R=\frac{r}{e}\frac{p-nb^2}{(p+nb)^2}\,. \tag{2}$$

Here r is assumed to be 1 for the sake of simplicity. From the above two equations, we obtain

$$\frac{n}{N_A}=\frac{1}{2(b+1)}\left\{2+c(b-1)\sqrt{1+\frac{4(c-1)}{2+c(b-1)}}-1\right\}, \tag{3}$$

where

$$c=R_{exh}/R,\quad R_{exh}=1/eN_A\,.$$

Denoting the term on the right hand side of Eq. (3) by $f(c, b)$, we can write

$$n=fN_A\,. \tag{4}$$

On the other hand

$$pn=CC'T^3\exp\left(-E_G/kT\right),$$

$$C=2(2\pi m_e kT/h^2)^{3/2}, \quad C'=2(2\pi m_h kT/h^2)^{3/2}\,, \tag{5}$$

where E_G is the width of the forbidden band, m_e and m_h are effective masses of the electron and the hole. Then from Eqs. (1), (4) and (5)

$$f(f+1)N_A{}^2=CC'T^3\exp(-E_G/kT) \tag{6}$$

and

$$\ln(N_A{}^2/T_c{}^3)=\ln CC'-\ln f(f+1)-E_G/kT_c\,. \tag{7}$$

We denote a temperature by T_c, at which the ratio of the value of a Hall coefficient curve to its exhaustion value becomes $1/c$, *i.e.* $R_{exh}/R=c$. For given c and given R_{exh} or N_A, T_c is obtained from the curves of Fig. 8. When curves of $\ln(N_A/T^{3/2})$ *vs.* $1/T$ are plotted for various values of c as a parameter, they must be a group of straight lines whose slopes are to give a value of E_G. They are shown in Fig. 9. The linearity of the curves is fairly good, and the value of E_G is determined as 0.34 ev.

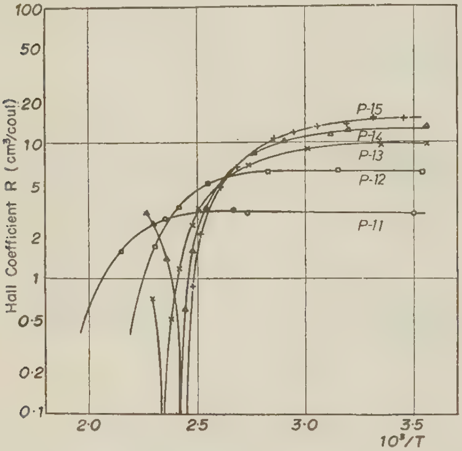

Fig. 8. Hall coefficient near the intrinsic reversal temperature.

The values of $CC'/f(f+1)$ for various values of c can be obtained from the intersections of the lines and the ordinate axis in Fig. 9, thus we can get $\ln CC'/f(f+1)$ *vs.* c relation from the experimental data. This relation is to be compared with the curves calculated from Eq. (3) for various values of b as a parameter. If, among the above theoretical curves, we find the curve which represents the experimental points well, the value of b corresponding to the curve must be one looked for as the mobility ratio. The theoretical curves and the experimental points are shown in Fig. 10. From this procedure b is estimated to be about 2.5, though this can give merely approximate value. The value of m_em_h/m^2 can be determined from the intersection of the curve and the ordinate axis in Fig. 9 after the value of b is determined. It is estimated to be 0.67.

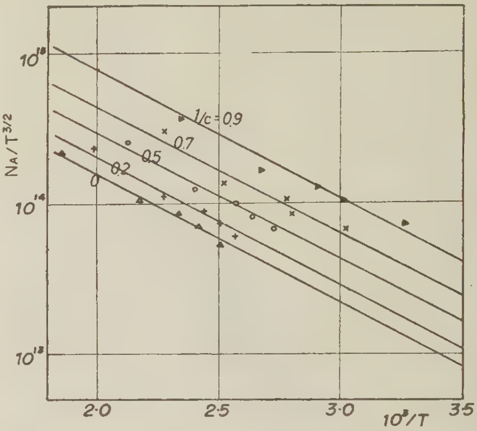

Fig. 9. Curves for determining the volue of E_G.

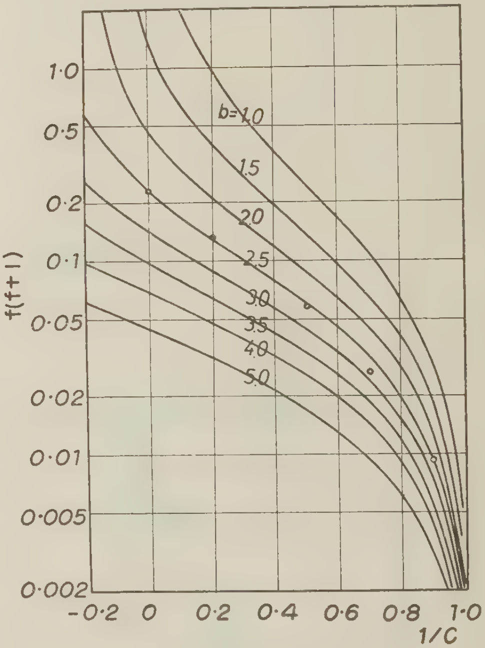

Fig. 10. Graph for determining the value of b, comparison between the theoretical curves and experimental points.

§ 5. Mobility

As is well known, this group of semiconductors has mobility proportional to $T^{-5/2}$. Petritz and Scanlon[6)] attempted to explain the mobility of PbS from the standpoint that it was affected principally by the optical mode of lattice vibration. However their attempt were not successful for higher temperatures. Difficulty of their interpretation at higher temperatures, they thought, was due to an inadequate expression of scattering cross section for electron whose energy was greater than $k\Theta$, Θ being the characteristic temperature.

Formerly they[13)] analyzed the mobility of PbS using the equation

$$\frac{1}{\mu}=\frac{1}{A\exp(\Theta/T)-1}+\frac{T^{3/2}}{B}, \qquad (8)$$

where the first term is related to the optical mode of lattice vibration and the second the acoustical mode. They found that Θ was about 1100°K and the effective mass was 0.17 m. On the other hand Hirahara and Murakami[4)] analyzed their mobility data of PbSe crystal by the equation

$$1/\mu=aT^{-3/2}+bT^{3/2}+c\{\exp(\Theta/T)-1\}^{-1}, \qquad (9)$$

where the first term represents the reciprocal of the mobility when scattering of ionized impurity centres only disturbs the motion of the carriers, the second concerns the acoustical mode of lattice vibration and the third the optical mode. They found that for characteristic temperature lower than 800°K Eq. (9) cannot represent the experimental data well.

An attempt to make Eq. (9) fit to our experimental data is made, and leads to the results that the characteristic temperature must be of the order of 1100°K in order to fit in the whole temperature range. This result is similar to the case of PbS[13)]. The characteristic temperature obtained is higher than the expected one. It was reported to be 194°K for PbS. As to PbTe approximately 150°K was given as the Debye temperature, which was deduced from specific heat measurement[14)]. In the above procedures the simple model of energy band structure is assumed tacitly. A consideration based on complicated band structure should be made in connexion to this point.

If the motion of the hole is affected mainly by the optical mode of lattice vibration and the value of $m_e m_h/m^2$ obtained in last section is assumed, the effective mass m_e of the electron in the conduction band is 0.51 m and m_h of the hole in the full band 0.94 m. Then the mean free path of the hole is estimated as shown in Fig. 11.

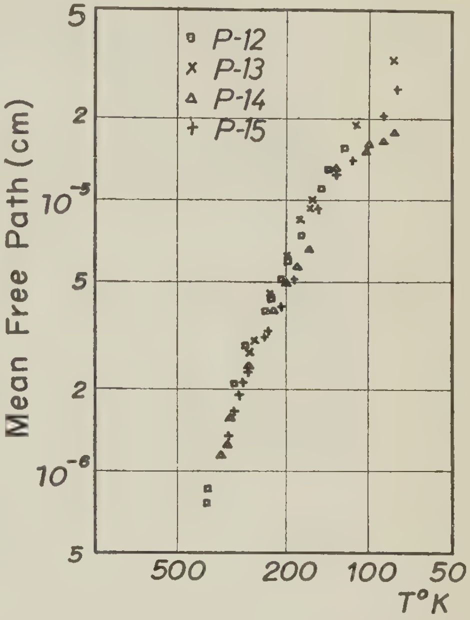

Fig. 11. Mean free path, corresponding to Figs. 4, 5 and 7.

§ 6. Discussion

It has been reported by many authors that this group of semiconductors undergoes an irreversible change of the electrical properties when it is heated above a certain temperature. This change depends upon the atmosphere in which the crystal is disposed during heat treatment. For instance, PbS changes to p-type in the sulphur vapour and n-type in vacuum. Our experiments showed that a crystal melted in the hydrogen atmosphere was of n-type and that heating of a p-type crystal to higher temperature in air causes the decrease of its Hall coefficient. These facts indicate that acceptors are principally due to excess tellurium or oxygen atoms or deficient lead atoms and that denors are due to excess lead or hydrogen atoms, though their precise situations in crystal structure cannot be known.

Heat treatment at moderate temperature, *e.g.* 400°K, even in air makes the Hall coefficient of a p-type crystal higher. And this effect is reported by Putley[1)] to be independent of the atmosphere. This may be due to reduction of some crystal imperfections such as defects or irregularities, hence a part of denors or acceptors may be due to the crystal imperfections in many crystals.

The activation energy of the acceptor levels is very small. This is thought to be connected with the high dielectric constant of this material. The refractive index, which is to be the square root of high frequency dielectric constant, is given to be $5^{15)}$. The energy gap of the forbidden band was not determined from the data in the intrinsic range, but it was estimated from other results of this experiment to be 0.34 ev., which proved to agree with those obtained from optical data$^{16)}$ and the recent data of intrinsic experiments$^{1)5)}$, while its variation with temperature was left untouched in this paper. The mobility ratio was determined in this paper. Smith$^{2)}$ stated that the mobility ratio was not constant but increased by fairly large amount with temperature. The value of the ratio calculated in this paper was obtained by using the data above 300°K.

The strong dependence of the mobility upon temperature has been already reported by many authors and is also verified in this paper. An explanation based on a conception that the mobility is affected by both acoustical and optical mode of lattice vibration gives good agreement between experimental and theoretical values, but it leads to a difficulty that the characteristic temperature must be assumed as high as 1100°K, as in the case of PbS. Difficulty might be removed if we introduce a consideration that the complexity of the band structure has some contribution to the temperature dependence of the mobility.

In conclusion, the writers wish to express their sincere acknowledgements to Professor Y. Sakaki and Professor K. Ariyama for their kind guidances and encouragements throughout the course of the work.

References

1) E. H. Putley: Proc. Phys. Soc. (London) **B68** (1955) 22; 35.
2) R. A. Smith: Physica **20** (1954) 910.
3) S. T. Silverman and H. Levinstein: Phys. Rev. **94** (1954) 871.
4) E. Hirahara and M. Murakami: J. Phys. Soc. Japan **9** (1954) 671.
5) R. F. Brebrick and W. W. Scanlon: Phys. Rev. **96** (1954) 598.
6) R. L. Petritz and W. W. Scanlon: Phys. Rev. **97** (1955) 1620.
7) T. Irie: J. Phys. Soc. Japan **11** (1956) 840.
8) E. H. Putley: Proc. Phys. Soc. (London) **B 65** (1952) 388; 993. R. P. Chasmar and E. H. Putley: Semiconducting Materials, ed. by H. K. Henish (Butterworth, London, 1951) 208.
9) W. W. Scanlon: Phys. Rev. **92** (1953) 1573.
10) W. D. Lawson: J. App. Phys. **22** (1951) 1444; **23** (1952) 495.
11) W. H. Mitchel: J. Sci. Instrum. **31** (1954) 147.
12) T. Fukuroi, S. Tanuma and S. Tobisawa: Sci. Pap. RITU. **A1** (1949) 373.
13) R. L. Petritz, W. W. Scanlon and F. L. Lummis: Bull. Amer. Phys. Soc. **29** (1954) 32.
14) D. H. Parkinson and J. E. Quarrington: Proc. Phys. Soc. (London) **A67** (1954) 569.
15) T. S. Moss: Photoconductivity in the Elements (Butterworth, London, 1952) 62.
16) A. F. Gibson: Proc. Phys. Soc. (London) **B 65** (1952) 378.

JOURNAL OF THE PHYSICAL SOCIETY OF JAPAN Vol. 12, No. 3, MARCH, 1957

On the Superstructure of the Ordered Alloy Cu_3Pd*
II. X-ray Diffraction Study

By Makoto HIRABAYASHI and Shiro OGAWA

The Research Institute for Iron, Steel and Other Metals, Tohoku University, Sendai

(Received September 25, 1956)

The structures of the ordered copper-palladium alloys in the composition range from 15.5 to 28.5 atomic per cent Pd were investigated by X-ray diffraction, using both single crystals and power specimens. The alloys with the composition of 20.8 to 25.8 atomic per cent Pd have an anti-phase domain structure in a fully ordered state cooled slowly from 450°C to room temperature in four months. This structure is formed from the elementary face-centered tetragonal lattice, in which the atoms arrange themselves as in the ordered alloy Cu_3Au but step-shifts occur at a definite period along the tetragonal axis. On the other hand, the alloys of 27.3 and 28.5 atomic per cent Pd were confirmed to possess a more complicated anti-phase domain structure characterized by the two kinds of out-of-step, which was already elucidated by the electron diffraction study in Part I. Variation of both the lattice parameters and the periods of anti-phase domain with composition were also studied.

§ 1. Introduction

The copper-palladium alloys in the vicinity of the composition Cu_3Pd have a disordered face-centered cubic lattice at temperatures above about 470°C. Below this temperature, according to Jones and Sykes[1], the ordered phase is in equilibrium and is subdivided into α' and α'' phases. According to them, the structure of α' phase, which exists in the composition range from about 8 to 18 %* Pd, is the face-centred cubic lattice with the atomic arrangement of the Cu_3Au type, while α'' phase, existing in the composition range from about 18 to 28 % Pd, is built up from the face-centered tetragonal cells in terms of the original disordered face-centered cubic cells. But the arrangement of atoms in this superlattice could not definitely be determined by them. In Part I[2], Watanabe and one of the present authors (S.O.) studied the superstructure of this alloy by electron diffraction, and elucidated a complicated anti-phase domain structure present stably in α'' phase. Recently Schubert, Kiefer, Wilkens and Haufler[3] studied the ordered structures with large periods of anti-phase domains in many binary and ternary systems, and reported that the structure of the ordered alloy Cu_3Pd seemed to coincide with the model proposed in our short communication[4]. On the other hand, Geisler and Newkirk[5] concluded that the Cu-Pd alloy, containing 20 % Pd, has an ordered structure of the modified Ni_4Mo-type. This structure was supported by the recent work of Jaumot and Sawatzky[6].

The present work was undertaken to examine the ordered structure of α'' phase by X-ray diffraction study, using single crystals mainly and powder specimens. In the present paper, it will be shown that the observed results essentially agree with those of the electron diffraction study, and then our results will be compared with the previous works and discussed.

§ 2. The Proposed Models of the Superstructure of α'' Phase

First of all, for the sake of interpretation of the results of the X-ray diffraction study described in § 4, we show several models of the structure of the ordered α'' phase proposed by various workers. Fig. 1 reproduces the model of the superstructure elucidated by the electron diffraction study in Part I[1]. This model is a two dimensional anti-phase domain structure, namely, as mentioned in Part I, this is thought of as formed from the elementary face-centered tetragonal lattice, in which the

---

* A short communication concerning this work has been published in Acta Cryst. 8 (1955) 510.

* In the present paper, all percentages refer to atomic per cent.

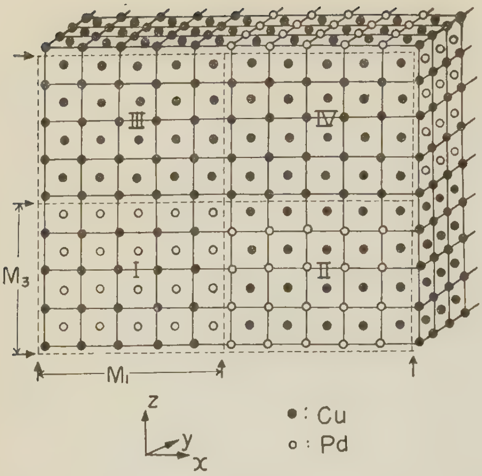

Fig. 1. Model of the two-dimensional anti-phase domain structure with $M_1=5$ and $M_3=4$. Out-of-steps occur at places indicated by arrows.

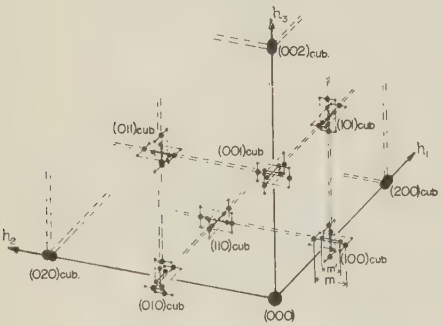

Fig. 2. Intensity distribution in reciprocal space for the actual crystal with the two-dimensional anti-phase structure. This figure is six-fold super-position of the fundamental reciprocal lattice corresponding to the model of Fig. 1.

atoms arrange themselves as in the structure of the ordered alloy Cu$_3$Au but "*the first kind*" and "*the second kind*" of step-shift, $\pm(\boldsymbol{a}_1 \pm \boldsymbol{a}_2)/2$ and $\pm(\boldsymbol{a}_3 \pm \boldsymbol{a}_1)/2$, occur at every M_3-th atom and M_1-th atom along the z and x directions respectively. $\boldsymbol{a}_1$, $\boldsymbol{a}_2$ and $\boldsymbol{a}_3$ are the fundamental lattice vector along the x, y and z axes in terms of the fundamental cells, and the fundamental tetragonal axis coincides with the z direction. Fig. 2 is the intensity distribution in reciprocal space corresponding to an actual crystal of α'' phase. In this figure the splits of the superlattice reflections have two distinct values of separation, m and m', being given by $(1/M_3)a_3^*$ and $(1/M_1)a_1^*$ respectively. a_1^* and a_3^* are reciprocal lattice constants corresponding to $\boldsymbol{a}_1$ and $\boldsymbol{a}_3$ respectively.

Fig. 3 shows the model of the structure of the fully ordered alloy Cu$_4$Pd, proposed by Newkirk and Geisler[5]. This structure belongs to the space-group $C_{4h}^2-P_{42/m}$, containing 20 atoms arranged in a tetragonal symmetry ($a=5.826$ Å, $c=7.328$ Å). It is easily seen that the intensity distribution in reciprocal space given by this structure is entirely different from that of our model depicted in Fig. 2.

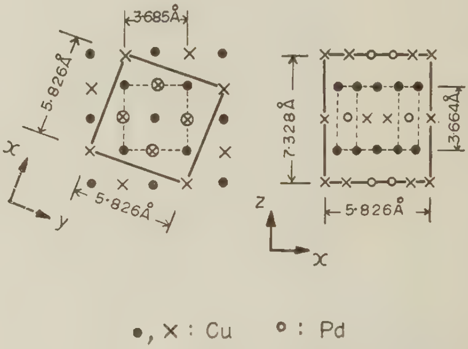

Fig. 3. The ordered structure of the alloy Cu$_4$Pd proposed by Geisler and Newkirk. Original cubic unit cell is shown by the dotted lines.

Schubert *et al.*[3], on the other hand, reported that the ordered alloys containing 18 to 25 % Pd have one-dimensional anti-phase domain structure, characterized by the first-kind of out-of-step, as shown in Fig. 4. The step-shift is lined up along the tetragonal axis of the fundamental cells. This structure has

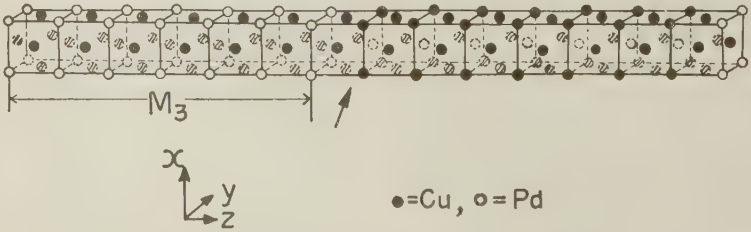

Fig. 4. The one-dimensional anti-phase domain structure with the period $M_3=7$. The arrow indicates the occurrence of step-shift.

also been reported for the alloy of 22 % Pd in our short communication[4] and resembles that found in the partially ordered states of Cu_3Au[7]. The intensity distribution in reciprocal space given by this structure is shown in Fig. 5(a), in which the tetragonal axis lies along the h_3 direction. For the actual case, since the tetragonal axis will distribute along the three original cubic axes, the reciprocal lattice has to be given as Fig. 5(b).

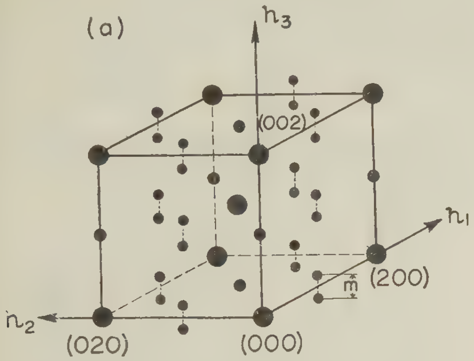

Fig. 5 (a). Fundamental intensity distribution in reciprocal space induced from Fig. 4.

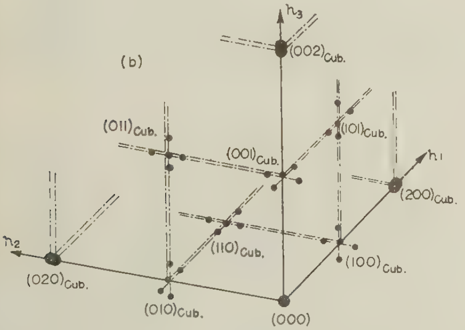

Fig. 5 (b). Three-fold superposition of the intensity distribution in (a), corresponding to the actual state of the ordered alloy.

§ 3. Experimental Procedures

a) Preparation of specimens

Seven specimens of the copper-palladium alloys, which possessed 15.5, 16.3, 20.8, 25.2, 25.8, 27.3 and 28.5 % Pd, were prepared from electrolytic copper (99.9 %) and pure palladium (99.9 %), each alloy weighing approximately 5 gr. The metals were melted in an evacuated thin quartz tube. The large crystals were often easily grown by slow cooling of ingots, but the single crystals were grown by the Tammann-Bridgman method in ceramic tubes, as previously reported[8]. After homogenization at temperatures below the solidus in vacuum, the single crystals were etched by $HCl+CrO_3$ aqueous solution or aqua regia and reduced to about 0.2 mm in diameter. The filed powder specimens were also used to determine the lattice parameters in both disordered and ordered states.

b) Heat treatment

The ordering process of the alloy of Cu_3Pd takes place so slowly that a very long period of heating below the transition temperature is necessary to obtain the fully ordered state[1,9]. To investigate preliminarily the well ordered state, the single crystals were annealed for two weeks in the temperature range between 450°C to 200°C, as follows; the specimens were initially brought to the disordered state, then heated at 450°C for 2 days, at 400°C and 350°C for 3 days, and at 300°C, 250°C and 200°C for 2 days respectively, and slowly cooled down to room temperature. In order to obtain the specimens in the completely ordered state, they were annealed over a period of four months, i.e. at 400°C for 23 days, at 350°C for 17 days, and at temperatures between 350°C and 200°C for 90 days, then slowly cooled in the furnace to room temperature. During the ordering treatment all specimens were sealed in evacuated glass ampules.

c) X-ray examination

Keeping either a [100] or a [110] direction of the original cubic crystal as the vertical axis, oscillation photographs were taken, and some series of stationary-crystal photographs were sometimes also taken to investigate in detail around certain reciprocal lattice points. With Cu or Fe radiation, X-ray diffraction patterns were recorded on the cylindrical films (Fuji non-screen 200 Type) of 10 cm or 8 cm in diameter. In the study of polycrystalline specimens, the lattice parameters were determined by means of the graphical-extrapolation method, using a 114.6 mm Debye-Scherrer camera. In some cases, in order to study the weak superlattice lines, a focusing camera was used together with a curved quartz monochromator.

§ 4. Experimental Results

a) Two weeks annealed state

The preliminary investigation was done for the two specimens, containing 20.8 and 25.2 %

Pd, after being annealed for 2 weeks. The observed results for the former crystal will be mainly described below. Photo. 1(a) and (b) are the oscillation photographs of the alloy of 20.8 % Pd. These patterns show that the superlattice reflections $(010)_{\text{cub.}}$ and $(110)_{\text{cub.}}$ split apparently into three and five spots, respectively. By comparing these photographs with Fig. 6(a) and (b), which are respectively the (100) and the $(1\bar{1}0)$ planes of the reciprocal lattice depicted in Fig. 5(b), it is clearly shown that the splitting of each superlattice reflection can well be interpreted by assuming the presence of one-dimensional anti-phase domains, characterized by the first kind of out-of-step and lined up along the tetragonal axis, as already given in Fig. 4. Therefore, indices of the splits of $(110)_{\text{cub.}}$ group in Photo. 1(a) are $(1\ 0\ 1\pm1/2M_3)$, $(0\ 1\ 1\pm1/2M_3)$ and (110), as described beside this pattern. Also the satellites of $(010)_{\text{cub.}}$ correspond to $(0\ 1\ \pm1/2M_3)$ and the central spot (001) is superposed by another pair of satellites $(1\ 0\ \pm1/2M_3)$*. While, in Photo. 1(b) the satellites of $(010)_{\text{cub.}}$ group are $(1\ 0\ \pm1/2M_3)$, and the central spot (001) is superposed by $(0\ 1\ \pm1/2M_3)$.

Table I.

Superlattice reflection $h\ k\ l$	Separation of satellites m	Period of aut-of-step M_3
1 0 0	0.062	6.7
1 1 0	0.060	7.0
2 1 0	0.060	7.0
2 1 1	0.056	7.5
3 0 0	0.060	7.0
2 2 1	0.058	7.2
3 1 0	0.058	7.2
3 2 0	0.058	7.2
4 1 0	0.060	7.0
3 2 2	0.060	7.0
	Mean value=7.1	

The period of out-of-step or the domain length, M_3, was determined from the splittings of certain superlattice reflections. For the alloy of 20.8 % Pd, Table I lists the separation of satellites in reciprocal space and the domain lengths determined from them. The mean value of M_3 is 7.1 and agrees quite well with that obtained from the powder photographs, using monochromatic focusing camera.

Further, the relative intensities of these splitting reflections were photometrically measured for both single and poly-crystal diffraction patterns and were compared with those calculated from the structural model shown in Fig. 4. Table II gives the observed and calculated relative intensities of the satellites of $(001)_{\text{cub.}}$ and $(110)_{\text{cub.}}$ groups, in which the intensity of either $(001)+(0\ 1\ \pm1/2M_3)$ or (110) reflection is taken as unity. The calculated values were obtained from $(\text{L.P.})F^2\cdot G_3{}^2$, where (L.P.) is the Lorentz-polarization factor, F the structure factor, and G_3 the Laue function along the z direction, being given by Guinier and Griffoul7) and by Raether7). The values calculated with $M_3=7$ agree almost well with the observed ones.

Table II. Relative intensities of satellites of superlattice reflections of the alloy containing 20.8 % Pd.

h	k	l	Relative intensities observed	Relative intensities calculated with $M_3=7$
1	0	$-1/2M_3$	0.25	0.23
0	0	1	1	1
0	1	$\pm1/2M_3$		
1	0	$+1/2M_3$	0.20	0.23
1	0	$1-1/2M_3$	0.35	0.46
0	1	$1-1/2M_3$	0.32	0.46
1	1	0	1	1
0	1	$1+1/2M_3$	0.25	0.37
1	0	$1+1/2M_3$	0.28	0.37

The alloy of 25.2 % Pd gave analogous diffraction patterns to those of the 20.8 % Pd alloy, except that the period of out-of-step was determined as 5.1 and the ratio c/a was 0.991.

b) *Four months annealed state*

Five single crystals containing 20.8, 25.2, 25.8, 27.3 and 28.5 % Pd were studied in the fully ordered state, cooled slowly in four months. In this state, the splitting manner of superlattice reflections was investigated to confirm in more detail the intensity distribution in reciprocal space. Photo. 2(a), (b) and (c) are the parts of oscillation photographs of the crystal of 20.8 % Pd using Cu radiation, showing split of some superlattice reflections. From these patterns, it was elucidated that the five splitting spots of superlattice reflections $(110)_{cub.}$ and $(011)_{cub.}$ lie on the (001) and (100) relplanes respectively, as just was represented in Fig. 6. In Photo. 2(a), the $(031)_{cub.}$ reflection

---

* Since the axial ratio c/a of this alloy is 0.993, the separation due to the tetragonality is so small that (001) is hardly distinguished from $(1\ 0\ \pm1/2M_3)$ in this photograph.

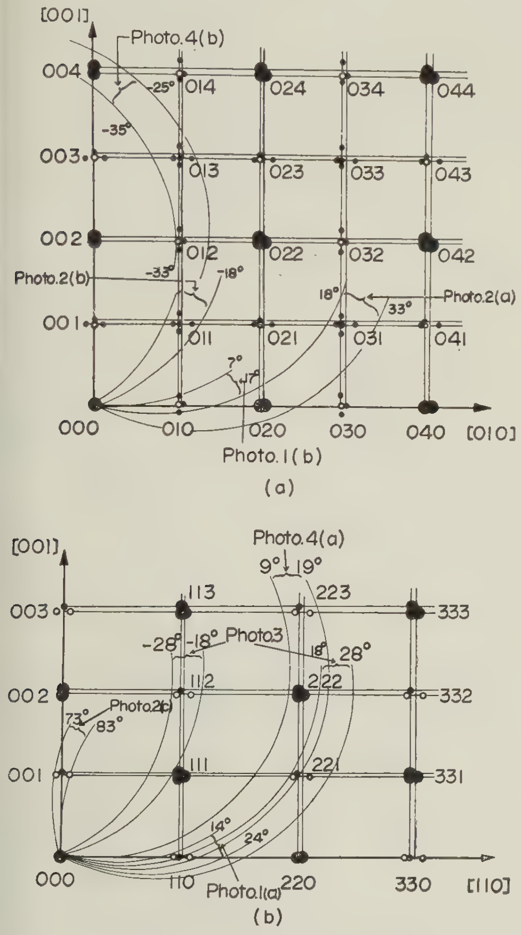

(a)

(b)

Fig. 6(a) and (b). (100) and $(1\bar{1}0)$ planes in the reciprocal lattice of Fig. 5 (b) respectively. The lune-shaped areas are sections through the relplanes swept out by the oscillating sphere of reflection of Cu Kα radiation, and each corresponds to each of Photos. 1～4. Full and open small circles show schematically the split superlattice points lying on and not on the planes concerned respectively.

plits appreciably in five spots lying on the 100) relplane, owing to the tetragonality, lthough the $(011)_{cub.}$ reflection in Photo. 2(b) plits only in three spots. Since the axial atio decreased to 0.991 at this stage, it is clearly seen, by comparison between Photo. 1 and Photo. 2(c), that the satellites of $(001)_{cub.}$ reflection displace towards the lower angle side than the central spot (001). Thus all these patterns are well interpreted by the anti-phase domain structure described in Fig. 4, as well as the pattern in Photo. 1 of the two weeks annealed state.

Table III. Relative intensities of the $(112)_{cub.}$ group in Photo. 3.

h	*k*	*l*	Relative intensities obs.	Relative intensities cal.
1	2	$1-{}^1\!/_2M_3$	0.47	0.45
2	1	$1-{}^1\!/_2M_3$	0.19	0.45
1	1	2	1	1
1	2	$1+{}^1\!/_2M_3$	0.37	0.41
2	1	$1+{}^1\!/_2M_3$	0.19	0.41

Table IV. Indices of the $(012)_{cub.}$ and $(013)_{cub.}$ groups in Photos. 5 and 6.

No. of spots in photographs		Index *h*	Index *k*	Index *l*
$(012)_{cub.}$ group	1	$1\pm{}^1\!/_2M_1$ 2	2 1	$-{}^1\!/_2M_3$ $-{}^1\!/_2M_3$
	2	$1\pm{}^1\!/_2M_1$ 2	2 1	$+{}^1\!/_2M_3$ $+{}^1\!/_2M_3$
	3	0 $1\pm{}^1\!/_2M_1$	1 0	$2-{}^1\!/_2M_3$ $2-{}^1\!/_2M_3$
	4	0 $1\pm{}^1\!/_2M_1$	1 0	$2+{}^1\!/_2M_3$ $2+{}^1\!/_2M_3$
	5	$2-{}^1\!/_2M_1$	0	1
	6	$2+{}^1\!/_2M_1$	0	1
	7	$+{}^1\!/_2M_1$	2	1
	8	$-{}^1\!/_2M_1$	2	1
	9	2	0	1
	10	Laue spot		
$(013)_{cub.}$ group	1	1	0	$3-{}^1\!/_2M_3$
	1′	$\pm{}^1\!/_2M_1$	1	$3-{}^1\!/_2M_3$
	2	1	0	$3-{}^1\!/_2M_3$
	2′	$\pm{}^1\!/_2M_1$	1	$3-{}^1\!/_2M_3$
	3	3	0	$1-{}^1\!/_2M_3$
	3′	$\pm{}^1\!/_2M_1$	3	$1-{}^1\!/_2M_3$
	4	3	0	$1+{}^1\!/_2M_3$
	4′	$\pm{}^1\!/_2M_1$	3	$1+{}^1\!/_2M_3$
	5	$3-{}^1\!/_2M_1$	1	0
	6	$1-{}^1\!/_2M_1$	3	0
	7	$1+{}^1\!/_2M_1$	3	0
	8	$3+{}^1\!/_2M_1$	1	0
	9	1	3	0

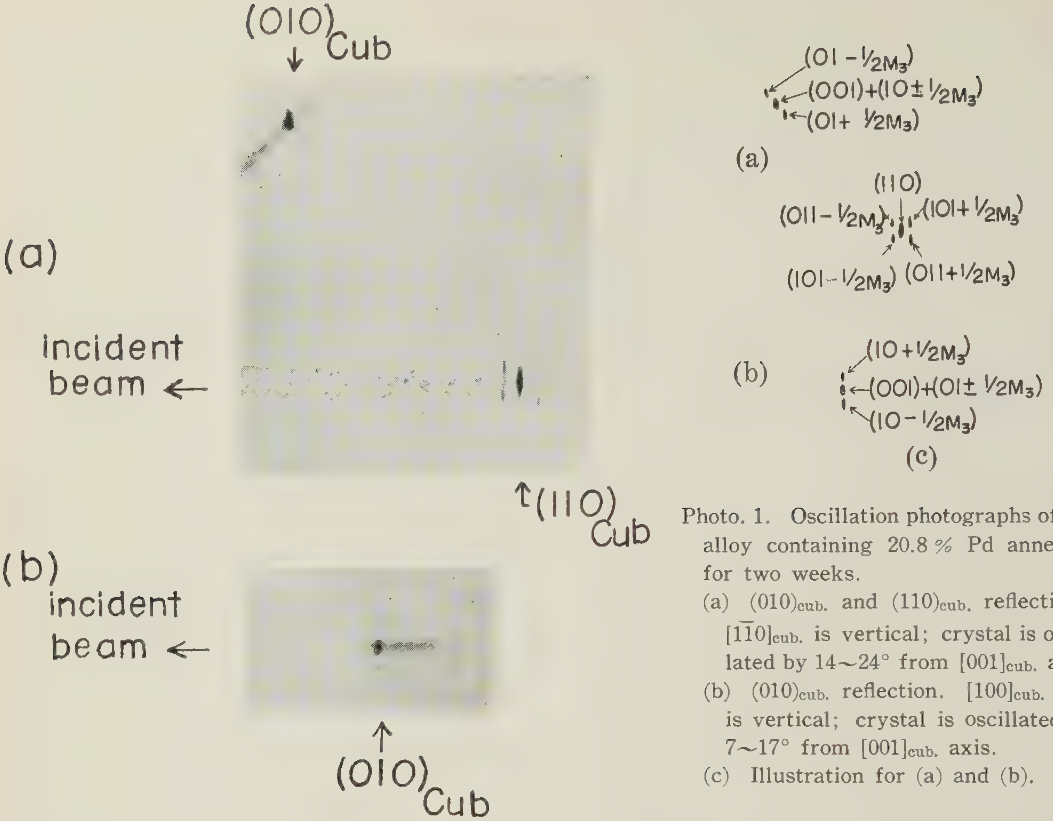

Photo. 1. Oscillation photographs of the alloy containing 20.8 % Pd annealed for two weeks.
(a) $(010)_{\text{cub.}}$ and $(110)_{\text{cub.}}$ reflections. $[1\bar{1}0]_{\text{cub.}}$ is vertical; crystal is oscillated by 14∼24° from $[001]_{\text{cub.}}$ axis.
(b) $(010)_{\text{cub.}}$ reflection. $[100]_{\text{cub.}}$ axis is vertical; crystal is oscillated by 7∼17° from $[001]_{\text{cub.}}$ axis.
(c) Illustration for (a) and (b).

The alloys of 25.2 and 25.8 % Pd also give closely analogous splitting of superlattice reflections to that of the 20.8 % Pd alloy. In Photo. 3, which shows the superlattice reflections of $(112)_{\text{cub.}}$, $(\bar{2}\bar{2}1)_{\text{cub.}}$ and the high angle side of $(\bar{1}\bar{1}0)_{\text{cub.}}$ of the 25.2 % Pd alloy, it should be noticed that the intensities of the two pairs of satellites of these reflections are considerably different from each other. The relative intensities of the splits of the $(112)_{\text{cub.}}$ group were photometrically measured, and the observed results are listed in the second column of Table III. This table shows that the relative intensities of the one pair of the satellites $(1\ 2\ 1 \pm 1/2M_3)$ to the central reflection (112) agree almost with the calculated ones, in which M_3 is assumed to be 5, but the other pair $(2\ 1\ 1 \pm 1/2M_3)$ has fairly less intensities. Hence we can conclude that the *c* axis of the ordered face-centered tetragonal lattice, i.e., the direction of line-up of anti-phase domains, is distributed not equally to three principal axes of the original cubic lattice. This circumstance is, however, special, and a uniform distribution of the tetragonal axis was observed in many cases.

Photo. 4(a) and (b) are the oscillation photographs of the alloy of 25.8 % Pd, giving some splitting groups of superlattice reflections, such as $(110)_{\text{cub.}}$, $(221)_{\text{cub.}}$, $(223)_{\text{cub.}}$, $(012)_{\text{cub.}}$ and $(013)_{\text{cub.}}$, besides the normal reflections. The vertical splittings of the normal spots, such as $(222)_{\text{cub.}}$, $(224)_{\text{cub.}}$ and $(004)_{\text{cub.}}$, seem to mean the occurrence of polycrystallization of the specimen caused by lattice distortion accompanying the ordering reaction.

From the following diffraction patterns of the alloys containing 27.3 and 28.5 % Pd, the complicated two-dimensional anti-phase domain structure depicted in Fig. 1 was confirmed to exist stably. Photo. 5 is a series of the stationary crystal photographs for the $(012)_{\text{cub.}}$ reflection of the alloy of 27.3 % Pd, with

---

* It is undeniable that the electron diffraction results do not compromise with the present X-ray diffraction results about the stable region of the two-dimensional anti-phase domain structure. The reason for this is, however, not clear at the present stage.

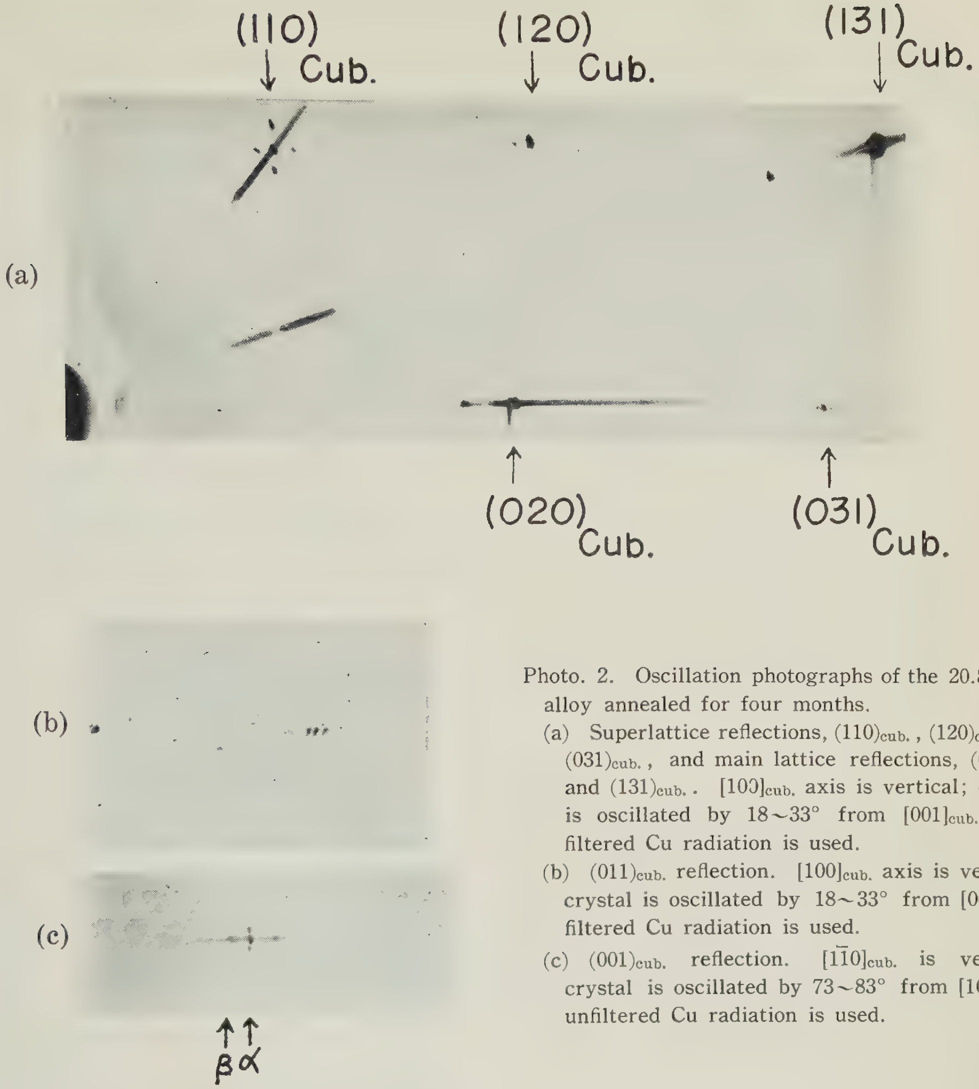

Photo. 2. Oscillation photographs of the 20.8 % Pd alloy annealed for four months.

(a) Superlattice reflections, $(110)_{cub.}$, $(120)_{cub}$, and $(031)_{cub.}$, and main lattice reflections, $(020)_{cub.}$ and $(131)_{cub.}$. $[100]_{cub.}$ axis is vertical; crystal is oscillated by 18～33° from $[001]_{cub.}$ axis; filtered Cu radiation is used.

(b) $(011)_{cub.}$ reflection. $[100]_{cub.}$ axis is vertical; crystal is oscillated by 18～33° from $[001]_{cub.}$; filtered Cu radiation is used.

(c) $(001)_{cub.}$ reflection. $[1\bar{1}0]_{cub.}$ is vertical; crystal is oscillated by 73～83° from $[100]_{cub.}$, unfiltered Cu radiation is used.

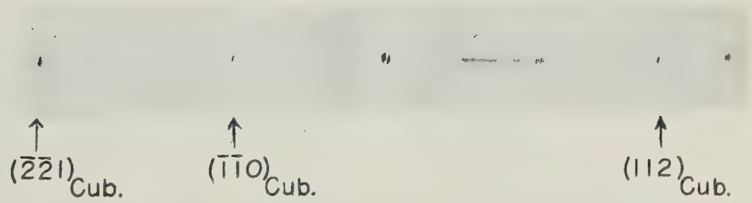

Photo. 3. Oscillation photograph of the ordered alloy of 25.2 % Pd. $[1\bar{1}0]_{cub.}$ is vertical; crystal is oscillated by 18～28° from $[001]_{cub.}$ axis. Unfiltered Cu radiation is used.

$[001]_{cub.}$ axis vertical. The $(012)_{cub.}$ reflection bears a resemblance to the $(110)_{cub.}$ reflection in the electron diffraction pattern in Fig. 8(a) of Part I and shows a double splitting of the satellites, whose indices are given in Table IV. Although the central spot, No. 9 in this table, has been observed also in the electron diffraction patterns, it can not be expected from the anti-phase domain model alone such as shown in Fig. 1. This fact, however, may

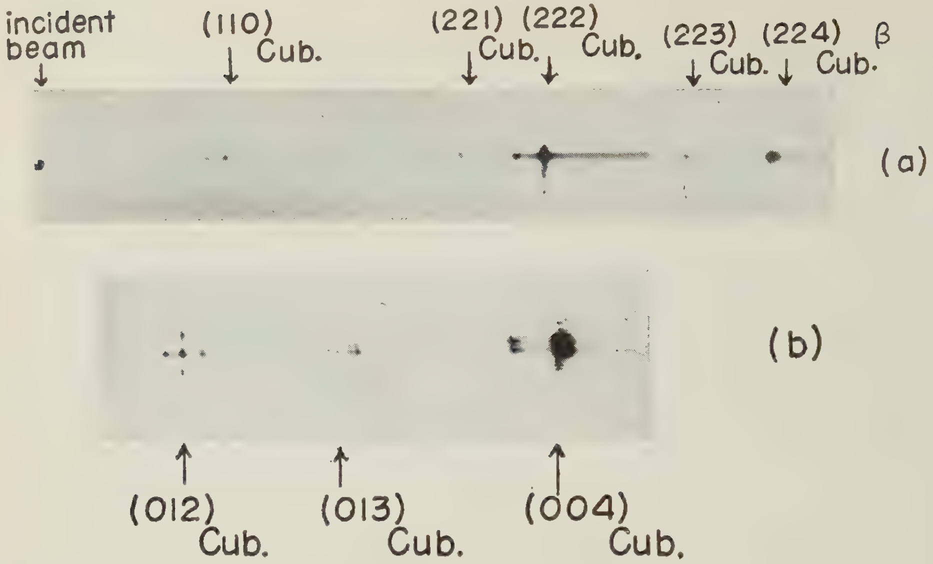

Photo. 4. Oscillation photographs of the ordered alloy of 25.8 % Pd. Unfiltered Cu radiation is used.

(a) $[1\bar{1}0]_{\text{cub.}}$ is vertical; crystal is oscillated by 9∼19° from $[001]_{\text{cub.}}$ axis.

(b) $[100]_{\text{cub.}}$ is vertical; crystal is oscillated by 25∼35° from $[001]_{\text{cub.}}$ axis.

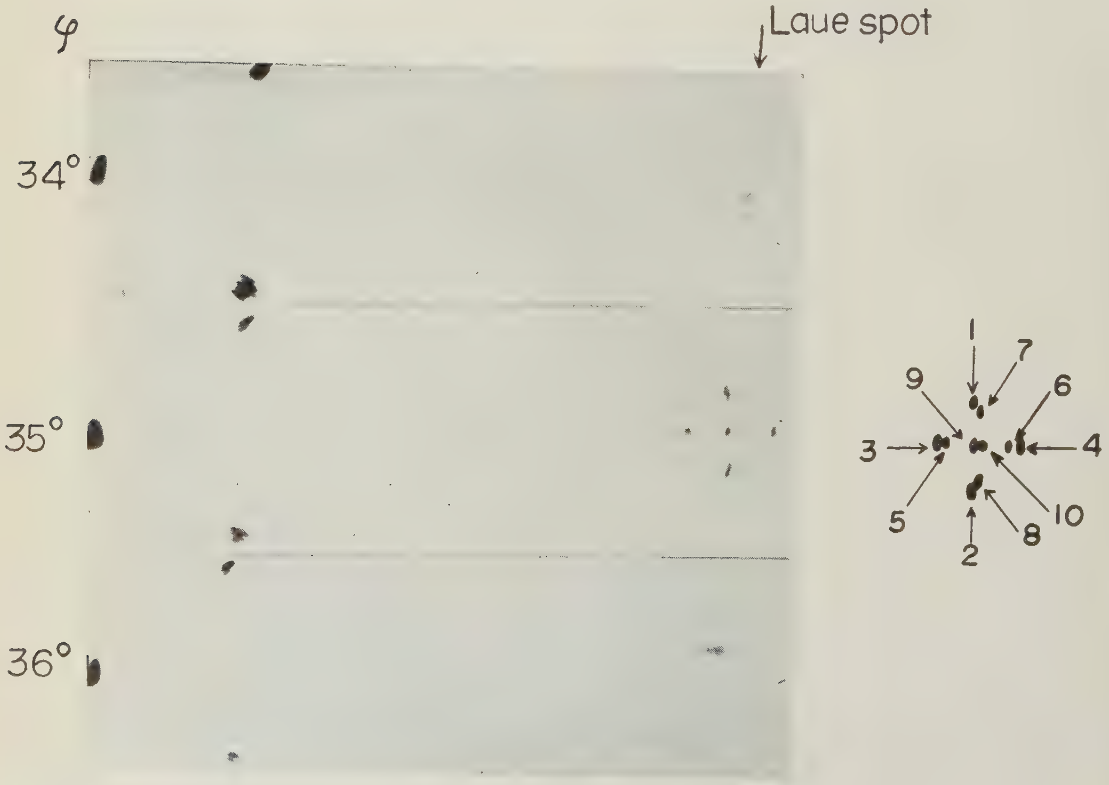

Photo. 5. Series of stationary crystal photographs of the $(012)_{\text{cub.}}$ reflection group of the alloy containing 27.3 % Pd. Unfiltered Fe radiation is used; $[100]_{\text{cub.}}$ axis is vertical; $[001]_{\text{cub.}}$ axis makes 34∼36° with beam direction. Indices of split spots are to be referred to Table IV.

be interpreted by considering coexistence of both the one-dimensional and the two-dimensional anti-phase domain structures, since the former type of anti-phase structure can give rise to the central spot, as mentioned before. Photo. 6 is an example of the oscillation photographs of this alloy, using unfiltered Fe radiation, and it shows the $(0\bar{1}3)_{\text{cub.}}$ reflection flanked by a new type of satellites. The difference between diffraction patterns of the one-dimensional and the two-dimensional anti-phase domain structures will clearly be seen by comparison between Photo. 2(a) or Photo. 4(b) and Photo. 6; namely in the last pattern the weak split spots, indicated by 1′, 2′, 3′ and 4′, are seen above and below the equatorial line, in addition to the spots on this line, while in the former two only five splits lying on this line are observable. The splits of the superlattice reflection in Photo. 6 can entirely be explained by the intensity distribution in reciprocal space as given in Fig. 2, and the indices of all splits are also given in Table IV. The two periods of anti-phase domain, M_1 and M_3, were obtained from the two kinds of separation of the satellites, being respectively 4.0 and 3.2 atomic distances.

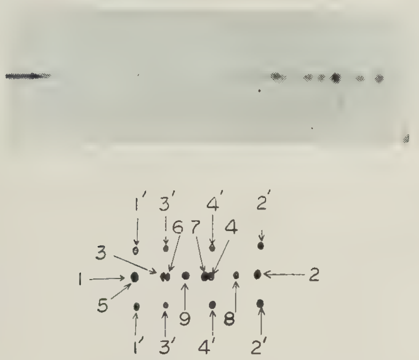

Photo. 6. Oscillation photograph of the alloy of 27.3 % Pd. Split $(013)_{\text{cub.}}$ reflection is shown. $[100]_{\text{cub.}}$ is vertical; crystal is oscillated by 11～21° from $[001]_{\text{cub.}}$ axis. Unfiltered Fe radiation is used. Indices of split spots are to be referred to Table IV.

The alloy containing 28.5 % Pd gave quite similar diffraction patterns to those of the alloy of 27.3 % Pd and possessed the superstructure characterized by both kinds of step-shift with the periods $M_1 \simeq 3.8$ and $M_3 \simeq 3.5$.

In X-ray diffraction patterns of any specimen, there have never been found such satellites flanking the normal reflections as observed in electron diffraction patterns.

Next, the data obtained from the present study will be summarized as a function of composition. Fig. 7 gives the periods of anti-phase, domain M_1 and M_3, as a function of composition for four months annealed state. Both values of M_1 and M_3 seem to agree well with the results of Schubert *et al.*[3] rather than with those of the electron diffraction study[2]. The periods of anti-phase domain decrease continuously with the increasing concentration of Pd atoms. These values in atomic distances are in general not integers. This fractional property of M's values is considered to prove that the different periods of anti-phase domain are mixed uniformly but probably with some irregularity. On this point, detailed discussions and calculations were recently developed[10] in the course of study on the alloy Ag_3Mg in our laboratory.

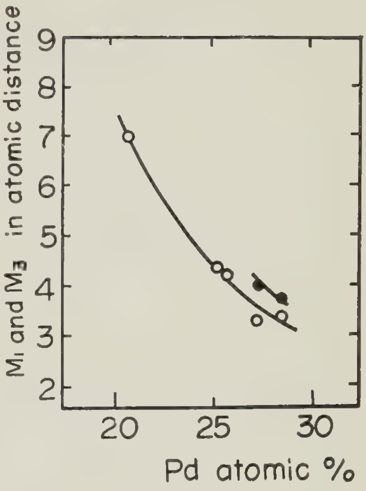

Fig. 7. Variation of the periods of anti-phase domain, M_1 and M_3, with composition. Open and full circles represent the values of M_3 and M_1 respectively.

Fig. 8(a) show the variation of lattice parameters with composition for the ordered and disordered states. The lattice parameters of the disordered alloys quenched from 600°C appear to be approximately linear with composition, but to deviate positively from Vegard's law. In this figure, $(a^2c)^{1/3}$ is also plotted, in addition to a and c, for the ordered tetragonal cell. These lattice parameters agree fairly well with the previous investigations [5],[6],[11]. The lattice contraction due to ordering is very

Table V. Comparison between observation and calculation for superlattice line positions and relative intensities of the 20 % Pd alloy.

Observed data by Geisler-Newkirk		Calculated data						
		Anti-phase domain model					2-*hi* inverted Ni_4Mo-type model	
$1/d^2$	I	$1/d^2$	(*L.P.*)× $F^2\cdot G_3^2\cdot p$**	h	k	l	$1/d^2$	$F^2\cdot p$
0.0751	M	0.0743	110	1	0	$\pm{}^1/_{14}$	0.0748	19
		0.0748	73	0	0	1	0.0778	24
0.1400	M	0.1385	47	1	0	$1-{}^1/_{14}$	0.1370	20
0.1488	M	0.1478	62	1	1	0	0.1479	30
0.1601	MW	0.1597	45	1	0	$1+{}^1/_{14}$	0.1666	18
0.1863	VW	0.1842	1	1	0	$1+{}^3/_{14}$	0.1978	18
							0.2274	16
							0.2553	16
							0.2849	14
							0.2865	14
0.3154	VVW	0.3122	1	1	0	$2-{}^3/_{14}$	0.3144	13
0.3224	VVW						0.3161	13
0.3544	VW	0.3522	12	1	0	$2-{}^1/_{14}$	0.3583	3
0.3714	M	0.3699	24	2	1	$\pm{}^1/_{14}$		
		0.3704	32	2	1	1	0.3705	40
0.3962	VW	0.3947	12	1	0	$2+{}^1/_{14}$	0.4031	24
							0.4048	12
0.4363	VW	0.4341	16	1	2	$1-{}^1/_{14}$	0.4344	12
0.4474	VW	0.4470	21	1	1	2	0.4470	36
0.4545	VVW	0.4553	15	1	2	$1+{}^1/_{14}$	0.4640	11
							0.5510	10
0.5590	VVW						0.5527	20
							0.5856	10
							0.6102	9
							0.6152	9
0.6506	VW	0.6478	8	2	1	$2-{}^1/_{14}$	0.6414	9
0.6675	W	0.6655	4	3	0	$\pm{}^1/_{14}$	0.6662	28
		0.6660	11	2	2	1		
		0.6732	3	0	0	3	0.6730	7
0.6860	VW	0.6903	8	2	1	$2+{}^1/_{14}$	0.7006	9
0.7172	VW	0.7152	4	1	0	$3-{}^1/_{14}$	0.7039	9
		0.7297	3	3	0	$1-{}^1/_{14}$	0.7335	8
0.7427	VW	0.7392	9	3	1	0	0.7393	26
		0.7509	4	3	0	$1+{}^1/_{14}$	0.7631	8
		0.7793	4	1	0	$3+{}^1/_{14}$	0.7876	16
							0.8763	16
							0.9076	8
							0.9372	14
							0.9405	7
0.9460	VW	0.9434	3	3	0	$2-{}^1/_{14}$	0.9456	7
0.9622	VW	0.9611	6	3	2	$\pm{}^1/_{14}$	0.9650	7
0.9685	VW	0.9688	8	2	0	3	0.9687	23
							0.9701	7

Table V. (Continued)

Observed data by Geisler-Newkirk		Calculated data						
		Anti-phase domain model					2-*hi* inverted Ni_4Mo-type model	
$1/d^2$	I	$1/d^2$	$(L.P.)\times F^2\cdot G_3^2\cdot p$**	h	k	l	$1/d^2$	$F^2\cdot p$
		0.9859	3	3	0	$2+{}^1/_{14}$	0.9751	7
							0.9997	7
1.0128	VW	1.0108	5	1	2	$3-{}^1/_{14}$	1.0242	7
1.0253	VVW	1.0253	5	3	2	$1-{}^1/_{14}$	1.0259	7
1.0377	VW	1.0384	15	3	1	2	1.0384	14
		1.0465	5	3	2	$1+{}^1/_{14}$	1.0588	7
1.0716	VVW	1.0675	5	1	2	$3+{}^1/_{14}$	1.0639	7
							1.0833	7
							1.1737	13
							1.2016	6
							1.2067	6
							1.2117	6
		1.2280	3	1	0	$4-{}^1/_{14}$	1.2312	12
		1.2391	6	2	3	$2-{}^1/_{14}$	1.2329	6
		1.2567	6	4	1	$\pm{}^1/_{14}$	1.2363	12
1.2565	MW	1.2572	8	4	0	1	1.2625	12
		1.2600	8	2	3	2	1.2644	19
		1.2815	6	2	3	$2+{}^1/_{14}$		
*1.3079	W	1.3064	3	3	0	$3-{}^1/_{14}$		
		1.3136	3	1	0	$4+{}^1/_{14}$		
		1.3209	6	1	4	$1-{}^1/_{14}$		
1.3284	W	1.3302	4	3	3	0	1.3308	9
1.3395	W	1.3421	6	1	4	$1+{}^1/_{14}$	1.3443	18
		1.3446	8	1	1	4	1.3495	6
							1.3512	6
1.3671	VW	1.3706	4	3	0	$3+{}^1/_{14}$	1.3808	11
							1.4678	5
							1.4974	5
							1.5062	5
							1.5075	5
*1.5229	MW	1.5236	13	1	2	$4-{}^1/_{14}$		
1.5309	VW	1.5426	13	4	2	$1-{}^1/_{14}$	1.5320	5
1.5486	M	1.5555	35	4	1	2	1.5534	34
							1.5565	10
1.5711	VW	1.5638	13	4	2	$1+{}^1/_{14}$	1.5861	10
1.5999	W	1.6020	21	3	2	$3-{}^1/_{14}$	1.6173	5
		1.6092	13	1	2	$4+{}^1/_{14}$		
1.6249	W	1.6294	28	3	3	2	1.6299	15
							1.6469	5
1.6590	W	1.6662	20	3	2	$3+{}^1/_{14}$	1.6553	10

** Relative intensities in this column were normalized on the basis of the intensity of the (200) reflection taken as 1000, while in the last column the intensity of the (200) reflection was taken as 840.

small, but it seems to reach a maximum value, about 0.08 %, in the vicinity of 25 % Pd. This value is greater than the value, 0.02 %, observed by Jaumot and Sawatzky[6], but agrees roughly with the result, 0.057 %, of dilatometric study by Sato[12]. In Fig. 8(b) it should be noticed that the c/a values have a minimum near the composition of Cu_3Pd rather than that of Cu_4Pd. The observed data plotted in Figs. 7 and 8 are summerized in Table VI.

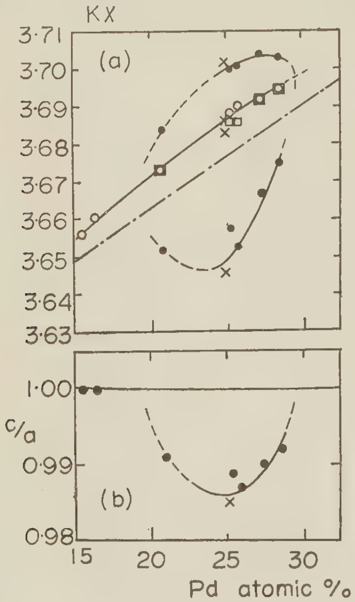

Fig. 8 (a). Lattice parameters as a function of composition.

○: quenched state,

●: four months annealed state,

□: $(a^2c)^{1/3}$ values,

×: after Jones and Owen,

—·—: Vergar's law

(b). Variation of the ratio c/a with composition.

●: present results,

×: after Jones and Owen.

The variation of the periods of anti-phase domain with temperatures was not completely examined, but it was found that the value of M_3 of the 25.2 % Pd alloy increases with temperature of annealing.

§ 5. Discussions

As already mentioned in § 1, Geisler and Newkirk[5] have proposed that the lattice of the fully ordered alloy Cu_4Pd has a "2-*hi* inverted Ni_4Mo-type" structure given in Fig. 3. Now, their data obtained from Debye-Scherrer patterns should be interpreted in terms of the present anti-phase domain model. In doing this, we assume that the ordered alloy of 20 % Pd possesses such a superstructure as characterized by the first kind of out-of-step with the period of 7 atomic distances, and that the dimensions of the elemental face-centered tetragonal cell are taken as $a=3.685$ Å $c=3.664$ Å according to Geisler and Newkirk. In Table V the first and the second columns list the values of $1/d^2$ and visual relative intensities of superlattice lines observed by them. The predicted positions, relative intensities and Miller indices of superlattice lines given by the present model are listed in the third, fourth and fifth columns of this table. The superlattice line positions and the relative intensities calculated by Geisler-Newkirk's model are also listed in the sixth and last columns. It is clearly seen that the experimental data, except two diffraction lines with VVW intensities, can quite well be explained on the basis of the one-dimensional anti-phase domain structure. The interpretation of Geisler and Newkirk is also good but not fully satisfactory, especially, two diffraction lines with W and

Table VI. Lattice parameters in the ordered and the disordered states of the copper-palladium alloys.

Composition Pd %	Disordered state	Ordered state (after 4 months annealing)				Period of aut-of-step	
	a_{kx}	a_{kx}	c_{kx}	$(a^2c)^{1/3}{}_{kx}$	c/a	M_1	M_3
15.5	3.656				1		
16.3	3.660				1		
20.8	3.673	3.684	3.652	3.673	0.991		7.0
25.2	3.688	3.700	3.658	3.686	0.989		4.4
25.8	3.689	3.701	3.653	3.686	0.987		4.2
27.3	3.692	3.704	3.670	3.692	0.990	4.0	3.2
28.5	3.694	3.703	3.675	3.694	0.992	3.8	3.5

MW intensities, marked with*, can not be explained by their model. Therefore, it can be said that the agreement between the observed data and the calculated results is better for the present model than for their model. Furthermore, their model can not explain the diffraction patterns of single crystals represented in the present paper. And, in the present experimental study, there is no evidence to support the fact that the Cu_4Pd composition is the most favorable composition for ordering.

Thus, it is concluded that the superlattice in the vicinity of 25 % Pd possesses in equilibrium state the anti-phase domain structure characterized by the first kind alone or both the first and the second kinds of out-of-step. The latter type of the anti-phase domain structure was observed over the composition range from 21 to 30 % Pd according to the electron diffraction study in Part I, while in the present X-ray study this structure was found only at the composition of 27.3 and 28.5 % Pd*. If the two-dimensional anti-phase domain structure is the same as the "*Komplexe Verwerfungsstruktur*" called by Schubert *et al.*[3], the results of the present study seem to support the stable region of each type of anti-phase domain structures proposed by them. Taking the results of the electron diffraction study into consideration, however, the region of the two-dimensional anti-phase domain structure should extend to less content of Pd at higher temperatures. Hence it can safely be said that the two-dimensional anti-phase domain structure is stable at higher temperatures and at higher concentrations of Pd than the region of the one-dimensional one, although there seems to be no discrete boundary between the stable regions of both structures. The presence of a well marked maximum at about 400°C in the specific heat-*vs.*-temperature curve obtained by Jones and Sykes[1] might probably correspond to the transition from the one-dimensional to the two-dimensional anti-phase superstructure. Both types of anti-phase domains gradually fade away with decreasing Pd content and completely vanish at about 18 % Pd together with the tetragonality of the fundamental lattice. To determine unconfirmed points in the phase diagram of this alloy, more detailed and conclusive investigations seem to be necessary.

§ 6. Conclusion

According to the present X-ray diffraction study on the ordered Cu_3Pd crystals, it was confirmed that the two-dimensional anti-phase superstructure characterized by two kinds of step shift, proposed in Part I, exists stably in the compositions of 27.3 and 28.5 % Pd after slow cooling from 450°C to room temperature in four months. The alloys containing 20.8 to 25.8% Pd, which were also annealed for four months, have the one-dimensional anti-phase superstructure. This structure is entirely different from the "2-*hi* inverted Ni_4Mo-type" structure proposed for the alloy Cu_4Pd by Geisler and Newkirk, but agrees with the result of Schubert *et al.*.

The lattice parameters as well as the periods of anti-phase domains were obtained as functions of Pd concentration. It is pointed out that changes of physical properties accompanying the order-disorder transformation and cold-work of this alloy should be considered on the basis of such rather unusual superstructures as mentioned above.

The authors wish to express their sincere thanks to Mr. D. Watanabe for his kind discussions.

This work has been supported in part by the fund of the Ministry of Education in Aid of Scientific Researches.

References

1) F. W. Jones and C. Sykes: J. Inst. Metals **65** (1939) 419.
2) D. Watanabe and S. Ogawa: J. Phys. Soc. Japan **11** (1956) 226.
3) K. Schubert, B. Kiefer, M. Wilkens and R. Haufler: Z. Metallk. **46** (1955) 692.
4) D. Watanabe, M. Hirabayashi and S. Ogawa: Acta Cryst. **8** (1955) 510.
5) A. H. Geisler and J. B. Newkirk: J. Met. **6** (1954) 1076.
6) F. E. Jaumot and A. Sawatzky: Acta Met. **4** (1956) 127.
7) A. Guinier and R. Griffoul: Rev. Métall. **45** (1948) 387.
H. Raether: Z. angew. Phys. **4** (1952) 53.
8) M. Hirabayashi and S. Ogawa: J. Phys. Soc. Japan **11** (1956) 907.
9) F. E. Jaumot and A. Sawatzky: Acta Met. **4** (1956) 118.
10) K. Fujiwara: J. Phys. Soc. Japan. **12** (1957) 7.
11) D. M. Jones and E. A. Owen: Proc. Phys. Soc. **B69** (1954) 297.
12) H. Sato: J. Japan Inst. Met. **6** (1942) 435. (in Japanese)

JOURNAL OF THE PHYSICAL SOCIETY OF JAPAN Vol. 12, No. 3, MARCH, 1957

Proton Magnetic Resonance in Chain Polymers

By Akira ODAJIMA, Junkichi SOHMA
Research Institute of Applied Electricity, Hokkaido University
and Mitsuru KOIKE
Department of Physics, Hokkaido University

(Received August, 13, 1956)

Proton magnetic resonance absorptions have been studied for several chain polymers. The experimental second moments of the absorption lines in the glassy state were compared with the calculated ones for the model of $(\text{-}\mathbf{CH_2 \cdot CHX}\text{-})_n$ type.

The temperature variations of the line widths were observed from room temperature to about 160°C. For PMMA and Polystyrene having large side chains, the line widths were found to narrow in two steps as temperature was raised. The first step of narrowing occured in neighbor of the glassy transition temperature T_g and is assigned to the onset of the "hindered rotation" of the side chain. The second step of rapid narrowing started at the higher temperature than T_g and is assigned to the "segmental rotation" of the main chain.

In contrast with these cases, the line width transition of PVC and of PVAc occured in a single step narrowing at the higher temperature than T_g which is assigned to the onset of the segmental motion.

Referring to another observations information of the movements and of the configurations of the side chain which was obtained from the proton magnetic study was discussed in the last section.

§ 1. Introduction

During the past few years much work has been done in the field of proton magnetic resonance study of long chain polymers. The main object of these this researches was in the investigation of the molecular structures and, especially, of the molecular movements.

A number of polymeric materials have been found to show merely amorphous diagrams under X-ray and electron diffraction examinations[1]. Therefore, the knowledge of the molecular structure of these materials is obtained less exactly than in the case of crystalline substances. It seems possible, however, that the proton magnetic spectroscopy permit a further insight into the structure of polymeric systems, for example, the relative position of the side chains to the main chains which is determined by examining a resonance line width which is due to the interactions between the neighbouring nuclear spins.

On the other hand, it is well known that all polymers consisting of flexible long chains show the apparent second order transition which separates the soft "rubbery" state from the hard "glassy" state. An explanation of this characteristic property based on the assumption of "quasi-free rotation" in the long chain molecules. However, concerning the existence and the nature of such internal motions we have only unsatisfactory knowledge. Hitherto, in order to study the characteristics of polymers in the transition region, various physical methods were employed, such as thermal[2], dynamical[3], and dielectrical[4] measurements. Especially, the latter two are very useful in studying the molecular behaviors responsible for this transition.

While, the proton magnetic resonance method demonstrates directly internal motions of the main chains and the side chains[5], this method is one of the most useful means of studying various inner motions of linear polymers in the transition region. Concerning the polymers having large substituents the possibilities of diversity in the transition are expected, for example, the possibility of the rotation of the side chains under circumstances which prevent the segmental motion of the main chain. Thus, it seems to be interesting to investigate how the side chains in polymers relate to the onset of the rotation of the main chain, and how they behave with each other in the "glassy" to "rubbery" transition in polymers.

Taking into account the relations between the side chains and the main chain, we have studied the line width of the proton magnetic resonance absorption for several chain polymers of the vinyl compounds and acryl ones, which are of similar construction except for the different nature and the size of the side chains. Moreover, we have tried to obtain information concerning the relative position of side chains and the nature of their rotational motion more accurately than in the past, and the semi-quantitative investigation described in the following has been developed.

§2. Experimental Procedure

Apparatus

Autodyne detector was used for observing the proton magnetic resonance line. The detector used was a cathode follower type[6]) which has high sensitivity and is the most useful of those so far tried. A block diagram of the whole apparatus is shown in Fig. 1.

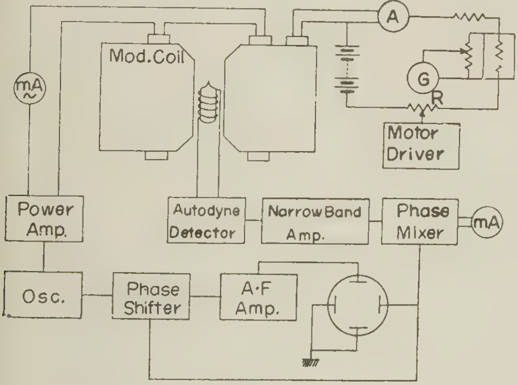

Fig. 1. Block diagram of apparatus.

The magnet used in this work was an electromagnet with 15 cm diameter pole face. The current to the magnet was supplied from storage batteries. The gap of the pole faces was 3 cm, and at this gap the inhomogeneity of the field was less than 0.3 gauss over the area of the sample used.

The experiments were performed at a fixed frequency with a variable applied magnetic field of about 3100 gauss. The linear variation of the magnetic field was accomplished through an electronic regulator extending over about 50 gauss range[6]). The magnetic field modulated at 50 cycles was applied and its intensity of less than 1.5 gauss was sufficient to obtain adequate signal strengths.

The narrow band amplifier and balanced mixer was used to observe the derivative of the absorption line as a function of the applied field. The line shapes were recorded by the automatic recording system.

Sample

The various samples used are shown in Table I. All samples have no plasticizer and are neither stretched nor orientated.

Table I.

Sample	Average Polymerization degree	Structure unit
Polyvinyl chrolide	1300	$-CH_2 \cdot CHCl-$*
Polystyrene	4200	$-CH_2 \cdot CHC_5H_5-$*
Polyvinyl Acetate	2000	$-CH_2 \cdot CHOCOCH_3-$*
Polymethyl Methacrylate		$-CH_2 \cdot CH_3$ $COOCH_3-$**
Polymethyl Acrylate		$-CH_2 \cdot CHCOOCH_3-$**

* These samples were manifactured by the Sekisui Kagaku and Co.

** These samples were supplied through the kindness of Dr. S. Iwayanagi and Mr. M. Hidejima, Scientific Research Institute.

These materials do not crystallize except PVC, and the crystallization of PVC is in such a small degree[1]) that it is not considered to affect the results of our experiment.

For the measurement, the powder or granular samples, of about 1 gram, were contained in a small glass tube of 1 cm inside diameter. And the radio frequency coil into which the glass tube was inserted was 1.1 cm inside diameter and 1 cm long, and was surrounded by a cylindical shield of 2.8 cm outside diameter. The temperature of the samples was measured with the copper constantan thermocouple embedded in the sample. The 3 cm gap of the available magnet prevented insertion of a heater, so heating was effected by conduction through the brass rod, the upper end of which was in contact with Ni–Cr heater placed too far above the magnetic pole to disturb the field homogeneity. And the shield tube containing the samples was thermally insulated from the surroundings. Thus the temperature of the samples was varied from room temperature to about 160°C. Within this extent satisfactory temperature control was obtained.

Hygroscopic samples were further desiccated in the vacuum desiccator for two days, and after this treatment they were desorbed by evacuating at 10^{-4} mmHg, having been kept in a heat bath of appropriately high temperature (100°C～160°C) for about 20 hours.

§ 3. Line Shapes and Line-width Changes

The derivatives of the absorption lines at room tempereture are shown in Fig. 2. All resonance lines are single-humped showing no fine structure. The second moments, half-widths and maximum slope widths are respectively listed in Table II. The experimental values of second moment $\langle\Delta H^2\rangle_{Av}$ and half-width $\Delta H_{1/2}$ of absorption lines are calculated through a graphical integration of the derivative curves replotted in a rectangular coordinate from the recording paper.

If the curve is the Gaussian type, there is the following well known relations⁷⁾.

$$\Delta H_{1/2}=2.35\langle\Delta H^2\rangle_{Av}^{1/2},\quad \Delta H_{m.sl.}=2\langle\Delta H^2\rangle_{Av}^{1/2}. \qquad (1)$$

Thus we obtain the ratio of $\Delta H_{1/2}$ to $\Delta H_{m.sl.}$

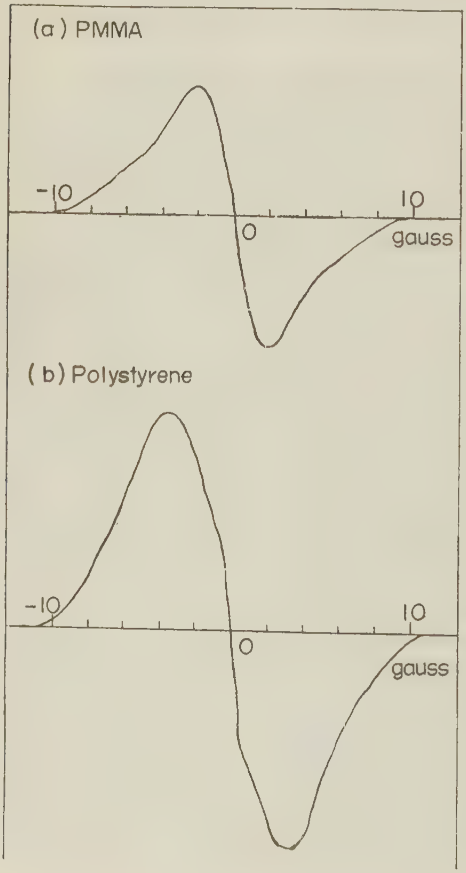

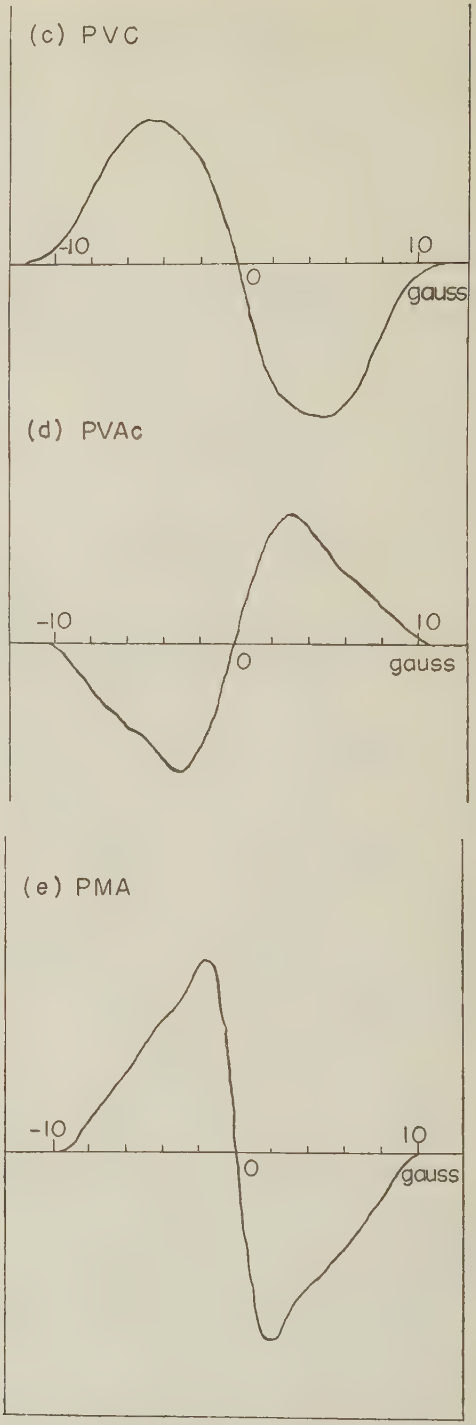

Fig. 2. Derivatives of the proton magnetic absorption line in PMMA, PS, PVC, PVAc and PMA at room temperature.

as 1.175. Referring to the experimental results, the line shapes for PVC and Polystyrene seem to be similar to the Gaussian type. On the other hand the line shapes for PMMA and

PVAc indicate sharper absorption line than the Gaussian type, in spite of the glass-like state at room temperature.

Table II.

	$\Delta H_{1/2}$	$\Delta H_{m.sl.}$	$\Delta H_{1/2}/\Delta H_{m.sl.}$	$\langle H^2\rangle_{Av}$	$\langle H^2\rangle_{Av}$ (narrowing)
	gauss	gauss		gauss^2	gauss^2
PMMA	6.2	3.8	1.6	9.0	6.9*
PS	8.9	7.3	1.2	11.9	9.1**
PVC	10.6	9.5	1.1	14.4	
PVAc	7.4	4.7	1.6	11.0	
PMA	6.8	3.5	2.0		

* at 103°C.

** at 105°C.

The line width behaviors as the temperature rises, are shown in Fig. 3 and 4. In each observation the values of the line width in the higher temperature region may be somewhat greater than the true ones because of the modulation broadening and the inhomogenity of the field.

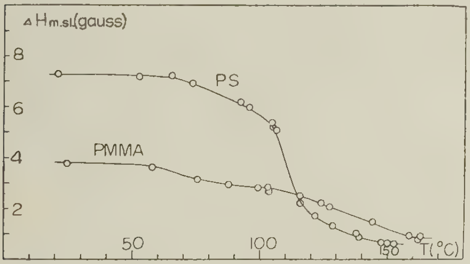

Fig. 3a. Max. Slope width vs. temperature curves for PMMA and PS.

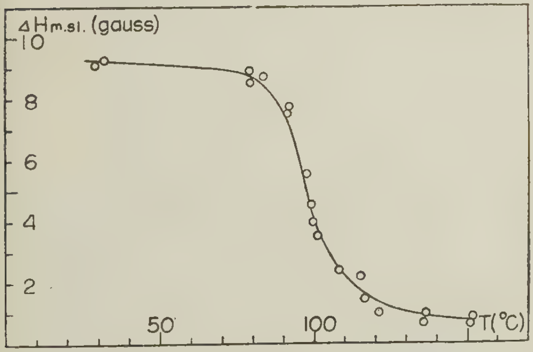

Fig. 3b. Max. Slope width vs. temperature curve for PVC.

Under the circumstances of thermal equilibrium, which was achieved by sufficiently slow variation of temperature, no hysteresis was apparent on the time scale of these experiments. The line width change for each material will be discussed in detail in a later part of this section.

(a) **PMMA.** The observed maximum slope width, $\Delta H_{m.sl.}$ of the absorption lines is plotted against temperature in Fig. 3a. The line width $\Delta H_{m.sl.}$ begins to narrow at about 60°C, which corresponds to the apparent second order transition temperature which is called, hereafter, T_g[2], and this result is consistent with that reported previously[9].

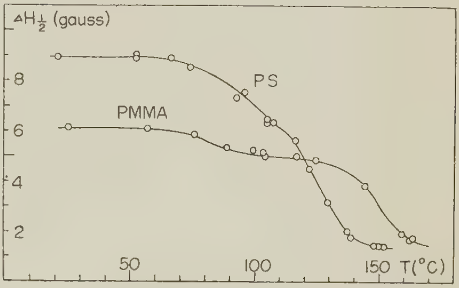

Fig. 4a. Half width vs. temperature curves for PMMA and PS.

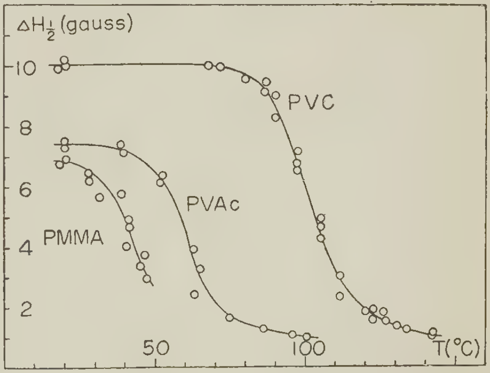

Fig. 4b. Half width vs. temperature curves for PVC, PVAc and PMA.

On the other hand, the observed half-width, $\Delta H_{1/2}$, vs. temperature curve is shown in Fig. 4a. In this case the line width transitions occur in two steps. At first step the narrowing of $\Delta H_{1/2}$ starts at about 65°C and is only 26% of the initial value of $\Delta H_{1/2}$ even at about 110°C, and after the first narrowing the curve enters into the second step of an abrupt decreasing at about 130°C, followed by the leveling off.

(b) **Polystyrene.** The maximum slope width and half-width vs. temperature curve are shown in Fig. 3a and Fig. 4a, respectively.

In this case the line width transitions also are shown to occur in two steps. The initial narrowing starts at about 80°C, which corresponds to the transition temperature T_g[2]. After this narrowing the curve enters into the second step of an abrupt decreasing at about 120°C followed by the leveling off.

(c) **PVC.** The line width vs. temperature curve for this material, given in Fig. 4b, shows typical one-step narrowing forming a contrast with those for the above two samples. That is, when the temperature rises the line width $\Delta H_{1/2}$ shows little change until about 85°C, which is higher than the transition temperature T_g, 75°C[2], and then it begins to fall rapidly to the leveling off.

(d) **PVAc.** The line width $\Delta H_{1/2}$ vs. temperature curve, given in Fig. 4b, begins to drop at about 50°C, and this temperature is higher than the transition temperature T_g of about 30°C[2].

Considering that PVAc has similar structure to PMMA, the line width transition might be supposed to occur in two steps as in the case of PMMA. Nevertheless the line width vs. temperature curve, shown in Fig. 4b, decreases not in two-steps but in one step.

(e) **PMA.** Although the unit of PMA is the isomer of that of PVAc, the line shape for this material at room temperature was a little different from those for PVAc and others. That is, even at room temperature the line shape, of which derivative curves are shown in Fig. 3, appears a little sharper than the shapes for PVAc, and the line width narrows at about 40°C being much higher than T_g of 3°C[2]. Considering that the transition temperature T_g of PMA is lower than room temperature, it seems not to be surprising that the above stated line shape appears for this material. For the purpose of studying whether the temperature variation of the line width shows another narrowing in the lower temperature region, the observation of the line width behavior in the lower temperature region seems to be interesting. Our results in this region, however, are not enough to draw any conclusion on this point.

§ 4. Second Moments for Rigid Chain Polymers

The second moment $\langle \Delta H^2 \rangle_{Av}$ of absorption line for the rigid lattice is given by Van Vleck. In case the chain axes in a material distribute at random in all directions, the second moment is given by the following equation[7]:

$$\langle H^2 \rangle_{Av} = \frac{6}{5}\frac{I(I+1)}{N}\frac{\mu^2}{I^2}\sum_{j>k} r_{jk}^{-6} + \frac{4}{15}\frac{1}{N}\sum_{j,f} I_f(I_f+1)\frac{\mu_f^2}{I_f^2} r_{jf}^{-6}. \qquad (2)$$

In this equation r is the distance between nuclei j and k, μ the magnetic moment of proton, I the proton spin and N the number of protons in the elementary cell over which the sum is taken. And the subscript f refers to all other nuclear species in sample. If the structure of a molecule is known and the lattice can be assumed rigid, **Eq.** (2) makes possible the calculation of the second ment.

The samples used in this experiment are the chain polymers of relatively simpl vinyl or acryl compounds of which chemical formulae are shown, respectively, in Table I. In the calculation of the second moment for the polymers in question $(-CH_2 \cdot CHX-)_n$, we consider two cases which are in the state of the planar zigzag chain and in the state of the randomly coiled chain respectively, as shown in Fig. 5. And we assume that the C–C and C–H distances are taken as 1.54 A and 1.094 A, respectively[9]. Then the intramolecular contributions to the second moment are found to be 12.64 gauss² in the case of the planar zigzag chain or 12.78 gauss² in the case of the randomly coiled chain, the necessary calculation for which being carried out in Appendix I.

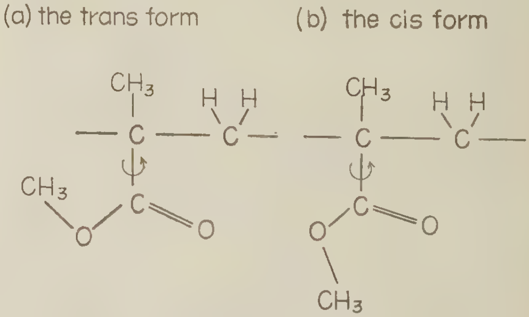

Fig. 5. Configurations of PMMA.

The chain molecules having large substituents are supposed not to be coiled up but to bend gradually on a scale of several bond lengths along the chain[1]. Therefore, in the following we will calculate the second moment based on the planar zigzag chain model.

The analysis[1)] of the X-ray and electron diffraction pattern for such polymers in stretched state suggests that steric hinderances are so great as to prohibit segments getting close to each other. Considering that the second moment is the inverse sixth power of the internuclear distances in **Eq.** (1) the contributions from the nuclei in external molecules are considered to be not sensitive to the intermolecular configuration.

This permits us to take the long chain molecule itself as the elementary cell in fairly good approximation, though the elementary cell should, in principle, include the neiboring molecules. Since all samples except PMA are glass-like at room temperature, they are supposed to be in a rigid state. Then a good estimate of their second moments can be obtained by adding up the contributions of each of the various structural groups in them.

(a) **PVC.** The monomer unit of PVC has 3 protons and a chlorine nucleus as the foreign nucleus. Considering the zigzag chain model, shown Fig. 5, **Eq.** (2) gives 12.7 gauss^2 as the second moment of PVC, of this only 0.1 gauss^2 is caused by chlorine nucleus.

The difference of 1.7 gauss^2 between the theoretical value and the experimental value, may come from the intermolecular interaction. This values would seem to be reasonable, though exact calculation of the intermolecular broadening is not possible.

(b) **Polystyrene.** Polystyrene shown in Fig. 6 contains 8 protons in its monomer unit, of these 5 are in the phenyl group of the side chain. CH_2 and CH groups in the main chain contribute 4.76 gauss^2 to the second moment. The phenyl group is a plane hexagon of carbon atoms, whose carbon-carbon length is known to be 1.39 A and the CH bond length is taken as 1.08 A[9)]. Thus the contribution to the second moment is obtained as $3.3\frac{4}{8}=1.65$ gauss^2. The experimental value is 11.9 gauss^2 being far larger than the sum of the contribution of the contribution of the above mentioned groups, 6.41 gauss^2. Moreover, it is neccesary to take account of the dipole interactions between the protons of the main chain and of the phenyl group, and between the protons of the different phenyl groups. In the Appendix II the broadening due to these interactions is calculated for the planar zigzag chain model and then $(3.97/8+1.87/4+1.27/4)=1.28$ gauss^2 is to be added to the second moment. However, the theoretical value which is combined with each of the above contributions is still less than the experimental value. This discrepancy seem to suggest that the planar structure does not represent the true picture of Polystyrene molecule[10)].

(c) **PMMA.** The monomer unit of PMMA has 8 protons, of these 6 are in 2 methyl groups which are found to rotate about their C_3 symmetry axis fast enough at room temperature. In the case of such rotation, the contribution of the methyl group to the second moment would be reduced by a factor of 1/4[11)].

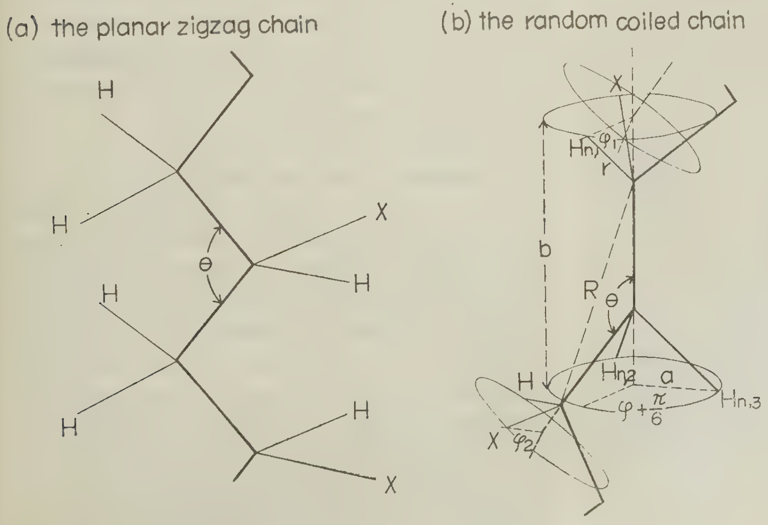

Fig. 6. The zigzag and random coiled chains.

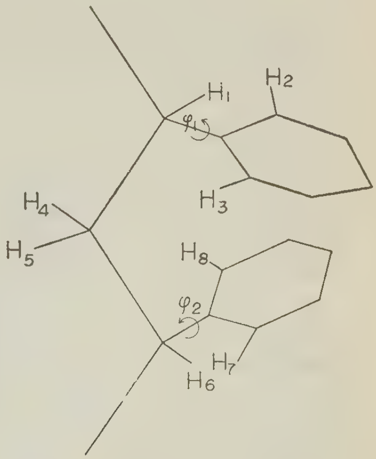

Fig. 7. The structure-model for Polystyrene.

Then the contribution of two methyl group to the second moment become $6/8\times(22.1/4)=4.14$ gauss². Combined with the contributions of the CH_2 group, we have an estimated second moment for PMMA of 6.90 gauss².

Another calculation can be obtained from the following consideration. The absorption line for PMMA can be interpreted to be a superposition of the line of the CH_2 group and the line of the CH_3 groups, because both groups are at a long distance from each other and because there is little interaction between the protons of each group. It is self-evident that the central part of the absorption line comes mainly from the line of the CH_3 group having the smaller second moment than the CH_2 group. Therefore, the maximum slope width of the line for PMMA is given by the broadening due to their external interactions. In the Appendix II, the relation of these broadenings to the meximum slope width of the CH_3 groups is calculated. As the result, we obtain $\alpha^2=3.35$ gauss² as the additional broadening of the CH_3 group, as shown in Fig. 8. We have then a predicated second moment for PMMA of $\langle\Delta H^2\rangle_{Av}=6.90+3.35\,\frac{6}{8}=9.41$ gauss². Comparing this theoretical value with the observed value agrees approximately with that predicted by adding the absorption of the various groups.

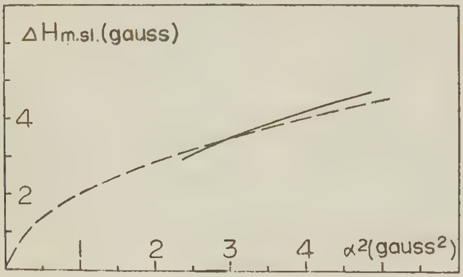

Fig. 8. Max. Slope width vs. external second moment for CH_3 group. The dashed line is the calculated curve based on the Eq. (9) of which the second term is neglected.

(d) **PVAc and PMA.** The each unit of PVAc and PMA has 6 protons, of these 3 belongs to the CH_3 group. The ambiguous distances of protons between those belonging to the side chain and main chain prohibit us to estimate the difference of the second moments for these materials.

The contribution from CH_3, CH_2 and CH are 2.76 gauss², 3.68 gauss² and 1.41 gauss², respectively. Adding up these values, the resultant value is 7.85 gauss². For PVAc, the difference 3.15 gauss² between the calculated value and experimental one comes presumably from the interactions between external protons.

For PMA in the rigid state, the accurate experimental value is not yet obtained. It is desirable to observe experimentally the difference of the second moments of PVAc and of PMA.

§ 5. Motional Narrowing

The line width of absorption is affected, in general, by both spin-spin relaxation time T_2 and spin-lattice relaxation time T_1.

But the effect of T_1 on the line width is considered to be negligible in the case of polymers[12], and we are able to confine our discussion to the effect of T_2 on the line width.

Bloembergen et al.[12] theoretically predicted how T_2 and the line width varies at the onset of the motion. It is pointed out, however, that as a measure of the line width, the maximum slope width or the root second moment are unable to be applied, since both quantities represent not exactly T_2 at the motional state. On the other hand Kubo and Tomita[14] derived the following equation predicting narrowing of half-width for motions.

$$(\Delta H_{1/2})^2=\frac{4\log 2}{\pi}\langle\Delta H_0^2\rangle_{Av}\tan^{-1}\left(\frac{\pi\tau}{4\log 2}\gamma\Delta H_{1/2}\right) \tag{3}$$

where $\langle\Delta H_0^2\rangle_{Av}$ stands for second moment of the rigid state, τ for the correlation time of the nuclear motion and γ for gyromagnetic ratio.

Therefore in this paper we adopt $\Delta H_{1/2}$ as the measure of the line width.

It is well known that motional narrowing of proton occurs when the correlation time of its Brownian motion is of the order of 10^{-5} sec[13]. Comparing narrowing temperature with the transition temperature T_g, given in Table II, it is found that the narrowing temperature are higher than the transition temperature T_g. This suggests that the segmental motion, of which rate is more rapid than 10^{-5} sec., occurs at the higher temperature than T_g. It is worthy to note, however, that apart from the narrowing to occur at the higher temperature both $\Delta H_{1/2}$'s of PMMA and of Polystyrene gradually narrow at first in the neighbourhood of T_g and show two-step narrowing, and that these polymers have large side chain containing several protons. The transition temperature T_g in the polymer could be associated with an increase of "free volume"[15]. And it is likely that in the vicinity of T_g, the free volume is too small to permit the rotation of the main chain as a whole, but may be sufficiently large to permit the localized rotation of the side chain itself.

If the correlation time of the latter rotation is of comparable order to the spin-spin relaxation time T_2, the line width of the absorption signal begins to narrow.

(1) Gradual Narrowing

(a) **PMMA.** For the sufficiently rapid rotation in the system containing a methyl group, the reduction of the second moment by this rotation is given by the following equation[11]

$$\langle \Delta H^2 \rangle_{Av} = \frac{9\mu^2}{10}(3\cos^2\psi - 1)^2\,, \qquad (4)$$

where ψ is the angle between the rotation axis of the side chain and C_3 symmetry axis of the methyl group. Referring to the structure of PMMA, shown in Fig. 5, two rotations about different axes except for C_3 axis, that is, C–O and C–C axis might be excepted to occur in a carboxyl group of the side chain as temperature is raised; there is however, evidence that the rotation about C–O axis is prohibited and that the only possible configuration of the carboxyl group in the side chain is approximately the cis form[16]. In this configuration the rotation of the side chain with increasing temperature is restricted to about C–C axis. As electron diffraction indicates that C–O–C plane is 25°±8° out of the cis planar configuration in methyl acetate[16], ψ becomes about 25° for this rotation axis, and then the reduction by this free rotation is estimated as 2.7 gauss² throug **Eq.** (4). The experimental value of narrowing is obtained as 2.1 gauss² at 103°C*. Since the actual motion seems to be a kind of oscillation, the reduction of this motion of the side chain is expected to be less than the above calculated value.

(b) **Polystyrene.** Following the similar procedure the reduction of the second moment for PS by the rotation of the phenyl group is theoretically expected to be 0.79 gauss² from **Eq.** (4), based on the assumption of the rapid, free rotation. The experimental value of narrowing is obtained as 2.8 gauss² at 105°C. In addition to the narrowing above calculated, the rotation also reduces the broadening contributed from the protons not in the same phenyl group but in the external group. However, the some part of narrowing must come from the reduction of the broadening contributed from the interaction of the protons in the main chain.

Simply speaking, the first narrowing may be closely related to the onset of the rotation of the side chain, and besides may be affected in some way by the motion of the main chain. That is, it is reasonable to assume that the rotation of the side chain is not completely independent of the motion of the main chain because of the steric hinderance, and that the rapid rotation of the side chain is accompanied by the localized motion of the main chain. Thus, this localized motion of the main chain is expected to contribute appreciably to the first narrowing.

(2) Rapid Narrowing

For PVC having a small side chain the narrowing as the temperature appears not in two steps but one rapidly narrowing due to the rotation of the segment in polymer. This fact supports quantitatively the above stated interpretation concerning the gradual narrowing.

On the other hand, the activation energy of the segmental rotation seems to be possibly estimated through **Eq.** (3) using the observed curve of the half-width. It should be noted, however, that in this equation the correlation time of the rotation is assumed to be only one kind, but for polymer the correlation time of the rotation is considered not to be one but to be distributed over some extent. Therefore, it is considered not to be correct way that the activation energy is estimated by **Eq.** (3) in which no distribution of the correlation times is included. We are now trying to estimate the activation energy assuming a reasonable distribution of the correlation times.

---

* For simplicity, we use the second moment as the measure of narrowing when we considere how the rotation of the side chain affect narrowing, though the second moment is known to represent narrowing not exactly.

Although PVAc has the larger side chain, this material alone shows one step narrowing. This exceptional line width transition for PVAc could be explained by assuming the hinderance of the independent motion of side chain. In this point we will discuss in the next section.

§ 6. Discussion

It is found that some polymers showing two-step transition of the line width, such as PMMA and PS, also show the secondary loss peak in the elastic[3)] or dielectric[4)] properties as temperature changes.

These anomalies would be interpreted by the movements of the side chain rather than the movement of the main chain. Concerning the details of the rotation of the carboxyl group, which is in the side chain of PMMA, some studies have been carried out with the substances containing the same group through the various experimental techniques. For example, it is known that for the carboxyl group in acetic ester two configuration (forms (a) and (b) of Fig. 5) are supposed to be possible in view of the possibility of resonance, though one has higher energy than the other[17)]. And the anomalous absorption and dispersion of the ultrasonics for the above substance[17)] suggest the existance of the transition to the higher energy state.

It is seen, however, from the infrared spectra study that the population of the higher energy level is very small for substances like these, because of the steric hinderance in the acetate. As a result it may be concluded that such a transition like this may not be detectable through the proton magnetic study. On the other hand, about the methyl methacrylate, that is the monomer of PMMA, the rotation about C–C axis is affirmed to be possible even in the crystalline state through the Raman spectra study[18)].

On the other hand, measureing the dielectric loss for PVAc and PMA, Mead and Fuoss[4)] found that the dielectric loss curve for PVAc is sharper and larger than that for PMA. And they pointed out that the side chain in PVAc may rotate more freely than PMA at the temperature higher than T_g.

The asymmetry of Cole-Cole diagram for PVAc also suggests the existance of the fast rotation of the side chain. Through our observation of the nuclear magnetic resonance line, the movements of the side chain and the main chain are in separable, and they are strongly coupled to each other and show rapid narrowing, as it was stated. It is worthy to note, however, that the large and sharp dielectric loss curve for PVAc would also seem to be interpreted to come from the simultaneous occurance of the rotations of the side and main chain.

For PMA, the line width vs. temperature curve shows one-step narrowing in the temperature region of our measurement. But the fact that the half-width appeared to reduce at room temperature suggests one more transition in the lower temperature region.

It is plausible from the molecular structure that steric hinderance for the rotation of the side chain in PMA may be smaller than that in PVAc, and that the rotation of the side chain is more independent from the motion of the main chain than in PVAc. These considerations lead us to the interpretation that the broad dielectric loss curve for PMA results from the rotation of the side chain under the circumstance of the hinderance of the movements of the main chain. And besides, this consideration may explain why the transition temperature T_g of PMA is lower than that of PVAc.

It is interesting to note that the line width transitions in proton magnetic resonance begin, in general, at a lower temperature than the temperature at which the dielectric or elastic anomaly occures in the same order of time scale.

This can be explained by the following consideration. Generally speaking, the temperature of the transition or of the anomaly in polymer is given the relation $\tau=\tau_0 \exp(E/RT)$ in which τ means the averaged correlations time.

In the case of dielectric properties the correlation time should belong to the resultant motions of each dipole vector.

On the other hand, in the case of the nuclear magnetic resonance it is known that the short range interaction is predominant for the line width. Therefore, the correlation time τ for the nulear magnetic resonance is supposed to be smaller than the dielectric relaxation time, and then the transition of the line width occurs at the lower temperature. The detailed discussion concerning these problems will be published later.

Acknowledgment

We wish to express our sincere thanks to Assistant Professor Y. Yokozawa of the Institute for his helpful advice. Moreover we would like to express gratitude for the encouragement given by Prof. J. Furuichi of Hokkaido University. We are also indebted to Mr. M. Nagai for his assistance in carrying out the measurements.

APPENDEX I.

For the chain polymer of $(\text{-CH}_2\cdot\text{CHX-})_n$ type, the contribution of the intramolecular interaction to the second moment is readily obtained in the following two cases.

(1) **Planar Zigzag Chain**

In the case of the planar zigzag chain, that is the configuration of the stretched out chain polymer, distances between each proton in a chain are estimated by assuming the tetrahedral distribution of the chain skelton. Taking into account the interaction of the protons, each distance of which is less than about 3.5 A, the intramolecular contribution is found to be $\langle \varDelta H^2\rangle_{Av}=12.62-3.97/n$ gauss² from the equation of the second moment (2). But it is possible to neglect the second term in the above expression because of the large n for polymer. Therefore $\langle \varDelta H^2\rangle_{Av}$ is assumed to be 12.62 gauss².

(2) **Randomly Coiled Chain**

We shall now discuss the case of the randomly coiled chain, in which chain segments orientate at random with the tetragonal bond angle. In this case, the distances between each proton have to be statistically averaged, excepting the constant distance of the proton pair in CH_2 group.

The distance r_{12} between the proton $H_{n,1}$ and the proton $H_{n,2}$ and the distance r_{13} between the proton $H_{n,1}$ and $H_{n,3}$, as it is illustrated in Fig. 6(b) are determined by the following relations, respectively,

$$r_{12}^2=b^2+2a^2\left(1-\frac{1}{2}\cos\varphi-\frac{\sqrt{3}}{2}\sin\varphi\right) \qquad \text{(A1)}$$

$$r_{13}^2=b^2+2a^2(1+\cos\varphi)$$

where a is 1.03 A and b is 2.20 A.

Using these two equation, we get in the average

$$\left\langle \frac{1}{r_{12}^6}+\frac{1}{r_{13}^6}\right\rangle_{Av(\varphi)}=0.673\,A^{-6}\,. \qquad \text{(A2)}$$

The distance $r_{n,n\pm1}$ between the proton $H_{n,2}$ or $H_{n,3}$ and the proton $H_{(n\pm1),2}$ or $H_{(n\pm1),3}$ belonging to the next monomer is determined by following equations,

$$r_{n,n\pm1}^2=2\{(X_1-x)^2+(Y_1-y)^2+(Z_1-z)^2\}\,, \qquad \text{(A3)}$$

$$\begin{aligned} &X_1=R\cos\theta\cos\varphi_1+r\sin\theta \quad \begin{cases} x=R\cos\varphi_2 \\ y=R\sin\varphi_2 \end{cases} \\ \text{and}\quad &Y_1=R\sin\varphi_1\,, \\ &Z_1=-R\cos\varphi_1\sin\theta+r\cos\theta+r\,. \end{aligned} \qquad \text{(A3')}$$

Therefore, we get

$$\left\langle \frac{1}{r^6}\right\rangle_{Av(\varphi)}=0.366\,A^{-6}\,. \qquad \text{(A4)}$$

In the case of the randomly oriented chain, the proton, that is to say $H_{n,n\pm m}$, belonging to the monomer labelled $(n\pm m)$ being far from the monomer n in question, it is possible for the proton $H_{(n\pm m),i}$ to get close to the proton $H_{n,i}$ in question. Thus we have to take this into account. If the m is large enough, the statistics of the random flights chain[19] with fixed bond lengths and fixed valence angles, tells us that the distribution of $r_{n,n\pm m}$ is Gaussian, and is given by the following equation

$$f(r)=\left(\frac{3}{2\pi R^2}\right)^2\exp\left(-\frac{3r^2}{2R^2}\right), \qquad \text{(A5)}$$

were R^2, the average of r^2, is,

$$R^2=N_q^2(1+\cos\theta)/(1-\cos\theta)\,. \qquad \text{(A5')}$$

Using this distribution, one can approximately evaluate through

$$\left\langle \frac{1}{6}\right\rangle_{Av}{}_{r_{n,n\pm m}}=\int_{r_0}^{r_{max}}\frac{1}{r^6}f(r)dr\,. \qquad \text{(A6)}$$

Table III.

	Planar zigzag (gauss²)	Random coil (gauss²)	Gaussian (gauss²)	
$\langle \varDelta H_{11}^2\rangle$	3.85	4.85		
$\langle \varDelta H_{12}^2\rangle$	3.63	2.64		
$\langle \varDelta H_{132}\rangle$			1.43	$(r_{max.})$ (5.0 A)
$\langle \varDelta H_{14}^2\rangle$			0.90	(6.8 A)

Actually, the lower limit of the integral in the above equation is somewhat arbitary. It may be reasonably assumed, however, that the proton is not possible to come close together within its Van der Waals redius and then the lower limit it taken as 2.4 A[20]. The values of the second moment for $m=3, 4$ as well as the previous results are listed in Table III.

APPENDEX II.

The Interaction Between Side Chain and Main Chain.

(1) **Polystyrene**

At first we assume that the main chain is fully stretched and it is in the state of polanar zigzag. The proton pairs which are consisted of protons in the phenyl group, protons in the main chain and a proton in a neighbouring phenyl group are H_1-H_2, H_3-H_6 and H_3-H_8, as it is shown in Fig. 7. We can certainly object to this assumption on physical grounds: however, it leads to the equations which given us the characteristic of the configuration in the rigid state. As protons in the phenyl groups are not possible to come close together within their Van der Waals radius 1.2 A, the groups do not orientate freely but presumably within the range of about 30°, thus the value of φ should be taken within this extent. For each proton pair H_i-H_j the distance r_{ij} is given respectively as follows.

$$\left.\begin{aligned} r_{12}^2 &= 9.92-4.26\cos\varphi \\ r_{36}^2 &= 11.29-10.78\sin\varphi \\ r_{38}^2 &= 23.14-3.05\cos\varphi_1\cos\varphi_2 \\ &\quad +4.28\sin\varphi_1\sin\varphi_2 \\ &\quad +10.79(\sin\varphi_1+\sin\varphi_2) \\ &\quad -6.85(\cos\varphi_1+\cos\varphi_2) \\ &\quad +4.95(\sin\varphi_1+\sin\varphi_2)^2 . \end{aligned}\right\} \qquad (A7)$$

Therefore we get in the average,

$$\begin{aligned} \langle \varDelta H_{12}^2\rangle_{Av(\varphi)} &= 3.94 \ \text{gauss}^2 \\ \langle \varDelta H_{36}^2\rangle_{Av(\varphi)} &= 1.87 \ \text{gauss}^2 \\ \langle \varDelta H_{38}^2\rangle_{Av(\varphi)} &= 1.27 \ \text{gauss}^2 . \end{aligned} \qquad (A8)$$

(2) **PMMA**

The absorption line for the triangular group is given by Andrew et al[21]. For the rotating triangular group the absorption line is given by the following expression

$$f(x)=\frac{1}{2\sqrt{2\pi\alpha}}\exp\left(-\frac{x^2}{2\alpha}\right) + \int_{-\infty}^{\infty} P_{\pm}(x_0)\exp\{-(x-x_0)^2/2\alpha^2\} , \qquad (A9)$$

where α^2 means the additional second moment due to the external broadening, and $P_{\pm}(x)$ of the shape function of the triangular group is

$$P_{\pm}(x)=\frac{1}{8\sqrt{3}\beta}(1\pm x/\beta)^{-1/2} \qquad (A10)$$

for

$$-\beta<\pm x\leqslant 2\beta .$$

As a result the second moment due to the external broadening is determined by obtaining the maximum slope width of the absorption line (A9). This relation is given by the solid line shown in the Fig. 8. For example, α^2 is 3.35 gauss² at $\varDelta H_{m.sl.}=3.8$ gauss for CH_3 group ($\beta=4.4$ gauss).

References

1) C. W. Buun: Advances in Colloid Science. I, P. 95. Interscience Publishers, Inc., New York, (1946).
C. D. Coumols: Proc. Roy. Soc. A. **182** (1943) 166.
2) R. F. Boyer and R. S. Spencer: Advances in Colloid Science II, P. I. Interscience Publishers, Inc., New York, (1946).
3) S. Iwayanagi and M. Hideshima: J. Phys. Soc. Japan **8** (1953) 368.
D. Schmieder and K. Wolf: Kolloid Z. **134** (1953) 157.
4) K. Deutsch, E. A. W. Hoot and W. Reddish: J. Polymer Sci. **13** (1954) 565.
D. J. Mead and R. M. Fuoss: J. Amer. Chem. Soc. **63** (1941) 2832.
5) A. Odajima, J. Sohma and M. Koike: J. Chem. Phys. **23** (1955) 1956.
6) A. Odajima, M. Nagai: Bull. Res. Inst. Appl. Elect. **6** (1954) 45 (in Japanese) ibid. **9** (1957) (will be published).
7) J. H. Van Vleck: Phys. Rev. **74** (1948) 61.
H. S. Gutowsky, G. B. Kistiakowsky, G. E. Pake and E. M. Purecell: J. Chem. Phys. **17** (1949) 87.
8) L. V. Holroyd, R. S. Codrington, B. A. Mrowca and E. Guth: J. Appl. Phys. **22** (1951) 696.
9) E. R. Andrew: J. Chem. Phys. **18** (1950) 607.
10) P. Debye and F. Buche: J. Chem. Phys. **19** (1951) 589.
11) H. S. Gutowsky and G. E. Pake: J. Chem. Phys. **18** (1950) 97.
12) V.R. Honnold, F. McCaffery and B.A. Mrowca: J. Appl. Phys. **25** (1954) 1219.
13) N. Bloembergen: Nuclear Magnetic Relaxation, Thesis, Leiden (1948).
14) R. Kubo and T. Tomita: J. Phys. Soc. Japan **9** (1954) 888.
15) J. G. Fox and P. J. Flory: J. Appl. Phys. **21** (1950) 58.
16) C. P. Smith: Dielectric Beharior and Structure, McGraw-Hill Book Company, Inc. New York, (1955).
17) J. Karpovish: J. Chem. Phys. **22** (1954) 1767.
18) M. Yasumi: J. Chem. Soc. Japan **63** (1942) 983 (in Japanese).
19) B. H. Zimm: J. Polymer Sci. **16** (1955) 245.
20) L. Pauling: The Nature of the Chemical Bond, Oxford Univ. Press, (1940).
21) E. R. Andrew and Bersohn: J. Chem. Phys. **18** (1950) 106.

JOURNAL OF THE PHYSICAL SOCIETY OF JAPAN Vol. 12, No. 3 MARCH, 1957

Nuclear Magnetic Resonance in Some Crystalline Polymers

By Atsuo NISHIOKA
Electrical Communication Laboratory, Musashino, Tokyo
Hachiro KOMATSU and Yoshinobu KAKIUCHI
Institute of Science and Technology, Tokyo University

(Received November 27, 1956)

Nuclear magnetic resonance absorption was studied for some linear crystalline polymers in the temperature range from liquid air temperature to the neighbourhood of the melting points of the samples. The second moments of the absorption curve observed for the rigid samples were in well accordance with the calculated moments about their assumed crystalline forms.

Recently the line width transitions of crystalline linear polymers such as polyethylene (P.E.) and polytetrafluoroethylene (P.T.F.E.) have been studied using the nuclear magnetic resonance technique by several workers.[1-3)

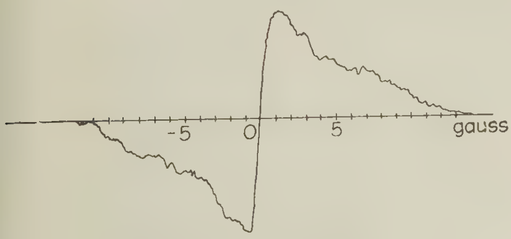

Fig. 1 (a). P.E., 1.2°C.

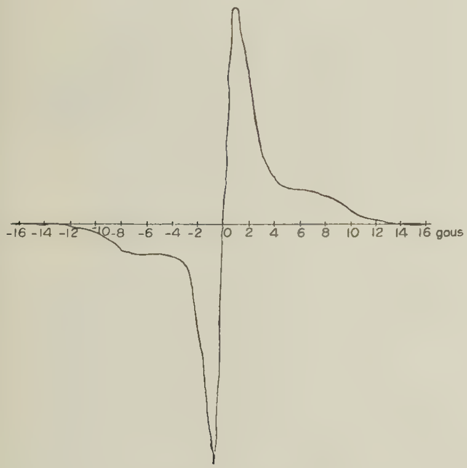

Fig. 1 (b). Polyethylene annealed for 30 min. at 100C°

We have studied these polymers and polytrifluorochloroethylene (P.T.F.C.E.) in further detail by nuclear magnetic resonance in wider temperature range from liquid air temperature to the neighbourhood of their melting points. Preliminarily, the polyvinylchloride (P.V.C.) has also been studied.

The derivatives of the absorption curves at room temperature are shown in Fig. 1~3 which show the composite structure with the sharp peak and long tail for P.E. and P.T.F.E., and broad bell shape for P.T.F.C.E. and P.V.C. Temperature dependences of the line widths defined as the separation between the maximum slopes ΔH_p, and the half maximum height width, $\Delta H_{1/2}$, of the absorption curves are shown in Fig. 4~6.

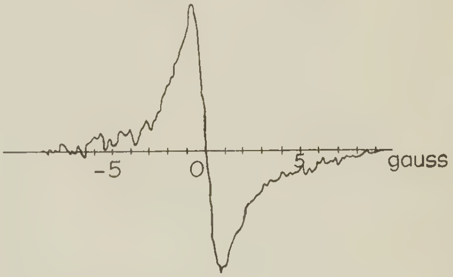

Fig. 2. P.T.F.E., 1.6°C.

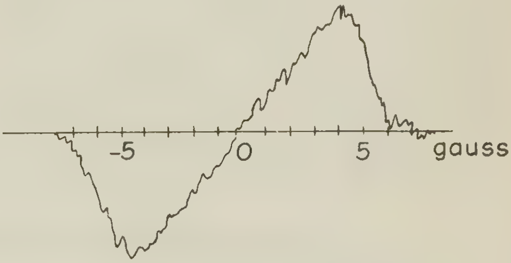

Fig. 3. P.T.F.C.E., 6°C.

The magnitude of ΔH_p or $\Delta H_{1/2}$ of the annealed samples of P.E. are comparable to those of the quenched specimen. In some cases, we observed the shoulder part pointed out by Wilson and Pake[2] in the annealed specimen as shown in Fig. 1 (b), whereas not in the quenched ones. With increasing temperature, the difference between ΔH_p and $\Delta H_{1/2}$ becomes larger. This is assumed to be due to the onset of the segmental motions of chain molecules. The tendencies of the changes of the line widths are very similar in P.E. and P.T.F.E. According to the results of Fig. 4, the "freezing temperature" of the segments, where the thermal motion of the segments begin to be stopped, is assumed around −100°C for both samples. With increasing temperature above this critical region, the line width decreases gradually in certain temperature range of −100°C∼0C°, and then drops markedly to a small value in the room temperature. Then the width continuously decreases with temperature from the room temperature to the melting point. On the other hand, P.T.F.C.E. has relatively monotonous decreasing curve as seen from Fig. 6 and the segments are frozen in about −30°C, but this temperature would depend upon the crystallinity of polymer. The behavior of P.V.C. are in well accordance with the results reported by Odajima.[4]

The observed second moment at the rigid state are shown in Table I. Assuming paraffine-like structure of plane zigzag molecule and further assuming that the expantion coefficient and axial ratio a/b of P.T.F.E. and P.T.F.C. are equal to that of P.E., we calculated the intra- and inter-molecular contribution to the second moment on the basis of the data of P.E. at liquid air temperature, and obtained the results shown in Table I, which are in well accordance with the observed values. These results may be considered to suggest that the chain molecules of these crystalline polymers have short range order in their rigid state.

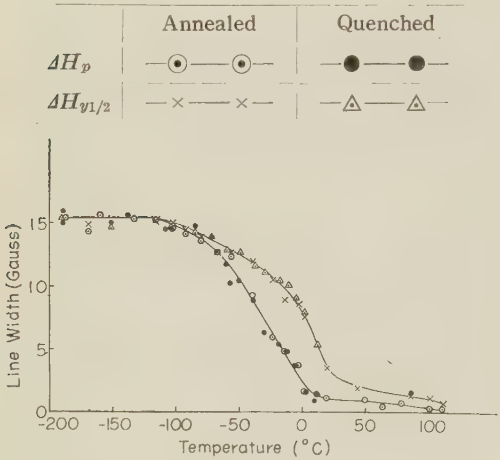

Fig. 4. Polyethylene.

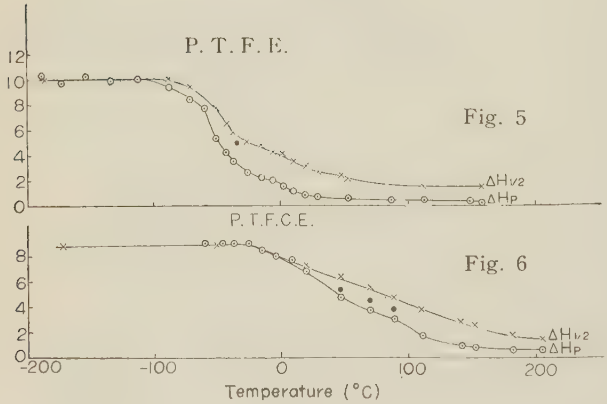

Fig. 5 (up) P. T. F. E. and 6 (lower) P. T. F. C. E.

Table I. Observed and calculated second moment at the rigid state.

Substances	T(°C)	Observed (gauss²)	calculated (gauss²)		
			intra	inter	total
P. E.	−189	26.3±2.7	17.8	7.7	25.5
P. T. F. E.	−173	11.7	9.2	2.4	11.6
P. T. F. C. E.	−172	7.7	(a) 7.4 (b) 6.4	0.6 0.5	8.0 6.9
P. V. C.	− 30	14.6	(a) 12.7 (b) 12.1		

(a) same side arrangement of F or H with Cl atom.
(b) alternative arrangement of F or H with Cl atom.

References

1) R. Newman: J. Chem. Phys. **18** (1950) 1303.
2) C. W. Wilson and G. E. Pake: J. Polymer Sci. **10** (1953) 503.
3) J. A. S. Smith: Discussions of the Farad. Soc. No. 19 (1955) 207.
4) A. Odajima, J. Sohma and M. Koike: J. Chem. Phys. **23** (1955) 1959.

JOURNAL OF THE PHYSICAL SOCIETY OF JAPAN Vol. 12, No. 3 MARCH, 1957

Self-consistent Field without Exchange for Doubly Ionized Cobalt

By Masataka ARIYAMA, Kunihusa KAYAMA and Masayoshi SUGIMOTO

Department of Physics, University of Tokyo

(Received December 7, 1956)

A self-consistent field without exchange for Co^{++} ion has been calculated and the tables of the results are given. Preliminary calculations were carried out with the aid of the differential analyzer, and the final results were obtained by the numerical integration. In the final approximation, the difference between estimated and calculated values of the contribution to Z_p from each subshell does not exceed 0.01 at any radius.

§ 1. Introduction

For the analysis of the atomic spectra, for the quantitative discussion of the properties of the fluoride, oxide, complex salts and intermetallic compounds of cobalt, and further for the calculation of the electronic structure of the metallic cobalt, it is desirable to know the atomic wave functions for Co as accurately as possible. The rough estimates of these atomic wave functions may be obtained by the interpolation between the wave functions for the atoms for which the calculations of the self-consistent field have already been carried out. The self-consistent field for Fe[1] and Cu^{+} [2] are available, and they may be used for the interpolation for Co. However, the interpolated wave functions are not sufficient for some applications. Therefore, it seems to be worth while to carry out a complete calculation of the self-consistent field without exchange for the paticular ion Co^{++}. The results of this calculation are reported in this paper, and they may be used for some applications which are mentioned above. Further, if it is found necessary to obtain the self-consistent field for the other electron configuration or the self-consistent field with exchange for this atom, the results for the Co^{++} ion will provide useful starting estimates of the wave functions.

In the present calculation, the electron configuration of the Co^{++} ion was assumed to be $(1s)^2\ (2s)^2\ (2p)^6\ (3s)^2\ (3p)^6\ (3d)^7$. Simultaneous integro-differential equations for six radial functions have been solved by the well known iterative method devised by Hartree[3]. Numerical work has been carried out partly with desk machines and partly with the diffferentical analyzer, which was recently designed and constructed in the Institute for Industrial Science, University of Tokyo. In using the differential analyzer, we followed in the technique used by Manning and others, who worked out several self-consistent field calculations with the aid of the differential analyzer in M.I.T.[1],[4],[5]

§ 2. Method and Procedure

As the detail of the practical procedure of calculating the Hartree field is reported in many literatures[3],[6],[7], only the outline of the method will be described here. In this paper, atomic units are used for all quantities except the eigenvalue for which the Rydberg unit is used.

The total wave function of the many electron atom is written as a product of one electron wave function of the type

$$\psi_{nl}=\frac{P_{nl}(r)}{r}\phi(\theta,\varphi)\,. \qquad (1)$$

The radial factor $P_{nl}(r)$ is the solution of the wave equation

$$\frac{d^2P_{nl}}{dr^2}+\left[2v^{(nl)}-\mathcal{E}_{nl}-\frac{l(l+1)}{r^2}\right]P_{nl}=0 \qquad (2)$$

where $\mathcal{E}_{nl}$ is the eigenvalue and $v^{(nl)}$ is the effective potential which is due to the nuclear charge and averaged charge distribution of that atom:

$$v^{(nl)}=\frac{1}{r}\left\{1+c+\sum_{n'l'}^{\text{all occupied subshells}}Z_p(n'l';r)-\frac{Z_p(nl;\ r)}{N_{nl}}\right\} \qquad (3)$$

where c is the degree of ionization and N_{nl} is the number of electrons in the subshell (nl). $Z_p(nl;\ r)$ is determined by the following relations.

$$\frac{dZ_p(nl;\ r)}{dr}=\frac{Z_p(nl;\ r)-Z(nl;\ r)}{r}, \qquad (4)$$

$$Z(nl;\ r)=N_{nl}\left\{1-\int_0^r P_{nl}^2\,dr\Big/\int_0^\infty P_{nl}^2\,dr\right\}. \qquad (5)$$

$Z(nl;\ r)$ is the contribution to the effective charge from N_{nl} electrons in the subshell (nl) and the corresponding positive charge on the nucleus. $Z_p(nl;\ r)$ is the contribution to the effective charge for potential, from N_{nl} electrons in the subshell (nl) and the corresponding positive charge on the nucleus.

It is convenient to start the self-consistent calculation from the estimated $Z_p(nl;\ r)$'s for each subshell. Then, $v^{(nl)}$ is calculated by (3) and the set of equations of the type of (2) is solved. The eigenvalue is determined by integrating the wave equation outwardly from $r=0$ and inwardly from large r with a trial values of $\mathcal{E}_{nl}$, and adjusting the value of $\mathcal{E}_{nl}$ so as to make the logaritymic derivatives of the solutions fit at a certain intermediate radius.

For the integration of Eq. (2), it is convenient to introduce a new independent variable $\rho=\log 1000r$ and new dependent variables $Y_{nl}=P_{nl}r^{-1/2}$ and $Q_{nl}=-\frac{1}{Y_{nl}}\frac{dY_{nl}}{d\rho}$, as has been suggested by Hartree5). With these variables, Eq. (2) is transformed into the following forms:

$$\frac{d^2Y_{nl}}{d\rho^2}+\left[2rZ_p^{(nl)}-\mathcal{E}_{nl}r^2+\left(l+\frac{1}{2}\right)^2\right]Y_{nl}=0, \qquad (6)$$

$$\frac{dQ_{nl}}{d\rho}=\left[Q_{nl}^2+2rZ_p^{(nl)}-\mathcal{E}_{nl}r^2-\left(l+\frac{1}{2}\right)^2\right], \qquad (7)$$

where $Z_p^{(nl)}=rv^{(nl)}$. Eq. (6) is used for the outward integration from $r=0$, and Eq. (7) is suitable for the inward integration from larger r.

When $P_{nl}(r)$'s are known, $Z(nl;\ r)$'s are calculated by (5) and the $Z_p(nl;\ r)$'s are obtained by solving Eq. (4) subject to the condition that $Z_p(nl;\ r)\rightarrow 0$ at large values of r. These calculated $Z_p(nl;\ r)$'s are compared with the estimated $Z_p(nl;\ r)$'s which are used to construct $v^{(nl)}$'s. The difference between the calculated and the estimated $Z_p(nl;\ r)$ for each subshell will be denoted by $\Delta Z_p(nl;\ r)$, and it is considered to be the measure of the consistency. These procedures form the one cycle of the interative process of our self-consistent field calculatirn, and it must be repeated until an estimate of the set of $Z_p(nl;\ r)$'s which makes the resulting $\Delta Z_p(nl;\ r)$'s sufficiently small is found.

In the present calculation, the consistency aimed at was 0.01 in $Z_p(nl;\ r)$, i.e. $\Delta Z_p(nl;r) < 0.01$ at any radius and for any subshell. The initial estimates of $Z_p(nl;\ r)$'s for Co^{++} were obtained by an interpolation4) between $Z_p(nl;\ r)$'s of Fe1) and those of Cu^{+} 2). To find the eigenvalue and eigenfunction for a paticular subshell, Eq. (2) was integrated for five different trial values of $\mathcal{E}_{nl}$ which were spread about the expected eigenvalue of that subshell.*) For a chosen value of $\mathcal{E}_{nl}$, integration was carried out by the following procedure.

For small values of r, $\frac{dY_{nl}}{d\rho}\Big/Y_{nl}$ can be expanded into a power series of r**). The value of $\frac{dY_{nl}}{d\rho}\Big/Y_{nl}$ at $\rho=0$ $(r=0.001)$ was found by this power series expansion, and from $\rho=0$, Eq. (6) was integrated outwardly with the aid of the differential analyzer. On the other hand, Eq. (7) was integrated inwardly with the aid of the differential analyzer. The starting point of this integration was taken well outside the range in which P_{nl} is appreciable, and the initial values were determined by the expansion of Q_{nl} in the power series of $1/r$.**)

---

*) This estimation was made from the X-ray term values for neutral Co. See, Manne Siegbahn; Spektroskopie der Röntgen strahlen, Berlin, 1931, p. 348.

**) As to the power series expansion, see Reference 1).

The eigenvalue was determined by graphical interpolation as follows. At a certain radius ρ_1, both $\left[\frac{dY_{nl}}{d\rho}\Big/Y_{nl}\right]_{\rho=\rho_1}$ obtained from outward integration and $Q_{nl}(\rho_1)$ obtained from inward integration are smooth functions of $\mathcal{E}_{nl}$. Thus $\left[\frac{dY_{nl}}{d\rho}\Big/Y_{nl}\right]_{\rho=\rho_1}$'s for each of the five values of $\mathcal{E}_{nl}$ were plotted and a curve of $\left[\frac{dY_{nl}}{d\rho}\Big/Y_{nl}\right]_{\rho=\rho_1}$ vs. $\mathcal{E}_{nl}$ was drawn. Similarly a curve of $-Q_{nl}(\rho_1)$ vs. $\mathcal{E}_{nl}$ was drawn. The value of $\mathcal{E}_{nl}$ with which $\left[\frac{dY_{nl}}{d\rho}\Big/Y_{nl}\right]_{\rho=\rho_1}=-Q_{nl}(\rho_1)$, was found from the intersection of those two curves. This procedure was carried out at two different values of the radius to check the accuracy of the determination, and it was confirmed that the eigenvalue can be determined to four or five significant figures by this crude graphical method, if trial values of $\mathcal{E}_{nl}$'s were chosen properly.

The eigenfunction was determined by an interpolation, with respect to the value of $\mathcal{E}_{nl}$, between the solutions which had already been obtained for several trial values of $\mathcal{E}_{nl}$. From the obtained eigenfunctions, $Z(nl;\,r)$'s and $Z_p(nl;\,r)$'s were caclulated. Using ρ as the independent variable, we have the explicit representation of the solution of Eq. (4) as follows,

$$Z_p(nl;\,\rho)=e^{\rho}\int_{\infty}^{\rho} Z(nl;\,\rho)\,e^{-\rho}\,d\rho\,.$$

These calculations were carried out with desk machines.

The maximum value of $\Delta Z_p(nl;\,r)$ was not less than 0.4 in the first approximation, and eight approximations were needed to obtain the consistency aimed at.

In the second and the third approximations, the calculated $Z_p(nl;\,r)$ of the preceding approximation was used as the estimate of $Z_p(nl;\,r)$ for the next approximation. This simple iterative process converged for inner shells, but oscillated for 3*s* and 3*p* shells, and diverged for 3*d* shell. Therefore, a revised estimate of $Z_p(nl;\,r)$ for 1*s*, 2*s*, 2*p*, 3*s*, and 3*p* electrons were made by averaging the results of 1st and 2nd approximations, and fixing these $Z_p(nl;\,r)$'s, $Z_p(3d;\,r)$ which was consistent with these revised estimates of $Z_p(nl;\,r)$ for other subshells was sought by the trial and error method. As had been reported by Manning and Goldberg,[1] once this approximate self-consistent field was found, the iterative process converged rapidly. From the 4th approximation, the average of the estimated and the calculated $Z_p(nl;\,r)$'s of the preceding approximation was used as the estimate of $Z_p(nl;\,r)$'s for the next approximation. This method of estimation

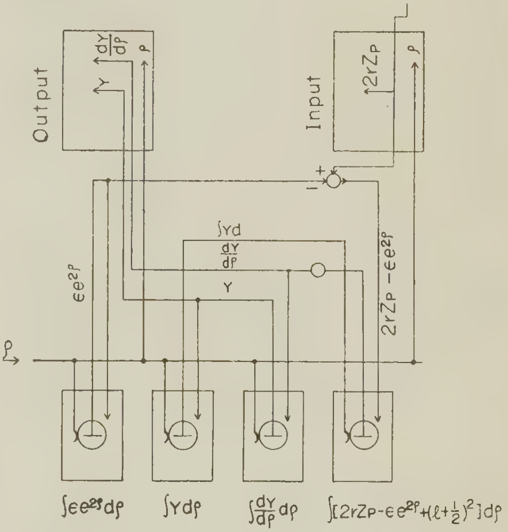
Output
Y
$\frac{dY}{d\rho}$
ρ
Input
$2rZ_P$
ρ
+
−
$\int Yd$
$\frac{dY}{d\rho}$
Y
$\epsilon e^{2\rho}$
$2rZ_P-\epsilon e^{2\rho}$
ρ
$\int \epsilon e^{2\rho}d\rho$
$\int Yd\rho$
$\int\frac{dY}{d\rho}d\rho$
$\int[2rZ_P-\epsilon e^{2\rho}+(l+\frac{1}{2})^2]d\rho$

Fig. 1. Schematic diagram of the differential analyzer for solution of equation:

$$\frac{d^2Y}{d\rho^2}+\left[2rZ_p-\varepsilon r^2-\left(l+\frac{1}{2}\right)^2\right]Y=0.$$

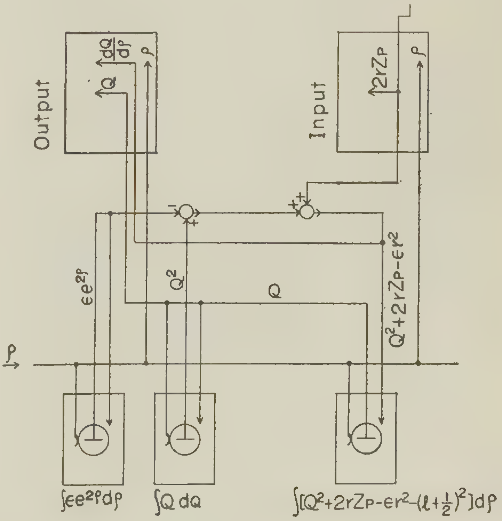

Fig. 2. Schematic diagram of the differential analyzer for solution of equation:

$$\frac{dQ}{d\rho}=Q^2+2rZ_p-\varepsilon r^2-\left(l+\frac{1}{2}\right)^2.$$

Table I. Values of $2Z_p$

ρ	$(1s)^2$	$(2s)^2$	$(2p)^6$	$(3s)^2$	$(3p)^6$	$(3d)^7$	Total
0.0	3.894	3.978	11.933	3.993	11.980	13.983	49.761
1	3.883	3.975	11.925	3.992	11.978	13.981	49.734
2	3·870	3.973	11.918	3.991	11.976	13.979	49.707
3	3.857	3.970	11.909	3.991	11.974	13.977	49.678
4	3.842	3.967	11.900	3.990	11.971	13.975	49.645
5	3.825	3.963	11.889	3.988	11.968	13.972	49.605
6	3.807	3.959	11.876	3.987	11.964	13.969	49.562
7	3.787	3.955	11.864	3.986	11.960	13.966	49.518
8	3.764	3.950	11.850	3.984	11.956	13.962	49.466
9	3.739	3.945	11.835	3.983	11.952	13.958	49.412
1.0	3.712	3.939	11.817	3.981	11.947	13.953	49.349
1	3.682	3.933	11.798	3.979	11.941	13.949	49.282
2	3.649	3.926	11.777	3.977	11.935	13.943	49.207
3	3.612	3.918	11.753	3.974	11.928	13.937	49.122
4	3.572	3.909	11.727	3.971	11.920	13.931	49.030
5	3.528	3.900	11.698	3.968	11.912	13.923	48.929
6	3.479	3.889	11.666	3.965	11.903	13.915	48.817
7	3.426	3.878	11.631	3.961	11.892	13.906	48.694
8	3.367	3.865	11.593	3.957	11.881	13.896	48.559
9	3.302	3.851	11.550	3.953	11.869	13.885	48.410
2.0	3.232	3.836	11.502	3.948	11.855	13.873	48.246
1	3.154	3.819	11.450	3.943	11.839	13.860	48.065
2	3.070	3.800	11.392	3.937	11.823	13.845	47.867
3	2.979	3.780	11.327	3.930	11.804	13.829	47.649
4	2.880	3.757	11.258	3.923	11.783	13.811	47.412
5	2.772	3.732	11.180	3.915	11.760	13.791	47.150
6	2.657	3.705	11.093	3.906	11.735	13.769	46.865
7	2.533	3.676	10.998	3.896	11.707	13.745	46.555
8	2.400	3.644	10.893	3.886	11.677	13.718	46.218
9	2.260	3.609	10.776	3.874	11.643	13.689	45.851
3.0	2.112	3.571	10.648	3.861	11.606	13.656	45.454
1	1.957	3.529	10.506	3.847	11.564	13.620	45.023
2	1.797	3.484	10.349	3.831	11.518	13.580	44.559
3	1.633	3.435	10.176	3.815	11.467	13.535	44.061
4	1.466	3.383	9.985	3.796	11.411	13.486	43.527
5	1.299	3.326	9.774	3.776	11.349	43.433	42.957
6	1.134	3.264	9.542	3.753	11.281	13.373	42.347
7	0.973	3.197	9.286	3.729	11.206	13.307	41.698
8	0.820	3.125	9.005	3.702	11.123	13.234	41.009
9	0.677	3.047	8.697	3.673	11.032	13.149	40.274
4.0	0.546	2.961	8.360	3.640	10.931	13.064	39.502
1	0.429	2.867	7.992	3.605	10.821	12.966	38.680
2	0.327	2.764	7.593	3.565	10.700	12.857	37.806
3	0.242	2.650	7.161	3.522	10.567	12.737	36.879
4	0.172	2.525	6.697	3.474	10.422	12.604	35.894
5	0.118	2.386	6.203	3.421	10.264	12.458	34.850
6	0.077	2.234	5.681	3.362	10.093	12.295	33.742
7	0.048	2.066	5.137	3.298	9.907	12.117	32.573
8	0.028	1.885	4.577	3.228	9.707	11.920	31.345
9	0.016	1.692	4.009	3.151	9.491	11.702	30.061
5.0	0.008	1.489	3.445	3.067	9.259	11.461	28.729
1	0.005	1.282	2.895	2.978	9.010	11.198	27.368
2	0.002	1.074	2.373	2.882	8.742	10.907	25.980
3	0.001	0.874	1.892	2.779	8.453	10.586	24.585
4	0.000	0.687	1.460	2.669	8.139	10.233	23.188
5		0.520	1.087	2.550	7.797	9.848	21.802
6		0.377	0.777	2.422	7.421	9.427	20.424
7		0.260	0.532	2.281	7.006	8.970	19.049
8		0.170	0.345	2.126	6.548	8.478	17.667
9		0.105	0.212	1.955	6.044	7.955	16.271
6.0		0.060	0.122	1.767	5.494	7.394	14.837
1		0.032	0.066	1.564	4.904	6.810	13.376
2		0.016	0.033	1.349	4.284	6.205	11.887
3		0.007	0.015	1.129	3.651	5.587	10.389
4		0.003	0.006	0.914	3.024	4.966	8.913
5		0.001	0.002	0.711	2.426	4.352	7.492
6		0.000	0.001	0.531	1.879	3.756	6.167
7			0.000	0.376	1.401	3.188	4.965
8				0.253	0.999	2.657	3.909
9				0.161	0.680	2.171	3.012
7.0				0.096	0.440	1.736	2.272
1				0.054	0.270	1,354	1.678
7.2				0.028	0.155	1.030	1.213
3				0.013	0.084	0.759	0.856
4				0.006	0.042	0.541	0.589
5				0.002	0.019	0.371	0.392
6				0.001	0.008	0.243	0.252
7				0.000	0.003	0.152	0.155
8					0.001	0.090	0.091
9					0.000	0.050	0.050
8.0						0.026	0.026
1						0.013	0.013
2						0.006	0.006
3						0.002	0.002
4						0.001	0.001
5						0.000	0.000
6							
7							
8							

Table II. Values of Y.

ρ	$(1s)$	$(2s)$	$(2p)$	$(3s)$	$(3p)$	$(3d)$
0.0	1000	1000	10.00	1000	10.00	0.0100
1	1048	1048	11.60	1048	11.60	0.0128
2	1099	1099	13.46	1099	13.46	0.0165
3	1151	1151	15.61	1151	15.61	0.0211
4	1205	1205	18.10	1205	18.10	0.0271
5	1262	1262	20.99	1262	20.99	0.0347
6	1320	1320	24.33	1320	24.33	0.0445
7	1381	1380	28.19	1380	28.19	0.0570
8	1443	1443	32.66	1443	32.66	0.0731
9	1508	1507	37.82	1507	37.82	0.0936
1.0	1574	1573	43.79	1573	43.79	0.1200
1	1642	1641	50.68	1641	50.68	0.1536
2	1712	1710	58.64	1710	58.63	0.1967
3	1782	1781	67.81	1781	67.80	0.2518
4	1854	1852	78.38	1852	78.37	0.3222
5	1927	1924	90.54	1924	90.53	0.4122
6	2000	1997	104.5	1996	104.5	0.5270
7	2074	2069	120.6	2068	120.6	0.6736
8	2146	2140	139.0	2140	139.0	0.8605
9	2218	2210	160.2	2210	160.1	1.099
2.0	2288	2278	184.4	2277	184.3	1.402
1	2356	2343	212.0	2342	211.9	1.788
2	2420	2403	343.5	2402	243.4	2.279
3	2480	2459	279.4	2457	279.2	2.901
4	2534	2508	320.1	2506	319.9	3.691
5	2582	2550	366.2	2546	366.0	4.692
6	2623	2582	418.3	2578	418.0	5.958
7	2655	2603	476.9	2598	476.5	7.557
8	2676	2611	542.7	2605	542.2	9.572
9	2685	2605	616.3	2597	615.7	12.11
3.0	2682	2582	698.3	2572	697.3	15.30
1	2664	2541	789.2	2528	787.8	19.29
2	2631	2479	889.5	2462	887.4	24.28
3	2581	2394	999.4	2374	996.4	30.51
4	2515	2286	1119	2261	1115	38.25
5	2430	2151	1249	2122	1243	47.84
6	2328	1990	1387	1955	1379	59.68
7	2209	1802	1535	1759	1523	74.24
8	2073	1587	1689	1536	1673	92.08
9	1923	1346	1849	1287	1827	113.8
4.0	1761	1080	2013	1012	1982	140.2
1	1590	794	2177	716	2135	172.0
2	1413	491	2337	404	2281	210.2
3	1234	177	2490	82	2416	255.6
4	1057	−142	2631	−242	2532	309.3
5	886	456	2753	559	2623	372.2
6	726	758	2853	858	2682	445.4

Table II. (Continued)

ρ	$(1s)$	$(2s)$	$(2p)$	$(3s)$	$(3p)$	$(3d)$
4.7	580	1038	2923	1127	2702	529.7
8	450	1286	2959	1355	2674	625.7
9	339	1493	2956	1529	2594	734.0
5.0	246	1651	2911	1638	2455	854.4
1	172	1756	2822	1675	2253	986.6
2	116	1802	2690	1632	1989	1130
3	74	1790	2517	1508	1664	1282
4	45	1724	2309	1306	1283	1440
5	26	1609	2072	1032	857	1602
6	14	1454	1816	700	398	1762
7	7	1272	1550	−326	−78	1915
8	5	1074	1287	+67	550	2056
9	2	875	1035	456	997	2177
6.0	1	685	805	816	1397	2273
1	0	514	603	1125	1731	2338
2		369	433	1363	1983	2366
3		252	298	1519	2142	2357
4		163	195	1588	2206	2310
5		100	121	1574	2179	2228
6		57	71	1488	2072	2115
7		31	39	1346	1901	1979
8		15	20	1169	1685	1824
9		7	10	974	1445	1659
7.0		3	4	779	1199	1488
1		1	2	598	961	1318
2		0	1	439	744	1151
3			0	309	555	991
4				207	399	840
5				131	274	700
6				79	180	572
7				45	113	457
8				24	67	356
9				12	37	269
6.0				5	19	197
1				2	9	139
2				1	4	94
3				0	2	60
4					1	37
5					0	21
6						11
7						6
8						3
9						1
9.0						0
1						
2						
3						
4						
5						

Table III. Expansion formulae of $Y(r)$ for $r < 0.001$

	$Y_{nl}(r)$
$1s$	$Y_{1s}(r)=32488.1\times r^{\frac{1}{2}}\times\{1-27r+368.6r^2\}$
$2s$	$Y_{2s}(r)=32490.5\times r^{\frac{1}{2}}\times\{1-27r+292.3r^2\}$
$2p$	$Y_{2p}(r)=32052.2\times r^{\frac{3}{2}}\times\{1-13{\cdot}5r+101.7r^2\}$
$3s$	$Y_{3s}(r)=32490.8\times r^{\frac{1}{2}}\times\{1-27r+283.8r^2\}$
$3p$	$Y_{3p}(r)=32052.3\times r^{\frac{3}{2}}\times\{1-13.5r+97.2r^2\}$
$3d$	$Y_{3d}(r)-31908.3\times r^{\frac{5}{2}}\times\{1-9r+51.8r^2\}$

Table IV. Values of $2Z$.

ρ	$(1s)^2$	$(2s)^2$	$(2p)^6$	$(3s)^2$	$(3p)^6$	$(3d)^7$	Total
0.0	4.000	4.000	12.000	4.000	12.000	14.000	50.000
1	〃	〃	〃	〃	〃	〃	〃
2	〃	〃	〃	〃	〃	〃	〃
3	〃	〃	〃	〃	〃	〃	〃
4	〃	〃	〃	〃	〃	〃	〃
5	〃	〃	〃	〃	〃	〃	〃
6	4.000	〃	〃	〃	〃	〃	50.000
7	3.999	〃	〃	〃	〃	〃	49.999
8	3.999	〃	〃	〃	〃	〃	49.999
9	3.999	〃	〃	〃	〃	〃	49.999
1.0	3.998	〃	〃	〃	〃	〃	49.998
1	3.998	〃	〃	〃	〃	〃	49.998
2	3.997	〃	〃	〃	〃	〃	49.997
3	3.996	〃	〃	〃	〃	〃	49.996
4	3.994	4.000	〃	〃	〃	〃	49.994
5	3.992	3.999	〃	〃	〃	〃	49.991
6	3.990	3.999	〃	〃	〃	〃	49.989
7	3.987	3.999	〃	〃	〃	〃	49.986
8	3.982	3.998	〃	〃	〃	〃	49.980
9	3.877	3.998	〃	〃	〃	〃	49.975
2.0	3.970	3.997	〃	4.000	〃	〃	49.967
1	3.960	3.996	〃	3.999	〃	〃	49.955
2	3.948	3.995	〃	3.999	〃	〃	49.942
3	3.932	3.994	〃	3.999	〃	〃	49.925
4	3.912	3.992	〃	3.999	〃	〃	49.903
5	3.887	3.990	〃	3.999	〃	〃	49.876
6	3.855	3.987	〃	3.998	〃	〃	49.840
7	3.815	3.984	12.000	3.998	〃	〃	49.797
8	3.764	3.979	11.999	3.997	〃	〃	49.739
9	3.702	3.974	11.999	3.996	〃	〃	49.671
3.0	3.626	3·968	11.998	3.995	〃	〃	49.587
1	3.534	3.960	11.997	3.994	12.000	〃	49.485
2	3.424	3.951	11.996	3.993	11.999	〃	49.363
3	3.293	3.941	11.994	3.992	11.999	〃	49.219
4	3.141	3.930	11.990	3.990	11.999	〃	49.050
5	2.966	3.917	11.985	3.988	11.998	〃	48.854
6	2.767	3.904	11.977	3.986	11.997	〃	48.631
7	2.547	3.890	11.965	3.984	11.995	〃	48.381
8	2.308	3.876	11.947	3.982	11.993	〃	48.106
9	2.054	3.864	11.920	3.981	11.989	〃	47.808
4.0	1.790	3.854	11.882	3.979	11.984	〃	47.489
1	1.523	3.846	11.827	3.978	11.977	〃	47.151
2	1.262	3.842	11.748	3.978	11.967	〃	46.797
3	1.014	3.841	11.639	3.978	11.953	〃	46.425
4	0.787	3.841	11.489	3.978	11.934	14.000	46.029
5	0.588	3.839	11.286	3.977	11.908	13.999	45.597
6	0.421	3.830	11.017	3.976	11.876	13.999	45.119
7	0.287	3.806	10.668	3.971	11.834	13.998	44.564
8	0.186	3.759	10.227	3.964	11.784	13.996	43.916
9	0.113	3.677	9.682	3.951	11.725	13.994	43.142
5.0	0.065	3.548	9.028	3.932	11.660	13.989	42.222
1	0.034	3.364	8.265	3.906	11.590	13.982	41.141
2	0.017	3.119	7.403	3.875	11.520	13.970	39.904
3	0.008	2.815	6.465	3.841	11.457	13.951	38.537
4	0.003	2.460	5.481	3.808	11.407	13.921	37.080
5	0.001	2.070	4.492	3.780	11.375	13.876	35.594
6	0.000	1.668	3.541	3.761	11.361	13.809	34.140
7		1.280	2.671	3.753	11.359	13.710	32.773
8		0.930	1.917	3.752	11.336	13.570	31.505
9		0.635	1.302	3.748	11.314	13.376	30.375
6.0		0.405	0.831	3.724	11.201	13.114	29.275
1		0.240	0.495	3.659	10.969	12.770	28.133
2		0.130	0.273	3.528	10.571	12.334	26.836
3		0.065	0.138	3.315	9.973	11.796	25.287
4		0.029	0.064	3.014	9.164	11.155	23.426
5		0.012	0.027	2.635	8.161	10.416	21.251
6		0.004	0.010	2.201	7.012	9.589	18.816
7		0.001	0.003	1.747	5.789	8.693	16.233
8		0.000	0.001	1.313	4.574	7.749	13.637
9			0.000	0.929	3.445	6.783	11.157
7.0				0.615	2.464	5.820	8.899
1				0.380	1.661	4.886	6.927

Table IV. (Continued)

ρ	$(1s)^2$	$(2s)^2$	$(2p)^6$	$(3s)^2$	$(3p)^6$	$(3d)^7$	Total
7.2				0.218	1.059	4.003	5.280
3				0.115	0.629	3.192	3.936
4				0.055	0·348	2.468	2.871
5				0.024	0.177	1.843	2.044
6				0.010	0.083	1.323	1.416
7				0.003	0.035	0.907	0.945
8				0.001	0.014	0.591	0.606
9				0.000	0.004	0.363	0.367
8.0					0.002	0.209	0.211
1					0.000	0.112	0.112
2						0.055	0.055
3						0.024	0.024
4						0.010	0.010
5						0.003	0.003
6						0.001	0.001
7						0.000	0.000
8							
9							
9.0							

quickens the convergence, and at the same time, has a merit of preventing the divergence which is apt to occur for the outer subshells.

In the 7th approximation, the consistency aimed at was obtained. The 8th approximation was carried out entirely by desk machines to refine the results and to check the systematic error of the differential analyzer. The systematic error was found to be very small, and if careful set-up is used, relative error of the solution will be less than 1% except at some singular points. The schematic diagrams for the set-up of the differential analyzer for the solution of the Eqs. (6) and (7) are shown in Fig. (1) and (2).[8]

§ 3. Results

Tables are given of the values of Y, $2Z$, and $2Z_p$ for each type of electrons as a function of ρ. Tables of ε_{nl}, $\int_{-\infty}^{\infty} Y^2 e^{2\rho}\,d\rho$, $-2v_0(nl)$, and the maximum value of $\Delta Z_p(nl; r)$ are also given. In the actual integrations, one or two more significant figures have been retained in the calculations than are tabulated. Slater Intetegrals F_2, F_4,[9] spin-orbit separation parameter ζ_{3d}[10] and several intermultiplet separations are calculated from the values tabulated in Tables II and IV, and are compared with those values estimated from optical data.[11] These results are tabulated in Table VI. The discrepancy between the calculated and estimated values is less than 5% of the magnitude of each of these quantities, but ^4P and ^2G levels are obtained in wrong order. These discrepancies would not be reduced even if more convergent solutions of Hartree equations were used for the calculation.

Table V. Values of ε_{nl}, $\int_{-\infty}^{\infty} Y_{nl}^2 e^{2\rho}\,d\rho$, $-2v_0(nl)$ and $2\Delta Z_p(nl; r)$

	$(1s)$	$(2s)$	$(2p)$	$(3s)$	$(3p)$	$(3d)$
ε_{nl}	567.07	67.357	59.558	8.7897	6.2520	2.1216
$\int_{-\infty}^{\infty} Y_{nl}^2 e^{2\rho}\,d\rho$	13869	15502×10	31552×10	10636×10^2	23205×10^2	39143×10^2
$-2v_0(nl)$	106.1	22.4	67.3	7.04	19.66	17.14
$2\Delta Z_p(nl; r)$	≤ 0.001	≤ 0.006	≤ 0.007	≤ 0.006	≤ 0.014	≤ 0.002

$v_0(nl)$ is the contribution from N_{nl} electrons in the subshell (nl) to the potential at the position of nucleus.

Table VI. F_2, F_4, ζ_{3d} and intermultiplet separations

	Calculated	Estimated from observation
F_2	1685.2 cm^{-1}	1598.8 * cm^{-1}
F_4	115.32	123.81*
ζ_{3d}	519.8	527.4 **
$^4P-{}^4F$	16630.5	14697.2
$^2G-{}^4F$	16541.3	16918.9
$^2H-{}^4F$	22084.8	21817.9

* The values of F_2 and F_4 are estimated by the least square method.

** The value of ζ_{3d} is estimated from the average of fine structure separations of ^4F levels.

§ 4. Acknowledgements

The authors would like to express their sincere gratitude to Prof. Kotani and the members of his laboratory for their helpful discussions and to Dr. Watanabe and Dr. Miita of Institute for Industrial Science for their instruction as to the use of the differential analyzer. They also wish to express their indebtedness to Misses S. Maniwa, J. Matsuoka and K. Murata for their assistance in carrying out the numerical work.

References

1) M. F. Manning and L. Goldberg: Phys. Rev. **53** (1938) 662.
2) D. R. Hartree: Proc. Roy. Soc. A**141** (1933) 282.
3) D. R. Hartree: Proc. Camb. Phil. Soc. **24** (1927) 89, 111.
4) M. F. Manning and J. Millman: Phys. Rev. **49** (1936) 848.
5) D. R. Hartree: Phys. Rev. **46** (1934) 738.
6) D. R. Hartree: Report on Progress in Physics XI (1946-7) 113.
7) E. U. Condon and G. H. Shortley: The Theory of Atomic Spectra (Cambridge, 1953) Chapter XIV Sec. 8, 9.
8) M. Watanabe and J. Miita: Seisan Kenkyu **6** (1954) 197, **7** (1955) 79.
9) See Reference 6) p. 177.
10) See Reference 6) p. 196.
11) Atomic Energy Levels Vol. 2 Circular of the National Bureau of Standards 467 Issued August 15, 1952 p. 85.

JOURNAL OF THE PHYSICAL SOCIETY OF JAPAN Vol. 12, No. 3, MARCH, 1957

The Forces Experienced by Two Circular Cylinders in a Uniform Flow at Small Reynolds Numbers

By Shinji KUWABARA

Department of Physics, Faculty of Science, University of Tokyo

(Received December 7, 1956)

Using Imai's general method of solving two-dimensional Oseen's equations, the drag and lift coefficients for one of two parallel circular cylinders in a uniform flow at small Reynolds numbers have been calculated. The general expressions for these coefficients become very simple when the two cylinders are placed symmetrically with respect to the uniform flow. Numerical calculations have been carried out in several cases for various values of the parameters.

§1. Introduction and Summary

As is well known, the motion of an incompressible viscous fluid past obstacles at small Reynolds numbers can be described by Oseen's approximate equations. With the aid of these Oseen's equations the viscous flow past a single obstacle such as a sphere, a circular cylinder, etc. has been studied by several authors, but there have been few works concerning the case of two obstacles. Here, the case of two circular cylinders placed in general configurations in a uniform flow, will be investigated with a, d, α and R as parameters, where a is the radius of the second circular cylinder (the radius of the first circular cylinder is normalized as unity), d the distance between the centres of the two cylinders, α the angle between the direction of the uniform flow and the vector drawn from the centre of the first cylinder to that of the second and R the Reynolds number based on the diameter of the first cylinder.

Prof. Imai proposed an elegant general method of solving Oseen's equations by introducing complex variables [1], and we shall make use of his method in our study. We calculate the drag and the lift coefficients of one of the two circular cylinders and then the resultant drag, lift and moment coefficients of the system of the two circular cylinders are related to these coefficients of each cylinder.

Numerical calculations were carried out in the following cases; (i) $a=1$; $d=5$, 10, 20; $\alpha=0°$, 90°, 180°; $R=0.04-1.0$. (ii) $a=1$; $d=5$; $\alpha=0°-180°$; $R=0.4$, 0.8 and (iii) $a=0-3.0$; $d=10$; $\alpha=0°$, 90°, 180°; $R=0.4$, 0.8. The qualitative results obtained from these calculations are as follows: (i) the drag coefficients for one of the two cylinders are smaller than that for a single cylinder at the same Reynolds numbers; (ii) the mutual interaction is attractive when the central line is parallel to the uniform flow and is repulsive when it is perpendicular; (iii) the force acting on the first cylinder is roughly in the direction of the flow induced when the second cylinder alone is in the uniform flow and (iv) if the two cylinders of the same radius connected rigidly are falling in a viscous fluid, there exists a tendency that the central line becomes perpendicular to the direction of fall.

§ 2. Imai's Method of Solving Oseen's Equations

Oseen's approximate equations and the equation of continuity for the two-dimensional steady motion of an incompressible viscous fluid can be written as

$$U\frac{\partial u}{\partial x}=-\frac{1}{\rho}\frac{\partial p}{\partial x}+\nu\Delta u\,, \qquad (2.1)$$

$$U\frac{\partial v}{\partial x}=-\frac{1}{\rho}\frac{\partial p}{\partial y}+\nu\Delta v\,, \qquad (2.2)$$

and

$$\frac{\partial u}{\partial x}+\frac{\partial v}{\partial y}=0\,, \qquad (2.3)$$

where $\Delta=\partial^2/\partial x^2+\partial^2/\partial y^2$, (x, y) are the cartesian co-ordinates, (u, v) the velocity components, U the velocity at infinity of a uniform flow in the direction of the x-axis, p the pressure, ρ the density and ν the kinematic viscosity.

Eliminating p from (2.1) and (2.2), we have

$$\Delta\omega-2k\frac{\partial\omega}{\partial x}=0\,, \qquad (2.4)$$

where ω is the vorticity defined by

$$\omega=\frac{\partial v}{\partial x}-\frac{\partial u}{\partial y}\,, \qquad (2.5)$$

and $2k=U/\nu$.

Introducing complex variables

$$z=x+iy,\quad z=x-iy\,, \qquad (2.6)$$

and

$$W=u-iv\,, \qquad (2.7)$$

we obtain from (2.3) and (2.5)

$$\frac{\partial W}{\partial\bar{z}}=-\frac{1}{2}i\omega\,. \qquad (2.8)$$

The general solution of (2.4) satisfying $\omega=0$ at infinity can be expressed as

$$\omega=\Re\sum_{n=0}^{\infty}C_n e^{kx}K_n(kr)e^{ni\theta}\,, \qquad (2.9)$$

where (r, θ) are polar co-ordinates, K_n is the modified Bessel function of the second kind, C_n is a complex coefficient and $\Re$ signifies "the real part of".

Inserting (2.9) into (2.8) and integrating with respect to $\bar{z}$, we have

$$W=\frac{i}{2k}e^{kx}\Big\{A_1K_0(kr)+\sum_{n=1}^{\infty}(A_{n+1}e^{ni\theta}-\bar{A}_n e^{-ni\theta})K_n(kr)\Big\}+\frac{df}{dz}\,, \qquad (2.10)$$

where $A_n=\sum_{p=n}^{\infty}C_p$ is a new complex coefficient and $f(z)$ is an arbitrary analytic function of z. In Oseen's approximation, $f(z)$ can be expressed in general as

$$f(z)=Uz+\frac{m+i\Gamma}{2\pi}\ln z+O\Big(\frac{1}{z}\Big)\,, \qquad (2.11)$$

where m and Γ are constants.

§ 3. Application of Imai's Method to the Case of Two Circular Cylinders

Since Oseen's equations are linear, the sum of the complex velocities (2.10) is also their solution. In the case of two circular cylinders we assume the following form for the complex velocity

$$W(z_1, z_2)=W_1(z_1)+W_2(z_2)+U\,, \qquad (3.1)$$

$$W_1=\frac{i}{2k}e^{kx_1}\Big\{A_1^{(1)}K_0(kr_1)+\sum_{n=1}^{\infty}(A_{n+1}^{(1)}e^{ni\theta_1}-\bar{A}_n^{(1)}e^{-ni\theta_1})K_n(kr)_1\Big\}+\frac{m_1+i\Gamma_1}{2\pi}\frac{1}{z_1}+\cdots\,, \qquad (3.2)$$

$$W_2=\frac{i}{2k}e^{kx_2}\Big\{A_1^{(2)}K_0(kr_2)+\sum_{n=1}^{\infty}(A_{n+1}^{(2)}e^{ni\theta_2}-\bar{A}_n^{(2)}e^{-ni\theta_2})K_n(kr_2)\Big\}+\frac{m_2+i\Gamma_2}{2\pi}\frac{1}{z_2}+\cdots\,, \qquad (3.3)$$

where

$$z_1=x_1+iy_1=r_1e^{i\theta_1},\quad z_2=x_2+iy_2=r_2e^{i\theta_2} \qquad (3.4)$$

are vectors drawn from the centres of the circular cylinders C_1 and C_2 to a point P in question respectively. The radius of the cylinder C_1 is normalized as unity and that of the cylinder C_2 is a. $de^{i\alpha}$ is a vector connecting the centres of C_1 and C_2 (*cf.* Fig. 1).

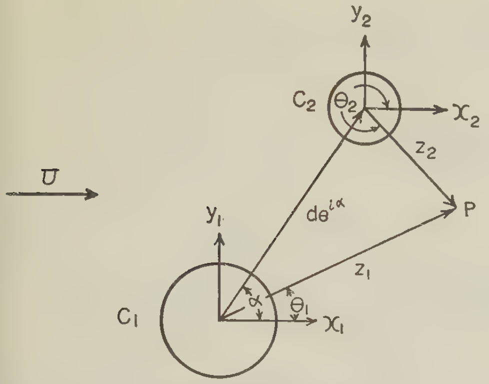

Fig. 1. The general configuration of two circular cylinders.

The boundary conditions are

$$W=0$$

at the surfaces of the cylinders C_1 and C_2, or

$$W_1(e^{i\theta})+W_2(-de^{i\alpha}+e^{i\theta})+U=0\ , \qquad (3.5)$$

$$W_1(de^{i\alpha}+ae^{i\theta})+W_2(ae^{i\theta})+U=0\ . \qquad (3.6)$$

Expanding these equations (3.5) and (3.6) with respect to $e^{i\theta}$, we have

$$\begin{aligned}\cdots&+e^{i\theta}\{A_2^{(1)}I_0(k)K_1(k)+O(k^2)\}\\ &+A_1^{(1)}I_0(k)K_0(k)-\bar{A}_1^{(1)}I_1(k)K_1(k)\\ &+e^{-kd\cos\alpha}I_0(k)^2\{A_1^{(2)}K_0(kd)+\bar{A}_1^{(2)}K_1(kd)e^{-i\alpha}\}\\ &+ik\frac{m_2+i\Gamma_2}{\pi}\frac{e^{-i\alpha}}{d}+O(k^2)\\ &+e^{-i\theta}\left\{-\bar{A}_1^{(1)}I_0(k)K_1(k)-ik\frac{m_1+i\Gamma_1}{\pi}+O(k^2)\right\}\\ &+\cdots=2ikU\ , \qquad (3.7)\end{aligned}$$

$$\begin{aligned}\cdots&+e^{i\theta}\{A_2^{(2)}I_0(ka)K_1(ka)+O(k^2)\}\\ &+e^{kd\cos\alpha}I_0(ka)^2\{A_1^{(1)}K_0(kd)-\bar{A}_1^{(1)}K_1(kd)e^{-i\alpha}\}\\ &+A_1^{(2)}I_0(ka)K_0(ka)-\bar{A}_1^{(2)}I_1(ka)K_1(ka)\\ &-ik\frac{m_1+i\Gamma_1}{\pi}\frac{e^{-i\alpha}}{d}+O(k^2)\\ &+e^{-i\theta}\left\{-\bar{A}_1^{(2)}I_0(ka)K_1(ka)\right.\\ &\left.-ik\frac{m_2+i\Gamma_2}{\pi}\frac{1}{a}+O(k^2)\right\}+\cdots=2ikU\ . \qquad (3.8)\end{aligned}$$

Here we have assumed that $k\ll 1$, $a\doteqdot 1$, $kd=O(1)$ and therefore $A_n=O(k^n)$. Retaining the terms of the order 1 and k and neglecting those of higher order in (3.7) and (3.8) as the first approximation, we have six algebraic equations for the complex numbers $A_1^{(1)}$, $A_2^{(1)}$, $A_1^{(2)}$, $A_2^{(2)}$, $m_1+i\Gamma_1$ and $m_2+i\Gamma_2$;

$$A_2^{(1)}I_0(k)K_1(k)=0\ , \qquad (3.9)$$

$$\begin{aligned}&A_1^{(1)}I_0(k)K_0(k)-\bar{A}_1^{(1)}I_1(k)K_1(k)+e^{-kd\cos\alpha}I_0(k)^2\\ &\quad\times\{A_1^{(2)}K_0(kd)+\bar{A}_1^{(2)}K_1(kd)e^{-i\alpha}\}\\ &\quad+ik\frac{m_2+i\Gamma_2}{\pi}\frac{e^{-i\alpha}}{d}=2ikU\ , \qquad (3.10)\end{aligned}$$

$$-\bar{A}_1^{(1)}I_0(k)K_1(k)-ik\frac{m_1+i\Gamma_1}{\pi}=0\ , \quad (3.11)$$

$$\bar{A}_2^{(2)}I_0(ka)K_1(ka)=0\ , \qquad (3.12)$$

$$\begin{aligned}&e^{kd\cos\alpha}I_0(ka)^2\{A_1^{(1)}K_0(kd)-\bar{A}_1^{(1)}K_1(kd)e^{-i\alpha}\}\\ &\quad+A_1^{(2)}I_0(ka)K_0(ka)-\bar{A}_1^{(2)}I_1(ka)K_1(ka)\\ &\quad-ik\frac{m_1+i\Gamma_1}{\pi}\frac{e^{-i\alpha}}{d}=2ikU\ , \qquad (3.13)\end{aligned}$$

$$-\bar{A}_1^{(2)}I_0(ka)K_1(ka)-ik\frac{m_2+i\Gamma_2}{\pi}\frac{1}{a}=0\ . \qquad (3.14)$$

Now the drag coefficients $C_D^{(1)}, C_D^{(2)}$ and the lift coefficients $C_L^{(1)}, C_L^{(2)}$ for the cylinders C_1, C_2 are respectively defined as

$$C_D^{(1)}=\frac{X_1}{\frac{1}{2}\rho U^2\times 2}\ , \qquad C_L^{(1)}=\frac{Y_1}{\frac{1}{2}\rho U^2\times 2}\ , \qquad (3.15)$$

$$C_D^{(2)}=\frac{X_2}{\frac{1}{2}\rho U^2\times 2a}\ , \qquad C_L^{(2)}=\frac{Y_2}{\frac{1}{2}\rho U^2\times 2a}\ , \qquad (3.16)$$

where X_1, X_2 and Y_1, Y_2 are the drags and the lifts for the cylinders C_1, C_2 respectively.

As is well known, the drag X and the lift Y of a cylinder are given by

$$X=\rho Um\ , \quad Y=\rho U\Gamma\ , \qquad (3.17)$$

where m and Γ are constants which appeared in (2.11).

If $C^{(1)}$ and $C^{(2)}$ are defined as

$$C^{(1)}=C_D^{(1)}+iC_L^{(1)}, \quad C^{(2)}=C_D^{(2)}+iC_L^{(2)}\ , \qquad (3.18)$$

we have, by (3.15), (3.16) and (3.17),

$$m_1+i\Gamma_1=UC^{(1)}, \quad m_2+i\Gamma_2=aUC^{(2)}\ . \qquad (3.19)$$

Since $k\ll 1$ and $ka\ll 1$, we can make use of the following approximate formulae;

$$\begin{aligned}K_0(k)=&-\ln(\tfrac{1}{2}k)-\gamma-(1/4)k^2\{\ln(\tfrac{1}{2}k)+\gamma-1\}\\ &+O(k^4), \qquad (3.20)\end{aligned}$$

$$K_1(k)=\tfrac{1}{2}(\tfrac{1}{2}k)^{-1}+\tfrac{1}{2}k\{\ln(\tfrac{1}{2}k)+\gamma-\tfrac{1}{2}\}+O(k^3)\ , \qquad (3.21)$$

and similar formulae as obtained by putting ka in place of k in (3.20) and (3.21), where

$\gamma=0.57721\cdots$ is Euler's constant. Then we can rewrite (3.10)–(3.14) as follows:

$$\tfrac{1}{2}C^{(1)}+S_1\overline{C}^{(1)}-a\left(K_1e^{-(Rd/4)\cos\alpha}-\frac{4}{Rd}\right)e^{-i\alpha}C^{(2)}$$
$$+aK_0e^{-(Rd/4)\cos\alpha}\overline{C}^{(2)}=\frac{8\pi}{R}, \qquad (3.22)$$

$$\left(K_1e^{(Rd/4)\cos\alpha}-\frac{4}{Rd}\right)e^{-i\alpha}C^{(1)}+K_0e^{(Rd/4)\cos\alpha}\overline{C}^{(1)}$$
$$+\tfrac{1}{2}aC^{(2)}+aS_2\overline{C}^{(2)}=\frac{8\pi}{R}, \qquad (3.23)$$

where

$$S_1=\ln\frac{8}{R}-\gamma, \quad S_2=\ln\frac{8}{Ra}-\gamma, \qquad (3.24)$$

$R=4k=2U/\nu$ is the Reynolds number based on the diameter of the cylinder C_1 and the argument $kd=Rd/4$ of the modified Bessel function $K_n(kd)$ is omitted for brevity in (3.22), (3.23) as well as in the following lines. (3.22), (3.23) and their complex conjugate equations determine $C^{(1)}, \overline{C}^{(1)}, C^{(2)}$ and $\overline{C}^{(2)}$. And then we obtain the drag and the lift coefficients by means of taking their real and imaginary parts of these coefficients. We consider, for example, only the coefficients of the first cylinder C_1 for brevity:

$$C_D^{(1)}=\frac{8\pi}{R}\frac{\Delta_X^{(1)}}{J}, \qquad (3.25)$$

$$C_L^{(1)}=\frac{8\pi}{R}\frac{\Delta_Y^{(1)}}{J}, \qquad (3.26)$$

with

$$J=o_1o_2o_3o_4+(p_1p_2-q_1^2)(p_3p_4-q_2^2)-o_1o_3p_2p_3$$
$$-o_2o_4p_1p_4+o_1o_4q_1q_2+o_2o_3q_1q_2, \qquad (3.27)$$

$$\Delta_X^{(1)}=o_2o_3o_4+p_2(p_3p_4-q_2^2)-o_3p_2p_3$$
$$-o_2o_4p_4+o_4q_1q_2, \qquad (3.28)$$

$$\Delta_Y^{(1)}=-q_1(p_3p_4-q_2^2)+o_3p_3q_1+(o_1-p_1)o_4q_2 \qquad (3.29)$$

where

$$o_1=S_1+\tfrac{1}{2}, \qquad (3.30)$$

$$o_2=S_1-\tfrac{1}{2}, \qquad (3.31)$$

$$o_3=S_2+\tfrac{1}{2}, \qquad (3.32)$$

$$o_4=S_2-\tfrac{1}{2}, \qquad (3.33)$$

$$p_1=K_0e^{(Rd/4)\cos\alpha}+\left(K_1e^{(Rd/4)\cos\alpha}-\frac{4}{Rd}\right)\cos\alpha, \qquad (3.34)$$

$$p_2=K_0e^{(Rd/4)\cos\alpha}-\left(K_1e^{(Rd/4)\cos\alpha}-\frac{4}{Rd}\right)\cos\alpha, \qquad (3.35)$$

$$p_3=K_0e^{-(Rd/4)\cos\alpha}+\left(K_1e^{-(Rd/4)\cos\alpha}-\frac{4}{Rd}\right)\cos\alpha, \qquad (3.36)$$

$$p_4=K_0e^{-(Rd/4)\cos\alpha}-\left(K_1e^{-(Rd/4)\cos\alpha}-\frac{4}{Rd}\right)\cos\alpha, \qquad (3.37)$$

$$q_1=\left(K_1e^{(Rd/4)\cos\alpha}-\frac{4}{Rd}\right)\sin\alpha, \qquad (3.38)$$

$$q_2=\left(K_1e^{-(Rd/4)\cos\alpha}-\frac{4}{Rd}\right)\sin\alpha. \qquad (3.39)$$

Making use of the asymptotic form of $K_n(kd)$:

$$K_n(kd)=\left(\frac{\pi}{2kd}\right)^{1/2}e^{-kd}\left(1+\frac{4n^2-1}{1!8kd}+\cdots\right),$$

we have the limiting form of (3.25) and (3.26) for $kd\to\infty$ $(k\ll 1)$ as

$$C_D^{(1)}=\frac{8\pi}{R}\frac{1}{S_1+\frac{1}{2}}, \quad C_L^{(1)}=0 \qquad (3.40)$$

which are the same in the case of a single circular cylinder.

(3.25) and (3.26) can be simplified in a few special cases, that is;

(i) $a=1$ (two circular cylinders of the same radius); $\alpha=90°$ (*cf.* Fig. 2a).

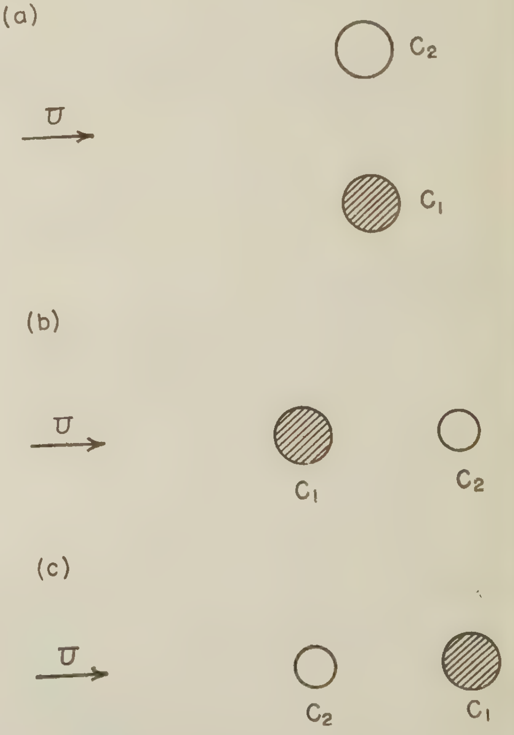

Fig. 2. Special configurations. (a) $a=1$, $\alpha=90°$; (b) $a\doteqdot 1$, $\alpha=0°$; (c) $a\doteqdot 1$, $\alpha=180°$. The drag and lift coefficients are concerned with the hatched cylinders.

$$C_D^{(1)}=\frac{8\pi}{R}\frac{S_1-\frac{1}{2}-K_0}{(S_1+\frac{1}{2}+K_0)(S_1-\frac{1}{2}-K_0)+\{K_1-(4/Rd)\}^2}\,, \qquad (3.41)$$

$$C_L^{(1)}=\frac{8\pi}{R}\frac{K_1-(4/Rd)}{(S_1+\frac{1}{2}+K_0)(S_1-\frac{1}{2}-K_0)+\{K_1-(4/Rd)\}^2}\,. \qquad (3.42)$$

(ii) $a\doteqdot 1$; $\alpha=0°$ (*cf.* Fig. 2b).

$$C_D^{(1)}=\frac{8\pi}{R}\frac{S_2+\frac{1}{2}-(K_0-K_1)e^{-(Rd/4)}-(4/Rd)}{(S_1+\frac{1}{2})(S_2+\frac{1}{2})-\{(K_0+K_1)e^{(Rd/4)}-(4/Rd)\}\{(K_0-K_1)e^{-(Rd/4)}+(4/Rd)\}}\,, \qquad (3.43)$$

and no lift.

(iii) $a\doteqdot 1$; $\alpha=180°$ (*cf.* Fig. 2c).

$$C_D^{(1)}=\frac{8\pi}{R}\frac{S_2+\frac{1}{2}-(K_0+K_1)e^{(Rd/4)}+(4/Rd)}{(S_1+\frac{1}{2})(S_2+\frac{1}{2})-\{(K_0+K_1)e^{(Rd/4)}-(4/Rd)\}\{(K_0-K_1)e^{-(Rd/4)}+(4/Rd)\}}\,, \qquad (3.44)$$

and no lift.

(iv) If $a=1$ and $k\ll kd\ll 1$, we can make use of (3.20) and (3.21) with respect to kd instead of k so that we have

$$C_D^{(1)}=\frac{8\pi}{R}\frac{2S_1-\frac{1}{2}-\ln d-\cos^2\alpha}{(2S_1+\frac{1}{2}-\ln d+\cos^2\alpha)(2S_1-\frac{1}{2}-\ln d-\cos^2\alpha)-\cos^2\alpha\sin^2\alpha}\,, \qquad (3.45)$$

$$C_L^{(1)}=-\frac{8\pi}{R}\frac{\cos\alpha\sin\alpha}{(2S_1+\frac{1}{2}-\ln d+\cos^2\alpha)(2S_1-\frac{1}{2}-\ln d-\cos^2\alpha)-\cos^2\alpha\sin^2\alpha}\,. \qquad (3.46)$$

Especially, for $\alpha=0°$, 90°, 180°, we have:

$$\alpha=90°; \qquad C_D^{(1)}=\frac{8\pi}{R}\frac{1}{2S_1+\frac{1}{2}-\ln d}\,, \qquad C_L^{(1)}=0\,, \qquad (3.47)$$

$$\alpha=0° \text{ and } 180°; \qquad C_D^{(1)}=\frac{8\pi}{R}\frac{1}{2S_1+\frac{3}{2}-\ln d}\,, \qquad C_L^{(1)}=0\,, \qquad (3.48)$$

which may also be obtained by expanding (3.41)–(3.44) in terms of kd.

If we are interested in the resultant drag X, lift Y and moment M of the system of the two circular cylinders with respect to the (geometrical) centre of gravity, we have

$$X=X_1+X_2\,, \qquad (3.49)$$

$$Y=Y_1+Y_2\,, \qquad (3.50)$$

$$M=d_1(X_1\sin\alpha-Y_1\cos\alpha)-d_2(X_2\sin\alpha-Y_2\cos\alpha)\,, \qquad (3.51)$$

where

$$d=d_1+d_2\,, \quad \frac{d_1}{d_2}=\frac{\pi a^2}{\pi}=a^2\,,$$

so that

$$d_1=\frac{a^2d}{1+a^2}\,, \qquad d_2=\frac{d}{1+a^2}\,. \qquad (3.52)$$

If we define the resultant drag, lift and moment coefficients of the system of the two circular cylinders as:

$$C_D=\frac{X}{\frac{1}{2}\rho U^2d}\,, \qquad (3.53)$$

$$C_L=\frac{Y}{\frac{1}{2}\rho U^2d}\,, \qquad (3.54)$$

$$C_M=\frac{M}{\frac{1}{2}\rho U^2 2d}\,, \qquad (3.55)$$

we can relate these resultant coefficients to those coefficients of each cylinders as follows:

$$C_D=\frac{2}{d}C_D^{(1)}+\frac{2a}{d}C_D^{(2)}\,, \qquad (3.56)$$

$$C_L=\frac{2}{d}C_L^{(1)}+\frac{2a}{d}C_L^{(2)}\,, \qquad (3.57)$$

$$C_M=\frac{a^2}{1+a^2}\{C_D^{(1)}\sin\alpha-C_L^{(1)}\cos\alpha-(1/a)(C_D^{(2)}\sin\alpha-C_L^{(2)}\cos\alpha)\}\,. \qquad (3.58)$$

In case when $a=1$, we have

$$C_D=\frac{2}{d}(C_D^{(1)}+C_D^{(2)})\,, \qquad (3.59)$$

$$C_L=\frac{2}{d}(C_L^{(1)}+C_L^{(2)})\,, \qquad (3.60)$$

$$C_M=\tfrac{1}{2}\{(C_D^{(1)}-C_D^{(2)})\sin\alpha-(C_L^{(1)}-C_L^{(2)})\cos\alpha\}. \qquad (3.61)$$

Since, in this case,

$C_D^{(2)}(\alpha)=C_D^{(1)}(\pi-\alpha),\ C_L^{(2)}(\alpha)=-C_L^{(1)}(\pi-\alpha),$

we have

$$C_D(\alpha)=C_D(\pi-\alpha)\ , \qquad (3.62)$$

$$C_L(\alpha)=-C_L(\pi-\alpha)\ , \qquad (3.63)$$

$$C_M(\alpha)=-C_M(\pi-\alpha)\ , \qquad (3.64)$$

that is, C_D is symmetric about $\alpha=\pi/2$, while C_L and C_M are antisymmetric about it.

§ 4. Numerical Discussions

Numerical calculations have been carried out for the cases: (i) $a=1$; $d=5$, 10, 20; $\alpha=0°$, 90°, 180°; $R=0.04$—1.0 by using (3.41)—(3.44), (ii) $a=1$; $d=5$; $\alpha=0°$—180°; $R=0.4$, 0.8 by using (3.25)—(3.39) and (3.59)—(3.61) and (iii) $a=0$—3.0; $d=10$; $\alpha=0°$, 90°, 180°; $R=0.4$, 0.8 by using (3.25)—(3.39), (3.41) and (3.42). They are shown in Figs. 5—7 and tabulated in Tables I—III.

Table I. Calculated values of $C_D^{(1)}$ and $C_L^{(1)}$ for various values of R.

(a) $a=1$; $d=5$

α	0°	90°		180°
R	$C_D^{(1)}$	$C_D^{(1)}$	$-C_L^{(1)}$	$-C_D^{(1)}$
0.04	72.742	75.316	6.146	61.766
0.08	44.631	45.044	5.980	34.168
0.2	25.026	24.106	5.698	15.457
0.4	17.092	15.860	5.481	8.322
0.6	14.014	12.744	5.419	5.685
0.8	12.336	11.049	5.468	4.247
1.0	11.285	9.956	5.622	3.297

(b) $a=1$; $d=10$

α	0°	90°		180°
R	$C_D^{(1)}$	$C_D^{(1)}$	$-C_L^{(1)}$	$C_D^{(1)}$
0.04	78.473	80.025	6.683	66.647
0.08	48.434	49.796	6.284	37.569
0.2	27.092	27.282	5.555	17.878
0.4	18.193	18.237	4.878	10.429
0.6	14.666	14.731	4.414	7.712
0.8	12.721	12.791	4.145	6.257
1.0	11.492	11.541	4.004	5.322

(c) $a=1$; $d=20$

α	0°	90°		180°
R	$C_D^{(1)}$	$C_D^{(1)}$	$-C_L^{(1)}$	$C_D^{(1)}$
0.04	85.776	89.835	8.153	70.845
0.08	53.282	55.273	7.229	40.889
0.2	29.569	30.612	5.563	20.216
0.4	19.423	20.240	4.039	12.378
0.6	15.411	16.074	3.188	9.487
0.8	13.226	13.761	2.692	7.932
1.0	11.859	12.294	2.413	6.942

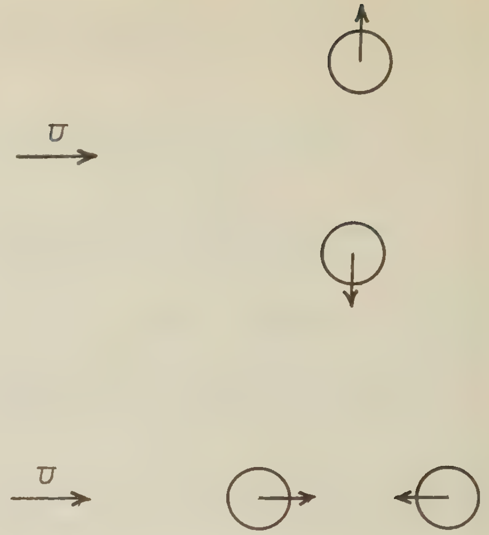

Fig. 3. The mutual interaction of the two circular cylinders in the case of a viscous fluid.

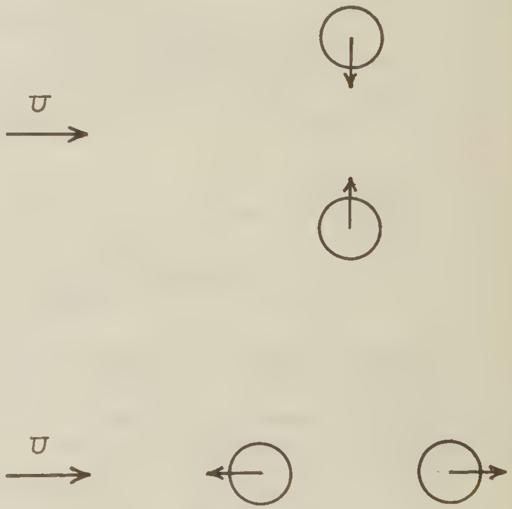

Fig. 4. The mutual interaction of the two circular cylinders in the case of an ideal fluid.

The qualitative results obtained from the numerical calculations are summarized as follows:

(1) The drag coefficient of the first cylinder is smaller than that for a single cylinder at the same Reynolds numbers. The greater or the nearer the second cylinder is, the smaller becomes the drag coefficient of the first cylinder (*cf.* Figs. 5 and 7).

(2) Comparing three cases when (i) the second cylinder is downstream of the first (*cf.*

Table II. Calculated values of $C_D^{(1)}$, $C_L^{(1)}$, $C_D^{(1)}+C_D^{(2)}$, $C_L^{(1)}+C_L^{(2)}$ and C_M for various values of α.

(a) $a=1$; $d=5$; $R=0.4$

α	$C_D^{(1)}$	$-C_L^{(1)}$	$C_D^{(1)}+C_D^{(2)}$	$-C_L^{(1)}-C_L^{(2)}$	C_M
0°	17.092	0	25.414	0	0
18°	16.786	1.669	26.240	2.723	1.425
36°	16.108	3.340	28.162	3.988	2.281
54°	15.582	4.850	30.090	3.506	2.255
72°	15.560	5.755	31.322	1.942	1.383
90°	15.860	5.481	31.720	0	0
108°	15.761	3.813	31.322	−1.942	−1.383
126°	14.508	1.344	30.090	−3.506	−2.255
144°	12.053	−0.648	28.162	−3.988	−2.281
162°	9.455	−1.054	26.240	−2.723	−1.425
180°	8.322	0	25.414	0	0

(b) $a=1$; $d=5$; $R=0.8$

α	$C_D^{(1)}$	$-C_L^{(1)}$	$C_D^{(1)}+C_D^{(2)}$	$-C_L^{(1)}-C_L^{(2)}$	C_M
0°	12.236	0	16.583	0	0
18°	12.018	1.523	17.515	2.514	1.260
36°	11.330	2.959	19.459	3.274	2.010
54°	10.751	4.304	21.100	2.407	1.985
72°	10.672	5.333	21.886	1.102	1.220
90°	11.049	5.468	22.097	0	0
108°	11.214	4.231	21.886	−1.102	−1.220
126°	10.350	1.898	21.100	−2.407	−1.985
144°	8.130	−0.316	19.459	−3.274	−2.010
162°	5.497	−0.991	17.515	−2.514	−1.260
180°	4.247	0	16.583	0	0

Fig. 2b), (ii) the central line is perpendicular to the uniform flow (*cf.* Fig. 2a), and (iii) the second cylinder is upstream of it (*cf.* Fig. 2c), it will be seen that the drag coefficient in the case (iii) is the smallest and those in the cases (i) and (ii) are almost of the same order (*cf.* Fig. 5). The former statement can be recognized by the fact that the first cylinder is in the wake of the second.

(3) The mutual interaction of the two cylinders is attractive when the central line is parallel to the uniform flow and is repulsive

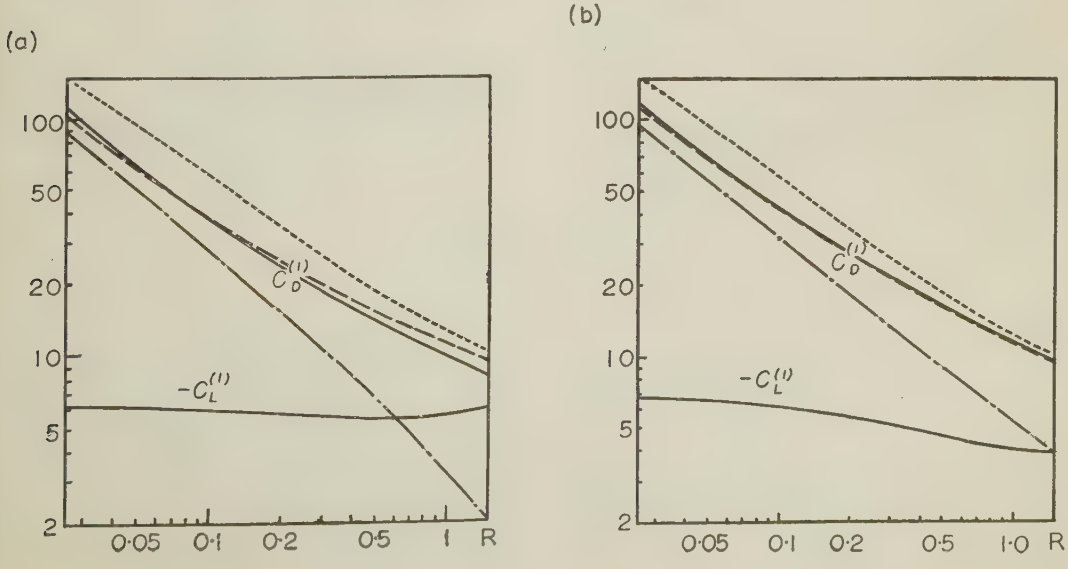

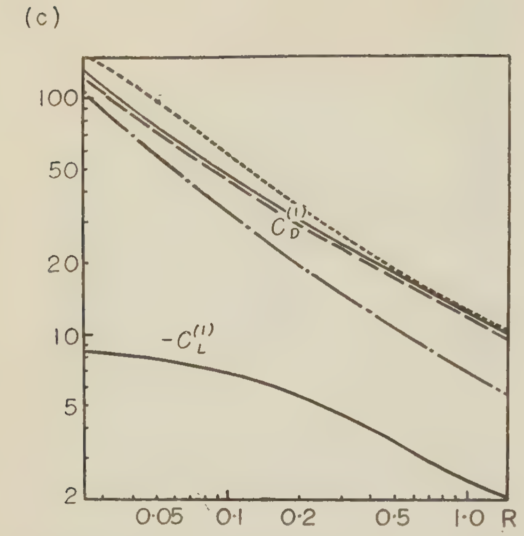

Fig. 5. $C_D^{(1)}$ and $C_L^{(1)}$ vs. R. (a) $a=1$, $d=5$; (b) $a=1$, $d=10$; (c) $a=1$, $d=20$.

— — — — $\alpha=0°$

———— $\alpha=90°$

—·—·— $\alpha=180°$

- - - - - - the drag of a single circular cylinder in a uniform flow.

Table III. Calculated values of $C_D^{(1)}$ and $C_L^{(1)}$ for various values of α.

(a) $d=10$; $R=0.4$

α	0°	90°		180°
a	$C_D^{(1)}$	$C_D^{(1)}$	$-C_L^{(1)}$	$C_D^{(1)}$
0	21.529	21.529	0	21.529
0.1	19.844	19.762	2.591	15.923
0.2	19.549	19.478	3.010	14.942
0.5	18.953	18.920	3.833	12.958
1.0	18.193	18.237	4.848	10.429
1.5	17.497	17.628	5.755	8.113
2.0	16.797	17.026	6.659	5.783
2.5	16.060	16.393	7.613	3.330
3.0	15.263	15.699	8.666	0.677

(b) $d=10$; $R=0.8$

α	0°	90°		180°
a	$C_D^{(1)}$	$C_D^{(1)}$	$-C_L^{(1)}$	$C_D^{(1)}$
0	14.117	14.117	0	14.117
0.1	13.483	13.553	2.026	10.544
0.2	13.358	13.438	2.392	9.843
0.5	13.092	13.182	3.146	8.343
1.0	12.721	12.792	4.145	6.257
1.5	12.347	12.333	5.118	4.150
2.0	11.932	11.692	6.201	1.811
2.5	11.445	10.594	7.576	−0.929
3.0	10.851	7.844	9.928	−4.274

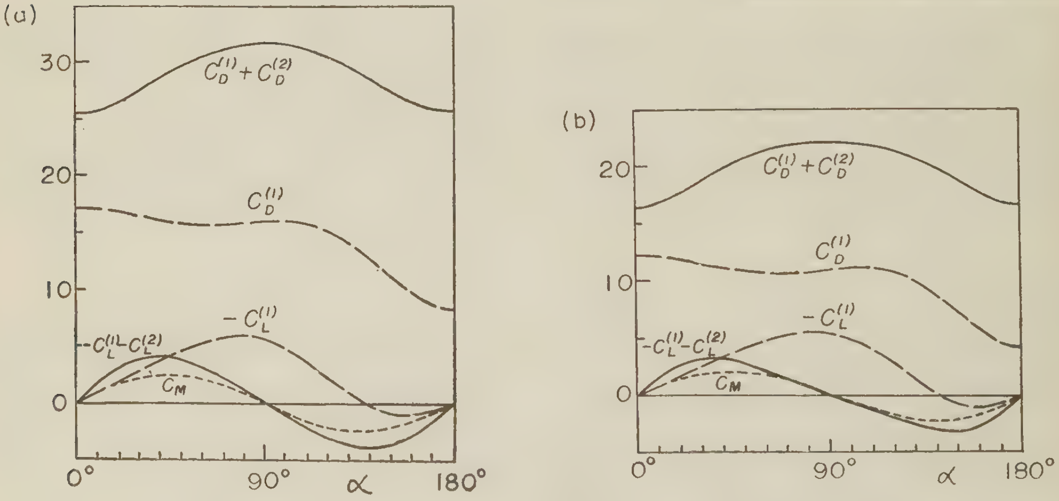

Fig. 6. $C_D^{(1)}$, $C_L^{(1)}$, $C_D^{(1)}+C_D^{(2)}$, $C_L^{(1)}+C_L^{(2)}$, and C_M vs. α. (a) $a=1$, $d=5$, $R=0.4$; (b) $a=1$, $d=5$, $R=0.8$.

when it is perpendicular (*cf.* Fig. 3).

These tendencies are opposite to the same cases of an ideal fluid (*cf.* Fig. 4).

(4) The force acting on the first cylinder is roughly in the direction of the flow induced when the second cylinder alone is placed in a uniform flow (*cf.* Fig. 6′).

(5) The resultant lift of the system of the two circular cylinders is positive (or negative) when α (the negative of the angle of attack) is negative (or positive). While, the resultant moment is negative or positive according as α is negative or positive, i. e., there is a tendency that the central line becomes perpendicular to the uniform flow (*cf.* Fig. 6).

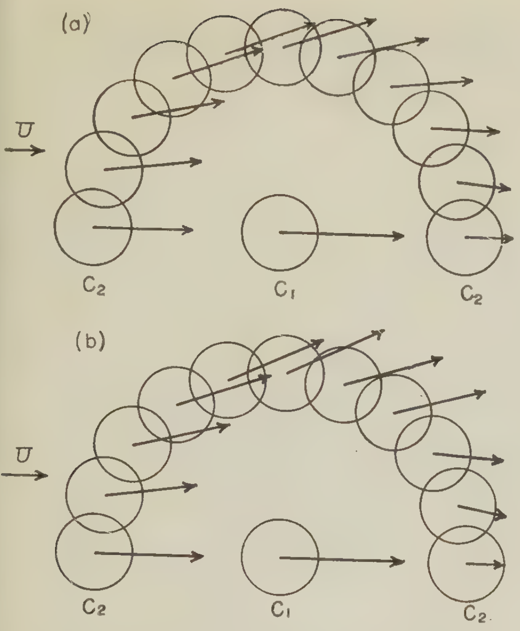

Fig. 6′. The force vectors experienced by C_2, compared with the drag in the case of a single cylinder which is shown on C_1. (a) $a=1$, $d=5$, $R=0.4$; (b) $a=1$, $d=5$, $R=0.8$.

Acknowledgement

The author wishes to express his sincere and profound thanks to Professor Isao Imai and Professor Takahiko Yamanouchi for their continual guidance and encouragement throughout this study. He is also indebted to Dr. Hidenori Hasimoto for his suggestion of this problem and detailed discussions and Dr. Mitutosi Kawaguti for his invaluable advice.

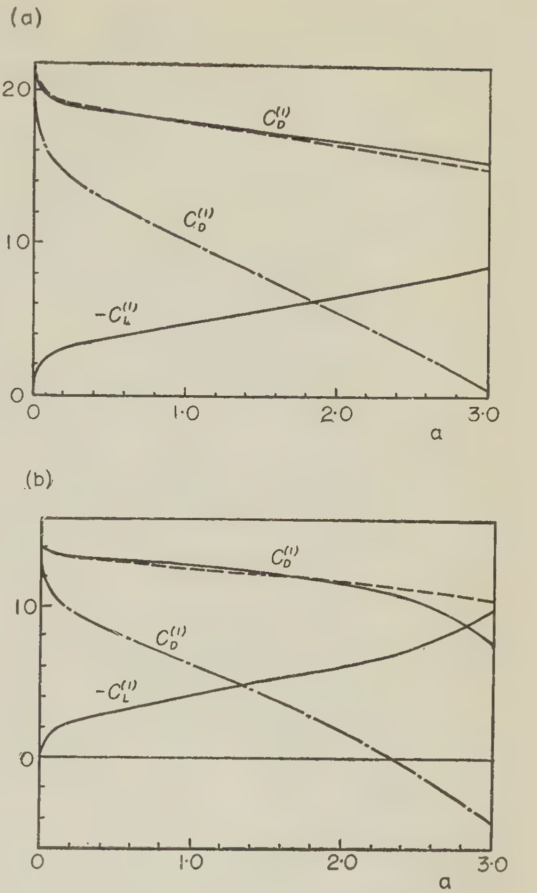

Fig. 7. $C_D^{(1)}$ and $C_L^{(1)}$ vs. a. (a) $d=10$, $R=0.4$; (b) $d=10$, $R=0.8$.

— — — — $\alpha=$ 0°
——— $\alpha=$ 90°
— - — - — $\alpha=$180°

References

1) I. Imai: Proc. Roy. Soc. A **224** (1954) 141.
2) I. Imai: Proc. Roy. Soc. A **208** (1951) 487.
3) S. Tomotika and T. Aoi: Quart. J. Mech. and Applied Math. **3** (1950) 140.
4) H. Fujikawa: J. Phys. Soc. Japan **11** (1956) 558.
5) H. Fujikawa: J. Phys. Soc. Japan **11** (1956) 690.
6) G. N. Watson: *Theory of Bessel Functions* (Cambr. Univ. Press, 1922).

JOURNAL OF THE PHYSICAL SOCIETY OF JAPAN Vol. 12, No. 3, MARCH, 1957

Theory of the Ultrasonic Absorption in Aqueous Solutions (II) Aqueous Solutions of Some Alcohols*

By Otohiko NOMOTO

Kobayasi Institute of Physical Research, Kokubunzi, Tokyo

(Received May 31, 1956)

Anomalous parts of the ultrasonic absorption coefficient have been calculated for aqueous solutions of methanol, ethanol and *n*-propanol as functions of the concentration by employing the result of the general theory described in part (I) of this paper (J. Phys. Soc. Japan **11** (1956) 827), which is based on the assumption that the pressure change of the sound wave accompanies a change in the existence ratio between the single and the associated molecules of water, that there takes place a molecular rearrangement among the single and the associated molecules of water and the solute molecules, accompanying changes in configurational entropy of the system, and that the irreversible entropy production takes place in the stage of energy transfer from the thermal motion to the configurational degree of freedom and vise versa. Calculations have been performed for two simplified model cases: (a) ignoring the difference in sizes of the single water molecule and the solute molecule, and (b) taking into account the difference in sizes of these molecules by approximating them by linear polymers each consisting of one kind of atoms. The value of the absorption peaks and the location of them have been found to be in semi-quantitative agreement with experiments, the agreement being somewhat better in case (b) as compared with (a).

§ 1. Introduction

Anomalous parts of the ultrasonic absorption coefficient are to be calculated in aqueous solutions of three sorts of alcohols (methanol, ethanol and *n*-propanol) by employing the result of the general theory developed in Part I (cited as (I) in the following) of this paper[1]. It becomes necessary for this purpose to estimate various quantities involved in theoretical formulas. These estimations are preformed in § 2 ~ § 5. By employing the values of the constants evaluated, we have calculated the values of the function f of the entropy of molecular rearrangement, apparent specific heat C_m, and the sound absorption coefficient (α/ν^2) as functions of the concentration. These calculations are executed in § 6~§ 8.

§ 2. Ratio Between the Numbers of Moles of the Associated and the Single Water-Molecules in Pure Water

According to Hall's theory[3] on ultrasonic absorption in pure water, the ratio between the number of moles of the associated water molecules n_{a0} and that of the single water molecules n_{s0} in pure water is given by

$$n_{s0}/n_{a0}=\exp(-\Delta F/RT) \qquad (2.1)$$

(cf. (I), eq. (3.5)), where ΔF means the difference in free energies (per mole) of the single and the associated molecules of water, R the universal gas constant and T the absolute temperature.

The value of ΔF is to be obtained from the expression given by Hall for the relaxational compressibility of pure water:

$$\beta_r=\beta_0-\beta_\infty=\frac{(v_a-v_s)^2}{2vRT\{1+\cosh(\Delta F/RT)\}}, \qquad (2.2)$$

where β_0 and β_∞ mean the static and the instantaneous compressibility respectively, v the molar volume and v_a and v_s the molar volumes of the associated and the single molecules of water respectively. This equation is easily to be obtained from (I), eq. (3.12).

Hall has estimated the value of ΔF to be 500 cal/mole. It depends, however, also on the temperature and on the assumed values of Δv and β_∞. Hall has determined the values of the constants so as to afford the ultrasonic absorption coefficients in agreement with experiment, the values at 20° being as follows:

---

* The text in Japanese of this paper will be published in "Bulletin of the Kobayasi Institute of Physical Research" somewhat in detail.

$$\left.\begin{array}{l}\beta_0=45.8\times10^{-12}\ \mathrm{cm^2/dyne}\ ,\\ \beta_\infty=(15\sim18)\times10^{-12}\quad\text{″}\quad ,\end{array}\right\}\begin{array}{l}\beta_r=(30.8\sim27.8)\\ \times10^{-12}\ \mathrm{cm^2/dyne};\end{array}$$

$$\left.\begin{array}{l}v_s=10.4\ \mathrm{cm^3}\ ,\\ v_a=18.0\sim19.6\ \mathrm{cm^3}\ ,\end{array}\right\}\ \Delta v=7.6\sim9.2\ \mathrm{cm^3}\ .$$

By employing various values for β_∞ and v_a, the values of ΔF were computed. These values are tabulated in Table I, together with the existence ratio

$$n_s/n_w=\frac{n_s}{n_a+n_s}=\frac{1}{1+\exp(\Delta F/RT)}\ . \qquad (2.3)$$

We have calculated the absorption coefficients corresponding to various values of the existence ratio tabulated, but adopted the value $n_s/n_w=0.175$ (the smallest one) for final calculation, because this gives the greatest absorption coefficients, i.e., the nearest to experimental results.

Table I. Difference in free energies per mole (ΔF) between the single and the associated molecules of water, and the existence ratio n_s/n_w of the single molecules as functions of v_a and β_∞ (20°C).

	$v_a=18.0\mathrm{cm^3}$		$v_a=18.8\mathrm{cm^3}$		$v_a=19.6\mathrm{cm^3}$	
β_∞	ΔF cal/mole	n_s/n_w	ΔF cal/mole	n_s/n_w	ΔF cal/mole	n_s/n_w
15×10^{-12}	296	0.376	613	0.259	808	0.200
16.5 ″	397	0.336	671	0.241	856	0.187
18 ″	482	0.305	728	0.223	904	0.175

Hall has assumed the associated molecules of water to be in a state of lower free energy, while the single molecules are in a state of higher free energy. On the contrary, Litovitz and Carnevale[4)] have recently deduced from the pressure dependence of the ultrasonic absorption in pure water that the associated molecules are in the state of higher free energy and the single molecules are of lower free energy. If we adopt this latter view, the existence ratio of $n_s:n_a$ becomes reversed and we have $n_s/n_w=0.825\sim0.624$. For example, $n_s/n_w=0.759$ for average value of β_∞ and that of v_a. This however, gives an absorption maximum only about 1/3 the experimental value for the ethanol-water mixture, when the magnitude of the associated molecule is so assumed as to give a relaxation time in agreement with the experiment. Also the estimation of n_s/n_a from the molar volumes of water, solute and the solutions deviates widely from the estimation from Litovitz-Carnevale's theory. The existing various estimations are not in accord with this, too.

So we have assumed, after Hall, the single water molecules to be in a state of higher free energy and the associated molecules to be of lower free energy, and adopted the following values of the parameters (at 20°C) in the following:

$$\left.\begin{array}{l}v_s=10.4\ \mathrm{cm^3}\ ,\\ v_a=19.6\ \mathrm{cm^3}\ ,\end{array}\right\}\ \Delta v=9.2\ \mathrm{cm^3}; \qquad (2.4)$$

$$\Delta F=904\ \mathrm{cal/mole}\ , \qquad (2.5)$$

and

$$n_{s0}/n_{w0}=0.175\ , \qquad n_{a0}/n_{w0}=0.825\ , \qquad (2.6)$$

where the suffix zero indicates the values at zero concentration of the solvent, i.e., the values for pure water.

§ 3. Concentration Dependence of the Number of Moles of the Associated Water-Molecules in Solvent Water

The number of moles of the associated water-molecules in aqueous solutions is to be estimated from the concentration dependence of the adiabatic compressibility in aqueous solutions. The procedure was described elsewhere (Nomoto[2)]) and we will employ the result in the following. The number of moles of the associated water-molecules (n_a) and that of the single water-molecules (n_s) in one mole of the aqueous solutions, of methanol, ethanol and n-propanol are represented as functions of the concentration (molar fraction of the solute n_F) in Fig. 1. As is to be seen in the figure, the value of n_a in aqueous methanol solution decreases monotonously with increasing concentration, while in ethanol-solution the decrease of n_a with increasing n_F becomes slow in the intermediate concentration, and the n-propanol solution shows even a slight minimum and a nearly flat region in the curve of n_a.

Although it may be supposed from these curves that the slowing down of the reduction of n_a in aqueous solutions of ethanol and n-propanol with increasing concentration may be due to the mutual association between water and alcohols, this idea must be rejected because the absorption curves, and especially, the relative heights of the absorption peaks and the concentrations for the absorption peaks, widely deviates from experiments if this view is adopted.

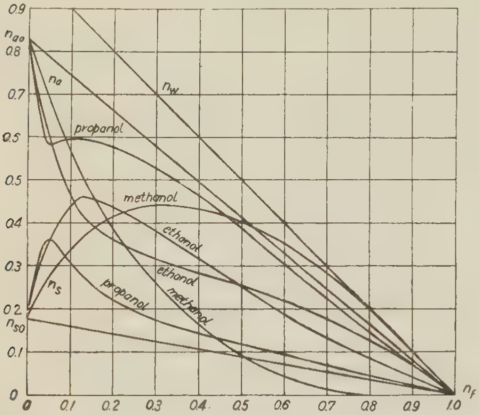

Fig. 1. Number of moles of the associated water-molecules (n_A) and that of the single water-molecules (n_s) in aqueous solutions of methanol, ethanol and n-propanol as functions of the concentration (20°C).

§ 4. Physical Constants of the Aqueous Alcohol Solutions

All calculations were performed for 20°C.

(a) density ρ

Jacobson's data[5] were employed for the values of the density. The values of the density are represented in Fig. 2 for the three alcohol solutions here considered as functions of the concentration.

As the data of Jacobson, however, are represented as functions of the volume fraction ϕ (ratio between the volumes of the solute and the solution), we have to transform the volume fractian into molar fraction. First we obtain the weight fraction p by

$$p=\phi\rho_2/\rho\ , \tag{4.1}$$

where ρ_2 means the density of the solute and ρ the density of the solution, and then obtain the molar fraction n_F by

$$n_F=m_F/(m_w+m_F)\ , \tag{4.2}$$

where

$$m_w=(1-p)/M_w;\quad m_F=p/M_F\ . \tag{4.3}$$

Here M_w and M_F mean the molecular weight of water and that of the solute respectively.

(b) thermal expansion coefficient ϑ

This was computed from the density data of ICT (=International Critical Tables) and also shown in Fig. 2. As is to be seen in the figure, the methanol solution shows an irregular behaviour with respect to the thermal expansion coefficient, and it seems that the smoothed values indicated by arrows are the more reliable ones. Also the computed values of γ and c_v become irregular by this effect, although the influence on the values of C_m, c_p and (α/ν^2) are not large, being masked by other irregularities due to the estimation of n_a, n_s, etc.

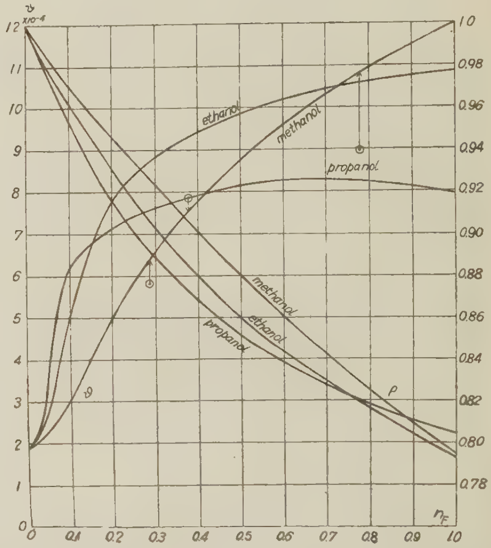

Fig. 2. Density and the thermal expansion coefficient in aqueous alcohol solutions in dependence on the concentration (20°C).

(c) sound velocity V

Jacobson's data were employed.

(d) specific heat at constant pressure c_p **and the ratio of the specific heats** γ

c_p was obtained from ICT by interpolation. Fig. 3 shows the concentration dependence of c_p and γ. The interpolation, however, is presumably not so exact because of the non-monotonous variation of c_p with temperature, c_p at lower concentration having a maximum at a certain temperature. C_p involved in the absorption formulars (I), (6.7) and (6.8) mean the molar specific heat at constant pressure, given by

$$C_p=Mc_p\ , \tag{4.4}$$

where M means the average molecular weight of the solution given by

$$M=(1-n_F)M_w+n_FM_F\ . \tag{4.5}$$

The ratio of the specific heats γ is to be calculated by (I), (5.8) from the known values of V, ϑ and c_p. Then we have c_v from c_p and γ. The values of γ are also shown in Fig. 3. As is to be seen, the calculated values of γ in methanol-solutions are scatterd by the influence of the scattered values of ϑ.

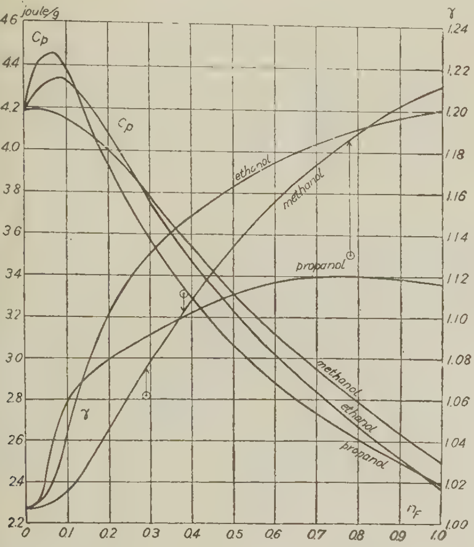

Fig. 3. The values of c_p and γ in aqueous solutions of methanol, ethanol and n-propanol as functions of concentration (20°C).

(e) **diffusion coefficient D**

The values of the diffusion coefficient are not so well investigated. Concerning the three alcohol solutions here considered, ICT gives the concentration dependence of D only for the ethanol solution at 10°C. The tabulated values are as follows (with indicated errors ±10%):

c (mole)	3.75	0.75	0.25	0.05	(0)
D (in 10^{-5} cgs)	0.50	0.70	0.78	0.83	($D_0=0.87$)

The value at zero (=infinitesimal) concentration D_0 was obtained here by extrapolation. By reducing the molarity c into the weight fraction by

$$p=M_F c/1000\rho\ , \qquad (4.6)$$

and then transforming p into the molar fraction n_F by (4.2) and (4.3), we can obtain the concentration dependence of D as indicated in Fig. 4, where D/D_0 is represented *vs.* n_F. Although this corresponds to the ethanol solution at 10°C, we have assumed that this curve is also valid for the aqueous solutions of methanol, ethanol and n-propanol at 20°C.

Now the ICT gives the diffusion coefficient at zero (=infinitesimal) concentration for the aqueous solutions of three sorts of alcohols at 15°C. This is reproduced in the third column of Table II (accuracy ±7%).

Table II. Diffusion coefficient at zero concentration (D_0 in 10^{-5} cgs) for aqueous alcohol solutions.

Solute	10° (extrapolated)	15° (ICT)	20° (estimated) (a)	20° (estimated) (b)
methanol		1.28	1.47	1.46
enthanol	(0.87)	1.00	1.16	1.14
n-propanol		0.87	1.01	0.99

Two estimations were made from this for the values of D_0 at 20°C. In the first place, if we assume the theoretical formula

$$D=kT/6\pi\eta a\ , \qquad (4.7)$$

where η means the viscosity coefficient of the solvent, a the molecular radius of the solute, and k the Boltzmann constant, we have $D\infty T/\eta$. This gives the values tabulated in column (a). In the second place, if we make graphical extrapolation from the extrapolated value of D_0 at 10° (for ethanol solution) and the ICT value at 15°, we obtain column (b). As both estimations are nearly in accord, we employed the results of (b) in the following. The diffusion coefficients at any concentration were obtained by multiplying this value by D/D_0 obtained from Fig. 4.

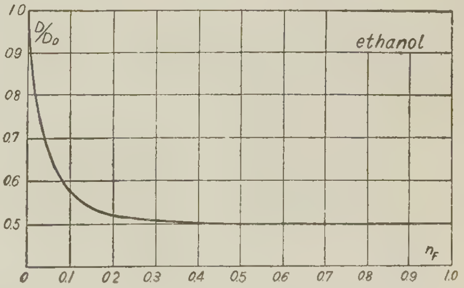

Fig. 4. Concentration dependence of the diffusion coefficient in aqueous ethanol solutions (10°C).

§ 5. Concentration Dependence of the Size of the Associated Molecules of Water in Aqueous Solutions

The only parameter in our theory to be determined directly from acoustic absorption experiment is the size of the associated water-molecules in aqueous solutions. This is to be estimated from the relaxation time by the relation, $\tau=0.783r^2/D$ (cf. (I) (7.14)), where D means the diffusion coefficient and r the radius of the groups of single water molecules produced under excess pressure by the collapse of the associated molecules. This radius is given by $r=s(3v_s/4\pi N_L)^{1/3}$ (cf. (I) (7.27)), where N_L means the Loschmidt number and s the ratio between the radius of the associated water molecules and the effective radius of the monomers constituting the associated molecules.

By employing the value of (2.4) for v_s, we have

$$r=s\times1.60\times10^{-8}\,\mathrm{cm} \qquad (5.1)$$

and accordingly

$$\tau=2.005\times10^{-16}\,\mathrm{cm}^2\,s^2/D\,. \qquad (5.2)$$

The relaxation frequencies are known experimentally in the neighbourhood of the absorption maximum for aqueous solutions of ethanol, n-propanol and phenol, as cited in (I), (1.2), (1.3) and (1.4). In the first place, we have for aqueous ethanol solution from Storey's measurements (cf. (I), (1.2)) by interpolation:

$$\nu_m=137\,\mathrm{Mc/sec} \quad \text{at } 20°\mathrm{C},\ 25\%\ (n_F)\,,$$

and accordingly by

$$\tau=1/2\pi\nu_m \qquad (5.3)$$

the experimental value of the relaxation time:

$$\tau_{\mathrm{exp}}=1.16\times10^{-9}\,\mathrm{sec}$$
$$\text{(ethanol solution, } 20°\mathrm{C},\ n_F=0.25) \qquad (5.4)$$

Then we have from Sette's absorption data at 24.5°C and 13.9% (n_F) the relaxation frequency $\nu_m=53.6$ Mc (cf. (I), (1.3)), for propanol-solution, and this gives $\tau=2.85\times10^{-9}$ sec (24.5°C). The value of τ at 20° was estimated from this by employing (5.2) and assuming the diffusion coefficient D to be proportional to T/η and ignoring the temperature dependence of s. This was calculated to be

$$\tau_{\mathrm{exp}}=3.23\times10^{-9}\,\mathrm{sec}$$
$$(n\text{-propanol solution, } 20°\mathrm{C},\ n_F=0.13 \qquad (5.5)$$

Finally, we have from Cevolani and Petralia's absorption data at 70°C for aqueous phenol solutions $\nu_m=35$ Mc (cf. (I), (1.4)). This gives

$$\tau=4.55\times10^{-9}\,\mathrm{sec}\ (70°\mathrm{C})\,.$$

Correcting for the temperature dependence of D, but not for s as before, we have from this

$$(\tau^*_{\mathrm{exp}}=13.2\times10^{-9}\,\mathrm{sec}) \quad \text{(hypothetical phenol solution, } 20°\mathrm{C},\ n_F=0.06) \qquad (5.6)$$

Then the values of s were calculated by (5.2) corresponding to these values of τ_{exp} at 20°C, and found to be

$$\left.\begin{array}{ll} s=5.92 & \text{(ethanol solution, } n_F=0.25)\,. \\ s=9.36 & (n\text{-propanol solution, } n_F=0.13)\,, \\ (s^*=19.1) & \text{(hypothetical phenol solution,} \\ & \qquad n_F=0.06) \end{array}\right\} \qquad (5.7)$$

The phenol solution, however, is known to separate into two phases below the critical mixing temperature at about 68°C, and there is no solution of the concentration $n_F=0.06$ at 20°C. So the values with asterisks are only extrapolated values corresponding to hypothetical solution. (The value of s^* was computed by employing $D_0=0.84$ (at 20°C) and assuming $D=(2/3)D_0$ at $n_F=0.06$.)

Also the mechanism of sound absorption may be somewhat different for critical mixtures. The mechanism is certainly different for non-aqueous mixtures near the critical point, the cluster formation playing an important role in this case. The mechanism, however, may not be so widely different for aqueous critical mixtures, from that for ordinary aqueous solutions. These points must be investigated in a separate research. Here we assumed the mechanism of the excess sound absorption in aqueous phenol solution near the critical solution temperature to be the same as in ordinary aqueous solutions.

Although it is not clear as yet what are the quantities which determine the seize (s) of the associated water molecules, it is to be seen from the above result that s decreases rapidly with increasing value of n_F. As we have no sufficient data to investigate the dependency of s on concentration in each of the aqueous solutions, we have assumed s to be a function of n_a, but not dependent on other quantities, and obtained the relation as indicated in Fig. 5. As the data for phenol solution is not exact, we assumed the curve a rather arbitrarily. The curve connecting ethanol and n-propanol gives straight line b. Here we adopted the curve a for further calculations because the experimental absorption curves at different frequencies seem to indicate that the concentration dependence of the relaxation time is only slight, at least in the neighbourhood of the absorption peak. The coincidence of the calculated absorption curves with experiments is also better for curve *a* than for curve *b*.

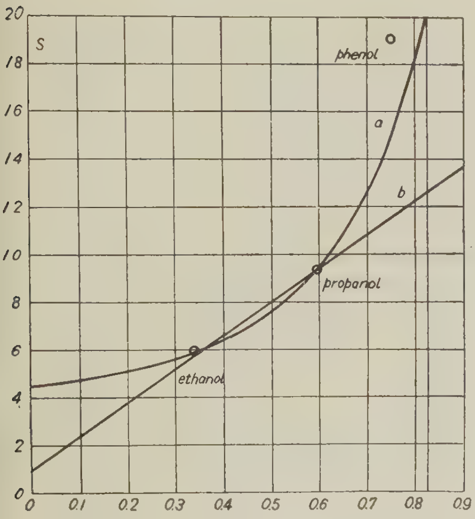

Fig. 5. Relation between s, the quantity proportional to the radius of the associated water molecules in aqueous solutions, and the molar fraction of the associated molecules (20°C).

As is to be seen in the figure, the value of s for pure water is comparatively large, becoming

$$s_0=20 \tag{5.8}$$

n case of curve *a*. Accordingly, the number of monomers constituting an associated molecule becomes

$$Z=8000 \tag{5.9}$$

by (I) (7.15).

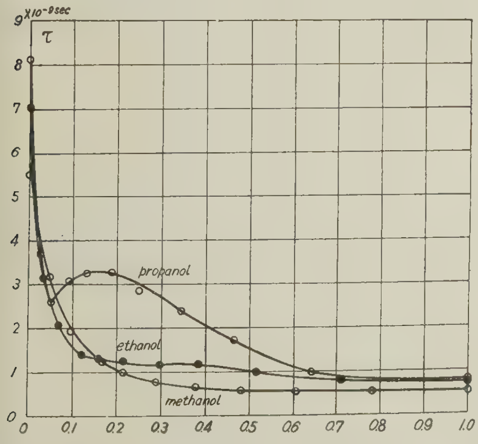

Fig. 6. Relaxation time of the molecular rearrangement in aqueous solutions of methanol, ethanol and n-propanol as functions of the concentration (20°C).

In order that a molecular diffusion may take place, it is necessary that the diameter ($2r$) of the groups of single water molecules produced by the sudden collapse of the associated water molecules under excess pressure are larger than the mean distance of the solute molecules in the solution (l_F), i.e.,

$$l_F<2r \tag{5.10}$$

This, condition, however, is always satisfied except at extremely low concentrations.

Fig. 6 shows the values of the relaxation time as functions of the concentration, calculated by (5.2) for the three sorts of alcohol solutions here considered.

§ 6. Entropy Change Due to the Molecular Rearrangement (Functions *f* and *f**)

Now we have all the quantities required to calculate the function $f=T\Delta S/\Delta p$ (cf. (I), (4.6)) proportional to the entropy change of the molecular rearrangement. In case when the difference in seizes of the various kinds of molecules are ignored, this function is given by (I), (4.7), i.e.,

$$f=\frac{(v_a-v_s)n_a\log(1+n_F/n_s)}{\{1+\exp(\Delta F/RT)\}} \tag{6.1}$$

Fig. 7 shown the values of f as functions of n_F for the three sorts of alcohol solutions here considered.

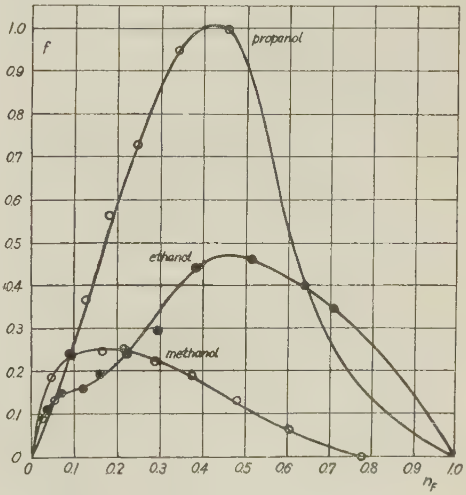

Fig. 7. Entropy function f in aqueous solutions of methanol, ethanol and n-propanol as functions of the concentration (20°C).

In case the effect of the difference in magnitudes of the molecules are taken into account, by regarding the single molecule of water and the solute molecule as linear polymers, each consisting of one kind of atoms, the entropy function becomes f^* given by (I), (4.13),

There may be problems as to the number of the nearest neighbours z surrounding an atom in an aqueous alcohol solutions. The number, however, cannot exceed 12. The number z may be also dependent on the kind of the atoms, and there are reasons to suppose that z is presmuably far smaller than 12 for carbon atoms in alcohol molecules. The increment of the configurational entropy ΔS, however, is not so largely dependent on the value of z, increasing slightly with increase in z. So we assumed

$$z=12 \tag{6.2}$$

in this calculation. The calculation gives, therefore, the upper limit of the entropy change under this liquid model.

The values of the constants r_s, q_s and r_F, q_F in eq. (I) (4.13), become by (I) (4.9) and (4.10) as follows:

$$\left.\begin{array}{lll} \text{water:} & r_s=3\,, & q_s=8/3; \\ \text{methanol:} & r_F=6\,, & q_F=31/6; \\ \text{ethanol:} & r_F=9\,, & q_F=23/3; \\ n\text{-propanol:} & r_F=12\,, & q_F=61/6. \end{array}\right\} \tag{6.3}$$

Here r_s and r_F mean the number of atoms constituting the molecules. By employing these values we obtain from (I) (4.13) the following expressions of the entropy function for the aqueous solutions.

methanol solution:

$$f^*=\frac{(v_a-v_s)n_a}{1+\exp(\Delta F/RT)}\left\{16\log\left(1+\frac{31}{16}\frac{n_F}{n_s}\right)-15\log\left(1+2\frac{n_F}{n_s}\right)\right\} \tag{6.4}$$

ethanol solution:

$$f^*=\frac{(v_a-v_s)n_a}{1+\exp(\Delta F/RT)}\left\{16\log\left(1+\frac{23}{8}\frac{n_F}{n_s}\right)-15\log\left(1+3\frac{n_F}{n_s}\right)\right\} \tag{6.5}$$

n-propanol solution:

$$f^*=\frac{(v_a-v_s)n_a}{1+\exp(\Delta F/RT)}\left\{16\log\left(1+\frac{61}{16}\frac{n_F}{n_s}\right)-15\log\left(1+4\frac{n_F}{n_s}\right)\right\}\,. \tag{6.6}$$

§7. Apparent Specific Heat Due to Molecular Rearrangement C_m

Once f is known, we can calculate C_m by (I), (5.9), i.e.,

$$C_m=\rho c_p f/T\vartheta\,. \tag{7.1}$$

Fig. 8 shows the values of C_m as functions of the concentration, for the three alcohol solutions here considered. The dependence of C_m on concentrations is widely different according to the kinds of the alcohols, methanol solution exhibiting higher values of C_m at low concentration as compared to other solutions.

In case the difference in sizes of the molecules are taken into account we have

$$C_m^*=\rho c_p f^*/T\vartheta\,. \qquad (7.2$$

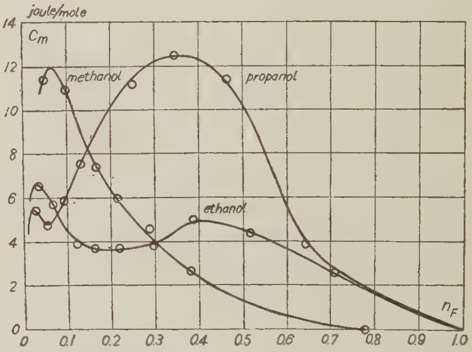

Fig. 8. Relaxational specific heat C_m due to the molecular rearrangement in aqueous solutions of methanol, ethanol and propanol in dependence on the concentration (20°C).

§8. Ultrasonic Absorption Coefficient

The ultrasonic absorption coefficient at sufficiently low frequency is to be calculated by (I), (6.7), i.e.,

$$\left(\frac{\alpha}{\nu^2}\right)_0=\frac{2\pi^2\rho\vartheta V}{C_p}\frac{C_v}{C_v-C_m}f\tau\,. \tag{8.1}$$

In case we take into account the difference in seizes of the molecules, we have to replace f with f^* and C_m with C_m^*. The corresponding value of α is to be written as α^*. The relaxation time being of the order of 10^{-9} sec, the equation (8.1) holds true within an error of 1% up to about 20 Mc/sec.

Fig. 9 shows the values of $(\alpha/\nu^2)_0$ for the three sorts of alcohol solutions here considered, and Fig. 10 shows $(\alpha^*/\nu^2)_0$. Table III summarizes the experimental and the theoretical results concerning the height and location of the absorption peaks.

Table III. Experimental and theoretical values of the height and location of the ultrasonic adsorption peaks in aqueous alcohol solutions.

Solute		methanol		ethanol		n-propanol	
		n_F	$(\alpha/\nu^2)_0$ (in 10^{-17})	n_F	$(\alpha/\nu^2)_0$ (in 10^{-17})	n_F	$(\alpha/\nu^2)_0$ (in 10^{-17})
Experiments	25∼27°C	(—)	(—)	0.27	190	0.14	960
	−10°C	0.3	110	—			
Calculation 20°C							
(a) point molecules		0.05	60	0.39	125	0.28	435
(b) linear polymer molecules		0.05	85	0.38	155	0.27	640

As seen in the table, the theoretical result is in qualitative agreement with the experiments. The tendency that the absorption peak increases in height with increase in seize of the solute molecules, is in agreement with experiment. The values of the absorption peaks, however, are not in agreement with the observed ones, being about half the experimental value for propanol solution, 2/3 for ethanol solution and somewhat heigher for methanol solution, in case of Fig. 9 (calculation (a)). Also the positions of the absorption maxima are somewhat displaced, the calculated absorption peaks being located at somewhat higher alcohol concentrations than observed ones in case of n-propanol and ethanol solutions, and at lower concentration for methanol solution. In case of Fig. 10 (calculation (b)) the agreement with experiment is somewhat improved, especially concerning the height of the absorption peaks, though the location of the absorption peaks remains nearly the same.

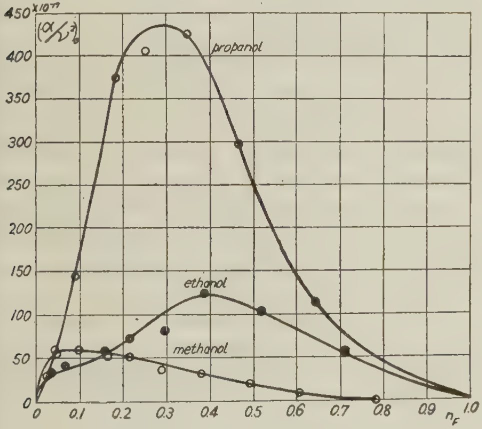

Fig. 9. Absorption curve of sound for aqueous solutions of methanol, ethanol and n-propanol (20°C).

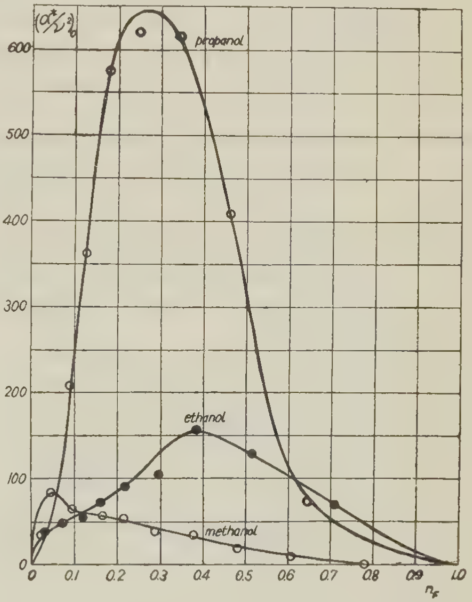

Fig. 10. Absorption curve of sound for aqueous solutions of methanol, ethanol and n-propanol (20°C). Calculation by taking into account the effect of the difference in magnitudes of the molecules.

This work was Financially assisted by the Grant for Sciencific Research of the Ministry of Education for the 1954 fiscal year.

References

1) O. Nomoto: J. Phys. Soc. Japan **11** (1956) 827.
2) O. Nomoto: J. Phys. Soc. Japan **11** (1956) 1146.
3) L. L. Hall: Phys. Rev. **73** (1948) 775.
4) T. A. Litovitz and E. H. Carnevale: J. Appl. Phys. **26** (1955) 816.
5) B. Jacobson: Arkiv for Kemi **2** (1950) 177.

Short Notes

This section is intended to secure prompt publication of important discoveries in physics. The reports should not exceed 800 words in length. A figure of size 7 cm × 7 cm will be counted as 150 words.

J. PHYS. SOC. JAPAN **12** (1957) 308

An Empirical Regularity of Energy Gap in Semiconductors

By Takeshi MIYAUCHI

Junior College of Engineering, University of Osaka Prefecture, Neyagawa, near Osaka

(Received January 8, 1957)

Fundamental properties of a semiconductor that determine its characteristics are width of energy gap and mobilities of electrons and holes. If their regularities could be known, these would be very useful and convenient to the study of semiconductors, specially, in the field of their applications. According to Goodman¹⁾, the energy gap of the compound with the zincblende structure increases with the increase in melting point and also with the increase in electronegativity difference between elements. However, this method has numerous exceptions in practice. For example, the melting point of GaSb (720°C) is lower than of InAs (936°C), but the gap of the former (0.8 ev) is greater than of the latter (0.47 ev).

In this paper, a trial will also be made for this purpose. The method is almost empirical as follows. A ratio (r_1/r_2) is dopted, where r_1 is half of the distance between the neighbouring elements in the crystal lattice and r_2 is average of the positive ionic radii of elements. For example, in the case of InSb, the distance between neighbours is 2.80A, the ionic raddii are: In^{+3} 0.81A, Sb^{+5} 0.62A, and therefore the ratio (r_1/r_2) becomes 1.96. When we examine dependence of the energy gap to this ratio, an unexpected simple relation results.

The results for several groups of compounds are shown in Fig. 1, where values of ionic radii are those by Pauling²⁾. The relation is satisfactorily linear, if it is taken into consideration that the values of gaps used in the figure are gathered from many literatures³⁾ and that they show small differences even in the similar measuring methods. Besides, they have temperature coefficients of the order of -10^{-4} to -10^{-3} ev/deg. It is interesting to get such a simple regularity although the physical reason is not known to the author.

In the figure, Si deviates from Sn-Ge line. A similar phenomenon also occurs in the case of Mg_2Si of the antifluorite lattice type group. This may be due to a chemical peculiarity of silicon. This method essentially involves that in the same group the band structures, as well as chemical properties, have resemblances to each other, and it may be desirable that the deviation is associated with their considerable variation. In fact, some workers⁴⁾ have pointed out remarked differences between band structures of germanium and silicon.

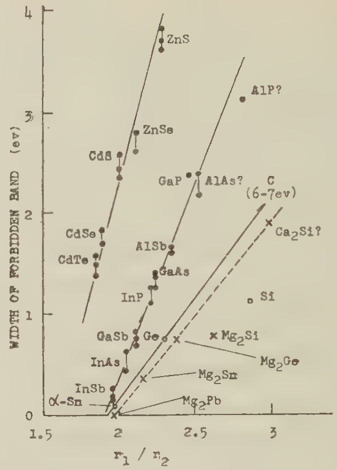

Fig. 1. Energy gap vs r_1/r_2. Dots, zincblende type; circles, diamond type; crosses, antifluorite type.

As to the zincblende type family including the diamond type the slope of the curve increases and the curve shifts to the left from the Group IV elements through the $A^{III}B^{V}$ group to the $A^{II}B^{VI}$ group with the increasing ionic character of bonding, corresponding to the electronegativity difference between elements mentioned by Goodman.

The utility of this regularity is to presume the energy gaps for several compounds, whose properties are unknown or uncertain. It seems that this method can be applied to other groups of compounds, but no systematic study in this field has been carried out up to now.

References

1) C. H. L. Goodman: Proc. Phys. Soc. **67B** (1954) 258.
2) L. Pauling: The Nature of the Chemical Bond.
3) Y. Kanai: Syposium on Intermetallic Compounds, Annual Meeting of Phys. Soc. Japan, Oct. 1955, etc.
4) E. R. Johnson and S. M. Christian: Phys. Rev. **95** (1954) 560; F. Herman: Phys. Rev. **95** (1954) 847; etc.

J. PHYS. SOC. JAPAN **12** (1957) 309

Nuclear Magnetic Resonance in Solid Solutions of Transition Metals in Copper and Aluminum

By Tadashi SUGAWARA

The Research Institute for Iron, Steel and Other Metals, Tohoku University, Sendai, Japan

It is known that the magnetic properties of the dilute solide solutions of transition metals in non-transition metals can be interpreted in terms of the localized 3d-state picture of the solute atoms[1]. When the localized $3d$-electrons have unpaired spins, the nuclear magnetic resonance absorption of the solvent nucleus will have the following characteristics. (1) *The line width.* At low temperatures each nucleus will be subjected to a local field arising from the magnetization of the solute atoms which is given by[2]

$$H_{\mathrm{loc}}=\sum_k g_k{}^2\mu_\beta{}^2 H_0 \frac{S_k(S_k-1)}{3k(T-\Theta)}(1-3\cos^2\theta_{ik})r_{ik}{}^{-3}\,. \tag{1}$$

The line shape and the width will be determined by the distribution of the local field. (2) *The Knight shift.* The Knight shift of the alloy will be expressed by

$$(\delta H/H)_l=(\chi_l/\chi_0)(\delta H/H)_0\,, \tag{2}$$

where χ_l is the spin susceptibility of conduction electrons in the alloy, χ_0 and $(\delta H/H)_0$ is the spin susceptibility and the Knight shift of the pure metal. (3) *The spin-lattice relaxation time.* The relaxation time T_1 will be given by

$$1/T_1=(1/T)_{ce}+(1/T_1)_S\,, \tag{3}$$

where $(1/T_1)_{ce}$ and $(1/T_1)_S$ are the contributions arising from the interaction of the nuclear spins with the conduction electron spins and with the localized $3d$-spins, respectively. Explicit expression for $(1/T_1)_S$ is given by Bloembergen[2].

The experiments were made on fine powders of Cu-Mn, Al-Mn, Cu-Fe and Cu-Ni at frequencies of about 8 Mc/sec. Variations of the line width, the Knight shift and T_1 with temperature are shown in Figs. 1, 2 and 3. The line widths in Cu-Fe and Cu-Mn showed the behavior expected from eq. (1). Temperature dependence of the Knight shift of Cu-Mn seems to support the prediction made by Owen et al[3]. T_1 at helium temperatures in Cu-Mn was smaller than that of pure Cu, showing the effect considered above. In Al-Mn, the width, the shift and T_1 did not show appreciable changes as compared with Al. T_1 in Cu-Ni with 1.5. and 3.5% Ni could not be determined owing to the anomalous saturation behaviors of these alloys, though T_1 in 0.07% alloy was the same as that of pure Cu.

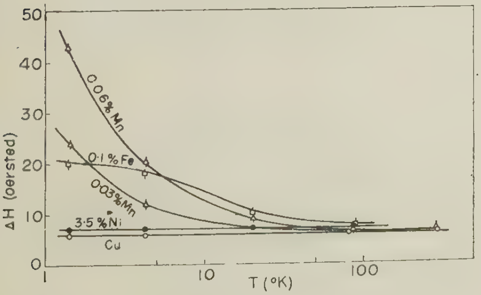

Fig. 1. The line width of Cu^{63} resonance in Cu-Mn, Cu-Fe, Cu-Ni and Cu.

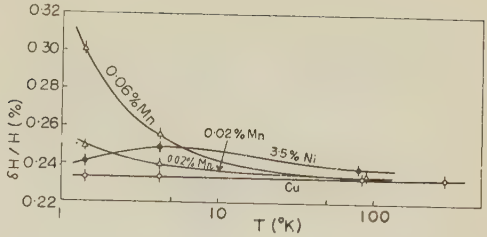

Fig, 2. The Knight shift of Cu^{63} resonance in Cu-Mn, Cu-Ni and Cu.

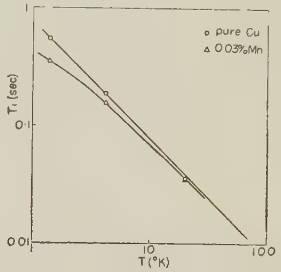

Fig. 3. The spin-lattice relaxation time of Cu^{63} in Cu-Mn and Cu.

References

1) W. Hume-Rothery and B. R. Coles: Adv. in Phys. **3** (1954) 149.
2) N. Bloembergen: Physica **15** (1949) 386.
3) J. Owen, M. Browne, W. D. Knight and C. Kittle: Phys. Rev. **102** (1956) 1501.

Note added in proof—It has been found that the shifts in Cu-Mn at helium temperatures are smaller than those shown in Fig. 2.

J. Phys. Soc. Japan **12** (1957) 310

Multiplication of Charge Carriers and Breakdown in Ge p-n Junction I

By Chiyoe Yamanaka and Tokuo Suita

Department of Electrical Engineering,
College of Engineering,
Osaka University

(Received November 26, 1956)

We have studied the relation between the current multiplication[1] and the breakdown voltage of Ge p-n junction at various temperatures. The junctions were prepared by alloying indium at 550°C on n type Ge, doped with arsenic, the resistivity of which was 5 Ω cm. The crystallographic direction of specimens was [100].

The drift of the current with time is shown in Fig. 1. At low voltage the collector current did not show any drift. At the voltage of about seventy percent of the breakdown value, the current decreased to a certain lower value in a period of ten minutes. At ninety percent, this drift disappeared. A little increase of voltage across this critical point provoked a current rise with time which turned itself to the breakdown.

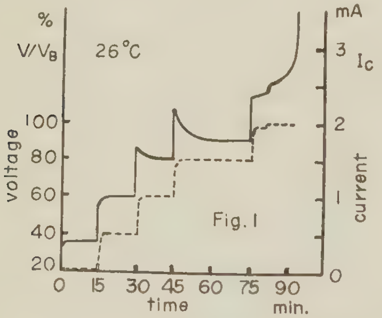

Fig. 1. The time dependent collector current. The real line indicates the collector current. The dotted line indicates the applied voltage.

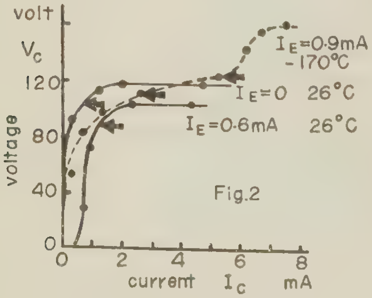

Fig. 2. Voltage-current characteristics. The arrows show the decrease in current with time.

As for the effect of temperature, at lower temperatures the breakdown voltage was higher and the current jumped more sharply at this critical point than in the case of higher temperature. In fact, the junctions were restorative at room temperature by a prompt cut of the after-current, but at −170°C they were non-restrative. In Fig. 2, we show the characteristics of current and voltage where the arrows indicate the drift with time. These results seem to show that at higher temperature the current multiplication and the breakdown process are much more influenced by the thermal effect. The mechanism of time dependent creep is not clear, but a possible interpretation might be as follows. As the applied field is increased, the surface current begins to appear. As the surface state is so changeable by the current, the surface leakage tends to decrease with time. Near the breakdown voltage, the avalanche current has a dominant role and masks the behavior of surface component.

The distribution of current pulses was measured by using an amplifier and a discriminator. Fig. 3 shows these results. At lower current density the distribution obeys the Furry-Wijsman's[2] formula which is observed in gasous ionization. But at higher current density the distribution was quite flat. This means the intermittent discharges which consists of rather large pulses of the same magnitude are prevailing. These phenomena may be the same ones as those observed by McKay[3] The mechanism of them may be the on-off process in the different discharge paths in junction which have nearly the same firing voltage.

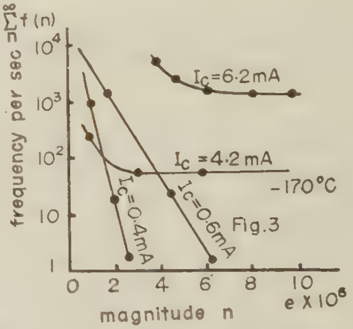

Fig. 3. The distribution of current pulses.

More experiments concerning the directional effect by using impulse voltages are being carried out.

References

1) C. Yamanaka, T. Suita: Tech. Rep. Osaka Univ. **6** (1956) 243.
2) R. A. Wijsman: Phys. Rev. **75** (1949) 833.
3) A. G. Chynoweth, K. G. McKay: Phys. Rev. **102** (1956) 369.

J. PHYS. SOC. JAPAN **12** (1957) 311

Molecular Sound Velocity of Aqueous Sugar Solutions

By Otohiko NOMOTO and Tadashi KISHIMOTO
Kobayasi Institute of Physical Research, Kokubunzi, Tokyo

(Received January 10, 1957)

One of the authors[1] has reported that Rao's molecular sound velocity[2] $R=(M/\rho)V^{1/3}$ becomes a linear function of the molar fraction (n) in most of the liquid mixtures. Here M is the mean molecular weight, ρ the density and V the sound velocity. Deviation from linearity has been observed in aqueous solutions, R becoming higher than the value corresponding to the straight line connecting the R-values of the both component liquids. This was attributed to the breaking of the bydrogen bonds of water in aqueous solutions by the influence of the solute molecules[3]. As some of the aqueous solutions show deviation from linearity rule of R, while others do not, we intended to investigate the behaviour of R also in other aqueous solutions than hitherto investigated.

Sound velocity (at 1.43 Mc/sec, by ultrasonic interferometry) and density were measured for some aqueous sugar solutions at various concentrations (0～20% weight) and temperatures (5°～30°C), and the values of R were computed. R was found to be a linear function of n for all the sugar solutions investigated within the accuracy of the experiments (cf. Fig. 1.).

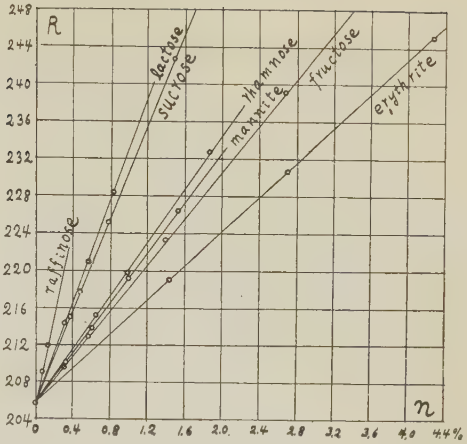

Fig. 1. Molecular sound velocity *vs.* molar fraction of the solute for aqueous sugar solutions (20°C).

When the linear relationship is extrapolated to $n=100\%$ we obtain the values of R for the pure solutes (corresponding to the supercooled liquid state). These values (average values over the temperature range 5°～30°) are indicated by R_{exp} in Table I, while R_{cal} indicates the values computed by assuming the additivity rule of R for the atomic increments and employing Rao's values[4] of the atomic increments (C=10, H=92.5, and O=74). As is to be seen in the table, R_{exp} is always lower than R_{cal}. This may presumably be due to the branching of the sugar molecules.

If the linear relationship of R holds true up to 100% concentration, we may conclude that the state of association of water molecules are effectively nearly the same as in pure water. This may presumably be due to the fact that the effect of the solvation (combination by hydrogen bonds of water molecules to the sugar molecules) on compressibility nearly compensates the effect of the partial destruction of the associated water molecules (destruction of hydrogen bonds) by the influence of the solute.

Table I. Molecular sound velocity of saccharides obtained by extrapolation from aqueous solutions and that calculated by employing the atomic increments

Sugars	Chemical formula	Molecular weight	R_{exp}	R_{cal}	$R_{\mathrm{exp}}/R_{\mathrm{cal}}$
erythrite	$C_4H_{10}O_4$	122.08	1129	1261	0.895
fructose	$C_6H_{12}O_6$	180.09	1452	1614	0.900
mannite	$C_6H_{14}O_6$	182.11	1553	1799	0.862
rhamnose	$C_6H_{12}O_5\cdot H_2O$	182.11	1644	1799	0.914
sucrose	$C_{12}H_{22}O_{11}$	342.17	2692	2969	0.907
lactose	$C_{12}H_{22}O_{11}\cdot H_2O$	360.19	2883	3228	0.893
raffinose	$C_{18}H_{32}O_{16}\cdot 5H_2O$	594.33	4540	5619	0.808

References

1) O. Nomoto: J. Phys. Soc. Japan **8** (1953) 553.
2) Rama Rao: Indian J. Phys. **14** (1940) 619.
3) O. Nomoto: J. Phys. Soc. Japan **11** (1956) 1146.
4) Rama Rao: J. Chem. Phys. **9** (1940) 682.

J. Phys. Soc. Japan **12** (1957) 312

Phase Transition of In_2Se_3

By Hisao Miyazawa and Suezo Sugaike
Matsuda Research Laboratory,
Tokyo-Shibaura Electric Co.,
Kawasaki-shi, Kanagawa-ken

(Received December 15, 1956)

Fairly large single crystals of In_2Se_3 grown by means of the double furnace techniques[1] in this laboratory were confirmed by X-ray examination to have the hexagonal lattice at room temperature, where $a=4.01$ Å, $c=19.2_4$ Å, and $c/a=4.80$, in good agreement with those reported by Hahn[2]. This is one exception among III_2VI_3 type compounds almost crystalizing in wurtzite, zincblende or their related structure, where the symbol III represents one of the third-B metals from aluminium to indium in Periodic Table, and VI one of the chalcogene elements that is sulphur, selenium or tellurium. It is therefore expected that the material shows different features from other families.

In the course of observations of several properties about these crystals, it was found at nearly 200°C that In_2Se_3 has a remarkable phase transition which might be first order. As shown in Fig. 1, electrical conductivity along (0001) plane of the crystal abruptly decreases by two orders of magnitude at the transition temperature T_c, while Hall constant* which is nearly constant up to T_c increases about sixfold discontinuously. Though it is not illustrated, thermoelectric power also jumps at T_c from 150~200 μV/deg to 600~700 μV/deg.

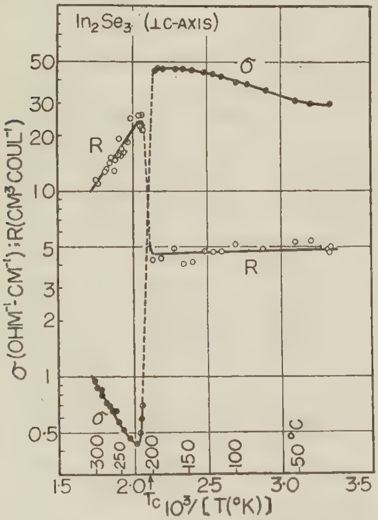

Fig. 1. Discontinuous changes of conductivity and Hall constant due to phase transition of In_2Se_3.

These changes are accompanied by extraordinary volume contraction of the crystal. This is obvious from Fig. 2, where thermal expansion measured in the direction perpendicular to the c axis is shown. One can see that the specimen does shorten by 0.5 percent in its length at T_c. Meanwhile, the thermal expansion appeared to be anisotropic and it was disclosed that in one case the rate of contraction along the c axis was about four times larger than that along (0001) plane.

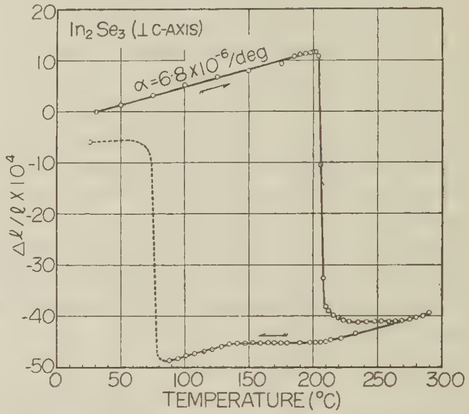

Fig. 2. Thermal expansion of In_2Se_3 characterized by marked contraction at T_c with increasing temperature and by striking supercooling with decreasing temperature.

Differential thermal analysis carried out on powdered sample, provided that temperature is slowly increased, indicates a sharp heat absorption process at T_c which may correspond to the latent heat. Supercooling is always characteristic to all quantities observed. As for the thermal expansion, for example, recovery to the lower temperature phase, when temperature is decreased, takes place below 100°C as seen in Fig. 2. Of course, simultaneous recovery of electrical quantities is confirmed.

Since the crystals easily cleave along (0001) plane somewhat like a mica sheet, it is difficult to cut out a specimen along the c axis which is long enough to set probes for electrical anisotropy measurements. However, it appears that current-voltage characteristics observed along the c axis suggest large anisotropy in conductivity, which is especially striking at the lower temperature phase and slightly diminishes at the higher temperature phase.

Further results and discussions will be published later.

References

1) D. C. Stockbarger: Rev. Sci. Instr. **7** (1936) 133.
W. D. Lawson: J. App. Phys. **22** (1951) 1444.
2) H. Hahn: Angew. Chemie **65** (1935) 538.

---

* The sign of Hall constant is negative in both phases.

J. Phys. Soc. Japan **12** (1957) 313~314

The Generation of EMF During Melting and Freezing of Ionic Crystalline Substances

By Kiyoshi Azuma and Hiroshi Kametani

Department of Metallurgy, Faculty of Engineering, Tokyo Univ.

(Received September 20, 1956)

The emf studies on ionic crystals during melting and freezing were carried out with the apparatus illustrated in Fig. 1. In a silica tube two platinum electrodes are placed 20 mm apart. A pre-heating coil is wound around the silica tube. This set is put in an electric furnace which is movable at a constant velocity. The pre-heating coil raised the temperature of the salt and maintained it at least over 660°C. This pre-heating method reduced the error due to the internal resistance of the KCl system to below 10%, and minimized the possibility of the damage to the tube by the expansion-contraction of the salt accompanying melting and freezing.

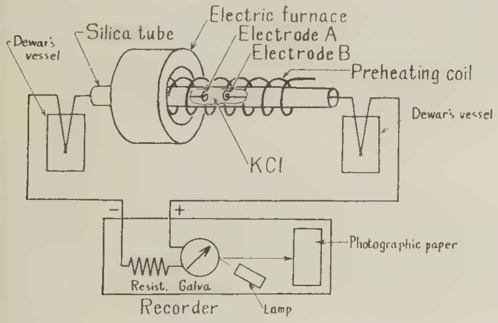

Fig. 1.

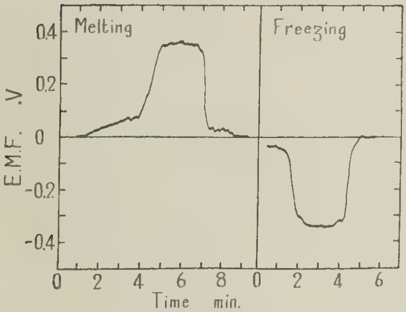

Fig. 2.

The KCl (Guaranteed Reagent) in the tube was melted and allowed to solidify. The furnace was moved from left to right, melting the salt. When the melting phase reached the electrode A, the emf appeared. The emf persisted as long as the solid phase existed between the electrodes A and B and disappeared when the melting phase reached the electrode B and only molten material remained between the electrodes. A freezing phase followed the passage of the furnace. When this freezing phase reached the electrode A, the oppositely polarized emf was developed which continued as long as molten salt remained between the electrodes. Fig. 2 illustrates the development and magnitude of the emf in the above sequence. The maximum emf obtained for KCl and similar substances are listed in Table I. A similar phenomenon has been noted for silicates such as glass, ferrous silicates etc$^{1)}$.

Table I.

Substance	EMF V	Substance	EMF V
KCl	0.33±0.03	NaCl	0.36±0.03
KBr	0.31±0.03	AgCl	0.29±0.03
KI	0.28±0.02		

The solid generally had a positive charge against the melt. Futher experiments show that the magnitude of the emf is independent of the shape of the electrodes, the distance between them and the rate of movement of the melting and freezing phases in the range of 0.3 to 3.4 cm/min., assuming that they travelled at the same velocity as the furnace. This was also true when the cooling rate was increased to 30 cm/min. by quenching the tube with water.

In another experiment the electrode B was maintained at 740°C and the electrode A at 830°C. When the temperature gradient was kept constant between the solid at one electrode and the melt at the other, the measured emf was negligible. It appears, then, that the emf is generated only when a phase change is taking place.

Workman and Reynolds$^{2)}$ and Gill$^{3)}$ have noted that the potential difference as great as 230 V accompany the freezing of dilute aqueous solutions. This phenomenon may be analogous to the one we have studied. However, there is a difference in the bonding nature of the water solution and the ionic crystals, and at high temperatures the determining factor is not "structure-sensitive lattice defects" but thermal vibration of atoms or ions. Taking into account the Schottky defects existing on the surface of the NaCl crystal in contact with its vapor, Lehovec$^{4)}$ calculated the surface potential to be −0.28 V. Though we are dealing with the solid-melt interface, it may be of some meaning that his calculated value is comparable to our result.

References

1) K. Azuma and H. Kametani: J. Mining Int. Japan **72** (1956) 577.
2) E. J. Workman and S. E. Reynolds: Phys.

Rev. **78** (1950) 254.
3) E. W. B. Gill: Brit. J. App. Phys. Sup. 2, S16 (1952)
4) K. Lehovec: J. Chem. Phys. **21** (1953) 1123.

J. PHYS. SOC. JAPAN **12** (1957) 314

Frequency Shift in Ammonia Absorption due to Self-broadening

By Kiyokata MATSUURA, Yoshikazu SUGIURA and G. M. HATOYAMA
Electrotechnical Laboratory, Nagata-cho, Tokyo

(Received December 25, 1956)

Although it is well known that the resonance frequencies of molecules in visible and infrared regions vary with pressure, and the amount of the shift is proportional to the line width, the corresponding shift in microwave region has not yet been observed. Theoretically, the shift due to collision broadening is expected to be much smaller in microwave region than in visible or infrared region. For example, Towness[1] estimates a shift of less than 5×10^{-2} Mc per Mc width.

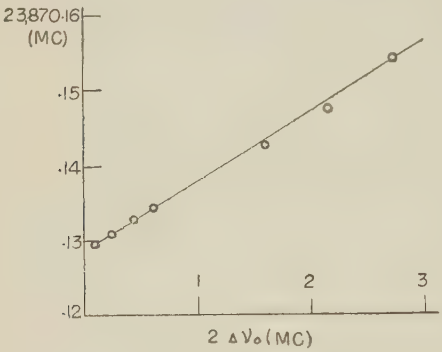

Fig. 1.

We have observed during the course of researches on atomic clock the shift in resonance frequency of ammonia (3,3) line with pressure.

An example of the measurements is shown in Fig. 1, where the apparent resonance frequency is plotted against the line width between half-power points. If the line-shape is assumed as

$$\gamma=\frac{\gamma_0}{(\nu-\nu_0-a\Delta\nu_0)^2+\Delta\nu_0^2},$$

where,

$1-e^{-\gamma}\approx\gamma$: absorption per cm for a plane wave,
$2\Delta\nu_0$: line width between half-power points,
ν: frequency of the incoming wave,
ν_0: resonance frequency of an isolated molecule,

we can estimate the value of a from the above measurement as

$$a=(1.8\pm0.1)\times10^{-2}.$$

The error given includes those coming from the uncertainties in the measurements of the resonance frequency and the line width. Errors from other sources such as coming from the purity of the gas should also be considered.

It has also been observed that the apparent resonance frequency varies with the foreign gases contained. Studies on such effects are now going on. The frequency shift reported previously[2] may come from either or both of these effects.

References

1) C. H. Townes and A. L. Schawlow: Microwave Spectroscopy (1955) p, 355.
2) K. Matsuura, Y. Sugiura and G. M. Hatoyama: J. Phys. Soc. Japan **12** (1956) 1301.

JOURNAL OF THE PHYSICAL SOCIETY OF JAPAN Vol. 12, No. 4, APRIL, 1957

Crystal Structure and Phase Transition of Some Metallic Halides (IV)

On the Anomalous Structure of α-AgI

By Sadao HOSHINO*

Department of Physics, Tokyo Institute of Technology,
Oh-Okayama, Meguro-ku, Tokyo

(Received September 22, 1956)

Intensities of X-ray diffraction from α-AgI at various temperatures were measured in the absolute scale by using a G-M counter spectrometer with the crystal monochromated Cu $K\alpha$ radiation. Measurements of the specific heat and the thermal expansion were also performed. A drastic temperature dependence of the intensities of Debye lines and the presence of a comparatively strong diffuse background were detected. The observed intensities of the Debye lines could be explained well by the disordered structure model (or the "averaged structure") proposed by Strock (Z. Physik. Chem., **B31** (1936) 132.), assuming fairly large Debye factors for silver and iodine atoms. The intensity of the diffuse background from such an averaged structure was calculated in the similar way as in the case of binary alloys having short range order, assuming appropriate probability functions for the presence of atoms in different sites. It was confirmed that the intensity curves of the diffuse background measured at 250° and 400°C were in fair agreements with the theoretical ones. The nature of the "averaged structure" having the random arrangement of silver atoms and the origin of the large displacements of atoms from their equilibrium positions were discussed.

§ 1. Introdution

Silver iodide (AgI) has three solid phases α, β and γ. The crystal structure of the α-phase for the highest temperature range, from 148°C to the melting point 555°C, was investigated by Strock¹⁾, and is famous as a typical example of the "averaged structure". According to his X-ray study, α-AgI has a cubic unit cell in which two silver atoms are distributed statistically over fourty two sites around the body centered arrangement of iodine atoms. He considered that the silver atoms may behave almost liquid-like, in accordance with the remarkably high ionic conductivity of this phase. However, since his result is still qualitative, further studies of the structure of this phase seems to be desirable.

The present author has studied α-AgI by thermal and X-ray methods, in which the intensity of Debye lines and also of the diffuse background of the Debye lines have been accurately measured in absolute scale by the use of a G-M counter spectrometer. Results of the intensity measurements have been compared with some possible models of the α-AgI structure.

§ 2. Experimental

1. *Preparation of Specimen*

The sample was prepared by the following chemical reaction.

$$AgNO_3aq.+KI\,aq.\rightarrow KNO_3aq.+AgI\downarrow$$

As was reported by Bloch and Möller²⁾, AgI samples prepared by this method at room temperature contain sometimes coexisting phases γ and β. When the amount of $AgNO_3$ in the solution is in excess over the stoichiometric proportion the solution tends to precipitate the cubic γ-phase of ZnS type. On the other hand, when the amount of KI is in excess the hexagonal β-structure of ZnO type tends to precipitate. The cubic γ-phase is stable at room temperature, while the hexagonal β-phase is only metastable since the stable range of the β-phase is from 136° to

---

* Now at Department of Physics, The Pennsylvania State University, University Park, Pennsylvania, U.S.A

148°C. In fact, the metastable hexagonal state at room temperature was found to transform readily to the cubic γ-phase by grinding the samples. It was confirmed that the structure of the α-phase is not affected by the forms of the precipitate at room temperature. We used, however, the sample obtained from the solution containing slightly excessive KI, because the sample prepared with excessive $AgNO_3$ showed a tendency to separate gradually free metallic silver at the surface of specimen.

2. *Specific Heat Measurement*

In order to confirm the transition temperature and to obtain some information about the phase transition of AgI, the temperature change of the specific heat was measured. AgI sample (14 gr. in weight) sealed in a hard glass vessel (3 gr. in weight) was set in an adiabatic calorimeter of modified Sykes's type[3]. The heat input given to the specimen was about 0.05 cal/sec. The specific heat vs. temperature curve (Fig. 1) shows only one transition peak at 148°C corresponding to the $\beta \rightarrow \alpha$ transition, wanting the peak corresponding to the $\gamma \rightarrow \beta$ transition at 136°C. This is because the sample was used for which the hexagonal β-phase was metastable at room temperature. The transition energy ΔQ and the entropy change ΔS obtained for the $\beta \rightarrow \alpha$ phase change are as follows:

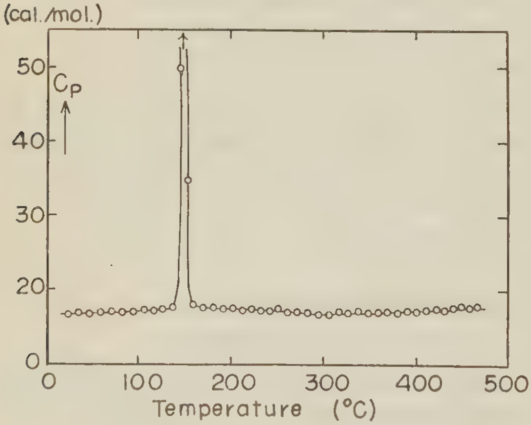

Fig. 1. Specific heat vs. temperature curve.

$$\Delta Q = 1.53 \text{ Kcal/mol.}$$
$$\Delta S = 3.6 \text{ cal/mol. degree.}$$

3. *Thermal Expansion*

The measurement of the lattice constant a_0 of cubic α-AgI at various temperatures was performed by the analysis of X-ray photographs from AgI powder coated on a Pt wire. Because the intensities of the reflexion lines of α-AgI decrease rapidly with diffraction angle especially at high temperatures, we were obliged to use the line (321) at a comparatively low angle of reflexion. The Pt wire served as the standard specimen. The result of this measurement is shown in Fig. 2.

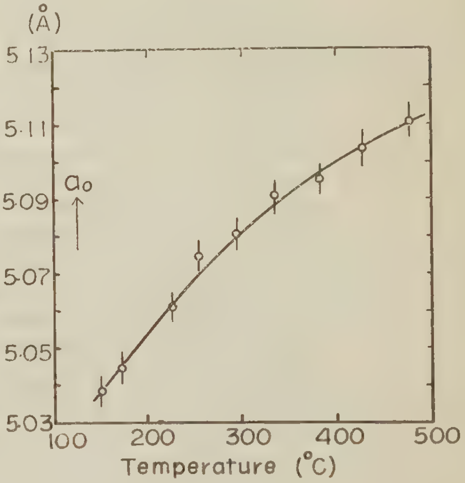

Fig. 2. Change of lattice constant a_0 with temperature.

In addition to the measurement of the lattice constant by X-ray method, we measured the thermal expansion by the ordinary dilatometric method. The sample used in the dilatometry was shaped to a cylinder of diameter 10 mm and length 35 mm by four ton weight press. As the crystal of α-AgI is highly plastic, we must avoid the deformation at the top of the sample caused by the weight of the silica tube touching there. To prevent this influence a very thin and light silica tube was used and a thin mica plate was inserted between the sample and the silica tube. The change of the linear expansion with temperature obtained by this method is shown in Fig. 3, where black circles show the values by the X-ray method. The results by the two methods show general agreement except for high temperatures.

4. *X-ray Intensity Measurement*

In the X-ray measurement a rotating copper anode X-ray tube[4] having a fine focus was used as the X-ray source, because the X-ray diffraction intensities from powdered specimen of α-AgI, especially the intensity of diffuse background, are very weak and, moreover, it was desired to use monochromatic beam in the present study. The tube was opetated with electron current about 70～80 mA and voltage 20～25 kV. Cu K radiation generated from this tube was momochromated by the (200) reflexion from a LiF crystal monochromator. Comparatively low tube voltage was applied in order to prevent the participation of higher harmonic terms.

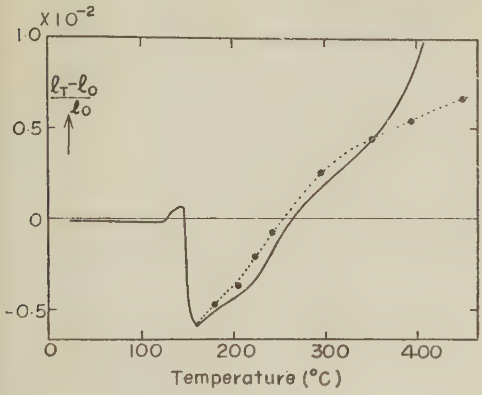

Fig. 3. Thermal expansion vs. temperature curve.

Measured values were standardized by using a monitor counter whicn detects the change of incident intensities by measuring a reflexion from Al foil set behind the first slit. Scheme of the measurement is shown in Fig. 4.

By pressing slightly the powder specimen in a metal case, a plate shape sample of 15 mm × 10 mm × 1 mm was made, and was set in a furnace made of isolite. Temperature of the sample was measured by an alumel-chromel thermocouple. The accuracy of temperature measurements was within about ±5°C even at high temperatures.

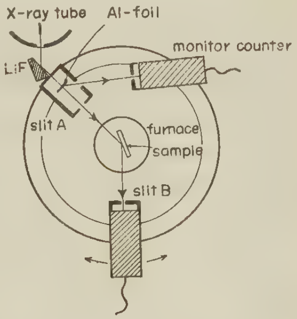

Fig. 4. Schematic diagram of X-ray intensity measurement.

Values of the height l and the breadth b of the slit B and the distance R from the center of the sample to the slit were chosen as inscribed in the following figures explaining each measurement. The slit breadth b was taken sufficiently wide to cover the whole

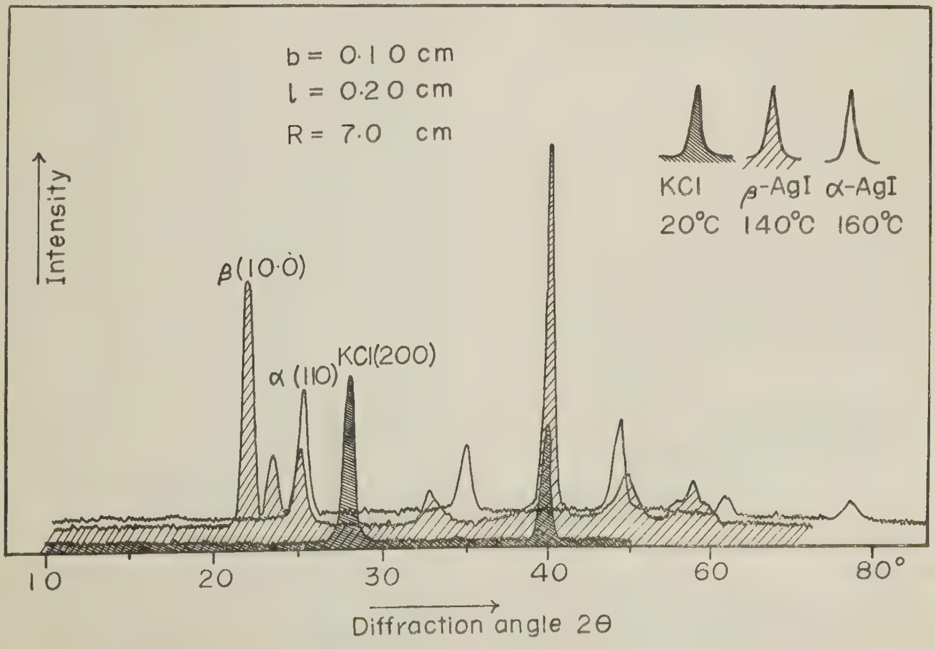

Fig. 5. Intensity curves with monochromated CuKα radiation.

width of each line so as to obtain the integrated intensity of the Debye lines.

Fig. 5 is the intensity curves obtained by the ordinary self recording method. The curves from β-AgI at 140°C and KCl at room temperature are also shown for comparison. It is readily seen in this figure that the diffuse background of α and β-AgI is considerably prominent compared with that of KCl.

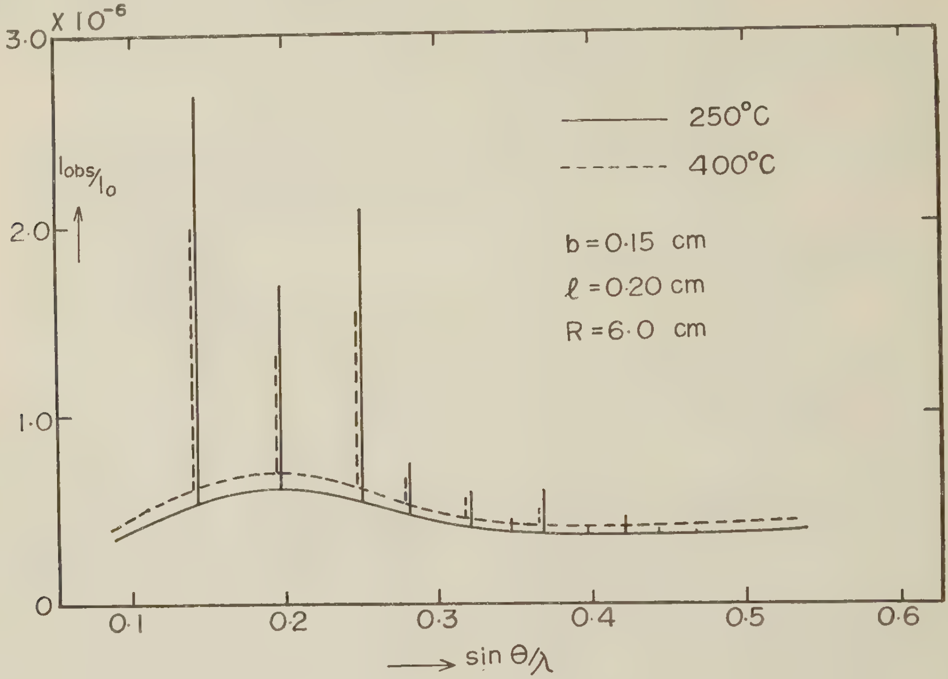

Fig. 6. Intensity curves at 250°C and 400°C measured by counting with monochromated CuKα, as functions of $\sin\theta/\lambda$.

More precise intensity measurement was performed by measuring the counts in a constant time-interval for the diffraction angle 2θ from 10° to 110°. Intensity curves obtained were transformed into an absolute intensity scale by the measurement of line intensities from standard specimens such as KCl, NaCl and CuI powdered crystals. The background proper to the apparatus, such as the scattering from air and the slit A and natural counts of the counter tube was subtracted. The intensity curves thus obtained for 250° and 400°C are shown in Fig. 6, in which the length of vertical lines represents the integrated intensity of Debye lines.

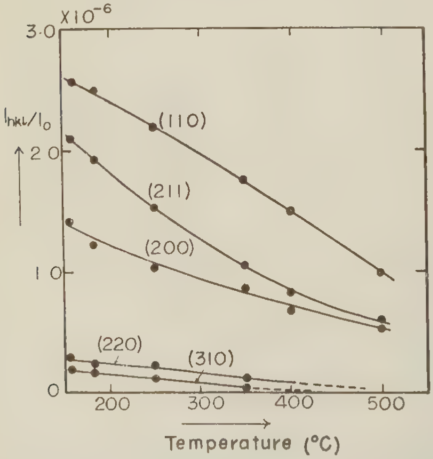

Fig. 7. Intensity change of Debye lines with temperature.

The integrated intensities of several Debye lines were measured at various temperatures. The result is shown in Fig. 7.

§ 3. Structure Model and Temperature Effect

1. *Intensities of Debye Lines and Structure Model*

In the structure model of α-AgI proposed by Strock (which is referred to as Model A), two silver atoms in the unit cell occupy the the following fourty sites of the space group $Im3m$ with an equal probability:

(0 0 0, 1/2 1/2 1/2)+
6(*b*) 0 1/2 1/2 ↺;
12(*d*) 1/4 0 1/2 ↺, 3/4 0 1/2 ↺;
24(*h*) 0 1/8 1/8 ↺, 0 7/8 7/8 ↺;
0 1/8 7/8 ↺, 0 7/8 1/8 ↺.

Strock showed that the relative intensities of Debye lines can be well explained by this model. On the other hand, the present author[5)] has previously proposed an alternative model of α-AgI which, referred to as Model B, is also in accordance with the observation so far as the relative intensities are concerned.* This circumstance implies the fact that in the case of α-AgI, for which only several lines are observable on account of a rapid intensity decrease with scattering angle, the relative intensties of the Debye lines can not supply a deciding information for the structure determination. However, the difficulty of finding the correct structure may be much reduced when the comparison of calculated and observed values is performed with respect to the absolute intensity.

The intensities of Debye lines, $I(hkl)$, reflected by a powdered block is calculated by the formula

$$I(hkl) = I_0(e^2/mc^2)^2 N_0 \frac{l}{2\mu} \frac{\lambda^3 j}{32\pi R a_0{}^3} \frac{1+\cos^2 2\theta \cos^2 2\mathcal{E}}{\sin^2\theta\cos\theta} |\overline{F^2}|, \tag{1}$$

where I_0 is the total intensity flux of the incident beam, N_0 the number of the unit cell in unit volume, l the height of the slit B, μ the linear absorption coefficient, a_0 the lattice constant, R the distance from the sample to the slit B, j the multiplicity, and $\mathcal{E}$ the Bragg angle for the monochromator crystal. $\overline{F}$ is the mean structure amplitude of the satistical structure, which is expressed as

$$\overline{F} = \Big< \sum_i f_i \exp[-B_i(\sin\theta/\lambda)^2] \exp[2\pi \boldsymbol{i}/\lambda(\boldsymbol{s}-\boldsymbol{s}_0\cdot\boldsymbol{r}_i-\boldsymbol{r}_{i'})] \Big> \tag{2}$$

where B_i is the Debye factor for the ith atom in a unit cell.

The results of calculations for the intensities of several lines are shown in Fig. 8 in comparison with the observed values. In this figure the solid curve corresponds to the observation at 250°C, and the broken curves *a* and *b* show the calculated values for the structures of Model A and B respectively. In these calculations the Debye factors, B_i, were chosen so as to bring the best agreement between the calculated and the observed relative intensities of the lines. They were put

$B_{Ag}=8$, $B_I=8$ for Model A, and
$B_{Ag}=3$, $B_I=2$ for Model B.

In Fig. 8, it is seen that the intensity values of Model A are in a good agreemenl with observation (with the reliability index $R=0.09$*) not only in the relative values but also

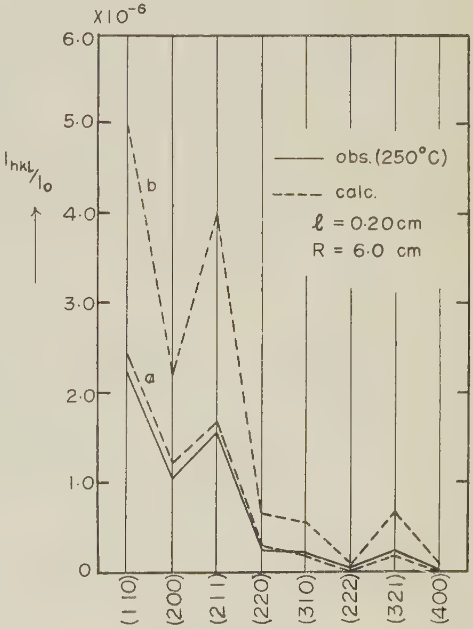

Fig. 8. Observed and calculated values of Debye line intensities.

---

* The proposed model is a partially disordered structure between a perfectly ordered and a perfectly disordered structure. The perfectly ordered structure has the tetragonal unit cell with the axial ratio $c/a=1$ and the space group $I\bar{4}m2$; iodine stoms are at (0 0 0), (1/2 1/2 1/2), and sliver atoms at (0 1/2 1/4), (1/2 0 3/4). The perfectly disordered structure has a cubic symmetry and belongs to the space group $Im3m$; iodine atoms are in the same positions as in the ordered structure, whereas the two silver atmos are distributed statistically over the 12(*d*) sites. The relative intensities of Debye lines could be explained well when the parameter of the degree of order S was put as 0.8 and values of the Debye factors were appropriately assumed.

* The index adopted here is defined as

$$R = \frac{\sum|I_{\rm obs}-I_{\rm calc}|}{\sum I_{\rm obs}}.$$

in the absolute values. On the other hand, Model B fails decidingly with respect to the absolute intensity.**

2. *Temperature Dependence of Line Intensity*

In the previous section we found that Model A is a more favourable model than model B for the structure of α-AgI. To get this agreement, however, we had to assume the anomalously large Debye factors in the calculation. Moreover, as seen in Fig. 7, the line intensities decrease drastically with increasing temperature, so that far larger Debye factors should be taken into account at higher temperatures. These facts seem to show that in α-AgI crystal the displacements of atoms from their mean positions are very large.

The Debye factor B_i in the equation (2) was introduced formally without accounting for its physical implication, assuming only the statistical displacements of atoms from their mean positions. It is natural to consider that the thermal vibration of atoms is the most important cause for the statistical displacements of atoms. However, since the anomalously large Debye factor assumed for α-AgI is in the outside of the scope of the ordinary theory of thermal vibration, we can not exclude some other origins of the statistical displacements. For instance, irregularities of the atomic positions associated with the disordered structure supposed for α-AgI might contribute to the large Debye factors.

The experimental result shows that the B-factor is the function of temperature whatever its implication may be. The change of the *mean* Debye factors, $\overline{B}$, can be deduced by the relation

$$\ln [I_F \exp(-2\overline{B}_{T_1}[\sin\theta/\lambda]^2)$$
$$\div I_F \exp(-2\overline{B}_{T_2}[\sin\theta/\lambda]^2)]$$
$$=2(\overline{B}_{T_2}-\overline{B}_{T_1})(\sin\theta/\lambda)^2\,,$$

where I_F corresponds to the intensity for a hypothetical state of crystal in which atoms are frozen in their equibrium positions, and $\overline{B}_{T_1}$ and $\overline{B}_{T_2}$ are the mean Debye factors at temperatures T_1 and T_2 respectively. Fig. 9 shows the temperature dependence of $(\overline{B}_{T_2}-\overline{B}_{T_1})$ calculated from the intensity change of (110), (200) and (211) shown in Fig. 4; T_1 is fixed at 160°C. If the origin of the ordinate in Fig. 9 is displaced so as the value at 250°C becomes 8 in accordance with the result in the previous section, we can find $\overline{B}$ value at any temperature. The calculations for the Debye line intensities with these $\overline{B}$ values at various temperatures showed fair agreements with observations up to the temperature of about 350°C. Above this temperature the deviation begins to appear, indicating the inadequacy of the use of the mean factor $\overline{B}$ for the two kinds of atoms.

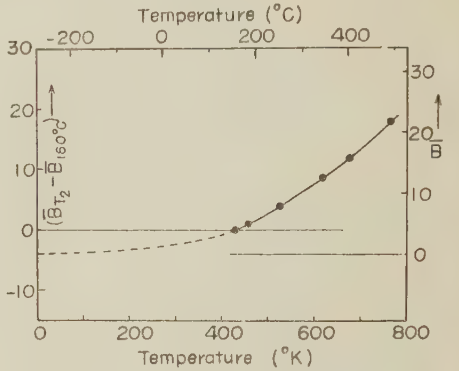

Fig. 9. $(\overline{B}_{T_2}-\overline{B}_{160°C})$ vs. temperature curve.

§ 4. Interpretation of Diffuse Background

In addititon to the absolute intensity measurement of the Debye lines, another helpful information is available for the structure determination of α-AgI. That is the measurement of the diffuse background due to the disordered structure supposed for α-AgI.

The intensity of the diffuse background I_B scattered by a crystal of a disordered structure may be written as

$$I_B=I_D+I_S+I_{\text{incoh.}}\,, \tag{3}$$

where I_D is the diffuse term due to the disordered structure, I_S the term due to the statistical displacements of atoms from their mean positions caused by thermal vibration and other origins, and $I_{\text{incoh.}}$ the term due to the incoherent scattering.

Since the first term in (3) is most important one in the present study, let us obtain a general expression of I_D for the "averaged

---

** Model B fails also in explaining the absolute intensity of the diffuse scattering (§ 4).

structure" in which the number of atomic sites is more abundant than that of atoms and the atoms are distributed statistically over these sites. It is conceived that in the structure of α-AgI only one kind of atom, silver atom, has the statistical arrangement. If this is the case, the disordered term I_D is solely due to the scattering from silver atoms, and may be expressed as

$$I_D=I_0k\sum_s\sum_{s'}\exp\left[2\pi i(\boldsymbol{b}\cdot\boldsymbol{R}_s-\boldsymbol{R}_{s'})\right]\Delta f_s\cdot\Delta f_{s'},\tag{4}$$

where k is a constant depending on the experimental conditions, $\boldsymbol{R}_s$ is the position vector of the sth site in the crystal and summation is taken over the unit volume of the crystal. Δf_s is defined as the deviation of the scattering amplitude f_s at the sth site from the mean scattering amplitude $\overline{f}$, namely

$$\Delta f_s=f_s-\overline{f}\,.$$

If all the sites are equivalent, the probability of finding the atom in any sites, W, is equal to the ratio of the number of atoms to the number of sites in the crystal, and we obtain

$$\overline{f}=Wf_{Ag}$$

and

$$\Delta f_s=f_s-Wf_{Ag}\,,\tag{5}$$

where f_{Ag} is the atomic scattering factor of silver atom and f_s is either f_{Ag} or 0.

The equation (4) can be treated in the similar way as in the case of binary alloy having short range order. The equation (4) in written as

$$I_D=I_0k\Big[\sum_s(\Delta f_s)^2+\sum_s\sum_{s'}{}'\Delta f_s\cdot\Delta f_{s'}\times\exp\left[2\pi i(\boldsymbol{b}\cdot\boldsymbol{R}_s-\boldsymbol{R}_{s'})\right]\Big],\tag{6}$$

in which the prime added to the summation symbol in the second term means to omit the term of $s=s'$. Since, from (5), Δf_s is $(1-W)f_{Ag}$ or $-Wf_{Ag}$, thus

$$(\Delta f_s)^2=(1-W)^2f_{Ag}^2\quad\text{or}\quad W^2f_{Ag}^2\,.$$

The probabilities for the two cases are W and $(1-W)$ respectively, so we have

$$\langle(\Delta f_s)^2\rangle=W(1-W)^2f_{Ag}^2+W^2(1-W)f_{Ag}^2=W(1-W)f_{Ag}^2\,.$$

Thus the first term of the summation in (6) is given as

$$\sum_s\langle(\Delta f_s)^2\rangle=pN_0W(1-W)f_{Ag}^2\tag{7}$$

where p is the number of sites in a unit cell.

In order to calculate the second term in (6), let us introduce the probability functions $\alpha(r)$ and $\beta(r)$ as follows: $\alpha(r)$ gives the probability of finding an atom at a site apart by a distance r from a site occupied by an atom, and $\beta(r)$ the probability of finding an atom at a site apart by r from a vacant site. By the use of these two functions we can obtain

$$\langle\Delta f_s\cdot\Delta f_{s'}\rangle=W(1-W)[\alpha(r_{s,s'})-\beta(r_{s,s'})]f_{Ag}^2\,,\tag{8}$$

where $r_{s,s'}$ denotes the distance between the sth and the s'th sites. Thus, by the use of atomic scattering amplitudes taking account of Debye factors, the disordered term of the diffuse scattering may be expressed as

$$I_D=I_0kN_0pW(1-W)f_{Ag}^2\exp\left[-2B_{Ag}(\sin\theta/\lambda)^2\right]\left[1+\frac{1}{pN_0}\sum_s\sum_{s'}{}'(\alpha-\beta)_{r_{s,s'}}\exp\left[2\pi i(\boldsymbol{b}\cdot\boldsymbol{R}_s-\boldsymbol{R}_{s'})\right]\right]\tag{9}$$

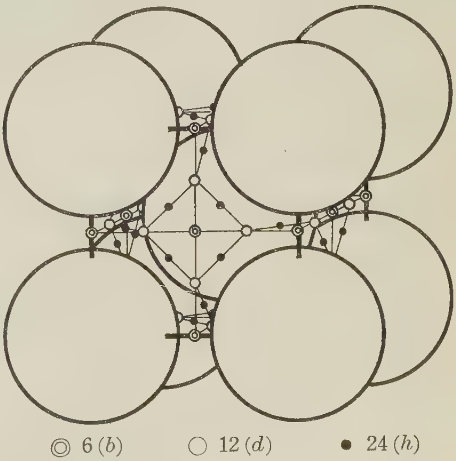

Fig. 10. Structure of α-AgI.

As mentioned in a previous section, the fourty two sites for silver atoms in Model A are classified into three kinds of positions (b), (d) and (h) (Fig. 10). Thus the summation in (9) for Model A is given by the three terms as follows:

$$\frac{1}{pN_0}\sum_{s}\sum_{s'}{}'(\alpha-\beta)_{r_{s,s'}}\exp\left[2\pi i(\boldsymbol{b}\cdot\boldsymbol{R}_s-\boldsymbol{R}_{s'})\right]=\frac{1}{pN_0}\Big[\sum_{s(b)}\sum_{s'}{}'(\alpha-\beta)_{r_{s(b),s'}}\exp\left[2\pi i(\boldsymbol{b}\cdot\boldsymbol{R}_{s(b)}-\boldsymbol{R}_{s'})\right]$$

$$+\sum_{s(d)}\sum_{s'}{}'(\alpha-\beta)_{r_{s,s'}}\exp\left[2\pi i(\boldsymbol{b}\cdot\boldsymbol{R}_{s(d)}-\boldsymbol{R}_{s'})\right]+\sum_{s(h)}\sum_{s'}{}'(\alpha-\beta)_{r_{s(h),s'}}\exp\left[2\pi i(\boldsymbol{b}\cdot\boldsymbol{R}_{s(h)}-\boldsymbol{R}_{s'})\right]$$

$$=\frac{1}{pN_0}\Big[p_bN_0\sum_{s'}{}'(\alpha-\beta)_{r_{s(b),s'}}\exp\left[2\pi i\,\boldsymbol{b}\cdot\boldsymbol{R}_{s(b),s'}\right]+p_dN_0\sum_{s'}{}'(\alpha-\beta)_{r_{s(d),s'}}\exp\left[2\pi i\,\boldsymbol{b}\cdot\boldsymbol{R}_{s(d),s'}\right]$$

$$+p_hN_0\sum{}'(\alpha-\beta)_{r_{s(h),s'}}\exp\left[2\pi i\,\boldsymbol{b}\cdot\boldsymbol{R}_{s(h),s'}\right]\Big] \tag{10}$$

where the index $s(b)$ specifies the sth of the (b) type sites and p_b is the number of the (b) type sites per unit cell, and so forth.

Expression (10) can be simplified in the case of powder samples. If we write $\frac{\sin(4\pi r\sin\theta/\lambda)}{4\pi r\sin\theta/\lambda}=S_r$, then the disordered term of the diffuse scattering from a powder sample is given by

$$I_D=I_0kN_0n(1-W)f_{Ag}{}^2\exp\left[-2B_{Ag}(\sin\theta/\lambda)^2\right]\Big[1+p_b/p\sum_{s'\neq0}Z_{s(b),s'}(\alpha-\beta)_{r_{s(b),s'}}S_{r_{s(b),s'}}$$

$$+p_d/p\sum_{s'\neq0}Z_{s(d),s'}(\alpha-\beta)_{r_{s(d),s'}}S_{r_{s(d),s'}}+p_h/p\sum_{s'\neq0}Z_{s(h),s'}(\alpha-\beta)_{r_{s(h),s'}}S_{r_{s(h),s'}}\Big] \tag{11}$$

where $n(=pW)$ corresponds to the number of silver atoms per unit cell and $Z_{s(b),s'}$ is the number of sites belonging to the s'th neighbor around a (b) type site.

The factor $(\alpha-\beta)_{r_{s,s'}}$ is an analogous function to the distribution function of the short range order in alloys. Let us consider two sites s and s' which are apart by the distance r. The probability of finding an atom in s and a vacancy in s' simultaneously is $W(1-\alpha_r)$, while the probability of finding a vacancy in s and an atom in s' is $(1-W)\beta_r$. Since these two probabilities should be equal, we find a relation

$$W(1-\alpha_r)=(1-W)\beta_r\,. \tag{12}$$

This equation gives a relation between α_r and β_r and will be used later for the calculation of I_D.

The kind and the number Z of neighboring sites around each kind of positions and the neighboring distances are as listed in Table 1, in which the distance is expressed by a fraction of the lattice constant, namely, by r_s/u, where $u=a_0/8$. The values of r_s at 160°C are given in Table 2.

The possibility of the simultaneous presence of silver ions in closer neighboring sites should be excluded on account of the finite radius of the siver ion. The ionic radius of Ag⁺ has been given by Goldschmidt and by Pauling and their values are 1.13 Å and 1.26 Å respectively. In our consideration Goldschmidt radius was adopted, though Pauling

Table I. The kinds and the number Z of neighboring sites around each kind of positions and the neighboring distances r_s. $u=a_0/8$.

neighbor	1st		2nd		3rd		4th		5th		6th		7th	
	Z	r/u	Z	r/u	Z	r/u	Z	r/u	Z	r/u	Z	r/u	Z	r/u
(b)	h 4	$\sqrt{2}$	d 4	$\sqrt{4}$	h 8	$\sqrt{10}$	b 4	$\sqrt{16}$	d 8	$\sqrt{20}$				
(d)	h 4	$\sqrt{2}$	b 2	$\sqrt{4}$	d 4	$\sqrt{8}$	h 4	$\sqrt{10}$	h 8	$\sqrt{14}$	d 2	$\sqrt{16}$		
(h)	d 2 b 1	$\sqrt{2}$	h 2	$\sqrt{4}$	h 4	$\sqrt{6}$	h 1	$\sqrt{8}$	d 2 b 2	$\sqrt{10}$	d 4	$\sqrt{14}$	h 10	$\sqrt{18}$

Table II. The values of r_s at 160°C.

r/u	$\sqrt{2}$	$\sqrt{4}$	$\sqrt{6}$	$\sqrt{8}$	$\sqrt{10}$	$\sqrt{12}$	$\sqrt{14}$	$\sqrt{16}$	$\sqrt{18}$	$\sqrt{20}$
r (Å)	0.89	1.26	1.54	1.78	1.99	2.18	2.35	2.52	2.67	2.81

radius gave almost the same result. By the mutual interference due to the ionic radius, α_r should be put zero for the following neighbors;

from the 1st to the 3rd neighbors around the (*b*) type sites,
from the 1st to the 4th neighbors around the (*d*) type sites,
from the 1st to the 5th neighbors around the (*h*) type sites,

From the relation $\alpha_r=0$ for these neighbors and the eqation (12), we have

$$(\alpha-\beta)_r=-\beta_r=-W/(1-W)=-1/20,$$

where $W=2/42$.

The functions of $(\alpha-\beta)_r$ for the other neighbors are difficult to estimate unless some approximations are introduced. For large r, both α_r and β_r may be equal to W and consequently $(\alpha-\beta)_r=0$. Thus, we assume $(\alpha-\beta)_r=0$ for the neighbors farther than the 5th neighbor for the (*b*) type positions, the 6th one for the (*d*) type positions and the 7th one for the (*h*) type positions. Finally, the functions for the 4th neighbor for (*b*), the 5th one for (*d*) and the 6th one for (*h*) can be given by the condition that the total of the probability functions, $\sum_s(\alpha-\beta)_{r_{s,s'}}$, is -1. Thus, they are determined as $-1/20$, $-3/80$ and $-3/40$, respectively.

We can now calculate the diffuse scattering I_D by using the above values of the probability functions. I_D is expessed as

$$I_D=I_0kN_0n(1-W)f_{Ag}{}^2\exp[-2B_{Ag}(\sin\theta/\lambda)^2]$$
$$\times\left[1-\left(\frac{6}{35}S_{u\sqrt{2}}+\frac{4}{35}S_{u\sqrt{4}}+\frac{4}{35}S_{u\sqrt{6}}+\frac{3}{35}S_{u\sqrt{8}}\right.\right.$$
$$\left.\left.+\frac{8}{35}S_{u\sqrt{10}}+\frac{9}{35}S_{u\sqrt{14}}+\frac{1}{35}S_{u\sqrt{16}}\right)\right] \tag{13}$$

where $n=2$ and

$$k=(e^2/mc^2)^2\frac{bl}{2\mu R^2}\frac{1+\cos^2 2\theta\cos^2 2\varepsilon}{2}$$

It is known that the diffuse background I_S from the powder sample is approximately expressed as

$$I_S=I_0kN_0\sum_i f_i{}^2(1-\exp[-2B_i(\sin\theta/\lambda)^2]).$$

In this equation, the correlations among the displacements of different atoms are neglected. In the case of α-AgI, I_S is given by

$$I_S=I_0kN_0n[f_I{}^2(1-\exp[-2B_I(\sin\theta/\lambda)^2])$$
$$+f_{Ag}{}^2(1-\exp[-2B_{Ag}(\sin\theta/\lambda)^2]) \tag{14}$$

The intensity of the diffuse background I_B from α-AgI is given by the sum of I_D ((13)), I_S ((14)) and the incoherent scattering $I_{incoh.}$

When the influence of the anomalous disperson is taken into account, the atomic scattering factor f is expressed as

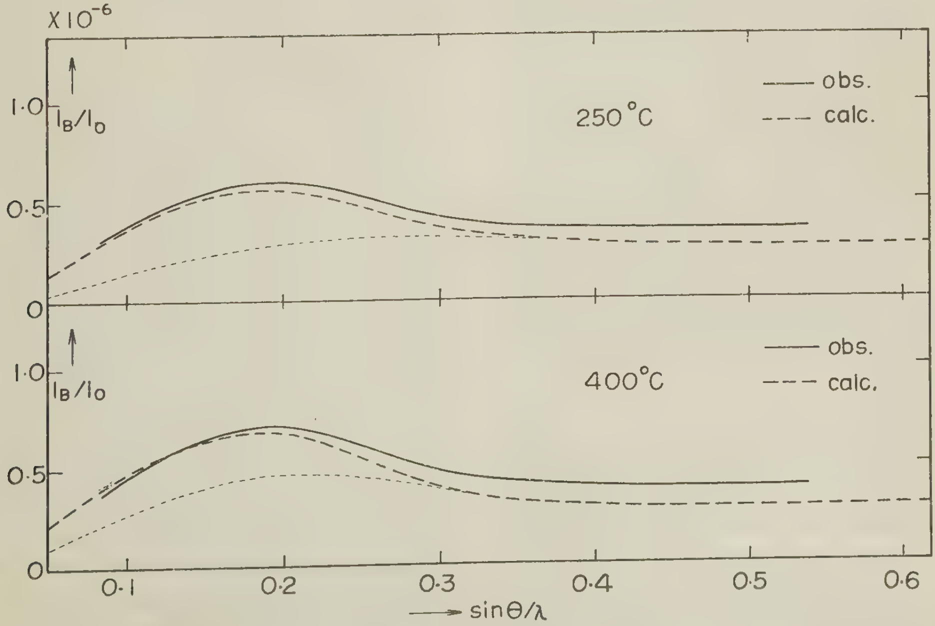

Fig. 11. Observed and calculaed intensities of the diffuse background of α-AgI.

$$f=f_0+\Delta f'+i\Delta f''.$$

In the present study in which the CuKα radiation is used, the imaginary term $\Delta f''$ for both the iodine and the silver atoms has an appreciable influence on the diffuse background, especially on the term I_S. The amounts of $\Delta f''$ are 7.2 for iodine and 4.7 for silver at $\theta=0$, while the values of f_0 are 53 and 47 respectively.[10] The square of $\Delta f''$ is not so large compared with that of f_0 at $\theta=0$, but at high diffraction angles its contribution to f^2 becomes important, because the value of $\Delta f''$ does not decrease appreciably with increasing angle. The real term $\Delta f'$ is negligibly small. Thus, I_S was calculated by using the corrected scattering factor $f=f_0+i\Delta f''$.

In Fig. 11 the calculated and the observed I_B/I_0 curves (drawn by the thick broken and solid curves respectively) are compared for 250° and 400°C. The thin broken curve indicates $I_S+I_{incoh.}$ Consequently, the difference between the thick broken curve and the thin broken one corresponds to the theoretical values of I_D. In the calculation, the Debye factors $\overline{B}$ are taken as 8 and 15 for 250° and 400°C respectively. In Fig. 11 we can see that, for both temperatures 250° and 400°C, the curves of the calculation and the observation are in a fair agreement in the smaller range of the diffraction angle, although the deviation of these curves increases gradually with increasing diffraction angle. The deviation seems to result from the rough approximation in the calculation of I_S neglecting the correlations among the displacements of atoms. In addition, as mentioned before (§ 3), there is some doubt about the use of the mean Debye factor $\overline{B}$ above 350°C. However, it seems to be difficult to give more refined expression for I_S in the present step of study.

§ 5. Discussion

As described in the foregoing sections, the result of the intensity comparison of the diffuse background as well as of the Debye lines in the absolute scale seems to favor Model A (or Strock's model) for the structure of α-AgI. This structure has the two remarkable features as follows:

(a) Statistical distribution of silver atoms over many sites.

(b) Large statistical displacements of silver and iodine atoms from their mean positions.

In model A, the probabilities of finding the atom in the sites (*b*), (*d*) and (*h*) are assumed to be equal. However, it is not appropriate to accept this assumption strictly, since we can obtain a good agreement of the intensity of diffuse background even when the assumption is properly modified. For instance, let us suppose that the two silver atoms in unit cell take only 12 (*d*) sites, but the probabilities of finding the atoms in (*b*) and (*h*) type sites are zero (Model C). The calculated intensity of diffuse scattering I_D due to this structure is shown in Fig. 12 by the dotted curve, in comparison with the curve for Model A. We can see by this figure that the assumption of different probabilities of finding atoms in the different kinds of site influences the intensity of diffuse scattering only little. Although Model C can not explain well the intensities of Debye lines, it is probable that we can find an intermediate structure between Model A and Model C which is capable of explaining the intensities of Debye lines as well as the intensities of diffuse background.

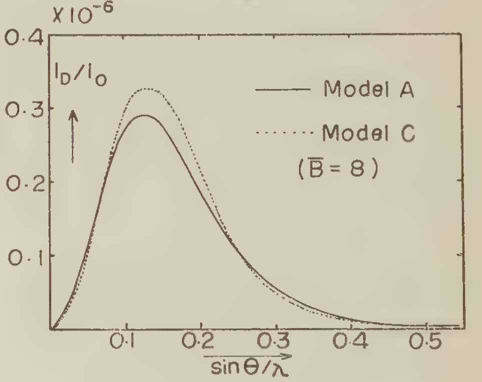

Fig. 12. Comparison of I_D curves for Model A and Model C.

In the case of the intermediate structure as above, it may be expected that the degree of disorder of the distribution of silver atoms over possible sites becomes larger with increasing temperature. If this is the case the specific heat in the α-phase will increase with rising temperature. However, since no such tendency can be found in the specific heat vs.

temperature curve shown in Fig. 1, the temperature change of the degree of disorder, if any, is supposed to be very small.

There is the following well known relation between the Debye factor B_i and the atomic displacement from the equilibrium position, ξ_i;

$$B_i = 8\pi^2 \langle \xi_i^2 \rangle .$$

If the atomic displacement in α-AgI is assumed as isotropic on the average, the temperature change of the *mean* atomic displacement ξ for iodine and silver atoms is obtained experimentally by using the $\overline{B}$ values for various temperatures. Fig. 13 shows $\sqrt{\langle \xi^2 \rangle}$ thus obtained. We can see that the atomic displacement from the equilibrium position at high temperature is very large, being comparable with the nearest neighboring distance between the sites of silver, about 0.9 Å.

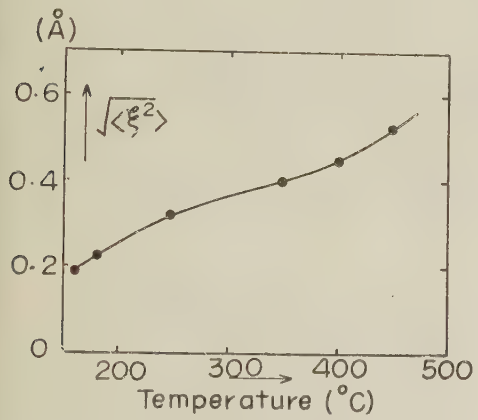

Fig. 13. Temperature change of $\sqrt{\langle \xi^2 \rangle}$.

We have studied previously the structures and the phase transitions of CuI⁽⁶⁾, CuBr⁽⁷⁾, CuCl, Ag_2HgI_4⁽⁸⁾ and Cu_2HgI_4.* In these crystals, only α-CuBr (which is stable in the temperature range from 470°C to the melting point 488°C) seems to possess the same structure as that of α-AgI, and the others have cubic ZnS type or hexagonal ZnO type structures. However, all of these crystals show a common nature that very large Debye factors for the metallic atoms must be introduced in order to explain the intensities of Debye lines at high temperatures so that the large amount of displacements of the metallic atoms is expected to occur. The origin of such common characteristic seems to be due to the thermal vibration mainly. On the other hand, in the α-AgI crystal the large value of B should be applied also to the iodine atom. This suggests that the large atomic displacements in α-AgI may be caused not only by the thermal vibration but also by the disordered structure. In fact, large local displacements of atoms are conceivable for the structure like α-AgI in which atoms are situated randomly and many sites in the lattice are left as vacant sites. Thus, we can consider that the liquid-like state of silver atoms as suggested by Strock may be an allowable picture of the structure of α-AgI in view of high randomness of the silver atoms due to the statistical distribution over many sites and the large statistical displacements from the mean positions of atoms.

In Fig. 3 showing the thermal expansion of AgI, the disagreement between the results from the ordinary dilatometry and the X-ray method is noted at high temperatures. From this fact, we may expect a possibility that a large number of vacancies of the negative ions are formed at high temperatures. However, this can not be concluded to be sure at present because the dilatometry might contain appreciable error due to the plastic deformation of the sample at these temperatures.

To study further details of the anomalous structure of α-AgI, the use of a single crystal seems to be necessary. The single crystal of α-AgI has not been obtained so far, while the single crystal of β-AgI can be prepared at room temperature in a solution of AgI with hydroiodic acid, by diluting gradually the solution with alcohl. When the single crystal of β-AgI was heated very slowly up to the temperature range of the α-phase in the furnace of the high temperature X-ray camera, it was found by Laue and rotation photographs that the crystal changed to an assembly of comparatively large grains of α-AgI orientating in nearly the same direction. This observation suggested that more perfect single crystals of α-AgI may be obtained by the similar method by refining the technique of thermal controle.

In conclusion the author wishes to express his best thanks to Prof. S. Miyake for his kind guidance and also to Dr. M. Takagi for her helpful discussions. Thanks are also due

---

* In these substances only CuCl has a single solid phase⁽⁹⁾.

to Dr. H. Maniwa for the facilities of the thermal expansion and the specific heat measurements.

This work was supported by a Grant in Aid for Fundamental Scientific Research from the Ministry of Education.

References

1) L. W. Strock: P. Zhysik. Chem. **B25** (1934) 441; **B31** (1936) 132.
2) R. Bloch und H. Mōller: Z. Physik. Chem. A **152** (1930) 245.
3) S. Nagasaki and Y. Takagi: J. App. Phys. Japan **17** (1948) 104.
4) S. Miyake and S. Hoshino: X-Rays **8** (1955) 45.
5) S. Hoshino: J. Phys. Soc. Japan **9** (1954) 245.
6) S. Miyake, S. Hoshino and T. Takenaka: J. Phys. Soc. Japan **7** (1952) 19.
7) S. Hoshino: J. Phys. Soc. Japan **7** (1952) 560.
8) S. Hoshino: J. Phys. Soc. Japan **10** (1955) 197.
9) M. R. Lorenz and J. S. Prener: Acta Cryst. **9** (1956) 538.
10) C. H. Dauben and D. H. Templeton: Acta Cryst., **8** (1955), 841.

JOURNAL OF THE PHYSICAL SOCIETY OF JAPAN Vol. 12, No. 4, APRIL, 1957

Radial Distribution Function of Fluids I

By Kazuo HIROIKE

Department of Physics, Tokyo Institute of Technology

(Received December 8, 1956)

The consistency of several approximate radial distribution functions of fluids is examined in the sense that the pressure and the internal energy derived from them satisfy the thermodynamical relation $\frac{\partial}{\partial T}\left(\frac{p}{T}\right)=\frac{\partial}{\partial V}\left(\frac{E}{T^2}\right)$, where T, p, V and E have the usual meanings. It is found that the original form of Green's linear theory is the only one which satisfies the above relation. It is also shown that Green's theory can be improved further without breaking the above relation.

§ 1. Introduction

The pressure p and the internal energy E of a classical fluid of volume V and temperature T which is composed of N molecules can be expressed in terms of the radial distribution function $g(r)$ as follows[1]:

$$\frac{p}{\rho kT}=1-\frac{\rho}{6kT}\int_0^\infty g(r)\frac{d\phi(r)}{dr}4\pi r^3dr\,, \quad (1)$$

$$\frac{E}{\frac{3}{2}NkT}=1+\frac{\rho}{3kT}\int_0^\infty g(r)\phi(r)4\pi r^2dr\,, \quad (2)$$

where ρ is the number density N/V, k the Boltzmann constant and $\phi(r)$ is the potential energy of interaction between two molecules, which is assumed to be a function of the distance r alone. The radial distribution function is normalized as

$$\lim_{r\to\infty} g(r)=1;$$

and we have the following relation[2]:

$$kT\left(\frac{\partial\rho}{\partial p}\right)_T=1+\rho\int_0^\infty [g(r)-1]4\pi r^2dr\,. \quad (3)$$

It is seen from these equations that the thermodynamical properties of a fluid can be obtained from the knowledge of the distribution function $g(r)$. However, when some approximate $g(r)$'s are made use of, it often occurs that self-consistency of the theory is broken, since certain thermodynamical relations exist among the quantities on the left sides of Eqs. (1), (2) and (3). In fact it has been pointed out by several authors[3][4] that Eqs. (1) and (3) cannot be consistent if $g(r)$ based on Kirkwood's superposition approximation is used. Rushbrooke and Scoins[3] showed that this inconsistency can be reduced by adopting the so-called "netted-chain approximation" which can be used in place of the superposition approximation. It is not the purpose of this paper to investigate this inconsistency. Rather it will be pointed out that there is another inconsistency which is supposed to be more serious.

There exists the thermodynamical relation

$$\frac{\partial}{\partial T}\left(\frac{p}{T}\right)=\frac{\partial}{\partial V}\left(\frac{E}{T^2}\right) \tag{4}$$

between p and E. It is needless to say that relation (4) is satisfied by the values of p and E, which are calculated from Eqs. (1) and (2), if the exact distribution function $g(r)$ is used. If, however, some approximate $g(r)$ is used to calculate p and E, relation (4) is not always satisfied. It is the purpose of this paper to examine whether relation (4) holds or not for the approximate $g(r)$'s hitherto derived and to improve the approximations if relation (4) is found not to be satisfied.

If p and E are known as the functions of T and V, the Helmholtz free energy A can be obtained by integrating

$$d\left(\frac{A}{T}\right)=-\frac{p}{T}\,dV-\frac{E}{T^2}dT\,.$$

Then Eq. (4) is the condition that the right side of the above equation is integrable. Therefore it can be said that our aim is to examine whether or not the free energy can be derived in a consistent way.

§ 2. Notations

It is convenient for our purpose to express the pressure p, the internal energy E and the radial distribution function $g(r)$ as power series in the number density ρ. Thus,

$$\frac{p}{\rho kT}=1+B\rho+C\rho^2+D\rho^3+\cdots\,, \tag{5}$$

$$\frac{E}{\frac{3}{2}NkT}=1+E_1\rho+E_2\rho+E_3\rho^3+\cdots\,, \tag{6}$$

$$g(r)=e^{-\phi(r)/kT}[1+g_1(r)\rho+g_2(r)\rho^2+\cdots]\,. \tag{7}$$

Equation (5) is the virial expansion of $p/\rho kT$ and B, C and D are the second virial coefficient, the third and the fourth respectively. The expressions of these coefficients are found in many text-books[5]. Equation (7) is due to Mayer and Montroll[6]. The expressions of coefficients of Eq. (6) can be derived from those of Eq. (5) by the use of Eq. (4). Only D, E_3 and $g_2(r)$ will be shown here, since these will play important roles in the following deductions. (The expressions of B, C and $g_1(r)$ will be found in Eq. (24).)

$$D=-\frac{3}{8}\square-\frac{3}{4}\boxslash-\frac{1}{8}\boxtimes\,, \tag{8}$$

$$E_3=\frac{1}{12}T\frac{d}{dT}\square+\frac{1}{6}T\frac{d}{dT}\boxslash+\frac{1}{36}T\frac{d}{dT}\boxtimes\,, \tag{9}$$

$$g_2(r)=\square+2\boxslash+\frac{1}{2}\boxslash+\frac{1}{2}\boxtimes\,. \tag{10}$$

The symbols written in the form of figures represent expressions as shown below:

$$\left.\begin{aligned}
\square&=2\pi\int_{-\infty}^{\infty}r^2a_1^2(r)dr=(2\pi)^4\int_{-\infty}^{\infty}u^2\beta^4(u)du\,,\\
\boxslash&=2\pi\int_{-\infty}^{\infty}r^2\alpha(r)a_1^2(r)dr=(2\pi)^4\int_{-\infty}^{\infty}u^2\beta^2(u)\gamma(u)du\,,\\
\boxtimes&=\iiint_{VVV}\alpha(r_{12})\alpha(r_{23})\alpha(r_{31})\alpha(r_{41})\alpha(r_{42})\alpha(r_{43})d\boldsymbol{r}_2d\boldsymbol{r}_3d\boldsymbol{r}_4\,,
\end{aligned}\right\} \tag{11}$$

$$\left.\begin{aligned}
\square&=(2\pi)^{5/2}\int_{-\infty}^{\infty}u\beta^3(u)\frac{\sin ur}{r}du\,,\\
\boxslash&=(2\pi)^{5/2}\int_{-\infty}^{\infty}u\beta(u)\gamma(u)\frac{\sin ur}{r}du\,,\\
\boxslash&=a_1^2(r)\,,\\
\boxtimes&=\iint_{VV}\alpha(r_{14})\alpha(r_{13})\alpha(r_{34})\alpha(r_{42})\alpha(r_{23})d\boldsymbol{r}_3d\boldsymbol{r}_4\,,\quad(r_{12}=r)\,,
\end{aligned}\right\} \tag{12}$$

where

$$\left.\begin{aligned} \alpha(r) &= e^{-\phi(r)/kT}-1 , \\ u\beta(u) &= \frac{1}{\sqrt{2\pi}}\int_{-\infty}^{\infty} r\alpha(r)\sin ur\,dr , \\ ra_1(r) &= 2\pi\int_{-\infty}^{\infty} u\beta^2(u)\sin ur\,du , \\ u\gamma(u) &= \frac{1}{(2\pi)^2}\int_{-\infty}^{\infty} r\alpha(r)a_1(r)\sin ur\,dr . \end{aligned}\right\} \qquad (13)$$

The function $\phi(r)$ and hence $\alpha(r)$, $\beta(u)$, $a_1(r)$, $\gamma(u)$ are defined also for negative values of the arguments, being assumed to be even functions. The notations in Eq. (13) as well as in Eq. (11) are the same as those used by Rushbrooke and Scoins[3)7)].

If Eqs. (5), (6) and (7) are inserted in both sides of Eqs. (1), (2) and (4) and the coefficients of ρ^3 are compared, the following relations are deduced:

$$D=\frac{\pi}{3}\int_{-\infty}^{\infty}\frac{d\alpha(r)}{dr}g_2(r)r^3dr , \qquad (14)$$

$$E_3=\frac{2\pi}{3}\int_{-\infty}^{\infty}T\frac{\partial\alpha(r)}{\partial T}g_2(r)r^2dr , \qquad (15)$$

$$E_3=-\frac{2}{9}T\frac{dD}{dT} . \qquad (16)$$

It is necessary for the validity of relation (4) to satisfy the relation (16). In the next section it will be examined whether relation (16), instead of relation (4), holds or not when some approximate $g_2(r)$'s are used in Eqs. (14) and (15).

When D and E_3 are expressed in an approximate way in terms of $\beta(u)$, $a_1(r)$ and $\gamma(u)$, it is sometimes difficult to see whether relation (16) holds or not, since these functions are not independent of each other. In such cases the difficulty will be avoided if D and E_3 are calculated explicitly in terms of a simplified interaction potential such as:

$$\begin{aligned} \phi(r) &= \Delta \quad (0<r<a) \\ &= 0 \quad (r>a) , \end{aligned} \qquad (17)$$

that is

$$\begin{aligned} \alpha(r) &= -z \quad (0<r<a) \\ &= 0 \quad (r>a) , \end{aligned}$$

where

$$z=1-e^{-\Delta/kT} .$$

This potential leads to the following expressions for $\beta(u)$, $a_1(r)$, B, C and D:

$$\left.\begin{aligned} u\beta(u) &= z\sqrt{\frac{2}{\pi}}\frac{d}{du}\left(\frac{\sin ua}{u}\right) , \\ a_1(r) &= \frac{z^2\pi}{12}(r^3-12a^2r+16a^3) \quad (0<r<2a) \\ &= 0 \qquad\qquad (r>2a) , \\ B &= bz , \\ C &= \frac{5}{8}b^2z^3 , \\ D &= -\frac{3}{8}\square-\frac{3}{4}\boxslash-\frac{1}{8}\boxtimes \\ &\frac{3}{8}\square=\frac{34}{35}b^3z^4=0.9714b^3z^4 \\ &\frac{3}{4}\boxslash=-\frac{6347}{4480}b^3z^5=-1.4167b^3z^5 \\ &\frac{1}{8}\boxtimes=0.1584b^3z^6 , \end{aligned}\right\} \qquad (18)$$

where

$$b=\frac{2\pi}{3}a^3$$

and the value of (1/8)⊠ is calculated conversely from the value of D in the case of hard spheres where it is known that $D=0.2869b^3$ [8)]. If we put $z=1$ in the above expressions, they are reduced to the case of hard spheres.

§ 3. Discussion of Several Approximate Expressions for $g(r)$

The following fact is important in examining an approximate distribution function. It can be seen from Eqs. (8), (9) and (10) that the function $g_2(r)$ has four terms of different types which are expressed as □, ⧄, ⊠, whereas the quantity D or E_3 is composed of three terms □, ⧄, ⊠ or $d\square/dT$, $d\boxslash/dT$, $d\boxtimes/dT$. When $g_2(r)$ given by Eq. (10) is inserted in Eq. (14) or (15), the term □ in $g_2(r)$ corresponds to the term □ in D or E_3, $2\boxslash+(1/2)\boxslash$ to ⧄, and ⊠ to ⊠. These correspondences may be expressed symbolically as

$$\square\rightarrow\square,\ (\boxslash+\boxslash)\rightarrow\square,\ \boxtimes\rightarrow\boxtimes . \qquad (19)$$

Thus the function $g_2(r)$ can be expressed as a sum of three terms □, ⧄ + ⧄ and ⊠, when used in calculation of D and E_3 and each of these terms contributes separately to the establishment of relation (16). Hence, as shown in later examples, relation (16) is valid even if use is made of some approximate $g_2(r)$'s with one or two of these terms omitted.

The following four kinds of approximations to $g(r)$ will be examined.

1. *The solution of the Born-Green non-linear integral equation*[9)10)]

This integral equation is based upon Kirkwood's superposition approximation. Its solution will be denoted by $g^{(1)}(r)$. The integral equation is given by

$$\log g^{(1)}(r)+\frac{\phi(r)}{kT}=\pi\rho\int_0^\infty\int_{-s}^{s}(s^2-t^2)\frac{t+r}{r} \times[g^{(1)}(t+r)-1]\,dt\,g^{(1)}(s)\frac{1}{kT}\frac{d\phi(s)}{ds}ds\,. \tag{20}$$

2. *Rodriguez's improved form of Green's linear theory*[11)]

The distribution function obtained in this theory will be denoted by $g^{(2)}(r)$. It is given

$$\left.\begin{aligned}&g^{(2)}(r)=\exp[-\phi(r)/kT+f^{(2)}(r)]\,,\\&\text{where}\\&rf^{(2)}(r)=\frac{1}{\sqrt{2\pi}}\int_{-\infty}^{\infty}\frac{\varepsilon^2u\beta^2(u)}{\lambda-\varepsilon\beta(u)}\sin ur\,du,\\&\frac{1}{\lambda}=(2\pi)^{3/2}\rho,\\&\varepsilon-1=\int_{-\infty}^{\infty}r^2f^{(2)}(r)\alpha(r)\,dr\bigg/\int_{-\infty}^{\infty}r^2\alpha(r)dr.\end{aligned}\right\} \tag{21}$$

3. *The netted-chain approximation*[3)]

The radial distribution function in this approximation is obtained by selecting particular terms from the right side of Eq. (7) and by smming them up. This will be denoted by $g^{(3)}(r)$. It is given by

$$\left.\begin{aligned}&g^{(3)}(r)=e^{-\phi(r)/kT}[1+f^{(3)}(r)]\,,\\&\text{where}\\&rf^{(3)}(r)=\frac{1}{\sqrt{2\pi}}\frac{1}{\lambda}\int_{-\infty}^{\infty}\frac{\left[\beta(u)+\dfrac{\gamma(u)}{\lambda}\right]^2}{1-\dfrac{\beta(u)}{\lambda}-\dfrac{\gamma(u)}{\lambda^2}}\\&\qquad\times u\sin ur\,du.\end{aligned}\right\} \tag{22}$$

4. *The original form of Green's linear theory*[10)]

The distribution function obtained in this theory will be denoted by $g^{(4)}(r)$. It is given by

$$\left.\begin{aligned}&g^{(4)}(r)=e^{-\phi(r)/kT}[1+f^{(4)}(r)]\,,\\&\text{where}\\&rf^{(4)}(r)=\frac{1}{\sqrt{2\pi}}\int_{-\infty}^{\infty}\frac{\varepsilon^2u\beta^2(u)}{\lambda-\varepsilon\beta(u)}\sin ur\,du\,,\\&\varepsilon=\text{constant}.\end{aligned}\right\} \tag{23}$$

Expansion of the above four approximate $g(r)$'s into power series in ρ in the form of Eq. (7) leads to the four approximate expressions for $g_2(r)$, which can be used in calculation of D and E_3 by Eqs. (14) and (15). Each way of approximations will be shown by superscript figures. For example $D^{(3)}, E_3{}^{(3)}$ and $g_2{}^{(3)}(r)$ express D, E_3 and $g_2(r)$ based on the netted-chain approximation, respectively.

The expressions for B, C and $g_1(r)$ in these approximations are expressed as follows:

$$\left.\begin{aligned}&B^{(1)}=B^{(2)}=B^{(3)}=B^{(4)}=B=-\frac{(2\pi)^{3/2}}{2}\beta(0)\,,\\&C^{(1)}=C^{(2)}=C^{(3)}=C=-\frac{(2\pi)^{5/2}}{3}\int_{-\infty}^{\infty}u^2\beta^3(u)du\,,\\&\qquad C^{(4)}=\varepsilon^2C\,,\\&g_1{}^{(1)}(r)=g_1{}^{(2)}(r)=g_1{}^{(3)}(r)=g_1(r)=a_1(r)\,,\\&\qquad g_1{}^{(4)}(r)=\varepsilon^2g_1(r)\,.\end{aligned}\right\} \tag{24}$$

It is seen that, except for Green's linear theory, $g_1(r)$'s and hence C and E_2 are correct.

The functions $g_2(r)$'s for these approximations can be expressed as:

$$g_2{}^{(1)}(r)=\square+2\boxslash+\tfrac{1}{2}\boxslash+(2\pi)^{1/2}\int_{-\infty}^{\infty}ds\,\alpha(s)\frac{da_1(s)}{ds} \times\int_0^s dt\cdot t\int_{-\infty}^{\infty}du\,\beta(u)\sin ut\frac{\sin ur}{r}\,, \tag{25–1}$$

$$g_2{}^{(2)}(r)=\square+\tfrac{1}{2}\boxslash+\frac{3C}{B}a_1(r)\,, \tag{25–2}$$

$$g_2{}^{(3)}(r)=\square+2\boxslash\,, \tag{25–3}$$

$$g_2{}^{(4)}(r)=\varepsilon^3\square\,. \tag{25–4}$$

Comparison of Eq. (10) with Eqs. (25–2), (25–3) and (25–4) shows clearly that they are not correct and hence cannot give the correct expressions for D and E_3. The last term of Eq. (25–1) corresponds to $\frac{1}{2}\boxtimes$ of Eq. (10). It differs, however, essentially from $\frac{1}{2}\boxtimes$, since the former has only four pairs of molecules in its integrand while the latter has five pairs. (Note that $\alpha(r)$ and $\beta(u)$ correspond to one pair of molecules and $a_1(r)$ to two pairs.) Therefore $g_2{}^{(1)}(r)$ can give no correct expressions for D and E_3. This conclusion for D has been already pointed out[7)]. Relation (16) between $D^{(1)}$ and $E_3{}^{(1)}$ fails to be valid due to the presence of the last term of $g_2{}^{(1)}(r)$. (See Eq. (26).) It fails to be valid also for $D^{(2)}$ and $E_3{}^{(2)}$ and for $D^{(3)}$ and $E_3{}^{(3)}$. It is due to the fact that, in $g_2^{(2)}(r)$ and $g_2^{(3)}(r)$, one of $\boxslash$ and $\boxslash$ is either missing or substituted by another term, since, as explained at the beginning of this section, it is necessary that both $\boxslash$ and $\boxslash$ are contained as one group. In $g_2^{(4)}(r)$ these terms are missing completely and this makes relation (16) between $D^{(4)}$ and $E_3^{(4)}$ hold again. Actually, it is not necessary to examine relation (16) as shown above so far as Green's linear theory is concerned, because, in this case, Green[10] has already confirmed relation (4) and calculated the free energy.

After all, it is found that, among the four approximations examined above, the original form of Green's linear theory is the only one which satisfies relation (4). It seems that the above conclusion remains valid, even if the solution of the integral equation proposed by Kirkwood[12] is added to these four cases, though this is not examined here.

Finally, the expressions for D and E_3 based on the above-mentioned approximations are shown in the following, first giving the expressions for the general form and then for the simplified form, Eq. (17), of the interaction potentials:

$$\left.\begin{aligned}
D^{(1)}&=\left(-\frac{3}{8}\square-\frac{3}{4}\boxslash\right)+\left(\frac{\pi}{6}\int_{-\infty}^{\infty}drr^3\alpha(r)\frac{da_1(r)}{dr}a_1(r)-\pi\int_{-\infty}^{\infty}dr\alpha(r)\frac{da_1(r)}{dr}\int_0^r ds\,s^2a_1(s)\right)\\
&=\left(-\frac{34}{35}b^3z^4+\frac{6347}{4480}b^3z^5\right)-\frac{493}{2240}b^3z^5\,,\\
E_3^{(1)}&=\left(\frac{1}{12}T\frac{d}{dT}\square+\frac{1}{6}T\frac{d}{dT}\boxslash\right)+\frac{\pi}{3}\int_{-\infty}^{\infty}dr\alpha(r)\frac{da_1(r)}{dr}T\frac{\partial}{\partial T}\int_0^r ds\,s^2a_1(s)\\
&=\left(\frac{272}{315}b^3z^3-\frac{6347}{4032}b^3z^4\right)T\frac{dz}{dT}+\frac{4819}{20160}b^3z^4T\frac{dz}{dT}\,,\\
E_3^{(1)}&+\frac{2}{9}T\frac{dD^{(1)}}{dT}=\frac{111}{20160}b^3z^4T\frac{dz}{dT}\,,
\end{aligned}\right\}\tag{26}$$

$$\left.\begin{aligned}
D^{(2)}&=-\frac{3}{8}\square+\frac{\pi}{6}\int_{-\infty}^{\infty}dr\,r^3\frac{d\alpha(r)}{dr}a_1^2(r)+\frac{3C^2}{B}\\
&=-\frac{34}{35}b^3z^4+\frac{25}{128}b^3z^5+\frac{75}{64}b^3z^5\,,\\
E_3^{(2)}&=\frac{1}{12}T\frac{d}{dT}\square+\frac{\pi}{3}\int_{-\infty}^{\infty}dr\,r^2\,a_1^2(r)\,T\frac{\partial\alpha(r)}{\partial T}-\frac{1}{2}\frac{T}{B}\frac{dC^2}{dT}\\
&=\frac{272}{315}b^3z^3T\frac{dz}{dT}-\frac{6347}{20160}b^3z^4T\frac{dz}{dT}-\frac{75}{64}b^3z^4T\frac{dz}{dT}\,,\\
E_3^{(2)}&+\frac{2}{9}T\frac{dD^{(2)}}{dT}=\frac{653}{20160}b^3z^4T\frac{dz}{dT}\,,
\end{aligned}\right\}\tag{27}$$

$$\left.\begin{aligned}
D^{(3)}&=\left(-\frac{3}{8}\square-\frac{3}{4}\boxslash\right)-\frac{\pi}{6}\int_{-\infty}^{\infty}dr\,r^3\frac{d\alpha(r)}{dr}a_1^2(r)\\
&=\left(-\frac{34}{35}b^3z^4+\frac{6347}{4480}b^3z^5\right)-\frac{25}{128}b^3z^5\,,\\
E_3^{(3)}&=\left(\frac{1}{12}T\frac{d}{dT}\square+\frac{1}{6}T\frac{d}{dT}\boxslash\right)-\frac{\pi}{3}\int_{-\infty}^{\infty}dr\,r^2a_1^2(r)\,T\frac{\partial\alpha(r)}{\partial T}\\
&=\left(\frac{272}{315}b^3z^3-\frac{6347}{4032}b^3z^4\right)T\frac{dz}{dT}+\frac{6347}{20160}b^3z^4T\frac{dz}{dT}\,,\\
E_3^{(3)}&+\frac{2}{9}T\frac{dD^{(3)}}{dT}=\frac{493}{5040}b^3z^4T\frac{dz}{dT}\,,
\end{aligned}\right\}\tag{28}$$

$$\left.\begin{aligned} D^{(4)} &= -\frac{3}{8}\varepsilon^3\square = -\frac{34}{35}\varepsilon^3 b^3 z^4 ,\\ E_3{}^{(4)} &= \frac{1}{12}\varepsilon^3 T\frac{d}{dT}\square = \frac{272}{315}\varepsilon^3 b^3 z^3 T\frac{dz}{dT} ,\\ E_3{}^{(4)} &+ \frac{2}{9}T\frac{dD^{(4)}}{dT} = 0 . \end{aligned}\right\} \tag{29}$$

Each of third equations of Eqs. (26), (27), (28) and (29) gives the values of $E_3+(2/9)T\times(dD/dT)$ for the simplified form of the interaction potential. As stated above, they should be zero if the theory is self-consistent.

§ 4. Attempt to Improve the Approximation I

As shown in the preceding section, only Green's linear theory satisfies relation (4). However this theory is not satisfactory from the quantitative point of view. It will be desirable that some approximate procedure will be found, which, while satisfying relation (4), gives better quantitative results than Green's theory.

In the following discussion, the free energy will be expressed in terms of $g(r)$, and $g(r)$ will be determined so as to minimize the free energy. Then the internal energy E and the pressure p will be derived from the free energy so that relation (4) will be automatically satisfied.

The configurational part S_τ of entropy is defined by

$$S_\tau = -\frac{k}{V^N}\int_V\cdots\int_V \times P_N(\boldsymbol{r}_1, \boldsymbol{r}_2,\cdots,\boldsymbol{r}_N)\log P_N(\boldsymbol{r}_1,\boldsymbol{r}_2,\cdots,\boldsymbol{r}_N) \times d\boldsymbol{r}_1\, d\boldsymbol{r}_2\cdots d\boldsymbol{r}_N , \tag{30}$$

where $P_N(\boldsymbol{r}_1, \boldsymbol{r}_2,\cdots,\boldsymbol{r}_N)$ denotes the distribution function at the point $(\boldsymbol{r}_1, \boldsymbol{r}_2,\cdots,\boldsymbol{r}_N)$ in the configuration space of N molecules and is normalized as

$$\frac{1}{V^N}\int_V\cdots\int_V P_N(\boldsymbol{r}_1, \boldsymbol{r}_2, \cdots, \boldsymbol{r}_N)d\boldsymbol{r}_1 d\boldsymbol{r}_2\cdots d\boldsymbol{r}_N = 1 .$$

The reduced distribution functions $P_n(\boldsymbol{r}_1, \boldsymbol{r}_2, \cdots, \boldsymbol{r}_n)$ for n molecules are defined by

$$P_n(\boldsymbol{r}_1, \boldsymbol{r}_2,\cdots,\boldsymbol{r}_n) = \frac{1}{V^{N-n}}\int_V\cdots\int_V \times P_N(\boldsymbol{r}_1, \boldsymbol{r}_2,\cdots,\boldsymbol{r}_n,\boldsymbol{r}_{n+1},\cdots,\boldsymbol{r}_N)d\boldsymbol{r}_{n+1}\cdots d\boldsymbol{r}_N ,\quad n=1, 2, 3,\cdots . \tag{31}$$

Then the function $P_2(\boldsymbol{r}_1, \boldsymbol{r}_2)$ is the same as $g(|\boldsymbol{r}_1-\boldsymbol{r}_2|)$. The functions $z_n(\boldsymbol{r}_1, \boldsymbol{r}_2,\cdots,\boldsymbol{r}_n)$ are defined in terms of P_n as follows:

$$\left.\begin{aligned} \log P_1(\boldsymbol{r}_1) &= z_1(\boldsymbol{r}_1) ,\\ \log P_2(\boldsymbol{r}_1, \boldsymbol{r}_2) &= z_2(\boldsymbol{r}_1, \boldsymbol{r}_2)+z_1(\boldsymbol{r}_1)+z_1(\boldsymbol{r}_2)\\ \log P_3(\boldsymbol{r}_1, \boldsymbol{r}_2, \boldsymbol{r}_3) &= z_3(\boldsymbol{r}_1, \boldsymbol{r}_2, \boldsymbol{r}_3)+z_2(\boldsymbol{r}_1, \boldsymbol{r}_2)+z_2(\boldsymbol{r}_2, \boldsymbol{r}_3)\\ &\quad +z_2(\boldsymbol{r}_3, \boldsymbol{r}_1)+z_1(\boldsymbol{r}_1)+z_1(\boldsymbol{r}_2)+z_1(\boldsymbol{r}_3) ,\\ &\cdots\cdots\cdots\cdots\cdots\cdots\cdots\cdots\\ \text{or conversely}\qquad &\\ z_1(\boldsymbol{r}_1) &= \log P_1(\boldsymbol{r}_1) ,\\ z_2(\boldsymbol{r}_1, \boldsymbol{r}_2) &= \log P_2(\boldsymbol{r}_1, \boldsymbol{r}_2)/P_1(\boldsymbol{r}_1)P_1(\boldsymbol{r}_2),\\ z_3(\boldsymbol{r}_1, \boldsymbol{r}_2, \boldsymbol{r}_3) &= \log\frac{P_3(\boldsymbol{r}_1, \boldsymbol{r}_2, \boldsymbol{r}_3)P_1(\boldsymbol{r}_1)P_1(\boldsymbol{r}_2)P_1(\boldsymbol{r}_3)}{P_2(\boldsymbol{r}_1, \boldsymbol{r}_2)P_2(\boldsymbol{r}_2, \boldsymbol{r}_3)P_2(\boldsymbol{r}_3, \boldsymbol{r}_1)}\\ &\cdots\cdots\cdots\cdots\cdots\cdots\cdots\cdots \end{aligned}\right\} \tag{32}$$

From Eqs. (30), (31) and (32) S_τ is written in terms of P_n's and z_n's as

$$S_\tau = -k\sum_{n=1}^{N}\frac{1}{V^n}\frac{N!}{n!(N-n)!}\int_V\cdots\int_V \times P_n(\boldsymbol{r}_1, \boldsymbol{r}_2,\cdots \boldsymbol{r}_n)z_n(\boldsymbol{r}_1, \boldsymbol{r}_2,\cdots,\boldsymbol{r}_n)d\boldsymbol{r}_1 d\boldsymbol{r}_2 \cdots d\boldsymbol{r}_n . \tag{33}$$

If use is made of the "generalized superposition approximation", which was adopted by Mayer[13], that is

$$z_n(\boldsymbol{r}_1, \boldsymbol{r}_2,\cdots,\boldsymbol{r}_n)=0 \quad \text{for } n\geqq 3 , \tag{34}$$

Eq. (33) becomes

$$S_\tau = -k\frac{N}{V}\int_V P_1(\boldsymbol{r})z_1(\boldsymbol{r})d\boldsymbol{r} - \frac{k}{2}\frac{N(N-1)}{V^2}$$
$$\times\iint_{VV} P_2(\boldsymbol{r}_1, \boldsymbol{r}_2)z_2(\boldsymbol{r}_1, \boldsymbol{r}_2)d\boldsymbol{r}_1 d\boldsymbol{r}_2$$

or

$$S_\tau = -k\frac{N(N-2)}{V}\int_V P_1(\boldsymbol{r})\log P_1(\boldsymbol{r})d\boldsymbol{r}$$
$$-\frac{k}{2}\frac{N(N-1)}{V^2}\iint_{VV} \tag{35}$$
$$\times P_2(\boldsymbol{r}_1, \boldsymbol{r}_2)\log P_2(\boldsymbol{r}_1, \boldsymbol{r}_2)d\boldsymbol{r}_1 d\boldsymbol{r}_2 .$$

Now the configurational part E_τ of the internal energy is expressed as

$$E_\tau = \frac{1}{2}\frac{N(N-1)}{V^2}\iint_{VV}\phi(\boldsymbol{r}_1, \boldsymbol{r}_2)P_2(\boldsymbol{r}_1, \boldsymbol{r}_2)d\boldsymbol{r}_1 d\boldsymbol{r}_2 \tag{36}$$

without any approximation. The configurational part A_τ of the free energy is obtained from Eqs. (35) and (36) as

$$A_\tau = E_\tau - TS_\tau$$
$$= kT\frac{N(N-2)}{V}\int P_1(\boldsymbol{r})\log P_1(\boldsymbol{r})d\boldsymbol{r}$$
$$+\frac{1}{2}\frac{N(N-1)}{V^2}\iint_{VV}$$
$$\times[\phi(\boldsymbol{r}_1, \boldsymbol{r}_2)+kT\log P_2(\boldsymbol{r}_1, \boldsymbol{r}_2)] \tag{37}$$
$$\times P_2(\boldsymbol{r}_1, \boldsymbol{r}_2)d\boldsymbol{r}_1 d\boldsymbol{r}_2 .$$

It is clear that the form of the function $P_2(\boldsymbol{r}_1, \boldsymbol{r}_2)$, which minimizes A_τ under the condition $P_1=\text{const.}=1$, is given by

$$P_2(\boldsymbol{r}_1, \boldsymbol{r}_2) = g(|\boldsymbol{r}_1-\boldsymbol{r}_2|)\propto e^{-\phi(\boldsymbol{r}_1, \boldsymbol{r}_2)/kT} . \tag{38}$$

This is the simplest form of the approximate expression for $g(r)$. Thus in our case the approximation has been found to be very poor, and it means that our attempt on the above line has not been successful. This is an example which shows that, if Mayer's superposition approximation (34) is adopted, it must be done with much care.

Recently Richardson[14] obtained the integral equation for $g(r)$ by a similar procedure as above. In place of the approximation (34) he used the approximation

$$z_3=\text{const.}=-\gamma , \quad z_n=0 \quad \text{for } n\geqq 4 . \tag{39}$$

Although the order of magnitude of γ is $O(1/N^2)$, yet the term containing z_3 on the right side of Eq. (33) cannot be neglected, since this term is multiplied by the quantity of the order of $O(N^3)$. Retaining this term, Richardson obtained the integral equation for $g(r)$ similar to the Born-Green non-linear integral equation. It is not clear at present how far his approximation is successful, but it seems to be necessary, if his idea should be carried out thoroughly, to apply similar procedures not only to z_3 but also to z_4, z_5 and so on.

§ 5. Attempt to Improve the Approximation II

In Green's linear theory the parameter ε appears, as shown in Eq. (23), where ε is supposed to be independent of T and V. In order to improve Green's theory, Rodriguez[11] determined ε by the equation

$$\varepsilon-1=\int_0^\infty r^2 f(r)\alpha(r)dr \Big/ \int_0^\infty r^2\alpha(r)dr , \tag{40}$$

considering that in Green's theory $\varepsilon-1$ is an average of the function $f(r)$ near $r=0$. Since $f(r)$ itself depends on ε, the parameter ε is given implicitly as a function of T and V. As shown in § 3, however, Rodriguez's procedure violates relation (4). To avoid this difficulty, it will be attempted to determine ε as a function of T and V in such a way that relation (4) remains valid.

The expressions of the pressure and the internal energy, when approximate expression (23) for $g(r)$ is inserted in Eqs. (1) and (2), become respectively

$$\left.\begin{aligned}
\frac{p}{\rho kT} &= 1-\frac{\beta(0)}{2\lambda}-\frac{1}{2\sqrt{2\pi}}\frac{1}{\lambda}\int_{-\infty}^{\infty}\left[-\frac{1}{2}\varepsilon\beta^2(u)+\frac{\lambda^2\beta(u)}{\lambda-\varepsilon\beta(u)}+\frac{\lambda^2}{\varepsilon}\log\left(1-\frac{\varepsilon}{\lambda}\beta(u)\right)\right]u^2du ,\\
\frac{E}{\frac{3}{2}NkT} &= 1+\frac{T}{3\lambda}\frac{\partial\beta(0)}{\partial T}+\frac{1}{3\sqrt{2\pi}}\frac{1}{\lambda}\int_{-\infty}^{\infty}\frac{\varepsilon^2\beta^2(u)T\dfrac{\partial\beta(u)}{\partial T}}{\lambda-\varepsilon\beta(u)}u^2du ,
\end{aligned}\right\} \tag{41}$$

where the superscript figures are dropped and the thermodynamical variables T and $\lambda=\{(2\pi)^{3/2}\rho\}^{-1}$ are used instead of T and V. Relation (4) is satisfied by these expressions when ε is assumed to be independent of T and λ. If ε is supposed to be a function of T and λ, it is found from Eqs. (4) and (41) that ε must satisfy the differential equation

$$\frac{\partial\varepsilon(T,\lambda)}{\partial T}\frac{\partial F(T,\lambda,\varepsilon)}{\partial\lambda}=\frac{\partial\varepsilon(T,\lambda)}{\partial\lambda}\frac{\partial F(T,\lambda,\varepsilon)}{\partial T}\,, \tag{42}$$

where

$$F(T,\lambda,\varepsilon)=\int_{-\infty}^{\infty}\left[-\frac{\beta^2(u)}{2\lambda}+\frac{\lambda}{\varepsilon^2}\log\left(1-\frac{\varepsilon}{\lambda}\beta(u)\right)+\frac{\lambda}{\varepsilon}\frac{\beta(u)}{\lambda-\varepsilon\beta(u)}\right]u^2du \tag{43}$$

and $\partial F/\partial T$ (or $\partial F/\partial\lambda$) is the derivative of F with respect to T (or λ) under the condition $\varepsilon=\text{const}$. The general solution of Eq. (42) is

$$\varepsilon=U(F)\,, \tag{44}$$

where $U(x)$ is any arbitrary function of x. Equation (44) determines ε implicitly as a function of T and λ, F itself depending on ε as seen from Eq. (43).

If the function $\overline{F}(T,\lambda,\varepsilon)$ is defined by

$$\begin{aligned}\overline{F}(T,\lambda,\varepsilon)&=F-\int_{-\infty}^{\infty}\left[\frac{\lambda}{\varepsilon}\frac{\beta(u)}{\lambda-\varepsilon\beta(u)}-\frac{\beta(u)}{\varepsilon}-\frac{\beta^2(u)}{\lambda}\right]u^2du\\&=\int_{-\infty}^{\infty}\left[\frac{\beta^2(n)}{2\lambda}+\frac{\beta(u)}{\varepsilon}+\frac{\lambda}{\varepsilon^2}\log\left(1-\frac{\varepsilon}{\lambda}\beta(u)\right)\right]u^2du\,,\end{aligned} \tag{45}$$

the expressions (41) become respectively

$$\left.\begin{aligned}\frac{p}{\rho kT}&=1-\frac{\beta(0)}{2\lambda}-\frac{1}{2\sqrt{2\pi}}\varepsilon\lambda\frac{\partial\overline{F}(T,\lambda,\varepsilon)}{\partial\lambda}\,,\\ \frac{E}{\frac{3}{2}NkT}&=1+\frac{T}{3\lambda}\frac{\partial\beta(0)}{\partial T}-\frac{1}{3\sqrt{2\pi}}\varepsilon T\frac{\partial F(T,\lambda,\varepsilon)}{\partial T}\,,\end{aligned}\right\} \tag{41'}$$

where $\partial\overline{F}/\partial T$ and $\partial\overline{F}/\partial\lambda$ have similar meanings as $\partial F/\partial T$ and $\partial F/\partial\lambda$ in Eq. (42). By the relation

$$d\left(\frac{A}{NkT}\right)=-\frac{3}{2}\frac{1}{T}\left(\frac{E}{\frac{3}{2}NkT}\right)dT-\frac{1}{\lambda}\left(\frac{p}{\rho kT}\right)d\lambda\,,$$

where A denotes the Helmholtz free energy, we finally obtain

$$\frac{A}{NkT}=-\log\lambda-\frac{3}{2}\log T-\frac{1}{2\lambda}\beta(0)+\frac{1}{2\sqrt{2\pi}}\left[\varepsilon\overline{F}(T,\lambda,\varepsilon)+\int_0^{F(T,\lambda,\varepsilon)}x\frac{dU(x)}{dx}dx\right]+C_0\,. \tag{46}$$

In this equation C_0 denotes a constant independent of T and λ and hence of T and V. Expression (46) for the free energy coincides in form with the one derived by Green[10] apart from the term with the integral $\int_0^F x\frac{dU}{dx}dx$.

Since $f(r)$ should tend to zero as ρ tends to zero or λ to a very large value, it is required that ε should have the property

$$\lim_{\lambda\to\infty}\varepsilon(T,\lambda)=1\,.$$

It is found from Eq. (43) that $\lim\limits_{\lambda\to\infty}F(T,\lambda,\varepsilon)=0$. Therefore, the function $U(x)$ of Eq. (44) must have the property that $U(0)=1$. The equation which determines ε becomes finally

$$\varepsilon=U(F)\,,\quad U(0)=1\,. \tag{47}$$

However, ε still cannot be determined uniquely since the form of $U(x)$ is arbitrary except for its initial value. It turns out that it is impossible to determine the function $U(x)$ so as to minimize the free energy. We have not yet found a method appropriate to the determination of $U(x)$. A similar situation occurs in Rodriguez's procedure as well, because there could be other expressions than Eq. (40) which have the meaning of the average of $f(r)$ near $r=0$; for example,

$$\varepsilon-1=\int_0^\infty f(r)\alpha(r)\,dr \Big/ \int_0^\infty \alpha(r)dr\,,$$

If it is assumed that $U(x)$ can be expanded in a power series in x, Eq. (47) gives, when ρ is small,

$$\varepsilon=1+0(\rho^2)$$

Thus ε does not vary so long as the first power of ρ is concerned, and the expression for $g_2(r)$ becomes equal to Eq. (25–4) with $\varepsilon=1$. If other forms of $U(x)$, for example, $U(x)=1+\sqrt{x}$, are used, the term of the first power of ρ can appear in the expression of ε and hence the expression for $g_2(r)$ can be made more accurate.

§ 6. Conclusion

Many attempts have been made thus far to obtain theoretically the radial distribution function of fluids. It may be said that one of their objects is to obtain the distribution function itself and hence to obtain the knowledge about the structure of fluids, especially of liquids, which can be compared with the structure determined experimentally by the method of X-ray scattering. The other object is to calculate the thermodynamical functions of fluids with the use of the distribution function obtained theoretically.

In either case the solution of the Born-Green non-linear integral equation has been supposed to be most preferable among different approximations and many authors have attempted to solve the integral equation analytically or numerically. However, it has been found in § 3 that this solution does not lead to relation (4) and hence is not suitable for use in the calculation of the thermodynamical quantities. We could say strictly that, for example, even if this solution is obtained exactly and used in Eq. (1) in the calculation of the pressure, it is doubtful whether the calculated one can be called the "pressure". This fact does not necessarily mean that the above solution is not a good approximation for the radial distribution function. On the contrary, it seems to be the most preferable approximation in the present stage of the theory.

Rushbrooke and Scoins showed that the inconsistency between Eqs. (1) and (3) can be reduced for the case of hard spheres by adopting the netted-chain approximation. As shown in § 3, this approximation violates relation (4). Moreover, it is not certain that this approximation will reduce the inconsistency between Eqs. (1) and (3) for more general forms of interaction potential.

The procedure proposed in § 5 may be said to offer an improvement of Green's linear theory, because the dependence of ε on temperature and volume is taken into account. At the same time our theory can be said to be an improved form of Rodriguez's theory, since relation (4) holds in the former while it does not in the latter. It is, however, desirable that more appropriate approximation will be found, in which relation (4) is satisfied, giving, at the same time, better quantitative results.

The author wishes to express his appreciation to Professor A. Harasima for his continual encouragement in the course of this work.

References

1) See, for example, T. L. Hill, "Statistical Mechanics" (McGraw-Hill, New York, 1956), pp. 189 and 190.
2) See, for example, Hill, *l.c.*, p. 236.
3) G. S. Rushbrooke and H. I. Scoins: Proc. Roy. Soc. **A216** (1953) 203.
4) B. R. A. Nijboer and L. van Hove: Phys. Rev. **85** (1952) 777.
5) See, for example, Hill, *l.c.*, p. 141.
6) J. E. Mayer and E. W. Montroll: J. Chem. Phys. **9** (1941) 2; see also J. de Boer: Rep. Progr. Phys. **12** (1949) 305 and reference 3.
7) G. S. Rushbrooke and H. I. Scoins: Phil. Mag. **42** (1951) 582.
8) R. H. Fowler and A. E. Guggenheim: "Statistical Thermodynamics" (Cambridge, London, 1939) § 717.
9) M. Born and H. S. Green: Proc. Roy. Soc. **A188** (1946) 10.
10) H. S. Green: Proc. Roy. Soc. **A189** (1947) 103.
11) A. E. Rodriguez: Proc. Roy. Soc. **A196** (1949) 73.
12) J. G. Kirkwood: J. Chem. Phys. **3** (1935) 300; J. G. Kirkwood and E. M. Boggs: J. Chem. Phys. **10** (1942) 394.
13) J. E. Mayer: J. Chem. Phys. **15** (1947) 187.
14) J. M. Richardson: J. Chem. Phys. **23** (1955) 2304.

JOURNAL OF THE PHYSICAL SOCIETY OF JAPAN Vol. 12, No. 4, APRIL, 1957

Note on Some Properties of Gamma Brass*

By Takao SATO and Seiichiro NOGUCHI

Department of Physics, Tokyo Metropolitan University, Tokyo

(Received November 20, 1956)

Electrical resistance and magneto-resistance of gamma brass were measured at liquid helium, liquid nitrogen and room temperature. Moreover, Hall coefficient and thermoelectric power of gamma brass were measured at room temperature. Data of the electrical resistance are presented for several samples having various concentrations. In the relation between specific resistivity and concentration, a minimum occurs at about 34 wt.% copper in the curve of resistivity *vs*. concentration. The value of the Hall coefficient and of the thermoelectric power are comparable to the values of pure metals. The magneto-resistance is small at room temperature but becomes large at liquid helium temperature. Differences of the physical properties between gamma brass and bismuth are discussed.

§ 1. Introduction

It is known as a Hume-Rothery rule that the crystal structures of the intermetallic compound are specified by their electron concentration. Especially, the intermetallic compound whose electron concentration is 21/13 possesses a crystal structure of gamma brass type. On this gamma brass type structure Westgren and Phragmen[1] carried out the structure analysis by means of X-ray diffraction and found its structure to be very similar to the body centered cubic structure except that 52 atoms are included in its unit cell.

Jones[2] discussed about the stability of gamma structure on the basis of the facts that alloys of gamma structure are usually brittle and have a large diamagnetic susceptibility and a large Hall coefficient. In his theory, alloys of gamma structure were regarded as analogous to bismuth which has nearly filled band. In this paper we shall demonstrate the dissimilarity between gamma brass and bismuth, on the basis of the specific resistivity versus concentration curve of gamma brass and other properties.

§ 2. Experiment

a) *Specimens and Procedure*

Purity of zinc used in the present investigation was of 99.95% and that of copper was of 99.98%. These alloys were melted under flux, mixture of sodium chloride and potassium chloride and were sucked up into quartz tubes of 1~2 mm diameter. Although a gamma brass is exceedingly brittle and improper to the machining, we have easily prepared a good shaped specimen by this sucking method. These specimens were sealed into quartz tubes with argon gas, and annealed for 50 hours at 550~600°C. The tubes were then cooled slowly down to room temperature. After this treatment one part of them was used for measurement and others for chemical analysis. It was confirmed by X-ray photography that each specimen consists of a homogeneous gamma phase.

Electrical resistance was measured by ordinary D-C method with potentiometer. Specimens for the measurement of Hall coefficient were about $10 \times 20 \times 0.5$ mm in size. Since the Hall coefficient was unexpectedly small, an apparatus with sensitivity of 7×10^{-9} volt was used, the details of which are the same as already reported.[3]

b) *Experimental results*

(1) Relation between specific resistivity and concentration

Specific resistivity of the specimens of 31.5, 33.3, 35.3, 38.0 and 41.6 wt.% copper were measured. The results of these experiments are given in the Fig. 1, which shows an occurrence of a minimum in resistance at gamma phase. Moreover, the specific resistivity is of the same magnitude as those of ordinary metals.

---

* This work performed by the equipments of very low temperature in the Research Laboratory of Iron, Steel and other metals of Tohoku University.

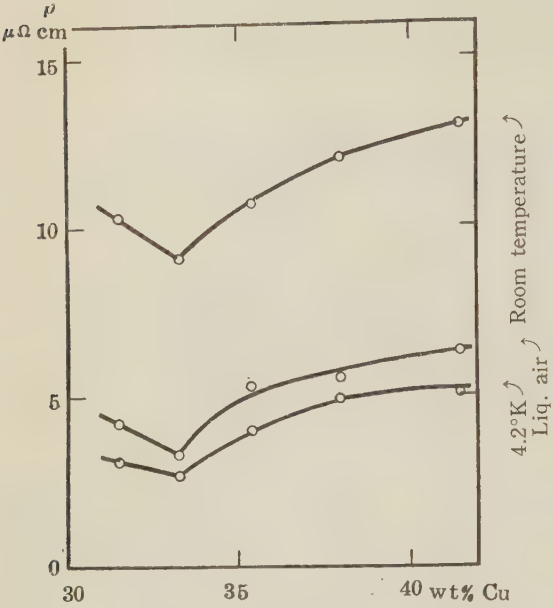

Fig. 1. Electrical resistivity *vs.* concentration curve of gamma brass.

(2) Relation between specific resistivity and temperature

Temperature dependence of the resistivity is shown in the Fig. 2. In the range from 4.2° K to 1.5° K the resistance of each specimen become almost constant. In the higher temperature range, the temperature coefficient was positive.

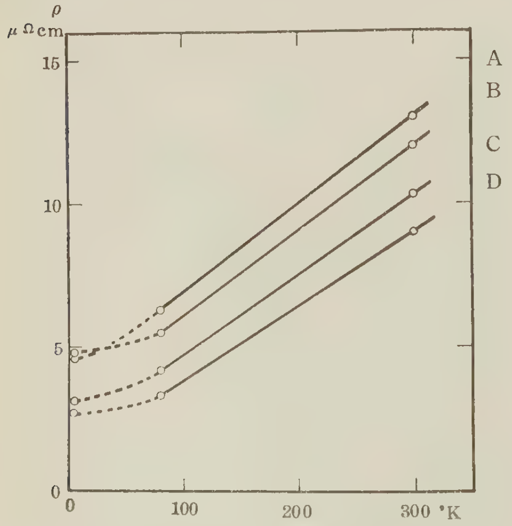

A: 41.6% Cu B: 38.0% Cu
C: 31.5% Cu D: 33.3% Cu

Fig. 2. Electrical resistivity *vs.* temperature curve of gamma brass.

(3) Hall coefficient

The Hall coefficient of gamma brass was very small. The Hall potential of the specimen (69 wt.% zinc) of 10×20×0.5 mm in size was about 2.3×10^{-8} volt for the magnetic field of 5000 gauss at room temperature. From this result $+2.9\times10^{-4}$ cgs. emu. of Hall coefficient was obtained. This value is the same order of magnitude as those of ordinary metals.

(4) Thermoelectric power

Thermoelectromotive force of gamma brass was also very small. For instance, absolute thermoelectric power of 69 wt.% zinc at room temperature was $+1.7\times10^{-6}$ volt/deg which was comparable to the values of pure metals.

(5) Magneto-resistance

The magneto-resistance of gamma brass was so small that it was hardly possible to measure it at room temperature. It was recognized, however, that the sign of the effect is negative at very low temperatures.[4)]

§ 3. Discussion

In order to discuss about the electronic structure of gamma brass and that of bismuth, we must be concerned with following physical properties: Diamagnetic susceptibility, de Hass-van Alphen effect, Hall coefficient, thermoelectric power and magneto-resistivity. It is well known that these properties of bismuth are extremely peculiar. Diamagnetic susceptibility of gamma brass has been measured by several investigators,[5),6)] and turned out to be about the same value as that of bismuth. De Haas-van Alphen effect and the Hall effect have not yet been observed for the gamma brass. Hall coefficient of the gamma phase of copper cadmium system was measured by Richard and Evans,[7)] and was found to be of the same order of magnitude as those of normal metals. In observation for gamma brass, the Hall coefficient was about $+2.9\times10^{-4}$ cgs. emu., although the large value is errorneously cited in some text books of metals. Absolute thermoelectric power is also very small and has the value $+1.7\times10^{-6}$ volt/deg.

Since Hall coefficient and thermoelectric power are proportional to electronic charge, holes and electrons have the opposite contributions to both effects and cancel out with each other. The small magnitude of the values would be caused from such reasons.

Basing upon the fact that the magneto-resistance effect was very small at room temperature, it may be concluded that the anisotropy of the energy surface of this substance may be negligibly small, since this effect is an important measure of the anisotropy of energy surface in this phase. An anomalous magneto-resistance effect observed at low temperature are similar to that observed in other substances, for instance, p-type indium antimonide⁸⁾ and the alloys of gold or copper containing a small amount of manganese or chromium.⁹⁾ However, it is difficult to interprete it on the present theoretical ground.

Thus the gamma brass does not resemble to the bismuth with respect to the various properties except diamagnetic susceptibility. Both of gamma brass and bismuth would have nearly filled band, but the behaviour of conduction electrons at Fermi surface would differ very much from each other.

These circumstances may be recognized when one compare the shapes of the Brillouin zone of bismuth and gamma brass. The Brillouin zone of gamma brass (Fig. 3) is 36-hedron and a sphere-like shape but the Brillouin zone of bismuth (Fig. 4) is not the same. According to this difference, the behaviour of positive holes in the first zone and the behaviour of electrons in the next zone would be nearly equal in the case of gamma brass, so that physical quantity which is proportional to electronic charge $\pm e$, may cancell out with each other. However, in the case of bismuth the contribution of the holes and the electrons to the conduction mechanism would be different very much.

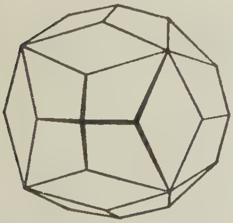

Fig. 3. The prominent zone boundary for the gamma structure.

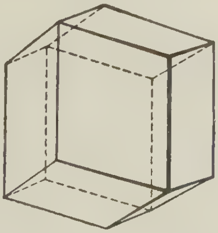

Fig. 4. The prominent zone boundary for bismuth.

It is usual that a minimum occurs in the curve of resistivity *vs.* concentration in cases of superlattice, whereas a maximum occurs in the case of intermetallic compound. The measurement of the resistivity of gamma brass has been performed by Puschen and Rjaschsky¹⁰⁾ who have found a maximum of resistivity at gamma phase on the contrary to our results. From our result it may be overhasty to conclude that gamma brass is superlattice-like. The reason of the occurrence of a minimum in resistivity might not be attributed to the ordered arrangement of atoms but to the special electronic structure of the material. Therefore, the measurement of Hall coefficient in various composition of gamma brass may be desirable, but it is not so easy to prepare a specimen for Hall coefficient.

The fact that the gamma brass, though it is a typical intermetallic compound in a certain sense, shows interesting anomalies as mentioned above, may play a significant role in future progress of our knowledge.

§ 4. Conclusions

1. It has been considered that gamma brass is similar to bismuth in electronic structure. Main experimental confirmation for this opinion is due to the fact that gamma brass has a large diamagnetic susceptibility and is very brittle. However, in other point, i.e. with respect to Hall coefficient, thermoelectric power and magneto-resistance, it is not similar to bismuth.

2. A minimum in the resistivity *vs.* composition curve of gamma brass was found. This result is opposite to the ordinary opinion for intermetallic compounds but rather similar to the superlattice alloys. However, it could not be attributed to the ordered arrangement of atoms but to the situation of its electronic structure.

With respect to the problem of the minimum in resistivity-composition curves, we have been studying other intermetallic compounds and also investigating the relation between intermetallic compound and superlattice alloy.

Moreover, we have observed the negative magneto-resistance effect in several gamma structures other than gamma brass, and so we want to investigate it in details in future.

Acknowledgement

We are indebted to Professor T. Hukuroi, Professor T. Hirone and Professor S. Ogawa for use of facilities in the Research Institute of Steel, Iron and other Metals of the Tohoku University and to the staff of their laboratory for continual help and encouragement. We wish to thank Professor Y. Takagi for valuable advice, and Mr. S. Nagasaki and Mr. M. Hirabayashi for their aid and helpful discussion.

References

1) A. J. Bradley and J. Thewlis: Proc. Roy. Soc. **A112** (1926) 678.
2) H. Jones: Proc. Roy. Soc. **A144** (1934) 225.
3) K. Yonemitsu and T. Sato: Oyo Butsuri (Japan) (to be published).
4) S. Noguchi and T. Sato: Busseiron Kenkyu **101** (1956) 122.
5) C. T. Lane: J. Appl. Phys. **8** (1937) 693.
6) J. A. Marcus: Phys. Rev. **76** (1949) 621.
7) E. Richard and J. Evans: Phil. Mag. **13** (1932) 201.
8) H. Fritzsche and K. Lark-Horovitz: Phys. Rev. **99** (1955) 400.
9) A. N. Gerritzen: Physica **19** (1953) 61.
10) N. Puschin and W. Rjaschsky: Z. anorg. Chem. **82** (1913) 50.

JOURNAL OF THE PHYSICAL SOCIETY OF JAPAN Vol. 12, No. 4, APRIL, 1957

On the Melting of Ionic Crystals

By Tatsumi KUROSAWA

Institute of Science and Technology, University of Tokyo

(Received December 1, 1956)

Comparing the data of AgCl and NaCl crystals, it is suggested that the contribution of lattice defects is more important than that of lattice vibrations, for the melting of ionic crystals. The coulombic interaction between defects can cause a sort of phase transition, and the transition temperature is near the melting point. Several experimental evidences: melting point, latent heat, viscosity and ionic conductivity of liquids, are also discussed on this ground.

§ 1. Introduction

The structure of liquids has been studied by many authors, but the knowledge about it is not so much and accurate as about solids and gases, owing to the complicated nature of liquids. Usually we regard liquids as the limiting case of the imperfect crystal or that of the imperfect gas, because of the difficulties accompanied to deal with the liquids as they are. The former picture seems to be appropriate to the liquid near the melting point, and the latter near the critical point. If the picture of the imperfect solid is a good approximation, we may expect that our knowledge about the imperfections in solids is useful for the study of liquid structures, especially of the mechanism of melting. The melting of the solid is to be explained by the abrupt increase of some kinds of imperfections. These imperfections may be, for instance, lattice vibrations, lattice defects, dislocations, grain boundaries or more complicated disorders which are often found in polymeric substances. Although such a classification of the imperfections in solids has not clear meaning in the case of liquids, it is an important problem to find which of them performs the main role in the melting process.

Above all, the pictures of lattice vibration mechanism have been investigated by many authors, e.g. Lindemann¹⁾, Braunbek,²⁾ Born and Thompson³⁾. On the other hand, Lennard-Jones⁴⁾ and others have developed the so-called "hole theory of liquids," which is somewhat similar to the picture of lattice defect mechanism. Mackenzie and Mott⁵⁾ regarded liquids as the limiting case of polycrystalline solids, and derived a relation on the basis of this picture. It is rather a dificult problem to decide which of these nechanisms is the most important one in a eal liquid, because each kind of liquids has ts own characteristics and the truth should not be a simple one, but a mixture of these nechanisms. This question can be answered nly by detailed comparisons between the heory and experiments in each case. And nversely such considerations will give some nformations about the imperfections in solids. Thus, we see that the study of the melting nechanism is important for those who have much interest in the liquid structure and also in the imperfections in solids. In this paper, we shall consider ionic crystals and shall suggest that the lattice defect mechanism may be most reasonable in ionic crystals.

§ 2. Lattice Vibrations and Lattice Defects

The melting of ionic crystals has been attributed to lattice vibrations. As its evidence it has been quoted that the Lindemann relation is satisfied in ionic crystals. If we consider alkali halides only, the Lindemann relation is really satisfied. However, if we consider alkali halides and silver halides at the same time, we find that this relation is no longer satisfied. As an example, let us take NaCl and AgCl crystals, which are known as nearly ideal ionic crystals and are the typical example of alkali halides and that of silver halides. Some data concerning these crystals are shown in Table I, where ω_t and ω_l are the angular frequencies of long transversal and longitudinal waves of the optical mode respectively, μ is the reduced mass, Θ_D is the Debye temperature determined from the specific heat at low temperatures, ρ is the density, ω_0 is the frequency of the sphere which vibrates homogeneously⁶⁾, e^2C is the coefficient of the repulsive force when both ions displace relative to each other⁷⁾, and K is the compressibility. Thus, $1/2\,\mu\omega^2$ means the hardness for the optical waves and $\rho\Theta_D^2$ means the hardness for the comparatively long acoustical waves.

These data suggest that AgCl is harder than NaCl, that is, AgCl has smaller amplitudes of lattice vibrations at the same temperature for most of the vibrational modes. The additional amplitude due to the quantum effect must be larger in NaCl, because of the smaller mass. Neverthless, NaCl has higher melting point. This fact seems to be contradictory to the view that melting occurs when the amplitude of thermal vibration reaches a certain fraction of the inter-atomic distance.

Table I. Comparisons of NaCl and AgCl.

	NaCl	AgCl
a	2.81	2.77×10^{-8} cm
Lattice	NaCl	NaCl
κ	5.62	12.30
κ_0	2.25	4.01
$\frac{\mu}{2}\omega_t^2$	1.10	1.05×10^4 erg/cm²
$\frac{\mu}{2}\omega_l^2$	2.76	3.23 〃
$\rho\Theta_D^2$	1.00	1.10*
$\frac{\mu}{2}\omega_0^2$	1.98	2.46×10^4 erg/cm²
e^2C	2.22	2.56 〃
K(0°K)	~3.3	
(20°C)	4.16	2.40×10^{-12} cm³/erg
α(20°C)	12.0	9.2×10^{-5} deg⁻¹
T_m	1073	728°K
E	1.8~2.0	0.8~1.0 ev
W_0	2.02	1.08 1.2 } ev

a: Lattice constant.
*: in arbitrary unit.
α: Volume expansion coefficient.
T_m: Melting point.

On the other hand, if higher derivatives of the interionic potential of AgCl were much greater than that of NaCl, it would be possible that thermal vibration and thermal expansion make AgCl unstable at lower temperature Such mechanisms of melting have been suggested by Born and Thompson³⁾. However, the comparison of the thermal expansion coefficients α does not support this assumption. The fact that α of AgCl is small comes from the smallness of the higher (the third) derivative of the potential energy compared with the second one, and decreases the effect of making the lattice unstable due to the thermal expansion. For a rough estimation, we use the Grüneisen relation

$$\gamma=-\frac{\partial\ln\omega}{\partial\ln V}\simeq\frac{\alpha V}{C_vK}, \qquad (2.1)$$

where V is the molar volume and C_v is the specific heat. In this relation we substitute the values of α, V, K at 20°C, and for C_v $6R$. Then we obtain

$$\gamma = 1.6\ (\text{NaCl}),\quad 1.9\ (\text{AgCl})\ . \tag{2.2}$$

And

$$-\frac{\partial \ln \omega}{\partial T} = \alpha\gamma \sim \begin{cases} 1.9\times 10^{-4}\ \text{deg}^{-1}\ (\text{NaCl}) \\ 1.8\times 10^{-4}\ \text{deg}^{-1}\ (\text{AgCl}) \end{cases} \tag{2.3}$$

In fact, the problem is so complicated that such a simple estimation gives no definite conclusion. However, it is evident that the explanation of melting on the basis of the conventional lattice vibration mechanism is not convenient to interpret such differences between NaCl and AgCl crystals.

In the next place, we consider the lattice defect mechanism. For this purpose, we compare the data in Table I again. In Table I E is the activation energy for ionic conduction, and W_0 is the formation energy of a pair of the Schottky or Frenkel defects, they are connected by a relation;

$$E = \frac{W_0}{2} + U\ , \tag{2.4}$$

where U is the activation energy of migration. Although the values of W_0 and U are not well known separately, the experiment of Etzel and Maurer[8] for NaCl gives the value of W_0 as 2.02 ev. On the other hand, any conclusive experiment is absent for AgCl, though Koch and Wagner[9] reported that the value of W_0 was about 1.08 ev and Breckenridge[10] 1.2 ev, which are appreciably smaller than that of NaCl. In NaCl the Schottky defects may predominate, and in AgCl the Frenkel defects may do so. The reason for the smallness of the formation energy of the Frenkel defects in AgCl may be as follows: (1) Strong van der Waals force between Ag^+ ions diminishes the formation energy about 1 ev, that is, when the Ag^+ ions are at the normal sites, the distance between neighbouring Ag^+ ions is $\sqrt{2}\,a$ and the van der Waals force is not so effective, but if one of the Ag^+ ions enters into an interstitial site, the distance becomes $(\sqrt{3}/2)a$ and the energy becomes $(2\sqrt{2}/\sqrt{3})^6 \simeq 19$ times larger. (2) κ is larger in AgCl, and the polarization energy diminishes the formation energy. In other words, for small displacements of ions about the equilibrium position the larger energy is necessary in AgCl, but for larger displacements such as defects the circumstances are not the same.

Generally speaking, there is a parallel tendency between E and T_m. These facts seem to support the assumption that ionic crystals melt when the concentration of defects reaches a certain amount.

§ 3 Interaction Between Defects

The concentration of defects in the state of equilibrium is given by

$$f = c\exp(-W_0/2kT), \tag{3.1}$$

where f is the fractional density of defects, W_0 is the formation energy of a pair of defects at 0°K, and c is a factor of the order of 10∼100. If we give the values 2.1 ev and 1.2 ev for W_0 of NaCl and AgCl respectively, and 30 for c, then we have the values of f at the melting point to be about 3×10^{-4} and 2×10^{-3} respectively. These values may be too small to cause a large change such as melting. Moreover we can not understand why the mere increase of the number of defects leads to the discontinuous change at the melting point.

The defects interact each other with the potential $\pm e^2/\kappa r$, r being the distance between defects. This interaction causes such a tendency that a defect is surrounded by a cloud with the charge of the opposite sign, as an ion in a strong electrolytic solution. It causes an apparent decrease of the formation energy, and this effect becomes appreciable at high temperatures. If we take into account this effect according to the Debye-Hückel's[11] theory, the equilibrium condition without the interaction,

$$W + 2kT\ln f = 0 \tag{3.2}$$

is replaced by

$$W + 2kT\ln f - 2\sqrt{\pi}\,\frac{e^2}{\kappa a}\left(\frac{e^2}{\kappa a k T}\right)^{1/2} f^{1/2} = 0\ , \tag{3.3}$$

where W is the formation free energy per pair of defects, and if we assume that

$$W = W_0 - \beta T\ , \tag{3.4}$$

we have

$$c = \exp(\beta/2k). \tag{3.5}$$

We can see from Eq. (3.3), that the exstence of the third term works to increase f, and causes a sort of phase transition. To see this more clearly, we transform Eq. (3.3) into

$$\frac{W_0}{2kT}-\sqrt{\pi}\left(\frac{e^2}{\kappa a\,kT}\right)^{3/2}f^{1/2}=\frac{\beta}{2k}-\ln f\,. \tag{3.6}$$

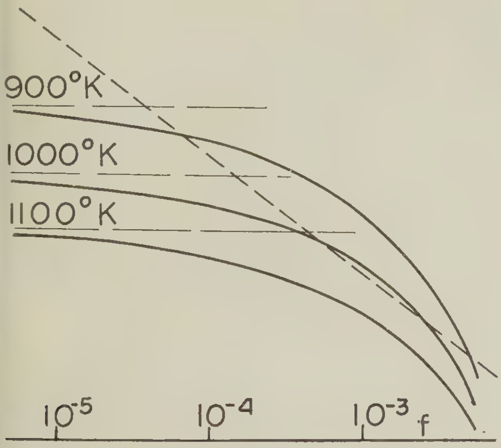

Fig. 1. The both hand sides of Eq. (3.6) for NaCl.

The results of numerical calculations for the case of NaCl are shown in Fig. 1, in which the full lines denote the left hand side of Eq. (3.6), the dotted lines are the right hand side and the broken lines are the left hand side without the second term, at several temperatures. We used the values $W_0=2.1$ ev and $c=30$. The points of intersection are the equilibrium concentrations at each temperature. From this figure, we can see that there is no solution above a certain critical temperature T_c, and this temperature is about 1000°K for NaCl, nearly equal to the melting point 1073°K. The values of W_0 and c have some ambiguities, but the change of T_c is not so large with the change of W_0 or c over a reasonable range. For instance, if the values $W_0=2.02$ ev and $c=5.4$ are used according to Etzel and Maurer,(8) T_c becomes 1170°K.

We must notice here that the true transition temperature should not be T_c, but be somewhat lower temperature, where the free energies of two phases are equal. Since we do not know about the other phase, it is impossible to calculate this temperature. We expect, however, that this true transition temperature may be nearly equal to T_c. Although it is not certain if such a transition exist really and corresponds to the melting, several experimental evidences, which are discussed in the next section, lead us to such a conclusion.

§ 4. Comparisons with Experiments

(1) The melting point and the formation energy of defects

If we denote the left hand side of Eq. (3.3) by $F(f, T)$, then T_c is given by the equations

$$F(f, T_c)=0 \tag{4.1}$$

and

$$\left[\frac{\partial F(f, T)}{\partial f}\right]_{T=T_c}=0\,, \tag{4.2}$$

that is

$$W(T_c)=2kT\left\{\ln\frac{\pi}{4}\left(\frac{e^2}{\kappa akT_c}\right)^3+2\right\} \tag{4.3}$$

and

$$f_c=c\exp\left(-\frac{W_0}{2kT_c}\right)=\exp(-2)\,\frac{4}{\pi}\left(\frac{\kappa akT_c}{e^2}\right)^3$$
$$=\exp(-2)f(T_c)\,, \tag{4.4}$$

where f_c is the fractional density of defects which is extrapolated to T_c from the values at lower temperatures. We calculate f_c or W_0 from Eqs. (4.3) and (4.4) under the expectation that $T_c \doteqdot T_m$, instead of solving T_c from Eq. (4.3). This procedure is rather convenient, because the values of W_0 are not

Table II. The values of f_c and W_0.

Crystal	T_m(°K)	$f_c(10^{-4})$		W_0(ev)	
		(Cal.)	(Exp.)	(Cal.)	(Exp.)
LiF	1129	3.8	5.2(12)	2.2	2.7(12)
NaF	1259	2.0		2.5	
NaCl	1073	1.8	1.02(3) 4.1(13)*	2.2	2.02(8)
NaBr	1018	2.2		2.0	
KCl	1041	1.3	0.7(14)	2.1	2.4(14) 2.1(15)
KBr	1002	1.5		2.1	
RbCl	989	1.6		2.0	
RbBr	955	1.6		1.9	
AgCl	728	5.7		1.2 ($\beta=4k$)	
AgBr	695	6.7		1.1 ($\beta=4k$)	
MgO	3070	1.5		6.3	
CaO	2850	3.0		5.5	
SrO	2700	4.5		5.0	

* This value may be rather $f(T_c)$ than f_c.

known in most substances. The calculated and observed values of W_0 and f_c are listed in Table II for several substances, where we put in general $\beta=6k$, or $c=20$ arbitrarily except for silver halides. We used the values of κ and a at room temperature. These calculated values have only approximate meaning, because the Debye-Hückel's theory may not be valid at high concentrations near T_c. Neverthless the agreement is satisfactory when the experimental values are available. The calculated values are also reasonable even when the experimental value is not available. It is to be noted that the values of f_c are always of the order of 10^{-4} in alkali halides and of 10^{-3} in silver halides.

The KCl-KBr system has the lowest melting point for the composition containing about 75 mole per cent KBr, where the ionic conductivity of the mixed crystals has the highest value[16]. The explanation for this fact is very easy from our view point.

According to Eq. (4.4) the real concentration at T_c is about seven times larger than the value extrapolated from the low temperatures. As mentioned in § 3, however, the real transition temperature is somewhat lower than T_c. Therefore we may expect that the difference is not so large as predicted by Eq. (4.4).

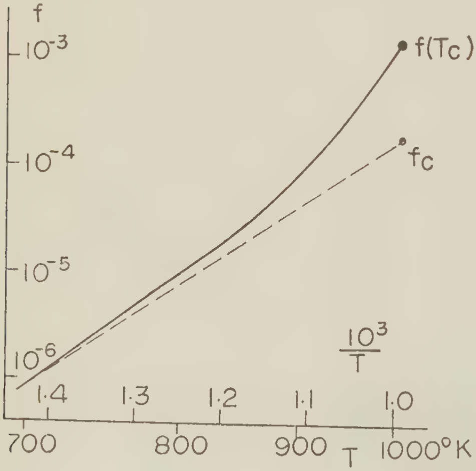

Fig. 2. ln f vs. T for NaCl.

In Fig. 2, f is plotted as a function of T for NaCl. Due to the interaction between defects, the relation of ln f vs. $1/T$ is no longer linear. Such a behaviour has not been observed in most experiments on the ionic conductivity except for a few cases. Although the reason of this discrepancy is not clear, this may be explained partley by the fact that the melting point is lower than T_c and the curvature of ln f vs. $1/T$ curve is rather small.

(2) Latent heat and volume change at melting

According to our theory, the melting of ionic crystals is to be explained by the abrupt increase of defects, and this abrupt increase may be the main structural change at melting. If this is true, the latent heat is to be close to the energy necessary to increase the defects.

When the concentration of defects is large, we estimate the interaction energy between defects by $-(\alpha_M e^2/\kappa a)f^{1/3}$, which is the interaction energy between defects in cubic array, where α_M is the Madelung constant. Thus the energy necessary to increase the concentration from f_s to f_l (the concentration of defects in solid and liquid respectively) is

$$\int_{f_s}^{f_l}\left[W_0-\frac{\alpha_M e^2}{\kappa a}f^{1/3}\right]df$$
$$=W_0(f_l-f_s)-\frac{3}{4}\frac{\alpha_M e^2}{\kappa a}(f_l^{4/3}-f_s^{4/3})\,. \tag{4.5}$$

Because $f_l \gg f_s$, we neglect f_s, and in virtue of the above discussion, we put

$$L_m \simeq W_0 f_l-\frac{3}{4}\frac{\alpha_M e^2}{\kappa a}f_l^{4/3}\,, \tag{4.6}$$

where L_m is the latent heat of melting.

On the other hand, if the volume change at melting is mainly due to defects, and the defects are predominantly Schottky defects, f_l may be nearly equal to the fraction of the volume change $\Delta V/V$. Hence we have

$$L_m \simeq W_0\left(\frac{\Delta V}{V}\right)-\frac{3}{4}\frac{\alpha_M e^2}{\kappa a}\left(\frac{\Delta V}{V}\right)^{4/3}\,. \tag{4.7}$$

In Table III the values of $\Delta V/V$ and L_m are listed, the data of the density and the latent heat are taken from "International Critical Tables". Since the density of solids at melting point is not known, we are obliged to use the extrapolated values from the room temperature. NaCl is the exception, for which the thermal expansion coefficient up to the melting point has been measured.[17] Although the values of $\Delta V/V$ and W_0 are not accurate and the formula (4.7) is only approximate, the agreement between theoretical and experimental values of the latent heat is comparatively good, especially for alkali halides. And the difference may be still more reduced, if we consider that the true interaction energy is less (algebraically) than the estimated value in Eq. (4.5). The agreement is less satisfactory for silver halides, where the calculated values are smaller than the experimental values. This may be explained as follows; in alkali halides the Schottky defects predominate, and it is a good approximation to take $f_l \cong \Delta V/V$, but in silver halides the Frenkel defects may be dominant, so that $f_l > \Delta V/V$ and the calculated latent heats become too small. As we see in Table III, the values of $\Delta V/V$ are about 20% in alkali halides but less than 10% in silver halides, this fact is consistent with the view that the former melts by the defects of Schottky type and the latter by the Frenkel type.

Table III. The latent heats.

Crystal	$V_l/V_{s'}$	$V_{s'}/V_s$	$\Delta V/V$	W_0 (ev)	L_m(ev)	
					(Cal.)	(Exp.)
LiF	1.47	(0.9)	(0.33)	2.7	(0.66)	
NaF	1.45	(0.87)	(0.26)	(2.5)	(0.43)	0.34
NaCl	1.40	0.88	0.23	2.02	0.30	0.31
NaBr	1.37	0.90	0.24	(2.0)	0.32	
KF	1.34	(0.89)	(0.19)	(2.2)	(0.30)	0.27
KCl	1.31	0.90	0.17	2.4	0.29	0.24
KBr	1.30	0.89	0.16	(2.1)	(0.22)	
RbCl	1.33	0.91	0.21	(2.0)	(0.27)	0.20
AgCl	1.14	<0.96	<0.09	1.1	<0.08	0.13 0.19
AgBr	1.17	<0.96	<0.11	(1.1)	<0.09	0.10

V_l: the molar volume of liquids at melting point.

V_s: the molar volume of solids at melting point.

$V_{s'}$: the molar volume of solids at room temperature.

W_0: experimental values if available, otherwise calculated values in Table II. In the latter case, we show them enclosing.

It is interesting to see that, generally the value of $\Delta V/V$ in alkali halides is very large compared with that in the other types of solids, for instance, in alkali metals 2∼3%, in noble metals 4∼5% and in molecular crystals 5∼10%. This seems to suggest that the mechanism of melting appreciably differs in the ionic crystals from the other crystals. Especially in alkali metals the defects will play no role because of the lack of such a strong interaction between defects as in ionic crystals.

(3) Viscosity and electrical conductivity in ionic liquids

Since ionic liquids contain a great amount of defects, very frequent migrations of ions are expected through or by these defects, and these will cause the fluidity and the high electrical conductivity of ionic liquids. First, we consider the viscosity on this line.

In most ionic crystals, positive ions are more mobile than negative ions, so that the fluidity of ionic liquids will be limited by the mobility of negative ions. In ionic liquids, the concentration of defects f, is near to 0.2, and an ion or a defect is surrounded by $6f\,(\geq 1)$ vacancies in average. Therefore, the migration of the negative ions in liquids will be similar to that of the pair vacancies in solids, rather than that of single vacancies, because the activation energy of migration is far smaller in the former.

Then the jump frequency of a negative ion to any one of the like neighbours will be

$$2f^2\nu z\cdot\exp(-Q_-/kT)\,, \tag{4.8}$$

where z is the number of like nearest sites, 12 for NaCl type crystals, fz of them are vacant, $2f$ is the probability that the jump to a like nearest vacant site is of the pair vacancy type and Q_- is the activation energy of migration, which will be more or less smaller than that of pair vacancy in solids. Here we neglected the complicated correlations between vacancies. Hence the diffusion constant of a negative ion is

$$D=8\nu f^2a^2\exp(-Q_-/kT)\,, \tag{4.9}$$

and the mobility μ is

$$\mu=\frac{D}{kT}=\frac{8\nu f^2a^2}{kT}\exp(-Q_-/kT). \tag{4.10}$$

The simplest but somewhat doubtful way to connect this μ with the viscosity η is as follows. We regard the motion of a negative ion under an external force F as the motion of a macroscopic ball of radius R in a viscous fluid, and use the Stokes' law

$$F=6\pi R\eta v=\frac{v}{\mu}\,. \tag{4.11}$$

Thus we have

$$\eta = \frac{kT}{48\pi f^2 \nu R a^2} \exp\left(\frac{Q_-}{kT}\right) . \tag{4.12}$$

If we take the values, $T \simeq 1000°\mathrm{K}$, $\nu \simeq 3 \times 10^{12}\,\mathrm{sec}^{-1}$, $a \simeq 3 \times 10^{-8}\,\mathrm{cm}$, $R \simeq 2 \times 10^{-8}\,\mathrm{cm}$ and $f \simeq 0.2$, we obtain

$$\eta \simeq 4.3 \times 10^{-4} \exp\left(\frac{Q_-}{kT}\right) \text{(poises)} . \tag{4.13}$$

On the other hand, the experimental values of η are fitted by a formula

$$\eta = \eta_0 \exp\left(\frac{Q_\eta}{kT}\right) , \tag{4.14}$$

and the values of η_0 and Q_η are tabulated in Table IV[18]. The values of η_0 are in rather good agreement with the calculated values in the order of magnitude. We expect that Q_η is nearly equal to the activation energy of the pair vacancy and somewhat smaller than that in solids. For KCl, this energy is calculated by Dienes,[19] and his result gives 0.375 ev, which is in good accord with Q_η. The values of Q_η for other liquids are also reasonable on this view. Although our estimation is very crude, the qualitative feature may be correct.

Table IV. The values of η_0 and Q_η.

Liquid	η_0(10^{-4} poises.)	Q_η(ev)
NaCl	2.11	0.40
NaBr	2.85	0.35
KCl	4.29	0.33
KBr	2.92	0.35

In the above discussion, we neglected the temperature dependence of the former factor of Eq. (4.12), especially of f, but we can expect that this factor may have little temperature dependence, i.e.

$$\frac{d \ln \eta}{d \ln T} = -\frac{Q_-}{kT} + 1 - \frac{d \ln \nu}{d \ln T} - 2\frac{d \ln f}{d \ln T} . \tag{4.15}$$

The last two terms may be estimated as follows. The thermal expansion coefficient of liquids is about $3 \times 10^{-4}\,\mathrm{deg.}^{-1}$, this may be divided approximately into two parts, that is, the part due to the increase of the vacancies α_v, and that due to the increase of the lattice constant α_l, which is the origin of the thermal expansion in solids. The value of α_l in solids is about $1 \times 10^{-4}\,\mathrm{deg}^{-1}$ at room temperature and $2 \times 10^{-4}\,\mathrm{deg}^{-1}$ near the melting point. As we expect that α_l is larger in liquids, α_v may be at most $1 \times 10^{-4}\,\mathrm{deg}^{-1}$ and $d \ln f / dT \simeq 5 \times 10^{-4}\,\mathrm{deg}^{-1}$. On the other hand,

$$-\frac{d \ln \nu}{d \ln T} \simeq \alpha_l \gamma T \simeq +0.5 , \tag{4.16}$$

so that the sum of the last three terms is about +0.5, which is much smaller than Q_-/kT (about 4~5).

In the next place, let us consider the ionic conductivity of liquids. It is mainly determined by the mobility of positive ions in most ionic liquids. In the same manner as above, we can derive

$$\sigma = \frac{4e^2 \nu f^2}{akT} \exp\left(-\frac{Q_+}{kT}\right) . \tag{4.17}$$

Inserting the same numerical values as (4.13),

$$\sigma \simeq 30 \exp\left(-\frac{Q_+}{kT}\right)\left(\frac{1}{\mathrm{ohm \cdot cm}}\right) . \tag{4.18}$$

The experimental values are fitted by a formula

$$\sigma = \sigma_0 \exp\left(-\frac{Q_\sigma}{kT}\right) , \tag{4.19}$$

and the data are tabulated in Table V. In this case Q_σ is small, so that the temperature dependence of the former factor can not be neglected and the meaning of Q_σ becomes somewhat obscure. However, as the general tendency of Q_σ, it is reasonable that in the case of larger negative ion or smaller positive ion Q_σ is smaller. The values of σ_0 are also acceptable.

Table V. The values of σ_0 and Q_σ.

Liquid	σ_0($\Omega^{-1}\,\mathrm{cm}^{-1}$)	Q_σ(ev)
NaCl	13.8	0.10
NaBr	10.0	0.08
NaI	(230)	(0.27)
KF	201	0.32
KCl	28.4	0.18
KBr	11.9	0.13
KI	10.1	0.13
RbCl	11.6	0.14

The experimental values are taken from "International Critical Tables".

§ 5. Discussions and Conclusions

At the beginning of the above discussions, we have assumed that the melting of ionic rystals is due to defects, and the interaction etween them is essential. We took the nteraction into account by the Debye-Hückel's heory. At the high concentrations near T_c, owever, the Debye-Hückel's theory is no onger correct.

According to the second approximation of the Debye-Hückel's theory[11], the third term of Eq. (3.3) is reduced by a factor $\left\{1+\sqrt{\frac{4\pi e^2}{\kappa k T a^3}f\cdot d}\right\}^{-1}$, where d is the closest distance of approach between defects theoretically, that is, in our case a for NaCl type crystals. If we consider d as an adjustable parametre, the theory agrees well with experiments in the case of electrolytic solutions, but d becomes generally very small and even negative. Then we should not expect that the inclusion of d with the real value a would give a better approximation than the calculation by means of Eq. (3.3). For the case of the high concentrations near T_c, all the theory can not be reliable quantitatively.

Neverthless, it has some meanings to calculate the equilibrium conditions according to the second approximation of the Debye-Hückel's theory for several values of d. The results for NaCl at 1000°K and 1100°K are in Fig. 3 and Fig. 4. The meanings of the figures are same as in Fig. 1. Roughly speaking, for $d<0.5\,a$ the transition can occur.

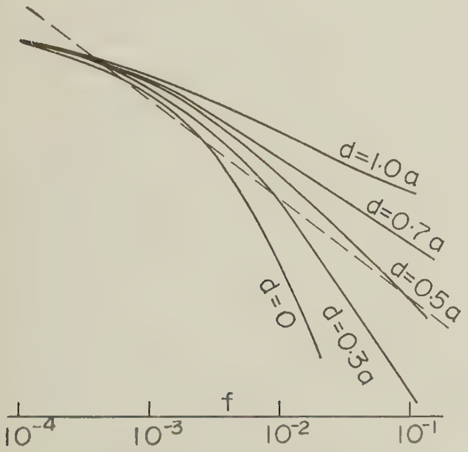

Fig. 3. NaCl 1000°K.

An electrolytic solution with $\kappa=5.6$, $T=1073$°K and $Z=1$ corresponds to a solution with the same concentration and $\kappa=80$, $T=300$°K, $Z=2$. On the other hand, the aqueous solution of bivalence ions obeys the Debye-Hückel's theory up to considerable concentrations (above 0.1 mol./lit., which corresponds to $f\sim 3\times 10^{-3}$ in our case, and κ of water at 300°K is 78), so long as we consider d as an adjustable parametre, and the values of d are very much smaller than the real values generally. Then we may expect a similar trend for the defects in ionic crystals.

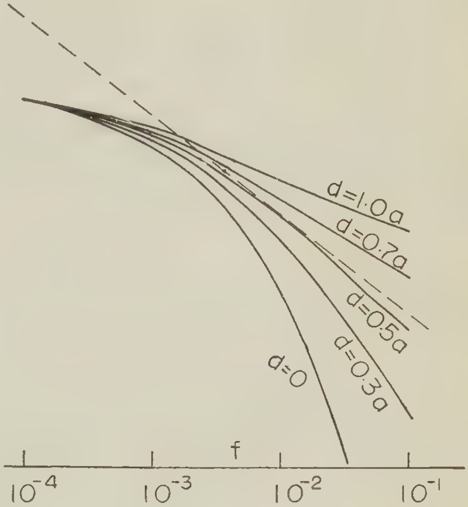

Fig. 4. NaCl 1100°K.

Although the theory contains several difficulties, it may be true that the apparent formation energy of defects decreases appreciably owing to the interaction between them, when f becomes of the order of 10^{-4}, and that f approaches this value near the melting point. Then the defects may play an important role in melting, though we may not deny the role of the lattice vibrations. And on this assumption, we can explain many facts, which can not be explained by the lattice vibration mechanism, at least qualitatively.

The author wishes to express his sincere thanks to Professor J. Yamashita for his helpful discussions.

References

1) F. A. Lindemann: Phys. Zs. **11** (1910) 609.
2) W. Braunbek: Zs. f. Phys. **38** (1926) 549.
3) M. Born: J. Chem. Phys. **7** (1939) 591.
M. Born: Proc. Camb. Phil. Soc. **39** (1943) 100.
J. H. C. Thompson: Phil. Mag. **44** (1953) 131.
4) J. E. Lennard-Jones and F. Devonshire: Proc. Roy. Soc. **A169** (1939) 317; **170** (1939) 464.

5) J. K. Mackenzie and N. F. Mott: Proc. Phys. Soc. **A63** (1950) 411.
6) H. Fröhlich: Theory of Dielectrics. § **18**.
7) J. Yamashita and T. Kurosawa: J. Phys. Soc. Japan **10** (1955) 610.
8) H. W. Etzel and R. J. Maurer: J. Chem. Phys. **18** (1950) 1003.
9) E. Koch and C. Wagner: Zs. f. Phys. Chem. **B38** (1937) 295.
10) R. G. Breckenridge: J. Chem. Phys. **16** (1943) 959.
11) For instance, Fowler and Guggenheim: Statistical Thermodynamics (1939) Chap. IX.
12) I. Haven: Rec. trav. chim. **69** (1950) 1259, 1471.
13) M. E. Straumanis: Am. Mineralogist **38** (1953) 662.
14) H. Kelting and H. Witt: Z. Physik **126** (1949) 697.
15) C. Wagner and P. Hantelmann: J. Chem. Phys. **18** (1950) 72.
16) H. Schulze: thesis, Göttingen University, 1952, this is quoted by F. Seitz in Rev. Mod. Phys. **26** (1954) 89.
17) P. G. Strelkow: Phys. Zeits. Sowj. Union **12** (1937) 35.
18) A. G. Ward: Trans. Faraday Soc. **33** (1937) 88.
19) G. J. Dienes: J. Chem. Phys. **16** (1948) 620.

JOURNAL OF THE PHYSICAL SOCIETY OF JAPAN Vol. 12, No. 4, APRIL, 1957

Rotational Lrttice Vibration in Complex Crystals[*]

Part I. Vicrational Modes and Specific Heat

Sumitada ASANO and Yasuo TOMISHIMA

Department of Physics, Faculty of Science, Okayama University

(Received January 12, 1957)

In complex crystals which contain groups of atoms bonded strongly with each other such as anionic radicals, complex ions and hydrated cations, low-frequency rotational vibrations of these groups of atoms may be expected to exist in addition to low-frequency translational vibrations, as in the case of ideal molecular crystals. By using an one-dimensional lattice, the modes of these vibrations are analysed. According to the results obtained, we may conclude that new additional modes appear, which is related to the rotational vibrations of the groups of atoms, and they may be classified, in general, into the optical and acoustical branches just as in the case of the translational vibrations. In addition, the effects of the introduction of these new modes upon the specific heat at low temperatures are investigated, by using the results of the analysis for the one-dimensional lattice.

§ 1. Introduction

In molecular crystals, in which the intra-molecular forces are much stronger than the intermolecular forces, there may be a set of $3N$ modes (N: total number of molecules) of low-frequency tortional vibrations as well as $3N$ modes of low-frequency translational vibrations[1]. On the other hand, in complex crystals[**], such as sulphates and phosphates etc., the ions constituting the radicals $[SO_4]^{2-}$ and $[PO_4]^{3-}$ may be considered as strongly bonded with each other, compared with the forces binding the radical groups with each other and that binding the radical group and the partner cation[2]. This is evidenced, to some extent, by several experimental facts: For example, the peak wave-length in vibration spectra of most of the isolated radicals are of the order of several microns[3], whereas the Reststrahlen wave-lengths of usual crystals are of the order of several tens microns. The absorption maxima characteristic to the internal vibrations of a particular radical in various types of complex crystals are nearly constant and are hardly affected by the binding with cations in the lattice. They often persist even in solution[4]. These complex crystals are dissociated into radicals and cations when they are dissolved in suitable solvents. The size of one particular radical is nearly constant regardless of the kind of the partner cation[5]. Therefore, the radical in such a complex crystal may suffer a rotational vibration around the equilibrium orientation except at a high temperature, besides a translational motion as a whole. (cf. Fig. 1) At a high temperature the radical may wander from one equilibrium orientation to another one passing through a potential barrier, when the coordination of the ions in the radical has a central symmetry.

---

[*] The results given in this paper were presented in part at the Tokyo Sectional Meeting of the Physical Society of Japan in November 1956.

[**] A complex crystal means here broadly a crystal containing groups of atoms (or ions) which are bonded with each other more tightly than with the lattice, such as anionic radicals, complex ions and hydrated cations (aquo-cations), whereas a simple crystal means an ordinary one consisting of single atoms (or ions).

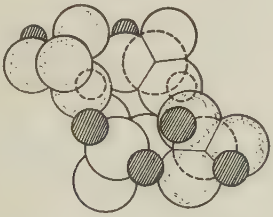

Fig. 1. A packing drawing of the atoms in a monoclinic unit cell of Li_2SO_4 crystal. The small hatched spheres are the lithium ions, the large spheres the oxygen ions; sulphur ions are hidden at the centers of the tetrahedra of their surrounding oxygen ions. Further, among the ions belonging to this unit cell two lithium ions and two oxygen ions are not seen also behind the oxygen ions. They are shown by the spheres with dotted outlines. The sizes of the spheres are proportional to the ionic radii[6].

In this part the vibrational modes in one-dimensional complex lattice are analysed and furthermore the deviation of its specific heat at low temperatures from that of the Debye model is discussed by making use of the results of the analysis.

§ 2. Rigid Rotor Model

For the sake of simplicity the following assumptions are made:

(1) The radical is regarded as a rigid rotor. Hence the additional high-frequency vibrational modes, i. e. the modes of internal vibrations which may be excited within the radical are ignored. The translational vibration of the radical as a whole may be separated from the rotational vibration and regarded as concerning with ordinary translational phonons, as stated later.

(2) Each ion constituting a radical is regarded as a point charge with the atomic mass, and furthermore the coordination of the ions in a radical has a central symmetry around the central ion such as tetrahedral or octahedral one.

(3) The motion of a radical consists of the translational motion and the rotational one around its center of mass. The radical at the equilibrium orientation may be brought into an arbitrary one by a single rotation, and if the angle θ of this rotation is small (to the extent that the square of θ is negligible for unity), we can define a vector $\boldsymbol{\theta}$ called angular displacement, which has the magnitude equal to θ and the direction pararell to the axis of rotation, satisfying the right-winding screw relation. The $\boldsymbol{\theta}$ determines the orientation of the radical uniquely and $\dot{\boldsymbol{\theta}}$ is identical with the angular velocity of the radical.

The effective potential energy Φ of the constituents i. e. the radicals and the cations of the crystal is given by

$$\Phi=\Phi(u_\alpha(k),\, \theta_p(k))\,, \tag{2.1}$$

where $u_\alpha(k)(\alpha=1, 2, 3)$ is the component of the Cartesian displacement of the center of mass of the kth constituent $(k=1, 2, \cdots, n)$ referring to its equilibrium position and $\theta_p(k)$ $(p=1, 2, 3)$ is the component of the angular displacement of the kth constituent. When the kth constituent is a cation, $\theta_p(k)$ should be omitted in (2.1), since the cation is regarded as a point charge. Let us introduce the notation

$$\begin{aligned} &\Phi_\alpha(k)\equiv(\partial\Phi/\partial u_\alpha(k))_0, \quad \Phi_p(k)\equiv(\partial\Phi/\partial\theta_p(k))_0 \\ &\Phi_{\alpha\beta}(kk')\equiv(\partial^2\Phi/\partial u_\alpha(k)\partial u_\beta(k'))_0\,, \\ &\Phi_{\alpha p}(kk')\equiv(\partial^2\Phi/\partial u_\alpha(k)\partial\theta_p(k'))_0\,, \end{aligned} \tag{2.2}$$

and

$$\Phi_{pq}(kk')\equiv(\partial^2\Phi/\partial\theta_p(k)\partial\theta_q(k'))_0\,,$$

where the index 0 signifies the configuration $u_\alpha(k)'\text{s}=0,\ \theta_p(k)'\text{s}=0$.

Then

$$\Phi_\alpha(k)=\Phi_p(k)=0\,. \tag{2.3}$$

So we may write

$$\Phi=\frac{1}{2}\sum_{k,k'}\Big[\sum_{\alpha,\beta}\Phi_{\alpha\beta}(kk')u_\alpha(k)u_\beta(k')$$

$$+\sum_{\alpha,p}\Phi_{\alpha p}(kk')u_\alpha(k)\theta_p(k')$$

$$+\sum_{p,q}\Phi_{pq}(kk')\theta_p(k)\theta_q(k')\Big]. \qquad (2.4)$$

We introduce the notations

$$D_{\alpha\beta}(kk')\equiv\frac{1}{(m_k m_{k'})^{1/2}}\Phi_{\alpha\beta}(kk),$$

$$D_{\alpha p}(kk')\equiv\frac{1}{(m_k I_{k'})^{1/2}}\Phi_{\alpha p}(kk'),$$

$$D_{pq}(kk')\equiv\frac{1}{(I_k I_{k'})^{1/2}}\Phi_{pq}(kk'), \qquad (2.5)$$

and

$$\omega_\alpha(k)\equiv m_k^{1/2}u_\alpha(k),$$

$$\omega_p(k)\equiv I_k^{1/2}\theta_p(k),$$

where m_k and I_k are the mass and the moment of inertia of the kth constituent respectively.

From the assumption (3) it may be deduced that the variable defined by

$$L(k)\equiv I_k\dot{\theta}(k) \qquad (2.6)$$

is canonically conjugate to $\theta(k)$, and then $L_p(k)$, and $\theta_p(k)$ satisfy the commutation relations quite similar to those which are satisfied by the components of the linear momentum and coordinate conjugate to one another. Therefore, $L(k)$ may be replaced with the differential operator

$$L_p(k)=-i\hbar\partial/\partial\theta_p(k). \qquad (2.7)$$

Furthermore, the rotational kinetic energy of the kth radical may be written in the form

$$(L(k))^2/2I_k. \qquad (2.8)$$

If $\omega_\alpha(k)$'s and $\omega_p(k)$'s are rewritten by the notations $\omega_{\alpha'}(k)$'s with the newly labeled indices α''s which are $1, 2, 3$ or $1, 2, \cdots, 6$ according as the kth constituent being a cation or a radical, and similarly $D_{\alpha\beta}(k,k')$, $D_{\alpha p}(k,k')$ and $D_{pq}(k,k')$ by $D_{\alpha'\beta'}(k,k)$, then the kinetic and potential energies T and Φ for the motion of the constituents can be written as follows:

$$T=\frac{1}{2}\sum_k\sum_{\alpha'}P_{\alpha'}{}^2(k),$$

$$\Phi=\frac{1}{2}\sum_{k,k'}\sum_{\alpha',\beta'}D_{\alpha'\beta'}(kk')\omega_{\alpha'}(k)\omega_{\beta'}(k), \qquad (2.9)$$

where

$$P_{\alpha'}(k)\equiv-i\hbar\,\partial/\partial\omega_{\alpha'}(k).$$

By introducing the normal coordinates q_j which are given by the appropriate linear combinations of $\omega_{\alpha'}(k)$'s, we obtain the usual expressions[7)]

$$T=\frac{1}{2}\sum_j P_j{}^2,$$

$$\Phi=\frac{1}{2}\sum_j\omega_j{}^2q_j{}^2, \qquad (2.10)$$

where

$$P_j\equiv-i\hbar\,\partial/\partial q_j,$$

and the Hamiltonian of the system is given by

$$H=T+\Phi=\frac{1}{2}\sum_j(P_j{}^2+\omega_j{}^2q_j{}^2). \qquad (2.11)$$

Thus the energy of the lattice vibrations (including the rotational energy) may be quantized as so-called phonons.

§ 3. One-dimensional Complex Lattice

In order to clarify the aspects of the rotational vibration of the radicals, we investigate the simplest model i. e. a chain of two different types of constituents occupying alternate sites, one is a sphere with finite radius d', mass M and moment of inertia I, and the other a point particle with mass m. The former corresponds to the radical and the latter to the partner cation. (cf. Fig. 2) If we consider only the transverse vibration of the chain, the displacement of each constituent may be refered to one transverse direction and the axis of rotation of each sphere may be taken as perpendicular to its displacement and the chain.

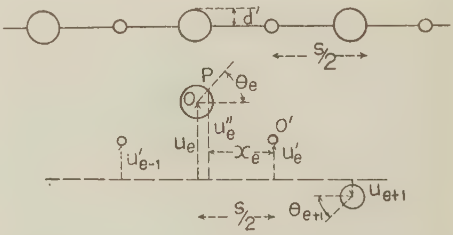

Fig. 2. One-dimensional complex lattice.

We assume two kinds of potential functions between nearest-neighbours in the lth unit cell

$$\phi_1(\overline{OO'})=\phi_1(\sqrt{(u_l-u_l')^2+(s/2)^2}),$$

$$\phi_2(\overline{PO'})=\phi_2(\sqrt{(u_l''-u_l')^2+x_l{}^2}). \qquad (3.1)$$

The meanings of the notations in (3.1) are illustrated in Fig. 2. Then the forces acting on the sphere from the adjacent particle are given by $-\partial\phi_1/\partial u_l$ and $-\partial\phi_2/\partial u_l''$; the former represents a central force acting on the radical and the latter a non-central one. When u_l, u_l'' and $u_l' \ll s/2$ and $s/2-d'$, and θ_l is small,

$$-\partial\phi_1/\partial u_l=-c_1(u_l-u_l')\ ,$$

and

$$-\partial\phi_2/\partial u_l''=-c_2(u_l+d'\theta_l-u_l')\ , \qquad (3.2)$$

where c_1 and c_2 are the force constants for the central and noncentral forces given by

$c_1=\phi_1'(s/2)/(s/2)\ ,\quad c_2=\phi_2'((s/2)-d')/((s/2)-d')\ .$

Then the equations of motion of the constituents in the lth cell are written as

$$\begin{aligned} M\ddot{u}_l&=(c_1+c_2)[(u_l'-u_l)-(u_l-u_{l-1}')]\ ,\\ m\ddot{u}_l'&=(c_1+c_2)[(u_{l+1}-u_l')-(u_l'-u_l)]\\ &\quad -c_2d'(\theta_{l+1}-\theta_l)\ ,\\ I\ddot{\theta}_l&=c_2d'(u_l'-u_{l-1}')-2d'^2c_2\theta_l\ . \end{aligned} \qquad (3.3)$$

By the following special substitutions

$$\left.\begin{aligned} u_l&\equiv u\\ u_l'&\equiv u'\\ \theta_l&\equiv\theta \end{aligned}\right\}\times\exp(2\pi iyl-i\omega t)\ , \qquad (3.4)$$

(3.3) is reduced to

$$\begin{aligned} &[M\omega^2-2(c_1+c_2)]u+(c_1+c_2)(1+e^{-2\pi iy})u'=0\ ,\\ &(c_1+c_2)(1+e^{2\pi iy})u+[M\omega^2-2(c_1+c_2)]u'\\ &\qquad\qquad +c_2d'(1-e^{2\pi iy})\theta=0\ ,\\ &c_2d'(1-e^{-2\pi iy})u'+[I\omega^2-2c_2d'^2]\theta=0\ . \end{aligned} \qquad (3.5)$$

From (3.5) we obtain the secular equation to determine ω

$$\{x^2-2(1+\sigma)x+4\sigma\sin^2\pi y\}\left(x-\frac{2B\sigma}{\alpha}\right)$$
$$-4(x-2\sigma)\frac{B^2\sigma}{\alpha}\sin^2\pi y=0\ , \qquad (3.6)$$

where

$$x\equiv(\omega/\Omega)^2\ ,\quad \Omega^2\equiv(c_1+c_2)/m$$
$$B\equiv c_2/(c_1+c_2)\ ,\quad \sigma\equiv m/M\ ,\quad \alpha\equiv I/Md'^2 \qquad (3.6a)$$

At long wave-length limit: $y\approx0$

$$[x]_{y\simeq0}=2\pi^2\frac{(1-B)\sigma}{1+\sigma}y^2$$
$$\times\left[1+\pi^2\frac{\Gamma}{(1+\sigma)^2}y^2+O(y^4)\right], \qquad (3.7a)$$

$$[x]_{y\simeq0}=2(1+\sigma)$$
$$\times\left[1-\pi^2\frac{\sigma\{(1+\sigma)\alpha-B(B+\sigma)\}}{(1+\sigma)^2\{(1+\sigma)\alpha-B\sigma\}}y^2\right]+O(y^4)\ , \qquad (3.7b)$$

$$[x]_{y\simeq0}=2\frac{B\sigma}{\alpha}$$
$$\times\left[1+\pi^2\frac{\alpha(\alpha-B)}{(1+\sigma)\alpha-B\sigma}y^2\right]+O(y^4)\ , \qquad (3.7c)$$

where

$$\Gamma\equiv\sigma(1-B)+(B-\alpha)(1+\sigma)-(1/3)(1+\sigma)^2\ . \qquad (3.7d)$$

The first two branches, (3.7 a and b), correspond to the usual acoustical and optical branches in translational mode which contains no rotational energy at $y=0$ (abbreviated as TA- and TO-branches respectively), whereas in the last one (3.7c) the rotational energy occupies, in general, the large portion of the total mechanical energy and the frequency depends less strongly upon wave-number, as stated later, therefore we will call this the optical branch in the rotational mode (abbreviated as RO-branch). When $c_1=0$, the TA-branch disappears and when $c_2=0$, the RO-branch does not exist.

At short wave-length limit: $y=1/2$ (3.6) can be solved simply as

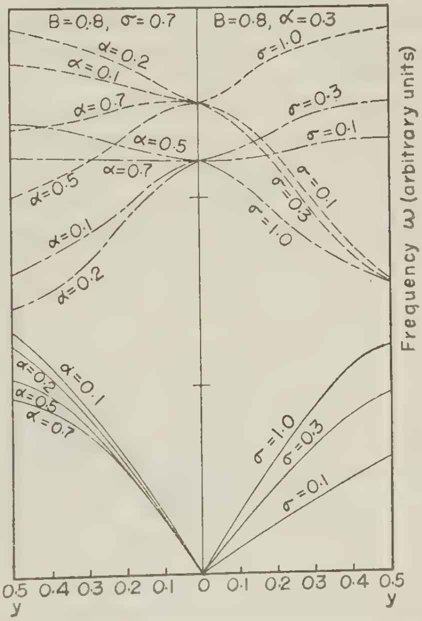

Fig. 3. Variation of frequency with wave-number.
Dotted curves: rotational optical mode.
Chain curves: translational optical mode.
Real curves: translational acoustical mode.

$$[x]_{y=1/2}=2\sigma\ , \qquad (3.8a)$$

and

$$[x]_{y=1/2}=1/\alpha\,[(\alpha+\sigma B)\pm\sqrt{(\alpha-\sigma B)^2+4B^2\alpha\sigma}]\ , \qquad (3.8b)$$

which correspond to these three branches.

We can solve (3.6) for given values of B, σ, α and y. Fig. 3 shows the actual dependence of ω upon y(wave-number$=|y/s|$,$-1/2\leq y\leq 1/2$) for various sets of B, σ and α. The values of ω at $y=0$ in the TO- and RO-branches are adjusted in such a way that they coincide with those in the case $\sigma=1$, $\alpha=0.3$, by multiplying an appropriate factor proper to each case. In general, the constancy of the frequency of the TO-branch ω_t, is realized for small values of σ, as in the case of the one-dimensional simple lattice (consisting of point particles), and that of the frequency of the RO-branch, ω_γ, also for small values of α and $\alpha\simeq B$.

In the model stated above, the rotational vibration of a radical is mainly due to the forces exerted by the adjacent cations. Therefore, in the RO-branch where the rotational vibrations of the radicals have the main contribution in the lattice vibrations, their frequencies are less dependent on whether the radicals in adjacent unit cells vibrate with the same or with the different phases, in other words on the wave-number y.

From (3.5) we obtain

$$\frac{u}{u'}=-(1+e^{-2\pi iy})\Big/\left(\frac{x}{\sigma}-2\right),$$

$$\frac{d'\theta}{u'}=-B(1-e^{-2\pi iy})\Big/\left(\alpha\frac{x}{\sigma}-2B\right). \qquad (3.9)$$

The real parts of (3.9) give the amplitude ratios of the actual displacements in the lattice vibration. Therefore, the ratio ρ of the rotational energy to the total mechanical energy is given, for each branch, by

$$\rho=\frac{4\alpha B^2\sin^4\pi y\Big/\left(\alpha\dfrac{x}{\sigma}-2B\right)^2}{4\cos^4\pi y\Big/\left(\dfrac{x}{\sigma}-2\right)^2+\sigma+4\alpha B^2\sin^4\pi y\Big/\left(\alpha\dfrac{x}{\sigma}-2B\right)^2}\ . \qquad (3.10)$$

Fig. 4 shows the dependence of ρ upon y. We can conclude that the contribution of the rotational energy in the TA- and TO-branches are considerably smaller than that of the translational one, in particular, for a long wave-length range, whereas in the RO-branch the large portion of the mechanical energy is contributed by the rotational motion of the radicals except for the intermediate values of α and σ. Moreover ρ tends to increase with increasing wave-number in all branches.

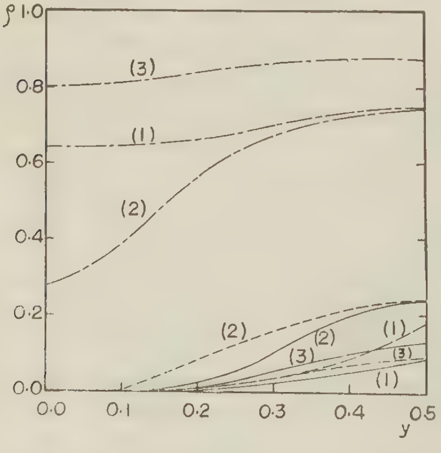

Fig. 4. Dependence of ρ upon y.
Chain curves: rotational optical mode.
Dotted curves: translational optical mode.
Real curves: translational acoustical mode.
(1) $B=0.8$, $\alpha=0.3$, $\sigma=0.1$.
(2) 〃 , 〃 , $\sigma=1.0$.
(3) 〃 , $\alpha=0.1$, $\sigma=0.7$.

From (3.7b and c) we obtain

$$[(\omega_r/\omega_t)^2]_{y=0}=\frac{B}{\alpha}\,\frac{\sigma}{1+\sigma}\ . \qquad (3.11)$$

Since $B\simeq\alpha$ and $\sigma\simeq 1$ in order of magnitude, $\omega_r\simeq\omega_t$ at $y=0$. According to the assumption (2) in § 2, the moment of inertia I of the radical around the axis passing through its center of mass i. e. the central ion is independent of the orientation of the axis relative to the radical and given by

$$I=M_c k_c d^2\ , \qquad (3.12)$$

where M_c is the mass of a coordinated ion, d the distance between a coordinated ion and the central ion of the radical, k_c a numerical constant peculiar to the symmetry of the coordination in the radical, i. e. 8/3 or 4 respectively according as it being tetrahedral or octahedral.

In identifying the sphere in our linear chain model with a real radical, we may put

$$M=M_0+n_cM_c$$

and

$$d'=d\,, \tag{3.13}$$

where M_0 is the mass of the central ion of the radical and n_c the coordination number. Putting (3.12) into last equation of (3.6a) and taking into account of (3.13), we obtain

$$\alpha=k_0(n_c+M_0/M_c)^{-1}. \tag{3.14}$$

Its values are listed in Table I for some anionic radicals with tetrahedral and octahedral structures.

Table I.

Radical	Molecular weight	α
$[BF_4]^{2-}$	86.82	0.58
$[SO_4]^{2-}$	96.00	0.44
$[ClO_4]^{-}$	99.46	0.43
$[MnO_4]^{-}$	118.94	0.36
$[PO_4]^{3-}$	94.98	0.31
$[MoO_4]^{2-}$	159.95	0.27
$[WO_4]^{2-}$	247.92	0.17
$[SiF_6]^{2-}$	407.97	0.53
$[PtCl_6]^{2-}$	247.92	0.35

Since σ may be expected to be considerably small, unless the partner cation is an extremely heavy metal, it would be reasonable, in general, to assume a small value of σ and α for a real complex crystal. Hence the assumptions on the constancy of the frequency and on the concentration of the rotational energy in the RO-branch would be allowable.

§ 4. Specific Heat at Low Temperatures

In this section, we will treat again only the isotropic complex crystals consisting of point-like cations and rigid anionic radicals. Then we have no need to take into account of the RA-branch (accoustical branch in rotational mode), as stated in App. II.

Blackman has used the linear chain model to discuss schematically the behaviors of the specific heat of simple crystals and shown its deviation from the Debye's continuum approximation[8]. Let us investigate now how affects the additional introduction of the rotational lattice-vibration the behavior of the specific heat at low temperatures, by using the results of the linear chain model calculated in § 3. Although there are $3(n-2)$ additional high-frequency modes of internal vibrations of each radical (n: the number of atoms in a radical), their contribution to the specific heat, which may be given by the sum of the Einstein functions, would be negligible at low temperatures. Therefore we may ignore these internal vibrations.

For a finte chain of L cells, there are

$$2L\Delta y=2L\left(\frac{dy}{d\nu}\right)\Delta\nu \tag{4.1}$$

vibrations in the frequency range $(\nu, \nu+\Delta\nu)$ with respect to each one of the three branches, i. e. TA-, TO- and RO-branches; the factor 2 in (4.1) takes account of the dual ranges for the y-value.

Accordingly the heat capacity C_V at T°K is given by

$$C_V=2Lk\int\frac{e^{h\nu/kT}}{(e^{h\nu/kT}-1)^2}\left(\frac{h\nu}{kT}\right)^2 \times\left[\left(\frac{dy}{d\nu}\right)_1+\left(\frac{dy}{d\nu}\right)_2+\left(\frac{dy}{d\nu}\right)_3\right]d\nu\,, \tag{4.2}$$

where $2\pi\nu=\omega$ and the suffixes appended to $(dy/d\nu)$ correspond to the three branches.

If we will apply Debye's approximation to this case, the relation between the frequency and y is given by, (cf. (3.7a))

$$\nu_{app}=\Omega\left[\frac{(1-B)}{2}\frac{\sigma}{1+\sigma}\right]^{1/2}y\,. \tag{4.3}$$

In the case of ideal molecular crystals, whose one-dimensional analogue was treated in App. I, $6N$ continuum modes will appear (N: the number of molecules), if we take into account the $3N$ translational modes and $3N$ torsional modes. Load et al[9] have calculated the specific heat of crystalline benzene taking into account these $6N$ modes and found that the observed molar heats are fitted by the single Debye function with $\Theta_D=150$°K even in fairly low temperatures. Since the RA-branch disappear in our case in which the cations are assumed to have infinitesimal size, the RO-branch have no corresponding continuum branch to be related with Debye's approximation. (cf. App. I and II) Accordingly we will determine the maximum frequency ν_D by the following normalization condition.

$$\int_0^{\nu_D}2L\left[\frac{\Omega^2(1-B)}{2}\frac{\sigma}{1+\sigma}\right]^{-1/2}d\nu=3L$$

or

$$\nu_D=\Omega\left[\frac{\sigma(1-B)}{2(1+\sigma)}\right]^{1/2}\frac{3}{2}\,. \tag{4.4}$$

Then the heat capacity in the continuum approximation is given by

$$(c_V)_{app}=3Lk\left(\frac{T}{\Theta_D}\right)\int_0^{\Theta_D/T}\frac{\xi^2e^\xi}{(e^\xi-1)^2}d\xi\,, \tag{4.5}$$

where

$$\Theta_D=h\nu_D/k\,. \tag{4.6}$$

C_V given in terms of (4.2) may be numerically computed using the results in §3. (cf. Fig. 3) Therefore, if we simply equate the accurate expression (4.2) to the approximate one (4.5), we can calculate a value for Θ_D for any particular T and then obtain the Θ_D-T curves for various sets of values of B, σ and α, which are analogous to those in the Blackman's computation[8]. We expect that the values of Θ_D calculated in this way will agree exactly with (4.6) only for very small T, and that for only this limiting case the Debye formula (4.5) is exact. These curves are actually shown in Fig. 5, in which the maximum frequency $\nu_m\left(=\frac{\Omega}{2\pi}\sqrt{x_m}\right)$ corresponding to the largest one, x_m, of the six roots of (3.6) at $y=0$ and 1/2, which are given by (3.7) and (3.8), is chosen in each case so that $h\nu_m/k=200°\text{K}$ by adjusting the constant Ω.

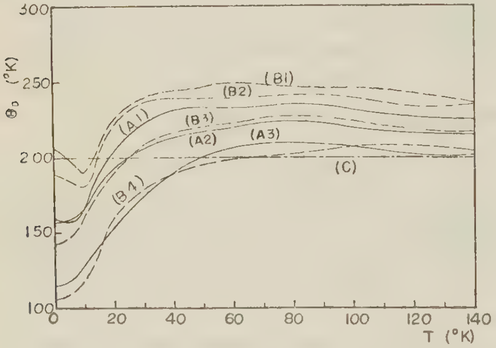

Fig. 5. Temperature dependence of Θ_D.
(A1) $B=0.8,\ \alpha=0.3,\ \sigma=1$
(A2) 〃 , 〃 , $\sigma=0.3$
(A3) 〃 , 〃 , $\sigma=0.1$
(B1) $B=0.8,\ \alpha=0.7,\ \sigma-0.7$
(B2) 〃 , $\alpha=0.5$, 〃
(B3) 〃 , $\alpha=0.2$, 〃
(B4) 〃 , $\alpha=0.1$, 〃
(C) Continuum approximation

In A-group B and α are constant and σ variable, whereas in B-group B and σ are constant and α variable. The curves (A1), (B1) and (B2) have minima, whereas the curves (A2), (A3), (B3) and (B4) have not.

Referring to Fig. 5, we note in particular the following points:

(1) θ_D is far from being independent of temperature and shows marked variations at low temperatures.

(2) At high temperatures, Θ_D tends to a fairly constant value proper to each case but it is considerably different from the low-temperature limit at $T=0$. That is, the specific heat at high temperatures can be fairly represented by means of the Debye formula with a suitably chosen value for the parameter Θ_D.

(3) The region for the linear law $C_V\propto T$, which is the analogue of the T^3-law in actual three-dimensional crystals, is extrememely narrow and only recognized as a horizontal tangent at $T=0$.

(4) Curves (A1), (B1) and (B2) have minima, where Θ_D is stationary. Since the corresponding temperatures are sufficiently low compared with Θ_D, we have in the neighbourhood of the minimum spurious T^3-variation quite unrelated to the real T^3-region at $T=0$, as observed always in real simple crystals.

(5) The remaining curves have no minima, although the curves rapidly increase above the low-temperature limit of Θ_D at $T=0$ with increase of T.

All the above features would be retained in the real three-dimensional cases in somewhat less exaggerated way.

§5. Conclusions

According to the above results we may assume that the frequency in the RO-branch is nearly independent on the wave-number and of order of magnitude comparable to the frequency of the Reststrahlen and that the mechanical energy of lattice vibration in this branch is considered as the rotational energy of the radicals approximately. A vibrational mode in RO-branch is characterized by the motion such that the rotational vibration of the radicals is much more conspicuous compared with the translational motions of the radicals and cations.

In the three-dimensional case, where a unit cell contains n radicals and n partner cations, $3\times3n=9n$ branches i. e. three TA- and $3(2n-1)$ TO-branches and $3n$ RO-branches will appear. ω_j's in §2 may be classified into these $9n$ branches. Therefore, the quantized energies of the lattice vibration in complex crystals may be classified as the TA-, TO- and RO-phonons. If the crystal structure of a complex crystal were an ideal one, the RO-phonons would be classified into transverse and longitudinal ones, as in the case of the TA- and TO-phonons.

When the binding forces between ions constituting a radical is not so strong that it is hardly regarded as a rigid rotor, then our model is not available. On the contrary, if the forces between radicals and cations and between different radicals are considerably weak and ω_r has a value small enough to be treated as a free rotor, it would be irrelevant to take into account the rotational vibration, since such a low-frequency vibration will give only a constant contribution to the specific heat even in a relatively low temperature range owing to the validity of the equipartion law. However, ω_r would be expected to have a fairly large value, since the binding forces between radicals and cations and between different radicals would be considered as too large in actual complex crystals to allow a nearly free rotation of the radicals, although they are much weaker than the intraradical forces.

In the complex salt crystals, which contain tetrahedral or octahedral complex ions such as $[MCl_4]^{n-}$ or $[M(CN)_6]^{n-}$ (M: metallic ion), the binding forces within these complex ions may be expected to be stronger than those with the lattice. Some crystals preferably take water of crystallization by forming the solid salts hydrates. The tendency of the hydration is comspicuous, in particular, for the metallic cation of small ionic radius and high ionic charge i.e. large polarizing power$^{10)}$. In the case such as $BeSO_4\cdot4H_2O$, $NiSO_4\cdot7H_2O$ and $CrCl_3\cdot6H_2O$ the water may be coordinated to the cation of the salt, not only in crystallographical sense, but to form a coordinated complex ion in the sense of Werner's theory, and we have actually the salts of hydrated cations (aquo-cations) $[Be(H_2O)_4]SO_4$, $[Ni(H_2O)_6]SO_4H_2O$ and $[Cr(H_2O)_6]Cl_3$. In aquo-cations $[Be(H_2O)_4]^{2+}$, $[Ni(H_2O)_6]^{2+}$ and $[Cr(H_2O)_6]^{3+}$ the coordinated water molecules would be strongly polarized by the central metallic ion. Accordingly the present theory would be applicable not only to the complex crystal containing anionic radicals but also to those containing complex ions or aquo-cations, if the binding forces within these complex ions and aquo-cations are considerably tight as in the case of anionic radicals. Only in the ideal complex crystals, whose unit cell consists of n rigid anionic radicals and n rigid aquo-cations, the three RA-branch of the lattice vibrations will appear. (cf. App. II)

The features on the Θ_D-T relation (except the item (5)), stated in § 4, are quite analogous to those in the case of simple ionic crystals, where the rotational mode is not necessary to be taken into account. As the striking difference caused by introducing the rotational modes we may mention that the Θ_D-T curve has no minimum occasionally at an intermediate temperature, even when the curve rises towards higher temperatures beyond the Θ_D value at $T=0$. (cf. curves (A2), (A3), (B3) and (B4) in Fig. 5) The Θ_D-T curve of a simple ionic crystals, in such a case, always has a minimum, although the minimum lies very close to $T=0$ and its existence may be not marked in some cases$^{11)}$.

This is due to the fact that the factor Γ in the coefficient of the second terms in (3.7a) may take a positive value for appropriate values of the three parameters B, σ and α, whereas the corresponding coefficient in the case of a one-dimensional simple lattice is always negative$^{11)}$. Referring to Fig. 5 and (3.7a), a positive coefficient occurs for small values of σ and α. Accordingly we could infer that in some actual complex crystals the Θ_D-T curve has no minimum and that they do not have the spurious T^3-region in the temperature dependence of the specific heat.

Unfortunately we cannot find suitable experimental data on the specific heats of complex crystals at low temperatures which are to be compared with the present theoretical conclusion. If the measurement is made accurately for complex crystals in the future, a clew for the problem mentioned above may be given.

In conclusion, the authors express their sincere thanks to Professor K. Umeda who read the manuscript and gave them valuable advices.

Appendix I.

Vibrational Modes in One-dimensional Lattice Consisting of Spheres of One Kind.

For the lattice consisting of spheres of one kind with finite radius d, mass M and moment of inertia I, the secular equation to determine the frequency as a function of the wave-number is given by

$$\alpha x^2-4(B\cos^2\pi y+\alpha\sin^2\pi y)x$$
$$+16\,B(1-B)\cos^2\pi y\sin^2\pi y=0\ , \qquad \text{(A-1)}$$

where

$$x\equiv(\omega/\Omega)^2,\quad \Omega^2\equiv(c_1+c_2)/M\ ,$$
$$\alpha\equiv I/Md^2\ ,\quad B\equiv c_2/(c_1+c_2)\ .$$

Then two branches appear, namely TA-branch and RA-branch (that is, accoustical branch in rotational mode), whose frequencies depend upon y as shown in Fig. 6a.

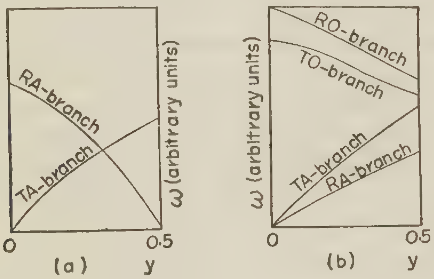

Fig. 6a and b. Schematic diagrams of the $\omega-y$ relation. $(-1/2\leq y\leq 1/2)$

If we expand $(\omega/\Omega)^2$ at $\omega\simeq 0$, we have in the TA-branch

$$(\omega/\Omega)^2_{TA}=4(1-B)\pi^2y^2+O(y^4) \qquad \text{(A-2a)}$$
$$\text{near}\quad y=0\ ,$$

and in the RA-branch

$$(\omega/\Omega)^2_{RA}=4(1-B)(B/\alpha)\pi^2\left(\frac{1}{2}-y\right)^2$$
$$+O\left(\left(\frac{1}{2}-y\right)^4\right)\qquad \text{near } y=1/2\ . \quad \text{(A-2b)}$$

Appendix II.

Vibrational Modes in One-dimensional Lattice Consisting of Spheres of Two Kinds.

In the case of the lattice consisting of spheres of two kinds occupying alternate sites, whose radii, masses and moments of inertia are d, d'; M, M'; and I, I' respectively, the secular equation is given by

$$[x^2-2(1+\sigma)x+4\sigma\sin^2\pi y]$$
$$\times[\alpha\alpha' x^2-2B(\alpha+\sigma\alpha')x+4B^2\sigma\sin^2\pi y]$$
$$-[(x-2\sigma)(\alpha' x-2B)+(x-2)(\alpha x-2B\sigma)]$$
$$\times 4B^2\sigma\sin^2\pi y$$
$$+16\,B^4\sigma^2\sin^2\pi y(\sin^2\pi y+2\cos^2\pi y)=0\ , \qquad \text{(A-3)}$$

where

$$x\equiv(\omega/\Omega)^2\ ,\qquad \Omega^2\equiv(c_1+c_2)/M'\ ,$$
$$\alpha\equiv I/Md^2\ ,\qquad \alpha'\equiv I'/M'd'^2\ ,$$
$$B\equiv c_2/(c_1+c_2)\ ,\quad \sigma\equiv M'/M\ .$$

In this case four branches appear as shown in Fig. 6b. In the TA- and RA-branches near $y=0$, ω^2 can be expressed such as

$$(\omega/\Omega)_{TA}{}^2=\frac{2(1-B)\sigma}{1+\sigma}\pi^2y^2+O(y^4) \qquad \text{(A-4a)}$$

and

$$(\omega/\Omega)_{RA}{}^2=\frac{2(1-B)B\sigma}{\alpha+\alpha'\sigma}\pi^2y^2+O(y^4)\ , \qquad \text{(A-4b)}$$

respectively. When $\alpha'\to\infty$, (A-3) coincides with (3.6) and RA-branch disappears. (cf. (A-4b)) This is the case treated in § 3.

References

1) F. Seitz: *Modern Theory of Solids* (McGraw-Hill Co. N. Y. 1940) p. 115.
2) H. W. Leverentz: *Introduction to Luminescence of Solids* (John Wiley and Sons Co. N. Y. 1950) p. 115.
3) M. G. Mellon: *Analytical Absorption Spectra* (John Wiley and Sons Co. N. Y. 1950) Chap. 8.
4) M. Born and K. Huang: *Dynamical Theory of Crystal Lattices* (Oxford 1954) p. 127.
C. Schaeffer and F. Matossi: *Das Ultrarote Spectrum* (Springer Berlin 1930) Table 54.
5) L. Pauling: *The Nature of Chemical Bond* (Cornell Univ. Press 1945) Chap. 7.
6) R. Wyckoff: *Crystal Structure* II (Interscience Publisher, N. Y. 1951) Chap. 8 Illust. p. 8-12.
7) M. Born and K. Huang: loc. cit. p. 173.
8) M. Blackman: Proc. Roy. Soc., **A148** (1935) 365.
9) R. C. Load, J. E. Ahlberg and D. H. Andrews: J. Chem. Phys. **5** (1937) 649.
10) H. J. Emeréus and J. S. Anderson: *Modern Aspects in Inorganic Chemistry* (D. Van Nostrand Co. N. Y. 1952) pp. 82, 191.
11) F. Seitz: loc. cit. p. 134.

JOURNAL OF THE PHYSICAL SOCIETY OF JAPAN Vol. 12, No. 4, APRIL, 1957

The Structure of Evaporated Barium Films

By Yoshihiko MIZUSHIMA, Zenjiro ODA and Osamu OCHI

Electrical Communication Laboratory, Nippon Telegraph and Telephone Public Corporation, Musashino-shi, Tokyo

(Received November 9, 1956)

The electrical resistance and nitrogen sorption at liquid oxygen temperature were measured for barium films evaporated and heat-treated under various conditions. The conditions which provided the properties of the film were:

1. Temperature of substrate during deposition, T_d,
2. Temperature of substrate at annealing, T_a, and
3. Pressure of residual gas during deposition, P_d.

Comparing the temperature variation of electrical resistance with sorption property for nitrogen, the authors reached the following conclusions:

1. Granular structure plays an important role in resistance as well as in nitrogen sorption,
2. The contribution of the imperfections included in each crystalline lattice is also remarkable at low temperature, but decays easily at higher temperature.

Discussions are also given on the mechanism of nitrogen sorption on barium film.

§ 1. Introduction

The complexity of the physical properties of an evaporated metal film can be more or less attributed to its structure-sensitivity, which is easily affected by treatment conditions. From this point of view, relations between factors during evaporation and the resulting film structure must be studied accurately, and the effects of the treatment conditions should be connected with the unified atomic model of the film construction. Recently, information on lattice imperfections has been markedly accumulated, so that the detailed results given here are able to be investigated systematically by the model of lattice imperfections.

Among the properties of evaporated barium film, the reaction with various gases[1] is most extensively investigated because of its practical application, and few is reported on the structure and the resulting adsorption properties of the barium film. Reimann[2] was the first investigator who pointed out the large capacity of the gas-evaporated film for various gases. He attributed this excess capacity to the large surface area of "black" deposit. The same phenomenon was found by Ehrke and Slack[3] and later by Haase[4].

On the other hand, investigations of evaporated metal films by the measurement of electrical resistance have been often reported[5-8]. The resistance is known to be sensitive to the condition of evaporation and the subsequent treatment. To interpret this, ideas[9],[10] have been proposed that in an evaporated film disordered parts contribute to the resistivity and the heat treatment diminishes such disorders.

Furthermore, a number of studies by electron diffraction[11] and electron microscope[12]-[15] show that evaporated metal films have a granular structure with a variety of crystallines.

The present series of studies were undertaken to illustrate the micro-structure of evaporated barium films produced and treated under various conditions.

§ 2. Electrical Resistance of Evaporated Barium Film

2.1. *Experimental*

Test tubes used in this measurement are shown in Fig. 1, in which two platinum electrodes are enamelled on glass wall for resistance measurement. As a barium source commercial barium tube getter was used and directly heated by passing electric current. To secure the uniform thickness and size of the film, a nickel cylinder with a slot was mounted around the source. After thorough glass baking and outgassing of metal parts by the ordinary vacuum techniques, the system was evacuated to 10^{-7} mmHg and the evaporation was carried out under a prepared condition and then evacuating to high vacuum again the bulb was sealed off. When necessary, another getter was evaporated previously in order to maintain the high vacuum during measurement. The weight of the evaporated amount or the thickness of the film was kept almost the same from sample to sample. The electrical resistance was measured by a Wheatstone bridge, where the power consumed in the film was below 10^{-8} watts on the average. When the fast change must be followed, an electronic automatic recorder was also used.

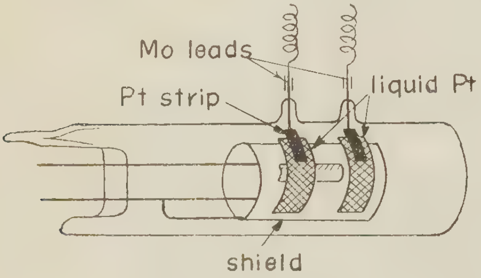

Fig. 1. Test tube for electrical resistance measurement.

Temperature was varied by using the following baths; liquid oxygen for −183°C, dry ice-propyl alchohol mixture connected to vacuum pump for about −110°C, dry ice-toluene mixture from −78°C to room temperature, transformer oil up to 100°C and small electric furnace for higher temperatures. When the temperature must be changed continuously, the rate of temperature change was controlled manually in the range 0.5∼2 degrees/min.

2.2. *Results on Resistance-Temperature Coefficient*

As will be introduced later, the resistance characteristics of an evaporated film are completely reversible so long as the temperature is varied below the highest one ever experienced by the film. Moreover, so far as the films maintain metallic character (positive temperature coefficient), the resistance vs temperature curves show themselves almost parallel with each other. In Fig. 2 are shown curves for films of various histories, to say, with reduced resistance by stabilization or by recrystallization, or with increased resistance by slight aggregation.

One can see that for this case a rule similar to the Mathiesen's holds good irrespective of the histories, and that the properties of the film may be infered from the residual resistance. Moreover, from these curves we can obtain the temperature coefficient of resistance for barium; $\alpha = 0.0035$ is almost the same as the usual temperature coefficient of bulky barium metal.

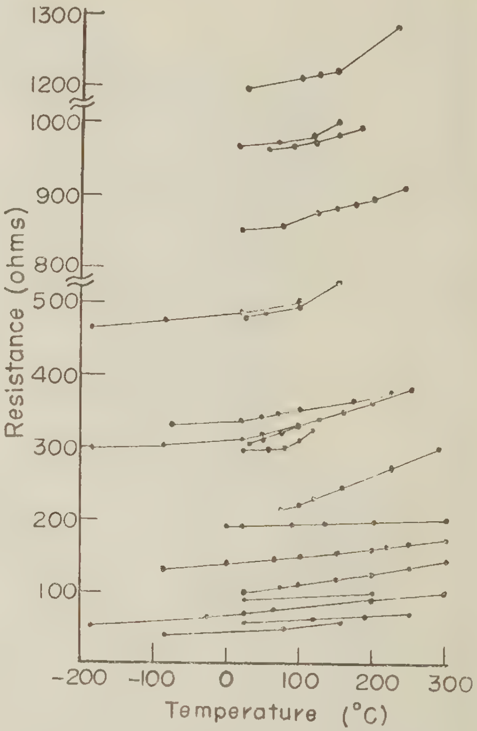

Fig. 2. Electrical resistance vs. temperature relations for various films.

2.3. *Recovery of Electrical Resistivity at Low Temperatures*

Barium films produced at low substrate temperature have large residual resistivity. However, when the film is brought to higher temperature, the excess resistivity decreases irreversibly. The rate of decrease increases at high temperature, and after long annealing near room temperature, the resistivity attains the lowest equilibrium value. We name this process as "stabilization" following Harris and his co-workars⁶⁾. As will be proved later, this process is attributed to the disappearance of lattice imperfections, existing in the evaporated film. An example of this stabilization process is shown in Fig. 3, where the temperature is raised stepwisely. Up to above room temperature these treatment is continued and the resistance attains to its lowest value so far as the recrystallization does not occur. To analyse this process, both rates before and after the sudden change of temperature are obtained. The analysis will be given in 3.2.

Furthermore, the degree of such stabilization is affected by the residual pressure during evaporation P_d. The result is shown in Fig. 4, where we take the ratio of the resistance value immediately after the evaporation to that after the annealing at 20°C for an hour. The result is underestimating, since the temperature coefficient is not taken into account. However, it is clear that the increase in P_d makes the unstable imperfections in the film richer.

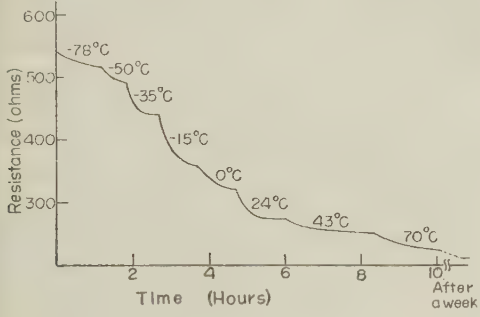

Fig. 3. Stabilization of a low-temperature evaporated film.

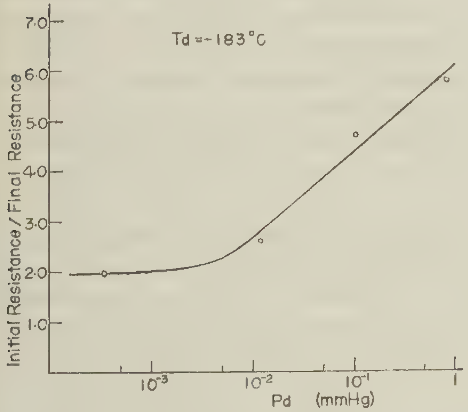

Fig. 4. Effect of residual gas pressure during evaporation on the stabilization of low-temperature evaporated film.

2.4. *Process of Recrystallization and Aggregation*

For the films already suffered the stabilization at or below room temperature, the resistance-temperature characteristics are completely reversible. However, when this film is heated to higher temperatures a new irreversible decrease of resistance regarded as recrystallization is observed above certain temperature. However, if the heat treatment is continued further, an irreversible increase regarded as oxidation or aggregation takes place. In Fig. 5 these tendencies are shown.

The recrystallization occurs in a narrow temperature range and has a different feature from the stabilization process. However, such a phenomenon is observed only in a few cases in total several tens of the experiments and at temperatures ranging from 100° to 300°C.

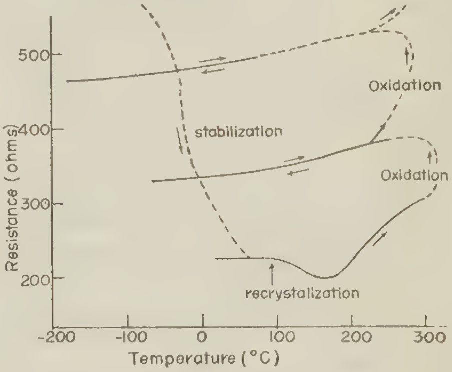

Fig. 5. Change of electrical resistance with aggregation (or oxidation) at high temperature.

The oxidation or the aggregation is observed between 100°C and the softening point of glass (~500°C), and we will call them as aggregation for convenience sake. The film, subjected to slight aggregation, keeps a metallic character in the plot of resistance vs temperature

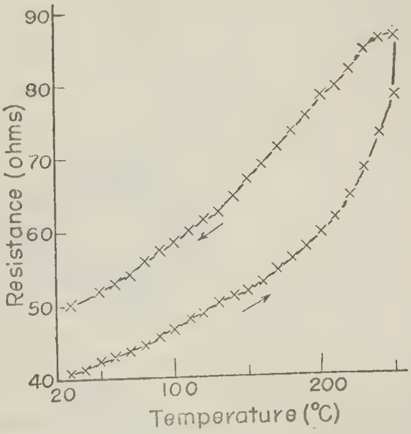

Fig. 6. Change of resistance with temperature.

as shown in Fig. 6 and the Mathiesens' rule still holds.

2.5. *State of Semi-Conducting Character*

As shown in Fig. 7, the aggregation (or oxidation) proceeds further until the film resistance becomes infinity, under the constant temperature. In such a case when the aggregation proceeds extensively and over some limits, the temperature dependency deviates from the metallic character to a stable semi-conducting one. When the film is further subjected to the aggregation at higher temperatures, another different semi-conducting character appears. The activation energies are shown in Fig. 8 and usually lie between 0.08 and 0.003 eV. The point of inflextion lies, if exists, around 150°C.

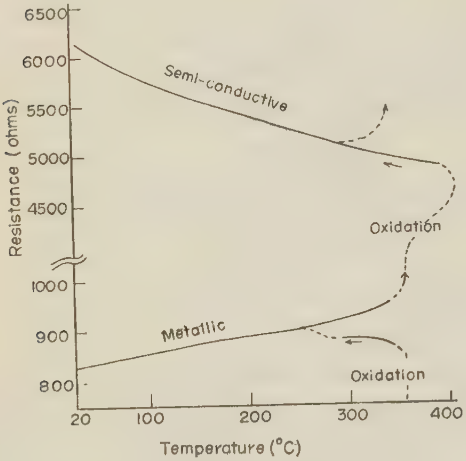

Fig. 7. Semi-conducting character of the film after extensive aggregation.

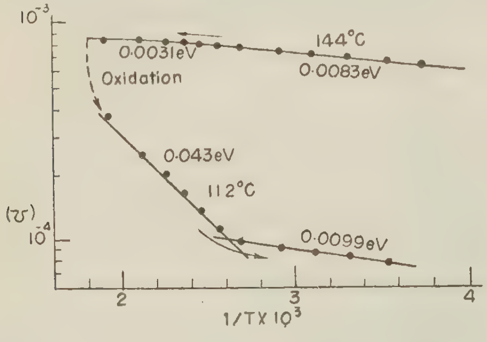

Fig. 8. Activation energy of semi-conducting film.

When the film is very thin, to say below 50 Å, the temperature dependency of resistance shows the similar semi-conducting properties, even evaporated at lower temperatures and without any heat treatment. This should be attributed not to the oxidation of film by residual oxygen but to the characteristics of the thin films, because the outgassing has been carried out extensively.

§ 3. Discussions

3.1. *Irreversible Decrease of the Low Temperature Evaporated Film*

In general, the factors contributing to the electrical resistance of the metal can be divided into;

1. temperature-independent component (residual resistivity), and
2. temperature-proportional component.

As mentioned above, the resistance of the evaporated barium film changes irreversibly by the heat-treatment at temperatures to which the film is not yet subjected. The nature of such a decrease in resistance is found to relate to the residual resistivity alone.

Furthermore, the temperature-independent component is, in our case, divided as follows;

1. electron scattering at grain boundaries and surfaces,
2. electron scattering at imperfect points in crystal lattice.

By the measurement of Hall coefficient it is roughly proved that the number of conduction electrons does not change so much as to explain such a large change of resistance.

In the evaporated metal films the irreversible decrease of resistance consists of two distinctly different processes. The first is the stabilization, which for barium with intermediate melting point according to the classification of Levinstein[13], occurs below room temperature. The second is the recrystallization, which is very similar to the sintering process of metallic powder. These two processes are not joined continuously, but are different in the temperature range and reaction rate. According to Wilkinson and Birks[8], in the temperature range of stabilization on gold film, there is a little change in X-ray diffraction pattern, but in the region of recrystallization at higher temperatures significant sharpening of the lines is observed. We may define here that the slow decrement process at lower temperatures is a recovering process in which imperfect lattice region tends to disappear and that the fast decreasing process at higher temperatures corresponds to the growth of the crystalline particles in the film. Since the latter process will require a higher activation energy, it is reasonable to appear at higher temperatures.

3.2. *Stabilization*

The kinetics of the stabilization for evaporated metal films have been already studied by Harris et al[6] with gold. They assumed that in all recovery region only one mechanism is prevailing, and that the imperfections can diffuse out to grain boundaries, where they disappear. However, refering to the recent data on the recovery of imperfections in metals, these assumptions is found to be incorrect. As the method of Vand[10] is also doubtful, another method of analysis following Overhauser[16] is employed. Let f be the density of imperfections in question, and Q an activation energy of recovery, then by the usual notations we can set

$$-\left(\frac{df}{dt}\right)_T = \text{const}\, e^{-Q/kT} \tag{1}$$

Let r_0 be the residual resistivity at the final equilibrium, then $r-r_0$ denotes the excess resistance due to the imperfection at any instant t. When T_1 and T_2 does not differ so much,

$$\log\left\{\frac{d(r-r_0)}{dt}\right\}_{T_1} \Big/ \left\{\frac{d(r-r_0)}{dt}\right\}_{T_2} = \frac{Q}{k}\left(\frac{1}{T_2}-\frac{1}{T_1}\right) \tag{2}$$

For convenience we take R as a resistance at any time and at any temperature,

$$\log\frac{\left(\frac{dR}{dt}\right)_{T_1}}{\left(\frac{dR}{dt}\right)_{T_2}} = \frac{Q}{k}\left(\frac{1}{T_2}-\frac{1}{T_1}\right) \tag{3}$$

Thus we can calculate the activation energies of recovery as a function of heat-treatment temperature irrespective of the recovery mechanism. In this case, it is assumed that in small temperature range from T_1 to T_2 the energy is nearly constant. The results are shown in Fig. 9, where, curves 1 with peak near 0°C correspond to the sample produced with high evaporating speed, and curves 2 without peak to the sample with low speed.

In the case of noble metals many reports are found on the recovery of residual resistivity induced by radiation damage or cold work[17],[18]. Comparing these results with the stabilization of evaporated metals[19],[20], it is supposed that nearly the same recovery mechanism is prevailing in both cases. If this is accepted, the energy corresponding to the flat portion of the curves in Fig. 9 can be attributed to the migration of interstitial atoms or lattice vacancies.

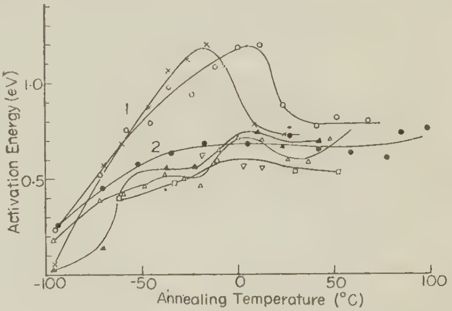

Fig. 9. Change of activation energy with heat treatment temperature. Curve 1; fastly evaporated films, curve 2; slowly evaporated films.

Following Overhauser[16] one can get theoretically

$$\frac{df}{dt} = -kf^m e^{\beta f} \tag{4}$$

where m is the true reaction order, and the last exponent a stress-induced extra term. This extra term makes the apparent reaction order larger. Plotting $\log\left\{\frac{d(r-r_0)}{dt}\right\}$ at any temperature against $\log(r-r_0)$ one can estimate the value of m. The values of m thus obtained are abnormally high, for instance 38.9 at −78°C, 17.9 at 20°C and 10.8 at 50°C, whereas with copper films[20] the values are 9.6 at −78°C, 4.0 at −8.5°C and 1.26 at 31.5°C. In the latter case, reaction order approaching unity indicates that this recovery is due to one agent, at least below room temperature. For barium, however, the reaction order is very high, indicating that this reaction is not an unique process, but readily affected by stresses induced by the deformation of lattice, probably because barium is softer than copper.

Furthermore, the fact that the activation energy is not constant shows that the diffusion process in barium is very complicated and different from noble metals. In f.c.c. metals vacancies are more readily created and more stable to diffusing out than interstitial atoms. In b.c.c. metals as barium, however, there are no large differences in mobilities between vacancies and interstitial atoms and hence combined processes may take place easily in a complicated manner. These facts afford facilities for discussing the recovery mechanism.

The possibility that imperfections other than point defects, to say dislocations or grain boundaries, play some roles in the stabilization, is almost negligible. In general, recovery of dislocations seems to occur at such high temperatures as recrystallization occurs. In addition, dislocations contribute very little to the resistivity than point defects[21] and are hardly possible to cause a large change of resistance ranging some hunderds per cents of the final equilibrium value.

3.3. *Recrystallization*

As shown in 2.4 the decrease of resistance due to the recrystalization takes place in the temperature range 100° to 300°C. On the other hand, non-transition metal of similar melting point, to say silver, has a recrystallization temperature of about 200°C, after cold-working. Empirical formula of Tamman[23], semi-empirical formula of Kramer[24], and theoretical formulas[25] give recrystallization temperature of metal as roughly 40 per cents of its melting point (absolute). The value estimated for barium is about 150°C and lies in the range of observed one. Electron-micrographs for other metal films show that the recrystallization makes the grain large.

However, such a recrystalization is not usually observed because of chemical reactivity of barium, that is, the minute oxidation products on the surface prevent the sintering of grain boundaries. Such influences of impurities or occluded gases on the recrystallization temperature after cold working is widely accepted. In other evaporated metals, for instance nickel films[26], the chemical reactivity is much lower, so recrystallization temperature has been easily observed. Furthermore, in a very thin film the aggregation of particles may also mask the contribution of recrystallization to the film resistance.

3.4. *Aggregation, Oxdation, and Semi-Conducting Property*

The resistivity-increasing tendency is defined here as the process of aggregation, or oxidation of the film. In this temperature range either the migration of metal atoms or a chemical reaction with the gas evolved from glass wall will take place. By any means, these processes increase the film resistance and when exceeding some limits, give semi-conducting character. In barium films, it is difficult to decide which mechanism is prevailing. However, in view of the experimental condition, it seems probable that the aggregation process is predominant, and only near the softening point of glass (~500°C) the oxidation by the gas evolved from glass wall becomes significant.

The activation energy of such a semi-conducting property is too small to be interpreted in terms of an energy-band model of normal oxide. Even in case of both a very thin barium film without suffering any oxidation and a film of noble metal[27),28], which have suffered appropriate heat treatment at and above room temperature, such a low activation energy also appears. By continual processing of aggregation the film resistance can reach any large value up to infinity without changing other properties appreciably, to say activation energy and visual appearance. All these facts indicate that the thin barium film has a granular structure composed of fine crystalline particles, and the contact between them becomes poorer with either aggregation or oxidation. The evidences for such a granular structure are also given by electron diffraction[29], electron micrograph[30] and by the gas sorption property described below. This semi-conducting property of metal film has been discussed theoretically by Mostovetch[31].

§ 4. Nitrogen Sorption at Low Temperature

4.1. *Experimental*

The vacuum apparatus comprised (i) a conventional pumping system, using Hickman pump and mechanical fore pump by means of which pressures below 10^{-6} mmHg were obtained, (ii) gas dosing systems and (iii) a sorption system containing a evaporation bulb and a Pirani gauge which was protected by a liquid oxygen trap and could be isolated by mercury cut-offs. Barium was evaporated from a commercial tube getter heated electrically. By changing the temperature of the glass wall during evaporation (T_d), and the residual gas pressure during evaporation (P_d) the structure of evaporated film was varied. T_d was provided with liquid oxygen, water bath and an electric furnace and P_d with the admission of argon previously purified by another barium getter. After extensive evacuation and glass baking, the trap was cooled with liquid oxygen and the evaporation source was outgassed carefully and then evaporation was carried out under prepared conditions. After immersing the bulb in liquid oxygen, under extensive evacuation, the sorption system was closed and pure nitrogen, prepared by thermal decomposition of BaN_6, was admitted and then the pressure change was followed. After the sorption experiment evaporated amount was determined mainly by the chemical analysis.

To examine the influence of the speed of evaporation, a new barium source appropriate for this purpose was designed. As shown in Fig. 10 metallic barium was loaded in a iron boat and covered with a protective film of nickel. The distance between evaporation source and the substrate was changed twofold, whereby the density of arriving atoms could be changed fourfold. Furthermore, the rate of evaporation was varied 100 times with the source temperature changed from 470° to 780°C.

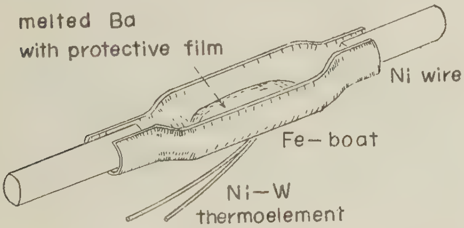

Fig. 10. Barium evaporation source convenient for controlling the rate of evaporation.

To investigate the influence of nitrogen adsorption on electrical resistance of the film, another type of bulb having two liquid platinum electrodes enamelled on the inner wall was used. Connecting this to the adsorption apparatus and after the same procedure as above, the electrical resistance of the film was recorded in the course of nitrogen adsorption. Gas pressure was measured by a McLeod gauge.

4.2. *Rate and Amount of Nitrogen Sorption at Low Temperature*

When the nitrogen is admitted to the film at liquid oxygen temperature, a very fast sorption is observed initially and then followed by a slow one, which reaches an equilibrium gradually after an hour or more. No more sorption takes place with added nitrogen. Some examples of the sorption for the films previously treated at different conditions are shown in Fig. 11.

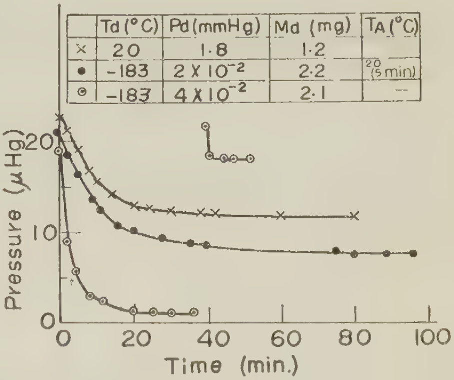

Fig. 11. Rate of nitrogen sorption at −183°C on films evaporated under various conditions.

The rate of sorption can be expressed by the following equation,

$$-\frac{dP}{dt}=kP(P-P_f) \qquad (5)$$

where P is a nitrogen pressure, P_f is a pressure after sufficiently long time. Integrating this equation, a linear relation between $\log(P-P_f)/P$ and t is obtained, thus making possible to calculate the rate constant k from the slope of the line kP_f.

The saturation amount of sorption S_1 is found to be almost independent of the equilibrium pressure and so we can take this amount

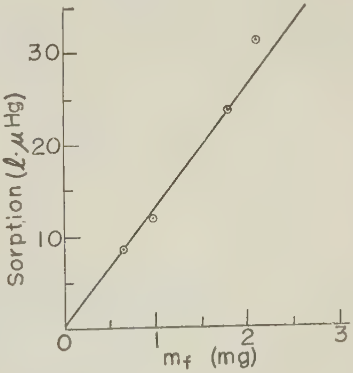

Fig. 12. Relation between deposited amount and sorption amount. Evaporation condition; $P_d=2.5\times10^{-2}$ mmHg, $T_d=-183$°C.

as a measure of the effective area of barium film. Following Beeck[32),33)], the low-temperature adsorption isotherm of nitrogen on evaporated metal films shows a long plateau in such a range of equilibrium pressure; hence the sorption amount in this range may be treated as a characteristic quantity of the film.

The relation between the amount of nitrogen sorption at low temperature and the weight of the film, which is evaporated at some fixed condition ($P_d=3.5\sim5\times10^{-2}$ mmHg, $T_d=-183$°C) is almost linear as shown in Fig. 12. In the following, therefore, we take the saturation amount of sorption divided by the film weight as a characteristic value intimately connected to the evaporation condition.

4.3. *Influence of the Residual Gas Pressure at Evaporation* (P_d)

The low temperature sorption of the film evaporated in various argon pressure is shown in Fig. 13. Vacuum-evaporated film shows rather poor sorption, whereas for the film produced in an atmosphere of inert gas S_1 increases markedly. The value for the film evaporated at $P_d=1.8$ mmHg is 9 times as large as that for the vacuum-evaporated film. The gas-evaporated film above 0.8 mmHg has a visual appearance of lamp-black.

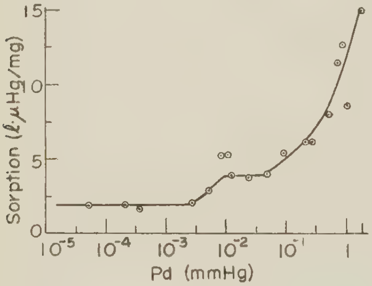

Fig. 13. Relation between the residual gas pressure at evaporation (P_d) and sorption amount. $T_d=20$°C.

4.4. *Influence of the Substrate Temperature* (T_d *and* T_a)

Setting P_d in the pressure range from 1×10^{-2} to 5×10^{-2}, nitrogen sorption is measured as a function of wall temperature during deposition. The result is shown in Fig. 14 by circle. Since the film evaporated at −183°C ($T_d=-183$°C) is very unstable, we examined the variation of sorption with stabilization. Fig. 15 shows the decrease of sorption with time when the film is kept in a bath of room temperature. Also crosses in Fig. 14 show the result when the film produced at $T_d=-183$°C was annealed at each desired temperature (T_a) for an hour in high vacuum prior to adsorption. The higher the temperature, the smaller becomes the distance between these two curves; this fact suggests that at high temperatures the stabilization becomes faster and almost accomplishes in an hour.

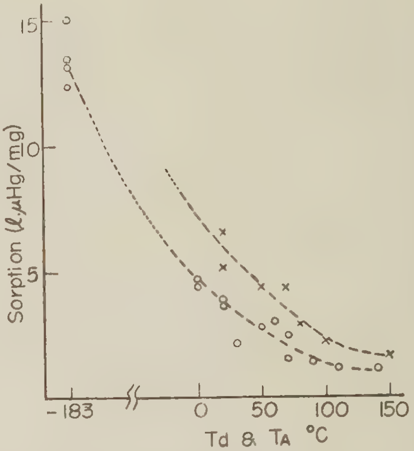

Fig. 14. Relation between the wall temperature at evaporation T_d and sorption amount (circles) and its change with annealing temperature T_A (crosses) at $P_d=1\sim5\times10^{-2}$ mmHg.

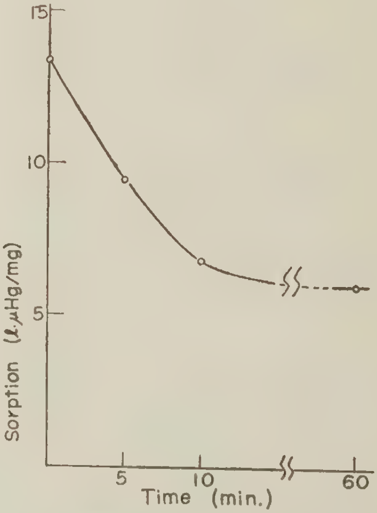

Fig. 15. Change of sorption amount for low-temperature evaporated film with stabilization at room temperature.

4.5. *Reversibility of Nitrogen Sorption*

Nitrogen sorption on barium film is not reversible. When the newly prepared film is saturated with nitrogen at −183°C (S_1) and then evacuated for an hour at that temperature, some fraction of sorbed gas can be desorbed only in the early stage. Admitting the gas again at the same temperature, the film takes up only a smaller amount (S_2) than that in the first. Although the first sorption cannot be repeated twice, the second sorption S_2 is completely reversible and can be tried many times. On the other hand, when the evacuation is carried out at room temperature (for an hour), larger desorption occurs and the capacity of low temperature sorption recovers partly. This third sorption S_3 can be also repeated. Always the relation $S_1 > S_3 > S_2$ holds. The rates of these three sorptions are shown in Fig. 16 and 17 where Eq. (5) can be fairly applied to the first and the third type of sorption, but the second type is generally too fast to be followed.

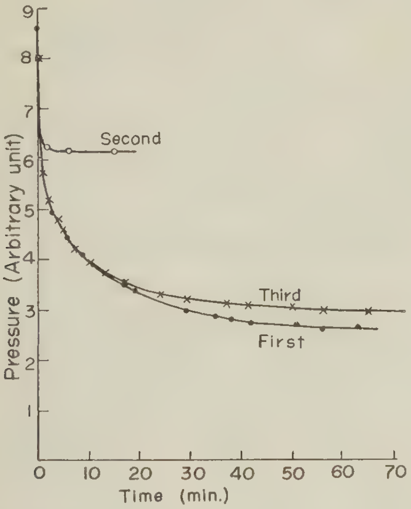

Fig. 16. Change of sorption rate after sorption-desorption cycles has been carried out.

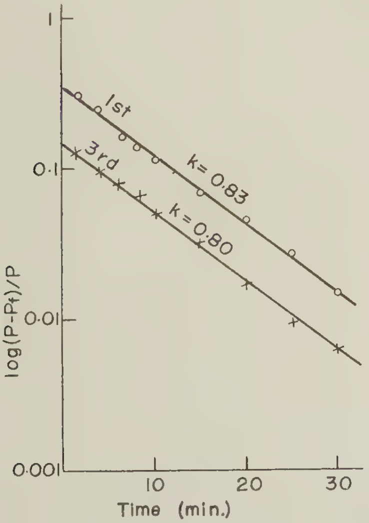

Fig. 17. Plots of Eq. (5) applied to first and third types of sorption.

Sorptions of the first and the second type measured for the film produced under various evaporation temperatures T_d are shown in Fig. 18. We see that the unstable large capacity of the low-temperature-evaporated film corresponds to the difference between the first and the second type, that is irreversible slow part of sorption.

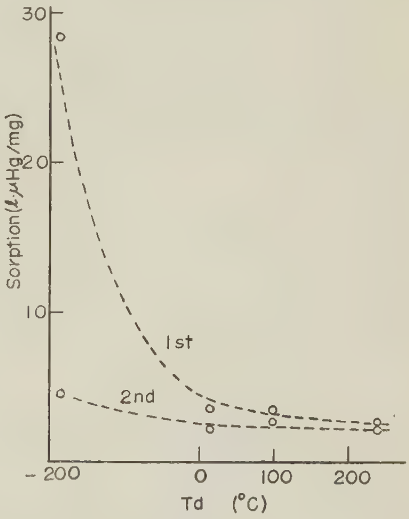

Fig. 18. Variation of first and second sorption with wall temperature T_d.

4.6. *Influence of Evaporation Rate*

The influences of evaporation rate and density of arriving atoms for the room-temperature-evaporated film are shown in Figs. 19 and 20, where solid marks correspond to the bulb with the evaporation source near to the substrate wall, blank marks to the bulb with the source further, triangles to the evaporation condition of $P_e = 0.1 \sim 0.13$ mmHg, and circles to the condition of high-vacuum evaporation. In this temperature range the evaporation changes 100-folds according to the data for vapor pressure of barium. While the temperature of evaporation source, i.e., the rate of evaporation has no effect on the sorption for the vacuum-evaporated film, there is a conceivable influence on the gas-evaporated film. In addition, these figures show that the density of depositing atoms has no influence on both films.

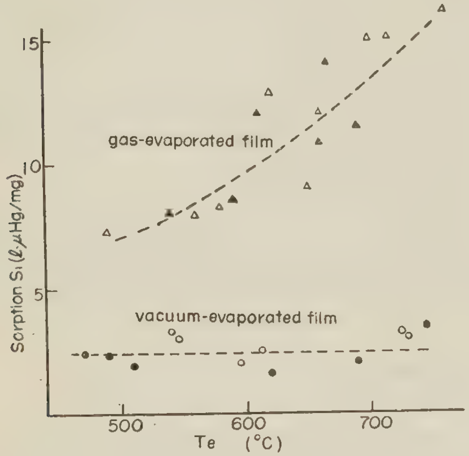

Fig. 19. Effect of evaporation rate on the first sorption amount.

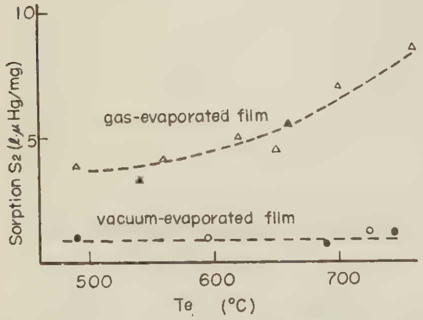

Fig. 20. Effect of evaporation rate on the second sorption amount.

4.7. *Nitrogen Sorption and Electrical Resistance of Film*

To know how nitrogen sorption affects on the electrical resistance of the film, simultaneous measurements of the two quantities were attempted. In Fig. 21 is shown the behavior of both nitrogen pressure and resistance for low-temperature high-vacuum-evaporated film, which has not been stabilized. Firstly, sorption were carried out at −183°C, and secondly stabilization applied and then the gas was admitted. Fig. 22 shows the behavior when the gas was admitted to a film previously stabilized at room temperature. From these curves one can see the following features:

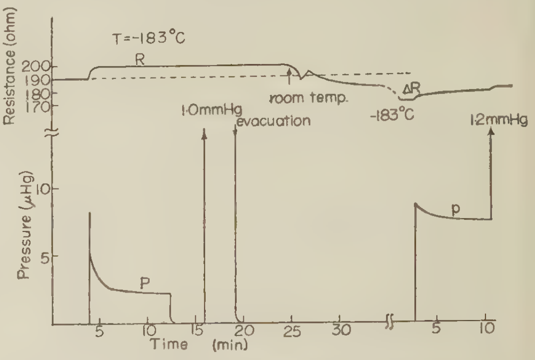

Fig. 21. Change of electrical resistance of film with nitrogen sorption at −183°C. The film has not been stabilized.

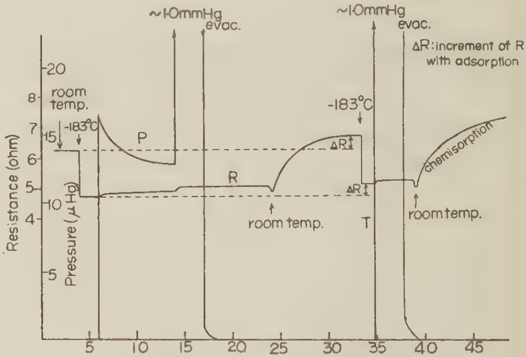

Fig. 22. Change of electrical resistance of film with nitrogen sorption. The film has been stabilized prior to sorption at room temperature.

1. Nitrogen sorption results in the increase of resistance which does not recover with desorption at low temperature.
2. The rate of sorption and the rate of resulting resistance-increase fall with the degree of stabilization and increase with nitrogen pressure.
3. Nitrogen, once sorbed at low temperature, prevents the stabilization significantly even in high vacuum. Therefore, nitrogen should be regarded as being occluded in the film.
4. Room-temperature evacuation partly recovers the sorption-induced resistivity, in quite a parallel manner with the behavior of sorption already mentioned in 4.5.
5. When the film, which has been already

saturated with nitrogen at low temperature, is brought up to room temperature, an instantaneous desorption and subsequent re-sorption take place with remarkable increase in resistivity. This fact suggests that the room-temperature sorption is of different nature from the low-temperature sorption.

5. Discussions

5.1. *Effects of Various Evaporation Conditions on the Gas Sorption Capacity*

Among many factors which may prescribe he film structure, the following is considered n this paper:

1. Rate of film growth (Density of arriving atoms),
2. Rate of evaporation (Temperature of the evaporation source),
3. Temperature of glass wall during evaporation T_d and annealing temperature T_a.
4. Residual gas pressure during evaporation P_d.

As described in 4.6 the first and second factors re almost insensitive to the low-temperature itrogen sorption in our experimental condiions, and so no comments are made hereafter.

The large sorption surface of low-temperaure-evaporated film is very unstable at high emperature and decreases with time. In the neasurement of electrical resistance the same henomenon has been already observed, and his similarity was also confirmed with nickel ilms[26], leading to the conclusion that the ame mechanism can be applied both for the ecay of adsorption capacity and stabilization f the film. Therefore, it may be possible to onsider that the unstable part of sorption is ue to crystal imperfections. If so, this is due ot to dislocations as discussed previously, ut to lattice vacancies (or their combinations), which can absorb nitrogen molecules. The ower the substrate temperature T_d, the more mperfect the deposited crystal structure beomes. The imperfections thus produced can nduce excess resistivity and absorb molecules. f the vacancies trap nitrogen molecules, the ubsequent stabilization may be hindered narkedly because of the reduced number of ree vacancies.

On the other hand, the large sorption capaty of the gas-evaporated film seems to be aused by another mechanism. Since this film is very stable even at room temperature, it is unreasonable to attribute this large capacity to lattice imperfections mentioned above and so other interpretation is made in the next.

5.2. *Structure of Gas-evaporated Film*

As reported by many investigators[2],[3],[27], evaporation in an atmosphere of inert gas makes so-called metal black. The origin of this black may be mainly due to the loss of kinetic energy of barium atoms by the collisions with gas molecules during flight. Following the calculation of Tsukagoshi[34], even in such a low pressure as 0.1 mmHg thermal energy of an evaporating atom is lowered to that of gas molecules by collisions of 100 times or more. However, the experimental results show that the black is formed only above 0.8 mmHg of inert gas, and that the film produced at 0.1 mmHg has already large capacity, whereas its appearance does not differ so markedly from that of vacuum-evaporated film. Furthermore, as shown in Fig. 19, when the kinetic energy of evaporating atoms is decreased by lowering the temperature of evaporation source, the sorption becomes rather smaller in contrast to the above implication. Therefore, the effect of the residual gas is not considered simply as to carry off the kinetic energy of barium atom.

On evaporating gold in an argon atmosphere of high pressure (~10 mmHg), one can observe a cloud of particles originating near the source and diffusing around away. Perhaps this may occur also in the case of barium. Near the evaporation source, evaporated atoms suffer sufficient collisions with argon atoms to prevent the tight binding of metal atoms and form aggregates, which diffuse onto the wall. Then the aggregates should stabilize corresponding to the temperature of the substrate or the gas. By means of electron microscope the metal black is revealed as large particles of irregular shape piled up randomly, and by electron diffraction, each particle is proved to be a fairly large crystalline and not amorphous as is easily imagined from its visual appearance. The average size of unit particle does not differ markedly both in gas- and vacuum-evaporated films. But the definite difference is found in the state of accumulation; in case of vacuum-evaporated film each particle has not always free surface and connected with each other, and in case of metal black each particle is isolated and has large free surfaces. This situation may explain the large and stable sorption capacity of the black.

5.3. *The Nature of Nitrogen Sorption at Low Temperature*

It has been generally considered that at −183°C nitrogen molecule adsorbs on a solid surface by the van der Waals forces, and this character has been used to the measurement of surface area of solid. However, nitrogen sorption on barium film cannot be regarded as simply physical adsorption due to van der Waals forces because of its slowness and irreversibility in the first sorption. However, the second sorption is instantaneous and completely reversible with rather smaller amount. The difference between the first and second sorption indicates the irreversible part at low temperature. The third sorption which occurs after evacuation at room temperature suggests that the heat of sorption for this irreversible part is not so large as for usual chemisorption. The capillary condensation is not responsible for this irreversibility, for it occurs at rather higher pressure and does not remain after evacuation in high vacuum.

Arizumi and Kotani[35] studied the sorption of carbon monoxide on barium film, and found that below −70°C the sorption was of physical nature and the gas partly diffused into crystal with slow rate. Their theoretical expression for the rate of sorption is

$$-\frac{dP}{dt}=-K_AP\left\{N_0-\frac{NV}{RT}(P_0-P)\right\}$$
$$-K_SP\left(K_AN_0t+\log\frac{P}{P_1}\right) \qquad (6)$$

where K_A, K_S, N_0, P_1 and P_0 are constants. The last term expresses absorption into interior. By a suitable abbreviation, Eq. (6) can be reduced to our empirical formula (5). This formula defines at first the fast sorption on the surface and then the succeeding slow absorption. The fact that this slow stage is not found at −183°C on many metal films other than barium[36),37)] may be due to the exceptionally large interatomic distance of barium, rather larger than the size of nitrogen molecule (∼4.0 A); owing to this special feature of barium the slow absorption into the crystallite may be very easy. According to our estimation given in the Appendix of this paper, the van der Waals heat of trapping at lattice deficiency is so large as not expected in an usual physical adsorption. This may be a reason why the irreversible sorption of nitrogen occurs on barium film at temperature. From this idea, it can be concluded that the irreversible part of sorption represents the absorption into lattice imperfections and results in the increment of electrical resistivity, but the reversible one represents the pure physical adsorption on the surface with almost no influence on electrical resistivity. However, in view of the feature of the adsorption of argon at −183°C and 10^{-2} mmHg, which takes place almost instantaneously with very small amount, it may be necessary to consider that this irreversible nitrogen sorption is, at least partly, of chemical nature, which is concluded by previous authors[36),37),38)] for other metals.

5.4. *Quantitative Study of Imperfection*

Up to date the quantitative measurement of lattice imperfection in metal is very scare. Hence we attempt here some discussions on the number of imperfections in evaporated barium film. If we assume that each nitrogen molecule occupys each barium vacancy, then for a film evaporated at −183°C there exist 2.5×10^{21} vacancies/cm^3, and for a film evaporated at room temperature, about a tenth of that. While these values for vacancy density seems too high, such a large value has been proposed in case of Kirkendahl diffusion[39)]. Especially, when evaporated at low temperature, the barium film has a large stress in it and therefore it may be rather probable to consider that nitrogen molecules enter not only into lattice vacancies but into strained interstitial positions, combined pairs of imperfections and others, so as to give apparently such a large value for lattice vacancy.

The measurement of specific resistivity due to imperfections could not be exactly consecuted, but under the assumption of the same contribution from vacancy and interstitial atom, the resistivity of the vacancy is roughly estimated as 0.3 Ωcm/per cent vacancies. This is qualitatively in agreement but slightly smaller than the one theoretically estimated for copper[40)]. If imperfections other than lattice vacancies are taken into account, the agreement will become fair. Because the presence of such a large number of imperfecions will cause a large stress in the low-temerature-evaporated film, effects of stress hould be considered in a kinetics of recovery s described in 3.2.

6. Conclusion

1. Evaporated barium film exhibits a character of granular structure in gas sorption and electrical resistivity.

2. When evaporated at low substrate temperature, the crystal structure becomes imperfect and this induces excess nitrogen sorption as well as excess resistivity.

3. At and below room temperature marked decreases of electrical resistivity and of low-temperature sorption of nitrogen take place with the recovery of imperfection.

4. Semi-conductive characteristics at high temperature is probably caused by aggregation or oxidation.

5. Gas-evaporated film has a large sorption area due to the special construction of the film.

The authors wish to express their sincere thanks to Mr. T. Ichimiya for his earnest guidance and discussions.

§ 7. Appendex

Energy of van der Waals adsorption at vacancy.

Suppose a simple situation, in which a nitrogen molecule occupies a vacant lattice point substitutionally in an infinite metallic lattice at 0°K. The centre of the nitrogen molecule is taken as an origin of polar coordinate. Smaller terms can be neglected such as zero point energy, change of distribution energy of electron after absorption, and that of thermal energy of lattice. We take into account three terms, that is, van der Waals attraction between the nitrogen molecule and the metal, repulsion between the molecule and the nearest-neighboring metal atoms, and the stress in the outside medium caused by the relaxation of metal atoms.

Van der Waals energy has been calculated by, for example, Margenau et al.[41] and Bardeen[42]. Their calculations assume the adsorption on a flat surface and therefore their integrals must be modified to spherically symmetrical way. The calculation is simple and the result shows that each term is increased 6 or 8 times larger than in their original equations. As a definition of metallic surface, one must take the relaxation of atoms into account.

For a repulsive term, we apply r^{-m} potential and its coefficient is calculated analytically by an usual method from compressibilities. For simplicity m is taken as 12, an average exponent for N_2, Ba and Ni. Following Hirschfelder[43] the coefficient can be taken as a geometrical mean of both metal and liquid nitrogen. For nitrogen molecule Kihara's potential[44] with rigid core is used. Total repulsive potential is calculated against the number of repulsion between nitrogen and nearest-neigboring atoms.

Thirdly, in the medium outside the nearest-neighboring atoms, a stress is caused by the relaxation of them. This potential is calculated with a model of continuous medium of spherical symmetry, and can be expressed simply by $\frac{12\pi r_0}{\beta}(r-r_0)^2$, where β is a compressibility, r_0 is an original interatomic distance of the nearest-neighbors. Thus the total potential is given by

$$-A(r-r_M)^{-3}+\sqrt{B_1B_2}(r-0.47)^{-12}+C(r-r_0)^2$$

The result of numerical calculations for barium is shown in Fig. 23, where energy minimum exists below zero, showing the possibility of van der Waals adsorption in a lattice vacancy. In this case the trapping energy is high because of loosely packed structure and large interatomic distance of barium, which insure less error of calculation than for other metals. With a rough approximation for the compression of electron cloud in nitrogen molecule, the same calculation is carried out for nickel,

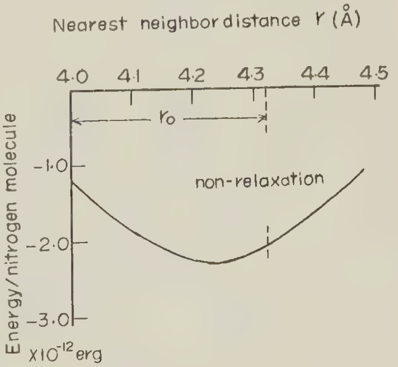

Fig. 23. Potential energy diagram for a nitrogen molecule trapped in a vacant lattice point of barium.

which gives the value of 11 Kcal/mole, which is consistent with the calorimetric heat of adsorption by Beeck[34], 10 Kcal/mole.

In general, the heat of adsorption larger than 20 Kcal/mole is said to prevent the desorption of adsorbed gas at room temperature. In the cases of nickel and barium which exhibit the complete and imcomplete desorption of nitrogen respectively, the calculations are in good accordance with the experimental situations by sorption and electrical resistance measurements.

References

1) For example: W. Espe, M. Knoll and M. P. Wilder, Electronics, **23** (1950, Oct.) 80; S. Wagener, Proc. I. E. E., **99** part III (1952) 135; Vacuum **3** (1953) 11.
2) A. L. Reimann: Phil. Mag. **18** (1934) 1117.
3) L. F. Ehrke and C. M. Slack: J. Appl. Phys. **11** (1940) 129.
4) G. Haase: Z. angew. Phys. **2** (1950) 188.
5) E. T. S. Appleyard: Proc. Phys. Soc. **49** Extra Part (1937) 118.
6) L. Harris, D. Jeffries and B. M. Siegel: J. Chem. Phys. **18** (1950) 261.
7) W. Buckel and R. Hilsch: Z. Phys. **138** (1954) 109, 136; W. Rühl, ibid, 121.
8) P. G. Wilkinson and L. S. Birks: J. Appl. Phys. **20** (1949) 261; P. G. Wilkinson: J. Appl. Phys, **22** (1951) 419.
9) R. Suhrmann and G. Barth: Z. Phys. **103** (1936) 10.
10) V. Vand: Proc. Phys. Soc. **55** (1943) 222.
11) For example, G. I. Finch: Proc. Phys. Soc. **49**, Extra Part (1937) 113.
12) L. Harris, D. Jeffries and B. M. Siegel: J. Appl. Phys. **19** (1948) 791.
13) H. Levinstein: J. Appl. Phys. **20** (1949) 306.
14) R. S. Sennett and G. D. Scott: J. Opt. Soc. Am. **40** (1950) 203.
15) C. S. Barret: Structure of Metals (McGraw-Hill Co. 1952).
16) A. W. Overhauser: Phys. Rev. **90** (1953) 393.
17) J. W. Glen: Adv. in Phys. **4** (1955) 381.
18) T. Bloom: Adv. in Phys. **3** (1954) 26.
19) N. S. Rasor: Phys. Rev. **98** (1955) 1555.
20) Y. Mizushima and O. Ochi: J. Phys. Soc. Japan **11** (1956) 893.
21) J. S. Koehler: Phys. Rev. **75** (1949) 106; J. K. Mackenzie, and E. H. Sondheimer: Phys. Rev. **77** (1950) 260.
22) R. W. Hoffman and H. S. Story: J. Appl. Phys. **27** (1956) 193.
23) G. Tamman: Z. Metallkunde **26** (1934) 97.
24) J. Kramer: Ann. Phys. **19** (1934) 37.
25) H. Althum: Z. Metallkunde **14** (1922) 414.
26) Z. Oda: J. Appl. Phys. Japan **22** (1953) 142.
27) S. Hirota, Y. Mizushima and H. Noake: J. Appl. Phys. Japan **25** (1956) 294.
28) Y. Mizushima and O. Ochi: unpublished data.
29) K. Ono and Y. Mizushima: J. Appl. Phys. Japan **25** (1956) 349.
30) K. Yazawa and H. Yakō: Report at the meeting of the Phys. Soc. Japan Oct. 1956.
31) N. Mostovetch: Ann. de Physique **8** (1953) 61.
32) O. Beeck, A. E. Smith and A. W. Wheeler: Proc. Roy. Soc. **A177** (1941) 62.
33) O. Beeck: Adv. in Catalysis II (1950) 151.
34) O. Tsukagoshi: Rep. Sci. Res. Inst. **25** (1949) 1.
35) T. Arizumi and S. Kotani: J. Phys. Soc. Japan **7** (1652) 152, 158, 163.
36) B. M. W. Trapnell: Proc. Roy. Soc. **A218** (1953) 566.
37) E. Greenhalgh, N. Slack and B. M. W. Trapnell: Trans. Farad. Soc. **52** (1956) 865.
38) Y. Ishikawa and Y. Sasaki: Oral representation at the Meeting of Society of Electron Emission, 1952.
39) F. Seitz: Acta Met. **1** (1953) 355; Phys. Rev. **79** (1950) 1002: R. W. Balluffi: Acta Met. **2** (1954) 194.
40) P. Jongenburger: Appl. Sci. Res. **3B** (1953) 1; D. L. Dexter: Phys. Rev. **89** (1952) 768; J. Jongenburger; Nature **175** (1955) 545.
41) H. Margenau and W. G. Pollard: Phys. Rev. **60** (1941) 128.
42) J. Bardeen: Phys. Rev. **58** (1940) 727.
43) R. H. Fowler and E. A. Guggenheim: Statistical Thermodynamics (Cambridge Univ. Press, 1939) p. 300.
44) T. Kihara: Proc. Phys. Soc. Japan **2** (1947) 11.

JOURNAL OF THE PHYSICAL SOCIETY OF JAPAN Vol. 12, No. 4, APRIL, 1957

Studies of High Polymers by Radioactive Method (II) Self-diffusion of Polystyrene in Its Dilute Solution

By Shintaro SUGAI and Jiro FURUICHI
Physics Department, Faculty of Science, Hokkaido University

(Received October 22, 1956)

Self-diffusion of high polymer in dilute solution was studied by use of C^{14}-labelled polystyrene. Especially the dependence of the self-diffusion coefficient of polystyrene upon its molecular weight was determined. Then, from the results, the molecular extension, the shielding ratio, and other molecular quantities of polystyrene molecule in the dilute solution were calculated by use of the diffusion theory of Debye and Bueche, and compared with the data obtained by other methods.

§ 1. Introduction

The molecular extension of the polymer in its dilute solution is one of the most important molecular quantities of the polymer solution. Therefore, many workers have recently attempted to study the molecular extension in the polymer solution from various measurements, mainly from viscometric and optical ones$^{1)}$. However, self-diffusion studies in dilute solutions seem to be, also, a very suitable method for the discussion of molecular extension and molecular form, because the most natural form of the polymer molecule in the solution can be investigated only by means of this method.

In the case of viscometric measurement, the molecular form is distorted by the shear stress. Similarly, in the case of optical measurement, the electronic excitation of the molecule is given by the light, and then variations of natural form and extension of the molecule seem, also, to be possible results.

On the other hand, self-diffusion of the molecule is caused only by its thermal motion, therefore self-diffusion studies are probably the most suitable method to use in making research on the molecular natures.

However, unfortunately, this appropriate method has never been employed, except in a few cases$^{2)}$. This is probably because the process of manufacturing the radioactive polymer was usually very difficult.

In the present studies, the self-diffusion of polystyrene in its dilute solution has been measured using C^{14}-labelled polystyrene made in England for the purpose of preparing the standard β-ray source, and then the natural extension and other molecular quantities of polystyrene molecule in its dilute solution have been calculated by use of the sphere model of chain polymer.

§ 2. Experimental Procedures

C^{14}-labelled polystyrene made in England was, firstly, fractionated by the ordinary method. Unfortunately, the specific radioactivity of the sample in the present case was considerably small, so carriers could not be added to it, and also sharp fractionation of itself could not be employed.

The average molecular weights of the fractionated radioactive polystyrene have been determined from the intrinsic viscosity measurements in their dilute benzene solutions$^{3)}$.

Then the fractionated radioactive polymer in its benzene solution, whose concentration is 1 gr/lit., was diffused into the same nonactive fractionated solution.

Nonactive polystyrene was fractionated by the same method as is used in the case of the fractionation of a radioactive one.

However these two samples were not of the same molecular weight distributions, and moreover the specific radioactivity of the present radioactive sample was very small as noted above, therefore it was very difficult to obtain the nonactive polystyrene fraction having the same average molecular weight and the same molecular weight distribution as the radioactive one.

In the present case, by fractionating the nonactive sample very sharp, approximately the same average molecular weight fraction as the radioactive one was obtained, although the molecular weight distributions of the two samples were probably different.

A diffusion cell of sintered glass type was employed[4]. The average diameter of the sintered glass hole was 0.05 cm. The upper limit of the molecular extensions of polystyrene used in the present case seems to be approximately 1500 A, then the polystyrene molecule is considered to diffuse freely through these holes.

The schematic diagram of cell is shown in Fig. 1.

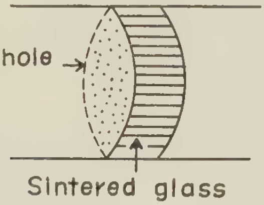

Fig. 1. Schematic diagram of the diffusion cell.

If, at the beginning of the experiments, radioactive solution is put into the left side compartment of the cell, and nonactive one is put into the right side compartment, then the self-diffusion coefficient D of the polystyrene molecule can be calculated by measuring the radioactive concentration of the two compartments after diffusion for the given duration of the time t:[5]

$$\log\{(C_l^t - C_r^t)/C_l^0\} = -KDt(1/V_l + 1/V_r) \quad (1)$$

where C_l^t and C_r^t are respectively the radioactive concentration of the left and right compartments at time t and C_l^0 is the initial radioactive concentration of the left compartment.

Furthermore, K is a cell constant and, previous to the experiments, should be determined using standard substances.

In the present case, K was determined from the diffusion of the aqueous solution of potassium chloride.

V_l and V_r are respectively the volume of the left and right compartments of the cell.

The values of diffusion coefficient D determined by such a method, however, did not exactly coincide one with another as the duration of time t of the diffusion varies, therefore the average value of D at various times had to be calculated.

The radioactivity of the solution was measured by the same method as was previously described[6].

§ 3. Experimental Results and Discussion

The experimental results of the self-diffusion of polystyrene in the dilute benzene solution at 30°C are indicated in Table I, in which the viscosity and the intrinsic viscosity of the solution are included.

Table I. Self-diffusion coefficient of polystyrene in its dilute benzene solution at 30°C.

Mol. Weight M	Concentration of Solution	Viscosity η	Intrinsic Viscosity	D
10^5	gr/lit.	10^{-3}poise		10^{-7} cm^2/sec
1.1	1.0	6.08	55	4.0
2.5	〃	6.36	100	2.4
8.0	〃	6.72	212	1.2
10.5	〃	6.82	255	1.0
	0(solvent)	5.95		

Viscosity of the solution was measured by Ostwald type viscometer, at the same temperature, under a small shear stress.

However extrapolation of the shear stress to zero was not employed.

Generally speaking, diffusion coefficient D of the molecule in the dilute solution can be expressed in the term of the frictional constant F of a polymer molecule as follows:

$$D = kT/F \quad (2)$$

where k and T have a well known meaning.

Of course, the viscosity of the solution η is related, also, to the frictional constant F. Therefore an important relation is judged to exist between the self-diffusion coefficient of the polymer molecule in the solution and the viscosity of the same solution.

R. L. Saxton and H. G. Drickamer have indicated such a relation in the case of polymeric liquid sulfer[7].

P. Debye and F. Bueche have checked similar circumstances even in the cases of some solid polymers[8], and pointed out the following empirical relation:

$$D\eta_b/\rho = \text{constant} \quad (3)$$

where η_b is the bulk viscosity of the solid polymer and ρ is its density.

If Debye's free draining model is used, diffusion coefficient D of the polymer molecule in the dilute solution is simply expressed in terms of the intrinsic viscosity of the solution and the molecular extension:

$$D[\eta]/\rho\cdot M/\langle r^2\rangle_{av}=\text{constant} \qquad (4)$$

'here $[\eta]$ is the intrinsic viscosity of the solu- on, M is the molecular weight of the poly- ıer, and $\langle r^2\rangle_{av}^{1/2}$ is the root mean square nd to end distance of the polymer molecule, ıat is, the molecular extension.

As for a solid polymer, the diffusion theory eems to be able to be developed by the same rgument as that in the case of the dilute olution.

F. Bueche has employed such procedure⁹⁾, nd obtained Eq. (3) by accepting the idea hat the relation $\langle r^2\rangle_{av}/M$ is nearly constant ı a solid polymer¹⁰⁾.

In the present case, $D[\eta]/\rho$ is not exactly onstant, as shown in Fig. 2.

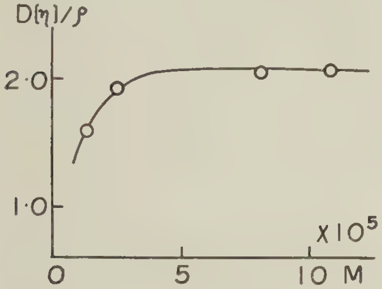

Fig. 2. Values of $D[\eta]/\rho$ at the various molecular weights. (Unit of $D[\eta]/\rho$ is arbitrary.)

Then, the polystyrene molecule cannot be considered to behave as a free draining randomly coiled chain polymer in the dilute benzene solution.

To analyse the molecular extension of polystyrene in the solution from the present results, therefore, the more generalized polymer models have to be employed.

By the way, many authors have previously attempted to develop the theory of high polymer solution¹¹⁾. In the present case, the sphere model devised by P. Debye and A. M. Bueche was used.

This was done because their theory is not essentially different from the other typical theories of polymer solution, and a more generalized application is possible.

P. Debye and A. M. Bueche have derived a theoretical relation between D and molecular weight M valid over a limited range M¹²⁾:

$$\left.\begin{array}{l} D=AM^{-\varepsilon}\\ \varepsilon=1/2+1/4\cdot\sigma/\psi\cdot d\psi/d\sigma \end{array}\right\} \qquad (5)$$

and also a relation between D and the viscosity of the solvent η_0:

$$D=kT/6\pi R_s\eta_0\psi(\sigma) \qquad (6)$$

where σ is shielding ratio, $\psi(\sigma)$ is a certain function of σ, and R_s is the radius of polymer sphere.

Applying Eq. (5), the average values of ε and σ of the present case can be determined from the dependence of $\log D$ upon $\log M$ as shown in Fig. 3.

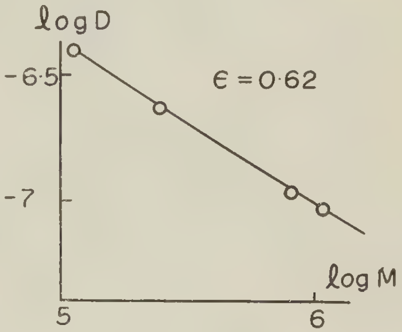

Fig. 3. Dependence of $\log D$ upon $\log M$.

Then if such a value of σ and the viscosity of the solvent are used, R_s can be calculated.

The results are presented in Table II, in which molecular extension $\langle r^2\rangle_{av}^{1/2}$ of polystyrene is determined from R_s, using the well relation of randomly coiled chain polymer as known follows:

$$R_s=(1/6\langle r^2\rangle_{av})^{1/2} \qquad (7)$$

However, it should be noted that the above value of σ is an average one, and also, generally σ must depend upon M.

Moreover, Eqs. (5) and (7) are based on the randomly coiled chain polymer, therefore in molecular extension in Table II the volume exclusion effect of chain elements of the molecule and the effect of interaction between

Table II. Molecular extension and average shielding ratio of polystyrene in benzene solution calculated from Eqs. (5) and (7).

Mol. Weight M	Shielding Ratio σ	ε	$\langle r^2\rangle_{av}^{1/2}$
10^5			A
1.1	3.2	0.62	364
2.5	〃	〃	627
8.0	〃	〃	1378
10.5	〃	〃	1647

the chain elements and the solvent molecules are not taken into consideration.

In order to investigate such circumstances, in the present case, the theory of intrinsic viscosity of Debye and Bueche has been combined with their diffusion theory.

According to Debye and Bueche's model, the intrinsic viscosity of the polymer solution is given by

$$[\eta]=CR_s{}^3\phi(\sigma)/M \qquad (8)$$

where $\phi(\sigma)$ is also a certain function of σ.

From Eqs. (6) and (8), in which the assumption of randomly coiled chain polymer is not used, one has

$$(D\eta_0)^3=C'\phi(\sigma)/\{\psi(\sigma)\}^3\cdot(kT)^3/M[\eta]^3 \qquad (9)$$

where C' is a numerical constant.

Therefore, from measurements of D, η_0 and $[\eta]$ of the solution, and from Eq. (9), the value of $\phi(\sigma)/\{\psi(\sigma)\}^3$ is calculated as a function of M.

The values of $\phi(\sigma)/\{\psi(\sigma)\}^3$ as a function of σ are listed in Table III.

Table III. Values of $\phi(\sigma)/\{\psi(\sigma)\}^3$.

σ	$\phi(\sigma)$	$\psi(\sigma)$	$\{\psi(\sigma)\}^3$	$\phi(\sigma)/\{\psi(\sigma)\}^3$
1	0.0947	0.176	0.00545	173.7
2	0.327	0.432	0.08062	4.056
3	0.600	0.600	0.2160	2.777
4	0.857	0.701	0.3447	2.487
5	1.07	0.770	0.4565	2.343
8	1.52	0.858	0.6316	2.406
10	1.70	0.890	0.7049	2.411
∞	2.50	1.000	1.000	2.500

In Table IV are shown the molecular radius R_s and the shielding ratio σ determined from Eqs. (9) and (6).

However, in this case, the molecular extension cannot easily be obtained from the value of the radius of polymer sphere by Eq. (7).

On the other hand, recently, many authors made theoretical studies on the relation between R_s and other molecular quantities considering the volume exclusion effect and so on[13].

For example, B. H. Zimm et al have proposed the following equation[14]:

$$R_s{}^2=R_0{}^2+0.0572A_2M^2/N_0R_0+\cdots \qquad (10)$$

where R_0 is the molecular extension of randomly coiled chain polymer, A_2 is the second virial coefficient, N_0 is Avogadro number and M is the molecular weight of the polymer.

However, it could be easily examined that the second and higher terms are considerably smaller than the first main term $R_0{}^2$ of the right side of Eq. (10) by using the value of A_2 for polystyrene-benzene pair[15], then the molecular extension can be considered to be connected, at the first approximation, with the polymer radius R_s by Eq. (7) even in the present case.

In Table V, the molecular extension calculated from the radius R_s in Table IV, by using Eq. (7), is shown.

Table IV. The radius of the polystyrene sphere R_s and the shielding ratio σ in the benzene solution determined from Eqs. (9) and (6).

Mol. Weight M	$\phi(\sigma)/\{\psi(\sigma)\}^3$	σ	R_s
10^5			A
1.1	2.71	3.2	146
2.5	2.65	3.5	233

Table V. Molecular extension of polystyrene $\langle r^2\rangle_{av}{}^{1/2}$ in the dilute benzene solution determined from R_s in Table IV and Eq. (7).

Mol. Weight M	$\langle r^2\rangle_{av}{}^{1/2}$
10^5	A
1.1	358
2.5	571

Table VI. Molecular extension and shielding ratio of polystyrene in the dilute solution determined by various authors.

Mol. Weight M	Solvent	$\langle r^2\rangle_{av}{}^{1/2}$	σ	Author	Method
10^5		A			
10.0	benzene	1125		Kirkwood[11]	viscosity
	〃	1110		Bueche[12]	light scattering
	〃	1030		〃	viscosity
	〃	914*	3.92	Debye[12]	〃
1.05	〃	383		Mizutani[1]	〃
3.55	〃	569		〃	〃
2.5	〃	571	3.5	Sugai and Furuichi	diffusion and visc.
10.5	〃	1647	3.2	〃	diffusion

* This value was calculated by the assumption $\sigma=0$.

The value of $\langle r^2\rangle_{av}^{1/2}$ in Table V is perhaps more exact than that in Table II.

Finally, the data obtained by other methods, for instance viscometric and optical ones, are shown in Table VI to be compared with the present results.

§ 4. Conclusion and Acknowledgements

Self-diffusion of polystyrene in the dilute benzene solution was measured by the radioactive method.

Self-diffusion coefficient depends approximately upon the molecular weight of the polystyrene so that the free draining randomly coiled chain approximation is not simply satisfied.

Therefore, using the general sphere model of the polymer molecule introduced by P. Debye and A. M. Bueche, the molecular extension and the shielding ratio are calculated as a function of the molecular weight of polystyrene from the present experimental results, and they are compared with other authors' data.

The present authors are exceedingly grateful for the discussion by other members belonging to the Research Institute of High Polymer Physics in Hokkaido University and also for a grant of financial aid from the Ministry of Education of the Japanese Goverment.

References

1) P. J. Flory: J. Poly. Science **14** (1954) 451. H. Mizutani: J. Phys. Soc. Japan **11** (1956) 245.
2) H. G. Drickamer: J. Chem. Phys. **21** (1953) 1364.
3) P. C. Pepper: J. Poly. Science **7** (1951) 347.
4) F. T. Wall: J. Chem. Phys. **20** (1952) 1200.
5) J. H. Wang: Radioactivity applied to Chemistry, John Wiley and Sons, Inc., New York (1951) 62.
6) S. Sugai and J. Furuichi: J. Phys. Soc. Japan **10** (1955) 1032.
7) R. L. Saxton and H. G. Drickamer: J. Chem. Phys. **21** (1953) 1362.
8) P. Debye and F. Bueche: J. Chem. Phys. **20** (1952) 1956.
9) F. Bueche: J. Chem. Phys. **20** (1952) 1959.
10) P. J. Flory: J. Chem. Phys. **17** (1949) 303.
11) J. G. Kirkwood: J. Chem. Phys. **16** (1948) 565. H. Kuhn: J. Poly. Science **14** (1954) 193.
12) P. Debye and A. M. Bueche: J. Chem. Phys. **16** (1948) 573.
13) E. Teramoto: Proceedings of the International Conference of Theoretical Physics, 1953, Kyoto and Tokyo, 409. H. I. Frish: J. Chem. Phys. **19** (1951) 1402.
14) B. H. Zimm *et al*: J. Chem. Phys. **21** (1953) 1716.
15) The authors applied the experimental result obtained by osmotic method in their laboratory.

JOURNAL OF THE PHYSICAL SOCIETY OF JAPAN Vol. 12, No. 4, APRIL, 1957

An Investigation of the Dynamic Mechanical Properties of Glassy Polymers by the Composite Oscillator Method

By Keiji YAMAMOTO and Yasaku WADA

Department of Applied Physics, Faculty of Engineering, Tokyo University, Tokyo

(Received December 18, 1956)

The dynamic Young's modulus and loss factor are determined by the composite oscillator method for several glassy polymers: phenol resin, polymethyl methacrylate, polystyrene, nylon 6 and polyester, in the temperature from −70° to +90°C at frequencies 50, 100 and 200 kc/s. The loss factor curve of polymethyl methacrylate shows an anomaly at ca. −20°C which is concluded to be due to the γ-transition, the activation energy being estimated as 7 kcal/mole. The moisture dependence of this transition is also shown and the molecular process involved is hypothetically proposed. For polyethylene a peak of loss factor is observed at 10°C. A procedure to eliminate the false attenuation peaks observed in applying the composite oscillator method to high polymers is described.

§ 1. Introduction

In studies of viscoelastic properties of polymeric materials, it is advisable to measure the dynamic modulus and loss factor over a wide range of temperature. At frequencies of the order of one hundred kilo-cycles the composite oscillator method[1] has a special advantage for this purpose, since the specimen used can be designed in a very small size and consequently the temperature of the specimen can easily be conditioned.

Though a few authors[2-4] have attempted to apply his method to high polymer research, no extensive results along this line have so far been available. In the present paper the data obtained by this method in our laboratory will be given for several polymers, together with possible interpretations on the molecular process of the observed viscoelastic behaviors.

§ 2. Experimental

The apparatus employed has been described previously[5]. Essentially, it consists of a device for applying voltage of variable frequency to a composite oscillator system and for observing the frequency dependence of the resultant current. A composite oscillator system is made by cementing a specimen rod of 3 mm square cross section to an X-cut quartz transducer of identical cross section by the use of Araldite cement and is set into longitudinal vibration, the nodal point of the quartz being supported. The dynamic Young's modulus and the associated loss factor of the specimen can be deduced from analysis of the current-frequency relation.

The composite oscillator technique has succefully been applied to a dynamical test of low loss materials, e.g., metals and inorganic glasses. In applying this method to high polymers, however, one has to take some additional cautions as in what follows.

In carrying out this method, the length of a specimen should be adjusted so as to make the resonant frequencies of the quartz(f_q) and the specimen (f_s) lie within about ten percent. Otherwise, the damping of the whole oscillator system would become abnormally large, thus causing an experimental error. In case of high polymers which often have a strong temperature dependence of elastic modulus, f_s for the specimen of a given length varies fairly rapidly with temperature and hence the discrepancy between f_q and f_s is apt to increase above the limit in both upper and lower sides of the experimental temperature. In the measurement over a wide temperature range, therefore, it is required to use specimens of different length, each of which being adapted for each temperature subdivision.

A further source of experimental errors takes place when f_s closely approaches to f_q. In this case a spurious increase of loss factor is generally observed, probably owing to the following reason: Since, in this case, the quartz/polymer interface nearly coincides with an antinodal plane, the appreciable difference in acoustic impedance between them will give rise to such an anomaly. This "spurious" peak of loss factor shifts along temperature axis if the specimen is slightly varied in length and thus can readily be distinguished from a "true" peak associated with material properties.

In the previous paper[5)], a peak of loss factor was reported at 30°C for phenol resin. This peak, however, was found to correspond to the above-mentioned spurious one. The corrected, new data obtained for this polymer will be given in detail in the next section.

In the composite oscillator method the length of the specimen should be large enough in comparison with its cross-sectional dimension. Since the sound velocity is of the order of 2×10^3 m/s for glassy polymers, a half wavelength is estimated as *ca.* 1 cm at 100 kc/s. In most of the present experiments, specimens in length of three half waves are used. For high loss polymers such as polyethylene, however, a specimen of one half wave length is used in order to avoid experimental difficulties, because, otherwise, the damping of the composite oscillator would be so large that the resonance might hardly be observed. In this case calculated values of both modulus and loss factor are thought to have some errors. No correction, however, is made to them, since the only effect of the correction is to change the results by a small factor, the over-all behavior remaining the same, while the temperature dependence of the properties is of particular interest in this research.

The composite bar with its holder is placed in a test tube which is immersed in a Dewer vessel containing a liquid—water above 0°C and alcohol-dry ice mixture below. The temperature in the test tube is measured by means of a mercury or pentane thermometer. Measurements are made after a steady state has been reached at each temperature.

All the specimens used are pure commercial products, including neither plasticizer nor filler and are annealed at 100°C for more than ten hours so as to remove unreacted monomers, other volatile impurities and, if any, residual thermal stress.

§ 3. Phenol Resin

In Fig. 1, a family of curves of loss factor are illustrated in case of phenol resin, being computed from the measurements without any consideration to the error sources discussed in the preceding section. Each curve corresponds to a specimen of different length respectively, f_s (kc/s) being shown beside each experimental point. As above predicted, a spurious increase of loss factor is found in the temperatures where f_s deviates too far from f_q or f_s closely approaches to f_q.

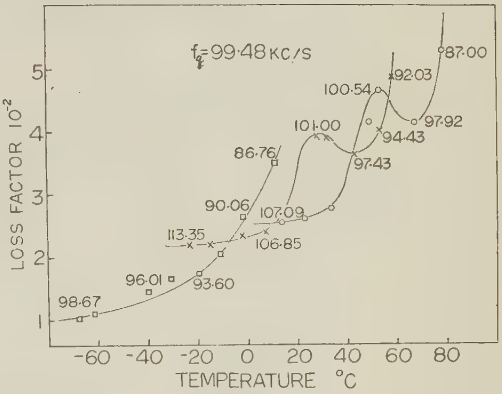

Fig. 1. Examples of erroneous measurements for phenol resin, f_s(kc/s) shown beside each experimental point.

Elliminating erroneous data from Fig. 1, the temperature dependence of the modulus and loss factor for phenol resin is presented in Fig. 2. As is seen, the loss factor increases

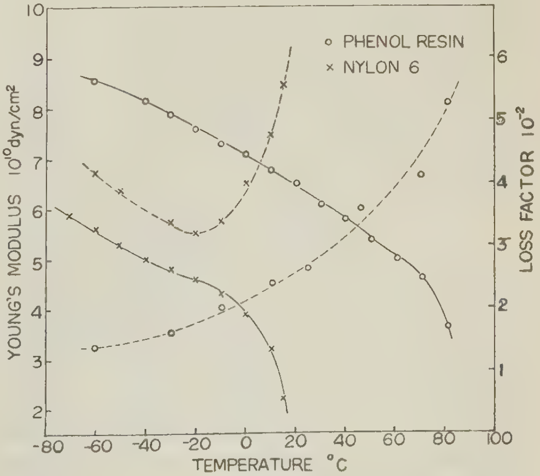

Fig. 2. Young's modulus (solid line) and loss factor (broken line) for phenol resin and nylon 6 at 100 kc/s.

monotonously with temperature and thus shows no anomalous maximum in the temperature range studied.

The results presented in the followings have all been obtained by taking care of the error sources before stated.

§4. Polymethyl Methacrylate

The data for polymethyl methacrylate (PMMA) are illustrated in Fig. 3, where the modulus is brought into a single curve since it does not vary with frequency within the experimental error.

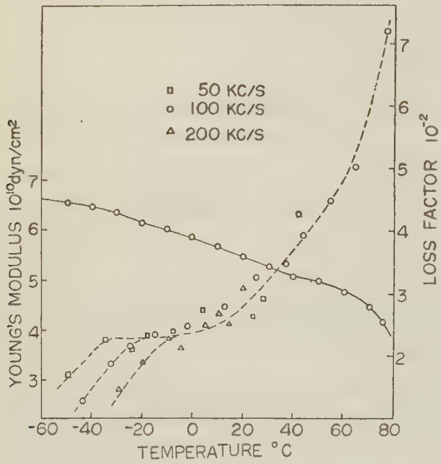

Fig. 3. Young's modulus (solid line) and loss factor (broken line) for polymethyl methacrylate.

Dynamic studies for PMMA in low frequency range[6-10] have related that, besides the glassy transition (or α-transition as is frequently called[8]), this polymer has a second (or β-) transition at lower temperature and the possible mechanism responsible for the latter is believed to be allied to the mobility of the side group ($-COOCH_3$) of this polymer[6,7]. In the ultrasonic measurement as is our case, however, the β-transition is expected to shift to a higher temperature and become undistinguishable from the α-transition, because the activation energy involved in the former, *ca.* 20 kcal/mole as generally accepted, is much smaller than that in the latter. As a consequence, the anomalous behavior of the loss factor observed at about −20°C in Fig. 3 should be regarded as not the β-transition, but a third (or γ-) transition.

While several investigators[8-10] have discussed on the γ-transition for PMMA, there exists so far no conclusive evidence whether or not this type of transition could be observed in this polymer. Among them, Hoff and others[9] have concluded a lack of this transition for PMMA on the basis of their audio-frequency dynamic data, which however have been presented only in an extremely small figure and probably may be too scattered to distinguish so small an anomaly as has been observed in our experiment. Recently Kawai[12], on the other hand, has suggested the existence of this transition in PMMA from the dielectric loss data.

Anyway, the apparent activation energy ΔH for the γ-transition can be evaluated from the present data as 7 kcal/mole, assuming the frequency of measurement is proportional to $\exp(-\Delta H/RT)$, where R is the gas constant and T the absolute temperature of the loss maximum. This estimate of ΔH, being much smaller than that of the β-transition, does not seem unreasonable to the hypothesis that the γ-transition of PMMA might be due to the rotation of a portion of the side group.

Fig. 4 illustrates the moisture dependence of the loss factor in the transition region. As can be observed, the transition shifts to a higher temperature with increase of moisture. Taking into account the above hypothesis, it might be said that the absorbed water makes hindrance to the rotation of the side group. In fact, Maeda[13] recently has reported that the absorbed water in PMMA, especially at low temperatures, occupies the free space between adjacent chains and consequently

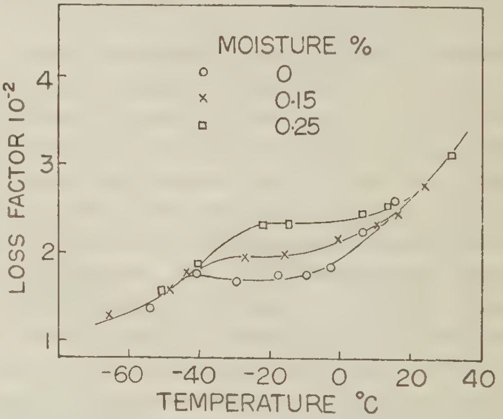

Fig. 4. Moisture dependence of loss factor for polymethyl methacrylate in the transition region (100 kc/s).

as a hindering effect on kinetic motions of he polymer chain.

Much more extensive data will be required efore the above hypothesis on the γ-transi- on can be considered anything more than ntative.

5. Polystyrene

The experimental results for polystyrene re shown in Fig. 5. It can be seen that the oss factor curve tends to rise gradually with

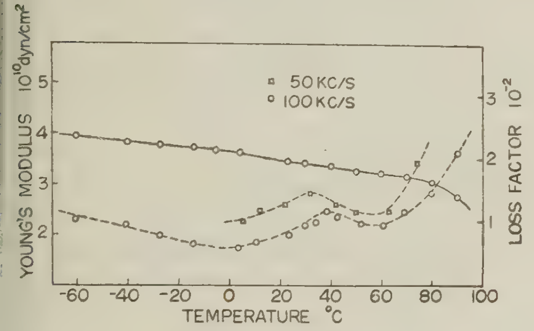

Fig. 5. Young's modulus (solid line) and loss factor (broken line) for polystyrene.

escending temperature and indicates the pos- ible existence of a peak below the test tem- erature. A similar behavior has been observ- d for this polymer by other authors[10,14].

The loss curve in Fig. 5 appears o exhibit a peak also at room tem- erature. This anomaly seem difficult o explain, since polystyrene mole- ule has no movable side group in ontradistinction to PMMA. In fact, he observed peak is so slight as to e reasonably ascribed to an ex- erimental error, but it may be vorthy to note that the curves here resented have good reproducibility. Nothing more can be said about this nomaly in the present stage.

6. Polyethylene and Other Plymers

The modulus and loss factor of olyethylene are illustrated in Fig. 6. It is vell established[5,15,16] that this polymer has a oss peak at room temperature when measured t ultrasonic frequencies. Also in the present tudy, a prominent peak is found in loss factor t 10°C. Combining this result with those in ther reports[5,16], a value of 28 kcal/mole is evaluated for the apparent activation energy. The molecular process involved in this transition is, as Mason[15] has stated, probably ascribed to the mobility of polymer chains in the amorphous region.

In the case of nylon 6 (see Fig. 2) which is also partially crystalline as polyethylene, the loss factor curve indicates the existence of a peak above room temperature.

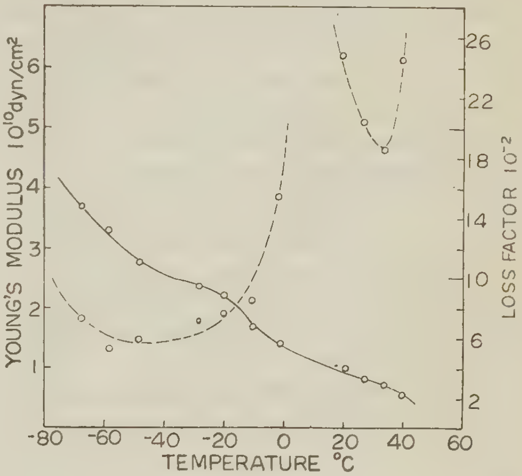

Fig. 6. Young's modulus (solid line) and loss factor (broken line) for polyethylene (100 kc/s).

Finally, the data are presented in Fig. 7 for two polyester samples of different crosslinking degree. While softening occurs at different temperatures for each sample, the modulus as well as the loss factor of both samples fall into a single curve respectively below the softening temperature. This indicates that, at the glassy state at least, the

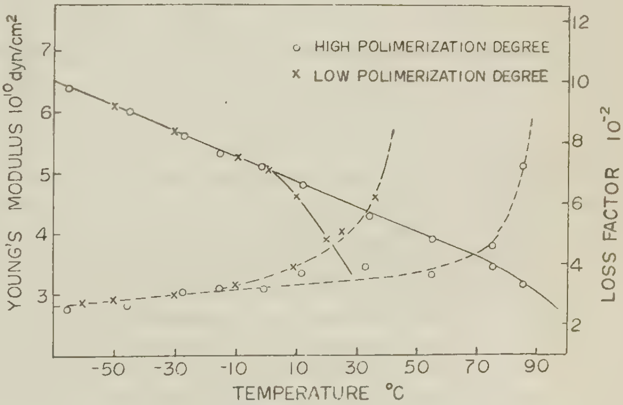

Fig. 7. Young's modulus (solid line) and loss factor (broken line) for two polyester samples. (100 kc/s).

dynamic elasticity of high polymers at ultrasonic frequencies almost energetics in nature, as has been discussed in detail in the previous paper[5].

§ 7. Acknowledgements

In conclusion, the authors express their sincere appreciation to Prof. Y. Suge for his continuous encouragement throughout this study. They also wish to thank to Dr. S. Iwayanagi and other members of the high polymer laboratory in the Scientific Research Institute for their valuable discussions.

References

1) J. Zacharias: Phys. Rev. **44** (1933) 116.
2) J. S. Rinehart: J. Appl. Phys. **12** (1941) 811.
3) S. V. Subrahmanyan: J. Chem. Phys. **22** (1954) 1562.
4) I. G. Mikhailov and V. A. Solov'ev: Akust. Zh. **1** (1955) 343.
5) Y. Wada and K. Yamamoto: J. Phys. Soc Japan **11** (1956) 887.
6) S. Iwayanagi and T. Hideshima: ibid. **8** (1953 368.
7) A. J. Staverman: Kolloid-Z. **134** (1953) 189.
8) K. Deutsch, E. A. W. Hoff and W. Reddish: J. Polym. Sci. **13** (1954) 565.
9) E. A. W. Hoff, D. W. Robinson and A. H Willbourn: ibid. **18** (1955) 161.
10) K. Schmieder and K. Wolf: Kolloid-Z. **134** (1953) 157.
11) B. Maxwell: J. Polym. Sci. **20** (1956) 551.
12) R. Kawai: Report given at the meeting on the thema: " High polymers and water ", held at Tokyo, Nov. 1956.
13) Y. Maeda: J. Appl. Phys. Japah **26** (1957) 22.
14) J. A. Sauer and D. E. Kline: J. Polym. Sci **18** (1955) 491.
15) W. P. Mason and H. J. McSkimin: Bell Sys Tech. J. **31** (1952) 122.
16) Y. Maeda: Report given at the annual meeting of the Phys. Soc. Japan, held at Sendai, July 1956.

JOURNAL OF THE PHYSICAL SOCIETY OF JAPAN Vol. 12, No. 4, APRIL, 1957

On the Effective Diffusion Tensor of a Segment in a Chain Molecule and its Application to the Non-Newtonian Viscosity of Polymer Solutions

By Yuichi IKEDA

*Kobayasi Institute of Physical Research, 2431 Kokubunzi, Tokyo**

(Received December 27, 1956)

The effect of hydrodynamic interaction between segments in a chain molecule plays an important role in the theory of the intrinsic viscosity of high polymer solutions. In this paper, the effect of hydrodynamic interaction is reflected into the concept of the effective diffusion tensor of a segment in a chain molecule. In performing the calculation, r_{iG}, the distance from the centre of gravity of the chain molecule to the cited segment, is considered as a parameter. In result, each segment has an anisotropic effective diffusion tensor, the radial component of which is about 10% larger than the transversal ones on the average. With this anisotropic diffusion tensor, the shear gradient dependence of the intrinsic viscosity of polymer solutions is deduced, making use of Rouse model. The agreement with experiments is satisfactory.

§ 1. Introduction

The molecular theory of the intrinsic viscosity of polymer solutions is now almost completed by Zimm[1], after many authors' efforts following Huggins[2], Kramers[3] and Debye[4]. The viscoelastic properties of dilute polymer solutions in alternating shear gradient are also well explained. However, the shear gradient dependence of the intrinsic viscosity is not satisfactorily explained, although some theories[5,6] have been given. Zimm's theory, the most exact one ever established, gives no shear gradient dependence of intrinsic viscosity, perhaps because of the complete linearity of the diffusion equation. It should be noted that in his theory the hydrodynamic effect is completely averaged using the probability distribution function in equilibrium. On the other hand, Kuhn and Kuhn[5] are the first who derived non-Newtonian intrinsic viscosity. They introduced the concept of internal viscosity into the dumb-bell model of the macromolecule, and in result, the dumb-bell model they took has an anisotropic diffusion tensor, which causes the non-Newtonian viscosity. However, the idea of "internal viscosity" is not clear. If it really exists, we might be able to derive it making use of Rouse model, considering hydrodynamic interactions.

---

* Present address: Fuji Spinning Co., Ltd., 2 Chōme 1, Honchô, Nihonbasi, Chūō-ku, Tokyo.

Having these circumstances in mind, we will attempt to estimate the effective diffusion tensor of a segment in a chain molecule, with specified position r_{iG} apart from the centre of gravity of the chain. In this case, when the effect of hydrodynamic interaction s taken into consideration, the effective diffusion tensor of a segment becomes an ansotropic one because of the anisotropic distribution of other segments around the cited segment. With this anisotropic diffusion tensor, we can get a higher approximation of the hydrodynamic interaction effect than Zimm's, in the theory based on a Rouse model. In result, we can get the non-Newtonian intrinsic viscosity of polymer solutions.

§2. The Effective Diffusion Tensor of a Segment

We will take a Rouse model with N identical segments, each of which is designated by an index i running from 1 to N. The root mean square of distance of neighbouring segments is l. The diffusion tensor D^{ij} can be defined by

$$\vec{j}^i=\sum_j \frac{D^{ij}}{kT}\vec{F}_j\,, \tag{1}$$

where $\vec{j}^i$ is the velocity of the ith segment minus the velocity of the unperturbed flow of olvent, and $\vec{F}_i$ is the force acting on the ith egment. The components of the diffusion tensor can be rewritten as

$$D^{ij}=kT\left\{\frac{1}{\zeta}\mathbf{1}^{ij}+\frac{1}{8\pi\eta_0 r_{ij}}\left[\mathbf{1}^{ij}+\frac{\vec{r}_{ij}{}^{i}\vec{r}_{ij}{}^{j}}{r_{ij}{}^{2}}\right]\right\}, \tag{2}$$

as Kirwood[7] has shown*. D^{ij} ($i \neq j$) vanishes when the hydrodynamic interaction can be neglected.

Firstly, we will consider the case where $\vec{F}_i$ has a value of $\vec{F}$ independent of i, then we have

$$\vec{j}^i=(\sum_j D^{ij})\vec{F}\,, \tag{3}$$

so we may define the effective diffusion tensor $\mathbf{D}^i{}_{\text{trans}}$ of the ith segment in the translational movement of the polymer as follows:

$$\mathbf{D}^i{}_{\text{trans}}=D^{ii}+\langle\sum_{j\neq i} D^{ij}\rangle_i\,, \tag{4}$$

where $\langle\ \ \rangle_i$ means the average taken over all other $\vec{r}_{jG}$ ($j=1, \cdots, i-1, i+1, \cdots, N$) except $\vec{r}_{iG}$, where $\vec{r}_{iG}$ is the vector running from the centre of gravity to the ith segment. Strictly speaking, Eq. (4) does not give the exact definition of $\mathbf{D}^i{}_{\text{trans}}$, because in the translational motion, the movement is represented not by $\vec{F}_i=\vec{F}$ but by $\vec{j}^i=$constant vector $\vec{j}$. However, the treatment for describing $\mathbf{D}^i{}_{\text{trans}}$ starting form $\vec{j}^i=\vec{j}$ is rather difficult. Fortunately, it is seen from some papers[1,9,10] that $\vec{F}_i$ does not so much depend on i, and it is natural to think that $\vec{F}_i$'s acting on two segments have almost same values when they are near each other, because the circumstances around each segment are nearly the same. Moreover, we can justify the definition Eq. (4) in another way. When we assume each segment has its diffusion constant $\overline{D^i{}_{\text{trans}}}$ which is given by averaging $\mathbf{D}^i{}_{\text{trans}}$ over $\vec{r}_{iG}$, we obtain the translational diffusion constant of a chain molecule D_{trans} in rigorous way as follows:

$$\vec{j}=\vec{j}^i=\frac{\overline{D^i{}_{\text{trans}}}}{kT}\vec{F}_i \text{ or } \vec{F}_i=\left(\frac{\overline{D^i{}_{\text{trans}}}}{kT}\right)^{-1}\vec{j}\,, \tag{5}$$

so consequently we have

---

* Eq. (2) is not so general as Kirkwood considered. Eq. (12) in his paper cannot be written generally, because F_α is determined not only by $\overset{\circ}{v}{}^{\beta}$'s and $\dot{q}^{\beta}$'s in the chain space but also by the components of $\mathbf{v}$ perpendicular to chain space. However if we take a Rouse model, the configuration space is identical to the whole space; so we may adopt Eq. (2) in this case[8].

$$\sum_i \vec{F} = \sum_i \left(\frac{\overline{D^i{}_{\text{trans}}}}{kT} \right)^{-1} \vec{j} = D^{-1}_{\text{trans}} \vec{j} \tag{6}$$

or

$$D_{\text{trans}} = \left[\sum_i \left(\frac{\overline{D^i{}_{\text{trans}}}}{kT} \right)^{-1} \right]^{-1} .$$

We can show that the value of D_{trans} calculated from Eq. (6) is in good agreement with the exact one[11] irrespectively of the degree of hydrodynamic interaction effect. This seems to justify the applicability of Eq. (4).

Now we will consider the effective diffusion tensor of a segment in the rotational motion of a polymer. In this case, the circumstances are analogous to the translational case; when the value of $\vec{r}_{iG}$ is near $\vec{r}_{jG}$, $\vec{F}$ does not differ so much from $\vec{F}_j$. However, as the chain rotates around the centre of gravity (strictly speaking, around the centre of resistance[1]), $\vec{F}_i$ will be nearly equal to $-\vec{F}_j$ when $\vec{r}_{iG} = -\vec{r}_{jG}$. Consequently, we may define $\mathbf{D}^i{}_{\text{rot}}$ by

$$\mathbf{D}^i{}_{\text{rot}} = D^{ii} + \alpha \langle \sum_{j \neq i} D^{ij} \rangle_i \, , \tag{7}$$

where α is a constant factor which can be determined from more detailed analysis. We will now take 1/4 for α, tentatively. Now, using the diffusion constant which is obtained by averaging Eq. (7), we can calculate the intrinsic viscosity, $[\eta]'$, employing Rouse model. The result is shown in Table I, compared with Kirkwood-Zwanzig-Plock's result[12]. The agreement is good through all degrees of hydrodynamic interaction effect, and hereafter we may use Eq. (7) as $\mathbf{D}^i{}_{\text{rot}}$, where $\alpha = 1/4$. More precise theories[1,9] give a little smaller values then Kirkwood-Zwanzig-Plock's. So, the value of α should be taken a little smaller than 1/4. However, as our theory is not so strict, it will be meaningless to decide the value of α in detail.

Table I. The values of $F(x)$ and $xF(x)$, where $F(x) = \left(\frac{N_a N^2 l^2 \zeta}{36 M \eta_0} \right) [\eta]'$ and $x = \lambda_0 N^{1/2}$; $\lambda_0 = \zeta / \{ (6\pi^3)^{1/2} \eta_0 l \}$.

x	$F(x) = \left(1 + \frac{2x}{3}\right)^{-1}$ (Eq. (15))		after Kirkwood-Zwanzig-Plock[12]	
	$F(x)$	$xF(x)$	$F(x)$	$xF(x)$
0	1.00	0.00	1.00	0.00
0.5	0.75	0.38	0.69	0.35
1.0	0.60	0.60	0.54	0.54
2.0	0.43	0.86	0.38	0.75
3.0	0.33	1.00	0.29	0.88
4.0	0.27	1.09	0.24	0.96
5.0	0.23	1.15	0.20	1.02
10.0	0.13	1.30	0.12	1.17
20.0	0.07	1.40	0.07	1.31
∞	0	1.50	0	1.48

We will now estimate Eq. (7) as a function of i. Substituting Eq. (2) into Eq. (7), with $\alpha = 1/4$, we have

$$\mathbf{D}^i{}_{\text{rot}} = \frac{kT}{\zeta} \mathbf{1} + \frac{1}{32 \pi \eta_0} \left\langle \sum_{j \neq i} \frac{1}{r_{ij}} \left\{ \mathbf{1} + \frac{1}{r_{ij}{}^2} \begin{pmatrix} x_{ij}{}^2 & x_{ij} y_{ij} & x_{ij} z_{ij} \\ y_{ij} x_{ij} & y_{ij}{}^2 & y_{ij} z_{ij} \\ z_{ij} x_{ij} & z_{ij} y_{ij} & z_{ij}{}^2 \end{pmatrix} \right\} \right\rangle_i . \tag{8}$$

The probability distribution functions $Z_N(\vec{r}_{ij};\ \vec{r}_{iG})$ of $\vec{r}_{ij}$ with $\vec{r}_{iG}$ fixed is given by[13,14]

$$Z_N(\vec{r}_{ij};\ \vec{r}_{iG}) = \frac{t_i{}^{3/2}}{(2\pi)^{3/2} (t_i t_{ij} - t_{i,ij}{}^2)} \exp\left[\frac{-t_i}{2(t_i t_{ij} - t_{i,ij}{}^2)} \left(\vec{r}_{ij} - \frac{t_{i,ij}}{t_i} \vec{r}_{iG} \right)^2 \right] , \tag{9}$$

where

$$\begin{aligned} t_i &= \frac{Nl^2}{3} \left\{ \frac{1}{3} - \frac{i}{N} \left(1 - \frac{i}{N} \right) \right\} , \\ t_{ij} &= \frac{Nl^2}{3} \left| \frac{i}{N} - \frac{j}{N} \right| , \\ t_{i,ij} &= \begin{cases} \dfrac{Nl^2}{6} \left(\dfrac{i}{N} - \dfrac{j}{N} \right) \left(\dfrac{i}{N} + \dfrac{j}{N} - \dfrac{1}{N} \right) & (i > j) \\ \dfrac{Nl^2}{6} \left(\dfrac{j}{N} - \dfrac{i}{N} \right) \left(2 - \dfrac{i}{N} - \dfrac{j}{N} + \dfrac{1}{N} \right) . & (i < j) \end{cases} \end{aligned} \tag{10}$$

Using Eqs. (9) and (10), Eq. (8) can be rewritten as

$$\mathbf{D}^{i}{}_{\mathrm{rot}}=\frac{kT}{\zeta}\begin{pmatrix} 1+\frac{\zeta}{12\pi\eta_0 l}A\left\{1+B\left(1-\frac{r_{iG}{}^2}{5t_i}\right)\right\}+\cdots & 0 & 0 \\ 0 & 1+\frac{\zeta}{12\pi\eta_0 l}A\left\{1+B\left(1-\frac{2r_{iG}{}^2}{5t_i}\right)\right\}+\cdots & 0 \\ 0 & 0 & 1+\frac{\zeta}{12\pi\eta_0 l}A\left\{1+B\left(1-\frac{2r_{iG}{}^2}{5t_i}\right)\right\}+\cdots \end{pmatrix}, \tag{11}$$

where we take x-axis parallel to $\vec{r}_{iG}$, and

$$A=\sqrt{\frac{6N}{\pi}}\left[\left(\frac{1}{2}-x\right)^{1/2}+\left(\frac{1}{2}+x\right)^{1/2}\right],$$
$$B=\frac{71}{2520}\frac{Nl^2}{t_i}\frac{(1/2-x)^{7/2}+(1/2+x)^{7/2}}{(1/2-x)^{1/2}+(1/2+x)^{1/2}}. \qquad \left(x=\frac{i}{N}-\frac{1}{2}\right) \tag{12}$$

Eq. (11) can be interpreted physically as follows: the hydrodynamic interaction effect causes a segment to move easily, if there are many segments moving in the same direction. The smaller the distance r_{iG} is, the more closely crowd the segments, and so the larger become the components of the effective diffusion tensor. Moreover, when the position of the ith segment from the centre of gravity is specified previously, the density distribution of other segments around the ith segment becomes anisotropic, with the result that the radial component of the effective diffusion tensor becomes larger than the transversal ones on account of the effect of hydrodynamic interaction.

If a polymer chain in a solution is under the shear flow, the chain will rotate and be deformed. In this case, we can calculate the intrinsic viscosity of a polymer chain molecule, solving the diffusion equation of the chain. If the diffusion constant of each segment remains constant, the non-Newtonian viscosity does not occur when we use the Rouse model, as is already pointed out[1,5,15]. But if the diffusion constant of a segment becomes an anisotropic effective diffusion tensor with variable components, non-Newtoninan viscosity may occur. However, Eq. (11) cannot be used in the above form. Under the shear flow, the chain is deformed, so that the distribution function in equilibrium (Eq. (9)) used to calculate Eq. (8) is to be replaced by the one of non-equilibrium. This circumstances make it difficult to apply the idea of effective diffusion tensor to the calculation of non-Newtonian intrinsic viscosity. So, hereafter, we may only use the anisotropic property of the effective diffusion tensor, which is essential whether the chain is deformed or not. Thus, we will average the component of the tensor in Eq. (11) on r_{iG}, then we have

$$\mathbf{D}^{i}{}_{\mathrm{rot}}=\frac{kT}{\zeta}\begin{pmatrix} 1+\frac{\zeta}{12\pi\eta_0 l}A\left(1+\frac{2}{5}B\right) & 0 & 0 \\ 0 & 1+\frac{\zeta}{12\pi\eta_0 l}A\left(1-\frac{1}{5}B\right) & 0 \\ 0 & 0 & 1+\frac{\zeta}{12\pi\eta_0 l}A\left(1-\frac{1}{5}B\right) \end{pmatrix}. \tag{13}$$

As A and B are slowly varying functions of i, we will again average Eq. (13) through i, to avoid the complexity which will occur otherwise in carrying out the calculation. Consequently, the averaged effective diffusion tensor, $\mathbf{D}_{\mathrm{rot}}$, becomes in its final form

$$\mathbf{D}_{\mathrm{rot}}=\frac{kT}{\zeta}\begin{bmatrix} 1+0.71\lambda_0 N^{1/2} & 0 & 0 \\ 0 & 1+0.64\lambda_0 N^{1/2} & 0 \\ 0 & 0 & 1+0.64\lambda_0 N^{1/2} \end{bmatrix}, \tag{14}$$

where $\lambda_0=\zeta/\{(6\pi^3)^{1/2}\eta_0 l\}$.

The average of the three diagonal elements is $kT/\zeta(1+2/3\cdot\lambda_0 N^{1/2})$. If we take this mean value for the diffusion constant of each segment, we get the intrinsic viscosity, $[\eta]'$, as follows:

$$[\eta]'=\frac{N_a N^2 l^2 \zeta}{36M\eta_0}\,\frac{1}{1+2/3\cdot\lambda_0 N^{1/2}}\,, \tag{15}$$

the value of which is shown in Table I as a function of $\lambda_0 N^{1/2}$.

§ 3. Non-Newtonian Intrinsic Viscosity

We will now treat the non-Newtonian intrinsic viscosity of polymer solutions. Here we will adopt the Rouse model. In this case, it is convenient to use the normal coordinates ξ_i, η_i, ζ_i $(i=1, \cdots, N-1)$ (the same ones for free-draining case in Zimm's paper[1], non-free-draining effect being taken into account in a different way in our paper), which are linear combinations of x_{iG}, y_{iG}, z_{iG} $(i=1, \cdots, N)$. The coordinates representing the position of the centre of gravity, ξ_0, η_0, ζ_0, do not enter in the following calculation. It is desirable to calculate the effective diffusion tensor in normal coordinates directly. But the functional form of $1/r_{ij}$ in normal coordinates is so complex, that we will try to derive the diffusion tensors in this case from the ones of ordinary x_{iG}, y_{iG}, z_{iG} coordinates. Though it is troublesome to seek the exact new form of diffusion tensors, it will be intuitively understood that the diffusion tensor of Eq. (14) can be used without changing its form for the new coordinates, when we consider the simple rotation of a chain around the centre of gravity, or the uniform radial deformation of the chain. So we may assume for each set of coordinates ξ_i, η_i, ζ_i the diffusion tensor to be of the same form as is given in Eq. (14).

Taking a laminar flow $(gy, 0, 0)$, where g is the shear gradient, we have

$$\begin{aligned}(\xi_i\eta_i)&=\frac{1}{D^r{}_{\mathrm{rot}}}\,\frac{g}{2}\,\langle\xi_i{}^2\rangle(\eta_i{}^2)+3\langle\xi_i{}^2\rangle\left(1-\frac{D^t{}_{\mathrm{rot}}}{D^r{}_{\mathrm{rot}}}\right)(\xi_i\eta_i/\rho_i{}^2)\,,\\(\eta_i{}^2)&=\frac{D^t{}_{\mathrm{rot}}}{D^r{}_{\mathrm{rot}}}\,\langle\xi_i{}^2\rangle+3\langle\xi_i{}^2\rangle\left(1-\frac{D^t{}_{\mathrm{rot}}}{D^r{}_{\mathrm{rot}}}\right)(\eta_i{}^2/\rho_i{}^2)\,,\end{aligned} \tag{16}$$

where $D^r{}_{\mathrm{rot}}$ and $D^t{}_{\mathrm{rot}}$ are the radial and transversal components of effective diffusion tensor, respectively, $\rho_i{}^2=\xi_i{}^2+\eta_i{}^2+\zeta_i{}^2$, and $\langle\ \rangle$ means the average in equilibrium. $(\ )$ means the average in the steady state. Eqs. (16) are derived from the diffusion equation of Rouse modified by anisotropic diffusion tensors, by multiplying $\xi_i\eta_i$ and $\eta_i{}^2$ to it and averaging, and $\langle\xi_i{}^2\rangle$ is introduced in Eqs. (16) because it comes from the spring constant of Rouse model given by equilibrium mean square separation. If $(1-D^t{}_{\mathrm{rot}}/D^r{}_{\mathrm{rot}})=0$, non-Newtonian viscosity disappears, and we will calculate $(\xi_i\eta_i)$ in a power series of $(1-D^t{}_{\mathrm{rot}}/D^r{}_{\mathrm{rot}})$. We may substitute $(\xi_i\eta_i/\rho_i{}^2)_0$ and $(\eta_i{}^2/\rho_i{}^2)_0$ into $(\xi_i\eta_i/\rho_i{}^2)$ and $(\eta_i{}^2/\rho_i{}^2)$ on the righthand term of Eqs. (16), respectively, for the first approximation. The subscript 0 indicates the value evaluated when we assume that $(1-D^t{}_{\mathrm{rot}}/D^r{}_{\mathrm{rot}})=0$. So we have

$$(\xi_i\eta_i/\rho_i{}^2)_0=\frac{1}{5}s_i-\frac{2}{15}s_i{}^3+\cdots\,, \tag{17}$$

$$\left(s_i=\frac{g}{2}\langle\xi_i{}^2\rangle\frac{1}{D^r{}_{\mathrm{rot}}}\right)$$

$$(\eta_i{}^2/\rho_i{}^2)_0=\frac{1}{3}-\frac{16}{105}s_i{}^2+\cdots\,, \tag{18}$$

and

$$(\xi_i\eta_i)=\frac{g}{2}\langle\xi_i{}^2\rangle^2\frac{1}{D^r{}_{\mathrm{rot}}}\left\{1+\frac{3}{5}\left(1-\frac{D^t{}_{\mathrm{rot}}}{D^r{}_{\mathrm{rot}}}\right)+\cdots\right\}\left[1-\frac{6}{7}\left(1-\frac{D^t{}_{\mathrm{rot}}}{D^r{}_{\mathrm{rot}}}\right)\left\{\frac{g}{2}\langle\xi_i{}^2\rangle\frac{1}{D^r{}_{\mathrm{rot}}}\right\}^2+\cdots\right], \tag{19}$$

From $(\xi_i\eta_i)$, we can get in a usual way the intrinsic viscosity $[\eta]$, that is

$$[\eta]=\frac{RT}{gM\eta_0}\sum_i\frac{(\xi_i\eta_i)}{\langle\xi_i^2\rangle}=\frac{RT}{2MD^r{}_{\mathrm{rot}}\eta_0}\{\Sigma\langle\xi_i^2\rangle\}\left\{1+\frac{3}{5}\left(1-\frac{D^t{}_{\mathrm{rot}}}{D^r{}_{\mathrm{rot}}}\right)+\cdots\right\}$$
$$\times\left[1-\frac{6}{7}\left(1-\frac{D^t{}_{\mathrm{rot}}}{D^r{}_{\mathrm{rot}}}\right)\frac{1}{D^r{}_{\mathrm{rot}}{}^2}\frac{\Sigma\langle\xi_i^2\rangle^3}{\Sigma\langle\xi_i^2\rangle}\frac{g^2}{4}+\cdots\right]. \tag{20}$$

where one has $\langle\xi_i^2\rangle=\frac{l^2}{3}\frac{N^2}{\pi^2 i^2}$, which leads immediately

$$\sum_i\langle\xi_i^2\rangle=\frac{l^2}{18}N^2, \tag{21}$$

and

$$\sum_i\langle\xi_i^2\rangle^3=\frac{8}{35}\{\Sigma\langle\xi_i^2\rangle\}^3. \tag{22}$$

Then, Eq. (20) can be rewritten as

$$[\eta]=[\eta]_{g\to0}\left[1-\frac{48}{245}\left(1-\frac{D^t{}_{\mathrm{rot}}}{D^r{}_{\mathrm{rot}}}\right)\left([\eta]_{g\to0}\,\eta_0\frac{M}{RT}\right)^2 g^2+\cdots\right]. \tag{23}$$

Remembering Eq. (14), we have

$$1-D^t{}_{\mathrm{rot}}/D^r{}_{\mathrm{rot}}=(1+0.07\lambda_0N^{1/2})/(1+0.71\lambda_0N^{1/2}). \tag{24}$$

When $\lambda_0\to\infty$, $(1-D^t{}_{\mathrm{rot}}/D^r{}_{\mathrm{rot}})\sim 0.1$. $[\eta]_{g\to0}$ is nearly the same as $[\eta]'$. $[\eta]_{g\to0}\propto 1/D^r{}_{\mathrm{rot}}\{1+3/5(1-D^t{}_{\mathrm{rot}}/D^r{}_{\mathrm{rot}})+\cdots\}$ and $[\eta]'\propto 1/D^r{}_{\mathrm{rot}}\{1+2/3(1-D^t{}_{\mathrm{rot}}/D^r{}_{\mathrm{rot}})+\cdots\}$, where $0<(1-D^t{}_{\mathrm{rot}}/D^r{}_{\mathrm{rot}})<0.1$.

§ 4. Discussion

Recently, Peterlin-Čopič[16,17] proposed a theory of the non-Newtonian viscosity of dilute polymer solutions. Their idea is essentially similar to that of this paper. But they started from the dumb-bell model, and discussed the anisotropic diffusion tensor according to it. On the other hand, we have started from the concept of the effective anisotropic diffusion tensor of one segment in a chain. In result, Peterlin and Čopič obtained the following result,

$$[\eta]=[\eta]_{g\to0}\left[1-\frac{53}{50}\left(1-\frac{D^t{}_{\mathrm{rot}}}{D^r{}_{\mathrm{rot}}}\right)\left([\eta]_{g\to0}\,\eta_0\frac{M}{RT}\right)^2 g^2+\cdots\right], \tag{25}$$

our result is shown in Eq. (23), where Rouse model is employed.

It is to be noted that $[\eta]/[\eta]_{g\to0}$ is a function of $[\eta]_{g\to0}\eta_0Mg/RT$, this corresponds to the fact that $[\eta]/[\eta]_{\substack{g\to0\\ \omega\to0}}$ is a function of $[\eta]_{\substack{g\to0\\ \omega\to0}}\eta_0M\omega/RT$ in the oscillating field. Though we cannot clarify the behaviour of a chain in the full range of shear gradient, we mayn ow suggest a formula for $[\eta]$ as follows:

$$[\eta]/[\eta]_{g\to0}=\left(1-\frac{[\eta]_{g\to\infty}}{[\eta]_{g\to0}}\right)\frac{6}{\pi^2}\sum_{i=1}^{N}\frac{1}{1+\beta\left[\frac{1}{i^2}\frac{6}{\pi^2}g[\eta]_{g\to0}\,\eta_0\frac{M}{RT}\right]^2}+\frac{[\eta]_{g\to\infty}}{[\eta]_{g\to0}}, \tag{26}$$

presuming the Philippoff-type non-Newtonian viscosity formula. Eq. (26) fits to Eq. (24) with the parameter $\beta=6/7(1-D^t{}_{\mathrm{rot}}/D^r{}_{\mathrm{rot}})(1-[\eta]_{g\to\infty}/[\eta]_{g\to0})^{-1}$, if g is small. This formula is suggested considering of many normal coordinates representing the configuration of a polymer chain.

We will now compare Eqs. (24) and (26) to the experimental data. Eq. (24) with $\lambda_0N^{1/2}\to\infty$ is applied to Čopič's data[17] and Wada's data[18] of non-Newtonian intrinsic viscosity of polystyrene and polymethylmethacrylate, respectively. Broadly speaking, the agreement is satisfactory. Eq. (26) is applied to Sharman-Sones-Cragg's data[19] where $g=0\sim10^4$ sec^{-1}. Many Sharman-Sones-Cragg's data are plotted in log η_r/c vs. g, but approximately holds the relation

$$\log \eta_r/c \simeq \frac{[\eta]}{c} \frac{(1-1/\eta_r{}^0)}{[\eta]_{g\to 0}} + \log \eta_r{}^0/c - \frac{1}{c}\left(1-\frac{1}{\eta_r{}^0}\right),$$

where η_r is the relative viscosity, $\eta_r{}^0$ is η_r at $g\to 0$, and c is the concentration of polymer solution, and hence Eq. (26) can be roughly compared with their data. Though the agreement with each experimental data is not so good, the trend of experimental curves, i.e., the fast decrease of $[\eta]$ followed by slow one with increasing shear rate is reasonably explained by Eq. (26). The tendency of dependence of non-Newtonian viscosity on molecular weight is also satisfactorily explained.

Acknowledgement

The writer would express his sincere thanks to Dr. S. Oka, Dr. N. Saitô, Mr. O. Nakada and others in Kobayasi Institute of Physical Research for their encouragement and valuable discussions. The present investigations has been supported partly by the Scientific Research Grant of the Ministry of Education.

References

1) B. H. Zimm: J. Chem. Phys. **24** (1956) 269.
2) M. L. Huggins: J. Phys. Chem. **42** (1938) 911.
3) H. A. Kramers: J. Chem. Phys. **14** (1946) 415.
4) P. Debye: J. Chem. Phys. **14** (1946) 636.
5) W. Kuhn and H. Kuhn: Helv. chim. acta **28** (1945) 1533; **29** (1946) 71.
6) F. Bueche: J. Chem. Phys. **22** (1954) 1570.
7) J. G. Kirkwood: Rec. trav. chim. **68** (1949) 649.
8) Y. Ikeda: Bull. Kobayasi Inst. Phys. Res. **6** (1956) 44.
9) P. L. Auer and C. S. Gardner: J. Chem. Phys. **23** (1955) 1545 and 1546.
10) J. G. Kirkwood and J. Riseman: J. Chem. Phys. **16** (1948) 565.
11) J. G. Kirkwood: J. Polymer Sci. **12** (1954) 1.
12) J. G. Kirkwood, R. W. Zwanzig and R. J. Plock: J. Chem. Phys. **23** (1955) 213.
13) Y. Ikeda: Bull. Kobayasi Inst. Phys. Res. **5** (1955) 230.
14) Y. Ikeda: Bull. Kobayasi Inst. Phys. Res. **6** (1956) 149.
15) A. Peterlin: J. Polymer Sci. **8** (1952) 473.
16) A. Peterlin and M. Čopič: J. Appl. Phys. **27** (1956) 434.
17) M. Čopič: J. chim. phys. **53** (1956) 440.
18) E. Wada: J. Sci. Res. Inst. (Tokyo) **47** (1953) 159; J. Polymer Sci. **14** (1954) 305.
19) L. J. Sharman, R. H. Sones and L. H. Cragg: J. Appl. Phys. **24** (1953) 703.

JOURNAL OF THE PHYSICAL SOCIETY OF JAPAN Vol. 12, No. 4, APRIL, 1957

On the Magnetic Properties of Chromium Sulfides*

By Motoyoshi YUZURI, Tokutaro HIRONE, Hiroshi WATANABE,
Seizo NAGASAKI and Seijiro MAEDA

*The Research Institute for Iron, Steel and Other Metals,
Tohoku University, Sendai*

(Received January 7, 1957)

The thermomagnetic properties of chromium sulfide $CrS_{1.17}$ were studied. The spontaneous magnetization of this compound, which is probably of the ferrimagnetic origin, suddenly disappears during cooling at −120°C. A slight heat absorption was observed at this transition point. By X-ray analysis excess diffraction lines besides those of the ideal crystal lattice of the nickel arsenide type were observed at room temperature, which shows a super-lattice structure with parameters of twice c and $2\sqrt{3}$ times of a, a and c being those of the original lattice. It was also found by X-ray analysis that there was no change of the crystal lattice at the magnetic transition temperature, −120°C. This compound showed a ferrimagnetic behavior with the asymptotic Curie temperature at 150°K. A peak in susceptibility *vs.* temperature curve was found by the thermomagnetic measurement in the temperature range from the liquid helium temperature to −120°C. Basing on these data, a short discussion on the nature of the above-mentioned transition is given.

§ 1. Introduction

It was reported by Haraldsen and Neuber¹⁾ that chromium sufide with the composition $CrS_{1.17}$ is ferromagnetic with the Curie temperature of about 30°C and its spontaneous magnetization disappears suddenly during cooling at −120°C and the compound becomes paramagnetic below that temperature. As to the mechanism of the abrupt disappearance of magnetization at −120°C many possibilities could be proposed, *e.g.* the change in crystal structure, the formation or vanishing of ordered arrangement of cations or vacancies in the crystal lattice, or that of ordered arrangement of spins. Because of the lack of thermal and crystallographic data, however, it is difficult to distinguish the most probable one from these possibilities. Hence, in the present studies magnetic, thermal, and X-ray analyses of this compound were undertaken. In the following pages the results of the measurements and a discussion of the nature of the magnetic transition mentioned above are given.

§ 2. Preparation of the Specimens

The specimens used were prepared by the usual ceramic method. Chromium powder (99.3%) and sulfur (99.99%) were mixed in the desired ratios and sealed doubly in an evacuated quartz tube and then heated in an electric furnace. To avoid explosion during heating, the mixtures were heated slowly during 24 hours till 400°C and held at this temperature for 24 hours, then heated till 1,000°C during 24 hours and kept at this temperature for 24 hours. After the reaction was completed, the specimens were cooled at the rate of 30°C per hour down to the room temperature. Sometimes, slight cracks occurred at the inner quartz tube during cooling due to the difference in thermal contraction between the specimens and the quartz tube, but the doubly sealed container mentioned above prevented the specimens from oxidation or decomposition. In order to obtain homogeneous specimens, the reaction products were crushed once more, mixed well and then pressed in a form of small bar under the pressure of about 1.5 tons per square cm and again heated above 900°C for more than 24 hours. Every portion of the specimen thus obtained showed the same thermomagnetic behavior.

---

* A part of this report is based upon the dissertation (Master Course (1955), Tohoku University) presented by Motoyoshi Yuzuri. This investigation was financed in part by the Grant-in-Aid of the Fundamental Scientific Research of the Ministry of Education.

§ 3. Thermomagnetic Measurements

An automatically recording magnetic balance was used for the measurements of the magnetic susceptibility[2]. The change of the susceptibility, χ, with temperature was measured with samples of various sulfur contents at the magnetic field of about 3,500 Oe. The susceptibility of the compound $CrS_{1.17}$ as measured in the temperature range from the boiling point of liquid nitrogen to 600°C, is shown in Fig. 1. As seen from the figure the reciprocal susceptibility decreases linearly with the fall of temperature in the high temperature range, and then falls rapidly just above the Curie point, below which the saturation in magnetization is observed. Such a behavior suggests that the magnetism of this compound is of ferrimagnetic origin. From the Curie constant obtained from the slope of the $1/\chi$-T curve, the effective Bohr magneton number per Cr ion was calculated to be 4.8. Assuming Lande factor g as 2, the mean spin quantum number S becomes 3.9/2. This observed value of S is considered to be a resonable one, since it may be supposed from the ionic picture of this compound that two kinds of chromium ions, Cr^{2+} and Cr^{3+}, whose spin quantum numbers are 4/2 and 3/2 respectively, coexist in the substance. The specific magnetization at 3,000 Oe below the Curie temperature is also shown in the same figure, which hows that the magnetization disappears suddenly at −120°C as stated above. The change of the specific magnetization σ with the magnetizing field obtained with the sample of $CrS_{1.17}$ is shown is Fig. 2, from which it can be seen that the complete saturation is reached at the field of 8000 Oe. A $\sigma_s - T^{3/2}$ plot made, based on such measurements at various temperatures is shown in Fig. 3, which indicates that the saturation magnetization varies linearly with $T^{3/2}$ below 250°K*. The saturation value at the absolute zero of temperature obtained by extrapolating the linear part of the $\sigma_s - T^{3/2}$ curve, is 0.35 Bohr magneton per Cr atom.

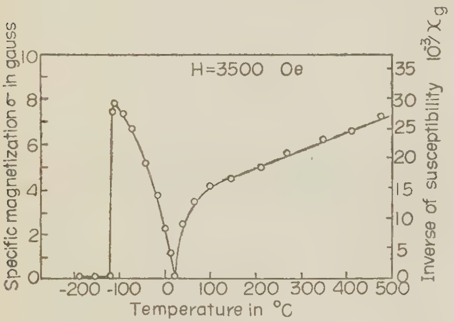

Fig. 1. The thermomagnetic curve of $CrS_{1.17}$.

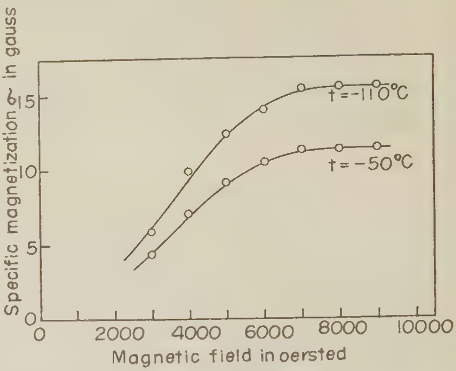

Fig. 2. The curves of specific magnetization versus magnetic field.

The behavior of the susceptibility below the transition temperature is shown in Fig. 4. As can be seen from the figure, there appears a maximum of susceptibility at −170°C. The emergence of this peak, however, was accompanied by a relaxation of the order of an hour. If the specimen was cooled rapidly to the boiling point of nitrogen and then heated without delay, such a peak did not appear. The necessary condition for observ-

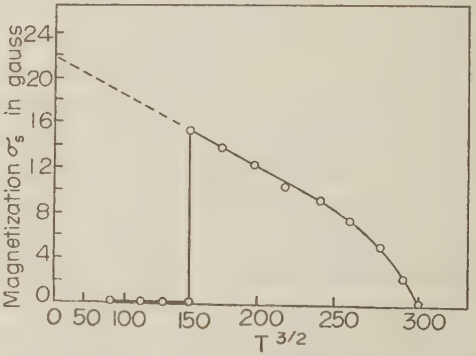

Fig. 3. The saturation magnetization versus (temperature $T^{3/2}$).

---

* Such a procedure for obstaining absolute saturation value with Bloch's $T^{3/2}$ law is justified in the case of ferrimagnetism by Prof. Kubo.

ng this peak was to keep the specimen at he boiling point of liquid nitrogen for a few ours or to cool it until the liquid helium emperature was reached. The origin of such relaxation phenomenon, however, is not yet lear.

4. Thermal Analysis

The measurement of specific heat in the ow temperature range was carried out by eans of an adiabatic method, the detailed escription of which was given by Nagasaki nd Takagi[3]. In this case a cylindrical essel made of paper was used as the specien container. The result of measurement s shown in Fig. 5. An anomalous peak of pecific heat at about 30°C corresponds to the Curie point of this compound, and the total eat absorption due to the vanishing of ferrimagnetism is 30 cal/mol.* In addition, a ery small peak was observed at about −120°C, corresponding to the vanishing point f magnetization at low temperature side. The total heat absorption under this peak is 7 cal/mol, the excess entropy change at this point being only 0.044 entropy unit.

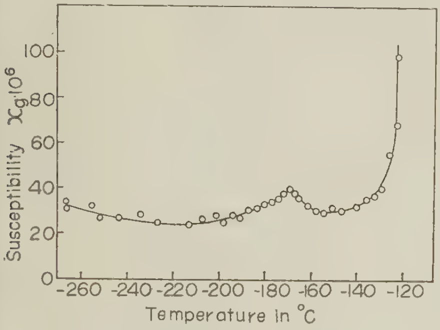

Fig. 4. The curves of susceptibility versus temperature.

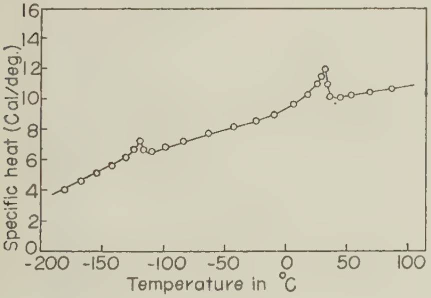

Fig. 5. The curve of the specific heat versus temperature of $CrS_{1.17}$.

§ 5. X-ray Analysis

For the purpose of detecting any change of crystal structure corresponding to the magnetic transition at −120°C, powder diffraction photographs were taken at room temperature and below −120°C. A modefied X-ray camera of the Ubbelohde[4] type was used, the detail of which is as shown in Fig. 6.

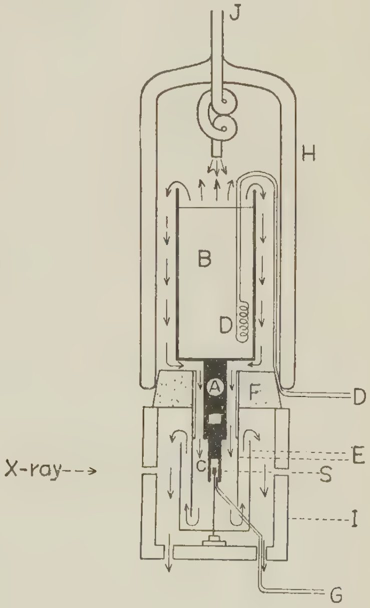

Fig. 6. The low temperature X-ray camera.
A, copper rod; B, copper container for cooling medium; C, copper rod; D, heater; E, cellophane sleeve with glass stiffing; F, corke table; G, thermocouple; H, Dewar vessel; I, cassette; J, glass tube for supply of cooling medium; S, specimen.

The diameter of the camera was 70 mm. Rotating specimen S was cooled by both the cooled copper rod A attached at the bottom of liquid air container and the flow of cooled air evaporated from it. The control of the temperature of the specimen was made by adjusting the contact between the copper rods C and A as well as the flow of cooled air. The evaporation control of liquid air was made by means of adjusting the power supply in the heater D in B, thus the adjustment of temperature of the specimen could range from −100°C to −150°C. As the X-

---

* Mean molecular weight 89.9 for $CrS_{1.17}$ is dopted here.

Table I. The result of X-ray analysis at room temperature.

Intensity	Scattering angle	*hkl*		$\sin^2\theta$	
	θ	*NiAs*-type	Super structure	Observation	Calculation
w	11°33′		002	0.0401	0.0398
w	14°30′		201	0.0589	0.0585
vw	17° 1′		210	0.0858	0.0850
w	18°00′		211	0.0955	0.0949
w	21°45′		203	0.1373	0.1380
s	22°30′	100	220	0.1465	0.1450
vs	25°30′	101	222	0.1853	0.1848
		002*	004		0.1590
vw	33°00′		205	0.2966	0.2967
vs	33°30′	102	224	0.3046	0.3090
vs	41°27′	110	600	0.4434	0.4390
s	45°00′	103	226	0.5000	0.5030
vw	49°54′	200	440	0.5852	0.5830
s	52° 7′	201	442	0.6227	0.6228
		112*	604		0.5980
s	52°30′	004	008	0.6295	0.6350
vs	59°24′	202	444	0.7408	0.7420
vw	61°45′	104	228	0.7760	0.7810

Notation of intensity; vs=very strong, s=strong, w=weak, vw=very weak.

* not to be observed.

ray scattering occurred by frost adhered to the circumference of the specimen, the freezing of frost was avoided by setting a cylindrical wall of selophan E and flowing cooled air in the direction of arrow sign in the figure. The result of X-ray analysis at room temperature is as shown in Table I. As it shows the compound $CrS_{1.17}$ has the crystal structure of NiAs type and the unit length of a and c axes are 3.45 Å and 5.76 Å respectively, its axial ratio c/a being 1.67. These results coincide with those of Haraldsen. The result of X-ray analysis below −120°C is as shown in Table II; any appreciable change of crystal structure from that at room temperature was not recognized and it was ascertained that the lattice contracts 0.29% and 0.39% along the directions of a and c axes respectively. Such a contraction is probably due to the ordinary thermal contraction, as the thermal expansion coefficient 1.8×10^{-5} in the direction of a axis and 2.2×10^{-5} in that of c axis are sufficient to reproduce such a contraction.

Table II. The result of X-ray analysis at −140°C.

NiAs-type	20°C		−140°C	
hkl	θ	$\sin^2\theta$	θ	$\sin^2\theta$
100	22°30′	0.1465	22°35′	0.1475
101	25°30′	0.1853	25°38′	0.1871
102	33°30′	0.3046	33°38′	0.3068
110	41°27′	0.4434	41°50′	0.4449
103	45°00′	0.5000	45°12′	0.5035
201	52° 7′	0.6227	52°29′	0.6290
004	52°30′	0.6295	52°50′	0.6351
202	59°24′	0.7760	59°56′	0.7489

temperature	a	c	c/a
20°C	3.45 Å	5.76 Å	1.67
−140°C	3.44 Å	5.74 Å	1.67
	$\Delta a/a=0.29\%$	$\Delta c/c=0.35\%$	

A power photograph at room temperature was also taken by using an X-ray camera with the diameter of 114 mm and the abovementioned results in Table I were confirmed. However, several diffraction lines besides the proper lines of this crystal lattice were recognized in the range of small diffraction angles. These, correspond to a super-lattice structure, whose c axis and a axes are, respectively, twice and $2\sqrt{3}$ times greater an those of the original nickel arsenide pe lattice. According to Haraldsen, the me super-structure* exists the composition ar $CrS_{1.00}$ but not at the composition of $S_{1.17}$.

6. Discussions

Now we discuss the mechanism of abrupt ange of magnetism at −120°C. The pos- bility of the structural change of crystal at is transition point may be excluded because the negligible difference of the X-ray wder patterns found above and below the ansition point and the very small heat sorption observed at this temperature (only cal/mol, cf. § 4 and 5).

It was suggested by Haraldsen and Neuber, at the ordered structure of ions or vacancies as found at the composition $CrS_{1.00}$ (para- agnetic), while, such super-lattice lines anished at the composition $CrS_{1.17}$. They nsidered from these results that the dis- ppearance of the super-structure is respon- ble for the appearance of ferrimagnetism. owever, as reported in section 5, the same iffraction lines corresponding to the above- entioned ordered structure were found by s both for paramagnetic and ferrimagnetic ompounds, and hence such a super-structure considered to have no direct relation to e observed ferrimagnetism and the magnetic ransition at −120°C.

As for the cause of the magnetic transi- ion mentioned above, some kind of the riangular arrangement of the magnetic oment of cations may be considered. In e compound $CrS_{1.17}$ two kinds of cations r^{2+} and Cr^{3+} coexist in the same crystal ttice. In such a case it was concluded pre- iously basing on the molecular field theory[5] at the magnetic moment of each kind of cations orient to different directions respectively, making the so-called triangular spin arrangement in the crystal lattice. It was also inferred from the same theory that more than two stable or metastable directions of the resultant magnetic moment of each kind of cations will occur at a certain temperature during heating or cooling, and an abrupt change of total magnetic moment of the substance will be expected owing to the discontinuous change of the angle between the magnetic moments of cations. The resultant magnetic moment of each kind of cations remain unchanged while the total magnetic moment of the crystal is largely changeable; such a magnetic transition will not be accompanied by any latent heat or heat absorption, this theoretical result coinciding with the fact that a very small heat absorption was observed at the transition. It was also shown previously that a ferrimagnetic behavior of the crystal can be expected from the model of the triangular spin arrangement, and then the above-mentioned abrupt decrease of the reciprocal susceptibility during cooling just above the Curie point is expected from the same point of view.

References

1) H. Haraldsen and A. Neuber: Z. anorg. u. allgem. Chem. **234** (1937) 337. Z. anorg. u. allgem. Chem. **234** (1937) 372.
H. Watanabe and N. Tsuya: Sci. Rep. RITU. **A2** (1950) 503, Sci. Rep. RITU. **A2** (1950) 764.
2) T. Hirone, S. Maeda and N. Tsuya: Rev. Sci. Instr. **25** (1954) 516.
3) S. Nagasaki and Y. Takagi: J. Appl. Phys. Japan, in Japanese **17** (1948) 104.
4) A. R. Ubbelohde and I. Woodward: Proc. Roy. Soc. **A188** (1946–47) 358.
5) T. Hirone and K. Adachi: to be published shortly in this journal.

---

* The coincidence of the intensity distribution f the extra-lines with those reported by Haraldsen ould not be confirmed by the present investigation.

JOURNAL OF THE PHYSICAL SOCIETY OF JAPAN Vol. 12, No. 4, APRIL, 1957

Preliminary Report on an Electromagnetic Isotope Separator

By Jun OKANO

Department of Physics, Faculty of Science, Osaka University

(Received October 16, 1956)

As a first step towards constructing a high intensity electromagnetic isotope separator, the focussing characteristics of the Smythe type magnetic lens was investigated. And for preliminary experiments of isotope separation, we constructed a small mass separator of this type. The apparatus has the ion radius of 50 cm in the magnet, and has two ion sources which can be operated independently and simultaneously. The ion source was a sort of Finkelstein type and its characteristics was investigated in conjunction with the electrostatic lens system. The maximum ion current on the collector that was attained was about 400 μa and 1 ma for neon and for magnesium respectively.

§ 1. Introduction

In 1934 Smythe et al[1] constructed a mass-spectrometer with a special type of magnetic lens capable of focussing on a collector all the positive ions of the definite mass from a wide area of the ion source. They separated alkaline metals emplying an ion current of 0.1 ma for K^{39}.

From 1938 to 1949 medium size electromagnetic separators were constructed by Walcher.[2] Koch,[3] Bergström[4] et al. The collector currents in these separators were of the order of 10–100 μa. Recently the intensity of the electromagnetic separator has been increased remarkably mainly due to the success in the neutralization of space charge in the ion beam. Bernas[5] constructed a 60° type electromagnetic separator and was able to increase the collector current up to about 10 ma. He used grids of negative potential in order to trap the electrons in the ion beams and succeeded in neutralizing the space charge of positive ions.

Kistemaker and Zilverschoon[6] built a large elcctromagnetic separator and operated the apparatus with a collector current of 1–10 ma. In Oak Ridge[7] and Harwell[8] large scale separators were constructed and the collector currents of these separators were of the order 10–100 ma.

With the recently constructed separators, the ion currents at the collectors are of the order of 1–100 ma. Because the collector current is firstly limited by the area of the source slit through which ions are drawn out, it is necessary to use an exist slit with a large area in order to get a high intensity. In the case of a magnetic lens of first order focussing, increasing the width of the source slit results in the corresponding broadening of the image and decreasing of the resolving power. It follows from this that in order to increase the area of the slit without decreasing the resolving power, an increase of the length of the slit is necessary. However, the increase of the length requires an increase of the magnet pole gap, which may be too expensive. Therefore, it may be more efficient to utilize as an analyzing field of an isotope separator a magnetic lens which is capable of focussing completely on a collector all the ions of the definite mass from a wider source slit.

From this standpoint Smythe type magnetic lens, which is able to focus completely a very wide incident beam of parallel ions on a collector, is considered to be one of the most appropriate as an analyzing field of the isotope separator. We investigated the focussing characteristics of the Smythe type magnetic lens and constructed a small mass separator of this type for preliminary experiments of isotope separation.

Practically, if we use a special type of ion source such as Kunsmann-source, a very wide source slit is available. However, when a more general type of source like arc source is used, it may be difficult to regulate by the electrical lens system the path of ions from the extremely large slit. Then it may be advantageous to employ instead of one source two or more independent sources that are parallel to each other, and to operate them multaneously and superpose the images from hese sources on one collector.

And also it is advantageous to use a multiource, because by adjusting the accelerating oltage slightly it is possible to avoid the roadening of the image due to the imperfecon of the homogeneity of the magnetic field nd because the multisource is beneficial for xchanging the charge material and for inimizing the time for the preparation.

In the following we describe the results of he consideration with respect to some haracteristics of this magnetic lens which re important when it is used as an analyzing ield of the electromagnetic separator and the esults of preliminary experiment of the isoope separation using a small separator of his type.

§ 2. The Characteristics of Smythe Type Magnetic Lens

Let us consider incident ions running parallel to each other and designate the direction of the path of incident ions as the x-axis. And let the mass and energy of the ions be M and eE respectively.

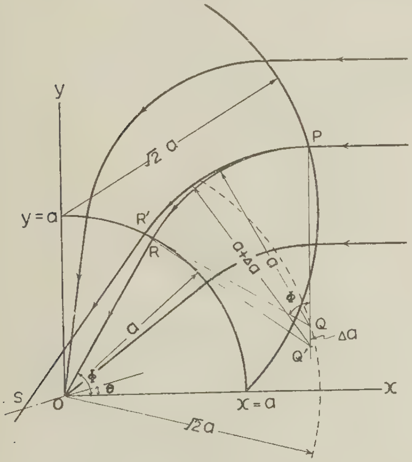

Fig. 1. Focussing property of Smythe-type magnetic lens.

As shown in Fig. 1 ions entering the magnetic field at P will run on a circle with center Q, and radius a, and be deflected by the angle Φ. After leaving the magnetic field at R, the ions pass through the point O. Ions of mass $M+\Delta M$ in the magnetic field run on a somewhat different circle with center Q', and radius $a+\Delta a$ where

$$\Delta a \approx \frac{a}{2}\,\frac{\Delta M}{M} \tag{1}$$

when

$$\frac{\Delta M}{M} \ll 1$$

They leave the magnetic field at R' and pass through the point S on a focal plane which crosses the x-axis at point 0 with an angle θ. The distance $\overline{OS}$ is the mass dispersion, δ_m, for mass difference $\Delta M/M$, and is given by

$$\overline{OS} = \delta_m \approx \frac{\Delta a(1-\cos\Phi+\sin\Phi)}{\sin(\Phi-\theta)} \tag{2}$$

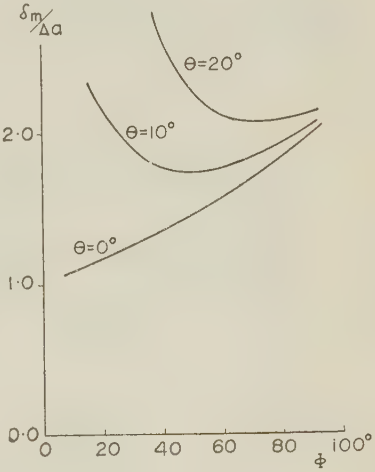

Fig. 2. Mass-dispersion of Smythe-type magnetic lens as a function of Φ. Parameter θ is the angle between the x-axis and the focal plane.

δ_m is plotted as a function of Φ in Fig. 2 for $\theta=0°$, 10° and 20°. As it is desirable to have a constant value of δ_m on a focal plane for the change of Φ, the angle θ for the most appropriate focal plane is determined from the minimum point of the curve plotting δ_m versus Φ. If the part of this magnetic lens, $\Phi=45°\sim90°$ is used, the appropriate value of θ is found between 10° and 25°. θ may also be determined by a graphical method. But in practice the actual focal plane will be somewhat different from that estimated by the above described method mainly due to the effect of the fringing field.

Fig. 3 shows the path of ions emitted from the point P at all angles within the range α. The resultant breadth at the focal plane is

$$\delta_\alpha = a\alpha\left(\frac{\sin\Phi+\cos\Phi}{\sin(\Phi-\theta)}\right), \quad \alpha \ll 1 \tag{3}$$

which determines the breadth of the image due to an imperfection in the parallelity of incident ions. The value of δ_α given by eq. (3) is plotted as a function of Φ in Fig. 4. If Φ increases, δ_α decreases and vanish at $\Phi=135°$ where a first order focussing with respect to α is accomplished but $\Phi=135°$ does not correspond to the practical case because the path of incident ions is tangentially to the boundary of the magnetic field.

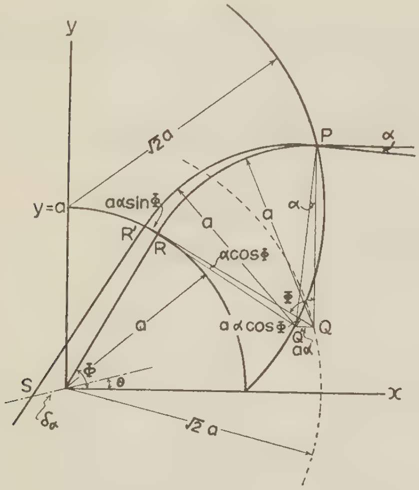

Fig. 3. Arration due to α. (δ_α)

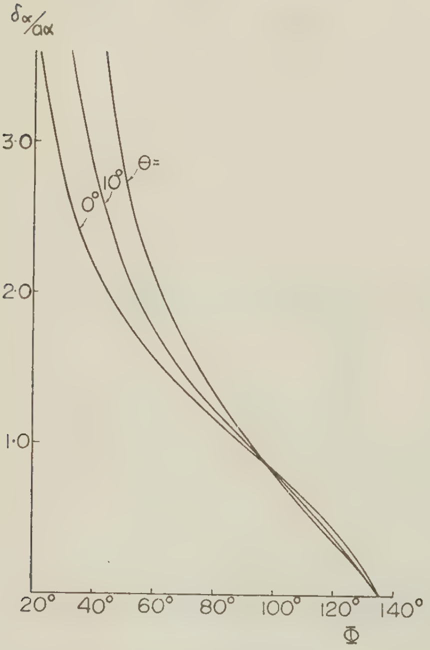

Fig. 4. Values of the aberration due to the imperfection of the parallelity of paths of incident ions as a function of Φ.

In the range of $\Phi=45°-90°$ δ_α is of the order of $a\alpha - 3a\alpha$ when θ is less than 20°.

If the path of incident ions is parallel to the x axis, an incident angle to the magnetic field, that is, the angle between the path of incident ions and a normal to the boundary of the magnetic field at the point of incidence is given by

$$\mathcal{E}'=\Phi-\frac{\pi}{4} \tag{4}$$

When $\mathcal{E}'\not\approx 0$, the magnetic lens has an action of three dimensional focussing. Let us take the Z-axis parallel to the direction of the magnetic field. Then the Z direction focal point is given by

$$G''=a(\operatorname{ctg}\mathcal{E}'-\Phi) \tag{5}$$

where G'' is the distance between the Z direction focal point and the boundary of the magnetic field.

In Fig. 5 G''/a is plotted as a function of Φ showing that it is infinity at $\Phi=45°$ and unity at $\Phi\approx 69° 20'$. And so three dimensional focussing is achieved when $\Phi\approx 69° 20'$. In Fig. 5 the Z-direction magnification factor m_z of the image is also plotted. m_z is larger or smaller than unity according as $\Phi<45°$ or $45°<\Phi<84°$. In the case of an electromagnetic separator the perfect three dimensional focussing is not necessary but it is

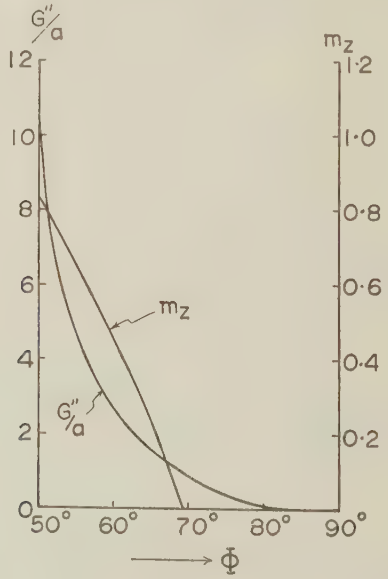

Fig. 5. Z-direction focal length G'' and z-direction magnification factor m_z of Smythe-type magnetic lens as a function of Φ.

desirable that the magnetic lens has Z-direction focussing action and the Z-direction magnification factor of the image is smaller than unity.

Although a Smythe type magnetic lens is considered one of the most appropriate magnetic lens for an analyzing field of an electromagnetic isotope separator, it is necessary to keep in mind the characteristics described above and to select the range of Φ from the practical standpoint.

In order to confirm the practical possibilities of focussing high current ion beam, a preliminary experiment has been carried out with a Smythe type mass-spectrometer which has two sources at $\Phi=53°$ and 67°. In Table I the mass dispersion δ_m, the aberration due to α and Z-direction magnification factor m_z of the image are given for $\Phi=53°$ and 67° assuming that the boundary of the magnetic field is sharp and there is no stray field.

Table I.

	θ \ Φ	53°	67°
δ_m $(\Delta a/a \ll 1)$	10°	$1.75\Delta a$	$1.82\Delta a$
	20°	$2.22\Delta a$	$2.08\Delta a$
$\delta\alpha$ $(\alpha \ll 1)$	10°	$2.05a\alpha$	$1.56a\alpha$
	20°	$2.55a\alpha$	$1.82a\alpha$
m_z		0.73	0.14

§ 3. Apparatus

The mass-spectrometer that was built in this work is shown schematically in Fig. 6.

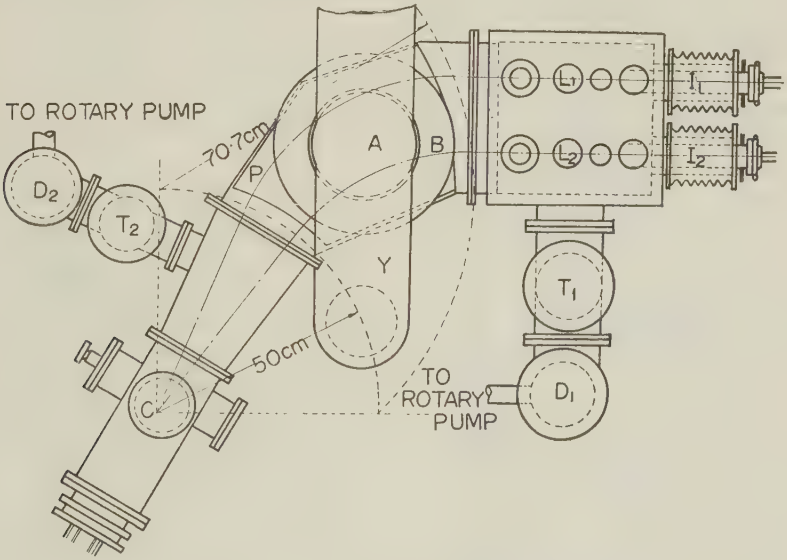

Fig. 6. Schematic diagram of the isotope separator constructed for this work. I_1, I_2: ion source; L_1, L_2: electrostatic lens; Y: yoke; A: core; B: coil; P: pole piece; C: collector; T_1, T_2: liquid air trap; D_1. D_2: diffusion pump.

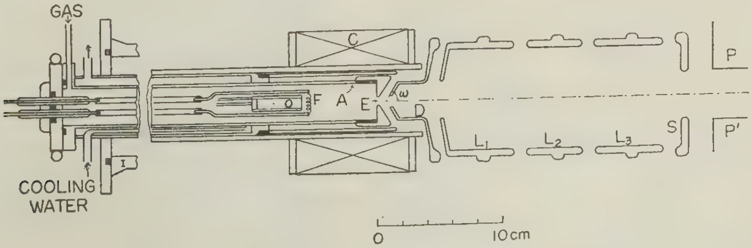

Fig. 7. Schematic diagram of the ion source and the electrostatic lens. I: insulator; O: oven; F: filament; A: anode; E: exit slit; D: draw out electrode; S: electrode for space charge neutralization; L_1, L_2, L_3: electrostatic lens; P, P': pole piece.

Two ion sources are placed 15 cm appart from each other in a casing with openings to a high vacuum pump. Ions are drawn from the plasma of the arc of the ion source by an electric field, and by passing through the electrostatic lens, consisting of three cylinders, a beam of ions is formed. Then the enter the magnetic field where they are deflected by the angle Φ (53° or 67°).

In Fig. 7 the ion source and the electrostatic lens are shown. The ion source is a sort of Finkelstein type. The anode is a copper cylinder, the inside diameter of which is 30 mm. At the end of the anode cylinder a stainless steel diaphragm is mounted which has in the center a hole of 6 mm diameter. From the hole ions are drawn out by an electric field. The filament is a 0.3 mm tungsten wire. When the element to be separated isotopically is a metal, an oven is inserted behind the filament as shown in Fig. 7. The inner wall of the oven is made of molybdenum sheet and the outer wall is an insulator surrounded by tungsten wire as a heater. At the filament side of the oven there is a small hole, of 2 mm diameter, from which metal vapor diffuses to the space where they are ionized by electron impact. Outside of the anode cylinder a coil is mounted which produces an axial magnetic field up to 600 gause in the ionizing space.

The angle ω between the conical surface of the ion draw out electrode and the beam axis, shown in Fig. 7, was determined experimentally so as to produce a high current ion beam with a small divergence. Now we choose $\omega = 60°$ as this angle. The electrostatic lens consists of three stainless steel cylinders, the inside diameter of which is 82 mm. As the diameter of the ion beam in the electrostatic lens is 20–30 mm in this experiment, the spherical aberration of this lens is considered fairly small. At the end of this electrostatic lens near the analyzing magnetic field a diaphram is placed, which has a circular hole of 36 mm diameter at the center. This diaphram is useful for neutralizing the space charge in the ion beam and for protecting the pole face of the magnet from the bombardment of ions. As the ion source and the electrostatic lens have high positive potentials, if there is on potential barrier, electrons in the ion beam escape to the source side, but if a barrier exists which is given by a negative potential supplied to this diaphragm, the electrons are retarded to the collector side, and trapped in the ion beam, compensating the positive space charge in the ion beam.

The radius of the path of ions in the magnetic field is 50 cm. The total weight of the magnet is about 500 kg and the gap between the pole faces is 40 mm. The maximum field is about 2500 gauss which limits practically the number of elements that can be separated with this apparatus. The pole pieces of the magnet are used at the same time as walls of the vacuum chamber.

The collector consists of pockets made of 0.5 mm thick copper sheets, the back side of which is in contact with the brass plate cooled by water as shown in Fig. 8. In front of the collector a shutter is placed. Ion beams are visible clearly at the front of the collector through windows of the collector chamber in two directions; one is vertical and another is horizontal. In practice this is very convenient for adjusting the conditions of the ion source and the electrostatic lens and for watching the intensity and the sharp-

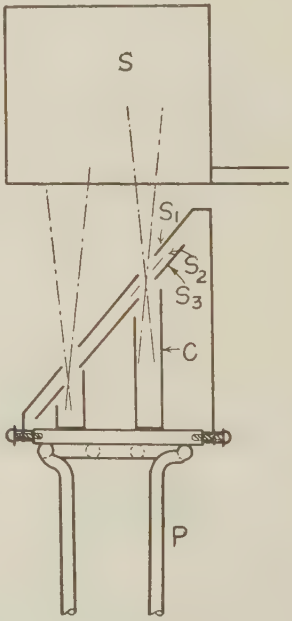

Fig. 8. Collector. S: shutter; S_1: collector cover; S_2: probe for detecting the deviation of the image position; S_3: secondary electron suppressor; C: collector pocket.

ness of the image during a separation run.

Two 6″ oil diffusion pumps are used. One is mounted on the casing of the ion source and another on the chamber placed between the pole chamber and the collector chamber. Liquid air traps are placed between the pumps and the chambers. The effective pumping speed is about 800 liters/sec. The pressure in the vacuum chamber is $(1-3)\times10^{-5}$ mmHg during operation.

The block diagram of the power supply and the control system is shown in Fig. 9. During the process of the adjustment the accelerating voltage is modulated by 60 cycles and the out put current from the collector is driven to the vertical deflection plates of an oscilloscope. A part of the modulated voltage taken from the earth side of the potential divider provides the horizontal deflection. By this device it is possible to observe mass spectra on the oscilloscope screen which gives immediately the information with respect to the sharpness of the image and the beam intensities of all the ions produced in the ion source.

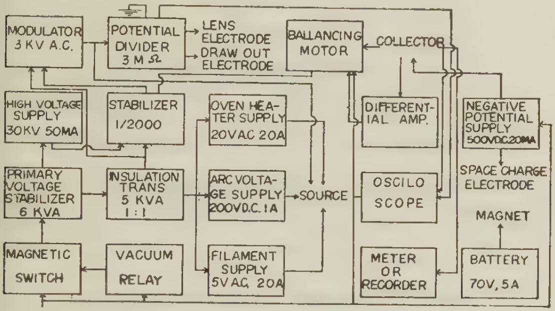

Fig. 9. Block diagram of the power supply and the control system.

During the operation time, a device similar to that used by Zilverschoon et al,6) for an automatic control of the image position was employed in order to compensate for the imperfection of the stabilities of the accelerating voltage and the magnetic field strength.

§ 4. Experimental Results

(1) Ion Source and Eectrostatic Lens

The gas pressure in the ion source 10^{-3}—10^{-4} mmHg. The gas was supplied from the reservoir at the rate of about 4.10^{-3} liters. mmHg/sec. Ion current drawn out of the source decreased exceedingly when the pressure in the source was below 2.10^{-4} mmHg. The optimum magnetic field strength of the source, which was a function of the arc voltage, was between 200 gauss and 500 gaues.

As shown in Fig. 10 the total ion current I_t drawn out of the source, which did not include the current flowing into the ion draw out electrode, increased with the increase of the arc current which was varied by changing filament current. But at some point it reached the maximum, and further increase of the arc current resulted in the decrease of the ion current. This might be caused by the fact that the ion beam diverged with the increase of the arc current and the greater part of the current flowed into the drawing

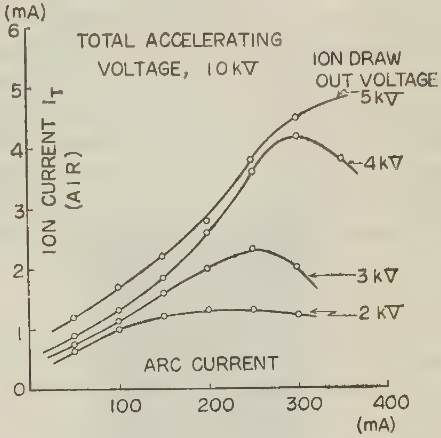

Fig. 10. Total ion current vs. arc current.

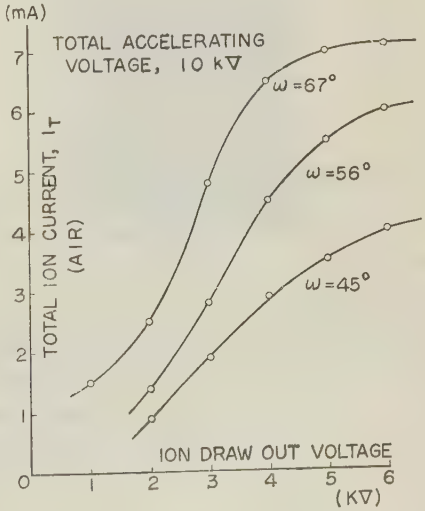

Fig. 11. Total ion current vs. ion draw out voltage.

out electrode. The results shown in Fig. 10 indicate also that the stronger electric field is capable of drawing out the larger ion current within the range of 2–5 kv.

Fig. 11 shows the relation between the total ion draw out voltage for three sorts of angles of the ion draw out electrode which is designated as ω in Fig. 7. The larger ω resulted in higher ion current but in weaker converging action of the ion beam, other conditions being the same. It was desirable to keep the diameter of the ion beam in the electrostatic lens less than one to three times the diameter of the diameter of the electrostatic lens electrode. We chose 60° for ω with a satisfactory result.

Fis. 12 shows the results for the focussing properties of the electrostatic lens. The ion current, which is designated as I_c in Fig. 12, was detected at the Faraday cage about 20 cm distant from the end of the electrostatic lens after passing through the circular slit of 20 mm diameter. Only at optimum conditions of both the lens potential and the ion draw out voltage a shap beam of parallel ions could be formed.

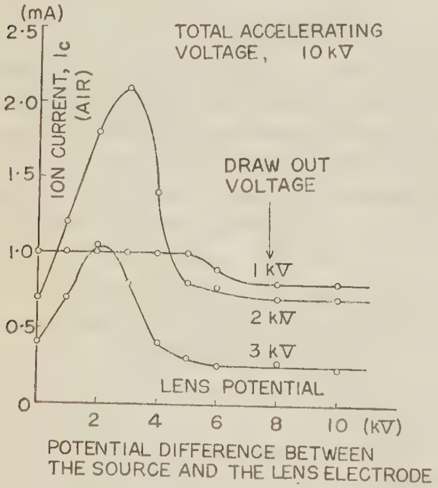

Fig. 12. Variation of ion current with the lens potential.

After adjusting the rats of gass supply, the arc current, the magnetic field of the source, the ion draw out voltage and the lens potential to an optimum condition for producing an intense beam of parallel ions, the accelerating voltage was varied and the ion current I_c was measured in the same way as the case of Fig. 12. The result is shown in Fig. 13. After all, several milliampares of beam current was obtained from our source and lens system. The diameter and the parallelity of the beam could be varied by changing the ion draw out voltage and the lens potential.

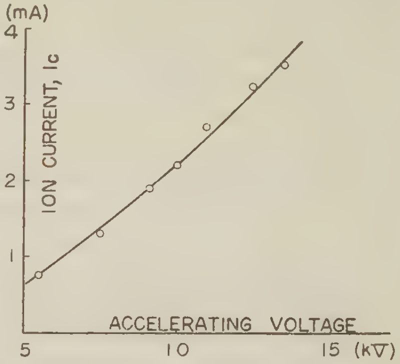

Fig. 13. Ion current vs. accelernting voltage.

(2) Neutralization of Space Change

After these experiments, the sources were mounted on the spectrometer. The image formed at the collector was observed on the oscilloscope screen by the way described previously, or viewed directly through the windows of the collector chamber. At first some tens of microampares of the ion current were obtained at the collector. But increasing the ion current still more resulted in an extremely large divergence of the ion beam due to space charge and therefore in a broadened image.

This result was expected from a rough estimation[3)] of the space charge divergence of the beam by the following relation. Let us consider a beam of parallel ions which has a circular cross section with radius r_0 passing at $Z=0$ and moving into a field free space along the Z axis. After passing through a distance Z, the radius r of the beam gets greater as a result of the mutual repulsion of the ions. The ratio r/r_0 is given by[19)3)]

$$r/r_0 \approx 1.137\cdot 10^{-2}\,(A.J_0^2/E^3)^{1/4}Z \qquad (6)$$

where

A: mass number of ions
E: accelerating voltage in kv
J_0: current density at $Z=0$ in microampare/cm²
Z: distance in cm

This relation has an accuracy of less than 10% in the interval of $1.3 < r/r_0 < 5$.

In Fig. 14 J_0 calculated from Eq. (6) is plotted as a function of A when the accelerating voltage is 10, 20 and 30 kv, Z=100 cm. r/r_0= 1.5. In this experiment an accelerating voltage in the range 10–12 kv was used and length of the path of ions was about 100 cm. And so in the case of ions of neon gas, A=20, it was expected from Fig. 14 to be impossible to obtain an ion current greater than some tens of microampares at the collector as a sharp beam without neutralizing the space charge there.

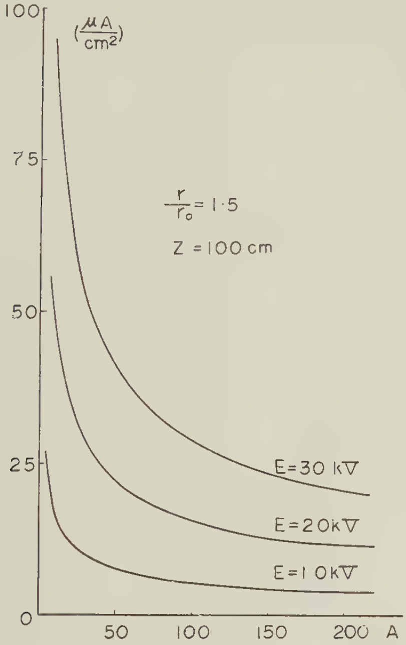

Fig. 14. Space charge divergence of ion beams having circular cross sections.

In order to compensate the space charge of ions by trapping electrons in the ion beam, a negative potential of several hundred volts with respect to the earth was supplied to the diaphram placed at the end of the electrostatic lens system and the potential barrier was prepared to prevent the electrons from escaping into the surce side.

The results were successful and a sharp image was obtained even at several hundred microampares of the collector current. In Fig. 15 are shown photographs of the horizontal view of the neon beam in front of the collector when the negative potential is supplied to the electrode (Fig. 15a) or not (Fig. 15b). The ion current in this case was about 200 microampares for the neon 20 beam, and the ion accelerating voltage was 12 kv. The resolving power was about 60. In Fig. 16 photographs of neon spectra on the oscilloscope screen are shown, taken when the negative potential was varied from 0 volt to −300 volts. When the negative potential increased more than −150 volts, change of

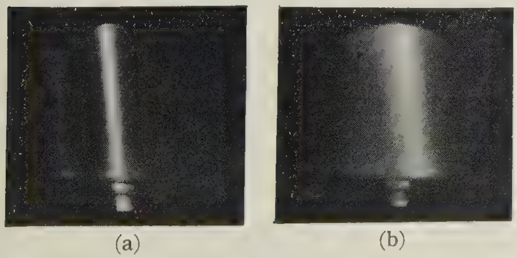
(a) (b)

Fig. 15. Ion beams of neon at the front of the collector. Space change is neutralized (a) and not (b).

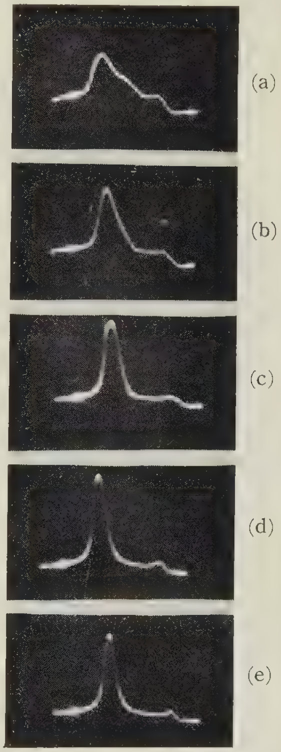

Fig. 16. Photographs of neon spectra on the oscilloscope screen. Negative potential supplied to the electrode for space charge neutralization: (a) 0 V, (b) −50 V, (c) −100 V, (d) −150 V, (e) −300 V; total collector current: 200 μa; accelerating voltage: 12 kV.

the image form was not remarkable. From the comparison of Fig. 15 a and b or Fig. 16 and d, it is obvious that the neutralization effect is important for getting sharp image and intense ion currents in this experiment.

(3) Characteristic of the Collector Current

In Fig. 17 photographs of mass spectra of neon on the oscilloscope screen showing the variation of the image form with change of the arc current and the magnetic field strength of the ion source are shown. It is seen from the comparison of Fig. 17–1 and 17–2 that the increase of the arc current gives image form somewhat similar to that due to the increase of the magnetic field strength. It is supposed that in both cases the change of the image form is mainly due to the deformation of the equipotential surface near the exit hole of the ion source.

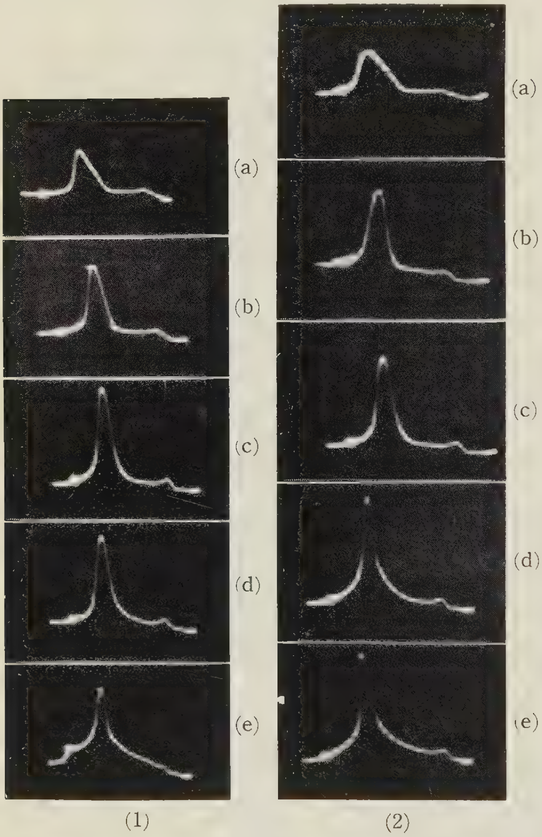

(1) (2)

Fig. 17–1. Variation of the image form with arc current. arc current: (a) 40 ma, (b) 60 ma, (c) 80 ma, (d) 100 ma, (e) 150 ma; arc voltage: 125 V; magnetic field of the source (coil current): 1.0 amp; accelerating voltage: 12 kV; collector current: 200 μa.

Fig. 17–2. Variation of the image form with the magnetic field strength of the source. coil current: (a) 0.8 amp., (b) 0.9 amp., (c) 1.0 amp., (d) 1.1 amp., (e) 1.3 amp.; arc current: 80 ma.; arc voltage: 125 V; accelerating voltage: 12 kV; collector current: 200 μa.

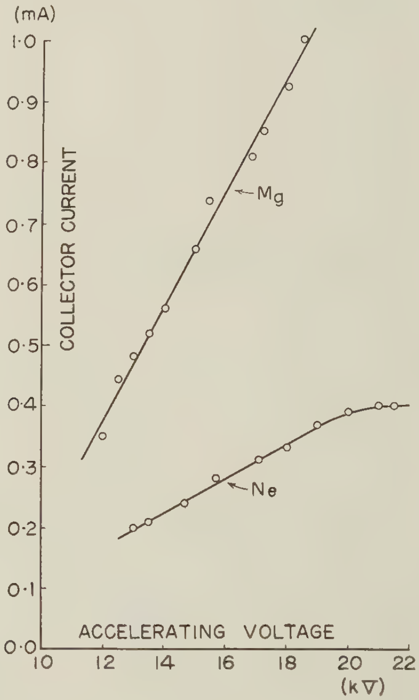

Fig. 18. Collector current vs. accelerating voltage.

The accelerating voltage was raised to about 20 kv and the collector current was measured for neon and magnesium. The results are shown in Fig. 18. Since in the case of magnesium the loss due to scattering by residual gas is smaller than in the case of neon, an ion current two or three times larger is obtained. The maximum collector current obtained from one source was about 1 ma for magnesium and 400 *μa* for neon.

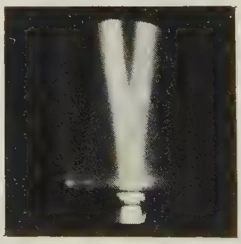

Fig. 19. Neon beams at the front of the collector from two independent sources. ion current (Ne^{20}): 400 μa.

In Fig. 19 is reproduced the photograph of neon beams at the front of the collector showing Ne^{20} beam from two independent sources which are superposed on the collector slit. From the photograph it is possible to determine the focal plane experimentally. The angle θ between the focal plane and the x axis is estimated at 17° by the graphical mathod or by the method of Fig. 2. In this apparatus two sources, which give $\Phi=53°$ and 67° respectively, are used and the experimental results obtained from the photograph give $\theta=25°$ which is somewhat larger than that obtained by the graphical method. In the graphical method or the method of Fig. 2, the boundary of the magnetic field is assumed to be sharp but in practice the radius of the circles of the bounderies are corrected for the fringing field by the length of the pole gap. It is considered that the difference between experimental and graphical θ is mainly due to the imperfection of the correction of the fringing field.

It was observed that the width of the ion beam in the Z-direction at the front of the collector coming from the source of $\Phi=67°$ was smaller than that from the source of $\Phi=53°$, which was reasonable result expected from the Z-direction focussing properties of this magnetic lens discussed in section 2. But no quantitative study on the Z-direction focussing has been carried out as yet.

§ 4. Example of the Separation of Neon and Magnesium

A few experimental separation run will be shown in order to get information for the stability of the instrument.

a. *Neon*

The operating conditions were:

charge material	neon gas
natural abundance	20 90.00% 21 0.27% 22 9.73%
accelerating voltage	15 kV
arc	170 V, 100 ma
source magnetic field	360 gauss
ion draw out voltage	1.5 kV
lens potential	14 kV
negative potential for space charge neutralization	−200 V
pressure in the vacuum chamber	3.10^{-5} mmHg
collector current (total)	200 μa
collector material	0.18 mm thick nickel sheet

The collection method was similar to that of Koch3). After degassing a nickel sheet by high frequency heating in high vacuum at about 800°C, it was mounted in the collector and irradiated to the ion beam for about one hour. Then it was taken out of the collector chamber and set in a small discharge tube as one of the electrodes. The discharge tube was evacuated and sealed off. After these procedures the electrode was heated up to about 800°C. A side tube of the discharge tube was cooled by dry ice and the discharge was started. We could observe the brilliant neon discharge. The volume of the discharge tube was about 10 cc and the neon pressure in the tube was 10^{-1} mmHg. The gas contained in the tube was analyzed by the mass-spectrometer, and the isotopic purities for neon 20 and 22 samples were measured and estimated at 99% and 80% respectively.

b. *Magnesium*

A ribbon of magnesium metal was inserted in the oven which was placed in the anode cylinder of the ion source, and the temperature of the oven was raised gradually up to about 500°C. During this process neon gas was supplied to the ion source as a starting gas and the source was kept at the operating state. When evaporation of magnesium began, the arc current increased suddenly, then the supply of the starting gas was stopped. The operating conditions were:

charge material	metallic magnesium
natural abundance	24 77.4% 25 11.5% 26 11.1%
arc	150 V, 300 ma
source magnetic field	300 gauss
ion draw out voltage	1.2 kV
lens potential	11 kV
negative potential for space charge neutralization	−200 V
pressure in the vacuum chamber	1.10^{-5} mmHg
collector current (total)	300 μa
collector material	0.5 mm thick copper sheet

After a separation run of about 3 hours, the target was taken out of the chamber, and a quantitative chemical analysis was carried out. About 500 micrograms of magnesium 24 were detected from the target. The check of the isotopic purity was not done.

§ 5. Conclusion

A consideration for some properties of the Smythe type magnetic lens was described and a preliminary experiment of the electromagnetic isotope separation was carried out. With an ion exit hole of 6 mm diameter we obtained maximum ion current of the order of 1 ma and the resolving power of about 60 under normal operating condition. In order to get higher resolving power it is necessary to adjust finely the incident direction of ion beams to the magnetic lens, and to move the collector so as to locate it on the actual focal plane. The energy spread of ions drawn out of the source, an imperfection of the alignment of source and lens system, the aberration of the electrostatic lens, a fringing field of the magnetic field, and the scattering of ions by residual gas are considered to have some effects on the broadness of the image, but they were not studied systematically in this experiment.

By increasing the accelerating voltage it is possible to minimize the broadening of the image caused by the energy spread of ions and the scattering by the residual gas. A part of the aberratian of the electrostatic lens may be avoided by an enlargement of the lens diameter. As for the fringing field effect it is necessary to carry out a systematic study.

As shown is Fig. 18 the collector current increases with the increase of the accelerating voltage up to 20 kV. But at about 20 kV it is saturated in the case of neon. This characteristics is similar to a space charge limited current of a diode. The saturation current may be limited mainly by the area of the ion exit hole unless this type of source is employed. It is necessary to use a high enough accelerating voltage to draw out the saturation current and to use as wide an area of the source slit as possible in order to get a high current and to operate an electromagnetic separator most efficiently.

The space charge in the ion beam is compensated successfully by trapping electrons in it and it is considered that the divergence of the ion beam caused by the space charge is no longer a serious obstacle for getting a high current and a sharp image at the collector.

Acknowledgement

The author is indebted to Prof. K. Ogata for his guidance and encouragement throughout this study. The auther wishes to express his gratitude to Prof. T. Hayakawa and Mr. S. Yamashita who kindly carried out the quantitative chemical analysis of the enriched magnesium and to Mr. Y. Kobayashi and Mr. Y. Yoshikawa for their kind help in the mass-spectrometric analysis of the enriched neon gas.

References

1) W. R. Smythe, L. H. Rumbaugh and S. S. West: Phys. Rev. **45** (1934) 724.
2) W. Walcher: Zeit. f. Phys. **108** (1938) 376.
3) J. Koch and B. Bendt-Nielsen: Kgl. Danske Vid. Sels. Mat-fys. Medd. **21** No. 8 (1944); Phys. Rev. **69** (1946) 238; Nature **160** (1947) 498; **161** (1948) 566; **162** (1948) 695; **164** (1949) 19.
4) I. Bergström, S. Thulin, N. Svartholm and K. Siegbahn: Ark. f. Fys. **1** (1949) 281.
5) R. Bernas: J. de Phys. **14** (1953) 34.
6) J. Kistemaker and J. Zilverschoon: N. B. S. Circular **522** (1953) 179.
C. J. Zilverschoon: An Electromagnetic Isotope Separator, Thesis. Univ. Amsterdam (1954) 98.
7) C. P. Keim: J. Appl. Phys. **24** (1953) 1255.
8) R. H. V. M. Dawton and M. L. Smith: Quarterly Review **9** (1955) 1.
9) F. K. Herzog: Acta Phyica Austriaca **4** (1951) 431.
10) E. E. Watson: Phil. Mag. **3** (1927) 849.

JOURNAL OF THE PHYSICAL SOCIETY OF JAPAN Vol. 12, No. 4, APRIL, 1957

On the Transonic Flow of a Compressible Fluid Past an Axisymmetric Slender Body at Zero Incidence

By Ken-ichi KUSUKAWA

Department of Physics, Faculty of Science, Tokyo Metropolitan University

(Received November 20, 1956)

The high subsonic flow past a slender body of revolution placed along the axis of a circular cylindrical wind tunnel at zero incidence is discussed. Neglecting the square of the perturbation velocity q'^2 in comparison with q' and the spatial derivatives of q'^2, making use of a certain transformation of variables, the fundamental equation for determining the perturbation stream function of this transonic flow can be reduced to the equation which is formally equal to the fundamental equation of transonic flow past a two-dimensional body placed along the center line between two parallel flat walls. Considering the transonic similar solution due to von Kármán and the general similarity rule of the axisymmetric transonic flow derived by Oswatisch and Berndt, we can obtain very easily the surface pressure coefficient C_{pax} of an axisymmetric flow, provided the surface pressure coefficient C_{p2} of a two-dimensional flow can be found.

As an example the pressure distribution on the surface of a paraboloid of revolution of finite length at Mach number 1 is obtained.

§ 1. Introduction

As is well known, the so-called linearized theory cannot be applied to the transonic flow of a compressible fluid, because the non-linear term in the fundamental equation becomes to contribute essentially to the character of the solution in the vicinity of the sonic point. In this case it is necessary to consider the fundamental equation of the transonic approximation due originally to von Kármán[1]. While the fundamental equation of the transonic flow in two dimensions can be reduced to a simple linear equation (so-called Tricomi's equation) in the hodograph plane, that of the axisymmetric transonic flow remains non-linear in the hodograph space as well as in the physical space. Owing to this reason there have been few examples of the axisymmetric flow treated by this transonic approximation: the discussion of the singularity of a particular solution at infinity,[2] the flow past a slender cone-cylinder[3] studied by the relaxation method, etc....

In this paper the fundamental equation is represented in a form for determining the perturbation stream function ψ instead of the perturbation velocity potential φ. Considering the fact that at the sonic point the square of the perturbation velocity q'^2 takes a minimum value which is zero and that the spatial derivative of q' may take a finite value where q' vanishes, we may neglect q'^2 in comparison with q' and the spatial derivatives of q'^2. Thus the fundamental equation for determining ψ can be reduced to an equation which is formally equal to the fundamental equation of transonic flow in two-dimensions. Considering the relation between the boundaries of axisymmetric and two-dimensional flows, the transonic similar solution due to von Kármán[1], and the general similarity rule due to Oswatisch and Berndt[4], we can obtain very easily the velocity distribution on the surface of an axisymmetric slender body, provided the velocity distribution on the surface of a corresponding two-dimensional symmetric body is known. The latter can be found, in principle, by solving Tricomi's differential equation.

As an example, we investigate the velocity distribution at Mach number 1 on the surface of a paraboloid of revolution of finite length.

§ 2. Fundamental Equations

We now consider the high subsonic flow past a slender body of revolution which is placed along the centre line (axis) of a circular cylindrical wind tunnel at zero incidence. We shall take the cylindrical coordinates o-xy, where the x-axis is taken along the axis of revolution of the body and y denotes the distance from the axis. If we denote by u, v, the velocity components along the x- and y- directions and by ρ the density of the fluid, the axisymmetric irrotational flow of a compressible inviscid fluid is governed by the equations:

$$\frac{\partial}{\partial x}(\rho y u)+\frac{\partial}{\partial y}(\rho y v)=0\,, \tag{2.1}$$

$$\frac{\partial v}{\partial x}-\frac{\partial u}{\partial y}=0\,. \tag{2.2}$$

We shall introduce Stokes's stream function Ψ satisfying (2.1) such that

$$\rho y u=\partial\Psi/\partial y,\quad \rho y v=-\partial\Psi/\partial x\,, \tag{2.3}$$

then using Bernoulli's equation

$$(a^2/\rho)d\rho+q\,dq=0\,, \tag{2.4}$$

where $a=(dp/d\rho)^{1/2}$ is the local speed of sound and q is the magnitude of the velocity, Eq. (2.2) bocomes

$$\begin{aligned}(1-u^2/a^2)\Psi_{xx}-2(uv/a^2)\Psi_{xy}\\ +(1-v^2/a^2)\Psi_{yy}-\Psi_y/y=0.\end{aligned} \tag{2.5}$$

Instead of the velocity components u, v, we shall make use of the magnitude q and the angle of inclination θ of the velocity vector such that

$$u=q\cos\theta,\quad v=q\sin\theta\,.$$

For a slender obstacle we may assume that θ is very small, so that Eqs. (2.3) and (2.5) can be respectively approximated to

$$\rho y q=\partial\Psi/\partial y,\quad \rho y q\theta=-\partial\Psi/\partial x\,, \tag{2.6}$$

$$(1-q^2/a^2)\frac{\partial^2\Psi}{\partial x^2}+\frac{\partial^2\Psi}{\partial y^2}-\frac{1}{y}\frac{\partial\Psi}{\partial y}=0\,. \tag{2.7}$$

Since we deal with the transonic flow in the present paper, the perturbation analysis may be carried out as follows. Taking conveniently the magnitude q of the flow velocity and the density ρ of the fluid at the sonic point as their units, the magnitude of the perturbation velocity q', the perturbation density ρ' and the perturbation stream function ψ are defined as

$$q'=q-1,\quad \rho'=\rho-1,\quad \psi=\Psi-y^2/2\,. \tag{2.8}$$

Neglecting higher order terms, we obtain the following relations

$$\rho q=1-\Gamma q'^2,\quad 1-q^2/a^2=-2\Gamma q' \tag{2.9}$$

where $\Gamma=(\gamma+1)/2$, γ being the ratio of the specific heats. By the use of Eqs. (2.8) and (2.9), the equations (2.6) and (2.7) become respectively

$$-\Gamma q'^2=\frac{1}{y}\frac{\partial\psi}{\partial y},\quad \theta=-\frac{1}{y}\frac{\partial\psi}{\partial x}\,, \tag{2.10}$$

$$\pm 2\sqrt{\Gamma}\sqrt{-\frac{1}{y}\frac{\partial\psi}{\partial y}}\frac{\partial^2\psi}{\partial x^2}+\frac{\partial^2\psi}{\partial y^2}-\frac{1}{y}\frac{\partial\psi}{\partial y}=0\,, \tag{2.11}$$

where the positive and negative signs refer respectively to the sub- and the supersonic local velocities.

Now, at infinity upstream the velocity is equal to the uniform velocity U, and on the surface of the obtacle and the tunnel wall the gas must flow tangentially along the surfaces. Thus the perturbation stream function must satisfy the following conditions:

$$\left.\begin{aligned}\frac{1}{y}\frac{\partial\psi}{\partial y}&=-\Gamma(1-U)^2\\ \frac{\partial\psi}{\partial x}&=0\end{aligned}\right\}\ \text{at}\quad x=-\infty\,, \tag{2.12}$$

$$\psi+\frac{y^2}{2}=\Psi=0 \tag{2.13}$$

on the surface of the obstacle,

$$\frac{\partial\psi}{\partial x}=0\qquad\text{at } y=L\,, \tag{2.14}$$

where L denotes the radius of the wind tunnel. In the extreme case, where $1/L$ tends to zero, the obstacle can be considered to be placed in an unbounded uniform flow.

§ 3. Transformation of Variables

Introducing the following transformation of the variables:

$$x=l\xi,\quad \frac{3}{2}y^{2/3}=k\eta,\quad \psi=k^{-3}\omega(\xi,\,\eta), \tag{3.1}$$

where l and k are constants Eq. (2.11) is transformed to

$$\pm 2\sqrt{\Gamma_1}\sqrt{-\frac{\partial\omega}{\partial\eta}}\frac{\partial^2\omega}{\partial\xi^2}+\frac{\partial^2\omega}{\partial\eta^2}+\frac{8}{9}k^6\Gamma q'^2\eta=0\,, \tag{3.2}$$

in which

$$\sqrt{\Gamma_1}=\sqrt{\Gamma}/l^2\,. \tag{3.3}$$

The boundary conditions (2.12), (2.13) and (2.14) are respectively transformed to

$$\left.\begin{aligned}\frac{9}{4}k^{-6}\eta^{-2}\frac{\partial\omega}{\partial\eta}&=-\Gamma(1-U)^2\\ \frac{\partial\omega}{\partial\xi}&=0\end{aligned}\right\}\ \text{at}\ \xi=-\infty\,, \tag{3.4}$$

$$\frac{4}{27}k^6\eta^3+\omega=0\quad\text{on curve C, say,} \tag{3.5}$$

$$\frac{\partial\omega}{\partial\xi}=0 \quad \text{at} \quad \eta=L_1, \tag{3.6}$$

where the curve C in the ξ,η-plane should correspond to the meridian curve of the body of revolution, and

$$L_1=\frac{3}{2k}L^{2/3} \tag{3.7}$$

§ 4. Approximate Solution of Eq. (3.2)

The solutions of Eq. (3.2) subject to the boundary conditions (3.4) at infinity upstream must take the following form:

$$\lim_{\xi\to-\infty}\omega=-\frac{4}{27}k^6\Gamma(1-U)^2\eta^3\,. \tag{4.1}$$

We now discuss the orders of magnitude of various terms in Eq. (3.2). In the first term $\sqrt{-\partial\omega/\partial\eta}$ is of the order of $\eta q'$, and the second term is of the order of $\partial(\eta^2 q'^2)/\partial\eta$. At the sonic point the square of the perturbation velocity q'^2 takes a minimum value which is equal to zero. On the other hand the spatial derivative of q' may take a finite value where q' vanishes. Therefore q'^2 can be neglected in comparison with q' and the spatial derivatives of q'^2. Thus the last term in Eq. (3.2) can be safely neglected in comparison with other terms except at a great distance from the obstacle, where the solution must take the form (4.1), and therefore the last term becomes larger than the first. Consequently, except at a great distance from the obstacle, Eq. (3.2) can be approximated to

$$\pm2\sqrt{\Gamma_1}\sqrt{-\frac{\partial\omega_1}{\partial\eta}}\frac{\partial^2\omega_1}{\partial\xi^2}+\frac{\partial^2\omega_1}{\partial\eta^2}=0\,, \tag{4.2}$$

where ω_1 represents ω to this approximation. If we suppose that ω_1 satisfies the following boundary conditions:

$$\left.\begin{aligned}&\frac{\partial\omega_1}{\partial\eta}=-\Gamma_1(1-U_1)^2\\&\frac{\partial\omega_1}{\partial\xi}=0\end{aligned}\right\}\quad \text{at} \quad \xi=-\infty\,, \tag{4.3}$$

$$\frac{4}{27}k^6\eta^3+\omega_1=0 \qquad \text{on curve C,} \tag{4.4}$$

$$\frac{\partial\omega_1}{\partial\xi}=0 \quad \text{at} \quad \eta=L_1\,, \tag{4.5}$$

where Γ_1 and L_1 were defined in Eqs. (3.3) and (3.7), and U_1 denotes an undetermined constant, the function

$$\omega^*=\omega_1+\Gamma_1(1-U_1)^2\eta-(4/27)k^6\Gamma(1-U)^2\eta^3$$

has the character of the solution at infinity expressed by Eq. (4.1). Considering the condition (4.5), it can be readily seen that the function ω^* satisfies the boundary condition (3.6) at the wall of the wind tunnel.

As mentioned above, Eq. (3.2) can be approximated by Eq. (4.2) near the obstacle, and their solution ω and ω_1 satisfy the same boundary conditions (3.5) and (4.4) respectively at the obstacle. Thus the solution ω can be approximately replaced by ω_1, and so by ω^*, if the following conditions can be satisfied near the obstacle:

$$\left|\frac{\partial\omega_2}{\partial\eta}\right|\ll\left|\frac{\partial\omega_1}{\partial\eta}\right|,\qquad \left|\frac{\partial^2\omega_2}{\partial\eta^2}\right|\ll\left|\frac{\partial^2\omega_1}{\partial\eta^2}\right|, \tag{4.6}$$

where

$$\omega_2=\Gamma_1(1-U_1)^2\eta-(4/27)k^6\Gamma(1-U)^2\eta^3\,.$$

It will be seen in consideration of Eq. (4.4) that ω_2 is of the order of $(1-U)^2\omega_1$ on the obstacle. Neglecting the terms of the order of $(1-U)^2$ and $(1-U_1)^2$, the conditions (4.6) are satisfied except at the sonic point, where

$$q'^2=(9/4)k^{-6}\eta^{-2}(\partial\omega/\partial\eta)\doteqdot(9/4)k^{-6}\eta^{-2}(\partial\omega_1/\partial\eta)$$

vanishes, but $(\partial\omega_2/\partial\eta)$ may take a finite value. To satisfy the relations (4.6) at the vicinity of the sonic point, we must add the following conditions:

$$\partial\omega_2/\partial\eta=\Gamma_1(1-U_1)^2-(4/9)k^6\Gamma(1-U)^2\eta^2=0$$
$$\text{at} \quad \eta=\eta_s \tag{4.7}$$

where η_s denotes the sonic point on the surface of the obstacle.

Especially, when the obstacle has a sharp shoulder at the point of maximum thickness, the velocity of fluid attains the local sound velocity at this point: $\eta_s=c\tau$, where c and τ denote the chord length and the half thickness ratio of the obstacle respectively. Thus in this case Eq. (4.7) can be expressed in the following form:

$$\begin{aligned}(1-M_1)^2/\Gamma_1&=\frac{4}{9}k^6c^2\tau^2(1-M)^2/\Gamma\\&=\frac{4}{9}k^6\tau^2\left(\frac{\Gamma_1}{\Gamma}\right)^{1/2}(1-M)^2/\Gamma\,,\end{aligned} \tag{4.8}$$

or

$$(1-M)=(3/2)\Gamma^{3/4}(1-M_1)/(k^3\tau\Gamma_1^{3/4})$$

where

$$1-M=\Gamma(1-U) \text{ and } 1-M_1=\Gamma_1(1-U_1)\,.$$

By this equation (4.8) the arbitrary constant U_1 is determined.

§ 5. Corresponding Two-dimensional Fluid Flow

Now we shall consider the two-dimensional symmetric transonic flow past a thin obstacle which is placed along a centre line between two parallel flat walls. Taking the cartesian coordinates o-$\xi\eta$, where the ξ-axis is taken along the axis of symmetry of the obstacle, the two-dimensional nearly parallel flow of a compressible fluid is governed by

$$(1-Q^2/a^2)\frac{\partial^2\Omega}{\partial\xi^2}+\frac{\partial^2\Omega}{\partial\eta^2}=0\,, \tag{5.1}$$

where Q and a denote the magnitude of the two-dimensional flow velocity and the local speed of sound respectively, and Ω is the stream function satisfying the following relations:

$$\rho Q=\partial\Omega/\partial\eta\,,\quad \rho Q\Theta=-\partial\Omega/\partial\xi \tag{5.2}$$

in which Θ is the angle of inclination of the velocity.

As in the axisymmetric case, taking the magnitude of the flow velocity and the density ρ of the fluid at the sonic point as their units conveniently, the magnitude Q' of the perturbation velocity, the perturbation density ρ' and the perturbation stream function Ω, are defined as follows,

$$Q'=Q-1,\quad \rho'=\rho-1,\quad \Omega_1=\Omega-\eta\,. \tag{5.3}$$

Neglecting higher order term, Eqs. (5.1) and (5.2) become respectively

$$\pm2\sqrt{\Gamma^*}\sqrt{-\frac{\partial\Omega_1}{\partial\eta}}\,\frac{\partial^2\Omega_1}{\partial\xi^2}+\frac{\partial^2\Omega_1}{\partial\eta^2}=0\,, \tag{5.4}$$

$$-\Gamma^*Q'^2=\frac{\partial\Omega_1}{\partial\eta}\,,\quad -\Theta=\frac{\partial\Omega_1}{\partial\xi}\,, \tag{5.5}$$

where $\Gamma^*=(\gamma^*+1)/2$, and γ^* denotes the ratio of specific heats of a gas considered here.

Since Eq. (5.4) is formally equal to Eq. (4.2), the solution of Eq. (4.2) subject to the boundary conditions (4.3), (4.4) and (4.5) can be recognized to be the perturbation stream function of the two-dimensional symmetric transonic flow of an imaginary gas, the ratio of the specific heats of which is determined by Eq. (3.3).

The condition (4.3) means that this two-dimensional flow has a uniform velocity U_1 at infinity upstream. While the boundary condition (4.5) is readily recognized to be the condition at the two parallel flat walls a distance $2L_1$ apart, the boundary condition (4.4) at the obstacle represents that the curve C cannot be the surface of an obstacle in the two-dimensional fluid flow, because the gas does not flow tangentially along the curve C but crosses it. (In fact, the condition that the gas flows tangentially along the curve C should be expressed by $\eta+\omega_1=0$.)

Instead of the boundary curve C, we shall consider a symmetric curve C_1 on which the following condition is satisfied:

$$\left(\frac{d\eta}{d\xi}\right)_{c_1}=\pm\tau h(\xi_1)\,, \tag{5.6}$$

where ξ_1 denotes ξ/c, and c is the chord length of the obstacle. Remembering the transformation (3.1), the corresponding chord length in the xy-plane is cl. If this chord length in the xy-plane is conveniently taken to be unity, we obtain

$$\left.\begin{aligned} c&=1/l\\ \text{and}\quad x&=\xi_1\end{aligned}\right\} \tag{5.7}$$

Integrating Eq. (5.6), we obtain

$$\eta_{c_1}=c\tau H(\xi_1)\qquad\text{on curve } C_1 \tag{5.8}$$

with

$$H(\xi_1)=\int_0^{\xi_1}h(\xi_1)$$

where τ denotes the half thickness ratio $\eta_{\max}/c$, and then the maximum value of the given function $H(\xi_1)$ becomes unity.

Instead of the boundary condition (4.4) on the curve C, we shall take the following one on the curve C_1 such that

$$\left(\frac{\partial\omega_1}{\partial\xi}\right)_{c_1}=-\Theta=-(\tau^m\Gamma_1{}^n)\tau h(\xi_1)\ \text{on}\ C_1 \tag{5.9}$$

where m and n denote certain constants. This condition (5.9) also represents that the gas does not flow tangentially along the curve C_1 except when both m and n vanish.

In the flow pattern given by the solution of Eq. (4.2) subject to the boundary conditions (4.3), (4.5) and (5.9), we shall find the form of the curve C on which the condition (4.4) is satisfied. From Eq. (4.4), we obtain

$$\begin{aligned}\left(\frac{d\eta}{d\xi}\right)_c&=\left\{-\frac{\partial\omega_1}{\partial\xi}\Big/\left(\frac{4}{9}k^6\eta^2+\frac{\partial\omega_1}{\partial\eta}\right)\right\}_c\\ &=\left\{-\frac{\partial\omega_1}{\partial\xi}\Big/\frac{4}{9}k^6\eta^2(1-\Gamma q'^2)\right\}_c\\ &\qquad\qquad\text{on curve C}\end{aligned} \tag{5.10}$$

As the order of q'^2 can be safely neglected, Eq. (5.10) is reduced to

$$\left(\eta^2\frac{d\eta}{d\xi}\right)_c=-\frac{9}{4k^6}\left(\frac{\partial\omega_1}{\partial\xi}\right)_c \quad \text{on curve C} \qquad (5.11)$$

If both the thickness ratios of the curves C and C$_1$ are very small, we may assume in the first approximation that at the two points having the same abscissa on the curves C and C$_1$, the values of $\partial\omega_1/\partial\xi$ will take almost the same values. Thus putting

$$\left(\frac{\partial\omega_1}{\partial\xi}\right)_c\doteqdot\left(\frac{\partial\omega_1}{\partial\xi}\right)_{c_1}\equiv-(\tau^m\Gamma_1{}^n)\tau h(\xi_1)\,, \qquad (5.12)$$

Eq. (5.11) becomes

$$\left(\eta^2\frac{d\eta}{d\xi}\right)_c=\frac{9}{4k^6}(\tau^m\Gamma_1{}^n)\tau h(\xi_1) \quad \text{on C} \qquad (5.13)$$

Integrating this equation, we obtain

$$\eta^3=\frac{27}{4k^6}(\tau^m\Gamma_1{}^n)c\tau H(\xi_1) \quad \text{on C} \qquad (5.14)$$

where

$$H(\xi_1)=\int_0^{\xi_1}h(\xi_1)d\xi_1$$

In compliance with Eq. (5.12), we shall take the thickness ratio of the curve C to be equal to that of the curve C$_1$, then

$$\frac{27}{4k^6}(\tau^m\Gamma_1{}^n)\tau c=c^3\tau^3 \quad \text{where } c=1/l\doteqdot(\Gamma_1/\Gamma)^{1/4},$$

and therefore the value of k can be determined as a function of τ, Γ_1 and Γ such that

$$k^6=(27/4)\tau^{m-2}\Gamma_1{}^{n-1/2}\Gamma^{1/2}\,, \qquad (5.15)$$

Then Eq. (5.14) becomes

$$\eta_c=c\tau H^{1/3}(\xi_1)\,. \quad \text{on C} \qquad (5.16)$$

Thus it is seen that the solution of Eq. (4.2) subject to the boundary conditions (4.3), (4.5) and (5.9) also satisfies the condition (4.4) on the curve C, which is represented by Eq. (5.16).

By the use of the transformation (3.1), we can find the meridian curve of the obstacle, which is corresponding to the curve C in the $\xi\eta$-plane, such that

$$y=tH^{1/2}(x) \qquad (5.17)$$

with

$$t=\sqrt{8/27}k^{3/2}c^{3/2}\tau^{3/2}=(2/\sqrt[4]{27})\tau^{1+m/4}\Gamma_1{}^{1/4+n/4}\Gamma^{-1/4}\,, \qquad (5.18)$$

where t denotes the half thickness ratio of this obstacle.

From the same transformation (3.1), we obtain the magnitude q' of the perturbation velocity on the surface of the obstacle:

$$q'=k^{-2}(\Gamma_1/\Gamma)^{1/2}Q_c'/y_c{}^{2/3}\,, \qquad (5.19)$$

where the sufix c represents the quantities on the curve C. By the use of Eqs. (5.17) and (5.7), we obtain

$$y_c=tH^{1/2}(x)=tH^{1/2}(\xi_1)\,. \qquad (5.20)$$

As both the curves C and C$_1$ in the $\xi\eta$-plane have the same thickness ratio, $Q_c'(\xi)$ can be approximately obtained in the following form:

$$Q_c'(\xi)\doteqdot Q_{c_1}'(\xi)+(\partial Q_c'/\partial\eta)(\eta_c-\eta_{c_1})\,. \qquad (5.21)$$

As the flow is irrotational, we obtain the relation

$$\frac{\partial Q_{c_1}'}{\partial\eta}=\frac{\partial\Theta_c}{\partial\xi}\cdot \qquad (5.22)$$

Remembering the boundary condition (5.9), we obtain

$$\partial\Theta_{c_1}/\partial\xi=(\tau^m\Gamma_1{}^n)(\tau/c)h'(\xi_1)\,. \qquad (5.23)$$

Substituting (5.8), (5.16) and (5.23) into (5.21), we obtain

$$Q_c'(\xi)=Q_{c_1}'(\xi)+\tau^{m+2}\Gamma_1{}^nh'(\xi_1)\{H^{1/3}(\xi_1)-H(\xi_1)\} \qquad (5.24)$$

Substitution of Eqs. (5.24) and (5.20) into Eq. (5.19) yields

$$\begin{aligned}q_c'=(1/\sqrt{3})\tau^{-m/2}\Gamma_1{}^{1/2-n/2}\Gamma^{-1/2}[Q_{c_1}'(\xi_1)\\+\tau^{2+m}\Gamma_1{}^nh'(\xi_1)\{H^{1/3}(\xi_1)-H(\xi_1)\}]H^{-1/3}(\xi_1),\end{aligned} \qquad (5.25)$$

where

$$x=\xi_1\,.$$

If the values of constants m and n are determined, we can find the perturbation velocity of the transonic axisymmetric fluid flow on the surface of a obstacle whose meridian curve is represented by Eq. (5.17), provided the perturbation velocity Q' of the corresponding two-dimensional transonic fluid flow can be known.

The character of the singularity at infinity in the transonic axisymmetric fluid flow is essentially different from that in the transonic two-dimensional fluid flow. This is represented as the difference between the transonic similarity laws' in both cases: The perturbation velocities q' and Q' of the axisymmetric and of the two-dimensional transonic fluid flows, which are connected by the relation (5.25), must satisfy respectively their own "transonic similarity laws", and by this fact we shall obtain the formulae for determining the constants m and n.

§ 6. Transonic Similarity Law

We shall consider again the two-dimensional transonic fluid flow which was discussed in § 5. Taking ω_1 in Eq. (4.2) as the perturbation stream function Ω_1 of the two-dimensional transonic flow, the fluid flow should be governed by Eq. (4.2). The boundary conditions are given by Eqs. (4.3), (4.5) and (5.9). Since the half thickness ratio τ of the curve C_1 is considered to be very small, the boundary condition (5.9) can be assumed to be satisfied on the ξ-axis within the accuracy considered here. Therefore, instead of Eq. (5.9) we can use

$$\frac{\partial\omega_1}{\partial\xi}=-\Theta=-(\tau^m\Gamma_1{}^n)\tau h(\xi_1) \text{ at } \eta=\pm 0\,. \quad (6.1)$$

Introducing the following affin transformation:

$$\left.\begin{aligned}&\xi=c\xi_1\,,\quad \eta=c\tau^{-p}\Gamma_1{}^{-q}\eta_1\,,\\&\omega_1=(c\Gamma_1{}^{-1})\tau^{-p}\Gamma_1{}^{-q}(1-M_1)^2F(\xi_1,\eta_1),\end{aligned}\right\} \quad (6.2)$$

where M_1 and c denote respectively the Mach number of the flow at infinity and the chord length of the curve C_1 and p, and q are certain constants, Eq. (4.2) becomes

$$\pm 2\frac{|1-M_1|}{\tau^{2p}\Gamma_1{}^{2q}}\sqrt{-\frac{\partial F}{\partial\eta_1}}\frac{\partial^2F}{\partial\xi_1{}^2}+\frac{\partial^2F}{\partial\eta_1{}^2}=0\,, \quad (6.3)$$

and the boundary conditions (4.3), (4.5) and (6.1) respectively become

$$\frac{\partial F}{\partial\eta_1}=-1,\quad \frac{\partial F}{\partial\xi_1}=0,\quad \text{at } \xi_1=-\infty, \quad (6.4)$$

$$\frac{\partial F}{\partial\xi_1}=0 \quad \text{at } \eta_1=L_1\tau^p\Gamma_1{}^q/c \quad (6.5)$$

and

$$\frac{\partial F}{\partial\xi_1}=-\frac{\tau^{m+p+1}\Gamma_1{}^{n+q+1}}{(1-M_1)^2}h(\xi_1) \quad \text{at } \eta_1=\pm 0. \quad (6.6)$$

The dependence of the preceding equations on τ, Γ_1 and M_1, can be eliminated by setting

$$\frac{1-M_1}{\tau^{2p}\Gamma_1{}^{2q}}=K_1\,, \quad (6.7)$$

$$\frac{\tau^{m+p+1}\Gamma_1{}^{n+q+1}}{(1-M_1)^2}=K'\,, \quad (6.8)$$

where K_1 and K' are constants. Eliminating $(1-M_1)$ from Eqs. (6.7) and (6.8), we obtain

$$K'K_1{}^2=\frac{\tau^{m+p+1}\Gamma_1{}^{n+q+1}}{\tau^{4p}\Gamma_1{}^{4q}}\,, \quad (6.9)$$

which shows that these equations hold for arbitrary values of τ, Γ_1 and M_1 only if

$$p=\frac{m+1}{3},\quad q=\frac{n+1}{3}, \quad (6.10)$$

in which case

$$K_1=(1-M_1)\tau^{-(2/3)(m+1)}\Gamma_1{}^{-(2/3)(n+1)}\,, \quad (6.11)$$

and

$$K'=\frac{1}{K_1{}^2}\,. \quad (6.12)$$

Substituting

$$f_1(\xi_1,\ \eta_1)=K_1{}^2F(\xi_1,\ \eta_1)\,, \quad (6.13)$$

Eq. (6.3) becomes

$$\pm 2\sqrt{-\frac{\partial f_1}{\partial\eta_1}}\frac{\partial^2 f_1}{\partial\xi_1{}^2}+\frac{\partial^2 f_1}{\partial\eta_1{}^2}=0\,, \quad (6.14)$$

and the boundary conditions (6.4), (6.5) and (6.6) respectively become

$$\frac{\partial f_1}{\partial\eta_1}=-K_1{}^2,\quad \frac{\partial f_1}{\partial\xi_1}=0 \quad \text{at } \xi_1=-\infty\,, \quad (6.15)$$

$$\frac{\partial f_1}{\partial\xi_1}=0 \quad \text{at } \eta_1=L_1\tau^p\Gamma_1{}^q/c\,, \quad (6.16)$$

$$\frac{\partial f_1}{\partial\xi_1}=-h(\xi_1) \quad \text{at } \eta=\pm 0 \quad (6.17)$$

The equation (6.14) and the boundary conditions (6.15) and (6.17), except for (6.16) depend merely on K_1. If the distance $2L_1$ between the two parallel walls can be expressed as a function of K_1 such that

$$L_1\tau^p\Gamma_1{}^q/c=\lambda_1(K_1)\,, \quad (6.18)$$

the value of $\lim\limits_{\eta\to 0}(\partial f_1/\partial\eta_1)$ should depend on ξ_1 and K_1 for given functional forms of $h(\xi_1)$ and $\lambda_1(K_1)$. Therefore putting

$$\lim_{\eta_1\to 0}(\partial f_1/\partial\eta_1)=-\Phi(\xi_1,\ K_1)\,,$$

from Eq. (5.5), we obtain the perturbation velocity at $\eta=0$ such that

$$\begin{aligned}Q'^2&=-\frac{1}{\Gamma_1}\left(\frac{\partial\omega_1}{\partial\eta}\right)=-\frac{(1-M_1)^2}{\Gamma_1{}^2}\frac{\partial F}{\partial\eta_1}\\&=\frac{-(1-M_1)^2}{\Gamma_1{}^2K^2}\frac{\partial f_1}{\partial\eta_1}=\frac{(1-M_1)^2}{\Gamma_1{}^2K^2}\Phi(\xi_1,\ K_1),\end{aligned}$$

or

$$\begin{aligned}Q'&=\pm\frac{|1-M_1|}{\Gamma_1K_1}\sqrt{\Phi(\xi_1,\ K_1)}\\&=\pm\tau^{(2/3)\cdot(m+1)}\Gamma_1{}^{(1/3)\cdot(2n-1)}\sqrt{\Phi(\xi_1,\ K_1)}\,. \quad (6.19)\end{aligned}$$

where the negative and positive signs refer to the sub- and the supersonic regions respectively.

In a special case for $m=n=0$, Eq. (6.19) becomes

$$Q'=\pm\tau^{2/3}\Gamma_1{}^{-1/3}\sqrt{\Phi(\xi_1,\ K_1)}\,, \quad (6.20)$$

and the boundary condition (6.1) can be reduced to

$$(\partial\omega_1/\partial\xi)_{c_1}=-\Theta=\tau h(\xi_1) \quad \text{at } \eta=\pm 0\,, \qquad (6.21)$$

which represents that the gas flows along the curve C_1. This result represents von Kármán's two-dimensional transonic similarity law[1]. Substituting Eq. (6.19) into Eq. (5.25), we obtain the magnitude q' of the perturbation velocity of transonic axisymmetric fluid flow on the surface of the body of revolution as

$$\begin{aligned} q' = \mp & \frac{1}{\sqrt{3}}\tau^{2/3+m/6}\Gamma_1^{1/6+n/6} \\ & \times\Gamma^{-1/2}\sqrt{\Phi(\xi_1, K_1)}\,H^{-1/3}(\xi_1) \\ & +\frac{1}{\sqrt{3}}\tau^{2+m/2}\Gamma_1^{1/2+n/2}\Gamma^{-1/2}h'(\xi_1) \\ & \times\{1-H^{2/3}(\xi_1)\}\,, \end{aligned} \qquad (6.22)$$

where the negative and positive signs refer respectively to the sub- and the supersonic local velocities. By the use of Eq. (5.18), Eq. (6.22) can be represented in the following form

$$\begin{aligned} q' = \mp & \frac{3}{4}t^2\tau^{-(4+m)/3}\Gamma_1^{-(1+n)/3}\sqrt{\Phi(\xi_1, K_1)}\,H^{-1/3}(\xi_1) \\ & +\frac{3}{4}t^2h'(\xi_1)\{1-H^{2/3}(\xi_1)\} \end{aligned} \qquad (6.23)$$

where

$$t^2=\frac{4}{3\sqrt{3}}\tau^{(4+m)/2}\Gamma_1^{(1+n)/2}\Gamma^{-1/2}\,. \qquad (5.18)$$

On the other hand the similar solutions of the axisymmetric transonic flow governed by Eqs. (2.10) and (2.11) can be obtained by introducing the following affin transformations:

$$\left.\begin{aligned} & x=x_1\,, \quad y=\frac{1}{t\sqrt{\Gamma}}y_1 \\ & \psi=t^2g(x_1,\ y_1) \end{aligned}\right\} \qquad (6.24)$$

By the use of this transformation, Eq. (2.11) becomes

$$\pm 2\sqrt{-\frac{1}{y_1}\frac{\partial g}{\partial y_1}}\frac{\partial^2 g}{\partial x_1^2}+\frac{\partial^2 g}{\partial y_1^2}-\frac{1}{y_1}\frac{\partial g}{\partial y_1}=0\,. \qquad (6.25)$$

Considering the obstacle to be slender, the boundary condition on the surface of the obstacle (2.13) can be replaced by the following condition:

$$-\frac{\partial\psi}{\partial x}=y\theta=\frac{1}{2}\frac{dy^2}{dx}=\frac{t^2}{2}\frac{dH(x)}{dx} \quad \text{at } y=0, \qquad (6.26)$$

where $y=tH^{1/2}(x)$ represents the meridian curve of the body of revolution. The boundary conditions (2.12), (6.26) and (2.14) are transformed respectively to

$$\left.\begin{aligned} & \frac{1}{y_1}\frac{\partial g}{\partial y_1}=-K_1^2\,, \\ & \frac{\partial g}{\partial x_1}=0 \end{aligned}\right\} \quad \text{at } x_1=-\infty\,, \qquad (6.27)$$

$$-\frac{\partial g}{\partial x_1}=\frac{1}{2}\frac{dH(x_1)}{dx}=\frac{1}{2}h(x_1) \quad \text{at } y_1=0\,, \qquad (6.28)$$

$$\frac{\partial g}{\partial x_1}=0 \quad \text{at } y_1=t\sqrt{\Gamma}\,L\,, \qquad (6.29)$$

where

$$K=(1-M)/t^2\Gamma\,. \qquad (6.30)$$

As the equation (6.25) and the boundary conditions (6.27) and (6.28) contain only one parameter K, there exists a similar solution $g(x_1,\ y_1,\ K)$, if the radius L of the circular wind tunnel can be expressed as a function of the transonic parameter K such that

$$Lt\sqrt{\Gamma}=\lambda(K)\,. \qquad (6.31)$$

Thus the magnitude q' of the perturbation velocity at a position $(x_1,\ y_1)$ can be found in the following similar form:

$$q'=\pm\sqrt{-\frac{1}{\Gamma}\frac{1}{y}\frac{\partial\psi}{\partial y}}=\pm t^2\sqrt{-\frac{1}{y_1}\frac{\partial g}{\partial y_1}} \qquad (6.32)$$

Putting

$$\sqrt{-\frac{1}{y_1}\frac{\partial g}{\partial y_1}}=f(x_1,\ y_1,\ K)\,, \qquad (6.33)$$

Eq. (6.32) can be described shortly as

$$q'=\pm t^2 f(x_1,\ y_1,\ K)\,. \qquad (6.34)$$

It should be noted here that this function $f(x_1,\ y_1,\ K)$ has singularities along the axis of the body, and that a point (x_1, y_1) which corresponds to one point on the surface of the body of revolution for one value of t, can never remain at the surface for any other value of t. Oswatisch and Berndt[4] considered the character of the affin transformation (6.24) and found the general similarity law. According to this law, the perturbation velocity $q'_{\text{surf.}}$ on the surface of a body of revolution of thickness ratio $2t$, is represented by the following form:

$$\begin{aligned} q'_{\text{surf.}}/t^2-\frac{d^2H}{dx^2}\log\sqrt[4]{\Gamma}\,t= & f(x_1,\ K) \\ & -\frac{d^2H}{dx^2}\log\sqrt[4]{\Gamma_0}\,t_0\,, \end{aligned} \qquad (6.35)$$

with

$$\Gamma=\frac{\gamma+1}{2}\,, \quad \Gamma_0=\frac{\gamma_0+1}{2}$$

where γ_0 and t_0 denote the ratio of the specific heats of a standard gas and a standard thickness ratio respectively, and where $f(x_1, K)$ denotes a similar solution (6.33).

Putting especially,

$$\sqrt[4]{\Gamma}\, t = \sqrt[4]{\Gamma_0}\, t_0 \tag{6.36}$$

Eq. (6.35) can be reduced to Eq. (6.34).

Comparing Eqs. (6.23) and (5.18) with (6.35) and (6.36) respectively, we can determine the values of constants m and n such that

$$m=-4\,, \quad n=-1\,. \tag{6.37}$$

By the use of these values, Eqs. (6.23) and (5.18) become respectively

$$\begin{aligned} q'_{\text{su.f.}} = &\mp \frac{3}{4} t^2 \sqrt{\Phi(\xi_1,\, K_1)} H^{-1/3}(\xi) \\ &+ \frac{3}{4} t^2 \frac{d^2H}{d\xi_1{}^2}(1-H^{2/3}(\xi_1)) \end{aligned} \tag{6.38}$$

$$t\Gamma^{1/4} = 2/\sqrt[4]{27} \tag{6.39}$$

and

$$\xi_1 = x\,.$$

Considering the similarity law (6.35), we obtain the perturbation velocity $q'_{\text{surf.}}$ on the surface of a body of revolution for general values of $t\sqrt[4]{\Gamma}$ such that

$$\begin{aligned} q'_{\text{surf.}} = &\mp \frac{3}{4} t^2 \sqrt{\Phi(x,\, K_1)} H^{-1/3}(x) \\ &+ \frac{3}{4} t^2 H''(x)\{1-H^{2/3}(x)\} \\ &- H''(x) \log\{2/(27\Gamma)^{1/4} t\}\,, \end{aligned} \tag{6.40}$$

where negative and positive signs refer to the sub- and the supersonic local fluid velocities respectively.

Substituting Eqs. (6.39) and (4.8) into Eq. (6.30), and remembering Eqs. (6.11), (6.37) and and (5.15), we obtain the following relation between the transonic parameters K and K_1:

$$\left.\begin{aligned} K &= \frac{1-M}{t^2\Gamma} = \frac{3}{2}\frac{(1-M_1)}{k^3\tau}\left(\frac{\Gamma}{\Gamma_1}\right)^{3/4}\frac{\sqrt{27}}{4}\Gamma^{-1/2} \\ &= (3/4)\tau^2(1-M_1) = (3/4)K_1\,, \end{aligned}\right\} \tag{6.41}$$

substituting Eqs. (6.39) and (3.7) into Eq. (6.31), remembering Eqs. (6.18), (6.37) and (5.15), we obtain the following relation between the functional forms $\lambda(K)$ and $\lambda_1(K_1)$:

$$\left.\begin{aligned} \lambda(K) &= Lt\sqrt{\Gamma} \\ &= \frac{2}{3}\sqrt{\frac{2}{3}}\, k^{3/2} L_1{}^{3/2} \frac{2}{4\sqrt{27}} \Gamma^{-1/4}\sqrt{\Gamma} \\ &= \frac{4}{3\sqrt{3}} [L_1\tau^{-1}/(\Gamma_1/\Gamma)^{1/4}]^{3/2} \\ &= \frac{4}{3\sqrt{3}} \lambda_1{}^{3/2}(K_1) \end{aligned}\right\} \tag{6.42}$$

By the use of the relations (6.40), (6.41) and (6.42), we can obtain the velocity distribution over the given body of revolution placed along the axis of a circular cylindrical wind tunnel (in the extreme case, in the uniform flow extended to infinity) if we want to find the entire axisymmetric flow pattern of a imaginary gas (whose gas constant must be determined by the relation (6.39)) past a slender body represented by Eq. (5.17) placed along the axis of a circular cylindrical wind tunnel, we need to find the two-dimensional transonic flow governed by Eq. (4.2) subject to the boundary conditions (4.3), (4.5) and (6.1), where we must put $m=-4$ and $n=-1$. However, the velocity distribution on the surface of the body of revolution can be readily obtained, provided the functional form

$$\Phi(\xi_1,\, K_1) \equiv \Phi\left(x,\, \frac{4}{3}K\right)$$

is known. Fortunately this function $\Phi(\xi_1, K_1)$ can be found from the velocity distribution of a real gas over the corresponding two-dimensional body, (which is given by solving Eq. (4.2) subject to the boundary conditions (4.3), (4.5) and (6.1), where we may put $m=0$ and $n=0$.) Thus we can obtain the velocity distribution represented by Eq. (6.38) and the relation between the functional forms $\lambda(K)$ and $\lambda_1(K_1)$ represented by Eq. (6.42), if there exists the relation (6.39) between the half thickness ratio t of the obstacle and the gas constant Γ. Considering the general similarity law expressed by Eq. (6.35), this result can be modified to the general form (6.40), which is useful for general values of Γ and t. It is worth while to mention here that the similarity law is not completely consistent with a Prandtl-Meyer expansion at the shoulder.

The pressure coefficient C_p on the surface of an obstacle considered here is given by

$$C_p = \frac{p-p_\infty}{(1/2)\cdot\rho_\infty U^2} = -2\{q'_{\text{surf.}} - q_\infty'\} \tag{6.43}$$

By the use of Eqs. (6.40) and (6.43), we obtain the pressure coefficient over a body of revolution such that

$$\left.\begin{aligned} C_p/t^2 = &\pm \frac{3}{2}\sqrt{\Phi\left(x,\, \frac{4}{3}K\right)} H^{-1/3}(x) \\ &- \frac{3}{2} H''(x)\{1-H^{2/3}(x,\} \\ &+ 2H''(x) \log\{2/\sqrt[4]{27\Gamma}\, t)\}\,, \end{aligned}\right\} \tag{6.44}$$

where the positive and negative signs refer to the sub- and the supersonic local fluid velocities respectively.

Corresponding two-dimensional formula becomes

$$C_{p_2}\Gamma_1^{1/3}\tau^{-2/3}=\pm 2\sqrt{\Phi(\xi_1,\ K_1)}-2K_1\,, \qquad (6.45)$$

with

$$K_1=(1-M_1)/\tau^{2/3}\Gamma_1^{2/3}\,,$$

where the double signs have the same meaning as in the former case.

The head drag coefficient C_d of a body of revolution is obtained by

$$C_d=\frac{1}{A_b}\int_0^1 2\pi C_p\left(\frac{dy}{dx}\right)y\,dx\,, \qquad (6.46)$$

where A_b denotes the area of the base section.

Substitution of Eqs. (6.44) and (5.17) into Eq. (6.46) yields

$$\left.\begin{aligned}C_D/t^2=&\int_0^1\left(\frac{3}{2}\sqrt{\Phi}\,H^{-1/3}+\frac{3}{2}H''H^{2/3}\right)H'\,dx-\left(\log\frac{(27)^{1/4}}{2}+\frac{3}{4}\right)(H'(1)^2-H'(0)^2)\\&+\{\log(\Gamma^{1/4}t)^{-1}\}\{H'(1)^2-H'(0)^2\}-2K\,.\end{aligned}\right\} \qquad (6.47)$$

§7. A Numerical Example

As is mentioned above, to find the velocity distribution on the surface of an axisymmetric obstacle, we need to obtain that on the surface of a certain two-dimensional obstacle which is symmetric with respect to the free-stream velocity.

As a typical example of two-dimensional transonic flows, the flow past a finite wedge at Mach number 1 was dealt with by Guderley and Yoshihara[5]. Starting from this solution, we shall obtain a certain axisymmetric flow. In this case, the function $H(\xi_1)$ in Eq. (5.8) becomes

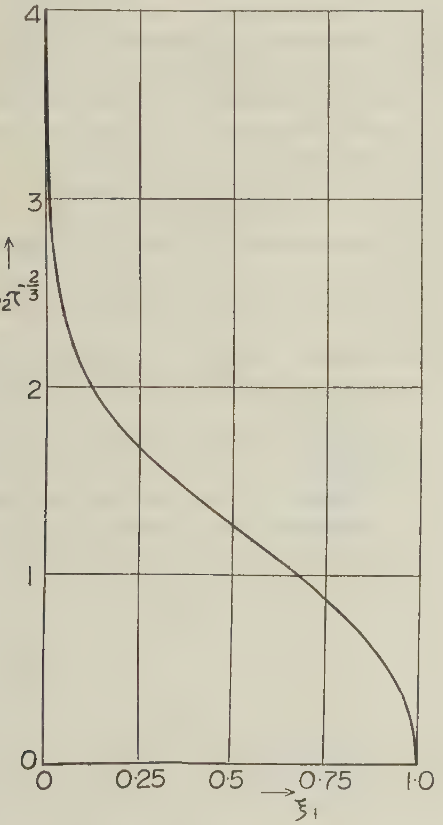

Fig. 1. Pressure distribution over a finite wedge at $M=1$, for $\gamma=1.4$ (Ref. (5)).

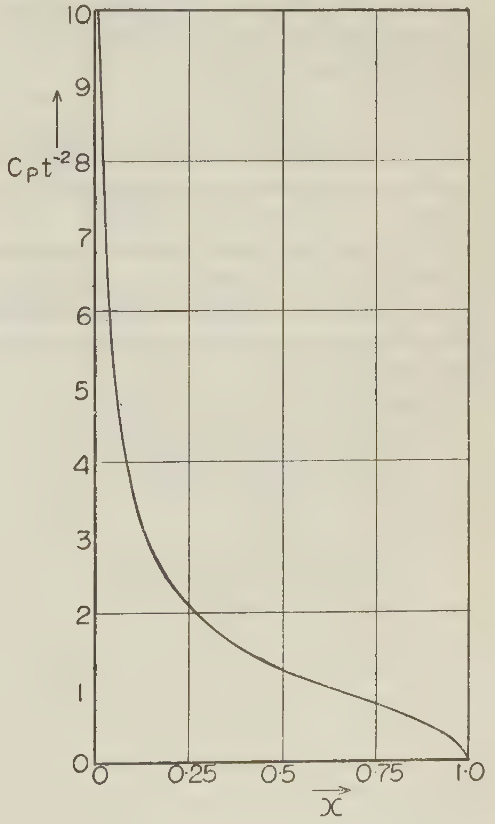

Fig. 2. Pressure distribution over a paraboloid of revolution of finite length at $M=1$.

$$H(\xi_1)=\begin{cases}\xi_1 & \text{for } 0\leqq\xi_1\leqq 1\\ 1 & \text{for } 1<\xi_1\,.\end{cases} \tag{7.1}$$

By the use of Eq. (5.17), the corresponding body of revolution is given by

$$y=\begin{cases}t\sqrt{x} & \text{for } 0\leqq x\leqq 1\\ t & \text{for } 1\leqq x\end{cases} \tag{7.2}$$

which represents a paraboloid of revolution of finite length. Guderley and Yoshihara calculated the function

$$C_{p_2}\tau^{-2/3}=2\Gamma_1{}^{(-1/3)}\sqrt{\Phi(\xi_1,\ 0)}$$

which is shown in Fig. 1. In this case the term of $H''(x)$ in Eq. (6.44) vanishes and we can obtain the pressure coefficient over the paraboloid in the following simple form:

$$C_p/t^2=\frac{3}{2}\sqrt{\Phi(x,\ 0)}/x^{1/3} \qquad \text{for } 0\leqq x\leqq 1. \tag{7.3}$$

This pressure distribution is shown in Fig. 2.

Integrating Eq. (6.46) graphically, we obtain the head drag coefficient of the paraboloid of revolution of finite length as

$$C_d=1.73\,t^2\,, \tag{7.4}$$

where t denotes the half thickness ratio.

Miles[6] evaluated the wave drag on a slender body in sonic flight by matching the result of the linearised theory with the asymptotic solution of Guderley and Yoshihara[7] along the sonic line. The head drag coefficient of a body of revolution of finite length is given by

$$\left.\begin{aligned} C_D/t^2=\frac{H'(1)^2}{4}&\left[\log\left\{1.786\left[\int_0^1 H(x)\,dx\right]^3\right.\right.\\ &\left.\left.\Big/H'(1)\right\}+\frac{7}{2}\right]\\ &+H'(1)^2\log\left(\Gamma^{1/4}t\right)^{-1}\,,\end{aligned}\right\} \tag{7.5}$$

where the meridian curve of the body is represented by

$$y=tH^{1/2}(x)\,. \tag{5.17}$$

Putting $K=0$ in Eq. (6.47), it should be compared with Miles's result (7.5). When the body of revolution considered has pointed nose, $H'(0)$ in Eqs. (6.47) and (7.5) vanishes. Thus for the pointed body both equations have the same coefficient in the term of $\log(\Gamma^{1/4}t)$. However, when $H'(0)$ does not vanish, their coefficients are quite different. Then it is probable that Miles's formula (7.5) fails for a body of revolution with a bluff nose. It seems to be the very reason for this failure that the solution of the linearized equation in the extreme case of $M=1$ is recognized as the extreme form of the solution of the hyperbolic equation for the supersonic flow rather than that of the elliptic equation for the subsonic flow, and that it cannot include the contribution of the bluff nose.

More interesting examples will be dealt with in another paper to be published shortly.

The writer wishes to express his heartiest gratitude to Professor I. Imai for many useful suggestions and kind advice.

References

1) Th. von Kármán: J. Math. Phys. **26** (1947) 182.
2) Barish and G. Guderley: J. Aero. Sci. **20** (1953) 491.
3) H. Yoshihara: WADC Tech. Rep. 52–295 (1952).
4) K. Oswatitsch and S. B. Berndt: KTH-AERO TN **15** (1950).
5) G. Guderley and H. Yoshihara: J. Aero. Sci. **17** (1950) 723.
6) J. W. Miles: J. Aero. Sci. **23** (1956) 146.
7) G. Guderley and H. Yoshihara: Quart. Appl. Math. **4** (1951) 333.

JOURNAL OF THE PHYSICAL SOCIETY OF JAPAN Vol. 12, No. 4, APRIL, 1957

On the Transonic Flow of a Compressible Fluid Past a Nearly Axisymmetric Slender Body

By Ken-ichi KUSUKAWA

Department of Physics, Faculty of Science, Tokyo Metropolitan University

(Received November 20, 1956)

The transonic flow of a compressible inviscid fluid past a nearly axisymmetric slender body is dealt with by dividing the perturbation velocity potential into two parts:—the one is governed by the fundamental equation of an axisymmetric transonic flow, and the other is determined by the two-dimensional Laplace's equation in the plane perpendicular to the free-stream velocity vector.

As the axisymmetric transonic flow can be dealt with by a new approximation offered in a previous paper[3], and the solution of the two-dimensional Laplace's equation is easily found, the present problem can be solved.

As examples the flow past an elliptic paraboloid of finite length is discussed and the head drag and the lift coefficients of a paraboloid of revolution of finite length are obtained.

§ 1. Introduction

As is well known, the nearly parallel flow of a compressible inviscid fluid past a slender obstacle of general cross section can be dealt with by the so-called slender body theory[1),2)], unless there exists any transonic region. But this method cannot be applied to the transonic flow, because the approximation of linearization of the equation, on which this method is based, fails in the transonic region.

In this paper we shall deal with the transonic flow of a compressible inviscid fluid past a nearly axisymmetric slender body. The perturbation velocity potential is divided into two parts:—the one refers essentially to the magnitude of the velocity of a transonic fluid flow, but is not sensitively influenced by the sectional form of the body, and the other is essentially determined by the sectional form of the body, but scarecely contributes to the magnitude of the fluid velocity. Thus the approximate equation for determining the former can be reduced to the fundamental equation for the transonic axisymmetric fluid flow, and that for determining the latter can be reduced to the two-dimensional Laplace's equation in the plane parpendicular to the free stream velocity vector.

As the two-dimensional Laplace's equation can be easily solved for any boundary condition corresponding to the form of the body, we can find the perturbation velocity potential of transonic flow past a slender body of general cross section, provided the transonic fluid flow past a suitable axisymmetric body can be known. An approximate method for solving the latter problem was offered by the present writer[3)], and we shall apply a solution given by this method to the numerical examples, which will be discussed in § 4.

§ 2. Fundamental Equations

We shall take the cartesian coordinates where the x-axis is taken along the uniform velocity. Taking conveniently the magnitude of the velocity and the density of the fluid at the sonic point as their units, the perturbation velocity components u', v' and w' along x, y and z-axis, the perturbation density ρ' and the perturbation velocity potential φ are defined as follows:

$$\left.\begin{aligned} &u'=u-1=\frac{\partial\varphi}{\partial x}, \quad v'=\frac{\partial\varphi}{\partial y}, \quad w'=\frac{\partial\varphi}{\partial z}, \\ &\rho'=\rho-1 \end{aligned}\right\} \qquad (2.1)$$

Assuming the flow to be nearly parallel, the equation for determining φ becomes

$$\left(1-\frac{u^2}{c^2}\right)\frac{\partial^2\varphi}{\partial x^2}+\frac{\partial^2\varphi}{\partial y^2}+\frac{\partial^2\varphi}{\partial z^2}=0\ , \qquad (2.2)$$

where c denotes the local speed of sound.

By the use of (2.1) and Bernoulli's theorem:

$$(c^2/\rho)d\rho+qdq=0\ ,$$

where q denotes the magnitude of the velocity, we obtain approximately the following relation:

$$1-u^2/c^2=-(\gamma+1)u' \qquad (2.3)$$

wehre γ denotes the ratio of the specific heats.

Substituting Eq. (2.3) into Eq. (2.2), we obtain

$$-(\gamma+1)\frac{\partial\varphi}{\partial x}\frac{\partial^2\varphi}{\partial x^2}+\frac{\partial^2\varphi}{\partial y^2}+\frac{\partial^2\varphi}{\partial z^2}=0\,, \tag{2.4}$$

which is the fundamental equation in the transonic approximation due originally to von Kármán[4].

Introducing the cylindrical coordinates such that

$$y=r\cos\theta\,,\qquad z=r\sin\theta\,,$$

Eq. (2.4) becomes

$$-(\gamma+1)\frac{\partial\varphi}{\partial x}\frac{\partial^2\varphi}{\partial x^2}+\frac{\partial^2\varphi}{\partial r^2}+\frac{1}{r}\frac{\partial\varphi}{\partial r}+\frac{1}{r^2}\frac{\partial^2\varphi}{\partial\theta^2}=0\,. \tag{2.5}$$

We shall expand the perturbation velocity potential φ into Fourier series as

$$\varphi=u_0(x,r)+\sum_{n=1}^{\infty}u_n(x,r)\cos(n\theta+\beta_n)\,, \tag{2.6}$$

where β_n are arbitrary constants.

At a great distance from the obstable φ must become $U(1-x)$, where U denotes the free-stream velocity, therefore the flow pattern becomes asymptotically axisymmetric. Since the body considered is nearly axisymmetric, we can assume the following relation between the values of u_0 and u_n (for $n\geqq1$) near the obstacle:

$$O(u_n)/O(u_0)=O(\varepsilon)\ll O(1)\qquad\text{for }n\geqq1 \tag{2.7}$$

As the body is very slender, the magnitudes of the axial and radial components of the velocity can be assumed to be of the order of $O(\varepsilon)$ according to the usual perturbation theory:

$$\left.\begin{aligned}O\left(\frac{\partial\varphi}{\partial x}\right)&=O\left(\frac{\partial u_0}{\partial x}\right)=O(\varepsilon)\,,\\ O\left(\frac{\partial\varphi}{\partial r}\right)&=O\left(\frac{\partial u_0}{\partial r}\right)=O(\varepsilon)\,.\end{aligned}\right\} \tag{2.8}$$

On the other hand the order of a diameter of the body denoted by $O(r)$ is also assumed to be of the order of $O(\varepsilon)$:

$$O(r)=O(\varepsilon) \tag{2.9}$$

Thus from Eqs. (2.7), (2.8) and (2.9), we obtain the following order estimations near the obstacle:

$$\left.\begin{aligned}O\left(\frac{\partial^2u_0}{\partial x^2}\right)&=O\left(\frac{\partial u_0}{\partial x}\right)=O(\varepsilon)\\ O\left(\frac{\partial^2u_n}{\partial x^2}\right)&=O\left(\frac{\partial u_n}{\partial x}\right)\\ &=O\left(\frac{\partial u_0}{\partial x}\right)\cdot O(\varepsilon)=O(\varepsilon^2)\\ O\left(\frac{\partial^2u_0}{\partial r^2}\right)&=O\left(\frac{1}{r}\frac{\partial u_0}{\partial r}\right)\\ &=O\left(\frac{\partial u_0}{\partial r}\right)\Big/O(r)=O(1)\\ O\left(\frac{\partial^2u_n}{\partial r^2}\right)&=O\left(\frac{1}{r}\frac{\partial u_n}{\partial r}\right)=O(u_n/r^2)\\ &=O\left(\frac{\partial u_n}{\partial r}\right)\Big/O(r)\\ &=O\left(\frac{\partial u_0}{\partial r}\right)O(\varepsilon)/O(\varepsilon)=O(\varepsilon)\end{aligned}\right\} \tag{2.10}$$

Substituting Eq. (2.6) into Eq. (2.5), and remembering Eq. (2.10), Eq. (2.5) can be reduced to

$$\begin{aligned}&-(\gamma+1)\frac{\partial u_0}{\partial x}\frac{\partial^2u_0}{\partial x^2}+\frac{\partial^2u_0}{\partial r^2}+\frac{\partial u_0}{r\partial r}\\ &+\sum_{n=1}^{\infty}\cos(n\theta+\beta_n)\left\{\frac{\partial^2u_n}{\partial r^2}+\frac{\partial u_n}{r\partial r}-\frac{n^2}{r^2}u_n\right\}\\ &+O(\varepsilon^3)=0\,.\end{aligned} \tag{2.11}$$

Neglecting the terms of the order of $O(\varepsilon^3)$, we can obtain the following equations for determining u_0 and u_n:

$$-(\gamma+1)\frac{\partial u_0}{\partial x}\frac{\partial^2u_0}{\partial x^2}+\frac{\partial^2u_0}{\partial r^2}+\frac{\partial u_0}{r\partial r}=0\,, \tag{2.12}$$

$$\frac{\partial^2u_n}{\partial r^2}+\frac{\partial u_n}{r\partial r}-\frac{n^2}{r^2}u_n=0\,.\qquad\text{for }n\geqq1 \tag{2.13}$$

Eq. (2.12) is formally equal to the fundamental equation for the transonic axisymmetric flow of a compressible fluid.

§ 3. Solutions and Boundary Conditions

As is well known, the general solutions of Eqs. (2.13) are given by

$$u_n=a_n(x)r^n+b_n(x)r^{-n}\,,\qquad\text{for }n\geqq1\,, \tag{3.1}$$

where $a_n(x)$ and $b_n(x)$ are arbitrary functions of x.

Thus the perturbation velocity potential φ is represented by

$$\varphi=u_0(x,r)+\sum_{n=1}^{\infty}\{a_n(x)r^n+b_n(x)r^{-n}\}\cos(n\theta+\beta_n)\,. \tag{3.2}$$

We shall consider the boundary conditions which φ must satisfy. Since $\partial\varphi/\partial x$ tends to $(U-1)$ as $x\to\infty$ or $r\to\infty$, we obtain

$$u_0(x,r)=(U-1)x\qquad\text{at infinity,} \tag{3.3}$$

and

$$a_n=0\qquad\text{for all }n\geqq1\,. \tag{3.4}$$

On the surface of the obstacle, the gas must flow tangentially along the surface. If the surface of the obstable is expressed by

$$R=F(x,\theta)\ , \tag{3.5}$$

this function $F(x, \theta)$ can be expanded into Fourier series as

$$R=F_0(x)+\sum_{n=1}^{\infty} F_n(x)\cos(n\theta+\alpha_n) \tag{3.6}$$

where α_n are certain constants.

We shall consider the following three points on the surface of the obstacle:

$$\mathrm{A}(x,\ R,\ \theta)\ ,\qquad \mathrm{B}(x,\ R+\Delta R,\ \theta+\Delta\theta)$$

and

$$\mathrm{C}(x+\Delta x,\ R+\Delta R,\ \theta)\ .$$

Since both the vectors $\overrightarrow{\mathrm{AB}}$ and $\overrightarrow{\mathrm{AC}}$ exist on the tangential plane of the surface at the point A, and the velocity vector should also be on this plane, we obtain the following condition:

$$\begin{vmatrix} 0 & \partial R/R\partial\theta & 1 \\ 1 & \partial R/\partial x & 0 \\ 1 & \partial\varphi/\partial r & \partial\varphi/r\partial\theta \end{vmatrix}=0 \tag{3.7}$$

Neglecting the higher order terms, Eq. (3.7) is reduced to

$$\partial\varphi/\partial r=\partial R/\partial x \qquad \text{at } r=R\equiv F(x,\theta)\ . \tag{3.8}$$

Substituting Eqs. (3.2) and (3.6) into Eq. (3.8), we obtain

$$\left.\begin{aligned} &\frac{\partial u_0}{\partial r}-\sum_{n=1}^{\infty}\frac{nb_n(x)}{r^{n+1}}\cos(n\theta+\beta_n) \\ &=\frac{dF_0}{dx}+\sum_{n=1}^{\infty}\frac{dF_n(x)}{dx}\cos(n\theta+\alpha_n) \\ &\qquad\qquad \text{at}\quad r=R\equiv F(x,\theta)\ . \end{aligned}\right\} \tag{3.9}$$

As the sectional form $R=F(x, \theta)$ is not very different from a circle, the boundary condition (3.8) at $r=R\equiv F(x, \theta)$ can be assumed, within the accuracy of the order of the usual slender body theory, to be satisfied at $r=F_0(x)$. Thus Eq. (3.8) can be approximated to

$$\left.\begin{aligned} &\left(\frac{\partial u_0}{\partial r}\right)_{r=F_0(x)}-\sum_{n=1}^{\infty}\frac{nb_n(x)}{F_0^{\,n+1}(x)}\cos(n\theta+\beta_n) \\ &=\frac{dF_0}{dx}+\sum_{n=1}^{\infty}\frac{dF_n(x)}{dx}\cos(n\theta+\alpha_n)\ . \end{aligned}\right\} \tag{3.10}$$

From this equation, we obtain the following conditions:

$$\left(\frac{\partial u_0}{\partial r}\right)_{r=F_0(x)}=\frac{dF_0(x)}{dx}\ , \tag{3.11}$$

and

$$\left.\begin{aligned} &\beta_n=\alpha_n \\ &b_n(x)=-\frac{F_0^{\,n+1}(x)}{n}\frac{dF_n(x)}{dx}\ . \end{aligned}\right\} \tag{3.12}$$

By the use of the conditions (3.3), (3.4), (3.11) and (3.12), the perturbation velocity potential φ of the transonic flow past a slender obstacle expressed by Eq. (3.6) is readily given by

$$\varphi=u_0(x,r)-\sum_{n=1}^{\infty}\frac{F^{n+1}(x)}{nr^n}\frac{dF_n(x)}{dx}\cos(n\theta+\alpha_n)\ , \tag{3.13}$$

provided the perturbation velocity potential $u_0(x, r)$ of the transonic flow of free-stream velocity U past an axisymmetric body expressed by $R=F_0(x)$ can be known.

§ 4. Examples

As examples we shall consider the following two cases. The one is the transonic flow of a compressible fluid past a slender elliptic paraboloid of finite length at zero angle of attack at $M_\infty=1$, and the other is the transonic flow past a slender paraboloid of revolution of finite length with small angle of attack at $M_\infty=1$.

(1) Elliptic Paraboloid

We shall consider an elliptic paraboloid of unit length expressed by

$$\left.\begin{aligned} &x=\frac{y^2}{a^2}+\frac{z^2}{b^2}\ ,\qquad 0\leq x\leq 1\ , \\ &e=\sqrt{a^2-b^2}/a\ , \end{aligned}\right\} \tag{4.1}$$

where a, b and e denote the semi-major and semi-minor axes and the eccentricity of the base section respectively.

Introducing the cylindrical coordinates such that

$$y=R\cos\theta\ ,\qquad z=R\sin\theta\ , \tag{4.2}$$

Eq. (4.1) can be expanded into the e^2-power series as

$$R=b\sqrt{x}\left(1+\frac{e^2}{2}\cos^2\theta+\frac{1.3}{2!\,2^2}e^4\cos^4\theta+\cdots\right) \tag{4.3}$$

After some elementary calculations Eq. (4.3) is reduced to Fourier series as

$$\left.\begin{aligned} &R=b\sqrt{x}\,(A_0+A_1\cos 2\theta \\ &\qquad\qquad +A_2\cos 4\theta+\cdots) \\ &\text{where} \\ &A_0=1+\frac{e^2}{4}+\frac{9}{64}e^4+\cdots\ , \\ &A_1=\quad\ \frac{e^2}{4}+\frac{12}{64}e^4+\cdots\ , \\ &A_2=\qquad\quad \frac{3}{64}e^4+\cdots\ . \end{aligned}\right\} \tag{4.4}$$

In our case it is sufficient, within the accuracy of the approximation in Eq. (3.10), to take terms up to e^2.

Comparing Eq. (4.4) with Eq. (3.6), we obtain

$$\left.\begin{aligned} &F_0(x)=A_0b\sqrt{x}\ , \quad F_1(x)=0\ , \\ &F_2(x)=A_2b\sqrt{x}\ , \quad F_n(x)=0 \ \text{for}\ n\geq 3\ . \end{aligned}\right\} \tag{4.5}$$

By the use of this equation, Eq. (3.13) becomes

$$\varphi=u_0(x,\ r)-\left\{\frac{A_0{}^3A_1b^4}{4}\frac{x}{r^2}\cos 2\theta\right\}\ . \tag{4.6}$$

Thus the axial, radial and tangential components $v_x{}'$, $v_r{}'$, $v_\theta{}'$ of the perturbation velocity are respectively represented by

$$v_x{}'=\frac{\partial\varphi}{\partial x}=\frac{\partial u_0}{\partial x}-\frac{A_0{}^3A_1b^4\cos 2\theta}{4r^2}\ , \tag{4.7}$$

$$v_r{}'=\frac{\partial\varphi}{\partial r}=\frac{\partial u_0}{\partial r}+\frac{A_0{}^3A_1b^4\cos 2\theta}{2r^3}\ , \tag{4.8}$$

$$v_\theta{}'=\frac{\partial\varphi}{r\partial\theta}=\frac{A_0{}^3A_1b^4x\sin 2\theta}{2r^3}\ . \tag{4.9}$$

For the sake of finding the velocity components on the surface of the elliptic paraboloid, putting approximately

$$r=R\doteqdot F_0(x)=A_0b\sqrt{x}\ ,$$

Eqs. (4.7) and (4.8) are reduced to

$$(v_x{}')_s=\left(\frac{\partial u_0}{\partial x}\right)_{r=F_0(x)}-\frac{A_0b^2A_1\cos 2\theta}{4x}\ , \tag{4.10}$$

$$(v_\theta{}')_s=\frac{bA_1\sin 2\theta}{2\sqrt{x}}\ . \tag{4.11}$$

The values of A_0 and A_1 for $a=0.1$, $b=0.09$, $e=(19)^{1/2}/10$, and those for $a=0.1$, $b=0.08$, $e=6/10$ are given in Table I.

Table I. The values of A_0 and A_1.

a	b	e	A_0	A_1
0.1	0.09	$(19)^{1/2}/10$	1.0475	0.0475
0.1	0.08	6/10	1.09	0.09

By an approximate method offered in the previous paper[3)], we can find the value of $(\partial u_0/\partial x)$ at $r=F_0(x)$, which represents the axial component of the perturbation velocity over a paraboloid of revolution of unit length and thickness ratio $t=2A_0b$. Thus by the use of Eq. (4.8), we can calculate the values of the axial and tangential components $v_x{}'$, $v_\theta{}'$ of the velocity on the surface of the elliptic paraboloid.

In the case of $a=0.1$ and $b/a=9/10$, the distributions of the tangential velocity components $v_\theta{}'$ at several chordwise stations are shown in Fig. 1, and the chordwise distributions of the axial component $v_x{}'$ in the several meridian planes are shown in Figs. 2–5. For comparison, there are also shown in these figures the distributions of the axial component $v_x{}'$ over the surface of the paraboloids of revolution whose meridian curves are the same as those of the elliptic paraboloid in every meridian planes. It is due to the influence of tangential flows, that at small values of θ, the absolute values of $v_x{}'$ on the elliptic paraboloid are smaller than those over the paraboloid of revolution, and at values near 90° the latter ones are smaller than the formers.

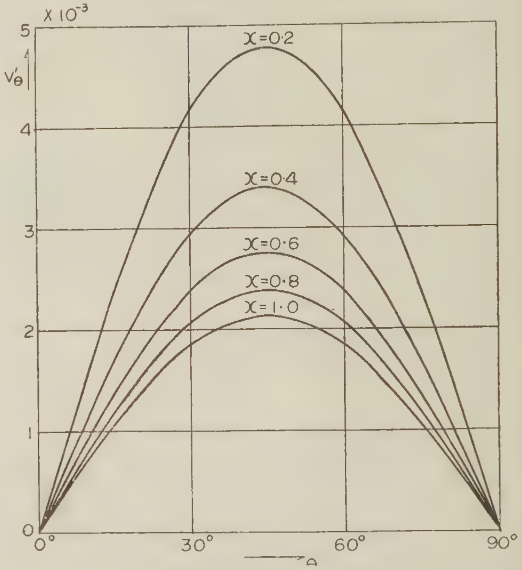

Fig. 1. The distribution of the tangential velocity component $v_\theta{}'$ over an elliptic paraboloid of $a=0.1$ and $b/a=9/10$.

In the case of $a=0.1$ and $b/a=8/10$, the distributions of the tangential component $v_\theta{}'$ of the velocity at several chordwise stations are shown in Fig. 6, and the chordwise distributions of the axial component $v_x{}'$ in the several meridian planes are shown in Figs. 7–10.

As the pressure coefficient C_p on the surface in the approximation considered here is given by

$$C_p=\frac{p-p_\infty}{p_\infty U^2/2}=-2v_x{}'\ , \tag{4.12}$$

we can find readily the values of C_p from those of $v_x{}'$, and they are also shown in Figs. 2–5, 7–10.

Since Prandtl-Meyer's expansion occurs locally at the shoulder of the finite elliptic para-

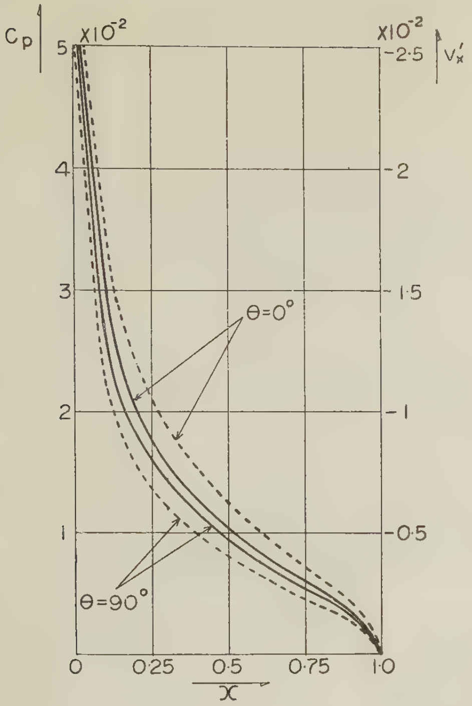

Fig. 2.

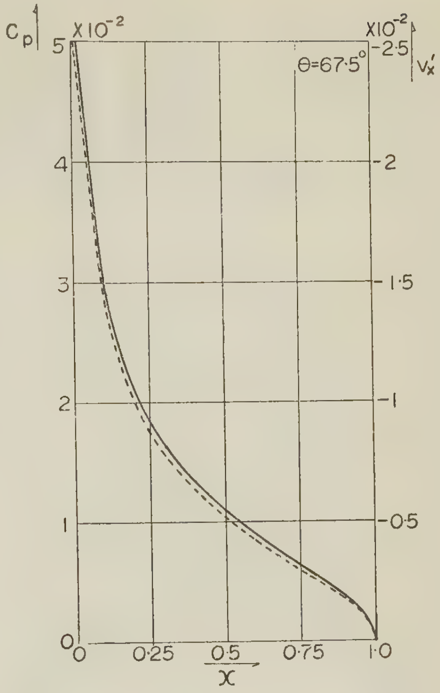

Fig. 3.

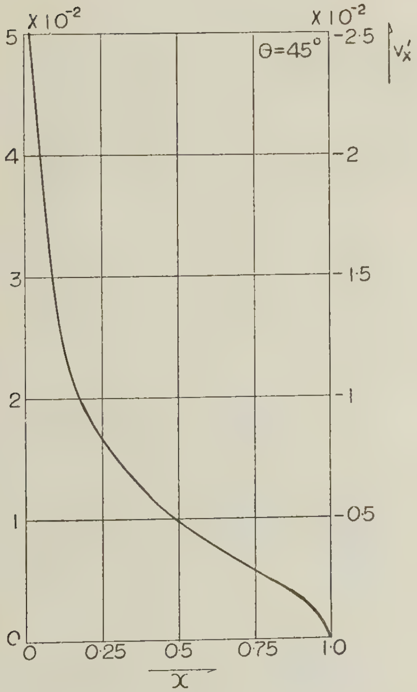

Fig. 4.

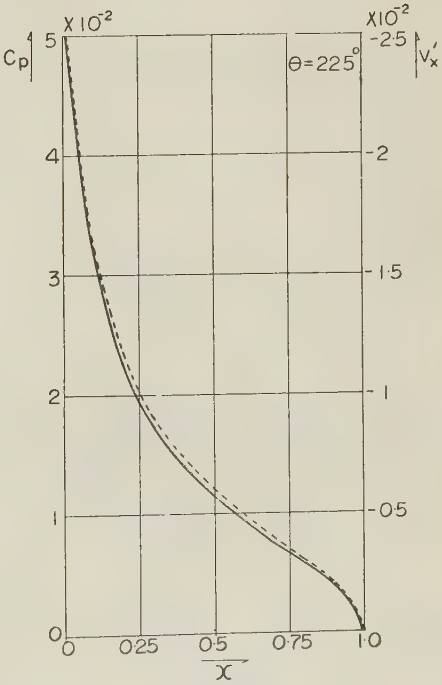

Fig. 5.

Figs. 2–5. Chordwise distributions of the pressure and the axial perturbation velocity component v_x' over an elliptic paraboloid of $a=0.1$ and $b/a=9/10$ in the several meridian planes.

The full-and the dotted lines refer to the elliptic paraboloid and the corresponding paraboloid of revolution.

boloid, the pressure coefficient C_p must, in principle, vanish there. In fact, the calculated values of the pressure coefficient at the shoulder become of such a vanishingly small order as 2/10000 in our case, therefore this approximate method is justified from this view point.

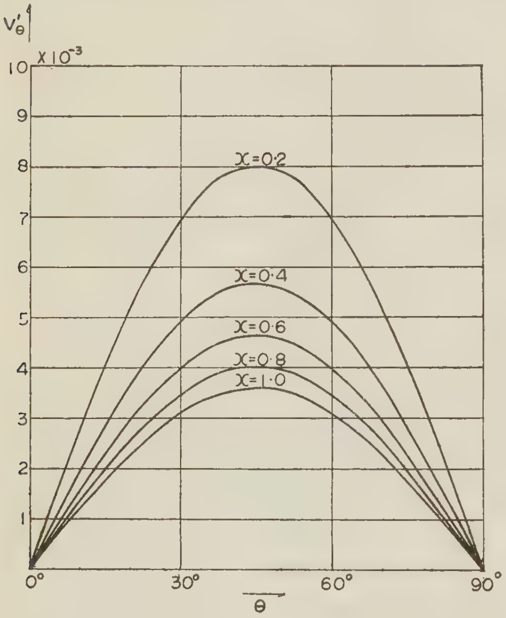

Fig. 6. The distributions of the tangential velocity component v_θ' over an elliptic paraboloid of $a=0.1$ and $b/a=8/10$.

(2) Paraboloid of Revolution at Small Incidence

We shall consider a slender paraboloid of revolution of unit length such that

$$x_1=\frac{y_1^2}{a^2}+\frac{z^2}{a^2}\,, \qquad 0\leqq x_1\leqq 1 \tag{4.13}$$

where a denotes the radius of the base section.

We shall introduce the angle of attack α. Taking the cartesian coordinates $o-x\,y\,z$ where the x-axis is taken along the free stream velocity, we obtain the following relations:

$$\begin{aligned} x_1&=x\cos\alpha-y\sin\alpha\,,\\ y_1&=x\sin\alpha+y\cos\alpha\,. \end{aligned} \tag{4.14}$$

Substitution of Eq. (4.14) into Eq. (4.13) gives

$$\begin{aligned} ax^2\cos\alpha-a^2y\sin\alpha&=(y^2+z^2)\\ &+(x^2-y^2)\sin^2\alpha+2xy\sin\alpha\cos\alpha\,. \end{aligned} \tag{4.15}$$

Introducing the cylindrical coordinates such that

$$y=R\cos\theta\,, \qquad z=R\sin\theta\,, \tag{4.16}$$

Eq. (4.15) becomes

$$R=\frac{1}{2A}[-B\pm\sqrt{B^2+4AC}\,]\,,$$

where

$$\left.\begin{aligned} A&=1-\sin^2\alpha\cos^2\theta\,,\\ B&=a^2\sin\alpha\cos\theta+x\sin 2\alpha\cos\theta\,,\\ C&=a^2x\cos\alpha-x^2\sin^2\alpha\,. \end{aligned}\right\} \tag{4.17}$$

Since $R\geqq 0$, neglecting the terms of the order smaller than $O(\alpha)$, Eq. (4.17) is reduced to

$$R=a\sqrt{x}-(1/2)(a^2+2x)\alpha\cos\theta\,. \tag{4.18}$$

Comparing this equation with Eq. (3.6), we obtain

$$F_0(x)=a\sqrt{x}\,, \qquad F_1(x)=-\frac{1}{2}(a^2+2x)\alpha\,. \tag{4.19}$$

Thus by the use of Eq. (3.13), we can obtain the perturbation velocity potential:

$$\varphi=u_0(x,\,r)+\alpha a^2x\cos\theta/r\,, \tag{4.20}$$

Then the axial and the tangential components v_x', v_θ' of the perturbation velocity on the surface of the obstacle are respectively given by

$$(v_x')_s=\left(\frac{\partial u_0}{\partial x}\right)_{r=F_0(x)}+\frac{\alpha a}{\sqrt{x}}\cos\theta\,, \tag{4.21}$$

$$(v_\theta')_s=-\alpha\sin\theta\,, \tag{4.22}$$

where $\partial u_0/\partial x$ at $r=F_0(x)$ represents the axial component of the velocity over the same paraboloid of revolution at zero incidence. The pressure coefficient C_p on the surface of the body is readily given by

$$C_p=-2v_x'=-2\left(\frac{\partial u_0}{\partial x}\right)_{r=F_0(x)}-2\frac{\alpha a}{\sqrt{x}}\cos\theta\,. \tag{4.23}$$

The head drag coefficient C_d of the obstacle is obtained as

$$C_d=\frac{1}{A_b}\iint C_p(dR/dx)Rd\theta dx\,, \tag{4.24}$$

where A_b denotes the area of the base section.

Substitution of Eq. (4.23) into Eq. (4.24) gives

$$C_d=\frac{1}{A_b}\left\{\iint C_{p_0}\frac{dR}{dx}Rdxd\theta+\iint C_{p_1}\frac{dR}{dx}Rd\theta dx\right\},$$

where

$$C_{p_0}=-2\left(\frac{\partial u_0}{\partial x}\right)_{r=F_0(x)}\,, \qquad C_{p_1}=-\frac{2\alpha a}{\sqrt{x}}\cos\theta\,. \tag{4.25}$$

Since the function C_p is symmetric with respect to the axis of revolution x_1, the first term in the right-hand side of Eq. (4.25) is calculated by

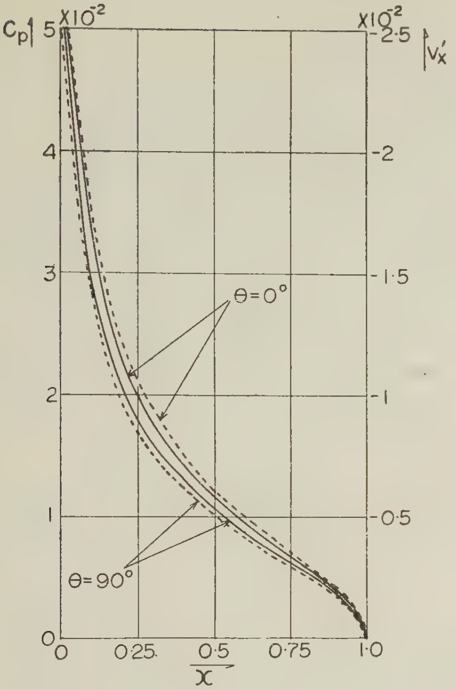

Fig. 7.

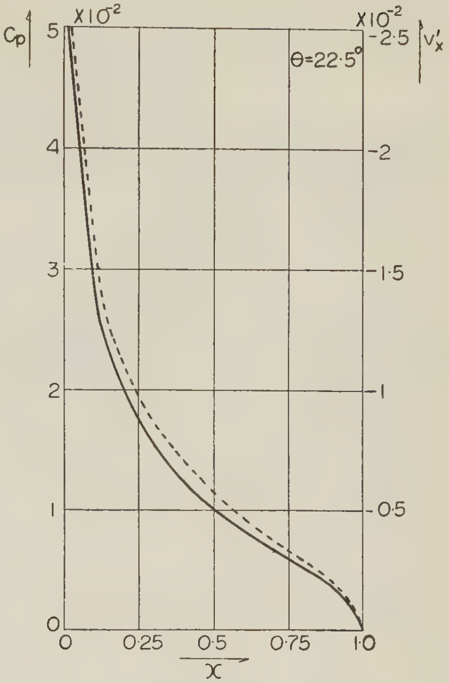

Fig. 8.

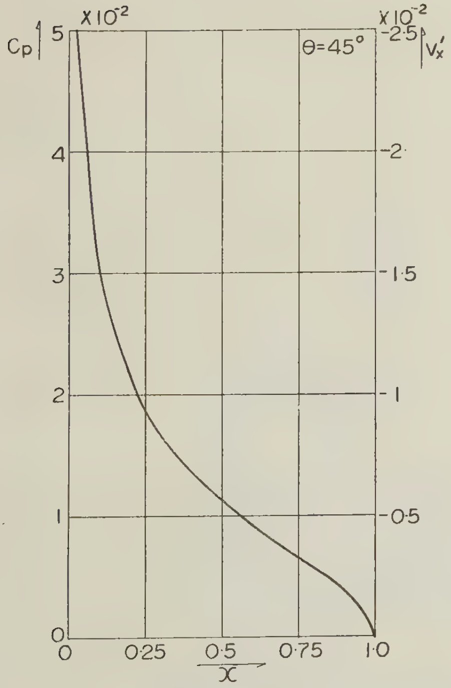

Fig. 9.

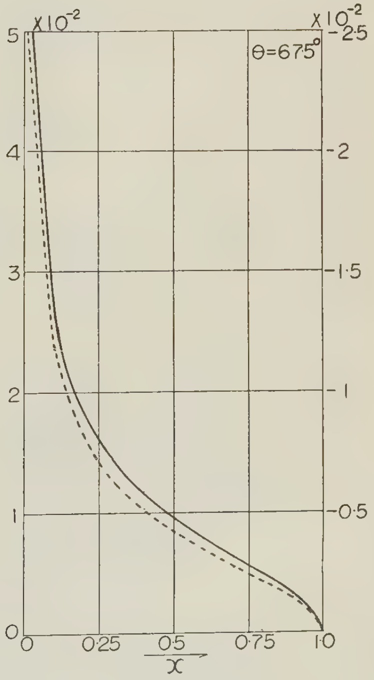

Fig. 10.

Figs. 7–10. Chordwise distributions of the pressure and the axial perturbation velocity component v_x' over an elliptic paraboloid of $a=0.1$ and $b/a=8/10$ in the several meridian planes.

The full-and the dotted lines refer to the elliptic paraboloid and the corresponding paraboloid of revolution.

$$\left\{\frac{1}{A_b}2\pi\int_0^1 C_{p0}\frac{dR}{dx_1}R(x_1)dx_1\right\}\cos\alpha$$
$$=\left(\int_0^1 C_{p_0}dx_1\right)\cos\alpha\ .$$

Neglecting the terms of the order of $O(\alpha^2)$, the second term is reduced to

$$-\iint\frac{2\alpha a\cos\theta}{\sqrt{x}}\frac{1}{2}\left(\frac{dR}{dx}\right)^2 d\theta dx$$
$$=-a^3\alpha\iint\frac{\cos\theta}{\sqrt{x^3}}d\theta dx=0\ .$$

Thus we obtain the head drag coefficient:

$$C_d=C_{d_0}\cos\alpha=C_{d_0}+O(\alpha^2)\ , \qquad (4.26)$$

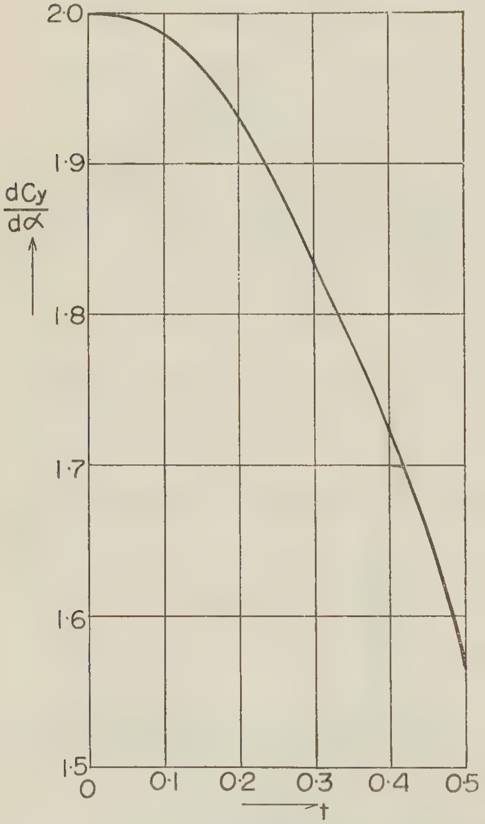

Fig. 11. The variation of $(dC_y/d\alpha)_{\alpha=0}$ for a finite paraboloid with the half thickness ratio t.

where $C_{d_0}=\int_0^1 C_{p_0}dx_1$ represents the head drag coefficient of the paraboloid of revolution of unit length at zero incidence. According to the previous paper[3)], C_{d_0} is given by

$$C_{d_0}=1.73t^2 \qquad (4.27)$$

where t denotes the half thickness ratio, so that it is the same as a in this case.

It is seen from Eq. (4.26) that the influence of the angle of attack α to the drag coefficient C_d is of the order of $O(\alpha^2)$.

As the lift is seriously influenced by the under pressure at the base, it cannot be estimated without the knowledge of the base pressure. Then we shall consider here the y-component P_y of the resultant of the pressure acting on the head of the obstacle such that

$$P_y=-\iint C_pR\cos\theta d\theta dx$$
$$=-\left[\iint C_{p_0}\cos\theta R d\theta dx+\iint C_{p_1}R\cos\theta d\theta dx\right]$$
$$=-\left[2\pi\int C_{p_0}R\frac{dR}{dx_1}dx_1\right]\sin\alpha$$
$$+\left[\iint\frac{2\alpha a}{\sqrt{x}}\cos^2\theta(a\sqrt{x})d\theta dx\right]$$
$$=-A_bC_{d_0}\sin\alpha+2\alpha A_b=A_b\alpha(2-C_{d_0}) \qquad (4.28)$$

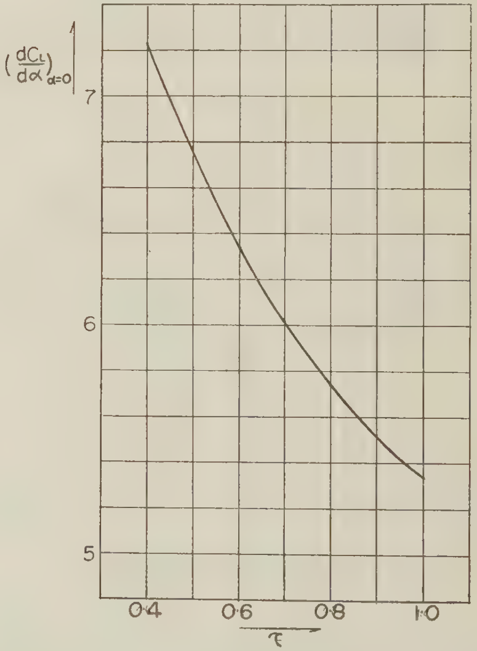

Fig. 12. The variation of $(dC_L/d\alpha)_{\alpha=0}$ for a double wedge with the thickness ratio τ. (Ref. (5)).

Introducing the non-dimensional coefficient $P_y/A_b=C_y$, we obtain

$$C_y=P_y/A_b=(2-C_{d_0})\alpha\ . \qquad (4.29)$$

Substitution of Eq. (4.27) yields

$$C_y=(2-1.73t^2)\alpha\ , \qquad (4.30)$$

and we obtain

$$(dC_y/d\alpha)_{\alpha=0}=2-1.73t^2\ , \qquad (4.31)$$

where t denotes the half thickness ratio of the paraboloid of revolution. The variation of $(dC_y/d\alpha)_{\alpha=0}$ with the half thickness ratio t is shown in Fig. 11.

Guderley and Yoshihara[5] investigated theoretically the transonic flow past a double wedge with small angle of attack α, at $M_\infty=1$ and calculated the lift coefficient C_L. For comparison the variation of $(dC_L/d\alpha)_{\alpha=0}$ with the thickness ratio τ of the double wedge is shown in Fig. 12.

Finally it will be of interest to mention here that by the slender body theory[1],[6], the lift coefficient of the pointed slender body of revolution in the supersonic fluid flow is given by

$$C_L=2\alpha+O(t^3\log^2 t)\ . \qquad (4.32)$$

It is the reason for the difference between Eqs. (4.30) and (4.32), that the surface velocity of a paraboloid of finite length in sonic flight is subsonic, while that of a pointed body at $M>1$ is supersonic.

The writer wishes to express his heartiest gratitude to professor I. Imai for his many useful suggestions and kind advice.

References

1) W. Sears: Quart. Appl. Math. **5** (1947) 89.
2) G. N. Ward: Quart. J. Mech. Appl. Math. **2** (1949) 75.
3) K. Kusukawa: J. Phys. Soc. Japan **12** (1957) 401.
4) Th. von Kármán: J. Math. Phys. **26** (1947) 182.
5) G. Guderley and H. Yoshihara: J. Aero. Sci. **20** (1953) 757.
6) H. S. Tsien: J. Aero. Sci. **5** (1938) 480.

JOURNAL OF THE PHYSICAL SOCIETY OF JAPAN Vol. 12, No. 4, APRIL, 1957

Experimental Studies of the Lift on Two Equal Circular Cylinders placed side by side in a Uniform Stream at Low Reynolds Numbers

By Sadatoshi TANEDA

Kobe University of Mercantile Marine

(Received December 26, 1956)

Lifts acting on two equal circular cylinders placed side by side in a uniform stream were measured by means of lamp scale and mirror method at Reynolds numbers from 0.01 to 1.6. The results obtained are as follows:

1. Each cylinder experiences a repulsive force.
2. The value of lift coefficient decreases monotonously as the Reynolds number is increased.
3. When the Reynolds number is sufficiently small, the value of lift coefficient increases first and then decreases as the ratio of the distance between two cylinders to the diameter of the cylinder increases.

These results are in good agreement with the theoretical conclusions which are led from the Oseen's linearized equations of motion.

The photographs of the actual flow pattern were also taken.

§ 1. Introduction

In a recent paper[1], the forces acting on two parallel circular cylinders of equal diameter with their axes in a plane perpendicular to a uniform flow have been discussed by Fujikawa on the basis of Oseen's linearized equations of motion, and several interesting results were obtained. The present author was interested especially in the conclusions that when two equal cylinders are placed side by side they repulse each other, and that when Reynolds number is small, the lift increases first and then decreases with the increase of the distance between the two cylinders. However, so far as is known to the author, there has been no experimental verification up to the present.

In the present experiments, the lifts acting on two equal circular cylinders placed side by side were measured for several cases when the ratio of the distance between the axes of the two cylinders to the diameter of the cylinder is equal to 4.6, 10, 18 and 50, the Reynolds number of the flow varying from 0.01 to 1.6. To obtain the flow with such a low Reynolds number, the glycerine-water solutions were used as the viscous fluid. And the lift, which was extremely small (order of 10^{-1} dyne), were sensibly detected by means of lamp scale and mirror method. The results were in good agreement with the theoretical one based on the Ossen's equations.

§ 2. Apparatus

The experiments were carried out with the moving metal vessel of 200 mm in length, 100 mm in width and 80 mm in depth. The general arrangement of the apparatus is shown in Fig. 1. The vessel is filled with the glycerine-water solution, and is set on the small carriage which is advanced uniformly along the straight rails by means of lead screw. The value of Reynolds number can be varied by changing the density of the glycerine-water solution.

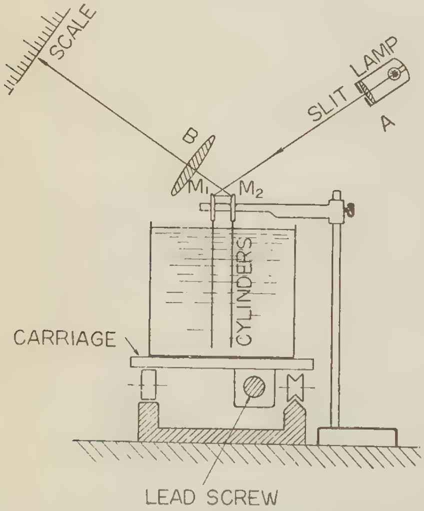

Fig. 1. Schematic diagram of the apparatus.
A, **B**: Convex lenses, $\mathbf{M}_1$, $\mathbf{M}_2$: Plane mirrors.

The two cylinders are hung as a pendulum on a horizontal bracket by means of needle edges so as to be free to swing only across the stream (see Fig. 2). When the vessel is at rest, the following adjustments have to be made:

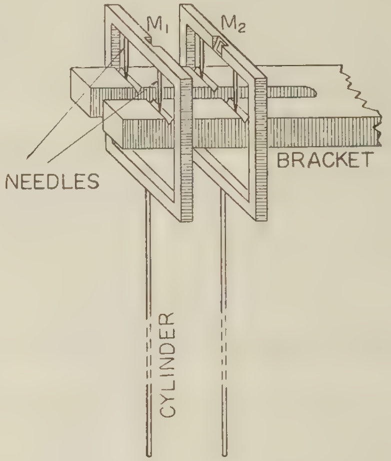

Fig. 2. Sketch of the pendulums.

1. The plane containing the two cylinders has to be made perpendicular to the direction about which the vessel is moved.
2. The two cylinders have to be inclined slightly each other so as to be exactly parallel when the vessel is in motion.
3. The ray of light from the lamp has to be thrown on to a scale after reflections in the mirrors $\mathbf{M}_1$ and $\mathbf{M}_2$ which are attached to the pendulums facing each other.
4. The image of the light source has to be formed on the mirror $\mathbf{M}_1$ by means of lens **A**.
5. The image of the slit has to be formed on the scale by means of lens **B**.

Then the vessel is set in motion, and the small inclination of the pendulum which is caused by the lift is measured by reading the movement of a spot of light on the scale.

The fine brass wires of four different sizes were used as the models, their diameters being 0.30 mm, 0.40 mm, 0.60 mm and 0.77 mm respectively. It must be noted that steel wire cannot be used as the model because it is strongly affected by the weak magnetism existing in the apparatus. The distance between two cylinders was varied from 1 mm to 15 mm at the interval of 1 mm.

On the other hand, the actual flow pattern around the two circular cylinders was photographed by means of aluminium dust method with the glass water tank of 100 cm in length, 20 cm in width and 30 cm in depth. A general description of the apparatus and an account of the photographic technique were given in the previous paper²⁾, and so need not be repeated here.

§ 3. Notations

m: mass of pendulum

l: distance between needle edge and center of gravity of the pendulum

l^*: distance between needle edge and center of lift

g: acceleration of gravity

x: displacement of spot of light on the scale

a: distance between two mirrors $\mathbf{M}_1$ and $\mathbf{M}_2$

b: distance from middle point of $\mathbf{M}_1$ and $\mathbf{M}_2$ to lens **B**

c: distance between lens **B** and scale

f: focal length of lens **B**

D: distance from middle point of $\mathbf{M}_1$ and $\mathbf{M}_2$ to scale

L: lift

C_L: lift coefficient

ρ: density of glycerine-water solution

d: diameter of cylinder

U: speed of carriage

s: span of cylinder (submerged portion of cylinder)

h: distance between axes of two cylinders

ν: kinematic viscosity of glycerine-water solution

R: Reynolds number based on diameter of the cylinder (Ud/ν)

§ 4. Results and Discussion

If the inclination of the pendulum is sufficiently small, then we have from the condition for balance of the forces

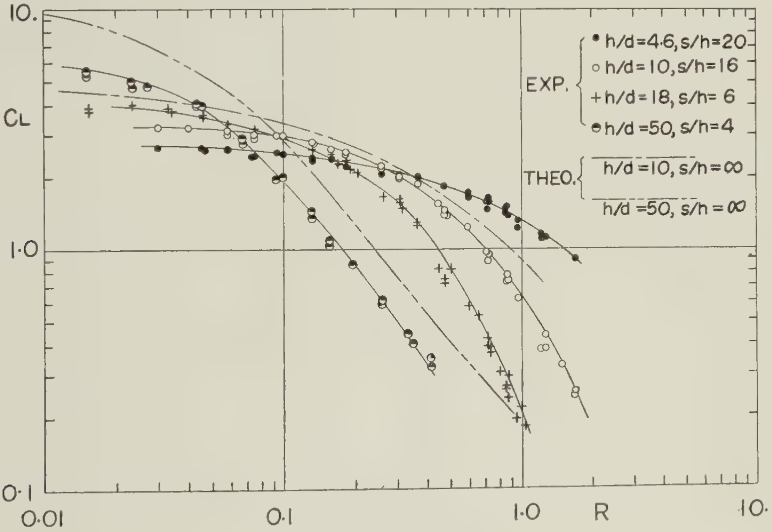

Fig. 3. Lift coefficient.

$$\frac{Dx}{\left(\frac{fb}{f-b}+c\right)\left(1-\frac{b}{f}\right)}=2\,\frac{Ll_1^*}{m_1gl_1}(a+D)+2\frac{Ll_2^*}{m_2gl_2}D\,.$$

Hence

$$L=\frac{Dgx}{2\left(\frac{fb}{f-b}+c\right)\left(1-\frac{b}{f}\right)\left\{\frac{l_1^*(a+D)}{m_1l_1}+\frac{l_2^*D}{m_2l_2}\right\}}\,,$$

and therefore

$$C_L=\frac{L}{d\rho U^2s}=\frac{Dgx}{2\rho dU^2s\left(\frac{fb}{f-b}+c\right)\left(1-\frac{b}{f}\right)\left\{\frac{l_1^*(a+D)}{m_1l_1}+\frac{l_2^*D}{m_2l_2}\right\}}\,.$$

Thus by measuring the value x, the lift coefficient C_L can be calculated. In the present experiments, the inclination of the pendulum which was caused by the lift was less than 1/200. When the Reynolds number R is higher than about 1.5, the lift is too small to be accurately measured by means of this method. On the other hand, when R is lower than about 0.02, the influence of the vessel wall is not so small as can be neglected. Therefore the measurements were made only at Reynolds numbers from 0.01 to 1.6.

Fig. 3 shows the experimental results, together with the theoretical values for the two cases $h/d=10$ and 50. The general conclusions drawn from the experiments are summarized as follows:

1. Two cylinders repulse each other.
2. Lift coefficient decreases monotonously as the Reynolds number is increased.
3. When Reynolds number is small, the value of lift coefficient increases first and then decreases as the ratio of the distance between the axes of the two cylinders to the diameter of the cylinder is increased.

These conclusions are in complete agreement with the theoretical. However, the observed lift coefficient is slightly lower than the theoretically calculated, the discrepancy being probably due to the end effect and the wall effect. The theoretical calculations apply to an unlimited field of fluid around the two cylinders of infinite length, while the experiments were made in a tank of finite size using the cylinders of finite length.

Photographs of the actual velocity field around the two equal parallel circular cylinders are shown in Fig. 4. It will be noticed that the wakes produced by two cylinders repulse each other.

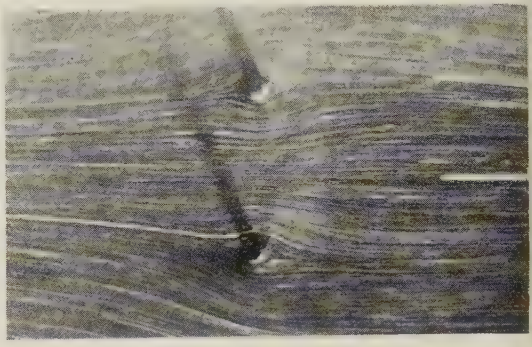

(a) $R=0.486$, $s/h=12$.

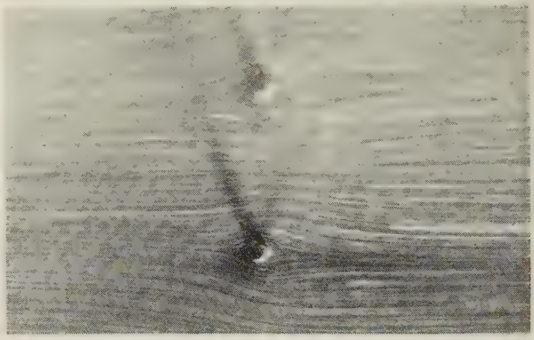

(b) $R=1.46$, $s/h=12$.

Fig. 4. Photographs showing flow pattern around the two equal parallel circular cylinders placed side by side in a uniform stream.

The author is indebted to Professor Hikoji Yamada for his valuable advice and encouragement in the course of this work. Thanks are also due to Dr. Hiroomi Fujikawa for his kind suggestions.

References

1) H. Fujikawa: J. Phys. Soc. Japan **11** (1956) 558.
2) S. Taneda: J. Phys. Soc. Japan **11** (1956) 302.

Journal of the Physical Society of Japan Vol. 12, No. 4, April, 1957

Expansion Formulae for the Forces acting on Two Equal Circular Cylinders placed in a Uniform Stream at Low Values of Reynolds Number

By Hiroomi Fujikawa

Junior College of Engineering, University of Osaka Prefecture, Neyagawa nr. Osaka

(Received December 30, 1956)

As a continuation of a previous paper¹⁾, a further discussion is made on the steady slow motion of a viscous fluid past two parallel circular cylinders of equal radius with their axes in a plane perpendicular to a uniform flow, confining ourselves to the case when the two cylinders are in close proximity to each other.

Expansion formulae in powers of Reynolds number R for the drag and lift acting on one of the cylinders are obtained correct to the lowest order of Reynolds number R. The coefficients of each term are expressed in power series of $a/2h$ and obtained as far as terms of $(a/2h)^4$, where a denotes the radius of the cylinders and $2h$ the distance between their centres.

Up to the order of $(a/2h)^2$, the results are found to be in complete agreement with expansion formulae for the drag and lift acting on the one cylinder placed near the other, which has been obtained directly by expanding the formulae useful for the case when the distance between the cylinders is great.

§1. Introduction and Summary

In a previous paper¹⁾, the writer treated a steady slow motion of a viscous fluid past two parallel circular cylinders of equal radius a, at a great distance apart, with their axes in one plane perpendicular to a uniform stream and obtained expansion formulae in powers of Reynolds number for the forces acting on one of the cylinders, up to the second term of Oseen's approximation. These formulae are valid for the case when the two cylinders are situated at a great distance apart, but they are not applicable to the case in which the cylinders are adjacent to each another.

Also, the writer expanded formally the above formulae in power series of the ratio $a/2h$ as far as terms of $(a/2h)^2$, where $2h$ is the distance between the centres of the cylinders. However, as was noted in the previous paper, such formal expansion formulae are not suitable for a detailed discussion, especially for the case of two adjacent cylinders. It is therefore desirable to obtain expansion formulae for the drag and lift acting on one of the cylinders correct to the order higher than $(a/2h)^2$.

In the present paper, expansion formulae useful for the case when the two circular cylinders are situated in close proximity to each other are obtained up to the order of $(a/2h)^4$ as well as to the lowest order of Reynolds number R. And it is shown that the expressions thus obtained are in complete agreement, up to the order of $(a/2h)^2$, with those which have been derived formally by expanding the formulae useful for the case when the distance between the two cylinders is great.

Making use of these formulae, detailed numerical discussion is made for several cases when the distance between the axes of the two cylinders is equal to 5/4, 3/2, 5/2, 5 and 10 times their diameter, the Reynolds number of the flow varying from 0 to 0.1. Further, as a limiting case, a similar discussion is made for the drag when the two cylinders touch each other, and compared with Tamada's results²⁾.

Thus, it is ascertained that, on increasing the distance between the two cylinders, the drag on one cylinder increases but the lift—the repulsive force—decreases first and then increases.

OUTLINE OF ANALYSIS

§ 2. Fundamental Solutions

For the sake of reference we shall first reproduce the outline of analysis which is necessary for our present purpose.

We consider two infinitely long parallel circular cylinders C, C_*, of equal radius a, set in a steady uniform stream of velocity U of an incompressible viscous fluid in such a manner that their axes lie in a plane perpendicular to the uniform stream.

Let Ox, Oy be the rectangular co-ordinate axes in the plane of fluid motion, the axis of x being taken along the direction of the uniform stream and the origin coinciding with the centre of the cylinder C. The centre of the other cylinder C_* is situated on the y-axis, its coordinates being denoted by $(0, -2h)$ (Fig. 1).

As is well known, the stream function ψ for the perturbation flow due to the presence of a single circular cylinder placed in an unlimited uniform flow has been given by Filon[3) in the form:

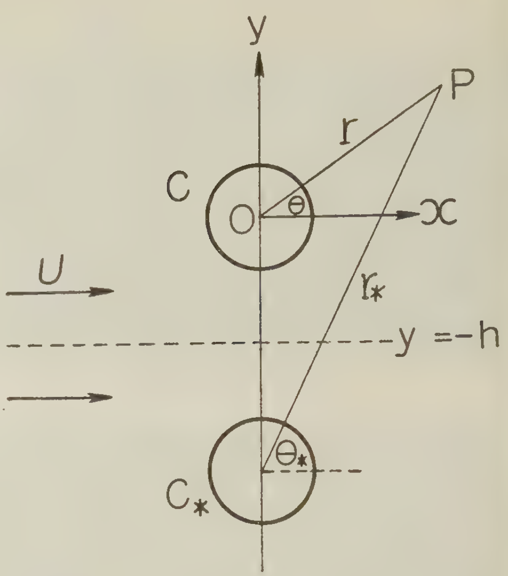

Fig. 1.

$$\psi = \psi_h + \psi_u \,,$$

with

$$\left.\begin{aligned} \psi_h &= \alpha_0 \log r + a_0\theta + \sum_{n=1}^{\infty} r^{-n}(\alpha_n \cos n\theta + a_n \sin n\theta) \,, \\ k\psi_u &= \beta_0 e^{kx} K_0(kr) + b_0 \int_0^{\theta} kr\{K_1(kr) + K_0(kr)\cos\theta\} e^{kr\cos\theta}\, d\theta \\ &\quad + e^{kx} \sum_{n=1}^{\infty} K_n(kr)(\beta_n \cos n\theta + b_n \sin n\theta) \,, \end{aligned}\right\} \tag{2.1}$$

where

$$x = r\cos\theta \,, \qquad y = r\sin\theta \,,$$

a_n, α_n, b_n, β_n being arbitrary real constants, $K_n(kr)$ the modified Bessel function of the second kind[†], and k is connected with the kinematic viscosity ν as

$$k = U/2\nu \,. \tag{2.2}$$

Then, putting

$$\left.\begin{aligned} A_0 = a_0 + i\alpha_0 \,, \qquad A_n = n(a_n - i\alpha_n) \,, \qquad (n \geqq 1) \\ B_n = b_n + i\beta_n \,, \qquad (n \geqq 0) \end{aligned}\right\} \tag{2.3}$$

the conjugate complex velocity W $(=u-iv)$ for the perturbation flow is generally expressed as follows:

$$\left.\begin{aligned} W &= W_h + W_u \,, \\ W_h &= \sum_{n=0}^{\infty} A_n z^{-(n+1)} \,, \\ W_u &= e^{kx}\{C_1 K_0(kr) + \sum_{n=1}^{\infty} (C_{n+1} e^{in\theta} + \overline{C}_n e^{-in\theta}) K_n(kr)\} \,, \end{aligned}\right\} \tag{2.4}$$

[†] The definition of the modified Bessel function used here is identical with those in G. N. Watson's "*A Treatise on the Theory of Bessel Functions*" (Cambridge, 1922).

where C_n's are arbitrary constants connected with B_n's as

$$C_1 = B_0 - \frac{1}{2} B_1 , \qquad C_n = \frac{1}{2}(B_{n-1} - B_n) , \qquad (n \geqq 2) \tag{2.5}$$

and $\overline{C}_n$ denotes the complex conjugate of C_n.

The expression (2.4) for W was first obtained by Prof. I. Imai[1] after integrating a general expression for vorticity.

Now, the conjugate complex velocity W for the perturbation flow due to the presence of the two cylinders in the uniform stream may be written in the following form:

$$W = W_h^{(1)} + W_h^{(2)} + W_u^{(1)} + W_u^{(2)} , \tag{2.6}$$

with

$$\left.\begin{aligned} &W_h^{(1)} = \sum_{n=0}^{\infty} A_n z^{-(n+1)} , \qquad W_h^{(2)} = \sum_{n=0}^{\infty} A_n^* z_*^{-(n+1)} , \\ &W_u^{(1)} = e^{kx}\{C_1 K_0(kr) + \sum_{n=1}^{\infty} (C_{n+1} e^{in\theta} + \overline{C}_n e^{-in\theta}) K_n(kr)\} , \\ &W_u^{(2)} = e^{kx}\{C_1^* K_0(kr_*) + \sum_{n=1}^{\infty} (C_{n+1}^* e^{in\theta_*} + \overline{C}_n^* e^{-in\theta_*}) K_n(kr_*)\} , \end{aligned}\right\} \tag{2.7}$$

where A_n, C_n, A_n^*, C_n^* etc. are arbitrary complex constants and

$$z_* = r_* e^{i\theta_*} = z + 2ih . \tag{2.8}$$

The flow field under consideration must be symmetric with respect to the straight streamline $y = -h$, i.e. $\Im(W) = 0$ along $y = -h$. This condition yields immediately the following relations between the constants in (2.7):

$$A_n^* = \overline{A}_n \qquad (n \geqq 0) , \qquad\qquad C_n^* = \overline{C}_n \qquad (n \geqq 1) . \tag{2.9}$$

§ 3. Determination of the Constants A_n, B_n

We now proceed to the consideration of the remaining boundary conditions at the surfaces of the two cylinders.

The flow is symmetric with respect to the straight streamline $y = -h$ and since the solution (2.6) together with (2.7) and (2.9) already satisfies this condition, it is sufficient to consider the fulfilment of the condition on one cylinder C ($z = a \exp(i\theta)$) only.

The resultant velocity $U + W$ must be zero on the surface of the cylinder, so that the required boundary condition is written as:

$$(W)_{r=a} = -U . \tag{3.1}$$

In order to apply this condition to W given by (2.6), we expand W in a Fourier series in θ on the surface ($r = a$) of the cylinder C. After several calculations, we get the following results† as

$$\left.\begin{aligned} &(W_h^{(1)})_{r=a} = \sum_{n=0}^{\infty} A_n a^{-(n+1)} e^{-i(n+1)\theta} , \\ &(W_h^{(2)})_{r=a} = \sum_{n=0}^{\infty} \sum_{m=0}^{\infty} (-1)^n \frac{(m+n)!}{m!\,n!} \left(\frac{a}{2ih}\right)^n \frac{\overline{A}_m}{(2ih)^{m+1}} e^{in\theta} , \\ &(W_u^{(1)})_{r=a} = \sum_{n=-\infty}^{\infty} \Big\{C_1 K_0 I_n + \sum_{m=1}^{\infty} K_m (C_{m+1} I_{n-m} + \overline{C}_m I_{n+m})\Big\} e^{in\theta} , \\ &(W_u^{(2)})_{r=a} = \sum_{n=-\infty}^{\infty} \Big\{\overline{C}_1 \lambda_{n,\,0} + \sum_{m=1}^{\infty} (\overline{C}_{m+1} \lambda_{n,\,m} + C_m \lambda_{n,\,-m})\Big\} e^{in\theta} , \end{aligned}\right\} \tag{3.2}$$

where

$$\lambda_{n,\,\sigma} = \sum_{s=-\infty}^{\infty} i^{s+\sigma} I_s I_{s-n} K_{s-\sigma}(2kh) , \qquad (\sigma = 0, \pm 1, \pm 2, \cdots) \tag{3.3}$$

---

† For details of the calculation reference should be made to the previous paper[1] of the present writer.

the argument ka of the modified Bessel functions I_n, K_n having been omitted for simplicity.

According to the boundary condition (3.1), every coefficient of $\exp(in\theta)$ $[n=0, \pm 1, \pm 2, \cdots]$ in the expansion should vanish except for the constant term ($n=0$), which must be equal to $-U$.

Thus, we have

$$\left.\begin{aligned}
&\sum_{m=0}^{\infty}(-1)^n \frac{(m+n)!}{m!n!}\left(\frac{a}{2ih}\right)^n \frac{\overline{A}_m}{(2ih)^{m+1}} \\
&\qquad +\mathrm{C}_1 I_n K_0+\sum_{m=1}^{\infty} K_m(\mathrm{C}_{m+1} I_{n-m}+\overline{\mathrm{C}}_m I_{n+m}) \\
&\qquad +\overline{\mathrm{C}}_1 \lambda_{n,\,0}+\sum_{m=1}^{\infty}(\overline{\mathrm{C}}_{m+1}\lambda_{n,\,m}+\mathrm{C}_m \lambda_{n,\,-m})=\begin{cases}-U, & (n=0) \\ 0, & (n=1, 2, \cdots)\end{cases} \\
&A_{n-1}a^{-n}+\mathrm{C}_1 I_n K_0+\sum_{m=1}^{\infty} K_m(\mathrm{C}_{m+1} I_{n+m}+\overline{\mathrm{C}}_m I_{n-m}) \\
&\qquad +\overline{\mathrm{C}}_1 \lambda_{-n,\,0}+\sum_{m=1}^{\infty}(\overline{\mathrm{C}}_{m+1}\lambda_{-n,\,m}+\mathrm{C}_m \lambda_{-n,\,-m})=0\,, \qquad (n=1, 2, \cdots)
\end{aligned}\right\} \tag{3.4}$$

where the argument ka of the modified Bessel functions has been dropped for simplicity. Further, elimination of A_m's from these equations gives

$$\begin{aligned}
&\sum_{m=0}^{\infty}\Bigg[\mathrm{C}_{m+1}\left\{I_{n-m}K_m+\lambda_{n,\,-(m+1)}-\sum_{s=0}^{\infty}(-1)^n \frac{(s+n)!}{s!n!}\left(\frac{a}{2ih}\right)^{s+n+1}(I_{s-m}K_{m+1}+\lambda_{s+1,\,-m})\right\} \\
&\quad +\overline{\mathrm{C}}_{m+1}\left\{I_{n+m+1}K_{m+1}+\lambda_{n,\,m}-\sum_{s=0}^{\infty}(-1)^n \frac{(s+n)!}{s!n!}\left(\frac{a}{2ih}\right)^{s+n+1}(I_{m+s+1}K_m+\lambda_{s+1,\,m+1})\right\}\Bigg] \\
&\qquad\qquad =\begin{cases}-U, & (n=0) \\ 0. & (n=1, 2, \cdots)\end{cases}
\end{aligned} \tag{3.5}$$

Equations (3.5) together with the second equation of (3.4) determine in principle the coefficients A_m's, C_m's and hence the solution of the present problem.

APPROXIMATE SOLUTION FOR THE FLOW AT SUFFICIENTLY SMALL REYNOLDS NUMBER

§ 4. Simultaneous Equations for the Constants b_n and β_n

Now, we shall determine the constants C_m's from the equations (3.5). However, it is difficult in practice to solve these equations exactly. On the other hand, Oseen's equation itself is valid for the whole field of flow only at small Reynolds numbers, and our main interest in the present investigation lies also in such flows. Therefore, in the present paper, we shall treat the case in which the two parameters ka $\left(=\frac{1}{4}R\right)$ and kh are very small.

Separating real and imaginary parts of the equations (3.5), we obtain the system of equation for determining B_n $(=b_n+i\beta_n)$ in the following form:

$$\left.\begin{aligned}
&C_{11}b_0+C_{12}\beta_0+C_{13}\left(\frac{b_1}{2}\right)+C_{14}\left(\frac{\beta_1}{2}\right)+C_{15}\left(\frac{b_2}{2}\right)+C_{16}\left(\frac{\beta_2}{2}\right)+\cdots=-U\,, \\
&C_{i1}b_0+C_{i2}\beta_0+C_{i3}\left(\frac{b_1}{2}\right)+C_{i4}\left(\frac{\beta_1}{2}\right)+C_{i5}\left(\frac{b_2}{2}\right)+C_{i6}\left(\frac{\beta_2}{2}\right)+\cdots=0\,. \\
&\qquad\qquad (i=2, 3, 4, \cdots)
\end{aligned}\right\} \tag{4.1}$$

The coefficients C_{ij}'s involve the functions $I_n(ka)$, $K_n(ka)$ and $K_n(2kh)$. In the previous paper[1], we have developed the analysis under the assumption that $ka \ll 1$, $(kh)^{-1}=O(1)$ and therefore we expanded only the functions $I_n(ka)$ and $K_n(ka)$ up to the order of $(ka)^2$.

However, in the case when $ka \ll 1$ and $kh \ll 1$, with which we are concerned in the present paper, the values of $(kh)^{-n}$ and $K_n(2kh)$ $(n=0, 1, 2, \cdots)$ in C_{ij}'s become very large, and therefore the previous analysis for small values of ka and kh should be modified.

Now, expanding every functions in powers of ka or kh and performing some tedious but traightforward calculations, we find that

$$\left.\begin{aligned}&C_{11},\ C_{13},\ C_{22},\ C_{24},\ C_{32},\ C_{34},\ C_{41},\ C_{43},\ C_{51},\ C_{53},\ C_{62},\ C_{64}=O(1)\ ,\\&C_{12},\ C_{21},\ C_{31},\ C_{42},\ C_{52},\ C_{61}=O(ka)\ ,\\&C_{14},\ C_{16},\ C_{23},\ C_{25},\ C_{33},\ C_{35},\ C_{44},\ C_{46},\ C_{54},\ C_{56},\ C_{63},\ C_{65}=O(k^{-1}a^{-1})\ ,\\&C_{15},\ C_{26},\ C_{36},\ C_{45},\ C_{55},\ C_{66}=O(k^{-2}a^{-2})\ ,\end{aligned}\right\}\tag{4.2}$$

cf. (4.3a)–(4.3c) and (4.5a)–(4.5c)].

These results suggest that the orders of magnitude of b_0, β_0, b_1, β_1, b_2, β_2, $\cdots$ are 1, ka, $ka)^2$, ka, $(ka)^2$, $(ka)^3$, $\cdots$, respectively. Therefore, to the lowest order in ka, we can deternine b_0, β_1, b_2, $\cdots$, separately from β_0, b_1, β_2, $\cdots$, by solving the following system of simulaneous equations:

$$\left.\begin{aligned}&C_{11}b_0+C_{14}(\beta_1/2)+C_{15}(b_2/2)+\cdots=-U\ ,\\&C_{41}b_0+C_{44}(\beta_1/2)+C_{45}(b_2/2)+\cdots=0\ ,\\&C_{51}b_0+C_{54}(\beta_1/2)+C_{55}(b_2/2)+\cdots=0\ ,\\&\qquad\cdots\cdots\cdots\cdots\ ,\end{aligned}\right\}\tag{4.3}$$

vhere

$$\left.\begin{aligned}&C_{11}=\left\{(2S-\tau)-\frac{1}{4}(a/2h)^4+\cdots\right\}+O(k^2a^2)\ ,\\&C_{41}=\left\{\frac{1}{2}(a/2h)^3+\cdots\right\}+O(k^2a^2)\ ,\\&C_{51}=\frac{1}{4}\{(a/2h)^2+2(a/2h)^4+\cdots\}+O(k^2a^2)\ ,\end{aligned}\right\}\tag{4.3a}$$

$$\left.\begin{aligned}&C_{14}=\{(a/2h)^3+\cdots\}(ka)^{-1}+O(ka)\ ,\\&C_{44}=\{1-2(a/2h)^2+4(a/2h)^4+\cdots\}(ka)^{-1}+O(ka)\ ,\\&C_{54}=\{3(a/2h)^3+\cdots\}(ka)^{-1}+O(ka)\ ,\end{aligned}\right\}\tag{4.3b}$$

$$\left.\begin{aligned}&C_{15}=2\{(a/2h)^2-4(a/2h)^4+\cdots\}(ka)^{-2}+O(1)\ ,\\&C_{45}=\{12(a/2h)^3+\cdots\}(ka)^{-2}+O(1)\ ,\\&C_{55}=2\{1-12(a/2h)^4+\cdots\}(ka)^{-2}+O(1)\ ,\end{aligned}\right\}\tag{4.3c}$$

vith

$$S=\frac{1}{2}-\gamma-\log(ka/2)\ ,\qquad \tau=\frac{1}{2}-\log(a/2h)\ ,\tag{4.3d}$$

vhere $\gamma=0.57721\ldots$ is Euler's constant.

Thus, we obtain

$$\left.\begin{aligned}&b_0=-\frac{1}{4}U\Delta\{1-2(a/2h)^2-8(a/2h)^4+\cdots\}+O(k^2a^2)\ ,\\&\beta_1=\frac{1}{4}U\Delta\{(a/2h)^3+\cdots\}(ka)+O(k^3a^3)\ ,\\&b_2=\frac{1}{16}U\Delta\{(a/2h)^2+\cdots\}(ka)^2+O(k^4a^4)\ ,\end{aligned}\right\}\tag{4.4}$$

vhere

$$\Delta=\frac{4}{2S-\kappa-1}\left\{1+2(a/2h)^2+\left(12+\frac{1}{4S-2\kappa-2}\right)(a/2h)^4+\cdots\right\}\ .\tag{4.4a}$$

Then, inserting (4.4) in (4.1), the remaining coefficients β_0, b_1, β_2, $\cdots$ can be determined rom the following equations:

$$\left.\begin{aligned}
&C_{22}\beta_0+C_{23}(b_1/2)+C_{26}(\beta_2/2)+\cdots=C_{20}\,,\\
&C_{32}\beta_0+C_{33}(b_1/2)+C_{36}(\beta_2/2)+\cdots=C_{30}\,,\\
&C_{62}\beta_0+C_{63}(b_1/2)+C_{66}(\beta_2/2)+\cdots=C_{60}\,,\\
&\cdots\cdots\cdots\cdots\,,
\end{aligned}\right\}\qquad(4.5)$$

where

$$\left.\begin{aligned}
&C_{22}=\frac{1}{4}\{4(\tau-1)+4(a/2h)^2-(a/2h)^4+\cdots\}+O(k^2a^2)\,,\\
&C_{32}=\frac{1}{2}\{2(a/2h)-3(a/2h)^3+\cdots\}+O(k^2a^2)\,,\\
&C_{62}=\frac{1}{4}\{3(a/2h)^2-8(a/2h)^4+\cdots\}+O(k^2a^2)\,,
\end{aligned}\right\}\qquad(4.5a)$$

$$\left.\begin{aligned}
&C_{23}=\{2(a/2h)-3(a/2h)^3+\cdots\}(ka)^{-1}+O(ka)\,,\\
&C_{33}=\{1-2(a/2h)^2+6(a/2h)^4+\cdots\}(ka)^{-1}+O(ka)\,,\\
&C_{63}=\{-3(a/2h)^3+\cdots\}(ka)^{-1}+O(ka)\,,
\end{aligned}\right\}\qquad(4.5b)$$

$$\left.\begin{aligned}
&C_{26}=2\{3(a/2h)^2-8(a/2h)^4+\cdots\}(ka)^{-2}+O(1)\,,\\
&C_{36}=\{-12(a/2h)^3+\cdots\}(ka)^{-2}+O(1)\,,\\
&C_{66}=2\{1-12(a/2h)^4+\cdots\}(ka)^{-2}+O(1)\,,
\end{aligned}\right\}\qquad(4.5c)$$

$$\left.\begin{aligned}
C_{20}=\frac{1}{16}&U\Delta(a/2h)^{-1}\{2S-2\tau+1-4(S-\tau+1)(a/2h)^2\\
&-2(8S-9\tau+3)(a/2h)^4+\cdots\}(ka)+O(k^3a^3)\,,\\
C_{30}=\frac{1}{32}&U\Delta\{4(2S-\tau)-3-8(2S-\tau-1)(a/2h)^2\\
&-(64S-32\tau-23)(a/2h)^4+\cdots\}(ka)+O(k^3a^3)\,,\\
C_{60}=\frac{1}{48}&U\Delta\{3(a/2h)-10(a/2h)^3+\cdots\}(ka)+O(k^3a^3)\,,
\end{aligned}\right\}\qquad(4.5d)$$

S, τ and Δ being the same as in (4.3d) and (4.4a) respectively.
Thus, we get

$$\left.\begin{aligned}
&\beta_0=\frac{1}{8}U\Delta\left(S-\tau+\frac{1}{2}\right)(\tau-1)^{-1}(a/2h)^{-1}[1+\Lambda_1(a/2h)^2+\Lambda_2(a/2h)^4+\cdots](ka)+O(k^3a^3)\,,\\
&b_1=\frac{1}{16}U\Delta(\tau-1)^{-1}[\{4S(2\tau-3)-4\tau^2+5\tau+1\}+\cdots](ka)^2+O(k^4a^4)\,,\\
&\beta_2=-\frac{1}{64}U\Delta(\tau-1)^{-1}[(6S-10\tau+7)(a/2h)+\cdots](ka)^3+O(k^5a^5)\,,
\end{aligned}\right\}\qquad(4.6)$$

with the abbreviations

$$\left.\begin{aligned}
&\Lambda_1=\frac{2\tau-1}{\tau-1}-\frac{8S-6\tau+3/2}{S-\tau+1/2}\,,\\
&\Lambda_2=\frac{3}{2}\,\frac{4\tau-5}{\tau-1}+\left(\frac{2\tau-1}{\tau-1}\right)^2-\frac{2\tau-1}{\tau-1}\,\frac{8S-6\tau+3/2}{S-\tau+1/2}+\frac{4S+4\tau-39/4}{S-\tau+1/2}\,.
\end{aligned}\right\}\qquad(4.6a)$$

On the other hand, solving the second equation of (3.4) for $A_0=a_0+i\alpha_0$, and separating the real and imaginary parts, we get the relations

$$\left.\begin{aligned}
&a_0/a=-b_0(ka)^{-1}\\
&\alpha_0/a=b_0\{(a/2h)+O(k^2a^2)\}+\beta_0\{(ka)^{-1}+O(ka)\}\\
&\quad+b_1\left[\left\{-(a/2h)+\frac{1}{2}(a/2h)^3\right\}+O(k^2a^2)\right]+\beta_1\{(a/2h)^2(ka)^{-1}+O(ka)\}\\
&\quad+b_2\{4(a/2h)^3(ka)^{-2}+O(1)\}+\beta_2[\{2(a/2h)^2-3(a/2h)^4\}(ka)^{-1}+O(ka)]\\
&\quad+\cdots\cdots\cdots\cdots\,.
\end{aligned}\right\}\qquad(4.7)$$

Inserting (4.4) and (4.6) into (4.7), we obtain

$$\left.\begin{aligned} a_0 &= \frac{1}{4}Ua\Delta\{1-2(a/2h)^2-8(a/2h)^4+\cdots\}(ka)^{-1}+O(ka)\,, \\ \alpha_0 &= \frac{1}{8}Ua\Delta\left(S-\tau+\frac{1}{2}\right)(\tau-1)^{-1}(a/2h)^{-1}\left[1+\left\{\Lambda_1-\frac{2(\tau-1)}{S-\tau+1/2}\right\}(a/2h)^2\right. \\ &\qquad \left.+\left\{\Lambda_2+\frac{4(\tau-1)}{S-\tau+1/2}\right\}(a/2h)^4+\cdots\right]+O(k^2a^2)\,, \end{aligned}\right\} \tag{4.8}$$

where Λ_1, Λ_2 and Δ are given by (4.6*a*) and (4.4*a*) respectively.

§ 5. The Forces on the Cylinder

We now proceed to the evaluation of the force acting on the cylinder C. As shown in the previous paper[1)], this force may be considered as composed of the drag D and the lift L in the directions of the x and y-axes respectively, which are expressed respectively as

$$D=2\pi\rho U a_0\,, \qquad L=2\pi\rho U\alpha_0\,, \tag{5.1}$$

where ρ is the density of the fluid concerned.

Therefore, making use of the expressions (4.8) for a_0 and α_0, we can obtain expansion formulae for the drag and lift. Thus, correct as far as terms of the lowest order of R, we have the drag and lift coefficients as:

$$\begin{aligned} C_D &= \frac{D}{2\rho U^2 a} \\ &= \frac{4\pi}{R(2S-\kappa-1)}\left\{1+\frac{1}{2(2S-\kappa-1)}\left(\frac{a}{2h}\right)^4\right. \\ &\qquad \left.+O\left(\frac{a^6}{h^6}\right)\right\}+O(R)\,, \end{aligned} \tag{5.2}$$

and

$$\begin{aligned} C_L &= \frac{L}{2\rho U^2 a} \\ &= \frac{\pi}{2\kappa}\,\frac{h}{a}\,\frac{2S-2\kappa-1}{2S-\kappa-1}\left[1+\left(\frac{1}{\kappa}-\frac{8S-5}{2S-2\kappa-1}\right)\right. \\ &\quad \times\left(\frac{a}{2h}\right)^2+\left\{\left(\frac{1}{\kappa}+\frac{1}{2}\right)\left(\frac{1}{\kappa}-4\right)\right. \\ &\quad \left.+\frac{1}{2}\,\frac{1}{2S-\kappa-1}+\left(\frac{1}{\kappa}-\frac{15}{2}\right)\frac{1}{2S-2\kappa-1}\right\} \\ &\quad \left.\times\left(\frac{a}{2h}\right)^4+O\left(\frac{a^6}{h^6}\right)\right]+O(R^2)\,, \end{aligned} \tag{5.3}$$

where as before

$$S=\frac{1}{2}-\gamma-\log\frac{R}{8}\,, \qquad \kappa=-\frac{1}{2}-\log\left(\frac{a}{2h}\right). \tag{5.4}$$

It will be seen that as was noted in the previous paper, these results are in perfect agreement, up to the first two terms, with the formulae which were obtained by considering formally the case $kh \ll 1$ in the previous results for the case of $(kh)^{-1}=O(1)$.

§ 6. Numerical Discussions

Making use of the formulae (5.2) and (5.3), the writer has calculated the values of $C_D/C_D{}^*$ and C_L for various values of the Reynolds number R $(=4ka)$ as well as for various values of the ratio $a/2h$, where $C_D{}^*$ denotes the drag coefficient for a single circular cylinder in an unbounded stream and is given by $C_D{}^*=4\pi/RS$. The results are given in Tables

Table I. Values of $C_D/C_D{}^*$.

R \ $a/2h$	1/10	1/5	1/3	2/5	1/2 Present writer	 Tamada
0.0001	0.5714	0.5519	0.5385	0.5340	0.5289	0.5287
0.001	0.5933	0.5672	0.5495	0.5436	0.5369	0.5367
0.01	0.6346	0.5950	0.5691	0.5606	0.5511	0.5508
0.02	0.6553	0.6086	0.5785	0.5687	0.5577	0.5575
0.04	0.6834	0.6266	0.5908	0.5793	0.5664	0.5661
0.06	0.7052	0.6403	0.6000	0.5871	0.5728	0.5725
0.08	0.7241	0.6519	0.6077	0.5936	0.5782	0.5780
0.1	0.7413	0.6623	0.6146	0.5995	0.5829	0.5825

Table II. Values of C_L.

R \ $a/2h$	1/10	1/5	1/3	2/5
0	4.21	3.08	2.67	2.95
0.0001	3.79	2.85	2.50	2.78
0.001	3.66	2.79	2.45	2.73
0.01	3.42	2.67	2.37	2.65
0.02	3.30	2.61	2.33	2.61
0.04	3.14	2.53	2.27	2.56
0.06	3.01	2.47	2.23	2.52
0.08	2.90	2.42	2.20	2.49
0.1	2.80	2.37	2.17	2.46

I–III and are also shown graphically in Figs. 2 and 3.

The values of C_D/C_D^* for the limiting case when $a/2h=1/2$ are also found to be in good agreement with Tamada's results[2] which are tabulated in the last column of Table I for the sake of reference. Further, the values of C_D/C_D^* and C_L for the case when $a/2h=1/20$ are tabulated for comparison in Table III together with the values calculated by the expansion formulae valid for $kh=O(1)$ which were obtained in the previous paper. In this table, the second and fourth columns with the heading I give the values of C_D/C_D^* and C_L calculated by the formulae in the present paper, while in the third and fifth columns with the heading II are given similar values calculated in the previous paper. In Figs. 2 and 3 the results for the case when $a/2h=1/20$ calculated by the expansion formulae valid for $kh=O(1)$ are also shown by dotted-line curves.

Table III. Values of C_D/C_D^* and C_L $(a/2h=1/20)$.

R	C_D/C_D^*		C_L	
	I	II	I	II
0	0.5000		6.24	
0.0001	0.5923		5.40	
0.001	0.6220		5.13	
0.01	0.6798	0.6793	4.60	4.60
0.02	0.7097	0.7080	4.33	4.34
0.04	0.7516	0.7461	3.95	3.99
0.06	0.7848	0.7737	3.65	3.74
0.08	0.8143	0.7965	3.38	3.53
0.1	0.8418	0.8155	3.13	3.34
0.2		0.8799		2.68
0.4		0.9423		1.88

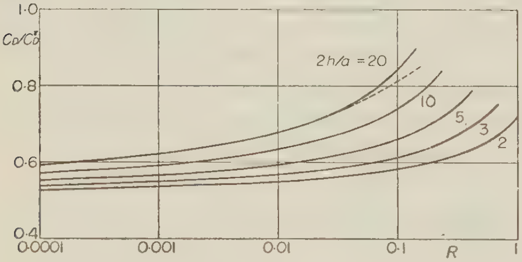

Fig. 2.

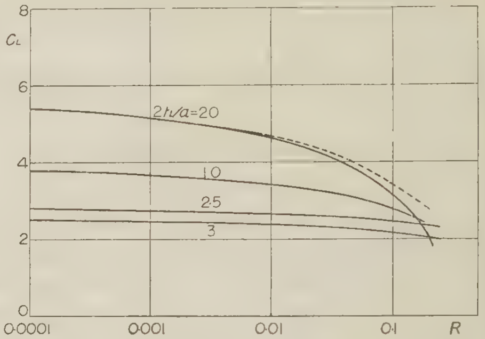

Fig. 3.

From these tables and figures, it will be seen that, as the distance between the cylinders decreases, the values of C_D for a sufficiently small Reynolds number decreases monotonously, while the value of C_L decreases first and then increases.

In conclusion, the writer wishes to express his cordial thanks to Professor S. Tomotika for his continual interest and encouragement throughout this work and especially for his kind inspection of the manuscript.

Also, the writer is much indebted to Professor K. Tamada for his invaluable advices and criticism, and also for his kindness in putting some of his unpublished results at the writer's disposal.

References

1) H. Fujikawa: J. Phys. Soc. Japan **11** (1956) 558.
2) K. Tamada: to be published.
3) L. N. G. Filon: Proc. Roy. Soc. **A, 113** (1926) 7.
4) I. Imai: Proc. Roy. Soc. **A, 224** (1954) 141.

Short Notes

This section is intended to secure prompt publication of important discoveries in physics. The reports should not exceed 800 words in length. A figure of size 7 cm × 7 cm will be counted as 150 words.

J. PHYS. SOC. JAPAN **12** (1957) 431

Anomalies of Electrical Properties of Lead Telluride Crystal

By Susumu UCHIYAMA and Kisaburo SHOGENJI
Faculty of Engineering, Nagoya University, Nagoya

(Received January 24, 1957)

It was reported by Putley1) that some PbSe and PbTe crystals reversed the signs of their Hall coefficient in addition to the intrinsic sign reversal. We looked for the sign reversal of PbTe crystals by heat treatment, but could not find it.2) However, a specimen, which was at first a normal p-type one and, after copper being added by evaporation, heat treated in vacuum at 500°K for 3 hours, showed the sign reversal in the extrinsic temperature range. The results obtained are shown in Fig. 1 and are similar to those reported by Putley1). Impurity levels with activation energy of the order of 0.1 ev. are seen, from the slope of resistivity curve, to appear in addition to the ordinary acceptor levels.

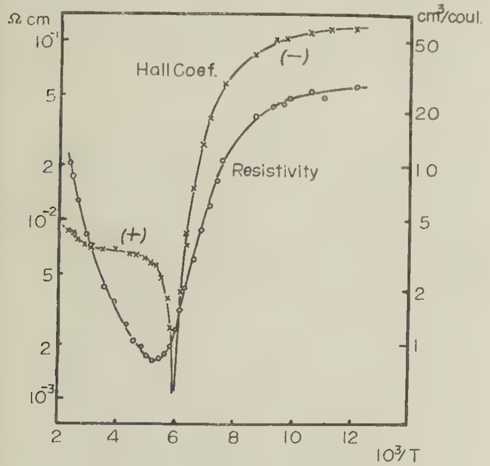

Fig. 1.

Besides the sign reversal some anomalies were found at lower temperatures. At some temperature below the sign reversal temperature, voltage *vs.* current rleation was not symmetrical with respect to the origin, and was not strictly linear even for smaller current. At the same temperature range, voltage drop across the two resistivity probes, for the same current through the specimen, changed by applying a magnetic field transversely. It increased or decreased according to the change of the direction of applied field. The phenomenon cannot be considered to represent magnetoresistive effect, since the change is not proportional to the square of the field but rather proportional to the field itself. The experiments were made with the greatest care. We concluded that the anomalies were not due to any experiment errors but they represented the real peculiarities of the specimen. We thought that these two anomalies arose from the inhomogeneity of the specimen, though the specimen proved to be homogeneous in electrical properties at room temperature. If the number of current carrier varies along the specimen, potential gradient also varies when a current flows. Then potential drop between two probes can be changed by applying a magnetic field, especially when the variation of potential gradient is large near the probes. The potential drop can be increased or decreased by changing the direction of magnetic field. This is, we think, the cause of the anomaly mentioned above. The non-ohmic properties obtained are considered to result from the inhomogeneity too. Moreover a p-n junction might be generated within the specimen at some temperature.

Let us now consider the reason why Hall coefficient changes its sign. Within the scope of our experiments, copper added seems to be responsible for the sign reversal. The surfaces were ground, before measurements, by using emery paper in order to avoid any disturbances due to the surface copper film. Impurity band conduction3) and surface conduction4) can be taken into account as the cause of the sign reversal. Impurity band conduction model proved to have several difficulties in quantitatively explaining the phenomena, although the characteristics obtained were, in several respect, similar to those of germanium with impurity conduction band. But we cannot entirely deny, at present, an occuarence of impurity band conduction, since the data are scanty and there are some uncertainties in the date due to the inhomogeneity.

Researches to get more informations on the cause of the sign reversal are now in progress.

References

1) E. H. Putley: Proc. Phys. Soc. (London) **B 66** (1955) 22.
2) K. Shogenji and S. Uchiyama: J. Phys. Soc. Japan **12** (1957) 252.
3) C. S. Hung and J. R. Gliesman: Phys. Rev. **96** (1954) 1226.
4) H. P. R. Faederikse, W. R. Hosler and D. E. Roberts: Phys. Rev. **103** (1956) 67.

J. PHYS. SOC. JAPAN **12** (1957) 432

Quasi-static Hysteresis in Barium-titanate Single Crystals

By KIYASU Zen'iti, Kazuo HUSIMI and
Keisuke KATAOKA
Electrical Communication Laboratory, Tokyo

(Received November 5, 1956)

The measurement of hysteresis curve and spontaneous polarization in barium-titanate single crystal have hitherto been carried out by polarization switching method. By this method, we cannot measure these characteristics quantitatively, because there may be asymmetries on the hysteresis loop, and we cannot detect the depolarized point.

The authors have developed a new ultrasonic measuring method which uses the piezoelectric property of ferroelectric materials to determine the absolute polarization. Using this method together with the conventional method we have obtained various important results.

The sample used, 0.14 mm in thickness, with 1 mm² electrode area, is a c-plate which contains a-domain a little, and has been produced by KF-process by Waku in this Laboratory.

After applying a positive half cycle of a sinusoidal field with a peak value of 2 kV/cm and the period of 6 minutes, we obtained minor loops for the field strengths of 0.3, 0.35, 0.4, 0.45 and 0.5 kV/cm. These quasi-static hysteresis loops are shown in Fig. 1.

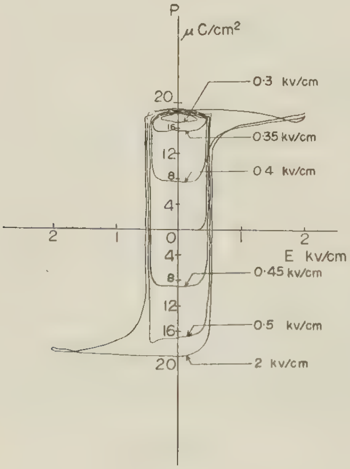

Fig. 1.

After applying 5 kV/cm d.c. field for several times, we measured the polarization at 5 kV/cm d.c. field for 2 seconds. These results are shown in Fig. 2.

1. Maximum slope of the hysteresis loop $\varepsilon_{\max}$ is virtually infinite. $\varepsilon_{\max}$ is found to follow the relaxation formula of Debye's type,

$$\varepsilon^* = \frac{a}{1+j\frac{f}{f_0}} + \varepsilon_\infty$$

with $f_0=0$, instead of the value 29 kc/s reported by Drougard¹⁾, that is, $\varepsilon_{\max}$ is represented by the formula

$$\varepsilon_{\max} = \frac{A}{jf} + \varepsilon_\infty .$$

2. In case of single crystals, the minor loops return to their original spontaneous value without any appreciable depolarization.

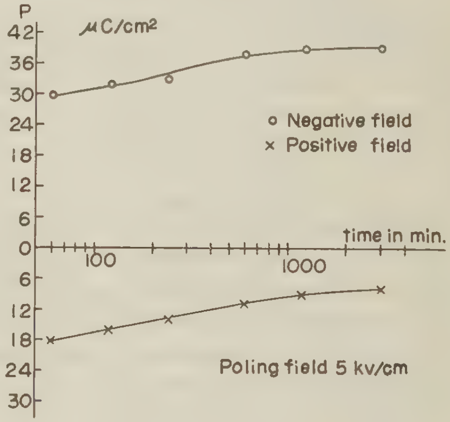

Fig. 2

3. The crystal contains slowly polarizing components which takes several hours to polarize even under a high electric field, whereas it has been believed that the reversal of polarization is completed within a very short time under such a field, although under a low field the polarization may be fairly slow, as Little observed²⁾.

4. There are asymmetries in polarization velocity under positive and negative fields. This characteristic is in the same polarity throughout a single plate crystal, and it is easier to polarize from outer to inner side of a butterfly pair.

5. The value of spontaneous polarization, 37.8×10^{-6} coulomb/cm² at room temperature, is much in excess of Merz's value 24×10^{-6}. The sum of positive and negative polarizations in Fig. 2, on the other hand, is always nearly 48×10^{-6} coulomb/cm² which is just twice the above value. From this we conclude that Merz has measured the high speed component only.

References

1) H. E. Drougard, H. L. Funk and D. E. Young: J. App. Phys. **25** (1954) 1166.
2) E. A. Little: Phys. Rev. **98** (1955) 978.

J. PHYS. SOC. JAPAN **12** (1957) 433

The Thermal Decomposition of Polyvinyl Alcohol Using Mass Spectrometer

By Hideo FUTAMA and Hidejirō TANAKA

Department of Physics, Faculty of Science, Hokkaidō University, Sapporo

(Received November 29, 1956)

It has been known that the thermal decomposition of polyvinyl alcohol (PVA) plays an important role in considering its properties[1]. Using the mass spectrometer (Hitachi RM-AA) which seems to be more convenient than to the customary chemical method[2], we have analysed the thermal decomposition products of PVA. Heating of PVA films is so controlled that the temperature is kept constant for a sufficiently long time and raised step by step.

Decomposed vapours are mainly water and acetaldehyde. Generation of vapours fit the first order reaction with reaction constant k of the order of $10^{-4}\,\mathrm{min}^{-1}$, $m=a[1-\exp(-kt)]$, where t is time and m is the mass of the generated vapour per unit mass of initial PVA. This equation holds for the generation which occurs by raising the tempera-true from $T-\Delta T$ to T and keeping it at T. For example, Fig. 1 shows the generation of acetaldehyde at 200°C. Dotted line is calculated from the equation, where a and k are chosen so as to fit the experimental curve.

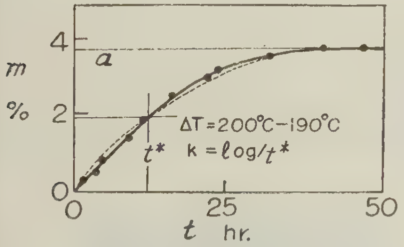

Fig. 1

Saturation value a is the function of T and ΔT, and by making $\Delta T\to O$ we may abtain $a(T,\Delta T)\fallingdotseq f(T)\cdot\Delta T$. Then we can assume the existence of certain distribution function $f(T)$ of the source of decomposed vapour in PVA. Thus it follows

$$a(T,\Delta T)=\int_{T-\Delta T}^{T} f(T)\cdot dT\fallingdotseq f(T)\cdot\Delta T\,.$$

Seeking $a(T,\Delta T)/\Delta T$ experimentally, we can obtain the approximate shape of $f(T)$ as showe in Fig. 2, where ΔT is about 10°C and curves ***A***, ***B*** and ***C*** are found to correspond to water, water and acetaldehyde respectively by the mass spectrometric analysis.

To examine curves ***A*** and ***B*** in Fig. 2, we prepared two samples. One (S_1) is immersed in the vapour of heavy water D_2O solution. Table I shows merely a qualitative tendency of the generation of DHO which consists in the generated aqueous vapour. In the sample (S_1), degree of heavy hydrogen exchange with PVA radical seems to be lower than that in (S_2). Further the curve ***B*** occurs in connection with the decomposition curve ***C***. Thus in Fig. 2, the curve ***B*** seems to correspond to the decomposition or rather to the cross linking (ether bond) in PVA structure, and the curve ***A*** to mere dehydration.

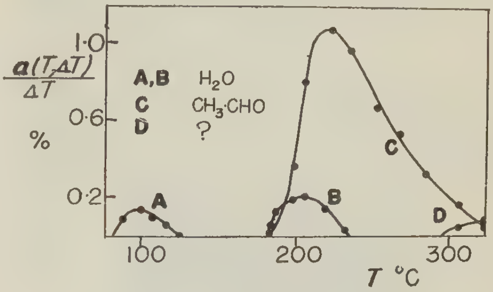

Fig. 2

In Fig. 2, the area of the curve ***B*** indicates 7% of PVA, which means 20% of O atoms in PVA, react into H_2O. The area of the curve ***C*** indicates 60% of PVA, and accumulated plots of a about this curve show 60~70°C lower generation temperature in comparison with more rapid heating[3]. The curve ***D*** in Fig. 2 consists of undetectable vapours which seem to be hydrocarbons. This part and the residue in the furnace indicate 25% of PVA. To detect them is a remaining task.

Table I. Concentration of DHO in the generated aqueous vapour

Sample	***A***	***B***
S_1	30~40%	2~ 3%
S_2	30~40%	40~50%

References

1) E. Nagai, N. Sagara and K. Uchikoshi: Kōbunshikagaku **10** (1953) 211, **11** (1954) 218.
"Polyvinylalcohol": Symposium at Ōsaka University, November (1955).
2) Noma and K. Taniguchi: Kōbunshikagaku **10** (1953) 271.
3) K. Harabayashi and J. Hiramatsu: ibid. **9** (1952) 33.

J. PHYS. SOC. JAPAN **12** (1957) 434

Resistivity and Hall Coefficient of Semiconductors

By Kisaburo SHOGENJI and Susumu UCHIYAMA
Faculty of Engineering, Nagoya University, Nagoya

(Received January 24, 1957)

Resistivity and Hall coefficient of semiconductors have been already calculated for the case in which the current carriers are scattered by acoustical mode of lattice vibration and ionized impurity centres.[1] We have made the calculation for the case where the current carries are affected by both acoustical and optical modes of lattice vibration. The scattering by impurity centres is neglected in this calculation. Since its effect becomes appreciable at lower temperatures, the calculation made here has some significance at rather high temperatures, especially for semiconductors with high dielectric constant.

The calculation is made on the basis of the following assumptions: *i*) electrons (or holes) which contribute to conduction are free; *ii*) they obey Boltzmann statistics; *iii*) scattering of electrons is due to acoustical and optical modes of lattice vibration, other scattering sources being neglected; *iv*) for scattering by optical mode, relaxation time of Fröhlich and Mott[2] exists. Using conventional notations, conductivity and Hall coefficient are expressed as follows:

$$\left.\begin{aligned} &\sigma=A+(B^2/A), \qquad R=-B/\{H(A^2+B^2)\},\\ &A=-\frac{4\pi e^2}{3}\int_0^\infty lv^3(1+s^{22})^{-1}\frac{\partial f}{\partial\varepsilon}dv,\\ &B=-\frac{4\pi e^2}{3}\int_0^\infty slv^3(1+s^2)^{-1}\frac{\partial f}{\partial\varepsilon}dv,\\ &s=elH/mv. \end{aligned}\right\} \quad (1)$$

Mean free path l of electron is given by

$$\left.\begin{aligned} &1/l=(1/l_a)+(1/l_0),\\ &l_a=3(2\pi mkT)^{1/2}/4e^2n\rho_a,\\ &l_0=(2m\varepsilon)^{1/2}/c^2n\rho_0, \end{aligned}\right\} \quad (2)$$

l_a is mean free path when the acoustical mode only scatters electron and ρ_a is the resistivity at that time; l_0 and ρ_0 correspond to the optical mode. Thus

$$\left.\begin{aligned} &A=\frac{2}{\rho_a}\int_0^\infty\frac{x^4(x+\beta)\exp(-x^2)}{(x+\beta)^2+\gamma}dx,\\ &B=\frac{2\sqrt{\gamma}}{\rho_a}\int_0^\infty\frac{x^4\exp(-x^2)}{(x+\beta)^2+\gamma}dx,\\ &\beta=\frac{3\sqrt{\pi}}{4}\frac{\rho_0}{\rho_a}, \qquad \gamma=\frac{9\pi}{16}\mu_a{}^2H^2, \end{aligned}\right\} \quad (3)$$

μ_a is the mobility corresponding to the acoustical mode. With Eqs. (1) and (3) we can calculate resistivity and Hall coefficient. Fig. 1 shows resistivity at no magnetic field, and ratio of Hall ceofficient to 1/ne. Fig. 2 shows the change of resistivity with magnetic field.

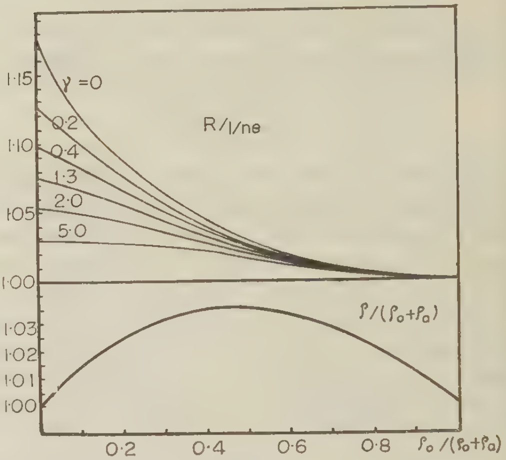

Fig. 1.

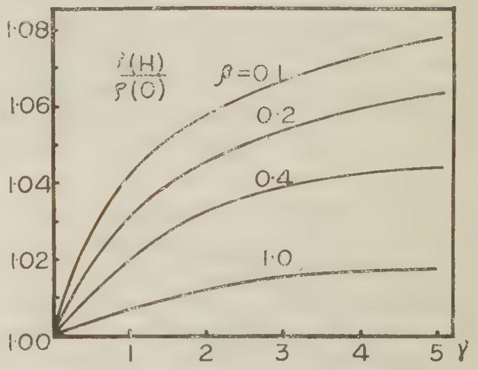

Fig. 2.

References

1) V. A. Johnson and K. Lark-Horovitz: Phys. Rev. **79** (1950) 176; **82** (1951) 977. H. Jones: *ibid*. **81** (1951) 149.
2) H. Fröhlich and N. F. Mott: Proc. Roy. Soc. **171** (1939) 496.

J. PHYS. SOC. JAPAN **12** (1957) 435

Manganese Impurities in Silver Halides Studied by the Paramagnetic Resonance Absorption

By Hidetaro ABE

Institute of Science and Technology, University of Tokyo, Tokyo

(Received February 8, 1957)

Silver halides, AgCl and AgBr, containing manganese impurities were examined by the method of paramagnetic resonance absorption at room temperature and at $\lambda=3.23$ cm. Specimens were prepared from the mixed melt with cooling velocities of 1°∼50°/min.

Table I. P.R.A. spectra of manganese in silver halides.

Base	AgCl		AgBr
Sort of spectrum	(a) 6 peaks	(b) single	(a) 6 peaks
g-value	2.006 ±0.003	2.000 ±0.003	2.006 ±0.010
Hfs splitting const. A in oer.	87±4	—	83±4
Line shape	≈Gaussian	Lorentzian	—
Line width in oer.	19±3	52±4	60±5
Mole Mn concentration in the sample	$10^{-4}\sim 10^{-2}$	$\sim 10^{-2}$	$10^{-4}\sim 10^{-2}$

The Mn/AgCl system gives two types of spectra as listed in Table I, though sometimes another type of absorption is accompanied which is very broad and weak. Spectrum (a) consists of six clearly resolved lines showing the hfs of Mn, three of which are shown in Fig. 1. Spectrum (b) can be only observed in the specimens having higher Mn concentration. Spectrum (a) should correspond to an impurity state of isolated ions whereas (b) can be explained as being caused by manganese aggregation[1) 2)]. So far as much diluted samples are concerned, it can be concluded from the measured intensity that nearly all the part of added Mn impurities appears to occupy the impurity state (a) and it is stable at room temperature over months. Situation differs somewhat from the case of Mn/NaCl, etc.[1) 3)] at room temperature. The observed hfs shows the crystalline field acting on the Mn ion at room temperature is cubic and the Mn^{++} in AgCl crystal is not accompanied by any Ag vacancy at least in its near neighbours. Mn/NH_4Cl crystal really shows in its P.R.A. spectrum the influence of a heavily distorted crystalline field acting on the Mn ions. In Mn/AgBr system, the six peaks of hfs can be just resolved as in Fig. 2. Assuming that each component line has Gaussian shape, the width of 60 oer. gives the best fit to the observed derivative curves (at 5×10^{-4} mole Mn).

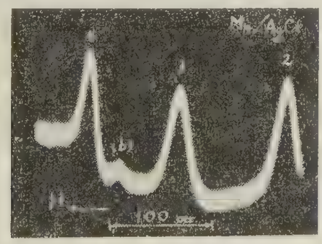

Fig. 1. CRO photo of Mn spectra at 3×10^{-3} mole Mn in AgCl. Large peaks correspond to the 2nd, 3rd and 4th peak of spectrum (a) whereas small peak is the spectrum (b).

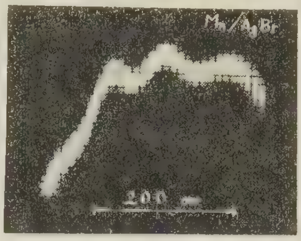

Fig. 2. Low field side of the Mn spectrum at 7×10^{-4} mole Mn in AgBr.

The width of line remains constant within our listed errors, being independent of Mn concentration, which can not be explained by the dipole width. The widths of hfs components in Mn/AgBr and in Mn/AgCl give a ratio of 3.2±0.8. These widths may be, at least mainly, attributed to the nuclear magnetic moments of neighbouring halogens, since the ratio of the nuclear magnetic moment of Br to Cl, $\mu Br/\mu Cl=2.7$, agrees with the above ratio. They are about ten times larger, however, to be explained by the local magnetic field caused by these nuclei. It may be considered that the origin of these widths is attributable to the unresolved substructures due to the halogen nuclei superposed to the main structure of Mn hfs, so that our total Hamiltonian may, presumably, be expressed in the following form:

$$\mathscr{H}=g\beta\boldsymbol{H}\cdot\boldsymbol{S}+A(\boldsymbol{S}\cdot\boldsymbol{I})_{Mn}+\sum A_x(\boldsymbol{S}_x\cdot\boldsymbol{I}_x) \qquad (1)$$

From the observed width of hfs components, the total probability of finding the unpaired spin on some halogen atoms is estimated to be about 0.10.

The author is very grateful to Prof. K. Ôno for his valuable discussions and to Mr. E. Mizuki of the Fuji Photo Film Co. Ltd. for supplying the pure silver halides.

References

1) Schneider et al: *Defects in Cryst. Solids*, (London, 1955), 74.
2) Abe et al: J. Chem. Phys. **25** (1956) 378.
3) Itoh et al: Report at the annual meeting of the Phys. Soc. Japan (Tokyo, 1955).

J. PHYS. SOC. JAPAN **12** (1957) 436

Observation of the Drift of Germanium Surface by Field Effect Experiment

By Makoto KIKUCHI

Electrotechnical Laboratory, Tokyo, Japan

(Received February 22, 1957)

It has been found out that an etched surface of n-type germanium shows "drift" in the room air. Experimental apparatus and measuring circuits are shown in Fig. 1. A chopped light beam is focused on the single crystal germanium rod through a thin mica plate, which is sandwhiched by the specimen and a fine metal mesh. d.c. voltage V_p is supplied to the mesh, and the variation of conductance of the sample and that of photoconductance are measured.

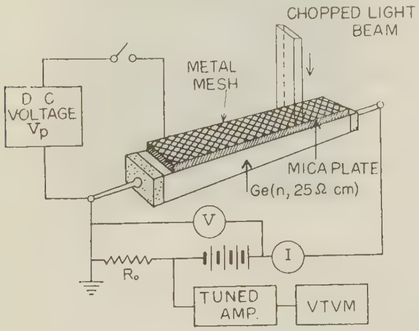

Fig. 1. Schematic representation of experimental apparatus.

At first, the sample was etched with $CP-4$, and after two days, it was again treated with HF for 10 minutes. Measurements were performed after (A) 5 minutes, (B) 17 hours, (C) 24 hours, and (D) 48 hours. Results are shown in Fig. 2. These results were quite well reproducible.

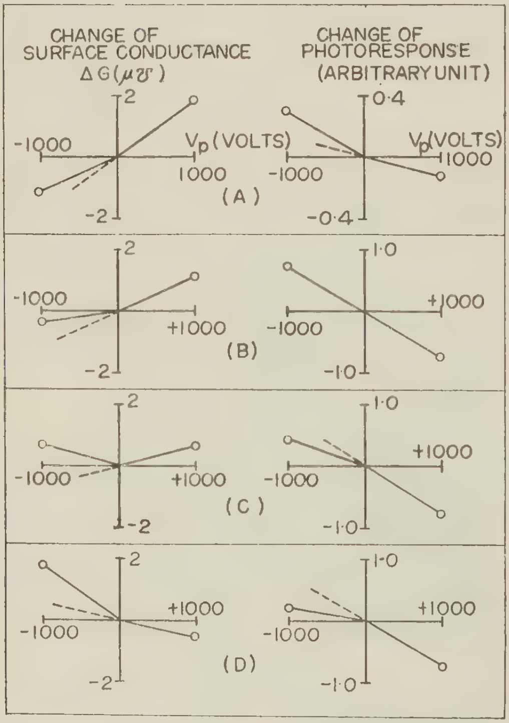

Fig. 2. Experimental results (A) 5 min, (B) 17 hours, (C) 24 hours, (D) 48 hours, after HF treatment.

The surface conductance can be calculated as a function of φ_s (i.e., the difference between the Fermi level and the middle of the energy gap at the surface), using Schrieffer's estimation of the mobility. Relative values of photoresponse may also be estimated from the Stevenson's calculation[1]. These curves are shown in Fig. 3.

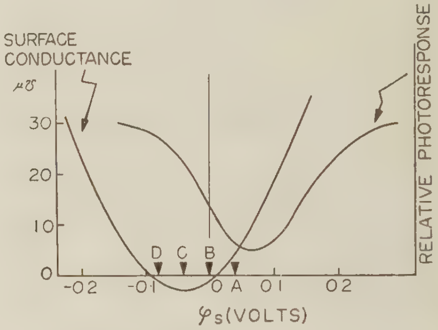

Fig. 3. Variation of surface conductance and photoresponse with φ_s.

From Fig. 2 and 3, we can obtain following conclusions:

1) The situations of the surface (A, B, C and D in Fig. 2) correspond to the positions A, B, C and D on the φ_s axis in Fig. 3, respectively.
2) The etched surface drifts towards the state of less φ_s value in the room air.
3) The maximum of the surface recombination velocity as a function of φ_s calculated by Stevenson must be shifted towards right, as independently pointed out by Harik[2] et al.

It seems likely that the drift of φ_s is caused or accompanied by the building up of oxide layer on the etched surface. We have also obtained some evidences for it.

Detailed discussions and other experimental results will be reported in the near future.

References

1) Stevenson: Physica. **20** (1954) 1041.
2) Harik et al: Phys. Rev. **101** (1956) 1434.

J. Phys. Soc. Japan **12** (1957) 437~438

Randomness of Microwave Gas Breakdown Voltage

By Kenji Mitani and Hiroshi Kubo
Yoshida College, University of Kyoto

(Received January 25, 1957)

R. Cooper[1] has made observation of the randomness of the microwave gas breakdown by using pulsed microwave. We have investigated the same phenomenon by continuous microwave, and here the results obtained together with some discussions will be given. The experimental apparatus used is the same as that reported in our previous paper.[2]

In Fig. 1 the curves (a) and (b) show the breakdown probabilities, corresponding respectively to the cases with and without irradiation by γ-rays of RaBr, the breakdown probability meaning the ratio of the number of the breakdowns occuring before a certain voltage V to the total number of breakdowns. Comparing these two curves, it will easily be seen that the case with irradiation by γ-rays has a sharper slope, meaning that in microwave, too, the so called statistical time lag is smaller in the case with irradiation than in the case without it. We find that the microwave breakdown voltage is not uniquely determined. When we take the potential corresponding to the breakdown probability of 50% as the breakdown voltage, as in the case of the direct current breakdown[3], the curves of the microwave breakdown voltage *versus* gas pressure become as shown in Fig. 2. It is found that these curves have the same character as the ones obtained by S. C. Brown and others in microwave[4].

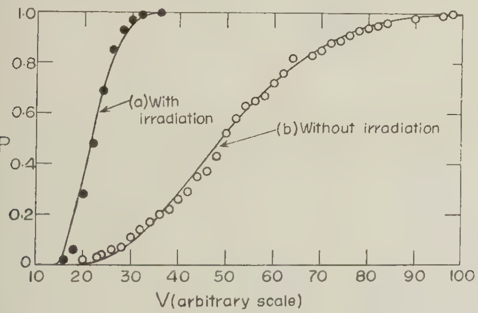

Fig. 1. Effect of irradiation on breakdown probability. ○ and ●: experimental values; ——: calculated curves.

Furthermore, the authors have investigated how these breakdown probability curves are expressed, and it has been found that, except in the range of very small breakdown voltages, these curves can be expressed very nearly by the same equation as that derived by H. Tamagawa[5] in the case of the d.c. breakdown, namely,

$$P(v)=\int_0^v W(v)dv$$
$$=\int_0^v \frac{v}{ak}\exp\left(-\frac{v^2}{2ak}\right)dv=1-\exp\left(-\frac{v^2}{2ak}\right),$$

where P is the breakdown probability, v the over-voltage, and a and k are certain constants. The above equation is based upon such an experimental condition that the applied voltage is raised linearly with respect to the time, and the authors' experiment was also carried out approximately in compliance with this condition. The solid lines in Fig. 1 show the above equation.

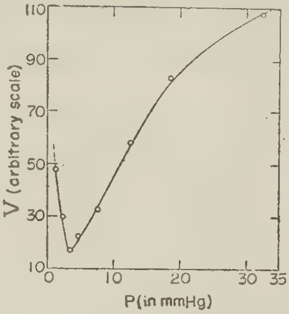

Fig. 2. Breakdown voltage *versus* gas pressure.

As shown by S. C. Brown and others[6], the mechanism of microwave breakdown is different from that of d.c. breakdown, mainly because the diffusion plays a predominant role in the microwave breakdown. Further, we have found from our experiment that the microwave breakdown voltages are distributed in a certain range and the breakdown probability can be expressed approximately by the same expression as in the d.c. breakdown. This result seems to give an important suggestion as to a more detailed breakdown mechanism in microwave, since the curves in Fig. 1 show the existence of the forming time of the avalanche in the microwave breakdown. On the other hand, one of the authors has already shown, in a previous paper[7], that the avalanche can occur in the microwave breakdown, but that its direct detection is very difficult because of its spherical form.

The authors greatfully acknowledge their indebtedness to Professor K. Honda and his coworkers for their encouragement and helpful discussions. The authors' thanks are also due to Professor I. Takahashi for his useful advice and encouragement.

References

1) R. Cooper: J. E. E., **94** (1947) 315.
2) K. Mitani: J. Phys. Soc. Japan, **7** (1952) 637.

3) L. B. Loeb: Rev. Mod. Phys. **20** (1948) 151.
4) For example, M. A. Herlin and S. C. Brown: Phys. Rev. **74** (1948) 291.
5) H. Tamagawa: Electrotech. Papers, **2** (1950) 9 (in Japan).
6) M. A. Herlin and S. C. Brown: ibid.
7) K. Mitani: Bulletin Inst. Chem. Res., Kyoto University, **32** (1954) 134.

J. PHYS. SOC. JAPAN **12** (1957) 438

A Possible Fusion Reactor

By Goro MIYAMOTO, Giiti IWATA, Sigeru MORI and Kenji INOUE

Department of Physics, Faculty of Science, University of Tokyo

(Received March 1, 1957)

Perfect focusing properties of an electromagnetic field for ion motion were investigated theoretically[1]) by one of the authors; a mass-spectrometer of such a focusing type, namely, of perfect velocity focusing and total direction focusing for the solid angle 4π, was constructed and tested with electrons. This principle may be applicable to an apparatus for producing effective nuclear reactions, i.e. nuclear fusion reactor.

In the homogeneous magnetic field $(0, 0, -H)$ and the electric field with potential represented by $k/2\cdot(-x^2-y^2+2z^2)$, a charged particle of mass m and charge e moves as the equations,

$$\ddot{x}=\frac{e}{m}kx-\frac{e}{m}\dot{y}H\ ,$$

$$\ddot{y}=\frac{e}{m}ky+\frac{e}{m}\dot{x}H\ ,$$

$$\ddot{z}=-2\frac{e}{m}kz\equiv-\omega^2z\ .$$

By putting $x+iy\equiv\exp(ieHt/2m)\cdot Z$, and transforming into rotating coordinates, the first two equations are transformed into

$$\ddot{Z}=-\left(\frac{1}{4}\frac{e^2}{m^2}H^2-\frac{e}{m}k\right)Z\equiv-s^2\omega^2Z\ .$$

The motion is composed of simple harmonic motions, and if s is selected as a rational number, for example, 1, then the particle can pass through the central point (0, 0, 0) any number of times, even though the particle changes by collisions its velocity and direction at the point.

If we inject ion beams (or a beam), e.g. deuteron beams, in such a way as to make them pass through the central point and compensate the space charge effect by sufficient quantity of electrons, then the ions will come back to that point again and again, till the ion mass changes its value by a nuclear reaction.

Losses of the ions would arise as a result of the neutralization or of the scattering by residual gases or ions outside the central part; especially the multiple Coulomb scattering is fearful.

If the ion density is constant in the small central region $r\leq r_0$ (r: distance from the center), and decreases as $1/r^2$ in the outer region $r_0<r\leq R$, then the occurrence number n of an ion passing the origin is represented approximately by $n^2\sim1/(2\rho\sigma_c r_0)$ where $n\rho$ is the ion density at the center, σ_c is the cross section of the Coulomb scattering. For example, by virtue of $\rho=2.0\times10^{12}i/(r_0^2\sqrt{E})$ and $\sigma_c\sim6\times10^{-13}/E^2$, we have $n^2\sim0.42\,r_0E^{5/2}/i$ where i is the injected total deuteron beams in ampere and E its energy in eV. Numerical expamples are shown in the Table

E (eV)	n	$n\rho$
10^4	4.6×10^4	3.7×10^{15}
10^5	8.1×10^5	2.0×10^{16}
10^6	1.5×10^7	1.2×10^{17}

for $2r_0=1$ and $i=1$. Accordingly the ions have sufficient probability of producing the nuclear reactions near the center. Moreover, if the rational number s is selected specifically, for example, as 4/3 or 4/5 or 7/12 etc. for deuteron mass, then the reaction products T^3 and He^3 are also refocused to the nearly same point again.

When applied static voltage is more than 1 MV and deuteron energy is originally small, then the product ions come to accelerate deuterons by Coulomb collisions near the center, till the nuclear transformation (D^2+T^3) or (D^2+He^3) takes place and T^3 and He^3 are consumed.

This fact suggests the possibility of the chain fusion reaction.

Reference

1) G. Iwata: Prog. Theor. Phys. **8** (1952) 183.

J. PHYS. SOC. JAPAN **12** (1957) 439

Noise from Ge PN Junction and γ ray Irradiation Effect

By Yoshio INUISHI

Faculty of Engineering, Osaka University

(Received February 18, 1957)

Two kinds of noise exist in Ge PN junction:

a) Shot noise

$$(\overline{\Delta i_s{}^2})_f=2eI\Delta f \qquad (1)$$

b) Flicker-like noise or excess noise or $1/f$ noise

$$(\overline{\Delta i_s{}^2})_f=kI^2\cdot\frac{1}{f}\Delta f \qquad (2)$$

where $\overline{\Delta i_s{}^2}$, I, f and k represent mean square short circuit noise current, mean current, frequency, and a material constant respectively.

In leaky or deteriorated diode, increase in reverse current at Zener voltage is not accompanied[1)3)] corresponding increase in noise current, as is shown in Fig. 1.

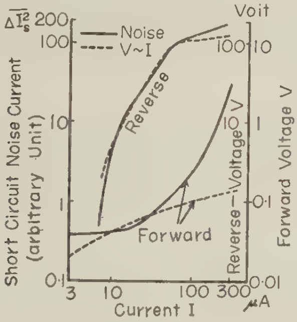

Fig. 1.

Also, carrier injection by light illumination at reversely biased junction does not increase current noise at leaky diode as expected from the increase in reverse current[1) 3)]. These facts suggest us that current through PN junction even over Zener voltage is rather noiseless in comparison with some other kind of excess current which might be produced at surface channel[2) 4)].

To clarify this point, noise from Ge PN junction which shows almost ideal saturation in backward current was investigated. These diodes were provided by the courtesy of G.E. Co., U.S.A.

In Fig. 2 the mean square short circuit noise current and reverse current were plotted as functions of reverse voltage.

In sample No. 1 which shows very clear saturation characteristics, the noise was extremely small and almost equal to the calculated value of shot noise (equation (1)), being nearly independent of applied voltage. Frequency spectrum of noise also supports this view at frequency larger than several KC.

In sample No. 2 at unirradiated state, noise was also small under Zener voltage, being of the same order as calculated shot noise. At Zener voltage, however, abnormal increase in $1/f$ noise current was observed. This might correspond to avalanche noise. These points are under detailed investigation.

No. 2 sample was irradiated by γ ray of 10^6 röntgen dose from CO^{60}, noise and reverse current were measured after irradiation. Reverse current increases and the junction becomes leaky by γ ray irradiation. Noise current also increases remarkably in comparsion with unirradiated samples. These increased noise were proved to obey the equation (2) of flicker-like noise having typical $1/f$ spectrum.

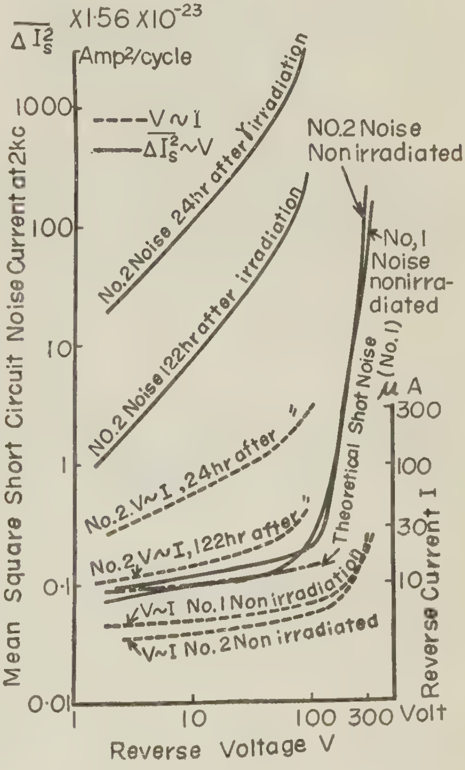

Fig. 2.

Namely γ ray irradiation produce some leaky channel in PN junction which produces remarkable flicker-like noise. In these irradiated sample increase of noise at Zener voltage was masked by the predominant flicker like noise just like the case of leaky diode Fig. 1. Irradiation effect can be annealed even in room temperatures as in shown in Fig. 2.

References

1) Y. Inuishi: Tech. Rept. Osaka Univ. **6** (in press) ibid. **3** 41 (1953).

2) A. Mcwhorter: Lincoln. Lab. Tech. Rept., No. **80** (May, 1955).
3) Y. Inuishi: Bullt. Jap. Phys. Soc. (semicond. sec. Spring Meeting, 1955.
4) A. Plummer: Proc. Phys. Soc. **69** 539 (1956).

J. Phys. Soc. Japan **12** (1957) 440

A Graphical Method for Determining the Coefficient of Viscosity of Newtonian Liquids using an Oscillating Cylinder Viscometer III

By Ali Abdel Kerim Ibrahim (Ph. D.)
Physics Department, Faculty of Science,
Uuiversity of Alexandria
Alexandria, Egypt

(Received December 15, 1956)

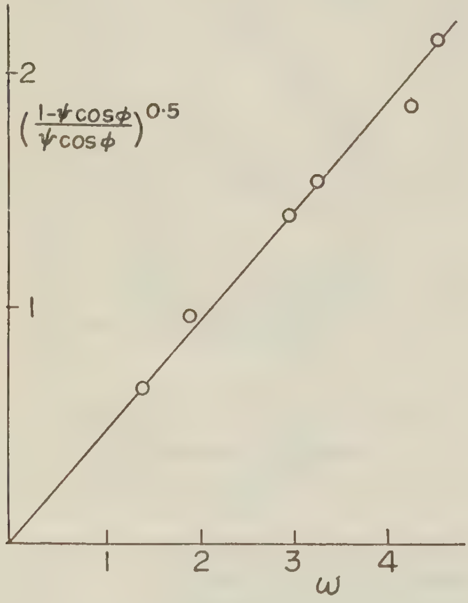

Fig. 1.

If a non-elastic liquid of coefficient of viscosity η in gm. cm.$^{-1}$ sec.$^{-1}$ is filling the annular gap between two coaxial cylinders, the outer being oscillating through very small angles with various frequencies n c.p.s., while the inner is suspended by a delicate copper wire of torsion constant τ then[1],

$$\eta = \frac{1}{\pi} \cdot \frac{d}{L} \cdot \frac{e^{-3d/R}}{a^3} \cdot \frac{I\omega^2-\tau}{\omega}\left(\frac{\psi\cos\phi}{1-\psi\cos\phi}\right)^{0\cdot5} \cdots(1)$$

where, $R=(b+a)/2$ $\omega=2\pi n$
$d=(b-a)/2$

b, is the inner radius in cms. of the outer cylinder, a, is the radius in cms. of an inner cylinder of moment of inertia I in gm. cm^2; and length of immersion L in cms.

$$\psi=\theta_0/\phi_0$$

ϕ_0 being the amplitude of the outer cylinder and θ_0 is that of the inner cylinder. Also, ϕ is the phase angle by which the inner cylinder lags the outer cylinder.

If τ is very small compared with $I\omega^2$, therefore,

$$\eta=k\omega\,[\psi\cos\phi/(1-\psi\cos\phi)]^{0\cdot5} \cdots\cdots\cdots(2)$$

where,

$$k=\frac{I}{\pi} \cdot \frac{d}{L} \cdot \frac{e^{-3d/R}}{a^3}$$

K is an apparatus constant.

Now, if $[(1-\psi\cos\phi)/(\psi\cos\phi)]^{0\cdot5}$ represents the Y-axis, and ω represents the X-axis, then the relation between Y and X is linear and may then be written as,

$$Y=(K/\eta)X \cdots\cdots\cdots\cdots\cdots(3)$$

i.e. a straight line relation from whose slope (K/η) the coefficient of viscosity η may be determined.

The figure shows the results taken by Markovitz[2] et al for standard oil obtained from the national bureau of standards.

The following table gives the results for the liquid under test.

K	(K/η)	η in poise	
		from graph	from table
0.376	0.47×10^{-2}	81	91.6

It is clear from graph and table that my equation represents the facts to a certain degree of accuracy.

References

1) Ali A. K. Ibrahim (in preperation).
2) Markovitz et al. Rev. Sci. Inst. **23**, 8 (1952).

J. Phys. Soc. Japan **12** (1957) 441

Anomalous Electrical Properties of Lead Telluride

By Yasuo Kanai and Riro Nii

The Electrial Communication Laboratory, Musashinoshi, Tokyo

(Received January 25, 1957)

Electrical properties of single crystals of lead telluride (PbTe) were measured from room temperature to liquid air temperature. In some p-type specimens, the same anomaly as previously reported by Putley[1], i.e., the reversal of the sign of the Hall coefficient at low temperature was found. A typical example of such anomalous behaviour is shown in Fig. 1.

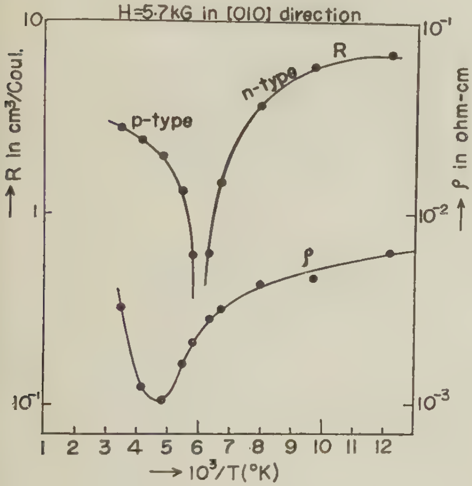

Fig. 1. Resistivity, ρ, and Hall coefficient, R, versus 1/T curves of a single crystal of PbTe. The electric current was applied in the [100] direction.

In such specimens further anomalous phenomena, i.e., the *magneto-conductive phenomena* was observed in the low temperature n-type region. Fig. 2 shows the magetic field dependency of the Hall coefficient and transverse magneto-conductance effect, $-\varDelta\rho/\rho(0)\equiv 1-\rho(H)/\rho(0)$, of the same sample whose electrical properties are shown in Fig. 1. The longitudinal effect of this sample is very small and this magneto-conductive effect varies as $\sin\theta$, where θ is the angle between the direction of electric current and that of magnetic field.

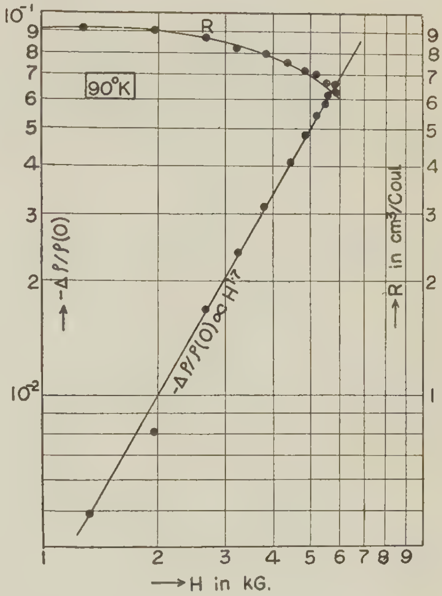

Fig. 2. Hall coefficient, R, and magneto-conductance effect, $-\varDelta\rho/\rho(0)$ versus magnetic field strength curves. Electric current was applied in the [100] direction, and the magnetic field in the [010] direction.

Further systematic investigations on these anomalous properties of PbTe are now in progress.

The authers thank to Mr. S. Uchiyama for valuable discussions.

Reference

1) E. H. Putley: Proc. Phys. Soc. B **68** (1955) 22.

J. PHYS. SOC. JAPAN **12** (1957) 442

Cross Section for Displacement of Atoms by Heavy Particle Irradiation

By Takeshi MORIMOTO

Department of Metallurgy, Kyoto University, Kyoto, Japan

(Received January 7, 1957)

The cross section Φ_d of displacement collision by heavy charged high energy particles in the case of $E > ME_{el}/m$ is expressed as follows¹⁾

$$\Phi_d = \frac{2\pi Z^2 z^2 e^4}{M_n V^2 \varepsilon_t}, \tag{1}$$

where Ze and M_n are the nuclear charge and mass of the stopping material, ze, V, E and M are respectively the full charge, the velocity, the kinetic energy and the mass of the incident particle, $\varepsilon_t (\approx 25\,eV)$ is the threshold energy of displacement, m is an electron mass, and $E_{el} = \frac{1}{2} m v^2$ (where v is the electron velocity), the ionization potential.

In the case of low energy, i.e., $E < ME_{el}/m$, the formula (1) is not valid because of the screening effect of the nuclear charge and the electron pick-up of the incident particle. Then, it may be safely said that the incident particle can be regarded electrically neutral rather than ion-like in sufficient low energy. Here, a calculation is presented, assuming that the interaction potential energy between two different neutral atoms $V(R)$ is of the form²⁾

$$V(R) = \frac{Zze^2}{R} \left\{ \frac{a_1^2 \exp(-R/a_2) - a_2^2 \exp(-R/a_1)}{a_1^2 - a_2^2} \right\}. \tag{2}$$

The momentum transfer ΔP in the collision having impact parameter b is given as follows:

$$\Delta P = \frac{2Zze^2}{V(a_1^2 - a_2^2)} \left\{ \frac{a_1^2}{a_2} K_1(b/a_2) - \frac{a_1^2}{a^2} K_1(b/a_1) \right\}, \tag{3}$$

where a_1 and a_2 are the radii of the atomic electron clouds of the incident and stopping atoms respectively, $K_1(x)$ the 1st order modified Bessel function of the second kind. Eq. (3) generally gives the momentum transfer of the interaction between two different atoms. When $a_1 \gg b$ and $a_2 \gg b$ (in high energy range), eq. (3) reduces to

$$\Delta P = \frac{2Zze^2}{Vb}, \tag{4}$$

and we can readily get eq. (1) from eq. (4). The variation of Φ_d for V can be found as shown in Fig. 1, by solving numerically the following eqs. (5) and (6):

$$\Phi_d = \pi b_t^2, \tag{5}$$

$$\frac{2Zze^2}{\Delta P_t (a_1^2 - a_2^2)} \left\{ \frac{a_1^2}{a_2} K_1(b_t/a_2) - \frac{a_2^2}{a_1} K_1(b_t/a_1) \right\} = V, \tag{6}$$

where $\Delta P_t^2 = 2M_n \varepsilon_t$. The low energy treatment mentioned above will be permissible if the condition $MV \geq \Delta P_t$ is fulfilled. This is satisfied by heavy particles to the extent of considerable low energy.

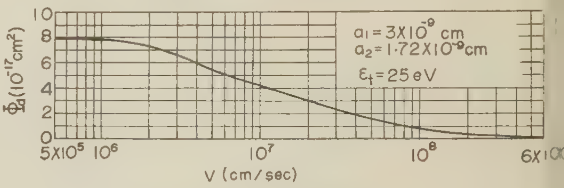

Fig. 1. Cross section for displacement of Atoms by α-Particle Irradiation in Cu.

The author wishes to express his thanks to Prof. J. Takamura for his helpful advice and guidance.

References

1) T. Morimoto: Busseiron Kenkyu **94** (1956) 92; **95** (1956), 120.
2) J. A. Brinkman: J. A. Phys. **25** (1954) 970.

Errata

On the Superstructure of the Ordered Alloy Cu_3Pd

II. X-ray Diffraction Study

By Makoto HIRABAYASHI and Shiro OGAWA
J. Phys. Soc. Japan **12** (1957) 259

P. 172 left column line 24
* should refer to the foot note in P. 264.

Effect of Plastic Deformation on the Dielectric Breakdown of Silver Chloride Crystals

By Noriaki ITOH and Tokuo SUITA
J. Phys. Soc. Japan **12** (1957) 214

Fig. 1 (kv/m) should be read (kv/cm)

JOURNAL OF THE PHYSICAL SOCIETY OF JAPAN Vol. 12, No. 5, MAY, 1957

Nuclear Reactions induced by the 14 MeV Neutrons

By Shinjirō YASUMI

Department of Physics, Kōnan University, Kōbe

(Received December 18, 1956)

The nuclear reactions of Al, Fe, Cu, Zn, Mo and Ag produced by the neutrons from the $T^3(d, n)$ He^4 reaction have been investigated by means of the activation technique. The absolute numbers of activated nuclei in samples were determined by measuring the beta-rays from the samples with a 4π-proportional counter and applying the "method of extrapolation."

By utilizing the variations of neutron energies in the laboratory system, an excitation curve of $Mo^{92}(n, 2n)Mo^{91}$ reaction was obtained. For the cases of Al, Cl, Zn and Ag, only the gradients of excitation curves were also found.

The experimental cross sections were determined as follows: 87.2 mb±8% for $Al^{27}(n, p)Mg^{27}$, 120 mb±12% for $Al^{27}(n, \alpha)Na^{24}$, 144 mb±13% for $Fe^{56}(n, p)Mn^{56}$, 556 mb±5% for $Cu^{63}(n, 2n)Cu^{62}$, 119 mb±12% for $Zn^{64}(n, 2n)Zn^{63}$, 60.2 mb±12% for $Zn^{66}(n, p)Cu^{66}$, 132 mb±16% for $Mo^{92}(n, 2n)Mo^{91}$, 458mb±11% for $Ag^{107}(n, 2n)Ag^{106}$, and 604 mb±11% for $Ag^{109}(n, 2n)Ag^{108}$. Comparing these results with the predictions by the statistical theory of Weisskopf *et al.* it was found that they agreed with each other within about factor 3, but in details, there were some discrepancies between them.

The relative behavior of excitation curve of the $Mo^{92}(n, 2n)Mo$ reaction seems to be consistent with the above theory, though with respect to the absolute values, the theoretical curve lies above the experimental one by about 2.4.

§1. Introduction

A study on the nuclear reactions induced by fast neutrons can provide us powerful informations about the mechanism of the nuclear process.

In recent years, the monoenergetic neutrons from the $T^3(d, n)He^4$ reaction have become easily available by using tritium-loaded zirconium targets[1]. The nuclear reactions by these neutrons have been studied by some workers[2] with the activation method.

Especially, Paul and Clarke[3] carried out these investigations for many nuclei. They found remarkable discrepancies between the theoretical and experimental cross sections of (n, p) and (n, α) reactions for heavy nuclei and suggested the existence of the direct process in these cases. However, the absolute beta-counting method adopted by them seems to be somewhat rough as pointed out by the workers themselves, and may have introduced appreciable errors in their results.

Thus we have attempted to determine more accurately the absolute cross sections and the excitation curves of these reactions by an improved method. The results obtained were discussed from the point of view whether the statistical theory of the nuclear reaction is valid or not for about 14 MeV neutrons.

§2. Experimental Procedures

If a nuclear reaction leads to the formation of an unstable isotope, the resulting activities may provide a means for determining the reaction cross section by absolute beta-counting which determines the total number of active nuclei in the sample. The activation method is still usable also in the case involving K-electron capture, if a fraction of the disintegration through β-emission is known.

(A) *Cross Section*

To determine the cross section, the following three points must be taken into account.

(1) *Number of Neutrons*

The number of neutrons was monitored by the α-particles emitted simultaneously in the T–*d* reaction which were counted by a ZnS-scintillation counter placed at 90° direction with respect to the deuteron beam. The angular distribution of the emitted neutrons is found to be isotropic[4] in the c. m. system at the deuteron energy under consideration.

The samples were irradiated for from several to several ten minutes according to the half-lives of the induced activities. The neutron intensity was obtained from the α-counts in every one minute or thirty seconds interval during irradiations for the purpose of correction for the small fluctuations of the neutron intensity.

In calculating the cross section it was assumed that the neutron intensity was constant in such small intervals. This approximation will introduce inappreciable errors, probably less than 1 per cent.

(2) *Absolute Beta-Counting*

In order to estimate the total number of the active nuclei in the sample plate of finite thickness, the following procedures were used. The net beta-counting rate c/m of a radioactive sample mounted in a given position may be represented as the product of the disintegration rate d/m of the sample multiplied by several factors which express the effects of beta-particle scattering, absorption and the counting geometry, that is, it will be written as follows:

$$c/\mathrm{m}=(d/\mathrm{m})\cdot f_S\cdot f_A\cdot f_B\cdot f_G\ , \tag{1}$$

where

f_S: factor for the effect of the mass of the sample itself in causing both scattering and absorption of beta-particles,

f_A: factor due to the effects of absorption and inscattering into the counter by the counter window and air,

f_B: factor due to the effects of backscattering by the sample holder and the housing,

f_G: geometrical factor.

(a) The correction factor f_S (the “extrapolation method”[5])

Samples of various thickness and the irradiation monitor, which was consisted of the same material and had the same diameter as the samples, were irradiated in juxtaposition, and their activities were counted by two Geiger counters.

The ratio $N_S/N_M\cdot w$ is proportional to the apparent specific activity, where N_S and N_M are the total net counts for the same time interval of a sample and a monitor respectively, w is the thickness of a sample in g/cm². When the curve of $(N_S/N_M\cdot w)$ vs w which represents the self-scattering and absorption of a sample is extrapolated to zero-thickness, the limiting value $\lim\limits_{w\to 0} N_S/N_M\cdot w\equiv S$ may be taken as the true specific activity ($f_S=1$).

(b) The product of the correction factors $(f_A\cdot f_B\cdot f_G)$

These factors were determined by using a 4π-proportional counter of the propan gas flow type.

Two comparatively thin samples of the same material and same thickness were irradiated in juxtaposition at 90° to the direction of the deuteron beam, and the beta-particles from the one sample was counted by an end-window Geiger counter and those from the other sample by the 4π-counter for the same time interval. Then the ratio of their counts $N_{4\pi}/N_G$ corresponds to the reciprocal of the product $(f_A\cdot f_B\cdot f_G)$.

(3) *Assignment of the Nuclear Reactions*

The nuclear reaction was assigned by the half-life of the product nucleus. When more than two reactions occurred simultaneously, the component activities were separated by the analysis of the compound decay curve or from the intensity of residual activity after an appropriate time lapse.

Finally, in order to calculate the cross section, the following equations were used in the cases of “one minute-treatment” and “thirty seconds-treatment”[*] respectively:

for one minute-treatment,

$$\sigma=\frac{M\cdot\left[N_M\Big/\sum\limits_{i=1}^{T} n_{\alpha i}\cdot\exp\{-(T-i+t_0)\lambda\}\right]\cdot S\cdot C_{G'}\cdot C_K}{N_0\cdot\eta\cdot\Omega\cdot[(1-\mathrm{e}^{-\lambda})(1-\mathrm{e}^{-10\lambda})/\lambda]\cdot(4\pi/\omega)}\ , \tag*{(2)$_1^*$}$$

and for thirty seconds-treatment,

---

[*] These referred to the cases in which the neutron intensities were taken to be constant for every one minute or thirty seconds, respectively.

$$\sigma=\frac{M\cdot\left[N_M\Big/\sum_{i=1}^{2T}2n_{\alpha i}\cdot\exp\left\{-\left(T-\frac{i}{2}+t_0\right)\lambda\right\}\right]\cdot S\cdot C_{G'}\cdot C_K}{N_0\cdot\eta\cdot\Omega\cdot[(1-e^{-\lambda/2})(1-e^{-10\lambda})/\lambda]\cdot(4\pi/\omega)}, \qquad (2)_2{}^*$$

where

N_0: Avogadro's number

M: molecular weight of the sample

η: isotopic abundance (%)

S: $=\lim_{w\to 0} N_S/N_M\cdot w$

$C_{G'}$: $=1/(f_A\cdot f_B\cdot f_G)$

Ω: solid angle of the sample under irradiation $=\frac{1}{4}\log\frac{R^2+a^2}{a^2}$

$n_{\alpha i}$: α-counts for one minute or 30 seconds of the i-th interval

T: time of irradiation

t_0: time elapsed from the end of irradiation to the beginning of beta-counting

i: number of the order of each time interval during bombardment (integer)

N_S: beta-counts per 10 minutes on the sample

N_M: beta-counts per 10 minutes on the monitor

C_K: correction factor concerning the branching ratio between the positron emission and the orbital electron capture, namely

$C_K=1$ for the case of β^--activity,
$C_K>1$ for the case of β^+-activity.

ω: solid angle which the α-detector subtends to the neutron source

λ: decay constant

(B) Excitation Curve

The neutron energy E_n in the laboratory system is given by the following equation

$$\sqrt{E_n}=\frac{1}{5}[\sqrt{2E_d}\cos\theta_n+\sqrt{2E_d\cos^2\theta_n+10E_d+20Q}\,], \qquad (3)$$

where E_d is the deuteron energy, θ_n is the emission angle of neutron to the deuteron beam, and Q is the liberation energy of the $T^3(d, n)He^4$ reaction which is equal to 17.6 MeV. At the 0.15 MeV deuteron, E_n varies from 13.3 MeV to 15.0 MeV according to the angle of emission with respect to the deuteron beam. Utilizing this effect, excitation curves near 14.1 MeV were obtained for a few reactions.

Two sheets of fairly thick samples were irradiated at different angles to the deuteron beam. These samples were of the same material and the same thickness, and the relative yield of each specimen is proportional to the relative cross sections at the corresponding neutron energies. Relative counting efficiency of the two Geiger counters used in this experiment was determined previously by a preliminary experiment.

The deuteron energy was kept constant within 2 per cent during the excitation study by stabilizing the exciting current of the beam analyser. Since various deposits on the T–Zr target diminish the deuteron energy considerably after a long bombardment, the excitation curve was always measured with a fresh target.

§ 3. Apparatus

The tritium-loaded zirconium target* was bombarded by the analysed beam of deuterons, which was accelerated by a 0.4 MV-Cockcroft generator. The deuteron energy was about 0.15 MeV and the beam intensity was limited to about 20 microamperes to prevent the local heating. The size of the beam spot was from 2 mm×6 mm to 3 mm×7 mm in an elliptic shape as the target was oblique to the deuteron beam. The total yields for these targets were found as several 10^7 neutrons per second per microampere for 0.15 MeV deuterons.

The target chamber is shown schematically in Fig. 1. The chamber has five irradiation windows covered with 0.2 mm thick copper plates situated respectively at 30°, 60°, 90°,

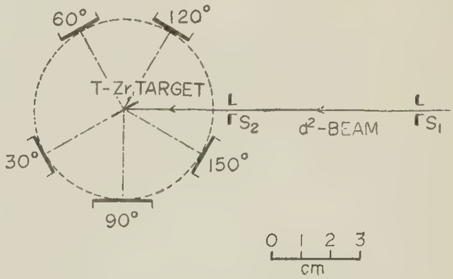

Fig. 1. Schematic drawing of the target chamber.

---

* For the derivation of Eq. (2), see Appendix (1).

* These targets were obtained from A.E.R.E. in England.

120° and 150° to the deuteron beam. For cross section measurements, samples of 20 mm in diameter were irradiated at the 90°-window only, while, for obtaining the excitation curve, samples of 14 mm in diameter were irradiated at all the five windows.

The neutron was monitored by counting α-particles emitted at 90° to the deuteron beam with a ZnS-scintillation counter. The scintillator was made by depositing RCA 33-Z-20A powder in a circular shape directly on the glass wall of a photomultiplier 931A. The thickness of the deposit layer was about 16 mg/cm², which gives the optimum pulse height distribution for the Polonium-α-particles. The scintillator was covered with two very thin aluminium foils (about 120 μg/cm² thick each) to prevent any light from reaching the scintillator.

To determine the discriminator bias the pulse height distribution of the reaction α-particles was measured by a Johnstone-type single channel pulse height analyser⁶⁾. During this measurement the neutron intensity was monitored by a plastic scintillation counter. The noise-level and the α-particle peak were found to be distinctly separated by a wide valley where the counting rate was nearly zero. Hence the bias voltage of the discriminator was set at about the middle point of this valley. The peak due to the proton emitted by the reaction $D^2(d, p)T^3$ was not found in the pulse height distribution curve.

For counting β-rays, we used three end-window type Geiger counters, whose absolute efficiencies were calibrated by a 4π-proportional counter. The counting geometries could be exactly reproducible by means of a proper "jig". All counting systems were placed at adequate distances from the neutron source.

The 4π-counter used is shown in Fig. 2. Propan gas flows through the counter tube at the atmospheric pressure, the flow rate being monitored by a simple flowmeter of the bubble-bottle type⁷⁾. The special feature of this counter is that it is able to put the specimen quickly into the counter without seriously disturbing the operating conditions. Preliminary experiments showed the disturbances of the operating conditions by insertion of samples were found to disappear after one or two minutes at the flow rate of about 60 bubbles per minute.

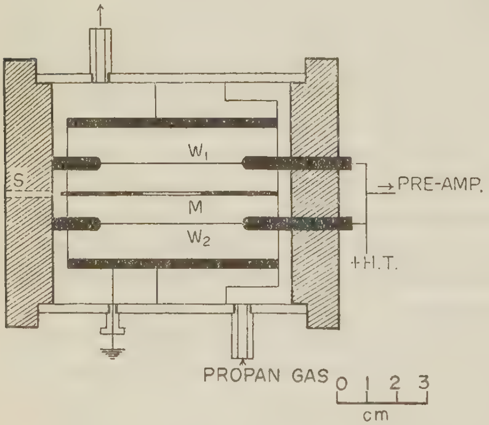

Fig. 2. Construction of the 4π-proportional counter. The plate M is the central separator between the two counters and serves also as a sample holder. It is at the ground potential. W₁ and W₂ are the tungsten wires of 0.05 mm in diameter, which are at positive 4950 volts. One of the end plates made of ebonite has a narrow slit S, which is closed with a strip of "celotape". To insert a sample into the counter, the separator is first taken out through S by removing the celotape strip. Then the sample is placed on the separator, and the latter is taken back into the counter. Finally the slit S should be again closed with the celotape strip.

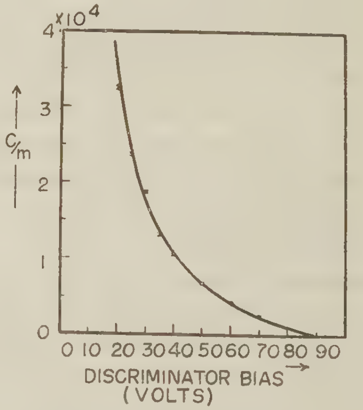

Fig. 3. The integral pulse height distribution of the tritium beta-rays measured by the 4π-proportional counter.

To count nearly all beta-rays emitted from the sample whose maximum energy is about 1 to 3 MeV, the discriminator bias must be set in such a way that the electrons of several keV or more are perfectly detected. For this purpose, the pulse height distribution of the tritium beta-rays was measured by this counter. The results are shown in Fig. 3.

The maximum energy of these beta-rays is about 18 keV, which will be seen from the figure to correspond to 87 volts of the discriminator bias. On the other hand, the noise counting rate per channel above 15 volts was practically negligible. Therefore the bias voltage was set at 20 volts, which corresponds to the electron energy of 4.1 keV.

Hence, the counting efficiency by this counter could be taken to be nearly 100 per cent for beta-rays under consideration. The analysis of the pulse height distribution of beta-rays by the proportional counter is given in Appendix (2).

§ 4. Results

(*1*) *Absolute Cross Section*

All data of the cross section measurements and the final results are tabulated in Table I with their standard errors. The decay constants used for the identification of product nuclei and the calculation of cross sections have been taken from the Table of Isotopes8).

Table I. Data of the cross section measurements and the final results

Reaction	Decay constant λ (min.$^{-1}$)	N_M/Σ*	S	$C_{G'}$	C_K	Cross section** (mb)
$Al^{27}(n, p)Mg^{27}$	0.0707	1.97 ±2%	5.33± 7%	5.31±3%	1.00	87.2± 8%
$Al^{27}(n, \alpha)Na^{24}$	0.000767	0.0426±9%	5.33± 7%	5.31±3%	1.00	120±12%
$Fe^{56}(n, p)Mn^{56}$	0.00448	0.191 ±2%	4.08±12%	4.80±5%	1.00	144±13%
$Cu^{63}(n, 2n)Cu^{62}$	0.0684	7.15 ±3%	2.84± 3%	4.79±2%	1.043	556±5 %
$Zn^{64}(n, 2n)Zn^{63}$	0.018	0.273 ±5%	3.80±10%	4.80±4%	1.075	119±12%
$Zn^{66}(n, p)Cu^{66}$	0.135	0.359 ±6%	3.80±10%	4.80±4%	1.00	60.2±12%
$Mo^{92}(n, 2n)Mo^{91}$	0.0425	0.287 ±2%	1.59±15%	4.80±5%	1.224	132±16%
$Ag^{107}(n, 2n)Ag^{106}$	0.0285	0.842 ±8%	5.03± 7%	4.72±3%	1.00	458±11%
$Ag^{109}(n, 2n)Ag^{108}$	0.295	3.52 ±8%	5.03± 7%	4.72±3%	1.00	604±11%

* (1) The abbreviation $\Sigma \equiv \left[\sum_{i=1}^{T} n_{\alpha i} \cdot \exp\{-(T-i+t_0)\lambda\}\right]$ is introduced.

(2) All values of (N_M/Σ) correspond to the "one minute-treatment" (see § 2). In the case of the "30 seconds-treatment" the values of $\left[\sum_{i=1}^{2T} 2n_{\alpha i} \cdot \exp\left\{-\left(T-\frac{i}{2}+t_0\right)\lambda\right\}\right]$ were multiplied by the factor $(1-e^{-\lambda/2}/1-e^{-\lambda})$ to reduce to the "one minute-treatment" (cf. eq. $(2)_2$).

** (1) The neutron energy used is 14.1 MeV.

(2) No traces of the reaction $Fe^{54}(n, 2n)Fe^{53}$ was observed with the 14.1 MeV neutrons. This is probably due to the fact that the threshold energy of this reaction is 14.1 MeV11).

The curve of the apparent specific activity vs the sample thickness is shown in Fig. 4 for the case of copper, as an example. In the figure, the arrow indicates the thickness of the sample which was used in the 4π-counter measurement. In all cases these curves have a peak at a certain small thickness. In order to estimate the *S*-value, the curve was linearly extrapolated to zero-thickness inside the peak value by means of the least square calculation.

In the cases of the positron emitters for which the branching ratios of the orbital electron capture are not known, the correction factors C_K are determined from the curves published by Feenberg and Trigg9).

The existence of the shorter half-life activity (65.5 sec.) of Mo^{91} was reported by L.

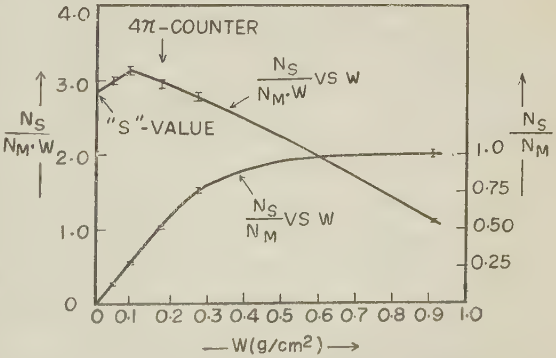

Fig. 4. The curve of the apparent specific activity vs the sample thickness for the case of Cu^{62}.

Katz and others[10] by their betatron experiments. This activity was investigated in the present experiment, but the existence was not found at all at the 14.1 MeV neutrons as reported by Brolley[10].

(2) *Excitation*

Results on the excitation of the reaction $Mo^{92}(n, 2n)Mo^{91}$ are shown in Fig. 5. In the figure the vertical bars show the standard deviations and the horizontal bars show the maximum energy spreads of the neutrons by which each sample is traversed. The solid curve represents the relative excitation function calculated theoretically.

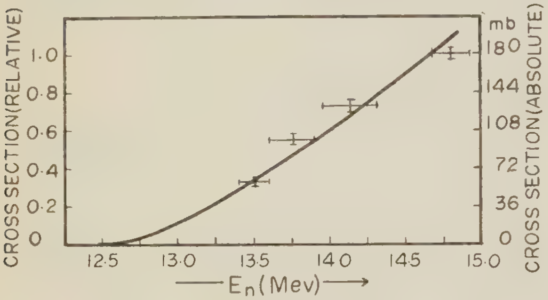

Fig. 5. The threshold behavior of the reaction $Mo^{92}(n, 2n)Mo^{91}$.

Only the gradients of excitation curves, i.e., $d\sigma/\sigma \cdot dE_n$ were measured for the cases of Al, Zn and Ag, because their yields showed no appreciable changes in the energy range considered, and for Cl because of the experimental difficulties due to its low yield. These results are shown in Table II.

Table II. Gradients of excitation curves

Reaction	E_n (MeV)	ΔE_n (MeV)	$\Delta\sigma/\sigma \cdot \Delta E_n \times 100$ (%·MeV^{-1})
$Al^{27}(n, p)Mg^{27}$	14.15	1.31	−21
$Zn^{64}(n, 2n)Zn^{63}$	14.0	1.04	+52
$Cl^{37}(n, p)S^{37}$	14.15	1.28	+ 6
$Ag^{109}(n, 2n)Ag^{108}$	14.15	1.31	−10.2

§ 5. Discussions

It is very interesting to compare the observed cross sections and the excitation curves with the predictions from the existing nuclear theory. The so-called "continuum theory" developed by Weisskopf and his collaborators[12] based on the compound nuclear formalism will be applicable to the present nuclear reaction, where a compound nucleus, if exists, is so highly excited that the conditions of the continuum theory are well fulfilled.

According to Bohr's assumption, the cross section of a nuclear reaction $X(a, b)Y$ can be written in a form

$$\sigma(a, b)=\sigma_C(a)G_C(b)\ , \qquad (4)$$

where $\sigma_C(a)$ is the cross section for the formation of a compound system by the particle a incident upon the target nucleus X and can be found by the wave-mechanical calculations. In the present experiments, however, since the incident particle is the 14 MeV neutron, $\sigma_C(n)$ may be taken to a good approximation to be the cross section for the inelastic collision which can be expressed by $\sigma_{in}(n)=\sigma_{total}-\sigma_{elastic}$. The values of $\sigma_{in}(n)$ used in the present calculations were obtained from the experimental results by Graves and Davis[13].

The second factor $G_C(b)$ is the probability that the compound nucleus C, once formed, decays by emission of a particle b, leaving a residual nucleus Y, and it does not depend on the way in which the compound nucleus has been produced. From the reciprocity theorem and Bohr's assumption, it is given by

$$G_C(b)=\sum_\beta{}' k_\beta^2\sigma_C(\beta)/\sum_\gamma k_\gamma^2\sigma_C(\gamma)\equiv F_b/\sum_c F_c\ , \qquad (5)$$

where $\sigma_C(\beta)$ and $\sigma_C(\gamma)$ are the cross sections for the formation of the compound nucleus through β- and γ-channels, k_β and k_γ being the wave numbers at these channels respectively. The summation $\sum_\beta{}'$ in the numerator of Eq. (5) is to be extended over all the open channels β leading to the emission of the particle b, while the summation $\sum_\gamma$ in the denominator should be extended over all the channels γ into which the compound nuclear system can decay (namely, the summation $\sum_c$ is extended over all particle types c emitted in this reaction).

Now, if we introduce the level density $w(E)$ of the residual nucleus and assume that the decay probabilities from the compound nucleus to various levels of the residual nucleus Y are all the same, i.e., the branching probabilities through β-channels are all equal, then the expression for the F-function will be given as follows:

$$F_b = F_b(\mathcal{E}_{bY}) = \frac{2M_\beta}{\hbar^2}\int_0^{\mathcal{E}_{bY}} \mathcal{E}_\beta \sigma_C(\mathcal{E}_\beta) w_Y(\mathcal{E}_{bY}-\mathcal{E}_\beta)d\mathcal{E}_\beta\ , \tag{6}$$

where M_β is the reduced mass in the channel β; $\mathcal{E}_\beta$ is the channel energy of the emitted particle b; $\mathcal{E}_{bY}$ is the maximum value of $\mathcal{E}_\beta$ and is expressed by the equation $\mathcal{E}_{bY}=\mathcal{E}+Q_{ab}$ using the incident channel energy $\mathcal{E}$ and the Q-value Q_{ab} for the reaction $X(a, b)Y$. $w_Y(E)$ is the level density of the nucleus Y at the excitation E and is given by Weisskopf from thermodynamical consideration, such that

$$w_Y(E) = C \exp\left[2\sqrt{aE}\,\right]\ , \tag{7}$$

where C and a are the constants to be determined to fit the various experimental results. In addition, for C, the following relation holds[14]:

$$4C_{\text{even-even}} = 2C_{\text{even-odd}} = C_{\text{odd-odd}}\ . \tag{8}$$

The Q-values of the (n, p) reactions were derived from the known total β-disintegration energies[15] of the product nucleus, and those for the (n, α) reactions were calculated from the semi-empirical mass data[16]. The values of F-functions can be obtained from the Final Report of the Fast Neutron Data Project[17] and the work of Heidmann and Bethe[18] except for the case of Al.

For Al, there have not yet been published any available data for theoretical estimations, and hence numerical calculations were performed by the author by Eq. (6) making use of the values of σ_C and C given in references (12) and (17) respectively. Further, the values of a were calculated from the semi-empirical formula given by Heidmann and Bethe[18], that is

$$a = \frac{0.14}{4}(A-12)\ \text{MeV}^{-1},$$

for $15<A<70$ where A is mass number.

A very simple formula can be given especially for the $X(n, 2n)Y$ reaction. In this case we may assume that the neutron emission is predominant as soon as it becomes energetically possible. Then the cross section $\sigma(n, 2n)$ will depend on the fraction of the first neutrons emitted from the compound nucleus with such a low energy that the residual nucleus is left with an energy of excitation sufficient to evaporate the second neutron. Then the following formula is obtained for the $(n, 2n)$ cross section:

$$\sigma(n, 2n) = \sigma_{\text{in}}(n)\left[1-\left(1+\frac{\mathcal{E}_c}{\Theta}\right)\exp\left(-\frac{\mathcal{E}_c}{\Theta}\right)\right], \tag{9}$$

where $\mathcal{E}_c$ is the excess energy over the threshold of the $(n, 2n)$ reaction, Θ is the nuclear temperature $\Theta(\mathcal{E}_{bY})$ of the intermediate residual nucleus Y and is put as $\Theta=(\mathcal{E}_{bY}/a)^{1/2}$.

The threshold energies of the $(n, 2n)$ reac-

Table III. $(n, 2n)$ Reactions

Reaction	$\sigma_{\text{in}}(n)$ (mb)	Threshold Energy (Mev)	ε_c (MeV)	a^* (MeV^{-1})	Θ (MeV)	ε_c/Θ	Theoretical cross section (mb)	$\frac{\sigma_{\text{exper.}}}{\sigma_{\text{theor.}}}$
$\text{Cu}^{63}(n, 2n)\text{Cu}^{62}$	1420	11.3	2.8	2.2 (F)	2.53	1.11	432	1.29
				1.8 (W) (H)	2.80	1.00	375	1.48
$\text{Zn}^{64}(n, 2n)\text{Zn}^{63}$	1460	11.9	2.2	1.9 (W)	2.73	0.806	280	0.425
				1.82(H)	2.78	0.792	274	0.434
$\text{Mo}^{92}(n, 2n)\text{Mo}^{91}$	1670	12.48(B)	1.62	3.16(B)	2.12	0.764	298	0.443
				4.3 (W)	1.81	0.895	376	0.351
$\text{Ag}^{107}(n, 2n)\text{Ag}^{106}$	1820	9.8 (M)	4.3	5.8 (W)	1.56	2.76	1390	0.330
$\text{Ag}^{109}(n, 2n)\text{Ag}^{108}$	1820	9.1	5.0	6.0 (W)	1.53	3.27	1520	0.397

* The values of a were taken from the following references:

(F) ····Fowler and Slye[20]

(B) ····Brolley, ref. (10)

(W)····Feld, Feshbach, Goldberger, Goldstein and Weisskopf, ref. (17)

(H) ····Heidmann and Bethe, ref. (18).

Table IV. (n, p) and (n, α) Reactions

Reaction	$\sigma_C(n)$ (mb)	Q_{np} (MeV)	$Q_{n\alpha}$ (MeV)	F_p/F_n	F_α/F_n	Theoretical cross section (mb)	$\sigma_{exper.}/\sigma_{theor.}$
$Al^{27}(n, p)Mg^{27}$	1000	-2.59	-2.18	0.262	0.914	120	0.73
$Al^{27}(n, \alpha)Na^{24}$	1000	-2.59	-2.18	0.262	0.914	420	0.29
$Fe^{56}(n, p)Mn^{56}$	1270	-3.65	$+1.43$	0.089	—*	104	1.38
$Zn^{66}(n, p)Cu^{66}$	1460	-2.63	$+1.71$	0.0875	0.040	113	0.53

* This value was neglected in calculations.

tions were obtained from the photoneutron thresholds[19] except for the case of Mo and Ag. The value for Mo was taken from Brolley's results[11] and that for Ag was taken from the semi-empirical mass data[16].

The theoretical cross sections thus calculated are tabulated in comparison with the observed values in Table III for the $(n, 2n)$ reactions, and in Table IV for the (n, p) and (n, α) reactions respectively.

In the case of the $(n, 2n)$ reactions, it is found from Table III that the observed cross sections agree with the theoretical values within about factor 3, and that the formers are always less than the latters except for the case of copper. The ratio $\sigma_{exper.}/\sigma_{theor.}$ for Mo^{92} shows no distinctive anomalies in spite of its neutron magic number 50. The $(n, 2n)$ reactions for two silver isotopes, Ag^{107} and and Ag^{109}, are 458 mb and 604 mb respectively. This coincides with the fact that these threshold energies for the $(n, 2n)$ reactions are about 9.8 MeV for Ag^{107} and 9.1 MeV for Ag^{109}.

The results of the excitation measurement for the $Mo^{92}(n, 2n)Mo^{91}$ reaction are shown in Fig. 5 and also in Table V. The solid curve in Fig. 5 represents the relative excitation function calculated theoretically with the threshold energy of 12.48 MeV and a of 3.16 MeV^{-1} [10]. As far as the relative behavior is concerned, these results show a fairly good agreement with the theoretical curve.

Table V. Excitation data (Threshold Behavior) of $Mo^{92}(n, 2n)Mo^{91}$

Neutron energy (MeV)	Relative cross section (exper.)	Absolute cross section (exper.)	Absolute cross section (theor.)	$\frac{\sigma_{exper.}}{\sigma_{theor.}}$
		mb	mb	
14.80 ± 0.13	$1.00 \pm 3\%$	$180 \pm 17\%$	484	0.372
14.14 ± 0.18	$0.733 \pm 5\%$	$132 \pm 16\%$	308	0.429
13.76 ± 0.18	$0.556 \pm 6\%$	$100 \pm 18\%$	209	0.479
13.51 ± 0.11	$0.334 \pm 7\%$	$60.1 \pm 18\%$	149	0.403

As to the absolute values, however, the theoretical curve lies always above the experimental curve approximately by factor 2.4. These results were also observed in the cross section measurements.

It should be remarked that the threshold energy of the $(n, 2n)$ reaction for Mo^{92} is less than the corresponding (γ, n) threshold energy which was reported as 13.28 MeV by Hanson *et al.*[21]

Moreover, as stated in § 4, the shorter activity of the Mo^{91} isomer is not found for the neutron energy of 14 MeV, and Brolley has observed a weak 65.5 sec. activity by 18 MeV neutrons[10]. Therefore the threshold energy of the $(n, 2n)$ reaction for the 65.5 sec. isomer production seems to be larger than that for the 16 min. isomer, being inconsistent with King's comment[15].

In the cases of the (n, p) and (n, α) reactions, the even-odd effect was taken into account for the nuclear level density. If correction was made for this effect, the theoretical predictions agreed with the experimental cross sections within factor 2 except for the case of the $Al^{27}(n, \alpha)Na^{24}$ reaction as shown in Table IV.

The relative cross section of the reaction $Al^{27}(n, p)Mg^{27}$ to $Al^{27}(n, \alpha)Na^{24}$ was found 1:1.38 by the present experiment; while the theoretical value not corrected for the even-odd effect is 1:1.74, and the corrected value is 1:3.5. Thus in the $Al^{27}(n, \alpha)Na^{24}$ reaction, it appears that the experimental cross section rather agrees with the theoretical one not corrected for the odd-odd nucleus.

It is found from Table II that the gradient of the excitation curve for the $Cl^{37}(n, p)S^{37}$ reaction was $+6\% \cdot MeV^{-1}$. This value will not contradict the data of Cohen and White[22]. According to Cohen and White, the theoretical excitation curves based on both the statistical theory using (the extrapolation of) Gugelot's level densities[23] and the direct interaction described by Austern *et al.*[24] should have negative gradient in the energy range under consideration. Therefore the experimental results show a remarkable disagreement with the theoretical predictions as already pointed out by Cohen and White.

§ 6. Acknowledgements

The author desires to express his sincere thanks for the encouragements and many valuable discussions given by Dr. B. Arakatsu, the president of Kōnan University, and Profs. K. Kimura, M. Sonoda and S. Kawata. It is pleasure to acknowledge his indebtedness to his colleagues, Messrs. K. Yuasa, M. Sakisaka, K. Sugiyama, B. Saeki and Y. Oyama, who have been in cooperation during these experiments. Further he is greatly indebted to Dr. K. Hisano of Denkishikenjō and Mr. T. Oshida of Kōbe Kōgyō Corporation for their kindness to lend him the precious samples.

This work was partly supported by a grant-in-aid for scientific researches of the Ministry of Education.

Appendix

(1) Calculation of the reaction cross section

For cross section measurements, the irradiation by neutrons is made in the geometry shown in Fig. 6 (in the 90° direction).

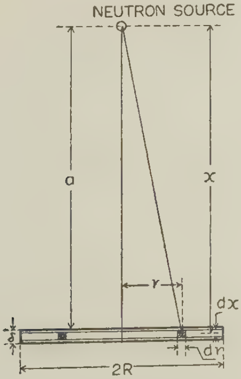

Fig. 6. Geometry of the irradiation by neutrons.

The number of the product nuclei generated by the neutrons in the "ring-element" of a sample of radius r and thickness dx can be written as follows:

$$\sigma\left\{\frac{n}{4\pi(r^2+x^2)}\right\}\cdot\{2\pi r\cdot dr\cdot dx\cdot m)dt\,,$$

where

σ = reaction cross section

m = number of the parent nuclei per unit volume (cm^{-3}) in the sample

n = total number of neutrons emitted from the Zr–T target per unit time (min^{-1})

dt = time of irradiation (min).

Hence, the number of the product nuclei in the sample disc of radius R is

$$dA=\sigma mndt\int_a^{a+\delta}dx\int_0^R\frac{r\cdot dr}{2(r^2+x^2)}$$
$$=\sigma mndt\cdot\frac{1}{4}\int_a^{a+\delta}\log\frac{R^2+x^2}{x^2}dx\,.$$

Immediately after the irradiations for a time interval T with constant intensity, the number of the existing active nuclei can be given by

$$A=\left[\frac{1}{4}\int_a^{a+\delta}\log\frac{R^2+x^2}{x^2}dx\right]$$
$$\times\int_0^T\sigma mn\exp\{-\lambda(T-t)\}dt$$
$$=\Omega'\sigma mn\frac{1-e^{-\lambda T}}{\lambda}\,,$$

where the abbreviation "Ω'" is used for the factor in the square bracket and λ is the decay constant for the beta-disintegration of the product nucleus. As mentioned in § 2 (A), it was assumed that the neutron intensity was constant for every one minute or 30 seconds interval during irradiations. Here let us consider the case of the "one minute-treatment". If the measurement of the activity of a sample is commenced t_0 minutes after the end of irradiation, the number of active nuclei existed in the sample at that time can be given by

$$A_0=\Omega'\sigma m\frac{1-e^{-\lambda}}{\lambda}\left[\sum_{i=1}^{T}n_i\exp\{-(T-i+t_0)\lambda\}\right],$$

where n_i is the total number of neutrons emitted from the target per minute in the i-th time interval.

The number n_i can be obtained from the net counts $n_{\alpha i}$ of α-particles per minute such that

$$n_i=n_{\alpha i}\times\frac{4\pi}{\omega}\,,$$

where ω is the solid angle which the α-detector subtends at the neutron source. Therefore

$$A_0=\Omega'\sigma m\cdot\frac{1-e^{-\lambda}}{\lambda}\cdot\frac{4\pi}{\omega}$$

$$\times\left[\sum_{i=1}^{T} n_{\alpha i}\exp\{-(T-i+t_0)\lambda\}\right].$$

As the β-activity is measured for ten minutes, the total number A_d of the nuclei which disintegrate by the beta-decay in that time interval is given by

$$A_d=\Omega'\cdot\sigma\cdot m\cdot(\lambda)\cdot\Sigma\cdot\frac{4\pi}{\omega}, \qquad (10)$$

where the abbreviations

$$\Sigma\equiv\left[\sum_{i=1}^{T} n_{\alpha i}\exp\{-(T-i+t_0)\lambda\}\right]$$

and

$$(\lambda)\equiv\frac{(1-e^{-\lambda})(1-e^{-10\lambda})}{\lambda}$$

are used.

On the other hand, by Eq. (1) the following relation holds between N_S and A_d:

$$N_S=\frac{f_S}{C_{G'}}\cdot A_d,$$

and accordingly, Eq. (10) now becomes

$$N_S=\frac{f_S\cdot\Omega'\cdot\sigma\cdot m\cdot(\lambda)\cdot\Sigma}{C_{G'}}\cdot\frac{4\pi}{\omega}.$$

If the beta-counts for the monitor irradiated in juxtaposition with the sample is designated by N_M, the apparent specific activity is proportional to $(N_S/N_M\cdot w)$ which is given by

$$\frac{N_S}{N_M\cdot w}=\frac{f_S\cdot\sigma\cdot m\cdot(\lambda)}{C_{G'}\cdot\rho}\cdot\frac{\Sigma}{N_M}\cdot\frac{4\pi}{\omega}\cdot\frac{\Omega'}{\delta}, \qquad (11)$$

where w and ρ are the thickness (in g/cm^2) and the density of the sample respectively.

Now, if w tends to zero, i.e., δ tends to zero, then $f_S\to 1$ and

$$\frac{\Omega'}{\delta}=\frac{1}{4\delta}\int_a^{a+\delta}\log\frac{R^2+x^2}{x^2}dx\xrightarrow[\delta\to 0]{}\frac{1}{4}\log\frac{R^2+a^2}{a^2}\equiv\Omega,$$

where it should be noted that (Σ/N_M) in Eq. (11) is constant irrespectively of the change of w.

From these relations the expression for the limiting value S of the apparent specific activity is given by

$$S\equiv\lim_{w\to 0}\frac{N_S}{N_M\cdot w}=\frac{\sigma\cdot(\lambda)\cdot\Omega}{C_{G'}}\cdot\frac{\Sigma}{N_M}\cdot\frac{4\pi}{\omega}\cdot\frac{m}{\rho}.$$

Then, if we use the relation $m/\rho=N_0\eta/M$, the reaction cross section can be written as

$$\sigma=\frac{M\cdot[N_M/\Sigma]\cdot S\cdot C_{G'}}{N_0\cdot\eta\cdot\Omega\cdot(\lambda)\cdot(4\pi/\omega)}.$$

Finally we obtain Eq. (2) by introducing the correction factor C_K concerning the branching ratio of the positive beta-decay to the orbital K-electron capture.

$$\sigma=\frac{M\cdot[N_M/\Sigma]\cdot S\cdot C_{G'}\cdot C_K}{N_0\cdot\eta\cdot\Omega\cdot(\lambda)\cdot(4\pi/\omega)}.$$

(2) Analysis of the pulse height distribution of the beta-rays measured by the 4π-proportional counter

Let us consider the typical pulse height distribution of β-rays by a proportional counter when a point source of β-rays is placed in the centre of the sample holder (see Fig. 2).

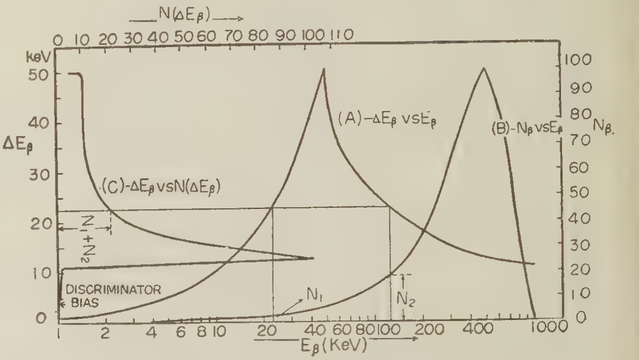

Fig. 7. Analysis of the pulse height distribution of the beta-rays measured by the 4π-proportional counter.

In Fig. 7, the curve A shows the energy loss in the counter gas ΔE_β plotted against the electron energy E_β on the logarithmic scale. The curve rises linearly to the maximum value determined by the dimension of the counter tube and then falls gradually towards the value corresponding to the minimum ionization. The range-energy relation for electrons used in this calculation was taken from the work by L. Katz and A. S. Penfold[25]. The curve B represents schematically an energy distribution of the beta-ray. The curve C was obtained from the curves A and B by the procedures indicated in Fig. 7. It shows the relation between ΔE_β and the number $N(\Delta E_\beta)$ of electrons which lose ΔE_β of their energies. The curve corresponds to the differential pulse height distribution to be expected for the β-rays shown by the curve B. The differential curve exhibits a peak at about $\Delta E_\beta=11$ keV corresponding to the neighbourhood of the minimum ionization.

Therefore the integral pulse height distribution curve appears to be nearly constant up to the bias-voltage corresponding to the peak point and then falls rapidly beyond this point. In the preliminary experiments, the integral pulse height distributions of the β-rays from La and K were observed and it was found that they were in good agreement with the above analysis.

References

1) E. R. Graves, A. A. Rodrigues, M. Goldblatt and D. I. Meyer: Rev. Sci. Inst. **20** (1949) 579.
2) E. B. Paul and R. L. Clarke: Can. Jour. Phys. **31** (1953) 267.
S. G. Forbes: Phys. Rev. **88** (1952) 1309.
J. E. Brolley, Jr., J. L. Fowler and L. K. Schlacks: Phys. Rev. **88** (1952) 618.
J. E. Brolley, Jr.: Phys. Rev. **89** (1953) 877.
A. V. Cohen and P. H. White: Nuc. Phys. **1** (1956) 73.
3) cf. 2)
4) H. V. Argo, R. F. Taschek, H. M. Agnew, A. Hemmendinger and W. T. Leland: Phys. Rev. **87** (1952) 612.
5) S. Shimizu: Mem. Coll. Sci. Kyoto Univ. **A25** (1949) 193.
S. Shimizu, S. Yasumi, Y. Saji and J. Muto: Mem. Coll. Sci. Kyoto Uuiv. **A26** (1950) 85.
6) C. W. Johnstone: Nucleonics **11** (1953) 36.
7) M. Sonoda: Mem. Coll. Sci. Kyoto Univ. **A25** (1949) 185.
8) J. M. Hollander, I. Perlman and G. T. Seaborg: Rev. Mod. Phys. **25** (1953) 469.
9) E. Feenberg and G. L. Trigg: Rev. Mod. Phys. **22** (1950) 399.
10) J. E. Brolley, Jr.: Phys. Rev. **89** (1953) 877.
11) L. McElhinney, A. O. Hanson, R. A. Becker, R. B. Duffield and B. C. Diven: Phys. Rev. **75** (1949) 542.
12) L. M. Blatt and V. F. Weisskopf: *Theoretical Nuclear Physics*, (John Wiley and Sons, New York, 1952).
13) E. R. Graves and R. W. Davis: Phys. Rev. **97** (1955) 1205.
14) V. F. Weisskopf and D. H. Ewing: Phys. Rev. **57** (1940) 472.
15) R. W. King: Rev. Mod. Phys. **26** (1954) 327.
16) C. N. Martin: *Tables Numériques de Physique Nucléaire*, (Gauthier-Villars, Paris, 1954).
17) B. T. Feld, H. Feshbach, M. L. Goldberger, M. Goldstein and V. F. Weisskopf: NYO-636 A.E.C., U.S.A., 1951.
18) J. Heidmann and H. A. Bethe: Phys. Rev. **84** (1951) 274.
19) E. Segrè: *Experimental Nuclear Physics* Vol. 2.
20) J. L. Fowler and J. M. Slye, Jr.: Phys. Rev. **77** (1950) 787.
21) A. O. Hanson, R. B. Duffield, J. D. Knight, B. C. Diven and H. Palevsky: Phys. Rev. **76** (1949) 578.
22) A. V. Cohen and P. H. White: Nuc. Phys. **1** (1956) 73.
23) P. C. Gugelot: Phys. Rev. **81** (1951) 51; **93** (1954) 425.
24) N. Austern, S. T. Butler and H. McManus: Phys. Rev. **92** (1953) 350.
25) L. Katz and A. S. Penfold: Rev. Mod. Phys. **24** (1952) 28.

JOURNAL OF THE PHYSICAL SOCIETY OF JAPAN Vol. 12, No. 5, MAY, 1957

Meson Showers by Heavy Primary Particles

By Senzo TOKUNAGA

Department of Physics, Saikyo University, Kyoto

(Received February, 7, 1957)

Meson showers by heavy primary particles which have energy of 500 BeV per nucleon were studied with nuclear emulsions. Dealing with the event, " the nuclear disintegration cascade by heavy primary particle ", it was possible to estimate the energy of the primary particle with much accuracy by two methods, one by usual median angle of shower particles and the other by the opening angle of the fragmentation products of heavy primary particle. The angular distribution of the shower particle was studied and compared with the theory of Fermi and that of Landau.

§ 1. Introduction

Studies on meson production by nucleon-nucleon or nucleon-nucleus collision with nuclear emulsions have been reported by many workers,1)-11) but studies on meson production by heavy primaries have been comparatively rare.12)-15) The former has given a good deal of knowledge, but there still remain some inconsistencies among their results,—for example, about the angular distribution of the produced mesons, the multiplicity of mesons, the inelasticity coefficient and so on. These discrepancies are considered to originate mainly in the attained statistical accuracy. For instance, when a few mesons are produced in a jet, it is very difficult to estimate the energy of the primary nucleon which caused the interaction with much accuracy.

When the interaction of a high energy heavy primary particle with a nucleus of emulsion is assumed to be the superposition of many simultaneous nucleon-nucleon collisions, or the collision of a certain number of nucleons among the incident heavy nucleus with the same number of those of the target nucleus in the emulsion, much information about nucleon-nucleon collision can be gained at one time, and it is possible to estimate the energy of the incident primary by the median angle method with more accuracy than in the case of simple nucleon-nucleon collision, owing to a greater number of mesons produced. Moreover, when the fragmentation products of heavy primary are accompanied in the interaction, it is also possible to estimate the energy of the primary particle by the opening angle of the fragmentation products, and the accuracy obtained by this method is better than the median angle method.

From these points of view we studied the meson production by heavy primaries. And the angular distribution of the produced meson was compared with the theory by Fermi16) and that by Landau.17) Having much to do with the mechanism of the meson production, the angular distribution of the produced meson is a very important problem.

§ 2. Experimental Procedure

§ *2.1 Emulsion Blocks and the Events Studied*

The stack we used consisted of 48 4-inch by 6-inch G5 600 microns pellicles and was flown with the emulsion surfaces vertical for 6 hours up to a maximum altitude of 33 km by a polyethylene balloon at Kobe in Japan in 1955.

In the stack were searched for events in which heavy primaries interacted with the nuclei of the emulsion causing meson showers. Fifteen examples of this kind have been found so far, but the events in which only a small number of mesons are produced were not suitable for our purpose, because it was not possible to estimate energies of the primary particles with sufficient accuracy by median angle method. Three events suitable for our analysis were selected among them and studied in detail. These were tabulated in Table I.

Table I. The events studied.

No. 1	$8+44_{\mathrm{Na}}$
No. 2	$19+9_{\mathrm{He}}$
No. 3	$17+120_{\mathrm{Li}}$

It is very remarkable that the events No. 1, 2 and 3 are nuclear disintegration cascade, which will be reported elsewhere.[18] As shown in Fig. 1, a heavy primary having charge Z 11, a Na nucleus, caused the event No. 1 at B, from which a He nucleus and a Li nucleus were emitted as a result of the fragmentation of the primary Na nucleus, and each caused the event No. 2 and No. 3 at C and D respectively.

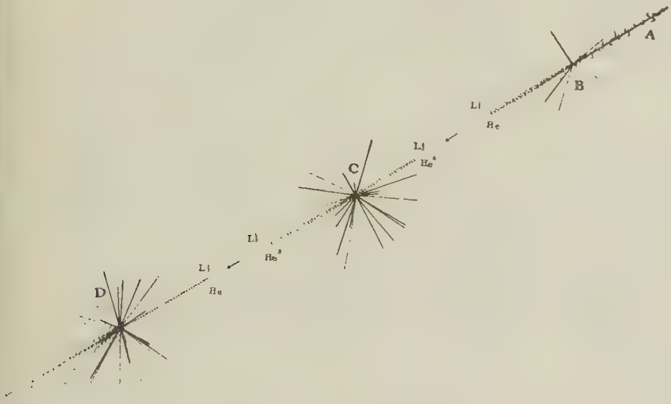

Fig. 1. Projection drawing of a nuclear disintegration cascade. A sodium nucleus producing a thin track at A continued to B, there causing a star $8+44_{\mathrm{Na}}$ (the event No. 1), from which a helium nucleus and a lithium nucleus were emitted, and each produced a star at C (the event No. 2) and D (the event No. 3) respectively.

§ 2.2 Determination of the Charge of the Heavy Primary Particle

The charge of the heavy primary particle was determined by δ-ray counting. The δ-rays with more than four grains were counted, and the charge of the primary was determined comparing with the result of Dainton et al.[19] When the number of charge is small as in the cases of a helium and a lithium nucleus, the gap-length method[20] was also used to get grain density of the track. The ratio of the charge of helium and lithium determined by two methods agreed so well as shown in Table II that it was possible to calibrate the relation between the number of δ-rays and the charge of particle.

Table II. The grain density and δ-ray density of the track of a helium and a lithium nucleus.

The grain density	
$g_{\mathrm{Li}}=144.0\pm6.1/100\,\mu$	$g^*_{\mathrm{Li}}=8.95\pm0.47$
$g_{\mathrm{He}}=61.2\pm2.6/100\,\mu$	$g^*_{\mathrm{He}}=3.80\pm0.20$
	$g^*_{\mathrm{Li}}/g^*_{\mathrm{He}}=2.35\pm0.14$
The δ-ray density	
$N_{\mathrm{Li}}=0.96\pm0.08/100\,\mu$	$N_{\mathrm{Li}}/N_{\mathrm{He}}=2.28\pm0.33$
$N_{\mathrm{He}}=0.42\pm0.05/100\,\mu$	

As the ratio of the square of the charge of lithium and of helium is 2.25, the results agree very well.

§ 2.3 Measurement of Angular Distribution of Shower Particles

In order to measure angles between the directions of secondary shower particles and primary particle, the primary track was aligned along the x-axis on a scattering microscope and y-coordinate of each secondary track was measured at several points on the track, and depth measurement of each track was also made. Making use of them the angles were calculated. By this method true angle between the primary particle and the secondary shower particle was possible to be measured with an error, the order of which is estimated to be 5×10^{-3} radians.

§ 2.4 Selection of Primarily Produced Mesons

Among the shower particles emitted in the interaction there would be included not only the primary produced mesons and protons which were constituents of the primary particle and had no concern with the interaction. In order to choose only the primarily produced mesons, the following two assumptions were made. Firstly, the number of protons which suffered no interaction was assumed to equal the difference between the charge of the incident nucleus and the sum of charge of multiply charged fragments. Secondly, the criterion by G. Bertolino,[8] which was used in his study of jet was adopted. The criterion is as follows: if the θ_n, the angle formed by the n-th track with the shower axis, is larger than twice of the θ_{n-2}, the angle formed by the $n-2$th track, the n-th track is not considered as the primarily produced meson. Taking the criterion into consideration, the results of the estimation of the energy of the primary particle of the event No. 1, 2 and 3 by median angle method agree very well.

§ 2.5 *Estimation of the Energy of the Primary Particle*

The estimation of the energy of the primary particle was made by kinematical method. We assume that the interaction of a heavy primary particle with a nucleus of emulsion is the superposition of simultaneous nucleon-nucleon collisions and that there exists the center of mass system for the interaction. By applying the Lorentz transformation assuming that the angular distribution of particles in the center of mass system is symmetric about a plane transverse to the direction of incident particle, we get

$$\tan\frac{\theta^*}{2}=\gamma_c\tan\theta \qquad (1)$$

$$\gamma=\frac{2}{\theta_F\theta_{1-F}} \qquad (2)$$

where θ^* and θ denote the angle of particle with the direction of motion of the incident particle in the c.m. system and laboratory system respectively, $\gamma_c=1/\sqrt{1-\beta_c^2}$, β_c, the velocity of the c.m. system, $\gamma=2\gamma_c^2-1$, energy per nucleon of the incident particle in the laboratory system, and the subscripts F and $1-F$ refer to the angles containing a fraction of the total number of produced mesons. The angle $\theta_{1/2}$ which has the greatest statistical accuracy was used in our analysis.

To check our assumptions concerning the angular distribution in the center of mass system, the integral angular distribution of the mesons in the laboratory system

$$F(\theta_F)=\frac{1}{N}\int_0^{\theta_F}N_\theta d\theta \qquad (3)$$

is plotted versus $\log\theta_F$, where N denotes the total number of particles, N_θ, the number of particles which is included within the angle θ with the direction of the incident particle, and θ_F, the angle containing a fraction of F of the total number of particles. The plots are shown in Fig. 2 and Fig. 3. It is seen that the plots are symmetric with respect to the reflection through the point $F=1/2$, $\log\theta_{1/2}$ as origin. The fact shows the consistency of our assumptions.

When some fragments are produced in the interaction, the estimation of the energy of the primary particle is also possible by measuring the opening angle of the fragmentation products. According to Kaplon et al. the root mean square angle which the shower particles of fragmentation products make with direction of the incident primary in the laboratory system is

$$<\theta^2>^{1/2}=0.06/E \qquad (4)$$

where E is the total energy per nucleon in BeV of the incident nucleus, and the largest observed angle of any particle in the laboratory system gives an upper limit for the energy of incident particle, which is given by:

$$E_{\max}\approx\frac{0.12}{\theta_{\max}} \qquad (5)$$

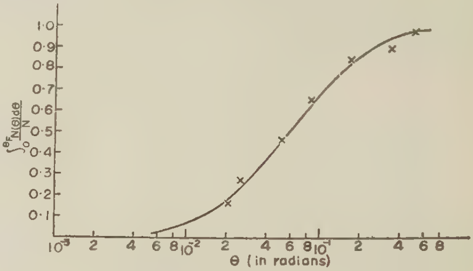

Fig. 2. Normalised integral angular distribution of mesons produced in the event No. 1 in the laboratory system.
Ordinate: Fraction of charged particles contained within the polar angle θ.
Abscissa: $\log\theta$.

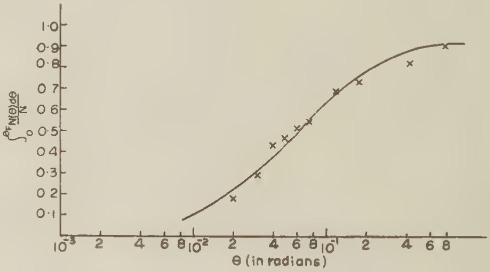

Fig. 3. Normalised integral angular distribution of mesons produced in the event No. 3 in the laboratory system.
Ordinate: Fraction of charged particles contained within the polar angle θ.
Abscissa: $\log\theta$.

The advantage of the method is that it gives results which have better accuracy than the median angle method. In the event No. 1 both methods were employed, and the values obtained agree very well with each other. Moreover, the energies obtained for the event No. 2 and No. 3 by the median angle of the shower particles also agree so well as shown in Table III, the value of the energy of the primary particle in the events No. 1, 2 and 3 seems to be certain. The fact that the results obtained by two methods agree shows our assumption to be correct.

Table III. Energy of the incident primary particles obtained by two methods.

	1. Energy obtained by the opening angle of the fragmentation products (BeV per nucleon)	2. Energy obtained by the median angle of shower particles (BeV per nucleon)
the event No. 1	336 (by eqn. (4)) 672 (by eqn. (5))	507
the event No. 2		507
the event No. 3		505

§ 3. The Angular Distribution of Mesons Produced in the Interaction by Heavy Primaries

Angular distributions in the center of mass system were shown in Fig. 4 and Fig. 5, in which the abscissa represents the ten parts that cover equal solid angle in the center of mass system, and I represents the forward direction and X the backward direction with respect to the direction of the incident particle. Among the particles which are emitted forwards there may be some protons which did not interact in the interaction as described in § 2.4. These protons being expected to be emitted making angles less than $\sim 10^{-4}$ radians with the incident particle, they always belong to the region I. We assumed the number of these protons to be equal to the difference in charge between that of the incident nucleus and the sum of charge of multiply charged fragments in the jet. In Fig. 4 and Fig. 5 the number of mesons is shown in full line, and the number of thin particles including protons is shown in dotted line.

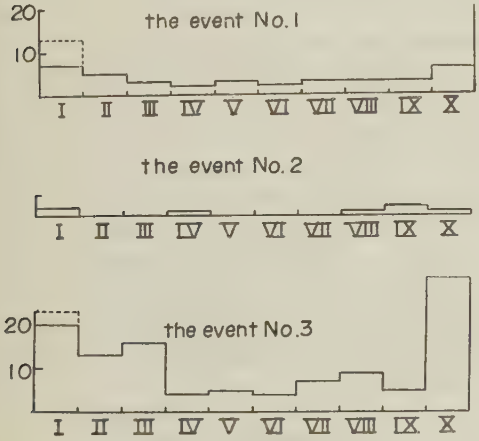

Fig. 4. The angular distribution of mesons produced in each event in c.m. system. The abscissa represent the ten parts which cover equal solid angle in c.m. system. *I* represents the forward direction and *X* the backward with respect to the incident particle.

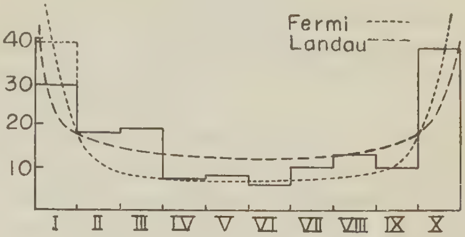

Fig. 5. The angular distribution of mesons produced in the event No. 1, 2 and 3. The dotted curve represents the theoretical angular distribution by Fermi, and the broken line by Landau.

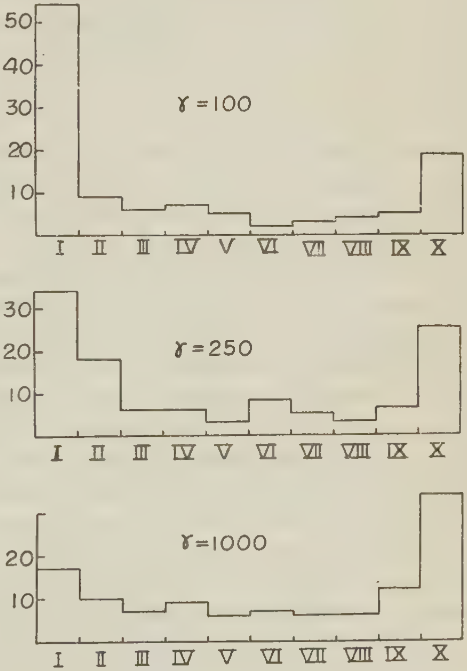

Fig. 6. The angular distribution of mesons produced in the event No. 3 in c.m. system for different γ.

From the results it is clearly seen that the angular distribution is not isotropic, and more mesons are emitted in the forward and backward direction than other directions.

The angular distribution was compared with the theory of Fermi and that of Landau. In Fig. 5 were shown the results of the calculation according to the theories, normalizing the total number of mesons with the experimental values. In the calculation with Fermi's theory the median impact parameter was taken. Though it is difficult to assert which theory is more fitted to the experimental results, it is seen that Landau's theory is rather fitted than Fermi's.

Though the angular distribution in the center of mass system varies with the values of γ, it would be recognized that, even if the value of γ changed more than a factor of two as shown in Fig. 6, more mesons are emitted in the forward and backward direction.

§ 4. Discussion

As our events are occuring by nucleus-nucleus collisions, it would not be right, strictly speaking, to look upon them as the superposition of nucleon-nucleon collisions, or the collisions of the same number of nucleons in the target nucleus with the same number of nucleons in the incident nucleus each other. It would be necessary to consider other mechanism concerning the events. However, the fact that the energy of the primary particle determined by the opening angle of the fragmentation products accords with the energy determined by the half-angle of the shower particles using the criterion of G. Bertolino shows that the events can be regarded approximately as the superposition of the simultaneous nucleon-nucleon collisions. Also, though the number of the grey and black prong is large in our events, their energies per nucleon of the primary particle are small comparing with the energy of the primary particle, so it would not be wrong to look upon them as the superposition of the nucleon-nucleon collisions. In the study of jet showers by nucleons, stars with black and grey prongs less than three are usually regarded as jets.

When we consider the events as the superposition of nucleon-nucleon collisions, a greater number of mesons being produced, it is a great advantage that much information can be obtained concerning the meson production by the incident nucleons having same energy at one time. It is also very favourable that the energy of the primary particle can be estimated by two methods, when the interaction is accompanying fragmentation products of heavy primary particle. In the events No. 1 the values of the energy per nucleon of the primary particle obtained by two methods agree well, and moreover, they are also in accord with those obtained for the events No. 2 and No. 3 by the median angle of shower particles. The fact shows that the estimation of the energy of the primary particle is reliable, and that the assumption of the superposition of nucleon-nucleon collisions is not wrong. As the method to determine the energy of the primary particle by the opening angle of the fragmentation products having comparatively a good accuracy, it is very profitable.

As stated in § 3, the angular distribution of the mesons is not isotropic, but more mesons are emitted in forward and backward directions, and the result favours Landau's theory. By G. Bertolino the angular distribution of mesons in the jet is isotropic.[8] It is inconsistent with our result. It seems that it is mainly due to the fact that owing to the many jets, each having different γ, his results are averaged over. In case of a small number of mesons being emitted in jet, the estimation of the energy of the primary particle by median angle method has much error. Collecting many jets for which the estimation of the energy is not possible with sufficient accuracy, it appeares that he obtained the isotropic angular distribution.

It is a characteristic of the present analysis that dealing with the event, "nuclear disintegration cascade by heavy primary particle," many nucleon-nucleon collisions, in which the incident particles have the same values of γ, are collected.

Acknowledgement

The author wishes to express his hearty gratitude to Prof. K. Kimura and Prof. O. Minakawa for their sustained interest and encouragement through the course of the work. Also, his sincere appreciation and thanks go to Dr. K. Nishikawa and Miss. T. Ishii for their cooperative efforts, and to the members of the Kansai Balloon Group for making possible the balloon flight.

This work was financially supported by the Grant for Scientific Research of the Ministry of Education for the 1955 fiscal year.

References

1) R. R. Daniel, J. H. Davies, J. H. Mulvey and D. H. Perkins: Phil. Mag. **43** (1952) 753.
2) J. H. Mulvey: Proc. Roy. Soc. **221** (1954) 367.
3) M. F. Kaplon and D. M. Ritson: Phys. Rev. **88** (1952) 386.
4) M. F. Kaplon, W. D. Walker and M. Koshiba: Phys. Rev. **93** (1954) 1424.
5) M. Koshiba and M. F. Kaplon: Phys. Rev. **97** (1955) 193.
6) C. Castagnoli, G. Cortini, C. Franzinetti, A. Manfredini and D. Moreno: Nuovo Cim. **10** (1953) 1939.
7) G. Bertolino and D. Pescetti: Nuovo Cim. **12** (1954) 630.
8) G. Bertolino: Nuovo Cim. **3** (1956) 141.
9) E. Lohrmann: Nuovo Cim. **3** (1956) 822.
10) S. Kaneko, O. Kusumoto and S. Matsumoto: Journ. Phys. Soc. Japan **11** (1956) 1129.
11) F. A. Brisbout, C. Dahanayake, A. Engler, Y. Fujimoto and D. H. Perkins: Phil. Mag. **1** (1956) 605.
12) D. Lal, Y. Pal, B. Peters and M. S. Swami: Phys. Rev. **87** (1952) 545.
D. Lal, Y. Pal, B. Peters and M. S. Swami: Proc. Ind. Acad. Sci. **A36** (1952) 75.
13) M. Teucher: Suppl. Nuovo Cim. **12** (1954) 361.
14) P. Freier and J. Naugle: Phys. Rev. **92** (1953) 1086.
15) J. H. Noon and M. F. Kaplon: Phys. Rev. **97** (1954) 769.
16) E. Fermi: Phys. Rev. **81** (1951) 683.
17) S. Z. Belen'kji and L. D. Landau: Suppl. Nuovo Cim. **1** (1956) 15.
18) S. Tokunaga, K. Nishikawa and T. Ishii: Nuovo Cim. **5** (1957) 517.
19) A. D. Dainton, P. H. Powler and D. W. Kent: Phil. Mag. **43** (1952) 729.
20) P. H. Fowler and D. H. Perkins: Phil. Mag. **46** (1955) 587.
21) M. F. Kaplon, B. Peters, H. L. Reynolds and D. M. Ritson: Phys. Rev. **85** (1952) 295.

JOURNAL OF THE PHYSICAL SOCIETY OF JAPAN Vol. 12, No. 5, MAY, 1957

The Surface Potential of Selenium and its Relation to the Rectification and the Photovoltaic Effects

By Umejiro YOSHIDA and Akira SUZUKI

Faculty of Engineering Yokohama National University

(Received November 8, 1957)

The surface potential of selenium was measured by Kelvin's methods and was found to be influenced by the ambient. The characteristics of a rectifier obtained by making metal electrode contact with the selenium surface depend on the surface potential. The variation of the surface potential under illumination is of the same maginitude as the photoelectromotive force of the selenium cell. From these results, it is concluded that a blocking layer is formed on the selenium surface during the heat treatment.

§1. Introduction

The rectification properties of the selenium cell are known to come from a blocking layer localized in the interface between the selenium and the metal. Notwithstanding many studies about the selenium rectifier, there is no complete knowledge about the composition of the blocking layer. The polarization and the creep effect of the selenium rectifier may result from the unstable components of the blocking layer[1]. There is an opinion that cadmium selenide CdSe is the main component of the blocking layer, as it is detected in some selenium cell. By coating the selenium surface with a thin film of CdSe, its rectification ratio can be increased[2)].

It is known that the characteristics of selenium rectifiers are controlled in the early stage of treatments in the industrial manufacturing process. The surface state of selenium after heat treatment has important factors on its rectification action. After coating with the front electrode, its characteristics is improved under many processes such as electric aging; but its final characteristics is widely affected by the surface states at the time of coating with the front electrode. The blocking layer existing in finished selenium rectifiers may be formed by combination of the selenium surface and front electrode metal, in the course of manufacturing process and therefore its composition may be of complex nature.

This paper treats the characteristics of selenium cells immediately after heat treatment for finding the nature of blocking layer formation in the early stage of manufacturing process. The surface stages of selenium after heat treatment is measured by its surface potentials. There are some researches about the surface potential of germanium[3)], but none about that of selenium at present. The present work was undertaken to find the relation of the surface potential of the selenium after the heat treatment to its rectification and photovoltaic effect.

The surface potential of the selenium is found to change slowly for long time after the heat treatment. A rectifier is prepared by contacting a rod of wood metal with the selenium surface to find the relation between the rectification property and the surface potential. It is found that the surface potential and the rectification ratio is nearly of a constant value for a long time in the atmosphere if the selenium surface is coated with a thin film of synthetic resin. The variation of the surface potential under illumination is measured for a long time after the heat treatment and is found to be of a nearly constant value. A photovoltaic cell is obtained by contacting a transparent cadmium film with the selenium. The electromotive force induced under illumination is found to be nearly equal to the variation of the surface potential under same intensity of illumination.

§ 2. Experimental Arrangement

The surface potential of selenium is measured by Kelvin's method from the difference of work function between the reference electrode and selenium[4)]. Gold plate is used for the reference electrode as the work function of gold is not much influenced by the atmosphere. An electromotive force E is applied in such a way as to oppose the contact potential difference between the selenium and the gold plate. As shown in Fig. 1, the gold plate is separated at about 1 mm from the selenium surface and is made in vibration at about 200 c.p.s. by means of an electromagnet. When potential E is not equal to the surface potential, current proportional to the difference is induced in the resistance R in Fig. 1. The voltage across R is amplified and detected by a cathode ray oscillograph or a telephone receiver.

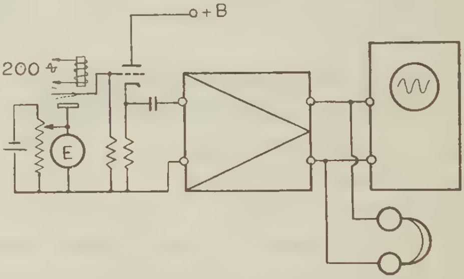

Fig. 1. Circuits of measurement apparatus.

When the electromotive force E is made equal to the contact potential difference, the output voltage of the amplifier becomes zero. The surface potential of selenium may be obtained from the value of E. For the measurement of the surface potential variation under illumination, this vibrating gold plate is replaced by a gold plate with a hole covered with fine mesh of gold wires, through which the selenium surface is irradiated with the light. In this experiment, a selenium plate of diameter 18 mm is used and the amplitude of vibration of the gold plate and mesh is controlled at about 0.1 mm. To measure the surface potential within the accuracy of 1 mv, the voltage gain of the amplifier is made larger than 120 d.b.

§ 3. The Surface Potential of Selenium after Heat Treatment

The selenium is melted evenly on an iron plate electroplated with nickel and is transformed into grey metallic stage by heat treatment at about 200°C. The surface potential of this surface is measured by the abovementioned Kelvin's method. The results of the measurement of the relation between the surface potential and the time after the heat treatment are shown in Fig. 2. As is seen from it, there is a rise and decay in the surface potential curve. For example, in the atmosphere of relative humidity 85%, the surface potential increases by about 0.16 V in 2 hours after the heat treatment and thereafter decreases gradually, as shown in the curve (1). In the atmosphere of lower relative humidity, the rise and decay of the surface potential becomes slower: the curve (2) and (3) show the surface potential of selenium exposed in the atmosphere of relative humidity 70% and 45%, respectively. When the surface of the selenium is oxidized by exposing in a stream of ozon, the surface potential increases by about 0.2 V from the initial value; and then decreases slowly in the same manner as the curve (1) or (2) according to the relative humidity of the atmosphere to which it is exposed. By exposing the surface in the saturated water vapour for a few seconds, its potential decreases suddenly by about 0.4 V. The surface potential decreases by about 0.4 V in the atmosphere of relative humidity 85% in 20 hours after the heat treatment. From these facts, it is seen that the surface potential increases by oxidization and decreases by absorption of moisture. As the surface of selenium is chemically active, it continues to oxidize with the oxygen in the atmosphere after the time of the heat treatment, and its surface potential increases. Then it absorbs water vapour from the atmosphere and the surface potential decreases depending on the relative humidity and hours exposed. The surface potential curve in Fig. 2 may be considered as coming from these oxidization and absorption of moisture. When the selenium surface is irradiated with light, its potential increases depending on the intensity of illumination. The amount of change in the surface potential is nearly independent of the time exposed in the atmosphere after the heat treatment. A plot of this variation of the surface potential against the intensity of illumination is shown in Fig. 3. The curve (1) shows results of measurements for the selenium surface immediately after heat treatment, curve (2) for that at 2 hours after heat treatment and curve (3) for that after a long time. It is evident that the linear relation does not hold between the variation of the surface potential and the intensity of illumination. The variation of the surface potential becomes about 0.2 V at high illumination. It is independent of the time exposed in the atmosphere.

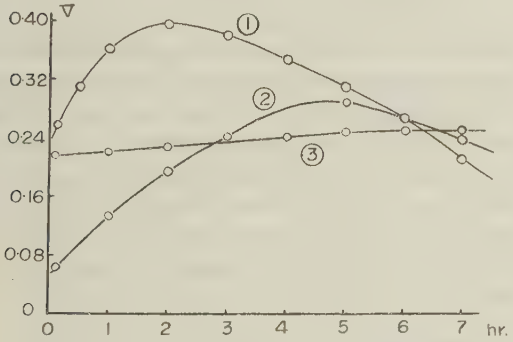

Fig. 2. Surface potential of Se after the heat treatment as a function of the time.

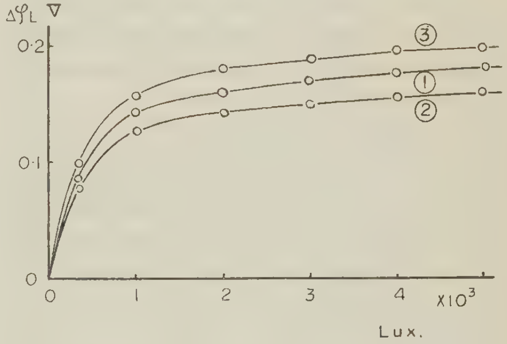

Fig. 3. Surface potential as a function.

§ 4. Rectification and the Surface Potential

The alloy of bismuth, cadmium and tin is used for the front electrode of a selenium rectifier as in the ordinary commercial type. The surface potential of this alloy is nearly of constant magnitude under exposure in the atmosphere. A rectifier is prepared by contacting a rod of alloy with the surface of selenium under a constant pressure to find the relation of the surface potential to the rectification. Fig. 4 shows the ratio of forward and backward current at 1 V. Corresponding to the increase in the surface potential in the atmosphere, the rectification ratio decreased slowly after heat treatment. It falls to the minimum value at the maximum surface potential. From this point, it becomes to be independent of the surface potential and the hours exposed in the atmosphere. From this curve it can be seen that the condition of the selenium surface after heat treatment has large effect on its rectification action. The electrostatic capacity of a rectifier prepared in the same manner is measured for finding the change occuring in the blocking layer. The electrostatic capacity is found to increase slowly after the time of contact, and in 5 hours it reaches the magnitude of 150–200% of that immediately after the contact. This may be due to the change of the surface potential in the interface.

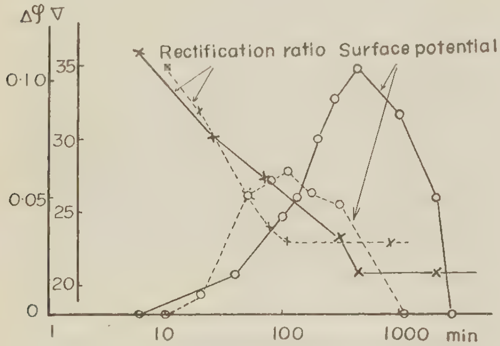

Fig. 4. Surface potential and rectification ratio.

In the process of industrial manufacture of rectifiers, the selenium surface is usually coated with a thin insulating film and the front electrode is placed on it. To find its effect on rectification action, the selenium surface is coated after heat treatment with a thin film of synthetic resin. Several synthetic resins different chemical composition are used for coating and the thickness of film is $10^{-6}\sim 10^{-5}$ cm. By coating with synthetic resin, the surface potential falls immediately after coating for all resins, and is nearly of constant magnitude for a long time, as shown in Fig. 5. From these curves, it can be seen that the insulating layer protects the selenium surface from the effect of the atmosphere. To find the effect of the insulating layer on the rectification action. A rectifier is obtained by contacting a rod of alloy with this surface under a constant pressure. In this rectifier there is no direct contact between the front electrode and the selenium surface, but for some synthetic resin its rectification ratio immediately after contact is larger than that of the direct contact type. Fig. 6, curve (1) shows the D.C. characteristics a rectified made on the free selenium surface, curve (2) and (3) that on the surface coated with insulating film of thickness about 5×10^{-6} cm. This shows that, also in the direct contact rectifier, the chemical combination between the metal and the selenium is no essential factor in the rectification action, at least in the earlier stage.

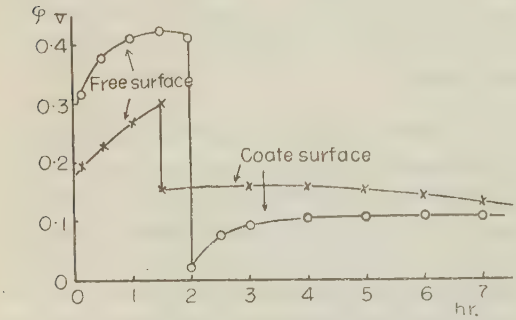

Fig. 5. Variation of surface potential after coating by synthetic resin as a function of the time.

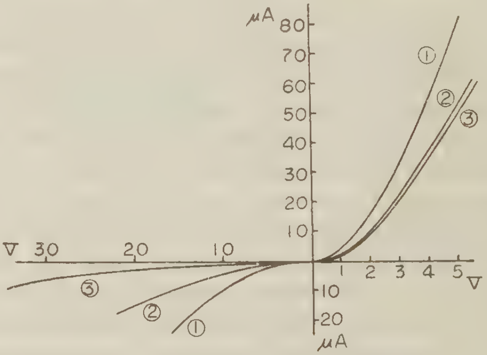

Fig. 6. D.C. characteristics of point contact rectifier.

§ 5. Photovoltaic Effect

By evaporating in vacuum or sputtering, a semitransparent cadmium film is obtained on a thin film made of a transparent synthetic resin. By contacting this film with the selenium surface a photovoltaic cell is prepared. A photoelectromotive force is induced between the film and the selenium by irradiating the surface with a light from a lamp through the synthetic resin. The current sensitivity of the cell is very low, but the voltage sensitivity is of the same magnitude at that of the commercial cell. The low current sensitivity may be explained by the small effective contact area between selenium and cadmium surfaces compared to the total surface of contact. The results of the measurement of the relation between the photoelectromotive force and the intensity of the illumination are shown in Fig. 7. Curve (1) shows the photoelectromotive force immediate after contact, and curve (2) that 2 hours after contact for the same cell; this may be considered to have occured by the change of surface states as in Fig. 3. This curve fits fairly well with the curve of the surface potential variation in Fig. 3. The photoelectromotive force is just of the same magnitude as the surface potential variation due to illumination at each intensity of illumination. A photovoltaic cell of the ordinary type is obtained by coating the surface of the selenium with a thin film of cadmium by sputtering in vacuum. The plot of the photoelectromotive force against the intensity of the illumination is shown in Fig. 8. Curves (1) and (2) show respectively the upper and lower limit of the range of sensitivity of these cells. For this type of cells, the photovoltaic current sensitivity is of the same magnitude as commercial cells, as the contact area between the front electrode and selenium is larger than that of the above-mentions contacting type; But there is no large difference in their voltage sensitivites between these photovoltaic cells.

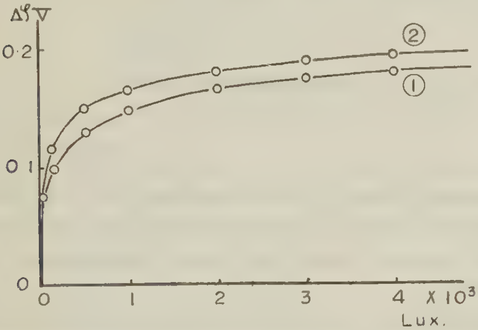

Fig. 7. Variation of surface potential under illumination for contact type cell.

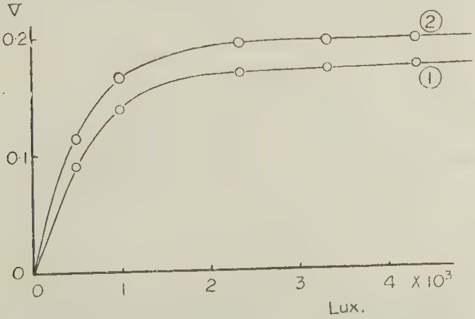

Fig. 8. Photovoltage of commercial type photovoltaic cell as a function of illumination.

§ 6. Conclusion and Acknowledgement

The surface of selenium is chemically active and its surface potential changes slowly under the effect of the ambient. The characteristic of the selenium rectifier made by contacting a rod of alloy on the surface is influenced by the surface condition. When the selenium surface coated with a thin insulating film is used, a rectifier of high rectification ratio is obtained. The surface potential of selenium under illumination varies in the same manner as the photoelectromotive force of selenium cells with the light intensity.

This work has been financially supported by the research expenditure of the group " The fundamental research on the physics of semiconducors " organized by Professor T. Muto, on the Institute of Science and Technology, Tokyo University.

References

1) M. Tomura: J. Phys. Soc. Japan **5** (1950) 349; **6** (1951) 359.
M. Tomura, Y. Abiko: ibid. **7** (1952) 220; **7** (1952) 624.
2) J. Yamaguchi, S. Katayama: ibid. **5** (1950) 386 **10** (1955) 234.
M. Tomura: ibid. **8** (1053) 477.
H. Strosche: ZS. f. Phys. **140** (1955) 409.
3) W. H. Brattain, J. Bardeen: Bell Syst. Tech. J. **27** (1953) 1.
J. Bardeen, S. R. Morrison: Physica **20** (1953) 873.
4) W. H. Brattain, J. Bardeen: Bell Syst. Tech. J. **32** (1953) 1.
U. Yoshida, A. Suzuki: Bull. Fac. Eng. Yokohama Natl. Univ. **1** (1941) 97.
S. R. Morrison: J. Phys. Chem. **57** (1953) 860.
5) W. K. Zworkin, E. G. Ramberg: Photoelctricity and its application (1949).
B. Lange: Die Photoelements und ihre Anwendung (1936).

JOURNAL OF THE PHYSICAL SOCIETY OF JAPAN Vol. 12, No. 5, MAY, 1957

On the 180°-type Domain Wall of $BaTiO_3$ Crystal

By Wataru KINASE and Hidetosi TAKAHASI
Department of Physics, Faculty of Science,
University of Tokyo, Tokyo

(Received December 28, 1956)

The energy of the 180°-type domain wall of $BaTiO_3$ crystal is obtained as 1.4 erg/cm^2 considering the dipole interaction and other interatomic energy of Born type.

The dipole interaction term has been obtained approximately from the difference of the energy of ferroelectric and antiferroelectric (stripes type) dipole configurations. The wall is found to be quite thin, that is, the change of polarization at the boundary is abrupt, in contrast with the ferromagnetic walls.

The structure of the 180° domains and their reversing process are also discussed.

§ 1. Introduction

Optical observations of single crystals of barium titanate have revealed a great deal about the domain structure of this crystal.[1)2)3)4)5)] In general, the domains are separated by two types of domain boundaries, that is, the 180°-wall and the 90°-wall which are boundaries between the two domains polarized respectively in antiparallel and perpendicular directions to each other (Fig. 1 (a) and (b)).

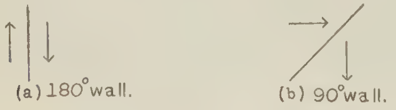
(a) 180°wall. (b) 90°wall.

Fig. 1.

The aim of our investigation is to find out the correct molecular model for the 180°-type domain boundary (or wall)*.

Treated in this paper are the atomic arrangement, the spontaneous deformation and polarization, the "thickness" and the energy of the 180°-type domain wall, considering the electrostatic dipole interaction and other interatomic forces of Born type.[6)] Of special interest is the fact that the dipole interaction energy at the boundary turns out to be nearly equal to that of the bulk crystal, resulting in an abrupt change of the dipole moments at the 180°-type boundary (Fig. 2) in contrast with the magnetic case, where more or less gradual change is found.

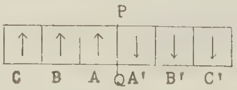

Fig. 2. Dipole arrangement near 180° boundary PQ.

We shall assume throughout this article that the dipole interaction is caused by the shift of Ti ions which are at the body-centres of the unit cells. The dipole moments by this shift will be shown by arrows as in Fig. 2.

§ 2. Ferro- and Antiferroelectric States

The calculation in the present paper makes use of the former results of the energy calculations for two periodic dipole configurations of $BaTiO_3$ crystal, that is, the ferroelectric configuration and one of the antiferroelectric configuration as shown in Figs. 3 and 4, respectively.

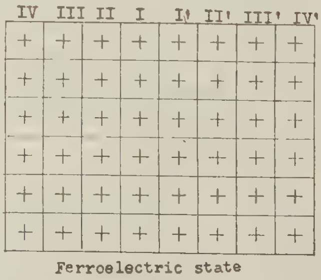

Fig. 3.

The energy and related quantities for these configurations have been calculated in a previous paper[8)] (Hereafter referred to as I) taking account of the electrostatic interaction among the sublattices.* There we obtained as the ratios γ and γ' of the electronic polarization of Ti ion (which is composed of the polarizations of the charge clouds of electrons) to the ionic polarization of Ti ion the values

---

* The two words "boundary" and "wall" will be used almost synonymously in this article.

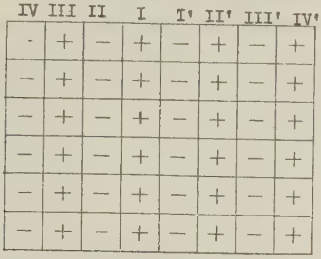

IV	III	II	I	I'	II'	III'	IV'
-	+	−	+	−	+	−	+
−	+	−	+	−	+	−	+
−	+	−	+	−	+	−	+
−	+	−	+	−	+	−	+
−	+	−	+	−	+	−	+
−	+	−	+	−	+	−	+

Antiferroelectric state

Fig. 4. + and − indicate upward and downward directions of dipoles perpendicular to the paper respectively.

0.1974 (eq. (15) in I) for the ferroelectric state and 0.1969 (eq. (19) in I) for the (stripes type) antiferroelectric state using the numerical values $c=64\times10^{-24}$c.c.$=(4\text{Å})^3$ for the volume of a unit cell and $4\pi\alpha_{\mathrm{Ti}}/c=0.0365$, $4\pi\alpha_{\mathrm{Ba}}/c=0.382$ and $4\pi\alpha_{\mathrm{O}}/c=0.470$ for the electronic polarizabilities of the ions[9], where the ionic polarization is defined as the sum of the moments of the dipoles contained in a unit volume[10], which correspond to the product of the effective charge ne and the shift from symmetrical position of Ti ion.** We can estimate the local fields acting on Ti ion caused by its own shift taking account of the above definition.

The local fields have been expressed in the preceding article[11]*** as

$$\gamma nex(1-8.17\Delta_a)/\alpha_{\mathrm{Ti}} \qquad (1)$$

for the ferroelectric state, where $\gamma=0.1974$, and

$$\gamma' nex(1-8.17\Delta_a)/\alpha_{\mathrm{Ti}} \qquad (2)$$

for the antiferroelectric state****, where $\gamma'=0.1969$, and x and Δ_a mean the shift of Ti ions and the fractional elongation of the lattice in the direction of the shift, that is, the lattice spacing is put as $4(1+\Delta_a)$ Å in this direction.

The potentials acting on Ti ion are obtained according to the usual definition of the "work" done to shift the Ti ion from the centre. Then multiplying eqs. (1) and (2) by a factor $-1/2$ and nex, we can get

$$\frac{-\gamma(ne)^2}{2\alpha_{\mathrm{Ti}}}\cdot(1-8.17\Delta_a)x^2 \qquad (3)$$

and

$$\frac{-\gamma(ne)^2}{2\alpha_{\mathrm{Ti}}}\cdot(1-8.17\Delta_a)x^2 \qquad (4)$$

as the potentials for the two states respectively.

§ 3. Local Fields at the Domain Wall

Figs. 5 (a) and (b) show schematically the dipole arrangement near a 180°-type domain boundary.

Let us consider the local field acting on Ti ion in the layer I and I' by the shift of Ti itself.

Here the method of the superposition of the local fields is useful for calculating the field in the domain boundary. For instance, the field acting on the point O by the ionic shift can be obtained if we know the field caused by the ionic shift of each layer in Fig. 6, which shows that the field in (a) is equal to the sum of those of (b), (c) and (d).

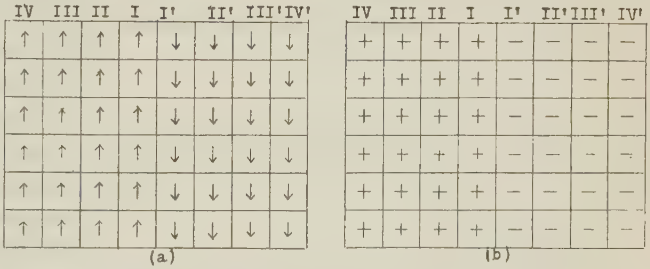

IV	III	II	I	I'	II'	III'	IV'
↑	↑	↑	↑	↓	↓	↓	↓
↑	↑	↑	↑	↓	↓	↓	↓
↑	↑	↑	↑	↓	↓	↓	↓
↑	↑	↑	↑	↓	↓	↓	↓
↑	↑	↑	↑	↓	↓	↓	↓
↑	↑	↑	↑	↓	↓	↓	↓

(a)

IV	III	II	I	I'	II'	III'	IV'
+	+	+	+	−	−	−	−
+	+	+	+	−	−	−	−
+	+	+	+	−	−	−	−
+	+	+	+	−	−	−	−
+	+	+	+	−	−	−	−
+	+	+	+	−	−	−	−

(b)

Fig. 5. Dipole arrangement near 180° wall.

Let us now consider the local field acting on Ti ion in the layer I in Fig. 5, where the ionic shift is $+x$ (upward arrows) and $-x$ (downward arrows) in the layer I, II, III,···· and I', II', III',····respectively.

For this purpose, we first consider Eqs. (1) and (2) which is for the cases of ferro- and antiferroelectric configurations shown in Figs. 3 and 4 respectively.

---

* Similar calculation was made independently by Y. Takagi.[7]

** ne means the "effective" charge of the Ti ion.

*** We refer to this paper as II.

**** Strictly speaking the two states have not the common factor $1-8.17\Delta_a$. However we neglect here this point, since the error is supposed to be small.

Now we shall put

$$ne(1-8.17\Delta_a)/\alpha_{\rm Ti}=k \qquad (5)$$

and apply the method of the superposition. Eqs. (1) and (2) are rewritten as

$$\begin{aligned} k\gamma x &= k\gamma_0 x+2\{k\gamma_1 x+k\gamma_2 x+k\gamma_3 x+\cdots\cdot\} \\ &= k\{\gamma_0+2(\gamma_1+\gamma_2+\gamma_3+\cdots\cdot)\}x \qquad (1)' \end{aligned}$$

and

$$\begin{aligned} k\gamma' x &= k\gamma_0+2\{k\gamma_1(-x)+k\gamma_2 x+k\gamma_2(-x)+\cdots\cdot\} \\ &= k\{\gamma_0+2(-\gamma_1+\gamma_2-\gamma_3+\cdots\cdot)\}x\,, \qquad (2)' \end{aligned}$$

where $\gamma_0, \gamma_1, \gamma_2, \gamma_3, \cdots\cdot$ are coefficients that characterize the effects of the shifts of the layers I, II (or I′), III (or II′), IV (or III′)···· in Figs. 3 and 4 on the layer I. The factor 2 before the parentheses in eqs. (1)′ and (2)′ means that the effects of the layers II and I′; III and II′; IV and III′; etc. are equivalent, and the alternate signs of $\gamma_0, -\gamma_1, \gamma_2, -\gamma_3, \cdots\cdot$ in eq. (2)′ correspond to the alternate directions of the shift in Fig. 4.

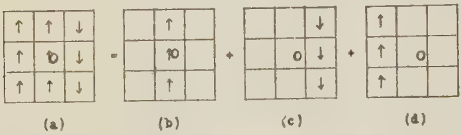

Fig. 6. Superposition of local fields caused by ionic shifts.

We get

$$\gamma=\gamma_0+2(\gamma_1+\gamma_2+\gamma_3+\cdots\cdot) \qquad (1)''$$

and

$$\gamma'=\gamma_0+2(-\gamma_1+\gamma_2-\gamma_3+\cdots\cdot)\,. \qquad (2)''$$

If we assume the relation

$$1:p=\gamma_0:\gamma_1=\gamma_1:\gamma_2=\gamma_2:\gamma_3=\cdots\cdot \qquad (6)$$

which certainly holds approximately, we obtain the relations

$$\gamma_0=\sqrt{\gamma\gamma'}\,, \qquad (7)$$

and

$$p=\frac{\sqrt{\gamma}-\sqrt{\gamma'}}{\sqrt{\gamma}+\sqrt{\gamma'}}\,. \qquad (8)$$

If we put $\gamma=0.1974$, $\gamma'=0.1969$ from eq. (1) and (2) we obtain

$$\gamma_0=0.19715 \qquad (9)$$

and

$$p=0.0006359=\frac{1}{1572.6} \qquad (10)$$

Here the smallness of p suggests that the local field acting on any Ti ion is mainly due to the shift of the ions within the same layer that contains the ion in question, the effect of the neighbouring layers being quite small. Our approximation may be inadequate in a general treatment of the local fields, but the error is considered to be small in cases where p is much smaller than unity.

The local field at the domain boundary can be found by using these values of γ_0 and p. The field in the layer I is

$$\begin{aligned} &k\gamma_0 x_1+k\gamma_1(x_2-x_1')+k\gamma_2(x_3-x_2') \\ &\quad +k\gamma_3(x_4-x_3')+\cdots\cdot \qquad (11) \end{aligned}$$

where

$$x_1, x_2, x_3, x_4, \cdots\cdot;\ x_1', x_2', x_3', x_4' \cdots\cdot$$

are the ionic shifts in the layers I, II, III, IV, ····; I′, II′, III′, IV′ ···· respectively. In a special case when the ionic shifts are all equal we can put the above x's as x. Then eq. (11) are rewritten simply as

$$k\gamma_0 x\,. \qquad (11)'$$

It may be admissible in a later treatment to take only the first term in eq. (11) into account and neglect the following term which are much smaller than $k\gamma_0 x_1$, because of the relation $\gamma_0 \gg \gamma_1 \cdots\cdot$ and $x_1 \gg x_2-x_1' \cdots\cdot$.

§4. The Lattice Spacings and the Ionic Shift at the Domain Boundary

We shall estimate here the lattice spacings in the domain wall.

The spontaneous deformation of the wall may be treated in a similar fashion as in II. The overlap, van der Waals' and Coulomb energy which were already discussed in the paper II are also available in the treatment of the domain wall. The dipole interaction may be taken from eq. (11), retaining only the first term, as already mentioned.

The potential acting on a Ti ion has been expressed as

$$(a'+a)x^2+bx^4 \qquad (12)$$

in the paper II, where $a'x^2$ is a negative term due to the dipole interaction and $|a'|>|a|$ in case of the "spontaneous" shift, while ax^2 and bx^4 are positive terms due to the van der Waals' and overlap interaction among the ions.[6)12)] The coefficients have been calculated in II for bulk crystals as

$$a'=\frac{-\gamma(ne)^2}{2\alpha_{\rm Ti}}\cdot(1-8.17\Delta_a)\,, \qquad (13)$$

$$a=10^5(5.1227-71.302\Delta_a+6.9541\Delta_{b1}+6.9541\Delta_{b2}+433.97\Delta_a{}^2-42.605\Delta_{b1}{}^2-42.605\Delta_{b2}{}^2) \tag{14}$$

and

$$b=10^{22}(1.8952-23.738\Delta_a-0.57603\Delta_{b1}-0.57603\Delta_{b2}+167.32\Delta_a{}^2+4.0873\Delta_{b1}{}^2+4.0873\Delta_{b2}{}^2)\ , \tag{15}$$

where γ, ne, α_{Ti} and Δ_a have the significance already mentioned, and Δ_{b1} and Δ_{b2} are the elongation of the cube edges relative to those of the standard cube in the two directions perpendicular to the ionic shift.

These coefficients must be somewhat modified in case of the domain boundary. Let us denote them by putting a bar on each symbol as $\bar{a}'$, $\bar{a}$ and $\bar{b}$. They are expressed as

$$\bar{a}'=\frac{-\gamma_0(ne)^2}{2\alpha_{\mathrm{Ti}}}\cdot(1-8.17\Delta_a)\ , \tag{13$'$}$$

$$\bar{a}=a+(6.8-47\Delta_{b2}) \tag{14$'$*}$$

and

$$\bar{b}=b+(-3+25\Delta_{b2})10^{16}\ . \tag{15$'$*}$$

Eq. (13)′ is obtained by putting γ_0 instead of γ in eq. (13). $\bar{a}$ is somewhat different from a, but the effect of this modification on the result is very small, the magnitude being expected to be about one-hundredth of the modification of a'. We also find that the difference between b and $\bar{b}$ is quite negligible. The above modification of a and b is due to van der Waals' and overlap interactions between Ti ions in the layers I and I′, and the interactions are so small as to leave a and b almost unchanged. Using the three coefficients $\bar{a}'$, $\bar{a}$ and $\bar{b}$ we can determine the lattice spacing and the ionic shift at the domain boundary by minimizing the energy for the domain boundary:

$$\bar{U}\doteq(\bar{a}'+\bar{a})x^2+\bar{b}x^4+\bar{U}_{\mathrm{overlap}}+\bar{U}_{\mathrm{Waals}}+\bar{U}_{\mathrm{Coulomb}} \tag{16}$$

as we have done in paper II for the bulk crystal.

The last three terms in eq. (16) represent the energy of the "unpolarized" tetragonal lattice, and do not contain x explicitly. Accordingly, by minimizing eq. (16) with respect to x, that is, by putting

$$0=\frac{\partial}{\partial x}\bar{U}, \tag{17}$$

we can obtain the spontaneous shift as

$$x=\pm\{(-\bar{a}'-\bar{a})/(2\bar{b})\}^{1/2}\ . \tag{18}$$

Substituting (18) into (16), the energy is rewritten as

$$\bar{U}=-(\bar{a}'+\bar{a})^2/(4\bar{b})+\bar{U}_{\mathrm{overlap}}+\bar{U}_{\mathrm{Waals}}+\bar{U}_{\mathrm{Coulomb}}\ , \tag{19}$$

the first term of `which corresponds to the "shift" energy.

It is reasonable to assume that the lattice spacings of the domain wall in the a and b_1 direction (that is, the direction parallel to the wall) are the same as in the bulk crystal, because the wall is clamped by the neighbouring lattices. Thus we have only to minimize the energy expression with respect to Δ_{b2} by solving the equation

$$0=\frac{\partial}{\partial\Delta_{b2}}\bar{U}\ . \tag{20}$$

We adopt here the values

$$\Delta_a=0.01951 \tag{21}$$

$$\Delta_{b1}=\Delta_{b2}=0.003723 \tag{22}$$

for Δ_a and Δ_{b1}, which has been obtained as the roots of the equations for the bulk crystal

$$0=\frac{\partial}{\partial\Delta_a}U\ , \qquad 0=\frac{\partial}{\partial\Delta_b} \tag{23 A, B}$$

in II, where U is the energy for the ferroelectric state of the bulk crystal. That is,

$$U=-(a+b)^2/(4b)+U_{\mathrm{overlap}}+U_{\mathrm{Waals}}+U_{\mathrm{Couloumb}}\ , \tag{24}$$

where we have assumed the effective charge of Ti ion to be 2.102* which corresponds to the value

$$\frac{\gamma(ne)^2}{2\alpha_{\mathrm{Ti}}}=5.4\times10^5 \tag{25}$$

in eq. (13) and to the total polarization 22 μ coul/cm² which may be compared with the observed value by W. J. Merz.[13]**

Putting these into eq. (20) we obtain

$$\Delta_{b2}=0.003745 \tag{26}$$

---

* In eq. (14)′ and (15)′ the factors 6.8 and −3 are due to the nearest neighbour Ti ion that is shifted in the antiparallel direction, while $-47\Delta_{b2}$ and $25\Delta_{b2}$ are due to the lattice deformation characteristic of the boundary.

* See Appendix A.

** The polarization reported is 15 μ (old) or 26 (new) μ coulomb/cm² at room temperature.

for the elongation of the spacing of lattice at the domain boundary and

$$x=\{(-a'-a)/(2b)\}^{1/2}=0.1402\ \text{Å} \tag{27}$$

for the shift of Ti ion in the adjacent layer. The above calculation leads therefore to the conclusion that the change of the lattice spacings and the ionic shift at the domain boundary are quite small, namely, 9×10^{-5} Å and -0.0007 Å which correspond to the relative differences 0.002 % and 0.5 % respectively.

Table I.

	Lattice spacings			Ionic shift
Bulk crystal	4(1+0.01951) Å	4(1+0.003723) Å	4(1+0.003723) Å	0.1409 Å
Domain boundary	〃	〃	4(1+0.003745) Å	0.1402 Å

We have hitherto considered only the shift of the Ti ions in the layers I and I′. Strictly speaking, we also had to take account of the modification of the shifts of the Ti ions in the layers II and II′, etc. These effects, however, are so small that they may be entirely neglected.

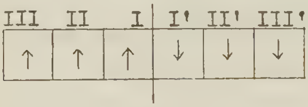

Fig. 7. Ionic shift at 180° wall.

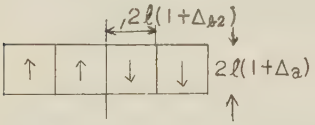

Fig. 8. Dipole moment by ionic shift.

§ 5. The Thickness and Energy of the 180°-Wall

We now calculate the ionic shifts in the layers near the domain boundary using the relation (11). The shift in the layers I, II, III etc. will be expressed as

$$x_1=(1-\delta_1)x_0\,,\quad x_2=(1-\delta_2)x_0\,,\quad x_3=(1-\delta_3)x_0\,,$$

etc. where x_0 is the shift in the normal ferroelectric state, $\delta_1=4.8\times10^{-3}$ from the last column in Table I. δ_2 is obtained as follows:

(i) For the uniformly polarized state the local field on the i-th layer is obtained as

$$k\gamma_0x_i+k\gamma_1(x_{i-1}+x_{i+1}) +k\gamma_2(x_{i-2}+x_{i+2})+\cdots \tag{28*}$$

from the eq. (11). If we retain only the first two terms and put

$$x=x_i=x_{i-1}=x_{i+1}=\cdots\,, \tag{29}$$

the eq. (28) is rewritten as

$$k\gamma_0x+2k\gamma_1x\,. \tag{30}$$

(ii) For the boundary layers I and I′ the ionic shift is $(1-\delta_1)x_0$.

The local field is obtained by putting

$$\left.\begin{aligned} &x_i=x\,,\qquad x_{i+1}=-x\\ \text{and}\qquad&\\ &x_{i-1}=\frac{x}{1-\delta_1}\,. \end{aligned}\right\} \tag{31}$$

Then eq. (28) is rewritten as

$$k\gamma_0x+k\gamma_1x\left(\frac{1}{1-\delta_1}-1\right)$$

$$\fallingdotseq k\gamma_0x+\delta_1k\gamma_1x\,.\ (\delta_1\ll1) \tag{32}$$

(iii) For the boundary layers II and II′ the ionic shift is $(1-\delta_2)x_0$. The local field is obtained by putting

$$\left.\begin{aligned} &x_1=x\,,\qquad x_{i+1}=x\cdot\frac{1-\delta_1}{1-\delta_2}\\ \text{and}\qquad&\\ &x_{i-1}=\frac{x}{1-\delta_2}\,. \end{aligned}\right\} \tag{33}$$

Then eq. (28) is rewritten as

$$k\gamma_0x+k\gamma_1x\left(\frac{1}{1-\delta_2}+\frac{1-\delta_1}{1-\delta_2}\right)$$

$$\fallingdotseq k\gamma_0x+(2-\delta_1)k\gamma_1x\,. \tag{34}$$

From eq. (30), (32) and (34) the difference of the local fields from the normal ferroelectric state are obtained as $(2-\delta_1)k\gamma_1x$ and $\delta_1k\gamma_1$ respectively for the layers I (or I′) and II (or II′). Taking account of the smallness of differences we can obtain the following relation of proportionality between the differences of the local fields and the ionic shifts from the normal ferroelectric state, that is,

---

* Eq. (28) is more general expression than eq. (11), since x_i means the ionic shift in an arbitrary layer.

$$\frac{(2-\delta_1)k\gamma_1 x}{\delta_1}=\frac{\delta_1 k\gamma_1 x}{\delta_2}. \qquad (35)$$

By putting $\delta_1=4.8\times10^{-3}$ we obtain

$$\delta_2=\frac{\delta_1^2}{2-\delta_1}=1.2\times10^{-5}. \qquad (36)$$

In the same manner we can obtain

$$\delta_3=2.8\times10^{-8}, \quad \delta_4=6.6\times10^{-11}. \qquad (36)'$$

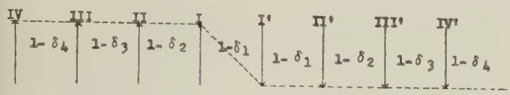

$$\delta_1=4.8\times10^{-3}, \qquad \delta_3=2.8\times10^{-8},$$
$$\delta_2=1.2\times10^{-5}, \qquad \delta_4=6.6\times10^{-11}.$$

Fig. 9. Relative ionic shift near 180° wall to the shift of uniformly polarized crystal.

Considering the smallness of δ's obtained above we may say that the wall thickness is practically "zero".*

From the above estimation we may regard the 180°-type domain wall will be very thin accompanied by a remarkable change of the dipole orientation there, which is in contrast with the magnetic domain wall whose thickness is estimated to be hundreds of lattices and where the gradual change of spin orientation is expected.[14)]

Of course our discussion is valid at room temperature, and more thorough consideration may be necessary in the transition temperature where the domains disappear.

The energy of the domain wall can be obtained from eq. (19) and (24). The difference between $\overline{U}$ and U means the energy required to form a domain boundary layer, that is, the wall energy, and is given by

$$\overline{U}-U=U_{\text{shift}}+U_{\text{lattice}}, \qquad (37)$$

where

$$U_{\text{shift}}=\{-(\overline{a}'+\overline{a})^2/(4\overline{b})\}-\{-(a'+a)^2/(4b)\}, \qquad (38)$$

$$U_{\text{lattice}}=\{\overline{U}_{\text{overlap}}+\overline{U}_{\text{Waals}}+\overline{U}_{\text{Coulomb}}\} -\{U_{\text{overlap}}+U_{\text{Waals}}+U_{\text{Coulomb}}\}. \qquad (39)$$

Here U_{shift} and U_{lattice} mean respectively the contributions of the shift and the lattice deformation to this difference. Taking eq. (14), (15), (14)′, (15)′, (21), (22), (26) and also Table I into account, we obtain

$$U_{\text{shift}}=1.179\times10^{-15}\,\text{erg}, \qquad (40)$$
$$U_{\text{lattice}}=-0.0336\times10^{-15}\,\text{erg}, \qquad (41)$$
$$\overline{U}-U=1.145\times10^{-15}\,\text{erg}. \qquad (42)$$

These energy expressions are concerned with the unit cells in the layer I or I′ in Fig. 9, so we must multiply them by a factor two. Then the wall energy per unit area (cm²) is obtained as

$$(\overline{U}-U)\times2\times\frac{1}{4l^2(1+\Delta_a)(1+\Delta_{b1})}$$
$$=1.40\,\text{erg/cm}^2, \qquad (43)$$

where $l=2$ Å and the fraction means the number of the unit lattice per cm².

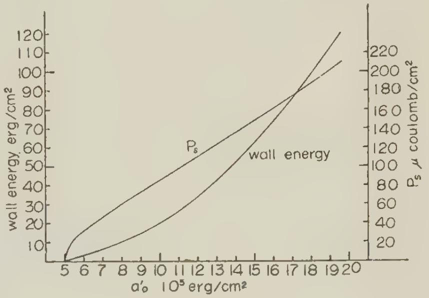

Fig. 10 (a). Wall energy and spontaneous polarization, which are calculated taking dipole interaction coefficient a_0' as a parameter.

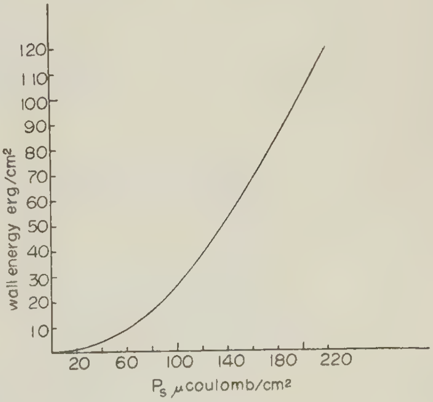

Fig. 10 (b). Wall energy vs. spontaneous polarization.

The calculated wall energy and polarization vs. the dipole interaction (the effective charge) are shown in Fig. 10 and Table II. The dependency of wall energy to polarization can be roughly obtained as $U=0.0032\,P_s^{1.96}$ from the figure and Table II.

---

* In the definition of the wall thickness we have adopted here the definition of a unit cell with a Ti ion at its centre. If, on the other hand, we define a unit cell so that a Ba ion is at its centre, the thickness would be "one layer".

Table II.

Dipole interaction	Polarization (μ coul/cm^2)	Wall energy (erg/cm^2)
−4.976	0	
−5	3.21	0.0229
−5.1	11.88	0.408
−5.2	16.24	0.761
−5.4	22.16	1.399
−6	33.36	3.07
−7	47.25	6.02
−8	60.18	9.71
−10	85.81	19.94
−14	137.4	51.6
−19.557	210.6	120.6

§ 6. Estimation of the Domain Width

Above results will now be used to determine the width of the domain of 180°-type from the condition of the counterbalance of the wall energy and the electrostatic energy caused by the free poles at the crystal surface, in the same manner as Kittel[14] did for magnetic domains.*

It is true that there is a difference between the magnetic and electric case, because of the existence of the neutralizing charges in the electric poles, so that in the equilibrium state the eletrostatic energy disappears and cannot be the cause of domain structure. However we must take account of the fact that the domain structures may be determined just at the instant of change to ferroelectric state, that is, before the neutralizing charges have enough time to wander on to the free poles.

Kittel's results, applied to the electrostatic energy, for three different configurations A, B and C in Fig. 11 are**

$$U_{\text{electric}}=\begin{cases}0.8525\ (\eta P_s)^2D\,, & (A)\\ 0.53\ \ (\eta P_s)^2D\,, & (B)\\ 0.374\ (\eta P_s)^2D\,, & (C)\end{cases}\qquad (44)$$

where D means the domain width, and P_s means the spontaneous polarization. The factor $(0\leqq\eta\leqq1)$ before P_s in (44) has been added in order to take account of the effect of partial neutralization of surface charges that may occur during the phase change.

If we assume the crystal shape as rectangular parallelepiped whose three edges are d_1, d_2 and d_3 respectively as in Fig. 12, the electrostatic energy at the surface and the domain wall energy is expressed as

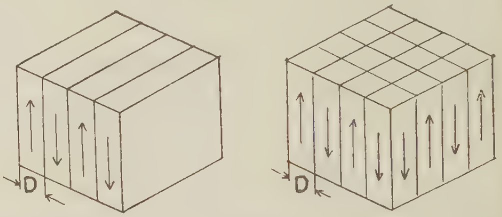

Stripes domain (A) Checker-board domain (B)

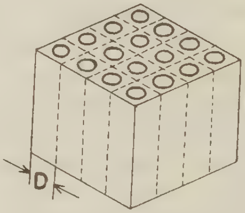

Cylindrical domain (C)

Fig. 11. Three domain configurations.

$$U_{\text{total}}=U_{\text{electric}}+U_{\text{wall}}$$
$$=\xi_i(\eta P_s)^2\cdot\frac{d_1}{N}\cdot d_1d_3+\zeta_iNd_2d_3\,,\qquad (i=1,2,3)\qquad (45)$$

where

$$\xi_1=0.8525,\quad \xi_2=0.53,\quad \xi_3=0.374$$

and

$$\zeta_1=1.40,\quad \zeta_2=2\times1.40,\quad \zeta_3=(2\pi)^{1/2}\times1.40\qquad (46)$$

according to Kittel. $i=1,2,3$ correspond respectively to the three domain configurations shown in Fig. 11.

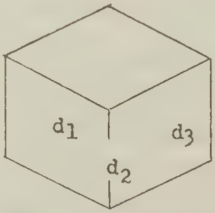

Fig. 12. Rectangular parallelepiped of the crystal.

---

* The discussion for KH_2PO_4 crystal was done by W. Känzing and R. Sommerhalder.[15]

** Recently the 180° domains were observed using the etching method by D.S.Campbell[16], J.A. Hooton and W.J.Merz[17]. Some of their etch patterns are circles, and some look more complicated in shape.

N is the number of domain stripes as seen on the $d_1\,d_2$ plane. So d_1/N in eq. (45) means the domain width D in cases (A) and (B), and the distance between the centres of the neighbouring cylinders in case (C), where the radius of the circle should be $D/(2\pi)^{1/2}$ so that total cross-section of the cylinders is half the area $d_1\,d_3$.

By solving the equation

$$0=\frac{\partial}{\partial N}(U_{\text{electric}}+U_{\text{wall}}) \qquad (47)$$

which is the condition of the minimum energy, we obtain the domain width

$$D=\frac{d_1}{N}=(1.40d_2\zeta_i/\xi_i)^{1/2}\cdot\frac{1}{\eta P_s}\quad (i=1,2,3)\,. \qquad (47)'$$

Table III shows some numerical results.

Table III. Domain Width (Unit in 10^{-4} cm).

	$\eta=1$			$\eta=0.5$			$\eta=0.1$		
	$d_2=1$ cm	$d_2=0.5$	$d_2=0.1$	$d_2=1$	$d_2=0.5$	$d_2=0.1$	$d_2=1$	$d_2=0.5$	$d_2=0.1$
(A) stripes	0.19	0.14	0.061	0.39	0.27	0.122	1.9	1.36	0.61
(B) checkerboard	0.35	0.24	0.109	0.69	0.49	0.22	3.5	2.4	1.09
(C) cylinder	0.46	0.33	0.146	0.92	0.65	0.29	4.6	3.3	1.46
(diameter)	0.37	0.26	0.116	0.74	0.52	0.23	3.7	2.6	1.16

The result is in the same order of magnitude with the observed domains, which are about 10^{-4} cm wide.[16)17)] Eq. (47)′ shows that the neutralizing charge has the effect of making the domain width larger. Since the actual shapes of the domains are generally more complicated, our result may give only a rough estimate of the domain size.

§ 7. Discussion

Comparison with Merz's theory

The wall energy 1.40 erg/cm² obtained by us differs substantially from the value 7 erg/cm² by W. J. Merz.[13)] The origin of this discrepancy lies mainly in the difference of the models of both theories, for we have started from the model of the wall accompanied by an abrupt change of the dipole direction, while Merz has simply brought the model for the Bloch wall of ferromagnetics, where a gradual change of the spin direction is effected by *rotation*, into dielectric case. In case of the 180° wall of $BaTiO_3$ the rotation of dipoles without change of magnitude is highly improbable because of the great anisotropy within the wall due to the clamping effect of spontaneous deformation of the bulk crystal, so that the analogy to the Bloch wall is not justified.

In order to make this comparison more directly, we can put the wall energy in the form

$$E_{\text{wall}}=AN+\frac{B}{N}$$

as Merz did (eq. (10) in his article).[13)] Merz regarded the first term as anisotropy energy and the second term as the dipole interaction energy. However this interpretation will be entirely inadequate, if we assume that the *magnitude* and sign of polarization changes without rotation.

We divide the dipole interaction energy in $BaTiO_3$ in two parts, that is, the interaction in the direction parallel and perpendicular to the polarization, which are the order of 10^{-14} erg and 10^{-15} erg per unit cell respectively from the calculation in § 5. It must be the latter one rather than total dipole interaction energy as Merz assumed, that mainly contributes to the wall energy and plays a role similar to the exchange energy in Bloch wall thickness, while the other term (proportional to N) tending to decrease the wall thickness is mainly the parallel part of the dipole interation rather than the anisotropy energy.

By putting proper values for A and B (5.88×10^{-14} erg and 2.36×10^{-15} erg respectively)*, we again have $N=0.2$ which is equal to saying that the thickness is "zero".

The lattice spacing within the 180° wall is almost equal to the bulk system as shown in

---

* The value of B is equal to $2U_{\text{shift}}$ in (40) (that is, for both sides of the boundary), while the value of A corresponds to $(a'+a)^2/(4b)$ in (38).

Table I. However this may not be necessary the case in the 90° wall, where the rotation of the dipoles occurs accompanied by the lattice deformation due to the tetragonality of the lattice. This tetragonality is about 1 %,[18][19] so the deformation energy may take some part in the 90° wall, adding to the dipole interaction energy. Anyhow the 90° wall is expected to be thicker, and its energy larger than 180° wall. The quantitative estimation of the energy and thickness of the 90° wall seems to be more complicated than the 180° wall.

Origin of domain formation

The domain width obtained from the consideration of electrostatic depolarizing field has been found to be in fair agreement with observation. However, our treatment applies only to the virgin state of a free crystal (without electrode) cooled from above the Curie temperature. The domains observed at room temperature in crystals in the way of its polarization reversal cannot be determined by equilibrium considerations. These are determined rather by the wedge shaped domain nuclei formed at the surfaces. Tentative explanation of the origin of these nuclei will be given later.

The origin of the 90° domains is more obvious. Since the 90° rotation of polarization is accompanied by a large deformation, a mechanically clamped crystal must be split into domains in order to relax its elastic stress. A quantitative discussion of the domain width would require, however, a knowledge about the energy of the 90° walls as well as a precise mathematical treatment of the elastic energy of multi-domain configurations.

Polarization reversal

Let us now discuss the field strength required to move the wall sideways. First we will estimate the field strength required to cause a simultaneous reversal of the polarization of a whole domain. The reversing field strength corresponds to the steepest gradient of the double minimum potential acting on Ti ion, that is, the gradient at the inflection-point P and P' in Fig. 13.

This is obtained from the equation

$$\frac{\partial^2}{\partial x^2}\{(a'+a)x^2+bx^4\}=0 \tag{48}$$

and is given by

$$x=\{(-a'-a)/(6b)\}^{1/2}\,. \tag{49}$$

The gradient of the potential curve at P is

$$\frac{\partial U}{\partial x}=\frac{4}{3}(-a'-a)\{(-a'-a)/(6b)\}^{1/2}\,. \tag{50}$$

The expression (50) represents the force which is required to act on each Ti ion in order to cause the reversal, and is related to the local field E_{local} at the Ti position by

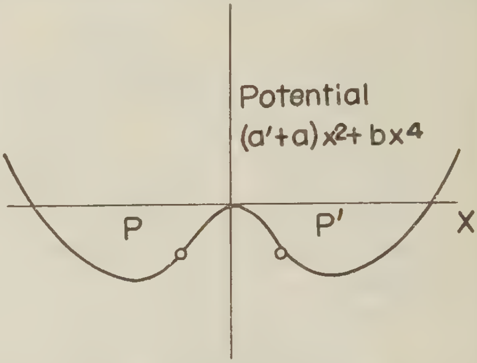

Fig. 13. Double minimum well of potential acting on Ti ion.

$$\frac{\partial U}{\partial x}=E_{\text{local}}\cdot ne\,, \tag{51}$$

where ne is the effective charge. E_{local} is equal to 3.246 E where E is the applied field strength (See Appendix B).[10][20]*

Taking as the numerical value $n=2.102$**, we obtain the field strength E required to reverse the polarization as

$$1.96\times10^4 \text{ e.s.u.}$$

or

$$5.88\times10^6 \text{ volt/cm.} \tag{52}$$

This value seems to be too large to have any correspondence with experimental data.

Then let us calculate the minimum field strength required to move a 180° wall. The mechanism of the movement of a 180° wall may be explained as follows.

When we apply the electric field which is strong enough, the reversing of the polarization at the boundary layer which is polarized in the opposite direction to the applied field will take place at first. In the reversing process the polarization of the boundary layer will decrease in magnitude and tend to zero at last, and then the layer will be polarized in the same direction of the applied field and complete the reversing. The change of the polarization of other layers will give little effect to the reversing, for the sideway interaction of the dipoles is much smaller than that of the dipoles in the same layer as discussed in the preceding sections. So we treat here the reversing of the boundary independently of other layers, considering only the potential acting on Ti ions at the boundary layer.

---

* These values are calculated for the cubic crystal (4Å). Strictly speaking, we must calculate for the more accurate lattice considering the lattice deformation. Moreover the electrostriction due to the applied field must be taken into account for the more precise estimation.

** This value 2.102 was used in the preceding sections when we discussed the wall energy.

The potential at the boundary is expressed as

$$(\overline{a}'+\overline{a})x^2+\overline{b}x^4 \text{ instead of } (a'+a)x^2+bx^4$$

in the bulk crystal as already mentioned, so we can obtain the field to move the wall in the same way as above, the result being

$$1.93\times10^4 \text{ e.s.u.}$$

or

$$5.79\times10^6 \text{ volt/cm .} \tag{53}$$

Note that there is no substantial difference between (52) and (53), that is, to move a 180° wall is no easier than to reverse the polarization of a whole domain, in sharp contrast with the ferromagnetic case. This difference is the result of the difference of the wall thickness.*

Actually the reversal of the polarization takes place at a very low field of the order of hundreds of volts per cm. And so we shall have to assume a certain mechanism that enable the motion of the wall in a substantially lower field. Although we are not going to give a complete discussion of the possible mechanism, we shall suggest a few of them. Namely

1. The domain wall may not be parallel to (001) axis. That is, microscopically, there may be many steps in the wall²³⁾. These steps may be able to move within the wall by a much lower external field, and may effectively shift the wall in the direction perpendicular to it. This mechanism may be responsible for the growth of wedge-shaped domains, which have been observed by Merz¹³⁾ and Little²¹⁾.

2. While usually these steps may disappear at the crystal boundary after it has travelled across the wall surface, there may by some steps which originate at the screw dislocations running perpendicular to the wall. These steps are permanently connected to the dislocation, and will move around the dislocation making spirals, but never disappear at the crystal boundary, causing effectively a parallel shift of the domain walls.*

3. Our results apply only to the inner part of the crystal. The situation would be quite different at the surfaces, especially at those perpendicular to the polarization, where the internal field is caused only by an array of semi-infinite dipole chains. In other words, the large spontaneous polarization gives rise to a large surface charge, which produces a strong depolarizing field. It is true that, in experimental conditions, these surfaces are always covered by conducting electrodes, and the depolarizing charges are completely canceled by the induced charge in the electrode, and therefore the surfaces are not all too different from the bulk. However, it is also probable that there are many pinholes and also small local gaps in the electrode, where the compensating charge are not effective. Since a slight decrease of the internal field is sufficient to make the crystal non-ferroelectric, these defects in the electrode will cause small non-ferroelectric specks on the crystal surface. The dipoles in the neighbourhood of these specks will have a gradual change as shown schematically in Fig. 14. Since a small field will be sufficient to reverse the polarization in these transition regions, they will act as the nuclei of the new domains. Eventually, these surface charges would have been neutralized by external charges.** In this case, the polarization in these parts will not be reversed by a reversed field, and will form small wedge-shaped domains around it.

---

* The polarization reversal taking into account of the shape of the hysteresis loop has been discussed by R. Landauer, D. R. Young and M. E. Drougard.²²⁾

* Refer to the article "T. Nakamura, Jour. Phys. Soc. Japan, 9 (1954) 425 about this mechanism.

** W. Känzig has assumed that these exist a surface layer which traps electrons as in the case of usual semiconductors. See Phys. Rev. 98 (1955) 549.

These will also act as nuclei when the field is again reversed.

4. Another possible cause of domain nuclei, which can be effective on the surface as well as within the crystal, is the edge dislocation. Since the 180° reversal of the polarization does not cause mechanical strain, a homogeneous stress in the crystal cannot have any effect on the 180° wall. However, inhomogeneous stress of the type found around an edge type dislocation will definitely favour the domains of one polarization against the domains of opposite polarization, and "trap" a small wedge domain polarized in that direction when the external field is in the opposite direction. These small trapped domains will also act as the nuclei when the field is again reversed. It is possible that the observed fine domain structure of real crystals is caused mainly by these inhomogeneous stresses rather than by the electrostatic energy of free poles.

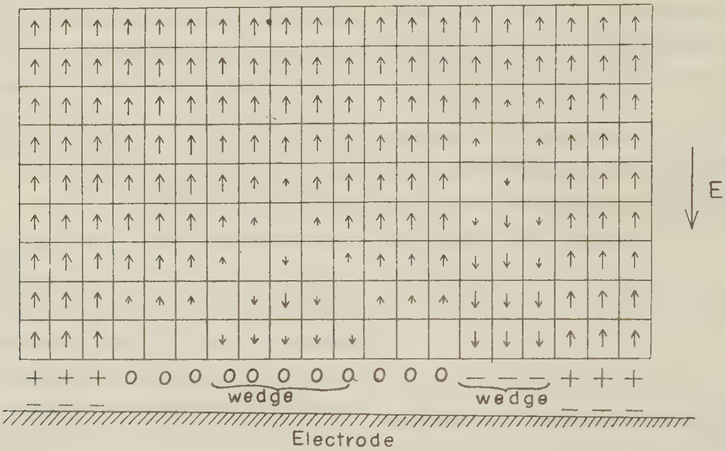

Fig. 14. The state of polarization at the surface, which is speculated tentatively. An external field E was applied downward just now, and the growth of wedge-type domains is shown. Electrodes are attached at the surfaces (In the figure only lower surface is found.), and generally neutralizing charges are induced at the Electrodes. + and − indicate the signs of charges, and O means that there exist no charges. Two types of the wedge-type domains are shown in the figure, one is polarized spontaneously at the surface and the other is not. Shorter arrows correspond to weaker polarizations, and the polarization has just induced at the surface of the wedge-type domain in the left side. The surface region indicated by − or O corresponds to the "speck" in the article, while that indicated by + is the normal region of the surface.

A crystal may contain edge dislocations of one sign in excess of ones of opposite sign. In such a case the crystal would have a tendency to polarize in one direction and will reveal asymmetrical hysteresis loops. This will explain the asymmetry of the hysteresis loops found in the crystal plates forming butterfly pairs.[24)]

5. Thermal motion of ions will cause the wall displacement by any mechanism discussed above in a still lower field. This would result in a "creep", that is, a gradual displacement of walls at a definite rate that depends on the applied field.[13)]

Summarizing our article, the 180° wall of $BaTiO_3$ is considered to be quite thin at room temperature, and its energy is estimated to be 1.4 erg/cm^2. The formation of the 180° domains can be explained by considering the electrostatic energy of the free poles, resulting in the domain width of the order of 10^{-4} cm for the possible domain configurations and the crystal sizes. The reversing process cannot be explained by the abrupt reversing, and some mechanisms for the nucleation and the growth of the reversed domains are suggested.

This work was supported by the Grant for Scientific Researches from Education Ministry.

Appendix A

Our previous article on spontaneous deformation of $BaTiO_3$ (J. P. S. J. 10 (1955) 942) has been found to contain some numerical mistakes and will be corrected as follows:—

The equations (20 A, B, C, D, E), which represent the relation between ionic and electronic polarizations taking account of the lattice deformation, should be read.

$$u=0.1974(1-8.17\Delta_a)u_0\,,$$
$$v=-0.0630(1-39.9\Delta_a)u_0\,,$$
$$w=1.9090(1-4.80\Delta_a)u_0\,,$$
$$x_1=0.1014(1-3.32\Delta_a)u_0\,,\quad (20\ A, B, C, D, E)$$
$$x_2=0.1014(1-3.32\Delta_a)u_0\,.$$

The changes are made for the coefficients of Δ_a.

Corresponding corrections should be made for Table I and Table II.

The corrected version is as follows:

Table I. Standard cube is (4 Å)^3.

Effective charge of Ti	Dipole interaction (C.G.S.)	Lattice deformation ratio//P	Lattice deformation ratio⊥P	Tetragonality	Volume excess	Ti shift (Å)
n	$a_0'\times10^{-5}$	Δ_a	Δ_b	$\Delta_a-\Delta_b$	$\Delta_a+2\Delta_b$	$\sqrt{\frac{-a'-a}{2b}}$
2.01766	−4.976	0.00811	0.00811	0	0.02433	0
2.02252	−5	0.009054	0.007807	0.001247	0.02467	0.02054
2.04264	−5.1	0.01227	0.006622	0.005648	0.02551	0.07604
2.06258	−5.2	0.01504	0.005558	0.009482	0.02616	0.1038
2.10186	−5.4	0.01951	0.003723	0.01579	0.02696	0.1409
2.21556	−6	0.02696	−0.0001386	0.02710	0.02668	0.2057
2.39307	−7	0.03021	−0.003932	0.03414	0.02235	0.2712
2.55831	−8	0.02919	−0.006377	0.03557	0.01644	0.3202
2.86027	−10	0.02396	−0.009960	0.03392	0.00404	0.3972
3.38432	−14	0.01363	−0.01582	0.02945	−0.01801	0.5103
4	−19.5572	0.003769	−0.02224	0.02601	−0.04071	0.6269

Table II. Standard cube is (4.03244 Å)^3.

Effective charge of Ti	Dipole interaction (C.G.S.)	Lattice deformation ratio//P	Lattice deformation ratio⊥P	Tetragonality	Volume excess	Polarization (μ coulomb per cm^2)
n	$a_0'\times10^{-5}$	Δ_a'	Δ_b'	$\Delta_a'-\Delta_b'$	$\Delta_a'+2\Delta_b'$	P
2.01766	−4.976	0	0	0	0	0
2.02252	−5	0.000936	−0.000301	0.00124	0.000335	3.210
2.04264	−5.1	0.00413	−0.00148	0.00560	0.00117	11.88
2.06258	−5.2	0.00687	−0.00253	0.00941	0.00181	16.24
2.10186	−5.4	0.01131	−0.00435	0.01566	0.00260	22.16
2.21556	−6	0.01870	−0.00818	0.02688	0.00233	33.36
2.39307	−7	0.02192	−0.01195	0.03387	−0.00197	47.25
2.55831	−8	0.02091	−0.01437	0.03528	−0.00783	60.18
2.86027	−10	0.01572	−0.01792	0.03365	−0.02013	85.81
3.38432	−14	0.00548	−0.02374	0.02921	−0.04200	137.4
4	−19.5572	−0.00431	−0.03011	0.02580	−0.06452	210.0

Appendix B

The local fields caused by the applied external field has been calculated by the method of J. C. Slater[10] and T. Oguchi.[20]

The local fields acting on ions are obtained by solving the following equations.

Field on Ti$=(c/\alpha_{\mathrm{Ti}})u$

$$=E+\frac{1}{\varepsilon_0}\left\{\frac{1}{3}u+\frac{1}{3}v+\left(q+\frac{1}{3}\right)w+\left(-q+\frac{2}{3}\right)x\right\}, \tag{A}$$

Field on Ba$=(c/\alpha_{\mathrm{Ba}})v$

$$=E+\frac{1}{\varepsilon_0}\left\{\frac{1}{3}u+\frac{1}{3}v+\left(-p+\frac{1}{3}\right)w+\left(p+\frac{2}{3}\right)x\right\}, \tag{B}$$

Field on Oa$=(c/\alpha_{\mathrm{O}})w$

$$=E+\frac{1}{\varepsilon_0}\left\{\left(q+\frac{1}{3}\right)u+\left(-p+\frac{1}{3}\right)v+\frac{1}{3}w+\left(p+\frac{2}{3}\right)x\right\}, \tag{C}$$

Field on Ob$=(c/\alpha_{\mathrm{O}})x$

$$=E+\frac{1}{\varepsilon_0}\left\{\left(-\frac{1}{2}q+\frac{1}{3}\right)u+\left(\frac{1}{2}p+\frac{1}{3}\right)v+\left(\frac{1}{2}p+\frac{1}{2}\right)w+\left(-p+\frac{2}{3}\right)x\right\}, \tag{D}$$

where c is the volume of a unit cell 64×10^{-24} C.C.,

α's the polarizabilities of Ti, Ba and Oxygen ions respectively ($\alpha_{\mathrm{Ti}}=2.34\times10^{-24}\varepsilon_0$ C.C., $\alpha_{\mathrm{Ba}}=24.42\times10^{-24}\varepsilon_0$ C.C. and $\alpha_{\mathrm{O}}=30.0\times10^{-24}\varepsilon_0$ C.C. in M.K.S. system), and u, v, w and x the polarization due to Ti, Ba, Oa and Ob ions respectively.

Solving these equations we get

$$u=0.1185\varepsilon_0 E, \tag{E}$$

$$v=0.9197\varepsilon_0 E, \tag{F}$$

$$w=1.4305\varepsilon_0 E, \tag{G}$$

$$x=1.1585\varepsilon_0 E. \tag{H}$$

By putting these values into (A), (B), (C) and (D), we obtain the local fields

$$(\text{Field on Ti})=3.246E, \qquad (\mathrm{J})$$

$$(\text{Field on Ba})=2.408E, \qquad (\mathrm{J})$$

$$(\text{Field on Oa})=3.044E, \qquad (\mathrm{K})$$

$$(\text{Field on Ob})=2.465E. \qquad (\mathrm{L})$$

References

1) B. T. Matthias and A. von Hippel: Phys. Rev. **73** (1948) 1387.
2) H. F. Kay: Acta Cryst. **1** (1948) 229.
3) P. W. Forsbergh: Phys. Rev. **76** (1949) 1187.
4) A. Nishioka: Jour. Phys. Soc. Japan **10** (1955) 535.
5) W. J. Merz: Phys. Rev. **88** (1952) 421.
6) M. Born: Ann. d. Phys. **61** (1919) 87.
7) Y. Takagi: Proceedings of the International Conference of Theoretical Physics Sep. 1953 in Kyoto.
8) W. Kinase: ibid. and Prog. Theor. Phys. **13** (1955) 529. We refer to this paper as I.
9) P. W. Anderson and W. Shockley: Unpublished. This was quoted also in 10).
10) J. C. Slater: Phys. Rev. **78** (1950) 748.
11) W. Kinase and H. Takahasi: Jour. Phys. Soc. Japan **10** (1955) 942.
12) A. F. Devonshire: Phil. Mag. **40** (1040) 1949.
13) W. J. Merz: Phys. Rev. **76** (1949) 1221; **91** (1953) 513; **95** (1954) 690.
14) C. Kittel: Rev. Modern Phys. **21** (1949) 541.
15) W. Känzing and R. Sommerhalder: Helv. Phys. Acta **26** (1953) 603.
16) D. S. Campbell: Phil. Mag. **46** (1955) 1261.
17) J. A. Hooton and W. J. Merz: Phys. Rev. **98** (1955) 409.
18) S. Miyake and R. Ueda: Jour. Phys. Soc. Japan **2** (1947) 93.
19) H. D. Megaw: Proc. Royal Soc. London **A189** (1947) 261.
20) T. Oguchi: Busseironkenkyu **65** (1953) 20 in Japanese.
21) E. A. Little: Phys. Rev. **98** (1955) 978.
22) R. Landauer, D. R. Young and M. E. Drougard: Private communication.
23) R. Abe: Busseironkenkyu **97** (1956) 117 in Japanese.
24) Z. Kiyasu, K. Husimi and K. Kataoka: Jour. Phys. Soc. Japan **12** (1957) 432.

JOURNAL OF THE PHYSICAL SOCIETY OF JAPAN Vol. 12, No. 5, MAY, 1957

After Effect of the Domain Motion in Rochelle Salt Crystal

By Terutaro NAKAMURA
Department of Physics, Faculty of Science,
University of Tokyo

(Received February 8, 1957)

After effect of the domain motion in rochelle salt crystal was observed for several hours. Quasi-static f–E hysteresis loop was obtained, where f is the fraction of the domain saturated in one direction to the total volume of the crystal. Comparing this with P–E hysteresis loop at 50 cps, differences are remarkable. A.c. hysteresis loop has shallow sloping sides and high coercivity, while quasi-static f–E hysteresis loop is almost square and shows much lower coercivity. f is time dependent and can be expressed in the formula:

$$f(t)=1-e^{-\alpha t}$$

where time constant $1/\alpha$ is about one hour for critical field about 60 v/cm, in the sample of thickness 0.6 mm at 10°C.

§ 1. Introduction

Recently the domain structure of rochelle salt crystal has been investigated in detail by several authors[1),2),3),4)].

It was reported by Mitsui and Furuichi[1)] that the domain motion showed after effect when an electric field of a square wave was applied, the frequency of which was 22 cps. It was also shown by Marutake[2)] that the polarization of the crystal was reversed, unlike ferromagnetics, not only by the sidewise motion of domain walls, but also by the nucleation of antiparallel domains, and that the motion of the domains were accompanied with a marked after effect, when one cycle was completed in 30∼90 min. Any closer study on the after effect of the domain motion in rochelle salt crystal, however, has not yet been made.

On the other hand, it has been known that polarization of rochelle salt crystal, if measured electrostatically, (not optically), also shows a marked after effect[5)]. This phenomenon was subsequently studied in detail by Takahasi and Hara[6)], and recently by Marutake[7)]. Electrical measurements of the after effect for an extremely long time, however, were impossible, since experiments were limited by such characteristics as resistivity of insulators. Change of polarization due to the domain motion was able to be measured by an optical method for a considerably long period of time.

The present article reports some measurements on the long time after effect of the domain motion in rochelle salt crystal by the optical method.

§ 2. Experimental

A-plate rochelle salt crystals of the size 0.6 mm × 20 mm × 10 mm, cut out from large crystals, were employed in experiments. The domain structure were observed by means of a polarization microscope through a hole of about 1 mm in diameter in silver foil electrodes attached to the crystals. The foiled crystal was placed between metal electrodes, as shown in Fig. 1. Measurements were made at room temperature.

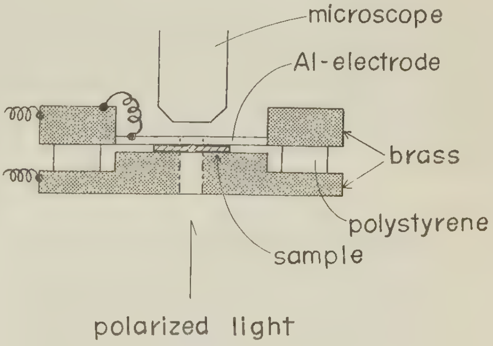

Fig. 1. Device for holding a sample under a microscope.

The schematic diagram in Fig. 2 shows the arrangement for the experimental observations. When Sw.1 moves from a to b, and then from b to c, and so on, the field applied to the crystal changes stepwise. The polarity of the field was controlled by Sw.2.

After a certain electric field had been attained, the domain structure was observed for a long time, taking photographs at successive intervals. Suppose a fraction f of the total volume of a crystal is saturated in one direction, then a fraction $(1-f)$ is saturated in the opposite direction. Then the net polarization P is expressed in terms of f and P_s:

$$P=fP_s-(1-f)P_s=(2f-1)P_s$$

where P_s denotes spontaneous polarization of the crystal. f or $(1-f)$ was obtained from the photograph, by cutting out the regions which point in one direction separating from those which point in the opposite direction, and by comparing the weight of those two by the use of a chemical balance.

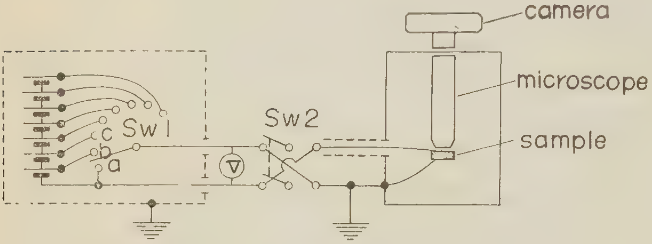

Fig. 2. Experimenatl arrangement for the observation of quasi-static domain motion.

For fields lower than 40 v/cm, no domain motion was observable. In Fig. 3 f was plotted as a function of electric field E, observations being made for a long time until no detectable change in the domain pattern was observed. From A to B or from C to D about 10 hours were taken. A group of photographs taken in the course from A to B are shown in plates (1)∼(6).

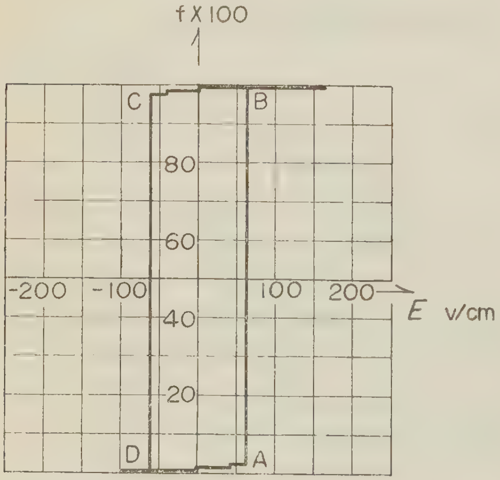

Fig. 3. Quasi-static f-E hysteresis loop for a 0.6 mm thick sample at 10°C.

It must be noted here that the quasi-static $f-E$ hysteresis loop is almost square. Coercive field seems to be somewhat different for different samples, being about 62.5 v/cm in Fig. 3. The actual critical value, however, will be lower than this value, because foil electrodes have holes, through which the domain structure is observed.

Figs. 5 contain hysteresis loops obtained at 50 cps by the usual Sawyer and Tower method, in the same scale of abscissa as $f-E$ hysteresis loops. There is no evidence that states of saturation attained in a.c. hysteresis loop actually correspond to states $f=0, 1$.

Comparing the quasi-static $f-E$ loop with the usual $P-E$ loop at 50 cps, differences prove to be remarkable. First, in the case of an electric field of 50 cps, a field lower than about 150 v/cm* gives almost linear $P-E$ curve, scarcely giving hysteresis loop as shown in Fig. 5(f), while electrostatic fields higher than about 60 v/cm give saturated hysteresis loop. Secondly, an a.c. field higher than about 150 v/cm* and lower than about 400 v/cm* gives hysteresis loop with shallow sloping sides and high coercivity, having the shape of parallelogram with rounded vertices, as shown in Fig. 5(e). Thirdly, a.c. fields higher than

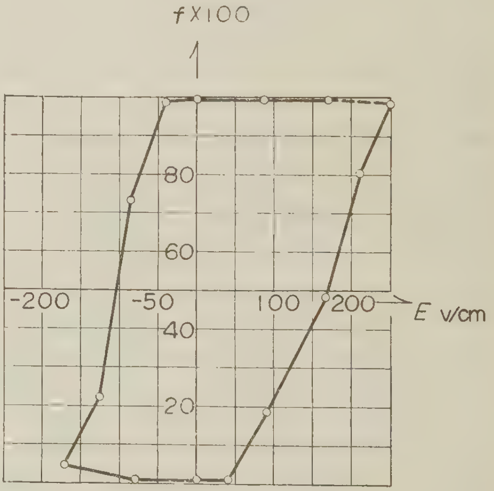

Fig. 4. f-E hysteresis loop for 0.6 mm thick sample at 10°C. One cycle was completed in 1h 27m.

---

* given by peak values.

about 400 v/cm* give saturated hysteresis loops, and complete saturation is attained at about 1000 v/cm* as shown in Figs. 5(b) and (c), while static fields higher than about 60 v/cm cause the saturation. The saturated hysteresis loop obtained by a.c. field also has shallow sloping sides and much higher coercivity than the quasi-static $f-E$ hysteresis loop.

Fig. 4 shows similar hysteresis loop as Fig. 3, but one cycle was completed in 1 h 27 m. Coercive field is larger than Fig. 3, the curve has rather shallow sloping sides. This curve is essentially consistent with Marutake's results²⁾, except that there is a little difference in the shape of the loop in the part near zero field. This difference may be due to the hystory of samples, but remains not fully explained.

Plates (1)~(6) clearly reveal that the motion of domains is very slow when the critical field is applied. In Fig. 6(a) f is plotted as a function of time in the course from A to B in Fig. 3. Fig. 6(b), logarithmic representation of Fig. 6(a), shows that $f(t)$ is fairly expressed in the form:

$$f(t)=1-e^{-\alpha t}$$

where α denotes a constant which generally depends on the field applied to the crystal.

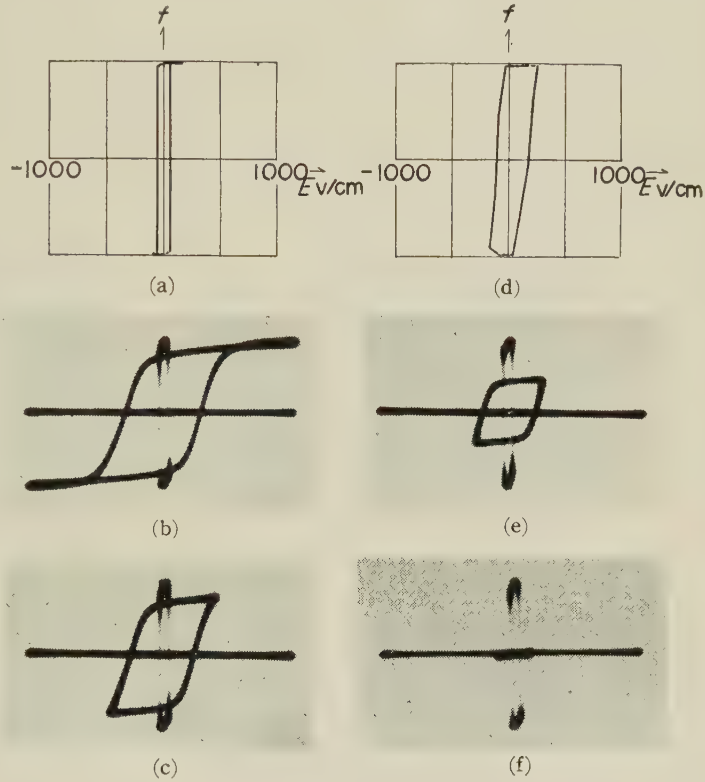

Figs. 5. P–E hysteresis loops obtained by Sawyer and Tower method at 50 cps, compared with f–E hysteresis loops, abscissa being presented in the same scale. At 10°C, the thickness of the sample 0.6 mm.
(a) Quasi-static f–E hysteresis loop, (b) 1200 v/cm a.c., (c) 440 v/cm a.c., (d) f–E hysteresis loop, one cycle completed in 1h27m, (e) 300 v/cm a.c., (f) 130 v/cm a.c. Voltage of 50 cps is given by the peak value.

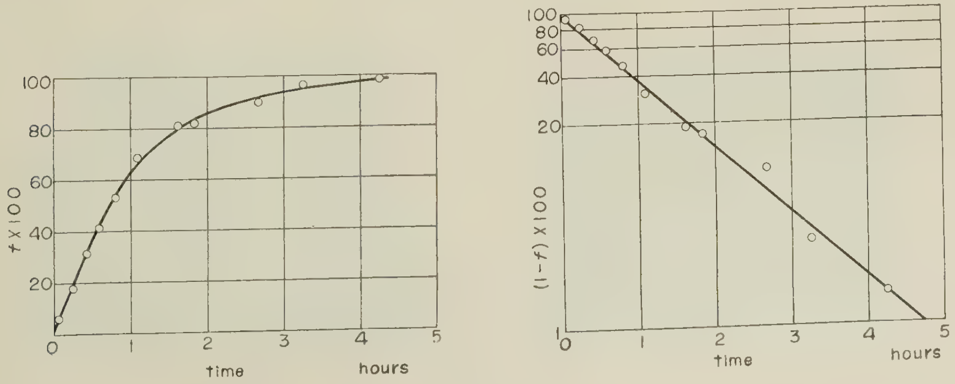

(a) (b)

Figs. 6. Time dependence of f, from A to B in Fig. 3.
(a) f as a function of time.
(b) $\log(1-f)$ as a function of time.

From Fig. 6(b) time constant $1/\alpha$ is obtained to be approximately 62 min for the sample of thickness 0.6 mm, at 10°C.

§ 3. Discussions

If an external field, which saturated a ferroelectric specimen, is reduced and reversed, domains of reverse polarization are nucleated in several regions of specimen and the irreversible domain motions begin. E_{ni} will be defined as the critical field strength for domain creation for i-th nucleus. It will be defined as positive if it is oriented in the direction of the polarization within the new domain. The polarization of the rochelle salt crystal is reversed by the irreversible motion of 180° domain walls, as well as nucleation of the domains[2]. E_{wi} will be defined as the critical field strength for irreversible motion of the walls which enclose the i-th necleus domain of reverse polarization.

Our experiments showed that

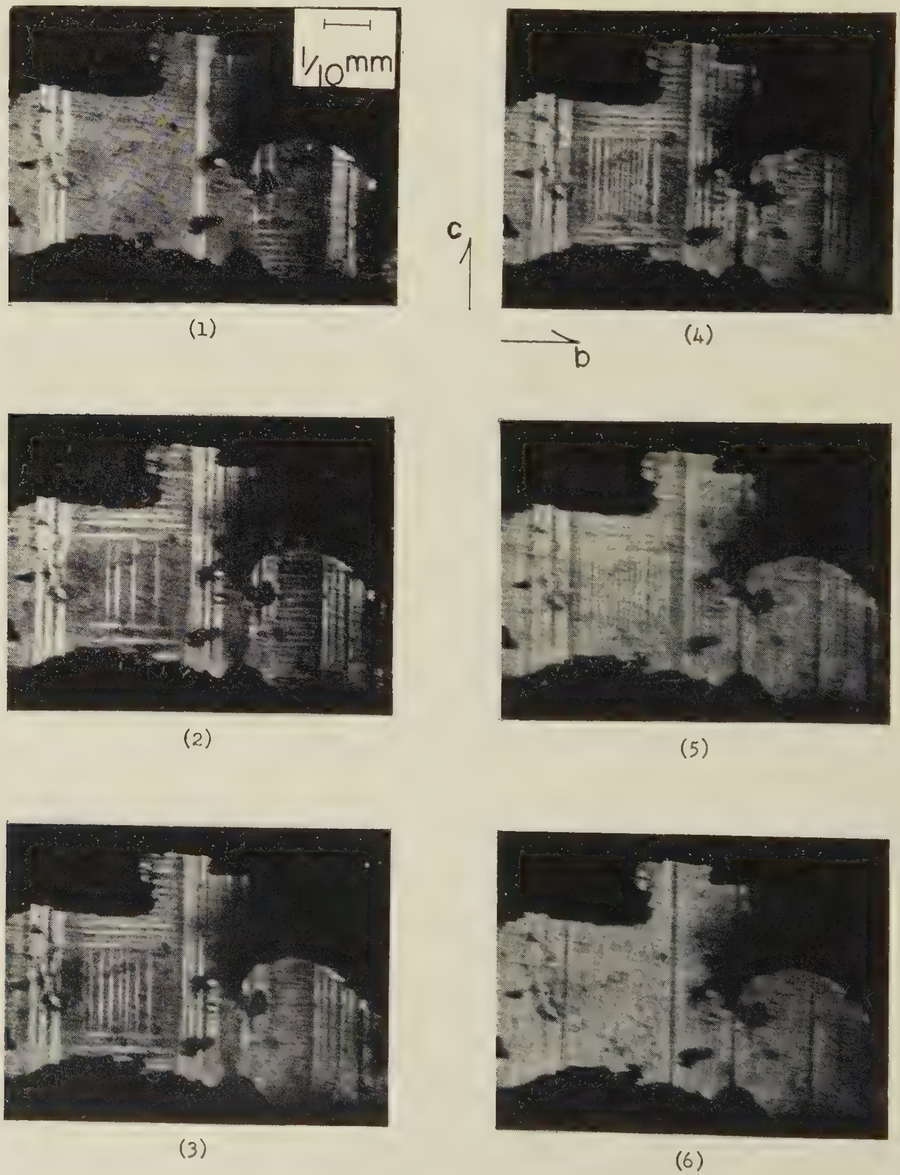

(1) (4)
(2) (5)
(3) (6)

Plates (1)~(6)
Relaxation phenomenon of the domain motion, in the course from A to B in Fig. 3.
(1) 15 min (2) 35 min (3) 48 min (4) 1h5m (5) 1h50m
(6) 3h15m after applying the field.

for $E<E_0$, f is effectively zero,

for $E\geqq E_0$, $f(t)=1-e^{-\alpha(E)t}$,

where $1/\alpha=62$ min for $E_0=62.5$ v/cm, in the sample of thickness 0.6 mm, at 10°C, and that E_{ni} and E_{wi} will be:

$$E_{ni}\approx E_{wi}\approx E_0\,.$$

The existence of the critical field E_0 causes an almost square hysteresis loop as shown in Fig. 3.

This implies that the after effect is remarkable and time constant is of the order of one hour. It is clear that the large difference between $P-E$ hysteresis loops at 50 cps and the quasi-static $f-E$ loop is due to the marked after effect. Hence, after effect of the domain motion must be taken into account, in discussing about the shape of the hysteresis loops, coercive field, and the energy dissipation which corresponds to hysteresis loop.

It will be interesting to note here that the photographs shown in Plates (1)∼(6) clearly indicate a process of polarization reversal, within a square area that is bounded by *b*-axis domains and *c*-axis domains. A few nuclei, which were formed in the first place, cannot broaden beyond a certain domain width. Instead of the growth of the first domains, many new domains are created. This phenomenon may be understood in a following way. Displacement (v, w), which is given by the expression:

$$y_{zs}=\frac{\partial v}{\partial z}+\frac{\partial w}{\partial y}$$

must be continuous on the domain boundary, where y_{zs} denotes spontaneous strain[8]. If the first nuclei broaden more and more, this boundary condition becomes unsatisfied, and hence, new domains must be created at the expense of domain wall energy and elastic energy.

Our experiments showed that for the sample of thickness 0.6 mm fields lower than 40 v/cm do not give rise to any detectable domain motion, and that the domain motion due to the critical field is accompanied with a marked relaxation phenomenon. These two facts seem to indicate that for a small field of a few v/cm and of frequency higher than or of the order of 50 cps domain motion must not occur for crystals of the thickness 0.6 mm. In measuring initial permittivity, accordingly, the domain must not contribute to the change of polarization. This view is also supported by following considerations:

(1) The motion of wedge-shaped domains due to weak fields are not detectable[2].

(2) Suppose that a crystal of size a cm × b cm × c cm is composed of domains of width h cm as shown in Fig. 7, polarization change due to sidewise motion of domain walls will be:

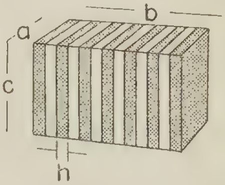

Fig. 7. A crystal composed of laminated domains perpendicular to *b*-axis.

$$\delta P=2P_s\delta x ac\left(\frac{b}{h}-1\right)\frac{1}{abc}\approx 2P_s\delta x\,\frac{1}{h}$$

where δx denotes average sidewise displacement of domain walls. If δx is proportional to field E, permittivity due to sidewise motion of the domain wall must be inversely proportional to h. It can be, therefore, said that the permittivity due to the sidewise motion of domain walls depends on h, hence on the domain structure of the crystals. Most careful measurements by Kawai[9] indicated that initial permittivity does not depend on the method of the preparation of the crystal, hence on h, or on the domain structure of the crystal.

(3) Measurements of dielectric after effect at low field by Marutake also gave a support of this view[7].

Thus it may be inferred that the initial permittivity appears to be independent of the domain motion, although the latter largely affects the shape of hysteresis loop.

Coercive field seems to be largely dependent upon the thickness of the specimen, i.e., the coercive field decreases with increasing thickness, but no detailed studies on this phenomenon were made.

The author's thanks are due to Prof. H. Takahasi for his helpful discussions, and also to Dr. M. Marutake for supplying samples of rochelle salt crystals. Progress of this study was facilitated by a Grant in Aid for Fundamental Scientific Research from the Ministry of Education.

References

1) T. Mitsui and J. Furuichi: Phys. Rev. **90** (1953) 193; Phys. Rev. **95** (1954) 558.
2) M. Marutake: J. Phys. Soc. Japan **7** (1952) 25.
3) R. Abe: Busseiron-Kenkyu. No. **88** (1955) 38 (in Japanese).
4) T. Nakamura: J. Phys. Soc. Japan **11** (1956) 624.
5) S. Miyake: "Rochelle Salt" (1949) Koyama Shoten (in Japanese).
6) H. Takahasi and S. Hara: J. Phys. Soc. Japan **4** (1949) 257; 261.
7) M. Marutake: Bull. Kobayasi Inst. Phys. Res. **6** (1956) 64, (in Japanese).
8) H. Takahasi: Kagaku **20** (1950) 495 (in Japanese).
9) H. Kawai: J. Phys. Soc. Japan **3** (1948) 105.

JOURNAL OF THE PHYSICAL SOCIETY OF JAPAN Vol. 12, No. 5, MAY, 1957

Study of Metallic Carbides by Electron Diffraction
Part I. Formation and Decomposition of Nickel Carbide

By Sigemaro NAGAKURA

Tokyo Institute of Technology, Oh-okayama, Meguro, Tokyo

(Received February 5, 1957)

Thin nickel films formed by evaporation were carburized in CO gas stream at temperatures from 250°C to 500°C and were studied by electron diffraction. Only Ni_3C was found to be formed. This has c.p.h. arrangement of nickel atoms with lattice constants $a_h=2.628$ Å and $c_h=4.306$ Å, but showed super-lattice reflections due to a hexagonal lattice of $a=\sqrt{3}a_h$ and $c=3c_h$, which is considered to be caused by a regular arrangement of carbon atoms.

The carbide was formed below 450°C in CO gas with slow rate and decomposed rapidly above 430°C in vacuum. The rate of the carbide formation was highest at about 350°C, although it depended very much on the texture of nickel films. Hydrogen atmosphere did not alter essentially the stability of the carbide.

It was found that nickel carbide is formed from metallic nickel with an epitaxial relation $(00.1)_{Ni_3C}//(111)_{Ni}$ and $[10.0]_{Ni_3C}//[10\bar{1}]_{Ni}$ (Ni_3C: c.p.h. indices) at the nucleation stage.

A mechanism of the lattice transformation from metallic nickel to the carbide was suggested. This mechanism explains the epitaxy and its destruction in the growth stage of the carbide crystal.

§ 1. Introduction

Carbides of transition elements, iron, cobalt and nickel are important substances in metallurgy and are considered to play an important rôle in Fischer-Tropsch synthesis. They are known to be interstitial compounds, but their structures have not yet been fully established. The present author has studied these carbides by the electron diffraction method and some results of metallurgical interest have already been published[1]. Fuller description will be reported in this series of papers, of which the first two papers (Part I and II) are concerned with nickel carbide.

The existence of nickel carbide was found by Bahr and Bahr[2]. They carburized fine nickel powder in CO gas at temperatures between 250° and 300°C and found a weight increase corresponding to formation of the carbide of a form of Ni_3C. Jacobson and Westgren[3] studied Ni_3C by the X-ray powder method and concluded that it has a hexagonal lattice having

$$a_h=2.649\text{ Å},\quad c_h=4.338\text{ Å}\quad\text{and}\quad c_h/a_h=1.636$$

with nickel atoms located at the close packed hexagonal positions (1/3, 2/3, 1/4) and (2/3, 1/3, 3/4) as shown in Fig. 1. Although positions of carbon atoms were difficult to be determined by the X-ray diffraction method, they proposed by a geometrical consideration that the carbon atoms should be distributed over the octahedral interstices (0, 0, 0) and (0, 0, 1/2).

The preparation of X-ray specimens requires very long time on account of slow rate of carbide formation. For example, Bahr and Bahr spent more than a hundred hours in carburizing fine nickel powder prepared by reducing nickel oxide with hydrogen. Jacobson and Westgren failed in producing the carbide by direct addition of carbon to molten nickel; they obtained it only from fine nickel powder carburized in CO gas for a week. On the other hand, since a very small amount of substance is sufficient to give rise to fairly strong electron diffraction patterns, carbide samples for electron diffraction studies can be more easily prepared by carburizing evaporated thin metal films. Even single-crystalline samples of carbides can be prepared by this method4). Furthermore, since the scattering power of carbon atom relative to that of nickel atom is more than twice larger for electrons than for X-rays, the electron diffraction is more favourable to study the structure of carbides than by the X-ray method.

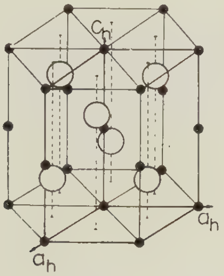

Fig. 1. The structure of Ni_3C. Large circles represent nickel atoms and small black circles represent octahedral interstices, possible positions for carbon atoms. (after Jacobson & Westgren)

In the present paper (Part I), the formation and the decomposition of the carbide Ni_3C and hydrogenation of carbidic carbon are described. Detailed structure analysis of the carbide, especially the determination of positions of carbon atoms will be reported in the next paper (Part II).

§ 2. Experimental Method

In the present experiment nickel carbide was produced by carburizing nickel films of thickness 200~300 Å in CO gas. The nickel films were prepared by evaporating commercial electrolytic nickel in vacuum. Hereafter, films without preferred orientation and films with single-crystalline orientation will be designated as 'P.C.' and 'S.C.' films, respectively. The former were prepared by evaporating nickel on cleavage faces of rock-salt kept at room temperature and the latter, on the faces kept at 450°~500°C. A transmission electron diffraction pattern of a P.C. film is reproduced in Photo. 1. The mean particle size of nickel in the film was estimated to be less than 50 Å from the half-breadth of Debye rings. Photo. 2 reproduces a diffraction pattern of a S.C. film taken with an incidence of electrons perpendicular to the film. It reveals that crystallites grow on the substrate with a preferred orientation $(001)_{Ni}//(001)_{NaCl}$ and $[100]_{Ni}//[100]_{NaCl}$.

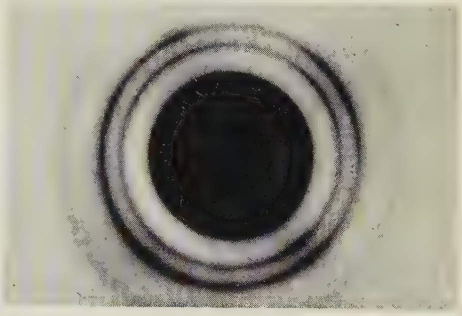

Photo. 1. Diffraction pattern of P.C. film of nickel evaporated on cleavage face of rock-salt kept at room temperature.

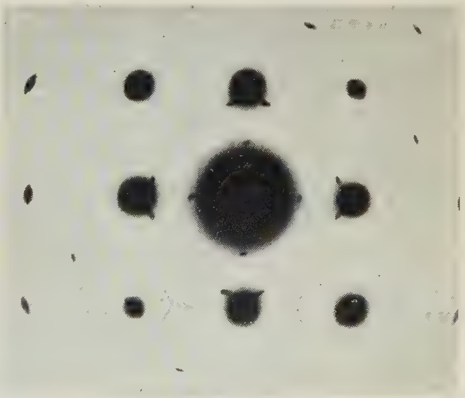

Photo. 2. Diffraction pattern of S.C. film of nickel evaporated on cleavage face of rock-salt kept at 450°C. Incident electrons are perpendicular to the film surface.

The apparatus used for cementation is shown in Fig. 2. CO_2 gas from the vessel A is reduced to CO through the converter furnace B which is filled with charcoal particles heated at 950°～1100°. CO gas, after purified through the stage C, is led to the reaction furnace D where nickel films are to be carburized. The purifying stage C consists of a series of cooled active carbon (-12°C), soda-lime and metallic sodium. The charcoal particles in the converter furnace were heated beforehand at 700°～800°C for 6～8 hrs. to eliminate impurities.

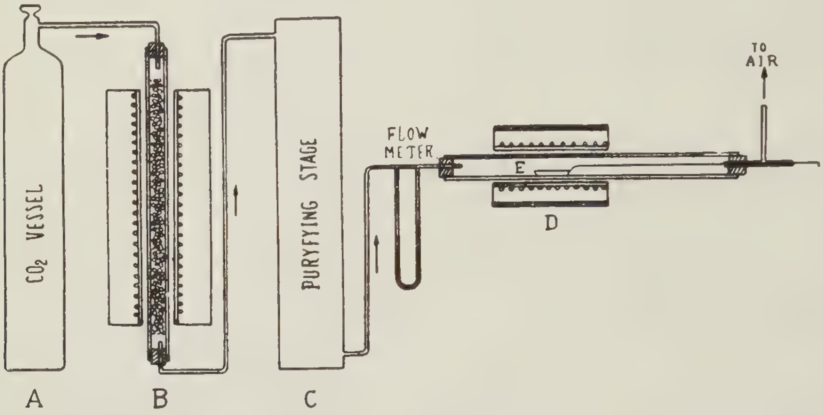

Fig. 2. Schematic diagram of apparatus used for cementation. A: CO_2 vessel, B: converter furnace (filled with charcoal particles) for producing CO gas, C: gas-purifying stage consisting of a series of cooled active carbon, soda-lime, calcium chloride and metallic sodium, D: reaction furnace, in which specimen films are carburized, E: porcelain boat, on which specimen films are put.

The procedure of cementation was as follows: Nickel films not detached from the substrates or transfered on nickel gauzes of about 150 meshes were put on the porcelain boat E and the boat was inserted into the quartz reaction tube kept at a desired temperature in a flow of CO gas. The heating temperature and the heating period were from 250° to 500°C and from 4 to 40 hrs., respectively. Rate of flow in the reaction tube was kept at about 100 cc per min.; the temperature fluctuation was kept within ±10°C. After the treatment, the boat was drawn out to a cold part and cooled down in the flow of CO gas as fast as possible by pouring water around the tube.

The study of thermal decomposition of nickel carbide in vacuum was carried out in two ways: (i) Carbide films were heated in a vacuum furnace for certain periods and examined by electron diffraction. (ii) The carbide films were heated in an electron diffraction camera and changes of the diffraction pattern were continuously observed. In both the methods the vacuum was of the order of 1×10^{-5} mmHg.

The study of decomposition of the nickel carbide due to hydrogen treatment was carried out with the same apparatus as used for the cementation (Fig. 2) by replacing CO gas with hydrogen gas. Hydrogen gas was produced by electrolysis of water and purified by red-heated copper and through the same purifying stage as used for the purification of CO gas.

An electron diffraction camera of the standard type of specimen-plate distance 250 mm having single focussing lens was used with an accelerating voltage 40 kV. Sometimes, however, a high resolution diffraction camera* with two focussing lenses and a specimen-plate distance 380 mm was also utilized with an accelerating voltage 50 kV. For high temperature examination, a high temperature specimen holder** attached to the high resolution camera was utilized. The temperature of specimen was measured by a thermo-couple placed as near as possible to the specimen film. In order to check possible differences between temperatures of the specimen film and the thermo-couple, the change of electron diffraction pattern due to melting was observed for evaporated tin films about 200 Å in thickness. It was found that the melting occurred when the thermo-couple indicated a temperature 220°C, which is 12°C lower than the known melting point of tin, 232°C. However, in view of Takagi's result⁶⁾ that the melting point of an evaporated thin metal film is always lower than that of bulk metal by an amount of this order, the accuracy of the thermo-couple indication may be a few degrees.

---

* Hillier type diffraction camera set in Miyake-Honjo Laboratory.

** Designed and constructed by G. Honjo and N. Kitamura. Its construction is a modification of the low temperature specimen holder reported by them[5].

§ 3. Formation of Nickel Carbide

1. Electron Diffraction Pattern of Ni_3C

In Photo. 3(a) and (b) electron diffraction patterns from P.C. films carburized at 350°C for 5 hrs. and 10 hrs. are reproduced. The latter is the pattern due to nickel carbide, while the former is composed of rings due to the carbide and residual nickel***. In Table I, observed spacings and visual intensities of the carbide rings are tabulated and compared with the X-ray data of Ni_3C given by Jacobson and Westgren.

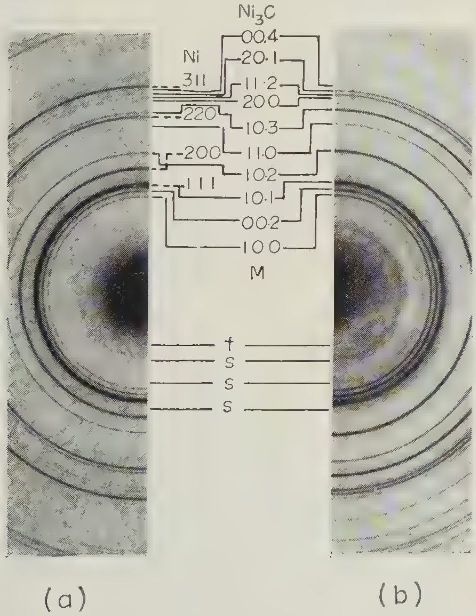

Photo. 3. Diffraction pattern of carburized P.C. films.
(a) Partly carburized at 350°C for 5 hrs.
(b) Completely carburized at 350°C for 10 hrs.
Indices of reflections are indicated. Classification of reflections such as *M*, *f* and *s*: see text.

The observed rings are classified into three groups '*M*' (main), '*f*' (forbidden) and '*s*' (super-lattice) reflections, as indicated in Photo. 3 and in Table I. The *M* reflections are strong and sharp, corresponding to a mean particle size 290 Å, and are well interpreted by the close packed hexagonal structure of Ni_3C proposed by Jacobson and Westgren. Their spacings correspond to the lattice constants (at 25°C)

$$a_h=2.628\ \text{Å},\quad c_h=4.306\ \text{Å}\quad \text{and}\ c_h/a_h=1.638,$$

which are smaller than Jacobson and Westgren's values only slightly (0.79% for a_h and 0.78% for c_h). The relative intensities of the rings agree in general with the X-ray data.

The "extra" rings *f* and *s*, which were not observed by Jacobson and Westgren, were found to coexist always with the *M* reflections in the electron diffraction patterns of the carburized nickel films. Moreover, the rings *M*, *f*, and *s* disappeared simultaneously when the carbide is decomposed (see Photo, 7). The *f* reflections are sharp but weak, and are indexed by the same unit cell for the *M* reflections, though they are forbidden reflections for the close packed hexagonal structure. The *s* reflections, which are weak and diffuse, can not be indexed by this unit cell. They, together with *M* and *f* reflections, can be indexed by the following hexagonal cell:

$$a=\sqrt{3}\,a_h=4.553\ \text{Å}\quad \text{and}\ c=3c_h=12.92\ \text{Å}\ .$$

The new hexagonal lattice is a super-lattice of the Jacobson and Westgren's as shown in Fig. 3. The indices of reflections corresponding to this unit cell and calculated spacings are tabulated in Table I. In Part II, where a detailed analysis of the observed intensity is given, it will be concluded that the above diffraction pattern is appropriate for Ni_3C having the crystal structure as depicted in Fig. 3. Here, large circles represent nickel atoms arranged in the close packed hexagonal positions and small circles represent carbon atoms located regularly in the positions of one-third of

---

*** Lattice constant of the residual nickel is 3.521 Å, which coincides very well with the known value of nickel $a_{Ni}=3.517$ Å.

Table I. Diffraction data of Ni_3C.

No.	Electron Diffraction(1)					X-ray Diffraction(2)		
	Classification(3)	*hkil*(4)	Int.(5)	d_{obs}(Å)(6)	d_{cal}(Å)(7)	*hk.l*(8)	Int.(5)	*d*(kX)(9)
1	*f*	(0003)	w	4.290	4.305	(00.1)	—	—
2	*s*	$01\bar{1}2$	w, br	3.358	3.365	—	—	—
3	*s*	$10\bar{1}4$	w, br	2.480	2.499	—	—	—
4	*M*	$11\bar{2}0$	m	2.274	2.276	10.0	m	2.292
5	*M*	0006	s	2.150	2.153	00.2	m	2.164
6	*M*	$11\bar{2}3$	vs	2.012	2.012	10.1	vs	2.025
7	*s*	$20\bar{2}2$	vw, br	1.885	1.884	—	—	—
8	*s*	$02\bar{2}4$	vw, br	1.685	1.683	—	—	—
9	*M*	$11\bar{2}6$	s	1.566	1.564	10.2	m	1.576
10	*s*	$01\bar{1}8$	vw, br	1.493	1.494	—	—	—
11	*s*	$12\bar{3}2$	vw, br	1.452	1.452	—	—	—
12	*f*	(0009)	vw	1.435	1.435	(00.3)	—	—
13	*s*	$21\bar{3}4$	—	—	1.353	—	—	—
14	*M*	$03\bar{3}0$	m	1.314	1.314	11.0	s	1.323
15	*f*	$(03\bar{3}3)$	vw	1.258	1.257	(11.1)	—	—
16	*s*	$20\bar{2}8$	vw	1.238	1.249	—	—	—
17	*s*	$10\bar{1}.10$			1.227	—	—	—
18	*M*	$11\bar{2}9$	s	1.214	1.214	10.3	s	1.221
19	*M*	$22\bar{4}0$	w	1.139	1.138	20.0		
20	*M*	$03\bar{3}6$	m	1.122	1.122	11.2		
21	*M*	$22\bar{4}3$	m	1.101	1.100	20.1		
22	*M*	000.12	w	1.077	1.076	00.4		
23	*M*	$22\bar{4}6$	vw	1.008	1.006	20.2		
24	*M*	$11\bar{2}.12$	w	0.973_6	0.9728	10.4		
25	*M*	$22\bar{4}9$	w	0.892_1	0.8913	20.3		
26	*M*	$14\bar{5}0$	vw	0.860_6	0.8606	21.0		
27	*M*	$14\bar{5}3$	m	0.844_7	0.8439	21.1		
28	*M*	$03\bar{3}.12$	w	0.832_8	0.8333	11.4		
29	*M*	$11\bar{2}.15$	w	0.805_2	0.8052	10.5		
30	*M*	$14\bar{5}6$	w	0.798_7	0.7987	21.2		

(1) First 30 reflections are tabulated. Only *M* reflections are shown below No. 19.
(2) Jacobson and Westgren's data.
(3) *M*: main reflection, *s*: super-lattice reflection, *f*: forbidden reflection.
(4) Indices of reflections. Indices in blackets correspond to *f* reflections.
(5) vs: very strong, s: strong, m: medium strong, w: weak, vw: very weak; br: broad.
(6) Observed spacings. Reference: reflection due to residual nickel assuming its lattice constant $a_{Ni}=3.517$ Å.
(7) Spacings calculated from lattice constants $a=\sqrt{3}a_h=4.553$ Å and $c=3c_h=12.92$ Å.
(8) Indices of reflections due to Jacobson and Westgren's lattice.
(9) Spacing calculated from Jacobson and Westgren's lattice constants $a_h=2.644$ kX and $c_h=4.329$ kX.

the octahedral interstices of nickel atoms. The structure is in accordance with that of Jacobson and Westgren so far as the nickel positions are concerned. In what follows, therefore, Jacobson and Westgren's unit cell will be utilized for the sake of convenience.

In Photo. 4, a diffraction pattern from a S. C. film carburized for 20 hrs. at 350°C is reproduced. A schematic diagram of the pattern is illustrated in Fig. 4. Besides spots due to metallic nickel having the same arrangement as observed in Photo. 2, there appears an array of slightly arced and elongated spots which are situated with a definite geometrical relation with respect to the nickel spots. The former spots are due to Ni_3C. The pattern reveals that the nickel carbide Ni_3C is produced from nickel metal with the orientational relation

$$(00.1)_{Ni_3C}//(111)_{Ni} \quad \text{and} \quad [10.0]_{Ni_3C}//[10\bar{1}]_{Ni}\,.$$

This means that the closest packed atomic planes and atomic rows of the both crystals are parallel to each other.

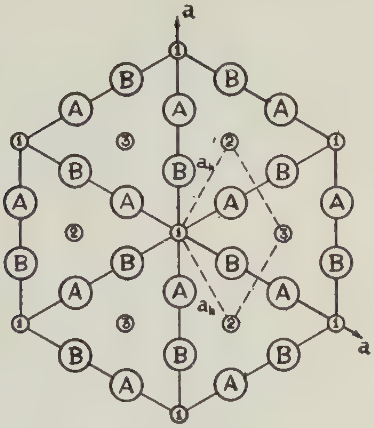

Fig. 3. Structure of Ni_3C. The figure shows projection of atomic arrangement on basal plane. Large circles represent nickel atoms (A and B) and small circles, carbon atoms (C_1, C_2, C_3). Unit cell is indicated by heavy lines and Jacobson and Westgren's unit cell, by dotted lines. Relation of lattice constants between the two lattice is $a=\sqrt{3}a_h$ and $c=3c_h$. Height of atoms: A(1/12, 5/12, 9/12); B(3/12, 7/12, 11/12); C_1(2/12, 8/12); C_2(4/12, 10/12); C_3(0/12, 6/12). A and B atoms form the close packed hexagonal arrangement and C atoms occupy one-third of the octahedral interstices regularly. The structure can be represented by the following stacking order $A(C_1)B(C_2)A(C_3)B(C_1)A(C_2)B(C_3)A\ldots$

It should be mentioned here that, in the whole course of the present study, Ni_3C is the only product formed by the cementation of nickel films, and the existence of any other carbide such as Ni_3C_x suggested by Bahr and Bahr was not recognized. It must be also added that the f reflections did not appear in the diffraction patterns when crystal size of Ni_3C was estimated to be smaller than about 100 Å. This seems to show the fact that f reflections are caused by multiple reflections of electrons, the effect which is considered to be remarkable when the crystal is large enough.

2. Progress of Carburization

The temperature range of carbide formation was determined by carburizing many P.C. films for 4～6 hrs. at various temperatures from 250°C to 500°C with an interval of 50°C. Below 450°C, the carbide was formed, though nickel rings of appreciable intensity always remain as already shown in Photo. 3(a). At 500°C, on the other hand, only amorphous

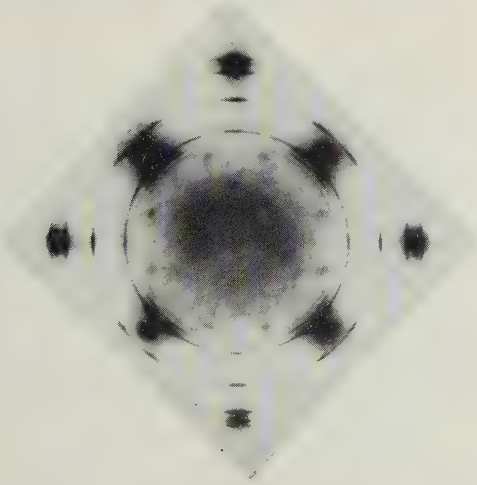

Photo. 4. Diffraction pattern of Ni_3C formed from S.C. film by the cementation at 350°C for 20 hrs. Note the epitaxial relation between Ni_3C reflections and nickel reflections. (cf. Fig. 4)

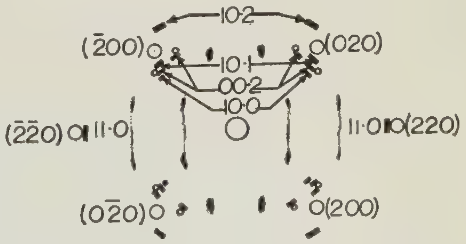

Fig. 4. Key diagram of Photo. 4. Large and small plain circles represent ($kh0$) main spots and (111) twin spots due to nickel, respectively. Short rods and elongated bars are M and s reflections due to Ni_3C, respectively. (Equivalent two orientations of Ni_3C relative to nickel are found in Photo. 4. But in this figure the spots due to one of them are shown.)

carbon was deposited on nickel films without the carbide formation. The electron diffraction patterns obtained in this case are similar to Photo. 7(d). From the intensities of the carbide rings, it was found that the maximum rate of the carbide formation is attained at about 350°C. Above 400°C and below 300°C, the rate was slower.

By prolonged treatments carried out at about 350°C for 10~20 hrs., some specimens were carburized completely and gave the diffraction patterns as already shown in Photo. 3(b). The completely carburized films, however, were not always obtained, though it was not so difficult to obtain partly carburized films: Of about 80 nickel films carburized for 20~40 hrs. at about 350°C, only 10 films gave diffraction patterns composed of the carbide rings alone, and patterns from the other films contained more or less nickel rings besides carbide rings. It is notable that the residual nickel does not grow up over 100 Å even after such prolonged heating. The degree of carburization was different from film to film, even when the films were treated under the same condition. It was observed that the carburization was delayed when the starting P.C. films were prepared on substrates kept at somewhat elevated temperatures ($\gtrsim$200°C), where they gave sharper diffraction rings corresponding to the particle size about 100 Å. However, any systematic difference could not be recognized between the films transfered on meshes and those not detached from the substrates.

The carburization was in general more difficult for S.C. films. For instance, while fairly strong carbide reflections were almost always obtained from P.C. films by 10 hrs. treatment, this was not always the case for the S.C. films.

Examination of degrees of carburization in the course of the cementation showed that a small amount of the carbide was formed initially but the carburization did not always proceed with a prolonged cementation.

The experiments on S.C. films revealed the following characteristic relation between the degree of orientation of the carbide crystals and the degree of carburization: In the initial stage of the carbide formation, the orientation is in general fairly good, but it is destroyed by further progress of the carburization. This can be seen from Photo. 5(a), (b) and (c), which are the diffraction patterns obtained

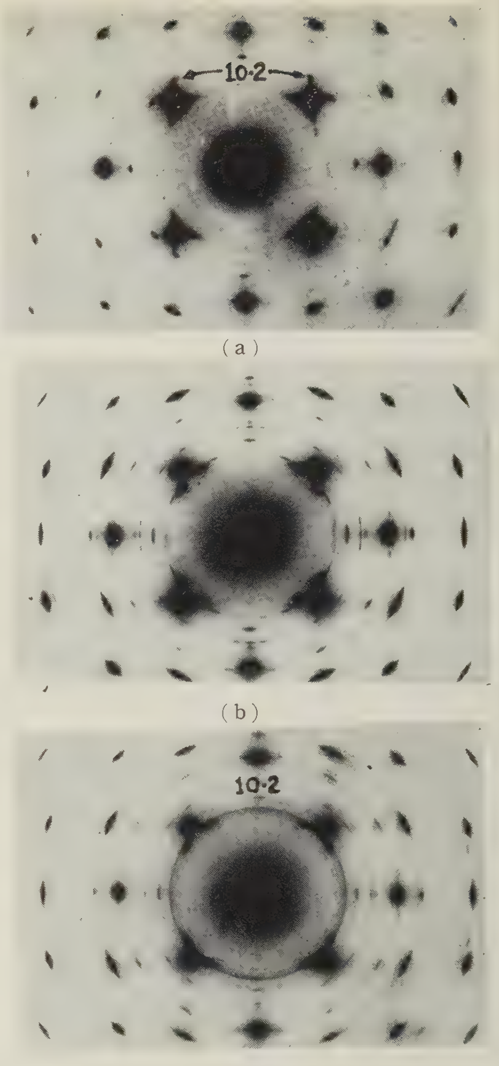

(a)

(b)

(c)

Photo. 5. Diffraction patterns of carburized S.C. films illustrating change of degree of orientation of Ni_3C with progress of carburization.

(a) Good orientation corresponding to the nucleation stage of the carbide crystal. Typical Ni_3C spots (10.2) are indicated by arrows. cf. Fig. 4. (carburized at 350°C for 10 hrs.)

(b) Partly destroyed orientation corresponding to development of crystal growth. (carburized at 380°C for 14.5 hrs.)

(c) Completely* destroyed orientation corresponding to growth stage of the carbide crystal. (carburized at 350°C for 20 hrs.) *For example, $(10.2)_{Ni_3C}$ reflections have turned into a continuous ring. Note the fact that the degree of the orientation of nickel is not changed by the progress of the carburization.

from S.C. films subjected to the cementation for 10 hrs. at 350°C, for 14.5 hrs. at 380°C and for 20 hrs. at 350°C, respectively. In Photo. 5(a), the carbide spots, which are weak and diffuse corresponding to the nucleation stage, are manifesting a good orientation of crystallites. The crystal size estimated is about 50 Å. In Photo. 5(c), the carbide reflections appear in a form of sharp Debye rings. This shows that the particles have grown larger than 200 ~300 Å and, at the same time, that the orientation has been completely destroyed. Photo. 5(b) corresponds to an intermediate stage of the above two cases. In these patterns it is seen that the degrees of the orientation of metallic nickel are not appreciablly changed by the treatment.

3. Electron Microscopic Observation

Electron microscopic observations were performed on some of nickel and carburized films. Photo. 6(a) and (b) reproduce electron micrographs of a S.C. film and a partly carburized S.C. film at 350°C for 26 hrs., respectively. It can be seen that a considerable aggregation of crystallites takes place during the cementation. The formed carbide crystallites have no characteristic shape. This coincides with the fact that the diffraction patterns do not show any fine structure such as due to the effect of refraction and shape transform.

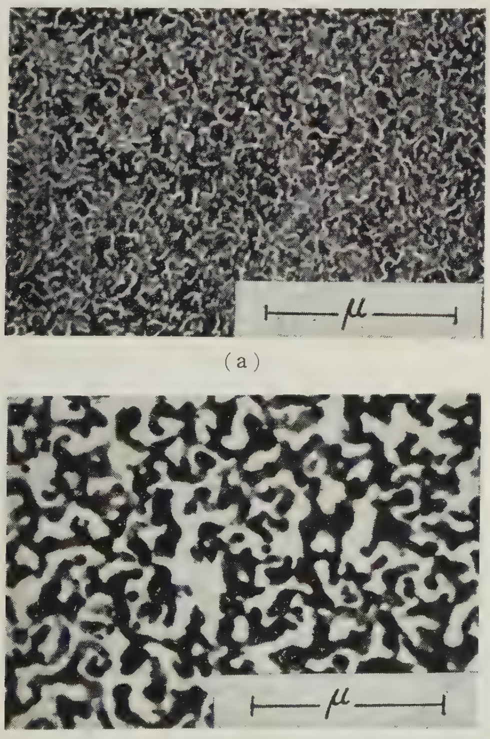

(a)

(b)

Photo. 6. Electron micrographs of (a) S.C. film prepared on cleavage face of rock-salt kept at 480°C and (b) S.C. film party carburized at 350°C for 26 hrs. Considerable aggregation of crystallites is observed to be caused by the prolonged treatment.

§ 4. Decomposition of Nickel Carbide

Bahr and Bahr reported that, when the carbide was heated in nitrogen at 380°~420°C, it decomposed to nickel and carbon, and that, when heated in hydrogen at 180°C, the carbidic carbon was completely hydrogenated to methane, leaving only metallic nickel.

In the present experiment, it was found that nickel carbide films kept in a desiccator over a year showed no appreciable change in electron diffraction pattern, indicating that the carbide is stable at room temperature. In order to investigate the stability of the carbide at elevated temperatures, the carbide films were heated in vacuum and in hydrogen stream.

1. Thermal Decomposition of the Carbide

When completely carburized P.C. films were kept at 300°C for 21 hrs., the diffraction pattern still consisted almost solely of the carbide rings, though a trace of nickel rings appeared. At 400°C, heating for 30 min. produced also no remarkable change but after 2~4 hrs. heating the carbide decomposed completely; the films gave patterns as shown in Photo. 7(d). At 500°C the decomposition occurred more rapidly than at 400°C.

Study of continuous change of the diffraction pattern of the carbide during heating was performed on partly carburized films having no preferred orientation using a high temperature electron diffraction camera. The rate of temperature rise was 2°~4°C per min.. Photo. 7(a)~(d) reproduce a series of photographic records. No difference is recognized between the patterns of Photo. 7(a) and (b) which were taken at 16°C and 192°C, respectively. Similar pattern persisted until 431°C, but at this temperature a considerable change took place. In Photo. 7(c) taken just after the change, the carbide rings weaken, while the nickel rings become stronger and diffuse carbon rings appear, showing that the decomposion of the carbide has been started. In Photo. 7(d) at 433°C, taken 2 min. after Photo. 7(c), any carbide rings are not found, showing that the decomposition has been completed. The disappearance of the carbide rings at this temperature proceeded very rapidly and completed within a few seconds.

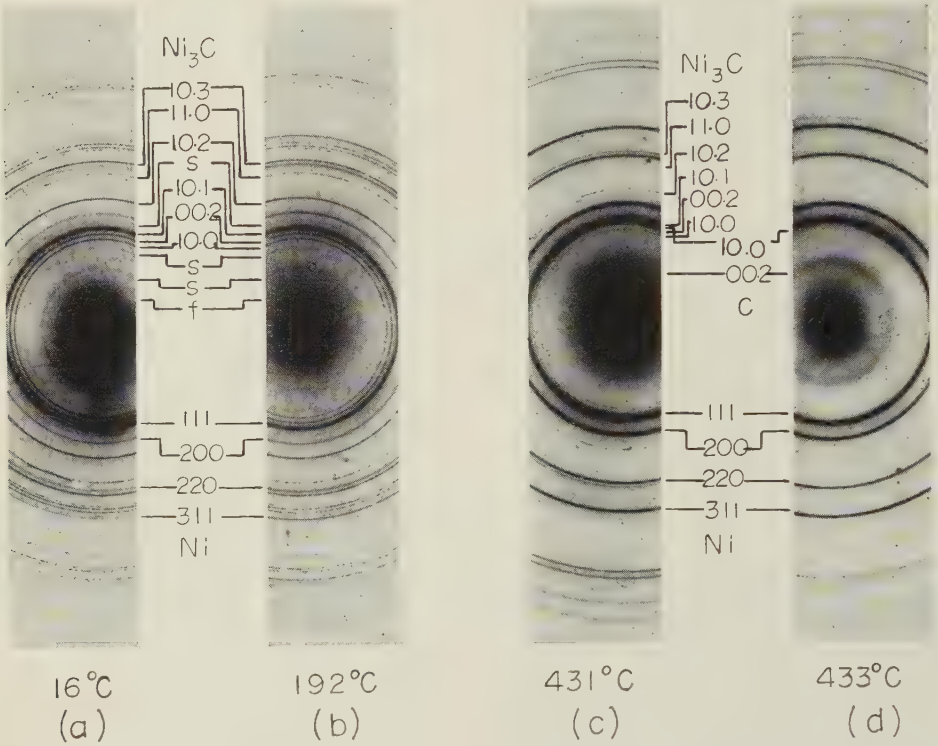

16°C (a)

192°C (b)

431°C (c)

433°C (d)

Photo. 7. A series of diffraction patterns at various temperatures taken by the high temperature electron diffraction camera. Between the pattern (a) at 16°C and (b) at 192°C, no appreciable change is observed. The pattern (c) at 431°C shows that the thermal decomposition of Ni_3C has started and the pattern (d) at 433°C, that the decomposition has completed. Note the fact that the *f* and *s* reflections disappear simultaneously together with *M* reflections.

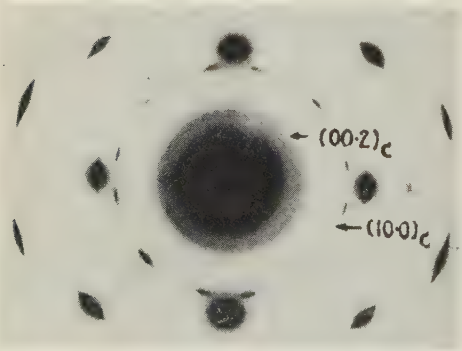

Photo. 8. Diffraction pattern after heating at 500°C for 10 min. of the carburized S.C. film of Photo. 4. Diffuse rings are due to amorphous carbon. Note the well-defined nickel spots showing the same disposition as Photo. 2.

From the half-breadth of the rings, it can be seen that the carbide particles of about 300 Å decompose to metallic nickel, particle size of which being less than 100 Å.

It was observed that films giving the patterns as reproduced in Photo. 4 changed by decomposition to films giving a pattern as reproduced in Photo. 8. This pattern is composed of diffuse rings due to amorphous carbon and regular array of the diffraction spots due to nickel, being arranged in the same disposition as in Photo. 2. From this observation it is seen that, when the carbide of single-crystalline orientation is decomposed, the produced metallic nickel restores its original orientation.

2. Hydrogen Treatment of the Carbide

Completely carburized films without preferred orientation were heated in hydrogen gas stream. At 300°C, after treatment for 18 hrs., the film produced weak nickel rings but their intensities did not change appreciably even after 26 hrs., showing that hydrogenation of the carbidic carbon takes place only very slowly at this temperature. At 400°C, for one specimen treated for 20 hrs., carbide rings were weakened and nickel rings became stronger without producing carbon rings. But for another specimen treated for 3 hrs., the carbide rings disappeared and nickel and diffuse carbon rings appeared. At 500°C, the films produced nickel and diffuse carbon rings after 3 hrs. treatment.

These results show that reaction of methane formation, $Ni_3C+2H_2=3Ni+CH_4$, may take place actually as reported by Bahr and Bahr, but its rate is very slow. The carbon deposition above 400°C indicates, however, that at higher temperatures the simple thermal decomposition predomiates over the hydrogenation of the carbidic carbon.

§ 5. Thermal Expansion of Nickel Carbide

From high temperature electron diffraction patterns at various temperatures such as reproduced in Photo. 7(a)∼(c), thermal expansion coefficients of nickel carbide were determined by taking reference to the lattice constant and the thermal expansion coefficient of metallic nickel as follows:

$$a_{\mathrm{Ni}}=3.5168\ \text{Å} \quad (\text{at } 25°\mathrm{C})$$

$$\alpha_{\mathrm{Ni}}=13.3\times10^{-6}/°\mathrm{C}\ .$$

The lattice constant of the carbide a_h was determined at various temperatures from (10.0), (20.0) and (11.0) rings and c_h, from (00.2) and (00.4) rings. The results are plotted in Fig. 5 against temperature t°C. They give the following relations for the thermal expansion of the carbide (using the least square method),

$$a_h=2.628(1+\alpha_\perp t)\ , \qquad \alpha_\perp=10\times10^{-6}/°\mathrm{C}\ ,$$

$$c_h=4.304(1+\alpha_\parallel t)\ , \qquad \alpha_\parallel=16\times10^{-6}/°\mathrm{C}$$

and

$$c_h/a_h=1.638\{1+(\alpha_\parallel-\alpha_\perp)t\}\ ,$$

$$\alpha_\parallel-\alpha_\perp=6\times10^{-6}/°\mathrm{C}\ .$$

This result shows a little anisotropy in the thermal expansion. Mean expansion coefficient $\bar{\alpha}$ was calculated from the above values using the relation

$$\bar{\alpha}=\overline{\alpha_\parallel\cos^2\theta}+\overline{\alpha_\perp\sin^2\theta}\ ,$$

where θ is the angle between c_h axis and the direction for which α is averaged. It gives

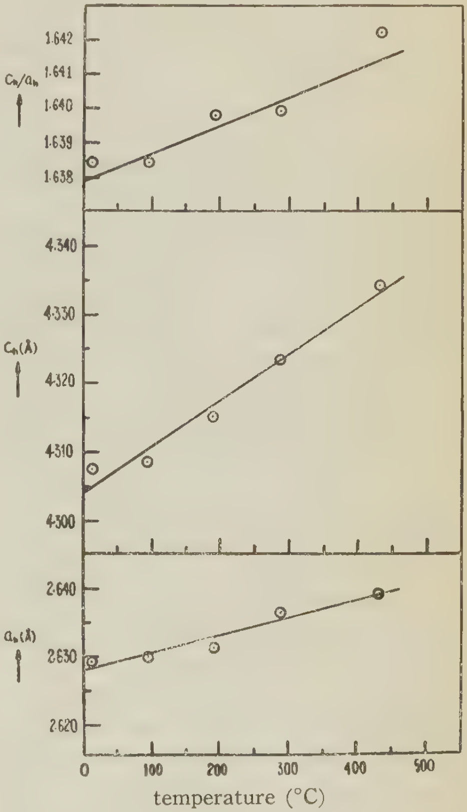

Fig. 5. Thermal change of lattice constants and axial ratio of Ni_3C.

$$\bar{\alpha}=12\times10^{-6}/°\mathrm{C}\ ,$$

which is sensibly close to α_{Ni}.

§ 6. Discussion

1. Formation and Decomposition of Nickel Carbide

The reaction of carbide formation

$$M+2CO=MC+CO_2$$

(M: metallic element, MC: its carbide) is considered to proceed by following processes: First, (1) CO molecules are adsorbed on the surface of specimen, and subsequently, (2) the molecules are decomposed and generate active carbon atoms, then (3) these carbon atoms diffuse into solid, and finally, (4) combine with metal atoms to form a carbide. The process

(4) is divided further into two processes: nucleation and growth.

As in the cases of many other solid reactions, the rate of carbide formation is considered to be determined mainly by the process (3). The diffusion process is accelerated by increasing temperature, so that the rate of the carbide formation increases with temperature rise. This may be the case below 350°C. At higher temperatures, however, the increasing rate of the diffusion is surmounted by increasing rate of the decomposition (§4.1), resulting in the maximum rate of the carbide formation at about 350°C (§3.2).

The diffusion process should be highly dependent on lattice imperfections such as vacancies, dislocations and grain boundaries. These imperfections may trap carbon atoms to form nuclei of the carbide crystals[7], and also may accelerate the diffusion of carbon atoms. In the films prepared on the substrates kept at elevated temperatures, the lattice imperfections must be much fewer than in the films prepared on the substrates kept at room temperature, since the former films are tempered by the heating during preparation[8]. Such a difference may be the main reason for the difference of the rate of carbide formation for P.C. and S.C. films (§3.2).

It was observed that the carbide was formed comparatively easily at the initial stage of the cementation but prolonged cementation did not always increase the amount of the carbide (§3.2). This may be partly due to the fact that the texture of the films is gradually improved during heating. Also the rate of diffusion of carbon atoms through the carbide crystal is considered to be slower than through nickel metal: The formation of the carbide layer on the surface prevents further progress of the carbide formation.

The thermal decomposition of the carbide and the hydrogenation of the carbidic carbon are considered to proceed as follows: The carbidic carbon atoms are driven out onto the crystal surface and, when the samples are heated in vacuum, the carbon atoms combine with one another on the surface to form amorphous carbon, while, when heated in hydrogen atmosphere, the atoms react with hydrogen on the surface to produce hydrocarbon such as methane which escapes out from the surface. So that the existence of hydrogen does not affect substantially the rate of the decomposition (§4.2).

2. Nucleation and Growth of Nickel Carbide

It was mentioned in §3.1 that the nuclei of carbide crystal are formed with a particular epitaxial relation to metallic nickel, $(111)_{\mathrm{Ni}}//(00.1)_{\mathrm{Ni_3C}}$ and $[10\bar{1}]_{\mathrm{Ni}}//[10.0]_{\mathrm{Ni_3C}}$, and in §4.1 that, when they decompose, produced metallic nickel restores the original orientation.

As well known, the face centred cubic lattice of metallic nickel is characterized by a stacking order ABCABC··· of the closest packed atomic planes, and the close packed hexagonal lattice of nickel atoms in $\mathrm{Ni_3C}$, by a stacking order ABAB···. Therefore, the nucleation of nickel carbide is considered to be a lattice transformation from the ABC··· stacking to the ABAB··· stacking and its decomposition is the reversed process.

Here, we suppose a lattice transformation by the following scheme:

$$\begin{array}{ccccccc}
\mathrm{A} & \to & \mathrm{C} & \to & \mathrm{B} & \to & \mathrm{A} \\
\mathrm{B} & \to & \mathrm{A} & \to & \mathrm{C} & \to & \mathrm{B} \\
\mathrm{C} & & \mathrm{C} & \to & \mathrm{B} & \to & \mathrm{A} \\
\mathrm{A} & & \mathrm{A} & \to & \mathrm{C} & \to & \mathrm{B} \\
\mathrm{B} & & \mathrm{B} & & \mathrm{B} & \to & \mathrm{A} \\
\mathrm{C} & & \mathrm{C} & & \mathrm{C} & \to & \mathrm{B} \\
\vdots & & \vdots & & \vdots & & \vdots
\end{array}$$

Namely, every two layer of nickel metal in the left hand side of the scheme slips by one step to produce the carbide lattice in the right hand side of the scheme. Each slip can be produced, as well known, by a half dislocation moving on the slip plane $\{111\}_{\mathrm{Ni}}$ or $\{00.1\}_{\mathrm{Ni_3C}}$ along the direction $\langle 112\rangle_{\mathrm{Ni}}$ or $\langle 21.0\rangle_{\mathrm{Ni_3C}}$. When the face centred cubic lattice and the close packed hexagonal lattice are transformed into each other by this mechanism, it is evident that they have the epitaxial relation as mentioned above. Therefore, it is very conceivable that the formation and the decomposition processes of nuclei of nickel carbide take place by the mechanism proposed above. The interplaner and interatomic distances of the closest packed atomic planes and atomic rows, which are kept parallel in the transformation, are tabulated in Table II. The fact that these values are very close, also favours the proposed mechanism.

Table II. Interatomic and interplaner distances of metallic nickel and nickel carbide.

	Ni	Ni_3C	Vernier period
Interatomic distance along the most densly packed atomic row (Å)	⟨110⟩ 2.488 $(=a_{Ni}/\sqrt{2})$	⟨10.0⟩ 2.628 $(=a_h)$	19 $(=a_h/(a_h-a_{Ni}/\sqrt{2}))$
Interplaner distance between the most densly packed atomic planes (Å)	{111} 2.030 $(=a_{Ni}/\sqrt{3})$	{00.1} 2.152 $(=c_h/2)$	18 $(=(c_h/2)/(c_h/2-a_{Ni}/\sqrt{3}))$

The mechanism of transformation by a series of microscopic slips is quite similar to that of martensitic transformation of cobalt from the face centred cubic to the close packed hexagonal structure[9]. In this case driving force is supplied by internal stress due to cooling. In the transformation of the carbide nucleation the driving force is considered to be supplied by internal stress produced by diffusing-in carbon atoms.

Differing from the case of cobalt metal, however, there exists a definite, though small, misfitness between the carbide and the nickel lattice. The vernier period[10] between them are tabulated in Table II. It means that 19 nickel atoms on the closest packed plane of the carbide crystal must face to 20 atoms on that of the nickel crystal and 18 layers of the closest packed plane of the carbide must join to 19 layers of the nickel. This relation is illustrated in Fig. 6, where atomic arrangement of nickel atoms (plain circles) on $(1\bar{1}0)_{Ni}$ plane of the matrix (left-lower region) and that on $(1\bar{2}.0)_{Ni_3C}$ plane of the epitaxially formed carbide crystal (right-upper region) are shown. Thus, on the boundary face between the two crystals there must exist one dislocation per one vernier period.

When the carbide crystal grows up, such dislocations are accumulated on the interface of the two crystals. They have the same sign and arranged on the same slip plane, so that they repel one another. As a result, the destruction of the epitaxial relation may take place as observed in the growth stage of the carbide crystal (§ 3.2). In fact the destruction of epitaxy was observed to occur when the crystal size of the carbide becomes larger than about 100 Å, which is a few multiples of the vernier period mentioned above.

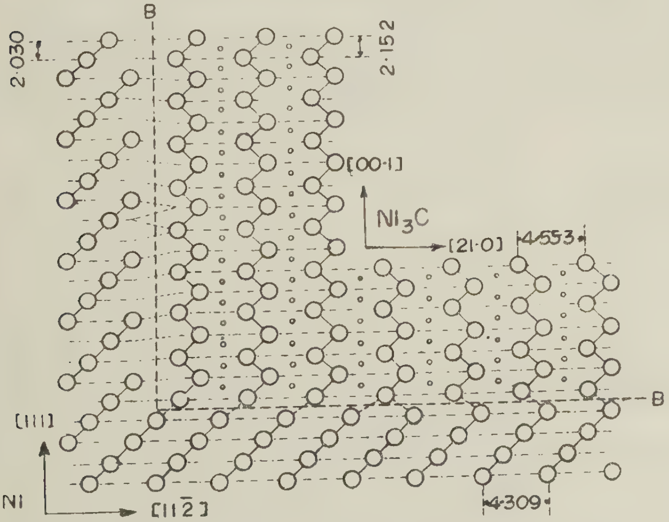

Fig. 6. Atomic arrangement of Ni_3C crystal (right-upper region) formed from nickel crystal (left-lower region). This figure shows the atomic arrangement on $(1\bar{2}.0)_{Ni_3C}$ and $(1\bar{1}0)_{Ni}$ planes, where large circles represent nickel atoms and small circles represent possible positions for carbon atoms. Interface of the two crystals are indicated by broken line *BB*, the nearest neighbour atoms are linked by full lines and the closest packed atomic planes are represented by chain lines. Dislocations are produced at the crystal boundary.

It has been reported many observations on the epitaxial growth of metallic films deposited on single crystal surfaces[11]. In these cases, the epitaxy is well preserved upto a crystal size of several hundred Ångströms even when the misfitness between the depositing crystals and the substrate crystals is much larger than the present case. In fact, the orientation of S.C. film of Photo. 2 was preserved in its own growth upto, at least, 400 Å, in spite of the very small vernier period of about 5. In the case of surface deposition, nuclei of deposited crystals, whose orientation is determined by the substrate, can grow up by themselves in free space incoherently with the substrates[12]. The nickel carbide, however, must grow up, not in free space but in the matrix of nickel, so that its growth produces necessarily dislocations at the interface. This results in the destruction of epitaxy when the carbide grows up more than a few multiple of the vernier period.

In the carburized P.C. films the carbide crystal grows upto about 300 Å in spite of the fact that residual nickel does not grow upto more than 100 Å. Therefore, in the process of the carbide formation, a considerable recrystallization must take place. On the contrary, in the decomposition process, such a large carbide crystal decomposed into several smaller crystals of metallic nickel (~100 Å) and no recrystallization of them was observed.

Acknowledgements

The author wishes to express his thanks to Professor S. Oketani for his guidance throughout this work. He also wishes to express his thanks to Professors S. Miyake and G. Honjo for their valuable discussions. This work was supported by a Grant in Aid for Fundamental Scientific Research from the Ministry of Education.

References

1) S. Oketani, S. Nagakura and K. Tsuchiya: J. Japan Inst. Metals **18** (1954) 325; S. Oketani and S. Nagakura: *ibid.* **18** (1954) 329; *ibid.* **20** (1956) 460; S. Nagakura: *ibid.* **20** (1956) 465. (in Japanese)
2) H. A. Bahr und Th. Bahr: Ber. Deut. Chem. Gesell. **61** (1928) 2177.
3) B. Jacobson und A. Westgren: ZS. f. phys. Chem. **B20** (1933) 361.
4) J. -J. Trillat et S. Oketani: Met. et Corr. **25** (1950), No. 302; *ibid.* **25** (1950), No. 308; Acta Cryst. **5** (1952) 469.
5) G. Honjo, N. Kitamura, K. Shimaoka and K. Mihama: J. Phys. Soc. Japan **11** (1956) 527.
6) M. Takagi: J. Phys. Soc. Japan **9** (1954) 359.
7) For example, A. H. Cottrel: *Dislocations and Plastic Flow in Crystals*, 1954.
8) S. Oketani and S. Nagakura: J. Japan Inst. Metals **17** (1953) 536. (in Japanese)
9) T. R. Anantharaman and J. Christian, Phil. Mag. **43** (1952) 1338.
10) F. C. Frank and J. H. van der Merwe: Proc. Roy. Soc. **A198** (1949) 205.
11) For example, G. P. Thomson and W. Cochrane: *Theory and Practice of Electron Diffraction*, (1939).
12) S. Miyake: *Busseiron Kenkyu* **4** (1941) 77; R. Uyeda; *Buturigaku Kōensyū* No. 4 (1943) 285. (in Japanese)

JOURNAL OF THE PHYSICAL SOCIETY OF JAPAN Vol. 12, No. 5, MAY, 1957

Studies on the Radial Distribution Analysis in Diffraction Methods

I. Errors due to the Approximation of Integration by Summation*

By Tadashi INO

The Institute of Polytechnics, Osaka City University, Osaka

(Received February 8, 1957)

In the calculation of a radial distribution function

$$rD(r)=(1/2\pi^2)\int_0^\infty sI(s)\sin sr\,ds$$

we usually approximate the integral by such a sum as

$$rD_\Sigma(r)=(\Delta s/2\pi^2)\sum_{n=1}^\infty n\Delta s\cdot I(n\Delta s)\cdot\sin(n\Delta sr)\,.$$

In this paper the mathematical property of $rD_\Sigma(r)$ is derived and the error due to the approximation is proved to be expressed as

$$rD_\Sigma(r)-rD(r)=\sum_{\substack{m=-1\\ \neq 0}}^{\infty}{}'\,(r+2m\pi/\Delta s)D(r+2m\pi/\Delta s)\,.$$

Furthermore, the formula for the estimation of the error is derived. It turned out that in order to obtain a high accuracy from the approximation we must make the spacing Δs less than π/R_0, where R_0 is the distance beyond which $rD(r)$ is regarded practically zero.

§ 1. Introduction

In order to analyze the diffraction data of gaseous, liquid, and amorphous substances we generally use two methods; the "*correlation*" and the "*radial distribution*" methods. The former is an empirical "*trial* and *error*" method, consisting in the theoretical calculations of scattering intensities for various models and the comparison of these values with the observed data. The latter consists in Fourier inversion of diffraction data which requires essentially the accurate intensity data and laborious numerical calculations, while it can offer the structural information straightforward. Recent advances in the experimental techniques of diffraction method and the availability of punched card methods[1] for the calculation have made it more practicable to carry out this method and made the results obtained more reliable and accurate. In this series of papers, problems concerning the radial distribution analysis will be discussed.

The intensity function $I(s)$ sensitive to the structure of the substance is connected with the radial distribution function $D(r)$[2] by the following relation,

$$sI(s)=4\pi\int_0^\infty rD(r)\sin sr dr \qquad (1)$$

where $s=(4\pi/\lambda)\sin\theta/2$, θ=scattering angle, and λ=wave length. The Fourier transform of eq. (1) becomes

$$rD(r)=(1/2\pi^2)\int_0^\infty sI(s)\sin srds \qquad (2)$$

In numerical calculation of eq. (2) we usually approximate the integral by the sum over evenly spaced s values as follows.

$$rD_\Sigma(r)=(\Delta s/2\pi^2)\sum_{n=1}^\infty n\Delta s\cdot I(n\Delta s)\cdot\sin(n\Delta sr)$$

The aim of the present paper is to make clear the nature of the error introduced by this approximation.

§ 2. Derivation of Formula

In practice, $I(s)$ cannot be obtained in the whole range of s, but is limited in a certain range of $0\leqslant s\leqslant s_{\max}$ and we are forced to treat the integrals of the type

$$(1/2\pi^2)\int_0^{s_{\max}} sI(s)\sin srds \qquad (3)$$

or

$$(1/2\pi^2)\int_0^{s_{\max}} sI(s)\exp(-a^2s^2)\sin srds\,, \qquad (4)$$

instead of the integral (2). To treat the errors introduced in the calculations of these integrals by approximation generally, we introduce a modification function $M(s)$*, a modified intensity function $\boldsymbol{I}(s)$, a modified radial distribution function $\boldsymbol{D}(r)$, and its approximation function $\boldsymbol{D}_{\Sigma}(r)$ given by following eqs.

---

* Read at the Meeting of Physical Society of Japan, Tokyo, April, 1955.

$$\boldsymbol{I}(s)=M(s)I(s) \tag{5}$$

$$r\boldsymbol{D}(r)=(1/2\pi^2)\int_0^{\infty} s\boldsymbol{I}(s)\sin srds \tag{6}$$

$$r\boldsymbol{D}_{\Sigma}(r)=(\Delta s/2\pi^2)\sum_{n=1}^{\infty} n\Delta s\cdot\boldsymbol{I}(n\Delta s)\cdot\sin(n\Delta s\cdot r) \tag{7}$$

With the use of the property of odd function of $r\boldsymbol{D}(r)$ and the Fourier inversion of eq. (6) as

$$s\boldsymbol{I}(s)=4\pi\int_0^{\infty} t\boldsymbol{D}(t)\sin stdt$$

eq. (7) can be transformed:

$$\begin{aligned} r\boldsymbol{D}_{\Sigma}(r)&=(\Delta s/\pi)\lim_{N\to\infty}\int_{-\infty}^{\infty} t\boldsymbol{D}(t)\sum_{n=1}^{N}\cos\{n\Delta s(t-r)\}dt \\ &=(\Delta s/\pi)\lim_{N\to\infty}\int_{-\infty}^{\infty} t\boldsymbol{D}(t)\frac{\sin\{(2N+1)\Delta s(t-r)/2\}}{2\sin\{\Delta s(t-r)/2\}}dt \end{aligned}$$

Since the sine part of the integrand has a period of $2\pi/\Delta s$, the integral can be conveniently transformed into an infinite series:

$$r\boldsymbol{D}_{\Sigma}(r)=(1/\pi)\lim_{M\to\infty}\sum_{m=-\infty}^{\infty}\int_{-\pi/2}^{\pi/2}\left(r+\frac{2m\pi}{\Delta s}+\frac{2x}{\Delta s}\right)\boldsymbol{D}\left(r+\frac{2m\pi}{\Delta s}+\frac{2x}{\Delta s}\right)\frac{\sin Mx}{\sin x}dx$$

where

$$t=r+\frac{2m\pi}{\Delta s}+\frac{2x}{\Delta s} \quad \text{and} \quad M=2N+1\,.$$

Suppose

$$\sum_{m=-\infty}^{\infty}\left(t+\frac{2m\pi}{\Delta s}\right)\boldsymbol{D}\left(t+\frac{2m\pi}{\Delta s}\right)$$

converges, a further transformation can be carried out by the theorem of Dirichlet's integral:

$$r\boldsymbol{D}_{\Sigma}(r)=\sum_{m=-\infty}^{\infty}(r+2m\pi/\Delta s)\boldsymbol{D}(r+2m\pi/\Delta s) \tag{8}$$

or

$$r\boldsymbol{D}_{\Sigma}(r)-r\boldsymbol{D}(r)=\sum_{\substack{m=-\infty\\ \neq 0}}^{\infty}{}'(r+2m\pi/\Delta s)\boldsymbol{D}(r+2m\pi/\Delta s)\,. \tag{9}$$

§ 3. Properties of the Approximation Function

a) According to eq. (7) or eq. (8) it is evident that $r\boldsymbol{D}_{\Sigma}(r)$ is periodic with a period $2\pi/\Delta s$ and is zero at the points

$$r=m\pi/\Delta s\,, \qquad m\text{: integer}\,.$$

Since eq. (7) is a sine series, it is antisymmetric about the zero points as illustrated in Fig. 1.

b) According to eq. (9) the error due to this approximation is expressed by:

$$\sum_{\substack{m=-\infty\\ \neq 0}}^{\infty}{}'(r+2m\pi/\Delta s)\boldsymbol{D}(r+2m\pi/\Delta s)\,.$$

Consequently if $r\boldsymbol{D}(r)$ is zero outside the range $(-\pi/\Delta s, \pi/\Delta s)$, all the values of $(r+2m\pi/\Delta s)\times\boldsymbol{D}(r+2m\pi/\Delta s)$ $(m\neq 0)$ are zero inside the range $(-\pi/\Delta s, \pi/\Delta s)$. Therefore $r\boldsymbol{D}_{\Sigma}(r)$ is identical with $r\boldsymbol{D}(r)$ inside the same range. On the contrary, if $r\boldsymbol{D}(r)$ is different from zero somewhere outside the range $(-\pi/\Delta s, \pi/\Delta s)$, it is not the case. These features are shown in Fig. 2 and Fig. 3 respectively. In Fig. 3 the value of $r\boldsymbol{D}_{\Sigma}(r)$ at a position, say Q_0, is quite different from the value of $r\boldsymbol{D}(r)$ at the same position Q_0, since the value of $r\boldsymbol{D}(r)$ is not zero at such positions as $Q_1, Q_{-1}, \cdots$ separated mutually by a distance $2\pi/\Delta s$. But in Fig. 2 the value of $r\boldsymbol{D}(r)$ is zero at those position, hence $r\boldsymbol{D}_{\Sigma}(r)$ is equal to $r\boldsymbol{D}(r)$.

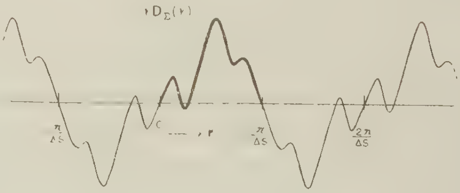

Fig. 1.

---

* In the case of (3):

$$\begin{aligned} M(s)&=1 && 0\leqslant s\leqslant s_{\max} \\ &=0 && s_{\max}<s \end{aligned}$$

In the case of (4):

$$\begin{aligned} M(s)&=\exp(-a^2s^2) && 0\leqslant s\leqslant s_{\max} \\ &=0 && s_{\max}<s \end{aligned}$$

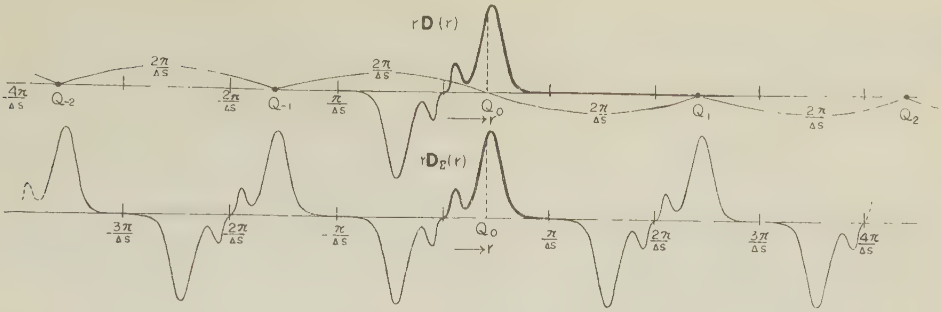

Fig. 2. non-zero range of $rD(r) \leq \pi/\Delta s$

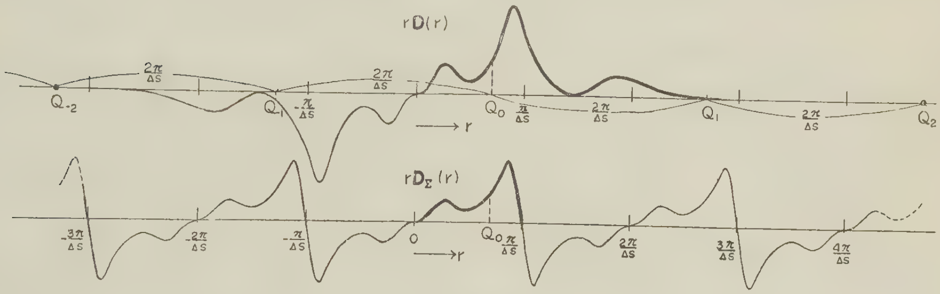

Fig. 3. none-zero range of $rD(r) > \pi/\Delta s$

§ 4. Estimation of Error

Since the approximation is considered as a modified trapezoidal law of numerical, integration, the error can be estimated by usual way as follows:

$$2\pi^2 r(D_\Sigma(r)-D(r))$$
$$=(\Delta s/2)(sI(s))_{s_{\max}} \sin(s_{\max} r)$$
$$+(s_{\max}/12)\Delta s^2 (sI(s)\sin sr)''_{s=\sigma}$$

or

$$2\pi^2 r(D_\Sigma(r)-D(r)) \sim (\Delta s/2)(sI(s))_{s_{\max}} \sin(s_{\max} r)$$
$$+(\Delta s^2/12)\{(sI(s)\sin sr)'_{s_{\max}}-(sI(s)\sin sr)'_0\}$$
$$-(\Delta s^4/720)\{(sI(s)\sin sr)'''_{s_{\max}}-(sI(s)\sin sr)'''_0\}$$
$$\cdots\cdots\cdots\cdots$$

where σ is a certain value in the range $(0, s_{\max})$.

However, eq. (8) being applied, a more convenient formula will be obtained. Since

$$2\pi^2 \rho D(\rho)=\int_0^{s_{\max}} sI(s)\sin s\rho\, ds$$

and $sI(s)$ is an odd function, then an asymptotic formula can be derived by repeated partial integration:

$$2\pi^2 \rho D(\rho) \sim -(sI(s))_{s_{\max}} \frac{\cos s_{\max}\rho}{\rho}$$
$$+(sI(s))'_{s_{\max}} \frac{\sin s_{\max}\rho}{\rho^2}$$
$$+(sI(s))''_{s_{\max}} \frac{\cos s_{\max}\rho}{\rho^3}$$
$$-(sI(s))'''_{s_{\max}} \frac{\sin s_{\max}\rho}{\rho^4}$$
$$\cdots\cdots\cdots \qquad (10)$$

Eq. (10) can be used successfully for the estimation of $\left(r+\frac{2m\pi}{\Delta s}\right)D\left(r+\frac{2m\pi}{\Delta s}\right)$ $(m \neq 0)$, if $L=2\pi/\Delta s$ is sufficiently large and $|r| \leqslant L/2$. Then according to eq. (9), the error can be expressed:

$$2\pi^2 r(D_\Sigma(r)-D(r)) \sim$$
$$-(sI(s))_{s_{\max}} \cos s_{\max} r \sum_{\substack{m=-\infty \\ \neq 0}}^{\infty}{}' (r+mL)^{-1}$$
$$+(sI(s))'_{s_{\max}} \sin s_{\max} r \sum_{\substack{m=-\infty \\ \neq 0}}^{\infty}{}' (r+mL)^{-2}$$
$$+(sI(s))''_{s_{\max}} \cos s_{\max} r \sum_{\substack{m=-\infty \\ \neq 0}}^{\infty}{}' (r+mL)^{-3}$$
$$-(sI(s))'''_{s_{\max}} \sin s_{\max} r \sum_{\substack{m=-\infty \\ \neq 0}}^{\infty}{}' (r+mL)^{-4}$$
$$\cdots\cdots\cdots \qquad |r| \leq L/2$$

With the help of the following relations;

$$e_1(z)=\sum_{\substack{m=-\infty \\ \neq 0}}^{\infty}{}' (z+m\pi)^{-1}=\cot z-1/z$$

$$
\begin{aligned}
e_{n+1}(z) &= \sum_{\substack{m=-\infty \\ \neq 0}}^{\infty}{}' (z+m\pi)^{-(n+1)} \\
&= \frac{(-1)^n}{n!} \frac{d^n}{dz^n} (\cot z - 1/z) ,
\end{aligned}
$$

the error can be transformed:

$$
\begin{aligned}
& 2\pi^2 r (D_\Sigma(r) - D(r)) \sim \\
& \quad -(sI(s))_{s_{\max}} (\Delta s/2) e_1(\Delta sr/2) \cos s_{\max} r \\
& \quad +(sI(s))'_{s_{\max}} (\Delta s/2)^2 e_2(\Delta sr/2) \sin s_{\max} r \\
& \quad +(sI(s))''_{s_{\max}} (\Delta s/2)^3 e_3(\Delta sr/2) \cos s_{\max} r \\
& \quad -(sI(s))'''_{s_{\max}} (\Delta s/2)^4 e_4(\Delta sr/2) \sin s_{\max} r \\
& \quad \cdots\cdots\cdots \qquad |r| \leqslant \pi/\Delta s \qquad (11)
\end{aligned}
$$

Hence the error can be estimated by a small number of terms in eq. (11), provided that Δs is sufficiently small. These terms are determined by the magnitude of Δs and values of $sI(s)$ and its derivatives simply *at* $s=s_{\max}$. This is characteristic of eq. (11), because the other equations mentioned before contain the additional terms determined by the derivatives of $sI(s)$ *at* $s=0$ or $s=\sigma$.

Since $z \cot z = 1 - \sum_{n=1}^{\infty} 2^{2n} B_n z^{2n}/(2n)!$ where $\pi > |z|$ (B_n: Bernoullian number), $e_n(z)$ is a monotonic functions of z in the same range and the first four functions are illustrated in Fig. 4. Therefore, the error is approximately expressed as a ripple consisting of $\sin s_{\max} r$ and $\cos s_{\max} r$ terms.

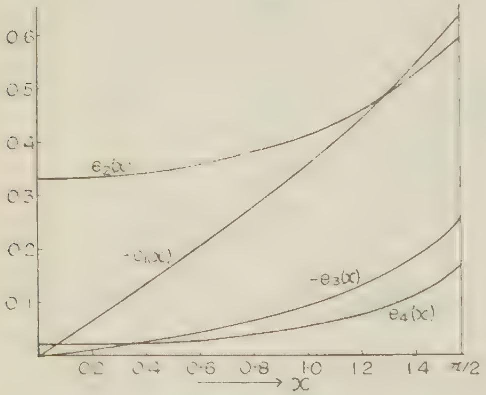

Fig. 4.

§ 5. Discussion

According to the mathematical properties of $rD_\Sigma(r)$, we can deduce facts to be noted in practical calculation of radial distribution function.

As mentioned before, the function obtained by this approximation has a periodicity which is not dependent upon the structure but only upon the magnitude of Δs. Then the functional behaviour outside the range $(-\pi/\Delta s, \pi/\Delta s)$ is simply the repetition of that in side the range $(-\pi/\Delta s, \pi/\Delta s)$. Therefore the function by no means gives the information of the structure outside the range $(-\pi/\Delta s, \pi/\Delta s)$. Consequently if we desire to obtain the information as far as $r=R'$ the spacing Δs must be taken as follows,

$$\Delta s < \pi/R' .$$

This condition however is not always a sufficient but a necessary one, as discussed in the following.

The error due to the approximation can be estimated according to eq. (11) if the values of the derivatives of $sI(s)$ at $s=s_{\max}$ can be determined. But according to eq. (8) one can derive a rule concerning the accuracy of the approximation: when $rD(r)$ may be regarded practically zero beyond R_0 (which may be called the *non-zero range*), a high accuracy can be expected from the computation where such a spacing given by

$$\Delta s \leq \pi/R_0$$

is used.

Since the integral given by (3) has extraneous ripples due to the termination effect[3], its non-zero range R_0 is much larger than that of $rD(r)$. Therefore the error is large, unless Δs is taken very small. On the other hand the convergence factor, for example, $\exp(-a^2s^2)$ improves the accuracy of the evaluation of radial distribution function, since it attenuates the amplitudes of the extraneous ripples and generally the coefficients of terms in eq. (11). Consequently the error due to the approximation of (4) is smaller than that of (3) if the same spacing is taken. In the radial distribution method the integral (4) is more advantageous than the integral (3) from the viewpoint of the accuracy of the approximation.

Since the integral given by (4) can be expressed as the convolution[4] of $rD(r)$ and $\exp(-r^2/4a^2)$, the non-zero range of the $rD(r)$ may be nearly equal to that of $rD(r)$. Therefore the suitable spacing Δs for a satisfactory approximation can be determined, when the non-zero range of $rD(r)$ can be estimated. From this discussion one can easily infer the following empirical rule to be reasonable:

taking a spacing $\Delta s=\pi/10$ and using the factor $\exp(-a^2s^2)$ (with 'a^2' chosen so that $\exp(-a^2s^2_{\max})=0.1$), one can obtain fully satisfactory results even for $r=7A$ in the electron diffraction study of gas1). Morito and Kuchitsu5) showed that the spacing $\Delta s=\pi/10$ gives sufficiently accurate result as well as the spacing $\Delta s=\pi/50$ in the electron diffraction study of acethyl chloride. This fact is in agreement with our result.

In the cases of liquid and amorphous substances the non-zero range of $rD(r)$ is as large as the size of the specimen. Hence the suitable spacing Δs for a satisfactory approximation must be taken very small and the calculation is too laborious to perform. On the other hand $r(D(r)-D_0)$ has a much smaller non-zero range than $rD(r)$ where D_0 is the volume average of $D(r)$6). Hence from the standpoint of the accuracy of the evaluation it is highly necessary that we should treat the intensity corresponding to $r(D(r)-D_0)$ instead of $rD(r)$ in these cases*. This requirement is satisfied by the usual procedure in the radial distribution analysis of liquid and amorphous substances6).

R. E. Franklin7) discussed briefly the problem on the spacing of summation in the study of the diffuse X-ray diagrams of carbon. Her result is also consistent with our conclusion.

§ 6. Acknowledgement

The author wishes to express his sincere thanks to Prof. J. Kakinoki and Mr. K. Katada for their kind advices and Prof. R. Uyeda for his valuable discussions. The author is also indebted to the Ministry of Education for the research grant.

References

1) P. A. Shaffer, Jr. V. Schomaker and L. Pauling: J. Chem. Phys. **14** L. (1946) 648.
2) P. Debye and M. H. Pirenne: Ann. d. Phys. **33** (1938) 617.
3) W. L. Bragg and J. West: Phil. Mag. **10** (1930) 823.
4) J. Waser and V. Schokamer: Rev. Mod. Phys. **25** (1953) 671.
5) Y. Morino and K. Kuchitsu: X-rays, **8** (1954) 37.
6) P. Debye and H. Menke: Ergebn. Tech. Röntgenk **2** (1931) 1.
7) R. E. Franklin: Acta Cryst. **3** (1950) 107.

---

* The difference between these intensities appears in the range of small scattering angles.

JOURNAL OF THE PHYSICAL SOCIETY OF JAPAN Vol. 12, No. 5, MAY, 1957

Radiative Collisions between Molecular and Electron Beams

II. Angular Momentum Distribution of OH* Radicals Splitting from H_2O_2 Molecules

By Tadao HORIE, Takayuki NAGURA and Masamoto OTSUKA

Faculty of Science, Osaka University

(Received December 6, 1956)

A molecular spectroscopic study of the radiative collision of electrons with H_2O_2 molecules leads to a pronounced abnormal rotation of the OH* radical split by electron impact from H_2O_2. A homogeneous electron beam is fired at right angles across a localized jet of H_2O_2 vapor in a vacuum chamber maintained at a pressure of about 1×10^{-4} mmHg. The angular momentum distribution curve obtained shows a single maximum which is located near the rotational quantum number of 20, and the rotational temperature corresponds to 20,100°K, being remarkably higher than the initial gas temperature. In comparison with the double maxima found for H_2O, there are two differences, namely—the absence of the first maximum and the shift of the second maximum towards higher rotational quantum numbers.

§ 1. Introduction

The earliest study of the abnormal rotation of the hydroxyl radical splitting away from H_2O_2 was reported in 1936 by A. A. Frost and O. Oldenberg[1]. They observed the OH absorption by the hydroxyl radicals left unrecombined immediately after interrupting an electrical discharge of brief duration through H_2O_2 vapor. After that in 1951, P. J. Dyne and D. W. G. Style[2] made a study of the OH emission from the OH* radicals present in a fluorescence cell through which a steady flow of hydrogen peroxide vapor at a few tenths of 1 mmHg was maintained. These observations seem to be in agreement with each other with respect to the qualitative property of the rotational intensity distribution. According to a comparison of the OH bands obtained in their experiments with H_2O_2 with that frequently observed in electrical discharges through H_2O, the band-tail representing the highest rotation is more intense in the former, while the band-head is much more intense in the latter.

As for H_2O, however, the OH (0, 0) band emitted from an electrical discharge through its vapour is widely variable in respect of the rotational intensity distribution depending upon the condition under which water molecules are excited. For instance, it has been proved by H. P. Broida and W. R. Kane[3] that the relative intensity of the first maximum to the second of the R_2 branch undergoes a remarkable change with varying discharge pressure even in one and the same tube of an electrodeless ring discharge. In order to avoid such a danger of fluctuation, the most fundamental collisions of electrons with water molecules have been taken up in Part I.[4] In such a simplified collision process, the rotational intensity distribution of the Q_1 branch exhibits double maxima almost independently of the energy of impinging electrons in the wide range from 20 to 1,000 volts, the second (abnormal) maximum near the tail being at all energies predominant over the first (thermal) maximum near the head.

As an origin of the double maxima, a tentative mechanism has been proposed in Part I[4] on the basis of a localized electron pair bond theory of the H_2O molecule. Briefly summarized, when either one of the hydrogen atoms within a water molecule flies off nearly in the direction along the line of centers of the two hydrogen atoms, the remaining hydrogen atom must, for the law of angular momentum conservation, start an abnormal rotation about the oxygen atom, the second maximum being caused by such a swarm of hydroxyl radicals. Alternatively, when a hydrogen atom flies off in the direction along the O–H bond concerned, the H atom left behind does show merely a thermal rotation, the first maximum resulting from such a swarm of hydroxyl radicals. In order to examine such a proposal, it may be desirable to compare the angular momentum distribution of the OH* radicals splitting away from H_2O_2 molecules excited by electron impact with that found for H_2O.

§ 2. Experimental

In order to realize the simplest condition of collision of electrons with molecules, a nearly homogeneous electron beam is fired at right angles to a beam of molecules in a vacuum of about 1×10^{-4} mmHg as depicted in Fig. 1. The OH* radicals appearing at the intersection of two beams—an electron beam ejected from an especially designed electron gun and a beam of H_2O or H_2O_2 molecules—emit a crowd of rotational lines of the (0, 0) band near λ 3,064, the intensity distribution among them giving full information about the angular momentum distribution under investigation.

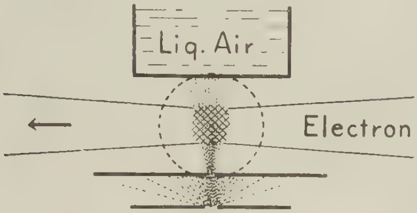

Fig. 1. The intersection of the two beams; the dotted circle means a quartz window.

Looking into the collision chamber through a quartz window, a reddish glow is visible around the intersection of an electron beam with a beam of water molecules. Its shape is more or less varied depending upon the strength of the focusing magnetic field of the electron gun, the width of the image slit, the intensity of the electron beam, the pressure of the collision chamber, and other experimental conditions, as shown in Fig. 2. The whole apparatus used is largely the same as described in detail in Part I.[4]

The preparation of the sample of H_2O_2 was made in two steps as follows. Firstly, the commercial 30% solution was concentrated after the recipe given by G. Brauer.[5] A glass flask, provided with a fine glass capillary to secure regular boiling and prevent superheating, containing 180 cc of the dilute solution was immersed in a water bath kept at 45–50°C. The side tube of the flask was connected with a pumping system via a spiral condenser and a receiving flask of about 150 cc. After a vacuum distillation for 3.5 hours at a pressure between 16 and 22 mmHg, the volume of the content was reduced down to about 45 cc, the residue being found to be about 90% H_2O_2 in weight. Secondly, the flask containing the residue was taken off and attached to another high vacuum system. Before the H_2O_2 vapour was used in the collision experiment, a vacuum distillation of long duration at much lower pressures was preceded to make the residue as free as possible of air and water dissolved into it.

Since H_2O_2 decomposes when in contact with stopcock grease, metals and harsh surfaces of ground glass, precautions were taken against the H_2O_2 vapour to contact with anything but smooth surfaces of clean glass walls both in the preparation procedure and in the collision experiment. From the reservoir of H_2O_2 to the image slit, all parts were made of glass. Without any stopcock, the pressure of the

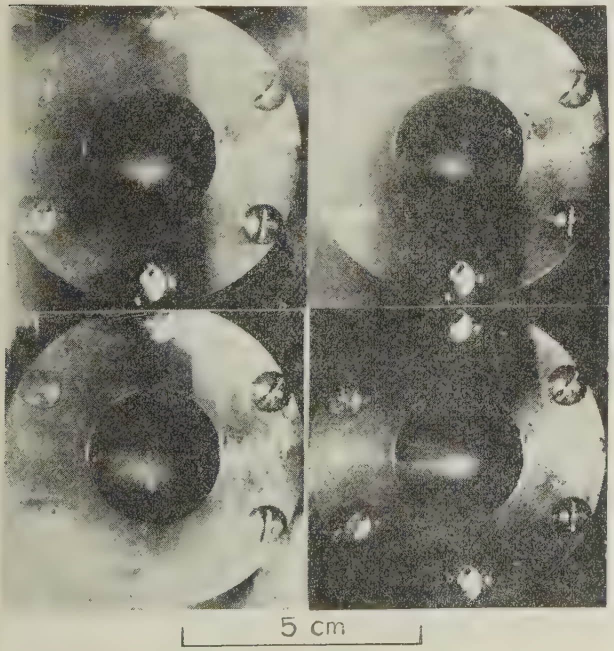

Fig. 2. Owing to the Balmer lines, a reddish glow is visible in various shapes under somewhat different conditions of operation at the intersection between an electron beam and a localized jet of water vapor.

H_2O_2 vapour was controlled only by cooling or heating the reservoir. The two metallic slits used in the preceding experiment with H_2O were also replaced with ones of glass as follows. After one end of a glass tube was closed in a blow-pipe flame, the thickness of the glass wall at the closed end was adjusted by blowing into the tube so as to become moderately thin. A slit was bored at the central portion of the closed end by a grinding device and sharp edges caused by grinding were all rounded off by a dilute solution of hydrogen fluoride.

§ 3. Result

The result of photographic photometry measurements for the rotational lines emitted from the OH* radicals splitting away from H_2O_2 molecules bombarded by electrons is compared in Fig. 3 with that observed in the experiment with H_2O. Both of them were obtained at sufficiently higher energies of impinging electrons ranging from 500 to 700 volts so that the ambiguity due to the possibility of what is called electron exchange collision might be set aside from the subject.

In general, $I(K')$, the intensity of the rotational line corresponding to the rotational quantum number K', is related to $N(K')$, the number of the excited radicals per unit volume at the rotational state with K', as follows:

$$N(K')=CI(K')(2K'+1)/i(K', K''),$$

where $i(K', K'')$ is the intensity factor. In the Q_1 branch considered, $C(2K'+1)/i(K', K'')$ varies quite gradually as a function of K' alone, the fluctuation of which does not exceed 1.3% of its magnitude in the range of K' from 3 to 30. These figures, therefore, may be able to be regarded as the distributions of number of radicals against rotational quantum number without any serious alteration, merely except for the range of K' less than 3.

Now in the case of H_2O_2, the distribution curve has a single maximum near the rotational quantum number K' of 20. The effective rotational temperature corresponds to 20,100K°, which is remarkably higher than the initial gas temperature. On the contrary, in the case of H_2O, in addition to the thermal maximum near K' of 5, the abnormal maximum is located near K' of 17 and the rotational temperature corresponds to about 14,000°K. On comparison of these figures it is seen that the thermal maximum found for H_2O is entirely absent for H_2O_2 and moreover the abnormal maximum is found at a higher rotational quantum number for H_2O_2 than it is for H_2O.

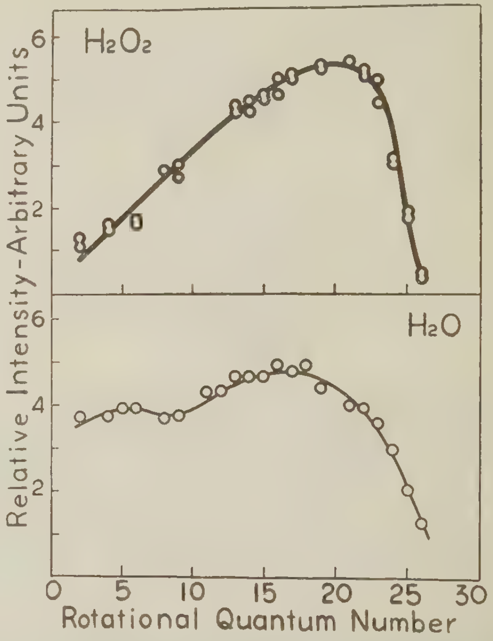

Fig. 3. Rotational intensity distributions of the Q_1 branch in the OH (0, 0) band excited in the radiative collision of elections with H_2O_2 and H_2O molecules.

In order to show the absence of the thermal maximum in the case of H_2O_2, the first fourteen members of the Q_1 branch in the OH (0, 0) band excited in several kinds of collision processes are compared with one another in Fig. 4, in which (a) was taken by the hydrogen canal ray impact experiment with water molecules,[7] (b) by the radiative collision of electrons with hydrogen peroxide molecules and (c) by the radiative collision of electrons with water molecules. These intensity dis tributions are undoubtedly quite different from one another, and it may be recognized that the $Q_1(2)$, $Q_1(4)$ and $Q_1(6)$ lines, for example, are very much fainter especially in the electron-impact excitation of H_2O_2, (b). On the other hand, the higher members, for example, the $Q_1(13)$ and $Q_1(14)$ lines in (b) and (c) are comparable with each other, while in (a) they fade out in rapid succession in

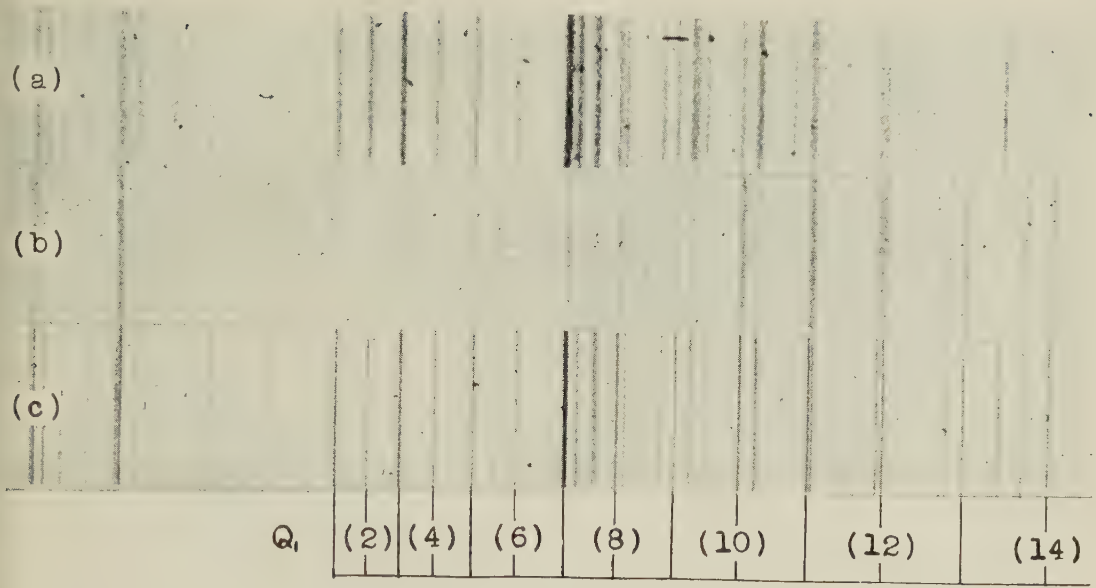

Fig. 4. The OH (0, 0) band; (a) hydrogen canal-ray-impact excitation of H_2O, (b) electron-impact excitation of H_2O_2, and (c) electron-impact excitation of H_2O.

contrast with the growing-up as seen in (b). It is also obviously doubtless that the gas temperature is not the main reason for such variations, because the parent molecules were certainly in all cases at room temperature.

§ 4. Discussion

As regards the molecular structure of the H_2O_2 molecule, three models have so far been suggested as depicted in Fig. 5.[6] Since in 1934 W. G. Penny and G. B. B. M. Sutherland[8] indicated theoretically that the nonplanar structure (c) was most probable, a number of works, as reviewed by J. T. Massey and D. R. Bianco,[9] tended to confirm their conclusion from both theoretical and experimental points of view. Especially the recent investigations by J. T. Massey *et al.*[9][10] with the microwave spectra and by P. A. Giguère *et al.*[11][12] with the infrared absorption spectra, all of them having been carried out in the *vapour* state, provided further strong confirmations for the nonplanar structure.

As is well known, H_2O_2 can be composed by various procedures of preparation, some of them being based on the association reaction of H atoms with O_2[13], and others on the recombination reaction of OH radicals liberated in electrical discharges through H_2O.[16] It was in 1932 that K. H. Geib and P. Harteck[13] proposed the existence of the isomer with the structure (b) in discussing about their experimental study of the former method. Since then the existence of such an isomer has long been the point in dispute for 20 odd years. Meanwhile, the recent work performed by P. A. Giguère and E. A. Secco[14] with the infrared absorption spectra in the *solid* state of hydrogen and deuterium peroxides produced in an electrodeless ring discharge revealed a new indication in favour of the existence of the isomer, $\begin{matrix}H\\H\end{matrix}\!>O^{+}-O^{-}$.

As far as the gaseous state is concerned, however, all the recent evidences cited above would allow us to set aside the model (b) from the question. And in fact, this model does not account for the absence of the first maximum, because it involves within itself a triangular configuration of HOH. Judging from this structure, whether it may be planar or pyramidal as suggested by A. D. Walsh,[15] the OH* radical must be produced as, for example,

$$\text{(A)}\quad H_2O_2 + e \rightarrow OH^* + \begin{cases} H + O + e \\ H^* + O + e \\ H^+ + O + 2e\,. \end{cases}$$

Accordingly, two different possibilities may exist for the direction of the recoiling hydrogen atom or proton, as has been indicated in the case of H_2O, namely—the direction along the line of centers of the two hydrogen atoms and that along either one of the O–H bonds respectively. If a recoiling hydrogen atom, whether it may be normal, excited, or ionized, were projected in the direction extending the O–H bond concerned, the OH* radical left behind would thermally rotate for the law of angular momentum conservation, such a swarm of OH* radicals leading to the thermal maximum. But, in point of fact, the experimental result does not give any evidence of the thermal maximum, as shown in Figs. 3 and 4.

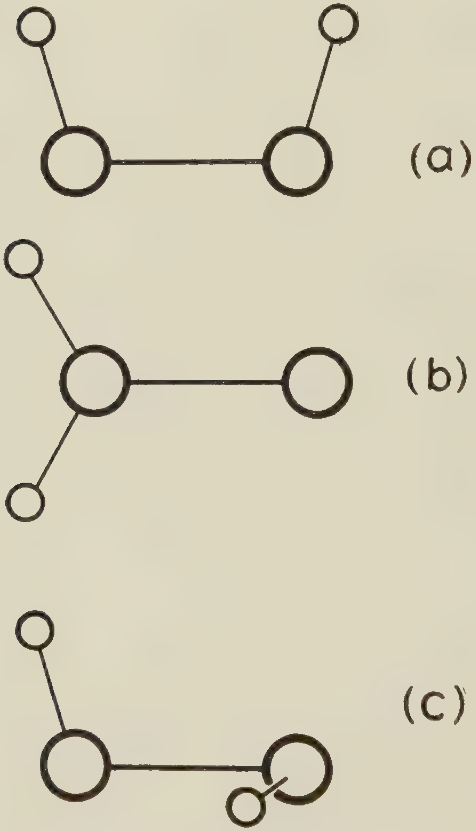

Fig. 5. Suggested models of H_2O_2; (c) is non-planar.

Such being the case, the absence of the first maximum must be attributed to the structures shown by the models (a) and (c). Owing to hindered rotation,[9)10)] the two OH bars within the H_2O_2 molecule in the ground state may take various orientations with respect to each other about the axis of the O–O bond; then the molecule may transitorily take various shapes, including the *cis* (a), the *trans* and the nonplanar (c) structures. In the case of such a structure, when excited by electron impact, the H_2O_2 molecule would be expected to split more probably into two hydroxyl radicals rather than into pieces as shown in (A). These considerations are in good agreement with the fact that the hydrogen Balmer series is very much weaker in the radiative collision of electrons with H_2O_2 than with H_2O as shown in Fig. 6. The faint traces of the Balmer lines in (b) may be due in part to a small quantity of H_2O impurities contained in the H_2O_2 molecular beam and in part to small probabilities for decompositions into pieces of the H_2O_2 molecule.

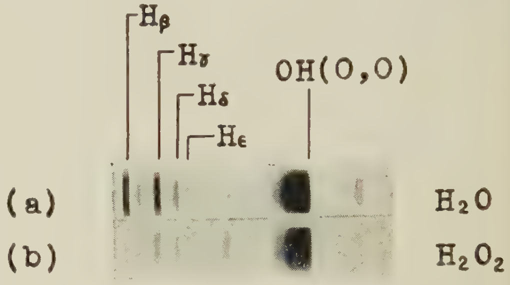

Fig. 6. Relative intensities of the hydrogen Balmer series to the OH (0, 0) band in the radiative collision of electrons with (a) H_2O and (b) H_2O_2 molecules.

Accordingly, the essential features in the angular momentum distribution curve observed in the experiment with H_2O_2, namely—the absence of the first (thermal) maximum and the shift of the second (abnormal) maximum towards higher rotational quantum numbers—may be attributable chiefly to the mechanism of the simultaneous excitation and dissociation by electron impact of H_2O_2 different from that of H_2O as follows:

$$\text{(B)}\qquad H_2O_2 + e \rightarrow OH^* + \begin{cases} OH + e \\ OH^* + e \\ OH^+ + 2e\,, \end{cases}$$

and

$$\text{(C)}\qquad H_2O + e \rightarrow OH^* + \begin{cases} H + e \\ H^* + e \\ H^+ + 2e\,. \end{cases}$$

The excitation by radiation of diatomic molecules is strictly governed by the Franck-Condon principle. If the relative positions of the potential-energy curves for a diatomic molecule in its lowest state and in an excited state were assumed as shown in Fig. 7, (a) or (b), excitation results in a molecule which at once dissociates into atoms. At that time, the relative kinetic energy of the two atoms with which they fly apart is given by the vertical distance of the horizontal line *AB* from the asymptote of the upper potential-energy curve.

Although the dissociation by electron impact of the HO–OH molecule may be in actuality a complex phenomenon, the qualitative feature of the process may likewise be understood. Now the two-dimensional potential-energy curves of the diatomic molecule must be replaced by polydimensional surfaces, but the Franck-Condon principle is still admittedly applicable to the process of excitation by electron. The potential energy above the asymptotic plane of the point on an upper potential-energy surface reached after the quantum jump must now be converted not only into the translational energies but also into the rotational energies of the fragment radicals. Accordingly, the surplus energy corresponding to *E* indicated in Fig. 7 must at all times be partly expended in enhancing the rotational energy of the H atom circling the O in the OH* radical splitting away from the H_2O_2 molecule excited by electron impact, thus the absence of the thermal maximum being brought about. It may be of interest to study the over-all distribution curve in more detail from a theoretical point of view.

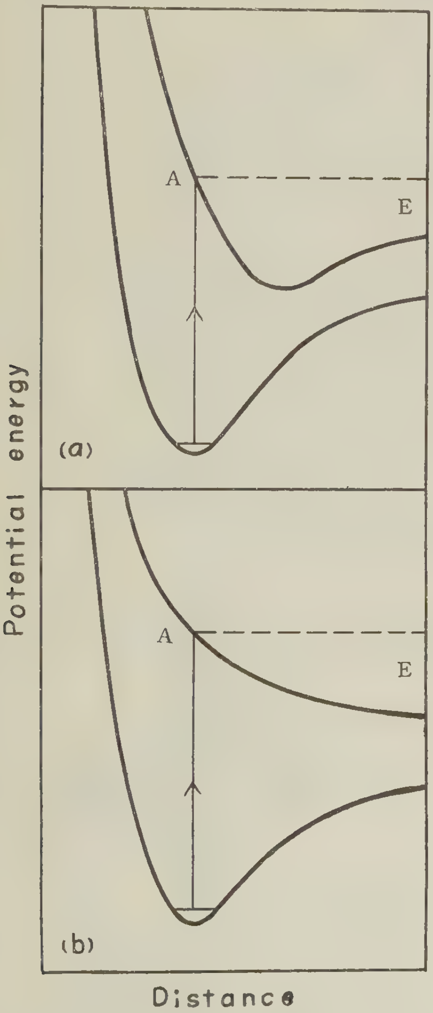

Fig. 7. Potential-energy curves for a diatomic molecule in its lowest state and in an excited state; excitation leads to dissociation.

Finally the authors wish to express their sincere thanks to Prof. T. Asada and Prof. T. Watanabe for placing the experimental facilities at their disposal. The authors have also pleasure in expressing their hearty thanks to Prof. M. Kotani of University of Tokyo and Prof. K. Niira of Tokyo Institute of Technology for their kind encouragements.

References

1) A. A. Frost and O. Oldenberg: J. Chem. Phys. **4** (1936) 781.
2) P. J. Dyne and D. W. G. Style: Nature, June 2 (1951) 899.
3) H. P. Broida and W. R. Kane: Phys. Rev. **89** (1953) 1053.
4) T. Horie, T. Nagura and M. Otsuka: Phys. Rev. **104** (1956) 547; J. Phys. Soc. Japan **11** (1956) 1157.
5) Georg Brauer: Handbuch der Präparativen Anorganischen Chemie, Ferdinand Enke Verlag Stuttgart (1954) 116.
6) G. Herzberg: "Molecular Spectra and Molecular Structure" II (1951) 301.
7) T. Horie, T. Nagura and M. Otsuka: Ann. Rep. Scient. Works, Fac. Sci. Osaka Univ. **4** (1956) 11.
8) W. G. Penny and G. B. B. M. Sutherland: J. Chem. Phys. **2** (1934) 492.
9) J. T. Massey and D. R. Bianco: J. Chem. Phys. **22** (1954) 442.
10) J. T. Massey and R. W. Hart: J. Chem. Phys. **23** (1955) 942.
11) P. A. Giguère: J. Chem. Phys. **18** (1950) 88.
12) P. A. Giguère and O. Bain: J. Phys. Chem. **56** (1952) 340.
13) K. H. Geib and P. Harteck: Ber. **65** (1932) 1551.
14) P. A. Giguère and E. A. Secco: J. Phys. Rad. **15** (1954) 508.
15) A. D. Walsh: Disc. Trans. Faraday Soc. **14** (1953) 140.
16) P. A. Giguère, E. A. Secco and R. S. Eaton: Disc. Trans. Faraday Soc. **14** (1953) 104.

JOURNAL OF THE PHYSICAL SOCIETY OF JAPAN Vol. 12, No. 5, MAY, 1957

Nuclear Magnetic Resonance Experiment on Solid Hexamethyldisilane

By Teruo YUKITOSHI*, Hirosi SUGA**, Syûzô SEKI**,
and Junkichi ITOH*
*Department of Physics, and **Department of Chemistry,
Osaka University, Osaka

(Received December 24, 1956)

Proton magnetic resonance of solid hexamethyldisilane was studied. Line width and spin-lattice relaxation time were measured in temperature range from liquid air to room temperature. By analysing these quantities following results were obtained: Even at liquid air temperature, each CH_3 group reorientates about its three-fold symmetry axis so rapidly as to narrow the dipolar width due to three proton interactions within itself (activation energy 2.6 kcal/mole). Then at about −120°C, reorientation of CH_3-groups about the axis joining two silicon atoms becomes rapid enough to narrow the width further (activation energy 5.7 kcal/mole). Spin-lattice relaxation time varies qualitatively in accordance with the above considered reorientational motions. At −51.3°C, this crystal changes its structure and at the same time rapid reorientational motion of the molecular axis is excited, resulting discontinuous decrease in the line width and discontinuous increase in the spin-lattice relaxation time. Above the transition temperature, self-diffusion of molecule as a whole starts and the line width decreases gradually to zero (activation energy 10 kcal/mole). No change in the line width was observed at the melting point.

§ 1. Introduction

Hexamethyldisilane is known as a typical plastic crystal in the sense first proposed by J. Timmermans[1] and the following properties have been revealed from the previous thermal and X-ray measurements[2][3]. (1) There is a remarkable anomaly in heat capacity at −51.3°C. In the high temperature phase, the substance becomes transparent perfectly in absence of air. On the other hand, the appearance of the sample brought into the low temperature phase is a white and opaque mass apparently composed of small crystals, probably with many craks. (2) The entropy change ΔS at the transition point is 10.5 cal/deg., mole, and this value is much larger than that at the melting point (14.5°C) where ΔS is 2.51 cal/deg., mole. A large scale disorder of lattice or molecule might be reasonably expected in the high temperature phase. (3) In the high temperature phase, the crystal structure determined from Laue and oscillation photographs using single crystals is body-centered cubic with the lattice constant of 8.47 Å (at 0°C) containing two molecules and the molecular axes are orientated at random over four body diagonals. On the other hand, it is very difficult to obtain single crystals below the transition temperature, but Debye-Sherrer photographs suggest that the low

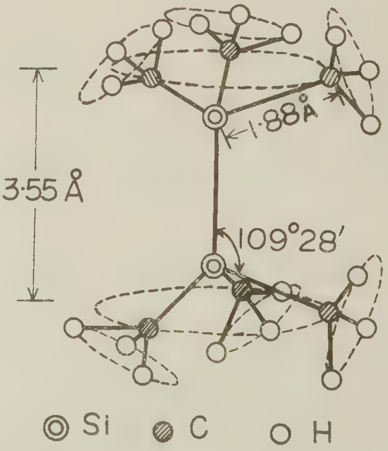

Fig. 1. Molecular structure of hexamethyldisilane in gaseous state determined by the electron diffraction measurement.

temperature modification is not at all "plastic" and belongs to lower symmetry.

It is the purpose of this work to investigate motions of the atomic groups or the molecule as a whole by the observations of the temperature dependence of proton magnetic resonance line width and spin-lattice relaxation time and also to relate them with the thermal and crystallographic data.

Electron diffraction study of the present molecule in gaseous state has been already published[4]. For the discussion of our experimental results, molecular parameters (shown in Fig. 1) determined by this electron diffraction experiment are assumed.

§ 2. Experimental Method and Procedure

The detection method of nuclear magnetic reasonance is similar to that of Watkins[5]. The sample (about 99.7% pure) was sealed by distillation under vacuum into a thin-walled glass tube (1 cm diameter and 3 cm long) which is inserted into the radio-frequency coil of a Watkins type oscillator. The experiments were carried out with the constant frequency of 5.35 Mc/sec., and by sweeping the magnetic field slowly, the derivatives of the absorption curves were recorded on a recording meter, after being amplified and detected by a phase sensitive detector. Most of the measurements were done by using a magnet whose inhomogeneity over the sample is about 0.1 gauss, and the magnetic field was modulated by 60 cycles per second.

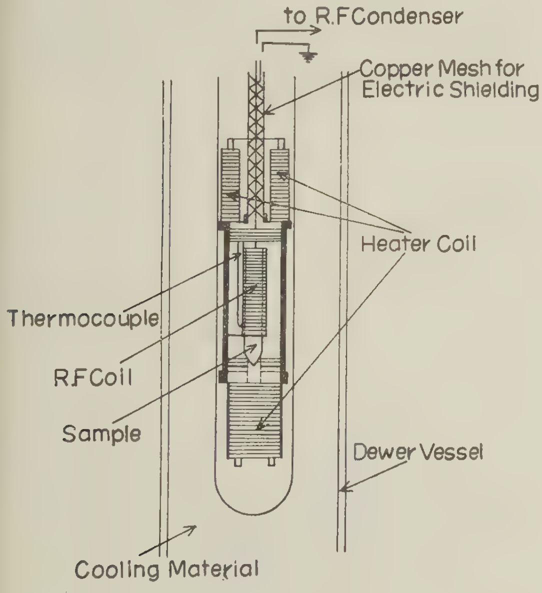

Fig. 2. The cryostat.

The cryostat used in our experiment is shown in Fig. 2. Liquid air or dry ice mixed with toluene was used as cooling material. The temperature of the sample was measured by means of a calibrated copper-constantan thermocouple located at a point very near the sample coil. Care was taken to assure good thermal equilibrium between the specimen and the surroundings and also to keep the temperature constant for enough time to do the measurements of line width or saturation curve. The specimen was cooled slowly by pouring cooling material into the Dewer vessel little by little and then was warmed gradually up to the desired temperature by increasing the currents of the heater coils. Data were taken after the temperature was in good equilibrium.

In the high temperature phase where the line width becomes very narrow, another highly homogeneous magnet was used for further precise measurement of the line width. The inhomogeneity of the magnetic field over the sample was about 6 milligauss. The magnetic field was modulated by 20 cycle per second to avoid distorsion of the resonance line by the modulation. In this case the temperature of the specimen was varied by the adjustment of the velocity of cold air flowing a glass tube surrounding the rf-coil. In order to avoid the occurrence of temperature gradient within the specimen, the specimen was sealed in a nearly spherical glass tube, about 6 mm in diameter.

The spin-lattice relaxation time T_1 was measured by usual saturation method, the sensitivity of the detector being calibrated by a calibrator of Watkins type[5]. The results obtained for long T_1 are not so reliable, because at very weak oscillator coil voltage, the detector output becomes very noisy. For the calibration of the oscillating field H_1, the line shape and saturation curve were measured for an aqueous solution of paramagnetic salt. Since the line shape is Lorentzian and $T_1=T_2$ in this case, we can calculate the value of H_1 using the formula given by Bloembergen, Purcell and Pound[6], which is found to be 9.4×10^{-2} oersted per unit coil voltage. Here the coil voltage was measured by a valve voltmeter. Although the relative values of the spin-lattice relaxation time are reliable, their absolute values may be in error within ±30%, for they imply many possible errors in the calibration of H_1, in the evaluation of T_2, and others.

§ 3. Experimental Results and Discussions

(*a*) The second moment

For the case in which similar nuclei are interacting with each other by magnetic dipole-dipole interactions and are considered to be rigid, the second moment of the absorption line is given by[7)8)]

$$<\Delta H^2>=\frac{3}{2}I(I+1)\,g^2\beta^2\frac{1}{N}\sum_{j>k}(3\cos^2\theta_{jk}-1)^2r_{jk}^{-3} \qquad (1)$$

where N is the number of nuclei interacting with each other, θ_{jk} is the angle between the external magnetic field and the line joining nuclei j and k, r_{jk} is the distance between nuclei j and k, I is the nuclear spin, and $g\beta I$ is the nuclear magnetic moment. For powder sample, taking the average over the angle θ_{jk} and inserting the numerical values for the case of protons, (1) becomes to be

$$<\Delta H^2>=7.16\times10^{-46}N^{-1}\sum_{j>k}r_{jk}^{-6}\,. \qquad (2)$$

Now, we shall consider the case of hexamethyldisilane molecule. The numerical value of the second moment for isolated rigid CH_3 group with H–H distance of 1.79 Å[9)] is $<\Delta H^2>=21.7$ gauss². The dipolar interactions between three CH_3 groups belonging to each one of silicon atoms are calculated by assuming that three protons lie randomly on a circle determined by three hydrogen atoms belonging to a CH_3 group, since the exact orientation of CH_3 group with respect to the three-fold symmetry axis, or, C_3 axis is not known. The second moment due to the interaction between CH_3 groups belonging to different silicon atoms in a molecule is calculated by assuming that relative orientations are at random, since exact molecular configuration, that is, cis, trans, or other type, is also not known.

When three protons in each CH_3 group reorientate about the C_3 symmetry axis, or, CH_3 groups reorientate about Si–Si axis (C'_3 axis), the reduced second moments are calculated by the formula given by Gutowsky and Pake[8)], or, by the equation (20) given in section (*C*). The calculated values of the second moments in each case are shown in Table I. The contribution of the intermolecular dipolar interactions to the second moment is impossible to be calculated exactly, owing to the lack of knowledge about the crystal structure. However, if we take body-centered cubic structure with the lattice constant of 8.47 Å which corresponds to that in the high temperature phase, and assume that the direction of the molecular axis is distributed randomly over the directions of four diagonals, we obtain about 1.0 gauss² as the second moment due to the intermolecular interactions. We assume tentatively this second moment also in the low temperature phase, because the packing of the crystal might not change violently

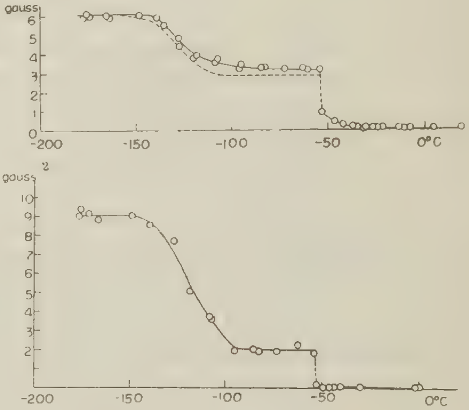

Fig. 3. Experimental line width between maximum and minimum slopes (upper curve) and the second moment for hexamethyldisilane plotted against temperature (lower curve). Dotted line represents the calculated curve.

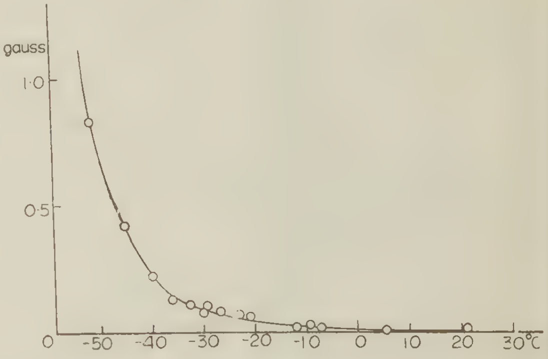

Fig. 4. Experimental line width of hexametyldisilane in high temperature phase measured by the use of homogeneous magnet.

Table I. The calculated second moments and the comparison with the experimental results.

Interaction / State of motion	Interaction between three protons in a methyl group	Interaction between protons belonging to three methyl groups bonded to one silicon atom	Interaction between protons belonging to methyl groups bonded to different silicon atoms	Inter-molecular interaction	Total	Exp.
	gauss^2					
Rigid	21.7	1.04	0.52	1.0	24.3	—
C_3-rotation	5.43	0.90	0.52	1.0	7.9	9.0
C_3'-rotation	0.64	0.23	0.33	0.6	1.8	2.0

by the transition. This value may be scarcely affected by the C_3 axis rotation, but it will be narrowed by the C'_3 axis rotation and we rather arbitrarily take the value 0.6 gauss^2 for the narrowed second moment.

From the experimentally obtained derivative curves, the second moments were computed and are shown in Fig. 3, together with the widths between maximum slopes. Fig. 4 shows the results of line width measurements in the high temperature phase, by the use of more homogeneous magnet. The second moment is constant in the temperature range between −180°C and −140°C, and also between −90°C and −55°C. These constant values are shown in Tab. I and are compared with the theoretical values.

From Tab. I, it is clear that even at the lowest temperature, this molecule cannot be considered to be rigid, since the measured second moment is much less than that calculated by the assumption of rigid lattice. On the contrary, the experimental second moment coincides nearly with the calculated one in the case of CH_3 group reorientating about its C_3 axis. Thus, it seems clear that even at liquid air temperature the methyl group reorientates about its C_3 axis with enough high frequency to narrow the line width due to dipolar interactions between three protons in each CH_3 group.

The gradual change in the line width which takes place around −125°C is due to some additional motion and this motion may be the reorientational motion of methyl groups about C_3' axis. In fact, the second moment in the temperature range between −90°C and the transition point coincides well with the caluculated value under the assumption of C'_3 axis rotation. Whether the structure of this molecule is cis, trans, or some other type is indeterminable by our experiments alone.

Just above the transition temperature*, the line width and also the second moment decrease suddenly to much smaller values, indicating that some additional rapid motion of the molecule or some groups in the molecule starts suddenly at the transition temperature. Now, in this higher temperature phase, X-ray determination of the crystal structure and lattice dimension have been already done, the result of which was given in the introduction. The caluclated second moment due to the intermolecular dipolar interaction alone, in the high temperature phase, yields about 0.55 gauss^2, if we assume that eighteen protons lie at the center of gravity of each molecule. If the line shape is Gaussian, the separation between the points of maximum and minimum slopes is calculated to be 1.4 gauss. Extrapolating the observed values in the high temperature phase to the transition point, 1.1 gauss is obtained for the line width. This suggests that the whole molecule will rotate around its center of gravity rapidly enough to average out the intramolecular interaction leaving only the intermolecular one. Narrowing of the line width above the transition temperature is caused by the self-diffusion of the molecule as a whole which will be discussed later.

(*b*) Spin-lattice relaxation time

Generally speaking, studies of the spin-lattice relaxation time will give more detailed informations about molecular motions. First, we shall give the results of some theoretical considerations about spin-lattice relaxation time, in this molecule.

---

* The temperature at which discontinuous change in the line width occurs is −53°C, which differs about 2°C from the thermal transition temperature. This discrepancy may probably arise from the errors in measuring the temperature of the sample in our measurement.

The spin-lattice relaxation time, T_1, due to molecular motion is expressed as follows:[9]

$$1/T_1=(3/2)\gamma^4\hbar^2 I(I+1)[J_1(\nu_0)+J_2(2\nu_0)] \qquad (3)$$

where γ is the gyromagnetic ratio and $J_1(\nu_0)$ and $J_2(2\nu_0)$ are the sum of the intensities of the Fourier spectra, of frequency ν_0 and $2\nu_0$, of $F_{1,ij}$ and $F_{2,ij}$ respectively, where

$$\left.\begin{aligned} F_{1,ij}&=\sin\theta_{ij}\cos\theta_{ij}\exp(i\phi_{ij})\, r_{ij}^{-3} \\ F_{2,ij}&=\sin^2\theta_{ij}\exp(2i\phi_{ij})\, r_{ij}^{-3} \end{aligned}\right\} \qquad (4)$$

Here $\boldsymbol{r}_{ij}$ is the vector joining the nuclei i and j with magnitude r_{ij}, θ_{ij} is the polar angle of $\boldsymbol{r}_{ij}$ taking the z-axis in the direction of the applied field, ϕ_{ij} is the azimuthal angle of $\boldsymbol{r}_{ij}$ measured from some fixed reference direction, and ν_0 is the Zeeman frequency. For the discussion of the change of the line width, which will begiven in the next section, one more function, $F_{0,ij}$ is needed, where

$$F_{0,ij}=(3\cos^2\theta_{ij}-1)\, r_{ij}^{-3} \qquad (5)$$

To each of these positional functions we can define a correlation function

$$K(\tau)=\langle F(t)\, F^*(t+\tau)\rangle \qquad (6)$$

where $F(t)$ represents any one of three functions, F_0, F_1 and F_2. Then the spectral intensity $J(\nu)$ is given by the sum of the Fourier transforms of $K(\tau)$:

$$J(\nu)=\sum_j \int_{\infty}^{-\infty} K(\tau)\exp(2\pi i\nu\tau)\, d\tau \qquad (7)$$

Next, we shall consider how the correlation function is expressed in the case of hindered rotation of methyl group. As for the narrowing of the line width, Powles and Gutowsky have already discussed the same problem[10]. We assume that the reorientation about C_3 axis among three equivalent orientations takes place stepwisely and the time spent during the rotation from one equivalent orientation to another one can be neglected, compared with the time during which the atomic group stays at an equivalent orientation. We shall define probabilities a_1, a_2 and a_3 for the molecule taking each of three equivalent orientations at a time t. Assuming that the direction of rotation is random, and that the rate per unit time of jumping is $1/\tau_c$, we can write

$$\frac{da_1}{dt}=\frac{1}{\tau_c}\left(-a_1+\frac{a_2}{2}+\frac{a_3}{2}\right) \qquad (8)$$

Two similar equations are obtained by cyclic permutations of the suffices. The solution of these equations, subject to the initial conditions, $a_1(0)=1$, $a_2(0)=0$ and $a_3(0)=0$, is

$$\left.\begin{aligned} a_1(t)&=(1/3)+(2/3)\exp[-(3/2)t/\tau_c] \\ a_2(t)=a_3(t)&=(1/3)-(1/3)\exp[-(3/2)t/\tau_c]. \end{aligned}\right\} \qquad (9)$$

In this case the correlation function is calculated to be

$$\begin{aligned} &\langle F(t)\, F^*(t+\tau)\rangle_{\mathrm{Av}} \\ &\quad=(1/3)[(a_1-a_2)(|F^1|^2+|F^2|^2+|F^3|^2)+a_2|F|^2], \end{aligned} \qquad (10)$$

where $F=F^1+F^2+F^3$ and F^i is the value of the position function F in the i-th orientation. Inserting (9) into (10), we obtain

$$\begin{aligned} &\langle F(t)\, F^*(t+\tau)\rangle_{\mathrm{Av}} \\ &\quad=|\langle F\rangle|^2+\{\langle|F|^2\rangle \\ &\qquad-|\langle F\rangle|^2\}\exp[-(3/2)\tau/\tau_c], \end{aligned} \qquad (11)$$

where $\langle\ \rangle$ means the average of the position function over three equivalent orientations. When $\tau\ll\tau_c$, $\langle F(t)F^*(t+\tau)\rangle$ is equal to $\langle|F|^2\rangle$ itself, while, when $\tau\gg\tau_c$, F itself is first averaged and the square of this averaged value remains.

Now, in the case of methyl group reorientating about its C_3 axis, (11) can be easily calculated as

$$\left.\begin{aligned} &b^6\langle F_0(t)F_0^*(t+\tau)\rangle \\ &\quad=(1/2)(3\nu_z^2-1)^2+(9/4)(1-\nu_z^2)^2\exp(-\tau/\tau_c') \\ &b^6\langle F_1(t)F_1^*(t+\tau)\rangle \\ &\quad=(1/2)\nu_z^2(1-\nu_z^2)+(1/4)(1-\nu_z^4)\exp(-\tau/\tau_c') \\ &b^6\langle F_2(t)F_2^*(t+\tau)\rangle \\ &\quad=(1/2)(1-\nu_z^2)^2 \\ &\qquad+(1/4)(1+6\nu_z^2+\nu_z^4)\exp(-\tau/\tau_c') \end{aligned}\right\} \qquad (12)$$

where ν_z is the cosine of the angle between the C_3 axis and the static magnetic field, b is the distance between protons in methyl group and

$$\tau_c'=(2/3)\,\tau_c\,. \qquad (13)$$

For crystal powder, taking average over the angles

$$\left.\begin{aligned} &b^6\langle F_0(t)\, F_0^*(t+\tau)\rangle_{\text{powder}} \\ &\quad=(2/5)[1+3\exp(-\tau/\tau_c')] \\ &b^6\langle F_1(t)\, F_1^*(t+\tau)\rangle_{\text{powder}} \\ &\quad=(1/15)[1+3\exp(-\tau/\tau_c')] \\ &b^6\langle F_2(t)\, F_z^*(t+\tau)\rangle_{\text{powder}} \\ &\quad=(4/15)[1+3\exp(-\tau/\tau_c')] \end{aligned}\right\} \qquad (14)$$

By (6) and (7), J in the case of crystal powder is calculated to be

$$\left.\begin{aligned} J_1(\nu_0) &= \frac{1}{5}\,\frac{2\tau_c'}{1+\omega_0^2\tau_c'^2}\,b^{-6} \\ J_2(2\nu_0) &= \frac{4}{5}\,\frac{2\tau_c'}{1+4\omega_0^2\tau_c'^2}\,b^{-6} \end{aligned}\right\} \tag{15}$$

where ω_0 is 2π times the Zeeman frequency.

Next, we shall consider the case when the C_3' axis rotation superposes on the C_3 axis rotation. In our case, since at the temperature where the C_3' axis rotation contributes to the narrowing of the line width or spin-lattice relaxation time, the C_3 axis rotation is already very rapid, the effects of the C_3 axis rotation and C_3' axis rotation can be treated separately. Then, (11) can be well applied also to the case of C_3' axis rotation, provided that F is replaced by $<F>_{c_3}$, where $<\ >_{c_3}$ means the average of F over C_3 axis rotation. If we write $<\ >_{c_3}'$ for the average over C_3' axis rotation, the correlation function in the case of the C_3' axis rotation can be expressed to be

$$\begin{aligned} &<F(t)F^*(t+\tau)>_{c_3,\,c_3'} \\ &\quad = |<<F>_{c_3}>_{c_3'}|^2+\{<|<F>_{c_3}|^2>_{c_3'} \\ &\qquad -|<<F>_{c_3}>_{c_3'}|^2\}\exp\left[-(3/2)\tau/\rho_c\right] \end{aligned} \tag{16}$$

where ρ_c is the correlation time for the C_3' axis rotation. (16) is a good approximation when $\rho_c \gg \tau_c$, and $\omega_0\tau_c \ll 1$. The powder averages of the correlation functions for three protons in one $\mathrm{CH_3}$ group are given by

$$\left.\begin{aligned} &b^6<F_0(t)F_0^*(t+\tau)> \\ &\quad =(1/10)[(1-3\cos^2\alpha)^2 \\ &\qquad +3(1+3\cos^2\alpha)(1-\cos^2\alpha)\exp(-\tau/\rho_c')] \\ &b^6<F_1(t)F_1^*(t+\tau)> \\ &\quad =(1/60)[(1-3\cos^2\alpha)^2 \\ &\qquad +3(1+3\cos^2\alpha)(1-\cos^2\alpha)\exp(-\tau/\rho_c')] \\ &b^6<F_2(t)F_2^*(t+\tau)> \\ &\quad =(1/15)[(1-3\cos^2\alpha)^2 \\ &\qquad +3(1+3\cos^2\alpha)(1-\cos^2\alpha)\exp(-\tau/\rho_c')] \end{aligned}\right\} \tag{17}$$

where α is the angle between the C_3- and C_3'-axis, and $\rho_c'=2\rho_c/3$. The spectral intensities can be calculated easily by (7) and (17).

Equations (11) and (16) are applicable also to more general cases. In the case of arbitrary reorientational motion of some atomic group, $<\ >$ in (11) should be taken as the average value of F over all equivalent orientations, and in (16), $<\ >_{c_3}$ and $<\ >_{c_3'}$ should correspond to the average value over equivalent orientations corresponding to the very fast rotation and that corresponding to the slower motion, respectively.

The spin-lattice relaxation time T_1 is given by

$$\frac{1}{T_1}=C\left[\frac{\tau_c'\ (\text{or}\ \rho_c')}{1+\omega_0^2\tau_c'^2(\text{or}\ \rho_c'^2)}+\frac{4\tau_c'\ (\text{or}\ \rho_c')}{1+4\omega_0^2\tau_c'^2\ (\text{or}\ \rho_c'^2)}\right] \tag{18}$$

where C is a constant which depends upon the configuration of the molecule and the mode of its motion, and is calculated easily by the expressions for J_1 and J_2. The numerical values of C calculated with the molecular parameters of hexamethyldisilane are shown in Tab. II. The intermolecular part is estimated by the same way as discussed in (*a*). It can be seen from Tab. I that the second moment calculated with the same parameters is about 14% smaller than the measured value. This discrepancy may arise from errors in the molecular parameters, such as H–H distance in each methyl group, or difference in the packing in the low temperature phase as compared with that in the high temperature phase, by which the intermolecular interaction will be changed. We tentatively correct the values of C by the amount just enough to compensate the discrepancy in the second moment. The corrected values are also shown in Tab. II.

Now, since in our case the molecular motion is the hindered reorientational one, we may

Table II. The calculated values of C.

Interaction / State of motion	Interaction between three protons in a methyl proup	Interaction between protons belonging to three methyl groups bonded to one silicon atom	Interaction between protons belonging to methyl groups bonded to different silicon atoms	Inter-molecular interaction	Total	Corrected
C_3-rotation	7.6×10^9	0.1×10^9	small	small	7.7×10^9	8.8×10^9
C_3'-rotation	2.2×10^9	0.4×10^9	0.1×10^9	0.2×10^9	2.9×10^9	3.3×10^9

assume that τ_c' (or ρ_c') varies with temperature as follows:

$$\tau_c' \text{ (or } \rho_c') = \tau_0' \text{ (or } \rho_0') \exp (E/RT). \quad (19)$$

The quantity E corresponds to the activation energy or the height of potential barrier hindering rotation. The values of E and τ_0' (or ρ_0') can be obtained by analysing the experimental results on T_1, as well as by analysing the narrowing of the line width which will be discussed in next section, and thus the confirmation of the mode of molecular motion can be done by comparing the values of E and τ_0' (or ρ_0') obtained from these two independent methods.

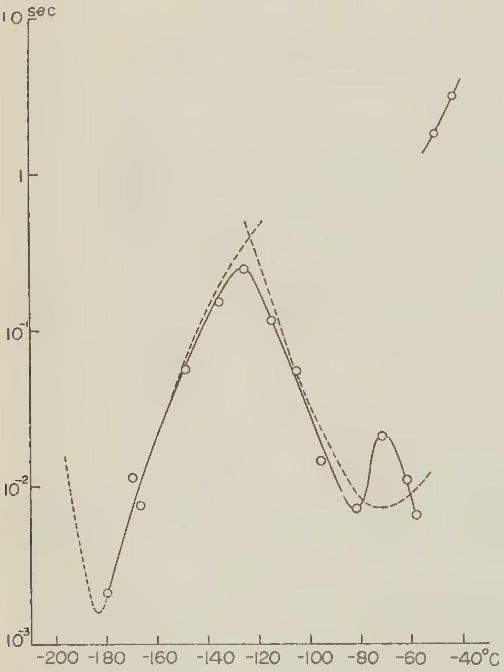

Fig. 5. Temperature dependence of the observed spin-lattice relaxation time, and the calculated curves with the parameters given in the text.

The experimental results of the measurement of T_1 is shown in Fig. 5. From the temperature dependence of T_1 in the temperature range between −180°C and −120°C and using the value of C in Tab. II, the activation energy and the value of τ_0' for the hindered rotation of each methyl group about its C_3 axis are determined to be 2.6 kcal/mole and 1.0×10^{-14} sec., respectively. Since the temperature range suitable for the determination of these quantities is rather narrow, error in E may be ±0.2 kcal/mole and correspondingly τ_0' may be in error within a factor of 5. Activation energy for this kind of motion has been estimated in various organic crystals by proton magnetic resonance method[8)10)11)] and their reported values are in agreement with each other and also with ours. At −180°C the correlation time τ_c is 1.1×10^{-8} sec. which is consistent with the narrowed line width discussed in (a). The calculated value of T_1 by the use of these values of E and τ_0' is shown in Fig. 5 by the dotted line, by which one might expect that there will be a minimum in T_1 around −185°C. It is hoped to carry out experiments below −180°C to ascertain the existence of this minimum and also to determine at what temperature the line width will broaden up to its full width corresponding to the rigid molecule.

According to the discussion in (a), the decrease of T_1 above −125°C will be caused by the hindered rotation of methyl groups about the C_3' axis, corresponding to the narrowing of the line width around −120°C. The general trend of the decrease of T_1 from −130°C to −90°C can be well accounted for by taking $E=5.7$ kcal/mole and $\rho_0'=1.4 \times 10^{-14}$ sec. with $C=3.3 \times 10^9$ (Tab. II). The calculated value of T_1 with these constants is shown in Fig. 5. However, there exists anomalous change of T_1 around −70°C which cannot be interpreted by any simple consideration of such reorientational motions as considered above. The actual behaviour of the molecular motion might be much more complicated than assumed here, especially in the vicinity of the transition temperature, by which the anomalous change of T_1 might be produced. But no further discussion can be made at the present stage. The inaccuracy in E and ρ_0' is comparatively large in the case of the C_3' axis rotation, about ±0.5 kcal/mole in E and a factor of 10 or so in ρ_0'. At −133°C, where the line width begins to narrow, ρ_c' is calculated to be 1×10^{-5} sec., which is just the same order as the inverse of the line width expressed in frequency scale, indicating our interpretation is the reasonable one.

As already described in (a), at the thermal transition point the line width and the second moment decrease suddenly, and above this temperature they continue to decrease until the width becomes narrower than 0.01 gauss. On the other hand, though we measured only two points, T_1 increases discontinuously at the transition point and it seems undoubtedly to increase with raising temperature. We found already from the analysis of the second moment that the vigorous reorientational motion of the molecular axis, which is enough to make the intramolecular interactions negligible, occurs abruptly at the transition point and then the width due to the intermolecular interaction decreases gradually with raising temperature by the self-diffusion of the molecules through the lattice. Just above the transition point, the rate of self-diffusion should not be so rapid as to narrow the intermolecular interaction appreciably. Therefore, the fact that T_1 increases with raising temperature above the transition point may suggest that the contribution to the relaxation of the reorientational motion of the molecular axis is larger than that of the self-diffusion. Some further discussion will be given in (*d*).

(*c*) The line width transition

The narrowing of the absorption line width due to the reorientational motion about the C_3 axis can be treated with just the same procedure as given in (*b*). The correlation function of $F_0=r^{-3}(3\cos^2\theta-1)$ is already given there. For a value of τ_c', the line width is given by[9]

$$(\Delta\omega)^2=2\log 2[(1/4)+(3/2\pi)\,\mathrm{arctg}\{(\pi\alpha/4\log 2)\,\tau_c'\Delta\omega\}]\langle\Delta\omega_0^2\rangle \tag{20}$$

where $\Delta\omega$ is the half of the half-value width, $\langle\Delta\omega_0^2\rangle$ is the second moment in the case of rigid configuration and α is a correction factor depending upon the line shape which is equal to 1 in the case of Gaussian shape. Actually, however, the line width is already narrowed at the lowest temperature of our measurements, and no discussion can be made concerning the C_3 axis rotation.

Narrowing of the line width around -120°C is caused by the reorientational motion about the C_3' axis, as already discussed in (*a*) and (*b*). In this case, the intra-methyl and also inter-methyl interactions are narrowed at the same time, as shown in Tab. I. The narrowing of the width can be calclulated in just the similar way as discussed in (*b*) for T_1, the result of calculation being given by

$$(\Delta\omega)^2=2\log 2\,[\langle\Delta\omega'^2_0\rangle+\{\langle\Delta\omega_0^2\rangle-\langle\Delta\omega'^2_0\rangle\}(2/\pi)\,\mathrm{arctg}\{(\pi\alpha/4\log 2)\,\rho_c'\Delta\omega\}] \tag{21}$$

where $\langle\Delta\omega^2\rangle$ and $\langle\Delta\omega_0'^2\rangle$ are the second moments before and after narrowing, respectively, and $\Delta\omega$ is the half of the half-value width corresponding to the correlation time ρ_c'. Expressing in magnetic field scale and using the experimental values 9.0 gauss^2 and 2.0 gauss^2 for the second moments before and after narrowing, the line width between maximum slopes is calculated with the values of E and ρ_0' obtained in (*b*), assuming the line shape is Gaussian. The best fit with the experimental results is obtained with $\alpha=2$, the calculted curve being shown in Fig. 3. Actually, the assumption of Gaussian shape is not exactly valid in the case of strong narrowing; after narrowing, the observed width between maximum slopes is 3.2 gauss which is not exactly equal to $2\sqrt{\langle\Delta H^2\rangle}=$ 2.8 gauss calculated from the observed second moment 2.0 gauss^2 with assumption of Gaussian shape, though, before narrowing, the line width 6.0 gauss is exactly equal to that calculated from the observed second moment 9.0 gauss^2. But the general discussion about the narrowing of the line width is not altered by this minute variation of the line shape.

The further decrease of the line width in the high temperature phase is considered to be caused by the self-diffusion of the molecule as a whole in a similar manner to that suggested by Andrew for cyclohexane and some other organic molecules[12]. At the transition point, the crystal structure undergoes the change from some structure of lower symmetry to body-centered cubic with large entropy change, 10.5 cal/deg. mole, and at the same time many vacancies might be produced in the crystalline lattice. Accordingly, in spite of comparatively large size of the molecule, the molecules change their equilibrium positions accompanying the still more rapid reorientation of the molecular axis, fast enough to affect the line width. Assuming that the self-diffusion has a correlation time τ_c', the equation (20) will be applicable also for the narrowing of the line width in this case. Using the calculated value of $\langle\Delta H^2\rangle$, which is 0.55 gauss^2, and assuming Gaussian shape, though it is not a good approximation, the activation energy and τ_0' for the self-diffusion are found to be 10 kcal/mole and 2.6×10^{-15} sec, respectively. Of course these values give only orders of magnitude. From the fact that the lattice energy of this subatance (sum of heat of vaporization and heat of fusion) is about 9.6 kcal/mole, this activation energy is considered to be reasonable in order*.

In addition, the line width at about 4°C (lower than the melting point, 14.4°C) where this crystal is still in a solid state, is as narrow as the one in liquid state (6 to 8 milligauss between maximum slopes which arises almost from the magnetic field inhomogeneity). Therefore, even in solid state these molecules behave effectively in the similar manner as Brownian motions in liquid state.

(*d*) Relaxation time at the high temperature phase and self-diffusion.

Assuming that the intramolecular interaction is completely averaged out, the spin-lattice relaxation time by self-diffusion is calculated by the formula given by Torrey[13] to be about 20 sec. at −46°C, using the correlation time obtained from the analysis of line width narrowing. Actually, however, just above the transition temperature, the contribution to the spin-lattice relaxation arises from two origins, the diffusion of the molecule as a whole, and the reorientational motion of the molecular axis. The observed T_1 at −46°C is about 2.5 sec., which is considerably smaller than the value calculated above by the self-diffusion alone, indicating that the reorientational motion of the molecular axis is probably the main origin of the spin-lattice relaxation. If the correlation time of this reorientational motion is of the order of 1×10^{-10} sec. at this temperature, the calculated value of T_1 can be brought to coincide with the experimental one. As the temperature increases, it is expected that T_1 will reach a maximum, then decrease to a minimum value and finally increase again, by the competation of the two contributions to T_1 arising from the motion of the molecular axis and of the self-diffusion. Unfortunately, however, it was impossible to measure the saturation curves above −40°C by our apparatus, because of long T_1 and narrow line width.

Recently, Nachtrieb and his collaborators[14] have proposed an experimental relation for self-diffusion in metals and also in molecular crystals which is

$$\Delta H_{\text{act}} = CL \qquad (22)$$

where ΔH_{act} is the activation enthalpy for self-diffusion, L is the latent heat of fusion and C is a constant having a value of 16.5 for body-centered cubic and face-centered cubic lattices. Inserting the observed value of latent heat of fusion 720 cal/mole into equation (22), ΔH_{act} is estimated to be 11.9 kcal/mole. This is consistent with the value obtained in the preceding section, 10 kcal/mole.

We may notice that the experiment of self-diffusion by the radioactive tracer method is planned to check the conclusion of our magnetic resonance experiments and to obtain more reliable activation energy.

In conclusion, we would like to thank Miss. H. Ibamoto for her collaboration in some part of the experimental work.

References

1) J. Timmermans: J. Chim. Phys. **35** (1938) 331.
2) H. Suga and S. Seki: Ann. Meeting of Chem. Soc. Japan (1955) (to be published).
3) Y. Chatani, H. Suga and I. Taguchi: Ann. Meeting of Chem. Soc. Japan (1955), (to be published).
Y. Chatani, H. Suga, I. Taguchi and S. Naya: Ann. Meeting of Chem. Soc. Japan (1955), (to be published).
4) M. L. Huggins: J. Am. Chem. Soc. **75** (1953) 4123.
5) G. D. Watkins: Thesis (Harvard, 1952) (unpublished).
6) N. Bloembergen, E. M. Purcell and R. V. Pound: Phys. Rev. **73** (1948) 679.
7) J. H. Van Vleck: Phys. Rev. **74** (1948) 1168.
8) H. S. Gutowsky and G. E. Pake: J. Chem. Phys. **18** (1950) 162.
9) R. Kubo and K. Tomita: J. Phys. Soc. Japan **9** (1954) 888.
10) J. G. Powles and H. S. Gutowsky: J. Chem. Phys. **23** (1955) 1692.
11) J. G. Powles and H. S. Gutowsky: J. Chem. Phys. **21** (1953) 1695.

---

* In X-ray investigation, a slight inflection exists in the thermal expansion coefficient vs temperature curve at −30°C (ref. 2). In our proton magnetic resonance experiment, however, no such anomaly was observed at this temperature. We might be able to detect some change if we could measure spin-lattice relaxation time.

12) E. R. Andrew: *Report of the Conference on Defect in Crystalline Solids* (1955), Proc. Roy. Soc. **A216** (1953) 398.

13) H. C. Torrey: Phys. Rev. **92** (1953) 962, Phys. Rev. **96** (1954) 690.

14) N. H. Nachtrieb and G. S. Hamdler: Acta Metallurgica **2** (1954) 797.

JOURNAL OF THE PHYSICAL SOCIETY OF JAPAN Vol. 12, No. 5, MAY, 1957

Magnetic Properties of Perovskites Containing Strontium

I. Strontium-Rich Ferrites and Cobaltites

By Hiroshi WATANABE

Research Institute for Iron, Steel and Other Metals,
Tohoku University

(Received January 28, 1957)

Magnetic susceptibilities and electrical conductivities of (La, Sr)(Fe/Co)O_x samples sintered in vacuo or in oxygen stream are measured here. Samples containing tetravalent magnetic ions in general have Curie contants smaller than those containing only trivalent ions. This fact and the high conductivity in the former specimens strongly support the combined effect of the double exchange and the usual exchange mechanism in these compounds. The parallel alignment of spins of magnetic ions due to double exchange is partly or completely hindered by the presence of the strongly negative trivalent-trivalent interionic interactions.

§ 1. Introduction

Since the ferromagnetic compounds with perovskite structure were discovered by Jonker and van Santen1), a considerable number of researches have been made on related compounds2–7), both on the experimental side and the theoretical side. The ferromagnetism is attributed to the positive exchange interaction between magnetic ions, and the magnetic properties of these compounds are generally affected strongly by the temperature and the atmosphere under which they have been prepared, since these factors influence the amount of oxygen in the crystal lattice, hence the valency of magnetic ions.

In their studies, Jonker and van Santen confined their samples to those "correctly prepared", as they call. For instance, $LaMnO_3$, when prepared correctly, should contain no Mn^{4+} ions, whereas $SrMnO_3$ shold have no Mn^{3+} ions. It is generally easy to obtain correct samples when the compound are rich in trivalent rare earth ions, whereas it is rather difficult to obtain correct samples from compounds with a large amount of divalent alkaline earth ions. This might be one of the reasons why Jonker and van Santen used samples with limited compositions of alkaline earth metals.

In the present study, we have selected the specimen without such a restriction, by studying the effect of sintering-atmosphere on the properties of a sample which has given cation composition. The effect becomes more remarkable according to an increase of the alkaline earth ions8); pure $SrFeO_x$ contains practically no Fe^{4+} ion, when sintered in vacuo, whereas it does contain 58% Fe^{4+}, if it is sintered and cooled in oxygen atmosphere. As a result there is a striking difference between these samples in their magnetic properties.

The second purpose of this study is to investigate the high temperature susceptibility of these compounds. Zener has proposed a mechanism of parallel alignment of spins of magnetic ions, called double exchange, and explained the ferromagnetism found in manganites. Anderson and Hasegawa9) pointed out that according to such a mechanism a behavior of the susceptibility above the Curie temperature would be different from that when merely usual exchange interactions are present. In a recent paper Jonker[10] states that no such effect can be found for manganites, and he seems to be inclined to put less weight on Zener's mechanism. We have examined this point for other compounds.

As a perliminary step for these purposes we have chosen (La, Sr) ferrites and (La, Sr) cobaltites as our samples. As was expected, the electrical conductivity is much increased with the coexistence of trivalent and tetravalent magnetic ions, and also the susceptibilities above the Curie temperature are changed from those where merely trivalent ions are present. This is not contradictory to the mechanism of double exchange, although complete alignment of ionic spins would not be realized in this case.

§ 2. Experimental Procedure and the Nature of the Samples

1. *Preparation of the samples*

All the samples were prepared by the usual ceramic method; the starting materials were pure La_2O_3, $SrCoO_3$, Fe_2O_3 prepared from FeC_2O_4, and Co_3O_4 prepared from cobalt sulphate. The starting materials were mixed in the desired proportions and milled in an agate mortar, prefired for two hours in air at about 1200°C, and then quenched. Then they were milled again and heated in air at about 1250°C for several hours. As for $SrFeO_x$, final heat treatments were carried out in various ways, in order to observe the change in character of this substance with x. For other compounds, the products were heat-treated in vacuo or in oxygen for several hours at 1100–1200°C. $SrCoO_x$, sintered in vacuo, showed a melting point lower than that of other compounds, and the sintering temperature was accordingly lowered (~1150°C). It showed a strong tendency to absorb oxygen in air even at room temperature, especially in the form of fine powder.

2. *Chemical analysis*

The chemical analysis was carried out by means of the procedure sketched in Yakel's paper[5] in the chemical analysis department of our institute. The result is listed in Tables I and II.

3. *X-ray powder patterns*

Crystal symmetry was studied for all the samples by means of the X-ray powder pat-

Table I. The relation between the amount of tetravalent ions and the crystal symmetry of $SrFeO_x$ samples.

No.	Heat-treated in	Chemical analysis		Crystal Symmetry
		% Fe^{4+} in tot. Fe	x	
1	Vacuo, 1300°C	0.49	2.50	Monoclinic
2	Vacuo, 1000°C	11.6	2.56	1+5
3	Air, 900°C	30.0	2.65	1+5
4	Air stream, 1150°C	45.3	2.73	1+5
5	Oxygen stream, 600°C	58.3	2.79	Neary cubic (Slightly tetragonal)

Table II. Crystal symmetry and the results of chemical analysis of (La, Sr)(Fe/Co)O_x samples.

Substance	Crystal symmetry		% Fe^{4+} or % Co^{4+}	
	Heat-treated in		Heat-treated in	
	Vacuo	Oxygen	Vacuo	Oxygen
$SrFeO_x$	Monoclinic	Neary cubic	0.5	58.3
$La_{0.5}Sr_{0.5}FeO_x$	Cubic	Cubic	0	47.6
$SrCoO_x$	Undetermined	Cubic	6.3	59.3
$La_{0.5}Sr_{0.5}CoO_x$	Undetermined	Cubic	11.3	61.0

tern technique, using a Fe anticathode tube and a 9 cm diameter camera. The result is listed in Tables I and II, together with that of the chemical analysis. It can be seen from Table I, that $SrFeO_x$ is monoclinic when x is small, but is almost cubic at the maximum value of x attained in our preparation. In the intermediate range of x values, the compounds were mixtures of both of the materials. The lattice parameters of the monoclinic and the nearly cubic phase, represented with respect to a single perovskite cell, were found to be:

monoclinic: $a \sim b = 3.95\text{Å}$, $c = 3.87\text{Å}$, $\gamma = 91°32'$;
nearly cubic (tetragonal): $a = 3.87\text{Å}$, $c = 3.85\text{Å}$.

The samples of $La_{0.5}Sr_{0.5}FeO_x$ are cubic, the lattice constants being

$La_{0.5}Sr_{0.5}FeO_x$ heat-treated in vacuo: $a = 3.90\text{Å}$;
$La_{0.5}Sr_{0.5}FeO_x$ heat-treated in oxygen stream: $a = 3.88\text{Å}$.

The powder patterns of these samples are shown in Photo. 1.

As for cobaltites, the difference in crystal structure was remarkable between samples heat-treated in vacuo and those heat-treated in oxygen stream. The latter samples are cubic, while we could not determine the crystal symmetry of the former. The system $SrCoO_x$ is more complicated than $SrFeO_x$, and

$SrFeO_x$, heat-treated in vacuo.

$SrFeO_x$, heat-treated in oxygen stream.

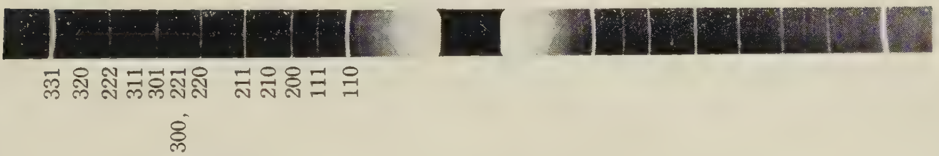

$La_{0.5}Sr_{0.5}FeO_x$, heat-treated in vacuo.

$La_{0.5}Sr_{0.5}FeO_x$, heat-treated in oxygen stream.

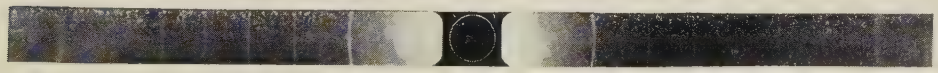

Photo. 1. X-ray powder patterns of (La, Sr) ferrites. Anticathode: Fe.

$SrCoO_x$, heat-treated in vacuo.

$SrCoO_x$, heat-treated in oxygen stream.

$La_{0.5}Sr_{0.5}CoO_x$, heat-treated in vacuo.

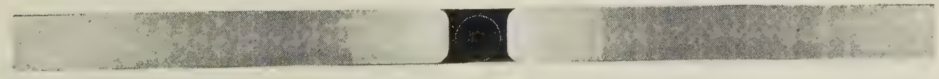

$La_{0.5}Sr_{0.5}CoO_x$, heat-treated in oxygen stream.

Photo. 2. X-ray powder patterns of (La, Sr) cobaltites. Anticathode: Fe.

the phase diagram has not yet been studied in detail at present. The powder patterns in this case is shown in Photo. 2. The lattice constants of the cubic samples are:

$SrCoO_x$ heat-treated in oxygen stream: $a=3.85$Å;

$La_{0.5}Sr_{0.5}CoO_x$ heat-treated in oxygen stream: $a=3.83$Å.

4. *Magnetic measurements*

A. High temperatures. Magnetic measurements above room temperature were carried out with a pendulum magnetometer and a de Bois type electromagnet. The sample was heated by a small platinum furnace and the temperature was read with a Pt-PtRh thermocouple. The sample container for samples treated in vacuo was a small hollow spherical silica globe with a small cock, attached to one end of the pendulum beam. It was detachable from the beam and could be evacuated after the sample was put in.

This container, however, could not be used for samples not treated in vacuo, since the oxygen in the crystal lattice of the sample was apt to escape from it during heating. To protect samples from oxygen emission, we had to use another type of container, which was sealed off leaving a dead space as small as possible. Then, the results of the measurements became almost reversible on heating from room temperature to 900°C and subsequent cooling, except for $SrCoO_x$, in which case heating above 600°C gave irreversible results.

B. Low temperatures. The low temperature magnetizations were measured with a magnetic balance and a cyclotron type electromagnet installed in the low temperature laboratory of our institute. The magnetic field used was about 15000 Oe. The temperature was read with a Cu-constantan thermocouple.

5. *Conductivity measurements*

Samples for the measurements of electrical conductivity were made from the sintered products stated in *1*. They were pressed in the form of rectangular bars of $5\,mm^2 \times 3\,cm$. Potential terminals were thin platinum wires inserted in the pressed bricket through pressing. These brickets were heat-treated under the same condition as when they had been prepared. After the heat-treatment, the attachment of the terminals to the specimen became very tight. It was only the specimen $SrCoO_x$ treated in vacuo that caused some difficulty in making such brickets. It was apt to disintegrate in the course of heat-treatment. So we used a melted mass with electrodes attached to it in a similar manner.

Measurements below room temperature were carried out in vacuo, whereas, those above room temperature were done in vacuo or in oxygen stream, according as the sample had been treated in vacuo or in oxygen. All of the results were reversible in heating and cooling in the temperature range of measurement.

§ 3. Experimental Results

1. *Magnetic properties*

Fig. 1 shows the effect of heat treatment on the susceptibilities of $SrFeO_x$. As can be seen from the figure, this substance, when it is poor in oxygen (specimen 1 of Table I) has an antiferromagnetic character with the Néel point near 400°C. As given in Table I, it contains practically no Fe^{4+} ion, *viz.*, its chemical formula is $SrFeO_{2.5}$, so the antiferromagnetism may be attributed to $Fe^{3+}-Fe^{3+}$ interaction in the substance. On the contrary, when it is rich in oxygen (specimen 5 of Table I), it has an approximate composition of $SrFeO_{2.8}$, and does not have any Néel point, while its susceptibilities are much greater. In

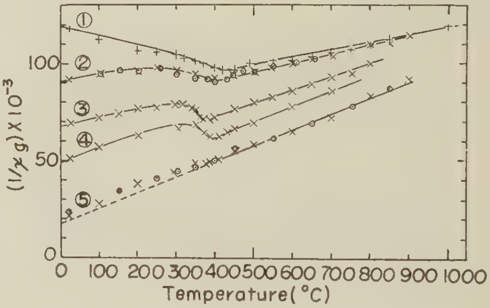

Fig. 1. Reciprocal susceptibility per gram $(1/\chi_g)$ *vs* temperature curves of $SrFeO_x$ samples.

① $x=2.50$.
② $x=2.56$.
③ $x=2.65$.
④ $x=2.73$.
⑤ $x=2.79$.

× and +, Experimental points measured during heating. ⊙, Those measured during cooling.

accordance with the phase relation given in Table I, the susceptibilities of the substances of intermediate values of x are what is to be expected for mixtures of those of $x=2.5$ and 2.8. In an earlier paper10), the specimens were quenched or slowly cooled in air, and these correspond to the intermediate mixtures. There the measurements were made with an open sample container. We have, however, ascertained that the results of the measurements were completely irrespective of the rate of cooling provided that the measurements were carried out with a sealed sample container as described in *4*. of § 2.

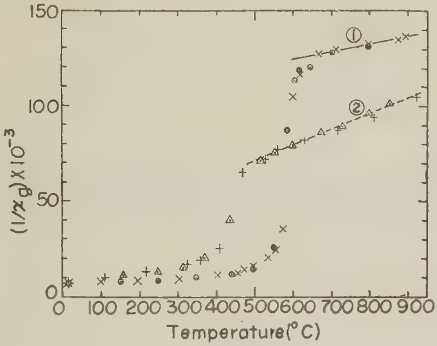

Fig. 2. $(1/\chi_g)$ *vs* temperature curves of $La_{0.5}Sr_{0.5}FeO_x$ samples, heat-treated in
① vacuo.
② oxygen stream.
× and +, Experimental points measured during heating. ⊙ and △ Those measured during cooling.

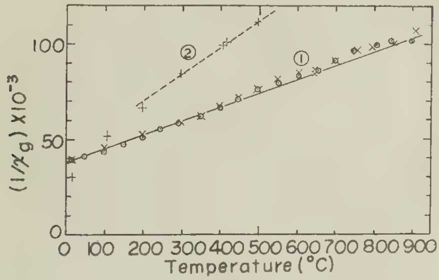

Fig. 3. $(1/\chi_g)$ *vs* temperature curves of $SrCoO_x$ samples, heat-treated in
① vacuo.
② oxygen stream

As for $La_{0.5}Sr_{0.5}FeO_x$, both the samples treated in vacuo and in oxygen is weakly ferromagnetic (Fig. 2). The origin of the ferromagnetism is not clear at present, but it is evident that it is the same as that found in $LaFeO_3$10),11). If we assume this ferromagnetism to be something like the parasitic ferromagnetism of α-Fe_2O_3, its Curie temperature might be identified with the Néel temperature. The behavior of the susceptibilities above this temperature for the substance treated in vacuo suggests that it is strongly antiferromagnetic, since its paramagnetic Curie temperature is as low as −2100°K. When the specimen is treated in oxygen, the Néel temperature becomes lower, and the high temperature susceptibilities become greater.

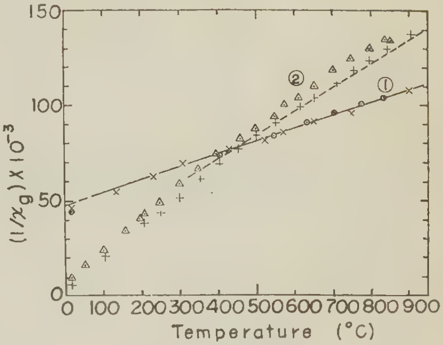

Fig. 4. $(1/\chi_g)$ *vs* temperature curves of $La_{0.5}Sr_{0.5}CoO_x$ samples, heat-treated in
① vacuo.
② oxygen stream.

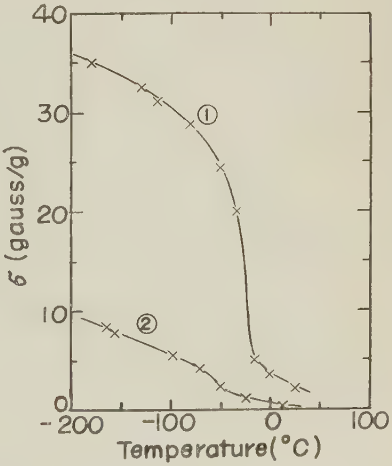

Fig. 5. Magnetization per gram (σ) at H=15000Oe *vs* temperature curves of
① $La_{0.5}Sr_{0.5}CoO_x$.
② $SrCoO_x$.
samples, heat-treated in oxygen stream.

In the case of cobaltites, samples treated in vacuo are probably antiferromagnetic, since they have negative paramagnetic Curie temperatures. (Figs. 3 and 4) On the contrary,

Table III. Magnetic properties of (La, Sr)(Fe/Co)O_x samples

Substance	*Bohr magneton number/magnetic ion				Paramagnetic Curie temperature		Ferro- or antiferro-magnetic Curie temperature	
	Heat-treated in vacuo		Heat-treated in oxygen		Heat-treated in vacuo	Heat-treated in oxygen	Heat-treated in vacuo	Heat-treated in oxygen
	Exp.	Spin-only	Exp.	Spin-only				
$SrFeO_x$	5.95	5.92	4.38	5.32	−1590	45	693	
$La_{0.5}Sr_{0.5}FeO_x$	6.45	5.92	4.59	5.41	−2120	−75	873	723
$SrCoO_x$	4.53	4.96	3.32	5.50	−238	−28		223
$La_{0.5}Sr_{0.5}CoO_x$	5.14	5.01	3.65	5.52	−445	−113		253

* Bohr magneton numbers of the samples treated in oxygen stream are calculated from those slopes of the $(1/\chi_g)$ *vs* temperature curves which are indicated by the broken lines shown in the figures.

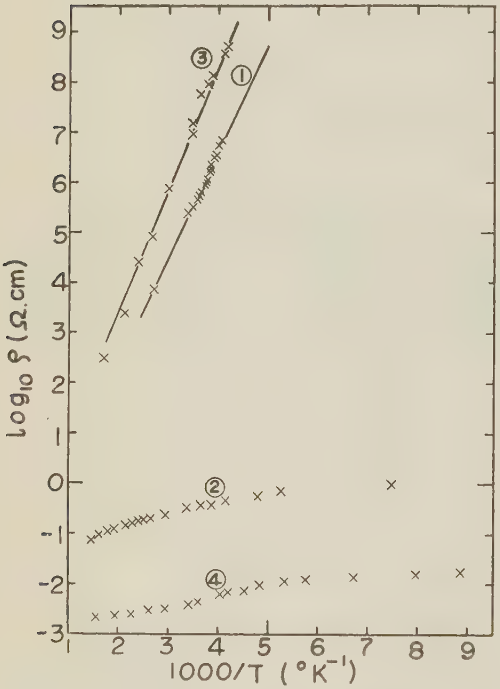

Fig. 6. Logarithm of electrical resistivity ρ *vs* inverse temperature curves of
① $SrFeO_x$, heat-treated in vacuo.
② $SrFeO_x$, heat-treated in oxygen stream.
③ $SrCoO_x$, heat-treated in vacuo.
④ $SrCoO_x$, heat-treated in oxygen stream.

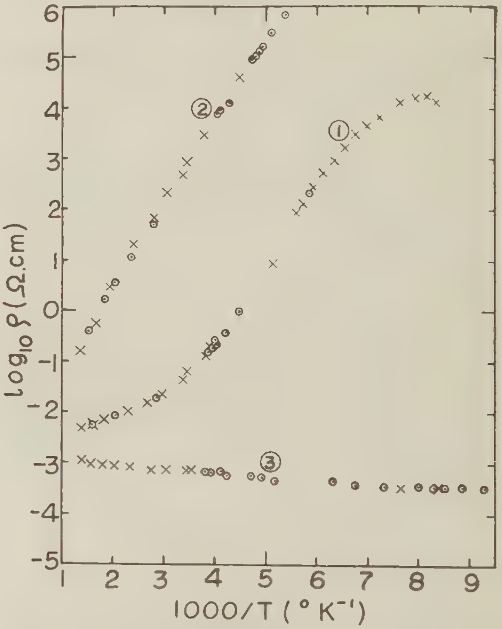

Fig. 7. Logarithm of electrical resistivity ρ *vs* inverse temperature curves of
① $La_{0.5}Sr_{0.5}FeO_x$, heat-treated in oxygen stream.
② $La_{0.5}Sr_{0.5}CoO_x$, heat-treated in vacuo.
③ $La_{0.5}Sr_{0.5}CoO_x$, heat-treated in oxygen stream.

those treated in oxygen have spontaneous magnetization below room temperature. (Fig. 5) The reciprocal susceptibility *vs* temperature curves are straight lines for samples treated in vacuo, whereas they are slightly curved and have a greater overall inclination against temperature axis for samples treated in oxygen. These data are summarized in Table III.

2. *Electrical conductivity*

There is a great difference in the magnitude of electrical conductivity between various substances (Figs. 6 and 7). $SrFeO_x$ treated in vacuo has a high activation energy and a high electrical resistivity, whereas that treated in oxygen has a low activation energy and a low electrical resistivity. Also, $La_{0.5}Sr_{0.5}FeO_x$ treated in vacuo had extremely high resisti-

Table IV. Electrical resistivity of (La, Sr)(Fe/Co)O_x samples.

Substance	20°C (Ω cm) Heat-treated in vacuo	20°C (Ω cm) Heat-treated in oxygen	Max. Act. Energy (eV) Heat-treated in vacuo	Max. Act. Energy (eV) Heat-treated in oxygen
$SrFeO_x$	2.3×10^5	3.3×10^{-1}	0.183	0.021
$La_{0.5}Sr_{0.5}FeO_x$	Very high	4.9×10^{-2}	Very high	0.143
$SrCoO_x$	8.9×10^6	3.9×10^{-4}	0.211	0.021
$La_{0.5}Sr_{0.5}CoO_x$	4.9×10^2	6.9×10^{-4}	0.138	Metallic

vity, and accurate measurement was impossible in our experiment, whereas that treated in oxygen could easily be measured, though it had fairly high resistivity at low temperatures.

As for $SrCoO_x$ the difference between samples treated in vacuo and in oxygen is even greater than in $SrFeO_x$. This might partly be due to the differences in crystal structure. Also the samples containing La behave just in the same way as ferrites, but here the temperature coefficient of resistivity is positive in accord with Jonker's result. These data are summarized in Table IV.

§ 4. Discussion and Conclusion

The ferromagnetism observed in the system of manganites has been ascribed by Zener to the double exchange between Mn^{3+} and Mn^{4+} ions. This type of exchange would be expected not only between manganese ions, but also between other transition metal ions. Jonker has found this for cobaltites, although the values of saturation magnetization are far below those predicted from the total contribution of spins of Co^{3+} and Co^{4+} ions. As for ferrites, ferromagnetism which can be considered to be caused by the interplay of Fe^{3+} and Fe^{4+} has not been found.

Such a situation would be considered to be as follows. In the case of manganites, not only the interaction $Mn^{3+}-Mn^{4+}$ is positive, but also the interaction $Mn^{3+}-Mn^{3+}$ is weakly positive in the cubic phase[10]. In the case of cobaltites, however, the interaction $Co^{3+}-Co^{3+}$ is negative, and may partly counteract the double exchange interaction $Co^{3+}-Co^{4+}$. With this idea, Kishi[12] has calculated the magnetism of manganites and cobaltites, taking into account the formation of triangular spin arrangement. His calculation, basing on the molecular field approximation, should be criticized, since it does not treat positive interaction of double exchange correctly. The low saturation values of cobaltites deduced from his theory, however, might be essentially correct. Since the negative interaction $Fe^{3+}-Fe^{3+}$ is very strong in ferrites, it is natural that the ferromagnetism due to double exchange is completely hidden.

From our data on electrical conductivity, it is highly probable that there is a positive interaction of double exchange between trivalent and tetravalent ions in cobaltites and ferrites. This can be seen apparently from the difference in conductivity between $La_{0.5}Sr_{0.5}FeO_x$ treated in vacuo and in oxygen. Here the crystal structure is the same for both samples, and also the difference in the lattice parameter, hence that in the interionic distance is very small. The high conductivity in the sample treated in oxygen is evidently caused by the coexistence of Fe^{3+} and Fe^{4+}.

From the data on paramagnetic susceptibilities, it can be seen that samples treated in vacuo obeys the Curie-Weiss law above their Curie temperatures, and the effective Bohr magneton numbers are not far from what would be expected for the spin-only values of magnetic ions. (Table III) On the contrary, the effective Bohr magneton numbers of samples treated in oxygen are smaller than those of the corresponding samples treated in vacuo, and, in cobaltites, there is an evidence that reciprocals of susceptibilities do not obey the Curie-Weiss law, but exhibit a slight curvature as found in ferrimagnetism. Such a behavior of susceptibilities may be accounted for either from the standpoint of double exchange, as calculated by Anderson and Hasegawa, or by the theory of ferrimagnetism. As for ferrimagnetism there are again two possibilities. One is that it may be due to a formation of unbalanced antiferromagnetic sublattices, tetravalent ions occupying preferably one of the sublattices. The other is that it may be due to the formation of triangular arrangement of spins of magnetic ions, as proposed by Kishi.

We have at present no definite grounds for supporting one mechanism in preference to the other between these possibilities. It should be noticed, here, that the susceptibilities showed no appreciable change on rapid cooling from high temperatures (provided the cooling was done without change in the value of x) This would mean that the time required for the redistribution of magnetic ions is much shorter than that required for technical cooling, because the redistribution involves only electron jumping. Then the distribution of trivalent and tetravalent ions is a unique function of temperature, determined by electrostatic energies, magnetic interaction energies, &c. In the mechanism of double exchange, the ions adjust their positions according to the positive magnetic interaction and temperature. This is the origin of the deviation from the Curie-Weiss law. On the contrary, this effect is completely neglected in Kishi's theory. The author believes that the theory would give an adequate explanation of experimental data, if it is corrected as to this neglection.

It is quite certain from our experiment that the interaction $Fe^{3+}-Fe^{4+}$ is positive, irrespective of which standpoint we adopt. Also we can expect the interaction $Co^{3+}-Co^{4+}$ to be positive from the standpoint of double exchange, However, we cannot deduce any definite conclusions about sign and strength of tetravalent—tetravalent interionic interactions, since the materials treated in our experiment do not contain a sufficient amount of tetravalent ions.

In conclusion, the author wishes to express his thanks to Prof. T. Hirone for his valuable advices, and also to Mr. K. Ito for his assistance in the experiments. This work has been supported in part by the Scientific Research Expenditure of the Ministry of Education.

References

1) G. H. Jonker and J. H. Van Santen: Physica **16** (1950) 337.
2) J. H. Van Santen and G. H. Jonker: Physica **16** (1950) 599.
3) G. H. Jonker and J. H. Van Santen: Physica **19** (1953) 120.
4) C. Zener: Phys. Rev. **82** (1951) 403.
5) H. L. Yakel: Act. Cryst. **8** (1955) 394.
6) M. G. Harwood: Proc. Phys. Soc. **68B** (1955) 586.
7) E. O. Wollan and W. C. Koehler: Phys. Rev. **100** (1955) 545.
8) G. H. Jonker: Physica **20** (1954) 1118.
9) P. W. Anderson and H. Hasegawa: Phys. Rev. **100** (1955) 675.
10) G. H. Jonker: Physica **22** (1956) 707.
11) H. Watanabe: Sci. Rep. RITU **8A** (1956) 14.
12) H. Kishi: Busseiron Kenkyu **69** (1953) 181 (in Japanese).

JOURNAL OF THE PHYSICAL SOCIETY OF JAPAN Vol. 12, No. 5, MAY, 1957

Nuclear Magnetic Resonance Experiment on Metal Cadmium*

By Yoshika MASUDA

Department of Physics, Kobe University

(Received January 29, 1957)

The Knight shift, the line width and shape, and the spin-lattice relaxation time of the resonance line in metal cadmium are measured employing a nuclear magnetic resonance technique. The resonance line is asymmetric indicating an anisotropy of the Knight shift. From the analysis of these line shapes, the asymmetry in p-character of the conduction electron is estimated. The shift perpendicular to the c-axis is 0.42 percent and the shift parallel to the c-axis is 0.46 percent. The isotropic shift is 0.43 percent. In appendix, skin effect in metallic foil is discussed.

§ 1. Introduction

Knight[1] discovered that the resonance frequency is higher for nuclei in metals than for that of the same isotope in a non-conducting material in the same magnetic field. Townes[2] pointed out that the enhancement of a local field produced at the position of the nucleus is attributable to the hyperfine interaction between the nuclear magnetic moment and the conduction electron in s state. Besides this isotropic shift, in non-cubic crystals, non s-character (p-, d-, etc.) of the electron orbitals gives rise to an anisotropy of the Knight shift.[3] Such an anisotropy usually leads to an anomalous broadening and asymmetry of resonance line, and this anisotropic Knight shift gives the measure of asymmetry in p-character of electron at the top of the conduction band.

The fact that the nuclear magnetic resonance line width in heavier metals may be broader than expected from magnetic dipole interaction alone was pointed out by Bloembergen and Rowland[4] for metal thallium and tin, and by us[5] for metal cadmium. Besides the line broadening by anisotropic Knight shift, this extra broadening could be attributed to the indirect exchange coupling between neighboring nuclei which involves conduction electrons. Additional broadening for nuclei with spin $I>1/2$ might be caused by the nuclear quadrupole interaction but cadmium nuclei with $I=1/2$ have zero quadrupole moment so that the quadrupolar effects are excluded. Natural cadmium contains, as the magnetic isotopes, Cd^{111} (abundance ratio 12.86 percent) and Cd^{113} (abundance ratio 12.34 percent).

We measured the Knight shift, the line width and shape, and the spin-lattice relaxation time of nuclear magnetic resonance in metal cadmium.

§ 2. Experiment

The experimental procedures and equipments employed for the measurement have been described elsewhere.[6] The Knight shift is defined as $(H_r-H_s)/H_r$ for a constant resonance frequency, where H_r and H_s are the magnetic fields necessary for resonance for the reference and the sample, respectively. The reference was an aqueous solution of the cadmium nitrate. The experiment was performed at the field of 6200 gauss with a permanent magnet described previously[6] whereas at 3900 gauss, with the other permanent magnet which was newly constructed by NKS-3 steel of 50 kgs and has a gap of 4 cm and the pole faces of 13 cm in diameter. Experiment at a higher field of 8350 gauss was carried out with a usual electromagnet.

The sample was consisted of fine powders which were passed through a 320 mesh sieve permitting the size small compared to the skin depth, and were suspended in paraffin oil. Other samples were consisted of foils rolled to a thickness of about 15 μ. Layers of foil were separated by insulating paper. Fe less than 0.01 percent was the dominant impurity, which does not affect the width and shape of the resonance.

---

* A report of this work was given at the annual meeting of the Physical Society of Japan, Sendai, July, 1956. Recently, T. J. Rowland reported the Knight shift for metal cadmium, in Phys. Rev., **103** (1956) 1670, independently. His results agree with ours within experimental error.

Table I. Experimental results in metal cadmium.

	Knight shift $\Delta H_{\mathrm{iso}}/H_0$	Line width (δH) max. sl.			T_1
		3900 gauss	6200 gauss	8350 gauss	
Cd^{111}	4.3×10^{-3}	1.8 ± 0.2 gauss	2.3 ± 0.2 gauss		0.5×10^{-3} sec
Cd^{113}	4.3×10^{-3}	1.9 ± 0.2	2.4 ± 0.2	2.9 ± 0.3 gauss	0.5×10^{-3}

§ 3. Results and Discussion

Experimental results are shown in Table I. The derivative curve of nuclear magnetic resonance line of metal cadmium is shown in Fig. 1 and its integrated line shape in Fig. 2.

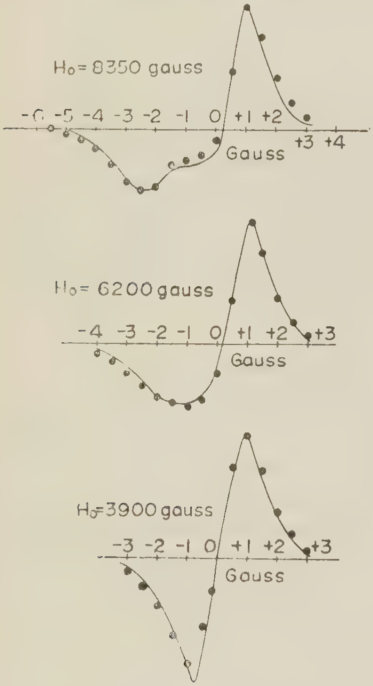

Fig. 1. The derivative of the Cd^{113} resonance line: comparison of theory and experiment. Solid curve: Derivative of the theoretical line shape. Dots: Experimental points taken from a typical recording beter plot.

The absorption curve is markedly asymmetric indicating an anisotropy of the Knight shift. Data were obtained at the field of 3900, 6200, and 8350 gauss and it is shown in Fig. 3 that the overall width is proportional to the applied field. Resonance figure of metals often becomes asymmetric due to the skin effect.[7] Asymmetry here observed is distinguished from the skin effect by two points; (1) Sharp rise of the resonance figure is in the high field side which is opposite to the case of the skin effect. (2) While the skin effect asymmetry is sensibly affected by the thickness of the foil, the asymmetry now in problem is not. In appendix we analyzed the asymmetry due to the skin effect both theoretically and experimentally.

Cadmium is a divalent metal, and it is expected that the electrons at the Fermi level have p-character considerably. The crystal structure of cadmium is the hexagonal close-packed whose c/a ratio being 1.886 is exceptionally much deviated from the ideal one (1.633). Each atom has twelve neighbors of which the six in the plane perpendicular to the c-axis are at the distance of 2.973 Å while the others at 3.286 Å. Naturally it has an axial symmetry about the c-axis but not a spherical symmetry.

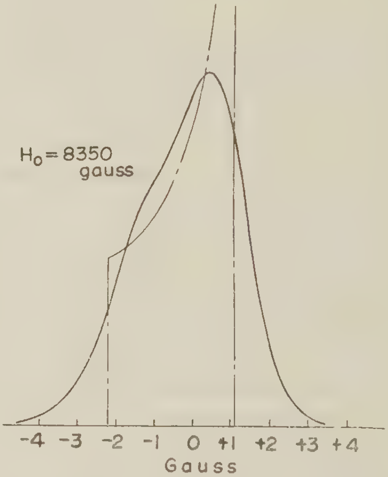

Fig. 2. The integrated experimental line shape of the Cd^{113} resonance is given by the full-drawn curve. The chain-line is the theoretical shape for powders with axial symmetry.

The electron in the solid may be adequately described by one-electron wave function of the Bloch type,

$$\Psi_k = e^{ik\cdot r}U_k(r)\,. \tag{1}$$

$U_k(r)$ has the periodicity of the lattice, and within the atomic polyhedron, it is assumed to be consisted of mixture of s- and p-type wave functions of the form

$$U_k(\mathbf{r}) \rightarrow a_s\varphi_s + a_1\varphi_{p_x} + a_2\varphi_{p_y} + a_3\varphi_{p_z}\ , \qquad (2)$$

where

$$|a_s|^2 + |a_1|^2 + |a_2|^2 + |a_3|^2 = 1\ .$$

In case of axial symmetry we can expect that

$$\langle |a_1|^2 \rangle = \langle |a_2|^2 \rangle = \eta\ ,$$

and by the way we put

$$\langle |a_s|^2 \rangle = \xi \quad \text{and} \quad \langle |a_3|^2 \rangle = \zeta\ ,$$

where $\langle\ \rangle$ means the average over the Fermi surface.

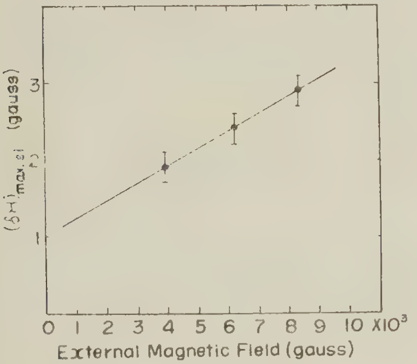

Fig. 3. The line width, measured between points of maximum slope, in the Cd^{113}, vs. the external magnetic field.

The Hamiltonian for the nuclear spin-electron spin interaction is given by

$$\mathscr{H} = \frac{16\pi}{3}\beta\beta_N g_N \mathbf{I}_i \cdot \mathbf{S}\delta(\mathbf{r}_i)$$

$$+ 2\beta\beta_N g_N \mathbf{I}_i \cdot \{\mathbf{S}r_i^{-3} - 3r_i^{-5}(\mathbf{S}\cdot\mathbf{r}_i)\mathbf{r}_i\}\ , \qquad (3)$$

where $\mathbf{r}_i$ is the radius vector of the electron with the nucleus at the origin and β is the Bohr magneton.

a) *Isotropic Knight shift*

The isotropic Knight shift is produced by the Fermi-type hyperfine interaction of the nuclear spin with the electron spin in s-state and is given by the first term of the Hamiltonian (3). It results in

$$\frac{\Delta H_{iso}}{H_0} = \frac{16\pi}{3}\beta^2\kappa\langle |u_k(0)|^2 \rangle \Omega N(E_0)\ , \qquad (4)$$

where κ is the relativistic correction (1.28 for $5s$, ${}^2S_{1/2}$), Ω is the atomic volume, and $N(E_0)$ is the density of states, the number of states per unit volume and per unit energy interval, at the Fermi level. $N(E_0)$ may be known, if available, from paramagnetic susceptibility χ_p or electronic specific heat C_v. Although the experimental value of χ_p of cadmium is listed in the reference (8), we estimated $N(E_0)$ by the formula

$$\Omega N(E_0) = \frac{3}{2}E_0^{-1}\ ,$$

which is deduced for divalent metal by the free electron model. Using the collective description of electron interaction introduced by Bohm and Pines,[9] E_0 was estimated to be 0.409 ry. It leads to χ_p of 1.36×10^{-6} c.g.s. volume unit whereas χ_p derived from the complete free electron model is 1.02×10^{-6} and the experimental value derived from measurement of electronic specific heat is 0.753×10^{-6}. Introducing Eq. (2), $|u_k(0)|^2$ in Eq. (4) is reduced to

$$|u_k(0)|^2 = \xi|\varphi_s(0)|^2\ .$$

It is very hard to obtain the exact wave functions φ_s and φ_p of metal cadmium and hereafter we will replace them, as a crude approximation, by the atomic s- and p-functions. Cadmium has two free electrons per atom and each will move in the field partially shielded by an another electron. φ_s seems to be better approximated by atomic $5s^2$ function of Cd I ${}^1S_0$-state than $5s^1$ of Cd II ${}^2S_{1/2}$-state but we refered to the states of Cd II because the atomic functions of Cd II are rather reliable than those of Cd I owing to the simple structure (one valence electron) of the former. In Table II the calculated value of $|\varphi_s(0)|^2$ are listed using the standard formula[10] for non-hydrogenic wave function. As a reference, the hyperfine splitting of the atomic spectrum $\lambda(8067)$ ($6s\ {}^2S_{1/2} - 6p\ {}^2P_{3/2}$) of Cd II was evaluated by the same way resulting in good agree-

Table II.

Atomic state	$\|\varphi_s(0)\|^2$	$\left\langle \frac{1}{r^3} \right\rangle$	ξ	η	ζ
Cd I	5.63×10^{25} cm^{-3}	3.00×10^{25} cm^{-3}			
Cd II	7.26×10^{25}	4.35×10^{25}	0.20	0.20	0.40

ment with the experimental value[11)] of $\Delta\nu=0.11\,\text{cm}^{-1}$. Using the experimental value of $\Delta H_{iso}/H_0$ and the calculated values of $|\varphi_s(0)|^2$ and $\Omega N(E_0)$, we determined the s-content ξ of the wave function to be about 20 percent. The fact that the p-character of the free electron of cadmium in the Fermi surface is as large as 80 percent is not so surprising as compared with the values: 65 percent for Na[12)] and more than 50 percent for Sn[3)].

b) *Anisotropic Knight shift*

The anisotropic Knight shift is produced by the nuclear spin-electron spin dipolar coupling when the charge distribution of electron is deviated from spherical symmetry about a nucleus and is deduced from the second term of the Hamiltonian (3). This anisotropic Knight shift is superimposed on the isotropic Knight shift. Since in first-order approximation only the component of the internal field parallel to the external field will affect the resonance, $\Delta H_{\parallel}$ and $\Delta H_{\perp}$, the shifts parallel and perpendicular to the c-axis, respectively, are given by the following formulae in case of axial symmetry:

$$\Delta H_{\parallel}=\Delta H_{\text{iso}}+2\beta^2\Omega N(E_0)qH_0\,,$$

$$\Delta H_{\perp}=\Delta H_{\text{iso}}-\beta^2\Omega N(E_0)qH_0\,,$$

and

$$\frac{\Delta H_{\parallel}-\Delta H_{\perp}}{H_0}=3\beta^2\Omega N(E_0)q\,, \qquad (5)$$

where

$$q=\left\langle\int u_k^*\frac{3\cos^2\theta-1}{r^3}u_k d\tau\right\rangle_{\kappa'}$$

$$=\frac{4}{5}\kappa'\left\langle\frac{1}{r^3}\right\rangle_p(\zeta-\eta)\,, \qquad (6)$$

is the quadrupole moment of the electrons near the Fermi level and κ' is again the relativistic correction (1.21 for $5p\ {}^2P_{1/2}$). The ratio of $(\Delta H_{\parallel}-\Delta H_{\perp})$ to ΔH_{iso} does not contain the ambiguous quantity $\Omega N(E_0)$ in its expression

$$\frac{\Delta H_{\parallel}-\Delta H_{\perp}}{\Delta H_{\text{iso}}}=\frac{9}{20\pi}\,\frac{\kappa'\left\langle\frac{1}{r^3}\right\rangle_p}{\kappa|\varphi_s(0)|^2}\,\frac{\zeta-\eta}{\xi} \qquad (7)$$

$(\Delta H_{\parallel}-\Delta H_{\perp})$ was determined by the experiment as discussed in section c) and it revealed that q is positive and hence $\zeta>\eta$. We again approximated the metallic p function by the atomic $5p$ function of Cd I, ${}^3P_1$-state or Cd II, ${}^2P_{1/2}$ and estimated $\left\langle\frac{1}{r^3}\right\rangle_p$ by the standard formula[10)] using the optically determined fine structure separation, $\delta({}^2P_{3/2}-{}^2P_{1/2})=2485\,\text{cm}^{-1}$ and $\delta({}^3P_2-{}^3P_0)=1714\,\text{cm}^{-1}$. In Table II are listed the values of $\left\langle\frac{1}{r^3}\right\rangle_p$ thus obtained as well as η and ζ estimated from Eq. (7) and the normalization condition of a's. The fact $\zeta>\eta$ corresponds to the charge distribution of the electron in the Fermi surface being elongated to the c-direction so that the atomic polyhedron is filled up by electron as uniformly as possible.

c) *Line shape and width*

The line shape in a polycrystalline sample is dominated by the anisotropic Knight shift when $(\Delta H_{\parallel}-\Delta H_{\perp})$ is larger than the symmetric width due to the dipole coupling and so on. Spatially random distribution of the crystalline axes determines the line shape whose analytic form in case of axial symmetry was given by Bloembergen,[3)]

$$I(H)\backsim(H-H_0-\Delta H_{\perp})^{-1/2}\ \text{if}\ \Delta H_{\perp}<H-H_0<\Delta H_{\parallel}\,, \qquad (8)$$

$I(H)=0$ outside this interval.

One may obtain true line shape by dressing a symmetric line broadening δ on the skeleton of the anisotropic shift given by Eq. (8). By proper choice of the magnitude of $(\Delta H_{\parallel}-\Delta H_{\perp})/H_0$ and δ, we can fit the theoretical line shape to all of the experimental lines at 3900, 6200, and 8350 gauss as shown in Fig. 2. The best fitted values are;

$$(\Delta H_{\parallel}-\Delta H_{\perp})/H_0=0.039\ \text{percent}$$

$$\delta\ \text{max. sl.}=1.5\ \text{gauss.}$$

Then the relative anisotropy of the Knight shift is as follows;

$$\frac{\Delta H_{\parallel}-\Delta H_{\perp}}{\Delta H_{\text{iso}}}=9.3\ \text{percent.}$$

This value was used for the determination of the anisotropy in p-character as stated in section b).

The second moment of the symmetric broadening δ assuming the Gaussian shape is 0.59 gauss^2 and is ten times as large as the second moment of the nuclear dipole coupling, 0.05 gauss^2. Subtracting further broadening by the field inhomogeneity and by T_1, there remains 0.52 gauss^2 which suggests the other origins of the broadening such as the indirect exchange coupling or the pseudo-dipolar coupling.[4,13)]

The indirect exchange coupling $A_{ij}\mathbf{I}_i\cdot\mathbf{I}_j$ is the coupling between the magnetic moments of two nuclei via their hyperfine interaction with the conduction electron. Taking $m^*=m$ and $\xi=1$, we estimated A_{ij} between nearest neighbors of Cd^{113} to be 2.78 gauss. If one takes ξ to be 0.65, the indirect exchange coupling would yield just the extra broadening 0.52 gauss^2 but if 0.20 it can interprete only one percent of the broadening. Since the second moment is proportional to the fourth power of ξ, its uncertainty affects so seriously to the broadening.

Pseudo-dipolar coupling between the spins i and j is given by

$$\mathscr{H}_{ij}^{\mathrm{dip}}=\{\mathbf{I}_i\mathbf{I}_j-3\mathrm{R}_{ij}^{-2}(\mathbf{I}_i\cdot\mathbf{R}_{ij})(\mathbf{I}_j\cdot\mathbf{R}_{ij})\}\mathrm{B}_{ij}$$

The coefficient B_{ij} is hardly estimated unless the band structure is known but the ratio B_{ij} to A_{ij} is, in its order of magnitude, given by the formula similar to Eq. (7),

$$\frac{\mathrm{B}_{ij}}{\mathrm{A}_{ij}}\sim\frac{9}{20\pi}\frac{\kappa'\left\langle\frac{1}{r^3}\right\rangle}{\kappa|\varphi_s(0)|^2}\frac{1-\xi}{\xi}\,.$$

The ratio was estimated to be 0.3 so that the pseudo-dipolar coupling will contribute to the broadening to some extent.

d) *Relaxation time*

The nuclear relaxation in metals is usually determined by interaction between nuclear spins and conduction electron spins. If one takes into account only the Fermi-interaction, the relation between the relaxation time and the Knight shift is usually refered to as the "Korringa relation",[14)]

$$T_1T(\varDelta H/H_0)^2=\frac{h}{\pi k}\left(\frac{\beta}{\gamma\hbar}\right)^2.$$

From the experimental value of the Knight shift, the relaxation time T_1 was estimated to be 1.1×10^{-3} sec. For the direct measurement we employed the ordinary saturation method and evaluated T_1 using the T_2 as determined from the symmetric line broadening δ. It results in T_1 of 0.5×10^{-3} sec. for Cd^{113} which is one half of the calculated one. This deviation from the Korringa relation may be due to the contribution of p-electron to the relaxation as suggested by Bloembergen.[15)]

In conclusion, the author wishes to express his hearty thanks to Professor T. Kanda for kind guidance and stimulating discussion throughout the course of this research. He is also indebted to Mr. T. Kojima for many helpful discussion, Dr. Y. Kitano for performing the chemical analysis of the sample, and Mr. K. Kuninobu for his technical assistance. This work has been supported in part by the Scientific Research Expenditure of the Ministry of Education.

Appendix

Note on the Skin Effect of the Magnetic Resonance Absorption in Metals.

It is well known that, in the nuclear magnetic resonance in metals, when the characteristic dimensions of the sample are not less than the rf skin depth, the line shape is distorted, whence the exact center of resonance is uncertain. This effect was analyzed by Bloembergen[7)], who pointed out that the phase shift of the rf fiield within the metal surface produces a mixture of the absorption and the dispersion components of the resonance.

We shall discuss only the case of the flat plate, which is of a convenient shape both experimentally and theoretically. The metal is considered to be infinite in the x and y directions, thus it occupies the region $-d\leqslant z\leqslant d$, where $2d$ is the thickness of the plate. We assume that the fields depend on z only so that the problem may be essentially one dimensional, and also that the magnetic field is equal on both sides of the plate. The power absorbed per unit area—the power is flowing in from both sides—is given by[7)]

$$W=Re\left(\frac{i\omega\mu}{4\pi K}H_0^2\tanh Kd\right), \qquad (9)$$

where K is the propagation constant,

$$K^2=(4\pi i\sigma\omega\mu-\omega^2\varepsilon\mu)/c^2\,.$$

The dielectric constant $\varepsilon=\varepsilon'-i\varepsilon''$ and the permeability $\mu=\mu'-i\mu''=1+4\pi\chi'-4\pi i\chi''$ may be complex. The classical skin depth is usually defined as $\delta^{-1}=ReK$. It is given approximately by

$$\delta=c/(2\pi\sigma\omega)^{1/2}\,,$$

where σ is the conductivity of the metal. Now, putting $d/\delta=x$, Eq. (9) becomes

$$W=\frac{\delta\omega H_0^2}{8\pi}\{(\mathscr{R}-\mathscr{J})+4\pi\chi'(\mathscr{R}-\mathscr{J})+4\pi\chi''(\mathscr{R}+\mathscr{J})\}, \qquad (10)$$

where

$$\left.\begin{aligned}\mathscr{R}&=\frac{\frac{1}{2}\sinh 2x}{\cosh^2 x\cos^2 x+\sinh^2 x\sin^2 x}\,,\\ \mathscr{J}&=\frac{\frac{1}{2}\sin 2x}{\cosh^2 x\cos^2 x+\sinh^2 x\sin^2 x}\,.\end{aligned}\right\}\qquad(11)$$

The experimentally observed quantity is the derivative of absorbed power with respect to the frequency and is given by the next formula under an assumption of the Lorentzian shape of resonance line:

$$\frac{dW}{d\omega}=-\frac{\delta\omega H_0^2}{4}\chi_0\omega_0T_2\left\{\frac{[1-T_2^2(\omega-\omega_0)^2]T_2}{[1+T_2^2(\omega-\omega_0)^2]^2}(\mathscr{R}-\mathscr{J})+\frac{2T_2^2(\omega-\omega_0)}{[1+T_2^2(\omega-\omega_0)^2]^2}(\mathscr{R}+\mathscr{J})\right\}\qquad(12)$$

where ω_0 is the resonance frequency satisfying the conditition $\hbar\omega_0=g\beta H_0$.

Employing Eq. (12), we can calculate the change with the thickness of the plate, of maximum slope separation, of the degree of asymmetry and of the position at which the derivative curve cuts the horizontal line. In Fig. 4 are given the calculated curves as well as the experimental points obtained by five kinds of samples consisted of well annealed aluminum foil of thickness 6, 15, 25, 50, and 100 μ respectively. When the resonance frequency is held constant, as x increases, the separation of the maximum slope increases and the resonance line shifts to the high field side. In pure aluminum no decrease in intensity after cold work was observed. The fact that the resonance in pure aluminum shows no effect of quadrupole broadening has been known.[15] The resonance line gained by very thin foil of pure aluminum is symmetric showing the lack of the anisotropy of the Knight shift and moreover the width is in good agreement with that calculated by pure dipolar coupling neglecting the atom diffusion. Accordingly, the line shape anomaly of the thick foil must be due only to the skin effect and, as seen in Fig. 4, it is completely interpreted by the simple theory of the skin effect.

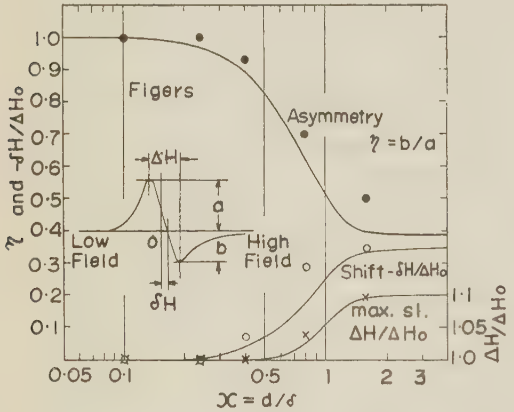

Fig. 4. Asymmetry η, shift $\delta H/\Delta H_0$, and max. slope separation $\Delta H/\Delta H_0$ vs. $x=d/\delta$.

References

1) W. D. Knight: Phys. Rev. **76** (1949) 1259.
2) Townes, Herring, and Knight: Phys. Rev. **77** (1950) 852.
3) N. Bloembergen and T. J. Rowland: Acta Metallurgica **1** (1953) 731.
4) N. Bloembergen and T. J. Rowland: Phys. Rev. **97** (1955) 1679.
5) The annual meeting of the Physical Society of Japan, Osaka, November, 1954.
6) Y. Masuda and T. Kanda: J. Phys. Soc. Japan **9** (1954) 82.
Y. Masuda: J. Phys. Soc. Japan **11** (1956) 670.
7) N. Bloembergen: J. App. Phys. **23** (1952) 1383.
8) W. D. Knight: *Electron Paramagnetism and Nuclear Magnetic Resonance in Metals*, p. 124 (Solid State Physics, Vol. 2, Academic Press, 1956).
9) D. Pines: Phys. Rev. **95** (1954) 1050.
10) H. Kopfermann, Kernmomente, Akademisch Verlagsgesellschaft, M.B.H. Leipzig, 1940.
11) G. Jones: Proc. Phys. Soc. **45** (1933) 625.
12) H. Jones and B. Schiff: Proc. Phys. Soc. **A411** (1954) 217.
13) M. A. Ruderman and C. Kittel: Phys. Rev. **96** (1950) 99.
14) J. Korringa: Physica **16** (1950) 601.
15) N. Bloembergen: *Report of the Conference on Defects in Crystalline Solids*, Bristol, July, 1954, p. 1.
16) T. J. Rowland: Acta Metallurgica **3** (1955) 74

Journal of the Physical Society of Japan Vol. 12, No. 5, May, 1957

On the Buckling of an Eliptic Plate with Clamped Edge, II

By Yoshio Shibaoka
Institute of Polytechnics, Osaka City University

(Received January 16, 1957)

The buckling of a uniform thin elliptic plate with clamped edge is dealt with in case when its periphery is subject to a uniform normal pressure in the plane of the plate, and the relationship between the critical buckling load and the eccentricity of the elliptic plate is shown graphically.

§ 1. Introduction

In a previous paper[1)], the fundamental normal mode of the buckling of a uniform thin elliptic plate with clamped edge was discussed formally in an exact manner in case when its periphery is subject to a uniform normal pressure in the plane of the plate. No detailed numerical discussions were carried out, however, and only an approximate formula giving the relationship between the critical buckling load and the eccentricity of the elliptic plate was derived correct to the fourth power of the eccentricity which may be adequately used in case when the eccentricity is not so large.

In the present paper, we have carried out rather laborious numerical calculations and the relationship between the critical buckling load of the fundamental normal mode of the buckling and the eccentricity of the elliptic plate is shown graphically.

§ 2. General Solution of the Fundamental Equation

Let the rectangular coordinate axes (x, y) be taken in the middle plane of an elliptic plate of uniform thickness, d, in such a way that the origin coincides with the centre of the plate and the axes are along the major and minor axes of the ellipse respectively. We denote Young's modulus and Poisson's ratio of the material of the plate, which is assumed to be homogeneous and isotropic, by E and σ respectively.

Then if w be the transverse displacement of a point on the middle plane, the differential equation for determining the deflection of the buckled plate subject to a uniform normal pressure P per unit length on its periphery is given by

$$\left.\begin{aligned} D\left(\frac{\partial^4 w}{\partial x^4}+2\frac{\partial^4 w}{\partial x^2\partial y^2}+\frac{\partial^4 w}{\partial y^4}\right) &= -P\left(\frac{\partial^2 w}{\partial x^2}+\frac{\partial^2 w}{\partial y^2}\right), \\ \text{with}\quad D=Ed^3/\{12(1-\sigma^2)\}\ . & \end{aligned}\right\} \tag{1}$$

If, for simplicity, we write $k_1{}^2=P/D$, equation (1) becomes

$$\left(\frac{\partial^2}{\partial x^2}+\frac{\partial^2}{\partial y^2}\right)\left(\frac{\partial^2}{\partial x^2}+\frac{\partial^2}{\partial y^2}+k_1{}^2\right)w=0\ . \tag{2}$$

Denoting the focal length of the ellipse by $2h$, we now introduce the elliptic coordinates (ξ, η) defined as:

$$x+iy=h\cosh(\xi+i\eta)\ .$$

Then, as explained in the previous paper[1)], if we restrict our attention to the normal mode of buckling in which the displacement is symmetrical about both axes, a formal general solution of equation (2) can be written in the form

$$w=\sum_{m=0}^{\infty}\left\{C_{2m}\cosh 2m\xi+\sum_{l=0}^{\infty}\overline{C}_{2l}A_{2m}^{(2l)}\,\mathrm{Ce}_{2l}(\xi,q)\right\}\times\cos 2m\eta\ , \tag{3}$$

with

$$q=\frac{1}{4}k_1{}^2h^2=\frac{P}{4D}h^2\ , \tag{4}$$

where C_{2m} and $\overline{C}_{2l}$ are arbitrary constants. If the clamped edge of the elliptic plate be expressed by $\xi=\xi_0$, the boundary conditions at this edge are given by

$$(w)_{\xi=\xi_0}=0\ ,\qquad \left(\frac{\partial w}{\partial\xi}\right)_{\xi=\xi_0}=0\ , \tag{5}$$

and substituting the expression (3) for w into these conditions, we have

$$\left.\begin{aligned} &\sum_{m=0}^{\infty}\left\{C_{2m}\cosh 2m\xi_0+\sum_{l=0}^{\infty}\overline{C}_{2l}A_{2m}^{(2l)}\mathrm{Ce}_{2l}(\xi_0,q)\right\}\\ &\qquad\qquad\times\cos 2m\eta=0\,,\\ &\sum_{m=0}^{\infty}\left\{2mC_{2m}\sinh 2m\xi_0\right.\\ &\quad\left.+\sum_{l=0}^{\infty}\overline{C}_{2l}A_{2m}^{(2l)}\mathrm{Ce}_{2l}'(\xi_0,q)\right\}\cos 2m\eta=0\,.\end{aligned}\right\} \tag{6}$$

In order that these two relations should be satisfied for all values of η between $-\pi/2$ and $\pi/2$, we must have, for any positive intergral value of m, zero inclusive,

$$\left.\begin{aligned} &C_{2m}\cosh 2m\xi_0+\sum_{l=0}^{\infty}\overline{C}_{2l}A_{2m}^{(2l)}\mathrm{Ce}_{2l}(\xi_0,q)=0\,,\\ &2mC_{2m}\sinh 2m\xi_0+\sum_{l=0}^{\infty}\overline{C}_{2l}A_{2m}^{(2l)}\mathrm{Ce}_{2l}'(\xi_0,q)=0\,.\end{aligned}\right\} \tag{7}$$

If we eliminate the constants C_{2m}'s from these equations, we get a system of simultaneous linear equations for determining the constants $\overline{C}_{2l}$'s. Thus

$$\sum_{l=0}^{\infty}a_{lm}\overline{C}_{2l}=0\,,\qquad (m=0,\,1,\,2,\,3,\,\cdots) \tag{8}$$

with

$$\begin{aligned} a_{lm}=A_{2m}^{(2l)}\{&2m\sinh 2m\xi_0\mathrm{Ce}_{2l}(\xi_0,q)\\ &-\cosh 2m\xi_0\,\mathrm{Ce}_{2l}'(\xi_0,q)\}\,.\end{aligned} \tag{9}$$

The solution of this system of simultaneous linear equations would in general yield the result that all the $\overline{C}_{2l}$'s are zero; but if a certain special relationship exists between the dimensions of the plate and the strength of the load P, namely, if the relation obtained by eliminating all the $\overline{C}_{2l}$'s from the system of simultaneous linear equation (8) exists, we can obtain a displacement in the normal mode of buckling, and with the aid of the said relationship the critical buckling load can be determined as a function of the dimensions of the plate and the elastic constants of the material of the plate.

By eliminating all the $\overline{C}_{2l}$'s from (8), we have the required relationship as:

$$\Delta=\begin{vmatrix} a_{00} & a_{10} & a_{20} & a_{30} & \cdots\\ a_{01} & a_{11} & a_{21} & a_{31} & \cdots\\ a_{02} & a_{12} & a_{22} & a_{32} & \cdots\\ a_{03} & a_{13} & a_{23} & a_{33} & \cdots\\ \vdots & \vdots & \vdots & \vdots & \end{vmatrix}=0\,. \tag{10}$$

If we obtain the numerical value of the root q of this infinite determinantal equation, the numerical value of $\sqrt{\frac{P}{D}}a$ can be obtained from the relation:

$$\sqrt{\frac{P}{D}}a=2\sqrt{q}/\varepsilon\,, \tag{11}$$

which follows immediately from (4), where a and ε are respectively a half-length of the major axis and the eccentricity of the ellipse.

When a, ε and D are fixed the only variable remaining in the determinant Δ is q, which is connected with the critical buckling load P by the relation (11), so that the smallest root of (10) will give the critical load of the fundamental normal mode of buckling, with which we are mainly concerned in the present paper.

The solution expressed by (10) is, however, merely formal. To find out whether it can be used to determine the actual value of buckling we must examine its convergence. For this purpose, we may form, as in Professor Tomotika's treatment of the transverse vibration of a square plate clamped at its four edges[2], a series of finite determinants Δ_1, Δ_2, Δ_3, $\cdots$, Δ_N by taking 1, 2, 3, $\cdots$, N rows and columns starting at the left-hand top corner of Δ, so that $\Delta_1=a_{00}$, $\Delta_2=\begin{vmatrix} a_{00} & a_{10}\\ a_{01} & a_{11}\end{vmatrix}$, etc. If it is found that the smallest root of $\Delta_N=0$ converges to a definite limit as N increases this root gives the required critical load of the fundamental normal mode of buckling of the elliptic plate under consideration.

§ 3. Search for Roots of $\Delta=0$

The writer has calculated the smallest roots q of $\Delta_1=0$, $\Delta_2=0$ and $\Delta_3=0$ in three cases in which the values of a/b are equal to 5/4, 2/1 and 3/1 respectively, with a view to finding out whether they converge to a definite limit, where b is a half-length of the minor axis of the ellipse.

Table I. Values of q_R.

a/b	ε	q_R
5/4	0.6	1.82
2/1	0.866	8.26
3/1	0.943	22.02

To this end, the values of Δ_1, Δ_2 and Δ_3 have been calculated for different values of q close to q_R, an approximate value of the smallest root, which can be found easily from Woinovsky-Krieger's results[3]. The values of q_R are shown in Table I. Then, plotting these values

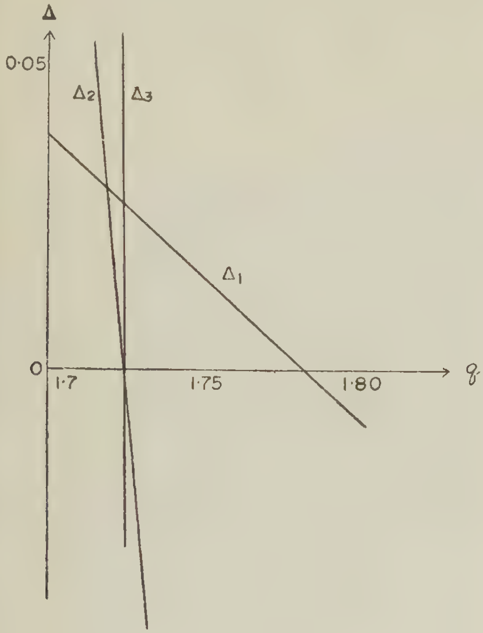

Fig. 1.

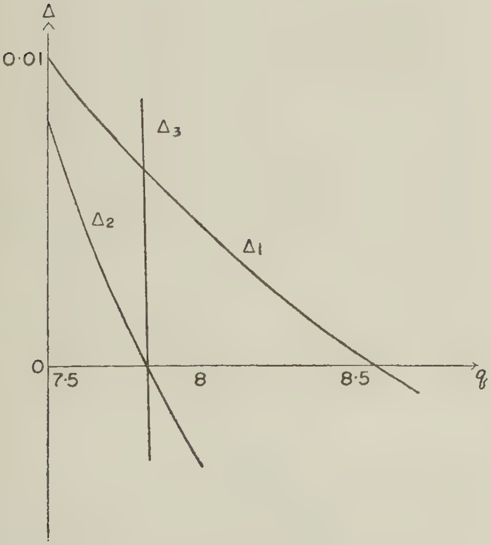

Fig. 2.

of Δ_1, Δ_2 and Δ_3 against q, the roots of the equations $\Delta_1=0$, $\Delta_2=0$ and $\Delta_3=0$ have been determined graphically as show in Figs. 1, 2 and 3*. The results are shown in Table II.

It may be added here that for the numerical calculations of the modified Mathieu functions $\mathrm{Ce}_{2n}(\xi_0, q)$ contained in the elements a_{in}'s of the determinant Δ use has been made of the following product series expressions because of their rapid convergency.

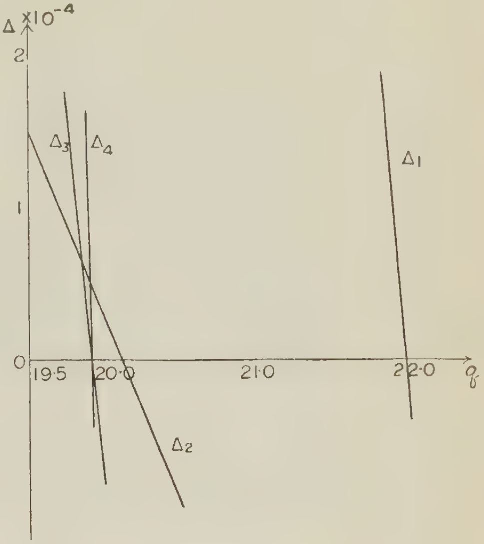

Fig. 3.

Table II. Roots of $\Delta_N=0$.

a/b	ε	Root of $\Delta_1=0$	Root of $\Delta_2=0$	Root of $\Delta_3=0$	Root of $\Delta_4=0$
5/4	0.6	1.785	1.725	1.725	—
2/1	0.866	8.57	7.825	7.825	—
3/1	0.943	22.0	20.13	19.93	19.91

$$\mathrm{Ce}_{2n}(\xi_0, q)=\frac{p_{2n}}{A_0^{(2n)}}\sum_{r=0}^{\infty}(-1)^r A_{2r}^{(2n)} J_r(v_1) J_r(v_2)\,,$$

where

$$v_1=\sqrt{q}\,e^{-\xi_0}\,,\qquad v_2=\sqrt{q}\,e^{\xi_0}\,,$$

$$p_{2n}=\mathrm{ce}_{2n}(0, q)\,\mathrm{ce}_{2n}\left(\frac{\pi}{2}, q\right)\Big/A_0^{(2n)}\,,$$

ξ_0 being connected with the value of a/b as:

$$\cosh\xi_0=\frac{a}{\sqrt{a^2-b^2}}=\frac{1}{\varepsilon}\,.$$

From Figs. 1, 2, 3 and Table II it will be seen that as N increases, the roots q of the equation $\Delta_N=0$ converge to 1.725 when $a/b=5/4$, to 7.825 when $a/b=2/1$ and to 19.91 when $a/b=3/1$.

Thus, substituting these limiting values of q into (11), we obtain ultimately the most probable values of $\sqrt{\frac{P}{D}}a$ as shown in Table III below.

---

* The values of Δ_4 have also been calculated in case when a/b is equal to 3/1 and the root of $\Delta_4=0$ has been obtained.

Table III. Valves of $\sqrt{\frac{P}{D}}a$.

a/b	ε	$\sqrt{\frac{P}{D}}a$
5/4	0.6	4.38
2/1	0.866	6.47
3/1	0.943	9.46

The curve of $\sqrt{\frac{P}{D}}a$ plotted against the eccentricity ε is shown by a thick-line curve in Fig. 4, where is also shown for reference the well-known values of $\sqrt{\frac{P}{D}}a$ equal to 3.8317 for a circular plate ($\varepsilon=0$) with clamped edge$^{4),5)}$.

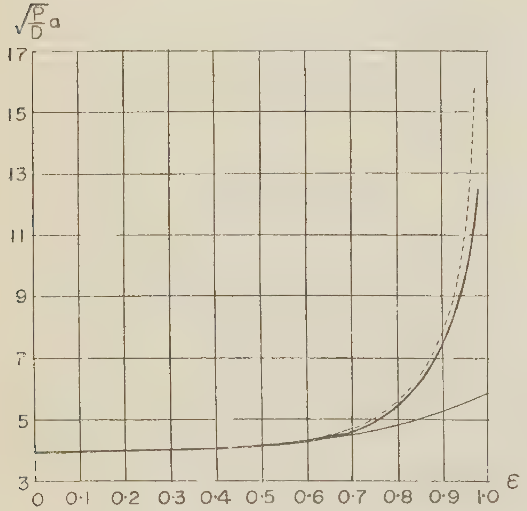

Fig. 4.

- present method
- expansion formula
- S. Woinovsky-Krieger's result (Rayleigh-Ritz method)

In the previous paper[1] we obtained an approximate formula for the relationship between the critical buckling load and the eccentricity of the elliptic plate. The result is

$$\sqrt{\frac{P}{D}}a=3.8317+0.9579\varepsilon^2+1.0382\varepsilon^4 . \tag{12}$$

The values calculated by using this expansion formula are shown by a thin-line curve in Fig. 4. The dotted-line curve shows the results that was obtained by S. Woinovsky-Krieger by the use of Rayleigh-Ritz method.

It will be seen that the expansion formula (12) is particularly useful for calculating the numerical values of $\sqrt{\frac{P}{D}}a$ in case when the plate is nearly circular.

§ 4. Summary

The fundamental normal mode of buckling of a uniform elliptic plate clamped at its edge is investigated in an exact manner. Carrying out detailed numerical calculations in three cases in which the eccentricity ε of the ellipse is equal to 0.6, 0.866 and 0.943 respectively, the relationship between $\sqrt{\frac{P}{D}}a$ and ε is shown graphically, where P is the strength of the critical load, a a half-length of the major axis of the ellipse and $D=Ed^3/\{12(1-\sigma^2)\}$, E and σ being respectively Young's modulus and Poisson's ratio of the material of the plate and d being the thickness of the plate.

§ 5. Acknowledgment

The present problem has been carried out at the suggestion of Professor S. Tomotika. The writer wishes to express his sincere gratitude to him for his helpful guidance and continual encouragement throughout this work and especially for his kind inspection of the manuscript. The writer's thanks are olso due to Professor K. Tamada for his many valuable advices and to Professor T. Okuda for his encouragement.

Finally, the writer is indebted to the Ministry of Education for a grant-in-aid for fundamental scientific researches.

References

1) Y. Shibaoka: On the buckling of an elliptic plate with clamped edge, I. J. Phys. Soc. Japan **11** (1956) 1088.
2) S. Tomotika: The transverse vibration of a square plate clamped at four edges. Phil. Mag. [7], **21** (1936) 745.
3) S. Woinovsky-Krieger: The stability of a clamped elliptic plate under uniform compression. J. Appl. Mech. **4** (1937) 177.
4) G. H. Bryan: Proc. London Math. Soc. **22** (1891) 54.
5) A. Nadai: Z. Ver. Deut. Ing. **59** (1915) 169.

JOURNAL OF THE PHYSICAL SOCIETY OF JAPAN Vol. 12, No. 5, MAY, 1957

Measurements of Pressure Fluctuation in the Wake of Cylinder

By Yasujiro KOBASHI

Faculty of Science, Hiroshima University

(Received February 4, 1957)

With a view to observing pressure fluctuations in turbulent flow of fluid, a new apparatus was constructed by using a condenser microphone as a transducer with a ratio-discriminator. The frequency response of the apparatus was calibrated by means of Kármán vortices produced by a circular cylinder. The Helmholtz resonance and the loss in the pressure duct were compensated electrically by a band-rejection filter and a high-frequency booster. By these devices, the overall frequency response of the pressure-measuring apparatus was made flat between 50 and 1500 cycles per second. Using the apparatus in combination with a single rotary type hot-wire anemometer, it proved succesful in determining the intensity of static pressure fluctuation as well as the correlation between pressure and velocity fluctuation. Consequently all the terms in the energy equation became measurable, and the energy equation for the fluctuating quantities was ascertained experimentally for the first time in the wake of a circular cylinder, 1 cm in diameter, placed in an airstream of the speed 14 m/s, at a section 42 times the cylinder diameter downstream.

§ 1. Introduction

Many experimental works[1),2),3),4)] have been done with fruitful results on the turbulence characteristics in the wake of a cylinder. All these experiments, however, were carried out by using the hot-wire technique. Consequently the quantities measured so far are concerned only with the temperature and velocity fluctuations. But a thorough understanding of the fundamental features of nonisotropic turbulence necessitates the knowledge of the contribution of other quantities, among which the most important seems to be that of pressure fluctuation. Indeed, Rotta[5),6)] has made an interesting theoretical approach, which has thrown light on the contribution of pressure to the trubulence mechanism.

From the experimental point of view, however, no attempt has ever been made to investigate the phenomena directly, because of the lack of an adequate apparatus for detecting the static pressure fluctuations. As a result, it was necessary for Townsend[7)] to determine the contribution of pressure fluctuation to the energy balance by the indirect method, in which all the terms in the energy equation except the pressure term were measured.

In view of these circumstances, the author has attempted to measure some turbulence characteristics in the wake of a cylinder by using a new pressure pick-up combined with a hot-wire anemometer. The pick-up consists of a condenser microphone and a fine duct, the latter being necessary for picking up a pressure signal at a small localized region. The effects due to Helmholtz resonance and due to the duct loss at high frequency range were eliminated by suitable electrical devices. Further, a new method of calibration was developed. The measured correlation between pressure and velocity agrees satisfactorily with that estimated from the equation of energy balance.

§ 2. Symbols

c: sound velocity
D: diameter of cylinder
f: frequency of fluctuation
f_r: frequency of Helmholtz resonance
f_o: cut-off frequency
G: amplification factor of hot-wire network
G_k: amplification factor of pressure pick-up network
H_θ: output of hot-wire anemometer
h_θ: input to hot-wire anemometer
K: output of pressure pick-up
k: input to pressure pick-up

l: length of static pressure tube
M: time constant
p: pressure fluctuation
q: velocity vector
q_n: velocity component normal to hot-wire
$\tilde{q}_n$: a.c. component of q_n
R_e: Reynolds number
S: Strouhal number
s: cross sectional area of pressure duct
S_θ: sensitivity of hot-wire
S_k: sensitivity of pressure pick-up
U_0: speed of general flow
U: mean longitudinal velocity
u: fluctuating velocity component in the direction of general flow
V: mean transverse velocity
v: fluctuating velocity component transverse to the general flow
w: fluctuating velocity component in the direction parallel to the cylinder
x: distance measured in the direction parallel to general flow
y: distance measured in the direction normal to general flow
z: distance measured in the direction parallel to cylinder
α: residual coefficient
ρ: air density
ν: kinematic viscosity
θ: angle of rotation of the hot-wire measured from yz-plane
φ: angle between z-axis and axis of rotation of hot-wire
Φ: error factor for single rotary type hot-wire anemometer

§ 3. Equipment and Procedure

(a) General description of the measuring apparatus

The experiments were carried out in the 50 cm × 30 cm open-jet wind tunnel at the Faculty of Science, Hiroshima University. The wind speed could be changed from about 0.5 m/s to 17 m/s.

The measurements of the turbulence characteristics were made in the airstream of the speed 14 m/s in the cross section 42 cm downstream of a circular cylinder of 1 cm diameter mounted at the exit of the nozzle.

The velocity distribution was measured with a total head tube of 1 mm outer diameter and a hot-wire anemometer. The latter was used especially for measuring the transverse component.

The fluctuating quantities were measured with a pressure pick-up in combination with a single rotary type hot-wire anemometer placed close to the pick-up tubing.

The hot-wire and the pressure pick-up were mounted on a microscrew mechanism which is movable along x-, y-, and z- directions. Here x-axis is in the direction of the general flow, z-axis in the direction parallel to the cylinder, and y-axis normal to x- and z-axes (Plate. 1).

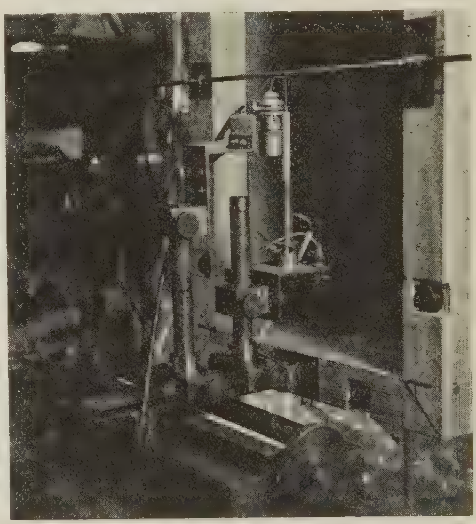

Plate 1. Arrangement of equipment.

The electric circuit for the pressure pick-up is composed of a ratio-detector type *F-M* discriminator and of an ordinary amplifier furnished with a band-rejection filter and with a compensating network. The circuit for the hot-wire anemometer is the same as that of Kovásznay.[8] Special computing networks are used for calculating various statistical quantities. The block-diagram of the circuit is shown in Fig. 1.

(b) Pressure measuring apparatus.

As a pressure transducer the condenser microphone with a ratio-detector type *F-M* discriminator is used because of its excellent sensitivity and reliability. But, in order to be used as a pick-up of local pressure in a wake, it must be combined with a tubing as a pressure duct. The scheme of the apparatus is shown in Fig. 2. Part A in the figure is a condenser microphone which serves as a transducer. The membrane A_1 made of aluminum sheet about 10 μ thick, is isolated electrically from the opposite electrode A_3 by the insulating sheet A_2 made of Valflon.* To control the sensitivity of the microphone, the space A_4 between the membrane and electrode can be varied by changing the thickness of A_2. The tension of the membrane A_1 is varied to a desired degree by screwing up the electrode A_3, thus shifting its resonance frequency to as high as 10,000 c/s. Part B shows the system of pressure duct, where the tube B_1 of 1.5 mm outer diameter has small static pressure holes B_2 on both sides. The combination of parts A and B leaves a small cavity B_3 between the membrane and the tubing.

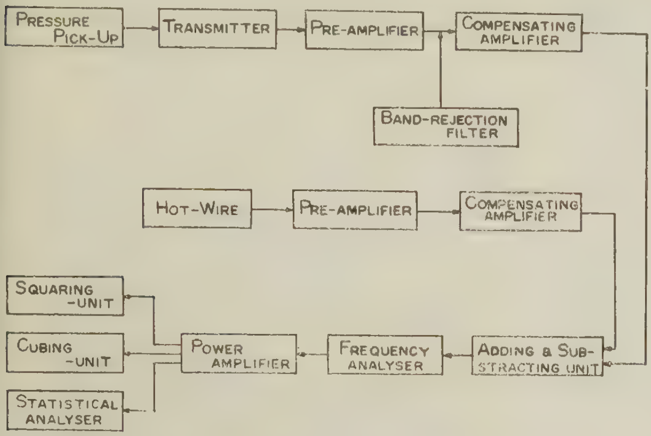

Fig. 1. Block diagram of circuit

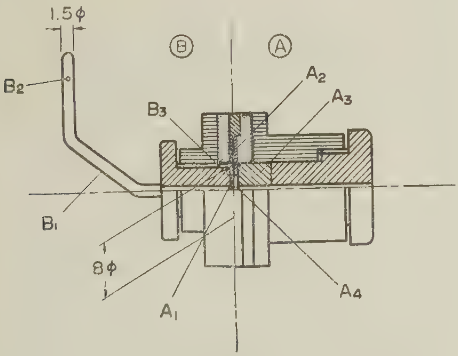

Fig. 2. Scheme of pressure pick-up.

In such a construction of the pressure pick-up, Helmholtz resonance and the duct loss cause secondary effects. The Helmholtz resonance[9] occurs theoretically at the frequency

$$f_r = \frac{c}{2\pi}\sqrt{\frac{s}{l V_{B_3}}}, \qquad (1)$$

where f_r is the resonance frequency of the cavity of volume V_{B_3} combined with a fine duct of length l and of cross section s, and c is the sound velocity. The loss by the tubing is expected to have the same characteristics as that of a hot-wire anemometer, increasing proportionally to the frequency at the high frequency range.[10]

In order to use such a pick-up as a measuring apparatus, these secondary effects must be compensated. For this purpose the following two ways can be considered:

(1) To shift the resonance frequency to the higher frequency range and to reduce the peak and the attenuation by changing the construction of the pick-up.

(2) To cancel out the resonance and the attenuation electrically by appropriate compensating networks.

In order to shift the resonance point to the higher frequency range, the dimension of the pick-up, especially the volume of the cavity B_3, must be reduced, and the duct must be made large in diameter and short in length. On the other hand, to reduce the resonance peak value, the duct must be made fine and long. These requirements not only contradict each other, but also reduce the sensitivity of the pick-up and therefore necessitate considerable improvement in the sensitivity of the subsequent circuits. This problem is now under study.

In the present work the second method was adopted by using a band-rejector and a compensating amplifier. The circuit of the band-rejector is shown in Fig. 3; the frequency band and degree of rejection can be varied at will.

Each amplifier is the same as that of Kovásznay with the exception that the circuit furnishes a cubing network in the output stage. The frequency characteristic of the amplifier is shown in Fig. 4 together with the response of the compensating network. In the same figure, the combined frequency response of the amplifier and discriminator is also shown, which is sufficiently flat over the range from 60 c/s to 3,000 c/s.

---

* Tokyo Shimoda Kogyo K.K.

(c) Calibration of the pressure pick-up

Various calibrating methods have been proposed to examine the dynamic response of the pressure pick-up. Some of the methods, based on mechanical principles, are inadequate for our purpose because they are limited to lower frequency range. On the other hand, acoustical methods, which are useful for a wider range, cannot be applied here because of the difficulty of getting a source of constant pressure. The method adopted by the author is to measure Kármán vortices in a wake of a circular cylinder.

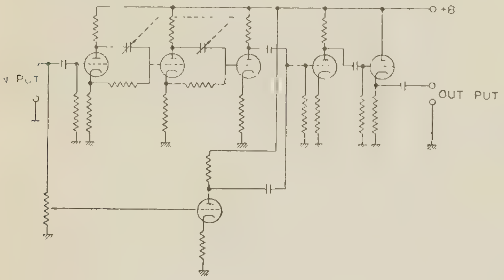

Fig. 3. Circuit of band-rejection filter.

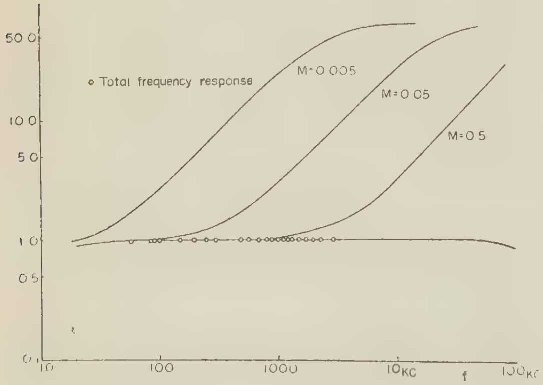

Fig. 4. Frequency characteristics of amplifier together with combined frequency response of amplifier and discriminator.

The frequency of Kármán vortices produced from a circular cylinder of diameter D is given by[11),12)]

$$f=S\frac{U_0}{D}\,, \tag{2}$$

where U_0 is the speed of general flow and S is the so-called Strouhal number which is nearly constant for the cylinder Reynolds number $R_e=\frac{U_0D}{\nu}$ between 10^2 and 10^4. The intensity of the vortex, $\overline{u}^2$, can be expressed in the form

$$\frac{1}{2}\rho\overline{u}^2\Big/\frac{1}{2}\rho U_0{}^2=F\left(R_e,\ \frac{x}{D},\ \frac{y}{D}\right), \tag{3}$$

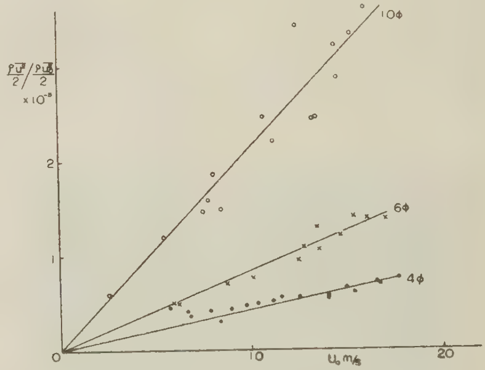

Fig. 5. Kármán vortex intensity measured by hot-wire anemometer.

where x and y are the distances measured in the directions parallel and normal to the general flow respectively. The results obtained by the hot-wire anemometer for various cylinder diameters are shown in Fig. 5, which suggests that the vortex intensity is proportional to the third power of U_0, that is

$$\overline{u}^2 \propto U_0{}^3\,. \tag{4}$$

Eq. (2) then gives

$$\overline{u}^2 \propto f^3\,. \tag{5}$$

For an isolated vortex, there must be a relation between its pressure defect p and its intensity $\overline{u}^2$ of the form[13)]

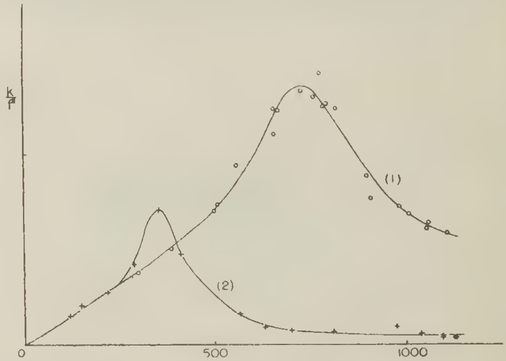

Fig. 6. Kármán vortex intensity measured by pressure pick-up without compensation.

$$p \propto \bar{u}^2 . \qquad (6)$$

If this is also valid in our case, we can expect

$$p \propto f^3 . \qquad (7)$$

Itokawa[14)] measured the pressure fluctuations in a separated flow from a flat plate inclined to the uniform flow, and some of his results seem to support our expectation.

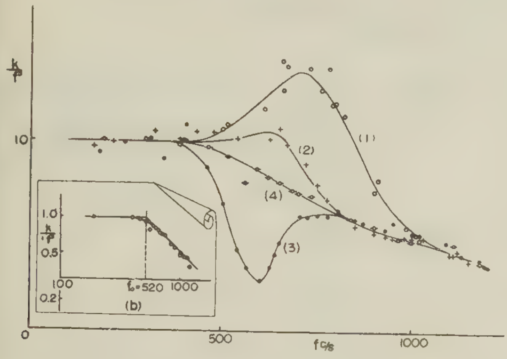

Fig. 7. Kármán vortex intensity measured by pressure pick-up with various rejection.

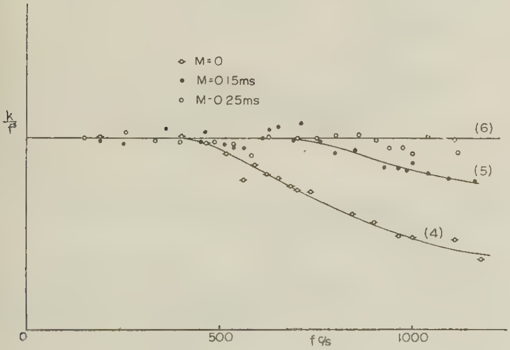

Fig. 8. Kármán vortex intensity measured by pressure pick-up with adequate compensation.

In Fig. 6 are shown the measured values of the pressure fluctuations at the same points at which the hot-wire measurements of Fig. 5 were obtained. The symbol k in the figure represents the input of the pressure pick-up, which is considered to be the sum of static pressure fluctuation and dynamic one arising from the velocity component normal to the holes. If the eqs. (5) and (7) are valied simultaneously, k must be proportional to f^3. The scale of the ordinate of the figure is taken arbitrarily for k/f^2. The two curves in the figure correspond to the different values of the cavity volume B_3. Each curve consists of three parts, namely, the part in which k/f^2 is proportional to f, the part of resonance, and the part in which attenuation is noticeable.

In Fig. 7 a, the curve (1) is the replot of the curve (1) of Fig. 6 while the curves (2), (3) and (4) correspond to the cases of over-rejection, under-rejection, and adequate rejection respectively. The curve of adequate rejection (4) is redrawn in logarithmic scale in Fig. 7 b, which shows

$$k/f^3 = \text{const} . \qquad (8)$$

in the low frequency range, and

$$k/f^3 \propto \frac{1}{f} \qquad (9)$$

in the high frequency range. This characteristic is to be expected from theoretical considerations, being quite similar as that of the hot-wire anemometer. The time constant of the pressure pick-up calculated from the curve (4) is

$$M = \frac{1}{2\pi f_0} = 0.3 \text{ ms} , \qquad (10)$$

which is of the same order of magnitude as that of the usual hot-wire anemometer. Here M is the time constant of the pressure pick-up and f_0 is the cut-off frequency. In Fig. 8, the curve (4) is the replot of the curve (4) of Fig. 7 a and the curves (5) and (6) are the results when the degree of compensation is changed. These results show a satisfactorily compensated response of the pick-up. Attention should also be paid to the phase characteristics, but in our case its effect is negligibly small.

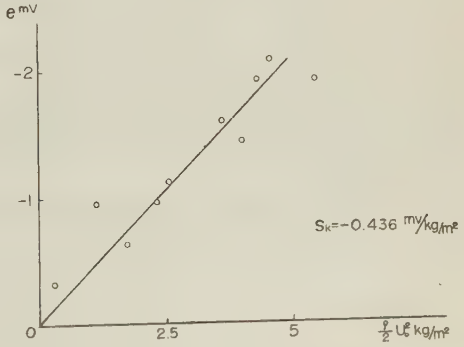

Fig. 9. Sensitivity of pressure pick-up.

In order to calibrate the sensitivity of the pressure pick-up, a static method was used. When the pick-up is used for fluctuating phenomena, a slight error may result because of the effect of compressibility. But the error is considered to be reduced by drilling a hole through the electrode as shown in Fig. 1, which allows the air in the cavity A_3 to pass freely. In Fig. 9 an example of the calibration curve is given, which shows that the sensitivity is fairly constant over a wide range of pressure change.

(d) Single rotary type hot-wire anemometer

The hot-wire anemometer used in our experiment is a single rotary type. The wire is carefully arranged so that its center coincides with the axis of rotation. This type of the hot-wire anemometer, although complicated for use and liable to introduce systematic errors when treated inadvertently, can be utilized for measuring various fluctuating quantities with high reliability if it is mounted and calibrated with the greatest care.

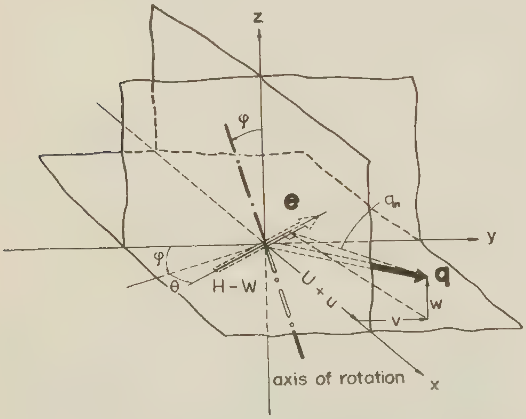

Fig. 10. Principle of measurement of turbulence characteristics by hot-wire anemometer.

The principle of measuring turbulence characteristics by a hot-wire anemometer of this type is described in the following together with the estimation of the error and of the limit of application.

Let the mean flow be in the direction of x-axis, and the hot-wire be rotated around the axis placed in the yz-plane (Figs. 10, 11). The angle between z-axis and the axis of rotation of the hot-wire is denoted by φ and the angle between the hot-wire and yz-plane by θ. If the instantaneous velocity vector is given by $\boldsymbol{q}$ and the direction of the hot-wire by the unit vector $\boldsymbol{e}$, the velocity component normal to the wire is

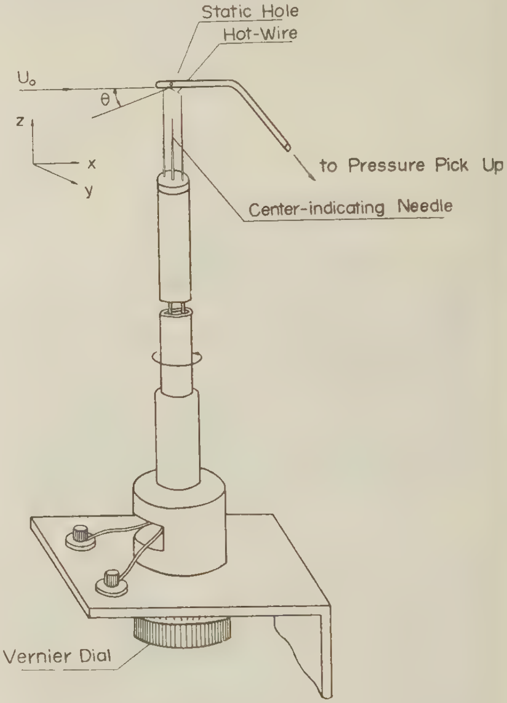

Fig. 11. Arrangement of pressure pick-up and hot-wire anemometer.

$$q_n = |\boldsymbol{q} \times \boldsymbol{e}| \, . \tag{11}$$

Since

$$\boldsymbol{e} = -\sin\theta\boldsymbol{i} + \cos\theta\cos\varphi\boldsymbol{j} + \cos\theta\sin\varphi\boldsymbol{k} \, ,$$

and

$$\boldsymbol{q} = (U_0 + u)\boldsymbol{i} + v\boldsymbol{j} + w\boldsymbol{k} \, ,$$

we have

$$q_n = U_0\cos\theta\left[\begin{array}{l} 1 + \dfrac{2}{U_0}(u + v\tan\theta\cos\varphi + w\tan\theta\sin\varphi) + \dfrac{1}{U_0}\{u^2 + v^2(\tan^2\theta + \sin^2\varphi)\} \\ +w^2(\tan^2\theta + \cos^2\varphi) + 2(uv\tan\theta\cos\varphi + uw\tan\theta\sin\varphi - vw\cos\varphi\sin\theta) \end{array}\right]^{1/2} . \tag{12}$$

Expanding the Eq. (12) into series, we obtain

$$q_n = U_0\cos\theta\left[\begin{array}{l} 1 + \dfrac{1}{U_0}(u + v\tan\theta\cos\varphi + w\tan\theta\sin\varphi) + \dfrac{1}{2U_0{}^2\cos^2\theta}(v^2\sin^2\varphi \\ +w^2\cos^2\varphi - 2vw\sin\varphi\cos\varphi) + \mathrm{o}(u^3) \end{array}\right] . \tag{13}$$

The a.c. component of q_n, denoted by $\tilde{q}_n$, is given by

$$\tilde{q}_n=(u\cos\theta+v\sin\theta\cos\varphi+w\sin\theta\sin\varphi)$$
$$+\left[\frac{1}{2U_0\cos\theta}(v^2\sin^2\varphi+w^2\cos^2\varphi-2vw\sin\varphi\cos\varphi)+\mathrm{o}(u^3)\right]. \tag{14}$$

If the term in the square bracket of Eq. (14) is neglected against the first term, the maximum error is estimated by the following equation.

$$\text{Error}=\frac{1}{2U_0\cos\theta}\frac{\overline{u^2}\sin^2\varphi+\overline{w^2}\cos^2\varphi\pm2|\overline{vw}|\sin\varphi\cos\varphi}{\sqrt{\begin{array}{l}\overline{u^2}\cos^2\theta+\overline{v^2}\sin^2\theta\cos^2\varphi+\overline{w^2}\sin^2\theta\sin^2\varphi\\ \pm(|\overline{uv}|\sin^2\theta\cos\varphi+|\overline{vw}|\sin^2\theta\sin^2\varphi+\overline{wu}\sin^2\theta\sin\varphi)\end{array}}} \tag{15}$$

The maximum errors can be evaluated provided appropriate assumptions are made conserning the magnitudes of cross products of the velocity components. For example, the estimated errors for typical cases are

(i) for isotropic turbulent flow

$$\left\{\begin{array}{l}\overline{u^2}=\overline{v^2}=\overline{w^2}\,,\ |\overline{uv}|=|\overline{vw}|=|\overline{wu}=0|\\ (\text{Error})_{\max}=\dfrac{1}{2\cos\theta}\dfrac{\sqrt{\overline{u^2}}}{U_0}\equiv\Phi_1(\theta,\varphi)\dfrac{\sqrt{\overline{u^2}}}{U_0}\end{array}\right. \tag*{(15)$'$}$$

(ii) for two-dimensional shear flow

$$\left\{\begin{array}{l}\overline{u^2}=\overline{v^2}=\overline{w^2}\,,\ |\overline{uv}|=0.4\overline{u^2}\,,\ |\overline{vu}|=|\overline{wu}|=0\\ (\text{Error})_{\max}=\dfrac{1}{2\cos\theta}\dfrac{1}{\sqrt{1-0.4\sin^2\theta\cos\varphi}}\dfrac{\sqrt{\overline{u^2}}}{U_0}\equiv\Phi_2(\theta,\varphi)\dfrac{\sqrt{\overline{u^2}}}{U_0}\end{array}\right. \tag*{(15)$''$}$$

(iii) for three-dimensional shear flow

$$\left\{\begin{array}{l}\overline{u^2}=\overline{v^2}=\overline{w^2}\,,\ |\overline{uv}|=|\overline{vw}|=|\overline{wu}|=0.4\overline{u^2}\\ (\text{Error})_{\max}=\dfrac{1}{2\cos\theta}\dfrac{1+0.4\sin^2\varphi}{\sqrt{1-0.4\{\sin^2\theta(\cos\varphi+\sin\varphi)+\sin\theta\sin^2\varphi\}}}\dfrac{\sqrt{\overline{u^2}}}{U_0}\equiv\Phi_3(\theta,\varphi)\dfrac{\sqrt{\overline{u^2}}}{U_0}\end{array}\right. \tag*{(15)$'''$}$$

The values of Φ_1, Φ_2 and Φ_3 are calculated and given in Table I. If we use the values of φ and θ in the domain bounded by thick lines in the table, then the error becomes less than the value of $\left|\dfrac{\sqrt{\overline{u^2}}}{U_0}\right|$.

From the input $h_{\theta,\varphi}$ corresponding to the angles φ and θ,

$$h_{\theta,\varphi}=u\cos\theta+(v\cos\varphi+w\sin\varphi)\sin\theta \tag{16}$$

values of $h^2_{\theta,\varphi}$ and $h^3_{\theta,\varphi}$ are computed electrically by the squaring and cubing networks respectively, and with the aid of these quantities various products of second and third orders can be obtained.

(e) Principle of obtaining the pressure fluctuation and its correlation to velocity fluctuation.

Let the output of the hot-wire anemometer, whose axis of rotation is parallel to the z-axis, be H_θ, and that of the pressure pick-up be K, then the input to each apparatus can be calculated respectively by

$$\left.\begin{array}{l}\dfrac{H_\theta}{S_\theta G}=h_\theta=u\cos\theta+v\sin\theta\,,\\ \dfrac{K}{S_k G_k}=k=p+\dfrac{\rho}{2}\alpha(v^2-\overline{v^2})\,.\end{array}\right\} \tag{17}$$

Here S_θ and G are the sensitivity and the amplification factor of the hot-wire, and S_k and G_k those of the pressure pick-up. The nondimensional coefficient α lies between zero and unity according to the stagnating effect of the hole. But since the value of p is of the order of

Table I. Values of error factor Φ_1, Φ_2 and Φ_3 and the limit of use for single rotary type hot-wire anemometer.

(i) isotropic case, Φ_1

θ	0	5	10	15	20	25	30	35	40	45
	0.500	0.502	0.508	0.518	0.532	0.552	0.577	0.610	0.653	0.707

(ii) two-dimensional case, Φ_2

φ \ θ	0	5	10	15	20	25	30	35	40	45
0	0.500	0.520	0.547	0.579	0.617	0.662	0.714	0.773	0.838	0.913
5	0.500	0.520	0.547	0.579	0.617	0.662	0.714	0.772	0.836	0.911
10	0.500	0.519	0.546	0.578	0.616	0.660	0.712	0.769	0.834	0.908
15	0.500	0.519	0.545	0.577	0.614	0.658	0.708	0.765	0.829	0.903
20	0.500	0.518	0.544	0.575	0.611	0.654	0.703	0.759	0.822	0.895
25	0.500	0.518	0.543	0.572	0.607	0.649	0.698	0.752	0.813	0.885
30	0.500	0.517	0.541	0.569	0.604	0.644	0.690	0.743	0.804	0.875
35	0.500	0.517	0.539	0.566	0.599	0.637	0.682	0.734	0.793	0.862
40	0.500	0.516	5.537	0.563	0.594	0.631	0.674	0.724	0.781	0.849
45	0.500	0.514	5.535	0.559	0.588	0.623	0.665	0.713	0.768	0.835

(iii) three-dimensional case, Φ_3

φ \ θ	0	5	10	15	20	25	30	35	40	45
0	0.500	0.520	0.547	0.579	0.618	0.665	0.715	0.773	0.840	0.914
5	0.535	0.560	0.592	0.632	0.682	0.739	0.804	0.878	0.960	1.053
10	0.568	0.599	0.639	0.688	0.743	0.819	0.902	0.996	1.100	1.212
15	0.600	0.637	0.682	0.742	0.814	0.901	1.000	1.123	1.255	1.400
20	0.629	0.671	0.722	0.791	0.878	0.980	1.100	1.259	1.428	1.610
25	0.653	0.699	0.750	0.837	0.935	1.060	1.233	1.398	1.615	1.840
30	0.673	0.723	0.797	0.873	0.984	1.126	1.308	1.533	1.796	2.083
35	0.688	0.741	0.812	0.903	1.024	1.180	1.383	1.646	1.966	2.317
40	0.697	0.751	0.824	0.919	1.047	1.211	1.433	1.721	2.080	2.481
45	0.700	0.755	0.829	0.926	1.054	1.225	1.451	1.749	2.124	2.547

$\rho u U_0$ and usually large compared to $\frac{\rho}{2}(v^2-\bar{v}^2)$, as confirmed by our measurement, we can approximately put $p=k$ independent of the value of α. Thus α may be conveniently put zero for calculating the pressure fluctuation.

When the pressure pick-up is used with a hot-wire anemometer which is mounted close to the static pressure hole, the correlation between pressure and velocity components can be obtained by

$$\left.\begin{aligned}\overline{pu}&=\frac{[(k+h_{\theta+})^2-(k-h_{\theta+})^2]+[(k+h_{\theta-})^2-(k-h_{\theta-})^2]}{8\cos\theta_+}-\frac{\rho}{2}\alpha\overline{uv^2}\\ \overline{pv}&=\frac{[(k+h_{\theta+})^2-(k-h_{\theta+})^2]-[(k+h_{\theta-})^2-(k-h_{\theta-})^2]}{8\sin_{\theta+}}-\frac{\rho}{2}\alpha\overline{v^3}\end{aligned}\right\}\qquad(18)$$

where θ_+ and θ_- denote the angles measured clockwise and anticlockwise respectively. Here the residual coefficient α can again be put equal to zero for the sake of convenience, since the contribution of the second term on the right-hand side of eq. (18) is negligible even if the value of α assumes its maximum value of unity.

§ 4. Results of Measurements in the Wake of a Cylinder

From the measurement at the cross section 42 cm downstream from a cylinder of 1 cm diameter, which was mounted in a uniform flow of the speed 14 m/s, the following quantities were obtained;

turbulent intensities: $\overline{u^2}, \overline{v^2}, \overline{w^2}$,

mean square of velocity derivative: $\overline{\left(\frac{\partial u}{\partial x}\right)^2}$

double velocity correlation: $\overline{uv}$,

triple velocity correlation: $\overline{u^3}, \overline{v^3}, \overline{u^2v}, \overline{w^2v}$,

pressure-velocity correlation: $\overline{pu}, \overline{pv}$.

Because of the two-dimensionality of the flow, the terms containing odd powers of w reduce to zero.

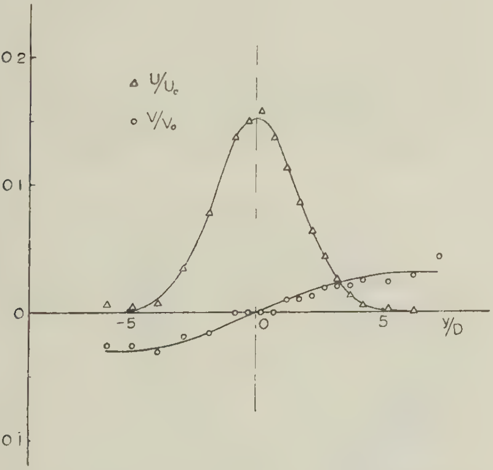

Fig. 12. Distribution of mean velocity components in nondimensional form.

In Fig. 12 are shown the distributions of mean velocity components $\frac{U}{U_0}$ and $\frac{V}{U_0}$. The figure shows that the jet velocity, V, is noticeable at the edge of the wake.

In Fig. 13 are shown in nondimensional forms the distributions of the components of the turbulent intensity and those of its diffusion.

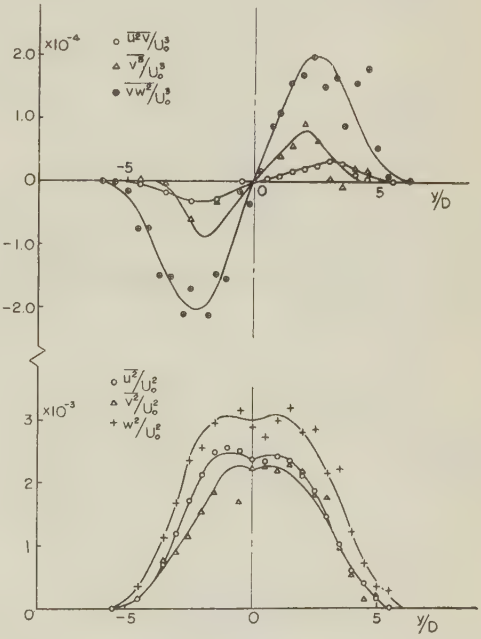

Fig. 13. Distribution of components of turbelent intensity and of its diffusion.

The distributions of turbulent intensity and its diffusion are shown in Fig. 14. In the same figure the turbulent intensity multiplied by the jet velocity is also shown. If the turbulent energy is transported by the jet velocity, as proposed by Townsend, the following relation must be expected

$$\overline{u^2v}+\overline{v^3}+\overline{w^2v}=V(\overline{u^2}+\overline{v^2}+\overline{w^2})\,. \qquad (19)$$

The measured results seem to support this proposition.

In Fig. 15 quantities such as $\overline{uv^2}$ and $\overline{v^3}$ are shown, which are used later for computing the pressure contributions.

The measured values of pressure fluctuation are shown in Fig. 16, in which $\frac{\rho}{2}\overline{v^2}\times 10$ is also given for comparison. The results show that the contribution of the dynamic pressure term to the pick-up input is so small that we can safely put $k=p$ as already mentioned in § 3. The figure also shows that the pressure fluctuation is of the order of $\rho U_0 u$ and has a bell-shaped distribution in the wake.

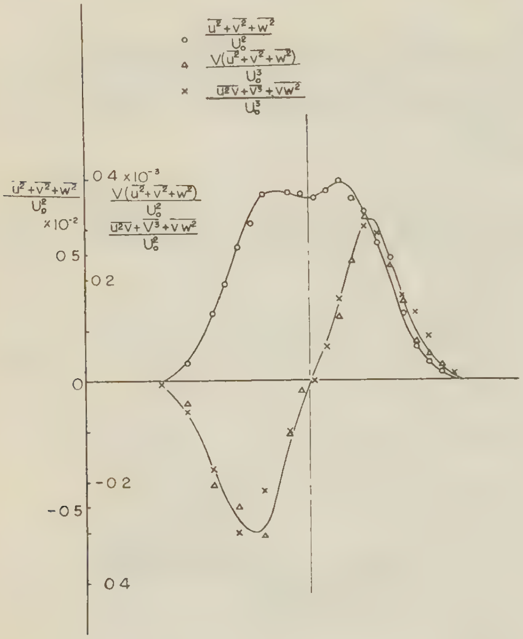

Fig. 14. Distribution of turbulent intensity and its diffusion.

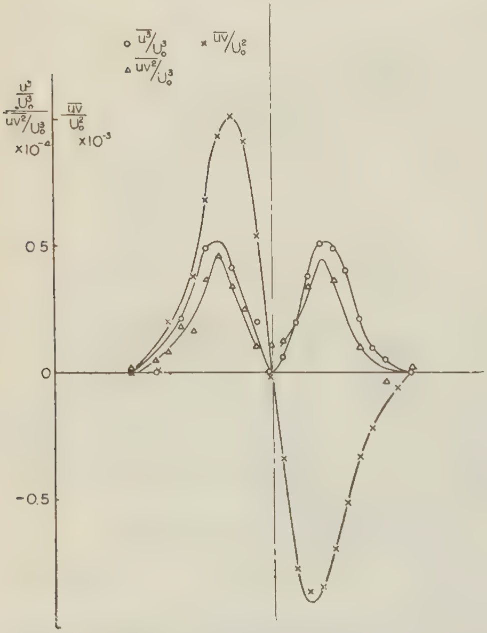

Fig. 15. Distribution of various turbulence characteristics in non dimensional form.

Fig. 17 shows the correlations between pressure fluctuation and velosity components.

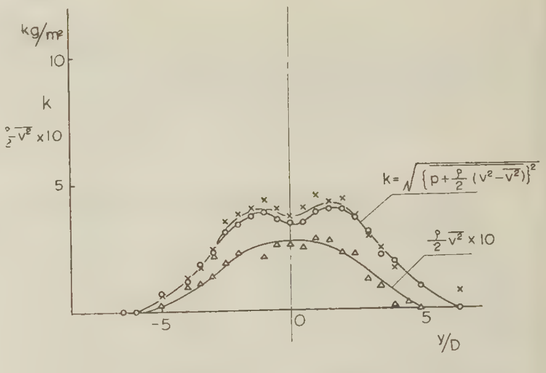

Fig. 16. Distribution of pressure fluctuation and energy component.

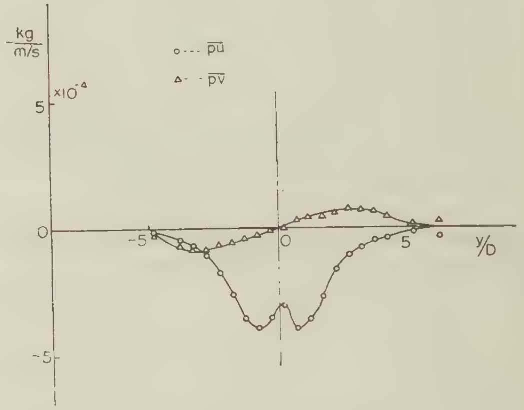

Fig. 17. Distribution of correlations of Pressure fluctuation to velocity components.

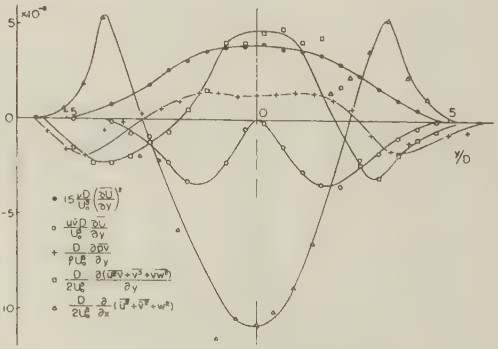

Fig. 18. Energy balance in non-dimensional form.

An interesting trend of the results is that $\overline{pu}$ has the sense such that a positive p corresponds to a negative u, while $\overline{pv}$ has the sense such that a positive p corresponds to a positive v. This tendency seems to be correlated with the fact that the increase in v corresponds to the decrease in u to produce a positive shear stress in the wake.

Since the turbulent energy must be conserved at each point in the wake, the equation of energy is expressed as

$$\left.\begin{aligned} &15\nu\overline{\left(\frac{\partial u}{\partial x}\right)^2}+\frac{U_0}{2}\frac{\partial}{\partial x}(\overline{u}^2+\overline{v}^2+\overline{w}^2)+\overline{uv}\frac{\partial U}{\partial y} \\ &+\frac{1}{2}\frac{\partial}{\partial y}(\overline{u^2v}+\overline{v}^3+\overline{w^2v})+\frac{1}{\rho}\frac{\partial\overline{pv}}{\partial y}=0 \end{aligned}\right\} \qquad (20)$$

on the assumption of the boundary-layer approximation and of local isotropy. Each term of the equation represents dissipation, advection, shear production, local diffusion and pressure flow, respectively. All these terms are plotted in nondimensional forms in Fig. 18, from which the validity of the relation (20) is confirmed. This in turn gives support to the reliability of the result obtained by the pressure pick-up.

§ 5. Concluding Remarks

The detailed description of the new pressure pick-up was given. The characteristics of the condenser microphone, the tubing and their combination was studied. The methods of compensating the secondary effects were considered and a band-rejection filter for the resonance and a compensating amplifier for the attenuation at the higher frequency range were introduced. By these means an apparatus with a sufficiently flat freqency response was obtained.

For the calibration of the apparatus, a new method was adopted in which Kármán vortices were used as reference, and the results were found to be satisfactory.

The principle of measuring turbulence characteristics by combined use of pressure pick-up and single rotary type hot-wire anemometer was discussed and the error and the limit of application were estimated.

The experimental results obtained are as follows;

(1) The pressure fluctuation is of the order of $\rho U_0 u$; this gives support to the fact that the input to the pick-up is equal to the pressure signal itself.

(2) The nature of the correlation between pressure and velocity fluctuation such as $\overline{pu}$ and $\overline{pv}$ is revealed for the first time both in the sense and the magnitude.

(3) The balance between gain and loss of various kinds of turbulence energy at a section in the wake is confirmed by the measurements of all terms in the energy equation. This fact, in turn, gives support to the reliability of the pressure pick-up.

Acknowledgement

The author wishes to express his thanks to Prof. I. Tani of Tokyo University for his kind advice and suggestion, especially for bringing the importance of the problem to his notice. His acknowledgement is also due to Prof. T. Maekawa for the continued interest and encouragement throughout the work.

The author is indebted to Mr. N. Kono and Mr. T. Nishi for their efficient assistance in carrying out the experiments. The work was partially supported by a research grant of the Ministry of Education.

References

1) A. A. Hall and G. S. Hislop: Proc. Camb. Phil. Soc. **34** (1949) 345-350.
2) L. S. G. Kovásznay: Proc. Roy. Soc. **A198** (1949) 174-190.
3) M. S. Uberoi and S. Corrsin: NACA TR 1142 (1953).
4) A. A. Townsend: *The Structure of Turbulent Shear Flow* Camb. Univ. Press (1956).
5) J. Rotta: Z. Phys. **129** (1951) 547-572.
6) J. Rotta: Ingen-Arch. **20** (1952) 195-207.
7) A. A. Townsend: Proc. Roy. Soc. **A197** 124-140.
8) L.S.G. Kovásznay: NACA TR 1209.
9) R. J. Lord Reighlay: *Theory of Sound* MacMillan (1929).
10) S. Takeda: Rep. Tech. Colledge, Hosei Univ. Japan **1** (1956).
11) A. Roshko: NACA TN 1953 (1953).
12) H. Komoda: To be published in Jour. Res. Inst. Tech. Nihon Univ.
13) H. Lamb: *Hydrodynamics* Camb. (1906).
14) H. Itokawa: Rep. Inst. Industrial Science, Univ. Tokyo **2** (1951).

JOURNAL OF THE PHYSICAL SOCIETY OF JAPAN Vol. 12, No. 5 MAY, 1957

Experimental Studies on the Stability of the Transonic Flow past Airfoils

By Fumio TAMAKI

Institute of Industrial Science, University of Tokyo

(Received February 7, 1957)

Local flow fluctuations near the airfoil surface have been measured in the speed range near critical Mach number, by using a Mach-Zehnder interferometer and a rotating-drum camera. Airfoils tested are Tomotika-Tamada airfoil, NACA-0012 and 10 per cent thick elliptic cylinder. Experiments show that amplitude and frequency of oscillation that appears when the local sonic speed is exceeded on the surface depend on the shape of the profile. In the cases of T.T.- and 0012-airfoils, the oscillation is of small amplitude and high frequency when the maximum local Mach number on the surface is not much above unity, and the time-mean pressure distribution on the surface is smooth and shows no appreciable distortion due to shock waves. In the case of the elliptic cylinder, slow oscillation of large amplitude involving distinct shock waves appears, as soon as sonic speed is exceeded on the surface.

§ 1. Introduction

Transonic flow with embedded supersonic region has been investigated theoretically by many authors, and it has been shown that a smooth, irrotational flow containing both subsonic and supersonic regions exists for some special shapes of the flow boundary. Wind tunnel experiments, however, contradict these theoretical findings in that the flow over the body surface either becomes unsteady or involves shock waves when the local sonic speed is exceeded anywhere on the surface. There have been many attempts to explain the reason for this discrepancy. (See references (1)–(5)). However, it seems to the present author that detailed experiments are still lacking in order to check these theories and to understand clearly the flow behavior at such critical speeds.

In the present paper, experiments are described, which have been carried out for obtaining some quantitative data as to the stability or instability of the flow in the local supersonic region and the process of formation of a steady shock wave.

§ 2. Experiments

Experiments were carried out in the I.I.S. high speed induced wind tunnel having a rectangular test section of 6 cm × 9.2 cm (Fig. 1). Compressed air was supplied to the injector from a reservoir of 10 m^3 volume and 10 atms. pressure. In order to prevent the flow at the test section from being influenced by the flow fluctuation at the injector slot, a variable throat was inserted between the test section and the slot, so as to make the flow sonic at the minimum section. Control of flow speed was effected by changing its area.

Models tested are: (1) Tomotika-Tamada airfoil$^{6)}$ for which a smooth irrotational flow with substantial supersonic region has been predicted; (2) NACA-0012; and (3) 10 per cent thick elliptic cylinder. Each has a chord of 3 cm and a span of 6 cm, which is equal to the tunnel width. Airfoil profile of Tomotika and Tamada changes with free-stream Mach number, but the profiles given for three Mach numbers, M=0.717, 0.745 and 0.752 differ quite little from each other, so only the profile for M=0.745 has been adopted for the model. The theoretical profile has a cusp at the trailing edge, but the model has a thickness of 0.2 mm there. Each model has a pressure hole on the surface, its position being 42, 40 and 50 per cent chord from the leading edge for airfoils (1), (2) and (3) respectively.

A Mach-Zehnder interferometer with a light source of high pressure mercury vapor lamp was used for measuring the density field. A monochromatic filter (5461 Å) was used for photographing the whole field, but it was removed for recording the flow fluctuations, in order to secure sufficient light intensity.

Flow fluctuations that appeared when the sonic speed was approached or exceeded on the surface were recorded by a rotating-drum camera. For this purpose, a diaphragm with a narrow slit was introduced into the light path, thus only the image of the fringes corresponding to a strip region parallel or perpendicular to the chord line was focused on a film wound on a rotating drum. (See Fig. 7). Fluctuations of flow in the wake were recorded by the same method. Width of the strip in the real flow field was 5 per cent of the chord. Peripheral speed of the drum was 19 m/sec, and the film length was 76 cm.

Experiments on the T.T.- and 0012-airfoils were carried out at zero incidence. A slight asymmetry was inevitable between the flow on the upper and the lower surface due to the presence of the support on the lower surface. Experiments on the elliptic cylinder were at first made for the case of small incidence ($\alpha \fallingdotseq 1°$), because the maximum speed of our tunnel was not high enough for obtaining a flow with any appreciable shock wave in the case of zero incidence. It will be called the A-case later on. Experiments at zero incidence were tried afterwards, by reducing the tunnel section to 6 cm × 8.6 cm. This will be called the B-case. In this case, however, the tunnel chokes as soon as the sonic speed is exceeded on the surface, so this case should be considered as a channel flow rather than a flow around a body in free air.

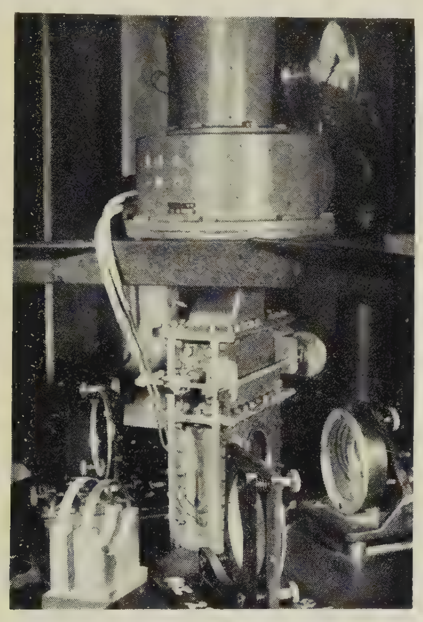
Fig. 1. Wind tunnel.

Reynolds number based on chord length was 4×10^5 at $M=0.75$. Boundary layer was in general laminar, and separation occurred immediately behind the point of minimum pressure. As such a flow was not suitable for any comparison with theory, the boundary layer was made turbulent by sticking a cellophane strip of 1 mm width and 0.1 mm thickness to each side of the airfoil near the leading edge. This caused an additional peak of negative pressure on its back; accordingly, its position and thickness were selected such that the sonic speed should not be exceeded there. It should be remarked that when the sonic speed is exceeded there, a shock wave appears and causes flow separation. For this reason, the trip was not applied to the elliptic cylinder.

§ 3. Discussion of Results

i) *Velocity distribution on the airfoil surface*

Fig. 2 shows one of the interferograms of the flow field. Distributions of pressure and velocity around the airfoil were determined from the density by assuming the isentropic relation. Even when the flow involves shock waves, the error due to entropy change is small, because we are only dealing with the case of weak shock waves in the present experiments. Figs. 3, 4 and 5 show examples of the velocity distribution on the airfoil surface. Here q is the velocity divided by the critical sound speed. In Fig. 3a, which represents the case of T.T. airfoil with boundary layer trip, theoretical curves for three Mach numbers are also included. Strictly speaking, these curves belong to three different profiles, but we may consider that these curves represent approximately the velocity distributions

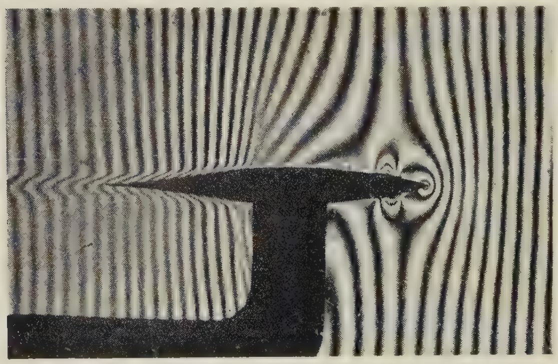
Fig. 2. Interferogram of the flow past T.T. airfoil ($M=0.754$).

on a fixed profile at different Mach numbers. It can be seen that experimental points lie fairly close to the corresponding theoretical curves. In the case without trip, experiments do not agree with theory as shown in Fig. 3b.

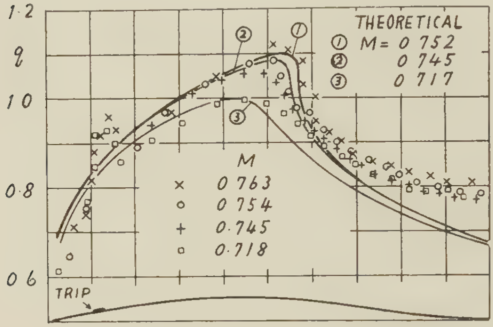

(a) with trip

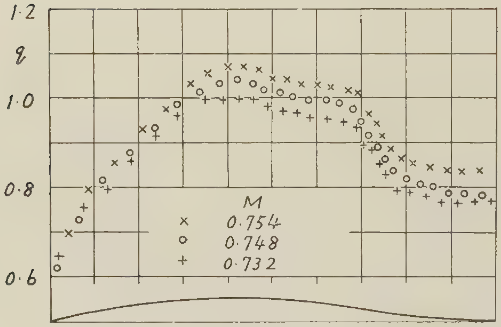

(b) without trip

Fig. 3. Velocity distribution on the surface: T.T. airfoil.

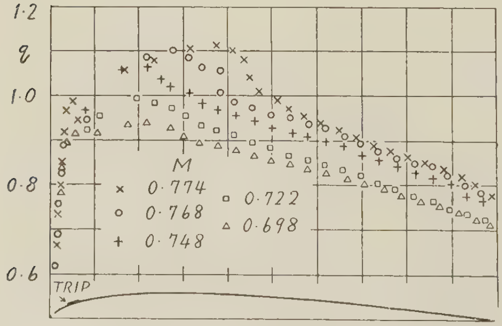

Fig. 4. Velocity distribution on the surface: NACA-0012 (with trip).

Fig. 5 represents the A-case of the elliptic cylinder, at which the pressure gradient along the surface is positive. The flow on the surface at M slightly above 0.80 fluctuates considerably due to the oscillating shock waves, as shown by the two different distributions for $M=0.803$.

ii) *Extent of the supersonic region*

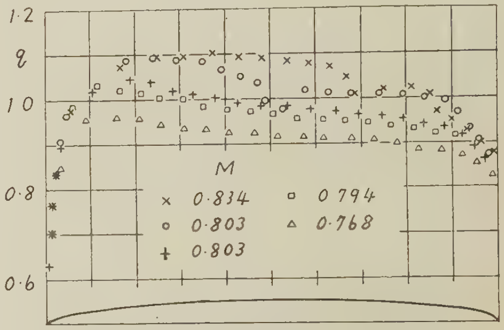

Fig. 5. Velocity distribution on the surface· 10 per cent thick elliptic cylinder ($\alpha \doteqdot 1°$).

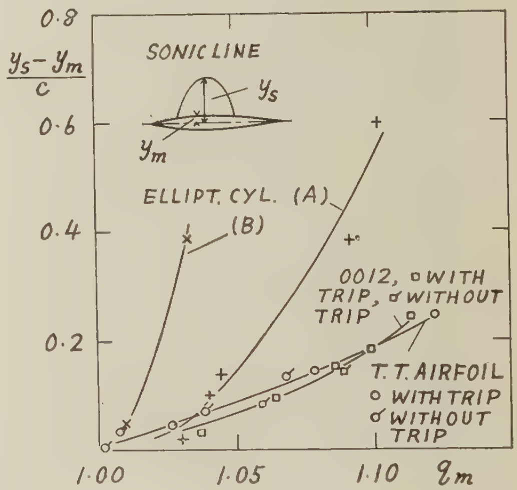

Fig. 6. Height of the sonic line.

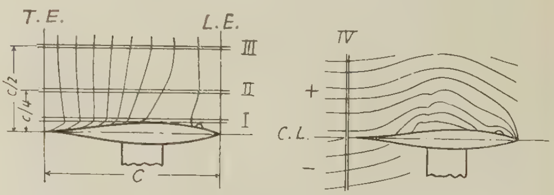

Fig. 7. Locations of the strip regions.

Based on the measurement of the density distribution in the whole field, equal-velocity contours have been drawn for each case. In Fig. 6, the height of the sonic line from the surface is plotted against the maximum velocity q_m on the surface. In this figure, y_s is the distance between the top of the sonic line and the chord line, y_m is the maximum ordinate of the profile and c the chord length.

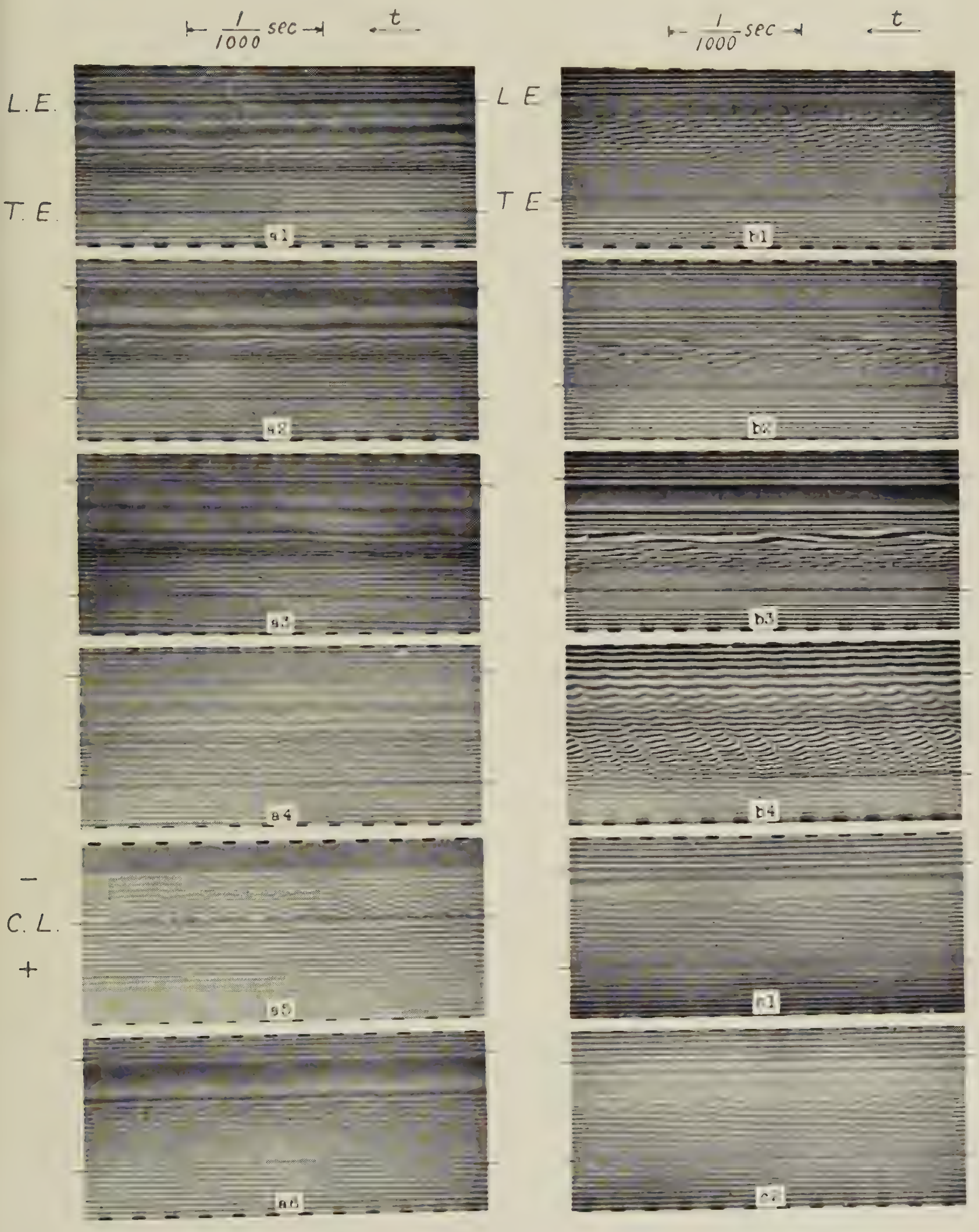

a. T.T. airfoil (1-5: with trip)
1. $M=0.731$, $\bar{q}_m=0.99$, Strip I
2. 0.742, 1.04, I
3. 0.759, 1.08, I
4. 0.768, 1.12, I
5. 0.726, 0.98, IV
6. 0.747, 1.03, I (without trip)

b. Elliptic cylinder: A-case
1. $M=0.765$, $\bar{q}_m=0.96$, Strip I
2. 0.803, 1.07, I
3. 0.803, 1.07, II
4. 0.800, 1.06, III

c. NACA-0012: with trip
1. $M=0.743$, $\bar{q}_m=1.05$, Strip I
2. 0.754, 1.08, I

Fig. 8. Records of the fringe fluctuations.

iii) *Flow fluctuations near the surface*

Fringe fluctuations in the strip regions shown in Fig. 7 were recorded by a rotating-drum camera. Short cuts of these records are shown in Fig. 8. These pictures correspond to the time interval of 3 milliseconds. Here $\bar{q}_m$ is the time mean of the maximum velocity on the surface estimated from the fringe analysis and the measurement of the static pressure at the hole. Accuracy of its value is rather poor when it approaches 1.1. Fringe records for the strip region tangential to the surface at the point of maximum thickness may be considered to represent approximately the flow fluctuations on the surface itself. These fluctuations are in general aperiodic and irregular, and the analysis is not easy. However, the following facts have been found.

(I) When the maximum velocity on the surface is subsonic but near to the sonic speed, there appears on the surface a series of weak unsteady shock waves traveling against the stream. This phenomenon has been already noticed by Hilton and Fowler[7]. Our preliminary experiments using spark photography also confirm this fact. Frequency of the unsteady shock is of the order of 5000 cps, as shown for example in Figs. 8a1 and b1. Fringe records for the strip perpendicular to the chord at the trailing edge show that the low frequency component in the wake has nearly the same frequency as the above-mentioned. From this, it may be concluded that these traveling shocks have their origin in the wake. Fig. 8a5 shows that there are also fluctuations of 10,000 to 20,000 cps behind the model support, but these do not affect the flow upstream due perhaps to their rapid decay.

(II) When the local sonic speed is slightly exceeded on the surface of T.T.- and 0012-airfoils, a flow oscillation occurs with a frequency lower and an amplitude larger than mentioned in (I). (Figs. 8a2 and c1). The frequency is 1000–1500 cps for the T.T. airfoil, and about 500 cps for the 0012. This type of oscillation does not occur on the elliptic cylinder; in the A-case, oscillation of the type that will be mentioned in (III) occurs, and in the B-case, a steady shock appears as soon as the sonic speed is exceeded on the surface.

(III) When the maximum local Mach number on the surface of T.T.- and 0012-airfoils approaches 1.1, there appears an oscillation whose frequency is of the order of 100 cps. In the A-case of the elliptic cylinder, the frequency is 30–40 cps. The flow involves oscillating shock waves, as shown in Figs. 8a3, b2 and c2, though these photographs are cut too short to see the whole periods.

(IV) These oscillations cease when the flow speed is raised further, and a flow involving a steady shock is formed (Fig. 8a4).

The oscillation mentioned in (II) may be considered as the repetition of the following processes. When the sonic speed is exceeded on the surface, the traveling shocks tend to accumulate at a certain point, but their pressure rise can be transferred upstream through the subsonic region outside, where the upstream movement of these shocks is still possible. This raises the pressure ahead of the accumulation point and smoothes the pressure jump. After that the flow returns to its initial state and repeats the same process.

The accumulation of the traveling shocks resembles the process described in Kuo's stability analysis (references (3) and (5)), but it should be noted that the process does not lead directly to the formation of a steady shock but causes flow oscillation at first. In view of the isolated character of the mixed potential flow, it is of course probable that the accumulation of the disturbances in the sense of Busemann's theory takes place at the end of the supersonic region, but it is impossible to distinguish it from the accumulation of the traveling shocks.

The above-mentioned two-dimensional shock diffusion exists also in stage (III), as clearly seen in Fig. 8b4 which shows the flow fluctuation in the subsonic region distant from the surface of the elliptic cylinder. Its effect on the flow ahead of the shock may be correlated to the extent of the local supersonic region. As shown in Fig. 6, it is much wider for the elliptic cylinder than for the two other airfoils. This seems to explain why a rapid oscillation of type (II) does not occur on the elliptic cylinder.

Fig. 9 shows the pressure fluctuations at certain points near the surface of the T.T. airfoil. Here p' is the fluctuation about the mean pressure and p_0 is the stagnation pressure. Two curves in the right of each diagram are the pressure distributions corresponding to the extreme values of p'. Pressure distribution on the surface is smooth as a time mean, and approximately agrees with the theoretical prediction, as shown by the interferograms taken under the exposure of the order of 1/100 sec. Also, the pressure distribution at the case when the steady shock appears nearly agrees with the theoretical one at the breakdown of the potential flow.

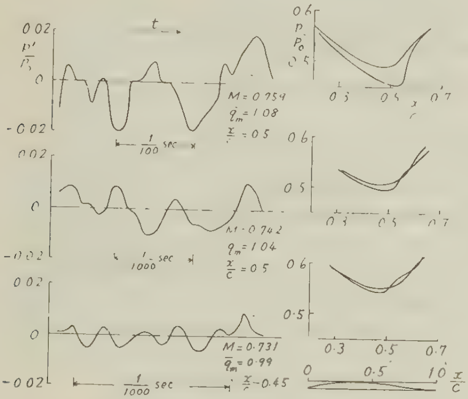

Fig. 9. Pressure fluctuation near T.T. airfoil (Strip region I).

Finally the maximum amplitude Δp of the pressure fluctuation in the region downstream of the point of minimum pressure is shown in Fig. 10. Steep rise of Δp corresponds to the appearance of the oscillation of type (III), and sudden fall corresponds to the settling down of the shock wave. Fluctuations on the 0012 are a little smaller than on the T.T. airfoil when q_m is near unity, but get larger as q_m is increased. It should be added here that in the case without the boundary layer trip fluctuations in the local supersonic region contain a considerable amount of high frequency components of about 5000 cps or more due to laminar separation, but the amplitude of low frequency oscillation is small (Fig. 8a6).

All these results have been obtained by using very small models. A certain kind of scale effect is expected to exist with respect to the frequencies and amplitudes of these oscillations. Such an effect will be a subject of future investigation.

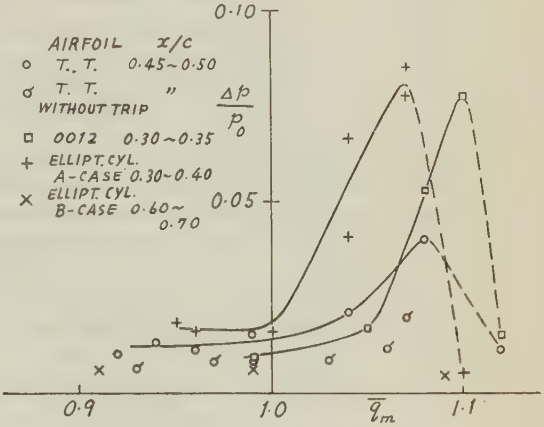

Fig. 10. Amplitude of the pressure fluctuation (strip region I).

The author wishes to express his cordial thanks to Mr. S. Nagai for his assistance during the course of the present work. This work has been partly aided by the fund of the Ministry of Education for scientific researches.

References

1) A. Busemann: J. Aero. Sci. **16** (1949) 337.
2) G. Guderley: Advances in Applied Mechanics, Vol. III, ed. R. von Mises and Th. von Kármán (1953) 145.
3) Y. H. Kuo: J. Aero. Sci. **18** (1951) 1.
4) W. F. Sears: J. Appl. Phys. **21** (1950) 771.
5) Y. H. Kuo and W. F. Sears: General Theory of High Speed Aerodynamics, ed. W. F. Sears (1954) 490.
6) S. Tomotika and K. Tamada: Quart. Appl. Math. **7** (1951) 381.
7) W. F. Hilton and R. G. Fowler: R. & M. No. 2692 (1947).

JOURNAL OF THE PHYSICAL SOCIETY OF JAPAN Vol. 12, No. 5, MAY, 1957

Studies on the Hypersonic Flow Using a Double-Diaphragm Shock Tube

By Fumio TAMAKI

Institute of Industrial Science, University of Tokyo

and KIM Chul-Soo

Department of Physics, Faculty of Science, University of Tokyo

(Received February 7, 1957)

A shock tube having two partition diaphragms is devised for generating a hypersonic flow free from air-liquefaction. The tube consists of a high and a medium pressure chambers of equal cross-section and a low pressure chamber with a narrow, slit-shaped inlet and a large area divergence. Hypersonic flow is generated by the expansion into the low pressure chamber of the air, which is initially contained in the medium pressure chamber and compressed to high pressure and temperature by the nearly clossed-wall reflection of the shock wave created by the rupture of the diaphragm between high and medium pressure chambers.

Flow of Mach number 6.4 with a duration of 1 millisecond is obtained and used for the studies of the flow past elliptic-nosed plates. Axis-ratios tested are 8, 1 (semi-circular nose) and 0 (square nose). Pressure distribution over the surface and head drag coefficient are determined by using a Mach-Zehnder interferometer.

§ 1. Introduction

One of the difficulties in hypersonic wind-tunnel techniques lies in the prevention of air-liquefaction caused by a considerable drop of temperature due to a large degree of adiabatic expansion. Supply air must be heated to a high temperature in order to be kept above the dew line after the expansion.

A shock tube method, utilizing a shock wave for heating the expanding air, has been devised by Hertzberg[1)], and a certain modification has been reported by Nagamatsu[2)]. An idea of a double-diaphragm shock tube with constant cross-section has been proposed by Bernstein[3)]. Although his method is excellent as to the gain in temperature at high Mach numbers, it requires considerable tube length, and so far as the present authors are aware, the experimental results have not been reported yet.

A divergent shock tube, having a diaphragm adjacent to the entrance of the divergent channel of the low pressure chamber, has been previously used by the present authors[4),5)] for the studies of supersonic flows of Mach numbers less than 6. In this shock tube, supersonic flow is obtained by the expansion of the air which is initially contained in the high pressure chamber, so the pre-heating of the air is necessary in order to use this shock tube for high Mach numbers. Addition of one more stage of high pressure chamber for this purpose has led us to a double-diaphragm shock tube somewhat different from the above mentioned. In order to obtain a flow of very high Mach number, maintaining its state above the dew line, and to secure sufficient duration of steady flow, it is of course necessary to use a long medium pressure chamber. The tube length is however shorter than the Bernstein's and the pressure adjustment of the low pressure chamber seems to be easier.

The shock tube here constructed has been used for the investigation of the flow past elliptic-nosed plates at $M \doteq 6.4$. Such experiments at low and moderate supersonic speeds have been reported by Holder and Chinneck[6)], A. Ferri[7)] and others[8),9)]. In the present experiments, the same types of the leading edge shape as those of Holder and Chinneck have been dealt with. As the Reynolds numbers in both experiments are nearly the same, the comparison of the results is significant and enables us to understand the Mach number effect on the flow character near the leading edge, particularly on the nose drag of the body moving with supersonic speed.

§ 2. Equipments

The schematic diagram of the present shock tube and dimensions of the main parts are shown in Fig. 1. High and medium pressure channels are of equal cross-section. Medium pressure channel is bent in rectangle, due to the limit in the available height of the room. Low pressure chamber consists of a rectangular tube and a receiver of a large volume. Straightly diverged nozzle is formed by wooden liners inside the tube. Test chamber has a rectangular cross-section of 15×6 cm². This cross-section is continued by a duct inserted into the receiver nearly to its mid-point. As for the partition diaphragms, three or four sheets of cellophane of 40 micron thickness are used for D_1, and a thin cellophane of 18 micron thickness is used for D_2. D_1 is broken by a needle, and D_2 by the shock wave.

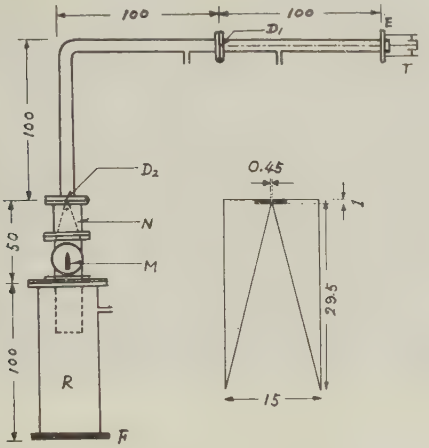

Fig. 1. Schematic diagram of hypersonic shock tube. T (Trigger), D_1 (1st draphragm), D_2 (2nd diaphragm), N (Nozzle), M (Model), R (Receiver), ED_1 (High pressure chamber), D_1D_2 (Medium pressure chamber), D_2F (Low pressure chamber), Dimensions in centimeter.

Models tested are three elliptic-nosed plates of axis-ratios $\lambda=2L/t=8$, 1 (semi-circular nose) and 0 (square nose). All the plates are 8 mm thick, and supported by thin stings attached to their mid-span. Mach-Zehnder interferometer with a light source of magnesium spark has been used for optical measurements. The shock tube has been operated at a Mach number of 6.4, and Reynolds number is 1.35×10^5 per centimeter.

§ 3. Theoretical Consideration

As shown in Fig. 1 the whole tube is divided into three parts by two diaphragms D_1 and D_2. The first two chambers constitute an ordinary shock tube. Actually, there is a bent at the middle of the second chamber, but it is simply neglected in the present consideration, assuming that the weakening of the incident shock and the disturbance to the flow behind it are small. Then, the shock generated in the second chamber by the rupture of D_1, together with the flow state behind it, can be predicted by the usual shock tube theory. Fig. 2 shows a wave diagram for the case of initial pressure ratio $p_2/p_1=13/4$, where p_2 and p_1 denote the initial pressure in high and medium pressure chambers, respectively. Abscissa is the distance x along the tube axis, and ordinate is the time t multiplied by the sound speed a_1 corresponding to the initial temperature. (It is assumed that the initial temperature is the same for all the chambers.)

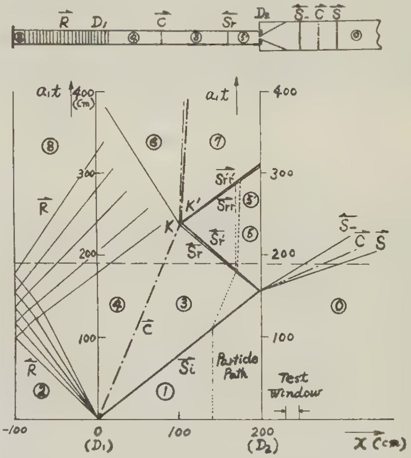

Fig. 2. Wave diagram.

The second diaphragm D_2 is situated at the end of the second chamber, i.e., just in front of the slit-shaped inlet of the third, low pressure chamber. There the shock is reflected, and at the same time, D_2 is broken by the pressure rise due to the shock reflection, and a certain amount of air compressed to high pressure and temperature expands through the divergent channel to a hypersonic speed. Shock reflection at the position of D_2 can be calculated by using shock polars under the assumptions: flow is sonic at the throat and one-dimensional steady flow relation holds between the throat and the upstream tube, and the shock reflection takes place so as to satisfy the condition that the flow Mach number behind the reflected shock is equal to the value determined by the area ratio A_*/A_1 of the throat to the upstream tube. As A_*/A_1 is small, we may expect that the shock reflection does not differ much from that at a closed wall. Assuming the initial pressure ratio $p_2/p_1=13/4$, we have, for the closed-wall reflection, $p_5/p_1=2.97$, $\rho_5/\rho_1=2.16$ and $T_5/T_1=1.38$, where 5 denotes the quantities behind the reflected shock; while in the case of real reflection, we have $p_{5'}/p_1=2.87$, $\rho_{5'}/\rho_1=2.11$, $T_{5'}/T_1=1.37$ and $u_{5'}/a_1=0.02$, where $u_{5'}$ is the flow velocity behind the reflected shock. Here and in Fig. 2, primes attached to the letters denote the case when the mass flow through the nozzle is taken into account. In this calculation, the effective value of A_* has been assumed to be 1.28 cm^2, which is about a half of the geometrical area of the nozzle inlet. This value of A_* has been estimated from the fact that a quasi-steady flow of $M=6.4$, which is considerably higher than expected from the geometrical area ratio of the test section to the nozzle inlet, has been obtained at the test section. This fact, which may be attributed to the viscosity effect at the throat was also experienced in our previous single-stage divergent shock tube[4),5)].

The wave propagation and the associated flow in the low pressure chamber can be calculated by the method of characteristics. However, for a rough estimation of the time of establishment of the quasi-steady flow at the end of the divergent channel, it is sufficient to approximate the continuous area change by one or two discontinuous steps. Procedure for such a calculation is given by Rudinger[10)]. Wave diagram in the right part of Fig. 2 has been obtained by replacing the whole area change by a single step at the inlet of the divergent channel. In this diagram, the initial condition is $p_2:p_1:p_0=13$ atms: 4 atms: 2 mmHg and $T_2=T_1=T_0=285°$K. A quasi-steady flow of high Mach number is obtained in the test section after the passage of the primary shock, contact surface and the secondary shock. Temperature of this flow is about 42°K for $M=6.4$ which is actually obtained in the experiment. This is nearly equal to the air-liquefaction temperature estimated by an extrapolation of Hausen's T-S diagram[11)]. However, since a certain degree of supersaturation is expected, there may be no fear of air-liquefaction.

§ 4. Results

Schlieren photographs showing the flow history at the test section are given in Fig. 3. These photographs have been obtained under the condition: $p_2=13$ atms, $p_1=4$ atms and $p_0=2$ mmHg. Fig. 3a shows the primary shock advancing toward the wedge. Fig. 3b shows the flow near the contact surface. Here the wide zone of mixing of cold and hot airs appears instead of a thin contact surface. Fig. 3c shows the flow near the secondary shock. After the secondary shock is swept downstream, a quasi-steady flow of $M=6.4$ is established with a duration of 1 milli-second. This is shown in Fig. 3d.

Mach number of the stationary flow has been determined by the measurement of Mach angle. For this purpose, several strips of cellophane tape have been sticked to each of the diverging walls, and the angle between the wave fronts originating from each side has been measured. This gives the value of $M=6.4$ for the initial condition given above. The same condition has been kept through the experiments.

The flows past elliptic-nosed plates have been investigated by schlieren method and interferometer. Photographs for the case of $\lambda=8$, 1 and 0 are shown in Figs. 4a, 4b and 4c, respectively. Results will be discussed separately according to the axis-ratio, and will be compared with the experiments of Holder and Chinneck at low supersonic speeds.

$\lambda=8$: Distribution of the static pressure p on the surface expressed in non-dimensional form by dividing it by the total pressure p_n behind a normal shock is given in Fig. 5. Results of Holder and Chinneck for $M=1.42$ and 1.79 are shown in the same figure. As seen in this figure, pressure falls monotoniously from the value at the nose, which is close to the theoretical total head p_n behind the normal shock, to the free stream value p_∞ far back on the plate. In Fig. 6, the pressure distribution along the surface in non-dimensional forms of $(p-p_\infty)/p_\infty$ is plotted against y, the coordinate normal to the free-stream direction. Dotted lines in the neighborhood of

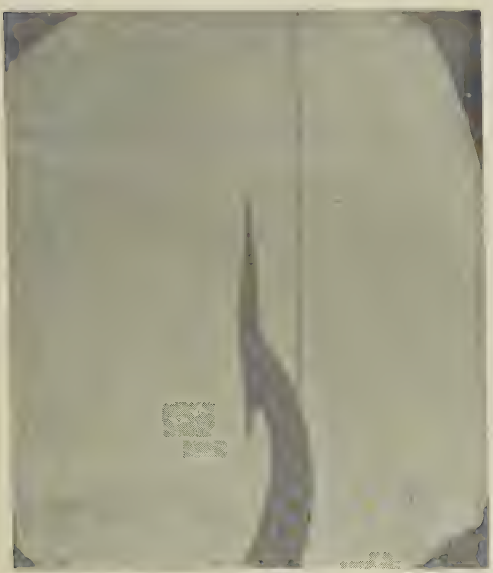

Fig. 3a.

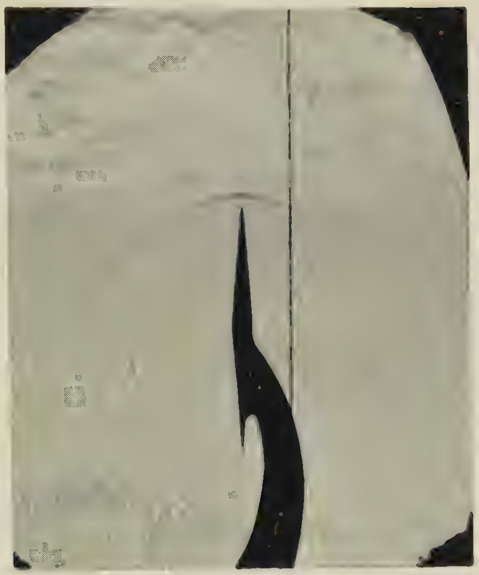

Fig. 3b.

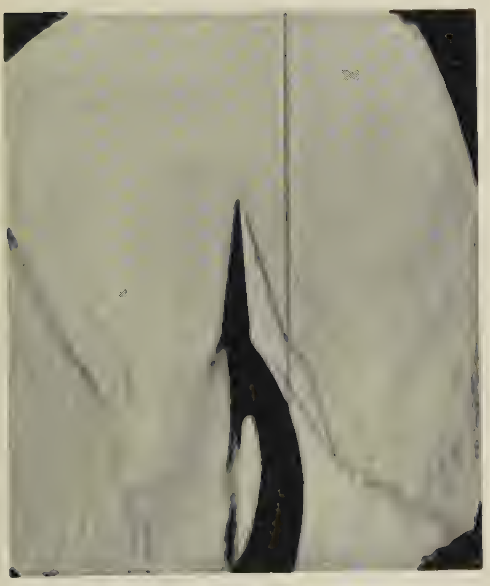

Fig. 3c.

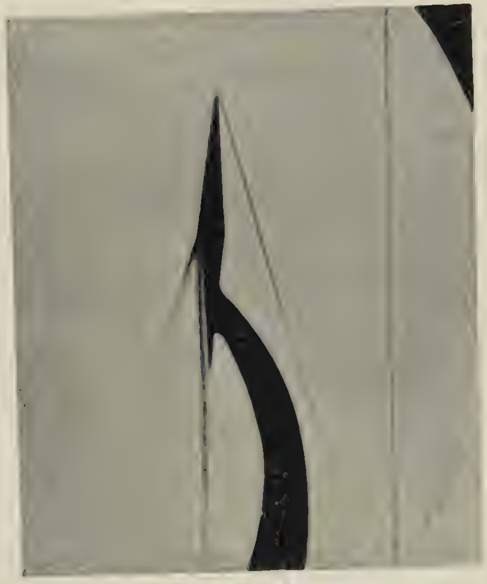

Fig. 3d.

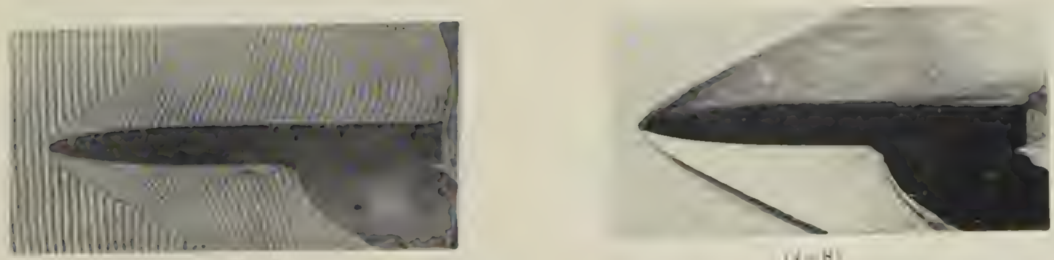

($\lambda=8$)

($\lambda=8$)

Fig. 4a.

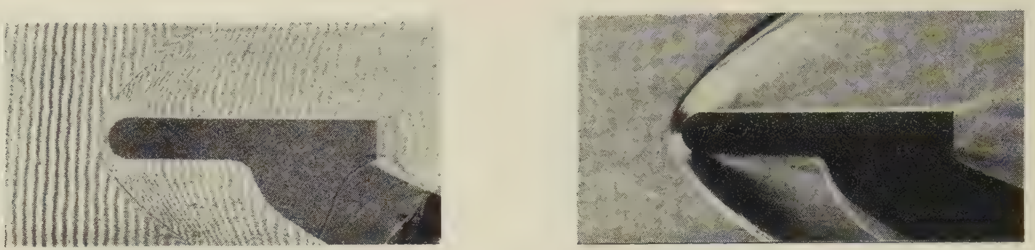
(λ=1) (λ=1)

Fig. 4b.

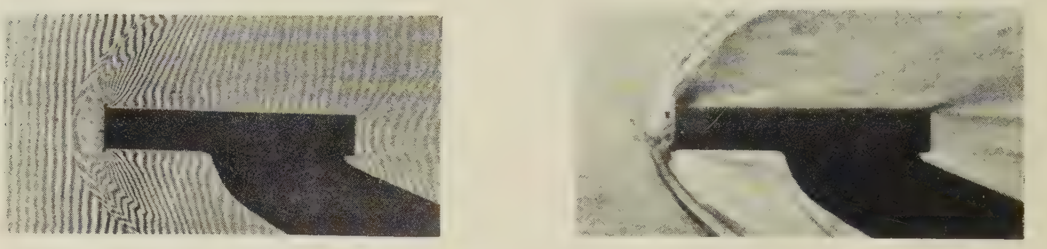
(λ=0) (λ=0)

Fig. 4c.

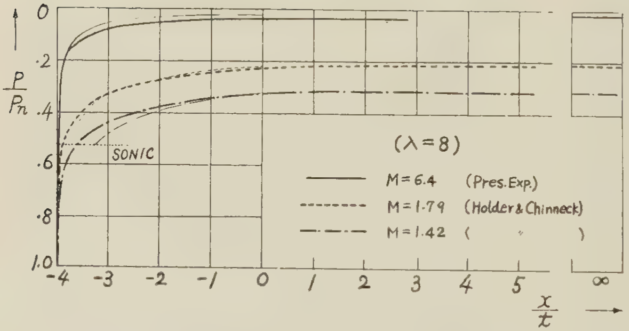

Fig. 5. Pressure distribution along the surface (λ=8). (Thin lines: Corresponding curves based on Busemann's theory.)

the nose denote our experimental values of $(p-p_\infty)/p_\infty$ for a circular cylinder, whose radius is taken to be equal to the radius of curvature at the nose. Chain lines in this figure and thin lines in Fig. 5 give the theoretical values of $(p-p_\infty)/p_\infty$ and p/p_n, respectively, calculated by Busemann's second order theory assuming that the pressure at the shoulder is equal to the free-strerm value. Even in the case of $M=6.4$, Busemann's theory shows good agreement with experiments except in the neighborhood of the nose.

$\lambda=1$: Experiments of Holder and Chinneck at low supersonic speed show that the minimum pressure occurs near the shoulder due to the over-expansion around it. But in our case, no striking peak of negative pressure is observed. (Fig. 7)

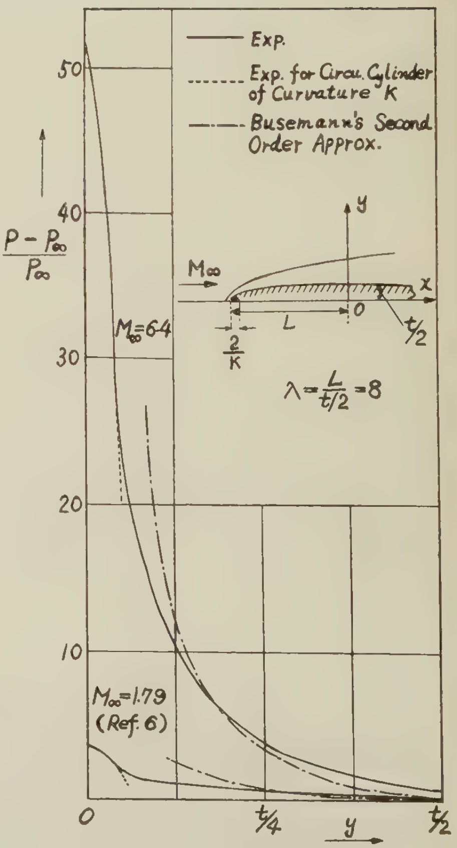

Fig. 6. $(p-p_\infty)/p_\infty$ vs. y ($\lambda=8$).

$\lambda=0$: In the low supersonic flow, negative pressure near the shoulder becomes more and more pronounced as the nose becomes blunter

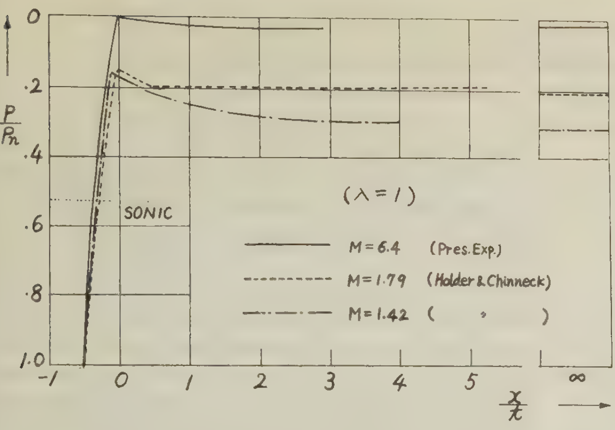

Fig. 7. Pressure distribution along the surface ($\lambda=1$).

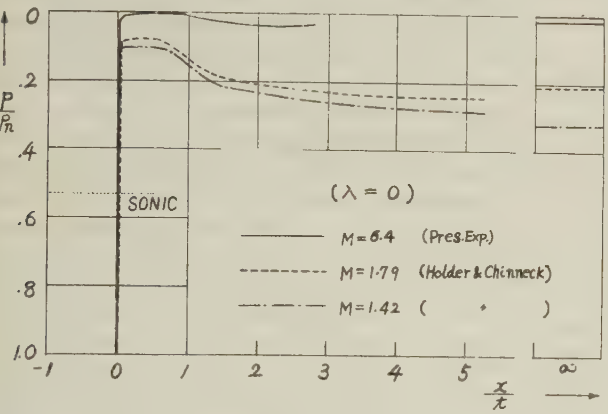

Fig. 8. Pressure distribution along the surface ($\lambda=0$).

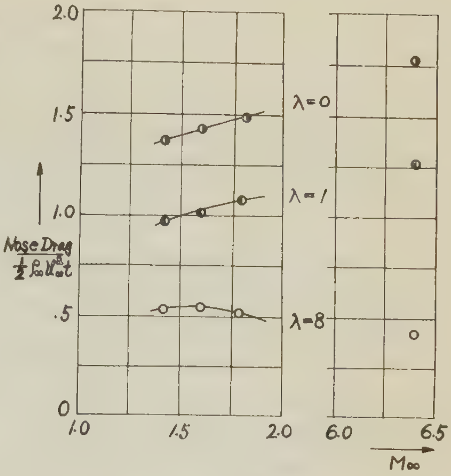

Fig. 9. C_{DN} vs. M.

and a distinct bubble caused by the separation and the reattachment of the flow appears at the shoulder. But in our case, these phenomena become less distinct due to a considerable thickening of the boundary layer. The pressure on the surface is shown in Fig. 8.

The nose drag coefficients defined by $C_{DN}=$ nose drag$/\frac{1}{2}\rho_\infty u_\infty^2 t$, where ρ_∞ and u_∞ are the density and the flow velocity of the free stream and t the thickness of the plate, are calculated from the pressure distribution, and are plotted aginst M together with the values at low supersonic speeds (reference 12) in Fig. 9. Since our interferograms for the case of $\lambda=0$ are rather indistinct as shown in Fig. 4c, the determination of the pressure distribution on the frontal surface is almost impossible, so the value of C_{DN} for this case is obtained by assuming that the pressure at the stagnation point is equal to the theoretical value and that the velocity increases linearly with the distance along the surface to the sonic speed at the shoulder. Experiments of Holder and Chinneck show that nose drag coefficient increases or decreases according to whether the nose is blunt or sharp, as expected from Ackeret's formulas. Our results show that this tendency holds even in the hypersonic flow. However, the change of C_{DN} with M seems to be smaller than in the low supersonic flow.

References

1) A. Hertzberg: J. Aero. Sci. **18** (1951) 803.
2) H. T. Nagamatsu: ibid. **22** (1955) 165.
3) H. Bernstein: ibid. **20** (1953) 790.
4) F. Tamaki: J. Phys. Soc. Japan **11** (1956) 434.
5) C. S. Kim: ibid. **11** (1956) 439.
6) D. W. Holder and A. Chinneck: Aero. Quart. **4** (1954) 317.
7) A. Ferri: Atti di Guidonia **67, 68, 69** (1942).
8) W. E. Moeckel: NACA TN **2418** (1951).
9) W. B. Fallis, G. W. Johnston, J. D. Lee, N. B. Tucker and J. H. Wade: UTIA Rep. **15** (1953).
10) G. Rudinger: *Wave Diagrams for Nonsteady Flow in Ducts*, D. Van Nostrand, New York (1954) 94.
11) L. Howarth: *Modern Developments in Fluid Dynamics, High Speed Flow*, Vol. **2** (1953) 538.
12) M. J. Lighthill: *Section E, General Theory of High Speed Aerodynamics*, edited by W. F. Sears, Princeton (1954).

Short Notes

This section is intended to secure prompt publication of important discoveries in physics. The reports should not exceed 800 words in length. A figure of size 7 cm × 7 cm will be counted as 150 words.

J. PHYS. SOC. JAPAN **12** (1957) 556

The Absorption Spectra of Ruby

By Y. TANABE

Department of Applied Physics, Tokyo University, Tokyo

and S. SUGANO

Department of Physics, Tokyo University, Tokyo

(Received March 16, 1956)

The absorption spectrum of Ruby (Cr^{3+}; Al_2O_3) in the opical region is quite analogous to that of Cr alum; it consists of two bands (obs. max. 18,000 cm^{-1}, 25,000 cm^{-1}) and several groups of lines situated at 14,000 cm^{-1} and 21,000 cm^{-1}.[1] Ruby shows, however, remarkable dichroism,[2] which is not clearly observed in the case of alum.

From the crystal structure of Al_2O_3, we see that the Cr^{3+} ion which substitutes the Al^{3+} ion is surrounded by six O^{2-}'s nearly octahedrally and therefore subjected to the strong cubic field as in the case of octahedral complex ion, besides the strong trigonal field which was weak in the latter.

This resemblance and the difference of the environment of the Cr^{3+} ion in these two cases lead us to expect that we can provide a firmer foundation of the theory of the absorption spectra of complex ions[3] by analyzing the spectra of dichroic Ruby.

We quote here several features of the spectrum.

(1) The first band and the characteristic doublet R_1 and R_2 show similar behaviour for linearly polarized light, i.e., the absorption is maximum for the light whose electric vector E is $\perp C_3$ (the optical axis) and minimum for $E//C_3$.[4] The emitted light of R_1 and R_2 is also polarized in the plane $\perp C_3$.[1][2]

(2) The sharp doublet R_1 (14,418 cm^{-1}) and R_2 (14,447 cm^{-1}) both show the Zeeman effect.[5] The pattern consists of an unshifted line and two nearly equally displaced side components when $H_0//C_3$ and $E\perp C_3$ (σ component). Contrary to the case of free ion spectra, the central component is stronger than the side components. When $H_0\perp C_3$ and $E\perp C_3$ (σ and π component), the pattern consists of four almost equally spaced components, their intensity being almost equal. Aside from several small differences for R_1 and R_2, these are features common to the Zeeman pattern of both R_1 and R_2.

We want to interprete these facts by using the model for the complex ion.

(1) The existence of sharp lines: The sharpness of the lines is probably due to the lack of the first order interaction between electron and nuclear motion in both the exited and ground state. That fact is peculiar to the half filled shell.

(2) The optical anisotropy: According to the theory of the absorption of the complex ion, the intensity of R_1, R_2 is stolen from that of the first band, so that it is quite reasonable that they show similar dichroism. The anisotropy of the first band is explained by assuming that the transition is that of the electric dipole coupled with the trigonal field V (F_{1uz}) whose exis is C_3. This assumption also explains the anisotropy of the second band. Thus we feel that the assignment (1st band: ${}^4A_2 \rightarrow {}^4F_2$, 2nd band: ${}^4A_2 \rightarrow {}^4F_1$) made in the previous paper is now almost established.

(3) The Zeeman pattern: The features of the Zeeman pattern enables us to conclude that R_1 and R_2 correspond respectively to the transition from the ground quartet to the doubly degenerate level (denoted as E') and the degenerate two levels (2A′) (Kramers' degeneracy) which are split from ${}^2E$ level by the interplay of the effects of the trigonal field and the spin orbit interaction. The g-values of these two exited states are anisotropic: $|g_{//}|=2$, $g_{\perp}=0$ for both of the levels. This explains the number of Zeeman components when $H_0//C_3$ and $H_0\perp C_3$. (The g-value of the ground quartet is almost isotropic and ~ 2.) The appear ance of the central line in the σ component when $H_0//C_3$ is explained by $g \sim -2$ for E' (R_1) and the transformation property of $2A'$ state wave function $\left(\sim \exp\left(\pm \frac{3}{2} i\varphi\right)\right)$ in spite of $g_{//} \sim 2$ for $2A'$ (R_2). Furthermore the intensity distribution in Zeeman pattern is nicely explained by this assignment. The observed asymmetry of the pattern can also be explained by taking the ground state natural splitting into account.

Details will be given in a later communication.

References

1) O. Deutschbein: Ann. d. Phys. (5) **14** (1932) 712, 729; ibid. (5) **20** (1934) 828.

2) B. V. Thosar: Phys. Rev. **60** (1941) 616. J. Chem. Phys. **10** (1942) 246.

3) Y. Tanabe and S. Sugano: J. Phys. Soc. Japan **9** (1954) 753, 766.

4) According to the preliminary experimental result obtained in the laboratory to which one of the authors S.S. belongs the absorption is maximum when $E//C_3$ and is minimum when $E\perp C_3$ for the 2nd band.

5) H. Lehmann: Ann. d. Phys. (5) **19** (1934) 99.

J. PHYS. SOC. JAPAN **12** (1957) 557

The Absolute Intensities of Cosmic Rays at 2840 Meters and Geomagnetic Latitude 25°N

By Masakazu MURAKAMI and Toshiro MAEDA
Department of Physics, Kobe University

(Received January 26, 1957)

In a previous note[1], refered to hereafter as (A), the absolute intensities of cosmic rays at sea level ($\lambda=25°$N) were reported by Kitamura and Minakawa.

Those at Mt. Norikura (altitude 2840 m. $\lambda=25°$N) were measured in the fall of 1955 by the same apparatus[2] as that used in (A).

The procedure of measurement and notation of counting rate are identical with those in (A), except for slight differences in both cases*.

The explanation of the notation and the corresponding energy intervals are tabulated in Table I, and the results are summalized in Table II and Fig. 1, where t is the average atmospheric pressure during the period of our experiment; i.e. 745.2 gr/cm².

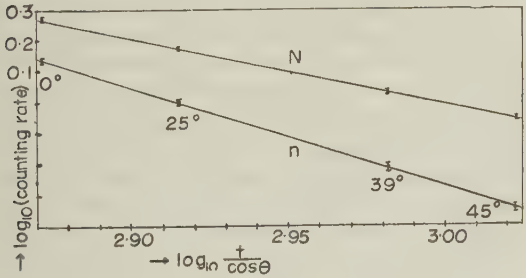

Fig. 1

In Fig. 1, it will be noted that the zenithal distribution of intensities are reported by the power of $\cos\theta$ between 0° and 45°, the exponent being 2.1±0.1 and 3.1±0.2 for the hard and soft components respectively.

We put $I_{(\theta)}=K\cdot N_{(\theta)}$, then the value of K's in respective cases were calculated as follows.

$K=1/2.65$ for the hard component
$K=1/2.58$ for the soft component

Using these relations, we obtained the following absolute intensities at 2840 m elevation;

$I_v=(1.17\pm0.01)\times10^{-2}\ \mathrm{cm^{-2}\,sec^{-1}\,sterad^{-1}}$ for the hard component

$I_v'=(0.90\pm0.02)\times10^{-2}\ \mathrm{cm^{-2}\,sec^{-1}\,sterad^{-1}}$ for the hard component

$I_v''=(2.07\pm0.02)\times10^{-2}\ \mathrm{cm^{-2}\,sec^{-1}\,sterad^{-1}}$ for the total

Table I. The explanation of the notation

notation	explanation
N	Counting rate per minute of hard component, which are mainly proportional to the number of protons and μ-mesons capable of penetrating 160 gr/cm² lead, whose energies are above 385 Mev and above 210 Mev for protons and mesons respectively.
n	Counting rate per minute of soft component, which are proportional to the number of protons, slow mesons and electrons capable of penetrating 4 gr/cm² aluminium but incapable of penetrating 160 gr/cm² lead. The energy ranges are between 385 Mev and 60 Mev, between 210 Mev and 23 Mev and above 6 Mev for protons, slow mesons and electrons respectively.
n'	Counting rate per minute of very soft component, mainly consisting of electrons, whose energies lie between 6 Mev and 1.5 Mev.

Table II. The results of counting rate against zenith angles

	0°	25°	39°	45°
$N+n$	3.28±0.03	2.46±0.02	1.69±0.02	1.36±0.01
N	1.87±0.01	1.49±0.01	1.08±0.01	0.90±0.01
n	1.39±0.03	0.97±0.03	0.62±0.02	0.47±0.02
n'**	1.12±0.06	0.60±0.05	0.77±0.03	0.44±0.03
$n+n'$	2.51±0.07	1.57±0.05	1.39±0.04	0.91±0.03

The above results are compared with those at sea level in (A) in Table III.

Table III. Ratio of the intensities at 2840 m and at sea level

	0°	25°	39°	45°
$N+n$	2.1±0.03	2.0±0.02	2.0±0.02	1.9±0.01
N	1.6±0.02	1.6±0.01	1.6±0.01	1.6±0.01
n	3.9±0.04	3.6±0.03	3.5±0.02	3.2±0.02

Acknowledgements

The authors wish to express our heartfelt gratitude to Profs. Minakawa and Kameda for their invaluable help. We also wish to thank Prof. Hirata, Director of the Norikura Cosmic Ray Laboratory, who permitted us to use that institute.

References

1) Y. Kitamura and O. Minakawa: Prog. Theor. Phys. **10** (1953) 239.
2) K. Greisen: Phys. Rev. **61** (1942) 212.

---

* The thickness of the roof was 1.5 gr/cm² of wood and 0.2 gr/cm² of copper plate at the Norikura hut, and 0.4 gr/cm² of wood 0.3 gr/cm² of iron plate at the pent house of Kobe University.

** Irregularities in this row may be due to the nonuniformity of the roof.

J. Phys. Soc. Japan **12** (1957) 558

Precise Frequency of the 3,3 Inversion Line of Ammonia

By Koichi Shimoda

Department of Physics, Faculty of Science, University of Tokyo

(Received March 8, 1957)

Recent runs of the absorption type Stark-Zeeman ammonia clock[1] during a period from March to November 1956 give the frequency of the 3,3 line on UT2 as

$$\nu_a=23,870,131.05\pm0.05 \text{ kc/sec.}$$

Since the center frequency was found to shift to higher frequency by $\Delta\nu_a=a\Delta\nu_p$, where $\Delta\nu_p$ is the width due only to pressure broadening*, the value of frequency extrapolated to zero-pressure is given above.

A note on the frequency of a molecular beam maser oscillator has appeared, reporting the value on UT2 (Sept. 1956) as[2]

$$\nu_m=23,870,129.42\pm0.05\pm0.12 \text{ kc/sec,}$$

which is 1.63 kc/sec or 7×10^{-8} smaller than ν_a.

In comparing these values frequency shift due to different distribution of populations in quadrupole hyperfine levels, $F_1=2$, 3 and 4, must be considered. This type of shift was not described in reference 3, since it had already been shown by Gordon[4]. Assuming that eqQ in the lower inversion state is 4 ± 1 kc/sec larger than that in the upper, the center line of the 3,3 line corresponding to the transition $\Delta F_1=0$ is made up of three components as shown in Fig. 1.

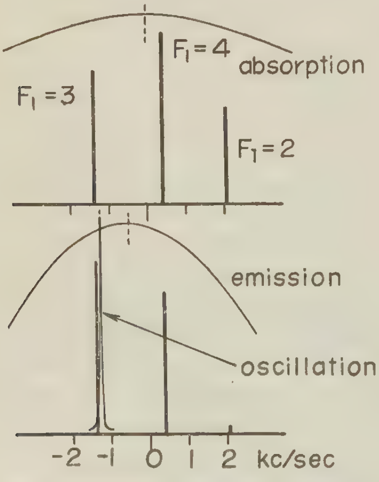

Fig. 1. Spectra of absorption, emission and oscillation of the 3,3 inversion line.

The ratio of intensities of components with $F_1=3$, 4 and 2 in the absorption line is 7:9:5, and hence the weighted average frequency coincides exactly with that undisplaced by hyperfine structure. The relative intensities of these components in a maser is determined by the relative number of focused molecules in the hyperfine levels. Since the focusing force is roughly proportional to M^2, an approximate intensity ratio of components with $F_1=3$, 4 and 2 is 45:37:2. Then the unresolved center of the emission line is shifted by $\Delta\nu_e=-0.48\pm0.12$ kc/sec. The situation in a maser oscillator is still different. Because of the regenerative amplification, the oscillation in a long cavity must start at a frequency much closer to the strongest emission line, $F_1=3$. Then the frequency shift of oscillation near the threashold would be closer to -1.24 ± 0.31 kc/sec. With increasing focuser voltage rf amplitude in the cavity increases and the saturation of $F_1=3$ component tends to introduce more contribution of ccmponents with $F_1=4$ and 2, which results in the shift approaching to $\Delta\nu_e$. The detail will be published.

Moreover, frequency shift caused by the presence of traveling wave is rather large for a long cavity as shown by (57) in reference 3. Because rf enery released from the beam is proportional to t^2 or z^2 in weak rf field, while the loss of rf energy is symmetrically distributed along the length of the cavity, the net flow of rf energy is opposite to the direction of the beam so that the frequency shift is negative. Taking $Q_t=1\sim2\times10^4$, $L=30$ cm, and $Q_l=10^7$, the shift caused by the traveling wave is $\Delta\nu_t=-(0.48\sim0.24)$ kc/sec.

Therefore, the frequency shift of the maser oscillator is estimated to be -1.6 kc/sec near the threshold and it is -0.7 kc/sec near the saturation limit. It may be concluded that the absorption line might be a better etalon in view of absolute accuracy, while each maser shows better resettability. The only so far uninvestigated source of systematic error of the absorption frequency is the shift relating to wall collision. But it does not vary with operating conditions. Accurate comparison of the absorption line with the maser has been planned in our laboratory. Since our maser can start oscillation at the focuser voltage of only 2.4 kV, while allowing the maximum of 21 kV, the above mentioned shifts will be studied in detail.

References

1) K. Shimoda: Journ. Phys. Soc. Japan **9** (1954) 567.
2) J. Bonanomi and J. Herrmann: Helv. Phys. Acta **29** (1956) 451.
3) K. Shimoda, T. C. Wang and C. H. Townes: Phys. Rev. **102** (1956) 1308.
4) J. P. Gordon: Phys. Rev. **99** (1955) 1253.

---

* The coefficient, a, decreases sensitively with the impurity gas in the cell, hence the tentative estimate for pure ammonia is $a=(4.0\pm0.5)\times10^{-2}$.

J. PHYS. SOC. JAPAN **12** (1957) 559

Technique of Obtaining a Minute Pinhole in a Metal Plate

By Tadasi NUMATA
Nagasaki University, Ohasi-Machi, Nagasaki

(Received April 15, 1957)

Hitherto, minute pinholes have been bored in metal by some methods[1]. By the following new method, the author was able to obtain easily very small circular pinholes of about 50 to 10 μ diameter in such metal plates as lead and Wood's metal. The pinholes obtained by this method may be applicable for optical and X-ray researches. The method is as follows:

(1) First fine long glass fibres of about 50 to 10 μ in diameter are produced by drawing out a larger hard glass rod not having bubbles and striae by usual ways[2]. Next among these fibres a fine straight glass fibre with a desirable diameter and a circular cross section is chosen by observing with a microscope. Then the needle of a fine straight glass fibre in length of about 3 cm is cut off from this selected long glass fibre.

(2) One end of a glass rod is tapered and the above needle is fixed on the tapered part of the glass rod parallel to the axis of the rod with a small piece of picein wax. Then the needle is cut again in a suitable length (2~0.5 cm), and the surface of the needle is covered with oil film by putting the needle into suitable oil. The picein wax connecting the needle with the glass rod is wrapped with cotton wetted by water in order to avoid softening of the picein wax. Then, the microscope in a travelling microscope instrument is replaced with the glass rod using rubber plug as a jointer.

(3) A circular hole of about 3 to 2 mm in diameter in a suitable metallic base plate of high melting point is covered with a molten metal of low melting point. The needle is then put into the molten metal at the center of the hole, until the tip of the needle comes out of the base metal plate, by lowering down carefully the needle perpendicular to the surface of the molten metal with the aid of the screw of the travelling microscope instrument.

(4) After congelation of the molten metal, the needle is slowly pulled up by turning the screw. In most cases, the needle smoothly comes out of the metal without snap of the needle. (Tensil strength of a glass fibre of 20 μ diameter is approximately 70 Kg/mm^2.)

By the above method, very small straight circular pinholes of about 50 to 10 μ diameter can be easily obtained on a metal plate. These pinholes have, of course, the same sizes and forms as those of the needles used. This method can be applied to the metals which have lower melting points than the strain temperature of the glass used.

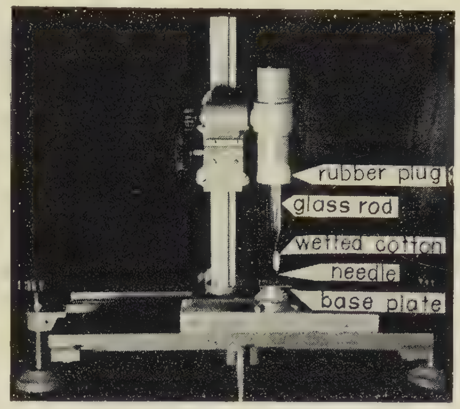

Fig. 1. Apparatus used in the method of obtaining a minute pinhole in a metal plate.

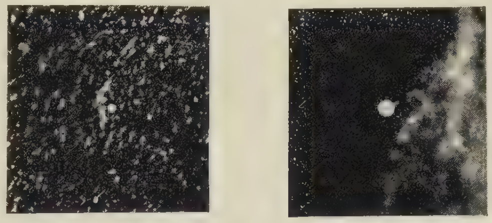

(*a*) (*b*)

Fig. 2. Microphotographs of pinholes. The white circles at the centers are the pinholes whose diameters are 15 (*a*) and 30 μ (*b*) respectively.

Figs. 1 and 2 show, respectively, the apparatus used for the above method, and the examples of the microphotographs of the pinholes obtained by the present method. The diameters of the pinholes are 15 and 30 μ respectively.

Finally, the author expresses his sincere thanks to Professor A. Okazaki of the Kyushu University for his encouragements.

References

1) H. S. Peiser and Others: X-Ray Diffraction by Polycrystaline Materials (1955) 283.
S. Shinozuka: Rev. Sci. Instr. **27** (1956) 542.
2) J. Strong: Procedures in Experimental Physics.

PROGRESS OF THEORETICAL PHYSICS

(Founded by H. Yukawa in 1946)

Published for the

Research Institute for Fundamental Physics

The Physical Society of Japan

Progress of Theoretical Physics Vol. 16, No. 3, September 1956

On the Quantum Field Theory of the Interaction between the Graviton and the Matter Field .... Toshiei KIMURA..157
Note on the Decay Interactions of Hyperons and Heavy Mesons .... Chikashi ISO and Masaaki KAWAGUCHI..177
On the Determination of the Spins of Λ^0 and θ^0 Particles .... Shoichi HORI..189
Partial Description of Quantum-Mechanical System .... Gentaro ARAKI..197
Free-Electron Model of Benzene .... Gentaro ARAKI..212
The Energy Band Structure of the Metallic Copper—*The Orthogonalized Plane Wave Method*— .... Mitsuru FUKUCHI..222
Extensions of Vibrational Methods, III—*Determination of Potential from Phase Shift Function*— .... Takashi OHMURA..231

Letters to the Editor:

State Vectors in the Collective Description .... T. NISHIYAMA..244
Some Remarks on the Nuclear Level Spacing .... Y. FUJIMOTO, F. FUKUZAWA and S. OKAI..246
Note on the Decay of Ξ Particles .... S. HATANO..248
On the Energy Dependence of the Cross Section for the Production of the Penetrating Shower Underground .... S. HIGASHI, M. ODA, S. OSHIO, H. SHIBATA, K. WATANABE and Y. WATASE..250
On the Nuclear Interaction of μ-Meson below Ground .... T. KITAMURA and M. ODA..252
Thermodynamic Properties of He^3 ...... V. S. NANDA and S. K. TRIKHA..254
On the Energy Matrix of the Tensor Forces .... T. SASAKAWA..256

Price	\$ 1.25 per copy
	\$ 15.00 per year (postage inclusive)
Annual dues for foreign members (individual subscribers)	
	\$ 12.00 (postage inclusive)
〃 for foreign members of the Physical Society of Japan	
	\$ 10.00 (postage inclusive)

Application for members, subscriptions and orders for back numbers should be sent, directly or through book-dealers, to

The Publication Office
in
Yukawa Hall, Kyoto University, Kyoto, Japan

JOURNAL OF THE PHYSICAL SOCIETY OF JAPAN Vol. 12, No. 6, JUNE, 1957

Elastic Scattering of 5.7 Mev Protons from Ni and Cu

By Minoru TAKEDA, Michiya KONDO, Syohei KATO,
Chuin HU, Ryuzo NAKASIMA and Shotaro YAMABE
Department of Physics, Osaka University, Osaka

(Received February 11, 1957)

Using 5.7 Mev protons from the cyclotron, we have studied the angular distributions of protons elastically scattered from Ni and Cu by means of nuclear emulsion technique. The angular distributions were measured from 14° to 161° at an interval of 5° in the laboratory system. The differential cross sections, in the ratio to the Rutherford cross section, have a minimum at about 85° in both cases, but at large scattering angles the cross section for Ni increases linearly, while there is a maximum at about 130° in the case of Cu. The results are in essential agreement with those of Bromley and Wall.

§ 1. Introduction

Bromley and Wall[1] investigated the elastic scattering of 5.25 Mev protons from Co, Ni, Cu and Zn, and discussed the angular dependence of the deviation from the Rutherford scattering. They found two characteristic features in the angular dependences. One was that the distribution had a minimum at about 85° in the relative cross sections in all cases, and the other was that it showed large deviations from the Rutherford scattering at large angles. As to the latter feature, the measured differential cross sections at large angles were larger than those expected from the Rutherford scattering in the case of Ni(Z=28) and Zn(Z=30), while they were smaller for Co (Z=27) and Cu(Z=29). They tried to explain these situations by the use of the complex potential well model[2], and succeeded in the case of Ni but did not in the case of nearby elements with the same parameters. Because of many adjustable parameters involved in the formula of this theory, it seems to be possible to obtain a considerable agreement between the experimental results and calculated values. Since the measured angular dependences seem to be different corresponding to target spin, Bromley and Wall suggested as an alternative possibility that if one assumed the spin dependent nuclear interaction, the different tendency might be explained.

It may be expected that the spread of the beam energy is sufficient to cover many levels of the compound nucleus in medium weight region such as Ni and Cu, and still the spacing of the lowest level of the target nucleus is large enough to allow an adequate resolution for the elastically scattered protons. We attempted to obtain further informations on the elastic scattering of protons by medium weight nuclei at incident energy of nearby Coulomb barrier height. The natural Ni and Cu targets were bombarded by 5.7 Mev proton beam from the 44-inch Osaka University cyclotron[3], and the elastically scattered protons were detected by nuclear plates.

§ 2. Experimental Arrangement and Procedure

The focused proton beam from the recently built cyclotron has been used for this work. The experimental arrangement is schematically illustrated in Fig. 1. The emergent beam from the cyclotron was passed through the wedge shaped magnet, placed at about 2 meters from the deflector exit, and was focused at the center of a scattering chamber set at about 5 meters from the magnet. The 60 cm diameter scattering chamber made of aluminium was used, and the scattering angles were measured by a precise goniometer. A collimating slit system defined the beam with an angular divergence of ±0.2°, forming an energy spread of about 50 kev, and the area of beam spot on the target was 4 mm × 10 mm.

The proton beam was collected by a negatively biased Faraday cage with a small magnet which suppressed the secondary electrons. The scattered protons were detected by Fuji ET-6B nuclear emulsions which were alike, in character, to Ilford C2. The thickness of the emulsion was 70 μ and the plates were put in a plate camera with plate holders spaced at an interval of 5° from −9° to −74° and from 6.5° to 161.5° in the laboratory system, and the glancing angles of the plates were 7.5°±0.1°. As shown in Fig. 2, the plate camera was set in the scattering chamber, and the centering was accurate within ±0.2 mm.

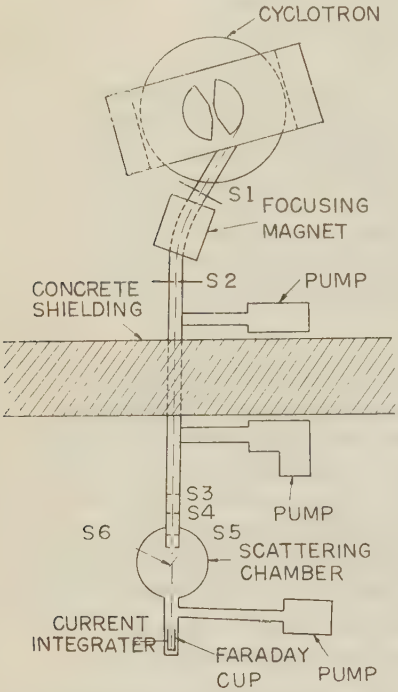

Fig. 1. The schematic illustration for present experimental arrangement.

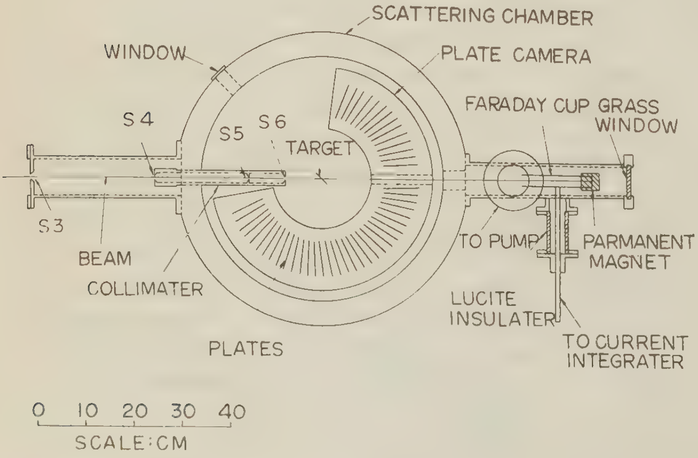

Fig. 2. The schematic diagram of the scattering chamber setting the plate camera.

The number of proton tracks in the emulsion was counted by using a microscope equipped with a ×40 objective and ×10 eyepieces. The microscope had an ocular microscope disk inserted in one eyepiece. Since the numbers of the elastically scattered protons at small angles were very large, the exposure at small angle plates was made about one-tenth in intensity of that of large angles by the shutter in front of the camera. A target equipped in the stainless steel holder with an area of 15 mm×15 mm, was set at 45°±1° to the beam direction, and the target was placed at the center of the scattering chamber with an accuracy of about±0.2 mm. The angular resolution of this work was about ±0.8°. The overall alignment was done within ±0.2°, and the geometrical errors were estimated to be about 1%.

The energy of the cyclotron beam was measured to be 5.7±0.1 Mev by the range of the elastically scattered protons from gold in C2 emulsion. It was believed that the energy used in both targets was the same within the spread of 0.1 Mev.

The Ni foil 1.5 mg/cm^2 thick was prepared by electroplating from an aqueous solution onto a polished plate of stainless steel. After it was peeled off from the backing, it was baked in vacuum. The Cu foil of 0.8 mg/cm^2 was prepared by evaporating onto a flat surface of sodium-chloride crystal, and then the crystal was dissolved into water.

§3. Results and Discussions

Our attempt was to measure the relative values of the differential cross sections, not to measure the absolute values. Since the Rutherford scattering is predominant at small angles, they were normalized to the Rutherford cross section at small angles. The number of the tracks observed in each plate was about one thousand, but about four thousand tracks were counted in the plates at small angles for which the normalization was done.

Since there are no excited levels below 500 kev in both elements except Ni^{61} (1.25% in natural), the resolution of our experiment was sufficient to distinguish the elastic peak from the inelastic one. The typical range distribution of the scattered protons from Ni target is shown in Fig. 3. For the first excited states at 1.45 Mev (2+) for Ni^{58} (67.76%) and at 1.33 Mev (2+) for Ni^{60} (26.16%), the proton groups could not be resolved. The similar spectrum of the scattered protons by Cu is shown in Fig. 4. Each level of Cu isotopes was not resolved in this experiment as shown in Fig. 4 because of their low intensities.

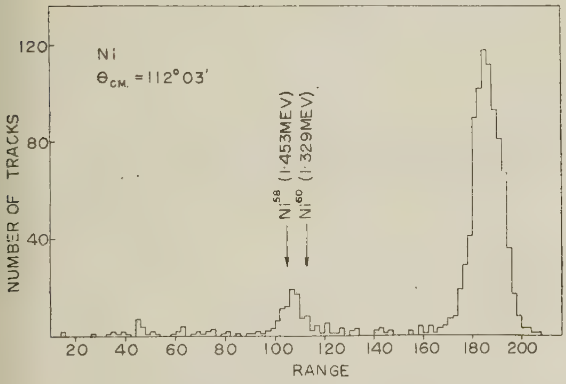

Fig. 3. The typical range distribution of the scattered protons from Ni at a center of mass angle of 112°03′. 1 div. = 1.2μ.

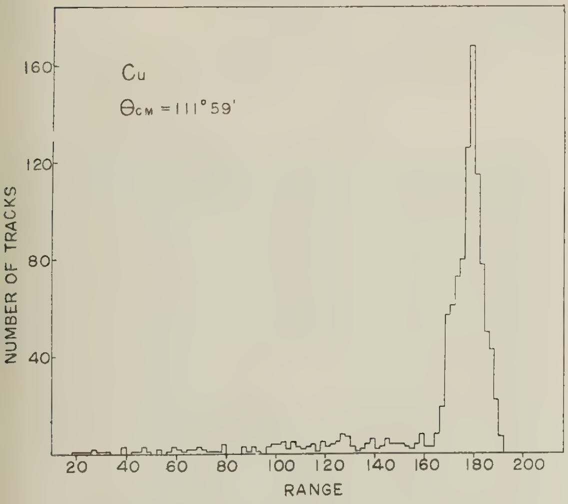

Fig. 4. The typical range distribution of the scattered protons from Cu at a center of mass angle of 111°59′. 1 div. = 1.2μ.

The amounts of the target impurities in both elements were negligible, but there was an appreciable background due to elastic protons which had escaped from the emulsion surfaces. The correction for this effect amounted to 4% of the elastic proton group. This correction was estimated by a preliminary measurement on the elastic scattering of protons from carbon by the same apparatus, because the inelastically scattered protons from carbon could not be detected energetically in our experiment. It is expected that the relative errors of the cross sections are about ±5%. The errors of the cross sections in the ratio to the Rutherford scattering are estimated to be ±12% because of the uncertainty of the beam direction.

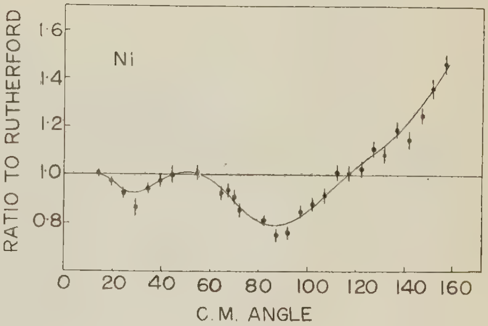

Fig. 5. Ratio of measured cross section in the center of mass system to the Rutherford for Ni.

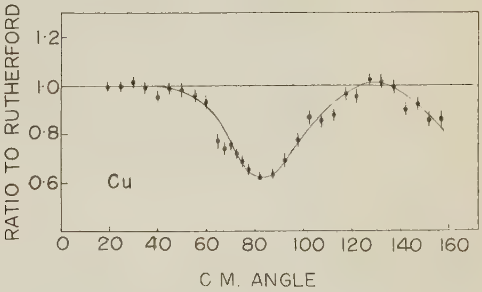

Fig. 6. Ratio of measured cross section in the center of mass system to the Rutherford for Cu.

The angular distributions obtained are shown in Figs. 5 and 6. As is seen in these figures, the angular dependences of the deviations from the Rutherford scattering are quite similar to those of Bromley and Wall. In the case of Ni, the shape of the measured angular distribution is in agreement with the calculated values by Saxon and Melkanoff$^{1)}$. Although the incident energy of our experiments (5.7 Mev) differs from that of Bromley and Wall's experiments (5.25 Mev), the present results are quite similar to theirs. The behavior of the angular dependences obtained by Schneider$^{4)}$ (6.0, 6.5 and 7.0 Mev) and Goldman$^{5)}$

(6.5 Mev) are also not so different from ours. Consequently, for Ni and Cu, it may be concluded that the behavior is not sensitive to the incident energy in these region.

Acknowledgments

The authors gratefully acknowledge the encouragement of Professor S. Kikuchi, Professor T. Wakatsuki, and Professor S. Yamaguchi who gave us kind advice throughout the course of this investigation. We also wish to express our appreciation to Fuji Film Corporation for the preparation of nuclear plates.

References

1) D. A. Bromley and N. S. Wall: Phys. Rev. **102** (1956) 1560.
2) Feshbach, Porter, and Weisskopf: Phys. Rev. **96** (1954) 448.
3) S. Kikuchi, et al.: Ann. Rep. Fac. Sci. Osaka Univ. **3** (1955) 1.
4) H. Schneider, et al.: Helv. Phys. Acta. **27** (1954) 170.
5) L. M. Goldman: Phys. Rev. **89** (1953) 349.

JOURNAL OF THE PHYSICAL SOCIETY OF JAPAN Vol. 12, No. 6, JUNE, 1957

Geometrical Theory of Convex Molecules in Non-Uniform Gases

By Taro KIHARA

Department of Physics, Faculty of Science,
University of Tokyo

(Received February 26, 1957)

Geometrical theory of convex molecules in uniform gases (T. Kihara, Revs. Modern Physics, **25** (1953) 831, **27** (1955) 412) is generalized to that in non-uniform gases when molecules are represented by rigid convex bodies without any additional intermolecular force. For this representation collisions between heavy molecules and light spherical molecules are treated exactly. Shape and size of several molecules are determined from diffusion coefficient. A " geometrical approximation " is suggested for more general cases.

§ 1. Introduction

After Enskog and Chapman¹⁾ had developed the kinetic theory of transport phenomena in dilute gases, several transport coefficients were calculated²⁾ for typical spherically symmetric intermolecular potentials and were compared with observation. The result was satisfactory for monatomic molecules. For non-monatomic molecules on the other hand there is no satisfactory treatment yet.

In 1950 Isihara³⁾ proved a geometrical identity for convex bodies and pointed out the fact that the identity is useful for treatment of molecular interaction in *uniform* gases and liquid-solutions. His work was improved and generalized by the present author⁴⁾. Owing to the generalization it became possible to treat the second virial coefficient for polyatomic molecules in a neat and simple manner.

Recently the author noticed that Hadwiger⁵⁾, a mathematician, had independently proved the same identity also in the year 1950. His result is constituted by three identities, one of which is the same as Isihara's. The chief objective of the present article is to show that the second identity by Hadwiger can be applied to molecular interactions in *non-uniform* gases.

It is to be noted that Curtiss⁶⁾ is developing a kinetic theory of non-uniform gases by use of the convex-body model of molecules. Owing to great difficulties of treating collisions between two convex bodies, however, he does not seem to have succeeded in obtaining a result capable of comparison with observations.

In this article a direct and simple proof of Hadwiger's relations and other necessary formulas will be given first. The former is an extension of the proof by the author of Isihara's identity. After preparing necessary tables, our mathematical results will be applied to transport phenomena, chiefly to diffusion; the shape and size of several polyatomic molecules will be determined as a result of comparison with observations.

§2. Geometry of Convex Bodies

A body is called convex if any segment whose end points are inside lies entirely in that body.

Let us choose a coordinate origin O inside a (fixed) convex body and take coordinates of polar angles θ and φ ($0 \leq \theta \leq \pi$, $0 \leq \varphi \leq 2\pi$). For any direction (θ, φ), there is one and only one plane which is in contact with the convex body and whose normal from the origin is in the direction (θ, φ). This plane is named the supporting plane in the direction (θ, φ); the perpendicular distance from the origin to the supporting plane is called the supporting function, when it is considered as a function of θ and φ. The supporting function will be denoted by $H(\theta, \varphi)$. Let us further denote by M the supporting function integrated over all directions,

$$M \equiv \int_0^{2\pi}\int_0^{\pi} H(\theta, \varphi) \sin\theta d\theta d\varphi \ . \qquad (1)$$

We shall later see that M is the mean curvature integrated over the whole surface of the convex body.

Let us first assume that convex body has a smooth surface and that each supporting plane has a contact of first order with the convex body. Let $\boldsymbol{r}(\theta, \varphi)$ be the radius vector from the origin to the contact point of the body with the supporting plane in the direction (θ, φ); compare Fig. 1(a). Then by use of the unit vector $\boldsymbol{u}(\theta, \varphi)$ in the direction (θ, φ) we have

$$H(\theta, \varphi) = \boldsymbol{r}(\theta, \varphi) \cdot \boldsymbol{u}(\theta, \varphi) \qquad (2)$$

and

$$M = \iint \boldsymbol{r} \cdot \boldsymbol{u} \sin\theta \, d\theta d\varphi = \iint \boldsymbol{r} \cdot \left(\frac{\partial \boldsymbol{u}}{d\theta} \times \frac{\partial \boldsymbol{u}}{\partial\varphi}\right) d\theta d\varphi \ . \qquad (3)$$

The surface area S and the volume V of the convex body are given by

$$S = \iint \left|\frac{\partial \boldsymbol{r}}{\partial\theta} \times \frac{\partial \boldsymbol{r}}{\partial\varphi}\right| d\theta d\varphi$$

or, since $(\partial \boldsymbol{r}/\partial\theta) \times (\partial \boldsymbol{r}/\partial\varphi)$ is parallel to $\boldsymbol{u}$,

$$S = \iint \boldsymbol{r} \cdot \left(\frac{\partial \boldsymbol{r}}{\partial\theta} \times \frac{\partial \boldsymbol{r}}{\partial\varphi}\right) d\theta d\varphi \qquad (4)$$

and

$$V = \frac{1}{3} \iint \boldsymbol{r} \cdot \left(\frac{\partial \boldsymbol{r}}{\partial\theta} \times \frac{\partial \boldsymbol{r}}{\partial\varphi}\right) d\theta d\varphi \ . \qquad (5)$$

Now we consider two convex bodies labelled A and B and in each body choose a coordinate origin O_A and O_B. The volume, the surface area, the M-value, and the $\boldsymbol{r}$-function will be denoted by

$$V_A, \quad S_A, \quad M_A, \quad \boldsymbol{r}_A(\theta, \varphi)$$

and

$$V_B, \quad S_B, \quad M_B, \quad \boldsymbol{r}_B(\theta, \varphi) \ ,$$

respectively. Keeping O_A and the orientation of A fixed, and keeping the orientation of B also fixed, let us move B around A keeping contact from outside. Then the locus of O_B forms the surface of another convex body, named AB, whose $\boldsymbol{r}$-function is

$$\boldsymbol{r}(\theta, \varphi) = \boldsymbol{r}_A(\theta, \varphi) + \boldsymbol{r}_B^*(\theta, \varphi) \ ,$$

with

$$\boldsymbol{r}_B^*(\theta, \varphi) \equiv -\boldsymbol{r}_B(\pi - \theta, \pi + \varphi) \ ,$$

see Fig. 1(b).

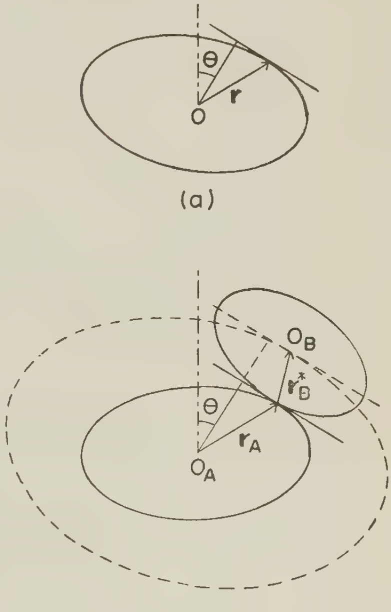

(a)

(b)

Fig. 1. Convex bodies and their supporting planes.

The volume of the last convex body AB,

$$V_{AB}=\frac{1}{3}\iint(\boldsymbol{r}_B+\boldsymbol{r}_B^*)\cdot\left[\left(\frac{\partial \boldsymbol{r}_A}{\partial\theta}+\frac{\partial \boldsymbol{r}_B^*}{\partial\theta}\right)\times\left(\frac{\partial \boldsymbol{r}_A}{\partial\varphi}+\frac{\partial \boldsymbol{r}_B^*}{\partial\varphi}\right)\right]d\theta d\varphi,$$

will be first evaluated. Making use of the identity

$$\frac{\partial}{\partial\theta}\left[\boldsymbol{r}_B^*\cdot\left(\boldsymbol{r}_A\times\frac{\partial \boldsymbol{r}_A}{\partial\varphi}\right)\right]+\frac{\partial}{\partial\varphi}\left[\boldsymbol{r}_B^*\cdot\left(\frac{\partial \boldsymbol{r}_A}{\partial\theta}\times\boldsymbol{r}_A\right)\right]$$
$$=2\boldsymbol{r}_B^*\cdot\left(\frac{\partial \boldsymbol{r}_A}{\partial\theta}\times\frac{\partial \boldsymbol{r}_A}{\partial\varphi}\right)-\boldsymbol{r}_A\cdot\left(\frac{\partial \boldsymbol{r}_B^*}{\partial\theta}\times\frac{\partial \boldsymbol{r}_A}{\partial\varphi}\right)$$
$$-\boldsymbol{r}_A\cdot\left(\frac{\partial \boldsymbol{r}_A}{\partial\theta}\times\frac{\partial \boldsymbol{r}_B^*}{\partial\varphi}\right)$$

we have

$$\iint\left[\boldsymbol{r}_A\cdot\left(\frac{\partial \boldsymbol{r}_B^*}{\partial\theta}\times\frac{\partial \boldsymbol{r}_A}{\partial\varphi}\right)+\boldsymbol{r}_A\cdot\left(\frac{\partial \boldsymbol{r}_A}{\partial\theta}\times\frac{\partial \boldsymbol{r}_B^*}{\partial\varphi}\right)\right]d\theta d\varphi$$
$$=2\iint\boldsymbol{r}_B^*\cdot\left(\frac{\partial \boldsymbol{r}_A}{\partial\theta}\times\frac{\partial \boldsymbol{r}_A}{\partial\varphi}\right)d\theta d\varphi\,,$$

since the integral of the divergence expression vanishes. Making use of this relation and another similar one, we obtain

$$V_{AB}=V_A+V_B+\iint\boldsymbol{r}_B^*\cdot\left(\frac{\partial \boldsymbol{r}_A}{\partial\theta}\times\frac{\partial \boldsymbol{r}_A}{\partial\varphi}\right)d\theta d\varphi$$
$$+\iint\boldsymbol{r}_A\cdot\left(\frac{\partial \boldsymbol{r}_B^*}{\partial\theta}\times\frac{\partial \boldsymbol{r}_B^*}{\partial\varphi}\right)d\theta d\varphi\,.$$

Up to this point the orientation of the convex body B has been kept fixed. The next step is to take the average with respect to the orientations of the body B. The integrand of the third term on the right-hand side can be replaced by

$$\boldsymbol{r}_B^*\cdot\boldsymbol{uu}\cdot\left(\frac{\partial \boldsymbol{r}_A}{\partial\theta}\times\frac{\partial \boldsymbol{r}_A}{\partial\varphi}\right).$$

When $\boldsymbol{r}_B^*\cdot\boldsymbol{u}$ is averaged with respect to orientations of the body B, the value no longer depends on (θ,φ) and is equal to $(4\pi)^{-1}M_B$. The average value of the third term is therefore $(4\pi)^{-1}M_BS_A$. Thus the average value of V_{AB} becomes

$$<V_{AB}>_{\mathrm{AV}}=V_A+V_B+\frac{1}{4\pi}(M_BS_A+M_AS_B)\,. \tag{6}$$

The surface area of the convex body AB,

$$S_{AB}=\iint\boldsymbol{u}\cdot\left[\left(\frac{\partial \boldsymbol{r}_A}{\partial\theta}+\frac{\partial \boldsymbol{r}_B^*}{\partial\theta}\right)\times\left(\frac{\partial \boldsymbol{r}_A}{\partial\varphi}+\frac{\partial \boldsymbol{r}_B^*}{\partial\varphi}\right)\right]d\theta d\varphi$$

can be transformed in a similar way into

$$S_{AB}=S_A+S_B+\iint\boldsymbol{r}_B^*\cdot\left(\frac{\partial \boldsymbol{r}_A}{\partial\theta}\times\frac{\partial \boldsymbol{u}}{\partial\varphi}\right)d\theta d\varphi$$
$$+\iint\boldsymbol{r}_B^*\cdot\left(\frac{\partial \boldsymbol{u}}{\partial\theta}\times\frac{\partial \boldsymbol{r}_A}{\partial\varphi}\right)d\theta d\varphi\,.$$

Replacing

$$\boldsymbol{r}_B^*\cdot\left(\frac{\partial \boldsymbol{r}_A}{\partial\theta}\times\frac{\partial \boldsymbol{u}}{\partial\varphi}\right)\quad\text{by}\quad\boldsymbol{r}_B^*\cdot\boldsymbol{uu}\cdot\left(\frac{\partial \boldsymbol{r}_A}{\partial\theta}\times\frac{\partial \boldsymbol{u}}{\partial\varphi}\right)$$

and taking the average with respect to orientations of the convex body B, we obtain

$$<S_{AB}>_{\mathrm{AV}}$$
$$=S_A+S_B+\frac{1}{4\pi}M_B\left[\iint\boldsymbol{u}\cdot\left(\frac{\partial \boldsymbol{r}_A}{\partial\theta}\times\frac{\partial \boldsymbol{u}}{\partial\varphi}\right)d\theta d\varphi\right.$$
$$\left.+\iint\boldsymbol{u}\cdot\left(\frac{\partial \boldsymbol{u}}{\partial\theta}\times\frac{\partial \boldsymbol{r}_A}{\partial\varphi}\right)d\theta d\varphi\right].$$

The [ ]-bracket expression can be reduced to

$$2\iint\boldsymbol{r}_A\cdot\left(\frac{\partial \boldsymbol{u}}{\partial\theta}\times\frac{\partial \boldsymbol{u}}{\partial\varphi}\right)d\theta d\varphi\,,$$

which, by virtue of (3), is equal to $2M_A$. Hence the result is

$$<S_{AB}>_{\mathrm{AV}}=S_A+S_B+(1/2\pi)M_AM_B\,. \tag{7}$$

The third relation

$$<M_{AB}>_{\mathrm{AV}}=M_A+M_B \tag{8}$$

is easy to see.

After we have obtained these relations it is no longer necessary to assume that the convex body has a smooth surface and that each supporting plane has a contact of first order with the convex body.

The formulas (6), (7) and (8) were given by Hadwiger[5]. The proof given above is partly due to Minkowski.[7]

The particular case when the convex body B is a sphere of radius b is well known. A convex body formed by all points whose distances from A are smaller than or equal to b is called the parallel body of A in the distance b. Its volume, surface area and the M-value are respectively given by

$$V_b=V+Sb+Mb^2+(4\pi/3)b^3\,, \tag{9}$$
$$S_b=S+2Mb+4\pi b^2\,, \tag{10}$$
$$M_b=M+4\pi b\,, \tag{11}$$

where V, S, M on the right-hand sides are constants of the convex body A. These three relations are called Steiner's formulas.

According to Gauss' theorem on spherical representation the surface area S can be expressed in another form

$$S=\iint R_1\,R_2\sin\theta\,d\theta\,d\varphi$$

where R_1 and R_2 are the principal radii of curvature at $\boldsymbol{r}(\theta,\varphi)$. The surface area of a parallel body is similarly

$$S_b=\iint(R_1+b)(R_2+b)\sin\theta\,d\theta\,d\varphi$$

$$=S+b\iint(R_1+R_2)\sin\theta\,d\theta\,d\varphi+4\pi b^2\ .$$

Comparing (10) we obtain therefore

$$M=\frac{1}{2}\iint(R_1+R_2)\sin\theta\,d\theta\,d\varphi$$

or, again by use of the Gauss theorem,

$$M=\int\frac{1}{2}\left(\frac{1}{R_1}+\frac{1}{R_2}\right)dS\ . \tag{12}$$

The last relation indicates that M is the mean curvature integrated over the whole surface of the convex body.

Values of V, S and M for several typical shapes are given in an article of the author[4] and in Hadwiger's book.[5]

§ 3. Convex Cores of Molecules

For applications of the geometry of convex bodies to molecules in gases it is useful to define an appropriate convex core within each molecule. In order to determine the core of a molecule, it is necessary to have information about the interatomic distances (and bond angles if any) of the molecule. We prepare, therefore, Table I. Consulting this table we fix our cores as in Table II. The volume V_0, the surface area S_0, and the surface integral of the mean curvature M_0 of the core are also tabulated.

Table I. Interatomic distances

Molecules		Bonds	Distance in A
Hydrogen	H_2	H–H	0.74
Nitrogen	N_2	N–N	1.094
Oxygen	O_2	O–O	1.10
Fluorine	F_2	F–F	1.44
Chlorine	Cl_2	Cl–Cl	2.01
Carbon dioxide	CO_2	C–O	1.15
Acetylene	C_2H_2	C–C	1.20
		C–H	1.06
Boron trifluoride	BF_3	B–F	1.30
Boron Trichloride	BCl_3	B–Cl	1.74
Ethylene	C_2H_4	C–C	1.33
		C–H	1.087
(Angle H–C–H is $2\tan^{-1}\sqrt{2}=109°30'$			
Benzene	C_6H_6	C–C	1.39
		C–H	1.08
Methane	CH_4	C–H	1.093
Carbon tetrafluoride	CF_4	C–F	1.36
Carbon tetrachloride	CCl_4	C–Cl	1.755
Silicon tetrafluoride	SiF_4	Si–F	1.54
Silicon tetrachloride	$SiCl_4$	Si–Cl	2.01
Sulfur hexafluoride	SF_6	S–F	1.56

The values are chiefly taken from L. Pauling, *Nature of the Chemical Bond* (Cornell Univ. Press, Ithaca, New York 1948). The value for SF_6 is due to H. Braune and S. Knocke, Z. physik. Chem. B **21** (1933) 297.

Table II. The cores of molecules

Molecules	Cores	V_0 (A³)	S_0 (A²)	M_0 (A)
N_2	thin rod joining 2N's	0	0	3.44
O_2	thin rod joining 2O's	0	0	3.45
CO_2	thin rod joining 2O's	0	0	7.23
CCl_4	tetrahedron joining 4Cl's	2.77	14.23	16.43
SF_6	octahedron joining 6F's	5.06	16.86	16.29
C_6H_6	hexagon joining mid-points of C–H	0	19.4	18.2

§ 4. Application to Transport Phenomena in Gases

In order to apply our theory of convex bodies to transport phenomena in gases let a molecule be representated by a rigid convex body without additional intermolecular force. In the following the representing convex body will be called molecule for brevity.

Diffusion between heavy convex molecules and light spherical molecules can be treated exactly so far as Enskog-Chapman's first approximation is concerned. Here we assume that the heavy molecule does not greatly change its linear and rotational velocities when it collides with a light molecule.

The coefficient of diffusion D in general is inversely proportional both to the total number-density N of gas molecules and to an effective cross section Q of collisions between two unlike molecules,

$$D=\frac{3}{4N}\left(\frac{2\pi kT}{m^*}\right)^{1/2}\frac{1}{Q}\ . \tag{13}$$

Here m^* is the reduced mass of a pair of unlike molecules; kT is the Boltzmann constant times temperature. Values of D at 0°C, 1 atmosphere and values of Q defined by (13) are given in Table III. When the two diffusing molecules are spheres of radii a and b, Q is equal to

$$Q=4\pi(a+b)^2\ , \tag{14}$$

which is the surface area of a sphere of collision radius.

The coefficient of diffusion between heavy molecules and light spherical molecules can be

Table III. Coefficients of diffusion D at 0°C, 1 atm. and the effective cross sections Q in Eq. (13)

Gases	D (cm^2/sec)	Q (A^2)	$S_A+S_B+\frac{1}{2\pi}M_AM_B$ (A^2)
H_2-N_2	0.674	114	
H_2-O_2	0.697	109	
H_2-CO_2	0.550	138	
H_2-CCl_4	0.293	255	
H_2-SF_6	0.420	178	
H_2-C_6H_6	0.318	236	
N_2-O_2	0.181	150	147
N_2-CO_2	0.144	176	179
O_2-CO_2	0.139	175	173
O_2-CCl_4	0.0636	320	304
O_2-C_6H_6	0.0797	278	283
O_2-O_2	0.189	139	141
CO_2-CO_2	0.104	215	208

The values of D are taken from

S. Chapman and T. G. Cowling: *Mathematical Theory of Non-Uniform Gases* (Cambridge Univ. Press, 1953).

W. Jost: *Diffusion* (Academic Press, New York, 1954).

J. O. Hirschfelder et al.: *Nolecular Theory of Gases and Liquids* (John Wiley and Sons, Inc., New York, 1954)

obtained if we replace $4\pi(a+b)^2$ by the expression (10):

$$Q=S+2Mb+4\pi b^2 . \tag{15}$$

Here S and M are the surface area and the surface integral of mean curvature of a heavy molecule, respectively, and b is the radius of a light molecule. This substitution is understood as follows. When a heavy molecule collides with a light spherical molecule the center of the light molecule is reflected at the surface of a parallel body in the distance b from the heavy molecule, which does not move during the collision. Two surface elements of equal amount on the parallel body reflect, in the average, equal number of light molecules into each scattering angle. In other words each surface element is independent of the shape of the whole surface. Therefore, the effective collision cross section is determined only by the total surface areas of the parallel body in the distance b from the heavy molecule.

For practical applications it is useful to choose as the convex body representing the heavy molecule a parallel body of its molecular core. Denoting by S_0 and M_0 the surface area and the surface integral of the mean curvature of the core respectively, we let namely

$$S=S_0+2M_0a+4\pi a^2 ,$$

$$M=M_0+4\pi a ,$$

where a is a parameter indicating the distance from the core to the molecular surface. Hence the relation (15) becomes

$$Q=S_0+2M_0(a+b)+4\pi(a+b)^2 . \tag{16}$$

Table IV. Constants of rigid convex-body model of molecules determined from coefficients of diffusion at 0°C.

Molecules	a (A)	S (A^2)	M (A)
N_2	1.48	37.7	22.0
O_2	1.41	34.7	21.2
CO_2	1.50	50.0	26.1
CCl_4	1.99	129	41.5
SF_6	1.24	76.6	31.9
C_6H_6	1.68	116	39.3

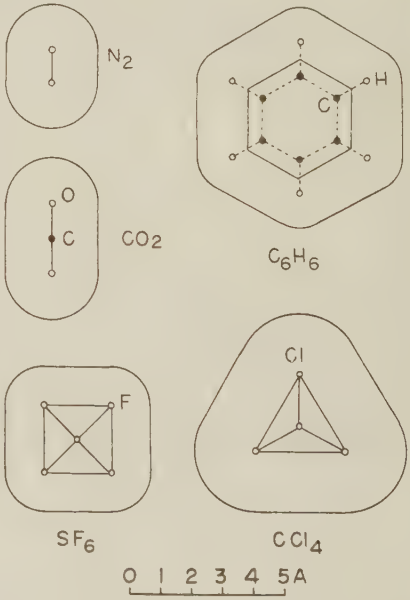

Fig. 2. Shape and size of molecules according to the rigid convex-body model determined from diffusion coefficients in hydrogen at 0°C.

The result obtained above can be applied to diffusion between hydrogen molecule (which may be assumed to be spherical) and several heavier molecules. From observed coefficient of self diffusion for hydrogen at 0°C we have $b=1.27$A. Then using the coefficient of mutual diffusion at 0°C, we can determine a of eral molecules. The result is given in ble IV and Fig. 2.

Thermal diffusion between heavy convex lecules and light spherical molecules can be ated similarly if the density of one of the mponents is much smaller than the density the other. (The last restriction is not nec- sary for ordinary diffusion,) For thermal fusion, however, our molecular model can used only at high temperatures, because the tractive part of the intermolecular potential ays an essential role at lower temperatures.

Collisions between two convex bodies in neral constitute a difficult dynamical problem ther than a mere geometrical one. Two lliding convex bodies rotate in a complicated anner, making several contacts in general; rrect treatment of this dynamical and atistical problem seems to be formidable. he present author, therefore, suggests a geometrical approximation" which is based on the assumption that the effect of mole- lar rotation vanishes in the average and the rmula (7) can be used. Thus, for the coef- cient of diffusion between A and B a sug- ested approximation to Q is

$$Q\approx S_A+S_B+(1/2\pi)M_AM_B\,. \tag{17}$$

Table III calculated value of the right-hand de are compared with observed values of the ft-hand side. Since equality holds within perimental accuracy our approximation seems to be close to the reality so far as rigid convex molecules are concerned.

Similar approximation to the viscosity η of a pure gas composed of rigid convex molecules with constants S and M and the mass m is

$$\eta\approx\frac{5}{4}(\pi kTm)^{1/2}\left(2S+\frac{1}{2\pi}M^2\right)^{-1}. \tag{18}$$

Refefences

1) See S. Chapman and T. G. Cowling: *Mathematical Theory of Non-Uniform Gases* (Cambridge Univ. Press, 1953).
2) See J. O. Hirschfelder et al.: *Molecular Theory of Gases and Liquids* (John Wiley and Sons, Inc., New York, 1954).
3) A. Isihara: J. Chem. Phys. **18** (1950) 1446; A. Isihara and T. Hayashida: J. Phys. Soc. Japan **6** (1951) 40; T. Kihara: J. Phys. Soc. Japan **8** (1953) 686.
4) T. Kihara: J. Phys. Soc. Japan **6** (1951) 289; T. Kihara: Revs. Modern Phys. **25** (1953) 831, **27** (1955) 412.
5) H. Hadwiger: Mh. Math. **54** (1950) 345; see also H. Hadwiger: *Altes und Neues über Konvexe Körper* (Birkhauser Verlag, Basel und Stuttgart, 1955).
6) C. F. Curtiss: J. Chem. Phys. **24** (1956) 225. C. F. Curtiss and Muckenfuss: University of Wisconsin, Naval Research Laboratory Report, (November 1955).
7) H. Minkowski: Math. Ann. **57** (1903) 447.

JOURNAL OF THE PHYSICAL SOCIETY OF JAPAN Vol. 12, No. 6, JUNE, 1957

Statistical-Mechanical Theory of Irreversible Processes. I.

General Theory and Simple Applications to Magnetic and Conduction Problems

By Ryogo KUBO

Department of Physics, University of Tokyo

(Received March 2, 1957)

A general type of fluctuation-dissipation theorem is discussed to show that the physical quantities such as complex susceptibility of magnetic or electric polarization and complex conductivity for electric conduction are rigorously expressed in terms of time-fluctuation of dynamical variables associated with such irreversible processes. This is a generalization of statistical mechanics which affords exact formulation as the basis of calculation of such irreversible quantities from atomistic theory. The general formalism of this statistical-mechanical theory is examined in detail. The response, relaxation, and correlation functions are defined in quantummechanical way and their relations are investigated. The formalism is illustrated by simple examples of magnetic and conduction problems. Certain sum rules are discussed for these examples. Finally it is pointed out that this theory may be looked as a generalization of the Einstein relation.

§ 1. Introduction

The principal purpose of the present paper is to develop a general scheme for the calculation of kinetic coefficient, or admittance for external forces such as electric or magnetic susceptibility for alternating field, electric conductivity, heat conductivity and so on. The most common method traditionally employed to calculate such non-equilibrium quantities is to set up the so-called kinetic equation or transport equation for the molecular distribution functions. This will be solved for stationary or periodic conditions. It is however to be remineded that the kinetic equation is itself an approximation and cannot be derived without a certain condition which is rather strict and is not often satisfied.[1] For weakly interacting particles, it may be justified if the nature of interaction is appropriate. But certainly it is not always true, and we may not be able even to write down any equation of that sort.

On the other hand, the recent development of the thermodynamic of irreversible processes[2] indicates the possibility of constructing a general statistical-mechanical theory at least for those irreversible processes which are not far apart from thermal equilibrium. In fact, there have been a number of attempts in this direction[3]. A remarkable progress has been made by Kirkwood[4] wl showed that the friction constant, for instanc of a Brownian particle is determined by th correlation of forces acting on the particl This may be looked as a particular case the so-called dissipation-fluctuation theorem As was discussed from a general point view by Callen, Welton,[5] Takahasi[6] an others, the general admittance for an externa disturbance is related to the expectation the square of Fourier component of certai physical quantity which fluctuates in time thermal equilibrium. Thus it is shown tha as far as linear responses are concerned, th admittance is reduced to the calculation time-fluctuations in equilibrium.

This idea was used by the present autho as the basis of the theory of magnetic r sonance problem. In a previous paper[7] th author developed a quantum-mechanical theor of this and has shown a certain method practical application. A straightforward a plication of this theory was made by Nakan for the conduction problem. He showed th the simplest approximation of the fundament expression of conductivity gives the we known Grüneisen's formula.

A generalized form of Nyquist's theore can be easily derived by application of pe turbation theory either classical or quantu echanical. The complete conductivity tensor r a given frequency of applied electric field an be rigorously expressed in terms of ectric current components fluctuating spon- neously in equilibrium state[9]. We emphaze here that this expression is quite rigorous hough admittedly somewhat abstract. It is owever of great value, because the tradional theory of conductivity has not been ware of existence of such rigorous expresion (although the Heisenberg-Kramers disperion formula is an equivalent). The abstract ature of the formula may be compared to hat of general theory of statistical mechanics. he statistical mechanics can give a rigorous xpression for the equation of state in terms f partition function, but its calculation is not ecessarily easy.

This theory of electric conduction has been ctively discussed in last two years in Japan ince the appearance of our paper on magnetic esonance[7] and its application to conduction roblem by Nakano. Feynman also discussed his when he visited Japan in the summer f 1955. Also it has been discussed by Lax, Luttinger, Kohn and possibly by some others n the United States. Recently Mori[20] has ublished a paper on the same problem.

In the present paper, which will be the first art of a series of papers devoted to the evelopment of statistical mechanics of ireversible processes along this line and to its pplications, we shall examine in detail the mplications of this new method.

In § 2, we shall treat the response of a ystem to an external force by simple perurbation method. In order to make the idea learer we first discuss the classical case. Quantum-mechanical formulation is quite in arallel with this classical theory. However, we notice a difficult problem of quantumechanical observation which might disturb he natural development of the motion. It vill be pointed out that the logical basis f the whole theory is closely related to the rgodic properties of the system and the hysical quantities we are concerned with. This is discussed in § 3 in connection with the efinition of relaxation functions which desribe the relaxation of the system after renoval of external disturbance.

In § 4, the correlation functions are introduced which describe the time correlation of two quantities at different time points. The relation between the correlation function and the relaxation function is derived. This is somewhat complicated in quantum-mechanical case.

§ 5 is devoted to the application of general argument to simple examples of magnetic and conduction phenomena. This is mostly to illustrate the general idea. The symmetry of the relaxation and response functions is discussed in § 6. The Onsager's reciprocity is seen most clearly by this formalism. The complete form of fluctuation-dissipation theorem will be given in § 7 taking the example of conductivity tensor.

As an interesting application of the theory, some general rules for the admittance is discussed in § 8. The most general sum rule is mentioned with regard to the symmetric part of conductivity tensor. The integration of this over the whole range of frequency must be constant irrespective of the presence of interactions or magnetic field and at any temperature. Another type of sum rule is derived for the antisymmetric part of conductivity. An interesting sum rule for the magnetic problem is that the integrated absorption intensity of circular wave by magnetic media is directly related to the gyromagnetic ratio of magnetic particles.

In § 9, it will be pointed out that the theory may be looked as a generalization of Einstein relation which relates the mobility and the diffusion constant. The general nature of Einstein relation is thus most clearly revealed.

In the present paper we confined ourselves to such type of external disturbance which can be expressed definitely as an additional term in the Hamiltonian of the system. Thus the heat flow, or mass flow phenomena under the gradient of temperature or chemical potential is logically out of the frame of this treatment. This problem has been treated recently by Mori.[10] We shall, however, discuss this in a forthcoming paper from a somewhat different point of view.

We also have applied the present theory to the galvanomagnetic effect at high magnetic field[11]. This is an example for which the traditional transport equation has to be modified. Our theory will be reported in another paper.

§ 2. Response Function and Admittance of an Isolated System

Let us consider an isolated system, the Hamiltonian of which is denoted by $\mathscr{H}$. The dynamical motion of the system determined by $\mathscr{H}$ is called the "*natural motion*" of the system. We suppose that an external force $F(t)$ is applied to the system, the effect of which is represented by the perturbation energy,

$$\mathscr{H}'(t)=-AF(t)\,. \tag{2.1}$$

The motion of the system is perturbed by this force, but the perturbation is small if the force is weak. We confine ourselves to weak perturbation and ask for the response of the system in the linear approximation. The response is observed through the change $\Delta B(t)$ of a physical quantity B. The problem is now to express $\Delta B(t)$ in terms of the natural motion of the system.

First, we shall treat this in classical mechanics. We conceive a statistical ensemble which is represented by a distribution function $f(p,q)$ in the phase space. The *natural motion* is described by the equation of motion,

$$\frac{\partial f}{\partial t}=-\sum\left(\frac{\partial f}{\partial q}\frac{\partial\mathscr{H}}{\partial p}-\frac{\partial f}{\partial p}\frac{\partial\mathscr{H}}{\partial q}\right)=(\mathscr{H},f), \tag{2.2}$$

where p and q mean the set of the canonical moments and coordinates and the bracket means the Poisson bracket,

$$(A,B)=\sum\left(\frac{\partial A}{\partial q}\frac{\partial B}{\partial p}-\frac{\partial A}{\partial p}\frac{\partial B}{\partial q}\right). \tag{2.3}$$

We assume that the distribution function is given by f at $t=-\infty$, that is, at the infinite past. It is assumed to be in equilibrium, that is, $(\mathscr{H}f)=0$. The perturbation (2.1) is inserted adiabatically at $t=-\infty(F(-\infty)=0)$. The distribution function $f'(t)$ obeys the equation

$$\frac{\partial f'(t)}{\partial t}=(\mathscr{H},f')+(\mathscr{H}'(t),f)\,. \tag{2.4}$$

Since we take the linear approximation, we put

$$f'(t)=f+\Delta f$$

and replace (2.4) by

$$\frac{\partial\Delta f}{\partial t}=(\mathscr{H},\Delta f)-F(t)(A,f)\,. \tag{2.5}$$

The solution is easily found to be

$$\Delta f(t)=-\int_{-\infty}^{t}e^{i(t-t')L}(A,f)\,F(t')\,dt' \tag{2.6}$$

where the operator L is defined by the operation4)

$$iLg\equiv(\mathscr{H},g)\,. \tag{2.7}$$

Therefore, the change $\Delta B(t)$ of a dynamical quantity B is statistically given by

$$\begin{aligned}\Delta B(t)&=\int\Delta f(t)\cdot B(p,q)\,d\Gamma\\&=-\int d\Gamma\int_{-\infty}^{t}\left\{e^{i(t-t')L}(A,f)\right\}\cdot F(t')B\,dt'\\&=-\int d\Gamma\int_{-\infty}^{t}(A,f)B(t-t')F(t')\,dt'\,,\end{aligned} \tag{2.8}$$

$d\Gamma$ being the volume element of the phase space. The last expression is obtained from the second remembering that the transformation $\exp(iLt)$ is the natural motion which conserves the measure of the phase space and that $B(t)$ means the dynamical motion of the phase function $B(p,q)$ which follows the equation

$$\dot{B}(p,q)=(B,\mathscr{H})\,.$$

This corresponds to the Heisenberg equation of motion in quantum-mechanics. Eq. (2.8) means that the response $\Delta B(t)$ is a superposition of the effects of pulses $F(t')\,dt'$, $-\infty<t'<t$. The response for an unit pulse will be called the ***response function*** or the ***after-effect function*** $\phi_{AB}(t)$. From Eq. (2.8) we find at once that it is given by

$$\phi_{BA}(t)=-\int d\Gamma(A,f)\,B(t) \tag{2.9}$$

which describes the response ΔB at the time t after the pulse. The response $\Delta B(t)$, (2.8), is written as

$$\Delta B(t)=\int_{-\infty}^{t}\phi_{BA}(t-t')\,F(t')\,dt'\,. \tag{2.10}$$

The above consideration applies even when the initial distribution is very sharp, as far the perturbation is weak enough. But our aim is rather to apply this for a macroscopic system, in which case the statistical average itself acquires a realistic meaning. If A and B are both macroscopic quantities, we may think the ensemble average $\Delta B(t)$ is what we actually observe, because a macroscopic system can be conceived to consist of smaller systems so that observed value of ΔB is a sum of a number of components and has only very small relative fluctuation.

Let us now turn to quantum mechanics. he distribution function in phase space is ow replaced by the density matrix ρ. The itial ensemble which represents statistically e initial state of the system is specified by he density matrix ρ satisfying $[\mathscr{H},\rho]=0$, hereas the motion of the ensemble under he perturbation (2.1) is represented by $\rho'(t)$, hich obeys the equation,

$$\frac{d}{dt}\rho'(t)=\frac{1}{i\hbar}[\mathscr{H}+\mathscr{H}'(t),\rho'(t)]. \qquad (2.11)$$

With the initial condition

$$\rho'(-\infty)=\rho,$$

we expand $\rho'(t)$ as

$$\rho'(t)=\rho+\Delta\rho(t).$$

The same procedure as we used for (2.5) leads us at once to

$$\Delta\rho(t)=-\frac{1}{i\hbar}\int_{-\infty}^{t}\exp(-i(t-t')\mathscr{H}/\hbar)[A,\rho]\times\exp(i(t-t')\mathscr{H}/\hbar)F(t')\,dt'. \qquad (2.12)$$

Incidentally, we note that it is sometimes very convenient to introduce the operator $a^\times$ operating on another operator b by following definition, i.e.,

$$a^\times b=[a,b], \qquad (2.13)$$

for which one find the rule,

$$e^{a^\times}b=e^a b e^{-a}. \qquad (2.14)$$

With this notation, Eq. (2.11) and (2.12) can be written as

$$\rho'(t)=\frac{1}{i\hbar}(\mathscr{H}^\times+\mathscr{H}'(t)^\times)\rho'(t) \qquad (2.15)$$

$$\Delta\rho(t)=-\frac{1}{i\hbar}\int_{-\infty}^{t}\exp(-i(t-t')\mathscr{H}^\times/\hbar)\times[A,\rho]F(t')\,dt' \qquad (2.16)$$

This will make clear the similarity of Eqs. 2.6) and (2.12).

The response $\Delta B(t)$ of the quantity B is statistically

$$\begin{aligned}\Delta B(t)&=\mathrm{Tr}\,\Delta\rho(t)B\\&=-\frac{1}{i\hbar}\mathrm{Tr}\int_{-\infty}^{t}\exp(-i(t-t')\mathscr{H}/\hbar)\\&\quad\times[A,\rho]\exp(i(t-t')\mathscr{H}/\hbar)BF(t')\,dt'\\&=-\frac{1}{i\hbar}\mathrm{Tr}\int_{-\infty}^{t}[A,\rho]B(t-t')F(t')\,dt'\end{aligned} \qquad (2.17)$$

where $B(t)$ is the Heisenberg representation of B following the equation

$$\dot{B}(t)=\frac{1}{i\hbar}[B(t),\mathscr{H}],\ B(0)=B. \qquad (2.18)$$

Eq. (2.17) corresponds to Eq. (2.8)

The response function or the after-effect function is now

$$\phi_{BA}(t)=-\frac{1}{i\hbar}\mathrm{Tr}\,[A,\rho]B(t) \qquad (2.19)$$

corresponding to Eq. (2.9). We naturally have Eq. (2.10) for (2.17) with the use of response function (2.19). If the force is periodic, i.e.,

$$F(t)=F_0\cos\omega t,$$

the response $\Delta B(t)$ will be conveniently written as

$$\Delta B(t)=\mathrm{Re}\,\chi_{BA}(\omega)F_0e^{i\omega t} \qquad (2.20)$$

with the complex admittance $\chi_{BA}(\omega)$, for which we have from Eq. (2.10)

$$\chi_{BA}(\omega)=\int_0^\infty\phi_{BA}(t)e^{-i\omega t}\,dt, \qquad (2.21)$$

or more exactly

$$\chi_{BA}(\omega)=\lim_{\varepsilon\to0+}\int_0^\infty\phi_{BA}(t)e^{-i\omega t-\varepsilon t}\,dt.$$

We summarize the above by the theorem:

Theorem 1. *The linear response of a physical quantity B to an external force F(t) is represented by Eq. (2.10) as the superposition of after-effects. The after-effect function or the response function is given by*

$$\begin{aligned}\phi_{BA}(t)&=\int d\Gamma(f,A)B(t)\quad\text{(classical)}\quad(2.22a)\\&=\frac{1}{i\hbar}\mathrm{Tr}[\rho,A]B(t)\quad\text{(quantal)}.\quad(2.22b)\end{aligned}$$

The admittance $\chi_{BA}(\omega)$ is given by

$$\chi_{BA}(\omega)=\lim_{\varepsilon\to0+}\int_0^\infty e^{-i\omega t-\varepsilon t}\,dt\int d\Gamma(f,A)B(t)\quad\text{(classical)}\quad(2.23a)$$

$$=\lim_{\varepsilon\to0+}\int_0^\infty e^{-i\omega t-\varepsilon t}\,dt\frac{1}{i\hbar}\mathrm{Tr}[\rho,A]B(t).\quad\text{(quantal)}\quad(2.23b)$$

Eqs. (2.22) may be written as

$$\begin{aligned}\phi_{BA}(t)&=\int d\Gamma f(A,B(t))\quad\text{(classical)}\quad(2.24a)\\&=\frac{1}{i\hbar}\mathrm{Tr}\,\rho[A,B(t)]\quad\text{(quantal)}\quad(2.24b)\end{aligned}$$

which are sometimes more convenient. One must however be careful about the boundary conditions of f or ρ, which may, however, be replaced by a suitable potential under certain circumstances.

As we mentioned before, there is no difficulty in classical cases to interprete the response thus obtained as the average which approximates closely the actual observation for large systems. In quantum-mechanical cases, however, we must note that there exists a certain difficulty. ΔB as given by Eq. (2.17) is the quantum-mechanical expectation of the first order change of B at the time t. This means that we prepare at $t=-\infty$ an ensemble of systems which corresponds to the statistical operator ρ. At a certain time t, we pick up a number of systems and observe B. The average of the observed values will be $\Delta B(t)$. We shall not follow these systems after this observation. At a later time point t', we choose different systems which have not been observed before. This is the way to follow the time change $\Delta B(t)$ to avoid the quantum-mechanical disturbance of observation process.

For the most of practical applications, we are rather interested in a continuous observation of a particular system, which is however macroscopic. The use of ensemble average for the actual observation will be justified by the same argument we made for the classical case. But the quantum-mechanical disturbance of observation is another thing. We may, however, expect for most of macroscopic quantities which we observe this disturbance can be neglected. This is a condition for macroscopic observations. Unfortunately, exact conditions for the existence of such quantities are not known.

Thus we shall rather introduce without proof the assumption that the identification of the statistically calculated $\Delta B(t)$ with the actully observed time variation is legitimate at least for those macroscopic quantities we shall be concerned with. We should howev make reservation that this assumption ma not be necessary for the identification of th admittance calculated by Eq. (2.23b) wit what will be actually observed, because th observation of admittance, for example, th refractivity and absorption in optical problem is not the observation of the response fun tion itself. As a matter of fact, Eq. (2.23 is equivalent to the well known dispersio formula of Heisenberg and Kramers[12] plu the absorption calculated by time-depende perturbation method.[7] The dispersion formul represents the oscillation of expectation val of dipole moments if the formula is applie to optical problems. This is not directl observed. We observe the refraction measuring the number of photons passe through the material. The logical relatio between this and that is not clear enough but the most common apologize is the use o correspondence principle. Any further analysis of this delicate problem is not our main purpose in this paper so we shall leave it for a future occasion.

Before concluding this section, we remark that the method employed here is also applicable to higher approximations than the linear. For this purpose we note Eq. (2.5) can be used for successive approximation, namely

$$\frac{\partial \Delta_k f}{\partial t}=(\mathscr{H},\ \Delta_k f)-F(t')(A,\ \Delta_{k-1} f)\,, \tag{2.25}$$

where $\Delta_k f$ means the k-th term of the expansion

$$f'(t)=f+\Delta_1 f+\Delta_2 f+\cdots\,. \tag{2.26}$$

The solution of Eq. (2.25) has the same from as Eq. (2.6), f being replaced by $\Delta_{k-1}f\,(t')$. Therefore we obtain the complete solution of Eq. (2.4) as

$$\begin{aligned} f'(t)=f+\sum_{k=1}^{\infty}(-)^k\int_{-\infty}^{t}\int_{-\infty}^{t_1}\cdots\int_{-\infty}^{t_{k-1}} e^{iL(t-t_1)}\Big(A,\ e^{iL(t_1-t_2)}(A,\ \cdots e^{iL(t_{k-1}-t_k)}(A,\ f))\cdots\Big) \\ \times F(t_1)\,F(t_2)\cdots F(t_k)\,dt_1\cdots dt_k \\ =f+\sum_{k=1}^{\infty}(-)^k\int_{-\infty}^{t}\int_{-\infty}^{t_1}\cdots\int_{-\infty}^{t_{k-1}} e^{iLt}\Big(A(t_1),\ (A(t_2),\cdots(A(t_k),\ f)\cdots\Big)F(t_1)\cdots F(t_k)dt_1\cdots dt_k\,. \end{aligned}$$

(2.27

where $A(t)$ is defined by

$$A(t)=A(p_t,\ q_t)\,,\quad p_{t=0}=p\,,\quad q_{t=0}=q\,.$$

ie same expression is obtained for quantum-mechanical case, namely

$$\rho'(t)=\rho+\sum_{k=1}^{\infty}\left(-\frac{1}{i\hbar}\right)^{k}\int_{-\infty}^{t}\int_{-\infty}^{t_1}\int_{-\infty}^{t_{k-1}}\exp(-it\mathscr{H}^{\times}/\hbar)\,A(t_1)^{\times}A(t_2)^{\times}\cdots A(t_k)^{\times}\rho F(t_1)\cdots F(t_k)\,dt_1\cdots dt_k \tag{2.28}$$

nere the cross means the commutator operation with the operation on its right hand side ee Eqs. (2.13) and (2.14)). These solutions allow us to write down the expression of re-onses in higher approximation. For instance, the second order change of B at the time can be written as

$$\Delta_2 B(t)=\left(\frac{1}{i\hbar}\right)^2 \mathrm{Tr}\int_{-\infty}^{t}\int_{-\infty}^{t_1}[A(t_1-t_2)[A,\rho]]\,B(t_1-t_2)F(t_1)F(t_2)dt_1dt_2 \tag{2.29}$$

he corresponding classical formula is similar so that it is omitted here.

3. Relaxation Function and Other Useful Formulae for Canonical Ensemble

In the following we consider quantum-echanical problems, because the classical mit is easily obtained from quantum-echanical formulae by replacing $[\ ,\ ]/i\hbar$ by oission bracket or by making $\hbar\to 0$.

First let us observe the behavior of the esponse function $\phi_{BA}(t)$ in the limit $t\to\infty$. t may approach to a limiting value or may ot approach to any definite value. If it oes, we must have

$$\lim_{t\to\infty}\phi_{BA}(t)=0 \text{ (if the limit exists).} \tag{3.1}$$

This is evident from Abel's theorem

$$\lim_{t\to\infty}\phi_{BA}(t)=\lim_{\varepsilon\to 0+}\varepsilon\int_0^{\infty}\phi_{BA}(t)\,e^{-\varepsilon t}\,dt \tag{3.2}$$

vhich holds if the left hand side exists. The ight hand side is zero unless $\phi_{BA}(t)$ has a inite Fourier-amplitude at zero frequency. If $_{BA}(t)$ has finite Fourier components for a set f discrete frequencies, $\phi_{BA}(t)$ will oscillate ndefinitely and does not have any limit. But, or calculation of admittance we have the onvergence factor $e^{-\varepsilon t}$ so that we may even n this case regard the relation (3.1) to hold. f $\phi_{BA}(t)$ is expressed by a Fourier integral vith continuous Fourier spectrum, Eq. (3.1) s generally true. This corresponds to actual ases of large systems, because the com-licated interaction within the system is lways enough to split the energy levels into structure so fine that the observation can ot discriminate. The error in the observa-ion of frequency certainly introduces an verage which allows us to replace the riginally discrete Fourier spectrum by con-inuous spectrum. Classically this corresponds to ellimination of long Poincaré cycles.

If the perturbation is applied continuously from $t=-\infty$ up to $t=0$ and is cut off at $t=0$, then the response ΔB will relax following the formula

$$\begin{aligned}\Delta B(t)&=\int_{-\infty}^{0}\phi_{BA}(t-t')dt'F\\&=F\int_t^{\infty}\phi_{BA}(t')dt',\qquad t>0\,.\end{aligned} \tag{3.3}$$

Therefore, the function

$$\Phi_{BA}(t)=\lim_{\varepsilon\to 0+}\int_t^{\infty}\phi_{BA}(t')\,e^{-\varepsilon t'}\,dt' \tag{3.4}$$

describes the relaxation of ΔB after removal of the outer disturbance. This will be called the relaxation function.

Here, for later reference we note the theorem:

Theorem 2. *The admittance $\chi_{BA}(\omega)$ can be calculated by the following formulae;*

$$\begin{aligned}\chi_{BA}(\omega)&=\lim_{\varepsilon\to 0+}\int_0^{\infty}\phi_{BA}(t)\,e^{-i\omega t-\varepsilon t}\,dt\\&=\lim_{\varepsilon\to 0+}\frac{1}{i\omega+\varepsilon}\left\{\phi_{BA}(0)+\int_0^{\infty}\dot{\phi}_{BA}(t)\,e^{-i\omega t-\varepsilon t}dt\right\}\\&=\Phi_{BA}(0)-i\omega\int_0^{\infty}\Phi_{BA}(t)\,e^{-i\omega t}\,dt\,.\end{aligned} \tag{3.5}$$

These transformations are rather evident.

The expression of $\phi_{BA}(t)$ has already been given by Eq. (2.22). We note here that other functions $\phi_{BA}(t)$ and $\Phi_{BA}(t)$ have convenient transform if the statistical ensemble is assumed to be *canonical*. For this purpose, we observe the identity

$$\begin{aligned}&[A,\exp(-\beta\mathscr{H})]\\&\quad=\exp(-\beta\mathscr{H})\int_0^{\beta}\exp(\lambda\mathscr{H})[\mathscr{H},A]\\&\qquad\qquad\times\exp(-\lambda\mathscr{H})\,d\lambda\end{aligned}$$

$$= \frac{\hbar}{i} \exp(-\beta \mathscr{H}) \int_0^S \exp(\lambda \mathscr{H})\, \dot{A} \times \exp(-\lambda \mathscr{H})\, d\lambda$$

$$= \frac{\hbar}{i} \exp(-\beta \mathscr{H}) \int_0^\beta \dot{A}(-i\hbar\lambda)\, d\lambda \tag{3.6}$$

or

$$[\rho_\beta, A] = i\hbar \int_0^\beta \rho_\beta \dot{A}(-i\hbar\lambda)\, d\lambda \tag{3.7}$$

which is easily seen by writing the expression in matrix form in the representation diagonalizing $\mathscr{H}$.

Let us now assume that the system we observe is statistically represented by the canonical density matrix,

$$\rho = \exp(-\beta(\mathscr{H} - \Psi)), \quad \beta = 1/kT,$$
$$\exp(-\beta\Psi) = \mathrm{Tr} \exp(-\beta\mathscr{H}). \tag{3.8}$$

By Eq. (2.22b) we have

$$\begin{aligned}\phi_{BA}(t) &= \frac{1}{i\hbar} \mathrm{Tr}\, [\rho, A] B(t) \\ &= \int_0^\beta \mathrm{Tr}\, \rho \dot{A}(-i\hbar\lambda) B(t)\, d\lambda \\ &= -\int_0^\beta \mathrm{Tr}\, \rho A(-i\hbar\lambda) \dot{B}(t)\, d\lambda \end{aligned} \tag{3.9}$$

and also

$$\begin{aligned}\dot{\phi}_{BA}(t) &= \frac{1}{i\hbar} \mathrm{Tr}\, [\rho, A] \dot{B}(t) \\ &= \frac{1}{i\hbar} \mathrm{Tr}\, \rho [A, \dot{B}(t)] = \frac{-1}{i\hbar} \mathrm{Tr}\, \rho [\dot{A}, B(t)] \\ &= \int_0^\beta \mathrm{Tr}\, \rho \dot{A}(-i\hbar\lambda) \dot{B}(t)\, d\lambda \end{aligned} \tag{3.10}$$

One may use any of these expressions depending on the nature of the quantities A and B. This will be illustrated later by examples.

With the aid of Eq. (3.9), the relaxation is transformed into

$$\Phi_{BA}(t) = \frac{i}{\hbar} \int_t^\infty \mathrm{Tr}\, \rho [B(t'), A]\, dt' \tag{3.11a}$$

$$= \int_0^\beta \mathrm{Tr}\, \rho A(-i\hbar\lambda) B(t) d\lambda - \beta \mathrm{Tr} \rho A^0 B^0 \tag{3.11b}$$

where A^0 and B^0 are the diagonal parts of A B with respect to $\mathscr{H}$. The second term on the right hand side of Eq. (3.11) is the limit

$$\begin{aligned}&\lim_{t\to\infty} \int_0^\beta \mathrm{Tr}\, \rho A(-i\hbar\lambda) B(t)\, d\lambda \\ &= \lim_{t\to\infty} \frac{1}{t} \int_0^t dt \int_0^\beta \mathrm{Tr}\, \rho A(-i\hbar\lambda) B(t)\, d\lambda \\ &= \beta\, \mathrm{Tr}\, \rho A^0 B^0 \end{aligned} \tag{3.12}$$

because this limit process selects the zer frequency component of $B(t)$. The limit the first expression, if it exists, must be equ to the last.

We may also define the function

$$\Phi^e{}_{BA}(t) = \int_0^\beta \mathrm{Tr}\, \rho A(-i\hbar\lambda)(B - B(t)) \tag{3.1}$$

which we shall call the *excitation* function convenience, because this describes the i crease of $\Delta B(t)$ when a constant force applied from $t=0$. Thus

$$\lim_{t\to\infty} \Phi^e{}_{BA}(t) = \Phi_{BA}(0). \tag{3.14}$$

In particular, for $t=0$, we have from Eq (3.11) and Eq. (3.5)

$$\begin{aligned}\chi_{BA}(0) &= \Phi_{BA}(0) = \Phi^e{}_{BA}(\infty) \\ &= \int_0^\beta \mathrm{Tr}\, \rho A(-i\hbar\lambda) B d\lambda - \beta\, \mathrm{Tr}\, \rho A^0 B^0 \\ &= \int_0^\beta \mathrm{Tr}\, \rho (A(-i\hbar\lambda) - A^0)(B - B^0)\, d\lambda \end{aligned} \tag{3.15}$$

where $\chi_{BA}(0)$ is the static admittance.

Eq. (3.15) is a little embarrassing, since the isothermal admittance, $\chi_{BA}{}^T$, is

$$\chi_{BA}{}^T = \int_0^\beta \mathrm{Tr}\, \rho (A(-i\hbar\lambda) - \overline{A})(B - \overline{B})\, d\lambda \tag{3.16}$$

where $\overline{A}$ and $\overline{B}$ and the equilibrium expectations of A and B in thermal equilibrium with $F=0$.

Eq. (3.16) is obtained by using the expansion

$$\exp\{-\beta(\mathscr{H} - FA\} = \exp(-\beta\mathscr{H})\{1 + \int_0^\beta A(-i\hbar\lambda) d\lambda F + 0(F^2)\}$$

for the expression

$$\Delta B = \frac{\mathrm{Tr} \exp\{-\beta(\mathscr{H} - FA)\} B}{\mathrm{Tr} \exp\{-\beta(\mathscr{H} - FA)\}} - \frac{\mathrm{Tr} \exp(-\beta\mathscr{H}) B}{\mathrm{Tr} \exp(-\beta\mathscr{H})}$$

$\chi_{BA}{}^T$ is defined by

$$\chi_{BA}{}^T = \Delta B / F.$$

Expressions (3.15) and (3.16) are different unless

$$\mathrm{Tr}\, \rho A^0 B^0 = \overline{A}\, \overline{B} = \mathrm{Tr}\, \rho A \cdot \mathrm{Tr}\, \rho B. \tag{3.17}$$

This will not however hold without certain restrictions imposed on A and B. In fact, $\chi_{BA}(0)$ as given by Eq. (3.15) is the static admittance of an isolated system on which the force F is inserted adiabatically. On the other hand $\chi_{BA}{}^T$, Eq. (3.16), is isothermal, hat gives the response when the system is in thermal contact with the heat reservoir. Thus they need not be equal.

But, there are situations in which the difference is quite negligible. For instance, suppose a magnetic system is magnetized by external field. If the magnetic energy is only a very small fraction of the total energy, the magnetization process treated by Eq. (3.15) is practically isothermal. This means that, if the heat capacities associated with A and B are only a small fraction of total heat capacity, the equality (3.17) must be practically satisfied.

It is noted here that this is concerned with the ergodic property of the system. Khinchin[13] has shown that the ergodicity for a quantity A, namely

$$\langle A\rangle=\lim_{t\to\infty}\frac{1}{t}\int_0^t A(t)\,dt \tag{3.18}$$

must hold if the autocorrelation of A satisfies the relation

$$\lim_{t\to\infty}\langle A(0)A(t)\rangle=\langle A\rangle^2\,. \tag{3.19}$$

Here $\langle A\rangle$ means the phase average of a phase function $A(p, q)$ over a microcanonical ensemble. The ergodicity of A, (3.18), means that the time average of A starting from any point P on the ergodic surface approaches to $\langle A\rangle$ independent of the initial point P. This will hold on the assumption of (3.19) for almost all of P except a set of measure zero. This Khintchin's theorem can be reversed. It can be proved that the correlation function $\langle A(0)A(t)\rangle$ satisfies Eq. (3.19) if (3.18) holds uniformly.

In classical limit, (3.11b) in replaced by

$$\Phi_{BA}(t)=\beta\{\langle A(0)B(t)\rangle-\langle A^0B^0\rangle\}\,, \tag{3.20}$$

where $\langle\ \ \rangle$ means the phase average, and A^0 means the invariant part of $A(p_{t},, q_t)$ with respect to the natural motion. Eq. (3.16) becomes classically

$$\chi_{BA}{}^T=\beta\langle(A-\langle A\rangle)(B-\langle B\rangle)\rangle\,. \tag{3.21}$$

In general we must expect

$$\begin{aligned}\Phi_{BA}(0)&=\Phi_{BA}{}^e(\infty)=\chi_{BA}(0)\\&=\beta\langle(A-\mathrm{A}^0)(B-B^0)\rangle\doteqdot\chi_{BA}{}^T\,.\end{aligned} \tag{3.22}$$

The left hand side is the static admittance for an isolated system. This means that

$$\lim_{t\to\infty}\langle A(0)(B(t)\rangle\doteqdot\langle A\rangle\langle B\rangle \tag{3.23}$$

and hence that the ergodicity (3.18) does not hold. This is quite true as one would easily understand by the example of magnetization process of an ideal magnetic system. The isothermal and adiabatic susceptibilities are different, the later being zero.

However, our aim is to apply the whole theory to realistic systems which contain various interactions. As we have mentioned before, we should expect that

$$\chi_{BA}(0)=\chi_{BA}{}^T \tag{3.24}$$

will hold if the total system is large enough compared to the degrees of freedom associated with the observed quantities A and B.

For a very large system, the canonical distribution is almost equivalent to a microcanonical distribution, the relative fluctuation being very small. The ensemble average in Eqs. (3.20), etc., can be regarded as that over an ergodic surface. Therefore, Eq. (3.24) must hold if the quantities A, B, and $A(0)B(t)$ are ergodic, namely

$$\begin{aligned}\langle A\rangle&=\lim_{t\to\infty}\frac{1}{t}\int_0^t A(t)\,dt\,,\\ \langle B\rangle&=\lim_{t\to\infty}\frac{1}{t}\int_0^t B(t)\,dt\,,\\ \langle A(0)\,B(t)\rangle&=\lim_{t'\to\infty}\frac{1}{t'}\int_0^{t'}\langle A(t')B(t'+t)\rangle\,dt'\end{aligned} \tag{3.25}$$

Here the right hand sides of the equations are primarily determined by the location of the initial point of time average, but they do not depend on that. That is the assertion of ergodicity.

If the requirement of ergodicity, (3.25), is fulfilled, we shall have

$$\begin{aligned}&\lim_{t\to\infty}\langle A(0)\,B(t)\rangle\\&=\lim_{t\to\infty}\lim_{t'\to\infty}\frac{1}{t'}\int_0^{t'}\langle A(t')B(t'+t)\rangle\,dt'\\&=\lim_{t\to\infty}\frac{1}{tt'}\int_0^t\int_0^{t'}\langle A(t')\,B(t'+t)\rangle\,dt'dt\\&=\langle\langle A\rangle\langle B\rangle\rangle=\langle A\rangle\langle B\rangle\,.\end{aligned} \tag{3.26}$$

Thus Eq. (3.22) holds.

The above arguments apply to quantum-mechanical cases with small modifications that the function $\int_0^\beta\langle A(-i\hbar\lambda)\,B(t)\rangle\,d\lambda$ enters in place of the correlation function.

Let us consider a magnetic system for illustration. The system, M, of the magnetic units are embedded in another large system,

R, with a certain interaction between M and R. The total system S we consider is $M+R$. If the heat capacity of R is large compared with M, R is a sort of heat bath for M. If we treat only M, assuming a canonical distribution and ignore the interaction between M and R, the relaxation function calculated by (3.11) describes only the internal process inside the subsystem M. The magnetic susceptibility, for instance, obtained from this, is adiabatic. For this canonical distribution, the ergodicity such as (3.25) will not hold.

If we consider the interaction and suppose, for instance, that it induces a Markoffian process for the transition of M among its various states, the ergodicity (3.25) will become true; the Markoffian assumption makes it easy to treat the relaxation process. The Markoffian assumption may be adequate if the interaction is weak and satisfies certain conditions which may be required. If such conditions are not satisfied, we are forced to deal directly with the combined system $M+R$. The relaxation function or the response function has to be treated with the complete Hamiltonian for $M+R$. In this case, the ergodicity (3.25) may be approximately true if the subsystem M is small compared to R. A rigorous formulation of mathematical proof of this is not easy, so that we merely anticipate this.

§ 4. Correlation Functions

We have seen in the previous section that the relations function $\Phi_{BA}(t)$ in classical case for canonical ensemble is essentially the correlation function of A and B; namely

$$\Phi_{BA}(t)=\beta\langle A(0)B(t)\rangle-\beta\langle A^0B^0\rangle \quad \text{(classical)} \tag{4.1}$$

where the bracket means the phase average over the canonical distribution. Or, the excitation function is

$$\Phi_{BA}{}^e(t)=\beta\langle A(0)(B-B(t))\rangle\,. \tag{4.2}$$

Other functions, for example, the response functions, are also proportional to certain correlation functions; e.g.

$$\phi_{BA}(t)=-\beta\langle A(0)\dot{B}(t)\rangle\,. \tag{4.3}$$

These are also valid for the microcanonical ensemble provided that the system in question is large.

Now the question arises how the correlation functions are defined in quantum-mechanics. We may define this by

$$\Psi_{BA}(t)=\mathrm{Tr}\,\rho\{A(0)B(t)\}=\mathrm{Tr}\,\rho\{A(t_1)B(t_1+t)\} \tag{4.4}$$

where ρ is the equilibrium density matrix, either canonical or microcanonical. The bracket means the symmetrized product,

$$\{AB\}=\frac{1}{2}(AB+BA)\,.$$

We may call this the time correlation of B and A at the time interval t, although it is not the correlation of two sets of actually observed values of B and A at different time points. The disturbance due to the observation is not taken into account. If the nature of the system and of A and B is such that this disturbance is not serious, which will be true for macrosopic systems and macroscopic observations, the function (4.4) describes the actual correlation. Since ρ is equilibrium density matrix, the time variation of A and B makes a stochastic time series which is stationary in time. For the sake of brevity, we rewrite the relaxation function as

$$\Phi_{BA}(t)=\int_0^\beta \mathrm{Tr}\,\rho(A(-i\hbar\lambda)-A^0)(B-B^0)\,d\lambda \tag{4.5}$$

and in the following we shall deal with quantities A and B which satisfy the condition

$$\mathrm{Tr}\,\rho A=\mathrm{Tr}\,\rho B=0\,, \tag{4.6}$$

which is achieved merely by substracting the invariant part from each of the quantities.

We can show easily that the relaxation function and the correlation function are mutually connected by the following theorem:

Theorem 3. *Let the Fourier transforms of $\Phi_{BA}(t)$ and $\Psi_{BA}(t)$ be*

$$f_{BA}(\omega)=\frac{1}{2\pi}\int_{-\infty}^{\infty}\Phi_{BA}(t)\,e^{-i\omega t}\,dt\,,$$

$$g_{BA}(\omega)=\frac{1}{2\pi}\int_{-\infty}^{\infty}\Psi_{BA}(t)\,e^{-i\omega t}\,dt\,, \tag{4.7}$$

then we have

$$g_{BA}(\omega)=E_\beta(\omega)f_{BA}(\omega) \tag{4.8}$$

where $E_\beta(\omega)$ is the average energy of the oscillator with the frequency ω at temperature $T=1/k\beta$,

$$E_\beta(\omega)=\frac{\hbar\omega}{2}\coth\frac{\beta\hbar\omega}{2}\,. \tag{4.9}$$

Eq. (4.8) is equivalent to

$$\Phi_{BA}(t)=\int_{-\infty}^{\infty}\Gamma(t-t')\Psi_{BA}(t')\,dt' \qquad (4.10)$$

where $\Gamma(t)$ *is defined*

$$\Gamma(t)=\frac{1}{2\pi}\int_{-\infty}^{\infty}\frac{e^{i\omega t}}{E_\beta(\omega)}\,d\omega=\frac{2}{\hbar\pi}\log\coth\frac{\pi}{2\beta\hbar}|t|\,, \qquad (4.11)$$

or to

$$\Psi_{BA}(t)=E_\beta\left(\frac{d}{idt}\right)\Phi_{BA}(t)\,. \qquad (4.12)$$

The easiest way of the proof is to write first the functions $\Phi_{BA}(t)$ and $\Psi_{BA}(t)$ as double series over the quantum states of $\mathscr{H}$ and rearrange the double sum. An alternative method is to assume a function-theoretical conditions, i.e.,

$$\lim_{Ret\to\pm\infty}\operatorname{Tr}\rho AB(t)=0\,, \qquad (4.13)$$

and that $\operatorname{Tr}\rho AB(t)$ is analytic in the domain

$$0\leqq \operatorname{Im} t\leqq\beta\hbar\,.$$

The condition (4.13) is fulfilled if one extends the meaning of the limit process as was discussed in § 2 and § 3. The second condition is equivalent to the existence $\operatorname{Tr}\rho AB$ and $\operatorname{Tr}\rho BA$.

Now Eq. (4.8) is derived as follows. By definition we can write

$$\begin{aligned}f_{BA}(\omega)&=\frac{1}{2\pi}\int_{-\infty}^{\infty}\int_0^\beta\operatorname{Tr}\rho AB(t+i\hbar\lambda)\exp(-i\omega t)d\lambda dt\\&=\frac{1}{2\pi}\int_{-\infty}^{\infty}\int_0^\beta\operatorname{Tr}\rho AB(t+i\hbar\lambda)\\&\qquad\times\exp\{-i\omega(t+i\hbar\lambda)-\lambda\hbar\omega\}\,d\lambda dt\\&=\frac{1}{2\pi}\int_0^\beta d\lambda\exp(-\lambda\hbar\omega)\\&\qquad\times\int_{-\infty+i\hbar\lambda}^{\infty+i\hbar\lambda}\operatorname{Tr}\rho AB(t)\exp(-i\omega t)\,dt\,.\end{aligned}$$

Thus interchanging the order of integration and shifting the path of integration, we obtain by the above-mentioned assumptions

$$f_{BA}(\omega)=\frac{1-\exp(-\beta\hbar\omega)}{\hbar\omega}\times\frac{1}{2\pi}\int_{-\infty}^{\infty}\operatorname{Tr}\rho AB(t)\exp(i\omega t)\,dt\,. \qquad (4.14)$$

Similarly we can show that

$$\int_{-\infty}^{\infty}\operatorname{Tr}\rho AB(t)e^{-i\omega t}\,dt=\exp(\beta\hbar\omega)\int_{-\infty}^{\infty}\operatorname{Tr}\rho B(t)\,A\exp(-i\omega t)\,dt \qquad (4.15)$$

by shifting the integration path to $-i\hbar\beta-\infty$ to $-i\hbar\beta+\infty$. In the above transformations, we took ρ as canonical given by Eq. (3.8).

Eqs. (4.15) gives

$$\int_{-\infty}^{\infty}\operatorname{Tr}\rho AB(t)e^{-i\omega t}\,dt=\frac{2}{1+\exp(-\beta\hbar\omega)}g_{BA}(\omega)\,,$$

so that Eq. (4.14) leads Eq. (4.8).

Eq. (4.10) is easily obtained from (4.8). The kernel $\Gamma(t)$, (4.11) is calculated using the partial fraction expansion of $\tanh z/z$. We note further that it has the property

$$\lim_{\hbar\to 0}\Gamma(t)=\beta\delta(t)\,, \qquad (4.16)$$

which in naturally to be expected.

§ 5. Simple Examples

It will be adequate to insert here simple examples to illustrate the general idea developed in the previous sections. The author has applied this in a previous paper[7] to the problem of magnetic resonance absorption. An uniform magnetic field $\boldsymbol{H}(t)$ is applied to a magnetic system, the total magnetic moment of which is denoted by $\boldsymbol{M}$. The perturbation energy due to $\boldsymbol{H}(t)$ is now

$$\mathscr{H}'(t)=-\boldsymbol{MH}(t)\,. \qquad (5.1)$$

The natural motion of the magnetic moment in the absence of the external field is represented by $\boldsymbol{M}(t)$. Then, the response function $\phi_{\mu\nu}(t)$ for the magnetization in μ-direction when the external field $\boldsymbol{H}(t)$ lies in ν-direction, is by Eq. (2.22).

$$\begin{aligned}\phi_{\mu\nu}(t)&=\frac{i}{\hbar}\langle[M_\mu(t),\ M_\nu]\rangle\\&=\int_0^\beta\langle\dot{M}_\nu(-i\hbar\lambda)M_\mu(t)\rangle d\lambda\,,\end{aligned} \qquad (5.2)$$

and the relaxation function is, by Eq. (3.11),

$$\Phi_{\mu\nu}(t)=\int_0^\beta\langle(M_\nu(-i\hbar\lambda)-M_\nu{}^0)(M_\mu(t)-M_\mu{}^0)\rangle\,d\lambda \qquad (5.3)$$

where $M_\nu{}^0$ and $M_\mu{}^0$ mean the diagonal parts of M_ν and M_μ with respect to the unperturbed Hamiltonian $\mathscr{H}$.

If we consider a system with unit volume, the admittance becomes the magnetic susceptibility. Thus the complex magnetic susceptibility tensor can be expressed either by $\phi_{\mu\nu}(t)$ or $\Phi_{\mu\nu}(t)$. The convenient expression is, by Eq. (3.5)

$$\chi_{\mu\nu}(\omega)=\Phi_{\mu\nu}(0)-i\omega\int_0^\infty\Phi_{\mu\nu}(t)\,e^{-i\omega t}\,dt\,. \qquad (5.4)$$

The static susceptibility is, in particular,

$$\chi_{\mu\nu}(0)=\int_0^\beta \langle (M_\nu(-i\hbar\lambda)-M_\nu{}^0)(M_\mu-M_\mu{}^0)\rangle\, d\lambda \tag{5.5}$$

which is the susceptibility for the isolated system and is not necessarily equal to the isothermal susceptibility,

$$\chi_{\mu\nu}{}^T=\int_0^\beta \langle M_\nu(-i\hbar\lambda)M_\mu\rangle d\lambda-\beta\langle M_\nu\rangle\langle M_\mu\rangle. \tag{5.6}$$

In the expression for $\chi_{\mu\nu}(0)$, the diagonal parts of M_ν and M_μ are substracted. This corresponds to the fact the magnetization in an isolated system proceeds adiabatically, the occupation probabilities of the levels remaining unchanged. On the other hand they are changed in isothermal process for $\chi_{\mu\nu}{}^T$. The difference becomes smaller if the environment is taken into account in greater extent.

In the classical limit, Eq. (5.5) becomes

$$\chi_{\mu\nu}(0)=\frac{1}{kT}\langle (M_\nu-M_\nu{}^0)(M_\mu-M_\mu{}^0)\rangle\,. \tag{5.7}$$

while Eq. (5.6) becomes

$$\chi_{\mu\nu}{}^T=\frac{1}{kT}\langle\, (M_\nu-\langle M_\nu\rangle)(M_\mu-\langle M_\mu\rangle)\,\rangle\,. \tag{5.8}$$

The last expression is first noticed by Kirkwood[14] for the classical theory of dielectric polarization. Eq. (5.7) is its extension to adiabatic susceptibility, and Eq. (5.4) to general complex susceptibility for non-equilibrium states. It is evident that the similar formulae are obtained for dielectric polarizations.

As a second example we shall consider the electric conductivity. For an electric $\boldsymbol{E}(t)$, the perturbation energy is

$$\mathscr{H}'(t)=-\sum_i e_i\boldsymbol{r}_i\boldsymbol{E}(t) \tag{5.7}$$

where e_i is the charge of the i-th particle in the system and $\boldsymbol{r}_i$ its position vector. The response of current in μ-direction when a pulse of electric field is applied in ν-direction at $t=0$ is, by Eq. (2.22) or Eq. (3.9)

$$\begin{aligned}\phi_{\mu\nu}(t)&=\frac{1}{i\hbar}\,\mathrm{Tr}\,[\rho,\,\sum_i e_i\, x_{i\nu}]\sum e_i\,\dot{x}_{i\mu}(t)\\ &=\int_0^\beta \langle\, J_\nu\,(-i\hbar\lambda)\,J_\mu(t)\,\rangle\, d\lambda\end{aligned} \tag{5.10}$$

where

$$J_\mu=\sum e_i\,\dot{x}_{i\mu}$$

is the total current in the system.

If we take the volume of the system as unity, the conductivity tensor $\sigma_{\mu\nu}(\omega)$ for periodic field is given by

$$\sigma_{\mu\nu}(\omega)=\int_0^\infty e^{-i\omega t}\,dt\int_0^\beta d\lambda\,\langle\, J_\nu(-i\hbar\lambda)\,J_\mu(t)\,\rangle\,. \tag{5.11}$$

This is an exact expression for the conductivity. In particular, for the static conductivity we have

$$\sigma_{\mu\nu}=\int_0^\infty\int_0^\beta d\lambda\,\langle\, J_\nu(-i\hbar\lambda)\,J_\mu(t)\,\rangle\,. \tag{5.12}$$

This may be expressed in another form,

$$\sigma_{\mu\nu}=\lim_{s\to0+}\frac{1}{s}\left\{\phi_{\mu\nu}(0)+\int_0^\infty\dot{\phi}_{\mu\nu}(t)\,e^{-st}\,dt\right\} \tag{5.13}$$

where

$$\dot{\phi}_{\mu\nu}(t)=-\frac{1}{i\hbar}\,\mathrm{Tr}\,\rho[J_\nu,\,J_\mu(t)]\,. \tag{5.14}$$

The above expressions of conductivity tensor are, as a matter of fact, what one would obtain by simple application of dispersion formula of Heisenberg and Kramers. But they are more convenient and much clearer for physical interpretation. Nakano[8] has shown that the Grüneisen formula is obtained from (5.11) as the first approximation. We emphasize again that the formulae given in the above are exact although they are admittedly rather abstract and have to be approximated in some way to deduce useful answers for assumed physical models. We can show that the usual method of employing Boltzmann-Bloch type transport equations makes a certain approximation to calculate these exact expressions. But the transport equation can not always be justified since the Markoffian assumption involved is only valid under rather strict conditions for the scattering processes.[1] The exact theory will certainly give a starting point of actual calculations when the traditional methods are not justified. A good example of this is provided by the problem of electronic conduction in strong magnetic field.[11] This will be treated in a forthcoming paper.

§ 6. Symmetry Relations

We note here some symmetry properties of the response and relaxation functions and those of the admittance. Let us consider for convenience the relaxtion function defined by Eq. (3.11), for which we have the theorem:

Theorem 4. *The relaxation function $\Phi_{BA}(t)$ has the following properties;*

1) *$\Phi_{BA}(t)$ is real* (6.1)

2) $\Phi_{BA}(-t)=\Phi_{AB}(t)$ (6.2)

3) *reciprocity law: if a static magnetic field* $\boldsymbol{H}$ *is present, the reversal of the direction of* $\boldsymbol{H}$ *results in*

$$\begin{aligned}\Phi_{BA}(t, \boldsymbol{H}) &= \mathcal{E}_A\mathcal{E}_B\Phi_{BA}(-t, -\boldsymbol{H})\\ &= \mathcal{E}_A\mathcal{E}_B\Phi_{AB}(t, -\boldsymbol{H})\end{aligned} \tag{6.3}$$

where $\mathcal{E}_A$ *or* $\mathcal{E}_B$ *is* $+1$ *or* -1 *according to the quantity* A *or* B *is even or odd with respect to the reversal of time.*

The proof is simple. The complex conjugate of $\Phi_{BA}(t)$ is calculated as follows.

$$\begin{aligned}\overline{\Phi}_{BA}(t) &= \int_0^\beta \mathrm{Tr}\,\rho B(t)\,A(i\hbar\lambda)\,d\lambda\\ &= \int_0^\beta \mathrm{Tr}\,\rho B(t-i\hbar\lambda)\,A\,d\lambda\\ &= \int_0^\beta \mathrm{Tr}\,\rho B(t-i\hbar(\beta-\lambda))\,A\,d\lambda\\ &= \int_0^\beta \mathrm{Tr}\,\rho AB(t+i\hbar\lambda)\,d\lambda = \Phi_{BA}(t)\,.\end{aligned}$$

The transformation from the second to the third line is simply the change of integration variable from λ to $\beta-\lambda$.

Similarly, we may proceed as

$$\begin{aligned}\Phi_{BA}(-t) &= \int_0^\beta \mathrm{Tr}\,\rho AB(-t+i\hbar\lambda)\,d\lambda\\ &= \int_0^\beta \mathrm{Tr}\,\rho A(t-i\hbar\lambda)\,B\,d\lambda\\ &= \int_0^\beta \mathrm{Tr}\,\rho BA(t+i\hbar\lambda)\,d\lambda = \Phi_{BA}(t)\,.\end{aligned}$$

Eq. (6.3) follows from the fact that the simultaneous reversal of t and $\boldsymbol{H}$ changes the q-representation of the Hamiltonian and the wave function to their complex conjugates. A corollary of the theorem is the symmetry of other functions such as $\phi_{BA}(t)=-\dot{\Phi}_{BA}(t)$. This is clear and so is omitted here.

The second corollary is the symmetry of admittance. We write down here the symmetry of the quantity defined by

$$\sigma_{BA}(\omega)=\int_0^\infty \Phi_{BA}(t)\,e^{-i\omega t}\,dt \tag{6.4}$$

for which we have

$$\mathrm{Re}\,\sigma_{BA}(\omega)=\mathrm{Re}\,\sigma_{BA}(-\omega)\,, \tag{6.5}$$

$$\mathrm{Im}\,\sigma_{BA}(\omega)=-\mathrm{Im}\,\sigma_{BA}(-\omega)\,, \tag{6.6}$$

$$\sigma_{BA}(\omega, -\boldsymbol{H})=\mathcal{E}_A\mathcal{E}_B\sigma_{AB}(\omega, \boldsymbol{H})\,. \tag{6.7}$$

Eq. (6.7) is the well-known Onsager's relation.[15] The derivation here made is very simple.

As examples, we note the symmetry of magnetic susceptibility tensor and that of the conductivity tensor. The susceptibility tensor has the symmetry

$$\begin{aligned}\mathrm{Re}\,\chi_{\mu\nu}(\omega, \boldsymbol{H}) &= \mathrm{Re}\,\chi_{\mu\nu}(-\omega, \boldsymbol{H})\\ &= \mathrm{Re}\,\chi_{\nu\mu}(\omega, -\boldsymbol{H})\,,\\ \mathrm{Im}\,\chi_{\mu\nu}(\omega, \boldsymbol{H}) &= -\mathrm{Im}\,\chi_{\mu\nu}(-\omega, \boldsymbol{H})\\ &= \mathrm{Im}\chi_{\nu\mu}(\omega, -\boldsymbol{H})\,.\end{aligned} \tag{6.8}$$

For the conductivity tensor we have the same relations

$$\begin{aligned}\mathrm{Re}\,\sigma_{\mu\nu}(\omega, \boldsymbol{H}) &= \mathrm{Re}\,\sigma_{\mu\nu}(-\omega, \boldsymbol{H})\\ &= \mathrm{Re}\,\sigma_{\nu\mu}(\omega, -\boldsymbol{H})\,,\\ \mathrm{Im}\,\sigma_{\mu\nu}(\omega, \boldsymbol{H}) &= -\mathrm{Im}\,\sigma_{\mu\nu}(-\omega, \boldsymbol{H})\\ &= \mathrm{Im}\,\sigma_{\nu\mu}(\omega, -\boldsymbol{H})\,.\end{aligned} \tag{6.9}$$

Thus, for the change ω to $-\omega$, the real part is even while the imaginary part is odd. For the reversal of $\boldsymbol{H}$, the symmetric part is even and the antisymmetric part is odd.

§ 7. Fluctuation-Dissipation Theorems

We have shown in § 4 that the response and relaxation functions can be expressed by correlation functions. Thus the admittance can also be expressed in terms of correlation functions. This is rather trivial for classical cases, but in quantum mechanics it becomes rather complicated. The relation between the admittance and the Fourier components correlation functions is usually called the fluctuation-dissipation theorem. Thus our aim here is to give this theorem in its complete form.

We treat as a typical example the case of electric conduction. Let us rewrite Eq. (5.11) in terms of the Fourier component of response function $\phi_{\mu\nu}(t)$, i.e.,

$$f_{\mu\nu}(\omega)=\frac{1}{2\pi}\int_{-\infty}^{\infty}\phi_{\mu\nu}(t)\,e^{-i\omega t}\,dt\,. \tag{7.1}$$

Eq. (5.11) is transformed as

$$\begin{aligned}\sigma_{\mu\nu}(\omega) &= \int_0^\infty \phi_{\mu\nu}(t)\,e^{-i\omega t}\,dt\\ &= \int_0^\infty dt\int_{-\infty}^{\infty} d\omega'\,f_{\mu\nu}(\omega')\,e^{i\omega' t-i\omega t}\\ &= \pi f_{\mu\nu}(\omega)+i\int_{-\infty}^{\infty}\frac{f_{\mu\nu}(\omega')}{\omega'-\omega}\,d\omega'\,.\end{aligned} \tag{7.2}$$

Thus we obtain at once

$$\mathrm{Re}\,\sigma^{s}{}_{\mu\nu}(\omega)=\pi f^{s}{}_{\mu\nu}(\omega)\equiv\frac{\pi}{2}\left\{f_{\mu\nu}(\omega)+f_{\nu\mu}(\omega)\right\}$$

$$\operatorname{Im}\sigma^{a}_{\mu\nu}(\omega)=\frac{\pi}{2}f^{a}_{\mu\nu}(\omega)\equiv\frac{\pi}{2i}\Big\{f_{\mu\nu}(\omega)-f_{\nu\mu}(\omega)\Big\} \tag{7.3}$$

$$\operatorname{Im}\sigma^{s}_{\mu\nu}(\omega)=\int_{-\infty}^{\infty}\frac{f^{s}_{\mu\nu}(\omega')}{\omega'-\omega}d\omega'$$

$$\operatorname{Re}\sigma^{a}_{\mu\nu}(\omega)=i\int_{-\infty}^{\infty}\frac{f^{a}_{\mu\nu}(\omega')}{\omega'-\omega}d\omega'\ , \tag{7.4}$$

where the superscript s or a means the symmetric or the anti-symmetric part of the tensor. By the theorem 4 one has the symmetry

$$\overline{f_{\mu\nu}}(\omega)=f_{\nu\mu}(\omega)\ , \tag{7.5}$$

which shows $f^{s}_{\mu\nu}(\omega)$ is real while $f^{a}_{\mu\nu}(\omega)$ is purely imaginary. Eqs. (7.3) and (7.4) give the well-known Kramers-Kronig relation. Note that it holds for each of the symmetric and antisymmetric parts separately.

Now let us introduce the correlation function of current components,

$$\Psi_{\mu\nu}(t)=\operatorname{Tr}\rho\{j_{r}(0)\,j_{\mu}(t)\}\ , \tag{7.6}$$

which describes the correlation of spontaneous current fluctuating in equilibrium. We can show the following theorem:

Theorem 5. *The conductivity tensor $\sigma_{\mu\nu}(\omega)$ is connected with correlation function of current components, (7.6), by the following relations:*

$$E_{\beta}(\omega)\operatorname{Re}\sigma^{s}_{\mu\nu}(\omega)=\pi g^{s}_{\mu\nu}(\omega)$$
$$=\int_{0}^{\infty}\Psi^{s}_{\mu\nu}(t)\cos\omega t\,dt \tag{7.7a}$$

$$E_{\beta}(\omega)\operatorname{Im}\sigma^{a}_{\mu\nu}(\omega)=\frac{\pi}{i}g^{a}_{\mu\nu}(\omega)$$
$$=-\int_{0}^{\infty}\Psi^{a}_{\mu\nu}(t)\sin\omega t\,dt \tag{7.7b}$$

$$\Psi^{s}_{\mu\nu}(t)=\frac{2}{\pi}\int_{0}^{\infty}E_{\beta}(\omega)\operatorname{Re}\sigma^{s}_{\mu\nu}(\omega)\cos\omega t\,d\omega \tag{7.8a}$$

$$\Psi^{a}_{\mu\nu}(t)=-\frac{2}{\pi}\int_{0}^{\infty}E_{\beta}(\omega)\operatorname{Im}\sigma^{a}_{\mu\nu}(\omega)\sin\omega t\,d\omega\ , \tag{7.8b}$$

and

$$\operatorname{Im}\sigma^{s}_{\mu\nu}(\omega)=\int_{-\infty}^{\infty}\frac{1}{E_{\beta}(\omega')}\cdot\frac{g^{s}_{\mu\nu}(\omega')}{\omega'-\omega}d\omega'$$
$$=-2\int_{0}^{\infty}\Gamma(\tau)\cos\omega\tau\,d\tau\int_{\tau}^{\infty}\Psi^{s}_{\mu\nu}(t)\sin\omega t\,dt$$
$$-2\int_{0}^{\infty}\Gamma(\tau)\sin\omega\tau\,d\tau\int_{0}^{\tau}\Psi^{s}_{\mu\nu}(t)\cos\omega t\,dt \tag{7.9a}$$

$$\operatorname{Re}\sigma^{a}_{\mu\nu}(\omega)=-\frac{1}{i}\int_{-\infty}^{\infty}\frac{1}{E_{\beta}(\omega')}\frac{g^{a}_{\mu\nu}(\omega')}{\omega'-\omega}d\omega'$$
$$=2\int_{0}^{\infty}\Gamma(\tau)\cos\omega\tau\,d\tau\int_{\tau}^{\infty}\Psi^{a}_{\mu\nu}(t)\cos\omega t\,dt$$
$$-2\int_{0}^{\infty}\Gamma(\tau)\sin\omega\tau\,d\tau\int_{0}^{\tau}\Psi^{a}_{\mu\nu}(t)\sin\omega t\,dt \tag{7.9b}$$

$$\Psi^{s}_{\mu\nu}(t)=\frac{2}{\pi}\int_{0}^{\infty}\operatorname{Im}\sigma^{s}_{\mu\nu}(\omega)\operatorname{Re}\Delta(\omega,t)\,d\omega \tag{7.10a}$$

$$\Psi^{a}_{\mu\nu}(t)=\frac{2}{\pi}\int_{0}^{\infty}\operatorname{Re}\sigma^{a}_{\mu\nu}(\omega)\operatorname{Im}\Delta(\omega,t)\,d\omega\ , \tag{7.10b}$$

where the kernel $\Delta(\omega,t)$ is defined by

$$\Delta(\omega,t)=\frac{1}{\pi}\int_{-\infty}^{\infty}\frac{du}{u-\omega}E_{\beta}(u)e^{iut}\ . \tag{7.11}$$

These expressions reduce, in classical limit, to

$$\operatorname{Re}\sigma_{\mu\nu}(\omega)=\int_{0}^{\infty}\Psi_{\mu\nu}(t)\cos\omega t\,dt$$
$$\operatorname{Im}\sigma_{\mu\nu}(\omega)=-\int_{0}^{\infty}\Psi_{\mu\nu}(t)\sin\omega t\,dt \tag{7.12}$$

First we note that the symmetry of $\Psi_{\mu\nu}(t)$ is the same as that we have for $\phi_{\mu\nu}(t)$ (Theorem 4). Eqs. (7.7) and the first parts of (7.9a) and (7.9b) are obvious from Eq. (4.8). Eq. (7.8a, b) is simply the inverse of Eq. (7.7a, b). We need some calculation to derive (7.9) and (7.10) but the details are omitted here. Only we note for the convenience of reference that the function (7.11) can be transformed to

$$\operatorname{Re}\Delta(\omega,t)=-E_{\beta}(\omega)\sin\omega t\cdot\operatorname{sign}t$$
$$+\frac{1}{\pi\beta}\sum_{n=1}^{\infty}\frac{(n\pi)^{2}\exp(-2n\pi|t|/\beta\hbar)}{(n\pi)^{2}+(\beta\hbar\omega)^{2}/4} \tag{7.13a}$$

$$\operatorname{Im}\Delta(\omega,t)=E_{\beta}(\omega)\cos\omega t\cdot\operatorname{sign}t$$
$$-\frac{1}{\pi\beta}\sum_{n=1}^{\infty}\frac{(n\pi/2)\beta\hbar\omega\exp(-2n\pi|t|/\beta\hbar)}{(n\pi)^{2}+(\beta\hbar\omega)^{2}/4}\operatorname{sign}t\ . \tag{7.13b}$$

An useful corollary of the theorem is the expression of static conductivity $\sigma_{\mu\nu}(0)$. We have the formulae;

$$\sigma^{s}_{\mu\nu}(0)=\beta\int_{0}^{\infty}\Psi^{s}_{\mu\nu}(t)\,dt\equiv\frac{\beta}{2}\int_{-\infty}^{\infty}\Psi^{s}_{\mu\nu}(t)\,dt \tag{7.14}$$

$$\sigma^{a}_{\mu\nu}(0)=2\int\Gamma(\tau)\,d\tau\int_{\tau}^{\infty}\Psi^{a}_{\mu\nu}(t)\,dt$$
$$=2\int_{0}^{\infty}\Psi^{a}_{\mu\nu}(t)\int_{0}^{t}\Gamma(\tau)\,d\tau\ . \tag{7.15}$$

Thus the symmetric part of the static conductivity is calculated either as the integration of the response function or as that of the correlation function. The situation is more complicated for the antisymmetric part. If one wishes to use the correlation function instead of the response function, one has to be careful about a quantum effect which appears as $\Gamma(\tau)$ in Eq. (7.15).

Another remark is that, even at finite frequencies, the symmetric part is easily obtained if the correlation function is known. This is, of particular interest, for instance, in the case of magnetic problem[7]. For a linearly polarized radiation, the absorption is determined by the imaginary part of susceptibility tensor, for which we have from Eq. (5.4)

$$\chi''_{xx}(\omega) = -\mathrm{Im}\,\chi_{xx} = \frac{\omega}{2E_\beta(\omega)}\int_{-\infty}^{\infty}\langle\{M_x(0)M_x(t)\}\rangle\cos\omega t\,dt\,. \tag{7.16}$$

The corresponding expression for conduction is (7.7a) itself, i.e.,

$$\sigma_{xx}(\omega) = \frac{1}{2E_\beta(\omega)}\int_{-\infty}^{\infty}\langle\{J_x(0)J_x(t)\}\rangle\cos\omega t\,dt \tag{7.17}$$

The last equation is the well-known Niquist's theorem[16]. If the fluctuating current is expanded into the Fourier components, Eq. (7.17) reduces to

$$\sigma_{xx}(\omega) = \frac{\pi}{E_\beta(\omega)}\langle|J_x(\omega)|^2\rangle\,. \tag{7.18}$$

§ 8. Sum Rules

It is interesting that the exact expressions of admittance derived in the above give proof of certain general laws. The simplest example of this is the well-known sum-rule of oscillator strength. This is generalized in the following way.

We consider the expression (6.4), from which we obtain

$$\frac{1}{\pi}\int_{-\infty}^{\infty}\sigma_{BA}(\omega)\,d\omega = 2\int_0^{\infty}\Phi_{BA}(t)\,\delta(t)\,dt = \Phi_{BA}(0)\cdot \tag{8.1}$$

and

$$\lim_{\omega\to\infty} i\omega\,\sigma_{BA}(\omega) = \Phi_{BA}(0) \tag{8.2}$$

by Abel's theorem if the left hand side does exist.

Let us now apply this for electric conduction. By Eq. (5.10) one can write

$$\phi_{\mu\nu}(t) = \frac{1}{i\hbar}\mathrm{Tr}\,\rho\left[\sum e_i x_{i\nu},\ \sum e_j \dot{x}_{j\mu}(t)\right] \tag{8.3}$$

If the Hamiltonian $\mathscr{H}$ has the general form

$$\mathscr{H} = \sum_i\left[p_{i\nu} - \frac{e_i}{c}A_\nu(\boldsymbol{r}_i)\right]^2\Big/2m_i + V(\boldsymbol{r}_1,\cdots\boldsymbol{r}_N),$$

$\boldsymbol{A}$ being the vector potential we have the commutation rule

$$[x_{i\nu},\ \dot{x}_{j\mu}] = \frac{i\hbar}{m_i}\delta_{ij}\,\delta_{\mu\nu} \tag{8.4}$$

which gives

$$\phi_{\mu\nu}(0) = \sum_{i=1}^{N}\frac{e_i{}^2}{m_i}\delta_{\mu\nu} = \sum_r\frac{n_r e_r{}^2}{m_r} \tag{8.5}$$

where r means the species of charge carriers, n_r being the number of carriers of r-th kind.

Eq. (8.3) is derived from Eq. (5.10) by changing the order in the trace operation. One might doubt whether this is justfied or not, pointing out that the operators $x_{i\nu}$ may be singular if one uses the Born-Karman boundary conditions. As a matter of fact this will not affect the validity of the proof, because the commutators are actually regular operators. It might be worth while to see what one has in classical case. Classically we may proceed as (see Eq. (2.22a))

$$\begin{aligned}\phi_{\mu\nu}(t) &= \int d\Gamma(f,\ \sum e_i x_{i\nu})\sum e_j\dot{x}_{j\mu}(t)\\ &= -\int d\Gamma\sum_i e_i\frac{\partial f}{\partial p_{i\nu}}\cdot\sum e_j\dot{x}_{j\mu}(t)\\ &= \int d\Gamma\,f\sum_i\sum_j e_i e_j\frac{\partial}{\partial p_{i\nu}}\dot{x}_{j\mu}(t)\,.\end{aligned} \tag{8.6}$$

Thus we have

$$\begin{aligned}\phi_{\mu\nu}(0) &= \int d\Gamma f\sum_i\sum_j e_i e_j\frac{\partial}{\partial p_{i\nu}}\cdot\frac{1}{m_j}\left\{p_{j\mu} - \frac{e_j}{c}A_\mu(\boldsymbol{r}_j)\right\}\\ &= \int d\Gamma f\sum_i e^2{}_i\,/\,m_i\,\delta_{\mu\nu}\end{aligned} \tag{8.7}$$

This is exactly the same as Eq. (8.5). This does not prove directly the validity of (8.3), but will be enough to make it convincing. As as proof one may introduce a suitable potential to avoid the difficulty of singular operators $x_{i\nu}$, and make it vanish if one wants.

Thus we have proved the sum rule

$$\frac{2}{\pi}\int_0^{\infty}\mathrm{Re}\,\sigma^s{}_{\mu\nu}(\omega)\,d\omega = \sum_r\frac{e^2{}_r n_r}{m_r}\delta_{\mu\nu} \tag{8.8}$$

and

$$\lim_{\omega\to\infty}\omega\,\mathrm{Im}\,\sigma^{s}_{\mu\nu}=-\sum_{r}\frac{e^{2}_{r}n_{r}}{m_{r}}\delta_{\mu\nu} \qquad (8.9)$$

which hold for any system irrespective of the interaction of particles, the temperature, the statistics and even in the presence of magnetic field. This is the most general form of the sum rule.

For a system of electrons, Eqs. (8.8) and (8.9) are written as

$$\frac{2}{\pi}\int_{0}^{\infty}\mathrm{Re}\,\sigma^{s}_{\mu\nu}(\omega)\,d\omega=\frac{ne^{2}}{m}\delta_{\mu\nu} \qquad (8.10)$$

$$\mathrm{Im}\,\sigma^{s}_{\mu\nu}(\omega)\to-\frac{e^{2}n}{m\omega}\delta_{\mu\nu}\quad(\omega\to\infty)\,. \qquad (8.11)$$

Here we should remember that m is the true mass of electrons. The integration of $\sigma(\omega)$ has to be carried over all range of frequencies.

If one considers electrons in a crystal and confines himself to the electrons in a particular band neglecting interband transitions, the sum rule has to be modified to

$$\begin{aligned}&\frac{2}{\pi}\int_{0}^{\infty}\mathrm{Re}\,\sigma^{s}_{\mu\nu}(\omega)\,d\omega\\&=-\lim_{\omega\to\infty}\omega\,\mathrm{Im}\,\sigma^{s}_{\mu\nu}(\omega)\\&=e^{2}\,\mathrm{Tr}\,\{\rho\cdot\partial^{2}E(p)/\partial p_{\nu}\partial p_{\mu}\}\,. \qquad (8.12)\end{aligned}$$

This holds if the electron system is described by the Hamiltonian

$$\mathscr{H}=\sum_{i}E(p_{i})+V(r_{1},\cdots r_{N}) \qquad (8.13)$$

where $E(p)$ is the energy of an electron with the crystal moments p. Also one has to omit the interband elements of the potential V. The theorem (8.12) is wider than that usually given in text books only for the oscillator strength connecting one-electron states.

Another interesting result is obtained from the second expression of (3.5) when applied to conduction problem. This give

$$\begin{aligned}&\frac{1}{\pi}\int_{-\infty}^{\infty}\{i\sigma_{\mu\nu}(\omega)\,\omega-\phi_{\mu\nu}(0)\}d\omega\\&=-\lim_{\omega\to\infty}\omega^{2}\left\{\sigma_{\mu\nu}(\omega)-\frac{\phi_{\mu\nu}(0)}{i\omega}\right\}=\dot{\phi}_{\mu\nu}(0)\end{aligned} \qquad (8.14)$$

The tensor

$$\dot{\phi}_{\mu\nu}(0)=-\frac{i}{\hbar}\,\mathrm{Tr}\,\rho\,[J_{\mu},J_{\nu}] \qquad (8.15)$$

is antisymmetric. Therefore Eq. (8.14) is rewritten as

$$\begin{aligned}&-\frac{1}{\pi}\int_{-\infty}^{\infty}\mathrm{Im}\,\sigma^{a}_{xy}(\omega)\,\omega d\omega\\&=\lim_{\omega\to\infty}\omega^{2}\sigma^{a}_{xy}(\omega)=-\sum_{r}\frac{n_{r}e_{r}^{3}H_{z}}{m_{r}^{2}c}\,. \qquad (8.16)\end{aligned}$$

Both sides of this equation are identically zero unless the system is in a magnetic field (or rotating, in which case $e_{r}H_{z}/m_{r}c$ must be replaced by the angular frequency of the rotation). This is seen from the fact that the velocity of charged particles in magnetic field is

$$v=\frac{1}{m}\left(p-\frac{e}{c}A\right)$$

and the commutation rule is now

$$[v_{x},v_{y}]=-\frac{eH_{z}}{m^{2}c}\frac{\hbar}{i}\,. \qquad (8.17)$$

This gives

$$\frac{i}{\hbar}\,\mathrm{Tr}\,\rho\,[J_{x},J_{y}]=\sum n_{r}e_{r}^{3}H_{z}/m_{r}^{2}c\,, \qquad (8.18)$$

which is the last expression in Eq. (8.16).

In particular, for electrons we have

$$\begin{aligned}\frac{2}{\pi}\int_{0}^{\infty}\mathrm{Im}\,\sigma^{a}_{\mu\nu}(\omega)\omega d\omega&=-\lim_{\omega\to\infty}\omega^{2}\sigma^{a}_{\mu\nu}(\omega)\\&=\frac{ne^{3}}{m^{2}c}H_{z}\,. \qquad (8.19)\end{aligned}$$

This is another type of sum-rule which holds quite generally, but is not usually remarked. Eq. (8.19) may also be written as

$$\sum_{l}\mathrm{Im}\,\langle k|J_{x}|l\rangle\langle l|J_{y}|k\rangle=-\frac{ne^{3}}{2m^{2}c}H_{z} \qquad (8.20)$$

for a system of n electrons.

Similar arguments can also be made for tensors of other kinds. For instance, the magnetic susceptibility tensor satisfies the rules,

$$-\frac{1}{\pi}\int_{-\infty}^{\infty}\mathrm{Im}\,\chi^{s}_{\mu\nu}(\omega)\frac{d\omega}{\omega}=\chi^{s}_{\mu\nu}(0)\,, \qquad (8.21)$$

$$\lim_{\omega\to\infty}\mathrm{Re}\,\chi^{s}_{\mu\nu}(\omega)=0\,, \qquad (8.22)$$

$$\begin{aligned}&\frac{1}{\pi}\int_{-\infty}^{\infty}\mathrm{Re}\,\chi^{a}_{\mu\nu}(\omega)\,d\omega\\&=-\lim_{\omega\to\infty}\omega\,\mathrm{Im}\,\chi^{a}_{\mu\nu}(\omega)=\frac{i}{\hbar}\,\mathrm{Tr}\,\rho[M_{\mu},M_{\nu}]\,.\end{aligned} \qquad (8.23)$$

The relation (8.21) is well-known. This states that the properly weighted integration of absorption intensity for linearly polarized radiation is equal to the static susceptibility. The third relation, (8.23), requires more attention.

If M_μ is written as

$$M_\mu=\sum_i \gamma_i I_{i\mu} \ ,$$

where I_i is the angular momentum associated with the magnetic moment, we have

$$\frac{i}{\hbar}[M_x, M_y]=-\sum \gamma_i^2 I_{iz} \ .$$

Therefore Eq. (8.23) can be written as

$$\frac{1}{2}\int_0^\infty \mathrm{Re}\, \chi^a{}_{xy}(\omega)\, d\omega$$

$$=-\lim_{\omega\to\infty} \omega\, \mathrm{Im}\, \chi^a{}_{xy}(\omega)=-\sum \gamma_i^2 \overline{I}_{iz}=-\sum \gamma_r \overline{M}_{rz} \tag{8.24}$$

where $\overline{M}_{rz}$ means the magnetization due to r-th component in the system.

For circularly polarized radiation, the rate of energy absorption per unit volume is

$$Q=\frac{\omega}{2} H_1^2\{\chi'_{xy}-\chi'_{yx}+\chi''_{xx}+\chi''_{yy}\}$$

H_1 being the amplitude of the magnetic field of radiation. Thus, $\mathrm{Re}\, \chi^a{}_{xy}(\omega)$ is related to the absorption intensity of circular waves. The total integration of the absorption intensity is directly connected with the gyromagnetic ratio γ. This may not be of much value if γ can be measured accurately by sharp resonance. But one has to remember that (8.24) is generally valid even in the presence of strong interaction between magnetic moments. Thus the effects related to the absorption of circular wave may be used for the determination of γ, for instance, for electronic magnetic moments in ferromagnets or paramagnets. This sort of experiments may be considered to corresponds in a sense to those of gyromagnetic effects.

§ 9. Einstein Relations

We note here that the expression of conductivity given by Eq. (5.12) or (7.14) is the most general form of Einstein relation, which connects the conductivity or the mobility with the diffusion constant.

To see this, let us take the simplest example of charged particles which are moving independently. By Eq. (7.14), the conductivity is

$$\sigma^s{}_{\mu\nu}=\frac{ne^2}{kT}\int_0^\infty \langle v_\nu(0)\, v_\mu(t)\rangle\, dt \ , \tag{9.1}$$

if we regard the system to be classical. If we admit

$$\lim_{t\to\infty} \langle v_\nu(0) v_\mu(t)\rangle=\langle v_\nu\rangle\langle v_\mu\rangle=0$$

we can transform the right hand side of Eq. (9.1) as

$$\int_0^\infty \langle v_\nu(0) v_\mu(t)\rangle\, dt$$

$$=\lim_{T\to\infty} \frac{1}{2T}\int_0^T\int_0^T \langle v_\nu(t') v_\mu(t)\rangle\, dt\, dt'$$

$$=\lim_{T\to\infty} \frac{1}{2T}\langle (x_\nu(T)-x_\nu(0))(x_\mu(T)-x_\mu(0))\rangle$$

$$=D_{\mu\nu} \ . \tag{9.2}$$

where $D_{\mu\nu}$ is the diffusion constant defined by the third expression of Eq. (9.2). Eqs. (9.2) and (9.1) give at once

$$\sigma^s{}_{\mu\nu}=e^2 n D_{\mu\nu}/kT \tag{9.3}$$

which is the well known Einstein relation.

For a system of interacting particles, the exact form of Einstein relation is

$$\sigma^s{}_{\mu\nu}=e^2\overline{\Delta n^2} D_{\mu\nu}/kT \tag{9.4a}$$

$$=e^2 D_{\mu\nu}\Big/\left(\frac{\partial\mu}{\partial n}\right)_T \tag{9.4b}$$

where $D_{\mu\nu}$ is the diffusion constant in isothermal conditions, $\overline{\Delta n^2}$ the average fluctuation of particle density, and μ the chemical potential of the particle. This relation gives, for the diffusion constant,

$$D^s{}_{\mu\nu}=\left(\frac{\partial\mu}{\partial n}\right)_T\int_0^\infty dt\int_0^\beta \mathrm{Tr}\, \rho I_\nu(-i\hbar) I_\mu(t) d\lambda$$

$$=\left(\frac{\partial\mu}{\partial n}\right)_T \frac{1}{2}\int_{-\infty}^\infty dt\, \mathrm{Tr}\, \rho\{I_\nu I_\mu(t)\} \tag{9.5}$$

where

$$I_\nu=\sum_i v_{i\nu}$$

is the total particle flow per unit volume. Eq. (9.5) can be used for the calculation of diffusion constant in gases and also condensed phases. This will be discussed further in a forthcoming paper.

It might be worth while to note that Eq. (9.4) indicates at once how the factor $1/kT$ appearing in the expression of electric conductivity, Eq. (7.14) cancels out for degenerate Fermi particles. In this case, $\overline{\Delta n^2}$ is proportional to T, or in other words $(\partial\mu/\partial n)_T$ is a constant of the order of μ_0/n, μ_0 being the Fermi-level at the absolute zero.

Acknowledgements

The author wishes to express appreciation to Dr. N. Hashitsume and other members of our research group at University of Tokyo for valuable discussions. This study was financed by the Scientific Research Fund of the Ministry of Education.

References

1) I. Prigogine: Proceedings of the International Conference on Electron Transport in Metals and Solids, Canadian J. Physics, **34**, No12A (1956) 1236; L. Van Hove: Physica **21** (1955) 517, **22** (1956) 343.
2) See for instance, S. R. de Groot, Thermodynamics of Irreversible Processes, North Holland Pub. Co. 1952.
3) See for instance, R. T. Cox, Statistical Mechanisc of Irreversible Change.
4) J. G. Kirkwood: J. Chem. Phys. **14** (1946) 180.
5) H. B. Callen and T. A. Welton: Phys. Rev. **83** (1951) 34.
6) H. Takahasi: J. Phys. Soc. Japan **7** (1952) 439.
7) R. Kubo and K. Tomita: J. Phys. Soc. Japan **9** (1954) 888.
8) H. Nakano: Prog. Theor. Phys. **15** (1956) 77, Busseiron-Kenkyu (in Japanese) **84** (1955) 25, **88** (1955) 53.
9) The preliminary reports by the author; R. Kubo: Proceedings of the International Conf. on Electron Transport in Metals and Solids, Canadian J. Phys. **34** No12A (1956) 1274, Kagaku (in Japanese) **27** (1957) 58, Busseiron-Kenkyu (in Japanese) **89** (1955) 79, R. Kub and M. Yokota: ibid. **89** (1955), 99, R. Kubo, N. Hashitsume and M. Yokota: ibid. **91** (1955) 32.
10) H. Mori: J. Phys. Soc. Japan **11** (1956) 1029.
11) Reported by R. Kubo at the Conference on Physics of Magnetic Phenomena, Moskow, 1956 May.
12) See for instance, G. Placzek: Handbuch der Radiologie, Bd VI, Teil ii, p. 211.
13) A. I. Khintchin: Mathematical Foundations of Statistical Mechanics.
14) J. Kirkwood: J. Chem. Phys. **7** (1939) 911, H. Frohlich: Theory of Dielectrics, 1949.
15) L. Onsager: Phys. Rev. **37** (1931) 405, **38** (1931) 2265.
H. B. G. Casimir: Rev. Mod. Phys. **17** (1945) 343.
16) H. Nyquist: Phys. Rev. **32** (1928) 110.

JOURNAL OF THE PHYSICAL SOCIETY OF JAPAN Vol. 12, No. 6, JUNE, 1957

Electron-Electron Interaction and Superconductivity. I*

By Ziro MIKURA

The Research Institute for Iron, Steel and Other Metals,
Tohoku University, Sendai

(Received January 11, 1957)

It is shown that an electron gas exhibits the Meissner-Ochsenfeld effect if a special type of electron-electron interaction, $e^2s_1\cdot s_2/r$, is assumed and if the motion of an electron is considered to obey Dirac's relativistic equation. (s_1 and s_2 are the spin operators belonging respectively to each interacting electron.) The perturbation method of statistical mechanics, when applied to this system, leads to the London equation though the coefficient is different from London's original one. The theory talks in principle about the feature at the absolute zero of temperature in the sense that the electron-phonon interaction is not taken into account. The penetration depth of the field calculated according to the present model is quantitatively in good agreement with experiment. The known type of electron-electron interaction due to Breit, does not lead to superconductivity even in the relativistic treatment. The proposed interaction is discussed in connection with some experimental facts, i.e. the existance of an impurity effect for the penetration depth and the smaller Knight shift in the superconducting than the normal state.

§ 1. Introduction

A perfectly free electron gas does not exhibit the Meissner-Ochsenfeld effect (M–O effect), and it has long been supposed that introduction of some kind of electron-electron interaction would be able to account for this phenomenon. But no one has ever succeeded to establish a theory substantiating this supposition.

Fröhlich¹⁾ and Bardeen²⁾ proposed a theory of superconductivity based on an indirect electron-electron interaction with phonons as intermediaries. The most prominent success of this theory was the prediction of the isotope effect³⁾. However, the most important feature of a superconductor, i.e. the Meissner-Ochsenfeld effect, has not yet been understood on the basis of this theory. In this connection we should note the work of Schafroth⁴⁾, who showed that Fröhlich's interaction does not lead to the M–O effect as long as the perturbation theory can be used. He showed besides that the Coulomb interaction cannot produce the M–O effect, and stated further that the absence of this effect is confirmed generally for any not explicitly spin-dependent two-body force⁵⁾. On the other hand, Schafroth⁶⁾ has shown in a recent paper that an ideal Bose-Einstein gas exhibits the M–O effect below its condensation temperature. Application of this model to an actual superconducting metal, however, is not easy, since the assembly of conduction electrons in a metal should be considered to be a Fermi gas as confirmed by various kinds of experimental evidence.

Several years ago, the author investigated the magnetic property of a non-interacting electron gas by means of the relativistic theory of an electron by Dirac and the quantum hydrodynamics by Born and Green⁷⁾, and suggested that the M–O effect would occur if one assumes between two electrons such an interaction that makes the antiparallel-spin orientation more favourable than the parallel-spin orientation**. According to this conjecture we are led to introduce an interaction of the form $e^2s_1\cdot s_2/r$, where s_1 and s_2 are the spin operators belonging respectively to each interacting electron and each has eigenvalues ±1/2. Applying the relativistic theory of an electron by Dirac and the perturbation theory in statistical mechanics by Schafroth⁴⁾ and

---

* Work Partly supported by the Grant-in-Aid for Fundamental Scientific Research from the Ministry of Education.

** Read at the Osaka meeting of the Physical Society of Japan, Nov. 2, 1950 (unpublished).

Nakajima[8)], we show in this paper that a stationary current is established in the system of electrons interacting each other through the above-mentioned interaction under the influence of a magnetic field. Since the electron-phonon interaction is not taken into account, the theory should be considered to hold only at the absolute zero of temperature. The equation connecting current and field has the same form as the London equation, but the coefficient is different from London's. The penetration depth of the field according to the present model is numerically of the same order of magnitude as that according to London, in spite of different appearences, and in good agreement with experiment.

The M–O effect does not occur for the well-known type of electron-electron interaction due to Breit[9)] even if the relativistic theoy is applied.

In § 2 the perturbation theory in statistical mechanics is re-formulated in terms of the Dirac theory of an electron. In § 3 the well-known result that the M–O effect is absent in a free electron gas is confirmed in a relativistic way. The subsequent two sections, §§ 4 and 5, are devoted to the theory of an electron gas with interaction. In § 6 some experimental facts are discussed in the light of the present theory.

§ 2. Notations and Fundamental Equations

(i) Relativistic wave mechanics of an electron

The wave function ψ for the stationar state of a free Dirac electron satisfies

$$(c\boldsymbol{\alpha}\cdot\boldsymbol{p}+mc^2\alpha_m)\psi=\mathcal{E}\psi\ , \qquad (2.$$

where $\boldsymbol{\alpha}(\alpha_x,\ \alpha_y,\ \alpha_z)$ and α_m are the Dirac ope rators and satisfy

$$\alpha_\mu\alpha_\nu+\alpha_\nu\alpha_\mu=2\delta_{\mu\nu} \qquad (\mu,\ \nu=x,\ y,\ z,\ m)\ . \qquad (2.$$

As well known, these α's can be represente by the following four-four matrices:

$$\alpha_x=\begin{pmatrix}0&0&0&1\\0&0&1&0\\0&1&0&0\\1&0&0&0\end{pmatrix},\quad \alpha_y=\begin{pmatrix}0&0&0&-i\\0&0&i&0\\0&-i&0&0\\i&0&0&0\end{pmatrix},$$
$$\alpha_z=\begin{pmatrix}0&0&1&0\\0&0&0&-1\\1&0&0&0\\0&-1&0&0\end{pmatrix},\quad \alpha_m=\begin{pmatrix}1&0&0&0\\0&1&0&0\\0&0&-1&0\\0&0&0&-1\end{pmatrix}. \qquad (2.3$$

The solution $\psi(\boldsymbol{x})$ of (2.1) has four component $\psi(\rho,\ \boldsymbol{x})$ ($\rho=1,\ 2,\ 3,\ 4$), so that (2.1) can be re garded as a set of four simultaneous equa tions for $\psi(\rho,\ \boldsymbol{x})$. The solution of (2.1) cor responding to a given momentum $\boldsymbol{p}=\hbar\boldsymbol{k}$ ca be given by

$$\psi(\boldsymbol{x})=u_k\exp[i\boldsymbol{k}\cdot\boldsymbol{x}]\ , \qquad (2.4$$

where u_k satisfies the equation

$$(c\hbar\boldsymbol{\alpha}\cdot\boldsymbol{k}+mc^2\alpha_m)u_k=\mathcal{E}u_k \qquad (2.5$$

and has four components $u_k(\rho)$. For a give $\boldsymbol{k}$, (2.5) has four independent solutions. typical set of these solutions is:

$$\left.\begin{array}{cccc}
u_k^{(1)} & u_k^{(2)} & u_k^{(3)} & u_k^{(4)} \\
\hline
1 & 0 & \dfrac{-c\hbar k_z}{mc^2+\mathcal{E}_k} & \dfrac{-c\hbar k_x+ic\hbar k_y}{mc^2+\mathcal{E}_k} \\
0 & 1 & \dfrac{-c\hbar k_x-ic\hbar k_y}{mc^2+\mathcal{E}_k} & \dfrac{c\hbar k_z}{mc^2+\mathcal{E}_k} \\
\dfrac{c\hbar k_z}{mc^2+\mathcal{E}_k} & \dfrac{c\hbar k_x-ic\hbar k_y}{mc^2+\mathcal{E}_k} & 1 & 0 \\
\dfrac{c\hbar k_x+ic\hbar k_y}{mc^2+\mathcal{E}_k} & \dfrac{-c\hbar k_z}{mc^2+\mathcal{E}_k} & 0 & 1
\end{array}\right\}\times D_k\ , \qquad (2.6$$

$$\mathcal{E}_k=(m^2c^4+c^2\hbar^2k^2)^{1/2}\ , \qquad D_k=(mc^2+\mathcal{E}_k)^{1/2}/(2\mathcal{E}_k)^{1/2}\ .$$

The eigenvalue $\mathcal{E}$ in (2.5) should be $\mathcal{E}_k$ for $u_k^{(1)}$ and $u_k^{(2)}$, and $-\mathcal{E}_k$ for $u_k^{(3)}$ and $u_k^{(4)}$, i.e. $\mathcal{E}_k^{(1)}=\mathcal{E}_k^{(2)}=\mathcal{E}_k$ and $\mathcal{E}_k^{(3)}=\mathcal{E}_k^{(4)}=-\mathcal{E}_k$. We call the eigenstates $u_k^{(1)}$ and $u_k^{(2)}$ the positive-energy states, and $u_k^{(3)}$ and $u_k^{(4)}$ the negative-energy states. The normalization is

$$\textstyle\sum_{\rho=1}^4 u_k^{(s)*}(\rho)u_k^{(t)}(\rho)\equiv(\boldsymbol{k}s|\boldsymbol{k}t)=\delta_{st}\ , \qquad (2.7$$

as easily confirmed by using the identity

$$\frac{mc^2+\mathcal{E}_k}{2\mathcal{E}_k}+\frac{c^2\hbar^2k^2}{2\mathcal{E}_k(mc^2+\mathcal{E}_k)}=1\ . \qquad (2.8$$

The velocity of an electron in the Dira

theory is given by

$$v=c\boldsymbol{\alpha}\ . \tag{2.9}$$

The wave equation for an electron in a magnetic field $\boldsymbol{A}$ is

$$(c\boldsymbol{\alpha}\cdot\boldsymbol{p}-e\boldsymbol{\alpha}\cdot\boldsymbol{A}+mc^2\alpha_m)\psi=\mathcal{E}\psi\ . \tag{2.10}$$

Note that the expression (2.9) represents the velocity not only for a free electron but also for an electron in a field. This forms a striking contrast to the non-relativistic case, in which the velocity explicitly depends on $\boldsymbol{A}$ and is given by the equation

$$v=(\boldsymbol{p}/m)+(e\boldsymbol{A}/mc)\ .$$

The Dirac relativistic electron has the spin angular momentum $\boldsymbol{s}\hbar$. $\boldsymbol{s}$ is called the spin operator and defined by

$$\boldsymbol{s}=\boldsymbol{\sigma}/2\ , \tag{2.11}$$

where $\boldsymbol{\sigma}$ is the spin matrix to be defined in terms of $\boldsymbol{\alpha}$ by the equations

$$\sigma_x=-i\alpha_y\alpha_z\ ,\quad \sigma_y=-i\alpha_z\alpha_x\ ,\quad \sigma_z=-i\alpha_x\alpha_y\ .$$

In the representation in which α's are expressed in the form (2.3), σ_z is diagonal and its eigenvalues are ±1.

In later sections we need the explicit values of matrix elements of the following types

$$\left.\begin{aligned}(\boldsymbol{k}'s'|\boldsymbol{k}''s'')&\equiv u_{\boldsymbol{k}'}{}^{(s')*}1u_{\boldsymbol{k}''}{}^{(s'')}\ ,\\ (\boldsymbol{k}'s'|\sigma_\mu|\boldsymbol{k}''s'')&\equiv u_{\boldsymbol{k}'}{}^{(s')*}\sigma_\mu u_{\boldsymbol{k}''}{}^{(s'')}\ ,\\ (\boldsymbol{k}'s'|\alpha_\mu|\boldsymbol{k}''s'')&\equiv u_{\boldsymbol{k}'}{}^{(s')*}\alpha_\mu u_{\boldsymbol{k}''}{}^{(s'')}\ ,\end{aligned}\right\}$$

$$(\mu=x,\ y,\ z;\ \ s',\ s''=1,\ 2,\ 3,\ 4.)$$

for $\boldsymbol{k}'=\boldsymbol{k}-\frac{1}{2}\boldsymbol{q}$ and $\boldsymbol{k}''=\boldsymbol{k}+\frac{1}{2}\boldsymbol{q}$. They are listed in Table II of the Appendix.

(ii) *Perturbation expansion in statistical mechanics*

A brief account of the perturbative expansion theorem in statistical mechanics is given. We follow the formulation developed by Nakajima[8]. The Hamiltonian is assumed to be composed of two parts, namely, the unperturbed H_0 and the perturbation H_I and thus to be given by

$$H=H_0+H_I\ . \tag{2.12}$$

For the canonical distribution the free energy of the system is

$$F=-\beta^{-1}\ln \mathrm{Tr}\,(\exp[-\beta H])\ , \tag{2.13}$$

where $\beta=(kT)^{-1}$. According to Nakajima we have the following expansion:

$$F=F_0+F_1+F_2+F_3+\cdots\ ,$$

$$\begin{aligned}&F_0=\text{Free energy of the unperturbed system},\\ &F_1=\langle H_I\rangle_\beta\ ,\\ &F_2=\frac{1}{2}\beta\langle H_I\rangle_\beta{}^2-\frac{1}{2}\int_0^\beta d\lambda_1\langle H_I(\lambda_1\rangle H_I\rangle_\beta\ ,\\ &F_3=\frac{1}{3}\beta^2\langle H_I\rangle_\beta{}^3-\frac{1}{2}\beta\langle H_I\rangle_\beta\int_0^\beta d\lambda_1\langle H_I(\lambda_1)H_I\rangle_\beta\\ &\qquad+\frac{1}{3}\int_0^\beta d\lambda_1\int_0^{\lambda_1}d\lambda_2\langle H_I(\lambda_1)H_I(\lambda_2)H_I\rangle_\beta\ ,\\ &\cdots\cdots\cdots\ ,\end{aligned} \tag{2.14}$$

where

$$H_I(\lambda_i)=\exp[\lambda_i H_0]H_I\exp[-\lambda_i H_0]\ , \tag{2.15}$$

$$\langle Q\rangle_\beta=\mathrm{Tr}\,(Q\exp[-\beta H_0])/\mathrm{Tr}\,(\exp[-\beta H_0])\ . \tag{2.16}$$

$\langle Q\rangle_\beta$ is the expectation value of Q with respect to the unperturbed canonical distribution.

(iii) *Second quantization*

We consider a system of N Dirac electrons and impose on the wave functions a periodic boundary condition with periodic volume V. The formalism of second quantization is used, and the wave function is expanded in terms of the eigenfunctions of the Dirac equation for a free electron which are given by (2.4) and (2.6). Thus we write

$$\left.\begin{aligned}\psi(\boldsymbol{x})&=V^{-1/2}\textstyle\sum_k\sum_s a_k{}^{(s)}u_k{}^{(s)}\exp[i\boldsymbol{k}\cdot\boldsymbol{x}]\ ,\\ \psi^*(\boldsymbol{x})&=V^{-1/2}\textstyle\sum_k\sum_s a_k{}^{(s)*}u_k{}^{(s)*}\exp[-i\boldsymbol{k}\cdot\boldsymbol{x}]\ ,\end{aligned}\right\} \tag{2.17}$$

where $a_k{}^{(s)}$ and $a_k{}^{(s)*}$ are the usual destruction and creation operators satisfying

$$\left.\begin{aligned}&[a_k{}^{(s)*},\ a_l{}^{(t)}]_+=\delta_{kl}\delta_{st}\ ,\\ &[a_k{}^{(s)},\ a_l{}^{(t)}]_+=[a_k{}^{(s)*},\ a_l{}^{(t)*}]_+=0\ ,\\ &a_k{}^{(s)*}a_k{}^{(s)}=n_k{}^{(s)}\ .\end{aligned}\right\} \tag{2.18}$$

According to statistical mechanics we see

$$\begin{aligned}\langle a_k{}^{(s)*}a_k{}^{(s)}\rangle_\beta&\equiv\langle n_k{}^{(s)}\rangle_\beta\equiv f_k{}^{(s)}\\ &=(\exp[\beta(\mathcal{E}_k{}^{(s)}-\eta)]+1)^{-1}\ ,\end{aligned} \tag{2.19}$$

where

$$\mathcal{E}_k{}^{(s)}=\begin{cases}\ \ \mathcal{E}_k\ , & s=1,\ 2,\\ -\mathcal{E}_k\ , & s=3,\ 4,\end{cases} \tag{2.20}$$

and η is determined by means of the equation

$$\textstyle\sum_k\sum_s^+ f_k{}^{(s)}=N\ . \tag{2.21}$$

$\sum_s^+$ stands for $\sum_{s=1,2}$. Note that $f_k{}^{(1)}=f_k{}^{(2)}$ and $f_k{}^{(3)}=f_k{}^{(4)}$, and that the latter is very nearly equal to 1 at ordinary temperatures. It is advantageous to use different notations for the distribution function in the positive- and negative-energy regions:

$$f_k \equiv f_k^{(1)} = f_k^{(2)}\ , \qquad g_k \equiv f_k^{(3)} = f_k^{(4)}\ . \quad (2.22)$$

Corresponding to the velocity of an electron expressed by (2.9), the current density is

$$\boldsymbol{j} = ce\psi^*\boldsymbol{\alpha}\psi\ , \quad (2.23)$$

which is compared with the non-relativistic expression

$$\boldsymbol{j} = -(ie\hbar/2m)(\psi^*\nabla\psi - \nabla\psi^*\psi) - (e^2/mc^2)\psi^*\psi\boldsymbol{A}\ . \quad (2.24)$$

Let the Hamiltonian be

$$H = H_0 + H_A + H'\ , \quad (2.25)$$

where

$$H_0 = c\int\psi^*(\boldsymbol{\alpha}\cdot\boldsymbol{p} + mc\alpha_m)\psi d^3\boldsymbol{x}\ , \quad (2.26)$$

$$H_A = -e\int\psi^*\boldsymbol{\alpha}\cdot\boldsymbol{A}\psi d^3\boldsymbol{x}\ , \quad (2.27)$$

and H' represents the electron-electron, electron-phonon and other interactions independent of the field $\boldsymbol{A}$. It is clear that the current density (2.3) can be obtained as the functional derivative of H with respect to $\boldsymbol{A}$:

$$j_\mu(\boldsymbol{x}) = -c\delta H/\delta A_\mu(\boldsymbol{x})\ .$$

The mean current density is then the functional derivative of the free energy:

$$\begin{aligned} J_\mu(\boldsymbol{x}) &= \mathrm{Tr}(j_\mu(\boldsymbol{x})\exp[-\beta H])/\mathrm{Tr}(\exp[-\beta H]) \\ &= -c\delta F/\delta A_\mu(\boldsymbol{x})\ . \end{aligned} \quad (2.28)$$

This expression was derived by Nakajima[8] in the non-relativistic case and the derivation in the relativistic case is much the same. Since, however, this current involves the infinite contribution from the vacuum, the actual current can be obtained by subtracting this contribution. Let F° be the free energy of the vacuum, then the mean current density should be written as

$$J_\mu(\boldsymbol{x}) = -c\delta\Phi/\delta A_\mu(\boldsymbol{x})\ , \quad (2.29)$$

instead of (2.28), in terms of the corrected free energy

$$\Phi = F - F^\circ\ .$$

(iv) *Criterion for the occurrence of the Meissner-Ochsenfeld effect*

According to Schafroth[4] the mean current density $J_\mu(\boldsymbol{x})$ in a weak magnetic field $\boldsymbol{A}(\boldsymbol{x})$ (in an arbitrary gauge) can be expressed by the equation

$$J_\mu(\boldsymbol{x}) = \sum\nolimits_\nu\int d^3\boldsymbol{x}'K_{\mu\nu}(\boldsymbol{x}-\boldsymbol{x}')A_\nu(\boldsymbol{x}')\ .$$

Its Fourier transform is

$$J_\mu(\boldsymbol{q}) = \sum\nolimits_\nu K_{\mu\nu}(\boldsymbol{q})A_\nu(\boldsymbol{q})\ . \quad (2.30$$

Assuming an isotropic system, gauge invariance and continuity of current require $K_{\mu\nu}(\boldsymbol{q}$ to take the form

$$K_{\mu\nu}(\boldsymbol{q}) = (q^2\delta_{\mu\nu} - q_\mu q_\nu)K(q)\ . \quad (2.31$$

The M–O effect is established when $K(q)$ ha a pole of order q^{-2} at the origin, that is, whe it has the form

$$K(q) = -K_0 q^{-2} + K_r(q^2) \quad (2.32$$

with K_0, a positive constant, and $K_r(q^2)$, regular function of q^2. Substituting (2.31) an (2.32) in (2.30) and going back to the ordinar space we have the London equation

$$\mathrm{curl}\,\boldsymbol{J}(\boldsymbol{x}) = -K_0\boldsymbol{B}(\boldsymbol{x})\ , \qquad \boldsymbol{B}(\boldsymbol{x}) = \mathrm{curl}\,\boldsymbol{A}(\boldsymbol{x})\ , \quad (2.33$$

apart from an ordinarily negligible correctio term related to $K_r(q^2)$.

§ 3. Absence of the Meissner-Ochsenfel Effect in a Free Electron Gas

It is shown that the M–O effect cannot b established in a free electron gas even if th motion of an electron is dealt with in th relativistic theory. It is a well establishe fact in the non-relativistic case, and at firs sight it appears trivial in the relativistic theor as well. But, as the calculations in this section will show, the manner in which the M– effect disappears in the relativistic case is ver instructive and suggestive, and enables on to presume a type of electron-electron interaction which is able to produce the M– effect. Before entering the actual calculatio we should point out an important differenc between the relativistic and non-relativisti cases. The curent density in the former cas is expressed by a single term while that i the latter consists of two terms, as indicate by eqs. (2.23) and (2.24). It is a well-know fact that the vanishing of the M–O effec in the non-relativistic theory is due to th exact cancellation of the contributions fro these two terms in (2.24) (apart from highe order effects involving Landau's diamagnetism). This sort of cancellation cannot occu in the relativistic case, because the expressio for current in the field contains only a singl term in this case. This does not mean, however, that the relativistic treatment of a fre electron gas leads to the M–O effect. Th object of this section is to make this poin clear.

The Hamiltonian for a free electron gas in the magnetic field takes the form

$$H = H_0 + H_A\,,$$

$$H_0 = \sum_k \sum_s \mathcal{E}_k{}^{(s)} a_k{}^{(s)*} a_k{}^{(s)}\,, \tag{3.1}$$

$$H_A = -eV^{-1}\int d^3x \sum_k \sum_q \sum_{s's''} (\boldsymbol{k}'s'|\boldsymbol{\alpha}|\boldsymbol{k}''s'')\boldsymbol{A}(x) \times a_{k'}{}^{(s')*} a_{k''}{}^{(s'')} \exp[i\boldsymbol{q}\cdot\boldsymbol{x}]\,, \tag{3,2}$$

where $\boldsymbol{k}' = \boldsymbol{k} - \frac{1}{2}\boldsymbol{q}$ and $\boldsymbol{k}'' = \boldsymbol{k} + \frac{1}{2}\boldsymbol{q}$ as before[*]. It follows immediately from (2.26) and (2.27) if (2.17) is substituted in $\psi(\boldsymbol{x})$.

We need to calculate the free energy to the second order of H_A in order to get the current linear in $\boldsymbol{A}$. Putting $H_I = H_A$ and avoiding higher order terms in (2.14) we have

$$F = F_0 + F_1 + F_2\,, \tag{3.3}$$

$$F_1 = \langle H_A \rangle_\beta = -eV^{-1} \sum_k \sum_s \int d^3\boldsymbol{x} (\boldsymbol{k}s|\boldsymbol{\alpha}|\boldsymbol{k}s)\cdot \boldsymbol{A}(\boldsymbol{x}) \langle a_k{}^{(s)*} a_k{}^{(s)} \rangle_\beta\,, \tag{3.4}$$

$$\begin{aligned} F_2 = \frac{1}{2}\beta\langle H_A\rangle_\beta{}^2 - \frac{1}{2} e^2 V^{-2} \sum_k \sum_q \sum_{s's''} \int_0^\beta d\lambda \exp[\lambda(\mathcal{E}_{k'}{}^{(s')} - \mathcal{E}_{k''}{}^{(s'')})] \\ \times \iint d^3\boldsymbol{x} d^3\boldsymbol{x}' (\boldsymbol{k}'s'|\boldsymbol{\alpha}|\boldsymbol{k}''s'')\cdot\boldsymbol{A}(\boldsymbol{x}) (\boldsymbol{k}''s''|\boldsymbol{\alpha}|\boldsymbol{k}'s')\cdot\boldsymbol{A}(\boldsymbol{x}') \\ \times \langle a_{k'}{}^{(s')*} a_{k''}{}^{(s'')} a_{k''}{}^{(s'')*} a_{k'}{}^{(s')} \rangle_\beta \exp[i\boldsymbol{q}\cdot(\boldsymbol{x}-\boldsymbol{x}')]\,. \end{aligned} \tag{3.5}$$

It is first noted that F_0 and F_1 do not contribute to the current. Since it is evident for F_0, we need only to show it for F_1. It can easily be shown that the summation with respect to s in (3.4) yields an odd function of $\boldsymbol{k}$, use being made of the explicit values for the matrix elements of $\boldsymbol{\alpha}$ given in the Appendix. In consequence, the right-hand side of (3.4) should vanish when the summation over $\boldsymbol{k}$ is performed. This happens in the respective contributions from the positive- and negative-energy states separately. It is concluded therefrom that the F_1-contribution of the vacuum and thus the corrected first-order free energy Φ_1 also vanish. F_2 is then the only term which might lead to a non-vanishing current.

Making use of (2.18) and (2.19) we find

$$\int_0^\beta d\lambda \langle a_{k'}{}^{(s')*} a_{k''}{}^{(s'')} a_{k''}{}^{(s'')*} a_{k'}{}^{(s')} \rangle_\beta \exp[\lambda(\mathcal{E}_{k'}{}^{(s')} - \mathcal{E}_{k''}{}^{(s'')})] = -\frac{f_{k'}{}^{(s')} - f_{k''}{}^{(s'')}}{\mathcal{E}_{k'}{}^{(s')} - \mathcal{E}_{k''}{}^{(s'')}}\,. \tag{3.6}$$

Substituting (3.6) in (3.5) gives

$$F_2 = \frac{e^2}{2V^2} \sum_k \sum_q \sum_{s's''} P(\boldsymbol{k}, \boldsymbol{q}, s', s'') \frac{f_{k'}{}^{(s')} - f_{k''}{}^{(s'')}}{\mathcal{E}_{k'}{}^{(s')} - \mathcal{E}_{k''}{}^{(s'')}}\,, \tag{3.7}$$

where

$$P(\boldsymbol{k}, \boldsymbol{q}, s', s'') = \iint d^3\boldsymbol{x} d^3\boldsymbol{x}' (\boldsymbol{k}'s'|\boldsymbol{\alpha}|\boldsymbol{k}''s'')\cdot\boldsymbol{A}(\boldsymbol{x}) (\boldsymbol{k}''s''|\boldsymbol{\alpha}|\boldsymbol{k}'s')\cdot\boldsymbol{A}(\boldsymbol{x}') \exp[i\boldsymbol{q}\cdot(\boldsymbol{x}-\boldsymbol{x}')]\,. \tag{3.8}$$

According to the definition of the vacuum its F_2-contribution is obtained by setting $f_k{}^{(1)} = f_k{}^{(2)} = 0$ and $f_k{}^{(3)} = f_k{}^{(4)} = 1$ in (3.7):

$$F_2{}^\circ = -\frac{e^2}{2V} \sum_k \sum_q \left\{ \sum_{s'}^+ \sum_{s''}^- P(\boldsymbol{k}, \boldsymbol{q}, s', s'') \frac{1}{\mathcal{E}_{k'} + \mathcal{E}_{k''}} + \sum_{s'}^- \sum_{s''}^+ P(\boldsymbol{k}, \boldsymbol{q}, s', s'') \frac{1}{\mathcal{E}_{k'} + \mathcal{E}_{k''}} \right\}\,, \tag{3.9}$$

where $\sum_s^+$ and $\sum_s^-$ mean the summations on $s = 1, 2$ and $3, 4$ respectively. Subtraction of (3.9) from (3.7) gives

$$\begin{aligned} \Phi_2 = \frac{e^2}{2V} \sum_k \sum_q \Bigg\{ \sum_{s'}^+ \sum_{s''}^+ P(\boldsymbol{k}, \boldsymbol{q}, s', s'') \frac{f_{k'}{}^{(s')} - f_{k''}{}^{(s'')}}{\mathcal{E}_{k'} - \mathcal{E}_{k''}} + \sum_{s'}^+ \sum_{s''}^- P(\boldsymbol{k}, \boldsymbol{q}, s', s'') \frac{f_{k'}{}^{(s')} + 1 - f_{k''}{}^{(s'')}}{\mathcal{E}_{k'} + \mathcal{E}_{k''}} \\ + \sum_{s'}^- \sum_{s''}^+ P(\boldsymbol{k}, \boldsymbol{q}, s', s'') \frac{f_{k''}{}^{(s'')} + 1 - f_{k'}{}^{(s')}}{\mathcal{E}_{k'} + \mathcal{E}_{k''}} - \sum_{s'}^- \sum_{s''}^- P(\boldsymbol{k}, \boldsymbol{q}, s', s'') \frac{f_{k'}{}^{(s')} - f_{k''}{}^{(s'')}}{\mathcal{E}_{k'} - \mathcal{E}_{k''}} \Bigg\}\,. \end{aligned} \tag{3.10}$$

---

[*] Hereinafter all singly and doubly primed wave numbers should be understood in an analogous way.

At ordinary temperatures we may put $f_k^{(3)}=f_k^{(4)}=g_k=1$ with complete accuracy, and then (3.10) becomes

$$\Phi_2=\frac{e^2}{2V^2}\Sigma_k\Sigma_q\Big\{\Sigma^+_{s'}\Sigma^+_{s''}P(\boldsymbol{k},\boldsymbol{q},s',s'')\frac{f_{k'}-f_{k''}}{\mathcal{E}_{k'}-\mathcal{E}_{k''}}$$
$$+\Sigma^+_{s'}\Sigma^-_{s''}P(\boldsymbol{k},\boldsymbol{q},s',s'')\frac{f_{k'}}{\mathcal{E}_{k'}+\mathcal{E}_{k''}}+\Sigma^-_{s'}\Sigma^+_{s''}P(\boldsymbol{k},\boldsymbol{q},s',s'')\frac{f_{k''}}{\mathcal{E}_{k'}+\mathcal{E}_{k''}}\Big\}. \tag{3.11}$$

An important fact is that the corrected second-order free energy (3.11) can be obtained by putting $f_k^{(3)}=f_k^{(4)}=g_k=0$ in the corresponding uncorrected expression (3.7).

Substituting (3.11) in (2.29) we find, for the mean current density in the Fourier space,

$$J_\mu(\boldsymbol{q})=-\frac{ce^2}{V}\Sigma_\nu\Sigma_k\Sigma^+_{s'}\Sigma^+_{s''}(\boldsymbol{k}'s'|\alpha_\mu|\boldsymbol{k}''s'')(\boldsymbol{k}''s''|\alpha_\nu|\boldsymbol{k}'s')A_\nu(\boldsymbol{q})\frac{f_{k'}-f_{k''}}{\mathcal{E}_{k'}-\mathcal{E}_{k''}}$$
$$-\frac{ce^2}{V}\Sigma_\nu\Sigma_k\Sigma^+_{s'}\Sigma^-_{s''}(\boldsymbol{k}'s'|\alpha_\mu|\boldsymbol{k}''s'')(\boldsymbol{k}''s''|\alpha_\nu|\boldsymbol{k}'s')A_\nu(\boldsymbol{q})\frac{f_{k'}}{\mathcal{E}_{k'}+\mathcal{E}_{k''}}$$
$$-\frac{ce^2}{V}\Sigma_\nu\Sigma_k\Sigma^-_{s'}\Sigma^+_{s''}(\boldsymbol{k}'s'|\alpha_\mu|\boldsymbol{k}''s'')(\boldsymbol{k}''s''|\alpha_\nu|\boldsymbol{k}'s')A_\nu(\boldsymbol{q})\frac{f_{k''}}{\mathcal{E}_{k'}+\mathcal{E}_{k''}}. \tag{3.12}$$

As we are only concerned here with the Meissner-Ochsenfeld effect and not with other magnetic effects generally small compared with it, it is sufficient to calculate the right-hand side of (3.12) in the limit of small q as discussed by Schafroth[4].

We now consider successively each term in (3.12). In the first term, $s'\neq s''$ does not contribute in the limit $q\to 0$ as easily confirmed making use of the explicit values of $(\boldsymbol{k}'s'|\alpha_\mu|\boldsymbol{k}''s'$ in the Appendix. For $s'=s''$ we have easily, for $q\to 0$,

$$-\frac{2c^3e^2\hbar^2}{V}\Sigma_\nu\Sigma_k\frac{k_\mu k_\nu}{\mathcal{E}_k^2}\frac{\partial f_k}{\partial\mathcal{E}_k}A_\nu(\boldsymbol{q}). \tag{3.13}$$

The summand for $\nu\neq\mu$ vanishes after the summation over $\boldsymbol{k}$ because it is an odd function with respect to k_μ and k_ν. When the summation over $\boldsymbol{k}$ is replaced by integration, it is easy to show for $\nu=\mu$, by integration by parts,

$$-\frac{2c^3e^2\hbar^2}{V}\Sigma_k\frac{k_\mu^2}{\mathcal{E}_k^2}\frac{\partial f_k}{\partial\mathcal{E}_k}A_\mu(\boldsymbol{q})=\frac{2ce^2}{V}A_\mu(\boldsymbol{q})\Sigma_k\frac{f_k}{\mathcal{E}_k}\Big(1-\frac{c^2\hbar^2k_\mu^2}{\mathcal{E}_k^2}\Big). \tag{3.14}$$

We now consider the second term in (3.12). As the matrix elements of α_μ listed in Table II of the Appendix are not symmetrical in μ, the calculations are difficult to be carried out without specifying μ. Taking $\mu=x$ and applying the values in Table II together with (A.2) and (A.3) of the Appendix, we have for $q\to 0$

$$-\frac{2ce^2}{V}A_x(\boldsymbol{q})\Big\{\Sigma_k(1-N_kk_x^2+iN_kk_xk_y)(1-N_kk_x^2-iN_kk_xk_y)\frac{f_k}{2\mathcal{E}_k}+\Sigma_kN_k^2k_z^2k_x^2\frac{f_k}{2\mathcal{E}_k}\Big\}. \tag{3.15}$$

In this expression, the first term in { } comes from 1⇄4 and 2⇄3 and the second from 1⇄3 and 2⇄4*. In both terms the non-vanishing contributions have only come from the case $\nu=\mu=x$. The expression (3.15) can be further simplified by applying (2.8) and considering the definition of N_k in (A.2). One finds

$$(1-N_kk_x^2+iN_kk_xk_y)(1-N_kk_x^2-iN_kk_xk_y)$$
$$=1-\frac{2c^2\hbar^2k_x^2}{\mathcal{E}_k(mc^2+\mathcal{E}_k)}-\frac{c^4\hbar^4(k_x^4+k_x^2k_y^2)}{\mathcal{E}_k^2(mc^2+\mathcal{E}_k)^2}=1-\frac{c^2\hbar^2k_x^2}{\mathcal{E}_k^2}-\frac{c^4\hbar^4k_z^2k_y^2}{\mathcal{E}_k^2(mc^2+\mathcal{E}_k)}.$$

According to this, (3.15) becomes

---

* We mean the scattering $s'=1$, $s''=4$ or $s'=4$, $s''=1$ by simply writting 1⇄4 or 4⇄1.

$$-\frac{ce^2}{V}A_x(\boldsymbol{q})\sum_k \frac{f_k}{\mathcal{E}_k}\left(1-\frac{c^2\hbar^2k_x^2}{\mathcal{E}_k^2}\right). \tag{3.16}$$

We have similar results for $\mu=y$ and z.

Now consider the third term in (3.12). It is an easy matter to show that its contribution is equal to that of the second term. This is guaranteed by the relation

$$\sum_{s'}^{-}\sum_{s''}^{+}(\boldsymbol{k}'s'|\alpha_\mu|\boldsymbol{k}''s'')(\boldsymbol{k}''s''|\alpha_\mu|\boldsymbol{k}'s')\frac{f_{k''}}{\mathcal{E}_{k'}+\mathcal{E}_{k''}}=\sum_{s'}^{+}\sum_{s''}^{-}(\boldsymbol{k}'s'|\alpha_\mu|\boldsymbol{k}''s'')(\boldsymbol{k}''s''|\alpha_\mu|\boldsymbol{k}'s')\frac{f_{k'}}{\mathcal{E}_{k'}+\mathcal{E}_{k''}},$$

which holds for any μ in the limit $q\rightarrow 0$. See Table II in the Appendix.

The sum of the second and third terms is thus equal to just twice the value given by (3.16) with x replaced by μ:

$$-\frac{2ce^2}{V}A_\mu(q)\sum_k \frac{f_k}{\mathcal{E}_k}\left(1-\frac{c^2\hbar^2k_\mu^2}{\mathcal{E}_k^2}\right). \tag{3.17}$$

The right-hand side of (3.12), which is the sum of (3.14) and (3.17), has then to vanish in the limit $q\rightarrow 0$, and this means

$$J_\mu(\boldsymbol{q})=0$$

in the same limit. This is the same result that obtained according to the usual non-relativistic theory, and means the absence of the M–O effect in a free electron gas. Note that the result is relativistically exact as we have not used any non-relativistic approximation. We should note further that the contribution in the first term of (3.12) comes from the virtual transitions between the electronic states with spins parallel while the main contribution in the second and third terms comes from those between the states with spins antiparallel to each other. Considering that the latter contribution is diamagnetic, we can presume that a spin-dependent electron-electron interaction can produce a diamagnetic current if it favours the antiparallel spin orientation of interacting electrons. This is just the conclusion reached in the earlier argument* by the author on the same reason as mentioned here.

§ 4. A Special Type of Electron-Electron Interaction which Produces the Meissner-Ochsenfeld Effect

As suggested in § 1 and at the end of § 3 we introduce a special type of electron-electron interaction of the form**

$$U_M=e^2\boldsymbol{s}_1\cdot\boldsymbol{s}_2/r\,, \tag{4.1}$$

where $\boldsymbol{s}_1$ and $\boldsymbol{s}_2$ are the spin angular momenta belonging respectively to each interacting electron, measured in the unit $\hbar$. They are related to the spin matrices $\boldsymbol{\sigma}_1$ and $\boldsymbol{\sigma}_2$ by eq. (2.11). r is a distance between interacting electrons. Choice is made of the special form (4.1) according to the following considerations. Firstly, we require the scalar product of the spin angular momenta as a factor, in order to secure the property that the interaction lowers the energy of the state with antiparallel spin orientation. Secondly, the r^{-1}-dependence is introduced to obtain the required singularity of the kernel $K(q)$ in (2.31), as discussed there. Finally, the analogy with the magnetic interaction

$$e^2\boldsymbol{\alpha}_1\cdot\boldsymbol{\alpha}_2/r \tag{4.2}$$

is considered. This is the Coulomb interaction multiplied by the product of velocities measured in the unit of the light velocity c, the universal unit of velocity. The proposed expression (4.1) has a resemblance to this in the sense that it is the Coulomb interaction multiplied by the product of spin angular momenta measured in $\hbar$, the universal unit of angular momentum. We shall show in this section that the interaction (4.1) brings upon the Meissner-Ochsenfeld effect of the correct order of magnitude.

---

* Footnote on p. 587.

** This interaction is not Lorentz invariant. It is to be considered as a part of some Lorentz invariant interaction.

Write the Hamiltonian of the system in a magnetic field as

$$H=H_0+H_I\ , \qquad H_I=H_A+H_M\ . \tag{4.3}$$

Here H_A is given by (3.2) and H_M by

$$H_M=\frac{\pi e^2}{2V}\sum_{kl}\sum_q\sum_{s's''t't''}\frac{(\boldsymbol{k}'s'|\boldsymbol{\sigma}|\boldsymbol{k}''s'')\cdot(\boldsymbol{l}''t''|\boldsymbol{\sigma}|\boldsymbol{l}'t')}{q^2}a_{k'}^{(s')*}a_{k''}^{(s'')}a_{l''}^{(t'')*}a_{l'}^{(t')}\ . \tag{4.4}$$

For convenience $\boldsymbol{\sigma}$ is used in place of $\boldsymbol{s}$.

The free energy should be calculated to the first order of H_M and to the second order of H_A. The expansion theorem (2.14) gives

$$F=F_0+F_1+F_2+F_3\ ,$$

$$F_1=\langle H_A\rangle_\beta+\langle H_M\rangle_\beta\ , \tag{4.5}$$

$$F_2=\frac{1}{2}\beta(\langle H_A\rangle_\beta+\langle H_M\rangle_\beta)^2-\frac{1}{2}\int_0^\beta d\lambda\langle(H_A(\lambda)+H_M(\lambda))(H_A+H_M)\rangle_\beta\ , \tag{4.6}$$

$$\begin{aligned}F_3=&\frac{1}{3}\beta^2(\langle H_A\rangle_\beta+\langle H_M\rangle_\beta)^3-\frac{1}{2}\beta(\langle H_A\rangle_\beta+\langle H_M\rangle_\beta)\int_0^\beta d\lambda\langle(H_A(\lambda)+H_M(\lambda))(H_A+H_M)\rangle_\beta\\&+\frac{1}{3}\int_0^\beta d\lambda_1\int_0^{\lambda_1}d\lambda_2\langle(H_A(\lambda_1)+H_M(\lambda_1))(H_A(\lambda_2)+H_M(\lambda_2))(H_A+H_M)\rangle_\beta\ .\end{aligned} \tag{4.7}$$

In the above equations $\langle H_A\rangle_\beta$ should vanish as discussed in § 3. After dropping all the terms independent of $\boldsymbol{A}$ as well as those equal to zero, we are left with

$$F_m=-\frac{1}{2}\int_0^\beta d\lambda\langle H_A(\lambda)H_A\rangle_\beta-\frac{1}{2}\beta\langle H_M\rangle_\beta\int_0^\lambda d\lambda\langle H_A(\lambda)H_A\rangle_\beta+\frac{1}{3}\int_0^\beta d\lambda_1\int_0^{\lambda_1}d\lambda_2{\sum}'_P\langle H_M(\lambda_1)H_A(\lambda_2)H_A\rangle_\beta\ , \tag{4.8}$$

where $\sum'_P$ means the summation over all different permutations of suffixes to H. We have here dropped terms of orders H_M^2, H_M^3 and H_A^3 as we are not concerned with these higher order terms. As concerns the first term on the right-hand side of (4.8), we have already developed a detailed discussion in § 3 and have shown that it has nothing to do with the M-O effect. We are thus left with

$$F_M=-\frac{1}{2}\beta\langle H_M\rangle_\beta\int_0^\lambda d\lambda\langle H_A(\lambda)H_A\rangle_\beta+\frac{1}{3}\int_0^\beta d\lambda_1\int_0^{\lambda_1}d\lambda_2{\sum}'_P\langle H_M(\lambda_1)H_A(\lambda_2)H_A\rangle_\beta\ . \tag{4.9}^*$$

It is convenient to write

$$F_M=F_{M0}+F_{M1}+F_{M2}+F_{M3}\ , \tag{4.10}$$

where F_{M0} stands for the first term in (4.9), and F_{M1}, F_{M2} and F_{M3} correspond to the permutations MAA, AMA and AAM respectively in the second term. Using (2.15), (3.2) and (4.4) and performing integrations with respect to λ_1 and λ_2 in the last three terms give

---

* The first term on the right-hand side vanishes for the particular interaction (4.1) because $\langle H_M\rangle_\beta$ vanishes in this case. This term is formally included here in order to apply in § 5 the expression for the current derived in this section also to the case where this term does not vanish. We should note that the corrected free energy corresponding to this term does not vanish in the general case where the statistical average of the perturbative Hamiltonian due to interaction does not disappear.

$$
\begin{aligned}
F_M &= F_{M0}+\sum_{\xi=1}^{3}F_{M\xi}\\
&= \frac{\pi e^4}{6V^3}\sum_q\sum_{kl}\sum_{s's''t't''}\sum_\xi Q_\xi\left(\frac{1}{q^2}-\frac{1}{|\boldsymbol{k}-\boldsymbol{l}|^2}\right)(\boldsymbol{k}'s'|\boldsymbol{\sigma}|\boldsymbol{k}''s'')\cdot(\boldsymbol{l}''t''|\boldsymbol{\sigma}|\boldsymbol{l}'t')\\
&\quad\times\iint d^3x d^3x'(\boldsymbol{k}''s''|\boldsymbol{\alpha}|\boldsymbol{k}'s')\cdot\boldsymbol{A}(\boldsymbol{x})(\boldsymbol{l}'t'|\boldsymbol{\alpha}|\boldsymbol{l}''t'')\cdot\boldsymbol{A}(\boldsymbol{x}')\exp\left[i\boldsymbol{q}\cdot(\boldsymbol{x}-\boldsymbol{x}')\right]+F_{M0}+F_{MR}\;, \qquad (4.11)
\end{aligned}
$$

where

$$
\begin{aligned}
Q_1 &= \left\{\frac{\exp[-\beta(\delta_1+\delta_2)]-1}{\delta_1(\delta_1+\delta_2)}-\frac{\exp[-\beta\delta_2]-1}{\delta_1\delta_2}+\frac{\exp[-\beta(\delta_1+\delta_2)]-1}{\delta_2(\delta_1+\delta_2)}-\frac{\exp[-\beta\delta_1]-1}{\delta_1\delta_2}\right\}\\
&\quad\times\langle a_{k'}^{(s')*}a_{k''}^{(s'')}a_{l''}^{(t'')*}a_{l'}^{(t')}a_{k''}^{(s'')*}a_{k'}^{(s')}a_{l'}^{(t')*}a_{l''}^{(t'')}\rangle_\beta \qquad (4.12)
\end{aligned}
$$

with

$$
\delta_1=\mathcal{E}_{k''}^{(s'')}-\mathcal{E}_{k'}^{(s')}\;,\qquad \delta_2=\mathcal{E}_{l'}^{(t')}-\mathcal{E}_{l''}^{(t'')}\;, \qquad (4.13)
$$

$$
\begin{aligned}
Q_2 &= \left\{\frac{\exp[-\beta\delta_1]-1}{\delta_1(\delta_1+\delta_2)}+\frac{\exp[\beta\delta_2]-1}{\delta_2(\delta_1+\delta_2)}+\frac{\exp[-\beta\delta_2]-1}{\delta_2(\delta_1+\delta_2)}+\frac{\exp[\beta\delta_1]-1}{\delta_1(\delta_1+\delta_2)}\right\}\\
&\quad\times\langle a_{l'}^{(t')*}a_{l''}^{(t'')}a_{k'}^{(s')*}a_{k''}^{(s'')}a_{l''}^{(t'')*}a_{l'}^{(t')}a_{k''}^{(s'')*}a_{k'}^{(s')}\rangle_\beta\;, \qquad (4.14)
\end{aligned}
$$

$$
\begin{aligned}
Q_3 &= \left\{\frac{\exp[\beta(\delta_1+\delta_2)]-1}{\delta_2(\delta_1+\delta_2)}-\frac{\exp[\beta\delta_1]-1}{\delta_1\delta_2}+\frac{\exp[\beta(\delta_1+\delta_2)]-1}{\delta_1(\delta_1+\delta_2)}-\frac{\exp[\beta\delta_2]-1}{\delta_1\delta_2}\right\}\\
&\quad\times\langle a_{k''}^{(s'')*}a_{k'}^{(s')}a_{l'}^{(t')*}a_{l''}^{(t'')}a_{k'}^{(t')*}a_{k''}^{(s'')}a_{l''}^{(t'')*}a_{l'}^{(t')}\rangle_\beta\;. \qquad (4.15)
\end{aligned}
$$

F_{MR} concerns those processes, in which H_M scatters electrons initially in $\boldsymbol{k}'$- and $\boldsymbol{l}''$-states into $\boldsymbol{l}''$- and $\boldsymbol{k}'$-states respectively, initial and final states of the system being thus identical. F_{MR} contributes a regular term to the kernel $K(q)$ at $q=0$ and has nothing to do with the M-O effect. F_{M0} also yields no required singularity in the kernel, as clearly seen from the appearence. The $1/|\boldsymbol{k}-\boldsymbol{l}|^2$ term, reqular in q, can be shown to vanish in the limit $q\to0$ when combined with the last two terms, F_{M0} and F_{MR}, as required by gauge invariance*. Making use of the definition (2.16) and of the invariance property of the trace of a product with respect to the cyclic change in the order of factors, gives the following equations:

$$
\begin{aligned}
&\langle a_{k'}^{(s')*}a_{k''}^{(s'')}a_{l''}^{(t'')*}a_{l'}^{(t')}a_{k''}^{(s'')*}a_{k'}^{(s')}a_{l'}^{(t')*}a_{l''}^{(t'')}\rangle_\beta\\
&\quad=\exp[\beta\delta_2]\langle a_{l'}^{(t')*}a_{l''}^{(t'')}a_{k'}^{(s')*}a_{k''}^{(s'')}a_{l''}^{(t'')*}a_{l'}^{(t')}a_{k''}^{(s'')*}a_{k'}^{(s')}\rangle_\beta\\
&\quad=\exp[\beta(\delta_1+\delta_2)]\langle a_{k''}^{(s'')*}a_{k'}^{(s')}a_{l'}^{(t')*}a_{l''}^{(t'')}a_{k'}^{(s')*}a_{k''}^{(s'')}a_{l''}^{(t'')*}a_{l'}^{(t')}\rangle_\beta\;. \qquad (4.16)
\end{aligned}
$$

With this one obtains

$$
\begin{aligned}
\sum_{\xi=1}^{3}Q_\xi &= 3\left\{\frac{\exp[-\beta(\delta_1+\delta_2)]-1}{\delta_1(\delta_1+\delta_2)}+\frac{\exp[-\beta(\delta_1+\delta_2)]-1}{\delta_2(\delta_1+\delta_2)}-\frac{\exp[-\beta\delta_1]-1}{\delta_1\delta_2}-\frac{\exp[-\beta\delta_2]-1}{\delta_1\delta_2}\right\}\\
&\quad\times f_{k'}^{(s')}(1-f_{k''}^{(s'')})f_{l''}^{(t'')}(1-f_{l'}^{(t')})\\
&= 3\frac{(\exp[-\beta\delta_1]-1)(\exp[-\beta\delta_2]-1)}{\delta_1\delta_2}f_{k'}^{(s')}(1-f_{k''}^{(s'')})f_{l''}^{(t'')}(1-f_{l'}^{(t')})\\
&= 3\frac{f_{k'}^{(s')}-f_{k''}^{(s'')}}{\mathcal{E}_{k'}^{(s')}-\mathcal{E}_{k''}^{(s'')}}\frac{f_{l'}^{(t')}-f_{l''}^{(t'')}}{\mathcal{E}_{l'}^{(t')}-\mathcal{E}_{l''}^{(t'')}}\;. \qquad (4.17)
\end{aligned}
$$

Substituting this in (4.11) gives

$$
\begin{aligned}
F_M &= \frac{\pi e^4}{2V^3}\sum_q\sum_{kl}\sum_{s's''t't''}\frac{(\boldsymbol{k}'s'|\boldsymbol{\sigma}|\boldsymbol{k}''s'')\cdot(\boldsymbol{l}''t''|\boldsymbol{\sigma}|\boldsymbol{l}'t')}{q^2}\frac{f_{k'}^{(s')}-f_{k''}^{(s'')}}{\mathcal{E}_{k'}^{(s')}-\mathcal{E}_{k''}^{(s'')}}\frac{f_{l'}^{(t')}-f_{l''}^{(t'')}}{\mathcal{E}_{l'}^{(t')}-\mathcal{E}_{l''}^{(t'')}}\\
&\quad\times\iint d^3x d^3x'(\boldsymbol{k}''s''|\boldsymbol{\alpha}|\boldsymbol{k}'s')\cdot\boldsymbol{A}(\boldsymbol{x})(\boldsymbol{l}'t'|\boldsymbol{\alpha}|\boldsymbol{l}''t'')\cdot\boldsymbol{A}(\boldsymbol{x}')\exp\left[i\boldsymbol{q}\cdot(\boldsymbol{x}-\boldsymbol{x}')\right]\;. \qquad (4.18)
\end{aligned}
$$

To obtain the corrected free energy Φ_M, we should take all $f^{(3)}$'s and $f^{(4)}$'s in (4.18) as equal to 0 as explained in § 3*. Write, for convenience,

---

* See Schafroth[4].

$$R_{\mu\nu}{}^{ij}(\boldsymbol{k}, \boldsymbol{l}, \boldsymbol{q}, s', s'', t', t'') = (\boldsymbol{k}'s'|\sigma_i|\boldsymbol{k}''s'')(\boldsymbol{l}''t''|\sigma_j|\boldsymbol{l}'t')(\boldsymbol{k}''s''|\alpha_\mu|\boldsymbol{k}'s')(\boldsymbol{l}'t'|\alpha_\nu|\boldsymbol{l}''t'') , \tag{4.19}$$

then, by applying (2.28) to the corrected free energy Φ_M and taking the Fourier transform, one gets the mean current density in the form

$$J_\mu(\boldsymbol{q}) = \sum_\nu K_{\mu\nu}(\boldsymbol{q}) A_\nu(\boldsymbol{q}) ,$$

$$\begin{aligned} K_{\mu\nu}(\boldsymbol{q}) = -\frac{\pi c e^4}{V^2}\frac{1}{q^2}\sum_{kl}\sum_j \Big\{ & \sum^+_{s's''}\sum^+_{t't''} R_{\mu\nu}{}^{jj}\frac{f_{k'}-f_{k''}}{\mathcal{E}_{k'}-\mathcal{E}_{k''}}\frac{f_{l'}-f_{l''}}{\mathcal{E}_{l'}-\mathcal{E}_{l''}} \\ & + \sum^+_{s's''t''}\sum^-_{t'} R_{\mu\nu}{}^{jj}\frac{f_{k'}-f_{k''}}{\mathcal{E}_{k'}-\mathcal{E}_{k''}}\frac{f_{l''}}{\mathcal{E}_{l'}+\mathcal{E}_{l''}} + \sum^+_{s's''t'}\sum^-_{t''} R_{\mu\nu}{}^{jj}\frac{f_{k'}-f_{k''}}{\mathcal{E}_{k'}-\mathcal{E}_{k''}}\frac{f_{l'}}{\mathcal{E}_{l'}+\mathcal{E}_{l''}} \\ & + \sum^+_{s''t't''}\sum^-_{s'} R_{\mu\nu}{}^{jj}\frac{f_{k''}}{\mathcal{E}_{k'}+\mathcal{E}_{k''}}\frac{f_{l'}-f_{l''}}{\mathcal{E}_{l'}-\mathcal{E}_{l''}} + \sum^+_{s't't''}\sum^-_{s''} R_{\mu\nu}{}^{jj}\frac{f_{k'}}{\mathcal{E}_{k'}+\mathcal{E}_{k''}}\frac{f_{l'}-f_{l''}}{\mathcal{E}_{l'}-\mathcal{E}_{l''}} \\ & + \sum^+_{s''t''}\sum^-_{s't'} R_{\mu\nu}{}^{jj}\frac{f_{k''}}{\mathcal{E}_{k'}+\mathcal{E}_{k''}}\frac{f_{l''}}{\mathcal{E}_{l'}+\mathcal{E}_{l''}} + \sum^+_{s''t'}\sum^-_{s't''} R_{\mu\nu}{}^{jj}\frac{f_{k''}}{\mathcal{E}_{k'}+\mathcal{E}_{k''}}\frac{f_{l'}}{\mathcal{E}_{l'}+\mathcal{E}_{l''}} \\ & + \sum^+_{s't''}\sum^-_{s''t'} R_{\mu\nu}{}^{jj}\frac{f_{k'}}{\mathcal{E}_{k'}+\mathcal{E}_{k''}}\frac{f_{l''}}{\mathcal{E}_{l'}+\mathcal{E}_{l''}} + \sum^+_{s't'}\sum^-_{s''t''} R_{\mu\nu}{}^{jj}\frac{f_{k'}}{\mathcal{E}_{k'}+\mathcal{E}_{k''}}\frac{f_{l'}}{\mathcal{E}_{l'}+\mathcal{E}_{l''}} \Big\} , \end{aligned} \tag{4.20}$$

where $R_{\mu\nu}{}^{jj}$ is the abbreviation of (4.19) for $i=j$. Note that $R_{\mu\nu}{}^{jj}$ is a function of s', s'', t' and t''. For the sake of convenience we write

$$K_{\mu\nu}(\boldsymbol{q}) = -\frac{\pi c e^4}{V^2}\frac{1}{q^2}\sum_{\xi=1}^{9} \Lambda_{\mu\nu}{}^{\xi} , \tag{4.21}$$

where $\Lambda_{\mu\nu}{}^1$, $\Lambda_{\mu\nu}{}^2$, $\cdots$, and $\Lambda_{\mu\nu}{}^9$ stand for the first, second, $\cdots$, and nineth terms respectively on the right-hand side of (4.20) apart from a trivial factor $-\pi c e^4/(Vq)^2$.

In order to study the M–O effect it is sufficient to look for the values of $\Lambda_{\mu\nu}{}^\xi$'s to the order of q^2 in the limit of small q. The calculations are elaborate but can be performed in a straight-forward way by applying the explicit values of matrix elements listed in Table II of the Appendix. We should note that the evaluation of $K_{\mu\nu}(q)$ can be restricted to a single case $\mu=\nu=x$ because the values for the other cases can readily be obtained according to the symmetry property of the kernel as mentioned in § 2, (iv).

In the first place, we consider $\Lambda_{xx}{}^1$ in which all the virtual transitions involved are those between positive-energy states. It is sufficient in this section to use approximate values correct to the first order of q_μ for all the matrix elements. Note that $(f_{k'}-f_{k''})/(\mathcal{E}_{k'}-\mathcal{E}_{k''})$ is an even function of $\boldsymbol{k}$, then one obtains

$$\begin{aligned} \Lambda_{xx}{}^1 = \sum_j & \Big\{ \sum_\pm \sum_k \sum^+_{s's''} (\boldsymbol{k}'s'|\sigma_j|\boldsymbol{k}''s'')_\pm (\boldsymbol{k}''s''|\alpha_x|\boldsymbol{k}'s')_\pm \frac{f_{k'}-f_{k''}}{\mathcal{E}_{k'}-\mathcal{E}_{k''}} \Big\} \\ & \times \Big\{ \sum_\pm \sum_l \sum^+_{t't''} (\boldsymbol{l}''t''|\sigma_j|\boldsymbol{l}'t')_\pm (\boldsymbol{l}'t'|\alpha_x|\boldsymbol{l}''t'')_\pm \frac{f_{l'}-f_{l''}}{\mathcal{E}_{l'}-\mathcal{E}_{l''}} \Big\} , \end{aligned} \tag{4,22}$$

where the (+) or (−) symbol attached to the matrix element means that the expression designates its even or odd part as a function of $\boldsymbol{k}$, and $\sum_\pm$ means the summation on both pairs of double signs. Applying the list in the Appendix together with (A.2) and (A.3) we have the following results which are correct to the first order of q_μ:

$$\begin{aligned} & \sum_\pm \sum_k \sum^+_{s'=s''} (\boldsymbol{k}'s'|\sigma_j|\boldsymbol{k}''s'')_\pm (\boldsymbol{k}''s''|\alpha_x|\boldsymbol{k}'s')_\pm \frac{f_{k'}-f_{k''}}{\mathcal{E}_{k'}-\mathcal{E}_{k''}} \\ & = \begin{cases} i\sum_k \{N_k k_z k_x(-K_k q_y + 2L_k k_y \boldsymbol{k}\cdot\boldsymbol{q}) + K_k N_k k_x(k_z q_y - k_y q_z)\} \dfrac{\partial f_k}{\partial \mathcal{E}_k} = 0 , & j=x , \\ i\sum_k K_k N_k (k_x{}^2 + N_k k_y{}^2 k_z{}^2) q_z \dfrac{\partial f_k}{\partial \mathcal{E}_k} , & j=y , \\ -i\sum_k K_k \{1 - 2N_k k_y{}^2 + N_k{}^2 k_y{}^2 (k_x{}^2 + k_y{}^2)\} q_y \dfrac{\partial f_k}{\partial \mathcal{E}_k} , & j=z , \end{cases} \end{aligned} \tag{4.23}$$

---

* This procedure corresponds to the subtraction from (4.18) of the sum of the free energies belonging to those cases where either $\boldsymbol{k}$- or $\boldsymbol{l}$- or both electrons belong to the vacuum.

$$\sum_{\pm}\sum_k\sum^{+}_{s'\neq s''}(\boldsymbol{k}'s'|\sigma_j|\boldsymbol{k}''s'')_{\pm}(\boldsymbol{k}''s''|\alpha_x|\boldsymbol{k}'s')_{\pm}\frac{f_{k'}-f_{k''}}{\mathcal{E}_{k'}-\mathcal{E}_{k''}}$$

$$=\begin{cases} i\sum_k N_k k_y k_x(K_k q_z-2L_k k_z\boldsymbol{k}\cdot\boldsymbol{q})\dfrac{\partial f_k}{\partial\mathcal{E}_k}=0\,, & j=x\,,\\ i\sum_k K_k\{1-N_k(k_x^2+2k_z^2)+N_k^2k_z^2(k_x^2+k_z^2)\}q_z\dfrac{\partial f_k}{\partial\mathcal{E}_k}\,, & j=y\,,\\ -i\sum_k K_k N_k^2k_y^2k_z^2q_y\dfrac{\partial f_k}{\partial\mathcal{E}_k}\,, & j=z\,,\end{cases} \tag{4.24}$$

where $\sum^{+}_{s'=s''}$ means the summation on pairs, (1, 1) and (2, 2), and $\sum^{+}_{s'\neq s''}$ the summation on pairs, (1, 2) and (2, 1). Combining (4.23) and (4.24) gives

$$\sum_{\pm}\sum_k\sum^{+}_{s's''}(\boldsymbol{k}'s'|\sigma_j|\boldsymbol{k}''s'')_{\pm}(\boldsymbol{k}''s''|\alpha_x|\boldsymbol{k}'s')_{\pm}\frac{f_{k'}-f_{k''}}{\mathcal{E}_{k'}-\mathcal{E}_{k''}}$$

$$=\begin{cases} 0\,, & j=y\,,\\ iq_z\sum_k K_k(1-2N_kk_z^2+N_k^2k^2k_z^2)\dfrac{\partial f_k}{\partial\mathcal{E}_k}\,, & j=y\,,\\ -iq_y\sum_k K_k(1-2N_kk_y^2+N_k^2k^2k_y^2)\dfrac{\partial f_k}{\partial\mathcal{E}_k}\,, & j=z\,,\end{cases}$$

$$=\begin{cases} 0\,, & j=x\,,\\ iq_z\sum_k K_kI_k\dfrac{\partial f_k}{\partial\mathcal{E}_k}\,, & j=y\,,\\ -iq_y\sum_k K_kI_k\dfrac{\partial f_k}{\partial\mathcal{E}_k}\,, & j=z\,,\end{cases} \tag{4.25}$$

where

$$I_k\equiv1-\frac{2}{3}N_kk^2+\frac{1}{3}N_k^2k^4=1-\frac{1}{3}\frac{c^2\hbar^2k^2}{\mathcal{E}_k^2}\,. \tag{4.26}$$

Inserting (4.25) into the first brackets on the right-hand side of (4.22) and applying the same expression with $\boldsymbol{l}$ and $-\boldsymbol{q}$ to the second brackets, we get

$$\Lambda_{xx}{}^1=(q_y^2+q_z^2)\sum_kK_kI_k\frac{\partial f_k}{\partial\mathcal{E}_k}\sum_lK_lI_l\frac{\partial f_l}{\partial\mathcal{E}_l}=(q_y^2+q_z^2)\Bigl(\sum_kK_kI_k\frac{\partial f_k}{\partial\mathcal{E}_k}\Bigr)^2 \tag{4.27}$$

Note that the second term in the last expression of (4.26) is a small quantity usually negligible compared to 1 for the conduction electrons in a metal. This is clearly seen from the estimate

$$2c^2\hbar^2k^2/\mathcal{E}_k^2\sim(v/c)^2\lesssim10^{-4}\,. \tag{4.28}$$

It is also obvious that this term should be interpreted as the usual relativistic correction.

We now proceed to the discussion of the next four terms, $\Lambda_{xx}{}^2\sim\Lambda_{xx}{}^5$, in (4.21). They all involve two kinds of virtual processes, of which one scatters the electron between positive-energy states and the other between positive- and negative-energy states. The details of calculation will be described only for the second term, $\Lambda_{xx}{}^2$, because from this result those for the other three can be easily derived and shown to equal it.

Note that

$$\Lambda_{xx}{}^2=\sum_j\Bigl\{\sum_{\pm}\sum_k\sum^{+}_{s's''}(\boldsymbol{k}'s'|\sigma_j|\boldsymbol{k}''s'')_{\pm}(\boldsymbol{k}''s''|\alpha_x|\boldsymbol{k}'s')_{\pm}\frac{f_{k'}-f_{k''}}{\mathcal{E}_{k'}-\mathcal{E}_{k''}}\Bigr\}$$
$$\times\Bigl\{\sum\sum^{+}_{t''}\sum^{-}_{t'}(\boldsymbol{l}''t''|\sigma_j|\boldsymbol{l}'t')(\boldsymbol{l}'t'|\alpha_x|\boldsymbol{l}''t'')\frac{f_l}{\mathcal{E}_{l'}+\mathcal{E}_{l''}}\Bigr\}\,. \tag{4.29}$$

The first brackets have already been dealt with, so the second alone are to be worked out.

The second brackets can be divided into two parts:

$$\begin{aligned}
&\Sigma_l \Sigma^+_{t''} \Sigma^-_{t'} (\boldsymbol{l}'t''|\sigma_j|\boldsymbol{l}'t')(\boldsymbol{l}'t'|\alpha_x|\boldsymbol{l}''t'')\,\frac{f_{l''}}{\varepsilon_{l'}+\varepsilon_{l''}} \\
&= \frac{1}{2}\Sigma_\pm \Sigma_l \Sigma^+_{t''} \Sigma^-_{t'} (\boldsymbol{l}'t''|\sigma_j|\boldsymbol{l}'t')_\pm (\boldsymbol{l}'t'|\alpha_x|\boldsymbol{l}''t'')_\pm \frac{f_{l'}+f_{l''}}{\varepsilon_{l'}+\varepsilon_{l''}} \\
&+ \frac{1}{2}\Sigma_\pm \Sigma_l \Sigma^+_{t''} \Sigma^-_{t'} (\boldsymbol{l}'t''|\sigma_j|\boldsymbol{l}'t')_\pm (\boldsymbol{l}'t'|\alpha_x|\boldsymbol{l}''t'')_\mp \frac{f_{l''}-f_{l'}}{\varepsilon_{l'}+\varepsilon_{l''}}\,.
\end{aligned} \tag{4.30}$$

As the first brackets in (4.29) have no zeroth order term of q_μ, calculations in the first order of q_μ are sufficient for the second brackets. We are then allowed to use the following approximations:

$$\frac{f_{l'}+f_{l''}}{\varepsilon_{l'}+\varepsilon_{l''}}=\frac{f_l}{\varepsilon_l}; \qquad \frac{f_{l''}-f_{l'}}{\varepsilon_{l'}+\varepsilon_{l''}}=\frac{c^2\hbar^2}{2\varepsilon_l}\frac{\partial f_l}{\partial \varepsilon_l}\boldsymbol{l}\cdot\boldsymbol{q}=\frac{1}{2}K_l{}^2\frac{\partial f_l}{\partial \varepsilon_l}\boldsymbol{l}\cdot\boldsymbol{q}\,, \tag{4.31}$$

in which the neglected terms are those of the second and higher orders of q_μ.

Making use again of the explicit values in Table II of the Appendix for treating the right-hand side of (4.30) we have

$$\Sigma_l \Sigma_{(t'',t')=(1,3),\,(2,4)} (\boldsymbol{l}''t''|\sigma_j|\boldsymbol{l}'t')(\boldsymbol{l}'t'|\alpha_x|\boldsymbol{l}''t'')\,\frac{f_{l''}}{\varepsilon_{l'}+\varepsilon_{l''}}
=\begin{cases} 0\,, & j=x\,, \\ -\dfrac{1}{2}\,iq_z\Sigma_l K_l{}^3 N_l l_x{}^2 l_z{}^2\dfrac{\partial f_l}{\partial\varepsilon_l}\,, & j=y\,, \\ 0\,, & j=z\,. \end{cases} \tag{4.32}$$

In the derivation of this result, it proves that the contribution from the first term on the right-hand side of (4.30) vanishes on account of the cancellation of those terms due to $(t'', t')=(1, 3)$ and $(2, 4)$ respectively. Similarly we obtain

$$\Sigma_l \Sigma_{(t'',t')=(1,4),\,(2,3)} (\boldsymbol{l}''t''|\sigma_j|\boldsymbol{l}'t')(\boldsymbol{l}'t'|\alpha_x|\boldsymbol{l}''t'')\,\frac{f_{l''}}{\varepsilon_{l'}+\varepsilon_{l''}}
=\begin{cases} 0\,, & j=x\,, \\ -\dfrac{1}{2}iq_z\Sigma_l K_l{}^3(1-N_l l_x{}^2)l_z{}^2\dfrac{\partial f_l}{\partial\varepsilon_l}\,, & j=y\,, \\ \dfrac{1}{2}\,iq_y\Sigma_l K_l{}^3 l_y{}^2\dfrac{\partial f_l}{\partial\varepsilon_l}\,, & j=z\,. \end{cases} \tag{4.33}$$

Only the second term in (4.30) gives again non-vanishing contributions. Combining (4.32) and (4.33) results in

$$\Sigma_l \Sigma^+_{t''} \Sigma^-_{t'} (\boldsymbol{l}''t''|\sigma_j|\boldsymbol{l}'t')(\boldsymbol{l}'t'|\alpha_x|\boldsymbol{l}''t'')\,\frac{f_{l'}}{\varepsilon_{l'}+\varepsilon_{l''}}
=\begin{cases} 0\,, & j=x\,, \\ -\dfrac{1}{2}iq_z\Sigma_l K_l{}^3 l_z{}^2\dfrac{\partial f_l}{\partial\varepsilon_l}\,, & j=y\,, \\ \dfrac{1}{2}\,iq_y\Sigma_l K_l{}^3 l_y{}^2\dfrac{\partial f_l}{\partial\varepsilon_l}\,, & j=z\,. \end{cases} \tag{4.34}$$

Substituting (4.25) and (4.34) in (4.29), with $l_z{}^2$ or $l_y{}^2$ in (4.34) replaced by $l^2/3$, gives

$$\Lambda_{xx}{}^2=\frac{1}{6}(q_y{}^2+q_z{}^2)\Sigma_{kl}K_k I_k K_l{}^3 l^2\frac{\partial f_k}{\partial\varepsilon_k}\frac{\partial f_l}{\partial\varepsilon_l}\,. \tag{4.35}$$

It is shown that the same result can be obtained for Λ_{xx}^3, Λ_{xx}^4 and Λ_{xx}^5. To show this for Λ_{xx}^3, note that this term is obtained if one interchanges t' with t'' and $f_{l'}$ with $f_{l''}$ in (4.30) and uses this result for the second factor on the right-hand side of (4.29). On the other hand, it is easily seen with the use of the table in the Appendix that the left-hand sides of (4.32) and (4.33) and, in consequence, that of (4.30) retain their original values for the simultaneous interchanges $t' \rightleftarrows t''$ and $f_{l'} \rightleftarrows f_{l''}$. This means that Λ_{xx}^3 can also be given by the right-hand side of (4.35). The same is true for Λ_{xx}^4 and Λ_{xx}^5, because they are obtained respectively merely by interchanging $\boldsymbol{k}$ and $\boldsymbol{l}$ in the expressions for Λ_{xx}^2 and Λ_{xx}^3.

We now proceed to the evaluation of the last four terms, $\Lambda_{xx}^6 \sim \Lambda_{xx}^9$. The virtual transitions involved are all those between positive- and negative-energy states. Applying (4.34) we readily obtain

$$\begin{aligned}\Lambda_{xx}^6 = \Sigma_j \Big\{ & \Sigma_k \Sigma_{s''}^{+} \Sigma_{s'}^{-} (\boldsymbol{k}'s'|\sigma_j|\boldsymbol{k}''s'')(\boldsymbol{k}''s''|\alpha_x|\boldsymbol{k}'s') \frac{f_{k''}}{\mathcal{E}_{k'}+\mathcal{E}_{k''}} \Big\} \\ \times \Big\{ & \Sigma_l \Sigma_{t''}^{+} \Sigma_{t'}^{-} (\boldsymbol{l}''t''|\sigma_j|\boldsymbol{l}'t')(\boldsymbol{l}'t'|\alpha_x|\boldsymbol{l}''t'') \frac{f_{l''}}{\mathcal{E}_{l'}+\mathcal{E}_{l''}} \Big\} \\ = & -\frac{1}{36}(q_y^2+q_z^2)\Sigma_{kl} K_k^3 K_l^3 k^2 l^2 \frac{\partial f_k}{\partial \mathcal{E}_k}\frac{\partial f_l}{\partial \mathcal{E}_l} \,. \end{aligned} \tag{4.36}$$

All the four terms $\Lambda_{xx}^6 \sim \Lambda_{xx}^9$ have the same contribution, as obvious from the argument developed in the discussion of the preceding terms.

Introducing (4.27), (4.35) and (4.36) into (4.21) with consideration of $\Lambda_{xx}^2 = \Lambda_{xx}^3 = \Lambda_{xx}^4 = \Lambda_{xx}^5$ and $\Lambda_{xx}^6 = \Lambda_{xx}^7 = \Lambda_{xx}^8 = \Lambda_{xx}^9$, we have

$$K_{xx}(\boldsymbol{q}) = (q_y^2+q_z^2) K_M(q) \,, \tag{4.37}$$

$$\begin{aligned} K_M(q) = -\frac{\pi c e^4}{V^2}\frac{1}{q^2}\Big\{ & \Big(\Sigma_k K_k I_k \frac{\partial f_k}{\partial \mathcal{E}_k}\Big)^2 \\ & + \frac{1}{3}\Sigma_{kl} K_k K_l (K_k^2 I_l k^2 + K_l^2 I_k l^2) \frac{\partial f_k}{\partial \mathcal{E}_k}\frac{\partial f_l}{\partial \mathcal{E}_l} - \frac{1}{9}\Big(\Sigma_k K_k^3 k^2 \frac{\partial f_k}{\partial \mathcal{E}_k}\Big)^2 \Big\} \,. \end{aligned} \tag{4.38}$$

According to the general discussion of the kernel described in § 2, (iv), we have by inspection, as the final result,

$$K_{\mu\nu}(\boldsymbol{q}) = (q^2 \delta_{\mu\nu} - q_\mu q_\nu) K_M(q) \,, \tag{4.39}$$

with $K_M(q)$ given by (4.33). The result obtained here is exact in the sense that our treatment does not involve any approximation to be allowed only for $(v/c)^2 \ll 1$. The second and third terms in the curly brackets of (4.38) provide respectively at most the first and second order relativistic corrections, in the ordinary sense, to the first term. These correction terms are, of course, of little importance for the conduction electrons in a metal as $(v/c)^2 \ll 1$ for these electrons. It might be argued that these terms could be discarded from the beginning by reason of their little importance in order to dispense with laborious calculations. In this connection, however, we should note that similar terms involving virtual transitions between positive- and negative-energy states are sometimes of the same importance as those involving only transitions among positive-energy states. It was the case, for instance, for a free electron gas discussed in § 3. Another example of such a case is that of the magnetic interaction which will be discussed in § 5. Thus, we have no right without calculation to regard those terms as small corrections.

In the present case, we can neglect in practice all the relativistic correction terms in (4.38). We can thus neglect the second and third terms in the curly brackets and further use the following approximations:

$$I_k = 1 \;; \qquad K_k = \hbar/mc \;; \qquad \mathcal{E}_k = mc^2 + (\hbar^2 k^2/2m) \,,$$

and

$$f_k = (\exp[\beta(\hbar^2 k^2/2m) - \beta\zeta] + 1)^{-1} \,.$$

Assuming temperatures sufficiently low compared with the degeneracy temperature and neglecting small temperature-dependent terms, we get

$$\Sigma_k K_k I_k \frac{\partial f_k}{\partial \varepsilon_k} = -\frac{V}{2\pi c\hbar}\left(\frac{3n}{\pi}\right)^{1/3}, \qquad (4.40)$$

were n is the number of electrons per volume. Introducing (4.40) into (4.38) and neglecting all the correction terms, we have, for the singular part of the kernel,

$$K_M(q) = -K_0/q^2 , \qquad (4.41)$$

$$K_0 = \frac{1}{4\pi}\left(\frac{3}{\pi}\right)^{2/3} \frac{n^{2/3}e^4}{c\hbar^2} . \qquad (4.42)$$

As discussed in § 2, (iv) the kernel given by (4.41) and (4.42) leads to the London equation of the form (2.33). It is of great interest that the expression for K_0 obtained here has quite a different form from that derived according to the London theory, i.e.

$$K_0 = ne^2/mc , \qquad (4.43)$$

while the order of magnitude is the same in both cases.

In order to examine the order of magnitude of the Meissner-Ochsenfeld effect to be expected in the present theory, it is convenient to derive the penetration depth of the field and to compare it with that obtained in the experiment on actual superconductors. As well known, the penetration depth, λ, is related to the constant K_0 by the equation

$$\lambda = (c/4\pi K_0)^{1/2} . \qquad (4.44)$$

From (4.42) and (4.44) the penetration depth according to the present model becomes

$$\lambda = (\pi/3)^{1/3}(c^2\hbar^2/n^{2/3}e^4)^{1/2} . \qquad (4.45)$$

Inserting (4.43) into (4.44) gives the penetration depth in the London theory:

$$\lambda_L = (1/4\pi)^{1/2}(mc^2/ne^2)^{1/2} . \qquad (4.46)$$

In Table I the theoretical values of λ according to (4.45) and (4.46) assuming one electron per atom are listed for several elements and compared with the experimental values extrapolated to the absolute zero of temperature. We should note that the penetration depth given by (4.45) is to be considered as giving the value at the absolute zero of temperature. The temperature variation will be discussed in Part II. It is rather surprising that (4.45) gets so good agreement with experiment, in view of the fact that the interaction (4.41) on which the whole theory is based has never been introduced in a quantitatively unambiguous way.

Table I. Theoretical values of λ assuming one electron per atom and experimental values at $T=0°$K taken from D. Shoenberg: Superconductivity 2. ed. (1952) 188.

	Element	In	Sn	Hg	Pb
$\lambda \times 10^6$ cm	The present theory: Eq. (4.50)	4.1	4.2	3.9	4.3
	The London theory: Eq. (4.51)	2.7	2.8	2.5	2.9
	Experiment: $T=0°$K	6.4	5.2	4.1	3.9

We have shown that the interaction (4.1) produces the M-O effect, but this is not the only one to bring upon this effect. The interaction of the form

$$U_M' = e^2(\boldsymbol{s}_1\cdot\boldsymbol{r})(\boldsymbol{s}_2\cdot\boldsymbol{r})/r^3 \qquad (\boldsymbol{r}=\boldsymbol{x}_2-\boldsymbol{x}_1) \qquad (4.47)$$

can be shown to have the same effect as (4.1). As simple mathematics shows, the perturbative term in the Hamiltonian due to this interaction is

$$H_M{}'=\frac{\pi e^2}{2V}\sum_q\sum_{kl}\sum_{s's''t't''}\frac{1}{q^2}\Big\{(\boldsymbol{k}'s'|\boldsymbol{\sigma}|\boldsymbol{k}''s'')\cdot(\boldsymbol{l}''t''|\boldsymbol{\sigma}|\boldsymbol{l}'t')$$
$$-\frac{2(\boldsymbol{k}'s'|\boldsymbol{\sigma}\cdot\boldsymbol{q}|\boldsymbol{k}''s'')(\boldsymbol{l}''t''|\boldsymbol{\sigma}\cdot\boldsymbol{q}|\boldsymbol{l}'t')}{q^2}\Big\}a_{k'}{}^{(s')*}a_{k''}{}^{(s'')}a_{l''}{}^{(t'')*}a_{l'}{}^{(t')}\,. \tag{4.48}$$

As we are considering the current linear in $H_M{}'$, the currents arising from separate terms in $H_M{}'$ are additive. The first term in { } on the right-hand side of (4.48) is identical to (4.4) and accordingly leads to the same M–O effect as already described. Only the second term in (4.48) is thus to be discussed here. The mean current density to be expected from this part of interaction is given, apart from a numerical factor, by replacing $R_{\mu\nu}{}^{jj}$ in (4.20) with

$$R_{\mu\nu}{}^{ij}(\boldsymbol{k},\boldsymbol{l},\boldsymbol{q},s',s'',t',t'')=(q_iq_j/q^2)(\boldsymbol{k}'s'|\sigma_i|\boldsymbol{k}''s'')(\boldsymbol{l}''t''|\sigma_j|\boldsymbol{l}'t')(\boldsymbol{k}''s''|\alpha_\mu|\boldsymbol{k}'s')(\boldsymbol{l}'t'|\alpha_\nu|\boldsymbol{l}''t'') \tag{4.49}$$

and summing over i. The quantity corresponding to $\Lambda_{\mu\nu}{}^{\xi}$ in (4.21) is designated by the same symbol with a prime. We are again confined to the calculation for the case $\mu=\nu=x$. We have then

$$\Lambda_{xx}{}^{1'}=q^{-2}\sum_{ij}q_iq_j\Big\{\sum_k\sum^+_{s's''}(\boldsymbol{k}'s'|\sigma_i|\boldsymbol{k}''s'')(\boldsymbol{k}''s''|\alpha_x|\boldsymbol{k}'s')\frac{f_{k'}-f_{k''}}{\varepsilon_{k'}-\varepsilon_{k''}}\Big\}$$
$$\times\Big\{\sum_l\sum^+_{t't''}(\boldsymbol{l}''t''|\sigma_j|\boldsymbol{l}'t')(\boldsymbol{l}'t'|\alpha_x|\boldsymbol{l}''t'')\frac{f_{l'}-f_{l''}}{\varepsilon_{l'}-\varepsilon_{l''}}\Big\}\,, \tag{4.50}$$

$$\Lambda_{xx}{}^{2'}=\Lambda_{xx}{}^{3'}=\Lambda_{xx}{}^{4'}=\Lambda_{xx}{}^{5'}$$
$$=q^{-2}\sum_{ij}q_iq_j\Big\{\sum_k\sum^+_{s's''}(\boldsymbol{k}'s'|\rho_i|\boldsymbol{k}''s'')(\boldsymbol{k}''s''|\alpha_x|\boldsymbol{k}'s')\frac{f_{k'}-f_{k''}}{\varepsilon_{k'}-\varepsilon_{k''}}\Big\}$$
$$\times\Big\{\sum_l\sum^+_{t''}\sum^-_{t'}(\boldsymbol{l}''t''|\sigma_j|\boldsymbol{l}'t')(\boldsymbol{l}'t'|\alpha_x|\boldsymbol{l}''t'')\frac{f_{l''}}{\varepsilon_{l'}+\varepsilon_{l''}}\Big\}\,, \tag{4.51}$$

$$\Lambda_{xx}{}^{6'}=\Lambda_{xx}{}^{7'}=\Lambda_{xx}{}^{8'}=\Lambda_{xx}{}^{9'}$$
$$=q^{-2}\sum_{ij}q_iq_j\Big\{\sum_k\sum^+_{s''}\sum^-_{s'}(\boldsymbol{k}'s'|\sigma_i|\boldsymbol{k}''s'')(\boldsymbol{k}''s''|\alpha_x|\boldsymbol{k}'s')\frac{f_{k''}}{\varepsilon_{k'}+\varepsilon_{k''}}\Big\}$$
$$\times\Big\{\sum_l\sum^+_{t''}\sum^-_{t'}(\boldsymbol{l}''t''|\sigma_j|\boldsymbol{l}'t')(\boldsymbol{l}'t'|\alpha_x|\boldsymbol{l}''t'')\frac{f_{l''}}{\varepsilon_{l'}+\varepsilon_{l''}}\Big\}\,. \tag{4.52}$$

Note that

$$q_iq_j\Big\{\sum_k\sum^+_{s's''}(\boldsymbol{k}'s'|\sigma_i|\boldsymbol{k}''s'')(\boldsymbol{k}''s''|\alpha_r|\boldsymbol{k}'s')\frac{f_{k'}-f_{k''}}{\varepsilon_{k'}-\varepsilon_{k''}}\Big\}$$
$$\times\Big\{\sum_l\sum^+_{t't''}(\boldsymbol{l}''t''|\sigma_j|\boldsymbol{l}'t')(\boldsymbol{l}'t'|\alpha_x|\boldsymbol{l}''t'')\frac{f_{l'}-f_{l''}}{\varepsilon_{l'}-\varepsilon_{l''}}\Big\}$$
$$=\begin{cases}0\,, & i\text{ or }j=x\,,\\ \left(\sum_kK_kI_k\dfrac{\partial f_k}{\partial\varepsilon_k}\right)^2q_y{}^2q_z{}^2\,, & i=j=y\text{ or }z\,,\\ -\left(\sum_kK_kI_k\dfrac{\partial f_k}{\partial\varepsilon_k}\right)^2q_y{}^2q_z{}^2\,, & i,\ j=y\text{ or }z;\ i\neq j\,,\end{cases} \tag{4.53}$$

$$q_iq_j\Big\{\sum_k\sum^+_{s's''}(\boldsymbol{k}'s'|\sigma_i|\boldsymbol{k}''s'')(\boldsymbol{k}''s''|\alpha_x|\boldsymbol{k}'s')\frac{f_{k'}-f_{k''}}{\varepsilon_{k'}-\varepsilon_{k''}}\Big\}$$
$$\times\Big\{\sum_l\sum^+_{t''}\sum^-_{t'}(\boldsymbol{l}''t''|\sigma_j|\boldsymbol{l}'t')(\boldsymbol{l}'t'|\alpha_x|\boldsymbol{l}''t'')\frac{f_{l''}}{\varepsilon_{l'}+\varepsilon_{l''}}\Big\}$$
$$=\begin{cases}0\,, & i\text{ or }j=x\,,\\ \dfrac{1}{6}\sum_{kl}K_kI_kK_l{}^3l^2\dfrac{\partial f_k}{\partial\varepsilon_k}\dfrac{\partial f_l}{\partial\varepsilon_l}q_y{}^2q_z{}^2\,, & i=j=y\text{ or }z\,,\\ -\dfrac{1}{6}\sum_{kl}K_kI_kK_l{}^3l^2\dfrac{\partial f_k}{\partial\varepsilon_k}\dfrac{\partial f_l}{\partial\varepsilon_l}q_y{}^2q_z{}^2\,, & i,\ j=y\text{ or }z;\ i\neq j\,,\end{cases} \tag{4.54}$$

and

$$q_iq_j\left\{\sum_k\sum^{+}_{s''}\sum^{-}_{s'}(\boldsymbol{k}'s'|\sigma_i|\boldsymbol{k}''s'')(\boldsymbol{k}''s''|\alpha_x|\boldsymbol{k}'s')\frac{f_{k''}}{\varepsilon_{k'}+\varepsilon_{k''}}\right\}$$
$$\times\left\{\sum_l\sum^{+}_{t''}\sum^{-}_{t'}(\boldsymbol{l}''t''|\sigma_j|\boldsymbol{l}'t')(\boldsymbol{l}'t'|\alpha_x|\boldsymbol{l}''t'')\frac{f_{l''}}{\varepsilon_{l'}+\varepsilon_{l''}}\right\}$$
$$=\begin{cases} 0\,, & i \text{ or } j=x\,,\\ -\frac{1}{36}\sum_{kl}K_k{}^3K_l{}^3k^2l^2\frac{\partial f_k}{\partial\varepsilon_k}\frac{\partial f_l}{\partial\varepsilon_l}q_y{}^2q_z{}^2\,, & i=j=y \text{ or } z\,,\\ \frac{1}{36}\sum_{kl}K_k{}^3K_l{}^3k^2l^2\frac{\partial f_k}{\partial\varepsilon_k}\frac{\partial f_l}{\partial\varepsilon_l}q_y{}^2q_z{}^2\,, & i,j=y \text{ or } z;\ i\neq j\,. \end{cases} \qquad (4.55$$

The derivations of these results are achieved by applying (4.25) and (4.34).

Substitution of (4.53), (4.54) and (4.55) in (4.50), (4.51) and (4.52) respectively reveals tha all the $A_{\tau x}{}^{\xi''}$s vanish. This means that the kernel $K_{xx}(\boldsymbol{q})$ and, in consequence, $K_{\mu\nu}($ vanish for the second part of $H_M{}'$ in (4.48) in the limit $q\to 0$. The current then arises onl from the first part, which is identical to the interaction (4.4). It is thus concluded that th interactions U_M and $U_M{}'$ give exactly the same Meissner-Ochsenfeld effect and that an linear combination of them, i.e. $aU_M+bU_M{}'$, brings on the M–O effect of the correct ord of magnitude provided that $a+b$ is a positive number of order 1.

§ 5. The Known Type of Interaction

According to Breit, the interaction energy between two moving electrons is given, in th order of $(v/c)^2$, by

$$U_B=\frac{e^2}{r}-\frac{e^2}{r}\boldsymbol{\alpha}_1\cdot\boldsymbol{\alpha}_2+\frac{e^2}{2r}\left\{\boldsymbol{\alpha}_1\cdot\boldsymbol{\alpha}_2-\frac{(\boldsymbol{\alpha}_1\cdot\boldsymbol{r})(\boldsymbol{\alpha}_2\cdot\boldsymbol{r})}{r^2}\right\}=U_{BI}+U_{BII}+U_{BIII}\,, \qquad (5.1)$$

where the first and third terms represent the retarded Coulomb interaction and the secon term the magnetic interaction. The Hamiltonian of the system of electrons interacting each other with this type of interaction is given by

$$H=H_0+H_A+H_B\,,$$

where H_A is the preturbation due to the magnetic field and

$$H_B=H_{BI}+H_{BII}+H_{BIII}\,,$$
$$H_{BI}=\frac{2\pi e^2}{V^2}\sum_{kl}\sum_q\sum_{s's''t't''}\frac{(\boldsymbol{k}'s'|\boldsymbol{k}''s'')(\boldsymbol{l}''t''|\boldsymbol{l}'t')}{q^2}a_{k'}{}^{(s')*}a_{k''}{}^{(s'')}a_{l''}{}^{(t'')*}a_{l'}{}^{(t')}\,, \qquad (5.2$$
$$H_{BII}=-\frac{2\pi e^2}{V^2}\sum_{kl}\sum_q\sum_{s's''t't''}\frac{(\boldsymbol{k}'s'|\boldsymbol{\alpha}|\boldsymbol{k}''s'')\cdot(\boldsymbol{l}''t''|\boldsymbol{\alpha}|\boldsymbol{l}'t')}{q^2}a_{k'}{}^{(s')*}a_{k''}{}^{(s'')}a_{l''}{}^{(t'')*}a_{l'}{}^{(t')}\,, \qquad (5.3)$$
$$H_{BIII}=\frac{2\pi e^2}{V^2}\sum_{kl}\sum_q\sum_{s's''t't''}\frac{(\boldsymbol{k}'s'|\boldsymbol{\alpha}\cdot\boldsymbol{q}|\boldsymbol{k}''s'')(\boldsymbol{l}''t''|\boldsymbol{\alpha}\cdot\boldsymbol{q}|\boldsymbol{l}'t')}{q^4}a_{k'}{}^{(s')*}a_{k''}{}^{(s'')}a_{l''}{}^{(t'')*}a_{l'}{}^{(t')}\,. \qquad (5.4$$

The object of this section is to show that none of the three parts of H_B exhibits the M– effect even if the relativistic theory of an electron is applied.

(i) *The Coulomb interaction, H_{BI}*

In order to obtain the mean current density in this case (apart from a trivial numerica factor) we replace $\sum_j R_{\mu\nu}{}^{jj}$ in (4.20) by

$$R_{\mu\nu}(\boldsymbol{k},\boldsymbol{l},\boldsymbol{q},s',s'',t',t'')=(\boldsymbol{k}'s'|\boldsymbol{k}''s'')(\boldsymbol{l}''t''|\boldsymbol{l}'t')(\boldsymbol{k}''s''|\alpha_\mu|\boldsymbol{k}'s')(\boldsymbol{l}'t'|\alpha_\nu|\boldsymbol{l}''t'')\,. \qquad (5.5$$

The equation obtained will be designated as (4.20′). It is again sufficient to evaluate $K_{\mu\nu}(\boldsymbol{q}$ only for the case $\mu=\nu=x$.

Applying the explicit values of the matrix elements in Table II of the Appendix, we can asily verify the following equations:

$$\left.\begin{aligned}&\Sigma_k\Sigma^+_{s'=s''}(\boldsymbol{k}'s'|\boldsymbol{k}''s'')(\boldsymbol{k}''s''|\alpha_x|\boldsymbol{k}'s')\frac{f_{k'}-f_{k''}}{\mathcal{E}_{k'}-\mathcal{E}_{k''}}=0\ ,\\&\Sigma_k\Sigma^+_{s'\neq s''}(\boldsymbol{k}'s'|\boldsymbol{k}''s'')(\boldsymbol{k}''s''|\alpha_x|\boldsymbol{k}'s')\frac{f_{k'}-f_{k''}}{\mathcal{E}_{k'}-\mathcal{E}_{k''}}=0\ .\end{aligned}\right\}\tag{5.6}$$

his implies that the first five terms on the right-hand side of (4.20′) vanish. We have urther

$$\begin{aligned}&\Sigma_l\Sigma^+_{t''}\Sigma^-_{t'}(\boldsymbol{l}''t''|\boldsymbol{l}'t')(\boldsymbol{l}'t'|\alpha_x|\boldsymbol{l}''t'')\frac{f_{l''}}{\mathcal{E}_{l'}+\mathcal{E}_{l''}}\\&=\frac{1}{2}\Sigma_\pm\Sigma_l\Sigma^+_{t''}\Sigma^-_{t'}(\boldsymbol{l}''t''|\boldsymbol{l}'t')_\pm(\boldsymbol{l}'t'|\alpha_x|\boldsymbol{l}''t'')_\pm\frac{f_{l'}+f_{l''}}{\mathcal{E}_{l'}+\mathcal{E}_{l''}}\ .\end{aligned}\tag{5.7}$$

$$\begin{aligned}&\Sigma_l\Sigma^+_{t'}\Sigma^-_{t''}(\boldsymbol{l}''t''|\boldsymbol{l}'t')(\boldsymbol{l}'t'|\alpha_x|\boldsymbol{l}''t'')\frac{f_{l'}}{\mathcal{E}_{l'}+\mathcal{E}_{l''}}\\&=\frac{1}{2}\Sigma_\pm\Sigma_l\Sigma^+_{t'}\Sigma^-_{t''}(\boldsymbol{l}''t''|\boldsymbol{l}'t')_\pm(\boldsymbol{l}'t'|\alpha_x|\boldsymbol{l}''t'')_\pm\frac{f_{l'}+f_{l''}}{\mathcal{E}_{l'}+\mathcal{E}_{l''}}\ .\end{aligned}\tag{5.8}$$

t is easy to show that the non-vanishing terms in (5.7) are just equal to the non-vanishing erms in (5.8) with opposite sign. This implies that the sixth and eighth terms in (4.20′) ancel the seventh and nineth terms respectively.

It is thus confirmed that the right-hand side of (4.20′) vanishes and that the M–O effect loes not occur for the Coulomb interaction.

ii) *The magnetic interaction, H_{BII}*

Since the exact calculation is very troublesome for this interaction, only the zeroth order erms of q_μ are evaluated exactly in the relativistic sense and the terms of order $q_\mu q_\nu$ are valuated in the approximation neglecting all the relativistic (in the ordinary sense) correcions. As will be seen, the calculation in the present approximation is sufficient to show hat the magnetic interaction cannot be considered to produce superconductivity.

The kernel $K_{\mu\nu}(\boldsymbol{q})$ for this interaction can be obtained (apart from a trivial numerical actor) when $R_{\mu\nu}{}^{jj}$ in (4.20) is replaced by the quantity

$$R_{\mu\nu}{}^{jj}(\boldsymbol{k},\boldsymbol{l},\boldsymbol{q},s',s'',t',t'')=(\boldsymbol{k}'s'|\alpha_j|\boldsymbol{k}''s'')(\boldsymbol{l}''t''|\alpha_j|\boldsymbol{l}'t')(\boldsymbol{k}''s''|\alpha_\mu|\boldsymbol{k}'s')(\boldsymbol{l}'t'|\alpha_\nu|\boldsymbol{l}''t'')\ .\tag{5.9}$$

he equation thus obtained will be quoted as (4.20″) and, corresponding to $\Lambda_{\mu\nu}{}^{\xi}$ in (4.21), e introduce $\Lambda_{\mu\nu}{}^{\xi''}$. The calculations are restricted to the case $\mu=\nu=x$.

We first consider

$$\Lambda_{xx}{}^{1''}=\Sigma_j\Sigma_{kl}\Sigma^+_{s's''}\Sigma^+_{t't''}R_{xx}{}^{jj}\frac{f_{k'}-f_{k''}}{\mathcal{E}_{k'}-\mathcal{E}_{k''}}\frac{f_{l'}-f_{l''}}{\mathcal{E}_{l'}-\mathcal{E}_{l''}}\ .\tag{5.10}$$

t is insufficient for the present purpose to evaluate the expression

$$\Sigma_k\Sigma^+_{s's''}(\boldsymbol{k}'s'|\alpha_j|\boldsymbol{k}''s'')(\boldsymbol{k}''s''|\alpha_x|\boldsymbol{k}'s')\frac{f_{k'}-f_{k''}}{\mathcal{E}_{k'}-\mathcal{E}_{k''}}\tag{5.11}$$

nerely in the first order of q_μ as in the preceding section. It is necessary to take further he second order terms of q_μ into account, because (5.11) has non-vanishing zeroth order erms of q_μ and the current consists of the products of two expressions of this type. Using he values of matrix elements in the Appendix we obtain the following results correct in the rder of $q_\mu q_\nu$:

$$\sum_k\sum^{+}_{s's''}(\boldsymbol{k}'s'|\alpha_k|\boldsymbol{k}''s'')(\boldsymbol{k}''s''|\alpha_x|\boldsymbol{k}'s')\frac{f_{k'}-f_{k''}}{\mathcal{E}_{k'}-\mathcal{E}_{k''}}$$

$$=\begin{cases}\sum_k\Big\{2K^2(\boldsymbol{k},\boldsymbol{q})k_x^2+2L^2(\boldsymbol{k},\boldsymbol{q})(k_y^2+k_z^2)+\dfrac{1}{2}K^2(\boldsymbol{k},\boldsymbol{q})(q_y^2+q_z^2) \\ \qquad\qquad -2K(\boldsymbol{k},\boldsymbol{q})L(\boldsymbol{k},\boldsymbol{q})\boldsymbol{k}\cdot\boldsymbol{q}\Big\}\dfrac{f_{k'}-f_{k''}}{\mathcal{E}_{k'}-\mathcal{E}_{k''}}\,, & j=x\,, \\ -\sum_k\Big\{\dfrac{1}{2}K^2(\boldsymbol{k},\boldsymbol{q})(q_xq_y+q_xq_z)+2L^2(\boldsymbol{k},\boldsymbol{q})(k_xk_y+k_xk_z) \\ \qquad\qquad -K(\boldsymbol{k},\boldsymbol{q})L(\boldsymbol{k},\boldsymbol{q})(k_zq_x+k_xq_z)\Big\}\dfrac{f_{k'}-f_{k''}}{\mathcal{E}_{k'}-\mathcal{E}_{k''}}\,, & j=y\,, \\ -\sum_k K(\boldsymbol{k},\boldsymbol{q})L(\boldsymbol{k},\boldsymbol{q})(k_zq_x+k_xq_z)\dfrac{f_{k'}-f_{k''}}{\mathcal{E}_{k'}-\pi_{k''}}\,, & j=z\,.\end{cases}\qquad (5.$$

We have to consider here $(f_{k'}-f_{k''})/(\mathcal{E}_{k'}-\mathcal{E}_{k''})$ in the second order with respect to q_μ, becau the brackets preceding this quantity contain a zeroth order term in q_μ for $j=x$. Substitu i

$$(f_{k'}-f_{k''})/(\mathcal{E}_{k'}-\mathcal{E}_{k''})=(\partial f_k/\partial\mathcal{E}_k)+\omega(\boldsymbol{k},\boldsymbol{q})\,,\qquad (5.$$

$$\omega(\boldsymbol{k},\boldsymbol{q})=\frac{c^2\hbar^2q^2}{8\mathcal{E}_k}\frac{\partial^2 f_k}{\partial\mathcal{E}_k^2}+\frac{c^4\hbar^4(\boldsymbol{k}\cdot\boldsymbol{q})^2}{24\mathcal{E}_k^2}\frac{\partial^3 f_k}{\partial\mathcal{E}_k^3}\,,\qquad (5.$$

in (5.12) and using the results, we have

$$\sum_{kl}\sum^{+}_{s's''}\sum^{+}_{t't''}R_{xx}{}^{jj}\frac{f_{k'}-f_{k''}}{\mathcal{E}_{k'}-\mathcal{E}_{k''}}\frac{f_{l'}-f_{l''}}{\mathcal{E}_{l'}-\mathcal{E}_{l''}}$$

$$=\begin{cases}4\sum_{kl}K_k^2K_l^2k_x^2l_x^2\dfrac{\partial f_k}{\partial\mathcal{E}_k}\dfrac{\partial f_l}{\partial\mathcal{E}_l}+\sum_{kl}K_k^2K_l^2(k_x^2+l_x^2)(q_y^2+q_z^2)\dfrac{\partial f_k}{\partial\mathcal{E}_k}\dfrac{\partial f_l}{\partial\mathcal{E}_l} \\ \qquad\qquad +4\sum_{kl}K_k^2K_l^2k_x^2l_x^2\Big\{\omega(\boldsymbol{l},\boldsymbol{q})\dfrac{\partial f_k}{\partial\mathcal{E}_k}+\omega(\boldsymbol{k},\boldsymbol{q})\dfrac{\partial f_l}{\partial\mathcal{E}_l}\Big\}\,, & j=x\,, \\ 0\,, & j=y\,, \\ 0\,, & J=z\,.\end{cases}\qquad (5.1$$

We should note that the second and third terms on the right-hand side are of order $q_\mu q_\nu$ a of the same order with respect to $(v/c)^2$, and further that the $q_\mu q_\nu$-terms of still high orders in $(v/c)^2$ are all neglected. Introducing this result into (5.10) and using

$$\sum_k K_k^2k_\mu^2\frac{\partial f_k}{\partial\mathcal{E}_k}=-\sum_k\left(1-\frac{c^2\hbar^2k_\mu^2}{\mathcal{E}_k^2}\right)\frac{f_k}{\mathcal{E}_k}=-\sum_k I_k\frac{f_k}{\mathcal{E}_k}\,,\qquad (5.1$$

give

$$\Lambda_{xx}{}^{1''}=4\sum_{kl}I_kI_l\frac{f_kf_l}{\mathcal{E}_k\mathcal{E}_l}-4\sum_{kl}K_k^2I_l\Big\{\frac{1}{2}(q_y^2+q_z^2)+2k_x^2\omega(\boldsymbol{k},\boldsymbol{q})\Big\}\frac{f_l}{\mathcal{E}_l}\,.\qquad (5.1$$

We proceed now to the next four terms on the right-hand side of (4.20′′). It is an ea matter to show that these four terms are equal to each other. We thus evaluate only t second term. We should note first

$$\sum_l\sum_{(t'',t')=(1,3),\,(2,4)}(\boldsymbol{l}''t''|\alpha_j|\boldsymbol{l}'t')(\boldsymbol{l}'t'|\alpha_x|\boldsymbol{l}''t'')\frac{f_{l''}}{\mathcal{E}_{l'}+\mathcal{E}_{l''}}$$

$$=\begin{cases}\sum_l\Big\{N^2(\boldsymbol{l},\boldsymbol{q})l_z^2l_x^2+\dfrac{1}{4}N^2(\boldsymbol{l},\boldsymbol{q})(l_z^2q_y^2+l_y^2q_z^2)\Big\}\dfrac{f_{l'}+f_{l''}}{\mathcal{E}_{l'}+\mathcal{E}_{l''}}\,, & j=x\,, \\ 0\,, & j=y\,, \\ \dfrac{1}{4}\sum_l N_l\Big\{M_l+N_l\Big(l_x^2-\dfrac{1}{2}l^2\Big)\Big\}q_zq_x\dfrac{f_{l'}+f_{l''}}{\mathcal{E}_{l'}+\mathcal{E}_{l''}}\,, & j=z\,,\end{cases}\qquad (5.1$$

$$\Sigma_l \Sigma_{(t'',t')=(1,4),\,(2,3)} (\boldsymbol{l}'t''|\alpha_j|\boldsymbol{l}'t')(\boldsymbol{l}'t'|\alpha_x|\boldsymbol{l}'t'') \frac{f_{l''}}{\varepsilon_{l'}+\varepsilon_{l''}}$$

$$= \begin{cases} \Sigma_l\Big[\Big\{M(\boldsymbol{l},\boldsymbol{q})+N(\boldsymbol{l},\boldsymbol{q})\Big(\frac{1}{2}l^2-l_x^2\Big)\Big\}^2+N^2(\boldsymbol{l},\boldsymbol{q})l_x^2l_y^2 & \\ \quad +\frac{1}{4}N_l\Big\{M_l+N_l\Big(\frac{1}{2}l^2-l_x^2\Big)\Big\}\Big(\frac{1}{2}q_x^2-q^2\Big)\Big]\frac{f_{l'}+f_{l''}}{\varepsilon_{l'}+\varepsilon_{l''}}\,, & j=x\,, \\ 0\,, & j=y\,, \\ \frac{1}{4}\Sigma_l N_l\Big\{M_l+N_l\Big(\frac{1}{2}l^2-l_x^2\Big)\Big\}q_zq_x\frac{f_{l'}+f_{l''}}{\varepsilon_{l'}+\varepsilon_{l''}}\,, & j=z\,. \end{cases} \tag{5.19}$$

t is then easily seen that all the $q_\mu q_\nu$-terms on the right-hand side of (5.18) and (5.19), when multiplied by the right-hand side of (5.12) with the same j, provide at most small quantities f order $(v/c)^2$ compared with the largest $q_\mu q_\nu$-term in (5.15). Accordingly in evaluating the second term of (4.20′′) in the same approximation as in the case of the first, we can neglect ll the $\boldsymbol{q}$-dependent terms in (5.18) and (5.19). From these equations we have then, using A.2) and (A.3),

$$\Sigma_l \Sigma^+_{t''} \Sigma^-_{t'} (\boldsymbol{l}'t''|\alpha_j|\boldsymbol{l}'t')(\boldsymbol{l}'t'|\alpha_x|\boldsymbol{l}'t'') \frac{f_{l''}}{\varepsilon_{l'}+\varepsilon_{l''}}$$

$$= \begin{cases} \Sigma_l I_l f_l/\varepsilon_l\,, & j=x\,, \\ 0\,, & j=y\,, \\ 0\,, & j=z\,, \end{cases} \tag{5.20}$$

where I_l is given by (4.26) with $\boldsymbol{k}$ replaced by l. From (5.12) and (5.19) we get

$$\Lambda_{xx}{}^{2''}=\Lambda_{xx}{}^{3''}=\Lambda_{xx}{}^{4''}=\Lambda_{xx}{}^{5''}=\Sigma_j\Sigma_{\boldsymbol{kl}}\Sigma^+_{s's''t''}\Sigma^-_{t'}R_{xx}{}^{jj}\frac{f_{k'}-f_{k''}}{\varepsilon_{k'}-\varepsilon_{k''}}\frac{f_{l''}}{\varepsilon_{l'}+\varepsilon_{l''}}$$

$$=2\Sigma_{\boldsymbol{kl}}K_k{}^2I_l\Big\{k_x{}^2+\frac{1}{4}(q_y{}^2+q_z{}^2)\Big\}\Big\{\frac{\partial f_k}{\partial\varepsilon_k}+\omega(\boldsymbol{k},\boldsymbol{q})\Big\}\frac{f_l}{\varepsilon_l}$$

$$=-2\Sigma_{\boldsymbol{kl}}I_kI_l\frac{f_kf_l}{\varepsilon_k\varepsilon_l}+\Sigma_{\boldsymbol{kl}}K_k{}^2I_l\Big\{\frac{1}{2}(q_y{}^2+q_z{}^2)\frac{\partial f_k}{\partial\varepsilon_k}+2k_x{}^2\omega(\boldsymbol{k},\boldsymbol{q})\Big\}\frac{f_l}{\varepsilon_l}\,. \tag{5.21}$$

Now we consider the last four terms in 4.20′′). It is also easy to see that these four terms are equal to each other. The $\boldsymbol{q}$-dependent terms in (5.18) and (5.19) can be neglected also in this case on account of the same reason as mentioned in the discussion preceding eq. (5.20). Then applying (5.20) twice gives

$$\Lambda_{xx}{}^{6''}=\Lambda_{xx}{}^{7''}=\Lambda_{xx}{}^{8''}=\Lambda_{xx}{}^{9''}$$

$$=\Sigma_j\Sigma_{\boldsymbol{kl}}\Sigma^+_{s''t''}\Sigma^-_{s't'}R_{xx}{}^{jj}\frac{f_{k''}}{\varepsilon_{k'}+\varepsilon_{k''}}\frac{f_{l''}}{\varepsilon_{l'}+\varepsilon_{l''}}$$

$$=\Sigma_{\boldsymbol{kl}}I_kI_lf_kf_l/\varepsilon_k\varepsilon_l\,. \tag{5.22}$$

From (5.17), (5.21) and (5.22) it follows

$$\Sigma_\xi\Lambda_{xx}{}^{\xi''}=0\,.$$

This result means that $K_{\mu\nu}(\boldsymbol{q})$ vanishes exactly with respect to the zeroth order term in q_μ and approximately with respect to the second order term. The approximation we have used leaves the possibility of the M–O effect with

$$K_{\mu\nu}(\boldsymbol{q})=-(\delta_{\mu\nu}-q_\mu q_\nu/q^2)K_0''\,,$$

$$K_0''\sim\Big(\frac{v}{c}\Big)^2\frac{4\pi ce^4}{V^2}\Sigma_{\boldsymbol{kl}}K_k{}^2K_l{}^2k_x{}^2\frac{\partial f_k}{\partial\varepsilon_k}\frac{\partial f_l}{\partial\varepsilon_l}$$

$$\sim\Big(\frac{v}{c}\Big)^4K_0\,, \tag{5.23}$$

where K_0 is the constant given by (4.42). (Compare the expression in the middle of the second line in (5.23) with the main contribution in (4.38).) Since the order of magnitude of this K_0 gave a very nice correspondence to that required from experiment, we can say that the magnetic interaction never leads to the M–O effect larger than 10^{-8} times that observed in superconductors and, in consequence, that it is never be responsible for superconductivity, at least, of real metals.

(iii) *The interaction term arising from the retardation effect in the Coulomb force,* H_{BIII}

In order to obtain $K_{\mu\nu}(\boldsymbol{q})$ belonging to this interaction, the $R_{\mu\nu}{}^{ij}$ in (4.20) should be replaced by

$$\sum_i R_{\mu\nu}{}^{ij}(\boldsymbol{k}, \boldsymbol{l}, \boldsymbol{q}, s', s'', t', t'') = \sum_i (q_iq_j/q^2)(\boldsymbol{k}'t'|\alpha_i|\boldsymbol{k}''s'')(\boldsymbol{l}''t''|\alpha_j|\boldsymbol{l}'t') \times(\boldsymbol{k}''s''|\alpha_\mu|\boldsymbol{k}'s')(\boldsymbol{l}'t'|\alpha_\nu|\boldsymbol{l}''t'') : \tag{5.24}$$

We need to carry out the actual calculation only for the case $\mu=\nu=x$. The sum of the contributions from $R_{xx}{}^{ij}$ with $i=j$ should give the same kernel as obtained for the magnetic interaction described in (ii) of this section, apart from a factor $q_x{}^2/q^2$, and, in consequence, it vanishes to the same degree of approximation as adopted there. We have now to investigate the contributions from $R_{\mu\nu}{}^{ij}$ with $i\neq j$ in the same approximation. For this purpose, the $\boldsymbol{q}$-dependent terms in (5.18) and (5.19) can be again neglected and the approximate result (5.20) can be applied. From (5.12) and (5.20) it is obvious that the non-vanishing contribution for $i\neq j$ might only arise in the two cases: $i=y$, $j=x$ and $i=x$, $j=y$. The contribution from these cases to the quantity corresponding to $\Lambda_{xx}{}^1$ is obtained from (5.12) as

$$-2(q_xq_y/q^2)\left\{\sum_k \frac{1}{2} K_k{}^2(q_xq_y+q_xq_z)\frac{\partial f_k}{\partial \varepsilon_k}\right\} \times\left\{\sum_l 2K_l{}^2 l_x{}^2 \frac{\partial f_l}{\partial \varepsilon_l}\right\} . \tag{5.25}$$

The contribution to the quantity corresponding to the sum $\sum_{\xi=2}^{5}\Lambda_{xx}{}^{\xi}$ is obtained from (5.12) and (5.20):

$$-4(q_xq_y/q^2)\left\{\sum_k \frac{1}{2} K_k{}^2(q_xq_y+q_xq_z)\frac{\partial f_k}{\partial \varepsilon_k}\right\} \times\left\{\sum_l l_l \frac{f_l}{\varepsilon_l}\right\} . \tag{5.26}$$

Since the quantity corresponding to $\sum_{\xi=6}^{9}\Lambda_{xx}{}^{\xi}$ has no contribution, the total contribution from the cases $i\neq j$ is the sum of those given by (5.25) and (5.26). Application of (5.16) shows that these two contributions cancel each other. Consequently, the whole contribution of H_{BIII} to the M–O effect vanishes to the same degree of approximation as in the preceding case, (ii). It is thus concluded that the retardation effect in the Coulomb interaction cannot also produce the M–O effect, a least, large enough to account for superconductivity.

Summarizing the results of this section, w conclude that the well-known type of electron electron interaction leads to no Meissner Ochsenfeld effect as long as the first orde effect is considered.

§ 6. Discussion

We have introduced in § 4 a special type o electron-electron interaction which brings upo the Meissner-Ochsenfeld effect in quantitativ agreement with experiment. It is, however of an unfamiliar type, and there seems to b two possible interpretations of it: one (i) t assume that the interaction originates from an inherent property of the electron, and the other (ii) to assume that it arises as a resul of modification, in a metal, of the known type of interaction, say (5.1). We do not want t discuss in this paper the physical foundation of this interaction and to decide which is the better of the above alternatives. However it seems worthwhile to discuss some other experimental facts besides the M–O effect in connection with the proposed interaction.

Pippard[10] introduced a concept of coherence length in order to account for his findings that the penetration depth of the field depends on the amount of impurity and begings to increase when the mean free path of an electron becomes as small as the penetration depth. Schafroth and Blatt[11] showed that in order to get agreement with this experiment, the kernel for the London equation should be modified as

$$K(q)=-K_0/q(q+\mu) \tag{6.1}$$

with μ of the same order of magnitude as the reciprocal mean free path. μ^{-1} was called the correlation length. The kernel (6.1) with $\mu=0$ corresponds of course to the London equation.

It is interesting to note that, if we assume a finite effective range of interaction and modify (4.1) in the form

$$U_M=e^2\boldsymbol{s}_1\cdot\boldsymbol{s}_2\exp\left[-r/d\right]/r\,, \quad (d>0) \tag{6.2}$$

we can well explain the experiment of Pippard. Indeed, the perturbative part of the Hamiltonian due to (6.2) becomes

$$H_M=\frac{\pi e^2}{2V}\sum_{kl}\sum_q\sum_{s's''l't''}$$

$$\times\frac{(\boldsymbol{k}'s'|\boldsymbol{\sigma}|\boldsymbol{k}''s'')\cdot(\boldsymbol{l}''t''|\boldsymbol{\sigma}|\boldsymbol{l}'t')}{q^2+\mu^2}$$

$$\times a_{\boldsymbol{k}'}{}^{(s')*}a_{\boldsymbol{k}''}{}^{(s'')}a_{\boldsymbol{l}''}{}^{(t'')*}a_{\boldsymbol{l}}{}^{(t')} \qquad (6.3)$$

with

$$\mu=d^{-1}\,. \qquad (6.4)$$

The corresponding kernel is given by

$$K(q)=-K_0/(q^2+\mu^2) \qquad (6.5)$$

with K_0 given by (4.42). It is clear that both kernels, (6.1) and (6.5), provide practically the same result as concerns the Meissner-Ochsenfeld effect in the case $\mu\lesssim\lambda_\infty^{-1}$ (λ_∞: penetration depth for $\mu^{-1}\to\infty$), because then the Fourier components of current, roughly speaking, contribute or do not contribute to this effect in both kernels according as the wave number q is larger or smaller than μ. As Pippard's experiment belongs to this case, his experimental results are well explained if we assume an effective range of interaction force, d, of the order of the mean free path. According to this consideration, we are led to conclude that the mean free path of an electron in the metal determines the effective range of the interaction causing superconductivity. This conclusion seems to be in favour of the second of the alternative interpretations of the interaction force mentioned at the beginning of this section, though not decisively. Comparing the two forms of kernel, (6.1) and (6.5), we should remark that, as mentioned above, the latter allows a simpler physical interpretation than the former. Since these kernels differ in detailed penetration law of the field, especially for a small mean free path, it is hoped to decide, by suitable experimental arrangements, which is the better form of the two.*

There is another interesting result to be expected from the assumption of (4.1) or (6.2) and to be correlated to experiment. Before discussing this, it is advantageous to give a brief account of the problem of the superconducting transition. (A detailed account of this topic will be given in Part II.) It can be shown that the M-O effect due to electron-electron interaction is suppressed by the disturbing effect of the electron-phonon interaction as the temperature increases. The superconducting-normal transition is considered to occur when the temperature becomes so high that the electron-phonon interaction makes the electron-electron interaction causing superconductivity completely ineffective. According to this consideration the interaction of the form (4.1) or (6.2) is supposed to be effective only in the superconducting state and ineffective in the normal. Since the above-mentioned interaction tempts the Pauli paramagnetism to decrease, we expect the smaller Pauli susceptibility in the superconducting than in the normal state. In order to check this prediction, it is most advantageous to use the data on the conduction-electron spin resonance, if available. Unfortunately, this type of resonance has not yet been found experimentally for any superconducting element. Recent observation of the Knight shift in mercury due to Reif$^{12)}$, however, provides some information of this subject. According to Townes *et al*$^{13)}$. the Knight shift in a simple metal should be proportional to the product of the Pauli spin susceptibility, χ_p, and the average probability density at the nucleus of conduction electrons on the Fermi surface, $\langle|\psi_F(0)|^2\rangle_{AV}$. In the experiment of Reif, a decrease of the shift was observed from 2.4% in the normal state to 1.5% in the superconducting state at 1.45°K. It is felt that one can hardly expect such a large change in $\langle|\psi_F(0)|^2\rangle_{AV}$ between the normal and superconducting states that accounts for the observed decrease in the Knight shift. On the other hand, if one assumes an electron-electron interaction of the form (4.1) or (6.2), it is not unlikely to expect such a large decrease of χ_p. In this connection it is interesting to quote the note of Dresdon$^{14)}$, which states that, if the electronic wave function differs considerably between the normol and superconducting states, the lifetime of positrons should be different between these states. Recent experiments$^{15),16)}$ revealed that, within the limits of experimental error, no such difference is observed. Independent determination by means of experiment either of χ_p or of $\langle|\psi_F(0)|^2\rangle_{AV}$ in superconductors is highly desirable.

---

* Note added on March 8, 1957. Quite recently this problem has fully been discussed by Schafroth and Blatt (Nuovo Cimento **4** (1956) 786). For the details of the penetration laws expected from both kernels readers are referred to this work.

Finally we should note that we have not discussed the convergence problem of our perturbation treatment which is of course open to discussion.

Appendix

In Table II, the explicit values of matrix elements $(\boldsymbol{k}'s'|\boldsymbol{k}''s'')$, $(\boldsymbol{k}'s'|\sigma_\mu|\boldsymbol{k}''s'')$ and $(\boldsymbol{k}'s'|\alpha_\mu|\boldsymbol{k}''s'')$ are listed for $\boldsymbol{k}'=\boldsymbol{k}-\frac{1}{2}\boldsymbol{q}$ and $\boldsymbol{k}''=\boldsymbol{k}+\frac{1}{2}\boldsymbol{q}$. For convenience, they are decomposed into two parts, one being an even function of $\boldsymbol{k}$ and the other its odd function. The former is quoted by a (+) symbol and the latter by a (−) symbol. The matrix elements connecting two negative-energy states are omitted, for they do not appear in the text.

The following abbreviations are used:

$$\left.\begin{aligned}
K(\boldsymbol{k},\boldsymbol{q})&=\frac{c\hbar}{2\mathcal{E}_{k'}^{1/2}\mathcal{E}_{k''}^{1/2}}\left\{\frac{(mc^2+\mathcal{E}_{k''})^{1/2}}{(mc^2+\mathcal{E}_{k'})^{1/2}}+\frac{(mc^2+\mathcal{E}_{k'})^{1/2}}{(mc^2+\mathcal{E}_{k''})^{1/2}}\right\},\\
L(\boldsymbol{k},\boldsymbol{q})&=\frac{c\hbar}{2\mathcal{E}_{k'}^{1/2}\mathcal{E}_{k''}^{1/2}}\left\{\frac{(mc^2+\mathcal{E}_{k''})^{1/2}}{(mc^2+\mathcal{E}_{k'})^{1/2}}-\frac{(mc^2+\mathcal{E}_{k'})^{1/2}}{(mc^2+\mathcal{E}_{k''})^{1/2}}\right\},\\
M(\boldsymbol{k},\boldsymbol{q})&=\frac{(mc^2+\mathcal{E}_{k'})^{1/2}(mc^2+\mathcal{E}_{k''})^{1/2}}{2\mathcal{E}_{k'}^{1/2}\mathcal{E}_{k''}^{1/2}},\\
N(\boldsymbol{k},\boldsymbol{q})&=\frac{c^2\hbar^2}{\mathcal{E}_{k'}^{1/2}\mathcal{E}_{k''}^{1/2}(mc^2+\mathcal{E}_{k'})^{1/2}(mc^2+\mathcal{E}_{k''})^{1/2}}.
\end{aligned}\right\}\quad\text{(A.1)}$$

It should be noted that $K(\boldsymbol{k},\boldsymbol{q})$, $M(\boldsymbol{k},\boldsymbol{q})$ and $N(\boldsymbol{k},\boldsymbol{q})$ are even functions of $\boldsymbol{k}$ and $\boldsymbol{q}$ while $L(\boldsymbol{k},\boldsymbol{q})$ is an odd function of each.

All the matrix elements in the table are correct for small $\boldsymbol{q}$ to the second order of q_μ when the following approximations are used:

$$\left.\begin{aligned}
K(\boldsymbol{k},\boldsymbol{q})&=K_k+\varDelta_K; && K_k=c\hbar/\mathcal{E}_k\,, \quad \varDelta_K=-K_k(\hbar^2q^2/8m^2c^2)\,,\\
L(\boldsymbol{k},\boldsymbol{q})&=L_k\boldsymbol{k}\cdot\boldsymbol{q}; && L_k=c^3\hbar^3/2\mathcal{E}_k^2(mc^2+\mathcal{E}_k)\,,\\
M(\boldsymbol{k},\boldsymbol{q})&=M_k+\varDelta_M; && M_k=(mc^2+\mathcal{E}_k)/2\mathcal{E}_k\,, \varDelta_M=-M_k(\hbar^2q^2/16m^2c^2)\,,\\
N(\boldsymbol{k},\boldsymbol{q})&=N_k+\varDelta_N; && N_k=c^2\hbar^2/\mathcal{E}_k(mc^2+\mathcal{E}_k)\,, \quad \varDelta_N=-N_k(3\hbar^2q^2/3m^2c^2)\,.
\end{aligned}\right\}\quad\text{(A.2)}$$

Table II.

s', s''		$(\boldsymbol{k}'s'\|\boldsymbol{k}''s'')_+$, $(\boldsymbol{k}'s'\|\sigma_\mu\|\boldsymbol{k}''s'')_+$ or $(\boldsymbol{k}'s'\|\alpha_\mu\|\boldsymbol{k}''s'')_+$	$(\boldsymbol{k}'s'\|\boldsymbol{k}''s'')_-$, $(\boldsymbol{k}'s'\|\sigma_\mu\|\boldsymbol{k}''s'')_-$ or $(\boldsymbol{k}'s'\|\alpha_\mu\|\boldsymbol{k}''s'')_-$
1, 1 2, 2	1	$M(\boldsymbol{k},\boldsymbol{q})+\frac{1}{2}N(\boldsymbol{k},\boldsymbol{q})\{k^2-(q^2/4)\}$	$\pm\frac{1}{2}iN(\boldsymbol{k},\boldsymbol{q})(k_xq_y-k_yq_x)$
	σ_x	$\pm N(\boldsymbol{k},\boldsymbol{q})\{k_zk_x-(q_zq_x/4)\}$	$\frac{1}{2}iN(\boldsymbol{k},\boldsymbol{q})(k_zq_y-k_yq_z)$
	σ_y	$\pm N(\boldsymbol{k},\boldsymbol{q})\{k_zk_y-(q_zq_y/4)\}$	$\frac{1}{2}iN(\boldsymbol{k},\boldsymbol{q})(k_xq_z-k_zq_x)$
	σ_z	$\pm M(\boldsymbol{k},\boldsymbol{q})\pm N(\boldsymbol{k},\boldsymbol{q})\{k_z^2-\frac{1}{2}k^2-(q_z^2/4)+(q^2/8)\}$	$\frac{1}{2}iN(\boldsymbol{k},\boldsymbol{q})(k_yq_x-k_xq_y)$
	α_x	$\pm\frac{1}{2}iK(\boldsymbol{k},\boldsymbol{q})q_y\mp iL(\boldsymbol{k},\boldsymbol{q})k_y$	$K(\boldsymbol{k}.\ \boldsymbol{q})k_x-\frac{1}{2}L(\boldsymbol{k},\boldsymbol{q})q_x$
	α_y	$\mp\frac{1}{2}iK(\boldsymbol{k},\boldsymbol{q})q_x\pm iL(\boldsymbol{k},\boldsymbol{q})k_x$	$K(\boldsymbol{k},\boldsymbol{q})k_y-\frac{1}{2}L(\boldsymbol{k},\boldsymbol{q})q_y$
	α_z	0	$K(\boldsymbol{k},\boldsymbol{q})k_z-\frac{1}{2}L(\boldsymbol{k},\boldsymbol{q})q_z$
1, 2 2, 1	1	0	$\pm\frac{1}{2}N(\boldsymbol{k},\boldsymbol{q})(k_zq_x-k_xq_z)$ $-\frac{1}{2}iN(\boldsymbol{k},\boldsymbol{q})(k_zq_y-k_yq_z)$
	σ_x	$M(\boldsymbol{k},\boldsymbol{q})+N(\boldsymbol{k},\boldsymbol{q})\{k_x^2-\frac{1}{2}k^2-(q_x^2/4)+(q^2/8)\}$ $\mp iN(\boldsymbol{k},\boldsymbol{q})\{k_xk_y-(q_xq_y/4)\}$	0
	σ_y	$\mp iM(\boldsymbol{k},\boldsymbol{q})\mp iN(\boldsymbol{k},\boldsymbol{q})\{k_y^2-\frac{1}{2}k^2-(q_y^2/4)+(q^2/8)\}$ $+N(\boldsymbol{k},\boldsymbol{q})\{k_xk_y-(q_xq_y/4)\}$	0
	σ_z	$N(\boldsymbol{k},\boldsymbol{q})\{k_zk_x-(q_zq_x/4)\}\mp iN(\boldsymbol{k},\boldsymbol{q})\{k_zk_y-(q_zq_y/4)\}$	0
	α_x	$\mp\frac{1}{2}K(\boldsymbol{k},\boldsymbol{q})q_z\pm L(\boldsymbol{k},\boldsymbol{q})k_z$	0
	α_y	$\frac{1}{2}iK(\boldsymbol{k},\boldsymbol{q})q_z-iL(\boldsymbol{k},\boldsymbol{q})k_z$	0
	α_z	$\pm\{\frac{1}{2}K(\boldsymbol{k},\boldsymbol{q})q_x-L(\boldsymbol{k},\boldsymbol{q})k_x\}-i\{\frac{1}{2}K(\boldsymbol{k},\boldsymbol{q})q_y-L(\boldsymbol{k},\boldsymbol{q})k_y\}$	0

Table II. (continued)

s', s''		$(\boldsymbol{k}'s'\vert\boldsymbol{k}''s'')_+$, $(\boldsymbol{k}'s'\vert\sigma_\mu\vert\boldsymbol{k}''s'')_+$ or $(\boldsymbol{k}'s'\vert\alpha_\mu\vert\boldsymbol{k}''s'')_+$	$(\boldsymbol{k}'s'\vert\boldsymbol{k}''s'')_-$, $(\boldsymbol{k}'s'\vert\sigma_\mu\vert\boldsymbol{k}''s'')_-$ or $(\boldsymbol{k}'s'\vert\alpha_\mu\vert\boldsymbol{k}''s'')_-$
1, 3 2, 4	1	$\mp\frac{1}{2}K(\boldsymbol{k},\,\boldsymbol{q})q_z\pm L(\boldsymbol{k},\,\boldsymbol{q})k_z$	0
	σ_x	$-\frac{1}{2}K(\boldsymbol{k},\,\boldsymbol{q})q_x+L(\boldsymbol{k},\,\boldsymbol{q})k_x$	$\mp iK(\boldsymbol{k},\,\boldsymbol{q})k_y\pm\frac{1}{2}iL(\boldsymbol{k},\,\boldsymbol{q})q_y$
	σ_y	$-\frac{1}{2}K(\boldsymbol{k},\,\boldsymbol{q})q_y+L(\boldsymbol{k},\,\boldsymbol{q})k_y$	$\pm iK(\boldsymbol{k},\,\boldsymbol{q})k_x\mp\frac{1}{2}iL(\boldsymbol{k},\,\boldsymbol{q})q_x$
	σ_z	$-\frac{1}{2}K(\boldsymbol{k},\,\boldsymbol{q})q_z+L(\boldsymbol{k},\,\boldsymbol{q})k_z$	0
	α_x	$\mp N(\boldsymbol{k},\,\boldsymbol{q})\{k_zk_x-(q_zq_x/4)\}$	$\frac{1}{2}iN(\boldsymbol{k},\,\boldsymbol{q})(k_yq_x-k_zq_y)$
	α_y	$\mp N(\boldsymbol{k},\,\boldsymbol{q})\{k_zk_y-(q_zq_y/4)\}$	$\frac{1}{2}iN(\boldsymbol{k},\,\boldsymbol{q})(k_xq_z-k_zq_x)$
	α_z	$\pm M(\boldsymbol{k},\,\boldsymbol{q})\pm N(\boldsymbol{k},\,\boldsymbol{q})\{\frac{1}{2}k^2-k_z^2-(q^2/8)\}$	$\frac{1}{2}iN(\boldsymbol{k},\,\boldsymbol{q})(k_yq_x-k_xq_y)$
3, 1 4, 2	1	$\pm\frac{1}{2}K(\boldsymbol{k},\,\boldsymbol{q})q_z\mp L(\boldsymbol{k},\,\boldsymbol{q})k_z$	0
	σ_x	$\frac{1}{2}K(\boldsymbol{k},\,\boldsymbol{q})q_x-L(\boldsymbol{k},\,\boldsymbol{q})k_x$	$\pm iK(\boldsymbol{k},\,\boldsymbol{q})k_y\mp\frac{1}{2}iL(\boldsymbol{k},\,\boldsymbol{q})q_y$
	σ_y	$\frac{1}{2}K(\boldsymbol{k},\,\boldsymbol{q})q_y-L(\boldsymbol{k},\,\boldsymbol{q})k_y$	$\mp iK(\boldsymbol{k},\,\boldsymbol{q})k_x\pm\frac{1}{2}iL(\boldsymbol{k},\,\boldsymbol{q})q_x$
	σ_z	$\frac{1}{2}K(\boldsymbol{k},\,\boldsymbol{q})q_z-L(\boldsymbol{k},\,\boldsymbol{q})k_z$	0
	α_x	$\mp N(\boldsymbol{k},\,\boldsymbol{q})\{k_zk_x-(q_zq_x/4)\}$	$\frac{1}{2}iN(\boldsymbol{k},\,\boldsymbol{q})(k_yq_z-k_zq_y)$
	α_y	$\mp N(\boldsymbol{k},\,\boldsymbol{q})\{k_zk_y-(q_zq_y/4)\}$	$\frac{1}{2}iN(\boldsymbol{k},\,\boldsymbol{q})(k_xq_z-k_zq_x)$
	α_z	$\pm M(\boldsymbol{k},\,\boldsymbol{q})\pm N(\boldsymbol{k},\,\boldsymbol{q})\{\frac{1}{2}k^2-k_z^2-(q^2/8)\}$	$\frac{1}{2}iN(\boldsymbol{k},\,\boldsymbol{q})(k_yq_x-k_xq_y)$
1, 4 2, 3	1	$-\{\frac{1}{2}K(\boldsymbol{k},\,\boldsymbol{q})q_x-L(\boldsymbol{k},\,\boldsymbol{q})k_x\}\pm i\{\frac{1}{2}K(\boldsymbol{k},\,\boldsymbol{q})q_y-L(\boldsymbol{k},\,\boldsymbol{q})k_y\}$	0
	σ_x	$\mp\frac{1}{2}L(\boldsymbol{k},\,\boldsymbol{q})q_z$	$\pm K(\boldsymbol{k},\,\boldsymbol{q})k_z$
	σ_y	$\frac{1}{2}iL(\boldsymbol{k},\,\boldsymbol{q})q_z$	$-iK(\boldsymbol{k},\,\boldsymbol{q})k_z$
	σ_z	$\pm\frac{1}{2}L(\boldsymbol{k},\,\boldsymbol{q})q_x-\frac{1}{2}iL(\boldsymbol{k},\,\boldsymbol{q})q_y$	$\mp K(\boldsymbol{k},\,\boldsymbol{q})k_x+iK(\boldsymbol{k},\,\boldsymbol{q})k_y$
	α_x	$M(\boldsymbol{k},\,\boldsymbol{q})+N(\boldsymbol{k},\,\boldsymbol{q})\{\frac{1}{2}k^2-k_x^2+(q_x^2/4)-(q^2/8)\}$ $\pm iN(\boldsymbol{k},\,\boldsymbol{q})\{k_xk_y-(q_xq_y/4)\}$	0
	α_y	$\mp iM(\boldsymbol{k},\,\boldsymbol{q})\mp iN(\boldsymbol{k},\,\boldsymbol{q})\{\frac{1}{2}k^2-k_y^2+(q_y^2/4)-(q^2/8)\}$ $-N(\boldsymbol{k},\,\boldsymbol{q})\{k_xk_y-(q_xq_y/4)\}$	0
	α_z	$-N(\boldsymbol{k},\,\boldsymbol{q})\{k_zk_x-(q_zq_x/4)\}\pm iN(\boldsymbol{k},\,\boldsymbol{q})\{k_zk_y-(q_zq_y/4)\}$	0
4, 1 3, 2	1	$\{\frac{1}{2}K(\boldsymbol{k},\,\boldsymbol{q})q_x-L(\boldsymbol{k},\,\boldsymbol{q})k_x\}\pm i(\frac{1}{2}K(\boldsymbol{k},\,\boldsymbol{q})q_y-L(\boldsymbol{k},\,\boldsymbol{q})k_y\}$	0
	σ_x	$\mp\frac{1}{2}L(\boldsymbol{k},\,\boldsymbol{q})q_z$	$\pm K(\boldsymbol{k},\,\boldsymbol{q})k_z$
	σ_y	$-\frac{1}{2}iL(\boldsymbol{k},\,\boldsymbol{q})q_z$	$iK(\boldsymbol{k},\,\boldsymbol{q})k_z$
	σ_z	$\pm\frac{1}{2}L(\boldsymbol{k},\,\boldsymbol{q})q_x+\frac{1}{2}iL(\boldsymbol{k},\,\boldsymbol{q})q_y$	$\mp K(\boldsymbol{k},\,\boldsymbol{q})k_x-iK(\boldsymbol{k},\,\boldsymbol{q})k_y$
	α_x	$M(\boldsymbol{k},\,\boldsymbol{q})+N(\boldsymbol{k},\,\boldsymbol{q})\{\frac{1}{2}k^2-k_x^2+(q_x^2/4)-(q^2/8)\}$ $\mp iN(\boldsymbol{k},\,\boldsymbol{q})\{k_xk_y-(q_xq_y/4)\}$	0
	α_y	$\pm iM(\boldsymbol{k},\,\boldsymbol{q})\pm iN(\boldsymbol{k},\,\boldsymbol{q})\{\frac{1}{2}k^2-k_y^2+(q_y^2/4)-(q^2/8)\}$ $-N(\boldsymbol{k},\,\boldsymbol{q})\{k_xk_y-(q_xq_y/4)\}$	0
	α_z	$-N(\boldsymbol{k},\,\boldsymbol{q})\{k_zk_x-(q_zq_x/4)\}\mp iN(\boldsymbol{k},\,\boldsymbol{q})\{k_zk_y-(q_zq_y/4)\}$	0

In the text, use is frequently made of the relations

$$L_k=\frac{1}{2}K_kN_k;\qquad M_k=1-\frac{1}{2}N_kk^2\,. \tag{A.3}$$

Note that K_k, L_k, M_k and N_k are all even functions of $\boldsymbol{k}$ and independent of $\boldsymbol{q}$. The correction terms Δ_K, Δ_M and Δ_N in (A.2) can be omitted when we want to calculate the matrix elements to the first order of q_μ.

When double signs (± or ∓) are used, the upper (or lower) sign always belongs to the upper (or lower) pair of s', s'' in the left column of the table.

References

1) H. Fröhlich: Phys. Rev. **79** (1950) 845; Proc. Roy. Soc. (London) **A215** (1952) 291.
2) J. Bardeen: Phys. Rev. **80** (1950) 567.
3) H. Fröhlich: Proc. Roy. Soc. (London) **A63** (1950) 778.
4) M. R. Schafroth: Helv. Phys. Acta **24** (1951) 645.
5) M. R. Schafroth: Nuovo Cimento **9** (1952) 291.
6) M. R. Schafroth: Phys. Rev. **100** (1955) 463.
7) M. Born and H. S. Green: Proc. Roy. Soc. (London) **A191** (1947) 168.
8) Nakajima: Advances in Phys. **4** (1955) 363.
9) G. Breit: Phys. Rev. **34** (1929) 553; **53** (1938) 153.
10) A. B. Pippard: Proc. Roy. Soc. (London) **A216** (1953) 547.
11) M. R. Schafroth and J. M. Blatt: Phys. Rev. **100** (1955) 1221.
12) F. Reif: Phys. Rev. **102** (1956) 1417.
13) C. H. Townes, C. Herring and W. D. Knight: Phys. Rev. **77** (1950) 852.
14) M. Dresden: Phys. Rev. **93** (1954) 1413.
15) B. Green and L. Madansky: Phys. Rev. **102** (1956) 1014.
16) S. M. Shafroth and J. A. Marcus: Phys. Rev. **103** (1956) 585.

JOURNAL OF THE PHYSICAL SOCIETY OF JAPAN Vol. 12, No. 6, JUNE, 1957

Diffuse Scattering of X-rays by a Point-Imperfection in Diamond Lattice

By Sigeo YOMOSA and Takeo NAGAMIYA

Department of Physics, Osaka University

(Received February 12, 1957)

The temperature independent diffuse scattering of X-ray by a diamond lattice, in which a few carbon atoms are missing or have been replaced by foreign atoms of valency four is investigated. By the method given by Matsubara the intensity of diffuse scattering is calculated in terms of the force constants which are related to changes in bond length and of bond angle. The diffuse patterns observed by Lonsdale and Smith in natural diamonds are of streak or spike type but ours are of lemniscate type. Our patterns may be observed in radiation damaged diamond crystals.

§ 1. Introduction

The object of this paper is to investigate theoretically the diffuse scattering of X-rays by a diamond lattice in which a few carbon atoms are missing or have been replaced by foreign atoms of valency four (Si, for example). Natural diamonds may or may not contain defects of such a kind, but a recent radiation damage experiment1) and its interpretation2) show an evidence of the creation of vacancies (as well as other kinks of defects) in the lattice. The original aim of the present paper was to explain the well-known temperature-independent diffuse scattering of X-rays observed by Lonsdale and Smith3) and recently by Hoerni and Wooster4) in natural diamonds of type I. This type is distinguished from type II by the existence of this diffuse scattering, as well as of certain infrared and ultra-violet absorption, and the absence of mosaic structure. The results of our calculation were, however, unfavourable, and this deterred the present authors from publishing the calculation, though the work was announced in 1952 in a paper by Matsubara5). Recently Frank6) successfully explained the diffuse scattering in diamonds of type I assuming segregated Si atoms on (100) planes. Formerly Olmer7) was also able to explain it assuming a suitable Fourier decomposition of the distortion which might exist in diamonds of type I. We have, however, some hope in testing our theory with the use of radiation damaged crystals, though we have so far no such data*.

We confine ourselves to point type defect and assume that the atomic displacements around the foreign atom or the vacancy have cubic symmetry. The method used in the present paper is based on that expounded by Matsubara[6] He sets up the equation of equilibrium determining the atomic displacements around the defect and, by constructing their Fourier transforms, finds a set of equations to be satisfied by the scattering amplitudes. This method enables one to find the intensity of diffuse scattering in terms of the force constants between the forign and normal atoms and those among normal atoms.

§ 2. Deformation around a Foreign Atom or Vacancy

When a carbon atom in a diamond crystal is replaced by a foreign atom of valency four, the nearest neighbouring four carbon atoms will be acted upon by radial forces and will be radially displaced. We shall denote these forces by $\gamma \boldsymbol{r}_1$, $\gamma \boldsymbol{r}_2$, $\gamma \boldsymbol{r}_3$ and $\gamma \boldsymbol{r}_4$, where $\boldsymbol{r}_i$'s are the vectors joining each atom to its neighbours in the normal lattice and γ a constant. We assume that the elastic force constant related with changes in bond angles, including the angle in (foreign atom)-(carbon)-(carbon) bonds, to be the same as that in the normal lattice. These simplifications will not seriously affect the result for the diffuse scattering, since the latter may arise mainly from a certain spread region of deformation around the foreign atom. In the case of a vacancy, the four unpaired electrons left in it will probably form the state of the highest multiplicity[2] and the same situation will be realized with a different value of γ.

We shall denote by d the atomic distance in the normal lattice and by a the lattice constant $(a=4d/\sqrt{3})$. Dividing the normal lattice into two interpenetrating face-centred cubic lattice, A and B, of lattice constant a, the lattice points are given by

$$A: \quad \boldsymbol{R}_l=l_1\boldsymbol{a}_1+l_2\boldsymbol{a}_2+l_3\boldsymbol{a}_3 \qquad (l_1+l_2+l_3=\text{even})$$

$$B: \quad \boldsymbol{R}_m'=m_1\boldsymbol{a}_1+m_2\boldsymbol{a}_2+m_3\boldsymbol{a}_3+\boldsymbol{r}_1 \qquad (m_1+m_2+m_3=\text{even})$$

where

$$\boldsymbol{a}_1=(a/2, 0, 0), \quad \boldsymbol{a}_2=(0, a/2, 0), \quad \boldsymbol{a}_3=(0, 0, a/2),$$

and $r_1=(a/4, a/4, a/4)$.

Let the displacement of the atom at $\boldsymbol{R}_l$ be denoted by $\boldsymbol{u}_l$ and that at $\boldsymbol{R}_m'$ by $\boldsymbol{u}_m'$. The change of length of the bond between, say, $\boldsymbol{R}_l'$ and $\boldsymbol{R}_l$ is $\boldsymbol{r}_1\cdot(\boldsymbol{u}_l'-\boldsymbol{u}_l)/d$, and the corresponding increase in potential energy will be written as

$$\frac{1}{2}k_1[\boldsymbol{r}_1\cdot(\boldsymbol{u}_l'-\boldsymbol{u}_l)/d]^2 . \tag{1}$$

The change of the bond angle between, say, $\boldsymbol{R}_l'-\boldsymbol{R}_l$ and $\boldsymbol{R}_m'-\boldsymbol{R}_l$ with $\boldsymbol{R}_m'=\boldsymbol{R}_l+\boldsymbol{r}_2$ is

$$\begin{aligned}\varDelta\vartheta=-\frac{1}{d^2\sin\vartheta_0}&[(\boldsymbol{r}_2-\boldsymbol{r}_1\cos\vartheta_0)\cdot(\boldsymbol{u}_l'-\boldsymbol{u}_l)\\ &+(\boldsymbol{r}_1-\boldsymbol{r}_2\cos\vartheta_0)\cdot(\boldsymbol{u}_m'-\boldsymbol{u}_l)] ,\end{aligned} \tag{2}$$

where $\cos\vartheta_0=-1/3$ and $\sin\vartheta_0=2\sqrt{2}/3$. The corresponding increase in potential energy will be written as

$$\frac{1}{2}k_2(d\varDelta\vartheta)^2 . \tag{3}$$

The total potential energy will be assumed to be the sum of the potential energies of type (1) and type (3). For a moment we drop those terms which represent the interactions between next-nearest neighbours, but later (in § 4) we shall take them into account. Then the potential energy can be written[8]

$$\begin{aligned}W=&\frac{1}{2}\sum_l\boldsymbol{u}_l\cdot\varPhi_0\cdot\boldsymbol{u}_l+\frac{1}{2}\sum_m\boldsymbol{u}_m'\cdot\varPhi_0\cdot\boldsymbol{u}_m'\\ &+\frac{1}{2}\sum_l\sum_{i=1}^{4}\boldsymbol{u}_l\cdot\varPhi_i\cdot\boldsymbol{u}_{li}'+\frac{1}{2}\sum_m\sum_{i=1}^{4}\boldsymbol{u}'\cdot\varPhi_i\cdot\boldsymbol{u}_{mi} ,\end{aligned} \tag{4}$$

where $\varPhi_0$, $\varPhi_1$, $\varPhi_2$, $\varPhi_3$, $\varPhi_4$ are symmetric diadics defined by

$$\begin{aligned}\varPhi_0=&\frac{k_1}{d^2}\sum_{i=1}^{4}\boldsymbol{r}_i\boldsymbol{r}_i+\frac{k_2}{d^2}\frac{(1-\cos\theta_0)^2}{\sin^2\theta_0}\sum_{i=1}^{i}\sum_{k(\neq i)}\\ &\times(\boldsymbol{r}_i+\boldsymbol{r}_k)(\boldsymbol{r}_i+\boldsymbol{r}_k) ,\end{aligned} \tag{5}$$

$$\begin{aligned}\varPhi_i=&-\frac{k_1}{d^2}\boldsymbol{r}_i\boldsymbol{r}_i-\frac{k_2}{d^2}\frac{2(1-\cos\theta_0)}{\sin^2\theta_0}\sum_{k(\neq i)}\\ &\times(\boldsymbol{r}_k+\boldsymbol{r}_i)(\boldsymbol{r}_k-\boldsymbol{r}_i\cos\theta_0) ,\\ &(i=1, 2, 3, 4;\ k=1, 2, 3, 4)\end{aligned} \tag{6}$$

$$\varPhi_0+\sum_{i=1}^{4}\varPhi_i=0 . \tag{7}$$

In (4), $\boldsymbol{u}_{li}'$ is the displacement of the atom at $\boldsymbol{R}_m'=\boldsymbol{R}_l+\boldsymbol{r}_i$, and $\boldsymbol{u}_{mi}$ that of the atom at $\boldsymbol{R}_l=\boldsymbol{R}_m'-\boldsymbol{r}_i$. If the atoms at $\boldsymbol{R}_l$ and $\boldsymbol{R}_m'$ are acted upon by external forces $\boldsymbol{F}_l$ and $\boldsymbol{F}_m'$, respectively, the equilibrium conditions are

---

* H. Kanzaki recently made calculations similar to ours (private communication).

$$\left.\begin{aligned}\boldsymbol{\Phi}_0\cdot\boldsymbol{u}_l+\sum_i\boldsymbol{\Phi}\cdot\boldsymbol{u}_{li}{}'&=\boldsymbol{F}_l\ ,\\ \boldsymbol{\Phi}_0\cdot\boldsymbol{u}_m{}'+\sum_i\boldsymbol{\Phi}_i\cdot\boldsymbol{u}_{mi}&=\boldsymbol{F}_m{}'.\end{aligned}\right\}\qquad(8)$$

We now suppose that a foreign atom or a vacancy is at the origin. Then, external forces act only upon those atoms which directly surround the origin, i. e.,

$$\begin{aligned}&\boldsymbol{F}_{000}{}'=\gamma\boldsymbol{r}_1\ , &&\boldsymbol{F}_{-1-10}{}'=\gamma\boldsymbol{r}_2\ ,\\ &\boldsymbol{F}_{-10-1}{}'=\gamma\boldsymbol{r}_3\ , &&\boldsymbol{F}_{0-1-1}{}'=\gamma\boldsymbol{r}_4\ ,\\ &\text{other}\quad \boldsymbol{F}_m{}'=0\ , &&\text{all}\quad \boldsymbol{F}_l=0\ .\end{aligned}\qquad(9)$$

(8) and (9) determine the deformation around the defect.

We define the Fourier transforms of the displacements by

$$\left.\begin{aligned}\boldsymbol{S}(\boldsymbol{b})&=\sum_l\boldsymbol{u}_l\exp\left[2\pi i\boldsymbol{b}\cdot\boldsymbol{R}_l\right]\ ,\\ \boldsymbol{S}'(\boldsymbol{b})&=\sum_m\boldsymbol{u}_m{}'\exp\left[2\pi i\boldsymbol{b}\cdot\boldsymbol{R}_m{}'\right]\ ,\end{aligned}\right\}\qquad(10)$$

where $\boldsymbol{b}$ is an arbitrary vector. From (8) we find

$$\begin{aligned}&\boldsymbol{\Phi}_0\cdot\boldsymbol{S}(\boldsymbol{b})+\Big(\sum_i\boldsymbol{\Phi}_i\exp\left[-2\pi i\boldsymbol{b}\cdot\boldsymbol{r}_i\right]\Big)\cdot\boldsymbol{S}'(\boldsymbol{b})\\ &\qquad=\sum_l\boldsymbol{F}_l\exp\left[2\pi i\boldsymbol{b}\cdot\boldsymbol{R}_l\right]\ ,\\ &\boldsymbol{\Phi}_0\cdot\boldsymbol{S}'(\boldsymbol{b})+\Big(\sum_i\boldsymbol{\Phi}_i\exp\left[2\pi i\boldsymbol{b}\cdot\boldsymbol{r}_i\right]\Big)\cdot\boldsymbol{S}(\boldsymbol{b})\\ &\qquad=\sum_m\boldsymbol{F}_m{}'\exp\left[2\pi i\boldsymbol{b}\cdot\boldsymbol{R}_m{}'\right]\ .\end{aligned}\qquad(11)$$

The right hand side of the first equation is zero and that of the second equation is

$$\gamma\sum_i\boldsymbol{r}_i\exp\left[2\pi i\boldsymbol{b}\cdot\boldsymbol{r}_i\right]\ .\qquad(12)$$

To solve (11), we write, after Begbie[9], Born[8] and Smith[10], the matrices of $\boldsymbol{\Phi}_0$ and $\boldsymbol{\Phi}_i(i=1, 2, 3, 4)$ explicitly as follows:

$$\boldsymbol{\Phi}_0=4\alpha\begin{pmatrix}1&0&0\\0&1&0\\0&0&1\end{pmatrix},\qquad \boldsymbol{\Phi}_1=-\begin{pmatrix}\alpha&\beta&\beta\\\beta&\alpha&\beta\\\beta&\beta&\alpha\end{pmatrix},$$

$$\boldsymbol{\Phi}_3=-\begin{pmatrix}\alpha&\beta&-\beta\\\beta&\alpha&-\beta\\-\beta&-\beta&\alpha\end{pmatrix},\qquad \boldsymbol{\Phi}_3=-\begin{pmatrix}\alpha&-\beta&\beta\\-\beta&\alpha&-\beta\\\beta&-\beta&\alpha\end{pmatrix},$$

$$\boldsymbol{\Phi}_4=-\begin{pmatrix}\alpha&-\beta&-\beta\\-\beta&\alpha&\beta\\-\beta&\beta&\alpha\end{pmatrix},\qquad(13)$$

where

$$\alpha=\frac{1}{3}(k_1+8\,k_2)\ ,\quad \beta=\frac{1}{3}(k_1-4k_2)\ .\qquad(14)$$

(13) and (14) can be derived easily by observing that

$$\begin{aligned}&\boldsymbol{r}_1=\frac{1}{4}(a, a, a), &&\boldsymbol{r}_2=\frac{1}{4}(\bar{a}, \bar{a}, a)\ ,\\ &\boldsymbol{r}_3=\frac{1}{4}(\bar{a}, a, \bar{a},\ ), &&\boldsymbol{r}_4=\frac{1}{4}(a, \bar{a}, \bar{a});\\ &\boldsymbol{r}_1+\boldsymbol{r}_2+\boldsymbol{r}_3+\boldsymbol{r}_4=0\ ,\end{aligned}$$

and that therefore $\boldsymbol{\Phi}$'s are simplified to

$$\begin{aligned}\boldsymbol{\Phi}_0&=\frac{k_1+8k_2}{d^2}\sum_{i=1}^{4}\boldsymbol{r}_i\boldsymbol{r}_i\ ,\\ \boldsymbol{\Phi}_i&=-\frac{(k_1-4k_2)}{d^2}\boldsymbol{r}_i\boldsymbol{r}_i-\frac{3k^2}{d^2}\sum_{k=1}^{4}\boldsymbol{r}_k\boldsymbol{r}_k\ .\end{aligned}$$

Then (11), with (12), can be written

$$\begin{pmatrix}S_x\\S_y\\S_z\end{pmatrix}-\begin{pmatrix}\vartheta_0{}^*&\vartheta_3{}^*&\vartheta_2{}^*\\\vartheta_3{}^*&\vartheta_0{}^*&\vartheta_1{}^*\\\vartheta_2{}^*&\vartheta_1{}^*&\vartheta_0{}^*\end{pmatrix}\begin{pmatrix}S_x{}'\\S_y{}'\\S_z{}'\end{pmatrix}=0\ ,$$

$$\begin{pmatrix}S_x{}'\\S_y{}'\\S_z{}'\end{pmatrix}-\begin{pmatrix}\vartheta_0&\vartheta_3&\vartheta_2\\\vartheta_3&\vartheta_0&\vartheta_1\\\vartheta_2&\vartheta_1&\vartheta_0\end{pmatrix}\begin{pmatrix}S_x\\S_y\\S_z\end{pmatrix}+\gamma'\begin{pmatrix}\vartheta_1\\\vartheta_2\\\vartheta_3\end{pmatrix}=0\ ,\qquad(15)$$

where

$$\begin{aligned}\vartheta_0&=\frac{1}{4}\sum_{i=1}^{4}\exp\left[2\pi i\boldsymbol{b}\cdot\boldsymbol{r}_i\right]\ ,\\ \vartheta_1&=\frac{\beta}{4\alpha}\big(\exp\left[2\pi i\boldsymbol{b}\cdot\boldsymbol{r}_1\right]-\exp\left[2\pi i\boldsymbol{b}\cdot\boldsymbol{r}_2\right]\\ &\qquad-\exp\left[2\pi i\boldsymbol{b}\cdot\boldsymbol{r}_3\right]+\exp\left[2\pi i\boldsymbol{b}\cdot\boldsymbol{r}_4\right]\big)\ ,\\ \vartheta_2&=\frac{\beta}{4\alpha}\big(\exp\left[2\pi i\boldsymbol{b}\cdot\boldsymbol{r}_1\right]-\exp\left[2\pi i\boldsymbol{b}\cdot\boldsymbol{r}_2\right]\\ &\qquad+\exp\left[2\pi i\boldsymbol{b}\cdot\boldsymbol{r}_3\right]-\exp\left[2\pi i\boldsymbol{b}\cdot\boldsymbol{r}_4\right]\big)\ ,\\ \vartheta_3&=\frac{\beta}{4\alpha}\big(\exp\left[2\pi i\boldsymbol{b}\cdot\boldsymbol{r}_1\right]+\exp\left[2\pi i\boldsymbol{b}\cdot\boldsymbol{r}_2\right]\\ &\qquad-\exp\left[2\pi i\boldsymbol{b}\cdot\boldsymbol{r}_3\right]-\exp\left[2\pi i\boldsymbol{b}\cdot\boldsymbol{r}_4\right]\big)\ ,\end{aligned}\qquad(16)$$

and

$$\gamma'=-\gamma a/4\beta\ .\qquad(17)$$

ϑ^*'s are the conjugate complexes of ϑ's.

Eliminating S from (15), we have

$$\begin{pmatrix}A-1&D&E\\D^*&B-1&F\\E^*&F^*&C-1\end{pmatrix}\begin{pmatrix}S_x{}'\\S_y{}'\\S_z{}'\end{pmatrix}=\gamma'\begin{pmatrix}\vartheta_1\\\vartheta_2\\\vartheta_3\end{pmatrix},\qquad(18)$$

where

$$\begin{aligned}A&=|\vartheta_0|^2+|\vartheta_2|^2+|\vartheta_3|^2\ ,\\ B&=|\vartheta_0|^2+|\vartheta_1|^2+|\vartheta_3|^2\ ,\\ C&=|\vartheta_0|^2+|\vartheta_1|^2+|\vartheta_2|^2\ ,\\ D&=\vartheta_0\vartheta_3{}^*+\vartheta_3\vartheta_0{}^*+\vartheta_2\vartheta_1{}^*;\\ E&=\vartheta_0\vartheta_2{}^*+\vartheta_3\vartheta_1{}^*+\vartheta_2\vartheta_0{}^*\ ,\\ F&=\vartheta_3\vartheta_2{}^*+\vartheta_0\vartheta_1{}^*+\vartheta_1\vartheta_0{}^*\ .\end{aligned}\qquad(19)$$

Solving (18) we get $\boldsymbol{S}'$, and putting it into the first equation of (15) we find $\boldsymbol{S}$. Further calculations will be given in the next section.

§ 3. Intensity of Diffuse Scattering

The intensity of the scattered X-ray with wave vector $\boldsymbol{k}$ when incident X-ray with wave vector $\boldsymbol{k}_0$ is passing through the diamond crystal is given by

$$I=I_e|f(\boldsymbol{b})\sum_l{}' \exp[2\pi i\boldsymbol{b}(\boldsymbol{R}_l+\boldsymbol{u}_l)]$$
$$+f(\boldsymbol{b})\sum_m \exp[2\pi i\boldsymbol{b}(\boldsymbol{R}_m'+\boldsymbol{u}_m')+f_0(\boldsymbol{b})|^2, \tag{20}$$

where $\boldsymbol{b}=\boldsymbol{k}-\boldsymbol{k}_0$, $f(\boldsymbol{b})$ the atom form factor of carbon (of a tetrahedral form when speaking rigorously), $f_0(\boldsymbol{b})$ that of the foreign atom at the origin of the coordinates, $\sum_l{}'$ indicating the sum with the exception of $\boldsymbol{R}_l=0$, and I_e the Thomson factor, i. e. the intensity of scattering by one electron.

Assuming $\boldsymbol{b}\cdot\boldsymbol{u}_l$ and $\boldsymbol{b}\cdot\boldsymbol{u}_m'$ to be very small compared with 1, (20) can be written, after expanding the exponential functions in power series and retaining the first order terms, as

$$I=I_e|G_0(\boldsymbol{b})+G_1(\boldsymbol{b})|^2\,, \tag{21}$$

where

$$G_0(\boldsymbol{b})=f(\boldsymbol{b})(\sum_l \exp[2\pi i\boldsymbol{b}\cdot\boldsymbol{R}_l]$$
$$+\sum_m \exp[2\pi i\boldsymbol{b}\cdot\boldsymbol{R}_m'])\,,$$
$$G_1(\boldsymbol{b})=2\pi i f(\boldsymbol{b})[(\boldsymbol{b}\cdot\boldsymbol{S})+(\boldsymbol{b}\cdot\boldsymbol{S}')]$$
$$+[f_0(\boldsymbol{b})-f(\boldsymbol{b})]\,. \tag{22}$$

$G_0(\boldsymbol{b})$ gives the Laue scattering and vanishes everywhere except at those $\boldsymbol{b}$ which coincide with reciprocal lattice vectors. Apart from the latter, I is given by

$$I=I_e|G_1(\boldsymbol{b})|^2\,. \tag{23}$$

We may further neglect $f_0(\boldsymbol{b})-f(\boldsymbol{b})$ in (22), since the diffuse scattering would arise from a certain spread deformed region around the defect. The intensity of diffuse scattering is given by

$$I_{\text{diffuse}}(\boldsymbol{b})=I_e|f(\boldsymbol{b})|^2|2\pi\boldsymbol{b}\cdot(\boldsymbol{S}+\boldsymbol{S}')|^2\,. \tag{24}$$

The quantity $2\pi\boldsymbol{b}\cdot(\boldsymbol{S}+\boldsymbol{S}')$ can be calculated from the formulas given in § 2.

In the following we shall confine ourselves to a simple case of $b_x=b_y$, and moreover only to those $\boldsymbol{b}$ which are in the neighbourhood of reciprocal lattice vectors with $b_x=b_y$; it can be shown generally that the diffuse scattering is intense in the neighbourhood of the Laue scattering vectors. We put

$$\xi=\pi ab_x\,,\quad \zeta=\pi ab_z\,, \tag{25}$$

and have

$$\vartheta_0=\frac{1}{2}(e^{i\zeta/2}\cos\xi+e^{-i\zeta/2})\,,$$
$$\vartheta_1=\frac{i\beta}{2\alpha}e^{i\zeta/2}\sin\xi\,,$$
$$\vartheta_2=\vartheta_1\,,$$
$$\vartheta_3=\frac{\beta}{2\alpha}(e^{i\zeta/2}\cos\xi-e^{-i\zeta/2}); \tag{26}$$

$$A=B=\frac{1}{4}(1+2\cos\zeta\cos\xi+\cos^2\xi)$$
$$+\frac{\beta^2}{2\alpha^2}(1-\cos\zeta\cos\xi)\,,$$
$$C=\frac{1}{4}(1+2\cos\zeta\cos\xi+\cos^2\xi)$$
$$+\frac{\beta^2}{2\alpha^2}\sin^2\xi\,,$$
$$D=-\frac{\beta}{2\alpha}\left(1-\frac{\beta}{2\alpha}\right)\sin^2\xi\,,$$
$$E=F=-\frac{\beta}{2\alpha}\left(1-\frac{\beta}{2\alpha}\right)\sin\xi\sin\zeta$$
$$-\frac{i\beta^2}{4\alpha^2}\sin\xi(\cos\xi-\cos\zeta)\,. \tag{27}$$

Solving (18) and (15) for $\boldsymbol{S}$ and $\boldsymbol{S}'$, we have

$$2\pi\boldsymbol{b}\cdot(\boldsymbol{S}+\boldsymbol{S}')=\frac{2\gamma'}{a}\frac{1}{(C-1)(A+D-1)-2|E^2|}$$
$$[2\xi\{[(C-1)\vartheta_1-E\vartheta_3](\vartheta_0{}^*+\vartheta_3{}^*+1)$$
$$+[(A+D-1)\vartheta_3-2E^*\vartheta_1]\vartheta_1{}^*\}$$
$$+\zeta\{[(C-1)\vartheta-{}_1E\vartheta_3]2\vartheta_1{}^*$$
$$+[(A+D-1)\vartheta_3-2E^*\vartheta_1](\vartheta_0{}^*+1)\}] \tag{28}$$

We expand this expression in the neighbourhood of reciprocal lattice vectors in powers of $(\xi-\xi_0)$ and $(\zeta-\zeta_0)$, where $(\xi_0/\pi, \xi_0/\pi, \zeta_0/\pi)$ represent a reciprocal lattice vector, or indices of the corresponding reflection. Further, we put

$$\xi-\xi_0=\frac{1}{\sqrt{2}}\rho\sin\varphi,\ \ \zeta-\zeta_0=\rho\cos\varphi\,. \tag{29}$$

If the expansion of (28) in ascending powers of ρ around a given reciprocal lattice point begins with a constant term or a term proportional to ρ, then we have practically no observable diffuse pattern around the corresponding Laue spot. If, on the other hand, the expansion begins with a term proportional to ρ^{-1}, we have an intense diffuse pattern around the corresponding Laue spot which fades away with increasing distance from the Laue spot. In the latter case, the structure of the diffuse pattern is mainly determined by the φ-dependence of that term. The infinite rise of the intensity for $\rho\to 0$ in this case results from our mathematical simplification of replacing $\exp(2\pi i\boldsymbol{b}\cdot\boldsymbol{u}_l)$ and $\exp(2\pi i\boldsymbol{b}\cdot\boldsymbol{u}_m')$ of (20) by $1+2\pi i\boldsymbol{b}\cdot\boldsymbol{u}_l$ and $1+2\pi i\boldsymbol{u}_m'$, respectively, and thus it should not be taken seriously.

The general expansion formula of (28) in powers ρ may not need be reproduced here. We summarize below our results obtained for several indices of reflection of lower degrees.

For reciprocal lattice points 000,001,002,112, where there are no normal Laue spots by extiction law, the expansion begins with a constant term (a function of φ). Therefore, there is no observable diffuse spot.

For 110, where we have also no normal Laue spot, the expansion begins with a term proportional to ρ. Therefore, we have also no observable diffuse spot.

For 111. 113, 220, where we have normal Laue spots and where anomalous patterns were observed in natural diamond of type I by Lonsdale and Smith[3)], and Hoerni and Wooster[4)], the expansion of (28) begins with a term proportional to ρ^{-1}. This term is as follows:

$$111:\quad -(1+i)\frac{4\pi\gamma'\beta'}{a}\times\frac{\sqrt{2}(1-\mu+2\mu\sin^2\varphi)\sin\varphi+(1+\mu\cos^2\varphi)\cos\varphi}{\Phi(\mu,\varphi)}\times\frac{1}{\rho},$$

$$113:\quad (1-i)\frac{4\pi\gamma'\beta'}{a}\times\frac{\sqrt{2}(1-\mu+2\mu\sin^2\varphi)\sin\varphi+3(1+\mu\cos^2\varphi)\cos\varphi}{\Phi(\mu,\varphi)}\times\frac{1}{\rho},$$

$$220:\quad -i\,\frac{16\sqrt{2}\,\pi\gamma'\beta'}{a}\,\frac{(1-\mu+2\mu\sin^2\varphi)\sin\varphi}{\Phi(\mu,\varphi)}\,\frac{1}{\rho}, \tag{30}$$

where

$$\Phi(\mu,\varphi)=1+\mu+\mu(1-4\mu)\sin^2\varphi+\mu^2(4-\mu)\sin^4\varphi,$$
$$\beta'=\beta/\alpha\,. \tag{31}$$

§ 4. Improved Treatment

We have so far neglected the forces between next-nearest neighbours. Considering them, we have to add to (4) the following terms:

$$\frac{1}{2}\sum_l\sum_{i,j=1}^{4}{}'\,\boldsymbol{u}_l\cdot\Phi_{ij}\cdot\boldsymbol{u}_{lij}+\frac{1}{2}\sum_m\sum_{i,j=1}^{4}{}'\,\boldsymbol{u}_m'\cdot\Phi_{ij}\cdot\boldsymbol{u}_{mij}'\,. \tag{4)'$$

Here $\sum'$ indicates summation with $i\neq j$; Φ_{ij} are symmetric diadics defined by

$$\Phi_{ij}=\frac{k_2}{d^2}\frac{1}{\sin^2\vartheta_0}(\boldsymbol{r}_j-\boldsymbol{r}_i\cos\vartheta_0)(\boldsymbol{r}_i-\boldsymbol{r}_j\cos\vartheta_0)\,. \tag{6)'$$

In (4)', $\boldsymbol{u}_{lij}$ is the displacement of the atom at $\boldsymbol{R}_{l'}=\boldsymbol{R}_l+\boldsymbol{r}_i-\boldsymbol{r}_j$, and $\boldsymbol{u}_{mij}$ that of the atom at $\boldsymbol{R}_{m'}'=\boldsymbol{R}_m'+\boldsymbol{r}_i-\boldsymbol{r}_j$. Then (7), (8) and (11) are replaced by

$$\Phi_0+\sum_{i=1}^{4}\Phi_i+\sum_{i,j=1}^{4}{}'\,\Phi_{ij}=0\,, \tag{7)'$$

$$\left.\begin{aligned}\Phi_0\cdot\boldsymbol{u}_l+\sum_i\Phi_i\cdot\boldsymbol{u}_{li}'+\sum_{i,j}{}'\Phi_{ij}\cdot\boldsymbol{u}_{lij}&=\boldsymbol{F}_l\,,\\ \Phi_0\cdot\boldsymbol{u}_m'+\sum_i\Phi_i\cdot\boldsymbol{u}_{mi}+\sum_{i,j}{}'\Phi_{ij}\boldsymbol{u}_{mij}'&=\boldsymbol{F}_m'\end{aligned}\right\} \tag{8)'$$

$$\begin{aligned}&(\Phi_0+\sum_{i,j}{}'\,\Phi_{ij}\exp[-2\pi i\boldsymbol{b}(\boldsymbol{r}_i-\boldsymbol{r}_j)])\cdot\boldsymbol{S}(\boldsymbol{b})\\&\quad+(\sum_i\Phi_i\exp[-2\pi i\boldsymbol{b}\cdot\boldsymbol{r}_i])\cdot\boldsymbol{S}'(\boldsymbol{b})\\&\quad=\sum_l\boldsymbol{F}_l\exp[2\pi i\boldsymbol{b}\cdot\boldsymbol{R}_l]\,,\\&(\Phi_0+\sum_{i,j}{}'\,\Phi_{ij}\exp[-2\pi i\boldsymbol{b}(\boldsymbol{r}_i-\boldsymbol{r}_j)])\cdot\boldsymbol{S}'(\boldsymbol{b})\\&\quad+(\sum_i\Phi_i\exp[2\pi i\boldsymbol{b}\cdot\boldsymbol{r}_i])\cdot\boldsymbol{S}(\boldsymbol{b})\\&\quad=\sum_m\boldsymbol{F}_m'\exp[2\pi i\boldsymbol{b}\cdot\boldsymbol{R}_m']\,.\end{aligned} \tag{11)'$$

To solve (11)' we write after (Begbie, Born and) Smith[10)] the matrices Φ_{ij} explicitly as follows:

$$\Phi_{12}=\Phi_{21}=-\begin{pmatrix}\mu&\nu&0\\\nu&\mu&0\\0&0&\lambda\end{pmatrix},\quad\Phi_{13}=\Phi_{31}=-\begin{pmatrix}\mu&0&\nu\\0&\lambda&0\\\nu&0&\mu\end{pmatrix},$$
$$\Phi_{14}=\Phi_{41}=-\begin{pmatrix}\lambda&0&0\\0&\mu&\nu\\0&\nu&\mu\end{pmatrix},\quad\Phi_{23}=\Phi_{32}=-\begin{pmatrix}\lambda&0&0\\0&\mu&-\nu\\0&-\nu&\mu\end{pmatrix},$$
$$\Phi_{24}=\Phi_{42}=-\begin{pmatrix}\mu&0&-\nu\\0&\lambda&0\\-\nu&0&\mu\end{pmatrix},\quad\Phi_{34}=\Phi_{43}=-\begin{pmatrix}\mu&-\nu&0\\-\nu&\mu&0\\0&0&\lambda\end{pmatrix}, \tag{13)'$$

where

$$\lambda=-2/3\,k_2\,,\quad\mu=\nu=1/6\,k_2\,. \tag{14)'$$

(14)' can be easily derived from (6)'. From

(7)′, Φ_0 is

$$\Phi_0=4(\alpha+\lambda+2\mu)\begin{pmatrix}1&0&0\\0&1&0\\0&0&1\end{pmatrix}.$$

Then we have

$$\begin{pmatrix}a&f&e\\f&b&d\\e&d&c\end{pmatrix}\begin{pmatrix}S_x\\S_y\\S_z\end{pmatrix}-\begin{pmatrix}\vartheta_0{}^*&\vartheta_3{}^*&\vartheta_2{}^*\\\vartheta_3{}^*&\vartheta_0{}^*&\vartheta_1{}^*\\\vartheta_2{}^*&\vartheta_1{}^*&\vartheta_0{}^*\end{pmatrix}\begin{pmatrix}S_x'\\S_y'\\S_z'\end{pmatrix}=0\,,$$

$$\begin{pmatrix}a&f&e\\f&b&d\\e&d&c\end{pmatrix}\begin{pmatrix}S_x'\\S_y'\\S_y'\end{pmatrix}-\begin{pmatrix}\vartheta_0&\vartheta_3&\vartheta_2\\\vartheta_3&\vartheta_0&\vartheta_1\\\vartheta_2&\vartheta_1&\vartheta_0\end{pmatrix}\begin{pmatrix}S_x\\S_y\\S_z\end{pmatrix}$$

$$+\gamma'\begin{pmatrix}\vartheta_1\\\vartheta_2\\\vartheta_3\end{pmatrix}=0\,, \tag{15$'$}$$

where

$$a=\left(1+\frac{\lambda}{\alpha}+\frac{2\mu}{\alpha}\right)-\frac{\lambda}{a}\cos\pi ab_y\cos\pi ab_z$$
$$-\frac{\mu}{\alpha}\cos\pi ab_x(\cos\pi ab_y+\cos\pi ab_z)\,,$$
$$b=\left(1+\frac{\lambda}{\alpha}+\frac{2\mu}{\alpha}\right)-\frac{\lambda}{\alpha}\cos\pi ab_z\cos\pi ab_x$$
$$-\frac{\mu}{\alpha}\cos\pi ab_y(\cos\pi ab_z+\cos\pi ab_x)\,,$$
$$c=\left(1+\frac{\lambda}{\alpha}+\frac{2\mu}{\alpha}\right)-\frac{\lambda}{\alpha}\cos\pi ab_x\cos\pi ab_y\,,$$
$$-\frac{\mu}{\alpha}\cos\pi ab_z(\cos\pi ab_x+\cos\pi ab_y)\,,$$
$$d=-(\nu/\alpha)\sin\pi ab_y\sin\pi ab_z\,,$$
$$e=-(\nu/\alpha)\sin\pi ab_z\sin\pi ab_x\,,$$
$$f=-(\nu/\alpha)\sin\pi ab_x\sin\pi ab_y\,. \tag{16$'$}$$

Solving (15)′, we get S and S'. Calculations similar to those before show that the expressions corresponding to (30) are as follows and that other things are qualitatively the same:

$$111:\quad -(1+i)\frac{4\pi\gamma'\beta'}{a}\frac{g(\varphi)}{f(\varphi)}\frac{1}{\rho}\,,$$
$$113:\quad (1-i)\frac{4\pi\gamma'\beta'}{a}\frac{h(\varphi)}{f(\varphi)}\frac{1}{\rho}\,,$$
$$220:\quad i\,\frac{16\sqrt{2}\,\pi\gamma'\beta'}{a}\frac{l(\varphi)}{f(\varphi)}\frac{1}{\rho}\,,$$

where

$$\begin{aligned}f(\varphi)=&(1-\beta'^2-4\mu')(1-4\lambda'-2\mu')\\&+\{(\beta'-2\lambda'+2\mu')(1-4\lambda'-2\mu')\\&-\beta'^2(5-4\beta'-4\mu')\}\sin^2\varphi\\&+\beta'^2(4-5\beta'+\beta'^2+2\lambda'-2\mu')\sin^4\varphi\,,\end{aligned}$$

$$\begin{aligned}g(\varphi)=&\sqrt{2}\{(1+\beta'^2-2\beta'-4\lambda')\\&-2(\beta'^2-\beta'-2\lambda'+2\mu')\sin^2\varphi\}\sin\varphi\\&+\{(1-\beta'-2\lambda'-2\mu')\\&-(\beta'^2-\beta'-2\lambda'+2\mu')\cos^2\varphi\}\cos\varphi\,,\end{aligned}$$

$$\begin{aligned}h(\varphi)=&\sqrt{2}\{(1+\beta'^2-2\beta'-4\lambda')\\&-2(\beta'^2-\beta'-\lambda'+2\mu')\sin^2\varphi\}\sin\varphi\\&+3\{(1-\beta'-2\lambda'-2\mu')\\&-(\beta'^2-\beta'-2\lambda'+2\mu')\cos^2\varphi\}\,,\end{aligned}$$

$$\begin{aligned}l(\varphi)=&\{(1+\beta'^2-2\beta'-4\lambda')\\&-2(\beta'^2-\beta'-2\lambda'+2\mu')\sin^2\varphi\}\sin\varphi\,,\end{aligned}$$

$$\lambda'=\lambda/\alpha\,,\quad \mu'=\mu/\alpha\,.$$

§ 5. Numerical Computation and Comparison with Experiment

(A) In the approximation of taking account of only the nearest neighbour interactions, the elastic constants are given in terms of α and β as

$$c_{11}=c_{22}=c_{33}=\alpha/a\,,$$
$$c_{12}=c_{13}=c_{23}=(2\beta-\alpha)/a\,,$$
$$c_{44}=c_{55}=c_{66}=\left(\alpha-\frac{\beta^2}{\alpha}\right)\Big/a. \tag{32}$$

Therefore, from (14), the approximate relations between the elastic constants and the force constants k_1 and k_2 are given by

$$c_{11}=\frac{1}{3a}(k_1+8k_2)\,,$$
$$c_{12}=\frac{1}{3a}(k_1-16k_2)\,,$$
$$c_{44}=\frac{8k}{a}\frac{k_1+2k_2}{k_1+8k_2}\,. \tag{33}$$

Determining the values of k_1 and k_2 from the experimental values[11] of c_{11} and c_{12},

$$c_{11}=9.5\times10^{12}\ \text{dyne/cm}^2\,,$$
$$c_{12}=3.9\times10^{12}\ \text{dyne/cm}^2\,, \tag{34}$$

we have

$$k_1=8.13\times10^5\ \text{dyne/cm}\,,$$
$$k_2=0.246\times10^5\ \text{dyne/cm}\,. \tag{35}$$

Using these values and calculating c_{44} from (33), we get

$$(c_{44})_{\text{cal}}=4.72\times10^{12}\ \text{dyne/cm}^2\,. \tag{36}$$

This nearly agrees with the experimental value[11] of $c_{44}=4.4\times10^{12}$ dyne/cm^2.

(B) When the next-neighbour interactions are taken into account, the elastic constants are, in terms of $\alpha, \beta, \lambda, \mu, \nu$,

$$c_{11}=(\alpha+8\mu)/a\,,$$

$$c_{12}=(2\beta-\alpha-4\lambda-4\mu+8\nu)/a\ ,$$

$$c_{44}=\left(\alpha-\frac{\beta^2}{\alpha}+4\lambda+4\mu\right)\Big/a\ .$$

The relations between these elastic constants and k_1 and k_2 are given by

$$c_{11}=(k_1+12\,k_2)/3a\ ,$$

$$c_{12}=(k_1-6\,k_2)/3a\ ,$$

$$c_{44}=\frac{1}{3a}\frac{18\,k_1k_2}{k_1+8\,k_1}\ . \tag{38}$$

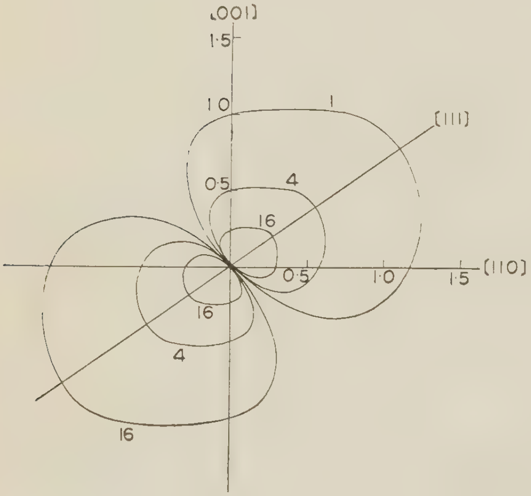

(a)

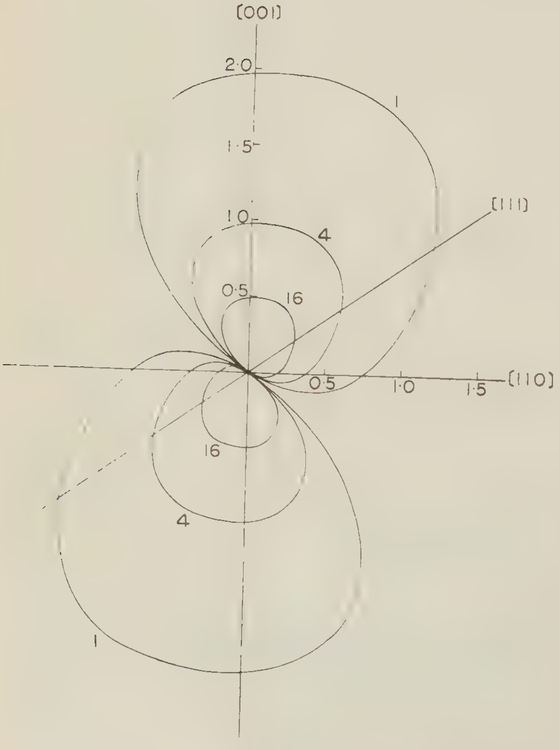

(b)

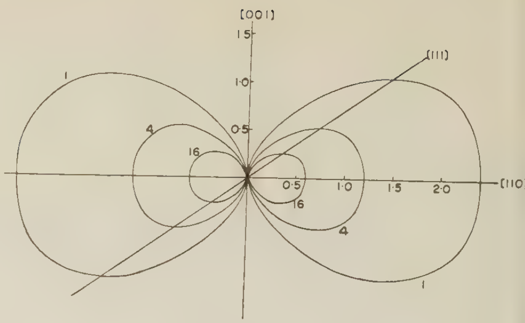

(c)

Fig. 1. The iso-diffusion curves calculated from the formula (30); (a) for 111, (b) for 113 and (c) for 220.

These coincide with the results given by Bhagavantam and Bhimasenachar. Determining the values of k_1 and k_2 from the experimental values of c_{11} and c_{12}, we get

$$k_1=6.16\times10^5\ \text{dyne/cm},$$

$$k_2=0.332\times10^5\ \text{dyne/cm}\ . \tag{39}$$

The value of c_{44} determined from (38) using these values is $(c_{44})_{\text{cal}}=3.92\times10^{12}\ \text{dyne/cm}^2$, which also nearly agrees with the experimental value of c_{44}. The value of parameter β' in (30) and (31) in the approximation (A) is, according to (35) and (14),

$$\beta'=\beta/\alpha=\frac{k_1-4k_2}{k_1+8k_2}=0.705\ ,$$

and the values of parameters $\beta',\lambda',\mu',\nu'$ in (30) and (31)′ of the approximation (B) are, according to (39), (14) and (14)′,

$$\beta'=\beta/\alpha=\frac{k_1-4k_2}{k_1+8k_2}=0.548\ ,$$

$$\lambda'=\lambda/\alpha=-\frac{2k_2}{k_1+8k_2}=-0.075\ ,$$

$$\mu'=\nu'=\mu/\alpha=\frac{k_2}{2(k_1+8\,k_2)}=0.019\ .$$

In making numerical computation of the scattering intensity, we take $2\pi|\gamma'|/a=1$. This corresponds to an elongation or a contraction of a $C-C$ bond ($C-C=1.54$Å) of the order of 10 % when one of the C atoms is replaced by a Si atom or a vacancy. In drawing the iso-diffusion curves, we take as the unit of intensity the following:

$$J=2I_ef_1^2\left(\frac{2\pi\gamma'\beta'}{a}\right)^2=\begin{cases}6.73\,I_e & \text{for (A)}\ ,\\ 4.07\,I_e & \text{for (B)}\ .\end{cases}$$

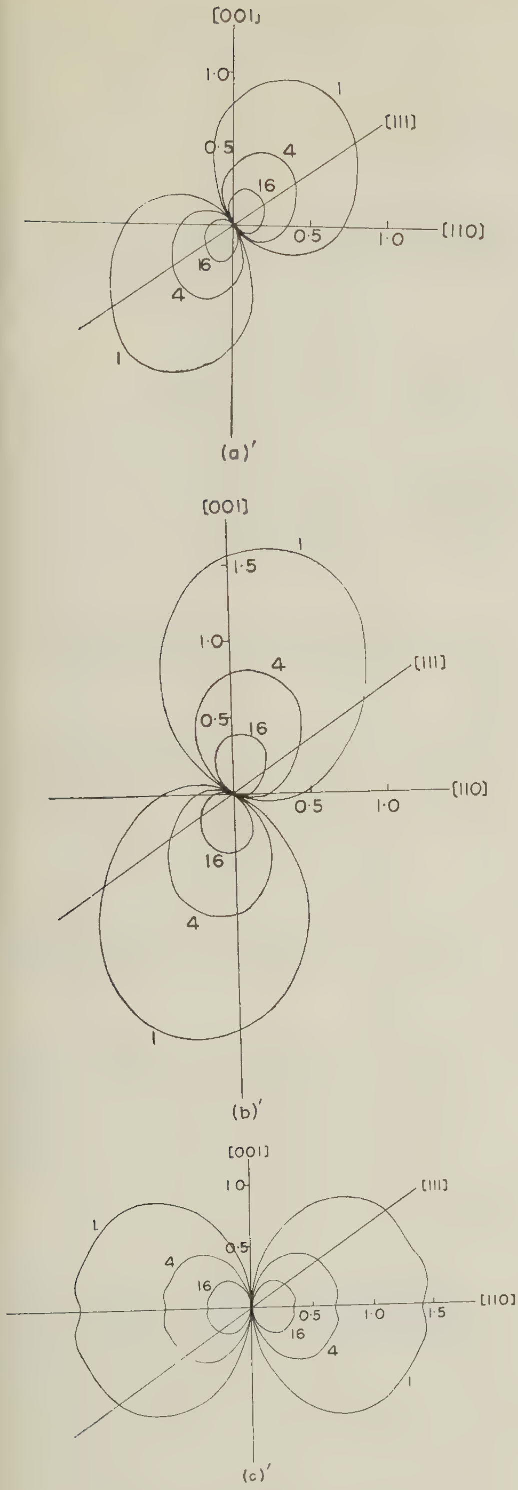

Fig. 2. The iso-diffusion curves calculated from the formula (30)′; (a)′ for 111, (b)′ for 113 and (c)′ for 220.

Accordingly, in (B) for example, the diffusion curves of intensity 1 around the reciprocal lattice points 111, 113 and 220 are given respectively as follows:

$$\rho_1=\left|\frac{g(\varphi)}{f(\varphi)}\right|, \quad \rho_3=\frac{f_3}{f_1}\left|\frac{h(\varphi)}{f(\varphi)}\right|=0.654\left|\frac{h(\varphi)}{f(\varphi)}\right|,$$

$$\rho_2=\frac{4f_2}{f_1}\left|\frac{l(\varphi)}{f(\varphi)}\right|=2.92\left|\frac{l(\varphi)}{f(\varphi)}\right|,$$

where f_1, f_2, and f_3 are the atomic structure factor at the reciprocal lattice points 111, 113, 220, respectively, and $f_1=2.60$, $f_3=1.70$ and $f_2=1.90$[12]. In Fig. 1 and Fig. 2 we show the iso-diffusion curves in the plane $\xi=\eta$ around these reciprocal lattice points. We see that the both approximations give qualitatively the same results.

The diffuse patterns observed by Lonsdale and Smith are as follows: at 111 six horns extend to the directions of the reciprocal axes, at 113 and 220 four horns extend to the directions [100] and [010] but [001] horns are missing, and the diffuse patterns are of streak or spike type (ours are of lemniscate type).

References

1) J. H. E. Griffiths, J. Owen and I. M. Ward: Defects in Crystalline Solids, Bristol Conference Report, London (1954) 81.
2) M. C. M. O'Brien and M. H. L. Price: ibid., 88.
3) K. Lonsdale and H. Smith: Nature **148** (1941) 112, 257.
4) J. A. Hoerni and W. A. Wooster: Acta Cryst. **8** (1955) 187.
5) T. Matsubara: J. Phys. Soc. Japan **7** (1952) 270.
6) F. C. Frank: Proc. Roy. Soc. A, **237** (1956) 168.
7) Ph. Olmer: Bull. Soc. franc. Miner. **72** (1949) 72.
8) G. H. Begbie and M. Born: Proc. Roy. Soc. **188** (1947) 179.
9) G. H. Begbie: Proc. Roy. Soc. **188** (1947) 189.
10) H. M. J. Smith: Phil. Trans. Roy. Soc. A, **241** (1948) 105.
11) S. Bhagavantam and J. Bhimasenachar: Proc. Roy. Soc. A, **187** (1946) 381.
12) R. W. James and G. W. Brindley: Phil. Mag. **12** (1931) 81.

JOURNAL OF THE PHYSICAL SOCIETY OF JAPAN Vol. 12, No. 6, JUNE, 1957

Effect of Inelastic Waves on Electron Diffraction

By Hide YOSHIOKA

Physical Institute, Nagoya University, Nagoya, Japan

(Received January 25, 1957)

The effect of inelastic scattering on electron diffraction by crystals is theoretically studied. It is proved that the effect of inelastic scattering gives rise to an additional complex term to Fourier coefficient of the inner potential. The imaginary part of the additional term explains qualitatively the observation that two components of a doubly refracted electron beam are subjected to different degrees of absorption (Honjo and Mihama, J. Phys. Soc. Japan **9** (1954) 184). The real part of the additional term gives a correction of about 6~7 % to the calculated value of mean inner potential at accelerating voltages of 30~40 kv. This explains the systematic difference between the mean inner potential experimentally obtained by electron diffraction and that calculated by the use of diamagnetic susceptibility (Miyake, Proc. Physico-Math. Soc. Japan **22** (1940) 666).

§ 1. Introduction

The high resolution method of electron diffraction revealed fine structures in Debye-Scherrer rings given by smoke particles of MgO and CdO, which particles show clear cut cubic shape in electron-microscope.[1),2),3)] The spot group due to a single crystallite appearing on a spotty diffraction ring is composed of a set of doublets. The doublet is caused by the double refraction effect which can be explained by the dynamical theory of electron diffraction.[4),5)] Honjo and Mihama[3)] observed that for a doublet the spot with larger deviation from the unrefracted position is always weaker than the other. This difference in intensity cannot be explained by the dynamical theory which assumes that the crystal is non-absorptive.

Honjo and Mihama[3)] explained this anomaly by the use of a complex periodic potential which was introduced by K. Molière[6)] as a phenomenological concept. In X-ray diffraction, the complex structure factor similar to the complex potential in electron diffraction could explain the anomalous intensity of the transmitted X-rays through the crystal at the setting of Bragg reflexion.[7),8),9),10)] This complex structure factor was established on the quantum-mechanical basis by G. Molière[11)], and can be calculated theoretically. On the other hand, the complex potential in electron diffraction has not yet been established theoretically.

In this paper, we derive the so-called complex potential from a quantum mechanical basis and estimate its numerical value. Our method is to take account of the effect of inelastic scattering on elastic scattering. It will be shown that this effect gives rise to an additional complex term to Fourier coefficients of the inner potential. The imaginary part of the additional term is due to the damping of incident and diffracted waves by inelastic scattering. The real part is due to virtual inelastic scattering process and may be interpreted as representing the dynamic polarization of the crystal induced by the incident electron.

§ 2. Effect of Inelastically Scattered Waves on Elastic Scattering

We consider the interaction of an incident electron with a crystal. The Schrödinger equation of our system is

$$\left(-\frac{\hbar^2}{2m}\nabla^2+H_c+H'\right)\Phi=E\Phi \tag{1}$$

where $-(\hbar^2/2m)\nabla^2$ is the kinetic energy of the electron, H_c the energy of the crystal and H' the interaction energy between the electron and the crystal. The interaction energy is given by

$$H'=\sum_j\frac{e^2}{|\boldsymbol{r}-\boldsymbol{r}_j|}-\sum_k\frac{Z_ke^2}{|\boldsymbol{r}-\boldsymbol{R}_k|}, \tag{2}$$

where $\boldsymbol{r}$ is the coordinate of the incident electron, $\boldsymbol{r}_j$ that of the jth electron of the crystal, $\boldsymbol{R}_k$ that of the kth nucleus with charge Z_ke in the crystal. The effect of thermal motion is neglected.

The wave function of our system Φ depends upon the coordinates $\boldsymbol{r}$ and $\boldsymbol{r}_j$. It can be expanded in the form

$$\Phi(\boldsymbol{r}, \boldsymbol{r}_1, \cdots, \boldsymbol{r}_N)=\varphi_n(\boldsymbol{r})a_n(\boldsymbol{r}_1, \cdots, \boldsymbol{r}_N)\ , \quad (3)$$

where a_n is the wave function representing the nth excited state of the crystal, satisfying the equation

$$H_c a_n = E_n a_n\ . \quad (4)$$

where E_n is energy of the nth state of the crystal. Function $\varphi_0(\boldsymbol{r})$ in (3) describes the elastic scattering, and $\varphi_n(\boldsymbol{r})$ the inelastic scattering which excites the crystal from the normal state to the nth state. Substituting (3) into (1), multiplying by a_n, integrating over $\boldsymbol{r}_j$'s, and then by the help of (4) we obtain

$$\nabla^2\varphi_0+\left(k_0^2+\frac{2m}{\hbar^2}H'_{00}\right)\varphi_0=\frac{2m}{\hbar^2}\sum_{m\neq0}H'_{0m}\varphi_m\ , \quad (5)$$

$$\nabla^2\varphi_n+\left(k_n^2-\frac{2m}{\hbar^2}H'_{nn}\right)\varphi_n=\frac{2m}{\hbar^2}\sum_{m\neq n}H'_{nm}\varphi_m\ , \quad (6)$$

where

$$k_n^2=(2m/\hbar^2)(E-E_n) \quad (7)$$

and

$$H'_{nm}=\int a_n^* H' a_m d\tau\ , \quad d\tau=d\boldsymbol{r}_1\cdots d\boldsymbol{r}_N\ . \quad (8)$$

The term on the right-hand side of (5) represents the effect of inelastic waves. In Bethe's theory of electron diffraction[4] this effect is neglected. On the contrary, in this paper Bethe's theory is modified by taking account of this term.

Terms $H'_{nm}\varphi_m$ $(m\neq0)$ in (6) give only the second order correction to Bethe's theory, because φ_n is small compared with φ_0 and $|2mH'_{nm}/\hbar^2|\ll k_n^2$. In our theory, these terms are neglected, thus (6) is reduced to

$$\nabla^2\varphi_n+k_n^2\varphi_n=(2m/\hbar^2)H'_{n0}\varphi_0\ . \quad (n\geq1)\ . \quad (9)$$

The equation has a solution representing an out-going wave

$$\varphi_n(\boldsymbol{r})=-\frac{m}{2\pi\hbar^2}\int\frac{\exp(ik_n|\boldsymbol{r}-\boldsymbol{r}'|)}{|\boldsymbol{r}-\boldsymbol{r}'|}H'_{n0}(\boldsymbol{r}')\varphi_0(\boldsymbol{r}')d\boldsymbol{r}'\ . \quad (10)$$

Substituting (10) into (5), we have

$$\nabla^2\varphi_0+\left(k_0^2-\frac{2m}{\hbar^2}H'_{00}(\boldsymbol{r})\right)\varphi_0+\frac{2m}{\hbar^2}\int A(\boldsymbol{r}, \boldsymbol{r}')\varphi_0(\boldsymbol{r}')d\boldsymbol{r}'=0 \quad (11)$$

where $A(\boldsymbol{r}, \boldsymbol{r}')$ is given by

$$A(\boldsymbol{r}, \boldsymbol{r}')=-\frac{m}{2\pi\hbar^2}\sum_{n\neq0}H'_{0n}(\boldsymbol{r})H'_{n0}(\boldsymbol{r}')\frac{\exp(ik_n|\boldsymbol{r}-\boldsymbol{r}'|)}{|\boldsymbol{r}-\boldsymbol{r}'|}\ . \quad (12)$$

The integral kernel $A(\boldsymbol{r}, \boldsymbol{r}')$ is considered to vanish for the values of $|\boldsymbol{r}-\boldsymbol{r}'|$ larger than a few interatomic distances*, and satisfies the periodic condition

$$A(\boldsymbol{r}, \boldsymbol{r}')=A(\boldsymbol{r}+\boldsymbol{a}, \boldsymbol{r}'+\boldsymbol{a})\ , \quad (13)$$

where $\boldsymbol{a}$ is the unit-cell vector of the lattice.

§ 3. Derivation of the Generalized Fundamental Equations

Inside the crystal, $H'_{00}(\boldsymbol{r})$ represents the periodic crystal potential and the integral over infinite domain in (11) can be restricted to over the crystal volume owing to the short range of $A(\boldsymbol{r}, \boldsymbol{r}')$. Then, it can be shown, using (13) and the periodicity of $H'_{00}(\boldsymbol{r})$, that $\varphi_0(\boldsymbol{r}+\boldsymbol{a})$ becomes a solution of (11) as well as $\varphi_0(\boldsymbol{r})$. This fact shows that the solution of (11) is given by a Bloch type function. Therefore, we can express the solution of (11) in the form

$$\varphi_0(\boldsymbol{r})=\sum_h\chi_h\exp(i\boldsymbol{K}_h\cdot\boldsymbol{r})\ , \quad (14)$$

where

$$\boldsymbol{K}_h=\boldsymbol{K}+2\pi\boldsymbol{h}\ ,$$

$\boldsymbol{h}$ being a reciprocal lattice vector. Expression

---

* When the crystal has a filled band electronic structure, $A(\boldsymbol{r}, \boldsymbol{r}')$ is easily transformed to

$$A(\boldsymbol{r}, \boldsymbol{r}')=-\frac{me^4}{2\pi\hbar^2}\frac{\exp(i\bar{k}|\boldsymbol{r}-\boldsymbol{r}'|)}{|\boldsymbol{r}-\boldsymbol{r}'|}\times\int_V\int_V|\sum\rho_l(\boldsymbol{r}_1, \boldsymbol{r}_2)|^2\left(\frac{1}{|\boldsymbol{r}-\boldsymbol{r}_1|}-\frac{1}{|\boldsymbol{r}-\boldsymbol{r}_2|}\right)\left(\frac{1}{|\boldsymbol{r}'-\boldsymbol{r}_1|}-\frac{1}{|\boldsymbol{r}'-\boldsymbol{r}_2|}\right)d\boldsymbol{r}_1d\boldsymbol{r}_2\ ,$$

where $\bar{k}$ is given by (38) and $\rho_l(\boldsymbol{r}, \boldsymbol{r}')$ is defined by (40) and the summation with respect to l is over all atoms in the crystal. Since $\rho_l(\boldsymbol{r}, \boldsymbol{r}')$ vanishes if $|\boldsymbol{r}-\boldsymbol{r}'|$ becomes larger than about an interatomic distance, $A(\boldsymbol{r}, \boldsymbol{r}')$ tends rapidly to vanish if $|\boldsymbol{r}-\boldsymbol{r}'|$ goes beyond about an interatomic distance. We exclude the case of metals where collective motion of valence electrons seems to nessecitate a special treatment.

(14) for φ_0 has the same form as that used by Bethe for describing the electron wave in the crystal. We expand the crystal potential $H'_{00}(\boldsymbol{r})$ in a Fourier series

$$H'_{00}(\boldsymbol{r})=\sum_h V_h \exp(i2\pi\boldsymbol{h}\cdot\boldsymbol{r}) . \tag{15}$$

Substituting (14) and (15) into (11), multiplying $\exp(-i\boldsymbol{K}_h\cdot\boldsymbol{r})$ and integrating over the whole volume, V, of the crystal, we obtain

$$\frac{\hbar^2}{2m}(\boldsymbol{K}_h{}^2-k_0{}^2)\chi_h+\sum_g V_{h-g}\chi_g+\sum_g C_{hg}\chi_g=0 , \tag{16}$$

where

$$C_{hg}=\frac{1}{V}\int_V\int_V A(\boldsymbol{r},\boldsymbol{r}')\exp(-i\boldsymbol{K}_h\cdot\boldsymbol{r}+i\boldsymbol{K}_g\cdot\boldsymbol{r}')d\boldsymbol{r}d\boldsymbol{r}' . \tag{17}$$

Equation (16) is the fundamental equation of the dynamical theory generalized by taking account of inelastic waves.

Green function in (10) is expressed in the integral form

$$\frac{1}{4\pi}\frac{\exp(ik_n|\boldsymbol{r}-\boldsymbol{r}'|)}{|\boldsymbol{r}-\boldsymbol{r}'|}=\frac{1}{(2\pi)^3}\int\frac{\exp[i\boldsymbol{K}'\cdot(\boldsymbol{r}-\boldsymbol{r}')]}{\boldsymbol{K}'^2-k_n{}^2}d\boldsymbol{K}' , \tag{18}$$

where the integration is over the whole $\boldsymbol{K}'$ space[18]. By the use of this form, the expression of C_{hg} turns out (Appendix I)

$$C_{hg}=C^r_{hg}+iC^i_{hg} . \tag{19}$$

Here, C^r_{hg} is the volume integral in K'-space

$$C^r_{hg}=-\frac{1}{V}\frac{m}{4\pi^3\hbar^2}\times\sum_{n\neq0}\iiint\frac{E_{0n}(\boldsymbol{K}_h-\boldsymbol{K}')E_{n0}(\boldsymbol{K}'-\boldsymbol{K}_g)}{\boldsymbol{K}'^2-k_n{}^2}d\tau(\boldsymbol{K}') , \tag{20}$$

taking the principal value with respect to the singularity at $|\boldsymbol{K}'|=k_n$. E_{0n} is defined by

$$E_{0n}(\boldsymbol{K}_h-\boldsymbol{K}')\equiv\int_V H'_{0n}(\boldsymbol{r})\exp[-i(\boldsymbol{K}_h-\boldsymbol{K}')\cdot\boldsymbol{r}]d\boldsymbol{r} , \tag{21}$$

and can be interpreted as the matrix element for inelastic scattering from the state $(\boldsymbol{K}_h, a_0)$ to the state $(\boldsymbol{K}', a_n)$. There holds the relation

$$E_{n0}(\boldsymbol{K}'-\boldsymbol{K}_h)=[E_{0n}(\boldsymbol{K}_h-\boldsymbol{K}')]^* . \tag{22}$$

Term C^i_{hg} is the surface integral

$$C^i_{hg}=-\frac{m}{4\pi^2\hbar^2V}\times\sum_{n\neq0}\iint\frac{E_{0n}(\boldsymbol{K}_h-\boldsymbol{K}')E_{n0}(\boldsymbol{K}'-\boldsymbol{K}_g)}{2k_n}d\sigma(\boldsymbol{K}') \tag{23}$$

where the integration is over the surface $|\boldsymbol{K}'|=k_n$.

We mention, here, that $|\boldsymbol{K}'|=k_n$ means the energy conservation in the transition $(\boldsymbol{K}_h, a_0)\to(\boldsymbol{K}', a_n)$ since, then, $E=E_n+\hbar^2\boldsymbol{K}'^2/(2m)$. Thus, we can interprete C^r_{hg} is due to virtual process of inelastic scattering, whereas C^i_{hg} is due to real process.

From (20), (22) and (23), it is evident that

$$\left.\begin{aligned}C^r_{hg}&=(C^r_{gh})^*\\ C^i_{hg}&=(C^i_{gh})^* .\end{aligned}\right\} \tag{24}$$

If the crystal has a center of symmetry, the wave function of the crystal $a_n(\boldsymbol{r}_1, \cdots, \boldsymbol{r}_N)$ can be chosen as a real function with a definite parity

$$a_n(\boldsymbol{r}_1, \cdots, \boldsymbol{r}_N)=\pm a_n(-\boldsymbol{r}_1, \cdots, -\boldsymbol{r}_N) .$$

Therefore, C^r_{hg} and C^i_{hg} are real, thus

$$\left.\begin{aligned}C^r_{hg}&=C^r_{gh}\\ C^i_{hg}&=C^i_{gh} .\end{aligned}\right\} \tag{25}$$

§ 4. Solution of the Generalized Fundamental Equation

(1) *No Bragg reflexion*

When no Bragg reflexion is excited in the crystal the generalized fundamental equation becomes simply

$$\frac{\hbar^2}{2m}(\boldsymbol{K}^2-k_0{}^2)\chi_0+V_0\chi_0+C_{00}\chi_0=0 .$$

Since

$$|\boldsymbol{K}|\sim k_0$$

we have

$$|\boldsymbol{K}|=k_0-(m/\hbar^2k_0)(V_0+C^r_{00}+iC^i_{00}) . \tag{26}$$

Vector $\boldsymbol{K}$ is determined by (26) and the tangential continuity of wave vector on the incident surface. For centrosymmetric crystals (26) indicates that inelastic waves result in the apparent increase of mean inner potential by C^r_{00} and the absorption of elastic wave with the absorption coefficient given by

$$\kappa=-\frac{2m}{\hbar^2k_0}C^i_{00} , \tag{27}$$

where the factor 2 is multiplied since the absorption coefficient is referred to intensity.

(2) *One Bragg reflexion*

When one Bragg reflexion of index $\boldsymbol{h}$ is excited, the generalized fundamental equations are reduced to

$$\left.\begin{aligned}&\left\{\frac{\hbar^2}{2m}(\boldsymbol{K}^2-k_0^2)+V_0+C_{00}\right\}\chi_0\\&\qquad\qquad+(V_{-h}+C_{0h})\chi_h=0\\&(V_h+C_{h0})\chi_0\\&\qquad+\left\{\frac{\hbar^2}{2m}(\boldsymbol{K}_h^2-k_0^2)+V_0+C_{hh}\right\}\chi_h=0\,.\end{aligned}\right\}\tag{28}$$

If we define resonance errors by

$$\left.\begin{aligned}\xi&=|\boldsymbol{K}|-k_0+\frac{m}{\hbar^2k_0}V_0\\\eta&=|\boldsymbol{K}_h|-k_0+\frac{m}{\hbar^2k_0}V_0\end{aligned}\right\}\tag{29}$$

and if we take into account

$$(\boldsymbol{K}^2-k_0^2)\sim 2k_0\{|\boldsymbol{K}|-k_0\}\,,$$

the equation of the dispersion surface is written as

$$\left(\xi+\frac{m}{\hbar^2k_0}C_{00}\right)\left(\eta+\frac{m}{\hbar^2k_0}C_{hh}\right)=\left(\frac{m}{\hbar^2k_0}\right)^2(V_h+C_{h0})(V_{-h}+C_{0h})\,.\tag{30}$$

If we neglect C_{00}, C_{hh} and C_{h0}, (30) is reduced to the dispersion surface in Bethe's approximation,

$$\xi^0\eta^0=\left(\frac{m}{\hbar^2k_0}\right)^2|V_h|^2\,.\tag{31}$$

It is convenient to determine the wave vector at first by Bethe's approximation, and then calculate the correction caused by C_{hg}. We consider the Laue case. The wave vectors in Bethe's approximation are determined by wave points Q_1 and Q_2 which are intersections of the dispersion surface and the normal $\boldsymbol{n}$ to the incident surface determinined by the tangential continuity of wave vectors (Fig. 1). We denote the wave vectors corresponding to Q_1 and Q_2 by $\boldsymbol{K}_1^0$ and $\boldsymbol{K}_2^0$ respectively, and their resonance errors by

$$\left.\begin{aligned}\xi_i^0&=|\boldsymbol{K}_i^0|-k_0+\frac{m}{\hbar^2k_0}V_0\\\eta_i^0&=|\boldsymbol{K}_{hi}^0|-k_0+\frac{m}{\hbar^2k_0}V_0\,.\quad(i=1,2)\end{aligned}\right\}\tag{32}$$

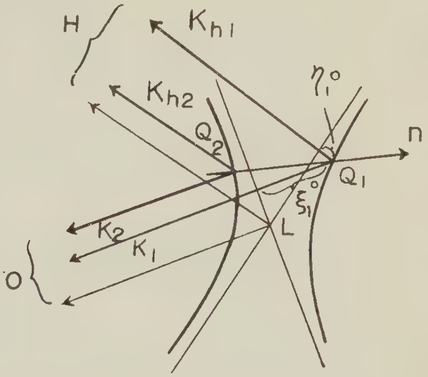

Fig. 1. Dispersion surface in Bethe's approximation.

Next, we consider the correction, $\Delta\boldsymbol{K}_i=\boldsymbol{K}_i-\boldsymbol{K}_i^0$, caused by C_{hg}. By the tangential continuity of the wave vector, correction $\Delta\boldsymbol{K}_i$ is in the direction of the normal $\boldsymbol{n}$, i.e. $\Delta\boldsymbol{K}_i=\varepsilon_i\boldsymbol{n}$. If we denote the angles between $\boldsymbol{n}$ and $\boldsymbol{K}_i^0$ by α_i, and $\boldsymbol{n}$ and $\boldsymbol{K}_{hi}^0$ by β_i, then

$$\left.\begin{aligned}\xi_i-\xi_i^0&=\varepsilon_i\cos\alpha_i\\\eta_i-\eta_i^0&=\varepsilon_i\cos\beta_i\,.\end{aligned}\right\}\tag{33}$$

Substituting (33) into (30), and neglecting higher orders of small quantities, we have

$$\varepsilon_i=\frac{-(m/\hbar^2k_0)(C_{00}\xi_i^0+C_{hh}\eta_i^0)+(m/\hbar^2k_0)^2(V_hC_{0h}+V_{-h}C_{h0})}{\xi_i^0\cos\beta_i+\eta_i^0\cos\alpha_i}\,.\tag{34}$$

The absorption coefficient κ_i is given by twice the imaginary part of ε_i. For centrosymmetric crystals the imaginary part comes from C_{00}^i, C_{hh}^i and C_{h0}^i.

We prove in the next section that, (1) C_{00}^i, C_{hh}^i and C_{h0}^i can be treated practically as constants in the range where the resonance error (ξ_i^0, η_i^0) is the order of $(m/\hbar^2k_0)V_0$, and that (2) C_{hh} are equal to C_{00}, and that (3) C_{h0}^i has the same sign as V_h.

Using

$$\cos\alpha_1\simeq\cos\alpha_2\simeq\cos\beta_1\simeq\cos\beta_2\,,$$

we obtain

$$\kappa_i=\frac{2m}{\hbar^2k_0}\left\{-\frac{C_{00}^i}{\cos\alpha}+\frac{2m}{\hbar^2k_0}\frac{V_hC_{0h}^i}{(\xi_i^0+\eta_i^0)\cos\alpha}\right\}.\tag{35}$$

Thus the absorption coefficient is smaller for ξ_i^0, $\eta_i^0<0$ than for ξ_i^0, $\eta_i^0>0$. In the former case the wave point lies on the branch nearer the origin. This fact agrees with the observed intensity difference in a refraction doublet.

§ 5. Evaluation of C_{hg}

In this section we assume that the crystal have a filled band electronic structure, and calculate the wave functions of each band by the approximation of tight binding. Then, neglecting the overlap integrals, we can transform the expressions (20) and (23) to (Appendix II)

$$C^{r}_{hg}=-\frac{8E_H}{\pi v_0}\iiint\frac{\sum_l s_l(2\pi(\boldsymbol{h}-\boldsymbol{g}),\ \boldsymbol{K}-\boldsymbol{K}'+\pi(\boldsymbol{h}+\boldsymbol{g}))\exp[2\pi i\boldsymbol{R}_l\cdot(\boldsymbol{h}-\boldsymbol{g})]}{(\boldsymbol{K}'^2-\bar{k}^2)(\boldsymbol{K}_h-\boldsymbol{K}')^2(\boldsymbol{K}_g-\boldsymbol{K}')^2}d\tau(\boldsymbol{K}') \tag{36}$$

$$C^{i}_{hg}=-\frac{4E_H}{\bar{k}v_0}\iint\frac{\sum_l s_l(2\pi(\boldsymbol{h}-\boldsymbol{g}),\ \boldsymbol{K}-\boldsymbol{K}'+\pi(\boldsymbol{h}+\boldsymbol{g}))\exp[2\pi i\boldsymbol{R}_l\cdot(\boldsymbol{h}-\boldsymbol{g})]}{(\boldsymbol{K}_h-\boldsymbol{K}')^2(\boldsymbol{K}_g-\boldsymbol{K}')^2}d\sigma(\boldsymbol{K}')\,. \tag{37}$$

Here, the summation is over the atoms in a unit-cell, and v_0 is the volume of the unit cell, E_H the atomic unit of energy $me^4/(2\hbar^2)$ and

$$\bar{k}=k_0-(m/\hbar^2k_0)\overline{\Delta E}\,, \tag{38}$$

where $\overline{\Delta E}$ is an appropriately weighted mean of excitation energy E_n-E_0 and is of the order of a half the ionization energy. Function s_l is given by

$$s_l(2\pi(\boldsymbol{h}-\boldsymbol{g}),\ \boldsymbol{K}-\boldsymbol{K}'+\pi(\boldsymbol{h}+\boldsymbol{g}))=2\Big[\int\rho_l(\boldsymbol{r},\ \boldsymbol{r})\exp[i2\pi(\boldsymbol{h}-\boldsymbol{g})\cdot\boldsymbol{r}]d\boldsymbol{r}$$
$$-\iint|\rho_l(\boldsymbol{r},\ \boldsymbol{r}')|^2\exp[i(\boldsymbol{K}_h-\boldsymbol{K}')\boldsymbol{r}-i(\boldsymbol{K}_g-\boldsymbol{K}')\boldsymbol{r}']d\boldsymbol{r}d\boldsymbol{r}'\Big]\,. \tag{39}$$

$\rho_l(\boldsymbol{r},\ \boldsymbol{r}')$ is Dirac's density matrix

$$\rho_l(\boldsymbol{r},\ \boldsymbol{r}')=\sum_n\phi_n{}^*(\boldsymbol{r})\phi_n(\boldsymbol{r}')\,, \tag{40}$$

where the summation is over all the orbitals occupied in the lth atom.

(1) C^{i}_{00} and C^{r}_{00}

From (36) and (37) coefficients C^{i}_{00} and C^{r}_{00} are written as

$$C^{i}_{00}=-\frac{4E_H}{v_0k_0}\iint\frac{\sum_l s_l(0,\ \boldsymbol{K}-\boldsymbol{K}')}{(\boldsymbol{K}-\boldsymbol{K}')^4}d\sigma(\boldsymbol{K}') \tag{41}$$

$$C^{r}_{00}=-\frac{8E_H}{\pi v_0}\iiint\frac{\sum_l s_l(0,\ \boldsymbol{K}-\boldsymbol{K}')}{(\boldsymbol{K}'^2-\bar{k}^2)(\boldsymbol{K}-\boldsymbol{K}')^4}d\tau(\boldsymbol{K}')\,. \tag{42}$$

Function $s_l(0,\ \boldsymbol{K}-\boldsymbol{K}')$ was calculated as a function of v_l by Bewilogua[12] using Thomas-Fermi model (Fig. 2), where

$$v_l=b_l|\boldsymbol{K}-\boldsymbol{K}'|$$
$$=\frac{0.176}{Z_l{}^{2/3}}\times10^{-8}\times|\boldsymbol{K}-\boldsymbol{K}'|\ cm^{-1}\,. \tag{43}$$

However, this approximation becomes bad for small values of $|\boldsymbol{K}-\boldsymbol{K}'|$. For small values we evaluate s_l by expanding exponentials in the integrand of (39) into power series of $\boldsymbol{K}-\boldsymbol{K}'$. The result is

$$s_l(0,\ \boldsymbol{K}-\boldsymbol{K}')=B_l|\boldsymbol{K}-\boldsymbol{K}'|^2+\cdots\,, \tag{44}$$

where B_l is given by

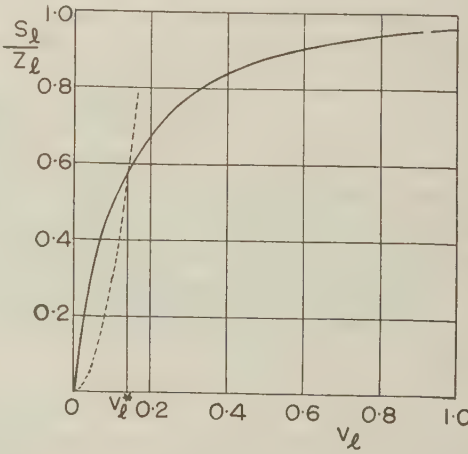

Fig. 2. $s_l(0,\ \boldsymbol{K}-\boldsymbol{K}')/Z_l$ as a function of $v_l=b_l|\boldsymbol{K}-\boldsymbol{K}'|$.

solid curve: utilizing Thomas-Fermi model.

dotted curve: utilizing power series expansion for Mg ion.

$$B_l=\frac{1}{3}\int\rho_l(\boldsymbol{r},\boldsymbol{r})\boldsymbol{r}^2d\boldsymbol{r}\,. \tag{45}$$

In Fig. 2 the value of s_l given by (44) is shown by a dotted curve. According to Koppe[13)], the above expansion is a good approximation for $|\boldsymbol{K}-\boldsymbol{K}'|<q_l^*$, while for $|\boldsymbol{K}-\boldsymbol{K}'|>q_l^*$ the Thomas-Fermi model gives a good approximation, where $q_l^*=b_l v_l^*$, v_l^* is the abscissa of intersection of the two curves in Fig. 2. The contribution to the integral of C^i_{00} and C^r_{00} from the domain $|\boldsymbol{K}-\boldsymbol{K}'|>q_l^*$ is very small and can be neglected. Thus we can calculated the integral by using (44) and obtain (Appendix IV)

$$C^i_{00}=-\frac{8\pi E_H}{v_0k_0}\sum_l B_l\log\frac{q_l^*}{|\boldsymbol{K}|-\bar{k}} \tag{46}$$

$$C^r_{00}=-\frac{4\pi^2E_H}{v_0k_0}\sum_l B_l\,. \tag{47}$$

Since C^r_{00} does not depend on $\boldsymbol{K}$, C^r_{00} can be treated as a constant. The expression of C^i_{00} depends on $\boldsymbol{K}$. This is given by

$$|\boldsymbol{K}|=k_0-(m/\hbar^2k_0)V_0$$

provided there is no Bragg reflexion. When one Bragg reflexion is excited, $|\boldsymbol{K}|$ is given by (29)

$$|\boldsymbol{K}|=k_0-\frac{m}{\hbar^2k_0}V_0+\xi\,,$$

or using (38),

$$|\boldsymbol{K}|-\bar{k}=(m/\hbar^2k_0)(\overline{\varDelta E}-V_0)+\xi\,,$$

where the resonance error ξ has the order of $(m/\hbar^2k_0)V_h$. Since, however, we have $\overline{\varDelta E}-V_0\gg|V_h|$, the change of C^i_{00} with $|\boldsymbol{K}|$ is so small that C^i_{00} is practically a constant within a deviation of a few percents.

Since the mean inner potential V_0 is expressed in the form

$$V_0=-\frac{2\pi e^2}{v_0}\sum_l B_l\,, \tag{48}$$

C^r_{00} is proportional to V_0,

$$\frac{C^r_{00}}{V_0}=\frac{2\pi E_H}{k_0e^2}=\frac{\lambda}{2a_0} \tag{49}$$

where λ is the wave length of the incident electron and a_0 is Bohr radius.

(2) C^i_{hh} and C^r_{hh}

Coefficients C^i_{hh} has the same form as C^i_{00} and C^r_{hh} the same as C^r_{00}, $\boldsymbol{K}$ in C^i_{00} and C^r_{00} being replaced by $\boldsymbol{K}_h$ in C^i_{hh} and C^r_{hh}. If $\boldsymbol{h}$-reflexion is excited, the difference between $|\boldsymbol{K}|$ and $|\boldsymbol{K}_h|$ is the order of resonance error. Thus, C^i_{hh} and C^r_{hh} can be treated as constants equal to C^i_{00} and C^r_{00}, respectively.

(3) C^i_{h0}

From (37), this coefficient is written as

$$C^i_{h0}=-\frac{4E_H}{k_0v_0}\times\iint\frac{\sum_l s_l(2\pi\boldsymbol{h},\boldsymbol{K}-\boldsymbol{K}'+\pi\boldsymbol{h})\exp(2\pi i\boldsymbol{h}\cdot\boldsymbol{R}_l)}{(\boldsymbol{K}-\boldsymbol{K}')^2(\boldsymbol{K}_h-\boldsymbol{K}')^2}d\sigma(\boldsymbol{K}'). \tag{50}$$

We evaluate (50) near $\boldsymbol{h}$-reflexion, i.e. assuming the resonance error (32) is small. Function $s_l(2\pi\boldsymbol{h},\boldsymbol{K}-\boldsymbol{K}'+\pi\boldsymbol{h})$ was calculated using Thomas-Fermi model (Appendix III) in the same way as $s_l(0,\boldsymbol{K}-\boldsymbol{K}')$[14)]. The result is shown in Fig. 3 as a function of $v_l=b_l|\boldsymbol{K}-\boldsymbol{K}'+\pi\boldsymbol{h}|$. Although Thomas-Fermi model gives inaccurate result for small value of $|\boldsymbol{K}-\boldsymbol{K}'+\pi\boldsymbol{h}|$*, the contribution from this range to the integral of C^i_{h0} may be less dominant than in the calculation of C^i_{00} on account of a finite value of the denominator of the integrand at $\boldsymbol{K}-\boldsymbol{K}'+\pi\boldsymbol{h}=0$. Therefore, the calculation using Thomas-Fermi model is not meaningless for a rough estimation of C^i_{h0}, though it is never exact.

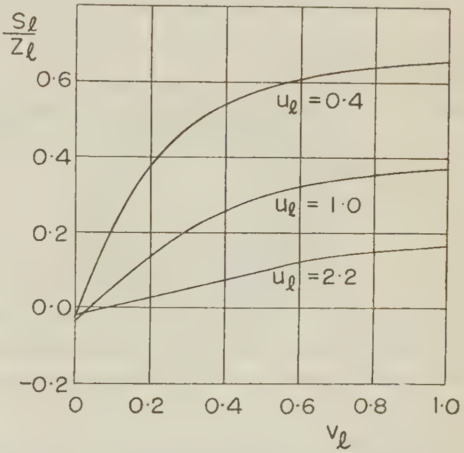

Fig. 3. $s_l(2\pi\boldsymbol{h},\boldsymbol{K}-\boldsymbol{K}'+\pi\boldsymbol{h})$ as a function of $v_l=b_l|\boldsymbol{K}-\boldsymbol{K}'+\pi\boldsymbol{h}|$ with the parameter $u_l=a_l|2\pi\boldsymbol{h}|$. ($Z_l=12$.).

The curve in Fig. 3 is almost linear in the range from the origin of v_l to about ten times of $b_l|\pi\boldsymbol{h}|$, and the contribution to the integral of (50) from the larger values of v_l is negligibly small owing to the large values of the denominator in the integrand. Hence, we can evaluate (50) approximately by replacing s_l by $T_l(\boldsymbol{h})(|\boldsymbol{K}-\boldsymbol{K}'+\pi\boldsymbol{h}|-|\pi\boldsymbol{h}|)$, where $T_l(\boldsymbol{h})$ is the tangent of $s_l(2\pi\boldsymbol{h}, q)$ at $q=0$, and given by

---

* Though Pauling and Sherman's method may be better for the calculation of this range, their method requires a very complicated calculation.

$$T_l(\boldsymbol{h})=\frac{3}{2}b_lZ_l\int_0^\infty \frac{\varphi(x)}{x}\frac{\sin u_lx}{u_lx}x^2dx \qquad (51)$$

where u_l is the parameter

$$u_l=a_l|2\pi\boldsymbol{h}|=\frac{0.468}{Z_l^{1/3}}\times10^{-8}\times|2\pi\boldsymbol{h}|\ cm^{-1}\ , \qquad (52)$$

and φ is the function given by Fermi (Appendix V). Thus, the integral turns out (Appendix V)

$$C^i_{h0}=-\frac{8\pi E_H}{v_0k_0}\frac{\log 2}{|2\pi\boldsymbol{h}|}\sum_l T_l(\boldsymbol{h})\exp(2\pi i\boldsymbol{h}\cdot\boldsymbol{R}_l)\ . \qquad (53)$$

This coefficient can also be treated as a constant.

Coefficient $T_l(\boldsymbol{h})$ has a similar behavior to the atomic scattering factor for X-rays $f_l(\boldsymbol{h})$ which is given by

$$f_l(\boldsymbol{h})=Z_l\int_0^\infty\left(\frac{\varphi(x)}{x}\right)^{3/2}\frac{\sin u_lx}{u_lx}x^2dx\ . \qquad (54)$$

Therefore, C^i_{h0} has a similar character to the crystal structure factor for X-rays and thus to V_h. C^i_{h0} is large, when V_h is large, and C^i_{h0} has the same sign as that of V_h when the crystal is centrosymmetric.

Numerical values for MgO

We calculate the coefficients C^i_{00}, C^r_{00} and C^i_{h0} for MgO crystal using (45), (46) and (53).

Table I. Values of C_{hg} and V_h for MgO. Values of V_0 and V_h are those obtained by Honjo and Mihama[3].

C^r_{00}		-0.59 (ev)			
C^i_{00}		-1.47 (ev)	V_0		-15.6 (ev)
C^i_{h0}	(111)	-0.016	V_h	(111)	~ -1.7
	(200)	-0.068		(200)	~ -7
	(220)	-0.027		(220)	-5.5
	(420)	-0.009		(420)	-4.2

The value of B_l can be calculated from the experimental value of diamagnetic susceptibility $\chi_{\text{mol},l}$ by the use of the relation

$$\chi_{\text{mol},l}=-\frac{Le^2}{6mc^2}B_l=-2.832\times10^{-10}B_l \qquad (55)$$

where L is Loschmidt number. Using the value of χ_{mol} in Van Vleck's book[15] we have $B_{Mg}=37.7\times10^{-18}\ cm^2$, $B_O=148\times10^{-18}\ cm^2$. The value of $\overline{\Delta E}$ is taken to be $25\ ev$ from the strongest peak in the energy loss curve reported by Watanabe[16]. The energy of the incident electron is taken to be $40\ kv$ corresponding to $\lambda=0.061A$. The results are shown in Table I.

§ 6. Comparison with Experiments

We have concluded above that inelastic waves result in the increase of V_0 by C^r_{00} and of V_h by C^r_{h0}, as well as the absorption due to C^i_{00} and C^i_{h0}. We compare these results with experiments.

(1) C^r_{00}

Previously, Miyake[17] calculated V_0 using the formula (48) with the value of B_l determined from the experimental value of diamagnetic susceptibility χ_{mol}. He found that for simple ionic crystals the calculated value is systematically smaller than the experimental value measured by electron diffraction. He inferred that the deviation is caused by the underestimate of B_l either through the neglect of temperature independent paramagnetic terms in χ_{mol} or through the effect of ferromagnetic impurity in the sample. However, our result indicates that the deviation may be explained by the correction term C^r_{00}, which amounts to 6∼7% of V_0 at accelerating voltages 30∼40 kv. Table II gives the values reported by Miyake together with our corrected values $V_0+C^r_{00}$. The agreement between the calculated values and the experimental values is fairly improved by the introduction of C^r_{00}. The origin of the large deviation for MgO even after the correction is not clear. It is to be mentioned, however, that the experimental value of V_0 of MgO is obtained by transmission method, while all the other values are obtained by the rotating crystal method.

(2) C^i_{00} and C^i_{h0}

When there is no Bragg reflexion, the absorption coefficient is given by (27). This result is the same as that obtained by Koppe[13], provided we neglect overlapping of neighbor atoms.

When $\boldsymbol{h}$-Bragg reflexion is excited, there exist two wave fields corresponding to the two wave points on the dispersion surface. The bsorption coefficients for these two wave ields are different and are given by (35). quation (35) implies that the difference is arge for large C^i_{h0}. Since C^i_{h0} is large for arge V_h, the intensity difference must be onspicuous for strong Bragg reflexions. This s in accordance with the observations of Ionjo and Mihama[3]. Their photograph for louble refraction implies that the order of C^i_{h0} is 1/3∼1/10 of the value of C^i_{00} for strong eflexions by MgO. The calculated value of C^i_{h0} in Table I is small compared with this rder. The discrepancy between the calculated alue and the experimental value is probably lue to the inaccuracy of the evaluation of C^i_{h0} described in § 5. We may expect that a etter agreement will be obtained by using auling and Sherman's method in the calcuation of C^i_{h0}.

The coefficient C^r_{h0} gives a correction for V_h. Although we cannot estimate its order wing to the difficulty of the integration in he formula (37), it is worth noting that Ionjo and Mihama report a deviation between he theoretical value of V_h and the value neasured by electron diffraction.

Table II. Calculated mean inner potential V_0, corrected value $V_0+C^r_{00}$, and mean inner potential obtained by electron diffraction V_{0e}.

	$-V_0$	$-C^r_{00}$	$-(V_0+C^r_{00})$	$-V_{0e}$
NaCl	7.1	0.4	7.5	7.3
NaF	7.4	0.5	7.9	8.3
NaBr	8.2	0.5	8.7	7.5
KCl	6.7	0.4	7.1	8.5
ZnS	10.6	0.6	11.2	12.5
PbS	11.2	0.6	11.8	13.2
PbO	11.9	0.7	12.6	12.3
ZnO	12.0	0.7	12.7	12.3
MgO	12.8	0.8	13.6	15.6

Values of V_0 for crystals except MgO are those calculated by Miyake[17]. Value of V_0 for MgO is from the paper of Honjo and Mihama[3]. Value of C^r_{00} for MgO is calculated from (49) using the above value of V_0 and, therefore, different from that given in Table I.

The author would like to thank Prof. R. Jyeda for his guidance and Dr. Y. Kainuma or his helpful discussions.

Appendix

(I) *Derivation of (19)*

Substituting (18) into (17) we find

$$C_{hg}=-\frac{m}{4\pi^3\hbar^2V}$$
$$\times\sum_{n\neq0}\iint\exp(-i\boldsymbol{K}_h\cdot\boldsymbol{r}+i\boldsymbol{K}_g\cdot\boldsymbol{r}')H'_{0n}(\boldsymbol{r})H'_{n0}(\boldsymbol{r}')$$
$$\times\int\frac{\exp[i\boldsymbol{K}'\cdot(\boldsymbol{r}-\boldsymbol{r}')]}{K'^2-k_n^2}d\boldsymbol{K}'d\boldsymbol{r}d\boldsymbol{r}'$$
$$=-\frac{m}{4\pi^3\hbar^2V}$$
$$\times\sum_{n\neq0}\int\frac{E_{0n}(\boldsymbol{K}_h-\boldsymbol{K}')E_{n0}(\boldsymbol{K}'-\boldsymbol{K}_h)}{K'^2-k_n^2}d\boldsymbol{K}'\ . \tag{A.1}$$

The last step is obtained by changing the order of integration and with definition (21).

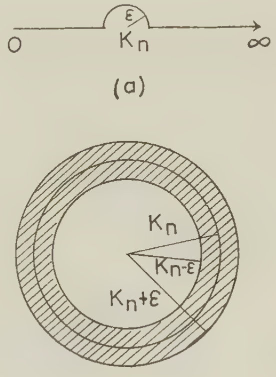

(a)

(b)

Fig. 4.

The volume element is $d\boldsymbol{K}'=\rho^2d\rho d\Omega$, and integration for ρ is carried out along the contour shown in Fig. 4a, which is devided into two parts, one is the part on the real axis and the other the semicircle around k_n[18]. The integration over the real axis results in a volume integral over the whole $\boldsymbol{K}'$-space except a shell shaded in Fig. 4b. In the limit of $\varepsilon\to0$ this integral becomes C^r_{hg} as defined by (20).

The integration along the semicircle becomes half the residue at $\rho=k_n$ in the limit of $\varepsilon\to0$. Thus the result is

$$\int\frac{[E_{0n}(\boldsymbol{K}_h-\boldsymbol{K}')E_{n0}(\boldsymbol{K}'-\boldsymbol{K}_g)]_{\rho=k_n}}{2k_n}k_n^2d\Omega$$
$$=\int_{|K'|=k_n}\frac{E_{0n}(\boldsymbol{K}_h-\boldsymbol{K}')E_{n0}(\boldsymbol{K}'-\boldsymbol{K}_g)}{2k_n}d\sigma(\boldsymbol{K}')\ .$$

This gives C^i_{hg} defined in (23).

(II) *Derivation of (36) (37).*

Using the formula[19]

$$\int \frac{\exp(i\boldsymbol{K}\cdot\boldsymbol{r})}{|\boldsymbol{r}-\boldsymbol{r}'|}\,d\boldsymbol{r}' = \frac{4\pi}{\boldsymbol{K}^2}\exp(i\boldsymbol{K}\cdot\boldsymbol{r})\ , \qquad (A.2)$$

(21) can be transformed into

$$\begin{aligned} &E_{0n}(\boldsymbol{K}_h-\boldsymbol{K}') \\ &= \frac{4\pi e^2}{|\boldsymbol{K}_h-\boldsymbol{K}'|^2}\int a_n^*\Big(\sum_j \exp\left[-i(\boldsymbol{K}_h-\boldsymbol{K}')\cdot\boldsymbol{r}_j\right]\Big)a_0 d\tau \\ &\equiv \frac{4\pi e^2}{|\boldsymbol{K}_h-\boldsymbol{K}'|}\,F_{0n}(\boldsymbol{K}_h-\boldsymbol{K}')\ . \qquad (A.3) \end{aligned}$$

Thus

$$\begin{aligned} &C^r_{hg} = -\frac{8E_H}{\pi V} \\ &\times \sum_{n\neq 0}\iiint \frac{F_{0n}(\boldsymbol{K}_h-\boldsymbol{K}')F_{n0}(\boldsymbol{K}'-\boldsymbol{K}_g)}{(\boldsymbol{K}'^2-k_n^2)(\boldsymbol{K}_h-\boldsymbol{K}')^2(\boldsymbol{K}_g-\boldsymbol{K}')^2}\,d\tau(\boldsymbol{K}') \\ &\qquad (A.4) \end{aligned}$$

$$\begin{aligned} &C^i_{hg} = -\frac{4E_H}{V} \\ &\times \sum_{n\neq 0}\iint \frac{F_{0n}(\boldsymbol{K}_h-\boldsymbol{K}')\,F_{n0}(\boldsymbol{K}'-\boldsymbol{K}_g)}{k_n(\boldsymbol{K}_h-\boldsymbol{K}')^2(\boldsymbol{K}_g-\boldsymbol{K}')^2}\,d\sigma(\boldsymbol{K}') \qquad (A.5) \end{aligned}$$

where $E_H = me^4/(2\hbar^2)$ is the atomic unit of energy. Since E_n-E_0 is small compared with the kinetic energy of the incident electron $\hbar^2k_0^2/(2m)$, we have from (7)

$$k_n = k_0 - m(E_n-E_0)/(\hbar^2 k_0)\ . \qquad (A.6)$$

We can obtain a simplified expression for C_{hg}, if we replace E_n-E_0 by an appropriately weighted mean of E_n-E_0, say $\overline{\varDelta E}$. According to Koppe[13)] the order of this mean excitation energy $\overline{\varDelta E}$ is roughly a half the ionization energy. Then using $\bar{k}$ which is given by

$$\bar{k} = k_0 - (m/\hbar^2 k_0)\overline{\varDelta E}\ , \qquad (A.7)$$

we have

$$\begin{aligned} &C^r_{hg} = -\frac{8E_H}{\pi V} \\ &\times \iiint \frac{S(\boldsymbol{K}_h-\boldsymbol{K}'\ \boldsymbol{K}_g-\boldsymbol{K}')}{(\boldsymbol{K}'^2-\bar{k}^2)(\boldsymbol{K}_h-\boldsymbol{K}')^2(\boldsymbol{K}_g-\boldsymbol{K}')^2}\,d\tau(\boldsymbol{K}') \\ &\qquad (A.8) \end{aligned}$$

$$\begin{aligned} &C^i_{hg} = -\frac{4E_H}{V} \\ &\times \iint_{|\boldsymbol{K}'|=\bar{k}} \frac{S(\boldsymbol{K}_h-\boldsymbol{K}',\ \boldsymbol{K}_g-\boldsymbol{K}')}{\bar{k}(\boldsymbol{K}_h-\boldsymbol{K}')^2(\boldsymbol{K}_g-\boldsymbol{K}')^2}\,d\sigma(\boldsymbol{K}') \qquad (A.9) \end{aligned}$$

where $S(\boldsymbol{K}_h-\boldsymbol{K}',\ \boldsymbol{K}_g-\boldsymbol{K}')$ is given by

$$\begin{aligned} &S(\boldsymbol{K}_h-\boldsymbol{K}',\ \boldsymbol{K}_g-\boldsymbol{K}') \\ &\quad = \sum_{n\neq 0} F_{0n}(\boldsymbol{K}_h-\boldsymbol{K}')F_{n0}(\boldsymbol{K}'-\boldsymbol{K}_g)\ . \qquad (A.10) \end{aligned}$$

The functions S was calculated by Kainuma[14)] in his study on Kikuchi patterns. According to him,

$$\begin{aligned} &S(\boldsymbol{K}_h-\boldsymbol{K}',\ \boldsymbol{K}_g-\boldsymbol{K}') \\ &\quad = N\sum_l s_l(2\pi(\boldsymbol{h}-\boldsymbol{g}),\ \boldsymbol{K}-\boldsymbol{K}'+\pi(\boldsymbol{h}+\boldsymbol{g})) \\ &\qquad \times \exp(-2\pi i(\boldsymbol{h}-\boldsymbol{g})\cdot\boldsymbol{R}_l)\ , \qquad (A.1 \end{aligned}$$

where $\boldsymbol{R}_l$ is the position of the lth atom i an unit cell relative to the lattice point, ar the sum is over the whole atoms in the un cell. The function s_l is that is called b Kainuma the atomic scattering factor fo Kikuchi lines. In the case of all spins couple it is given by (39), if we neglect overlappi of atomic orbitals between neighbor atoms[14,

(III) *Calculation of* $s_l(2\pi\boldsymbol{h},\ \boldsymbol{K}-\boldsymbol{K}'+\pi\boldsymbol{h})$ *usin Thomas-Fermi model.*

Equation (39) can be written as

$$\begin{aligned} s_l(\boldsymbol{Q},\boldsymbol{q}) = 2\iint |\rho_l(\boldsymbol{r},\boldsymbol{r}')|^2 \Big\{&\exp\Big(-i\frac{\boldsymbol{Q}}{2}\cdot(\boldsymbol{r}-\boldsymbol{r}' \\ &- \exp(-i\boldsymbol{q}\cdot(\boldsymbol{r}-\boldsymbol{r}'))\Big\} \\ &\times \exp\Big(i\frac{\boldsymbol{Q}}{2}\cdot(\boldsymbol{r}+\boldsymbol{r}')\Big)d\boldsymbol{r}d\boldsymbol{r}'\ , \qquad (A.1 \end{aligned}$$

where we put

$$\left.\begin{aligned} &\boldsymbol{Q} = 2\pi(\boldsymbol{h}-\boldsymbol{g}) \\ &\boldsymbol{g} = \boldsymbol{K}-\boldsymbol{K}'+\pi(\boldsymbol{h}+\boldsymbol{g})\ . \end{aligned}\right\} \qquad (A.1$$

In the Thomas-Fermi model, we put

$$\rho(\boldsymbol{r},\boldsymbol{r}') = \frac{1}{h^3}\int d\boldsymbol{p}f(\boldsymbol{p})\exp\left\{\frac{i}{\hbar}\boldsymbol{p}\cdot(\boldsymbol{r}-\boldsymbol{r}')\right\} \qquad (A.1$$

where

$$\left.\begin{aligned} &f(\boldsymbol{P}) = 1 \quad \text{for} \quad |\boldsymbol{P}| < P_m\Big(\frac{\boldsymbol{r}+\boldsymbol{r}'}{2}\Big) \\ &f(\boldsymbol{P}) = 0 \quad \text{for} \quad |\boldsymbol{P}| > P_m\Big(\frac{\boldsymbol{r}+\boldsymbol{r}'}{2}\Big) \end{aligned}\right\} \qquad (A.1$$

and $P_m((\boldsymbol{r}+\boldsymbol{r}')/2)$ is maximun of the momentu allowed at the point $(\boldsymbol{r}+\boldsymbol{r}')/2$. Then $s_l(\boldsymbol{Q},$ becomes

$$s_l(\boldsymbol{Q},\boldsymbol{q}) = Z_l(G(u_l, v_{0l}) - G(u_l, v_l))\ . \qquad (A.1$$

Here,

$$\begin{aligned} &G(u, v) \\ &= \int_0^{x_0}\Big(v-\sqrt{\frac{\varphi(x)}{x}}\Big)^2\Big(\frac{1}{2}v+\sqrt{\frac{\varphi(x)}{x}}\Big)\frac{\sin ux}{ux}x^2dx \\ &\qquad (A.1 \end{aligned}$$

where $\varphi(x)$ is the function given by Fermi an

$$u_l = a_l|\boldsymbol{Q}|\ , \qquad v_l = b_l|\boldsymbol{q}|\ , \qquad v_{0l} = b_l\left|\frac{\boldsymbol{Q}}{2}\right|\ ,$$

with a_l, b_l defined by (53) and (43). Th upper limit of integration x_0 is determined b $v = [\varphi(x_0)/x_0]^{1/2}$.

For $\boldsymbol{Q}=0$, we have

$$s_l(0, \boldsymbol{q}) = Z_l - Z_l G(v) \,, \tag{A.18}$$

vhich is the same function obtained by ewilogua[12]. Our expression for s_l, (A.16), s a little different from that given by Kai-uma since we applied the approximation A.14) to both the term in (39). Our procedure s needed to guarantee that s_l vanishes when $\boldsymbol{K}' = \boldsymbol{K}_h$ or $\boldsymbol{K}' = \boldsymbol{K}_g$.

IV) *Derivation of (46), (47).*

Coefficient C^i_{00} is given by (41),

$$C^i_{00} = -\frac{4E_H}{v_0 k_0} \sum_l \iint \frac{s_l(0, \boldsymbol{q})}{|\boldsymbol{K}-\boldsymbol{K}'|^4} d\sigma(\boldsymbol{K}') \,. \tag{A.19}$$

ince the contribution to the integral is al-nost from the neighborhood of $\boldsymbol{K}$, we can eplace the sphere $|\boldsymbol{K}'| = k$ by its tangential lane. Then, we obtain immediately (46),

$$C^i_{00} = -\frac{8\pi E_H}{v_0 k_0} \sum_l B_l \log \frac{q_l^*}{q_0} \,,$$

vhere

$$q_0 = |\boldsymbol{K}| - \bar{k} \,. \tag{A.20}$$

For coefficient C^r_{00} given by (42)

$$C^r_{00} = -\frac{8E_H}{\pi v_0} \sum_l \iiint \frac{s_l(0, \boldsymbol{q})}{(\boldsymbol{K}'^2 - \bar{k}^2)(\boldsymbol{K}-\boldsymbol{K}')^4} d\tau(\boldsymbol{K}') \,, \tag{A.21}$$

we can replace the $|\boldsymbol{K}'| = \bar{k}$ by its tangential lane, and put

$$\boldsymbol{K}'^2 - \bar{k}^2 \doteqdot 2k_0(|\boldsymbol{K}'| - \bar{k})$$

since

$$q_l^* \ll \bar{k} \,.$$

Then, using the cylindrical coordinates, we have

$$C^r_{00} = -\frac{4E_H}{\pi v_0 k_0} \left(\sum_l B_l \iint \frac{2\pi r dr dz}{(z + k_0 - \bar{k})(r^2 + z^2)} \right) .$$

The integral becomes after integration of r

$$2\pi \int_{-q_l^*}^{q_l^*} \frac{\log (q_l^*/|z|)}{z + k_0 - \bar{k}} dz \,.$$

This integral can be shown by means of con-tour integration to be equal to

$$2\pi[\pi^2/2 - 2\sinh\{(K_0 - \bar{k})/q_l^*\}] \,.$$

Thus we have, neglecting the small quantity f order $(K_0 - \bar{k})/q_l^*$,

$$C^r_{00} = -\frac{4\pi^2 E_H (\sum B_l)}{v_0 k_0} \,. \tag{A.22}$$

V) *Deviation of (52), (54).*

The tangent $T_l(\boldsymbol{h})$ of $s_l(Q, \boldsymbol{q})$ at $\boldsymbol{q} = 0$, is btained from (A.17)

$$\begin{aligned} T_l(\boldsymbol{h}) &= -Z_l \left(\frac{\partial G(u, v)}{\partial v} \right)_{v=0} b_l \\ &= \frac{3}{2} b_l Z_l \int_0^\infty \frac{\varphi(x)}{x} \frac{\sin u_l x}{u_l x} x^2 dx \end{aligned} \tag{A.23}$$

which is (51).

Expression (50) for C^i_{h0} becomes, by the use of the approximation (51),

$$\begin{aligned} C^i_{h0} = &-\frac{4E_H}{v_0 k_0} \sum_l \exp(i2\pi \boldsymbol{h} \cdot \boldsymbol{R}_l) T_l(\boldsymbol{h}) \\ &\times \iint \frac{|\boldsymbol{K}-\boldsymbol{K}'+\pi\boldsymbol{h}| - |\pi\boldsymbol{h}|}{(\boldsymbol{K}-\boldsymbol{K}')^2(\boldsymbol{K}_h-\boldsymbol{K}')^2} d\sigma(\boldsymbol{K}') \,. \end{aligned}$$

Since the Bragg angle is usually small, we can consider the surface of the integration to be a plane as in the above case. In the case of $|\boldsymbol{K}_h| = |\boldsymbol{K}|$, the above integral becomes

$$\begin{aligned} &\int_0^\infty \int_0^{2\pi} \frac{\{(r^2+q_0^2)^{1/2} - h\} r dr d\theta}{(r^2+q_0^2+h^2) - 4r^2h^2 \cos\theta} \\ &= 2\pi \int_{q_0}^\infty \frac{(q-h) q dq}{(q^2+h^2)\{(q^2-h^2)^2 + 4q_0^2 h^2\}^{1/2}} \end{aligned}$$

where $q_0 = |\boldsymbol{K}| - \bar{k}$ and $h = |\pi\boldsymbol{h}|$. We can neglect q_0 in the above integral, since the error caused by the neglect is very small as long as $q_0 \ll h$. Then, the integration is easily carried out with the result

$$C^i_{h0} = -\frac{8\pi E_H}{v_0 k_0} \frac{\log 2}{|2\pi\boldsymbol{h}|} \sum_l T_l(\boldsymbol{h}) \exp(2\pi i \boldsymbol{h} \cdot \boldsymbol{R}_l) \,. \tag{A.24}$$

Though we have assumed $|\boldsymbol{K}_h| = |\boldsymbol{K}|$, this assumption is not necessary because the final result is obtained with the neglect of q_0. We can consider the formula (A.24) holds as long as $||\boldsymbol{K}| - \bar{k}|$ and $||\boldsymbol{K}_h| - \bar{k}|$ are both $\ll |\pi\boldsymbol{h}|$.

References

1) L. Sturkey: Phys. Rev. **73** (1948) 183.
2) J. M. Cowley and A.. L G. Rees: Proc. Phys. Soc. **59** (1947) 287.
3) G. Honjo and K. Mihama: J. Phys. Soc. Japan **9** (1954) 184.
4) H. A. Bethe: Ann. d. Phys. Lpz. **87** (1928) 55.
5) N. Kato: J. Phys. Soc. Japan **7** (1952) 397.
6) K. Molière: Ann. d. Phys. Lpz. **34** (1939) 461.
7) G. Borrmann: Phys. Z. **42** (1941) 157; Z. Phys. **127** (1950) 297.
8) H. N. Campbell: J. A. P. **22** (1951) 1139.
9) H. Yoshioka: J. Phys. Soc. Japan **9** (1954) 636.
10) M. v. Laue: Acta Cryst. **2** (1949) 106.
11) G. Molière: Ann. d. Phys. Lpz. **35** (1939) 272.

12) L. Bewilogua: Phys. Z. **32** (1931) 740.
13) H. Koppe: Z. Phys. **124** (1948) 658.
14) Y. Kainuma: Acta Cryst. **8** (1955) 247.
15) J. H. Van Vleck: Theory of Electric and Magnetic Susceptibilities, p. 225 (Oxford, 1932).
16) H. Watanabe: J. Phys. Soc. Japan **9** (1954) 920.
17) S. Miyake: Proc. Physico-Math. Soc. Japan (1940) 666.
18) L. I. Schiff: Quantum Mechanics, p. 1 (McGraw-Hill Book Co., New York, 1949).
19) H. A. Bethe: Ann. d. Phys. Lpz. **87** (193 55.

JOURNAL OF THE PHYSICAL SOCIETY OF JAPAN Vol. 12, No. 6, JUNE, 1957

Fine Structures of X-ray Absorption Spectra of Cobalt in the Face Centered Cubic Lattice and Close-packed Hexagonal Lattice

By Masao SAWADA, Kenjiro TSUTSUMI and Akira HAYASE

Department of Physics, Faculty of Science, University of Osaka

(Received February 18, 1957)

Samples of cobalt of the α-modification (hexagonal close-packed lattice) and the β-modification (face centered cubic lattice) and their mixtures were prepared, and their crystal structures were examined by means of the X-ray diffraction method. Fine structures of the X-ray K absorption spectra of these cobalt samples were photographed by a bent crystal spectrograph and the mass absorption coefficients in the X-ray K absorption spectral region were measured by using the North American Philips Diffraction Unit and Wide Range Spectrometer modified to a tube spectrometer with a Geiger-Müller counter. By comparing these photometer curves of these spectrograms or the recorded curves, the fine structures of the absorption spectra of these cobalt samples were found to be very similar. The wavelength values and the mass absorption coefficient of the fine structures of the absorption spectra also nearly coincided within experimental errors, and thus the position and the form of the maximum and minimum of these structures were found to be the same. We conclude that this is due to the fact that atoms in the α-cobalt have the same immediate surroundings as those in the β-cobalt

§ 1. Introduction

According to Kronig's theory[1] of the fine structure of X-ray K absorption edge in solid crystalline substances, the phenomenon of the fluctuation of the absorption coefficient in the short wave-length side of the absorption edge (so-called "fine structure") is as follows. The X-rays are absorbed by the electrons, which make transitions from the X-ray K levels to empty levels lying above the Fermi distribution. These empty levels are grouped into zones and exist as forbidden and allowed bands caused by the periodic field in the crystal. As the absorption coefficient is proportional to the product of the transition probability and the state density, a fine structure occurs. From Kronig's theory it must concluded that the fine structure should highly dependent upon the type of the cryst lattice in which the absorption element is im bedded. This can experimentally be teste in several ways[2] and many peculiarities the fine structure of X-ray absorption edge can fully be understood on the basis Kronig's theory. However in some specia cases, there seemed to be at first sight som discrepancy between theory and experimen and it has been demonstrated that the im mediate surroundings in the crystal lattice the atoms in question are also of great im portance.[3] Rigorously speaking, we may sa that the fine structures are identical (apa from the usual reduction) only for elements which have identical positions in the same crystal or in the same type of the crystal lattice. However, the surroundings of atoms which crystallize in a cubic close-packed crystal lattice are very similar to those of atoms which crystallize in a hexagonal close-packed crystal lattice, and it is therefore of some importance to compare the fine structures of these two kinds of crysral lattices. Thus, Coster[4] compared the absorption edge of Ti (hexagonal) to that of Ca (f.c.c.) and also the edge of α-brass (f. c. c.) to that of ε-brass (hexagonal) and concluded that the positions of the maximum and minimum relative to the main edges are the same. But there remained still some typical differences in the forms of the maximum and minimum of the photometer curves for these two cases, which had to be ascribed to the difference between the cubic and hexagonal close-packed lattices. However, Ti and ε-brass are not exactly hexagonal closed-packed ($c/a=1.59$ for Ti and 1.56 for ε-brass respectively instead of 1.63 for the ideal close-packed hexagonal), and the distance of the neighboring atoms are not the same in these cases of the hexagonal close-packed and face centered cubic lattices, though some reduction can be done at the comparison. Besides, the atomic numbers of the two elements are different in the case of Ti (22) and Ca (20), and in the case of α-brass and ε-brass, the surrounding atoms in the crystal lattices of the atoms in question consist of two kinds of element, Zn (30) and Cu (29).

The fact that the cobalt metal has two allotropic modifications, α (hexagonal close-packed lattice) and β (face contered cubic lattice), was found by A. W. Hull,[5] and it was ascertained later by H. Masumoto[6] and others that each modification has its own stable temperature region. Though these facts have already been well-known, it has been experienced actuality by many investigators that the β-modification (stable at high temperatures) is often observed at room temperature in a mixed state with the α-modification. For instance, a sample of cobalt prepared by electrolysis, reducing the oxide in hydrogen at 600°C, crystallized almost in the face centered cubic lattice.[5] Similar phenomena have been reported by several investigators also in the case of electrodeposited cobalt, which suggests itself that the electrodeposited cobalt is a mixture of the hexagonal close-packed and face centered cubic crystals, their contents differing in accordance with the electrolytic condition. Okuno[7] investigated the crystal structure of the cobalt electrodeposited from cobalt-sulfate solution at various electrolytic current densities and with various P_H of the solution. He concluded that, at low current densities and high P_H, the deposits are always of the hexagonal close-packed lattice, while in all other cases the deposits are always of mixtures of the hexagonal close-packed lattice and the face centered cubic lattice, in general the former modification tending to deposit more easily at high P_H than at law P_H and *vice versa* for the latter modification. In the face centered cubic cobalt, the lattice constant is 3.554Å and the distance to the nearest neighboring atom is 2.514Å, while in the hexagonal close-packed cobalt the lattice constants are $a=2.514$Å, $c=4.105$Å, corresponding to the axial ratio $a:c=1:1.633$ (which corresponds to that of the ideal hexagonal close-packed lattice), and the distance to the nearest neighbor is 2.514 Å, exactly being equal to that of the face centered cubic cobalt. For this reason we compared directly, without reduction, the fine structures of the X-ray K absorption edges of these two modifications of cobalt.

§ 2. Experiments

Preparation of the specimen. Following Okuno's method, we made electrolyte of the following composition: $CoSO_4 \cdot 7H_2O$ ··· 150 g, NaCl···6 g, H_3BO_3···13 g and water···1000 cc. The P_H of the electrolyte was regulated with sulfuric acid or ammonia-water. The electrodeposition was carried out in a 500 cc beaker kept in the water bath held at 30°C. We used a stainless steel cathode 4.5 cm wide immersed to a depth of 7 cm placed 4 cm apart from a cobalt anode. The contents of the α-cobalt and β-cobalt depended on the current density and P_H of the electrolyte. These conditions are shown in Table I. The time of electrolysis was 0.2–1 hour to obtain a suitable thickness for the X-ray absorption spectrum. Some of them were annealed in a vaccum furnace at 600°C for 3–5 hours in order to increase the content of β-cobalt.

Table I. Electrolytic conditions and contents of each deposits.

Contents	almost all α (hex.)	$\alpha > \beta$	$\alpha \sim \beta$	$\alpha > \beta$	almost all β (f.c.c.)
Current Densities Amp./cm^2	0.03	0.03	0.03	0.03	0.005
P_H	5.0	2.0	2.1	2.1	1.2
Time of Electrolysis Miniuts	8	5	8	12	60
Time of Heat Treatment Hours	—	—	3	5	1

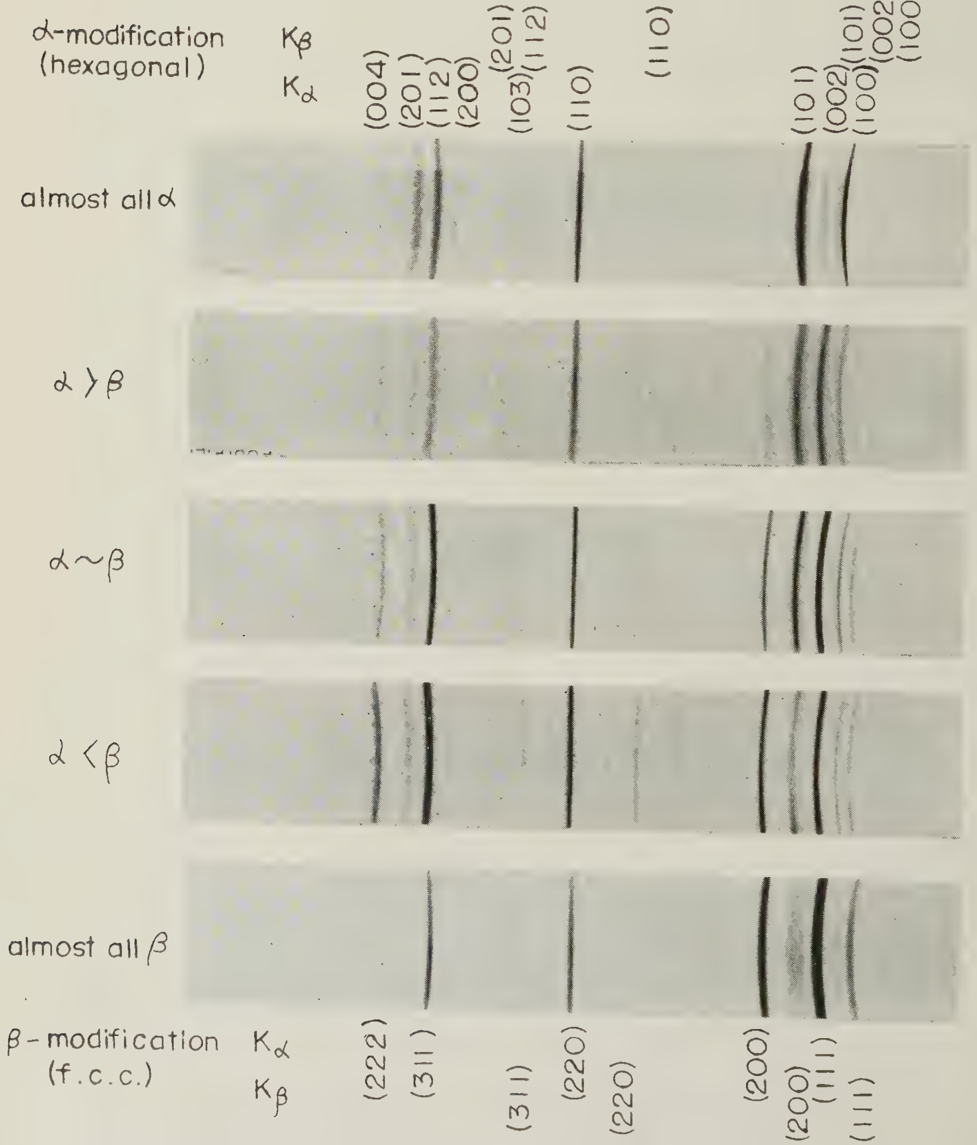

Photo. 1. X-ray diffraction patterns of cobalt in α-(hexagonal) and β-(f.c.c.) modifications and their mixed states.

They are also listed in Table I. Deposits are 7μ—11μ in thickness and could easily be stripped from the cathode plate together with a cigarette paper pasted on them. This paper was used to protect brittle samples without the loss of X-ray transmission.

Diffraction pattern. For the diffraction study, the electrodeposit stripped from the cathode was cut into sheets of 0.2–0.5 mm width and about 3 mm length and several

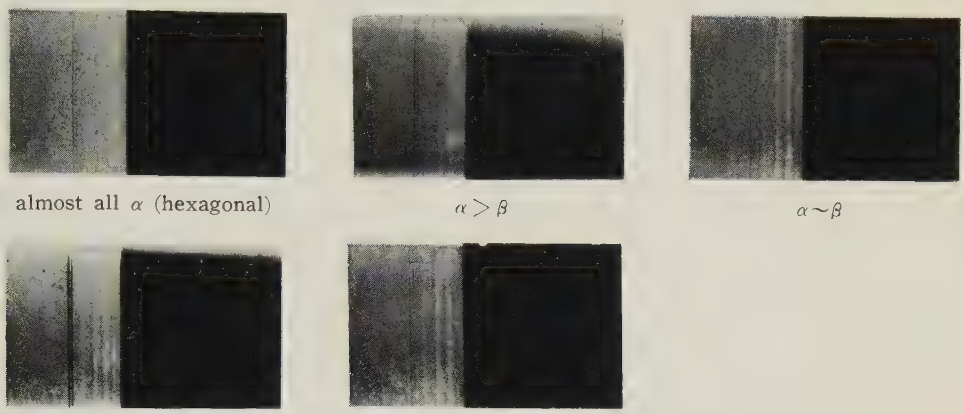

almost all α (hexagonal)

$\alpha > \beta$

$\alpha \sim \beta$

$\alpha < \beta$

almost all β (f.c.c.)

Photo. 2. X-ray K absorption spectra of cobalt in α-(hexagonal) and β-(f.c.c) modifications and their mixed states.

Table II. Wavelength values of fine structures of X-ray K absorption spectra of cobalt.

	almost all α (hexagonal)	$\alpha > \beta$	$\alpha \sim \beta$	$\alpha < \beta$	almost all β (f.c.c.)
	x.u.	x.u.	x.u.	x.u.	x.u.
K	1604.7_6	1604.5_2	1604.4_8	1604.4_8	1604.7_4
K'	1601.7	1601.4	1601.8	1601.4	1602.1
A	1600.7	1600.6	1601.0	1600.7	1601.0
α	1600.6	1600.4	1600.3	1600.3	1600.6
B	1599.5	1599.2	1599.0	1599.0	1599.3
β	1598.0	1597.7	1597.6	1597.5	1597.7
B'	1597.1	1596.6	1596.5	1596.3	1596.6
β'	1596.3	1596.1	1596.0	1595.8	1596.0
C	1594.8	1594.1	1594.5	1594.6	1594.7
γ''	1592.1	1592.1	1592.0	1592.1	1592.2
γ	1590.8	1590.4	1590.8	1591.3	1591.0
C'	1589.3	1589.3	1590.0	1590.2	1590.3
γ'	1588.4	1588.5	1589.1	1589.1	1588.8
D	1584.4	1583.9	1584.3	1584.5	1584.1
δ''	1580.8	1580.8	1580.4	1580.5	1580.9
δ	1579.1	1578.8	1578.8	1578.8	1579.0
D'	1576.9	1576.5	1576.1	1576.1	1576.0
δ'	1575.6	1575.5	1574.6	1574.6	1574.3
E	1571.2	1570.8	1571.3	1570.8	1571.1
ε	1566.2	1565.8	1566.0	1566.0	1566.1
E'	1561.5	1561.4	1563.1	1563.0	1563.0
ε'	1559.2	1558.7	1558.5	1558.8	1559.3
F	1554.1	1554.1	1555.0	1555.0	1555.1

Table III. Energy-separations of fine structures from principal K absorption edges of cobalt.

	almost all α (hexagonal)	$\alpha > \beta$	$\alpha \sim \beta$	$\alpha < \beta$	almost all β (f.c.c.)
K	−eV.	−eV.	−eV.	−eV.	−eV.
K'	14.9	14.9	12.9	14.4	12.0
A	19.7	18.7	16.8	17.8	17.3
α	20.2	19.7	20.2	19.8	19.7
B	25.5	25.5	26.4	26.0	26.0
β	32.8	32.7	33.2	33.3	33.7
B'	37.1	38.0	38.5	39.1	39.0
β'	41.0	40.4	40.9	41.5	41.9
C	48.2	50.1	48.2	47.3	48·2
γ''	61.4	59.9	60.4	59.5	60.4
γ	67.7	68.2	66.2	63.4	67.3
C'	75.0	73.5	70.1	68.7	69.6
γ'	79.4	77.4	74.5	74.1	77.0
D	99.0	100.0	98.0	96.6	100.0
δ''	116.8	115.3	117.2	116.3	115.8
δ	125.2	125.2	125.1	124.7	125.1
D'	136.1	136.6	138.6	138.1	140.0
δ'	142.5	141.5	145.5	145.6	148.5
E	164.5	165.0	162.5	164.5	164.5
ε	189.5	190.1	189.0	188.6	189.5
E'	213.3	212.3	203.7	203.8	205.2
ε'	224.9	226.0	227.0	225.0	223.9
F	250.9	249.4	244.8	244.4	245.3

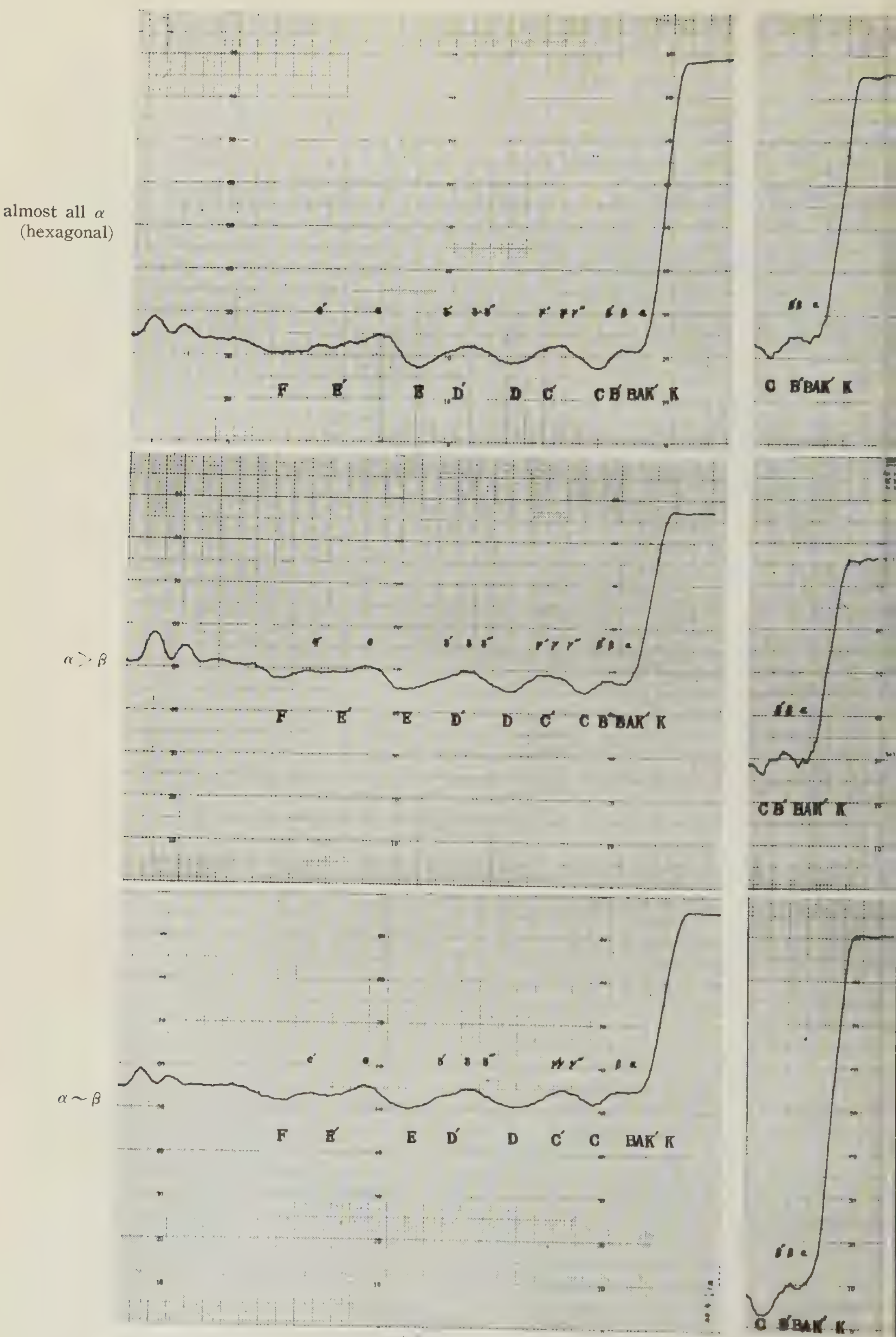

(a) (b)

Photo. 3. (to be continued)

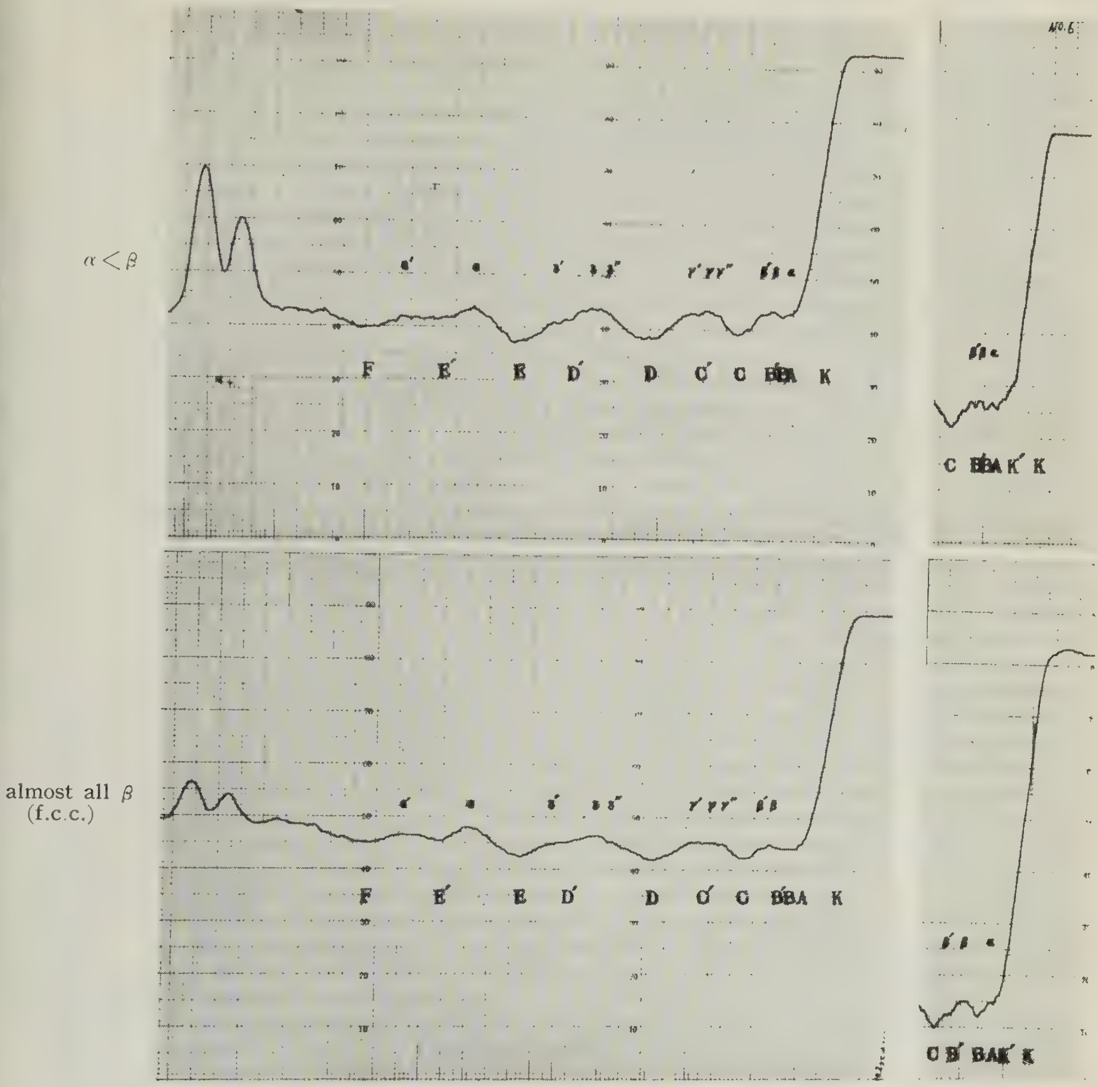

(a) (b)

Photo. 3. Photometer curves of X-ray K absorption spectra of cobalt in α-(hexagonal) and β-(f.c.c.) modifications and their mixed srates.
(a) Showing the curves taken by the photometer with a slit of 0.1 mm width.
(b) Showing the curves taken by the photometer with a slit of 0.025 mm width.

sheets were pasted one over the other.

The radius of the powder camera was 57.3 mm. The X-ray tube with a cobalt-target was loaded with 30 kV, 10 mA. The time of exposure ranged from about 2 to 3 hours. The specimens were rotated in order to avoid the influence of preferred orientations. Photo. 1 shows these diffraction patterns. The contents of α-cobalt and β-cobalt were compared by the intensities of the diffraction lines (101) K_α from α-cobalt and (200) K_α from β-cobalt following Okuno's method,⁷⁾ that is, (1) for almost all β, α (101) K_α is weak as compared even with β (200) K_β; (2) for $\beta > \alpha$, α (101) K_α is fainter than β (200) K_α but more intense than β (200) K_β; (3) for $\beta \sim \alpha$, α (101) K_α has about the same intensity as β (200) K_α. For opposite inequalities to the above apply similar criteria. The intensities of diffraction lines were also measured by the Geiger-counter method using the North American Philips Diffraction Unit and Wide Range Goniometer.

Absorption spectrum. The fine structures of X-ray *K* absorption spectra of cobalt were taken with a bent crystal focusing spectrograph of the Cauchois type. The diameter of the focal circule was 20 cm, and the second order reflection by (100) plane of a quartz crystal was used. Generally a current 10 mA at 10 kV was passed through an ion-type X-ray tube. The time of exposure was varied from 15 to 20 hours. The spectrograms and the microphotometer curves of the *K* absorption spectral region of cobalt are reproduced in Photo. 2 and Photo. 3. Photo. 3a shows the microphotometer curves taken by the photometer with a rather large slit width (0.1 mm) which was used in order to avoid the influence of the grain size of the photographic plate, and Photo. 3b shows the microphotometer curves taken by a photometer with a slit 0.025 mm wide in order to measure exactly the fine structure near the absorption edge. The measurements of wavelengths were carried out referring to the Co K_{α_1} and Cu K_{α_2} lines photographed on the same plate.

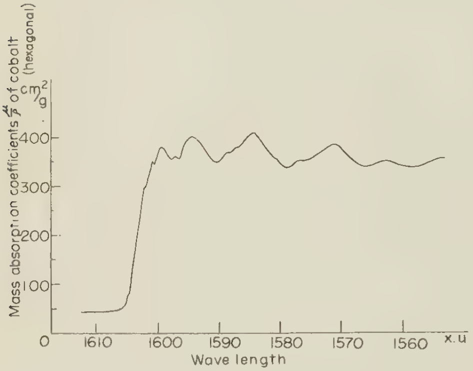

Fig. 1a. Curve of mass absorption coefficients with wavelengths of cobalt in close-nacked hexagonal lattice.

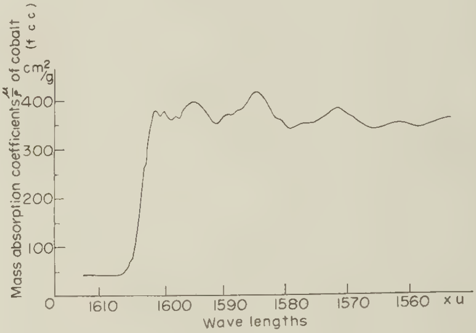

Fig. 1b. Curve of mass absorption coefficients with wavelengths of cobalt in face centered cubic lattice.

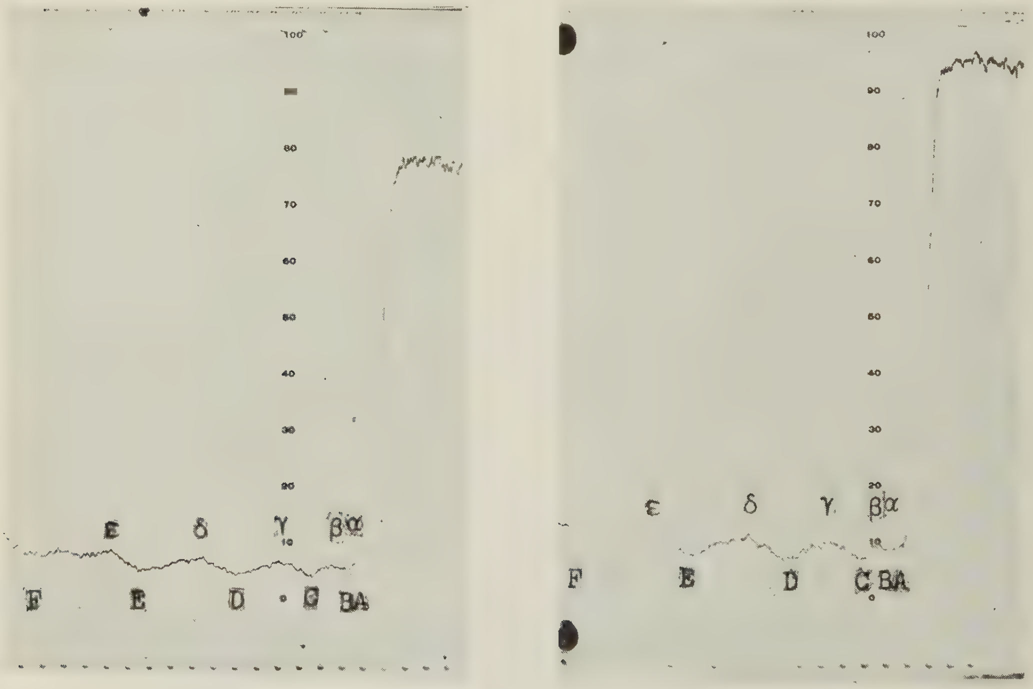

almost all α

$\alpha < \beta$

Photo. 4. Recorded curves of X-ray *K* absorption spectra of α-(hexagonal) and β-(f.c.c.) cobalt.

he wavelength values of reference lines are ken from the Table in Y. Cauchois and H. ulubei's[8] “ Longueurs d'Onde des Emissions et des Discontinuites d'Absorption X ”. he wavelength values of the fine structures *K* absorption edges of cobalt are shown in able II. Table III shows the energy-separa- ons from the *K* principal absorption edges. In rder to measure the mass absorption coefficient $/\rho$, the fine structures of absorption spectra of ese specimens were recorded automatically y using the North American Philips Diffrac- on Unit and Wide Range Spectrometer. This nit is an installation to record the ordinary owder diffraction Unit and Wide Range pectrometer. This unit is an installation to ecord the ordinary powder diffraction pattern.

Table IV. Wavelength values and mass absorption coefficients of fine structures of X-ray *K* absorption spectra of cobalt by recording method.

	Wavelengths		Mass absorption coefficients	
	almost all α	$\alpha<\beta$	almost all α	$\alpha<\beta$
	x.u.	x.u.	46.2*cm²/g	45.7*cm²/g
K	1604.8	1604.6	—	—
K'	1601.4	1601.4	—	—
A	1600.8	1600.9	351	382
α	1600.6	1600.0	345	365
B	1599.7	1599.0	380	382
β	1597.6	1597.8	355	359
B'	1597.1	1596.8	—	—
β'	1596.3	1596.5	—	—
C	1594.7	1594.7	403	405
γ''	1592.4	1592.3	—	—
γ	1590.2	1591.0	348	352
C'	1588.8	1589.8	—	—
γ'	1588.2	1588.7	—	—
D	1584.2	1584.3	412	419
δ''	1580.6	1580.6	355	361
δ	1579.1	1579.1	338	334
D'	1577.0	1576.2	352	356
δ'	1575.8	1574.9	—	—
E	1571.2	1571.1	388	394
ε	1566.0	1566.0	342	332
E'	1561.8	1562.3	351	352
ε'	1558.7	1558.6		344
F	1554.3	1555.1	—	357

* This value is not the mass absorption coeffi- ent at the principal *K* edge of cobalt but is that the wavelength of 1610 x. u.

The unit is mechanically so arranged as to maintain a 1:2 ratio of rotational speed between the crystal holder of the center of the spectrometer and Geiger-Müller counter as required for Bragg reflections. We used this unit as the tube spectrometer described by Coster and De Lang.[9] The details of our modified method will be published in another paper.[10] The divergency of the slit system of this instrument is about 0.0004 radians. LiF is used as a reflecting crystal. As we can directly measure the primary X-ray intensity I_0 and the transmitted X-ray intensity I, it is easier to get the mass absorption coefficient μ/ρ from the equation

$$\frac{\mu}{\rho}=\frac{1}{\rho x}(\log I_0-\log I)\,,$$

where x and ρ are the thickness and density of the material, respectively, and I_0 is the intensity of the spectrum without the absorber in the same condition in which the absorption spectrum is recorded. Now ρx is about 7.7 mg/cm² in the case of $\beta>\alpha$-cobalt and 8.7 mg/cm² in the case of α-cobalt. Fig. 1 shows the μ/ρ curves near the absorption edges of $\beta>\alpha$-cobalt and α-cobalt thus measured and photo. 4 shows the recorded curves of the fine structures in the X-ray *K* absorption spectral region of these cobalts. Table IV shows the wavelength values and values of the mass absorption coefficients obtained by this method.

§ 3. Results and Discussions

By comparing photometer curves in Photo. 3 or recorded curves in Photo. 4, it will be seen that the fine structures of the absorption spectra of these sorts of cobalt are very similar. The wavelength values and the mass absorption coefficients of these fine structures also nearly coincide within the limit of experimental errors as seen from Table II, III and IV. In our case, the form of the maximum and minimum of the fine structures of the absorption edges are also the same contrary to Coster's case. This seems to be due to the fact mentioned in introduction. α-cobalt is of an ideal close-packed hexagonal lattice, the neighboring atoms being of the same kind and the distance to the nearest neighbor being equal to that in β-cobalt (f.c.c.). This is clearly seen in Table V which gives the successive shells of atoms in the case of α- and β-cobalt. The number of surrounding atoms and their distances from the central atom are identical in the first two shells. In our previous paper[11] on the fine structures of X-ray absorption spectra of amorphous substances, we found that the fine structures of the absorption spectra in amorphous state have similar forms and positions to those in substances which have undergone crystallization. We considered such results to be due to the fact that an amorphous substance is not an irregular assembly of atoms but has a certain definite structure, i.e., it has the same surroundings of atoms as in its crystalline state. Kiestra[12] remarks that the fine structure is determined by the immediate surroundings of the atom in question in t region about 40 eV to 150 eV from the absor tion edge. This is well supported by o experimental results.

Table V. Different successive shells of atom surrounding a definite cobalt atom in a close-packed hexagonal and face centered cubic lattice.

Number of Atoms		Distance	
f.c. cubic	hexagonal	f.c. cubic	hexagonal
12	12	2.513	2.514
6	6	3.554	3.555
	2		4.105
24	18	4.353	4.354
	12		4.814
12		5.025	

References

1) R. de Kronig: Zs. f. Phys. **70** (1931) 317, **7** (1932) 191.
2) D. Coster and R. Smoluchowski: Physica (1935) 1.
3) D. Coster and G. H. Klammer: Physica (1934) 145. V. P. Barton and G. A. Lindsa Phys. Rev. **46** (1934) 362.
4) D. Coster: Physica **2** (1935) 606.
5) A. W. Hull: Phys. Rev. **14** (1919) 540, **1** (1921) 571.
6) H. Masumoto: Sci. Rep. Tohoku Imp. Uni **15** (1926) 449. Kinzoku-no-kenkyu, **2** (192 877.
7) Okuno: Bulletin Univ. Osaka Prefecture **A** (1956) 89.
8) Y. Cauchois and H. Hulubei: Longueu d'Onde des Émissions X et des Discontinuit d'Absorption X. Herman, Paris (1947).
9) D. Coster and H. De Lang: Physica **13** (194 379.
10) K. Tsutsumi, M. Sawada and A. Hayase Norelco Reporter, to be published.
11) M. Sawada, K. Tsutsumi, T. Shiraiwa and M Obashi: J. Phys. Soc. Japan **10** (1955) 459.
12) S. Kiestra: A Conference on the Applicatio of X-ray Spectroscopy to Solid State Problem 23–25 Oct. (1950).

JOURNAL OF THE PHYSICAL SOCIETY OF JAPAN Vol. 12, No. 6, JUNE, 1957

Variation of Electron Diffraction Intensity with Crystal Size

By Shigeya KUWABARA

Department of Physics, Faculty of Science, Hiroshima University, Hiroshima, Japan

(Received September 12, 1956)

Intensity of electron diffraction Debye-Scherrer rings was studied for evaporated films of Al, Ag, Au, NaCl, KCl and MgO of various thicknesses and crystal sizes. The observed intensity deviates from the value calculated by the kinematical theory of diffraction at crystal sizes less than 100 Å for all the materials examined. This result agrees with the conclusion of Blackman's dynamical theory (Proc. Roy. Soc. **173** (1939) 68).

Yamzin & Pinsker's conclusion (Dokl. Akad. Nauk **65** (1949) 645) that the kinematical theory can hold for films of thickness up to 500 Å, apparently contradicts the present result. It was pointed out that Yamzin & Pinsker's conclusion resulted from the fact that they neglected the effect of the temperature factor.

§1. Introduction

Intensity of electron diffraction Debye-Scherrer rings was first studied by G. P. Thomson[1] and later by several investigators[2-7]. Thomson, Mark and Wierl[2] and Shirai[3] found that the observed intensity is proportional to the square of structure factor in accordance with the kinematical theory, but Ornstein *et al.*[4,5] and Friesen and Lennander[6,7] found that the observed intensity deviates from the kinematical value. Blackman[8] treated these results theoretically and concluded that the deviation found by Ornstein *et al.* is caused by the dynamical effect of the diffraction.

In the diffraction of electrons, which interact with matter very strongly, the kinematical theory fails and the dynamical theory must be refered to even for comparatively small crystals. According to Blackman, the crystal size of Thomson's specimens was small enough for the holding of the kinematical theory. However, in the specimen of Mark and Wierl and Ornstein *et al.* the crystal size was not so small, as was indicated by the sharpness of their Debye-Scherrer rings. Blackman pointed out that the deviation found by Ornstein *et al.* could be explained by the dynamical theory but the agreement with the kinematical theory found by Mark & Wierl could not be explained.

Recently, crystal analysis by electron diffraction was developed mainly by Soviet investigators[9]. They assumed the holding of the kinematical theory, and in order to examine the assumption, Yamzin[10] and Yamzin and Pinsker[11] carried out an experiment similar to that of G. P. Thomson. Specimen studied by Yamzin were Al, Cu, Ag, Au, Zn and Sn, and the accelerating voltage was from 38 to 56 kV. Although he measured crystal size, he stated his conclusion not in terms of crystal size but in terms of film thickness. He concluded that the kinematical theory holds for thickness less than 500Å, except for the material so heavy as Au. According to him, the apparent failure of the kinematical theory as observed by Ornstein *et al.*[4,5] and Friesen and Lennander[6] might be attributed to textures in the specimen films. Based upon the experimental result of Yamzin, Pinsker[12] concluded that Blackman's treatment is not sound. On the other hand, the dynamical theory was proved by many experiments[13] and we could not understand why Blackman's treatment is not sound.

The aim of the present investigation is to elucidate this contradiction. Specimens studied were Al, Ag, Au, NaCl, KCl and the accelerating voltage was from 32 to 60kV. First, the relation between intensity and thickness was studied to check the result of Yamzin and Pinsker. Against their conclusion it was found that the dynamical effect appears for films thinner than 100Å for all the materials examined. Next, the relation between intensity and crystal size was studied and it was found that the intensity varies with crystal size in accordance with Blackman's theory.

In analysing the intensity data the temperature effect, which was neglected by Yamzin and Blackman, was taken into account. The contradicting conclusions of Yamzin and Pinsker seems to have been resulted from the neglecting of the temperature effect.

§ 2. Experimentals

Specimens. Specimen films of Al, Ag, Au, NaCl and KCl were prepared by evaporation in high vacua of the order of 10^{-5} mmHg. Substrate for sepcimen was collodion film put on the standard specimen grid for electron microscope. The range of thickness was 100–1000 Å for Al, 10–150 Å for Ag and Au, and 100–150 Å for NaCl and KCl. Specimen film films of MgO were prepared by evaporating Mg in low vacua of the order of 10^{-3} mmHg. Thus the evaporated Mg, which would produce Mg-film of thickness from 50 to 300 Å, was oxidized into MgO as confirmed by electron diffraction. If the condition of evaporation was kept the same, the crystal size increased with film thickness. To control the crystal size at a given film thickness, the rate of evaporation and the temperature were changed. The time of evaporation was varied from 1 seconds to 10 minutes. The temperature the substrate was changed from room tempera ture to 230°C. The crystal size was large for high substrate temperature and high evap ration rate. To prevent the crystal growt after the evaporation, film was quickly coole in vacuum by taking it away from the furna after the evaporation.

Prefered orientation was examined carefull by tilting the specimen film up to about 40° Diffraction patterns were photometered alon two directions, one is parallel and the othe perpendicular to the tilting axis. For Al, A Au and MgO no prefered orientation was foun while for NaCl and KCl there was a tren that (001) plane becomes parallel to the sub strate film plane.

Diffraction equipment. The electron diffrac tion equipment used in the present experimen was constructed in our laboratory. The specimen-plate distance was 338 mm. The ac celerating voltage was from 32 to 60 kV.

Method of intensity measurement. Intensity of Debye-Scherrer rings was measured by the photographic method which was almost the same as that of Karle and Karle[14].

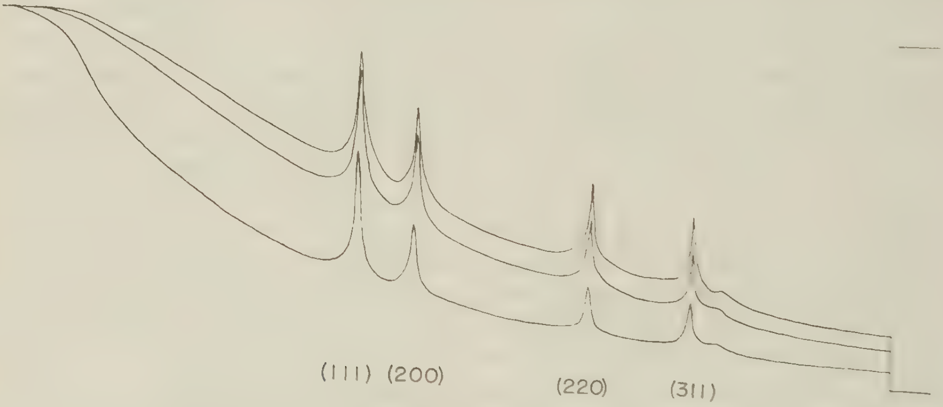

Fig. 1. Microphotometer curves of Debye-Scherrer rings of Al (Accelerating voltage 48 kV).

Fig. 1 shows an example of microphotometer curves. In this example three records with different exposure times are shown.

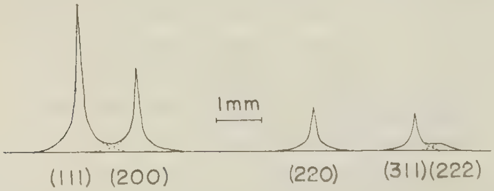

Fig. 2. Intensity curves of Debye-Scherrer rings obtained from Fig. 1.

Intensity curves of Debye-Scherrer rings were obtained by substracting the background from the total intensity.

For very thin specimen, the effect of halos due to collodion film was substracted by the method described by Kimoto[15]. For thicker specimen the effect of hales was negligible. Fig. 2 shows an example of intensity curves obtained from Fig. 1.

Determination of crystal size. Integral breadth B of a Debye-Scherrer ring is defined by

$$B=\int P(r)\,dr/P_m-B_0\;, \tag{1}$$

where r is the radius, $P(r)$ the intensity, P_m the maximum value of $P(r)$ and B_0 the diameter of the incident spot (0.13 mm).

Crystal size $\bar{A}$ is calculated by

$$\bar{A}=\lambda L/B\cos\theta\;,^{*} \tag{2}$$

where L is the specimen-plate distance (338 mm) and θ is Bragg angle which is so small that $\cos\theta$ can be taken as equal to unity. An example of crystal size and integrated intensity determination is shown in Table I, which was obtained from the microphotometer curve Fig. 1.

Table I. Example of integrated intensity, integral breadth and crystal size of Al (Accelerating voltage 48kV).

	hkl	(111)	(200)	(220)	(311)	mean
Integrated intensity		48_7	20_1	100	9_1	
		43_8	22_1	100	9_0	46_5 20_8 100 9_0
		47_2	20_2	100	8^8	
Integral breadth B (mm)		0.11_9	0.11_4	0.12_0	0.10_7	
		0.10_3	0.12_6	0.09_8	0.10_2	0.11_5
		0.11_7	0.14_5	0.10_6	0.12_5	
Crystal size (Å)		15_4	16_0	15_3	17_1	
		17_8	14_5	18_7	17_9	16_0
		15_6	12_6	17_3	14_6	

Determination of integrated intensity. Integrated intensity I was obtained by measuring the area of the intensity curve. For all specimens (220)-intensity was normalized to 100.

§ 3. Theoretical Formulas

In the kinematical theory the integrated intensity of a Debye-Scherrer ring is given by

$$I_h{}^K \backsim |S_h|^2\cdot p\cdot e^{-2M}/\theta^2\;, \tag{3}$$

while in the dynamical theory it is given by

$$I_h{}^D \backsim |S_h|\cdot p\cdot e^{-M}/\theta^2\;, \tag{4}$$

where the superfixes K and D indicate kinematical and dynamical, respectively; h is the index of a ring, S_h the structure factor for electrons and p the lattice plane multiplicity. Factors e^{-2M} and e^{-M} are the temperature factors for the kinematical and dynamical cases, respectively. Yamzin mentioned that the temperature effect is so small that it can be neglected for low order reflections. Actually, however, it is not small as is shown in Table II[17]. Thus in the following section the temperature effect is taken into account.

Table II. Calculated values of temperature factor

Specimen		(111)	(200)	(220)	(311)	(400)	(420)
Al	e^{-2M}	0.92_1	0.89_6	0.80_3	0.74_0	0.64_4	0.58_9
	e^{-M}	0.96_0	0.94_6	0.89_6	0.86_0	0.80_3	0.76_7
Ag	e^{-2M}	0.93_5	0.91_4	0.83_3	0.78_0	0.69_5	0.63_4
	e^{-M}	0.96_6	0.95_6	0.91_3	0.88_3	0.83_2	0.79_7
Au	e^{-2M}	0.94_8	0.93_1	0.86_7	0.82_3	0.75_2	0.69_8
	e^{-M}	0.97_4	0.96_5	9.93_2	0.90_7	0.86_8	0.83_5
NaCl	e^{-2M}	0.93_0	0.90_9	0.82_1	0.77_0	0.68_3	0.62_0
	e^{-M}	0.96_5	0.95_3	0.90_8	0.87_8	0.82_6	0.78_7
KCl	e^{-2M}	0.93_7	0.91_5	0.83_7	0.78_3	0.70_2	0.64_0
	e^{-M}	0.96_8	0.95_6	0.91_5	0.88_5	0.83_8	0.80_0

According to Blackman[8], the integrated intensity for parallel sided single crystal is given by

$$I \backsim I_0|S_h|\lambda^2/(v_0\theta)\int_0^A J_0(2x)\,dx\;, \tag{5}$$

where v_0 is the volume of the unit cell, J_0 the zeroth order Bessel function and

$$A=|S_h|D\lambda/v_0\;, \tag{6}$$

where D means the thickness of the single crystal. For small values of A, Eq. (5) becomes

$$I \backsim I_0|S_h|^2 D\lambda^3/(v_0{}^2\theta)\;, \tag{5$'$}$$

which is characteristic of the kinematical theory. For large value of A Eq. (5) becomes

$$I \backsim I_0|S_h|\lambda^2/(2v_0\theta)\;. \tag{5$''$}$$

Adopting Eq. (5), the intensity of Debye-Scherrer rings becomes

$$I_h \backsim I_0\frac{|S_h|}{\theta^2}\cdot e^{-M}\cdot p\int_0^{Ae^{-M}} J_0(2x)\,dx\;. \tag{7}$$

The numerical integration of this equation gives the relation between intensity and crystal size. In Fig. 4 the values calculated by Eq. (7) are shown by fully lines.

---

* In the previous paper[16] the crystal size was estimated too small, since the evaluation of B_0 was incorrect.

§ 4. Experimental Results

(a) *Intensity variaton with film thickness.* The variation of intensity with film thickness was studied at first, the evaporation being carried out under the same evaporation speed and the same temperature of the substrate.

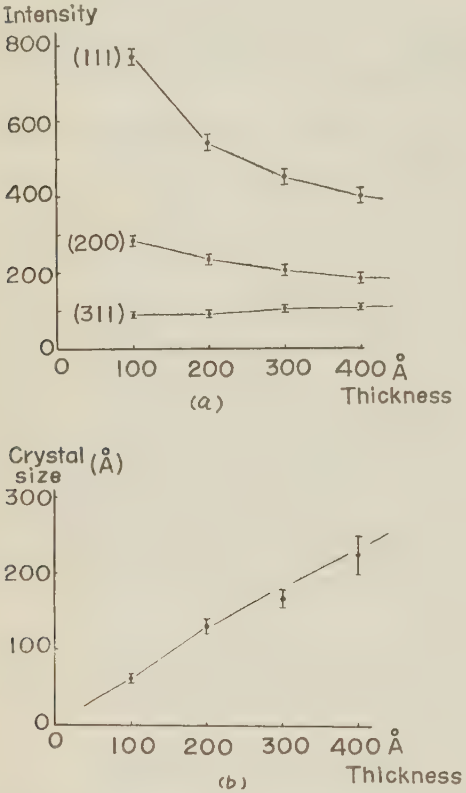

Fig. 3. (a) Intensity variation with film thickness of Al (Accelerating voltage 40 kV).
(b) Relation between crystrl size and film thickness of this specimen.

The result obtained from Al is shown in Figs. 3 a and b. The intensity ratios are plotted against the thickness of the film in (a), and the relation between crystal size and thickness is plotted in (b). The experimental errors are shown by the vertical line segments in each figure. As the thickness of film is increased the crystal size becomes larger, and at the same time, the intensity ratios vary appreciably.

b) *Intensity variation with crystal size.* Next, the intensities were measured for many specimens of the same thickness but of various crystal sizes. For all the specimens except NaCl and KCl, intensity of (111)-, (200)-, (220)-, and (311)- or (222)-reflections were studied. For NaCl and KCl only (hk0)-reflections wer studied to avoid the effect of the texture.

The result is shown in Figs. 4 a–f. In eac figure the experimental errors of intensity an crystal size are shown by vertical and horizontal line segments, respectively. The curve obtained from Fq. (7) are shown for accelerating voltage of 48 kV. Except for MgO, th temperature effect was taken into account i the calculation of Eq. (7). $(hkl)^K$ shows th kinematical intensities from Eq. (3), an $(hkl)_0{}^K$ shows the kinematical intensities without the temperature effect (*cf.* Tables II an III).

Table III. Kinematical intensity ratios with and without the temperature factor.

Specimen		(111)	(200)	(220)	(311)	(400)	(420)
Al	with	77_2	28_9	100	89	—	—
	without	67_5	26_0	100	97	—	—
Ag	with	52_7	22_6	100	95	—	—
	without	46_9	20_8	100	10_1	—	—
Au	with	48_5	21_0	100	98	—	—
	without	44_2	19_4	100	10_3	—	—
NaCl	with	—	22_3	100	—	9	19
	without	—	20_2	100	—	11	26
KCl	with	—	20_5	100	—	9	20
	without	—	18_8	100	—	11	26

The observed values do not exactly coincide with the theoretical values. However, it is obviously recognized that the observed intensities vary appreciably with crystal size and the reflections, the structure factors of which are larger than that of the standard reflection, have an inclination to decrease in their intensities as the crystal size becomes larger, and the ones, the structure factors of which are smaller than that of the standard one, tc increase in their intensities for the larger crystal size. This fact coincides at least qualitatively with the theoretical result and can be considered to be due to the dynamical effect.

§ 5. Discussions

Comparison with Yamzin's result. Materials studied both by Yamzin and the present author are Al, Ag and Au. Yamzin performed the experiment with various film thicknesses

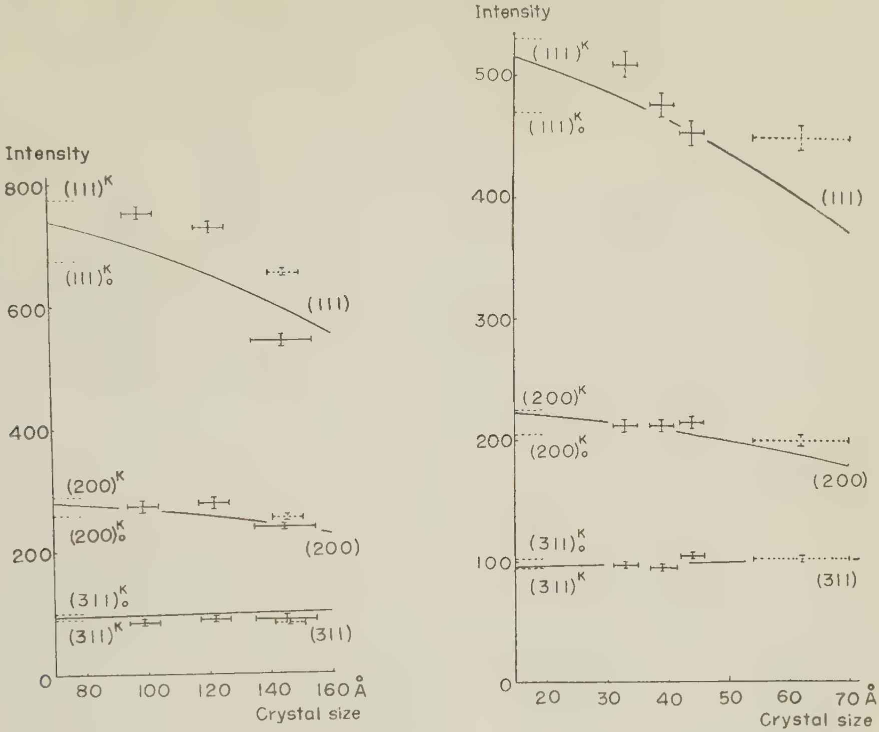

(a) Al (150Å in thickness).　　(b) Ag (20Å in thickness).

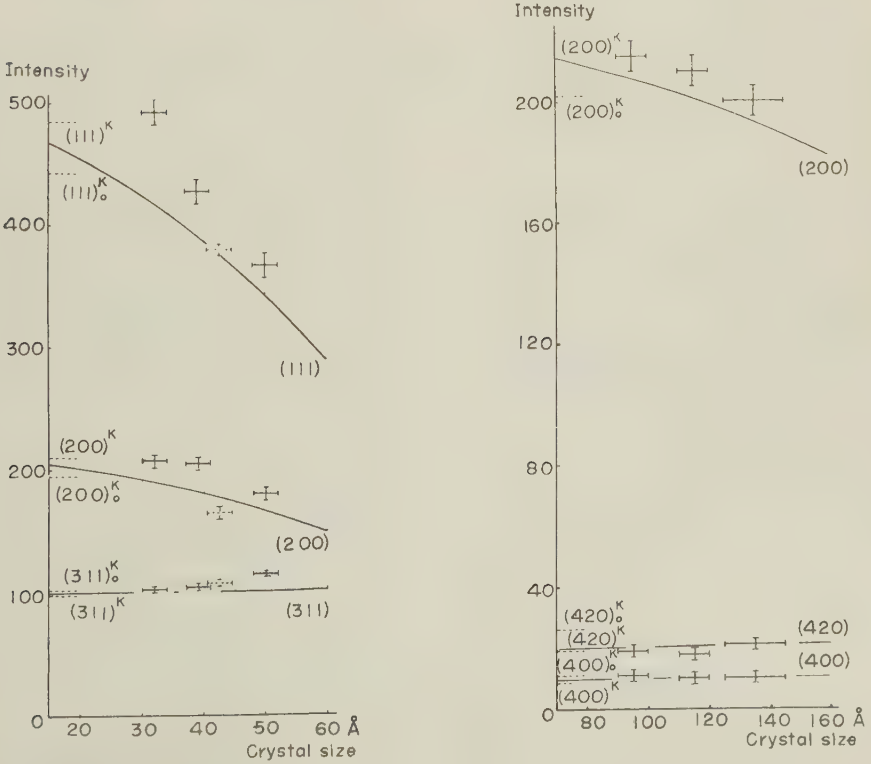

(c) Au (15Å in thickness).　　(d) NaCl (400Å in thickness).

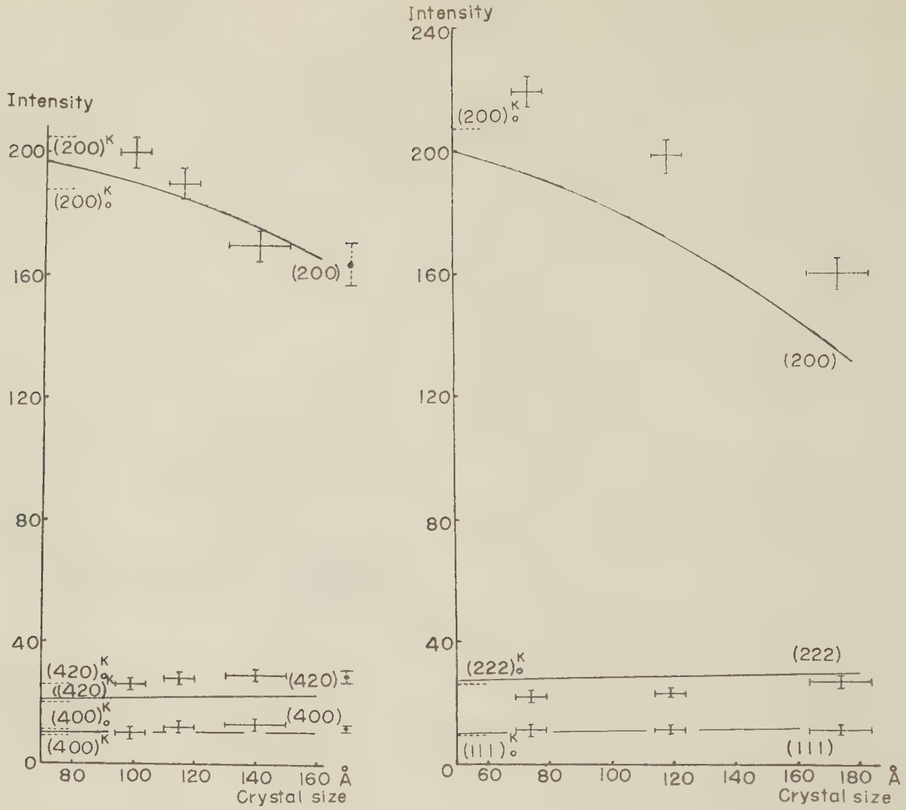

(e) KCl (300Å in thickness). (f) MgO (Mg, 100Å in thickness).

Fig. 4. Intensity variation with crystal size. (Accelerating voltage, 48 kV). Dotted plots show the results obtained from Yamzin and Shirai's experiments. Shirai did not show his result in terms of crystal size. Then only the intensity ratios should be compared with our result in the case of KCl.

and he did not observe any remarkable intensity change with the film thickness. His experimental values are plotted in Figs. 4 a–c.*

As is seen in these figures, his values do not deviate from those of the present investigation. They coincide with the kinematical values except the case of Au, if the temperature factor is not taken into account. This agreement, however, does not mean the holding of the kinematical theory.

Comparison with the results of the other investigators. G. P. Thomson[1)], Mark and Wierl[2)] and Shirai[3)] reported that the observed intensity agreed with the values expected by the kinematical theory, but all of them neglected the temperature factor. The results obtained by them are tabulated in Table IV. Comparing these results with Table III and Fig. 4, it can be said that their results contain the dynamical effect for low order reflections as (111) and (200) except the case of Al.

Ornstein *et al.*[4,5)] and Lennander *et al.*[6,7)] reported that the kinematical theory could not be applied for their specimen films. The results obtained by them are also shown in Table IV. Their values show much more deviation from the kinematical values than those of G. P. Thomson and others.

In conclusion, the kinematical theory can be applied when the crystal size of the specimen is very small, and the intensity varies gradually when the crystal size becomes larger. In analysing the data it is necessary to take into account the temperature effect which is too large to be neglected.

Acknowledgements

The present experiment was suggested by

---

* Yamzin calculated the crystal size by using half-width. The accelerating voltage in his experiment was 45, 53 and 42 kv for Al, Ag and Au, respectively.

Table IV. Intensity ratios reported by the previous investigators.

	Specimen	(111)	(200)	(220)	(311)	(222)	(400)	(331)	(420)	(422)	(333)
Thomson (30kV)	Au	518		100	120		(12)	51		22	
Mark & Wierl (50–60kV)	Al	798	280	100	75	—	—	16	—	10	10
	Ag	504	214	100	93	—	—	24	—	15	18
	Au	430	181	100	84	—	—	28	—	17	11
Tol & Ornstein (30kV)	Ag	302	145	100	109	—	—	26	24	15	—
	Au	343	125	100	100	—	—	31	27	—	—
Lennander (30kV)	Al	480	187	100	92	—	—	16	14	—	—
	Ag	410	171	100	106	—	—	26	23	15	—
	Au	353	132	100	107	—	—	38	29	23	—
Shirai (44–67kV)	KCl	—	164	100	—	24	12	—	29	14	—

Prof. S. Miyake of Tokyo Institute of Technology, whom the author wishes to express his hearty thanks. He is also indebted to Prof. Ryozi Uyeda of Nagoya University and Assist. Prof. G. Honjo for their kind advices and discussions. Thanks are also due to Prof. H. Tazaki of Hiroshima University for his kind interest and encouragement throughout this experiment.

References

1) G. P. Thomson: Proc. Roy. Soc. **125** (1929) 352.
2) H. Mark and R. Wierl: Zeits. Physik **60** (1930) 741.
3) S. Shirai: Proc. Phys.-Math. Soc. Japan **15** (1933) 420.
4) L. S. Ornstein, H. Brinkman, A. Hauer and T. Tol: Physica **5** (1938) 693.
5) T. Tol and L. S. Ornstein: Physica **7** (1940) 685.
6) S. Friesen and S. Lennander: Ark. Math. Ast. Fys. **A 33** (1946) 16.
7) S. Lennander: Ark. Fys. **8** (1954) 551.
8) M. Blackman: Proc. Roy. Soc. **173** (1939) 68.
9) Communications au III Cong. Int. Cryst. (1954) Paris.
10) I. I. Yamzin: Trudy Inst. Krist. Akad. Nauk **5** (1949) 69.
11) I. I. Yamzin and Z. G. Pinsker: Dokl. Akad. Nauk **65** (1949) 645.
12) Z. G. Pinsker: *Electron diffraction* (1953) London.
13) G. Honjo: Jour. Phys. Soc. Japan **8** (1953) 776; **9** (1954) 184.
R. Uyeda, T. Ichinokawa and Y. Fukano: Acta Cryst. **7** (1954) 216; 217.
S. Miyake and R. Uyeda: Acta Cryst. **8** (1955) 335.
14) J. Karle and I. I. Karle: Jour. Chem. Phys. **18** (1950) 957.
15) K. Kimoto: Jour. Phys. Soc. Japan **8** (1953) 762.
16) S. Kuwabara: Jour. Phys. Soc. Japan **10** (1955) 416.
17) *International Tables for the Determination of Crystal Structures* Vol. 2 (1939).

JOURNAL OF THE PHYSICAL SOCIETY OF JAPAN Vol. 12, No. 6, JUNE, 1957

Effect of the Basic Strength of Attached Groups on Light Absorption Spectra I.

Light Absorption of Triphenylmethane Dyes

By Reikiti ITOH*

Kobayasi Institute of Physical Research Kokubunzi, Tokyo

(Received August 28, 1956)

The electronic energy levels of typical triphenylmethane dyes, Döbner's Violet and Rosaniline, are calculated through the simple LCAO MO method. The electron densities and the bond orders in the ground states are also computed. Then, with these values of electron densities and the bond orders, the differences of the coulomb and of the resonance integrals, $\Delta\alpha_i$ and $\Delta\beta_{ij}$, respectively, as well as those between the carbon and the nitrogen atoms are taken into account and the electronic energy levels calculated above are modified by perturbation method. The differences of the coulomb integrals between the carbon and the nitrogen atoms cause profound effects to the absorption energy which amount to 23~27 Kcal (40~50 %), whereas those of different carbon atoms affect to the absorption only 4 Kcal (10 %). The energy levels of the various derivatives of Döbner's Violet and Rosaniline, e.g. dimethyl and diethyl derivatives of Döbner's Violet, Malachite Green, Brilliant Green, Hoffmann's Violet, Crystal Violet, Ethyl Violet etc. are also calculated by the method of perturbation. The values of the coulomb integrals of attached end groups are estimated through the basicity of the groups. The calculated absorption energies for these derivatives are compared with the observed light absorptions and it is shown that the course of the calculations is reasonable.

§ 1. Introduction

It is well known that the absorption spectra of triphenylmethane dyes e.g. Döbner's Violet and Rosaniline vary in wave length[1] and intensities with the terminal groups attached to phenyl groups. Although there are evidences that three phenyl groups are not in the same plane, Brickstock and Pople[2] calculated the resonance energies and charge distributions of triphenylmethyl group by means of semi-empirical molecular orbital method in S. C. F. scheme, asuming as if they were planer, and their treatment seems to be allowable in the first order approximation. In this paper, the absorption spectra and charge distributions of triphenylmethyl group with two or three substituents are calculated by the perturbation method in the simple semi-empirical MO theory. In the latter part of this paper (§ 5, 6), the correlations between the basicities of terminal groups and the absorption spectra of the triphenylmethane dyes are investigated. The data of absorption spectra and pK_b of these dyes are collected in Table I and IX.

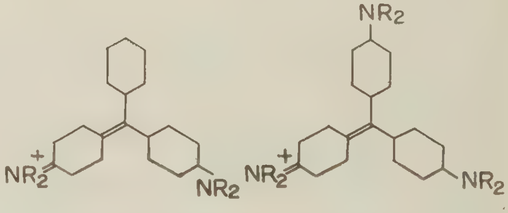

Fig. 1. Cations of Triphenylmethane dyes.

In these dyes, altering basicity of the terminal groups influences the light absorption as it does in the dyes of cyanine type; increasing basicity shifts the absorption band towards longer wave lengths. Thus, Döbner's Violet (I) and its dimethyl (II) and diethyl (III) derivatives absorb the light of higher frequencies than Malachite Green (IV), while the tetraethyl derivative, Brilliant Green (V), absorbs at lower frequencies. In the same manner, Rosaniline (I′) derivatives, i.e. Hoffmann's Violet (III′), Crystal Violet (IV′) and Ethyl Violet (V′), also absorb the light of

---

* Previous name R. Miyasaka was altered by R. Itoh.

Table I. The light absorption of Triphenylmethane dyes[1].

NR_2 group	No. of Days	absorption wave length	No. of Days	absorption wave length
NH_2	I	5616 A	I′	5430 A
$NH(CH_3)$	II	5870	II′	——
$NH(C_2H_5)$	III	5898	III′	5850
$N(CH_3)_2$	IV	6160	IV′	5905
$N(C_2H_5)_2$	V	6230	V′	5961

longer wave lengths than Rosaniline in this order.

In the first place, the light absorptions of the dyes (I) and (I′) will be computed by semi-empirical LCAO MO method with first order perturbation. In the second place, the light absorptions of other dyes (11), (111), ···(IV′) and (V′) etc. will be computed by the use of pK_b data of their terminal groups.

§ 2. Theoretical Preparations

It is assumed that electronic absorption bands of these dyes arise from transitions involving only the π electrons, not the σ electrons, and our attention will be restricted to the former. It is convenient to express the molecular orbitals (MO) of the electrons as linear combinations of suitable atomic orbitals (LCAO approximation). Each MO is then written in the form

$$\psi=\sum_{r} c_r\phi_r\,, \qquad (1)$$

where ϕ_r is the $2p\pi$ orbital of the r-th atom. The predictions will all be made by the following prescription;

(1) Compute the roots, x, of the secular equation determining the LCAO MO's, neglecting overlap integrals, and setting all coulomb integrals α_i and all resonance integrals β equal.

(2) Compute the one electron energies corrected for $\Delta\alpha_1$, which is the difference in coulomb integral between carbon atoms and nitrogen atoms and is assumed to be

$$\Delta\alpha_1=1.6\beta^{6)}.$$

(3) These energies are expressed in terms of β. Then put $\beta=-3\,\text{eV}$.

With these assumptions, the equations determining the MO's take the form

$$(\alpha-\mathcal{E})c_r+\sum_{\substack{s\text{ bonded}\\ \text{to } r}}\beta_{rs}c_s=0\,, \qquad (2)$$

or, more briefly,

$$-xc_r+\sum_{\substack{s\text{ bonded}\\ \text{to } r}}c_s=0\,, \qquad (3)$$

where $x=(\mathcal{E}-\alpha)/\beta$ and c_r is the MO coefficient of the r-th atom.

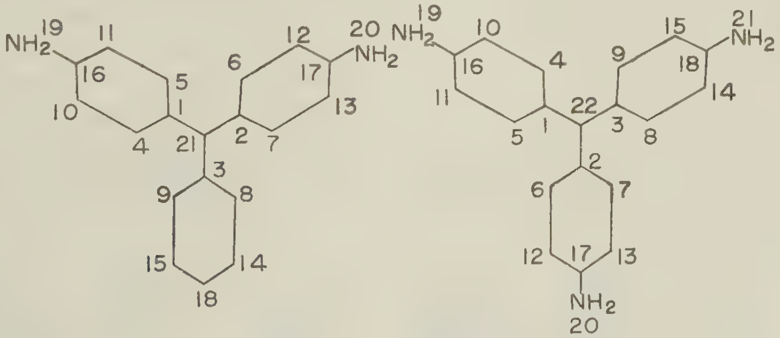

Fig. 2. The ith atom is denoted by number i in the figures of Döbner's Violet and Rosaniline.

1) Molecular Orbitals in Döbner's Violet

The molecule of Döbner's Violet consists of triphenylmethyl radical and two amino groups as shown in Fig. 1, and the symmetry group of this dye is C_{2v} as shown in Fig. 2, if assuming the planer configuration, and it has 21 atoms of which the number is shown in Fig. 2. The π MO's are, by definition, all antisymmetric with respect to the molecular plane and therefore belong to the species A_2 and B_2 as follows. From the character table of the irreducible representations of this group we have for the splitting of $\Gamma(C_{2v})$ representation

$$\begin{array}{lcccc} \text{operation} & E & C_2 & \sigma_v & \sigma_{v'} \\ \Gamma(C_{2v}) & 21 & -3 & -21 & 3 \end{array}$$

into its irreducible components

$$\Gamma(C_{2v})=9A_2+12B_2\ ,$$

Species of B_2: the molecular orbitals of species B_2 may be written in the form

$$\begin{aligned}\psi(B_2)=&c_1(\phi_1+\phi_2)+c_2(\phi_5+\phi_6)+c_3(\phi_4+\phi_7)\\&+c_4(\phi_{11}+\phi_{12})+c_5(\phi_{10}+\phi_{13})\\&+c_6(\phi_{16}+\phi_{17})+c_7(\phi_{19}+\phi^{20})+c_8\phi_3\\&+c_9(\phi_8+\phi_9)+c_{10}(\phi_{14}+\phi_{15})\\&+c_{11}\phi_{18}+c_{12}\phi_{21}\end{aligned}$$

We see $c_2=\pm c_3$, $c_4=\pm c_5$ (the double signs are to be read in the same order) and the approximate MO's are of the forms

$$\begin{aligned}\psi(B_2)=&c_1(\phi_1+\phi_2)+c_2(\phi_4+\phi_5+\phi_6+\phi_7)\\&+c_3(\phi_{10}+\phi_{11}+\phi_{12}+\phi_{13})\\&+c_4(\phi_{16}+\phi_{17})+c_5(\phi_{19}+\phi_{20})\\&+c_6\phi_3+c_7(\phi_8+\phi_9)+c_8(\phi_{14}+\phi_{15})\\&+c_9\phi_{18}+c_{10}\phi_{21}\\ \psi'(B_2)=&c_1(\phi_4-\phi_5-\phi_6+\phi_7)\\&+c_2(\phi_{10}-\phi_{11}-\phi_{12}+\phi_{13})\end{aligned}$$

Species A_2: the MO's of species A_2 have the nodal planes through atoms 21, 3, 18 and they have the form

$$\begin{aligned}\psi(A_2)=&c_1(\phi_2-\phi_1)+c_2(\phi_7-\phi_5)+c_3(\phi_6-\phi_4)\\&+c_4(\phi_{13}-\phi_{10})+c_5(\phi_{12}-\phi_{11})\\&+c_6(\phi_{17}-\phi_{16})+c_7(\phi_{20}-\phi_{19})\\&+c_8(\phi_8-\phi_9)+c_9(\phi_{14}-\phi_{15})\end{aligned}$$

but, since there is no interaction between the group of the atoms 8, 9, 14 and 15, and the other atoms, the MO's will be the form with $c_2=\pm c_3$, $c_4=\pm c_5$ (the double signs are to be read in the same order):

$$\begin{aligned}\psi(A_2)=&c_1(\phi_2-\phi_1)+c_2(\phi_6+\phi_7-\phi_5-\phi_4)\\&+c_3(\phi_{12}+\phi_{13}-\phi_{10}-\phi_{11})\\&+c_4(\phi_{17}-\phi_{16})+c_5(\phi_{20}-\phi_{19})\\ \psi'(A_2)=&c_1(\phi_4-\phi_5+\phi_6-\phi_7)\\&+c_2(\phi_{10}-\phi_{11}+\phi_{12}-\phi_{13})\\ \psi''(A_2)=&c_1(\phi_8-\phi_9)+c_2(\phi_{14}-\phi_{15})\end{aligned}$$

Thus the secular equation of π MO can be reduced and the determinants of $5(A_2)$, $2(A_2)$, $2(A_2)$, $10(B_2)$ and $2(B_2)$ ranks are obtained. In the case of $5(A_2)$, equation (3) gives

$$\begin{aligned}-xc_1+2c_2&=0\ ,\\-xc_2+\ c_1+c_3&=0\ ,\\-xc_3+\ c_2+c_4&=0\ ,\\-x_4+2c_3+c_5&=0\ ,\\-xc_5+\ c_4&=0\ .\end{aligned}$$

Eliminating the coefficients c_r, we have

$$\begin{vmatrix}-x&2&0&0&0\\1&-x&1&0&0\\0&1&-x&1&0\\0&0&2&-x&1\\0&0&0&1&-x\end{vmatrix}=-x^5+6x^3-7x=0$$

As this equation gives five roots x_i $(i=1, 2, 3, 4, 5)$, there are 5 MO's of specy A_2, with energies $\varepsilon_i=\alpha+\beta x_i$. The ratios of the coefficients c_r for each of these are obtained by substituting the appropriate x_i back into the linear equations, and their absolute magnitudes are determined by the normalized condition of MO;

Table II. The normalized AO coefficients and energy levels of MO in species B_2 of C_{2v}, where most of higher vacant orbitals are omitted.

C_{2v}, B_2, 10 ranks

$x=$	2.408088	2.040468	1.663987	1.079817	0.320359	−0.320359
c_1	0.357080	0.098895	−0.254779	−0.182179	0.120938	0.120938
c_2	0.210532	0.139689	−0.040681	−0.156559	−0.187087	0.187087
c_3	0.149900	0.186137	0.187086	0.013124	−0.180874	−0.180874
c_4	0.150440	0.240117	0.351990	0.170730	0.129143	−0.129143
c_5	0.062473	0.117678	0.211534	0.158110	0.403119	0.403119
c_6	0.342548	−0.356104	−0.060501	0.490046	−0.109594	−0.109594
c_7	0.193072	−0.324516	0.120940	0.206373	−0.224027	0.224027
c_8	0.122387	−0.306060	0.261743	−0.267202	0.037825	0.037825
c_9	0.101647	−0.299990	0.314597	−0.494902	0.236144	−0.236144
c_{10}	0.438816	−0.077587	−0.342587	0.116399	0.412919	−0.412919

$$\begin{aligned}\psi(B_2)=&c_1(\phi_1+\phi_2)+c_2(\phi_4+\phi_5+\phi_6+\phi_7)+c_3(\phi_{10}+\phi_{11}+\phi_{12}+\phi_{13})+c_4(\phi_{16}+\phi_{17})+c_5(\phi_{19}+\phi_{20})\\&+c_6\phi_3+c_7(\phi_8+\phi_9)+c_8(\phi_{14}+\phi_{15})+c_9\phi_{18}+c_{10}\phi_{21}\end{aligned}$$

Table III. The normalizid AO coefficients of MO in species A_2 of C_{2v}, except those of vacant levels.

C_{2v}, A_2, 5 ranks

$x=$	2.101004	1.259280	0.000000
c_1	0.237981	0.397052	0.267261
c_2	0.250000	0.250000	0.000000
c_3	0.287270	−0.082232	−0.267261
c_4	0.353554	−0.353554	0.000000
c_5	0.168279	−0.280758	0.534522

$$\psi(A_2)=c_1(\phi_2-\phi_1)+c_2(\phi_6+\phi_7-\phi_5-\phi_4)$$
$$+c_3(\phi_{12}+\phi_{13}-\phi_{10}-\phi_{11})+c_4(\phi_{17}-\phi_{16})+c_5(\phi_{20}-\phi_{19})$$

2 ranks

$x=$	1.00000	−1.00000
c_1	0.50000	0.50000
c_2	0.50000	−0.50000

$$\psi''(A_2)=c_1(\phi_8-\phi_9)+c_2(\phi_{14}-\phi_{15})$$

Table IV. AO coefficients of MO's and their energy levels in species A_2 and B_2 of C_{2v}.

C_{2v}, A_2, B_2, 2 ranks

$x=$	1.00000	−1.00000
c_1	0.35355	0.35355
c_2	0.35355	−0.35355

$$\psi'(A_2)=c_1(\phi_4-\phi_5+\phi_6-\phi_7)+c_2(\phi_{10}-\phi_{11}+\phi_{12}-\phi_{13})$$
$$\psi(B_2)=c_1(\phi_4-\phi_5-\phi_6+\phi_7)+c_2(\phi_{16}-\phi_{11}-\phi_{12}+\phi_{13})$$

$$2c_1^2+4c_2^2+4c_3^2+2c_4^2+2c_5^2=1\,.$$

The values of x_i and the corresponding values of c_r are given in Table II, III and IV.

2) Molecular Orbitals in Rosaniline

As shown in Fig. 2, the spatial symmetry of Rosaniline is D_{3h}, if we assume the planer configuration as before, and it has 22 atoms of which the number is shown in the figure. MO's are of species A_1'', A_2'' and E'' as shown in the following. From the character table and the character of $\Gamma(D_{3h})$ representation

operation	E	$2IC_6$	$2C_3$	σ_h	$3U$	$3\sigma_v$
$\Gamma(D_{3h})$	22	−1	1	−22	−4	4

we have the splitting of $\Gamma(D_{3h})$ representation into its irreducible components;

$$\Gamma(D_{3h})=2A_1''+6A_2''+7E''.$$

The MO's of these species have the form

$$\psi(A_1'')=c_1(\phi_4-\phi_5+\phi_6-\phi_7+\phi_8-\phi_9)$$
$$+c_2(\phi_{10}-\phi_{11}+\phi_{12}-\phi_{13}+\phi_{14}-\phi_{15})\,,$$
$$\psi(A_2'')=c_1\phi_{22}+c_2(\phi_1+\phi_2+\phi_3)$$
$$+c_3(\phi_4+\phi_5+\phi_6+\phi_7+\phi_8+\phi_9)$$
$$+c_4(\phi_{10}+\phi_{11}+\phi_{12}+\phi_{13}+\phi_{14}+\phi_{15})$$
$$+c_5(\phi_{16}+\phi_{17}+\phi_{18})+c_6(\phi_{19}+\phi_{20}+\phi_{21})\,.$$

As the MO's of specy E'' occur in degenerated pairs, there is a certain freedom in the choice of the form of MO (though the energy of each pair is uniquely determined) and we will use the following form:

$$\psi_1(E'')=c_1(\phi_1+\omega\phi_2+\omega^2\phi_3)+c_2(\phi_4+\omega\phi_6+\omega^2\phi_8)$$
$$+c_3(\phi_5+\omega\phi_7+\omega^2\phi_9)$$
$$+c_4(\phi_{10}+\omega\phi_{12}+\omega^2\phi_{14})$$
$$+c_5(\phi_{11}+\omega\phi_{13}+\omega^2\phi_{15})$$
$$+c_6(\phi_{16}+\omega\phi_{17}+\omega^2\phi_{18})$$
$$+c_7(\phi_{19}+\omega\phi_{20}+\omega^2\phi_{21})\,,$$
$$\psi_2(E'')=\psi_1^*(E'')\,.$$

where $\omega=\exp(2\pi i/3)$ and $\psi_1^*(E'')$ is the conjugated complex of $\psi_1(E'')$. In the case of specy E'' it is obvious that $c_2=\pm c_3$, $c_4=\pm c_5$ and we have the form:

$$\psi_1(E'')=c_1(\phi_1+\omega\phi_2+\omega^2\phi_3)$$
$$+c_2(\phi_4+\phi_5+\omega\phi_6+\omega\phi_7+\omega^2\phi_8+\omega^2\phi_9)$$
$$+c_3(\phi_{10}+\phi_{11}+\omega\phi_{12}+\omega\phi_{13}$$
$$+\omega^2\phi_{14}+\omega^2\phi_{15})$$
$$+c_4(\phi_{16}+\omega\phi_{17}+\omega^2\phi_{18})$$
$$+c_5(\phi_{19}+\omega\phi_{20}+\omega^2\phi_{21})$$
$$\psi_1'(E'')=c_1(\phi_4-\phi_5+\omega\phi_6-\omega\phi_7+\omega^2\phi_8-\omega^2\phi_9)$$
$$+c_2(\phi_{10}-\phi_{11}+\omega\phi_{12}-\omega\phi_{13}$$
$$+\omega^2\phi_{14}-\omega^2\phi_{15})$$

and now

$$\psi_2(E'')=\psi_1^*(E'')\,,\quad \psi_2'(E'')=\psi_1'^*(E'')\,.$$

Table V. AO coefficients and energies in MO of species A_2'' in D_{3h}, most of higher vacant levels being omitted.

D_{3h}, A_2'', 6 ranks

$x=$	2.41422	1.73205	0.414214	−0.414214
c_1	0.43301	0.35355	0.43301	−0.43301
c_2	0.34846	0.20412	0.05979	0.05979
c_3	0.20412	0.00000	−0.20412	0.20412
c_4	0.14434	−0.20412	−0.14434	−0.14434
c_5	0.14434	−0.35355	0.14434	−0.14434
c_6	0.05979	−0.20412	0.34846	0.34846

$$\psi(A_2'')=c_1\phi_{22}+c_2(\phi_1+\phi_2+\phi_3)+c_3(\phi_4+\phi_5+\phi_6$$
$$+\phi_7+\phi_8+\phi_9)+c_4(\phi_{10}+\phi_{11}+\phi_{12}+\phi_{13}$$
$$+\phi_{14}+\phi_{15})+c_5(\phi_{16}+\phi_{17}+\phi_{18})$$
$$+c_6(\phi_{19}+\phi_{20}+\phi_{21})$$

Table VI. AO coefficients and energies of MO's of species E'' in D_{3h}, vacant levels being omitted.

D_{3h}, E'', 5 ranks

$x=$	2.101000	1.259280	0.000000
c_1	0.194311	0.324920	0.218218
c_2	0.204124	0.204124	0.000000
c_3	0.234554	−0.067142	−0.218218
c_4	0.288675	−0.288675	0.000000
c_5	0.137399	−0.229238	0.436436

$$\psi_1(E'')=c_1(\phi_1+\omega\phi_2+\omega^2\phi_3)+c_2(\phi_4+\phi_5+\omega\phi_6+\omega\phi_7+\omega^2\phi_8+\omega^2\phi_9)+c_3(\phi_{10}+\phi_{11}+\omega\phi_{12}+\omega\phi_{13}+\omega^2\phi_{14}+\omega^2\phi_{15})+c_4(\phi_{16}+\omega\phi_{17}+\omega^2\phi_{18})+c_5(\phi_{19}+\omega\phi_{20}+\omega^2\phi_{21}),$$

$$\psi_2(E'')=\psi_1{}^*(E'').$$

Table VII. AO coefficients and eneagy levels in MO's of species A_1'' and E'' in D_{3h}.

D_{3h}, A_1'', E'', 2 ranks

$x=$	1.00000	−1.00000
c_1	0.288675	0.288675
c_2	0.288675	−0.288675

$$\psi(A_1'')=c_1(\phi_4-\phi_5+\phi_6-\phi_7+\phi_8-\phi_9)+c_2(\phi_{10}-\phi_{11}+\phi_{12}-\phi_{13}+\phi_{14}-\phi_{15})$$

$$\psi_1'(E'')=c_1(\phi_4-\phi_5+\omega\phi_6-\omega\phi_7+\omega^2\phi_8-\omega^2\phi_9)+c_2(\phi_{10}-\phi_{11}+\omega\phi_{12}-\omega\phi_{13}+\omega^2\phi_{14}-\omega^2\phi_{15})$$

$$\psi_2'(E'')=\psi_1'{}^*(E'').$$

As described above, the spatial symmetry o the molecule leads to secular determinants o $2(A_1'')$, $6(A_2'')$, $5(E'')$ and $2(E'')$ ranks. Th values of x and c_r are readily obtained. Th results are given in Table V, VI and VII.

§ 3. Electron Densities and Bond Orders in Döbner's Violet and Rosaniline

It must be re-emphasized that the abov values of the energy parameter, x, and th AO coefficient, c_r, have been calculated on th assumption that all the nitrogen atoms an the carbon atoms have the same value o coulomb imtegral. Under this assumption, le us calculate the electron densities and mobil bond orders in the ground state. These ar defined by

$$q_r=\sum_{occ} c_r{}^2,\quad p_{rs}=\sum_{occ} c_rc_s \qquad (4$$

respectively, where the summations are taken over all the electrons in the occupied orbitals As there are 22π electrons in Dobner's Viole cation, each of the 10 MO's of positive x wil contain 2 electrons while there are 2 electron in the MO for which $x=0$. On the othe hand, as there are 24π electrons in the Rosaniline cation, 10 MO's of positive x (4 of them have no degeneracy, 3 pairs are doubly degenerated) and 2 MO's of $x=0$ (doubly degenerated) are occupied by 2 electrons each.

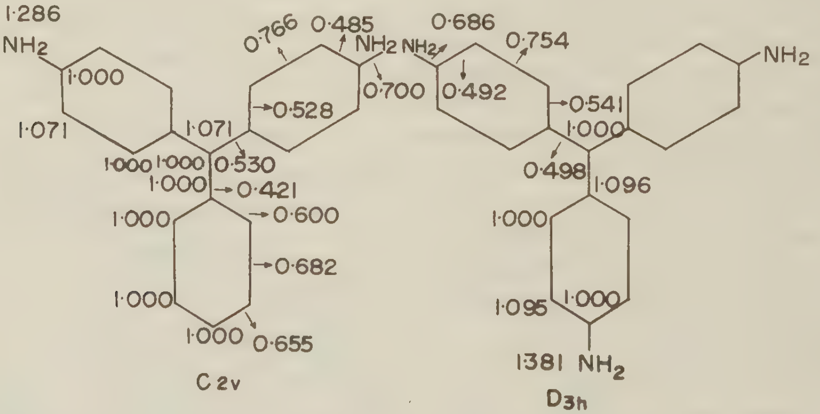

Fig. 3. Molecular diagrams of Döbner's Violet and Rosaniline. Values in the left hand side of the figures are those of π charge densities and the values denoted by an arrow are those of bond orders.

Summing over these orbitals, we obtain the values given in Fig. 3 for the electron densities and bond orders. It is intresting to note that π electron density is the highest on the atoms of terminal groups, even though no allowance has been made in the calculations for the greater electron affinity of nitrogen than carbon. This suggests two things. Firstly, this piling up of the electrons may reduce the electron affinity of nitrogen atoms and, hence, it may not be a poor approximation to set the coulamb integrals of nitrogen atoms equal to those of carbon atoms. Seondly, the basic strength of terminal groups vhich depends on the σ charge density of itrogen atoms, has some correlations with π harge density of the atoms. If the terminal roups becomes more basic, the non-bonding electrons (lone pair) of nitrogen are decreas-d by the induction effects of alkyl groups ttaching to the nitrogen atom.

4. Perturbation Treatments

In Döbner's Violet, f level (the highest oc-upied orbital) corresponds to the one with $x=0$ in A_2 species of C_{2v}, and g level (the low-st vacant orbital) corresponds to the one vith $x=--0.320359$ in B_2 species of C_{2v}. Electronic transition from one to another is llowed from symmetry consideration. It is lso readily known that in Rosaniline the lectronic transition between f level which is he one with $x=0$ in E'' of D_{3h} and g level which is the one with $x=--0.414214$ in A_2 of he same group is allowed from symmetry.

Up to this point, the common coulmb in-egral α is used for all atoms, but this is, of ourse, not correct, as nitrogen is more lectronegative than carbon, it has certainly ower value of α. Matsen[6] has indicated hat in the case of aniline the value of $\alpha_N-\alpha_c=\Delta\alpha_1=-4.8$ eV, is compatible with the spec-roscopic data. Here, too, the value of -4.8 eV, is used for $\Delta\alpha_1$, in both of Döbner's Vio-et and Rosaniline, where amino groups are he substituents for benzene rings. The value f resonance integral β is taken to be -3 eV.

By the first order perturbation theory the erturbed energy levels are given by

$$\mathcal{E}'=\mathcal{E}+\Delta\mathcal{E}\,, \qquad (5)$$

vhere $\Delta\mathcal{E}$ is given from the perturbed one lectron Hamiltonian H' as follows,

$$\Delta\mathcal{E}=(\psi(R)|H'|\psi(R)) = \sum_i c_i^2\Delta\alpha_i+\sum_{i,j} c_ic_j\Delta\beta_{ij}\,. \qquad (6)$$

In this expression, the second term can be estimated by the relation[3]

$$2\beta_{ij}=E_d-E_s + \frac{((1-p)/p)^2(k_s/k_c)^2-(k_s/k_d)}{1+(k_s/k_d)((1-p)/p)}(x_s-x_d)^2, \qquad (7)$$

where E_d and E_s are the bond energies -146 and -83 Kcal[4]; x_d and x_s are the bond lengths 1.34 and 1.54 A[5]; k_d and k_s are the force constants, $k_d=9.5\times10^5$ dyn/cm², $k_d/k_s=0.765$[3], suffixes d and s being refered to the double and the single bond respectively, and p is the bond order between the ith and jth atom. The standard value of β is taken to be -40.36 Kcal, which corresponds to the bond order of $p=2/3$, and the values of $\Delta\beta_{ij}$ are listed in Table VIII. With these values it can be shown that the effect of $\Delta\beta_{ij}$ on the calculated value of absorption energy is less than 2 Kcal. The first term of expression (6) is most important since it includes the nitrogen's large $\Delta\alpha_r$. $\Delta\alpha$'s for carbon atoms can be estimated by the following expression[7] to be also the same order as $\Delta\beta_{ij}$; in other words, the effects of $\Delta\alpha$'s other than $\Delta\alpha_1$ and $\Delta\beta$'s to the absorption energy are less than 10%:

$$\alpha_r=I_r+\left\{\frac{1}{2}\sum_{occ} c_i^2(E_r-I_r)\right\} \qquad (8)$$

where I_r is the ionization potential[8], -11.17 eV, of carbon atom from the valence state $C(sp^3, V_4)$ to $C^+(sp^2, V_3)$, and E_r is the electron affinity[8], -0.69 eV, of carbon atom in the valence state from $C^-(sp^4, V_3)$ to $C(sp^3, V_4)$. The standard value of α_r is taken to be -136.7 Kcal which corresponds to the atom with $q_r=1.00$, while $\Delta\alpha_r$'s of nitrogens are dominating terms in expression (6), the effect of the latter to the absorption energy being 23 ~ 27 Kcal, i.e. 40 ~ 50%. Therefore, we take only the main part of equation (6) into consideration, and the results obtained through

Table VIII. Values of bond orders and resonance integral differences computed by equation (7). Standard value of β is taken to -40.36 Kcal/Mol which corresponds to the bond order of 0.667.

C_{2v}	i–j	21–4	1–4	4–10	10–16	16–19	21–3	3–9	9–15	15–18
	p_{ij}	0.530	0.528	0.766	0.485	0.700	0.421	0.600	0.682	0.655
	$-\beta_{ij}$	34.46	35.28	44.25	31.72	46.16	31.29	40.20	45.23	43.71
	$\Delta\beta_{ij}$	5.90	5.08	−3.89	8.64	−5.80	9.07	0.16	−4.87	−3.35
D_{3h}	i–j	22–1	1–4	4–10	10–16	16–19				
	p_{ij}	0.498	0.541	0.754	0.492	0.686				
	$-\beta_{ij}$	32.98	34.97	43.81	32.70	41.14				
	$\Delta\beta_{ij}$	7.38	5.39	−3.45	7.66	−0.78				

simple perturbation with $\Delta\alpha_1 = -4.8$ eV and the resonance integral $\beta = -3$ eV are given in Table X.

§ 5. Relation between $\Delta\alpha_r$ and pK_b of Amino Groups

Various derivatives of Döbner's Violet and Rosaniline of the types II, III, IV, V and II′, III′, IV′, V′, etc. have the alkyl substituted amino groups as their end groups, and the existence of the correlation of the basic strength of these groups with the electronic absorption spectra is reasonably expected. If bases, B_i and B_j, correspond to the dye of the type I and J $(I<J)$, respectively, the terminal groups of B_j are more basic than those of B_i because of the electron donating character of NR_2 groups, and this causes the diminution of coulomb integrals of these groups, that is, if α_i and α_j are the coulomb integrals of the terminal groups in the bases B_i and B_j, respectively,

$$|\alpha_i| > |\alpha_j| \,. \tag{9}$$

In comparing the dissociation constants of two bases B_i and B_j in a given solvent at a given temperature, we consider the equilibrium

$$B_iH^+ + B_j = B_i + B_jH^+ \,. \tag{10}$$

Longuett-Higgins[9] has pointed out that the potential energy change occuring in reaction (10) is principally due to the difference in resonance energy between the species on the right hand side of the equation and those on the left. When the difference in resonance energy between B_iH^+ and B_i is indicated by $\Delta\mathcal{E}_i$, the above postulate may be written in the equation

$$\Delta\mathcal{E}_j - \Delta\mathcal{E}_i = 2.3RT(pK_{a_i} - pK_{a_j}), \tag{11}$$

where

$$pK_a = -\log K_a;\ K_a = \frac{[H_3O^+][B]}{[BH^+]} \,.$$

pK_a corresponds to the logarithmic equilibrium constant of the reaction

$$BH^+ + H_2O = B + H_3O^+. \tag{12}$$

In comparing the coulomb integral of terminal groups in B_i with that in B_j, it is convenient to postulate that the magnitude of coulomb integral α_i of NR_2 group depends up on the σ charge density on the group, the magnitude of which being proportional to the basic strength pK_b of NR_2 groups, in orde words, coulomb integral of terminal grou NR_2 is proportional to basicity, pK_b, of amin NHR_2, where

$$pK_b = -\log_{10} K_b;\ K_b = \frac{[BH^+][OH^-]}{[B]} \,,$$

K_b corresponds to the logarithmic equil brium constant of reaction (12). Then, pK and pK_b are related each other by

$$pK_a + pK_b = 14 \,.$$

Now it can be shown that if r is an ator in a conjugated system and if coulomb integra of atom r is altered by a small amount o $\Delta\alpha_r$, then the change in resonance energy o the system is given by[10]

$$\Delta\mathcal{E} = q_r \Delta\alpha_r \,,$$

where q_r is the π electron density at th position of atom r. This may be true in th case of bases B_i and B_j, where the differen ce, $\Delta\alpha_i - \Delta\alpha_j$, in coulomb integral of NR groups causes the difference in resonanc energy in B_i and B_j, and the above postulate may be summarized in the equations

$$\Delta\alpha_i - \Delta\alpha_j = k(pK_{b_i} - pK_{b_j}), \quad (13$$

$$\Delta\mathcal{E}_i - \Delta\mathcal{E}_j = q_r(\Delta\alpha_i - \Delta\alpha_j), \quad (14$$

where pK_b is the basic strength of amin NHR_2 and its values are shown in Table IX As it seems difficult to estimate the value o k in the exact manner, it was determine empirically by the data of Crystal Violet, an the value of $k = 0.4605$ eV was obtained.

Summarizing the above consideration on th situation of electronic sturcture, we rely o the two assumptions:

1) the differences in magnitudes of pK_b o NR_2 groups owing to σ charge density do no change appreciably the π electron density while 2) the induction effect of alkyl group which changes the ionization potential of NR groups correlates with coulomb integral o the groups, α_i, and the changes in α_i and α cause the resonance energy differences $\Delta\mathcal{E}$ $\Delta\mathcal{E}_j$ as shown in the above equations.

§ 6. Computed Absorption Spectra of Vari ous Derivatives

The terminal groups in the dyes of th types I, II, III, IV, V and I′, II′ III′, IV′, V are indicated in Table IX, in which the relat ve magnitudes in coulomb integrals and basi strengths of various NR_2 groups are given.

Table IX. Valtes of coulomb integrals and pK_b in alkyl substituted amino groups.

Dyes	NR_2 group	$\Delta\alpha_i K$ cal/mol	pK_b	literature
I, I′	NH_2	−110.64	4.75	a
II, II′	$NH(CH_3)$	−95.89	3.36	b
III, III′	$NH(C_2H_5)$	−95.57	3.33	c
IV, IV′	$N(CH_3)_2$	−95.15	3.29	a
V, V′	$N(C_2H_5)_2$	−92.28	3.02	b

a; Handbook of Chemistry (" *Kagaku Binran* "), Chem. Soc. of Japan, (1954) Maruzen.
b; I. M. Kolthoff: *Acid-Base Indicator*, Macmillan, N. Y. (1937) p. 384.
c; H. C. Brown and M. D. Talor: J. A. C. S. **69** (1947) 1332.

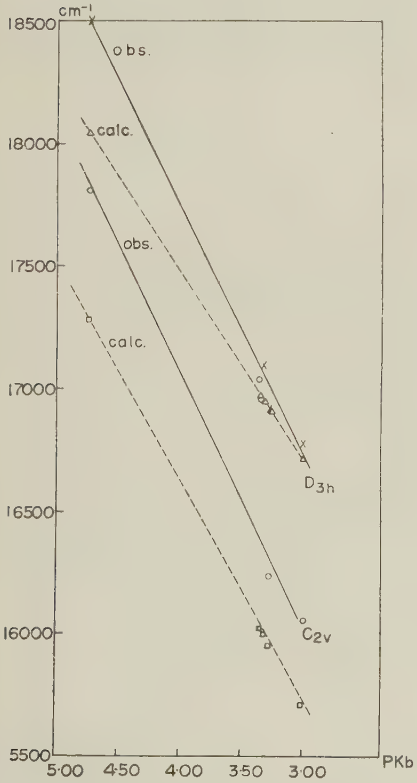

Fig. 4. The absorption frequencies, m⁻¹, of triphenylmethane dyes against the basic strength, pK_b, of their terminal groups NR_2 are shown by full lines (observed) and dotted lines (calculated).

The pK_b values in Table IX are based on activity in place of conceneration. The coulomb integral of the ith NR_2 groups is given by $\alpha_i = \alpha + \Delta\alpha_i$, where $\Delta\alpha_1$ is taken to be −4.8 eV from the data of Matsen and the other $\Delta\alpha_i$'s can be computed by equation (13). With the above values of $\Delta\alpha_i$ the predicted electronic transition energies are obtained in the same manner as in Döbner's Violet and Rosaniline by the simple perturbation method from the orbital coefficients of AO's in the present molecules which are iso-electronic with the Dye I and I′. The results are assembled in Table X.

The absorption frequencies of these dyes are compared in Table XI with experimental values in cm⁻¹ unit.

Table X. Calculated absorption energies of various derivatives in K cal/mol.

Base B_i	I	II	III	IV	V
C_{2v} Symmetry	49.42	45.79	45.71	45.60	44.90
Base B'	I′	II′	III′	IV′	V′
D_{3h} Symmetry	51.55	48.50	48.43	48.35	47.75

Table XI. Values of calculated and observed frequencies in cm⁻¹ unit.

NR_2	NH_2	$NHCH_3$	NHC_2H_5	$N(CH_3)_2$	$N(C_2H_5)_2$
Dye	I	II	III	IV	V
$\tilde{\nu}_{obs.}$	17810	17040	16960	16230	16050
$\tilde{\nu}_{calc.}$	17290	16020	15990	15960	15710
Dye	I′	II′	III′	IV′	V′
$\tilde{\nu}_{obs.}$	18510	—	17090	16920	16780
$\tilde{\nu}_{calc.}$	18040	16970	16950	16920	16710

These values are plotted in Fig. 4, where ordinate is absorption frequency in cm⁻¹ and abscissa is pK_b of NR_2 groups. It is now expected that electronic absorption energy is linear function of basic strength of terminal groups NR_2. In this diagram dyes of type II and III are somewhat deviated from the line for C_{2v} groups, but as the linear relation between absorption frequencies and basic strengths of substituents, NR_2, has been confirmed by the author[11)] in various aniline derivatives, the linearity will not be so far from the truth. Thus, it may be plausible to say that the computed transitions are in good agreement with experimental values within the error caused by slovent effects, and we may conclude that relative basic strength of alkyl substituted amino groups will be able to use as a measure of the relative magnitude in coulomb integral of the group.

The author would like to express his grati-

tude to Professor I. Oshida and Mr. Y. Ooshika for much stimulating and helpful discussions. This work was supported by the Scientific Research Fund granted by the Ministry of Education.

References

1) M. J. S. Dewar: *The Electronic Theory of Organic Chemistry*, McGraw-Hill, N. Y. 1949.
2) A. Brickstock and J. A. Pople: Trans. Farad. Soc. **50** (1949) 901.
3) C. A. Coulson: Proc. Roy. Soc. **A169** (1938) 413, Y. Ooshika: Busseiron Kenkyu No. **33** (1950) 95 (in Japanese).
4) C. A. Coulson: *Valence*, Oxford 1951, p. 18
5) ibid., p. 193.
6) F. A. Matsen: J. A. C. S. **72** (1950) 5243.
7) Y. Ooshika: Private communication. Fo references, see J. A. Pople: Trans. Fara Soc. **49** (1953) 1375, R. G. Parr and R. Pariser J. Chem. Phys. **23** (1955) 711, or reference 2
8) R. S. Mulliken: J. Chem. Phys. **2** (1934) 78
9) H. C. Longuett-Higgins: J. Chem. Phys. **1** (1950) 275.
10) C. A. Coulson and H. C. Longuett-Higgins Proc. Roy. Soc. **A 191** (1947) 39.
11) R. Miyasaka: Bull. of Kobayashi Inst. o Phys. Res. **6** (1956) 43, or see Part II of thi Paper.

JOURNAL OF THE PHYSICAL SOCIETY OF JAPAN Vol. 12, No. 6, JUNE, 1957

Structural Investigation by Means of Nuclear Quadrupole Resonance I

(Determination of Crystal Symmetry)

By Kenji SHIMOMURA

Minami Branch, Hiroshima University, Hiroshima

(Received October 13, 1956)

The number of nonequivalent directions of the z-axes of the field gradient in the crystal for every symmetry class is calculated. It is shown that we may discuss about the symmetry of the crystal and may determine the orientations of nonequivalent directions with respect to the axes of symmetry through the Zeeman analysis of nuclear quadrupole resonance line.

§ 1. Introduction

As was briefly reported[1], one may obtain the possible arrangements of resonant atoms by studying the multiplicity of pure quadrupole resonance spectrum and the intensity ratio of the multiplet. The values for the resonance frequency and asymmetry parameter of the field gradient at the resonant nucleus may give the percentage of ionic, single, and double bond character, which gives the bond distance.

A resonance line is attributed to all the resonant atoms which occupy the equivalent positions in crystal but the bond, or strictly speaking, the z-axis of the field gradient, at each equivalent position may have one of many different sorts of directions, called tentatively "*nonequivalent directions* (abbreviated to *N. E. D.*)". Since the behavior of th Zeeman splitting of nuclear quadrupole resonance line in the external magnetic field depends on the angle between the z-axis of th field gradient and the magnetic field, *N.E.D* may be determined through the investigatio of the Zeeman splitting. On the other hand since the positive and negative z-axes of th field gradient have the same behavior of Zeeman splitting, it will be noted that paralle and antiparallel directions of z-axis of the fiel gradient are not distinguished by this method Accordingly, these are called "*equivalent direction* (abbreviated to *E. D.*)". Bond direction which are usually coincident with the z-axes o the field gradient are decided through th Zeeman analysis of the resonance line, and fro these the orientation of axis of symmetry (o plane of symmetry), the molecular and crystal structure may be discussed.

§ 2. Calculations and Discussions

Since translations do not alter the bond (the z-axis of the field gradient) directions, so far as the number of *N. E. D.* is concerned, screw-axis and glide-plane are equivalent to simple axis and plane of symmetry, respectively. Consequently, the number of *N. E. D.* is the same in all space-groups which are derived from the same point-group. So it is only necessary to consider the simple space-group such as $C_1^1, C_2^1, C_{2h}^1, \ldots$ which may be built up by hanging one of the 32 point-groups at the lattice points of the simple space-lattice having appropriate symmetry characteristics.

Let the resonant atom whose coordinate is $(x_1y_1z_1)$ be covalently bonded to the partner atom whose coordinate is $(x_2y_2z_2)$, then each pair of atoms which situate at the positions which are crystallographically equivalent to $(x_1y_1z_1)$ and $(x_2y_2z_2)$ and correspond to the same coordinate of the point-group, e. g., $(x_1y_1\bar{z}_1)$ and $(x_2y_2\bar{z}_2)$, may also be bonded to each other, but the direction coefficient ratios of these bonds, such as $(x_1-x_2):(y_1-y_2):(z_1-z_2)$, are different from each other, hence the total number of *N. E. D.* at the resonant atoms which occupy the equivalent positions is generally equal to the number of coordinates of the point-group of the crystal. On the other hand, if the point-group contains the coordinates (xyz) and $(\bar{x}\bar{y}\bar{z})$, such as in the case of C_{2h}, the bond directions that correspond to (xyz) and $(\bar{x}\bar{y}\bar{z})$ are equivalent, hence in this case the number of *N. E. D.* is equal to one half the number of coordinates of the point-group.

On the other hand, when the bond lies along a special orientation, the number of *N. E. D.* will be less than the maximum number for the general case. For example, when the bond lies in a plane $z=$const. which is parallel to the (001) plane, if the point-group contains the coordinates $(xyz), (xy\bar{z})$ and the coordinates $(\bar{x}\bar{y}\bar{z}), (\bar{x}\bar{y}z)$ specifing the antiparallel bonds of the former two, respectively, it is very easy to verify that all bond directions which correspond to them are equivalent.

Generally, the special orientations in which the number of *N. E. D.* will decrease, may be constituted by 2-combinations of the following nine cases: $x=$const., $y=$const., $z=$const., $x=y$, $y=z$, $z=x$, $x=-y$, $y=-z$, $z=-x$, when each case may be repeated, where xyz are the coordinates refered to the reference axes XYZ of the space-group, and in this paper Wyckoff's notation[2] is adopted. So the number of special cases is equal to ${}_9H_2=45$ but all the independent cases among them are listed in Table I. In this Table, $x=c, x=y$, and $x=-y$ mean that the pair of atoms lie in the plane that satisfies $x_1=x_2, x_1-x_2=y_1-y_2$, and $x_1-x_2=y_2-y_1$, respectively. In such special cases, it is very easy to verify that the directions which correspond to the coordinates in Table IV in the appendix are equivalent. In these cases, the number of *N. E. D.* is equal to the total number of coordinates of the point-group divided by that which correspond to the equivalent directions. The results are listed in Table II. In each Table the second row is

Table I. Special cases.

Symbol	B_1	B_2	B_3	C_1	C_2	C_3	D_1	D_2	D_3	E_1	E_2	E_3	F_1	F_2	F_3	F_4	G_1	G_2	G_3	H_1	H_2	H_3
Specification	$z=c$	$x=c$	$y=c$	$x=c$ $z=c$	$x=c$ $y=c$	$y=c$ $z=c$	$x=y$	$y=z$	$z=x$	$x=-y$	$y=-z$	$x=-z$	$x=y$ $y=z$	$x=-y$ $x=-z$	$x=-y$ $x=z$	$x=y$ $x=-z$	$z=c$ $x=y$	$x=c$ $y=z$	$y=c$ $x=z$	$z=c$ $x=-y$	$x=c$ $y=-z$	$y=c$ $x=-z$

Table II. Number of *N.E.D.* of the *z*-axes of field gradient in the general and special orientations.

Triclinic System
C_1, C_i

Number of *N.E.D.*	1
Orientation of *z*-axis	General

Monoclinic System
C_s, C_2, C_{2h}

Number of *N.E.D.*	2	1
Orientation of *z*-axis	General	$\mathbf{B}_3$, $\mathbf{C}_1$ ∥ (010) , ⊥ (010)

Orthorhombic System
C_{2v}, D_2, D_{2h}

Number of *N.E.D.*	4	2	1
Orientation of *z*-axis	General	$\mathbf{B}_1$, $\mathbf{B}_2$, $\mathbf{B}_3$ ∥ (001) (100) (010)	$\mathbf{C}_1$, $\mathbf{C}_2$, $\mathbf{C}_3$ ⊥ (010) (001) (100)

Tetragonal System
S_4, C_4, C_{4h}

Number of *N.E.D.*	4	2	1
Orientation of *z*-axis	General	$\mathbf{B}_1$ ∥ (001)	$\mathbf{C}_2$ ⊥ (001)

D_{2d}, C_{4v}, D_4, D_{4h}

Number of *N.E.D.*	8	4	2	1
Orientation of *z*-axis	General	$\mathbf{B}_1$, $\mathbf{B}_2$, $\mathbf{B}_3$, $\mathbf{E}_1$, $\mathbf{D}_1$ ∥ (001) (100) (010) (110) $(1\bar{1}0)$	$\mathbf{C}_1$, $\mathbf{C}_3$, $\mathbf{G}_1$, $\mathbf{H}_1$ ⊥ (010) (100) (110) $(1\bar{1}0)$	$\mathbf{C}_2$ ⊥ (001)

Cubic System
T, T_h

Number of *N.E.D.*	12	6	4	3
Orientation of *z*-axis	General	$\mathbf{B}_1$, $\mathbf{B}_2$, $\mathbf{B}_3$ ∥ (001) (100) (010)	$\mathbf{F}_1$, $\mathbf{F}_2$, $\mathbf{F}_3$, $\mathbf{F}_4$ ⊥ (111) $(\bar{1}11)$ $(1\bar{1}1)$ $(11\bar{1})$	$\mathbf{C}_1$, $\mathbf{C}_2$, $\mathbf{C}_3$ ⊥ (010) (001) (100)

T_d, O, O_h

Number of *N.E.D.*	24	12	6	4	3
Orientation of *z*-axis	General	$\mathbf{B}_1$, $\mathbf{B}_2$, $\mathbf{B}_3$ $\mathbf{D}_1$, $\mathbf{D}_2$, $\mathbf{D}_3$ $\mathbf{E}_1$, $\mathbf{E}_2$, $\mathbf{E}_3$ ∥ (001) (100) (010) $(1\bar{1}0)$ $(01\bar{1})$ $(\bar{1}01)$ (110) (011) (101)	$\mathbf{G}_1$, $\mathbf{G}_2$ $\mathbf{G}_3$, $\mathbf{H}_1$ $\mathbf{H}_2$, $\mathbf{H}_3$ ⊥ (110) (011) (101) $(1\bar{1}0)$ $(01\bar{1})$ $(10\bar{1})$	$\mathbf{F}_1$, $\mathbf{F}_2$ $\mathbf{F}_3$, $\mathbf{F}_4$ ⊥ (111) $(\bar{1}11)$ $(1\bar{1}1)$ $(11\bar{1})$	$\mathbf{C}_1$ $\mathbf{C}_2$ $\mathbf{C}_3$ ⊥ (010) (001) (100)

Table II. (continued)

Hexagonal System

A. Rhombohedral Division

C_3, C_{3i}

Number of *N.E.D.*	3	1
Orientation of z-axis	General	$\mathbf{F}_1$
		$\perp(111)$

C_{3v}, D_3, D_{3d}

Number of *N.E.D.*	6	3	1
Orientation of z-axis	General	$\mathbf{C}_1$, $\mathbf{C}_2$, $\mathbf{C}_3$, $\mathbf{D}_1$, $\mathbf{D}_2$, $\mathbf{D}_3$	$\mathbf{F}_1$
		Parallel to the reference axes, $\parallel (1\bar{1}0)\ (01\bar{1})\ (\bar{1}01)$	$\perp(111)$

B. Hexagonal Division

C_{3h}, C_6, C_{6h}

Number of *N.E.D.*	6	3	1
Orientation of z-axis	General	$\mathbf{B}_1$	$\mathbf{C}_2$
		$\parallel(0001)$	$\perp(0001)$

D_{3h}, C_{6v}, D_6, D_{6h}

Number of *N.E.D.*	12	6	3	1
Orientation of z-axis	General	$\mathbf{B}_1$, $\mathbf{D}_1$, $\mathbf{E}_1$	$\mathbf{G}_1$, $\mathbf{H}_1$	$\mathbf{C}_2$
		$\parallel$ $(0001)\ (11\bar{2}0)$ $(1\bar{1}00)$	$\perp$ $(11\bar{2}0)$ $(1\bar{1}00)$	$\perp(0001)$

the symbols that specify the orientation of the z-axis of the field gradient and are defined in Table I, while the third row is another expression of the orientation; $\parallel(010)$ means that the z-axis lies in a plane parallel to the (010) plane, and $\perp(010)$ means that the z-axis is perpendicular to the (010) plane.

In the above discussion the resonant atom and its partner are assumed to be placed in the general positions, but even in the special cases in which the number of the equivalent coordinates of these atoms will be less than the maximum number of generally equivalent points, we may suppose that a pair of these atoms are moved to the general positions keeping the bond direction unaltered and that the other pairs of equivalent atoms are shifted simultaneously, maintaining the equivalent condition, then the results above-mentioned may be applied to this case, while since the bond directions are not altered in this process, the number of *N. E. D.* must be unaltered before and after this process. So to these cases the above-mentioned results can be applied. And in the above discussion, the z-axis of the field gradient is assumed to coincide with the bond axis, but even when this does not hold, we may assume an imaginary partner atom on the z-axis of the field gradient, so these results are applicable to these cases also.

Accordingly we may discuss about the crystal symmetry by studying the number and the relative orientations of *N.E.D.* For example, 2-*N. E. D.* is generally possible in the case of monoclinic symmetry but the crystals of orthorhombic or tetragonal symmetry may have 2-*N. E. D.* in the special cases; in the case of orthorhombic system 2-*N. E. D.* must lie in a plane perpendicular to one of the a-, b-, and c-axes and in the case of tetragonal system 2-*N. E. D.* must be perpendicular to each other. The *N. E. D.* of the x- and y-axes of the field gradient tensor may be useful in determining the crystal symmetry, if we have few *N. E. D.* But generally speaking, in order to determine the crystal symmetry, all *N. E. D.* of the z-axes of the field gradient must be found out.

By this method crystal of low symmetry can be treated rather easily than that of high symmetry, because in the low symmetry case few *N. E. D.* are expected to be found.

While, by means of Zeeman effect there is no distinction between positive and negative directions of the z-axis of the field gradient. The equivalence of these two directions means that, judged by the Zeeman effect, all crystals will seem to have a center of symmetry. The symmetry of the crystal judged by this method will therefore be that of one of the eleven point-groups of Table III.

Table III. The relation between crystallographic symmetry and symmetry judged by the Zeeman effect.

Crystallographic Symmetry	Symmetry judged by the Zeeman Effect.
1. Triclinic System	
C_1 C_i	C_i
2. Monoclinic System	
C_s C_2 C_{2h}	C_{2h}
3. Orthorhombic System	
C_{2v} D_2 D_{2h}	D_{2h}
4. Tetragonal System	
S_4 C_4 C_{4h}	C_{4h}
D_{2d} C_{4v} D_4 D_{4h}	D_{4h}
5. Cubic System	
T T_h	T_h
T_d O O_h	O_h
6. Hexagonal System	
A. Rhombohedral Division	
C_3 C_{3i}	C_{3i}
C_{3v} D_3 D_{3d}	D_{3d}
B. Hexagonal Division	
C_{3h} C_6 C_{6h}	C_{6h}
D_{3h} C_{6v} D_6 D_{6h}	D_{6h}

This relation is quite similar to that of the Laue symmetry2) in the X-ray crystallography. The zerosplitting-direction-pattern1)3) of Zeeman line corresponds to the Laue pattern i the X-ray analysis, and the Zeeman analys correspond to the Laue method in the X-ra crystallography.

§ 3. Summary

The number of *N. E. D.* of the z-axes

Table IV. Coordinates of the point-group that correspond to the *E. D.* in the special cases.

Special case	Coordinates that correspond to the *E.D.*
B$_1$	$(xyz),(\bar{x}\bar{y}\bar{z}),(xy\bar{z}),(\bar{x}\bar{y}z)$.
B$_2$	$(xyz),(\bar{x}\bar{y}\bar{z}),(\bar{x}yz),(x\bar{y}\bar{z})$.
B$_3$	$(xyz),(\bar{x}\bar{y}\bar{z}),(x\bar{y}z),(\bar{x}y\bar{z})$.
C$_1$	(xyz), $(xy\bar{z})$, $(\bar{x}yz)$, $(\bar{x}y\bar{z})$, $(\bar{x}\bar{y}\bar{z})$, $(\bar{x}\bar{y}z)$, $(x\bar{y}\bar{z})$, $(x\bar{y}z)$, (zyx), $(zy\bar{x})$, $(\bar{z}yx)$,$(\bar{z}y\bar{x})$, $(\bar{z}\bar{y}\bar{x})$, $(\bar{z}\bar{y}x)$, $(z\bar{y}\bar{x})$, $(z\bar{y}x)$.
C$_2$	(xyz), $(\bar{x}yz)$, $(x\bar{y}z)$, $(\bar{x}\bar{y}z)$, $(\bar{x}\bar{y}\bar{z})$, $(x\bar{y}\bar{z})$ $(\bar{x}y\bar{z})$, $(xy\bar{z})$, (yxz), $(\bar{y}xz)$, $(y\bar{x}z)$, $(\bar{y}\bar{x}z)$, $(\bar{y}\bar{x}\bar{z})$, $(y\bar{x}\bar{z})$, $(\bar{y}x\bar{z})$,$(yx\bar{z})$, $(x-y\ xz)$, $(x-y\ x\bar{z})$, $(x-y\ yz)$, $(x-y\ y\bar{z})$, $(x-y\ \bar{y}z)$, $(x-y\ \bar{y}\bar{z})$, $(x\ x-y\ z)$, $(x\ x-y\ \bar{z})$,$(\bar{x}\ x-y\ z)$, $(\bar{x}\ x-y\ \bar{z})$, $(y\ x-y\ z)$,$(y\ x-y\ \bar{z})$, $(\bar{y}\ x-y\ z)$, $(\bar{y}\ x-y\ \bar{z})$, $(x-y\ \bar{x}z)$, $(x-y\ \bar{x}\bar{z})$ } And the coordi nates havin the opposite up per signs t them.
C$_3$	(xyz), $(x\bar{y}z)$, $(xy\bar{z})$, $(x\bar{y}\bar{z})$, $(\bar{x}\bar{y}\bar{z})$, $(\bar{x}y\bar{z})$, $(\bar{x}\bar{y}z)$, $(\bar{x}yz)$, (xzy), $(x\bar{z}y)$, $(xz\bar{y})$, $(\bar{x}\bar{z}\bar{y})$, $(\bar{x}z\bar{y})$, $(\bar{x}\bar{z}y)$, $(\bar{x}zy)$, $(x\bar{z}\bar{y})$.
D$_1$	(xyz), $(\bar{x}\bar{y}\bar{z})$, (yxz), $(\bar{y}\bar{x}\bar{z})$.
D$_2$	(xyz), $(\bar{x}\bar{y}\bar{z})$, (xzy), $(\bar{x}\bar{z}\bar{y})$.
D$_3$	(xyz), $(\bar{x}\bar{y}\bar{z})$, (zyx), $(\bar{z}\bar{y}\bar{x})$.
E$_1$	(xyz), $(\bar{x}\bar{y}\bar{z})$, $(\bar{y}\bar{x}z)$, $yx\bar{z})$.
E$_2$	(xyz), $(\bar{x}\bar{y}\bar{z})$, $x\bar{z}\bar{y})$, $(\bar{x}zy)$.
E$_3$	(xyz), $(\bar{x}\bar{y}\bar{z})$, $(\bar{z}y\bar{x})$, $(z\bar{y}x)$.
F$_1$	(xyz), (xzy), (yzx), (yxz), (zxy), (zyx), $(\bar{x}\bar{y}\bar{z})$, $(\bar{x}\bar{z}\bar{y})$, $(\bar{y}\bar{z}\bar{x})$, $(\bar{y}\bar{x}\bar{z})$, $(\bar{z}\bar{x}\bar{y})$, $(\bar{z}\bar{y}\bar{x})$.
F$_2$	(xyz), (xzy), $(\bar{y}\bar{x}z)$, $(\bar{y}z\bar{x})$, $(\bar{z}\bar{x}y)$, $(\bar{z}y\bar{x})$, $(\bar{x}\bar{y}\bar{z})$, $(\bar{x}\bar{z}\bar{y})$, $(yx\bar{z})$, $(y\bar{z}x)$, $(zx\bar{y})$, $(z\bar{y}x)$.
F$_3$	(xyz), $(x\bar{z}\bar{y})$, $(\bar{y}\bar{x}z)$, $(\bar{y}\bar{z}x)$, $(z\bar{x}\bar{y})$, (zyx), $(\bar{x}\bar{y}\bar{z})$, $(\bar{x}zy)$, $(yx\bar{z})$, $(yz\bar{x})$, $(\bar{z}xy)$, $(\bar{z}\bar{y}\bar{x})$.
F$_4$	(xyz), $(x\bar{z}\bar{y})$, $(y\bar{z}\bar{x})$, (yxz), $(\bar{z}x\bar{y})$, $(\bar{z}y\bar{x})$, $(\bar{x}\bar{y}\bar{z})$, $(\bar{x}zy)$, $(\bar{y}zx)$, $(\bar{y}\bar{x}\bar{z})$, $(z\bar{x}y)$, $(z\bar{y}x)$.
G$_1$	(xyz), $(\bar{x}\bar{y}\bar{z})$, (yxz), $(\bar{y}\bar{x}\bar{z})$, $(xy\bar{z})$, $(\bar{x}\bar{y}z)$, $(yx\bar{z})$, $(\bar{y}\bar{x}z)$.
G$_2$	(xyz), $(\bar{x}\bar{y}\bar{z})$, $(\bar{x}yz)$, $(x\bar{y}\bar{z})$, (xzy), $(\bar{x}\bar{z}\bar{y})$, $(\bar{x}zy)$, $(x\bar{z}\bar{y})$.
G$_3$	(xyz), $(\bar{x}\bar{y}\bar{z})$, $(x\bar{y}z)$, $(\bar{x}y\bar{z})$, (zyx), $(\bar{z}\bar{y}\bar{x})$, $(z\bar{y}x)$, $(\bar{z}y\bar{x})$.
H$_1$	(xyz), $(\bar{x}\bar{y}\bar{z})$, (yxz), $(\bar{y}\bar{x}\bar{z})$, $(\bar{y}\bar{x}z)$, $(yx\bar{z})$, $(\bar{x}\bar{y}z)$, $(xy\bar{z})$.
H$_2$	(xyz), $(\bar{x}\bar{y}\bar{z})$, $(\bar{x}yz)$, $(x\bar{y}\bar{z})$, $(\bar{x}zy)$, $(\bar{x}\bar{z}\bar{y})$, (xzy),
H$_3$	(xyz), $(\bar{x}\bar{y}\bar{z})$, $(x\bar{y}z)$, $(\bar{x}y\bar{z})$, $(\bar{z}y\bar{x})$, $(z\bar{y}x)$, $(\bar{z}\bar{y}\bar{x})$, (zyx).

field gradient was calculated for every symmetry class. By studying the Zeeman splitting of the nuclear quadrupole resonance line one may discuss about the crystal symmetry and may determine the relative orientation of *N. E. D.* of the bond with respect to the symmetry axes of the crystal. It is concluded that, judged by the Zeeman analysis, all crystals will seem to have a center of symmetry, and that the crystal symmetry will therefore be that of one of the eleven point-groups and is quite similar to the symmetry of Laue photograph.

The author wishes to express his sincere thanks to Professor H. Tazaki for his kind guidance and Professor T. Fujiwara, Professor Y. Seiki of Hiroshima University and Professor R. Kiriyama of Ōsaka University for their helpful advices and encouragement. This work has been partly supported by the Scientific Research Expenditure of the Ministry of Education.

Appendix

The coordinates of the point-group that correspond to the *E. D.* in the special cases are listed in Table IV.

References

1) K. Shimomura: J. Chem. Phys. in press.
2) R. W. G. Wyckoff: *The Structure of Crystals*, second edition, Chem. Cat. Co. Inc., New York (1931) pp. 25–38, 127.
3) K. Shimomura: this journal.

JOURNAL OF THE PHYSICAL SOCIETY OF JAPAN Vol. 12, No. 6, JUNE, 1957

Structural Investigation by Means of Nuclear Quadrupole Resonance II

(Tin Tetrabromide)

By Kenji SHIMOMURA

Minami Branch, Hiroshima University, Hiroshima

(Received November 13, 1956)

Details of the universal quadrupole resonance crystal analyzer were described, and using this apparatus the crystal structure of SnBr was studied at room temperature (15°～20°C). The $SnBr_4$ molecule is an almost exact tetrahedron, and each of the four resonance lines is assigned to each bromine atom situated at the apexes of the tetrahedron, and the value of asymmetry parameter of the field gradient at the bromine nucleus is less than 0.025. The crystal has monoclinic symmetry and one of the Sn-Br bond in one molecule is perpendicular to the *b*-axis and the other two orient at the same angle to the *b*-axis. All atoms including Sn in a molecule have nonequivalent general positions in the crystal, and the number of molecules in a unit-cell is equal to the maximum number of equivalent coordinates of the space-group. The existence of pair of two molecules is suggested, and the origin of the splitting of the spectrum is discussed. $SnBr_4$ may be assigned to the symmetry class C_{2h}. The crystal symmetry of the low temperature phase is assigned to the cubic or hexagonal class.

§ 1. Introduction

The energy levels of interaction between a nuclear quadrupole moment Q and electric field V in a crystal for nuclear spin $I=3/2$ are[1]

$$E_{m=\pm 1/2}=-\frac{eQ}{4}q_{zz}\left(1+\frac{\eta^2}{3}\right)^{1/2}, \qquad (1)$$

$$E_{m=\pm 3/2}=\frac{eQ}{4}q_{zz}\left(1+\frac{\eta^2}{3}\right)^{1/2}, \qquad (2)$$

where η is an asymmetry parameter and is defined as

$$\eta=\left|\frac{q_{xx}-q_{yy}}{q_{zz}}\right| , \quad q_{xx}=\frac{\partial^2 V}{\partial x^2} , \quad q_{yy}=\frac{\partial^2 V}{\partial y^2} , \quad \text{etc.},$$

and x, y, z are the principal axes of the field gradient tensor, and z-axis is usually chosen so that

$$|q_{zz}|>|q_{yy}| , \quad |q_{xx}| .$$

If the static magnetic field is applied, the 2-fold degeneracy of the pure quadrupole energy levels is removed, and $E_{\pm 3/2}$ and $E_{\pm 1/2}$ are split into the energy levels $E_{+3/2}$, $E_{-3/2}$ and $E_{+1/2}$, $E_{-1/2}$, respectively. Consequently each resonance line for a given nucleus is split into four components (Fig. 1).

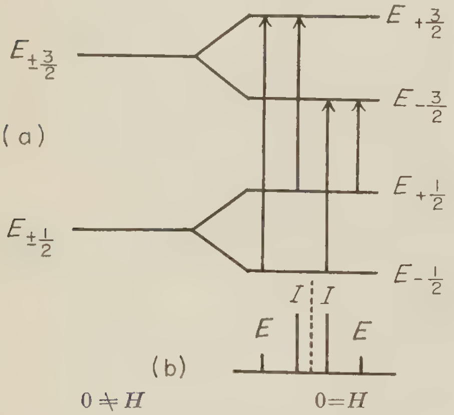

Fig. 1. (a) The energy diagram showing Zeeman splitting in the external magnetic field.
(b) Diagram illustrating the spacings of Zeeman lines. I and E denote the internal and external components, respectively.

The splitting depends on the orientation of the magnetic field with respect to the electric field gradient at that nucleus. In the special orientation of the magnetic field which satisfies the following relation

$$E_{+3/2}-E_{+1/2}=E_{-3/2}-E_{-1/2} , \tag{3}$$

the inner component lines coalesce to a single line. For $I=3/2$, this relation is satisfied when[2)]

$$\sin^2\theta=\frac{2}{3-\eta\cos 2\phi} , \tag{3'}$$

where θ, ϕ are the polar coordinates of the magnetic field with respect to the principal axes xyz (Fig. 2).

The relations between the multiplicity and the intensity ratio of the pure quadrupole resonance lines and crystal structure have been discussed in the previous paper[3)] whose notation will be employed here.

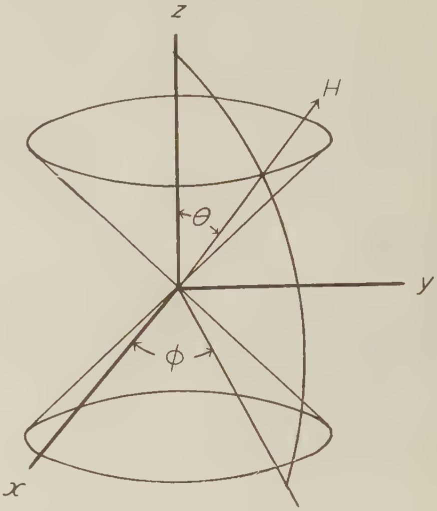

Fig. 2. Diagram illustrating a pair of zerosplitting cones. H denotes a direction of the magnetic field when the zerosplitting is observed. θ is called zerosplitting angle.

In this experiment, the method used in the author's previous measurement[4)] of the angle between the two nonequivalent directions[3)] of the bond in iodine crystal was employed, the apparatus, however, being improved in order to yield more exact determination of the bond angles.

The nuclear quadrupole resonance spectrum[5)6)] of $SnBr_4$ consists of three lines grouped together with a fourth line at noticeably lower frequency and there is a striking similarity[6)] in the spectra of $SnBr_4$, $SnCl_4$[7)], $GeCl_4$[7)], and $SiCl_4$[7)] which suggests that these substances may be isomorphous.

Since most of Group IV tetrahalides are liquid at room temperature and moreover easy to hydrolyze when exposed to moisture, the analysis of the crystal structure is difficult in the usual way.

§ 2. Determination of Structure

(a) Determination of field gradient orientation

Since Eq. (3′) does not contain the magnitude of the static magnetic field H, the zerosplitting angle θ is independent of the magnitude of the magnetic field, while, when $\eta\neq 0$, θ depends on ϕ, but when $\eta=0$, zerosplitting angle θ does not depend on ϕ and is equal to 54°44′. In a general case, zerosplitting is observed when the magnetic field orientates at angle θ that satisfies Eq. (3′), to the z-axis. The locus of zerosplitting direction is a circular cone ($\eta=0$) or roughly elliptical one ($\eta \neq 0$) about the z-axis. This cone is called "*zerosplitting cone*".

Let XYZ be the orthogonal coordinate system fixed to the crystal where Z-axis is chosen to be the rotational axis of the crystal. Let the laboratory coordinate system $X'Y'Z'$ be so chosen that Z'- and X'-axes lie in a horizontal plane, that Y'-axis is perpendicular to the $Z'X'$-plane, and that Z'-axis coincides with the Z-axis. The crystal is rotated about Z, and the external magnetic field H is rotated in a horizontal $Z'X'$-plane. Θ, Φ are the polar coordinates of H with respect to the XYZ axes (Fig. 3).

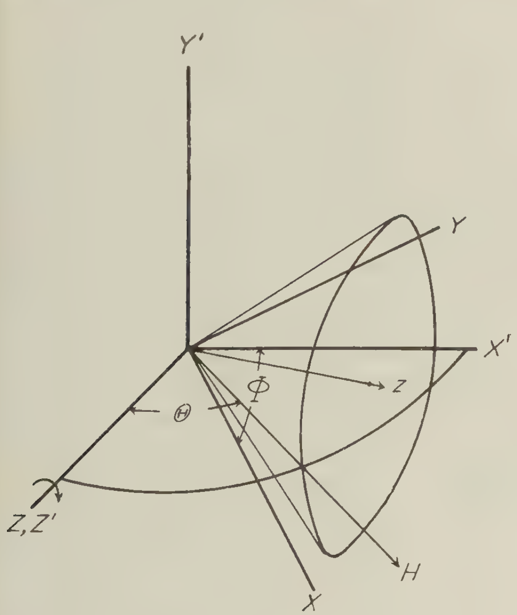

Fig. 3. The relative orientation of the two coordinate systems YYZ, $X'Y'Z'$. H represents the direction of the magnetic field which satisfies the zerosplitting condition (3′). Θ, Φ are the polar coordinates of H with respect to the XYZ system.

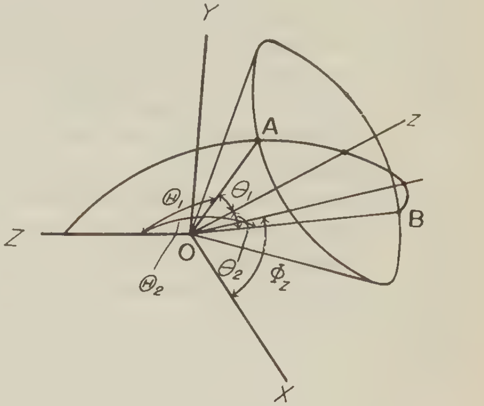

Fig. 4. The relation between zerosplitting cone and the plane which contains the z-axis and satisfies Φ=const.

When any independent values of Θ and Φ are chosen, any relative orientation of H with respect to the XYZ axes may be obtained. Consequently, in principle, the location of any zerosplitting direction is possible by this method. In order to determine the direction of the z-axis of the field gradient from the zerosplitting cone, let us suppose a plane that contains the z-axis and satisfies Φ=const. (Fig. 4), then this plane will intersect the zerosplitting cone along the two directions **OA** and **OB** which make the angles θ_1 and θ_2 with the z-axis, respectively. Since these two directions satisfy $\phi_1=\phi_2$, it is concluded that $\theta_1=\theta_2$ from Eq. (3′). Accordingly, the z-axis must lie in a locus of direction bisecting the angle between the intersecting lines of the zerosplitting cone with plane Φ=const. In the case of Θ=const. (Fig. 5) the same procedure may be applied when $\eta=0$, but

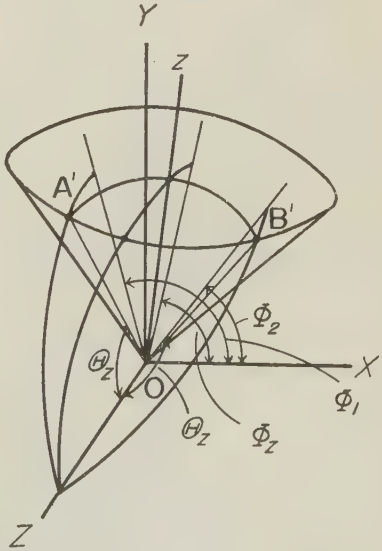

Fig. 5. The relation between zerosplitting cone and the surface which contains the z-axis and satisfies Θ=const.

when $\eta \neq 0$, this procedure is rather approximate, because the surface Θ=const. is not a plane. But in either of the following cases when (1) the z-axis is nearly perpendicular to the Z-axis, (2) either x- or y-axis lies nearly in a plane Φ=const., and (3) η is small and zerosplitting cone may be considered to be a spherical cone, we have good reason to do this. Thus, the orientation of the z-axis is determined from the two loci.

An alternate method was used to obtain the direction of the z-axis. The direction of H is made to coincide with the X'-axis, and then the crystal is rotated until the z-axis comes to be perpendicular to H (Fig. 6). This is easily found by the characteristic spectrum, i.e., the four components of Zeeman lines that are ascribed to one of the *N.E.D.**[3] coalesce into two lines. In that case the z-axis is expected to lie in the $Z'Y'$-plane. Let the crystal be rotated further by 90°, then the z-axis lies in the $Z'X'$-plane. And next, let the magnetic field be rotated in the $Z'X'$-plane, then the zerosplitting directions **AO**, **A′O** and the direction **BOB′** that is perpendicular to the z-axis are easily found. Consequently, the direction of the z-axis may be decided as a line perpendicular to **BOB′** or as the bisector of the angle $\angle$**AOA′**.

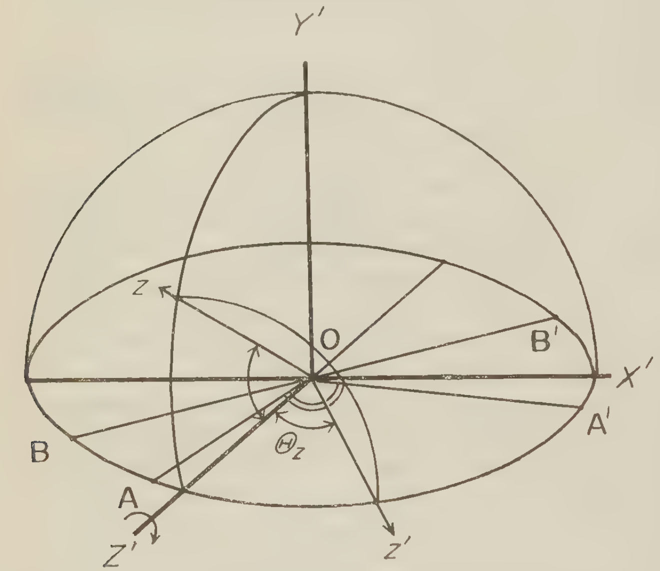

Fig. 6. Diagram illustrating an alternate way determining the direction of field gradient. z, z' denote the directions of the z-axis when it lies in the $Z'Y'$-, $Z'X'$-planes, respectively, hence $\angle Z'Oz' = \angle Z'Oz = \Theta_z$.

Let the z-axis be specified by the polar coordinates $(\Theta_z \Phi_z)$ where the angle Θ_z is measured from the Z-axis, and values for angle Φ_z is determined from a divided circle mounted on the shaft of the crystal holder. An excellent agreement was found between the results obtained by the two methods. But in the present experiment the former was chiefly employed.

(b) **Calculation of angle**

The angle α between the two directions $(\Theta_1 \Phi_1)$ and $(\Theta_2 \Phi_2)$ is calculated from the following equation:

$$\cos\alpha = \sin\Theta_1 \sin\Theta_2 \cos(\Phi_1 - \Phi_2) + \cos\Theta_1 \cos\Theta_2 . \qquad (4$$

(c) **Determination of orientation of two-fold axis of symmetry (or a line perpendicular to the plane of symmetry)**

Nonequivalent directions are systematically arranged about the axis of symmetry, which can be determined from the nonequivalent directions. In this paper we are concerned only with 2-fold axis of symmetry. This symmetry axis should bisect the angle between two proper *N.E.D.* of the z-axes, or be perpendicular to them, and it is easily found by plotting the directions of the z-axes on a globe. Three possible types of orientations of the axis of symmetry, i.e., **U**, **V** and **W** (Fig. 7) are calculated by the following equations where **U** and **V** are the internal and external

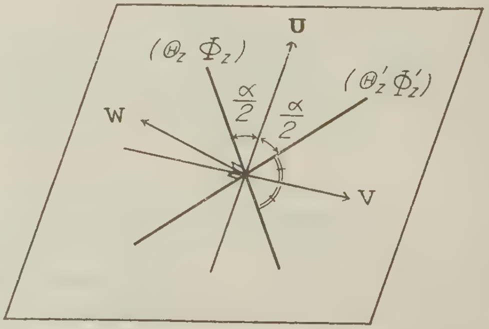

Fig. 7. Three possible types of 2-fold symmetry axis. $(\Theta_z \Phi_z)$, $(\Theta_z' \Phi_z')$ are the two proper *N.E.D.* of the z-axes.

---

* "*Nonequivalent directions of the z-axes of the field gradient tensor*" is abbreviated to *N.E.D.*

isectors of the angle between the two direcions of the z-axes $(\Theta_z\Phi_z)$, $(\Theta_z'\Phi_z')$, respectively, nd **W** is a perpendicular to them,

U:

$$\frac{\sin\Theta_z\cos\Phi_z+\sin\Theta_z'\cos\Phi_z'}{2\cos(\alpha/2)}=\sin\Theta_{\text{sym.}}\cos\Phi_{\text{sym.}}\,,$$

$$\frac{\sin\Theta_z\sin\Phi_z+\sin\Theta_z'\sin\Phi_z'}{2\cos(\alpha/2)}=\sin\Theta_{\text{sym.}}\sin\Phi_{\text{sym.}}\,,$$

$$\frac{\cos\Theta_z+\cos\Theta_z'}{2\cos(\alpha/2)}=\cos\Theta_{\text{sym.}}\,, \tag{5}$$

V: + should be replaced by − in the above equations.

W:

$$\frac{m_1n_2-m_2n_1}{\sin\alpha}=\sin\Theta_{\text{sym.}}\cos\Phi_{\text{sym.}}\,,$$

$$\frac{n_1l_2-n_2l_1}{\sin\alpha}=\sin\Theta_{\text{sym.}}\sin\Phi_{\text{sym.}}\,,$$

$$\frac{l_1m_2-l_2m_1}{\sin\alpha}=\cos\Theta_{\text{sym.}}\,,$$

$$l_1=\sin\Theta_z\cos\Phi_z\,,\quad m_1=\sin\Theta_z\sin\Phi_z\,,$$

$$n_1=\cos\Theta_z\,,\quad l_2=\sin\Theta_z'\cos\Phi_z'\,,\quad \text{etc.}, \tag{6}$$

where α denotes the angle between the two directions $(\Theta_z\Phi_z)$, $(\Theta_z'\Phi_z')$; and $(\Theta_{\text{sym.}}\Phi_{\text{sym.}})$ represents the direction of the symmetry axis.

(d) Determination of η

The angle θ between the z-axis $(\Theta_z\Phi_z)$ and the generating line of zerosplitting cone is calculated from Eq. 4. Using the maximum and minimum values for θ, η is determined from the formula[2)]

$$\eta=\frac{3(\sin^2\theta_{\text{max.}}-\sin^2\theta_{\text{min.}})}{\sin^2\theta_{\text{max.}}+\sin^2\theta_{\text{min.}}}\,. \tag{7}$$

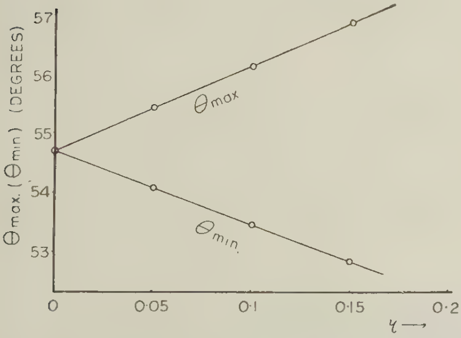

Fig. 8. $\theta_{\text{max.}}$ $(\theta_{\text{min.}})$ as a function of η. This graph was obtained by putting $\phi=0$ $(\phi=\pi/2)$ into Eq. (3).

The alternate method for obtaining the value of η is shown in Fig. 8. From the value of $\theta_{\text{max.}}$ or $\theta_{\text{min.}}$, the value of η may be determined. This method is easier than the former.

§ 3. Experimental Procedure

$SnBr_4$ was prepared by dropping bromine on tin metal, and was distilled at 201°C and sealed in a glass cylinder[8)] (diameter 2.5 cm) with a bottom tapered to a capillary tube of about 15 cm long (inside diameter 1 mm). The single crystal was obtained by descending the container slowly (at about 1 cm/hour) into water through a vertical furnace (at about 75°C) which has a large temperature gradient.

The apparatus was a frequency-modulated superregenerative detector of the CV6×2 push-pull Lecher-wire tuned type[6)], and the absorption lines for Br^{81} were observed on a persistent-screen cathode-ray oscilloscope. The spectrum was obtained with the sample at room temperature (15°~20°C).

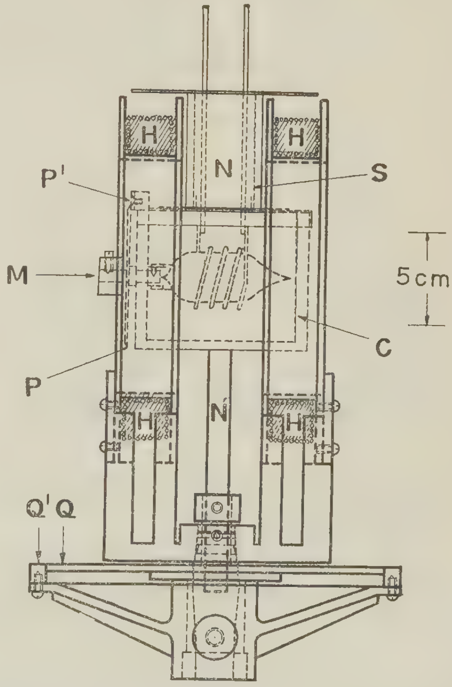

Fig. 9. The universal quadrupole resonance crystal analyzer. **H** denotes the Helmholtz coil.

As Fig. 9 shows, the crystal was set on the shaft **M** in a brass cylinder **C** which had been proved to be non-magnetic, and could be rotated about **M** as one pleases. No particular relative orientation of the sample with respect to the shaft **M** was needed in this apparatus. Values for angle Φ could be measured to

±0.1° from a divided circle **P**, which is mounted on the shaft **M**, and its vernier **P′**.

The external magnetic field, which was provided by a Helmholtz coil **H**, could be rotated about the axis of cylinder **C**, i.e., **N**-**N′** and the values for angle Θ could be measured to ±1′ from a divided circle **Q** and its vernier **Q′**.

Copper static shield **S** was used in order to eliminate the electrostatic effect on the Lecher-wire produced by the rotation of the Helmholtz coil. In order to keep the effect of still surviving faint magnetism constant during the rotation of the external magnetic field, axial symmetry was given to **C** and non-magnetic substance was used as much as possible.

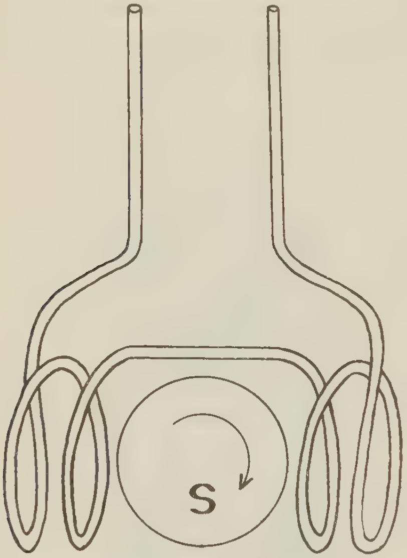

Fig. 10. The special coil used at the second step of the experiment. The sample S is rotated as this figure shows.

In the present experiment, two kinds of hf coils were used. At the first step, the axis of hf coil of usual type was taken nearly parallel to the rotation axis **M**, and the zerosplitting directions were observed on each line of $SnBr_4$. The intensity of the resonance line varies as the square of the sine of the angle between the rf magnetic field and the z-axis of the field gradient, accordingly, if the z-axis is nearly parallel to the hf coil axis (and therefore to the rotation axis **M**), the Zeeman line that is ascribed to it may be missed. In order to remove such apprehension, at the second step of the experiment another hf coil was used, the axis of which was taken perpendicular the rotation axis **M** (see Fig. 10). Then th zerosplitting line that was observed with di ficulty at the first step, became comparativel strong, and the variation of its intensity wit rotation of the sample was reduced, hence th possibility of missing the zerosplitting lin might be deminished. At the second step the experiment, the intensity variation of th resonance line with rotation of the sample i the absence of the external magnetic field wa observed. This results give a rough estimat of orientation of the z-axis of field gradient.

§ 4. Results Obtained

The pure quadrupole resonance absorptio of polycrystalline $SnBr_4$ in the absence o external magnetic field shows $M=4$ an $m_1:m_2:m_3:m_4=1:1:1:1$. Consequently one obtains the following five cases from Eqs (1), (2), and (3) of the previous paper[3] (see Table I). In the seventh column of Table I

Table I. Possible arrangements of **Br** atoms which satisfy Eqs. (1), (2), and (3).

Case	n_1	n_2	n_3	n_4	N	p_{ij}
a	4	0	0	0	1	$p_{11}=p_{12}=p_{13}=p_{14}=1$
b	3	1	0	0	2	
c	2	2	0	0	2	$p_{11}=p_{12}=p_{21}=p_{22}=2$
d	2	1	1	0	3	$p_{11}=p_{12}=2,\ p_{21}=p_{31}=4$
e	1	1	1	1	4	$p_{11}=p_{21}=p_{31}=p_{41}=4$

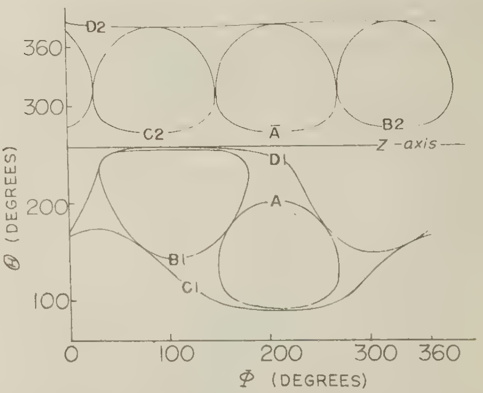

Fig. 11. Zerosplitting-direction-patterns of Zeeman lines of $SnBr_4$. Θ, Φ are polar coordinates with respect to the orthogonal coordinate axes XYZ fixed to the sample. Equivalent patterns are omitted in order to avoid confusion. **A**, **B1**, **B2**, etc. represent the zerosplitting-directions of Zeeman lines at the nuclei $\mathbf{Br_A}$, $\mathbf{Br_{B1}}$, $\mathbf{Br_{B2}}$, etc., respectively.

the arrangements of atoms that do not satisfy the intensity relation are not included. The quartet lines of $SnBr_4$ (in the absence of external magnetic field) are called ***A***, ***B***, ***C***, and ***D*** from the higher to the lower frequency.

Let the bromine atoms that contribute to the line ***B***, etc., be labeled as $\mathbf{Br_{B1}}$, $\mathbf{Br_{B2}}$, etc., briefly, where the latter subscript is used to discriminate the *N.E.D.* At the first step of the determination of zerosplitting direction on each line, it has been shown that ***A*** has only one *N.E.D.*, while $\mathbf{Br_{B1}}$ and $\mathbf{Br_{B2}}$ contribute to the line ***B***; $\mathbf{Br_{C1}}$, $\mathbf{Br_{C2}}$ to the line ***C***; and $\mathbf{Br_{D1}}$ to the line ***D***. While at the second step $\mathbf{Br_{D2}}$ has also been proved to contribute to the line ***D***.

These experimental results are shown in Fig. 11 in which the closed or unclosed contour shows zerosplitting direction of each line. The orientations of the *z*-axes are plotted on a globe. As is shown in Plate 1, an axis of 2-fold symmetry (or a plane of symmetry) can be found.

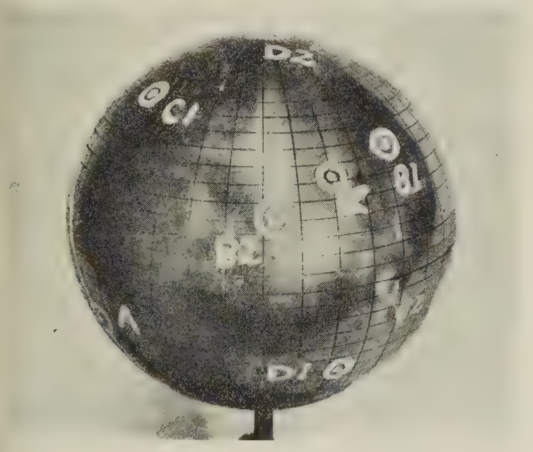

Plate 1. Plotting of directions of the *z*-axes of the field gradient on a globe. **A, B1, B2**, etc. represent the directions of the *z*-axes of the field gradient at the nuclei $\mathbf{Br_A}$, $\mathbf{Br_{B1}}$, $\mathbf{Br_{B2}}$, etc., respectively.

The intensity variation with rotation of the crystal at the second step of the experiment is shown in Fig. 12.

In the temperature range between about 10°C and the dry-ice temperature two closely spaced lines were observed; the resonance frequency being 161.15 Mc, 160.95 Mc for Br^{81} at 12°C. The higher frequency resonance line is three times more intense than the lower one (Fig. 13). This spectrum is noticeably different from those of the SnI_4 type crystals in the two points, namely the spacing and the intensity distribution of the doublets. These lines seem to be in good agreement with an earier measurement[5]. This spectrum suggests the existence of another phase of the crystal structure, which is tentatively called β-phase, while the high temperature phase so far studied mainly is called α-phase. When the β-phase of the crystal is heated near room temperature, an increase in volume occurs often resulting in the fracture of the glass container. This fact seems to correspond to the phase transformation.

In the temperature range between the liquid nitrogen and liquid air temperature, the striking four-lines spectrum indicates that the crystal has the same structure as that of the α-phase.

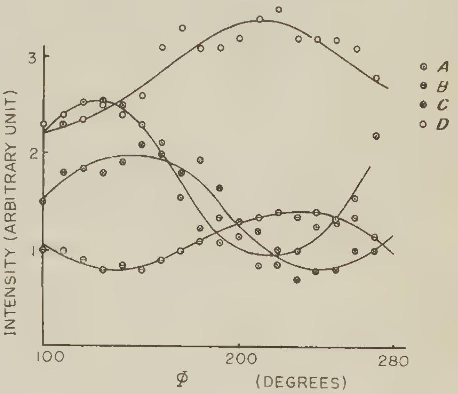

Fig. 12. The intensity variation of resonance lines with rotation of the sample in the hf field as shown in Fig. 10. The relative intensity of each line has no significance since each line was measured under different conditions, e.g., different quenching frequencies.

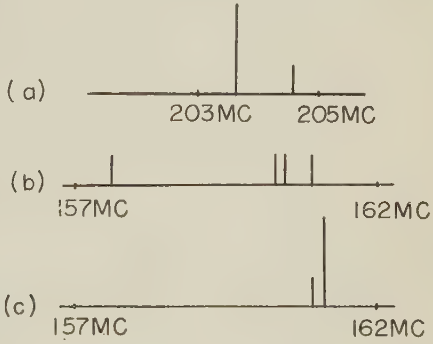

Fig. 13. Resonance spectra of SnI_4 and $SnBr_4$. (a) SnI_4, (b) α-$SnBr_4$, (c) β-$SnBr_4$.

§ 5. Discussions

The number of *N.E.D.* of the lines *A*, *B*, *C*, and *D* are 1, 2, 2, and 2, respectively. Accordingly the single crystal must have been perfect, since otherwise the line *A* could not have only one *N.E.D.* Moreover, one might expect no missed line, since at the second step, only $\mathbf{Br}_{\mathrm{D2}}$ was newly added and moreover $\mathbf{Br}_{\mathrm{A}}$, $\mathbf{Br}_{\mathrm{B1}}$, $\mathbf{Br}_{\mathrm{B2}}$, $\mathbf{Br}_{\mathrm{C1}}$, $\mathbf{Br}_{\mathrm{C2}}$, $\mathbf{Br}_{\mathrm{D1}}$ that had already been found at the first step and were expected to absorb weakly this time, were also observed, and since the positions of maxima and minima of each resonance line in Fig. 12 are compatible with Fig. 11. Accordingly, one may conclude that the crystal has monoclinic symmetry, because each line has 2-*N.E.D.*9) generally, and as Plate 1 shows, the crystal has only one 2-fold symmetry axis; i.e., *b*-axis, or a plane of symmetry.

And the fact that *A* has only 1-*N.E.D.* shows that cases (c), (d), and (e) are impossible, because in these cases the line *A* also must have more than 2-*N.E.D.* Consequently only case (a) is possible; each bromine and **Sn** atoms in a $\mathrm{SnBr_4}$ molecule situate at their own crystallographically general positions which are nonequivalent to each other, because each atom of $\mathrm{SnBr_4}$ molecule must possess the same number of equivalent positions in a unit cell from the relations $p_{11}=p_{12}=p_{13}=p_{14}=1$ and five atoms including **Sn** in the molecule cannot situate simultaneously at their own special positions10) having fewer equivalent points than the maximum number of generally equivalent ones in the monoclinic crystal. So the number of molecules in a unit-cell is equal to the maximum number of equivalent positions of the space-group of the crystal. If the number of molecules per unit-cell is determined from the density and dimensions of the unit-cell which are obtained by the X-ray method, the space-group may be discussed.

The angles between any two **Sn-Br** bond directions calculated from Eq. 4 using the data obtained from Fig. 11 are listed in Table II, where the value in parenthesis is the supplementary angle of the other. These two possibilities of the bond angle are due to the fact that the Zeeman effect cannot distinguish between the positive and negative directions of the *z*-axis of the field gradient. In order to determine the true one of these two possibilities one must rely on other data. Since the gas molecule of $\mathrm{SnBr_4}$ has been found to be an exact tetrahedron11), one may expect that this molecule is nearly an exact tetrahedron in the solid state also.

Table II. The angles between all the **Sn–Br** bonds in the crystal.

Sn	$\mathbf{Br}_{\mathrm{A}}$	$\mathbf{Br}_{\mathrm{B1}}$	$\mathbf{Br}_{\mathrm{B2}}$	$\mathbf{Br}_{\mathrm{C1}}$	$\mathbf{Br}_{\mathrm{C2}}$	$\mathbf{Br}_{\mathrm{D1}}$
$\mathbf{Br}_{\mathrm{A}}$						
$\mathbf{Br}_{\mathrm{B1}}$	70°19′ (109°41′)				Bond Angle	
$\mathbf{Br}_{\mathrm{B2}}$	70° 7′ (109°53′)	39°36′ (140°24′)			α $(180°-\alpha)$	
$\mathbf{Br}_{\mathrm{C1}}$	69°11′ (110°49′)	109°11′ (70°49′)	122°52′ (57° 8′)			
$\mathbf{Br}_{\mathrm{C2}}$	70°13′ (109°47′)	56°43′ (123°17′)	110°10′ (69°50′)	55°56′ (124° 4′)		
$\mathbf{Br}_{\mathrm{D1}}$	109°14′ (70°46′)	70°28′ (109°32′)	54°22′ (125°38′)	71°38′ (108°22′)	39° 2′ (140°58′)	
$\mathbf{Br}_{\mathrm{D2}}$	70°43′ (109°17′)	55°13′ (124°47′)	71°19′ (108°41′)	139°54′ (40° 6′)	109° 0′ (71° 0′)	122°35′ (57°25′)

Taking this into consideration, we find from Table II that each of the groups $\mathbf{Br}_{\mathrm{A}}$, $\mathbf{Br}_{\mathrm{B1}}$, $\mathbf{Br}_{\mathrm{C1}}$, $\mathbf{Br}_{\mathrm{D1}}$ and $\mathbf{Br}_{\bar{\mathrm{A}}}$, $\mathbf{Br}_{\mathrm{B2}}$, $\mathbf{Br}_{\mathrm{C2}}$, $\mathbf{Br}_{\mathrm{D2}}$ belongs to each molecule where the symbols **A**, $\bar{\mathbf{A}}$ mean that the atoms that contribute to the resonance line *A* have *E.D.* of the *z*-axis. This fact is more easily verified in Fig. 11, where the contours that correspond to $\mathbf{Br}_{\mathrm{A}}$, $\mathbf{Br}_{\mathrm{B1}}$, $\mathbf{Br}_{\mathrm{C1}}$, $\mathbf{Br}_{\mathrm{D1}}$ (or $\mathbf{Br}_{\bar{\mathrm{A}}}$, $\mathbf{Br}_{\mathrm{B2}}$, $\mathbf{Br}_{\mathrm{C2}}$, $\mathbf{Br}_{\mathrm{D2}}$)

ontact with each other, which means that $r_A Br_{B1} Br_{C1} Br_{D1}$, etc., may be an almost xact tetrahedron and that the value of η may e small, because two times of the zerosplitting angle $\theta = 54°44'$ corresponding to $\eta = 0$, is qual to 109°28′ which is the tetrahedral bond ngle. The relative orientation of each **Sn-Br** ond with respect to the b-axis is obtained by sing Eq. 5. The results are given in Fig. 14.

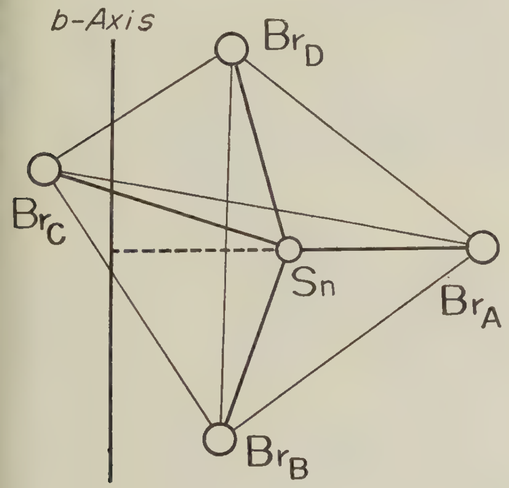

Fig. 14. Relative orientation of $SnBr_4$ tetrahedron with respect to the b-axis.

$\angle \mathbf{Br_A}\text{-}\mathbf{Sn}\text{-}\mathbf{Br_B} = 109°47' \pm 6'$,

$\angle \mathbf{Br_A}\text{-}\mathbf{Sn}\text{-}\mathbf{Br_C} = 110°18' \pm 31'$,

$\angle \mathbf{Br_B}\text{-}\mathbf{Sn}\text{-}\mathbf{Br_C} = 109°40' \pm 29'$,

$\angle \mathbf{Br_D}\text{-}\mathbf{Sn}\text{-}\mathbf{Br_A} = 109°16' \pm 2'$,

$\angle \mathbf{Br_D}\text{-}\mathbf{Sn}\text{-}\mathbf{Br_B} = 109°\ 7' \pm 25'$,

$\angle \mathbf{Br_D}\text{-}\mathbf{Sn}\text{-}\mathbf{Br_C} = 108°41' \pm 19'$,

$\mathbf{Sn}\text{-}\mathbf{Br_C}$, $\mathbf{Sn}\text{-}\mathbf{Br_D}$, $\mathbf{Sn}\text{-}\mathbf{Br_B}$, $\mathbf{Sn}\text{-}\mathbf{Br_A}$ orient at the angles $62°2' \pm 9'$, $61°18' \pm 24'$, $19°48' \pm 14'$, and $90°0' \pm 20'$, respectively, to the b-axis.

From Fig. 14 we may conclude that the molecule is an exact tetrahedron within the experimental accuracy, and that the predominant configuration of electron of covalent bond of **Sn** atom is $4s\,(4p)^3$.

As in the case of SnI_4[11)12)], the **Sn-Br** bond length in the solid state is assumed to be nearly equal to that of the gas molecule, i.e., 2.44Å[11)], and considerable amount of double ond character[6)] may be expected, nevertheless, it is concluded that the value of η at the r_A nucleus does not exceed 0.025, from Fig. using the value of zerosplitting angle of ig. 15. The small value of η is ascribed to he 3-fold symmetry character of the $SnBr_4$ olecule about the $\mathbf{Sn}\text{-}\mathbf{Br_A}$, etc. Consequently, we may conclude that each **Sn-Br** bond length is nearly equal. As Fig. 14 shows $\mathbf{Sn}\text{-}\mathbf{Br_A}$ is perpendicular to the b-axis (this is the reason why the line A has only 1-$N.E.D.$)[9)], while $\mathbf{Sn}\text{-}\mathbf{Br_C}$ and $\mathbf{Sn}\text{-}\mathbf{Br_D}$ have almost the same angle between the b-axis, and the plane $\mathbf{Br_B Br_C Br_D}$ may be almost parallel to the b-axis.

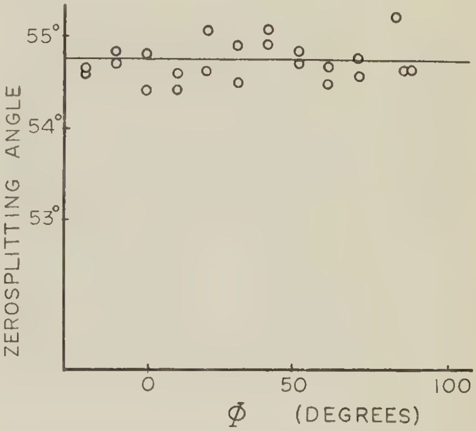

Fig. 15a. The zerosplitting angle θ as a function of Φ. The straight line at 54°44′ corresponds to $\eta = 0$.

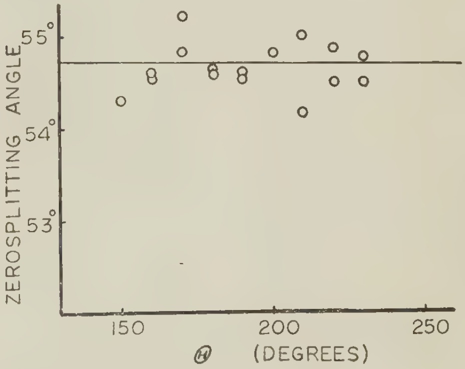

Fig. 15b. The zerosplitting angle θ as a function of Θ.

Unfortunately, the nuclear quadrupole resonance itself always introduces into the Zeeman analysis the effect of adding a center of symmetry to the crystal.[9)] It is therefore impossible on the basis of the Zeeman analysis alone to distinguish between C_s, C_2, and C_{2h}. But the resonance spectrum may discriminate these point-groups. The resonance frequency of $\mathbf{Br_D}$ atom is considerably lower (1.8%) than those of $\mathbf{Br_A}$, $\mathbf{Br_B}$, and $\mathbf{Br_C}$. The spacing of the multiplets is too large to be ascribed only to the difference of the nuclear sites* in the crystal. So it is concluded that the bond character of $\mathbf{Br_D}$ may be slightly different from those of $\mathbf{Br_A}$, $\mathbf{Br_B}$, and $\mathbf{Br_C}$.

The electric field gradient, that is produced primarily by the valence electron, at a given nucleus may be affected by the change in ionic character of the bonds due to electrostatic interactions[1)13)] between neighbouring ions. The consideration on the feature of the spectrum consisting of three lines grouped together with a fourth line at noticeably lower frequency indicates that the arrangement of surrounding molecules must have approximately three-fold symmetry character about the $\mathbf{Sn}$-$\mathbf{Br_D}$ bond. As concluded before, this substance has monoclinic symmetry, which has not three-fold axis, so we may deduce the existence of *pair of tetrahedral molecules*, whose interactions with each other are more prominent than those with the other neighbouring molecules, and which contribute three-fold symmetrical fields to each other. The three-fold symmetrical field will be given by the two neighbouring tetrahedral molecules whose $\mathbf{Sn}$-$\mathbf{Br_D}$ bond-directions are coincident. The models which are compatible with the striking pure quadrupole spectrum and with the relative orientation of the $SnBr_4$ tetrahedron with respect to the b-axis, are shown in Fig. 16. In the model (a) of Fig. 16, the base of each tetrahedron, i.e., $\mathbf{Br_A}$-$\mathbf{Br_B}$-$\mathbf{Br_C}$-$\mathbf{Br_A}$, sites opposite to that of the other one, and the edges $\mathbf{Br_A}\rightarrow\mathbf{Br_B}$, $\mathbf{Br_B}\rightarrow\mathbf{Br_C}$ and $\mathbf{Br_C}\rightarrow\mathbf{Br_A}$ of one tetrahedron are antiparallel to that of the other one, respectively, while in the other model (b), the two $\mathbf{Br_D}$ atoms in a pair of tetrahedrons face to each other along the line connecting the two $\mathbf{Sn}$ atoms. This pair of molecules which satisfy the relative orientation with respect to the b-axis can be realized in the crystal which has C_{2h} symmetry among the three possible symmetry class mentioned above.

While, in SnI_4[12)14)], GeI_4[12)14)], and SiI_4[12)14)] which have structures of the type (a) of Fig. 16, six $\mathbf{I}$ atoms which form the facing planes of the two tetrahedrons contribute to the low frequency line of the doublets[6)]. Hence, on the basis of the existence of pair of molecules of the type (a) the resonance frequencies of $\mathbf{Br_A}$, $\mathbf{Br_B}$, and $\mathbf{Br_C}$ may be expected to be lower than that of $\mathbf{Br_D}$ independently of the crystal structure. This conclusion is opposite to the spectrum, so we prefer the model (b). And moreover in the β-phase the stronger resonance line has higher frequency than the other, and this may also be interpreted by the use of the model (b).

While, in order to estimate the influence of the partner molecule in contrast with that of the other neighbouring molecules, let us consider the difference of the values of the following quantity at each resonant nucleus

$$u=\left|\frac{eQq}{(eQq)_{\mathrm{atom}}}\right|^{*}$$

where q is the magnitude of the field gradient at the resonant nucleus and $(eQq)_{\mathrm{atom}}$ is the atomic coupling constant.

Using the data on the resonance frequencies, one finds that Δu, the difference of the value of u at $\mathbf{Br_D}$ and the mean value of those at $\mathbf{Br_A}$, $\mathbf{Br_B}$, and $\mathbf{Br_C}$, is 9.7×10^{-3}. On the other hand, in SnI_4 in which the $\boldsymbol{A}$, $\boldsymbol{B}$, and $\boldsymbol{C}$ lines coalesce into a single line, Δu is 4.2×10^{-3}. Accordingly, Δu, the intermolecular interaction of $SnBr_4$, is about the same order of that of SnI_4.

On the other hand, Δu in the β-phase is 6.1×10^{-4}. This small value of Δu in the β-phase indicates that the origin of Δu in the α-phase is not due to the covalent bond between the pair of molecules but due to electrostatic interaction between neighbouring ions tending to lower the energy of the ionic form

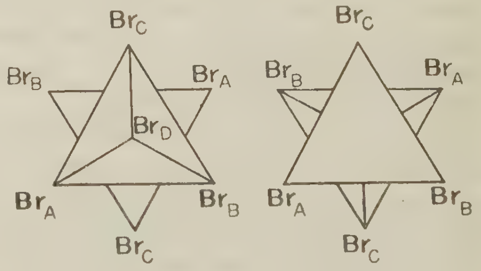

(a) (b)

Fig. 16. Proposed models of pair of molecules.

---

* The moderate spacings of the lines, $\boldsymbol{A}$, $\boldsymbol{B}$, and C, are ascribed to the nonequivalency of sites of the atoms, $\mathbf{Br_A}$, $\mathbf{Br_B}$, and $\mathbf{Br_C}$, which have almost the same bond character.

* On the estimation of the unbalanced p-electron, eQq in the numerature is usually evaluated from the mean value of the resonance frequencies of component lines of the multiplets.

of each **Sn**-**Br** bond, because if the former is the true origin of Δu, the same order of magnitude of Δu is expected also in the β-phase as in the α-phase.

The arrangements of molecules which are shown in Fig. 16 are possible in the space-groups of C_{2h}^2, C_{2h}^4, C_{2h}^5, and C_{2h}^6, and are impossible in the C_2 symmetry class. Fig. 17 shows an illustration of the arrangements of molecules.

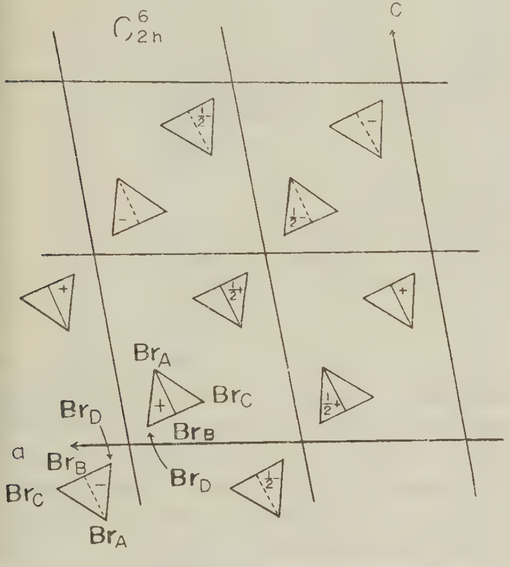

Fig. 17. An illustration of arrangement of $SnBr_4$ tetrahedrons. The b-axis is taken upwards from the plane of the paper, while the directions of the a- and c-axes which cannot be determined from this experiment, are drawn arbitrarily.

From the analysis of the spectrum of the β-phase, one may reasonably conclude that $p_{11}=3$, and $p_{12}=1$, and that the structure must have cubic or hexagonal symmetry. The bond direction connecting the central **Sn** atom with one of the four **Br** atoms in one molecule is coincident with three-fold symmetrical axis of this crystal, and the other three bromine atoms occupy the three equivalent positions about the three-fold axis. The small value of Δu in the β-phase is interpreted as follows; the neighbouring molecules distributed about the three-fold axis contribute the same order of magitude of intermolecular interaction as that between the pair of molecules.

A. E. Nordenskjöld[15] (1863) showed that the crystals form rhombic pyramids with axial ratios a : b : c = 0.556 : 1 : 1.487. But we cannot give orthorhombic symmetry on the basis of Zeeman analysis. This substance is so hygroscopic that the treatment in the air is very difficult, and the optical study has not yet been made with any success by us. The study of the crystal structure by the optical and X-ray methods will be performed in near future.

§ 6. Acknowledgement

The author wishes to express his sincere thanks to Professor R. Kiriyama of Osaka University for his helpful discussions, Professor H. Tazaki for his kind guidance and encouragement and Professor Y. Seiki of Hiroshima University for his interest and helpful discussions. A part of this work was supported by the Scientific Research Expenditure of the Ministry of Education.

References

1) C. H. Townes: J. Chem. Phys. **20** (1952) 35.
2) C. Dean: Phys. Rev. **96** (1954) 1053.
3) K. Shimomura: J. Chem. Phys. (in press).
4) K. Shimomura: Read April, 1954 at the Meeting of the Phys. Soc. of Japan (not yet published).
5) Kojima, Tsukada, Ogawa, and Shimauchi: J. Chem. Phys. **21** (1953) 1415.
6) K. Shimomura: J. Sci. Hiroshima Univ. Ser. A, **17** (1954) 383.
A. L. Schawlow: J. Chem. Phys. **22** (1954) 1211.
7) R. Livingston: J. Phys. Chem. **57** (1953) 496.
8) C. Cean: thesis, Harvard University (1952) (unpublished).
9) K. Shimomura: J. Phys. Soc. Japan (this journal).
10) W. P. Davey: *A Study of Crystal Structure and its Applications*, McGraw-Hill Book Co., New York (1934) p. 662.
11) P. W. Allen and L. E. Sutton: Acta Cryst. **3** (1950) 46.
12) R. W. G. Wyckoff: *Crystal Structure*, Vol. 1, Interscience Publishers, Inc., New York (1948).
13) C. H. Townes and A. L. Schawlow: *Microwave Spectroscopy*, McGraw-Hill Book Co., New York (1955) p. 228.
14) H. Robinson, H. G. Dehmelt, and W. Gordy: J. Chem. Phys. **22** (1954) 511.
15) P. Groth: *Chemische Krystallographie*, Teil 1, Wilhelm Engelmann, Leipzig (1906) S. 230.

JOURNAL OF THE PHYSICAL SOCIETY OF JAPAN Vol. 12, No. 6, JUNE, 1957

Microwave Studies of the Internal Motion and the Structure of Methyl Amine

By Tetsuji NISHIKAWA*

Department of Physics, Faculty of Science, University of Tokyo, Tokyo, Japan

(Received January 19, 1957)

This is the final report of a series of papers from this laboratory on the internal motion and the structure of methyl amine. Most of the observed lines including $J=1\leftarrow0$, $K=0\leftarrow0$ lines were analyzed in the frequency range between 4 and 50 kMc/sec. The barrier height of internal rotation has been determined to be 691.1 cm^{-1} as well as the molecular structure, $d_{\mathrm{CN}}=1.474$ A, $\angle\mathrm{HNC}=112°10'$, $\angle\mathrm{HNH}=105°50'$, $\angle\mathrm{HCH}=109°30'$ and the angle between CN and methyl axis$=3°30'$ on the assumption that $d_{\mathrm{CH}}=1.093$ A and $d_{\mathrm{NH}}=1.014$ A. These results were compared with the barrier height and the structure of other $\mathrm{CH_3\,MH}_n$ type molecules, methyl alcohol and methyl mercaptan.

The inversion doubling of the observed lines was also analyzed satisfactorily. The quadrupole coupling constant of N^{14} along the charge symmetry axis has been obtained as -3.6 ± 0.3 Mc/sec, with the direction of the axis, 90°±8, from the methyl axis.

§ 1. Introduction

Methyl amine is a unique molecule in microwave spectroscopy because of the remarkable effects of both internal rotation and inversion. The spectrum was observed in the frequency range between 4 and 34 kMc/sec by several workers[1,2,3]. Since the spectrum is very much complicated by the internal motion, former analyses were entirely incomplete. A previous study[1]**, however, showed that the internal rotation of the molecule can be treated by a theory similar to those of Dennison and others for methyl alcohol[4,5,6], with an additional treatment on the coupling between the internal rotation and inversion. The molecular structure calculated from frequencies of several lines by use of the theoretical method was reported by Itoh[7]. After these previous studies, the frequency range of observation has been extended to the millimeter wave region, where many important lines for the complete analysis, such as $J=1\leftarrow0$ line, have been found.

§ 2. Experimental Results

The spectrometer used and the frequencies of the lines previously observed were already reported in SNI. Since the spectrum of methyl amine consists of many lines due to complicated transitions, it was important to study the Stark effects of the lines precisely. All the observed lines can be classified into five classes according as they show whether

1) the first-order Stark effect with stronger outer components, 1(o),
2) the first-order effect with stronger inner components, 1(i),
3) the second-order Stark effect with positive Stark shift, 2(+),
4) the second-order effect with negative Stark shift, 2(−), or
5) the first-order effect similar to 1(o) in a weaker field ($\lesssim 100$ V/cm), and nearly the second-order effect, 2(+), in a stronger field, 1→2.

A high sensitivity Stark-modulation spectrometer for the millimeter wave region was also constructed. A frequency multiplier using a commercial crystal mixer, 1N 26, driven by a K-band klystron, 2K 33, was employed as the power source. The conversion loss of the multiplier was estimated to be less than 15 db for the second harmonics. A K-band waveguide absorption cell of one meter long sealed by teflon sheets of 1 mil thick was used. The Stark electrode was supported by teflon plates of 20 mils thick in a usual manner. The loss was as small as 0.7 db/ft at 48 kMc/sec. A detector current of more than 50 μA was ob-

---

* Present address: Institute for Nuclear Study, University of Tokyo, Tanashimachi, Tokyo, Japan.

** We shall refer it as SNI in this paper.

Table I. Microwave Spectrum of methyl amine, I. Lines in millimeter wave region.

	Frequency (Mc/sec)	Intensity	Stark-effect
q_2	41615.12	S	1→2
q_2	41615.76	S	1→2
	41658.42	MS	2(−)
s_2	41830.54	W	2(+)
r_2	42101.94	MW	2(+)
	42104.30	W	1(i)
s_2	42622.36	MW	2(+)
r_1	42720.94	S	2(+)
	42804.58	M	1(i)
	43040.72	M	1(i)
s_2	43220.12	MW	2(+)
q_1	43346.58	MW	1→2
	43404.8	WW	1(i)
	43498.32	W	2(−)
	43711.80	W	2(+)
	43728.61	W	2(+)
s_2	44188.60	M	2(+)
	44205.	WW	2(+)
	44214.	WW	2(+)
	44286.56	W	2(+)
	44462.1	WW	2(+)
s_2	44573.06	MW	2(+)
	44826.66	W	2(+)
	44967.40	WW	1(i)?
	45256.68	WW	1(i)?
q_2	45324.22	S	1→2
q_2	45325.04	S	1→2
	45336.60	WW	2?
	45458.06	W	2(+)
s_2	45759.26	MW	2(+)
r_2	45769.96	MW	2(+)
s_2	45865.08	M	2(+)
	45957.66	MW	1(i)
	45994.56	MS	1(i)
	46163.84	WW	2(+)
	46368.42	W	2(+)
	46544.84	MW	2(+)?
r_1	46575.18	S	2(+)
	46771.70	W	2(+)
	46855.6	WW	2?
q_1	47032.08	MW	1→2
s_2	47075.84	MW	2(+)
s_2	47239.84	MW	2(+)
	47334.60	W	1(i)
	47608.08	W	1(i)
	47732.44	W	1(i)?
	48082.01	MW	2(−)?
s_2	48180.38	MW	2(+)
	48243.46	W	2(+)
	48385.	W	2?
	48387.02	MS	2(+)
	48400.	WW	2?
	48404.06	W	1(i?)
	48414.83	M	1(i)
s_2	48547.14	MW	2(+)
	48715.82	W	2(+)
	48857.40	W	2(+)
q_2	49085.76	S	1→2
q_2	49086.38	S	1→2
s_2	49148.90	MW	2(+)
	49229.64	M	1(i)
	49426.06	W	1(i)
r_2	49560.00	M	2(+)
s_2	49614.02	MW	2(+)
	49914.58	MS	2(−)
s_2	49952.46	MW	2(+)
s_2	50399.24	W	2(+)
r_1	50423.40	MS	2(+)
s_2	50558.60	W	2(+)
q_1	50658.48	MW	1→2
s_2	50875.60	W	2(+)
s_2	50934.64	W	2(+)
s_2	51048.46	W	2(+)

tained at the output end of the absorption cell. About one hundred lines were found in the region between 40 and 50 kMc/sec. Their observed frequencies and Stark effects are listed in Table I.

After a careful study, some additional lines have also been found in the frequency range between 11 and 28 kMc/sec; they are given in Table II.

Table II. Microwave spectrum of methyl amine, II. Additional lines in centimeter wave region. (See also Table II in SNI.)

Frequency (Mc/sec)	Intensity	Stark-effect
11786.82	MW	2(+)
11819.80	W	2(+)
12445.	W	1(i)
13175.80	MW	1(i)
13177.04	MW	1(i)
14961.12	WW	1(i)?
16228.00	WW	1(i)?
16373.56	WW	1(i)?
17148.36	MW	2?
18308.64	MW	1(i)
18348.40	MW	2(+)
18476.	WW	2?
18486.	WW	2?
18928.16	WW	1?
20302.80	W	1(i)
22060.71	MW	2(+)
22082.37	W	1(i)
22369.95	W	1(i)
22381.96	W	1→2?
22507.42	WW	1(i)
22637.08	W	2(−)?
22818.83	W	1(i)
23071.58	W	2(+)
23090.83	WW	1(i)
23106.34	WW	1(i)
23608.52	W	2(+)
24037.31	W	1(i)
24465.58	WW	1(o?)
24472.77	WW	2(+)?
24634.0	WW	2?
24647.1	WW	2?
27553.24	WW	2(+)

§ 3. Theoretical Consideration

The energy level of methyl amine type molecule may be written as

$$W^{JK\mu n\pm}=W_0^{JK\mu n\pm}+\tilde{W}^{JK\mu n\pm} \tag{1a}$$

and $$W_0^{JK\mu n\pm}=W^{JK}+W^{K\mu n}+W^{n\pm}\,, \tag{1b}$$

where J and K are the usual rotational quantum numbers, n is the quantum number of torsional vibration, and $\mu(=0,\ \pm1)$* is the quantum number of hindered rotation; + or − indicates the inversion state, i.e. whether it corresponds to the triplet or singlet nuclear spin state of the two hydrogen nuclei in the amino group.

In equation 1(b), W^{JK} expresses the rotational energy when the molecule is assumed to be a rigid symmetric rotor, $W^{K\mu n}$ is the energy of internal rotation, and $W^{n\pm}$, which is also affected by K and μ because of the interaction with the internal rotation, is the energy of inversion. $\tilde{W}^{JK\mu n\pm}$ in equation 1(a) is the perturbation energy due to asymmetry.

From the theory developed by Itoh[7], W^{JK}, $W^{K\mu n}$, and $W^{n\pm}$ can be expressed by

$$W^{JK}=\frac{A+B}{2}(J(J+1)-K^2)-CK^2\,, \tag{2}$$

$$W^{K\mu n}=VR^{K\mu n}\,, \tag{3}$$

$$W^{n\pm}=\pm\frac{1}{2}(-1)^K\Delta_0\int_0^{2\pi}Q^{K\mu n*}(x)Q^{K\mu n}(x-\pi)dx\,, \tag{4}$$

where

$$A=\frac{h^2}{8\pi^2I_x}\,,\qquad B=\frac{h^2I_y}{8\pi^2(I_y^2+D^2)}\,,$$

$$C=\frac{h^2}{8\pi^2}\left(\frac{I_y+I_z}{I_yI_z-D^2}-\frac{I_y}{I_y^2+D^2}\right),$$

$$V=\frac{h^2}{8\pi^2}\frac{I_yI_z-D^2}{I_2(I_yI_1-D^2)}$$

I_x, I_y, and I_z are the moments of inertia about x, y and z axes, and D is the product of inertia with respect to y and z axes, z axis being parallel to the symmetry axis of methyl group, y axis being comprised in the bisecting plane of HNH angle, and the origin being taken at the center of masses of the molecule. I_1 is defined as $I_1=I_z-I_2$, where I_2 is the moment of inertia of methyl group about its symmetry axis. $R^{K\mu n}$ and $P^{K\mu n}(x)=e^{iKx}Q^{K\mu n}(x)$ are respectively the eigen value and the eigen function of the internal rotation which were introduced by Koehler and Dennison[4], whereas $\alpha=\frac{2\pi^2}{h^2}H_0\frac{I_1I_2}{I_z}$ and $\sigma=-\frac{I_1}{I_z}K$ in their equation are replaced by $\alpha'=\frac{2\pi^2}{h^2}H_0\left(\frac{I_2(I_yI_1-D^2)}{I_yI_z-D^2}\right)$ and $\sigma'=-\left(1-\frac{I_2\sqrt{I_y^2+D^2}}{I_yI_z-D^2}\right)K$. The potential barrier is assumed to be a sinusoidal form, $\frac{H_0}{2}(1-\cos 3x)$. The energy of inversion doubling can be calculated from equation (4), where the constant, Δ_0, would correspond to the hypothetical inversion splitting if the coupling between inversion and internal rotation were absent.

The perturbation energy $\tilde{W}^{JK\mu n\pm}$ in equation (1.a) consists of the terms due to the K, $K\pm1$ off-diagonal elements of the Hamiltonian and of the terms due to the K, $K\pm2$ elements. It can be expressed by

$$\begin{aligned}\tilde{W}^{JK\mu n\pm}&=\tilde{W}^{K}_{K\pm1}+\tilde{W}^{K}_{K\pm2}\\&=S^2\left[\frac{\left(K-\frac{1}{2}\right)^2(J-K+1)(J+K)(I^{K-1\mu n}_{K\ \ \mu n})^2}{W_0^{JK\mu n\pm}-W_0^{JK-1\mu n\pm}}+\frac{\left(K+\frac{1}{2}\right)^2(J-K)(J+K+1)(I^{K+1\mu n}_{K\ \ \mu n})^2}{W_0^{JK\mu n\pm}-W_0^{JK+1\mu n\pm}}\right]\\&+\frac{1}{4}(A-B)^2\left[\frac{(J+K)(J+K-1)(J-K+1)(J-K+2)}{W_0^{JK\mu n\pm}-W_0^{JK-2\mu n\pm}}I(^{K-2\mu n}_{K\ \ \mu n})^2\right.\\&\left.+\frac{(J-K)(J-K-1)(J+K+1)(J+K+2)}{W_0^{JK\mu n\pm}-W_0^{JK+2\mu n\pm}}(I^{K+2\mu n}_{K\ \ \mu n})^2\right],\end{aligned} \tag{5}$$

where $S=\frac{h^2}{8\pi^2}\frac{D}{I_y^2+D^2}$ and $I^{K'\mu n}_{K\ \mu n}=\int_0^{2\pi}Q^{K\mu n*}(x)Q^{K'\mu n}(x)dx$.

$W_0^{JK0n\pm}$ is equal to $W_0^{J-K0n\pm}$, so that the asymmetry of the molecule yields the K-type doublet for $\mu=0$ and $K\neq0$ states as in a rigid asymmetric rotor. When the effect of internal rotation is not so large as in the ground torsional state in methyl amine, the magnitude of the doublet splitting is approximately given by Wang's formula8),

---

* $K-\tau+\mu=1$ (mod. 3), where $\tau(=1, 2, 3)$ is the quantum number used by Dennison and others.

$$\Delta W=\frac{A-B}{2}\left(\frac{\delta}{1-\frac{1}{2}\delta}\right)^{K-1}$$
$$\times\frac{(J+K)!}{16^{K-1}(J-K)!(K-1)!(K-1)!}\ . \qquad (6)$$

The asymmetry parameter δ is

$$\delta=\frac{A-B}{C-A}\ . \qquad (7)$$

It must be noted that the denominator of the $K\leftrightarrow K\pm 2$ interaction term in equation (5) is sometimes too small to use the perturbation method. For example, if $\mu=0$, the perturbation energy due to $K=1\leftrightarrow -1$ interaction is replaced by

$$\Delta W_{J\ \ 10n}^{J-10n}=\frac{A-B}{2}I_{\ 10n}^{-10n}J(+1)\ , \qquad (8)$$

from equation (6), including the effect of internal rotation.

For $\mu=\pm 1$, Burkhard and Dennison5) showed that the energy level $W^{JK\mu n\pm}$ always degenerates to the level $W^{J-K-\mu n\pm}$ belonging to a degenerate symmetry class, E, while the degeneracy of K and $-K$ levels for the same J, μ, n, and inversion state is already removed by the tunneling effect due to the internal rotation even in the symmetric top approximation. However, in some cases as $|K|=1$, ΔW in equation (6) may be as large as the magnitude of $W_0^{JK\mu n\pm}-W_0^{J-K\mu n\pm}$. In such case, the energy level $W^{JK\mu n\pm}$ must be calculated by solving a secular equation,

$$\begin{vmatrix} W_0^{JK\mu n\pm}-W & \frac{\Delta W}{2} \\ \frac{\Delta W}{2} & W_0^{J-K\mu n\pm}-W \end{vmatrix}=0 \qquad (9)$$

Again, the perturbation energy due to $K=1\leftrightarrow -1$ interaction must be excluded from equation (5), when its effect is taken account by means of equation (9).

The selection rules for allowed transitions are $\Delta J=0$ or ± 1, $\Delta K=0$ or ± 1, $\Delta n=0$, $\Delta\mu=0$, and $+\leftrightarrow+$, or $-\leftrightarrow-$.

§ 4. Analysis of the Spectrum

a) Assignment of the series

Eight well-defined series of lines have been found in the observed range; seven of them, p_1, p_2, q_1, q_2, r_1, r_2 and s_1, were already reported in SNI, the remaing one, s_2, having been found later in the millimeter wave region.

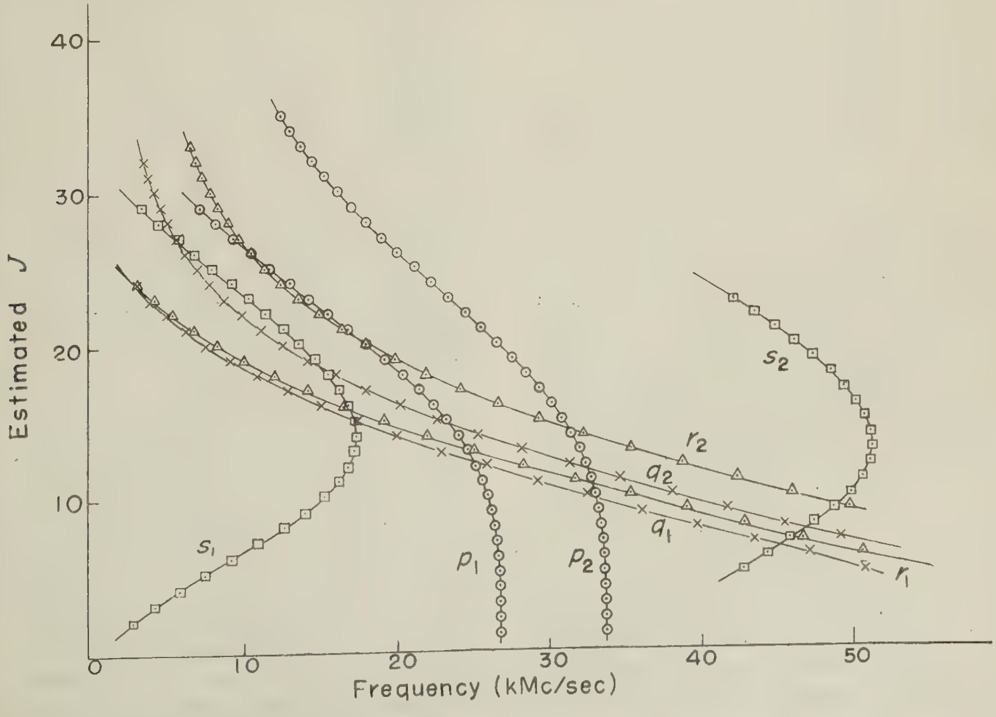

Fig. 1. Frequencies of the lines of series plotted against their rotational quantum number J. J values are only approximate except for p series.

The Stark effect for p series is 1(o), that for q series is 1→2, and those for r and s series are 2(+).

These series correspond to the transitions, $\Delta J=0$ and $\Delta K=\pm 1$, and member lines of a series correspond to successive J values. The frequencies of the observed lines are plotted against estimated J values in Fig. 1. Among the observed series the initial lines were observed only for p_1 and p_2 series. The frequencies of initial lines of theoretically possible series were calculated as functions of the barrier height as shown in Fig. 2 of SNI. The first-order Stark effect of p series indicates that the series belongs to the transitions between degenerated levels of internal rotation, $\mu=\pm 1$. From the study of the Stark pattern of a few low J lines of p_1 series and also from the intensity consideration, p series were previously assigned to the transition $J \leftarrow J$, $K=1\leftarrow 0$, $\mu=1\leftarrow 1$, and $n=1\leftarrow 1$; p_1 correspond to the stronger inversion partner, $+\leftarrow +$ while p_2 to the weaker partner, $-\leftarrow -$.

The Stark pattern of some low J lines of series have also been resolved, and the mea frequency of the initial lines of s_1 and series can be estimated to be nearly 20 kMc sec. If one takes the barrier height of abou 700 cm^{-1} which is infered from the assignmen of p series, s series can be uniquely assigne to the transitions, $J \leftarrow J$, $K=0\leftarrow 1$, $\mu=0\leftarrow$ and $n=1\leftarrow 1$; s_1 to $+\leftarrow +$ and s_2 to $-\leftarrow -$.

On the other hand, the initial lines of q an r series are in the higher frequency regio than the observed range, and a few sets c assignments are possible. The previous ten tative assignments in SNI, however, wer found to be incorrect, and the present assign ments are given in Table III. The most im portant difference lies in the assignment of for q series. Even by the crude theory in SNI, it could be expected that the frequencies of member lines of $\mu=0$, $K=1\leftarrow 0$ series ($n=0$) would greately deviate from the frequency of the initial line (80∼90 kMc/sec). Thus q series was assigned to this transition, though its peculiar Stark effect (1→2) was rather inconsistent with the assignment. The Stark effect of $\mu=0$ lines should be simple second-order as observed in s series.

Table III. Assignments of series.

Series	Assignment			Frequency of initial line		Inversion state	Magnitude of inversion doubling	
	$K' \leftarrow K$	μ	n	Obs. (Mc/sec)	Calc. (Mc/sec)		Obs.(Mc/sec)	Calc.(Mc/sec
p_1	1←0	1	1	26734*	26734	+	6903*	6903
p_2	1←0	1	1	33637*	33637	−		
q_1	1←0	−1	0	—	70428	−	∼5000	8641
q_2	1←0	−1	0	—	79069	+		
r_1	1←0	0	0	—	79171	+	∼10000	10690
r_2	1←0	0	0	—	89861	−		
s_1	0←1	0	1	∼2000	2743	+	∼36000	38064
s_2	0←1	0	1	∼38000	40807	−		

If the $K=1\leftrightarrow -1$ interaction in $\mu \neq 0$ lines is taken into account, however, it is found that the frequencies of member lines of $\mu=-1$, $K=1\leftarrow 0$ series ($n=0$) also deviate to the lower frequency region from the frequency of initial line (70∼80 kMc/sec). The Stark effect of this series should be primarily first-order, 1(o), similar to p series, but should become second-order, 2(+), because of the $K=1\leftrightarrow -$ interaction. This just accounts for the pecu liar Stark effect of q series, 1→2. From theoretical considerations, the q_1 series is as signed to be the weaker inversion partner $-\leftarrow -$, whereas q_2 series to $+\leftarrow +$. These assignments differ from the previous ones no only in respect to μ, but also to the inversion states. Since the intensities of lines in q_1 and q_2 series were almost equal in the spectrum of centimeter wave region, it was difficult in SNI to decide from the experimental results which of q_1 and q_2 series belongs to the stronger inversion state. But it has been clearly confirmed from the millimeter wave spectrum that the q_2 series belongs to the stronger state because the intensity difference of the lines becomes more significant as the

J value decreases.

Now the transitions $\mu=0$, $K=1\leftarrow 0$, and $n=0$ are assigned to r series instead of q series; r_1 is the stronger inversion partner $+\leftarrow+$ and r_2 is $-\leftarrow-$. The lines of $\mu=0$, $K=2\leftarrow 1$, and $n=1$ series, that was assigned to r series in SNI, are considered to be so weak that the series could not be taken out from the observed spectrum; its initial line lies at a very high frequency region ($\sim$100 kMc/sec) and it belongs to the excited torsional state.

b) Analysis of $4_2\leftarrow 5_{\pm 1}$ and $6_{\pm 1}\leftarrow 5_2$ lines

From the study of Stark effects some ten lines, which were expected to correspond to the transitions, $J_K=4_2\leftarrow 5_{\pm 1}$ or $6_{\pm 1}\leftarrow 5_2$ in the ground torsional state, were found. In case of $\mu=0$, these lines show either 2(+) or 2(−) Stark effect according to the lower or higher frequency partner of the K-type doublet. Lide[2] assigned the lines at 23341, 23450 and 36452 Mc/sec to $4_{22}\leftarrow 5_{14}$, $6_{15}\leftarrow 5_{23}$, and $4_{23}\leftarrow 5_{15}$ transitions, respectively. He also found their weaker inversion partners at 17476, 29312 and 30566 Mc/sec[9].

Table IV. Assignments of $\varDelta J=\pm 1$, $\varDelta K=\mp 1$ lines (I).

$J'_{K'}\leftarrow J_K$	μ	n	γ^a	Obs. freq. (Mc/sec)		Calc. freq. (Mc/sec)	
				+State	−State	+State	−State
$4_2\leftarrow 5_1$	0	0	0	23341*	17476*	23341	17476
	0	0	1	36452*^{b}	30566*^{b}	36442	30576
	1	0		14438	10262	14301	10342
	−1	0		19777	29771^b	20003	29795
$4_2\leftarrow 5_{-1}$	1	0		28534	—	28440	—
$6_1\leftarrow 5_2$	0	0	0	23450*	29312*^{b}	23449	29313
	−1	0		21931	12593	21709	12303
$6_{-1}\leftarrow 5_2$	1	0		13176	—	13272	—

a. $\gamma=0$ or 1 as $J+K_{+1}-K_{-1}$ is even or odd.

b. These frequencies are taken from reference 9.

In case of $\mu\neq 0$, however, it was very difficult to obtain a proper assignment, since all lines show similar Stark effect, 1(i), both for $\mu=+1$ and $\mu=-1$. If one takes into account the effect of $K=1\leftrightarrow -1$ interaction, however, it is shown as in the following section that the magnitudes of the Stark effect coefficient and the quadrupole hyperfine splitting would differ for each line. The consistent assignments, which have been obtained from the study of these effects, are shown in Table IV. The transitions $K=-1\leftrightarrow 2$, assigned to the lines at 13176 Mc/sec and 28533 Mc/sec, were forbidden by the crude theory neglecting the $K=1\leftrightarrow -1$ interaction. Due to this interaction, however, K is not a good quantum number and the state of $K=-1$ merges to $K=1$ state. Then the transition $K=-1\leftrightarrow 2$ becomes to be allowed. It is also noted that the magnitude of inversion doubling largely depends on the quantum number, J, through the $K=1\leftrightarrow -1$ interaction. The present assignments considerably differ from those by Lide[9]. The latter seems to have been given without proper consideration on the effect of $K=1\leftrightarrow -1$ interaction on $\mu\neq 0$ lines.

Recently, the molecular constants, A, B, C, D, V and $\varDelta_0$ have been calculated by Itoh[7] from the observed frequencies of initial lines of p series, $4_2\leftarrow 5_1$ ($\mu=0$) lines, and $6_1\leftarrow 5_2$ ($\mu=0$) lines. The results are also shown here in Table V. By use of these values, the frequencies of other $4_2\leftarrow 5_{\pm 1}$ and $6_{\pm 1}\leftarrow 5_2$ ($\mu=\pm 1$) lines as well as those of the initial lines of q, r and s series have been calculated. They agree well with the observed values as shown in Table III and IV.

Table V. Molecular parameters calculated from the observed frequencies marked by * in Table III and Table IV.

$A+B$	44329.2 Mc/sec
$\dfrac{A-B}{2}$	461.46 Mc/sec
C	10314.8 Mc/sec
S	−135. Mc/sec
V	456609. Mc/sec
$\varDelta_0$	28604. Mc/sec ($n=0$) 29358. Mc/sec ($n=1$)
$\alpha'\left(=\dfrac{2\pi^2 H_0}{h^2}\dfrac{I_2(I_y I_1-D^2)}{I_y I_z-D^2}\right)$	11.3444
$\sigma'\left(=1-\dfrac{I_2\sqrt{I_y^2+D^2}}{I_y I_z-D^2}\right)$	0.344724

c) The $J=1\leftarrow 0$ line

To verify the above analysis, it is most important to find the line for which $J=1\leftarrow 0$ and $K=0\leftarrow 0$. Edwards, Gilliam, and Gordy[10] tentatively assigned the line at 45325 Mc/sec to this transition. However, that line is definitely assigned to a member of q_2 series in the present analysis. Using the millimeter wave Stark-modulation spectrometer, the author found the line at 44286.56±0.20 Mc/sec, which showed the correct Stark effect of $J=1 \leftarrow 0$ transition. For methyl amine, the component of the dipole moment parallel to the methyl axis, $\mu_{\parallel}$, is as small as a quarter of the perpendicular component, $\mu_{\perp}$, so that the intensity of this line is very weak, perhaps as small as 10^{-7} cm^{-1}.

The fine structure due to internal rotation and inversion could not be resolved for this line ($n=0$), but two satellite lines were found, which are expected to belong to the excited torsional state, $n=1$. Their frequencies are 44214±1 and 44205±1 Mc/sec. Similar vibrational fine structures were also observed in $J=1 \leftarrow 0$ lines of other molecules with internal rotation. The method, which was presented by the author11) for the purpose of the analysis of the fine structure of methyl alcohol spectra, will also be applicable to this molecule. In order to obtain the complete analysis of the present case, at least three satellite lines have to be observed, because the line, for which $\mu=0$ and $n=1$, is expected to be observed as an inversion doublet separated by several megacycles on account of the appreciable $K, K\pm1$ perturbation energy. However, an approximate calculation shows that the value of $A+B$ including the vibrational correction should be about 40 Mc/sec larger than the observed frequency of $n=0$ line; hence $A+B \approx 44325$ Mc/sec. This value is close to the value 44329.2 Mc/sec in Table V, calculated on the basis of a rigid hindered rotor model. The difference between two values is within the error of the approximation used.

d) *K*-type doublet lines

Some lines corresponding to the transition from one to the other partner of a K-type doublet should be observed in case of $\mu=0$, as in spectra of usual rigid asymmetric rotors.

However, the tentative assignments given in SNI were incorrect. After a careful study, lines corresponding to the transitions, for which $J=6$, 7, and 10 ($|K|=1$), have been found, while their intensities are very weak ($\sim 5\times 10^{-8}$ cm^{-1} for $J=6$). Each transition consists of two lines due to the inversion doubling.

Their frequencies are theoretically given by equation (8). The values of $\Delta\nu/J(J+1)$ are listed in the third column of Table VI. Thus the value of $\frac{A-B}{2} I_{1\ \ 00}^{-100}$ is obtained as 440.0 Mc/sec from their mean value. Using the calculated value of $I_{1\ \ 00}^{-100}$ ($=0.9510$), one obtains $\frac{A-B}{2}=462.7$ Mc/sec. This value is consistent with that in Table V, 461.46 Mc/sec, calculated from the frequencies of $4_2 \leftarrow 5_1$ and $6_1 \leftarrow 5_2$ transitions.

Table VI. Assignments of K-type doublet lines ($|K|=1$).

J	$\Delta\nu$ (Mc/sec)	$\frac{\Delta\nu}{J(J+1)}$ (Mc/sec)
6	18476.	439.90
	18486.	440.15
7	24634.0	439.89
	24647.1	440.13
10	48385.	439.86
	48400.	440.00

e) Additional strong lines

The remaining strong lines, which are rather irregularly spaced in the observed range, will be assigned to the transitions, $\Delta J=\pm1$ and $\Delta K=\mp1$ ($J\gtrsim7$ and $K\gtrsim2$). The frequencies of such lines were calculated using the values of molecular parameters in Table V.

Following procedures were used for the simplicity of calculation.

1) As pointed out by Dennison and others4)-7), the energy of internal rotation, $W^{K\mu n}=VR^{K\mu n}$, is a periodic function of $\gamma=\frac{2\pi}{3}\left(\frac{I_2\sqrt{I_y^2+D^2}}{I_yI_z-D^2}K+\mu\right)$. Hence, $R^{K\mu n}$ can be expanded as a Fourier series in γ. The expansion formula,

$$R^{K\mu n}(\text{cm}^{-1})=-13.185372-0.018873\cos\gamma$$
$$+0.000012\cos 2\gamma\ , \qquad (10a)$$
$$\gamma=78°38'K+120°\mu \qquad (10b)$$

were used for $n=0$ states.

2) Itoh7) showed that the inversion energy $W^{n\pm}$ is also a periodic function of $\gamma'=\pi/3\left(\frac{I_2\sqrt{I_y^2+D^2}}{I_yI_z-D^2}K-2\mu\right)=39°19'K-120°\mu$. The overlap integral which expresses the coupling between the inversion and the internal rotation is approximately given by,

$$\int_0^{2\pi} Q^{K\mu n*}(x)Q^{K\mu n}(x-\pi)dx \quad (\text{cm}^{-1})$$
$$=0.210803\cos\gamma' - 0.000377\cos 3\gamma'$$
$$+0.000001\cos 5\gamma' \qquad (11)$$

for the ground torsional state, $n=0$.

3) The perturbation energy due to K, $K\pm1$ off-diagonal elements of Hamiltonian, $\tilde{W}^{K}_{K\pm1}$, can be neglected since their magnitudes are of the order of 10 Mc/sec.

4) The perturbation energy due to K, $K\pm2$ off-diagonal elements, $\tilde{W}^{K}_{K\pm2}$, cannot be neglected, because it may amount to a few hundred megacycles even in large K levels. The denominators of $\tilde{W}^{K}_{K\pm2}$, however, were replaced by $W^{JK}-W^{JK\pm2}$ in the present calculation. This results in errors of several ten megacycles in the calculated frequencies.

Table VII. Assignments of $\varDelta J=\pm1$, $\varDelta K=\mp1$ lines (II).

$J'_{K'}\leftarrow J_K$	μ	n	γ	Obs. freq. (Mc/sec)		Calc. freq. (Mc/sec)	
				+State	−State	+State	−State
$7_3\leftarrow 8_2$	0	0	0	48387	46545	48088	46445
	0	0	1	49915	48082	49660	48017
$8_3\leftarrow 9_2$	0	0	1	5767[a]	—	5505	—
	1	0		4660[a]	6867[a]	−4441	6857
	−1	0		15908	6450[a]	16047	6378
$10_2\leftarrow 9_3$	0	0	0	41658	43498	42051	43694
	1	0		49230	—	49257	—
	−1	0		28515	—	28378	—
$11_4\leftarrow 12_3$	0	0	0	23683	32104[b]	23776	32171
	0	0	1	23861	32283[b]	23958	32353
	1	0		43041	32708[b]	43355	32536
$13_3\leftarrow 12_4$	0	0	0	20831	12444	20800	12405
	0	0	1	20547	12162	20509	12114
	1	0		—	11961	—	11985
	−1	0		8412	6270[a]	8770	6326
$14_3\leftarrow 13_4$	1	0		45995	—	45731	—
$15_5\leftarrow 16_4$	0	0	0	23409	12239	23754	12424
	0	0	1	23429	12259	23773	12443
	1	0		21713	27504	21427	27637
	−1	0		—	16682	—	16256
$17_4\leftarrow 16_5$	0	0	0	21052	32187[b]	20770	32100
	0	0	1	21019	32155[b]	20739	32069
	1	0		22723	16948	23091	16881
	−1	0		33152[b]	—	33416	—
$18_6\leftarrow 19_5$	0	0	0	49426	—	49106	—
	0	0	1		—	49107	—
	1	0		45958	47335	45711	46949
	−1	0		48415	—	48262	—
$19_6\leftarrow 20_5$	0	0	0	4858[a]	13415	4611	13775
	0	0	1	4860[a]	13417	4613	13777
	−1	0		—	6500[a]	—	−6625
$21_5\leftarrow 20_6$	0	0	0	—	30566[b]	—	30745
	0	0	1	—	30565[b]	—	30742
	1	0		42805	—	43302	—

a: These lines are quoted from reference 3.

b: These lines are quoted from the private communication sent by Dr. D. R. Lide, Jr.

5) The energy of K-type doubling, $\varDelta W$, is not so small for $|K|=2$ levels that it is necessary to calculate the effect of $-K\leftrightarrow K$ interactions by equation (9) for $\mu=\pm1$ states. As K increases, $\varDelta W$ rapidly decreases by $(\delta)^K\approx(0.1)^K$ so that this effect can be neglected for $|K|\geq3$.

The calculated frequencies based upon these procedures have fitted successfully the observed frebuencies. About fifty lines, which have J ranging from 7 to 21 and K from 2 to 6, have been assigned and are listed in Table VII. The errors of two to three hundred megacycles in the calculated frequencies are not surprising in view of the approximation used, since the interactions of internal rotation with the other vibrations than torsion and inversion have been neglected, as well as other smaller interactions.

Some experimental evidence for these assignments have been given as follows:

(1) The Stark effect patterns of the stronger inversion partners of $7_3\leftarrow8_2$, $8_3\leftarrow9_2$ and $10_2\leftarrow9_3$ lines have been partially resolved. The J values of these lines could be estimated from the splittings of resolved component lines.

(2) The Stark pattern of higher J lines ($J\geq14$) could not be resolved. The Stark effect of most lines are similar to 1(i) since in case of $\mu=0$ the forbidden lines appear near the allowed lines even in a lower Stark field. The Stark pattern, however, shows an unsymmetrical feature about the center of the line in case of $\mu=0$, whereas a symmetrical feature in case of $\mu=\pm1$. This gives a check for the assignment of μ.

(3) The magnitude of K-type splitting for a $\mu=0$ line is almost independent of the energy of internal rotation and inversion. Thus the magnitude gives a good verification for the value of J and K in case of $\mu=0$.

(4) The magnitude of inversion doubling for these lines depends on K and μ, but is almostly independent of J, since the effect due to $-K\leftrightarrow K$ interaction on the inversion energy is small as theoretically expected. This confirms the choice of inversion pairs.

§ 5. Molecular Parameters

The molecular dimensions of methyl amine calculated from the rotational constants in Table V are $d_{CN}=1.474\pm0.005$ A, $\angle$CNH$=112°10'\pm1°$, $\angle$HCH$=109°30'\pm1°$, and $\angle$HNH$=105°50'\pm1°$, on the assumption of $d_{NH}=1.014$ A and $d_{CH}=1.093$ A. The direction of methyl axis does not coincide with that of CN axis and passes through the NH_2 triangle having an angle of $3°30'\pm20'$ to the CN axis. The height of potential barrier hindering internal rotation has been found to be 691.1 ± 1 cm^{-1}. This value is between the previous value from the calorimetric data[12], 1000 cm^{-1}, and that from the infrared spectrum[13], 530 cm^{-1}. Recently, Aston and others[14] reexamined the barrier height from the entropy measurement and obtained the value of 665 ± 140 cm^{-1}, which was close to the present value.

The magnitude of inversion doubling is considerably large. The Δ_0 in equation (4) (the hypothetical inversion splitting in case of no significant internal rotation) has been calculated to be 28,604 Mc/sec for $n=0$ and 29,358 Mc/sec for $n=1$. If one assumes that the reduced mass is proportional to the inverse square of the frequency of the NH_2 wagging vibration, the value of 3,300 Mc/sec is calculated from Dennison and Uhlenbeck's formula[15]. The observed inversion splitting is much larger than the calculated value, but the difference can be explained, at least qualitatively, from the large CNH angle, which facilitates the inversion motion. If one takes a fictitious ammonia type symmetric top molecule, NM_3, which has the same reduced mass as methyl amine and a MNM angle of about 110°30′ ($d_{NM}=1.014$ A), the inversion splitting is calculated to be about 30,000 Mc/sec, consistent with the observed value.

§ 6. Dipole Moment and Quadrupole Coupling Constant

a) Stark effect and dipole moment

The Stark patterns of the lines, for which $\mu=0$, $J_K=4_2\leftarrow5_1$ and $6_1\leftarrow5_2$, were measured by Lide[2]. From the Stark coefficients he gave the component of dipole moment parallel to the z axis, $\mu_{\parallel}$, to be 0.304 D and the perpendicular component, $\mu_{\perp}$, to be 1.232 D. These values are consistent with the Stark coefficient of the third and forth lines of p_1 series, which have been measured by the author.

The first-order Stark energy of $\mu=\pm1$ levels is given from the diagonal matrix element,

$$W_s=\mu_{\parallel}\frac{KE}{J(J+1)}\ , \qquad (12)$$

neglecting the perturbation term from the K, $K\pm1$ off-diagonal matrix element. However, if the effect of $-K\leftrightarrow K$ interactions is taken into account, K is no longer a good quantum number. The mixing of the wave functions ψ_{+K} and ψ_{-K} is expressed by

$$c_+\psi_{+K}+c_-\psi_{-K}\ , \qquad (13)$$

taking $c_+^2+c_-^2=1$. Hence K, which is used in equation (12), should be replaced by

$$c_+^2K-c_-^2K\ . \qquad (14)$$

The Stark coefficient, b_{JK}, for a observed line is approximately given by

$$b_{JK}=\mu_{\parallel}\left(\frac{(c_+^2-c_-^2)}{J(J+1)}K-\frac{(c'^2_+-c'^2_-)}{J'(J'+1)}K'\right)\ , \qquad (15)$$

where JK and $J'K'$ mean the final and initial states of the transition, respectively. The Stark shift, $\Delta\nu_s$, is

$$\Delta\nu_s=\frac{1}{h}b_{JK}ME\ , \qquad (16)$$

where M is the projection of $\boldsymbol{J}$ on the direction of the applied field.

The calculated Stark coefficients are compared with the observed values for $4_2\leftarrow5_1$ and $6_1\leftarrow5_2$ lines in Table VIII. The agreement gives a good verification for the present assignment.

Table VIII. Stark effect coefficient and quadrupole hyperfine splitting.

$J'_{K'}\leftarrow J_K$	μ γ	Inv. st.	Stark coeff. (Mc/esu) Obs.	Stark coeff. (Mc/esu) Calc.	Quad. Spl.* (Mc/sec) Obs.	Quad. Spl.* (Mc/sec) Calc.
$4_2\leftarrow5_1$	0 0	+	—	—	−0.64	−0.68
	1	+	3.8	4.0	−0.51	−0.61
	−1	+	4.0	4.0	+1.34	+1.28
$4_2\leftarrow5_{-1}$	1	+	5.2	5.1	+1.32	+1.28
$6_1\leftarrow5_2$	0 0	+	—	—	+0.78	+0.79
	−1	+	2.7	2.8	−1.29	−1.19
$6_{-1}\leftarrow5_2$	1	+	3.3	3.4	−1.24	−1.19

* The sign of the splitting is plus when the frequency of the stronger component is higher than that of the weaker component, and vice versa.

b) Quadrupole hyperfine structure

The quadrupole energy, W_Q, due to the nuclear quadrupole moment, Q, of N^{14} can be written by

$$W_Q = eQ\left\langle\frac{\partial^2 V}{\partial Z^2}\right\rangle_{Av} \frac{\frac{3}{4}C(C+1) - I(I+1)J(J+1)}{2J(2J-1)I(2I-1)}\,, \tag{17}$$

where

$$C = F(F+1) - I(I+1) - J(J+1)\,,$$

and

$$F = J+I\,,\ J+I-1\,,\ \cdots,\ |J-I|\,.$$

$I(=1)$ is the nuclear spin of N^{14}. The field gradient averaged over the rotational wave function, $\left\langle\frac{\partial^2 V}{\partial Z^2}\right\rangle_{Av}$, is given by

$$\left\langle\frac{\partial^2 V}{\partial Z^2}\right\rangle_{Av} = \langle\alpha_{Zx}{}^2\rangle\frac{\partial^2 V}{\partial x^2} + \langle\alpha_{Zy}{}^2\rangle\frac{\partial^2 V}{\partial y^2} + \langle\alpha_{Zz}{}^2\rangle\frac{\partial^2 V}{\partial z^2} + 2\langle\alpha_{Zx}\alpha_{Zy}\rangle\frac{\partial^2 V}{\partial x\partial y} + 2\langle\alpha_{Zy}\alpha_{Zz}\rangle\frac{\partial^2 V}{\partial y\partial z} + 2\langle\alpha_{Zz}\alpha_{Zx}\rangle\frac{\partial^2 V}{\partial z\partial x}\,, \tag{18}$$

referred to the x, y and z axes. The direction cosine matrix element $\langle\alpha_{Zz}\rangle$ is diagonal with respect to K, whereas $\langle\alpha_{Zx}\rangle$ and $\langle\alpha_{Zy}\rangle$ have only K, $K\pm1$ off-diagonal elements. Thus the last two terms vanish and the remaining cross term, $2\langle\alpha_{Zx}\alpha_{Zy}\rangle\frac{\partial^2 V}{\partial x\partial y}$ is also zero since y axis is implied in the symmetry plane which bisects HNH angle and x axis is perpendicular to this plane. Using the relations,

$$\alpha_{Zx}{}^2 + \alpha_{Zy}{}^2 + \alpha_{Zz}{}^2 = 1 \tag{19}$$

and

$$\frac{\partial^2 V}{\partial x^2} + \frac{\partial^2 V}{\partial y^2} + \frac{\partial^2 V}{\partial z^2} = 0\,, \tag{20}$$

the following equation is obtained;

$$\left\langle\frac{\partial^2 V}{\partial Z^2}\right\rangle_{Av} = \frac{1}{2}\langle 3\alpha_{Zz}{}^2 - 1\rangle\frac{\partial^2 V}{\partial z^2} + \frac{1}{2}\langle\alpha_{Zy}{}^2 - \alpha_{Zx}{}^2\rangle\left(\frac{\partial^2 V}{\partial y^2} - \frac{\partial^2 V}{\partial x^2}\right). \tag{21}$$

The first term is diagonal with respect to K and the second term has only K, $K\pm2$ off-diagonal elements. The second term becomes significant when $|K|=1$, through $K=1\leftrightarrow-1$ interactions. Hence equation (21) becomes

$$\left\langle\frac{\partial^2 V}{\partial Z^2}\right\rangle_{Av} = \frac{3K^2 - J(J+1)}{(J+1)(2J+3)}\frac{\partial^2 V}{\partial z^2} \pm \delta_{|K|,1} \times \frac{J}{2J+3}\left(\frac{\partial^2 V}{\partial y^2} - \frac{\partial^2 V}{\partial x^2}\right)c_+c_-\,. \tag{22}$$

Using equations (17) and (22), the quadrupole hyperfine splitting, $\Delta\nu_Q$, for $4_2\leftarrow5_1$ lines is given by

$$\Delta\nu_Q = eQ\left[0.1865\frac{\partial^2 V}{\partial z^2} \pm 0.3744\left(\frac{\partial^2 V}{\partial y^2} - \frac{\partial^2 V}{\partial x^2}\right)c_+c_-\right], \tag{23a}$$

and for $6_1\leftarrow5_2$ lines

$$\Delta\nu_Q = eQ\left[-0.1223\frac{\partial^2 V}{\partial z^2} \mp 0.3736 \times \left(\frac{\partial^2 V}{\partial y^2} - \frac{\partial^2 V}{\partial x^2}\right)c_+c_-\right]. \tag{23b}$$

These formula have been obtained on the assumption that the doublet separation is given by the difference in frequencies between $F=J$ line and the weighted mean of $F=J\pm1$ lines, because the $F=J+1$ and $J-1$ lines are close to each other. The double sign of the second term should be the upper one when the $|K|=1$ level is the upper state ($\mu=1$ for $K=1$ and $\mu=-1$ for $K=-1$), and the lower one when the $|K|=1$ level is the lower state ($\mu=-1$ for $K=1$ and $\mu=1$ for $K=-1$).

The quadrupole coupling constants $eQ\frac{\partial^2 V}{\partial z^2}$ and $eQ\left(\frac{\partial^2 V}{\partial y^2} - \frac{\partial^2 V}{\partial x^2}\right)$ have been determined so as to give the best fit calculated values to the observed splittings. The results are

$$eQ\left(\frac{\partial^2 V}{\partial z^2}\right) = 1.8 \pm 0.2\ \text{Mc/sec}\,, \tag{24a}$$

$$eQ\left(\frac{\partial^2 V}{\partial y^2} - \frac{\partial^2 V}{\partial x^2}\right) = -5.4 \pm 0.3\ \text{Mc/sec}\,. \tag{24b}$$

The comparison between the observed and the calculated splittings are also given in Table VIII, confirming the present analysis.

It is also interesting to transform the coupling constants to the charge symmetry axis around the nitrogen nucleus. The charge symmetry axis, ζ, is naturally comprised in the bisecting plane of the HNH angle, with an angle Θ between z and ζ axes. Hence the transformation is expressed by

$$\frac{\partial^2 V}{\partial x^2} = -\frac{1}{2}\frac{\partial^2 V}{\partial \zeta^2} \tag{25a}$$

$$\frac{\partial^2 V}{\partial y^2} = \frac{3\sin^2\Theta - 1}{2}\frac{\partial^2 V}{\partial \zeta^2} \tag{25b}$$

$$\frac{\partial^2 V}{\partial z^2} = \frac{3\cos^2\Theta - 1}{2}\frac{\partial^2 V}{\partial \zeta^2}\,. \tag{25c}$$

From equation (20), (24a, b), and (25a), the coupling constant along ζ direction is

$$eQ\frac{\partial^2 V}{\partial \zeta^2} = -3.6 \pm 0.3\ \text{Mc/sec}\,. \tag{26}$$

This value is rather close to that of ammonia,

−4.10 Mc/sec.[16] The angle Θ can also be determined by a relation

$$3\frac{\cos^2\Theta-1}{3\cos^2\Theta-1}=\frac{\dfrac{\partial^2 V}{\partial x^2}-\dfrac{\partial^2 V}{\partial y^2}}{\dfrac{\partial^2 V}{\partial z^2}}=\eta\,. \tag{27}$$

The left term of this equation takes a value from 0 to $-\infty$ as Θ increases from 0 to Θ_0, and it takes a value from $+\infty$ to 3 as Θ increases from Θ_0 to 90°, as shown in Fig. 2.

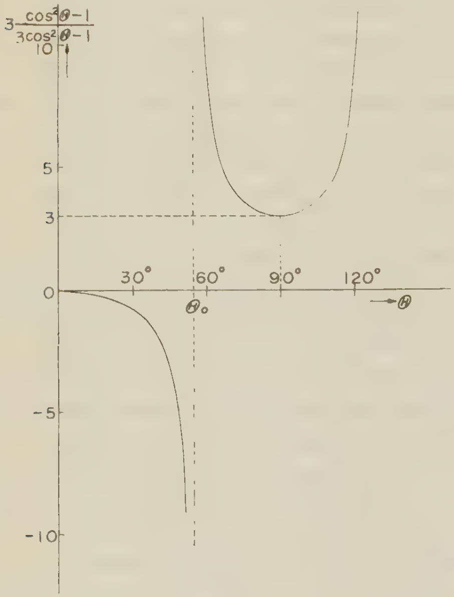

Fig. 2.

Θ_0 (∼54°45′) is the angle for which $\cos^2\Theta_0=1/3$. From the experimental values in (24a, b), η is 3.0 ± 0.2. This value gives the direction of charge symmetry axis to be 90° ± 8° to z axis.

On the other hand, we can calculate the direction of charge symmetry axis from the bond angles using the orthogonal conditions for bonding orbitals. If no ionic structure is assumed, Θ is calculated to be 105° ± 5°* from the molecular dimension described in the preceding section. Θ determined from the quadrupole coupling constant is smaller than the calculated volue, even if the experimental errors are taken into account. However, if the ionic structure or the hyperconjugation effect is considered, the symmetry exis probably in clines towards the perpendicular direction to CN axis.

§ 7. Discussion

Most of the important lines in the spectrum have been analyzed, giving the molecular parameters of methyl amine. The error of a few hundred megacycles in the calculated frequencies of lines may be attributed to higher order effects. For example, the effect of other vibrations than torsion and inversion were entirely neglected in the calculated frequencies. The assumption of a cosine form of the barrier to internal rotation, $H=H_0(1-\cos 3x)$, and a simple treatment of the coupling of internal rotation and inversion may also cause some errors in the calculation of frequencies. The remaining weaker lines, which have not been assigned, will be attributed to the excited torisonal states ($n\geq1$), to the very high rotational states ($J\geq20$, $K\geq6$), or to other isotopic species. Further study on the lines belonging to the excited torsional states would give more precise knowledge on the potential barrier to internal rotation, such as the contribution of six-fold potential barrier term.

It is interesting to compare the structure of methyl amine with other CH_3MH_n type mole-

Table IX. Molecular structure, barrier height, and dipole moment of CH_3MH_n type molecule.

Molecule	CH_3NH_2	CH_3OH	CH_3SH
d_{CM}(A)	1.474	1.427	1.819
Sum of covalent radii	1.471	1.431	1.811
d_{MH}(A)	1.014†	0.953	1.336
d_{CH}(A)	1.093†	1.096	1.091
∠CMH	112°10′	108°24′	96°30′
∠HMH in MH_{n+1} molecule	106°47′ (ammonia)	104° (water)	92°30′ (hydrogen sulfide)
∠HMH	105°50′	—	—
∠HCH	109°30′	109°4′	109°45′
θ*	3°30′	3°18′	2°0′
H_0(cm^{-1})	691	373	444
H_0 calculated by Lassetree-Dean's method	740	340	490
$\mu_{\parallel}$(D)	0.304	0.893	1.35
$\mu_{\parallel}$ (Sum of bond moments)	0.21	0.70	1.30
	(1.01)	(0.10)	(0.50)
$\mu_{\perp}$(D)	1.232	1.435	0.64
$\mu_{\perp}$ (Sum of bond moments)	1.20	1.45	0.71

* θ is the angle between CM and methyl axis.
† Assumed values.

---

* Θ is measured from the z axis in the clockwise direction.

cules, such as methyl alcohol[11] and as methyl mercaptan[17]. The molecular structures, barrier heights, and dipole moments of these molecules are listed in Table IX. First, the bond lengthes, d_{CM}, agree well with the sums of the Pauling's covalent radii, which are also shown in the table. Secondly, the bond angles ∠CMH are about five degrees larger than the bond angles ∠HMH in MH_{n+1} type molecules, that is ammonia, water and hydrogen sulfide corresponding to methyl amine, methyl alcohol, and methyl mercaptan, respectively. It is also noted that the CM directions are not on the symmetry axis of methyl group and that the angles between CM and methyl axes, θ's, are almost equal for these molecules. These characteristics in the angles, ∠CMH and θ, are probably explained by the repulsive effect between the MH_n group and methyl group.

Several theories on the potential barrier to internal rotation have already been given. Among them, Lassettre and Dean's method[18] on the electrostatic potential due to the dipole-dipole, dipole-quadrupole, and quadrupole-quadrupole interactions between MH and CH bonds seems to be valid for these simple molecules. They calculated the barrier height for methyl amine and methyl alcohol assuming a tetrahedral value, 109°28′, for CMH angles. The approximation is fairly good and they obtained the value of 740 cm^{-1} for methyl amine and 340 cm^{-1} for methyl alcohol, which show good agreement with the observed values. The bond angle of methyl mercaptan (∠CSH =96°20′) is considerable less than the tetrahedral value, so that their method should be slightly modified. The value of 490 cm^{-1} has been calculated by a modified Lassettre and Dean's method for methyl mercaptan, showing the consistency with the experimental value (440 cm^{-1}).

In these calculations, the direction of CH bond dipole moment was taken to be $\mathrm{C}^- \rightarrow \mathrm{H}^+$. It is also interesting to compare the observed values of the components of dipole moments with the calculated values using the molecular structures and the bond dipole moments by Pauling and others[19]. Table IX also shows good agreement between the observed and calculated values, confirming the direction of CH bond moment, $\mathrm{C}^- \rightarrow \mathrm{H}^+$. If we take the reverse direction $\mathrm{C}^+ \leftarrow \mathrm{H}^-$, the agreement is completely destroyed as shown in parenthesis. The perpendicular components, $\mu_\perp$, depend predominantly on the MH bond moments, so that the agreement also verifies the values of MH bond moments given by Pauling and others.

Acknowledgement

The author expresses his hearty thanks to Professor Koichi Shimoda for his continuous guidance and advice, and to Professors Masao Kotani and Charles H. Townes for their interests throughout this work. His thanks are also due to Dr. Takashi Itoh for his valuable discussion and help on the theoretical treatment and the numerical calculation. He is also grateful to Dr. David R. Lide, Jr. for his kind informations of his unpublished worthful results.

APPENDIX

Expansion Coefficients of *p* Series

The positions of the lines of p series are expressed by means of a power series, $\nu=\nu_0+aJ(J+1)+bJ^2(J+1)^2+\cdots$. The expansion coefficients, a, b, $\cdots$, can also be calculated from the molecular parameters. The value of a is mainly determined by the centrifugal distorsion effect, and the contribution from the asymmetry is small. Although the rigorous treatment of the centrifugal effect is difficult, a rough estimation shows that its contribution is about −0.72 Mc/sec while the contribution from the asymmetry is less than 0.1 Mc/sec. These values are compared with the observed value of a, −0.77 Mc/sec.

On the other hand, the coefficient, b, springs from $\tilde{W}^K_{K\pm2}$ and can be calculated more precisely by the second-order perturbation method. The observed and the calculated values of b are −0.0614 and −0.0601 Mc/sec, respectively.

The above discussion concerns the mean values between p_1 and p_2 series, though it is also right for the coefficients of each series.

References

1) K. Shimoda, T. Nishikawa, and T. Itoh: J. Phys. Soc. Japan **9** (1954) 974; J. Chem. Phys. **22** (1954) 1456.
2) D. R. Lide, Jr: J. Chem. Phys. **20** (1952) 1812, **21** (1953) 571.
3) A. Miyahara, H. Hirakawa, and K. Shimoda: J. Phys. Soc. Japan **11** (1956) 334.
4) J. S. Koehler and D. M. Dennison: Phys. Rev.

57 (1940) 1006.
5) D. G. Burkhard and D. M. Dennison: Phys. Rev. **84** (1951) 408.
6) E. V. Ivash and D. M. Dennison: J. Chem. Phys. **21** (1953) 1804.
7) T. Itoh: J. Phys. Soc. Japan **11** (1956) 264.
8) S. C. Wang: Phys. Rev. **34** (1929) 243.
9) D. R. Lide, Jr: J. Chem. Phys. **22** (1954) 1613.
10) H. E. Edwards, O. R. Gilliam, and W. Gordy, cited in P. Kisliuk and C. H. Townes: Molecular Microwave Spectra Tables, N.B.S. Circular 518, 1952.
11) T. Nishikawa: J. Phys. Soc. Japan **11** (1956) 781.
12) J. G. Aston, C. W. Siller, and G. H. Messerly: J. Am. Chem. Soc. **59** (1937) 1743.
13) J. G. Aston and P. M. Doty: J. Chem. Phys. **8** (1940) 743.
14) J. G. Aston and F. L. Gitter: J. Am. Chem Soc. **77** (1955) 3175.
15) D. M. Dennison and G. E. Uhlenbeck: Phys Rev. **41** (1932) 333.
M. T. Weiss and M. W. P. Strandberg: Phys Rev. **83** (1951) 567.
16) C. H. Townes and A. L. Shawlow: Microwav Spectroscopy, McGraw-Hill, 1955, p. 242.
17) T. Kojima and T. Nishikawa: J. Phys. Soc Japan **12** (1957) 680.
18) E. N. Lassettre and L. B. Dean, Jr: J. Chem Phys. **17** (1949) 317.
19) L. Pauling: The Nature of Chemical Bond Cornell Univ. Press, 1939, p. 68; C. P. Smyth J. Phys. Chem, **41** (1937) 209, J. Am. Chem Soc. **60** (1938) 183.

JOURNAL OF THE PHYSICAL SOCIETY OF JAPAN Vol. 12, No. 6, JUNE, 1957

Potential Barrier and Molecular Structure of Methyl Mercaptan from its Microwave Spectra

By Takeshi KOJIMA
Department of Liberal Arts, Toyama University, Toyama, Japan
and Tetsuji NISHIKAWA*
Department of Physics, Faculty of Science, University of Tokyo, Tokyo, Japan

(Received February 9, 1957)

The microwave spectrum of normal methyl mercaptan has been studied in the frequency range from 14 to 29 kMc/sec. The potential barrier height hindering internal rotation has been determined as $444 \pm 10\,\mathrm{cm}^{-1}$, from the analysis of the lines corresponding to the transitions involving both over-all and internal rotations. The fine structures of $J=1 \leftarrow 0$, $K=0 \leftarrow 0$ lines of the various isotopic species have also been analysed and discussed. The molecular structure of methyl mercaptan has been calculated to be $d_{\mathrm{SH}}=1.336 \pm 0.01\,\mathrm{A}$, $d_{\mathrm{CS}}=1.819 \pm 0.005\,\mathrm{A}$, $d_{\mathrm{CH}}=1.091 \pm 0.01\,\mathrm{A}$, $\angle\mathrm{CSH}=96°30' \pm 1°$, $\angle\mathrm{HCH}=109°45' \pm 30'$ and the angle between CS bond and methyl axis, $\theta=2°0' \pm 30'$.

§1. Introduction

The resent development of microwave spectroscopy has made it possible to study the internal rotation of free molecules and to determine the height of potential barrier with good accuracy. The internal rotation in methyl alcohol[1),2),3)] and methyl amine[4),5)] has been studied with precision by several workers. It will be interesting to study the mo lecular structure and the behaviour of th internal rotation of methyl mercaptan as i has the structural similarity to methyl alcoho and also in some respects to methyl amine.

The barrier height, V_0, of methyl mercapta was determined as about $510\,\mathrm{cm}^{-1}$ by Russe and others[6)] by the calorimetric method. B the microwave spectroscopic method, it wa determined to be $371 \pm 43\,\mathrm{cm}^{-1}$ by Solimen

---

* Present Address: Institute for Nuclear Study, University of Tokyo, Tanashi-machi, Tokyo, Japan.

Table I. Microwave Spectrum of Methyl Mercaptan.

Table I. (Continued).

Frequency (Mc/s)	Stark Effect	Intensity	Assignment
14146.3	1(o)	W	q
14548.4	1(o)	W	q
14643.1	2(+)	W	$7_{16}\leftarrow 7_{17}$
14764.5	1	W	$1_1 \leftarrow 2_0$
14865.1	1(i)	W	
14888.0	1(i)	W	
15089.3	1	W	
15102.2	2(+)	W	
15103.5	1	W	
15123.2	2(+)	MW	
15165.1	1(o)	W	q
15335.9	2(+)	W	r
15339.4	2(−)	W	
16057.0	1(i)	W	
16059.8	2(+)	W	
16066.1	1(o)	W	q
16796.4	1(i)	W	
17320.4	1(o)	MW	q
18039.5	1(i)	MW	$8_2\leftarrow 9_1$
18257.8	1(i)	W	
18396.0	1(o)	W	p
18417.6	1	W	
18431.8	1(i)	MW	
18446.3	1(o)	W	p
18494.1	2(+)	MW	
18499.7	1(i)	W	
18509.7	1(o)	W	p
18586.1	1(o)	W	p
18675.6	1(o)	W	p
18778.6	1(o)	W	p
18806.4	1(i)	MW	
18824.2	2(+)	W	$8_{17}\leftarrow 8_{18}$
18895.7	1(o)	MW	p
18991.8	1(o)	W	q
19027.1	1(o)	MW	p
19173.0	1(o)	MW	p
19273.6	1	WW	
19334.0	1(o)	MW	p
19510.4	1(o)	MW	p
19568.3	2(+)	W	r
19702.9	1(o)	MW	p
19912.2	1(o)	MW	p
19999.9	2(+)	W	
20052.6	1(i)	MW	
20138.6	1(o)	MW	p
20241.9	1(i)	MW	
20383.2	1(o)	MW	p
20646.4	1(o)	MW	p
20928.9	1(o)	MW	p
21057.4	2(+)	W	
21131.1	1(o)	W	q
21231.7	1(o)	MW	p
21519.9	1(i)	W	
21555.6	1(o)	MW	p
21734.6	1(i)	W	
21766.6	1(i)	W	
21865.5	1(i)	M	
21877.1	1(i)	MW	
21901.0	1(o)	M	p
21943.5	2(+)	W	
21973.2	1(i)	MS	
22269.4	1(o)	M	p
22329.8	1(i)	MW	
22560.2	1(i)	W	
22661.4	1(o)	MW	p
22827.3	2(+)	MW	
23073.8	1(i)	W	
23078.2	1(o)	MW	p
23230.3	1(i)	M	
23256.9	2(+)	M	$5_{05}\leftarrow 4_{14}$
23339.2	1(i)	W	$2_1 \leftarrow 3_0$
23494.4	1(i)	W	
23520.4	1(o)	MW	p
23526.2	2(+)	W	$9_{18}\leftarrow 9_{19}$
23566.6	2(+)	MW	r
23617.3	2(+)	M	
23773.8	1(o)	M	q
23801.8	1(i)	M	
23989.0	1(o)	MW	p
24067.5	1(i)	M	
24485.0	1(o)	MW	p
24988.5	1(i)	W	
25009.0	1(o)	W	p
25121.4	1	W	
25126.9	2(+)	W	$1_{01}\leftarrow 0_{00}$
25142.2	2(+)	W	
25143.7	2(+)	MW	
25154.9	2(+)	MW	
25206.8	2(+)	M	
25219.7	2(+)	M	
25290.8	2(+)	MS	
25291.8	2(+)	MS	
25562.0	1(o)	W	p
25659.7	2(−)	MW	$9_{28}\leftarrow 10_{19}$
25917.5	1	W	
26077.4	1(i)	MW	
26144.7	1(o)	W	p
26388.4	1(i)	M	
26758.1	1(o)	W	p
26947.0	1(o)	W	q
26994.2	1(i)	M	$5_0\leftarrow 4_1$
27235.8	2(+)	W	
27333.9	2(+)	M	r
27364.5	2(−)	M	
27402.2	1(o)	W	p
27419.4	1	W	
27444.5	1(i)	MW	
27911.9	1(i)	MW	
28078.2	1(o)	W	p
28275.1	1(i)	W	
28530.1	2(+)	W	
28593.5	1(i)	MW	
28686.8	1(o)	W	
28747.9	2(+)	W	$10_{19}\leftarrow 10_{1,10}$
28786.0	1(o)	W	p
28910.8	1(i)	MW	
28990.3	1(i)	MW	
29073.9	2(+)	W	
29074.4	1(o)	MW	
29091.9	2(−)	MW	$2_1\leftarrow 3_0$
29436.3	1	W	
29526.2	1(o)	W	p
29574.4	1(i)	MW	
29593.1	2(+)	MW	

and Dailey[7] from the relative intensities of the satellites of $J=1\leftarrow0$, $K=0\leftarrow0$ line. However, since the measurements of intensities of spectral lines can not be very accurate, it is preferable to determine the barrier height from the frequency measurement. Kilb[8] obtained the height as 247 cm^{-1} from the analysis of the doublet separation of $J=1\leftarrow0$, $K=0\leftarrow0$ line in the ground torsional state. Kojima and Nishikawa[9] also estimated the height to be 280 cm^{-1} from a tentative assignment of the series originated at 18300 Mc/sec. These studies, however, were too crude to determine the reliable value of V_0.

§ 2. Experimental Results

The spectrum of methyl mercaptan has been observed in the frequency range from 14 to 29 kMc/sec, using an ordinary Stark-modulation spectrometer with an X-band waveguide cell of three meters in length.

The sample of methyl mercaptan was prepared by adding sodium hydroxide to methyl-iso-thio-urea sulfate, and that of CH_3SD was prepared by adding deuterated sodium hydroxide.

About one hundred and forty lines and their Stark effects have been observed as listed in Table I. The observed lines are classified into four kinds corresponding to their Stark effects. The lines which show first-order Stark effects are denoted by 1(i) or 1(o), according as the inner or outer Stark components are stronger. The lines which show second-order Stark effects are denoted by 2(+) or 2(−), according as the components shift to higher or lower frequency side with increasing Stark field.

Four kinds of transmissions can be considered: (1) $\Delta J=0$, $\Delta K=\pm1$ (2) $\Delta J=\pm1$, $\Delta K=\mp1$ (3) $\Delta J=\pm1$, $\Delta K=0$ (4) $\Delta J=0$, $\Delta K=0$.

(1) $\Delta J=0$, $\Delta K=\pm1$ lines

Three series of lines belonging to this kind ($\Delta J=0$, $\Delta K=\pm1$) have been found in the observed range and are designated as p, q and r in Table I. The p series showing the Stark effect, 1(o), has its origin at about 18300 Mc/sec. The member lines could not be resolved into distinct Stark patterns because of the weakness of their intensities. The lines arise from molecules in an excited torsional state, not in the ground state as was reported in our preliminary report[9].

The origins of q and r series seem to lie far beyond the observed range. The Stark effect of q series is also 1(o), while that of r series is 2(+). From their Stark effects, the internal rotation states of p and q series must be degenerate ($\mu^*=\pm1$), and r series non-degenerate ($\mu=0$).

(2) $\Delta J=\pm1$, $\Delta K=\mp1$ lines

All of 1(i) lines and many of 2(+) and 2(−) lines belong to this kind ($\Delta J=\pm1$, $\Delta K=\mp1$). The μ's of 1(i) lines are ±1 and the μ's of 2(+) and 2(−) lines are 0. These lines are irregularly distributed over the microwave

Table II. Lines of $\Delta J=\pm1$, $\Delta K=\mp1$.

Frequency (Mc/s)	Stark Effect	Assignment μ	$J_K\leftarrow J'_{K'}$*
23339.2	1	1	$2_1\leftarrow3_0$
26994.2	1	1	$5_0\leftarrow4_1$
14764.5	1	−1	$1_1\leftarrow2_0$
29091.9	2	0	$2_{12}\leftarrow3_{03}$
23256.9	2	0	$5_{05}\leftarrow4_{14}$
25659.7	2	0	$9_{28}\leftarrow10_{19}$
18039.5	1	1	$8_2\leftarrow9_1$

* Both $K_{-1}(=K)$ and K_{+1} are listed for $\mu=0$ lines as in the spectrum of a rigid asymmetric-top molecule.

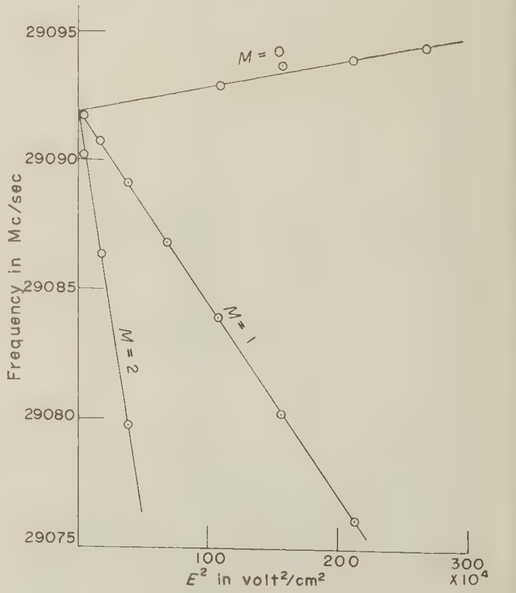

Fig. 1. Stark effect of 29091.9 line.

---

* μ is related by $\mu=-(K+\tau-1)$ mod. 3 to the quantum number, τ, used by Dennison and others. see reference 4).

region. Several low J lines, which are listed in Table II, have been resolved into Stark components for determination of J value. The frequencies of Stark components of 29091.9 line were carefully measured and plotted against the square of field strength (E^2) in Fig. 1.

(3) $\Delta J=\pm 1$, $\Delta K=0$ lines

The $J=1\leftarrow 0$ and $K=0\leftarrow 0$ line is the only one of this kind in the observed region. This line was first found by Shaw and Windle[10], and some vibrational satellites of the line were assigned by Solimene and Dailey[7], who also observed similar fine structures for several isotopic species. Their assignment for CH_3SH was confirmed by the present study, while a misassignment for CH_3SD was detected.

(4) $\Delta J=0$, $\Delta K=0$ lines

The transition from one to the other partner of a K-type doublet belongs to this kind ($\Delta J=0$, $\Delta K=0$). Six lines ($J=5$ to 10 and $K=1$) have been observed and assigned as shown in Table VI. The frequencies of these lines are proportional to $J(J+1)$ and their Stark effects are 2(+).

§ 3. Determination of the Barrier Height

The heights of potential barriers of methyl alcohol and methyl amine were determined from the series of lines which belong to $\Delta J=0$, $\Delta K=\pm 1$ transitions. Similar series of lines in the methyl mercaptan spectrum were too weak to be given the definite assignment in the observed range.

The lines which belong to $\Delta J=\pm 1$, $\Delta K=\mp 1$ transitions are more appropriate to determine the barrier height for this molecule, as their frequencies are also sensitive to the barrier height.

First, the line at 29091.9 Mc/sec could easily be assigned as $2_{12}\leftarrow 3_{03}$. The frequency can be calculated using the theory on the internally rotating molecules such as methyl alcohol and methyl amine. It is approximately given by

$$29091.9=\frac{h^2 I_z}{8\pi^2 I_1 I_2}(R^{100}-R^{000})-3\nu_0-\frac{\Delta_{J=2}}{2}$$

where I_z, I_1 and I_2 are moments of inertia of the molecule, SH group and methyl group respectively along the methyl axis. $R^{J\mu n}$ is a solution of Mathieu's equation corresponding to K, μ and n state. ν_0 is the frequency of $J=1\leftarrow 0$, $K=0\leftarrow 0$ line. $\Delta_{J=2}$ is a K-type separation at $J=2$, $K=1$ which is calculated from the lines of $\Delta J=0$, $\Delta K=0$ transitions.

The similar analysis was applied to the other six lines listed in Table II. As a result, the value of the potential barrier height was determined as 444 cm^{-1}.

The frequencies of the origins of p, q and r series were also estimated using the barrier height determined above. Their assignments are shown in Table III, while some ambiguity still remains since the origins of q and r series could not be observed.

Table III. Assignments of series.

Series	Stark Effect	Assignment	Frequency of the Origins in Mc/sec	
		$K\ \mu\ n \leftarrow K'\ \mu'\ n'$	Observed	Calculated
p	1	$5\ -1\ 2 \leftarrow 6\ -1\ 2$	18300	20000
q	1	$1\ -1\ 0 \leftarrow 0\ -1\ 0$	.....	65000
r	2	$1\ \ 0\ 1 \leftarrow 2\ \ 0\ 1$	.....	60000

We are now studying the spectrum in the millimeter wave region and have observed two series of lines showing first-order Stark effect which have their origins at about 32000 Mc/sec and 32820 Mc/sec respectively. They are assigned to be K, μ, $n=0$, 1, 1 $\leftarrow$ 1, 1, 1 and K, μ, $n=3$, -1, 1 $\leftarrow$ 2, -1, 1, respectively, confirming the above value of the barrier height. Their data and discussions will be reported later in this Journal.

The value of barrier height is also confirmed by the analysis of the vibrational fine structure of $J=1\leftarrow 0$, $K=0\leftarrow 0$ line. The vibrational satellite lines arise from molecules in different torsional states denoted by n and furthermore, the line in each torsional state splits into a doublet, $\mu=\pm 1$ and $\mu=0$, due to the internal rotation.

Kivelson[11] developed a theory of the interaction between internal rotation and vibrations to explain the similar fine structure of $J=1\leftarrow 0$ line for symmetric rotor. However, the fine structure of methyl mercaptan will occur even when we assume a rigid SH group attached at an arbitrary angle to the rigid methyl group because of asymmetry. Kilb[8] attempted to explain the doublet separation in the torsional ground state for the various isotopic species by this asymmetry effect, and he proposed that the barrier height might be 247 cm^{-1}. But it seems that he did note take account of the vibration-internal rotation interaction.

The method presented by one of us[3] (T.N.), which took into account these two effects, was applied successfully to this molecule as well as to methyl alcohol. The splitting due to the asymmetry was calculated to be of order of 0.1 Mc/sec or less for the barrier height 440 cm^{-1} in $C^{12}H_3S^{32}H$ and $C^{13}H_3S^{32}H$. Hence the vibration-internal rotation interaction is predominant as for normal methyl alcohol. The calculated and observed frequencies of $C^{12}H_3S^{32}H$ and $C^{13}H_3S^{32}H$ listed in Table IV and Table V is in good agreement. Appreciable contribution of the asymmetry effect found in the deuterated molecules will be described in § 4.

Table IV. Lines of $J=1\leftarrow0$, $K=0\leftarrow0$ of $C^{12}H_3S^{32}H$.

n	μ	Observed Frequency in Mc/sec	Calculated Frequency in Mc/sec
0	0	25290.8	(25290.8)
0	±1	25291.8	25291.8
1	0	25219.7	25219.3
1	±1	25206.8	(25206.8)
2	0	25143.6	(25143.6)
2	±1	25154.8	25154.2
3	±1	25142.2	25140.5
3	0	25126.9	25124.3

Three frequencies in parentheses were used to determine the three parameters in Kivelson's theory; $B_v=12666.3$ Mc/sec, $F_v=-61.41$ Mc/sec, and $G_v=-0.980$ Mc/sec.

Table V. Lines of $J=1\leftarrow0$, $K=0\leftarrow0$ of $C^{13}H_3S^{32}H$.

n	μ	Observed Frequency[a] in Mc/sec	Calculated Frequency[b] in Mc/sec
0	0	24389.1	24389.0
0	±1	24388.0	(24388.0)
1	0	24318.5	(24318.5)
1	±1	24306.2	24306.5
2	0	24245.0	24244.6
2	±1	24256.2	(24256.2)

a) The data are quoted from Solimene and Dailey.

b) Three parameters are $B_v=12214.45$ Mc/sec, $F_v=-53.82$ Mc/sec and $G_v=-0.937$ Mc/sec.

§ 4. Determination of the Molecular Structure

The approximate value of $\frac{1}{I_x}+\frac{1}{I_y}$ and $\frac{I_z}{I_1I_2}$ were determined from the frequencies of $J=1\leftarrow0$, $K=0\leftarrow0$ line and $\Delta J=\pm1$, $\Delta K=\mp1$ lines. Using the relations, $I_z=I_1+I_2$ and $I_1=$ I_x-I_y, the molecular structure was roughly calculated. The frequencies of the $\Delta J=0$, $\Delta K=0$ lines (transitions between the levels of K-type doublets) which are proportional to $\frac{1}{I_x}-\frac{1}{I_y}$ were also calculated and listed in Table VI.

Table VI. Lines of $\Delta J=0$, $\Delta K=0$ of $C^{12}H_3S^{32}H$.

Assignment $J_{K_{-1}K_{+1}}\leftarrow J'_{K_{-1}K'_{+1}}$	Observed Frequency in Mc/sec	Calculated Frequency in Mc/sec
$5_{14}\leftarrow5_{15}$	7846.0	7700
$6_{15}\leftarrow6_{16}$	10983.4	10800
$7_{16}\leftarrow7_{17}$	14643.1	14400
$8_{17}\leftarrow8_{18}$	18824.2	18500
$9_{18}\leftarrow9_{19}$	23526.2	23200
$10_{19}\leftarrow10_{1,10}$	28747.9	28200

To determine the exact structure of the molecule, it is necessary to determine D value which is the product of inertia in CSH plane. We have found that the contribution of the asymmetry effect to the frequency of the $J=1\leftarrow0$, $K=0\leftarrow0$, $\mu=\pm1$, $n=1$ line of CD_3SH is about 1.4 Mc/sec as shown in Table VII. The asymmetry effect is larger for CH_3SD

Table VII. Lines of $J=1\leftarrow0$, $K=0\leftarrow0$ of $C^{12}D_3S^{32}H$.

Assignment n	μ	ν[a]	Asymmetry Effect	Calculated[b] Frequency	Observed Frequency
0	0	20732.5	−0.1	20732.4	20732.0
0	±0	20733.0	−0.2	(20732.8)	20732.8
1	0	20678.9	0.0	(20678.9)	20678.9
1	±1	20672.7	1.4	20674.1	20674.8
2	0	20620.7	0.0	20620.7	20619.0
2	±1	20627.6	0.0	(20627.6)	20627.6

a) $\nu=2B_v+2F_v(m|1-\cos3\theta|m)+2G_v(m|\Pi_z{}^2|m)$ where $B_v=10381.2$ Mc/sec, $F_v=-47.33$ Mc/sec and $G_v=-0.718$ Mc/sec.

b) The calculation was done assuming $\alpha=8.8$ and $\frac{h}{8\pi^2c}\frac{D}{B^2}=80$ Mc/sec.

because of its large D value.

We tried to determine the D value of CH_3SD from the fine structure of $J=1\leftarrow0$, $K=0\leftarrow0$ line measured by Solimene and Dailey[7] but failed. Then we have remeasured the fine structure and detected the true $n=0$ line which they missed. The measured and calculated frequencies agree very well and the D value of CH_3SD has been determined as -0.78 amu A². They are listed in Table VIII.

Table VIII. Lines of $J=1\leftarrow0$, $K=0\rightarrow0$ of $C^{12}H_3S^{32}D$.

Assignment n	μ	ν[a)]	Asymmetry Effect	Calculated[b)] Frequency	Observed Frequency
0	0	24456.7	−0.9	(24455.8	24456.0
0	±1	24457.1	−1.0	24456.1)	
1	0	24392.5	−4.8	24387.7	24388.3
1	±1	24388.1	−1.8	24386.3	24385.9
2	0	24322.0	+0.2	(24322.2)	24322.2
2	±1	24330.3	0.0	(24330.3)	24330.3
3	0	24302.2	0.0	24302.2	24302.9
3	±1	24293.8	0.0	24293.8	....

a) $\nu=2B_v+2F_v(m|1-\cos 3\theta|m)+2G_v(m|\Pi_z{}^2|m)$ where $B_v=12245.7$ Mc/sec, $F_v=-58.83$ Mc/sec and $G_v=-0.839$ Mc/sec.

b) The calculation was done assuming $\alpha=10.6$ and $\frac{h}{8\pi^2c}\frac{D}{B^2}=250$ Mc/sec.

From the D value, the angle between CS bond and methyl axis has been determined as 2°0′±30′. Then the other molecular parameters have been determined taking account of all the frequencies of $J=1\leftarrow0$ lines of various isotopic species as follows:

$$d_{SH}=1.336\pm0.01\ \text{A}$$
$$d_{CS}=1.819\pm0.005\ \text{A}$$
$$d_{CH}=1.091\pm0.01\ \text{A}$$
$$\angle CSH=96°30'\pm1°$$
$$\angle HCH=109°45'\pm30'$$

The CS bond length is very close to the sum of covalent radii, 1.82 A. It is also interesting to see that the bond angle ∠CSH is somewhat smaller than formerly reported,[7),8)] while it is about 4° larger than ∠HSH of hydrogen sulfide, (92°30′). On the other hand, the structure of the methyl group does not differ from that of methane within experimental error. The similar tendencies were also found in the structures of methyl alcohol and methyl amine.

Lassetree and Deans[12)] developed a theory, in which they pointed out that the interaction due to the quadrupole moments of CH and MH (M is O for methyl alcohol, and M is S for methyl mercaptan) bond take a considerable part in forming potential barrier to internal rotation. Since the bond quadrupole moment is approximately proportional to the square of the bond length, a larger moment is expected in SH bond than in OH bond ($d_{OH}=$ 0.95 A). Besides, since the bond angle ∠CSH is considerably smaller than the bond angle ∠COH (108°50′), the distances between the midpoints of CH and MH bond does not differ so much as expected from the difference in the CM bond lengths of the two molecules. Hence the relatively high barrier of methyl mercaptan is conceivable when we consider the quadrupole-quadrupole and the quadrupole-dipole interactions. We have obtained the barrier height of 490 cm^{-1} for this molecule by a modified Lassetree-Dean's method using the molecular structure determined above.

The components of the dipole moment parallel and perpendicular to the methyl axis have been determined as $\mu_{\parallel}=1.35\pm0.05\,D$ and $\mu_{\perp}=0.64\pm0.05\,D$ respectively from the Stark patterns of $\Delta J=\pm1$, $\Delta K=\mp1$ lines. These values are also consistent with those calculated from the bond dipole moment ($\mu_{\parallel}=1.30\,D$ and $\mu_{\perp}=0.71\,D$).

Acknowledgement

We wish to express our hearty thanks to Prof. K. Shimoda for his valuable advice and encouragement throughout this work. Also thanks are due to Mr. T. Itoh who gave us valuable discussion and to Mr. H. Hirakawa for the preparation of deuterated methyl mercaptan. This work was financially supported by grants in aid for Fundamental Scientific Research of the Ministry of Education.

References

1) J. S. Koehler and D. M. Dennison: Phys. Rev. **57** (1940) 1006.
D. G. Burkhard and D. M. Dennison: Phys. Rev. **84** (1951) 408.
E. V. Ivash and D. M. Dennison: J. Chem. Phys. **21** (1953) 1804.
2) P. Venkateswarlu, H. D. Edwards and W. Gordy: J. Chem. Phys. **23** (1955) 1195.

3) T. Nishikawa: J. Phys. Soc. Japan **11** (1956) 781.

4) K. Shimoda, T. Nishikawa and T. Ito: J. Chem. Phys. **22** (1954) 1456; J. Phys. Soc. Japan **9** (1954) 974.
T. Nishikawa, T. Ito and K. Shimoda: J. Chem. Phys. **23** (1955) 1735.
T. Ito: J. Phys. Soc. Japan **11** (1956) 264.
T. Nishikawa: J. Phys. Soc. Japan **12** (1957) 668.

5) D. R. Lide Jr.: J. Chem. Phys. **20** (1952) 1812; **21** (1953) 571; **22** (1954) 1613.

6) H. Russell Jr., D. W. Osborne and D. M. Yost: J. Amer. Chem. Soc. **64** (1942) 165.

7) N. Solimene and B. P. Dailey: J. Chem. Phys. **23** (1955) 125.

8) R. W. Kilb: J. Chem. Phys. **23** (1955) 1736.

9) T. Kojima and T. Nishikawa: J. Phys. Soc. Japan **10** (1955) 240.

10) T. M. Shaw and J. J. Windle: J. Chem. Phys. **19** (1951) 1063.

11) D. Kivelson: J. Chem. Phys. **22** (1954) 1733.

12) E. N. Lassettre and L. B. Dean Jr.: J. Chem. Phys. **17** (1949) 317.

JOURNAL OF THE PHYSICAL SOCIETY OF JAPAN Vol. 12, No. 6, JUNE, 1957

Fluctuations in Amplification of Quanta with Application to Maser Amplifiers

By Koichi SHIMODA, Hidetosi TAKAHASI, and Charles H. TOWNES*

Department of Physics, Faculty of Science, University of Tokyo

(Received February 15, 1957)

Fluctuations in the amplification and absorption of waves by quantum processes are considered. Assuming for each quantum the probability (per unit time) a of producing another quantum, probability b of being absorbed, and assuming a probability c that a new quantum is introduced, a set of differential equations is obtained. By solving these equations, a complete expression for the probability of distribution of quanta is obtained, as well as expressions for the average values and fractional fluctuation.

The expressions developed are applied in particular to maser-type amplifiers, and certain fluctuations in the amplification of electromagnetic waves are pointed out which are important when their quantum character becomes significant. This condition can occur in maser-type amplifiers, where thermal and extraneous noises may be very small. For such an amplifier, a is proportional to the number of excited molecules, whereas b consists of a term proportional to the number of molecules in the ground state plus terms due to certain other losses. The noise temperature of a maser-type traveling-wave amplifier is the "effective temperature" $a(a-b)^{-1}h\nu/k$. In superregenerative and regenerative amplifiers using resonant cavities, the noise temperature is rather similar, if losses through the input coupling hole are excluded from b. In any case, the limiting noise for an ideal amplifier corresponds to a classical noise temperature of $h\nu/k$.

§ 1. Introduction

The intensity of a classical wave may increase or decrease continuously with time, or as the wave progresses. The intensity of a quantized wave, on the other hand, can change only by discrete amounts, and the extent of these changes is governed by probabilities. Hence a measurement of the number of quanta which it contains may give a variety of values. An evident example is a cosmic ray shower, in which a single initial electron may

---

[*] Fulbright Professor, May–Aug. 1956. Permanent address, Department of Physics, Columbia University.

roduce other electrons as it progresses through atter. The expectation value for the number f particles in the shower after a certain ath length may have some definite non-integral value, but the number of particles counted n the shower will of course be integral, and ay have a wide variety of values. It is his general type of fluctuation, associated ith quantum effects, with which the following discussion is primarily concerned.

A system involving stimulated emission and bsorption of low energy photons by matter ffords a particularly simple case for study f these fluctuations, since every such photon as the same energy, and the same probability er unit time of producing further absorption r emission. This case is also of interest ecause it allows discussion of the ultimate ensitivity of maser-type amplifiers, to which ome application of the theory developed below will be made. However, the equation used and their solutions apply to certain simple cases of a variety of experiments, such as fluctuations in the number of mutants of some organism[1)], in the growth of neutrons in fissionable material, in the multiplication of electrons by secondary emission, as well as variations in cosmic ray showers[2)].

§ 2. Definitions and Fundamental Equations

Consider an initial number of particles, n, each of which has a probability per unit time, a, for producing another similar particle, and a probability per unit time, b, of being absorbed or destroyed. Also let c be the constant rate at which additional particles may be added from some unspecified source. If the total number of particles, m, could increase continuously, it would then follow the equation

$$\frac{dm}{dt}=(a-b)m+c\,, \tag{1}$$

with the initial condition, $m=n$ for $t=0$. Solution of this equation, corresponding to the change in intensity of a classical wave, is

$$m=\left(n+\frac{c}{a-b}\right)e^{(a-b)t}-\frac{c}{a-b}\,. \tag{2}$$

Hence the quantity $m+\frac{c}{a-b}$ increases or decreases exponentially with time. However, since m must be integral, equation (1) does not apply precisely*, and it is convenient to consider the probability $P_{n,m}(t)$ for having a total of m particles at a time t. Since $(am+c)P_{n,m}$ is the probability per unit time that the number of particles are increased from m to $m+1$ and $bmP_{n,m}$ the probability for a decrease from m to $m-1$, the $P_{n,m}$ are related by the set of differential equations

$$\begin{aligned}\frac{dP_{n,m}}{dt}=&-[(a+b)m+c]P_{n,m}\\&+[a(m-1)+c]P_{n,m-1}\\&+b(m+1)P_{n,m+1}\end{aligned} \tag{3}$$

with initial conditions that for $t=0$, $P_{n,m}=\delta_{nm}$ Evidently, this equation is satisfied by any probability distribution corresponding to an arbitrary initial state, although the initial condition may differ from that given above.

§ 3. Distributions when Absorption or Emission Occurs Alone

Since general solutions for the set of equations (3) are rather complicated, it is instructive to first consider solutions of the simplified cases when only emission or only absorption occurs ($b=0$ or $a=c=0$ respectively). For emission only,

$$\frac{dP_{n,m}}{dt}=-(am+c)P_{n,m}+[a(m-1)+c]P_{n,m-1}\,. \tag{4}$$

Solutions satisfying the initial conditions, $P_{n,m}=\delta_{nm}$ for $t=0$ are

$$\begin{aligned}P_{n,m}(t)=&\frac{\Gamma(m+c/a)}{(m-n)!\,\Gamma(n+c/a)}e^{-at(n+c/a)}\\&\times(1-e^{-at})^{m-n}\end{aligned} \tag{5a}$$

or

$$\begin{aligned}P_{n,m}=&\frac{\Gamma(m+c/a)}{(m-n)!\,\Gamma(n+c/a)}\left(\frac{1}{K}\right)^{n+c/a}\\&\times\left(1-\frac{1}{K}\right)^{m-n}\,,\end{aligned} \tag{5b}$$

where $K=e^{at}$ is the classical growth or amplification factor from (2). When there is absorption or attenuation only,

$$P_{n,m}=\frac{n!}{m!\,(n-m)!}e^{-btm}(1-e^{-bt})^{n-m} \tag{6a}$$

or

---

* It will been seen below, in equation (11), that even when the number of particles is finite and does not increase continuously, the average number of particles still changes with time in precisely the same manner given by the classical expression.

$$P_{n,m}=\frac{n!}{m!\,(n-m)!}(K)^m(1-K)^{n-m} \tag{6b}$$

where $K=e^{-bt}$ is from (2) the classical attenuation factor.

After a very long time (6a) gives, as expected, a probability zero for finding any number of particles other than $m=0$. However, the asymptotic behavior of (5a) is more interesting. In the limit where e^{at} or K is very large,

$$P_{n,m}\to\frac{m^{n+c/a-1}e^{-m/K}}{K^{n+c/a}\,\Gamma(n+c/a)}\,. \tag{7}$$

This probability is a maximum when $m=K(n+c/a-1)$, but from it the average value of m can be shown to be $\bar{m}=K(n+c/a)-c/a$, which is identical with the classical expression (2). Furthermore when K is so large that (7) is a good approximation, the distribution does not change shape, but is a function of $\frac{m}{K}=n+c/a-1$. The fluctuations then depend, after a large amplification, only on the number n of initial particles and on c/a, which is the number of new particles introduced during the time required for the amplification to increase by a factor e.

A special property of equation (6), or of (5) when $c/a=1$, is that an exponential probability distribution remains exponential after amplification or attenuation. The latter case $c/a=1$ is important, as will be shown below, for distributions of photons where c is due only to spontaneous emission. Let there be initially a probability $p_n(0)=(1-u_0)u_0^n$ that n particles are introduced, where $u_0<1$. The probability p_m of m particles after amplification is

$$\begin{aligned}p_m&=\sum_n P_{n,m}p_n(0)\\&=\frac{(1-u_0)}{K}\sum_n\frac{m!}{n!(m-n)!}\left(\frac{u_0}{K}\right)^n\left(1-\frac{1}{K}\right)^{m-n}\\&=\frac{(1-u_0)}{K}\left(\frac{K+u_0-1}{K}\right)^m.\end{aligned} \tag{8a}$$

This is just another exponential distribution with somewhat larger spread, since u_0 is replaced by $u=\frac{K+u_0-1}{K}$, and $u\geq u_0$ when $K\geq 1$. Equation (8a) can be written in the form

$$\frac{u}{1-u}=K\left(\frac{u_0}{1-u_0}+1\right)-1\,. \tag{8b}$$

Since $\frac{u_0}{1-u_0}$ and $\frac{u}{1-u}$ represent the averag value of n and m respectively, (8b) mean that the classical relation (2) is again satisfie for the average values.

Similarly, when attenuation occurs, a distr bution $(1-u_0)u_0^n$ is changed into $(1-u)u^m$ where

$$u=\frac{Ku_0}{1-u_0(1-K)}\,. \qquad (9$$

Here $u\leq u_0$ since now $K\leq 1$. (9a) may b written as

$$\frac{u}{1-u}=\frac{Ku_0}{1-u_0} \qquad (9$$

which again corresponds to the classical re lation (2) with $a=c=0$. When $c/a=0$ in ex pressions (6a) or (6b), an exponential distri bution can be shown to again remain ex ponential after amplification, with exceptio of the unique case of $m=0$. The case o $m=0$ is exceptional when $c/a=0$, since it probability must remain constant, while pro babilities for all other values of m may be changed by the effect of amplification. These properties will prove useful in a later section

Expressions (5) and (6) giving the distri bution in the number of particles are quite general in the sense that they do not depend on the particular mechanism of attenuation or amplification. Thus if a group of particles strike a partially reflecting surface, each particle having a probability K of being re flected, the probability that m particles in al are reflected is given by (6b). Expressions (5b) and (6b) do not include time as a para meter, but simply the total amplification o attenuation, and their validity can be shown not to depend on constant values of a or b However, they do require that only emission or only absorption be present, and not both a once.

§ 4. The General Case — Moments of the Distribution and Average Fluctuation

When $K=1$, expressions (5b) and (6b) show that there is no change from the initial values of the probabilities. This is because no ampli fication or absorption has occurred, so no disturbances are introduced. However, the net amplification may also be unity in a system where both amplifying and absorbing processes occur simultaneously, and hence introduc uctuations. Hence when neither a nor b is ro, equations (5) and (6) may need con-derable modification. Since a general solution (3) in this case is complex, it is convenient examine first the various moments of the stribution and properties of the fluctuations hich can be easily deduced from them.

Behavior of the average value of m, $=\sum_m mP_{n,m}$, can be obtained by multiplying quation (3) with m, summing over m, and aking substitutions of the type,

$$\sum_m f(m)P_{n,m-1}=\sum_m f(m+1)P_{n,m}$$
$$\sum_m f(m)P_{n,m+1}=\sum_m f(m-1)P_{n,m}\,. \tag{10}$$

This gives

$$\frac{d\overline{m}}{dt}=\overline{m}(a-b)+c\,. \tag{11}$$

By a similar process, one obtains

$$\frac{d\overline{m^2}}{dt}=2(a-b)\overline{m^2}+(a+b+2c)\overline{m}+c \tag{12}$$

$$\frac{d\overline{m^r}}{dt}=\sum_{s=1}^{r}\frac{r!}{s!\,(r-s)!}\left\{\overline{m^{r-s+1}}[a+(-1)^s b]+\overline{m^{r-s}}c\right\}. \tag{13}$$

olutions of (11) and (12) are

$$\overline{m}=\left(\overline{n}+\frac{c}{a-b}\right)e^{(a-b)t}-\frac{c}{a-b} \tag{14}$$

$$\overline{m^2}=\left[\overline{n^2}-\frac{c(b+c)}{(a-b)^2}+\left(\overline{n}+\frac{c}{a-b}\right)\frac{(a+b+2c)}{a-b}\right]e^{2(a-b)t}$$
$$-\left(\overline{n}+\frac{c}{a-b}\right)\frac{(a+b+2c)}{a-b}e^{(a-b)t}+\frac{c(b+c)}{(a-b)^2}\,, \tag{15}$$

here $\overline{n}$ and $\overline{n^2}$ are values of $\overline{m}$ and $\overline{m^2}$ respectively at $t=0$. The average or expectation alue, $\overline{m}$, follows the same equation (2) which is obtained for a classical wave. It may be oted that when $\overline{n}=-\frac{c}{a-b}$ and $\overline{n^2}=\frac{c(b+c)}{(a-b)^2}$, $\overline{m}$ and $\overline{m^2}$ are constant. This equilibrium ondition can occur only when $b>a$, and will be shown below to represent thermal equiibrium in the case of photons. Furthermore, if $b>a$, (14) and (15) show that $\overline{m}$ and $\overline{m^2}$ pproach these equilibrium values after a long time.

The most significant quantity for a ready measure of fluctuations is $\frac{\overline{m^2}-\overline{m}^2}{\overline{m}^2}$. This is the quare of what is usually called the coefficient of variation or more loosely the fractional luctuation $\mathcal{E}$. $\mathcal{E}^2$ can be obtained from (14) and (15). If amplification occurs, so that $a>b$, hen after a long time the first terms of expressions (14) and (15) are the only important nes. Neglecting other terms,

$$\mathcal{E}^2=\frac{\overline{m^2}-\overline{m}^2}{\overline{m}^2}=\frac{\overline{n}\left(\frac{a+b}{a-b}\right)+\frac{ac}{(a-b)^2}}{\left(\overline{n}+\frac{c}{a-b}\right)^2}+\frac{\overline{n^2}-\overline{n}^2}{\left(\overline{n}+\frac{c}{a-b}\right)^2}\,. \tag{16}$$

number of special cases are of interest. uppose that there are a fixed number of nitial particles n, and no new ones are added, e., $\overline{n^2}=\overline{n}^2$ and $c=0$. Then

$$\mathcal{E}=\frac{1}{\sqrt{n\left(\frac{a-b}{a+b}\right)}}\,. \tag{17}$$

f amplification alone occurs ($b=0$), then $=n^{-1/2}$. The fluctuation $\mathcal{E}$ is not due to any ncertainty in the initial number n, but simply o fundamental processes in the amplification of particles. This fluctuation occurs also in amplification of an electromagnetic wave, even in the absence of thermal noise, and represents a lower limit to fluctuation of any amplifying process. If both emission and absorption occur, (17) shows that fluctuations may be appreciably larger than $n^{-1/2}$.

In many cases such fluctuations are negligible, particularly at low frequencies where the number of photons in thermal noise is large. Any degree of freedom of an electrical circuit has average energy kT and hence $kT/h\nu$

photons. Hence as long as $kT \gg h\nu$, and $(a-b)/(a+b)$ is not very small, fluctuations of this type will be negligible. On the other hand, the discussion of amplifiers of electromagnetic waves below will show that thermal noise at low frequencies is just the limiting case of the fluctuations discussed here when $kT/h\nu$ becomes large and $(a-b)/(a+b)$ becomes small as $h\nu/kT$.

A second special case of interest occurs when $c/(a-b) \gg \bar{n}$. Since $c/(a-b)$ is the number of new particles introduced during the time required for the amplification to increase by e, this condition represents the case where the initial number of particles can hardly be regarded as fixed, but is dominated by the entrance of $c/(a-b)$ new particles during the time required for an appreciable amplification. In this case

$$\varepsilon=\sqrt{\frac{a}{b}}\,. \qquad (18)$$

Note that the fluctuations are determined not by $c/(a-b)$, the number of particles entering during time for amplification, but by c/a, the smaller number which enters during the time required for appreciable emission (or absorption if $a-b \ll a$, for then $b \approx a$).

§ 5. Complete Solution for the Distribution Function

Values of the first few moments of m may be all that is usually needed for practical purposes, and these can be conveniently calculated from the set of equations (13). However, a complete solution of (3) may be useful in some cases, and will be given in the following. The solution has been obtained for the general case of arbitrary values of a, b and c by use of a generating function. However, the cases $c=a$ and $c=0$, which have the special property mentioned above, can be dealt with in a somewhat different and more physical way. Since these are also quite important cases, they will be considered in some detail.

i) Case $c=a$

It has been shown above that, when $c=$ the exponential form of probability distributi is invariant and that there is a linear relatic ship, (8b) or (9b), between the average numbe of quanta before and after either amplificati alone or attenuation alone. Hence this i variance of an exponential distribution a the same type of linear relationship mu remain valid for any combination of succe sive absorption and amplification and, as limiting case, for simultaneous absorption ar amplification. It may then be assumed tha some solution of the fundamental differenti equation

$$\frac{dp_m}{dt}=-[a(m+1)+bm]p_m + amp_{m-1}+b(m+1)p_{m+1} \qquad (19$$

has the form

$$p_m=(1-u)u^m\,. \qquad (20$$

Equation (19) is the form taken by (3) whe $c=a$. When expression (20) is substituted int (19), a factor depending on m drops out fron both sides of the equation, and a single equation independent of m is obtained:

$$\frac{du}{dt}=(1-u)(a-bu)\,.$$

Integration of this expression yields a linea relation between the average numbers o quanta, i.e.,

$$\frac{u}{1-u}=\frac{Ku_0}{1-u_0}+\frac{a}{a-b}(K-1) \qquad (21$$

where $K=e^{(a-b)t}$ is the classical amplificatio factor and u_0 is the initial value of u (fo $t=0$).

Since (20) is the probability distribution corresponding to the initial distribution $(1-u_0)u_0$ we have

$$(1-u)u^m=\sum_n P_{n,m}(1-u_0)u_0^n \qquad (22$$

or

$$\sum_n P_{n,m}u_0^n=\frac{1-u}{1-u_0}u^m=\frac{(a-b)a^m(K-1)^m}{(aK-b)^{m+1}\left[1-\frac{b(K-1)}{aK-b}u_0\right]}\left[1+\frac{\frac{(a-b)^2Ku_0}{a(K-1)(aK-b)}}{1-\frac{b(K-1)}{aK-b}u_0}\right]^m. \qquad (23$$

Since (23) holds for any u_0 (less than unity), it may be used to evaluate $P_{n,m}$ by expandin the right hand side in powers of u_0 and equating coefficients of u_0^n on each side of th uation. Such an expansion gives a convergent series when $u_0<1$, since always $\frac{b(K-1)}{aK-b}>1$. ter carrying out the expansion, one obtains the probability distribution

$$P_{n,m}=\frac{(a-b)a^m b^n (K-1)^{m+n}}{(aK-b)^{m+n+1}}\sum_{j=0}^{m \text{ or } n}\frac{m!n!}{j!(m-j)!j!(n-j)!}\left[\frac{(a-b)^2K}{ab(K-1)^2}\right]^j . \tag{24}$$

re the upper limit of the summation should be n for $n\leq m$ and m for $n\geq m$.

When $a=0$, expression (24) becomes $\frac{n!}{m!(n-m)!}K^m(1-K)^{n-m}$ for $n\geq m$, and 0 for $n<m$, agreement with the previous result (6b). Similarly, when $b=0$, (24) becomes $\frac{m!}{(m-n)!n!}$ $\frac{(K-1)^{m-n}}{K^{m+1}}$ for $m\geq n$, and 0 for $m<n$, in agreement with (5b) when $c=a$.

Case $c=0$

It has already been shown that the same type of invariance of the exponential distribution lds also when $c=0$, with the exception of the case $m=0$. Accordingly, one can proceed in way similar to that above for $c=a$, but with a few modifications. Since $m=0$ is exceptional, e probabilities may be written in the form

$$\begin{aligned} p_m&=\alpha(1-u)u^m \qquad (m\neq 0)\\ p_0&=1-\alpha u\ , \end{aligned} \tag{25}$$

sing a positive parameter α. The lowest state $m=0$ is more or less populated than is reuired by the strictly exponential distribution according as $\alpha>1$ or $\alpha<1$. One again obtains e relation between u and u_0:

$$\frac{u}{1-u}=\frac{Ku_0}{1-u_0}+K-1\ , \tag{26}$$

hich is identical with (8b). However, it should be noted that here the average number of uanta $\overline{m}$ is no longer $u/(1-u)$ but rather $\alpha u/(1-u)$ and the physical meaning of (26) is quite ifferent. The proper equation for $\overline{m}$ is

$$\overline{m}=\frac{\alpha u}{1-u}=K\frac{\alpha_0 u_0}{1-u_0}\ , \tag{27}$$

here α_0 is the initial value of α at $t=0$. Note that (27) just corresponds to (14) when $c=0$. 7) may be used to determine the additional parameter α.

From these equations, one obtains after a little calculation for $m\neq 0$

$$\sum_{n=1}^{\infty}P_{n,m}u_0^{\,n}=\frac{(a-b)^2Ku[a(K-1)+(a-bK)u]^{m-1}}{[(aK-b)-b(K-1)u_0]^{m+1}} \tag{28}$$

nd for $m=0$

$$\sum_{n=1}^{\infty}P_{n,0}u_0^{\,n}=\frac{b(K-1)u_0}{(aK-b)-b(K-1)u_0}\ .$$

xpansion of the right hand side gives

$$P_{n,m}=\frac{a^m b^n (K-1)^{m+n}}{(aK-b)^{m+n}}\sum_{j=0}^{m \text{ or } n}\frac{n!(m-1)!}{j!(n-j)!(j-1)!(m-j)!}\left[\frac{(a-b)^2K}{ab(K-1)^2}\right]^j . \tag{29}$$

i) General Case

The form of $P_{m,n}$ for the general case might he conjectured from expressions (24) and (29), r it may be rigorously derived by use of a generating function. It is

$$P_{n,m}=\frac{(a-b)^{c/a}a^m b^n (K-1)^{m+n}}{(aK-b)^{m+n+c/a}}\sum_{j=0}^{m\text{ or }n}\frac{n!\Gamma(m+c/a)}{j!(n-j)!(m-j)!\Gamma(j+c/a)}\left[\frac{(a-b)^2K}{ab(K-1)^2}\right]^j, \qquad \text{(3}$$

where the sum is to m when $m\leq n$ or to n when $n\leq m$. The generating function and deta of the derivation of (30) are given in the Appendix. Expression (30) holds for any positi values of K, a, b, and c. However, there are a number of special cases listed below whi warrant separate consideration.

(a) Case $a=b$, $K=1$

Expression (30) holds for $K>1$ as well as for $K<1$. However, the equation cannot used directly for the limiting case $K=1$, that is, the case with neither amplification nor a tenuation. By the appropriate limiting process, $K=(a-b)t+1$ and $a\rightarrow b$, (30) can be broug to the following from

$$P_{n,m}=\frac{(at)^{m+n}}{(at+1)^{m+n+c/a}}\sum_{j=0}^{m\text{ or }n}\frac{n!\Gamma(m+c/a)}{j!(n-j)!(m-j)!\Gamma(j+c/a)}\left(\frac{1}{at}\right)^{2j}. \qquad \text{(3}$$

(b) Case $a=0$, $c\neq 0$

Another limiting case occurs when there is no amplification but a constant rate of generat of new quanta. Then

$$P_{n,m}=\frac{c^m(1-K)^{n+m}}{b^m}e^{-(1-K)c/b}\sum_{j=0}^{n\text{ or }m}\frac{n!}{j!(n-j)!(m-j)!}\left(\frac{bK}{c(1-K)^2}\right)^j. \qquad \text{(32}$$

(c) $K\rightarrow\infty$, $m\rightarrow\infty$, $K/m=$finite

The asymptotic behavior of (30) for large K and m is of special interest since such a cas is related to a macroscopic observation of a small number of quanta by means of very larg amplification, as in the case of photo-multiplier tubes, or perhaps in a maser amplifier.

The asymptotic form in this case is

$$P_{n,m}=\frac{1}{m}\left(\frac{a-b}{a}\frac{m}{K}\right)^{c/a}\left(\frac{b}{a}\right)^n\exp\left(-\frac{a-b}{a}\frac{m}{K}\right)\sum_{j=0}^{n}\frac{n!}{j!(n-j)!\Gamma(j+c/a)}\left[\frac{(a-b)^2}{ab}\frac{m}{K}\right]^j. \qquad \text{(33}$$

When $c=a$, the right hand side becomes a Laguerre polynomial and

$$P_{n,m}=\frac{a-b}{aK}\left(\frac{b}{a}\right)^n\exp\left(-\frac{a-b}{ab}\frac{m}{K}\right)L_n\left[-\frac{(a-b)^2}{ab}\frac{m}{K}\right]. \qquad \text{(34}$$

When $a\gg b$, the highest term of the sum in (33) prevails and the distribution is nearly identical with the one given by (7). However, as the ratio b/a increases, the peak becomes broader and the value of $P_{n,m}$ does not vanish at $m=0$ corresponding to the fact that there is always some probability that all particles vanish during the process.

(d) Equilibrium

The distribution reaches an equilibrium after a long time only if $a<b$. $P_{n,m}$ may be evaluated in this case either by setting $dP_{n,m}/dt=0$ in the fundamental equation (3) and solving the equation by a mathematical induction, or by letting K approach zero in the general solution (30). This gives

$$P_{n,m}=(1-a/b)^{c/a}\frac{\Gamma(m+c/a)(a/b)^m}{m!\Gamma(c/a)} \qquad (35)$$

which is independent of n and finite for a values of m, since $a<b$.

Finally, attention should be called to th generality of the expression of the type (30 In case $c=a$ and $c=0$, it can be shown tha any succession of absorption and emissio leaves the exponential form of distributio invariant and leads to a linear relation betwee $u/(1-u)$ and $u_0/(1-u_0)$. The expression co tains two independent parameters K and $a/$ and represents the most general linear relatio between $u/(1-u)$ and $u_0/(1-u_0)$. Hence follows that the forms (24) and (29) represe the general case involving any arbitrary su cession of absorption, amplification, or mixtu of both, provided appropriate values of K a a/b are used.

The same argument does not apply to t

eneral case represented by (30), but it will e shown in the appendix, that this is true ven in this case, that is, when both a and depend on time, but c/a remains constant.

6. Applicability of Results to Maser-type Amplification

Equation (3) and solutions discussed above pply well to a group of photons which may ncrease or decrease in number as a result of ormal absorption, stimulated emission, or pontaneous emission. Consider some atomic r molecular system which may exist in one f two nearby levels, between which photons nay induce transitions. The probability of bsorption of a photon by a molecule in the ower state is the same as that for emission timulated by the photon from a molecule in he upper state. Under normal conditions, an nsemble of such molecules is in thermal quilibrium, there are more molecules in the ower than in the upper state, and hence the nsemble attenuates a wave packet of photons. However, spontaneous emission also occurs and is responsible for maintaining the thermal radiation of photons by the molecules. Moreover, if an abnormal ensemble can be created n which there are more molecules in the upper than in the lower state, a wave packet of photons passing through such an ensemble will be amplified rather than attenuated. This type of phenomenon occurs in a maser$^{3)}$, and gives promise of allowing construction of amplifiers which are exceptionally free of noise. To show that equation (3) applies to such amplifiers, two somewhat idealized cases will be discussed.

Consider first a cavity with perfectly reflecting walls and containing molecules of the type described above with n_a molecules in the upper state and n_b in the lower state. For simplicity, suppose that the response of these molecules is independent of frequency over the range of frequencies considered, which includes the frequency of a normal mode of the cavity. If there are m photons of this frequency in the cavity, the probability of one of the photons being absorbed per unit time is proportional to m and to n_b or hence has the form Amn_b, where A is a constant. The probability per unit time for a photon to be produced by stimulated emission is correspondingly Amn_a.

Spontaneous emission may also provide new photons. When an excited atomic or molecular system interacts with one of the normal modes of an electromagnetic field in some enclosure, the probability for emission of a photon (of the same frequency as that of the normal mode) is proportional to $n+1$, where n is the number of quanta present in the mode. The finite probability for emission when $n=0$ represents spontaneous emission, or the effect of zero-point fluctuations of the electromagnetic field which have one-half the energy of one quantum. Hence the spontaneous emission is given by An_a.

From the above, it may be seen that the number of photons in a perfectly reflecting cavity containing molecules of the type discussed will follow equations (3) with $a=An_a$, $b=An_b$, and $c=a$. If the walls are not perfectly reflecting, but absorb and emit photons, they may be replaced in principle by perfectly reflecting walls and a suitable number of molecules n_a and n_b in the upper and lower states. Hence, with appropriate modification of the effective number of molecules involved, a cavity with absorbing walls is equivalent to the case with perfectly reflecting walls already considered. If there is a coupling hole in the cavity, this allows photons to escape and corresponds simply to an increase in n_b or in b provided no new photons enter through the coupling hole. If a signal is introduced through the coupling hole, this corresponds to an increase in c, the rate of introduction of new photons, so that $c>a$. However, as will be seen below, some care must be taken to allow for possible interference of the waves of incoming and outgoing photons in this case.

As a second example, consider a packet of m photons traveling along a waveguide filled with material containing the molecules in question with a density n_a of molecules in the upper state and a density n_b in the lower state. For simplicity, let the wave associated with the m photons be a packet of constant amplitude and finite length, with Δt the time required for the entire packet to pass a given point in the waveguide. Now the probability of one of the photons being absorbed per unit time is again proportional to m and to n_b, or $A'mn_b$. The probability per unit time for production of a photon by stimulated emission is correspondingly $A'mn_a$. Again for simplicity, the molecular systems will be assumed to respond uniformly over a wide range of frequencies so that A' is independent of frequencies to be considered.

The ratio of induced emission to spontaneous emission may be seen from the discussion above to be determined by the ratio of the energy density associated with photons to twice that of zero-point fluctuations of the normal modes which have appropriate frequencies to produce emission.

A waveguide may be considered an enclosure, and the energy density of normal modes calculated, by assuming it has some arbitrary long length. Or, such a calculation may be circumvented by use of the well known relation for the power flow P of noise along a waveguide.

$$P = kT\Delta\nu\ , \tag{36}$$

where $\Delta\nu$ is the bandwidth to which the amplifying system responds. Since each normal mode has energy kT (when $kT \gg h\nu$, which may be assumed for this derivation), and each mode may be considered as two traveling waves moving in opposite directions, it can be seen from (36) that the power which might be considered to flow in one direction due to zero-point vibration is

$$P_0 = \frac{h\nu\,\Delta\nu}{2}\ .$$

The power flow due to the wave packet of m photons is $\frac{mh\nu}{\Delta t}$. Now a wave packet of duration Δt has a frequency spectrum with the power per unit bandwith given as a function of frequency by

$$\Phi(\nu)d\nu = \Phi(\nu_0)\left[\frac{\sin(\nu-\nu_0)\pi\Delta t}{(\nu-\nu_0)\pi\Delta t}\right]^2 d\nu\ . \tag{37}$$

Integration of (37) gives the total power flow and allows evalution of $\Phi(\nu_0)$

$$\frac{mh\nu}{\Delta t} = \int \Phi(\nu)d\nu = \frac{\Phi(\nu_0)}{\Delta t}$$

since $\int_{-\infty}^{\infty} \frac{\sin^2 x}{x^2}dx = \pi$. Hence the ratio of stimulated to spontaneous emission at the frequency ν is

$$r = \frac{\Phi(\nu)\Delta\nu}{2P_0} = \frac{\Phi(\nu)}{h\nu} = m\left[\frac{\sin(\nu-\nu_0)\pi\Delta t}{(\nu-\nu_0)\pi\Delta t}\right]^2.$$

Under the optimum condition, which occurs when $\nu=\nu_0$, $r=m$. Thus if the stimulate emission is given by $A'mn_a$ as indicated abov the spontaneous emission is $A'n_a$. This co responds to the case $c=a$ in (3). If emissio and absorption of photons by the waveguid walls occur, they may be again regarded a due to some equivalent number of absorbin or emitting molecules, so that the above dis cussion applies, but with modified number n_a and n_b of molecules in the two states.

Photons in Equilibrium

If there is an equilibrium distribution o particles, so that $dP_{n,m}/dt=0$ for all $P_{n,}$ then according to (35)

$$P_{n,m} = (1-a/b)^{c/a}\frac{\Gamma(m+c/a)}{m!\,\Gamma(c/a)}(a/b)^m\ .$$

If new photons are introduced into the system only as a result of spontaneous or stimulate emission then, as shown above, $c/a=1$, and (35) becomes

$$P_{n,m} = (1-a/b)(a/b)^m\ . \tag{39}$$

This is just the probability distribution for thermal equilibrium of photons with the molecules, since $a/b=e^{-h\nu/kT}$ where T is the temperature of the molecules.

§ 7. Fluctuations in a Traveling-wave Maser

Fluctuations in an amplifier of the maser type may now be related to the coefficients a, b, and c. In many cases, fluctuations which determine the limiting sensitivity of such an amplifier depend only on the ratio a/b, which is conveniently expressed in terms of an effective temperature T_e defined by

$$\frac{a}{b} = \exp\left(\frac{-h\nu}{kT_e}\right)\ . \tag{40}$$

Here $h\nu$ is the energy gap between upper and lower levels and k is Boltzmann's constant T_e may be positive or negative depending on the relative magnitude of a and b, but the fluctuations are primarily dependent on the absolute value of T_e.

Consider first the waveguide case, where for amplification to occur $a>b$. From (16) if exactly n photons are introduced into the amplifier, after a large amplification a measure of the fractional fluctuation is

$$\varepsilon^2 = \frac{\overline{m^2}-\overline{m}^2}{\overline{m}^2} = \frac{n\left(\frac{a+b}{a-b}\right)+\frac{ac}{(a-b)^2}}{[n+c/(a-b)]^2}\ . \tag{41}$$

Since in the present case $c=a$,

$$\mathcal{E}^2=\frac{n\dfrac{1+e^{h\nu/kT_e}}{1-e^{h\nu/kT_e}}+\dfrac{1}{(1-e^{h\nu/kT_e})^2}}{[n+(1-e^{h\nu/kT_e})^{-1}]^2}\,. \qquad (42)$$

If $h\nu/k|T_e|\gg 1$, (42) becomes

$$\mathcal{E}^2\approx\frac{1}{n+1} \qquad (43)$$

nd the probability distribution is given by 7) with $c=a$, or

$$P_{n,m}\approx\frac{1}{K}\left(\frac{m}{K}\right)^n\frac{e^{-m/K}}{n!}\,. \qquad (44)$$

quation (43) and (44) represent the behavior f a perfect amplifier, where the absolute alue of the temperature approaches zero and nly emission processes occur ($b\to 0$). In this ase there remain fluctuations due to quantum ffects. The fractional variations which occur pproach zero when the number of quanta to e amplified is large, which is normally the ase for very low frequencies. It should be oted that the effective temperature need not e actually zero to approach a perfect amplifier, but $k|T_e|$ must be small compared with he energy $h\nu$ of one quantum. In the case f 1-centimeter radiation, $k|T_e|=h\nu$ when $T_e|\approx 1.5$°K. $|T_e|$ in an ammonia maser[3], or example, can be smaller than this value, ince ammonia molecules in a well focused eam flowing into the cavity are predominanty in the upper inversion state and $a\gg b$.

In the other extreme case where a is almost qual to b, or $h\nu/k|T_e|\ll 1$,

$$\mathcal{E}^2\approx\frac{2nh\nu/k|T_e|+1}{(nh\nu/k|T_e|+1)^2}\,. \qquad (45)$$

A measure of the minimum detectable number f quanta under such conditions can be obtained rom the equations (14) or (21). After large mplification

$$\overline{m}=\left(\overline{n}+\frac{a}{a+b}\right)K \qquad (46)$$

here K is the classical amplification factor $e^{(a-b)t}$. For the signal to equal background oise

$$n_{\min}=\frac{a}{a-b}\approx\frac{k|T_e|}{h\nu}\,, \qquad (47)$$

f $a\approx b$ or $h\nu/k|T_e|\ll 1$. This value reresents just the magnitude of thermal noise t a temperature $|T_e|$. The thermal power evel in the same time interval Δt as the input ignal may be expressed by $P_t=k|T_e|\Delta\nu_e$, here $\Delta\nu_e$, the effective bandwidth corresponding to the length of wave packet of the signal, is $1/(\Delta t)$ by (37). The thermal noise level in terms of number of photons in time Δt is then

$$n_t=\frac{P_t\Delta t}{h\nu}=\frac{k|T_e|}{h\nu}\,.$$

Thus the signal level which doubles the background output of an amplifier has just the magnitude of the usual thermal noise at temperature $|T_e|$. From (45), if the number of photons is s times the thermal noise level, $n=sk|T_e|/h\nu$, the fluctuation is given by

$$\mathcal{E}^2=\frac{2s+1}{(s+1)^2}\,. \qquad (48)$$

Hence the signal level must be considerably larger than $k|T_e|/h\nu$ before the fractional fluctuations become small.

The probability distribution for this case is obtained from (33) as

$$P_{n,m}=\frac{1}{m_0}\,e^{-(s+m/m_0)}I_0\!\left(2\sqrt{\frac{m}{m_0}s}\right). \qquad (49)$$

where m_0 is the average number of quanta for the background noise only, and I_0 is the modified Bessel function of order zero. Note that equations (48) and (49) agree precisely with the classical expressions for the fluctuation of power for the waves obtained by superposition of a sinusoidal wave and a thermal noise.

It is important to note that $|T_e|$ may have very little to do with any ordinary idea of the temperature of the amplifying system. Suppose, for example, that the waveguide walls are at absolute zero temperature, but absorb photons. Suppose also that the material inside the waveguide is at a very small negative temperature, so that for it $b=0$, and one might expect to have an ideal amplifier. However, absorption of photons by the waveguide adds to the net value of b, and if this absorption is of sufficient size, the entire system may have b almost equal to a, so that $|T_e|$ would be extremely large and the amplifier very noisy.

§ 8. Regenerative Amplifier Using a Cavity

In the case of a resonant microwave cavity containing amplifying materials, the same equations (14) and (15) for $\overline{m}$ and $\overline{m^2}$ apply, but their physical significance is somewhat different. m then represents the total number of photons in the cavity, which does not give directly the magnitude of the energy delivered by the amplifier. Furthermore, if a signal is fed into the cavity continuously, c must represent both this signal and spontaneous emission. Two general types of operation of an amplifier using a cavity are important:

1) Superregenerative amplification where $a>b$ and amplification results from an exponentially increasing pulse initiated by the signal. The exponentially increasing pulse is quenched, and the build-up from the input signal is then repeated in a so-called quenching cycle.

2) Stable amplification where $a<b$. This gives continuous amplification without any exponential build-up.

Consider first the case of a stable amplifier made up of a perfectly conducting cavity with input and output coupling holes and containing material with active molecules or atoms which responds uniformly to electromagnetic radiation at all frequencies of interest. If photons are put into the cavity, they will be absorbed in the material or escape from the input coupling holes. They may also stimulate emission and create new photons. As a result, their average number $\overline{m}$ will decay (since $a<b$) in accordance with the expression

$$-\frac{d\overline{m}}{dt}=(b-a)\overline{m}=(b_u+b_i+b_o-a)\overline{m}\ , \qquad (50)$$

where b_u represents loss in the material, b_i and b_o losses through the input and output coupling holes respectively. The loaded Q for the cavity is easily shown to be $Q=2\pi\nu/(b-a)$. Similarly the unloaded Q, and Q's for the coupling holes are $Q=2\pi\nu/(b_u-a)$, $Q_i=2\pi\nu/b_i$, and $Q_o=2\pi\nu/b_o$. Here Q_u may be negative, since the active material would have $a<b$ to provide amplification or the equivalent of a negative resistance.

Assume now an input signal of power P_i per unit frequency interval. Standard theory for cavity resonators, which may be extended to the case where Q_u is negative, gives for the power per unit bandwidth emerging from the output

$$P_o=P_i\frac{2\pi\nu QR(\nu)}{Q_iQ_o}\ , \qquad (51)$$

where $R(\nu)$ is the resonant expression

$$R(\nu)=\left(\frac{1}{2\pi\nu Q}\right)\frac{1}{\left(\frac{1}{2Q}\right)^2+\left(\frac{\nu-\nu_0}{\nu_0}\right)^2} \qquad (52)$$

with ν_0 the resonance frequency of the cavity. Similarly, power reflected back to the input waveguide is

$$P_r=P_i\frac{2\pi\nu QR(\nu)}{4}\left[\left(\frac{1}{Q}-\frac{2}{Q_i}\right)^2+4\left(\frac{\nu-\nu_0}{\nu_0}\right)^2\right] \qquad (53)$$

and the energy stored in the cavity as a result of the input signal is

$$W_i=P_i\frac{Q}{Q_i}R(\nu)\ . \qquad (54)$$

The gain of this type of amplifier is, from (51)

$$G=\frac{P_o}{P_i}=\frac{2\pi\nu Q}{Q_iQ_o}R(\nu) \qquad (55)$$

which becomes

$$G=\frac{4Q^2}{Q_iQ_o}=\frac{4b_ib_o}{(b-a)^2} \qquad (56)$$

at the resonance frequency, $\nu=\nu_0$.

It is important now to note the difference in the reemission of an input signal from the cavity, and the escape of spontaneous emission from the coupling holes. If the input signal is a long train of coherent waves $\left(\Delta\nu<\frac{\nu_0}{2Q}\right)$, then there is an interference between the wave which is reflected from the input coupling hole without entering the cavity, and that which enters the cavity and is reemitted from the input hole. For example, in the case of a "matched" input, where $1/Q=2/Q_i$ equation (53) shows that there is no power reflected from the input when $\nu=\nu_0$. Hence in this case none of the power W_i accumulated in the cavity can escape from the input hole which might lead one to suppose that $b_i=0$ However, the spontaneous emission within the cavity undergoes no interference of this type and is emitted from the input according to the value $b_i=\frac{2\pi\nu}{Q_i}$ indicated above. Because of these same interference effects, it is also not immediately clear what values of c should be attributed to the input signal. There are $P_i/h\nu$ photon/sec. per unit bandwidth flowing towards the cavity input, but since the wave reflected directly from the input is indistinguishable from that reemitted from the cavity through the input coupling, the number of photons actually entering the cavity is subject to various interpretations.

For use of equation (3) and its solutions, the effective value of c corresponding to a certain input power P_i is the rate at which photon vould have to be released in the cavity to roduce an equivalent total number of photons r an equivalent power output. Now if c_i hotons/sec. are released within the cavity, t can be shown by standard methods that hey produce the total output power which s $h\nu c_i\frac{Q}{Q_o}$. Letting this power equal the total utput power due to the input as given by 51), the equivalent rate of introduction of hotons by the input signal is

$$c_i=\int P_0(\nu)d\nu=\frac{2\pi P_i}{hQ_i}=\frac{P_i b_i}{h\nu}\,. \tag{57}$$

Fluctuations in the power output may now e obtained from expressions (14) and (15). he result is somewhat different from that f equation (16) because, in the case of a table amplifier, $a<b$ and the exponentials in 14) and (15) decrease with time so that, under onstant conditions

$$\bar{m}=\frac{c}{b-a}\,,$$

$$\overline{m^2}=\frac{c(b+c)}{(b-a)^2}\,,$$

$$\mathcal{E}^2=\frac{\overline{m^2}-\bar{m}^2}{\bar{m}^2}=\frac{b}{c}\,. \tag{58}$$

ubstituting appropriate values into (58) one as

$$\mathcal{E}^2=\frac{b}{a+c_i}=\frac{b}{a+\dfrac{2\pi P_i}{hQ_i}}\,. \tag{59}$$

ere it is assumed that P_i is constant over he frequency range for which $R(\nu)$ is of apreciable magnitude. For an amplifying system f reasonably large gain, $a\approx b$, so that

$$\mathcal{E}^2=\frac{1}{1+\dfrac{2\pi P_i}{ahQ_i}} \tag{60}$$

nd for $\mathcal{E}$ to be small, $\dfrac{2\pi P_i}{ahQ_i}\gg 1$.

As in the waveguide amplifier, there are ackground noise fluctuations due to spontaneus emission even when no signal is present. or the output power to be doubled as a esult of an input signal, c_i must equal a, or rom (57)

$$\frac{2\pi P_i}{hQ_i}=a\,. \tag{61}$$

terms of a noise temperature T_n for the mplifier, this gives

$$P_i=kT_n=\frac{ahQ_i}{2\pi}=\frac{ah\nu}{b_i}\,. \tag{62}$$

Since $b=b_i+b_u+b_o$, and $a\approx b$ for large amplification, (62) becomes

$$T_n=\frac{bh\nu}{k(b-b_u-b_o)}\,. \tag{63}$$

An effective temperature $T_e(<0)$ for the molecular system can be defined which includes all gains and losses except those due to the input coupling, that is

$$\frac{a}{b_u+b_o}=\exp\left(-\frac{h\nu}{k|T_e|}\right). \tag{64}$$

Hence, when $h\nu\ll k|T_e|$, the noise temperature (63) is simply

$$T_n=|T_e| \tag{65}$$

and if $h\nu\gg k|T_e|$, the limiting noise temperature becomes, from (63) and (64),

$$T_n=\frac{h\nu}{k}\,. \tag{66}$$

Now a noise temperature $T_n=h\nu/k$ is based on the classical assumption that the flow of power per unit bandwidth is $kT\Delta\nu$. An amplifier with this ideal noise temperature is capable, as is the ideal waveguide amplifier, to "detect a single photon." This may be demonstrated from the fact that the noise temperature $h\nu/k$ corresponds to a rate of power flow $h\nu\Delta\nu$ in a bandwidth $\Delta\nu$, or to $\Delta\nu$ quanta per unit time. But an amplifier of bandwidth $\Delta\nu$ can amplify a pulse of minimum length $1/\Delta\nu$ which would then contain just one photon at this minimum detectable power level.*

From (63) and (64), it may be noted that the lowest noise temperature is obtained for an amplifier by making the output coupling very small, and that the limiting noise temperature when $b_o=0$ just corresponds to the effective temperature of the active material. Furthermore, as in the case of a waveguide amplifier, additional coupling holes or losses in the cavity can produce a very high noise temperature even when the cavity and its active material are at low temperatures. Of course it is also possible to dispense with the output coupling entirely and use the wave reflected from the input as the amplified signal.

---

* This does not mean the possibility of unambiguously observing a single photon as an individual pulse.

§ 9. Superregenerative Amplifier Using a Cavity

To consider the noise properties of a superregenerative cavity amplifier, assume that the rate of induced emission a is zero until time $t=0$, when suddenly a is made larger than b so that an exponential build-up of energy in the cavity is begun. There are on the average n photons in the cavity at $t=0$. Then equation (14) describes the growth of the number of photons in the cavity during the amplification period. For large gain $(a-b)t \gg 1$ and the average number of photons in the cavity after amplification lasting time t_1 is

$$\overline{m}=\left(\overline{n}+\frac{c_i}{a-b}+\frac{a}{a-b}\right)e^{(a-b)t_1}, \tag{67}$$

where c_i is again given by (57). Since the initial number of photons n is determined by the input power before $t=0$, it is from equation (14) for $a=0$

$$\overline{n}=\frac{c_i}{b}, \tag{68}$$

where a term with exponential decay factor may be neglected. Whether the contribution of initial number of photons due to input signal before $t=0$, or that of continuing flow of photons during build-up denominates depends on the relative size of $1/b$ and $1/(a-b)$, assuming c_i is same for $t<0$ and $t>0$.

Putting (68) into (67), one obtains

$$\overline{m}=\left[\frac{c_i}{b}+1\right]\frac{a}{a-b}e^{(a-b)t_1}. \tag{69}$$

Or, if the the cavity is operated as a stable regenerative amplifier until $t=0$ with $a=a_0<b$ and after that a is suddenly increased so that $a>b$, $\overline{n}$ is equation (67) is given by

$$\overline{n}=\frac{1}{b-a_0}(c_i+a_0) \tag{68a}$$

instead of (68). Then one obtains from (67)

$$\overline{m}=\frac{b(a-a_0)}{(a-b)(b-a_0)}\left[\frac{c_i}{b}+1\right]e^{(a-b)t_1} \tag{69a}$$

The background noise due to spontaneous emission when no photon is introduced from coupling holes is given by the second term, $+1$, in the brackets of (69) and (69a). The threshold signal is that which gives the same amount of output or the same number of quanta $\overline{m}$ as the background noise. Then

$$\frac{ci}{b}=1 \quad \text{or} \quad \frac{b_iP_i}{bh\nu}=1$$

and the noise temperature of the amplifier at the resonance is

$$T_n=\frac{P_i}{k}=\frac{h\nu}{k}\frac{b}{b_i}. \tag{70}$$

It may be noted that the noise temperature in a superregenerative amplifier is essentially the same form as (63) in a regenerative amplifier, and that more detailed discussion is allowed by the application of general solutions developed in § 5.

The discussion of noise and the number of quanta in the cavity has dealt with a continuous range of frequencies. The amplifier gain of course varies with frequency, but in any small part of its bandwidth the signal to noise ratio is equivalent. The gain varies as

$$\left[\left(\frac{1}{2Q}\right)^2+\left(\frac{\nu-\nu_0}{\nu_0}\right)^2\right]^{-1}$$

and at maximum, $\nu=\nu_0$, it is

$$G=\frac{4ab_ib_0}{b(a-b)^2}e^{(a-b)t_1} \tag{71}$$

for the case described by equation (69), and

$$G=\frac{4(a-a_0)b_ib_0}{(b-a_0)(a-b)^2}e^{(a-b)t_1} \tag{71a}$$

for the case to which equation (69a) applies.

These results differ somewhat from the conclusions of Gordon, Zeiger, and Townes,[33] partly because the earlier work did not take into account spontaneous emission from the molecules. Although this random spontaneous emission is generally small compared with the stimulated emission occuring in the cavity, it is amplified and therefore may become an important source of noise. Consider, for example, a group of molecules which are entirely in the upper state. Let them be in a cavity made of lossless and hence non-radiative material and let no photons enter through the coupling hole. One might then suppose that no noise would exist in the cavity. This is true only if there is no spontaneous emission $(c=0)$. Actually $c=a$ and if the system is stable, the noise level is given by $\overline{m}=a/(b-a)$, which is equivalent to the input noise temperature $b/b_i\cdot(h\nu)/k$.

Other differences between the present results and those of Gordon, Zeiger, and Townes come from the fact that they consider effects of thermal radiation which may enter the amplifier through input or output coupling holes

Although this type of noise is quite important in some cases, it is not fundamental o the amplification process, and has been neglected in the above discussion. Appropriate design of input and output circuits can in most cases prevent such noise which is not essentially associated with the signal from entering the amplifier.

Many varieties of design are possible for maser-type amplifiers, each of which needs analysis for a precise evaluation of sensitivity. However, the above results for certain idealized cases should indicate qualitatively the results which may be obtained, and illustrate the application to maser amplifiers of the general expressions for fluctuations developed in the former sections.

In conclusion we would like to acknowledge a helpful correspondence on the subject of noise between one of the authors and Mr. Marcel Muller.

Appendix. Derivation of Solution (30)*

The equation (3) will be solved here by use of a generating function for the most general case that a and b are functions of time and c/a is any positive constant.

The generating function for $P_{n,m}$ is very similar to (23) and is defined by

$$f_n=\sum_m P_{n,m}x^m\,. \qquad \text{(A1)}$$

By substituting (A1) into (3), one obtains a partial differential equation satisfied by $f_n(x,t)$:

$$\frac{\partial f_n}{\partial t}=(1-x)(b-ax)\frac{\partial f_n}{\partial t}-c(1-x)f_n \qquad \text{(A2)}$$

This is linear in f_n and may be solved by standard methods. The characteristic equation for (A2) is given by

$$\frac{-dx}{(1-x)(b-ax)}=dt=\frac{-df_n}{c(1-x)f_n} \qquad \text{(A3)}$$

The desired solution of (A2) is obtained by solving (A3) with the initial conditions: $x=x_0$ and $f_n=x_0{}^n$ for $t=0$, and then eliminating x_0.

The equation (A3) may be solved by putting

$$y=\frac{1}{1-x} \qquad \text{(A4)}$$

Then (A3) becomes

$$\frac{-dy}{(b-a)y+a}=dt=\frac{-y\,df_n}{cf_n}\,. \qquad \text{(A5)}$$

The left part of the equation (A5) is

$$dy/dt=(a-b)y-a \qquad \text{(A6)}$$

which is linear in y. The solution is given by

$$y=e^{\int(a-b)dt}\left(\int -ae^{-\int(a-b)dt}dt+y_0\right) \qquad \text{(A7)}$$

where y_0 is the initial value of y for $t=0$, i.e.

$$y_0=\frac{1}{1-x_0}$$

Using the notations

$$K=e^{\int(a-b)dt}\,, \qquad \text{(A8)}$$

$$G=K\int\frac{a}{Kdt}\,, \qquad \text{(A9)}$$

(A7) is written in the form

$$y=Ky_0-G \qquad \text{(A10)}$$

Evidently, K is the classical amplification factor.

f_n is obtained from the right part of (A5), i.e.

$$\frac{1}{f_n}\frac{df_n}{dt}=-\frac{c}{y} \qquad \text{(A11)}$$

By (A7), the equation takes the form

$$\frac{1}{f_n}\frac{df_n}{dt}=-\frac{c}{a}\frac{a}{K}\Big/\left(-\int\frac{a}{K}dt+y_0\right) \qquad \text{(A12)}$$

Integrating (A12), one obtains

$$f_n=\left(-\int a/K\,dt+y_0\right)^{c/a}\times\text{const}$$
$$=(-G/K+y_0)^{c/a}\times\text{const.} \qquad \text{(A13)}$$

Considering the initial condition $f=x_0{}^n=(1-1/y_0)^n$ at $t=0$, (A13) becomes

$$f_n=\left(1-\frac{G}{Ky_0}\right)^{c/a}\left(1-\frac{1}{y_0}\right)^n \qquad \text{(A14)}$$

Eliminating y_0 by use of (A10), the generating function is finally given by

$$f_n=\left(\frac{y}{y+G}\right)^{c/a}\left(1-\frac{K}{y+G}\right)^n$$
$$=\left(\frac{1}{1+G(1-x)}\right)^{c/a}\left(\frac{1+(G-K)(1-x)}{1+G(1-x)}\right)^n \qquad \text{(A15)}$$

Expansion of the numerator and denominator in powers of x gives

---

* A derivation similar to that indicated here was obtained independently by Dr. L. R. Walker and kindly communicated to one of the authors.

$$P_{n,m}=\frac{G^m(G-K+1)^n(K-1)^{m+n}}{(G+1)^{m+n+c/a}}$$
$$\times\sum_{j=0}^{m\text{ or }n}\frac{n!\Gamma(n+m+c/a-j)}{(n-j)!\,j!\,(m-j)!\,\Gamma(n+c/a)}\left[\frac{(G+1)(G-K)}{G(G-K+1)(K-1)^2}\right]^j. \qquad \text{(A16}$$

Or, if (A15) is put into a form like that of (23) and similarly expanded, one obtains a mor convenient expression

$$P_{n,m}=\frac{G^m(G-K+1)^n(K-1)^{m+n}}{(G+1)^{m+n+c/a}}$$
$$\times\sum_{j=0}^{m\text{ or }n}\frac{n!}{j!\,(n-j)!\,(m-j)!}\,\frac{\Gamma(m+c/a)}{\Gamma(j+c/a)}\left[\frac{K}{G(G-K+1)}\right]^j. \qquad \text{(A17}$$

When a and b are constant, K and G are given by

$$K=e^{(a-b)t},$$
$$G=\frac{a}{a-b}(e^{(a-b)t}-1)=\frac{a}{a-b}(K-1) \qquad \text{(A18)}$$

and substituting this into (A17), one obtains the expression (30) as a result.

References

1) D. E. Lee and C. A. Coulson: Journal of Ge netics, **49** (1949) 264.
2) W. Furry: Phys. Rev. **52** (1937) 567.
3) J. P. Gordon, H. J. Zeiger and C. H. Townes Phys. Rev. **99** (1955) 1264.

JOURNAL OF THE PHYSICAL SOCIETY OF JAPAN Vol. 12, No. 6, JUNE, 1957

Magnetic Susceptibility of Iron-Nickel Alloys in Liquid and Solid States

By Yasuaki NAKAGAWA

Department of Physics, Faculty of Science, University of Tokyo

(Received March 2, 1957)

The magnetic susceptibilities of various Fe-Ni alloys have been measured through their melting points up to 1600°C. The susceptibilities of the alloys with less than 60 % Ni increase discontinuously on melting, while those of the alloys with more than 60 % Ni decrease. The temperature variation of the susceptibilities is approximately expressed by the Curie-Weiss law in the liquid state as well as in the solid state, but the Curie constants and the paramagnetic Curie temperatures of liquids are in general different from those of solids.

These results can be explained by assuming that the atomic magnetic moments remain unaltered and that the magnetic interaction varies with the interatomic distance as indicated by the Bethe-Slater curve. The change of susceptibility at the melting point is solely due to the difference in interatomic distance between the liquid and the solid.

It is expected, in some cases, that the especially strong dependence of the magnetic interaction on the interatomic distance results in an appreciable change of interaction with temperature through the thermal expansion. It can account for the anomalously large Curie constants of pure γ-Fe and Fe-rich alloys in the solid state.

§1. Introduction

As reported previously¹⁾, the magnetic susceptibilities of various transition metals and alloys decrease or increase on melting, depending on whether the interatomic interactio favours parallel alignment of atomic magneti moments or not. This result may indicate hat the interaction is always weaker in liquid han in solid. Some Fe-rich alloys with face-entred cubic lattice, however, form excep-ions to the simple rule mentioned above, *i.e.* their susceptibilities increase on melting though they are ferromagnetic at low temperatures. These exceptions can be also explained, if the Bethe-Slater interaction curve is taken into ccount*.

The magnetic interaction is expressed as a function of the ratio R of the interatomic distance D to the diameter of $3d$-shall δ, as shown in Fig. 1. The value of the interaction has a maximum at $R=R_m$ and vanishes at $R=R_0$. If $R_0<R<R_m$, the interaction is ferromagnetic and may become larger on melting, since R may be larger in liquid than in solid.

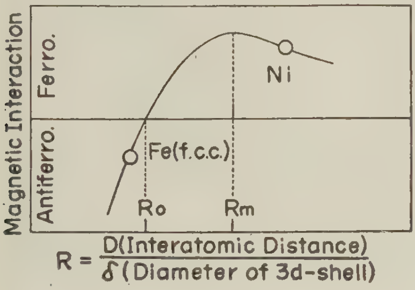

Fig. 1. Interaction Curve.

In the Fe-Ni system, the values of R for Ni-rich alloys are larger than R_m, while those for Fe-rich alloys are smaller. It was supposed in the previous paper[1)] that the susceptibility of the alloy with about 65% Ni might remain unaltered at the melting point, since this alloy might correspond to the maximum point on the Bethe-Slater curve. This supposition, however, was based upon rough measurements on merely three alloys. In the present paper, detailed experimental data on Fe-Ni alloys will be reported together with further discussions about the Bethe-Slater curve.

Up to the present, several investigations on the susceptibility of solid Fe-Ni alloys have been reported. Wohlfarth[3)] discussed the experimental data of Peschard[4)] and of Fallot[5)] on the basis of the collective electron theory of ferromagnetism. This theory, however, seems less satisfactory for Fe-Ni alloys than for Ni-Cu or Ni-Co alloys. At the present stage, the collective electron theory is unlikely to be suitable to account for the properties of the ferromagnetic metals which have more than two holes in $3d$-shell per atom. Thus the Heitler-London theory will be used in the present discussion though it also encounters some difficulties.

§ 2. Experimental Procedures and Results

The experimental method is the same as that described previously[1)]. The susceptibilities of nine different alloys ranging in composition from 10 to 89% of Ni were measured through their melting points up to 1600°C. These alloys were prepared by T. Nagashima by melting pure Fe and Ni together in a vacuum induction furnace for the purpose of other investigations[6)]. The impurities in Fe and Ni used and the composition of alloys are listed in Table I and Table II respectively.

Table I. Impurities in electrolytic Fe and Ni used
(Spectroscopic analysis)

	Al	Ca	Co	Cu	Fe	Mg	Mn	Ni	Pb	Si
Fe	trace	trace	trace	0.01	—	0.001	0.01	0.001	trace	none
Ni	0.1	trace	0.1	0.01	0.1	0.1	none	—	none	trace

(in weight %)

As can be seen in the phase diagram[7)], all alloys investigated are face-centred cubic at high temperatures. The susceptibilties of Fe-Ni alloys at low temperatures show anoma-

---

* After publishing the previous paper, the author found Weil's[2)] experimental data on the susceptibilities of some liquid alloys of transition elements. Among these alloys, those of homogeneous solid solutions such as Cu-Mn, Cu-Ni and Ag-Mn are interesting in view of the change of susceptibility on melting. Weil's results can be also accounted for by the general rule given in the previous paper.

Table II. Composition of specimens
(Chemical analysis)

Specimen	No. 1	2	3	4	5	6	7	8	9
Fe (weight %)	89.26	79.01	69.02	59.27	49.82	40.02	30.22	20.65	10.30
Ni (weight %)	10.36	20.69						79.18	
Fe (atomic %)	90	80	70	60	51	41	31	22	11
Ni (atomic %)	10	20	30	40	49	59	69	78	89

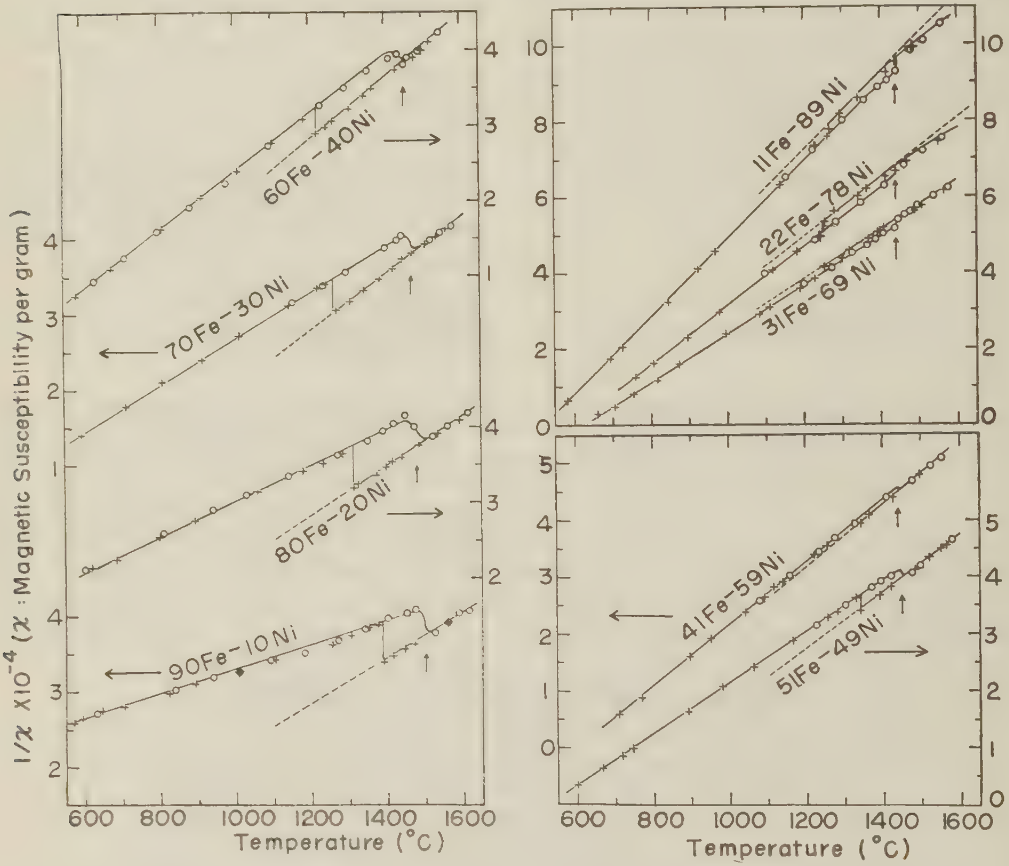

Fig. 2. Susceptibility Curves.
o: Value of susceptibility measured during heating.
+: Value of susceptibility measured during cooling.
↑: Melting point (Mean value of liquidus and solidus temperature).

lously large values owing to the transformation into the body-centred cubic phase.

Figure 2 shows the experimental results on the temperature variation of the susceptibilities per gram. The change of susceptibility on melting, $\Delta\chi=\chi_l-\chi_s$, is plotted against composition in Fig. 3 together with its relative value $\Delta\chi/\chi_s$. $\Delta\chi$ changes its sign at about 60% Ni, as has been supposed.

The susceptibilities of these alloys are approximately expressed by the Curie-Weiss law,

$$\chi=C'/(T-\theta)\,, \qquad (1)$$

in the liquid state as well as in the solid ate. The Curie constants per gram C' and e paramagnetic Curie temperatures θ are termined from the straight lines shown in ig. 2. C_s' and θ_s are those of solid, while $'$ and θ_l are those of liquid. Each of them is lotted as a function of composition in Fig. 4. nstead of C', the Curie constant per mole is shown for convenience. C is equal to $'M$, where M is the 'mean' atomic weight f the alloy. The C vs composition curve, however, is not essentially different from the C'vs omposition curve, since there is no large diference in atomic weight between Fe and Ni. It should be mentioned that remarkable supercooling of liquid was observed in all casse. As shown in the previous paper[1], the magnetic behaviours of supercooled liquids are not different from those of ordinary liquids. Thus the values of C_l and θ_l can be determined precisely enough.

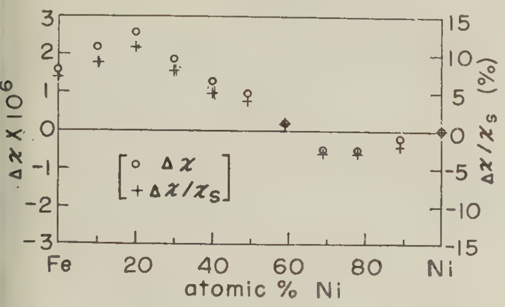

Fig. 3. Change of Susceptibility on melting.
$\Delta\chi=\chi_l-\chi_s$.
χ_l: Susceptibility per gram of liquid at melting point.
χ_s: Susceptibility per gram of solid at melting point.

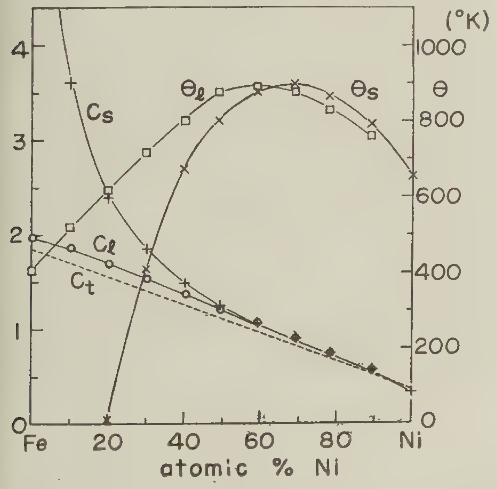

Fig. 4. Curie constant per mole C and paramagnetic Curie temperature θ.
Solid: ——+—— C_s ——×—— θ_s
Liquid: ——○—— C_l ——□—— θ_l
Theoretical: -------------- C_t

For pure Fe and Ni, the data reported before[1] are used. The susceptibility of Ni, however, shows a large deviation from the Curie-Weiss law at high temperatures, and so the Curie constant and the paramagnetic Curie temperature of liquid Ni are quite uncertain.

The very small deviations from the Curie-Weiss law for the alloys are somewhat systematic: the $1/\chi$ *vs* T curves for Ni-rich alloys are concave downwards, while those for Ferich alloys are convex.

It is to be noted that Peschard's[4] and Fallot's[5] results on the susceptibilities of Fe-Ni alloys in the solid state are in good agreement with those reported here.

§ 3. Theoretical Interpretation

The experimental results summarized in Fig. 4 may be explained on the basis of the following assumptions:

(I) The magnetic susceptibilities of these alloys can be treated with Weiss' molecular field theory.

(II) The atomic magnetic moments of Fe and Ni in Fe-Ni alloys are 3 and 1 Bohr magneton respectively, not depending on the composition of alloys. These moments remain unaltered on melting.

(III) The magnetic interaction varies with the ratio R of the interatomic distance D to the diameter of $3d$-shell δ, as indicated by the Bethe-Slater curve (Fig. 1). In order to treat the liquid and the solid together, the cubic root of atomic volume is used as the value of D, being larger in liquid than in solid. In cases where the slope of the Bethe-Slater curve is very steep, the interaction varies appreciably with temperature owing to the thermal expansion.

Discussions about these assumptions will be presented in the next section.

It is deduced from the assumption (I) that the susceptibility per mole χ_M can be expressed as

$$\chi_M=C_t/(T-C_tW)\,, \qquad (2)$$

where C_t is the 'theoretical' Curie constant and W the coefficient of molecular field. For a pure metal,

$$C_t = \frac{N\mu^2}{3k}4S(S+1)\,, \qquad (3)$$

where N is the Avogadro number, μ the Bohr magneton, k the Boltzmann constant and S the resultant spin of the atom. According to the assumption (II), S is equal to 3/2 for Fe and 1/2 for Ni.

For the Fe-Ni alloys,

$$C_t = (1-x)C_{Fe} + xC_{Ni}\,, \qquad (4)$$

where C_{Fe} and C_{Ni} are the 'theoretical' Curie constants of Fe and Ni respectively, and x is the atomic concentration of Ni. The values of C_t, given by Eq. (4), are shown in Fig. 4 with a dotted line.

If the molecular field coefficient W is independent of temperature, it is found easily that $C = C_t$ and $\theta = C_t W$ by comparing Eq. (2) with Eq. (1). This is the case of the alloys with more than 50% Ni, since both C_s and C_l are about equal to C_t as shown in Fig. 4. Thus the change of susceptibility at the melting point is solely due to the difference in W between liquid and solid.

This difference may be explained on the basis of the assumption (III). As has been suggested by Bozorth[8)], the Curie temperature θ, instead of W, is expressed as a function of $R(=D/\delta)$. Since it has been assumed that the values of R for the alloys depend linearly on the composition, the θ *vs* composition curve should be analogous to the Bethe-Slater curve. According to Slater[9)], the value of R for pure Ni is about 10% larger than that for pure Fe (with face-centred cubic lattice). On the other hand, R may be about 1% larger in liquid than in solid owing to the volume expansion on melting[10)]. Thus the increase in R due to melting corresponds to that due to 10% increase in Ni content. Therefore, the θ_l *vs* composition curve must coincide with the θ_s *vs* composition curve if the former is shifted along the composition axis by about 10%. This conclusion is in agreement with the experimental result on the alloys with more than 50% Ni, as shown in Fig. 4.

For the alloys with less than 50% Ni, however, the above theory is not satisfactory, because C_s is much larger than C_t while C_l is not so different from C_t. In this case the temperature dependence of W should be taken into account.

Since it is expected that these alloys in t solid state correspond to the steep range the Bethe-Slater curve, even the small chan in interatomic distance, caused by the therm expansion, can produce an appreciable effe on the magnetic interaction. This effect w first treated by Néel[11)].

The temperature dependence of W can expressed approximately by the formula,

$$W = W_0 + (dW/dT)_0(T-T_0)\,, \qquad \text{(5}$$

near an arbitrary temperature T_0. By su stituting (5) in (2), one obtains again the Curi Weiss law [Eq. (1)], where

$$C = \frac{C_t}{1-C_t(dW/dT)_0}\,, \qquad \text{(6}$$

and

$$\theta = T_0 - \frac{T_0 - C_t W_0}{1-C_t(dW/dT)_0}\,. \qquad \text{(7}$$

If T_0 is chosen to be equal to θ, Eq. (7) be comes

$$\theta = C_t W_0\,. \qquad \text{(8}$$

When the value of $C_t(dW/dT)_0$ approache unity, the apparent Curie constant C become much greater than the 'theoretical' one C This is the case of the alloys with less tha 50% Ni in the solid state. The value o $(dW/dT)_0$, calculated from the experimenta Curie constant $C(=C_s)$ by using Eq. (6), be comes larger with decreasing Ni content.

The value of $(dW/dT)_0$ can be also estimat ed from the change of ferromagnetic Curi point with hydrostatic pressure. It is interest ing to note that the two results are closel similar.

The interaction W is expressed as a func tion of the interatomic distance D which de pends on both temperature T and pressure *i.e.*

$$W = f\{D(p,\,T)\}\,, \qquad \text{(9}$$

The ferromagnetic Curie point, equal to θ i Eq. (8), is given implicitly as a solution o the equation,

$$\theta = C_t f(p,\,\theta)\,. \qquad \text{(10}$$

Therefore,

$$\frac{d\theta}{dp} = \left[\frac{C_t(\partial f/\partial p)_T}{1-C_t(\partial f/\partial T)_p}\right]_{T=\theta}. \qquad \text{(11}$$

From Eq. (9) it is found that

$$\frac{(\partial f/\partial p)_T}{(\partial f/\partial T)_p} = \frac{(\partial D/\partial p)_T}{(\partial D/\partial T)_p} = \frac{-\kappa/3}{\alpha}\,, \qquad \text{(12}$$

where κ is the compressibility and α the linear thermal expansion coefficient. Since $(\partial f/\partial T)_p$ is equal to $(dW/dT)_0$ in Eq. (6), one obtains finally,

$$\frac{d\theta}{dp} = -\frac{\kappa}{3\alpha}\left(\frac{C}{C_t}-1\right). \qquad (13)$$

If the values of κ and α at the Curie point re known, $d\theta/dp$ can be calculated from the experimental Curie constant $C(=C_s)$.

For the 70 Fe–30 Ni alloy, for example, it may be estimated that $\alpha=1.3\times10^{-5}$ (per degree) and $\kappa=0.55\times10^{-6}$ (per atm.), and the value of C_s/C_t is about 1.31 as shown in Fig. 4. Thus $d\theta/dp=-4.4\times10^{-3}$ (degrees/atm.). On the other hand Patrick[12] has shown by a direct measurement that $d\theta/dp=-5.8\times10^{-3}$ degrees/atm.). It may be said that these two values are in good agreement with each other. Patrick has also shown that $d\theta/dp$ decreases with increasing Ni content and becomes nearly zero for the 32 Fe–68 Ni alloy, as can be expected from the present susceptibility data.

These results are consistent with the Bethe-Slater curve. Moreover, the curvature of the Bethe-Slater curve can account for the experimental fact that the $1/\chi$ *vs* T curves for Fe-rich alloys are slightly convex downwards.

It is to be mentioned here that the susceptibility data on Fe-Co and Co-Ni alloys, reported in the previous paper[1], can be also explained by the above assumptions. The atomic moment of Co is assumed to be 2 Bohr magnetons, *i.e.* $S=1$ in Eq. (3). The 'theoretical' Curie constants C_t for these alloys are given by a similar equation to (4). For the Co-Ni alloys both C_l and C_s are not so different from C_t. For the Fe-Co alloys, on the other hand, C_l is not so different from C_t, while C_s is much larger than C_t, just as for the Fe-Ni alloys with less than 50% Ni.

§ 4. Discussions

Although the susceptibilities of these alloys can be consistently explained by using the above-mentioned assumptions, these assumptions may be open to some objections.

(I) The assumption that the susceptibility can be simply treated with Weiss' molecular field theory is questionable in the case of the alloys containing two kinds of transition elements. In order to calculate the susceptibilities of these alloys on the basis of the Heitler-London theory, three kinds of the nearest neighbor interactions between two kinds of atoms should be taken into account. It follows from this that the susceptibilities do not obey the Curie-Weiss law except at very high temperatures. According to Néel[13], the $1/\chi$ *vs* T curve should be a hyperbola, the asymptotic line of which corresponds to the Curie-Weiss law [Eq. (2)], where the Curie constant is given by Eq. (4). It is not so hopeless, however, that a more careful treatment of this statistical problem would prove the applicability of Eq. (2) to the present case.

(II) The second assumption is based on the electronic configuration of the atoms $(3d)^n(4s)^1$, where n is equal to 7 for Fe, 8 for Co and 9 for Ni*. Although the lowest-energy configuration of these atoms in the isolated state is expressed as $(3d)^{n-1}(4s)^2$, the former configuration can be more stable than the latter in the metallic state. According to Pauling[15], there is no large difference in cohesion among various transition metals of Fe-group, and Cu $[(3d)^{10}(4s)^1]$ is much more cohesive than Zn $[(3d)^{10}(4s)^2]$. These facts indicate that the number of $3d$-electrons per atom is not an important factor in cohesion and that the configuration $(4s)^1$ is more stable than the configuration $(4s)^2$.

This conclusion is based on the assumption that the number of $3d$-electrons per atom in the metallic state should be an integer. Although this assumption may be quite natural as far as the Heilter-London theory is adopted, it seems to conflict with the fact that the ferromagnetic saturation moment per atom is not equal to an integral multiple of the Bohr magneton. In the ferromagnetic state, however, the magnetic moment due to the localized $3d$-electrons might be partly compensated by that due to the non-localized $4s$-electrons**.

According to Shull and Wilkinson[17], the neutron diffraction experiments on Fe-Ni alloys in the ferromagnetic state have shown that the difference in atomic moment between Fe and Ni amounts to about 2 Bohr magnetons, being nearly independent of the composition of alloys. This result is consistent with the present theory.

---

* The magnetic resonance experiment by Bagguley and Harrick[14] has proved that the g-factor of Ni is equal to 2.0 in the paramagnetic state, *i.e.* the orbital magnetic moment is completely quenched.

** Zener[16] has considered that the non-localized $4s$-electrons participate in the ferromagnetic saturation moment of a metal. According to his theory, however, the resultant moment due to the $4s$-electrons should be parallel to that due to the $3d$-electrons.

(III) Although it may be valid that the magnetic interaction in a transition metal varies with the interatomic distance as indicated by the Bethe-Slater curve, it is very doubtful whether a 'single' Bethe-Slater curve can be applicable in common to all the transition metals and alloys.

For the Fe-Ni alloys, however, Bozorth[8] has suggested that the magnetic interaction energy, assumed to be proportional to the Curie temperature, may be expressed as a unique function of $R(=D/\delta)$*. Although Bozorth's suggestion is unlikely to be based on any plausible theory, it can well account for various experimental results, *e.g.* the change of ferromagnetic Curie point with hydrostatic pressure, the anomalous thermal expansion near the Curie point, the volume magnetostriction *etc.* The present experiment on the magnetic susceptibility is also explained by Bozorth's interaction curve, as shown in the preceding section. This interaction curve, however, cannot be applied to other metals and alloys. It may be rather fortuitous that Bozorth's suggestion has been helpful in the case of Fe-Ni alloys. In general, different interaction curves for different metals should be looked for, as proposed by Dehlinger[18].

It should be emphasized here that the anomalously large Curie constant of pure γ-Fe (face-centred cubic) can be explained by the present theory as due to the temperature dependence of the magnetic interaction. If this effect were not taken into account, very large atomic moment (6 Bohr magnetons) and very large negative interaction ($\theta=-2500$°K) would be derived from the Curie-Weiss law [Eq. (1)]. According to Wilkinson and Shull[19], however, the neutron diffraction experiment on Fe at high temperatures has shown that there is no remarkable difference in atomic moment between γ-Fe and α-Fe; the atomic momen of α-Fe may be 2 or 3 Bohr magnetons Moreover, such large negative interaction i likely to conflict with the fact that the antiferromagnetism has not been confirmed i γ-Fe*. These contradictions are overcome b the present theory: the anomalously larg Curie constant is solely due to the temperature dependence of the interaction W, an the value of W at 900°C is only slightly negative if it is calculated from Eq. (2) by using the experimental value of χ_M and the theoretical value of C_t.

§ 5. Conclusions

The magnetic susceptibilities of Fe-Ni alloys follow the Curie-Weiss law in the liquid state as well as in the solid state. The Curie constants are approximately equal to the theoretical values calculated from the atomic magnetic moments, 3 Bohr magnetons for Fe and 1 Bohr magneton for Ni, except in the case of pure γ-Fe and Fe-rich alloys in the solid state.

In this case the temperature variation of the magnetic interaction is expected to be large, resulting in the anomalously large value of the apparent Curie constant. This effect can be related quantitatively to the especially sensible change of ferromagnetic Curie points of these alloys with hydrostatic pressure.

Since there is no difference in atomic moment between liquid and solid, the change of susceptibility on melting is only due to the difference in magnetic interaction. The interaction varies with the interatomic distance, as indicated by the Bethe-Slater curve, and the interatomic distance is larger in liquid than in solid.

The alloys with less than 60% Ni, corresponding to the left-hand side of the maximum on the Bethe-Slater curve, show an increase in susceptibility on melting, and the opposite in true for the alloys with more than 60% Ni. Thus the slope of the Bethe-Slater curve can be found out experimentally by using the susceptibility change on melting.

---

* According to Néel[13], the molecular field coefficient W can be expressed as a function of $D-\delta$ for various transition metals and alloys. His interaction curve, however, seems to be inconsistent with the experiment on the change of ferromagnetic Curie point with hydrostatic pressure.

* According to Corliss, Hastings and Weiss [*cf.* reference 20)], a weak antiferromagnetism with low Néel temperature (~80°K) is suggested for pure γ-Fe by extrapolation of the properties of the Fe-Mn system.

The author wishes to express his sincere anks to Professor S. Kaya for his valuable ggestions and encouragement. The author also indebted to Mr. T. Nagashima of lectrotechnical Laboratory for his kindness in pplying the specimens.

References

1) Y. Nakagawa: J. Phys. Soc. Japan **11** (1956) 855.
2) L. Weil: Thèse, Univ. de Strasbourg (1941).
3) E. P. Wohlfarth: Phil. Mag. **40** (1949) 1095.
4) M. Peschard: Rev. Métallurgie **22** (1925) 490.
5) M. Fallot: J. Phys. Rad. **5** (1944) 153.
6) T. Nagashima *et al*: Rep. Electrotech. Lab. Japan **19** (1955) 19.
7) Amer. Soc. Metals: *Metals Handbook* (1948).
8) R. M. Bozorth: Bell System Tech. J. **19** (1940) 1.
9) J. C. Slater: Phys. Rev. **36** (1930) 57.
10) O. Kubaschewski: Trans. Faraday Soc. **45** (1949) 931.
11) L. Néel: Ann. Physique **8** (1937) 237.
12) L. Patrick: Phys. Rev. **93** (1954) 384.
13) L. Néel: Ann. Physique **5** (1936) 232.
14) D. M. S. Bagguley and N. J. Harrick: Proc. Phys. Soc. **67A** (1954) 648.
15) L. Pauling: Phys. Rev. **54** (1938) 899.
16) C. Zener: Phys. Rev. **81** (1951) 440.
17) C. G. Shull and M. K. Wilkinson: Phys. Rev. **97** (1955) 304.
18) U. Dehlinger: Z. Metallkunde **28** (1936) 232.
19) M. K. Wilkinson and C. J. Shull: Phys. Rev. **103** (1956) 516.
20) R. J. Weiss and K. J. Tauer: Phys. Rev. **102** (1956) 1490.

JOURNAL OF THE PHYSICAL SOCIETY OF JAPAN Vol. 12, No. 6, JUNE, 1957

Electronic Structure of Simple Homonuclear Diatomic Molecules

I. Oxygen Molecule

By Masao KOTANI, Yukio MIZUNO, Kunihusa KAYAMA
Department of Physics, University of Tokyo, Tokyo
and Eiichi ISHIGURO
Department of Physics, Ochanomizu University, Tokyo

The wave functions of the ground state and several lower excited states of O_2 and O_2^+ are calculated non-empirically at $R=2.3$ a.u. by LCAO MO method, where all sixteen electrons are taken into consideration and Slater type $1s$, $2s$, and $2p$ atomic orbitals are used. For the ground state of O_2, various approximate treatments are investigated. Further, for $^1\Delta_g$, $^1\Sigma_g^+$, $^1\Sigma_u^-$, $^3\Sigma_u^+$, and $^3\Sigma_u^-$ states, improved calculations are performed by mixing several configurations. By using the wave functions thus obtained, dissociation energy D_e, excitation energies ΔE, molecular quadrupole moment Q, magnetic hyperfine structure parameters $\langle\psi^2(0)\rangle$ and $\langle P_2/r^3\rangle$, oscillator strengths f, diamagnetic second order Zeeman term $\chi_{\text{dia.}}$, and polarizabilities $\alpha_{//}$ and $\alpha_\perp$ are calculated and compared with the observed values. The results are found to be improved appreciably by mixing a small number of configurations. Finally, several of the wave functions of the O_2 ground state are analyzed by the population analysis method developed by Mulliken.

§ 1. Introduction

Since the classical work of Heitler-London-Sugiura on the hydrogen molecule, mechanism of chemical binding and the electronic structure of molecules in general have been understood in principle. Useful concepts in molecular quantum theory, such as electron pair bond, hydridization, valence states of atoms in molecules, were introduced in early days, and have been extensively employed in theoretical interpretation of molecular electronic structure. However, on account of the mathematical difficulty of quantum mechanics of many electron systems, the early developments were of more or less semi-empirical nature except in the case of the hydrogen molecule, and very often in the formulation of the theory some drastic approximations had to be introduced, which were not easy to justify; particularly the neglect of non-orthogonality of orbitals localized on two adjacent atoms, which was made commonly in the generalization of Heitler-London method to more complex molecules, has been criticized by Slater and others.

Under these circumstances, rigorous, non-empirical treatment of molecules with more than two electrons seems to be highly desirable. The possibility of calculating quantum-mechanically properties of molecules with a fairly large number of electrons within manageable amount of labour has been shown by the recent developments of molecular orbital theory; success of MO SCF calculations of CO_2, H_2O, N_2 etc., extensive studies of configuration interaction by Parr, Craig and Ross, members of Slater's laboratory in M.I.T.1), and others have encouraged us to undertake purely non-empirical, detailed study of simple molecules of the first row atoms and their hydrides. We chose Li_2 and O_2 as objects of our first study; the reason of this choice is as follows: Li_2 is the simplest molecule having 2-quantum σ bond, which may have characteristics quite different from those of $1s$ bond in H_2, while O_2 is particularly rich in spectroscopic and other data, including microwave data on magnetic hyperfine structure of $O^{17}O^{16}$. In the first and second papers of this series, the results of our study of O_2 and Li_2 will be reported, and the third paper will contain summarizing discussions on these and similar diatomic molecules.

The calculation which is described in this series of papers is based on the so-called MOCI method. Taking all electrons into account, we calculate energies of the ground and lower excited states, on different choice of configurations, and comparing the results, discuss the relative merits of various approximation procedures. Further we evaluate various physical quantities such as electronic quadrupole moment, electric polarizability, transition probability, constants in microwave hfs spectra, etc., with different wave functions.

As is well-known, wave functions in Heitler London approach can be covered by MOC procedure, as long as in the former method the same atomic orbitals are used irrespectively of the degree of ionization of atom concerned, and in this way we shall be abl to discuss, among others, the relative superiority between Heitler-London and molecula orbital methods.

Very interesting results, particularly on excitation energies, have recently been obtained by Moffitt2), Mulliken3), Ohno-Itoh4) and others on the assumption that atoms will preserve their properties of their different states even in molecules. In orbital approximation this requires the use of different atomic orbitals according as the amount of charge which happens to be located on the atom concerned. This sort of refinement of Heitler-London method is not covered by our MOCI procedure. However, their methods are either semi-empirical, or involve approximations, which make the exact estimate of their effect more or less difficult.

To develop the theory on unambiguous basis, it seemed to us inevitable to carry out MOCI calculation, taking, at least, important configurations constructed out of $1s$, $2s$, and $2p$ AO's. We hope that, even for those interested in such refined approaches of HL type as mentioned above, our results will provide reliable data useful for their study.

MOCI study of the oxygen molecule has already been made by Meckler5). Meckler used Gaussian type atomic orbitals, while we employ Slater type ones, as building blocks of molecular orbitals. Further he did not consider the configurations in which $2s$ core electrons are excited. We shall show that $2s$ excitation is by no means negligible.

§ 2. Construction of Molecular Orbitals

The two oxygen nuclei will be denoted by A and B and the AO's of atoms A and B are denoted by χ_a and χ_b respectively. Since the electronic configuration of the ground state of an oxygen atom is $(1s)^2(2s)^2(2p)^4$, we confined ourselves to $1s$, $2s$, and $2p$ type AO's. Further, we adopted for these AO's the normalized Slater-type AO's, namely,

$$
\left.\begin{aligned}
&1s_a(1)=(\delta_1{}^3/\pi)^{1/2}\exp(-\delta_1 r_{a1})\ ,\\
&2s_a(1)=(\delta_2{}^5/3\pi)^{1/2}\, r_{a1}\exp(-\delta_2 r_{a1})\ ,\\
&\left.\begin{matrix}2p\sigma_a(1)\\ 2p\pi_a{}^+(1)\\ 2p\pi_a{}^-(1)\end{matrix}\right\}=(\delta_2{}^5/\pi)^{1/2} r_{a1}\exp(-\delta_2 r_{a1})\left\{\begin{matrix}\cos\theta_{a1}\\ \sin\theta_{a1}\exp(+i\varphi_1)\\ \sin\theta_{a1}\exp(-i\varphi_1)\ .\end{matrix}\right.
\end{aligned}\right\}\qquad(1)
$$

$_b$(1)'s are defined in a similar way. Here $_{a1}$, r_{b1}, θ_{a1}, θ_{b1}, and φ_1 have meanings as hown in Fig. 1, and δ_1 and δ_2 are the orbital xponents. For the orbitals 2*s*, 2*pσ*, and 2*pπ* ne same value of the orbital exponent, δ_2, is ssumed. Throughout this paper, unless othervise noticed, we shall use the atomic units,

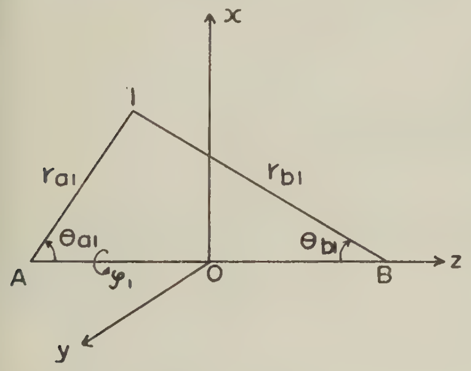

Fig. 1. Diagram of notation of coordinates.

(energy: 27.206 e.v., length: 0.5292Å). The equilibrium internuclear distance *R* of the O_2 molecule in its ground state $^3\Sigma_g{}^-$ is 2.282 a.u., and according to Slater's rule δ_1 and δ_2 are equal to 7.70 and 2.275 respectively. But the molecular integrals involving Slater-type AO's (1) are expressed in terms of $\alpha=\delta_1 R$, $\beta=\delta_2 R$, and *R*. Hence, for convenience of numerical work, we have chosen the following values, $\alpha=17.75$, $\beta=5.25$, and $R=2.30$ a.u. The corresponding values of δ_1 and δ_2 are 7.717 and 2.283 respectively.

From the AO's (1) we set up the unnormalized symmetry orbitals

$$
\left.\begin{aligned}
(\sigma 1s)_{g,u}&=1s_a\pm 1s_b\ ,\\
(\sigma 2s)_{g,u}&=2s_a\pm 2s_b\ ,\\
(\sigma 2p)_{g,u}&=2p\sigma_a\pm 2p\sigma_b\ ,\\
(\pi^\pm 2p)_{g,u}&=2p\pi_a{}^\pm\mp 2p\pi_b{}^\pm\ .
\end{aligned}\right\}\qquad(2)
$$

Orthogonalized molecular orbitals (OMO's) can be constructed as linear combinations of these symmetry orbitals in various ways; OMO's most commonly used are those of the following form, which we shall call "Schmidt-orthogonalized molecular orbitals*" (abbreviated as Schmidt-OMO's)

$$
\left.\begin{aligned}
\sigma_{1g}&=\alpha_{11}(\sigma 1s)_g\ ,\\
\sigma_{2g}&=\alpha_{21}(\sigma 1s)_g+\alpha_{22}(\sigma 2s)_g\ ,\\
\sigma_{3g}&=\alpha_{31}(\sigma 1s)_g+\alpha_{32}(\sigma 2s)_g+\alpha_{33}(\sigma 2p)_g\ ,\\
\pi_g{}^\pm&=\gamma_g(\pi^\pm 2p)_g\ ,\\
\sigma_{1u}&=\beta_{11}(\sigma 1s)_u\ ,\\
\sigma_{2u}&=\beta_{21}(\sigma 1s)_u+\beta_{22}(\sigma 2s)_u\ ,\\
\sigma_{3u}&=\beta_{31}(\sigma 1s)_u+\beta_{32}(\sigma 2s)_u+\beta_{33}(\sigma 2p)_u\ ,\\
\pi_u{}^\pm&=\gamma_u(\pi^\pm 2p)_u\ .
\end{aligned}\right\}\qquad(3)
$$

In the above equations, the coefficients α_{ij}, β_{ij}, γ_g, and γ_u are determined by the conditions of orthonormality and are given in Table I.

Table I. Values of coefficients α, β, and γ in OMO[a)].

α_{11}	0.70710 59	β_{11}	0.70710 76
α_{21}	−0.16451 50	β_{21}	−0.18141 32
α_{22}	0.64420 46	β_{22}	0.85443 12
α_{31}	0.01656 28	β_{31}	−0.05226 28
α_{32}	−0.15659 10	β_{32}	0.40917 14
α_{33}	0.63726 88	β_{33}	0.94154 01
γ_g	0.76305 78	γ_u	0.66189 67

a) See Eq. (3).

The evaluation of the molecular integrals involving the AO's (1) is laborious, but the method of integration and the numerical values of them are already published and need not be repeated here.[6),7)] Then the molecular integrals concerning the unnormalized symmetry orbitals are evaluated easily. Finally we have calculated from these the integrals involving Schmidt-OMO's. These values have been published in another paper[12)].

§ 3. Methods of Calculation

The number of electrons contained in the O_2 molecule is sixteen, and the Hamiltonian of our problem is

---

* Such procedure of orthonormalization as employed in (3) is known as Schmidt method among mathematicians. See, for example, R. Courant und D. Hilbert: Methoden der Mathematischen Physik I, p. 34.

$$H=-\frac{1}{2}\sum_{i=1}^{16}\Delta_i-\sum_{i=1}^{16}\left(\frac{8}{r_{ai}}+\frac{8}{r_{bi}}\right)+\sum_{i>j}^{16}\frac{1}{r_{ij}}+\frac{64}{R}\,. \tag{4}$$

Since this Hamiltonian has $D_{\infty h}$ symmetry, its eigenfunctions are bases of an irreducible representation of $D_{\infty h}$ group and may be classified by the quantum numbers Λ, I, and v, specifying the component of the orbital angular momentum of the electrons along the internuclear axis, the character of the inversion at the center, and the character of the reflection at any plane passing through both nuclei (for the case of $\Lambda=0$), respectively. A set of these quantum numbers Λ, I, and v is abbreviated as Ω. Moreover, as the Hamiltonian (4) is free from spin operators, the total spin quantum number S and its component along a fixed axis M are good quantum numbers. Accordingly the eigenfunctions of (4) have the symmetry character specified by (Ω, S, and M). We impose this property also on the approximate solutions of (4) which are composed of Schmidt-OMO's.

As is usually accepted, we suppose that the orbital energies of Schmidt-OMO's increase in the order of σ_{1g}, σ_{1u}, σ_{2g}, σ_{2u}, σ_{3g}, $\pi_u{}^{\pm}$, $\pi_g{}^{\pm}$, and σ_{3u}, so we assume that the wave functions of the normal state and of lower excited states of the O_2 molecule are composed mainly of configurations which contain two electrons in each of σ_{1g}, σ_{1u}, σ_{2g}, σ_{2u}, and σ_{3g} orbitals and no electron in σ_{3u} orbital. Within these limitations it is sufficient to consider only six electrons accomodated in $\pi_u{}^{\pm}$ and $\pi_g{}^{\pm}$ orbitals, and the molecular states compatible with this assumption are shown in Table II.

Table II. Electronic states arising from $(\sigma_{1g})^2(\sigma_{1u})^2(\sigma_{2g})^2(\sigma_{2u})^2(\sigma_{3g})^2[\pi]^6$ [a].

π_u^+	π_u^-	π_g^+	π_g^-	States
		1	1	$^3\Sigma_g^-$; $^1\Sigma_g^+$
		2		$^1\Delta_g$
			2	
	1	1		$^1\Sigma_u^-$; $^3\Sigma_u^-$; $^3\Sigma_u^+$; ($^1\Sigma_u^+$)
1			1	
1		1		($^1\Delta_u$); ($^3\Delta_u$)
	1		1	

a) Electron configurations are shown by specifying the unoccupied orbitals.

In Table II, electron configurations a shown by their electron holes and the state with the parenthesis are those not observe experimentally. In this paper we shall con sider those nine states shown in Table I which are the same as those considered b Fumi-Parr[8] and Itoh-Ohno[4].

We shall explain briefly the method of con structing a complete set of orthonormaliz wave functions, which have a symmetr character specified by (Λ, I, (v), S, M) an are convenient both for calculations and fo their physical understanding, from ten kin of Schmidt-OMO's given by (3)[6].

In the first place, we pick up from these ten Schmidt-OMO's all the sets of sixteen orbitals, whose products have the given sym metry (Λ, I), considering that each orbita can only accomodate at most two electrons Then we make a product function of these sixteen orbitals for each set, in which sixteen orbitals are arranged in the order to be explained later. Then by multiplying these products by various spin functions with the symmetry (S, M) and by antisymmetrizing these results, we can obtain the required wave functions with the given symmetry (Λ, I, S, M) for $\Lambda\neq0$. When $\Lambda=0$, we can easily find the required wave functions with the given symmetry (Λ, I, v, S, M) by taking the real parts (for Σ^+) or the imaginary parts (for Σ^-) of the product functions of sixteen orbitals and then performing the same procedure as for the case of $\Lambda\neq0$. In this paper the spin-free functions having the orbital symmetry Ω correctly, such as the ones mentioned above, are called "primitive functions," in the sense that they can give wave functions with the complete symmetry character only after being multiplied by the spin functions and then antisymmetrized. Generally, many primitive functions exist for a given Ω. Then they are denoted by A, B, C, $\cdots$, and the normalized forms of them are written as $\Psi_\Omega^{\rm A}$, $\Psi_\Omega^{\rm B}$, $\Psi_\Omega^{\rm C}$ $\cdots$, respectively.

Secondly we shall consider spin functions. The number of spin functions that correspond to given values of S and M is independent of M and amounts to

$$f_S{}^N=\frac{(2S+1)\cdot N!}{(N/2+S+1)!\,(N/2-S)!}\,,$$

where N is the total number of electrons. These spin functions are denoted by $\Theta_{S,M;k}$

$=1, 2, \cdots, f_S{}^N$). Let P be any permutation mong $N!$ permutations of N electrons, then $\Theta_{S,M;k}$ is expressed linearly in terms of ^{N} functions $\Theta_{S,M;k}$:

$$\mathrm{P}\Theta_{S,M;k}=\sum_{h=1}^{f_S^N}\mathrm{V}^S_{hk}(\mathrm{P})\Theta_{S,M;h}\ , \tag{5}$$

here $\mathrm{V}^S(\mathrm{P})$ is called the representation maix of the permutation group $\mathfrak{S}_N$. Further e put

$$\mathrm{U}^S(\mathrm{P})=\varepsilon_{\mathrm{P}}\mathrm{V}^S(\mathrm{P}^{-1})^{\dagger}\ , \tag{6}$$

here † means the transposition of matrix and $_{\mathrm{P}}=(-1)^{\mathrm{P}}$. Then we have antisymmetric ave functions specified by letters A, k, Ω, , and M of the following form

$$\Phi^{\mathrm{A},k}_{\Omega,S,M}=\frac{1}{(N!)^{1/2}}\sum_{\mathrm{P}}\sum_{h}\overline{U}^S_{hk}(\mathrm{P})\mathrm{P}\Psi^{\mathrm{A}}_{\Omega}\cdot\Theta_{S,M;h}\ . \tag{7}$$

Now, we consider the case of the O_2 molecule. As we must assign sixteen electrons to ten Schmidt-OMO's, each of which can accomodate at most two electrons, the number of orbitals which contain only one electron is at most four. These orbitals are called unpaired ones. The orbitals appearing in the primitive function $\Psi^{\mathrm{A}}_{\Omega}$ are divided into paired orbitals and a few (two or four) unpaired ones. In writing $\Psi^{\mathrm{A}}_{\Omega}$, we put the unpaired orbitals first and then the paired ones. For example

$$\begin{aligned}\Psi^{\mathrm{F}}_{\Sigma_g^-}=\frac{1}{\sqrt{2}}\{&\pi_g{}^+(1)\pi_u{}^-(2)\sigma_{3g}(3)\sigma_{3u}(4)\pi_g{}^-(5)\pi_g{}^-(6)\pi_u{}^+(7)\pi_u{}^+(8)\\&-\pi_g{}^-(1)\pi_u{}^+(2)\sigma_{3g}(3)\sigma_{3u}(4)\pi_g{}^+(5)\pi_g{}^+(6)\pi_u{}^-(7)\pi_u{}^-(8)\}\\&\times\sigma_{2u}(9)\sigma_{2u}(10)\sigma_{2g}(11)\sigma_{2g}(12)\sigma_{1u}(13)\sigma_{1u}(14)\sigma_{1g}(15)\sigma_{1g}(16)\ .\end{aligned} \tag{8}$$

Generally, if we assume that r paired orbitals are present in $\Psi^{\mathrm{A}}_{\Omega}$, it is invariant with respect o the interchange between electrons in each pair. The number of such permutations is 2^r nd they are expressed as

$$\mathrm{Q}=(N-2r+1, N-2r+2)^{\lambda_1}(N-2r+3, N-2r+4)^{\lambda_2}\cdots(N-1, N)^{\lambda_r}\qquad(\lambda_i=0\text{ or }1)\ . \tag{9}$$

f we select $s=\frac{N!}{2^r}$ permutations $\mathrm{P}_0, \mathrm{P}_1, \cdots, \mathrm{P}_{s-1}$ out of $N!$ permutations of N electrons, n such a way that each of all $N!$ elements can be expressed uniquely in the form $\mathrm{P}_u\mathrm{Q}$ ($u=0, 1, \cdots, s-1$), we have, in general, s mutually independent functions $\mathrm{P}_u\Psi^{\mathrm{A}}_{\Omega}$ among $!$ $\mathrm{P}\Psi^{\mathrm{A}}_{\Omega}$.

On the other hand, since 2^r elements Q are ll commutable and $\mathrm{Q}^2=1$, we can transform (Q) to the following form

$$V_{kh}(\mathrm{Q})=0\qquad(k\neq h)\ ,$$
$$V_{hh}(\mathrm{Q})=\pm1\ .$$

In this case we can assign the suffix k so that if $k\leqq g$, $V_{kk}(\mathrm{Q})=-1$ for every Q and if $k>g$, $V_{kk}(\mathrm{Q})=+1$ for at least one Q. Then it is proved that $\Phi^{\mathrm{A},k}_{\Omega,S,M}$'s for $k\leqq g$ are linearly independent, and those for $k>g$ vanish identically. The spin functions of these first g numbers must be of the form

$$\begin{aligned}\Theta_{S,M;h}&(1, 2, \cdots, N)\\&=\Theta_{S,M;h}(1, 2, \cdots, N-2r)\\&\quad\times\frac{1}{2^{1/2}}\{\alpha(N-2r+1)\beta(N-2r+2)\\&\qquad-\beta(N-2r+1)\alpha(N-2r+2)\}\\&\quad\cdots\cdots\\&\quad\times\frac{1}{2^{1/2}}\{\alpha(N-1)\beta(N)-\beta(N-1)\alpha(N)\}\\&\qquad\qquad(1\leqq h\leqq g)\ .\end{aligned} \tag{10}$$

able III. Adopted forms of spin functions Θ_h(1, 2, 3, 4)[a].

or $S=1$, $M=1$

$$\Theta_1=\frac{1}{\sqrt{2}}\alpha(1)\alpha(2)\{\alpha(3)\beta(4)-\beta(3)\alpha(4)\}$$

$$\Theta_2=\frac{1}{\sqrt{2}}\{\alpha(1)\beta(2)-\beta(1)\alpha(2)\}\alpha(3)\alpha(4)$$

$$\begin{aligned}\Theta_3=\frac{1}{2}\{&\alpha(1)\beta(2)\alpha(3)\alpha(4)+\beta(1)\alpha(2)\alpha(3)\alpha(4)\\&-\alpha(1)\alpha(2)\alpha(3)\beta(4)-\alpha(1)\alpha(2)\beta(3)\alpha(4)\}\end{aligned}$$

r $S=0$, $M=0$

$$\Theta_1=\frac{1}{2}\{\alpha(1)\beta(2)-\beta(1)\alpha(2)\}\{\alpha(3)\beta(4)-\beta(3)\alpha(4)\}$$

$$\begin{aligned}\Theta_2=\frac{1}{\sqrt{3}}[&\alpha(1)\alpha(2)\beta(3)\beta(4)+\beta(1)\beta(2)\alpha(3)\alpha(4)\\&-\frac{1}{2}\{\alpha(1)\beta(2)+\beta(1)\alpha(2)\}\{\alpha(3)\beta(4)+\beta(3)\alpha(4)\}]\end{aligned}$$

a) See Eq. (10).

Here $\Theta_{S,M;k}$ $(1, 2, \cdots, N-2r)$'s are the spin functions of $(N-2r)$ electrons, and their explicit forms adopted in this paper are given in Table III. Then we can construct g antisymmetrized wave functions $\Phi^{A,k}_{\Omega,S,M}$ with quantum numbers Ω, S, and M from the primitive function Ψ^{A}_{Ω}. The explicit form of these functions is

$$\Phi^{A,k}_{\Omega,S,M}(1, 2, \cdots, N) = \frac{1}{(N!\,2^r)^{1/2}} \sum_{\mathrm{P}} \sum_{h} \overline{U}^{S}_{hk}(\mathrm{P})\mathrm{P}\Psi^{A}_{\Omega}\Theta_{S,M;h} \quad (1 \leqq k \leqq g) . \tag{11}$$

The factor in (11) appears on account of normalization. In general we have many primitive functions $\Psi^{A}_{\Omega}, \Psi^{B}_{\Omega}, \cdots$, for each of which the functions of the form (11) can be constructed. The best wave function in our approximation is therefore a suitable linear combination of them, namely

$$\Phi_{\Omega,S,M}(1, 2, \cdots, N) = \sum_{A,k} c_{A,k}\Phi^{A,k}_{\Omega,S,M}(1, 2, \cdots, N) . \tag{12}$$

As is well known, the coefficients $c_{A,k}$ of (12) and the total energy E are determined from the following linear algebraic equations

$$\sum_{B,k} \{H_{(A,k),(B,h)} - E\Delta_{(A,k)(B,h)}\}c_{B,h} = 0 , \tag{13}$$

where $H_{(A,k),(B,h)}$ and $\Delta_{(A,k),(B,h)}$ are the matrix elements of the Hamiltonian (4) and the unity, respectively, referring to the functions (11). The evaluation of these matrix elements is performed according to the following formulae

$$H_{(A,k),(B,h)} = \sum_{\mathrm{P}_u} U_{hk}(\mathrm{P}_u)\int \mathrm{P}_u\Psi^{A*}_{\Omega}H\Psi^{B}_{\Omega}dv \tag{14}$$

$$\Delta_{(A,k),(B,h)} = \sum_{\mathrm{P}_u} U_{hk}(\mathrm{P}_u)\int \mathrm{P}_u\Psi^{A*}_{\Omega}\Psi^{B}_{\Omega}dv . \tag{15}$$

In the above equations $U_{hk}(\mathrm{P}_u)$ can be obtained according to the rules explained in KAIK⁶⁾.

As the primitive functions $\Psi^{A}_{\Omega}, \Psi^{B}_{\Omega}, \cdots$ are constructed simply from Schmidt-OMO's, the integrals in (14) and (15) can be reduced easily and are expressed in terms of one or two electron integrals involving Schmidt-OMO's. We notice here that this reduction can not be done so easily without the help of orthogonality of orbitals.

§ 4. Calculation of the Energy of the Ground State ${}^3\Sigma_g^-$

As can be shown by actual examination, we can construct thirty wave functions (11) havi ${}^3\Sigma_g^-$ symmetry from Schmidt-OMO's (3) a the spin functions given in Table III. T wave functions are denoted by A_1, B_1, $\cdots$ E_1, E_2, $\cdots$ and so on, where suffices 1, 2, · refer to the choice of spin functions Table III. Each of these functions correspon to a "configuration." In case for a giv primitive function the wave functions (1 with suffices other than 1 vanish, we om the suffix 1, for example, we write simply A instead A_1. Among thirty configuratio seventeen are shown explicitly in Table I where the product functions, contained the primitive functions Ψ^{A}, Ψ^{B}, $\cdots$ with pos tive coefficients are specified by the numbe and the orders of electrons accomodated i each Schmidt-OMO written on the first lin The whole primitive function can be co structed from this product function easily symmetry considerations. Configuration corresponds to the usual antisymmetrize orthogonalized-molecular-orbital wave functio (ASOMO) built from linear combinations atomic orbitals (LCAO). In nine configuration from A to F_3 in Table IV, Schmidt-OMO σ_{1g}, σ_{1u}, σ_{2g}, and σ_{2u} are fully occupied b eight electrons, while in the remaining twenty one configurations it is not the case.

Now, a lot of proposals have been put fo ward hitherto on the procedure of calculatin non-empirically the electronic ground state a molecule and we actually applied several these methods to the O_2 molecule. To explai our calculations it is convenient to divide the into sixteen cases.

Case 1. A (*single configuration*)

The total energy for single configuratio A, calculated by the formula (A.1), is foun to be -149.00734 a.u.

Case 2. A+C (π *electron configuratio* *interaction*

In the π electron theory, π electrons a considered to be loosely bound to the m lecular framework and play an importa role to the electronic structure of the groun state and lower excited states. In fact, almo all the calculations hitherto made on the molecule except perhaps Meckler's one⁵⁾, a based on the π electron theory. Since th π electron theory is widely accepted in i simplicity and usefulness, we have studie the configurational interaction within this a able IV. Configurations used in CI calculation and their coefficients in normalized wave function for ground state ${}^3\Sigma_g^-$.

	Configurations[a)]										Coefficients c_i [b)]		
i	π_u^+	π_u^-	π_g^+	π_g^-	σ_{3g}	σ_{3u}	σ_{2g}	σ_{2u}	σ_{1g}	σ_{1u}	Case 8	Meckler	Case 10
A	2	2	1	1	2		2	2	2	2	0.9629	0.9749	0.9490
B	2	2	1	1		2	2	2	2	2	−0.0959	−0.0826	−0.0735
C	1	1	2	2	2		2	2	2	2	−0.1719	−0.1352	−0.1521
D	1	1	2	2		2	2	2	2	2	0.0515	0.0329	
E_1	$\bar{1}$	$\bar{1}$	$\underline{1}$	$\underline{1}$	2	2	2	2	2	2	0.0027	0.0026	
E_2	$\underline{1}$	$\underline{1}$	$\bar{1}$	$\bar{1}$	2	2	2	2	2	2	0.0259	0.0233	0.0272
F_1	$\bar{1}$	2	2	$\bar{1}$	$\underline{1}$	$\underline{1}$	2	2	2	2	0.1716	0.1473	0.1465
F_2	$\underline{1}$	2	2	$\underline{1}$	$\bar{1}$	$\bar{1}$	2	2	2	2	−0.0309	−0.0263	−0.0226
F_3	$\bar{1}$	2	2	$\bar{1}$	$\bar{\bar{1}}$	$\bar{\bar{1}}$	2	2	2	2	0.0179	0.0178	0.0184
H	2	2	1	1	2	2	2		2	2			−0.0005
J_1	2	2	$\bar{1}$	$\bar{1}$	2	$\underline{1}$	2	$\underline{1}$	2	2			−0.2118
J_3	2	2	$\bar{1}$	$\bar{1}$	2	$\bar{\bar{1}}$	2	$\bar{\bar{1}}$	2	2			−0.0438
L	2	2	1	1	2	2		2	2	2			−0.0162
M_1	$\bar{1}$	2	2	$\bar{1}$	2	$\underline{1}$	$\underline{1}$	2	2	2			0.0202
M_2	$\underline{1}$	2	2	$\underline{1}$	2	$\bar{1}$	$\bar{1}$	2	2	2			0.0132
M_3	$\bar{1}$	2	2	$\bar{1}$	2	$\bar{\bar{1}}$	$\bar{\bar{1}}$	2	2	2			−0.0073
O_1	2	2	$\bar{1}$	$\bar{1}$	$\underline{1}$	2	$\underline{1}$	2	2	2			0.0156

a) The product function contained with the positive coefficient in the primitive function of each configurational wave function is shown by specifying the numbers of electrons occupying each orbital. Further in this product function, it is assumed that the i-th unpaired orbital ($i=1, 2, \cdots, 2r$), if numbered from left to right, accomodates the i-th electron, and the j-th paired orbital ($j=1, 2, \cdots, 8-r$) accomodates the $(2j+2r-1)$th and the $(2j+2r)$th electrons.

b) See Eq. (12).

roximation. Then the configurations which iust be considered are only A and C. The ormalized wave function determined by the rinciple of minimun energy is

$$0.9629\mathrm{A}-0.2698\mathrm{C}\,, \tag{16}$$

nd the corresponding total energy is lower ian that of Case 1 by 1.403 e.v.

'ase 3. A+J_1 (*s-p hybridization*)

Contrary to Case 2, we consider in Case 3 ie configurations, whose primitive functions iffer from that of A only in the σ orbital art. B, H, J_i, $\cdots$ belong to such configu- itions. Since, however, the orbital energy f σ_{3u} is far above those of σ_{3g}, σ_{2u}, and σ_{2g}, ie contribution of B, H, $\cdots$ except J_i may e considered small. Among J_i's, it is shown y actual examination that the contribution f J_1 is most important. The wave function otained by taking into account only J_1 be- des A is

$$0.9704\mathrm{A}-0.2414\mathrm{J}_1\,, \tag{17}$$

id the total energy is lower than that of Case 1 by 2.1687 e.v. Since in J_1, σ_{2u} and σ_{3u} are coupled to a singlet, the mixing of J_1 may be taken in some sense as the *s-p* hybridization in the molecular orbital scheme, and is outside the scope of Meckler's approximation (cf. Case 8).

Case 4. $(u)^2$ *approximation*

In spite of the much higher orbital energy of σ_{3u} than σ_{2u}, the contribution of J_1 turns out to be so large that we are not always permitted to neglect J_1. While, we are allowed to use some other OMO's instead of Schmidt-OMO's (3) as the building block of our primitive functions. Then configuration A, if composed of suitable OMO's, may be accepted to give in general a better result than Case 1, and the corresponding best OMO's are nothing but the Roothaan's self-consistent field molecular orbitals (SCFMO)[9)]. Now the result does not depend upon the form of σ_g orbitals as they are fully occupied in A, while it depends of course upon the form of σ_u orbitals we employed. Here we shall limit ourselves to the case where 1*s* AO's are fully occupied, and the form of σ_{1u} orbital is fixed to Schmidt-OMO (3). Then among the OMO's included in A, only the form of σ_{2u} orbital is left undetermined. The best σ_{2u} orbital, determined by the principle of minimum energy with σ_{1u} held fixed to Schmidt-OMO (3), will be called here *u* orbital. The variational calculation shows that the form of *u* is

$$u=0.9855\sigma_{2u}-0.1698\sigma_{3u}\ , \qquad (18)$$

where σ_{2u} and σ_{3u} are Schmidt-OMO's defined by (3), and the total energy obtained is lower than that of Case 1 by 2.108 e.v. The wave function here obtained can be expressed in terms of the configurations in Table IV as follows

$$0.9712\mathrm{A}-0.2367\mathrm{J}_1+0.0288\mathrm{H}\ . \qquad (19)$$

By comparing this result with that of Case 3, we can confirm that the contribution of configuration J_1 can be much reduced, if we adopt a suitable *u* orbital instead of σ_{2u}.

Case 5. A+J$_1$+H (*u′u″ approximation*)

In Case 4, paired electrons are assigned to the same molecular orbital *u*, but we can generalize this treatment by introducing two different orbitals *u′* and *u″*. This generalization has in some sense a nature of the so-called in-out effect, although it must be mentioned that the same values of the orbital exponents δ_1 and δ_2 are taken for *u′* and *u″*. After the variation, we found

$$\left.\begin{aligned} u'&=0.9426\sigma_{2u}-0.3339\sigma_{3u}\ ,\\ u''&=1.0000\sigma_{2u}+0.0027\sigma_{3u}\ ,\end{aligned}\right\} \qquad (20)$$

and the corresponding total energy is lower than that of Case 1 by 2.1689 e.v. *u′* and *u″* can be shown to represent the outer and inner orbitals respectively. The wave functions here obtained can be written down also in terms of the configurations in Table IV as follows

$$0.9705\mathrm{A}-0.2412\mathrm{J}_1-0.0009\mathrm{H}\ . \qquad (21)$$

Case 6. *The* LCAO SCF *method*

As the O$_2$ molecule does not have a closed shell configuration of electrons, we have carried out a LCAO SCF calculation by modifying slightly Roothaan's method[9]. We have assumed the wave function as

$$\begin{aligned}\frac{1}{(16!)}&\sum_P(-1)^P\mathrm{P}(1\pi_g{}^+)(1\pi_g{}^-)(1\pi_u{}^+)^2(1\pi_u{}^-)^2\\ &\times(3\sigma_g)^2(2\sigma_u)^2(2\sigma_g)^2(1\sigma_u)^2(1\sigma_g)^2\\ &\times\alpha(1)\alpha(2)\alpha(3)\beta(4)\cdots\alpha(15)\beta(16)\ , \qquad (22)\end{aligned}$$

where $\alpha(i)$ and $\beta(i)$ are the spin functions electron *i* corresponding to the spin parall and antiparallel to a fixed direction, respe tively. Further we assumed that $1\sigma_g$, $1\sigma_u$, · are the molecular orbitals whose symmetri are σ_g, σ_u, ··· respectively, and can be e pressed in terms of Schmidt-OMO's (3) as

$$\left.\begin{aligned} 1\sigma_g&=c_{11}\sigma_{1g}+c_{12}\sigma_{2g}+c_{13}\sigma_{3g}\ ,\\ &\cdots\cdots\\ 1\sigma_u&=c_{41}\sigma_{1u}+c_{42}\sigma_{2u}+c_{43}\sigma_{3u}\ ,\end{aligned}\right\} \qquad (2$$

and so on. By the help of Eq. (A.1) and t principle of minimum energy, we can set the equations, by which the coefficients in (2 are determined. Adopting Roothaan's no tions, we can write the quations as

$$\left.\begin{aligned} &\{h+\sum_k(2J_k-K_k)+\tfrac{1}{2}\sum_a(2J_a-K_a)\}\varphi_j\\ &\qquad\qquad-\mathcal{E}_j\varphi_j=0\ ,\\ &\{h+\sum_k(2J_k-K_k)+(J_b-K_b)\}\varphi_a\\ &\qquad\qquad-\mathcal{E}_a\varphi_a=0\ .\end{aligned}\right\} \qquad (2$$

In the above equations, φ_k's denote the ful occupied orbitals in (22) and φ_a's are $1\pi_g{}^+$ ar $1\pi_g{}^-$. φ_k's and φ_a's are often abbreviate simply as *k*'s and *a*'s respectively. *h*, J and K$_k$ are the one electron, Coulomb, an exchange operators respectively. $\mathcal{E}_j$ and $\mathcal{E}_a$ a the orbital energies. Inserting (23) into (24 we can obtain the equations involving coe ficients c_{ij}. These can be determined follov ing Roothaann's self-consistent method. Th values of orbital energies $\mathcal{E}_j$'s, and the coe ficients c_{ij}'s are shown in Table V. Tot energies thus obtained is lower than in Case by 2.167 e.v.

The wave function for Case 5 is superio to that for Case 4 in so far as the former more flexible than the latter on account adopting different *u* orbitals and the wav function for Case 6 is superior to that for Cas 4 in so far as it takes into account the co figurations in which 1*s* electrons do not for a closed shell. The amount of the improve ment in the total energy is 0.061 e.v. for th former and 0.059 e.v. for the latter.

Case 7. A+F$_1$ (*σ-π interaction*)

In the *π* electron approximation, on whic our calculation till now has been based, th primitive functions can be written, even configurational mixing is taken into conside ation, in the form of the product of a *π* pa and a *σ* part, and so the correlation betwee able V. Expansion coefficients[a] of SCF MO's of ground state $^3\Sigma_g^-$ with respect to Schmidt-OMO's[b] and unnormalized symmetry orbitals[c], and orbital energies (R=2.3 a.u.).

SCF MO	Schmidt-OMO[a]				Unnormalized symmetry orbital[c]				Orbital energy (in a. u.)
	$\sigma_{1g,u}$	$\sigma_{2g,u}$	$\sigma_{3g,u}$	$\pi^{\pm}_{g,u}$	$(\sigma 1s)_{g,u}$	$(\sigma 2\bar{s})^{d)}_{g,u}$	$(\sigma 2p)_{g,u}$	$(\pi^{\pm}2p)_{g,u}$	
$1\sigma_g$	0.9998	0.0188	0.0004		0.7067	0.0117	0.0002		−20.5951
$2\sigma_g$	−0.0182	0.9646	0.2631		−0.0315	0.5641	0.1677		− 1.5219
$3\sigma_g$	0.0046	−0.2631	0.9648		−0.0125	−0.3117	0.6148		− 0.5564
$1\pi_u^{\pm}$				1				0.7631	− 0.3944
$1\sigma_u$	0.9999	0.0148	0.0049		0.7075	0.0142	0.0046		−20.5927
$2\sigma_u$	−0.0137	0.9850	−0.1717		0.0009	0.7500	−0.1617		− 0.9782
$3\sigma_u$	−0.0073	0.1717	0.9851		0.0408	0.5345	0.9275		0.7392
$1\pi_u^{\pm}$				1				0.6619	− 0.5499

a) See Eq. (23).
b) See Eq. (3).
c) See Eq. (2).
d) See Eq. (30).

electrons and π electrons, usually called the -π interaction, is not taken into account.

We have attempted here to improve this oint by mixing to A configuration F_1, which s derived from A by replacing one σ_{3g} by σ_{3u} nd one $\pi_u{}^{\pm}$ by $\pi_g{}^{\pm}$. The wave function obained by the variational method is

$$0.9739A+0.2269F_1\,, \tag{25}$$

nd the corresponding total energy is lower han that of Case 1 by 2.339 e.v.

ase 8. *p electron configurational interaction (Meckler's case)*

In this case, we considered the nine configuations from A to F_3 in Table IV, which are quivalent as a whole to those considered by leckler[5] in studying the O_2 molecule. If 1*s* nd 2*s* AO's can be considered fully occupied ctually, a wave function derived by the varition from a linear combination of these nine onfigurations will be a good approximation. he wave function obtained is shown in Table V, where the coefficients (cf. Eq. (12)) in our vave function are listed in column 3, and for omparison the coefficients obtained by interolating Meckler's ones to R=2.3 a.u. are iven in column 4. It is interesting to notice hat the coefficients here obtained agree well vith the corresponding Meckler's ones, though his seems rather fortuitous as the latter were alculated with the use of the AO's of Gausian type. The depression of the total energy rom Case 1 is 3.424 e.v. in our calculation, ompared with 2.29 e.v. in Meckler's one.

Case 9. Five dimensional configurational interaction

Judging from the coefficients of Case 8 in Table IV, we can expect that configurations A, F_1, C, and B contribute dominantly to the result. Further from the result of Case 3 we know that configuration J_1 is also very important. Thus it is likely that a rather simple but comparatively good wave function can be constructed from configurations A, B, C, F_1, and J_1. Here we examined this approximation. The resulting wave function after the variational calculation turned out to be

$$0.9526A-0.0774B-0.1541C \\ +0.1481F_1-0.2023J_1\,, \tag{26}$$

and the corresponding total energy is lower than that of Case 1 by 4.781 e.v.

Case 10. Fifteen dimensional configurational interaction

In order to obtain the best wave function within our framework, we must take into account all the thirty configurations. As this requires, however, a considerably laborious work, we selected only those fifteen configurations which have non-vanishing matrix elements between the main configuration A and themselves. From the standpoint of the second order perturbation theory, this selection seems to be reasonable. The configurations given in Table IV, except D and E_1, correspond to these fifteen ones. The wave function obtained by the variational calculation is given in Table IV. The corresponding total energy is lower than that in Case 1 by 5.000 e.v. The difference between the total energies of Case 9 and Case 10 is 0.219 e.v., whereas the number of configurations involved is only five for the former in contrast with fifteen for the latter.

Case 11. *Pure* HL *approximation*

The wave function for the Heitler-London (HL) approximation can be obtained by the following primitive function

$$\left.\begin{aligned}&\Psi=(\text{normalization constant})\times\{\Psi_{a,b}+\Psi_{b,a}\}\ ,\\&\Psi_{a,b}=\{\pi_a{}^+\pi_b{}^-(\pi_a{}^-)^2(\pi_b{}^+)^2-\pi_a{}^-\pi_b{}^+(\pi_a{}^+)^2(\pi_b{}^-)^2\}\\&\qquad\times\sigma_a\sigma_b(2s_a)^2(2s_b)^2(1s_a)^2(1s_b)^2\ .\end{aligned}\right\}\tag{27}$$

This wave function is shown to be expressed with the configurations of Table IV as

$$0.7265\text{A}-0.3328\text{B}-0.5466\text{C}+0.2504\text{D}\ .\tag{28}$$

By using this relation we have calculated the energy and this is found to be 4.160 e.v. higher than that in Case 1. Thus, unexpectedly, in the case of the O_2 molecule ground state, the straightforward application of the HL method proves to be not superior to that of the MO method. In part III of this series we shall explain the reason for this result.

Case 12. σ-HL, π-MO *approximation*

We have found that the pure HL method is a much poorer approximation compared with the pure MO method mentioned in Case 1. So we here examined an intermediate approximation shown by the following primitive function,

$$\left.\begin{aligned}&\Psi=(\text{normalization constant})\\&\times\{(\Psi_{a,b}+\Psi_{b,a})-\text{complex conjugate}\}\ .\\&\Psi_{a,b}=\pi_g{}^+\pi_g{}^-(\pi_u{}^+)^2(\pi_u{}^-)^2\\&\qquad\times\sigma_a\sigma_b(2\overset{\circ}{s}_a)^2(2\overset{\circ}{s}_b)^2(1s_a)^2(1s_b)^2\ .\end{aligned}\right\}\tag{29}$$

In the above, $2\overset{\circ}{s}_a$ is the orthonormalized $2s$ function of the following form

$$2\overset{\circ}{s}_a(1)=c_1 1s_a(1)+c_2 2s_a(1)\ ,\tag{30}$$

where c_1 and c_2 are the constants to be determined by the conditions of orthogonality of $2\overset{\circ}{s}_a$ and $1s_a$ and of normalization. In our case c_1 and c_2 are $-0.24051\ 76$ and $1.02851\ 77$, respectively. In Eq. (29), atomic orbitals are used for $1s$, $2\overset{\circ}{s}$, and $2p\sigma$, but for $2p\pi$, molecular orbitals are used. Accordingly we may call this treatment σ-HL, π-MO approximation. The total energy obtained turns out to be still 3.033 e.v. higher than that of Case 1. The wave function in this case is expresse in terms of the configurations of Table IV a

$$\Phi_{\sigma\text{-HL},\pi\text{-MO}}=0.9091\text{A}-0.4165\text{B}\ .\qquad(3$$

Case 13. π-HL, σ-MO *approximation*

Contrary to the previous case, we shall trea here the σ electrons by the MO scheme an the π electrons by the HL scheme. Then ou primitive function is

$$\begin{aligned}&\Psi=(\text{normalization constant})\times\{\Psi_{a,b}+\Psi_{b,a}\},\\&\Psi_{a,b}=\{\pi_a{}^+\pi_b{}^-(\pi_a{}^-)^2(\pi_b{}^+)^2-\pi_a{}^-\pi_b{}^+(\pi_a{}^+)^2(\pi_b{}^-)^2\}\\&\qquad\times(\sigma_{3g})^2(\sigma_{2u})^2(\sigma_{2g})^2(\sigma_{1u})^2(\sigma_{1g})^2\ .\end{aligned}\qquad(3$$

The energy value obtained by (32) is highe than that of Case 1 by 1.141 e.v. The wav function obtained can be written as

$$\Phi_{\pi\text{-HL},\sigma\text{-MO}}=0.7991\text{A}-0.6012\text{C}\ .\qquad(3$$

Summarizing the results of Cases 11, 12 and 13, we can conclude that (i) the MO method is superior to the HL method for th σ electrons as well as for the π electrons, an (ii) the MO method is more appropriate fo the σ electrons than for the π electrons.

Case 14. σ (*s-p hybridized*)-HL, π-MO *ap proximation*

We here attempted to improve Case 12 b taking into consideration the *s-p* hybridization that is, by using the primitive function

$$\begin{aligned}&\Psi=(\text{normalization constant})\\&\times\{(\Psi_{a,b}+\Psi_{b,a})-\text{complex conjugate}\},\\&\Psi_{a,b}=\pi_g{}^+\pi_g{}^-(\pi_u{}^+)^2(\pi_u{}^-)^2(\sigma_a+\lambda 2\overset{\circ}{s}_a)\\&\times(\sigma_b+\lambda 2\overset{\circ}{s}_b)(2\overset{\circ}{s}_a-\lambda\sigma_a)^2(2\overset{\circ}{s}_b-\lambda\sigma_b)^2(1s_a)^2(1s_b)^2,\end{aligned}\qquad(34$$

where λ is the variational parameter showin the degree of *s-p* hybridization. The tota energy obtained is still higher than that o Case 1 by 0.061 e.v., and the correspondin value of λ is found to be 0.2557. The improvement due to this second order hybridization is 2.972 e.v. (cf. Cases 3, 4, and 6) The wave function here obtained is expresse in terms of configurations in Table IV as follows,

$$\begin{aligned}&0.9095\text{A}-0.2991\text{B}+0.0377\text{H}\\&\qquad-0.2619\text{J}_1-0.0214\text{L}+0.1133\text{O}_1\ .\end{aligned}\qquad(35$$

If the degree of *s-p* hybridization is define by $\lambda^2/(1+\lambda^2)$, it can be estimated from the above value of λ as 6.1%.

Case 15. σ-SO, π-MO *approximation*

In general, a better approximation than the

O method as well as than the HL method n be obtained by the semilocalized orbital ethod (SO). We here applied this method the σ electrons, by replacing the σ_a and e σ_b orbitals in (29) by the orbitals of the rm

$$\sigma_a^{sl}=\sigma_a+\mu\sigma_b\ , \qquad \sigma_b^{sl}=\sigma_b+\mu\sigma_a\ , \tag{36}$$

the above μ represents the degree of semicalization and is obtained by the variational inciple. The energy depression from Case was found to be 0.881 e.v., and the value μ to be 0.2912. The wave function thus tained is decomposed into the configurations Table IV as follows:

$$\Phi_{\sigma\text{-SO},\pi\text{-MO}}=0.9906\mathrm{A}-0.1367\mathrm{B}\ . \tag{37}$$

Further the ionic character of the σ-bond can be seen by reexpressing wave function (37) as

$$\Phi_{\sigma\text{-SO},\ \pi\text{-MO}}$$
$$=(1/d_\sigma)(\Phi_{\sigma\text{-HL},\ \pi\text{-MO}}+c_\sigma\Phi_{\sigma\text{-ion},\ \pi\text{-MO}})\ ,$$

where $\Phi_{\sigma\text{-ion},\ \pi\text{-MO}}$ is the normalized wave function having σ-ionic, π-MO character, and we have found $d_\sigma=1.4105$ and $c_\sigma=0.5369$.

Finally, it is worth while to notice that the π-SO, σ-MO method is identical with Case 2, and Eq. (16) can be constructed from the following primitive function

$$\Psi=(\text{normalization constant})\times\{\Psi_{a,b}+\Psi_{b,a}\}\ ,$$
$$\Psi_{a,b}=\{(\pi_a{}^{+}+\nu\pi_b{}^{+})(\pi_b{}^{-}+\nu\pi_a{}^{-})(\pi_a{}^{-}-\nu\pi_b{}^{-})^2(\pi_b{}^{+}-\nu\pi_a{}^{+})^2$$
$$-(\pi_a{}^{-}+\nu\pi_b{}^{-})(\pi_b{}^{+}+\nu\pi_a{}^{+})(\pi_a{}^{+}-\nu\pi_b{}^{+})^2(\pi_b{}^{-}-\nu\pi_a{}^{-})^2\}(\sigma_{3g})^2(\sigma_{2u})^2(\sigma_{2g})^2(\sigma_{1u})^2(\sigma_{1g})^2\ , \tag{38}$$

ith $\nu=0.2420$.

Further the ionic character of the π-bond can be seen by reexpressing wave function (16) btained in Case 2 as

$$\Phi_{\sigma\text{-MO},\ \pi\text{-SO}}=(1/d_\pi)(\Phi_{\sigma\text{-MO},\ \pi\text{-HL}}+c_\pi\Phi_{\sigma\text{-MO},\ \pi\text{-ion}})\ ,$$

here $\Phi_{\sigma\text{-MO},\ \pi\text{-ion}}$ is the normalized wave inction having σ-MO, π-ionic character, and e have found $d_\pi=1.2093$ and $c_\pi=0.4573$.

ase 16 A′(*assuming* $S(2s, 2p\sigma)=S(2s, 1s)=0$)

Here we have calculated the energy using e wave function obtained by replacing σ_{3g} y the normalized symmetry orbital $(\sigma 2p)_g$ in onfiguration A and assuming the overlap tegrals, of $2p\sigma$ with $1s$ and $2s$ to be zero. his treatment is similar to that assumed by reenhow and Smith[10] in calculating the Q alues of the O_2 molecule and to that by Rosen d Ikehara[11] in treating the Li_2 molecule. he total energy obtained is -149.3898 a.u., d this is lower than that of Case 1 by .406 e.v.

The energies obtained by the various appromations are illustrated in Fig. 2. Matrix ements of Hamiltonian for the configurations nsidered in this section will be published sewhere[12].

5. Calculation of the Energies of the Excited States

As shown in Table II, we have eight excited ates by distributing six electrons into four MO's. The primitive function of the most

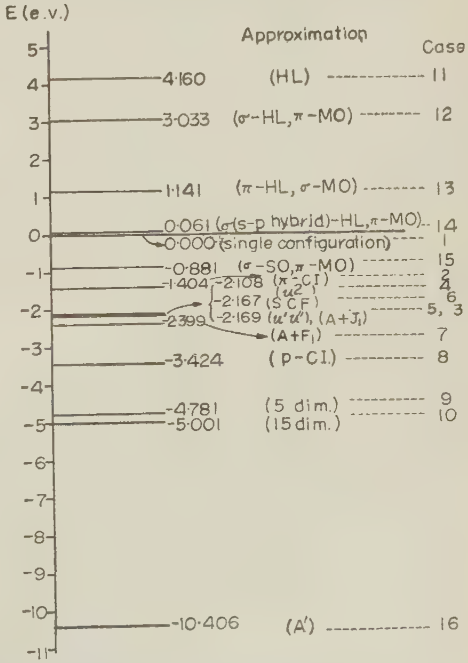

Fig. 2. Comparison of energy values of ground state.

important configuration for each excited state can be written down from Table II as

$$\begin{array}{lll}
{}^1\Delta_g & (\pi_g{}^+)^2(\pi_u{}^+)^2(\pi_u{}^-)^2 & \times(\sigma_{3g})^2(\sigma_{2u})^2(\sigma_{2g})^2(\sigma_{1u})^2(\sigma_{1g})^2 \\
{}^1\Sigma_g{}^+ & \frac{1}{2}\{\pi_g{}^+\pi_g{}^-(\pi_u{}^+)^2(\pi_u{}^-)^2 & \\
 & \quad +\text{complex conjugate}\} & \cdots \\
{}^1\Sigma_u{}^- & \frac{1}{\sqrt{2}}\{\pi_g{}^+\pi_u{}^-(\pi_g{}^-)^2(\pi_u{}^+)^2 & \\
 & \quad -\text{complex conjugate}\} & \cdots \\
{}^3\Delta_u & \pi_g{}^+\pi_u{}^+(\pi_g{}^-)^2(\pi_u{}^-)^2 & \cdots \\
\left.\begin{array}{l}{}^3\Sigma_u{}^+\\ {}^3\Sigma_u{}^-\end{array}\right\} & \frac{1}{\sqrt{2}}[\pi_g{}^+\pi_u{}^-(\pi_g{}^-)^2(\pi_u{}^+)^2 & \\
 & \quad \pm\text{complex conjugate}\} & \cdots \\
{}^1\Delta_u & \pi_g{}^+\pi_u{}^+(\pi_g{}^-)^2(\pi_u{}^-)^2 & \cdots \\
{}^1\Sigma_u{}^+ & \frac{1}{\sqrt{2}}\{\pi_g{}^+\pi_u{}^-(\pi_u{}^+)^2(\pi_g{}^-)^2 & \\
 & \quad +\text{complex conjugate}\} & \cdots\,.
\end{array} \qquad (39$$

For the $O_2{}^+$ molecular ion, the ground state, ${}^2\Pi_g$, and the three lower excited states, ${}^4\Pi_u$, ${}^2\Pi_u$, and ${}^4\Sigma_g{}^-$, are found by the spectroscopic measurements. For these states, the primitiv functions of the main configurations may be the following

$$\begin{array}{lll}
{}^2\Pi_g & \pi_g{}^+(\pi_u{}^-)^2(\pi_u{}^+)^2(\sigma_{3g})^2 & \times(\sigma_{2u})^2(\sigma_{2g})^2(\sigma_{1u})^2(\sigma_{1g})^2 \\
\left.\begin{array}{l}{}^4\Pi_u\\ {}^2\Pi_u\end{array}\right\} & \pi_g{}^+\pi_g{}^-\pi_u{}^-(\pi_u{}^+)^2(\sigma_{3g})^2 & \cdots \\
{}^4\Sigma_g{}^- & 1/2\{\pi_g{}^+\pi_g{}^-\sigma_{3g}(\pi_u{}^+)^2(\pi_u{}^-)^2 & \\
 & \quad -\text{complex conjugate}\} & \cdots
\end{array} \qquad (40$$

Table VI. Vertical excitation energies[a)] relative to the ground state ${}^3\Sigma_g^-$ of O_2 in e.v.

		Single configuration	(SCF)′	CI(π)	CI(π−σ)	obs.	Itoh-Ohno[b)]	Fumi-Parr[c)]	Moffitt[d)]
O_2^+	${}^4\Sigma_g^-$	14.765	16.184			18.3[e)]			
	${}^2\Pi_u$	14.410	15.859			17.7[e)]			
	${}^4\Pi_u$	10.303	11.752			16.8[e)]			
	${}^2\Pi_g$	10.108	11.040			12.5[e)]			
O_2	${}^1\Sigma_u^+$	18.452	18.969				14.5	13.6	
	${}^1\Delta_u$	15.817	16.334				11.7	11.7	
	${}^3\Sigma_u^-$	13.182	13.699	14.587	10.748	9.5[e)]	8.9	9.3	5.7
	${}^3\Sigma_u^+$	3.419	3.936	4.824	5.677	7.5[f)]	6.9	8.6	4.8
	${}^3\Delta_u$	3.293	3.810				6.7	8.4	
	${}^1\Sigma_u^-$	3.166	3.683	4.570	5.376	7.9[g)]	6.6	8.2	
	${}^1\Sigma_g^+$	2.969	2.969	1.423	1.986	1.6[e)]	2.3	1.8	1.7
	${}^1\Delta_g$	1.484	1.484	0.764	1.120	1.0[e)]	1.3	0.9	1.0
	${}^3\Sigma_g^-$	0	0	0	0	0[e)]	0	0	0

a) These values are those calculated at $R=2.3$ a.u.

b), c), and d) These values are those calculated at the equiliblium internuclear distance 2.282 a.u. See references (4), (8) and (2), respectively.

e) From references (13) and (2).

f) From reference (15).

g) From reference (14).

or each primitive function (39) or (40), we n determine the spin function Θ $(1, 2, \cdots,$ $-2r)$ uniquely, except the case of $^2\Pi_u(O_2^+)$. the latter case, we have adopted, as the in function of the main configuration, the ne in which the spins of two electrons in $_g^-$, and π_u^- couple to a triplet, because this nction is simple and its contribution to the est one was found to amount even to 99.96 %. This fact can be expected from the beginning, if we notice that the exchange integral volving π_g^- and π_u^- is considerably large mpared with the other exchange integrals volving π orbitals.

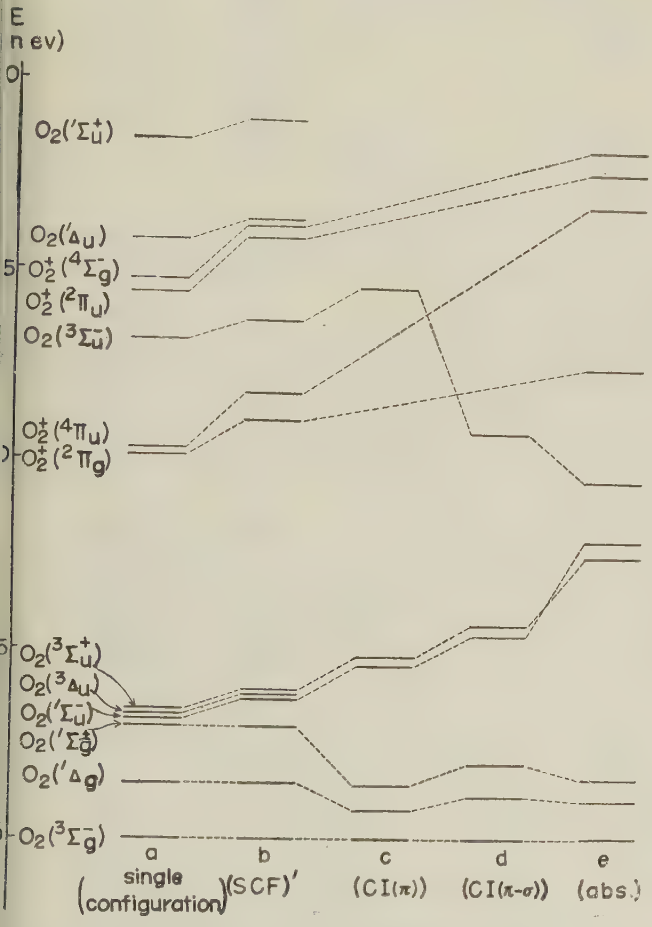

ig. 3. Comparison of energy levels calculated by various approximations with experiment.

Then we can construct the wave function om (39) and (40). Since these functions rrespond to that considered in Case 1 of the evious section, we shall denote them by A d give the formulae of H_{AA}'s in Appendix . 1). The values of H_{AA}'s are calculated at the fixed internuclear distance 2.30 a. u., using the same orbital exponents as used in the previous section. Numerical values of H_{AA} relative to the H_{AA} of the ground state of the O_2 molecule are given in column 2 in Table VI and also in Fig. 3a.

If, in the above calculation, we use SCF MO's obtained for the ground state instead of Schmidt-OMO's, we shall have a different approximation for the excited and ionized states. These calculations were actually performed and the results are shown in the column indicated by (SCF)′ in Table VI, and Fig. 3b.

As to the five excited states $^3\Sigma_u^-$, $^3\Sigma_u^+$, $^1\Sigma_u^-$, $^1\Sigma_g^+$, and $^1\Delta_g$ of the O_2 molecule, the spectroscopic data are available and various methods have hitherto been examined of calculating the respective excitation energies. Since these calculations assumed usually the π electron approximation, we also have, for the sake of comparison, carried out a similar calculation to Case 2 of the previous section for each state. The results are shown in the column indicated by CI(π) in Tables VI–X. In Tables VII–X, the coefficients of the linear combination and the total energy, relative to that of configuration A, for each state are given. In Table VI and in Fig. 3c. the excitation energies obtained by this π electron approximation are given.

Finally for the above five excited states we have performed the calculations which, as Case 9 for the ground state, are simple but may probably give the total energies in quite satisfactory agreement with fuller calculations. Configurations which are expected to play an important role can be easily selected from the experience in the previous section and are listed in column 1 in Tables VII–X. The rough meaning of the approximations of considering each configuration besides configuration A can be understood by seeing the last columns of the same tables. The matrix elements of the Hamiltonian operator for these configurations are to be published elsewhere[12].

Table VII. Configurations used in CI calculation and its results for $^1\Delta_g$ state.

i	Configurations[a)]										Coefficients c_i[b)]			Remarks[c)]
	π_u^+	π_u^-	π_g^+	π_g^-	σ_{3g}	σ_{3u}	σ_{2g}	σ_{2u}	σ_{1g}	σ_{1u}	Single configuration	CI(π)	CI(π-σ)	
A	2	2	2		2		2	2	2	2	1	0.9470	0.9464	
C	2		2	2	2		2	2	2	2		−0.3212	−0.2089	π-semiloc.
D	2	2	2			2	2	2	2	2			−0.0723	σ-semiloc.
G_1	$\underline{1}$	2	$\underline{1}$	2	$\underline{\underline{1}}$	$\underline{\underline{1}}$	2	2	2	2			−0.1426	σ-π
J	2	2	2		2	1	2	1	2	2			−0.1873	s-p hybrid.
										ΔE[d)]	0	−0·0781	−0.1891	

a) and b) See the caption in Table IV.

c) The physical meaning of mixing the respective configuration to configuration A is qualitativel shown in the remarks column, in terms of π-semilocalication, σ-semilocalization, σ-π interactio and s-p hybridization which are explained in Section 4.

d) ΔE is the difference of the calculated total energy for each case, E, from that of the single co figuration E_0, in atomic unit; that is, $\Delta E = E - E_0$. Here $E_0 = -148.9528$ a.u., including the nuclea repulsion. $|\Delta E|$ means the depression of energy due to CI.

Table VIII. Configurations used in CI calculation and its results for $^1\Sigma_g^+$ state.

i	Configurations[a)]										Coefficients c_i[b)]			Remarks[c)]
	π_u^+	π_u^-	π_g^+	π_g^-	σ_{3g}	σ_{3u}	σ_{2g}	σ_{2u}	σ_{1g}	σ_{1u}	Single configuration	CI(π)	CI(π-σ)	
A	2	2	1	1	2		2	2	2	2	1	0.9309	0.9333	
B	1	1	2	2	2		2	2	2	2		−0.3653	−0.2683	π-semiloc.
E	2	2	1	1		2	2	2	2	2			−0.0813	σ-semiloc.
J_1	$\underline{1}$	2	2	$\underline{1}$	$\underline{\underline{1}}$	$\underline{\underline{1}}$	2	2	2	2			0.1109	σ-π
N_1	2	2	$\underline{1}$	$\underline{1}$	2	$\underline{\underline{1}}$	2	$\underline{\underline{1}}$	2	2			−0.1952	s-p hybrid.
										ΔE[d)]	0	−0.1084	−0.2118	

a) and b) See the caption in Table IV.

c) and d) See the caption in Table VII. For this state, $E_0 = -148.8982$ a.u.

Table IX. Configurations used in CI calculation and its results for $^1\Sigma_u^-$ state.

i	Configurations[a)]										Coefficients c_i[b)]			Remarks[c)]
	π_u^+	π_u^-	π_g^+	π_g^-	σ_{3g}	σ_{3u}	σ_{2g}	σ_{2u}	σ_{1g}	σ_{1u}	Single configuration	CI(π)	CI(π-σ)	
A	2	1	1	2	2		2	2	2	2	1	1	0.9695	
B	2	1	1	2		2	2	2	2	2			−0.1136	σ-semiloc.
I_1	2	$\underline{1}$	$\underline{1}$	2	2	$\underline{\underline{1}}$	2	$\underline{\underline{1}}$	2	2			−0.2170	s-p hybrid.
										ΔE[d)]	0	0	−0·0945	

a) and b) See the caption in Table IV.

c) and d) See the caption in Table VII. For this state, $E_0 = -148.8909$ a.u.

The coefficients of configurations and the total energy relative to that of configuration A, obtained for each state, are given in the column indicated by CI (π-σ) in the same tables. The excitation energies are also listed in the column indicated by CI (π-σ) in Table VI, and in Fig. 3d. The observed values of the excitation energies are written in column 6 in Table VI, and in Fig. 3e. They have been derived by fitting the spectroscopic data to Morse curves. We notice here that the real potential curves cannot be reproduced very closely by the Morse curves, so that some ambiguity is left for these experimental values.

Table X. Configurations used in CI calculation and its results for ${}^3\Sigma_u^+$ and ${}^3\Sigma_u^-$ states.

i	Configurations a)										Coefficients c_i b)						Remarks c)
											${}^3\Sigma_u^+$			${}^3\Sigma_u^-$			
	π_g^+	π_g^-	π_u^+	π_u^-	σ_{3g}	σ_{3u}	σ_{2g}	σ_{2u}	σ_{1g}	σ_{1u}	Single configuration	CI(π)	CI(π-σ)	Single configuration	CI(π)	CI(π-σ)	
A	1	2	2	1	2		2	2	2	2	1	1	0.9707	1	1	0.9087	
B	1	2	2	1		2	2	2	2	2			−0.1143			0.0025	σ-semiloc.
E_1	$\bar{1}$	$\bar{1}$	2	2	$\underline{1}$	$\underline{1}$	2	2	2	2						0.3447	σ-π
F_1	2	2	$\bar{1}$	$\bar{1}$	$\underline{1}$	$\underline{1}$	2	2	2	2						0.1855	σ-π
G_1	$\bar{1}$	2	2	$\bar{1}$	2	$\underline{1}$	2	$\underline{1}$	2	2			−0.2113			−0.1450	s-p hybrid.
										ΔE d)	0	0	−0.0928	0	0	−0.2652	

a) and b) See the caption in Table IV.

c) and d) See the caption in Table VII. For ${}^3\Sigma_u^+$ state $E_0=-148.8816$ a.u., and for ${}^3\Sigma_u^-$ state $E_0=-148.5228$ a.u.

specially for the ${}^3\Sigma_u^-$, ${}^1\Sigma_u^-$14), and ${}^3\Sigma_u^+$15) tates, whose potential curves are very steep n the neighbourhood of the equiliblium disnce of the ground state, the resulting error ight possibly be rather large.

6. Molecular Quantities

The wave functions obtained by the above alculations will serve to calculate the physial quantities of the O_2 molecule. Further by omparing these results with the experiments, e can study the validity, usefulness, and eatures of our approximations. Among the onstants of the O_2 molecule, we have conidered here the dissociation energy D_e, moleular quadrupole moment Q, magnetic yperfine structure parameters, $\langle\psi^2(0)\rangle$ and $P_2/r^3\rangle$, oscillator strengths f_{lk}, and diamagnec second order Zeeman term χ_{dia}16). Also r the polarizability α we have tried a rough stimation. The necessary matrix elements, eferring to the configurational wave functions efined earlier, can be calculated easily and eir numerical values are given elsewhere12).

1) *Dissociation Energy D_e*

In principle, the dissociation energy D_e can e obtained by

$$D_e=E(R_\infty)-E(R_e)\ , \tag{41}$$

here $E(R_\infty)$ is the energy of a pair of nonteracting atoms in the ground state, and (R_e) is the total energy of the molecule at e equiliblium internuclear distance. In aplying (41), we must remark that very accurate alues of $E(R_\infty)$ and $E(R_e)$ are required, since ese quantities are of comparable magnitude d both are very large compared with D_e. However, the calculated value of $E(R_e)$ has usually an error much larger than the magnitude of D_e. Therefore, to obtain a reasonable value of D_e, it is inevitably necessary to find a suitable value of $E(R_\infty)$ that is calculated in the same degree of approximation as $E(R_e)$.

Now we shall here adopt for $E(R_e)$, the values calculated at $R=2.30$ a.u. by using the various approximations in Section 4, though the observed equilibrium internuclear distance is slightly smaller than 2.3 a.u. Then it seems appropriate, for our purpose, to use the value of $E(R_\infty)$ calculated by the same atomic orbitals (1) as were used for the calculation of $E(R_e)$. The values of D_e obtained in such a manner are listed in Table XI. D_e obtained by our best wave function (Case 10) is 3.629 e.v. compared with the observed value of 5.08 e.v. Further Table XI shows that all the calculated values of D_e, exept that of Case 16, do not exceed the observed value. This means that the approximation for the calculation of $E(R_\infty)$ is, in our case, better than that of $E(R_e)$. In the exceptional Case 16, D_e calculated is very large compared with the observed one, since in this case the exchange repulsion between the valence electrons and the closed shell electrons is neglected.

(2) *Molecular Quadrupole Moment of the O_2 Molecule Q*

Though the O_2 molecule is non-polar, it can possess the quadrupole moment

$$\begin{aligned} Q&=\int r^2(3\cos^2\theta-1)\rho dv \\ &=8R^2-2\langle z^2\rangle+\langle x^2+y^2\rangle\ , \\ \rho&=\rho_n+\rho_{el}\ . \end{aligned} \tag{42}$$

Table XI. Molecular constants.

Case		D_e a) (e.v.)	$\langle x^2+y^2\rangle$ b) / R^2	$\langle z^2\rangle$ b) / R^2	Q b) (a.u.)	$\langle P_2/r^3\rangle$ c) (a.u.)	$\langle\psi^2(0)\rangle$ d) (a.u.)	χ_{dia} e) cm³/mol
1	(A)	−1.372	2.3183	5.1448	0.152	−0.8504	0	−31.28
2	π-CI	0.032	2.3142	5.1527	0.046	−0.8359	0	−31.29
3	(A+J₁)	0.797	2.3108	5.3186	−1.726	−0.8504	0	−31.97
4	u^2	0.736	2.3108	5.3204	−1.745	−0.8504	0	−31.98
5	$u'u''$	0.797	2.3108	5.3182	−1.723	−0.8504	0	−31.97
6	SCF	0.795	2.3108	5.3214	−1.757	−0.8504	0	−31.99
7	(A+F₁)	1.027	2.3156	5.1453	0.132	−0.8453	0	−31.27
8	p-CI	2.052	2.3082	5.1340	0.213	−0.8346	0.0025 (0.0022) f)	−31.27
9	(5 dim.)	3.409	2.3100	5.2903	−1.431	−0.8435	0	−31.85
10	(15 dim.)	3.629	2.3091	5.2994	−1.533	−0.8589	0.1948 (0.1732) f)	−31.89
11	(HL)	−5.532	2.2896	5.1692	−0.259	−0.7784	0	−31.26
12	(σ-HL, π-MO)	−4.405	2.3101	5.1297	0.268	−0.8504	0	−31.1
13	(π-HL, σ-MO)	−2.513	2.2978	5.1843	−0.375	−0.7784	0	−31.36
14	(σ(s-p hybrid.)-HL, π-MO)	−1.433	2.3039	5.3499	−2.094	−0.8504	0	−32.08
15	(σ-SO, π-MO)	−0.491	2.3174	5.1431	0.165	−0.8504	0	−31.27
16	(A′)	9.034	2.3231	4.8731	3.053	−0.8504	0	−30.16
	obs.	5.08			$\lvert Q\rvert<0.82$	−1.32	0.187	

a) See Eq. (41). b) See Eq. (42). c) See Eq. (43). d) See Eq. (44). e) See Eq. (49).
f) The values within parenthesis are those obtained by using the H-F orbital. See also subsection (3) of § 6.

Here ρ_n and ρ_{el} are the charge densities of the nuclei and the electrons respectively, r is the distance to the charge from the center of the molecule, θ is the angle between the symmetry axis and r, and the meaning of x, y, and z is explained in Fig. 1. Further, $\langle z^2\rangle=\int z^2\rho_{el}dv$ and $\langle x^2+y^2\rangle=\int(x^2+y^2)\rho_{el}\,dv$. We shall here study this quantity.

In Table XI, the values $\langle x^2+y^2\rangle/R^2$, $\langle z^2\rangle/R^2$, and Q obtained with the use of the various approximations explained earlier are given. From this table we can see that the values of Q calculated, except the one of Case (16), can be classified into two groups, namely, one group consisting of values around 0.1 and the other one around −1.5, and that the latter values are obtained only by the use of the wave functions taking into account s-p hydridization. Table XI shows, moreover, that the value of $\langle x^2+y^2\rangle/R^2$ does not vary appreciably from one approximation to another. So the said difference of the values of Q is chiefly ascribed to that of $\langle z^2\rangle/R^2$. This difference of $\langle z^2\rangle/R^2$ can be easily understood on the valence bond theory as follows. As two O atoms approach each other, two $2p\sigma$ electrons suffer a positive hybridization but four $2s$ ones suffer correspondingly a negative hybridization, and so the net charge density in the outer region becomes larger than that obtained without s-p hybridization.

Next we shall consider the value of Q in Case 16, which is much the largest of all. From Table XI, we can see that this situation comes mainly from the fact that $\langle z^2\rangle/R^2$ is by far the smallest of all. This implies that the charge density of the symmetry orbital $(\sigma 2p)_g$ is inside of that of Schmidt-OMO σ_{3g}. Greenhow and Smith[10] have also performed a similar calculation by neglecting $1s$ electrons, and have obtained $Q=3.1103$ a.u. for the case of no s-p hydridization and this value agrees well with our result. On this occasion, we shall point out a strange property of Schmidt-OMO. By comparing the Q value of Case 12 or Case 15 with that of Case 1, it can be found that the former are larger than that of the latter. This means that the charge density of the σ_{3u} orbital is larger than that of σ_{3g} in the region between two nuclei.

Now the value of Q obtained by our best wave function (Case 10) is −1.533. On the her hand the observed value is reported by ownes and Schawlow,17), and Gordy, Smith, nd Trambarulo18) as $|Q|<0.82$ a.u. Accord- ngly the agreement of the theory with the bservation seems not to be so satisfactory. his does not, however, necessarily lead to the onclusion that our calculation should be criti- ized. As a matter of fact, the observed value bove quoted is open to some questions, be- ause this value has been derived from the ne width measurement of the microwave pectrum, which is accompanied with the dif- culty of the experimental technique and of he analysis of the measurement. Therefore, nore refined observations and their analysis re desirable.

3) *Magnetic Hyperfine Structure Parameters* $\langle P_2/r^3\rangle$ *and* $\langle\psi^2(0)\rangle$

From the microwave absorption measure- nents on $O^{16}O^{17}$ gas, Miller and Townes19) letermined the values of the following quan- ities

$$\left\langle\frac{P_2}{r^3}\right\rangle=\int\left(\frac{3\cos^2\theta_a-1}{2r_a{}^3}\sigma\right)\rho(\boldsymbol{r}_a,\sigma)d\tau\ , \tag{43}$$

nd

$$\langle\psi^2(0)\rangle=\int\{\delta(\boldsymbol{r}_a)\sigma\}\rho(\boldsymbol{r}_a,\sigma)\,d\tau\ , \tag{44}$$

vhere $\boldsymbol{r}_a$ is the position vector with its origin aken at the nucleus A, θ_a is the angle bet- veen $\boldsymbol{r}_a$ and the symmetry axis, and σ is the pin variable. Further $\rho(\boldsymbol{r}_a,\sigma)$ is the total umber density of electrons at $(\boldsymbol{r}_a,\sigma)$ which is ummarized as τ. In this subsection these uantities will be investigated.

As can be seen from (43) and (44), only the npaired orbitals contribute to the values of $P_2/r^3\rangle$ and $\langle\psi^2(0)\rangle$. Moreover, π electrons o not contribute to $\langle\psi^2(0)\rangle$. Therefore $\langle\psi^2(0)\rangle$ anishes in the simple valence bond theory or he single configuration of MO (Case 1) and as a finite value only after introducing con- gurations which have unpaired σ-orbitals. 'hus $\langle\psi^2(0)\rangle$ depends on a very "fine-struc- ure" of the electronic wave function and rovides an important clue for the study of he configurational mixing.

In the paper succeeding to that of Miller nd Townes, they and one of us, Kotani20), ave already estimated the value of $\langle P_2/r^3\rangle$ rom the standpoint of the simple valence bond heory. They considered that the experimental value of this quantity could be explained approximately by taking into account the contribution from the unpaired electron, which is accomodated in a π AO of the nucleus considered˙ Then it was shown that

$$\left\langle\frac{P_2}{r^3}\right\rangle=-\frac{1}{5}\int\pi_a{}^*(1)\frac{1}{r_a{}^3}\pi_a(1)dv$$
$$=-\frac{1}{5}\left\langle\frac{1}{r^3}\right\rangle_{av}, \tag{45}$$

and it amounts to 71 and 78 percent of the observed value by the use of the Hartree-Fock atomic orbital21) and Yamanouchi-Horie's data22) based on the atomic fine structure analysis, respectively. If we now use the Slater-type π orbital employed in our paper instead of the Hartree's one, we have 60 percent of the observed value. According to Miller, Townes, and Kotani20), the agreement with the experiment may be improved by a few percent, if the overlapping of atomic orbitals is taken into account.

Kleiner23) also calculated $\langle P_2/r^3\rangle$ and $\langle\psi^2(0)\rangle$ by the use of Meckler's wave function5). He found that the calculated value of $\langle P_2/r^3\rangle$ is almost determined by configuration A of Table IV, which, however, afforded only 27 percent of the observed value. Kleiner showed, however, that if the Hartree-Fock AO's were adopted instead of the Gaussian-type AO's in calculating the integral $\int\pi_a{}^*\frac{1}{r_a{}^3}\pi_a dv$, this result could be improved to 85–90 percent of the observed value. The inclusion of the remaining eight configurations did not alter the matter seriously and rather made the agreement worse. The value of $\langle\psi^2(0)\rangle$ found by Kleiner using Meckler's wave function was too small to explain the experiment. If the Hartree-Fock AO's were used instead of the Gaussian-type orbitals, the result was improved appreciably, but still accounted only for at most one percent of the observed value ($\langle\psi^2(0)\rangle<0.001$).

Since the previous calculations are only a rough estimation or based on the Gaussian-type AO's we have tried to study these quantities again with the use of the wave functions described in Section 4. The results of calculations are summarized in Table XI.

The differences between the values of $\langle P_2/r^3\rangle$ calculated by various approximations are rather small and indeed most of the contribution to this quantity comes from configuration A. More precisely speaking, the values of $\langle P_2/r^3\rangle$, in Cases, 1, 3, 4, 5, 6, 12, 14, 15, and 16, come solely from unpaired $\pi_g{}^+$ and $\pi_g{}^-$ electrons and coincide with one another. This situation does not change appreciably for the other cases, in which the mixing of the configurations with the unpaired orbitals different from those of configuration A is taken into account. The value of $\langle P_2/r^3\rangle$ obtained is about 65 percent of the observed one and the difference from 60 percent estimated by the single atom approximation (45) is due to the overlapping of orbitals. If we assume that the overlapping effect can be taken into account by multiplying the factor 65/60 to the results of the single atom approximation, Miller, Townes, and Kotani's values are improved to 77 and 85 percent from 71 and 78 percent, respectively. These values are a little smaller than that estimated by Kleiner. The remaining discrepancy of about 15% might be expected to result from contraction of π orbitals in a molecule due to the molecular formation. Then it requires the change of the orbital exponent δ_2 from 2.283 to 2.410, and it seems difficult energetically to explain the change of δ_2 of this magnitude. We might well expect another possiblity of eliminating this discrepancy on the fact that the ground state of O_2 is half-ionic in character and the orbitals in the positive ion O^+ will probably contract compared with those in neutral atom O, even if embedded in the molecule. A rough estimation of this effect shows that the discrepancy can be reduced to 5%.

The situation is quite different for the case of $\langle\psi^2(0)\rangle$. We can see in Table XI that $\langle\psi^2(0)\rangle=0$ except Cases 8 and 10. This is because there is no unpaired σ orbital in all the configurations except F_2, F_3, J_3, M_2, and M_3 of Table IV. The value obtained by the p electron configurational wave function (Case 8) which includes only F_2 and F_3 among the above five configurations, is far smaller than that observed and agrees in its order of magnitude with the Kleiner's estimation. On the other hand the fifteen configurational wave function (Case 10) gives a quite satisfactory result. In Table XII, the contributions of each configuration and of their cross terms are shown. From this table we can see that the cross terms with the main configuration A give an important contribution. A similar fact found also by Abragam, Horowitz, and Price in connection with a similar problem concer ing a paramagnetic ion. Further we can s that the contribution of configurations F_2 ar F_3 is small compared with that of J_3 and M in spite of the fact that the coefficients them in the fifteen configurational wave fun tion are almost comparable. However this ca be explained as follows. Since the values the nodeless Slater-type $2s$ and $2p$ orbita vanish at the nucleus, the values of Schmid OMO's at the nucleus are mainly due to th $1s$ orbital involved in them. Then from th coefficients of Schmidt-OMO's (3), we can ex pect that $|\sigma_{2u}(0)|$ and $|\sigma_{2g}(0)|$ are much large than $|\sigma_{3g}(0)|$ and $|\sigma_{3u}(0)|$. Since, however, un paired σ orbitals considered are σ_{3g} and σ_{3u} i F_2 and F_3, while they are σ_{2u} and σ_{3u} in J and σ_{2g} and σ_{3u} in M_3, the above situation i what should be so. Thus we can see that fo $\langle\psi^2(0)\rangle$, the configurations not so importan for the energy, make remarkable contributions Hence a satisfactory agreement of our resul with the observed value seems a little for tuitous.

Table XII. Numerical details of calculation o $\langle\psi^2(0)\rangle$ (values of $c_i{}^2\langle\psi^2(0)\rangle_{ii}$ and $2c_ic_j\langle\psi^2(0)\rangle$ $(i>j)$).[a]

ij	Case 8		Case 10	
	Slater	*H-F*[b]	Slater	*H-F*[b]
AJ_3			0.12839	0.11401
F_1F_3	0.00188	0.00166	0.00164	0.00145
F_2F_2	0.00051	0.00045	0.00027	0.00024
F_3F_3	0.00009	0.00008	0.00009	0.00008
HJ_3			0.00008	0.00006
J_1J_3			0.05838	0.05202
J_3J_3			0.00520	0.00463
M_1M_3			−0.00070	−0.00063
M_2M_2			0.00074	0.00067
M_3M_3			0.00012	0.00010
F_1M_3			0.00068	0.00062
F_2M_2			−0.00027	−0.00024
F_3M_1			0.00024	0.00021
F_3M_3			0.00006	−0.00006
Sum	0.0025	0.0022	0.1948	0.1732

a) c_i's are the expansion coefficients given i Table IV.

b) From reference (21).

In this respect it is interesting to calculat

$\psi^2(0)\rangle$ by using some other suitable AO's an the Slater's ones. We adopt here the artree-Fock (H-F) AO's[21] which are likely to ve a more reliable result of $\langle\psi^2(0)\rangle$ than the ater's ones. It is difficult, however, to construct the wave function built from the H-F AO's including the CI, by carring out a variational calculation. Accordingly a simplified calculation is attempted here. Namely, the expressions for $\langle\psi^2(0)\rangle$ associated with the p

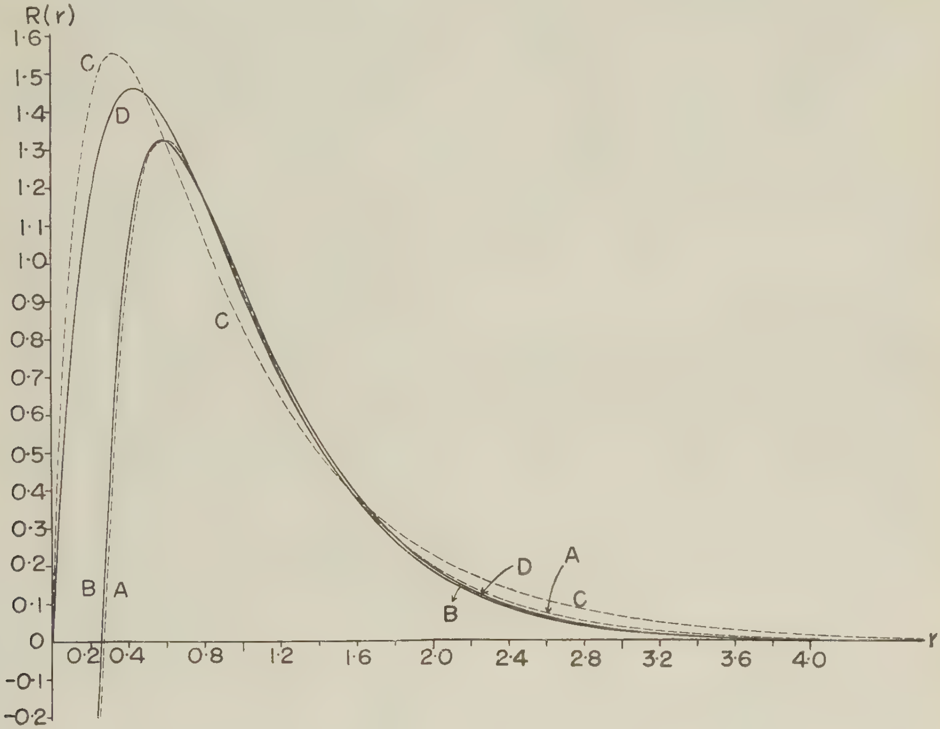

(a)

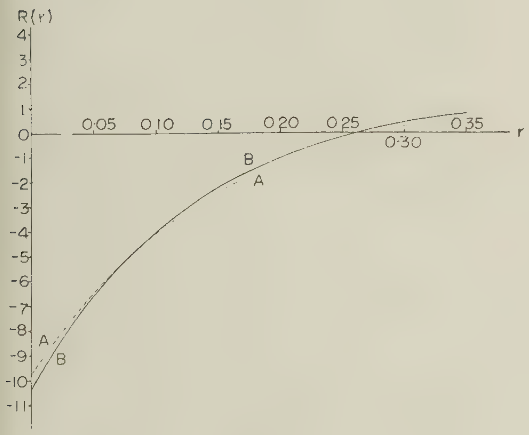

(b)

Fig. 4. Comparison of normalized Slater type radial functions $R(2\mathring{s})$ and $R(2p\pi)$ used in this paper with the corresponding Hartree-Fock functions. A: $R(2\mathring{s})$ of Hartree-Fock, B: $R(2\mathring{s})$ of Slater, C: $R(2p)$ of Hartree-Fock, D: $R(2p)$ of Slater. r is measured in a.u.

lectron configurational and fifteen configu- ational wave functions are at first written ı terms of the values of the orthogonalized later's AO's, 1s, 2$\mathring{s}$, and 2$p\sigma$ at the nucleus onsidered, which are then replaced by those of he corresponding H-F AO's. This procedure may be justified, provided that coefficients of the configurational wave functions and the values of the overlapping integrals between the AO's do not change appreciably for the case of the H-F AO's from the case of the Slater's AO's. The values of $\langle\psi^2(0)\rangle$ calculated by the method just explained are 0.0022 and 0.1732 for the p electron configurational and fifteen configurational wave functions, respectively, while the corresponding values obtained previously are 0.0025 and 0.1948. The reason for this good agreement of the values obtained by the different methods is that the values of the Slater's $2\mathring{s}$ AO and the H-F $2s$ AO are not so different even in the neighbourhood of the nucleus. This situation can be seen from Fig. 4, where the radial parts of the H-F and Slater's AO's are shown. The contribution to the value of $\langle\psi^2(0)\rangle$ of each configuration and their cross parts is shown in Table XII.

(4) *Oscillator Strengths f_{lk}*

The oscillator strength f_{lk} with respect to the transition from a state k to an energetically higher level l is expressed, in atomic units, as

$$f_{lk}=2/3\cdot|(\sum_i \boldsymbol{r}_i)_{lk}|^2(\Delta E)_{lk}\ , \qquad (46)$$

where $(\Delta E)_{lk}=E_k-E_l$. Eq. (46) can also b expressed as

$$f_{lk}=2/3\cdot|(\sum_i \nabla_i)_{lk}|^2/(\Delta E)_{lk}\ . \qquad (47)$$

Accordingly, in calculating f_{lk} we may use an of these equations. When approximate wave functions are used these two equations give in general, different results. The method o calculation by (46) is called the dipole length method and that by (47) is called the dipol velocity method.

Concerning the nine states of O_2 considere in this paper, neither x nor y components o the dipole length and velocity introduce an transition, but their z components give rise to the transitions ${}^3\Sigma_g{}^- - {}^3\Sigma_u{}^-, {}^1\Delta_g - {}^1\Delta_u$, an ${}^1\Sigma_g{}^+ - {}^1\Sigma_u{}^+$, all of which correspond to th one electron jump $\pi_u{}^\pm - \pi_g{}^\pm$. We have calculated the f-values concerning these transition by using four kinds of approximations, single configuration, (SCF)′, CI(π), and CI($\pi-\sigma$), explained in the calculation of the excitation energies. These values are listed in Table XIII. Column 4 shows the values of $(\Delta E)_{lk}$, found by the calculation of the previous section. $1/R\langle z\rangle_{lk}$ and $R\langle d/dz\rangle_{lk}$ are given in columns 5 and 6. f_{lk} obtained by the dipole length method (46) and the dipole velocity method (47) are shown in the next two columns In the last column of Table XIII are shown the values of $\langle\Delta E\rangle_{lk}$ which have been obtained

Table XIII. Oscillator strength f_{lk}.

k	l	Method	$(\Delta E)_{lk}$[a]	$\frac{\langle z\rangle_{lk}}{R}$[b]	$R\langle d/dz\rangle_{lk}$[c]	f_{lk} (d)	f_{lk} (e)	Obs.	$(\Delta E)_{lk}$[f]
${}^3\Sigma_g^-$	${}^3\Sigma_u^-$	Single configuration	0.4846	0.7143	0:6379	0.872	0.106		0.1688
		(SCF)′	0.5035	0.7143	0.6379	0.907	0.102		0.1688
		CI(π)	0.5362	0.4950	0.7864	0.464	0.145		0.3003
		CI($\pi-\sigma$)	0.3951	0.3303	0.1806	0.152	0.010		0.1033
		Obs.	0.35					0.19[g]	0.35
${}^1\Delta_g$	${}^1\Delta_u$	Single configuration	0.5269	−0.7143	−0.6379	0.948	0.097		0.1688
		(SCF)′	0.5458	−0.7143	−0.6379	0.983	0.094		0.1688
		Obs.	~					~	~
${}^1\Sigma_g^+$	${}^1\Sigma_u^+$	Single configuration	0.5691	0.7143	0.6379	1.025	0.090		0.1688
		(SCF)′	0.5881	0.7143	0.6379	1.059	0.087		0.1688
		Obs.	~					~	~

a), b), c) and f) measured in atomic units.
d) by the dipole length method (Eq. (46)).
e) by the dipole velocity method (Eq. (47)).
f) obtained by Eq. (48).
g) From reference (25).

om the following formula

$$\langle \Delta E\rangle_{lk}=\left|\left(\sum_i \nabla_i\right)_{lk}/r_{lk}\right|\ . \tag{48}$$

rom this table, we can see that the configu- tional interaction reduces the values of $\langle z\rangle$ nd the corresponding f_{lk}, and that for the tter quantity this reduction is very remark- ble. The observed value of f_{lk} for ${}^3\Sigma_g^-$ -${}^3\Sigma_u^-$ (Schuman-Runge bands) was reported s 0.19[25] and this agrees well with that cal- ulated by the use of the dipole length method nd CI(π-σ). It is known that the similar tuation occurs in the ${}^1A_{1g}-{}^1E_{1u}$ transition of e C_6H_6[26] molecule and the ${}^1A_{1g}-{}^1B_u$ transi- on of the C_4H_6[27] molecule. Concerning the ipole velocity method, we mention here that, ough we obtained f values of reasonable agnitude by the single configuration, (SCF)′, nd CI(π), CI(π-σ) makes the result, unfortu- ately, very wrong. The effect of the con- gurational interaction to ΔE obtained by (48) also not so satisfactory. Further we can e that f-values from the dipole length ethod are much larger than those from the elocity method. The studies on other mole- ules by several authors[1b)28)], however, show at this is not always the case.

) *Diamagnetic Second Order Zeeman Term* $\chi_{\rm dia}$

The temperature independent part of the usceptibility is given as the sum of two rms, the paramagnetic high-frequency term $_{\rm H\text{-}F}$ and the diagmagnetic second order eeman term $\chi_{\rm dia}$. Tinkham and Strandberg[16] stimated the value of $\chi_{\rm H\text{-}F}$ with the use of e data on the rotational magnetic moment f the the O_2 molecule and obtained (24.6 ± 1.7) $\times10^{-6}$ cm³/mol for it. $\chi_{\rm dia}$, on the other hand, given by the following formula

$$\chi_{\rm dia}=-0.7922\times\langle r^2\rangle\times10^{-6}\ {\rm cm^3/mol}\ , \tag{49}$$

here $\langle r^2\rangle$ is measured in atomic units.

With the use of Meckler's wave function[5] nd (49), Tinkham and Strandberg obtained -29.5×10^{-6} cm³/mol as the value of $\chi_{\rm dia}$, so e temperature independent part of the usceptibility estimated by them becomes $-4.9\pm1.7)\times10^{-6}$ cm³/mol.

Now we have calculated $\chi_{\rm dia}$ by using the arious approximate wave functions considered Section 4 and the results are given in Table I. $\chi_{\rm dia}$ calculated by our fifteen configura- onal wave function together with $\chi_{\rm H\text{-}F}$ estimated by Tinkham and Strandberg, yields the temperature independent part of the susceptibility of -7.3×10^{-6} cm³/mol. This value is of the same order as that of Tinkham and Strandberg, and seems to support their interpretation that the departure of the observed total susceptibility from Curie's law, found by Woltjer, Coppoolse, and Wiersma[29], would be due to the experimental error.

(6) *Polarizabilities $\alpha_{//}$ and $\alpha_\perp$*

The Hamiltonian of a molecule in the presence of a static field $\boldsymbol{F}$ is written down as follows

$$H=H_0+F\left(\frac{\boldsymbol{F}}{F}\cdot\sum_i \boldsymbol{r}_i\right), \tag{50}$$

where H_0 is the field free Hamiltonian of the molecule (4). Following the second order perturbation theory, the total energy E is expressed to the second order of F as follows

$$E=E_0-F^2\sum_n\frac{1}{E_n-E_0}\left|\left(\frac{\boldsymbol{F}}{F}\cdot\sum_i\boldsymbol{r}_i\right)_{n0}\right|^2. \tag{51}$$

Therefore the polarizability parallel to the molecular axis, $\alpha_{//}$, and that perpendicular to it, $\alpha_\perp$, become

$$\alpha_{//}=2\sum_n\frac{|(\sum_i z_i)_{n0}|^2}{E_n-E_0}\ , \tag{52.1}$$

$$\alpha_\perp=2\sum_n\frac{|(\sum_i x_i)_{n0}|^2}{E_n-E_0}\ . \tag{52.2}$$

In order to calculate α by means of Eq. (52), we have to know, in advance, the exact energy values and the corresponding wave functions of all the eigenstates of H_0. Therefore, the straightforward application of Eq. (52) is practically impossible. Hence we have here tried an approximate calculation by taking into account only the nine states of O_2 considered in Section 5 and using the eigenvalues and the eigen-functions obtained there by the various approximations. The values of the polarizabilities calculated by this procedure are listed in the column indicated by "perturbation" in Table XIV. The observed values are also added in the same table.[30] From this table we see that $\alpha_{//}$ decreases appreciably by introducing the CI. Further from the fact that $\alpha_{//}$ of CI(π–σ) is very small compared with the observed value and all the calculated values of $\alpha_\perp$ vanish, it seems necessary to take into account other states besides the above mentioned nine states. In

Table XIV. Polarizabilities (in a. u.)

	Method	Perturbation[a)]		Kirkwood's approximation[b)]			Obs.[c)]
		α	$<\Delta E>$ (a.u.)	$\alpha(N=16)$	$\alpha(N=12)$	$\alpha(N=6)$	α
//	Single configuration	11.140	0.995	15.634	20.548	11.195	
	(SCF)′	10.720	0.888	12.464	16.368	11.195	
	CI(π)	4.835	0.824	10.716	14.044	4.996	
	CI(π-σ)	2.922	0.661	6.908	9.017	7.638	
	Obs.						15.9
⊥	Single configuration	0	0.889	3.323	4.311	8.157	
	(SCF)′	0	0.897	3.378	4.396	8.157	
	CI(π)	0	0.888	3.314	4.298	8.105	
	CI(π-σ)	0	0.894	3.358	4.356	1.133	
	Obs.						8.2

a) See Eqs. (51), (52), and (53).
b) See Eqs. (54) and (55).
c) From reference (30).

order to investigate this situation, we estimated the values of $(\Delta E)_{//}$ and $(\Delta E)_{\perp}$ defined by the relations

$$\alpha_{//}=2\,\frac{1}{(\Delta E)_{//}}|\{(\sum_i z_i)^2\}_{00}|\,, \tag{53.1}$$

$$\alpha_{\perp}=2\,\frac{1}{(\Delta E)_{\perp}}|\{(\sum_i x_i)^2\}_{00}|\,, \tag{53.2}$$

using the observed values of $\alpha_{//}$ and $\alpha_{\perp}$, and the calculated values of $|\{(\sum_i z_i)^2\}_{00}|$ and $|\{(\sum_i x_i)^2\}_{00}|$. These values of (ΔE)'s represent some average values of the energy denominators (E_n-E_0) of Eq. (52), and suggest that we must take into account excited levels higher than the ground state at least by these amounts. In Table XIV are listed these calculated values.

The polarizabilities can be derived also by variational treatment. In fact, the simplest method along this line was given by Kirkwood[31)]. The perturbed wave function adopted is

$$\Phi=\left\{1+aF\left(\frac{F}{F}\cdot\sum_i r_i\right)\right\}\Phi_0\,, \tag{54}$$

where a is a parameter to be determined by the energy minimum condition, and Φ_0 is the eigenfunction of the unperturbed Hamiltonian H_0. By picking up the coefficients of F^2 in the total energy expression, we obtain the following formulae for the polarizabilities, $\alpha_{//}$ and $\alpha_{\perp}$,

$$\alpha_{//}=\frac{4}{N}[\{(\sum_i z_i)^2\}_{00}]^2\,, \tag{55.1}$$

$$\alpha_{\perp}=\frac{4}{N}[\{(\sum_i x_i)^2\}_{00}]^2\,, \qquad (55.$$

where N is the number of the electrons co sidered. Thus in Kirkwood's approximatio we can calculate the polarizabilities from on the knowledge of the wave function of th ground state. Using the wave functions single configuration, (SCF)′ CI(π), and CI(π– for the ground state, we have calculated α and $\alpha_{\perp}$, and the results are listed in th column indicated by $N=16$ in Table XIV. Fro these values we can see that

(i) the effect of the CI on $\alpha_{//}$ is appreciab also here, while that on $\alpha_{\perp}$ is not so importan and

(ii) $\alpha_{//}$ and $\alpha_{\perp}$ obtained for our best wa function, CI(π–σ), are very small compare with the observed values. However, this di crepancy may be ascribed to some extent the fcat that, in Kirkwood's approximatio each orbital involved is assumed to suffe a similar change governed by the same facto ar due to the perturbation caused by the applie electric field. Hence we may improve Kir wood's approximation by allowing to multipl each orbital φ_i by a different modulation fa tor $a_i r_i$. It is, however, laborious to carry ou this procedure strictly, and so we have aime to take into account this effect by omittin the inner shell electrons, which would be ver difficult to suffer any polarization. Namel we have applied Kirkwood's approximation (i) the twelve electrons except $\sigma_{1g}{}^2$ and σ_1

ectrons, and (ii) the six π electrons. The sults are shown in the column indicated by $=12$ and 6 respectively in Table XIV. As has ready been expected, the value of $\alpha_{//}$ in- eases from $N=16$ to 12, and also that of $\alpha_{\perp}$ creases from $N=16$ to 12 and to 6. Con- dering that Kirkwood's approximation is ther crude, we may say that the agreement ith the experiment of the value of $\alpha_{//}$ for I(π-σ), $N=12$) and that of $\alpha_{\perp}$ for (CI(π-σ), $=6$) is satisfactory.

7. Population Analysis

In order to obtain a useful insight for the ave function of the molecule, Mulliken[32),33)] eveloped a population analysis method, and is method was already applied to N_2[1c)], O[32),34)], BH[35)], and H_2O[32),1b)]. We also at- mpted the similar analysis for the O_2 wave nctions obtained in Case 1 (single configura- on), Case 7 (SCF MO), and Case 4 (u^2 appro- imation) of Section 4. For the sake of onvenience we introduced specific overlap opulations and specific AO populations in rthonormalized MO

$$\varphi_i=\sum_{rk} c_{i,rk}\chi_{rk} \qquad (r=a,b;\ k=1s, \overset{\circ}{2s}, 2p\sigma, 2p\pi^{\pm}) \quad (56)$$

s follows

$$n'(i;\ k,\ l)=\sum_{rs} 2c_{i,rk}c_{i,sl}S_{rk,sl} \qquad (57.1)$$

$$n'(i)=\sum_{k\geqq l} n'(i;\ k,\ l) \qquad (57.2)$$

$$N'(i;\ k)=\sum_{r} \{c_{i,rk}(c_{i,rk}+\sum_{l\neq k} c_{i,sl}S_{rk,sl})\}\ , \qquad (57.3)$$

where $S_{rk,sl}=\int \chi_{rk}\chi_{sl}dv$. Then the overlap population $n(i)$ and the gross AO population $N(i;\ k)$ in each orbital and the total overlap population n are given by

Table XV. Coefficients $c_{i,rk}$[a)] in MO φ_i.

	$(\sigma 1s)_{g,u}$[b)]	$(\sigma \overset{\circ}{2s})_{g,u}$[b)c)]	$(\sigma 2p)_{g,u}$[b)]
σ_{1g}	0.70711	0	0
σ_{2g}	−0.01387	0.62634	0
σ_{3g}	−0.02006	−0.15225	0.63727
σ_{1u}	0.70711	0	0
σ_{2u}	0.01839	0.83074	0
σ_{3u}	0.04342	0.39783	0.94154
u	0.01075	0.75111	−0.15990
u'	0.00284	0.65025	−0.31435
u''	0.01851	0.83183	0.00258
σ_{2u}'	0.01212	0.76669	−0.13214
σ_{3u}'	0.04557	0.51048	0.93222

a) See Eq. (56).
b) See Eq. (2).
c) See Eq. (30).

Table XVI. Specific overlap populations $n'(i;\ k,\ l)$[a)]

	$n'(i;\ 1s_a, 1s_b)$	$n'(i;\ 1s_a, \overset{\circ}{2s}_b)$ $+(a\longleftrightarrow b)$	$n'(i;\ 1s_a, 2p\sigma_b)$ $+(a\longleftrightarrow b)$	$n'(i;\ \overset{\circ}{2s}_a, \overset{\circ}{2s}_b)$	$n'(i;\ \overset{\circ}{2s}\ , 2p\sigma_b)$ $+(a\longleftrightarrow b)$	$n'(i;\ 2p\sigma\ , 2p\sigma_b)$	$n'(i;\ 2p\pi_a^{\pm}, 2p\pi_b^{\pm})$
σ_{1g}	0.00000	0	0	0	0	0	
σ_{2g}	0.00000	−0.00077	0	0.21577	0	0	
σ_{3g}	0.00000	0.00027	−0.00188	0.01275	−0.11849	0.24796	
σ_{1u}	0.00000	0	0	0	0	0	
σ_{2u}	0.00000	−0.00135	0	−0.37958	0	0	
σ_{3u}	0.00000	−0.00153	−0.00601	−0.08705	−0.45744	−0.54127	
$1\sigma_g$	0.00000	0.00073	0.00002	0.00010	0.00000	0.00000	
$2\sigma_g$	0.00000	−0.00158	−0.00078	0.17503	0.11551	0.01717	
$3\sigma_g$	0.00000	0.00035	−0.00113	0.05342	−0.23400	0.23080	
$1\sigma_u$	0.00000	−0.00089	−0.00048	−0.00011	−0.00008	−0.00001	
$2\sigma_u$	0.00000	−0.00007	0.00003	−0.30938	0.14811	−0.01597	
$3\sigma_u$	0.00000	−0.00193	−0.00556	−0.15714	−0.60546	−0.52530	
u	0.00000	−0.00072	0.00025	−0.31030	0.14667	−0.01561	
σ_{2u}'	0.00000	−0.00082	0.00024	−0.32330	0.12372	−0.01066	
σ_{3u}'	0.00000	−0.00206	−0.00625	−0.14333	−0.58116	−0.53061	
$\pi_u^{\pm}$							0.12379
$\pi_g^{\pm}$							−0.16452

a) See Eq. (57.1).

$$n(i)=N(i)n'(i)\ , \tag{58.1}$$

$$N(i;\,k)=N(i)N'(i;\,k)\ , \tag{58.2}$$

and

$$n=\sum_i n(i)\ , \tag{58.3}$$

respectively.

The coefficients in Eq. (56) are summarized in Table V and Table XV. The values of various populations obtained by using these values of $c_{i,rk}$ are listed in Tables XVI–XVIII.

Table XVII. Specific gross AO populations $N'(i;\,k)$[a] and specific overlap populations $n'(i)$[b] in each orbital.

i	$N'(i,1s)$	$N'(i;2s)$	$N'(i;2p\sigma)$	$n'(i)$
σ_{1g}	1	0	0	0.00000
σ_{2g}	0	1	0	0.21501
σ_{3g}	0	0	1	0.14061
σ_{1u}	1	0	0	0.00000
σ_{2u}	0	1	0	−0.38094
σ_{3u}	0	0	1	−1.09330
$1\sigma_g$	0.99925	0.00074	0.00001	0.00085
$2\sigma_g$	0.00082	0.86842	0.13076	0.30535
$3\sigma_g$	−0.00007	0.13084	0.86923	0.04944
$1\sigma_u$	1.00044	−0.00019	−0.00025	−0.00157
$2\sigma_u$	−0.00002	0.88962	0.11040	−0.17728
$3\sigma_u$	−0.00042	0.11057	0.88985	−1.29539
u	0	0.89101	0.10899	−0.17970
σ_{2u}'	0	0.91376	0.08624	−0.21083
σ_{3u}'	0	0.08624	0.91376	−1.26340
$\pi_u^{\pm}$				0.12379
$\pi_g^{\pm}$				−0.16452

a) See Eq. (57.3).
b) See Eq. (57.2).

The amounts of s–p promotion obtained by the population analysis method for the wave functions of single configuration, SCF, and u^2 approximations, together with the total overlap populations n are listed in Table XIX. The corresponding values of the N_2, CO, and BH molecules are also shown in the same table. From this table we can see that

(i) the charge distribution is nearly the same for SCF and u^2 wave functions,

(ii) the values of n for SCF and u^2 wave functions are much larger than that for the single configurational wave function, which manifests well that the bonding power increases due to s–p promotion, and

(iii) the amount of s–p promotion for O_2 is smaller than that for N_2, as is usually s posed.

Next we have examined the relation s gested by Mulliken[32)]

$$\frac{n_k-n_0}{n_0}=2\frac{R_k-R_0}{R_0}\ .$$

Here n_0 and R_0 are respectively the total ov lap population and the equiliblium internucl distance in the O_2 ground state, and n_k a R_k are those in the excited or ionized stat Here it is worth while to note that the re tion (59) tells us the equiliblium internucl

Table XVIII. Occupation numbers $N(i)$, over populations $n(i)$[a)] in each orbital, and $n'(i)/n$.

1). Single configuration (Case 1).

i	$N(i)$	$n(i)$	$n'(i)/n$
σ_{1g}	2	0.00000	0.0000
σ_{2g}	2	0.43002	1.8620
σ_{3g}	2	0.28122	1.2177
σ_{1u}	2	0.00000	0.0000
σ_{2u}	2	−0.76188	−3.2990
σ_{3u}	0	0	−9.4683
$\pi_u^{\pm}$	4	0.49514	1.0720
$\pi_g^{\pm}$	2	−0.32903	−1.4247

2). u^2 approximation (Case 4).

i	$N(i)$	$n(i)$	$n'(i)/n$
σ_{1g}	2	0.00000	0.00000
σ_{2g}	2	0.43002	0.41512
σ_{3g}	2	0.28122	0.27147
σ_{1u}	2	0.00000	0.00000
u	2	−0.35940	−0.34694
$\pi_u^{\pm}$	4	0.49514	0.23899
$\pi_g^{\pm}$	2	−0.32903	−0.31763

3). LCAO SCF (Case 6).

i	$N(i)$	$n(i)$	$n'(i)/n$
$1\sigma_g$	2	0.00170	0.00164
$2\sigma_g$	2	0.61070	0.58756
$3\sigma_g$	2	0.09888	0.09513
$1\sigma_u$	2	−0.00314	−0.00302
$2\sigma_u$	2	−0.35456	−0.34113
$3\sigma_u$	0	0	−2.49262
$\pi_u^{\pm}$	4	0.49514	0.23819
$\pi_g^{\pm}$	2	−0.32903	−0.31656

a) See Eq. (58.1).
b) See Eqs. (57.2) and (58.2).

able XIX. Total overlap populations n[a] and s-p promotion in percent.

ethod		O_2	N_2[b]	CO[c]	BH[d]
ingle onfigu-ation	n	0.11547			
	s-p	0			
SCF	n	0.51969	1.27553	1.018	0.5204
	s-p	11.02	26.13		9.78
u^2	n	0.51795			
	s-p	10.90			
I(π-σ)	n	0.38562			
	s-p	8.57			

a) See Eq. (58.3).
b) From reference (1c).
c) From reference (32).
d) From reference (35).

istances of all the states with the same orbital ssignment to be equal, although this statement can also be derived by only assuming e (SCF)′ approximation to be valid for all ese states. In Table XX are shown the experimental values of $(R_k-R_0)/R_0$ and the alues of $(n_k-n_0)/n_0$ calculated by using the SCF)′ wave functions. From this table we nd the relation (59) to hold satisfactorily.

Table XX. Comparison between values of $(n_k-n_0)/n_0$ calculated by (SCF)′ and experimental values of $2(R_k-R_0)/R_0$.[a]

k	$\dfrac{n_k-n_0}{n_0}$	$2\dfrac{R_k-R_0}{R_0}$	Remarks
O_2^+ $(^4\Sigma_g^-)$	0.09513	0.119	one σ_{3g} electron in $^3\Sigma_g^-$ (O_2) being ionized.
O_2^+ $(^4\Pi_u)$	0.23819	0.288	one $\pi_u^\pm$ electron in $^3\Sigma_g^-$ (O_2) being ionized.
O_2^+ $(^2\Pi_g)$	−0.31656	−0.140	one $\pi_g^\pm$ electron in $^3\Sigma_g^-$ (O_2) being ionized.
O_2 $(^3\Sigma_u^-)$	0.55475	0.648	one electron in $^3\Sigma_g^-$ (O_2) being excited from $\pi_u^\pm$ to $\pi_g^\pm$.
O_2 $(^3\Sigma_u^+)$	0.55475	0.541	one electron in $^3\Sigma_g^-$ (O_2) being excited from $\pi_u^\pm$ to $\pi_g^\pm$.
O_2 $(^1\Sigma_u^-)$	0.55475	0.645	one electron in $^3\Sigma_g^-$ (O_2) being excited from $\pi_u^\pm$ to $\pi_g^\pm$.
O_2 $(^1\Sigma_g^+)$	0	0.026	same orbital assignment.
O_2 $(^1\Delta_g)$	0	0.013	same orbital assignment.

a) See Eq. (59).

Finally we wish to investigate the electron distribution in the wave function obtained in Case 9 of Section 4 (CI(π–σ)). For this purpose, we have applied the population analysis method to the natural orbitals φ_i'[36], which are constructed by diagonalizing the one electron density materix in the following way,

$$\rho(1)=\int \Phi^*\Phi d\sigma_1 d\tau_2\cdots d\tau_N=\sum_{i,j}\varphi_i^*(1)\mu_{ij}\varphi_j(1)$$
$$=\sum_i \varphi_i'^*(1)N(i)\varphi_i'(1)\ , \tag{60}$$

where μ_{ij} is the matrix element of $\rho(1)$ for Schmidt-OMO's $\varphi_i(1)$, and $\varphi_i'(1)$ and $N(i)$ are respectively the eigenfunction and the eigenvalue. From Eq. (60), $N(i)$ may be taken as the effective number of electron occupying natural orbital $\varphi_i'(1)$. The natural orbitals for the wave function of CI(π–σ) are the same as Schmidt-OMO (3) except the higher two σ_u orbitals which are here designated as σ_{2u}' and σ_{3u}'. The coefficients $c_{i,rk}$ in σ_{2u}' and σ_{3u}' are listed in Table XV. The various populations in these orbitals are given in Tables XVI, XVII, and XXI. The amount of s–p promotion and the total overlap population n in CI(π–σ) wave function were calculated by using the natural orbitals and the results are shown in Table XIX. From his table, we can see that the value of n is maller in this case than in SCF case. Thus e find that electron correlation decreases the onding power. It is interesting to notice ere that we can expect the similar situation lso in the H_2 molecule by comparing the equiliblium internuclear distance calculated by ASMO wave function, 0.850Å (0.732Å)[37], with that by ASMO CI wave function, 0.884Å (0.750Å)[38]; the values within parenthesis being those found by taking into account the screening effect.

Table XXI. Occupation numbers $N(i)$, gross AO populations $N(i;\ k)$,[a] and overlap populations $n(i)$[b] in each orbital, for the case of five dimensional configurational interaction CI(π-σ) (Case 9).

i	$N(i)$	$N(i;\ 1s)$	$N(i,\ 2s)$	$N(i;\ 2p\sigma)$	$n(i)$
σ_{1g}	2	2	0	0	0.00000
σ_{2g}	2	0	2	0	0.43002
σ_{3g}	1.96608	0	0	1.96608	0.27645
σ_{1u}	2	2	0	0	0.00000
σ_{2u}'	1.99770	0	1.82542	0.17228	−0.42118
σ_{3u}'	0.03622	0	0.00312	0.03310	−0.04576
$\pi_u^{\pm}$	3.93056				0.48654
$\pi_g^{\pm}$	2.06944				−0.34045
Sum	16	4	3.82854	2.17146	0.38562

a) See Eqs. (58.2) and (57.3).
b) See Eqs. (58.1) and (57.2).

§ 8. Summary

The results of our calculations hitherto made are compared with the observations in Table XXII by taking the ratio of the computed to observed values. From this table, it is seen that all the results of the single configuration theory, except the f value calculated by the dipole velocity method, are improved as well though not fully, taking into acco the mixing of a relatively small numbe configurations. Especially satisfactory res are obtained for $\langle\psi^2(0)\rangle$ and for f va calculated by the dipole length method.

By examining the CI(π–σ) wave functio

Table XXII. Ratio of computed to observed value of each molecular quantity.
A). Total energy E, D_e, Q, $\langle P_2/r^3\rangle$, and $\langle\psi^2(0)\rangle$ of ground state.[a]

Case	E	D_e	Q[b]	$\langle P_2/r^3\rangle$	$\langle\psi^2(0)\rangle$
1 (A)	0.9907	−0.27	−0.19	0.644	0
2 π-CI	0.9910	0.01	−0.06	0.633	0
3 (A+J_1)	0.9912	0.16	2.10	0.644	0
4 u^2	0.9912	0.14	2.13	0.644	0
5 $u'u''$	0.9912	0.16	2.10	0.644	0
6 SCF	0.9912	0.16	2.14	0.644	0
7 (A+F_1)	0.9913	0.20	−0.16	0.640	0
8 p-CI	0.9915	0.40	−0.26	0.632	0.013 (0.012)[c]
9 5 dim.	0.9919	0.67	1.75	0.639	0
10 15 dim.	0.9919	0.71	1.87	0.651	1.042 (0.926)[c]
11 (HL)	0.9897	−1.09	0.32	0.590	0
12 (σ-HL, π-MO)	0.9900	−0.87	−0.33	0.644	0
13 (π-HL, σ-MO)	0.9904	−0.49	0.46	0.590	0
14 (σ(s-p hybrid.)-HL, π-MO)	0.9907	−0.28	2.55	0.644	0
15 (σ-SO, π-MO)	0.9909	−0.10	−0.20	0.644	0
16 (A′)	0.9932	1.78	−3.72	0.644	0

a) See Table XI.
b) In this column are listed the values found by taking $Q_{\text{obs.}} = -0.82$.
c) The values within parenthesis are those obtained by using the H-F orbital. See also subsection (3) of § 6.

Table XXII. (continued)

B). Excitation energies from the ground state of O_2, $^3\Sigma_g^-$.

	$O_2^+(^4\Sigma_g^-)$	$O_2^+(^2\Pi_u)$	$O_2^+(^4\Pi_u)$	$O_2^+(^2\Pi_g)$	$O_2(^3\Sigma_u^-)$
Single configuration	0.807	0.812	0.614	0.806	1.387
(SCF)′	0.884	0.894	0.700	0.880	1.441
CI(π)					1.535
CI(π-σ)					1.131
	$O_2(^3\Sigma_u^+)$	$O_2(^1\Sigma_u^-)$	$O_2(^1\Sigma_g^+)$	$O_2(^1\Delta_g)$	$O_2(^3\Sigma_u^-)$[a]
Single configuration	0.455	0.402	1.817	1.515	0.483
(SCF)′	0.524	0.468	1.817	1.515	0.483
CI(π)	0.642	0.581	0.871	0.780	0.860
CI(π-σ)	0.755	0.683	1.216	1.144	0.296

a) From Eq. (48)

C). f_{lk}[a] of transition from $^3\Sigma_g^-$ to $^3\Sigma_u^-$, $\alpha_{//}$, and $\alpha_{\perp}$.[b]

	f_{lk} (length)	f_{lk} (velocity)	$\alpha_{//}$ Perturb.	$\alpha_{//}$ Kirkwood ($N=12$)
Single configuration	4.59	0.558	0.701	1.292
(SCF)′	4.77	0.537	0.674	1.029
CI(π)	2.44	0.763	0.304	0.883
CI(π-σ)	0.80	0.053	0.184	0.567
	$\alpha_{//}$ Kirkwood ($N=6$)	$\alpha_{\perp}$ Perturb.	$\alpha_{\perp}$ Kirkwood ($N=12$)	$\alpha_{\perp}$ Kirkwoord ($N=6$)
Single configuration	0.704	0	0.526	0.995
(SCF)′	0.704	0	0.536	0.995
CI(π)	0.314	0	0.524	0.988
CI(π-σ)	0.480	0	0.531	0.992

a) See Table XIII.
b) See Table XIV.

one can see that the interatomic correlation among valence electrons, above all among π and σ electrons, plays an important role in the present ASMO CI treatment.

Further from this table, one can see that the MO approach yields better results than the HL one in so far as the total energy is concerned (compare Case I with Cases 11, 12, and 13).

These interesting results, will be discussed* in Part III of this series of papers, for various diatomic molecules in a summarized form.

Acknowledgements

The authors would like to express their gratitudes to Dr. T. Nakamura for informing us his similar calculation on the N_2 molecule before publication, and to Drs. K. Ohno and T. Itoh for their helpful discussions. They further appreciate the valuable and kind assistance, in our numerical work, of Misses. N. Mizushima, N. Sugawara, K. Matsuoka, S. Noguchi, S. Maniwa, J. Matsuoka, K. Murata, and H. Komuro, and moreover the secretary assistance of Mrs. Y. Yuminami.

---

* A brief account of the last topic was already given in the Progress Report No. 6 of our research group.

They are also indebted to the Ministry of Education and to the members of Kota Laboratory for their financial aids.

Appendix 1. Some Matrix Elements H_{ij} (i=A, j=A,B,$\cdots$)

We shall list for each state the formulae for the diagonal elements of the Hamiltonia matrix for the main configurational wave function, relative to that of the ground state of O_2.

$$H_{AA}({}^3\Sigma_g^-)=\sum_l(\mathcal{E}_l+h_l)+\frac{64}{R}=\sum_l(2h_l)+\Big[\sum_k\sum_j\{2J(k,j)-K(k,j)\}$$

$$+\sum_k\sum_a\{2J(k,a)-K(k,a)\}+\{J(\pi_g^+\pi_g^-)-K(\pi_g^+\pi_g^-)\}\Big]+\frac{64}{R}.$$

$$(l=\sigma_{1g},\ \sigma_{1u},\ \sigma_{2g},\ \sigma_{2u},\ \sigma_{3g},\ \pi_u^\pm,\text{ and }\pi_g^+\text{ or }\pi_g^-)$$

$$(j,\ k\neq\pi_g^\pm;\ a=\pi_g^\pm)$$

$$\left.\begin{array}{ll}
\text{State} & H_{AA}\\
O_2({}^3\Sigma_g^-) & 0\\
O_2({}^1\Delta_g) & K(\pi_g^+\pi_g^-)\\
O_2({}^1\Sigma_g^+) & 2K(\pi^+\pi^-)\\
O_2({}^1\Sigma_u^\pm) & (\mathcal{E}_{\pi_g^\pm}-\mathcal{E}_{\pi_u^\pm})+J(\pi_g^+,\pi_g^+)-J(\pi_g^+,\pi_u^+)+K(\pi_g^+,\pi_g^-)+\frac{3}{2}K(\pi_g^+,\pi_u^-)\\
 & \qquad +\frac{1}{2}K(\pi_g^+,\pi_u^+)\pm\{(\pi_g^+\pi_g^-|\pi_u^-\pi_u^+)+(\pi_g^+\pi_u^+|\pi_g^+\pi_u^+)\}\\
O_2({}^3\Sigma_u^\pm) & (\mathcal{E}_{\pi_g^\pm}-\mathcal{E}_{\pi_u^\pm})+J(\pi_g^+,\pi_g^+)-J(\pi_g^+,\pi_u^+)+K(\pi_g^+,\pi_g^-)-\frac{1}{2}K(\pi_g^+,\pi_u^-)\\
 & \qquad +\frac{1}{2}K(\pi_g^+,\pi_u^+)\pm\{(\pi_g^+\pi_g^-|\pi_u^-\pi_u^+)-(\pi_g^+\pi_u^+|\pi_g^+\pi_u^+)\}\\
O_2({}^3\Delta_u) & (\mathcal{E}_{\pi_g^\pm}-\mathcal{E}_{\pi_u^\pm})+J(\pi_g^+,\pi_g^+)-J(\pi_g^+,\pi_u^+)+K(\pi_g^+,\pi_g^-)+\frac{1}{2}K(\pi_g^+,\pi_u^-)\\
 & \qquad -\frac{1}{2}K(\pi_g^+,\pi_u^+)\\
O_2({}^1\Delta_u) & (\mathcal{E}_{\pi_g^\pm}-\mathcal{E}_{\pi_u^\pm})+J(\pi_g^+,\pi_g^+)-J(\pi_g^+,\pi_u^+)+K(\pi_g^+,\pi_g^-)+\frac{1}{2}K(\pi_g^+,\pi_u^-)\\
 & \qquad +\frac{3}{2}K(\pi_g^+,\pi_u^+)\\
O_2^+({}^2\Pi_g) & -\mathcal{E}_{\pi_g^\pm}\\
O_2^+({}^4\Pi_u) & -\mathcal{E}_{\pi_u^\pm}-\frac{1}{2}K(\pi_g^+,\pi_u^-)-\frac{1}{2}K(\pi_g^+,\pi_u^+)\\
O_2^+({}^2\Pi_u) & -\mathcal{E}_{\pi_u^\pm}+K(\pi_g^+,\pi_u^-)-\frac{1}{2}K(\pi_g^+,\pi_u^+)+\frac{3}{2}K(\pi_g^+,\pi_g^-)\\
O_2^+({}^4\Sigma_g^-) & \mathcal{E}_{\sigma_{3g}}-K(\sigma_{3g},\pi_g^\pm)
\end{array}\right\}\qquad\text{(A.1)}$$

in the above

$$(\varphi_k|h|\varphi_l)=\int\varphi_k^*\,h\varphi_l\,dv\,,\qquad h=-\frac{1}{2}\Delta-\left(\frac{8}{r_a}+\frac{8}{r_b}\right)$$

$$h_l=(\varphi_l|h|\varphi_l)$$

$$(\varphi_i\varphi_j|\varphi_k\varphi_l)=\int\varphi_i^*(1)\varphi_k^*(2)\frac{1}{r_{12}}\varphi_j(1)\,\varphi_l(2)\,dv_1dv_2$$

$$J(k,l)=(\varphi_k\varphi_l|\varphi_k\varphi_l)\quad\text{(Coulomb integral)}$$

$$K(k,l)=(\varphi_k\varphi_l|\varphi_l\varphi_k)\quad\text{(Exchange integral)}$$

$$\mathcal{E}_j=h_j+\sum_k\{2J(k,j)-K(k,j)\}+\frac{1}{2}\sum_a\{2J(a,j)-K(a,j)\}\qquad(j,k\neq\pi_g^\pm,\ a=\pi_g^\pm)$$

$$\mathcal{E}_a=h_a+\sum_k\{2J(k,a)-k(k,a)\}+\{J(b,a)-K(b,a)\}\qquad(a,b=\pi_g^\pm,\ k\neq\pi_g^\pm)\,,$$

and φ_l's mean Schmidt-OMO's (3). $\mathcal{E}_j$'s and $\mathcal{E}_a$'s may be taken as the orbital energies.

Next we shall list for each state the non-diagonal elements between the main configuration and the configurations considered in the present CI calculation.

$^3\Sigma_g{}^-$

$$
\left.\begin{aligned}
&H_{\mathrm{AB}}=(\sigma_{3g}\sigma_{3u}|\sigma_{3g}\sigma_{3u})\\
&H_{\mathrm{AC}}=(\pi_g{}^+\pi_u{}^+|\pi_g{}^-\pi_u{}^-)-(\pi_g{}^+\pi_u{}^-|\pi_g{}^-\pi_u{}^+)\\
&H_{\mathrm{AD}}=0\\
&H_{\mathrm{AE}_1}=0\\
&H_{\mathrm{AF}_2}=-\sqrt{2}\,(\sigma_{3u}\pi_u{}^+|\sigma_{3u}\pi_u{}^-)\\
&H_{\mathrm{AF}_1}=-2(\sigma_{3g}\sigma_{3u}|\pi_g{}^+\pi_u{}^+)+(\sigma_{3g}\pi_g{}^+|\sigma_{3u}\pi_u{}^-)\\
&H_{\mathrm{AF}_2}=(\sigma_{3g}\pi_g{}^+|\sigma_{3u}\pi_u{}^-)\\
&H_{\mathrm{AF}_3}=-\sqrt{2}\,(\sigma_{3g}\pi_g{}^+|\sigma_{3u}\pi_u{}^-)\\
&H_{\mathrm{AH}}=(\sigma_{2u}\sigma_{3u}|\sigma_{2u}\sigma_{3u})\\
&H_{\mathrm{AJ}_1}=\sqrt{2}\,\{(\sigma_{2u}|h|\sigma_{3u})+2(\sigma_{2u}\sigma_{3u}|\pi_g{}^+\pi_g{}^+)+4(\sigma_{2u}\sigma_{3u}|\pi_u{}^+\pi_u{}^+)+(\sigma_{2u}\sigma_{3u}|\sigma_{2u}\sigma_{2u})\\
&\qquad\qquad+2(\sigma_{2u}\sigma_{3u}|\sigma_{3g}\sigma_{3g})+2(\sigma_{2u}\sigma_{3u}|\sigma_{2g}\sigma_{2g})+2(\sigma_{2u}\sigma_{3u}|\sigma_{1u}\sigma_{1u})\\
&\qquad\qquad+2(\sigma_{2u}\sigma_{3u}|\sigma_{1g}\sigma_{1g})-(\sigma_{2u}\pi_g{}^+|\sigma_{3u}\pi_g{}^-)-2(\sigma_{2u}\pi_u{}^+|\sigma_{3u}\pi_u{}^-)\\
&\qquad\qquad-(\sigma_{3g}\sigma_{2u}|\sigma_{3g}\sigma_{3u})-(\sigma_{2g}\sigma_{2u}|\sigma_{2g}\sigma_{3u})-(\sigma_{1u}\sigma_{2u}|\sigma_{1u}\sigma_{3u})-(\sigma_{1g}\sigma_{2u}|\sigma_{1g}\sigma_{3u})\}\\
&H_{\mathrm{AJ}_3}=2(\sigma_{2u}\pi_g{}^+|\sigma_{3u}\pi_g{}^-)\\
&H_{\mathrm{AL}}=(\sigma_{2g}\sigma_{3u}|\sigma_{2g}\sigma_{3u})\\
&H_{\mathrm{AM}_1}=-2(\sigma_{2g}\sigma_{3u}|\pi_g{}^+\pi_u{}^+)+(\sigma_{2g}\pi_g{}^+|\sigma_{3u}\pi_u{}^-)\\
&H_{\mathrm{AM}_2}=-(\sigma_{2g}\pi_g{}^+|\sigma_{3u}\pi_u{}^-)\\
&H_{\mathrm{AM}_3}=\sqrt{2}\,(\sigma_{2g}\pi_g{}^+|\sigma_{3u}\pi_u{}^-)\\
&H_{\mathrm{AO}_1}=-\sqrt{2}\,(\sigma_{2g}\sigma_{3u}|\sigma_{3g}\sigma_{3u})
\end{aligned}\right\}\quad\text{(A.2)}
$$

$^3\Sigma_u{}^\pm$

$$
\left.\begin{aligned}
&H_{\mathrm{AB}}=(\sigma_{3g}\sigma_{3u}|\sigma_{3g}\sigma_{3u})\\
&H_{\mathrm{AE}_1}=\begin{cases}-2(\sigma_{3g}\sigma_{3u}|\pi_g{}^+\pi_u{}^+)+(\sigma_{3g}\pi_u{}^+|\sigma_{3u}\pi_g{}^-) & (\text{for }{}^3\Sigma_u{}^-)\\ \Phi^{\mathrm{E}_1}=0 & (\text{for }{}^3\Sigma_u{}^+)\end{cases}\\
&H_{\mathrm{AF}_1}=\begin{cases}-2(\sigma_{3g}\sigma_{3u}|\pi_g{}^+\pi_u{}^+)+(\sigma_{3g}\pi_g{}^+|\sigma_{3u}\pi_u{}^-) & (\text{for }{}^3\Sigma_u{}^-)\\ \Phi^{\mathrm{F}_1}=0 & (\text{for }{}^3\Sigma_u{}^+)\end{cases}\\
&H_{\mathrm{AI}_1}=\sqrt{2}\,\{(\sigma_{2u}|h|\sigma_{3u})+3(\sigma_{2u}\sigma_{3u}|\pi_g{}^+\pi_g{}^+)+3(\sigma_{2u}\sigma_{3u}|\pi_u{}^+\pi_u{}^+)+(\sigma_{2u}\sigma_{2u}|\sigma_{2u}\sigma_{3u})\\
&\qquad\qquad+2(\sigma_{2u}\sigma_{3u}|\sigma_{3g}\sigma_{3g})+2(\sigma_{2u}\sigma_{3u}|\sigma_{2g}\sigma_{2g})+2(\sigma_{2u}\sigma_{3u}|\sigma_{1u}\sigma_{1u})\\
&\qquad\qquad+2(\sigma_{3u}\sigma_{2u}|\sigma_{1g}\sigma_{1g})-\tfrac{3}{2}(\sigma_{2u}\pi_g{}^+|\sigma_{3u}\pi_g{}^-)-\tfrac{3}{2}(\sigma_{2u}\pi_u{}^+|\sigma_{3u}\pi_u{}^-)\\
&\qquad\qquad-(\sigma_{3g}\sigma_{2u}|\sigma_{3g}\sigma_{3u})-(\sigma_{2g}\sigma_{2u}|\sigma_{2g}\sigma_{3u})-(\sigma_{1u}\sigma_{2u}|\sigma_{1u}\sigma_{3u})-(\sigma_{1g}\sigma_{2u}|\sigma_{1g}\sigma_{3u})\}.
\end{aligned}\right\}\quad\text{(A.3)}
$$

$^1\Sigma_g{}^+$

$$
\left.\begin{aligned}
&H_{\mathrm{AB}}=(\pi_g{}^+\pi_u{}^+|\pi_g{}^-\pi_u{}^-)+(\pi_g{}^+\pi_u{}^-|\pi_g{}^-\pi_u{}^+)\\
&H_{\mathrm{AE}}=(\sigma_{3g}\sigma_{3u}|\sigma_{3g}\sigma_{3u})\\
&H_{\mathrm{AJ}_1}=-2(\sigma_{3g}\sigma_{3u}|\pi_g{}^+\pi_u{}^+)+(\sigma_{3g}\pi_g{}^+|\sigma_{3u}\pi_u{}^-)\\
&H_{\mathrm{AN}_1}=H_{\mathrm{AJ}_1}({}^3\Sigma_g{}^-)
\end{aligned}\right\}\quad\text{(A.4)}
$$

$^1\Delta_g$

$$
\left.\begin{aligned}
&H_{\mathrm{AC}}=(\pi_g{}^+\pi_u{}^+|\pi_g{}^+\pi_u{}^+)\\
&H_{\mathrm{AD}}=(\sigma_{3g}\sigma_{3u}|\sigma_{3g}\sigma_{3u})\\
&H_{\mathrm{AG}_1}=2(\sigma_{3g}\sigma_{3u}|\pi_g{}^+\pi_u{}^+)-(\sigma_{3g}\pi_g{}^+|\sigma_{3u}\pi_u{}^-)\\
&H_{\mathrm{AJ}}=H_{\mathrm{AJ}_1}({}^3\Sigma_g{}^-)
\end{aligned}\right\}\quad\text{(A.5)}
$$

$^1\Sigma_u{}^-$

$$
\left.\begin{aligned}
&H_{\mathrm{AB}}=(\sigma_{3g}\sigma_{3u}|\sigma_{3g}\sigma_{3u})\\
&H_{\mathrm{AI}_1}=H_{\mathrm{AI}_1}({}^3\Sigma_u{}^\pm)
\end{aligned}\right\}\quad\text{(A.6)}
$$

References

1a) J. F. Mulligan: J. Chem. Phys. **19** (1951) 347 (CO_2).

1b) F. O. Ellison and H. Shull: J. Chem. Phys. **21** (1953) 1420, **23** (1955) 2358 (H_2O).

1c) C. W. Scherr: J. Chem. Phys. **23** (1955) 569 (N_2).

1d) R. G. Parr, D. P. Craig, and I. G. Ross: J. Chem. Phys. **18** (1950) 1561 (C_6H_6).

1e) J. C. Slater: Recent issues of Quarterly Progress Report, M. I. T. (1951–1957).

2) W. Moffitt: Rroc. Roy. Soc. **A210** (1951) 224, 245, Rep. on Prog. in Phys. **17** (1954) 173.

3) R. S. Mulliken: Symposium on Molecular Physics, Nikko, Japan (1953).

4) T. Itoh and K. Ohno: J. Chem. Phys. **25** (1956) 1098.
K. Ohno and T. Itoh: J. Chem. Phys. **23** (1955) 1468.

5) A. Meckler: J. Chem. Phys. **21** (1953) 1750.

6) M. Kotani, A. Amemiya, E. Ishiguro, and T. Kimura: Table of Molecular Integrals, Maruzen Co., Ltd., Tokyo, 1955. This book will be referred as KAIK.

7) E. Ishiguro T. Arai, M. Sakamoto, and K. Takayanagi: Nat. Sci. Rep. Ocha. Univ. **5** (1955) 157.

8) F. G. Fumi and R. G. Parr: J. Chem. Phys. **21** (1953) 1864.

9) C. C. Roothaan: Rev. Mod. Phys. **23** (1951) 69.

10) C. G. Greenhow and W. V. Smith: J. Chem. Phys. **19** (1951) 1298.

11) N. Rosen and S. Ikehara: Phys. Rev. **43** (1933) 5.

12) E. Ishiguro, Y. Mizuno, K. Kayama, T. Arai, and M. Sakamoto: Nat. Sci. Rep. Ocha. Univ. **7** (1956) 63.

13) G. Herzberg: Molecular Specra and Molecular Structure, I Spectra of Diatomic Molecules, D. Van Mostrand Comp. Inc., New York, 1950.

14) G. Herzberg: Canad. J. Phys. **31** (1953) 657.

15) G. Herzberg: Canad. J. Phys. **30** (1952) 185.

16) M. Tinkham and M. W. P. Strandberg: Phys. Rev. **97** (1955) 951.

17) C. H. Townes and A. L. Shawlow: Microwave Spectroscopy, Mc.Grow-Hill Book Comp. Inc., New York, 1955.

18) W. Gordy, W. V. Smith and R. F. Trambarulo: Microwave Spectroscopy, John Wilky and Sons, New York, 1953.

19) S. L. Miller and C. H. Townes: Phys. Rev. **90** (1953) 537.

20) S. L. Miller, C. H. Townes, and M. Kotani: Phys. Rev. **90** (1953) 542.

21) D. R. Hartree. W. Hartree, and B. Swirles: Phil. Trans. Roy. Soc. (London) **A238** (1939) 229.

22) T. Yamanouchi and H. Horie: J. Phys. Soc. Japan **7** (1952) 52.

23) W. H. Kleiner: Quarterly Progress Report M.I.T. July 15 (1953) 39.

24) A. Abragam, J. Horowitz, and M. H. L. Pryce: Proc. Roy. Soc. **A230** (1955) 169.

25) R. Radendurg, C. C. Van Voorhis, and J. C. Boyce: Phys. Rev. **40** (1932) 1018, **43** (1933) 315.
R. S. Mulliken: J. Chem. Phys. **7** (1939) 20.

26) C. A. Bevan and D. P. Craig: Trans. Faraday Soc. **47** (1951) 564.

27) C. A. Coulson and J. Jacobs: Proc. Roy. Soc. **A206** (1951) 287.

28) H. Shull: J. Chem. Phys. **20** (1952) 18, 1095.

29) H. R. Woltjer, C. W. Copoolse, and E. C. Wiersma: Proc. Amsterdam Acad. **32** (1929) 1329.
J. H. Van Vleck: The Theory of Electric and Magnetic Susceptibilities, Oxford, 1932.

30) J. O. Hirschfelder, C. F. Curtiss, and R. Bird: Molecular Theory of Gases and Liquids, John Wiley and Sons, New York, 1954.

31) J. G. Kirkwood: Physik. Z. **33** (1932) 57.

32) R. S. Mulliken: J. Chem. Phys. **23** (1955) 1833, 1841.

33) R. S. Mulliken: J. Chem. Phys. **23** (1955) 2338, 2343.

34) R. C. Sahni: Trans. Faraday Soc. **49** (1953) 1.

35) R. C. Sahni: J. Chem. Phys. **25** (1956) 332.

36) P. O. Löwdin: Phys. Rev. **97** (1955) 1474.

37) C. A. Coulson: Trans. Faraday. Soc. **33** (1937) 1479.

38) S. Weinbaum: J. Chem. Phys. **1** (1933) 593.

Short Notes

This section is intended to secure prompt publication of important discoveries in physics. The reports should not exceed 800 words in length. A figure of size 7 cm × 7 cm will be counted as 150 words.

J. PHYS. SOC. JAPAN **12** (1957) 737

Hartree-Fock Values of Diamagnetic Susceptibilities of Neon-like Ions*

By Shigehiro KOBAYASHI

Department of Physics, Kagawa University, Takamatsu

(Received March 25, 1957)

On the basis of the Thomas-Fermi-Dirac (TFD) model Thomas and Umeda[1)] have recently investigated the dependence on degree of ionization of the molar diamagnetic susceptibilities χ_{TFD} by calculating these for the neutral atom as well as positive ions up to quadruply ionized, all homologous to inert gases.

It may be of some interest to compare this result with that based on the Hartree-Fock (HF) method. We have done it for neon-homologue for which alone the HF fields are known at present up to quadruple ionization, by calculating anew the values of χ_{HF} for F^-, Al^{3+} and Si^{4+}. For completeness the values for Ne, Na^+ and Mg^{2+} were also recalculated more accurately than hitherto. The results are given in Table I.

Since neon-homologue has not sufficient number of electrons to make the statistical treatment valid, there are some deviations between χ_{HF} and χ_{TFD} which decrease, however, with the increasing degree of ionization, as seen from Fig. 1. This can be reasoned from the fact that the higher ionization causes the larger electron density due to stronger contraction of the electron cloud.

Table I. Molar diamagnetic susceptibility χ in unit of 10^{-6} cm³.

Ion	Ionization degree	$-\chi_{HF}$				$-\chi_{TFD}$
		1s	2s	2p	Total	
F^-	−1/9	0.066	2.21_1	14.80_3	17.08	
Ne	0	0.053	1.75_6	6.24_3	8.06^a	14.33
Na^+	1/11	0.044	1.15_9	3.88_2	5.08^b	7.83
Mg^{2+}	1/6	0.036	0.908	2.79_9	3.74^c	5.24
Al^{3+}	3/13	0.031	0.724	2.12_1	2.88	3.81
Si^{4+}	2/7	0.026	0.594	1.67_2	2.29	2.92

a: previously 8.8 by P. Gombás[3)]

b: previously 5.7 by P. Gombás[3)] and 4.9 by D. R. Hartree and W. Hartree[2)]

c: previously the same value by W. J. Yost[2)]

Note: These three values of a and b are not in favor to the smooth dependence of χ on the degree of ionization.

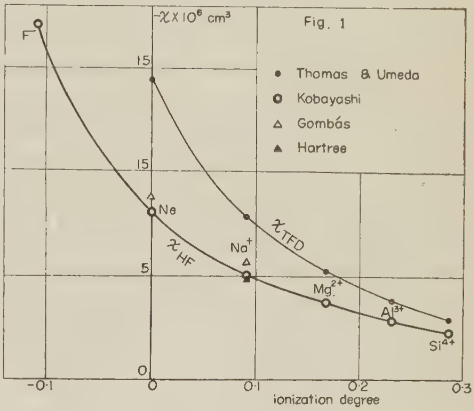

Fig. 1

The author wishes to express his sincere thanks to Professor K. Umeda of Okayama University for his suggestion of this calculation and his kind guidance.

References

1) L. H. Thomas and K. Umeda: J. Chem. Phys. **24** (1956) 1113.

2) Hartree-Fock field for
F^-, Ne; F. W. Brown: Phys. Rev. **44** (1933) 214.
Na^+ ; D. R. Hartree and W. Hartree: Proc. Roy. Soc. A **193** (1947) 299.
Mg^{2+} ; W. J. Yost: Phys. Rev. **58** (1940) 557.
Al^{3+} ; K. Katterbach: Z. Astrophys. **32** (1953) 165.
Si^{4+} ; W. Hartree, D. R. Hartree and M. F. Manning: Phys. Rev. **60** (1941) 857.

3) P. Gombás: *Die statistische Theorie des Atoms und ihre Anwendungen* (Wien, 1949) Tab. 29.

---

* Supported by the Scientific Research Expenditure of the Ministry of Education.

J. PHYS. SOC. JAPAN **12** (1957) 738

Beta Interaction in the Decay of Cs^{137}

By Toshio KATOH, Masao NOZAWA,
Yasukazu YOSHIZAWA

Department of Physics, Faculty of Science, Osaka University, Osaka

and Yujiro KOH

Faculty of Science-Engineering, Osaka City University, Osaka

(Received April 5, 1957)

Recently it has been said that the ratio of $|G_S/G_T|$ in beta interaction is close to one.[1] Its sign, however, has not been determined, though some attempts have been done.[2],[3] The present paper concerns a trial for this problem, investigating the spectrum of the higher component of beta rays from Cs^{137}.

A two directional focusing beta ray spectrometer of mushroom type with the mean radius of 40 cm was used. Theresolution of the spectrometer was 0.17~0.5%. It could be concluded from the measurements of P^{32} and Y^{90} spectra that the distortion due to the spectrometer was negligible. The thickness of the source was about 0.2 mg/cm².

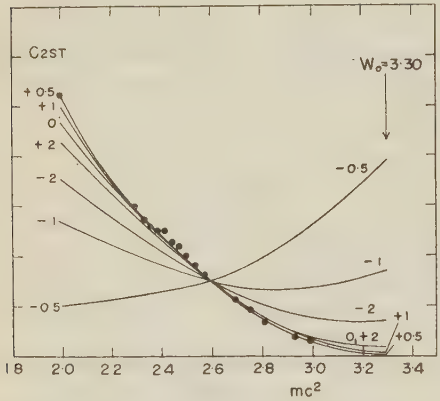

Fig. 1. The experimental and theoretical correction factors of the higher component of beta rays. Points show experimental values, $N/(B\rho f q^2)$ in arbitrary ordinate axis. The values in Figure indicate Y. Curves are theoretical ones normalized at 2.6 mc², and for each Y, parameters except Y were selected to fit them to experimental points.

The experimental results and the calculated correction factors of the higher component of beta rays are shown in Fig. 1. This spectrum was analysed in the following ways. First, measured spins and estimated parities of the ground states of Cs^{137} and Ba^{137} were to be reliable, i.e., the higher component was analysed on the basis of the second forbidden transition $\Delta I=2$, no parity change. Second, the linear combination of the scalar and tensor interactions was used. Third, the maximum energy of the higher component, 1176±2 kev, was taken to be the sum of precisely measured gamma ray energy, 662 kev, and the maximum energy of the lower component, 514±2 kev, which was observed in our experiment

It was the important feature that this spectrum became a straight line in the Kurie plot using the correction factor $C=q^2$ within the experimental error, where q was the momentum of neutrino.

When the lower component was analysed, this correction factor was used to subtract the higher component from the total spectrum and was obtained the straight corrected Kurie plot of the lower component using unique first forbidden correction factor. The branching ratio of the lower and the higher component was 92.4/7.6 which agreed with the result of Langer and Moffat.[4]

We tried to determine the value of $Y=(iG_S R_{ij})/(G_T T_{ij})$ in the approximate formula for the correction factor of Konopinski and Uhlenbeck.[5] The experimental correction factor was found to agree with the theoretical one in the region $2 \gtrsim Y > 0$, but was not in the region $Y < 0$. Assuming the time reversal property and the single particle model approximation, $R_{ij}/T_{ij}=i/2$[3] in the case of Cs^{137}. Then $Y=-G_S/2G_T$, and $Y=+0.5$ was rather good as shown in Fig. 1, whereby $|G_S/G_T|\simeq 1$. It was concluded that the negative sign of G_S/G_T was better than another, as Morita, Fujita and Yamada[3] had pointed out. Details of experiments and discussions will be published in near future.

References

1) E. J. Konopinski: Rev. Mod. Phys. **27** (1955)254.
2) Porter, Freedman, Novey and Wagner: Phys. Rev. **103** (1956) 921 and 942.
3) M. Morita, J. Fujita and M. Yamada: Prog. Theor. Phys. **10** (1953) 630.
4) L. M. Langer and R. J. D. Moffat: Phys. Rev. **82** (1951) 635.
5) E. J. Konopinski and G. E. Uhlenbeck: Rhys. Rev. **60** (1941) 308. E. J. Konopinski: Beta-and Gamma-Ray Spectroscopy, ed. by K. Siegbahn (North-Holland Co., Amsterdam, 1955) p. 292.

J. PHYS. SOC. JAPAN **12** (1957) 739

Intermolecular Free Length in Liquids in Relation to Sound Velocity

By Otohiko NOMOTO

Kobayasi Institute of Physical Research, Kokubunzi, Tokyo

(Received March 29, 1957)

Jacobson[1] has found an empirical relation

$$\beta = kL^p \qquad (1)$$

(k and p=constants, slightly dependent on temperature) between the compressibility (adiabatic or isothermal) β and the intermolecular free length L of the organic liquids, defined by

$$L = 2v_a/Y = 2(v-v_0)/Y\,, \qquad (2)$$

where v_a means the available volume, v the molar volume and v_0 the actual volume of the molecules in one mole, and Y is the total surface area of the molecules in one mole of the liquid, given by

$$Y = (36\pi N_L v_0^2)^{1/3}\,, \qquad (3)$$

where N_L denotes the Loschmidt number. In case β is the adiabatic compressibility, p and k in (1) becomes as $p=2.083$ and $\log k=7.097$ at 20°C, when the value of L is determined by adopting as v_a the difference of the molar volumes at 20°C and 0°K. The approximation $p=2$ leads to the relation

$$VL\rho^{1/2} = \text{const.} = K \qquad (4)$$

by (1).

Explanation for this relation has been put forward by Wada[2] by employing the hole-theory of Eyring et al.[3] and giving the expression of the constant K as

$$K_W = (6/\pi N^L)^{1/3}(\gamma_g RT)^{1/2}v^{-1/6}\,, \qquad (5)$$

where γ_g means the ratio of the specific heats of the gas or vapour of the corresponding liquid, R the universal gas constant and T the absolute temperature. The factor $\gamma_g^{1/2}v^{-1/6}$ being only slightly dependent on the various kinds of the liquids, K is expected to be nearly independent of the kinds of liquids and proportional to $T^{1/2}$, as has been pointed out and ascertained by Wada by employing Jacobson's data.

The numerical value of the constant K calculated by Wada, however, is about twice the experimental value. The reason for this discrepancy seems to be involved in the use of Eyring's liquid model for the calculation. So we performed a similar calculation by employing Toncks' equation of state[4], which becomes

$$pv_a = 3RT \qquad (6)$$

for liquids, where p means the pressure. The corresponding sound velocity is given by Kittel[5] as

$$V_K = (v/v_a)\gamma_l^{1/2}(3RT/M)^{1/2}\,, \qquad (7)$$

where M is the molecular weight and γ_l the ratio of the specific heats of the liquid, being equal to $(C_v+3R)/C_v$ in this case, where C_v is th molar specific heat at constant volume. The constant K in (4) becomes in this case as

$$K_K = \frac{2v^{1/2}}{(36\pi N_L v_0)^{1/3}}\gamma_l^{1/2}(3RT)^{1/2}\,. \qquad (8)$$

Comparing this constant with that of Wada, we have

$$K_K/K_W = (1/\sqrt{3})(\gamma_l/\gamma_g)^{1/2}(v/v_0)^{2/3}\,. \qquad (9)$$

Jacobson's empirical value is $K=618$ at 20°C, and we have $K/\sqrt{T}=36.1$, while Wada's value of K affords $K_W/\sqrt{T}=69$, when it is assumed that $v=90\,\text{cm}^3$ and $\gamma_g=1.2$. The relation (9) gives, on the other hand, $K_K/\sqrt{T}=46$, if it is assumed that $\gamma_l=\gamma_g$ and $v/v_0=1.25$.

Collins and Navidi[6] has obtained the expression of the sound velocity also by employing Toncks' equation of state, but without employing the geometrical assumption of the sound propagation model and directly from the thermodynamical equation of the sound velocity. Expanding their expression in terms of (v_a/v) and conserving the first order terms, we have as the sound velocity

$$V_c = \{1-(1/3)(v_a/v)(\gamma_l-1)\}V_K\,, \qquad (10)$$

where V_K means Kittel's sound velocity given by (7). This gives the value of K given by

$$K_C/K_W = (1/\sqrt{3})(\gamma_l/\gamma_g)^{1/2}\left\{1-\frac{1}{3}(v_a/v)(\gamma_l-1)\right\}\,, \qquad (11)$$

the corresponding value of $K/\sqrt{T}$ becoming

$$K_C/\sqrt{T} = 45\,, \qquad (12)$$

nearly in agreement with the empirical value.

References

1) B. Jacobson: Acta Chemica Scandinaviaca **5** (1951) 1214, **6** (1952) 1485, J. Chem. Phys. **20** (1952) 927.
2) Y. Wada: J. Phys. Soc. Japan **9** (1954) 641.
3) J. F. Kincaid and H. Eyring: J. Chem. Phys. **6** (1938) 620.
4) L. Toncks: Phys. Rev. **50** (1936) 955.
5) Ch. Kittel: J. Chem. Phys. **14** (1946) 614.
6) F. C. Collins and M. H. Navidi: J. Chem. Phys. **22** (1954) 1254.

J. PHYS SOC. JAPAN **12** (1957) 740

On the Conducting Mechanism of Oxide Coated Cathode

By Hiroyuki MIZUNO

Matsushita Electronics Corporation Takatsuki

(Received March 15, 1957)

We have pointed out that the theory of Loosjes-Vink can be applied on the rectification theory at the interface of oxide cathode[1]. Referring to this consideration we have studied some rectification properties between sleeve and coated oxide. Experimental cathodes consist of nickel circular sleeve*) coated with oxide, and double probes embedded in it. Direct voltage was applied through the contact between sleeve and first probe, first probe and second probe were used to measure the currents**) and temperature was measured simultaneously by using thermo-couple and micropyrometer. The difference between these two measured currents was taken as the conducting current through blocking layer. Fig. 1 shows the logarithm of current as a function of $(1/T)$ for forward direction. The curves consist of two regions. The one is the low temperature region (below 700° K) and the other is the high temperature region (beyond 700° K). There are some fluctuations according to different tubes but these tendencies are similar. In Fig. 2 we ploted $\log I/T^2$ as a function of $1/T$ in the high temperature region. Fig 3 and 4 show the logarithms of the currents in reverse direction in low temperature region ($<700°$ K) and of current divided by T^2 in high temperature region ($>700°$ K) respectively. Contrary to the case of forward flow, the gradients change with applied voltages in high temperature region and do not change in low temperature region. From these results, it can be assured that the low temperture conduction is attributed to the electrons moving through a granule to a granule, while high temperature conduction is attributed to electron gas emitted from granules. However the critical temperature is about 700° K, not 800° K as pointed by Loosjes and Vink.

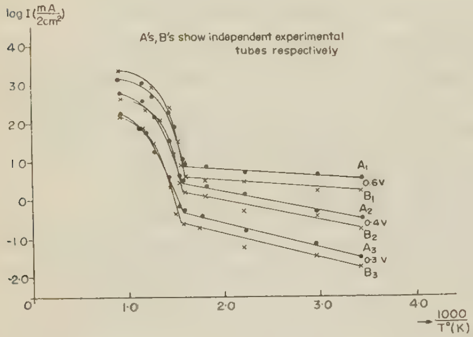

Fig. 1. Log I-$1/T$ curves for forward direction flow.

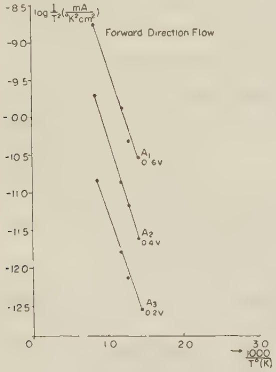

Fig. 2. Log $I/T^2-1/T$ curves for high temperatures.

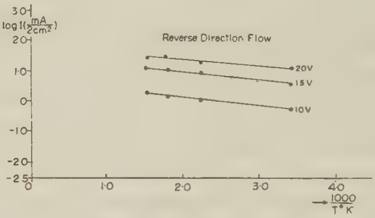

Fig. 3. Log. $I-1/T$ curves for low temperatures.

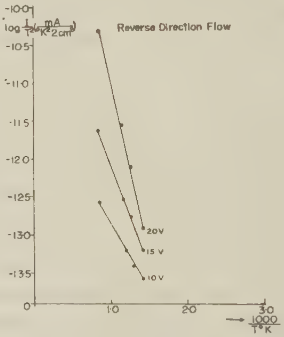

Fig. 4. Log. $I/T^{\frac{1}{2}}-1/T$ curves for high temperatures.

Reference

1) H. Mizuno: J. Phys. Soc. Japan **11** (1956) 1125

---

* It is to be noted that the sleeve must be cleaned completely. If there should be oxide films on the surface, the rectification property was something curious.

** Note: The rectifying area between sleeve and coating is computed by substraction of the contact area between probe and coating from the total contact area between sleeve and coating.

J. Phys. Soc. Japan **12** (1957) 741

On the Carrier Recombination through Nickel Impurities in Germanium

By Jun'ichi Okada

Matsuda Research Laboratory, Tokyo-Shibaura Electric Co., Kawasaki-city, Japan

(Received April 2, 1957)

Several recent experiments indicate that there exist impurities which act as both recombination and trapping centers in germanium: examples are Cu, Au, Fe and Ni[1]. These results have been explained by assuming that such impurities each introduce at least two acceptor levels whose charge distribution affects capture cross-sections for free carriers. A proposal will be presented here that there is a temperature range where carrier recombination through these impurities can be interpreted without above assumption.

The samples used in this study were prepared by diffusing nickel into originally n-type germanium. This method permits us to control the concentration of nickel and the position of Fermi level in germanium.

Figure 1 shows experimental results characteristic of high-resistivity p-type samples. Intrinsic photoconductivity $\Delta\sigma$ and resistivity ρ are plotted as a function of temperature T. Results indicate that $\Delta\sigma$ increases with decreasing temperature but saturates gradually. This fact cannot be interpreted by simple recombination theory[2], but we can explain it by assuming that each nickel atom introduces two acceptor levels, and applying the theory of recombination through multiple levels of constant capture cross-sections.[3] Rather simple explanations proposed here are as follows.

Assume that, for high-resistivity nickel-doped germanium, there exist two independent levels, one (upper level) 0.3eV below the bottom of the conduction band, the other (lower level) 0.22eV above the top of the valence band[4]. In the case of high-resistivity p-type samples, upper level captures excess electrons which recombine with free holes through this level. Therefore, in steady state, $p_0\gamma_{p1}\Delta N_1^- \simeq \Delta n\gamma_{n1}N_t$, where γ_{n1} is the rate of filling an empty site of upper level per unit electron concentration, γ_{p1} is the rate of emptying an occupied site per unit hole concentration, p_0 is the equilibrium free hole concentration, ΔN_1^- is the change of the density of electron captured in this level and N_t is the concentration of nickel. On the other hand, lower level acts as hole trapping centers. Thus, $p_2\gamma_{p2}\Delta N_2^+ \simeq \Delta p\gamma_{p2}N_t$, where γ_{p2} is the capture constant for holes, p_2 is the free hole concentration when the Fermi level equals to the lower level and ΔN_2^+ is the change of the density of empty sites in this level. In this case, we have two carrier lifetimes principally determined by the recombination rate U at upper level which is given by $\Delta n\gamma_{n1}N_t$ and neutrality condition requires $\Delta n+\Delta N_1^- = \Delta p+\Delta N_2^+$. Then, if we define an effective lifetime τ^* by the equation

$$\tau^*(\mu_n+\mu_p) = \tau_{n1}[\mu_n+\mu_p\{1+(\gamma_{n1}/\gamma_{p1})N_t/p_0\}/(1+N_t/p_2)], \quad (1)$$

photoconductivity $\Delta\sigma$ is given by

$$\Delta\sigma = \Delta n\mu_n+\Delta p\mu_p = L\tau^*(\mu_n+\mu_p), \quad (2)$$

where $\tau_{n1}=1/\gamma_{n1}N_t$ and L is the rate of excitation. In this expression, N_t and p_0 are obtained from resistivity data and p_2 can be calculated by assuming the position of lower level. γ_{n1} and γ_{p1} are determined by comparing the effective lifetimes. At room temperature, we have obtained, using two p-type samples of different concentrations of nickel, $\gamma_{n1}=0.9\times10^{-9}$ cm³/sec and $\gamma_{p1}=1.8\times10^{-9}$ cm³/sec. Figure 1 also shows the $\Delta\sigma$ curve calculated from Eq. (2) with $N_t=7\times10^{14}$/cm³. This is in good agreement with the experiment. Moreover, from Hall coefficient measurements, we have obtained $\Delta p/\Delta n \simeq 3$ for above sample at room temperature, while calculated value is 2.9.

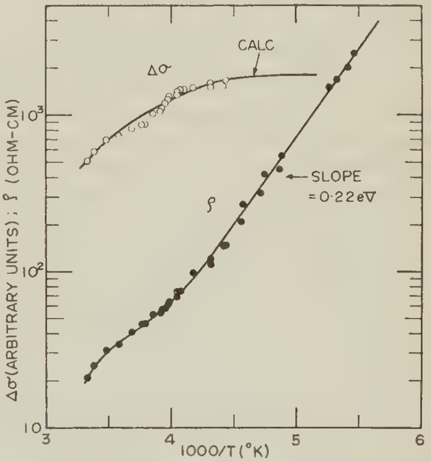

Fig. 1. Photoconductivity and resistivity *vs* temperature for high-resistivity p-type Ni-doped sample.

The author thanks Mr. M. Takabayashi for his kindness of preparing the samples.

References

1) See for example, M. L. Schultz and G. A. Morton: Proc. IRE **43** (1955) 119.
2) W. Shockley and W. T. Read, Jr.: Phys. Rev. **87** (1952) 835.
3) To be published later.
4) W. W. Tyler, R. Newman an H. H. Woodbury: Phys. Rev. **93** (1955) 461; J. F. Batteey and R. M. Baum: Phys. Rev. **100** (1955) 1634.

J. Phys. Soc. Japan **12** (1957) 742

Magnetic Annealing Effect in Iron-Nickel Ferrites

By Yoshimichi AIYAMA, Hisashi SEKIZAWA
and Shûichi IIDA
Department of Physics, Faculty of Science, Tokyo University, Tokyo, Japan

(Received April 15, 1957)

It has been shown by us[1,2] that the magnetic annealing effect in iron-cobalt ferrites can well be accounted for by the mechanism of the directional short range order, which is analogous to the case of metallic solid solution,[3] among Co^{2+} ions and cation vacancies on 16d sites of the spinel structure. The details will be published soon.[2] One of the experimental facts which lead us to this conclusion is that the magnetic annealing effect disappears after the specimens have been heat-treated in a high vacuum and recovers again by oxidizing the specimens, and the magnitude of the uniaxial anisotropy depends strongly on the degree of oxidation of the specimens. According to the phase diagram established by one of the authors[4], it is certain that the specimens after the vacuum heat-treatment are almost stoichiometric and the oxidation of the specimens means the oxidation of iron ions from Fe^{2+} to Fe^{3+}, accompanied by the increase of cation vacancies in the spinel matrixes. It is presumed that the orbital of Co^{2+} ion neighbouring a vacancy of a cation suffers the axial crystalline field and hence, combined with the spin-orbit coupling, the electronic energy of the Co^{2+} ion depends considerably on the direction of magnetization. According to this mechanism, every kind of mixed ferrites of magnetite and other ferrites are expected to show the magnetic annealing effect to some extent after appropriate oxidation heat-treatment, although the magnitude of the induced uniaxial anisotropy is to depend on both the manner of splitting of the orbital energy levels under the influence of the crystalline field and the strength of the spin-orbit coupling of the metal ions concerned.

Our preliminary experiments have shown that the magnetic annealing is effective in Fe-Ni ferrites, and also in Fe–Mn and Fe–Cu ferrites to some extent. It seems probable that the uniaxial anisotropy of these ferrites is also induced by the above mechanism. In order to confirm this presumption in the case of Fe–Ni ferrites, the dependence of the magnitude of the uniaxial anisotropy on the concentration of vacancies, i.e. the degree of oxidation of specimens, has been studied with the same method as in the case of Fe–Co ferrites[1].

Eight disk-shaped polycrystalline specimens, ranging in composition from Ni/(Fe+Ni)=0,083 to 0,417, were prepared by using cobalt-free carbonyl nickel and electrolytic iron. After prepared by sintering at 1400°C under an appropriate pressure of oxygen, they were heated up to 1000°C in a high vacuum, kept for one hour and then cooled slowly to room temperature. The cation-anion ratio of the specimens at this stage is thought to be almost stoichiometric. Then they were heated up to 400° in a high vacuum, kept ten minutes and cooled with an applied magnetic field of about 5000 Oe. The uniaxial anisotropy constants measured after this treatment are shown by curve (I) in figure. Similar magnetic annealing treatments from 400°C were repeated four times in various atmospheres. The anisotropy constants measured after each heat-treatment are shown in figure by curves (2), (3), (4) and (5), respectively. The atmospheres used are also indicated in the figure.

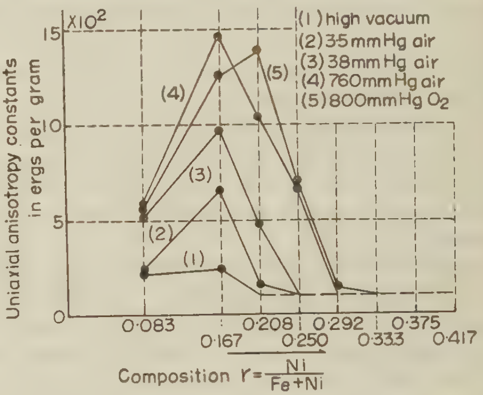

These results show that the magnitude of the uniaxial anisotropy of iron-nickel ferrites also depends essentially on the degree of oxidation of the specimens and the mechanism of this magnetic anneling effect will be the same as in the case of iron-cobalt ferrites. Contrary to the case of iron-cobalt ferrites, the magnetic annealing is ineffective in nickel rich specimens. It is perhaps due to the insufficiency of the vacancy concentration, for the ionization potential of Ni^{2+} ion is higher than that of Co^{2+} ion and the specimens were not so much oxidized as to have sufficient vacancies in our heat-treatments.

The authors wish to express their hearty thanks to Prof. S. Kaya for his constant encouragement. The authors are also indebted to Mr. H. Yamato who helped them in some parts of this work.

References

1) S. Iida, H. Sekizawa and Y. Aiyama: J. Phys. Soc. Japan **10** (1955) 907.
2) S. Iida, H. Sekizawa and Y. Aiyama: J. Phys. Soc. Japan (to be published).
3) S. Taniguchi and M. Yamamoto: Sci. Rep. RITU, **A6** (1954) 330.
S. Taniguchi: Sci. Rep. RITU, **A7** (1955) 269.
L. Néel: J. de phys. **15** (1954) 225.
4) S. Iida: J. Phys. Soc. Japan **11** (1956) 846.

J. PHYS. SOC. JAPAN **12** (1957) 743

Magnetic and Electrical Anisotropies of the Iron Sulfide Single Crystal

Tadamiki HIHARA
Department of Physics, Faculty of Science, Hiroshima University, Hiroshima,
Miyuki MURAKAMI and Eiji HIRAHARA
Department of Applied Physics, Faculty of Engineering, Hiroshima University, Hiroshima

(Received March 6, 1957)

We have reported on the behavior of the magnetic[1] and electrical[2] anisotropies of iron sulfide single crystal at the α-transformation temperature ($T\alpha$), and are now studying it in the temperature range over the Néel point (T_N, about 330°C).

The thermal variation of susceptibility is shown in Fig. 1, in which curve 1 and 2 are results when an applied magnetic field H, is perpendicular and parallel to the c-axis of the single crystal respectively. At temperatures above the Néel point there still remains a small but obvious anisotropy of susceptibility. Oxidation of the specimen was carefully avoided, because even very small quantities of oxide would disturb the measurements. The results shown in Fig. 1 may be explained qualitatively in the following way.

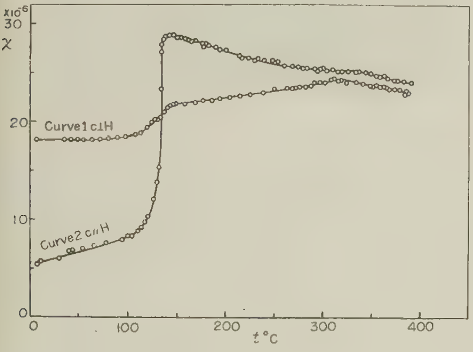

Fig. 1. Anisotropy of magnetic susceptibility.

As mentioned in [1] (the reference 1 will be denoted as [1]), the direction of antiferromagnetism is parallel to the c-axis at temperatures below T_α and is perpendicular to the c-axis at temeratures above T_α. On the basis of the fact that the crystal contracts along the c-axis as temperature rises through the α-transformation point, we may suppose that a super-exchange interaction between antiparallel spin pairs decreases and hence it causes an abrupt increase of susceptibility.

After the transformation the super-exchange energy would again increase on account of the usual lattice expansion and the gradual decrease of susceptibility follows in the temperature range between T_α and T_N, as seen in curve 2 in Fig. 1. In the same range of temperature curve 1 gradually increases, and hence we suppose that spins in the c-plane take two or more different directions in two or more sublattices (or domains) in the c-plane and their components parallel to the field contribute to the increment of susceptibility in this temperature range.

We now remark that the presence of two or more sublattices (or domains) is prerequisite in order to expain the constant susceptibility for the rotating measurements of [I] (curve B′ of Fig. 2), though in [I] we concluded incorrectly that spins in the c-plane turn easily keeping themselves perpendicularly to the external field H.

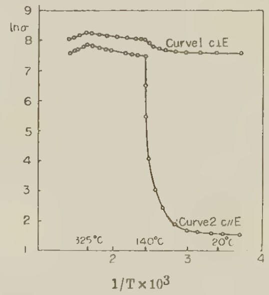

Fig. 2. Anisotropy of electrical conductivity.

The thermal variation of electrical conductivity is shown in Fig. 2, in which curves 1 and 2 are the results when an applied electric field is perpendicular and parallel to the c-axis respectively. The explanation for the anisotropy of conduction may be as follows.

In the range of temperature below T_α an easy flow of current will take place along a direction perpendicular to the c-axis because the spins in this direction are arrayed in parallel with each other, and a hard flow will be expected along the c-axis because the spins in this direction are arrayed in antiparallel with each other. In the range of temperature between T_α and T_N, the spins are disposed in the c-plane as mentioned above, and hence a flow of current along the c-axis increases to the same amount as a flow along a direction perpendicular to the c-axis. Above the Néel point the electrons released from antiferromagnetic interaction behave as ones in the conduction band and contribute to the metallic conduction as seen in Fig. 2. This work was partially supported by the Scientific Research Expenditure of the Ministry of Education.

References

1) T. Kamigaichi, T. Hihara, H. Tazaki and E. Hirahara: J. Phys. Soc. Japan **11** (1956) 1123.
2) T. Kamigaichi, T. Hihara, H. Tazaki and E. Hirahara: J. Phys. Soc. Japan **11** (2956) 606.
2) F. K. Lotgering: Philips Res. Rep. **11** (1956) 190.

J. PHYS. SOC. JAPAN **12** (1957) 744

A Density Filter Improving Aberrant Optical Image

By Jumpei TSUJIUCHI
Government Mechanical Laboratory, Tokyo, Japan

(Received April 12, 1957)

In the image-forming optical system, the complex amplitude of the image of an axial point source can be calculated, apart from constant factors, as follows:

$$U(\rho)=2\int_0^1 T(r)\exp[ikW(r)]\,J_0(\rho r)\,rdr\,, \qquad (1)$$

where r and ρ are the normalized radial coordinates in the pupil and image plane respectively, $T(r)$ the amplitude transmittivity, $W(r)$ the wave aberration, and $k=2\pi/\lambda$, then the intensity is

$$I(\rho)=U(\rho)\,U^*(\rho)\,. \qquad (2)$$

In case of the density filter attached to the ordinary optical system with $T(r)=1$, it is not introduced but the variation of absorption, so it is said that $T(r)$ is real and positive. Taking

$$T(r)=\frac{1}{2}\{1+\cos[kW(r)+\delta]\}\,, \qquad (3)$$

$T(r)\exp[ikW(r)]$ in (1) can be changed into the summation of two terms, of which one contains $W(r)$ and δ, and another contains δ only, so it is expected that the effect of $W(r)$ on the image can be reduced by the suitable choice of δ value.

We took (3) as the filter which improved the image formed by the aberrant system and was specified by the parameter δ, and studied the effect of this filter about the defocused system with

$$W(r)=ar^2\,. \qquad (4)$$

As to the evaluation of the optical image, Strehl's *definition*[1] has been used, and the *definition* in this case is obtained by setting $\rho=0$ in (2), which is calculated by (3), (4) and (1), and finally we have, with $\operatorname{sinc} t=\sin t/t$,

$$D(\delta)=I(0)=\frac{1}{4}\Big[\operatorname{sinc}^2\frac{ka}{2}+\frac{1}{4}\operatorname{sinc}^2 ka+\frac{1}{4}+\operatorname{sinc}\frac{ka}{2}(1+\operatorname{sinc}ka)\cos\Big(\frac{ka}{2}+\delta\Big)+\frac{1}{2}\operatorname{sinc}ka\cos 2\Big(\frac{ka}{2}+\delta\Big)\Big]\,. \qquad (5)$$

Taking $dD/d\delta=0$, the following values of δ are obtained corresponding to the extremums of $D(\delta)$;

$$\delta_1=2n\pi-\frac{ka}{2}\,,\quad \delta_2=\delta_1+\pi\,. \qquad (6)$$

On the other hand, the transmitted flux of the system with this filter can be calculated, using that without filter as unit;

$$E(\delta)=2\int_0^1\frac{1}{4}\{1+\cos[kar^2+\delta]\}^2\,rdr$$
$$=\frac{1}{4}\Big[\frac{3}{2}+2\operatorname{sinc}\frac{ka}{2}\cos\Big(\frac{ka}{2}+\delta\Big)+\frac{1}{2}\operatorname{sinc}ka\cos 2\Big(\frac{ka}{2}+\delta\Big)\Big]\,.$$

Here we take

$$D_0(\delta)=\frac{D(\delta)}{E(\delta)}$$

as the normalized *definition*, and the relations b tween a and D_0 for the filters of δ_1 and δ_2 a shown in Fig. 1, where we find that the *definiti* with the suitable filter is larger than that withou filter, or in other words, such a filter can improv the aberrant image. For $2n\lambda<a<(2n+1)\lambda$ the filte of δ_1 makes the *definition* maximum and that o δ_2 makes it mimium, whereas for $(2n+1)\lambda<a<2n$ the relations become contrary.

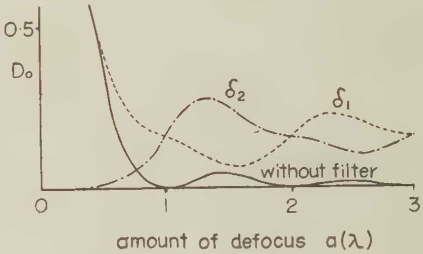

Fig. 1. Strehl's *definition* of defocused optica system with filter of δ_1, δ_2 and without filter.

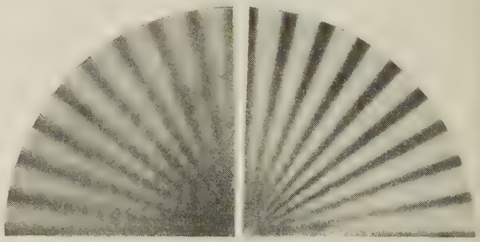

(A) without filter (B) with δ_1-filter

Fig. 2. Images of $3/4\,\lambda$ defocused system.

In order to ascertain the effect of this filter, w used as an appoximate filter the developed phot graphic plate of interferogram taken by Twyman lens interferometer, in which the objective to b tested was arranged to show the half amount o aberration due to defocusing, and the value of was adjusted by slight variation of the optical pat difference between two beams.

Thus, Fig. 2 (A) shows the nearly axial imag formed by $3\lambda/4$-defocused objective without filte and (B) with the filter of $\delta_1=5\pi/4$. The effect o improving the image is well recognized.

References

1) K. Strehl: Z. Instrumentenkunde, **15** (189 364, **22** (1902) 214.

J. PHYS. SOC. JAPAN **12** (1957) 745

Angular Distribution of Proton Groups from the Reaction F^{19} (*d,p*) F^{20}

Kazuo ÔNO, Junji SHIMADA, Keiichi KURODA
and Shigeya TANAKA

Institute of Science & Technology,
University of Tokyo

Bromley et al(1) at Rochester University measured the angular distribution of the protons from the reaction F^{19} (*d,p*) F^{20} using 3.6 Mev. deuterons. From the results they concluded that the proton group from the reaction in the ground state of F^{20} was interpreted with a mixture of $1_n=0$ and $1_n=2$ stripping. After that, the same reaction was also investigated by Takemoto et al(2) with 0.75–1.45 Mev. deuterons and by Black(3) with 14.3 Mev. deuterons. These two results can not be available to determine whether F^{20} in the ground state is formed by capturing *s*-neutron or not, because in Takemoto's experiment the proton angular distribution is nearly isotropic, and in the other one's the angular distribution has been measured from 20 to 100 degrees, which indicates only the existence of captured *d*-neutrons.

Our experiments were begun in order to probe the angular distribution characterized by two 1_n values, which were obtained by Bromley et al. So we measured the proton angular distribution near angles of zero degree with great precautions.

Deuterons of energy 1.92 and 2.03 Mev. from the 16-inch variable energy cyclotron were used to bombard a thin PbF_2 target. The out-going protons were detected from −10° to 160° with 100 micron Sakura nuclear plate. The proton group of P_0 corresponding to the F^{20} in the ground state, and that of P_1 corresponding to the 0.65 Mev. level were clearly resolved. The proton angular distributions of our experiments are shown in Fig 1. The group P_1 shows a large peak at about 60°(c.m. angle) and it seems to be caused by the stripping process of *d*-neutrons in good agreement with the results obtained hitherto.

On the contrary, the angular distribution of P_0 shows no peak at 0° and a large peak in the backward direction. These results at our bombarding energies indicate that the reaction proceeds mostly by compound nucleus formation. Recently, Rochester group(4) has repeated the previous experiment with the deuteron energy in the range 3.5–4.0 Mev. and they have obtained the same results with ours.

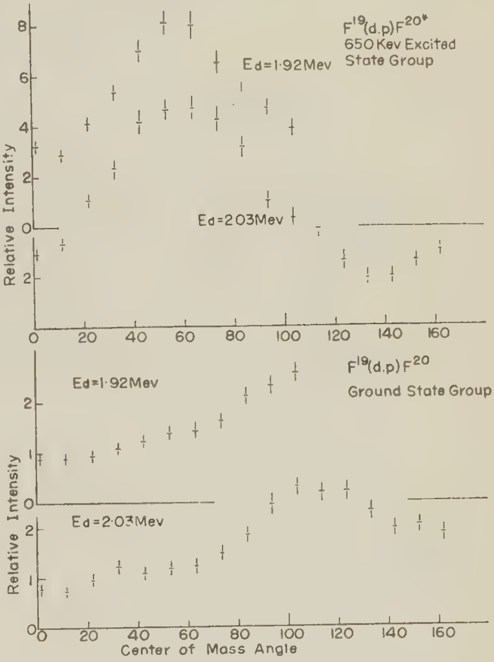

Fig. 1. Angular distribution of protons leaving F^{20} from F^{19} (*d,p*) F^{20}.

We are indepted to Professor T. Muto and Professor H. Kumagai for valuable discussions and contineous encouragements. We also thank to Mr. Y. Wakabayashi of Konishiroku Photo Manufacturing Co. for supplying nuclear plates for us.

References

1) Bromley, Bruner, and Fulbright: Phys. Rev. **89** (1953) 396
2) S. Takemoto et al.: Phys. Rev. **101** (1956) 772.
3) C. F. Black, Ph. D. Thesis: Massachusetts Institute of Technology 1953 (unpublished)
4) F. D. Seward (private comminucation)

PROGRESS OF THEORETICAL PHYSICS

(Founded by H. Yukawa in 1946)

Published for the

Research Institute for Fundamental Physics
The Physical Society of Japan

Progress of Theoretical Physics Vol. 16, No. 4, October 1956

The Range of the Interaction between Different Fermions .... Michiji KONUMA..259
Free-Electron Ring Model of Polyacenes .... Gentaro ARAKI..265
On the Grand Canonical Distribution Method of Statistical Mechanics .... T. YAMAMOTO and H. MATSUDA..269
A Relativistic Wave Equation for a Particle with Two Mass States of Spin 1 and 0 .... Haruo SHIMAZU..287
General Theory of Deuteron Induced Reaction, I—*(d, p) and (d, n) Reactions*— .... Haruo UI..299
Nuclear Deformability and Shell Structure .... T. MARUMORI, S. SUEKANE and A. YAMAMOTO..320
On the Theory of Condensation .... Kazuyoshi IKEDA..341
Nuclear Reactions in the Later Stage of the Stellar Evolution .... K. NAKAGAWA, T. OHMURA, H. TAKEBE and S. OBI..389

Letters to the Editor:

A Lattice Model of Liquid Helium ..... T. MATSUBARA and H. MATSUDA..416
On the Effects of Heavy Unstable Particles to the Anomalous Magnetic Moments of Nucleous .... C. ISO and S. IWAO..417

Price $ 1.25 per copy
$ 15.00 per year (postage inclusive)
Annual dues for foreign members (individual subscribers)
$ 12.00 (postage inclusive)
〃 for foreign members of the Physical Society of Japan
$ 10.00 (postage inclusive)

Application for members, subscriptions and orders for back numbers should be sent, directly or through book-dealers, to

The Publication Office
in
Yukawa Hall, Kyoto University, Kyoto, Japan

JOURNAL OF THE PHYSICAL SOCIETY OF JAPAN Vol. 12, No. 7, JULY, 1957

On the Analysis of the Slow Particles Emitted from Cosmic-Ray Stars (II)

By Shigeo NAKAGAWA, Eiji TAMAI, Humiaki HUZITA and Kiyoaki OKUDAIRA

Department of Physics, Rikkyo (St. Paul's) University, Ikebukuro, Tokyo, Japan

(Received February 21, 1957)

Observations have been made on the heavy fragments from stars produced by cosmic-rays and 6.2 BeV protons from the Bevatrons. The charges of the heavy fragments were determined by measuring the width of tracks.[1] The charge distribution of the heavy fragments emitted from silver or bromine nuclei seems approximately to decrease exponentially. The energy distributions of lithium and beryllium nearly agreed with the curves deduced from the evaporation model, assuming the appropriate nuclear temperatures and Coulomb barrier heights. The angular distributions of them were nearly isotropic. According to these results, the process of slow fragment emission seems to be interpreted as that of evaporation.

§ 1. Introduction

Studies of heavy fragments associated with cosmic ray stars have been made by several investigators.[2] Perkins[3] analysed the heavy fragments, both stable and unstable, emitted from heavy nuclei contained in C2 and G5 emulsions exposed at high altitude. He found that fragment emission might be interpreted in terms of an asymmetric fission process. Recently, Munir[4] reported[8] Li fragments from proton induced stars at 950 MeV, and found that they were ejected as part of the cascade process in the heavy nuclei. In the present paper we have also examined the fragments emitted from heavy nuclei (Ag or Br) of G5 emulsions exposed to cosmic rays in the high altitude and 6.2 BeV proton beam of Bevatron. 155 heavy fragments have been analysed from 1450 cosmic ray stars of more than 8 prongs. In the plates exposed to the Bevatron beam, 62 measurable heavy fragments have been observed in 680 stars. Distributions of charges, energies, and emission angles of the heavy fragments obtained from these two exposures were examined and in this paper the analysis of the relatively slow fragments were discussed.

§ 2. Experimental Procedure

G5 emulsions 600 microns thick were exposed for 3.5 hours to cosmic rays at 27,000 m in England* and to 6.2 BeV proton beam of the Berkeley Bevatron.** As the emulsion contains several elements and the determination of the light target nuclei is rather difficult in the analysis of stars, we only measured the stars produced by Ag and Br in selecting those which had more than 8 prongs (grey tracks +black tracks). Moreover, as written in the previous paper,[1] the analysis of star prongs were made by selecting those which fitted to the following restrictions:

i) the tracks terminated in the emulsions,
ii) location of tracks were more than 20 microns apart from the surface and bottom of the emulsions,
iii) the dip angles of the tracks were less than 12.5° before processing of emulsion.

The mean width over 6 microns lengths of the track was measured step by step along the track from its end point using an eyepiece with secrew micrometer. Since it was found in the previous analysis[1] that the width of track was approximately proportional to $\sqrt{Z}$ (Z: atomic number), in this experiment also the charge of the stable fragments was determined by the track width. Fig. 1 shows one example of the distribution of the track width and from this figure, we can see that the separation of each group is good enough to identify the charge of the fragment. The identification of the unstable fragments was also made according to the method given by Perkins.3) In the analysis we observed only

---

* These plates were furnished through the courtesy of Professor C. F. Powell.

** These plates we owed to Professor Y. Yamaguchi and these were exposed and processed at Berkeley.

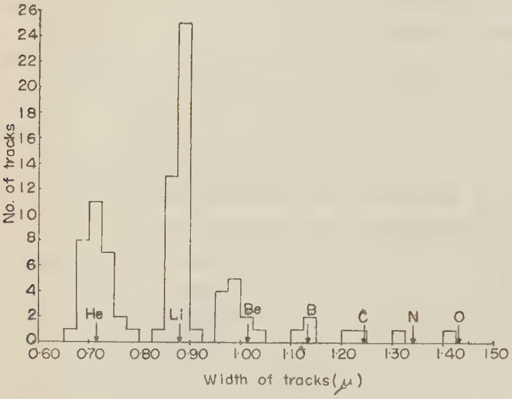

Fig. 1. Distribution of track width. The arrows show the estimated width of the each group by assuming the proportionality of the width to $\sqrt{Z}$. In the case of He we analysed the tracks from Radio Thorium stars in the emulsion.

the simpler cases such as

i) ^{8}Be→2^{4}He disintegration,

ii) ^{9}B →2^{4}He+H^1 disintegration,

and in the more complex cases we could not obtain any clear event. Besides these, we have of course observed the "hammer tracks" due to ^{8}Li and ^{8}B. However, as the "recoil fragments" always have ranges of less than 10 microns,5) our observations were restricted to the fragments of ranges in excess of 25 microns.

§3. Experimental Results

3·1. *Charge distribution of heavy fragments*

In this experiments we analysed the fragments which have charge $Z \geqq 3$. The number of fragments, are given in Table I (A) and I (B). In these Tables, (A) represents the charge distribution of heavy fragments emitted from cosmic ray stars and (B) shows that from the stars produced by the Bevatron proton beam. Total number of observed fragments of (A) and (B) are 155 and 62, respectively.

Table I. (A) Cosmic ray

Z	3	4	5	6	7	8	—	13	total
Observed	95	38	16	2	2	1	—	1	155
Corrected	468±47	179±29	73±18	11±8	7±5	4±4	—	4±4	750
Frequency/star	0.32	0.12	0.05	—	—	—	—	—	—

(B) Accelerator (Bevatron) beam

Z	3	4	5	6	7	total
Observed	37	14	5	4	2	62
Corrected	168±27	63±17	22±10	18±9	9±6	280
Frequency/star	0.25	0.09	0.03	—	—	—

These frequencies were corrected for

(i) geometrical loss of long tracks out of the emulsion layer, (ii) restriction in dip angle ($\theta \leqq 12.5°$), (iii) location of star in the emulsion, on the assumption that the distribution of tracks is isotropic. The assumption of isotropic distribution seems to be correct in the case of the slow fragments as will be seen in section 3·3.

The corrected frequencies of heavy fragments ($Z \geqq 3$) in both (A) and (B) case are equally about 0.5 per star and it seems to show that the emission probability does not depend on the incident proton energy above 6.2 BeV.

Fig. 2 shows the charge distributions of the fragments which have the energies greater than the Coulomb potential barrier heights experimentally deduced, as indicated in Fig. 3 and 4, and the three plots were done according to the star sizes (1) 9–14 prongs, (2) 15–28 prongs, (3) 9–28 prongs in the case of cosmic ray stars. In the Bevatron case we obtained the curve (4). It is seen that the four curves are similar in shape and show a exponential decrease when the charge Z increases, although the statistical error is yet large at the region of higher charges. This decrease can be represented approximately by the following formula:

$$F \propto \exp(-Z)\,,$$

where F is the frequency of the heavy fragment of the charge Z.

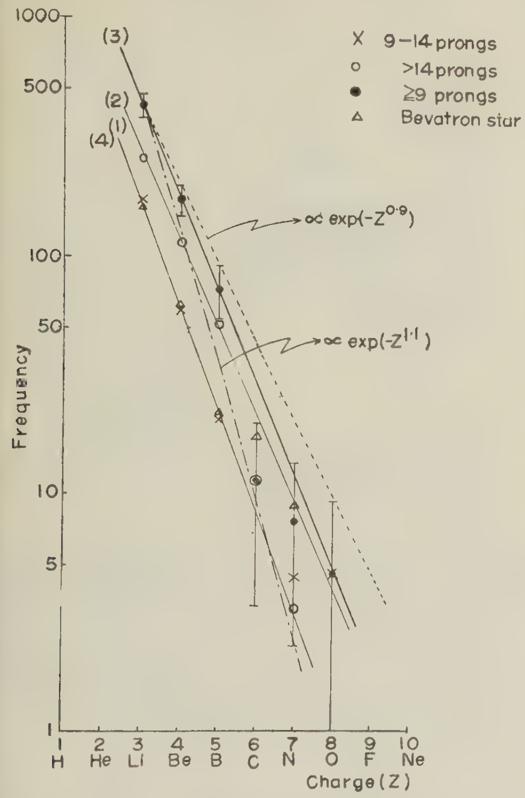

Fig. 2. Charge distribution of heavy fragments from cosmic ray stars with (1) 9 to 14 prongs; (2) >14 prongs; (3) ≥9 prongs. The plot of (4) was obtained from 6.2 BeV proton induced stars.

3·2. *Energy distribution of fragments*

The energies of the heavy fragments were obtained by measuring their ranges. Although the range-energy relation is not well established for slow heavy particles, some uncertainty of energies of the slower particles does not appreciably change the energy distribution. The energy distribution of Li fragments emitted from cosmic ray stars in the center of mass system is shown in Fig. 3. The full curve shows the theoretical evaporation distribution and is plotted after the following formula[6]:

$$N(E)dE = \frac{(E-V)}{T^2}\cdot\exp\left(-\frac{E-V}{T}\right)dE \qquad \text{for } E>V,$$

in which V means the average Coulomb barrier height during the evaporation process and T is the nuclear temperature. The value of V was calculated as 15 MeV (corresponding to $Z=34$, $A=79$) and that of T was given as 10 MeV to fit to the experimental histogram. Fig. 4 shows the energy distribution histogram of Be fragments in the center of mass system. In this case since the data of Be fragments from the cosmic ray induced stars were not sufficient in number, those from 6.2 BeV proton stars were added. In this figure, also the full curve was obtained from the evaporation theory, using the values $T=10$ MeV, $V=19$ MeV. It is found that the both experimental distributions are in good agreement with the calculated ones, except the lower energy region.

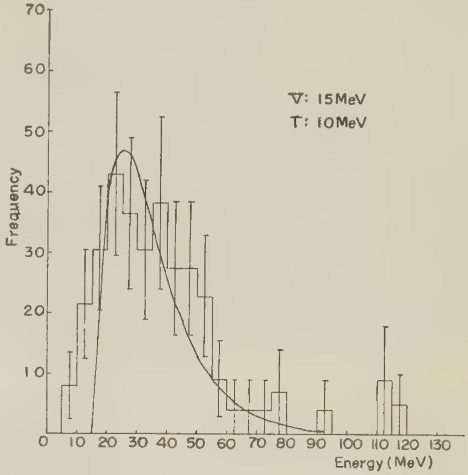

Fig. 3. Energy distribution of Li fragments in the center of mass system.

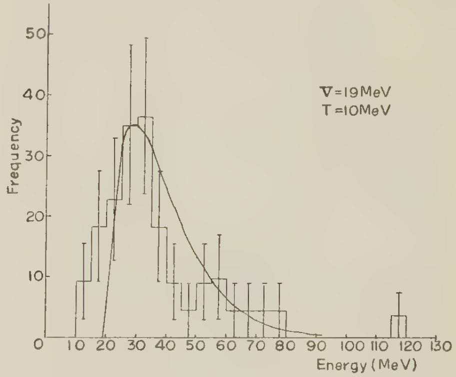

Fig. 4. Energy distribution of Be fragments in the center of mass system.

This excess of slow particles was discussed by several authors[7] on the case of α-particle.

They suggested that these slow particles may be due to expansion of nuclear volume or to secondary emission from the fragment emitted by the fission of mother nuclei. On the case of Li and Be, also slow particle excess was shown but we are not sure whether this is due to the above suggestion or to the emission at the near end of successive evaporation process.

We observed about ten more energetic fragments emitted from the stars and whether these fragments form a tail of the main distribution or are generated by a knock-on process is not certain. This point will be further studied. Fig. 5 and 6 show the energy distributions of protons and α-particles. There were plotted in the center of mass system from that in the laboratory of the previous paper.[1] The temperatures deduced from this figures are 3 and 5 MeV in proton and α-particle cases respectively. It seems to be interesting that the mean temperature is lower in emitting lighter particles than heavier ones.

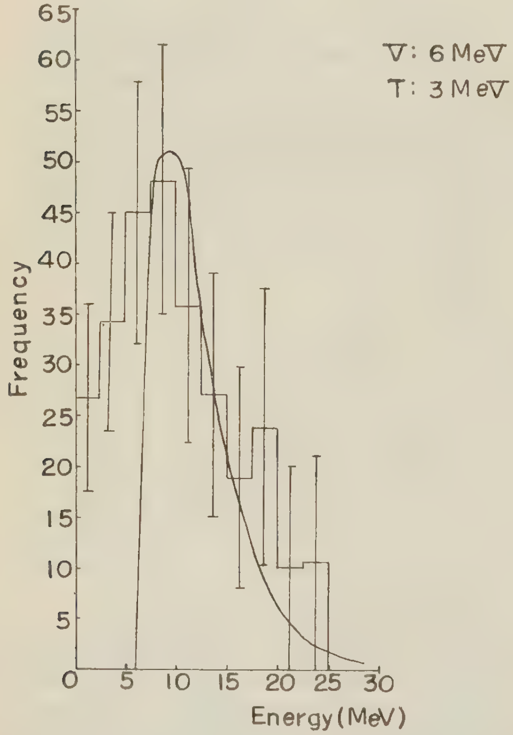

Fig. 5. Energy distribution of protons in the center of mass system.

For the fragments with charge $Z \geqq 5$ the statistics are now poor for describing the energy distribution.

3·3. *Angular distribution of fragments*

For obtaining the angular distribution, the analysis of the nuclear plates exposed to the Bevatron beam is available. In this case the incident protons lay nearly in the plane paral- lel to the emulsion surface and the dip angles of the heavy fragments in our measurement are less than 12.5°, so that measured angular distribution may approximately indicate the true distribution. Fig. 7 shows the angular distribution of the fragments $Z \geqq 3$ emitted from 6.2 BeV proton induced stars. The histogram seems to indicate nearly the isotropic angular distribution. In Fig. 8 the data is replotted in the center of mass system by correcting the forward motion of target nucleus. Considering the slower particles emitted backwards lost in the measurement by the forward motion of target nucleus, these two figures

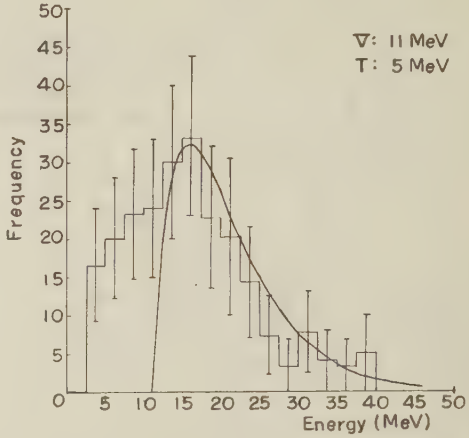

Fig. 6. Energy distribution of α-particles in the center of mass system.

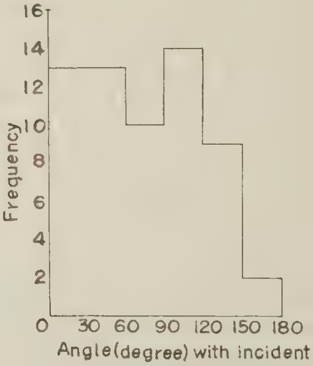

Fig. 7. Angular distribution of the fragments ($Z \geqq 3$) emitted from 6.2 BeV proton induced stars.

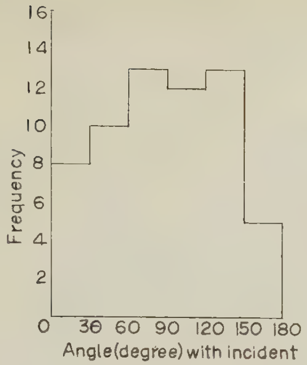

Fig. 8. Corrected angular distribution for the distribution of Fig. 7.

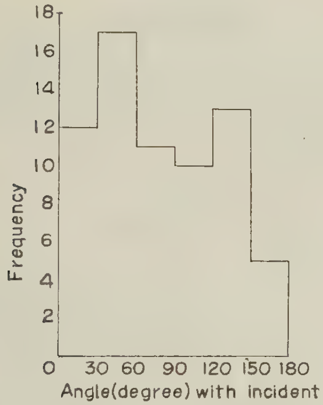

Fig. 9. Angular distribution of Li fragments (slow) emitted from the cosmic ray stars.

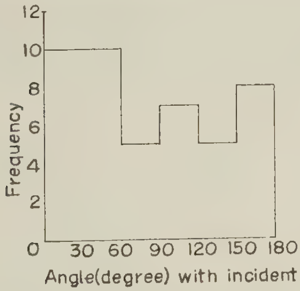

Fig. 10. Angular distribution of the higher charged fragments ($Z\geq 4$) emitted from the cosmic ray stars.

fairly represent the isotropic distributions of the emitted fragments. In Fig. 9 and 10, the distributions of fragments from the cosmic ray stars are shown. These figures also shows the nearly same distributions as in the case of the Bevatron exposure. So it seems to be that the angular distribution of the slow fragments emitted from the stars is isotropic and according to this conclusion, we corrected the frequency and energy distributions as was described in 3·1 and 3·2. In Fig. 11, the angular distribution of the more energetic fragments of $Z\geq 3$ is shown, although the data are poor. This distribution shows strongly collimated in the direction of the star-producing particle.

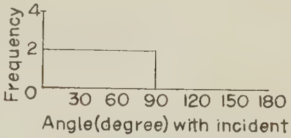

Fig. 11. Angular distribution of the more energetic fragments ($Z\geq 3$) from cosmic ray stars.

§ 4. Interpretation

The results of the measurements may be summarized as follows:

(a) At high excitation energies (the number of star prong is more than 8), a heavy fragment is emitted from a silver or bromine nucleus, with a probability of 0.5.

(b) The charge distribution of these emitted at high excitation energy ($U\sim 800$ MeV) seems nearly to decrease exponentially.

(c) The both energy spectra of the lithium and the beryllium fragments (slow) approximately agree with the calculated spectra assuming the appropriate nuclear temperature and Coulomb potential.

(d) The angular distribution of the Li fragments and that of the fragments of $Z\geq 4$ are nearly isotropic, except the more energetic fragments.

On the basis of the above results described in (c) and (d), the most suitable model to explain the emission of the slow fragments, at least Li and Be fragments, from the nuclei Ag or Br seems to be due to the evaporation process. The most suitable value of nuclear temperature T is 10 MeV in both cases of Li and Be, although, on account of poor statistics, the nuclear temperature could not be analysed more precisely by classifying the star size. We can estimate the excitation energy U of the parent nucleus (Ag or Br) using the following relation,8)

$$U=aT^2\lesssim 800\text{ MeV}, \quad a=\text{const},$$

assuming the Fermi gas model. And this value is comparable to the total nuclear binding energy of Ag or Br nucleus. In the cases of proton and α-particle emissions, the nuclear temperatures were evaluated as 3 and 5 MeV (Fig. 5 and Fig. 6), respectively, so the excitation energy of nucleus becomes higher for emission of heavy fragments. We are not assured that in both Li and Be cases the 10 MeV temperature indicates the true one, however, it seems to be probable that the emission of heavy fragments takes place at higher excitation energy state than proton and α-particle. As the temperature of nucleus is roughly same for Li and Be and it amounts nearly to the highest excitation state of nucleus, we can consider that the more heavier particles may probably be emitted at nearly same condition of nucleus. On discussion more detail, the data of heavier fragments $Z \geqq 5$ are not yet sufficient and we are now accumulating more data on these.

However, it is very interesting to examine the emission probability of various particles from the definite excited state of nuclei and to obtain some informations, especially on the existence or formation probabilities of heavy fragments in the nucleus. From this point of view the exponential decrease of Z dependence of emitted fragments may give us some clue, provided that more precise knowledge may be obtained. Above obtained results indicate only the mean value of emission probability, and so it is necessary to obtain more precise knowledge, that is, by classifying the star size. And also the investigation of more energetic particles emitted from the nuclei may give us important data.

Acknowledgement

We should like to express our sincere thanks to Professor C. F. Powell of the University of Bristol for kindly sending us the nuclear plates exposed to cosmic rays at high altitude, and we are much indebted to the Berkeley Bevatron group to give the chance to analyse the plates exposed to the Bevatron beam. Also the assistance of Mr. S. Nomoto is highly appreciated. This work was partially financed by the Scientific Research Fund from the Ministry of Education.

References

1) S. Nakagawa, E. Tamai, H. Huzita, and K. Okudaira: J. Phys. Soc. Japan **11** (1956) 191
2) G. Occhialini and C. F. Powell: Nature **159** (1947) 93.
P. Hodgson, and D. H. Perkin: Nature **163** (1949) 439.
A. Bonetti, and C. Dilworth: Phil. Mag. **40** (1949) 585.
S. O. C. Sörensen: Phil. Mag. **40** (1949) 947.
3) D. H. Perkins: Proc. Roy. Soc. **A203** (1950) 399.
4) B. A. Munir: Phil. Mag. **1** (1956) 355.
5) J. B. Harding: Phil. Mag. **50** (1949) 530.
6) K. J. Le Couteur: Proc. Phys. Soc. **A63** (1950) 259.
7) W. Heisenberg: Kosmische Strahlung (Springer, 1953) p. 201.
8) J. M. Blatt and V. F. Weisskopf: Theoretical Nuclear Physics, John Wiley & Sons, New York, (1952) p. 371.

JOURNAL OF THE PHYSICAL SOCIETY OF JAPAN Vol. 12, No. 7, JULY, 1957

Cluster Variation Method of Cooperative Phenomena and its Generalization I

By Tohru MORITA

Physics Department, Tokyo Institute of Technology

(Received March 6, 1957)

The cluster variation method of approximation for the cooperative phenomena in the lattice system is generalized so as to be applicable to the cases where the range of the interaction is long compared to the distance of neighboring (lattice) points.

The cluster variation method*) was originally proposed by Kikuchi[1)] and Kurata, Kikuchi and Watari[2)] and applied to lattice systems with the nearest neighbor interaction[1)2)], and then extended by Kikuchi[3)] to those with the 2nd and 3rd neighbor interactions. However, it is difficult to apply this method in its original form to cases where the interaction is of much longer range. In this paper a formulation of the method will be proposed which is valid independently of the kind of lattice structure and is applicable to cases where the range of interaction is long compared to the distance of neighboring (lattice) points.

The system to be considered in this paper is one which is characterized by the following three conditions: 1) The configuration of the system is described by the configurations of L fixed points in it. 2) The possible configurations x_i for the i-th point $(i=1, 2, \cdots, L)$ are denoted by $\alpha_i, \beta_i \cdots, \nu_i$. 3) The potential energy of the system is given by

$$\Phi(x_1, x_2, \cdots, x_L) = \sum_{i=1}^{L} V^{(1)}(x_i) + \frac{1}{2} \sum_{\substack{i=1 \\ (i \neq j)}}^{L} \sum_{j=1}^{L} V^{(2)}(x_i, x_j) + \frac{1}{3!} \sum \sum \sum V^{(3)} + \cdots \tag{1}$$

for the configuration $(x_1, x_2, \cdots, x_L)$.

Our problem is to calculate the free energy of the system. The free energy is given by the minimum value of

$$F = \sum_{x_1=\alpha_1}^{\nu_1} \sum_{x_2=\alpha_2}^{\nu_2} \cdots \sum_{x_L=\alpha_L}^{\nu_L} \rho^{(L)}(x_1, x_2, \cdots, x_L) \times \Phi(x_1, x_2, \cdots, x_L) + kT \sum_{x_1=\alpha_1}^{\nu_1} \sum_{x_2=\alpha_2}^{\nu_2} \cdots \sum_{x_L=\alpha_L}^{\nu_L} \rho^{(L)}(x_1, x_2, \cdots, x_L) \times \ln \rho^{(L)}(x_1, x_2, \cdots, x_L) \tag{2}$$

for the variation of the probability distribution function $\rho^{(L)}(x_1, \cdots, x_L)$, the variation being restricted by the normalization condition

$$\sum_{x_1=\alpha_1}^{\nu_1} \sum_{x_2=\alpha_2}^{\nu_2} \cdots \sum_{x_L=\alpha_L}^{\nu_L} \rho^{(L)}(x_1, x_2, \cdots, x_L) = 1 . \tag{3}$$

Some approximate procedures will be necessary to find the minimum value of F.

For this purpose we introduce clusters of points, a cluster meaning any set of points from L fixed points. Then we introduce several functions connected with a cluster $(i_1, \cdots, i_n)$, $(1 \leq i_1 < i_2 < \cdots < i_n \leq L;\ n=1, 2, \cdots, L)$: The probability distribution function $\rho^{(n)}(x_{i_1}, \cdots, x_{i_n})$ defined by

$$\rho^{(n)}(x_{i_1}, \cdots, x_{i_n}) = \sum_{x_1'=\alpha_1}^{\nu_1} \cdots \sum_{x_L'=\alpha_L}^{\nu_L} \prod_{s=1}^{n} \delta_{x_{i_s}, x_{i_s}'} \rho^{(L)}(x_1', \cdots, x_L'), \tag{4}$$

the correlation function $g^{(n)}(x_{i_1}, \cdots, x_{i_n})$ defined by

$$\rho^{(2)}(x_i, x_j) = \rho^{(1)}(x_i) \rho^{(1)}(x_j) g^{(2)}(x_i, x_j) \tag{5''}$$

$$\rho^{(3)}(x_i, x_j, x_k) = \rho^{(1)}(x_i) \rho^{(1)}(x_j) \rho^{(1)}(x_k) g^{(2)}(x_i, x_j) \times g^{(2)}(x_j, x_k) g^{(2)}(x_i, x_k) g^{(3)}(x_i, x_j, x_k) \tag{5'''}$$

$$\cdot \quad \cdot \quad \cdot \quad \cdot \quad \cdot \quad \cdot$$

$$\rho^{(L)}(x_1, \cdots, x_L) = \prod_{i=1}^{L} \rho^{(1)}(x_i) \prod_{i>j} g^{(2)}(x_i, x_j) \times \Pi\, g^{(3)} \cdots g^{(L)}(x_1, \cdots, x_L) , \tag{5^L}$$

and the function $G^{(n)}(i_1, \cdots, i_n)$ defined by

$$\ln G^{(n)}(i_1, \cdots, i_n) = - \sum_{x_{i_1}=\alpha_{i_1}}^{\nu_{i_1}} \cdots \sum_{x_{i_n}=\alpha_{i_n}}^{\nu_{i_n}} \rho^{(n)}(x_{i_1}, \cdots, x_{i_n}) \times \ln \rho^{(n)}(x_{i_1}, \cdots, x_{i_n}) . \tag{6}$$

The last function $G^{(n)}(i_1, \cdots, i_n)$ has been introduced by the following considerations. When we consider an ensemble of M ($M\to\infty$) similar systems to ours, $[G^{(n)}(i_1,\cdots,i_n)]^M$ is equal to the number of ways in which each of the M systems can be in one of the configurations $(x_{i_1},\cdots,x_{i_n})$ in such a way that $M\rho^{(n)}(x_{i_1}\cdots,x_{i_n})$ systems among M systems are in configuration $(x_{i_1},\cdots,x_{i_n})$, so that $[G^{(n)}(i_1,\cdots,i_n)]^M$ is equal to

---

* Full references on this method are found in reference 2.

$$M!\Big/\prod_{x_{i_1}=\alpha_{i_1}}^{\nu_{i_1}}\cdots\prod_{x_{i_n}=\alpha_{i_n}}^{\nu_{i_n}}(\rho^{(n)}(x_{i_1},\cdots,x_{i_n})M)!$$

and (6) follows from this in the limit $M\to\infty$. It will be noticed that $\ln G^{(n)}(i_1,\cdots,i_n)$ is of a nature of entropy for cluster $(i_1,\cdots,i_n)$. Next, we introduce functions $F^{(n)}(i_1,\cdots,i_n)$ given by

$$G^{(2)}(i,j)=G^{(1)}(i)\,G^{(1)}(j)F^{(2)}(i,j) \qquad (7'')$$

$$G^{(3)}(i,j,k)=G^{(1)}(i)G^{(1)}(j)\,G^{(1)}(k)\,F^{(2)}(i,j)\times F^{(2)}(j,k)F^{(3)}(i,k)F^{(3)}(i,j,k)$$

$$\cdots\cdots \qquad (7''')$$

$$G^{(L)}(1,\cdots,L)=\prod_{i=1}^{L}G^{(1)}(i)\prod_{i>j}F^{(2)}(i,j)\times\prod F^{(3)}\cdots F^{(L)}(1,\cdots,L)\,, \qquad (7^L)$$

and note that from these difinitions we have

$$\ln F^{(n)}(i_1,\cdots,i_n)=-\sum_{x_{i_1}=\alpha_{i_1}}^{\nu_{i_1}}\cdots\sum_{x_{i_n}=\alpha_{i_n}}^{\nu_{i_n}}\rho^{(n)}(x_{i_1},\cdots,x_{i_n})\times\ln g^{(n)}(x_{i_1},\cdots,x_{i_n})\,. \qquad (8)$$

In the following we will adopt the approximations that $F^{(n)}=1$ for most of the clusters, so that it is desired to get some knowledges about the plausibility of the assumption $F^{(n)}=1$. First, from the definitions of $G^{(n)}$ and $F^{(n)}$ and the meaning of $G^{(n)}$, $F^{(n)}$ for a cluster composed of groups of points far apart from each other can be taken to be nearly equal to unity. Secondly, some plausible discussions are found in Takagi's[4)] and Kikuchi's[1)2)] papers that $F^{(n)}$ for a large n may be approximated to 1.

By means of these functions, we rewrite (2) as

$$F=\sum_{i=1}^{L}\sum_{x_i=\alpha_i}^{\nu_i}\rho^{(1)}(x_i)V^{(1)}(x_i)+\frac{1}{2}\sum_{i=1}^{L}\sum_{\substack{j=1\\(i\neq j)}}^{L}\sum_{x_i=\alpha_i}^{\nu_i}\sum_{x_j=\alpha_j}^{\nu_j}\rho^{(2)}(x_i,x_j)V^{(2)}(x_i,x_j)+\frac{1}{3!}\sum\cdots\sum\rho^{(3)}V^{(3)}$$
$$+\cdots+kT\left[\sum_{i=1}^{L}\ln G^{(1)}(i)+\sum_{i>j}\ln F^{(2)}(i,j)+\sum\sum\sum\ln F^{(3)}+\cdots+\ln F^{(L)}(1,\cdots,L)\right]. \qquad (9)$$

The minimum value of this cannot be calculated if no approximate procedures are adopted.

The cluster variation method is as follows: We divide 2^L-1 clusters into two groups, "preserved clusters" and "not-preserved clusters". In the following, if the cluster of points $(i_1,\cdots,i_n)$ belongs to the group of preserved clusters, $F^{(n)}(i_1,\cdots,i_n)$, $G^{(n)}(i_1,\cdots,i_n)$, $\rho^{(n)}(x_{i_1},\cdots,x_{i_n})$ and $g^{(n)}(x_{i_1},\cdots,x_{i_n})$ will be called functions for a preserved cluster or briefly the preserved $F^{(n)}$, $G^{(n)}$, $\rho^{(n)}$ and $g^{(n)}$, and if otherwise they will be called not-preserved functions. Using (5) and (7) we rewrite the right-hand side of (9) so as to express the first row in terms of the preserved $\rho^{(n)}$ and the not-preserved $g^{(n)}$ with no not-preserved $\rho^{(n)}$ or preserved $g^{(n)}$ and the second row in terms of the preserved $G^{(n)}$ and the not-preserved $F^{(n)}$ with no not-preserved $G^{(n)}$ or preserved $F^{(n)}$. In the expression for F thus obtained, we equate $F^{(n)}$ and $g^{(n)}$ to 1**), and make use of (6) for the preserved $G^{(n)}$. Then function F can be expressed in terms of the preserved $\rho^{(n)}$'s only. Now we let this approximate expression for F take the minimum value with respect to the preserved $\rho^{(n)}$'s, where we notice that there exist the recurrence relations

$$\rho^{(s-1)}(x_{i_1},\cdots,x_{i_{s-1}})=\sum_{x_{i_s}=\alpha_{i_s}}^{\nu_{i_s}}\cdots\sum_{x_{i_n}=\alpha_{i_n}}^{\nu_{i_n}}\rho^{(n)}(x_{i_1},\cdots,x_{i_{s-1}},x_{i_s},\cdots,x_{i_n}) \qquad (10)$$

between two preserved $\rho^{(s-1)}$ and $\rho^{(n)}$ and the normalization conditions

$$\sum_{x_{i_1}=\alpha_{i_1}}^{\nu_{i_1}}\cdots\sum_{x_{i_n}=\alpha_{i_n}}^{\nu_{i_n}}\rho^{(n)}(x_{i_1},\cdots,x_{i_n})=1 \qquad (11)$$

for preserved $\rho^{(n)}$'s; Eqs. (10) and (11) follow from the definition of $\rho^{(n)}$, Eq. (4), and the normalization condition for $\rho^{(L)}$, Eq. (3). The minimum value obtained can be considered to be an approximate value to the exact free energy.

Which clusters are to be the "preserved" ones is to be decided from the physical considerations. The approximation will generally become better if we have more preserved clusters in our theory*).

---

* To equate $g^{(n)}$ for any configuration for not-preserved clusters constitutes an extension of the superposition approximation introduced by Kirkwood.

In the development by Kikuchi et al., the preserved clusters are lattice points, bonds of nearest neighbor lattice points and also polygons and polyhedrons which are composed of the bonds; the approximation has been shown to be generally improved as larger clusters are preserved*). It is easily shown that for nearest neighbor interacting systems, their bond approximation is equivalent to our pair approximation where the preserved clusters are all pairs of L points.

As to the degree of approximation of our method, nothing can be said from our formulation, but if the method is applied to a case where our approximations $F^{(n)}=1$ for not-preserved clusters are justified for $\rho^{(L)}=\exp[(F-\Phi)/kT]$, our variation gives an underestimated value for the free energy.

We have considered a system which satisfies 1), 2) and 3). However, we can easily generalize the method to apply to cases where the possible configurations x_i are continuous.

Our scheme of formulation to introduce $G^{(n)}$ is due to Kikuchi. An equivalent formulation is obtained as follows: We substitute from (5^L) into $\ln\rho^{(L)}$ in Eq. (2) so as to obtain

$$\begin{aligned}F=&\sum_{i=1}^{L}\sum_{x_i=\alpha_i}^{\nu_i}\rho^{(1)}(x_i)V^{(1)}(x_i)+\sum_{i>j}\sum_{x_i=\alpha_i}^{\nu_i}\sum_{x_j=\alpha_j}^{\nu_j}\rho^{(2)}(x_i,x_j)V^{(2)}(x_i,x_j)+\sum\cdots\sum\rho^{(3)}V^{(3)}+\cdots\\&+kT\Bigg[\sum_{i=1}^{L}\sum_{x_i=\alpha_i}^{\nu_i}\rho^{(1)}(x_i)\ln\rho^{(1)}(x_i)+\sum_{i>j}\sum_{x_i=\alpha_i}^{\nu_i}\sum_{x_j=\alpha_j}^{\nu_j}\rho^{(2)}(x_i,x_j)\ln g^{(2)}(x_i,x_j)+\sum\cdots\sum\rho^{(3)}\ln g^{(3)}\\&+\cdots+\sum\cdots\sum\rho^{(L)}\ln g^{(L)}\Bigg],\end{aligned}\tag{9'}$$

and express the right-hand side in terms of the preserved $\rho^{(n)}$ and the not-preserved $g^{(n)}$ with no not-preserved $\rho^{(n)}$ or preserved $g^{(n)}$, and finally equate $g^{(n)}$ to 1 in the expression for F**): it should be noted that to equate $g^{(n)}(x_{i_1},\cdots,x_{i_n})$ for any of configurations $(x_{i_s}=\alpha_{i_s},\cdots,\nu_{i_s};\ s=1,\cdots,n)$ to unity is to assume much more than to equate $F^{(n)}$ to unity for the same cluster**).

We have assumed in the above considerations that any configuration x_i is not degenerate. In case configuration x_i is $n(x_i)$-fold degenerate so that point i represents configuration x_i in $n(x_i)$ ways, $\rho^{(L)}\ln\rho^{(L)}$ in the second term in the right-hand side of (2) should be replaced by $\rho^{(L)}\ln\left[\rho^{(L)}(x_1,\cdots,x_L)/\prod_{i=1}^{L}n(x_i)\right]$ and so in the right-hand side of (9) and (9′) the term

$$-kT\sum_{i=1}^{L}\sum_{x_i=\alpha_i}^{\nu_i}\rho^{(1)}(x_i)\ln n(x_i)\tag{12}$$

should be added. (This is obtained if we consider that allowed configurations of point i are $\alpha_{i1},\alpha_{i2},\cdots,\alpha_{in(\alpha_i)},\cdots,\nu_{i1},\cdots,\nu_{in(\nu_i)}$, which are all simple, and x_{ij} and x_{ik} $(j,k\leq n(x_i))$ are equally probable.)

In conclusion, it should be emphasized again that this scheme of approximation is applicable to the cases where the range of interaction is long compared to the distance of neighboring points. Applications of this method will be published in the near future for lattice gases composed of molecules with hard core and for liquids. The latter constitutes an example of the case of continuous configuration for points.

The author wishes to express his cordial thanks to Prof. A. Harasima and Dr. K. Hiroike for the former's continual guidance and the latter's suggestive discussions and also for their kind inspection of the manuscript.

References

1) R. Kikuchi: Phys. Rev. **81** (1951) 988.
2) M. Kurata, R. Kikuchi and T. Watari: J. Chem. Phys. **21** (1953) 434.
3) R. Kikuchi: J. Chem. Phys. **19** (1951) 1230.
4) Y. Takagi: Proc. Phys. Math. Soc. Japan **23** (1941) 44.

---

* This point is illustrated for nearest neighbor interacting cases in ref. 1 and 2. An exception is also given in ref. 1.

** Note that $g^{(n)}=1$ for any configuration is followed by $F^{(n)}=1$, while the converse is not true: see Eq. (8).

JOURNAL OF THE PHYSICAL SOCIETY OF JAPAN Vol. 12, No. 7, JULY, 1957

Some Experiments on the Surface Field Effects in Germanium Single Crystals

By Makoto KIKUCHI

Electrotechnical Laboratory, Tokyo, Japan

(Received March 19, 1957)

From the combined measurements of the field effect on the surface conductance G and on the surface recombination velocity s, it has been found that φ_s (i.e., the difference between the Fermi level and the middle of the energy gap at the surface) drifts towards a negative value when the surface is kept in room air after being submitted to CP-4 etching. This drift is accompanied by a gradual growth of oxide layer on the surface, which has been checked by the observation of the relaxation effect. It is suggested from the results that $s\sim\varphi_s$ curves calculated by Stevenson el al[16] must be shifted by 0.1–0.2 Volts towards right.

§ 1. Introduction

It has already been observed that the surface conductance of a germanium single crystal varies with the electric field applied perpendicular to the surface. The first experiment of this kind was performed by Pearson and Shockley[1], which gave strong evidence for the existence of the "surface states". The remarkable progress in the experiments and theories on the surface field effect, however, has been made in these three years.

By using suitable experimental apparatus, Montgomery[2] succeeded in seeing the variation of the surface conductance with applied transverse field directly on an oscilloscope. Thomas and others[3] performed the similar experiments on the variation of surface recombination velocity s using an alloyed junction diode, taking the saturation current as a measure of s. A number of experimental results on the field effect have been reported in these three years[4–17].

On the other hand, the models for the interpretation of surface phenomena have become quite clear. For instance, we can calculate the variation of the surface conductance G as a function of φ_s (the difference between the Fermi level and the middle of energy gap at the surface), using Schrieffer's calculation of the mobility[18]. As for the surface recombination velocity s, we have a work by Stevenson et al[19] on the basis of Shockley-Read model[20] for the recombination through deathnium centers.

The purposes of this paper are to find more evidences for the models accepted at present, and to find informations for clarifying the mechanisms underlying "relaxation effects." The experiment was at first planned

1. to find variation of surface recambination velocity s with applied field,
2. to measure the accompanying chang of s and G,
3. to observe the relaxation effects in G and s.

On the course of the study, however, it has been found out that it is possible to see the variation of φ_s qualitatively from the experimental results. It has also been intended, therefore, to observe the change of φ_s in the room air after CP-4 etching.

On the other hand, the experimental results on the relaxation effect has shown that the oxide layer gradually grows up in the room air after the etching.

The experimental apparatus and the results are mentioned in the following sections, and the discussions will be given in the last section in some detail.

§ 2. Experimental Procedures

The experimental apparatus is shown in Fig. 1 with schematic diagrams of the measuring circuits. A light beam of about 50 microns in width which is chopped at 200 c.p.s. is focused on the upper surface of the specimen. A thin mica plate is sandwiched between the specimen and a fine metal mesh, as a spacer. A voltage V_p of either plus or minus 1,000 volts are applied to this mesh plate from the d.c. voltage source to cause the field effect. A constant d.c. current I is supplied to the specimen and the variation of the surface conductance G is measured as the variation of the voltage across the specimen by means of a d.c. V.T.V.M. The voltage signal of 200 c.p.s. across the resistor R_0 is measured as a measure of surface recombination velocity. Of course, leakage current through the mica spacer and undesirable disturbances of 50 c.p.s. are checked by inserting high sensitivity ampere-meters in proper places in the circuits.

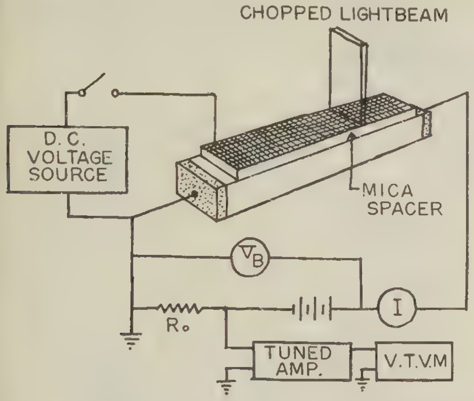

Fig. 1. Experimental apparatus and the measuring circuits.

For the p-n junction experiments, the rod specimen in Fig. 1 is replaced by a germanium grown p-n junction bar.

The specimens used in this work are a grown p-n junction bar and a single crystal rod. The junction was prepared by zone leveling, whose n-side is Sb-doped 2Ω cm, and p-side is In-doped 40Ω cm. The rod specimen is n-type 25Ω cm, which was cut from an Sb-doped pulled single crystal. When the photoresponse is measured as a function of distance, the specimen is moved by the micromanipulator on which it is mounted.

§ 3. Experimental Results

A. *p-n junction experiments*

The photoresponse was measured as a function of distance along the reverse biased p-n junction. When the voltage V_p of +1000 volts is suddenly applied, the photoresponse R_p decreases nearly instantaneously[21] on the n-side and the magnitude of this decrease is greater for larger distances from the junction. On the p-side, however, almost no change is observed in the photoresponse. The results are shown in Fig. 2. (Similar result was observed when the open-circuited photovoltage across the junction was measured instead of the photocurrent.)

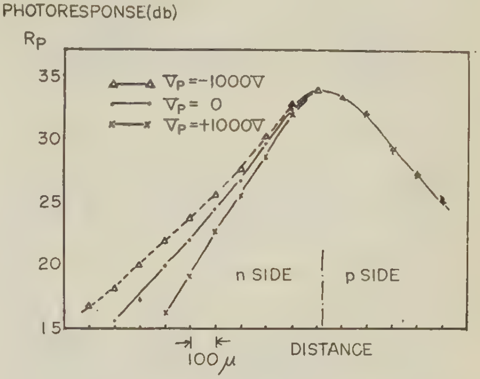

Fig. 2. The local photoresponse as a function of distance along the junction bar with and without the applied voltage V_p.

When V_p of either +1000 or −1000 volts is applied, also the voltage across the junction (V_B) varies instantaneously. It has been observed that these instantaneous change in V_B and R_p is followed by slow decay as shown Fig. 3.

These relaxation effects in V_B and R_p occur in a sense that they tend to recover the values before applying voltage V_p. In the

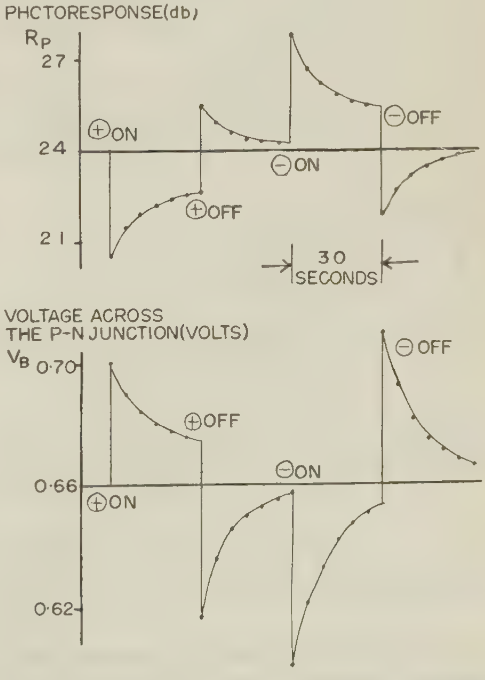

Fig. 3. Accompanying variation of R_p and V_B and the relaxation effect on the p–n junction.

case of Fig. 3, they reach the equilibrium values in 40–50 seconds, but the decay curves can not in general be expressed in a simple exponential function. An example of the time dependence of the photoresponse after "on" and "off" of −1000 volts is shown in Fig. 4.

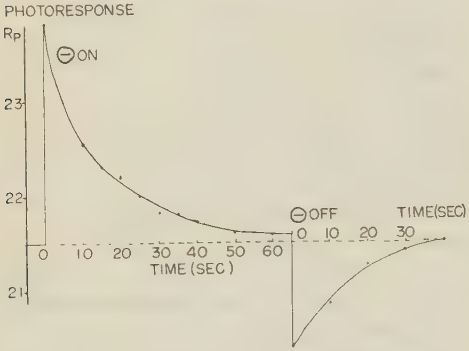

Fig. 4. Example of the relaxation effect.

The time constant, although it can not be defined well, has been found to change under certain surface treatments. For instance, when the surface is etched by CP-4 for 15 minutes, the decay occurs in a very short time. Sometimes, it is very difficult to observe the first "instantaneous" change by applied field just after the CP-4 etching, since the recovery time constant becomes much less than the time constant of the indicator of the V.T.V.M.

If the surface is exposed to the room air, however, the time constant gradually increases as shown in Fig. 5. The decay time increases with the time of exposure in the room air after CP-4 etching. When the surface is exposed to O_3 just after CP-4 etching, the decay curve becomes as shown in th figure by a broken line (*e*).

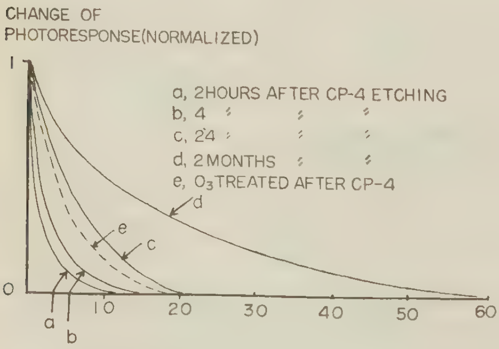

Fig. 5. Time dependence of the relaxation effect for different exposure time to the room air after CP-4 etching.

B. *Single crystal rod experiments*

Fig. 6 shows the results of the photoresponse as a function of distance along the single crystal rod for five different times after HF surface treatment. As is shown, the photoconductance increases after HF treatment, which shows that the surface recombination velocity *s* decreases also monotonically.

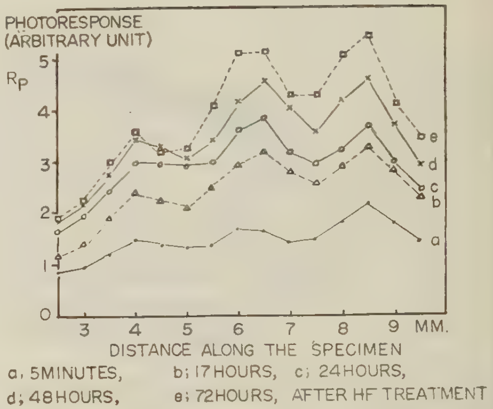

Fig. 6. Local photoresponse along the single crystal rod for different times after HF surface treatment.

When the d.c. voltage V_p is applied to the mesh plate, the photoresponse R_p and the surface conductance *G* vary with time as shown in Fig. 7.

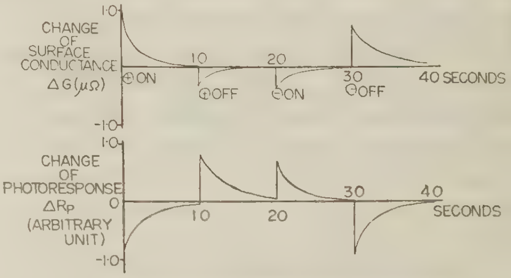

Fig. 7. Accompanying variation of surface conductance *G* and the surface recombination velocity *s* with the voltage V_p, and the "relaxation effect" on the single crystal rod.

It should be noticed that the result shown in Fig. 7 is the case of (b) in Fig. 6, i.e. 17 hours after HF treatment. In this case the relaxation effect occurs in about 10 seconds.

It has been observed that the instantaneou variations of the surface conductance and th photoresponse depend on the polarity of th applied voltage V_p both in sign and magnitude. The results are shown in Fig. 8 for the cases of a, b, c, d in Fig. 6, respectively.

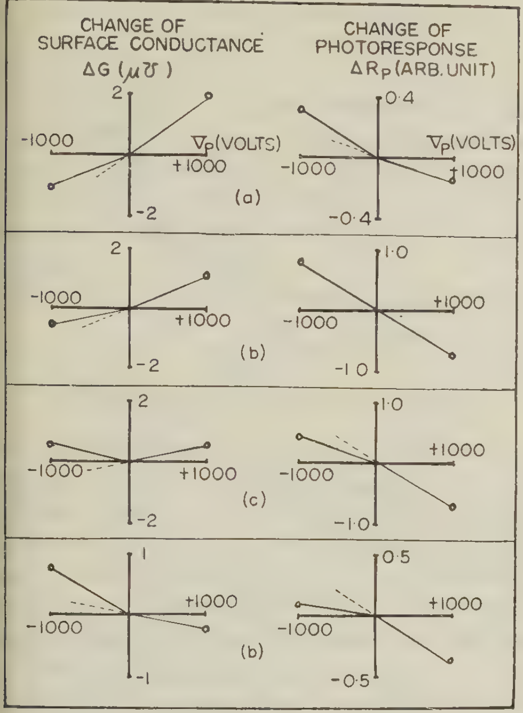

Fig. 8. The field effect on G and R_p of the single crystal rod. (a), (b), (c), (d) corresponding to (a), (b), (c), (d) in Fig. 6.

As is shown, the surface conductance increases with +1000 volts of V_p in the case of (a), while it decreases in (d). In the case of (c), it increases either with +1000 volts or −1000 volts in nearly the same magnitude. On the other hand, the magnitude of the variation of photoresponse R_p is greater for −1000 volts than +1000 volts of V_p in (a), while it becomes opposite in the case of (d). Since the accuracy of the measurements is high enough, above mentioned analysis is quite meaningful.

Fig. 9 shows the results of the same kind of measurements. Fig. 9 (a) is the result when the specimen is kept in high humidity ambient (~95% RH). When it is taken out from the high humidity ambient to the room air, it returns to the state shown in (c) within few minutes, passing through (b). It should be noted that the variation of G is larger in this case than in Fig. 8.

The time dependence of the relaxation effects is shown in Fig. 10 for the single crystal rod. These are the relaxation of the photoresponse (normalized), when +1000 volts of V_p is abruptly applied, for the cases of a, b, c, d and e in Fig. 6, respectively. The general trend is quite similar to the result observed on *p-n* junction.

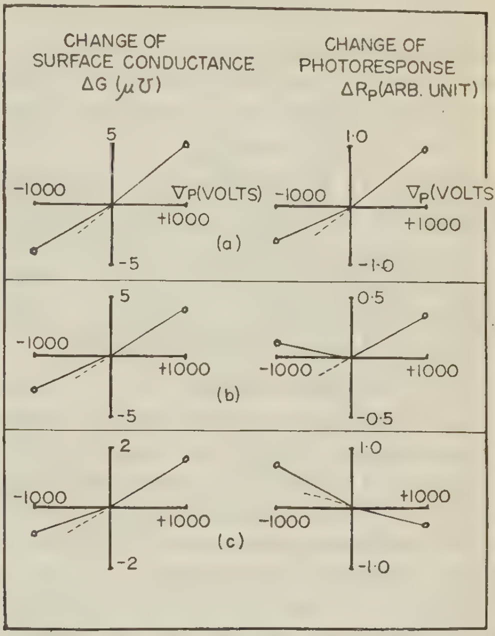

Fig. 9. The field effect on G and R_p of the single crystal rod. (a); in high humidity, (b), (c); when returned into the room air.

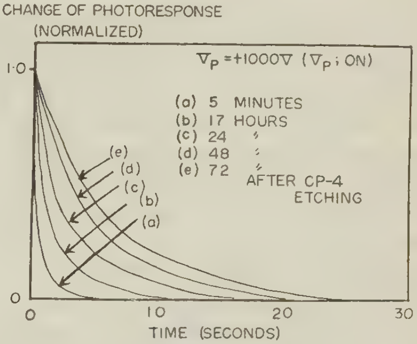

Fig. 10. Time dependence of the relaxation effect. (a), (b), (c), (d), (e) correspond to (a), (b), (c), (d), (e) in Fig. 6.

§ 4. Discussion

A. *Field effect on the surface recombination velocity s*

From the experimental results shown in Fig. 2 on *p-n* junction bar, we can conclude directly that the surface recombination velocity s on the n-side varies with the applied voltage V_p. The photoresponse R_p may be roughly written as a function of distance

$$R_p(x)=Ae^{-\frac{|x|}{L_p}}\,, \qquad (1)$$

where x is the distance from the junction, A is a constant, and L_p is the effective diffusion length, which in turn may be written;

$$L_p=\sqrt{D_m\tau_m} \qquad (2)$$

D_m, τ_m are the diffusion constant and effective lifetime of the minority carriers, respectively. As has been calculated by Shockley[23)], τ_m depends on the bulk lifetime τ_b, the surface recombination velocity s and also on some geometrical factors. Hence, in general,

$$\tau_m=F(\tau_b,\ s,\ \text{geometry})\,. \qquad (3)$$

It may well be expected that τ_m is a monotonic function of s, which decreases with increasing s. Since D_m, τ_b, and geometrical factors are kept constant during the field effect experiment, the result shown in Fig. 2, i.e., the variation of the slope of $\log R_p\sim x$ curve with V_p, may serve as a direct evidence for the field effect on the surface recombination velocity.

In Fig. 2, no field effect on s can be seen on the p-side, which will be discussed later.

B. *Accompanying variation of conductance G and surface recombination velocity s*

As are shown in Fig. 3, 4, for p-n junction and in Fig. 7 for single crystal rod, surface conductance G and surface recombination velocity s show accompanying variation in the field effect. These experimental results are qualitatively in good agreement with the work of Harrik et al[13)].

These results give also strong evidence for the fact that both the surface conductance and the surface recombination velocity are determined by common factors, one of which is the quantity φ_s as discussed later. The experimental fact, that the time dependence of the relaxation effect is almost same for G and s, shows that the relaxation occurs also through that common factor φ_s. The details are discussed in the following paragraph.

C. *The "drift" of φ_s in the room air*

Discussions on the results of Fig. 6, 8 and 9 will be given here. First, the quantity φ_s is defined as the energy difference between the Fermi level and the middle of the energy gap at the surface (Fig. 11). Roughly speaking, the sign of φ_s is plus for n-type surfac and minus for p-type surface.

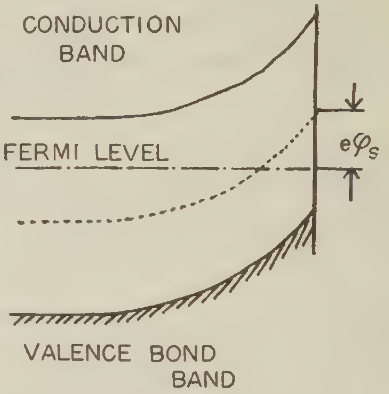

Fig. 11. Schematic energy diagram.

For simplicity, only the experimental result on single crystal rod are discussed. In thi case, the photoresponse R_p is proportional t the usual photoconductance, which in turn i a function of effective lifetime τ_m, since th thickness of the rod is much smaller tha the diffusion length of minority carriers an the d.c. current flowing in the specimen i small enough that sweeping-out effect is negligible. Hence,

$$R_p=A\Delta\sigma_p \qquad \text{(4}$$

$$=B\int_0^\infty e^{-\frac{\xi}{L_p}}d\xi=c\sqrt{\tau_m}\,. \qquad \text{(5}$$

According to Shockley's estimation[24)], th effective lifetime τ_m of a rod specimen whos cross-sectional dimensions are $2X$ and $2Y$ ma be expressed by;

$$\frac{1}{\tau_m}=\frac{1}{\tau_b}+\nu_s\,, \qquad \text{(6}$$

where τ_b is the bulk lifetime, and ν_s is written in the form;

$$\nu_s=s\left(\frac{1}{X}+\frac{1}{Y}\right), \qquad s\to 0 \qquad \text{(7}$$

$$\nu_s=\frac{\pi^2D_m}{4}\left(\frac{1}{X^2}+\frac{1}{Y^2}\right), \qquad s\to\infty\,. \qquad \text{(8}$$

Therefore, τ_m can be expressed;

$$\tau_m=\frac{1}{\frac{1}{\tau_b}+\alpha s}\,, \qquad s\to 0 \qquad \text{(9}$$

$$\tau_m=\frac{1}{\frac{1}{\tau_b}+\beta}\,, \qquad s\to\infty \qquad \text{(10}$$

where α, β are constants which includes th factor that s is varied only on one surface of the rod. Taking Eqs. (9), (10) and (4), (5) into consideration, $R_p \sim s$ curve is plotted qualitatively in Fig. 12.

On the other hand, according to the result of Stevenson's calculation[19)], s varies with φ_s as shown in Fig. 13 by a broken line. Combining the curves of $R_p \sim s$ in Fig. 12 with $s \sim \varphi_s$ in Fig. 13, we can obtain the shape of $R_p \sim \varphi_s$ curve as shown in Fig. 14. The position of the minimum of R_p in Fig. 14 is shifted towards right, which will be discussed later.

As for the surface conductance G, we can calculate it using the Schrieffer's estimation of the mobility[18)]. The solid curve in Fig. 14 is the $\Delta G \sim \varphi_s$ curve for n-type 25Ω cm sample.

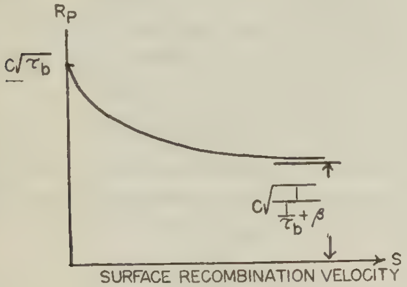

Fig. 12. Qualitative plotting of $R_p \sim s$ curve.

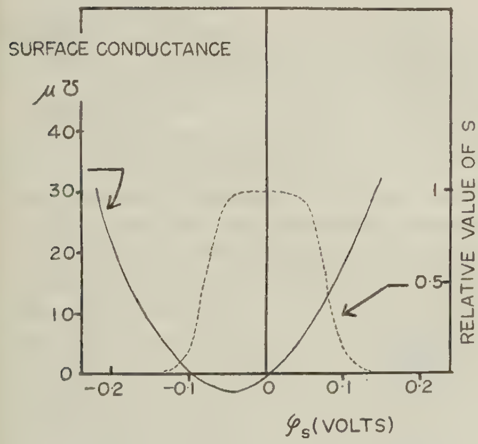

Fig. 13. $G \sim \varphi_s$, $s \sim \varphi_s$ curves.

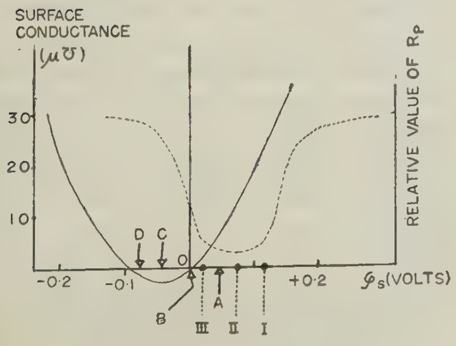

Fig. 14. $G \sim \varphi_s$, $R_p \sim \varphi_s$ curves.

Comparing the results of Fig. 8 with the curves in Fig. 14, it may be directly concluded, that the value of φ_s drifted from the point A to D on the φ_s axis in Fig. 14 when the etched surface was kept in the room air, since positive and negative values of V_p corresponds to the increase and decrease of φ_s, respectively. This conclusion is consistent with the result of Fig. 6.

If, in this process of estimation, the $R_p \sim \varphi_s$ curve were plotted without shifting towards right, it is impossible to obtain one unique point on the φ_s axis for one pair of the results of ΔG and ΔR_p. This means, therefore, that the curves obtained by Stevenson must be shifted towards right, which has been independently suggested by Harrik et al[13)].

The similar procedure applies to the result of Fig. 9, which shows that φ_s increases to the value of (I) in Fig. 14 in the high relative humidity ambient, and goes back to (III) passing through the point of R_p minimum when the specimen is again taken out to the room air.

From this standpoint, the result in Fig. 2, that no change of photoresponse occurs with V_p on the p-side of p-n junction bar, can be explained as that φ_s is just near the minimum point of $R_p \sim \varphi_s$ curve in Fig. 14.

This kind of procedure is quite reliable since it is qualitative rather than quantitative. For instance, the minimum of G or R_p can be directly checked by experiments.

D. *The relaxation effect*

The relaxation effects are already discussed by Kingston, Mcwhorter, and other workers on the model of two kinds of surface states. These surface states are usually called " fast " states and " slow " states. " Fast " states are localized between the germanium bulk and the germanium oxide layer and has the density of about 10^{11}/cm^2. They have time constant comparable to the lifetime of minority carriers, and they are believed to be responsible for the surface recombination. On the other hand, " slow " states exist in or on the outer surface of the oxide layer and have large density of about 10^{13}/cm^2.

When the external voltage V_p is applied, φ_s is changed in the time which is necessary for the readjustment of the carrier distribution through "fast" states. After that, gradual recovery of φ_s to the initial value occurs as the transport of electrons to the "slow" states goes on. This is the relaxation effect on the above mentioned model.

There are two standpoints in explaining the slow transport of electrons to the "slow" states. One is the jumping of electrons over the potential barrier of oxide layer with kinetic energy. The time constant τ of this process may be written in the form;

$$\tau=\tau_0 e^{-\frac{eH}{kT}}, \tag{11}$$

where H is the height of the potential barrier. Therefore, τ must be quite temperature dependent. Experimental results show, however, that τ is not temperature sensitive, so this may be not a predominant process.

The other standpoint is the transport by the tunnel effect. In this case, τ will have the form,

$$\tau=\tau_0 e^{\gamma W}, \tag{12}$$

where W is the thickness of the oxide layer.

According to the result in Fig. 5 and 10, the time constant is drastically decreased by CP–4 etching or *HF* treatment, both treatments are effective in removing the oxide layer on the surface. The time constant tends to increase when the etched surface is kept in the room air, which seems to show that W in Eq. (12) is increased. Brattain et al[25] have quoted the results of Heidenreich. Measuring the thickness of the oxide layer on germanium surface, he found it was 10 Å just after CP–4 etching, while it was increased to 20–50 Å after being aged in the air. Kingston[4] has reported that Green et al found 3 layers of the oxide 5 minutes after etching, and 6 layers after 3 days' exposure to the room air. These results are in agreement with our observations.

The experimental result in Fig. 5 that O_3 treatment increases the time constant of relaxation effect may be another evidence for the above mentioned model[26].

It might be concluded that the drift of φ_s in the air after *HF* treatment is either caused or accompanied by the gradual growing up of the oxide layer on the freshly etched surface.

As is well known, there are also two different theories for the explanation of non-exponential decay of relaxation effect. One is Mcwhorter's theory of multi-time-constants and the other is the theory of non-linea equation by Morrison. Both theories are clo sely related with the $1/f$ noise in semicon ductors. However, nothing has been checke on these problems in this work.

§ 5. Conclusion

By observing combined field effect on th surface conductance and surface recombinatio velocity, it has been found that φ_s drifts to wards some negative value when the surfac is kept in the room air after being submitte to CP–4 etching or *HF* treatment. This drif is accompanied by the gradual growth o oxide layer on the surface, which has bee verified by the observation of the relaxatio time constant of the field effect.

Acknowledgement

The author wishes to express his thank to the members of his group for their discus sions and encouragements.

References

1) Pearson and Shockley: Phys. Rev. **74** (1948 232.
2) Montgomery et al: Phys. Rev. **103** (1956) 865
3) Thomas et al: Phys. Rev. **101** (1956) 984.
4) Kingston: J. A. P. **27** (1956) 101.
5) Henisch: Proc. Phys. Soc. **68** (1955) 353.
6) Low: Proc. Phys. Soc. **68** (1955) 10.
7) Clarke: Phys. Rev. **99** (1955) 1899.
8) de Mars et al: Phys. Rev. **98** (1955) 539.
9) Statz: Phys. Rev. **98** (1955) 540.
10) Brown: Phys. Rev. **100** (1955) 590.
11) Low: Proc. Phys. Soc. **68** (1955) 1154.
12) Many et al: Phys. Rev. **101** (1956) 1433.
13) Harrik et al: Phys. Rev. **101** (1956) 1434.
14) Bardeen et al: Phys. Rev. **104** (1956) 47.
15) Nixon et al: Proc. Phys. Soc. **69** (1956) 487
16) Kingston et al: Phys. Rev. **103** (1956) 534.
17) Brattain et al: B. S. T. J. **35** (1956) 1019.
18) Schrieffer: Phys. Rev. **97** (1955) 641.
19) Stevenson et al: Physica **20** (1954) 1041.
20) Shockley et al: Phys. Rev. **87** (1952) 835.
21) The term "instantaneous" is used for the time much shorter than the time constant o relaxation effect.
22) Goucher: Phys. Rev. **81** (1951) 475.
23) Shockley: "Electrons and Holes in Semi conductors"
24) ref. (23) p. 323.
25) Brattain et al: B. S. T. J. **32** (1953) 1.
26) Though the decay of relaxation effect can no be expressed as a simple exponential function above discussions are still valid.

JOURNAL OF THE PHYSICAL SOCIETY OF JAPAN Vol. 12, No. 7, JULY, 1957

Electron Coupled Interaction in Solid Iodine

By Takashi ITOH*
Department of Physics, Faculty of Science,
University of Tokyo, Tokyo
By Kenjiro KAMBE
University of Electro-Communications, Tokyo

(Received March 25, 1957)

Hyperfine structure in the nuclear quadrupole resonance spectrum of solid iodine observed by Kojima, Ogawa, Hagiwara, Abe and Minematsu is analysed in terms of electron coupled interaction between nuclear spins. Theoretical expression for the Hamiltonian of the electron coupled interaction between two nuclei in an iodine molecule is derived, having the form of $JI_{Az}I_{Bz}+K(I_{Ax}I_{Bx}+I_{Ay}I_{By})$, where z is the bond axis. Electron coupled interactions between nuclei belonging to different molecules in the crystal are neglected. Values of the coupling constants J and K are determined to be both equal to 3.0 kc from the comparison with the experimental data.

Electronic structure of the chemical bond is discussed on the basis of the above coupling constants in combination with the previously known quadrupole coupling constants. It is concluded that the bond in an iodine molecule has 22% s character and 33% d character. It is also concluded that there are auxiliary bonds between neighboring molecules with a fractional importance of 10%.

§1. Introduction

Nuclear quadrupole resonance spectrum of solid iodine has been observed by Dehmelt,[1] Pound[2] and Kamei.[3] Two lines have been found, and their frequencies are 332 Mc and 644 Mc. Recently Kojima and Tsukada[4] found that the lower frequency line has a hyperfine structure with an overall spreading of about 80 kc. Tsukada[5] investigated the Zeeman effect on this line, and observed a very complicated pattern in the case of weak magnetic field where Zeeman energy is comparable with the hyperfine energy. This hyperfine structure has been studied more precisely by Kojima, Ogawa, Hagiwara, Abe and Minematsu.[6] The same pattern has also been observed independently by Watkins and Walker.[7]

Solid iodine is a molecular crystal of orthorhombic symmetry.[8] The lattice constants are $a=4.78$ Å, $b=7.25$ Å and $c=9.77$ Å. A unit cell contains four molecules, whose centers of gravity are located at $(0,0,0)$, $(\frac{1}{2}a, \frac{1}{2}b, 0)$, $(\frac{1}{2}a, 0, \frac{1}{2}c)$ and $(0, \frac{1}{2}b, \frac{1}{2}c)$. The direction of the bound axes of the molecule at $(0,0,0)$ and $(\frac{1}{2}a, \frac{1}{2}b, 0)$ is $(\sin\varphi, 0, \cos\varphi)$, and that of the molecules at $(\frac{1}{2}a, 0, \frac{1}{2}c)$ and $(0, \frac{1}{2}b, \frac{1}{2}c)$ is $(-\sin\varphi, 0, \cos\varphi)$, where $\varphi=32°4'$. All the nuclei are equivalent in the sense that they can be superimposed on each other by a symmetry operation of the crystal. Therefore, no multiplet structure would appear if there were no interaction between nuclear spins. Thus the hyperfine structure observed by Kojima and others must be due to some kind of interaction between nuclear spins.

There are various interactions between nuclear spins, which might give rise to a hyperfine structure such as observed by Kojima and others. Among them, the direct interaction between nuclear magnetic moments is of the order of 1 kc. This is too small to account for the observed spreading. Also the interaction between nuclear quadrupole moments is very small. However, there is another type of interaction between nuclear spins, which is called electron coupled interactions. This is the second order perturbation energy of the interaction between nuclei and electrons. This has been often invoked to explain the hyperfine structure in nuclear magnetic resonance spectra of liquids.[9][10] In the case of iodine crystal, the second order energy of the magnetic interaction between nuclei and electron proves to be of a reasonable order of magnitude to explain the observed spreading. The second order energy of quadrupole interactions and the crossed second order energy of magnetic and quadrupole interactions are so small as to be negligible.

---

* Present address: Department of Physics, University of Chicago, Chicago, Illinois, U.S.A.

§ 2. Electron Coupled Interation Between Nuclear Spins

Theory of the electron coupled interaction between nuclear spins has been developed by Ramsey[9] and Gutowsky, NcCall and Slichter.[10] The coupling constant for this interaction depends on the electronic structure of the chemical bond. In our paper, we consider an iodine molecule in which an electron pair bond between s-p hybridized orbitals of the constituent atoms is assumed. Since intermolecular bond is weak, the electron coupled interaction between nuclei of different molecules can be neglected.

The Hamiltonian for the magnetic interaction between nuclei and electrons is given by

$$H=\sum_N H_N\,, \tag{1}$$

$$H_N=\sum_j H_{Nj}\,, \tag{2}$$

$$H_{Nj}=2\beta\gamma\hbar\left\{\frac{\boldsymbol{I}_N\cdot\boldsymbol{l}_{jN}}{r_{jN}^3}-\frac{(\boldsymbol{I}_N\cdot\boldsymbol{s}_j)r_{jN}^2-3(\boldsymbol{I}_N\cdot\boldsymbol{r}_{jN})(\boldsymbol{s}_j\cdot\boldsymbol{r}_{jN})}{r_{jN}^5}+\frac{8\pi}{3}\delta(r_{jN})\boldsymbol{I}_N\cdot\boldsymbol{s}_j\right\}, \tag{3}$$

where β is the Bohr magneton, γ the magnetomechanical ratio of the nucleus, $\boldsymbol{I}_N$ the spin of the N th nucleus, $\boldsymbol{s}_j$ the spin of the j th electron, $\boldsymbol{l}_{jN}$ the angular momentum of the j th electron around the N th nucleus, and $\boldsymbol{r}_{jN}$ is the radius vector joining the N th nucleus and the j th electron. The electron coupled interaction between the nuclei A and B is given by

$$H_{AB}=-\sum_n\frac{(0|H_A|n)(n|H_B|0)+(0|H_B|n)(n|H_A|0)}{E_n-E_0} \tag{4}$$

where E_0 and E_n are the energies of the ground state and n th excited state of the molecule. To simplify the calculation, we replace the denominator E_n-E_0, as usual, by a certain average excitation energy ΔE, obtaining

$$H_{AB}=-\frac{(0|H_AH_B+H_BH_A|0)}{\Delta E} \tag{5}$$

The calculation of this demands essentially the knowledge about the ground state electronic wave function only. The ground state function is assumed to have the form

$$\Phi_0=\Psi_0\chi_0 \tag{6}$$

$$\Psi_0=(1/\sqrt{2})(\psi_A(1)\psi_B(2)+\psi_B(1)\psi_A(2)) \tag{7}$$

$$\chi_0=(1/\sqrt{2})(\alpha(1)\beta(2)-\beta(1)\alpha(2)) \tag{8}$$

where ψ_A and ψ_B are the s-p hybridized orbitals of the two iodine atoms:

$$\left.\begin{aligned}\psi_A&=\sqrt{s}\,\psi_{5sA}+\sqrt{1-s}\,\psi_{5p\sigma A}\\ \psi_B&=\sqrt{s}\,\psi_{5sB}+\sqrt{1-s}\,\psi_{5p\sigma B}\end{aligned}\right\} \tag{9}$$

s is the s character of ψ_A and ψ_B. α and β in Eq. (8) are spin functions. We neglect the overlapping between ψ_A and ψ_B, which ensures the normality of Ψ_0. The above wave function represents the electron pair bonded state. We do not consider inner core electrons, since their contribution to electron coupled interaction is not important.

Eq. (5) can further be rewritten as

$$H_{AB}=-\sum_{jk}\frac{(0|H_{Aj}H_{Bk}+H_{Bk}H_{Aj}|0)}{\Delta E}\,, \tag{10}$$

where j and k may be 1 and 2. H_{Aj} is appreciable only when the electron j is near the nucleus A, and similarly H_{Bk} is appreciable only when the electron k is near the nucleus B. Therefore, when $j=k$, $H_{Aj}H_{Bk}$ is small everywhere. We neglect this type of terms in (10). When $j\neq k$, H_{Aj} and H_{Bk} commute, so that the two terms $H_{Aj}H_{Bk}$ and $H_{Bk}H_{Aj}$ in (10) make equal contributions on account of the antisymmetry property of the wave function. Thus we obtain

$$H_{AB}=-\frac{4(0|H_{A1}H_{B2}|0)}{\Delta E}\,. \tag{11}$$

Now we consider the integral

$$\int\Psi_0H_{A1}H_{B2}\Psi_0dv_1dv_2\,, \tag{12}$$

where Ψ_0 is the spatial wave function given by (7). From the forms of (7) and (12) it is obvious that the second term of Ψ_0 can safely be omitted. Then we obtain

$$\int\Psi_0H_{A1}H_{B2}\Psi_0dv_1dv_2=\frac{1}{2}\int\psi_A(1)H_{A1}\psi_A(1)dv_1\int\psi_B(2)H_{B2}\psi_B(2)dv_2\,. \tag{13}$$

(3) and (9) give

$$\int \psi_A(1) H_{A1} \psi_A(1) dv_1 = P I_{Az} s_{1z} + Q(I_{Ax} s_{1x} + I_{Ay} s_{1y}) \,, \tag{14}$$

and a similar equation for $\int \psi_B(2) H_{B2} \psi_B(2) dv_2$, where

$$\left.\begin{aligned} P &= 2\beta\gamma\hbar\left\{\frac{8\pi}{3} s|\psi(0)|^2 + \frac{4}{5}(1-s)\left\langle\frac{1}{r^3}\right\rangle\right\} \,, \\ Q &= 2\beta\gamma\hbar\left\{\frac{8\pi}{3} s|\psi(0)|^2 - \frac{2}{5}(1-s)\left\langle\frac{1}{r^3}\right\rangle\right\} \,. \end{aligned}\right\} \tag{15}$$

$|\psi(0)|$ is the absolute value of the ψ_{5s} atomic orbital function at the position of the nucleus, and $\left\langle\frac{1}{r^3}\right\rangle$ is the average value of $\frac{1}{r^3}$ for the ψ_{5p} orbital. Z axis in (14) is taken in the direction of the chemical bond, and x axis is for convenience taken in the direction of the crystalline b axis.

Substituting (14) into (13) and averaging over the spin state (8), we have

$$(0|H_{A1} H_{B2}|0) = -\frac{1}{8} P^2 I_{Az} I_{Bz} - \frac{1}{8} Q^2 (I_{Ax} I_{Bx} + I_{Ay} I_{By}) \,. \tag{16}$$

Thus the final expression for the electron coupled interaction between A and B becomes

$$H_{AB} = J I_{Az} I_{Bz} + K(I_{Ax} I_{Bx} + I_{Ay} I_{By}) \,, \tag{17}$$

where

$$\left.\begin{aligned} J &= \frac{2}{\Delta E}(\beta\gamma\hbar)^2\left\{\frac{8\pi}{3} s|\psi(0)|^2 + \frac{4}{5}(1-s)\left\langle\frac{1}{r^3}\right\rangle\right\}^2 \,, \\ K &= \frac{2}{\Delta E}(\beta\gamma\hbar)^2\left\{\frac{8\pi}{3} s|\psi(0)|^2 - \frac{2}{5}(1-s)\left\langle\frac{1}{r^3}\right\rangle\right\}^2 \,, \end{aligned}\right\} \tag{18}$$

§ 3. Analysis of the Hamiltonian for the Electron Coupled Interaction and the Experimental Results

The Hamiltonian of the nuclear spin system is

$$\mathscr{H} = H_Q + H_{AB} \,. \tag{19}$$

Here H_Q is the Hamiltonian for the quadrupole coupling

$$H_Q = \sum_{N=A,\,B} eQq_{zz} \frac{3I_{Nz}^2 - I(I+1) + \eta(I_{Nx}^2 - I_{Ny}^2)}{4I(2I-1)} \tag{20}$$

with $\eta = (q_{xx} - q_{yy})/q_{zz}$, where q's are the principal values of the electric field gradient tensor, and H_{AB} is the Hamiltonian for the electron coupled interaction given by (17). Rigorously speaking, the x,y,z axes in (20) may be different from the x,y,z axes defined in the preceding section, that is, the former ones are the principal axes of the electric field gradient tensor, whereas the latter ones are the principal axes of the electron coupled interaction and these two sets of axes may not necessarily coincide with each other. However, according to the Zeeman effect study of Tsukada[5] the principal axes of the field gradient tensor coincide with the x,y,z axes defined in the preceding section within experimental error, so that we may use common axes in (17) and (20).

The Hamiltonian (19) has certain symmetry properties. It is not only symmetrical with respect to two nuclear spins, but also invariant under the reflection in the *ac* plane. The eigenvalue problem can be greatly simplified if we take into account these symmetries. The eigenfunctions must therefore be symmetrical or antisymmetrical with respect to these symmetry operations. Now, if we regard the term H_{AB} in (19) as a perturbation, the unperturbed eigenfunctions with the above symmetry properties are given by

$$\left.\begin{aligned} \Psi(m, m', A_1, \pm) &= C\{\psi_m(A)\psi_{m'}(B) + \psi_{m'}(A)\psi_m(B) \pm \psi_{-m}(A)\psi_{-m'}(B) \pm \psi_{-m'}(A)\psi_{-m}(B)\} \,, \\ \Psi(m, m', A_2, \pm) &= C\{\psi_m(A)\psi_{m'}(B) - \psi_{m'}(A)\psi_m(B) \pm \psi_{-m}(A)\psi_{-m'}(B) \mp \psi_{-m'}(A)\psi_{-m}(B)\} \,. \end{aligned}\right\} \tag{21}$$

where ψ_m are the eigenfunctions of the quadrupole coupling of individual nuclei, $m(=\pm 5/2, \pm 3/2, \pm 1/2)$ being the approximate quantum number corresponding to the z component of the nuclear spin angular momentum, and A_1, A_2 and $\pm$ indicate whether the wave function is symmetrical with respect to the exchange of two nuclei and with respect to the reflection about the *ac* plane respectively. C is the normalization factor, equal to $1/2\sqrt{2}$ when $m = \pm m'$ and $1/2$ when $m \neq \pm m'$.

The energy of electron coupled interaction is to be calculated on the basis of the above wave functions. Since two functions $\Psi(m, m', A_{1,2}, \pm)$ and $\Psi(m, -m', A_{1,2}, \pm)$ have equal unperturbed energies, we should take into account the mixing of these two states, if there were interaction between them. However, in the case of the spin quantum number equal to a half odd integer as in the present case, the off diagonal element connecting the above two states vanishes identically, so that the wave functions of (21) are by themselves correct eigenfunctions. The hyperfine energies for them are

$$\left.\begin{aligned}E(m, m', A_1, \pm)&=C^2[(m, m'|H_{AB}|m, m')+(m, m'|H_{AB}|m', m)\\&\qquad\pm(m, m'|H_{AB}|-m, -m')\pm(m, m'|H_{AB}|-m', -m)]\ ,\\E(m, m', A_2, \pm)&=C^2[(m, m'|H_{AB}|m, m')-(m, m'|H_{AB}|m', m)\\&\qquad\pm(m, m'|H_{AB}|-m, -m')\mp(m, m'|H_{AB}|-m', -m)]\ ,\end{aligned}\right\}\tag{22}$$

where $|m, m')$ means the wave function $\psi_m(A)\psi_{m'}(B)$ and so on. Although rigorous calculation of (22) is somewhat tedious, we may neglect the terms of higher order than η since η is sufficiently small; $\eta=-0.15$. First, we consider the case of $m\neq m'$. Then (22) is rewritten as

$$\left.\begin{aligned}E(m, m', A_1, \pm)&=Jmm'+Kf(m, m')\pm\eta Kg(m, m')\pm\eta Kh(m, m')\ ,\\E(m, m', A_2, \pm)&=Jmm'-Kf(m, m')\pm\eta Kg(m, m')\mp\eta Kh(m, m')\ ,\end{aligned}\right\}\tag{23}$$

where the four terms correspond to the four terms of (22) in that order. Nonvanishing values of f, g, h are

$$\left.\begin{aligned}f(m, m\pm1)&=\frac{1}{2}(I\mp m)(I\pm m+1),\\g\left(\pm\frac{3}{2}, \pm\frac{1}{2}\right)&=g\left(\pm\frac{1}{2}, \mp\frac{3}{2}\right)=\frac{1}{12}\left(I-\frac{1}{2}\right)\left(I+\frac{1}{2}\right)^2\left(I+\frac{3}{2}\right),\\h(m, -m\mp1)&=\left\{\frac{1}{8}+\frac{I(I+1)}{24m(m\pm1)}\right\}(I\mp m)(I\pm m+1)\ .\end{aligned}\right\}\tag{24}$$

Next, in the case of $m=\pm m'$, it can be proved that Eq. (23) and (24) still hold, although the correspondence between the terms of (22) and (23) is not as above in this case.

Hyperfine energies of the eigenstates calculated by (23) and (24) are listed in Table I.

Table I. Hyperfine energy levels $\left(I=\frac{5}{2}\right)$.

m,	m'	$E(m, m', A_1, +)$	$E(m, m', A_1, -)$	$E(m, m', A_2, +)$	$E(m, m', A_2, -)$
$\frac{5}{2}$	$\frac{5}{2}$	$\frac{25}{4}J$	$\frac{25}{4}J$		
$\frac{5}{2}$	$\frac{3}{2}$	$\frac{15}{4}J+\frac{5}{2}K$	$\frac{15}{4}J+\frac{5}{2}K$	$\frac{15}{4}J-\frac{5}{2}K$	$\frac{15}{4}J-\frac{5}{2}K$
$\frac{5}{2}$	$\frac{1}{2}$	$\frac{5}{4}J$	$\frac{5}{4}J$	$\frac{5}{4}J$	$\frac{5}{4}J$
$\frac{5}{2}$	$-\frac{1}{2}$	$-\frac{5}{4}J$	$-\frac{5}{4}J$	$-\frac{5}{4}J$	$-\frac{5}{4}J$
$\frac{5}{2}$	$-\frac{3}{2}$	$-\frac{15}{4}J+\frac{10}{9}\eta K$	$-\frac{15}{4}J-\frac{10}{9}\eta K$	$-\frac{15}{4}J-\frac{10}{9}\eta K$	$-\frac{15}{4}J+\frac{10}{9}\eta K$
$\frac{5}{2}$	$-\frac{5}{2}$	$-\frac{25}{4}J$			$-\frac{25}{4}J$
$\frac{3}{2}$	$\frac{3}{2}$	$\frac{9}{4}J$	$\frac{9}{4}J$		
$\frac{3}{2}$	$\frac{1}{2}$	$\frac{3}{4}J+4K$	$\frac{3}{4}J+4K$	$\frac{3}{4}J-4K$	$\frac{3}{4}J-4K$
$\frac{3}{2}$	$-\frac{1}{2}$	$-\frac{3}{4}J+\frac{98}{9}\eta K$	$-\frac{3}{4}J-\frac{98}{9}\eta K$	$-\frac{3}{4}J+\frac{10}{9}\eta K$	$-\frac{3}{4}J-\frac{10}{9}\eta K$
$\frac{3}{2}$	$-\frac{3}{2}$	$-\frac{9}{4}J$			$-\frac{9}{4}J$
$\frac{1}{2}$	$\frac{1}{2}$	$\frac{1}{4}J-12\eta K$	$\frac{1}{4}J+12\eta K$		
$\frac{1}{2}$	$-\frac{1}{2}$	$-\frac{1}{4}J+\frac{9}{2}K$			$-\frac{1}{4}J-\frac{9}{2}K$

Allowed transitions between these states are listed in Table II and III with their frequencies and relative intensities. Intensities of some hyperfine component lines depend on the direction of the radiation field, but since the dependence is not so prominent, we consider in the following only the average spectrum over all the directions of the radiation field, although slight variation of the spectrum with the direction of the radiation field has been observed in qualitative agreement with our theory.

The pattern of the hyperfine structure

Table II. Hyperfine component lines for the transition $m=\frac{3}{2}\rightarrow\frac{1}{2}$

m'	Symmetry	Frequency	Intensity*
$\frac{5}{2}$	$A_1,\pm\rightarrow A_1,\pm$	$-\frac{5}{2}J-\frac{5}{2}K$	1
	$A_2,\pm\rightarrow A_2,\pm$	$-\frac{5}{2}J+\frac{5}{2}K$	1
$\frac{3}{2}$	$A_1,\pm\rightarrow A_1,\pm$	$-\frac{3}{2}J+4K$	2
$\frac{1}{2}$	$A_1,\pm\rightarrow A_1,+$	$-\frac{1}{2}J-(4+12\eta)K$	1
	$A_1,\pm\rightarrow A_1,-$	$-\frac{1}{2}J-(4-12\eta)K$	1
$-\frac{1}{2}$	$A_1,+\rightarrow A_1,+$	$\frac{1}{2}J+\left(\frac{9}{2}-\frac{98}{9}\eta\right)K$	X
	$A_1,-\rightarrow A_1,+$	$\frac{1}{2}J+\left(\frac{9}{2}+\frac{98}{9}\eta\right)K$	Y
	$A_2,+\rightarrow A_2,-$	$\frac{1}{2}J-\left(\frac{9}{2}+\frac{10}{9}\eta\right)K$	Y
	$A_2,-\rightarrow A_2,-$	$\frac{1}{2}J-\left(\frac{9}{2}-\frac{10}{9}\eta\right)K$	X
$-\frac{3}{2}$	$A_1,+\rightarrow A_1,+$	$\frac{3}{2}J+\frac{98}{9}\eta K$	X
	$A_1,+\rightarrow A_1,-$	$\frac{3}{2}J-\frac{98}{9}\eta K$	Y
	$A_2,-\rightarrow A_2,+$	$\frac{3}{2}J+\frac{10}{9}\eta K$	Y
	$A_2,-\rightarrow A_2,-$	$\frac{3}{2}J-\frac{10}{9}\eta K$	X
$-\frac{5}{2}$	$A_1,+\rightarrow A_1,\pm$ $A_2,-\rightarrow A_2,\pm$	$\frac{5}{2}J-\frac{10}{9}\eta K$	1
	$A_1,-\rightarrow A_1,\pm$ $A_2,+\rightarrow A_2,\pm$	$\frac{5}{2}J+\frac{10}{9}\eta K$	1

* $X=\cos^2 xH_{rad.}$, $Y=\cos^2 yH_{rad.}$.

Here $xH_{rad.}$ and $yH_{rad.}$ denote the angles between the direction of the radiofrequency field and the x and y axes respectively.

Table III. Hyperfine component lines for the transition $m=\frac{5}{2}\rightarrow\frac{3}{2}$

m'	Symmetry	Frequency	Intensity*
$\frac{5}{2}$	$A_1,\pm\rightarrow A_1,\pm$	$-\frac{5}{2}J+\frac{5}{2}K$	2
$\frac{3}{2}$	$A_1,\pm\rightarrow A_1,\pm$	$-\frac{3}{2}J-\frac{5}{2}K$	2
$\frac{1}{2}$	$A_1,\pm\rightarrow A_1,\pm$	$-\frac{1}{2}J+4K$	1
	$A_2,\pm\rightarrow A_2,\pm$	$-\frac{1}{2}J-4K$	1
$-\frac{1}{2}$	$A_1,\pm\rightarrow A_1,+$	$\frac{1}{2}J+\frac{98}{9}\eta K$	$\frac{1}{2}$
	$A_1,\pm\rightarrow A_1,-$	$\frac{1}{2}J-\frac{98}{9}\eta K$	$\frac{1}{2}$
	$A_2,\pm\rightarrow A_2,+$	$\frac{1}{2}J+\frac{10}{9}\eta K$	$\frac{1}{2}$
	$A_2,\pm\rightarrow A_2,-$	$\frac{1}{2}J-\frac{10}{9}\eta K$	$\frac{1}{2}$
$-\frac{3}{2}$	$A_1,+\rightarrow A_1,+$ $A_2,-\rightarrow A_2,-$	$\frac{3}{2}J-\frac{10}{9}\eta K$	$2X$
	$A_1,-\rightarrow A_1,+$ $A_2,+\rightarrow A_2,-$	$\frac{3}{2}J+\frac{10}{9}\eta K$	$2Y$
$-\frac{5}{2}$	$A_1,+\rightarrow A_1,+$ $A_2,-\rightarrow A_2,-$	$\frac{5}{2}J+\frac{10}{9}\eta K$	$2X$
	$A_1,+\rightarrow A_1,-$ $A_2,-\rightarrow A_2,+$	$\frac{5}{2}J-\frac{10}{9}\eta K$	$2Y$

* X and Y are the same as in Table II.

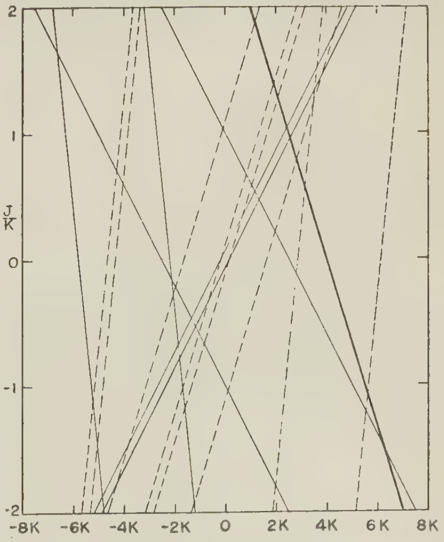

Fig. 1. Frequencies of hyperfine component lines for the transition $m=3/2\rightarrow1/2$ as function J/K. Bold lines, solid lines and broken lines represent the frequencies of hyperfine component lines with a unit intensity, a half intensity and a quarter intensity, respectively.

depends on the ratio J/K. In Figs. 1 and 2 the frequencies of hyperfine component lines are plotted as functions of J/K. Best agreement with experiment has been obtained for the pattern of the $m=3/2\rightarrow 1/2$ transition by putting $J=K=3.0$ kc. Comparison of observed and calculated spectra is shown in Figs. 3 and 4 for the transitions $m=3/2\rightarrow 1/2$ and $m=5/2\rightarrow 3/2$ respectively. The observed spectrum for the $m=5/2\rightarrow 3/2$ transition has not a well resolved structure, and it may be due to a large broadening of hyperfine component lines.

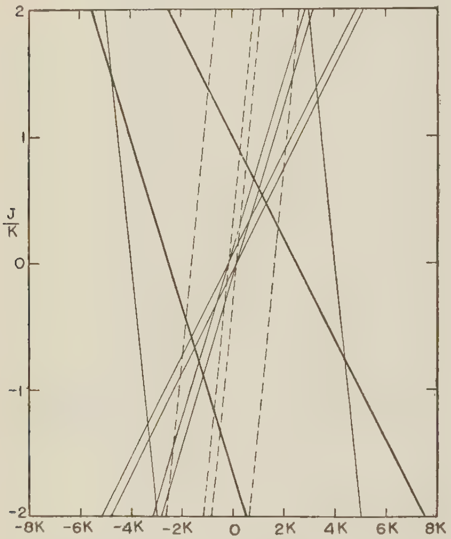

Fig. 2. Frequencies of hyperfine component lines for the transition $m=5/2\rightarrow 3/2$ as functions of J/K. Three types of lines indicate the same intensities as in Fig. 1.

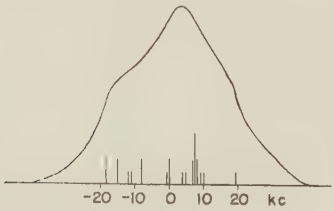

Fig. 3. Hyperfine structure of the $m=3/2\rightarrow 1/2$ spectrum. The smooth continuous curve represents the observed spectrum while the sharp vertical lines represent the calculated spectrum.

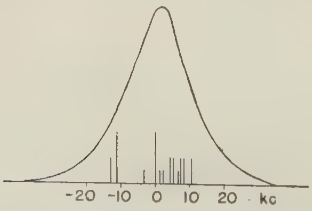

Fig. 4. Hyperfine structure of the $m=5/2\rightarrow 3/2$ spectrum.

§ 4. Discussion of the Electric Structure of the Chemical Bond

In the preceding section values of J and K have been determined to be both equal to 3.0 kc. According to (18), the equality of J and K would be ensured only when $s=1$, that is, only when the bond has 100 % s character. However, (18) can not be considered as very accurate, since we have introduced various approximations in deriving it. Thus, we must confine ourselves to the discussion of the order of magnitude of these constants. Now, since J and K are sensitive functions of s, we can obtain a rather precise value of s from the observed magnitude of J and K. Before doing so, we must estimate the values of several quantities involved in (18). The value of $\beta\gamma\hbar\left\langle\frac{1}{r^3}\right\rangle$ is very accurately known to be $\frac{15}{16}\times 827.265$ Mc[11] from the hyperfine structure of the atomic spectra of iodine, but $\beta\gamma\hbar|\psi(0)|^2$ can only be estimated by the conventional approximate formula $|\psi(0)|^2=Z\delta^2/\pi a_0^3 n'$,[12] where Z is the atomic number, δ Slater's orbital exponent, n' the effective principal quantum number, and a_0 is the Bohr radius. $\varDelta E$ may be put equal to be about 5 ev.[13] Then the values of J and K in (18) are functions of s. If we put $s=1$, J and K become about 78 kc, while if we put $s=0$, J becomes about 0.6 kc. To fit J and K with the observed magnitude, s must be about 0.22, that is, the s character of the bond is about 22 %.

We can discuss the electronic structure of the chemical bond in an iodine crystal in more detail by also using the previously known quadrupole coupling constants. Solid iodine has a layer structure[8] and the molecules in each layer are believed to be held together by auxiliary bonds, since the internuclear distance between nuclei of neighboring molecules is smaller than the sum of van der Waals radii. According to the crystalline structure, each atom is involved in two auxiliary bonds, one directed nearly along the z axis while the other directed nearly along the y axis. The auxiliary bonds have been discussed by Townes and Dailey[14] as due to the resonance switching of the bonds, and later by Robinson, Dehmelt and Gordy,[15] as due to the excitation of electrons to d orbitals. In this paper, we postulate that the auxiliary bonds are formed by excitation of electrons to d orbitals, since the resonance switching of the bonds would be accompanied with the rotation of the principal axes of field gradient tensor in contradiction to the experiment.

We denote by a the fractional importance with which the auxiliary bond is formed, and denote by d the d character of the intramolecular bond. Then theoretical expression for the quadrupole coupling constants are

$$\left.\begin{aligned} eQq_{zz} &= eQq_{\text{atom}}\left(1-s+d-\frac{1}{2}a\right), \\ \eta &= -\frac{3}{2}a\,. \end{aligned}\right\} \qquad (25)$$

We have neglected higher order terms such as sd, sa in the above expression. eQq_{atom} means the quadrupole coupling constant for an iodine atom. Its value is known to be -2×1146.356 Mc.[11] Putting $eQq_{zz}=-2157$Mc,[1,2,3] $\eta=-0.15$ and $s=0.22$, we obtain $a=0.1$ and $d=0.33$.

The nature of the bonds in halogen molecules has been discussed theoretically by Mulliken,[16] and it has been concluded that the s character in the F_2 molecule is about 2% and the s character in the Cl_2 molecule is about 10%, so that the present value of 22% for the s character in the I_2 molecule is quite reasonable. The value of d and a are also of reasonable order of magnitude.

We express our hearty thanks to Prof. M. Kotani and Prof. C. H. Townes for their encouragements and discussions, and to Prof. S. Kojima for suggesting this problem.

References

1) H. G. Dehmelt: Z. Physik **130** (1951) 346.
2) R. V. Pound: Phys. Rev. **82** (1951) 343.
3) T. Kamei: J. Phys. Soc. Japan **7** (1952) 649.
4) S. Kojima and K. Tsukada: J. Phys. Soc. Japan **10** (1955) 591.
5) K. Tsukada: J. Phys. Soc. Japan **11** (1956) 956.
6) S. Kojima, S. Ogawa, S. Hagiwara, Y. Abe and M. Minematsu: J. Phys. Soc. Japan **11** (1956) 964.
7) G. D. Watkins and R. M. Walker: Bull. Am. Phys. Soc. Ser. **III 1** (1956) 11.
8) R. W. Wykoff: Crystal Structures, Int. Sci. Pub. Inc., New York (1940). Crystal structure of iodine is shown in Fig. 2 of reference 6.
9) N. F. Ramsey: Phys. Rev. **91** (1953) 303.
10) H. S. Gutowsky, D. W. McCall and C. P. Slichter: J. Chem. Phys. **21** (1953) 279.
11) V. Jaccarino, J. G. King, R. A. Satten, and H. H. Stroke: Phys. Rev. **94** (1954) L 798.
12) K. Kopfermann: Kernmomente, Akademische Verlagsgesellschaft, Leipzig (1940) p. 20.
13) G. Herzberg: Spectra of Diatomic Molecules, D. Van Nostrand Co. Inc., New York (1950) p. 540.
14) C. H. Townes and B. P. Dailey: J. Chem. Phys. **20** (1952) 35.
15) H. Robinson, H. G. Dehmelt and W. Gordy: J. Chem. Phys. **22** (1954) 511.
16) R. S. Mulliken: J. AM. Chem. Soc. **77** (1955) 884.

JOURNAL OF THE PHYSICAL SOCIETY OF JAPAN Vol. 12, No. 7, JULY, 1957

Some Factors Affecting the Decay of Secondary Electron Emission of Silver-Magnesium Alloys

By Masaki HIRASHIMA* and Shoichi MIYASHIRO

Research Laboratories, Tokyo-Shibaura Electric Co.,
Kawasaki City

(Received April 6, 1957)

The secondary emission yield is observed to decay very rapidly under electron bombardment especially during the exhaust process using oil diffusion pump. In this paper, factors affecting the decay, a method of remedy to make the decayed yield to recover, and effects of various gases and vapors on the yield are discussed. A major cause of the secondary yield decay is attributed to the deposition of amorphous carbon, which is produced on the dynode surface through the decomposition of hydrocarbon or carbon-containing gases by the electron beam. Heating the contaminated dynode at high temperatures in oxygen atmosphere for some period results in a recovery of the yield. Keeping the dynode at high temperatures during electron bombardment is effective in bringing about a marked decrease in the decay. From the data on the temperature dependence of the decay, the heat of adsorption of a gas which is considered to be the source of contamination, is calculated to be about 1.6 kcal/mole. N_2, CO and CO_2 do not exert any harmful effects upon activated dynodes, while H_2 exerts somewhat harmful effects, and, particularly, electric discharge in H_2 should be avoided. The most unfavorable gas is the grease vapor. The process of contamination is briefly discussed.

§ 1. Introduction

In the course of experiments carried out to determine optimum activating conditions of silver-magnesium alloy secondary electron emitters, using water vapor and oxygen as oxidizing agents, we were confronted with some difficulty in obtaining reproducible results. It was also noticed that the secondary electron yield, δ, decayed so rapidly during the measurements that the values of yield measured at the beginning and at the end of the experiment under the same condition differ considerably from each other. It was considered necessary, therefore, to search into factors affecting the decrease in the yield prior to the determination of optimum activating conditions.

It is the object of this paper to describe the results thus obtained. A probable cause of the decay of secondary yield will be discussed in some detail, and effects of various gases or vapors on the yield will also be described.

§ 2. Measurements of Secondary Yield on the Pump

2.1 *Apparatus*

The description which follows pertains to the measurements on experimental tubes on the pump, except where otherwise noted. In order to save time and labor for making a number of experimental tubes to be used to determine optimum activating conditions, we carried out experiments with experimental tubes on the pump in place of sealed-off tubes. A schematic diagram of the apparatus used is shown in Fig. 1. Water vapor or oxygen was employed as oxidizing agent, and such gases as carbon monoxide, carbon dioxide, hydrogen, and nitrogen were used to study their effects on the secondary yield. The pressure of these gases was measured by the Pirani gauge. Most of the experimental tubes used in the following experiments were of usual construction with an exception of the provision of a shutter for protecting the contamination deposits on the dynode from the tungsten filament, as roughly sketched in the figure. The specimens used were Ag-Mg ribbons 20 mm in length, 5 mm in width, and about 0.1 mm in thickness and contained about 2 per cent Mg in weight. The Mg content has nothing to do with the following discussions.

---

* Now at Department of Communication Engineering, Tokai University, Tomigaya, Yoyogi, Shibuya-ku, Tokyo.

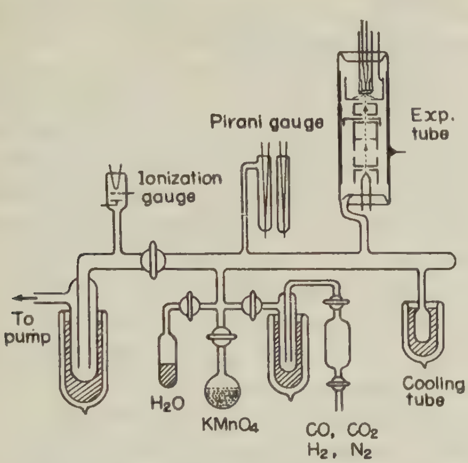

Fig. 1. Schematic view of the apparatus for measuring the yield decay and the effect of various gases on the yield.

These specimens were well polished before formed into ⊔ shape, by the polishing process described in a previous paper.[1)]

2.2. *Dependence of the Secondary Yield on Activating Time.*

At the start, the secondary yield was measured with a dynode not subjected to an activating treatment. It was assumed that since the dynode was not activated, the maximum secondary yield would be of the order of unity. This was, however, not the case, and somewhat larger value of the yield could perhaps be attributed to MgO film formed on the surface during glass-working and bulb-baking stages. Water vapor was then admitted into the experimental tube at a certain pressure; the dynode was heated at the desired temperature for a prescribed period by passing an electric current through the ribbon, and the temperature was measured by means of a thermojunction welded to its back; the current was stopped and the tube evacuated. After the bulb was baked out, the electrodes were degassed by induction heating, and the tungsten filament was flashed as usual, with the shutter closed, and the experimental tube was ready for measurement of the yield against primary voltage. These measurements were carried out in succession as many times as desired. The curves of Fig. 2 are typical results of such measurements. If maxima of these curves, δ_{max}, are plotted against the activating time, an activation curve such as shown in Fig. 3 is obtained. The curve shows a pronounced maximum, and even with prolonged activation with water vapor as the oxidizing agent, the yield could not be recovered.

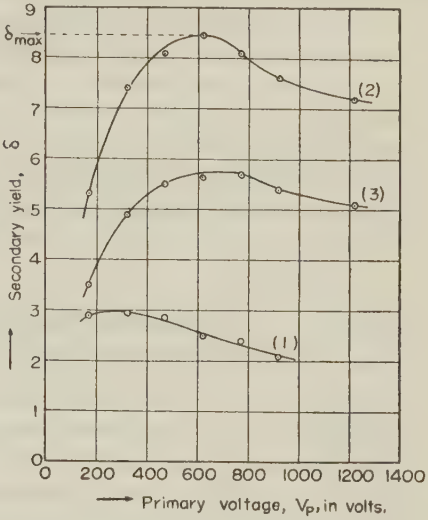

Fig. 2. Yield vs. primary voltage curves. Activating condition: $P_{H_2O} \approx 6 \times 10^{-2}$ mmHg.; Temp. = 620°C; Time: 0 min. (curve 1), 3 min. (curve 2), 6 min. (curve 3).

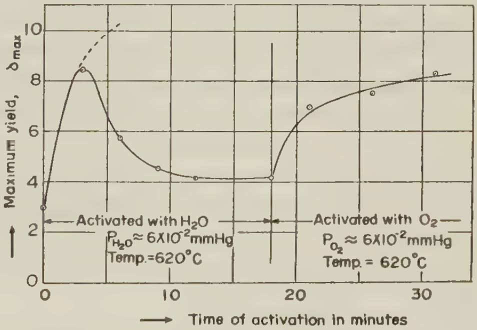

Fig. 3. Activation curve of Ag–Mg dynode.

When oxygen was employed in place of water vapor as the oxidizing agent at this stage, the secondary yield recovered to a higher value, reaching a nearly steady value after 15 to 30 minutes of activating time according to the oxygen pressure and the dynode temperature.

After a number of similar experiments were carried out with a variety of water vapor pressures and dynode temperatures, it was found that the maxima of the activation curves always occurred at the first measuring points. This fact seems to suggest that something unfavorable to secondary electron emission was produced on the dynode surface upon bombardment by primary electrons even for a short time during the yield measurement. In fact, when the dynode was taken out of the experimental tube, purple- or blue black-colored staining was observed on the portion of the surface bombarded by the primary beam, and the diameter of the stain was quite equal to the primary beam diameter.

2.3. *Decay of the Secondary Yield and Primary Electron Bombardment.*

It was our next step to determine whether the contamination deposit stated above is formed only through the bombardment by primary electron beam, or due to evaporation of contaminant from the tungsten filament. The simplest way to do this is to cut off the primary beam for a short time during the course of the decay. If the contamination deposit in question came from the filament, it would have nothing to do with the primary electron bombardment. Curve A of Fig. 4 shows, however, that this is not the actual case. The fact that the cessation of the primary beam with the filament being lit resulted in no decay of the secondary yield indicated that the evaporation of contaminants from the filament need not be taken into account in the present case. The only cause of contamination deposit is then attributed to the primary electron bombardment. This point was also confirmed by experiments carried out with experimental tubes of special construction using magnetically deflected primary electron beams.

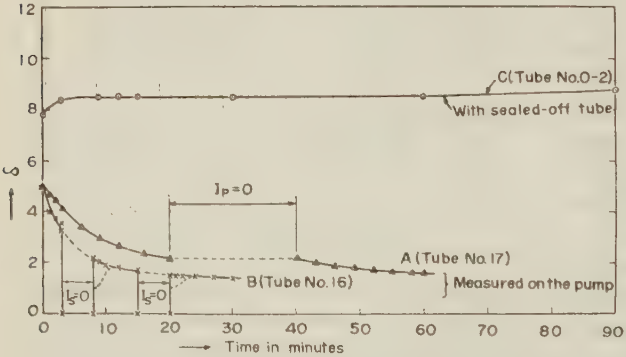

Fig. 4. Effect of cessation of primary electron bombardment and of secondary electron extraction on decay characteristics.

Intermittent suppression of the secondary electrons by applying the collector a negative potential with respect to the dynode, while the primary beam was held constant throughout the measurements, gives no effect upon the yield decay as shown by curve B of the same figure. On suddenly recovering the collector voltage from a negative value with respect to the dynode ($V_c=-15$ volts) to the normal positive value ($V_c=50$ volts), the gradual rise of the curves as shown dotted in Fig. 4 B was observed in cases where insulators such as glass exposed to stray electrons were present; stored charge on these is believed to be the cause of this phenomenon.

The result of a similar experiment with a sealed-off tube is also illustrated in the same figure by curve C. No decay is observed in this case, and only with prolonged primary electron bombardment a normal decay due to the decomposition of MgO into Mg and O_2 was noticed.

2.4. *Effects of Primary Electron Energy and Current Density on the Yield Decay.*

As it has become evident that the primary electron beam plays a major role in producing the contamination deposit, it is important next to know the effect of the primary electron energy and current density on the yield decay. As seen from Fig. 5, yield decay does not depend too much on electron energy in the range covered by our experiments.

On the other hand, the primary current density exerts a marked effect on the yield decay, as seen from Fig. 6. In this figure, curves A and B have been obtained with the same primary voltage ($V_p=620$ volts) but with different values of primary current ($I_p=1\mu A$ and $2\mu A$, respectively). Comparison of these two curves indicates that the time required for the yield to decay to the same value of δ is inversely proportional to the primary current, and that the same quantity of charge laid down by the bombarding beam on the dynode gives rise to equal decay of the secondary yield when the primary voltages are kept equal.

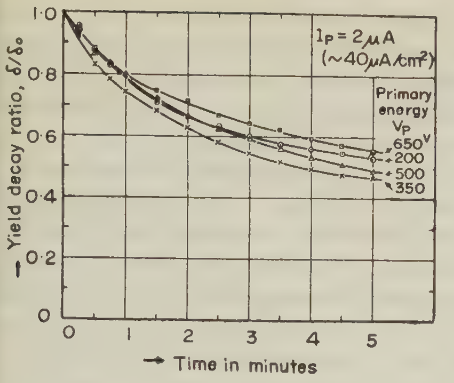

Fig. 5. Effect of primary electron energy on the decay.

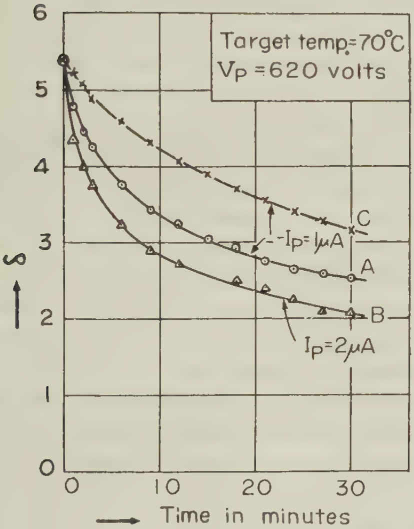

Fig. 6. Effect of primary current density on the yield decay.
Curves A and B: on oil diffusion pump
Curve C: on mercury diffusion pump.

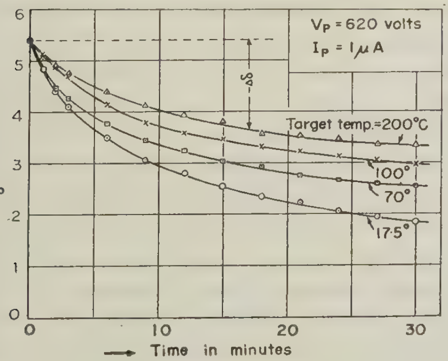

Fig. 7. Effect of target temperature on the decay.

2.5. *Effect of the Dynode Temperature on the Decay.*

In order to see the effect of the dynode temperature on the decay, dynode temperature was varied over the range from room temperature to 200°C. In the range of temperatures covered by our experiments, keeping the dynode at higher temperatures during the primary electron bombardment resulted in a considerable decrease in the decay of the yield, as shown in Fig. 7.

§ 3. The Cause of the Yield Decay during Primary Electron Bombardment

It is evident that the cause of the yield decay should be attributed to residual gases in the system, as shown by curve C of Fig. 4 for a sealed-off tube. A glance at Fig. 3 through Fig. 7 affords an impression that electron bombardment gives rise to something on the bombarded surface which is a poor secondary electron-emitting substance. Fig. 3 indicates definitely that the yield decay is not caused by the decomposition of MgO into Mg and O_2 by electron bombardment. A number of papers have been published on the so-called "electron-bombardment contamination" in the field of electron microscopy.[2)3)4)5)] In the field of secondary electron emission, Lempicki seems to be the first to publish the result of experiments on the yield decay during primary electron bombardment,[6)7)8)] and he attributed this to the deposition of silicone on the surface which was decomposed by electron bombardment from the silicone vapor originated from the pump oil. The pump oil used in the present experiments was not the silicone oil but the alkyl-naphthalene oil, although silicone grease was used in the taps. These taps were cooled with water during the experiments.

The curve of Fig. 3 seems likely to reveal that something deposited on the dynode surface by electron bombardment does not have great enough affinity for oxygen to deprive oxygen of water molecules. Referring to Fig. 8 which represents the relation between the dissociation pressure of various oxides and the reciprocal of temperature,[9)] it is considered that the substance deposited on the dynode surface by electron bombardment must form an oxide whose dissociation pressure should lie above the H_2O curve. Therefore, the probable substance is assumed to be carbon. The fact that the contamination deposits disappear completely when they were heated in air to about 800°C for about one minute indicates this to be the actual case. Although an electron diffraction study is unable to give any concrete conclusion to its identification, the patterns obtained reveal that it is amorphous and of carbonaceous nature. The gas that is produced by subjecting the stained dynode to activation with oxygen, therefore, will be either CO or CO_2.

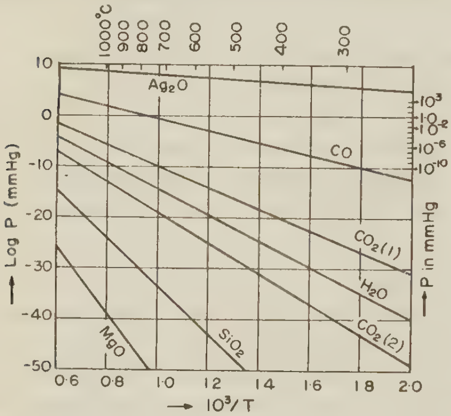

Fig. 8. Dissociation pressure of various oxides.
$CO_2(1)$: $C+O_2=CO_2$
$CO_2(2)$: $2\,CO+O_2=2\,CO_2$

§ 4. The Process of Contamination of the Dynode Surface

In conformity with the work of Hillier[2], and of König[3] the present investigation has shown that the contamination deposit has an amorphous structure and is of carbonaceous nature as stated above. This suggests that the source material is organic in nature or carbon-containing gas, and that contamination is formed by the reaction of the electron beam with the vapor or gas molecules on the dynode. The source of these organic vapors or gases may come from oil, grease, etc. in the system. The conversion of these organic substances to form the contamination deposit must take place on the surface of the dynode and not in the vapor, because the contamination deposit is formed only on the portion of the surface bombarded by primary electron beam. On the dynode surface, there may exist an adsorbed layer of hydrocarbon or carbon-containing gas which effectively increases the concentration of molecules. Whatever electronic mechanism causes the formation of contamination, the orignal organic or gas molecules are effectively fixed by the electron beam. The electron energies necessary to bring about the chemical reactions are relatively small in comparison with the beam energies employed,[10] which would explain why there is no great dependence of contamination on the electron energy (see Fig. 5).

The contamination process is continuous with time for so long as the electron beam is operative, so that a steady state condition must be set up between the rate of conversion of hydrocarbon molecules to contamination on the surface, and the net rate of supply of fresh molecules from outside. It has been established that no build-up of carbon layer takes place on the surface in the absence of the electron beam. And if any hydrocarbon or carbon-containing gas is present on the surface, it must result from an equilibrium between molecules arriving on the surface and those leaving it. At low surface concentrations, the contamination rate will be directly proportional to the surface concentration of molecules and to the current density. We have already seen that this was the actual case (Fig. 6).

We agree with A. E. Ennos[4] in attributing the replenishment of the hydrocarbon or carbon-containing gas film to the arrival of hydrocarbon or gas molecules by condensation from the surrounding vapor or gas. The concentration of these molecules, which are in dynamic equilibrium with the vapor, is dependent upon the pressure of the vapor, the temperature of the surface and the binding energy of the vapor molecules on the surface. At very high temperatures, no vapor molecules can exist for a significant time on the surface, but as the temperature is lowered, the average time for which a molecule can stay on it increases, with consequent increase in surface concentration. The degree of adsorption will be directly proportional to the pressure of the vapor since for the low vapor pressures which exist in a normal kinetic vacuum system, it is reasonable to assume that the surface concentration of vapor molecules never exceeds monolayer except under conditions of very low surface temperature. The fraction of the surface covered with molecules will then be given by a formula due to Langmuir:[11]

$$\theta=\frac{ap}{1+ap}\approx ap=\frac{\alpha_0\varepsilon^{Q/RT}}{k_0(2\pi MRT)^{1/2}}p, \qquad (1)$$

since p is very small in the present case

($\sim 10^{-6}$ mm Hg). Here α_0 is the condensation coefficient, Q is the activation energy necessary to evaporate 1 mole of the condensate or the heat of adsorption, R the gas constant, M the molecular weight of the condensate, k_0 a constant, T the absolute temperature and p the pressure.

In view of the experimental results obtained by Ennos[5] showing that the thickness of contamination deposit is nearly a linear function of bombarding time in the initial stage, it will not be unreasonable, as a first approximation, to assume that the square of the drop in the secondary yield from the initial value, $(-\Delta\delta)^2$, is proportional to the quantity of deposited carbon. m:

$$(-\Delta\delta)^2 \propto m. \tag{2}$$

On the other hand, the contamination rate, dm/dt, should be proportional to the primary current, i_p, and also to θ:

$$\frac{dm}{dt} \propto i_p \theta \,. \tag{3}$$

Taking K as the proportional constant, we obtain

$$\frac{dm}{dt} = K i_p \theta \approx K i_p \frac{\alpha_0 \varepsilon^{Q/RT}}{k_0 (2\pi MRT)^{1/2}} p \,. \tag{4}$$

Squaring both sides and assuming i_p and p constant, the following relation is obtained:

$$\log\left(\frac{dm}{dt}\right)^2 T = \text{constant} + \frac{2Q}{RT} \times 0.4343. \tag{5}$$

In Fig. 9 $(-\Delta\delta)^2$, taken from Fig. 7, is plotted against time. The slope of the linear parts of these curves gives dm/dt. If we plot $\log (dm/dt)^2 T$ against $1/T$, a straight line is obtained as shown in Fig. 10, whose slope giving Q, the heat of adsorption, as 1.6 kcal/mole. In the absence of data on the heat of adsorption of gases on MgO surface, we can not deduce from the above result what kind of gases plays the major role in the contamination in question.

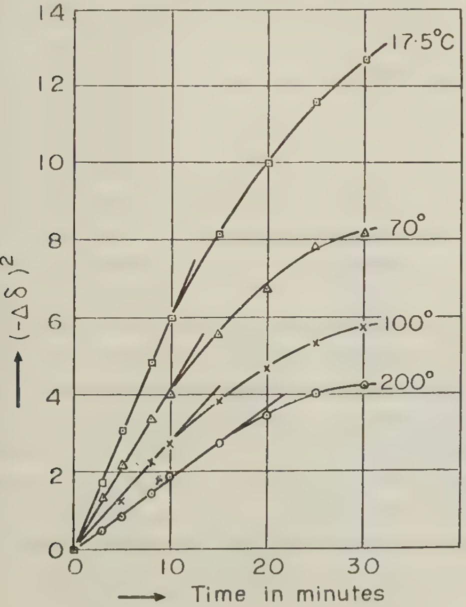

Fig. 9. $(-\Delta\delta)^2$ vs. time plot.

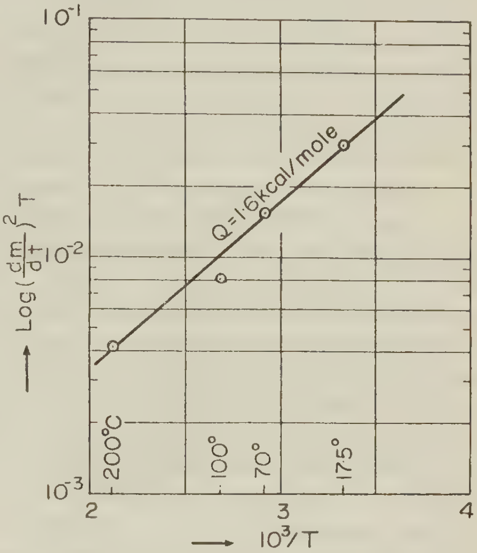

Fig. 10. Heat of adsorption.

When the oil diffusion pump is replaced by a mercury diffusion pump, it is observed that the yield decay shows a marked decrease as shown by curve C of Fig. 6. From this, we may conclude that gases or vapors originated from the pump oil play a significant role in producing contamination deposit in the present case.

§ 5. Effects of Heating Well-Activated Dynodes in Various Gases upon the Yield

5.1. *Effect of Heating in Vacuo.*

It is important to know the effect of heat treatment of an activated dynode in vacuum upon its secondary yield. From our experiments it has been shown that heat treatment at 300°C for about 5 minutes in vacuum causes the yield to increase slightly, but heating up to higher temperatures (over ca. 500°C) causes a considerable decrease in the yield.

5.2. *Effect of Air.*

Short-time exposure of an activated dynode kept at 590°C to air did not produce any change in the yield.

5.3. *Effect of Heating in Hydrogen and of Electric Discharge in Hydrogen.*

Heating of an activated dynode in line hydrogen at 1 atmospheric pressure up to about 600°C for 30 minutes causes the yield to decrease by approximately 30% or more, while a similar heat treatment in dry hydrogen at a pressure of the order of 10^{-2} mm Hg. does not affect the yield to a marked degree. This is probably due to partial decomposition of MgO film by hydrogen.

A more pronounced effect on the secondary yield is produced by subjecting the dynode to an electric discharge in an atmosphere of hydrogen. Furthermore, it was observed that the effect was more pronounced with the dynode negative and the collector positive, than with the dynode positive and the collector or the other electrodes negative. A decrease in the yield of about 40% was not rare. The reason for this effect might be considered as roughening of the dynode surface due to positive ion bombardment, giving rise to labyrinth-like structure of the surface.

5.4. *Effect of Heating in Nitrogen.*

Heating an activated dynode in dry nitrogen to about 600°C has no noticeable effect upon the secondary yield.

5.5. *Effect of Heating in Carbon Monoxide and Carbon Dioxide.*

At first, it was expected that such gases as CO and CO_2 would be decomposed on the dynode surface by being deprived oxygen atoms by magnesium atoms, thereby giving rise to carbon deposit on that surface. Contrary to our expectation, however, heating an activated dynode at 400–600°C for about 15 minutes or so in an atmosphere of dry CO or CO_2 at a pressure of about 1×10^{-2} mm Hg did not result in a decrease in the secondary yield. Rather, in conformity with the data obtained by Wargo et al,[12)13)] a virgin dynode is activated in CO and CO_2 atmospheres.

5.6. *Effect of Grease Vapors.*

From our preliminary experiments carried out some time ago it has been known that the vapor of grease used in taps has unfavorable effects upon the secondary yield. This has been confirmed again by the following experiment.

An experimental tube containing a dynode activated with oxygen is evacuated on the pump. The vacuum system is equipped with an appendage in which a small quantity of vacuum grease* is contained. Within this grease is embedded a Ni-W thermojunction by which the temperature of the grease may be measured. After the vacuum system was evacuated to as perfect a vacuum as possible, the system is shut off from the pump by a tap, the grease is heated from outside of the appendage by a gas flame, the vapor of the grease is admitted into the system directly or through a liquid-air trap, and then the dynode is heated to the desired temperature for a prescribed period. After the system has been exhausted again, the degassing of the bulb and of the electrodes is done as usual, and then the secondary yield is measured as a function of the primary voltage. It is found from this experiment that the grease vapor has the most influence in causing the secondary yield to decrease, and the dynode seems to be permanently damaged by the silicone grease vapor, as reported by Lempicki[6)].

A mass spectrographic study of the vapor of the silicone grease at 100°C gives the following result:

Table I

Components	Percentage
H_2	7.57
H_2O	69.85
CO	16.50
N_2	2.50
O_2	None
CO_2	1.05
Mass No. 73	2.55
Others	Trace

The vapor from the grease above 100°C was not measured because of the perplexing effects of the grease on the apparatus. Table I does not contain any harmful components of the grease vapor for the dynodes in question except for an unknown component of mass number 73, so far as our experiments on the effects of gases on the secondary yield are concerned. The component with mass number 73 seems to be hydrocarbon vapor, and along with vapors evolved from the grease at higher temperatures than 100°C which might contain some unfavorable components, it is very likely to be the source of the contamination deposit in the present case.

---

* Dow Corning High Vacuum Grease (silicone grease).

§ 6. Concluding Remarks

It has been found that the major cause of the yield decay of Ag-Mg alloy secondary electron emitters under electron bombardment during exhaust on the pump is not the decomposition of MgO film due to electron bombardment, but is the deposition of contaminant which is believed to be amorphous carbon decomposed from hydrocarbon vapors or carbon-containing gases by the electron beam. The contamination deposit is formed only on the portion of the surface of the dynodes bombarded by the primary electron beam. It seems to be very probable that the same phenomena occur more or less even in sealed-off tubes. Therefore, this should be taken into account, in connection with the interpretation of life test result of dynode materials.

Acknowledgments

We wish to take this opportunity to express our hearty thanks to Dr. N. Saito, who, together with Mr. K. Motoyama, has provided us with the data on the analysis of the grease vapor by means of a mass spectrograph, and to whom we are indebted for the many illuminating discussions throughout the present investigation. We also wish to thank Mr. Y. Fukao for the electron diffraction study of the contamination deposits; Messrs. Y. Nakayama, K. Noga, and M. Kondo for their discussions; and Mr. H. Muramatsu for preparing the Ag-Mg alloys. Many thanks are also due to Mr. S. Satoh for his ever willing assistance on the various phases of the experimental work.

References

1) M. Hirashima: J. Phys. Soc. Japan **10** (1955) 1055.
2) J. Hillier: J. Appl. Phys. **19** (1948) 226.
3) H. König and G. Helwig: Zeits. f. Phys. **129** (1951) 491; **129** (1951) 33.
4) A. E. Ennos: British J. Appl. Phys. **4** (1953) 101.
5) A. E. Ennos: ibid. **5** (1954) 27.
6) A. Lempicki A. B. McFarlane: Nature **167** 1951) 813.
7) A. Lempicki: J. Sci. Instr. **32** (1955) 221.
8) P. H. Dowling and J. R. Sewell: J. Appl. Phys. **25** (1953) 228.
9) M. Kawakami: *Physics and Chemistry of Metals* (Sankaido, Tokyo, 1946), Vol. 1, p. 245 (in Japanese).
10) e. g. D. A. Wright: British J. Appl. Phys. **5** (1954) 108.
11) e. g. S. Brunauer: *The Adsorption of Gases and Vapors* (Princeton University Press, 1945), p. 60.
12) P. Wargo: Phys. Rev. **96** (1954) 837 (A).
13) P. Wargo, B. V. Haxby and W. G. Shepherd: J. Appl. Phys. **27** (1956) 1311.

JOURNAL OF THE PHYSICAL SOCIETY OF JAPAN Vol. 12, No. 7, JULY, 1957

Conical Spiral Structure and Laminar Cleavage of Graphite

By Takuro TSUZUKU*

Tokai Electrode Research Laboratory, Daigiri, Fujisawa-City, Japan

(Received January 30, 1957)

Apparently circular crystals of graphite prepared from carbon black were investigated by electron microscope. These crystals show circular growth patterns and produce spotty electron diffraction rings accompanied by ellipses and diffuse bands. Moreover, the circular crystal folded in half presents a fan-shaped appearance instead of a semi-circular form; *i.e.*, two radii along the folded line makes an angle smaller than 180°.

These facts verify that the apparently circular crystal is really a stack of conical graphite sheets, each of which is successively rotated about the common axis in *c*-direction. It is pointed out that such a conical crystal can be formed by a spiral mechanism.

Laminar cleavage of conical crystals was observed, and the gliding mechanism connected with the spiral structure has been explained in terms of dislocations. From the spots distribution on the electron diffraction rings produced by some cleft sheets, the crystal has been concluded to be in the form of polygonal cone.

§ 1. Introduction

Previously the present author and his co-worker[1] have reported that hexagonal single crystals of graphite 1–5 μ in diameter were produced by heat treatment of carbon black 'Seast 116**' at 2500°C. From the pyramidal structure stepped by 150–300 A in height, the crystals were concluded to be grown by Frank's spiral mechanism[2].

In the subsquent course of the study by electron microscope, apparently circular crystals were found besides the hexagonal ones. A set of round growth patterns was observed on the face of each crystal, suggesting that the crystal might be formed also by the spiral mechanism. It should be remarked that the circular crystals produce spotty Debye-Scherrer rings while the ordinary spiral mechanism leads to the formation of pyramidal monocrystals which may produce single crystal diffraction patterns. This apparent discrepancy suggests that there exist some unknown aspects of the crystal structure, which will be investigated and revealed in the following sections.

The experimental work has been mainly carried out by means of a three-stage electron microscope[3] (HU-9 Type made by the Hitachi Co., Ltd***.) which enables us to observe a micrograph and a diffraction diagram from the same small object in the restricted area about 2×2 sq. microns.

§ 2. Conical Spiral Structure

2*A*. *General Observations*

Photo. 1 reproduces a pair of electron micrograph and diffraction diagram of an apparently circular crystal of graphite.

A set of circular loops observed in the micrograph (Photo. 1a) represents the growth front of each layer. Since the central part is hardly penetrated by the electron beam, it is concluded that the crystal has a pyramidal form stepped by the circular growth fronts. Two straight lines running toward the centre from the round external edges, *A* and *B*, are worthy of special attention in the respect that the fan-shaped portion bounded by these two lines (*A* and *B*) and the round edge (arc *AB*) is more transparent for electron beam than the rest. This suggest that the fan-shaped portion adheres to the surface of the supporting mount (collodion film) intersecting the incident beam nearly vertically while the rest are so appreciably inclined as to lengthen the

---

* Now at the Chuetsu Factory of the Tokai Electrode Mfg. Co., Ltd., Namerikawa-City, Toyama-Ken, Japan.

** Reinforcing-furnace black made by the Tokai Electrode Mfg. Co.

*** The writer is indebted to Dr. B. Tadano and to Mr. T. Komoda of Hitachi Central Laboratory for kindly allowing to utilize their electron microscope apparatus.

path of electron beam in the crystal.

In the diffraction diagram (Photo. 1b) we can see spotty Debye-Scherrer rings accompanied by elliptic arcs and diffuse bands. Since all the rings have indices of the type (*hko*), the crystal has been concluded to consist of numerous thin graphite layers each of which has the common axis in *c*-direction but is disoriented in *a*-direction. This seems, at first sight, to be associated with Warren's *turbostratic structure*[4] which implies stacking of graphitic monolayers parallel one to another but with random orientation about the layer normal. However, the *turbostratic structure* is generally seen in poorly- or non-graphitized carbons, and it produces quite diffuse patterns of (*hk*) 2-dimensional reflections in the diffraction diagram. All the rings obtained in this experiment are too clear to be those of turbostratic carbon.

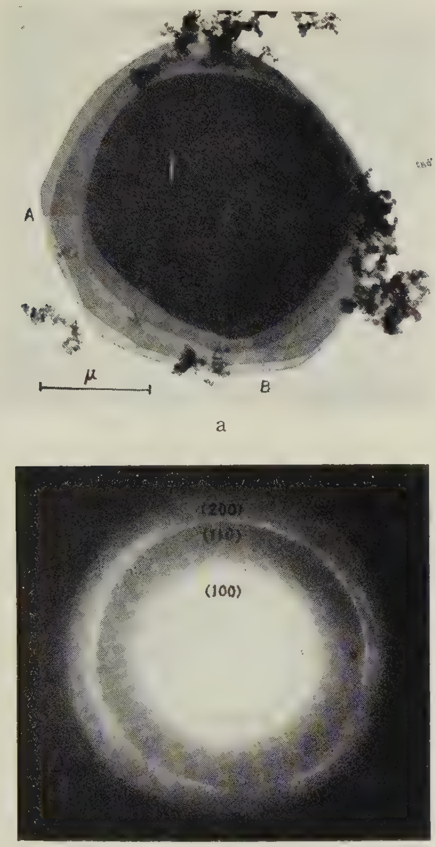

a

b

Photo. 1. Original form of conical crystal.

As well known, elliptic diffraction patterns are produced when electron beam is obliquely projected to the basal plane of thin layered crystal of fibrous structure. A typical elliptic pattern is reproduced in Photo. 2b. It is seen in the corresponding micrograph (Photo. 2a) that the crystal is obliquely suspended on the grid-mesh. The oblique angle, α, is given by

$$\alpha=\cos^{-1}(L_s/L_l)\ , \qquad (1)$$

where L_s and L_l represent the length of two principal axes of the ellipse, short and long respectively. For Photo. 2 the angle α is computed at 19°±2°, 26°±3° and 32°±3°.

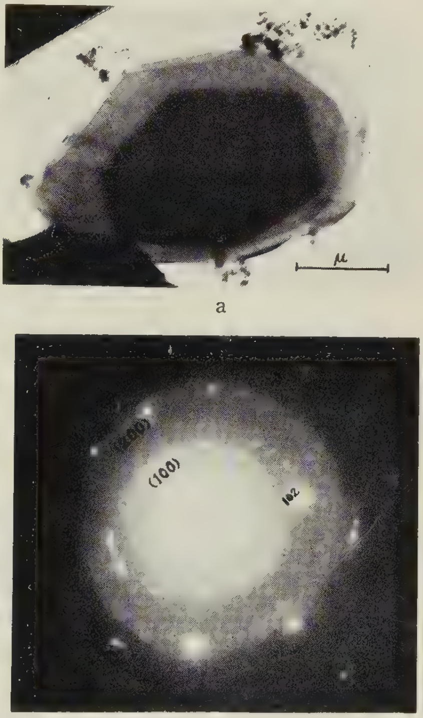

a

b

Photo. 2. Typical oblique photograph of graphite.

Conclusively, we can suppose that the spotty diffraction rings in Photo. 1b are produced by the abovesaid fan-shaped portion in Photo. 1a where the basal plane is vertical to the electron beam, and that the three ellipses are produced by the rest which are oblique to the electron beam. It should be remarked, moreover, that all the diffraction patterns are to be ascribed to the thin peripheral parts of the crystal because the central part is hardly penetrated by the electron beam as observed in the micrograph.

2B. *Evidences of Conical Form*

In order to explain the ellipses and diffuse bands indicated in Photo. 1b, it is convenient to assume that the crystal is not merely a stack of thin graphite layers but of conical form. The setting pose of the conical crystal is illustrated in Fig. 1. The fan-shaped portion bounded by dotted lines A and B in the figure may correspond to those in Photo. 1a, adhering to the supporting film, and the thin peripheral parts are expected to be quite flexible and wavy somewhat like a lolus leaf.

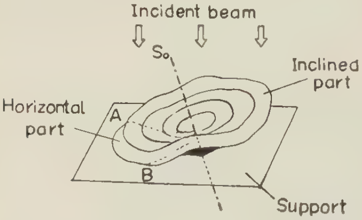

Fig. 1. Setting pose of a conical crystal corresponding to Photo. 1.

An important microscopic image consistent with these expectations is given in Photo. 3 where the crystal form is clearly exhibited by metallic (germanium) shadow-casting. It is very striking that the crystal is so concave as to prove the conical structure, and the peripheral parts are surely in wavy form and seem quite flexible. On the other hand, the conical form is confirmed by another fact that the folded crystals do not show perfect semi-circles but indicate fan-shaped appearance. In Photo. 4a, for example, two radii along the folded lines make an angle of 167.5° instead of 180°. From this, the angle φ made by the cone axis and the perpendicular to the generating line of the original cone is computed at

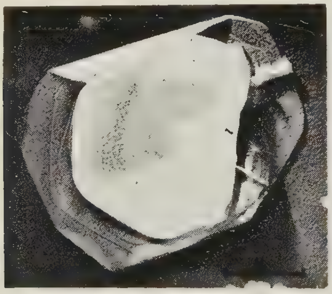

Photo. 3. Lotus-leaf-like form exhibited by metallic shadowing.

$$\varphi=\cos^{-1}(167.5/180)\approx 21.5°,$$

which gives a measure of the shapness of the cone.

Thus, the apparently circular crystal is concluded to be a stack of conical graphite sheets which intersects with electron beam (Fig. 1] so as to produce Debye-Sherrer diffraction rings, ellipses and diffuse bands together with

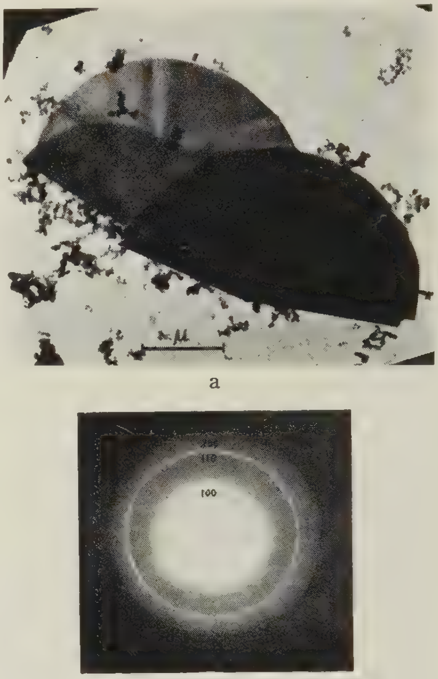

a

b

Photo. 4. Folded conical crystals.

2C. *Spiral Formation Mechanism*

Such a conical crystal can be formed by spiral growth mechanism as follows: When a thin graphite layer is twisted after the mechanical buckling producing the centra screw dislocation, it partly overlaps by an angle θ (*i. e.* rotational slip proposed by Wil-man[5]), forming a cone as shown in Fig. 2(a). The further growth of the crystal results in the conical spiral structure as in Fig. 2(b) where a helical twist boundary is introduced between the succesive layers. This mechanism seems particularly to conform to graphite because the interplanar binding is very weak in contrast with the extremly strong cohesion in the aromatic net plane.

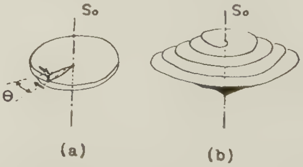

Fig. 2. Formation of conical crystal by spiral mechanism.

The twisting angle θ can be estimated from the microscopic observation and diffraction data. For example, θ of the specimen in Photo. 4a is $2\times(180°-167.5°)=25°$ on the assumption that the crystal is folded in completely flat form. Exactly speaking, however, this assumption is not suitable, because, in Photo. 4b, the Debye-Scherrer diffraction rings split into two maxima in the direction corresponding to that nearly vertical to the folded line in Photo. 4a. This means that the folded halves are inclined one to another, and the angle of inclination, α, is computed at about 15° from the distance between the two maxima. The geometrical relation between θ and α is illustrated in Fig. 3, by which the correct value of θ is computed at about 22°. In connection with this, the value of angle φ mentioned in the last sub-section should be revised as follows,

$$\varphi=\cos^{-1}\{\pi-(\theta/2)\}/\pi \quad \text{(general expression)}$$
$$=\cos^{-1}(169/180)\approx 20°.$$

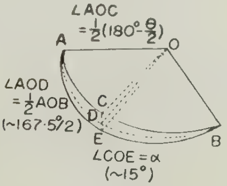

Fig. 3. Imperfectly folded crystal, illustrating the case of Photo. 4.

§ 3. Laminar Cleavage

3A. *Gliding of Conical Csystal*

In Photo. 5 we can observe nearly circular crystal flakes arranged in a row extending over up to 80 microns. The similar forms exhibited by adjacent flakes prove that they have been generated by the gliding of a crystal which is probably of such conical structure as mentioned in the last section. The shearing force promoting the glide might have been given in the process of specimen preparation for microscopy (rubbing method), because some scratches running nearly parallel

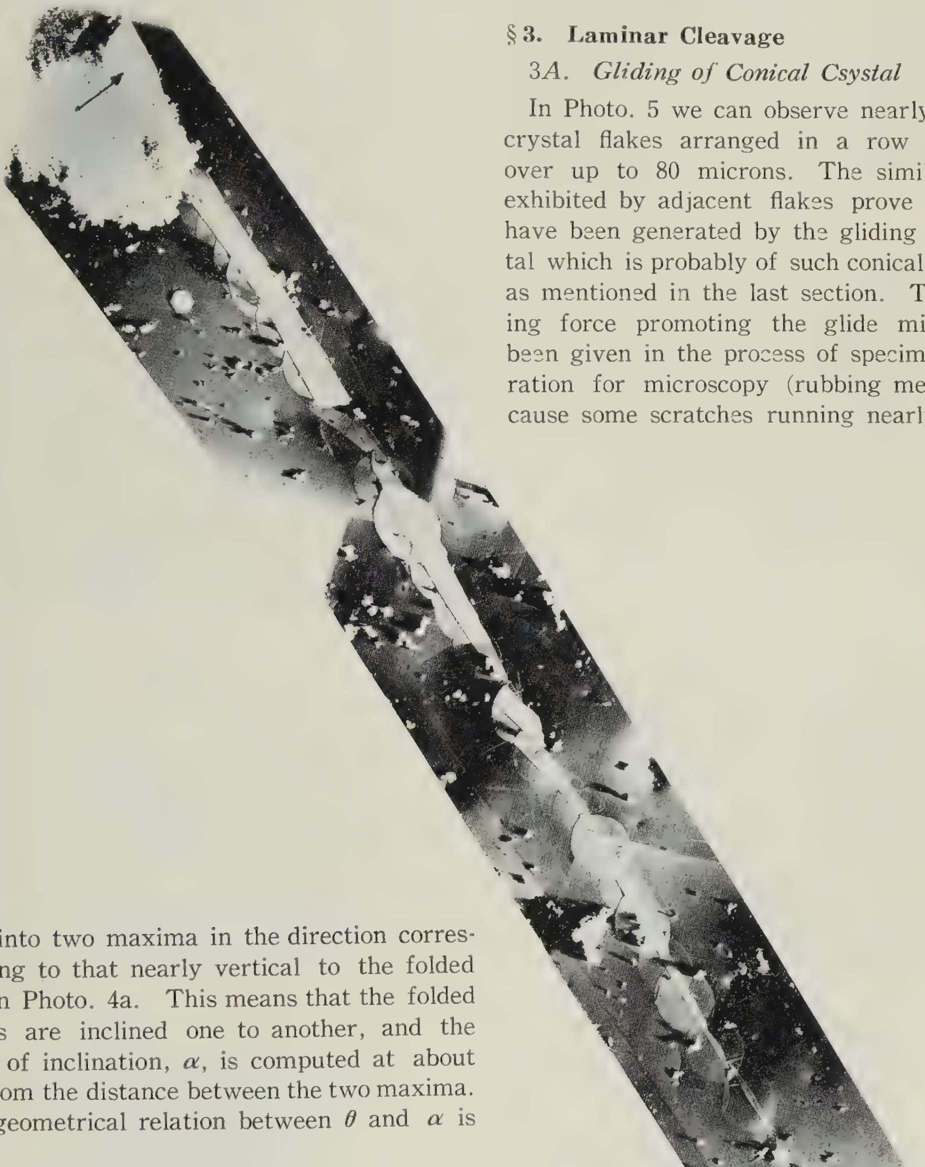

Photo. 5. Remarkable gliding a conical crystal.

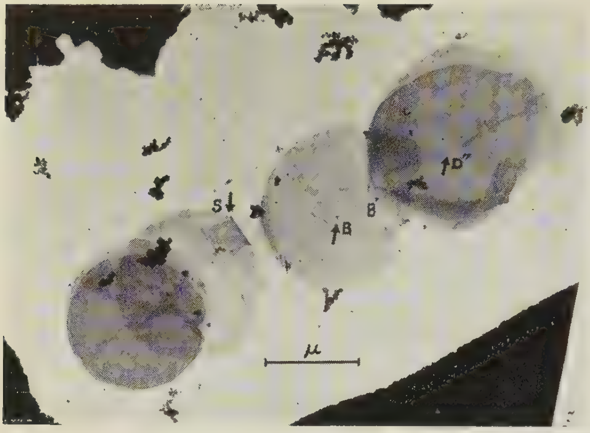

a

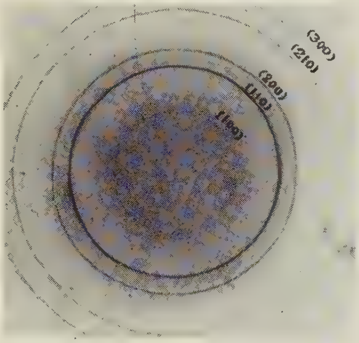

b

Photo. 6. Ceavage of a conical crystal presenting the mechanism in Fig. 6.

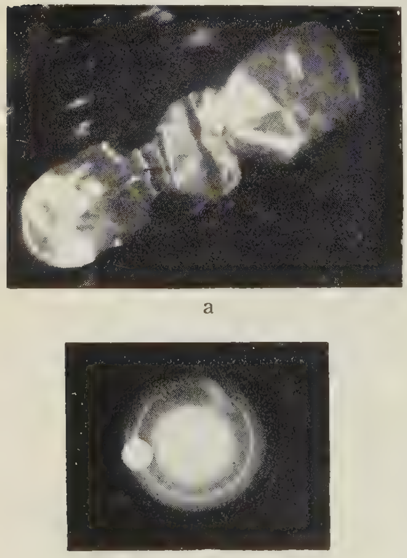

a

b

Photo. 7. A dark-field image corresponding to Photo. 6.

to the gliding direction are observed on the supporting film in the micrograph.

It is noticeable that some flakes in the upper-left part of the row exhibit each two radii making an angle smaller than 180°, somewhat like the folded crystal shown in Photo. 4a. This provides an evidence of the conical structure. On the other hand, the flakes in the under-right part are nearly circular and are traversed by a midrib-like fold along the gliding direction. Since the folded crystals are larger in diameter than circular ones, the original conical crystal, the parent of these flakes, might have been situated at the upper-left corner of the micrograph (indicated by arrow).

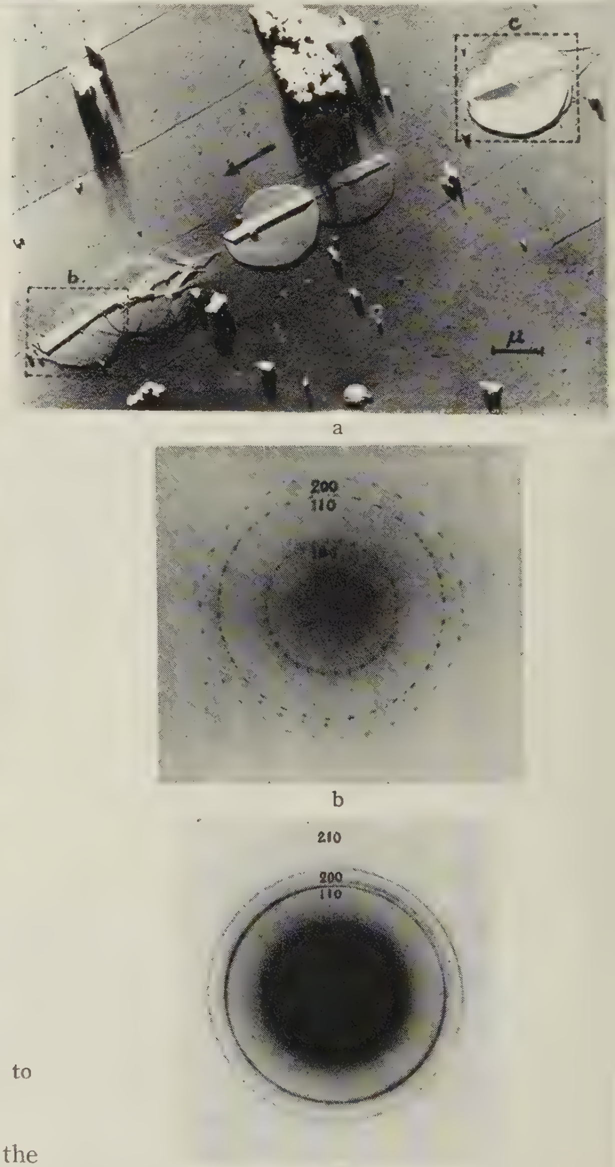

a

b

c

Photo. 8. Cleft sheets of two types, flat and concave ones.

At first sight, it would seem improbable that these flat discs glide away from a conical spiral. This is possible, however, if one assumes the mechanism as follows (*cf.* Fig. 4):

a) The central screw dislocation S_0 intersecting the active slip plane (conical plane) is so immobile that each gliding sheet may get over it successively, cancelling the initial spiraled structure of the sheet one by one.

b) The cancellation of the screw dislocation is similar to that demonstrated by Dawson and Anderson[6] on *n*-nonatriacontane crystal.

c) In order that each conical sheet is developed into flat one, a fairly sharp fold should be produced along the direction of the locus of the central screw axis, which may surely correspond to the abovesaid midrib-like one.

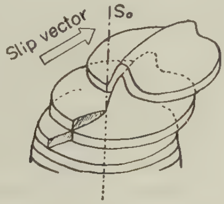

Fig. 4. Diagramatic representation of gliding of a conical spiraled crystal.

3B. *Another Mode of Cleavage*

In Photo. 6a. one can see another important aspect of the gliding of a conical crystal. Some broken sheets are observed at the place indicated by the arrow *S*, which suggests that the gliding in this case is not so simple. Besides, it should be remarked that the midrib-like striations are terminated at the centres of circular flakes indicated by the arrows *B* and *D''*. In order to explain these facts, another gliding mechanism of spiraled crystal should be introduced.

Firstly, if each glinding sheet gets over the central screw axis, it breaks itself into two semi-circular platelets (Fig. 5).

Secondly, if adjacent several sheets glide as a whole over the underneath, the initial screw dislocation is not cancelled but is cut into some shorter segments holding the conical spiral structure in each cleft sheet.

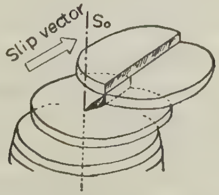

Fig. 5. Gliding of a spiraled crystal different from that shown in Fig. 4.

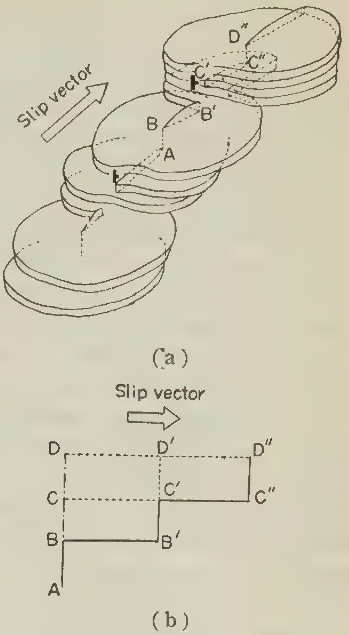

Fig. 6. Schematic illustration of the gliding shown in Photo. 6a; the central screw dislocation AD becomes zig-zag form.

These mechanisms are used to explain Photo. 6a. The arrows *B* and *D''* in Fig. 6 (a), corresponding to those in Photo. 6a, indicate the positions of emergence of such dislocation segments on the cleavage surfaces. A schematic picture representing the behavior of the dislocation line in this case is drawn in Fig. 6(b); the initial dislocation *AD* is transformed into such zigzag one consisting of five segments as below,

$$AD \longrightarrow AB + BB' + B'C' + C'C'' + C''D''$$

(screw) (screw) (edge) (screw) (edge) (screw),

where the signs in the round brackets denote the types of those dislocation segments just above them. Among these segments, *BB'* and *B'C'* are so to say imaginary dislocations lying on the upper and side exposed surfaces respectively. *AB* and *C''D''* are the very segments of screw type considered above. Thus, the midrib-like striations in this case can be attributed not only to the locus of the central screw axis but to the ledges of the edge-type components *BB'* and *C'C''* which terminate at the centres of discs. In connection with this, the diagramatic representation in Fig. 6

(a) enables us to understand the reason why the striation BB' in Photo. 6a is apparently jointed to the round edge of the right-hand adjacent disc.

Photo. 6b is the diffraction diagram corresponding to Photo. 6a, in which the Debye-Scherrer rings exhibit two intensity maxima respectively, suggesting that the two halves of each disc are slightly inclined one to another.

Photo. 7a reproduces a dark-field micrograph of the same specimen as that in Photo. 6a, and it is participated by only such a portion of the diffracted electron wave that passes through the aparture corresponding to the circular restricted area in Photo. 7b. Although the resolution is lowered owing to aberations, the above mentioned structural markings (midrib-like folds, dislocation ledges and other bending lines) are rather distinctly observed than in Photo. 6a. From the nearly uniform brightness of this image, it is concluded that any restricted portion of the diffraction rings corresponds to the whole parts of the specimen projected on the paper surface. Furthermore, can see numerous *double diffraction fringes* nearly all over the dark-field image, which have been discussed by Finch-Wilman and Mitsuishi-Nagasaki-Uyeda[7] independently. These observations are well consistent with our proposal, *i. e.* stacking of thin crystal layers successively rotated about the common axis in *c*-direction.

3C. *Glide Motion of Dislocations along Helical Interface*

As pointed out by Read[8] and other authors, the translational slip of a spiraled crystal along the helical plane leads to the intersection of moving dislocations with the screw axis and produces the dislocation jogs which generally slow down the glide motion. Moreover, except in the special case where the moving dislocations are of pure edge-type, each jog leaves behind a trail of lattice vacancies or interstitial atoms which may require considerable energy for the creation. At first sight, these difficulties would seem to make immpossible to explain the gliding of conical crystals in terms of the dislocation theory.

These difficulties can be removed, however, by introducing an assumption that the dislocation density is kept uniform all over the helical slip plane throughout the gliding process. The simplest example is schematically illustrated in Fig. 7, where the crystal is represented by a continuous plane in the form of a helicoid and the dislocations lie on the successive layers one to one as indicated by A_0D_0, C_0D_0, $E_0F_0\cdots$. When the shearing force is exerted on the crystal, these dislocations glide over the spiral ramp from right to left (as shown by arrows) and get to split in every two segments through the intersection with the central screw axis. It may be convenient to express this splitting process in the following formulae,

$$A_1B_1 \rightarrow A_1S + SB_1\ ,$$
$$C_1D_1 \rightarrow C_1S + SD_1\ ,$$
$$\cdots\cdots\cdots\cdots\ etc.\ ,$$

where S denotes the central screw axis. In ordinary circumstances, further glide makes those segments to move on the different levels of the spiral ramp, and the jogs are inevitably formed. In the present case, however, none of jog is necessarily produced, because the foregoing split of moving dislocations can be immediately followed by the recombination between the segments lying on the same levels of the spiral, which are to be expressed as below,

$$A_1S + SD_1 \rightarrow A_1D_1\ ,$$
$$C_1S + SF_1 \rightarrow C_1F_1\ ,$$
$$\cdots\cdots\cdots\cdots\ etc.$$

In the other words, the recombination forms again the system of moving dislocations which can continue to glide over the helical plane, as indicated by A_2D_2, $C_2F_2\cdots$. in Fig. 7.

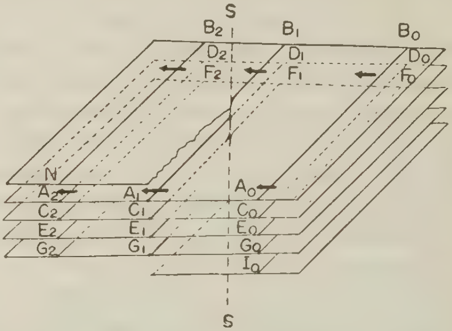

Fig. 7. 'Split and recombination' of moving dislocations.

In the case of the conical crystal, the slip along the helical twist boundary is generally represented by a moving set of crossed grid of screw dislocations. Parallel dislocations forming the grid sweep over the spiral ramp, repeating the aforesaid 'split and recombination' one after the another, so as to keep the dislocation density uniform all over the interface. This means that the orientation difference between the adjacent conical layers, defined by $\theta=2\tan^{-1}(b/h)$ (b; Burgers vector, h; dislocation spacing), is not altered throughout the gliding process, and that a local distortion is not produced anywhere on the helical interface. Therefore, in principle, it is expected that a conical crystal is ultimately resolved into individual monocrystal sheets, each of which has the unit thickness corresponding to one revolution of the spiral. In the actual case, however, the glide motion is usually so turbulent that the abovesaid theoretical expectation may not be satisfactorily realized. For example, as observed in Photo. 6a, the continuous spiral layer is broken off at places into flakes, which consists of multiple layeas producing spotty electron diffraction rings.

§ 4. Polygonization of Cone

4A. *Microscopic Observation*

Photo. 8a gives an image of gliding in which a conical crystal has been cleft so remarkably that individual sheets are almost separated from each other. Most of the cleft sheets are in flat form accompanying the midrib-like folds mentioned in the last section; *e.g.* the sheet indicated by the notation b. The sheet denoted by c is exceptionally thick, and is not flat but concave upward. Comparison between the largest diameters suggests that the sheet c is the parent of other flat ones.

4B. *Equidistant Spot Distribution on Diffraction Rings*

Photo. 8b reproduces the diffraction diagram of the sheet b. Each diffraction ring consists of thirty principal spots making angular intervals of 12° at the centre and those weak spots which are slightly displaced from the principals. The angular interval of these diffraction spots is closely related to the twisting angle θ at the first stage of the cone formation. Photo. 8b can be explained by assuming, for example, that the sheet consists of five revolutions of a conical spiral layer, θ of which is equal to 12°. However, this explanation is not necessarily unique, because the microscopic image shows that the sheet is folded into three. If a conical monocrystal layer of graphite corresponding to one revolution of the spiral is folded into flat form as shown in Figs. 8 (a) and (b), two halves on the both sides of the midrib-like fold are mutually disoriented by $\theta/2$ in a-direction. Accordingly, if the sheet b consists of three revolutions of the conical spiral and θ is equal to 24°, it may produce the diffraction spots at intervals of 12° similar to those in Photo. 8b.

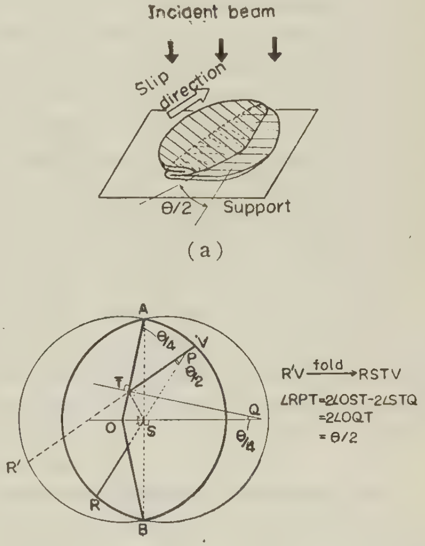

(a)

(b)

Fig. 8. Remarkable veining during the glide leads to triple folding of sheet in nearly flat form.

It is noteworthy that the thickness of the cleft sheet is expected to be multiple of the spiral pitch defined by the Burgers vector of the initial screw dislocation. This is consistent with the prediction on the gliding mechanism described in sub-section 3*C*. On the other hand, one finds that the numerical value of θ supposed here, either 12° or 24°, is in simple relation with the three-fold symmetry of graphite lattice. This suggests that the rotational slip is governed by certain crystallographic law to some extent, but requires for its affirmation further investigations in future.

The weak spots accompanying the principals are firstly due to the midrib-like fold (△OAB in Fig. 8(b)), but may partly be of seperate origin, *e.g.* the contribution of the right-hand neighbour sheets partly projecting into the rectangular area (broken lines in the micrograph) restricted by the aperture.

4C. *Evidence of Polygonal Form*

Photo. 8c gives the diffraction diagram of the sheet *c* in Photo. 8a. The spotty diffraction rings and the accompanying elliptic arcs suggest, in connection with the concave form observed in the micrograph, that the conical structure is held to some extent. It should be remarked, moreover, that in this diagram the diffraction spots on (100)-, (110)- and (200)-rings are counted to two hundred and fourty respectively. These observations present another important aspect of the conical crystal as described in the following paragraphs.

Let suppose a conical crystal laid on the supporting mount as one puts a bowler. As mentioned before, only the peripheral part which is turned up like the rim of bowler participates in electron diffraction. Then, let trace a spiral path arround the cone axis starting from the most exterior layer of the conical crystal toward the centre. Then, one finds that the crystal orientation in *a*-direction changes successively with the shift of the position (the angular displacement about the cone axis) at the rate of θ per 2π (in radians). Accordingly, so long as θ is not much large, one revolution of the spiral layer corresponding to one round of the path may produce every six arcs of (100)-, (110)- and (200)-reflections in the diffraction diagram, and each arc makes an angle as large as θ at the centre. When θ is 24°, for example, one revolution corresponds to six arcs making the central angle of 24°, twice to successive 24° (48° in total), and finally the third revolution may complete a set of continuous diffraction rings.

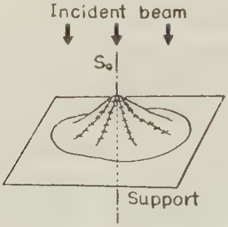

Fig. 9. Polygonization of conical crystal.

From such a viewpoint, it is of considerable importance that the diffraction rings observed are not continuous but spotty. This means that the peripheral part discretely changes the orientation arround the cone axis (along the spiral path considered before), and can be explained only by assuming that the cone is in polygonal form as illustrated in Fig. 9; *i. e.*, the discrete change in orientation is expected to occur at intervals of $2\pi/N$ radians, where N denotes number of the spots on each diffraction ring. For example, in the case of Photo. 8c, the interval is computed at 1.5° (=360°/240), and if θ is equal to 24° the crystal should be a hexadecagonal cone (24/1.5 =16) consisting of two and half revolution of the spiral layer at least.

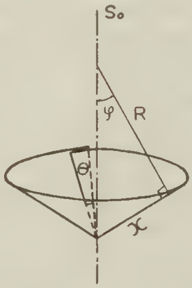

Fig. 10. Schematic illustration of $R-x$ relation.

4D. *Considerations*

It is easily understood that the aforesaid polygonization is closely associated with those edge dislocations of one sign which are produced by the plastic bend deformation of lattice into conical form. According to the schematic illustration given in Fig. 10, the radius of curvature and the average density of dislocations are expressed by

$$R=x/\tan\varphi=x/\sqrt{\{2\pi/(2\pi-\theta)\}^2-1} \qquad (3)$$

and

$$\rho=1/Rb=\tan\varphi/xb=\sqrt{\{2\pi/(2\pi-\theta)\}^2-1}/xb\,, \qquad (4)$$

where x is the distance from the cone top and b is the magnitude of the Burgers vector. Substituting $\theta=24°$ and $b=10^{-8}$ cm to eq. (4), for example, one can obtain a typical $\rho-x$ relation curve in Fig. 11. As seen there, the dislocation density rapidly decreases with increasing x, from the central part toward the exterior. The average density $\bar{\rho}$ is calculated by substituting half length of the generating line of the cone, $\bar{x}$, into eq. (4). For the example shown in Fig. 11, assuming $\bar{x}=0.5\,\mu$ (taken from the sheet *c* in Photo. 8a), $\bar{\rho}$ is computed at about $8\times10^{11}\text{cm}^{-2}$ which is of same order as in cold-worked metals.

The polygonization occurs through the climb motion of these dislocations in order to form the tilt boundaries, involving the migration of point lattice defects to or from the edges of their half planes. Since the specimen were treated at about 2500°C, well above the temperature at which graphite softens[9] (about 2000°C) this self-diffusion process is expected to occur quite rapidly. According to the schematic illustration in Fig. 12, the orientation difference ϕ at the polygonization boundary is approximately expressed by

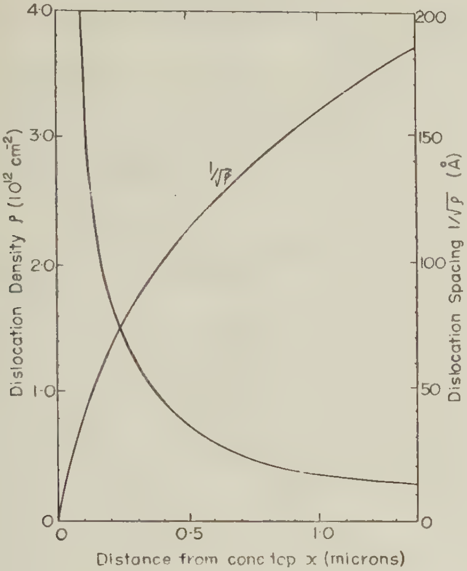

Fig. 11. $\rho-x$ and $1/\sqrt{\rho}-x$ relation curves when $\theta=24°$ and $b=10^{-8}$ cm.

$$\begin{aligned}\phi &\approx 2\cos^{-1}[\sin(2\pi/n)\cdot\cos\varphi/\sin\{(2\pi-\theta)/n\}]\\ &=2\cos^{-1}[\sin(2\pi/n)\{1-(\theta/2\pi)\}\\ &\quad\times 1/\sin\{(2\pi-\theta)/n\}]\,,\end{aligned}\tag{5}$$

where n is number of the polygonized domains. Substituting $\theta=24°$ and $n=16$ to this, ϕ is computed at about 9° for the sheet c in Photo. 8, which implies that the dislocation spacing in the boundary is about 12.5 b.

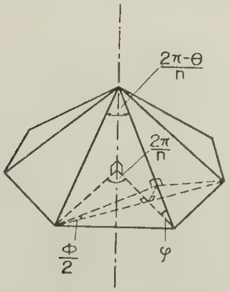

Fig. 12. Geometrical relation between ϕ, φ and θ.

On the other hand, one has to take note of the following fact; when the crystal is extremely thin it is only elastically bent, producing no dislocation. As a rough approximation, one can assume that the average dislocation spacing $1/\sqrt{\rho}$ gives the critical thickness deciding whether the bent crystal contains dislocations or not. A $1/\sqrt{\rho}$ *vs.* x relation curve is also indicated in Fig. 11. This curve suggests that if the thickness of the spiraled layer is about 100 A, for example, the central-side part of $x<0.4\,\mu$ is subjected to plastic deformation which may lead to the polygonization, whereas the exterior-side only to elastic circumferential bending.

It should be noted, however, that the foregoing discussion has revealed only the so-called geometrical aspect of the problem, taking no account of the energy condition and other mechanical circumstances associated with the creation of dislocations. In order to reveal the physical aspect, the author thinks, it must be settled first to overcome the general difficulties similar to those in the problem of fracture mechanism, which is to be attempted in future.

§ 5. Summary and Conclusion

By means of electron microscope apparently circular crystals of graphite were found. They have round growth patterns and show laminar cleavage accompanied by the formation of midrib-like folds. Moreover, they produced spotty electron diffraction rings accompanied by ellipses and diffuse bands. All these facts support that the apparently circular crystals are of conical layered structure.

Such a conical crystal can be formed by the spiral growth mechanism, if a thin monocrystal layer is mechanically buckled, producing the central screw dislocation, and then subjected to the *rotational slip* arround the screw axis so as to overlap by an angle.

The laminar cleavage has been explained also in terms of the dislocation theory by supposing that the gliding of conical sheets occurs along the helical interface so as to keep the density of moving dislocations uniform.

From the spots distribution on the diffraction rings produced by some cleft sheets, the crystal is concluded to be in the form of polygonal cone. It is theoretically verified that the polygonization of this kind is probable to occur under some restrictions concerning the thickness and the curvature of the conical spiral layer.

These results suggest that some important aspect of structure and properties of graphite can be revealed from the viewpoint of the dislocation theory, and further investigations along this course are expected to be attemted in future.

Acknowledgement

The writer wishes to express his hearty thanks to Prof. Ryozi Uyeda of Nagoya University, Prof. A. Ookawa of Gakushuin University and Dr. N. Kato of Kobayashi Institute of Physical Research for their kind guidance and valuable discussions. He also thanks Mr. M. Nomaguchi of our laboratory for the continuous encouragement throughout the entire course of this study.

References

1) T. Tsuzuku & T. Komoda: J. Phys. Soc. Japan **10** (1955) 81.
2) F. C. Frank: Discussions of Faraday Society, No. 5 (1949) 48.
3) For example, M. E. Haine, R. S. Page & R. G. Garfitt: J. App. Phys. **21** (1950) 173.
4) J. Biscoe & B. E. Warren: J. App. Phys. **13** (1942) 364.
5) H. Wilman: Nature **165** (1950) 321.
6) I. Dawson & H. G. Anderson, Proc. Roy. Soc. **A218** (1953) 255.
7) T. Mitsuishi, H. Nagasaki & R. Uyeda: Proc Japan Acad. **27** (1951) 86.
8) W. T. Read, Dislocations in Crystals (1953) Chap. 6.
9) C. Malmstrom, R. Keen & L. Green: J. App. Phys. **22** (1951) 583.

JOURNAL OF THE PHYSICAL SOCIETY OF JAPAN Vol. 12, No. 7, JULY, 1957

Fine Structures of X-ray Absorption Spectra of Crystalline and Amorphous Germanium

By Toshio SHIRAIWA, Tsutomu ISHIMURA and Masao SAWADA

Department of Physics, Faculty of Science, Osaka University

(Received March 18, 1957)

The X-ray absorption spectra of crystalline and amorphous germanium were photographed and fine structures at the K absorption edges were observed to 500 ev. in the crystalline and to 350 ev. in the amorphous state. The shape of the fine structure of amorphous germanium is like that of crystalline germanium though the small fluctuations disappear and the energy values measured from the main edge are smaller than the values of corresponding absorption maxima and minima of the crystalline germanium. From the comparison of the fine structures of both states we suggest that a structure which is like the diamond lattice of crystalline Ge with the smaller spacing exists in the amorphous Ge and this result coincides with the result of analysis of the X-ray diffraction pattern by Richter.

§1. Introduction

It has been reported that the fine structures existed even in the absorption spectrum of an amorphous substance¹⁾. The amorphous samples used in the above experiment was electrodeposited nickelsulfur and the fine structure obtained was of nearly the same form but of less appearance in the higher energy region as that of crystalline state. However, for reasons of their crystalline states being two-phase region of Ni and Ni_3S_2 which complicated the analysis of the fine structures, and also of the low resolving power of the spectrograph, the comparison between both states was not accomplished in detail. In the present experiment we treated germanium, as its amorphous state is that of a single element and the crystal structure was a comparatively simple diamond lattice.

The amorphous germanium can be prepared by evaporation method as a form of a thin film ($< 10^{-4}$ cm) and it is stable at room temperature[3]. The electron[2] and X-ray diffraction patterns have been studied by few authors and especially the Fourier analysis of the X-ray diffraction pattern has been done by Richter and Fürst according to Debye and Menke's method.

§ 2. Experiment

The crystalline or metallic germanium was 99.999% pure and the amorphous samples were prepared by evaporation in high vacuum. The furnace was made of tungsten plate and the substrate was a collodion film formed on a copper plate. The copper plate was a part of the bottom of a container of liquid air (A) and the radiation from outside to the substrate was interrupted by a wall of another liquid air bottle (B) except a hole (C) for the molecular beam of evaporated material. (See Fig. 1)

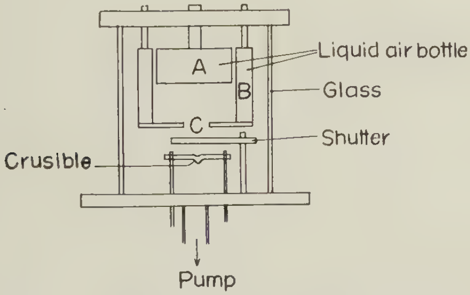

Fig. 1. A schematic diagram of the evaporation apparatus.

The prepared amorphous samples were studied by X-ray diffraction with a vacuum camera and Cu $K\alpha$ radiation monochromatized by a pentaerithrit crystal. But, as a pattern of the collodion film overlapped on the amorphous haloes, we dare not analyse them. Amorphous haloes coincided with other author's results in their positions but were accompanied by diffuse weak lines. The small angle part of the diffraction was photographed by a Guinier's type camera, which had a bended quartz monochrometer and the distance from the sample to the film was 20 cm, and the small angle diffraction pattern was not recognized and this fact showed that there was no small particle. According to Richter the evaporated germanium exists in an amorphous state only in a case of a thin film and in a thick film it is in a crystalline state. So, in our sample it was assumed that the process of crystalization partly had been developed but there were no perfect crystalline particle and the amorphous phase was still maintained.

The spectrograph was Johann's type and a radius of Rowland circle was 25 cm. The crystal was a quartz plate of 0.1 cm thickness and the first order reflection of (130) plane was used. The half width of Cu $K\alpha_1$ line was 0.6 x.u. with 7 mm opening of crystal surface and it can be thought that the crystal was bended considerable precisely. The dispersion at germanium K edge was 4.14 x.u./mm. In order to avoid the disturbing strong W $L\gamma$ series lines an X-ray tube of a gas-ion type with Mo target was used and for the reference lines W $L\gamma_3$ and other lines of shorter wavelength of W $L\gamma$ series were photographed after an exposure of the absorption spectrum was finished. The photo-plate was Fuji A–1 and situated tangentially to the Rowland circle. The angle between a photoplate and a tangent to the Rowland circle at the center of the crystal was computed from intervals between three reference lines.

The time of exposure was about 80∼100h. with 20 k.v.p. and 8 mA for the crystalline specimen. For the specimen of amorphous samples a few tens sheet of thin films were assembled and the fairly larger exposure time was needed because of the absorption of collodion films.

For the measurement of intensity, absorbers of aluminium foil of four sorts of thickness were put in front of a photo-plate and spectrograms of various relative intensities were photographed on the same plate.

The photometer curves were recorded by a pen recorder type microphotometer with a photo-cell and the effect of grains were eliminated by registering records of about twenty curves on the same chart paper. (Photo. 1)

§ 3. Results and Discussion

The values of wavelengths of K absorption edge and absorption maxima and minima of the fine structure and energy separations measured from the main edge are listed in Table I. Wavelengths of reference lines were referred to Cauchois and Hulubei's table[4].

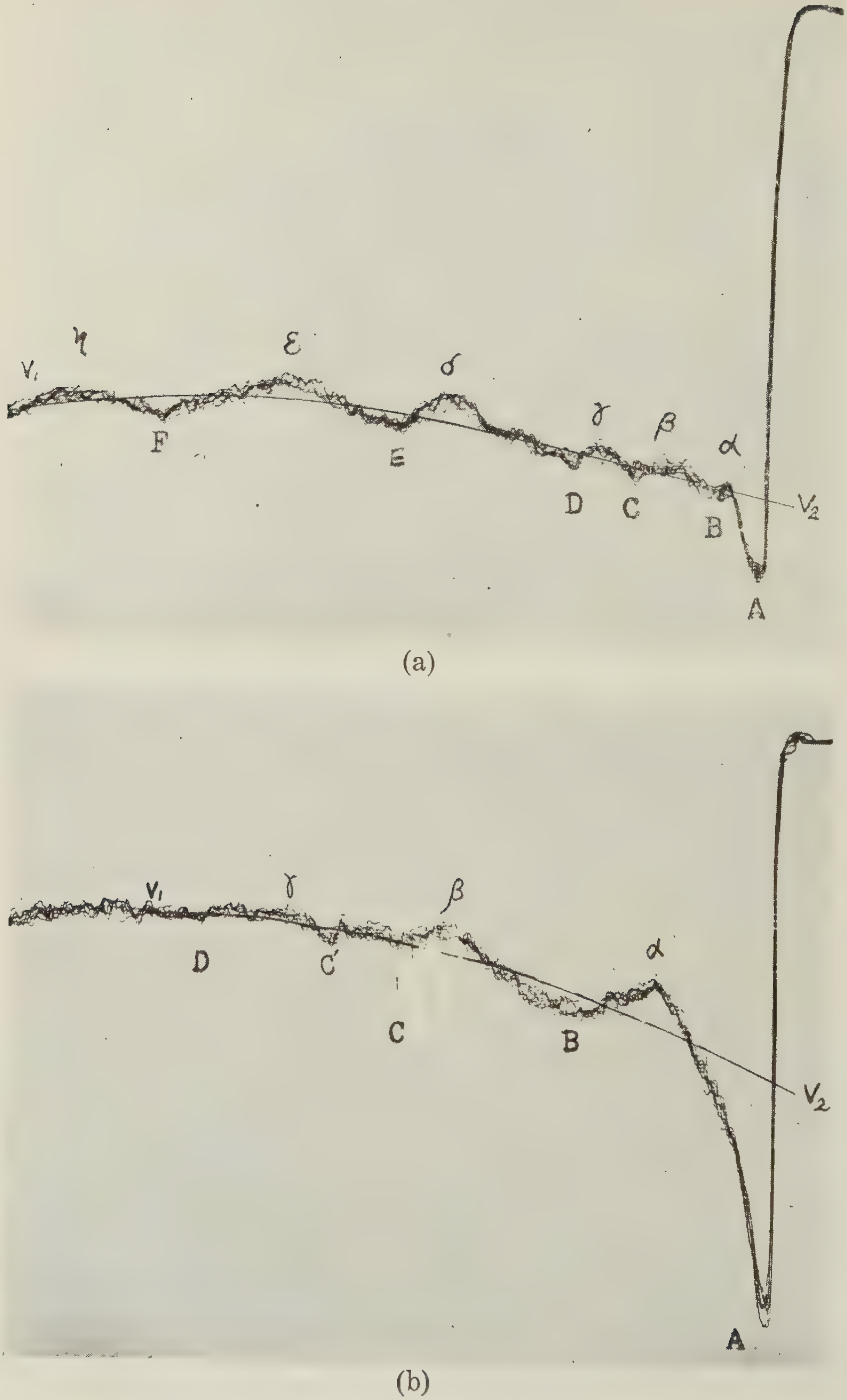

(a)

(b)

Photo. 1. Photometer curves of the absorption spectra near the *K* absorption edges of (a) crystalline Ge and (b) amorphous Ge.

The absorption spectrogram of a crystalline germanium has been photographed by Hulubei and Cauchois[5] and a fine structure extended to 300 eV. from the edge was observed. They resolved the structure more finely than us in the neighbourhood of the edge, and in higer energy region than 70 eV. their result coincided with our measurement.

Table I. The wavelengths of *K* absorption edges and absorption maxima and minima of fine structures and their energy values measured from the edges for crystalline and amorphous Ge.

	Crystalline Ge			Amorphous Ge		
	Wavelength in x.u.	Energy value from edge in eV.		Wavelength in x.u.	Energy value from edge in eV.	Energy value multiplied by 1.036
Kabs.	1114.2_6	0	Kabs.	1114.6_2	0	
A	1113.6	6.6	*A*	1114.1	5.2	
α	1112.7	15.5				
B	1111.8	25				
β	1110.1	41	α	1110.2	44	
C	1109.0	53				
γ	1107.6	67				
D	1106.5	78	*B*	1107.0	76	79
δ	1102.2	121	β	1102.8	119	123
E	1099.9	145	*C*	1100.8	139	144
			C'	1097.8	170	
ε	1095.5	190	γ	1096.4	184	191
F	1091.2	234	*D*	1092.7	222	230
η	1087.5	272	δ	1089.0	260	270
G	1083.5	314	*E*	1084.8	304	315
ζ	1079.2	360	ε	1080.7	349	362
H	1075.4	400				
θ	1072.0	436				
I	1068.3	476				

Fig. 2 (a) and (b) show the curves of values $\mu_r=\mu-\mu_0/\mu_{edge}-\mu_0$, of a crystalline and an amorphous Ge respectively. In the above formula μ is the absorption coefficient and μ_0 is the value if the fine structure does not occur and this value was obtained from the point on the line V_1V_2 in Photo. 1 which was drawn to path the mean points of the fine structure. The μ_{edge} is the absorption coefficient at longer wavelength side of the edge, that is $\mu_{edge}-\mu_0$ is the difference at the edge.

The abnormal absorption minima A appeares next to the edge which has been noticed by Cauchois and Mott[6] as a white line in a crystalline states is also present strongly in the amorphous phase.

The wavelength of the edge slightly increases in the amorphous phase and this shows that the germanium atom in the amorphous structure have the isolated atomic feature compared to the crystalline phase.

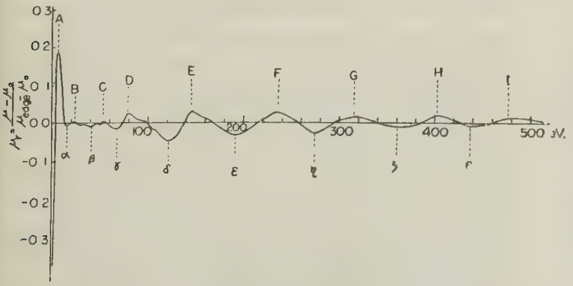

Fig. 2 (a). Showing the behavior of the fine structure of crystalline Ge. μ_γ is the ratio of the change of the absorption coefficient to the *K* absorption jump.

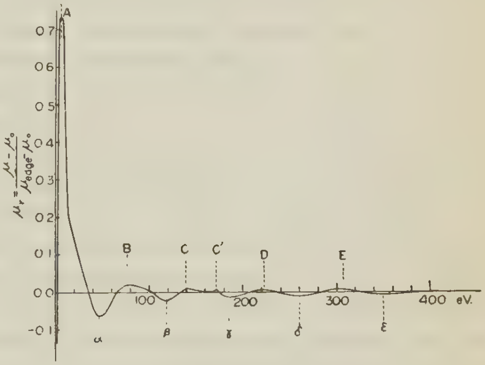

Fig. 2 (b). Showing the behavior of the fine structure of amorphous Ge.

In the case of crystalline state, the weak absorption minima (α, β, γ) appear next to the white line A and in the amorphous phase the broad band α appears instead of these weak structures. From the results of Fourier analysis, Richter suggested that the tetrahedron composed by five atoms which constitutes the diamond lattice in the crystalline germanium is still retained in the amorphous phase (Fig. 3), and he called this tetrahedron as a structure unit (Baueinheit) and combining these structure units he considered a model of the amorphous structure like diamond lattice but of less regularity. If the fine structure of the absorption spectrum is caused by the regular atomic arrangement increase of the irregularity in the amorphous substance will obscures the fine structure and this suggesion illustrates the phenomena that the α, β and γ of the crystal phase change into a broad band α in the amorphous phase, and small structures appeared between D and δ in the crystalline phase disappear in the amorphous phase.

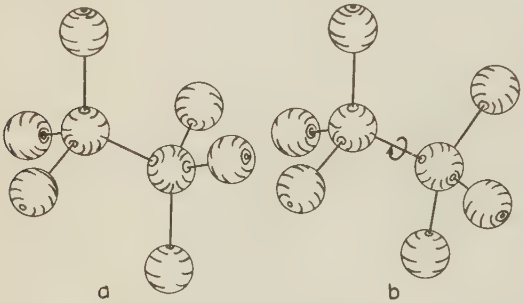

Fig. 3. Tetrahedron bonds (a) in a crystalline Ge and (b) in an amorphous Ge. Richter illustrated that the irregularity of the amorphous Ge was due to the rotations of tetrahedrons around the axis combining centeral atoms of the tetrahedrons.

In the higher energy region than 100 eV. the curves of μ_r in both phase are similar and when the values of abscissa of Fig. 2 (b) are multiplided by 1,036 for the amorphous phase, both maxima and minima are almost coincident though the magnitude in the amorphous phase is smaller than the crystalline. Their reduced values are listed in the last column in Table I. On the other hand it has well been known that the energy values of the fine structure measured from the main edge are inversely proportional to the square of the lattice constant when the crystal lattice is the same. So we may say that the structure of amorphous germanium is nearly the same structure with larger spacing than the crystalline germanium.

Generally (for ex. As, Se, etc.) the density in amorphous phase is smaller than in the crystalline and Richter analysed the X-ray diffraction patten on the assumption that the density decreased 20% in the amorphous phase. From our result the decrease of density is estimated at 5.4% but the real density will deviate from this value by the absorbed atoms or molecules which constitute partly the amorphous structure in the process of the condensation of germanium atoms.

Richter's result that the structure units of tetrahedrons constitute the amorphous germanium agrees with our result apart from the displacement of the wavelength of the edge, that is, in our result the bonds of atoms are weak in the amorphous phase, which suggest the increase of the inter atomic distance but in Richter's result the distance to the first nearest neighbors decreases.

In the higher energy region the magnitude of variation of μ_r becomes smaller in the amorphous state compared to that of the crystalline state with increasing energy. This phenomenon was recognized in an earlier experiment on Ni–S and these phenomenon will be probably due to the decrease of regularity of atomic positions or finite crystal size.

According to Richer the regularity of atomic positions was recognized within about 7 Å from a centered atom and this distance corresponds to the distance to the mid point between the third and the fourth nearest neighbors in the lattice of metallic germanium. Therefore, if the sample used by us and by Richter are the same the fine structure are determined by some ndighboring atoms surrounding the atom which absorbs X-ray energy in the region to the considerably high energy.

§4. Summary

The *K* X-ray absorption spectra of metallic and amorphous germanium were photographed and from the comparison of both fine structures the structure of amorphous germanium was infered, as a one coincident with Richter's result, namely, the structure unit like lattice was retained in the amorphous phase, and it was shown that the fine structure of the absorption spectrum was determined by the neighboring atoms arround the atom which absorbed the X-ray quantum.

References

1) M. Sawada, K. Tsutsumi, T. Shiraiwa and M. Obashi: J. Phys. Soc. Japan **10** (1955) 464.
2) H. König: Optik **3** (1948) 201.
3) O. Fürst, R. Glocker and H. Richter: Z. Naturforsch. **4**a (1949) 540.
H. Richter and O. Fürst: Z. Naturforsch. **6**a (1951) 38.
4) Y. Chauchois and H. Hulbei: "Longueurs d'Onde des Émissions X et des Discontinutes X." (1947) Hermann, Paris.
5) H. Hulbei and Y. Cauchois: C. R. Acad. Sci. Paris **211** (1940) 316.
6) Y. Chauchois and N. F. Mott: Phil. Mag. **40** (1949) 1260.

JOURNAL OF THE PHYSICAL SOCIETY OF JAPAN Vol. 12, No. 7, JULY, 1957

Fine Structures of X-ray K Absorption Spectra of Copper in Various Copper Compounds

By Kenjiro TSUTSUMI, Akira HAYASE and Masao SAWADA
Department of Physics, Faculty of Science, University of Osaka

(Received April 1, 1957)

By using the North American Philips Diffraction Unit and Wide Range Goniometer modified to a tube spectrometer described by Coster and De Lang, the fine structures of the X-ray K absorption edges of copper in following compounds were recorded: cupric chloride ($CuCl_2$), cupric chloride dihydrate ($CuCl_2 \cdot 2H_2O$), cupric bromide ($CuBr_2$), cupric sulfate pentahydrate ($CuSO_4 \cdot 5H_2O$), cupric nitrate trihydrate ($Cu(NO_3)_2 \cdot 3H_2O$), cupric carbonate ($CuCO_3$), cupric formate tetrahydrate ($Cu(HCOO)_2 \cdot 4H_2O$), cupric acetate monohydrate ($Cu(CH_3COO)_2 \cdot H_2O$), bis glycino copper monohydrate ($Cu(C_2H_4NO_2)_2 \cdot H_2O$), bis glycino copper hydrate ($Cu(C_2H_4NO_2)_2 \cdot H_2O$), copper phthalocyanine β-form ($CuC_{32}H_{16}N_8$), copper phthalocyanine α-form ($CuC_{32}H_{16}N_8$), cuprous chrloride ($CuCl$), cuprous bromide ($CuBr$) and cuprous iodide (CuI). The recorded curves of the fine structures of the Cu K absorption edges of these compounds, except α- and β-phthalocyanine, were found to be very similar in forms and the wavelength values of these structures also nearly coincided within experimental errors. We consider that this is due to the fact that the copper atom is surrounded by the various kinds of atoms in octahedral configuration in many cases and above exceptional case (α- and β-phthalocyanine) in planer configuration. We conclude that the fine structures of the Cu K absorption edges of these compounds are mainly determined by the immediate surroundings of the atom in question in our experimental energy region from the main edges.

§ 1. Introduction

On the short wavelength side of the X-ray absorption edges, typical for a certain element, the absorption coefficient has not a monotonic variation but fluctuates over a distance of several hundred volts from the main edge in the case of crystalline solids or polyatomic molecules in which the absorption element forms a constituent. This phenomenon, the so-called "fine structure of X-ray absorption edges," finds its explanation in the scattering of a K photoelectron in the crystalline solid or in the polyatomic molecule that contains the absorbing atom. According to Kronig¹⁾ the origin of this phenomenon in the case of crystalline solids is as follows. X-rays are absorbed by the electrons which make transitions from the X-ray K levels to empty levels lying above the Fermi distribution. When atoms are grouped in the crystal lattice, these empty levels are grouped into zones, characteristic of the crystal as a whole and extended sometimes several hundred volts out beyond the ordinary atomic optical levels, and exist as forbidden and allowed bands. As the absorption coefficient is proportional to the product of the transition probability and state density, a fine structure occurs. From the Kronig's theory the fine structures of the absorption edge must be highly depend upon the type of the crystal lattice in which the absorbing element is imbeded. This can experimentally be tested in several ways²⁾ and many peculiarities of the fine structures of the X-ray absorption edges can be fully understood in the basis of Kronig' theory. However, there seemed to be at first sight some discrepancy between theory and experiment in some special cases, for instance in the case of ionic crystals and complex compounds, and it has been demonstrated that the immediate surroundings in the crystal lattice of the atoms in question are also of great importance.³⁾ Thus in the case of the chemical compounds, the situation is more complex due to the presence of several kinds of atoms, the greater complexity of the lattice structure and the fact that a given sort of atom may have different valences and even different surroundings in the same lattice. Many investigations[4)] have been carried out on compounds of the various elements for the various purposes. It is therefore of some importance to extend the experimental data of the fine structures of the X-ray absorption edges of various chemical compounds, and to investigate the relation of the fine structures of the absorption edges to the chemical bond to the absorbing elements, the immediate surroundings in the crystal lattice of the atom in question and the crystal lattice in which the absorbing element is imbeded. Therefore the present authors investigated the fine structures of the X-ray *K* absorption edges of copper in following cupric and cuprous compounds: cupric chloride ($CuCl_2$), cupric chloride dihydrate ($CuCl_2 \cdot 2H_2O$), cupric bromide ($CuBr_2$), cupric sulfate pentahydrate ($CuSO_4 \cdot 5H_2O$), cupric nitrate trihydrate ($Cu(NO_3)_2 \cdot 3H_2O$), cupric carbonate ($CuCO_3$), cupric formate tetrahydrate ($Cu(HCOO)_2 \cdot 4H_2O$), cupric acetate monohydrate ($Cu(CH_3COO)_2 \cdot H_2O$) bis glycino copper monohydrate ($Cu(C_2H_4NO_2)_2 \cdot H_2O$), bis glycino copper hydrate ($Cu(C_2H_4NO_2)_2 \cdot xH_2O$), copper phthalocyanine α-form ($CuC_{32}H_{16}N_8$), copper phthalocyanine β-form ($CuC_{32}H_{16}N_8$), cuprous chloride ($CuCl$), cuprous bromide ($CuBr$) and cuprous iodide (CuI).

§ 2. Experiments

X-ray Diffraction Unit and Wide Range Goniometer of North American Philips Company Inc. (Norelco)[5)] are used. The unit is mechanically so arranged as to maintain a 1:2 ratio of the rotational speed between the crystal holder of the center of the goniometer and the Geiger-Müller counter as required for Bragg reflections. This unit is an installation to record the ordinary powder diffraction pattern. This unit is modified to a tube spectrometer described by Coster and De Lang[6)] who used the customary single crystal spectrometer removing its slit and used the line focus of the X-ray tube as the source and also as the slit, and could get the sufficient resolving power and intensity by their method. We attached Geiger-Müller counter to their method and let the crystal and the counter rotate automatically, therefore we could get the absorption spectrum by recording automatically on the strip-chart. The details of this modified method will be published in another paper[7)]. The effective target area of this unit is about $1.2 \times 10\ \text{mm}^2$, and we take off X-rays in 3° angle to the target surface, then the width of the effective target is about 0.06 mm. The X-rays of various wavelengths which satisfy the Bragg condition in the center of the spectrometer will be able to pass the receiving slit in front of the Geiger-Müller counter (Fig. 1). The width of the receiving slit was 0.003 in. and the distance between the focus of the X-ray tube and the center of the spectrometer and that between the center of the spectrometer and the receiving slit are 17 cm each. The X-ray divergency caused by the width of the effective target area and the width of the receiving slit (collimating slit system) has a relation[8)] to the resolving power of this spectrometer. In our case the maximum divergency of the slit system is about 0.0004 radians. As a reflecting crystal LiF was used. The resolving power of this instrument is rather well, and taking into consideration the undesirable influences of the slit width of the photometer and the grain size of the photographic plate it is sufficient to use this instrument for such research of the extended fine structures of the X-ray absorption spectra. The fine structures of the X-ray Cu *K* absorption spectra of the substances already described in introduction were recorded on the strip-charts. They are reproduced in Fig. 2 to Fig. 16. The X-ray tube with a cobalt taget at hand was loaded with 15 kV, 10 mA. Considering the time constants of the rate-meter and the recorder,

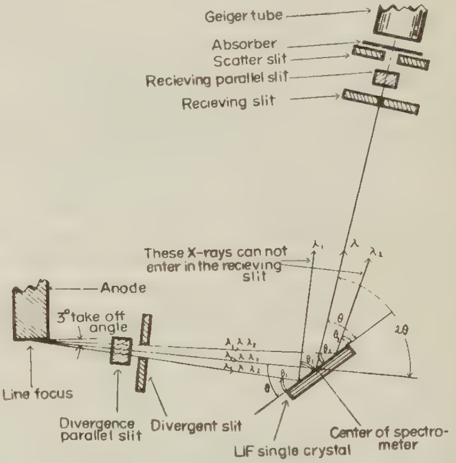

Fig. 1. Schematic diagram of the X-ray spectrometer.

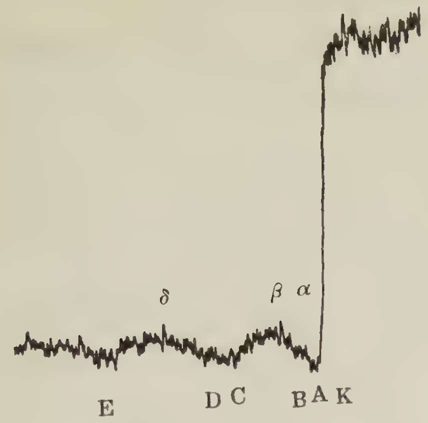

Fig. 2. $CuCl_2$

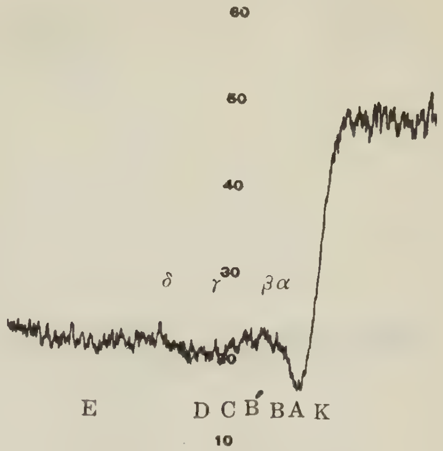

Fig. 5. $CuSO_4 \cdot 5H_2O$

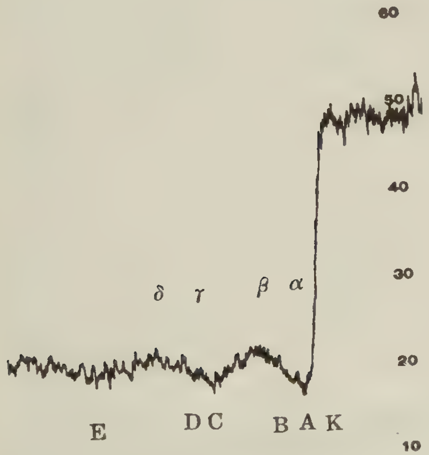

Fig. 3. $CuCl_2 \cdot 2H_2O$

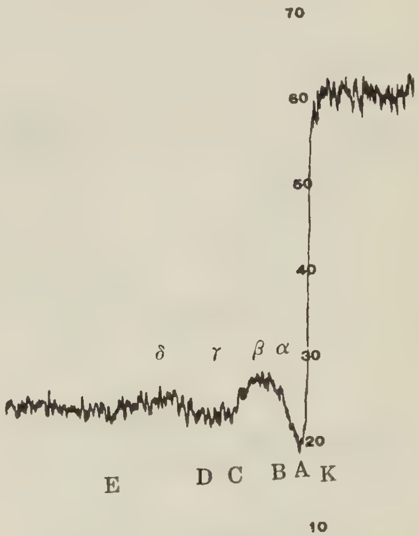

Fig. 6. $Cu(NO_3)_2 \cdot 3H_2O$

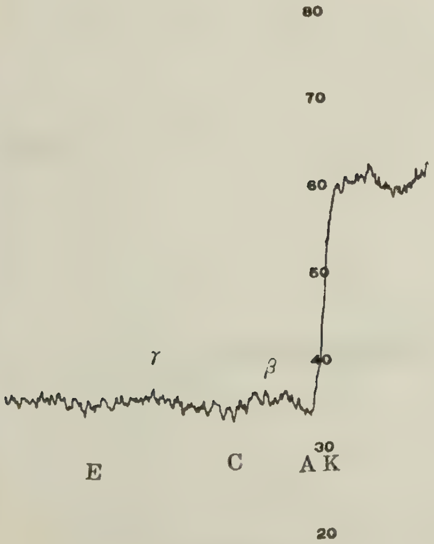

Fig. 4. $CuBr_2$

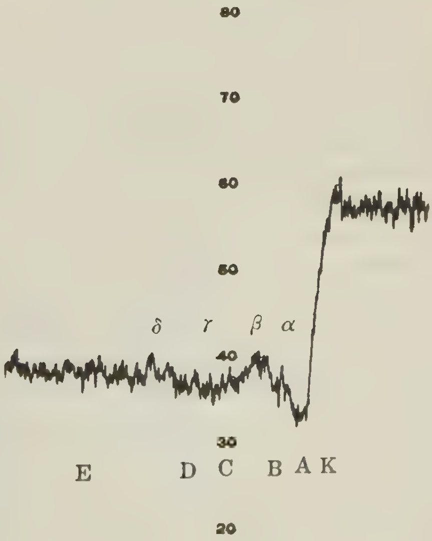

Fig. 7. $CuCO_3$

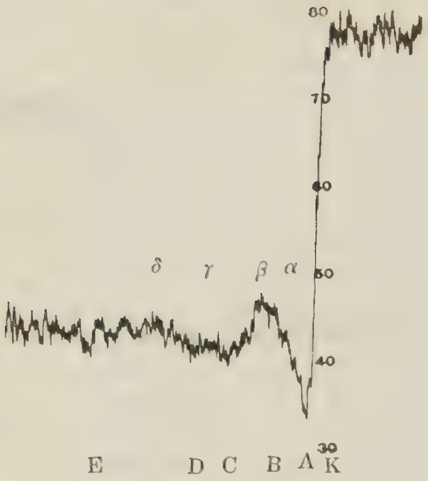

Fig. 8. $Cu(HCOO)_2 \cdot 4H_2O$

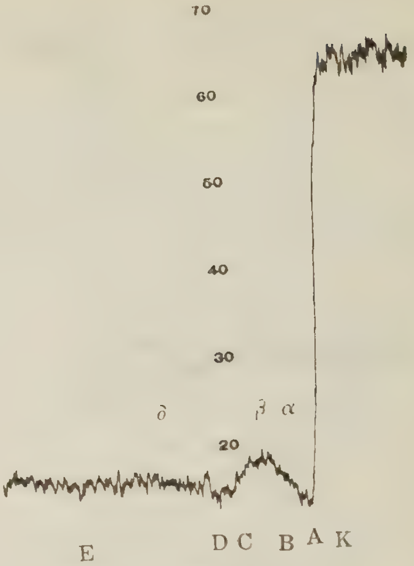

Fig. 10. $Cu(C_2H_4NO_2) \cdot H_2O$

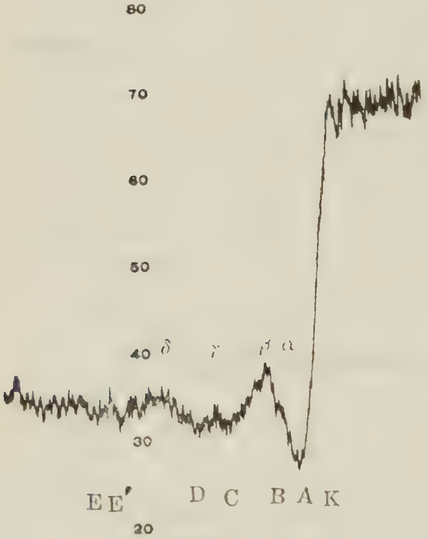

Fig. 9. $Cu(CH\ COO \cdot H_2O)_2$

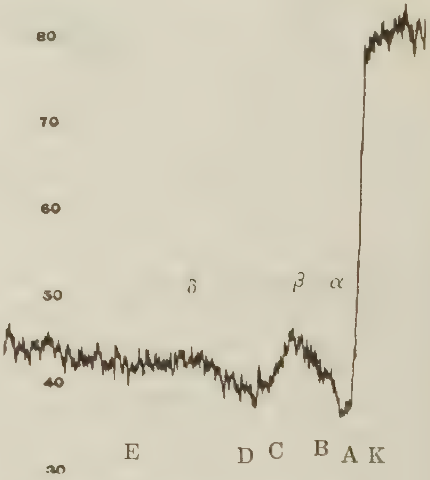

Fig. 11. $Cu(C_2H_4NO_2)_2 \cdot xH_2O$

the scanning speed of the Geiger-Müller tube 1/8° per min was used in all cases, and the time constant of the rate-meter was 2 or 4 sec, and one scale division of the stripchart correspondings about 9 X-ray quanta. The absorbers were held in front of the Geiger-Müller tube, and the best results were obtained by mixing a small amount of grease for vacuum seal with the powdered sample and spreading the mixture on a thin paper up to the required amount 10 mg/cm² to 30 mg/cm². This grease also protect against the various chemical attack with moisture. The first order reflection of general rays from the cobalt target was used. As we can directly measure the primary X-ray intensity and the

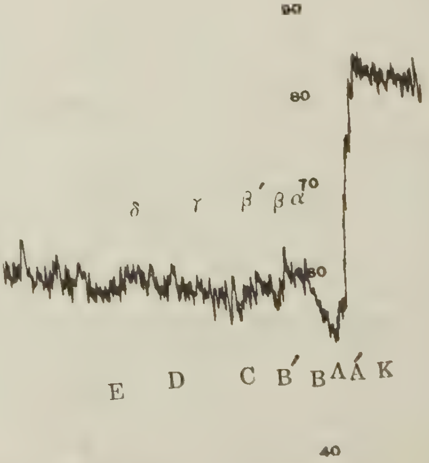

Fig. 12. $CuC_{32}H_{16}N_8$ α-form

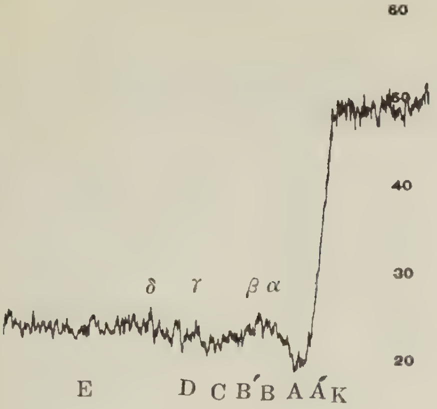

Fig. 13. $CuC_{32}H_{16}N_8$ β-form

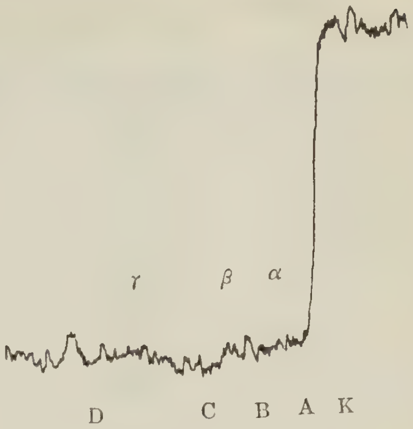

Fig. 15. CuBr

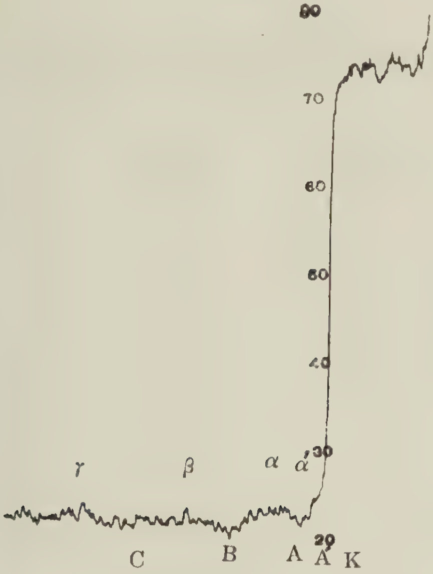

Fig. 14. CuCl

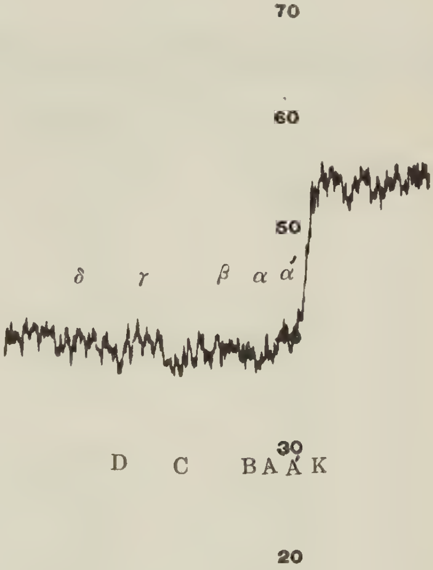

Fig. 16. CuI

Table I. Wavelength values of the fine structures of Cu *K* absorption edges of cupric compounds

	$CuCl_2$	$CuCl_2 \cdot 2H_2O$	$CuBr_2$	$CuSO_4 \cdot 5H_2O$	$Cu(NO_3)_2 \cdot 3H_2O$
	x.u.	x.u.	x.u.	x.u.	x.u.
K	1377.1	1377.1	1376.9	1376.9	1377.1
K'	1375.1				
A	1374.8	1375.0	1374.9	1374.8	1374.9
α	1374.2	1373.5		1373.1	1373.3
B	1373.7	1372.7		1372.3	1372.8
β	1370.4	1370.9	1370.8	1370.9	1371.2
B'				1370.1	
C	1366.0	1367.0	1367.8	1368.6	1368.1
γ	1365.0			1366.9	1366.2
D	1364.2	1364.4	1365.3	1365.2	1364.9
δ	1360.4	1360.9	1360.4	1360.8	1361.4
E	1354.5	1354.2	1354.0	1354.2	1354.2

Table II. Wavelength values of the fine structures of Cu *K* absorption edges of cupric compounds

	$CuCO_3$	$Cu(HCOO)_2 \cdot 4H_2O$	$Cu(CH_3COO)_2 \cdot H_2O$	$Cu(C_2H_4NO_2)_2 \cdot H_2O$	$Cu(C_2H_4NO_2)_2 \cdot xH_2O$
	x.u.	x.u.	x.u.	x.u.	x.u.
K	1377.2	1376.9	1377.1	1377.1	1377.1
A	1375.4	1375.0	1374.8	1374.8	1375.0
α	1373.5	1373.2	1372.9	1373.2	1373.1
B	1372.9	1372.5	1372.5	1372.4	1372.7
β	1371.1	1370.9	1370.1	1370.9	1370.9
C	1367.8	1367.3	1368.0	1367.7	1367.5
γ	1366.4	1365.7	1366.7		
D	1364.7	1364.5	1365.0	1366.5	1366.4
δ	1360.6	1360.7	1361.0	1360.9	1361.4
E′			1358.1		
E	1354.0	1354.1	1354.2	1353.7	1354.2

Table III. Wavelength values of the fine structures of Cu *K* absorption edges of copper phthalocyanines

	$CuC_{32}H_{16}N_8$ α-form	$CuC_{32}H_{16}N_8$ β-form
	x.u.	x.u.
K	1377.2	1377.3
A′	1375.4	1375.6
A	1374.3	1374.5
α	1371.9	1371.6
B	1371.3	1371.0
β	1370.5	1370.6
B′	1368.8	1368.5
β′	1367.7	
C	1365.4	1366.9
γ	1362.2	1365.6
D	1358.9	1364.3
δ	1357.3	1359.8
E	1353.0	1354.2

Table IV. Wavelength values of the fine structu of Cu *K* absorption edges of cuprous compoun

	CuCl	CuBr	CuI
	x.u.	x.u.	x.u.
K	1377.5	1377.4	1377.5
A′	1376.3	1376.3	1376.4
α′	1375.2		1375.8
A	1374.0	1375.3	1374.8
α	1371.4	1373.8	1374.3
B	1367.6	1372.1	1373.5
β	1362.4	1370.0	1370.7
C	1359.3	1368.0	1367.2
γ		1363.5	1364.8
D		1359.4	1363.1
δ			1360.7
E			1358.6

Table V. Energy separations of the fine structures of Cu *K* absoption edges of cupric compounds from the main edges

	$CuCl_2$	$CuCl_2 \cdot 2H_2O$	$CuBr_2$	$CuSO_4 \cdot 5H_2O$	$Cu(NO_3)_2 \cdot 3H_2O$
	eV.	eV.	eV.	eV.	eV.
K	0	0	0	0	0
K′	13				
A	15	14	13	14	15
α	19	24		25	25
B	23	29		30	28
β	44	41	40	40	39
B′				45	
C	73	66	60	54	59
γ	79			65	72
D	85	83	76	77	80
δ	110	107	109	107	103
E	150	152	152	152	152

Table VI. Energy separations of the fine structures of Cu K absorption edges of cupric compounds from the main edges

	$CuCO_3$	$Cu(HCOO)_2\cdot 4H_2O$	$Cu(CH_3COO)_2\cdot H_2O$	$Cu(C_2H_4NO_2)_2\cdot H_2O$	$Cu(C_2H_4NO_2)_2\cdot xH_2O$
	eV.	eV.	eV.	eV.	eV.
K	0	0	0	0	0
A	12	13	15	15	14
α	24	24	28	26	26
B	28	30	30	31	29
β	40	40	46	41	41
C	62	63	60	62	63
γ	71	73	68		
D	82	81	79	69	70
δ	109	107	106	107	103
E'			125		
E	154	151	152	155	152

Table VII. Energy separations of the fine structures of Cu K absoption edges of copper phthalocyanines from the main edges

	$CuC_{32}H_{16}N_8$ α-form	$CuC_{32}H_{16}N_8$ β-form
	eV.	eV.
K	0	0
A'	12	11
A	19	18
α	35	37
B	39	41
β	44	44
B'	55	58
β'	62	
C	77	68
γ	99	77
D	121	85
δ	131	115
E	160	153

Table VIII. Energy separations of the fine structures of Cu K absorption edges of cuprous compounds from the main edges

	CuCl	CuBr	CuI
	eV.	eV.	eV.
K	0	0	0
A'	8	7	7
α'	15		11
A	23	14	18
α	40	24	21
B	65	35	26
β	99	48	44
C	120	62	68
γ		91	83
D		118	95
δ			111
E			124

transmission X-ray intensity in this case, this recording method is easily changed so as to enable the measurement of the absorption coefficient. Table I, II, III and IV show the wavelength values of the fine structures of Cu K absorption edges of these compounds thus measured and Table V, VI, VII and VIII show energy separations of these fine structures from the K main absorption edges of copper. In the case of cuprous bromide and cuprous iodide, the fine structures of the Cu absorption edges were very faint so that we took the photographs of the Cu absorption edges of copper halide (CuI, CuBr, CuCl, $CuBr_2$, $CuCl_2$) with a bent crystal focusing spectrograph of the Cauchois type. The fine structures of the Cu absorption edges of CuI and CuBr were also very faint on the photographic plates, but we measured the wavelength values by means of a comparater with low magnification approximately five. These results fairly well coincided with those of recording method.

§ 3. Results and Discussions

The various compounds which have been treated in this paper are classified in three cases and discussed respectively as follows.

Case A. Cupric compounds:

$CuCl_2$, $CuCl_2\cdot 2H_2O$, $CuBr_2$, $CuSO_4\cdot 5H_2O$, $Cu(NO_3)_2\cdot 3H_2O$, $CuCO_3$, $Cu(HCOO)_2\cdot 4H_2O$, $Cu(CH_3COO)_2\cdot H_2O$, $Cu(C_2H_4NO_2)_2\cdot H_2O$, and $Cu(C_2H_4NO_2)_2\cdot xH_2O$.

In the case of the above compounds, it will be seen that the fine structures of the Cu K absorption edges of those compounds are very similar in forms by comparing each recorded curve in Fig. 2 to Fig. 11. As one sees from Table I and Table II, the wavelength values of the large absorption minima β, δ and maxima A, C, E, nearly coincide within the limit of experimental errors. This is clearly seen in Fig. 17 which shows a diagram of energy separations of the fine structures of the Cu absorption edges of these compounds from the main edges. It is regarded that this is due to the following facts. In these compounds the copper atom is bounded to the surrounding atoms by the bonds which one considered to be essentially ionic bond or essentially covalent bond or their mixture, and the bonding types are not the same in the all compounds. But, in these compounds the copper atom is surrounded by four atoms of nitrogen, oxygen, or halogens at the corners of the pseudo-square, and by two atoms of various kinds which situated upwards and downwards of the central copper atom at a little larger distance from the copper atom than those of four atoms at the corners of the square from the same copper atom. By these six atoms the elongated pseudo-octahedron[9] is formed. If the fine structures of the absorption edges are mainly determined by the immediate surroundings, they must be similar in all cases of these compounds. The little differences of forms of the fine structures of absorption edges of these compounds are du to the differences of the forms of these pseudo octahedrons. The crystal structures of thes compounds and their bonding types are ver complicated and are not the same in all com pounds but in the energy region here studie we can not find any difference which is cause by the crystal lattice as expected from Kronig' theory and also by bonding types. The distanc from the immediate surroundings to the ator in question has not also significant influenc on the fine structures of the absorption edges It is rather probable that the fine structure are determined by the radii of copper atom in question which are considered to be nearl equal in all these cases.

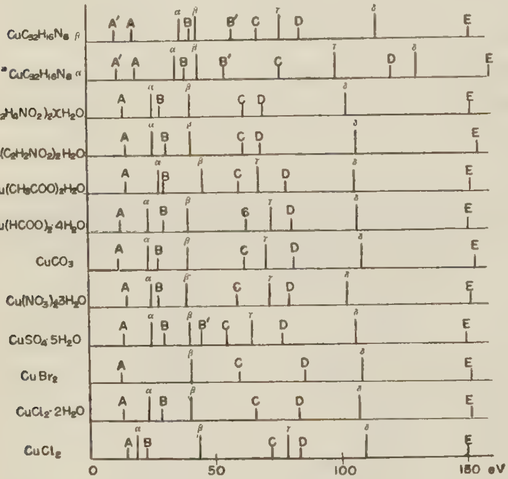

Fig. 17. Diagram of the energy separations of fine structures of absorption edges from the main edges.

Case B. Copper phthalocynaine (α- and β form)

In the case of β-phthalocyanine (Kienle' nomenclature) this is in the metastable state and its crystal structure and the atomic ar rangement of this molecule are not well studied In the case of α-phthalocyanine[10] the atomic arrangement is very much resemble as the preceding compounds, namely the copper atom is surrounded by four nitrogen atoms at the coners of the pseudo-square but in this case the distances of two copper atoms coordinated upwards and downwards the central one are each 4.76 Å. As this distance (Cu–Cu) is larger compared to that of the nitrogen atom from the central copper atoms (Cu–N) it is considered that these two copper atoms have less influence on the electric field around the centra copper atom than four nitrogen atoms. I seems to us that this is the reason why the fine structures of the Cu K absorption edges of phthalocyanines differ from those of preceding cupric compounds.

Case. C; CuI, CuBr, *and* CuCl

Among above cuprous compounds, the fine structures of Cu K absorption edges of Cu and CuBr were very faint. As all these com pounds crystallize in the lattice of Zn–S type (Zincblende type)[11] and the copper atom ha the identical position in all cases, the similarity of the fine structures of absorption edges ac cording to Kronig's theory was expected. Bu we failed to compare well these structures Stephenson[4] reported that the fine structure of the Cu K absorption edges of CuBr are n repeatable structures.

Summary

In general the wavelengths of main edges of copper do not greatly change in every cases, but tend to slightly displace towards the shorter wavelength sides with valencies than that of pure metallic copper. In the energy regions here studied the fine structures of absorption edges of copper are mainly determined by the immediate surroundings of the atom in question. There are no difference which should be caused by the crystal lattice according to the Kronig's theory. Coster¹²⁾ and others¹³⁾ show that even the fine structures of absorption edges of metals are influenced by the surrounding atoms. Also Kiestra¹⁴⁾ remarks that the fine structures are determined by the immediate surroundings of the atom in question in the regions about 40 eV to 150 eV from the main absoption edges. This statement is well supported in our present experimental results.

Recently we saw the manuscript by Cotton and Hanson¹⁵⁾ after we had written this paper. In our cases the fine structures close to the main edges were not studied and some of the small maxima and minima of these structures might not be measured. As many compounds in our experiment are not the perfectly ionic crystals, Cotton and Ballhausen's theory¹⁶⁾ can not directly be applied to these compounds.

We wish to express our sincere thanks to the members of Nitta and Watanabe laboratory where some of the samples were prepared.

References

1) R. de Kronig: Zs. f. Phys. **70** (1931) 317, **75** (1932) 191.
2) D. Coster and R. Smoluchowski: Physica **2** (1935) 1.
3) D. Coster and G. H. Klammer: Physica **1** (1934) 145.
V. P. Barton and G. A. Lindsay: Phys. Rev. **46** (1934) 362.
4) G. A. Lindsay and Voorhees: Phil. Mag. **6** (1928) 910.
S. Aoyama and T. Fukuroi: Sci. Rep. Tohoku Imp. Univ. **28** (1940) 410.
C. Kurylenko: J. Phys. et Rad. **8** (1940) 133.
S. T. Stephenson: Phys. Rev. **58** (1940) 873.
S. Yoshida: Sci. Paper Inst. Phys. Chem. Research, Tokyo **38** (1941) 272.
V. H. Sanner: Thesis Uppsala. 1941.
H. Hanson and W. W. Beeman: Phys. Rev. **76** (1949) 118.
5) Instruction Book for Installation and Operation of Norelco: North American Philips Comp. Inc. New York.
6) D. Coster and H. De Lang: Physica **13** (1947) 379.
7) K. Tsutsumi, M. Sawada and A. Hayase: Norelco Reporter. to be published.
8) F. K. Richtmyer: Phys. Rev. **26** (1925) 724.
9) C. A. Beevers and H. Lipson: Proc. Roy. Soc. **A 146** (1934) 570.
D. Harker: Zs. f. Krist. **A 93** (1936) 136.
H. Lindsay: J. A. C. S. **69** (I) (1947) 886.
A. F. Wells: J. C. S. (1947) 1670.
J. N. van Nickerk and F. R. L. Schoening: Acta cryst. **6** (1953) 227.
R. Kiriyama, H. Ibamoto and K. Matsuto: Acta cryst. **7** (1954) 482.
10) J. M. Robertson: J. C. S. (1935) 165.
11) R. W. G. Wyckoff: The Structure of Crystals New York (1924).
12) D. Coster: Physica **2** (1935) 606.
13) M. Sawada, K. Tsutsumi and A. Hayase: J. Phys. Soc. Japan. **12** (1957) 628.
14) S. Kiestra: A Conference on the Applications of X-Ray Spectroscopy to Solid State Problems 23-25 Oct. 1950.
15) F. A. Cotton and H. P. Hanson: J. C. P. **25** (1956) 619.
16) F. A. Cotton and C. J. Ballhausen: J. C. P. **25** (1956) 617.

JOURNAL OF THE PHYSICAL SOCIETY OF JAPAN Vol. 12, No. 7, JULY, 1957

Influence of Temperature on the Pure Nuclear Quadrupole Resonance in Hexachloroethane

By Itaru TATSUZAKI and Yasaburo YOKOZAWA

Research Institute of Applied Electricity, Hokkaido University, Sappro

(Received January 18, 1957)

The temperature dependences of the frequencies and the widths of absorption lines of pure nuclear quadrupole resonances in hexachloroethane were studied. The change of resonance frequencies with temperature was explained as influences both of a torsional vibration of one end of CCl_3 groups with respect to the other end and of a rotational vibration of those groups as a whole around the C–C axis, the frequency of the latter vibration being changed with temperature owing to a thermal expansion of the lattice. The line widths at half-maximum intensity were about 2 Kc/s at temperatures of 77°K and 90°K, and about 10 Kc/s at 196°K, although no absorption was detected at room temperature. The broadening of the resonance spectrum seems to be explainable by a reorientational motion around the C–C axis with much lower frequency than the resonance one.

§ 1. Introduction

Although the resonance spectra of pure nuclear quadrupole of $Cl_3C \cdot CCl_3$ were observed at 20°K and 77°K by R. Livingston1), no absorption spectrum was detected at room temperature. The melting point of this molecule is 185°C and any phase transition which disturbs the observation of the spectra between 77°K and the room temperature has not been known. The purpose of the present work is to find the cause which may disturb the observation at room temperature, by the study of the temperature dependences of both the frequencies and the widths of absorption lines measured at 77°K, 90°K and 196°K. The temperature dependences on the resonance frequencies are explained as influences both of a torsional vibration of one end of CCl_3 groups with respect to the other and of a rotational vibration of the groups as a whole around the C–C axis, the frequency of the latter vibration being changed with temperature owing to a thermal expansion of the lattice. The full line widths at half-maximum intensity were about 2Kc/s at 77°K and 90°K, and about 10 Kc/s at 196°K. The broadening of the resonance line widths can not be explained by relaxation mechanisms due to these vibrations, which are given first by H. Bayer2) for ClHC=CHCl. Y. Ayant3),4) reported that the reorientational motion with much lower frequencies that the resonance one could broaden the line width exponentially with the increase of temperature. If the effect of this reorientational motion is applied to the width at 196°K, it is found that the resonance line is never detected at room temperature.

§ 2. Experimental Apparatuses and Procedures

The spectrometer used in this work was a super regenerative type with a Collpitts circuit which was similar to that reported by K. Torizuka5). A frequency modulation was applied for the oscillator and a detected signal was observed either on a C.R.O. or an automatic recorder, the latter employing the method of a narrow band amplifier and a phase sensitive detector. The modulation frequency was 270 c/s and the band width of the narrow band amplifier was about 10 c/s. The time constant of recording system was about 1 sec. The velocity of frequency sweep was about 0.1∼0.2 Kcps/sec and its sweeping was established with a capacitor driven by a phonomotor. The shape of the detected signal very sensitively depended both on the quench amplitude and on quench frequency as pointed by K. Tsukada6). In order to obtain the derivative curve of pure absorption, both the quench amplitude and quench frequency had to be experimentally adjusted by observing the signal. The resonance frequency was determined by observing the beat frequency between the oscillation of spectrometer and a higher harmonic of a heterodyne frequency meter. For the measurement of the width, signals of the higher harmonic frequency modulated by 4 Kc/s was occasionally recorded. Both the heterodyne frequency meter and the modulating frequency were calibrated through radio station, J. J. Y.. The sample used in this work was Kanto Chemical Company reagent grade powdered material and had a melting point of 185°C in a sealed capillary tube. The powder of $Cl_3C{\cdot}CCl_3$ put in a thin glass tube was placed inside the six turned r–f coil of tuning circuit and was cooled to 77°K, 90°K and 196°K, being immersed in liquid nitrogen, liquid oxygen and solid carbon dioxide respectively. In order to avoid the broadening of the absorption line owing to the temperature inhomogeneity in the sample, the measurements were made about one hour after the sample was placed in a cooled Dewer vessel.

§ 3. Preliminary Discussions

A) *Temperature Dependence of the Resonance Frequency*

It is well known that the quadrupole resonance frequency generally decreases in magnitude with the increase of temperature*. This effect was explained by H. G. Dehmelt, H. Krüger⁷⁾ and Bayer²⁾ as an influence of the lattice vibration in solid. Recently, T. Kushida⁸⁾ extended their theory to more general case. According to Bayer's model the direction of the maximum principal axis of field gradient tensor (z′-axis) vibrates around the z-axis.

The z-axis is the direction of the maximum principal axis when there is neither molecular vibration nor lattice vibration. If the z′-axis inclines by a small angle θ from the original direction, z-axis, the Hamiltonian operator of interaction between the field gradient tensor and the nuclear quadrupole moment is given by

$$\boldsymbol{H}=\frac{eQq}{4I(2I-1)}\left\{\left(1-\frac{3}{2}\theta^2\right)(3\boldsymbol{I}_z^2-I(I+1))+3\theta(\boldsymbol{I}_z\boldsymbol{I}_y+\boldsymbol{I}_y\boldsymbol{I}_z)-\frac{3}{4}\theta^2(\boldsymbol{I}_+^2+\boldsymbol{I}_-^2)\right\} \quad (1)$$

assuming the asymmetery parameter is zero.

The notations in Eq. (1) have their usual meanings. The frequencies of the molecular vibration and the lattice vibration are much higher than the resonance frequency. Therefore, θ^2 in the first term of Eq. (1) can be replaced by its average $\overline{\theta^2}$. Accordingly, the resonance frequency $\nu(T)$ is expressed as

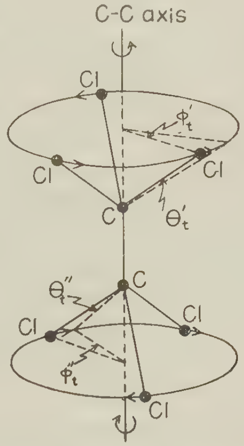

Fig. 1. Molecular structure of hexachloroethene and its torsional vibration. The parameters¹¹⁾ at 15°C are C–Cl=1.76 Å~1.77 Å, C–C=1.54 Å and ∠ClCCl=109.8°.

$$\nu(T)=\nu_0\left(1-\frac{3}{2}\overline{\theta^2(T)}\right), \quad (2)$$

where ν_0 is the resonance frequency when $\theta=0$ and equals to $eQq/2h$ for a nucleus with spin 3/2. The symmetry of $Cl_3C{\cdot}CCl_3$ is D_{3d} as shown in Fig. 1 and the frequencies of normal vibrations in the molecular vibration are well known⁹⁾ except A_{1u} mode of a torsional vibration. The A_{1u} mode is both Raman and infra-red inactive owing to D_{3d} symmetry of $Cl_3C{\cdot}CCl_3$. However, the height of potential wall against this vibration is estimated approximately 7~15 Kcal/mole by an electron diffraction investigation¹⁰⁾. It is assumed that the potential function hindering the torsional vibration has the form of

$$V=\frac{1}{2}V_0(1-\cos 3\phi_t) \quad (3)$$

where, ϕ_t is the relative angle of rotation of two groups CCl_3 and V_0 is the wall height. It follows that the torsional frequency ν_t is given by

$$\nu_t=\frac{3}{2\pi}\sqrt{\frac{V_0}{2I_r}} \quad (4)$$

---

* It is reported there are some exceptions.: $K[Cu(CN)_2]$, (Krüger and M. Berkhaut: Zeit. für Physik **132** (1952) 171), WCl_6 (R. P. Hamlen and W. S. Koski: J. Chem. Phys. **25** (1956) 360).

where I_r is the reduced moment of inertia, 243.5×10^{-40} gr-cm². The available structure parameters to determine I_r is refered to the results of X-ray analysis[11]. From Eq. (4), ν_t is 60 cm⁻¹ assuming $V_0=10$ Kcal/mole. This frequency is much lower than any other normal frequency of $Cl_3C\cdot CCl_3$. Therefore, it may be assumed that the contribution to the resonance frequency of any other normal vibration is negligible compared with that of the torsional vibration among molecular vibrations. Considering the symmetry of this molecule, it is assumed that a rotational vibration around the C–C axis is the most favourable lattice vibration in solid state. From these points of view, θ can be expressed as

$$\theta=\theta_t+\theta_r\ , \tag{5}$$

where θ_t and θ_r are deflection angles of the maximum principal axis of the field gradient tensor due to the torsional and the rotational vibration respectively. The direction of the maximum principal axis of the field gradient tensor is assumed to coincide with the direction of the C–Cl bond. For simplicity, assuming that the torsional vibration is incoherent with the rotational vibration, θ_t is independent of θ_r. Taking the time average, it follows

$$\overline{\theta^2}=\overline{\theta_t^2}+\overline{\theta_r^2}\ , \tag{6}$$

where

$$\overline{\theta_t^2}=\frac{1}{3}\sin^2\frac{A}{2}\frac{1}{I_r}\frac{h}{4\pi^2\nu_t}\left(\frac{1}{2}+\frac{1}{\exp(h\nu_t/kT)-1}\right) \tag{7}$$

and

$$\overline{\theta_r^2}=\frac{4}{3}\sin^2\frac{A}{2}\frac{1}{I}\frac{h}{4\pi^2\nu_r}\left(\frac{1}{2}+\frac{1}{\exp(h\nu_r/kT)-1}\right) \tag{8}$$

respectively, (cf. Appendix), and I is the moment of inertia of $Cl_3C\cdot CCl_3$ around the C–C axis, which is equal to $4I_r$ and A is the angle ∠CClC which is taken as 109.8°. Inserting the Eq. (6), (7) and (8) in Eq. (2), the next relation is obtained.

$$\frac{\nu_0-\nu(T)}{\nu_0}=\frac{1}{2}\sin^2\frac{A}{2}\frac{h}{4\pi^2I_r}\times\left\{\frac{1}{\nu_t}\left(\frac{1}{2}+\frac{1}{\exp(h\nu_t/kT)-1}\right)+\frac{1}{\nu_r}\left(\frac{1}{2}+\frac{1}{\exp(h\nu_r/kT)-1}\right)\right\} \tag{9}$$

B) *Temperature Dependences of the Line Width*

The causes of line broadening in a pure quadrupole resonance were reported by Bayer[2], Ayant[3),4] and E. R. Andrew[12]. These causes are (a) magnetic dipolar interaction between neighbouring nuclei and Zeeman effect in the terrestrial magnetic field, (b) fluctuation of θ^2 in the first term of Eq. (1) which does not give a relaxation, but has a relation with line broadening, (c) fluctuation of θ in the second term of Eq. (1) which induces a transition of $|\Delta m|=1$, (d) fluctuation of θ^2 in the third term of Eq. (1) which induces a transition of $|\Delta m|=2$, (e) imperfections in a crystal lattice which cause the field gradient to vary somewhat from molecule to molecule and (f) reorientational motion of CCl_3 group around the C–C axis, which limits a mean life time of the energy levels at each position, and gives a line broadening intensively depending on temperature.

The features of these causes are as follows. (a) does not depend on temperature. (b) and (d) depend on temperature and the line width is approximately proportional to square of temperature. (c) gives a negligible effect on the line width compared with (d). (f) depends on temperature remarkably. The full line width increases exponentially with the increase of temperature and is approximately, at half-maximum intensity[3),4],

$$(\Delta\nu)_{1/2}=\frac{\lambda}{\pi}\qquad \lambda=2\nu\exp\left(-\frac{W}{kT}\right), \tag{10}$$

where λ is a transition probability of the reorientational motion and W is a height of potential wall in which the molecule vibrates with frequency ν.

§ 4. Experimental Results and Discussions

The results of the experiment are listed in Table I. The resonance frequencies at 20°K and 77°K are quoted from Livingston's research[1] and values at 77°K are in agreement with those of the results of the present work within the experimental error of ±0.001 Mc/s.

The resonance absorption of Cl^{37} were observed at the frequencies expected from the known ratio of quadrupole moments. The existence of four absorption lines is in agreement with the result of X-ray analysis[11] which reported that this crystal contained four molecules in the unit cell. The value of ν_0 for each absorption line was determined by the extrapolation of the curve of resonance frequency against temperature to absolute

Table I. Resonance frequency and line width in $Cl_3C\cdot CCl_3$.

Temperature (°K)	Frequency (Mc/s)				line width (Kc/s) $(\Delta\nu)_{1/2}$
	ν_1	ν_2	ν_3	ν_4	
20*	40.885	40.823	40.798	40.652	—
70*	40.761	40.714	40.685	40.551	2.0±0.2
90	40.725±0.001	40.681	40.651	40.520	2.0±0.2
196	40.350±0.01	40.305	40.273	40.150	10.1±1.0

* From R. Livingston[1] for resonance frequency.

zero as shown in Fig. 2. They are 40.920, 40.852, 40.825 and 40.676 Mc/s respectively. As there is no available data, unfortunately, to determine the frequency of rotational vibration ν_r, the validity of Eq. (9) could not be examined directly from the resonance frequencies. If ν_r was calculated from Eq. (9) by the use of resonance frequency conversely, some informations would be obtained concerning the employed model in § 3. In the calculation of Eq. (9), the frequency of torsional vibration ν_t was assumed to be 60 cm^{-1} at each temperature, because the frequency of molecular vibration does not change with temperature. The calculated results are listed in Table II. As seen in Table II, each resonance line gives slightly different value for ν_r at the same temperature and moreover, each ν_r increases with the decrease of temperature. The small differences among ν_r's calculated from resonance frequencies seem to be due to the existence of anisotropic van der Waals interaction[11] between molecules in the crystal lattice. The variation of ν_r with temperature is explained by the consideration of variation of cohesive forces caused to the thermal expansion as suggested by B. Dreyfus and D. Dautreppe[13] in paradichlorobenzene. Assuming that the Grüneisen's formula is valid in the rotational vibration, γ is given by

$$\gamma = -\frac{d\log\nu_r}{d\log V}, \tag{11}$$

hence,

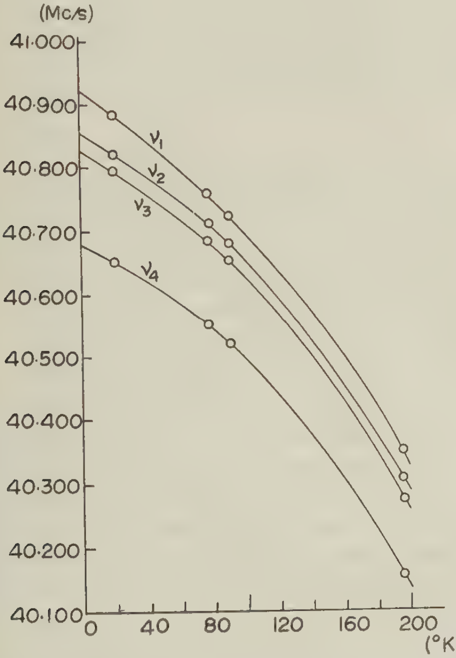

Fig. 2. Variation of the resonance frequency of Cl^{35} in $Cl_3C\cdot CCl_3$ with temperature.

Table II. Calculated values using Eq. (9).

	77°K			90°K			196°K		
	$\frac{\nu_0-\nu}{\nu_0}\times10^3$	$\left(\frac{\nu_0-\nu}{\nu_0}\right)_r \times10^3$	ν_r cm^{-1}	$\frac{\nu_0-\nu}{\nu_0}\times10^3$	$\left(\frac{\nu_0-\nu}{\nu_0}\right)_r \times10^3$	ν_r cm^{-1}	$\frac{\nu_0-\nu}{\nu_0}\times10^3$	$\left(\frac{\nu_0-\nu}{\nu_0}\right)_r \times10^3$	ν_r cm^{-1}
ν_1	3.89	2.63	40.4	4.77	3.32	38.6	13.92	10.96	31.0
ν_2	3.38	2.12	45.4	4.18	2.74	42.7	13.38	10.42	31.8
ν_3	3.43	2.17	45.1	4.26	2.82	42.1	13.52	10.56	31.6
ν_4	3.07	1.81	49.4	3.84	2.40	45.7	12.93	9.97	32.5
$\langle\nu_r\rangle_{Av}$			$\langle 45.1\rangle_{Av}$			$\langle 42.3\rangle_{Av}$			$\langle 31.7\rangle_{Av}$

* $\left(\frac{\nu_0-\nu}{\nu_0}\right)_r$ is contribution of rotational vibration to $\frac{\nu_0-\nu}{\nu_0}$.

$$\frac{\nu_r(t_1)}{\nu_r(t_2)} \simeq \exp\left[\gamma\alpha_v(t_2-t_1)\right] . \tag{12}$$

Where γ represents Grüneisen constant, V, volume and α_v, volume expansion coefficient, and $\nu_r(t_1)$ and $\nu_r(t_2)$ represent ν_r at temperatures of t_1 and t_2 respectively. γ is found to be 2.9 from Eq. (12) using the following sets of values: $\langle\nu_r(77)\rangle_{Av}=45.1\,\text{cm}^{-1}$, $\langle\nu_r(196)\rangle_{Av}=31.7\,\text{cm}^{-1}$ and $\alpha_v \simeq 1\times10^{-3}$[14]. Each $\langle\nu_r(t)\rangle_{Av}$ is given in Table II. In a similar way, from the values of $\langle\nu_r(90)\rangle_{Av}$, $42.3\,\text{cm}^{-1}$ and $\langle\nu_r(196)\rangle_{Av}$, γ becomes 2.7. Taking the mean value, γ is 2.8. On the other hand, Grüneisen constant, using thermodynamical relations, can be expressed as follows.

$$\gamma=\frac{\alpha_v V}{\kappa C_v} \qquad C_p-C_v=\frac{\alpha_v{}^2 VT}{\kappa} , \tag{13}$$

where κ is the compressibility, and C_p and C_v the molar heat at constant pressure and constant volume respectively.

By the X-ray analysis[11], the unit cell of this crystal at 15°C has a dimension of $a=11.56$ Å, $b=10.18$ Å, $c=6.42$ Å, and it contains four molecules and belongs to the space group Pnma. There is no data about C_p at 15°C but it has been measured at 22.25°C and is equal to 48.9 cal/mole[15]. The volume per mole is calculated to be 114.12 cc/mole using the volume expansion coefficient. From Eq. (13), using the numerical values, $\gamma=2.8$, $C_p=48.9$ cal/mole, $\alpha_v=1\times10^{-3}$, $V=114.12$ cc/mole and $T=295.25$°K, the value of κ is obtained as $37\times10^{-6}\,\text{Atm}^{-1}$, which is compatible with the compressibility of other organic compounds listed in Table III[16], taking the difference between solid and liquid into consideration. Recently, it is reported that the temperature dependence of the resonance frequency at atmospheric pressure has to be considered including the contribution of the effect of volume expansion on $|q|$[17]. Then, in order to do an adequate analysis of the observed temperature variation of the resonance frequency, it is required that the resonance frequency has to be measured as a function of volume for a series of different temperatures. From this point of view, the value of compressibility which is obtained by the present analysis seemes somewhat fortuitous.

Table III. Compressibility of organic molecule[16].

	Tem. (°C)	Pressure	$(\text{Atm}^{-1})\times10^6$
C_6H_6	0 (Solid)	100～300 Kg/cm²	31.69
	20 (liquid)	100～300 Kg/cm²	77.68
$CHCl_3$	18 (liquid)	0～8 Atm	97.43
C_6H_5Cl	17 (liquid)	0～8 Atm	71.41

The line widths of four absorption lines coincide with each other within an experimental error and their mean values are listed in Table I. Fig. 3 shows the derivative curves of absorption lines at 90°K and 196°K. The line width is defined as the interval between the two points where the integrated curve falls to half the maximum value. The difference between the widths at 77°K and 90°K is negligible, within the experimental error. The total width which is caused by b), c) and d) in § 3 is at most 50 c/s at 77°K and 90°K and is on the order of 500 c/s at 196°K, which are roughly estimated by considering the effect of a torsional and a rotational vibration using the formula given by Ayant[4]. Hence, it might follow that the main causes of the line widths at 77°K and 90°K are those stated in the item a) and e). It seems reasonable to consider that the causes of the broadening of

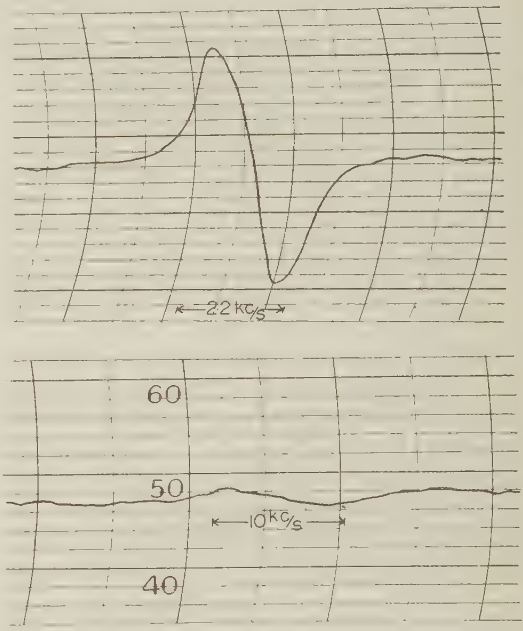

Fig. 3. Derivative curves of $Cl_3C{\cdot}CCl_3$. Upper curve, at 90°K. Frequency was swept at a rate about 0.1 Kc/s per second and the paper speed was six divisions per minute. Lower curve, at 196°K. Frequency was swept at a rate about 0.2 Kc/s per second and the paper speed was two divisions per minute.

absorption line at 196°K are those stated in the item a), e) and f). Among these causes, it is estimated that the one stated in the item f) is the most important, which represents a slow reorientational motion around the C–C axis, because the item a) and e) are nearly independent of temperature.

From this point of view, the line width due to the reorientational motion is of the order of 8±1 Kc/s at 196°K. It is expected that the reorientational motion consists of the torsional and the rotational reorientation. The line width is given by

$$(\varDelta\nu)_{1/2}=\frac{2\nu_t \exp\left(-\frac{V_0}{kT}\right)}{\pi}+\frac{2\nu_r \exp\left(-\frac{W}{kT}\right)}{\pi}\,, \tag{14}$$

where W is the height of potential wall where $Cl_3C\cdot CCl_3$ vibrates as a whole and the numerical values of other parameters are given above.

In Eq. (14), it is found that the contribution of the first term is negligibly small, and that the reorientational frequency is 25±3 Kc/s and using $\langle\nu_r(196)\rangle_{Av}=31.7\,\mathrm{cm}^{-1}$, W becomes to be about 7.0 Kcal/mole. Through out the present work, it is assumed that $|q|$ does not change with volume expansion. Actually, however, $|q_0|$ will increase as volume expands. In molecular crystals such as paradichlorobenzene, it is considered, $|q_0|\propto V^n$, with $0<n<0.04$[17]. Assuming $|q_0|\propto V^{0\sim0.04}$ also in $Cl_3C\cdot CCl_3$, the value of ν_r is between 26 and 31.8 cm⁻¹ at 196°K in the absorption line ν_2 by the use of Eq. (9), where $\nu_0\propto V^{0\sim0.04}$. If the value $\nu_r=26\,\mathrm{cm}^{-1}$ is inserted in Eq. (14), it is found that the value of W is nearly equal to 7.0 Kcal/mole, the value of which is obtained with $\nu_r=31.7\,\mathrm{cm}^{-1}$. The intermolecular distance are of the order of 3.7∼4.1 Å, as given by Sasada and Atoji[11]. These distances are slightly larger than the two times of van der Waals radius of Cl atom, 3.6 Å. It is plausible that the reorientational motion as a whole is apt to occur than the torsional reorientation. Being accepted the above broadening mechanism at 196°K, it was clarified that the absorption line could not be detected at room temperature, because of an extraordinary broadening with the increase of temperature.

The measurements reported in this paper yield some information about the temperature dependences of the resonance frequencies and the line widths of $Cl_3C\cdot CCl_3$. There are many molecular crystals whose pure quadrupole resonance are not detected at room temperature, though the large signals are detected at the temperature of liquid oxygen. This failure of detection is not explained by the decrease of population difference, accompanied with the increase of temperature, between the two energy levels which are concerned in transition.

$Cl_3C\cdot CCl_3$ in this work was chosen only for reason that this molecule was employded broadly in other fields of study, such as, X-ray analysis, Raman and infra-red spectra, electron diffraction, and specific heat etc. The measurements were carried out only at temperatures of 77°K, 90°K and 196°K, because of difficulty of keeping temperature constant in other temperatures within ±0.01°C, which was necessary for measuring of the line width.

Appendix

In a torsional vibration, ϕ_t' and ϕ_t'' are angles specifying the twist of the two parts of the molecule. The classical energy of the torsional vibration is given by

$$\frac{1}{2}I_r\dot{\phi}_t^2+\frac{1}{2}V_0\frac{9}{2}\phi_t^2\,, \tag{A1}$$

where

$$\phi_t=\phi_t'-\phi_t''\,,\qquad |\phi_t'|=|\phi_t''|\,. \tag{A2}$$

The normal coordinate is given by

$$q_t=\sqrt{I_r}\,\phi_t\,. \tag{A3}$$

Assuming that the time dependency of q_t is simple harmonic, q_t is expressed as

$$q_t(t)=D_t\sin 2\pi\nu_t t\,. \tag{A4}$$

Being the mean energy of the classical harmonic oscillator equated with the mean energy of the corresponding Planck's oscillator as usual, the following relation is derived.

$$h\nu_t\left(\frac{1}{2}+\frac{1}{\exp(h\nu_t/kT)-1}\right)=4\pi^2\nu_t^2\overline{q_t^2(t)}\,. \tag{A5}$$

With assumptions, $|\phi_t'|=|\phi_t''|$ and ϕ_t' is coherent with ϕ_t'',

$$\overline{q_t^2(t)}=I_r\overline{\phi_t^2}=4I_r\overline{\phi_t'^2}\,. \tag{A6}$$

From the geometrical configulation, θ_t is connected with ϕ_t' as follows,

$$\theta_t=\phi_t'\frac{2}{\sqrt{3}}\sin\frac{A}{2}\,. \tag{A7}$$

Hence Eq. (7) is obtained. In the similar way, Eq. (8) is obtained.

Acknowledgement

The authors wish to express hearty thanks, to the members of the Symposium on the Nuclear Quadrupole held in May 1956 at Research Institute for Fundamental Physics of Kyoto University, for their kind discussions and valuable suggestions. They thank Mr. Junichi Hori of Hokkaido University who has benefited them with many illuminating discussions. They also thank Mr. Yoshio Shindo of this institute for the aid in the construction of the frequency meter. The present work was supported in part by a Grant of Aid for Developmental Scientific Research in the Ministry of Education.

References

1) R. Livingston: J. Phys. Chem. **57** (1953) 496.
2) H. Bayer: Zeit. für Phys. **130** (1951) 227.
3) Y. Ayant, M. Buyle-Bodin and F. Lurcat: C. R. **237** (1953) 1551.
4) Y. Ayant: Ann. de Physique **10** (1955) 487.
5) K. Torizuka: Reser. Report of Tokyo Gakugei Univ. **5** (1953) 13.
6) K. Tsukada: J. Phys. Soc. Japan **11** (1956) 956.
7) H. G. Dehmelt and B. Krüger: Zeit. für Phys. **129** (1951) 401.
8) T. Kushida: J. Scien. Hiroshima Univ. **A19** (1955) 327.
9) S. Mizushima, Y. Morino, T. Simanouti and K. Kuratani: J. Chem. Phys. **17** (1949) 838.
10) Y. Morino and M. Iwasaki: J. Chem. Phys. **17** (1949) 216.
D. A. Swick, I. L. Karle and J. Karle: J. Chem. Phys. **22** (1954) 1242.
11) Y. Sasada and M. Atoji: J. Chem. Phys. **21** (1953) 145.
12) E. R. Andrew: Nuclear Magnetic Resonance (1955) 219.
13) B. Dreyfus and D. Dautreppe: C. R. **239** (1954) 1618.
14) M. Atoji and W. N. Lipscomb: J. Chem. Phys. **21** (1953) 1480.
15) S. Seki and M. Momotani: Bull. J. Chem. Soc. Japan **23** (1950) 30.
16) Landort Bernstein: Physikalische Chemische Tabellen (1927) 56.
17) T. Kushida, G. B. Benedek and N. Bloembergen: Technical Report No. 250, Harvard Univ. (1956).

Note:

After this paper was prepared, we found that M. Buyle-Bodin (Ann. de Physique **10** (1955) 533) treated the reorientational motion of $Cl_3C \cdot CCl_3$. He found the height of potential wall was about 6 Kcal/mole insead of our 7 Kcal/mole. Taking the difficulty accompanied with a measuring of the line width it seems that these values give a reasonable order of the height of potential wall.

JOURNAL OF THE PHYSICAL SOCIETY OF JAPAN Vol. 12, No. 7, JULY, 1957

Effect of the Basic Strength of Attached Groups on Light Absorption Spectra II: Near Ultraviolet Absorption Spectra of Para-substituted Aniline Derivatives

By Reikiti ITOH

Kobayashi Institute of Physical Research
Kokubunzi, Tokyo

(Received January 25, 1957)

The absorption spectra of para-substituted aniline derivatives of the type of $A_lC_6H_4B$, where A_l is one of the electron donating groups such as NH_2, $NHCH_3$, NHC_2H_5, $N(CH_3)_2$, $N(C_2H_5)_2$ etc. and B is one of the electron attracting groups such as COOH, $COCH_3$, CHO, NO_2 etc., change with the basic strength of the group A_l. The first absorption maxima of these molecules between 2800 and 4000 A are originated from the second absorption maxima of unsubstituted molecules (in 2600～2900 A region) under the influence of the group A_l. This is explained by semi-empirical MO theory with perturbation. The effects of B groups are taken into consideration by the delocalization of the molecular orbitals of benzene molecule, while the effects of A_l groups are calculated through the method of electron migration, in which the non-bonding π electrons on the nitrogen atom of A_l migrate to the parent molecule. The induction effect of the substituted alkyl group in A_l, which determines the degree of the electron migration, can be estimated from the relative basic strength of the end group, i.e. dissociation constant of amine NHR_2. The calculated absorption energies are in good agreement with the observed values if we take the solvent effect into consideration.

1. Introduction

In most of the previous discussions of ab-
orption spectra in aromatic molecules1), there
no quantitative consideration concerning the
ffect of basic character of substituents on
bsorption energies. There exists qualitative
elation between the shift of the absorption spec-
ra of substituted products of aromatic mole-
ules and the basicities of the substituents. In
he previous paper2), the author derived a qu-
ntitative relation between the absorption fre-
uencies of triphenylmethane dyes3) and the
asicities of the substiuted aminoalkyl groups
R$_2$ on the ground of semi-empirical LCAO
O method. It was found that the fre-
uencies of absorption vary linearly with the
asicities of the terminal groups attached to
he derivatives of Döbner's Violet and Rosani-
ne. The similar correlation is found for
arasubstituted aniline derivatives4), in which
eplacement of amino group NH_2 with one of
he more basic amino alkyl groups NR_2
auses a red shift of the main absorption
aximum. We denote this type of molecule
y $B(C_6H_4)A_l$, where B is an electron attract-
g group such as H, COOH, $COCH_3$, CHO, NO_2, etc. and A_l is one of the electron donating, alkyl substituted amino groups, such as HN_2, $NHCH_3$, NHC_2H_5, $N(CH_3)_2$, $N(C_2H_5)_2$, etc..

The present work is concerned with the study of the relation between basic strength of substituted amino-alkyl group and the position of absorption maximum using the semi-empirical MO method, in which the interaction between the NR_2 radical and the rest of the molecule, C_6H_4B, is taken into account through the second order perturbation. Thus, in the following sections, the theoretical explanation of electronic spectra in para-substituted aniline derivatives is extended.

§ 2. Interaction between the Parent Molecule and NH_2 Group

In the molecules $BC_6N_4NH_2$, the amino group is an electron donor on account of its non-bonding electron pair on the N atom which is in the valence state of trivalent sp^3. Then, the attachment of NH_2 to BC_6H_4 causes a perturbation to electronic states of the molecule due to the effect of electron migration from the amino group to the parent molecule. In our case, we owe the method of calculation for the perturbation to the theory of electron migration which is orignated by Sklar[5)] and later discussed by Herzfeld[6)] on monosubstituted benzene derivatives.

Here, we assume that the wave function of the migrating electron, $\Phi(\nu)$, is

$$\Phi(\nu)=\sum a_k\psi_k+b\phi_N \qquad (1)$$

with the normalization condition

$$\sum a_k^2+2b\sum a_kT_k+b^2=1, \qquad (2)$$

$$T_k=(\psi_k|\phi_N)=\int\psi_k\phi_N\,d\tau\,,$$

where ψ_k's are vacant orbitals of parent molecule and ϕ_N is $2p\pi$ orbital of non-bonding electrons in N atoms, and T_k is the overlap integral between ψ_k and ϕ_N. The Hamiltonian is the form of

$$H(\nu)=H_p(\nu)+H_s(\nu), \qquad (3)$$

where H_p is the potential of parent molecule and H_s is that of amino group for the migrating electron. Here, interaction parameters a_k and b are determined by the variational method minimizing the energy of orbital $\Phi(\nu)$ by the use of expressions (1), (2) and (3), and are given by the formula

$$a_k/b=\frac{\rho_k+T_k\chi}{\chi-\omega_k}\,, \qquad (4)$$

were

ρ_k: resonance integral between ψ_k and ϕ_N,
χ: coulomb integral of the amino group,
ω_k: energy levels of vacant orbitals ψ_k.

These are given as follows:

$$\begin{aligned}2\rho_k&=2(\psi_k|H|\phi_N)\\&=(\psi_k|H_p|\phi_N)+(\phi_N|H_e|\psi_k)+T_k(\chi+\omega_k), \qquad (5)\\ \chi&=(\phi_N|H_s|\phi_N),\quad \omega_k=(\psi_k|H_p|\psi_k).\end{aligned}$$

Thus for non-zero values of a_k, the energy of parent molecule goes down by the amount of ΔU which is calculated by the expressions (2) and (4), and neglecting $(\psi_k|H_s|\psi_l)$ and $(\phi_N|H_p|\phi_N)$

$$\begin{aligned}\Delta U&=(\Phi|H|\Phi)-(\phi_N|H|\phi_N)\\&=\sum a_k^2\omega_k+2b\sum a_k\rho_k+b^2\chi-\chi\\&=\sum a_k^2(\chi-\omega_k). \qquad (6).\end{aligned}$$

Corresponding to the two non-bonding electrons in the substituent and two electronic states of the parent molecule, the ground state g and the excited state e, there are two expressions for ΔU, that is,

$$\Delta U_g=2\sum a_k^2(\chi-\omega_k),$$

$$\Delta U_e=a_1^2(\chi-\omega_1)+2\sum a_k^2(\chi-\omega_k)-a_2^2(\chi-\omega$$

ΔU_g and ΔU_e are the stabilization energies d to the migration to the parent molecule in t ground state and in the excited state spectively, where suffixes 1 and 2 mean t highest occupied orbital in the ground and the excited state respectively. Then it easily found that $\chi<\omega_1<\omega_2<0$, and the sh of absorption energy due to the substituti of NH_2 is given by

$$\Delta Ue-\Delta Ug=a_1^2(\chi-\omega_1)-a_2^2(\chi-\omega_2). \qquad ($$

Here we simplify the expression by introdu ing the assumption that b is close to uni and a_k is very small. Then we have

$$hc\,\Delta\tilde{\nu}_{01}=\frac{(\rho_1-T_1\chi)^2}{\chi-\omega_1}-\frac{(\rho_2-T_2\chi)^2}{\chi-\omega_2}\,,$$

where $\Delta\tilde{\nu}_{01}$ is the shift of the absorbed wa number from that of the parent molecule d to the substitution of NH_2 and h is Planck constant and c the velocity of light.

§ 3. Effects of Alkyl-substituted Ami Groups

Up to this point, we have ignored the di ference among the substituents A_i, but no let us consider the various electron donati groups A_i as follows[2)]:

i	1	2	3	4	5
A_i	NH_2	$NHCH_3$	NHC_2H_5	$N(CH_3)_2$	$N(C_2H$
pK_{b_i}	4.75	3.36	3.33	3.29	3.02

where pK_b, the basic strength of amine NHR is calculated with activity coefficient in th place of concentration. If A_j group is mo basic than A_i, the density of σ electrons N atom of A_j will be larger than that of and this causes the difference in the exte of π electron migration to the parent mol cule by induction effects. Then coulomb i tegrals of A_i and A_j are different by a sma amount $\Delta\chi_{ij}$;

$$\chi_j=\chi_i+\Delta_{ij}, \qquad (9$$

where $\Delta\chi_{ij}$ is positive if A_j is more basic tha A_i, and expression (8) becomes

$$hc\,\Delta\tilde{\nu}_{0j}=\frac{(\rho_1-T_1\chi_j)^2}{\chi_j-\omega_1}-\frac{(\rho_2-T_2\chi_j)^2}{\chi_j-\omega_2}\,. \qquad (1$$

In the following we ignore the differen between the overlap integrals T_1 and T_2 ar use a single T in common. Now, we ca calculate the expression (8) for i and j using the relation (9). Expanding with $\Delta\chi$

and neglecting higher order terms of $\Delta\chi_{ij}$ we have the following expressions:

$$hc\,\Delta\tilde{\nu}_{ij}=hc(\tilde{\nu}_j-\tilde{\nu}_i)=hc(\Delta\tilde{\nu}_{0j}-\Delta\tilde{\nu}_{0i}), \qquad (11)$$

$$\Delta\tilde{\nu}_{ij}=-A\,\Delta\chi_{ij}-B(\Delta\chi_{ij})^2, \qquad (12)$$

where

$$A=\frac{(\rho_1-T\chi_i)T}{\chi_i-\omega_1}-\frac{(\rho_2-T\chi_i)T}{\chi_i-\omega_2}+\frac{(\rho_1-T\chi_i)^2}{(\chi_i-\omega_1)^2}-\frac{(\rho_2-T\chi_i)^2}{(\chi_i-\omega_2)^2},$$

$$B=-\frac{T}{4}\left(\frac{1}{\chi_i-\omega_1}-\frac{1}{\chi_i-\omega_2}\right)-\frac{(\rho_1-T\chi_i)T}{(\chi_i-\omega_1)^2}+\frac{(\rho_2-T\chi_i)T}{(\chi_i-\omega_2)^2}-\frac{(\rho_1-T\chi_i)^2}{(\chi_i-\omega_1)^3}+\frac{(\rho_2-T\chi_i)^2}{(\chi_i-\omega_2)^3}. \qquad (13)$$

In our case, according to the condition

$$\chi_i<\chi_j<\omega_1<\omega_2<0$$

we have

$$(\chi_i-\omega_2)<(\chi_i-\omega_1)<0\,.$$

From this and the inequality $\rho_1<\rho_2<0$ which can be seen from the expression (5), it follows that $A>B>0$ and $\tilde{\nu}_j<\tilde{\nu}_i$, which gives the qualitative explanation for that the molecule with A_j has the absorption maxima at lower frequencies than those with A_i, if A_j is more basic than A_i.

Ih the previous paper the author has shown that the coulomb integrals of NH_2 groups can be estimated by their relative basic strength pK_b by the formula

$$\Delta\chi_{ij}=k(pK_{b_i}-pK_{b_j}), \qquad (14)$$

where k is a parameter determined by the expression (12) so as to agree with the observed shift of absorption maximum between aniline and dimethyl aniline. As shown later, $k=0.4146$ is obtained in eV unit which is nearly equal to the k value in the case of triphenylmethane dyes, i.e., $k=0.4605$ eV.

Using the expression (14), we are able to rewright the expressions (11) and (12) in the following form

$$\tilde{\nu}_j=\tilde{\nu}_i-A\,(pK_{b_i}-pK_{b_j})-B\,(pK_{b_i}-pK_{b_j})^2, \qquad (15)$$

where $A>B>0$ and A is smaller than unity. This leads to the observed linear relation between the absorption wave numbers and pK_b of the substituents.

§ 4. Forms of the Orbitals ψ_1 and ψ_2

For the evaluation of numerical values in the expressions (8) and (12), it is necessary to determine the values of ω_1, ω_2, χ_1 and ρ_k which are given by

$$(\psi_1|H_p|\psi_1)=\omega_1,\ (\psi_2|H_p|\psi_2)=\omega_2,\ (\phi_N|H_s|\phi_N)=\chi_1,$$
$$2\rho_k=(\psi_k|H|\phi_N)+T(\chi_1+\omega_k),\quad T=(\psi_k|\phi_N),$$

respectively. The value of ω_1 is taken to the ionization potential of parent molecule BC_6H_5 and ω_2 is determined by

$$\omega_2-\omega_1=hc\,\tilde{\nu}_0\,. \qquad (16)$$

where $\tilde{\nu}_0$ is the absorption wave number of the secondary band in BC_6H_5 molecule. Further, χ_1 is taken to the ionization energy[12)] of N atom in the valence state, from $N(sp^4, V_3)$ to $N^+(sp^3, V_4)$, this is -12.24 eV. Values of ρ_k and T depend on the form of MO's in the parent molecule, and it is convenient to choose the linear combinations of atomic orbitals for MO's in the following form

$$\psi_1=c\psi_1'+(1-c^2)^{1/2}\,\phi_B\,,$$
$$\psi_2=c\psi_2'+(1-c^2)^{1/2}\,\phi_B\,, \qquad (17)$$

where[5)]

$$\psi_1'=\frac{1}{\sqrt{12}}(2\phi_1+\phi_2-\phi_3-2\phi_4-\phi_5+\phi_6)\,,$$

$$\psi_2'=\frac{1}{\sqrt{12}}(2\phi_1-\phi_2-\phi_3+2\phi_4-\phi_5-\phi_6)\,, \qquad (18)$$

ϕ_i is the $2p\pi$ orbital on the ith atom and ϕ_B is molecular orbital of the electron attracting group B in the system of nomenclature

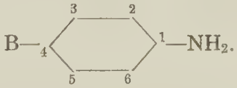

Here, the parameter c gives a measure of degree of localization of electrons in the benzene ring against the electron attracting group B. If we assume that the degree of localization in ψ_1' and ψ_2' can be expressed by the same parameter c which is closed to unity and ϕ_B is normalized molecular orbital, then, ψ_1 and ψ_2 constitute a nearly orthonormal system and will be able to be used as the orbitals of the parent molecule in the ground and the first excited state respectively. Nagakura[7)] has determined the parameter c in the case of intra-molecular charge transfer spectra by the variation method using LCAO MO for the ground state of monosubstituted benzene derivatives. These spectra are nearly equal to the primary bands of the molecules, however, it is allowed to use the same parameter c to the secondary absorption of that molecule about which ψ_1 and ψ_2 orbitals are concerned, because of the approximations in the theory of LCAO MO in benzene where four observed spectra are degenerated under the difference in energies of ψ_1' and ψ_2' orbitals. These spectra are shown in Table I for comparison.

Table I. Comparison of the spectra and values of c.

group B	observed secondary band in eV		calculated intramolecular charge transfer spectra in eV		values of c
	ω_1	ω_2	W_n	W_e	
NO_2	10.15	5.75	9.76	6.33	0.912
CHO	9.82	5.39	9.84	5.31	0.931
$COCH_3$	9.77	5.31	9.82	5.16	0.936
COOH	10.12 (9.52)	5.56 (4.96)	11.34	3.35	0.968
H	9.52	4.66	—	—	1.000

Literatures:

a) As for ionization potentials of C_6H_5B, see the reference (10) and as for the secondary absorption band see the references (8) and (9).

b) For the charge transfer spectra, see reference (7).

That the ionization potential of C_6H_5COOH is not known experimentally is probably due to the fact that it likely dissociates into anion $C_6H_5COO^-$ in the solution, and here value 10.12 eV is estimated from the values of analogous molecules, and for the anion $C_6H_5COO^-$, the value of 9.52 eV in parenthesis is assumed. Though existence of the secondary bands for nitrobenzene and benzaldehyde is not certain in the absorption spectra of these molecules, there are shoulders which are considered to be the positions of the secondary bands as shown in Fig. 1.

Using the orbitals ψ_1 and ψ_2 of the expressions (17) and (18), we have for ρ_k and T in the first order approximation

$$\rho_k=\frac{c}{\sqrt{12}}\cdot\frac{s}{s_0}\left[\gamma_0+s_0(\chi_1+\omega_k)\right],$$

$$T=\frac{c}{\sqrt{12}}\cdot\frac{s}{s_0}, \tag{19}$$

where γ_0 and s_0 are the resonance and overlap integrals of the $2p\pi$ atomic orbitals in benzene (C–C distance 1.39 A) respectively, and for aniline we make use of the relation proposed by Wheland[11], $\gamma/\gamma_0=s/s_0=0.8$, where γ_0 and s_0 are taken to be -5 eV and 0.2 respectively.[18]

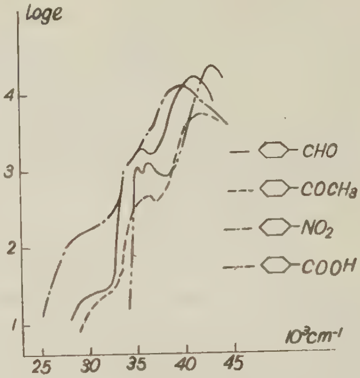

Fig. 1. The absorption maxima at 40000 cm^{-1} region are the primary bands of monosubstituted benzene derivatives. Those of 35000 cm^{-1} region are the secondary bands and those of 30000 cm^{-1} region are the bands due to $n-\pi$ transition. The solvents of the above two solutes are ethylalcohol and those of remains are hexane.

§ 5. Comparison between the Calculated and the Observed Spectra

As the orbitals ψ_1 and ψ_2 and values of their energies ω_1 and ω_2 and coulcomb integrals χ_i were given in § 4, interactions between the parent molecules and substituents A_i can be determind completely. There remains only one parameter k unknown. Now, k is determind so as expression (12) to match with observed spectral shift, for example, from aniline to dimethyl aniline, and thus $k=0.4146$ eV is obtained. In the cases of triphenylmethane dyes $k=0.4605$ eV was obtained. Relative values of χ for various A_i groups are shown in Table II.

Table II. Difference of pK_b and corresponding $\Delta\chi_{ij}$

i–j	pK_b	$\Delta\chi$ in eV
1–1	0	0
1–2	1.39	0.332
1–3	1.42	0.347
1–4	1.46	0.460
1–5	1.73	0.514

Using equations (8) and (12), we compute the absorption wave number $\tilde{\nu}_j$ by the relation

$$\tilde{\nu}_1=\tilde{\nu}_0+\Delta\tilde{\nu}_{01}\,,$$
$$\tilde{\nu}_j=\tilde{\nu}_1+\Delta\tilde{\nu}_{1j}\,. \tag{20}$$

Results are assorted in Table III, IV and V. These results are shown in Fig. 2, 3, 4 and

5, where the absorption wave numbers are plotted against the basicity of the substituents.

Table III. Values of A and B

3 group	H	COOH	COCH$_3$	CHO	NO$_2$
A	0.250	0.371 (0.231)	0.259	0.265	0.336
B	0.105	0.196 (0.098)	0.118	0.125	0.179

Values in parenthesis correspond to $\omega_1 = -9.52$ eV. A and B are defined by Eq. (13).

Table IV. Calculated spectral shifts in cm^{-1} unit.

B	H	COOH	COCH$_3$	CHO	NO$_2$
0–1	2404	3130 (2210)	2348	2380	2807
1–2	1444	2251 (1339)	1517	1573	2041
1–3	1476	2299 (1371)	1565	1605	2098
1–4	1525	2428 (1412)	1605	1654	2154
1–5	1880	2961 (1743)	1993	2049	2686

Values in parenthesis correspond to $\omega_1 = -9.52$ eV.

Table V. Comparison with experiment in cm^{-1} unit.

	B=H		B=COOH		B=COCH$_3$		B=CHO		B=NO$_2$	
$\tilde{\nu}_i$	calc.	obs.	calc.	obs.	calc.	obs.	calc.	obs.	calc.	obs.
0	—	39216	— (—)	36765*	—	35971	—	35714	—	35461
1	36812	35088	33635 (34555)	34722	33623	31546	33334	30488	32654	26667
2	35368	33898	31384 (33216)	—	32106	—	31761	—	30614	25907
3	35336	33898	31336 (33184)	—	32058	30120	31729	—	30556	25641
4	35287	33557	31207 (33143)	32468	32018	29674	31680	29240	30500	25641
5	34932	—	30674 (32812)	32051	31630	—	31285	28736	29968	25000

The observed values are taken mostly from the paper of W. D. Kumler[4)] except the case of B=COOH, the value of which is taken from the paper of W. W. Robertson[13)]. The solvent is ethyl-alchol in all cases. Value with asterisk is an assumed one based on the estimation from general spectral shifts given by Lewis[4)] who found an average shift of 130 A in a large number of dyes occuring when an alkyl group replaces a hydrogen and that of 30 A average when an ethyl replace a methyl group. Values in parenthsis corespond to $\omega_1 = -9.52$ ev.

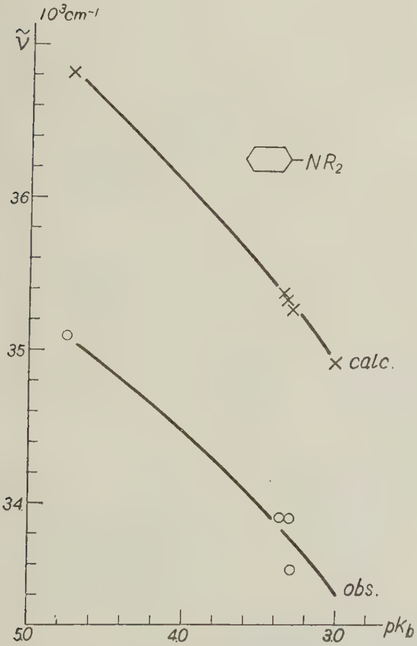

Fig. 2. Comparison with experiment. If the calculated absorption energies in vacuum are stabilized in ethylalcohol by about 2000 cm^{-1}, $\tilde{\nu}_{\text{calc}}$ agrees well with observation within the variance of the solvent effects.

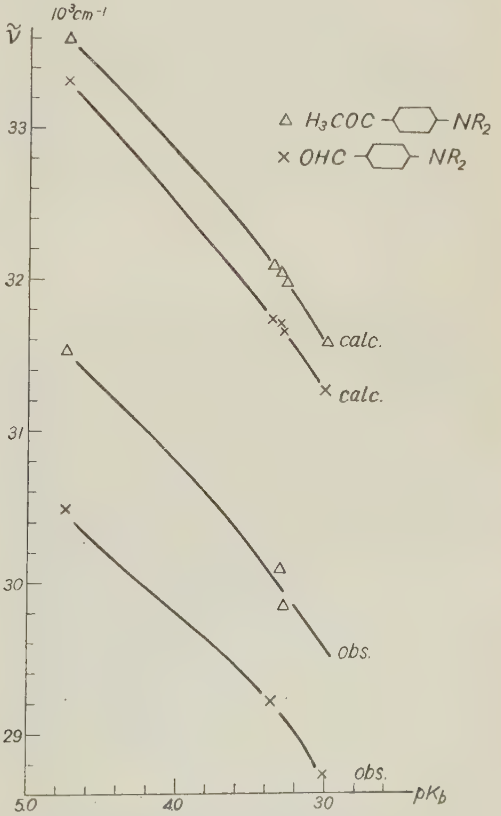

Fig. 3. Comparison with experiment. $\tilde{\nu}_{\text{calc}}$'s for the two cases agree with observations within the variance of the solvent effects.

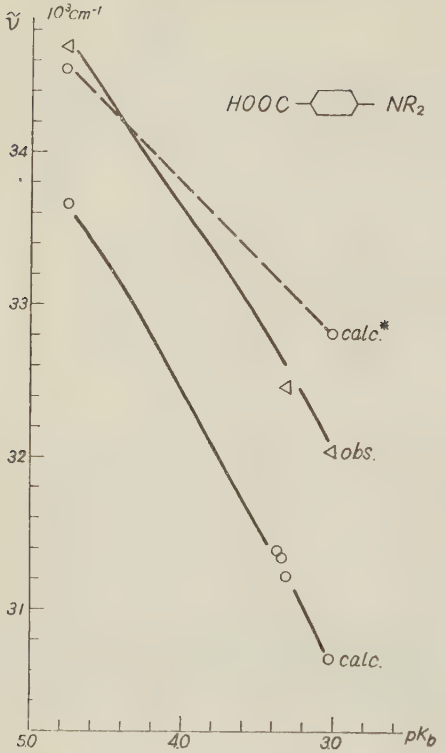

Fig. 4. Comparison with experiment. That $\tilde{\nu}_{obs}$'s are higher than $\tilde{\nu}_{calc}$'s is probably due to the dissociation of proton in the carboxyl group in alcohol. If we change the value of ionization potential from $\omega_1 = -10.12$ eV to $\omega_1 = -9.52$ eV taking the dissociation effect into consideration, $\tilde{\nu}_{calc}$'s move to the dotted line.

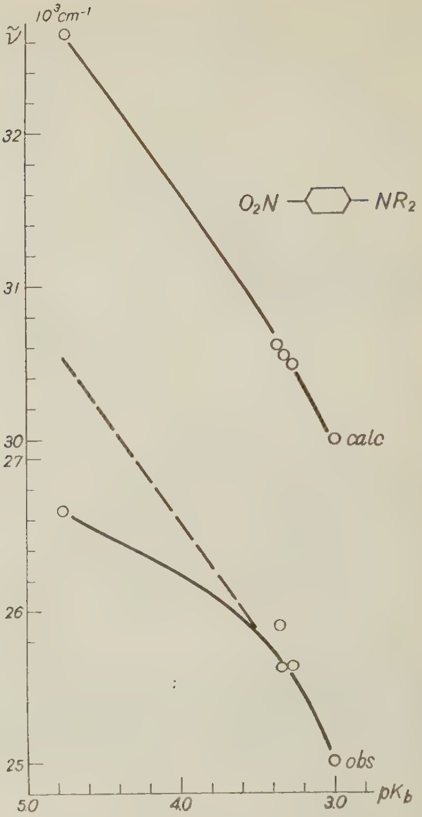

Fig. 5. Comparison with experiment. In this case, differences between $\tilde{\nu}_{calc}$ and $\tilde{\nu}_{obs}$ amount to 5000–6000 cm^{-1} owing to the two sort of solvent effects, the one is due to the dielectric character of solvent being about 2000 cm^{-1}, the other is due to the hydrogen bond formations with nitro group causing the shift of about 3000 cm^{-1} and with amino group causing the shift of about 1000 cm^{-1} which is shown by the deviation from the dotted line in the figure.

§ 6. Discussions

As seen from the comparison with observation, there are several points we have to put considerable importance on the solvent effect which seems to appear in two ways. The one is the dielectric character of solvents which shifts the absorption maxima towards lower frequencies and the other is the effect of the hydrogen bond formed between the solute and solvent molecules which produces the larger shift towards longer wave length. As in our calculation these effects have not been taken into consideration, it should be necessary to discuss the magnitude of these effects separately for the sake of comparing our result with the observation.

1) Derivatives of aniline, *p*-aminoacetphenone and *p*-aminoacetaldehyde.

In these groups, the calculated absorptio energies, $\tilde{\nu}_j$, are in good agreement with th observation, if we take the solvent effect int consideration, which makes the calculate frequencies in vacuum shift to lower values[15 by the amount of 2000 cm^{-1}. Here it shoul be noted two things:

a) The values of absorption wave lengt for each B group is in the order of

$$H < COOH < COCH_3 < CHO < NO_2 ,$$

which coincides to the order of electron attracting character of B groups and agree well with observation.

b) The parallelism between the calculate and the observed $\tilde{\nu}_i$'s against pK_{b_i} in Figs 2, 3, 4 and 5 shows the applicability of th expression (14) and possibility of estimatin the values of coulomb integrals of A_i fro their pK_b data.

) Derivatives of *p*-aminobenzoic acid.

Molecules in this group are probably in nic forms in solution owing to the dissocia-on of proton in COOH group, and the ioni-ation potential of benzoic acid has not been easured. This suggests two things:

a) The calculated $\tilde{\nu}_i$'s should be larger than he observed values as in the case of B groups ther than COOH. This contradiction may rise from the assumed value of the ioniza-ion potential ω_1 of benzoic acid, and if we hange ω_1 tentatively from -10.12 eV to -9.52 eV and ω_2 from -5.56 eV to -4.96 eV, $_{\text{calc}}$ comes to the higher value than $\tilde{\nu}_{\text{obs}}$ as hown by the dotted line in Fig. 4.

b) If these molecules are anions, induction ffects of alkyl groups may be greater than hose in the neutral molecules because of the egative charge. This fact explains the arger slope $\tilde{\nu}_i - pK_b$ line in this case.

) Derivatives of *p*-nitroaniline.

In these molecules, there may be formed ne or two hydrogen bonds between the solute nd the solvent molecules, one side at NH_2 roup (in dioxane) and other side, if any, at O_2 group (in alcohol or water). Kumler nd Strait[16)] pointed out that the shift in he absorption wave length with different olvents in the case of *p*-nitroaniline is in uch closer relation with the ability of the ydrogen bond formation of the solvent with he solute than it is with the dielectric con-tant of the solvent. Thus in going over rom hexane to dioxane the shift in wave ength is 350 A, i.e., from 3200 A to 3550 A, nd from hexane to water it is 380 A, i.e., rom 3550 A to 3930 A. The difference in the ielectric constant of the first two solvents is .3 and that of the second two is 78.9. On he other hand, *p*-nitroaniline can not form ydrogen bond with hexane, but can form hem at one end of the molecule with dioxane nd at both ends with water. These effects uggest the following:

a) There are the differences of about 000 cm^{-1} between the observed absorption nergies with singly hydrogen bonded cases for example, *p*-dimethylamino- and *p*-diethyl-minonitrobenze, etc.) and the calculated ab-orption energies. The difference may be artly attributed to the hydrogen-bonded ffect mentioned above being about 3000 cm^{-1} and partly to the normal solvet effects which amount to about 2000 cm^{-1}.

b) If hydrogen bonds are responsible for the solvent effect, then one can expect smaller shift for *p*-nitrodimethylaniline, which can form hydrogen bond only at one end by changing the solvent from hexane to alcohol than for *p*-nitroaniline, which can form hydrogen bonds at both ends, by changing the solvent similary. This is observed to be the case, the shift for the fomer being the 380 A (from 3520 A to 3900 A) and for the latter 550 A (from 3200 A to 3750 A). The effect of the second hydrogen bond of *p*-nitroaniline can be seen in Fig. 5 where the deviation from the datted line is about 1000 cm^{-1}, corresponding to the hydrogen bond effect between amino group and alcohol. The shift is also observed in the absorption of aniline[17)] for which the energy shift is also of the order of 1000 cm^{-1} going over from heptene (2853 A) to dioxane (2906 A). These solvent effects appearing in $\tilde{\nu}_{\text{obs}}$ - pK_b diagrams about which several points were mentioned above show that the $\tilde{\nu}_{\text{calc}}$ - pK_b lines are probaly true in vacuum or in the non-polar solvent and thus our conclusion that the first primary bands of $BC_6H_4NR_2$ molecules are caused by the substitution effect of NR_2 groups on the secondary bands of BC_6H_5 molecules would be accepted.

This work was supported by the Scientific Research Fund granted by the Ministry of Education.

References

1) A. L. Sklar: J. Chem. Phys. **7** (1939) 984, K. F. Herzfeld: Chem. Rev. **41** (1947) 233, F. A. Matsen: J. A. C. S. **72** (1950) 5243, S. Nagakura and H. Baba: J. A. C. S. **74** (1952) 5693.
2) R. Itoh: J. Phys. Soc. Japan **12** (1957) 644.
3) M. J. S. Dewar: *The electronic Theory of Organic Chemistry* McGraw-Hill N.Y. 1949.
4) W. D. Kumler: J. A. C. S. **68** (1946) 1184.
5) A. L. Sklar: See reference 1).
6) K. F. Herzfeld: See reference 1).
7) S. Nagakura and J. Tanaka: Bulletin of Chem. Soc. Japan **75** (1954) 331 (in Japanese).
8) Landolt-Börnstein, Bd. 1, Teil 3, Molekeln III.
9) *Kagaku Binran* (Hand Book of Chemistry), Chem. Soc. Japan, (Maruzen, Tokyo 1953) (in Japanese).
10) J. D. Morrison and A. J. C. Nicholson: J. Chem. Phys. **20** (1952) 1021.

11) G. W. Wheland: J. A. C. S. **64** (1942) 900.
12) R. S. Mulliken: J. Chem. Phys. **2** (1934) 782.
13) W. W. Robertson and F. A. Matsen: J. A. C. S. **57** (1950) 1543.
14) G. N. Lewis: J. A. C. S. **67** (1945) 770.
15) Y. Ooshika: J. Phys. Soc. Japan **9** (1954) 594.
16) W. D. Kumler and L. A. Strait: J. A. C.
65 (1943) 2349.
17) R. Miyasaka: Bussiron Kenkyu No. **62** (19
94 (in Japanese).
18) C. J. Roothaan and R. S. Mulliken: J. Che
Phys. **16** (1948) 118.

Journal of the Physical Society of Japan Vol. 12, No. 7, July, 1957

A Study on the Effects of Off-Resonance on the Spin-Echo Signals

By T. Ghose, S. K. Ghosh and D. K. Roy

Institute of Nuclear Physics, Calcutta, India

(Received March 11, 1957)

A comprehensive study of the off-resonance effects on the different spin-echo signals obtained with three rf-pulses has been made—both theoretically and experimentally. The main experimental bearing of this investigation lies in choosing the most suitable angles of the rf-pulses for which the fluctuations in the current, driving the electromagnet, will cause minimum effect on the amplitudes of the echo signals used for relaxation time measurements. Besides this, the above study has also been used for explaining another phenomenon associated with offresonance.

§ 1. Introduction

The spin echo technique is now being widely used for relaxation time measurements. Hahn(1) first introduced methods of measuring relaxation times T_1 and T_2 from the primary and stimulated echoes. Relaxation time T_2 is measured from the variation of the primary echo amplitude with the interval between the two pulses. T_1, the spin-lattice relaxation time can be measured from the variation of the stimulated echo $P_{(123)}$ by changing the interval between the second and third pluse, while the interval between the first and the second pulse is held fixed. A high degree of stability of the magnetic field is essential in these studies of the growth or decay of any echo signal in order to avoid the change in amplitude due to off-resonance during the time of observation. As this condition is not perfectly satisfied in the case of an electromagnet, the angle of the-pulses should be so chosen that the echo amplitude vs. off-resonance curve has the flattest peak. Hence the need arises for studying the off-resonance. Pfeifer(2) has formerly treated the case of the primary echo from such a consideration. He
the treatment has been applied to the case
the stimulated echo $P_{(123)}$. The investigati
also brings out the fact that the maximum
this echo does not necessarily occur at t
resonance value of the field for differe
angles of the rf-pulses—as is true for t
case of the primary echo. Moreover, by e
tending the theoretical analysis to the oth
echoes obtained with three rf-pulses, anoth
observed phenomenon associated with t
superposition of different echoes has been e
plained.

§ 2. Effects of Off-resonance on the Amp
tude of the Stimulated Echo $P_{(123)}$

The classical analysis of the spin ec
phenomena has previously been done
Hahn(1) and also by Das and Saha(3) under t
simplifying conditions of exact resonance a
H_r, the rf-field amplitude $\geqslant(\Delta H)_{Av}$, the latt
being the average value of the inhomogenei
over the sample volume. Under these si
plifying assumptions, contribution of the
mode to the total signal comes out as ze

when the average was taken over different isochromatic groups $\Delta\omega$. But in the case of off-reasonance, the contribution of the U-term does not vanish, the assumption $H_r \gg (\Delta H)_{Av}$ remaining intact. The U and V terms for the case of the stimulated echo at the echo maxima, i.e. at $t-\tau_1+\tau_2$ are then given by:

$$\begin{aligned} U_{t=\tau_1+\tau_2} &= \frac{\omega^* \omega_r^3}{\alpha^4} \left[\frac{4\omega^{*2}}{\alpha^2} \sin^2 \frac{\alpha t_{\omega_1}}{2} \sin^2 \frac{\alpha t_{\omega_2}}{2} \sin^2 \frac{\alpha t_{\omega_3}}{2} \right. \\ &\quad + \sin \alpha t_{\omega_1} \sin^2 \frac{\alpha t_{\omega_2}}{2} \sin \alpha t_{\omega_3} \\ &\quad - \sin \alpha t_{\omega_1} \sin \alpha t_{\omega_2} \sin^2 \frac{\alpha t_{\omega_3}}{2} \\ &\quad \left. + \sin^2 \frac{\alpha t_{\omega_1}}{2} \sin \alpha t_{\omega_2} \sin \alpha t_{\omega_3} \right] \\ &\quad \exp\left[-(\tau_2-\tau_1) \left(\frac{1}{T_1} - \frac{1}{T_2} \right) - (\tau_1+\tau_2) \frac{1}{T_2} \right] \end{aligned} \tag{1}$$

$$\begin{aligned} V_{t=\tau_1+\tau_2} &= \frac{1}{2} \frac{\omega_r^3}{\alpha^3} \left[-\frac{4\omega^{*2}}{\alpha^2} \sin^2 \frac{\alpha t_{\omega_1}}{2} \sin^2 \frac{\alpha t_{\omega_2}}{2} \sin \alpha t_{\omega_3} \right. \\ &\quad + 4 \frac{\omega^{*2}}{\alpha^2} \sin \alpha t_{\omega_1} \sin^2 \frac{\alpha t_{\omega_2}}{2} \sin^2 \frac{\alpha t_{\omega_3}}{2} \\ &\quad + \sin \alpha t_{\omega_1} \sin \alpha t_{\omega_2} \sin \alpha t_{\omega_3} \\ &\quad \left. + 4 \frac{\omega^{*2}}{\alpha^2} \sin^2 \frac{\alpha t_{\omega_1}}{2} \sin \alpha t_{\omega_2} \sin^2 \frac{\alpha t_{\omega_3}}{2} \right] \\ &\quad \exp\left[-(\tau_2-\tau_1) \left(\frac{1}{T_1} - \frac{1}{T_2} \right) - (\tau_1+\tau_2) \frac{1}{T_2} \right] \end{aligned} \tag{2}$$

where, $\omega^* = \gamma H_0 - \omega$, H_0 being the central value of the magnetic field distribution,

$$\omega_r = \gamma H_r$$

$$\alpha^2 = \omega^{*2} + \omega_r^2$$

and t_{ω_1}, t_{ω_2}, t_{ω_3} are the widths of the three rf-pulses.

If all the pulses are of equal width t_ω, we have

$$\begin{aligned} U_{t=\tau_1+\tau_2} &= \frac{\omega^* \omega_r^3}{\alpha^4} \sin^2 \frac{\alpha t_\omega}{2} \left[\frac{4\omega^{*2}}{\alpha^2} \sin^4 \frac{\alpha t_\omega}{2} + \sin^2 \alpha t_\omega \right] \\ &\quad \exp\left[-(\tau_2-\tau_1) \left(\frac{1}{T_1} - \frac{1}{T_2} \right) - (\tau_1+\tau_2) \frac{1}{T_2} \right] \\ V_{t=\tau_1+\tau_2} &= \frac{1}{2} \frac{\omega_r^3}{\alpha^3} \sin \alpha t_\omega \left[\frac{4\omega^{*2}}{\alpha^2} \sin^4 \frac{\alpha t_\omega}{2} + \sin^2 \alpha t_\omega \right] \\ &\quad \exp\left[-(\tau_2-\tau_1) \left(\frac{1}{T_1} - \frac{1}{T_2} \right) - (\tau_1+\tau_2) \frac{1}{T_2} \right] \end{aligned} \tag{3}$$

The theoretical and experimental curves of the stimulated echo amplitude with different amounts of off-resonance are shown in Fig. 1 for different angles ($\gamma H_r t_\omega = \pi/2$ and $2\pi/3$). It is evident that for $\gamma H_r t_\omega = \pi/2$, there is very little change in the tip of the signal amplitude with off-resonance and the top of the curve is quite flat indicating that the measurements of relaxation time T_1 with stimulated echo has to be performed near about such an angle. It is also evident from the curve for $\gamma H_r t_\omega = 2\pi/3$, that the maximum does not occur at $\omega^* = 0$, wereas for the corresponding curve for the primary echo as given by Pfeifer shows that the maximum does occur at this point.

Experimental measurements of the amplitude variation of echoes with different off-resonance values were carried out by observ-

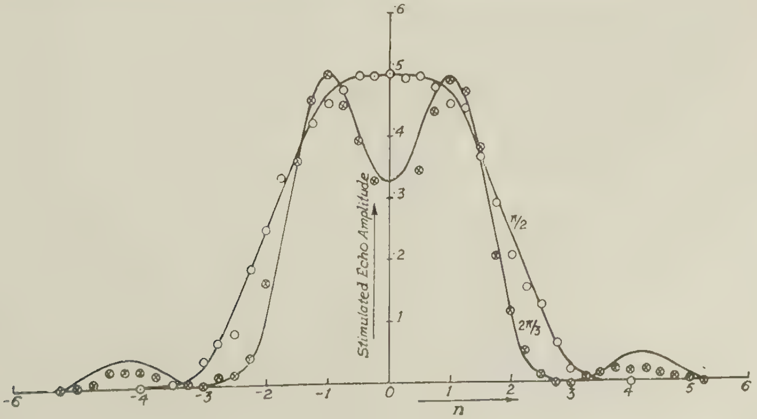

Fig. 1. Curves showing the variation of the stimulated echo amplitude with off-resonance. The theoretical curves are denoted by continuous lines; the encircled points represent the experimental values. $n = \omega^*/\omega_r$.

ing simultaneously the steady signal of a fluorine compound viewed on another oscilloscope. The steady signal was produced by an autodyne detector circuit having stable and easily variable frequency output. This frequency was accurately measured by beating with the signal produced by a 805C GR Signal Generator. Different amounts of off-reasonance was recorded accurately by noting the change in fluorine resonance frequency.

§ 3. Application of the Off-resonance Study

The analysis of the off-resonance signal amplitude of different echoes with three pulse system can be extended to the three other echoes at $t=2\tau_1$, $2\tau_2$ and $\tau_2-\tau_1$ and yields the following results,

$P_{(12)}$:

$$U=[a\cos\omega^*(t-2\tau_1)-b\sin\omega^*(t-2\tau_1)]\exp[-2\tau_1/T_2]$$
$$V=[b\cos\omega^*(t-2\tau_1)+a\sin\omega^*(t-2\tau_1)]\exp[-2\tau_1/T_2] \tag{4}$$

$P_{(13)}$:

$$U=[c\cos\omega^*(t-2\tau_2)-d\sin\omega^*(t-2\tau_2)]\exp[-2\tau_2/T_2]$$
$$V=[d\cos\omega^*(t-2\tau_2)+c\sin\omega^*(t-2\tau_2)]\exp[-2\tau_2/T_2] \tag{5}$$

$P_{(23)}$:

$$U=[e\cos\omega^*(t-2\tau_2+\tau_1)-f\sin\omega^*(t-2\tau_2+\tau_1)]\exp[-2\tau_2-2\tau_1/T_2]$$
$$V=[f\cos\omega^*(t-2\tau_2+\tau_1)+e\sin\omega^*(t-2\tau_2+\tau_1)]\exp[-2\tau_2-2\tau_1/T_2] \tag{6}$$

where,

$$a=\frac{1}{4}\frac{\omega^*\omega_r^3}{\alpha^4}(1-\cos\alpha t_{\omega_2})\Big[-\frac{\omega^{*2}}{\alpha^2}(1-\cos\alpha t_{\omega_1})(1-\cos\alpha t_{\omega_3})$$
$$+(1-\cos\alpha t_{\omega_1})-2\sin\alpha t_{\omega_1}\sin\alpha t_{\omega_3}+(1-\cos\alpha t_{\omega_1})\cos\alpha t_{\omega_3}\Big]$$

$$b=\frac{1}{2}\Big[\frac{\omega^{*2}\omega_r^3}{\alpha^5}(1-\cos\alpha t_{\omega_1})(1-\cos\alpha t_{\omega_2})\sin\alpha t_{\omega_3}$$
$$-\frac{1}{2}\frac{\omega^{*2}\omega_r^3}{\alpha^5}\sin\alpha t_{\omega_1}(1-\cos\alpha t_{\omega_2})(1-\cos\alpha t_{\omega_3})$$
$$-\frac{1}{2}\frac{\omega^{*2}\omega_r}{\alpha^3}\sin\alpha t_{\omega_1}(1-\cos\alpha t_{\omega_2})(1+\cos\alpha t_{\omega_3})$$
$$+\frac{1}{2}\frac{\omega_r}{\alpha}\sin\alpha t_{\omega_1}(1-\cos\alpha t_{\omega_2}\cos\alpha t_{\omega_3})$$
$$+\frac{1}{2}\frac{\omega_r}{\alpha}\sin\alpha t_{\omega_1}(\cos\alpha t_{\omega_3}-\cos\alpha t_{\omega_2})\Big]$$

$$c=\frac{1}{2}\frac{\omega^*\omega_r}{\alpha^2}(1-\cos\alpha t_{\omega_3})\Big[\frac{1}{2}\frac{\omega^{*4}}{\alpha^4}(1-\cos\alpha t_{\omega_1})(1-\cos\alpha t_{\omega_2})$$
$$+\frac{\omega_r^2}{\alpha^2}\sin\alpha t_{\omega_1}\sin\alpha t_{\omega_2}+\frac{1}{2}(1-\cos\alpha t_{\omega_1})\cos\alpha t_{\omega_2}$$
$$+\frac{1}{2}\frac{\omega_r^2}{\alpha^2}(1-\cos\alpha t_{\omega_1})-\frac{1}{2}\frac{\omega^{*2}}{\alpha^2}(1-\cos\alpha t_{\omega_1})\Big]$$

$$d=\frac{1}{4}\frac{\omega_r^3}{\alpha^3}\Big[-\frac{\omega^{*2}}{\alpha^2}(1-\cos\alpha t_{\omega_3})\Big\{\sin\alpha t_{\omega_1}(1-\cos\alpha t_{\omega_2})+2(1-\cos\alpha t_{\omega_1})\sin\alpha t_{\omega_2}\Big\}$$
$$+\sin\alpha t_{\omega_1}(1-\cos\alpha t_{\omega_2}\cos\alpha t_{\omega_3})+\sin\alpha t_{\omega_1}(\cos\alpha t_{\omega_2}-\cos\alpha t_{\omega_3})\Big]$$

$$e=2W(c)\frac{\omega^*\omega_r^3}{\alpha^4}\sin^2\frac{\alpha t_{\omega_2}}{2}\sin^2\frac{\alpha t_{\omega_3}}{2}$$

$$f=W(c)\frac{\omega_r^3}{\alpha^3}\sin\alpha t_{\omega_2}\sin^2\frac{\alpha t_{\omega_3}}{2}$$

$$W(c)=1+\frac{\omega_r^2}{\alpha^2}(\cos\alpha t_{\omega_1}-1)\exp(-\tau_1/T_1)$$

Now, if the third Pulse be applied very close (within T_2^*) to the second pulse, all the echoes due to the third pulse will be superimposed on each other. A single echo having approximately a gaussian shape will then be observed experimentally. If all the three pulses be of 90°, and third pulse be applied practically at the end of the second pulse then the total signal will be of double the magnitude due to the first two pulses alone if resonance be maintained. With a slight off-resonance and gradually increasing interval between the second and third pulses, the tip of the total signal goes through maxima and minima. The position of the tip also changes slightly due to increased separation between the two pulses. In case of exact resonance, there is no change in the amplitude of the total signal. The number of times that the total signal goes through maxima and minima depends on the amount off-resonance and the interval between the two pulses. Mathematically this can be seen from the expression for the total signal which is obtained by the superposition of all the terms shown in equations (4, 5, 6). As is evident, the echoes differ by phase factors of $\omega^*(\tau_2-\tau_1)$. By varying $(\tau_2-\tau_1)$, i.e. the interval between the third and the second pulse, the relative phases will change and hence there will be maxima and minima at intervals determined by multiples of $2\pi/\omega^*$. It is also seen from above that the number of times that the total signal passes through maxima and minima before the echoes are completely separated out depends on ω^*, i.e. the amount of off-resonance, and $\tau_2-\tau_1$.

The enhancement of the signal amplitude when the third pulse is applied near the second pulse may be used also for determining accurately the resonance value of the magnetic field. In the resonance condition, there will be no change of the amplitude if the interval between the third pulse and the second pulse be varied slightly.

The authors express their thanks to Prof. A. K. Saha for his encouragement during the progress of the work.

References

1) E. L. Hahn: Phys. Rev. **80** (1950) 580.
2) V. H. Pfeifer: Ann. Physik (Leipzig), **17** (1955) 23.
3) T. P. Das and A. K. Saha: Phys. Rev. **93** (1954) 749.

JOURNAL OF THE PHYSICAL SOCIETY OF JAPAN Vol. 12, No. 7, JULY, 1957

Microwave Spectrum of BrCN and Dependence of Quadrupole Coupling Constant on the Vibrational State

By Takeshi OKA and Hiromasa HIRAKAWA

Department of Physics, Faculty of Science,
University of Tokyo, Tokyo, Japan

(Received April 8, 1957)

The hyperfine structure of the J=1←0 and J=2←1 rotational transitions of BrCN has been measured. The values of eqQ(Br^{79}) and eqQ(Br^{81}) for each vibrational state were obtained as follows.

	Vibrational State (v_1, v_2, v_3)	From the frequencies of the J=1←0 transition	From the frequencies of the J=2←1 transition
eqQ(Br^{79}) in Mc/sec	(0,0, 0)	685.6±0.4	685.3±0.8
	(1,0, 0)	687.9±0.6	689.1±0.7
	$(0,2^0,0)$	681.6±0.7	680.2±0.9
eqQ(Br^{81}) in Mc/sec	(0,0, 0)	572.8±0.2	572.7±0.6
	(1,0, 0)	576.1±0.9	574.2±0.7
	$(0,2^0,0)$	568.9±1.5	567.3±1.5

Considerable increase of eqQ for the stretching vibration ($v_1=1$) is explained in terms of the decrease of the double bond character of Br–C bond, and the decrease of eqQ for the excitation of the bending vibration ($v_2=1$) is ascribed to the variation of the z component of q tensor.

§1. Introduction

The measurement of the quadrupole hyperfine structure of the spectrum of pure rotational transitions in a simple molecule gives the quadrupole coupling constant with considerable accuracy. As is well known, molecules in different vibrational states have different rotational constants, and if the microwave spectrum of a molecule in the excited vibrational state is measurable, it gives the quadrupole coupling constants in the excited vibrational states.

Tetenbaum and Javan measured the hyperfine structure of the $J=6\leftarrow5$ transition of BrCN and the $J=4\leftarrow3$ transition of ICN, respectively, and found the variation of eqQ with the excitation of the bending vibration[1),2)]. The hyperfine components of the $J=1\leftarrow0$ and the $J=2\leftarrow1$ transitions of ICN molecule in the (0, 0, 0), (1, 0, 0) and $(0, 2^0, 0)$ vibrational states were reported by the present authors, and the variation of eqQ was found to come not only from the excitation of the bending vibration but also from the excitation of the stretching vibration[3)]. Lower J transitions are more appropriate for this type of investigation.

In the present paper, the results of the measurement of the hyperfine components of the $J=1\leftarrow0$ and the $J=2\leftarrow1$ transitions of BrCN are described. The three vibrationa frequencies of BrCN are $\nu_1=580\ \mathrm{cm}^{-1}$, $\nu_2=$ 368 cm^{-1} and $\nu_3=2187\ \mathrm{cm}^{-1}$. The microwav spectrum of the molecule in the (0, 0 ,0), (1 0, 0) and (0, 2, 0) states were observed bu the study of the molecule in (0, 1, 0) state was given up as they show the complicate Stark behavior of the l-type doublets.

§2. Experiments and Results

The measured frequencies are listed i Tables I, II, III and IV. The errors of th observed frequencies mainly come from th weakness of the lines and from the hyperfin splittings due to the quadrupole moment o N^{14}. The errors are expected to be less tha 0.1 Mc/sec for almost all lines.

From these measured frequencies, the rotational constant B and the quadrupole couplin constant eqQ in each vibrational state wer derived by means of the least square fit t the formula

$$\nu=2(J+1)B+Y(F)\mathrm{eqQ}+Z(F)(\mathrm{eqQ})^2/B\ .$$

Some lines with large experimental error were not used in the analysis. In addition t the hyperfine structures due to the quadrupol moment of Br, some lines show further splittings due to the quadrupole moment of N^{1} From these splittings, eqQ(N^{14}) in BrCN i

Table I. Frequencies of the hyperfine components of the $J=1\leftarrow 0$ rotational transition of $Br^{79}CN$ molecule in Mc/sec.

F_i		F_f		observed	calculated	calculated absorption coefficient in cm^{-1}
F_1	F_2	F_1	F_2			
				(0, 0, 0) lines		
3/2,	5/2	5/2,	7/2	8206.92	8207.05	2.7×10^{-6}
3/2,	5/2	5/2,	5/2	8206.18	8206.24	
3/2,	5/2	5/2,	3/2	8207.39	8207.40	
3/2,	3/2	3/2,	5/2	8377.95	8377.91	1.9×10^{-6}
3/2,	3/2	3/2,	3/2	8378.58	8378.53	
3/2,	3/2	3/2,	1/2	8379.38	8379.31	
3/2		1/2		8070.45	8070.43	0.9×10^{-6}
				(1, 0, 0) lines		
3/2		5/2		8183.87	8183.97	1.7×10^{-7}
3/2		3/2		8356.48	8356.38	1.2×10^{-7}
3/2		1/2		8047.08	8047.08	0.6×10^{-7}
				(0, 2^0, 0) lines		
3/2		5/2		8245.29	8245.39	8.0×10^{-8}
3/2		3/2		8416.30	8216.22	5.7×10^{-8}
3/2		1/2		8109.78	8109.75	2.8×10^{-8}

Table II. Frequencies of the hyperfine components of the $J=2\leftarrow 1$ rotational transition of $Br^{81}CN$ molecule in Mc/sec.

F_i		F_f		observed	calculated	calculated absorption coefficient in cm^{-1}
F_1	F_2	F_1	F_2			
				(0, 0, 0) lines		
3/2,	5/2	5/2,	7/2	8165.68	8165.74	2.5×10^{-6}
3/2,	5/2	5/2,	5/2	8164.96	8164.93	
3/2,	3/2	3/2,	5/2	8308.27	8308.27	1.8×10^{-6}
3/2,	3/2	3/2,	3/2	8308.89	8308.89	
3/2,	3/2	3/2,	1/2	8309.67	8309.67	
3/2		1/2		8051.48	8051.47	0.8×10^{-6}
				(1, 0, 0) lines		
3/2		5/2		8142.89	8142.74	1.5×10^{-7}
3/2		3/2		8286.87	8286.95	1.1×10^{-7}
3/2		1/2		8028.04	8028.11	0.5×10^{-7}
				(0, 2^0, 0) lines		
3/2		3/2		8346.07	8346.07	5.2×10^{-8}
3/2		1/2		8090.25	8090.25	2.4×10^{-8}

Table III. Frequencies of the hyperfine components of the $J=2\leftarrow 1$ rotational transition of $Br^{79}CN$ molecule in Mc/sec.

F_i		F_f		observed	calculated	calculated absorption coefficient in cm^{-1}
F_1	F_2	F_1	F_2			
				(0, 0, 0) lines		
5/2		7/2		16466.35	16466.64	$27\ \times 10^{-6}$
3/2		5/2				
5/2		5/2		16638.40	16638.19	4.0×10^{-6}
5/2		3/2		16517.8	16517.25	0.4×10^{-6}
3/2,	5/2	3/2,	5/2	16345.38	16345.35	4.6×10^{-6}
3/2,	3/2	3/2,	3/2	16346.17	16346.10	
3/2,	5/2	1/2,	3/2	16172.90	16172.82	0.7×10^{-6}
3/2,	3/2	1/2,	3/2	16172.30	16172.20	
3/2,	1/2	1/2,	3/2	16173.40	16173.60	
1/2		3/2		16653.58	16653.62	3.7×10^{-6}
1/2		1/2		16480.92	16481.11	3.6×10^{-6}

F_i F_1	F_i F_2	F_f F_1	F_f F_2	observed	calculated	calculated absorption coefficient in cm^{-1}
				(1, 0, 0) lines		
5/2 3/2		7/2 5/2		16420.97	16420.91	17 $\times 10^{-7}$
5/2		5/2		16593.38	16593.40	2.5×10^{-7}
3/2		3/2		16299.07	16299.10	2.8×10^{-7}
1/2		3/2		16608.6	16608.93	2.3×10^{-7}
1/2		1/2		16435.3	16435.46	2.2×10^{-7}
				(0, 2^0, 0) lines		
5/2 3/2		7/2 5/2		16542.45	16542.38	8.0×10^{-7}
5/2		5/2		16712.9	16712.64	1.2×10^{-7}
1/2		3/2		16727.97	16727.96	1.1×10^{-7}
1/2		1/2		16556.67	16556.75	1.1×10^{-7}

Table IV. Frequencies of the hyperfine components of the $J=2\leftarrow 1$ rotational transition of $Br^{81}CN$ molecule in Mc/sec.

F_i F_1	F_i F_2	F_f F_1	F_f F_2	observed	calculated	calculated absorption coefficient in cm^{-1}
				(0, 0, 0) lines		
5/2 3/2		7/2 5/2		16375.43	16375.18	25 $\times 10^{-6}$
5/2		5/2		16518.62	16518.52	3.6×10^{-6}
5/2		3/2		16417.0	16417.25	0.4×10^{-6}
3/2,	5/2	3/2,	5/2	16273.00	16272.99	4.4×10^{-6}
3/2,	3/2	3/2,	5/2	16273.62	16273.61	
3/2,	1/2	3/2,	3/2	16274.38	16274.39	
3/2		1/2		16129.96	16129.75	0.7×10^{-6}
1/2		3/2		16531.31	16531.32	3.5×10^{-6}
1/2		1/2		16387.20	16387.30	3.4×10^{-6}
				(1, 0, 0) lines		
5/2 3/2		7/2 5/2		16329.72	16329.55	15 $\times 10^{-7}$
5/2		5/2		16473.20	15473.25	2.2×10^{-7}
3/2		3/2		16227.73	16227.88	2.7×10^{-7}
1/2		3/2		16486.04	16486.09	2.2×10^{-7}
				(0, 2^0, 0) lines		
5/2 3/2		7/2 5/2		16451.27	16451.27	7.5×10^{-7}
1/2		3/2		16605.92	16605.92	1.1×10^{-7}

calculated by means of Bardeen and Townes's theory[4]. The values of quadrupole coupling constants and the rotational constants ar listed in Tables V and VI, respectively.

Table V. Values of $eqQ(Br^{79})$, $eqQ(Br^{81})$ and $eqQ(N^{14})$ in Mc/sec.

Vibrational State	Transition	$eqQ(Br^{79})$	$eqQ(Br^{81})$
(0, 0, 0)	$J=1\leftarrow 0$ $J=2\leftarrow 1$	685.6 ± 0.4 685.3 ± 0.8	572.8 ± 0.2 572.7 ± 0.6
(1, 0, 0)	$J=1\leftarrow 0$ $J=2\leftarrow 1$	687.9 ± 0.6 689.1 ± 0.7	576.1 ± 0.9 574.2 ± 0.7
(0, 2^0, 0)	$J=1\leftarrow 0$ $J=2\leftarrow 1$	681.6 ± 0.7 680.2 ± 0.9	568.9 ± 1.5 567.3 ± 1.5

$eqQ(N^{14}) = -3.89$ Mc/sec.

Table VI. Values of rotational constants used in the calculation of the frequencies in Mc/sec.

Vibrational State	Transition	$Br^{79}CN$	$Br^{81}CN$
(0, 0, 0)	$J=1\leftarrow 0$ $J=2\leftarrow 1$	4120.32 4120.278	4096.92 4096.825
(1, 0, 0)	$J=1\leftarrow 0$ $J=2\leftarrow 1$	4108.93 4108.864	4085.74 4085.425
(0, 2^0, 0)	$J=1\leftarrow 0$ $J=2\leftarrow 1$	4139.49 4139.189	4115.83 4115.820

§ 3. Discussions

From Table V it is seen that eqQ increases when the stretching vibration is excited. This is reasonable in view of the variation of the double bond character of Br–C bond. When the stretching vibration is excited, Br–C bond is elongated owing to the anharmonicity of the potential, and the double bond character of the Br–C bond decreases, and thus eqQ increases. The elongation of the bond is calculated from the variation of the moment of inertia of the molecule with the vibrational excitation. Since ν_1 vibration is concerned mainly with the stretching of the Br–C bond, C–N distance may be assumed to be constant. Accordingly, the elongation of the Br–C bond is calculated to be

$$\delta R=(M_{\mathrm{Br}}+M_{\mathrm{C}}+M_{\mathrm{N}})(I'-I)/2M_{\mathrm{Br}}[M_{\mathrm{C}}l_1+M_{\mathrm{N}}(l_1+l_2)]\ ,$$

where M_{Br}, M_{C}, M_{N} are the masses of Br, C and N atoms, l_1 and l_2 are the bond lengths of Br–C and C–N bonds in the ground vibrational state, and I' and I are the moments of inertia of the molecule in the (1, 0, 0) and the (0, 0, 0) states, respectively. I' is calculated from the values of B_v obtained by Tetenbaum taking into account the effect of Fermi resonance¹⁾. Substituting $l_1=1.789$ A, $l_2=1.160$ A⁵⁾ and $I'-I=0.465$ a.m.u. A², δR was calculated to be 0.0049 A both for Br^{79}CN and Br^{81}CN. It was reported in the preceding paper that the variation of q is given by the formula³⁾

$$\frac{q+\delta q}{q}=1+\frac{[\frac{1}{2}-\mathcal{E}(\frac{1}{2}-s+d)]x(2x+1)}{[-(1-s+d)(1-x)-(\frac{1}{2}-s+d)(1+\mathcal{E})x]}\cdot\frac{\delta R}{(R-R_1)}\ .$$

Using the values $s-d=0.15$⁶⁾, $\mathcal{E}=0.15$⁵⁾, $x=0.15$⁶⁾ and $\delta R=0.0049$, it is found that

$$(q+\delta q)/q=1.0044\ .$$

This is in fair agreement with the experimental values of $(\mathrm{eqQ})_{v_1=1}/(\mathrm{eqQ})_0$ listed in Table VII.

Tabla VII. Values of $(\mathrm{eqQ})_v/(\mathrm{eqQ})_0$

		Transition	(1, 0, 0)	(0, 2^0, 0)
observed	Br^{79}CN	$J=1\leftarrow0$	1.0034	0.9942
		$J=2\leftarrow1$	1.0055	0.9924
	Br^{81}CN	$J=1\leftarrow0$	1.0058	0.9905
		$J=2\leftarrow1$	1.0026	0.9932
calculated			1.0044	0.9910

It is seen from Table V that eqQ decreases when the bending vibration is excited. This decrease is expressed by the formula²⁾,

$$q_v=(1-3\bar{\theta}^2/2)q_0\ .$$

In the case of BrCN, $1-3\bar{\theta}^2/2$ is calculated to be 0.9910, using the data from the vibrational analysis. This should be compared with the experimental values of $(\mathrm{eqQ})_{v_2=2}/(\mathrm{eqQ})_0$ listed in Table VII.

§ 4. Acknowledgement

The authors are indebted to Prof. K. Shimoda for his kind guidance and encouragement during the course of this investigation. They are also grateful to Prof. Y. Morino of the Department of Chemistry for his continued interest in this work.

References

1) S. J. Tetenbaum: Phys. Rev. **86** (1952) 440.
2) A. Javan: Phys. Rev. **99** (1955) 1302.
3) T. Oka, H. Hirakawa, and A. Miyahara: J. Phys. Soc. Japan **12** (1957) 39.
4) J. Bardeen and C. H. Townes: Phys. Rev. **73** (1948) 97.
5) C. H. Townes and A. L. Schawlow: "*Microwave Spectroscopy*" (McGraw-Hill Book Co. Inc. 1955) p. 240.
6) C. H. Townes and B. P. Dailey: J. Chem. Phys. **17** (1949) 782.

Short Notes

This section is intended to secure prompt publication of important discoveries in physics. The reports should not exceed 800 words in length. A figure of size 7 cm × 7 cm will be counted as 150 words.

J. Phys. Soc. Japan **12** (1957) 824

A Simpler Method for Removing Copper from Germanium

By Makoto Kikuchi and Sigeru Iizima
Electrotechnical Laboratory, Tokyo, Japan

(Received April 18, 1957)

On the course of study on the "thermal conversion" phenomenon, it has been found out that lattice defects (e.g. dislocations) act as *sinks* of Cu atoms. For instance, when the surface of a slice of n-type germanium single crystal was wetted with $Cu(NO_3)_2$ solution and then heated to 650°C, one portion of the specimen, where the dislocation density was very high, was not converted to p-type.

Utilizing this feature of lattice defects on the precipitation of Cu atoms, we have found out a new simpler method for removal of Cu from germanium crystal.⁽¹⁾ Experimental results are as follows.

After wetting the surface with $Cu(NO_3)_2$ solution, the specimens are heated to 650°C and Cu atoms of about $4\sim7\times10^{-14}/cm^3$ are introduced into the crystals. Surface contaminations are etched off with CP4.

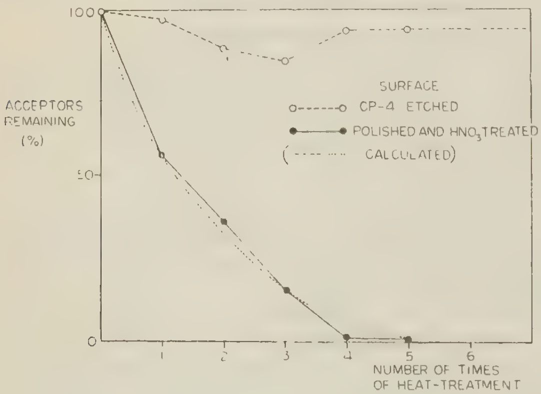

Fig. 1. Experimental results of Cu removal from germanium. Upper curve is for the case of CP4 etched surface, lower curve is for the "roughened" surface.

The surface of a specimen is polished with emery paper, washed with alcohol and de-ionized water, and then immersed into conc. HNO_3 for 1 hour. The roughened surface is washed and dried. The specimen is then heated at 650°C for 1.5 hours in Ar gas. The surface is again etched with CP-4.

As is shown in Fig. 1 (solid line), about 45% of Cu atoms are taken out from the specimen after this treatment. Repeating the treatment 4~5 times, almost all of the Cu atoms are removed. The results of Fig. 1 were obtained from the resistivity measurements, while Fig. 2 shows the recovery of the minority carrier lifetime along the repeated treatment.

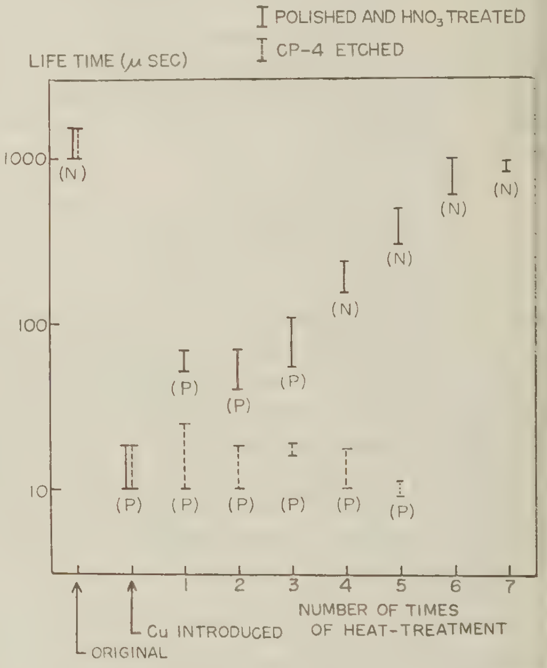

Fig. 2. Recovery of the minority carrier lifetime by the repeated heat-treatment (corresponding to Fig. 1).

As is shown, nearly the same value of the lifetime is restored after repeating the treatment six times.

The results of the heat treatment with normal CP4 etched surface are shown in Fig. 1 and 2 for comparison. The effect of the surface roughening method for the removal of Cu is quite evident.

If we take a quantity "relative distribution coefficient" into account as an analogy to the segregation phenomena, the removal effect can be calculated for the first approximation. The dotted line in Fig. 1 is the calculated curve.

The details will be presented elsewhere in the near future.⁽²⁾

References

1) Blodgett: J. A. P. **26** (1955) 1520.
Logan, et al: J. A. P. **26** (1955) 1287.
2) Bull. Electrotechnical Lab. (in Japanese).

J. PHYS. SOC. JAPAN **12** (1957) 825

On the Mechanism of Deformation Twin in fcc Crystal

By Akiya OOKAWA

Department of Physics and Chemistry, Gakushuin University, Mejiro, Tokyo.

(Received April 24, 1957)

With the pole mechanism suggested by Cottrell and Bilby[1], the deformation twin in bcc crystal is expected to grow easily in its width, while that in fcc crystal can not be expected to form any more than in a single atomic plane. It is reported[2], however, that single crystal of copper shows when cold worked at low temperature (4.2°K) an apparent twin with {111} as twinning plane at stresses 12–16 kg/mm². Here, we suggest a similar mechanism of deformation twin in fcc crystal, with reference to the Lomer-Cottrell barrier.

When a dislocation segment on a (111) plane dissociates according to the reaction

$$(a/2)[110] \rightleftarrows (a/3)[111] + (a/6)[11\bar{2}]$$

and the twin dislocation $(a/6)[11\bar{2}]$ sweeps once around the segment, a stacking fault on the (111) is formed but further repitition in the state is impossible (see Fig. 3 in *ref.* 1). As the perfect dislocation $(a/2)$ [110] after the rejoinment is movile on (1$\bar{1}$0), the dislocation segment, if happened to lie along [11$\bar{2}$], can glide out of the (111). If the segment displaces itself parallel to a neighbouring (111) plane, another stacking fault on the new (111) plane can be formed.

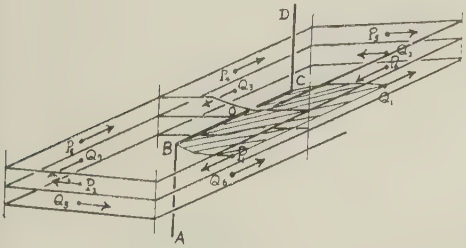

Fig. 1.

In the above treatment, two dislocation lines connected by the segment are tacitly assumed to emerge on the same side of the (111) plane. When the two dislocations emerge on different sides, the one on lower side and the other on upper side, the (111) planes look like a scheme in Fig. 1. It is characteristic to this state, that the sweeping dislocations BP_1 and CQ_1, both starting from the mother segment BC, rotate on different net planes consecutively. The one dislocation BP_1 sweeps in the sequence $BP_1 \rightarrow BP_2 \rightarrow BP_3 \rightarrow BP_4 \rightarrow BCP_5 \rightarrow CP_6 \rightarrow \cdots$, and afterwards the twin dislocation CP_6 rotates around the pole dislocation CD, resulting in growth of deformation twin on upper side of the reference plane. The growth on lower side is maintained by BQ_6 as consequence of CQ_1.

According to the above mechanism, neither the original segment is extended nor the two partial dislocations have elastic interaction after dissociation. The critical stress for twinning is, therefore, governed in main by the critical stress $\sigma_0 \sim \mu b/l$ needed to expand a dislocation segment of length l and the stress $\sigma_s \sim \varepsilon_s/b$ necessary to drag the twin dislocation trailing the stacking fault of energy ε_s. With $\varepsilon_s \sim 20$ erg/cm² for copper, we have $\sigma_s \sim 10^9$ dyne/cm², in the same order of magnitude as the experimental value. As the stress $\sigma_0 \sim 10^8$ dyne/cm² estimated for $l \sim 10^{-4}$ cm is much smaller than this value of σ_s, we can interpret the apparent twin in copper with the present mechanism, if provided the mother segment is sufficiently long.

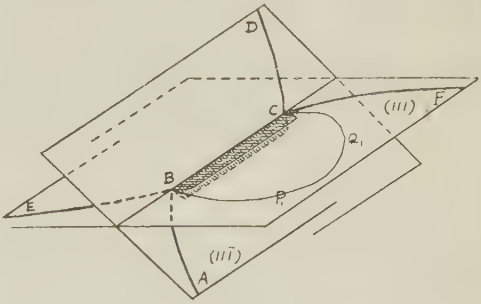

Fig. 2

A dislocation segment on (111) sufficiently long is realized in the Cottrell-Lome barrier[3], stabilized under dissociation

$$(a/2)[110] \rightleftarrows (a/6)[11\bar{2}] + (a/6)[110] + (a/6)[112].$$

When the twin dislocation $(a/6)[11\bar{2}]$ sweeps on (111), the dislocation lines AB and CD on the crossing (11$\bar{1}$) stand for the pole dislocations. In contrast to Fig. 1, however, the growth on either side is suppressed by the intrinsic fault on (11$\bar{1}$).

It is to be noted that at low temperature the induced deformation twin is expected stable, because the thermal energy does not suffice to activate the sessile dislocation $(a/6)[110]$ to dissociate; this is the mode prefered at high temperature[4].

References

1) A. H. Cottrell, B. A. Bilby: Phil. Mag. **42** (1951) 573.
2) T. H. Blewitt, R. R. Coltman, J. K. Redman: *Defects in crystalline solids* (1955) 489.
3) W. M. Lomer: Phil. Mag. **42** (1951) 1327; A. H. Cottrell: ibid. **43** (1952) 645.
4) A. N. Stroh: Phil. Mag. **1** (1956) 489.

J. Phys. Soc. Japan **12** (1957) 826

Nuclear Magnetic Resonance in Irradiated Teflon

By Hazime Kusumoto*

Institute of Science and Technology
University of Tokyo, Tokyo

(Received March 27, 1957)

We have examined at room temperature the F^{19} magnetic resonance in Teflon (polytetrafluoroethylene, PTFE) irradiated with deuterons from the cyclotron of our institute. The Teflon was commercial thin film and was irradiated repeatedly in vacuum at room temperature so much that it was powdered easily. The another four sheets were irradiated in the same condition of irradiation for 20 sec., 1 min., 3 min. and 10 min. respectively. They seem to have no change apparently. These samples were very kindly furnished by Prof. K. Ōno and H. Abe of this institute.

Table I. The experimental values of line width and second moment of PTFE's and PTFE*-1.

	PTFE*-1	PTFE	A.N.*	J.A.S.S.*
Line width (gauss)				
ΔH (m.sl.)	2.8	0.7	0.7	2.6
ΔH (1/2)	4.1	2.8	2.9	—
Second Moment (gauss^2)	2.4	1.8	2.8	3.8

* These values of A.N.(2) and J.A.S.S.(1) were interpolated approximately in their data.

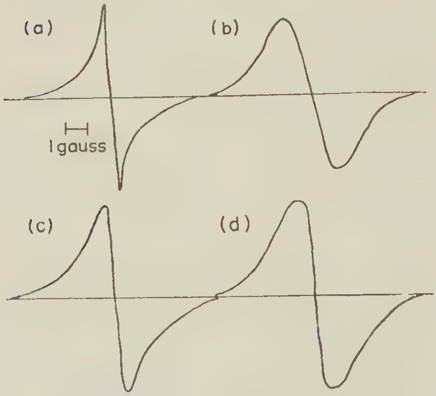

Fig. 1. F^{19} magnetic resonance in (a) PTFE, (b) PTFE*-1 (irradiated to be powdered), (c) PTFE*-2 (irradiated for three min.) and (d) PTFE*-3 (irradiated for ten min.).

In Fig. 1 there are reproduced the observed li shapes. The experimental values of line wid and second moment of the original PTFE an irradiated PTFE (PTFE*-1) are described in Tab I compared with such values obtained by anoth authors.

As shown in Fig. 1 the sharp central peak b came broad with increasing of irradiation ti and line shape would become similar to that PTFE*-1.

According to Charlesby3), the energy absorbed Teflon breaks it mainly at C-C bond to make smaller molecules. However, the experimental r sults suggest that the motion of F^{19} nuclei, name the segmental motion of the molecules, in PTF is more disturbed compared with the origin molecules. Therefore, it might be supposed th such structures that disturb segmental motion ha been produced in irradiated Teflon.

In irradiated Teflon: (1) at a broken C-C bon producing a free radical, oxygen atom might b trapped4),5) during aging in air after irradiati and/or double bond might be produced. Further more there would exist possibility for a broke chain to form some of ring5), (2) some of C- bonds must be broken releasing gases3) to leave free radical, which might produce double bon make a cross-linkage with a free radical produce in other molecule as at the case of polyethylen Unfortunately, since the irradiation dose and th quantity of released gas3) were not known, estimation of cross-linkage could not be done.

Though Teflon molecules become smaller b irradiation, these double bond, cross-linkage an rings produced sametime disturb the segmenta motion and cause broadening of line width. Further measurement on variation of line width an second moment vs. temperature has been done The results will be published later.

The author wishes to express his sincere thank to Prof. K. Oshima for his suggestions of thi work.

References

1) J. A. S. Smith: Discuss. Faraday Soc. No. 1 (1955) 207, 251.
2) A. Nishioka: Rp. Electr. Commun. Lab. No 889 (1956).
3) A Charlesby: Nucleonics, 12. No. 6 (1954) 1
4) E. E. Shneider: J. Chem. Phys. **23** (1955) 97
5) W. B. Ard, H. Shields and W. Gordy: Chem. Phys. **23** (1955) 1727.

---

* Now at University of Illinois, Urbana, Illinois, U.S.A.

J. PHYS. SOC. JAPAN **12** (1957) 827

Some Comments on the Theory of Coercive Force of Fine Particles

By Tetuo OHOYAMA

Department of Physics, Faculty of Science, Tokyo Metropolitan University

(Received April 26, 1957)

It is well known that the coercive force H_c of ferromagnetic fine particles increases with decreasing diameter d of the particle, and that a theoretical explanation of this variation has been given by Kittel1).

Recently Néel2) raised a theoretical objection against it, but it seems not to be absolutely correct to conclude that Kittel's model must lead to a constant H_c independent of d, on the basis of Néel's discussion. The model on which Néel carried out his calculation (Fig. 2) differs somewhat from Kittel's model (Fig. 1). Moreover, Néel's expression for the magnetostatic energy has an ambiguity connected with the conditional convergency.

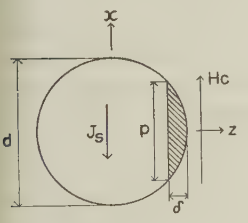

Fig. 1.

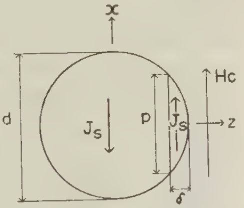

Fig. 2.

In Fig. 1, the spherical cap is a wall itself, but in Fig. 2, it is a domain of reversed magnetization bounded by an infinitely thin wall. In Fig. 1, δ has a definite meaning, the wall thickness, but in Fig. 2, its physical meaning is not very clear.

In both cases, the energy blance is given by the equation

$$\sigma(\pi p^2/4)=H_c(\bar{J}_x+J_s)v+(-\varDelta U)\,. \qquad (1)$$

Here σ is the surface energy density of a domain wall, $\bar{J}_x$ is the average of the x-component of the magnetization in the interior of the spherical cap. v is its volume. $-\varDelta U$ is the gain in magnetostatic energy due to the varied magnetization. $\bar{J}_x=J_s$ in Fig. 2.

Kittel put $\bar{J}_x=0$ and $-\varDelta U=(1/2)\cdot J_s^2\cdot(4\pi/3)(d/2)^3\cdot(\delta/2d)$ as a crude estimate in his model, coming to the expression $H_c/H_c^\infty=1-d/d_0$. As Néel pointed out, he would have come to an expression for H_c independent of d, if he had put $(\delta/2d)^2$ instead of $(\delta/2d)$.

The magnetostatic energy of a system shown in Fig. 2 has been calculated by Néel3) and can be written*, with an abbreviation $1-2\delta/d=u$,

$$U=\frac{\pi^2J_s^2d^3}{2}\times\left\{\frac{(u^3-3u)^2}{18}\right.$$
$$\left.+(1-u^2)^2\sum_{n=2}^{\infty}n(n+1)[\mathrm{P}_n^{-2}(u)]^2\right\}. \qquad (2)$$

According to Néel2), U can be written, if $\delta\ll d$, as**

$$U=(\pi^2d^3J_s^2/9)[1-12(\delta/d)^2+\cdots]\,, \qquad (3)$$

thus $-\varDelta U\propto d^3(\delta/d)^2$, leading to the d-independent H_c.

After some calculations we come, however, to infinitely large coefficients*** of $(\delta/d)^4, (\delta/d)^5, \cdots$, in the expansion of U in the power series in δ/d. It seems that we can not trace the energy curve as a function of δ/d, without numerical calculations.

This difficulty might be avoided by breaking off the series (2) after a finite number of terms. Then we can neglect the terms of higher order in δ/d unambiguously, if δ/d is sufficiently small. But if we reserve one more higher order term than Néel, we have, using geometrical identities $v=(1/2)\pi(d\delta^2-2\delta^3/3)$ and $p^2=4\delta(d-\delta)$,

$$H_c=\left(\frac{\sigma}{J_s\delta}-\frac{4\pi J_s}{3}\right)-\frac{\sigma}{3J_sd}\,,\quad(\delta\ll d)\,.$$

The last term on the right might be, in some cases, comparable to the quantity in the parenthesis****, and, with constant values of σ and δ, it makes H_c even decrease with decreasing d.

As Néel pointed out, H_c would become, to the first approximation, independent of d in the Kittel's model, if, and only if, $-\varDelta U\propto d^3(\delta/d)^2$. But Néel's calculation corresponds to an infinitely thin wall and another calculation seems to be necessary to decide the question that $-\varDelta U$ in the Kittel's model be proportional to $d^3(\delta/d)^2$.

References

1) C. Kittel: Phys. Rev. **73** (1948) 810.
2) L. Néel: J. de phys. et rad. **17** (1956) 250.
3) L. Néel: Cahiers de physique No. **25** (1944) 21.

---

* c_1 in the literatures (2) and (3) is equal to $(u^3-3u)/2$.

** $\mathrm{O}(2\delta/d)^4$ in the literature (2) might be a misprint of $\mathrm{O}[(2\delta/d)^3]$.

*** This does not mean that Eq. (2) is a divergent series.

**** This is what appeared in the Néel's discussion and are independent of d.

J. Phys. Soc. Japan **12** (1957) 828~829

Electron Transport in Metals

By Mikio Tsuji

General Education Department, Kyusyu University, Fukuoka, Japan

(Received May 13, 1957)

Barrie[1] has calculated the change produced in the conductivity and thermoelectric power of metals when one uses Bohm and Pines' $E_k \sim k$ curve[2] instead of the usual parabolic curve of free electrons. Barrie's calculation is confined to the case of high temperatures and pure metals, and there is a mistake in Barrie's paper. We have calculated the conductivity and thermoelectric power for the general case of arbitrary temperatures and arbitrary concentrations of impurities.

If the spherical energy surface is assumed, the energy of electron E_k may be expanded as follows,

$$E_k=\zeta+\alpha(k-k_0)+(1/2)\beta(k-k_0)^2, \qquad (1)$$

where k is the wave number vector of electrons, ζ the energy of Fermi level, and k_0 the wave number at the Fermi level. We derive Boltzmann's equation for the distribution function of electrons whose energy surface are given by Eq. (1). The lattice scattering term in the equation is identical to that given by Klemens[3], and in the impurity scattering term we expand the scattering cross section Q as $Q=Q_0\ \{1+\gamma_1(E-\zeta)+\gamma_2(E-\zeta)^2+\cdots\}$. We solve the Boltzmann equation by a variational method similar to that of Sondheimer[4], and obtain the electrical conductivity σ and thermoelectric power S as follows,

$$1/\sigma=\rho=\rho_0+\rho_r\ , \qquad \rho_0=A\frac{1}{\alpha^2}\left(\frac{T}{\Theta}\right)^5 J_5\left(\frac{\Theta}{T}\right)\ , \qquad \text{(2}$$

$$\rho_r=B(1/\alpha^2)\ , \qquad \text{(3}$$

$$S=-\frac{2\pi^2\beta}{3e\alpha^2}\kappa^2 T\frac{\left(1-\frac{\alpha^2}{2\beta}\gamma_1\right)+\frac{\rho_0}{\rho_r}\left\{\left(1+\frac{2\alpha}{\beta k_0}\right)-\frac{1}{2\pi^2}\left(1+\frac{\alpha}{2\beta k_0}\right)\frac{J_7}{J_5}+\frac{3}{\pi^2}\frac{k_0^2}{q_0^2}\left(\frac{\Theta}{T}\right)^2\right\}}{1+\frac{\rho_0}{\rho_r}\left\{1-\frac{J_7}{2\pi^2 J_5}+\frac{3}{\pi^2}\frac{k_0^2}{q_0^2}\left(\frac{\Theta}{T}\right)^2\right\}}\ , \qquad (4)$$

where A is a constant proportional to the interaction between electrons and lattice waves, q_0 the maximum wave number of phonons, Θ the Debye temperature, κ Boltzmann's constant, J_n Grüneisen's function and B a constant proportional to Q_0.

Eqs. (2) and (3) show the well known fact that the conductivity is proportional to $(dE/dk)^2$ at the Fermi surface. Eq. (4) is our new expression for the thermoelectric power.

In the case of high temperatures and pure metals, (2) and (4) reduce to

$$\sigma=\frac{4}{A}\frac{\Theta}{T}\alpha^2\ , \qquad (5)$$

$$S=-\frac{2\pi^2}{3e}\left(\frac{2}{\alpha k_0}+\frac{\beta}{\alpha^2}\right)\kappa^2 T\ . \qquad (6)$$

Eqs. (5) and (6) are different from the results of Barrie. (The error of Barrie is due to his Eq. (3), which should be replaced by $\tau=ck^3(m^*)^{-1}$.) We calculate the values of α and β in (1) from the $E \sim k$ relation obtained by Bohm and Pines, and use these values in (5) and (6); then we obtain the numerical results given in the first two rows of Table I.

In the Table σ_0 and S_0 are the values for the standard parabolic bands, and σ and S are the values for the band modified by the theory of Bohm and Pines. σ/σ_0 is decreased considerably from Barrie's results, but S/S_0 is only slightly different from Barrie's result. The values of σ/σ_0 do not depend on temperatures and impurity concentrations, but the values of S/S_0 depend on them.

Table I. Conductivity and thermoelectric power of alkali metals.

	Li	Na	K	Rb	Cs
σ/σ_0	1.43	1.23	1.14	1.12	1.08
$(S/S_0)_H$	0.82	0.91	0.97	0.99	1.02
$(S/S_0)_L$	0.80	0.91	1.04	1.11	1.14

At low temperatures (4) gives the following result for pure metals:

$$S=-\frac{2\pi^2\beta}{3e\alpha^2}\kappa^2 T\ . \qquad (7)$$

The values of S/S_0 calculated from (7) are shown in the last row of Table I. It is seen that the effect of modification of the band on S/S_0 is more appreciable at low temperatures than at high temperatures, but the effect is not so large. For impure metals at low temperatures, the values of S/S_0 are nearer to unity than those for pure metals.

Our conclusion is that, for any temperature and any concentration of impurity, the modification of the $E \sim k$ curve by the theory of Bohm and Pines dose not have very large influence on the electron transport phenomena of metals.

Eq. (4) shows that deviations of the band structure from the free electron model have very important effect on the thermoelectric power. In fact if $\beta<0$, the sign of thermoelectric power may become positive. The detailed calculations will be published in this journal.

References

1) R. Barrie: Phys. Rev. **103** (1956) 1581. [Quoted by D. Pines, in Canad. Jour. Phys. **34** (1956) 1376.]
2) D. Pines: Phys. Rev. **92** (1953) 626.
3) P. G. Klemens: Handbuch der Physik, Bd. **14**, Berlin (1956) 233.
4) E. H. Sondheimer: Proc. Roy. Soc. A **203** (1950) 75.

J. PHYS. SOC. JAPAN **12** (1957) 829

A Method of Evaluating the Dissociation Constant in the Excited State of a Molecule

By Reikiti ITOH

Kobayasi Institute of Physical Research
Kokubunzi, Tokyo

(Received May 13, 1957)

If a molecule liberates a proton in the excited state as well as in the ground state, one can evaluate the dissociation constant of the molecule from the pK value of the molecule in the ground state and the absorption spectra of the molecule in the acid and alkali solution. It is naturally expected that the dissociation of proton is easier in the excited state than in the ground state. Then, the excited molecule, if it is meta stable, has the smaller pK value than that of ground state. For the sake of comparison of the dissociation constants of the two states in a given solvent at a given temperature, we consider the equilibrium

$$GH+E^- = G^- + EH\,,$$

where GH and EH correspond to the ground and the excited state of a molecule respectively. Hammet[1] and lately Longuet-Higgins[2] have discussed in detail how the equilibrium constant for such a reaction is related to the kinetic and potential energies of the reacting species. If we ignore the entropy difference between the states in the right and left hand sides of the reaction, the standard free energy change in the reaction can be expressed by the difference in resonance energy of the π-electrons between the species on the right hand side of the equation and those of the left. This assumption may be expressed by the equation

$$(\varepsilon_{EH}-\varepsilon_{GH})-(\varepsilon_{E}-\varepsilon_{G}) = -2.303\,RT(pK_e - pK_g),$$

where ε_A is the π-electron energy of the specy A and pK is the logarithmic equilibrium constant of the molecule for the proton dissociation, and suffixes g and e correspond to the ground and the excited state of the molecule respectively. Then, the left hand side of the equation can be replaced by

$$hc\,\tilde{\nu}_{\text{acid}} - hc\tilde{\nu}_{\text{alkali}} = hc\,\varDelta\tilde{\nu}\,,$$

where $\tilde{\nu}_{\text{acid}}$ and $\tilde{\nu}_{\text{alkali}}$ are the absorption wave numbers in the acidic and alkaline solution of the molecule respectively, and h and c are the Planck's constant and the light velocity. For example, we take β-Naphthol for which the pK data have been reported, i.e., $pK_g=9.49$[3] and $pK_e=2.82$[3] (at 25C°), and the absorption wave numbers are $\tilde{\nu}_{\text{acid}} = 31250$[4] cm^{-1} (solvent HCl, 1/100 N) and $\tilde{\nu}_{\text{alkali}} = 28570$[4] cm^{-1} (solvent NaOH, 1/100 N). From the difference of the absorption wave numbers between the two solutions, one can obtain 5.62 for the value of $pK_g - pK_e$, which is near the observed value, that is $9.49-2.82=6.67$. The small difference between the calculated and the observed value may be attributed to the effects of hydration and entropy change of the reaction.

The author thanks to Prof. I. Oshida for valuable discussion.

References

1) L. P. Hammet: *Physical Organic Chemistry*, McGraw-Hill, N. Y. 1940.
2) H. C. Longuet-Higgins: J. Chem. Phys. **18** (1950) 275.
3) M. Koizumi and S. Shida: *Gendai-Kagaku, Photochemistry*, p. 57, Iwanami, Tokyo, 1956 (in Japanese); Weeler: Z. Elektrochem. **56** (1952) 662.
4) G. W. Ewing and E. A. Steck: J. A. C. S. **68** (1946) 2181.

J. PHYS. SOC. JAPAN **12** (1957) 830~831

Electrical Resistance of CuAu$_3$ and Cu$_3$Au at Low Temperatures*

By Makoto HIRABAYASHI and Yoshio MUTÔ
The Research Institute for Iron, Steel and Other Metals, Sendai.

(Received May 16, 1957)

One of the present authors¹⁾ has previously reported that the electrical resistance of CuAu$_3$ is larger in the ordered state than in the disordered state near room temperature. The behaviour seems to have an opposite sense to that of usual ordered alloys, so that it is of interest to clarify the dependence of the residual resistance of CuAu$_3$ on the degree of order. Although Passaglia and Love²⁾ found no difference in the residual resistance between the quenched and annealed states of CuAu$_3$ in contrast with Cu$_3$Au or CuAu, it seems rather doubtful whether the annealing imposed on this alloy was sufficient to attain the highly ordered state. Thus, we measured the electrical resistivities of CuAu$_3$, CuAu, and Cu$_3$Au in quenched and annealed states from about 2°K to room temperature.

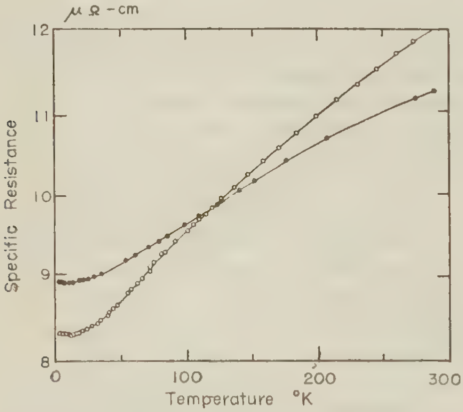

Fig. 1. Specific resistance-temperature curves for CuAu$_3$. Open and closed circles correspond to the highly ordered and disordered states, respectively. Specific resistance values were calculated by using dimensions measured at room temperature, taking no account of temperature change of the dimensions.

In Fig. 1 the specific resistance of CuAu$_3$ containing 75.06 atomic per cent gold, is plotted against temperature. The highly ordered state was obtained by slow cooling from about 200°C to room temperature in four months and the disordered state was obtained by quenching from 450°C to ice water. As shown in this figure, the resistivity-temperature curves for both states each other at about 120°K. It should be noticed, therefore, that the residual resistance is lower in the ordered state than in the disordered one, in the same way as in Cu$_3$Au and CuAu. Ratios of the residual resistance to the ice point resistance are 0.699 and 0.793 for the highly ordered and quenched states, respectively. The resistivity-temperature curves were obtained for various states after different heat-treatments, though not represented here, and it was established that in the partially ordered state the resistance becomes once larger than in the quenched state and again decreases as ordering proceeds. The initial increase might be due to the short-range order effect³⁾. The temperature-dependent portion of the resistance decreases approximately as T^5 below about 20°K for the ordered as well as disordered states. Above this temperature the temperature coefficient of resistance increases as ordering proceeds, similary to Cu$_3$Au and CuAu.

The results for Cu$_3$Au and CuAu almost agree with the work of Passaglia and Love. However, for Cu$_3$Au alloy, containing 25.07 atomic per cent gold, the so-called resistance minimum appeared at about 13°K in the resistance-temperature curves as depicted in Fig. 2. The temperature of the minimum point seems to be little affected by ordering. Such a minimum may probably occur from the presence of very small amounts of specific impurities, such as Fe, Mn, Mg and Si, which were spectroscopically detected. A detailed report will shortly be published elsewhere.

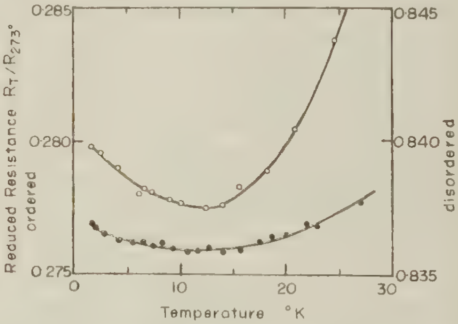

Fig. 2. Reduced resistance $R_T/R_{273K°}$-temperature curves for Cu$_3$Au. Open and closed circles correspond to the ordered and disordered states, respectively.

The authors wish to express their sincere thanks to Professor S. Ogawa and Professor T. Fukuroi, whose guidance and encouragement have made this work possible.

---

* The results given in this note were presented in part at the Sectional Meeting of the Physical Society of Japan in November 1956.

References

1) M. Hirabayashi: J. Phys. Soc. Japan **6** (1951) 129; Nippon Kinzoku Gakkai-si **16** (1955) 67.

2) E. Passaglia and W. F. Love: Phys. Rev. **98** (1955) 1006.
3) J. B. Gibson: J. Phys. Chem. Solids **1** (1956) 27.

J. Phys. Soc. Japan **12** (1957) 831

Barium Supplied Oxide Coated Cathodes

By Tetsuji Imai

Electrical Communication Laboratory,
Nippon Telegraph & Telephone Public
Corporation, Tokyo, Japan

(Received April 22, 1957)

In the oxide coated cathodes, it is believed that stoichiometric excess Ba in the coating layer acts as an active center and its density influences remarkably upon the activity of the cathode. "Stoichiometric excess" allows the possibility of existence of two type of imperfect crystaline states of the cathode coating. The one type is the barium atoms situated in the interstitial positions and the other is the oxygen vacancies.

Though it is quite difficult to decide which is more probable, it is clear that the free Ba is important in any case. In this point of view, many studies have been made on cathode base metals so as to obtain high activity coating. The base metal with large reducing power, however, has the tendency to form the high resistive interface layer which gives rise to many wrong influences upon the vacuum tube characteristics. Therefore, a new attempt is proposed to supply the Ba atom directly into the oxide coating without any chemical reactions between the oxide coating and the base metal.

(1) Supply through the Ni sleeve: Sleeve is constructed duplicately with electrolytic pure Ni, and the Ba source is sealed in the gap between the inner sleeve and the outer one on which oxide emitter is coated. In present experiments Ba getter is utilized as the Ba source.

The emission characteristics of two cathodes which have the same structure except for the existence of Ba source are examined. In each cathode, a deactivation process is produced at first due to flashing of the cathode at high temperature, because in each cathode electrolytic pure Ni are used as the base metal. However, after this heat treatment, if the cathode temperature is decreased to the normal operating condition, the rapid increase of emission is brought about in the cathode occluding Ba source. These aspects are shown in Fig. 1 (a). Life test for these two cathodes are also undertaken at about 700°C quiescently, and the remarkable difference of the emission durability is observed between them as seen in Fig. 1 (b).

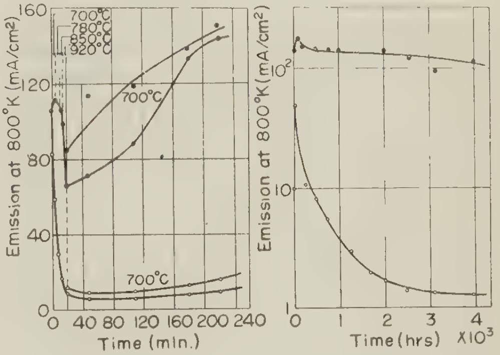

(a) (b)

Fig. 1. Vatiation of emission for the two type of cathodes. The closed points indicate the cathode in which Ba is supplied through a pure Ni sleeve and the open points indicate the one with no Ba source.

(a) Represents the inital stage of heat treatment, and

(b) represents the quiescent life test undertaken at about 700°C of cathode temperature.

(2) Supply through the porous metal: The effect of the Ba supply is examined for the cathode with L-cathode type Ni sleeve on which upper side porous metal (in this case porous pure Ni) is welded and with the Ba source which is sealed in the same manner as the previous case. In this case, we found that the activation is taken place from the begining at very lower temperature and the special high temperature treatment is not necessary for the activation process.

Thus the effect of the Ba supply is obvious and by the proper choice of the rate of Ba supply, low temperature activation and low temperature cathode operation may be possible and much more long life may be expected for the oxide coated cathode.

J. Phys. Soc. Japan **12** (1957) 832

Note on Collective Energy Losses in Metals

By Takao Sato
Department of Physics
Tokyo Metropolitan University, Tokyo

(Received April 4, 1957)

On the theoretical treatments of the collective behavior of electrons in metals, thorough investigations have been done by Bohm and Pines[1], while the experimental evidences thereof have been furnished first by Ruthemann, then by many authors[2]. That is, when a fast charged particle excites such collective oscillations, we are dealing with energy transfer to a number of electrons moving cooperatively in consequence of their mutual interaction. The energy of a plasmon is in the neighborhood of $\hbar\omega_p=\hbar(4\pi ne^2/m)^{1/2}$ where n is the valence electron density and m is the free electron mass.

We now will consider the experimental evidence for plasmon excitation in metals. It was clear from the experimental results that two kinds of situations prevail in the characteristic loss spectrum of a thin metal film; e.g. A group which shows comparatively good agreement between theory (calculated on the assumption that the valence electrons are free) and experiment, and B group metals do not coincide with the frequency $\hbar\omega_p$, and also there has been frequently observed only a single broad loss line.

The interpretation to the A group was provided by Mott[3], who showed that if the valence electrons are weakly bound, and the core electrons are strongly bound (with respect to the free electron plasmon energy $\hbar\omega_p$), the solid state environment would not greatly affect the plasmon energy. One interpretation to the B group was provided by Wolff[4], showed that the coupling of the plasmons to the core electrons in noble metals and transition metals would be expected to broaden the plasma resonance and increase the plasmon energy substantially. He is then led to the conclusion that loss lines continue to broaden as one goes through the transition elements in order of increasing valency. The conclusion, however, is not in agreement with the experiment done by Marton and Leder[5].

It seems that the discrepancies for the B group metals are the consequence of the situation inherent of the transition metals, and are closely related to the substantial problems concerning to their electronic structure. The reason, why the disagreement prevails mainly in noble metals and transition metals, will be attributed to the fundamental problem; what their valency means or what electrons are which contribute to plasma oscillation. It is to be noted that in the A group metals we obtain good agreement between theory and experiment by assuming simply that the valence electrons and the number of electrons which contributed to plasma excitation are equal.

So far the valencies has been considered only formally for the A group elements this may have some substantial meaning. For the B group metals, however, we might consider that the formal valencies lose its meaning. The latter group forms a new scheme of metallic valencies proposed by Pauling[6], in which the significance of formal valency has been in dispute. According to Pauling's theory of new valency scheme, the valencies have the substantial meaning that they concern directly with bond in metals.

A comparison of $\hbar\omega_p$ (eV) with E_{obs} (eV) for metals. Z denotes the number of Pauling's valence.

	Cr	Mn	Fe	Co	Ni	Cu	Zn	Ga
Z	5.78	5.78	5.78	5.78	5.78	5.44	4.44	3.44
E_{obs}	24	22	21	21	23	20	23	—
$\hbar\omega_p$	25	25	26	26	27	25	20	15
	Mo	**Ma**	**Ru**	**Rh**	**Pd**	**Ag**	**Cd**	**In**
Z	5.78	5.78	5.78	5.78	5.78	5.44	4.44	3.44
E_{obs}	25	—	—	—	22	23	20	12
$\hbar\omega_p$	22	—	24	24	23	21	16	13
	W	**Re**	**Os**	**Ir**	**Pt**	**Au**	**Hg**	**Tl**
Z	5.78	5.78	5.78	5.78	5.78	5.44	4.44	3.44
E_{obs}	22	—	—	—	23	24	—	17
$\hbar\omega_p$	22	23	24	24	23	22	16	13

When one calculates $\hbar\omega_p$ for the B group on the basis of Pauling's new valency scheme, the obtained values come closer to the observed ones, as one sees in the table. Although the agreement is not perfect, of course, this seems to provide some indication to the problems of plasmon excitation in transition metals.

It is a great pleasure to thank Professor M. Sasaki for his helpful discussions and encouragements.

References

1) See for instance, D. Pines: Solid State Physics **1** (1955) 368–449.
D. Pines: Rev. Mod. Phys. **28** (1956) 184.
2) See for instance, Marton, Leder, and Mendlowitz: Advances in Electronics **7** (1955) 183–238.
3) N. F. Mott: Proceedings of the Tenth Solvey Congress, Bruxelles (1954).
4) Wolff: Phys. Rev. **92** (1953) 18.
5) L. Marton and L. B. Leder: Phys. Rev. **94** (1954) 203.
6) L. Pauling: Phys. Rev. **54** (1938) 899, Jour. Amer. Chem. Soc. **69** (1947) 542.

J. PHYS. SOC. JAPAN **12** (1957) 833

Absorption Band due to Colloidal Silver

By Ryosuke YOKOTA and Kazuo SHIMIZU
Matsuda Research Laboratory,
Tokyo Shibaura Electric Company,
Kawasaki-city, Japan

(Received May 14, 1957)

Photosensitive glass is one of the most remarkable progress in the field of glass in recent years[1]. But very little has been studied about this interesting and useful glass.

We have discovered a very sharp absorption band due to silver colloid in this glass.

From the pure chemicals we prepared the photosensitive glass containing silver and cerium whose concentrations are about 6.4×10^{16} cm^{-3} and 1.6×10^{18} cm^{-3} respectively.

The oxide composition of the base glass in weight per cent is: SiO_2 82.5, Li_2O 12.5, K_2O 2.5 and Al_2O_3 2.5.

The glass whose size is $15 \times 6 \times 1$ mm^3 was irradiated with the ultra-violet light emitted from the high pressure mercury arc lamp. By this exposure the latent image was formed.

The irradiated glass was quickly inserted into the electric furnace which was maintained at any temperature from 510 to 590°C within ±1°C, and was held for some time, say, about 20 minutes. Then it was quickly withdawn and cooled in air to room temperature. Yellow color was developed.

We have discovered a very sharp absorption band whose half-width is 22 mμ by the use of Beckman DU spectrophotometer. The increase of absorption is given in Fig. 1 in the full line. In this case the dosage of the effective spectral region of the irradiated light was about 2×10^3 erg/cm^2 and the time and temperature of development were 20 minutes and 560°C, respectively.

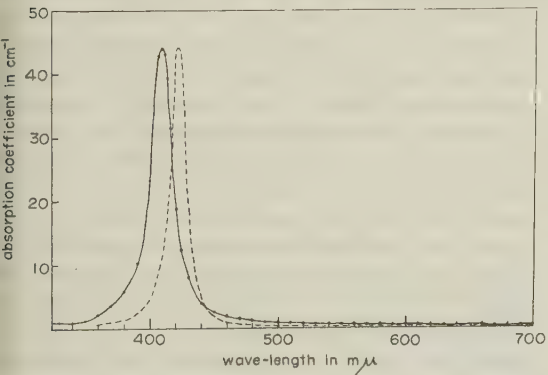

Fig. 1.

The shape and location of this band do not change by cooling down to 80°K, and by heating to 200°C, and by the irradiation of light lying in this band. The absorption bands produced by the ionizing radiation, for example, X-irradiation[2], have changed by the above treatments.

We prepared the glass which does not contain silver but the other compositions are the same. No band was developed in this glass by the same exposure and development.

Therefore this band is due to the silver colloid, especially that of diameter much less than the wave-length of the incident light, because no scattering of light was observed.

In this case the shape and location of this band can be calculated from the equation[3])

$$K=\frac{36\pi N_V V \dfrac{n^2\kappa}{n_u\lambda}}{\left[\left(\dfrac{n}{n_u}\right)^2+\left(\dfrac{n\kappa}{n_u}\right)^2\right]^2+4\left[\left(\dfrac{n}{n_u}\right)^2-\left(\dfrac{n\kappa}{n_u}\right)^2+1\right]}$$

Where K is absorption coefficient, N_V is the number of particles per unit volume; V is the volume of single particle; λ is the wave-length in air for which K is sought; n_u and n are the refractive indices of the glass and silver respectively and $n\kappa$ is the "absorption coefficient" of silver.

Our measured value of n_u for this glass was 1.513 at the wave-length of 420 mμ. The dispersion of n_u is so small that it can be neglected in this case.

It may be the most appropriate to employ in this calculation the optical constants of the silver measured by Schulz[4]) and by Schulz and Tangherlin,[5]) because they measured in an annealed state of the silver film evaporated on glass.

The calculated curve is given in Fig. 1 in the dotted line. In this case neither N_V nor V is known, the maximum value of K was set equal to the measured value.

A good agreement is obtained between the shapes and locations of the observed and calculated bands, although there is small difference of 12 mμ in their locations of peaks.

This small difference is supposed to originate in the circumstance that the colloidal silver in this glass has some different values of n and $n\kappa$ with those measnred by Schulz *et al.*

References

1) S. D. Stookey: Ind. Eng. Chem. **41** (1949) 856; ibid. **45** (1953) 115.
2) R. Yokota: Phys. Rev. **95** (1954) 1145; ibid. **101** (1956) 522.
3) R. W. Pohl: "Einführung in die Optik" Springer, Berlin, 1943.
4) L. G. Schulz: J. Opt. Soc. Amer. **44** (1954) 357.
5) L. G. Schulz and F. R. Tangherlin: ibid. **44** (1954) 362.

J. Phys. Soc. Japan **12** (1957) 834~835

Effect of Heat Treatments on the Magnetic Properties of the $FeTiO_3$–Fe_2O_3 Solid Solution Series

By Yoshikazu Ishikawa
Institute of Science and Technology University of Tokyo, Tokyo
and Syun-iti Akimoto
Geophysical Institute Tokyo University, Tokyo

(Received April 30, 1957)

It has been recently reported that the complete solid solutions between ilmenite ($FeTiO_3$) and hematite (Fe_2O_3), $x TiFeO_3 \cdot (1-x) Fe_2O_3$ can be prepared in the whole range of $0 \leq x \leq 1$ when the mixture of pure Fe_2O_3 and $FeTiO_3$ in an appropriate ratio sealed in a quartz tube evacuated approximately to 10^{-3} mm mercury is quenched from above 1200°C[1]. Although their Curie point temperatures and lattice parameters vary continuously with their compositions, the intensity of magnetization changes discontinuously near $x=0.5$; that is, very strong ferromagnetic (30~70 gauss/gram at 80°K) for $x>0.6$, while feeble ferromagnetic (1~2 gauss/gram) for $x<0.55$[2].

In the course of comprehensive research on the magnetic properties of the $FeTiO_3$–Fe_2O_3 solid solution series, we have found that the intensity of magnetization of the specimens of which chemical composition is near 0.5 is remarkably affected by the heat treatments. Before heat treatments, the specimen of $x=0.5$ which was prepared by the quench method from above 1200°C had the intensity of magnetization of about 2 gauss/gram at room temperature. We have carried out the following heat treatments upon this specimen; that is, the specimen sealed again in an evacuated quartz tube was either quenched or slow-cooled naturally in the furnace from the appropriate high temperatures after being maintained at these temperatures for five hours. Remarkable change in the intensity of magnetization for a magnetic field of 9350 Oe was found after such heat treatments. In Fig. 1, the cross marks show the case of quenching from high temperatures, while the hollow circles show the case of slow-cooling. In this figure, the abscissa shows the temperatures in which the specimen was maintained for five hours.

X-ray analysis carried out by a Norelco diffractometer shows that hardly any changes can be seen in the diffraction patterns as long as the temperature of heat treatment does not exceed 1100°C. On the contrary, when the specimen is cooled slowly from 1100°C, the positions of the diffraction line on the Norelco chart are shifted in the appreciable quantity, corresponding to the decrease of x by 0.05. Consequently, the sharp decrease in the curve B of Fig. 1 when the temperature of heat treatment is 1100°C is due to change of the composition. The Curie point of the specimen which acquired the strong ferromagnetism by means of the above-mentioned procedure is higher than that of the feeble ferromagnetic one by 30°C, but their magnetic susceptibilities above Curie points coincide with each other at high temperatures.

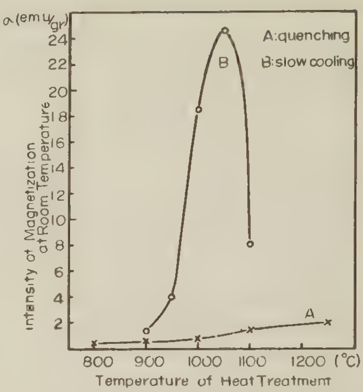

Fig. 1. Effect of heat treatments on the intensity of magnetization of $0.5\,TiFeO_3 \cdot 0.5\,Fe_2O_3$.

It may be very probable that the discontinuous change of the magnetization of the solid solutions with their compositions is closely related to the ordering of Ti and Fe ions, which is established in pure ilmenite[3] and is expected to be responsible for the strong ferrimagnetism. Such an effect of the heat treatments as described in this short note may also be related to an order-disorder transformation phenomenon. There are certain reasons, not described here, to infer that the order-disorder transformation temperature of this specimen is near 600°C. Hence, the fact that the strong ferromagnetism can be acquired only when the specimen was cooled slowly from above 1000°C may be interpreted as follows. It is necessary to maintain the specimen at the temperatures higher than 1000°C in order to create some short range order, without which ordering of Ti and Fe ions can not be attained even if the specimen is cooled slowly through the transformation temperature near 600°C. Furthermore, we have found that the intensity of magnetization of the original specimen can be increased three or four times even in the case of cooling from 600°C if the magnetic field is exerted in the cooling process. This phenomenon can be explained consistently if we assume that in the magnetic field the short range order can be created even at low temperatures.

Detailed investigation is now progressing and the understanding of the mechanism of this phenomenon may give us some information about the origin of ferromagnetism of this solid solution series.

References

1) T. Nagata and S. Akimoto: Geofis. pura appl. **34** (1956) 36.
2) Y. Ishikawa and S. Akimoto: Journal Phys. Soc. Japan, in the press.
3) T. F. W. Barth and E. Posnjak: Zeits. für Krist., **88** (1934) 265.

J. Phys. Soc. Japan **12** (1957) 835

Frequency Shift in Ammonia Absorption due to Foreign Gases

By Kiyokata Matsuura, Yoshikazu Sugiura and G. M. Hatoyama

Electrotechnical Laboratory, Nagatacho, Tokyo

(Received May 11, 1957)

We have already reported the frequency shift in ammonia (3,3) absorption line due to self-broadening[1]). We have also studied the frequency shift of the same line due to foreign gases present in the absorption cell.

The measurements were done with an absorption cell first filled with NH_3 to an amount corresponding to $2\Delta\nu_0 \approx 200$ to 300 kc, to which foreign gases were introduced, and the shift, line width and the pressure were measured similtaneously. The results are tabulated in Table I.

K. Tomita[2]) has calculated theoretically the shift due to impact between molecules, based on dipole-dipole interaction. He gives the value of $a=0.18$ for the shift due to self-broadening, which is some ten times larger than our observed value. Moreover, his calculations do not lead to any negative value of a. Some other types of interaction seem to be taken into account.

Table I. The shift due to foreign gases in ammonia

Gas	Molecular dipole (Debye unit)	$\Delta\nu/p$ (Mc/mmHg)	$a\times 10^2$ (Mc/Mc Width)
(NH_3)	1.47	27	1.8
H_2	0	3.0	− 0.6
A	0	2.0	− 0.6
O_2	0	2.3	− 0.7
N_2	0	4.5	− 1.8
CH_4	0	3.4	− 0.7
CO_2	0	6.6	− 3.8
C_3H_8	0	6.9	− 4.2
$C_6H_5CH_3$	0.5	8.5	− 2.6
H_2O	1.8	4.3	− 3.6
CH_3OH	1.7	9.0	− 3.9
C_2H_5OH	1.7	12.5	− 3.9
CH_3COCH_3	2.7	22	−12

References

1) K. Matsuura, Y. Sugiura and G. M. Hatoyama: J. Phys. Soc. Japan **12** (1957) 314.
2) Reported at the Spring Meeting of the Society, Hiroshima, 1957.

J. PHYS. SOC. JAPAN **12** (1957) 836~837

Some Aspects of Wedge-shaped Domains in $BaTiO_3$ Crystal

By Terutaro NAKAMURA, Wataru, KINASE
and Yoshinori KATŌ*
Department of Physics, Faculty of Science,
University of Tokyo

(Received May 6, 1957)

Domain structure in barium titanate crystals has been investigated by a number of authors.[1] This communication is a record of observations of a domain structure in a barium titanate crystal, which has yielded some aspects hitherto not yet reported.

Our observation of a barium titanate crystal through a polarization microscope, at about 20°C, gave patterns shown in Fig. 1, at a position 45° rotated from the extinction positions. Fig. 1*a* shows the top view, while *b* the bottom. The fact that fringes were observable, and the locations of fringes, which were the same either viewed from the top side or the bottom, indicates that the domain arrangement must be as shown in Fig. 2. The crystal showed remarkable bending, favorable to the structure suggested (Fig. 2). Some irregularities of fringes in Fig. 1*b* (shown by an arrow) were useful for distinguishing between the "top" surface and the "bottom", in consistent with the sense of bending.[2] The thickeess of the sample was 0.15 mm.

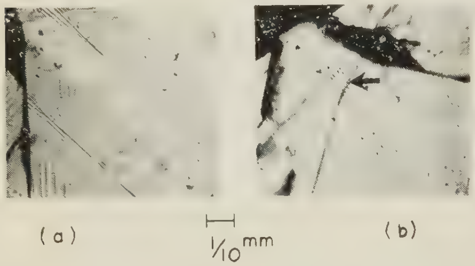

Fig. 1. (*a*) top and (*b*) bottom views at 20°C.

The process of the formation of this type of domain structure will be presumably as follows. At high temperatures, the crystal had been subject to mechanical or thermal stressess, which had caused bending of the plate-like crystal, in the course of the preparation of the specimen. Cooled through the 120°C Curie point, cubic crystal metamorphosed into tetragonal, and the domains assumed the arrangement shown in Fig. 2 so as to decrease the elastic energy.

Near a grain boundary, a number of stripes 45° to prismatic axes were observed, which were confirmed to be plate-like domains showing extinction at the positions parallel and perpendicular to prismatic axes. These plate-like domains were existent only in the regions of which c-axis is parallel to the crystal surface (part A in Fig. 2), and the plates of these domains were perpendicular to the crystal surface. These domains may have been created by mechanical stressess, which probably arised on the grain boundary.

Where "45°-stripe-domains" were existent, there it was observable that the fringe of the middle position was split into two and a new fringe was created between them, or that the fringe of the middle position became thicker. These effects may be understood as follows. The interference fringe of the middle position is not the zero-th order, but there is a minute distance between the crystal surface and the top of the prisms. Mechanical stressess may affect the distance and cause the splitting of the fringes.

Cooled down to 0°C through the transition point 5°C, the patterns which differ markedly from Fig. 1 were observed, as shown in Fig 3, photographed at 3°C. The prismatic domains split up into fine domains, the arrangement of which is supposed to be as shown in Fig. 4. Warmed back up to about 20°C, the previous patterns never reappeared and the bending was removed. This may be because in the orthorhombic phase the mechanical stressess had been relaxed.

The authors wish to thank Prof. H. Takahasi for his helpful discussions. They are also indebted

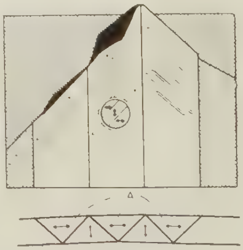

Fig. 2. Schematic arrangement at 20°C.

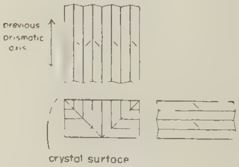

Fig. 4, Schematic of supposed domain structure at 3°C.

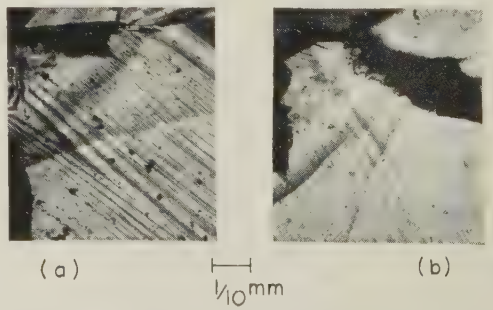

Fig. 3. (*a*) top and (*b*) bottom views at 3°C.

---

* Now at Electrical Communication Laboratory, Musashino, Tokyo.

to Messrs. E. Sawaguchi, A. Nishioka and T. Sakudo for the preparation of the crystals. This work was supported in part by a Grant in Aid for the Fundamental Scientific Research from the Ministry of Education.

References

1) See, for example: G. Shirane, F. Jona and R. Pepinsky, Proc. I. R. E. **43** (1955) 1738.
2) P. W. Forsbergh: Jr., Phys. Rev. **76** (1949) 1187.

J. Phys. Soc. Japan **12** (1957) 837

Paramagnetic Resonance of Silicocarbon

By Yoshikazu Sugiura and George Mitio Hatoyama

Electrotechnical Laboratory, Tokyo

(Received June 8, 1957)

When silicone resins are heated in vacuum to over 900°C, they become semiconductors[1]. We call them silicocarbon. The conductivity seems to arise from the carbon atoms present in the resin. Actually, resins with higher carbon content show conductivity at lower treatment temperatures.

At moderate treatment temperatures, hydrogen will come out of the resin leaving broken bonds in the carbon atoms. At higher temperatures, the carbon atoms will be rearranged so that the wave functions for these broken bonds may overlap. Such phenomena might be observed by resonance absorption experiments.

Dow Corning Silicone No. 2104 was used as samples. This material contains roughly 4 carbon atoms per one silicon atom. The resin was treated at temperatures between 600 and 1000°C and the microwave resonance absorption was observed at 1.25 cm. The number of unpaired electrons as a function of the treatment temperature is plotted as Curve A, Fig. 1. Probable errors in relative values are shown in the figure by bars. The number is deduced from the area of the absorption curve compared with that for $ZnAl_2O_4$ with a known amount of Mn^{++}. The absolute number may be in error by a factor of less than 2. Specific resistivity of the samples at room temperature is also shown in the figure as Curve C. It can be seen that the number of unpaired electrons first increases with the treatment temperature and then decreases at temperature range where the conduction becomes appreciable. The general feature is similar to those obtained by Ingram and others[2)3)] with carbohydrates.

The width between the maximum slope of the absorption is plotted as Curve B in the figure. It is seen that the width decreases suddenly as the number of unpaired electrons approaches its maximum. This is also similar to the results obtained by Combrisson and Uebersfeld[3)] with carbohydrates, and hence it seems that the exchange narrowing is happening.

The g-value was measered in reference with DPPH, giving a value 2.0027 ± 0.0005 for a sample treated at 1100°C. No appreciable change in g-value with the treatment temperature was observed.

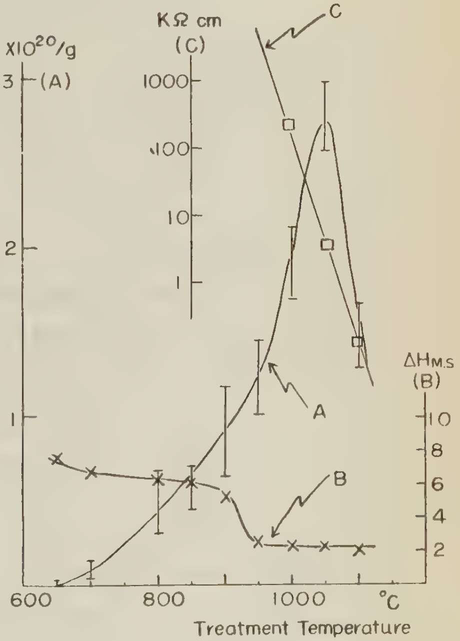

Fig. 1.

References

1) G. M. Hatoyama, W. Sasaki and Z. Ishii, J. Phys. Soc. Japan **8** (1953), 134.
2) D. J. E. Ingram and J. E. Bennett, Phil. Mag. **45** (1954) 545; D. J. E. Ingram, J. G. Tapley, R. Jackson, R. L. Bond and A. R. Murnaghan, Nature **174** (1954) 797; D. J. E. Ingram, Discuss. Farady Soc. **19** (1955) 179.
3) J. Combrisson and J. Uebersfeld, Discuss. Faraday Soc. **19** (1955) 181; J. Physique **16** (1955) 340.

Errata

Crystal Structure and Phase Transition of Some Metallic Halides (IV) On the Anomalous Structure of α-AgI

By Sadao HOSHINO

J. Phys. Soc. Japan **12** (1957) 315.

P. 318 right column line 25 ....the following fourty sites
should be read ....the following forty-two sites

P. 319 Eq. (1) $|\overline{F}^2|$ should be read $|\overline{F}|^2$

P. 322 Eq. (10) second line $+\sum_{s(d)}\sum_{s'}{}'(\alpha-\beta)_{r_{s,\,s'}}\exp[\cdots\cdot$
should be read $+\sum_{s(d)}\sum_{s'}{}'(\alpha-\beta)_{r_{s(d),\,s'}}\exp[\cdots\cdot$

Cross Section for Displacement of Atoms by Heavy Particle Irradiation

By Takeshi MORIMOTO

J. Phys. Soc. Japan **12** (1957) 442.

Eq. (3) $$\Delta P=\frac{2Zze^2}{V(a_1{}^2-a_2{}^2)}\left\{\frac{a_1{}^2}{a_2}K_1(b/a_2)-\frac{a_1{}^2}{a^2}K_1(b/a_1)\right\}$$

should be read

$$\Delta P=\frac{2Zze^2}{V(a_1{}^2-a_2{}^2)}\left\{\frac{a_1{}^2}{a_2}K_1(b/a_2)-\frac{a_2{}^2}{a_1}K_1(b/a_1)\right\}$$

PROGRESS OF THEORETICAL PHYSICS

(*Founded by H. Yukawa in 1946*)

Published for the
Research Institute for Fundamental Physics
The Physical Society of Japan

Progress of Theoretical Physics Vol. 16, No. 5, November 1956

On a Solution of Field Equations in Einstein's Unified Field Theory, I .... N. N. GHOSH..421

Deuteron Stripping and the Compound Nucleus ....Masayuki NAGASAKI..429

Theory of Bose-Einstein Condensation of an Imperfect Bose-Einstein Gas...... ....T. MATSUBARA, A. MORITA and N. HONDA..447

Two-Nucleon Problem with Pion Theoretical Potential, I—*Determination of Coupling Constant and Deuteron Problem*— ....J. IWADARE, S. OTSUKI, R. TAMAGAKI and W. WATARI..455

Two-Nucleon Problem with Pion Theoretical Potential, II—*Singlet Even State*— ....J. IWADARE, S. OTSUKI, R. TAMAGAKI and W. WATARI..472

The Creation of an Electron Pair by a Fast Charged Particle .... T. MUROTA, A. UEDA and H. TANAKA..482

On the Foundation and the Applicability of Williams-Weizsäcker Method..... ....T. MUROTA and A. UEDA..497

Helium Capturing Reactions in Stars ....S. HAYAKAWA, C. HAYASHI, M. IMOTO and K. KIKUCHI..507

Letters to the Editor:

Charge Independence Hypothesis and Leptons ....T. OUCHI and K. SENBA..528

Integral over Path Formulation of Statistical Theory of Irreversible Processes ....D. FALKOFF..530

On the Bethe-Salpeter Equation for the Salpeter-Spinor Particle System .... R. SUGANO and Y. MUNAKATA..532

Constraint in a Quantum System ....Y. WATANABE..534

Progress of Theoretical Physics Vol. 16, No. 6, December 1956

On an Extended Framework for the Description of Elementary Particles...... ....M. IKEDA and Y. MIYACHI..537

Meson-Nucleon Scattering in Low Energy Region ....D. ITO and S. MINAMI..548

Quantum Field Theory of the Interaction between the Graviton and the Matter Field, II—*Formulation without the Coordinate Condition*— .... Toshiei KIMURA..555

A Lattice Model of Liquid Helium, I ....T. MATSUBARA and H. MATSUDA..569

Some Consequences of the Compound Hypothesis for Elementary Particles ....Ken-iti MATSUMOTO..583

On the Bose-Einstein Condensation...........................Shigetoshi KATSURA..589

Two-Nucleon Problem with Pion Theoretical Potential, III—*p-p Scattering at 18.2 Mev*—........J. IWADARE, S. OTSUKI, R. TAMAGAKI and W. WATARI..604

Formation of Light Nuclei in the Expanding Universe ....C. HAYASHI and M. NISHIDA..613

The Composite Model for New Unstable Particles, I ....Sho TANAKA..625

The Composite Model for New Unstable Particles, II.................Sho TANAKA..631
Nuclear Magnetic Relaxation in Antiferromagnetics, II ....Toru MORIYA..641
Two-Nucleon Problem with Pion Theoretical Potential. IV—*Photodisintegration of Deuteron at 20 Mev*— ....J. IWADARE, S. OTSUKI, M. SANO, S. TAKAGI and W. WATARI..658
On a Theory of the Composite Model of Elementary Particles ....Ziro MAKI..667

Letters to the Editor:

A New Formation on the Electromagnetic Field.............T. OHMURA..684
Stability of the Electron ....T. OHMURA..685
On a Composite Model for the New Particles ....S. SAKATA..686
Special Theory of Relativity and the Structure of Elementary Particles ....H. YUKAWA..688
Contents and Authors Index to Volume 16 ....i~vi

---

Progress of Theoretical Physics Vol. 17, No. 1, January 1957

Coulomb Interactions and the Diamagnetism of Free Electrons, II ....Hideo KANAZAWA.. 1
The Functional Integrals in Quantum Theory ....T. KANKI, K. MURATA and S. SUNAKAWA.. 7
A Lattice Model of Liquid Helium, II ....H. MATSUDA and T. MATSUBARA.. 19
A Method of Renormalization for Unstable Particles....T. OKABAYASHI and S.SATO.. 30
Relation between the Nuclear Collective Model and the Individual Particle Model with Configurational Mixing......S. HAYAKAWA and T. MARUMORI.. 43
On the Bethe-Salpeter Equation and the Excited States of the Hydrogen Atom ....H. KITA and M. WAKANO.. 63
Electromagnetic Properties of Deuteron, II.......................Kiyomi ITABASHI.. 80
On the Spins and Decay Interactions of K$_{\mu3}$ and K$_{e3}$ ....S. FURUICHI, T. KODAMA, S. OGAWA, Y. SUGAHARA, A. WAKASA and M. YONEZAWA.. 89
On the Universality of the Weak Interactions ....Suteo GOTÔ..107

Letters to the Editor:

Elastic Scattering of 24.6 Mev Alpha Particles by Au ....S. IGARASI and T. TAKANO..124
On the Effective Normal Fluid Density of Solution of He^3 in He^4 ....S. K. TRIKHA and V. S. NANDA..126
Errata 129

Price $ 1.25 per copy
$ 15.00 per year (postage inclusive)
Annual dues for foreign members (individual subscribers)
$ 12.00 (postage inclusive)
〃 for foreign members of the Physical Society of Japan
$ 10.00 (postage inclusive)

Application for members, subscriptions and orders for back numbers should be sent, directly or through book-dealers, to

The Publication Office

in

Yukawa Hall, Kyoto University, Kyoto, Japan

JOURNAL OF THE PHYSICAL SOCIETY OF JAPAN Vol. 12, No. 8, AUGUST, 1957

On the Neutrons from the N^{14} (d, n) O^{15} Reaction-II

By Itaru NONAKA*, Susumu MORITA, Nawoyuki KAWAI,
Toshiyuki ISHIMATSU, Kenji TAKESHITA,
Yutaka NAKAJIMA and Nawoyuki TAKANO

Department of Physics, Faculty of Science, Kyushu University,
Fukuoka, Japan

(Received May 1, 1957)

The angular distribution of the neutrons from the $N^{14}(d, n)O^{15}$ reaction leading to O^{15} ground state was investigated in the angular range from 0 to 165 degrees (lab. system) by the photographic method. The energy of the bombarding deuterons was 1.96 MeV, and the Q-value was found to be $Q_0=(5.13\pm0.05)$ MeV.

The angular distribution shows a maximum at about 30 degrees (c. m. s.) and decreases considerably beyond this maximum, in accordance with what is characteristic to the stripping process corresponding to $l_p=1$. In the backward direction, the intensity of neutrons increases remarkably and reaches the value almost three times as large as that of the forward maximum. The absolute cross section of this reaction was estimated to be $\sigma(0°)=(2.4\pm0.7)$ mb/sterad. and $\sigma=(38\pm7)$ mb.

§ 1. Introduction

It is important to measure the angular distribution of particles emitted through the deuteron induced reaction in order to obtain the information concerning the mechanism of the nuclear reaction and the structure of nucleus. Many measarements of this sort have been performed so far on various nuclei and their theoretical interpretation have also been reported.

In our previous work[1], we measured the angular distribution of the neutron from the $N^{14}(d, n)$ O^{15} reaction leading to O^{15} ground state at angles ranging from 0 to 105 degrees (lab. system). The energy of bombarding deuterons was 1.85 MeV and the result was interpreted satisfactorily by Butler's theory. That is, the angular distribution had a maximum at about 20 degrees (c.m.s.), showing the contribution from the stripping process corresponding to $l_p=1$, in agreement with the results of other authors.

Most of the measurements of the neutron angular distributions in (d, n) reactions have so far been restricted to the relatively narrow angular ranges in the forward direction. The backward angular distribution, however, may be as useful as the forward in the analysis of nuclear reaction. Accordingly, we have tried to extend the measured angular range of our previous work on $N^{14}(d, n)O^{15}$ reaction to the more backward direction. In addition, the absolute value of the cross section of this reaction was estimated taking the ratio of the neutron yield of this reaction to that of the $D(d, n)$ reaction.

§ 2. Experimental Arrangements and Procedures

The experimental arrangements were similar to the previous ones except at a few points. As is shown in Fig. 1, the target chamber filled with nitrogen gas was made of glass cylinder of 3 cm in diameter and 4 cm in length and the bottom plate of silver of 1 mm thickness. The entrance to the chamber was of an aperture of 0.8 cm in diameter and sealed with a nickel foil of 1.6 mg/cm² thick. Any portion of the target chamber exposed to the direct deuteron beam was covered with silver plates to minimize the neutron background. The deuterium gas of 4.3 cm Hg in partial pressure was mixed to the nitrogen gas of 23.2 cm Hg in the target chamber, and the neutrons emitted from these two substances were detected simultaneously. Thus, it was possible to estimate the absolute cross section of the $N^{14}(d, n)O^{15}$ reaction comparing the neutron yield of this reaction with that of the D (d, n) He^3 reaction.[2] Commercial nitrogen gas was used as the target gas. The mass-spectrometric analysis* of the target showed traces of argon and oxygen besides nitrogen and deuterium,

---

* Now at the Institute for Nuclear Study, University of Tokyo.

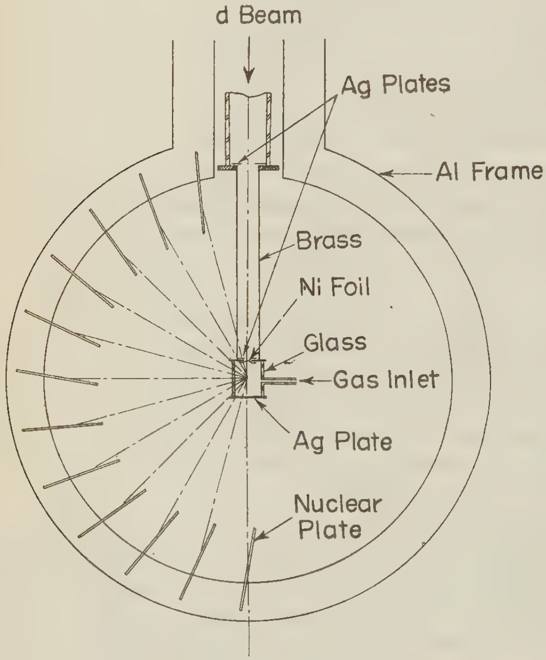

Fig. 1. Arrangements of the target chamber and photographic plates.

but these impurities would not affect the neutron spectrum.

Deuterons were accerelated to (2.31±0.01) MeV by means of the Van de Graaff accelerator at Kyushu University, whose voltage was calibrated with the resonances of F^{19} $(p, \alpha)\, O^{16**}\, (\gamma)\, O^{16}$ reaction. The mean energy of the beam in the target chamber was estimated to be 1.96 MeV, considering the energy loss of 190 keV in the nickel foil and that of 320 keV in target gas. These values of energy loss were caluculated from the data by Allison and Warshaw[3].

The slit system allows the whole deuteron beam to pass through the entrance aperture into the target chamber, so it was possible to use the target chamber as a collector cup for the deuteron beam, and the chamber was connected to a current integrator and microammeter in series. The intensity of the magnetically analyzed deuteron beam had been 1μA in average during the bombardment of about three hours. The background run, without the target gas, was carried out in such a way that the total integrated beam currents were equal to the true run.

Sakura NR-MI nuclear plates, 200 micron emulsion thickness, were used to detect the neutrons. The shrinkage factor of this emulsion was measured to be 2.0±0.1. Each plate was wrapped in a thin black paper after being covered with an aluminium foil. As is shown in Fig. 1, these plates were placed on an circular aluminium frame centered to the target chamber at intervals of 15 degrees in the angular range from 0 to 165 degrees with respect to the incident deuteron beam. The glancing angle of each plates was chosen to be 10 degrees.

The center of each scanned area was 3 cm distant from the inner edge of the plate and 19 cm from the center of the target chamber. The observed tracks were treated by the precedures described in the previous work. The range-energy relation for the NR-MI emulsion was determined with the energy of neutrons emitted from D (d, n) He^3 reaction and observed ranges in the emulsion of their recoil protons. As shown in Fig. 2, this rang-energy relation gives three percent smaller energy than that given by the previously calculated relation to the recoil

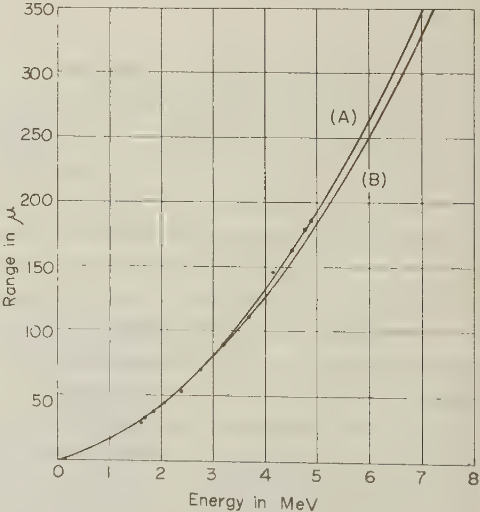

Fig. 2. Proton range-energy relation for Sakura NR-M1 emulsion. Curve (A) was determined with the energy of neutrons emitted from D (d, n) He reaction, and Curve (B) was calculated by Webb' method[1].

---

* This mass-spectrometric analysis was performed by Mr. M. Yokota. The authors wish to express their thanks to him for his kind assistance.

protons of the same range in the energy region up to 5 MeV.

When neutrons emerging from the target pass through the matter of the target chamber, some of the neutrons were scattered out of the neutron beam. As the thickness of the matter passed through by neutrons was different in each observing angle, the proportion of the lost neutrons was also different. The correction for these scattered out neutrons was also different. The correction for these scattered out neutrons were carried out as follows. The attenuation of neutron intensity in the materials which were present between the target and plates was estimated by considering their total cross sections for the neutron. The correction was found to become maximum at 165 degrees and amounted to 9 per cent for the D (d, n)-neutron and 10 per cent for the $N^{14}(d, n)$-neutron which leaves the residual nucleus in its ground state. These corrections, however, would be somewhat overestimated, because all the scattered neutrons were assumed to be lost entirely. But the errors introduced by this assumption would be negligible.

§ 3. Results and Discussions

Some of the typical energy spectra of neutrons are shown in Fig. 3, (A), (B) and (C), which were obtained at angles of 15, 90 and 165 degrees (lab. system), respectively. In each spectrum, the group of neutrons with higher energy are from the $N^{14}(d, n)O^{15}$ reactions leading to the ground state of O^{15} nucleus, and those with intermediate energy from $D(d, n)He^3$ reaction. Moreover, those with lower energy below 2 MeV consist of the neutrons emitted from the $C^{12}(d, n)N^{13}$ reactions due to carbon contamination and probably from the $N^{14}(d, n)O^{15}$ reaction leading to the first excited state of O^{15} nucleus.

The positions of the neutron groups from the $N^{14}(d, n)O^{15}$ reactions leading to the ground state in O^{15} nucleus, gave the Q-value of this reaction of $Q_0 = (5.13 \pm 0.05)$ MeV. The discrepancy between this value and our previous one (5.21±0.07) MeV is attributed to the different range-energy relations used.

In order to estimate the intensity of the neutrons of higher energy group from the $N^{14}(d, n)O^{15}$ reaction, the slope of the lower energy side of the spectrum was extrapolated to zero intensity and this extrapolated energy was assumed to be the lower end of this group. For examples, these values were found to be 5.60, 5.10 and 4.70 MeV as are shown by arrows in Fig. 3 (A), (B) and (C) respectively. It was found that in almost all spectra these energy values were smaller than those corresponding to the peaks by the amount of 20 per cent of the latter. The same procedures were also applied to the neutrons from the D (d, n) reaction. As is shown in Fig. 3, however, a part of the neutron spectrum from the D (d, n) reaction overlapped with that from the $N^{14}(d, n)$ reaction at smaller angles, and with that due to the carbon contamination at larger angles. The corrections for these overlappings of the groups were estimated simply assuming that

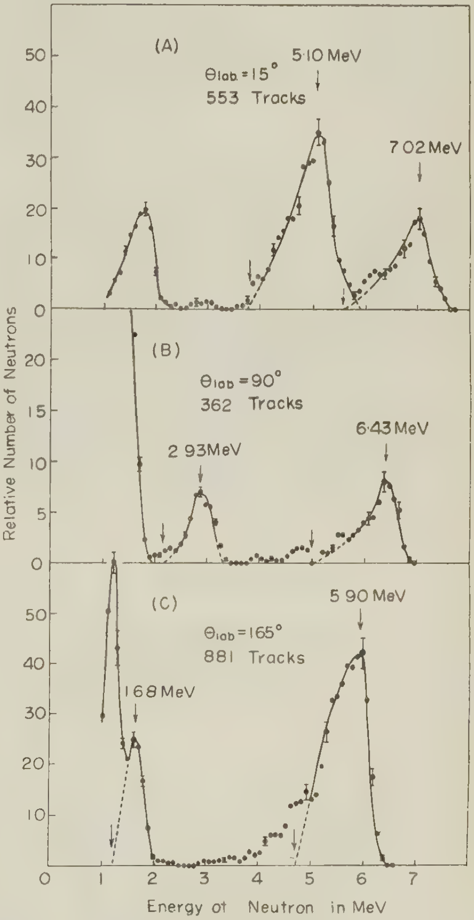

Fig. 3. Energy spectra of neutrons for $E_d = 1.96$ MeV, obtained by eliminating the background. (A), (B) and (C) were obtained at angles of 15, 90 and 165 degrees (lab. system), respectively.

all the neutron groups concerned have the same shapes irrespective of their positions and reactions they refer to. For instance, this correction for the intensity of the neutrons emitted at 15 degrees from D(d, n) reaction amounts to 7 per cent (see Fig. 3 (A)).

The angular distribution of neutrons was obtained from the intensity thus determined at each angle. The angular distribution of neutrons from the D(d, n)He^3 reaction is shown in Fig. 4, where indicated errors are the statistical ones. As is expected from kinematics, it is almost symmetrical about a plane perpendicular to the direction of the incident beam in the center-of-mass system. But the yield of neutrons in the backward directions seems to be some what smaller than that in the forward directions. The origin of this deviation cannot be attributed to the misalignment of experimental arrangement. For this deviation from the symmetry about 90 degrees, the following interpretations would be possible. Firstly, some of deuterium gas in the target chamber may have been absorbed onto the silver plate at the bottom of the chamber, and the neutrons from this deuterium contamination may have been detected in addition to that due to the target gas. Secondly, at the backward directions, the resolution between two groups referred to the D(d, n) and C$^{12}(d, n)$ reactions is very poor, as can be seen in Fig. 3 (C). Then the systematic errors may have been introduced into the estimation of the intensities of neutrons emitted in the D(d, n) reaction at the larger angles. In Fig. 4, the measure of ordinate was determined by comparing the observed intensities of neutrons at three forward angles to the known values of the differential cross section.

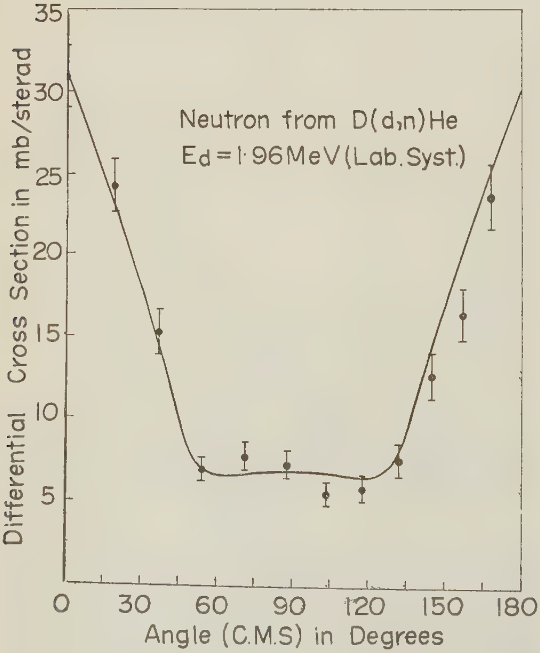

Fig. 4. Angular distribution of neutrons from D(d, n)He^3 reaction for $E_d=1.96$ MeV.

The angular distribution of neutrons from the N$^{14}(d, n)$O^{15} reaction leading to the ground state in O^{15} nucleus is shown in Fig. 5 where the indicated errors are the statistical ones. The forward distribution having a peak at about 30 degrees can be well fitted to the stripping theory using Bhatia's curve with $R=7.0\times10^{-13}$ cm and $l_p=1$. The absolute values of the differential and total cross sections of the N$^{14}(d, n)$O^{15} reaction leading to the ground state in O^{15} nucleus are evaluated from the mixing ratio of nitrogen and

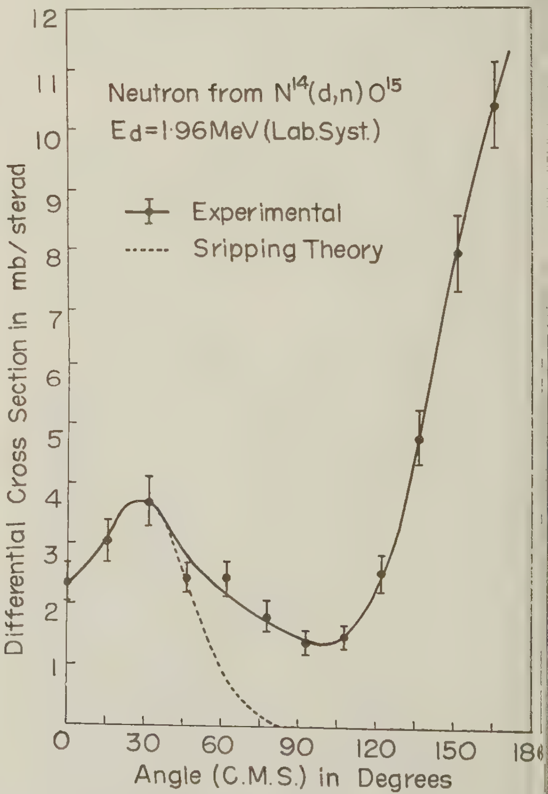

Fig. 5. Angular distribution of neutrons from N$^{14}(d, n)$O^{15} reaction leading to the ground state in O^{15} nucleus, for $E_d=1.96$ MeV. The dotted curve shows the Bhatia's curve with $R=7.0$ $\times10^{-13}$ cm and $l_p=1$.

deuterium gases, referring to the known value of cross section of the D(d, n)He^3 reaction, and found to be $\sigma(0^0)=(2.4\pm0.7)$ mb/sterad. and $\sigma=(38\pm7)$ mb, respectively. The measure of ordinate in Fig. 5, thus determined, is expected to have an uncertainty of 20 per cent. The unexpected behavior of the angular distribution is the large increase in the backward direction and the intensity of neutrons at 165 degrees comes up to almost three times as large as that of the forward maximum at 30 degrees. It is suspected that the considerable part of the reactions induced by deuterons of 1.96 MeV would be due to the process of compound nucleus formation. And the interference between the compound nucleus formation and the stripping processes may contribute appreciably. In conclusion, it seems interesting to investigate the angular distribution of neutrons at various energies of the bombarding deuterons, and also it would be much useful for the theoretical interpretation to know the variance of angular distribution with the bombarding energy.

The authors with to express their cordial thanks to Mr. Y. Wakabayashi of the Chemical Research Laboratory of Konishi-Roku Photographic Industry for his kind preparation of nuclear plates. Thanks are also due to Miss Hirakura and Miss J. Yoshida for their skilful scanning of the nuclear plates. This work has been supported by the Scientific Research Expenditure of the Ministry of Education.

References

1) I. Nonaka, S. Morita, N. Kawai, T. Ishimatsu, S. Suematsu, K. Takeshita, Y. Nakajima and Y. Wakuda: Jour. Phys. Soc. Japan **11** (1956) 1.
2) J. L. Fowler and J. E. Brolley Jr.: Rev. Mod. Phys. **28** (1956) 103.
3) S. K. Allison and S. D. Warshaw: Rev. Mod. Phys. **25** (1953) 779.
4) A. B. Bhatia, K. Huang, R. Huby and H. C. Newns: Phil. Mag. **43** (1952) 485.

JOURNAL OF THE PHYSICAL SOCIETY OF JAPAN Vol. 12, No. 8, AUGUST, 1957

Cosmic Ray Nuclear Interactions in Nitrogen Gas

By Saburo MIYAKE, Kensaku HINOTANI,
Itsuo KATSUMATA and Tatsunosuke KANEKO
Institute of Polytechnics, Osaka City University, Osaka

(Received February 26, 1957)

The natural rate of occurence of nuclear interactions of cosmic ray N-component in which more than 5 Mev are given to charged secondary particles have been measured in the nitrogen filled high pressure cloud chamber at Mt. Norikura (2840 m above sea level and 25°N geomagnetic latitude). From the rate of occurence of number interactions, the vertical intensity of N-component was estimated at $(2.4\pm40\%)\cdot10^{-3}\cdot E^{-1.4}\mathrm{cm}^{-2}\mathrm{s}^{-1}$ $\mathrm{sr}^{-1}\mathrm{Mev}^{-1}$ for the energy range from 10 Mev to 100 Mev by assuming the geometrical cross section. These events may be considered to be the source of the cosmic ray N-component with an energy less than that sufficient to produce nuclear interactions in the atmosphere, and it was shown that the spectrum of secondary particles was in accord with that of the latter. The absolute intensity of N-component was also consistent with that expected from the data of other energy regions in our previous paper. A possible scheme of the nuclear cascade was discussed in relation to the size distribution of the observed stars.

§ 1. Introduction

In this paper an experiment of the nuclear interactions in nitrogen gas is described and the intensity of cosmic ray N-component in the atmosphere is also estimated, assuming the geometrical cross section.

In the previous paper[1)], the energy spectrum of cosmic ray neutrons of energy range from 1 ev to 10 Gev and the general aspects of nuclear cascade in atmosphere have been discussed. However, a greater part of the spectral curve still remains unmeasured. Nuclear interactions with light nuclei such as nitrogen have not been studied to enable the understanding of the process of nuclear cascade in cosmic ray phenomena. The present paper will show one of the examples of experimental analysis for such problems.

The experimental method employed is to observe the cosmic ray nuclear interactions in a randomly operated high pressure cloud chamber filled with nitrogen gas.

The comparison of stars in ordinary emulsion with those occuring in nitrogen gas may allow an unambiguous interpretation of each observed events, namely, the observed events in emulsion can be extraporated to low energy events and discussed for light and heavy nuclear elements separately, using the data presented in this paper. In the case of emulsion, low energy events may be overlooked, because of the insufficient scanning efficiency.

Because photographic emulsions consist of a variety of elements, it is often impossible to ascribe with certainty an individual event observed in the ordinary emulsion to the disintegration of the nucleus of a particular element. The knowledge of the star characteristics, which vary with the atomic number of the nucleus and the energy of the incident particles, is also of importance in the interpretation of the existing data on stars in emulsions, as well as in understanding the nuclear interaction processes themselves.

§ 2. Experimental Procedure

The high pressure cloud chamber[2)] (50 cm in dia and 20 cm in depth) filled with nitrogen gas up to 55 atm was used. Usually this chamber is used at 100–150 atm but for the present purpose the pressure was decreased to be able to observe low energy secondaries. At this decreased pressure the range of proton of 5 Mev was about 5 mm. The experimental arrangement and procedure are the same with those as described in the previous paper, except the pressure and the gas of the chamber. The stopping power is shown in Fig. 1. The sensitive volume and the sensitive time were determined to be 12.5 liters and 5.2 sec, respectively by similar methods described in the previous paper.

To correct the effect of the surrounding materials, twice the geometrical mean free path was used as the absorption mean free

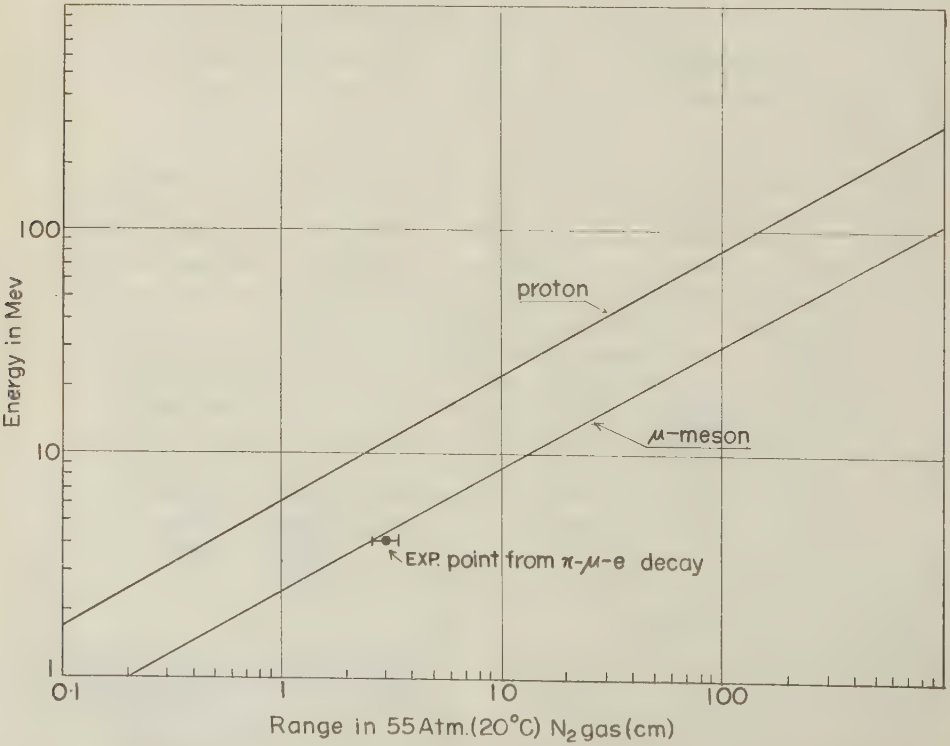

Fig. 1. Range-Energy relations for proton and μ meson in 55 atm (20°C) nitrogen gas.

path for the star producing component. The frequency of one prong stars which have long secondary tracks was corrected for the geometry of the instrument. All these corrections are also similar to those in the previous paper.

The purity of the nitrogen gas was 99.5% and the events by impurity nuclei such as alcohol vapor are negligible. The total sensitive time in this case is given by the product of the chamber sensitive time and the number of photographs taken. The chamber sensitive time is estimated from the width distribution of tracks using the diffusion constant of ions in nitrogen gas.

The observation covered by the total sensitive time may be considered to be equivalent to that of all cosmic ray nuclear events in the atmospheric air of about 690 liters at the mountain altitude during about 1.2 hours.

§ 3. Experimental Results

Throughout the experiment, 805 cloud chamber photographs were taken and 560 nuclear interactions in total were observed. The events which have at least one charged secondary particles and the particles have energies greater than 5 Mev were taken as the nuclear interactions. In Table I the results are listed according to the total number of charged particles observed in each interaction, whether they are primary or secondary. All tracks longer than 5 mm were counted, because of the unclear direction and of the insufficient detection efficiency for shorter ones. Under these conditions the protons with an energy less than 5 Mev and the alpha particles less than 20 Mev are likely to be missed, but the number of such prongs can be estimated from the energy distribution of secondaries, as described in later section. The effects due to radioactive contaminations can be excluded, because of the shorter track of only about 1 mm.

Fig. 2 shows some of the photographic records of the nuclear interactions occuring in the gas of the cloud chamber.

The integral rate of occurence of all nuclear interactions in the gas at 2840 m elevation and 25°N geomagnetic latitude, computed from the corrected data of Table I, was $1.78\cdot10^{-4}g^{-1}s^{-1}$.

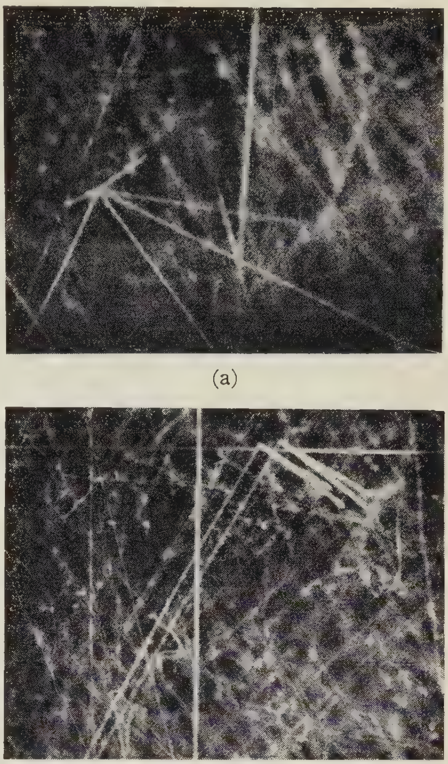
(a)

(b)

Fig. 2. a) An interaction of a neutral particle with a nitrogen nucleus in which seven charged secondaries are produced.

b) Three charged secondary particles are produced and separated track by sweeping electric field are seen.

1) *Size distribution*

The differential star size distribution corrected is shown in Fig. 3 where the rate of stars with m prongs observed per target nucleus is plotted semi-logarithmically against

Table I. Frequencies of events for each group, classified according to prong number and charged or neutral primaries. The corrected number for 1-prong stars are indicated in parenthesis.

Prong No.	1	2	3	4	5	6	7	8	total
Neutral primaries	332 (362)	126	42	17	8	1	1	1	528 (558)
Charged primaries	8	19	4	1	0	0	0	0	32
Total*	332 (362)	134	61	21	9	1	1	1	560 (590)

* In the third row, the total number of events in which the all charged particles are counted as secondaries regardless of characteristics of the prongs are indicated.

m. Statistical probable errors are indicated in the graph, as well as limits for the best straight line fit from which were found constant of a distribution of the form

$$M(m)=M_0\exp(-\alpha m) \qquad (1)$$

where α is 0.85 ± 0.12. Since the target nuclei are of single element, the distribution should be explained by the energy spectrum of the primaries and the character of the nuclear disintegration.

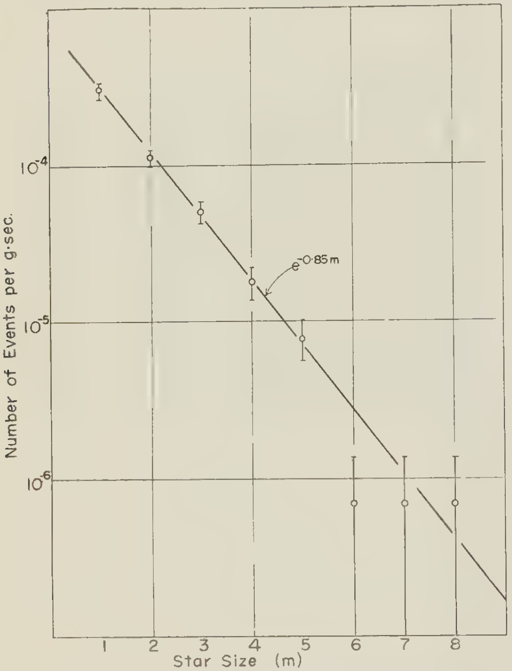

Fig. 3. Differential star size distribution: number of events per g. sec. plotted against star size.

The real size distribution can be computed as follows: The probability of the observation that n prong stars were observed as m prong stars is

$$P(n,m)=\frac{n!}{m!(n-m)!}p^m(1-p)^{n-m} \qquad (2)$$

where p is the probability that the length of each prong is longer than 2 mm. (As above mentioned, single tracks shorter than 5 mm were not counted, but the tracks longer than 2 mm in the multi-prong stars could be clearly distinguished.) If the real size distribution is expressed by the form of

$$N(n)=N_0\exp(-\lambda n) \qquad (3)$$

where λ is a constant. The observed size distribution, $M(m)$, is related to the real size distribution, $N(n)$, by the following equation:

$$M(m)=\sum_n P(n,m)N(n) \qquad (4)$$

From Eq. (1), (2) and (3), one can show easily following relations:

$$\lambda=\ln(pe^{\alpha}+(1-p)) \qquad (5)$$

$$N_0=(M_0\alpha/\lambda)(1-(1-p)e^{-\lambda}) \qquad (6)$$

where p is found to be about 0.9 by the estimation of number of undetected particles from energy distribution assuming that the distribution is expressed in the form of $(E-V)/T^2\exp-(E-V)/T$ even in the low energy region. From Eq. (5) one can show approximately $\lambda=\alpha p$. Then, the real size distribution is

$$N(n)=N_0\exp(-0.76\,n)\,. \qquad (7)$$

The similar star size distribution for light nuclei has been obtained from the data of photographic emulsion excluding the contribution of stars of heavy nuclei. In this case, α is about 0.6 at mountain altitude and about 0.4 at balloon height. These data are plotted in Fig. 10.

In the case of emulsion, in which 1 and 2 prong stars are not recorded, the frequency of the stars with 3 and 4 prongs are somewhat lower than those expected from the exponential relation Eq. (1), which was derived from the star frequencies of prong number larger than 4. This is probably due to the insufficient scanning efficiency for small size stars. The determination of the constant α in Eq. (1) is not so accurate for light nuclei in emulsion, but it does not contradict the present data.

There are small periodic increase of frequencies, in the present data, at 1, 3 and 5 prongs as compared with those at 2, 4 and 6 (the mean value of the increase is about 15%). This may be explained by the stability of the residual nuclei, namely, the nuclei with even atomic number are more stable than those with odd atomic number. But the quantitative explanation based on the shell model of light nucleus is difficult.

2) *Angular distribution*

The zenith angles of the trajectories of the charged particles involved in each nuclear interaction occuring in the gas were measured as follows. The cloud chamber photographs were projected onto a screen as the images have real size at the center of the cloud chamber and we get the angles from stereoscopic analysis of two photographs.

Fig. 4 shows the zenith angle distributions in which the distributions of tracks having ionization less than about twice minimum (lightly ionizing particles), medium ionization and those greater than about several times of the minimum (heavily ionizing particles) have been plotted separately. Since the direction of motion of the more lightly ionizing particles, some of which may be initiating particles, could not be determined, they were regarded, for the purpose of above measurement, as emanating from the points of origin of the nuclear interactions.

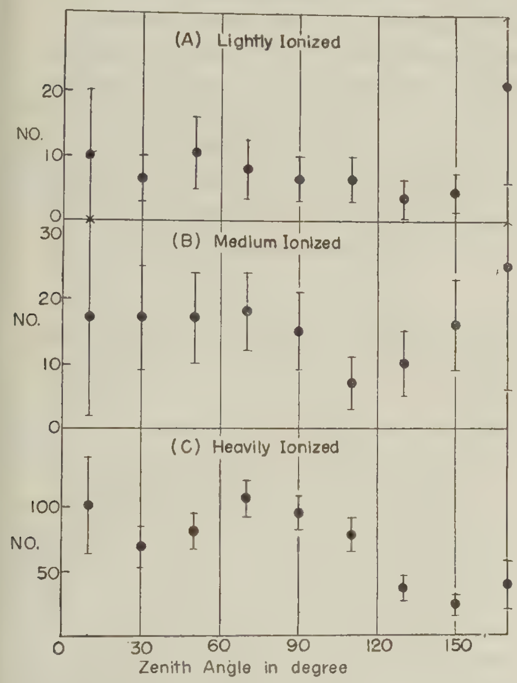

Fig. 4. Zenith angle distributions (A) Lightly ionized particles (B) Medium ionized particles (C) Heavily ionized particles

The heavily ionizing particles show a preference for the downward (zenith angles less than 90°) over the upward hemisphere and the lightly ionizing particles show more sharp downward pattern.

For the events with only one charged particle of range longer than 5 mm, whose both ends can be observed in the gas, the angular distribution is shown in Fig. 5 apart the other events. Since the most of their ends cannot be distinguished whether they were starting points or terminating ones, the zenith angles are obtained by assuming that the all tracks have downward direction (less than 90°).

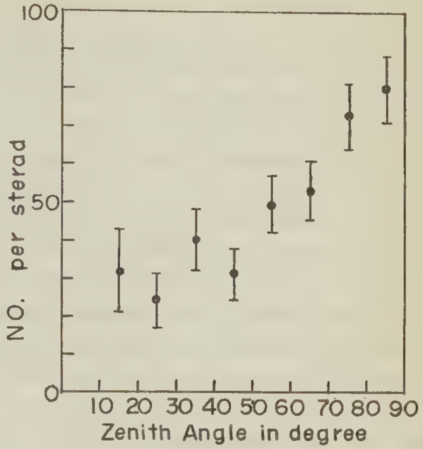

Fig. 5. Zenith angle distribution for one prong stars.

In the each angular distribution of the 1 and 2 prong stars, a maximum can be seen at about 80°−90°. It may be explained as follows. The perpendicular direction to the chamber axis favors the incident particles due to the minimum thickness of surrounding material of the chamber which they have to pass. And the secondary particles are inclined to be emitted in somewhat large angle to the incident particles by the Pauli's exclusion principle in Fermi's gas model of nucleus. Because the spirit of the model, representing all nucleons are free, clearly requires that the momentum of the two collision partners after the collision lie in an unoccupied region of the momentum space and so evidently a small momentum transfer to the struck nucleon is forbidden unless the nucleon initially lies very near the edge of the sphere in momentum space of radius P_F (Fermi momentum). This tendency is also in azimuthal angle distribution, namely, the secondaries are dominant in forward and backward direction of the chamber.

For the stars with more than 3 prongs, the angular distribution of black tracks show a preference for the downward over the upward hemisphere. It may be explained as follows. As the mean energy of the incident particles is thought to be greater than that of 1 and 2 prong stars, the directions which the direct knock-on secondaries are emitted are advantageous to the direction of incident particles. Slow particles may also posess such tendency by the Doppler effect of the bomberded and moving target nucleus.

In Fig. 5, some of the particles which show upward direction may be incident charged primaries. In the observed energy region, the intensity of the incident proton is so small and the obtained data are also so insufficient that the intensity of the proton cannot be discussed. Even in the energy range of emulsion stars (200 Mev to 1000 Mev), the intensity is only one fourth of neutrons.

3) *Energy distribution of secondary particles*

From the emulsion work, among the secondary charged particles there are protons, alpha particles and a group of deuterons and tritons with the proportions of 4, 2 and 1 respectively[4]. In this experiment the tracks were not distinguished whether they were protons or other particles, but the contribution of α particles to the total number of secondaries is not expected to be so large. Because most of the recorded tracks are longer than 5 mm and the lowest energy is about 20 Mev for α particles.

Assuming that the secondary charged particles are protons only, the energy distribution of the secondaries is obtained from the range of the tracks. The distribution is shown in Fig. 6 for the each group of prong number normalizing as area enclosed by the curve is equal to each other. It seems that the energy distributions have similar character.

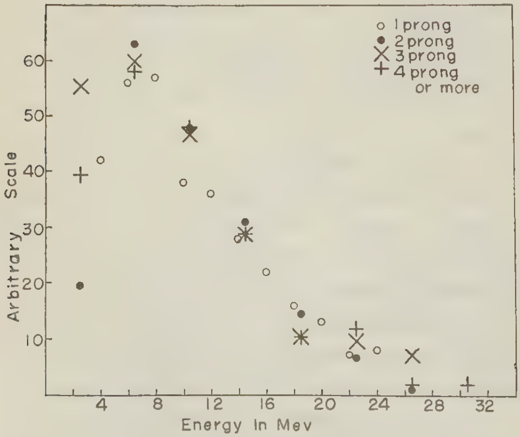

Fig. 6. Energy distribution for the each group of prong number normalizing as total number is equal.

Fig. 7 shows the approximate expression of the energy distribution in the form of $(E-V)/T^2 \exp(-(E-V)/T)$ where V is a Coulomb potential barrier of the nitrogen nucleus and T is a mean temperature of compound nucleus. This is well known expression as the spectrum of protons evaporated from the compound nucleus of the heavy element. The fundamental idea of the above expression may not be applied to the light nuclei as nitrogen, but it shows good approximation for the energy spectrum of secondaries of the stars of the light element. The mean temperature obtained from the gradient of the

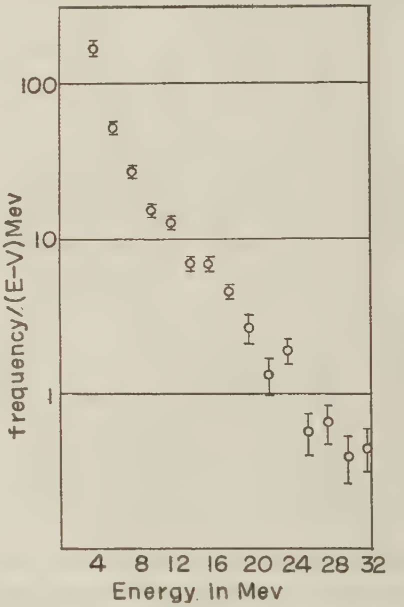

Fig. 7. Energy distribution expressed in the form of $(E\text{-}V)/T^2 \exp(-(E\text{-}V)/T.)$

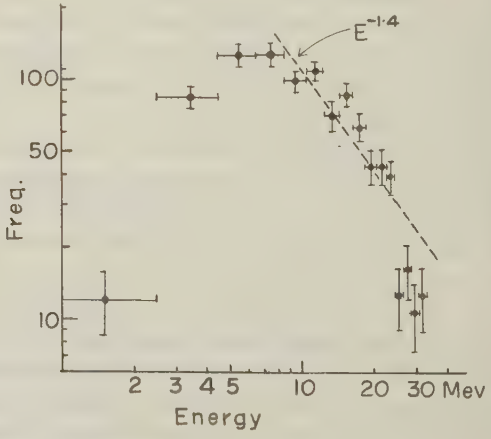

Fig. 8. Corrected differential energy spectrum of charged secondaries.

curve in Fig. 7 in the energy region from 5 to 10 Mev is about 2.7 Mev and is in accord with that obtained from the energy distribution of cosmic ray neutrons of such energy region[1)].

Fig. 8 shows the differential energy spectrum of the charged secondaries in logarithmic scale. The straight lines drawn through the points indicate that it is reasonable to represent the data over limited energy regions by the formula $F(E)=\text{const.}\,E^{-m}$ where m is 1.4 in this experiment. This is qualitative agreement with the results of emulsion work in which the distribution of the secondary protons are expressed as $k/(E+50)^2$ in the energy range from 50 to 1000 Mev.

4) *Energy distribution of primary particles*

The energy distribution of the primary particles, which initiating the nuclear interactions in the nitrogen gas, were obtained as follows. To estimate the absolute intensity of the star producing component, it is assumed that the cross section for nuclear interaction is geometric. The energy of the primary particle is obtained by the assumption that multiplicity and the energy distribution of the neutral secondaries are equal to those of the charged secondaries and each secondary particle is emitted independently. Finally, the energies for the thin, gray and black tracks which went out of the chamber are thought to be able to estimate from the energy spectrum of secondaries.

According to the above assumptions, the frequency of the stars which have n secondaries, including the neutral particles, is expressed approximately as follows:

$$K(n+1)\exp(-\alpha n)\Big(=\sum_{n_p+n_n=n} k\exp(-\alpha n_p)\exp(-\alpha n_n)\Big) \qquad (8)$$

In this expression, the factor $(n+1)$ is derived from the fact that the probability, that a event with n_p secondary protons and n_n secondary neutrons occures, is thought to be independent upon n_p and n_n. However, the probability has maximum value at $n_p=n_n$, because the residual nucleus is most stable at $n_p=n_n$, and the difference of the probabilities of occurence of $n-p$ and $n-n$ or $p-p$ interactions supports also such tendency in the process of the nuclear cascade. So, from the practical point of view the factor $(n+1)$ in Eq. (8) is thought to be too large. The energy spectrum of incident particles which produce the stars with n secondaries is thought to be equal to the visible energy spectrum dissipated for charged secondaries in each star which has equal number of prongs. The total energy dissipated for charged secondaries in each star is a sum of the following energies; the observed energies of black tracks which stopped in the chamber, the estimated energies of 70 and 350 Mev for gray-black and thin tracks, respectively, which went out of the chamber, and $n-1$ times the binding energy of nucleons in target nucleus. The variety of the estimated value does not give large change of the curve because it moves the curve to the direction of E^{-1} in the graph (45°).

In Fig. 9, the curves show the energy spectra of primaries for 1 prong stars, 2 prong stars, 3 prong stars and stars of more than 4 prongs and total sum of their intensities in the scale of $1/2\pi$ of total flux as they show the vertical intensities if their angular distributions are isotropic. Then the ratio of intensity to the estimated vertical flux which is described in the previous paper shows the angular distribution. If the ratio is m, the angular distribution of N-component at the

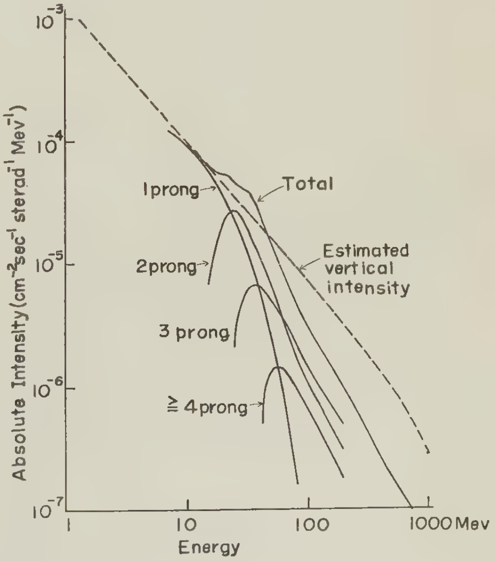

Fig. 9. Energy spectra of primary for 1 prong stars, 2 prong stars, 3 prong stars, stars of more than 4 prongs and total sum of their intensities in the scale of $1/2\pi$ of total flux. The dotted line indicates the energy spectrum of of cosmic ray neutrons given in reference 1).

energy region is thought to be $\cos^{m+1}\theta$. It is concluded from the figure that the angular distribution is isotropic at energy region lower than about 10 Mev and it changes to $\cos^5\theta$ according as the energy increases to 1 Gev.

There is no experiments to give the energy spectrum and absolute intensity of N-component in cosmic ray of these energy range. Then the present data were compared with another data of both side (higher and lower) of the energy range, and they agreed with each other within the limits of their errors, but at high energy region the accuracy of the present data is not good.

§ 4. Discussion and Conclusion

In this experiment, the tracks which displaced from the chamber wall to the illuminated region by the sweeping electric field are thought to be one of the stars occuring in the chamber wall. But such tracks have been probably counted as 1 prong stars. The ratio of such the tracks to the total 1 prong stars is estimated as below as 5%. In the case of 2 prong stars, the tracks which scattered by the nitrogen nucleus may be counted as 2 prong stars. The estimated number of such the events is below about 5% of 2 prong stars. These corrections have not so influence on the size distribution.

Brown[5)] finds for ion-cloud chamber stars, the size distribution varying uniformly down to the smallest stars, and also finds for stars of $n \geq 2$ a variation with atomic weight less rapid than $A^{2/3}$. The data differ from the present ones only in the part of smaller prongs than 3. The difference will be due to the bias of the selection in ion-cloud chamber. And the present result, though lightly ionizing particles are included in Table I, is also qualitatively in agreement with the conclusion from sandwich emulsion work[3)] that has analyzed nuclear interactions (stars) generated in the oxygen and smaller nuclei of the emulsion which have less than 6 heavily ionizing prongs.

In the observed events, various processes were mixing, namely, meson-producing collision and their secondary collision in the nucleus, a knock-on process or nuclear cascade in which particles of moderate energy are ejected, and a final process in which any particles, associated with these interaction, whose energies have degraded until they cannot escape from the nucleus, contribute to the excitation of the whole nucleus and its evaporation of low energy particles.

Insight into the operation of all above three types of interaction may be expected from investigation of how various characteristics of nuclear disintegrations depend on the primary energies.

Since we are dealing in the cosmic radiation with a particles whose De Broglie wave length is less than that of the nuclei involved, a semi-classical approach to the theoretical consideration of the origin of these fast protons can be expected to be fairly satisfactory.

In this approach, a high energy nucleon is considered as a particle which interact independently with a single nucleon in the nucleus having the same cross section as a free nucleon-nucleon interaction. Each particle from such a collision can in turn collide with other nucleon or escape from the nucleus. Then any nucleon has insufficient energy to escape, it is considered as contributing to the excitation of the whole nucleus and the subsequent evaporation.

Goldberger[6)] has calculated by the Monte Carlo method, effect of the exclusion principle for the nucleon-nucleon collision resulting when 90 Mev neutrons are incident on such a Fermi gas of nucleons and finds a reduction of the effective cross section in the ratio of 1 to $1-7E_f/5E_i$, where E_f is the Fermi energy and E_i is the energy of the incident neutron. A similar calculation was carried out at 400 Mev by Bernardini et al[7)]. The mean free path in the nuclear matter is a function of energy only, and is a constant of $4 \cdot 10^{-13}$ cm in the present energy region[8)].

About the nuclear cascade, in the energy region that is sufficient for growth of nuclear cascade and has not enough probability to produce the mesons, the number of secondary particles will be expressed as Furry function at first approximation.

If we take the mean free path of $4 \cdot 10^{-13}$ cm[8)] in nuclear matter, and treat as one dimentional problem in the average thickness of nucleus. It is sufficient in this discussion to assume that the nucleus is sphere, and average path length in nucleus is not much differ from average thickness of nucleus. The thickness is $0 \cdot 4 \cdot A^{1/3}$ in units of mean free path and the probability, $W(n)$, which a star has n secondary particles, is calculated as:

$$W(n)=k\exp(n\cdot\ln(1-e^{-0.4A^{1/3}})) \qquad (9)$$

Eq. (1) is compared with this expression and α is obtained as follows:

$$-\alpha=\ln(1-\exp(-0.4A^{1/3})) \qquad (10)$$

The data for size distribution obtained by sandwich emulsion technique at balloon height and other emulsion data are shown in Fig. 10 and the curve by Eq. (10) is also shown and best fit curve for the data of moutain altitude is calculated from the deformed Furry function considering the absorption of secondary particles in the nucleus. This result is as follows:

$$-\alpha=\ln(1-\exp(-aA^{1/3}))-\ln b \qquad (11)$$

where a is $0.4b$ and b is chosen as 1.2 to match the curve to experimental points of mountain altitude.

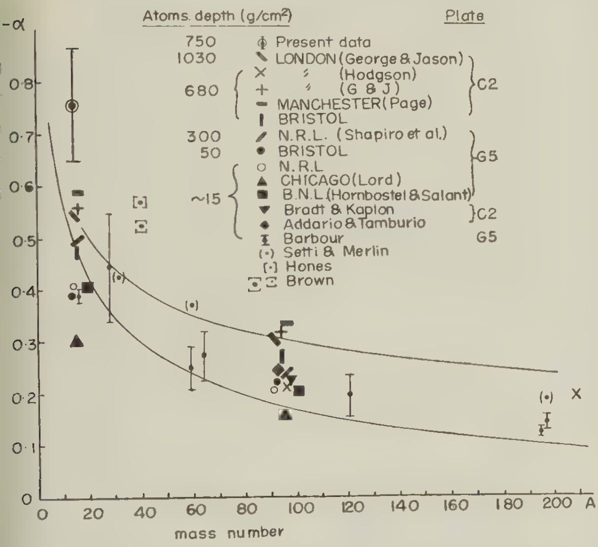

Fig. 10. Exponent, α, of size distribution is plotted as a function of mass number. The curves indicate the calculated value from Eq. (8) and (9). The experimental points except the present data are reproduced from reference 3).

In general, the effect of the difference in the incident energy spectrum at balloon and mountain altitude is clearly reflected in the graph. In other chamber experiment, in which the light nuclei are bomberded by 90 Mev neutrons, α was 1.2[9].

It is not strange that the calculated curve shows good approximation for the experimental points, because, since the gray-black track group includes protons of energies than 25 Mev it can contain relatively few evaporation particles. For light nuclei, however, the separation is not clear cut. The present data also show that the black track group has salient anisotropy of angular distribution and this fact indicate that the origin of the considerable parts of the group are not in an evaporation process but a knock-on process. Even in the evaporation prongs, their number will be proportional to excitation energy which is thought to be proportional to the frequency of inelastic collisions in the target nucleus. Then, it can be said that the size distribution is related mainly to a knock-on process.

Above explanation would in any case be dubious for nuclei as well as $A=14$, since no allowance is made for the alpha particle model or nucleon pair structure of the light elements or for the depletion of the nucleus during the cascade, which represents a significant change in the case of small nuclei. And the explanation is only qulitative one for the general stars which treated in Fig. 10.

In this experiment, the total interaction cross section is assumed to be geometric and it contradicts to the mean free path of $4\cdot10^{-13}$ cm in nuclear matter. This discrepancy means that there are many cases (about 30% of total) in which the incident particles pass through the nucleus with no interaction. It is also caused to crude approximation of the independent particle model which does not cover all interactions. Other model of interaction should be considered for low energy excitation of target nucleus, but detailed discussion is not reasonable from such crude conclusion in this paper which give us out-line of the interaction character.

The authors express their sincere thanks to Prof. Y. Watase for his continuous interest. This study has been supported in part by a Grant in Aid for Fundamental Scientific Research from the Ministry of Education and from Cosmic Ray Observatory of Tokyo University.

References

1) S. Miyake, K. Hinotani and K. Nunogaki: J. Phys. Soc. Japan **12** (1957) 113.

2) S. Miyake: J. Phys. Soc. Japan **11** 195 (1956)
3) I. G. Barbour: Phys. Rev. **93** (1954) 535.
4) U. Camerini, W. O. Lock and D. H. Perkins: "Progress in Cosmic Ray Physics" edited by J. G. Wilson North-Holland publishing co. Amsterdam (1952) P. 49.
5) W. W. Brown: Phys. Rev. **93** (1954) 528.
6) M. Goldberger: Phys. Rev. **74** (1948) 1268.
7) Bernardini, Booth and Lindenbaum: Phys Rev. **88** (1952) 1017.
8) S. Hayakawa, M. Kawai and K. Kikuchi Prog. Theor. Phys. **13** (1955) 415.
9) W. Horning: Phys. Rev. **75** (1949) 378.

JOURNAL OF THE PHYSICAL SOCIETY OF JAPAN Vol. 12, No. 8, AUGUST, 1957

On the Range Spectrum of μ-Mesons at Sea-Level at Geomagnetic Latitude 24°N

By Shūji FUKUI,
Department of Physics, Osaka University, Osaka
Takashi KITAMURA and Yōjirō MURATA
Institute of Polytechnics, Osaka City University, Osaka

(Received March 4, 1957)

Differential intensities of μ-mesons at sea-level at 24°N have been measured for the residual range equivalent to from 44 to 430 g/cm^2 of the air using a delayed coincidence method. It was found that the obtained range spectrum was nearly flat for present ranges and was 20 per cent lower than Rossi's curve which should be valid at geomagnetic latitude greater than 45°. The effect of the lateral displacement as well as the angular deflection of particles in the absorber was taken into account for the scattering correction. Mesons locally produced in the absorber was found to be at most a few per cent of all mesons that stop and decay in the apparatus. This fact suggests that the discrepancy between μ-meson spectra by the absorption method and by the magnetic cloud chamber method can not be accounted for only by the local π-meson production.

§1. Introduction

We have reported the differential momentum spectrum of μ-mesons at sea-level at geomagnetic latitude 24°N obtained by means of a magnetic cloud chamber in the preceding paper[1)] (hereafter referred to as *I*). The momentum spectrum of μ-mesons described in *I* showed some contradiction with what derived from the production spectrum theoretically obtained by Olbert[2)] in the low momentum part, and it appeared to disagree with the frequency of stopped μ-mesons in the emulsion at sea-level measured by Kaneko *et al*[3)]. It has been pointed out[4)] that, in general, all absorption methods give results somewhat higher than those obtained by magnetic cloud chamber methods. As a possible interpretation for this discrepancy, we have suggested in *I* the local π-meson production by the N-component in the thick absorber used in t absorption method.

In the present experiment, the intensities μ-mesons at sea-level have been measure over ranges 44 to 430 g/cm^2 air equivalent b the delayed coincidence method which is th most usable for identifying low energy mesons. At the same time, the contributio of locally produced π-mesons to μ-meso intensity has been examined with the hodoscope tray arranged under the absorber.

§2. Apparatus

The experimental arrangement is schematically shown in Fig. 1. GM counter trays and be define the incident beam. Each consist of 8 counters of 4 cm diameter and has th effective area of 33×44 cm^2. The distanc between them is 100 cm. The effective soli angle area of the counter telescope is estimated to be 193 sr cm^2 for the $\cos^2\theta$ zenith angle dependence of the flux.

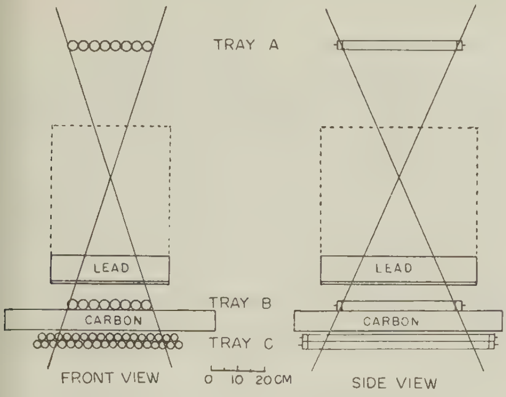

Fig. 1. Experimental arrangement.

A lead absorber between counter trays A and B, which determined the range of the incident particle, was placed on a 1 cm iron plate and its thickness was varied from 5 to 60 cm. If, as has usually been the case, the absorber covers little more than solid angle defined by telescope tray, the effect of scattering out predominates over that of scattering in. Then, in order to reduce a difference between both effects, it is desirable to use a sufficiently wide absorber.

The absorber S, in which slow μ-mesons come to rest and succeedingly decay into electrons, is the graphite slab of 8 cm (13.4 g/cm^2) in thickness.

The block diagram of the circuits employed in this experiment is shown in Fig. 2.

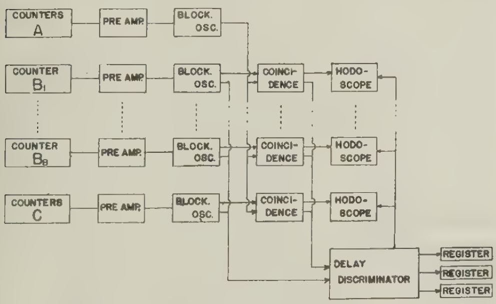

Fig. 2. Block diagram of the circuit.

Counters in tray A are joined at an input of the pre-amplifier stage and then connected to a blocking oscillator. Pulses from each of counters in tray B, through the individual pre-amplifier, trigger each corresponding blocking oscillator. Each of counters in tray B is individually in coincidence with tay A through a diode-coincidence circuit which has a resolving time of 0.6μs. Counters in tray C are connected to one blocking oscillator similarly to tray A.

Delayed coincidences $AB+(B \text{ or } C)_d$, i.e., events in which a coincidence AB was followed by a pulse from counters in tray B or C with a delay of 1.9 to 9.2 μs were recorded by a 3-channel delay discriminator. Each channel of the delay eiscriminator corresponds to delay of 1.9 to 4.4 μs, 4.4 to 6.7 μs and 6.7 μs and 6.7 to 9.2 μs, respectively.

If the blocking oscillator for tray C is triggered by a prompt pulse, tray C is insensitive for the detection of a decay electron because of the dead time of the blocking oscillator. Thus, μ-mesons which came to rest in the carbon absorber S after passing through trays A and B were detected, if their decay electrons traversed any one of counters in tray B or C during the selected time interval.

Each counter in tray B and counters in tray C were hodoscoped. The neon tube of the hodoscope panel was lighted by a prompt coincidence pulse between the corresponding counter and counters in tray A, whenever a delayed coincidence occurred. The probability that a neon tube of the hodoscope is lighted by chance is extremely small, i.e., $\sim 10^{-4}$ per delayed coincidence.

Rates of coincidence AB were recorded simultaneously to normalize rates of stopped μ-mesons.

This experiment was performed under a thin wooden roof (1 g/cm^2 of air equivalent).

§ 3. Experimental Results

a) *Delayed coincidence rate*

The measurements were performed with six different thicknesses of the lead absorber, i.e., 5, 10, 15, 30, 40 and 60 cm. Delayed coincidences accompanied by AC prompt coincidences, $ABC+(B)_d$, are considered almost to be accidental delayed coincidences due to random pairs of the threefold coincidence ABC and the single pulse from counters in tray B. These events are excluded in calculating the μ-meson intensity. Background rates unaccompanied by AC were obtained from measurements without the carbon absorber S for each thickness of the lead absorber. The background may be attributed to the following causes, i) the decay of mesons which stop in materials between trays *B* and *C*, ii) delayed discharges of counters of tray *C* and iii) accidental delayed coincidences unaccompanied by coincidence *AC* due to the inefficiency of tray *C*.

Measured rates of stopped mesons are listed in Table I. These values were obtained by subtracting background counts from rates of delayed coincidences with the absorber *S*.

Table I. Measured rates of stopped mesons. These values were obtained by subtracting rates of background from rates of delayed coincidence with the carbon absorber *S*.

Absorber thickness	Number of hours	Rate per hour
5 cm Pb	63.9	4.13±0.31
10	64.1	4.75±0.32
15	54.4	4.47±0.34
30	75.3	5.18±0.34
40	67.4	5.18±0.32
60	64.8	4.02±0.29

b) *Decay life time of mesons*

All observed rates were subdivided into three channels of delay discriminator. Results are shown in Fig. 3. The mean life time of μ-mesons was obtained to be 2.22±0.20 μs from our measurements. This is in fair agreement with values of the mean life time of μ-mesons in carbon obtained by other workers[5].

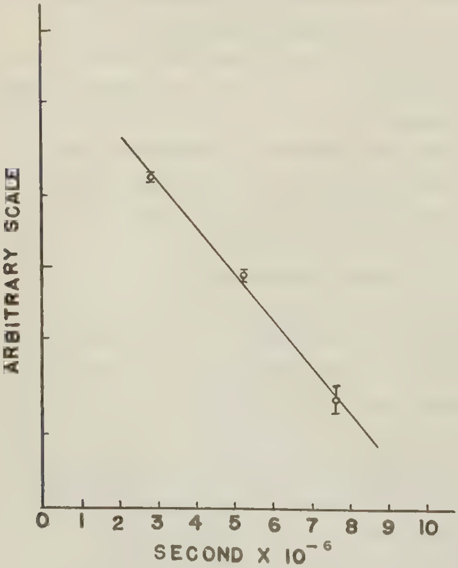

Fig. 3. Differential time distribution of delayed coincidence counts. The straight line corresponds to a mean life time of 2.22 μs. Errors are standard statistical ones.

§ 4. Corrections

It is necessary to consider various corrections that must be performed on the results.

a) *The extension of the range*

A slow meson is in a zig-zag motion through matter because of the multiple Coulomb scattering. Consequently, its actual path length *R* becomes longer than the thickness *T* of the absorber. The relation between *R* and *T* is given by the following expression, according to Koenig[6],

$$R(p_0/mc)-T(p_0/mc)=\int_0^{p_0/mc}\frac{\theta_m'}{2}\frac{dR}{d(p/mc)}d(p/mc)\,, \qquad (1$$

where the r.m.s. angle of scattering θ_m is a function of momentum p of the meson and p_0 is its initial momentum. We obtained values of *R* for thicknesses of the absorber employed in this experiment from this expression. The first and the second colums of Table II show thicknesses of the absorber and corresponding ranges *R* in air equivalent for the meson stopped in the corbon absorber, respectively.

b) *Barometer effect*

The intensity of μ-mesons at sea-level is affected by the variation of the atmospheric pressure through changes of the absorption and the decay probability of μ-mesons in the atmosphere. Therefore, counting rates of delayed coincidence must be corrected for this effect. Assuming a simple barometric regression, we figured out the barometer effect for each momentum of μ-mesons corresponding to the absorber thickness on a basis of the calculation of Trefall[7]. Values of atmospheric pressure during the experiment were offered from the Osaka Meteorological Observatory. Correction factors for the barometer effect are given in the third column of Table II.

c) *The effect of scattering in absorber on the measurement of the flux of mesons*

In such an arrangement that an absorber is placed between the counters of a telescope, the effective solid angle is in general distorted in a complicated way by the effect of Coulomb scattering in the absober, because some of mesons originally in the solid angle of the arrangement are scattered out, while some originally out of the solid angle are scattered in. This effect is remarkable for slow mesons. The absorption method always concerns with mesons which are near the ends of their ranges. Therefore, the correction for the effect of the multiple Coulomb scattering is significant, but is difficult to evaluate accurately. So far, in almost all experiments of the range spectrum, no careful consideration was paied for the effect of scattering of particles. Recently, Brini *et al.*[8] suggested the method to calculate this scattering effect by the Monte Carlo method. However, the effect of lateral displacement of particles was not taken into account in their method. The effect of the lateral displacement becomes important especially in the case of a thick absorber and a smaller area of an absorber than that of a counter tray. Eyges[9] gives the distribution function of the angular and lateral displacement due to the multiple Coulomb scattering including the energy loss of particles through the material. The effect of Coulomb scattering was computed using the distribution function of Eyges (cf. Appendix). In the course of computation we assumed the value of 70 MeV/c as the momentum of meson emerging from the lead absorber. The fourth column of Table II indicates the decreasing rates, C, of the effective solid angle due to the scattering effect, i.e., the ratio of the number of mesons coming off counter tray A which fall into counter tray B, by considering the scattering, to the number of the same mesons (from tray A) falling into tray B without considering the scattering. If, neglecting the term of the lateral displacement, our method to compute the scattering correction is directly applied to the arrangement of Brini *et al.*, our result is in agreement with their value for the scattering correction.

Table II. Some quantities pertinent to corrections for the barometer effect and the multiple Coulomb scattering effect. R is the range obtained from eq. (1) for mesons which come to rest in the carbon absorber. B is the correction percentage for the barometer effect evaluated on the basis of the calculation of Trefall. C is the decreasing rate of the effective solid angle due to the scattering effect.

Absorber thickness	R (in air eq.)	B	C
5 cm Pb+1 cm Fe	44 g cm^{-2}	$+0.48\times10^{-2}$	0.948
10 cm Pb+1 cm Fe	80 〃	+4.21 〃	0.912
15 cm Pb+1 cm Fe	112 〃	+2.90 〃	0.890
30 cm Pb+1 cm Fe	220 〃	+0.19 〃	0.833
40 cm Pb+1 cm Fe	295 〃	+1.74 〃	0.792
60 cm Pb+1 cm Fe	430 〃	+4.48 〃	0.710

Table III. The corrected rates of stopped mesons and the corresponding absolute differential intensities normalized to the value of $4.45\times10^{-6}\,\mathrm{g^{-1}\,s^{-1}\,sr^{-1}}$ at the range of 166 g/cm² air-equivalent.

Range (g cm^{-2} air eq.)	Corrected rate per hour	Absolute differential intensity ($\mathrm{g^{-1}\,s^{-1}\,sr^{-1}}\times10^{-6}$)
44	4.38±0.33	3.41±0.35
80	5.42±0.30	4.23±0.35
112	5.17±0.33	4.03±0.37
220	6.23±0.31	4.85±0.45
295	6.66±0.35	5.16±0.41
430	5.91±0.36	4.60±0.41

Rates of stopped mesons corrected for effects described above are shown in the second column of Table III.

§ 5. Normalization

In order to determine the absolute intensity of μ-mesons from the obtained rates of delayed coincidence, it is necessary to estimate the detection efficiency of counter trays for the decay electron. However, the accuracy of this estimation is very questionable mainly on account of the uncertainty concerning the range distribution of the decay electrons. Thus, the AB rates were used to normalize the stopped meson rates. The AB rates were concurrently recorded with the delayed coincidence rates at various thicknesses of the lead absorber. In the fifth column of Table IV are listed the AB coincidence rates corrected for accidental coincidences and for the barometer effect.

Table IV. Rates of two-fold coincidence AB.

Absorber thickness* (cm Pb)	Duration (minute)	Uncorrected number	Correction factor for barometer effect (%)	Rate** per minute
5	2120	195208	+1.37	92.93±0.22
10	1406	124419	+1.43	89.36±0.26
15	6510	556021	+0.10	85.08±0.10
30	3221	260024	+1.00	79.51±0.16
40	1892	143609	+1.01	76.26±0.21
60	1726	119726	+0.56	69.35±0.21

* Lead absorbers were put on an iron plate of 1 cm thickness.

** These rates were corrected for rates of accidental coincidence, too.

For the absorber thinner than 10 cm lead, a part of electron and nucleon components may contribute to the incident flux. On the other hand, the accuracy of the correction for the scattering decreases with increasing thickness of the absorber. From these reasons, the difference between the AB rates at the 15 cm and the 30 cm lead absorbers was used to determine the absolute differential intensity at the average range between them. After making the correction for the scattering, the AB rates are reduced to values of $(7.35\pm0.20)\times10^{-3}\,\text{cm}^{-2}\,s^{-1}\,sr^{-1}$ and $(6.87\pm0.25)\times10^{-3}\,\text{cm}^{-2}\,s^{-1}\,sr^{-1}$ for the integral vertical intensities of mesons penetrating the 15 cm and the 30 cm lead absorbers, respectively. The above value for the 15 cm lead is in agreement with other worker's values; namely, $(7.2\pm0.1)\times10^{-3}\,\text{cm}^{-2}\,s^{-1}\,sr^{-1}$ at 25°N by Kitamura and Minakawa[10], and $(7.3\pm0.1)\times10^{-3}\,\text{cm}^{-2}\,s^{-1}\,sr^{-1}$*) at 19°N (for 10 cm lead) by Gokhale and Balasubrahmanyan[11].

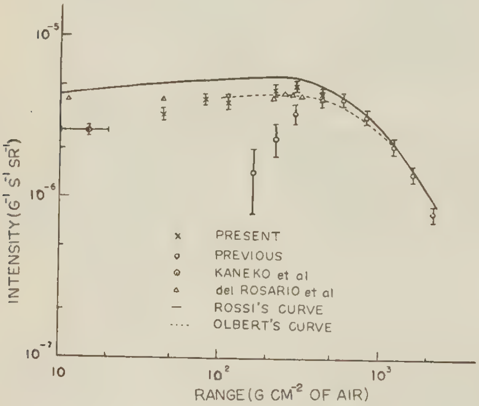

Fig. 4. Differential range spectra of μ-mesons at sea-level.

Obtained rates of delayed coincidence indicate that the differential vertical intensity of low energy μ-mesons is a slowly varying function of the range. Then, we obtained the absolute differential vertical intensity as follows,

$$\frac{I_v(15\text{ cm lead})-I_v(30\text{ cm lead})}{\text{Range between 30 and 15 cm lead}}=(4.45\pm0.12)\times10^{-3}\,\text{cm}^{-2}\,s^{-1}\,sr^{-1}$$

for mesons with range of 22.5 cm lead (=166 g/cm² air equivalent), where the symbol $I_v(T\,\text{cm lead})$ indicates the absolute vertical intensity of mesons penetrating a T cm lead absorber. Making use of this value as the normalization point, the absolute value of differential vertical intensities of μ-mesons at various ranges are given in the third column of Table III. The resultant differential range spectrum of μ-mesons is shown in Fig. 4.

§ 6. Local π-meson Production

The N-component (protons and π-mesons) which exists among cosmic rays at sea-level may undergo nuclear interactions in the lead absorber, giving rise to secondary π-mesons which stop in the carbon absorber and subsequently decay into electrons through π-μ-e process. Because of the very short mean life time of π-mesons, such π-mesons locally produced, ion addition to μ-mesons from the atmosphere, are capable of causing delayed coincidences. Thus, these events are recorded as those due to μ-mesons with the range corresponding to the thickness of the lead absorber. The π-meson production are frequently accompanied by other ionizing particles. Therefore, events of this kind cause simultaneous discharge in two or more counters in tray B. But electromagnetic interactions (electronic cascade showers and eletron productions by knock on processes) by μ-mesons can not be phenomenologically distinguished from penetrating showers only by the hodoscope picture in the present experiment. The rate of the former should be computed by an analytical consideration. In what follows we shall discuss about the contribution of π-mesons locally produced to the number of μ-mesons stopped in the carbon absorber.

---

* This value was reduced to sea-level by them from the value of $(7.55\pm0.10)\times10^{-3}\,\text{cm}^{-2}\,s^{-1}\,sr^{-1}$ at 124 m above sea-level.

The obtained data of hodoscope pictures are summarized in Tables V-a and V-b. Whole events were classified as "*Group I*" and "*Group II*" according to whether the event was accompanied by the prompt coincidence AC or not, respectively.

a) "*Group I*"

The majority of events which belong to this group are most likely due to accidental delayed coincidences caused by pairs of particles penetrating the whole absorber and other delayed particles. The mean energy of the penetrating particles is estimated to be about 2 GeV.

With a cloud chamber containing five 1.27 cm lead plates, Brown *et al.*12) observed an average number of 0.069 knock-on electrons (per meson) emerging from heavy materials and found that the distribution of the projected angle α between the trajectory of the incident meson and that of the knock-on electron emerging from the lead is represented by $\cos^n\alpha$, most likely, with $n=2.5$.

In the present experiment, we obtained a value of 0.044±0.005 for a ratio of the number of the ($B=2$) events, in which any two of counters in tray B were struck simultaneously, to the total number of events. If the angular distribution of knock-on electrons obtained by Brown *et al.* is applied to the geometry of our experimental arrangement, it is expected that 55 per cent of knock-on electrons emerging from the lead absorber strike another counter in tray B than that traversed by the primary meson. If one assumes that the ($B=2$) events are due to productions of knock-on electrons, the average number of secondary electron is estimated to be 0.080±0.009 per meson from this experiment. In the cloud chamber experiment of Brown *et al.*, 0.02 "back scattered" electrons (per meson) emerging from the surface through which the mesons enter the lead plate were observed. Making allowance for the existence of "back scattered" electrons from the absorber S in our case, the above value for the average number of secondary electrons is in fair agreement with the result of Brown *et al.*

Moreover, a ratio of the number of ($B=2s$) events to that of ($B=2a$) events was 0.27±0.07, as is seen in Table V-a. The ($B=2s$) indicates an event in which two counters in tray B separated by more than one counters were struck and the ($B=2a$) an event in which any two adjacent counters in tray B were struck. This value should be compared with a value of 0.32 which is figured out for a ($B=2s$)-to-($B=2a$) ratio by applying the angular distribution of secondary electrons obtained by Brown *et al.* to the geometry of our experimental ar-

Table V–a. Number of events accompanied by prompt coincidences AC, versus number of counters struck in tray B.

Type of coincidence	Absorber S	Number of counters struck in tray B			
		$B=1$	$B=2$		$B=3$
			$B=2a$*	$B=2s$**	
$AB+(B)_a$***	absent	297	11	2	1
$ABC+(B)_a$	absent	712	26	8	3
$ABC+(B)_a$	present	737	27	7	9
total:		1746	64	17	13
			81		

* Events in which any two adjacent counters in tray B were struck.

** Events in which two counters in tray B separated by more than one counters were struck.

*** This measurement was carried out without tray C.

rangement.

From the above discussions, it is concluded that almost all ($B=2$) events in "*Group I*" can be attributed to secondary electron production by knock-on processes in the lead absorber.

The ($B \geq 3$) events, in which three or more counters in tray B were simultaneously discharged, are probably accounted for in terms of double knock-ons, soft and hard showers.

b) "*Group II*"

The probability for a μ-meson of kinetic energy E to produce a secondary electron of energy between E' and $E'+dE'$ by a knock-on process is given by the follwing expression[13]:

$$\phi(E, E')dE' = \frac{2Cm_ec^2}{\beta^2}\frac{dE'}{E'^2}\left[1-\beta^2\frac{E'}{E'_m} + \frac{1}{2}\left(\frac{E'}{E+mc^2}\right)^2\right], \qquad (2)$$

where E'_m is the maximum transferable energy to a secondary electron and C is a constant which depends on the material. Let $g(E)$ represent the differential energy spectrum o μ-mesons. For the average number $n(E_c')$, o the knock-on electrons with energies large than E_c' produced by a cosmic ray μ-meso with energy larger than $\mathcal{E}$, one obtains

$$n(E_c') = \int_{\varepsilon}^{\infty}\int_{E_c'}^{E_m'} \phi(E, E')g(E)\, dE'dE \Big/ \int_{\varepsilon}^{\infty} g(E)dE\, . \quad (3$$

If $E_c' \ll E_m'$ for μ-mesons with kineti energies more than 76 MeV, which is th minimum energy required for μ-meson t penetrate the carbon of 13.4 g/cm² thickness eq. (3) may be written approximately a follows:

$$n(E_c') \simeq 2Cm_ec^2/E_c'\, . \qquad (4$$

Since C is 0.06 for lead, substituting th value of 0.08 obtained in "*Group I*" fo $n(E_c')$, one gets a value of 0.8 MeV for E_c' fo from eq. (4). This estimate suggests that th knock-on electron detected in our apparatu must have at least the kinetic energy o 0.8 MeV.

Table V–b. Number of events unaccompanied by prompt coincidences AC, versus number of counters struck in tray B.

Type of coincidence	Absorber S	Number of counters struck in tray B			
		$B=1$	$B=2$		$B=3$
			$B=2a$*	$B=2s$**	
$AB+(B \text{ or } C)_d$	present	2060	63	1	3

* Events in which any two adjacent counters in tray B were struck.

** Events in which two counters in tray B separated by more than one counters were struck.

*** This measurement was carried out without tray C.

In "*Group II*", the fraction of the ($B=2$) events was 0.030±0.004 of the total events. The probability for a μ-meson which comes to rest in S to produce a knock-on electron of energy larger than 0.8 MeV is considerably small. Moreover, only one ($B=2s$) event was observed among 64 ($B=2$) events of "*Group II*". From these evidences, it is suggested that ($B=2$) events in this group are attributed rather to large angle deflections which slow mesons undergo in passing through the lead absorber, than to production of knock-on electrons. For instance, in the case of 15 cm lead absorber, the r.m.s. angle of deflection of μ-mesons which come to rest at the center of S is estimated to be 29° and hence the probability that the mesons traverse obliquely two adjacent counters in tray B is 0.031.

c) *Local π-meson production*

12 ($B \geq 3$) events were obtained during th run with S (cf. Tables V-a and V-b). It i expected that ($B \geq 3$) events include doubl knock-ons, soft showers and hard shower (local and extensive), but our apparatus is n able to distinguish between them. Even if on assumes that all of ($B \geq 3$) events were du to local hard showers originating in the lea absorber, the number of those which coul trigger the apparatus was at most only 0. per cent of the number of stopped mesons.

In order to find the fraction of mesons tha are produced locally, it is necessary to es timate the relative efficiency for our apparatu to detect them. Because counters struck b shower particles become inactive for a decay electron, the detection efficiency for a stopped meson in the local shower is less than that for a single stopped meson. If N counters in tray B are struck by shower particles, the efficiency is approximately $\frac{1}{2}\{1+(8-N)/7\}$ for "*without AC*" and $\frac{1}{2}(8-N)/7$ for "*with AC*", respectively.

Moreover, owing to the nuclear copture for the negative π-mesons by carbon nuclei, the detection efficiency for π-mesons is about one half of that for μ-mesons.

Thus, from the obtained distribution on N (the number of discharging counters in tray B) we estimated the detection efficiency for π-mesons locally produced to be on the average about 1/6 of that for μ-mesons from the atmosphere. After this correction, it was found that mesons locally produced were at most 3.5 per cent of mesons stopped in the carbon absorber. Although, in ($B=2$) events, there may partly exist events due to local showers, their fraction is expected to be appreciably small from the previous discussion. Then, the fraction of mesons locally produced is consistent with one expected in I from Olbert's production spectrum.

§7. Discussion

As shown in Fig. 4, the present differential range spectrum is nearly flat in the interval of ranges from 44 to 430 g/cm^2 of air equivalent, and can consistently be extended to the data of Kaneko *et al*. Our data are about 20 per cent lower than Rossi's curve based on many experimental results measured at geomagnetic latitude greater than 45°. Some of recent measurements on intensities of low energy μ-mesons at high geomagnetic latitude have given values slightly higher than Rossi's curve, so that it can not be concluded that the variation of intensities of low energy mesons due to the geomagnetic effect between 24°N and 50°N is equal to 20 per cent.

Open circles in Fig. 4 show the range spectrum converted from the momentum spectrum (measured by a magnetic cloud chamber) described in I by making use of the theoretical momentum-range relation. (Hereafter, we shall call this range spectrum *the converted spectrum*.) It is seen in the figure that the present spectrum is consistently connected with *the converted spectrum* for ranges greater than 430 g/cm^2 of air equivalent, but there is a noticeable discrepancy for ranges lower than 430 g/cm^2. However, the present range spectrum is in good agreement with the range spectrum of μ-mesons at sea-level derived from Olbert's production spectrum at 24°. The low range part of Olbert's production spectrum has been based on results of altitude and latitude dependence of slow μ-meson intensity measured by the delayed coincidence and anticoincidence methods of detection.

Recent results[4)8)15)] by delayed coincidence method have indicated that the range spectrum of low energy μ-mesons is nearly flat, and have not been inconsistent with ones derived from Olbert's production spectra for each corresponding latitude.

Very recently, Nagoya University group has obtained a momentum spectrum of cosmic rays penetrating 15 cm lead at Mt. Norikura (2840 m altitude, 25°N geomagnetic latitude) by means of a magnetic cloud chamber. The resulting spectrum falls below that derived from Olbert's production spectrum at momenta lower than 1·5 GeV/c and decreasing momentum, while the latter still increases.

When we calculate the momentum spectrum at sea-level from that at Mt. Norikura under the consideration of the momentum loss due to ionization and the spontaneous decay of μ-mesons in traversing the atmosphere between the two places, we obtain a spectrum which agrees with our previous momentum spectrum.

These results provide evidence that there exists a consistency between the sea-level and altitude spectra obtained by the same kind of the method of detection.

The possible explanation for higher values in the differential range method is that π-mesons locally produced contribute to the number of μ-mesons from the atmosphere. Besides, since the effect of scattering becomes large for increasing thickness of a lead absorber, an insufficient correction for this effect tends to result in a flat spectrum. But these effects were found, as already discussed, to be too small to remove the discrepancy mentioned above, even though, in the present experiment, our paticular attention was given on these subjects.

The other approach to remove the discrepancy between the "present" and "previous" spectra is a modification of the range-momentum relation of μ-mesons. If, under the assumption that the range and momentum spectra are correct respectively, one calculates the momentum loss of μ-mesons in air as a function of momentum from both spectra, the momentum loss of μ-mesons should be a few times as large as the theoretical curve cited in Rossi's book[17)] at low momentum region. This conclusion yields an improbable result that the mass of μ-mesons should be considerably heavier than that is accepted at present. On the other hand, various theoretical range-energy relation have been exprerimentally confirmed within an error of a few per cent[18)].

We have, at present, no other explanation to remove the discrepancy between the "range" and "momentum" spectra of μ-mesons at low momentum region.

Acknowledgement

This research was conducted under the direction of Prof. Y. Watase, without whose constant guidance and encouragement this project would be impossible. The writers express their thanks to Prof. W. L. Kraushaar of the Massachusetts Institute of Technology, with whom authers have enjoyed the discussion and the collaboration during his stay in this laboratory as a Fullbrighter, for the design and the construction of electronic circuits. Thanks are also due to Prof. M. Oda and Prof. Y. Yamaguchi, who have made many helpful criticisms and suggestions. This study was supported in part by a Grant in Aid for Fundamental Scientific Research (Institutional Research) from the Ministry of Education.

Appendix

Let us consider one of projections of the motion of a particle on two vertical planes parallel with each side of the rectangular counter-tray (cf. Fig. 5), and let a, b and d be the length of one side of tray, the distance between two trays and the distance between the lower surface of the absorber and tray B. Consider that a particle enters toward a point P at an angle ω with the vertical direction and emerges from the absorber at a point T, suffering the multiple scattering. Let $F(t, y, \theta)d\theta dy$ represent the scattering probability for the particle to travel at an angle in $d\theta$ at θ with the original direction and to undergo a latera displacement in dy at y after traversal of th absorber of a thickness t. Taking into accoun energy loss of the particle in the substance Eyges[9)] gives the following expression for th scattering probability,

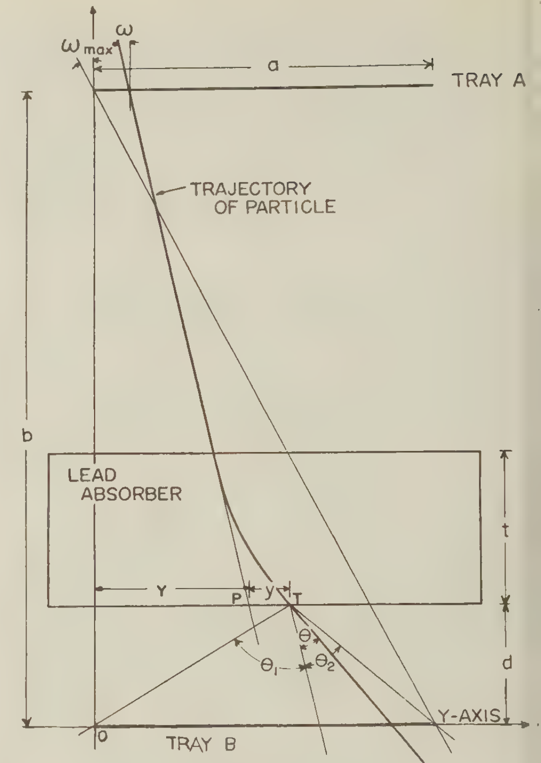

Fig. 5. Illustrating the computation of the scattering effect of the meson flux in the absorber.

$$F(t, y, \theta)=\frac{1}{2\pi[B(t)]^{1/2}}$$
$$\times\exp\left[-\frac{\theta^2 A_2-2y\theta A_1+y^2 A_0}{4B(t)}\right], \quad \text{(A-1}$$

where

$$\left.\begin{aligned} &A_0=\int_0^t\frac{d\eta}{w^2(\eta)}, \qquad A_1=\int_0^t\frac{(t-\eta)d\eta}{w^2(\eta)}, \\ &A_2=\int_0^t\frac{(t-\eta)^2 d\eta}{w^2(\eta)}, \quad B(t)=A_0A_2-A_1^2, \\ &w(\eta)=\frac{2p\beta}{E_s} \quad \text{and} \quad E_s=21\,\text{MeV}. \end{aligned}\right\} \quad \text{(A-2}$$

We got the values of A_0, A_1 and A_2 by th numerical integration using the range-momen tum relation of μ-mesons. Henceforce, w assume $\cos\omega\simeq 1$ to simplify the calculatio For our geometry, an error introduced b this assumption is negligible.

In Fig. 5, let us take the Y-axis of a sys tem of coordinates, whose origin O is at an edge of the tray B, in the horizontal direction. We shall denote by $\phi(Y, \omega)$ the probability that a particle toward the point $P(0, Y)$ passes through tray B after traversing the absorber. The expression for $\phi(Y, \omega)$ is given by

$$\phi(Y, \omega)=\int_{-\infty}^{\infty} dy \int_{\theta_1}^{\theta_2} F(t, y, \theta)\, d\theta\,, \qquad \text{(A-3)}$$

where

$$\theta_1=\tan^{-1}\frac{-(Y+y)}{d}-\omega$$

and

$$\theta_2=\tan^{-1}\frac{a-(Y+y)}{d}-\omega\,.$$

Put

$$D\equiv\sqrt{2A_2} \quad\text{and}\quad q(\theta, y)\equiv\sqrt{\frac{A_2}{2B}}\left(\theta-\frac{A_1}{A_2}y\right).$$

Eq. (A-3) becomes

$$\phi(Y, \omega)=\frac{1}{\sqrt{2\pi}D}\int_{-\infty}^{\infty}\int_{q_1}^{q_2} e^{-(y^2/2D^2+q^2/2)}\, dydq\,. \qquad \text{(A-4)}$$

where

$$q_1=q(\theta_1, y) \quad\text{and}\quad q_2=q(\theta_2, y)\,.$$

In eq. (A-4), the integral concerning q can be easily obtained from the table of the error function. After the numerical integration over y in eq. (A-4), we can obtain the value of $\phi(Y, \omega)$.

Let Φ be the relative number of particles which can pass through both trays A and B, to particles which are originally in the aperture defined by trays A and B. The expression for Φ is

$$\Phi=\int_0^{\pi/2}\int_{Y_0}^{Y_0+a}\phi(Y, \omega)\, dY d\omega \Big/ \int_0^{\omega_{\max}}(Y_1-Y_0)\, d\omega \qquad \text{(A-5)}$$

where $Y_0=(b-d)\tan\omega$ and $Y_1=b-d\tan\omega$.

The integral concerning Y must be limited within the region occupied by the absorber. Total triggering efficiency for the two fold coincidence AB is given by the product of two Φ's for each projection.

References

1) S. Fukui, T. Kitamura and Y. Murata: J. Phys. Soc. Japan **10** (1955) 735.
2) S. Olbert: Phys. Rev. **96** (1954) 1400.
3) S. Kaneko, T. Kubozoe and M. Takahata: J. Phys. Soc. Japan **10** (1955) 915.
4) A. Fafarman and M. H. Shamos: Phys. Rev. **96** (1954) 1096.
5) M. Conversi: Phys. Rev. **79** (1950) 749; H. A. Morewitz and M. H. Shamos: Phys. Rev. **92** (1953) 134.
6) H. P. Koenig: Phys. Rev. **69** (1946) 590.
7) H. Trefall: Proc. Phys. Soc. (London) **A68** (1955) 953.
8) D. Brini, L. Peli, O. Rimondi and P. Veronesi: Nuovo Cimento **12** (1955) 613.
9) L. Eyges: Phys. Rev. **74** (1948) 1534.
10) Y. Kitamura and O. Minakawa: Prog. Theo. Phys. (Kyoto) **10** (1953) 237.
11) G. S. Gokhale and V. K. Balasubrahmanyan: private communication.
12) W. W. Brown, A. S. McKay and E. D. Palmatier: Phys. Rev. **76** (1949) 506.
13) B. Rossi: *High Energy Particls* (Prentice-Hall, Inc., New York, 1952) p. 16.
14) B. Rossi: *ibid*, p. 40 ff.
15) L. del Rosario and J. Dávila-Aponte: Phys. Rev. **88** (1952) 998;
A. Fafarman: Phys. Rev. **104** (1956) 1116.
16) I. Miura, T. Matano, T. Murayama, H. Tanooka and G. Tanahashi: private communication.
17) B. Rossi: *ibid*, p. 25.
18) O. Heinz: Phys. Rev. **94** (1954) 1728; S. K. Allison and S. P. Warshaw: Rev. Mod. Rhys. **25** (1954) 779; G. Baroni, C. Castagnoli, G. Cortini, C. Franzinetti and A. Manfredini: CERN communication BS 9, 1954.

JOURNAL OF THE PHYSICAL SOCIETY OF JAPAN Vol. 12, No. 8, AUGUST 1957

Radial Distribution Function of Fluids II

By Kazuo HIROIKE

Department of Physics, Tokyo Institute of Technology

(Received April 6, 1957)

It is shown that the radial distribution function of fluid can be derived from the expression for the free energy in the form of a "functional derivative" with respect to the pair interaction potential. Three examples are treated on the line of the theory: (1) the simple chain approximation of classical fluid, (2) the second quantization and (3) the lowest state of the spinless bosons derived by Bogolyubov and Zubarev. A procedure, which differs from the usual one, is given in the derivation of the expressions by which the pressure and the internal energy are expressed in terms of the radial distribution function.

§1. Introduction

In a previous paper[1)] the consistency of several approximate radial distribution functions of fluid was examined in the sense that the pressure and the internal energy derived from them should satisfy the relation

$$\frac{\partial}{\partial T}(p/T)=\frac{\partial}{\partial V}(E/T^2)\,,$$

where T, p, V and E denote the temperature, the pressure, the volume and the internal energy of fluid respectively. It was found that the original form of Green's linear theory is the only one among them that satisfies the above relation. Although this theory was further improved without breaking the above relation, it was still a poor approximation from the quantitative point of view.

This situation shows that it is difficult to calculate the thermodynamical quantities without inconsistency when use is made of any approximate distribution function, because the Helmholtz free energy cannot be derived in a consistent way from the expressions of p and E unless they satisfy the relation above mentioned. In the present paper, attempts on the line considered in the previous paper are abandoned and, on the contrary, it is attempted to derive a relation which should hold between the free energy and the radial distribution function and which can be used to derive the approximate distribution function from an approximate expression for the free energy.

The Hamiltonian of a system composed of N molecules is assumed to be expressed in the form:

$$H=K+\frac{1}{2}\sum_{i\neq j}^{N}\phi_{ij} \qquad (1)$$

where K stands for the kinetic energy and $\phi_{ij}\equiv\phi(\boldsymbol{r}_i-\boldsymbol{r}_j)$ is the potential energy of interaction between two molecules at the positions $\boldsymbol{r}_i$ and $\boldsymbol{r}_j$ respectively, which is assumed to be the function of the distance $r_{ij}\equiv|\boldsymbol{r}_i-\boldsymbol{r}_j|$ alone. The average of any quantity X, which is expressed as an operator in quantum mechanics, over a canonical ensemble will be denoted by

$$\langle X\rangle=\mathrm{T}_r Xe^{-H/\kappa T}/Z\,, \qquad (2)$$

where

$$Z=\mathrm{T}_r\, e^{-H/\kappa T} \qquad (3)$$

and κ is the Boltzmann constant and $\mathrm{T}_r\ X$ means the trace of an operator X. In classical statistical mechanics, the trace should be replaced by the integration over the phase space. The Helmholtz free energy A of the system is given by

$$A=-\kappa T\log Z\,. \qquad (4)$$

The radial distribution function $g(r)$ and the structure factor $S(k)$ are defined respectively by

$$g(|\boldsymbol{r}-\boldsymbol{r}'|)=\left(\frac{V}{N}\right)^2\left\langle\sum_{i\neq j}^{N}\delta(\boldsymbol{r}-\boldsymbol{r}_i)\delta(\boldsymbol{r}'-\boldsymbol{r}_j)\right\rangle \qquad (5)$$

and

$$S(k)=1+\frac{N}{V}\int_V[g(r)-1]e^{i\boldsymbol{k}\boldsymbol{r}}\,d\boldsymbol{r} \qquad (6)$$

or, conversely,

$$g(r)=1+\frac{1}{(2\pi)^3}\frac{V}{N}\int[S(k)-1]e^{-i\boldsymbol{k}\boldsymbol{r}}\,d\boldsymbol{k}, \qquad (6')$$

where $\delta(\boldsymbol{r})$ is Dirac's δ-function and r and k are the absolute values of the vectors $\boldsymbol{r}$ and $\boldsymbol{k}$ respectively. The fact that $g(r)$ or $S(k)$ depends on the absolute value r or k alone is due to the circumstance that the interaction energy between two molecules is assumed to be dependent only on their distance. The functions $g(r)$ and $S(k)$ have the properties

$$\lim_{r\to\infty} g(r)=1 \quad \text{and} \quad \lim_{k\to\infty} S(k)=1\ .$$

§ 2. The Relation between the Free Energy and the Radial Distribution Function

The variation of the free energy, corresponding to a variation $\varDelta\phi$ of the interaction potential, will be denoted by $\varDelta A$. $\varDelta A$ can be written as follows:

$$\varDelta A=F[\varDelta\phi(\boldsymbol{r}')]+O(\varDelta\phi)^2\ . \tag{7}$$

The first term on the right-hand side of this equation is a functional of the function $\varDelta\phi$ and is linear with respect to $\varDelta\phi$. Actually this functional has the form

$$F[f(\boldsymbol{r}')]=\left\langle \frac{1}{2}\sum_{i\neq j}^{N} f(r_{ij}) \right\rangle \tag{8}$$

and Eq. (7) becomes, when explicitly written,

$$\varDelta A=\left\langle \frac{1}{2}\sum_{i\neq j}^{N} \varDelta\phi_{ij} \right\rangle+O(\varDelta\phi)^2\ . \tag{7'}$$

Whenever a functional of the form given by Eq. (8) appears it will be related with a variation of the free energy A.

The quantity $\left\langle \frac{1}{2}\sum_{i\neq j}^{N} e^{i\boldsymbol{k}(\boldsymbol{r}_i-\boldsymbol{r}_j)} \right\rangle$ can be transformed with the helf of Eq. (5) as

$$\left\langle \frac{1}{2}\sum_{i\neq j}^{N} e^{i\boldsymbol{k}(\boldsymbol{r}_i-\boldsymbol{r}_j)} \right\rangle$$

$$=\frac{1}{2}\iint_{VV} e^{i\boldsymbol{k}(\boldsymbol{r}-\boldsymbol{r}')} \left\langle \sum_{i\neq j}^{N} \delta(\boldsymbol{r}-\boldsymbol{r}_i)\delta(\boldsymbol{r}'-\boldsymbol{r}_j) \right\rangle d\boldsymbol{r}d\boldsymbol{r}'$$

$$=\frac{1}{2}\left(\frac{N}{V}\right)^2\iint_{VV} g(|\boldsymbol{r}-\boldsymbol{r}'|)e^{i\boldsymbol{k}(\boldsymbol{r}-\boldsymbol{r}')}d\boldsymbol{r}d\boldsymbol{r}'$$

$$=\frac{N}{2}\left\{\frac{N}{V}\int_V [g(r)-1]e^{i\boldsymbol{k}\boldsymbol{r}}\, d\boldsymbol{r}+\frac{N}{V}\int_V e^{i\boldsymbol{k}\boldsymbol{r}} d\boldsymbol{r}\right\}\ .$$

Hence from Eq. (6):

$$\left\langle \frac{1}{2}\sum_{i\neq j}^{N} e^{i\boldsymbol{k}(\boldsymbol{r}_i-\boldsymbol{r}_j)} \right\rangle$$

$$=\frac{N}{2}\left[S(k)-1+(2\pi)^3\frac{N}{V}\delta(\boldsymbol{k})\right]. \tag{9}$$

On the other hand $\left\langle \frac{1}{2}\sum_{i\neq j}^{N} e^{i\boldsymbol{k}(\boldsymbol{r}_i-\boldsymbol{r}_j)} \right\rangle$ can also be written be written by Eq. (8) in an alternative form:

$$\left\langle \frac{1}{2}\sum_{i\neq j}^{N} e^{i\boldsymbol{k}(\boldsymbol{r}_i-\boldsymbol{r}_j)} \right\rangle=F[e^{i\boldsymbol{k}\boldsymbol{r}'}]\ .$$

Comparison of this equation with Eq. (9) leads to

$$S(k)=1-(2\pi)^3\frac{N}{V}\delta(\boldsymbol{k})+\frac{2}{N}F[e^{i\boldsymbol{k}\boldsymbol{r}'}]\ .$$

When this expression is inserted in Eq. (6′) and the linear property of F is noticed, the expression for $g(r)$ is obtained as

$$g(r)=\frac{2V}{N^2}F[\delta(\boldsymbol{r}-\boldsymbol{r}')]\ ,$$

where the functional F operates on the variable $\boldsymbol{r}'$. This relation can be obtained directly from Eq. (5).

It is seen from these equations together with Eqs. (7) and (8) that the functions $g(r)$ and $S(k)$ can be related to the variation of the free energy A. Thus the expressions for $g(r)$ and $S(k)$ can be written symbolically as

$$g(r)=\frac{2V}{N^2}\left(\frac{\delta A}{\delta\phi}\right)_r, \tag{10}$$

$$S(k)=1-(2\pi)^3\frac{N}{V}\delta(\boldsymbol{k})+\frac{2}{N}\left(\frac{\delta A}{\delta\phi}\right)_k, \tag{11}$$

where

$$\left.\begin{aligned} \left(\frac{\delta A}{\delta\phi}\right)_r &\equiv F[\delta(\boldsymbol{r}-\boldsymbol{r}')] \\ \text{and}\qquad & \\ \left(\frac{\delta A}{\delta\phi}\right)_k &\equiv F[e^{i\boldsymbol{k}\boldsymbol{r}'}]\ . \end{aligned}\right\} \tag{12}$$

The functional $\left(\frac{\delta A}{\delta\phi}\right)_r$ or $\left(\frac{\delta A}{\delta\phi}\right)_k$ is similar to but somewhat different from the usual functional derivative. However, the terminology "functional derivative" will be used hereafter because of the lack of a suitable one. This terminology will be further generalized to quantities other than the free energy. The functional derivative of a quantity B, which is a functional of ϕ, will be defined in a similar way as above. Namely, when ϕ is varied by $\varDelta\phi$, the corresponding first order variation, with respect to $\varDelta\phi$, of B is denoted be $G[\varDelta\phi(\boldsymbol{r}')]$, which is a linear functional of $\varDelta\phi$. Then

$$\left.\begin{aligned} \left(\frac{\delta B}{\delta\phi}\right)_r &\equiv G[\delta(\boldsymbol{r}-\boldsymbol{r}')] \\ \text{or}\qquad & \\ \left(\frac{\delta B}{\delta\phi}\right)_k &\equiv G[e^{i\boldsymbol{k}\boldsymbol{r}'}]\ . \end{aligned}\right\} \tag{13}$$

If B depends also on another functional C of ϕ, it is seen from the above definition that the following relation is valid:

$$\left.\begin{array}{l}\left(\dfrac{\delta B}{\delta\phi}\right)_r=\left(\dfrac{\delta B}{\delta\phi}\right)_{r,\,C=\text{const.}}+\dfrac{\partial B}{\partial C}\left(\dfrac{\delta C}{\delta\phi}\right)_r\\ \text{or}\\ \left(\dfrac{\delta B}{\delta\phi}\right)_k=\left(\dfrac{\delta B}{\delta\phi}\right)_{k,\,C=\text{const.}}+\dfrac{\partial B}{\partial C}\left(\dfrac{\delta C}{\delta\phi}\right)_k,\end{array}\right\}\qquad(14)$$

Equation (10) is the relation which is to hold between the free energy and the radial distribution function, and it has been the object of this section to derive the relation. The function $g(r)$ measures the correlation between the positions of two molecules. Such a correlation arises from the presence of the interaction potential ϕ apart from the symmetry effect of the wave functions. Therefore it will be plausible to express $g(r)$ in the form of a functional derivative of the free energy with respect to ϕ. The relation under consideration is still valid in the case where $\phi(r)$ has no spherical symmetry and where many-body forces exist. In such cases the distribution function must be considered not only as a function of r but also of the direction of the vector $\boldsymbol{r}$.

There also exist similar formulas as Eqs. (10) and (11) when a grand canonical ensemble is considered. In this case the thermodynamic potential is pV and the following formulas can be derived:

$$g(r)=-\frac{2V}{N^2}\left(\frac{\delta(pV)}{\delta\phi}\right)_r\qquad(15)$$

and

$$S(k)=1-(2\pi)^3\frac{N}{V}\delta(k)-\frac{2}{N}\left(\frac{\delta(pV)}{\delta\phi}\right)_k,\qquad(16)$$

where N is to be interpreted as the average number of molecules over a grand canonical ensemble.

§ 3. Examples

The relations derived in the preceding section can be used to obtain the approximate distribution function if an approximate expression for the free energy is known, while these relations are valid between the exact free energy and the exact distribution function. Several examples will be shown in the following.

1. *Simple chain approximation to the free energy*

In a classical statistical mechanics the free energy A of fluid can be expressed as follows[2)]:

$$\frac{A}{N\kappa T}=\log\left(\frac{h^2}{2\pi m\kappa T}\right)^{3/2}\frac{\rho}{e}-\sum_{n=1}\frac{1}{n+1}\beta_n\rho^n,\qquad(17)$$

where ρ is the number density N/V and β_n's are the irreducible integrals. The irreducible integrals β_n's are composed of terms of various types, among which there are terms expressed symbolically as 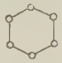. When only such terms are used in place of β_n in the right-hand side of Eq. (17), an approximate expression A_0 for the free energy is obtained. (See Appendix I). This approximation will be named the simple chain approximation to the free energy. It gives the free energy the following expression:

$$\begin{aligned}\frac{A_0}{N\kappa T}&=\log\left(\frac{h^2}{2\pi m\kappa T}\right)^{3/2}\frac{\rho}{e}\\&\quad-\frac{\rho}{2}\left[(2\pi)^{3/2}\beta(0)-\pi\int_{-\infty}^{\infty}u^2\beta^2(u)du\right]\\&\quad+\frac{1}{\rho}\frac{1}{8\pi^2}\int_{-\infty}^{\infty}u^2\log[1-(2\pi)^{3/2}\rho\beta(u)]du\\&\quad+\frac{1}{2\sqrt{2\pi}}\int_{-\infty}^{\infty}u^2\beta(u)du,\end{aligned}\qquad(18)$$

where

$$u\beta(u)=\frac{1}{\sqrt{2\pi}}\int_{-\infty}^{\infty}r[e^{-\phi(r)/\kappa T}-1]\sin ur\,dr\qquad(19)$$

and $\phi(r)$ is assumed to be an even function.

The functional derivative of A_0 is given from Eq. (18), with the help of Eq. (14), by

$$\begin{aligned}\frac{1}{N\kappa T}\left(\frac{\delta A_0}{\delta\phi}\right)_r&=-\frac{\rho}{2}(2\pi)^{3/2}\left(\frac{\delta\beta(0)}{\delta\phi}\right)_r-\frac{(2\pi)^{5/2}}{2}\rho^2\\&\quad\times\int_{-\infty}^{\infty}\frac{u^2\beta^2(u)}{1-(2\pi)^{3/2}\rho\beta(u)}\left(\frac{\delta\beta(u)}{\delta\phi}\right)_r du\,.\end{aligned}\qquad(20)$$

In order to calculate $\left(\dfrac{\delta\beta(u)}{\delta\phi}\right)_r$ or $\left(\dfrac{\delta\beta(0)}{\delta\phi}\right)_r$, it is convenient to write the right-hand side of Eq. (19) as

$$u\beta(u)=\frac{1}{(2\pi)^{3/2}}\int[e^{-\phi(r')/\kappa T}-1]\frac{\sin ur'}{r'}d\boldsymbol{r}'\,.$$

Then from definition (13)

$$\begin{aligned}&u\left(\frac{\delta\beta(u)}{\delta\phi}\right)_r\\&=-\frac{1}{(2\pi)^{3/2}}\frac{1}{\kappa T}\int e^{-\phi(r')/\kappa T}\delta(\boldsymbol{r}-\boldsymbol{r}')\frac{\sin ur'}{r'}d\boldsymbol{r}'\end{aligned}$$

$$=-\frac{1}{(2\pi)^{3/2}}\frac{e^{-\phi(r)/\kappa T}}{\kappa T}\frac{\sin ur}{r}$$

and

$$\left(\frac{\delta\beta(0)}{\delta\phi}\right)_r=-\frac{1}{(2\pi)^{3/2}}\frac{e^{-\phi(r)/\kappa T}}{\kappa T}\,.$$

When these expressions for $\left(\frac{\delta\beta(u)}{\delta\phi}\right)_r$ and $\left(\frac{\delta\beta(0)}{\delta\phi}\right)_r$ are inserted in Eq. (20) and use is made of Eq. (10), the following expression for $g(\boldsymbol{r})$ is obtained:

$$g(\boldsymbol{r})=e^{-\phi(r)/\kappa T}\times\left[1+2\pi\rho\int_{-\infty}^{\infty}\frac{u^2\beta^2(u)}{1-(2\pi)^{3/2}\rho\beta(u)}\frac{\sin ur}{ur}du\right]. \tag{21}$$

The above expression is identical to one which is obtained by putting $\varepsilon=1$ in Green's theory[3]. It is also identical to one[4,5] obtained by the procedure that only the terms expressed symbolically as 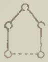 are taken in the exact expression for $g(r)$ which is a power series in ρ similar to Eq. (17). Such a procedure has been named the simple chain approximation by Rushbrooke[5], which will be called here the simple chain approximation to the distribution function in order to be distinguished from the approximation adopted in the derivation of Eq. (18). The fact that Eq. (21) is derived from Eq. (18) shows that both approximations are equivalent to each other. It can be shown that the netted-chain approximation, proposed by Rushbrooke and Scoins[6], to the distribution function is not the same as the netted-chain approximation to the free energy. This case will be treated in later occasion.

2. *The second quantization*

The Hamiltonian in the formalism of the second quantization $\boldsymbol{H}$, corresponding to Eq. (1), is written as

$$\boldsymbol{H}=\int\Psi^*(x)H(x)\Psi(x)dx+\frac{1}{2}\iint\Psi^*(x)\Psi^*(x')\phi(\boldsymbol{r}-\boldsymbol{r}')\Psi(x')\Psi(x)dxdx'\,, \tag{22}$$

where $H(x)$ is the kinetic energy which corresponds to K in Eq. (1), $\Psi(x)$ is a quantized wave function, $\Psi^*(x)$ the Hermitian adjoint of $\Psi(x)$ and $x\,(x')$ stands for both the configurational coordinates and the spin coordinates. The quantized wave functions satisfy the following commutation rules

$$\Psi(x')\Psi^*(x)-\varepsilon\Psi^*(x)\Psi(x')=\delta(x-x')\,,$$
$$\Psi(x')\Psi(x)-\varepsilon\Psi(x)\Psi(x')=0\,,$$
$$\Psi^*(x')\Psi^*(x)-\varepsilon\Psi^*(x)\Psi^*(x')=0\,,$$

where ε is taken to be either $+1$ or -1 according to the bosons or the fermions.

The grand partition function is

$$e^{pV/\kappa T}=\mathrm{T}_r\,e^{[\mu N-H]/\kappa T}\,, \tag{23}$$

where μ denotes the chemical potential. In the present subsection the average over the grand canonical ensemble will be denoted by $\langle\cdots\rangle$. Then, with the help of Eqs. (13), (22) and (23), $\left(\frac{\delta(pV)}{\delta\phi}\right)_r$ is calculated in the following manner:

$$\frac{1}{\kappa T}\left(\frac{\delta(pV)}{\delta\phi}\right)_r=-\frac{1}{2\kappa T}\left\langle\iint\Psi^*(x_1)\Psi^*(x_2)\delta(\boldsymbol{r}-\boldsymbol{r}_1+\boldsymbol{r}_2)\Psi(x_2)\Psi(x_1)dx_1dx_2\right\rangle$$

and hence from Eq. (15)

$$g(\boldsymbol{r})=\frac{V}{\langle N\rangle^2}\left\langle\iint\Psi^*(x_1)\Psi^*(x_2)\delta(\boldsymbol{r}-\boldsymbol{r}_1+\boldsymbol{r}_2)\Psi(x_2)\Psi(x_1)dx_1dx_2\right\rangle\,. \tag{24}$$

Equation (24) is the exact expression for $g(r)$ in the case that the Hamiltonian is given by Eq. (22). If the spinless bosons are considered, Eq. (24) is reduced to

$$g(\boldsymbol{r})=\frac{V}{\langle N\rangle^2}\left\langle\int\Psi^*(\boldsymbol{r}+\boldsymbol{r}')\Psi^*(\boldsymbol{r}')\Psi(\boldsymbol{r}')\Psi(\boldsymbol{r}+\boldsymbol{r}')\,d\boldsymbol{r}'\right\rangle\,, \tag{25}$$

which is usually known expression. Equation (25) can be transformed further into

$$g(r)=1+\frac{1}{\langle N\rangle^2}\sum_{\boldsymbol{k}_1}\sum_{\boldsymbol{k}_2\neq0}\langle N_{\boldsymbol{k}_1}N_{\boldsymbol{k}_2+\boldsymbol{k}_2}\rangle e^{i\boldsymbol{k}_2\boldsymbol{r}}+\frac{1}{\langle N\rangle^2}\sum_{\boldsymbol{k}_1}\sum_{\boldsymbol{k}_2\neq0}\sum_{\boldsymbol{k}_3\neq\boldsymbol{k}_1+\boldsymbol{k}_2}\langle a_{k_1}{}^*a_{k_3}{}^*a_{k_3-k_2}a_{k_1+k_2}\rangle e^{i\boldsymbol{k}_2\boldsymbol{r}}\,, \tag{25'}$$

where terms of the order of $\langle N\rangle^{-1}$ are omitted and N_k, a_k and $a_k{}^*$ are defined as follows:

$$\Psi(\boldsymbol{r})=\sum_k a_k\frac{1}{\sqrt{V}}e^{i\boldsymbol{kr}}\,,$$

$$\Psi^*(\boldsymbol{r})=\sum_k a_k{}^*\frac{1}{\sqrt{V}}e^{-i\boldsymbol{kr}}\,,$$

$$N_k=a_k{}^*a_k\,.$$

3. *The lowest state of the spinless bosons derived by Bogolyubov and Zubarev*

Bogolyubov and Zubarev[7] have derived approximate expressions for the energy E_0 and th wave function φ_0 for the lowest state of a system composed of spinless bosons, whic are

$$E_0=\frac{N^2}{2V}\nu(0)+\frac{1}{2}\sum_{k\neq0}\left(E(k)-\frac{\hbar^2k^2}{2m}-\frac{N}{V}\nu(k)\right), \qquad (26$$

$$\varphi_0=\exp\left\{-\frac{1}{4}\sum_{k\neq0}\left(\frac{1}{\lambda_k{}^2}-1\right)\rho_k\rho_{-k}\right\}, \qquad (27$$

where $\nu(k)$, $E(k)$ and ρ_k are defined by

$$\left.\begin{aligned}\nu(k)&=\int\phi(r)e^{-i\boldsymbol{kr}}d\boldsymbol{r}\,,\\ E(k)&=\sqrt{\frac{N}{V}\nu(k)\frac{\hbar^2k^2}{m}+\left(\frac{\hbar^2k^2}{2m}\right)^2}\,,\\ \lambda^2{}_k&=\frac{\hbar^2k^2}{2m}\Big/E(k)\,,\\ \rho_k&=\frac{1}{\sqrt{N}}\sum_{j=1}^{N}e^{-i\boldsymbol{kr}_j}\,,\end{aligned}\right\} \qquad (28$$

At temperature $T=0$, the free energy is the same with the energy and hence $g(r)$ an $S(k)$ in the lowest state are given from Eqs. (10) and (11) by

$$g(r)=\frac{2V}{N^2}\left(\frac{\delta E_0}{\delta\phi}\right)_r \qquad (29$$

and

$$S(k)=1-(2\pi)^3\frac{N}{V}\delta(\boldsymbol{k})+\frac{2}{N}\left(\frac{\delta E_0}{\delta\phi}\right)_k, \qquad (29'$$

of which the former expression is found in the paper of Bogolyubov and Zubarev*. Wit the help of

$$\left(\frac{\delta\nu(k')}{\delta\phi}\right)_k=\int e^{i\boldsymbol{kr}}e^{-i\boldsymbol{k'r'}}d\boldsymbol{r}=(2\pi)^3\delta(\boldsymbol{k}-\boldsymbol{k}')$$

and

$$\left(\frac{\delta E(k')}{\delta\phi}\right)_k=\frac{1}{2}\frac{N}{V}\frac{\hbar^2k'^2}{m}\frac{1}{E(k')}\left(\frac{\delta\nu(k')}{\delta\phi}\right)_k=\frac{(2\pi)^3}{2}\frac{N}{V}\frac{\hbar^2k^2}{m}\frac{1}{E(k)}\delta(\boldsymbol{k}-\boldsymbol{k}')\,,$$

Eq. (29′) is reduced to

$$S(k)=\frac{\hbar^2k^2}{2m}\Big/E(k)=\lambda_k{}^2 \qquad (30$$

and by Eq. (6′) $g(r)$ is obtained as

$$g(r)=1+\frac{V}{N}\frac{1}{(2\pi)^3}\int(\lambda_k{}^2-1)e^{-i\boldsymbol{kr}}d\boldsymbol{k}\,, \qquad (30'$$

---

* The starting point of the present investigation was an attempt to clarify the meaning of this expression

hich can be also obtained from the direct alculation of $(\delta E_0/\delta\phi)_r$.

As pointed out by Bogolyubov and Zubarev, q. (30) is identical to the relation derived by eynman[8] provided that $E(k)$ is interpreted o be a spectrum of excitation.

Comparison of the definition of ρ_k with Eq 9) leads to

$$S(k)=\langle\rho_k\rho_{-k}\rangle \quad \text{for} \quad k\neq 0\,. \tag{31}$$

Vhile Eq. (31) is valid for more general cases, ts right-hand side should be considered in ur case to be

$$\langle\rho_k\rho_{-k}\rangle=\frac{\int_V\cdots\int_V \rho_k\rho_{-k}\varphi_0{}^2 d\boldsymbol{r}_1\cdots d\boldsymbol{r}_N}{\int_V\cdots\int_V \varphi_0{}^2 d\boldsymbol{r}_1\cdots dd\boldsymbol{r}_N}\,. \tag{32}$$

f $\langle\rho_k\rho_{-k}\rangle$ is calculated by means of

$$\langle\rho_k\rho_{-k}\rangle=\frac{\int_{-\infty}^{\infty}\cdots\int(\sigma_k{}^2+\tau_k{}^2)\varphi_0{}^2\prod_{k'}d\sigma_{k'}d\tau_{k'}}{\int_{-\infty}^{\infty}\cdots\int\varphi_0{}^2\prod_{k'}d\sigma_{k'}d\tau_{k'}}\,,$$

where σ_k and τ_k are the real numbers defined y

$$\rho_k=\sigma_k+i\tau_k\,,\quad \sigma_{-k}=\sigma_k \text{ and } \tau_{-k}=-\tau_k\,,$$

a false result follows from Eq. (31), *i.e.*,

$$S(k)=\frac{\lambda_k{}^2}{1-\lambda_k{}^2}\,. \tag{33}$$

A calculation of Eq. (32) leading to Eq. (30) will be shown in Appendix II.

§4. The Expressions for the Pressure and the Internal Energy

In classical fluid the pressure p and the nternal energy E can be witten in terms of (r) by the following well-known expressions[9]:

$$\frac{p}{\rho\kappa T}=1-\frac{\rho}{6\kappa T}\int_0^\infty g(r)\frac{d\phi(r)}{dr}4\pi r^3 dr \tag{34}$$

nd

$$\frac{E}{(3/2)N\kappa T}=1+\frac{\rho}{3\kappa T}\int_0^\infty g(r)\phi(r)4\pi r^2 dr\,. \tag{35}$$

The above expressions are usually derived by making use of definition (5) of $g(r)$. Even if $g(r)$ is defined by Eq. (10), the same expressions ought to be derived as far as an exact theory is concerned, since then Eq. (10) is equivalent to Eq. (5). Therefore, as far as an exact theory is concerned, the following derivation is an alternative to the usual one of Eqs. (34) and (35). In addition to this, it has the advantage of being usable also in an approximate expression to the free energy. For the sake of completeness the quantum statistical mechanics will be considered.

The expression for the free energy will be assumed to have the following form:

$$\frac{A}{N\kappa T}=\log\frac{\lambda^3}{V}+a\left[\frac{\phi(Lx')}{\kappa T},\,\beta,\,\lambda^*\right], \tag{36}$$

where $V=L^3$, $\lambda^2=h^2/2\pi m\kappa T$, $\lambda^*=\lambda/L$ and Lx' is the position vector $\boldsymbol{r}'$ of a molecule and β is the parameter determined so as to minimize A under the condition of $T=$const. and $V=$const. and further functional a does not depend on T and V except for the form shown explicitly. With the help of Eqs. (10) and (14), $g(r)$ is written in terms of a as

$$\begin{aligned} g(r)&=\frac{2V\kappa T}{N}\left(\frac{\delta a}{\delta\phi}\right)_r+\frac{2V\kappa T}{N}\frac{\partial a}{\partial\beta}\left(\frac{\delta\beta}{\delta\phi}\right)_r \\ &=\frac{2V\kappa T}{N}\left(\frac{\delta a}{\delta\phi}\right)_r\,, \end{aligned} \tag{37}$$

where use has been made of the property of β to minimize A and $(\delta a/\delta\phi)_r$ should be interpreted as the functional derivative with respect to ϕ under the condition of $\beta=$const. It is more convenient for the present purpose to go back to the notation corresponding to $F[\delta(\boldsymbol{r}-\boldsymbol{r}')]$ in Eq. (12). Thus $g(r)$ is expressed as

$$g(r)=\frac{2V\kappa T}{N}f[\delta(\boldsymbol{r}-\boldsymbol{r}')]\,, \tag{37'}$$

where functional f is defined by the variation $\varDelta a$ in the similar way as F by $\varDelta A$ and it depends also on T, V, β and λ^*, though it is not shown explicitly. The essential point is that f is a linear functional with respect to the argument shown explicitly.

Now

$$\begin{aligned} \frac{p}{\rho\kappa T}&=-V\frac{\partial}{\partial V}\left(\frac{A}{N\kappa T}\right)=1-\frac{L}{3}\frac{\partial a}{\partial L} \\ &=1+\frac{\lambda^*}{3}\frac{\partial a}{\partial\lambda^*}-\frac{L}{3}\lim_{\varDelta L\to 0}\frac{a\left[\frac{1}{\kappa T}\left\{\phi(Lx')+x'\frac{\partial\phi}{\partial r'}\varDelta L\right\},\beta,\lambda^*\right]-a\left[\frac{\phi(Lx')}{\kappa T},\beta,\lambda^*\right]}{\varDelta L}\,. \end{aligned} \tag{38}$$

The third term in the last line of Eq. (38) can be transformed, by the use of the definition of f and Eq. (37′), in the following manner:

$$-\frac{L}{3}f\left[x'\frac{\partial\phi}{\partial\boldsymbol{r}'}\right]=-\frac{1}{3}f\left[\boldsymbol{r}'\frac{\partial\phi}{\partial\boldsymbol{r}'}\right]=-\frac{1}{3}f\left[\int_V\delta(\boldsymbol{r}-\boldsymbol{r}')\boldsymbol{r}\frac{\partial\phi}{\partial\boldsymbol{r}}d\boldsymbol{r}\right]$$

$$=-\frac{1}{3}\int_V f[\delta(\boldsymbol{r}-\boldsymbol{r}')]\boldsymbol{r}\frac{\delta\phi}{\partial\boldsymbol{r}}d\boldsymbol{r}$$

$$=-\frac{N}{6V\kappa T}\int_V g(r)\boldsymbol{r}\frac{\partial\phi}{\partial\boldsymbol{r}}d\boldsymbol{r}$$

$$=-\frac{\rho}{6\kappa T}\int_0^\infty g(r)\frac{d\phi}{dr}4\pi r^3dr\,.$$

Hence Eq. (38) becomes

$$\frac{p}{\rho\kappa T}=1+\frac{\lambda^*}{3}\frac{\partial a}{\partial\lambda^*}-\frac{\rho}{6\kappa T}\int_0^\infty g(r)\frac{d\phi}{dr}4\pi r^3dr\,. \qquad (39$$

In an analogous way the expression for E is obtained as

$$\frac{E}{(3/2)N\kappa T}=1+\frac{\lambda^*}{3}\frac{\partial a}{\partial\lambda^*}+\frac{\rho}{3\kappa T}\int_0^\infty g(r)\phi(r)4\pi r^2dr\,. \qquad (40$$

Equations (39) and (40) agree with Eqs. (34) and (35) respectively in the classical case, wher the second terms of the right-hand sides of Eqs. (39) and (40) are missing.

It might be supposed that the special form of the free energy assumed in (Eq. (36) limit the validity of) Eq. (39) or (40). However, the expression for the free energy will generall be written in the form given by Eq. (36) so far as it is calculated, even if approximately from the knowledge of $\phi(r)$. As an example we shall consider Eq. (18). It is rewritten as

$$\frac{A_0}{N\kappa T}=\log\frac{\lambda^3}{V}+\log\frac{N}{e}-\frac{N}{2}\left[(2\pi)^{3/2}\bar{\beta}(0)-\pi\int_{-\infty}^{\infty}y^2\bar{\beta}^2(y)dy\right]$$

$$+\frac{1}{N}\frac{1}{8\pi^2}\int_{-\infty}^{\infty}y^2\log[1-(2\pi)^{3/2}N\bar{\beta}(y)]dy+\frac{1}{2\sqrt{2\pi}}\int_{-\infty}^{\infty}y^2\bar{\beta}(y)dy\,,$$

where

$$y\bar{\beta}(y)=\frac{1}{\sqrt{2\pi}}\int_{-\infty}^{\infty}x[e^{-\phi(Lx)/\kappa T}-1]\sin xy\,dx\,.$$

Obviously the above expression has the form given by Eq. (36). It can be shown that even Eq. (26) has the form under consideration, provided that a proper limit is taken.

§ 5. Discussion

Formula (10) can be used to obtain the approximate distribution function when the approximate expression for the free energy is known. The function thus derived is consistent with the approximation used in the derivation of the free energy. However, this function is not necessarily equal to the one derived from Eq. (5) based on the same approximation. Such an example is given by the third example considered in § 3. Equation (29′) is equivalent to Eq. (10), while Eq. (31) is equivalent to Eq. (5). In order to obtain Eq. (30) from the calculation of the right-hanc side of Eq. (31) or Eq. (32), a further appro ximate procedure must be introduced. A detailed calculation is shown in Appendix II In such cases, it can be said that the distri bution function based on Eq. (10) is preferabl to one based on Eq. (5), since the former i consistent with the approximation used in th derivation of the free energy.

Generally speaking, an approximate proce dure can be introduced more properly in th derivation of the free energy than in th derivation of the distribution function. It i often difficult for the true character of th approximation used in the latter case to b revealed and this approximation often leads t the results having the self-inconsistency a discussed in the previous paper.

An interesting application of Eq. (10) is ound in the cell theory of liquid state, where t is difficult to apply Eq. (5) and more intuiive procedures are usually adopted in order o derive the distribution function. This is lue to the fact that Eq. (10) is applicable irespective of underlying models upon which he theory is based.

Formula (10) has the drawback that it is not applicable to the case where the expression of the free energy is not known as the functional of interaction potential. Especially t becomes powerless in the case of quantum ideal gases, where the interaction potential ϕ does not exist and $g(r)$ differs from unity due to the symmetry effect alone. Ideal gases must be considered as the limiting case where ϕ tends to zero if it is tried to apply Eq. (10). However, such a method cannot be carried out unless the theory of quantum fluid is given.

The author would like to express his appreciation to Professor A. Harasima for his continual encouragement and helpful discussions throughout this work.

Appendix I

Expression (18) for the approximate free energy will be derived here. The following procedure is analogous to one which was used by Montroll and Mayer[4] in calculation of $g(r)$. The free energy A of classical fluid is given by Eq. (17), *i. e.*,

$$\frac{A}{N\kappa T}=\log\left(\frac{h^2}{2\pi m\kappa T}\right)^{3/2}\frac{\rho}{e}-\sum_{n=1}\frac{1}{n+1}\beta_n\rho^n\,. \tag{I-1}$$

The irreducible integrals β_n's are defined by[2]

$$\beta_n=\frac{1}{n!\,V}\iint\cdots\int\sum_{\substack{\text{All products which are more}\\ \text{than singly connected}}}\prod_{n+1\geq i>j\geq 1}\alpha_{ij}\,d\boldsymbol{r}_1 d\boldsymbol{r}_2\cdots d\boldsymbol{r}_{n+1}$$

where

$$\alpha_{ij}=\alpha(r_{ij})=e^{-\phi(r_{ij})/\kappa T}-1\,.$$

Among many terms composing β_n, only the terms of the following type will be considered:

$$\frac{1}{n!\,V}\iint\cdots\int\alpha_{12}\alpha_{23}\cdots\alpha_{n+1,\,1}\,d\boldsymbol{r}_1 d\boldsymbol{r}_2\cdots d\boldsymbol{r}_{n+1}\,.$$

There exist $n!/2$ such terms in β_n. Then approximate irreducible integral β_{n0} which involves only terms as shown above, is

$$\beta_{n0}=\frac{n!}{2}\frac{1}{n!\,V}\iint\cdots$$
$$\times\int\alpha_{12}\alpha_{23}\cdots\alpha_{n+1,1}d\boldsymbol{r}_1 d\boldsymbol{r}_2\cdots d\boldsymbol{r}_{n+1}$$
$$=\frac{1}{2}\iint\cdots\int\alpha_{12}\alpha_{23}\cdots\alpha_{n+1,1}d\boldsymbol{r}_1 d\boldsymbol{r}_2\cdots d\boldsymbol{r}_n\,,$$

which can be calculated by the use of $\beta(u)$ defined by Eq. (19) as follows:

$$\beta_{n0}=\frac{1}{2}(2\pi)^{(3n-1)/2}\int_{-\infty}^{\infty}u^2\beta^{n+1}(u)du\,,\ \text{for } n\geqq 2\,. \tag{I-3}$$

The above procedure is not valid for $n=1$. The correct expression should be used for β_{10}:

$$\beta_{10}=\beta_1=2\pi\int_{-\infty}^{\infty}r^2\alpha(r)dr=(2\pi)^{3/2}\beta(0)\,. \tag{I-3′}$$

The simple chain approximation to the free energy is to use β_{n0} instead of β_n in the right-hand side of Eq. (I−1). Then the summation with respect to n can be carried out as follows:

$$\sum_{n=1}\frac{1}{n+1}\beta_{n0}\rho^n=\frac{1}{\rho}\int_0^{\rho}\left[\sum_{n=1}\beta_{n0}\,x^n\right]dx$$

$$=\frac{1}{\rho}\int_0^{\rho}\left[\frac{1}{2}\frac{1}{\sqrt{2\pi}}\sum_{n=1}\int_{-\infty}^{\infty}u^2\beta(u)\{(2\pi)^{3/2}x\beta(u)\}^n du+\left\{(2\pi)^{3/2}\beta(0)-\pi\int_{-\infty}^{\infty}u^2\beta^2(u)\,du\right\}x\right]dx$$

$$=\frac{1}{\rho}\int_0^{\rho}\left[\frac{1}{2\sqrt{2\pi}}\int_{-\infty}^{\infty}\frac{u^2\beta^2(u)(2\pi)^{3/2}x}{1-(2\pi)^{3/2}x\beta(u)}du+\left\{(2\pi)^{3/2}\beta(0)-\pi\int_{-\infty}^{\infty}u^2\beta^2(u)du\right\}x\right]dx$$

$$=-\frac{1}{\rho}\frac{1}{8\pi^2}\int_{-\infty}^{\infty}u^2\log\left[1-(2\pi)^{3/2}\rho\beta(u)\right]du-\frac{1}{2\sqrt{2\pi}}\int_{-\infty}^{\infty}u^2\beta(u)du$$
$$+\frac{\rho}{2}\left[(2\pi)^{3/2}\beta(0)-\pi\int_{-\infty}^{\infty}u^2\beta^2(u)du\right].$$

Hence the approximate expression A_0 for the free energy is obtained as follows:

$$\frac{A_0}{N\kappa T}=\log\left(\frac{h^2}{2\pi m\kappa T}\right)^{3/2}\frac{\rho}{e}-\frac{\rho}{2}\left[(2\pi)^{3/2}\beta(0)-\pi\int_{-\infty}^{\infty}u^2\beta^2(u)du\right]$$
$$+\frac{1}{\rho}\frac{1}{8\pi^2}\int_{-\infty}^{\infty}u^2\log\left[1-(2\pi)^{3/2}\rho\beta(u)\right]du+\frac{1}{2\sqrt{2\pi}}\int_{-\infty}^{\infty}u^2\beta(u)du\,, \tag{I-4}$$

which is the one given by Eq. (18).

Appendix II

Equation (30) for $S(k)$ will be derived here from Eq. (32). The method of our calculatio is taken from Zubarev's paper[10]. Our object is to calculate

$$\langle\rho_k\rho_{-k}\rangle=\frac{\int\cdots\int\rho_k\rho_{-k}\varphi_0^2\,d\boldsymbol{r}_1\cdots d\boldsymbol{r}_N}{\int\cdots\int\varphi_0^2 d\boldsymbol{r}_1\cdots d\boldsymbol{r}_N}\,. \qquad \text{(II-1}$$

For brevity we shall write the wave function given by Eq. (27) as

$$\varphi_0=\exp\{-\tfrac{1}{2}\sum_k{}'\,a_k\,\rho_k\rho_{-k}\}\,, \qquad \text{(II-2}$$

where

$$a_k=\frac{1}{\lambda_k^2}-1 \qquad \text{(II-3}$$

and $\sum_k{}'$ means that the summation is carried out over the semi-infinite region of $\boldsymbol{k}$ in whic z-component $\boldsymbol{k}_z$ is positive.

The denominator of Eq. (II-1) can be written as follows:

$$\int\cdots\int\varphi_0^2 d\boldsymbol{r}_1\cdots d\boldsymbol{r}_N=\int_{-\infty}^{+\infty}\cdots\int_{-\infty}^{+\infty}\exp\Big\{-\sum_k{}'\,a_k\rho_k\rho_{-k}\Big\}\times D(\cdots,\rho_k,\cdots)\prod_k{}'\,d\sigma_k d\tau_k\,, \qquad \text{(II-4)}$$

where

$$D(\cdots,\rho_k,\cdots)=\int\cdots\int\prod_k{}'\,\delta\Big(\sigma_k-\frac{1}{\sqrt{N}}\sum_j\cos\boldsymbol{k}\boldsymbol{r}_j\Big)\,\delta\Big(\tau_k-\frac{1}{\sqrt{N}}\sum_j\sin\boldsymbol{k}\boldsymbol{r}_j\Big)d\boldsymbol{r}_1\cdots d\boldsymbol{r}_N \qquad \text{(II-5)}$$

and

$$\rho_k=\sigma_k+i\tau_k,\ \sigma_{-k}=\sigma_k,\ \tau_{-k}=-\tau_k$$

and $\prod_k{}'$ is the product of which meaning is similar to $\sum_k{}'$. The function $D(\cdots,\rho_k,\cdots)$ is a kind of Jacobian for the transformation from $(\boldsymbol{r}_1,\cdots,\boldsymbol{r}_N)$ to $(\cdots,\rho_k,\cdots)$. Use of the Fourier representation of δ-function leads to

$$D(\cdots,\rho_k,\cdots)=\int_{-\infty}^{+\infty}\cdots\int_{-\infty}^{+\infty}e^{i\pi\sum_k\omega_k\rho_k}\Big\{\int\exp\Big[-\frac{i\pi}{\sqrt{N}}\sum_k\omega_k e^{i\boldsymbol{k}\boldsymbol{r}}\Big]d\boldsymbol{r}\Big\}^N\prod_k{}'\,d\alpha_k d\beta_k\,. \qquad \text{(11-6)}$$

where

$$\omega_k=\alpha_k-i\beta_k,\ \alpha_{-k}=\alpha_k,\ \text{and}\ \beta_{-k}=-\beta_k\,.$$

When the expansion

$$\frac{1}{V}\int\exp\Big\{-\frac{i\pi}{\sqrt{N}}\sum_k\omega_k e^{i\boldsymbol{k}\boldsymbol{r}}\Big\}d\boldsymbol{r}=1-\frac{\pi^2}{2N}\sum_k\omega_k\omega_{-k}+\frac{1}{3!}\Big(\frac{-i\pi}{\sqrt{N}}\Big)^3\sum_{k_1+k_2+k_3=0}\omega_{k_1}\omega_{k_2}\omega_{k_3}+\cdots,$$

is used in the integrand of Eq. (II-6), $D(\cdots,\rho_k,\cdots)$ is expressed as:

$$D(\cdots,\rho_k,\cdots)=\Big\{1-\frac{1}{3!}\frac{1}{\sqrt{N}}\sum_{k_1+k_2+k_3=0}\frac{\partial^3}{\partial\rho_{k_1}\partial\rho_{k_2}\partial\rho_{k_3}}+\cdots\Big\}D_0(\cdots;\rho_k,\cdots)\,, \qquad \text{(II-7)}$$

where

$$D_0(\cdots,\rho_k,\cdots)=V^N\int_{-\infty}^{+\infty}\int_{-\infty}^{+\infty}\exp\Big\{i\pi\sum_k\omega_k\rho_k-\frac{\pi^2}{2}\sum_k\omega_k\omega_{-k}\Big\}\prod_k{}'\,d\alpha_k d\beta_k \qquad \text{(II-8)}$$

The integration of the right-hand side of Eq. (II–8) can easily be carried out:

$$D_0(\cdots,\rho_k,\cdots)=V^N\exp\Big\{-\sum_k{}'(\rho_k\rho_{-k}+\log\pi)\Big\}\,. \tag{11–9}$$

As the first approximation we use $D_0(\cdots,\rho_k,\cdots)$ in place of $D(\cdots,\rho_k,\cdots)$ in Eq. (II–4). Then

$$\begin{aligned}\int\cdots\int\varphi_0{}^2d\boldsymbol{r}_1\cdots d\boldsymbol{r}_N &\approx\int_{-\infty}^{+\infty}\cdots\int_{-\infty}^{+\infty}\exp\Big\{-\sum_k{}'a_k\rho_k\rho_{-k}\Big\}D_0(\cdots,\rho_k,\cdots)\prod_k{}'\,d\sigma_kd\tau_k\\ &=V^N\prod_k{}'\left[\frac{1}{\pi}\int_{-\infty}^{+\infty}\cdots\int_{-\infty}^{+\infty}\exp\{-(a_k+1)(\sigma_k{}^2+\tau_k{}^2)\}d\sigma_kd\tau_k\right]\\ &=V^N\prod_k{}'\frac{1}{a_k+1}=V^N\prod_k{}'\lambda_k{}^2\,.\end{aligned} \tag{II–10}$$

In the same way, the numerator of Eq. (II–1) is calculated as

$$\int\cdots\int\rho_k\rho_{-k}\varphi_0{}^2d\boldsymbol{r}_1\cdots d\boldsymbol{r}_N\approx V^N\lambda_k{}^2\prod_{k'}{}'\lambda_{k'}{}^2\,. \tag{II–11}$$

Therefore we finally obtain, as the first approximation to $\langle\rho_k\rho_{-k}\rangle$,

$$\langle\rho_k\rho_{-k}\rangle\approx\lambda_k{}^2 \tag{II–12}$$

which is identical to Eq. (30) for $S(k)$.

References

1) K. Hiroike: J. Phys. Soc. Japan **12** (1957) 326

2) See, for example, J. E. Mayer and M. G. Mayer: "Statistical Mechanics" (Wiley, New York, 1940) Chapter 13.

3) H. S. Green: Proc. Roy. Soc. **A189** (1947) 103.

4) E. W. Montroll and J. E. Mayer: J. Chem. Phys. **9** (1941) 626.

5) G. S. Rushbrooke: Phil. Mag. **43** (1952) 1276.

6) G. S. Rushbrooke and H. I. Scoins: Proc. Roy. Soc. **A216** (1953) 203.

7) N. N. Bogolyubov and D. N. Zubarev: J. Exp. Theor. Phys. U. S. S. R. **28** (1955) 129.

8) R. P. Feynman: Phys. Rev. **94** (1954) 262.

9) See, for example, T. L. Hill: "Statistical Mechanics" (McGraw-Hill, New York, 1956) Chapter 6.

10) D. N. Zubarev: Dok. Akad. Sci. U. S. S. R. **95** (1954) 757.

JOURNAL OF THE PHYSICAL SOCIETY OF JAPAN Vol. 12, No. 8, AUGUST, 1957

Submicroscopic Topography of Oxidized Surface of Stibnite and Etched Surface of Zincblende

By Masaru WATANABE

Japan Electron Optics Laboratory Co., Ltd.
Kamirenjaku, Mitaka, Tokyo, Japan

(Received December 8, 1956)

Submicroscopic topographies of oxidized stibnite and of etched zincblende were examined by electron microscopes. Crystallites of antimony oxide formed on stibnite have a roof-like shape bounded by two well-developed and four less developed {111} faces. This is in agreement with the conclusion drawn previously from electron diffraction study (Miyake, Sc. Pap. I. P. C. R. **34** (1938), 565). The direct observation by electron microscope gives some further information on the growth of the oxide. Zincblende surfaces etched by hydrochloric acid has a shape which is slightly different from the negative triakis tetrahedron inferred from electron diffraction study (Uyeda et al., Proc. Phys.-Math. Soc. Japan **24** (1941) 1049). In the diffraction patterns from this surface, structures of reflexion spots finer than those previously reported were observed and analysed by the theory of the dynamical refraction effect.

§ 1. Introduction

When crystallites have a well-defined external shape, the electron diffraction spots show fine structures. By observing such fine structures submicroscopic topography of crystal surfaces were studied before the advent of the electron microscopy[1]. The results obtained in this way seem to be convincing, but they are after all indirect. Therefore, it is of interest to re-examine by electron microscopy the surfaces which were previously studied by electron diffraction. In the present paper the following two surfaces are examined.

(i) Oxidized surface of stibnite (Sb_2S_3)

Miyake[2] concluded that crystallites of antimony oxide, Sb_2O_3, which were formed on cleavage faces of stibnite grew into characteristic roof-like protrusions elongated along [001]-axis of stibnite and bounded by octahedral planes as illustrated in Fig. 1.

(ii) Etched surface of zincblende (ZnS)

Uyeda et al[3]. concluded that when cleavage face (110) of zincblende is etched b hydrochloric acid it consisted of minute face of the negative triakis tetrahedron[4], a for composed of {211} faces (Fig. 2). When, how ever, the same surface was etched by nitri acid it consisted of minute faces of positiv and negative triakis tetrahedrons.

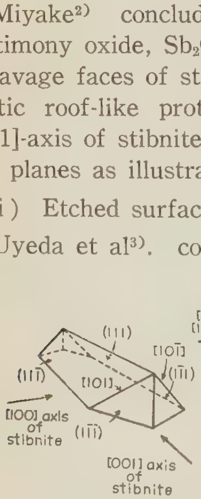

Fig. 1.

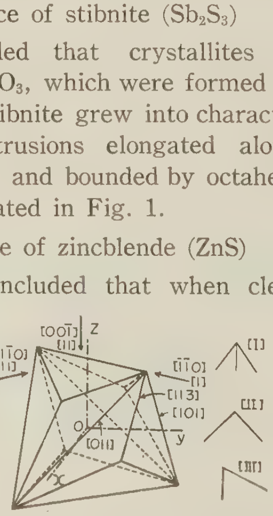

Fig. 2

In the present paper it will be shown a first that the antimony oxide grows in th form exactly as concluded by Miyake and the the zincblende surface etched by hydrochlori acid is made up of faces slightly differen from those of negative triakis tetrahedron In a later part of this paper structures o diffraction pattern finer than that observed b Uyeda et al. will be discussed in detail.

§ 2. Experimentals

(i) *Specimen Preparation*

The specimens were prepared following th methods adopted by the original observers.

a) Oxidized surfaces of stibnite

Small pieces of stibnite, about 1×1 sq. cm in area and 1~2 mm. in thickness, were clef off from larger crystals and oxidized for fron 1 to 60 min. in an open electric furnace a temperatures about 280°C.

b) Etched surfaces of zincblende

Small pieces of zincblende, about 1×1 sq cm. in area and 1~3 mm. in thickness, wer cleft off from a crystal block, and etched b hydrochloric acid at about 80°C and by nitric acid at room temperatures.

ii) *Method of Observation*

The surfaces prepared were studied with EM-5 electron microscope by the transmission method utilizing a replica technique and by the reflexion method as well. Each specimen was ascertained before electron microscopy that it gave electron diffraction patterns of the characteristic fine structures as described by the original observers.

iii) *Replica Technique*

Specimens of stibnite became so fragile by heating that it was difficult to apply the conventional replica techniques. Among other alternatives, metallic collodion negative replica[5] backed by reinforcing ethocel film gave the best result. Chromium-shadow was cast from the direction of [100]-axis of stibnite.

For zincblende specimens, a composite metallic film replica was prepared as follows: A mould of the specimen surface was made of a polystyrene plate of thickness about 2 mm., which was heated up to 150°～160°C with compressed to the specimen surface, and then the mould was chromium-shadowed from the direction of [$1\bar{1}0$]-axis of zincblende. Finally, an aluminum film was deposited on it. The composite metallic film was separated from polystyrene by immersing in benzene.

§ 3. Results

i) *Antimony Oxide formed on Stibnite*

Photos. 1a and 1b show two transimission electron micrographs of the surface. Photos. 2a and 2b reproduce reflexion micrographs obtained with incidences of electrons nearly perpendicular and parallel to [001]-axis of stibnite, respectively.

In Photos. 1a and 1b, it can be found that a number of parallel roof-like oxide protrusions stand out in relief from the substrate*. The angle between the two edges at the ends of the protrusion (Photo. 1a) is about 110° as illustrated in Photo. 1a and this agrees well with the calculated angle 109° 28′ between the projections of [101]- and [$10\bar{1}$]- axes to the cleavage surface. Thus Miyake's conclusion

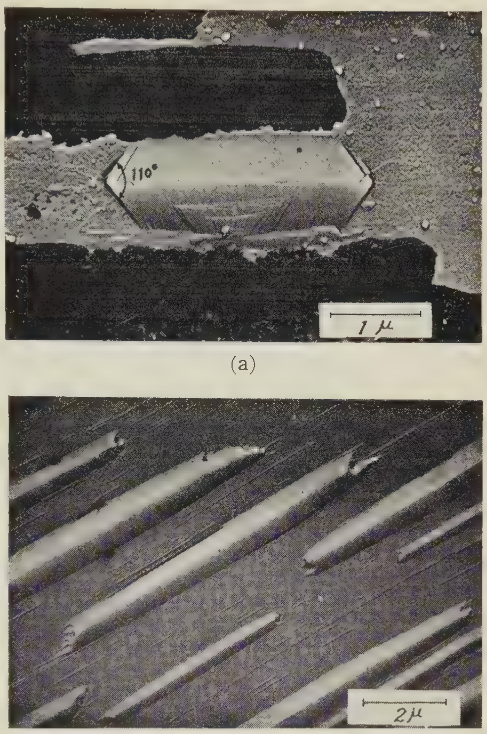

(a)

(b)

Photo. 1. Antimony oxide (Sb_2O_3) formed on the cleavage surface of stibnite (Sb_2S_3) heated at 280°C for 30 min. in atmosphere.

Note the lamellar growth of the octahedral faces.

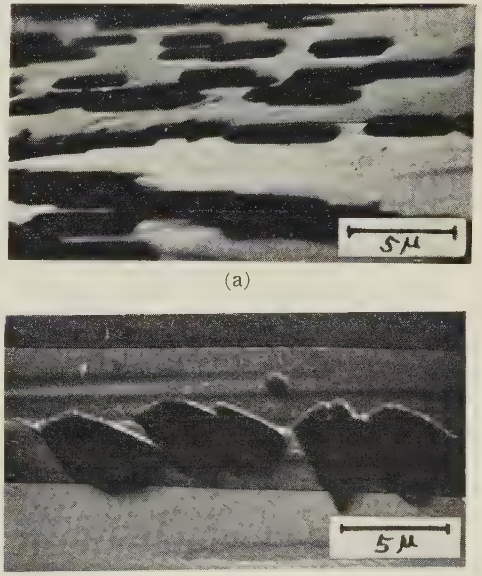

(a)

(b)

Photo. 2. Reflexion electron micrographs of Sb_2O_3 crystals formed on stibnite cleavage face (010). Electron incidences nearly parallel to (a) [100]- and (b) [001]-axes of stibnite.

---

* In our previous experiment[6] utilizing collodion one step replica, only a round edge was observed at the top of oxide roofs on account of the unfaithfulness of the replica.

is clearly verified. Photos. 2a and 2b show also the existence of such protrusions, though it is less obvious because of the fore-shortening of the image and poor resolusion.

In Photo. 1b, which is a surface heated for 30 minutes, it can be seen that, besides well developed oxide protrusions of lateral size about 1 micron, there are many much thinner protrusions of lateral size of a few hundred Å, having an external form similar to that of larger ones. After oxidation of less than 5 minutes, only such thinner protrusions were observed on the surface, and such surfaces gave the most clearly the characteristic fine structures of diffraction spots as found by Miyake. When the time of oxidation was longer than 5 minutes, protrusions of a larger size appeared. However, protrusions of lateral size larger than 1 micron were scarce even after one hour oxidation. In spite of variation of oxidation time, the lateral sizes of almost all protrusions were either a few hundred Å or about 1 micron. Thus it seems that 1 micron is the limit of the lateral size of the protrusion and that the lateral growth from a few hundred Å to the limit is very rapid.

(ii) *Etched Surface of Zincblende*

Photo. 3 shows the transmission electron micrograph of a surface of zincblende etched by hydrochloric acid. Photos. 4a and 4b are reflexion electron micrographs of the same surface. Photos. 5 and 6 are electron diffraction patterns produced from the same surface. The directions of electron incidence for Photos. 5 and 6 were almost the same as those for the micrographs Photos. 4a and 4b, respectively. The reflexions in these electron diffraction patterns show in general streak-like elongations as observed by Uyeda et al.*.

In Photo. 3, there can be found wedge shapes with an angle of about 70°. A faint line bisects each of the wedges. The apex angle of the wedges observed in Photo. 4a and the angle between the streaks of diffraction spots in Photo. 5 are equal to 90°. The wedge found in Photo. 4b is composed of two edges, one being vertical and the other meeting the vertical one at an angle of 56°~57°. The streaks in Photo. 6 are elongated exactly perpendicular to these two edges.

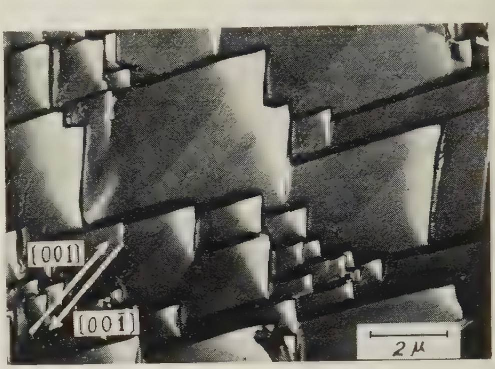

Photo. 3. (110) surface of zincblende (ZnS) etched by hydrochloric acid at about 80°C.

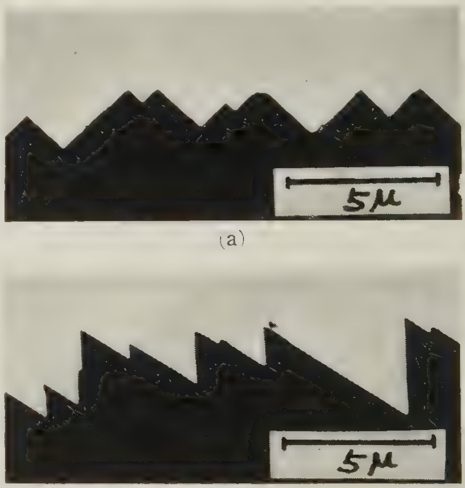

(a)

(b)

Photo. 4. Reflexion electron micrographs of etched (110) surface of zincblende with electron incidences parallel to (a) $[00\bar{1}]$- and (b) $[\bar{1}10]$-axes.

When we look at the negative triakis tetrahedron along [I] $[\bar{1}\bar{1}0]$-, [II] $[00\bar{1}]$- and [III] $[1\bar{1}0]$-directions, there will appear wedge shapes as follows (Fig. 2): [I] a wedge of apex angle 70°34′, bounded by edges [011]- and [101]-axes. It is bisected by the edge line [113]-axis, [II] a wedge of apex angle 90° bounded by [011]- and [101]-axes and [III] a wedge of apex angle 64°50′ bounded by [113]- and [001]-axes.

The wedge shapes found in Photos. 3 and 4a agree exactly with the wedges [I] and

---

* Uyeda et al. considered that the streaks of diffraction spots were due to the refraction effect. Thus the streak should be elongated along the direction perpendicular to the edge at which the two boundary faces penetrated by the electron beam intersect each other. More detailed observations and discussions will be given in §4 and §5.

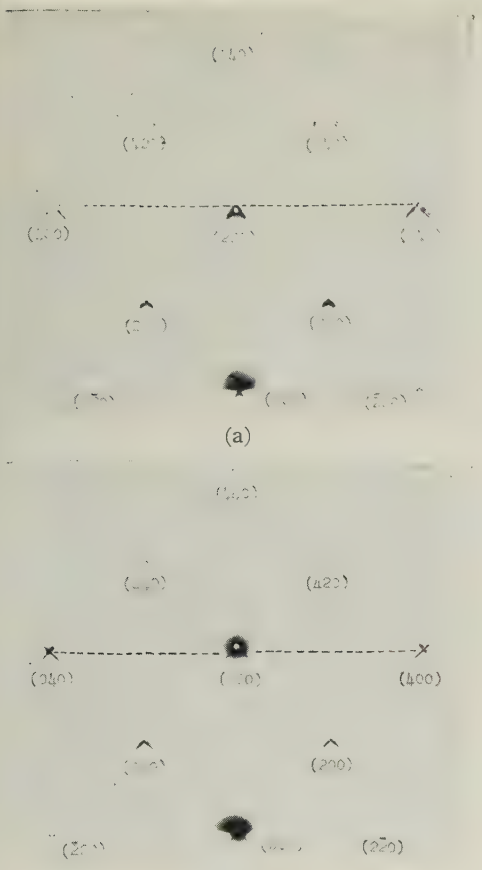

(a)

(b)

Photo. 5. Electron diffraction patterns of etched (110) surface of zincblende. (a) and (b) are taken, respectively, with a- and b-incidences defined in § 4.

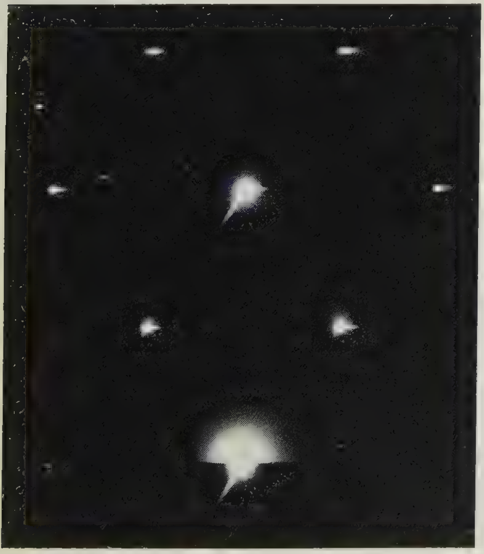

Photo. 6. Electron diffraction pattern of etched (110) surface of zincblende with electron incidence parallel to [$\bar{1}$10] axis.

[II], respectively. The apex angle of wedges in Photo. 4b, however, is different decidedly from that of the wedge [III]. Thus, we see that the protrusions on the etched zincblende surface have a form which is slightly different from the negative triakis tetrahedron. If we assume a form composed of {655} faces, there appears in the third view a wedge bounded by the edges [001]- and [55 11] -axes, the angle between them being 57°14′. In the other two views, this form gives the same wedges as those of the negative triakis tetrahedron. Thus we conclude that the etched surface of zincblende is composed of {655} faces.

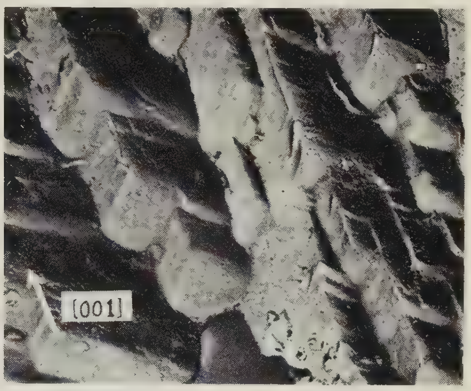

Photo. 7. (110) surface of zincblende etched by nitric acid.

Photo. 7 shows an electron micrograph of (110) face of zincblende etched by nitric acid. In this case, rough faces having indices {100} and {112} are revealed in the electron micrograph, but clean-cut feature as supposed by Uyeda et al. can not be detected.

§ 4. Fine Structure of Electron Diffraction Pattern of Etched Zincblende Surface

Photos. 5a and 5b were taken with incident electron beams in plane of incidence (1$\bar{1}$0). In both cases Bragg condition was exactly satisfied for (220)-reflexion. In Photo. 5a the electron beam was along [001]-direction (a-incidence) and in Photo. 5b, along [00$\bar{1}$]-direction (b-incidence).

Each streak (Photos. 5a and 5b) shows a fine structure containing two or more spots. The fine structure depends not only on indices of reflexions but also on the direction of the incident electrons. The relative position of reflexions is different in the two patterns

(Photos. 5a and 5b); for example, the halation spot of (220) reflexion is under (Photo. 5a) or above (Photo. 5b) the dashed lines joining the cross points of streaks in (400) and (040).

It is found that such details of reflexions vary considerably according to slight variations of the crystal setting. A series of variations of (400) and (420) reflexions are reproduced in Photos. 8 and 9*. There, the angle of incidence was varied without changing the plane of incidence. Numbers 1, 2, ···, 5 correspond, respectively, to the crystal settings for which Ewald's sphere intersects the (hh0) reciprocal lattice plane along circles 1, 2, ···, 5 shown in Fig. 3. The circle with a dot in each photograph indicates the position of reflexion due to the simple Bragg's law. One division of the scale in the photographs corresponds to 0.1 mm. on the original plates which were taken by a diffraction camera with specimen-plate distance 29 cm. and with an accelerating voltage 50 kV.

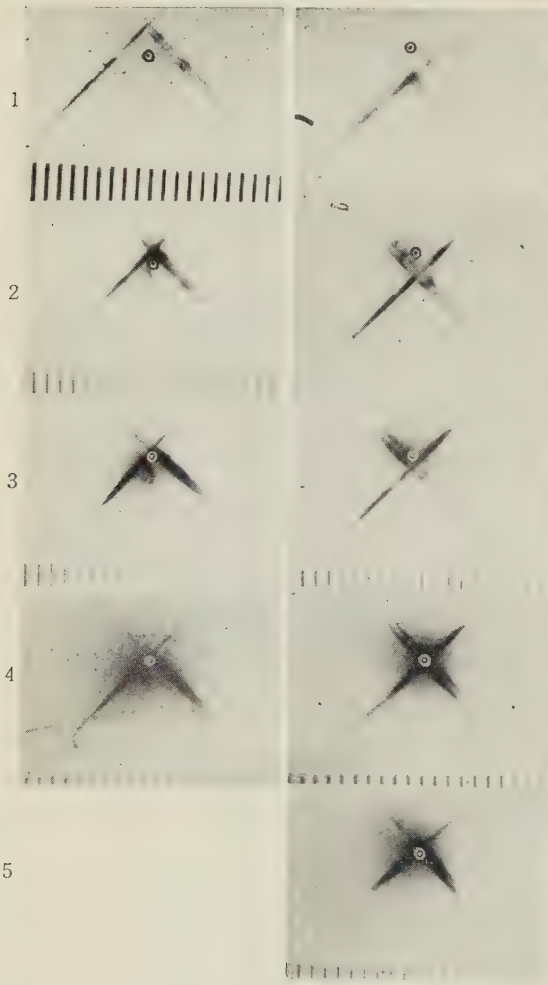

(a) (b)

Photo. 8. Variation of fine structures of {400} reflexions. (a) and (b) are taken, respectively, with a- and b-incidences defined in § 4. Numbers 1, 2, ..., 5 indicate settings of crystals given in Fig. 3.

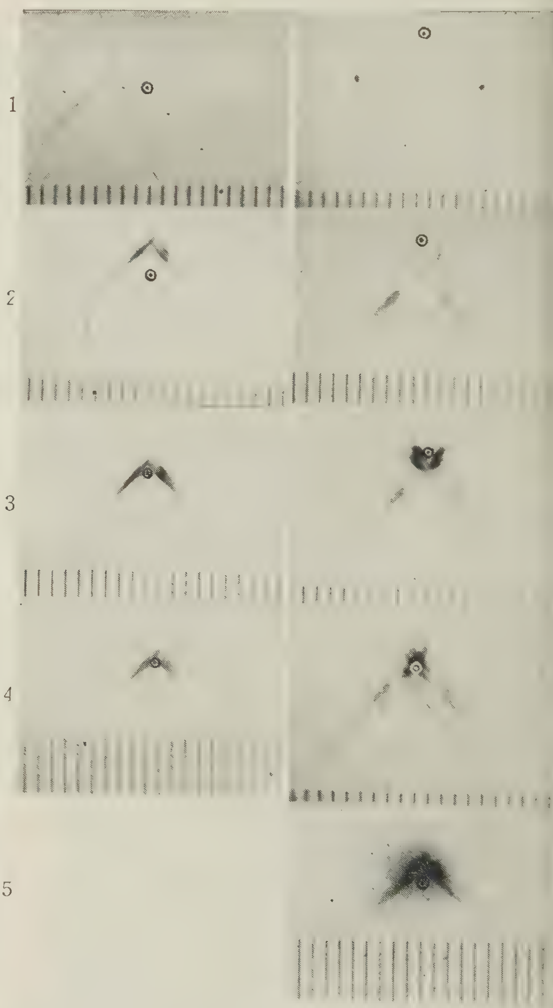

(a) (b)

Photo. 9. Variation of fine structures of {420} reflexions. (a) and (b) are taken, respectively, with a- and b-incidences defined in § 4. Numbers 1, 2, ..., 5 indicate settings of crystals given in Fig. 3.

It can be seen that the cross point of the streaks deviates in general vertically from the position of simple Bragg reflexion and the

---

* Duplicated parallel streaks of very small separations (Photos. 8 and 9) are considered to be due to domains of slightly different orientations.

Table I.

a) a-incidence**

* (hkl)	1	2	3	4	5
(200)	0.05 mm.	−0.05 mm.	−0.07 mm.	−0.09 mm.	
(220)	0.04	−0.07	−0.12	−0.16	−0.17 mm.
(400)	0.26	0.11	0.07	0.04	0.02
(420)	0.25	0.11	0.05	−0.07	−0.16
(440)	0.39	0.21	0.12	−0.07	−0.04

b) b-incidence**

* (hkl)	1	2	3	4	5
(200)	−0.11 mm.	−0.09 mm.			
(220)	−0.26	−0.15	0.02 mm.	0.07 mm.	
(400)	−0.31	−0.23	−0.11	−0.02	0.09 mm.
(420)		−0.42	−0.21		
(440)		−0.59	−0.35	−0.18	0.12

* Number 1, 2, ..., 5 indicate the crystal settings defined in Fig. 3.
** a- and b-incidences are defined at the beginning of § 4.

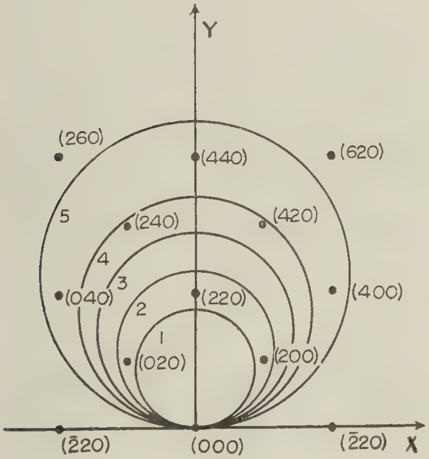

Fig. 3. The definition of settings of crystal in § 4.

deviation varies according to the angle of incidence. Observed values of the deviation are tabulated in Table I, where + and − signs indicate up- and down-ward shifts, respectively.

§ 5. Theoretical Consideration

A Bragg reflexion from a crystallite of a well-defined external form splits into a multiplet, since it is deviated from the position of simple Bragg reflexion by the prism action of edges of the crystallite. If there exist some minute irregularities or curvature on the faces of the prism, the deviation may have various magnitudes resulting in a set of streaks. Through such a consideration, which is originally pointed out by T. Yamaguti⁷⁾, Uyeda et al. explained the streaks in the diffraction pattern of etched zincblende surface.

At the data of the study of Uyeda et al., only the effect of simple refraction was known. At present, however, it is well known that there occurs the double refraction effect which is explained by the dynamical theory of electron diffraction. For this effect, which was originally pointed out by Sturkey⁸⁾, Kato⁹⁾ has given a refined theory. Experimentally it was studied in detail by Honjo and Mihama¹⁰⁾,¹¹⁾ and by Molière et al.¹²⁾,¹³⁾,¹⁴⁾. It may be of interest to examine the observed details of reflexions (See § 4) in the light of this theory.

According to Honjo and Mihama¹¹⁾, the deviation of a reflexion from the directions predicted by simple Bragg law can be calculated by refering to a co-ordinate system (ξ, η, ζ), where ζ-axis is the normal to the reflecting lattice plane, ξ-axis is the intersection of the lattice plane with the plane of incidence, and η-axis is perpendicular to ξ and ζ. The angular deviation is given by

$$\left.\begin{aligned} \alpha_\eta^{(1),(2)} &= -\{\varepsilon\cdot\delta_h\cdot S_\eta+(\delta_0\pm\delta_h\sqrt{1+\varepsilon^2}\,)t_\eta\}\ , \\ \alpha_\zeta^{(1),(2)} &= -\{\varepsilon\cdot\delta_h\cdot S_\zeta+(\delta_0\pm\delta_h\sqrt{1+\varepsilon^2}\,)t_\zeta\}\ , \end{aligned}\right\} \tag{1}$$

where α_η and α_ζ are η- and ζ-components of the angular deviation, respectively; and the superscripts (1) and (2) correspond to + and − signs, respectively.

$$\delta_0 = V_0/2E, \quad \delta_h = V_h/2E ,$$

V_0 being the mean inner potential of the crystal; V_h, the h-th Fourier coefficient of the periodic potential of the crystal; and E, the accelerating voltage of the electron. $s_{\eta\cdot\zeta}$ and $t_{\eta\cdot\zeta}$ are parameters which are given by

$$s_\eta = (m/l + m'/l') ,$$
$$s_\zeta = (n/l + n'/l') ,$$
$$t_\eta = (m/l - m'/l') ,$$
$$t_\zeta = (n/l - n'/l') ,$$

where (l, m, n) and (l', m', n') are the direction cosines of the outward normals to the entrance and exit faces of the prism, respectively. ε is a parameter which represents the resonance error. It is defined by

$$\varepsilon \cdot \delta_h = \Theta \cdot \Delta\Theta , \qquad (2)$$

where Θ is the Bragg angle and $\Delta\Theta$, the deviation from Bragg angle.

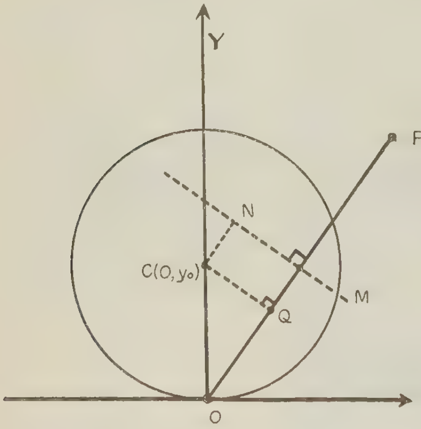

Fig. 4. (X, Y)-plane is (hh0) reciprocal lattice plane. $P(x_1, y_1)$ is a reciprocal lattice point (hk0). $C(0, y_0)$ is the center of circle along which Ewald's sphere intersects (hh0) reciprocal lattice plane.

When the plane of incidence is $(1\bar{1}0)$, ε for reflexion (hk0) can be calculated as follows: Under the present condition Ewald's sphere intersects (X, Y)-plane along a circle having the center $C(0, y_0)$ on Y-axis (Fig. 4). If Bragg condition is satisfied exactly, the center of the intersecting circle is on line $\overline{MN}$, $\overline{MN}$ being the perpendicular bisecthor of $\overline{OP}$. Thus $\Delta\Theta$ is given by

$$\Delta\Theta = (\overline{OQ} - \overline{OP}/2)/K ,$$

Since $\Theta = \overline{OP}/2K$, $\Theta \cdot \Delta\Theta$ is given by

$$\Theta \cdot \Delta\Theta = \frac{1}{4K^2}(y_1 y_0 - x_1^2 - y_1^2) , \qquad (3)$$

where K is the length of wave number vector of electrons. Values of V_0 is known to be 12 volts[15] and V_h are calculated from the known atom form factors as follows.

(hkl)	(200)	(220)	(400)	(420)	(440)
V_h	1.79 V	7.02 V	4.49 V	1.06 V	2.78 V

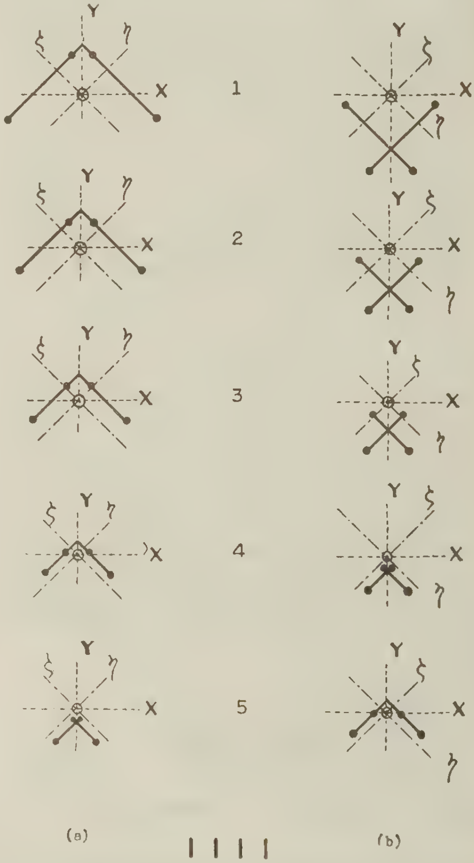

Fig. 5. Double refraction multiplet of {400} reflexions calculated for (a) a- and (b) b-incidences. Numbers 1, 2, ..., 5 correspond to settings of crystals given in Fig. 3.

$s_{\eta\cdot\zeta}$ and $t_{\eta\cdot\zeta}$ can be calculated easily from the known external form of crystallite. Thus, the theoretical multiplet structure can be known if the parameter y_0 is given.

The results for (400) and (420) reflexions are shown in diagrams of Figs. 5 and 6, respectively. Figs. 5 and 6 correspond to Photos. 8 and 9, respectively, and they are given in the same scale. In these diagrams two spots caused by a double refraction are joined by a thick line and the position of simple Bragg reflexion is indicated by white circles.

The following facts are in qualitative agreement with the observation.

(i) The separations between two spots of doublet are from 0.05 to 0.8 mm., which are the same order of magnitude found in Photos. 8 and 9.

(ii) The cross point of lines joining doublets deviates vertically from the position of simple Bragg reflexion. Values of the deviations are tabulated in Table II. They agree with the values in Table I in the order of magnitude.

(iii) The arrangement of component spots around the cross point is different considerably for a- and b-incidences of the same resonance error.

Diagrams (Figs. 5 and 6) are calculated under the assumption that only one strong reflexion is excited. Practically, however, many reflexions are excited simultaneously because the observation was made for plane of incidence $(1\bar{1}0)$ which is highly symmetric. Under such condition, there should occur more complicated effects than double refraction, resulting in a considerable variation of the effective values of V_0 and V_h[16]. Thus we must satisfy with the qualitative agreement.

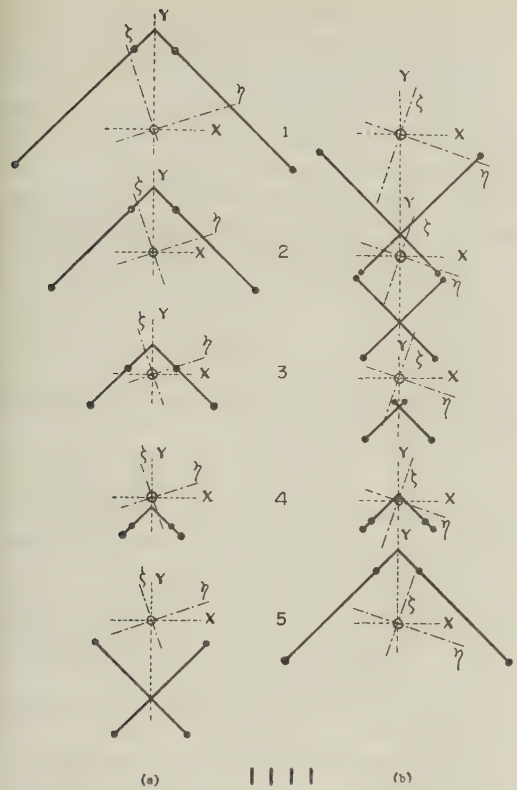

Fig. 6. Double refraction multiplet of {420} reflections calculated for (a) a- and (b) b-incidences. Numbers 1, 2, ..., 5 correspond to settings of crystals given in Fig. 3.

Table II*

(hkl)	1	2	3	4	5
(200)	±0.01 mm.	∓0.01 mm.	∓0.01 mm.	∓0.06 mm.	
(220)	±0.04	∓0.03	∓0.10	∓0.15	∓0.32 mm.
(400)	±0.20	±0.15	±0.10	±0.05	∓0.05
(420)	±0.47	±0.31	±0.14	∓0.03	∓0.35
(440)		±0.44	±0.31	±0.15	∓0.13

* Numbers 1, 2, ..., 5 indicate the crystal settings defined in Fig. 3 and upper and lower signs correspond to a- and b-incidences respectively.

The fact that the observed reflexions are different for a- and b- incidences can be explained neither by the simple theory of refraction nor by Sturkey's theory of double refraction. In these theories, the deviation of a reflexion spot from the position of simple Bragg reflexion is given by a vector sum of two deviations at the entrance and exit surface, the sum being a vector along $\boldsymbol{t}(t_\eta, t_\zeta)$. This quantity is independent of the directions of incident electrons, (a) or (b). According to the theory of Kato, the refractive index is different for entrance and for exit of electrons, as pointed out by Honjo and Mihama. Each deviation at an entrance and exit is a sum of two vectors, one along $\boldsymbol{s}(s_\eta, s_\zeta)$ and the other along $\boldsymbol{t}(t_\eta, t_\zeta)$. Since the change of $\boldsymbol{s}$ and $\boldsymbol{t}$ is asymmetric for the interchange of the entrance and exit faces, the asymmetry of the reflexions for a- and b- incidences appears. The asymmetry disappears only when Bragg condition is satisfied exactly, i. e. $\varepsilon=0$.

The present author examined also the fine structure of reflexions from Sb_2O_3. They could not, however, find any structure finer than that was observed by Miyake which was interpreted by himself by the simple theory of refraction. This fact seems to contradict the theory of double refraction. It can be reconciled, however, when we assume that one of spots of the refraction doublet is so weak that it cannot be observed. Such an effect was first pointed out by Honjo and Mihama¹¹⁾ for low order reflexions of cadmium oxide and was explained as due to the imaginary inner potential. The theoretical basis of the imaginary inner potential was recently given by Yoshioka¹⁷⁾. It is highly conceivable that the effect is more predominant in antimony oxide than in cadmium oxide, since the atomic weight of antimony oxide is larger than that of cadmium oxide.

Acknowledgement

The author wishes to express his sincere thanks to Dr. G. Honjo for his suggestions and discussions in this work. The author's thanks are also due to Dr. R. Ueda of Waseda University for his encouragement and interest, at whose Laboratory earlier parts of this work was carried out.

References

1) G. P. Thomson and W. Cockrane: Theory and Practice of Electron Diffraction (1939) London, Macmillan and Co.
2) S. Miyake: Sc. Pap. I. P. C. R. **34** (1938) 565.
3) R. Uyeda, S. Takagi and H. Hagihara: Proc. Phys.-Math. Soc. Japan **23** (1941) 1049.
4) A. E. H. Tutton: Crystallography and Practical Measurement Vol. 1 (1922) London, Macmillan and Co.
5) A. Fukami: Electron Microscope, Japan **1** (1953) 28.
6) M. Watanabe and R. Ueda: Acta Cryst. **6** (1953) 95.
7) T. Yamaguti: Proc. Phys.-Math. Soc. Japan **17** (1953) 443.
8) L. Sturky: Phys. Rev. **73** (1948) 183.
9) N. Kato: J. Phys. Soc. Japan **7** (1952) 406.
10) G. Honjo: J. Phys. Soc. Japan **8** (1953) 776.
11) G. Honjo and K. Mihama: J. Phys. Soc. Japan **9** (1954) 184.
12) K. Molière and H. Niehrs: Zeit. f. Phys. **137** (1954) 445.
13) H. J. Altenhein and K. Molière: Zeit. f. Phys. **139** (1954) 103.
14) K. Molière and H. Niehrs: Zeit. f. Phys. **140** (1955) 581.
15) S. Miyake: Proc. Phys.-Math. Soc. Japan **22** (1940) 666.
16) S. Miyake and G. Honjo: Nature **165** (1950) 644.
17) H. Yoshioka: to be published in J. Phys. Soc. Japan **12** (1957) No. 6.

JOURNAL OF THE PHYSICAL SOCIETY OF JAPAN Vol. 12, No. 8, AUGUST, 1957

Impedance of Bulk Semiconductor in Junction Diode

By Toshio MISAWA*

Central Labs., Matsushita Elec. Ind. Co., Ltd.
Kadoma-cho, Kitakawachi-gun, Osaka-fu

(Received March 9, 1957)

The impedance of bulk semiconductor in a junction diode, as defined as the "imref drop" for majority carrier divided by the total current through the junction, is calculated by using the low-level solution of minority carrier and is shown to have an inductive reactance, which becomes more and more dominant over the capacitive reactance of the impedance of the junction proper so that the impedance of the whole diode turns inductive as the injection level rises.

§ 1. Introduction

In discussing the small signal current voltage relation of the forward-biased junction diode, it is a common practice to treat the junction as consisting of the junction proper and the pure resistance of bulk semiconductor. The junction proper was studied by Shockley and his co-workers[1),2)] both theoretically, and experimentally, and can be represented by the equivalent circuit of a parallel connection of a resistance and a capacitance. But it is only a custom since the "pre-transistor" age to regard the bulk impedance as purely resistive. In the junction diode made of transistor material, the majority carrier density is modulated, according to the electrical neutrality condition, by those injected minority carriers which are essentially responsible for the rectification property of the junction. Also, while the current is carried by both majority and minority carriers in the vicinity of the barrier layer of the junction, its minority carrier component becomes less and less as a result of recombination of minority carriers, with increase in distance from the barrier. The situation in the bulk semiconductor is rather complicated. The purpose of this paper is to treat the process in bulk semiconductor.

---

* Now at Tokyo Tsushin Kogyo, Ltd., 351 Kitashinagawa-6, Shinagawa-ku, Tokyo.

The calculation, which is valid only at small forward bias current, shows that the impedance of bulk semiconductor is inductive and becomes comparable to that of the junction proper as the bias current increases. These results are qualitatively correct even if one takes into account the various high injection level effects, for the corrections due to these effects are of a small factor in the light of the high level behavior of the emitter junction in a transistor.[3)]

§ 2. Definition of Bulk Impedance

There has been used an expression "IR drop in bulk semi-conductor". But it is used rather vaguely. We must give it a clear-cut definition. In doing this we follow Shockley's imref method.

The imrefs, or quasi Fermi levels for electrons, φ_n, and holes, φ_p, are a very convenient tool in discussing the problem where both the drift and the diffusion currents are involved. According to Shockley the current densities carried by electrons and holes, I_n and I_p, are expressed in terms of imrefs by

$$I_n = -q\mu_n n \operatorname{grad} \varphi_n , \qquad (1)$$

$$I_p = -q\mu_p p \operatorname{grad} \varphi_p , \qquad (2)$$

where q is the elementary charge, μ_n and μ_p are mobilities of electrons and holes, and n and p are electron and hole densities. The formulae are the same as that for the current density in terms of electrostatic potential in an ordinary conductor in which only the drift current exists. The convenient point is that we can discuss the problem, at least formally, without particular knowledge of whether the current is by drift or by diffusion.

The important properties of the imrefs, which are apparent from their definition and which we shall use in the following discussion, are

(1) Their gradients are much larger in the minority region* than in the majority region.*

(2) φ_n and φ_p merge into the Fermi level where carrier densities assume thermal equilibrium values.

Using these properties, we can figure out the behavior of φ_n and φ_p in a forward-biased junction diode, as shown in Fig. 1. The externally applied bias, $\delta\varphi$, is the difference of Fermi levels in the contact electrodes. Beneath the contacts, where the minority carriers injected through the barrier layer of the junction have died away, φ_n and φ_p coincide according to (2) and assume the same values as the Fermi levels in the contacting electrode metals. Both φ_n and φ_p must change by $\delta\varphi$ in going from the p-region contact to the n-region contact. But there is considerable difference in the way of changing between φ_n and φ_p. According to (1) φ_n changes mainly in the p-region and φ_p in the n-region. As a result we have a bow-shaped figure. The width of the bow at the barrier layer, $\delta\varphi_j$, is the effective part in

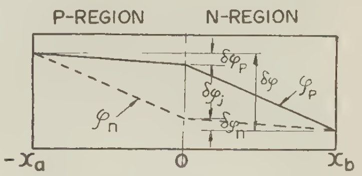

Fig. 1. Imref diagram of a forward-biased junction diode. The externally applied bias, $\delta\varphi$, is divided into $\delta\varphi_j$, the effective part in biasing the junction, and $\delta\varphi_n$ and $\delta\varphi_p$, the IR drops, in bulk semiconductors.

---

* We shall call a region as the majority or the minority region of the carrier according to weather the carrier under consideration is of majority or of minority in that region.

biasing the junction. The rest of $\delta\varphi$, $\delta\varphi_n$ and $\delta\varphi_p$, which are wasted in bulk semiconductors, are the *IR* drops.

When a small *ac* current $\tilde{I}\exp(i\omega t)$ is superposed on the bias current, the $\varphi_n-\varphi_p$ pattern vibrates about the steady state one. The phase of the vibration is different according to location in semiconductor. Therefore *ac* parts of $\delta\varphi_n$, $\delta\varphi_p$ and $\delta\varphi_j$ may have different phase with each other. Impedance of bulk are obtained by dividing $\delta\tilde{\varphi}_n$ and $\delta\tilde{\varphi}_p$ by the current $\tilde{I}$,

$$Z_n=\delta\tilde{\varphi}_n/\tilde{I}\,, \tag{3}$$

$$Z_p=\delta\tilde{\varphi}_p/\tilde{I}\,, \tag{4}$$

where the wave sign designates the *ac* part.

§ 3. Calculation of Bulk Impedance

Procedures of calculating a bulk impedance, Z_n for example, are as follows.

(1) Solving the continuity equations for minority carriers at a given value of $\delta\varphi_j$, one obtains $n(x)$ and $I_n(x)$ in the *p*-region, $p(x)$ and $I_p(x)$ in the *n*-region and the total current through the junction, I_0. This is a usual step followed in the theory of *p-n* junctions.

(2) Using results obtained in (1), one calculates $n(x)$ and $I_n(x)$ in the *n*-region from the electrical neutrality condition and constancy of current throughout the semiconductor, $I_n(x)=I_0-I_p(x)$, respectively.

(3) Insertion of $n(x)$ and $I_n(x)$ into and integration of Eq. (1) give $\delta\varphi_n$ in the *n*-region. We obtain Z_n from Eq. (3).

These procedures are followed successively.

Continuity equations for minority carriers have been solved by Shockly when $\delta\varphi_j$ consists of *dc* and small *ac* components,

$$\delta\varphi_j=\delta\bar{\varphi}_j+\delta\tilde{\varphi}_j\exp(i\omega t)\,, \tag{5}$$

where the bar means *dc* component. The hole density in the *n*-region

$$\bar{p}=p_n+p_0\exp(-x/L_p)\,, \tag{6}$$

$$\tilde{p}=p_1\exp[-x(1+i\omega\tau_p)^{1/2}/L_p]\,, \tag{7}$$

where

$$p_0=p_n[\exp(q\delta\bar{\varphi}_j/kT)-1]\,, \tag{8}$$

$$p_1=(qp_n\delta\tilde{\varphi}_j/kT)\exp(q\delta\bar{\varphi}_j/kT)\,, \tag{9}$$

τ_p and L_p are the lifetime and the diffusion length of holes in the *n*-region, p_n is the thermal equilibrium hole density in the *n*-region. The *ac* hole current in the *n*-region is

$$\tilde{I}_p=\frac{qD_pp_1}{L_p}\sqrt{1+i\omega\tau_p}\exp\left(-\frac{x\sqrt{1+i\omega\tau_p}}{L_p}\right). \tag{10}$$

Hole currents through the junction are

$$\bar{I}_{p0}=qD_pp_0/L_p\,, \tag{11}$$

$$\tilde{I}_{p0}=(qD_pp_1/L_p)(1+i\omega\tau_p)^{1/2}\,. \tag{12}$$

The corresponding expressions for electrons in the *p*-region are obtained by interchanging *p* and *n*.

From expressions derived in the preceding paragraph,

$$\begin{aligned}\tilde{n}&=\tilde{p}\\&=p_1\exp[-x(1+i\omega\tau_p)^{1/2}/L_p]\end{aligned} \tag{13}$$

and

$$\tilde{I}_n=\tilde{I}_0-\tilde{I}_p\,. \tag{14}$$

The constancy of the total current throughout the semiconductor used in Eq. (14) is easily verfied as in Appendix I.

Equation (1) is rewritten for *ac* components as

$$\tilde{I}_n=-q\mu_n\left(\tilde{n}\frac{d\bar{\varphi}_n}{dx}+\bar{n}\frac{d\tilde{\varphi}_n}{dx}\right). \tag{15}$$

The imref drop for electrons in the *n*-region can be obtained by

$$\delta\tilde{\varphi}=-\int_0^{x_b}\frac{d\tilde{\varphi}_n}{dx}dx_n\,. \tag{16}$$

In performing the above integration, we assume that the low injection level condition prevails in the *n*-region, namely, the electron density is not appreciably changed from its thermal equilibrium value, n_n:

$$\bar{n}=n_n\,. \tag{17}$$

Then

$$\delta\tilde{\varphi}=\frac{1}{q\mu_nn_n}J_1+\frac{1}{n_n}J_2\,, \tag{18}$$

where

$$\begin{aligned}J_1&=\int_0^{x_b}\tilde{I}_n dx\\&\simeq\tilde{I}_0x_b-\tilde{I}_{p0}L_p/(1+i\omega\tau_p)^{1/2}\,,\end{aligned} \tag{19}$$

$$\begin{aligned}J_2&=\int_0^{x_b}\tilde{n}\frac{d\bar{\varphi}_n}{dx}dx\\&\simeq\frac{p_1}{q\mu_nn_n}\left(-\frac{\bar{I}_0L_p}{\sqrt{1+i\omega\tau_p}}+\frac{\bar{I}_{p0}L_p}{1+\sqrt{1+i\omega\tau_p}}\right).\end{aligned} \tag{20}$$

The aprroximations are for the case when $x_b\gg L_p$.

The impedance of the n-region, Z_n, is

$$\begin{aligned} Z_n &= \delta\tilde{\varphi}_n / I\,, \\ &= Z_{n1} + Z_{n2} + Z_{n3}\,, \end{aligned} \tag{21}$$

where

$$Z_{n1} = \frac{x_b}{q\mu_n n_n} \tag{22}$$

$$\begin{aligned} Z_{n2} &= -\frac{L_p}{q\mu_n n_n} \frac{\tilde{I}_{p0}}{\tilde{I}_0} \frac{1}{\sqrt{1+i\omega\tau_p}} \\ &= -\frac{L_p}{q\mu_n n_n} \frac{1}{1+\tilde{I}_{n0}/\tilde{I}_{p0}} \frac{1}{\sqrt{1+i\omega\tau_p}}\,, \end{aligned} \tag{23}$$

$$\begin{aligned} Z_{n3} &= -\frac{L_p}{q\mu_n n_n n_n} p_1 \left(\frac{\bar{I}_0}{\tilde{I}_0} \frac{1}{\sqrt{1+i\omega\tau_p}} - \frac{\bar{I}_{p0}}{\tilde{I}_0} \frac{1}{1+\sqrt{1+i\omega\tau_p}} \right) \\ &= -\frac{L_p}{q\mu_n n_n} \frac{p_0}{n_n} \frac{1}{1+\tilde{I}_{n0}/\tilde{I}_{p0}} \\ &\quad \times \left[\left(1 + \frac{\bar{I}_{n0}}{I_{p0}} \right) \frac{1}{1+i\omega\tau_p} \right. \\ &\quad \left. - \frac{1}{(1+\sqrt{1+i\omega\tau_p})\sqrt{1+i\omega\tau_p}} \right]. \end{aligned} \tag{24}$$

Z_{n1} is purely resistive and its magnitude is what is expected from conductivity, $q\mu_n n_n$, and length, x_b, of the n-region. The magnitude-determining factor in Z_{n2}, $L_p/(q\mu_n n_n)$, is the resistance of bulk semiconductor whose conductivity is $q\mu_n n_n$ and length L_p. Namely only that part of the n-region which lies within L_p from the barrier layer contributes to this term. The phase factor of Z_{n2} is the same as that of the junction impedance with its sign reversed. Hence, Z_{n2} has an inductive reactance. Z_{n3} is also an inductive impedance but it has another factor, p_0/n_n, which is the ratio of the injected hole density to the thermal equilibrium electron density, P,

$$P \equiv p_0/n_n\,. \tag{25}$$

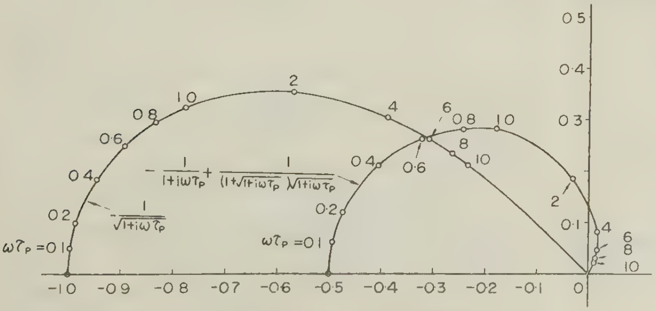

Fig. 2. Bulk impedance of the alloyed junction diode plotted on the complex plane with frequency as a parameter.

The radio of three terms is

$$|Z_{n1}| : |Z_{n2}| : |Z_{n3}| \sim x_b/L_p : 1 : P\,. \tag{26}$$

The impedance of the p-region is obtained by interchanging n and p,

$$\begin{aligned} Z_p &= \delta\tilde{\varphi}_p / \tilde{I} \\ &= Z_{p1} + Z_{p2} + Z_{p3}\,, \end{aligned} \tag{27}$$

where

$$Z_{p1} = \frac{x_a}{q\mu_p p_p}\,, \tag{28}$$

$$Z_{p2} = -\frac{L_n}{q\mu_p p_p} \frac{1}{1+\tilde{I}_{p0}/\tilde{I}_{n0}} \frac{1}{\sqrt{1+i\omega\tau_p}}\,, \tag{29}$$

$$\begin{aligned} Z_{p3} &= -\frac{L_n}{q\mu_p p_p} \frac{n_0}{p_p} \frac{1}{1+\tilde{I}_{p0}/\tilde{I}_{n0}} \\ &\quad \times \left[\left(1 + \frac{\bar{I}_{p0}}{I_{n0}} \right) \frac{1}{1+i\omega\tau_n} \right. \\ &\quad \left. - \frac{1}{(1+\sqrt{1+i\omega\tau_n})\sqrt{1+i\omega\tau_n}} \right]. \end{aligned} \tag{30}$$

Their ratio is

$$|Z_{p1}| : |Z_{p2}| : |Z_{p3}| \sim x_a/L_n : 1 : N\,, \tag{31}$$

where

$$N \equiv n_0/p_p\,. \tag{32}$$

For the symmetrical p–n junction where $I_{n0} = I_{p0}$,

$$Z_{n2} = -\frac{1}{2} \frac{L_p}{q\mu_n n_n} \frac{1}{\sqrt{1+i\omega\tau}}\,, \tag{33}$$

$$\begin{aligned} Z_{n3} &= -\frac{L_p}{q\mu_n n_n} \frac{p_0}{n_n} \\ &\quad \times \left(\frac{1}{1+i\omega\tau} - \frac{1}{2} \frac{1}{(1+\sqrt{1+i\omega\tau})\sqrt{1+i\omega\tau}} \right) \end{aligned} \tag{34}$$

and the similar ones for the p-region, where

$$\tau = \tau_n = \tau_p\,.$$

In the alloy junction in which p-region is heavily doped, most of the current through the junction is carried by holes, i.e.,

$$I_0 = I_{p0}\,.$$

The p-region impedance is negligible and the n-region one is

$$Z_{n2} = -\frac{L_p}{q\mu_n u_n} \frac{1}{\sqrt{1+i\omega\tau_p}}\,, \tag{35}$$

$$\begin{aligned} Z_{n3} &= -\frac{L_p}{q\mu_n n_n} \frac{p_0}{n_n} \times \left(\frac{1}{1+i\omega\tau_p} \right. \\ &\quad \left. - \frac{1}{(1+\sqrt{1+i\omega\tau_p})\sqrt{1+i\omega\tau_p}} \right). \end{aligned} \tag{36}$$

In Fig. 2, Eqs. (35) and (36) are plotted on the complex plane with frequency as a parameter.

§ 4. Discussion

In order to obtain more understanding on the subject, we shall investigate the inductive nature of the bulk impedance from another standpoint. We consider the transient response after the sudden increase of bias current.

First consider the steady state of a forward biased junction diode. In a junction diode which is biased in the direction of easy flow, the minority carrier densities have maxima on the both sides of the barrier layer and decrease monotonically with the distance from it. The minority carriers flow away from the barrier by the diffusion process, the rate of which is determined by their concentration gradients. On the other hand the majority carrier flow must be in the direction to the barrier in order to supply the opposite region of the barrier with the minority carriers. This direction of majority carrier flow is opposite to what is expected from the distribution and the diffusion process, for the majority carrier distribution which has the same gradient with that of minority carriers owing to the electrical neutrality condition is favorable to flowing-away from the barrier. Actually an electric field exists in the bulk semiconductor and produces the drift current to overshadow the diffusion component of the majority carrier current. The effect of this field on the minority carrier flow is negligible at small currents, because the drift current is proportional to the carrier density and the minority carrier density is much smaller than that of the majority carriers at low level. Thus the minority carrier current is by diffusion and the majority one is by drift. When injection level rises and the density of injected minority carriers becomes comparable to the thermal equilibrium one of majority carriers, the field which corrects the direction of the majority carrier flow grows up and its effect on the minority carriers becomes appreciable. Thus at high injection level the minority carrier current is composed of diffusion and drift components, both of which are of comparable magnitude and have the *same* flow direction.

Now let us consider the transient after the bias current through the diode is suddenly increased by ΔI. At the moment just after the application of the step current, the distributions of minority carriers and hence the minority carrier currents remain unchanged. ΔI is carried only by majority carriers. For example, in the n-region, p and I_p remain unchanged but I_n increases immediately by ΔI, since the electron current in the n-region is by drift and can change its magnitude in a very short time by an inertia-less change in the field. In the differential of Eq. (1),

$$\Delta I_n = -q\mu_n\left(\Delta n\cdot \frac{d\varphi_n}{dx} + n\cdot\Delta\frac{d\varphi_n}{dx}\right), \tag{37}$$

$\Delta I_n = \Delta I$ is responsible for the immediate increase in $|\Delta(d\varphi_n/dx)|$,

$$\begin{aligned}|\Delta(d\varphi_n/dx)|_{t=0} &\equiv \Delta(d\varphi_n/dx)_1 \\ &= \Delta I/q\mu_n n\,,\end{aligned} \tag{38}$$

with $\Delta n=0$, where Δ designates the change after the increase in I. Similarly in the p-region, the hole current increases immediately and the rate of hole injection into the n-region rises suddenly. These extra holes which are due to the increased rate of injection begin to increase p and I_p in the n-region. This re-distribution of holes is by the slow process of diffusion. At the same time Δn increases and ΔI_n decreases gradually, due to the electrical neutrality condition and the constancy of current through the diode, respectively. This stage of transient is charging-up of the so-called diffusion capacitance of the junction. Finally all quantities assume new values which correspond to the new value of current. Increase in Δn and decrease in ΔI_n during the whole transient entail the decrease in $|\Delta(d\varphi_n/dx)|$ from its initial value just after the application of the step current. Namely $|\Delta(d\varphi_u/dx)|$ decreases from its initial value given by Eq. (38) by

$$\Delta(d\varphi_n/dx)_2 = (\Delta I_p)_{t=\infty}/q\mu_n n \tag{39}$$

due to the gradual decrease in ΔI_n by $(\Delta I_p)_{t=\infty}$, and by

$$\Delta(d\varphi_n/dx)_3 = (\Delta n)_{t=\infty}|(d\varphi_n/dx)|/n \tag{40}$$

due to the gradual increase in n by

$$(\Delta n)_{t=\infty} = (\Delta p)_{t=\infty}\,.$$

This behavior of the gradual decrease after the sudden increase in $\delta\varphi_n$ after the application of the step current means that the small signal impedance of the n-region has an inductive reactance. It is shown in Appendix II that $\Delta(d\varphi_n/dx)_1$ is due to a pure resistance and $\Delta(d\varphi_n/dx)_2+\Delta(d\varphi_n/dx)_3$ to an impedance which has a negative resistance and inductive reactance at least at low frequencies. As is easily seen from their deduction, Z_{n2} in § 3 originates from the decrease in ΔI and Z_{n3} from the increase in Δn.

As is seen from the last part in Appendix II, integration and division by ΔI of Eqs. (38), (39), and (40) determine the magnitudes of Z_{n1}, Z_{n2}, and Z_{n3}, respectively. Using this, we can estimate the dependency of the latter upon the injection level. $(\Delta I_p)_{t=\infty}$ and ΔI are proportional to P, as is seen from Eqs. (9) and (12) and their counterparts for electrons. Therefore as long as the injection level is low, i.e. $n\simeq n_n$, $\Delta(d\varphi_n/dx)_2$ is proportional to, and the magnitude-determing factor in Z_{n2} is independent of P. As for $\Delta(d\varphi_n/dx)_3$, both Δn and $d\varphi_n/dx$ are proportional to P, and so Z_{n3} to P. When we substantialize this idea analytically for the alloy diode for example, the following expressions are obtained.

$$\frac{\Delta\varphi_{n1}}{\Delta I}=\frac{x_b}{q\mu_n n_n}\left[1-\frac{L_p}{x_b}\ln(1+P)\right], \qquad (41)$$

$$\frac{\Delta\varphi_{n2}}{\Delta I}=\frac{L_p}{q\mu_n n_n}\frac{\ln(1+P)}{P}, \qquad (42)$$

and

$$\frac{\Delta\varphi_{n3}}{\Delta I}=\frac{L_p}{q\mu_n n_n}\left[1-\frac{\ln(1+P)}{P}\right], \qquad (43)$$

where we took into account the conductivity modulation and used

$$\begin{aligned} n&=n_n+(p-p_n)\\ &=n_n(1+P\exp(-x/L_p)) . \end{aligned} \qquad (44)$$

These can als be obtained if we set $\omega=0$ in the calculation in § 3 and use Eq. (44). In the limit of $P\to 0$ they are in accordance with the results in § 3.

When injection level rises, the minority carrier current is enhanced by the above-mentioned electric field to a considerable degree. This changes the dependency on P of the quantities used in the calculation in the preceding paragraph and the rate at which the transient proceeds. But correction factors which are due to modification of the continuity equation, may be of the order of unity. This is analogized from the high level behavior of the emitter junction of a transistor. In the emitter junction those deviations from the low level expressions which are to the field (excluding other high level effects) did originate from the doubled effective diffusion constant of the minority carrier in the base region and were at most by a factor of 2.[3] In an (alloy) junction diode the situation is indeed, somewhat different from that in the emitter junction in a transistor. In a transistor the minority carrier distribution in the base region is artificially determined by another negatively biased junction (collector) which is near enough to the emitter for the ratio of minority carrier current density to majority carrier current density to be nearly constant and very large throughout the base region. While in the diode it is determined by the natural recombination of the injected minority carriers in the course of diffusion and drift away from the barrier and the whole current is carried by majority carriers at last, however high the injection efficiency may be. These differences are reflected in the diffusion capacitance. In the emitter junction the charge of the injected minority carriers in the base region behaves as if it were the charge on one of the condenser plates and the diffusion capacitance is obtained by differentiating it with the emitter bias[3] while in the diode only a part of the injected carriers is active and the capacitance is a half of the charge differentiated with bias.[4] This shows, however, the difference is not drastic and we can guess the behavior of a diode with the aids of knowledge of transistors. Therefore we are safe in concluding that the frequency and P dependencies of Z_n do not appreciably deviate from the results in § 3 and the preceding paragraph.

In this point it may be of interest to compare this bulk impedance with that of the junction proper, Z_j,

$$\begin{aligned} Z_j&=\delta\tilde{\varphi}_j/\tilde{I}_0\\ &=(\delta\tilde{\varphi}_j/\tilde{I}_{p0})/(1+\tilde{I}_{n0}/\tilde{I}_{p0})\\ &\simeq\frac{L_p}{q\mu_n p_0}\frac{1}{1+\tilde{I}_{n0}/\tilde{I}_{p0}}\frac{1}{\sqrt{1+i\omega\tau_p}} . \end{aligned} \qquad (45)$$

For the alloy junction

$$\begin{aligned} Z_j&=\frac{L_p}{q\mu_n p_0}\frac{1}{\sqrt{1+i\omega\tau_p}}\\ &=\frac{L_p}{q\mu_n n_n}\frac{1}{P}\frac{1}{\sqrt{1+i\omega\tau_p}} . \end{aligned} \qquad (46)$$

Therefore we have

$$|Z_{n2}|:|Z_{n3}|:|Z_j| \sim \frac{\ln(1+P)}{P} : \left[1-\frac{l(1n+P)}{P}\right] : \frac{1}{P} \,. \tag{47}$$

In Fig. 3 we show the P-dependent factors in Z's. At low injections level ($P \ll 1$), where the above calculations are valid rigorously, Z_j and $Z_{n1}+Z_{p1}$ are predominant and the equivalent circuit of the whole diode is a series connection of a capacitive impedance and a pure resistance. As level rises, the junction impedance becomes less and less important and the reactance of the whole diode is turned inductive, as is seen from Fig. 3. For $P \gtrsim 1$, Z_j decreases in a slower rate than the low level expression, Eq. (46), predicts, mainly due to the decrease in minority carrier injection. In this case also the essential nature of Eq. (45) does not change substantially, in the light of the behhavior of the emitter junction of the transistor.[3] It is very probable that at high injection level the reactance of the whole diode becomes inductive. Actually the inductive nature of the impedance of the junction diode was observed by many workers[6-8] at large bias currents.

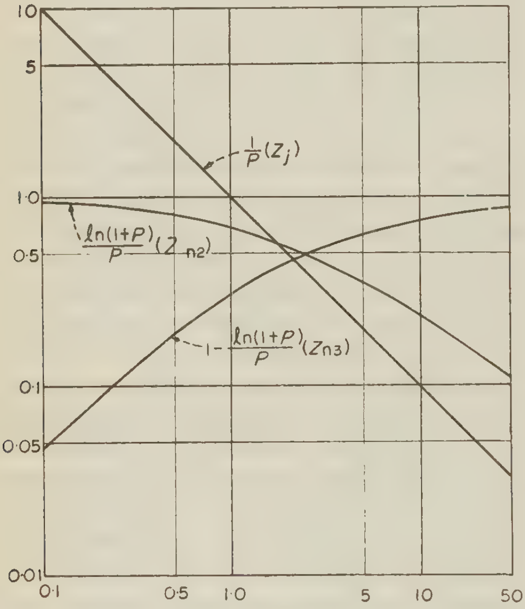

Fig. 3. Variation of Z_{n2}, Z_{n3} and Z_j with the injection level, P, for an alloy diode.

§ 5. Conclusion

The small signal impedance of bulk semiconductor in a junction diode was shown to have an inductive reactance by using the low level formulae. Although the reactance is small compared to the resistive part of the impedance, it becomes comparable to the junction impedance and makes the impedance of the whole diode reactive, as the injection level rises.

Appendix I

In this Appendix we prove that the current in semiconductor is source-free, i.e. constant in one dimension. The continuity equations for electrons and holes are

$$\frac{\partial n}{\partial t} = q_n + \frac{1}{q} \operatorname{div} I_n \,, \tag{A1}$$

$$\frac{\partial p}{\partial t} = q_p - \frac{1}{q} \operatorname{div} I_p \,, \tag{A2}$$

where g_n and g_p are the rates of generation for electrons and holes. The time-dependent parts in n and p are equal according to the electrical neutrality condition,

$$\frac{\partial n}{\partial t} = \frac{\partial p}{\partial t} \,.$$

The generation in this case is the mutual recombination of electrons and holes, therefore the rates are equal,

$$g_n = g_p \,.$$

Subtracting Eq. (A2) from Eq. (A1), we obtain

$$\operatorname{div}(I_n + I_p) = 0 \,,$$

which was to be proved.

Appendix II

We shall investigate the nature of an impedance $Z(i\omega)$, when the voltage, $v(t)$, developed on it increases suddenly by v_1 and later decreases gradually by v_2 after the application of unit step current as shown in Fig. 4.

According to the Laplace transform theory,[9] there exists the relation,

$$Z(s)(1/s) = \mathscr{L}[v(t)] \,, \tag{A3}$$

where $\mathscr{L}$ is the operator for the Laplace transformation, s the complex variable in the Laplace transform and $1/s$ the Laplace transform of the unit step function. Upon differentiating Eq. (A3) with t, we obtain

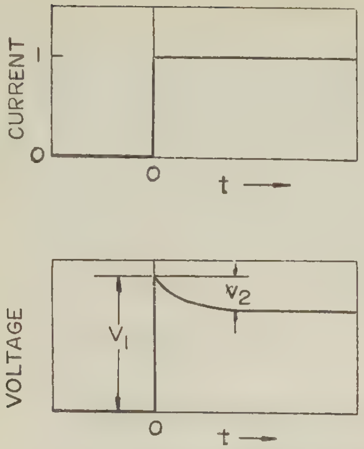

Fig. 4. Transient voltage developed on $Z(i\omega)$ after the application of unit step current.

$$Z(s)-v(0)=\mathscr{L}[v'(t)],$$

or

$$Z(s)=\int_0^\infty v'(t)\,e^{-st}\,dt+v_0\,. \qquad (A4)$$

The second term means that $Z(i\omega)$ has a component of pure resistance, which originates from the initial increase of the voltage developed on the impedance. The first term is analysed as was done by Shockley in discussing the negative resistance in a transistor structure.[10] The resistance part is

$$\mathrm{Re}[Z(i\omega)]=\frac{1}{2}\int_0^\infty v'(t)\cos\omega t\,dt$$
$$=-\frac{1}{2}\,\frac{1}{\omega}\int_0^\infty v''(t)\sin\omega t\,dt \qquad (A5)$$

and the reactance part is

$$\mathrm{Im}[Z(i\omega)]=-\frac{1}{2}\int_0^\infty v'(t)\sin\omega t\,dt\,. \qquad (A6)$$

All that we know is that $v'(t)<0$ for $t>0$. If the transient substantially finishes in the first half cycle of sine function, Eq. (A6) becomes positive and the reactance is inductive, and for such a low frequency that the transient fades away in the first quarter of the cosine function the resistance is negative. This is easily seen with the aid of Fig. 5. At higher frequencies we cannot obtain a definite conclusion only from negative $v'(t)$ for $t>0$; we must know the detail about the decrease rate of $v(t)$.[10] Anyway an impedance has the negative resistance and the inductive reactance at least for low frequencies, when its transient behavior is as shown in Fig. 4. The impedance of bulk semiconductor which was discussed in the text is of this kind.

Now we shall find the initial and final value of the voltage developed on Z_n in Eqs. (21), (22), (35), and (36) for an alloy diode when unit step current is applied. When $F(s)$ is the Laplace transform of $g(t)$, the following relations are valid.[11]

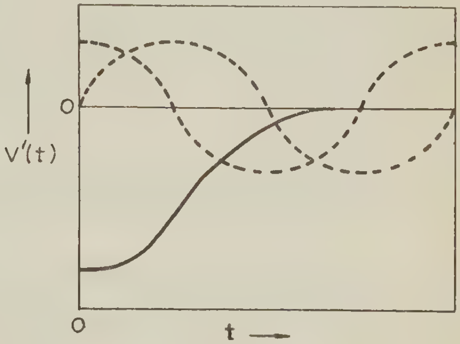

Fig. 5. Factors of integrands in Eqs. (A 5) and (A 6) for a small value of ω.

$$\lim_{s\to 0} sF(s)=\lim_{t\to\infty} g(t)$$

and

$$\lim_{s\to\infty} sF(s)=g(+0)\,.$$

Applying these relations to Eq. (A3) with $Z=Z_n$, one obtains

$$v_1=Z_n(\omega\to\infty)$$
$$=Z_{n1} \qquad (A7)$$

and

$$v_1-v_2=Z(\omega=0)$$
$$=Z_{n1}-\frac{L_p}{q\mu_n n_n}-\frac{1}{2}\,\frac{L_p}{q\mu_n n_n}P$$

or

$$v_2=\frac{L_p}{q\mu_n n_n}+\frac{1}{2}\,\frac{L_p}{q\mu_n n_n}P\,. \qquad (A8)$$

References

1) W. Shockley: Bell Sys. Tech. J. **28** (1949) 435.
2) F. S. Goucher, G. L. Pearson, M. Sparks, G. L. Teal, and W. Shockly: Phys. Rev. **81** (1951) 637.
3) W. M. Webster: Proc. IRE **42** (1954) 914; T. Misawa: J. Phys. Soc. Japan **11** (1956) 728.
4) W. Shockley: *Electrons and Holes in Semiconductors* (D. Van Nostrand Co., Inc., New York, 1950), p. 316. The proof can be easily extended to finite values of V_0.
5) G. Kohn and W. Nonnenmacher: Arch. Elekt.

Übertragung **8** (1954) 561.
6) Y. Kanai: J. Phys. Soc. Japan **10** (1955) 719.
7) J. Yamaguchi: 1955 Spring Meeting of the Phys. Soc. Japan, March 29, 1955.
8) M. Kikuchi: 1956 Fall Meeting of the Phys. Soc. Japan, October 31, 1956.
9) H. H. Skilling: *Transient Electric Currents* (McGraw-Hill Book Co., Inc., New York, 1952), second edition, Chap. X.
10) W. Shockley: Bell Sys. Tech. J. **33** (1954) 799.
11) H. M. James, N. B. Nichols, and R. S. Philips: *Theory of Servomechanism, MIT Radiation Laboratory Series* (McGraw-Hill Book Co., Inc., New York, 1948), p. 55.

JOURNAL OF THE PHYSICAL SOCIETY OF JAPAN Vol. 12, No. 8, AUGUST, 1957

Rotational Lattice Vibration in Complex Crystals

Part II. Vibrational Modes in Optical Branches and Interaction with a Conduction Electron

Sumitada ASANO and Yasuo TOMISHIMA
Department of Physics, Faculty of Science, Okayama University

(Received April 3, 1957)

Under the assumption that the anionic radical may be regarded as a rigid symmetric rotor, both the translational and the rotational lattice vibrations in the optical branches, which may be excited in isotropic complex crystals, are described on a macroscopic basis. By using the results obtained on it, the relative magnitudes of the mechanical and the radiative energy densities in the crystal are discussed for transverse vibrational modes. In addition, the interaction of a conduction electron witn the rotational lattice vibration is investigated on the standpoint that the radiation field serves as a medium of the interaction.

§ 1. Introduction

In the previous part¹⁾, we have investigated the modes of the rotational lattice vibrations in complex crystals by using the one-dimensional lattice and its effects upon the specific heat at low temperatures. This part deals with (1) the macroscopic theory of the translational and rotational lattice vibrations in optical branches which may be excited in isotropic complex crystals; the natural generalization of the Huang's theory on the translational optical lattice vibrations in simple ionic crystals, (2) the relative magnitudes of the mechanical (translational and rotational) and the radiative energy densities in the crystal which intermix with each other in the transverse lattice vibrations, and (3) the interaction of a conduction electron with the rotational lattice vibration in the optical branch.

Here we will concern ourselves only with the iosotropic complex crystals, whose unit cell consists of a point-like cation and a rigid anionic radical with central symmetry. Then we have no need to take into account the RA-branch (that is, the acoustical branch in the rotational mode), as shown in part I¹⁾.

§ 2. Lattice Vibrations in the Optical Branches

Just as in the case of isotropic simple crystals²⁾, for isotropic complex ones the macroscopic theory of the translational vibration is also fully embodied in the following equations:

$$\ddot{\boldsymbol{w}}=b_{11}\boldsymbol{w}+b_{12}\boldsymbol{E}\,, \tag{2.1a}$$

$$\boldsymbol{P}=b_{21}\boldsymbol{w}+b_{22}\boldsymbol{E}\,, \tag{2.1b}$$

where $b_{11}=-\omega_{tt}{}^2$, $b_{12}=b_{21}=\left(\frac{\varepsilon_0-\varepsilon_\infty}{4\pi}\right)^{1/2}\omega_{tt}$, $b_{22}=\frac{\varepsilon_\infty-1}{4\pi}$, and

$$\boldsymbol{w}=\eta\sqrt{N'\overline{M}}\,. \tag{2.2}$$

E and ***P*** are the macroscopic electric field and the macroscopic dielectric polarization in the crystal, respectively. ω_{tt} is the Reststrahlen frequency, and $\mathcal{E}_0$ and $\mathcal{E}_\infty$ are the static and the optical dielectric constants respectively. η is the displacement of a cation relative to the adjacent radical, N' the number of cation-radical pairs per unit volume, and $\overline{M}$ the reduced mass of the cation and the radical.

In quite a similar manner, the macroscopic theory of the rotational lattice vibration may be embodied in the following equations:

$$\ddot{\boldsymbol{u}}=c_{11}\boldsymbol{u}-c_{12}\boldsymbol{H}\,, \tag{2.1c}$$

$$\boldsymbol{I}=c_{21}\dot{\boldsymbol{u}}\,, \tag{2.1d}$$

where

$$c_{11}=-\omega_{rt}{}^2\,,\qquad \boldsymbol{u}=\Theta\sqrt{N'I}\,,$$

$$c_{21}=\frac{\beta_M}{\hbar}\sqrt{N'I}\,,\qquad \beta_M=\frac{Z_c e\hbar}{2M_c c}\,. \tag{2.3}$$

$\boldsymbol{H}$ and $\boldsymbol{I}$ are the macroscopic magnetic field and the macroscopic magnetization in the crystal respectively. Θ is the angular displacement[1] of each radical with the moment of inertia I. $\boldsymbol{I}$ is induced by the rotational vibration of the radicals, then c_{21} may be derived on the basis that the symmetric radical which has some point-like coordinated ions with mass M_c and effective charge $Z_c e$ (e: electronic charge), rotates around the center of mass with the angular velocity $\dot{\Theta}$. In reality, the deformation of the electron cloud on the radical will influence the magnetic moment induced by the rotation of the radical, but this effect may be ignored here since they are quite negligible on account of the smallness of the electronic polarizability of the ions. The physical meaning of ω_{rt} and the value of c_{12} are discussed later. (cf. Fig. 1 and (3.12))

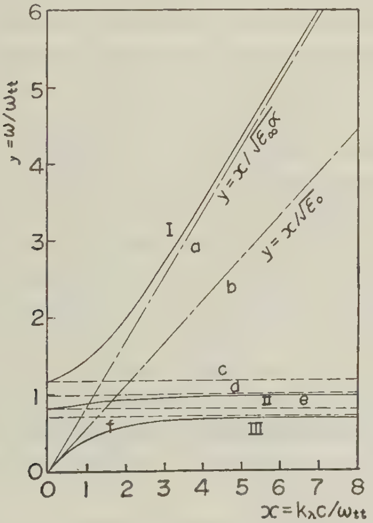

Fig. 1. Optical waves and lattice vibrations.

a: light wave (trans.) without dispersion.
b: light wave (trans.) with dispersion at long-wave limit.
c: translational lattice vibration (long.)
d: 〃 〃 〃 (trans.) ...approx.
e: rotational lattice vibration (long.)
f: 〃 〃 〃 (trans.) ...approx.

$\varepsilon_0=3.2$, $\varepsilon_\infty=2.0$, $\alpha=0.7$, $\sigma=0.5$

Let us seek the solutions, which satisfy the joint set of the lattice equations (2.1a, b c and d) and the following electromagnetic equations,

$$\operatorname{div}\boldsymbol{D}=0\,, \tag{2.4a}$$

$$\operatorname{div}\boldsymbol{B}=0\,, \tag{2.4b}$$

$$c\operatorname{curl}\boldsymbol{E}=-\dot{\boldsymbol{B}}\,, \tag{2.4c}$$

$$c\operatorname{curl}\boldsymbol{H}=\dot{\boldsymbol{D}}\,, \tag{2.4d}$$

$$\boldsymbol{D}=\boldsymbol{E}+4\pi\boldsymbol{P}\,,\quad \boldsymbol{B}=\boldsymbol{H}+4\pi\boldsymbol{I} \tag{2.4e}$$

and have the following sinusoidal forms:

$$\left.\begin{aligned}\boldsymbol{w}&=\boldsymbol{w}_0\\ \boldsymbol{P}&=\boldsymbol{P}_0\\ \boldsymbol{E}&=\boldsymbol{E}_0\\ \boldsymbol{u}&=\boldsymbol{u}_0\\ \boldsymbol{I}&=\boldsymbol{I}_0\\ \boldsymbol{H}&=\boldsymbol{H}_0\end{aligned}\right\}\times\exp\left[i(\boldsymbol{k}_\lambda\boldsymbol{r}-\omega t)\right]\,. \tag{2.5}$$

Substituting (2.5) into (2.1a and c), we obtain

$$\boldsymbol{w}=\frac{b_{12}}{-\omega^2-b_{11}}\boldsymbol{E}\,, \tag{2.6a}$$

$$\boldsymbol{u}=\frac{-c_{12}}{-\omega^2-c_{11}}\dot{\boldsymbol{H}}\,. \tag{2.6b}$$

Inserting (2.6a and b) into (2.1b and d) respectively, we obtain

$$\boldsymbol{P}=\left[b_{22}+\frac{b_{12}b_{21}}{-\omega^2-b_{11}}\right]\boldsymbol{E}\,, \tag{2.7a}$$

$$\boldsymbol{I}=\left[\frac{c_{12}c_{21}\omega^2}{-c_{11}-\omega^2}\right]\boldsymbol{H}\,. \tag{2.7b}$$

Using (2.7) and (2.5), we may transform (2.4) as follows.

$$(\boldsymbol{k}_\lambda\boldsymbol{E})\left[1+4\pi b_{22}+\frac{4\pi b_{12}b_{21}}{-b_{11}-\omega^2}\right]=0\,, \tag{2.8a}$$

$$(\boldsymbol{k}_\lambda\boldsymbol{H})\left[1+\frac{4\pi c_{12}c_{21}\omega^2}{-c_{11}-\omega^2}\right]=0\,, \tag{2.8b}$$

$$[\boldsymbol{k}_\lambda,\boldsymbol{E}]=\frac{\omega}{c}\left(1+\frac{4\pi c_{12}c_{21}\omega^2}{-c_{11}-\omega^2}\right)\boldsymbol{H}\,, \tag{2.8c}$$

$$[\boldsymbol{k}_\lambda, \boldsymbol{H}] = -\frac{\omega}{c}\left(1+4\pi b_{22}+\frac{4\pi b_{12}b_{21}}{-b_{11}-\omega^2}\right)\boldsymbol{E}\,. \tag{2.8d}$$

ω satisfying (2.8a, b, c and d) simultaneously may be obtained as follows[3]:

(I) When

$$1+4\pi b_{22}+\frac{4\pi b_{12}b_{21}}{-b_{11}-\omega^2}=0\,.$$

$$\omega^2=\left(\frac{\varepsilon_0}{\varepsilon_\infty}\right)\omega_{tt}^2\equiv\omega_{tl}^2\,. \tag{2.9}$$

Then

$$\boldsymbol{u}=\boldsymbol{I}=\boldsymbol{H}=0 \quad \text{and} \quad \boldsymbol{k}_\lambda /\!/ \boldsymbol{E} /\!/ \boldsymbol{P} /\!/ \boldsymbol{w}\,.$$

In this case only the longitudinal translational mode with the frequency ω_{tl} may exist.

(II) When

$$1+\frac{4\pi c_{12}c_{21}\omega^2}{-c_{11}-\omega^2}=0\,,$$

$$\omega^2=\frac{\omega_{rt}^2}{\alpha}\equiv\omega_{rl}^2\,, \tag{2.10}$$

where

$$\alpha=1-4\pi c_{12}c_{21}\,. \tag{2.11}$$

Then

$$\boldsymbol{w}=\boldsymbol{P}=\boldsymbol{E}=0 \quad \text{and} \quad \boldsymbol{k}_\lambda /\!/ \boldsymbol{H} /\!/ \boldsymbol{I} /\!/ \boldsymbol{u}\,.$$

In this case only the longitudinal rotational mode with the frequency ω_{rl} may appear.

(III) When $(\boldsymbol{k}_\lambda\boldsymbol{E})=0$ and $(\boldsymbol{k}_\lambda\boldsymbol{H})=0$, $(\boldsymbol{E}\boldsymbol{H})=0$ are concluded from (2.8c). Therefore, if we eliminate $\boldsymbol{E}$ and $\boldsymbol{H}$ from the equations (2.8c) and (2.8d), then we obtain

$$\frac{k_\lambda^2c^2}{\omega^2}=\left(\varepsilon_\infty+\frac{\varepsilon_0-\varepsilon_\infty}{\omega_{tt}^2-\omega^2}\omega_{tt}^2\right)\left(1+\frac{1-\alpha}{\omega_{rt}^2-\omega^2}\omega^2\right)\,. \tag{2.12}$$

This equation gives three branches of ω as a function of k_λ. At $k_\lambda=0$, (2.12) has three roots 0, ω_{rl} and ω_{tl}, and for $k_\lambda\to\infty$, there are also three types of solutions $\omega\to\omega_{rt}$, $\omega\to\omega_{tt}$, $\omega\to\infty\left(=\frac{c}{\sqrt{\varepsilon_\infty\alpha}}k_\lambda\right)$. For the question which one of the former three ω values at $k_\lambda=0$ continues to one of the latter three ω values for $k_\lambda\to\infty$, we cannot answer in general. There are several cases according as the magnitudes of ω_{tt}, ω_{tl}, ω_{rt} and ω_{rl}, and one example is shown in Fig. 1 for a set of given values of ε_0, ε_∞, α and $\kappa_t\equiv(\omega_{rt}/\omega_{tt})^2$. Hereafter, when we want to discuss the characters of these six branches for the limiting cases $k\to0$ and $k_\lambda\to\infty$, we will call them 0-, ω_{rl}- and ω_{tl}-branches (for $k_\lambda\to0$) and ω_{rt}-, ω_{tt}-, and ∞-branches (for $k_\lambda\to\infty$).

In this case, non vanishing $\boldsymbol{E}$, $\boldsymbol{H}$, $\boldsymbol{w}$ and $\boldsymbol{u}$ are all perpendicular to $\boldsymbol{k}_\lambda$, so there must coexist the electromagnetic wave, the transverse translational and the transverse rotational lattice vibrations.

§ 3. Equations of Motion

As well known, the effective electric field $\boldsymbol{E}_{\text{eff}}$ exerted on a particular cation of radical is related to the macroscopic field $\boldsymbol{E}$ by

$$\boldsymbol{E}_{\text{eff}}=\boldsymbol{E}+\frac{4\pi}{3}\boldsymbol{P} \tag{3.1}$$

and the equation of translational motion of a cation-radical pair is written as

$$\overline{M}\ddot{\boldsymbol{\xi}}=-k_t\boldsymbol{\xi}-Ze\boldsymbol{E}_{\text{eff}}\,, \tag{3.2}$$

where we have used for the later convenience $\boldsymbol{\xi}=-\boldsymbol{\eta}$; that is, the displacement of the radical relative to the adjacent cation, and Ze is the effective charge of the cation. (e: electronic charge, $Z<0$)

The first term on the right-hand side of (3.2) originates from the overlap forces and second term from all the elelctrostatic and the radiation field exerted on the cation-radical pair.

The equation of rotational motion of a particular radical may be written as

$$I\ddot{\boldsymbol{\Theta}}=-k_r\boldsymbol{\Theta}+Z_0e\sum_i[\boldsymbol{d}_i, \boldsymbol{E}_i]\,, \tag{3.3}$$

where $\boldsymbol{d}_i(|\boldsymbol{d}_i|=d)$ is the vector pointing from the center of the radical to the ith coordinated ion in the equilibrium orientation and $\boldsymbol{E}_i$ is the electric field of the radiation field exerted upon the ith ion. The summation is to be extended over all the coordinated ions belonging to the radical under consideration. The first term on the right-hand side of (3.3) represents the moments of the overlap forces and all the electrostatic forces exerted on the radical from the other constituents of the crystal.

If we denote the electric field at the center of the radical by $\boldsymbol{E}$, then $\boldsymbol{E}_i$ is expressed as

$$\boldsymbol{E}_i=\sum_{n=0}\frac{1}{n!}(\boldsymbol{d}_i\nabla)^n\boldsymbol{E}\,, \tag{3.4}$$

and

$$\sum_i[\boldsymbol{d}_i, \boldsymbol{E}_i]=\sum_{n=0}\sum_i\left[\boldsymbol{d}_i, \frac{1}{n!}(\boldsymbol{d}_i\nabla)^n\boldsymbol{E}\right]\,. \tag{3.5}$$

The first term with $n=0$ will vanish because of the symmetry of the radical, and the second term with $n=1$ will give

$$\frac{1}{2}d^2k_c \operatorname{curl} \boldsymbol{E}\,, \tag{3.6}$$

where k_c is a numerical constant peculiar to the type of the symmetry. (cf. (3.12) of part I.)

Omitting the higher order terms, we may rewrite (3.3) in the following form.

$$\begin{aligned} I\ddot{\Theta} &= -k_r\Theta + \frac{I\beta_M c}{\hbar} \operatorname{curl} \boldsymbol{E} \\ &= -k_r\boldsymbol{\Theta} - \frac{I\beta_M}{\hbar}\dot{\boldsymbol{B}}\,, \end{aligned} \tag{3.7}$$

where the relation $I = k_c d^2 M_c$ is used.

(3.7) may be considered as the equation of rotational motion of a particular radical, which corresponds to (3.2) in the case of translational motion.

It is advisable here to mention some complementary explanations on the equations of motion (3.2) and (3.7). We have neglected in (3.2) all the interactions of the multipole moments on the radical with the effective field acting on it, and in (3.7) the interactions of the multipole moments of higher order on the radical both with radiation field and with the external electrostatic field from additional free charges such as conduction electrons, since these interactions would be much smaller than the others effective to the translational and rotational motions of the radical. However, it should be noted that the electrostatic interactions of the multipole moments on the radical with the other constituents of the crystals, in particular in its neighbourhood, are retained in the first term in the right-hand side of (3.7), since they have a considerable effect upon the rotational motion of the radical together with the overlap forces as a result of superposition of the interactions in accordance with the crystal symmetry. This will actually be shown in part III.

If we insert $\boldsymbol{E}$ given by (3.1) into (2.1a and b), and eliminate $\boldsymbol{P}$ from the resulting two equations by taking account of (2.2), we may get

$$\begin{aligned} \ddot{\eta} &= -\left(\frac{\varepsilon_0+2}{\varepsilon_\infty+2}\right)\omega_{tt}^2\eta \\ &\quad + \frac{1}{\sqrt{N'\overline{M}}}\frac{3\omega_{tt}}{\varepsilon_\infty+2}\left(\frac{\varepsilon_0-\varepsilon_\infty}{4\pi}\right)^{1/2}\boldsymbol{E}_{\text{eff}}\,. \end{aligned} \tag{3.8}$$

Comparing the coefficients of η in the equations (3.2) and (3.8), we have the well-known relation

$$k_t = \overline{M}\left(\frac{\varepsilon_0+2}{\varepsilon_\infty+2}\right)\omega_{tt}^2\,. \tag{3.9}$$

On the other hand, (2.1c) may easily be transformed as follows:

$$\ddot{\Theta} = -\omega_{rl}^2\Theta - \frac{c_{12}}{\alpha\sqrt{N'I}}\dot{\boldsymbol{B}}\,, \tag{3.10}$$

where we have taken account of (2.1d), (2.3), (2.4e), (2.10) and (2.11). If we compare the coefficients in the equations (3.7) and (3.10), we may obtain

$$k_r = I\omega_{rl}^2 = I\omega_{rt}^2/\alpha\,, \tag{3.11}$$

and

$$c_{12} = \alpha\frac{\beta_M}{\hbar}\sqrt{N'I} = \alpha c_{21}\,. \tag{3.12}$$

Combining (3.12) with the definition of α (2.11), we may estimate α as follows.

$$\alpha = (1 + 4\pi N' I \beta_M^2/\hbar^2)^{-1}\,. \tag{3.13}$$

From (2.1a) we can easily derive the macroscopic equations of translational motion. (cf. App. I) In a similar manner we can obtain as below the corresponding macroscopic equations of rotational motion, which will be utilized for the later discussion.

We may deduce from (2.46)

$$\boldsymbol{B}_l = \boldsymbol{H}_l + 4\pi\boldsymbol{I}_l = 0\,.$$

Then

$$\boldsymbol{H}(=\boldsymbol{H}_t + \boldsymbol{H}_l) = \boldsymbol{H}_t - 4\pi\boldsymbol{I}_l\,, \tag{3.14}$$

where the suffixes l and t indicate the irrotational and solenoidal parts of the vector to which they are appended, respectively. Substituting (3.14) into (2.1c) and using the relations (2.1d), (2.3) and (2.10), we immediately obtain the macroscopic equations of motion:

$$\ddot{\boldsymbol{Q}}_l + \omega_{rl}^2\boldsymbol{Q}_l = 0 \tag{3.15a}$$

and

$$\gamma_{rt}(\ddot{\boldsymbol{Q}}_t + \omega_{rt}^2\boldsymbol{Q}_t) = -\dot{\boldsymbol{H}}_t\,, \tag{3.15b}$$

where

$$\boldsymbol{Q} \equiv IN'\beta_M/\hbar\cdot\boldsymbol{\Theta} \tag{3.16a}$$

and

$$1/\gamma_{rt} \equiv \alpha IN'\beta_M^2/\hbar^2\,. \tag{3.16b}$$

Starting from (3.10), (3.15b) takes the alternative expression such as

$$\gamma_{rl}(\ddot{\boldsymbol{Q}}_t + \omega_{rl}\boldsymbol{Q}_t) = -\dot{\boldsymbol{B}}_t\,, \tag{3.15b$'$}$$

where

$$1/\gamma_{rl} = IN'\beta_M^2/\hbar^2 = (c_{21})^2\,. \tag{3.17}$$

§ 4. Energy Density

If we define the energy density U in the lattice under vibration by the equation;

$$\frac{c}{4\pi}\int \operatorname{div}[\boldsymbol{E},\boldsymbol{H}]\,d\tau=-\int\left(\frac{dU}{dt}\right)d\tau\,,$$

then with the help of the Maxwell equation we may obtain

$$\frac{dU}{dt}=\frac{1}{4\pi}(\boldsymbol{E}\dot{\boldsymbol{E}}+\boldsymbol{H}\dot{\boldsymbol{H}})+\boldsymbol{E}\dot{\boldsymbol{P}}+\boldsymbol{H}\dot{\boldsymbol{I}}\,. \tag{4.1}$$

It is clear from the lattice equations (2.1) that different volume elements are coupled in the macroscopic theory only through their electrostatic and electromagnetic interaction, thus dU/dt must be equal to the rate of change of the total energy, including the kinetic energy of the lattice particles as well as all the electromagnetic and potential energies in the system. U satisfying (4.1) is given by

$$U=E_M+(\boldsymbol{H}\boldsymbol{I})+\frac{1}{8\pi}(\varepsilon_\infty\boldsymbol{E}^2+\boldsymbol{H}^2)\,, \tag{4.2}$$

where

$$E_M\equiv\frac{1}{2}\,(\dot{\boldsymbol{w}}^2-b_{11}\boldsymbol{w}^2)+\frac{1}{2}\,(\dot{\boldsymbol{u}}^2-c_{11}\boldsymbol{u}^2)\,\frac{1}{\alpha}\,. \tag{4.3}$$

By differentiating (4.2) with respect to time and taking account of (2.1), we can easily verify that (4.2) actually satisfies (4.1). From (A1-2), (2.1c) and (3.14), we obtain, when there are no free charges,

$$\boldsymbol{E}_l=\frac{-4\pi b_{21}}{1+4\pi b_{22}}\,\boldsymbol{W}_l\,, \tag{4.4}$$

and

$$\boldsymbol{H}_l=-4\pi\boldsymbol{I}_l=-4\pi c_{21}\dot{\boldsymbol{u}}_l\,. \tag{4.5}$$

If each vector in (4.2) is decomposed into the irrotational and solenoidal parts and the relations (2.9), (2.10), (4.4) and (4.5) are used, we may write U in the form

$$\begin{aligned}U=&\frac{1}{2}\,(\dot{\boldsymbol{w}}_l^2+\omega_{tl}^2\boldsymbol{w}_l^2)+\frac{1}{2}\,(\dot{\boldsymbol{u}}_l^2+\omega_{rl}^2\boldsymbol{u}_l^2)\\&+\frac{1}{2}\,(\dot{\boldsymbol{w}}_t^2+\omega_{tt}^2\boldsymbol{w}_t^2)+\frac{1}{2}\,(\dot{\boldsymbol{u}}_t^2+\omega_{rl}^2\boldsymbol{u}_t^2)\\&+\frac{1}{8\pi}(\varepsilon_\infty\boldsymbol{E}_t^2+\boldsymbol{B}_t^2)\,.\end{aligned} \tag{4.6}$$

When the longitudinal vibrations do not exist, the first and second terms vanish and the energy density is simply given by

$$\begin{aligned}U_t=&\frac{1}{2}\,(\dot{\boldsymbol{w}}_t^2+\omega_{tt}^2\boldsymbol{w}_t^2)+\frac{1}{2}(\boldsymbol{u}_t^2+\omega_{rl}^2\boldsymbol{u}_t^2)\\&+\frac{1}{8\pi}(\varepsilon_\infty\boldsymbol{E}_t^2+\boldsymbol{B}_t^2)\end{aligned} \tag{4.7}$$

The first and second terms are the densities of the mechanical energies in the translational and rotational transverse vibrations respectively, whereas the last term represents the density of the radiative energy.

Inserting (2.6) and (2.7) into (4.7) and taking account of (2.8c), we easily obtain

$$\begin{aligned}8\pi U_t/\overline{\boldsymbol{H}_t^2}=&(\varepsilon_0-\varepsilon_\infty)\frac{(1+y)(\kappa_t-\alpha y)}{(1-y)(\kappa_t-y)(\varepsilon_0-\varepsilon_\infty y)}\\&+(1-\alpha)\frac{y(\kappa_t+\alpha y)}{(\kappa_t-y)^2}\\&+\left[\varepsilon_\infty\frac{(1-y)(\kappa_t-\alpha y)}{(\kappa_t-y)(\varepsilon_0-\varepsilon_\infty y)}+\frac{(\kappa_t-\alpha y)^2}{(\kappa_t-y)^2}\right],\end{aligned} \tag{4.8}$$

where

$$y\equiv(\omega/\omega_{tt})^2\,,\qquad \kappa_t\equiv(\omega_{rt}/\omega_{tt})^2$$

and $\overline{\boldsymbol{H}_t^2}$ means the time average of $\boldsymbol{H}_t^2$. The first and second terms of (4.8) correspond to the densities of translational and rotational mechanical energies respectively, and the last one in the square brackets to the density of the radiative energy. For the set of the values of ε_0, ε_∞, α and κ_t, L_m, the ratio of the mechanical (translational and rotational) energy to the total energy and L_r, that of the rotational energy to the total energy are plotted in Fig. 2 against wave-number for each one of the three branches given in Fig. 1, (L_m-L_r indicates the ratio of the translational energy to the total energy.) In Fig. 2, the three vertical distances between the

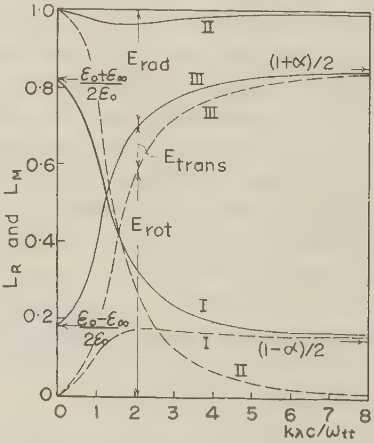

Fig. 2. Ratios of mechanical energy and rotational energy in the transverse modes.

$\varepsilon_0=3.2$, $\varepsilon_\infty=2.0$, $\alpha=0.7$, $\sigma=0.5$.
Real curves: L_m (mechanical energy/total energy)
Dotted curves: L_r (rotational energy/total energy)
The curve numbers correspond to those in Fig. 1.

base-line of the diagram and a dotted curve, between the dotted curve and the real curve with the same curve number, and between the real curve and the upside of the diagram indicate the ratios of the rotational, translational and radiative energies to the total energy for a particular transverse branch, respectively.

Referring to Fig. 2, we may point out in particular the following facts. In the ∞-branch, the radiative energy is predominant in short-wave region, that is, this branch represents the optical waves, whereas the ω_{tt}- and ω_{rt}-branches may be regarded as the translational and predominantly rotational lattice vibrations respectively, since the mechanical energy is predominant in short wave region of these branches. On the other hand, in long-wave region, the ω_{tl}- and ω_{rl}-branches are of predominantly translational and of rotational energies respectively, whereas in the 0-branch the radiative energy is predominant.

In short-wave region the rotational energy is not separated but mixed with the radiative one in the ω_{rt}- and ∞-branches, whereas the translational energy is lodged solely in the ω_{tt}-branch. On the other hand, in long-wave region the translational energy mixes with the radiative one in the ω_{tl}- and 0-branches, whereas the rotational energy is isolated in the other ω_{rl}-branch. As easily understood, the ratio ($\simeq(1-\alpha)/2$) of the radiative energy in the ω_{rt}-branch is markedly decreased when $\alpha(<1)$ approaches to unity, and the waves in this branch may be considered as purely mechanical rotational vibration with frequency ω_{rt}, which enables us to define the transverse rotational phonon.

§ 5. Interaction with a Conduction Electron

The interaction of a conduction electron with the translational lattice vibrations may be separated from that with the rotational ones as shown in (4.6) and treated by the usual manner. Hence we restrict ourselves to the optical modes of rotational vibration, assuming the constancy of the frequency.

Then the Hamiltonian of the system consisting of a conduction electron and the rotational phonon field is given by (cf. App. II)

$$
\begin{aligned}
H=&\frac{1}{2\kappa}\int[\boldsymbol{\pi}_t{}^2+\kappa^2c^2(\mathrm{curl}\,\boldsymbol{A}_t)^2]d\tau\\
&+\frac{1}{2\gamma_{rl}}\int[(\boldsymbol{P}_r-\mathrm{curl}\,\boldsymbol{A}_t)^2+\omega_{rl}{}^2\gamma_{rl}{}^2\boldsymbol{Q}^2]d\tau\\
&+\frac{1}{2m}\Big(\boldsymbol{p}_e-\frac{e}{c}\boldsymbol{A}_t(\boldsymbol{r}_e)\Big)^2\\
&-\boldsymbol{\mu}\cdot\mathrm{curl}\,\boldsymbol{A}_t(\boldsymbol{r}_e)\\
&+\frac{1}{2mc}\left[\boldsymbol{\mu},\frac{1}{c\kappa}\boldsymbol{\pi}_t(\boldsymbol{r}_e)\right]\boldsymbol{p}_e\,,
\end{aligned}
\tag{5.1}
$$

where $\boldsymbol{\mu}=\beta\boldsymbol{\sigma}$, $\kappa=1/4\pi c^2$ and $\boldsymbol{\sigma}$ is Pauli spin operator, β Bohr magneton. $(\boldsymbol{\pi}_t, \boldsymbol{A}_t)$ $(\boldsymbol{P}_r, \boldsymbol{Q})$ and $(\boldsymbol{p}_e, \boldsymbol{r}_e)$ are the sets of canonically conjugate momentum and coordinate of photon field, rotational phonon field, and electron respectively.

Making use of the Hamiltonian (5.1) we obtain the following field equations:

$$\Box\boldsymbol{A}_t=-\frac{4\pi e}{c}\dot{\boldsymbol{r}}_e{}^{(t)}\delta(\boldsymbol{r}-\boldsymbol{r}_e)-\frac{4\pi}{c}\boldsymbol{J}_s{}^{(t)}-\frac{4\pi}{c}\boldsymbol{J}_r\,, \tag{5.2}$$

and

$$\gamma_{rl}(\ddot{\boldsymbol{Q}}+\omega_{rl}{}^2\boldsymbol{Q})=-\mathrm{curl}\,\dot{\boldsymbol{A}}_t=c\,\mathrm{curl}\,\boldsymbol{E}_t\,, \tag{5.3}$$

where

$$\boldsymbol{J}_s{}^{(t)}=\frac{c}{4\pi}\Delta\boldsymbol{A}_s{}^{(m)}+\frac{1}{4\pi}\mathrm{curl}\,\dot{\boldsymbol{A}}_s{}^{(e)}\,, \tag{5.4}$$

$$\boldsymbol{J}_r=c\,\mathrm{curl}\,\dot{\boldsymbol{Q}}\,, \tag{5.5}$$

$$\boldsymbol{A}_s{}^{(m)}=\left[\boldsymbol{\mu},\,\mathrm{grad}_r\frac{1}{|\boldsymbol{r}-\boldsymbol{r}_e|}\right], \tag{5.6}$$

$$\boldsymbol{A}_s{}^{(e)}=\left[\frac{[\boldsymbol{\mu},\dot{\boldsymbol{r}}_e]}{2c},\,\mathrm{grad}_r\frac{1}{|\boldsymbol{r}-\boldsymbol{r}_e|}\right]. \tag{5.7}$$

$\dot{\boldsymbol{r}}_e{}^{(t)}$ means the solenoidal component of $\dot{\boldsymbol{r}}_e$. Here it should be noted that (5.3) is quite identical with the equations of motion (3.15a) and (3.15b)′.

Treating the interaction between the electron and the phonon as a perturbation, we can compute the probability when the electron absorbs or emits a phonon. Exactly speaking, this process is carried out by means of the interchange of virtual photons, so we need to calculated the second order perturbation. If we allow to neglect, however, the small contribution in transition probability, we may eliminate $\boldsymbol{A}_t$ from (5.1) by using (5.2).

Since the longitudinal rotational phonon does not interact with the radiation field and therefore also with the electron, we may consider only the transverse components of $\boldsymbol{P}_r$ and $\boldsymbol{Q}$. Introducting a solenoidal vector potential $\boldsymbol{A}_r$ such as

$$\dot{\boldsymbol{Q}}_t=\frac{1}{4\pi}\mathrm{curl}\,\boldsymbol{A}_r\,, \tag{5.8}$$

the Hamiltonian H can be transformed as follows.

$$H=H_0+H_{\text{int}}\,,$$

$$H_0=\frac{1}{2\gamma_{rl}}\int[\boldsymbol{P}_{rt}^2+\omega_{rl}\gamma_{rl}\boldsymbol{Q}_t^2]+\frac{1}{2m}\boldsymbol{p}_e^2\,, \tag{5.9}$$

$$H_{\text{int}}=-\frac{e}{c^2}\int\frac{\dot{\boldsymbol{r}}_e\boldsymbol{J}_r(\boldsymbol{r})}{|\boldsymbol{r}-\boldsymbol{r}_e|}d\tau-\frac{1}{c^2}\int\frac{\boldsymbol{J}_s^{(t)}(\boldsymbol{r}')\boldsymbol{J}_r(\boldsymbol{r})}{|\boldsymbol{r}-\boldsymbol{r}'|}d\tau d\tau' \tag{5.9a}$$

$$=-\frac{e}{mc}\boldsymbol{p}_e\boldsymbol{A}_r(\boldsymbol{r}_e)-\boldsymbol{\mu}\,\mathrm{curl}\,\boldsymbol{A}_r(\boldsymbol{r}_e)\,, \tag{5.9b}$$

where the self-energies of the electron and the phonon are neglected.

In (5.9a), the transverse rotational phonon field is destined to be purely mechanical vibration with the frequency ω_{rl}. This fact contradicts the conclusions of the last section that in short-wave region the transverse rotational branch i.e. ω_{rt}-branch has the frequencies near ω_{rt} somewhat different from ω_{rl}. (cf. the curve III in Fig. 1) and that it mixes with a considerable amount of radiative energy (cf. the dotted curve III in Fig. 2). However, $1/\gamma_{rl}\ll 1$ in actual complex crystals, as stated later. Then α is regarded as nearly equal to unity and $\gamma_{rl}\simeq\gamma_{rt}$. Since the radiative energy mixed may be ignored and $\omega_{rl}\simeq\omega_{rt}$ in such case, the difficulty mentioned above will not be serious in practice. Thus the first term in (5.9a) may be considered approximately as the Hamiltonian of the transverse rotational phonon field.

According to the usual procedure, $W_{12}^{(e)}$ the transition probability from the state $1(\boldsymbol{k},+,n_W)$, where the electron has the wave-number $\boldsymbol{k}$ and up spin, and the number of the phonons belonging to the wave-number $\boldsymbol{W}$ is n_W, to the states $2(\boldsymbol{k}',\pm,n_W+1)$ and $W_{12}^{(a)}$ that from the state $1(\boldsymbol{k},+,n_W)$ to the states $2(\boldsymbol{k}',\pm,n_W-1)$ may be obtained as follows:

$$W_{12}^{(e,a)}=\frac{2\pi}{\hbar}U_{12}^{(e,a)}\delta(E_1-E_2)\,, \tag{5.10}$$

$$\left.\begin{matrix}U_{12}^{(e)}\\ U_{12}^{(a)}\end{matrix}\right\}=(4\pi\beta)^2\frac{\hbar\omega_{rl}}{\gamma_{rl}V}\left\{\begin{matrix}(n_W+1)\delta_{\boldsymbol{k}',\boldsymbol{k}-\boldsymbol{W}}\\ n_W\delta_{\boldsymbol{k}',\boldsymbol{k}+\boldsymbol{W}}\end{matrix}\right\}$$

$$\times(1+2k^2\sin^2\theta/W^2)\,, \tag{5.11}$$

where θ is the angle between $\boldsymbol{k}$ and $\boldsymbol{W}$, and the two independent directions of $\boldsymbol{Q}_t$ belonging to each wave-number $\boldsymbol{W}(\boldsymbol{W}\perp\boldsymbol{Q}_t)$ are taken into account.

By integrating the above results in $\boldsymbol{W}$-space, we obtain the scattering probability $1/\tau_r$ of a conduction electron, as a function of its wave number k, due to the rotational phonon.

For large values of k, $1/\tau_r$ takes the following form.

$$1/\tau_r\sim 8\alpha_r\omega_{rl}(2n_W+1)g_r\eta\log(2v_0\eta)\,, \tag{5.12}$$

where

$$\alpha_r=\frac{2\pi e^2u_r}{\hbar\gamma_{rl}\omega_{rl}}\,,\quad u_r^2=\frac{2m\omega_{rl}}{\hbar}\,,\quad g_r=\frac{\hbar\omega_{rl}}{4mc^2}$$

$$\eta=k/u_r\,,\qquad v=w/u_r\,, \tag{5.13}$$

and v_0 is the cut-off value of the reduced wave number v of the rotational phonon.

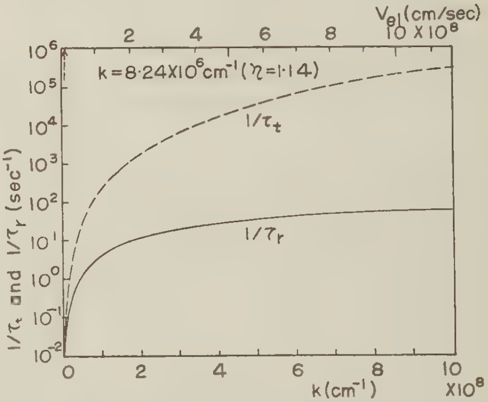

Fig. 3. Scattering probabilities of conduction electron due to rotational and transverse translational phonons *versus* wave number or velocity of the conduction electron.
$\omega_{tt}=\omega_{rl}=3\times10^{13}\,\mathrm{sec}^{-1}$, $\alpha_t=1$,
$v_0=6.10$ (for both cases), $\alpha_r=10^{-8}$, $T=300°K$
The arrow on the upside of the diagram indicates the point corresponding to thermal electron at 300°K.

Fig. 3 shows the dependence of $1/\tau_r$ upon the wave number k of a conduction electron for the given values of ω_{rl}, α_r and T. Besides, for the purpose of comparison, the dependence of the scattering probability $1/\tau_t$ by transverse translational phonons is plotted in the same figure. (cf. App. III) In contrast to the behavior of $1/\tau_t$, $1/\tau_r$ increases with increasing η values as $\eta\log\eta$. (cf. (5.12) and (AIII–4))

Referring to (3.17), let us estimate the order of magnitude of γ_{rl}, by using, as an example, the radical $[SO_4]^{2-}$ which has the tetrahedral structure around the central S-ion[4,5]. Since the binding force within an anionic radical would be essentially covalent, and the binding state of the radical may be expected to be formed by the resonance of several electronic states[6], the estimation of the effective charge on a coordinated ion in the radical, in general, would be difficult. But if we assume the state $S^{2+}(O^-)_4$ as the most predominant binding state for $[SO_4]^{2-}$ radical, then the effective charge on the oxygen atom may be infered to be approximately equal to e. Then $d=1.51$ Å[6)], $k_c=8/3$, $Z_c=1$, and $M_c=16M_H$ (M_H: mass of a H-atom). Furtuer we may take $N'=\mathfrak{N}\rho_0/M_m$, wher $\mathfrak{N}$ is Loschmidt number, ρ_0 and M_m the density and the molecular weight of the crystal respectively. In the case of the orthorhombic $PbSO_4$ crystal, $\rho_0=6.38\,g/cm^3$ [7)], and $M_m=303.27$. Therefore we obtain $1/\gamma_{rl}=1.87\times10^{-11}$. Then $\gamma_{rl}\simeq\gamma_{rt}$ and $\omega_{rl}\simeq\omega_{rt}$.

If we take $\omega_{rl}\simeq10^{13}\,\text{sec}^{-1}$ and $1/\gamma_{rl}\simeq10^{-11}$, then $\alpha_r\simeq10^{-8}$, $g_r\simeq10^{-8}$ and $\alpha_r g_r\simeq10^{-16}$. For the case of the scattering by transverse translational phonons, the factor corresponding to $\alpha_r g_r$ is $\alpha_t g_t^2$ which has the order of $10^{-15}\sim10^{-16}$. (cf. (5.12) and (AIII–4)) Therefore, we may conclude that the scattering probability due to rotational phonons would be comparable to that of transverse phonons for $\eta\simeq1$, if ω_{rl} is of order of magnitude $10^{13}\,\text{sec}^{-1}$. (cf. (5.12) and (AIII–4))

§ 6. Conclusions

In the ω_{tt} -branch the translational energy of lattice particles is abnormally high relative to the electromagnetic energy flux. (cf. the real curve II in Fig. 2.) In such a case, a stong absorption of the optical wave with frequency ω_{tt} must occur. In a steady state, whatever energy is lost by the lattice vibration must be supplied by the electromagnetic enery flux, and under such circumstances a small percentage energy loss by the former through a small coupling such as anharmonic potentials drastically reduces the latter.[8)]

Let us investigate the optical properties in infrared region in the case, where the rotational lattice vibration is taken into account. For this purpose, it is convenient to consider the dispersion formula which takes account of the energy dissipation. Namely, we add the simple damping terms $-\sigma_t\boldsymbol{W}$ and $-\sigma_r\dot{\boldsymbol{u}}$ to the right-hand sides of the equations of motion (2.1a) and (2.1c) respectively, where σ_t and σ_r are positive constants with dimension of frequency. Then, for the periodic solutions (2.5), we obtain

$$-\omega^2\boldsymbol{w}=(b_{11}+i\omega\sigma_t)\boldsymbol{w}+b_{12}\boldsymbol{E}\,, \tag{6.1a}$$

$$-\omega^2\boldsymbol{u}=(c_{11}+i\omega\sigma_r)\boldsymbol{u}+i\omega c_{12}\boldsymbol{H}\,. \tag{6.1b}$$

The addition of these damping terms is thus equivalent to the replacements of b_{11} and c_{11} by $b_{11}+i\omega\sigma_t$ and $c_{11}+i\omega\sigma_r$, respectively. Hence, we obtain

$$\begin{aligned}\mathcal{E}(\omega)&=(\boldsymbol{E}+4\pi\boldsymbol{P})/\boldsymbol{E}=1+4\pi b_{22}+\frac{4\pi b_{12}b_{21}}{-b_{11}-i\omega\sigma_t-\omega^2}\\&=\mathcal{E}_\infty+\frac{\mathcal{E}_0-\mathcal{E}_\infty}{1-y-i\sqrt{y}\,\Gamma_t}\,,\end{aligned} \tag{6.2a}$$

and

$$\begin{aligned}\mu(\omega)&=(\boldsymbol{H}+4\pi\boldsymbol{I})/\boldsymbol{H}=1+\frac{4\pi c_{12}c_{21}\omega^2}{-c_{11}-i\omega\sigma_r-\omega^2}\\&=1+\frac{(1-\alpha)y}{\kappa_t-y-i\sqrt{y}\,\Gamma_r}\,,\end{aligned} \tag{6.2b}$$

where

$$\Gamma_t\equiv\sigma_t/\omega_{tt}\,,\qquad \Gamma_r\equiv\sigma_r/\omega_{tt}\,.$$

If we denote by $\bar{n}$ the complex refractive index,

$$\bar{n}=n(1+i\kappa)=\sqrt{\mathcal{E}(\omega)\mu(\omega)}\,, \tag{6.3}$$

where n and κ are the optical constants of the absorbing medium. Inserting (6.2a and b) into (6.3) and squaring it, we obtain

$$\begin{aligned}n^2(1-\kappa^2)=&\left[\mathcal{E}_\infty+(\mathcal{E}_0-\mathcal{E}_\infty)\frac{1-y}{F_t(y)}\right]+\mathcal{E}_\infty(1-\alpha)\frac{y(\kappa_t-y)}{F_r(y)}\\&+(\mathcal{E}_0-\mathcal{E}_\infty)(1-\alpha)\frac{y[(1-y)(\kappa_t-y)-y\Gamma_t\Gamma_r]}{F_t(y)F_r(y)}\,,\end{aligned} \tag{6.4a}$$

$$\begin{aligned}2n^2\kappa=&(\mathcal{E}_0-\mathcal{E}_\infty)\Gamma_t\frac{\sqrt{y}}{F_t(y)}+\mathcal{E}_0(1-\alpha)\Gamma_r\frac{y\sqrt{y}}{F_r(y)}\\&+(\mathcal{E}_0-\mathcal{E}_\infty)(1-\alpha)\frac{y\sqrt{y}[\Gamma_t(\kappa_t-y)+\Gamma_r(1-y)]}{F_t(y)F_r(y)}\,,\end{aligned} \tag{6.4b}$$

where

$$F_t(y)\equiv(1-y)^2+\Gamma_t^2y\,,$$

$$F_r(y)\equiv(\kappa_t-y)^2+\Gamma_r^2y\,.$$

As well known, n gives the usual refractive index of the medium and $4\pi n\kappa$ the absorbancy coefficient in unit of reciprocal vacuum wavelength. If Γ_t and Γ_r are given numerically besides $\mathcal{E}_0$, $\mathcal{E}_\infty$, α and κ_t, we may compute n

and $n\kappa$ for an arbitrary wave-length by making use of (6.4a and b). Thus we may clarify the general features of infrared dispersion and absorption in the case, where the translational and rotational lattive vibrations simultaneously contribute to them.

The first terms in (6.4a and b) purely originate from the translational vibration, whereas the second and third terms in both equations appear first by taking account of the rotational vibration. Since in actual complex crystals $1/\gamma_{rl}\simeq 1/\gamma_{rt}=1-\alpha\sim 10^{-11}$ (cf. § 5, (3.13) and (3.16b)), the energy density of the ω_{rt}-branch is lodged predominantly in the radicals of the crystal as mechanical energy of lattice vibration rather than in the electromagnetic field just as in the case of the ω_{tt}-branch. (cf. § 4 and curves III in Fig. 2) Then a strong absorption due to the rotational vibration may be expected to exist. However, if $\Gamma_t\sim\Gamma_r$ and $\kappa_t\sim 1(\omega_{rt}\sim\omega_{tt})$, the second and third terms in (6.4a and b) may be neglected in this case, compared with the first terms in these equations, since we may expect the magnitude of $\varepsilon_0-\varepsilon_\infty$ to be of order of unity. Furthermore, the former terms will be still much smaller than the latters even in the neighbourhood of $y=\kappa_t(\omega=\omega_{rt})$. Hence, the former terms will not have any appreciable contribution to the values of n and $n\kappa$.

Accordingly we would not be able to recognize experimentally the definite existence of the absorption band due to the rotational lattice vibration, since this weak band will be covered by the strong absorption band resulting from the translational lattice vibration.

With respect to the scattering probability of conduction electrons we may conclude as follows: According to the order estimation in § 5, if ω_{rl} is of the order of magnitude 10^{13} sec^{-1}, the interaction of conduction electron with rotational phonons is of order comparable to that with transverse translational phonons at $\eta\simeq 1$, although the scattering probability due to rotational phonons increases with η as $\eta\log\eta$, whereas that due to transverse translational phonons as η^3. (cf. Fig. 3 and App. III)

Finally, the authors are indebted to Prof. K. Umeda for reading the manuscript in part and giving them valuable advices.

Appendix I

If free charges exist,

$$\mathrm{div}\,(\boldsymbol{E}+4\pi\boldsymbol{P})=4\pi\rho\ .$$

Therefore

$$\mathrm{div}\,\boldsymbol{E}=\frac{4\pi}{1+4\pi b_{22}}\,(-b_{21}\,\mathrm{div}\,\boldsymbol{w}_l+\rho(\boldsymbol{r},t))\ . \qquad \text{(cf. (2.1b))} \quad \text{(AI–1)}$$

If we put

$$\boldsymbol{D}_l(\boldsymbol{r},t)=-\mathrm{grad}\int\frac{\rho(\boldsymbol{r}',t)}{|\boldsymbol{r}'-\boldsymbol{r}|}d\tau'\ ,$$

we have

$$\boldsymbol{E}=\frac{-4\pi b_{12}}{1+4\pi b_{22}}\,\boldsymbol{w}_l+\frac{\boldsymbol{D}_l}{1+4\pi b_{22}}+\boldsymbol{E}_t\ . \qquad \text{(AI–2)}$$

Inserting (AI–2) into (2.1a) and (2.1b), we obtain

$$\ddot{\boldsymbol{w}}_l=-\omega_{tl}^2\boldsymbol{w}_l+\frac{b_{12}}{\varepsilon_\infty}\boldsymbol{D}_l\ , \qquad \text{(AI–3a)}$$

$$\ddot{\boldsymbol{w}}_t=-\omega_{tt}^2\boldsymbol{w}_t+b_{12}\boldsymbol{E}_t\ , \qquad \text{(AI–3b)}$$

$$\boldsymbol{P}_l=\frac{1}{\varepsilon_\infty}\,b_{21}\boldsymbol{w}_l+\frac{b_{22}}{\varepsilon_\infty}\boldsymbol{D}_l\ , \qquad \text{(AI–3c)}$$

and

$$\boldsymbol{P}_t=b_{21}\boldsymbol{w}_t+b_{22}\boldsymbol{E}_t\ . \qquad \text{(AI–3d)}$$

Further, from (2.2) and (AI–3c and d) we obtain, for the atomic polarization $\boldsymbol{P}_A$,

$$\boldsymbol{P}_{Al}=\frac{1}{\varepsilon_\infty}\left(\frac{\varepsilon_0-\varepsilon_\infty}{4\pi}\right)^{1/2}\omega_{tl}\boldsymbol{w}_l\ , \qquad \text{(AI–4a)}$$

and

$$\boldsymbol{P}_{At}=\left(\frac{\varepsilon_0-\varepsilon_\infty}{4\pi}\right)^{1/2}\omega_{tt}\boldsymbol{w}_t\ . \qquad \text{(AI–4b)}$$

Substituting (AI–4) into (AI–3a and b), we may get finally the macroscopic equations of motion:

$$\ddot{\boldsymbol{P}}_{Al}+\omega_{tl}^2\boldsymbol{P}_{Al}=\frac{\omega_{tl}^2}{4\pi}\left(\frac{1}{\varepsilon_\infty}-\frac{1}{\varepsilon_0}\right)\boldsymbol{D}_l\ , \qquad \text{(AI–5a)}$$

$$\ddot{\boldsymbol{P}}_{At}+\omega_{tt}^2\boldsymbol{P}_{At}=\frac{\omega_{tt}^2}{4\pi}(\varepsilon_0-\varepsilon_\infty)\boldsymbol{E}_t\ . \qquad \text{(AI–5b)}$$

Appendix II

Derivation of the Hamiltonian of the Rotational Phonon in the Electromagnetic Field.

We denote the position of the center of a radical by $\boldsymbol{r}$, and the displacement of the ith coordinated ion belonging to this radical from its equilibrium position by $\boldsymbol{r}_i$, then we have the following Hamiltonian of the system consisting of such radicals of the same kind.

$$H_r=\frac{N'}{2M_c}\int\sum_i\left\{\left(\boldsymbol{p}_i-\frac{Z_ce}{c}\boldsymbol{A}_i\right)^2+\omega_{rl}^2M_c^2\boldsymbol{r}_i^2\right\}d\tau\ , \qquad \text{(AII–1)}$$

where $\boldsymbol{p}_i$ is the canonically conjugate momentum of $\boldsymbol{r}_i$. The summation is to be taken over all the coordinated ions belonging to the radical at $\boldsymbol{r}$.

The equations of motion for each ion are thus written as

$$\partial H_r/\partial \boldsymbol{P}_i = N'\dot{\boldsymbol{r}}_i\,,\quad \partial H_r/\partial \boldsymbol{r}_i = -N'\dot{\boldsymbol{p}}_i\,. \qquad \text{(AII–2)}$$

When the magnitude of the angular displacement $\boldsymbol{\Theta}$ of the radical is small, $\boldsymbol{r}_i$ may be written as

$$\boldsymbol{r}_i = [\boldsymbol{\Theta}, \boldsymbol{d}_i]\,. \qquad \text{(AII–3)}$$

By using (3.16a) and (AII–3), we obtain

$$\frac{\delta H_r}{\delta Q_x} = \sum_{\beta=x,y,z}\sum_i \frac{\delta H_r}{\delta r_{i\beta}}\frac{\partial r_{i\beta}}{\partial Q_x} = \frac{\hbar}{I\beta_M}\sum_i [\dot{\boldsymbol{p}}_i, \boldsymbol{d}_i]_x\,.$$

Using the relations

$$\sum_i [[\boldsymbol{s}, \boldsymbol{d}_i], \boldsymbol{d}_i] = -k_c d^2 \boldsymbol{s},\ \text{(for arbitrary } \boldsymbol{s}) \qquad \text{(AII–4)}$$

and

$$\boldsymbol{p}_i - \frac{Z_c e}{c}\boldsymbol{A}_t = M_c\dot{\boldsymbol{r}}_i = \frac{M_c\hbar}{N' I\beta_M}[\dot{\boldsymbol{Q}}, \boldsymbol{d}_i]\,, \qquad \text{(AII–5)}$$

we may transform the above equation into

$$\delta H_r/\delta \boldsymbol{Q} = -\dot{\boldsymbol{P}}_r\,, \qquad \text{(AII–6)}$$

where

$$\boldsymbol{P}_r \equiv \gamma_{rt}\dot{\boldsymbol{Q}} + \text{curl}\,\boldsymbol{A}_t\,. \qquad \text{(AII–7)}$$

On the other hand, we can easily prove the equation

$$\delta H_r/\delta \boldsymbol{P}_r = \dot{\boldsymbol{Q}}\,. \qquad \text{(AII–8)}$$

Equations (AII–6) and (AII–8) indicate that $\boldsymbol{P}_r$ and $\boldsymbol{Q}$ are canonically conjugate.

Substituting (AII–3) (AII–5) and (AII–7) into (AII–1), the Hamiltonian changes into the second term in (5.1).

Appendix III

Scattering Probability of a Conduction Electron due to the Transverse Translational Phonon.

The Hamiltonian of the system consisting of a conduction electron and the transverse translational phonon field will be given by

$$H = H^0 + H_{\text{int}}^{(t)}\,, \qquad \text{(AIII–1)}$$

$$H^0 = \frac{1}{2\gamma_t}\int [\mathfrak{P}_t^2 + \omega_{tt}^2\gamma_t^2\boldsymbol{P}_t^2]\,d\tau + \frac{1}{2m}\boldsymbol{p}_e^2\,, \qquad \text{(AIII–1a)}$$

$$H_{\text{int}}^{(t)} = -\frac{e}{mc}\boldsymbol{p}_e\boldsymbol{A}_t(\boldsymbol{r}_e) - (\boldsymbol{\mu}\,\text{curl}\,\boldsymbol{A}_t(\boldsymbol{r}_e))\,, \qquad \text{(AIII–1b)}$$

where

$$\Delta \boldsymbol{A}_t = -\frac{4\pi}{c}\dot{\boldsymbol{P}}_t$$

and

$$1/\gamma_t = \frac{\omega_{tt}^2}{4\pi}(\varepsilon_0 - \varepsilon_\infty)\,.$$

$\boldsymbol{P}_t$ is the solenoidal component of the polarization $\boldsymbol{P}$, and $\mathfrak{P}_t$ is the momentum canonically conjugate to $\boldsymbol{P}_t$.

Treating this interaction Hamiltonian as a perturbation, we may calculate $W_{12}^{(e)}$, the transition probability from the state $1(\boldsymbol{k}, +, n_W)$ to the states $2(\boldsymbol{k}', \pm, n_W+1)$ and $W_{12}^{(a)}$, that from the state $1(\boldsymbol{k}, +, n_W)$ to the states $2(\boldsymbol{k}', \pm, n_W-1)$, where n_W is the number of transverse translational phonons with wave number $\boldsymbol{W}$.

$$W_{12}^{(e,a)} = \frac{2\pi}{\hbar}U_{12}^{(e,a)}\delta(E_1 - E_2)\,, \qquad \text{(AIII–2)}$$

$$\left.\begin{array}{l} U_{12}^{(e)} \\ U_{12}^{(a)} \end{array}\right\} = \frac{16\pi^2\hbar\omega_{tt}}{\gamma_t V}\frac{\beta^2}{c^2 W^2}\left\{\begin{array}{l}(n_W+1)\delta_{\boldsymbol{k}',\,\boldsymbol{k}-\boldsymbol{W}} \\ n_W\delta_{\boldsymbol{k}',\,\boldsymbol{k}+\boldsymbol{W}}\end{array}\right\}$$
$$\times(1 + 2k^2\sin^2\theta/W^2)\,. \qquad \text{(AIII–3)}$$

Integrating the above results in $\boldsymbol{W}$-space, we may obtain the scattering probability $1/\tau_t$ as a function of the electron wave number $\boldsymbol{k}$, which is shown in Fig. 3 in order to compare with $1/\tau_r$. With increasing $\boldsymbol{k}$ values, $1/\tau_t$ behaves such as

$$1/\tau_t \sim 16\alpha_t\omega_{tt}(2n_W+1)g_t^2\eta^3\,, \qquad \text{(AIII–4)}$$

where

$$\alpha_t = \frac{2\pi e^2 u_t}{\hbar\gamma_t\omega_{tt}^3}\,,\quad g_t = \frac{\hbar\omega_{tt}}{4mc^2}\,,\quad u_t^2 = 2m\omega_{tt}/\hbar$$

$$\eta = k/u_t \quad\text{and}\quad v = w/u_t\,. \qquad \text{(AIII–5)}$$

References

1) S. Asano and Y. Tomishima: J. Phys. Soc. Japan **12** (1957) 346.
2) K. Huang: E.R.A. Report L/T 239 (1950). Proc. Roy. Soc. **A208** (1951) 352.
3) M. Born and K. Huang: *Dynamical Theory of Crystal Lattices* (Oxford, Clarendon Press, 1954) p. 93.
4) H. J. Emeréus and J. S. Anderson: *Monern Aspects of Inorganic Chemistry* (D. Van Nostrand Co. N. Y. 1952) p. 82.
   K. Fajans and J. Baner: J. Chem. Phys. **10** (1950) 410.
5) R. Wyckoff: *Crystal Structure* II (Interscience Publisher, N.Y. 1951) Chap. 8 illus. page 8–12.
6) L. Pauling: *The Nature of Chemical Bond* (Cornell Univ. Press 1945). Chap. 7.
7) J.D.H. Donnay and W. Nowacki: *Crystal Data* (Geolog. Soc. Amer. 1954) p. 313.
8) M. Born and K. Huang: loc. cit. p. 120.

JOURNAL OF THE PHYSICAL SOCIETY OF JAPAN Vol. 12, No. 8 AUGUST, 1957

Rotational Lattice Vibration in Complex Crystals

Part III. Vibrational Frequencies in Cubic NaClO$_4$ Crystals

By Sumitada ASANO and Yasuo TOMISHIMA

Department of Physics, Faculty of Science, Okayama University

(Received April 3, 1957)

The frequencies of the translational and rotational vibrations (in optical branches) in the cubic NaClO$_4$ crystal, which is one of the complex crystals with simplest structure, are expressed in terms of the force constants of the interionic forces. The expression obtained with respect to the translational vibration is quite similar to that in the case of isotropic simple crystals, which is already known. Furthermore, by assuming reasonable values for these force constants, the orders of magnitudes of the both frequencies are estimated and compared with one another. The comparison shows that the both frequencies are nearly of the same order of magnitude.

§ 1. Introduction

In the preceding papers[1,2], we have assumed that the frequencies of the rotational vibrations in optical branches are of the same order of magnitude as those of the translational ones. Therefore, we will here determine the orders of magnitudes of the frequencies of both the rotational and the translational vibtrations for an actual crystal cubic NaClO$_4$ which is stable above 380°C[3]. This has one of the simplest structure in the complex crystals, which is obtained by replacing Cl-ions in NaCl crystal with tetrahedral $[\mathrm{ClO}_4]^-$ radicals, as shown in Fig. 1.

In such a crystal which has one cation and one anionic radical in a unit cell, the rotational lattice vibrations may be idealized by the motion such that all the radicals perform rotational vibrations in phase and all the cations are at rest. (There is only the optical branch in this case as discussed in part I.) On the other hand, the translational vibrations in optical branch are characterized by the motion such that all the radicals make the same translation remaining their orientation unchanged, and all the cations are at rest.

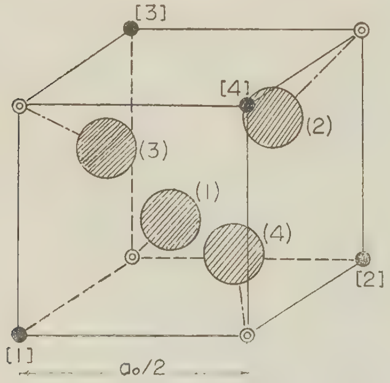

Fig. 1. Sketch illustrating the atomic arrangement in the cubic NaClO$_4$ crystal.
Dots: Na-ions. Double circles: Cl-ions.
Large hatched circles: O-ions.

Assuming an appropriate form, including adjustable parameters, for exchange potentials between constituent ions, we will first calculate the forces and their moments acting on a particular radical for the idealized translation and rotation stated above, and then determine the frequency of the rotational lattice vibration for some reasonable values of these parameters.

§ 2. Forces Acting on One Radical

Let us consider one cation-radical pair $\mathrm{Na}^+-[\mathrm{ClO}^4]^-$. We shall call them the central Na$^+$-ion and the central $[\mathrm{ClO}_4]^-$-ratical, and designate by $\boldsymbol{x}(i)$ the vectors specifying the positions of the Cl-ion ($i=0$) and the four coordinated O-ions ($i=1, 2, 3, 4$) relative to the equilibrium position of the Cl-ion, and the vector specifying the position of the central Na-ion ($i=5$) relative to its equilibrium position. (cf. Fig. 2) Further, we will use $\boldsymbol{x}_0(i)$ to signify $\boldsymbol{x}(i)$ for the equilibrium configuration, then

$$\boldsymbol{x}_0(0)=0\,, \tag{2.1a}$$

$$\boldsymbol{x}_0(5)=0\,, \tag{2.1b}$$

and

$$\left.\begin{aligned} \boldsymbol{x}_0(1)&=(\ \ ua_0,\ \ \ ua_0,\ \ \ ua_0)\,,\\ \boldsymbol{x}_0(2)&=(\ \ ua_0,\ -ua_0,\ -ua_0)\,,\\ \boldsymbol{x}_0(3)&=(-ua_0,\ \ \ ua_0,\ -ua_0)\,,\\ \boldsymbol{x}_0(4)&=(-ua_0,\ -ua_0,\ \ \ ua_0)\,, \end{aligned}\right\}\qquad(2.1\text{c})$$

where $a_0=7.25\,\text{Å}$ and $u=0.1314$. (cf. Fig. 1 and App. I)

In order to simplify the later calculation, all the ions are classified into groups, each of which consists of the ions sitting at a constant distance $r(ki)$ from the i-th ion ($i=0, 1, \cdots, 5$) in equilibrium and is called ki-group, where k is a positive integer labeling each group as $r(ki)>r(k'i)$ for $k>k'$. We should mention that with the variation of the standard ion, namely, with the variation of i from 0 to 5 there are six kinds of different classifications. Further we will define $\boldsymbol{y}(j;\,ki)$, a vector specifying the position of the j-th ion of the ki-group relative to the same origin as that of $\boldsymbol{x}(i)$; therefore the origin of $\boldsymbol{y}(j;\,ki)$ is the equilibrium position of the Cl-ion of the central radical for $i=0, 1, \cdots, 4$ and that of the central Na-ion for $i=5$. (cf. Fig. 2) Then, regardless of j, we have

$$|\boldsymbol{y}_0(j;\,ki)-\boldsymbol{x}_0(i)|=r(ki)\,,\qquad(2.2)$$

where $\boldsymbol{y}_0$ is the vector $\boldsymbol{y}$ in the equilibrium configuration.

In the interest of simplicity, Na-, O- and Cl-ions in the crystal are regarded as point charges with effective charges $-e$ (e: electronic charge), Z_ce and $(1-4Z_c)e$, respectively. If we assume that the potential between two ions may be expressed as the sum of the Coulomb and the overlap potentials and that the latter is also a function of only the distance between the two ions, then the potential between the i-th ion and the j-th ion belonging to the ki-group may be written as

$$\phi_{ki}(|\boldsymbol{y}(j;\,ki)-\boldsymbol{x}(i)|)\equiv\phi_{ki}(r(j;\,ki))\,,\qquad(2.3)$$

where only the suffixes i and k are appended to ϕ, because all the ions belonging to the ki-group are of the same kind regardless of j, and the form of potential function ϕ is dependent on the kinds of the both ions only.

In the equilibrium configuration, the atomic arrangements of the crystal around the four O-ions of the central radical are completely similar to each other owing to the crystal symmetry. Therefore, we may conclude

$$\left.\begin{aligned} &r(ki)=r(ki')\equiv r(k)\,,\\ &\phi_{ki}(r(ki))=\phi_{ki'}(r(ki'))\equiv\phi_k(r(k))\,,\\ &\qquad\qquad(i,\,i'=1, 2, 3, 4;\ i\neq i') \end{aligned}\right\}\qquad(2.4)$$

where $r(k)$ and $\phi_k(r(k))$ are independent of i.

The x-component* of $\boldsymbol{F}(j;\,ki)$, the force acting on the ith ion of the central radical from the jth ion of the ki-group is given by

$$F_1(j;\,ki)=-\frac{\partial}{\partial x_1(i)}\phi_{ki}(r(j;\,ki))\,.$$
$$(i=0, 1, 2, 3, 4)\qquad(2.5)$$

If we denote by $\delta\boldsymbol{x}(i)$ and $\delta\boldsymbol{y}(j;\,ki)$ the displacements of the ith ion and the jth ion of the ki-group from their own equilibrium positions respectively, we may obtain the following relations:

$$\left.\begin{aligned} &\boldsymbol{x}(i)=\boldsymbol{x}_0(i)+\delta\boldsymbol{x}(i)\\ \text{and}\ \ &\boldsymbol{y}(j;\,ki)=\boldsymbol{y}_0(j;\,ki)+\delta\boldsymbol{y}(j;\,ki) \end{aligned}\right\}$$
$$(\text{cf. Fig. 2})\ (2.6)$$

Inserting (2.3) and (2.6) into (2.5) and expanding the right-hand side of (2.5), we may get the following approximate expression:

$$F_1(j;\,ki)=F_1^{(0)}(j;\,ki)+F_1^{(1)}(j;\,ki)\,,\qquad(2.7)$$

where

$$F_1^{(0)}(j;\,ki)\equiv\left[\frac{\partial}{\partial y_1(j;\,ki)}\,\phi_{ki}(r(j;\,ki))\right]_0,\qquad(2.7\text{a})$$

$$F_1^{(1)}(j;\,ki)\equiv\sum_{\beta=1}^{3}\left[\frac{\partial^2}{\partial y_1(j;\,ki)\partial y_\beta(j;\,ki)}\right.$$
$$\left.\times\,\phi_{ki}(r(j;\,ki))\right]_0\{\delta y_\beta(j;\,ki)-\delta x_\beta(i)\}\,.\qquad(2.7\text{b})$$

The suffix 0 represents the value for the equilibrium configuration: $\boldsymbol{x}(i)=\boldsymbol{x}_0(i)$ and $\boldsymbol{y}(j;\,ki)=\boldsymbol{y}_0(j;ki)$.

$\boldsymbol{N}(j;\,ki)$, the moment of $\boldsymbol{F}(j;\,ki)$ with respect to the center of the central radical, is given by

$$\boldsymbol{N}(j;\,ki)=\boldsymbol{N}^{(0)}(j;\,ki)+\boldsymbol{N}^{(1)}(j;\,ki)\,,\qquad(2.8)$$

where

$$\boldsymbol{N}^{(s)}(j;\,ki)\equiv[\boldsymbol{x}_0(i)+\delta\boldsymbol{x}(i)-\delta\boldsymbol{x}(0),\ \boldsymbol{F}^{(s)}(j;\,ki)]$$
$$(s=0,\ 1;\ i=1,\ 2,\ 3,\ 4)\qquad(2.8\text{a})$$

The total force $\boldsymbol{F}$ and the total moment $\boldsymbol{N}$ acting on the central radical are given by

$$\left.\begin{aligned} \boldsymbol{F}&=\sum_{i=1}^{4}\sum_{k}\sum_{j=1}^{n(ki)}\boldsymbol{F}(j;\,ki)\,,\\ \text{and}\quad\boldsymbol{N}&=\sum_{i=1}^{4}\sum_{k}\sum_{j=1}^{n(ki)}\boldsymbol{N}(j;\,ki)\,, \end{aligned}\right\}\qquad(2.9)$$

---

* x-, y- and z-components of a vector are indicated hereafter by the suffixes 1, 2 and 3 respectively.

respectively, where $n(ki)$ is the total number of the ions belonging to the ki-group.

On the other hand, we have, owing to the T_d symmetry,

$$\sum_{i=1}^{4}\sum_{j=1}^{n(ki)}\boldsymbol{F}^{(0)}(j;ki)=\sum_{j=1}^{n(k0)}\boldsymbol{F}^{(0)}(j;\,k0)=0\ , \tag{2.10}$$

and

$$\sum_{i=1}^{4}\sum_{j=1}^{n(ki)}[\boldsymbol{x}_0(i),\ \boldsymbol{F}^{(0)}(j;\,ki)]=0\ . \tag{2.11}$$

Substituting (2.7) and (2.8) into (2.9), we have

$$\left.\begin{aligned} F_1=&-\sum_{i=1}^{4}\sum_{k}\sum_{j=1}^{n(ki)}\sum_{\beta=1}^{3}T_{1\beta}(j;\,ki)[\delta x_\beta(i)\\ &-\delta y(j;\,ki)]\ ,\\ N^1=&\sum_{i=1}^{4}\sum_{k}\sum_{j=1}^{n(ki)}[\{\delta x_2(i)-\delta x_2(0)\}F_3{}^{(0)}(j;\,ki)\\ &-\{\delta x_3(i)-\delta x_3(0)\}F_2{}^{(0)}(j;\,ki)]\\ &-\sum_{i=1}^{4}\sum_{k}\sum_{j=1}^{n(ki)}\sum_{\beta=1}^{3}[x_{02}(i)T_{3\beta}(j;ki)\\ &-x_{03}T_{2\beta}(j;\,ki)]\{\delta x_\beta(i)-\delta y_\beta(j;ki)\} \end{aligned}\right\} \tag{2.12}$$

where

$$T_{\alpha\beta}(j;\,ki)\equiv\left[\frac{\partial^2}{\partial y_\alpha(j;\,ki)\partial y_\beta(j;\,ki)}\phi_{ki}(\boldsymbol{r}(j;\,ki))\right]_0\ . \tag{2.13}$$

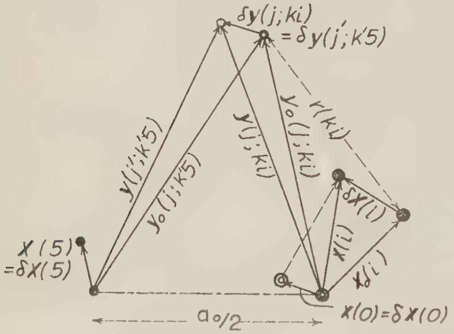

Fig. 2. Schematic diagram illustrating the relations among the vectors $\boldsymbol{x}(i)$, $\boldsymbol{x}_0(i)$, $\boldsymbol{y}(j;\,ki)$ and $\boldsymbol{y}_0(j;\,ki)$.
Hatched Circles: ith O-ion of central radical. ($i=1,\ 2,\ 3,\ 4$)
Double Circles: Cl-ion of central radical.
Dots: Central Na-ion.
Single Circles: jth ion of ki-group.

In deriving (2.12), we have used the relations (2.10) and (2.11), and furthermore neglected the small terms such as the squares of $\delta x_\alpha(i)$ and the cross products of $\delta x_\alpha(i)$ and $\delta y_\beta(j;\,ki)$.

When the ki-group is of O-ions, we may decompose the vector $\boldsymbol{y}_0(j;\,ki)$ into two parts as follows:

$$\boldsymbol{y}_0(j;\,ki)=\boldsymbol{y}_L(j;\,ki)+\boldsymbol{x}_0(j;\,ki)\ . \tag{2.14}$$

where $\boldsymbol{y}_L(j;\,ki)$ is the vector specifying the equilibrium position of the parent Cl-ion (to which the j-th O-ion belongs) relative to the same origin as that of $\boldsymbol{y}_0(j;\,ki)$, and $\boldsymbol{x}_0(j;\,ki)$ is the vector pointing from this Cl-ion to the j-th O-ion. Then $\boldsymbol{x}_0(j;\,ki)$ has the components similar to one of (2.1c). When the ki-group is of Na-ions or Cl-ions, $\boldsymbol{x}_0(j;\,ki)=0$ and $\boldsymbol{y}_0(j;\,ki)=\boldsymbol{y}_L(j;\,ki)$,

As stated in §1, for the optical branches we may assume the idealized displacements:

$$\left.\begin{aligned} &\delta\boldsymbol{x}(i)=\boldsymbol{\xi}+[\boldsymbol{\Theta},\,\boldsymbol{x}_0(i)] \qquad (i=0,1,2,3,4)\\ &\delta\boldsymbol{y}(j;\,ki)=\begin{cases}\boldsymbol{\xi}+[\boldsymbol{\Theta},\,\boldsymbol{x}_0(j;\,ki)] & \text{(for radicals)}\\ 0 & \text{(for cations),}\end{cases} \end{aligned}\right\} \tag{2.15}$$

where $\boldsymbol{\xi}$ respresents the translation common to all the radicals, relative to the Na-ions, and $\boldsymbol{\Theta}$ is the angular displacement[1] of each radical.

Further let us define the symmetric tensors $\boldsymbol{T}(ki)$ and $\boldsymbol{T}^\gamma(ki)$, whose components $T_{\alpha\beta}(ki)$ and $T_{\alpha\beta}{}^\gamma(ki)$ are defined as follows:

$$T_{\alpha\beta}(ki)\equiv\sum_{j=1}^{n(ki)}T_{\alpha\beta}(j;\,ki)\ , \qquad (i=0,1,2,3,4) \tag{2.16}$$

$$T_{\alpha\beta}{}^\gamma(ki)\equiv\frac{1}{ua_0}\sum_{j=1}^{n(ki)}T_{\alpha\beta}(j;\,ki)x_{0\gamma}(j;\,ki)\ . \qquad (i=1,2,3,4;\ \gamma=1,2,3) \tag{2.17}$$

We should mention that $T^\gamma(ki)$ vanishes unless the members of the ki-group are O-ions, acording to the definition of $\boldsymbol{x}_0(j;\,ki)$. Owing to the T_d symmetry, we have

$$\left.\begin{aligned} &\sum_{i=1}^{4}T_{\alpha\beta}(ki)=0\ (\alpha\neq\beta)\ , \quad T_{\alpha\beta}{}^\gamma(k0)=0\ ,\\ &\text{and}\\ &\sum_{i=1}^{4}\sum_{j=1}^{n(ki)}[\boldsymbol{\Theta},\,\boldsymbol{x}_0(i)],\,\boldsymbol{F}^{(0)}(j;\,ki)]=0\ . \end{aligned}\right\} \tag{2.18}$$

Substituting (2.15) into (2.12), and using the relations (2.16), (2.17), (2.18) and (AII-1 and 3), we obtain finally

$$F_1=-\sum_{k}^{(+)}[4T_{11}(k1)+T_{11}(k0)]\xi_1 \tag{2.19a}$$

$$\begin{aligned} N_1=-8\Big\{&\sum_{k}[T_{11}(k1)-T_{23}(k1)]-\sum_{k}^{(-)}T_{11}{}^3(k1)\\ &-T_{23}{}^2(k1)]\Big\}u^2a_0{}^2\theta_1\ , \end{aligned} \tag{2.19b}$$

where $\sum\limits_{k}^{(+)}$ and $\sum\limits_{k}^{(-)}$ mean the summations with respect to Na-ion groups only and O-ion groups only respectively.

§ 3. Vibrational Frequencies

Let us correlate F_1 and N_1 given by (2.19) to the frequencies of the translational and the rotational vibrations of the radical.

By using (2.3), (2.4), (2.13), (2.16) and (2.17), the tensor components in (2.19) may be written in the follwing forms:

$$\left.\begin{aligned} T_{11}\,(k1)&=A(k)\,\Phi_k{}^{(+)}\,,\\ T_{11}\,(k0)&=C(k)\,\Phi_{k0}{}^{(+)}\,,\\ T_{11}{}^3(k1)&=A(k)'\,\Phi_k{}^{(+)}\,,\\ T_{23}\,(k1)&=B(k)\,\Phi_k{}^{(-)}\,,\\ T_{23}{}^2(k1)&=B(k)'\,\Phi_k{}^{(-)}\,,\end{aligned}\right\}\tag{3.1}$$

where

$$\left.\begin{aligned} \Phi_k{}^{(+)}&\equiv\phi_k''(r(k))+\phi_k'(r(k))\,\frac{2}{r(k)}\\ &=\Delta\phi_k(r(k))\\ \Phi_{k0}{}^{(+)}&\equiv\phi_{k0}''(r(k0))+\phi_{k0}'(r(k0))\,\frac{2}{r(k0)}\\ &=\Delta\phi_{k0}(r(k0))\\ \Phi_k{}^{(-)}&\equiv\phi_k''(r(k))-\phi_k'(r(k))\,\frac{1}{r(k)}\end{aligned}\right\}\tag{3.2}$$

and $A(k)$ $B(k)$ $C(k)$ $A(k)'$ and $B(k)'$ are the numerical constants, whose general expressions are given in App. III.

As easily seen in (3.1) and (3.2), the Coulomb interactions of the ion-pairs do not enter into $T_{11}(k1)$ and $T_{11}(k0)$, accordingly into F_1 expressed by (2.19a). If we neglet all the overlap forces but those between an O-ion of the central radical and the three nearest Na-ions ((1) and (1) (2) (3) in Fig. 1) and those between the O-ion and the three nearest O-ions ((1) and (2) (3) (4) in Fig. 1), then $T_{11}(k0)=0$, Furthermore, F_1 given by (2.19a) contains the former overlap forces only, for $\overset{(+)}{\sum\limits_{k}}$ means the summation over Na-ion groups only. Then the summation sign in (2.19a) may be removed, by identifying the $k1$-group with three nearest Na-ions, and the expression (2.19a) becomes quite similar to that in the case of isotropic simple crystals[4].

However, long-range Coulomb interactions unfavorably remain in N_1 given by (2.19b), since in $T_{23}(k1)$ and $T_{23}{}^2(k1)$ the Coulomb interactions do not vanish. (cf. (3.1) (3.2)) Referring to (2.8a), the moment, $\boldsymbol{N}^{(c)}(j;\,ki)$, due to the electrostatic field $\boldsymbol{E}(j;\,ki)$ on the central radical from the jth ion of the ki-group may be given by

$$\boldsymbol{N}^{(c)}(j;\,ki)=Z_ce\sum_{i'=1}^{4}[\boldsymbol{x}(i')_r,\ \boldsymbol{E}_{i'}(j;\,ki)]\,,\tag{3.3}$$

where the suffix i' appended to $\boldsymbol{E}(j;\,ki)$ indicates its value at the i'-th O-ion of the central radical, and

$$\left.\begin{aligned}\boldsymbol{x}(i')_r=\boldsymbol{x}(i')-\boldsymbol{x}(0)&=\boldsymbol{x}(i')-\boldsymbol{\xi}\\ &=\boldsymbol{x}_0(i')+[\boldsymbol{\Theta},\,\boldsymbol{x}_0(i')]\end{aligned}\right\}$$

(cf. (2.6) and (2.15))

Expanding $\boldsymbol{E}_{i'}(j;\,ki)$ in (3.3) around the Cl-ion of the central radical, we obtain

$$\boldsymbol{N}^{(c)}(j;\,ki)=Z_ce\sum_{n=0}^{\infty}\sum_{i'=1}^{4}\frac{1}{n!}\times[\boldsymbol{x}(i')_r,\,(\boldsymbol{x}(i')_r,\,\boldsymbol{\nabla})^n\boldsymbol{E}_0(j;\,ki)]\,,\tag{3.4}$$

where $\boldsymbol{E}_0(j;\,ki)$ is the value of $\boldsymbol{E}(j;\,ki)$ on the Cl-ion sitting at $\boldsymbol{x}(0)=\boldsymbol{\xi}$. The terms with $n=0$ and 1 in (3.4) vanish, if the relations $\sum\limits_{i'=1}^{4}\boldsymbol{x}(i')_r=0$ and curl $\boldsymbol{E}_0(j;\,ki)=0$ are taken into account. Then we have

$$\boldsymbol{N}^{(c)}(j;\,ki)=Z_ce\sum_{n=2}^{\infty}\sum_{i'=1}^{4}\frac{1}{n!}\times[\boldsymbol{x}(i')_r,\,(\boldsymbol{x}(i')_r,\,\boldsymbol{\nabla})^n\boldsymbol{E}_0(j;\,ki)]\,.\tag{3.5}$$

(3.5) represents the moment acting on the radical due to the electrostatic interactions between the multipole moments of higher order (than dipole) on the radical and the jth ion of the ki-group.

Even when the jth ion is located in the vicinity of the radical, $\boldsymbol{N}^{(c)}(j;\,ki)$ given by (3.5) wouldn't have so large order of magnitude. But the sum of these moments originating from a number of ions in the vicinity of the central radical may have a contribution to its rotational motion comparable to that from the overlap forces, being enhanced as a result of superposition i. e. the summation with respect to j in each ki-group. This is autually shown in the later calculation.

However, the electrostatic field from all the ion comparatively distant from the central radical will be small and approximately replaced by a central field around the equilibrium position of the Cl-ion of the central radical. If we denote by $\varphi\{|\boldsymbol{x}(i)|\}$ the potential of this central field at the ith ion, $\boldsymbol{E}(\boldsymbol{x}(i))$, the field acting on it is given by

$$\boldsymbol{E}(\boldsymbol{x}(i))=-\mathrm{grad}\,\varphi(|\boldsymbol{x}(i)|)\,,\tag{3.6}$$

Since $\boldsymbol{x}(i)=\boldsymbol{x}(i)_r+\boldsymbol{\xi}$, $\boldsymbol{E}(\boldsymbol{x}(i))$ may be expanded approximately as

$$\boldsymbol{E}(\boldsymbol{x}(i))=\boldsymbol{E}(\boldsymbol{x}(i))+(\boldsymbol{\xi}\boldsymbol{\nabla})\boldsymbol{E}(\boldsymbol{x}(i)_r)\,,\tag{3.7}$$

where

$$\boldsymbol{E}(\boldsymbol{x}(i)_r) \equiv -\mathrm{grad}\,\varphi(|\boldsymbol{x}(i)_r|)\,. \tag{3.7a}$$

Similarly to (3.3), $\boldsymbol{N}^{(c)}$, the moment due to the fields $\boldsymbol{E}(\boldsymbol{x}(i))$'s ($i=1, 2, 3, 4$) is given by

$$\boldsymbol{N}^{(c)} = Z_c e \sum_{i=1}^{4} [\boldsymbol{x}(i)_r, \boldsymbol{E}(\boldsymbol{x}(i))]\,. \tag{3.8}$$

Substituting (3.7) and (3.7a) into (3.8) and taking account of the relations

$$\sum_{i=1}^{4} \boldsymbol{x}(i)_r = 0$$

$$\varphi'(|\boldsymbol{x}(i)|) = \varphi'(|\boldsymbol{x}(i')|)$$

and

$$\varphi''(|\boldsymbol{x}(i)|) = \varphi''(|\boldsymbol{x}(i')|) \quad (i \neq i';\ i, i' = 1, 2, 3, 4)\,,$$

we may easily verify that $\boldsymbol{N}^{(c)}$ vanishes.

According to the inferences stated above, we may take the summations $\sum\limits_k$ and $\overset{(-)}{\sum\limits_k}$ in (2.19b) only over some groups near the central radical, neglecting the effect from the other groups comparatively distant from it. Therefore in our actual calculation, these summations are taken up to the eight radicals sitting at $(\pm a_0/2, \pm a_0/2, \pm a_0/2)$. (cf. Fig. 1)

As stated in § 3 of part II, the equations of translational and rotational motion of a particular radical are given by

$$\overline{M}\,\ddot{\boldsymbol{\xi}} = -k_t \xi - Ze\boldsymbol{E}_{eff}\,, \tag{3.9a}$$

$$I\,\ddot{\boldsymbol{\Theta}} = -k_r \boldsymbol{\Theta} - \frac{I\beta_M}{\hbar}\dot{\boldsymbol{B}}\,, \tag{3.9b}$$

respectively, where $-k_t\boldsymbol{\xi}$ and $-k_r\boldsymbol{\Theta}$ represent the overlap force acting on the radical, and the moment of the overlap force and electrostatic forces from the other constituents in the crystal respectively. Accordingly F_1 and N_1 given by (2.19) should be identified with $-k_t\xi_1$ and $-k_r\theta_1$ respectively. Furthermore, k_t and k_r in (3.9) are given by

$$k_t = \left(\frac{\varepsilon_0+2}{\varepsilon_\infty+2}\right)\overline{M}\omega_{tt}^2 \tag{3.10a}$$

$$k_r = I\,\omega_{rt}^2/\alpha \tag{3.10b}$$

respectively, where $\overline{M} = M_R M_K/(M_R+M_K)$, $I = 8/3\, M_c(\sqrt{3}\, u a_0)^2$, M_R, M_K and M_c are the masses of a radical, a Na-ion and a coordinated O-ion respectively. (cf. § 3 in part II) Then we immedinately obtain

$$\omega_{tt}^2\left(\frac{\varepsilon_0+2}{\varepsilon_\infty+2}\right) = \overset{(+)}{\sum_k}[4T_{11}(k1) + T_{11}(k0)]/\overline{M}\,, \tag{3.11a}$$

$$\omega_{rt}^2/\alpha = \left\{\sum_k [T_{11}(k1) - T_{23}(k1)] - \overset{(-)}{\sum_k}[T_{22}{}^3(k1) - T_{23}{}^2(k1)]\right\}\Big/ M_c\,. \tag{3.11b}$$

We will assume the overlap potentials for the Na-O pair and for the O-O pair to be expressed by

$$b_1 \exp(-r/\rho_1) \text{ and } b_2 \exp(-r/\rho_2) \tag{3.12}$$

respectively, where r is the interionic distance, and b_1, b_2, ρ_1 and ρ_2 are the adjustable parameters.

If we substitute (3.1) (3.2) and (3.12) into (3.11) and calculating it with the actual $NaClO_4$ crystal, we may obtain the following forms:

$$\omega_{tt}^2 = 4\left[\left(\frac{1}{\rho_1} - \frac{2}{r_1}\right)s_1\right]\Big/\overline{M}Q^2\,, \tag{3.13a}$$

$$\omega_{rt}^2 = \left[\left(\frac{1.4671}{\rho_1} - \frac{1.5329}{r_1}\right)s_1 - \frac{3s_2}{r_2} + f_1(Z_c)\right]\alpha\Big/M_c\,, \tag{3.13b}$$

where

$$s_1 \equiv \frac{b_1}{\rho_1}\exp\left(-\frac{r_1}{\rho_1}\right), \qquad s_2 = \frac{b_2}{\rho_2}\exp\left(-\frac{r_2}{\rho_2}\right),$$

$$Q \equiv \left(\frac{\varepsilon_0+2}{\varepsilon_\infty+2}\right)^{1/2}, \qquad \overline{M} = 18.69 M_H \text{ and}$$

$M_c = 16.00 M_H$ (M_H: mass of a H-atom). $r_1 (= 2.993\times 10^{-8}\text{ cm})$ and $r_2 (= 2.432\times 10^{-8}\text{ cm})$ are the equilibrium distances of the Na-O pair and the O-O pair respectively. $f_1(Z_c)$ originates from the Coulomb interactions and depends on the effective charge $Z_c e$ of the O-ion as

$$f_1(Z_c) \equiv -(4.935 Z_c^2 + 0.729 Z_c)\times 10^4 \ (\text{erg/cm}^2) \tag{3.13c}$$

§ 4. Cohesive Energy and Compressibility

If the state consisting of free Na^+-ions and free $[ClO^4]^-$-radicals is taken as the reference level of the energy, the cohesive energy per cation-radical pair, E_p, for an arbitrary lattice constant a, is expressed by

$$E_p = \frac{1}{2}\sum_{i=0}^{5}\sum_k \sum_{j=1}^{n(ki)} \phi_{ki}(\bar{r}(j;ki)) - \frac{(M_\alpha + p)e^2}{a}\,, \tag{4.1}$$

where

$$\bar{r}(j;\,ki) \equiv |\boldsymbol{y}_L(j;\,ki)'a + \boldsymbol{x}_0(j;\,ki)'a_0 - \boldsymbol{x}_0(i)|\,,$$

(cf. (2.2) and (2.16))

$$\boldsymbol{y}_L(j;\,ki) \equiv \boldsymbol{y}_L(j;\,ki)'a_0$$

and

$$\boldsymbol{x}_0(j;\,ki) \equiv \boldsymbol{x}_0(j;\,ki)'a_0\,.$$

The summation sign with respect to k means the summation up to the third neighbours. M_α is the Madelung constant (=3.4951) and

$p\,(=-4.2668)$ the numerical constant to cancell the summation of the Coulomb interactions up to the third neighbours, which is included also in the first term.

In (4.1) the size and the orientation of the radical are assumed to remain unchanged with the variation of the parameter a on account of its rigidity and the crystal symmetry, and furthermore radicals are regarded as point charges with the electronic charge e, when the distance between two different radicals or between a radical and a Na-ion is larger than the third-neighbour distance $(=\sqrt{3}\,a_0/2)$.

From (4.1) $(E_p)_{a=a_0}$ is given actually by

$$(E_p)_{a=a_0}=\left[12b_1\exp\left(-\frac{r_1}{\rho_1}\right)+6b_2\exp\left(-\frac{r_2}{\rho_2}\right)+f_2(Z_c)\right]. \tag{4.2}$$

$f_2(Z_c)$ in (4.2) represents the Coulomb interaction and has the form:

$$f_2(Z_c)\equiv-(0.440Z_c^2-0.048Z_c+0.256) \tag{4.2a}$$

when the energy is expressed in atomic units. (1 atomic unit of energy equals 4.354×10^{-11} ergs or 623.96 Kcal/mol).

As well-known, E_p should satisfy the following relations[5)]

$$\left(\frac{\partial E_p}{\partial a}\right)_{a=a_0}=0 \tag{4.3}$$

and

$$\frac{1}{\beta_c}=\frac{a_0^2}{9v_0}\left(\frac{\partial^2 E_p}{\partial a^2}\right)_{a=a_0}, \tag{4.4}$$

where $v_0\equiv a_0^3/8$ and β_c is the compressibility of the crystal.

Substituting (4.1) into (4.3) and (4.4), we obtain

$$\left(\frac{\partial E_p}{\partial a}\right)_{a=a_0}=\frac{1}{2}\sum_{i=0}^{5}\sum_{k}\sum_{j=1}^{n(ki)}\phi'_{ki}(r(ki))\times\left(\frac{\partial\overline{\mathbf{r}}(j;ki)}{\partial a}\right)_{a=a_0}+\frac{(M_\alpha+p)e^2}{a_0^2}=0 \tag{4.5}$$

$$\frac{9v_0}{a_0^2\beta_c}=\left(\frac{\partial^2 E_p}{\partial a^2}\right)_{a=a_0}=\frac{1}{2}\sum_{i=0}^{5}\sum_{k}\sum_{j=0}^{n(ki)}\left[\phi_{ki}''(r(ki))\times\left(\frac{\partial\overline{\mathbf{r}}(j;ki)}{\partial a}\right)^2+\phi_{ki}'(r(ki))\left(\frac{\partial^2\overline{\mathbf{r}}(j;ki)}{\partial a^2}\right)\right]_{a=a_0}-\frac{2(M_\alpha+p)e^2}{a_0^3}, \tag{4.6}$$

where

$$\left.\begin{aligned}
&\left(\frac{\partial\overline{\mathbf{r}}(j;ki)}{\partial a}\right)_{a=a_0}\\
&=(\mathbf{y}_L(j;ki)',\ \mathbf{y}_0(j;ki)'-\mathbf{x}_0(i)')/r(ki)'\\
&\left(\frac{\partial^2\overline{\mathbf{r}}(j;ki)}{\partial^2 a}\right)_{a=a_0}\\
&=\left[\mathbf{y}_L(j;ki)'^2-\left(\frac{\partial\overline{\mathbf{r}}(j;ki)}{\partial a}\right)_{a=a_0}\right]\Big/r(ki)\\
&\mathbf{y}_0(j;ki)'\equiv\mathbf{y}_L(j;ki)+\mathbf{x}_0(j;ki)'\\
&r(ki)\equiv a_0r(ki)'\quad\text{and}\quad\mathbf{x}_0(i)\equiv a_0\mathbf{x}_0(i)'
\end{aligned}\right\} \tag{4.7}$$

When the ith ion is a Cl-ion or a Na-ion ($i=0$ or 5) and the ki-group is of Na-ions or Cl-ions also, then $\mathbf{x}_0(i)'=0$ and $\mathbf{y}_L(j;ki)'=\mathbf{y}_0(j;ki)'=r(ki)'$.

Therefore, $\left(\frac{\partial\overline{\mathbf{r}}(j;ki)}{\partial a}\right)_{a=a_0}=r(ki)'$ and $\left(\frac{\partial^2\overline{\mathbf{r}}(j;ki)}{\partial a^2}\right)_{a=a_0}=0$. Substituting (4.7) into (4.5) and (4.6) and calculating them with the actual NaClO$_4$ crystal, we obtain

$$10.2308s_1+3.8092s_2=f_3(Z_c)\,, \tag{4.8}$$

$$\frac{1}{\beta_c}=\frac{a_0^2}{9v_0}\left[\left(\frac{2.3923}{\rho_1}-\frac{0.6077}{r_1}\right)s_1+\left(\frac{0.5970}{\rho_2}-\frac{2.4030}{r_2}\right)s_2+f_4(Z_c)\right], \tag{4.9}$$

where $f_3(Z_c)$ and $f_4(Z_c)$ are the contributions from Coulomb interaction and given by

$$f_3(Z_c)\equiv(28.882Z_c^2-3.855Z_c+3.036)\times10^{-4}\ \text{(dyne)} \tag{4.8a}$$

and

$$f_4(Z_c)\equiv-(10.139Z_c^2-0.969Z_c-0.368)\times10^{-4}\ \text{(erg/cm}^2\text{)}\,, \tag{4.9a}$$

respectively.

§ 5. Conclusion

(3.13a), (3.13b), (4.2), (4.8) and (4.9) contain the four unknown parameters b_1, b_2, ρ_1 and ρ_2 together with Z_c. Therefore it is necessary to know four experimental data for ω_{tt}, ω_{rt}, $(E_p)_{a=a_0}$ and β_c besides $\mathcal{E}_0$, $\mathcal{E}_\infty$ and α, in order to determine these parameters unambiguously from these five equations. Unfortunately we cannot find none of them for the cubic NaClO$_4$ crystal. However, we can obtain some suggestions on the order of magnitude of ω_{rt} as well as that of ω_{tt}, by surveying the general aspects of the overlap forces in other crystals, which have been investigated with considerable accuracy.

We may infer as below that the overlap force of the O-O pair is attractive and its magnitude is nearly of the same order as that of the repulsive overlap force of the Na-O pair.

Referring to (3.13b) and (3.13c), the term $f_1(Z_c)$ originating from the Coulomb interactions, to which those of the O-O pairs ((1) and (2) (3) (4) in Fig. 1) considerably contribute, takes a negative value for a value of Z_c within the range 0~1 and the magnitude of the quantity in the square brackets in (3.13b) accordingly ω_{rt} is sensitively decreased with increasing Z_c value. Thus the Coulomb interaction tends to make unstable the equilibrium orientation of the radical.

The ionic radius of the coordinated O-ion with effective charge Z_ce ($Z_c=0\sim1$) may be roughly estimated to be 0.66~1 Å, since the ionic radii of the neutral O-atom and O^{2-}-ion are 0.66 Å and 1.40 Å respectively. The sum of the ionic radii of the two ions constituting the ion-pair is 1.3~2 Å for the O-O pair with the interionic distance $r_2=2.432$ Å and 1.6~2 Å for the Na-O pair with the interionic distance $r_1=2.993$ Å. (Ionic radius of Na^+-ion: 0.95 Å) Therefore the O-ions of the O-O pair would overlap at least to the extent that this overlap cannot be ignored for that between the Na-ion and the O-ion of the Na-O pair. Accordingly, it would be somewhat unreasonable to assume a much smaller magnitude for s_2, compared with that of s_1.

The overlap forces of the Na-O pairs are obviously repulsive ($b_1>0$), whereas those of the O-O pairs will be attractive ($b_2<0$). If it were not so ($b_2<0$), the cubic $NaClO_4$ crystal would be unstable or not exist, in particular, at high temperatures, since the quantity in the square brackets in (3.13b) takes a very small posive value or even a negative value for reasonable orders of magnitudes of ρ_1, s_1 (>0) and s_2 (>0). The fact that the overlap force of the O-O pair may be attractive has been infered also in the cubic MgO crystal⁶⁾. Therefore, we assume that b_2 accordingly s_2 are negative, whereas b_1 and s_1 are positive.

As regards the repulsive overlap forces for the ion-pairs of the cubic sodium halide crystals, the orders of magnitudes of $b/\rho\exp(-r_0/\rho)$ and ρ are about $1.25\sim0.64\times10^{-4}$ dyne and $0.29\sim0.36\times10^{-8}$ cm respectively⁷⁾, where r_0 is the equilibrium distance of the ion-pair. For the attractive overlap force of the O-O pair in the cubic MgO crystal, the values of $b/\rho\exp(-r_0/\rho)$ and ρ, giving the reasonable cohesive energy have been estimated to be about 1.33×10^{-4} dyne and 0.20×10^{-8} cm respectively⁶⁾.

If we fix s_1, $s_1/s_2\equiv q(<0)$ and ρ_1 at given values, we can find the corresponding Z_c value by means of (4.8) and (4.8a) and furthermore the value of $f_1(Z_c)$ corresponding to this Z_c value by using (3.13c). Therefore, the values of $\omega_{tt}Q$ and $\omega_{rt}/\sqrt{\alpha}$ may be calculated numerically by means of (3.13a) and (3.13b) respectively. Fig. 3 shows the curves of $\omega_{tt}Q$ and $\omega_{rt}/\omega_{tt}Q\sqrt{\alpha}$ thus obtained, in the case where ρ_1 is fixed at the reasonable value 0.3×10^{-8} cm and s_1 and q at various values within the probable ranges $0.5\sim1.5\times10^{-4}$ dyne and $-0.50\sim-2.00$ respectively. $f_3(Z_c)$ takes a minimum value f_m at $Z_c=0.066$ and the corresponding Z_c values in the above procedure are taken within the range 0.066~1. Since the selection of the set of the values of s_1 and q is restricted by the condition that $f_3(Z_c)$ in (4.8) $\geq f_m$, the $\omega_{rt}/\omega_{tt}Q\sqrt{\alpha}$ curves with $q=-1.50$ and -2.00 are cut off at intermediate points.

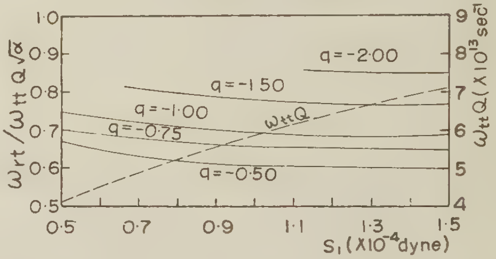

Fig. 3. Dependences of $\omega_{tt}Q$ and $\omega_{rt}/\omega_{tt}Q\sqrt{\alpha}$ upon s_1.
The real curves show $\omega_{rt}/\omega_{tt}Q\sqrt{\alpha}$ and the dotted curve $\omega_{tt}Q$. $\rho_1=0.3\times10^{-8}$ cm.

Referring to the curves of $\omega_{rt}/\omega_{tt}Q\sqrt{\alpha}$ in Fig. 3, we may point out that they are nearly insensitive to the selection of s_1 value, so far as q is kept constant. $\omega_{rt}/\omega_{tt}Q\sqrt{\alpha}$ slowly increases with increasing magnitude of q and lies within the range 0.6~0.8. Since $Q\gtrsim1$ and $\alpha\doteqdot1$ (cf. § 6 in part II) we may mention that the frequency of the rotational vibration ω_{rt} has an order of magnitude comparable to the frequency of the translational vibration ω_{tt}, that is, to the Reststrahlen frequency.

Therefore, the order estimation which has been made on the scattering probability of a conduction electron by the rotational phonon field (cf. § 6 in part II) would be reasonable.

When $q=-1$, $\rho_1=0.3\times10^{-8}$cm and $s_1=1\times10^{-4}$ dyne, the corresponding Z_c value is 0.41, $\omega_{tt}Q=5.86\times10^{13}\,\mathrm{sec}^{-1}$ and $\omega_{rt}/\sqrt{\alpha}=4.10\times10^{13}\,\mathrm{sec}^{-1}$. Then the cohesive energy per cation-radical pair and the compressibility of the cubic $NaClO_4$ crystal, which are calculated by making use of (4.2), (4.2a), (4.9) and (4.9a) and by using 0.3×10^{-8} cm also for ρ_2, are about 0.27 in atomic unit (=168 Kcal/mol) and 1.40×10^{-12} barye^{-1} respectively.

If the electronic structure assumed for $[SO_4]^{2-}$ radical is available also for $[ClO_4]^-$ radical, the normal state of the latter is considered to be the reasonce of several electronic structures which contain single and double covalent bonds and double ionic bonds and in which the effective charge on a coordinated O-ion is estimated to be 0, 0.25e, 0.5e, 0.75e and e8). The most typical one of them may be represented by the structure such as 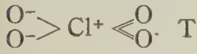 $\begin{smallmatrix}O^-\\O^-\end{smallmatrix}\!>Cl^+\!\lessdot\begin{smallmatrix}O\\O\end{smallmatrix}$. Therefore, the effective charge 0.41e on a coordinated O-ion which is estimated in our calculation would be reasonable.

Appendix I.

The atomic arrangement in the cubic $NaClO_4$ crystal is as follows:

Na:	$\frac{1}{2}\ 0\ 0$;	$0\ \frac{1}{2}\ 0$;	$0\ 0\ \frac{1}{2}$;	$\frac{1}{2}\ \frac{1}{2}\ \frac{1}{2}$
Cl:	$0\ 0\ 0$;	$\frac{1}{2}\ \frac{1}{2}\ 0$;	$\frac{1}{2}\ 0\ \frac{1}{2}$;	$0\ \frac{1}{2}\ \frac{1}{2}$
O :	$u\ u\ u$;	$u\ \bar{u}\ \bar{u}$;	$\bar{u}\ u\ \bar{u}$;	$\bar{u}\ \bar{u}\ u$

and the twelve equivalent points about the Cl-ion sites $(\frac{1}{2}\ \frac{1}{2}\ 0)$ $(\frac{1}{2}\ 0\ \frac{1}{2})$ and $(0\ \frac{1}{2}\ \frac{1}{2})$.

Appendix II.

The four tensors $\boldsymbol{T}(\boldsymbol{k}i)$ $(i=1, 2, 3, 4)$ and the twelve tensors $\boldsymbol{T}^\gamma(\boldsymbol{k}i)$ $(i=1, 2, 3, 4: \gamma=1, 2, 3)$ are dependent with each other. The components of $\boldsymbol{T}(\boldsymbol{k}i)$ and $\boldsymbol{T}^\gamma(\boldsymbol{k}i)$ $(i=2, 3, 4)$ may be expressed in terms of those of $\boldsymbol{T}(\boldsymbol{k}1)$ and $\boldsymbol{T}^\gamma(\boldsymbol{k}1)$ respectively by the ordinary transformation formulae:

$$\left.\begin{aligned}
&T_{\alpha\beta}(\boldsymbol{k}i)=\sum_{\xi,\eta=1}^{3}C_{\alpha\xi}^{(i)}C_{\beta\eta}^{(i)}T_{\xi\eta}(\boldsymbol{k}1)\\
&T_{\alpha\beta}^{\gamma}(\boldsymbol{k}i)=\begin{cases}\displaystyle\sum_{\xi,\eta=1}^{3}C_{\alpha\xi}^{(i)}C_{\beta\eta}^{(i)}T_{\xi\eta}^{\gamma}(\boldsymbol{k}1)\\ \quad(\text{for }\gamma=i-1)\\ \displaystyle-\sum_{\xi,\eta=1}^{3}C_{\alpha\xi}^{(i)}C_{\beta\eta}^{(i)}T_{\xi\eta}^{\gamma}(\boldsymbol{k}i)\\ \quad(\text{for }\gamma\equiv i\ (\mathrm{mod.}\ 3)\\ \quad\ \text{and }\gamma\equiv i+1\ (\mathrm{mod.}\ 3))\end{cases}\\
&\qquad(i=2,\ 3,\ 4:\ \gamma=1,\ 2,\ 3),
\end{aligned}\right\}\quad(\mathrm{AII\text{-}1})$$

where the transformation matrices $C^{(i)}$ are given by

$$C^{(2)}=\begin{pmatrix}1&0&0\\0&-1&0\\0&0&-1\end{pmatrix},\quad C^{(3)}=\begin{pmatrix}-1&0&0\\0&1&0\\0&0&-1\end{pmatrix},$$

$$C^{(4)}=\begin{pmatrix}-1&0&0\\0&-1&0\\0&0&1\end{pmatrix}.$$

Relations between the components of $\boldsymbol{T}(\boldsymbol{k}0)$, $\boldsymbol{T}(\boldsymbol{k}1)$ and $\boldsymbol{T}^\gamma(\boldsymbol{k}1)$ $(\gamma=1, 2, 3)$ are as follows: For an arbitrary orientation of the coordinate system,

$$\left.\begin{aligned}
&T_{\alpha\beta}(\boldsymbol{k}0)=0\quad(\alpha\neq\beta)\\
&\text{and}\\
&T_{11}(\boldsymbol{k}0)=T_{22}(\boldsymbol{k}0)=T_{33}(\boldsymbol{k}0)\ .
\end{aligned}\right\}\quad(\mathrm{AII\text{-}2})$$

If the principal axes of the crystal are taken as the coordinate axes (cf. (2.1c), Fig. 1 and App. I), then

$$\left.\begin{aligned}
&T_{11}(\boldsymbol{k}1)=T_{22}(\boldsymbol{k}1)=T_{33}(\boldsymbol{k}1)\ ,\\
&T_{11}^{\gamma}(\boldsymbol{k}1)=T_{22}^{\gamma}(\boldsymbol{k}1)=T_{33}^{\gamma}(\boldsymbol{k}1)\ ,\\
&T_{\alpha\alpha}^{\gamma}(\boldsymbol{k}1)=T_{\alpha\alpha}^{\gamma'}(\boldsymbol{k}1)\quad(\gamma\neq\gamma')\ ,\\
&\text{and}\\
&T_{12}(\boldsymbol{k}1)=T_{23}(\boldsymbol{k}1)=T_{31}(\boldsymbol{k}1)\ ,\\
&T_{12}^{1}(\boldsymbol{k}1)=-T_{23}^{1}(\boldsymbol{k}1)=T_{31}^{1}(\boldsymbol{k}1)\\
&=T_{12}^{2}(\boldsymbol{k}1)=T_{23}^{2}(\boldsymbol{k}1)=-T_{31}^{2}(\boldsymbol{k}1)\\
&=-T_{12}^{3}(\boldsymbol{k}1)=T_{23}^{3}(\boldsymbol{k}1)=T_{31}^{3}(\boldsymbol{k}1)\ .
\end{aligned}\right\}\quad(\mathrm{AII\text{-}3})$$

Appendix III.

Expressions for $A(\boldsymbol{k})$, $B(\boldsymbol{k})$, $C(\boldsymbol{k})$, $A(\boldsymbol{k})'$ and $B(\boldsymbol{k})'$.

$$\left.\begin{aligned}
&A(\boldsymbol{k})=\frac{1}{r(\boldsymbol{k})^2}\sum_{j=1}^{n(k1)}[y_1(j;\,\boldsymbol{k}1)-x_1(1)]^2\ ,\\
&B(\boldsymbol{k})=\frac{1}{r(\boldsymbol{k})^2}\sum_{j=1}^{n(k1)}[y_2(j;\,\boldsymbol{k}1)-x_2(1)]\\
&\qquad\times[y_3(j;\,\boldsymbol{k}1)-x_3(1)]\ ,\\
&C(\boldsymbol{k})=\frac{1}{r(\boldsymbol{k}0)^2}\sum_{j=1}^{n(k0)}[y_1(j;\,\boldsymbol{k}0)]^2\ .
\end{aligned}\right\}\quad(\mathrm{AIII\text{-}1})$$

$$\left.\begin{aligned} A(k)' &= \frac{1}{ua_0 r(k)^2}\sum_{j=1}^{n(k1)}[y_1(j;\,k1)-x_1(1)]^2 \\ &\quad\times x_3(j;\,k1) \\ B(k)' &= \frac{1}{ua_0 r(k)^2}\sum_{j=1}^{n(k1)}[y_2(j;\,k1)-x_2(1)] \\ &\quad\times[y_3(j;\,k1)-x_3(1)]x_2(j;\,k1) \end{aligned}\right\}\quad\text{(AIII-2)}$$

$A(k)'$ and $B(k)'$ have non-zero values for O-ion groups only.

References

1) S. Asano and Y. Tomishima: J. Phys. Soc. Japan **12** (1957) 346.
2) S. Asano and Y. Tomishima: J. Phys. Soc. Japan **12** (1957) 890.
3) R. W. G. Wyckoff: *The Crystal Structure of Crystals* (Chem. Catalog. Co. Inc. N. Y. 1931) p. 285.
4) B. Szigeti: Proc. Roy. Soc. **A204** (1950) 51. M. Born and K. Huang: *Dynamical Theory of Crystal Lattices* (Oxford Clarendon Press, 1954) p. 110.
5) For instance, F. Seitz: *Modern Theory of Solids* (McGraw-Hill Co. N. Y. 1940) p. 76.
6) J. Yamashita and T. Kurosawa: J. Phys. Soc. Japan **9** (1954) 944.
7) M. Born and K. Huang: loc. cit. p. 26 Table 9.
8) L. Pauling: *The Nature of the Chemical Bond* (Cornell Univ. Press, Ithaca 1945) Chap. 7.

JOURNAL OF THE PHYSICAL SOCIETY OF JAPAN Vol. 12, No. 8, AUGUST, 1957

Electronic States of the *F*-Center in Lithium Fluoride. I

By Tadanobu KOJIMA*

Department of Physics, Osaka University

(Received April 24, 1957)

The electronic states of the *F*-center in LiF are theoretically investigated taking account of the detailed atomic structure of the crystal. The Hamiltonian of an *F*-center including polarization effects is presented. The polarizabilities of the ions in the crystal are determined from the static and high-frequency dielectric constants and the reststrahl frequency. Approximate eigenfunctions and energy levels are calculated with the use of variational wave functions comprising linear combinations of the $2s$ and $2p$ atomic functions on the six lithium ions adjacent to the missing negative-ion site. For both the ground and excited states, the resulting wave functions have larger coefficients of the $2p$ functions than those of the $2s$ functions. The first optical excitation energy is obtained to be somewhat smaller than the experimental value; possible sources of this discrepancy are discussed. The g-factor of the *F*-center is also computed. A more satisfactory theory will be given in the next paper.

§ 1. Introduction

The electronic structure of the *F*-centers in alkali halide crystals has been explored theoretically by various authors since it was first treated by Tibbs[1]. In all the former theories, except that of Inui and Uemura, the crystal was replaced by a continuous dielectric medium with a spherical hole which represented a negative ion vacancy. It has remained an open question, however, to what extent such a continuum approximation could be legitimate from the atomistic view-point; actually, the wave functions obtained by this method were not very accurate as indicated by electron spin resonance experiments[2][3]. It is therefore desirable to make a more detailed calculation, taking full account of the atomic structure of the crystal. Inui and Uemura's work may be considered to have made a step toward this direction. In their work, however, the displacements and deformations of ions were entirely neglected, and the wave functions were chosen merely so as to satisfy the symmetry requirements (without solving the wave equation). The primary purpose of this and next papers is to carry through detailed calculations which are based on the atomistic standpoint and to clarify the nature of the approximations hitherto employed. Calculations were made on LiF, which is the simplest crystal of alkali halides for the purpose of making numerical calculations, but the methods developed here may equally be adapted to other alkali halides, with certain appropriate modifications.

---

* Present address: Research Institute for Atomic Energy, Osaka City University, Awaza-Nakadori Osaka.

The method of the present calculation is essentially a variational method: We first take a trial function of a suitable symmetric form for the wave function of the trapped electron, fix a variational parameter to an arbitrary value, look for the displacements and induced dipole-moments of all the ions which are consistent with the assumed wave function, and calculate the total energy of the crystal. In this way, we get the energy of the crystal as a function of the parameter. Then, finding the minimum of this energy, we obtain the desired energy and wave function.

In § 2 the ionic polarizabilities of the crystal are discussed, in § 3 the Hamiltonian for an *F*-center including polarization effects is presented, in § 4 the eigenfunctions and eigenenergies of the Hamiltonian are computed in the *LCAO* approximation, and in § 5 the *g*-factor is calculated making use of the obtained wave function.

§ 2. Polarizabilities of the Ions in the Crystal

The polarizabilities of the ions in crystals differ from those of the ions in free space owing to their interactions with the surroundings. Let α_+^o and α_-^o be the polarizabilities of the positive and negative ions, respectively, when the crystal is subject to a high-frequency electric field for which no displacements of the ions occur. These polarizabilities are related to the high-frequency dielectric constant κ_0 by the Lorenz-Lorentz formula:

$$\alpha_+^o+\alpha_-^o=\frac{3v}{4\pi}\,\frac{\kappa_0-1}{\kappa_0+2} \qquad (1)$$

where v $(=2a^3)$ is the volume per ion pair in the crystal. Now a static field be applied to the crystal. The polarization then arises not only from ionic deformations but also from displacements of the ions. Let the contribution of the latter to the polarizability be α_d, and the contribution of the former α_+^s and α_-^s, for the positive and negative ions respectively. These quantities and the static dielectric constant κ are related by Clausius-Mosotti formula:

$$\alpha_+^s+\alpha_-^s+\alpha_d=\frac{3v}{4\pi}\,\frac{\kappa-1}{\kappa+2}\,. \qquad (2)$$

Further, defining e^*_{sphere} for a spherical specimen by the expression:

$$e^*_{\text{sphere}}=\frac{(\alpha_+^s+\alpha_-^s+\alpha_d)-(\alpha_+^o+\alpha_-^o)}{\alpha_d} \qquad (3)$$

we have between e^*_{sphere} and κ, κ_0, ω_t (=the angular frequency of transverse lattice wave) the Lyddane-Sachs-Teller relation[4]:

$$\kappa-\kappa_0=4\pi\left(\frac{\kappa_0+2}{3}\right)^2\frac{e^{*2}_{\text{sphere}}}{\overline{M}v\omega_t^2}\,, \qquad (4)$$

$\overline{M}$ being the reduced mass of the ions.

Using the experimental values for LiF: $\kappa=9.27$, $\kappa_0=1.92$, $\omega_t=5.78\times10^{13}\,\text{sec}^{-1}$ and $a=2.01\text{Å}$, we obtain from the above relations

$$\begin{aligned}&\alpha_d=2.34_9\text{Å}^3\,,\\&\alpha_+^s+\alpha_-^s=0.49_6\text{Å}^3\,,\\&\alpha_+^o+\alpha_-^o=0.91_0\text{Å}^3\,.\end{aligned} \qquad (5)$$

To separate the contributions from the positive and negative ions, we first notice that the requirements $\alpha_+^f<\alpha_+^o<\alpha_+^s$ and $\alpha_-^f>\alpha_-^o>\alpha_-^s$ should be satisfied, where α_+^f and α_-^f denote the polarizabilities of the positive and negative ions in free space. Adopting Pauling's values[5]: $\alpha_+^f=0.029\text{Å}^3$ and $\alpha_-^f=1.04\text{Å}^3$ (Pauling's value of α_+^f is very close to that obtained by a variational method: 0.031Å^3 [6]) and setting $\alpha_+^o=0.04\text{Å}^3$ and $\alpha_+^s=0.07\text{Å}^3$ as reasonable values, we get values shown in Table I. It is interesting to compare these values with those given by other authors. Shockley[7] assumed α^o to be a quantity characteristic of each ion, irrespectively of the sort of the crystal which contains the ion, and so determined α^o's of the alkali and

Table I. Polarizabilities of Li^+ and F^- ions in Å^3

	α^f	α^o	α^s
α_+	0.03	0.04	0.07
α_-	1.04	0.87	0.42_6
α_d			2.35

halogen ions as to get a best fit of the Lorenz-Lorentz formula for all the alkali halides. His values for Li^+ and F^- are $\alpha_+{}^o=0.045\text{Å}^3$ and $\alpha_-{}^o=0.86\text{Å}^3$. The method used by Mott and Littleton[8)] is essentially to calculate $\alpha_+{}^s$, $\alpha_-{}^s$ and α_d, assuming that

$$\alpha_+{}^s:\alpha_-{}^s:\alpha_d=\alpha_+{}^f:\alpha_-{}^f:\alpha_d{}' ,$$

(which contradicts with the requirement $\alpha_+{}^f<\alpha_+{}^s$) where $\alpha_d{}'$ is given from the expression

$$\kappa-\kappa_0=\frac{4\pi\beta}{1-4\pi\beta/3} , \qquad \beta=\frac{\alpha_d{}'}{v} .$$

These are derived under the assumption that the polarizations due to displacement and deformation do not interfere one another, $\alpha_d{}'$ corresponds to α_d for an effective field which cares for the overlap effect between neighboring ions. Their method when applied to LiF yields $\alpha_+{}^s=0.02\text{Å}^3$, $\alpha_-{}^s=0.77\text{Å}^3$ and $\alpha_d=2.06\text{Å}^3$. This value of $\alpha_-{}^s$ is presumably too large (compare with given in Table I).

Now, resorting to the continuum approximation, let Maxwell's displacement vector be $\boldsymbol{D}$, whose spatial variation in the crystal is assumed to be sufficiently slow in the range of interatomic distances. When a high-frequency field is applied, there is an induced dipole of strength per ion pair of $(v/4\pi)(1-1/\kappa_0)\boldsymbol{D}$. Then, if we denote the contributions of the positive and negative ions to this dipole by $M_+{}^o\boldsymbol{D}a^3$ and $M_-{}^o\boldsymbol{D}a^3$, respectively, $M_\nu{}^o(\nu=+$ or $-)$ can be expressed as

$$M_\nu{}^o=\frac{1}{4\pi}\left(1-\frac{1}{\kappa_0}\right)\frac{\alpha_\nu{}^o}{\alpha_+{}^o+\alpha_-{}^o} . \qquad (6)$$

When a static field is applied, there is an induced dipole of $(v/4\pi)(1-1/\kappa)\boldsymbol{D}$ per ion pair, so that, denoting the contributions of the positive and negative ions to this dipole by $M_+\boldsymbol{D}a^3$ and $M_-\boldsymbol{D}a^3$, respectively, $M_\nu(\nu=+$ or $-)$ can be expressed as

$$M_\nu=\frac{1}{4\pi}\left(1-\frac{1}{\kappa}\right)\frac{\alpha_\nu{}^s+\alpha_d\overline{M}/\overline{M}_\nu}{\alpha_+{}^s+\alpha_-{}^s+\alpha_d} , \qquad (7)$$

where $\overline{M}_\nu$ is the mass of the ν-th ion. If we assumed, with Mott and Littleton, equal amounts of displacement for ions of the two kinds for a static field, it would have turned out that a strain field was produced in the crystal for an inhomogeneous $\boldsymbol{D}$. In (7) we assumed that the center of gravity does not displace when a static field is applied, in order to separate the effect of strain.

The above assumptions are applicable only if $\boldsymbol{D}$ varies slightly from ion to ion and the effect of the vacancy on the polarizabilities can be ignored. This does not seem very satisfactory especially for those ions which are immediate neighbors of the vacancy. Neverthless we apply these assumptions in the following calculations taking $\boldsymbol{D}=e\boldsymbol{r}/r^3$ (Mott and Littleton's zeroth approximation). In the next paper, however, we shall proceed to higher approximations, where it will be shown that most results of the zeroth approximation are not appreciably affected.

While this zeroth approximation is used throughout this paper, for simplicity, in discussing polarization effects, all the necessary expressions applicable to higher approximations are given. One has merely to replace M_ν and $M_\nu{}^o$ of the next section by more accurate values.

§ 3. The Hamiltonian

The Hartree-Fock Hamiltonian and its expectation value for an F-center in its ground state consist of the following terms, neglecting the effects of lattice vibrations and magnetic interactions:

I. *Kinetic Energy of the Trapped Electron.*—This contributes to the Hamiltonian,

$$\mathscr{H}_1=-(\hbar^2/2m)\nabla^2 , \qquad (8)$$

and to the energy,

$$\int\psi\mathscr{H}_1\psi d\tau=-(\hbar^2/2m)\int\psi\nabla^2\psi d\tau , \qquad (8a)$$

where $\psi(\boldsymbol{r})$ denotes the wave function of the trapped electron in the ground state.

II. *Interactions between the Trapped Electron and the Ions.*

(a) *The interactions not concerned with polarization effects.*—Disregarding the overlap between ions, these contribute to the Hamiltonian

$$\mathscr{H}_2=-e^2\sum_\nu\frac{Z_\nu}{|\boldsymbol{r}-\boldsymbol{R}_\nu|}+2e^2\sum_{\nu,j}\int\frac{\chi_{\nu j}{}^2(\boldsymbol{r}')}{|\boldsymbol{r}-\boldsymbol{r}'|}d\tau', \qquad (9)$$

in which $\boldsymbol{R}_\nu$ is the position vector of the ν-th lattice site, Z_ν the atomic number of the ν-th ion, and $\chi_{\nu j}$ is the undistorted j-th core wave function of the ν-th ion. The corresponding energy is

$$\int\psi\mathscr{H}_2\psi d\tau=-e^2\sum_\nu Z_\nu\int\frac{\psi^2(\boldsymbol{r})}{|\boldsymbol{r}-\boldsymbol{R}_\nu|}d\tau$$

$$+2e^2\sum_{\nu,j}\iint\frac{\psi^2(\boldsymbol{r})\chi_{\nu j}{}^2(\boldsymbol{r}')}{|\boldsymbol{r}-\boldsymbol{r}'|}d\tau d\tau' . \qquad (9a)$$

The effect of overlap between ion cores might be calculated by the method of Löwdin[9] which was developed in his theory of the cohesive energy of ionic crystals. However, we shall neglect it since the overlap integrals between core functions are no greater than about 0.05.

(b) *Interactions between the trapped electron and the polarizations induced by the vacancy.*—A dipole of strength $-M_\nu e a^3 \nabla_\nu R_\nu^{-1}$ is induced on the ν-th ion by the vacancy charge e. The interaction between the trapped electron and all such dipoles in the Hamiltonian is

$$\mathscr{H}_3 = \sum_\nu M_\nu e^2 a^3 \nabla_\nu \frac{1}{|\boldsymbol{r}-\boldsymbol{R}_\nu|} \cdot \nabla_\nu \frac{1}{R_\nu}, \tag{10}$$

and the corresponding interaction energy is

$$\int \psi \mathscr{H}_3 \psi d\tau = -\sum_\nu \frac{M_\nu e^2 a^3}{R_\nu^2} \frac{\partial}{\partial R_\nu} \int \frac{\psi^2(\boldsymbol{r})}{|\boldsymbol{r}-\boldsymbol{R}_\nu|} d\tau. \tag{10a}$$

Contributions from higher multipoles will be small and may safely be neglected. In the above expressions all the displacement dipoles and ion-core dipoles have been assumed to be point dipoles; although this approximation is fairly good for the calculation of the interaction energy, it cannot be used in a more careful calculation as that given in the next paper.

(c) *Interactions between the trapped electron and the optical polarizations induced by it.*—The optical dipole moment induced on the ν-th ion by the charge element $-e\psi^2(\boldsymbol{r})d\tau$ of the trapped electron is given by

$$M_\nu^o e a^3 \nabla_\nu \frac{\psi^2(\boldsymbol{r})}{|\boldsymbol{r}-\boldsymbol{R}_\nu|} d\tau,$$

and the time-average electric field at $\boldsymbol{R}_\nu$ due to the trapped electron is

$$e\nabla_\nu \int \frac{\psi^2(\boldsymbol{r})}{|\boldsymbol{r}-\boldsymbol{R}_\nu|} d\tau.$$

Hence the contribution from such dipoles is

$$\mathscr{H}_{4a} = -\sum_\nu M_\nu^o e^2 a^3 \nabla_\nu \int \frac{\psi^2(\boldsymbol{r})}{|\boldsymbol{r}-\boldsymbol{R}_\nu|} d\tau \cdot \nabla_\nu \frac{1}{|\boldsymbol{r}-\boldsymbol{R}_\nu|}, \tag{11}$$

and the interaction energy,

$$\int \psi \mathscr{H}_{4a} \psi d\tau = -\sum_\nu M_\nu^o e^2 a^3 \left| \nabla_\nu \int \frac{\psi^2(\boldsymbol{r})}{|\boldsymbol{r}-\boldsymbol{R}_\nu|} d\tau \right|^2. \tag{11a}$$

(d) *Interaction between the trapped electron and the infrared polarization induced by it.*—The infrared part of the polarization is defined as a difference between the total polarization and the optical part of the polarization. Accordingly, the necessary expressions are obtained merely by inserting $M_\nu - M_\nu^o$ in place of M_ν^o in (11) and (11a). Writing explicitly,

$$\mathscr{H}_{4b} = -\sum_\nu (M_\nu - M_\nu^o) e^2 a^3 \times \nabla_\nu \int \frac{\psi^2(\boldsymbol{r})}{|\boldsymbol{r}-\boldsymbol{R}_\nu|} d\tau \cdot \nabla_\nu \frac{1}{|\boldsymbol{r}-\boldsymbol{R}_\nu|}, \tag{12}$$

$$\int \psi \mathscr{H}_{4b} \psi d\tau = -\sum_\nu (M_\nu - M_\nu^o) e^2 a^3 \times \left| \nabla_\nu \int \frac{\psi^2(\boldsymbol{r})}{|\boldsymbol{r}-\boldsymbol{R}_\nu|} d\tau \right|^2. \tag{12a}$$

(e) *Exchange interactions between the trapped electron and the core electrons.*—The exchange interactions contribute to the Hamiltonian,

$$\mathscr{H}_5 = -e^2 \sum_j \int \frac{\psi(\boldsymbol{r}')\chi_{\nu j}(\boldsymbol{r}')}{|\boldsymbol{r}-\boldsymbol{r}'|} d\tau' \frac{\chi_{\nu j}(\boldsymbol{r})}{\psi(\boldsymbol{r})}, \tag{13}$$

and to the energy,

$$\int \psi \mathscr{H}_5 \psi d\tau = -e^2 \times \sum_{\nu, j} \iint \frac{\psi(\boldsymbol{r})\chi_{\nu j}(\boldsymbol{r})\psi(\boldsymbol{r}')\chi_{\nu j}(\boldsymbol{r}')}{|\boldsymbol{r}-\boldsymbol{r}'|} d\tau d\tau'. \tag{13a}$$

III. *Internal Energy of the Polarized Lattice.*—This is composed of the self-energy of the ion-core dipoles induced by the trapped electron and the change in interaction energy among all the ions due to this polarization. This energy can be expressed as

$$\int \psi \mathscr{H}_6 \psi d\tau = -\frac{1}{2} \int \psi (\mathscr{H}_{4a} + \mathscr{H}_{4b}) \psi d\tau. \tag{14a}$$

For the derivation of this expression, see Appendix A. (14a) suggests an equivalent Hamiltonian for the internal energy:

$$\mathscr{H}_6 = -\frac{1}{2} (\mathscr{H}_{4a} + \mathscr{H}_{4b}). \tag{14}$$

The total energy of the F-center in its ground state is thus given by

$$E = \int \psi \mathscr{H} \psi d\tau, \tag{15}$$

where $\mathscr{H}$ stands for the complete Hamiltonian:

$$\mathscr{H} = \mathscr{H}_1 + \mathscr{H}_2 + \cdots + \mathscr{H}_6. \tag{16}$$

For excited states, we must distinguish between two cases, *i.e.*, optically excited states in which all the ions are fixed, by the Franck-Condon principle, to their positions in the ground state, and thermally excited states in which they are allowed to move to new equilibrium positions. For optically excited states, we have to use the infrared polarization of the ground state, when calculating the interaction energy with the trapped electron. Thus, for optically excited states, we use, instead of (11), (13) and (14),

$$\mathscr{H}_{4a}^{e}=-\sum_{\nu} M_{\nu}^{0}e^{2}a^{3}$$

$$\times \nabla_{\nu}\int\frac{\psi_{e}^{2}(\boldsymbol{r})}{|\boldsymbol{r}-\boldsymbol{R}_{\nu}|}d\tau\cdot\nabla_{\nu}\frac{1}{|\boldsymbol{r}-\boldsymbol{R}_{\nu}|}, \tag{17}$$

$$\mathscr{H}_{5}^{e}=-e^{2}\sum_{j}\int\frac{\psi_{e}(\boldsymbol{r}')\chi_{\nu j}(\boldsymbol{r}')}{|\boldsymbol{r}-\boldsymbol{r}'|}d\tau'\ \frac{\chi_{\nu j}(\boldsymbol{r})}{\psi_{e}(\boldsymbol{r})}, \tag{18}$$

$$\mathscr{H}_{6}^{e}=-\frac{1}{2}\mathscr{H}_{4a}^{e}, \tag{19}$$

where $\psi_e(\boldsymbol{r})$ is the wave function of the excited state. The corresponding total energy is

$$E_{e}=\int\psi_{e}\mathscr{H}^{e}\psi_{e}d\tau-\frac{1}{2}\int\psi\mathscr{H}_{4b}\psi d\tau, \tag{20}$$

with

$$\mathscr{H}_{e}=\mathscr{H}_{1}+\mathscr{H}_{2}+\mathscr{H}_{3}+\mathscr{H}_{4a}^{e}+\mathscr{H}_{4b}+\mathscr{H}_{5}^{e}+\mathscr{H}_{6}^{e}. \tag{21}$$

The optical excitation energy is E_e-E. For thermally excited states, all the expressions are the same as for the ground state.

In all previous theories of the continuum model, the interaction energy between the trapped electron and the optical polarization induced by it has been assumed to be a constant independent of the electronic state, whether ground or excited. This assumption corresponds to putting $\mathscr{H}_{4a}=\mathscr{H}_{4a}^{e}=\text{const.}$ in our Hamiltonian. We shall refer to this approximation as 'quasi-adiabatic', against the conventional Hartree-Fock approximation. The quasi-adiabatic approximation in the continuum model is based on the idea that, if the motion of the trapped electron is much slower than that of the ion-core electrons, the induced optical polarization will follow quite easily, or adiabatically, the motion of the trapped electron, so that the interaction between them will be independent of the positions of the trapped electron. This idea has proved to be fruitful for donors and acceptors in most valence semiconductors, in which cases the orbit of the trapped carrier is large compared with the interatomic distance of the host crystal. In the case of *F*-centers, however, the optical polarization due to the trapped electron will not easily follow the motion of the electron. Furthermore, the presence of a negative ion vacancy will affect the optical polarization induced by the trapped electron and hence gives rise to an interaction between the negative ion vacancy and the trapped electron. It would, however, be very difficult to deal duly with the interaction between the electron and the induced optical polarization from the atomistic standpoint, since it is essentially the calculation of the correlation energy between the trapped electron and the core electrons that comes out of the second and higher order perturbation terms taking the interaction as the perturbation.

Notwithstanding all these, use is made of the quasi-adiabatic approximation in the present paper, in line with previous theories, but a comparison of both the approximations will be made in the next paper where it will be shown that they lead to not radically different results.

§4. The *LCAO* Approximation

We shall now calculate the eigenfunctions of the Hamiltonian described in the preceding section using a variation method. As a trial wave function for the trapped electron, we take a linear combination of the 2*s* atomic orbitals, *s*, and the 2*p* atomic orbitals, p_x, p_y and p_z, each localized on one of the six Li$^+$ ions which surround the negative ion vacancy. Numbering the six ions as illustrated in Fig. 1, the wave function for the ground state may be written,

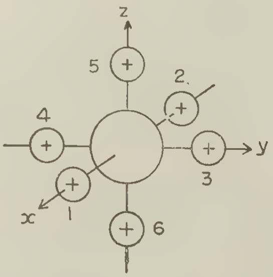

Fig. 1. Numbering the six positive ions around a negative ion vacancy.

$$\psi(\boldsymbol{r})=a_1\sum_{k=1}^{6}s(\boldsymbol{r}-\boldsymbol{R}_k)+a_2\{p_x(\boldsymbol{r}-\boldsymbol{R}_1)-p_x(\boldsymbol{r}-\boldsymbol{R}_2)+p_y(\boldsymbol{r}-\boldsymbol{R}_3)-p_y(\boldsymbol{r}-\boldsymbol{R}_4)+p_z(\boldsymbol{r}-\boldsymbol{R}_5)-p_z(\boldsymbol{r}-\boldsymbol{R}_6)\}, \tag{22}$$

in which, and also in the next expression, the sign of each p function is so chosen that its positive lobe points toward the positive lobe points toward the positive direction of the coordinate axis on which it locates. The first excited states which combine optically with the ground state are triply degenerate. The wave function for one of them may be written

$$\psi_e(\boldsymbol{r})=b_1\{s(\boldsymbol{r}-\boldsymbol{R}_5)-s(\boldsymbol{r}-\boldsymbol{R}_6)\}+b_2\sum_{k=1}^{4}p_z(\boldsymbol{r}-\boldsymbol{R}_k)+b_3\sum_{k=5}^{6}p_z(\boldsymbol{r}-\boldsymbol{R}_k). \tag{23}$$

In (22) and (23), a_i and b_i are variational parameters which are to be so determined as to minimize the corresponding expectation value of the Hamiltonian.

The trial functions constructed in such a way, are not strictly orthogonal to the ion core functions and hence violate the Pauli exclusion principle. As a consequence, it might occur that the energy obtained by minimizing the expectation value of the Hamiltonian becomes much lower than the actual energy value. Since the extension of the wave function and so its overlap with the core functions are larger for the excited state than for the ground state, the above-mentioned lowering of the energy would be more appreciable for the excited state. One would therefore obtain a too low value of the excitation energy by using our trial functions. A possible way of getting out this difficulty would be to orthogonalize the trial functions to the core functions, or as it is practically the same thing, to construct complete determinantal wave functions for the whole crystal. Obviously, however, this procedure is very complicated since we have to use from the start trial functions composed of a large number of atomic orbitals. Another way to go round the difficulty, which is actually adopted in this paper, is to suitably modify the potential function, leaving the trial functions unaltered. We simply replace the ions, to whose core functions the atomic orbitals composing the trial functions are not orthogonal, by point charges.

The atomic orbitals chosen in our actual calculation are the Hartree-Fock functions for a free Li atom[10]. Details of the method of calculation are given in Appendix B. The results are summarized in Table II. The optical first excitation energy obtained is 4.18 ev when polarizations are neglected, and 3.50 ev when they are included. The agreement with experimental value, 4.96 ev, is rather poor. The main source of this discrepancy can be seen by comparing the results with those of a more detailed calculation presented in the next paper. A large part of the discrepancy was found to come from the following: the ground state energy obtained is somewhat too low, and still more so for the excited state. First, our modification of the potential to avoid the nonorthogonality difficulty was not very satisfactory. Second, an additional discrepancy when polarization was included resulted from our use of Mott-Littleton's zeroth approximation. If the positions and deformations of the ions were rearranged to attain the equilibrium configuration, the excited level would have been lowered, but still more lowering would have occured with the ground level. Third, another possible source of the discrepancy may be due to our use of the quasi-adiabatic approximation, as will be discussed in the next paper.

It may be interesting to note that the contribution of the p functions predominates over that of the s functions, as indicated in the caption of Table II, and that by mixing the

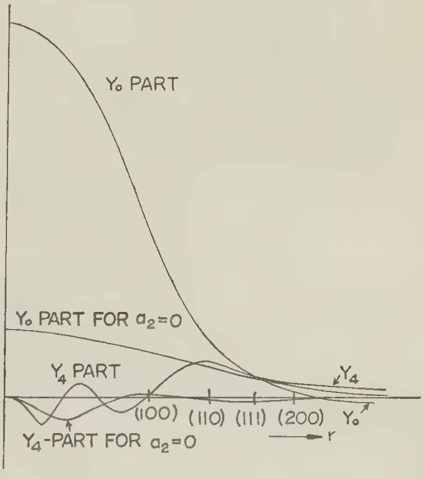

Fig. 2. Behavior of the Y_0 parts and Y_4 parts of the ground state wave function and of the contribution to it from the s functions alone ($a_2=0$).

p functions the ground state energy is lowered by as large as 1.9 ev. Fig. 2 shows the Y_0 and Y_4 parts of the ground state wave function, and for comparison also those parts when only the s functions are used for the linear combination. It may be seen that the Y_0 part is very similar in shape to that obtained by the continuum model, whereas the Y_4 part oscillates violently. It is also noted that the wave function constructed of the s functions only is widely spread over many surrounding ions. This is the main reason why this function gave poor energy levels. In Fig. 3, we have plotted the charge distribution of the trapped electron, $Q(r)=\int_{r'<r}\psi^2(\boldsymbol{r}')d\tau'$, against r. The wave functions obtained will be seen to be somewhat too diffuse when one compares these curves with those in the next paper.

Table II. Calculated energy levels in a.u. The minimum of the expectation value of the Hamiltonian is attained at $a_1=0.064_5$ and $a_2=-0.303$ for the ground state and $b_1=0.174$, $b_2=0.312$ and $b_3=-0.339$ for the first excited state. The values when some of the atomic functions composing the trial functions are omitted are also given for comparison.

State	Atomic Function Employed	Neglecting Polarization	Including Polarization
Ground State	2s only ($a_2=0$)	−0.176	−0.022
	2p only ($a_1=0$)	−0.261	−0.084
	2s and 2p	−0.271	−0.094
First Excited State	2s only ($b_2=b_3=0$)	0.075	0.220
	2p only ($b_1=b_3=0$)	−0.076	0.052
	2p only ($b_1=b_2=0$)	−0.102	0.041
	2s and 2p	−0.118	0.035

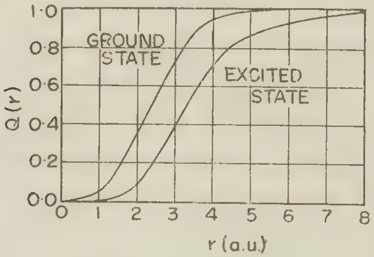

Fig. 3. Charge distributions of a trapped electron.

As is seen in Fig. 2, the computed wave function for the ground state have an extraneous nodal surface, which is unlikely to occur in reality. This evidently comes from the dominant contribution of the p functions or rather a superfluous admixture of them. An improvement might be made by mixing more atomic orbitals located on further ions, but to manipulate a large number of then appearing complicated many-center integrals would make such a calculation very cumbersome.

§ 5. The *g*-Value

In order to obtain the spectroscopic splitting factor, g, for the F-center, we include in the Hamiltonian two additional terms

$$\mathscr{H}_7=\frac{\hbar}{4m^2c^2}[\boldsymbol{\sigma}\times\nabla(-eV)]\cdot\boldsymbol{p}, \tag{24}$$

$$\mathscr{H}_8=\frac{e\hbar}{2mc}\left(\frac{[\boldsymbol{r}\times\boldsymbol{p}]}{\hbar}+\boldsymbol{\sigma}\right)\boldsymbol{H}, \tag{25}$$

where $-eV=\mathscr{H}_2+\mathscr{H}_3+\mathscr{H}_4$, $\boldsymbol{\sigma}$ the Pauli spin vector, and $\boldsymbol{H}$ the external magnetic field. If one already had the eigenfunction, ϕ, of the Hamiltonian which includes $\mathscr{H}_7$ but not $\mathscr{H}_8$, one could calculate the g-value by

$$g\frac{e\hbar}{2mc}H=\frac{\int(\phi\alpha)^*\mathscr{H}_8\phi\alpha d\tau}{\int|\phi\alpha|^2d\tau}-\frac{\int(\phi\beta)^*\mathscr{H}_8\phi\beta d\tau}{\int|\phi\beta|^2d\tau}, \tag{26}$$

where α and β are the usual spin functions. To obtain this ϕ, let us now take the trial function of the form:

$$\phi\alpha=(1+\lambda\mathscr{H}_7)\psi\alpha \tag{27}$$

for the spin state α, and minimize the expectation value of the energy

$$E=\frac{\int(\phi\alpha)^*(\mathscr{H}+\mathscr{H}_7)\phi\alpha d\tau}{\int|\phi\alpha|^2d\tau} \tag{28}$$

with respect to the variational parameter λ. Denoting the minimizing value of λ by λ_m, we have

$$\lambda_m=\frac{4JL^2}{K^2-4L(JK-JL-L^2)}, \tag{29}$$

with

$$J=\int\psi^*\mathscr{H}\psi d\tau,$$

$$K=3\left(\frac{e\hbar^2}{4m^2c^2}\right)^2\int[\nabla V\times\nabla]_z\psi\mathscr{H}[\nabla V\times\nabla]_z\psi d\tau,$$

$$L=3\left(\frac{e\hbar^2}{4m^2c^2}\right)^2\int|[\nabla V\times\nabla]_z\psi|^2d\tau,$$

in which $[\nabla V\times\nabla]_z$ denotes the component of the vector operator, $\nabla V\times\nabla$, along the direction of the magnetic field. Putting $\xi=(e\hbar^2/$

$4m^2c^2)\lambda_m$, the wave function is given by

$$\phi\alpha=\psi\alpha+i\xi\{[\nabla V\times\nabla]_z\psi\alpha+[\nabla V\times\nabla]_x\psi\beta +i[\nabla V\times\nabla]_y\psi\beta\}\,. \tag{30a}$$

Similarly, we have for the spin state β,

$$\phi\beta=\psi\beta+i\xi\{-\nabla V\times\nabla]_z\psi\beta+[\nabla V\times\nabla]_x\psi\alpha -i[\nabla V\times\nabla]_y\psi\alpha\}\,. \tag{30b}$$

Then $\varDelta g(=g-2)$ becomes

$$\varDelta g=-4\xi\int[\nabla V\times\nabla]_z\psi\cdot[\boldsymbol{r}\times\nabla]_z\psi d\tau\,, \tag{31}$$

neglecting terms of the order of ξ^2.

A rough estimation (see Apendix B) using these expressions and the wave function found in §4 yields $\varDelta g\simeq-10^{-3}$. Recently, Lord[11)] has made very careful measurements of the g-factor upon LiF and obtained a positive value, $\varDelta g=+6.2\times10^{-4}$, contrary to our prediction.* However, our theory when applied to KCl, assuming the same value for $a_1:a_2$ as that obtained for LiF, gives a g-value fairly close to the observed one. Kahn and Kittel[2)] state that when the wave function of the ground state is developed in spherical harmonics, in the form

$$\psi=\text{const.}\times[\psi_S+b(\psi_{G^4}+\psi_{G^{-4}})]\,, \tag{32}$$

where ψ_S, $\psi_{G^{-4}}$ and $\psi_{G^{-4}}$ are normalized functions possessing the symmetry properties of Y_0, $Y_{4,4}$ and $Y_{4,-4}$ respectively, the value of b to explain the g-value observed for KCl should be much larger than unity. However, our wave function yields $b=0.13$ and still gives a correct order-of-magnitude value of the g-factor. It should be emphasized that use of an accurate potential function in (31) is of vital importance.

To evaluate the electron resonance line width of the F-center, which is associated with the hyperfine interaction of the trapped electron with the nuclei of the ions surrounding the vacancy and hence with the values of the wave function at these nuclei, we have to use a wave function orthogonalized to all the ion-core functions. Our wave function is only partially orthogonal to the core functions, and so its values at the nuclei can not be expected to be satisfactory. A calculation of the line width using an orthogonalized wave function will be performed in the next paper.

§6. Summary and Conclusions

We used variational wave functions composed of the $2s$ and $2p$ atomic functions of the six lithium ions adjacent to the vacancy to calculate the energy levels and also the g-value. The contribution of the p functions was found to be much larger than that of the s functions, as seen in Table II; wave functions composed of only the s atomic functions gave very poor energy levels, probably because they extend over many ions as indicated in Fig. 2. Our *LCAO* method yielded a value of the first excitation energy which is in fair agreement with experiment but this method does not seem to be convenient for more accurate computations, primarily because we have to deal with complicated many-center molecular integrals. The g-value was also calculated. Although our method of approach presented in §5 will be able to explain the observed g-value of F-centers in most alkali halides, a complicated situation seems to exist in the case of LiF and a more careful investigation will be necessary.

The author would like to express his sincere thanks to Professor T. Nagamiya for his kind interest and encouragement during the course of this work. Thanks are also expressed to Mrs. K. Kojima for helpful discussions and assisting with numerical calculations.

Appendix A. Derivation of (14a)

The Maxwell's displacement vector in the Hartree approximation produced by the trapped electron is

$$\boldsymbol{D}(\boldsymbol{r})=e\nabla\int\frac{\psi^2(\boldsymbol{r}')}{|\boldsymbol{r}-\boldsymbol{r}'|}d\tau'\,. \tag{A1}$$

Through this $\boldsymbol{D}(\boldsymbol{r})$ ions deform and displace to their new equilibrium configurations. Considering the displacements and deformations of the ions separately, denote the components of the corresponding dipole moments by x_i ($i=1,2,\cdots 6N$; N: the total number of the ions). Their origin be so chosen that $x_i=0$ in the absence of the trapped electron. Let the component of $\boldsymbol{D}$ associated with x_i be D_i, and imagine the quantity, $\lambda D_i (0 \leqslant \lambda \leqslant 1)$. x_i will vary approximately linearly with λ. The total energy of the crystal, U, may then be written in the form

---

* F. J. Adrian (private communication) also made a similar calculation using a perturbation technique and obtained a value $\varDelta g\approx-5\times10^{-3}$. He suggested that holes produced by the deformation of the surrounding ions may be responsible for the positive $\varDelta g$ value.

$$U = U_0 + U_1\lambda + \sum_{i,j} k_{ij} x_i x_j + \sum_i k_i x_i \lambda \ , \tag{A2}$$

where k_{ij} and k_i are the coefficients which may depend on ψ but not on x_i; $U_1\lambda$ is the energy associated with $\mathscr{H}_1$, $\mathscr{H}_2$, $\mathscr{H}_3$ and $\mathscr{H}_5$. The third term comprises the self-energy of the dipoles induced by the trapped electron and the interaction energy among these dipoles. The fourth term is the interaction between these dipoles and the trapped electron. Now the values of x_i is so determined that U attains an extremum for a fixed ψ, we have for these values of x_i,

$$\sum_{i,j} k_{ij} x_i x_j = -\frac{1}{2} \sum_i k_i x_i \lambda \ ,$$

which states the relation (14a).

Appendix B. Evaluation of Integrals and Lattice Sums

1. Kinetic energy integrals are reduced to sum of one-center integrals and two-center integrals over atomic functions. Each two-center integral was calculated by expanding one atomic function in spherical harmonics around the center of the other atom. Similar convension was adopted also for overlap integrals. Each one-center integral, together with the corresponding one-center potential energy integral (the first term of (A8)), was substituted by the negative of the ionization energy of a free Li atom.

2. Potential energy integrals were calculated through the following two steps:

(a) First, all the ions were replaced by point charge with $\pm e$, and the atomic functions were expanded in spherical harmonics around the center of the vacancy. For example, we write $\psi(\boldsymbol{r})$ in the form:

$$\psi(\boldsymbol{r}) = a_1 \sum_{lm} f_{lm}{}^{(1)}(r) Y_{lm}(\theta,\varphi) + a_2 \sum_{lm} f_{lm}{}^{(2)}(r) Y_{lm}(\theta,\varphi) \ , \tag{A3}$$

in which the first sum comes from the $2s$ functions, the second from the $2p$ functions. Then (9a) reduces to $\sum_n \sum_{n'} a_n a_{n'} U_{nn'}$, with

$$U_{nn'} = -e^2 \sum_{lm} \sum_{l'm'} \sum_{\nu} \varepsilon_\nu \int \frac{f_{lm}{}^{(n)}(r) f_{l'm'}{}^{(n')}(r)}{|\boldsymbol{r}-\boldsymbol{R}_\nu|} \times Y_{lm}(\theta,\varphi) Y_{l'm'}(\theta,\varphi) d\tau \ , \tag{A4}$$

where ε_ν takes $+1$ or -1 according to the sign of the ν-th ion. When $|\boldsymbol{r}-\boldsymbol{R}|^{-1}$ is also expanded in spherical harmonics, integrals appear which contain products of three spherical harmonics. These integrals were evaluated by using the formula

$$Y_{lm}(\theta,\varphi) Y_{l'm'}(\theta,\varphi) = \sum_{L=|l-l'|}^{l+l'} \sum_{M=-L}^{L} \left[\frac{(2l+1)(2l'+1)}{4\pi(2L+1)} \right]^{1/2} \times (ll'00|ll'L0)(ll'mm'|ll'LM) Y_{LM}(\theta,\varphi) \tag{A5}$$

for normalized Y_{lm}12); $(ll'mm|ll'LM)$ are the Clebsch-Gordan (vector addition) coefficients which are tabulated elsewhere13).

Integrals appearing below (10) were also computed with a similar method.

(b) Second, the values of the integrals of the type $\int u^2(\boldsymbol{r}-\boldsymbol{R}_k)|\boldsymbol{r}-\boldsymbol{R}_k|^{-1} d\tau$ (u is the $2s$ or $2p$ atomic function) were revised in accordance with the prescription described in § 4. For this purpose, we expand u as

$$u(\boldsymbol{r}-\boldsymbol{R}_k) = \sum_{lm} g_{lm}(r) Y_{lm}(\theta,\varphi) \ , \tag{A6}$$

and from (A4) subtract

$$-e^2 \sum_{lm} \sum_{l'm'} \int \frac{g_{lm}(r) g_{l'm'}(r)}{|\boldsymbol{r}-\boldsymbol{R}_k|} Y_{lm}(\theta,\varphi) Y_{l'm'}(\theta,\varphi) d\tau \ , \tag{A7}$$

and add to it

$$(\hbar^2/2m) \int u(\boldsymbol{r}-\boldsymbol{R}_k) \nabla^2 u(\boldsymbol{r}-\boldsymbol{R}_k) d\tau - I_u \ , \tag{A8}$$

in which I_u is the ionization energy of a free Li atom corresponding to this u orbital. The ionization energies employed were 5.391 ev for the $2s$ function and 3.544 ev for the $2p$ function. The revision of the integrals of the type $\int u(\boldsymbol{r}-\boldsymbol{R}_k) u'(\boldsymbol{r}-\boldsymbol{R}_{k'}) |\boldsymbol{r}-\boldsymbol{R}_k|^{-1} d\tau$, on the other hand, cannot be made in an unambiguous way. In the present calculation,

$$-e^2 \sum_{lm} \sum_{l'm'} \int \frac{g_{lm}(r) g'_{l'm'}(r)}{|\boldsymbol{r}-\boldsymbol{R}_k|} Y_{lm}(\theta,\varphi) \times Y_{l'm'}(\theta,\varphi) d\tau \tag{A9}$$

was subtracted from (A4) and

$$\frac{1}{2} \left[-e \int u(\boldsymbol{r}-\boldsymbol{R}_k) u'(\boldsymbol{r}-\boldsymbol{R}_{k'}) V_+(\boldsymbol{r}-\boldsymbol{R}_k) d\tau - e^2 \int \frac{u(\boldsymbol{r}-\boldsymbol{R}_k) u'(\boldsymbol{r}-\boldsymbol{R}_{k'})}{|\boldsymbol{r}-\boldsymbol{R}_k|} d\tau \right] \tag{A10}$$

was added, where by $V_+(\boldsymbol{r}-\boldsymbol{R}_k)$ means the Hartree-Fock potential due to a free Li$^+$ ion at $\boldsymbol{R}_k$. These integrals being two-center integrals, the integration can be performed in an analogous way to that of the kinetic energy integrals.

3. Summations over lattice points were carried out as follows:

(a) $\sum(\varepsilon_\nu/R_\nu)F(R_\nu)$ ($F(R)$ represents any function which tends monotonously to unity with increasing R, and $\varepsilon_+=1$, $\varepsilon_-=-1$). This type of summation is evaluated most conveniently by dividing the crystal into cubes of volume a^3 with centers at lattice points and placing a point charge of magnitude $-(\varepsilon_\nu/8)F(R_{\nu i})$ at the i-th corner $R_{\nu i}$ of the ν-th cube each. These point charges approximately cancel one another in each cube except in the cube which contains the vacant lattice point. The summation therefore converges very rapidly when first summed over nine point charges in each cube and then over ν.

(b) $\sum(M_\nu/R_\nu^4)F(R_\nu)$. If $F(R_\nu)$ were all equal to unity, the summation would have been[14)]

$$\frac{1}{a^4}(10.1977M_+ + 6.3346M_-) \qquad \text{(A11)}$$

Correction for $(M_\nu/R_\nu^4)[1-F(R_\nu)]$ was calculated for each lattice point and summed over ν.

(c) $\sum_v(\varepsilon_\nu/R_\nu^5)F(R_\nu)Y^4(\theta,\varphi)$. This was calculated one by one and added in a straightforward manner. This type of sum was found to be so small that it could be neglected in most cases.

4. Expansion in spherical harmonics was actually retained up to the fourth order, Y_4, in every case; the contributions of the Y_4 terms to the energy integrals were found to be certainly much smaller than those of the Y_0 terms. Also, a rapid convergence of the expansions was made sure by comparing the values of the normalization integrals calculated exactly by the method described in Appendix B. 1., and those calculated using the functions expanded in spherical harmonics up to the fourth order. The difference in values between two methods was below 1% for the ground state and below 3.5% for the excited state throughout the varied ranges of a_i and b_i.

5. Calculation of the integrals appearing in the expression for the g-factor could also be made similarly. But now it is expedient to expand the potential, V, in spherical harmonics around each lattice point and integrate within the sphere of volume a^3 surrounding it. This is because the contribution to the integrals comes mainly from the vicinity of each nucleus. Since the Hartree-Fock potential for a free Li atom does not give the correct value of the $2p$ doublet splitting of the atom, the potential was adjusted by multiplying a constant factor that makes the calculated doublet interval agree with the experimental value, 0.3366 cm^{-1}[15)]. A rough estimate was obtained by taking only the six spheres adjacent to the vacancy. When integrating within a given sphere, we employed the wave function modified as follows: those constituent atomic functions whose centers lie outside the sphere are omitted, and the wave function so simplified is renormalized within the sphere to the value which the initial wave function ψ gives in the same sphere.

References

1) S. R. Tibbs: Trans. Faraday Soc. **35** (1939) 1471; R. Kubo: J. Phys. Soc. Japan **3** (1948) 254; J. H. Simpson: Proc. Roy. Soc. **A197** (1949) 269; T. Inui and Y. Uemura, Prog. Theor. Phys. **5**, (1950) 252; L. Pincherle: Proc. Phys. Soc. **A64** (1951) 648; S. I. Pekar: *Untersuchungen über die Elektonentheorie der Kristalle* (Akademie-Verlag, Berlin, 1954).

2) A. H. Kahn and C. Kittel: Phys. Rev. **89** (1953) 315.

3) Kip, Kittel, Levy and Portis: Phys. Rev. **91** (1953) 1066.

4) Lyddane, Sachs and Teller: Phys. Rev. **58** (1940) 1008; H. Fröhlich, *Theory of Dielectrics* (Clarendon Press, Oxford, 1949), p. 156. e^* is generally defined as the ratio of the infrared polarization to the polarization due to the displacements of ions for a given external field; therefore it depends on the shape of the specimen. For a spherical specimen, this definition leads to (3). Denoting its value for a slab by e^*_{slab}, there holds the relation: $e^*_{\text{slab}} = [(\kappa_0+2)/3]\, e^*_{\text{sphere}}$. e^* appearing in Lyddane *et al*'s paper means e^*_{slab}, and that appearing in Fröhlich's book e^*_{sphere}.

5) N. F. Mott and R. W. Gurney, *Electronic Processes in Ionic Crystals* (Clarendon Press, Oxford, 1949), p. 14.

6) L. Pauling and E. B. Wilson, Jr.: *Introduction to Quantum Mechanics* (McGraw-Hill Book Company, Inc., New York, 1935), p. 229.

7) M. Born and K. Huang: *Dynamical Theory of Crystal Lattices* (Clarendon Press, Oxford, 1954), p. 107. See also, Tessman, Kahn and Shockley: Phys. Rev. **92** (1953) 890.

8) N. F. Mott and M. J. Littleton: Trans Faraday Soc. **34** (1938) 485.

9) P. O. Löwdin, Arkiv. f. mat., astr. o. fysik, **35A** (1948) 30; J. Chem. Phys. **18** (1950) 365.
10) V. Fock and M. J. Petrashen: Phys. Zeits. d. Sowjet. 8 (1935) 547.
11) N. W. Lord: Phys. Rev. **105** (1957) 756.
12) The definition follows L. I. Schiff: *Quantum Mechanics* (McGraw-Hill Book Company, Inc., New York, 1955), p. 73.
13) E. U. Condon and G. H. Shortley: *The Theory of Atomic Spectra* (Cambridge University Press, Cambridge, 1953), p. 75; O. Racah: Phys. Rev. **62** (1942) 438.
14) J. E. Ingham and A. E. Jones: Proc. Roy. Soc. **A107** (1927) 636.
15) C. E. Moore: *Atomic Energy Levels* (National Bureau of Standards, Washington, 1949), Vol. I, p. 8.

JOURNAL OF THE PHYSICAL SOCIETY OF JAPAN Vol. 12, No. 8, AUGUST, 1957

Electronic States of the *F*-Center in Lithium Fluoride. II

By Tadanobu KOJIMA*

Department of Physics, Osaka University

(Received April 24, 1957)

The electronic structure of the *F*-center in LiF is investigated by making use of a variational wave function for the trapped electron which is orthogonal to all the ion-core functions. The variational parameters are so determined as to minimize the total energy of the whole crystal, including exchange interactions, polarization effects and van der Waals interactions. The equilibrium positions of the surrounding ions and the ion-core dipoles are determined in a self-consistent manner with the *F*-center wave functions. The resulting wave function shows correct oscillatory behaviors around each nucleus. The calculated first optical excitation energy is in excellent agreement with experiment. The associated oscillator strength is also evaluated. The line-width of the electron spin resonance is computed, yielding a value twice as large as the experimental value. A source of this discrepancy and other sources of errors which might have affected the energy levels are examined.

In the preceding paper¹⁾, we approximated the wave functions of a trapped electron in an *F*-center by linear combinations of atomic orbitals and calculated the energy levels. As mentioned there, an approach along this line is not very profitable to obtain better results by going to higher approximations, since the nonorthogonality of the wave functions with ion-core functions cannot practically be taken into account in any satisfactory way. Therefore it seems more profitable to start with another type of wave functions which is free from the above dismerit but still tractable. In this paper we shall make an attempt to find such wave functions and calculate with them the energy levels and the electron spin resonance line width, again for LiF.

§ 1. Polarization around a Negative Ion Vacancy

In I, the polarization around a vacancy was treated in Mott and Littleton's zeroth approximation, so that the deformations and displacements of the ions were assumed to be determined only by macroscopic quantities κ, κ_0 and ω_t, even for the ions in the immediate neighborhood of the vacancy. This assumption is actually not correct, because the electric field produced by a vacancy and a trapped electron is far from being uniform over a space large enough compared with the interatomic distance, and besides the dielectric constants must be different from those of the perfect crystal in a uniform field, as there is a lattice distortion caused by the lattice defect.

---

[*] Present address: Research Institute for Atomic Energy, Osaka City University, Awaza-Nakadori, Osaka.

Accordingly, in order to treat properly the polarization around the lattice defect, the polarizabilities of the ions in a strained lattice subjected to a nonuniform external field must be investigated. However, instead of doing this, we shall deal with the polarizations within the framework of Mott and Littleton's approximation²⁾, and proceed as follows.

In the first approximation, we take as unknowns the displacements $\xi_1 a$ and the ion-core dipoles $m_1 ea$ for the six ions adjacent to the vacancy, assuming that for all the other ions values given by the zeroth approximation are still valid. We assume also that the polarizability $\alpha_+{}^s$ of the (100) ions is unaffected by the presence of the vacancy and that the overlap repulsive potentials between ions of opposite signs have, as usual, the exponential form $Ae^{-r/\rho}$. The repulsive force exerted outwards on a (100) ion is then given by

$$F_r=\frac{A}{\rho}\left[-\exp\left\{\left(-1+\xi_1+\frac{M_-'}{4}\right)\frac{a}{\rho}\right\}\right.$$
$$\left.+\frac{4a}{d}\left(\xi_1+\frac{M_-'}{2\sqrt{2}}\right)e^{-d/\rho}\right], \qquad (1)$$

where

$$\left(\frac{d}{a}\right)^2=\left(1-\frac{M_-'}{2\sqrt{2}}\right)^2+\left(\xi_1+\frac{M_-'}{2\sqrt{2}}\right)^2,$$

and

$$M_\nu'=\frac{1}{4\pi}\left(1-\frac{1}{\kappa}\right)\frac{\alpha_d}{\alpha_+{}^s+\alpha_-{}^s+\alpha_d}\frac{\overline{M}}{M_\nu} \qquad (2)$$

is the displacement of the ion ($\nu=+$ or $-$) in units of a for the field of strength e/a^2, $\overline{M}$ being the reduced mass of the ions and $\overline{M}_\nu$ the mass of the ν-th ion. The constant A can be eliminated by making use of the equilibrium condition for the perfect crystal:

$$6Ae^{-a/\rho}/\rho=\alpha_M e^2/a^2\ ,$$

in which $\alpha_M=1.7476$ is the Madelung constant. The electrostatic force outward on the same ion is, aside from the Madelung field which is virtually zero for small displacements,

$$F_e=\frac{e^2}{a^2}\left[\frac{1+\sqrt{2}+0.25}{(1+\xi_1)^2}-\frac{4(1+\xi_1)}{(2+2\xi_1+\xi_1{}^2)^{3/2}}\right.$$
$$-\frac{1}{(2+\xi_1)^2}-\frac{2.3713\,m_1}{(1+\xi_1)^3}-0.3881\,M_+'$$
$$\left.-1.9652\,M_-'\right]. \qquad (3)$$

The unknowns m_1 and ξ_1 are determined from the conditions

$$F_r+F_e=0\ ,$$
$$m_1e^2a=\alpha_+{}^sF_e\ . \qquad (4)$$

In the second approximation, the displacements $\xi_2 a$ and ion-core dipoles $m_2 ea$ for the twelve (110) ions, as well as those for the (100) ions, are taken as unknowns which may be determined from additional conditions analogous to (4).

In order to practise the above calculations, it is necessary to know the value of ρ, which may be determined from the observed dielectric constant and reststrahl frequency as follows: When a uniform electrostatic field is impressed along the [100] direction of the perfect crystal, the overlap repulsive force exerted on a positive ion is given by

$$F_r=\frac{\alpha_M e^2}{6a^2}\left[e^{-x/\rho}-e^{x/\rho}\right.$$
$$\left.+\frac{4x}{\sqrt{a^2+x^2}}e^{-\surd(a^2+x^2-a)/\rho}\right], \qquad (5)$$

in which x denotes the relative displacements of the ions of unlike signs. The force due to the electrostatic field is $F_e=eE_{\text{loc}}$, where E_{loc} means the local field at the positive ion, which is related to x by $ex=\alpha_d E_{\text{loc}}$. Eliminating x from (5) with the use of the equilibrium condition, $F_r+F_e=0$, we have

$$\frac{1}{\alpha_d}=\frac{\alpha_M}{3a^2}\left(\frac{1}{\rho}-\frac{2}{a}\right). \qquad (6)$$

Inserting in this expression the value of α_d given in I, we finally obtain $\rho=0.253$ Å, which is employed throughout the present work.

Usually the value of ρ is determined from the observed compressibility, making use of a formula such as³⁾

$$\frac{1}{\beta}=\frac{\alpha_M e^2}{18a^3}\left(\frac{1}{\rho}-\frac{2}{a}\right), \qquad (7)$$

where β is the compressibility. Inserting the observed value 1.52×10^{-11}/barye for β into (7), we find $\rho=0.296$Å. The measered compressibility, however, is that for room temperature, whereas in fact we must use the value at 0°K. Since β decreases with decreasing temperature, the value of ρ should be lower than 0.296Å. Furthermore, a value of ρ obtained in this way corresponds to the repulsion between unpolarized ions and so would be larger than the value between the polarized ions with which we are actually concerned.

It is noted that our value of ρ, 0.253 Å, is valid for uniform electric field, and thus may not necessarily be satisfactory in applying to our problem of defect lattice. Fortunately, however, an accurate knowledge of ρ was found not very important when calculating the energy levels of the F-center, though it would be important in determining precisely the equilibrium positions of the surrounding ions.

The potential at a missing negative ion site due to the static polarization produced by it is given, in the zeroth, first and second approximations, by

$$V_0{}^s = -\frac{e}{a}(10.1977 M_+ + 6.3346 M_-)\,, \tag{8a}$$

$$V_1{}^s = -\frac{e}{a}\left[4.1977\, M_+ + 6.3346\, M_- + 6 - \frac{6}{1+\xi_1} + \frac{6m_1}{(1+\xi_1)^2}\right], \tag{8b}$$

$$V_2{}^s = -\frac{e}{a}\left[4.1977\, M_+ + 3.3346\, M_- + 6 - \frac{12}{\sqrt{2}} - \frac{6}{1+\xi_1} + \frac{12}{\sqrt{2}+\xi_2} + \frac{6m_1}{(1+\xi_1)^2} + \frac{12\, m_2}{(\sqrt{2}+\xi_2)^2}\right], \tag{8c}$$

respectively. In Table I are given our results of calculation. For reference, also the results of our similar calculation for optical polarization are included, *i. e.*, for the case where all the ions are held fixed to their own lattice points. In the latter calculation the optical polarizabilities of all the ions were assumed to be those for uniform electric field applied to the perfect crystal, and their values were taken from I.

Rittner *et al*⁴⁾ have made a similar calculation for the optical polarization of NaCl up to the tenth approximation. Considering the convergence in their calculation, it appears that our values of V^o converge to about -3.67 ± 0.02 ev. Therefore our second approximation seems to be satisfactory. On the other hand, the convergence of V^s seems rather poor. Rough evaluations were also made up to the fourth order in this case; it appears that V^s converges to a value between -9.2 ev and -9.7 ev⁵⁾. In spite of this poor convergence, the energy levels of the F-center can be computed fairly accurately, because the F-center is electrically neutral and the role of the polarization effects is not so important as in the case of a vacancy. In view of this and the uncertainty of the repulsive potential mentioned above, it was decided to make detailed calculations only to the *second* approximation.

§ 2. Wave Functions

Let us now take the wave function of the trapped electron in the form:

$$\psi(\boldsymbol{r}) = f(\boldsymbol{r}) - \sum_{\nu,j} C_{\nu j}\chi_{\nu j}(\boldsymbol{r})\,. \tag{9}$$

For the ground state, $f(\boldsymbol{r})$ is taken to be

$$f(\boldsymbol{r}) = C\frac{\sin kr}{kr} \quad (r<R)\,, \tag{10a}$$

$$f(\boldsymbol{r}) = C' e^{-\alpha r} \quad (r>R)\,, \tag{10b}$$

in which α is a variational parameter, and C, C' and k are determined from the condition that the two branches of $f(\boldsymbol{r})$ should join smoothly at $r=R$ and from the normalizing condition for $\psi(\boldsymbol{r})$. $\chi_{\nu j}$ denotes the j-th atomic function attached to the ν-th ion, and $c_{\nu j}$ are chosen so that $\psi(\boldsymbol{r})$ is orthogonal to all the core functions, *i.e.*, $c_{\nu j} = \int f(\boldsymbol{r})\chi_{\nu j}(\boldsymbol{r})d\tau$ neglecting the overlaps of different ions. For the first excited state, $f(\boldsymbol{r})$ is taken to be

$$f(\boldsymbol{r}) = C_e\left(\frac{\sin k_e r}{k_e{}^2 r^2} - \frac{\cos k_e r}{k_e r}\right)\cos\theta \quad (r<R), \tag{11a}$$

$$f(\boldsymbol{r}) = C_e' r e^{-\alpha_e r}\cos\theta \quad (r>R), \tag{11b}$$

where θ is the polar angle referred to a [100] axis. C_e, C_e' and k_e are determined similarly as mentioned above for the ground state. R may be taken as a variational parameter as well as α or α_e, but we fix its value, for simplicity, to $0.9\,a$ after Mott and Littleton. The final energy values were actually found to be rather insensitive to the value of R.

For $\chi_{\nu j}$ it is convenient to use simple analytic wave functions. We use therefore the approximate solutions of Hartree-Fock equations for the isolated lithium and fluorine ions⁶⁾:

$$\chi_{\mathrm{Li}^+,1\mathrm{s}}(r_i) = (2.69^3/\pi)^{1/2} e^{-2.69 r_i}\,,$$

$$\chi_{\mathrm{F}^-,2\mathrm{p}z}(r_i) = (2.35^5/\pi)^{1/2} r e^{-2.35 r_i}\cos\theta_i\,,\ \text{etc.},$$

$$\chi_{\mathrm{F}^-,2\mathrm{s}}(r_i) = (2.495^5/2.776\,\pi)^{1/2} \times (r_i e^{-2.495 r_i} - 0.8021 e^{-7.48 r_i})\,, \tag{12}$$

$$\chi_{\mathrm{F}^-,1\mathrm{s}}(r_i) = (8.75^3/\pi)^{1/2} e^{-8.75 r_i}\,, \qquad \text{(in a.u.)}$$

The wave functions of the core electrons may suffer slight changes when the ions aggregate to form a crystal, but we shall neglect such possible changes in our calculation. Furthermore, we shall ignore the effect of the displacements and deformations of the ions due to polarization in orthogonalizing $f(\boldsymbol{r})$ to the core functions. Both these approximations should be satisfactory for our purposes.

§3. Energy Levels

Among the various terms entering into the Hartree-Fock energy, the sum of the terms which are not related to polarization, (8a), (9a) and (13a) in I, can be rewritten by inserting (9) into them as follows, provided the overlaps of the core functions on different ions are ignored:

$$\int\psi(\mathscr{H}_1+\mathscr{H}_2+\mathscr{H}_5)\psi\, d\tau$$

$$=E_1+E_2+E_3+E_4+E_5\,, \tag{13}$$

$$E_1=-(\hbar^2/2m)\int f\nabla^2 f\, d\tau\,, \tag{13a}$$

$$E_2=\sum_{\nu,j}c_{\nu j}{}^2\left(-\frac{\varepsilon_\nu\alpha_M}{a}+\frac{1}{R_\nu}\right), \tag{13b}$$

$$E_3=\sum_{\nu,j}c_{\nu j}{}^2 I_{\nu j}\,, \tag{13c}$$

$$E_4=\int f^2\left[-e^2\sum_\nu\frac{Z_\nu}{|\boldsymbol{r}-\boldsymbol{R}_\nu|}+2e^2\sum_{\nu,j}\int\frac{\chi_{\nu j}{}^2(\boldsymbol{r}')}{|\boldsymbol{r}-\boldsymbol{r}'|}d\tau'\right]d\tau, \tag{13d}$$

$$E_5=-e^2\sum_{\nu,j}\iint\frac{f(\boldsymbol{r})\chi_{\nu j}(\boldsymbol{r})f(\boldsymbol{r}')\chi_{\nu j}(\boldsymbol{r}')}{|\boldsymbol{r}-\boldsymbol{r}'|}d\tau d\tau'. \tag{13e}$$

In (13b), ε_ν takes $+1$ or -1 according to the sign of the ν-th ion. $I_{\nu j}$, which appears in (13c), is the negative of the interaction energy between an electron in $\chi_{\nu j}$ and the rest of the ν-th ion, and may be put equal to the ionization energy of the orbital $\chi_{\nu j}$: $I_{\mathrm{Li}^+,1\mathrm{s}}=2.779$ a. u., $I_{\mathrm{F}^-,2\mathrm{p}}=0.131$ a. u., $I_{\mathrm{F}^-,2\mathrm{s}}=0.975$ a. u., $I_{\mathrm{F}^-,1\mathrm{s}}=26.15$ a. u. It is to be noted that, so far as experimental values or theoretical values calculated with much more accurate functions are employed for $I_{\nu j}$, detailed forms for $\chi_{\nu j}$ are of little importance in evaluating the energy levels. The methods of evaluating the overlap and exchange integrals are given in Appendix A.

Next we shall consider the terms associated with polarization. Although actual calculation was performed to the second approximation, we describe here, for simplicity, the method of calculation only to the first approximation, since the method can readily be extended to the second approximation. Setting

$$Q(r)=\int_{r'<r}\psi^2(\boldsymbol{r}')d\tau'\,, \tag{14}$$

we find for the term of $\mathscr{H}_3$, in terms of ξ_1 and m_1 which were worked out in §2,

$$\int\psi\mathscr{H}_3\psi d\tau$$

$$=\frac{6(\xi_1+m_1)e^2}{a}Q(a)+\sum_\nu{}'\frac{M_\nu e^2a^3}{R_\nu{}^4}Q(R_\nu)\,, \tag{15}$$

where the sum is taken over all the lattice points except the (100) set. In order to evaluate the term of $\mathscr{H}_4$, we take as unknowns the displacements $\xi_1'a$ and the ion-core dipoles $m_1'ea$ for the (100) ions, and assume for all other ions in the lattice the values in the zeroth approximation, namely, $-M_\nu'ea^3R_\nu{}^{-2}Q(R_\nu)$ for their displacements and $-(M_\nu-M_\nu')ea^3R_\nu{}^{-2}Q(R_\nu)$ for theirdeforma tions. Putting

$$q_n=1-Q(\sqrt{n}\,a)\,,$$

we find for the repulsive force exerted outward on a (100) ion,

$$F_r(\xi_1',\alpha)=\frac{\alpha_M e^2}{6a^2}\left[-\exp\left\{\left(\xi_1'+\frac{1}{4}\,q_4M_-'\right)\frac{a}{\rho}\right\}+\frac{4a}{d}\left(\xi_1'+\frac{q_2M_-'}{2\sqrt{2}}\right)\exp\left(\frac{a}{\rho}-\frac{d}{\rho}\right)\right], \tag{16}$$

where

$$\left(\frac{d}{a}\right)^3=\left(1-\frac{q_2M_-'}{2\sqrt{2}}\right)^2+\left(\xi_1'+\frac{q_2M_-'}{2\sqrt{2}}\right)^2,$$

and for the electrostatic force⁷⁾,

$$F_e(\xi_1',\alpha)=\frac{e^2}{a^2}\left[\frac{1+\sqrt{2}+0.25}{(1+\xi_1')^2}-\frac{4(1+\xi_1')}{(2+2\xi_1'+\xi_1'^2)^{3/2}}-\frac{1}{(2+\xi_1')^2}-\frac{2.3713m_1'}{(1+\xi_1')^3}-\frac{Q(a+\xi_1'a)}{(1+\xi_1')^2}\right.$$
$$\left.+\left(-1.2879\frac{q_3}{3}+0.22901\frac{q_5}{5}+\cdots\right)M_+ +\left(-4.5749\frac{q_2}{2}+1.4966\frac{q_4}{4}+\cdots\right)M_-\right]. \tag{17}$$

m_1' and ξ_1' are uniquely determined as functions of α from the conditions $F_r+F_e=0$ and

$m_1'e^2a=\alpha_+{}^sF_c$. Using the values of m_1' and ξ_1' so determined, we finally find for the term of $\mathscr{H}_4$,

$$\int\phi\mathscr{H}_4\phi d\tau=\frac{6(\xi_1'+m_1'-\xi_1-m_1)e^2}{a}Q(a)-\sum_\nu{}'\frac{M_\nu e^2a^3}{R_\nu{}^4}Q^2(R_\nu)\,. \tag{18}$$

For the first excited state, the situation is somewhat complicated because the charge distribution of the trapped electron has a lower symmetry (tetragonal); ions which lie at an equal distance from the vacancy do not always have an equal ion-core dipole strength, unlike the case of the ground state, and moreover, each ion-core dipole is not necessarily parallel to the vector joining the vacancy to that ion. It was estimated, however, that both these effects scarcely affect the final energy levels, so that we are justified to regard the induced optical polarization as if it were caused by a spherically symmetrical charge distribution which is obtained by averaging the true charge distribution of the trapped electron over solid angles. Therefore, denoting

$$Q_e(r)=\int_{r'<r}\psi_e{}^2(\boldsymbol{r}')d\tau,\quad q_{en}=1-Q_e(\sqrt{n}\ a)\,, \tag{19}$$

the term of $\mathscr{H}_{4a}{}^e$ can be evaluated as follows: Taking as an unknown the average of the optical dipole moments induced by the trapped electron on the six (100) ions, $m_{e1}{}^{o\prime}ea$, and assuming that for any other ion, ν, the induced optical dipole moment due to the trapped electron is still given by $-M_\nu{}^oea^3R_\nu{}^{-2}Q_e(R_\nu)$ and that it points toward the vacancy, $m_{e1}{}^{o\prime}$ is determined as a function of α_e from the equation:

$$m_{e1}{}^{o\prime}=\frac{\alpha_+{}^o}{\alpha^3}\Big[-Q_e(a+\xi_1'a)-\frac{2.3713\,m_{e1}{}^{o\prime}}{(1+\xi_1')^3}+\Big(0.3881-1.2879\frac{q_{e3}}{3}+0.22901\frac{q_{e5}}{5}+\cdots\Big)M_+{}^o$$
$$+\Big(1.9652-4.5749\frac{q_e{}^2}{2}+1.4966\frac{q_e{}^4}{4}+\cdots\Big)M_-{}^o\Big]\,, \tag{20}$$

We have then

$$\int\psi_e\mathscr{H}_{4a}{}^e\psi_e d\tau=\frac{6m_{e1}{}^{o\prime}e^2}{a}Q_e(a)-\sum_\nu{}'\frac{M_\nu{}^oe^2a^3}{R_\nu{}^4}Q_e{}^2(R_\nu)\,. \tag{21}$$

The term of $\mathscr{H}_{4b}$ is similarly expressed as

$$\int\phi_e\mathscr{H}_{4b}\psi d\tau=\frac{6(\xi_1'+m_1'-\xi_1-m_1-m_1{}^{o\prime})e^2}{a}Q_e(a)-\sum_\nu{}'\frac{(M_\nu-M_\nu{}^o)e^2a^3}{R_\nu{}^4}Q(R_\nu)Q_e(R_\nu)\,, \tag{22}$$

where $m_1{}^{o\prime}$ is given by the equation obtained by dropping the suffix e from Eq. (20). Expressions analogous to Eqs. (21) and (22) also hold, dropping the suffix e.

In the second approximation, we take as unknowns the displacements and the ion-core dipoles for the second neighbors, as well as for the first neighbors, and proceed in an entirely analogous way to the first approximation. Detailed expressions are omitted here because they are rather lengthy though it is easy to write them down.

So far we have approximated all the displacements of the ions by point dipoles. This might not be a good approximation if the displacements are large. We shall now briefly outline the method of calculation for this case though this effect was evetually found to be rather unimportant. These finite displacements can be taken into account without difficulty for the expressions of $\mathscr{H}_3$ and $\mathscr{H}_4$, in which one has only to replace $Q(a)$ and $Q_e(a)$ by other appropriate quantities according to circumstances. For example, the first term of Eq. (15) may be replaced by

$$\frac{6e^2}{a}\Big[\xi_1\Big(1+\frac{\xi_1}{2}\Big)^{-2}Q\Big(a+\frac{\xi_1}{2}a\Big)$$
$$+m_1(1+\xi_1)^{-2}Q(a+\xi_1a)\Big]\,.$$

On the other hand, the situation concerning the internal energy is much involved, for one can no longer use the relationship, $\mathscr{H}_6=-\mathscr{H}_4/2$, which has been derived under the approximation of point dipoles. To find the change of the internal energy, imagine a process in which the six first neighbors at $(1+\xi_1)$ a are removed to their new equilibrium positions $(1+\xi_1')$ a, and simultaneously an electron is brought into the vacancy from the outside of the crystal, then regard the accompanying change of charge density as a source of electric displactment $\boldsymbol{D}$, which would give rise to a polarization in the surrounding medium. More specifically, one can write in place of Eq. (A1) in I,

$$\boldsymbol{D}(\boldsymbol{r})=e\nabla\int\frac{\psi^2(\boldsymbol{r})'}{|\boldsymbol{r}-\boldsymbol{r}'|}d\tau' \\ -\sum_\nu\nabla V_+(\boldsymbol{r}-\boldsymbol{R}_\nu-\xi_1'\boldsymbol{R}_\nu)+\sum_\nu\nabla V_+(\boldsymbol{r}-\boldsymbol{R}_\nu-\xi_1\boldsymbol{R}_\nu),$$

where the sum is over the six (100) ions and V_+ stands for the Hartree-Fock potential due to a free Li$^+$ ion. Then, for the system composing the source of the electric displacement, the change in internal energy and of the interaction energy with the remaining part of the crystal can be calculated in a straightforward manner with the use of the known interatomic potentials. For the remaining part of the crystal, the change in internal energy may be put equal to $-1/2$ times the change of its interaction energy with the system composing the source of $\boldsymbol{D}$. An estimate shows, however, that these corrections for $\mathscr{H}_3$ and $\mathscr{H}_4$ nearly cancel with that for $\mathscr{H}_6$. Therefore, we conclude that the point-dipole approximation is effectively adequate even when the ionic displacements are not very small. All figures given in the next section are thus referred to the point-dipole approximation.

In calculating the energies related to polarization, we have entirely neglected the contributions from higher spherical harmonics, since they were expected to be negligibly small as in the case of the wave functions employed in I.

Next we shall consider the correction to the exchange energy E_5 which arises from the displacements of the ions; this was not considered in I. In the first approximation, this correction is made only for the first neighbors, in the second approximation, up to the second neighbors, and so on. The exchange integral between f and $\chi_{\nu j}$ will be nearly proportional to the value of f^2 at the nucleus of the ν-th ion if the displacement of the latter is small. Hence, for the ground state for instance, the correction will be given by

$$-e^2\sum_{\nu,j}\left[\frac{f^2(\boldsymbol{R}_\nu+\xi_\nu'\boldsymbol{R}_\nu)}{f^2(\boldsymbol{R}_\nu)}-1\right] \\ \times\iint\frac{f(\boldsymbol{r})\chi_{\nu j}(\boldsymbol{r})f(\boldsymbol{r}')\chi_{\nu j}(\boldsymbol{r}')}{|\boldsymbol{r}-\boldsymbol{r}'|}d\tau d\tau' ,$$

where the sum is over only the first or up to the second neighbors according as the first or second approximation is used.

In the frame of the Hartree-Fock approximation, the correlation between the trapped electron and the core electrons is not taken into account. Unfortunately, no satisfactory method to deal with this correlation is known. We shall compute this correlation energy by expanding it into van der Waals (or multipole) interactions; of course this approach can not entirely be satisfactory. The van der Waals energies can be found by making use of a variational method (Appendix B), the result of which can be written,

$$E_{\text{v.d.w.}}=E^{(1)}_{\text{v.d.w.}}+E^{(2)}_{\text{v.d.w.}}+\cdots , \tag{23}$$

$$E^{(1)}_{\text{v.d.w.}}=-e^2\sum_\nu\frac{\alpha_\nu{}^0}{R_\nu{}^6}\left(\int_{r<R_\nu}r^2\psi^2d\tau\right)^2 \\ \Big/\left(\int r^2\psi^2d\tau+\sqrt{\frac{\alpha_\nu{}^0}{mn_\nu}}\frac{3\hbar}{2e}\right), \tag{23a}$$

$$E^{(2)}_{\text{v.d.w.}}=-e^2\sum_\nu\frac{3\alpha_\nu{}^0}{2R_\nu{}^8}\left(\int_{\nu<R\nu}r^4\psi^2d\tau\right)^2 \\ \Big/\int r^4\psi^2d\tau , \tag{23b}$$

where n_ν denotes the number of electrons in

Table I. Comparison of the various approximations employed, for the static and optical polarizations around a negative ion vacancy.

Order of Approximation	Static Polarization					Optical Polarization		
	V^s(ev)	ξ_1	m_1	ξ_2	m_2	V^o(ev)	$m_1{}^o$	$m_2{}^o$
0	-8.92	0.086	0.003_5	-0.016	0.011	-3.55	0.003_4	0.036
1	-8.82	0.091	0.004_5	-0.016	0.011	-3.59	0.004_2	0.036
2	-9.62	0.087	0.004_2	-0.041	0.005_3	-3.69	0.003_9	0.039

the outermost shell of the ion ν. In this expression, $E^{(1)}_{\text{v.d.w.}}$ corresponds to the dipole-dipole interaction, $E^{(2)}_{\text{v.d.w.}}$ the dipole-quadrupole interaction, and so on. We can show that the same expression with ψ_e in place of ψ also holds for the excited state.

§ 4. Results of Calculation

The energy values for the ground and the first excited states worked out to the second approximation are plotted in Figs. 1a and 1b, respectively, as functions of each variational parameter. The minimizing values of α and α_e, and the corresponding final energy levels are shown in Table II. The first optical excitation energy obtained is 4.96 ev. which is in close agreement with the observed value, 4.96 ev. Such an excellent agreement would, however, be somewhat fortuitous in view of our approximations made, as will be discussed in § 6.

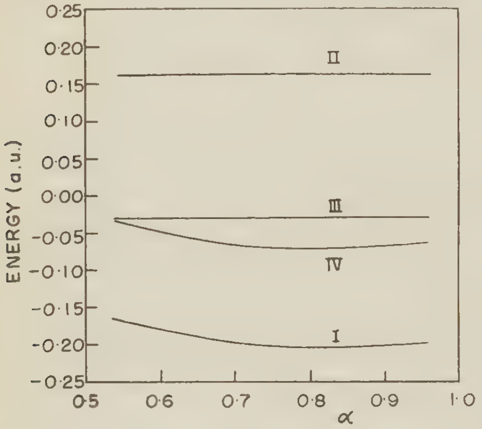

(a) Ground State

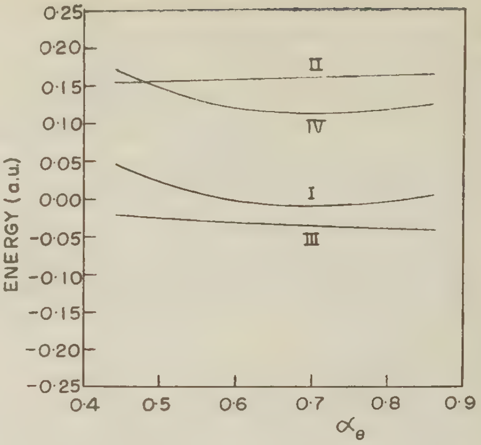

(b) Excited State

Fig. 1. Energies of an *F*-center.

I. Energy not associated with polarization.
II. Energy associated with polarization.
III. Van der Waals energy.
IV. Total energy (I+II+III).

Table II. Energy levels and optimum values of variational parameters for various kinds of approximations, worked out to the second order. (Energies in a.u.)

Approximation	Ground State		First Excited State		Excitation Energy
	α	Energy	α_e	Energy	
Polarization neglected	0.818	−0.2054	0.704	−0.0126	0.1928
Quasi-adiabatic approx.	0.811	−0.0106	0.697	0.1624	0.1730
All terms included	0.809	−0.1053	0.720	0.0769	0.1822

In Table II are also included for comparison the values when the polarization and van der Waals interactions are entirely neglected and the values for quasi-adiabatic approximation. With the former approximation, the first excitation energy comes out to be higher by about 0.3 ev with no appeciable changes in α and α_e. The qnasi-adiabatic approximation is just what was

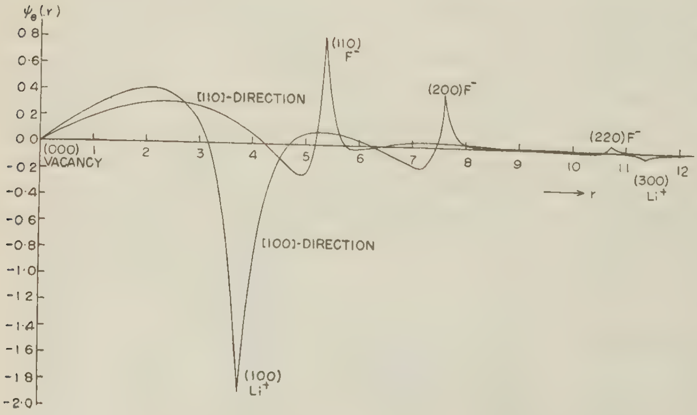

Fig. 2. (a) Ground State

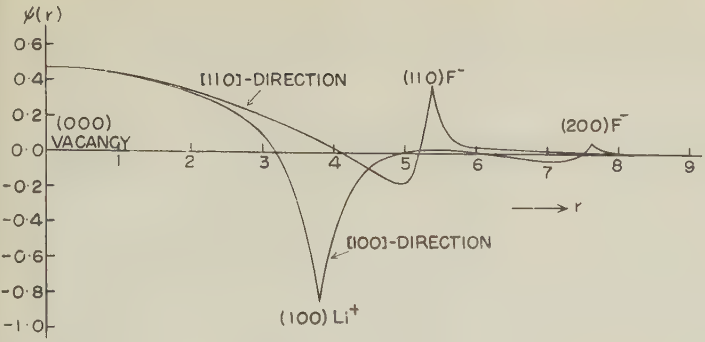

(b) Excited State

Fig. 2. Wave functions of a trapped electron along one of the [100]- and one of the [110]-directions.

employed in I and corresponds to neglecting $\mathscr{H}_{4\alpha}$ and the van der Waals interactions. Since both the neglected energies are rather insensitive to the variation of α or α_e, and besides this neglect lowers the first excitation energy by only 0.25 ev, we may conclude that the quasi-adiabatic approximation does not give appreciably different results compared with the Hartree-Fock approximation, as far as the excitation energy is concerned.

In Figs. 2a and 2b are depicted the wave functions along a [100] and a [110] direction for both the ground and excited states, and in Fig. 3, the charge distributions $Q(r)$ and $Q_e(r)$ defined by Eqs. (14) and (19). The mean orbital radii of the trapped electron turn out to be 2.4 a. u. for the ground state and 3.6 a. u. for the first excited state (note that a=3.8 a. u.). These figures indicate that the charge distributions are appreciably concentrated within the vacancy, as contrasted to earlier treatments. As Figs. 2a and 2b shows, our wave functions behave like a 2*s* function around each lithium nucleus and like a 3*s* function around each fluorine nucleus as might have been expected. The displacemets and ion-core dipole moments of the (100) and (110) ions for the ground state are listed in Table III.

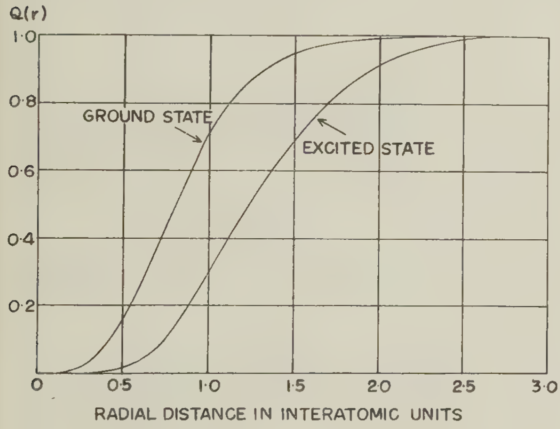

Fig. 3. Charge distributions of a trapped electron.

Table III. Values of displacement and core-dipole parameters for the ground state in the case of all energy terms included.

Neighbors	ξ	m
(100)	-0.074	0.002
(110)	-0.026	0.006

The oscillator strength associated with the lowest optical excitation is given by the expression $(2m/\hbar)^2[(E_e-E)/h](\int\psi_e x\psi d\tau)^2$, which was evaluated using our wave functions to be 0.85. No measurements have so far been made for the oscillator strength in LiF. However, a value of 0.81 was obtained for KCl by Kleinschrod[8], and 0.85 and 0.87 for KCl and NaCl respectively (with an accuracy of ±5%) by paramagnetic experiments[9]; one might expect for LiF a value not much different from these values, inasmuch as the shape of the *F*-band of LiF closely resembles that of NaCl or KCl. The oscillator strength being a quantity rather sensitive to the values of the variational parameters, an accurate measurement of it for LiF is desired to test our calculation.

We have made estimates of the first excitation energy in the zeroth and first approximations to compare with the result of the second approximation. The first approximation yields a value about 0.1 ev higher and the zeroth approximation a value about 1/4 ev lower than the second approximation. Somewhat rough evaluations were made up to the fourth approximation in order to see the speed of convergence. The values of excitation energy in the third and fourth approximations agree with that the second approximation within about 0.06 ev. Our successive approximations thus appear to converge rapidly, and the *second* approximation is already satisfactory for our purposes.

§ 5. Electron Spin Resonance

Kip et al[10] have shown that the line-width of electron spin resonance in F-centers arises from the hyperfine interactions between the trapped electron and the nuclear magnetic moments on the surrounding nuclei:

$$\mathscr{H}_9=-\frac{16\pi\mu_B}{3}\sum_\nu\frac{\mu_\nu}{I_\nu}|\psi(\boldsymbol{R}_\nu)|^2, \tag{24}$$

in which μ_ν denotes the magnetic moment and I_ν the spin quantum number of the ν-th nucleus. These interactions lead us to the rms width:

$$\langle(\Delta H)^2\rangle_{\text{Av}}{}^{1/2}=\frac{8\pi}{3^{3/2}}\left[\sum_\nu\mu_\nu{}^2\frac{I_\nu+1}{I_\nu}|\psi(\boldsymbol{R}_\nu)|^4\right]^{1/2}. \tag{25}$$

Our wave function yields a value $|\psi(\text{Li})|^2=0.0485$ a. u. at a (100) lattice site, and $|\psi(\text{F})|^2=0.0083$ a. u. at a (110) site. Assuming a relative abundance of Li^6 and Li^7 to be 1:11.5[11] and neglecting small contributions from more distant nuclei, Eq. (24) gives 82 oersteds for the rms width[12], which is about twice as large as the observed value 39 oersteds by Lord[13]. Lord also obtained for the charge densities $|\psi(\text{Li})|^2=0.0228$ a. u. and $|\psi(\text{F})|^2=0.0031$ a. u. by analyzing their data of the line-width.

The principal reason for this discrepancy appears to lie in that we have constructed the wave functions by means of the Schmidt's method of orthogonalization, without solving exactly the wave equation around each nucleus. According to our oalculation performed on metallic lithium[14], the value $|\psi(0)|^2$ for the lowest conduction electrons ($\boldsymbol{k}=0$) computed with a single orthogonalized plane wave was found to be 2.0 times as large as the value obtained with a more elaborate variational method. Therefore, the discrepancy may substantially disappear if the wave equation is solved more accurately in the neighborhood of each atomic nucleus.

§ 6. Discussions

We shall enumerate several sources of errors which might have been introduced and estimate their order of magnitude wherever possible.

(1) We have made the wave functions orthogonal to the core functions by the Schmidt's process. Obviously this is not the only possible method of orthogonalization, therefore one can expect lower energy values by taking some better procedure. An estimate of this lowering can be made on the basis of the calculation on metallic lithium mentioned at the end of § 5. The result is as follows: a lowering of 0.010 to 0.015 ev is expected per (100)Li^+ atomic cell, therefore a total lowering of about 0.1 ev for the ground level and of 0.2 to 0.3 ev for the first excited level. It is noted that this point is intimately connected with the problem on electron resonance line-width, as discussed in § 5.

(2) We have consistently neglected the non-orthogonality between different core functions when constructing the wave functions and deriving expressions for the energy. To take account of this non-orthogonality would in principle be possible, but the corresponding computations would be impractical owing to the appearence of a large number of many-center integrals. Non-orthogonality integrals between core functions are small, as mentioned in I, and inclusion of them will scarcely affect the final energy levels.

(3) The choice of the joining radius R also can affect the energy levels. Recalculations with different joining radii showed that the ground state lowered by no more than about 0.1 ev. A similar magnitude of lowering may be expected for the excited state. We might thus conclude that the first excitation energy is virtually unaltered by choosing some better value of R.

Furthermore, choice of the repulsive potential between ions and the shape of the trial functions f and f_e would to some extent affect the final results. Our line of attack on the correlation effects between a trapped electron and core electrons, consisting of expansion of the Coulomb interactions into a series of van der Waals interactions, would not also be entirely satisfactory.

The method of approach presented in this paper is applicable to other alkali halides if more laborious practical calculations could be made. It will also be possible to construct a complete configuration coordinates diagram for an F-center by extending the present calculation, but we shall postpone this program to another occasion.

The author wishes to express his gratitude to Professor T. Nagamiya for his continued interest and encouragement throughout this work. The author is indebted also to Mrs.

K. Kojima for helpful discussions and valuable assistance in the numerical calculations.

Appendix A. Evaluation of Integrals

Evaluation of various integrals appeared in the text were carried out in the following way:

1. Overlap integrals $c_{\nu j}$.

If the branch of $f(\boldsymbol{r})$ going with $r>R$ were extended into the region $r<R$, the calculation of $c_{\nu j}$ could have been executed analytically with ease[15]. Actually $f(\boldsymbol{r})$ takes a different form in $r<R$, so that we must correct for this difference. For this purpose, $\chi_{\nu j}$ was expanded into spherical harmonics around the missing lattice point, and the overlap integrals between $\chi_{\nu j}$ and the two kinds of $f(\boldsymbol{r})$ were evaluated numerically within the sphere $r=R$. The difference between these overlap integrals gave the desired correction.

2. Coulomb integrals in Eq. (13d).

Coulomb integrals between f and $\chi_{\nu j}$ can also be calculated analytically[15] for each $\chi_{\nu j}$ if the outer branch of $f(\boldsymbol{r})$ could be extended into the region $r<R$. Correction for the deviation from this extended $f(\boldsymbol{r})$ was evaluated analytically by expanding the potential due to $\chi_{\nu j}^2$ into spherical harmonics around the missing lattice point. Summation over j was most conveniently performed by the method described in Appendix B. 3 of I.

3. Exchange integrals in Eq. (13e).

The exchange integrals associated with (100) and (110) ions were evaluated after Landshoff[16] by expanding $f(\boldsymbol{r})$ into spherical harmonics around the vacant lattice point. Contributions from those associated with more remote ions are less important, so that the following simplified method was employed to evaluate them: Exchange integrals were first calculated using Slater's free electron approximation[17], but since this method was found to give values not accurate enough for our purposes, a correction factor γ was introduced into Slater's approximation such that

$$\sum_j \int \frac{f(\boldsymbol{r})f(\boldsymbol{r}')\chi_{\nu j}(\boldsymbol{r})\chi_{\nu j}(\boldsymbol{r}')}{|\boldsymbol{r}-\boldsymbol{r}'|}\,d\tau'$$

$$=3\gamma\left\{\frac{3}{8\pi}\sum_j \chi_{\nu j}^2(\boldsymbol{r})\right\}^{1/3} f^2(\boldsymbol{r})\,. \tag{A1}$$

γ can vary with α. It can also vary from ion to ion with which we are concerned, but we assumed a common value for all the positive ions and another common value for all the negative ions, and these values were determined at the (100) and (110) ions for each value of α.

It is needless to say that the above methods are also applicable to the excited state, provided some obvious modifications are made.

Appendix B. Van der Waals Energy

Let the total electronic wave function for the whole crystal containing an F-center be $\Psi=\psi(r)\prod_{\nu,j}\chi_{\nu j}(r_{\nu j})$, and let the deviation of the interaction between the trapped electron and core electrons from the Hartree-Fock Hamiltonian, $\mathscr{H}_{\mathrm{HF}}$,

$$\mathscr{H}_{\mathrm{corr}}=e^2\sum_{\nu,j}\left[\frac{1}{|\boldsymbol{r}-\boldsymbol{r}_{\nu j}|}-\iint\frac{\psi^2(\boldsymbol{r})\chi_{\nu j}^2(\boldsymbol{r}_{\nu j})}{|\boldsymbol{r}-\boldsymbol{r}_{\nu j}|}\,d\tau d\tau_{\nu j}\right]-e^2\sum_\nu Z_\nu\left[\frac{1}{|\boldsymbol{r}-\boldsymbol{R}_\nu|}-\int\frac{\psi^2(\boldsymbol{r})}{|\boldsymbol{r}-\boldsymbol{R}_\nu|}\,d\tau\right] \tag{A2}$$

be treated as a perturbation. We take as a trial function

$$\Phi=\left[1+\sum_{\nu,j}\lambda_{\nu j}{}^{(1)}u_{\nu j}{}^{(1)}(\boldsymbol{r},\boldsymbol{r}_{\nu j})+\sum_{\nu,j}\lambda_{\nu j}{}^{(2)}u_{\nu j}{}^{(2)}(\boldsymbol{r},\boldsymbol{r}_{\nu j})+\cdots\right]\Psi \tag{A3}$$

where $\lambda_{\nu j}{}^{(n)}$ are variational parameters and

$$u_{\nu j}{}^{(1)}=\frac{\boldsymbol{r}\cdot\overline{\boldsymbol{r}}_{\nu j}}{R_\nu{}^3}-\frac{3(\boldsymbol{r}\cdot\boldsymbol{R}_\nu)(\overline{\boldsymbol{r}}_{\nu j}\cdot\boldsymbol{R}_\nu)}{R_\nu{}^5}\,,$$

$$u_{\nu j}{}^{(2)}=\frac{3}{2}\left[\frac{r^2\overline{\boldsymbol{r}}_{\nu j}\cdot\boldsymbol{R}_\nu-\overline{r}_{\nu j}{}^2\boldsymbol{r}\cdot\boldsymbol{R}_\nu}{R_\nu{}^5}+\frac{\boldsymbol{r}\cdot\boldsymbol{R}_\nu-\overline{\boldsymbol{r}}_{\nu j}\cdot\boldsymbol{R}_\nu}{R_\nu{}^2}\left\{\frac{2\boldsymbol{r}\cdot\overline{\boldsymbol{r}}_{\nu j}}{R_\nu{}^3}-\frac{5(\boldsymbol{r}\cdot\boldsymbol{R}_\nu)(\overline{\boldsymbol{r}}_{\nu j}\cdot\boldsymbol{R}_\nu)}{R_\nu{}^5}\right\}\right], \tag{A4}$$

with an abbreviation $\overline{\boldsymbol{r}}_{\nu j}=\boldsymbol{r}_{\nu j}-\boldsymbol{R}_\nu$. $\lambda_{\nu j}{}^{(n)}$ are determined so as to minimize the variational integral:

$$\Delta E=\int\Phi(\mathscr{H}_{\mathrm{HF}}+\mathscr{H}_{\mathrm{corr}})\,\Phi d\tau\Big/\int\Phi^2 d\tau-\int\Psi\mathscr{H}_{\mathrm{HF}}\Psi d\tau\,. \tag{A5}$$

The result may be written

$$\begin{aligned}
\Delta E&=E^{(1)}_{\mathrm{v.d.w.}}+E^{(2)}_{\mathrm{v.d.w.}}+\cdots,\\
E^{(1)}_{\mathrm{v.d.w.}}&=-\sum_{\nu j}\frac{4me^4}{9\hbar^2}\langle\overline{r}_{\nu j}{}^2\rangle^2\frac{1}{R_\nu{}^6}\left(\int_{r<R_\nu}r^2\psi^2 d\tau\right)^2\Big/\left[\int r^2\psi^2 d\tau+\langle\overline{r}_{\nu j}{}^2\rangle\right],\\
E^{(2)}_{\mathrm{v.d.w.}}&=-\sum_{\nu j}\frac{2me^4}{3\hbar^2}\frac{1}{R_\nu{}^8}\left[\langle\overline{r}_{\nu j}{}^2\rangle\int_{r<R_\nu}r^4\psi^2 d\tau+\langle\overline{r}_{\nu j}{}^4\rangle\int_{r<R_\nu}r^2\psi^2 d\tau\right]^2\\
&\qquad\Big/\left[\int r^4\psi^2 d\tau+\frac{20}{3}\langle\overline{r}_{\nu j}{}^2\rangle\int r^2\psi^2 d\tau+\langle\overline{r}_{\nu j}{}^4\rangle\right],
\end{aligned} \tag{A6}$$

where $\langle\overline{r}_{\nu j}{}^2\rangle$ is an abbreviation for $\int\chi_{\nu j}(\boldsymbol{r})\times\overline{r}_{\nu j}{}^2\chi_{\nu j}(\boldsymbol{r})d\tau$. $E^{(1)}_{\mathrm{v.d.w.}}$ and $E^{(2)}_{\mathrm{v.d.w.}}$ correspond to instaneous dipole-dipole and dipole-quadrupole interactions, respectively. $\langle\overline{r}_{\nu j}{}^2\rangle$ can be expressed in terms of the polarizability $\alpha_\nu{}^0$ by means of the Kirkwood's formula[18]:

$$\alpha_\nu{}^0=\frac{4}{9}\sum_j\langle\overline{r}_{\nu j}{}^2\rangle^2\frac{me^2}{\hbar^2} \tag{A7}$$

Neglecting small terms in the expression of $E^{(2)}_{\mathrm{v.d.w.}}$ and assuming that only the electrons in the outermost shells contribute to the polarizabilities and van der Waals interactions, we arrive at Eq. (22).

References

1) T. Kojima: J. Phys. Soc. Japan **12** (1957) 908. We shall quote this as I hereafter. Notations used in the present paper follow those in I.
2) N. F. Mott and M. J. Littleton: Trans. Faraday Soc. **34** (1938) 485.
3) M. Born and K. Huang: *Dynamical Thory of Crystal Lattices* (Clarendon Press, Oxford, 1954), p. 25
4) Rittner, Hutner and du Pré, J. Chem. Phys. **17** (1949) 198.
5) If we start with the assumption that the ions of both types at an equal distance from the vacancy displace toward opposite directions by an equal amount, as was done by Mott and Littleton, we have to the zeroth approximation $V_0{}^s=-8.16$ ev, so that this assumption gives poorer values than ours.
6) Morse, Young and Haurwitz: Phys. Rev. **48** (1935) 948. A. Tubis, Phys. Rev. **102** (1956) 1049 gives differet, screening constants, but the differences between them are insignificant and so of little importance.
7) The coefficients of q_n are given in reference (4).
8) F. G. Kleinschrod: Ann. d. Physik **27** (1936) 97. See also, C. J. Rauch and C. V. Heer, Phys. Rev. **105** (1957) 914.
9) R. H. Silsbee: Phys. Rev. **103** (1956) 1675.
10) Kip, Kittel: Levy and Portis, Phys. Rev. **91** (1953) 1066.
11) D. A. Hutchison: Phys. Rev. **96** (1954) 1018.
12) The values of the nuclear magnetic moments are taken from N. F. Ramsey, *Nuclear Moments* (John Wiley and Sons, Inc., New York, 1953), p. 79.
13) N. W. Lord: Phys. Rev. **105** (1957) 756.
14) K. Kojima and T. Kojima: to be published elsewhere.
15) C. C. Roothaan: J. Chem. Phys. **19** (1951) 1445.
16) R. Landshoff: Z. f. Physik **102** (1936) 201.
17) J. C. Slater: Phys. Rev. **81** (1951) 385.
18) J. G. Kirkwood: Phys. Z. **33** (1932) 57.

JOURNAL OF THE PHYSICAL SOCIETY OF JAPAN Vol. 12, No. 8, AUGUST, 1957

The Magnetic Properties of Iron Selenide Single Crystals

By Kinshiro HIRAKAWA

Department of Physics, Kyushu University, Fukuoka, Japan

(Received September 22, 1956)

Large single crystals of Fe_7Se_8 and Fe_3Se_4 were prepared, and their magnetic properties below the Curie point were investigated by a torque magnetometer. The results obtained on Fe_7Se_8 at room temperature show similar characterics to that of natural pyrrhotite (Fe_7S_8), i.e. the crystals can be magnetized only in the *c*-plane. As the temperature is lowered, however, the *c*-axis becomes the direction of easy magnetization. This change in direction seems to occur gradually. In the case of Fe_3Se_4, such a change in direction of easy magnetization does not take place. The obtained saturation magnetizations for Fe_7Se_8 and Fe_3Se_4 are respectively 68 and 80 gauss at the liquid air temperature.

§ 1. Introduction

The original purpose of this investigation was to make clear the peculiar magnetic behavior of pyrrhotite.[1] In the course of an attack of this problem, it has been found that the properties of $FeSe_x$, which has selenium as an anion instead of surphur, have a close resemblance to those of pyrrhotite, because the anions in such a NiAs type crystal commonly have an important role in the super exchange interaction between iron atoms. We have already obtained an experimental evidence for the ordered arrangement of the lattice defects,[2] i.e. selectively missing iron ions in the alternating *c*-plane in the NiAs type structure. This may be a strong support for the occurence of ferrimagnetism in this substance. The magnetic properties of powdered $FeSe_x (x=1.00\sim1.35)$ have been studied by Hirone and his co-workers,[3] and they observed its ferrimagnetism-like behavior. After their experiments, $FeSe_{1.14}$ and $SeSe_{1.35}$ have Curie point at about 175°C and 40°C and the saturation magnetization at low temperature of about 35 and 15 gauss respectively. It is our purpose to obtain further informations about the anisotropy, saturation magnetization and their temperature dependence with the single crystals of Fe_7Se_8 and Fe_3Se_4.

§ 2. Preparation of Specimens

Single crystals were obtained by the following process: the electrolytic iron powder of about 50 mesh was fully reduced by electrolytic hydrogen gas at about 1000°C. A mixture of the proper proportion of this powder and redistilled selenium, which is more than 99.99% pure, was sealed into an evacuated thick silica tube. The inside of the tube was previously coated with thin carbon film by the decomposition of benzol gas. The tube was then put into the furnance horizontally so as to complete a full reaction and to avoid the cracking of the tube due to the anomalous contraction during the cooling. After keeping at 1100∼1150°C for 4∼5 days, it was cooled very slowly from one end of the container down to room temperature during about 7 days. The largest crystal thus obtained was a flat pole of hexagon of about $20\times20\times10$ mm. From each product, several circular disks were cut out. Crystallographic orientations of them are listed in Table I.

The compositions of specimens have been ascertained by chemical analysis of a small piece of the disks (about 15 mg), the results being listed in Table II. In each case, both selenium content and total weight are lower than the values expected. These disagreements may come from the situation that some amounts of selenium had been lost during the process of analysis, although it is not yet certified. The composition calculated from the iron weight is also listed in the last column of the table. No. 1∼3 show a good agreement to the expected composition of Fe_7Se_8, whereas No. 4 and No. 5 have surely excess content of iron. The remainder of the product, from which the specimens No. 4 and No. 5 were cut out, has also been examined and it proved to show a poor content of iron, as can be seen in the last row in that table. It has the Curie point of about −10°C which is lower than that of No. 4 and No. 5, although

Table I. The dimention and the planes of specimens.

In this table, a, c and V mean respectively the diameter, thickness and volume. The volume was determined from the weight of the disk and the density calculated from the X-ray data. N is the demagnetization factor with respect to the direction of applied field parallel to the plane of the disk, which is approximated to an oblate spheroid. In the last column of the table the indices of plane of the disks are listed, the possible error of which being within 2°.

Specimens number	Composition	a(mm)	c(mm)	V(cm^3)	N	Plane of the disk
No. 1	Fe_7Se_8	8.2	1.1_7	0.0603	1.2_0	$\{10\bar{1}0\}$
No. 2	〃	8.6	1.3_7	0.0785	1.2_5	{0001}
No. 3	〃	10.4	1.8_2	0.152_2	1.3_2	{0001}
No. 4	Fe_3Se_4	8.0	1.3_2	0.0653	1.3_5	{0001}
No. 5	〃	7.1	1.2_2	0.0481	1.4_0	{0001}

Table II. Chemical analysis of the specimens.

The ideal contents of Fe_7Se_8 and Fe_3Se_4 are shown in the brackets. * The remainder of the products from which the specimens No. 4 and No. 5 were cut out.

Specimens	Contents of Fe in weight %	Contents of Se in weight %	Total in weight %	Composition determined from the contents of Fe
No. 1~3	38.1_5(38.23)	60.7_1(61.77)	98.86	$Fe_7Se_{8.02}$
No. 4, 5	35.1_4(34.66)	63.6_0(65.34)	98.80	$Fe_3Se_{3.92}$
*	34.1_4(34.66)	65.1_6(65.34)	99.30	$Fe_3Se_{4.09}$

the details are not yet studied.

§ 3. Experimental Procedure

The measurements were carried out by means of the torque magnetometer which was the same type as that used by Kaya and Miyahara.[4] In order to see the saturation effect, we measured the normal component of magnetization $\boldsymbol{I}_\perp$ to the external field $\boldsymbol{H}$, because it should vanish for the field strength of complete saturation. Here $\boldsymbol{I}_\perp$ is given by

$$\boldsymbol{I}_\perp = \boldsymbol{D}/\boldsymbol{VH}\,, \qquad (1)$$

in which $\boldsymbol{D}$ denotes the exerted torque, which is measured by setting the disk horizontally in the uniform horizontal field as shown in Fig. 1 (a). From the amplitude of the torque curves which was obtained under a field strength sufficient to saturate, we can directly obtain the anisotropy constants.

As the crystals are hexagonal and expected to be strongly anisotropic, the following process may be applicable to obtain the saturation magnetization: first, we set the disk vertically and one of the directions of easy magnetization, which is in the plane of the disk, parallel to the direction of the external field. Next, the plane of the disk is turned through a small angle δ from the original position (Fig. 1 (b)). Then the torque in this case is given by

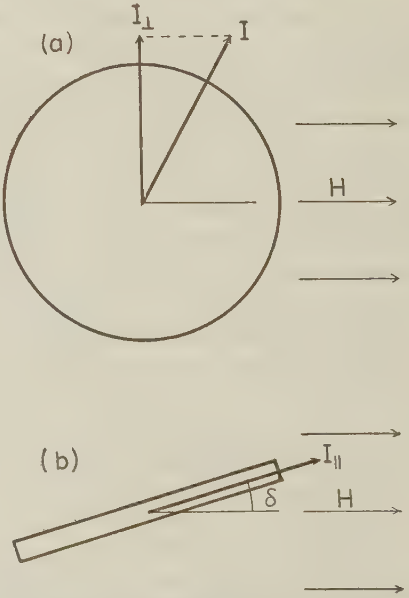

Fig. 1. Method of holding the specimen disk in the magnetic field. The torque is exerted in the plane of the paper. (a) for the measurement of the normal component and (b) of the saturation magnetization.

$$D = VI_{\parallel}H\sin\delta - \frac{\chi_{\perp}}{1+4\pi\chi_{\perp}}VH^2\sin\delta\cos\delta\ , \tag{2}$$

where $I_{\parallel}$ is the induced magnetization in the direction of easy magnetization, and $\chi_{\perp}$ the susceptibility in the direction normal to the plane of the disk when the crystal is regarded as paramagnetic in this direction. For small angle δ, Eq. (2) can be written as

$$D/VH\sin\delta = I_{\parallel} - \frac{\chi_{\perp}}{1+4\pi\chi_{\perp}}H\ , \tag{3}$$

which decreases with increasing H in the region of saturation. We can therefore obtain the saturation magnetization I_s by plotting the measured values of $D/VH\sin\delta$ as a function of H and by extrapolating it to $H=0$. Practically δ was taken as ±5° around the original position of $D=0$. The torque constant of the phosphorbronze string was determined by the method of oscillation. Magnetic field was produced by a rotatable electromagnet, and the field was measured by a search coil calibrated by proton resonance. The damping bath was not used, because the eddy current induced in the specimen holder played a role in damping-actions. The temperature was measured by a very fine copper-constantan thermocouple, which was attached very closely to the specimen.

§ 4. Experimental Results on Fe_7Se_8

a) Torque curves in the plane $\{10\bar{1}0\}$. (Specimen No. 1)

As the crystal of Fe_7Se_8 has a hexagonal symmetry, the anisotropy energy E, in the

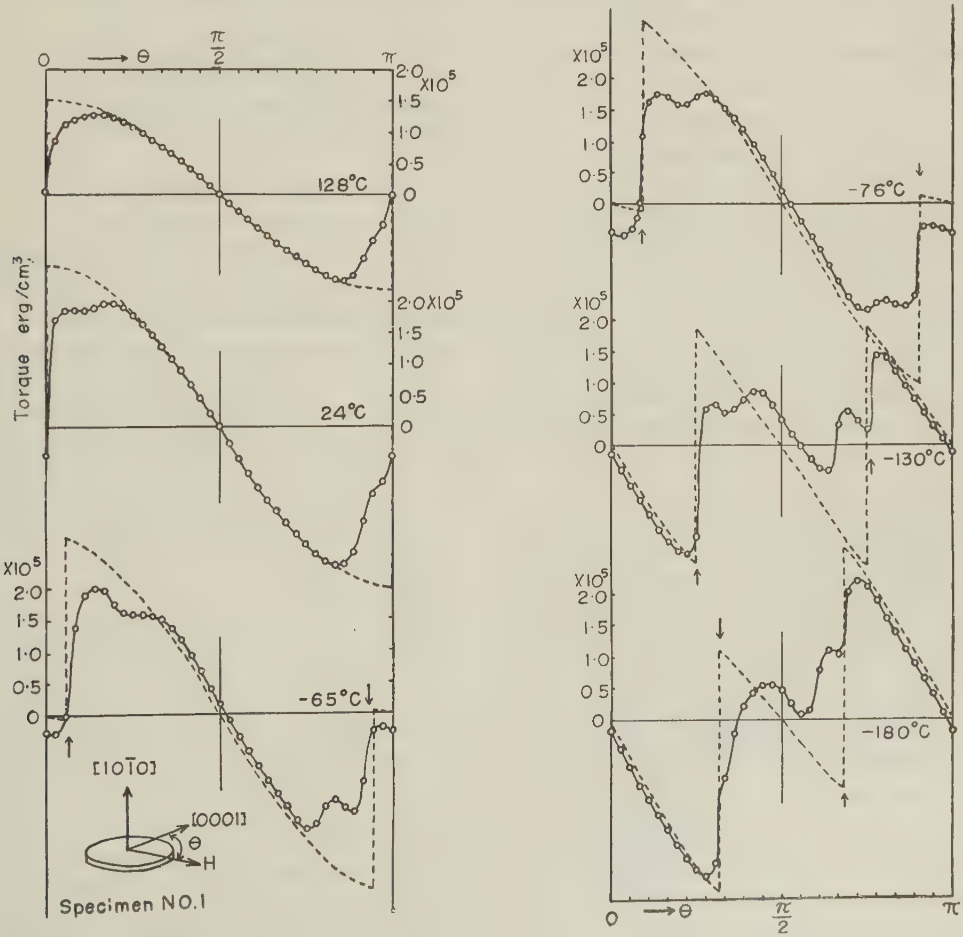

Fig. 2. Temperature variation of the torque curves of Fe_7Se_8 in the plane $\{10\bar{1}0\}$ under a constant field of 5650 Oe. The white circles are the observed points. The anomalous dents are marked by the arrows. The dotted curves are the suggested curves under the simple assumptions described in § 7 (i).

case when the crystal is magnetized, is given by

$$E=K_1\sin^2\theta+K_2\sin^4\theta+K_3\sin^6\theta$$
$$+K_3'\sin^6\theta\cdot\sin^2 3\varphi+\cdots\,, \qquad (4)$$

where $K_1, K_2, \cdots$ are the anisotropy constants and θ is the angle between the direction of magnetization and the c-axis. For the field strength higher than for saturation, the torque per unit volume in the plane $\{10\bar{1}0\}$ is

$$D/V=-\frac{\partial E}{\partial\theta}=-K_1\sin 2\theta$$
$$-2K_2\sin 2\theta\cdot\sin^2\theta-\cdots\,. \qquad (5)$$

At first, we examined the normal component of magnetization $I_\perp$ in this plane for the various field strength up to 11500 Oe. Up to this field strength, any decrements of $I_\perp$ was not observed at all. This fact means that the used field is too weak to analyse the torque curves quantitatively by means of Eq. (5).

Fig. 2 shows the temperature variation of the torque curves in this plane $\{10\bar{1}0\}$ which was obtained under the constant field of 5650 Oe. The direction of easy magnetization can be found out from the stable equilibrium position of $D=0$. At higher temperatures this is in the c-plane, but in the c-axis at lower temperatures. The torque curves thus obtained show a gradual change in their form. We suppose therefore that the direction of easy magnetization changes gradually with decreasing temperature as will be discussed in § 7.

b) *Torque curve in the plane {0001}.* (Specimen No.2)

The temperature variation of the torque curves in the c-plane under a constant field strength of 5650 Oe. can be seen in Fig. 3, where φ denotes the angle between the direction of external field and the axis $[10\bar{1}0]$. From the stable equilibrium positions of $D=0$, it seems that the directions of easy magnetization in the c-plane are parallel to the axis $[1\bar{1}20]$ or its equivalents. As expected from the hexagonal symmetry, all these curves have a six-fold symmetry, although a small component with two-fold symmetry is also contained. This fraction of two-fold symmetry is too large to come from the probable errors in cutting the specimen, so that there may be a small deformation from the hexagonal symmetry of an undetected order. As the temperature is lowered, a continuous decreasing of the amplitude of the torque curves can be seen. This decreasing of the amplitude is considered to have a close connection to the curves in Fig. 2 as will be discussed in § 7.

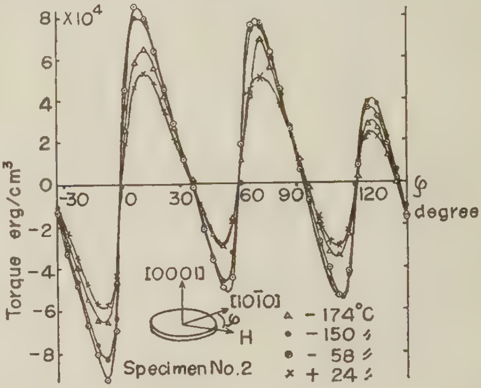

Fig. 3. Temperature variation of the torque curves in the plane {0001} obtained at a constant field strength of 5650 Oe.

c) *Saturation magnetization of Fe_7Se_8* (Specimen No. 1 and No. 3)

According to the method described in § 3, the saturation magnetization I_s of Fe_7Se_8 at various temperatures was measured. The specimen No. 3 was used at higher temperatures than −120°C and No. 1 at the lower temperatures, because below this temperature the specimen No. 3 is forced to rotate by 90°

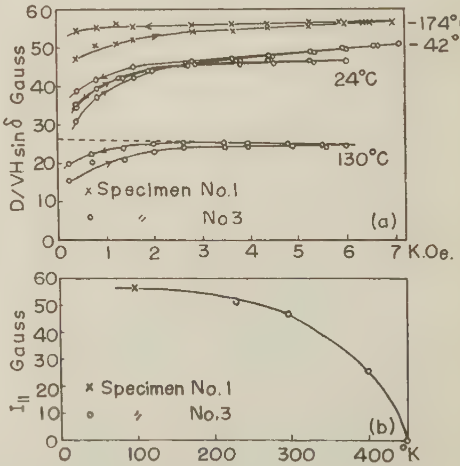

Fig. 4. (a) $D/VH\sin\delta$ and (b) the parallel component of magnetization in the directions of the $[11\bar{2}0]$ axis (○) and of the [0001] axis (×) as the functions of temperature.

to orient so as to make its surface normal to the direction of the field. Fig. 4 (*a*) shows the measured values of $D/VH \sin\delta$ as a function of H. As described in § **3**, the value of $D/VH \sin\delta$ decreases linearly in the region of high field at 128°C. At lower temperatures, however, it tends to increase with field strength, as if the crystal were not saturated. In such a case, we can not obtain the correct value of I_s. Neglecting the second term in Eq. (3), we took up, therefore, the maximum values of $D/VH \sin\delta$ as a value of $I_{\|}$ at 7000 Oe., which is shown in Fig. 4 (*b*). Thus, these values may somewhat, but not too much, be smaller than the saturation magnetization.

§ 5. X-ray Measurements

In order to examine any structural change in Fe_7Se_8, the X-ray diffraction study on the single crystal was carried out at liquid air temperature by the method of Lonsdale and Smith.[5)] But we could not find any marked change in the crystal structure and in the ordered arrangement of the lattice defects. Only a small contraction of the lattice parameters was observed as shown in Table III.

Table III. Lattice parameters of Fe_7Se_8

	Room temp.	Liq. air temp.	Fraction of contraction
B(2*a*)*	7.23_4	7.17_0	0.88%
C(3*c*)*	17.65	17.62	0.17%
c/*a*	1.62_5	1.63_8	

* The capital and small letters designate the unit cell lengths of the super and fundamental lattices, respectively.

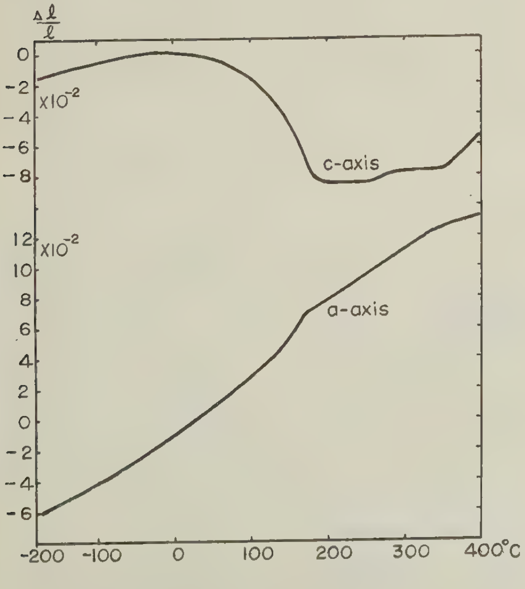

Fig. 5. Thermal expansion of Fe_7Se_8 along the direction parallel to the a- and c-axes.

The thermal expansion of Fe_7Se_8 was measured by a dilatometer and the results are shown in Fig. 5. There is no discontinuous change at low temperatures, but an anomalous change was observed at 170°C, which is a ferrimagnetic Curie point. Immediately below this temperature, on heating, the crystal expands along the *a*-axis while contracts along the *c*-axis.

At about 350°C there is an anomalous kink in both curves, suggesting the existence of a crystal transformation.*

§ 6. Experimental Results on Fe_3Se_4 (Specimen No. 4 and 5)

Fig. 6 shows the measured torque curves in the plane {0001} of the NiAs type structure under the various field strengths and temperatures. These curves show a strong two-fold symmetry besides the symmetry having a period of 60°. This may be possible, because Fe_3Se_4 has a pseudo- NiAs type structure or correctly monoclinic structure with $A = 6.16_7$ Å ($\approx\sqrt{3}\,B$), $B = 3.53_7$ Å, $C = 11.1_7$ Å ($\approx 2c$) and $\beta = 92.0°$.[2)] After the torque and X-ray studies, it was found that the direction of easy magnetization was in the *c*-plane. Contrary to the case of Fe_7Se_8, the saturation effect in this plane was not observed up to 11000 Oe. as well as in the plane $\{11\bar{2}0\}$. In the present case, the change of the direction of easy magnetization was not observed at all. In Fig. 7 are shown the measured values of $D/VH \sin\delta$ and of the saturation magnetization obtained by the method described in § **3**.

---

* The temperatures of 170°C and 350°C at which the anomalies occur agree well with those observed in thermal analysis by Hirone and Chiba[3)].

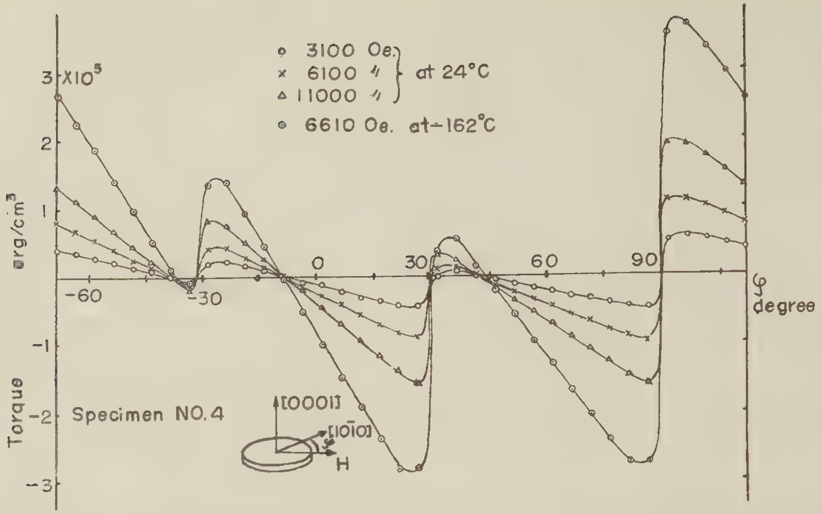

Fig. 6, Torque curves of Fe_3Se_4 in the plane {0001} under the various field strengths.

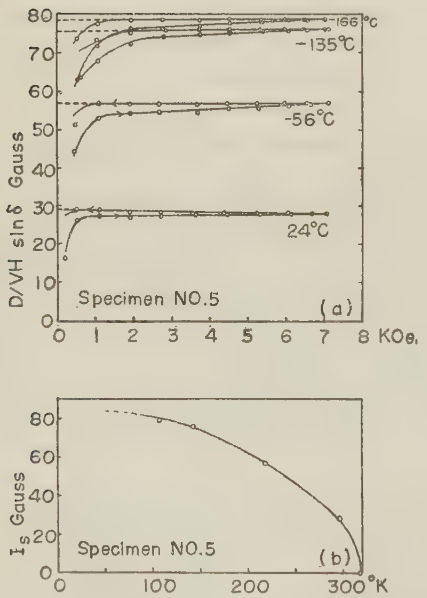

Fig. 7. $D/VH \sin\delta$ and I_S of Fe_3Se_4 as functions of temperature.

§ 7. Discussions of the Results

From the results described above, it seems that Fe_3Se_4 does not show any peculiar property and the obtained thermo-magnetic curve is similar to that of usual ferrimagnetic materials, while Fe_7Se_8 shows a change in direction of the easy magnetization at about −120°C. But the change is not likely to be simple. In the common case, when the contribution of the first term in the anisotropy expression (4) is dominant, the sudden change of the direction of easy magnetization occurs at a definite temperature at which K_1 changes its sign, and consequently the phase of the torque curve in the plane {10$\bar{1}$0} abruptly changes by an amount of $\pi/2$.* At the same temperature, the abrupt change in the torque amplitude in the plane {0001} may also be expected if the applied field were not so strong. Our results show, however, that the changes of the torque curves in both plane {10$\bar{1}$0} and {0001} are continuous over a wide temperature range.

We propose here that the direction of easy magnetization rotates progressively from one direction to another with decreasing temperature. Now, from this standpoint, we shall give an interpretation of the observed torque curves as follows:

(i) *Interpretation of the torque curves in Fig. 2.*

The torque curves in the plane {10$\bar{1}$0} change their forms according to the various field strengths. As an example, the torque curves of the crystal in which the direction of easy magnetization is in the *c*-plane and for the cases where the terms other than that of K_1 in Eq. (4) are negligible are shown schematically in Fig. 8. (a) is the case for the field strengths higher than for saturation. This curve can be expressed by $-\partial E/\partial\theta = -K_1 \sin 2\theta$. (c) is the case for a sufficiently weak field. In such a case where the field is very weak,

---

[*] See Fig. 9 (a) and (e).

the direction of magnetization remains in the c-plane, when the angle θ between the direction of the external field and the c-axis is varied.

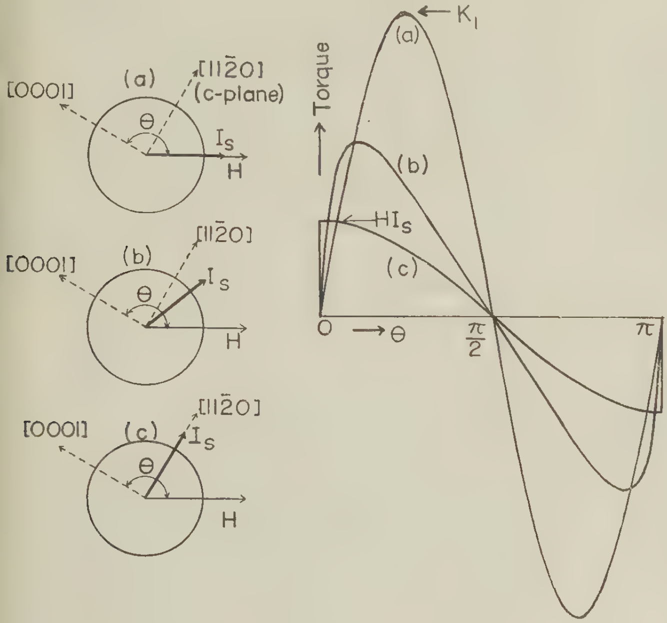

Fig. 8. The torque curves in the plane $\{10\bar{1}0\}$ of the crystal in which the direction of easy magnetization is in the c-plane.

(a) is the case for the field strength higher than for saturation. This torque can be expressed by $-K_1 \sin 2\theta$.

(c) is the case for the field fur weaker than the anisotropy field. The curve can be expressed by $HI_s \cos\theta$. At $\theta=0$, π a reversal of the sense of magnetization occurs, resulting a sudden change in torque.

(b) is the case for the intermediate field strength.

(b) is the case for an intermediate field strength. The torque curves observed at 128°C and 24°C in Fig. 2 resemble to the cases of (b) or (c). Regarding these two observed curves as the case of (c) ....as shown by the dotted curves in Fig. 2 ...., we can obtain the values of I_s, which are shown in Fig. 11. The values of I_s thus obtained agree well with the values those obtained in § 4 (**c**). As the temperature is lowered, however, a couple of anomalous dents appears in the vicinity of $\theta=0, \pi$ and it moves toward the position of $\theta=\pi/2$ with further decreasing temperatures. These dents are marked by the arrows in Fig. 2.

As an interpretation of these anomalous dents, we propose that the direction of easy magnetization rotates progressively from the direction in the c-plane at high temperatures towards the direction of c-axis at low temperatures. Such a progressive change is possible when the K_2 term plays a considerable contribution to the anisotropy expression of Eq. (4).* The torque curves for the various magnitude of K_1 and K_2 are shown schematically in Fig. 9 (the case of strong field). Now, let the polar angles which denote the direction of easy magnetization be θ_0 and $\pi-\theta_0$, which are the functions of temperature, then the torque becomes zero at the directions of $\theta=0$, θ_0, $\pi/2$, $\pi-\theta_0$, π, $\cdots$, as can be seen in Fig. 9.

Under a weak field, however, the forms of the torque curves in Fig. 9 will not immediately give those of the obtained curves, because the latter would greatly be modified, especially in the cases when the domain structures remain as yet. We shall set up, therefore, the forms of the torque curves which would be observed under a weak field and compare them with those observed.

In an actual crystal there exists, perhaps in equal proportions, two kinds of domains, one is magnetized in θ_0 direction and the other in $\pi-\theta_0$ direction. When such a crystal is rotated in a weak field, we assume that the transfer of the domains (domain $(\theta_0)\rightleftarrows$domain $(\pi-\theta_0)$ does not occur,** but the reversal of the sense of magnetization in each domain is permitted. Then the torque for the whole crystal can be expressed by a superposition of the two torque curves of the type of Fig. 8 (c), each of which corresponding respectively to the domain (θ_0) and the domain $(\pi-\theta_0)$, as shown in Fig. 10 (b). As can be seen in Fig. 10 (b), the torque decreases abruptly at $\theta=\pi/2\pm\theta_0$, where the direction of easy magnetization is just perpendicular to the external field.

---

* The direction of easy magnetization is neither in the c-plane nor in the c-axis, when the conditions $\frac{1}{2}|K_1|<|K_2|$ and $K_1K_2<0$ are satisfied. The possibility of these conditions from the atomic theory will not be discussed at present.

** The transfer of the domain will cause a change in the elastic deformation, resulting the increase in crystalline energy.

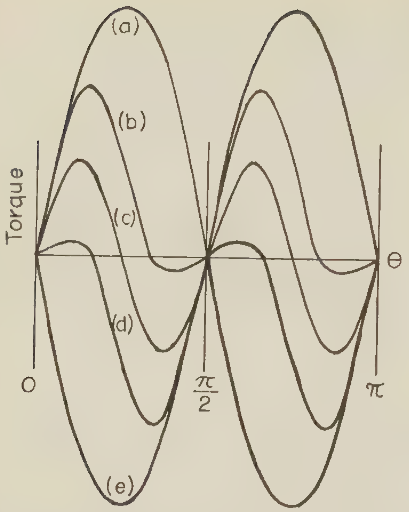

Fig. 9. The forms of the torque curves for the various values of K_1 and K_2 represented by Eq. (5).

(a) $|K_1| \gg |K_2|$, $K_1 < 0$
(b) $1/2|K_1| < |K_2| < |K_1|$, $K_1K_2 < 0$
(c) $K_1 = -K_2$
(d) $|K_1| < |K_2|$, $K_1K_2 < 0$
(e) $|K_1| \gg |K_2|$, $K_1 > 0$

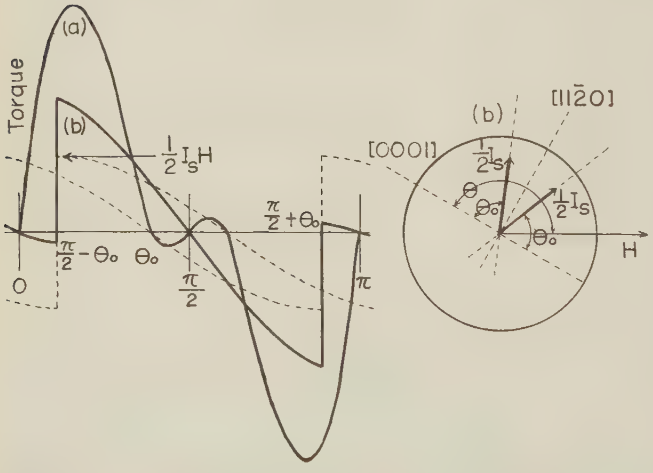

Fig. 10. An example of the forms of the torque curves for the crystal in which the directions of easy magnetization θ_0 and $\pi-\theta_0$ are not in the crystal axes. (a) is the case for a strong field. (b) is the supposed torque curve for a weak field, assuming that a half of the volume of the specimen is magnetized in the direction of θ_0 and the other half in the direction of $\pi-\theta_0$. This torque curve is composed by the superposition of two torque curves (dotted lines) of the type Fig. 8 (c).

The supposed torque curve in Fig. 10 (b) is very different from the curve of Fig. 10 (a) which is the case for a strong field, but Fig. 10 (b) gives the forms which resemble to the observed at −65°C. As can be seen in Fig. 10 (b), the positions of the anomalous dents appeared in Fig. 2 can be expressed by θ_0, while the magnitude of the observed torque, can be fit by a suitable choise of the magnitude of $\boldsymbol{I}_s$. The supposed torque curves thus obtained are represented by the dotted curves in Fig. 2. The used values of θ_0 and $\boldsymbol{I}_s$ are shown in Fig. 11 as functions of temperature.

At low temperatures the value of $\boldsymbol{I}_s$ thus chosen are larger than $\boldsymbol{I}_{\parallel}$ which was obtained in § 4. As $\boldsymbol{I}_{\parallel}$ is the component of $\boldsymbol{I}_s$ in the direction of the *c*-plane or the *c*-axis, $\boldsymbol{I}_s$ can be obtained by using $\boldsymbol{I}_{\parallel}$ and θ_0. At −180°C, for instance, $\boldsymbol{I}_s$ calculated from $\boldsymbol{I}_{\parallel}$ and θ_0 is

$$\boldsymbol{I}_s = \boldsymbol{I}_{\parallel}/\cos\theta_0 = 57 \text{ gauss}/\cos(33°) = 68 \text{ gauss},$$

which is in good agreement with the value of 68 Gauss at −180°C in Fig. 11.

The supposed and the observed torque curves, as can be seen in Fig. 2, deviate from each other in the neighbourhood of the maximum torque. These deviations may come from the fact that the model used (Fig. 8 (c) and the dotted curves in Fig. 10) is not adequate in the vicinity of the maximum torque. The appearence of the other small dents in the observed curves is not understood at present. Some orders of asymmetries in the observed curves can not be understood either, although a small order of lower crystal symmetry, as suggested in § 4 (b), may be the origin of the observed phenomenon.

Although any numerical evaluation of $\boldsymbol{K}_1$ and $\boldsymbol{K}_2$ can not be made under the field strengths lower than 10^4 Oe., $\boldsymbol{K}_1+\boldsymbol{K}_2$ will change from a large negative aluev at room temperature into a positive value with decreasing temperature. For the numerical evaluation of the anisotropy energy, a sufficiently strong field such as to bring the crystal into saturation is required. If $\boldsymbol{K}_1$ of the crystal is the same order of magnitude as that of MnBi[6] ($10^6 \sim 10^7$ erg/cm^3), the orders of 10^5 Oe. will be necessary to saturate Fe_7Se_8 with a small value of saturation magnetization of about 70 gauss.

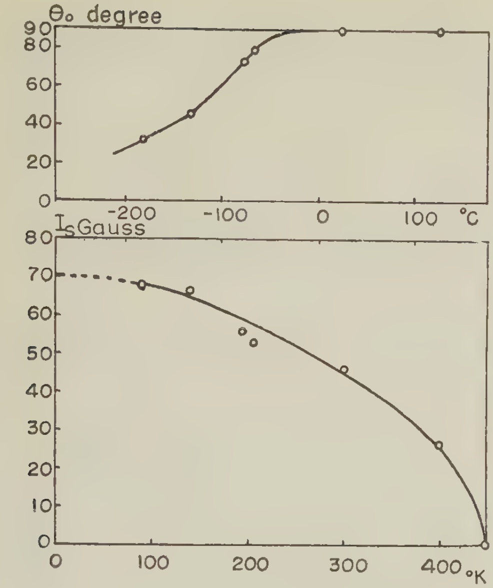

Fig. 11. The direction of easy magnetization and the saturation magnetization I_s in the direction θ_0 as the functions of temperature obtained by taking the observed torque curves in Fig. 2 as the supposed one in Fig. 10 (b).

(ii) *Interpretation of the torque curves in Fig. 3.*

The amplitude of the torque curve in the plane {0001} is proportional to $K_3' \sin^6 \theta$ in Eq. (4). As discussed in the previous case (i), the direction of magnetization θ induced by the weak field (5650 Oe.) is supposed to be nearly in the direction of easy magnetization θ_0. Thus if the change in the direction of easy magnetization takes place abruptly at a definite temperature, the torque amplitude would become zero abruptly at that temperature. The gradual decrement of our torque amplitude towards the lower temperatures (Fig. 3) may mainly depend upon the change of the direction of magnetization θ rather than that of K_3'. Thus the gradual decrement of our torque amplitude in the plane {0001} agrees qualitatively with the fact discussed in the previous case (i).

Pauthenet⁷⁾ has also observed a similar phenomenon on the natural crystal of Fe_7S_8, i.e. the c-axis, which is the direction of difficult magnetization at room temperature, becomes progressively the direction of easy magnetization at lower temperatures. As a change of the direction of easy magnetization commonly takes place suddenly, Néel¹⁾ has pointed out that the origin of the observed phenomenon in Fe_7S_8 may possibly be the local inhomogeneties of the specimen which contains many impurities. We took up, therefore, the measurements again on Fe_7Se_8 of high purity*, but the results was the same as before.

Next, we shall discuss the saturation magnetization of Fe_7Se_8 and Fe_3Se_4. Let us tentatively divide the lattice made of cations into two sublattices⁸⁾ consisting of layers parallel to the c-plane alternatively along the c-axis. One of them contains lattice defects, ferric and ferrous ions, and the other ferrous ions only. By assuming further that the magnetic moments in one sublattice are all antiparallel to those of the other, we obtain the resultant magnetization of Fe_7Se_8 of 69 gauss. This value is in good agreement with the extrapolated value of 70 gauss at 0°K in Fig. 11. Fe_3Se_4 can not be explained by such a model, because the calculated value becomes too large to give the experimental value of 80 gauss.

Acknowledgement

The writer wishes to express his sincere thanks to Prof. T. Nagamiya of Osaka University for his kind advices and encouragements. He wishes also to express his much thanks to Prof. A. Okazaki for the many advantages throughout the work, to Assist. Prof. T. Okada for his continuous guidance, to Assist. Prof. K. Kumada of Tokyo University for the chemical analysis, to Mr. A. Okazaki for the X-ray measurements and to Mr. H. Suzuki for the assistance of measurements. This work is indepted to the Scientific Research Expenditure of the Ministry of Education.

References

1) L. Néel: Rev. Mod. Phys. **25** (1953) 58.
2) A. Okazaki and K. Hirakawa: J. Phys. Soc. Japan **11** (1956) 930.
3) T. Hirone, S. Maeda and N. Tsuya: J. Phys. Soc. Japan **9** (1954) 496.
T. Hirone and S. Chiba: J. Phys. Soc. Japan **11** (1956) 666.
4) S. Kaya and S. Miyahara: Sci. Rep. Tohoku Univ. **27** (1939) 450.

---

* Selenium (99.997% pure) and iron rods (Johnson Matthey, Spectrographically Standardised Iron Rod) were directly reacted in the high frequency furnace and then crystallized.

H. J. Williams: Rev. Sci. Inst. **8** (1937) 56.

5) K. Lonsdale and H. Smith: J. Sci. Inst. **18** (1941) 133.

6) Williams, Sherwood and Boothby: Am. Phys. Soc. Ser. II, **1** (1956) 132.

7) R. Pauthenet: Compt. Rend. **234** (1952) 2261.

8) F. K. Lotgering: Philips Res. Rep. **11** (1956) 190.

On the Electronic Structure of the BH Molecule

By Kimio OHNO*

Department of Physics, Faculty of Science,
University of Tokyo, Tokyo

(Received March 20, 1957)

A nonempirical calculation of the electronic structure of the BH molecule based on a simple Heitler-London method is attempted. It is found that the results are in rather poor agreement with experiment and configuration interaction (CI) must be invoked. In the CI calculation we take into account all the configurations in which two electrons are retained in the 1*s* orbital of the boron atom. Thus we get $13\,{}^1\Sigma^+$, $12\,{}^3\Pi$, $11\,{}^1\Pi$, $9\,{}^3\Sigma^-$, $6\,{}^3\Sigma^+$, $6\,{}^1\Delta$, $3\,{}^5\Sigma^-$, $3\,{}^3\Delta$, $3\,{}^1\Sigma^-$ and $1\,{}^5\Pi$ configurations. In constructing the energy matrices, the orthogonalized atomic orbitals are used and we get the eigenvalue and eigenfunction of the lowest energy state of each symmetry by solving the secular equation. The results show marked improvements on those of the single configuration calculation.

A new nonempirical modification, in which intra-atomic energies are evaluated with atomic orbitals whose orbital exponents are adjusted according to an ionicity of the atom, is tried and leads to satisfactory results.

§1. Introduction

About twenty years ago, Stehn[1)] and King[2)] applied the conventional, extremely simplified form of the Heitler-London theory to the energy levels of the molecules BH, CH, NH, OH and FH. The authors made use of the Hamiltonian of the form

$$\mathscr{H}=\sum_{j>i} J_{ij}-\sum_{j>i}\tfrac{1}{2}\langle 1+4\boldsymbol{s}_i\cdot\boldsymbol{s}_j\rangle K_{ij}\,, \quad (1)$$

which is usually derived by neglecting overlaps between atomic orbitals. They determined the Coulomb (J_{ij}) and exchange (K_{ij}) integrals empirically to make the theory fit the known levels and found these values were smooth functions of the atomic numbers. Moreover, the empirically determined values for $K_{\pi h}$ were close to the calculated values. From these facts, Stehn and King concluded that the success of their theory was not entirely due to the fact that they had adjusted parameters to get the best fit.

It now seems clear that one cannot neglect overlaps between atomic orbitals at least in quantitative arguments and so we can hardly justify the Hamiltonian (1) in the usual way. However, it has been used often not only in the theory of molecules but also in the theory of solids. Recently Carr[3)] made an interesting analysis to determine under what conditions, and with what modifications, the Hamiltonian of the form (1) could be used.

It is of some interest, therefore, to choose one simple hydride molecule as an example and carry out a nonempirical calculation in order to compare its results with those of the semiempirical theory so as to get some insight into the validity of the Hamiltonian (1).

Thus we take up the BH molecule here and start from a calculation based on a simple Heitler-London scheme (§2). It is found, however, that the calculated dissociation and excitation energies are in rather poor agreement with experiment and we cannot rely upon the single configuration theory, so we are forced to proceed to a more refined treatment in which configuration interaction (CI) is included (§ 3).

---

* Present address: Department of Chemistry, University College of North Staffordshire, keel, Staffordshire, England.

The results of the CI calculation are much better than those of the single configuration calculation but still give a somewhat unsatisfactory dissociation energy. In view of this, a new modified nonempirical calculation is proposed and applied to the BH molecule (§ 4). The gist of the modified calculation is to use intra-atomic energies evaluated with the atomic orbitals whose orbital exponents are adjusted according to an ionicity of the atom. The results of our calculations are discussed and compared with experiment (§ 5).

§ 2. Single Configuration Calculation

In this section, a simple form of the Heitler-London or the valence-bond method is applied to the four states $^1\Sigma^+, {}^3\Pi, {}^1\Pi, {}^3\Sigma^+$ of the BH molecule, which were considered also by Stehn and King. The simple form means that we take only one electron configuration to represent each state and neglect all other electron configurations including ionic ones. In order to save computational labour, we calculate the energies of all states at the equilibrium internuclear distance, 1.2325 A, of the ground state, that is, the calculated energy differences are the vertical excitation energies.

In almost all quantum mechanical treatments of molecules, the building bricks are atomic orbitals. The following Slater type atomic orbitals are used for the $1s, 2s, 2p\sigma, 2p\pi$ orbitals of the boron atom and the $1s$ orbital of the hydrogen atom respectively:

$$\left.\begin{aligned}
u&=\sqrt{\frac{Z^3}{\pi}}e^{-Zr}\,,\\
s&=\sqrt{\frac{\delta^5}{3\pi}}re^{-\delta r}\,,\\
\sigma&=\sqrt{\frac{\delta^5}{\pi}}r\cos\theta\, e^{-\delta r}\,,\\
\pi_+&=\sqrt{\frac{\delta^5}{2\pi}}r\sin\theta\, e^{i\phi}e^{-\delta r}\,,\\
\pi_-&=\sqrt{\frac{\delta^5}{2\pi}}r\sin\theta\, e^{-i\phi}e^{-\delta r}\,,\\
\text{or}\quad \pi_x&=\sqrt{\frac{\delta^5}{\pi}}r\sin\theta\cos\phi\, e^{-\delta r}\,,\\
\pi_y&=\sqrt{\frac{\delta^5}{\pi}}r\sin\theta\sin\phi e^{-\delta r}\,,\\
h&=\sqrt{\frac{Z'^3}{\pi}}e^{-Z'r}\,.
\end{aligned}\right\}\qquad (2)$$

The polar axis is taken to coincide with the internuclear axis. Throughout this paper the unit of length is the first Bohr radius of the hydrogen atom: $a_0=0.529172\times10^{-8}$ cm[4]; the unit of energy is e^2/a_0: 1 a. u. $=27.20976$ eV[4] unless otherwise noted. These forms of atomic orbitals are chosen because they are most convenient for evaluation of molecular integrals.

In actual construction of molecular wave functions, instead of s, we make use of the orbital v which is orthogonalized to u,

$$v=\frac{1}{\sqrt{1-S^2}}[s-Su]\,,$$

where S is the overlap integral between s and u: $S=\int u(1)s(1)dv_1$. The reason for this is that v is not only expedient for the computation of energy because of its orthogonality to $1s$, but also v can be considered to be nearer to the best atomic $2s$-like orbital function. In fact, Fischer concluded from her calculation on LiH[5] that, if all the electrons of the molecule are represented explicitly in the wave function, the $2s$ orbit must have a node; while if the inner shells are accounted for by suitable screening constants only, the s-orbits of the valence shell should be nodeless.

The values of the orbital exponents Z, δ have to be determined, in principle, to make the total energy of the boron atom a minimum, but are chosen here to be 4.7 and 1.3 respectively as Slater rules indicate. Using these values, we get -666.503 eV as the total energy of boron atom in its ground state, while the more refined treatment of Tubis[6] gives -666.707 eV by varying these parameters. This means we adopt the suggestion made by Fischer that the wisest course consists in choosing the same screening constants as those obtained for the atomic problem.

We assume almost the same type of wave functions as Stehn and King assumed;

$$\left.\begin{aligned}
\varPhi(^1\Sigma^+)&=\frac{1}{\sqrt{6!}}\sum_P(-1)^P Pu(1)\alpha_1u(2)\beta_2l(3)\alpha_3l(4)\beta_4b(5)h(6)\frac{\alpha_5\beta_6-\beta_5\alpha_6}{\sqrt{2}}\\
&=|u\bar{u}l\bar{l}\,[bh]|\,,
\end{aligned}\right.$$

$$\left.\begin{aligned}\varPhi({}^3\Pi)&=\frac{1}{\sqrt{6!}}\sum_P(-1)^P P u(1)\alpha_1 u(2)\beta_2 v(3)\alpha_3 v(4)\beta_4 \pi(5)\alpha_5 h(6)\alpha_6\\&=|u\bar{u}v\bar{v}\pi h|\ ,\\ \varPhi({}^1\Pi)&=\frac{1}{\sqrt{6!}}\sum_P(-1)^P P u(1)\alpha_1 u(2)\beta_2 v(3)\alpha_3 v(4)\beta_4 \pi(5)h(6)\frac{\alpha_5\beta_6-\beta_5\alpha_6}{\sqrt{2}}\\&=|u\bar{u}v\bar{v}[\pi h]|\ ,\\ \varPhi({}^3\Sigma^+)&=\frac{1}{\sqrt{6!}}\sum_P(-1)^P P u(1)\alpha_1 u(2)\beta_2 v(3)\alpha_3 v(4)\beta_4 \sigma(5)\alpha_5 h(6)\alpha_6\\&=|u\bar{u}v\bar{v}\sigma h|\ .\end{aligned}\right\}\quad(3)$$

Here, b and l are the *s-p* hybridized orbitals of the following form,

$$\left.\begin{aligned}b&=\mu v+(1-\mu^2)^{1/2}\sigma\ ,\\ l&=(1-\mu^2)^{1/2}v-\mu\sigma\ .\end{aligned}\right\}\quad(4)$$

The u orbital is included in (3) explicitly because the calculation of Kotani[7] on simple hydride molecules, which treated the 1*s* electrons as point charges coinciding with the nuclei, led to negative binding energies, a result which is very unsatisfactory.

The only difference between the wave functions (3) and those of Stehn and King is that *s-p* hybridization is allowed in $\varPhi({}^1\Sigma^+)$ of (3) in order to get a good single determinant wave function.

The next step is to evaluate the expectation values of the Hamiltonian

$$\mathscr{H}=\sum_{i=1}^{6}\left(-\frac{1}{2}\varDelta-\frac{5}{r_{Bi}}-\frac{1}{r_H}\right)+\sum_{j>i}^{6}\frac{1}{r_{ij}}+\frac{1}{R_{BH}}\qquad(5)$$

with the use of the wave functions (3).

This is carried out for the ground state by three different methods in order to compare their usefulness. The first method is to enumerate all the permutations which make contributions to the expectation values. Although there is only one non-orthogonal orbital h, we have to consider 50 such permutations of 17 different types, so it is not easy to list all the necessary permutations. The second one is to make use of the orthogonalized orbit h' instead of h. h' is defined as

$$h'=\frac{1}{\sqrt{1-S_u^2-S_l^2-S_b^2}}[h-S_u u-S_l l-S_b b]\,,$$

where S_u, S_l, S_b are the overlap integrals between h and u, l, b, respectively.

Then we see

$$\begin{aligned}\varPhi({}^1\Sigma^+)&=|u\bar{u}\,l\,\bar{l}[bh]|\\&=|u\bar{u}\,l\,\bar{l}[bh']|+\sqrt{2}S_b|u\bar{u}\,l\,\bar{l}\,b\bar{b}|\\&=A+\sqrt{2}S_b B\end{aligned}$$

and

$$\begin{aligned}H({}^1\Sigma^+)&=\int\varPhi({}^1\Sigma^+)^*\mathscr{H}\varPhi({}^1\Sigma^+)d\tau\\&=H_{AA}+2\sqrt{2}S_b H_{AB}+2S_b^2H_{BB}\ .\end{aligned}$$

H_{AA}, H_{AB}, H_{BB} can be expressed in terms of molecular integrals more easily because they contain the orthogonal orbits only. The molecular integrals which involve h' can be decomposed into the normal ones; for example

$$\begin{aligned}(bh'|h'b)=(1-S_u^2-S_l^2-S_b^2)^{-1}\{&(bh|hb)\\&+S_u^2(bu|ub)+S_l^2(bl|lb)+S_b^2(bb|bb)\\&-2S_u(bh|ub)-2S_l(bh|lb)-2S_b(bh|bb)\\&+2S_uS_l(bu|lb)+2S_uS_b(bu|bb)\\&+2S_lS_b(bl|bb)\}\ .\end{aligned}$$

Here $(ab|cd)$ is the electron repulsion integral:

$$(ab|cd)=\int a^*(1)b(1)\frac{1}{r_{12}}c^*(2)d(2)dv_1dv_2\ .$$

The second method is compared favourably with the first one because of its simplicity but is still rather cumbersome, since it is necessary to calculate the molecular integrals involving b and/or l for various values of the parameter μ.

In order to avoid this difficulty, the third method was devised. We can transform and decompose the wave functions as follows:

$$\begin{aligned}\varPhi({}^1\Sigma^+)&=\sqrt{1-\mu^2}\,|u\bar{u}v\bar{v}[\sigma h]|+\mu|u\bar{u}\sigma\bar{\sigma}[vh]|\\&=\sqrt{1-\mu^2}\,\varPhi_\alpha+\mu\varPhi_\beta\ ,\\ \varPhi_\alpha&=|u\bar{u}v\bar{v}[\sigma h_0]|+\sqrt{2}S_\sigma|u\bar{u}v\bar{v}\sigma\bar{\sigma}|\\&=\varPhi_a+\sqrt{2}S_\sigma\varPhi_b\ ,\\ \varPhi_\beta&=|u\bar{u}\sigma\bar{\sigma}[vh_0]|+\sqrt{2}S_v|u\bar{u}\sigma\bar{\sigma}v\bar{v}|\\&=\varPhi_c+\sqrt{2}S_v\varPhi_b\ ,\\ H({}^1\Sigma^+)&=(1-\mu^2)H_{\alpha\alpha}+2\mu\sqrt{1-\mu^2}\,H_{\alpha\beta}\\&\quad+\mu^2H_{\rho\beta}\ ,\\ H_{\alpha\alpha}&=H_{aa}+2\sqrt{2}S_\sigma H_{ab}+2S_\sigma^2H_{bb}\ ,\\ H_{\beta\beta}&=H_{cc}+2\sqrt{2}S_vH_{bc}+2S_v^2H_{bb}\ ,\end{aligned}$$

$$H_{\alpha\beta}=H_{ac}+\sqrt{2}\,S_\sigma H_{bc}+\sqrt{2}\,S_v H_{ab}+2S_\sigma S_v H_{bb}\ ,$$

where

$$h_0=\frac{1}{\sqrt{1-S_u{}^2-S_v{}^2-S_\sigma{}^2}}\,[h-S_u u-S_v v-S_\sigma \sigma]\ . \qquad (6)$$

After some manipulation H_{aa}, H_{ab}, H_{bb}, H_{cc}, H_{bc}, and H_{ac} can be expressed as linear combinations of molecular integrals which involve neither b nor l.

We have neglected the *s*-*p* hybridization in the wave functions $\Phi(^3\Pi)$, $\Phi(^1\Pi)$, and $\Phi(^3\Sigma^+)$, so that the energies of these states can be calculated most easily by the second method.

All molecular integrals are evaluated exactly by means of the method developed by Roothaan, Ruedenberg and Jauzemis[8-10]. Details of the computation and the values of integrals are given in Appendix I.

The electronic energy of the $^1\Sigma^+$ state for various values of the hybridization parameter μ is given in Table I and illustrated in Fig. 1. We can see that the effect of *s*-*p* hybridization is rather small. In fact, even for the optimum value of μ^2 (0.060), the energy gain compared with the case of a pure $p\sigma$ bond is only 0.485 ev.

In Table II, the calculated binding and excitation energies are compared with those of the semiempirical theory and experiment[11]. The order of levels is in agreement between two calculations but quantitatively they show very poor agreement. For the $^1\Pi$ state, the semiempirical value is correct undoubtedly, but there are no detinite grounds for trusting the value predicted by the semiempirical theory for the $^3\Pi$ and $^3\Sigma^+$ states. On the other hand, for the nonempirical calculation, a question arises about whether the choice of the wave functions (3) is at all suitable or not. Therefore we try to find another wave functions which seem to have lower energies. The following wave functions are possibilities, since they preserve the σ-h bond although one $2s$ electron is promoted to the $2p\pi$ state:

$$\Phi(^3\Pi)'=|u\bar{u}v\pi\,[\sigma h]|\ ,$$
$$\Phi(^1\Pi)'=|u\bar{u}\,[v\pi]\,[\sigma h]|\ . \qquad (7)$$

The calculation of the energies with the use of these functions is straightforward but again somewhat tedious and details are not given here*.

We find the new $^3\Pi$ and $^1\Pi$ levels to be 2.93 ev and 8.35 eV above the $^1\Sigma^+$ state respectively. Thus the new $^3\Pi$ level is lower than the old one, while the new $^1\Pi$ is higher. If we adhere to the single configuration theory, we had better choose the new wave function to represent the $^3\Pi$ state, and Stehn and King's theory loses ground at least for the $^3\Pi$ state.

Table I. Electronic energy of the $^1\Sigma^+$ state of BH (in eV).

μ^2	E	μ^2	E	μ^2	E
0.0	−681.5569	0.3	−681.5015	0.7	−679.7612
0.060	−682.0419	0.4	−681.1566	0.8	−679.0713
0.1	−682.0108	0.5	−680.7621	0.9	−678.0819
0.2	−681.7962	0.6	−680.3058	1.0	−675.0661

Table II. Binding and excitation energies of BH.

states	nonempirical[a]	semiempirical[b]	obs.[c]
$^3\Sigma^+$	11.47	4.46	—
$^1\Pi$	5.78	2.85	2.86
$^3\Pi$	5.13	1.61	–
$^1\Sigma^+$	(0.00)	(0.00)	(0.00)
D_e	1.94	3.59	<3.66

a. The result of the single configuration calculation.
b. See reference 1.
c. See reference 11.

---

* All the results obtained in this section can also be obtained by transforming the energy matrices of the next section into the non-orthogonal basis.

The results of the present nonempirical calculation are very unsatisfactory as there are still marked discrepancies between the theory and experiment in the $^1\Sigma^+-{}^1\Pi$ energy interval and in the dissociation energy.

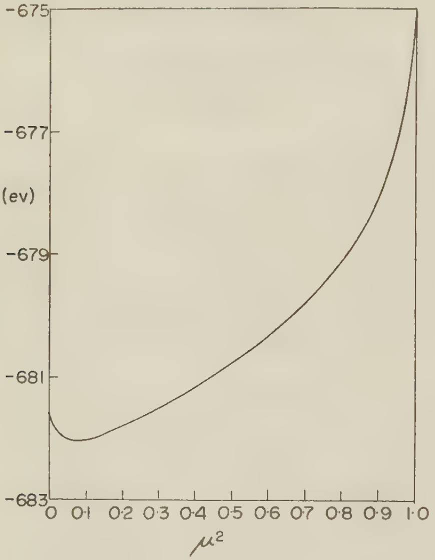

Fig. 1. Electronic energy of the $^1\Sigma^+$ state of the BH molecule.

If we want to improve on these points, we have to make more precise calculation and take account of configuration interaction. In the next section we digress from our primary aim of investigating the basis of the semiempirical single configuration theory and proceed to a many configuration calculation in order to get the most reliable result within the limits imposed by the available computational facilities*.

§ 3. Configuration Interaction Calculation

In this section, we take into account all the configurations in which two electrons are retained in the 1*s* orbital of the born atom. This limitation is imposed in order to reduce the number of configurations. However, from the results of the MO CI study of O_2[12] and the LCAO SCF study of N_2[13] and BH[14], we may suppose it has little influence on the final result.

Thus distributing 4 electrons among the 10 spin orbitals, $v\alpha$, $v\beta$, $\sigma\alpha$, $\sigma\beta$, $\pi_+\alpha$, $\pi_+\beta$, $\pi_-\alpha$, $\pi_-\beta$, (or sometimes $\pi_x\alpha$, $\pi_x\beta$, $\pi_y\alpha$, $\pi_y\beta$) $h\alpha$,

Table III. Basic functions*

		$^1\Sigma^+$			
1	$v\bar{v}\sigma\bar{\sigma}$	2	$v\bar{v}h\bar{h}$	3	$\sigma\bar{\sigma}h\bar{h}$
4	$v\bar{v}[\sigma h]$	5	$\sigma\bar{\sigma}[vh]$	6	$[v\sigma]h\bar{h}$
7	$v\bar{v}[\pi_+\pi_-]$	8	$\sigma\bar{\sigma}[\pi_+\pi_-]$	9	$h\bar{h}[\pi_+\pi_-]$
10	$[v\sigma][\pi_+\pi_-]$	11	$[vh][\pi_+\pi_-]$	12	$[\sigma h][\pi_+\pi_-]$
13	$\pi_+\bar{\pi}_+\pi_-\bar{\pi}_-$				
		$^3\Pi$			
1	$v\bar{v}\pi_x\sigma$	2	$v\bar{v}\pi_x h$	3	$\sigma\bar{\sigma}\pi_x v$
4	$\sigma\bar{\sigma}\pi_x h$	5	$h\bar{h}\pi_x v$	6	$h\bar{h}\pi_x\sigma$
7	$h\sigma[\pi_x v]$	8	$[h\sigma]\pi_x v$	9	$((h\sigma)(\pi_x v))$
10	$\pi_x\bar{\pi}_x\pi_y v$	11	$\pi_x\bar{\pi}_x\pi_y\sigma$	12	$\pi_x\bar{\pi}_x\pi_y h$
		$^1\Pi$			
1	$v\bar{v}[\pi_x h]$	2	$v\bar{v}[\pi_x\sigma]$	3	$\sigma\bar{\sigma}[\pi_x v]$
4	$\sigma\bar{\sigma}[\pi_x h]$	5	$h\bar{h}[\pi_x\sigma]$	6	$h\bar{h}[\pi_x v]$
7	$[h\sigma][\pi_x v]$	8	$[(h\sigma)(\pi_x v)]$	9	$\pi_x\bar{\pi}_x[\pi_y v]$
10	$\pi_x\bar{\pi}_x[\pi_y\sigma]$	11	$\pi_x\bar{\pi}_x[\pi_y h]$		
		$^3\Sigma^+$			
1	$v\bar{v}\sigma h$	2	$\sigma\bar{\sigma}vh$	3	$h\bar{h}v\sigma$
4	$v\sigma[\pi_+\pi_-]$	5	$vh[\pi_+\pi_-]$	6	$\sigma h[\pi_+\pi_-]$
		$^3\Sigma^-$			
1	$v\bar{v}\pi_+\pi_-$	2	$\sigma\bar{\sigma}\pi_+\pi_-$	3	$h\bar{h}\pi_+\pi_-$
4	$[v\sigma]\pi_+\pi_-$	5	$[vh]\pi_+\pi_-$	6	$[\sigma h]\pi_+\pi_-$
7	$((v\sigma)(\pi_+\pi_-))$	8	$((vh)(\pi_+\pi_-))$	9	$((\sigma h)(\pi_+\pi_-))$
		$^1\Delta$			
1	$v\bar{v}\pi_+\bar{\pi}_+$	2	$\sigma\bar{\sigma}\pi_+\bar{\pi}_+$	3	$h\bar{h}\pi_+\bar{\pi}_+$
4	$[v\sigma]\pi_+\bar{\pi}_+$	5	$[\sigma h]\pi_+\bar{\pi}_+$	6	$[vh]\pi_+\bar{\pi}_+$
		$^5\Sigma^-$			
1	$v\sigma\pi_+\pi_-$	2	$vh\pi_+\pi_-$	3	$\sigma h\pi_+\pi_-$
		$^3\Delta$			
1	$v\sigma\pi_+\bar{\pi}_+$	2	$vh\pi_+\bar{\pi}_+$	3	$\sigma h\pi_+\bar{\pi}_+$
		$^1\Sigma^-$			
1	$[(v\sigma)(\pi^+\pi^-)]$	2	$[(vh)(\pi_+\pi_-)]$	3	$[(\sigma h)(\pi_+\pi_-)]$
		$^5\Pi$			
1	$v\sigma\pi h$				

* Spins of two orbitals in square brackets and in parenthesis are coupled to form a singlet and a triplet respectively. Similarly $[(h\sigma)(\pi_x v)]$ (or $((h\sigma)(\pi_x v))$) means that a singlet (triplet) should be made from the two triplet $(h\sigma)$ and $(\pi_x v)$; actually in these cases we should use spin functions

$$\{\alpha\alpha\beta\beta-(\alpha\beta+\beta\alpha)(\alpha\beta+\beta\alpha)/2+\beta\beta\alpha\alpha\}/\sqrt{3}$$

for a singlet and

$$\{\alpha\alpha\alpha\beta+\alpha\alpha\beta\alpha-\alpha\beta\alpha\alpha-\beta\alpha\alpha\alpha\}/2$$

for a triplet.

---

* Actually all the calculations were made using desk machines.

$h\beta$, we obtain 13 $^1\Sigma^+$, 12 $^3\Pi$, 11 $^1\Pi$, 6 $\Delta^3\Sigma^+$ configurations and further 9 $^3\Sigma^-$, 6 $^1\Delta$, 3 $^5\Sigma^-$, 3 $^3\Delta$, 3 $^1\Sigma^-$ and 1 $^5\Pi$ configurations. Summing up the number of independent states, which is the number of configurations times their degeneracy, we get $210={}_{10}C_4$, thus we can see there is no other independent state. These wave functions are explicitly given in Table III. We use π_+ and π_- in Σ and Δ states and π_x and π_y in Π states. This choice makes the energy matrices a little simpler. Throughout this paper π without any suffix can be replaced by any one of π_+, π_-, π_x, and π_y.

In constructing the energy matrices, we make use of the orthogonalized orbital h_0 defined in § 2 (6), instead of h. We need not here transform or reduce the wave functions, all we need to do is replace the orbital h wherever it appears by the orbital h_0. This corresponds to the transformation from the non-orthogonal basic wave functions to the orthogonal ones and the eigenvalue E and the state function Ψ are invariant under such a transformation. If we denote the non-orthogonal and orthogonal basic wave functions by the row vector Φ and Φ_0, the following equations hold:

$$\left.\begin{aligned}(H_0-E)\Gamma_0=(H-EM)\Gamma=0\ ,\\ \Psi=\Phi_0\Gamma_0=\Phi\Gamma\ ,\\ \Gamma_0{}^\dagger\Gamma_0=l\ ,\quad \Gamma^\dagger M\Gamma=l\ ,\\ \Phi_0=\Phi T,\quad \Phi=\Phi_0 S\ ,\\ H=S^\dagger H_0 S\ ,\\ M=S^\dagger S\ .\end{aligned}\right\}\qquad(8)$$

By this replacement, we can make the CI calculation very much easier, in fact it seems to be almost impossible to set up many energy matrices by using non-orthogonal orbits. calculation of the matrix elements of the energy matrices H_0 are straightforward. The results are available in mimeographed form and will be sent on request to those interested in this problem.

Solving the secular equation of each symmetry by the iteration method, we can get its lowest eigenvalue and the corresponding eigenfunction.

The results will be discussed in § 5, together with those of the modified treatment which will be explained in the next section.

§ 4. Modified CI Calculation with an Intra-Atomic Correction

The importance of a correct estimate of intra-atomic energy in the molecular energy calculation was pointed out by Moffitt, who, has developed the method of atoms in molecules (AIM)$^{15)}$ from his experience of the calculation on the oxygen molecule. He recommended the use of the Hamiltonian

$$H(\mathrm{AIM})=H+\tfrac{1}{2}[M(W_e-W)+(W_e-W)M]\ ,\qquad(9)$$

where H and M are the usual energy and overlap matrix, W is an asymptotic form of H for large nuclear separations, and W_e is also a diagonal matrix formed from the energy of dissociation products in their valence states estimated by an appeal to the spectroscopic atomic term values.

For large nuclear separations, H tends to W and M tends to unity, and therefore H (AIM) tends to W_e. Thus use of the Hamiltonian (9) separates the whole energy into that of atoms and interactions between them and replaces the atomic energy W by the corresponding empirical value W_e: in effect, only the interactions are calculated from the usual wave function. Applying this method to the π-electron states of oxygen, ethylene, cyclobutadiene and benzene, Moffitt and Scanlan$^{15-16)}$ obtained much better agreement with experiment than in the case of the usual ASMO method. On the other hand, it must be noted that, in their application to the excitation energies of Li_2 and the ground state energy of H_2, Rahman$^{17)}$ and Hurley$^{18)}$ did not get reasonable results.

Recently Hurley$^{19)}$ and Arai$^{20)}$ criticized Moffitt's method and proposed the method of intra-atomic correlation correction and the method of deformed atoms in molecules respectively.

All these methods have a semiempirical character as they make use of the experimental term values. In an earlier paper, Itoh and the author$^{21)}$ proposed a modification of the nonempirical atomic orbital method, in which the use of different atomic orbitals for covalent and ionic structure of molecules is suggested in order to assess more correctly the energies of ionic structures. We applied this modified form to the lower excitation energies of $C_2H_4$$^{21)}$ and $O_2$$^{22)}$ with considerable success. In this section we try another modification within the scope of nonempirical calculation, namely the use of the Hamiltonian of the following form:

$$H(\text{modified})=H+\tfrac{1}{2}[M(W'-W)+(W-W)M], \tag{10}$$

where W' is a diagonal matrix formed from the energy of dissociation products in their valence states calculated with the use of different orbital exponents in atomic orbitals for polar and homopolar states. The purpose of using the Hamiltonian (10) is to replace the energy of the intra-atomic part by the more precise estimates W'. Thus applying this modification, we follow the general idea of Moffitt and are able to introduce it into the nonempirical theory.

In actual calculation, it is convenient to represent the Hamiltonian (10) in the orthogonal basis Φ_0;

$$H_0(\text{modified}) =H_0+\tfrac{1}{2}[S(W'-W)T+\{S(W'-W)T\}^{\dagger}]\,, \tag{11}$$

where $\{S(W'-W)T\}^{\dagger}$ is the Hermitian conjugate of $S(W'-W)T$. In calculating W', we use the same values of the orbital exponents for all states of a given atom with the same ionicity and determine these values from Slater rules. Accordingly, we take, for the BH molecule,

$$\delta^-=1.125, \quad \delta^+=1.475, \quad Z'^-=0.7,$$

while Z is considered to be unchanged.

Comparing this modification with our previous modified AO method, we may say the merits of the present modification are the simplicity of calculation and the circumvention of somewhat arbitrary approximations in calculating the complicated heteropolar integrals. On the other hand, the present modification has something dubious in its nature, because the calculated energy is not gained as an expectation value of the original Hamiltonian (5) with a given wave function. Therefore, the calculated energy may go below the true value in this treatment while this cannot occur with the previous method.

The present modification aims to assess properly the relative locations of covalent and ionic structures, but we can see from the result of the CI calculation that the state functions are essentially of covalent character for almost all levels of BH. Therefore we cannot expect a much improved result by this modification in BH. Nevertheless, we performed numerical calculations in order to see what it turns out to be. The necessary integrals are given in Appendix II and the resulting energy levels are illustrated in Figs. 2 and 3, with those of the preceding section. In Fig. 2, the zero of energy is shifted to −683.248 eV, which is the total energy of BH in its ground state calculated by the CI method. In Fig. 2 and Fig. 3 the energy of the lowest configuration of each symmetry is shown under the column (a).

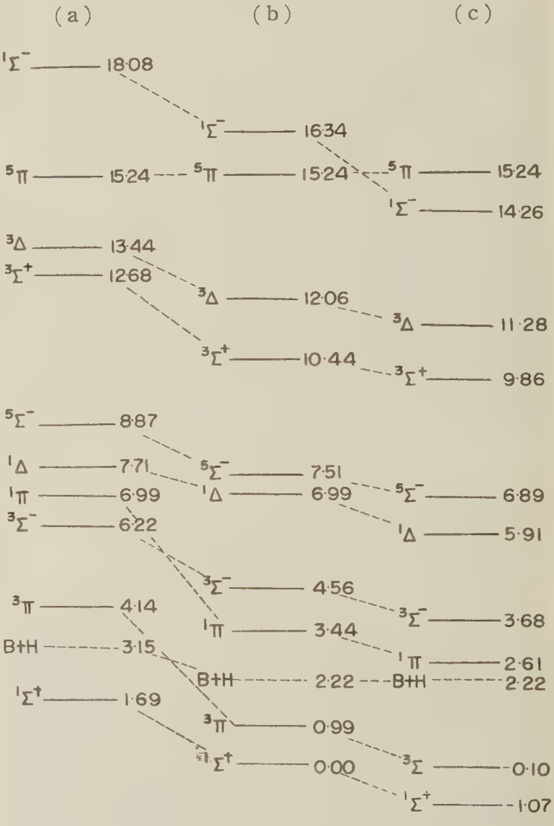

Fig. 2. Electronic energy levels of the BH molecule.

(a) The single configuration calculation.

(b) The CI calculation.

(c) The CI calculation with the intra-atomic correction.

In Table IV, the coefficients of the wave function for the lowest energy state of each symmetry are listed, both in the orthogonal and non-orthogonal representation without and with the intra-atomic correction.

Table IV. Coefficients of the lowest energy function of each symmetry

(a) The CI calculation in the orthogonal representation.

(b) The CI calculation in the non-orthogonal representation.

(c) The CI calculation with the intra-atomic correction in the orthogonal representation.

(d) The CI calculation with the intra-atomic correction in the non-orthogonal representation.

$^1\Sigma^+$

	(a)	(b)	(c)	(d)
1	0.77072	0.0624$\bar{5}$	0.77580	0.28400
2	0.08471	0.14100	0.16412	0.27316
3	−0.01297	−0.02298	0.02141	0.03793
4	0.56010	0.66053	0.52816	0.38111
5	0.11514	0.16549	0.08968	−0.03147
6	−0.03372	−0.06273	−0.10160	−0.18902
7	−0.07684	−0.01771	−0.08608	−0.05602
8	−0.16803	−0.02535	−0.17506	−0.07300
9	−0.01969	−0.04797	−0.05257	−0.12805
10	−0.11861	0.02890	−0.12283	−0.02534
11	−0.05983	−0.06334	−0.05686	0.01512
12	−0.13512	−0.1979$\bar{5}$	−0.11883	−0.10254
13	−0.00996	−0.00996	−0.01310	−0.01310

$^3\Pi$

	(a)	(b)	(c)	(d)
1	0.68317	0.05988	0.68348	0.26209
2	0.32877	0.36581	0.29936	0.20754
3	−0.49289	−0.03584	−0.50654	−0.20361
4	−0.08573	−0.10177	−0.07797	−0.00920
5	−0.05149	−0.10367	−0.15767	−0.31747
6	0.01137	0.02362	0.08718	0.18109
7	−0.04442	−0.04398	−0.03636	0.02093
8	−0.36790	−0.49673	−0.34839	−0.18535
9	−0.16493	−0.20622	−0.13498	−0.07774
10	−0.0027$\bar{5}$	0.01927	−0.01559	0.01616
11	−0.07127	−0.03414	−0.07519	−0.04572
12	−0.04556	−0.07110	−0.0361$\bar{5}$	−0.05642

$^1\Pi$

	(a)	(b)	(c)	(d)
1	0.4447$\bar{5}$	0.55843	0.38708	0.39607
2	0.76652	0.10422	0.78500	0.32379
3	−0.33311	−0.01172	−0.36411	−0.16777
4	−0.12007	−0.14676	−0.11120	−0.05478
5	0.01202	0.02497	0.08593	0.17849
6	−0.0135$\bar{5}$	−0.02728	−0.09116	−0.18356
7	−0.20259	−0.29575	−0.19151	−0.05446
8	0.17934	0.24442	0.14717	0.08039
9	−0.03803	0.02427	−0.03231	0.01754
10	−0.09626	−0.0384$\bar{5}$	−0.10350	−0.05724
11	−0.07093	−0.11070	−0.05675	−0.08858

$^3\Sigma^+$

	(a)	(b)	(c)	(d)
1	0.84342	0.75531	0.81647	0.63171
2	−0.26840	−0.18662	−0.3230$\bar{5}$	−0.15158
3	0.10032	0.15658	0.21036	0.32832
4	0.36058	0.03026	0.36163	0.08399
5	0.17061	0.22011	0.14499	0.18706
6	−0.21774	−0.28980	−0.18155	−0.24164

$^3\Sigma^-$

	(a)	(b)	(c)	(d)
1	0.62852	0.07487	0.64296	0.25712
2	0.11262	−0.01767	0.13209	0.076$\bar{5}$0
3	0.00891	0.02171	0.12204	0.29728
4	0.53531	0.07271	0.56432	0.26964
5	0.45125	0.78833	0.38642	0.4205$\bar{5}$
6	0.11817	0.18998	0.11757	−0.04070
7	−0.20686	−0.0425$\bar{5}$	−0.20442	−0.07608
8	−0.21251	−0.27416	−0.17497	−0.22574
9	−0.01014	−0.01350	−0.01627	−0.02166

$^1\Delta$

	(a)	(b)	(c)	(d)
1	0.66972	0.12252	0.68518	0.32373
2	0.13207	−0.02197	0.14644	0.07969
3	0.02141	0.0521$\bar{5}$	0.13540	0.32981
4	0.55346	0.07701	0.57584	0.28780
5	0.14597	0.21357	0.13594	−0.03545
6	0.45381	0.76512	0.37508	0.37053

$^5\Sigma^-$

	(a)	(b)	(c)	(d)
1	0.83461	0.32448	0.87256	0.43437
2	0.54580	0.70415	0.48617	0.62722
3	−0.07428	−0.09887	−0.04771	−0.06351

$^3\Delta$

	(a)	(b)	(c)	(d)
1	0.83041	0.28002	0.87944	0.42544
2	0.54359	0.70130	0.46895	0.60500
3	−0.12217	−0.16260	−0.08169	−0.10873

$^1\Sigma^-$

	(a)	(b)	(c)	(d)
1	0.81908	0.62937	0.86611	0.88412
2	0.51187	0.66038	0.35600	0.45929
3	0.25904	0.34478	0.35089	0.46702

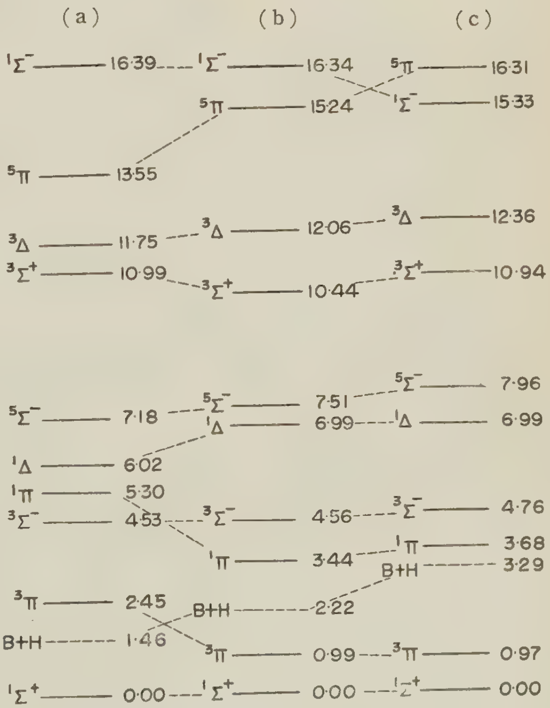

Fig. 3. Excitation energies of the BH molecule.

(a) The single configuration calculation.

(b) The CI calculation.

(c) The CI calculation with the intra-atomic correction.

§ 5. Discussion of Results

Carrying out nonempirical calculation based on the assignment of electron wave functions by Stehn and King, we found that assignment was not necessarily suitable. Therefore, we can say the basis of their semiempirical theory is open to question. In addition, the predicted value of the $^3\Sigma^+$ state by the theory seems to be too low, as is seen from the comparison with the results of these more detailed calculation.

From Table V, we see that by including configuration interaction the agreement with experiment is much improved as to the excitation energies but still rather unsatisfactory as to the dissociation energy and the $^1\Sigma^{+\prime}-{}^1\Pi$ separation. With the intra-atomic correction the calculated dissociation energy becomes very close to the observed value but the $^1\Sigma^{+\prime}-{}^1\Pi$ separation shows only a little improvement.

When the s–p hybridization is allowed, the single configuration calculation gave −682.042 eV as the total energy of the molecule, the figure already compares favourably with Sahni's LCAO SCF value −681.899 eV* and we get −683.248 eV by the CI calculation. On the other hand, the single configuration $(1s)^2(2s)^2(2p)$ P' of the boron atom gives -666.497 eV as its energy, while by the inclusion of the configuration $(1s)^2(2p)^3$ ^2P, the energy becomes −667.426 eV. Therefore, the calculated dissociation or binding energy increases only by 0.762 eV** when CI is applied consistently, i.e. to atom and molecule alike.

With the intra-atomic energy correction, the energy of the molecule goes down 1.075 eV further and the energy of the separated atoms remains unchanged, so that the resulting gain of dissociation energy, 1.075 eV, makes the agreement with experiment much better as was mentioned above.

Table V. Dissociation and excitation energies of the BH molecule (in eV)

	Calculated			Observed
	a	b	c	d
$^1\Pi-{}^1\Sigma^{+\prime}$	—	5.10	4.76	3.63
$^1\Sigma^+-{}^1\Pi$	5.30	3.44	3.68	2.86
$^3\Pi^--{}^3\Sigma^-$	2.08	3.57	3.79	3.35
De	1.46	2.22	3.29	<3.66
Total energy	−681.557	−683.248	−684.323	<-688.05

a. The single configuration calculation.
b. The CI calculation.
c. The CI calculation with the intra-atomic correction.
d. See reference 11. As for the total energy of the boron atom, see Atomic Energy Levels (the United State Department of Commerce, National Bureau of Standards, 1949) p 16.
e. $^1\Sigma^{+\prime}$ means the second lowest state among 13 $^1\Sigma^+$ eigenfunctions.

The electronic level scheme illustrated in Figs. 2 and 3 shows also there are marked differences between the results of the single configuration and the CI calculation, for example, the location of $^3\Pi$, the order of $^1\Pi$ and $^3\Sigma^-$ but small differences between those of CI and the modified CI except for the order of $^1\Sigma^-$ and $^5\Pi$. We can seen from Tables III and IV that the state function $^1\Sigma^-$ has a large contribution from ionic structure, while $^5\Pi$ is of purely covalent character, so that the reversal of the order of these two levels is not unreasonable.

Next we will try to interprete the coefficient of each state function given in Table IV. This is more easily done in the case of the non-orthogonal representation, because we can make use of our chemical intuition. Let us take the ground state $^1\Sigma^+$ for example. Configuration 4 was taken in the single configuration calculation (§ 2) and is the most important. Configuration 12 is the only one which interacts with 4 in the atomic problem and the coefficient of which is the second largest. The coefficient of 5 is the third largest and this represents the degree of *s–p* hybridization whose amount is about the same as was found in § 2. The coefficient of 2 is the fourth largest and represents the contribution of the ionic structure B $(1s)^2(2s)^2$+H $(1s)^2$. Comparing the coefficients in the column (b) and (d) in Table IV, however, we can see clearly that the coefficient in the non-orthogonal representation are very unstable with respect to the intra-atomic correction. Judging from the change of (a) and (c), we know that the difference of the direction of the vector Ψ in Hilbert space is not so large, but it looks large in the non-orthogonal representation, because the basis vectors are not mutually orthogonal. Another point in favour of the orthogonal representation is that the simple relation $\Gamma_0{}^*\Gamma_0=\sum_i c_i{}^2=1$ holds in this representation and this makes the importance of each configuration very clear.

---

* This is slightly different from the original value given in reference 14, as the conversion factor from the atmic unit to eV used in this paper is not the same as one used by Sahni.

** Relative to the $vv\,[\sigma h]$ ground state. This increase is 0.277 eV relative to the single configuration with hybridization.

Calculated dissociation energies of some simple molecules are given in Table VI, from which we can see evidence of a very difficult situation arising in this type of nonempirical molecular calculation: the dissociation energy is the difference between two large figures, and the errors of our calculation are of the same order as the binding energy. Consequently the much more refined treatments do not necessarily show greatly improved results.

Table VI. Dissociation energy of some simple molecules (in eV)

Method / Molecule	S.S.[a] AO	S.S.[a] MO	LCAO SCF MO	CI[b] AO	CI[b] AO	CI[b] MO	CI[b] MO	obs.
H_2	2.87			2.90(2)		2.90(2)		4.72
LiH[c]		1.96						2.63
BH[d]	1.46	1.37	1.80	1.94(2)	2.22(13)			<3.66
CH[e]			2.27		2.51(8)			3.65
NH[f]			1.40					4.01
OH[g]			0.98	0.86(5)	1.03(10)	0.41(6)	1.25(16)	4.58
FH[h]				1.03(2)	1.96(6)			6.08
Li_2[i]	0.17	−0.19	0.11			0.20(3)	0.75(8)	1.14
N_2[j]			1.20					9.90
O_2[k]	−5.53	−1.37	0.80			0.80(2)	3.63(15)	5.08

a. S. S. means a single structure or single configuration calculation.
b. A number in parenthesis is the number of configuration considered.
c. See reference 5.
d. The results of the present calculation except the LCAO SCF value which is taken from reference 14 and the S. S. MO value which is due to Mr. Kayama of our Laboratory.
e. J. Higuchi: J. Chem. Phys. **22** (1954) 1339.
f. J. Higuchi: J. Chem. Phys. **24** (1956) 535.
g. A. J. Freeman: Quarterly Progress Report, Solid State and Molecule Theory Group, M. I. T. July 15 (1956) p. 8.
h. D. Kastler: J. Chim. Phys. **50** (1953) 556.
i. M. Kotani, E. Ishiguro, Y. Mizuno and K. Kayama: To be published.
j. See reference 13.
k. See reference 12.

Acknowledgements

The author would like to express his hearty thanks to Dr. T. Itoh, with whom the work was originally begun and who kindly checked almost all the formulae used in this paper. He is very grateful to Prof. M. Kotani for his valuable discussions and continual encouragement throughout this work. He also wishes to thank members of Kotani Laboratory for their discussions and economical help, Prof. K. Kambe, Dr. R. McWeeny and Mr. J. Eve for reading the manuscript and

making valuable comments. He is indebted greatly to Mrs. H. Komuro and Miss K. Murata for their help in numerical calculations.

Appendix I. Evaluation of Moleculars Integral

The atomic orbital functions used in the calculation were given in § 2, (2). We take, for the sake of computational convenience, the following values for parameter ZR, δR, $Z'R$

$$ZR=10.95\ ,\quad \delta R=3.03\ ,$$
$$Z'R=2.33\ .$$

As all integrals are calculated at the equilibrium internuclear distance for the ground state:

$$R=1.2325\ \mathrm{A}$$
$$=2.329114785\ \mathrm{a.u.}^{11)}\ ,$$

the above choice of parameters means we choose the orbital exponents

$$Z=4.701356958\ ,$$
$$\delta=1.300923432\ ,$$
$$Z'=1.00038006\bar{5}\ .$$

One electron, one centre and Coulomb integrals are evaluated using the formulae of Roothaan[8], to seven decimal places.

Exchange integrals are calculated by the formulae, of Ruedenberg[9]. Taking 5 or 6 terms in the expansion, we can get the value accurate to six decimal places. The convergence is slow for the integrals containing the u orbital.

For the computation of hybrid integrals, we find Ruedenberg and others' formulae, especially those given in the unabridged paper in the Technical Report of the Chicago group, are very convenient. This type of integral is also calculated accurately to seven decimal places.

The numerical values obtain-

Table A1.

Numerical values of molecular integrals.

A. Overlap Integrals		$(\chi_a\|\chi_b)=\int\chi_a^*(1)\chi_b(1)dv_1$	
$(u\|h)=S_u=$	0.0769992060	$(u\|s)=S=$	0.2100630556
$(s\|h)=S_s=$	0.5647579843		
$(\sigma\|h)=S_\sigma=$	0.5207141127	$(v\|h)=S_v=$	0.5611027088
B. Kinetic Energy Integrals		$(\chi_a\|-(1/2)\Delta\|\chi_b)=-1/2\int\chi_a^*(1)\Delta_1\chi_b(1)dv_1$	
$(u\|-(1/2)\Delta\|u)=$	11.0513786	$(v\|-(1/2)\Delta\|v)=$	0.9571451
$(s\|-(1/2)\Delta\|s)=$	0.2820670	$(u\|-(1/2)\Delta\|v)=$	−2.7279251
$(\sigma\|-(1/2)\Delta\|\sigma)=$	0.8462009	$(v\|-(1/2)\Delta\|h)=$	0.0964887
$(h\|-(1/2)\Delta\|h)=$	0.5003801		
$(u\|-(1/2)\Delta\|s)=$	− 0.3455729	$(h_0\|-(1/2)\Delta\|h_0)=$	1.2999763
$(u\|-(1/2)\Delta\|h)=$	− 0.0025682	$(h_0\|-(1/2)\Delta\|v)=$	−0.3608524
$(s\|-(1/2)\Delta\|h)=$	0.0937964	$(h_0\|-(1/2)\Delta\|\sigma)=$	−0.3551954
$(\sigma\|-(1/2)\Delta\|h)=$	0.2137226		
C. Nuclear Attraction Integrals		$(\chi_a\|Z/r_a\|\chi_b)=Z\int\chi_a^*(1)\frac{1}{r_a}\chi_b(1)dv_1$ $(\chi_b\|Z/r_a\|\chi_b')=Z\int\chi_b^*(1)\frac{1}{r_a}\chi_b'(1)dv_1$	
$(u\|5/r_\mathrm{B}\|u)=$	23.5067848	$(u\|1/r_\mathrm{H}\|\sigma)=$	0.0148930
$(s\|5/r_\mathrm{B}\|s)=$	3.2523086	$(s\|1/r_\mathrm{H}\|\sigma)=$	0.1603522
$(h\|1/r_\mathrm{H}\|h)=$	1.0003801	$(v\|5/r_\mathrm{B}\|v)=$	3.5639812
$(u\|5/r_\mathrm{B}\|s)=$	2.1014289	$(v\|1/r_\mathrm{H}\|v)=$	0.4041857
$(u\|5/r_\mathrm{B}\|h)=$	0.9022706	$(u\|5/r_\mathrm{B}\|v)=$	−2.9012104
$(u\|1/r_\mathrm{H}\|h)=$	0.0359470	$(u\|1/r_\mathrm{H}\|v)=$	−0.0000034
$(s\|5/r_\mathrm{B}\|h)=$	1.5505170	$(v\|1/r_\mathrm{H}\|\sigma)=$	0.1608117
$(s\|1/r_\mathrm{H}\|h)=$	0.3762470	$(v\|5/r_\mathrm{B}\|h)=$	1.3920428
$(\sigma\|5/r_\mathrm{B}\|h)=$	1.2574748	$(v\|1r_\mathrm{H}\|h)=$	0.3771100
$(\sigma\|1/r_\mathrm{H}\|h)=$	0.4740974		
$(u\|1/r_\mathrm{H}\|u)=$	0.4293477	$(h_0\|5/r_\mathrm{B}\|h_0)=$	2.3548146
$(s\|1/r_\mathrm{H}\|s)=$	0.4052946	$(h_0\|1/r_\mathrm{H}\|h_0)=$	1.0664881
$(\sigma\|1/r_\mathrm{H}\|\sigma)=$	0.4881262	$(h_0\|5/r_\mathrm{B}\|v)=$	−0.6016179
$(\pi\|1/r_\mathrm{H}\|\pi)=$	0.3638788	$(h_0\|1/r_\mathrm{H}\|v)=$	0.1042290
$(h\|5/r_\mathrm{B}\|h)=$	2.0790660	$(h_0\|5/r_\mathrm{B}\|\sigma)=$	−0.6825832
$(u\|1/r_\mathrm{H}\|s)=$	0.0901868	$(h_0\|1/r_\mathrm{H}/\sigma)=$	0.2012217
D. Coulomb Repulsion Integrals		$(\chi_a\chi_a'\|1/r\|\chi_b\chi_b')=\iint\chi_a^*(1)\chi_a'(1)\frac{1}{r_{12}}\chi_b^*(2)\chi_b'(2)dv_1dv_2$	
$(uu\|uu)=$	2.9383481	$(hh\|\pi\pi)=$	0.3512022
$(ss\|ss)=$	0.4726011	$(vv\|vv)=$	0.4616330
$(\sigma\sigma\|\sigma\sigma)=$	0.5091896	$(vv\|\sigma\sigma)=$	0.4664713
$(uu\|ss)=$	0.6467778	$(v\sigma\|v\sigma)=$	0.1010426
$(uu\|us)=$	0.3726643	$(uu\|uv)=$	−0.2501556
$(us\|ss)=$	0.1315166	$(uu\|vv)=$	0.6484862
$(us\|us)=$	0.0606970	$(vv\|uv)=$	−0.0082943
$(u\sigma\|u\sigma)=$	0.0128751	$(v\sigma\|u\sigma)=$	0.0177863
$(s\sigma\|s\sigma)=$	0.1044578	$(\sigma\sigma\|uv)=$	−0.0044467
$(u\sigma\|s\sigma)=$	0.0200940	$(uv\|uv)=$	0.0353498
$(\pi\pi\|\sigma\sigma)=$	0.4543069	$(hh\|vv)=$	0.3700476
$(\sigma\pi\|\sigma\pi)=$	0.0274414	$(hh\|v\sigma)=$	0.1127653
$(\pi_+\pi_+\|\pi_-\pi_-)=$	0.4817482	$(hh\|uv)=$	−0.0006648
$(\pi_+\pi_-\|\pi_-\pi_+)=$	0.0548827		
$(hh\|hh)=$	0.6252375	$(uu\|h_0h_0)=$	0.4593193
$(hh\|uu)=$	0.4149220	$(vv\|h_0h_0)=$	0.3722729
$(hh\|us)=$	0.0865098	$(\sigma\sigma\|h_0h_0)=$	0.4126373
$(hh\|ss)=$	0.3717547	$(\pi\pi\|h_0h_0)=$	$0.355954\bar{5}$
$(hh\|u\sigma)=$	0.0120078	$(v\sigma\|h_0h_0)=$	0.0941898
$(hh\|s\sigma)=$	0.1127717	$(h_0h_0\|h_0h_0)=$	0.6374427
$(hh\|\sigma\sigma)=$	0.4128595		
E. Exchange Integrals		$(\chi_a\chi_b\|1/r\|\chi_a'\chi_b')=\iint\chi_a^*(1)\chi_b(1)\frac{1}{r_{12}}\chi_a'(2)\chi_b'^*(2)dv_1dv_2$	
$(hs\|hs)=$	0.156778	$(hv\|h\sigma)=$	0.161938
$(h\sigma\|h\sigma)=$	0.186273	$(hv\|hu)=$	0.022887
$(hs\|h\sigma)=$	0.162744		
$(hu\|hs)=$	0.024238	$(h_0u\|h_0u)=$	0.010628
$(hu\|h\sigma)=$	0.021039	$(h_0v\|h_0v)=$	0.028210
$(hu\|hu)=$	0.008859	$(h_0\sigma\|h_0\sigma)=$	0.056821
$(h\pi\|\pi h)=$	0.020577	$(h_0\pi\|\pi h_0)=$	0.013769
$(hv\|hv)=$	0.153772	$(h_0v\|h_0\sigma)=$	0.028899

ed are compared with the values of Sahni[14] who calculated almost all the integrals used here, except for those involving the π orbital, at the same R but took $Z=4.7$, $\delta=1.3$, $Z'=1$. The agreement is generally quite satisfactory but for the five hybrid integrals, $(u\sigma|uh)$, $(u\sigma|\sigma h)$, $(u\sigma|sh)$, $(s\sigma|uh)$ and $(\sigma\sigma|uh)$, we could not get reasonable agreement. These five are common in that they involve a factor $\sigma(1)h(2)$ and at least one u orbital. We therefore took as an example $(u\sigma|sh)$ and calculated this using Barnett and Coulson's formulae[23], getting a result identical with the previous value to 10 decimal places. It seems to us, therefore, that there may be a systematic error in Sahni's evaluation of this type of hybrid integral.

Our values are also compared with those, when available, interpolated from the table of Kotani and others[24], they coinside to three decimal places. Computed numerical values are given in Table AI.

F. Hybrid Integrals $(\chi_a\chi_a'|1/r|\chi_a''\chi_b)=\iint\chi_a^*(1)\chi_a'(1)\frac{1}{r_{12}}\chi_a''^*(2)\chi_b(2)dv_1dv_2$

$(uu|uh)=$ 0.1471641
$(uu|sh)=$ 0.3084578
$(uu|\sigma h)=$ 0.2511809
$(ss|uh)=$ 0.0482372
$(ss|sh)=$ 0.2434696
$(ss|\sigma h)=$ 0.2131519
$(us|uh)=$ 0.0228683
$(us|sh)=$ 0.0632581
$(us|\sigma h)=$ 0.0522363
$(u\sigma|uh)=$ 0.0014587
$(u\sigma|sh)=$ 0.0062973
$(u\sigma|\sigma h)=$ 0.0116057
$(s\sigma|uh)=$ 0.0028939
$(s\sigma|sh)=$ 0.0468917
$(s\sigma|\sigma h)=$ 0.0789777
$(\sigma\sigma|uh)=$ 0.0485759
$(\sigma\sigma|sh)=$ 0.2545193
$(\sigma\sigma|\sigma h)=$ 0.2351885
$(\pi\pi|uh)=$ 0.0480918
$(\pi\pi|sh)=$ 0.2379448
$(\pi\pi|\sigma h)=$ 0.2021336
$(u\pi|\pi h)=$ 0.0070253
$(s\pi|\pi h)=$ 0.0405827
$(\sigma\pi|\pi h)=$ 0.0094624
$(hh|hu)=$ 0.0338437
$(hh|hs)=$ 0.2871229
$(hh|h\sigma)=$ 0.3295737
$(uu|vh)=$ 0.2838780
$(vv|uh)=$ 0.0472065
$(vv|vh)=$ 0.2365059

$(vv|\sigma h)=$ 0.2116282
$(uv|uh)=-0.0082290$
$(uv|vh)=$ 0.0001595
$(uv|\sigma h)=-0.0005396$
$(u\sigma|vh)=$ 0.0061276
$(v\sigma|uh)=$ 0.0026465
$(v\sigma|vh)=$ 0.0471038
$(v\sigma|\sigma h)=$ 0.0782866
$(\sigma\sigma|vh)=$ 0.2498909
$(\pi\pi|vh)=$ 0.2330422
$(v\pi|\pi h)=$ 0.0399994
$(hh|hv)=$ 0.2864038

$(uu|vh_0)=-0.0950620$
$(uu|\sigma h_0)=-0.1340054$
$(vv|vh_0)=-0.0342490$
$(vv|\sigma h_0)=-0.0439496$
$(uv|uh_0)=-0.0137787$
$(u\sigma|uh_0)=-0.0082113$
$(v\sigma|vh_0)=-0.0086230$
$(v\sigma|\sigma h_0)=$ 0.0316548
$(\sigma\sigma|vh_0)=-0.0180098$
$(\sigma\sigma|\sigma h_0)=-0.0468890$
$(\pi\pi|vh_0)=-0.0443845$
$(\pi\pi|\sigma h_0)=-0.0538969$
$(v\pi|\pi h_0)=-0.0282793$
$(\sigma\pi|\pi h_0)=-0.0075556$
$(h_0h_0|vh_0)=$ 0.0323659
$(h_0h_0|\sigma h_0)=$ 0.0750103

Appendix II. Atomic Integrals for the Positive and Negative Ions of Boron

The orbital exponents

$$\delta^-=1.124890889$$

$$\delta^+=1.474809237$$

are used for the negative and positive ions of boron so as to make the parameters δ^-R and δ^+R round numbers for the equilibrium internuclear distance of the ground state:

$$\delta^-R=2.62\ ,\quad \delta^+R=3.435\ .$$

As we need only the integrals of atomic nature, the evaluation is very simple and the numerical values are given in Table AII,

where the one electron operator

$$F'=-\frac{1}{2}\Delta-\frac{5}{r_B}$$

is used.

Table AII. Numerical values of atomic integrals for boron ions

	Negative Ion δ^-	Positive Ion δ^+
$(u\|s)=S$	0.1645150489	0.256418397$\bar{5}$
$(s\|F'\|s)$	-2.6013306	-3.3245127
$(\sigma\|F'\|\sigma)$	-2.1795375	-2.5994920
$(u\|F'\|s)$	-1.9135351	-2.9914287
$(v\|F'\|v)$	-2.3730553	-2.7929858
$(u\|F'\|v)$	0.1374393	0.2093665
$(ss\|ss)$	0.4086518	0.5357705
$(\sigma\sigma\|\sigma\sigma)$	0.4402893	0.5772496
$(uu\|ss)$	0.5604025	0.7313569
$(uu\|us)$	0.2850418	0.4652233
$(us\|ss)$	0.0899347	0.1801453
$(us\|us)$	0.0361370	0.0930612
$(u\sigma\|u\sigma)$	0.0076654	0.0197403
$(s\sigma\|s\sigma)$	0.0903233	0.1184200
$(u\sigma\|s\sigma)$	0.0127550	0.0291528
$(\pi_+\pi_+\|\pi_-\pi_-)$	0.4165612	0.5461403
$(\sigma\sigma\|\pi\pi)$	0.3928330	0.5150310
$(\pi_+\pi_-\|\pi_-\pi_+)$	0.0474563	0.0622185
$(\sigma\pi\|\pi\sigma)$	0.0237282	0.0311093
$(vv\|vv)$	0.4022725	0.5189812
$(vv\|\sigma\sigma)$	0.4051946	0.5260611
$(v\sigma\|v\sigma)$	0.0887356	0.1121406
$(uu\|uv)$	-0.2011008	-0.2981930
$(uu\|vv)$	0.5613348	0.7342479
$(vv\|uv)$	-0.0042612	-0.0142709
$(v\sigma\|u\sigma)$	0.0116527	0.0249243
$(\sigma\sigma\|uv)$	-0.0022912	-0.0076436
$(uv\|uv)$	0.0224852	0.0510304

References

1) J. R. Stehn: J. Chem. Phys. **5** (1937) 186.
2 G. W. King: J. Chem. Phys. **6** (1938) 378.
3) W. J. Carr, Jr.: Phys. Rev. **92** (1953) 28.
4) E. R. Cohen, J. W. M. DuMond, T. W. Layton and J. S. Rollett: Rev. Mod. Phys. **27** (1955) 363.
5) I. Fisher: Arkiv für Fysik **5** (1952) 349.
6) A. Tubis: Phys. Rev. **102** (1956) 1049.
7) M. Kotani: Private communication.
8) C. C. J. Roothaan: J. Chem. Phys. **19** (1951) 1445.
9) K. Ruedenberg: J. Chem. Phys. **19** (1951) 1459.
10) K. Ruedenberg, C. C. J. Roothaan and W. Jauzemis: J. Chem. Phys. **24** (1956) 201; see also the Technical Report of the Laboratory of Molecular Structure and Spectra, The University of Chicago, (1952–1953) Part Two.
11) G. Herzberg, Spectra of Diatomic Molecules (D. Van Nostrand Company, Inc., New York 1945) p. 510.
12) M. Kotani, E. Ishiguro, Y. Mizuno and K. Kayama: J. Phys. Soc. of Japan **12** (1957) 707.
13) C. W. Scherr: J. Chem. Phys. **23** (1955) 569.
14) R. C. Sahni: J. Chem. Phys. **25** (1956) 332.
15) W. Moffitt: Proc. Roy. Soc. (London) **A 210** (1951) 224; **A210** (1951) 245.
16) W. Moffitt and J. Scanlan: Proc. Roy. Soc. (London) **A 218** (1953) 464; **A 220** (1953) 530.
17) A. Rahman: Physica **20** (1954) 623.
18) A. C. Hurley: Proc. Phys. Soc. **A 68** (1955) 149.
19) A. C. Hurley: Proc. Phys. Soc. **A 69** (1956) 49; **A 69** (1956) 301.
20) T. Arai: J. Chem. Phys. **26** (1957) 435.
21) K. Ohno and T. Itoh: J. Chem. Phys. **23** (1955) 1468.
22) T. Itoh and K. Ohno: J. Chem. Phys. **25** (1956) 1098.
23) M. P. Barnett and C. A. Coulson: Phil. Trans. Roy. Soc. (London) **243** (1951) 221.
24) M. Kotani, A. Amemiya, E. Ishiguro and T. Kimura: Tables of Molecular Integrals (Maruzen Co. Ltd., Tokyo 1955).

JOURNAL OF THE PHYSICAL SOCIETY OF JAPAN Vol. 12, No. 8, AUGUST, 1957

On Some Transition Phenomena in Aqueous Solution of Polyvinylalcohol

By Teruko SOEYA and Ryusuke KŌNO

Department of Applied Physics, Defence Academy

(Received April 6, 1957)

In order to obtain an information about the configurational state of molecule in an aqueous solution of P.V.A., the measurements of the specific volume, the ultrasonic velocity and the dielectric constant were carried out over a certain range of the concentration and the temperature, and the experimental result was discussed from a view point of transition phenomena.

The result seems to show that in a region of concentration higher than a certain critical value (C_m) the configurational state of molecule in the solution is similar to that in solid P.V.A. plasticized by a solvent type plasticizer possessing no transition point, while in the region of concentration lower than C_m, only above a certain critical temperature T_β, a model of spherical coiled molecule is applicable. The heat of cross-linking estimated experimentally by making use of Eldridge and Ferry's formula with respect to an apparent melting temperature of gel is about 12 k.cal./mol.

§1. Introduction

At present, it is allowed to consider that[1] the configurational states of long chain polymer molecules in the solution take two different types depending on the concentration of high polymer, that is to say: in a very dilute solution, each molecule coils independently and behaves as if a small isolated particle in a suspension, while in the case of relatively large concentration, the molecules form a loose irregular network structure by random cross-linking of each other. On the other hand, these configurational shapes of molecules are also affected by temperature changes. Accordingly, the changes in the configurational state of molecules will probably be detected in the concentration and temperature dependences of various physical properties of the solution through the changes of segmental motion.

From such a view point, the measurements of the specific volume, the ultrasonic velocity and the dielectric constant of the solution were carried out over a certain range of the concentration and the temperature.

The results of the experiment are regarded to show that if the concentration is higher than a certain critical value (C_m), in the solution there also takes place the change of segmental motion similar to the one which occurs at the second order transition point of solid P.V.A. plasticized by a solvent type plasticizer and there exist not only the critical concentration (C_m) but also the critical temperature (T_β) to the validity of the model of suspending coiled molecules. That is to say: if temperature is lower than T_β, even in the case of concentration lower than C_m, the weak inter-molecular cross-linkings exist between the segments belonging to different molecules, and the solution rather takes a network structure. Furthermore, in this paper, heat of cross-linking was estimated experimentally.

§ 2. Method of Experiment

The density of the solution was measured by a pycnometer. For the measurement of the ultrasonic velocity, the method of acoustic interferometer of Hubbard type[2)] was used. The frequency of the ultrasonic waves was 1000 k.c./sec. The measurement of the dielectric constant was carried out by means of the exchange method using a quartz oscillator. The used specimens were the aqueous solutions of P.V.A. (the average value of the degree of polymerization was about 4550).

§ 3. Experimental Results

(1) *Specific volume*

The specific volume (v) obtained from the density measurements of the solution is plotted against temperature as shown in Fig. 1. These curves have a look of the typical volume-temperature curve which is obtained in the experiment for the second order transition phenomena of high polymers in solid state. Each curve consists of two straight line portions connected by a curved part. Now, if we denote the temperature corresponding to the point of intersection of two straight lines by T_v, T_v increases linearly with the concentration of P.V.A. as shown in Fig. 2.

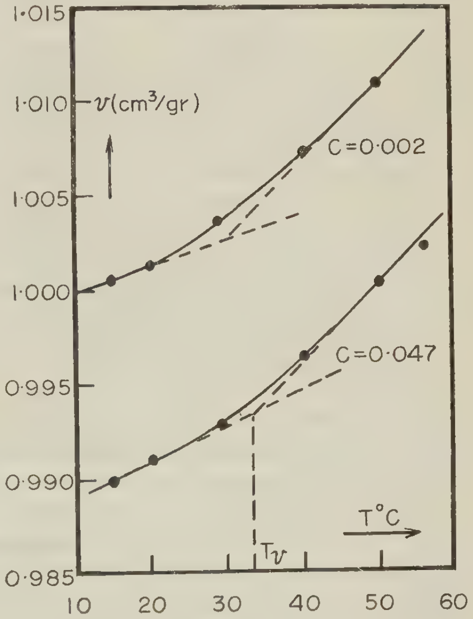

Fig. 1. Typical relations between specific volume and temperature.

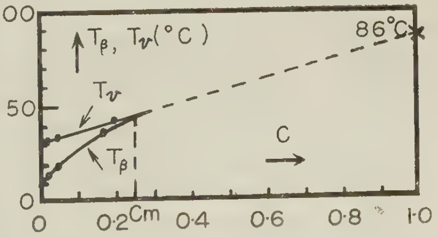

Fig. 2. Concentration dependence of T_β and T_v.

(2) *Ultrasonic velocity*

In Fig. 3, the ultrasonic velocity (V) and the adiabatic compressibility (β), which is obtained from $V=\sqrt{1/\rho\beta}$ using the experimental data of V and ρ (density), are plotted as the functions of temperature. As it will be seen from Fig. 3, there appears a certain anomalous range of temperature where the variation of V or β for temperature is especially distinguished. Now, let us denote the temperature at the middle point of the above anomalous range by T_β. In that case, as shown in Fig. 2, T_β depends upon the concentration of P.V.A. and the curve of $(T_\beta - C)$ relation coincides with the line of $(T_v - C)$ at the concentration about $C=0.25$.

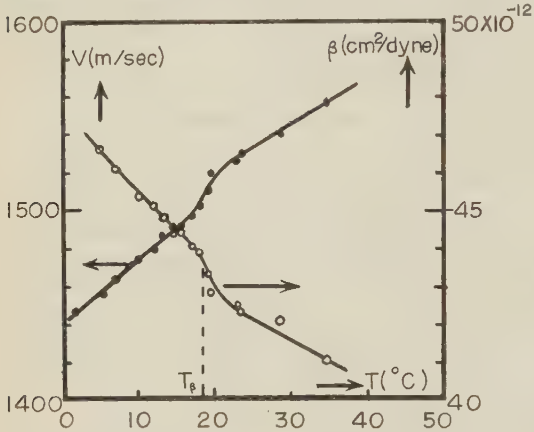

Fig. 3. Temperature dependence of ultrasonic velocity and adiabatic compressibility.

(3) *Dielectric constant*

The relations between the dielectric constant (ε) and temperature are shown in Fig. 4 and Fig. 5. Each curve in Fig. 4 has an obvious flexion point at a certain temperature. Now if we denote the temperature corresponding to the flexion point by T_ε, $T_\varepsilon = T_\beta$ is approximately satisfied. As shown in Fig. 5, however, the flexion point becomes indistinct with decreasing of frequency and seems to disappear almost entirely in the case of frequency 364 k.c./sec.

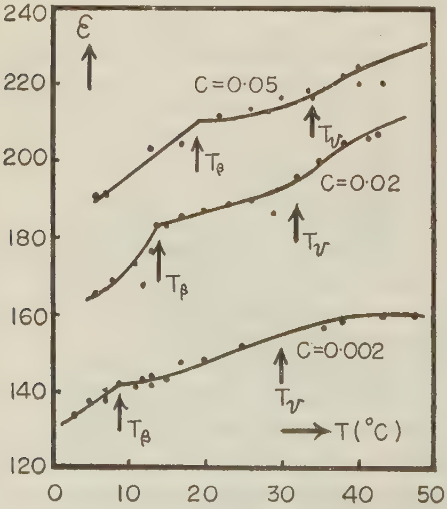

Fig. 4. Temperature dependence of dielectric constant. Frequency=1000 *k.c./sec.*

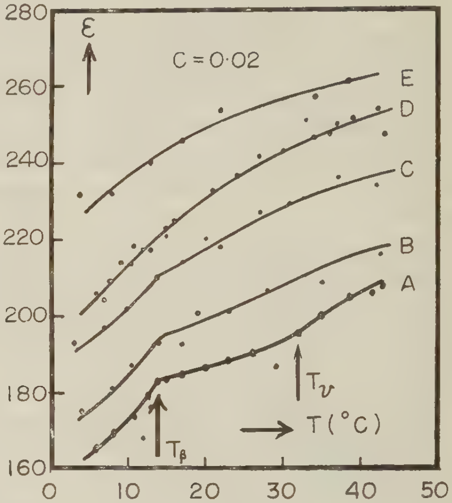

Fig. 5. Temperature dependence of dielectric constant. Concentration of P.V.A.=0.02. Curve A (1000 *k.c./sec*), B (700 *k.c./sec*), C (600 *k.c./sce*), D (364 *k.c./sec*), E (150 *k.c./sec*).

§4. Discussion of Results

As already described, T_β and T_v depend upon the concentration. Now, if the experimental curves $(T_\beta - C)$ and $(T_v - C)$ are extended to $C=1$, they coincide with each other at about $C=0.25$ and intersect the ordinate of $C=1$ at $T_\beta = T_v = 86°\text{C}$. This roughly extrapolated value $(T_\beta = T_v = 86°\text{C})$ is considered to be fairly close to the second order transition temperature[3] of pure solid P.V.A. (=85°C). This fact seems to suggest that the phenomena characterized by T_β or T_v may probably be caused by the molecular process which is similar to that of ordinary second order transition of solid P.V.A.

On the other hand, as it has been already known, the second order transition temperature of high polymer is much affected by the addition of the plasticizer and especially, if the solvent type plasticizer possessing no transition point is added, the second order transition temperature becomes lower. Accordingly, it seems to be reasonable to consider that in our solution water probably plays the same role as the solvent type plasticizer.

Next, in Fig. 1, we write as follows;

$$\Delta\gamma = \left(\frac{\Delta v}{\Delta T}\right)_{T>T_v} - \left(\frac{\Delta v}{\Delta T}\right)_{T<T_v} .$$

Then, the value of $\Delta\gamma$ obtained in this experiment is shown by solid curve in Fig. 6.

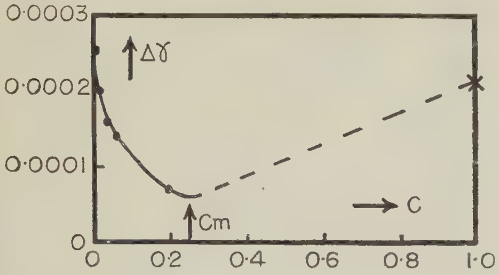

Fig. 6. Relation between $\Delta\gamma$ and concentration. Solid curve: experimental.

So far as concerns the concentration used in this experiment, $\Delta\gamma$ decreases with increasing concentration of P.V.A.. The value of $\Delta\gamma$ for the pure solid P.V.A., however, is in the neighbourhood of 0.0002. Consequently, it is natural to consider that the solid curve in Fig. 6 will rise for further increasing of C through a minimum point and approach to the corresponding value of solid P.V.A. at $C=1$ (dotted line in Fig. 6). In regard to this problem, it has been already found experimentally that[4] $\Delta\gamma$ for the molecular mixture of high polymer and solvent type plasticizer possessing no transition point approaches zero linearly with the amount of plasticizer added. On the other hand, our experimental result shows that, in the case of concentration lower than C_m $(=0.25)$, two anomalous points (T_β and T_v) are observed but in the case of concentration higher than C_m, one anomalous point only observed ($T_\beta=T_v$). These facts seem to support a presumption that in the region of concentration higher than C_m the aqueous solution of P.V.A. has a structure, as it were, of the molecular mixture of long chain polymer and solvent type plasticizer possessing no transition point. In consequence, the change of segmental motion at T_v $(=T_\beta)$ would probably be the same kind with that of the second order transition of solid P.V.A. plasticized by solvent type plasticizer.

In the next place, we describe with phenomena in the region of concentration lower than C_m $(=0.25)$. In this case, it is expected that the changes of segmental motion at T_β and T_v will be reflected sensitively in the dielectric properties of the solution because P.V.A. is polar polymer. Actually, the curves of $(\varepsilon-T)$ relation indicate the anomalies at T_β and T_v as shown in Figs. 4 and 5. In this case, if we make a presumption that even in the case of concentration lower than C_m if $T<T_\beta$, the solution has a network structure (i.e., so-called gel structure), we can interpret the result shown in Figs. 4 and 5 as follows. If temperature rises and approaches to T_β, the liberations of inter-molecular cross-linkings between the segments belonging to different polymer molecules would begin to take place and at the temperature T_β almost all inter-molecular cross-linkings would be liberated. As the result of this liberation each molecule would coil up independently to be regarded as a small spherical particle. This coiling up of molecules would bring on an increase of the number of intra-molecular cross-linkings and as a matter of course, the segmental motion would rather be suppressed to some extent. That is to say: as the result of the change in the configurational state of molecules at T_g $(=T_\beta)$, the activation energy for the segmental rotation would increase, and this means the increase of a relaxation time for the segmental rotation.

In regard to this problem, it was experimentally confirmed that while there is a distinct flexion point in the case of frequency $=1000$ k.c./sec, the flexion point becomes gradually indistinct with decreasing of frequency and disappears almost entirely in the case of frequency $=364$ k.c./sec. This experimental fact seems to allow to estimate the relaxation time (τ) for the segmental rotation as follows; i.e., in the region $T_\beta<T<T_v$, τ is in the neighbourhood of 2×10^{-6} sec, while in the region $T<T_\beta$, $\tau<10^{6}$ sec. Furthermore, if temperature rises beyond T_v, then in each coiled molecule, the liberation of the intra-molecular cross-linkings would take place and the hindered rotation of segments would again become active. This would cause the relatively rapid increase of ε at about T_v.

On the other hand, with respect to the relation between the apparent melting temperature of gel and the concentration, the following formula has been derived theoretically by Eldridge and Ferry[5]

$$\log C=\frac{\Delta H}{RT_m}+\text{constant}$$

where ΔH is heat of cross-linking. Making use of our experimental data, $\log_{10}C$ was plotted against $1/2.303RT_\beta$ as shown in Fig. 7

and from the linear part of the relation ΔH was estimated. The obtained value of ΔH is about 12 k.cal./mol. This value of ΔH is roughly close to the value obtained by Kawai[6] and co-workers. This fact is considered to support our previous presumption that even $C < C_m$, if $T < T_\beta$, the solution takes the network structure (gel structure).

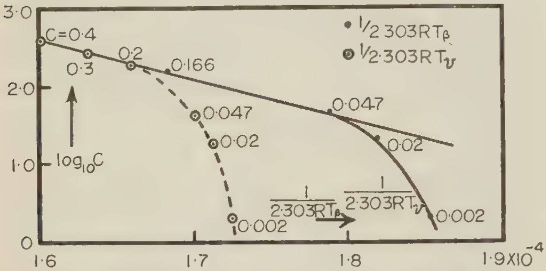

Fig. 7. Relation between $\log_{10} C$ and $1/2.303\,RT_\beta$ or $1/2.303\,RT_v$.

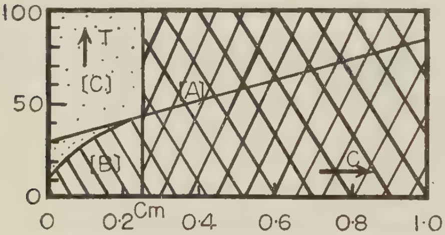

Fig. 8. Diagram illustrating the configurational state of molecules in aqueous solution of P.V.A.

Finally, we can summarize briefly the consequences of this experiment as follows.

(*1*) A diagram with respect to the configurational state of molecules in the aqueous solution of P.V.A. is obtained as shown in Fig. 8. In this temperature-concentration diagram, [*A*] represents the domain where the solution takes the irregular network structure which will be similar to that of solid P.V.A. plasticized by the solvent type plasticizer possessing no transition point, [***B***] represents the domain of network structure (i.e., so-called thermal recovery gel) and [*C*] represents the domain where the model of spherical coiled molecule is applicable.

(*2*) In the domain [*A*], for temperature variation, the change of molecular motion takes place only once at T_v $(=T_\beta)$. This is considered to take place in like manner with the second order transition of solid P.V.A. plasticized by the solvent type plasticizer possessing no transition point. On the contrary, in the region of concentration $C < C_m$, the changes of molecular motion occur twice at T_β and T_v. The one at T_β would be ascribed to the separation of inter-molecular cross-linkings and T_β is considered to represent the melting temperature of gel, while the another at T_v would be related with the separation of intra-molecular cross-linkings in the coiled molecules. This molecular process in each coiled molecule would also occur in like manner with the second order transition.

(*3*) Eldridge and Ferry's formula on the apparent melting temperature of gel is approximately satisfied in the range of concentration from $C=0.047$ to $C=0.4$. The obtained value of ΔH is about 12 k.cal./mol.

In conclusion, we wish to express our sincere thanks to Prof. Y. Ikeda for his continuous encouragement throughout this work.

References

1) P. J. Flory: J. Chem. Phys. **13** (1945) 453.
2) J. C. Hubbard and A. L. Loomis: Phys. Rev. **31** (1928) 295; Phil. Mag. **5** (1928) 1177.
3) H. Mark and A. V. Tobolsky: *Physical Chemistry of High Polymeric Systems* (1950) 347.
4) R. F. Boyer and R. S. Spencer: J. App. Phys. **15** (1944) 398.
5) J. E. Eldridge and J. D. Ferry: J. Phys. Chem. **58** (1954) 992.
6) Presented by Kawai, Maeda and Kashiwagi at the Tokyo annual meeting of the Society of Polymer Science of Japan June 1955.

JOURNAL OF THE PHYSICAL SOCIETY OF JAPAN Vol. 12, No. 8, AUGUST, 1957

On the Magnetic Aging of Commercial Pure Iron

By Mitsuru ASANUMA
Department of Physics, Faculty of Science, University of Hokkaido
and Shinji OGAWA
Research Institute of Applied Electricity, University of Hokkaido

(Received April 10, 1957)

The origin of magnetic aging in commercial pure iron is clarified by means of magnetic initial susceptibility and internal friction. It is due to very small amounts of carbon and nitrogen in iron, and the effect of nitrogen is more remarkable than that of carbon and it is dominant especially in the period of formation of intermediate nitride. Some possiblities that the different effect of nitrogen and carbon can be interpreted are suggested.

§ 1. Introduction

It has been known that the magnetic initial susceptibility of commercial pure iron decreases remarkably on tempering in the vicinity of 130°C, but the origin has not yet been clarified.

In the past Y. Shimizu[1] explained that small amounts of sulphur in iron was responsible for the decrease. According to him, sulphur has little solubility to iron, and forms the inclusion of iron-sulphide, therefore, when iron is heated up to about 130°C, the lattice parameter in C axis of FeS varies and this might cause the decrease of magnetic initial susceptibility. Moreover he concluded that this decrease was hindered by quenching.

However his explanation is unsuitable, because the transformation of lattice parameter in FeS is of the second kind, and is not generally hindered by quenching. In his experiment, he added FeS to pure iron and measured the thermal expansion and magnetic initial susceptibility in each step of rising the temperature to 130°C. But his experiment does not provide a direct proof about its origin, because it may be natural that the specimen which contains much FeS than commercial pure iron shows the decrease of magnetic initial susceptibility, and it does not provide any proof on the assertion that in pure iron FeS is main cause of the decrease of the susceptibility.

Then one must study in the new view point about this problem. The commercial pure iron contains always very small amounts of carbon and nitrogen in interstitial position of iron crystal. The precipitation of carbon and nitrogen from solid solution is accompanied by change in many physical properties. The effects of the precipitation of carbon and nitrogen in α-iron on physical properties, for example, elastic after effect, magnetic after effect, etc. were investigated by Snoek[2]. The change in coercive force during aging was also measured by Köster[3] in order to investigate the kinetics of precipitation. The same measurement was also made by Wert[4]. The structure sensitive magnetic properties, for example, the coercive force and the initial susceptibility may depend on the particle size or the shape of precipitates. The investigation along this problem was partly investigated by Néel[5].

In order to discuss the decrease of magnetic initial susceptibility or coercive force of these alloys during aging, the knowledge of the structure of the produced precipitates is necessary. Dijkstra[6] has demonstrated that the aging of N_2 in α-iron takes place by two stage process: metastable precipitation are first formed, then they dissolve and reprecipitate as Fe_4N. Jack[7] has shown the metastable precipitates to be $Fe_{16}N_2$.

In the investigation of the precipitation of carbon and nitrogen from solid solution, Wert[8] has pointed out that the volume of precipitates is proportional to $t^{3/2}$, $t^{5/2}$ and $t^{1/2}$, where t is aging time, for sphere-, diske- and cylinder-like shape, respectively. He also showed that the intermediate phase $Fe_{16}N_2$ is of the disk-like shape and Fe_3C is of the sphere-like shape.

The effect of the carbide or the nitride itself on the magnetic aging, however, has not yet been investigated in detail.

In the present paper the origin of the aging of magnetic, initial susceptibility will be clarified and the difference of the effect on aging between nitride and carbide will be discussed.

§ 2. Experimental Details

The iron which was supplied by Research Institute of the Mitsubishi Minning Co. Ltd. was used as specimen. The amounts of carbon and nitrogen in solid solution was determined by the measurement of internal friction and sulphur contents of specimen was determined by chemical analysis. The apparatus for measuring the internal friction was well known torsion pendulum, and the frequency used was about 1.0 c.p.s. The background damping Q^{-1} of the pendulum was 0.001. The strain on the surface of specimen at maximum deflection was 4×10^{-5}. The size of specimen was 1.0 mm in diameter and 300 mm in length. The magnetic initial susceptibility was measured by balistic galvanometer.

In order to separate the effect of carbon and nitrogen on the magnetic aging, the specimens were first purified by heating in a wet hydrogen atmosphere at 720°C for several hours and then carbon or nitrogen was separately dissolved into the specimens.

The carbon was dissolved into the purified specimens by heating at appropriate temperature in the mixing gases of carbon dioxide and monoxide, and nitrogen was added to the specimens by heating in the mixture of hydrogen and ammonia gases.

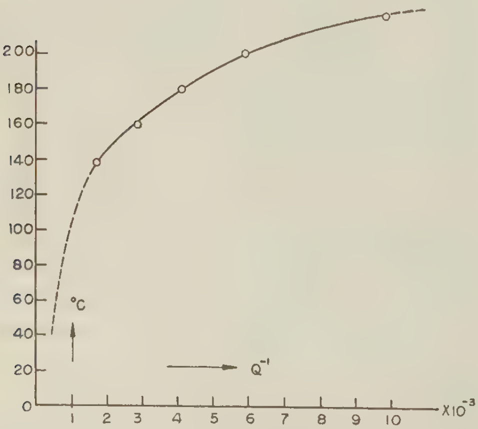

Fig. 1. The phase diagram of *Fe–N* system.

The phase diagram of Fe-N system was determined in our specimens by internal friction, although this had been investigated by Dijkstra[9] and Paranjpe[10]. This result was shown in Fig. 1.

§ 3. Experimental Results and Discussions

The specimens of the commercial pure iron which contain the amount of nitrogen corresponding to $Q^{-1}=0.0037$, less carbon and 0.003 wt % sulphur were annealed at 950°C for an hour and cooled down in the furnace to 750°C and then quenched in water. Thereafter the magnetic initial susceptibilities were measured for these specimens at every 10°C from 80°C to 200°C in the course of tempering. These results were shown in Figs. 2 and 3.

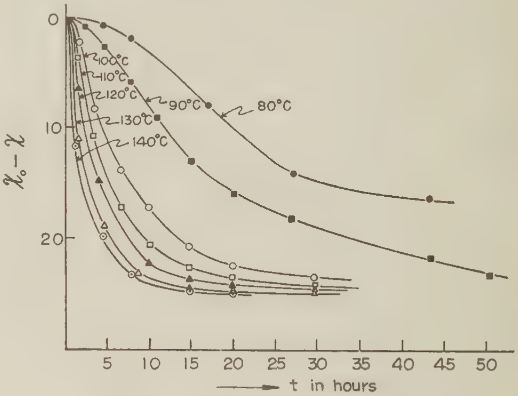

Fig. 2. The decrease of magnetic initial susceptibility *vs* tempering time.

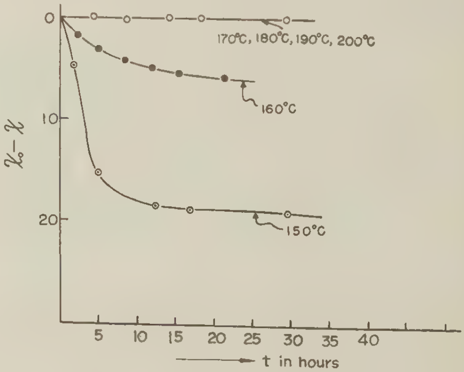

Fig. 3. The decrease of magnetic initial susceptibility *vs* tempering time.

The effect of the tempering on the magnetic initial susceptibility was most remarkable at 140°C, while it was not found above 170°C. In the specimen which was annealed in a wet hydrogen atmosphere to remove the impurities, the decrease of magnetic initial susceptibility was not observed during the tempering at 140°C where the magnetic aging would be the most effective. Fig. 4 (a) shows this result.

The specimen before and after hydrogen treatment contains 0.003 wt % and 0.002 wt % sulphur, respectively, which shows that the sulphur contents of this specimen was hardly changed. These facts mean that the small amounts of sulphur are not responsible for the decrease of magnetic initial susceptibility. Therefore, the interstitial impurities such as carbon and nitrogen is considered to be the possible origin.

In Fig. 1, the temperature corresponding the value $Q^{-1}=0.0037$ is about 170°C, and it seems that the interstitial impurity, nitrogen does not precipitate from the matrix above this temperature. On the basis of this fact, together with the facts that are showed in Figs. 2 and 3, it may be concluded that the magnetic aging of commercial pure iron is accompanied by the precipitation of carbide and nitride from solid solution, or segregation of carbon and nitrogen.

In order to investigate the effect of carbon separately, the initial susceptibilities of carbrized specimen was measured in the course of aging treatment at 140°C. This result is shown in Fig. 4 (b), where carbon contents correspond to $Q^{-1}=0.0022$. Fig. 4 (c) shows the result of nitride specimen, where nitrogen contents correspond to $Q^{-1}=0.0060$.

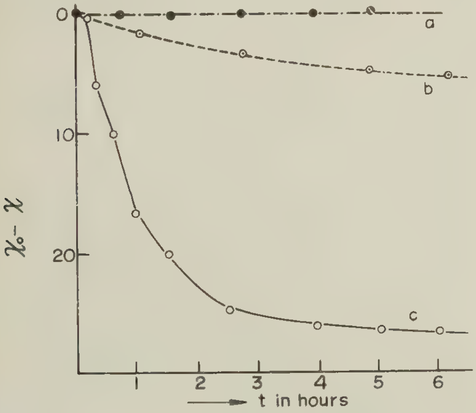

Fig. 4. The decrease of magnetic initial susceptibility *vs* tempering time.
a: the specimen after hydrogen treatment
b: the specimen to which was added the carbon after hydrogen treatment
c: the specimen to which was added the nitrogen after hydrogen treatment
Aging temperatures are 140°C.

According to Pitch and Lücke[11], carbon contents corresponding to $Q^{-1}=0.0033$ is about 0.005 wt % and according to Åstrom and Borelius[12] the Q^{-1} value of damping by nitrogen in α-iron is nearly equal to the contents of nitrogen in α-iron in weight per cent, in the region of small amounts of nitrogen. Therefore, in our both specimens carbon contents and nitrogen contents are considered to be 0.005 wt % and 0.006 wt % respectively. In Fig. 4, it is shown that the magnetic againg of nitrided specimen is more remarkable than that of carbrized specimen, although they have nearly the same amount of impurity. In other word, the effect of nitrogen on magnetic aging is more remarkable than that of carbon.

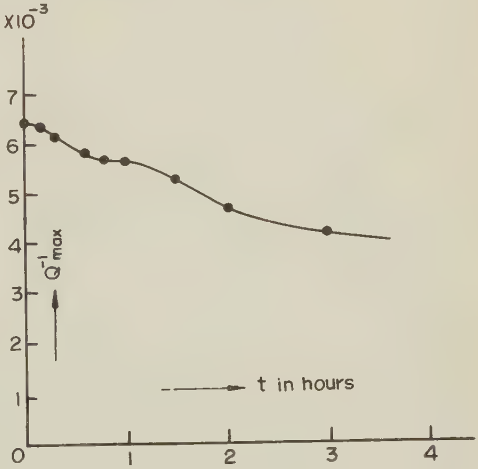

Fig. 5. International friction during precipitation of nitrogen at 140°C.

On the other hand, the aging of nitrided specimen was investigated at 140°C by means of internal friction method as shown in Fig. 5. It is noticed that the precipitation from supersaturated solid solution takes place according to different successive process. This result agrees with that of Dijkstra[6]. Fig. 6 is the curve of transformed fraction vs. growth time obtained from Fig. 5. The transformed fraction q is represented in terms of Q^{-1} as follows:

$$q=(Q_0^{-1}-Q^{-1})/(Q_0^{-1}-Q_f^{-1}),$$

where Q_0^{-1} and Q_f^{-1} are initial and final values of Q^{-1}, respectively and Q^{-1} corresponds to the cocentration of the solute at any time. The power of t, n, is determined according the equation[13]

$$q=1-\exp[-kt^n]$$

by the slope of the curve in Fig. 6. Thus the value of n obtained is 2.4 in the first stage and 1.1 in the second stage. If there is some stage before first stage, the value of n in it would be about 2/3, which means a formation of Cottrell atmospheres[14] in dislocations, though it is not quite accurate because of the difficulty of the measurement.

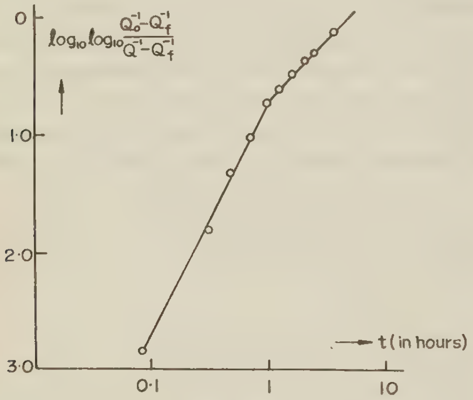

Fig. 6. $\log_{10}\log_{10}\frac{Q_0^{-1}-Q_f^{-1}}{Q^{-1}-Q_f^{-1}}$ vs log t curve. The nitrogen contents of the specimen is 0.0060%. From the slope of this curve n is determined. The aging time is 140°C.

Considering the aging of the magnetic initial susceptibility of the specimen which containg the same amount of nitrogen as that used for internal friction measurement, the following conclusions are obtained by comparing Figs. 4 (c) and 6. The process of precipitation which is proportional to t have completely accomplished during an hour after the aging treatment at 140°C, while in the same period, the decrease of the magnetic initial susceptibility was about three-fifth of total change. So that it would be concluded that the precipitation of the intermediate phase $Fe_{16}N_2$ is rather dominantly responsible for the decrease of magnetic initial susceptibility and Fe_4N more or less have also an influence on it. Moreover, even if the stage of $n=2/3$ takes place in present precipitation process, which corresponds to from 0 to about 5 minutes, the decrease of magnetic initial susceptibility would be insensitive in this stage.

It is not yet satisfactory clarified why the effect of nitrogen on the magnetic aging is more remarkable than that of carbon, but there are a few possibilities for the interpretation of this problem. That is (a) the difference of the shape between the precipitates of carbide and nitride, (b) the difference of the solubility limit of nitrogen and carbon in α-iron, and (c) the difference of the saturation magnetization of these.

§ 4. Conclussion

The magnetic aging in the commercial pure iron is due to very small amounts of carbon and nitrogen, and the effet of nitrogen is more remarkable than that of carbon. Though the reason of different effect of nitrogen and carbon is not clear, some possibilities are considered for these phenomenon, that is, the difference of the shape, the saturation magnetization of carbide and nitride and the difference of the solubility limit of carbon and nitrogen in α-iron.

Acknowledgements

The authors wish to express their thanks to Professor S. Miyahara for valuable advice during the course of present work. They also wish to acknowledge their indebtedness to Dr. E. Watanabe in the Research Institute of the Mitsubishi Minning Co. Ltd. for supply of the specimen. A part of the expenses of this research has been defrayed from the Scientific Research Expenditure of the Educational Ministry.

References

1) Y. Shimizu: Jour. Japan. Inst. Met. **5** (1941) 175 (in Japanese).
2) J. L. Snoek: Physica **8** (1941) 745.
3) W. Köster: Archiv. f. Eisenhütt. **2** (1928–9) 503 **3** (1930) 553, **3** (1930) 145, **4** (1930) 289.
4) C. Wert: Act. Metal. **2** (1954) 361.
5) L. Néel: Cahiers Phys. **25** (1944) 21.
6) L. Dijkstra: Trans. AIME **185** (1949) 252.
7) K. Jack: Act. Cryst. **3** (1950) 392.
8) C. Wert: J. Appl. Phys. **20** (1949) 943.
9) L. Dijkstra: J. Metals **1** (1949) 252.
10) V. Paranjpe, M. Cohen, M. Biever, C. Floe: Trans. AIME **183** (1950) 261.
11) W. Pitch and K. Lücke: Zeits. f. Physik **139** (1954) 413.
12) U. Åstrom and G. Borelius: Acta Metall. **2** (1954) 547.
13) H. K. Hardy and T. J. Heal: Prog. in Metal Phys. **5** (1954) 143.
14) Cottrell and Bilby: Proc. Phys. Soc. **A62** (1949) 49.

JOURNAL OF THE PHYSICAL SOCIETY OF JAPAN Vol. 12, No. 8, AUGUST, 1957

Application of the Thin-Wing-Expansion Method to the Compressible Flow past Profiles of Arbitrary Shape

By Humio NARUSE

Department of Physics, Faculty of Science,
Tokyo Metropolitan University

(Received May 10, 1957)

The formulae for the velocity distribution over the surface of an obstacle of arbitrary shape are given to the transonic third approximation by the use of Imai's thin-wing-expansion method. These formulae are applied to the flow past an elliptic cylinder and it has been found that the results are in accord with the other authors's results within the order of the approximation used. Further, these formulae, together with the Ψ- and the $\Phi\Psi$-procedures, are applied to the flow past Tomotika-Tamada's profiles. Calculated velocity distributions are compared with Tomotika-Tamada's exact solutions as well as with Takami's numerical results obtained by various approximate methods.

These formulae seem to be very useful, because their convergency and accuracy are very good up to considerably high Mach numbers.

§ 1. Introduction

A great many investigations have been made so far about the thin-wing-expansion method by which the compressible flow past a two-dimensional thin aerofoil can be treated successfully. Namely, Kaplan has calculated the flow past a cusped symmetrical aerofoil which is called the Kaplan bump[1)], a circular arc aerofoil[2)] and an elliptic cylinder[3)], taking account of the effects of their thickness or camber up to the third order.

On the other hand, more than ten years ago Imai established independently his thin-wing-expansion method, by which he gave the analytical expressions for the velocity and the pressure distributions, the lift and the moment of an aerofoil placed in the flow of a compressible fluid up to the second approximation[4)], and investigated in detail the characteristics of general Joukowski profiles[5)]. By that method, we can easily calculate the influences of an obstacle on the flow, even when its shape cannot be given in an analytical form. Later, Imai and Ōyama have given the formulae for the third approximation.[6)]

On the basis of these formulae, several examples have been treated up to the third approximation: the flow along a sinusoidal wall by Imai and Ōyama[7)], the flow past an elliptic cylinder by Hasimoto[8)], the flow past a Kaplan bump by Matunobu[9)], and the flow past a symmetrical circular arc aerofoil by Asaka in a somewhat modified and extended form[10)].

Recently, as an extension of von Kármán's transonic similarity rule, Imai developed a method called transonic thin-wing-expansion method[11)]. Matunobu has applied it to the compressible flow past a Kaplan bump and has calculated the velocity distribution over the profile up to the fourth approximation[12)].

In this paper, the formulae for the velocity distribution over the surface, which are convenient for both the analytical and the numerical calculations for an obstacle of arbitrary shape, have been given to the transonic third approximation by the use of Imai's method. These formulae are applied to the flow past an elliptic cylinder as an example of the analytical calculations and also to the flows past Tomotika-Tamada's profiles[13)], for which the exact solutions are known, as examples of the numerical calculations. The calculated velocity distributions are compared with Tomotika-Tamada's exact solutions as well as with Takami's numerical results obtained by various approximate methods[14)], in order to investigate the limitation of the validity of the thin-wing-expansion method. Further, the Ψ- and the $\Phi\Psi$-procedures associated with the thin-wing-expansion method are applied to the flow past these profiles.

§ 2. Basic Formulae of the Thin-Wing-Expansion Method

For the sake of convenience, a brief account of Imai's thin-wing-expansion method for a symmetrical profile will be given here.

The two-dimensional irrotational flow of a compressible fluid which obeys the adiabatic law is governed by the equations:

$$u=\frac{\partial \Phi}{\partial x}=\frac{\rho_\infty}{\rho}\frac{\partial \Psi}{\partial y}, \qquad v=\frac{\partial \Phi}{\partial y}=-\frac{\rho_\infty}{\rho}\frac{\partial \Psi}{\partial x}, \tag{2.1}$$

$$\frac{\rho}{\rho_\infty}=\left[1-\frac{\gamma-1}{2}M^2\left(\frac{q^2}{U^2}-1\right)\right]^{1/(\gamma-1)}, \tag{2.2}$$

where (u, v) are the component velocities in the x- and the y- directions respectively, q the magnitude of the velocity, ρ the density, ρ_∞ that of the undisturbed fluid, Φ the velocity potential, Ψ the stream function, U and M the magnitude of the velocity and the Mach number of the undisturbed flow respectively, and γ is the ratio of the specific heats.

Then the undisturbed flow will be given as

$$\Phi=x, \quad \Psi=y.$$

On the assumption of the small disturbance, Φ and Ψ can be expanded as follows:

$$\begin{aligned}\Phi&=x+\phi_1+\phi_2+\phi_3+\cdots,\\ \Psi&=y+\psi_1+\psi_2+\psi_3+\cdots,\end{aligned} \tag{2.3}$$

where ϕ_1, ψ_1; ϕ_2, ψ_2; ϕ_2, ψ_3; $\cdots$ are quantities of the order $t, t^2, t^3, \cdots$ respectixely ,t being a small parameter representing the thickness-ratio of the profile. Substituting from (2.2) and (2.3) into (2.1) and comparing terms of the same powers of t, we obtain a set of differential equations for ϕ_m and ψ_m $(m=1, 2, \cdots)$ suitable for the iterative method.

Here let us introduce the following quantities:

$$\xi=x, \quad \eta=\mu y, \quad \psi_m=\mu\chi_m, \quad \mu=\sqrt{1-M^2}, \tag{2.4}$$

$$\zeta=\xi+i\eta, \quad \overline{\zeta}=\xi-i\eta; \quad G_n=\phi_n+i\chi_n, \tag{2.5}$$

and transform the differential equations for ϕ_m and ψ_m in terms of complex quantities.

As the solutions of the transformed differential equations, we have the following expressions for G_1 and G_2:

$$G_1(\zeta)=f(\zeta), \tag{2.6}$$

$$G_2(\zeta, \overline{\zeta})=H_2(\zeta, \overline{\zeta})+g_2(\zeta), \tag{2.7}$$

$$H_2(\zeta, \zeta)=\frac{M^2}{4}\left[\lambda f'^2\overline{\zeta}+(1+\lambda)\{2f'\overline{f}+\int\overline{f}'^2d\overline{\zeta}\}\right]. \tag{2.8}$$

If we neglect those terms smaller than $O(t^3/\mu^5)$, as in Imai's transonic thin-wing-expansion method[11)], we have the following expression for G_3:

$$G_3(\zeta, \overline{\zeta})=H_3(\zeta, \overline{\zeta})+g_3(\zeta), \tag{2.9}$$

$$\begin{aligned}H_3(\zeta, \overline{\zeta})=\left\{\frac{M^2}{4}(1+\lambda)\right\}^2\Big\{&12f'^2\overline{f}+4ff'\overline{f'}+2f''\overline{f}^2+2f\overline{f'^2}+14f'\int\overline{f}'^2d\overline{\zeta}\\ &+\frac{16}{3}\int\overline{f}'^3d\overline{\zeta}+2f'g_2(\zeta)+2g_2'(\zeta)\overline{f}+2\int\overline{f}'\,\overline{g_2'(\zeta)}\,d\overline{\zeta}\Big\}+g_3(\zeta),\end{aligned} \tag{2.10}$$

where $f(\zeta)$, $g_2(\zeta)$ and $g_3(\zeta)$ are analytic functions of ζ, which must be determined by the boundary conditions, and $\overline{f}$ and f' are the complex conjugate and the derivative with respect to ζ of f respectively and $\lambda=(\gamma+1)M^2/4(1-M^2)$.

§ 3. Boundary Conditions

The region outside profile: $(\xi_p, \eta_p)=(x_p, \mu y_p)$ in the ζ-plane may be mapped conformally onto the region outside the unit circle: $Z=e^{i\theta}$ in fhe Z-plane by means of an analytic function of the form:

$$\zeta=C_{-1}Z+C_0+C_1/Z+\cdots, \quad |Z|>1. \tag{3.1}$$

The boundary conditions by which f, g_2 and g_3 are to be determined are as follows:

(i) $\partial G_m/\partial\zeta$ is one-valued and continuous throughout the flow field,

(ii) as $\zeta\to\infty$, $\partial G_m/\partial\zeta\to 0$, and

(iii) on the surface of the profile, $\mathfrak{J}(\zeta/\mu^2+G)=0$, where $\mathfrak{J}$ means "the imaginary part of". This condition is equivalent to the statement that $\Psi=0$ on the surface.

Then, it can easily be shown that $f=-(1/\mu^2)(\zeta-C_0-C_1Z-\overline{C}_{-1}/Z)$ satisfies the conditions (i), (ii) and (iii), and that dg_n/dZ is regular and one-valued for $|Z|>1$ and tends to 0 as $Z\to\infty$, if we consider the above-mentioned conditions and the behaviour of

$\partial H_n/\partial Z$ as $Z\to\infty$. Since the flow is symmetrical, the circulation is absent, and f and g_n may be expanded in the form:

$$\frac{b_1}{Z}+\frac{b_2}{Z^2}+\cdots . \tag{3.2}$$

Hereafter, let us confine ourselves to the boundary of the profiles where G_n, H_n and g_n may be decomposed as

$$G_n(e^{i\theta}, e^{-i\theta})=\phi_n(\theta)+i\chi_n(\theta)\ , \tag{3.3}$$

$$H_n(e^{i\theta}, e^{-i\theta})=P_n(\theta)+iQ_n(\theta)\ , \tag{3.4}$$

$$g_n(e^{i\theta})=R_n(\theta)+iI_n(\theta)\ . \tag{3.5}$$

Referring to the theory of the conjugate Fourier series and (3.2), we have

$$\phi_1(\theta)=\chi_1{}^*(\theta), \tag{3.6}$$

$$R_n(\theta)=I_n{}^*(\theta), \tag{3.7}$$

where asterisk denotes the conjugate Fourier series. Since $\chi_n(\theta)$ can be determined by taking account of the boundary condition (iii), $\phi_n(\theta)$ and $g_n(\theta)$ are determined as follows:

$$\phi_1(\theta)=\chi_1{}^*(\theta)\ , \tag{3.8}$$

$$\left.\begin{aligned} &\phi_n(\theta)=P_n(\theta)-Q_n{}^*(\theta)+\chi_n{}^*(\theta)\ , && (3.9)\\ &g_n(\theta)=\chi_n{}^*(\theta)+i\chi_n(\theta)\\ &\qquad-\{Q_n{}^*(\theta)+iQ_n(\theta)\}\ , && (3.10)\end{aligned}\right\} n\geqq 2\ .$$

§ 4. Approximate Boundary Conditions

An arbitrary aerofoil P can be parametrically represented by

$$x_p=\cos\vartheta\ ,\quad y_p=g(\vartheta)\ , \tag{4.1}$$

$\vartheta=0$, π corresponding to the leading and the trailing edges respectively.

The region outside the profile P′ in the ζ-plane may be mapped onto the region outside the unit circle in the Z-plane by an analytic function:

$$\zeta=\tfrac{1}{2}(Z+1/Z)+C(Z)\ , \tag{4.2}$$

where

$$C(Z)=C_{-1}Z+C_0+C_1/Z+\cdots\ ,\quad C_n=A_n+iB_n\ , \tag{4.3}$$

$C(Z)$ and hence C_n being $O(t)$.

Putting $C(e^{i\theta})=A(\theta)+iB(\theta)$, we have from (4.2)

$$\xi_p=\cos\theta+A(\theta)\ ,\quad \eta_p=B(\theta)\ . \tag{4.4}$$

Since the function: $C(Z)-C_{-1}Z-C_0$ is regular for $|Z|>1$ and tends to 0 as $Z\to\infty$, we have on the unit circle: $Z=e^{i\theta}$

$$A(\theta)=B^*(\theta)+2(A_{-1}\cos\theta-B_{-1}\sin\theta)+A_0\ , \tag{4.5}$$

taking account of the theory of the conjugate Fourier series. Further, from (2.4), (4.1) and (4.4), we have

$$A(\theta)=\cos\vartheta-\cos\theta=-\sin\theta(\vartheta-\theta)-\tfrac{1}{2}\cos\theta(\vartheta-\theta)^2+O(t^3)\ , \tag{4.6}$$

$$B(\theta)=\mu g(\vartheta)=\mu\{g(\theta)+g'(\theta)(\vartheta-\theta)+\tfrac{1}{2}g''(\theta)(\vartheta-\theta)^2\}+O(t^4)\ . \tag{4.7}$$

Considering that $A(0)=0$, $A(\pi)=0$ and $A'(0)=0$, $A(\theta)$, $B(\theta)$ and $(\vartheta-\theta)$ are determined from (4.5), (4.6) and (4.7) by the iterative method as follows:

$$A(\theta)=\mu h(\theta)+\mu k(\theta)+O(t^3)\ , \tag{4.8}$$

$$B(\theta)=\mu g(\theta)-\mu^2\frac{h(\theta)}{\sin\theta}g'(\theta)-\mu^2\left[\frac{g'(\theta)k(\theta)}{\sin\theta}+\frac{\mu}{2}\,\frac{h^2(\theta)}{\sin^2\theta}\left\{\cot\theta g'(\theta)-g''(\theta)\right\}\right]+O(t^4)\ , \tag{4.9}$$

$$\vartheta-\theta=-\frac{\mu}{\sin\theta}h(\theta)-\frac{\mu}{\sin\theta}\left\{k(\theta)+\frac{1}{2}\mu\,\frac{\cos\theta}{\sin^2\theta}h^2(\theta)\right\}+O(t^3)\ , \tag{4.10}$$

$$\cos\vartheta=\cos\theta+\mu h(\theta)+\mu k(\theta)+O(t^3)\ , \tag{4.11}$$

where

$$h(\theta)=g^*(\theta)-\tfrac{1}{2}\{g^*(0)-g^*(\pi)\}\cos\theta-g^{*\prime}(0)\sin\theta-\tfrac{1}{2}\{g^*(0)+g^*(\pi)\}\ , \tag{4.12}$$

$$k(\theta)=H^*(\theta)-\tfrac{1}{2}\{H^*(0)-H^*(\pi)\}\cos\theta-H^{*\prime}(0)\sin\theta-\tfrac{1}{2}\{H^*(0)+H^*(\pi)\}\ , \tag{4.13}$$

$$H(\theta)=-\mu\frac{h(\theta)}{\sin\theta}g'(\theta)\ . \tag{4.14}$$

§ 5. Velocity Potential

From (4.4), (4.9) and the boundary condition (iii) in § 3, $\chi_n(\theta)$ can be determind as follows:

$$\chi_1(\theta)=-g(\theta)/\mu\ , \tag{5.1}$$

$$\chi_2(\theta)=\frac{h(\theta)}{\sin\theta}g'(\theta)\ , \tag{5.2}$$

$$\chi_3(\theta)=\frac{g'(\theta)k(\theta)}{\sin\theta}+\frac{\mu}{2}\frac{h^2(\theta)}{\sin^2\theta}\{\cot\theta g'(\theta)-g''(\theta)\}\,. \tag{5.3}$$

Thus we have from (2.6), (3.3), (3.8) and (5.1) as the first approximation:

$$\phi_1(\theta)=-g^*(\theta)/\mu\,, \tag{5.4}$$

$$f(e^{i\theta})=f_0/\mu,\quad f_0=-\{g^*(\theta)+ig(\theta)\}\,. \tag{5.5}$$

Further, from (2.7), (2.8), (4.3), (3.9) and (5.2), we have

$$\phi_2(\theta)=\frac{M^2(1+\lambda)}{2\mu^2}\left\{\Re\int\left(\frac{df_0}{d\theta}\right)^2\frac{d\theta}{d\sigma}e^{-i\omega}\,d\theta+p_2(\theta)-q_2{}^*(\theta)\right\}+\chi_2{}^*\,, \tag{5.6}$$

where

$$e^{i\omega}\,d\sigma=d\zeta_p\,, \tag{5.7}$$

$$p_2(\theta)+iq_2(\theta)=2ig\frac{df_0}{d\theta}\frac{d\theta}{d\sigma}e^{-i\omega}\,, \tag{5.8}$$

and $\Re$ means "the real part of."

Neglecting terms smaller than $O(t^3/\mu^5)$, we have from (2.9), (2.10), (3.4), (3.9), (3.10) (5.3) and (5.7).

$$\phi_3(\theta)=\frac{M^4(1+\lambda)^2}{16\mu^3}\left[\frac{32}{3}\Re\int\left(\frac{df_0}{d\theta}\right)^3\left(\frac{d\theta}{d\sigma}\right)^2e^{-2i\omega}\,d\theta+8\Re\int\frac{df_0}{d\theta}\frac{dF}{d\theta}\frac{d\theta}{d\sigma}e^{-i\omega}d\theta+p_3'(\theta)-q_3'(\theta)\right], \tag{5.9}$$

where

$$\begin{aligned}p_3(\theta)+iq_3(\theta)=&12\bar{f}_0\left(\frac{df_0}{d\theta}\right)^2\left(\frac{d\theta}{d\sigma}\right)^2e^{-2i\omega}+4f_0\left|\frac{df_0}{d\theta}\frac{d\theta}{d\sigma}e^{-i\omega}\right|^2+2\bar{f}^2\left\{\frac{d^2f_0}{d\theta^2}\left(\frac{d\theta}{d\sigma}\right)^2e^{-2i\omega}\right.\\&\left.-\frac{df_0}{d\theta}\frac{d^2\zeta_p}{d\theta^2}\left(\frac{d\theta}{d\sigma}\right)^3e^{-3i\omega}\right\}+2f\overline{\left(\frac{df_0}{d\theta}\right)^2\left(\frac{d\theta}{d\sigma}\right)^2e^{-2i\omega}}+14\frac{df_0}{d\theta}\frac{d\theta}{d\sigma}e^{-i\omega}\overline{\int\left(\frac{df_0}{d\theta}\right)^2\frac{d\theta}{d\sigma}e^{-i\omega}\,d\theta}\\&+4\frac{df_0}{d\theta}\frac{d\theta}{d\sigma}e^{-i\omega}\bar{F}+4\bar{f}\frac{dF}{d\theta}\frac{d\theta}{d\sigma}e^{-i\omega}\,,\end{aligned} \tag{5.10}$$

and

$$F(\theta)=-\{q_2{}^*(\theta)+iq_2(\theta)\}\,. \tag{5.11}$$

§ 6. Velocity Distributions

The velocity distribution over the surface of the aerofoil is given by

$$q=\frac{d\phi}{ds}=\frac{d\phi}{d\vartheta}\frac{d\vartheta}{ds}=\left\{\frac{dx_p}{d\vartheta}+\left(\frac{d\phi_1}{d\theta}+\frac{d\phi_2}{d\theta}+\frac{d\phi_3}{d\theta}\right)\frac{d\theta}{d\vartheta}\right\}\frac{d\vartheta}{ds}\,, \tag{6.1}$$

where

$$\frac{ds}{d\vartheta}=\sqrt{\left(\frac{dx_p}{d\vartheta}\right)^2+\left(\frac{dy_p}{d\vartheta}\right)^2}=\sqrt{\sin^2\vartheta+\{g'(\vartheta)\}^2}\,,$$

$$\frac{dx_p}{d\vartheta}=-\sin\vartheta\,,\qquad \frac{d\vartheta}{d\theta}=1-\left\{\frac{\mu}{\sin\theta}h(\theta)\right\}'$$

and $d\phi_1/d\theta$, $d\phi_2/d\theta$ and $d\phi_3/d\theta$ are given by (5.4)~(5.11).

For the simplicity of the calculation, it is convenient to use the following formulae. Neglecting terms smaller than $O(t^3/\mu^5)$, we have from (4.10) and (6.1)

$$q=\{\sin\vartheta+g^{*\prime}(\vartheta)/\mu+S'(\vartheta)+\nu T(\vartheta)+\tfrac{1}{4}\mu\nu^2R(\vartheta)\}[\sin^2\vartheta+\{g'(\vartheta)\}^2]^{-1/2}\,, \tag{6.2}$$

where

$$S(\theta)=g^{*\prime}(\theta)\frac{h(\theta)}{\sin\theta}-\left\{g^{*\prime}(\theta)\frac{h(\theta)}{\sin\theta}\right\}^*\,, \tag{6.3}$$

$$T(\theta)=-\left[\Re\left\{\left(\frac{df_0}{d\theta}\right)^2\frac{d\theta}{d\sigma}e^{-i\omega}\right\}+p_2'(\theta)-q_2{}^{*\prime}(\theta)\right], \tag{6.4}$$

$$R(\theta)=-\left[\frac{32}{3}\Re\left\{\left(\frac{df_0}{d\theta}\right)^3\left(\frac{d\theta}{d\sigma}\right)^2 e^{-2i\omega}\right\}+8\Re\frac{df_0}{d\theta}\frac{dF}{d\theta}\frac{d\theta}{d\sigma}e^{-i\omega}+p_3'(\theta)-q_3^{*\prime}(\theta)\right], \tag{6.5}$$

$$\nu=\frac{1}{2}\frac{M^2}{(1-M^2)}\left\{1+\frac{(\gamma+1)M^2}{4(1-M^2)}\right\}, \tag{6.6}$$

and $h(\theta)$, $f_0(\theta)$, $p_2(\theta)+iq_2(\theta)$, $p_3(\theta)+iq_3(\theta)$ and $F(\theta)$ are given in (4.12), (5.5), (5.8), (5.10) and (5.11).

§ 7. The Ψ-Procedure and the $\Phi\Psi$-Procedure

The Ψ-procedure and the $\Phi\Psi$-procedure in which the velocity is obtained from the stream function or the combination of the velocity potential and the stream function respectively, were developed by Imai[15]. These procedures were applied, together with the M^2-expansion method, to the cases of a circular cylinder and a circular arc aerofoil by Imai himself and to the cases of Cherry's profile and Tomotika-Tamada's profile by Takami[16],[14] and it has been shown that the $\Phi\Psi$-procedure may give the most adequats results within the order of the approximation employed.

Now these procedures can be applied also to the thin-wing-expansion method as well as to the M^2-expansion method as follows. Let the velocity q, the stream function Ψ and the density ρ be expanded as

$$q=1+q_1+q_2+q_3+\cdots,$$

$$\Psi=\psi_0+\psi_1+\psi_2+\psi_3+\cdots,$$

$$1-\frac{\rho}{\rho_\infty}=\rho_1+\rho_2+\rho_3+\cdots, \tag{7.1}$$

where

$$\rho_1=M^2q_1,$$

$$\rho_2=M^2(\tfrac{1}{2}q_1^2+q_2)-\tfrac{1}{2}(2-\gamma)M^4q_1^2,$$

$$\rho_3=M^2(q_3+q_1q_2)-\tfrac{1}{2}(2-\gamma)M^4q_1(q_1^2+2q_2)$$
$$+\tfrac{1}{6}(2-\gamma)(3-2\gamma)M^6q_1^3. \tag{7.2}$$

Then, inserting (7.1) into the relation

$$\frac{\partial\Psi}{\partial n}=-\frac{\rho}{\rho_\infty}\frac{\partial\Phi}{\partial s}, \tag{7.3}$$

we get

$$\frac{\partial\psi_0}{\partial n}=1, \qquad \frac{\partial\psi_1}{\partial n}=q_1-\rho_1,$$

$$\frac{\partial\psi_2}{\partial n}=q_2-\rho_1q_1-\rho_2,$$

$$\frac{\partial\psi_3}{\partial n}=q_3-\rho_1q_2-\rho_2q_1-\rho_3. \tag{7.4}$$

From (7.2) and (7.4), $\partial\psi_n/\partial n$ can easily be calculated if we know q_1, q_2, $q_3\cdots$ in the Φ-procedure by the method of § 6. When $\partial\Psi/\partial n$ is known, we get the values of q in the Ψ-procedure by using the following relation:

$$\frac{\rho q}{\rho_\infty}=q\left\{1+\frac{\gamma-1}{2}M^2(1-q^2)\right\}^{1/(\gamma-1)}=\frac{\partial\Psi}{\partial n},$$

and in the $\Phi\Psi$-procedure by the relation: $q=(\rho_\infty/\rho)\partial\Psi/\partial n$, where the values from the Φ-procedure are substituted for q in ρ_∞/ρ.

In this paper these procedures are applied to Tomotika-Tamada's profiles and the results will be given in § 9.

§ 8. Flow past an Elliptic Cylinder

The formula (6.2) can be applied to the analytical and the numerical calculations for an obstacle of an arbitrary shape, and here, as an example of the analytical one, we consider the flow past an elliptic cylinder with its major axis parallel to the undisturbed flow.

Let the ellipse be given by

$$x_p=\cos\vartheta, \quad y_p=t\sin\vartheta. \tag{8.1}$$

Then we have from (4.1)

$$g(\vartheta)=t\sin\vartheta \quad \text{and} \quad g^{*\prime}(\vartheta)=t\sin\vartheta,$$

from (5.11)

$$f_0(\vartheta)=t(\cos\vartheta-i\sin\vartheta),$$

from (4.12) and (6.3)

$$h(\vartheta)=0 \quad \text{and} \quad S(\vartheta)=0,$$

from (5.8) and (6.4)

$$T(\vartheta)=t^2\frac{2\sin^3\vartheta-\sin\vartheta}{\sin^2\vartheta+\mu^2t^2\cos^2\vartheta}$$

and from (5.10) and (6.5)

$$R(\vartheta)=-t^3\left\{-\frac{128}{3}\sin\vartheta+64\frac{\sin\vartheta}{\sin^2\vartheta+\mu^2t^2\cos^2\vartheta}\right.$$
$$\left.-28\frac{\tan^{-1}\left(\frac{\sqrt{1-\mu^2t^2}}{\mu t}\sin\vartheta\right)}{\sin^2\vartheta+\mu^2t^2\cos^2\vartheta}\right\}.$$

Then from (6.2)

$$q=\left\{\sin\vartheta+\frac{t}{\mu}\sin\vartheta+\nu t^2\frac{2\sin^3\vartheta-\sin\vartheta}{\sin^2\vartheta+\mu^2t^2\cos^2\vartheta}\right.$$
$$+\mu\nu^2t^3\left[\frac{32}{3}\sin\vartheta-\frac{1}{\sin^2\vartheta+\mu^2t^2\cos^2\vartheta}\right.$$

$$\times\left\{16\sin\vartheta-7\tan^{-1}\left(\frac{\sqrt{1-\mu^2t^2}}{\mu t}\sin\vartheta\right)\right\}\Bigg]\Bigg\}$$

$$\times(\sin^2\vartheta+\mu^2t^2\cos^2\vartheta)^{-1/2}\,.$$

Further simplification can be achieved for $\vartheta\neq 0$ and π,

$$q=\left\{1+\frac{t}{\mu}+\nu t^2\left(2-\frac{1}{\sin^2\vartheta}\right)+\mu\nu^2t^3\right.$$

$$\left.\times\left(\frac{32}{3}-\frac{1}{\sin^2\vartheta}+\frac{7\pi}{2}\frac{1}{\sin^3\vartheta}\right)\right\}(1+\mu^2t^2\cot^2\vartheta)^{-1/2}\,.$$

This result is in accord with Imai's11) and Hasimoto's8) results based on Imai's thin-wing-expansion method and Kawaguti's results based on the M^2-expansion method.17)

§ 9. The Flow past Tomotika-Tamada's Profiles

As an example of the numerical calculations, we consider the flow past Tomotika-Tamada's profiles, for which the exact solutions have already been obtained by the hodograph method for a certain hypothetical gas satisfying the adiabatic gas relation approximately13). The shapes of these profiles, which have been calculated for the Mach numbers of the undisturbed flow equal to 0.717, 0.745 and 0.752, are slightly different from each other, and are symmetrical with respect to the direction of the oncoming flow

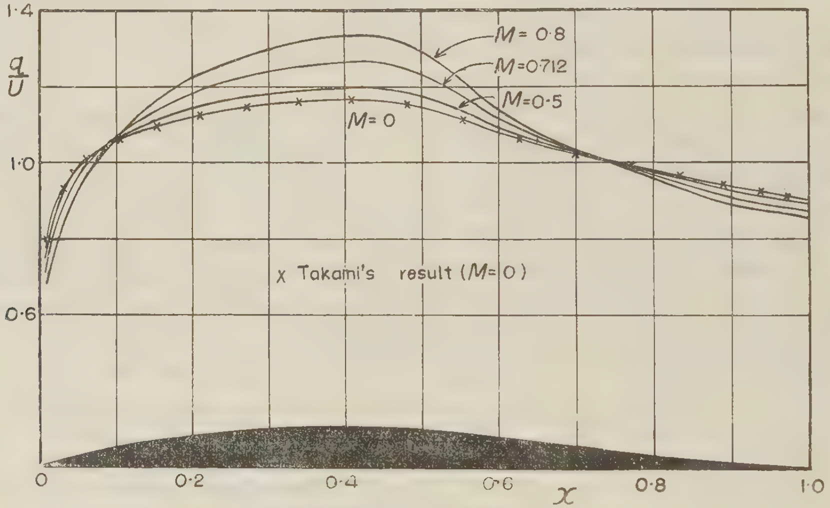

Fig. 1. The velocity distributions over the surface of the profile I for various Mach numbers (2nd approx.).

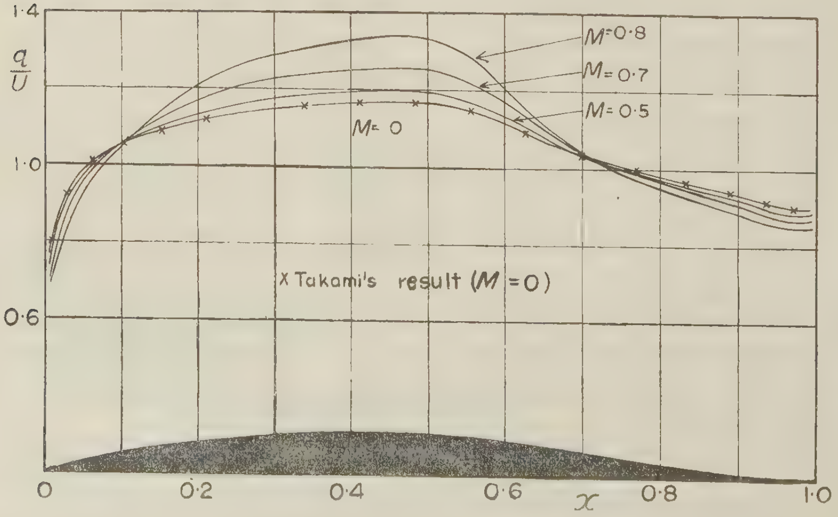

Fig. 2. The velocity distributions over the surface of the profile II for various Mach numbers (2nd approx.).

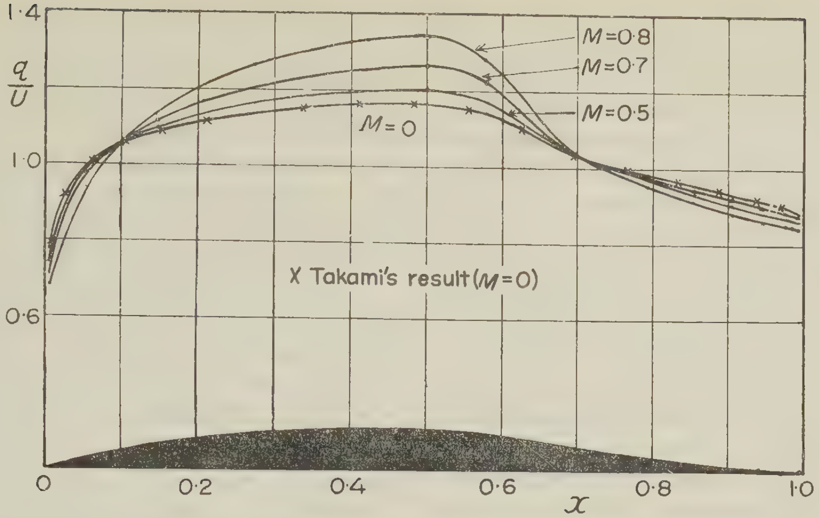

Fig. 3. The velocity distributions over the surface of the profile III for various Mach numbers (2nd approx.).

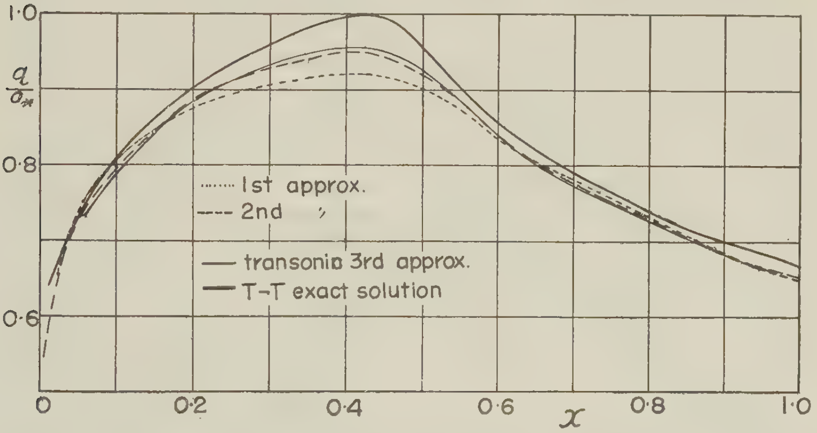

Fig. 4. The velocity distribution over the surface of the profile I ($M=0.717$).

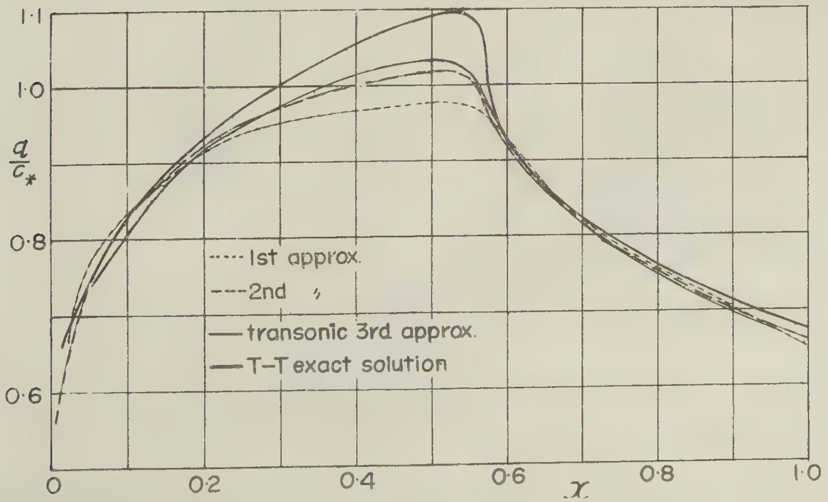

Fig. 5. The velocity distribution over the surface of the profile III ($M=0.752$).

and have a finite angle at the leading edge and a cusp at the trailing edge. It should be noticed that the flow past profile I with $M=0.717$ has the sonic speed at the point of the maximum velocity on the surface and the flow past profile III with $M=0.752$ has the infinite velocity gradient at a point of the surface.

Numerical calulations have been performed with 20 equipartitions of ϑ (the interval being 9°) for the three following cases:

(I) In order to investigate the change of the velocity distributions with the change of the Mach number, the velocity distributions over the surface of the profiles I, II, and III have been calculated to the second approximation by using (6.2) and taking $\gamma=1.4$ for various Mach numbers. These results are given in Figs. 1–3.

(II) In order to investigate the range of the validity of the thin-wing-expansion method, the velocity distributions over the surfaces of the profiles I and III have been calculated to the transonic third approximation by using (6.2) and taking as before $\gamma=1.4$ for the same Mach numbers as for the exact solutions. These results are given in Figs. 4 and 5.

(III) In order to investigate the validity of the Ψ- and the $\Phi\Psi$-procedures the velocity distribution over the surface of profile I has been calculated to the third approximation by using the method of § 7 and taking $\gamma=1.4$ for the same Mach number as for the exact solution. These results are given in Fig. 6.

The following may be concluded from Figs. 1–3. The velocity distributions over these

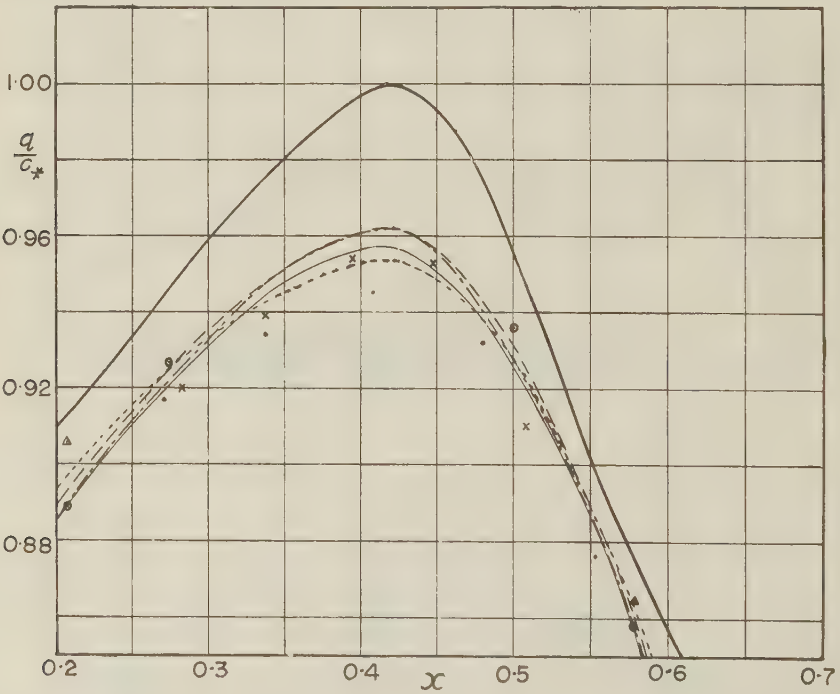

Fig. 6. The velocity distribution over the surface of the profile I near the point of the maximum velocity ($M=0.717$).

the thin-wing-expansion method:

——— the Φ-procedure (transonic 3rd approx.),
······· the $\Phi\Psi$-procedure (1st approx.),
— — — 〃 (2nd approx.),
-—-—- 〃 (transonic 3rd approx.),
△ the Ψ-procedure (2nd approx.),
⊙ 〃 (transonic 3rd approx.).

Takami's results:

× the WKB method,
● the $\Phi\Psi$-procedure in the M^2-expansion method (2nd approx.).
━━━ Tomotika-Tamada's exact solution.

profiles are fairly different from each other even for the same Mach number, and the higher the Mach number of the undisturbed flow becomes, the more the difference becomes conspicuous. In the case of $M=0$, the values from the second approximation agree very well with the exact ones calculated numerically by Takami and thus it follows that the calculation for the incompressible flow is sufficient with the second approximation.

From Figs. 4–5 it may be inferred that these solutions converge in the range of the local Mach number less than 1, but diverge in the range of the local Mach number larger than 1. Although the values to which the velocity seems to converge are generally somewhat lower than that of Tomotika-Tamada's exact solutions, the difference may be, due chiefly to the fact that the characteristics assumed in the exact solutions deviate from those of the adiabatic gas with $\gamma=1.4$. In fact, when the differences of the characteristics of the both gases are calibrated, it can be shown that our solutions are in very good agreement with the exact ones except for the neighbourhood of the sonic point.* Generally speaking, the convergency is very good in the range of the local Mach number lower than 0.9 where both the results calculated by (6.2) and Takami's numerical ones obtained by various approximate methods seem to be sufficiently reliable.

From Fig. 6 it is concluded that the behaviours of the solutions in the Ψ- and the $\Phi\Psi$-procedures agree very well with that by the M^2-expansion method. In fact it is worth noticing that in the $\Phi\Psi$-procedure the convergency is remarkably well even for a high subsonic velocity and the second approximation in the $\Phi\Psi$-procedure gives very good results in almost entire flow region (naturally except for the neighbourhood of the tip) in spite of the simplicity of the calculation.

§ 10. Conclusion

The formulae for the velocity distribution over the surface of an obstacle of arbitrary shape have been given to the transonic third approximation by the use of Imai's thin-wing-expansion method. As an example of the analytical calculations, these formulae are applied to the flow past an elliptic cylinder and it has been found that the results are in accord with the other authors's results within the approximation used. Further, as an example of the numerical calculations, these formulae, together with the Ψ- and the $\Phi\Psi$-procedures, are applied to the flow past Tomotika-Tamada's profiles. Although the calculated values are generally somewhat lower than those of Tomotika-Tamada's exact solutions, their convergency and accuracy are very good up to considerably high Mach numbers. Consequently, these formulae, particularly the second approximation in the $\Phi\Psi$-procedure, seem to be very useful, because of their good accuracy and simplicity of the calculation.

Acknowledgements

The writer would like to express his hearty thanks to Professor Isao Imai who suggested the problem and has guided and encouraged him throughout this study. The writer's thanks are also due to Professor Toshimitu Nagakura, Professor Saburo Asaka, Dr. Mitutosi Kawaguti and Dr. Hidenori Hasimoto for their advice and kind inspection of the manuscript, and to Mr. Hideo Takami who kindly showed him the numerical data and gave him much advice.

References

1) C. Kaplan: N. A. C. A. Tech. Rep. No. 768 (1943).
2) C. Kaplan: ibid. No. 794 (1944).
3) C. Kaplan: ibid. No. 834 (1946).
4) I. Imai: Rep. Aero. Res. Inst.; Tokyo Imp. Univ. No. 294 (1944).
5) I. Imai: Kagaku (Science) **14** (1944) 44 (in Japanese).
6) I. Imai and S. Ōyama: Rep. Inst. Sci. Tech., Univ. Tokyo **2** (1948) 37.
7) I. Imai and S. Ōyama: ibid. **2** (1948) 39.
8) H. Hasimoto: J. Phys. Soc. Japan **7** (1952) 322.
9) Y. Matsumoto: J. Phys. Soc. Japan **10** (1955) 814.
10) S. Asaka: J. Phys. Soc. Japan **10** (1955) 482.
11) I. Imai: J. Phys. Soc. Japan **9** (1954) 103.
12) Y. Matunobu: J. Phys. Soc. Japan **11** (1956) 452.
13) S. Tomotika and K. Tamada: Quart. Appl. Math. **9** (1951) 129.

---

[*] These results will be shown in a paper by Takami and the present writer, which will be published shortly.

14) H. Takami: J. Phys. Soc. Japan **11** (1956) 446.
15) I. Imai: Read at the monthly meeting of the Phys.-Math. Soc. Japan, Tokyo (May 1944).
16) H. Takami: J. Phys. Soc. Japan **11** (1956) 145.
17) M. Kawaguti: J. Phys. Soc. Japan **6** (1951) 168.

JOURNAL OF THE PHYSICAL SOCIETY OF JAPAN Vol. 12, No. 8, AUGUST, 1957

Notes on the Calculation of Electrophoresis of Polyelectrolytes with Partial Free-Drainage

By Hiroshi FUJITA

Physical Chemistry Laboratory, Department of Fisheries, University of Kyoto, Maizuru

(Received May 4, 1957)

This paper presents detailed numerical evaluation of the Hermans-Fujita's general equation for the electrophoretic mobility of a coiled polyelectrolyte molecule in salt solution. Values of the electrophoretic mobility u_p are obtained as functions of values of two basic parameters σ and β; here σ is Debye's "shielding ratio," and β is the radius of the polymer coil relative to the thickness of the diffuse double layer. It is shown that the criticism offered recently by Overbeek and Stigter for the validity of Hermans-Fujita's u_p equation is doubtlessly incorrect. A procedure is demonstrated by means of which u_p *vs.* β curves for different fixed values of σ can be reduced approximately to a single curve. The approximate solution for the same problem obtained by Overbeek and Stigter is discussed and compared with the rigorous treatment in relation to this reduction procedure.

§ 1. Introduction

Hermans and Fujita[1] extended the theory of Brinkman[2] and of Debye and Bueche[3] for the sedimentation of uncharged polymer molecules to the calculation of electrophoretic mobility of polyelectrolyte molecules in simple salt solutions. The model used was a porous sphere in which the density of polymer segments, and therefore also that of the fixed charges, is constant. For the charge density due to mobile ions an expression was used which had been derived for this model by Hermans and Overbeek[4] on the assumption that the approximation of Debye and Hückel is applicable. Relaxation effects were ignored. The calculation was made without any mathematical approximations. The final expression for the electrophoretic mobility, u_p, was obtained as a function of two dimensionless parameters, β and σ. Here β is the ratio of the molecular radius to the thickness of the diffuse electric double layer around the polyion, and σ is Debye-Bueche's "shielding radio." Various limiting forms as well as an asymptotic expression of the u_p equation useful for large enough values of β and σ were derived. No numerical discussion of the analytic results obtained was made, however.

In a recent article dealing with the same problem in a somewhat different manner, Overbeek and Stigter[5] have pointed out that the u_p equation of Hermans and Fujita yields a u_p value smaller than the segment's electric mobility for some intermediate values of σ and β. They state that this is clearly impossible to obtain, and therefore comparison of their approximate solution with Hermans-Fujita's rigorous treatment must await a correction of the latter.

Careful re-examination of the mathematical analysis described in reference (1) was made,[6] and it was confirmed that the results of Hermans and Fujita involve no error at all, at least so far as the mathematical aspects are concerned. This would imply that Overbeek and Stigter must have made some error in their numerical examination of Hermans-Fujita's u_p equation. This is largely probable because the physical models used in both calculations were essentially the same. To check this point critically detailed numerical calculation of the u_p equation in question was carried out, and the results obtained are presented below. It is shown that, in contrast with the criticism offered by Overbeek and Stigter, no particular paired values σ and β are likely to exist for which the electrophoretic mobility of a polyelectrolyte calculated from Hermann-Fujita's equation assumes a value smaller than the electric mobility of its segment (or monomer) unit.

§ 2. The Equation for the Electrophoretic Mobility u_p

The exact equation for the electrophoretic mobility of a polyelectrolyte derived by Hermans and Fujita[1] reads

$$u_p = \frac{\rho}{\nu f}\left[1+\frac{\Phi(\sigma,\beta)}{1-\tanh\sigma/\sigma}\right], \tag{1}$$

where

$$\Phi(\sigma,\beta)=\frac{2}{3}\left(\frac{1+\beta}{\beta^2-\sigma^2}\right)e^{-\beta}[F(\sigma,\beta)+G(\sigma,\beta)]$$
$$+\frac{2}{3}(e^{-\beta}/\beta^2)(\cosh\beta-\sinh\beta/\beta)H(\sigma,\beta)\,, \tag{2}$$

$$F(\sigma,\beta)=\left(1+\frac{2}{3}\sigma^2\right)(1-\sigma^2/\beta^2)\cosh\beta$$
$$+\left(\sigma^2/\beta^2+\frac{2}{3}\sigma^4/\beta^2-1+\frac{1}{3}\sigma^2\right)\sinh\beta/\beta\,, \tag{3}$$

$$G(\sigma,\beta)=[(\sigma^2/\beta^2-1-\sigma^2)\cosh\beta$$
$$+(1-\sigma^2/\beta^2)\sinh\beta/\beta]\tanh\sigma/\sigma\,, \tag{4}$$

$$H(\sigma,\beta)=\frac{1}{3}\sigma^2(1+\beta)$$
$$-(\sigma^2\beta+1+\beta)(1-\tanh\sigma/\sigma)\,. \tag{5}$$

The symbols in Eq. (1) have the following significance:

u_p = electrophoretic mobility of a polyion (at infinite dilution),
ρ = density of fixed charges inside the polyion,
ν = density of polymer segments,
f = frictional factor per polymer segment,
σ = Debye-Bueche's shielding ratio,
$\beta=\kappa R$, where κ is the reciprocal characteristic length of the theory of Debye and Hückel and R is the mean radius of the coiled polyion sphere.

It is noted that $\rho/\nu f$ represents the electric mobility of an individual polymer segment (or monomer). The shielding ratio is expressed in terms of ν, f, R and solvent viscosity η by

$$\sigma^2=\nu f R^2/\eta\,. \tag{6}$$

When Eqs. (3), (4) and (5) are substituted in Eq. (2) and the resulting equation is arranged properly, we find

$$\Phi(\sigma,\beta)=\frac{2}{3}(\sigma^2/\beta^2)\,e^{-\beta}\cosh\beta\{(1-\tanh\beta/\beta)$$
$$\times(1+\beta\tanh\sigma/\sigma)+[\beta^2(1+\beta)/(\beta^2-\sigma^2)]$$
$$\times(\tanh\beta/\beta-\tanh\sigma/\sigma)\}\,. \tag{7}$$

This form of $\Phi(\sigma,\beta)$ is much more tractable for numerical calculation than its original appeared in reference (1). For numerical work the ratio of u_p to $(\rho/\nu f)$ is computed as functions of σ and β. This ratio represents how the electrophoretic mobility of a coiled polyelectrolyte molecule differs from that of its constituent segment, in accordance with the degree of free-drainage, σ, and the ionic strength of the surrounding medium, β.

§ 3. Limiting Forms

Hermans and Fujita[1] derived from Eq. (1) its various limiting forms for large or small values of σ and β. Those are summarized below, together with some approximate expressions of Eq. (1) derived newly in the present study.

(a) When $\sigma\to 0$, Eq. (1) yields for any positive β

$$u_p=\rho/\nu f\,. \tag{8}$$

(b) When $\beta\to 0$, Eq. (1) reduces to

$$u_p=\frac{2}{9}\,\frac{\rho}{\nu f}\,\frac{\sigma^2}{\psi(\sigma)}\,, \tag{9}$$

where $\psi(\sigma)$ is the characteristic function of σ in the theory of Debye and Bueche[3] for the sedimentation of uncharged polymer molecules, i.e,

$$\psi(\sigma)=\frac{1-\tanh\sigma/\sigma}{1+(3/2\sigma^2)(1-\tanh\sigma/\sigma)}\,. \tag{10}$$

(c) When β becomes infinite but σ remains finite, Eq. (1) reduces to the same form as Eq. (8), i.e.,

$$u_p=\rho/\nu f\,. \tag{11}$$

(d) When σ becomes infinite, the limiting form is

$$u_p = \frac{\rho R^2}{\eta} \frac{2}{3} (e^{-\beta}/\beta^2) \cosh \beta (1 - \tanh \beta/\beta). \tag{12}$$

This is in complete agreement with Henry's formula[7] for a compact sphere whose electric conductivity is the same as that of the medium. This is expected because in this limit the polymer molecule behaves like a compact sphere.

(e) For σ and β large enough compared with unity, Eq. (1) gives asymptotically

$$u_p = \frac{\rho}{\nu f} \left[1 + \frac{\sigma^2}{3\beta^2} \left(\frac{2\beta+\sigma}{\beta+\sigma} \right) \right]. \tag{13}$$

In deriving this, both $\tanh \sigma$ and $\tanh \beta$ have been set equal to unity, and moreover both $1/\sigma$ and $1/\beta$ have been neglected compared with unity. This latter neglect is much more crude than the former approximation; the approximation that $\tanh x=1$ is quite accurate for x larger than about 4. If use is made of this approximation only, Eq. (1) becomes

$$u_p = \frac{\rho}{\nu f} \left\{ 1 + \frac{\sigma^3}{3\beta^2(\sigma-1)} \left[\frac{2\beta+\sigma}{\beta+\sigma} - \frac{(\beta+\sigma)^2+\beta^2}{\beta\sigma(\beta+\sigma)} \right] \right\}. \tag{14}$$

(f) For σ and β sufficiently small compared with unity, Eq. (1) is expanded in a double series in σ and β to give

$$u_p = \frac{\rho}{\nu f} \left[1 + \frac{4}{15} \sigma^2 - \frac{2}{9} \sigma^2 \beta + \left(\frac{4}{35} \sigma^2 \beta^2 - \frac{2}{1575} \sigma^4 \right) + \cdots \right]. \tag{15}$$

Eqs. (14) and (15) have newly been derived in this study.

§ 4. Numerical Results and Discussion

Numerical values of u_p were computed from Eq. (1) with $\Phi(\sigma, \beta)$ given by Eq. (7) over ranges of σ and β that are of practical importance (see Table I). For paired values of σ and β sufficiently small compared with unity, Eq. (15) was also used to check the results from the exact equation (1). For paired values of σ and β larger than 5, Eq. (14) was found to yield values identical with those from Eq. (1) within a practical accuracy.*

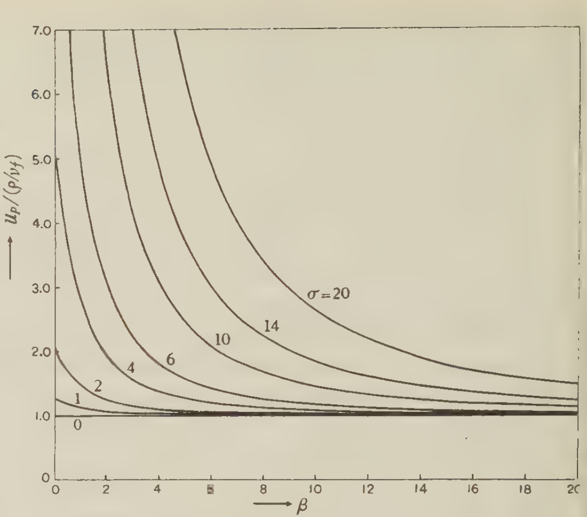

Fig. 1. Electrophoretic mobility u_p of a polyelectrolyte molecule relative to the mobility of its segment $\rho/\nu f$ as a function of β for different fixed values of σ.

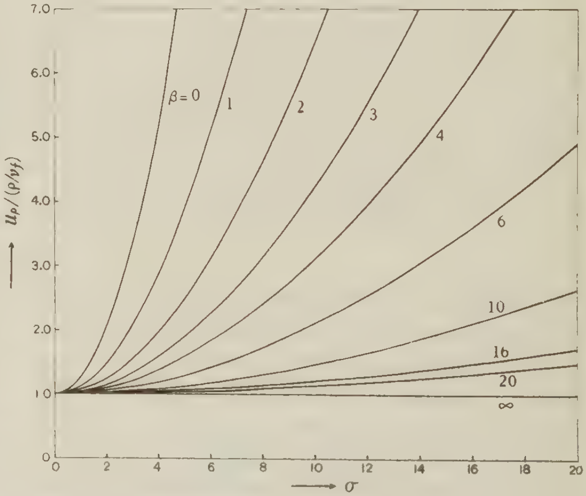

Fig. 2. Electrophoretic mobility u_p of a polyelectrolyte molecule relative to the mobility of its segment $\rho/\nu f$ as a function of σ for different fixed values of β.

The results obtained are shown graphically in Fig. 1 and 2. Fig. 1 gives the calculated u_p *vs.* β curves for several fixed values of σ. Fig. 2 shows the u_p *vs.* σ curves for different fixed values of β. To avoid confusion of the graph, only the curves for typical values of σ and β are presented here. Complete numerical values obtained are recorded in Table I. It is seen that for all pairs of the parameters treated in this calculation the u_p values are larger than or equal to $\rho/\nu f$. It is quite unlikely that there exist paired

---

* For the range σ and β both larger than 20, Eq. (13) can be satisfactorily used to predict values of u_p. Obviously, Eq. (13) yields u_p larger than $\rho/\nu f$ for any paired σ and β in this region.

Table 1. Values of the ratio $u_p/(\rho/\nu f)$ as functions of σ and β.

β \ σ	0	0.05	0.1	0.5	1.0	1.5	2.0	3.0	4.0	6.0	7.0	8.0	9.0	10.0	11.0	12.0	14.0	16.0	20.0	∞
0.0	1.0000	1.0006	1.0027	1.0666	1.2654	1.5942	2.0494	3.3333	5.0730	9.9333	13.037	16.587	20.583	25.025	29.911	35.242	47.239	61.015	93.901	∞
0.1	1.0000	1.0006	1.0025	1.0617	1.2443	1.5501	1.9649	3.1361	4.7358	9.1754	12.006	15.241	18.880	22.923	27.368	32.217	43.122	55.640	85.505	∞
0.2	1.0000	1.0005	1.0023	1.0612	1.2232	1.5039	1.8890	2.9655	4.4332	8.4970	11.084	14.038	17.359	21.046	25.100	29.519	39.454	50.852	78.033	∞
0.4	1.0000	1.0004	1.0019	1.0482	1.1923	1.4299	1.7577	2.6716	3.9131	7.3356	9.5076	11.984	14.765	17.849	21.237	24.928	33.219	42.721	65.359	∞
0.8	1.0000	1.0003	1.0015	1.0360	1.1432	1.3191	1.5616	2.2339	3.1417	5.6243	7.1912	8.9728	10.969	13.178	15.601	18.237	24.148	30.912	46.994	∞
1.0	1.0000	1.0002	1.0012	1.0313	1.1244	1.2775	1.4878	2.0704	2.8544	4.9915	6.3369	7.8648	9.5744	11.465	13.538	15.790	20.839	26.610	40.320	∞
1.5	1.0000	1.0002	1.0009	1.0226	1.0899	1.2004	1.3519	1.7695	2.3286	3.8413	4.7886	5.8611	7.0584	8.3800	9.8257	11.395	14.906	18.911	28.403	∞
2.0	1.0000	1.0001	1.0007	1.0169	1.0672	1.1495	1.2623	1.5724	1.9867	3.0985	3.7923	4.5781	5.4490	6.4110	7.4618	8.6011	11.145	14.042	20.893	∞
2.5	1.0000	1.0001	1.0005	1.0130	1.0514	1.1148	1.2013	1.4385	1.7542	2.6003	3.1262	3.7191	4.3785	5.1040	5.8954	6.7525	8.6632	10.835	15.963	∞
3.0	1.0000	1.0001	1.0004	1.0102	1.0406	1.0903	1.1584	1.3449	1.5926	2.2550	2.6658	3.1282	3.6417	4.2061	4.8210	5.4862	6.9673	8.6485	12.610	∞
4.0	1.0000	1.0001	1.0003	1.0069	1.0268	1.0596	1.1044	1.2273	1.3905	1.8261	2.0955	2.3981	2.7336	3.1015	3.5017	3.9339	4.8940	5.9811	8.5340	∞
5.0	1.0000	1.0001	1.0002	1.0047	1.0188	1.0419	1.0735	1.1602	1.2755	1.5832	1.7731	1.9865	2.2227	2.4815	2.7637	3.0658	3.7382	4.4979	6.2772	∞
6.0	1.0000	1.0000	1.0001	1.0035	1.0138	1.0310	1.0543	1.1187	1.2043	1.4334	1.5749	1.7337	1.9094	2.1017	2.3104	2.5354	3.0335	3.5955	4.9087	∞
8.0	1.0000	1.0000	1.0001	1.0021	1.0084	1.0188	1.0331	1.0724	1.1251	1.2661	1.3541	1.4524	1.5611	1.6829	1.8089	1.9477	2.2546	2.6000	3.4044	∞
10.0	1.0000	1.0000	1.0001	1.0014	1.0056	1.0126	1.0222	1.0487	1.0844	1.1806	1.2404	1.3075	1.3817	1.4630	1.5510	1.6458	1.8552	2.0905	2.6374	∞
12.0	1.0000	1.0000	1.0000	1.0010	1.0040	1.0090	1.0159	1.0350	1.0681	1.1306	1.1740	1.2229	1.2771	1.3363	1.4006	1.4697	1.6224	1.7939	2.1919	∞
14.0	1.0000	1.0000	1.0000	1.0008	1.0030	1.0068	1.0119	1.0263	1.0503	1.0988	1.1320	1.1692	1.2105	1.2558	1.3049	1.3577	1.4744	1.6054	1.9092	∞
16.0	1.0000	1.0000	1.0000	1.0006	1.0024	1.0053	1.0093	1.0205	1.0387	1.0775	1.1035	1.1320	1.1656	1.2013	1.2401	1.2819	1.3741	1.4778	1.7181	∞
20.0	1.0000	1.0000	1.0000	1.0004	1.0015	1.0034	1.0061	1.0135	1.0250	1.0513	1.0687	1.0884	1.1103	1.1343	1.1603	1.1885	1.2506	1.3205	1.4825	∞
30.0	1.0000	1.0000	1.0000	1.0002	1.0007	1.0016	1.0028	1.0062	1.0113	1.0239	1.0322	1.0415	1.0520	1.0634	1.0760	1.0895	1.1948	1.1533	1.2318	∞
50.0	1.0000	1.0000	1.0000	1.0001	1.0003	1.0006	1.0010	1.0023	1.0041	1.0090	1.0121	1.0157	1.0197	1.0242	1.0290	1.0343	1.0460	1.0593	1.0903	∞
∞	1.0000	1.0000	1.0000	1.0000	1.0000	1.0000	1.0000	1.0000	1.0000	1.0000	1.0000	1.0000	1.0000	1.0000	1.0000	1.0000	1.0000	1.0000	1.0000	

values of σ and β for which u_p becomes smaller than $\rho/\nu f$. We may thus conclude almost definitely that the criticism offered by Overbeek and Stigter for the electrophoretic mobility equation of Hermans and Fujita is errorneous.

Besides this principal conclusion, some interesting property of the u_p curves shown in Fig. 1 may be pointed out. This is found by plotting the ratio of $u_p(\rho/\nu f)-1$ to $(u_p)_0/(\rho/\nu f)-1$ against β for various fixed values of σ. Here $(u_p)_0$ stands for the value of u_p at the limit of $\beta=0$, and is given by Eq. (9). Fig. 3 shows such plots.* It is rather surprising that the values of this ratio for considerably different σ fall approximately on a single curve over the entire range of β herein shown. This suggests that, to a first approximation, u_p may be written in the form

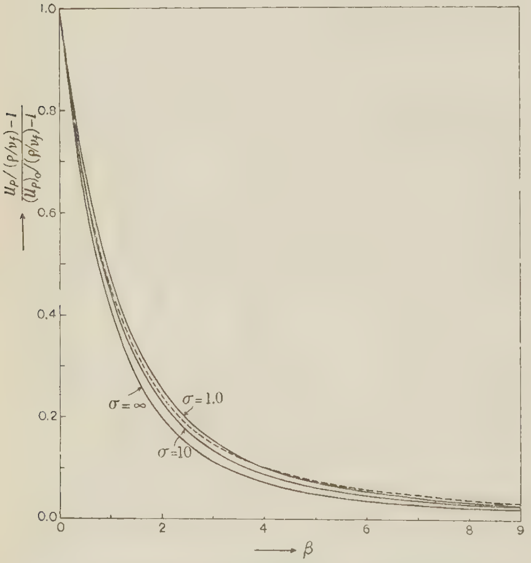

Fig. 3. Reduced electrophoretic mobility curves for different fixed values of σ; $(u_p)_0$ represents the values of u_p in the limit of zero ionic strength ($\beta=0$). The dashed line indicates the approximate reduced curve calculated from Eq. (19).

$$u_p=\frac{\rho}{\nu f}\left\{1+\left[\frac{(u_p)_0}{\rho/\nu f}-1\right]B(\beta)\right\}. \tag{16}$$

Here $B(\beta)$ is a function of β only. Actually, it may be taken as a mean curve running through the bundle of curves shown in Fig. 3.

The approximate equation for u_p obtained by Overbeek and Stigter[5)] may be written, in the notations of this article,

$$u_p=\frac{\rho}{\nu f}\left\{1+\left[\frac{(u_p)_0}{\rho/\nu f}-1\right]\right.$$
$$\left.\times\left[1-\frac{(2/9)\sigma^2}{(u_p)_0(\nu f/\rho)-1}\left(\frac{\beta}{1+\beta}\right)\right]C(\beta)\right\}, \tag{17}$$

where $C(\beta)$ stands for

$$C(\beta)=\frac{3}{2\beta^3}[(1+\beta)^2e^{-2\beta}-1+\beta^2]. \tag{18}$$

Numerical examination shows that the function $(2/9)\sigma^2/[(u_p)_0(\nu f/\rho)-1]$ varies very slowly with σ; it starts with 0.83333 (actually, 5/6) at $\sigma=0$, increases monotonically, and tends to unity for infinitely large σ. Accordingly, to a first approximation, we may replace it by some mean value between these two limits. Here, tentatively, a value of 0.90 is assigned to it. Then Eq. (17) reduces to

$$\frac{u_p/(\rho/\nu f)-1}{(u_p)_0/(\rho/\nu f)-1}$$
$$=\frac{3}{2\beta^3}[(1+\beta)e^{-2\beta}-1+\beta](1+0.1\beta). \tag{19}$$

Thus we find that a family of u_p *vs.* β curves for a series of fixed σ obtained from the equation of Overbeek and Stigter can also be reduced to a single curve if we replot those curves in the form of Fig. 3. The function of β in the right-hand side of Eq. (19) is indicated by a dashed line in Fig. 3. It is observed that this dashed line runs through or near-by the bundle of the solid curves calculated from the exact equation. This implies that the approximations used by Overbeek and Stigter permit remarkably accurate evalution of u_p as functions of σ and β.

Recently, Nagasawa[8)] reported interesting electrophoresis data on samples of sodium salt of sulphonated polyvinyl alcohol in aqueous sodium chloride solutions. When the ionic strength of the added electrolyte in

---

* From Eqs. (12) and (9) the limiting form of this ratio for $\sigma=\infty$ is obtained to give

$$\text{the ration}=3(e^{-\beta}/\beta^2)(\cosh\beta-\sinh\beta/\beta).$$

Similarly, by expanding the equations for u_p and $(u_p)_0$ in powers of σ, the limiting form of the ratio for $\sigma=0$ is obtained as

$$\text{the ratio}=15/2(e^{-\beta}/\beta^2)\cosh\beta\{(1+\beta)/3$$
$$-(1-\tanh\beta/\beta)[(\beta/3)+(1+\beta)/\beta^2]\}.$$

The curves for $\sigma=0$ and ∞ in Fig. 3 have been computed using these equations.

solution is decreased, his u_p data first go up following a curve quite similiar to the type shown in Fig. 1, but reaches a maxium at a certain finite ionic strength, then come down rapidly, and approach at the limit of zero ionic strength a value corresponding to the mobility of the monomer ion. At the limit of high enough ionic strength the curve again tends to the value equal to the mobility of the monomer ion. When comparing this behavior with the theory of Hermans and Fujita outlined above, it should be borne out in mind that the curves in Fig. 1 refer to fixed values of σ. As well known, the effective radius of the flexible polyelectrolyte molecule depends on the ionic strength κ^2, hence β, of the surrounding medium. This means that degree of free-drainage, σ, of the polyion changes with changing ionic strength of the external solution. At very low ionic strength the polymer coil becomes more expanded; therefore it becomes more free-drained so that σ becomes smaller. This explains that the electrophoretic mobility comes down again after passing through a maximum, when the electrolyte content of the solution is decreased down to zero.

Grateful acknowledgment is made for the assistance of Mr. K. Ninomiya and Miss A. Segawa of this Laboratory in the numerical calculation. This work was supported in part by a grant from the cooperative research project on the chemistry of polyelectrolytes under the supervision of Professor I. Kagawa, Department of Applied Chemistry, Nagoya University, and in part by a National Science Foundation Grant-G3599. Mention should be made that a brief description of the results obtained above has been presented elsewhere.⁹⁾

References

1) J. J. Hermans and H. Fujita: Proc. Acad. Amsterdam **B58** (1955) 182.
2) H. C. Brinkman: Proc. Acad. Amsterdam **50** (1947) 618.
3) P. Debye and A. M. Bueche: J. Chem. Phys. **16** (1948) 573.
4) J. J. Hermans and J. Th. G. Overbeek: Rec. trav. chim. **67** (1948) 762; Bull. soc. chim. Belg. **57** (1948) 154.
5) J. Th. G. Overbeek and D. Stigter: Rec. trav. chim. **75** (1956) 543.
6) J. J. Hermans: private communication.
7) D. C. Henry: Proc. Roy. Soc. (London) **A133** (1931) 106.
8) M. Nagasawa: J. Polymer Sci. (in press).
9) H. Fujita: Rec. trav. chim. (in press).

Short Notes

This section is intended to secure prompt publication of important discoveries in physics. The reports should not exceed 800 words in length. A figure of size 7 cm × 7 cm will be counted as 150 words.

J. PHYS. SOC. JAPAN **12** (1957) 974

On the Variational Problem connected with the Thomas Fermi Method

By Yukito TANABE

Department of Applied Physics, Faculty of Engineering, Tokyo University, Tokyo

(Received June 13, 1957)

The Thomas-Fermi method has been applied not only to the problems of free atoms and ions but also to those of molecules and solids. To solve the appropriate three dimensional Thomas-Fermi (T.F.) equation in the latter problems is, however, extremely difficult because of the lack of the sperical symmetry[1]. In order to avoid this difficulty the problem is usually reduced to that of spherical symmetry under a suitable approximation. However, whether this approximation is good or not is not clear, and to improve the result by including the angle-dependent terms in the T.F. function is still more difficult. Therefore it seems desirable to apply the variational technique to these problems.

The attempt to connect the T.F. equation and the variational principle has been done by Umeda[2] and more recently by Ikebe and Kato[3] for neutral atom, but it seems to the wrinter that the relation between the variational principle for the T.F. equation and the principle of energy minimum is not fully realized by these authors. The purpose of this note is to derive the variational principle for the T.F. equation of the many centre system from the principle of energy minimum and to show how the result could be used to find the degree of approximation.

Consider the molecular system consisting of several atomic nuclei and N electrons. Using the conventional notations, the total energy E in the statistical treatment is written in the following way:

$$E\left[\frac{1}{4\pi}\nabla V_e, e\rho, T\right]=\int d\tau\left\{\frac{1}{8\pi}(\nabla V_e)^2+\frac{1}{4\pi}\nabla V_e\cdot\nabla V_N\right\}+\int_T d\tau\kappa\rho^{5/3}, \qquad (1)$$

where T is the total volume occupied by each electron. The first term on the right hand side is the potential energy and the second is the kinetic energy of the electron system. The well-known relation between the charge density and the potential is obtained[4] by minimizing the above expression with respect to $\frac{1}{4\pi}\nabla V_e, e\rho$ and T under the subsidary conditions

$$\nabla\cdot\frac{1}{4\pi}\nabla V_e=\begin{cases}e\rho & \text{in } T\\ 0 & \text{otherwise,}\end{cases}$$

and

$$\int_T e\rho d\tau=N_e\,.$$

By introducing Lagrange's multipliers, the problem is converted to the minimum problem without the subsidary conditions and, imposing the natural condition on this problem, our problem is reduced to the maximization of the following functional (involutory transformation):

$$I[U,T]=N_eU(\infty)-\int d\tau\frac{1}{8\pi}(\nabla U-\nabla V_N)^2-\frac{1}{4\pi}\int_T d\tau\frac{2}{5}\mu U^{5/2*}, \qquad (2)$$

which is just the functional used by the above mentioned authors. From this maximum problem we can derive the usual T.F. equation together with the boundary conditions.

If we denote the correct T.F. energy by E_0, the above derivation ensures, for approximate U and ∇V_e, the inequality[5]

$$I[U,T']\leq E_0\leq E\left[\frac{1}{4\pi}\nabla V_e, T\right] \qquad (3)$$

This is equivalent to the inequality used by Ikebe and Kato to estimate the upper and lower bound of B_0. Furthermore, $8\pi\left\{E\left[\frac{1}{4\pi}\nabla V_e\right]-I[U]\right\}$ gives the upper bound of the mean square error of the approximate U or ∇V_e, as is easily shown[6].

The practical application of the variational priciple (2) is now being carried out for the problem of octahedral complex ion[7] and the details will be given in a later communication.

References

1) N. H. March: Proc. Camb. phil. Soc. **48** (1952) 655.
2) K. Umeda: J. Phys. Soc. Japan **9** (1954) 290.
3) T. Ikebe and T. Kato: J. Phys. Soc. Japan **12** (1957) 201.
4) P. Gombas: Die Statistische Theorie des Atoms, Wien, 1949.
5) See, for example: R. Courant and D. Hilbert: Methods of Mathematical Physics, Interscience Publishers, New York, Vol. 1, 1953.
6) The writer is greatly indebted to Professor T. Kato for pointing out this method of estimation.
7) Progress Report No. 6 (Dec. 1956) of the Research Group for the Study of Molecular Structure.

---

* $\mu=4\pi e(3e/5\kappa)^{3/2}$.

J. PHYS. SOC. JAPAN **12** (1957) 975

Magnetic Anisotropy in Connection with Rolling in the Course of Producing Single Crystals of Silicon Steel

By Tadayoshi YAMASHITA* and Eiji TATSUMOTO**

**Department of Physics, National Defense Academy*

***Department of Physics, Faculty of Science, Hirohima University*

(Received June 5, 1957)

In the single crystal strips (⊥) (001)-[100](1) produced by the special strain anneal method* from the commercial silicon steel sheets it has been discovered by one of the authors(2) that the energy is lower by 4×10^2 erg/cc, which corresponds to about 100 gr/mm^2 of the internal stress when the magnetization is in the perpendicular direction than in the parallel direction of the strips. In the present experiment, the cause of this anisotropy was investigated by means of the optical and electron microscopies.

Fig. 1. Optical microphotograph of electropolished surface. ×560.

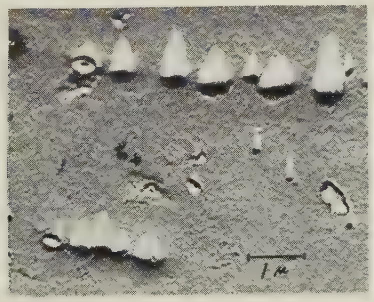

Fig. 2. Electronmicrograph of pits.

On the electropolished surfaces of the single crystals as well as the annealed polycrystals many arrays of the small pits are observed by the optical microscope as shown in Fig. 1. These pits are the nearly spherical holes as shown in Fig. 2 which is observed by the electron microscope by means of the carbon replica method shadowed by chromium. The arrays of the holes are always parallel to the rolling direction of the sheets. They are not influenced by the heatings before and after the preparation of the single crystals and are independent upon the crystal orientation and the processes of electropolishing. It is, thus, unquestionable that these holes are not produced by electropolishing, but the ones originally existed.

Magnetostatic energy due to the free poles appearing on the surfaces of the holes depends upon the direction of magnetization with respect to the arrays of the holes(3). The energy is the greatest and the smallest in the cases that the angles are 90° and 0° respectively. The energy difference between both extreme cases can be regarded as the anisotropy energy obtained already by one of us(2). It can be estimated easily with the average size, separation and density of the holes indicated in Fig. 3, and it is about 5×10^2 erg/cc. This value agrees satisfactorily with the observed 4×10^2 erg/cc.

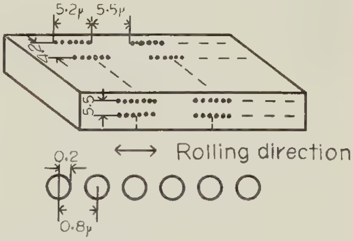

Fig. 3. Schematic diagram of average dimension and arrangement of holes.

In conclusion, the magnetic anisotropy associated with rolling may be attributed to the small pin holes linning up in groups parallel to the rolling direction of the sheets.

References

1) The mark (⊥) denotes that the rolling direction of the sheet is perpendicular to the lengthwise direction of the strips.
2) E. Tatsumoto: J. Sci. of Hiroshima Univ. **17** (1953) 229.
3) R. M. Bozorth: Ferromagnetism P. 423.

---

* Note added in proof: It means the recrystallization of cold-rolled sheet developed from the nucleus which is previously orientated in a desired crystallographic direction.

J. PHYS. SOC. JAPAN **12** (1957) 976

Etch Pits in Silicon Single Crystals

By Yasuo MATUKURA and Takeaki SUZUKI
Electrotechnical Laboratory, Tokyo, Japan

(Received May 21, 1957)

Since it is known that dislocations affect certain properties of semiconductors, a visual method for determining the number and distribution of such imperfections would have useful application both for practical tecknique and fundamental research. F. L. Vogel and L. C. Lovell[1] reported that the etching solution containing a small amount of mercuric nitrate was suitable to form clear etch pits in silicon. Presented here are some results of an investigation of methods for producing clearly defined dislocation etch pits in silicon with the etching solution containing potassium nitrate.

The composition of the etching solution is as follows:

4 parts HF (48%)
5 parts HNO$_3$ (75%)
2 parts glacial acetic acid
1/3 parts 1 mol % aqueous KNO$_3$.

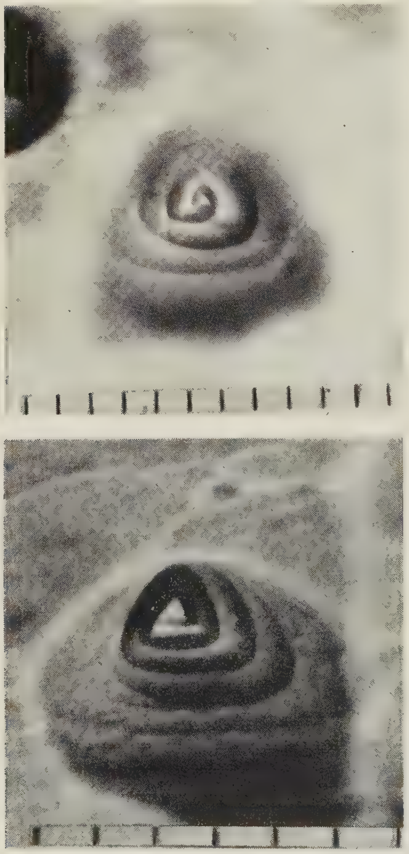

Fig. 1. Upper- and lower-handed screw etch pits on (111) surface of silicon crystal. One division of the scale is $10\,\mu$.

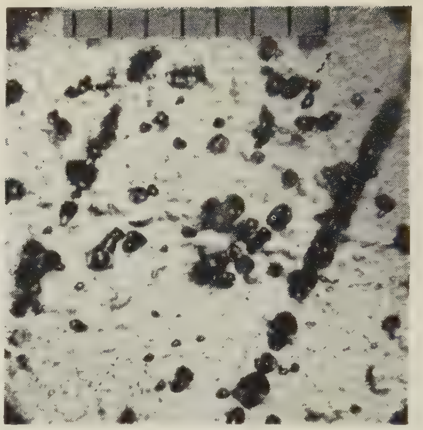

Fig. 2. Dislocation etch pits in slip lines. One division of the scale is $100\,\mu$.

Deionized water is used to make the potassium nitrate solution, and it has been found that excess water roughen the final surface.

The etching technique used is as follows. First, crystals are oriented and cut to expose the (111) surface. The surface is then lapped with 800 mesh carborundum on a glass plate. A light preliminary etching in CP-4 proved to be helpful in many cases in providing a smoother surface. Immersion in the etching solution for 20 minutes usually yields a well-defined, reproducible pits. In many cases, satisfactory results are obtained by etching for few seconds in CP-4 after the main etching.

The features of pits obtained are that its depth is reached to several ten microns and while the outline of shallow etch pits is trigonal, the upper outline of the deep ones is nearly circular, and that large pits with terraces or spiral terreces develop accasionally. Fig. 1 shows typical spiral etch pits which seem to indicate a screw dislocation[1], [2] or a lameller growth[3]. It is noticed that both upper- and lower-handed screw terraces are observed and the step heights are roughly reached to $10\,\mu$. Fig. 2 shows the array of dislocation etch pits, which may correspond to one of the slip lines.

The authors wish to express their gratitude to Mr. M. Kikuchi for various inspiring discussions.

References

1) F. L. Vogel and L. C. Lovell: J. Appl. Phys. **27** (1956).
2) W. Bardsley and B. W. Straughan: J. Electronics **1** (1956) 561.
3) A. R. Lang: J. Appl. Phys. **28** (1957) 497.

J. Phys. Soc. Japan **12** (1957) 977

A Characteristic of Tomotika-Tamada's Gas as Affecting the Velocity Distribution Around a Profile

By Hideo Takami
Department of Physics, Faculty of Science, University of Tokyo
and Humio Naruse
Department of Physics, Faculty of Science, Tokyo Metropolitan University

(Received June 8, 1957)

In previous papers [2] [3], present authors studied the compressible flow past a Tomotika-Tamada profile [4] by the use of various approximate methods. But certain discrepancy was seen to exist between their results and that of Tomotika and Tamada in the velocity distributions.

Here it will be shown that this discrepancy is attributed to the difference between the characteristics of Tomotika-Tamada's and the adiabatic gases.

(A) In our previous papers, the values of q/c_* were obtained from q/q_∞ by multiplying q_∞/c_* ($=0.748$ for $M_\infty=0.717$) corresponding to the adiabatic gas with $\gamma=1.4$. For comparison, however, we ought to have calculated $q/c_{*T}=(q/q_\infty)(q_\infty/c_{*T})$, where c_{*T} denotes the critical sound velocity for Tomotika-Tamada's gas. The factor q_∞/c_{*T} is calculated to be 0.769 from the pressure-density relation of this hypothetical gas.

(B) It has been shown by Imai [1] that, in applying the M^2-expansion or thin-wing-expansion method, a gas for which $p=p(\rho)$ (p: pressure, ρ: density) can be regarded, with high accuracy, as a gas with the adiabatic exponent $\gamma=1+[(\rho/c^2)\times d^2p/d\rho^2]_\infty$, where c is the sound velocity and the suffix ∞ denotes the value in the uniform flow. Using the (p, ρ)-relation for Tomotika-Tamada's gas we calculated $1+(\rho/c^2)\,d^2p/d\rho^2$ for various values of q/c_{*T} (Fig. 1). The value of $1+[(\rho/c^2)\,d^2p/d\rho^2]_\infty$ for our case is found to be 1.822 from Fig. 1, so that our previous values of q/q_∞ must be modified in the second approximation, because γ appears for the first time in this approximation.

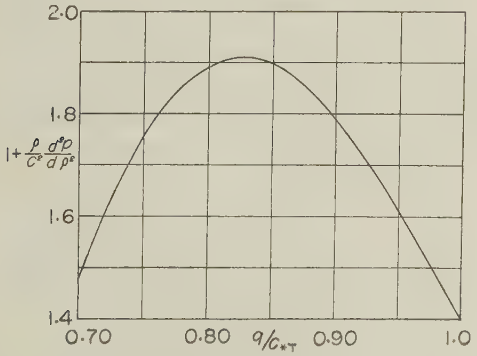

Fig. 1. $1+(\rho/c^2)d^2p/d\rho^2$ for various values of q/c_{*T}, calculated by using the (p, ρ)-relation for Tomotika-Tamada's gas.

The final results are shown in Fig. 2. (For comparison, one of the previous results for the adiabatic gas is also shown.) Modification due to (A) results in an increase of the velocity about 3%, while the increment due to (B) is less than 0.4%, so that we can say that the discrepancy was mainly due to the difference between the critical sound velocities of the two kinds of gases.

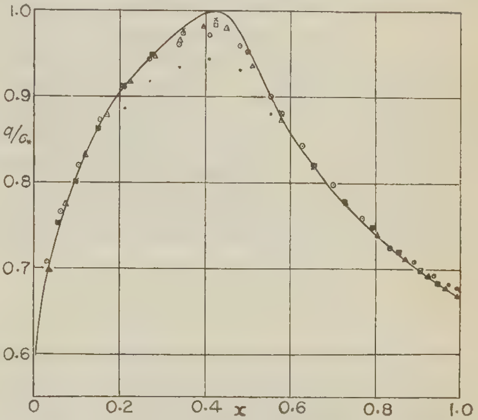

Fig. 2. The velocity distributions over the surface of Tomotika-Tamada's profile ($M_\infty=0.717$), modified due to (A).

— Tomotika-Tamada's exact solution [4],
△ the WKB method,
⊙ the M^2-expansion method, 2nd approximation in the $\Phi\Psi$-procedure,
• the M^2-expansion method, 2nd approximation (adiabatic gas of $\gamma=1.4$),
⊡ the thin-wing-expansion method, 3rd transonic approximation in the Φ-procedure,
× the thin-wing-expansion method, 3rd transonic approximation in the $\Phi\Psi$-procedure.

The authors would like to thank Professor Isao Imai for much valuable advice, and also to thank Professor Kô Tamada who kindly furnished them with the numerical data about the hypothetical gas.

References

1) I. Imai: Sûri-buturigaku Kenkyû (Studies in Mathematical Physics), **2** (1952, Iwanami, Tokyo) 103–5 (in Japanese). Also University of Maryland Tech. Note BN-95 (1957) Part I, 104–5.
2) H. Naruse: J. Phys. Soc. Japan **12** (1957) 959.
3) H. Takami: J. Phys. Soc. Japan **11** (1956) 446.
4) S. Tomotika and K. Tamada: Quart. Appl. Math. **9** (1951) 129.

J. PHYS. SOC. JAPAN **12** (1957) 978

Notes on the Ground State of Antiferromagnetism

By Ôjirô NAGAI

Department of Physics, Faculty of Science,
Kyusyu University

(Received June 11, 1957)

Recently, Marshall[1] and Taketa and Nakamura[2] generalized Hulthen's[3] and Kasteleijn's[4] methods of obtaining the ground state of antiferromagnetism to the cases of two and three dimensional lattices.

In particular, Kasteleijn and Taketa and Nakamura studied the anisotropic exchange Hamiltonian

$$\mathscr{H}=(1-a)J\sum_{<j,k>}(S_j{}^+S_k{}^-+S_j{}^-S_k{}^+)+2J\sum_{<j,k>}S_j{}^zS_k{}^z$$

where all the notations in this note are the same as those of Taketa and Nakamura. They obtained the critical values of the anisotropic parameter a at which the system becomes antiferromagnetic. In Taketa and Nakamura's calculation, it was found that with increasing coordination number the critical value decreases rapidly.

On the other hand, Marshall calculated the ground energy by a method different from Taketa and Nakamura's. He took into account partly the correlation among the spins neighbouring to a spin pair, which was neglected in Taketa and Nakamura's procedure. If the correlation among the spins could stabilize the antiferromagnetic ordering, the critical values from Marshall's treatment should be smaller than those from Taketa and Nakamura's.

Hence the writer calculated the critical values in Marshall's treatment. They are pretty higher than those from Taketa and Nakamura's as can be seen in Table I. In actual matters, spins are ordering without or with very small anisotropic effective fields.

In Table II, we should note that the numbers of antiparallel pairs from Marshall's and Taketa and Nakamura's treatments are decreasing with increasing coordination number. These results are contrary to our anticipation that with increasing number of neighbouring magnetic atoms the antiparallel orientations of spin pairs should be bound more tightly[5]. The results from the spin wave theory[6] prove our correct anticipation.

Table I. The critical values of a. z is the coordination number.

Method	$z=2$	$z=4$	$z=6$	$z=8$
Taketa and Nakamura	0.517	0.108	0.046	0.024
Marshall	0.517	0.193	0.080	—

Table II. The numbers of antiparallel pairs, $q/\frac{1}{2}Nz$, where q denotes the number of antiparallel pairs and N is the total number of spins.

Method	$z=2$	$z=4$	$z=6$	$z=8$
Taketa and Nakamura	0.774	0.637	0.589	0.566
Marshall	0.774	0.681	0.624	0.609
Spin Wave Theory	—	0.607	0.844	0.882

From the above facts, we may conclude that both Marshall's and Taketa and Nakamura's treatments overestimate the quantum effect arising from the non-diagonal elements of Hamiltonian and especially Marshall's method is not always better than Taketa and Nakamura's method.

The writer wishes to express his sincere thanks to Dr. T. Nakamura for his continual interest and and encouragement.

Also, the writer is much indebted to Professor T. Tanaka for his kind inspection of the manuscript and to Mr. S. Tosima for his helpful discussions.

References

1) W. Marshall: Proc. Roy. Soc. London **A 232** (1955) 48.
2) H. Taketa and T. Nakamura: J. Phys. Soc. Japan **11** (1956) 919.
3) L. Hulthen: Ark. Mat. Astr. Fys. **26 A No. 1** (1938).
4) P. W. Kasteleijn: Physica **18** (1952) 104.
5) P. W. Anderson: Phys. Rev. **83** (1951) 1260.
6) P. W. Anderson: Phys. Rev. **86** (1952) 694.

J. PHYS. SOC. JAPAN **12** (1957) 979

Acoustoelectric Effect in n-type Germanium

Wataru SASAKI and Eiichi YOSHIDA
Electrotechnical Laboratory, Nagatacho, Tokyo

(Received June 8, 1957)

Parmenter[1] suggested that electrons in a conductive crystal could be dragged by progressive acoustic waves in the crystal. We have observed this effect in an n-type germanium crystal.

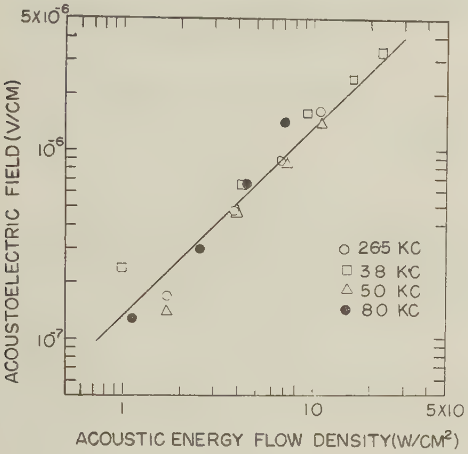

Fig. 1.

Longitudinal acoustic wave was excited by a magnetostrictive oscillator attatched on one end of the acoustic system, and the acoustic energy passed through the specimen was dissipated in copper wire on the other end. The copper wire was put in a water bath and the acoustic energy flow was estimated by the temperature rise of this bath.

The specimen used was a single crystal of n-type germanium of about 5.5 ohm-cm, and was 1.5 cm in length with cross sectional dimensions of 0.2 cm.

The open circuit voltage induced in the specimen by chopped acoustic wave was measured by a tuned phase sensitive amplifier. The frequency of the acoustic wave was varied from 26.5 kc to 80 kc/sec, thus the wave length of these waves was far beyond the dimensions of the specimen. The result of the experiment at room temperature is shown in Fig. 1.

Following features are noticeable.

a) The sign of the induced electric field is such that the short circuitted current is carried in the crystal by majority carriers moving in the same direction with acoustic wave.

b) The induce electric field is proportional to the acoustic energy flow density.

c) The induced electric field per unit acoustic energy flow density varies little with acoustic frequency.

In regard to (a), our observation agree with the prediction by Parmenter[1], but not with the revision of his theory by Weinreich[2]. As for the magnitude of the effect, our observation is extremely smaller than Parmenter's estimation, and Weinreich's comment on Parmenter's treatment of the problem should be justified.

The authors wish to represent their thanks to G. M. Hatoyama and M. Shibuya for their interest and discussions to this work.

References

1) R. H. Parmenter: Phys. Rev. **89** (1953) 990.
2) Gabriel Weinreich: Phys. Rev. **104** (1956) 321.

J. PHYS. SOC. JAPAN **12** (1957) 979~980

Elastic Scattering of 5.7 MeV Protons

By Minoru TAKEDA, Michiya KONDO, Ryuzo NAKASIMA, Chuin HU, Atsutomo TOI*, Takashi YAMAZAKI and Shotaro YAMABE
Department of Physics, Osaka University, Osaka
**Kobe University of Mercantile Marine, Kobe*

(Received May 17, 1957)

It has been pointed out experimentally[1),2)] that the angular dependences of the deviations from the Rutherford scattering for Cu and Ni have characteristic features. In particular, the behaviors at large angles are very different for both elements. Bromley and Wall[1)] suggested that these pronounced differences may be due to the spin dependent nuclear interaction.

We have extended these investigations for other adjacent elements in order to check the suggestion of Bromley and Wall by means of nuclear emulsion technique. The experimental arrangement and procedure were same as our previous work[2)]. Fe($Z=26$), Cr($Z=24$) and Ti($Z=22$) were chosen as the targets, and also the elastic scattering of 5.7 MeV protons on gold was examined. The Fe target was a self-supporting foil of 3.8 mg/cm^2 thick and the thickness of Au target was 1.9 mg/cm^2.

The results obtained are shown in Fig. 1. In the case of gold, the differential cross section agrees with that of the Rutherford scattering as is expected. For iron, however, the differential cross section, in the ratio to the Rutherford cross section, increases linearly at large angles. The shape of this rise at large angles is quite similar to that of previous results on Ni. Preliminary results on Cr and Ti show also the same situations.

Although our present experiments are restricted in the target nuclei with zero spin (even-even nuclei), the data of the elastic scattering of protons from neighbouring odd-A nuclei (with non-zero spin) should be accumulated in order to emphasize the presence of these characteristics in even-even nuclei of medium weight region.

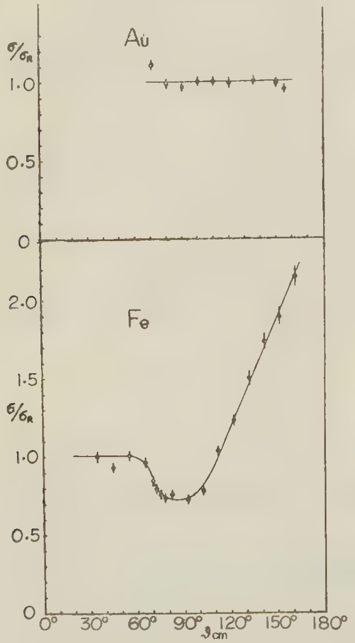

Fig. 1. Angular dependences of the deviations from the Rutherford scatterings for Au and Fe.

We are now scanning the plates for Cr and Ti to establish more complete data, and the report of these results will be published in near future.

References

1) D. A. Bromley and N. S. Wall: Phys. Rev. **102** (1956) 1560.
2) M. Takeda, et al.: Jour. Phys. Soc. Japan **12** (1957) 561.

J. Phys. Soc. Japan **12** (1957) 980

Series Expansion of the Fermi Part η_0 of the TF Function[*]

By Shigehiro Kobayashi

Department of Physics, Kagawa University, Takamatsu

(Received June 25, 1957)

The Fermi part $\eta_0(x)$ in the Thomas-Fermi (TF) function $\phi(x)$ for free positive ion expressed approximately with the ordinary TF function $\phi_0(x)$ as

$$\phi(x)=\phi_0(x)+k\eta_0(x)\,,$$

where k is a constant depending on the ionization degree q roughly as $k=-0.0542\cdot q^{2.86}$[**], is given numerically in a table refined recently by the present author1).

In the course of evaluation of some physical quantities, for example atomic scattering factor etc., using its tabulated values, the series expansion of it near the origin is often needed. Thus, it has been calculated here up to the term $x^{19/2}$ as follows.

$$\begin{aligned}\eta_0(x)=&\,x+\frac{2}{5}x^{5/2}+\frac{3}{35}B_0x^{7/2}+\frac{2}{15}x^4-\frac{1}{84}B_0^2x^{9/2}+\frac{2}{175}B_0x^5+\frac{1}{33}\left(\frac{31}{45}+\frac{1}{8}B_0^3\right)x^{11/2}+\frac{4}{525}B_0^2x^6\\&+\frac{1}{286}B_0\left(\frac{557}{175}-\frac{15}{32}B_0^3\right)x^{13/2}+\frac{4}{693}\left(1-\frac{29}{35}B_0^3\right)x^7+\frac{7}{520}B_0^2\left(-\frac{89}{225}+\frac{1}{16}B_0^3\right)x^{15/2}\\&+\frac{4}{3003}B_0\left(-\frac{23}{15}+\frac{17}{7}B_0^3\right)x^8+\frac{1}{20}\left(-\frac{113}{58905}+\frac{153173}{1455300}B_0^3-\frac{21}{2176}B_0^6\right)x^{17/2}\\&+\frac{2}{3465}B_0^3\left(\frac{523}{65}+4B_0^3\right)x^9+\frac{1}{76}B_0\left(\frac{101523673}{58351293}-\frac{38221171}{104264160}B_0^3+\frac{99}{4352}B_0^6\right)x^{19/2}\\&+\cdots\cdots\cdots,\end{aligned}$$

where $B_0=1.5880710$ is the initial slope of $\phi_0(x)$, as given previously by the present author and others2).

The author wishes to express his sincere thanks to Professor K. Umeda of Okayama University for his kind guidance.

References

1) S. Kobayashi: J. Phys. Soc. Japan **11** (1956) 609; S. Kobayashi and T. Taima: Mem. Fac. Lib. Arts and Educ. of Kagawa Univ., Part II, No. 33 (1956).
2) S. Kobayashi, T. Matsukuma, S. Nagai and K. Umeda: J. Phys. Soc. Japan **10** (1955) 759; R. Latter: J. Chem. Phys. **24** (1956) 280.

---

[*] Supported by the Scientific Research Expenditure of the Ministry of Education.

[**] This is a more correct expression than hitherto given and has been newly obtained by the present author and will be published shortly in this journal.

J. PHYS. SOC. JAPAN **12** (1957) 981

Supplementary Note to "On the Transonic Flow past a Nearly Axisymmetric Slender Body"

By Ken-ichi KUSUKAWA

Department of Physics, Faculty of Science
Tokyo Metropolitan University

(Received July 5, 1957)

In a recent paper[1], the perturbation velocity potential φ of the transonic flow of a compressible fluid past a nearly axisymmetric slender body was expanded into Fourier series as

$$\varphi=u_0(x,r)+\sum_{n=1}^{\infty}u_n(x,r)\cos(n\theta+\beta_n)\ , \qquad (1)$$

and the surface of the body was represented by

$$R=F(x,\theta)=F_0(x)+\sum_{n=1}^{\infty}F_n(x)\cos(n\theta+\alpha_n)\ , \qquad (2)$$

where x, r, θ denote the cylindrical coordinates.

Considering the singularity along the axis, the order estimation of the usual slender body theory[2],[3] may be available near the surface. Since the body is nearly axisymmetric, we can assume $O(F_n)=O(t)O(F_0)$ and $O(u_n)=O(t)O(u_0)$, where t is the thickness ratio. Thus the pressure coefficient C_p on the surface of the body is given by

$$C_p=-2(\partial\varphi/\partial x)-(\partial\varphi/\partial r)^2+O(t^4\log^2 t)\ , \qquad (3)$$

and the use of the linearized equation (4.12) of Reference [1] does not give the correct value of the pressure. The boundary condition on the surface of the body is expressed by

$$(\partial\varphi/\partial r)_{r=F}=dF/dx\ . \qquad (4)$$

In the previous paper[1], the left hand side of Eq. (4) was approximately replaced by the value on the surface of a body of revolution represented by $r=F_0(x)$. However, for the purpose of evaluating the correct pressure by Eq. (3), we have to refine the treatment as follows:

$$\left(\frac{\partial\varphi}{\partial r}\right)_{r=F}=\left(\frac{\partial\varphi}{\partial r}\right)_{r=F_0}-\frac{1}{F_0}\frac{dF_0}{dx}(F-F_0)\ , \qquad (5)$$

$$\left(\frac{\partial\varphi}{\partial x}\right)_{r=F}=\left(\frac{\partial\varphi}{\partial x}\right)_{r=F_0}+\frac{1}{F_0}\frac{d}{dx}\left(F_0\frac{dF_0}{dx}\right)(F-F_0)\ . \qquad (6)$$

Consequently the pressure on the surface is given by

$$C_p=C_{p0}+2\sum_{n=1}^{\infty}\left[\frac{1}{nF_0{}^n}\frac{d}{dx}\left\{F_0{}^n\frac{d}{dx}(F_0F_n)\right\}-\frac{dF_0}{dx}\frac{dF_n}{dx}-\frac{F_n}{F_0}\frac{d}{dx}\left(F_0\frac{dF_0}{dx}\right)\right]\cos(n\theta+\alpha_n)\ , \qquad (7)$$

where C_{p0} denotes pressure coefficient on the surface of the body of revolution. The distributions of C_{p0} were obtained by Yoshihara[4] for a cone-cylinder (relaxation method), and by the present author[5],[6] for several bodies of revolution with a curved surface (approximate treatment).

Finally we shall study the transonic flow past a body of revolution with a flat base at a small incidence α. Assuming $O(\alpha/t)=O(t)$, Eq. (7) becomes

$$C_p=C_{p0}-4\alpha F_0'(x)\cos\theta\ . \qquad (8)$$

Integrating Eq. (8), and taking account of the base pressure, the drag and the lift coefficients C_d, C_L are obtained as follows:

$$C_d=C_{d0}+O(t^4\log^2 t)\ , \qquad (9)$$

$$C_L=2\alpha+O(t^3\log^2 t)\ , \qquad (10)$$

where C_{d0} denotes the value at zero incidence, and is of the order of $O(t^2\log t)$ for a pointed body. (cf. Eq. (6.47) of Reference [5].) These results are consistent with those for the supersonic flow obtained by the slender body theory[3]. On the other hand, the head drag coefficient of a paraboloid of revolution of finite length at sonic and high subsonic speeds is of the order of $O(t^2)$[1],[5],[6].

References

1) K. Kusukawa: J. Phys. Soc. Japan **12** (1957) 411.
2) Mac. C. Adams and W. R. Sears: J. Aero Sci. **20** (1953) 85.
3) G. N. Ward: Quart. Journ. Mech. and Appl. Math. **2** (1949) 75.
4) H. Yoshihara: WADC Tech. Rep. 52-295 (1952).
5) K. Kusukawa: J. Phys. Soc. Japan **12** (1957) 401.
6) K. Kusukawa: to be published.

J. PHYS. SOC. JAPAN **12** (1957) 981~982

Theory of the Wiedemann Effect

By Mikio YAMAMOTO

The Research Institute for Iron,
Steel and Other Metals,
Tôhoku University

(Received May 27, 1957)

As regards the classical problem of the Wiedemann effect in ferromagnetic polycrystalline substance, any satisfactory theory has not yet been proposed, except Fromy's[1] theory for the case of a thin-walled tube specimen which has been almost entirely neglected in the literature. I give here a theory of the effect for the case of a cylindrical rod specimen, which involves Fromy's theory as a limiting case.

Let us consider a ferromagnetic cylindrical-rod specimen with the diameter a which is fixed at its one end. When this rod is magnetized under longitudinal magnetic field, $\vec{H}_l$, parallel to, and circular field, $\vec{H}_c$, centered at, the rod axis, the resultant magnetic field, H_r, at a point P in the specimen apart from the rod axis by the distance r, is given by $(H_l{}^2+H_{cr}{}^2)^{1/2}$ (H_{cr} is H_c at P), pointing to a direction which makes an angle $\varphi_r=\tan^{-1}(H_{cr}/H_l)$ against the direction of $\vec{H}_l$. The magnetization, $\vec{I}_r$, at P takes a direction for which the sum of the magnetic field and elastic energies is minimum and thus the direction of $\vec{I}_r$ generally does not coincides with that of $\vec{H}_r$ but makes a small angle ε_r with the direction of $\vec{H}_r$ in the $(\vec{H}_l, \vec{H}_{cr})$ plane. Of the components of magnetostrictive strain tensor associated with $\vec{I}_r$, referred to the cylindrical coodinate system (r, z, θ), of which the z axis is the rod axis and the r axis is the direction of radius passing through P, e_{rr}, $e_{\theta\theta}$, e_{zz}, and

$$e_{\theta z}=2\{\lambda_l(I_r)-\lambda_t(I_r)\}\cdot I_{rl}I_{rc}/I_r{}^2 \qquad (1)$$

are not zero, where $\lambda_l(I_r)$ and $\lambda_t(I_r)$ are, respectively, the longitudinal and transverse magnetostrictions associated with $\vec{I}_r$, $I_{rl}=I_r\cos(\varphi_r+\varepsilon_r)$, and $I_{rc}=I_r\sin(\varphi_r+\varepsilon_r)$. $e_{\theta z}$ expresses the shear of unit volume at P along the direction of the rod axis and that along the direction normal to it and the unit volume may be regarded as fixed at its one face, so that $e_{\theta z}$ results the torsion

$$\theta_r=e_{\theta z}/r=(2/r)\{\lambda_l(I_r)-\lambda_t(I_r)\}\cdot I_{rl}I_{rc}/I_r{}^2\,, \qquad (2)$$

this torsion being the Wiedemann effect.

Now, for normal ferromagnetic substances, in which the elastic energy is far smaller than the magnetic field energy and hence the direction of $\vec{I}_r$ coincides with that of $\vec{H}_r$, Eq. (2) may be written as

$$\theta_r=(2/r)\{\lambda_l(H_r)-\lambda_t(H_r)\}\cdot H_lH_{cr}/H_r{}^2\,, \qquad (3)$$

which becomes, for the surface of the rod,

$$\theta_a=(2/a)\{\lambda_l(H_a)-\lambda_t(H_a)\}\cdot H_lH_c{}^a/H_a{}^2\,. \qquad (4)$$

Eq. (4), which holds also for a thin-walled tube, is the expression derived already by Fromy[1] through an elementally and hence lengthy consideration.

Further, if the volume magnetostriction may be neglected as in normal ferromagnetics, Eq. (4) reduces simply to

$$\theta_a=(3/a)\lambda_l(H_a)\cdot H_lH_{ca}/H_a{}^2\,. \qquad (5)$$

It can be shown that Eq. (5) explains quantitatively well all of available experimental facts regarding the Wiedemann effect of cylindrical rod specimens.

Reference

1) E. Fromy: J. de phys., [6] **7** (1926) 13

Frrata

A Simpler Method for Removing Copper from Germanium

By Makoto KIKUCHI and Sigeru IIZIMA
J. Phys. Soc. Japan **12** (1957) 824

Left column line 17 $4\sim7\times10^{-14}/\mathrm{cm}^3$ should be read $4\sim7\times10^{14}/\mathrm{cm}^3$

PROGRESS OF THEORETICAL PHYSICS

(Founded by H. Yukawa in 1946)

Published for the
Research Institute for Fundamental Physics
The Physical Society of Japan

Progress of Theoretical Physics Vol. 17, No. 2, February 1957

On a Solution of Field Equations in Einstein's Unified Field Theory, II .... N. N. GHOSH..131
Note on the Isotopic Spin of the Antiparticle ....Shinzo NAKAI..139
A Method of Calculation of Electrical Conductivity ....Huzio NAKANO..145
One-Center Expansion of Molecular Wave Function, II—*Lower Excited States of H_2*— ....Sigeru HUZINAGA..162
One-Center Expansion of Molecular Wave Function, III—*He-He Repulsive Potential*— ....Sigeru HUZINAGA..169
Theory of the Magnetic Properties of Ferrous and Cobaltous Oxides, I ....Junjiro KANAMORI..177
Theory of the Magnetic Properties of Ferrous and Cobaltous Oxides, II .... Junjiro KANAMORI..197
Antiferromagnetism of Zn-Ferrite.....................M. TACHIKI and K. YOSIDA..223
Hydrodynamical Treatment of Multiple Meson Production in High Energy Nucleon-Nucleus Collisions....S. AMAI, H. FUKUDA, C. ISO and M. SATO..241
Note on Models of Multiple Meson Production at Extremely High Energy ....Ziro KOBA..288

Letters to the Editor:

The Surface Tension of Liquid He^3......S. K. TRIKHA and O. P. RUSTGI..303
Note on Bloch-Nordsieck Transformation and Electron-Lattice Interaction ....H. KANAZAWA..304
On the Exchange Effect in the Stripping Reactions ....T. KAMMURI, R. NAKASIMA and S. TAKAGI..306
A Model for the Inelastic Scattering of Nucleons ....S. OKAI..308

Progress of Theoretical Physics Vol. 17, No. 3, March 1957

An Attempt of Generalizing the Hypothesis of Charge Independence, I—*Selection Rule for the Decay Process*— ....O. HARA and Y. FUJII..313
Effect of Hard Cores on the Binding Energies of H^3 and He^3, II ....T. OHMURA, M. MORITA and M. YAMADA..326
On the Origin of the Magnetic Anisotropy Energy of Ferrites ....K. YOSIDA and M. TACHIKI..331
Pion Theory of Three-Body Forces ....J. FUJITA and H. MIYAZAWA..360
Spin-Orbit Coupling in Heavy Nuclei..................J. FUJITA and H. MIYAZAWA..366
Effects of the Central Spin on Planetary Motion..................Anadijiban DAS..373
Low's Scattering Equation and S-Matrix.........................Hideo FUKUTOME..383
General Integral Formula of Perturbation Term in the Quantized Field Theory

....Noboru NAKANISHI..401
Quantum Field Theory of Unstable Particles ....
................H. ARAKI, Y. MUNAKATA, M. KAWAGUCHI and T. GOTÔ..419
The Magnetic Octupole Moments of Nuclei ....S. SUEKANE and Y. YAMAGUCHI..443
The Hexadecapole Moments of Atomic Nuclei......S. SUEKANE and Y. YAMAGUCHI..449
On the Wave Propagation in the Non-Linear Fields ....Tosiya TANIUTI..461
Theory of the Susceptibility and Specific Heat of He^3 ....Sigeo YOMOSA..487

Letters to the Editor:

Antiproton-Nucleus and Antiproton-Proton Interactions.............
...............M. NOZAWA, T. GOTÔ, N. YAJIMA and R. NAKASIMA..504
Remarks on the Elastic Scattering of Deuterons by Heavy Nuclei...
....Y. NISHIDA..506
K-π Interactions and K^+-N Scattering ....S. MINAMI..508
Quantum Numbers for Lepton Processes ....Y. KATAYAMA..510
He-He Repulsive Potential...............................S. HUZINAGA..512
Equivalence between the Line Width and the Rate of Energy Relaxation in the Inversion Spectrum of Ammonia.............K. TOMITA..513
The Coupling Constants of Strong Interactions...............S. MIYACHI..515
A Remark on the Lepton Processes...........................S. GOTÔ..517
On a Classification of Light Particles ....K. SENBA..519
Some Identities for Renormalization Constants in S(S) and PS(PS) Meson Theories..K. HIIDA..520
Errata...522

Price $ 1.25 per copy
$ 15.00 per year (postage inclusive)
Annual dues for foreign members (individual subscribers)
$ 12.00 (postage inclusive)
〃 for foreign members of the Physical Society of Japan
$ 10.00 (postage inclusive)

Application for members, subscriptions and orders for back numbers should be sent, directly or through book-dealers, to

The Publication Office
in
Yukawa Hall, Kyoto University, Kyoto, Japan

JOURNAL OF THE PHYSICAL SOCIETY OF JAPAN Vol. 12, No. 9, SEPTEMBER 1957

Multichannel Angular Correlation Measurement of Gamma Rays from the Disintegration of Ag^{110m} and Spin Assignment of Excited Levels of Cd^{110}

By Mitsuo SAKAI*, Haruko OHMURA and Teruo MOMOTA

Department of Physics, Faculty of Science, University of Tokyo

(Received May 9, 1957)

The angular correlation of gamma rays from the disintegration of Ag^{110} has been studied with scintillation spectrometers. Ten correlation functions were measured by taking advantage of multichannel characteristic of a twenty-channel pulse height analyzer. The spin values of Cd^{110} in 2.93, 2.48, and 1.54-MeV excited states were found to be 3−, 2+ and 2± respectively and the radiation characteristic of three gamma rays of energies 0.885, 0.935 and 1.390-MeV were also determined.

§1. Introduction

The energy levels of Cd^{110} have been studied on the basis of the decay schemes of Ag^{110}, Ag^{110m} In^{110}, and In^{110m} by a number of investigators. Especially, the complex radiations from the disintegration of Ag^{110m} were studied very carefully by K. Siegbahn, measuring conversion electrons and photoelectrons with beta-ray spectrometer and a decay scheme was proposed by help of Ritz's law in nuclear spectroscopy and of the intensity ratio of gamma rays[1),2)]. The proposed decay scheme is presented in Fig. 1. Since then scintillation counter techniques being developed remarkably, it seems worth while to reexamine the level scheme of the daughter nuclide Cd^{110} by using these techniques. Moreover the advanced angular correlation technique makes one possible for assigning spin values to this complex level system.

In the pursuit of the present work, use of a multi-channel pulse height analyzer is believed to have been essential for the reduction of errors which is due to long-term variation of experimental conditions. In the present work, a twenty-channel pulse height analyzer was used, and the angular correlation functions of several energy intervals in the pulse height spectrum taken by this spectrometer were analyzed on the basis of the decay scheme newly confirmed by the present gamma-gamma scintillation coincidence measurements.

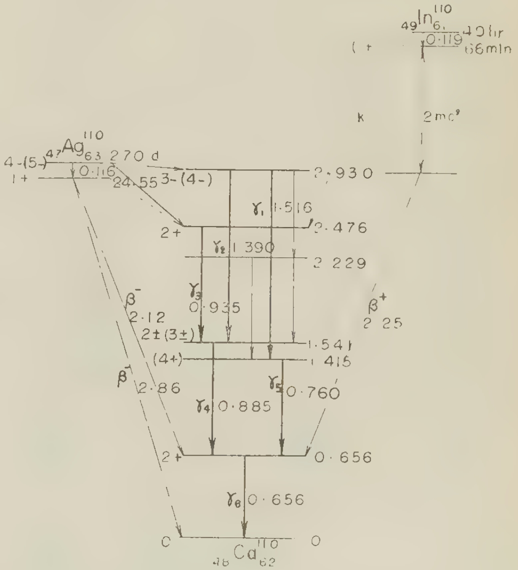

Fig. 1. Level Scheme of Cd^{110}. The studies of In^{110} have not been performed precisely.

§2. Genetic Relation of Gamma Rays

The apparatus consisted of a single channel pulse height analyzer (reference analyzer) and an Atomic twenty-channel pulse height analyzer (main analyzer). The former selected pulses of a certain pulse height from the reference counter and sent to the coincidence unit in the main analyzer. The latter sorted those pulses from the main counter which coincided with the reference channel pulses. The gamma-ray detector attached to the main analyzer was a DuMont 6292 photo-multiplier tube coupled with a mounted 1½″×1″ NaI (Tl) crystal and that of the reference analyzer was a RCA 5819 photo-multiplier tube coupl-

---

* Now at the Institute for Nuclear Study, University of Tokyo

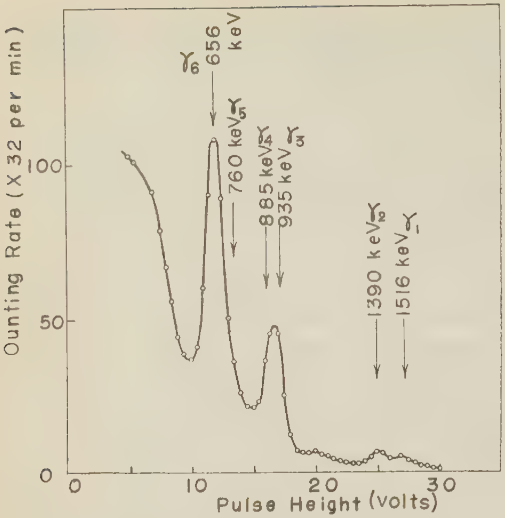

Fig. 2. Pulse-height distribution of gamma rays from Ag^{110m}.

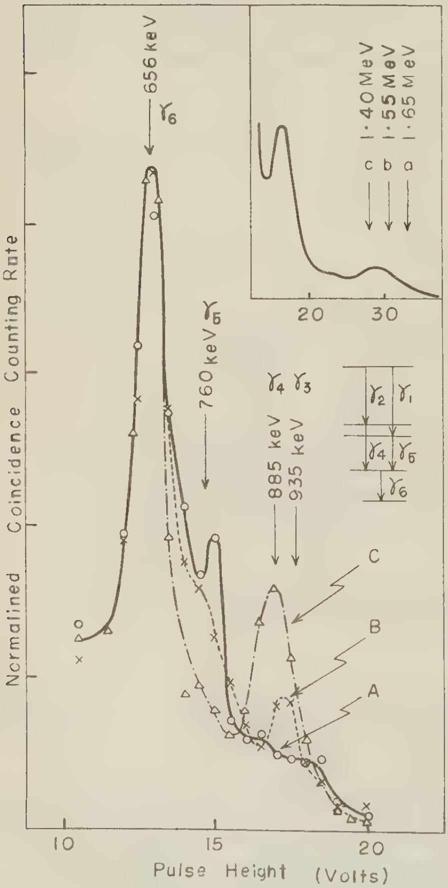

Fig. 3. Coincidence spectra. A, B and C are the coincidence spectra taken by setting the reference gate at a, b and c. The curves are normalized to the same counting rate N' of reference channel.

ed with a $1\frac{1}{2}'' \times 1\frac{1}{2}''$NaI(Tl) crystal. Fig. 2 shows the total pulse height spectrum taken by the main analyzer. Arrows show the pulse-height positions of the full-energy peaks of gamma rays which are indicated as γ_1 through γ_6 (see Fig. 1.)

The genetic relations of γ_1 and γ_2 to the other gamma rays were first investigated. A, B and C in Fig. 3 are the coincidence pulse height spectra taken with the gate of the reference analyzer set at a(1.65-MeV), b(1.55-MeV) and c(1.40-MeV) respectively. The ordinate shows counting rate of the main analyzer relative to the normalized counting rate of the reference analyzer. From these spectra following facts are revealed.

1) The genetic relation between γ_1 and γ_6 is the same as that between γ_2 and γ_6 because the height of each spectrum at 0.65-MeV are almost equal.
2) The coincidence rate at 0.76-MeV decreases in order of A, B and C. This fact can be explained by the genetic relation between γ_1 and γ_5.
3) The coincidence counting rate at 0.885-MeV region increases rapidly in order of A, B and C. The presence of the genetic relation between γ_2 and γ_4 is evident. The partial scheme in the inset of Fig. 3 is thus confirmed.

Next the genetic relation of γ_3 and γ_4 was investigated. In this case the gate of the reference analyzer was set at d(0.96-MeV), e(0.89-MeV) and f(0.82-MeV). (See Fig. 4 inset). The coincidence spectra taken with the main analyzer are presented in Fig. 4 as D, E and F respectively. From these curves one is led to the following conclusions.

4) The coincidence peak at 0.65-MeV shows the presence of the genetic relation of γ_3 and γ_4 to γ_6 and the fact that this peak diminished in order of D, E and F indicates that γ_4 coincides with γ_6, and partly with γ_3. This means that the emission of γ_3 is earlier than that of γ_4.
5) The width of the 0.65-MeV peak of the D-curve is narrower than those of the others. This seems to indicate the coincidence of γ_4 with weak gamma rays of 0.706-MeV and 0.671-Mev reported by K. Siegbahn[1].
6) The peak at about 0.9-MeV moves to the high energy side in order of D, E and F,

This fact indicates the cascade relation of γ_3 and γ_4. The partial decay scheme inserted in Fig. 4 is thus confirmed.

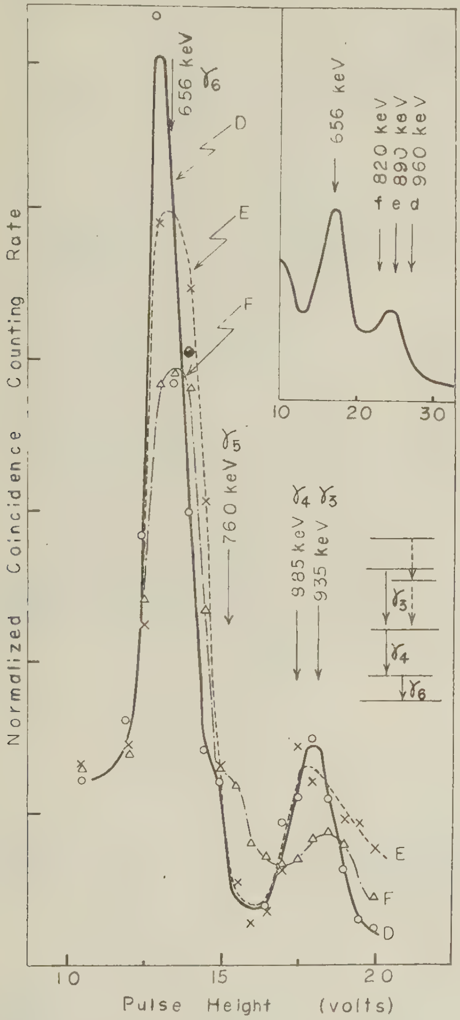

Fig. 4. Coincidence spectra. D, E and F are the coincidence spectra taken by setting the reference gate at d, e and f. The normalization of the curves is same as that in Fig. 3.

By combining above two measurements the main scheme of gamma ray transitions as proposed by K. Siegbahn[1] is established.

§ 3. Angular Correlation Experiment

The angular correlation function is usually written in the form:

$$W(\theta)=1+G_2A_2P_2(\cos\theta)+G_4A_4P_4(\cos\theta), \quad (1)$$

where A_2 and A_4 are the correlation coefficients and G_2* and G_4* are the geometrical attenuation coefficients. The same apparatus was used as in the preceding section. The coefficients G_2, G_4 were deduced from the resolution curve of the annihilation radiation of Co^{56} by Church and Kraushaar's method[3], and their magnitudes were found to be 0.930 and 0.782 respectively. The characteristic of the apparatus was checked by measuring the well-known angular correlation function of gamma rays from Co^{60}. The result is presented in Fig. 5. The agreement with theory is satisfactory.

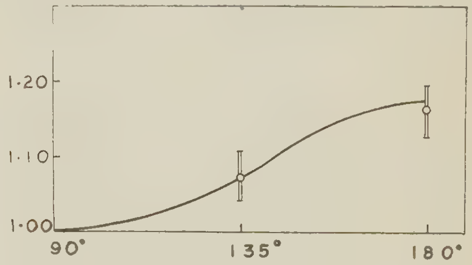

Fig. 5. Angular correlation of Co^{60}. The curve presents the theoretical correlation function. The probable errors at 135° and 180° are taken account of the propagation of error at 90°.

For the Ag^{110m} experiment, the gate of the reference analyzer was set at three positions P_A', P_3' and P_4' shown in Fig. 6b. When the gate was set at P_4', the pulses resistered by the main pulse sorter were composed in the coincidence pulses with those pulses which corresponded to the full energy peak of γ_4 and a certain portions of continuous pluse height spectra of γ_3, γ_2 and γ_1. Similarly, when the gate was set at P_3', pulses corresponding to full energy peak of γ_3 and a portion of Compton plateaus of γ_2 and γ_1 were permitted to pass to the main pulse sorter; while at P_A', Compton pulses of γ_2 and γ_1 only.

For each gate setting of the reference analyzer, coincidence rates in four regions of the pulse height spectrum were taken with the main counter at angles of 90°, 135°, and 180° with respect to the reference one. The four regions mentioned above consisted of R_I'', R_{II}'', R_{III}'' and R_{IV}'', as shown in Fig. 6a, the first of which comprised Compton plateaus of six gamma rays; the second the full energy peak of γ_6 and Compton plateaus

---

* The attenuation due to the extra-nuclear field was not considered in the present paper, because the source was used in the form of an aqueous silver nitrate solution.

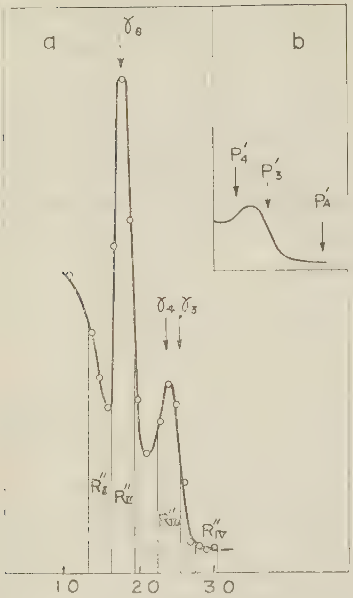

Fig. 6. Pulse-height intervals concidered in the angular correlation masurement of gamma rays from the disintegration of Ag^{110m}. The figure b shows the gate settings in the reference channel.

of γ_5 through γ_1; the third full energy peaks of γ_4 and γ_3 and Compton plateaus of γ_2 and γ_1; while the fourth Compton plateaus of γ_2 and γ_1 only. By this procedure ten possible correlation data were obtained.
They are presented in Table I.

Table I. Coincidence Counting Rate per 10 min.

	90°	135°	180°
$\langle P_A', R_{III}''\rangle$	5.98±0.16	5.24±0.15	4.61±0.14
$\langle P_A', R_{II}''\rangle$	20.18±0.42	17.79±0.40	14.64±0.37
$\langle P_A', R_I''\rangle$	11.14±0.36	9.16±0.30	8.73±0.29
$\langle P_3', R_{III}''\rangle$	29.52±0.62	28.82±0.60	29.91±0.62
$\langle P_3', R_{II}''\rangle$	81.30±0.98	82.44±1.03	78.60±0.97
$\langle P_3', R_I''\rangle$	38.52±0.68	37.87±0.70	37.49±0.72
$\langle P_4', R_{IV}''\rangle$	7.64±0.34	6.83±0.32	5.89±0.30
$\langle P_4', R_{III}''\rangle$	44.38±0.82	43.79±0.81	45.06±0.83
$\langle P_4', R_{II}''\rangle$	156.88±1.54	161.58±1.56	166.39±1.59
$\langle P_4', R_I''\rangle$	67.45±1.01	65.53±1.00	68.06±1.01

The mentioned coincidence counting rates can be written down as the sum of partial ones according to the decay scheme confirmed in the preceding section.

$$\langle P_A', R_{III}''\rangle=\langle n_2(P_A'), n_4(R_{III}'')\rangle \tag{2}$$

$$\begin{aligned}\langle P_A', R_{II}''\rangle=&\langle n_2(P_A'), n_4(R_{II}'')\rangle+\langle n_2(P_A'), n_6(R_{II}'')\rangle\\&+\langle n_1(P_A'), n_5(R_{II}'')\rangle+\langle n_1(P_A'), n_6(R_{II}'')\rangle\end{aligned} \tag{3}$$

$$\begin{aligned}\langle P_A', R_I''\rangle=&\langle n_2(P_A'), n_4(R_I'')\rangle+\langle n_2(P_A'), n_6(R_I'')\rangle\\&+\langle n_1(P_A'), n_5((R_I'')\rangle+\langle n_1(P_A'), n_6(R_I'')\rangle\end{aligned} \tag{4}$$

$$\langle P_3', R_{III}''\rangle=\langle n_3(P_3'), n_4(R_{III}'')\rangle+\langle P_A', R_{III}''\rangle \tag{5}$$

$$\langle P_3', R_{II}''\rangle=\langle n_3(P_3'), n_6(R_{II}'')\rangle+\langle n_3(P_3'), n_4(R_{II}'')\rangle+\langle P_A', R_{II}''\rangle \tag{6}$$

$$\langle P_3', R_I''\rangle=\langle n_3(P_3'), n_6(R_I'')\rangle+\langle n_3(P_3'), n_4(R_I'')\rangle+\langle P_A', R_I''\rangle \tag{7}$$

$$\langle P_4', R_{IV}''\rangle=\langle n_4(P_4'), n_2(R_{IV}'')\rangle \tag{8}$$

$$\langle P_4', R_{III}''\rangle=\langle n_3(P_4'), n_4(R_{III}'')\rangle+\langle n_4(P_4'), n_3(R_{III}'')\rangle+\langle P_4', R_{IV}''\rangle+\langle P_A', R_{III}''\rangle \tag{9}$$

$$\begin{aligned}\langle P_4', R_{II}''\rangle=&\langle n_4(P_4'), n_6(R_{II}'')\rangle+\langle n_3(P_4'), n_6(R_{II}'')\rangle\\&+\langle n_3(P_4'), n_4(R_{II}'')\rangle+\langle n_4(P_4'), n_3(R_{II}'')\rangle+\langle P_4', R_{IV}''\rangle+\langle P_A', R_{II}''\rangle\end{aligned} \tag{10}$$

$$\begin{aligned}\langle P_4', R_I''\rangle=&\langle n_4(P_4'), n_6(R_I'')\rangle+\langle n_3(P_4'), n_6(R_I'')\rangle\\&+\langle n_3(P_4'), n_4(R_I'')\rangle+\langle n_4(P_4'), n_3(R_I'')\rangle+\langle P_4', R_{IV}''\rangle+\langle P_A', R_I''\rangle,\end{aligned} \tag{11}$$

where $\langle X, Y\rangle$ represents the coincidence rate between pulses with height specified by notation X and those specified by Y; $n_i(X)$ or $n_i(Y)$ are their partial counting rate, that is, counting rate due to the ith γ ray; and $\langle n_i(X), n_j(Y)\rangle$ stands for the coincidence rate between $n_i(X)$ and $n_j(Y)$. The following approximations were used for deriving the above formulas;

$$n_1(P_A')\approx n_1(P_3')\approx n_1(P_4'),$$

$$n_2(P_4')\approx n_2(P_3')\approx n_2(P_4')$$

and

$$n_2(R_{\rm I}'')\approx n_2(R_{\rm II}'')\approx n_2(R_{\rm III}'')\approx n_2({\rm R}_{\rm IV}'').$$

The correlation function for a cascade $\gamma_i-\gamma_j$ which is represented by $\langle n_i, n_j\rangle$ can be deduced from the above ten equations. $\langle n_2, n_4\rangle$ is given directly by Eqs. (2) or (8). The agreement between both results is perfect. $\langle n_3, n_4\rangle$ is obtained from Eqs. (5) or (9), by introducing Eqs. (2) or (8) to them. $\langle n_3, n_6\rangle$ can be derived by subtracting Eqs. (6) from (7), namely:

$$\begin{aligned}&\langle n_3(P_3'),\ n_6(R_{\rm II}''-R_{\rm I}''))\rangle\\&\quad=\langle P_3',\ R_{\rm II}''\rangle-\langle P_3',\ R_{\rm I}''\rangle+\langle P_4',\ R_{\rm I}''\rangle\\&\qquad-\langle P_4',\ R_{\rm II}''\rangle\end{aligned}\tag{12}$$

where an approximation $n_4(R_{\rm I}'')\approx n_4(R_{\rm II}'')$ is made. In the same procedure the following equation is obtained from Eqs. (10) and (11),

$$\begin{aligned}&\langle n_4(P_4'),\ n_6(R_{\rm II}''-R_{\rm I}''))\rangle+\langle n_3(P_4'),\\&\quad n_6(R_{\rm II}''-R_{\rm I}'))\rangle=\langle P_4',\ R_{\rm II}''\rangle-\langle P_4',\ R_{\rm I}''\rangle\\&+\langle P_4',\ R_{\rm I}''\rangle-\langle P_4',\ R_{\rm II}''\rangle\cdots\end{aligned}\tag{13}$$

Then the correlation function $\langle n_4, n_6\rangle$ is given by the following formula:

$$\begin{aligned}&\langle n_4(P_4'),\ n_6(R_{\rm II}''-R_{\rm I}''))\rangle\\&\qquad=\langle\beta\rangle-\frac{n_3(P_4')}{n_3(P_3')}\langle\alpha\rangle\ ,\end{aligned}$$

where $\langle\alpha\rangle$ and $\langle\beta\rangle$ denote the quantities expressed by (12) and (13) respectively. The ratio $n_3(P_4')/n_3(P_3')$ can not be estimated exactly. But this ambiguity scarcely influences on the anisotropy of $\langle n_4, n_6\rangle$. For instance, its variation from 0.4 to 0.7 produces a difference of only few per cent in the anisotropy. The experimental correlation functions are plotted in Fig. 7, and the numerical data are presented in Table II.

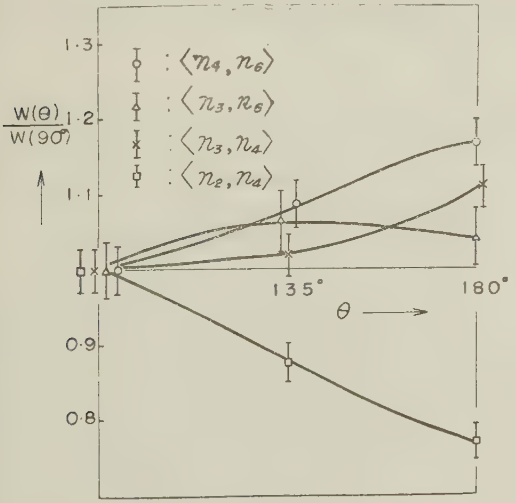

Fig. 7. Angular correlation functions.

Table II.

	90°	135°	180°
$\langle n_2, n_4\rangle$	1.000±0.027	0.876±0.025	0.770±0.023
$\langle n_3, n_4\rangle$	1.000±0.028	1.018±0.028	1.100±0.028
$\langle n_3, n_6\rangle$	1.000±0.038	1.064±0.040	1.042±0.038
$\langle n_4, n_6\rangle$	1.000±0.032	1.087±0.032	1.168±0.032

§ 4. Analysis of the Results

For analyzing the results of the preceding section, G_2A_2 and G_4A_4 were first calculated by making use of Eq. (1) and Table II. G_2 and G_4 being the known quantities, the values of A_2 and A_4 were obtained. The Table III is the list of A_2 and A_4.

Table III.

	A_2	A_4
$\langle n_4, n_6\rangle$	0.1151±0.0316	−0.0032±0.0339
$\langle n_3, n_4\rangle$	0.0577±0.0286	0.0366±0.0308
$\langle n_3, n_6\rangle$	0.0460±0.0381	−0.0486±0.0413
$\langle n_2, n_4\rangle$	−0.1835±0.0282	0.0114±0.0304

The characteristics of gamma rays γ_1 to γ_6 were analyzed according to Biedenharn and Rose's paper[4),5)] and Krohn and Roboy's paper[6)]. The former treated the mixed gamma-mixed gamma angular correlation and the latter treated the mixed gamma correlation with the intermediate radiation unobserved. The essential points of this analysis are as follows.

1) The first excited level was assumed to be 2+ because all first excited levels of even-even nuclei have spin 2+ with very few exceptions[7)].

2) The spin value of the third 1.54-MeV excited level was investigated for the possible cases of 2, 3 and 4.

The last possibility was, however, eliminated in this stage. The experimental A_2 and A_4 values of $\langle n_4, n_6\rangle$ agreed with the theoretical values for this case which were 0.102 and 0.0091 respectively. But if this spin sequence of 0–2–4 is the case, $\langle n_3, n_6\rangle$ should always be equal to $\langle n_3, n_4\rangle$. This fact can be easily verified by a simple calculation and the experimental values are in contradiction to this theorem[8]. Therefore we were led to the conclusion that this level did not have the spin value of 4.

So we have to seek the possibility for the case of spin 2 or 3, by searching the possible domain of the mixing ratio δ_4 of γ_4 which gives the correlation function consistent with the experimental data, where δ_4 is defined as the ratio of transition matrix element of $E2$ to that of $M1$[4]. The possible domains of δ_4 were found to be $0.12 < \delta_4(-) < 0.20$ and $0.22 < \delta_4(-) < 0.34$ for the cases of spin 2 and 3 respectively. (See Fig. 8).

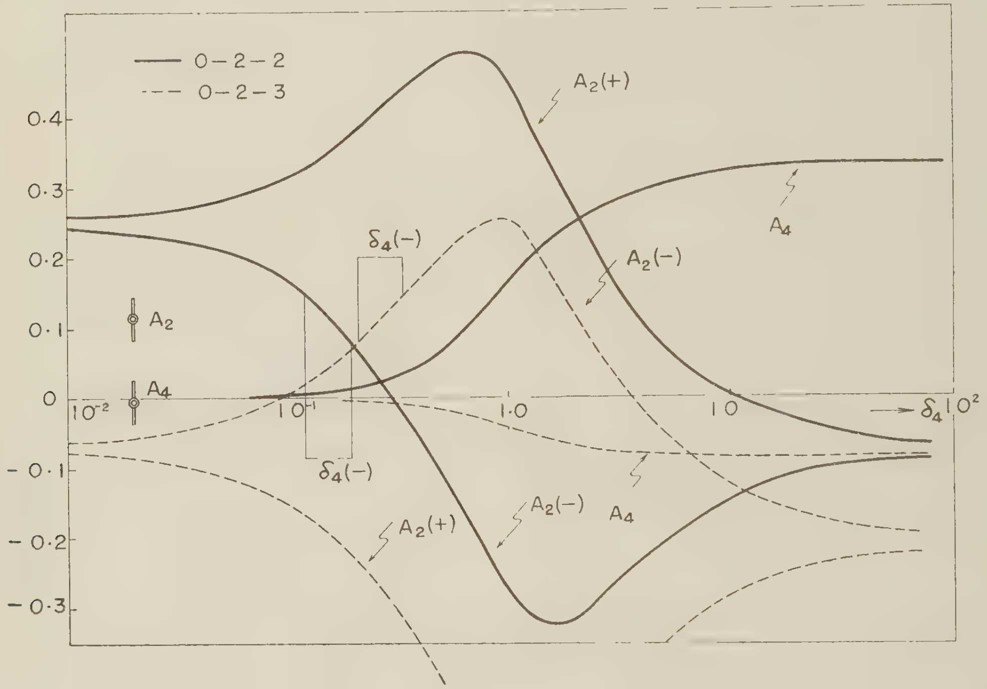

Fig. 8. Theoretical curves of A_2 and A_4 for the decay sequences of $2(\delta_4)2(Q)0$ and $3(\delta_4)2(Q)0$. The experimental values of A_2 and A_4 and the regions of probable mixing ratio are also indicated in the same figure.

3) The results of $\langle n_3, n_6\rangle$ and $\langle n_3, n_4\rangle$ enable use to make the cross check on the assignment for the fourth 2.48-MeV excited level. This means that for the fixed δ_4 obtained from the analysis of 2), we have to have the δ_3 value of γ_3 which can explain both of the correlation behavior of $\langle n_3, n_6\rangle$ and $\langle n_3, n_4\rangle$ at the same time. The analysis were made for the cases of the spin value 2, 3, 4 and 5. By this procedure many combinations of δ_4 and δ_3 were excluded.*

4) Using δ_4 consistent with the analysis of 2) and 3) the analysis was extended to the determination of spin value of the fifth 2.93-MeV excited level by using the data of $\langle n_2, n_4\rangle$ and the consistent domain of δ_2 was determined. The results of 3) and 4) are summarized in Table IV, a and b.

The possible spin sequence obtained from these analyses were listed in Table V.

Up to present, the spin sequence was discussed purely by the information from the gamma-gamma angular correlation experiments. For the further analysis, it is helpful to make use of the knowledges from the beta disintegration. As is well known, the spin of the ground state of Ag^{110} is 1+ because of the allowed characteristic of the two beta decays involved in this state to the ground and to the first excited state of the daughter nucleus of Cd^{110}. The K/L ratio of 116-KeV gamma ray from the isomeric state

---

* For this case the sign of δ_4 deduced from 2) should be changed in the deduction of the theoretical correlation function, according to its definition in Biedenharn and Rose's paper[4].

Table IV. a.

0-2-2 Sequence $0.12 < \delta_4(-) < 0.20$

Spin Sequence		$A_2(34)$	$A_4(34)$	$A_2(36)$	$A_4(36)$	$A_2(24)$	$A_4(24)$
	Experimental value	0.0577 ± 0.0286	0.0366 ± 0.0308	0.0460 ± 0.0381	-0.0486 ± 0.0413	-0.1835 ± 0.0283	0.0114 ± 0.0304
0- 2-2-2	Theoretical value	$\left\{\begin{matrix}-0.5532\\-0.6321\end{matrix}\right\}\alpha_{22}(\delta_3)$	$\left\{\begin{matrix}0.0013\\0.0036\end{matrix}\right\}\beta_{22}(\delta_3)$	$\left\{\begin{matrix}-0.2926\\-0.2826\end{matrix}\right\}\alpha_{22}(\delta_3)$	$\left\{\begin{matrix}-0.2125\\-0.2056\end{matrix}\right\}\beta_{22}(\delta_3)$	$\left\{\begin{matrix}-0.5532\\-0.6321\end{matrix}\right\}\alpha_{22}(\delta_2)$	$\left\{\begin{matrix}0.0013\\0.0036\end{matrix}\right\}\beta_{22}(\delta_2)$
	Remark	The possible region for δ_3 around -0.27 is found. The theoretical values for this case are as follows, $0.040 < A_2(34) < 0.046$, $0.0001 < A_4(34) < 0.0003$, $0.0206 < A_2(36) < 0.0213$ and $-0.0144 < A_4(36) < -0.0139$				The possible domains for δ_2 are $0.56 < \delta_2(-) < 0.72$ and $4.3 < \delta_2(-) < 10.0$	
0-2-2-3	Theoretical value	$\left\{\begin{matrix}-0.5532\\-0.6321\end{matrix}\right\}\alpha_{23}(\delta_3)$	$\left\{\begin{matrix}-0.0003\\-0.0009\end{matrix}\right\}\beta_{23}(\delta_3)$	$\left\{\begin{matrix}-0.2926\\-0.2826\end{matrix}\right\}\alpha_{23}(\delta_3)$	$\left\{\begin{matrix}0.0531\\0.0514\end{matrix}\right\}\beta_{23}(\delta_3)$	$\left\{\begin{matrix}-0.5532\\-0.6321\end{matrix}\right\}\alpha_{23}(\delta_2)$	$\left\{\begin{matrix}-0.0003\\-0.0009\end{matrix}\right\}\beta_{23}(\delta_2)$
	Remark	The remarkable contradiction of the theoretical $A_4(36)$ against the experimental one and a small discrepancy of $A_4(34)$ between the theoretical and the experimental one exclude the possibility of this spin sequence.				The δ_2 value in the domains of $0.10 < \delta_2(+) < 0.18$, $50 < \delta_2(+)$ and $13 < \delta_2(-)$ makes the experimental value consistent with the theoretical one.	
0-2-2 4	Theoretical value	$\left\{\begin{matrix}0.0946\\0.1081\end{matrix}\right\}$	$\left\{\begin{matrix}0.00004\\0.0001\end{matrix}\right\}$	$\left\{\begin{matrix}0.0500\\0.0483\end{matrix}\right\}$	$\left\{\begin{matrix}-0.0059\\-0.0057\end{matrix}\right\}$	$\left\{\begin{matrix}0.0946\\0.1081\end{matrix}\right\}$	$\left\{\begin{matrix}0.00004\\0.0001\end{matrix}\right\}$
	Remark	The theoretical values of $A_2(34)$, $A_4(34)$ and $A_4(36)$ are just outside of the experimental ones. Therefore this spin sequence must be eliminated.				The positive theoretical correlation function excludes this spin sequence.	

$\alpha_{ij}(\delta_k)$ and $\beta_{ij}(\delta_k)$ are defined as follows.

$$\alpha_{22}(\delta_k)=\frac{-0.4183-1.226\delta_k+0.1281\delta_k^2}{1+\delta_k^2}, \qquad \alpha_{23}(\delta_k)=\frac{0.1195+1.310\delta_k+0.3415\delta_k^2}{1+\delta_k^2}$$

$$\beta_{22}(\delta_k)=\beta_{23}(\delta_k)=\frac{\delta_k^2}{1+\delta_k^2}$$

Table IV. b.

0-2-3 Sequence $0.22 < \delta_4(-) < 0.34$

Spin sequence		$A_2(34)$	$A_4(34)$	$A_2(36)$	$A_4(36)$	$A_2(24)$	$A_4(24)$
	Experimental value	0.0577 ± 0.0286	0.0366 ± 0.0308	0.0460 ± 0.0381	-0.0486 ± 0.0413	-0.1835 ± 0.0282	0.0114 ± 0.0304
0 2-3-2	Theoretical value	$\left\{\begin{matrix}-0.074\\-0.281\end{matrix}\right\}\alpha_{32}(\delta_3)$	$\left\{\begin{matrix}0.0207\\0.0466\end{matrix}\right\}\beta_{32}(\delta_3)$	$\left\{\begin{matrix}-0.480\\-0.458\end{matrix}\right\}\alpha_{32}(\delta_3)$	$\left\{\begin{matrix}-0.2653\\-0.2220\end{matrix}\right\}\beta_{32}(\delta_3)$	$\left\{\begin{matrix}-0.074\\-0.281\end{matrix}\right\}\alpha_{32}(\delta_2)$	$\left\{\begin{matrix}0.0207\\0.0466\end{matrix}\right\}\beta_{32}(\delta_2)$
	Remark	The possible region of δ_3 is found around $+0.26$. For this case the theoretical A_2 and A_4 are as follows: $0.0107 < A_2(34) < 0.0406$, $0.0013 < A_4(34) < 0.0030$; $0.0663 < A_2(36) < 0.0694$, $-0.0168 < A_4(36) < -0.0141$				The region of $0.11 < \delta_2(-) < 2.5$ gives the theoretical correlation function consistent with the experimental one.	
0-2-3 3	Theoretical value	$\left\{\begin{matrix}-0.074\\-0.281\end{matrix}\right\}\alpha_{33}(\delta_3)$	$\left\{\begin{matrix}-0.0139\\-0.0312\end{matrix}\right\}\beta_{33}(\delta_3)$	$\left\{\begin{matrix}-0.480\\-0.458\end{matrix}\right\}\alpha_{33}(\delta_3)$	$\left\{\begin{matrix}0.177\\0.148\end{matrix}\right\}\beta_{33}(\delta_3)$	$\left\{\begin{matrix}-0.074\\-0.281\end{matrix}\right\}\alpha_{33}(\delta_2)$	$\left\{\begin{matrix}-0.0139\\-0.0312\end{matrix}\right\}\beta_{33}(\delta_2)$
	Remark	The signs of the theoretical $A_4(34)$ and $A_4(36)$ are in contradiction to the experimental values. Therefore the possibility of this sequence can be excluded.				The theoretical $A_2(24)$ is not compatible with the experimental one.	
0-2-3-4	Theoretical value	$\left\{\begin{matrix}-0.074\\-0.281\end{matrix}\right\}\alpha_{34}(\delta_3)$	$\left\{\begin{matrix}0.0046\\0.0104\end{matrix}\right\}\beta_{34}(\delta_3)$	$\left\{\begin{matrix}-0.480\\-0.458\end{matrix}\right\}\alpha_{34}(\delta_3)$	$\left\{\begin{matrix}-0.0589\\-0.0492\end{matrix}\right\}\beta_{34}(\delta_3)$	$\left\{\begin{matrix}-0.074\\-0.281\end{matrix}\right\}\alpha_{34}(\delta_2)$	$\left\{\begin{matrix}0.0046\\0.0104\end{matrix}\right\}\beta_{34}(\delta_2)$
	Remark	The common domain of δ_3 is found for this case to be $2.9 < \delta_3(-) < 3.3$. For the value of $\delta_3(-) = 3.1$, we find the following values: $0.0095 < A_2(34) < 0.0359$, $0.0042 < A_4(34) < 0.0094$; $0.0586 < A_2(36) < 0.0614$, $-0.0533 < A_4(36) < -0.0446$				We find a possible correlation function for the domain of $0.28 < \delta_2(+) < 6.0$	
0 2-3-5	Theoretical value	$\left\{\begin{matrix}0.0152\\0.0585\end{matrix}\right\}$	$\left\{\begin{matrix}-0.001\\-0.002\end{matrix}\right\}$	$\left\{\begin{matrix}0.0990\\0.0944\end{matrix}\right\}$	$\left\{\begin{matrix}0.0120\\0.0101\end{matrix}\right\}$	$\left\{\begin{matrix}0.0152\\0.0585\end{matrix}\right\}$	$\left\{\begin{matrix}-0.001\\-0.002\end{matrix}\right\}$
	Remark	The theoretical values of $A_4(34)$, $A_2(36)$ and $A_4(36)$ are outside of the probable error of the experimental values. So this possibility is eliminated.				The theoretical positive tendency is in contradiction to the experimental value.	

$\alpha_{ij}(\delta_k)$ and $\beta_{ij}(\delta_k)$ are defined as follows.

$$\alpha_{32}(\delta_k) = \frac{0.3464 - 1.897\delta_k - 0.1237\delta_k^2}{1+\delta_k^2}, \qquad \alpha_{33}(\delta_k) = \frac{-0.4330 - 0.868\delta_k + 0.2268\delta_k^2}{1+\delta_k^2}, \qquad \alpha_{34}(\delta_k) = \frac{0.1443 + 1.445\delta_k + 0.3093\delta_k^2}{1+\delta_k^2}$$

and

$$\beta_{32}(\delta_k) = \beta_{33}(\delta_k) = \beta_{34}(\delta_k) = \frac{\delta_k^2}{1+\delta_k^2}$$

was deduced by the careful interpolation of the Rose's Table[9]. The values obtained for the cases of $E3$, $M3$, $E4$, $M4$, $E5$ and $M5$ are presented in Table VI with the experimental value. From this table the $E3$ transition seems to be more probable than other possibilities. But, of course $M4$ transition could not entirely be excluded. Then the spin of the isomeric state of Ag^{110m} may be 4− or 5−. Since the 87-KeV beta transition involved in this level is allowed type it seems reasonable to assign 3−, 4− or 5− to the 2.93-MeV level. Therefore the spin sequences of D, E and F in Table V are eliminated. The 530-KeV beta transition has a $f-t$ value of 10^8, indicating even parity and possible spin value 2+, 3+, 6+ and 7+ for the 2.48-MeV level. On the other hand, there is an indication[10] which shows the ground state of Ag^{110} decays partially to this level. This fact may exclude the spin sequence C of the Table V.

Table V. The most probable spin and parity assignments in order of decreasing probability.

Energy (MeV) / Scheme	2.93	2.48	1.541	0.656	0
A	3−	2+	2±	2+	0
B	4−	2+	3±	2+	0
C	4−	4+	3±	2+	0
D	2−	2+	2±	2+	0
E	2−	2+	3±	2+	0
F	2−	4+	3±	2+	0

Table VI. K/L ratio for 116-KeV gamma ray.

Theoretical value						Experimental value
$E3$	$M3$	$E4$	$M4$	$E5$	$M5$	
1.63	3.61	0.46	1.73	0.185	1.04	1.3

Therefore we have two probable spin assignment, A and B for the excited levels of Cd^{110}. As one can see from the Table IV, a and b, the theoretical $A_4(34)$ of A and B is out side of the experimental value. But in reality, the determination of A_4 from the angular correlation work is very delicate and we can not say that this discrepancy is very serious. In the present experimental stage we can not choose the one of these alternatives. However it seems that we have a reason to prefer A over B. In progress of experimental technique, the decay scheme becomes clearer, and the spin doublet of 2+ and 4+ due to the core excitation[11] can be found in many nuclei, for instance, Fe^{56}, Co^{60}, Kr^{84}, Cd^{114} and Hg^{198}. And the application of this spin doublet idea[12] for this case is very attractive. Especially it is interesting to compare the decay scheme of Cd^{114} recently explored by Motz[13]. By this comparison the second 1.415-MeV excited state of Cd^{110} may have the spin 4+. Then the reason why the gamma transition from the third level to the ground level did not exist or it was scarcely detected could be explained by the difficulty of two phonon transition. But of course the possibility of the sequence B is not excluded. This ambiguity will be reduced if the exact knowledge on the beta disintegration of Ag^{110} and In^{110,110m} could be obtained. A more elaborate measurements are desired in future.

The authors would like to express their sincere thanks to Dr. M. Morita for the valuable theoretical discussions.

References

1) K. Siegbahn: Phys. Rev. **77** (1950) 233.
2) M. Goldhaber and R. D. Hill: Revs. Modern Phys. **24** (1952) 179.
3) E. L. Church and J. J. Kraushaar: Phys. Rev. **88** (1952) 419.
4) L.C. Biedenharn and M.E. Rose: Revs. Modern Phys. **25** ('53) 729.
5) M. E. Rose: Phys. Rev. **93** (1954) 477.
6) V. E. Krohn and S. Roby: Phys. Rev. **97** (1955) 1017.
7) M. Goldhaber and A. Sunyar: Phys. Rev. **83** (1951) 906.
G. Scharff-Goldhaber: Phys. Rev. **90** (1953) 587.
8) M. Sakai: J. Phys. Soc. Japan **10** (1955) 729.
9) M. E. Rose: in K. Siegbahn, "Beta and Gamma Ray Spectroscopy".
10) F. I. Boley: Phys. Rev. **94** (1954) 1078.
11) G. Scharff-Goldhaber and J. Weneser: Phys. Rev. **98** (1955) 212.
12) Alder et al.: Rev. Modern Phys. **28** (1956) 432 §V. C. 3.
13) H. T. Motz: Phys. Rev. **104** (1956) 1353.

JOURNAL OF THE PHYSICAL SOCIETY OF JAPAN Vol. 12, No. 9, SEPTEMBER, 1957

Temperature Variation of Mayer's Cluster Integrals

By Taro KIHARA and Shobu KANEKO

Department of Physics, Faculty of Science, University of Tokyo

(Received June 8, 1957)

By use of the square-well model of intermolecular potential, temperature variation of Mayer's cluster integrals, b_l for $l=2, 3, \cdots$, has been investigated (except the region of very high temperature where soft repulsive potential must be taken into account). The b_2 is monotone; b_3 has a minimum near the Boyle temperature T_B; b_4 has a minimum below T_B and a maximum above T_B; b_5 has a sharp minimum below T_B, a maximum near T_B, and a minimum above T_B; and so forth. Curves are shown up to b_6.

By use of Mayer's cluster integrals, b_l for $l=1, 2, \cdots$, the equation of state of gases is expressed in the form of parameter representation ($b_1=1$)

$$P=kT(z+b_2z^2+b_3z^3+\cdots)\ ,$$

$$N=V(z+2b_2z^2+3b_3z^3+\cdots)\ .$$

Here P is the pressure, T the temperature, k Boltzmann's constant, N the number of molecules in the volume V. The parameter z is a kind of fugacity or activity. Eliminating z from these two series we obtain an expansion in $v^{-1}\equiv N/V$

$$P=kT\left(v^{-1}-\frac{1}{2}\,\beta_1 v^{-2}-\frac{2}{3}\,\beta_2 v^{-3}-\cdots\right),$$

β_l being called lth irreducible integral. Relations between the cluster integrals and the irreducible integrals are the following[1]:

$$b_2=\frac{1}{2}\beta_1\ ,$$

$$b_3=\frac{1}{2}\beta_1^2+\frac{1}{3}\beta_2\ ,$$

$$b_4=\frac{2}{3}\beta_1^3+\beta_1\beta_2+\frac{1}{4}\beta_3\ ,$$

$$b_5=\frac{25}{24}\beta_1^4+\frac{5}{2}\beta_1^2\beta_2+\beta_1\beta_3+\frac{1}{2}\beta_2^2+\frac{1}{5}\beta_4\ ,$$

$$b_6=\frac{9}{5}\beta_1^5+6\beta_1^3\beta_2+3\beta_1^2\beta_3+\beta_1\beta_4+3\beta_1\beta_2^2$$
$$+\beta_2\beta_3+\frac{1}{6}\beta_5\ .$$

The second and third cluster integrals have been calculated in detail for adequate intermolecular potentials; the results explain temperature variations of the corresponding observed values. As regards fourth and higher cluster integrals detailed calculation is still lacking. In fact minute evaluation may not be needed, because their observed values are not accurate at all. It is desirable, however, to know characteristic feature of the temperature variation of cluster integrals, partly because the cluster integrals play an essential role in theories of condensation.

The characteristic feature of the cluster integrals for simple gases can be obtained by calculating them for the square-well potential[2]

$$U(r)=\begin{cases}\infty & \text{for}\quad r<r_0\\ -U_0 & \text{for}\quad r_0<r<gr_0\\ 0 & \text{for}\quad gr_0<r\end{cases}\qquad(1)$$

between two molecules, which potential is assumed to be additive in a system of three and more molecules. Here r is the intermolecular distance, r_0 is the diameter of the hard core of a molecule, U_0 denotes the depth of the potential well, and g is a parameter indicating the width of the well, appropriate value of g being probablly between 1.5 and 2. The second cluster integral for this model is simply given by

$$b_2=4v_0[(g^3-1)x-1]\ ,$$

where

$$x\equiv\exp(U_0/kT)-1\ ,$$

and

$$v_0\equiv(\pi/6)r_0^3$$

is the volume of the hard core of a molecule. The third cluster integral is a polynomial of third order in x:

$$b_3=v_0^2[27+(g^6-18\,g^4-32\,g^3+49)x$$
$$+(34\,g^6-36\,g^4-32\,g^3+18\,g^2+16)x^2$$
$$+(6\,g^6-18\,g^4+18\,g^2-6)x^3]\quad\text{for}\ g\leqq 2\ ,$$

$$b_3=v_0^2[27-(64\,g^3-81)x$$
$$+(32\,g^6-96\,g^3+18\,g^2+80)x^2$$

$$+(5g^6-32g^3+18g^2+26)x^3] \quad \text{for } g \leq 2.$$

There is a temperature, T_B, called Boyle temperature, below which b_2 is positive and above which it is negative. In connection to the Boyle temperature, let us define a volume v_B by the negative derivative of b_2 with respect to T/T_B:

$$v_B = -\left(T\frac{db_2}{dT}\right)_{T=T_B}.$$

For our square-well potential, these quantities are related to the model constants by the relations

$$\frac{U_0}{kT_B} = \ln\frac{g^3}{g^3-1}, \quad \frac{v_B}{4v_0} = g^3 \ln\frac{g^3}{g^3-1}.$$

Taking the characteristic values T_B and v_B as units, let us consider dimensionless "normalized cluster integral"

$$b_l^* = b_l/v_B^{l-1}$$

as functions of T/T_B. Owing to this procedure we can eliminate model constants, r_0 and U_0. The normalized second and third cluster integrals are shown in Fig. 1. Curves for $g=\infty$ indicate the limits for $g\to\infty$ and $U_0\to 0$, g^3U_0 being kept constant, at which

$$kT_B = g^3U_0, \quad v_B = 4v_0.$$

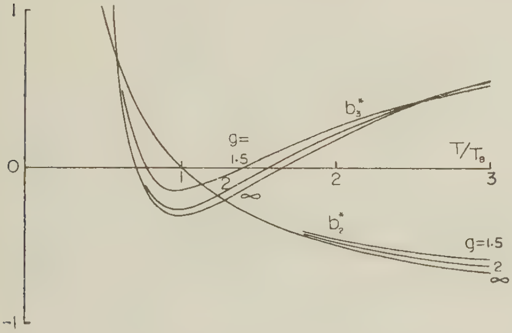

Fig. 1. Normalized second and third cluster integrals for the square-well potential.

They are given by

$$b_2^* = \frac{T_B}{T} - 1,$$

$$b_3^* = 2\left(\frac{T_B}{T} - 1\right)^2 - \frac{5}{16}.$$

It is important to notice that normalized cluster integrals are not very sensitive to the parameter g so far as $g \geq 2$. Hence general characteristics of the fourth and higher cluster integrals can be obtained by calculating them in the limiting case of $g=\infty$. Fortunately, the cluster integrals in this limiting case can be obtained by virtue of the following theorem.

The third and higher irreducible integrals, β_l for $l \geq 3$, for the square-well potential (1) with $g\to\infty$ and $U_0 \to g^{-3}kT_B$ are equal to the corresponding quantities for rigid spheres of the diameter r_0:

$$U(r)\begin{cases}\infty & \text{for } r<r_0 \\ 0 & \text{for } r>r_0.\end{cases}$$

In other words, attractive part of the intermolecular potential in this limiting case does not influence the third and higher irreducible integrals. A proof can easily be made when we use Mayer's expression for the irreducible integrals.

Thus in our limiting case, higher irreducible integrals are independent of the temperature:

$$\beta_2 = -\frac{15}{16}v_B^2, \quad \beta_3 = -\gamma_4 v_B^3, \quad \beta_4 = -\gamma_5 v_B^4, \cdots.$$

Here numerical values of γ_4 and γ_5 are[3,4]

$$\gamma_4 = 0.383, \quad \gamma_5 = 0.14.$$

By use of relations between cluster integrals and irreducible integrals we finally obtain

$$b_4^* = \frac{16}{3}\left(\frac{T_B}{T}-1\right)^3 - \frac{15}{8}\left(\frac{T_B}{T}-1\right) - \frac{1}{4}\gamma_4,$$

$$b_5^* = \frac{50}{3}\left(\frac{T_B}{T}-1\right)^4 - \frac{75}{8}\left(\frac{T_B}{T}-1\right)^2 - 2\gamma_4\left(\frac{T_B}{T}-1\right) + \frac{1}{2}\left(\frac{15}{16}\right)^2 - \frac{1}{5}\gamma_5.$$

These are continuations of the expressions for

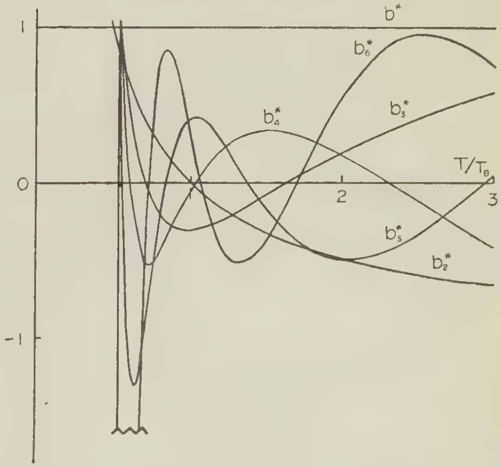

Fig. 2. Normalized cluster integrals for the square-well potential with $g=\infty$.

b_2^* and b_3^* given before. Curves representing these functions are shown in Fig. 2.

The numerical value of γ_5 is not accurate, but it does not influence the curve of b_5^*. Moreover we can draw the curve of

$$b_6^* = \frac{288}{5}\left(\frac{T_B}{T}-1\right)^5 - 45\left(\frac{T_B}{T}-1\right)^3 - 12\gamma_4\left(\frac{T_B}{T}-1\right)^2 + 2\left\{3\left(\frac{15}{16}\right)^2 - \gamma_5\right\}\left(\frac{T_B}{T}-1\right) + \frac{15}{16}\gamma_4 - \frac{1}{6}\gamma_6 \,.$$

without knowing the numerical value of γ_6, which curve is also included in Fig. 2.

References

1) J. E. Mayer and M. G. Mayer: *Statistical Mechanics* (1940) p. 288.
2) T. Kihara: Revs. Modern Phys. **25** (1953) 831.
3) See R. H. Fowler and E. A. Guggenheim: *Statistical Thermodynamics* (1939) p. 289.
4) M. N. Rosenbluth and A. W. Rosenbluth: J. Chem. Phys. **22** (1954) 881.

JOURNAL OF THE PHYSICAL SOCIETY OF JAPAN Vol. 12, No. 9, SEPTEMBER, 1957

Stress-Strain Relations for Viscoelastic Large Deformation

By Wataru SEGAWA

Training Institute for Education, Mishima, Shizuoka-ken

(Received March 18, 1957)

Stress-strain relation for non-homogeneous, three-dimensional and infinitesimal deformation were given by T. Alfrey[1] as follows:

$$d\gamma_i/dt = \frac{1}{G}\sum_j a_{ij}dS_j/dt + \frac{1}{\eta}\sum_j a_{ij}S_j \qquad \text{for Maxwellian material}$$

$$\sum_j a_{ij}S_j = G\gamma_i + \eta d\gamma_i/dt \qquad \text{for Voigtian material}$$

In this paper, the relations corresponding to above two equations are extended so as to be valid for large deformation. For example, the equations for incompressible Maxwellian material having a single relaxation time are as follows:

$$\partial(2\varepsilon_{xx})/\partial t = 1/\mu\cdot\partial/\partial t\cdot(P_{xx}+\mu\varphi) + 1/\eta(P_{xx}+\mu\varphi)$$

$$\partial(\varepsilon_{yz})/\partial t = 1/\mu\cdot\partial/\partial t\cdot(P_{yz}) + 1/\eta\cdot(P_{yz})$$

and corresponding equations for the other stress components.

These equations are then applied to three cases (constant stress, constant strain, and constant strain rate), results of which can be reduced to those of the ordinary case, if higher terms of strain can be neglected.

§ 1. Introduction

Stress-strain relations for Maxwellian and Voigtian material were given by T. Alfrey[1] as follows:

$$\frac{d\gamma_i}{dt} = \frac{1}{G}\sum_j a_{ij}\frac{dS_j}{dt} + \frac{1}{\eta}\sum_j a_{ij}S_j$$

for Maxwellian material (1)

$$\sum_j a_{ij}S_j = G\gamma_i + \eta\frac{d\gamma_i}{dt}$$

for Voigtian material (2)

These equations can be derived by combining the equation of elasticity,

$$\gamma_i = \frac{1}{G}\sum_j a_{ij}S_j \qquad (3)$$

which holds for purely elastic material, with the viscosity relationship.

Equations (1) and (2) are valid for infinitesimal deformation of incompressible isotropic material as well as equation (3) is.

Thus, if we want to extend the equation (1) or (2) to the case of large deformation, we must replace equation (3) by another equation which is valid for large deformation.

In this paper, we shall use the stress-strain relation of rubber[2),3)] in the Neo-Hookian theory, instead of equation (3). First we shall construct the stress-strain relations of incompressible isotropic materials for large deformation and then some simple applications of them will be done.

§ 2. Fundamental Equations

According to the Neo-Hookian theory, the stress-strain relation of rubber[2),3)] is given by the following equations:

$$\left.\begin{aligned} P_{xx}&=\mu\left(\frac{1+2\varepsilon_{xx}}{\det T}-\varphi\right) \\ P_{yz}&=\mu\cdot\varepsilon_{yz}/\det T \end{aligned}\right\} \qquad (4)$$

and corresponding equations for the other stress conponents, where T is given by

$$T=\begin{pmatrix} \frac{\partial X}{\partial x} & \frac{\partial X}{\partial y} & \frac{\partial X}{\partial z} \\ \frac{\partial Y}{\partial x} & \frac{\partial Y}{\partial y} & \frac{\partial Y}{\partial z} \\ \frac{\partial Z}{\partial x} & \frac{\partial Z}{\partial y} & \frac{\partial Z}{\partial z} \end{pmatrix} \qquad (5)$$

and $\det T$ represents the volume dilation, and φ is the undetermined isotropic component of stress.

In this paper, we treat only the incompressible case, so we can use the condition $\det T=1$, and the equation (4) results in the next equation.

$$\left.\begin{aligned} 1+2\varepsilon_{xx}&=\frac{1}{\mu}(P_{xx}+\mu\varphi) \\ \varepsilon_{yz}&=\frac{1}{\mu}P_{yz} \end{aligned}\right\} \qquad (4')$$

and corresponding equations for the other strain components.

Thus, by the same procedure as we convert equations (3) to (1), we can derive the following equations from equations (4′):

$$\left.\begin{aligned} \frac{\partial(2\varepsilon_{xx})}{\partial t}&=\frac{1}{\mu}\frac{\partial}{\partial t}(P_{xx}+\mu\varphi)+\frac{1}{\eta}(P_{xx}+\mu\varphi) \\ \frac{\partial\varepsilon_{yz}}{\partial t}&=\frac{1}{\mu}\frac{\partial P_{yz}}{\partial t}+\frac{1}{\eta}P_{yz} \end{aligned}\right\} \qquad (6)$$

and corresponding equations for the other strain components. Here we presumed that the volume viscosity can be neglected.

Similarly as above, we can gain the equations corresponding to equation (2) as follows:

$$\left.\begin{aligned} P_{xx}+\mu\varphi&=\mu(1+2\varepsilon_{xx})+\eta\frac{\partial(2\varepsilon_{xx})}{\partial t} \\ P_{yz}&=\mu\varepsilon_{yz}+\eta\frac{\partial\varepsilon_{yz}}{\partial t} \end{aligned}\right\} \qquad (7)$$

The equations for the shearing components in equation (6) and (7) are the same as the ordinary equation, except here strains are not infinitesimal but finite. If we use either of them, together with the equation of motion, the definition of finite strains and the boundary conditions as well as in the ordinary elasticity theory and $\det T=1$, we can solve the problems in incompressible large deformation, in principle.

§ 3. Simple Applications

Consider the incompressible deformation of rod- like material in the direction of its length, which we can select as the direction of x-axis. Then, x, y, and z axis becoming the principal axis, we need not the equation for shearing components and it can be assumed the following relations hold.

$$P_{yy}=P_{zz}=0 \qquad (a)$$

$$\varepsilon_{yy}=\varepsilon_{zz} \qquad (b)$$

$$\det T=1 \qquad (c)$$

Put

$$1+2\varepsilon_{xx}=\lambda^2 \qquad (d)$$

then, λ represents elongation ratio. From (b) and (c), we have

$$1+2\varepsilon_{yy}=1+2\varepsilon_{zz}=1/\lambda \qquad (e)$$

Under the above assumptions and relations, let us apply the above-obtained equations ((6) and (7)) to well-known three cases:

(1) $dP_{xx}/dt=0$,

(2) $d\varepsilon_{xx}/dt=0$,

(3) $2d\varepsilon_{xx}/dt=d(\lambda^2)/dt=\text{const.}$

The calculations are comparatively easy, so we will not describe their precise process. The results of calculations are listed belows. (It was proved that the behaviours for $d\varepsilon_{xx}/dt=0$ were the same as those in the ordinary case, so they are neglected belows.)

(1) When $dP_{xx}/dt=0$

From (6) $$\lambda^2-\frac{1}{\lambda}=\frac{P_{xx}}{\eta}t+\text{const.} \qquad (8)$$

From (7) $$\lambda_2-\frac{1}{\lambda}=\frac{P_{xx}}{\mu}(1-e^{-t/\tau}) \qquad (9)$$

(2) When $2d\varepsilon_{xx}/dt=d(\lambda^2)/dt=\text{const.}=a$

From (6)
$$P_{xx}=\mu\exp(-\lambda^2/\tau a)\int_0^\lambda d\left(\lambda^2-\frac{1}{\lambda}\right)\Big/d\lambda\cdot\exp(\lambda^2/\tau a)d\lambda \tag{10}$$

From (7)
$$P_{xx}=\mu\left(\lambda^2-\frac{1}{\lambda}\right)+\eta a\,d\left(\lambda^2-\frac{1}{\lambda}\right)\Big/d\lambda\cdot\frac{1}{2\lambda} \tag{11}$$

Where $\tau=\eta/\mu$

We can easily prove that if strains are small and higher terms of them can be neglected, these results can be reduced to those in the ordinary theory. Let us show this for equation (8) and (10). For example, next relations can hold.

$$\lambda=(1+2\varepsilon_{xx})^{1/2}=1+\varepsilon_{xx}$$
$$\lambda^2-1/\lambda=1+2\varepsilon_{xx}-(1+2\varepsilon_{xx})^{-1/2}=3\varepsilon_{xx}$$

Thus, from equation (8), we have

$$3\varepsilon_{xx}=\frac{P_{xx}}{\eta}t+\text{const.}$$
$$\therefore\quad \varepsilon_{xx}=\frac{P_{xx}}{3\eta}t+\text{const.} \tag{12}$$

and from equation (10) we have

$$P_{xx}=\mu\exp\left(-\frac{1+2\varepsilon_{xx}}{2\tau\dot{\varepsilon}_{xx}}\right)$$
$$\cdot\left[\int\frac{d(3\varepsilon_{xx})}{d\varepsilon_{xx}}\exp\left(\frac{1+2\varepsilon_{xx}}{2\tau\dot{\varepsilon}_{xx}}\right)d\varepsilon_{xx}+\text{const.}\right]$$
$$\therefore\quad P_{xx}=3\mu\tau\dot{\varepsilon}_{xx}\left[1-\exp\left(-\frac{\varepsilon_{xx}}{\tau\dot{\varepsilon}_{xx}}\right)\right] \tag{13}$$

References

1) T. Alfrey: Mechanical Behaviour of High Polymers. (1948) pp. 205.
2) R. S. Rivlin: Philos. Trans. Roy. Soc. London. **A240** (1948) 459.
3) F. R. Eirich: Rheology, Theory and Applications. Volume 1. (1956) pp. 367.

Erratum

Notes on the Calculation of Electrophoresis of Polyelectrolytes with Partial Free-Drainage

By Hiroshi FUJITA

J. Phys. Soc. Japan **12** (1957) 968

The curve with $\sigma=1.0$ in Fig. 3 should be accepted as that for $\sigma=0.0$. However, the numerical data obtained indicate that the difference between the plots for these two σ values lies practically within the thickness of the drawn line on a graph of this scale.

JOURNAL OF THE PHYSICAL SOCIETY OF JAPAN Vol. 12, No. 9, SEPTEMBER, 1957

On the Twin Structure of Nickel Films Electrodeposited on Single Crystals of Copper

By Shiro OGAWA, Joji MIZUNO, Denjiro WATANABE and F. Eiichi FUJITA*

The Research Institute for Iron, Steel and Other Metals,
Tohoku University, Sendai, Japan

(Received April 1, 1957)

Single-crystal-like nickel films electrodeposited on copper single crystals were examined by electron diffraction and electron microscopy after films were detached from the substrates. The twin structure in the films which has so far been observed only through diffraction patterns revealed themselves in electron micrographs. In films deposited on electropolished surfaces well marked {111} twin lamellae were observed and their directions satisfied the crystallographical relation. They were scatteringly located and their width ranged from less than 100 Å to several thousand Å. They grew up sometimes to be more than 10 μ in length. In films deposited on etched surfaces, on the other hand, such a coarse twin structure was hardly found and the finer one took place. The finer twins were in general 100 Å or less in width and were finely spaced at intervals somewhat larger than the width. The above results were obtained in films deposited on (110) and (001) faces of copper. Films deposited on surfaces with higher indices, (310) and (531), also showed high epitaxy and marked twin structures.

§ 1. Introduction

As Cochrane observed[1], face-centred cubic metals such as nickel, copper and silver electrodeposited on a single crystal of face-centred cubic metal, say copper, are oriented following the substrate, that is, epitaxy occurs. On that occasion, {111} twins are found in deposited layers. These circumstances are quite similar to those in thin films of face-centred cubic metals evaporated on rocksalt[2]. Reflection patterns of electron diffraction so far observed with electroplated surfaces gave indeed a positive evidence for the twin formation, but could inform us little of the width of twin lamellae and the frequency of their formation. These quantities will be known from electron micrographs of electroplated surfaces. Ueda, Kawai and Watanabe[3] carried out electron microscopic observations of nickel-plated surfaces of copper single crystal using replicas, but reported little about the twin structure. If electrodeposited films are thin enough to transmit electrons and are detached from substrates, their transmission electron micrographs will give more information about the twin formation than replicas. Weil and Read[4] and recently Reimer[5] detached nickel films from nickel-plated copper by a suitable reagent and examined them by electron microscope. They electroplated, however, polycrystalline copper and they did not examine the twin structure.

In order to examine the twin formation in nickel films electrodeposited on single crystals of copper, we detached the films from the nickel-plated crystals in a similar way to Weil and Read and observed them by electron diffraction and electron microscopy. The results obtained were almost satisfactory in giving detailed information about the twin formation.

§ 2. Experimental Method

Single crystal discs of copper 2 mm. in thickness and 10 to 20 mm². in area were cut, parallel to (110) or (001), out of rectangular rods 3 mm. in diameter. These rods of single crystal were kindly dispensed by Dr. H. Suzuki who prepared them by melting in a graphite mold. Their orientations were roughly determined by the light figure method. The discs were carefully cut out by a fret saw, polished by emery paper till 05, electropolished and, if necessary, etched. Then, the orientations were determined by the X-ray Laue method. Misorientations were found to be about 2° in (110) and (001) discs. Specimens were electropolished in aqueous solution of 600 cc/l H_3PO_4 and immediately, or after being etched in 5% KCN solution, plated with nickel in aqueous solution of 300 gr. $NiSO_4 6H_2O$, 3.1 gr. NaCl and 6.2 gr. H_3BO_3 in 1l. Plating current density ranged from 22 to 31 $\mu A/cm^2$. Current density less than these values caused no appreciable plating. Nickel films deposited were left after the copper was dissolved in aqueous solution of 500 gr. CrO_3 and 50 gr. H_2SO_4 in 1l. They were washed and scooped on meshes. It was difficult to obtain films of large area, and the largest film was only about 1 mm^2. in area.

---

* Now at the Japan Atomic Energy Research Institute, Tokyo, Japan.

Electron microscopy and electron diffraction were carried out by the apparatuses previously used[2)], except cases where defocused diffraction patterns of selected area were needed. In these cases an electron microscope, JEM-5C type of the Japan Electron Optics Laboratory Co., was used. The accelerating voltage of 80 KV was applied to this microscope.

§ 3. Experimental Results and Their Interpretation

(*a*) *Nickel films deposited on (110) face of copper*

At an early stage of the present work, copper surfaces were plated after etching in 5% KCN solution for about 5 min., because there was an anxiety that a good orientation of nickel layer could not probably be obtained on an electropolished surface owing to an oxide layer present there. A nickel-plated (110) face gave a single-crystalline reflection pattern shown in Fig. 1*a* which proved the epitaxial growth. Twin spots and junction spots[6)] are clearly visible in this pattern. The nickel film was then detached from the substrate. It gave a transmission pattern shown in Fig. 1*b*, where, though fairly strong Debye rings appeared, two kinds of extra spots, *e.g.*, such as weak E_1 lying in the oblique direction from a main spot M and strong E_2 lying in the vertical direction from the relevant spot M, were visible.

The relation between the twin spots in the reflection pattern and those in the transmission pattern is seen from Figs. 2*a* and *b*. In Fig. 2*a*, ABCD is parallel to the specimen surface and OBF, OCF, OBC and FBC are {111} planes on which twinning can occur. Fig. 2*b* represents a reciprocal lattice corresponding to the lattice containing four kinds of twins. The twin spots lie on the body-diagonals of the reciprocal lattice. When the incident beam is parallel to BC in the reflection case, the pattern obtained will almost be in agreement with the intensity distribution in OC′G′H′. On the other hand, when the incident beam is perpendicular to the film surface, *i.e.*, parallel to FO in the transmission case, the pattern obtained will almost be in agreement with the intensity distribution in A′B′C′O. The twin spots in Fig. 1*a* must have, therefore, arisen from twin lattices different from those causing twin spots in Fig. 1*b*. In the latter case, only the extra spots of the weak kind represented by E_1, lying on the body-diagonals in A′B′C′O, can be expected as the twin or junction spots, but those of the strong kind represented by E_2 cannot. If considerable rotations of crystallites took place, however, the latter spots can also be identified as the twin or junction spots. That is, the twin or junction spots lying on the reciprocal planes parallel to OC′G′H′ come to reflecting positions due to the rotations. In this case, these spots are doubled in intensity, owing to the two symmetrical positions referring to A′B′C′O.

In Fig. 1*b*, the spot E_2 lies on a direction parallel to A′B′ through the relevant main spot $(1\bar{1}1)$ in Fig. 2*b* and, after detailed observation, it was found that the spot E_2 was often separated into two parts. This fact means that there are two rotation axes in the film plane. Thus, four kinds of {111} twin lamellae were proved to exist in nickel films formed on (110) face of copper single crystal. The twin spots due to twins on OBF and OCF, *i.e.*, the kind represented by E_1 in the transmission pattern, are far weaker in intensity than those due to twins on OBC and FBC which appeared in the reflection pattern as well as in the transmission pattern. This means that twin lamellae oblique to the film plane are more frequently formed than those perpendicular to this plane, even if the doubled intensity of E_2 is considered.

Next, the detached films were examined by transmission electron microscopy. Micrographs obtained showed, however, very much complex structures, so that twin lamellae could scarcely be identified, against our expectation. Since this condition was considered to originate from etching before plating, immediate nickel-plating after electropolishing was tried. The detached nickel film exhibited an excellent single-crystalline diffraction pattern showing the epitaxial growth, in spite of our initial anxiety. The intensity of twin spots was, however, much weaker than in the case of etching. One of the electron micrographs of this film is shown in Fig. 3. Such a structure as observed in Fig. 3 was rarely observed through the whole film. In Fig. 3, a wide bright stripe runs, making an angle of about 54° with several narrow stripes about 300Å in width. This angular relation can clearly be understood, if the former stripe is parallel to BC in Fig. 2*a*, which is the intersection of OBC with the film

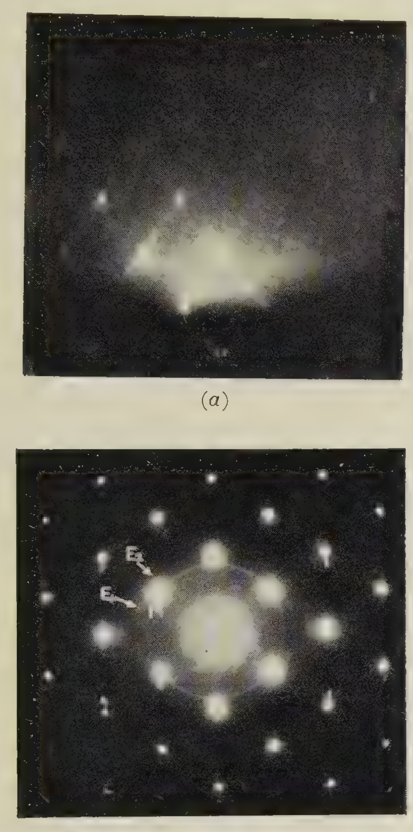

(*a*)

(*b*)

Fig. 1. Electron diffraction patterns from a nickel film on etched (110) face of copper. Electrodeposited with current density 23μA/cm² for period 11 hr.

a: Reflection pattern. Electron beam is parallel to [1$\bar{1}$0].

b: Transmission pattern. Normal incidence.

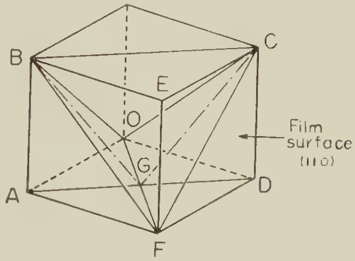

Fig. 2. *a*: Geometrical relation between (110) film surface and four {111} planes.

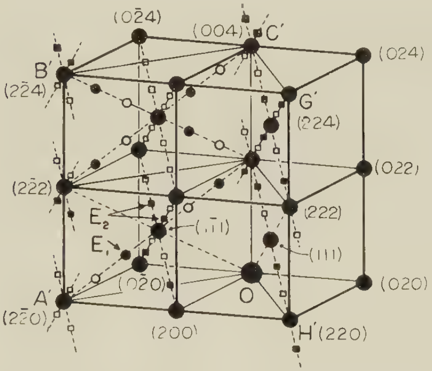

Fig. 2. *b*: Reciprocal lattice corresponding to the lattice containing four kinds of twins. Large full circles are main lattice points, small full circles and squares are twin spots, and small open circles and squares are junction spots. Small circles are caused by twins on OBF and OCF in *a*, and small squares by twins on OBC and FBC.

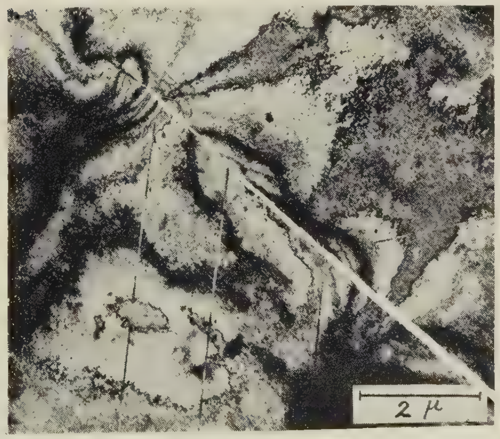

Fig. 3. Electron micrograph of a nickel film on electropolished (110) face of copper. Electrodeposited with current density 30μA/cm² for period 7 hr.

plane, and if the latter stripes are parallel to BG (or CG), which is the intersection of OBF (or OCF) with the film plane. BC makes an angle of 54°44′ with BG or CG. Thus, the wide stripe can be thought to represent a twin lamellae oblique to the film plane and hence to appear wider than its true thickness (this stripe seems, however, to change into a rip in its middle), and the narrow stripes can be thought to represent twin lamellae perpendicular to the film plane and hence to show their true width. The contrast changes along the narrow stripes, owing to the change of condition of Bragg reflections due to bending. Thus, it is sure that the stripes in Fig. 3 reveal the twin lamellae growing in the nickel film, and the fact that similar stripes were rarely observed explains the weak intensity of the twin spots in the diffraction pattern.

The facts stated above connot be, however, a conclusive evidence of the stripes representing the twin lamellae. The proof should be given by defocused diffraction patterns, just as given by Fischer and Richter⁷⁾. They observed the stripes similar to those in Fig. 3 in evaporated germanium films irradiated with electron beam and proved by the said method that they arose from the twin lamel-

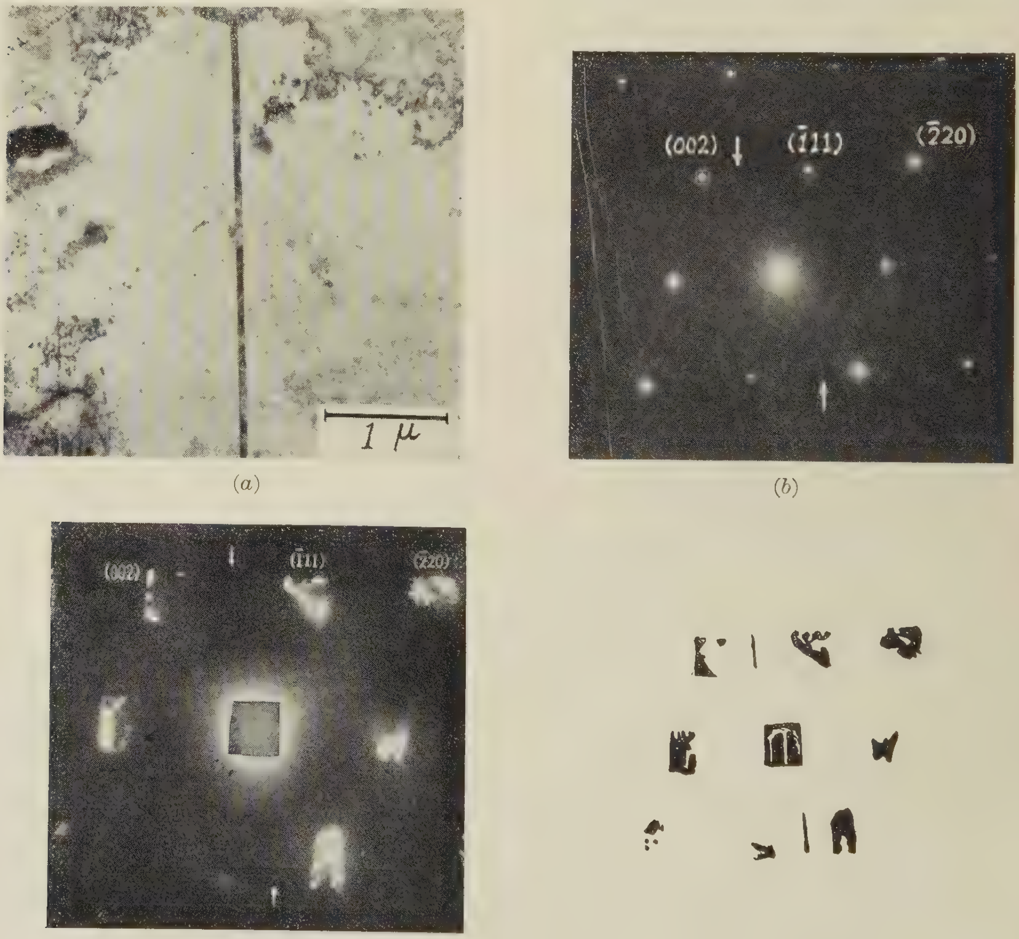

(*a*) (*b*)

(*c*) (*c*′)

Fig. 4. Electron micrograph and diffraction patterns of a (110) nickel film prepared under the same condition as in Fig. 3. In *a*, *b* and *c*, the specimen was placed at the usual position, *i.e.*, before the objective lens. *b* and *c* were taken without an objective aperture. Defocusing was carried out by adjusting the current of the intermediate lens. In *a*, faint stripes are also visible, running parallel to the intense stripe. In *c*, dark field images appear at positions corresponding to the diffraction spots in *b*. The arrows in *b* and *c* indicate the twin spots and the stripes due to twins, respectively.

lae. Fig. 4a* is an electron micrograph of a nickel film deposited on (110) copper face, Fig. 4b a selected area diffraction pattern of Fig. 4a, Fig. 4c the defocused pattern of Fig. 4b and Fig. 4c′ an illustration of Fig. 4c. The central small region of Fig. 4c is a reduced image of Fig. 4a. A dark stripe is seen through its middle. This stripe reveals itself, however, as a bright one in the defocused diffraction pattern, and its position corresponds just to that to be expected for the twin spot. Thus, the stripes in the micrographs were proved to arise from the twin lamellae.

(b) *Nickel films deposited on (001) face of copper*

Nickel films were very difficult to be detached from etched (001) faces, so that most works were carried out by plating without etching. The diffraction patterns exhibited the epitaxial growth also in this case. The twin spots were in general faint in reflection as well as in transmission, especially, scarcely visible in the latter case. There appeared, however, many dark and bright stripes in the transmission electron micrograph taken from a selected region (Fig. 5). The stripes are several hundred to several thousand Å in width and were classified into two groups perpendicular to each other. These stripes are similar to those obtained previously from thin films of face-centred cubic metals evaporated on cleavage surface of rocksalt[2]), though the former stripes are more coarsely spaced than the latter. Thus, it can be concluded that the stripes in Fig. 5 are caused by the twin lamellae and their directions are [110] and [$\bar{1}$10] respectively which represent the directions of intersection of {111} planes with (001) film plane. Fig. 6 shows another example of (001) nickel films. Here we see, besides such stripes as in Fig. 5, several square frameworks of different sizes which are connected with the stripes. The following suggestion may be permitted concerning the origin of these frameworks, remembering the directions of the stripes to be face-diagonal: Twin lamellae of nickel grew up on four faces of octahedral pits existing originally on the copper surface. At places where lamellae growing on neighbouring faces collided, the lattice epitaxial to the substrate was formed due to the symmetry relation. This suggestion seems to be supported by the fact that broad, curved dark lines due to Bragg reflections are seen inside the frameworks and straight dark lines are marked at the corners of the frameworks as if these places had the lattice continued from the outside region of the frameworks.

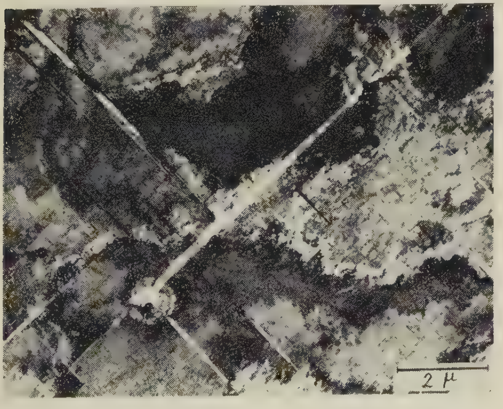

Fig. 5. Electron micrograph of a nickel film on electropolished (001) face of copper. Electrodeposited with current density 24 μA/cm² for period 14 hr.

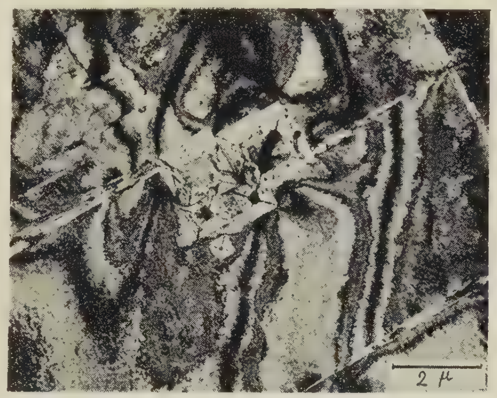

Fig. 6. Electron micrograph of a nickel film deposited on electropolished (001) face of copper which was slightly etched before plating. Plated with current density 23 μA/cm² for 31 hr.

It was proved also in the (001) case by the same method as used in the (110) case that the stripes arose from the twin lamellae.

(c) *Nickel films deposited on other faces of copper*

In order to examine whether the epitaxial growth occurred or not on crystal faces of higher indices and to see the aspect of the twin formation if this occurred, (310) and (531) discs were cut out. Misorientations were 5~6° in both cases.

---

* For photographing of Fig. 4a, b and c, we are much indebted to Dr. M. Watanabe.

Diffraction patterns obtained from nickel films formed on electropolished surfaces of these discs inform us that the orientations of the substrates were well followed by the deposited films. In these patterns and also in the transmission patterns obtained from the detached films the twin spots appear faint, but when the films were tilted in the latter case, they became strong. Fig. 7*a* shows a reflection pattern of the (310) case. Transmission electron micrographs obtained from the detached films showed the twin lamellae in both (310) and (531) cases. Fig. 7*b* was obtained from the (310) film. Most of lamellae appear bright, being in agreement with the fact that the twin spots in the diffraction patterns were faint in the normal incidence. The angles between the stripes satisfy the crystallographical relation.

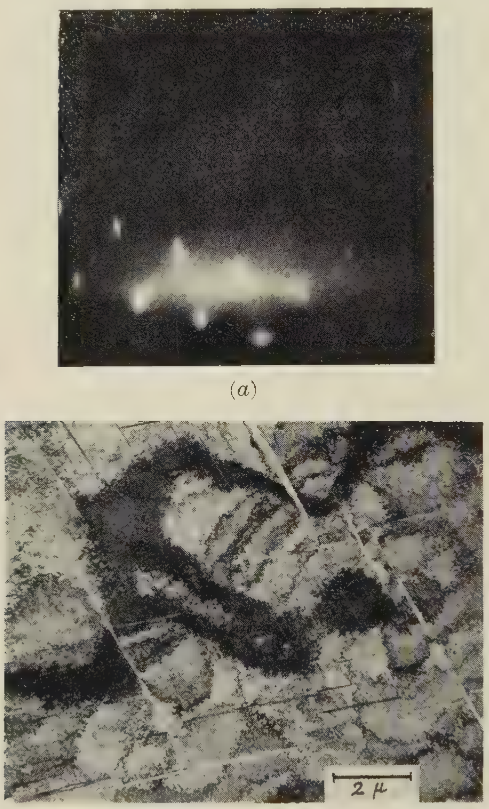

(*a*)

(*b*)

Fig. 7. Electron diffraction pattern and electron micrograph of a nickel film deposited on electropolished (310) face of copper. In a electron beam is nearly parallel to [1$\bar{3}$3]. The micrograph in *b* was obtained from the detached film. Plated with current density 30μA/cm^2 for 6.5hr.

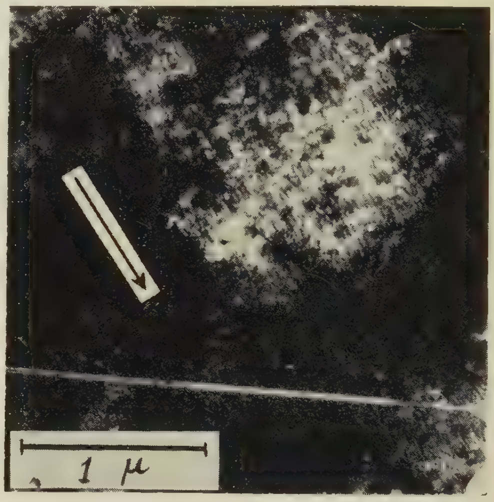

Fig. 8. Electron micrograph of a nickel film on etched (110) face of copper. Etching was carried out in 5% KCN solution for 1 min. Electrodeposited with current density 26μA/cm^2 for period 20hr.

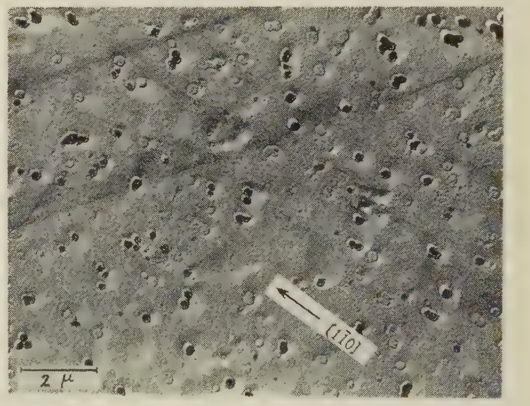

Fig. 9. Electron micrograph of a replica of nickel-plated (110) face of copper. Two-stage replica of methylmethacrylate and chromium was used. Chromium metal was evaporated along the direction making an angle of 30° with the surface and whose projection on the surface made an angle of 27° with [1$\bar{1}$0] lying on the surface.

Among the twin lamellae mentioned in subsections (a), (b) and (c), those with comparatively short length (~0.5μ) had, in general, a tendency to decrease in number with the increase of the depositing current density, while this increase was not the case with longer lamellae.

(*d*) *Nickel films deposited on etched faces of copper*

As already described in (a), every nickel film deposited on copper faces etched for about 5 min. in KCN of 5% gave comparatively strong diffraction spots due to twins, but its electron microscopic structure was so complex that the twin lamellae could not be identified. In order to obtain a simpler electron microscopic structure, (110) face was nickel-plated, etching duration being shortened and varied from 15 to 60 sec. Even when the etching was done for the shortest duration, the stripes as seen in Fig. 3 almost vanished. (But such twin lamellae were rarely observed even on the substrate etched for 3 min., if the depositing current density was high, *i.e.*, about 30 $\mu A/\text{cm}^2$.) Detailed observation enabled us, however, to find stripes caused by twin lamellae, even when the familiar stripes vanished. In Fig. 8, many dark fine stripes are observed along the direction of the arrow. They are in general 100Å or less in width and are spaced at intervals somewhat larger than the width. A bright stripe of the familiar type remains in the middle of the dark region of the figure. The angle between the direction of this stripe and that of the above-mentioned fine stripes is about 54°, which convinces us that the latter stripes represent nothing but the fine twin lamellae very frequently formed, if the angular relation in Fig. 3 is remembered. Such fine stripes were found, after detailed observation, in most places of the micrographs, and therefore, they could yield strong diffraction spots due to twins in spite of their indistinct microscopic pattern, while the distinct twin lamellae as seen in Fig. 3 yielded only faint twin spots, due to their small total volume. The fine twin lamellae have never been found in films formed without etching of the substrate.

§ 4. Discussion

Twins occurring in crystals are classified into two kinds[7]. One is named "growth twin", which occurs as a result of stacking disorder of (111) plane in the course of crystal growth, and the other "deformation twin", which is formed under stress as a mode of deformation. The coarse twin lamellae of the films formed on electropolished surfaces were occasionally more than 10μ in length. Such lamellae seemed at first sight to be deformation twins which occurred at the time of detachment of the films. A micrograph shown in Fig. 9, however, denies this conjecture. This micrograph was taken from a replica of nickel-plated (110) copper face and shows several diffuse stripes. These are classified into two groups of parallel stripes which intersect each other with an angle somewhat larger than 50°. Moreover, it is seen from the shadowing direction that the one group runs parallel to $[1\bar{1}0]$ lying on the surface. As the contrast in a replica micrograph mean some unevenness formed on the original surface, the said stripes may be considered as marks due to the twin lamellae, if these lamellae cause the surface to be uneven. Thus, the coarse twin structure seems to exist originally in the deposit*.

From the above consideration it is concluded that the twin structure of films electrodeposited on electropolished faces of copper are considerably different from and far coarser than that of the evaporated films. The twin structure of films electrodeposited on etched faces are, on the other hand, extremely fine and similar to that of the evaporated films in width as well as in spacing. The reason why the aspect of the twin formation depends on the surface condition of the substrate is not clear, but the following supposition may be allowed: According to Setty and Wilman[8], who examined the epitaxial growth of silver electrodeposited on electropolished (110), (001) and (111) faces of a silver single crystal, the twinned structure developed more frequently when the current density was increased. Now that etched surfaces are submicroscopically rough, on the top of projections it is likely that the current density is higher than the average. Then, chance for the twin formation will increase at such places, according to the results of Setty and Wilman. Moreover, the twins will be cut in pieces by surface irregularity. Thus, minute twinned lattices can frequently grow up on etched surfaces. On the other hand, electropolished surfaces have atomic smoothness, and hence only coarse twins grow up scatteringly.

---

* In single crystal discs of copper employed in the present work, twin layers were not found by X-ray and electron diffraction.

The above consideration seems to suggest that we deal with growth twins in the cases of electropolished as well as etched faces, as it is difficult to consider in the course of growth the occurrence of any stress other than that which is induced by unfitness between the lattices of the deposit and the substrate. The latter stress cannot be a cause of the twin formation, because twins are formed even when the same substance as substrate is deposited as in the case of Setty and Wilman.

We wish to express our sincere thanks to Dr. H. Suzuki for his kind dispensation of copper single crystals. We are much indebted also to the Japan Electron Optics Laboratory Co. and its member, Dr. M. Watanabe, for their kindness which they did us in photographing some electron micrographs.

The present work has been supported partly by the fund of the Ministry of Education in Aid of Scientific Researches.

References

1) W. Cochrane: Proc. Phys. Soc. **48** (1936) 723.
2) S. Ogawa, D. Watanabe and F. E. Fujita: J. Phys. Soc. Japan **10** (1955) 429.
3) R. Ueda, S. Kawai and M. Watanabe: Read at the Meeting of the Physical Society of Japan, Osaka, April 1953.
4) R. Weil and H. J. Read: J. Appl. Phys. **21** (1950) 1068.
5) L. Reimer: Z. Metallk. **47** (1956) 631.
6) O. Goche and H. Wilman: Proc. Phys. Soc. **51** (1939) 625.
7) E. W. Fischer and H. Richter: Ann. Phys. **16** (1955) 193.
8) T. H. V. Setty and H. Wilman: Trans. Far. Soc. **51** (1955) 984.

JOURNAL OF THE PHYSICAL SOCIETY OF JAPAN Vol. 12, No. 9, SEPTEMBER, 1957

Characteristics of the Beam Type Maser I

By Koichi SHIMODA

Department of Physics, Faculty of Science, University of Tokyo

(Received May 29, 1957)

Velocity distribution of molecules in the beam type maser is considered fairly completely, though the mathematical approach is rather approximate. Because slower molecules spend longer time in the cavity, the effective average velocity of molecules is considerably smaller than the most probable velocity, when the rf power level and the focuser voltage are low. Amplitude vs. focuser voltage and vs. frequency characteristics are obtained, which seem to be in good agreements with experiments. Finally frequency shift due to the unresolved hyperfine structure is discussed and shown to be appreciable (a few parts in 10^8).

§ 1. Introduction

A type of devices which utilize atomic processes of induced emission as oscillators, frequency converters, and amplifiers has been called a MASER. It has become feasible at first by a molecular beam type maser[1] and secondly by a solid state maser[2][3]. This paper is concerned with the characteristics of the beam type maser, particularly of ammonia maser. Molecules other than ammonia have not yet been used successfully for the maser.

Theories of the beam type maser have already been given[4][5][6]. However experimental results show that these theories are not satisfactory in describing the characteristics of ammonia masers. Particularly, Helmer has recently reported considerable frequency variations of an ammonia maser oscillator with source pressure and with focuser voltage[7]. It is shown in the following discussion that, if the presence of unresolved hyperfine components and velocity distribution of molecules are taken into account, this type of frequency shift can be predicted and other characteristics are also obtained in better agreement with experimental results. A preliminary discussion of this consideration was briefly reported[8] concerning the frequency difference between an absorption type frequency standard by the present author and a maser oscillator by Bonanomi[9]. Theoretical discussions of the beam type maser are described in this paper, while the experimental results will appear in part II.

§ 2. Velocity Distribution

Velocity distribution of molecules in the beam was first taken into account in the theory of the maser by Helmer[4]. However, his treatment was incomplete, because only the distribution of speeds was taken into consideration and the distribution of directions of velocities was neglected. Here a more complete treatment is described.

Velocity distribution of molecules which are effused from a molecular beam source may be assumed as that of Maxwell-Boltzmann type, since highly directional source has been found very difficult to realize. The number of molecules in a unit volume with velocity components, v_x, v_y, and v_z, is

$$N(v_x, v_y, v_z)dv_xdv_ydv_z=\frac{2N}{\alpha^3\pi^{3/2}}e^{-v^2/\alpha^2}dv_xdv_ydv_z, \tag{2.1}$$

where N is the number density of molecules in a particular energy level of interest independent of their velocities, α the most probable velocity given by

$$1/2\cdot m\alpha^2=kT \quad \text{or} \quad \alpha=(2kT/m)^{1/2}$$

and

$$v^2=v_x^2+v_y^2+v_z^2 \, .$$

If z-axis is chosen along the direction of the beam, v_x and v_y may take any values but v_z must be positive. Using a cylindrical coordinate, radial component is given by $v_r^2=v_x^2+v_y^2$, and the velocity distribution is

$$N(v_r, v_z)dv_rdv_z=\frac{4Nv_r}{\alpha^3\sqrt{\pi}}e^{-v^2/\alpha^2}dv_rdv_z \, . \tag{2.2}$$

The focuser exerts radial force outwards for ammonia molecules in the lower inversion state, while inwards for those in the upper state. Electro-static potential in a $2n$-pole focuser can be approximately expressed by

$$\phi=\frac{V}{2R^n}\mathrm{Re}(x+iy)^n \, , \tag{2.3}$$

where R is the radius of the focusing field and $\pm V/2$ the voltages of the alternate electrodes. That is, when the every other electrodes are grounded, the applied focuser voltage is V. Then the electro-static field in the focuser is

$$E_s=\frac{nr^{n-1}}{2R^n}V \, , \tag{2.4}$$

and the maximum field intensity is

$$E_m=\frac{n}{2R}V \, . \tag{2.5}$$

Fig. 1 shows the distribution of E^2, which is roughly proportional to the potential energy of molecules.

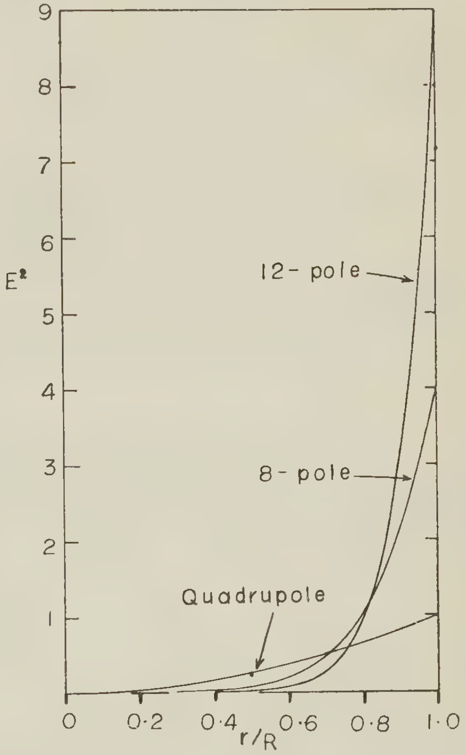

Fig. 1. Distribution of E^2 in a $2n$-pole focuser.

The molecules in the upper inversion state are focused, when the radial kinetic energy is smaller than the maximum Stark energy, which is

$$\varDelta W_E=\left[\left(\frac{h\nu_0}{2}\right)^2+\left(\frac{\mu MK}{J(J+1)}E_m\right)^2\right]^{1/2}-\frac{h\nu_0}{2} \, . \tag{2.6}$$

Then the focusing criterion is given by

$$\frac{1}{2}mv_r^2<\varDelta W_E\equiv\frac{1}{2}mv_c^2 \, . \tag{2.7}$$

If $\varDelta W_E \ll h\nu_0$, the critical radial velocity, v_c, is proportional to the focuser voltage, since

$$v_c \simeq \frac{\mu MK}{J(J+1)} E_m \left(\frac{2}{mh\nu_0} \right)^{1/2} \tag{2.8}$$

However, when the z-component of the velocity is large, the molecule cannot spend enough time to be focused within the focuser and also the molecules in the lower state cannot be sufficiently removed from the beam. Since $\frac{\pi}{2} \frac{R}{v_c} v_z$ is just half the focal length in a quadrupole focuser, the condition determined by the length of the focuser, l, may be written approximately as

$$\frac{l}{v_z} > \frac{\pi}{2} \frac{R}{v_c} \tag{2.9}$$

Thus the velocity of molecules to be focused should satisfy the conditions,

$$v_r < v_c \quad \text{and} \quad v_z < \frac{2}{\pi} \frac{l}{R} v_c$$

though the second condition is rather approximate. More accurate evaluation should of course be carried out by computing trajectories of molecules.

The number of focused molecules entering the cavity resonator in a unit time with velocity components, v_r and v_z, is

$$n(v_r, v_z) = A_i v_z N(v_r, v_z) , \tag{2.10}$$

where A_i is the area of the inlet hole through which the uniform density of molecules is assumed to pass. Then the rf power emitted from the beam of molecules is given by

$$\Delta P = \int_0^{v_c} \int_0^{(2/\pi)(l/R)v_c} n(v_r, v_z) |a_1(\tau)|^2 dv_z dv_r \tag{2.11}$$

where $|a_1(\tau)|^2$ is the transition probability[5)]. This equation should be modified when a long cavity is used as in the ordinary maser. In such a case, Eq. (2.1) may be divided into two parts, ΔP_1 and ΔP_2: One is the contribution of molecules which pass through the whole length of the cavity, and the other is that of molecules which collide with the cavity wall before it can pass through the cavity. Duration of interaction with the rf field in the cavity is $\tau = L/v_z$ in the former case, while it is approximately $\tau = R/v_r$ in the latter case, where L and R are the length and radius of the cavity.

In order that the molecules can pass through the cavity before they collide with the cavity wall, an approximate condition

$$\frac{v_z}{L} > \frac{v_r}{R}$$

must be satisfied. This condition is accurate for the molecules just focused at the center of inlet hole of the cavity, while for other molecules it may be considered as an average condition. For finite sizes of source and of inlet hole of the cavity each focused molecule generally takes different values of v_r before and after it passes the focuser, but as a statistical average, v_r can be considered as almost unchanged. Thus we may use the velocity distribution of Eq. (2.2) for the molecules flowing into the cavity with $v_r < v_c$.

From equation (4) in reference 5, hereafter referred as SWT, when the oscillation frequency is equal to that of molecular resonance, we obtain

$$|a_1(\tau)|^2 = \sin^2 \frac{x\tau}{2} , \tag{2.12}$$

where $x = E\bar{\mu}/\hbar$ and E is the intensity of rf field in the cavity.

Emitted Power

Assuming $x\tau/2 \ll 1$ so that $\sin \frac{1}{2}x\tau = \frac{1}{2}x\tau$, the power emitted from the molecules which pass through the cavity is obtained from Eqs. (2.2), (2.10), (2.11), and (2.12).

$$\begin{aligned} \Delta P_1 &= \frac{x^2}{4} h\nu_0 \frac{4NL^2A_i}{\sqrt{\pi}\,\alpha^3} \int_0^{v_c} \int_{(L/R)v_r}^{(2/\pi)(l/R)v_c} \frac{v_r}{v_z} e^{-v^2/\alpha^2} dv_z dv_r \\ &\cong x^2 h\nu_0 \frac{NR^2A_i}{\sqrt{\pi}\,\alpha} \int_0^a \int_\eta^b \frac{\eta}{\xi} e^{-\xi^2} d\xi d\eta , \end{aligned} \tag{2.13}$$

where

$$\xi = \frac{v_z}{\alpha} \cong \frac{v}{\alpha} , \qquad \eta = \frac{L}{R} \frac{v_r}{\alpha} ,$$

$$a = \frac{L}{R} \frac{v_c}{\alpha} , \quad \text{and} \quad b = \frac{2}{\pi} \frac{l}{R} \frac{v_c}{\alpha} .$$

As the length of the focuser, l, is considerably longer than that of the cavity, L, in masers so far constructed, we may assume $a<b$. The integration in (2.13) can be expressed in terms of exponential integrals, so that

$$\varDelta P_1=\frac{x^2}{4}h\nu_0\frac{NR^2A_i}{\sqrt{\pi}\,\alpha}[1-e^{-a^2}-a^2Ei(-a^2)+a^2Ei(-b^2)]\,. \tag{2.14}$$

Secondly, the emitted power from the molecules which collide with the cavity wall is calculated. The result is

$$\varDelta P_2=x^2h\nu_0\frac{NR^2A_i}{\sqrt{\pi}\,\alpha^3}\int_0^{v_c}\int_0^{(L/R)v_r}\frac{v_z}{v_r}e^{-v^2/\alpha^2}\,dv_zdv_r$$

$$=\frac{x^2}{4}h\nu_0\frac{NR^2A_i}{\sqrt{\pi}\,\alpha}[2\ln a-Ei(-a^2)+C]\,. \tag{2.15a}$$

Here $C=0.577216$ is the Euler's constant. Eq. (2.15a) may be expressed in a power series of a^2 as

$$\varDelta P_2=\frac{x^2}{4}h\nu_0\frac{NR^2A_i}{\sqrt{\pi}\,\alpha}\sum_{n=1}^{\infty}\frac{(-1)^{n-1}a^{2n}}{n\cdot n!}\,. \tag{2.15b}$$

The cavity loss including power flow from the output waveguide is

$$\varDelta P'=\frac{\omega W}{Q}=\frac{x^2h^2\nu_0LA}{16\,\pi^2\mu^2Q}\,, \tag{2.16}$$

where W is the stored energy, Q the loaded-Q and A the effective cross-section of the cavity. Then the threshold or the starting condition of maser oscillation is obtained from $\varDelta P'\leq\varDelta P=\varDelta P_1+\varDelta P_2$.

$$\frac{hLA}{4\pi^2\bar{\mu}^2Q}=\frac{NR^2A_i}{\sqrt{\pi}\,\alpha}\left[\sum_{n=1}^{\infty}(-1)^{n-1}\frac{n+1}{n\cdot n!}\,a^{2n}-a^2Ei(-a^2)+a^2Ei(-b^2)\right]. \tag{2.17}$$

In ammonia masers, the starting focuser voltage is not so large that $v_c\ll\alpha$ and $a^2\ll1$ may be a good approximation. In such a case higher order terms of a^2 can be neglected and Eq. (2.17) is expressed in the form,

$$\frac{hLA}{4\pi^2\bar{\mu}^2Q}=\frac{NR^2A_i}{\sqrt{\pi}\,\alpha}\,2a^2\left(1+\ln\frac{b}{a}\right)$$

$$=\frac{2\pi L^2}{\sqrt{\pi}\,\alpha^3}v_c^2\left(1+\ln\frac{2l}{\pi L}\right). \tag{2.18}$$

The critical radial velocity v_c is approximately proportional to the focuser voltage according to Eq. (2.8). It is noted that the starting condition, Eq. (2.17), includes the length of the focuser in a rather simple form.

The effective Average Velocity

The effective average velocity of molecules in the beam contributing to the oscillation is calculated. The weighted average velocity, $\langle v\rangle=\alpha\langle\xi\rangle$, is given by

$$\langle\xi\rangle=\frac{\displaystyle\int_0^a\int_\eta^b\xi\cdot\frac{\eta}{\xi}\,e^{-\xi^2}d\xi d\eta+\int_0^a\int_0^\eta\xi\cdot\frac{\xi}{\eta}\,e^{-\xi^2}d\xi d\eta}{\displaystyle\int_0^a\int_\eta^b\frac{\eta}{\xi}\,e^{-\xi^2}d\xi d\eta+\int_0^a\int_0^\eta\frac{\xi}{\eta}\,e^{-\xi^2}d\xi d\eta}\,. \tag{2.19}$$

The integrals in the denominator have already been given in Eqs. (2.14) and (2.15). The integrals in the numerator denoted by I_1 and I_2 are expressed in power series of a^2 as

$$I_1=\frac{\sqrt{\pi}}{4}a^2\Phi(b)-a^3\sum_{n=0}^{\infty}\frac{(-1)^n a^{2n}}{(2n+1)(2n+3)n!}, \tag{2.20}$$

and

$$I_2=a^3\sum_{n=0}^{\infty}\frac{(-1)_u a^{2n}}{(2n+3)^2 n!}, \tag{2.21}$$

where $\Phi(b)$ is the error integral. Then the numerator of (2.19) is

$$I_1+I_2=\frac{\sqrt{\pi}}{4}a^2\Phi(b)-2a^3\sum_{n=0}^{\infty}\frac{(-1)^n a^{2n}}{(2n+1)(2n+3)^2 n!}. \tag{2.22}$$

Now $\langle v\rangle=\alpha\langle\xi\rangle$ can be computed from (2.19) with (2.14), (2.15), and (2.22).

The ammonia masers hitherto constructed have the focuser about 2 to 3 times longer than the cavity. Therefore, almost all the reasonable designs of masers seem to fall in the range from $b=a$ to $b=5a$. Numerical computations of $\langle\xi\rangle$ for $a\leq b\leq 5a$ show that Eq. (2.19) may be approximated by a simple expression,

$$\langle\xi\rangle=(a+b)/4 \tag{2.23}$$

within the accuracy of about ±10%, when $b<1.4$. Using this approximation, the effective average velocity of molecules is expressed by

$$\langle v\rangle=\frac{\pi L+2l}{4\pi R}v_c. \tag{2.24}$$

This approximation is useful because of its simplicity.

Because slower molecules spend longer time in the cavity and have larger transition probabilities, the weighted average velocities of molecules contributing to induced emission is considerably smaller than the most probable velocity. However, this is not contradictory to the observed line width which corresponds to the molecular velocity approximately equal to the most probable velocity. In this section the effective average velocity has been calculated for $\omega=\omega_0$. On the other hand, when the emission line shape is observed by sweeping the frequency of incident microwaves, the contribution of slow molecules is rather small at the wing of the line $(\omega\not\doteqdot\omega_0)$, because the transition probability is

$$|a_1(\tau)|^2\cong\frac{x^2}{(\omega-\omega_0)^2}\sin^2(\omega-\omega_0)\frac{L}{2v}$$

in this case, and the contribution of slower molecules does not predominate when $(\omega-\omega_0)\times L/2v\gtrsim 1$.

§ 3. Saturation Characteristics

Oscillation amplitude of the ammonia maser is derived in this section as a function of focuser voltage, density of molecules, and dimensions of the cavity and the focuser. It is assumed here that the hyperfine structures do not exist, and the effects of unresolved hyperfine components will be discussed in the next section.

If the hyperfine effects are negligible, the Stark energy of ammonia in the upper inversion state is given by (2.6). The projection of J along the direction of electro-static field, M, takes $2J+1$ different values, from $-J$ to $+J$. The numbers of focused molecules are proportional to M^2, and the maximum radial velocities of focused molecules are different for those in different M states. Instead of calculating the sum of contributions from different M states, the weighted average of M^2 may be used to simplify the calculation.

$$\langle M^2\rangle=\frac{\Sigma M^2\cdot M^2}{\Sigma M^2}=\frac{6J^3+9J^2+J-1}{5(2J+1)}. \tag{3.1}$$

For the strongest line of ammonia $J=3$ gives $\langle M^2\rangle=7$. In equation (3.1) the deviation of the relative number of focused molecules from M^2 was neglected which would give only higher order small corrections in the further calculation.

The calculated maximum radial velocity, v_c, for the 3,3 line of ammonia is shown in Fig. 2, where the abscissa is the quadrupole focuser voltage, V_4, for $R=0.5$ cm. For the $2n$-pole focuser the voltage, V_{2n}, that produces the same maximum field as V_4 is from Eq. (2.5)

$$V_{2n}=\frac{2}{n}V_4. \tag{3.2}$$

In order to obtain approximate value of v_c for each value of M from Fig. 2, the scale in the ordinate should be multiplied by $M/7^{1/2}$.

The induced emission of molecules with velocity distribution may be considered as equivalent to that of uniform average velocity, $\langle v\rangle$, which was obtained in § 2. In the following discussion a variable θ defined by

$$\theta=[(\omega-\omega_0)^2+x^2]^{1/2}\,L/2\,\langle v\rangle \tag{3.3}$$

will be used. Although $\langle v\rangle$ has been obtained for small values of θ, the change of $\langle v\rangle$ by considering the effect of saturation can be regarded as the second order correction.

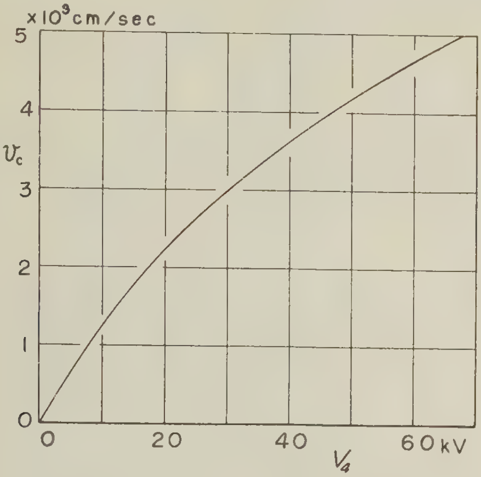

Fig. 2. Critical radial velocity of ammonia for $J=K=3$, $\langle M^2\rangle=7$, and $R=0.5$ cm.

The saturation characteristics was given by Eq. (31) in SWT as $n/n_{th}=\theta^2/\sin^2\theta$. However, in order to allow for the velocity distribution and the change of effective average velocity with operating conditions, this equation should be somewhat modified.

The transition probability of a molecule with the velocity equal to $\langle v\rangle$ is expressed as

$$|a_1(\tau)|^2=\frac{L^2x^2}{4\langle v\rangle^2\theta^2}\sin^2\theta \tag{3.4}$$

from Eq. (4) in SWT. Thus the emitted power from a beam of n molecules in a unit time is given by

$$\Delta P=\frac{x^2}{4}h\nu_0\frac{nL^2}{\langle v\rangle^2}\frac{\sin^2\theta}{\theta^2}\,. \tag{3.5}$$

The emitted power must be equal to the loss of the cavity given by (2.16), so that

$$\frac{Ah}{4\pi^2\overline{\mu}^2QL}=\frac{n}{\langle v\rangle^2}\frac{\sin^2\theta}{\theta^2}\,. \tag{3.6}$$

The threshold intensity of moleculer beam, n_0, is obtained from Eq. (3.6) by putting $\sin\theta=\theta$.

$$n_0=\frac{h\langle v_0\rangle^2A}{4\pi^2\overline{\mu}^2QL}\,. \tag{3.7}$$

This is almost the same as (30) in SWT except that here $\langle v_0\rangle$ is the effective average velocity at the threshold which is much smaller than the most probable velocity.

Using (3.7), we can write for the finite values of θ

$$\frac{n_0}{n}\frac{\langle v\rangle^2}{\langle v_0\rangle^2}=\frac{\sin^2\theta}{\theta^2}\,, \tag{3.8}$$

which is not same as Eq. (31) in SWT. Since n is approximately proportional to v_c^4 as

$$n=\int_0^{v_c}\int_0^{(2/\pi)(l/R)v_c} n(v_r,\,v_z)dv_zdv_r$$
$$=\frac{NA_i}{\sqrt{\pi}\,\alpha}v_c^2(1-e^{-b^2})\simeq\frac{4NA_i}{\pi^{5/2}\alpha^3}\frac{l^2}{R^2}v_c^4\,, \tag{3.9}$$

the saturation characteristics is expressed in the form

$$\frac{v_{c0}}{v_c}=\frac{\sin\theta}{\theta}\,. \tag{3.10}$$

Now the amplitude of oscillation, x, can be calculated as a function of focuser voltage, using Eqs. (2.7), (3.3), and (3.10). A typical example for the focuser length $l=30$ cm, cavity length $L=11$ cm, focuser radius $R=0.5$ cm, and the starting voltage $V_{4,0}=5$ kV with a quadrupole focuser is shown in Fig. 3. Saturation characteristics given by the uni-velocity theory in SWT and velocity distribution theory by Helmer[4] are also shown for comparison.

In this example the present theory gives $\langle v\rangle=15.0\,v_c$ from Eq. (2.24). This approximation is applicable when $b=38.2\,v_c/\alpha$ is smaller than 1.4, or when $V_4<16$ kV. Beyond this voltage the magnitude of $\langle v\rangle$ computed from complicated integrations in (2.19) tends to be smaller than the simple approximation. However, if the starting voltage is fairly small, the finite rf amplitude must be taken into account when b becomes large. In such a case $|a_1(\tau)|^2$ can not be approximated by $(xL/2v)^2$ which increases infinitely with decreasing v, but it must be $\sin^2(xL/2v)$. This factor takes a maximum value when $v=xL/\pi$ and becomes zero when $v=xL/2\pi$, taking oscillating values between 0 and 1 for the smaller values of v. Therefore, when $xL/2v\gtrsim 1$, the saturation effect will result in the increase of the effective average velocity.

Since the two sources of deviations from (2.24) requires corrections of different sign at nearly the same region, they more or less compensate each other, and the approximation, (2.24), may be used up to higher focuser voltage and larger amplitude of oscillation than $b=1.4$ or $xL/2v=1$. Of cource $\langle v\rangle$ would be nearly α for large values of V and x, and a plausible estimate is shown by a broken line in Fig. 3.

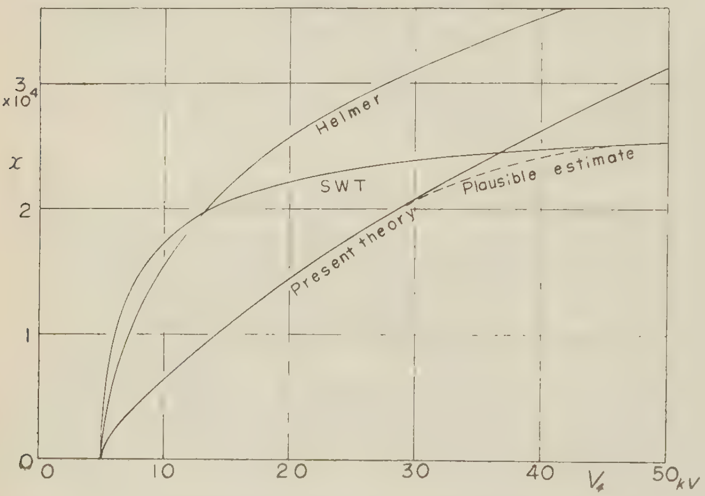

Fig. 3. Theoretical saturation characteristics of a maser oscillator.

The present theory has been found to agree with experimental results better than the former ones as will be described in part II.

It must be remembered that the relative numbers of molecules in each M state changes in a complex way with increasing focuser voltage. The number of focused molecules in a larger M state saturates faster than that in a smaller M state, and also their transition probability saturates faster with increasing x. Hence the contribution of smaller M states will increase in a large signal region discussed above.

§ 4. Effects of Unresolved Hyperfine Structure

Each inversion pair of energy levels of ammonia is split into hyperfine levels by the coupling with the quadrupole moment of nitrogen nucleus, N^{14}. Quadrupole hyperfine levels are designated by an angular momentum $F_1=J+I$. Inversion transitions corresponding to $\Delta F_1=\pm 1$ are the two pairs of satellites. The center line consists of three $\Delta F_1=0$ components which have not yet been resolved.

However, Gordon observed[10)] a significant asymmetry of the magnetic hyperfine structures about the center line, and it was ascribed to the change of quadrupole coupling constant eqQ in the upper and lower inversion states. He found the increase of $\Delta eqQ=4\pm1$ kc/sec in the lower state for the 3,3 line. The change of eqQ results in the separation of three components in the center inversion lines, with a sole exception for the 3,2 line in which the quadrupole hyperfine structure is absent.

When the molecules are in thermal equilibrium, the relative intensities of these three components are proportional to $2F_1+1$, and the weighted average frequency just coincides with that not displaced by hyperfine structure. The ratio of intensities of three components with $F_1=3, 4$, and 2 of the 3,3 line is 7:9:5 as shown in Fig. 4 (a).

The relative intensities of these three components in the maser are different from those in thermal equilibrium, since the number of molecules in respective F_1 states are determined by the focusing force which is approximately proportional to M^2 in the strong field region*. Assuming that the transition from the intermediate to strong field case is adiabatic, relative numbers of focused molecules in the weak field F_1 states are calculated as approximately $\sum M^2$, where the summation

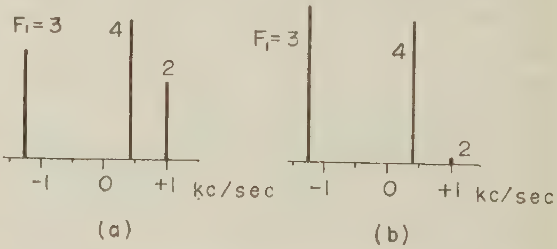

Fig. 4. Relative intensities of hyperfine components in the 3,3 center line of ammonia. (a): Thermal equilibrium, (b): In the maser.

---

* See Eq. (2.6). M_J is written simply M, but it is not M_F.

is for all levels which go to respective F_1 level in weak field. The approximate ratio of focused molecules for $F_1=3$, 4, and 2 in the 3,3 line is 45:37:2.

The probability of the transition $\Delta F_1=0$ has a factor,

$$f(F_1)=\frac{[F_1(F_1+1)+J(J+1)-I(I+1)]^2}{F_1(F_1+1)} \quad (4.1)$$

which is 121/3: 45: 128/3 for $F_1=3$, 4, and 2. Then the relative intensity is given by $c(F_1)=f(F_1)\cdot\sum M^2$, and the ratio for the 3,3 line is 1: 0.9174: 0.0470, as illustrated in Fig. 4 (b).

In observing the emission spectrum, these three components cannot be resolved, so far as the cavity is not extremely long, and the center line is observed at the frequency very close to the weighted average of the three components. Since the hyperfine shifts are -1.25, $+0.42$, and $+1.00$ kc/sec for $F_1=3$, 4, and 2, using the value $\Delta eqQ=4$ kc/sec*, the center frequency of the emission line is calculated to be -0.42 kc/sec.

The frequency of maser oscillator would be somewhat different, particularly near the threshold of oscillation where the oscillation amplitude is small and the focuser voltage is low. As discussed in § 2, the effective average velocity is so small in this case that the starting frequency might be near the strongest hyperfine component, $F_1=3$.

As a general extension of Eq. (44) in Appendix, the condition of oscillation with several hyperfine components can be expressed in the form

$$c_0\left(1+2iQ\frac{\omega-\omega_c}{\omega_c}\right) =\sum_j \frac{c_j}{\theta_j^2}\left[\sin^2\theta_j-i(\omega-\omega_j)\frac{L}{2\langle v\rangle} \times\left(1-\frac{\sin 2\theta_j}{2\theta_j}\right)\right], \quad (4.2)$$

where c_j is the relative intensity corresponding to $c(F_1)$ and also to $n/\langle v\rangle^2$, $\omega_j/2\pi$ the frequency of j-th hyperfine component, also

$$\theta_j=[(\omega-\omega_j)^2+x^2]^{1/2}\frac{L}{2\langle v\rangle}, \quad (4.3)$$

and c_0 is a constant corresponding to the relative intensity at the threshold of oscillation. Other notations are the same as in SWT and in § 2.

From the real part of Eq. (4.2) the amplitude of oscillation is obtained as

$$c_0=\sum_j c_j\frac{\sin^2\theta_j}{\theta_j^2}. \quad (4.4)$$

The imaginary part of Eq. (4.2) gives the frequency of oscillation by

$$2c_0Q\frac{\omega_c-\omega}{\omega_c} =\sum_j \frac{c_j}{\theta_j^2}(\omega-\omega_j)\frac{L}{2\langle v\rangle}\left(1-\frac{\sin 2\theta_j}{2\theta_j}\right). \quad (4.5)$$

It seems rather difficult to express amplitude and frequency of oscillation in explicit forms from (4.4) and (4.5). Then a typical case of the 3,3 line of ammonia will be numerically given. Because the relative intensity of the $F_1=2$ component is much smaller than the other two, as discussed above, calculation with only two components, $F_1=3$, and 4, would give fairly accurate results.

Amplitude vs. Frequency Characteristics

The amplitude of oscillation, x, due to the emission of two hyperfine components at ω_1 and ω_2 is determined from

$$\theta_1=[(\omega-\omega_1)^2+x^2]^{1/2}L/2\langle v\rangle,$$
$$\theta_2=[(\omega-\omega_2)^2+x^2]^{1/2}L/2\langle v\rangle, \quad (4.6)$$

and

$$c_0=c_1\frac{\sin^2\theta_1}{\theta_1^2}+c_2\frac{\sin^2\theta_2}{\theta_2^2}. \quad (4.7)$$

The ratio c_1: c_2 is known to be 1: 0.9174 in the case of the 3,3 line of ammonia, if the effect of saturation is neglected.

Since $\sin^2\theta_1/\theta_1^2=c_1/c_0=$const. is presented by a circle in the ω-x plane with its center at $\omega=\omega_1$, while $\sin^2\theta_2/\theta_2^2$ by another circle with its center at $\omega=\omega_2$, a set of θ_1 and θ_2 can be determined from Eq. (4.7) by a graphical method. Each set of θ_1 and θ_2 determine a set of ω and x from (4.6). Thus the amplitnde vs. frequency characteristics is obtained. An example for $V_4=14$ kV, $\langle v\rangle=15\,v_c=2.6\times10^4$ cm/sec is shown in Fig. 5, where the parameter is the beam intensity.

It is evident that by increasing the focuser voltage the characteristic curves in ω-x plane tend to be circular like those in the absence of hyperfine structure. The curves in Fig. 5 are very close to ellipses (note that the vertical scale is expanded) inconsistent with the observation by Helmer[7]. However, it must have come from the use of a single effective average velocity which is not a good approximation for large θ, as already discussed at the end of § 3.

---

* Bonanomi has recently obtained a somewhat smaller value as 3 kc/sec. Private communication.

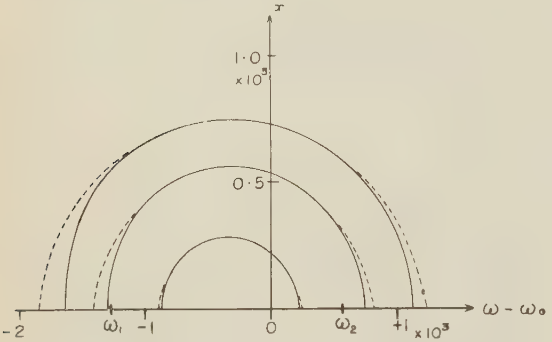

Fig. 5. Amplitude vs. frequency characteristics. Dotted curves show plausible modifications corresponding to those in Fig. 6.

The expression $\sin^2\theta/\theta^2$ must be somewhat modified when $\theta \gtrsim \pi/2$ as shown by a dotted curve in Fig. 6. This modification will spread the characteristic curve at the region where θ_1 or θ_2 is large, and then it will be consistent with experimental results. Because the higher frequency component ($F_1=4$) is weaker, there would occur more spread at the lower frequency wing of the characteristic curve where θ_2 is larger than θ_1 in the other wing.

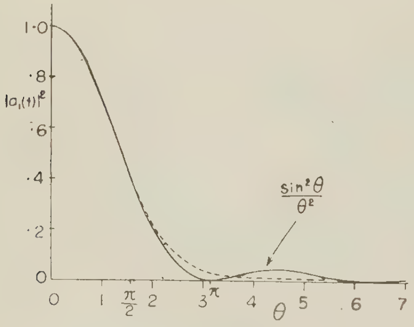

Fig. 6. Transition probability, $\sin^2\theta/\theta^2$ and its modification.

Frequency Shift

The frequency of oscillation, $\omega/2\pi$, due to the emission of two unresolved components is obtained from Eq. (4.5). It can be seen that the frequency pulling by the cavity occurs in a similar manner as described before[1)5)4)]. In this paper we are interested in the center frequency of oscillation which can be found or defined by putting $\omega_c=\omega$, although experimental determination of the corresponding line center needs a little troublesome procedure. Then Eq. (4.5) becomes

$$c_1\frac{\omega-\omega_1}{\theta_1^2}\left(1-\frac{\sin 2\theta_1}{2\theta_1}\right)+c_2\frac{\omega-\omega_2}{\theta_2^2}\left(1-\frac{\sin 2\theta_2}{2\theta_2}\right)=0. \tag{4.8}$$

Taking $x=0$ in order to find the starting frequency,

$$\theta_1=|\omega-\omega_1|L/2\langle v\rangle,\quad \theta_2=|\omega-\omega_2|L/2\langle v\rangle\ , \tag{4.9}$$

Eq. (4.8) is written as

$$\frac{c_1}{2\theta_1}\left(1-\frac{\sin 2\theta_1}{2\theta_1}\right)=\frac{c_2}{2\theta_2}\left(1-\frac{\sin 2\theta_2}{2\theta_2}\right), \tag{4.10}$$

since $\omega_1<\omega<\omega_2$, when $\omega_1<\omega_2$. The ratio c_1: c_2 is known and also

$$\theta_1+\theta_2=|\omega_2-\omega_1|L/2\langle v\rangle \tag{4.11}$$

is a known constant. Then the frequency of oscillation can be obtained from Eqs. (4.9), (4.10), and (4.11) as a function of $\langle v\rangle$.

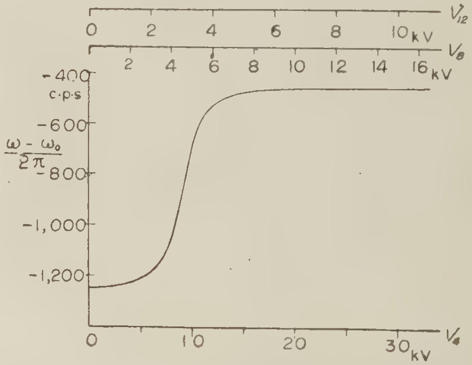

Fig. 7. Calculated frequency shift of the 3,3 line due to unresolved hyperfine structure. Changes of relative intensities by saturation effect are neglected.

An example for the 3,3 line of ammonia was calculated by plotting functions of the type, $(1-\sin 2\theta/2\theta)/2\theta$. The result is shown in Fig. 7, where the abscissa is the focuser voltage. Scales for the 8- and 12- pole focuser voltages, V_8, and V_{12}, as well as the quadrupole focuser voltage, V_4, are indicated for convenience. The conversion from $\langle v\rangle$ to V was done by Eqs. (2.24) and (2.7) or Fig. 2, using following values: $l=30$ cm, $L=11$ cm, $R=0.5$ cm, $\mu=1.44$ D, and $\langle M^2\rangle=7$. The frequency shift is shown in c.p.s. with respect to the center frequency not displaced by hyperfine structure.

The calculated frequency shown in Fig. 7 is the starting frequency as a function of the focuser voltage. Frequency shift for the finite amplitude of oscillation has to be computed from (4.8) instead of (4.10). The computation can be carried out by a graphical method, and it may be conjectured that the oscillation frequency in this case changes nearly the same way as Fig. 7 with increasing focuser voltage under a constant beam source hence with increasing amplitude of oscillation. Suppose, for example, a maser with threshold voltage of $V_{4,0}=10$ kV, it will start oscillation at the frequency 690 c.p.s. lower than the true center, and the frequency increases up to about -450 c. p. s.* at high voltages.

The frequency shift beyond the quadrupole focuser voltage of 15 kV is shown to be considerably small, of the order of 1 c. p. s./kV. On the other hand, it is appreciable below 15 kV, and its change is seen to amount to 2 to 3 parts in 10^8. Therefore, the frequency shift of this type would be studied better by a maser with lower starting voltage.

Of course the calculations used was not very accurate, but the conclusion such as that shown in Fig. 7 would be correct at least qualitatively. In particular, changes of the relative abundance of molecules in different F_1 states with increasing V and x, as described at the end of § 3, must cause considerable shift.

Since $F_1=3$ component has the lowest frequency and the largest value of $\sum M^2$, saturation effect tends to have less contribution of $F_1=3$ component and more of $F_1=2$ component, hence the oscillation frequency will be increased. Increasing the length of the cavity increases the saturation effect, because $\theta \propto L$, and will increase the oscillation frequency. Of course actual frequency shift of the maser oscillator includes other types of shifts such as those due to traveling wave component in the cavity, cavity pulling, and collision of molecules. Therefore, determination of the absolute shift seems to be very difficult, and the maser on the 3,3 line of ammonia may not be a good primary standard of frequency. However, excellent resettability of about 10^{-10} is practicable and it must be quite useful.

Appendix

It is shown that Eq. (46) in SWT can easily be obtained without any restriction of the frequencies. On page 1313 of SWT from line 28 should read as follows:
a slight deviation from Eq. (41). Therefore the following result is obtained.

$$\tfrac{1}{2}E=-i\frac{4\pi Q}{L}\left(1+2iQ\frac{\omega-\omega_c}{\omega_c}\right)^{-1}\int_0^L P^\dagger(z)dz\ . \tag{42}$$

By using Eq. (38), Eq. (42) may be written

$$\tfrac{1}{2}E=-i\frac{4\pi nQ}{vAL}\left(1+2iQ\,\frac{\omega-\omega_c}{\omega_c}\right)^{-1}\int_0^L p^\dagger(z)dz\ . \tag{43}$$

Since $p(z)$ has been given as a function of $x=E\bar{\mu}/\hbar$, the condition of stationary oscillation is obtained from Eqs. (43) and (37) as

$$\begin{aligned}\frac{x}{2}=&\frac{4\pi^2Qn\bar{\mu}^2}{vhAL}\left(1+2iQ\,\frac{\omega-\omega_c}{\omega_c}\right)^{-1}\frac{x}{[(\omega-\omega_0)^2+x^2]^{1/2}}\\ &\times\int_0^L\left\{\sin[(\omega-\omega_0)^2+x^2]^{1/2}\,\frac{z}{v}\right.\\ &-i\,\frac{\omega-\omega_0}{[(\omega-\omega_0)^2+x^2]^{1/2}}\\ &\left.\times\left[1-\cos[(\omega-\omega_0)^2+x^2]^{1/2}\frac{z}{v}\right]\right\}dz\ .\end{aligned} \tag{44}$$

From the real part of Eq. (44), the amplitude of oscillation $E=x\hbar/\bar{\mu}$ can be obtained as

$$n/n_{th}=\theta^2/\sin^2\theta\ .$$

This is the same as Eq. (31), but now

$$\theta=[(\omega-\omega_0)^2+x^2]^{1/2}\,L/2v\ , \tag{45}$$

including the case when $\omega\not\fallingdotseq\omega_0$.
The imaginary part of Eq. (44) gives

$$\frac{\omega-\omega_0}{\omega_0}=2Q\,\frac{(v/L)}{\omega_0}\,\frac{1-\cos 2\theta}{1-\sin 2\theta/2\theta}\,\frac{\omega_c-\omega}{\omega_c}\ . \tag{46}$$

References

1) J. P. Gordon, H. J. Zeiger, and C. H. Townes: Phys. Rev. **99** (1955) 1264.
2) N. Bloembergen: Phys. Rev. **104** (1956) 324.
3) H. E. D. Scovil, G. Feher, and H. Seidel: Phys. Rev. **105** (1957) 762.
4) J. C. Helmer: M. L. Report No. 311, Stanford Univ. (1956).
5) K. Shimoda, T. C. Wang, and C. H. Townes: Phys. Rev. **102** (1956) 1308.

---

* The difference of this value from -0.42 kc/sec given as the center of the emission line comes from the neglect of $F_1=2$ component.

6) R. P. Feynman F. L. Vernon, and R. W. Hellwarth: Journ. Appl. Phys. **28** (1957) 49.
7) J. C. Helmer: Journ. Appl. Phys. **28** (1957) 212.
8) K. Shimoda: Journ. Phys. Soc. Japan **12** (1957) 558.
9) J. Bonanomi and J. Herrmann: Helv. Phys. Acta **29** (1956) 451.
10) J. P. Gordon: Phys. Rev. **99** (1955) 1253.

JOURNAL OF THE PHYSICAL SOCIETY OF JAPAN Vol. 12, No. 9, SEPTEMBER, 1957

One-Center Molecular Orbital Wave Function for Methane

By Shoichiro KOIDE
Institute of Physics, College of General Education, University of Tokyo
Hisao SEKIYAMA and Toshio NAGASHIMA*
Department of Physics, Faculty of Science, University of Tokyo

(Received June 8, 1957)

The validity of the spherical approximation for the potential due to nuclei used in the calculation of molecules with good symmetry by means of one-center MO method is examined for methane molecule. Molecular orbital wave functions are set up as harmonic expansion about the central carbon nucleus, and energy expectation values are calculated with respect to the exact Hamiltonian. Results obtained by using various approximations are compared. It is shown that while the effect of the angular dependent part of the nuclear potential on the energy value is not so large as is expected, the electron charge distribution has fairly large directional dependence caused by the non-central part of the potential.

§ 1. Introduction

Most of the molecular orbital calculations heretofore performed have been based on the so-called LCAO approximation. The main difficulty of this method is that if we want to get sufficiently accurate results it requires extensive numerical work especially in the evaluation of many-center integrals. To avoid this difficulty, several attempts have been made concerning the one-center method[1] in which each molecular orbital is expressed as a series of spherical harmonics times a radial function about a single center. Thus

$$\psi(i)=\sum_{a} A_{a\alpha} r_i^{-1} P_{n_a l_a}(r_i) Y_{l_a m_a}(\theta_i, \phi_i) . \quad (1)$$

The most famous work in this direction is the self-consistent field calculation of methane molecule carried out by Buckingham, Massey and Tibbs[2]. Considering the high degree of symmetry of this molecule, they used spherically averaged nuclear potential and reduced the problem to the atomic one. The configuration used was $(1s)^2(2s)^2(2p)^6$, and this corresponds to the product of one-center molecular orbitals each of which is approximated by a single harmonic term in the expansion (1).

A similar calculation was made by Bernal using analytic radial functions[3]. In his calculation he took account of the exchange terms which were neglected in the calculation by Buckingham et al.

Quite recently, Carter has calculated the one-center molecular orbitals for methane and silane taking account of the higher harmonic terms in the expansion of the molecular orbitals[4]. According to his results, the total energy of the methane is predicted very well by taking just the first term in each series, but higher terms are important in the calculation of some other molecular quantities such as angular momentum and diamagnetic susceptibility.

If we use the one-center expansion of molecular orbitals, it will be difficult to obtain wave functions with uniform accuracy throughout all regions of the molecule. One cannot therefore expect good results for the calculation of such properties for which contribution from the outer atoms is considerable. Carter's result reveals this situation.

---

* Now at the Research Laboratory, Asahi Glass Company, LTD., Yokohama, Japan.

In all these calculations, the potential due to nuclei has been approximated by spherically smoothed one. By using this approximation, however, the effect of the attraction by the outer atomic nuclei will be considerably reduced. This defect of smoothing approximation has been revealed in the calculation of electron distribution in CCl_4 molecule carried through by March and his colaborators using the Thomas-Fermi method[5]. In their result, the electrons have an inclination to concentrate to the central carbon atom. The same tendency may occur in the calculation of wave functions. Of course, one can by no means calculate the directional variation of the valence electron distribution in this smoothing approximation.

In view of these circumstances, it may be highly desirable to consider the angular dependence of the nuclear potential in the calculation of the one-center molecular orbitals. In order to reflect this effect in the wave functions, we must take account of the higher harmonic terms of the expansion as far as possible.

In Bernal's calculation, the exchange terms lower the total energy of methane molecule by ca 0.9 a.u. which is comparable to the binding energy 0.74 a.u. observed for this molecule.

Although the numerical calculation of the self-consistent field would yield the best result, it requires a tremendous effort since the Hartree or the Hartree-Fock equations become a set of simultaneous equations coupled with each other in a complicated way.

In this paper, therefore, we will restrict the problem to the simplest one, i.e. that of methane, and simple analytic radial functions will be employed so as to enable us to estimate the effects of angular dependent nuclear potential by using the antisymmetrized total wave function.

§2. Nuclear Potential and Wave Functions

If we choose the coordinate axes as shown in Fig. 1, the potential energy of an electron due to all nuclei can be expanded as

$$V_n(r, \theta, \phi) = V_0(r) + V_c(r)A(\theta, \phi) + V_t(r)B(\theta, \phi) + V_h(r)C(\theta, \phi) + \cdots \, . \qquad (2)$$

The first term $V_0(r)$ is nothing but the spherically averaged potential used in the previous calculations. Here and in the following we use the atomic units, so the unit of length is the Bohr radius a_0. Since four protons are at a distance $2a_0$ from the central carbon nucleus, terms on the right hand side of Eq. (2) can be determined as

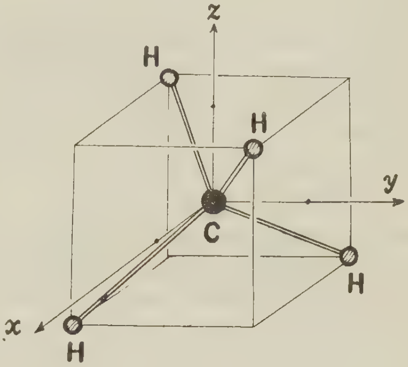

Fig. 1.

$$V_0(r) = \begin{cases} -2 - \dfrac{6}{r} & \text{if } r < 2 \, , \\ -\dfrac{10}{r} & \text{if } r > 2 \, , \end{cases} \qquad (3)$$

$$V_c(r) = \begin{cases} -\dfrac{(35\pi)^{1/2}}{42} r^3 & \text{if } r < 2 \, , \\ -\dfrac{64(35\pi)^{1/2}}{21} r^{-4} & \text{if } r > 2 \, , \end{cases} \qquad (4)$$

$$A(\theta, \phi) = -2^{-1/2} i \{ Y_{32}(\theta, \phi) - Y_{3-2}(\theta, \phi) \} \, , \qquad (4a)$$

$$V_t(r) = \begin{cases} -\dfrac{(21\pi)^{1/2}}{108} r^4 & \text{if } r < 2 \, , \\ -\dfrac{128(21\pi)^{1/2}}{27} r^{-5} & \text{if } r > 2 \, , \end{cases} \qquad (5)$$

$$B(\theta, \phi) = -\left(\frac{5}{24}\right)^{1/2} \{ Y_{44}(\theta, \phi) + Y_{4-4}(\theta, \phi) \} - \left(\frac{7}{12}\right)^{1/2} Y_{40}(\theta, \phi) \, , \qquad (5a)$$

$$V_h(r) = \begin{cases} -\dfrac{(26\pi)^{1/2}}{468} r^6 & \text{if } r < 2 \, , \\ -\dfrac{2048(26\pi)^{1/2}}{117} r^{-7} & \text{if } r > 2 \, , \end{cases} \qquad (6)$$

$$C(\theta, \phi) = -\left(\frac{7}{16}\right)^{1/2} \{ Y_{64}(\theta, \phi) + Y_{6-4}(\theta, \phi) \} + \left(\frac{1}{8}\right)^{1/2} Y_{60}(\theta, \phi) \, . \qquad (6a)$$

Corresponding to the atomic configuration $(1s)^2(2s)^2(2p_x)^2(2p_y)^2(2p_z)^2$, we may take the ground state configuration of our ten-electron system as

$$(1a_1)^2(2a_1)^2(2t_{2x})^2(2t_{2y})^2(2t_{2z})^2 .$$

Here a_1 and t_2 denote the irreducible representations A_1 and T_2 of the tetrahedral group corresponding to the respective molecular orbitals.

Since the influence of surrounding hydrogen atoms is considered to be small on the inner K-shell electrons of the carbon atom, $1a_1$ function may safely be assumed to be spherically symmetric; i.e.

$$(1a_1): \quad \psi_1(\boldsymbol{r})=C_1r^{-1}P_1(r)Y_{00}(\theta, \phi) . \tag{7}$$

In the molecular orbitals of the valence electrons, we will include the higher harmonic terms up to the third order ($l=3$). Then, by using the group character table, we can assume the following form for our $2a_1$ and $2t_2$ functions:

$$(2a_1): \quad \psi_2(\boldsymbol{r})=C_2r^{-1}P_2(r)Y_{00}(\theta, \phi) + C_3r^{-1}P_3(r)A(\theta, \phi) , \tag{8}$$

$$(2t_{2x}): \quad \psi_x(\boldsymbol{r})=C_4r^{-1}P_4(r)T_x^{(1)}(\theta, \phi) + C_5r^{-1}P_5(r)T_x^{(2)}(\theta, \phi) + C_6r^{-1}P_6(r)T_x^{(3)}(\theta, \phi) , \tag{9}$$

with similar expressions for $2t_{2y}$ and $2t_{2z}$. In these expressions, $A(\theta, \phi)\equiv f_{xyz}$ is the function defined by (4a) and is proportional to xyz/r^3, and

$$T_x^{(1)}=p_x , \quad T_x^{(2)}=d_{yz} , \quad T_x^{(3)}=f_{x(5x^2-3)} \tag{10}$$

are the functions proportional to x/r, yz/r^2 and $x(5x^2-3r^2)/r^3$ and they are expressed as proper linear combinations of the spherical harmonics $Y_{lm}(\theta, \phi)$ with $l=1, 2, 3$ respectively.

Since each of the angular and radial functions is taken to be normalized as

$$\iint|A|^2 \sin\theta \, d\theta d\phi = \iint|T_\xi^{(i)}|^2 \sin\theta \, d\theta d\phi = \int_0^\infty |P_i(r)|^2 dr=1 , \tag{11}$$

the coefficients C's must satisfy the conditions

$$C_1=1 , \quad C_2^2+C_3^2=C_4^2+C_5^2+C_6^2=1 . \tag{12}$$

For simplicity, the same functions as the Bernal's may be adopted as the radial functions of the leading terms in (7), (8) and (9):

$$P_1(r)=2\alpha^{3/2}re^{-\alpha r} \tag{13}$$

$$P_2(r)=\{12\beta^5/(\alpha^2-\alpha\beta+\beta^2)\}^{1/2} \times\{(\alpha+\beta)r/3-1\}re^{-\beta r} \tag{14}$$

$$P_4(r)=(4\gamma^5/3)^{1/2}r^2e^{-\gamma r} , \tag{15}$$

though the functions used by Carter appear to give somewhat better results.

As we know nothing in advance about the radial parts of the additional functions, some preliminary calculations about the Hartree equations for $P_3(r), P_5(r), P_6(r)$ were carried out using the initial fields obtained from numerical functions of Buckingham et al. As a result, it has been concluded that each of these functions seems to have a maximum in the neighborhood of the C–H bond length, i.e. $r=2$. Thus we may eventually assume the following form for these functions:

$$P_3(r)=(2048/315)^{1/2}r^4e^{-2r} \tag{16}$$

$$P_5(r)=(243/80)^{1/2}r^3e^{-3r/2} \tag{17}$$

$$P_6(r)=P_3(r) . \tag{18}$$

§ 3. Variation Calculations

The total energy of the molecule is the sum of the electronic energy E and the classical nuclear repulsion energy E_N:

$$E=\int\Psi^*\mathscr{H}\Psi d\boldsymbol{r}_1 d\boldsymbol{r}_2\cdots d\boldsymbol{r}_{10} , \tag{19}$$

$$E_N=\{40+3(3/2)^{1/2}\}/2 , \tag{20}$$

where $\mathscr{H}$ is the Hamiltonian of the electron system

$$\mathscr{H}=\sum_{i=1}^{10} H(i)+\sum_{i<j}^{10}\frac{1}{r_{ij}} , \tag{21}$$

$$H(i)=-\frac{1}{2}\Delta_i+V_n(r_i, \theta_i, \phi_i) , \tag{22}$$

and Ψ is the Slater determinant given by

$$\Psi=(10!)^{-1/2}\,\mathrm{Det}[\psi_1\bar{\psi}_1\psi_2\bar{\psi}_2\psi_x\bar{\psi}_x\psi_y\bar{\psi}_y\psi_z\bar{\psi}_z| , \tag{23}$$

where electrons in the orbitals with upper bar have an opposite direction of spin to those in the orbitals without bar.

The electronic energy E is expressed in terms of one- and two-electron integrals as follows:

$$\begin{aligned} E=&2I(1a_1)+2I(2a_1)+6I(2t_{2x})+F_0(11) \\ &+4F_0(12)C_2^2+4F_0(13)C_3^2+12F_0(14)C_4^2 \\ &+12F_0(15)C_5^2+12F_0(16)C_6^2+F_0(22)C_2^4 \\ &+2F_0(23)C_2^2C_3^2+F_0(33)C_3^4+\frac{4}{7}G_3(23)C_2^2C_3^2 \\ &+\frac{84}{1089}F_4(33)C_3^4+\frac{800}{20449}F_6(33)C_3^4 \\ &+12F_0(24)C_2^2C_4^2-\frac{48\sqrt{21}}{49}I_3(23:45)C_2C_3C_4C_5 \\ &+12F_0(25)C_2^2C_5^2+\frac{23}{7}I_3(23:56)C_2C_3C_5C_6 \end{aligned}$$

$$
\begin{aligned}
&+12F_0(26)C_2^2C_6^2+12F_0(34)C_3^2C_4^2 \\
&-\frac{32\sqrt{21}}{99}I_4(33:46)C_3^2C_4C_6+12F_0(35)C_3^2C_5^2 \\
&+\frac{16}{33}F_4(35)C_3^2C_5^2+12F_0(36)C_3^2C_6^2 \\
&-\frac{56}{121}F_4(36)C_3^2C_6^2+\frac{12000}{61347}F_6(36)C_3^2C_6^2 \\
&+15F_0(44)C_4^4-\frac{6}{5}F_2(44)C_4^4+30F_0(45)C_4^2C_5^2 \\
&+\frac{12}{7}F_2(45)C_4^2C_5^2+30F_0(46)C_4^2C_6^2 \\
&-\frac{2}{5}F_2(46)C_4^2C_6^2-\frac{36}{25}\sqrt{\frac{3}{7}}I_2(44:46)C_4^3C_6 \\
&+15F_0(55)C_5^4-\frac{30}{49}F_2(55)C_5^4-\frac{60}{441}F_4(55)C_5^4 \\
&+30F_0(56)C_5^2C_6^2+\frac{2}{7}F_2(56)C_5^2C_6^2 \\
&-\frac{100}{77}F_4(56)C_5^2C_6^2 \\
&+\frac{362}{35}\sqrt{\frac{3}{7}}I_2(55:46)C_4C_5^2C_6 \\
&-\frac{200}{63}\sqrt{\frac{3}{7}}I_4(55:46)C_4C_5^2C_6+15F_0(66)C_6^4 \\
&-\frac{7}{30}F_2(66)C_6^4-\frac{65125}{245388}F_6(66)C_6^4 \\
&-\frac{54}{25}\sqrt{\frac{3}{7}}I_2(46:66)C_4C_6^3 \\
&+\frac{100}{33}\sqrt{\frac{3}{7}}I_4(46:66)C_4C_6^3+\frac{684}{245}G_3(45)C_4^2C_5^2 \\
&-\frac{424}{35}\sqrt{\frac{3}{7}}I_3(45:56)C_4C_5^2C_6 \\
&-\frac{54}{25}G_2(46)C_4^2C_6^2+\frac{50}{21}G_4(46)C_4^2C_6^2 \\
&+\frac{394}{105}G_3(56)C_5^2C_6^2-\frac{7500}{7623}G_5(56)C_5^2C_6^2 \\
&-2G_0(12)C_2^2-\frac{2}{7}G_3(13)C_3^2-2G_1(14)C_4^2 \\
&-\frac{6}{5}G_2(15)C_5^2-\frac{6}{7}G_3(16)C_6^2 \\
&-2G_1(24)C_2^2C_4^2-\frac{6}{7}G_1(35)C_3^2C_5^2 \\
&+4\sqrt{\frac{3}{7}}I_1(24:35)C_2C_3C_4C_5 \\
&-\frac{6}{5}G_2(25)C_2^2C_5^2-\frac{18}{35}G_2(34)C_3^2C_4^2 \\
&-\frac{8}{15}G_2(36)C_3^2C_6^2 \\
&+\frac{12}{5}\sqrt{\frac{3}{7}}I_2(25:34)C_2C_3C_4C_5 \\
&-\frac{8}{5}I_2(25:36)C_2C_3C_5C_6 \\
&+\frac{8}{5}\sqrt{\frac{3}{7}}I_2(34:36)C_3^2C_4C_6-\frac{6}{7}G_3(26)C_2^2C_6^2 \\
&-\frac{8}{21}G_3(35)C_3^2C_5^2-\frac{8}{7}I_3(26:35)C_2C_3C_5C_6 \\
&-\frac{8}{21}G_4(34)C_3^2C_4^2-\frac{2}{121}G_4(36)C_3^2C_6^2 \\
&+\frac{8}{33}\sqrt{\frac{3}{7}}I_4(34:36)C_3^2C_4C_6 \\
&-\frac{680}{2541}G_5(35)C_3^2C_5^2-\frac{5600}{184041}G_6(36)C_3^2C_6^2 \\
&+\frac{24}{5}G_1(45)C_4^2C_5^2-\frac{72}{35}G_1(56)C_5^2C_6^2 \\
&+\frac{48}{5}\sqrt{\frac{3}{7}}I_1(45:56)C_4C_5^2C_6\ , \qquad (24)
\end{aligned}
$$

where one-electron integrals are expressed as usual:

$$I(1a_1)=\iint\psi_1^*(\boldsymbol{r})H(\boldsymbol{r})\psi_1(\boldsymbol{r})d\boldsymbol{r}\ , \qquad (25a)$$

$$I(2a_1)=\int\psi_2^*(\boldsymbol{r})H(\boldsymbol{r})\psi_2(\boldsymbol{r})d\boldsymbol{r}\ , \qquad (25b)$$

$$I(2t_{2x})=\int\psi_x^*(\boldsymbol{r})H(\boldsymbol{r})\psi_x(\boldsymbol{r})d\boldsymbol{r}=I(2t_{2y})=I(2t_{2z})\ . \qquad (25c)$$

Since our orbital functions are not of single term, two-electron integrals have the following form in general

$$I_n(ij:kl)=\iint\frac{r_<^n}{r_>^{n+1}}P_i(r)P_j(r)P_k(r')P_l(r')drdr'\ , \qquad (26)$$

and F and G are the special cases of this general form

$$F_n(ij)=I_n(ii:jj)\ , \qquad (27a)$$

$$G_n(ij)=I_n(ij:ij)\ . \qquad (27b)$$

Following the variational method, the electronic energy E is minimized with respect to the parameters, α, β, γ, C_1, C_2, $\cdots$, C_6 under the condition of Eq. (12). The calculation of Buckingham et al shows that the $1a_1$ function does not differ much from the self-consistent function for the free carbon atom. For this reason, the minimization with respect to α was not carried out. Comparing the results of Buckingham et al and of Bernal, we took $\alpha=5.52$. For several sets of the values of β and γ numerical calculations of the one- and two-electron integrals were carried out, and the coefficient C's were determined so as to minimize the value of E for each set of β and γ.

§4. Results and Discussion

The results are listed in Table I. From these values, we can find that the minimum value of the total energy occurs at $\beta=1.73$ and $\gamma=1.3$, as

$$E+E_N=-39.64\ \text{a.u.}$$

The coefficients C's corresponding to this minimum energy value were found to be $C_2=0.9851$, $C_3=0.172$, $C_4=0.9718$, $C_5=0.227$ and $C_6=-0.064$.

Table I. Calculated Expectation Values of the Total Energy.

β	γ	A	B	C	ΔE
1.50	1.30	−38.095	−38.964		
1.70	1.20	−38.424	−39.270	−39.581	0.311
1.70	1.30	−38.401	−39.314	−39.636	0.322
1.70	1.40	−38.286	−39.257		
1.75	1.125	−38.385	−39.178	−39.487	0.309
1.75	1.20	−38.426	−39.277	−39.588	0.311
1.75	1.30	−38.394	−39.315	−39.636	0.321
1.75	1.40	−38.270	−39.252	−39.576	0.324
1.80	1.20	−38.424	−39.279	−39.588	0.309
1.80	1.30	−38.383	−39.312	−39.623	0.311
1.80	1.40	−38.250	−39.244		
1.90	1.30	−38.353	−39.295		
1.90	1.40	−38.201	−39.214		

A: values obtained by using spherical approximation (without exchange).
B: values obtained by using spherical approximation (with exchange).
C: values obtained by taking account of angular dependent terms of the nuclear potential (with exchange).
$\Delta E=B-C$.

If we take $C_2=C_4=1$ and $C_3=C_5=C_6=0$, contribution from the angular dependent terms of the nuclear potential vanishes because of the properties of the spherical harmonics, and the results thus obtained, which are also shown in Table I in the fourth column, column, coincide with those given by Bernal's approximation. In this table, we can see that our results are lower about 0.3 a.u. than those of Bernal's approximation.

According to Carter's estimation, even when C_5 and C_6 terms and the non-central part of the nuclear potential are neglected, the minimum energy can be lowered by ca 0.2 a.u. if we take account of the second term of Eq. (8). Thus we can see that the effect of the non-central part of the nuclear potential is not so large as we have expected, though our results would be improved further to some extent by using more appropriate form for the additional functions.

In Table II, energy values obtained by the various workers are tabulated with approximations involved. As is pointed out by Carter, there is a numerical error in the total energy value calculated by Buckingham et al. Hence the calculated binding energy, which is given by subtracting the total energy $E+E_N$ from that for C+4H calculated by Torrance⁶⁾, becomes slightly negative. Since Torrance's calculation is based on the numerical computation of the self-consistent field without exchange, it is of little meaning to compare it with the $E+E_N$ values obtained by using other approximations. If, however, the non-central terms of the nuclear potential were took into account in the calculation of Buckingham et al, their result would be improved

Table II. Comparison of the Various Calculations.

Author	Radial functions	Angular dependence of the nuclear potential	Higher harmonic terms of MO's	Exchange terms	Total energy
B.M.T.*	numerical	neglected	neglected	neglected	−39.47 a.u.**
Bernal	analytic	neglected	neglected	considered	−39.33 〃
Carter	analytic***	neglected	considered	neglected	−39.68 〃
Present calculation	analytic	considered	considered	considered	−39.64 〃

* Buckingham, Massey and Tibbs²⁾.
** Corrected value.
*** Carter's functions are different from those adopted by Bernal and by the present authors.

and, as we have seen in the above consideration, the calculated total energy of methane would be lowered by at least ca 0.3 a.u., yielding the positive binding energy of about 0.1 a.u. = 2.7 eV.

In order to see the effect of angular dependent part of the nuclear potential on the electron distribution, we may divide the whole space into eight regions by xy-, yz- and zx-planes, and calculate the number of electrons belonging to each of these divisions. As is seen in Fig. 1, protons are located in four of those, and the number of electrons lying in one of them can be easily calculated as

$$\begin{aligned} n_+ = \frac{10}{8} &+ 4C_2C_3(4\pi)^{-1/2}\int_0^{\pi/2}\int_0^{\pi/2} A(\theta, \phi)\sin\theta\, d\theta d\phi \int_0^\infty P_2P_3dr \\ &+ 12C_4C_5\int_0^{\pi/2}\int_0^{\pi/2} T_x^{(1)}T_x^{(2)}\sin\theta\, d\theta d\phi \int_0^\infty P_4P_5dr \\ &+ 12C_6C_6\int_0^{\pi/2}\int_0^{\pi/2} T_x^{(2)}T_x^{(3)}\sin\theta\, d\theta d\phi \int_0^\infty P_5P_6dr \\ &+ 12C_4C_6\int_0^{\pi/2}\int_0^{\pi/2} T_x^{(1)}T_x^{(3)}\sin\theta\, d\theta d\phi \int_0^\infty P_4P_6dr = 1.25+0.25\ . \end{aligned} \tag{28a}$$

Similarly, the number of electrons in one of the remaining four divisions is

$$n_- = 1.25 - 0.25\ . \tag{28b}$$

If we use the simplest Heitler-London method and neglect the non-orthogonality of the hydrogen atomic orbitals with each other and with carbon atomic orbitals, ten electrons are accommodated as $(1s)^2 \cdot \phi_1 : h_1 \cdot \phi_2 : h_2 \cdot \phi_3 : h_3 \cdot \phi_4 : h_4$. Here ϕ_i denotes one of the sp^3 hybridized orbitals which points to the i-th hydrogen atom whose atom orbital is expressed by h_i; e.g.

$$\phi_1 = [(2s) + \{(2p_x) + (2p_y) + (2p_z)\}]/2\ ,$$

and the colons express the bondings between the orbitals connected by them. In this rough approximation, electron distribution is given by

$$\begin{aligned} \rho(\boldsymbol{r}) = 2(1s)^2 &+ (2s)^2 + (2p_x)^2 + (2p_y)^2 + (2p_z)^2 \\ &+ h_1^2 + h_2^2 + h_3^2 + h_4^2\ . \end{aligned}$$

Since the first five terms give the charge distribution of spherical symmetry, angular dependence comes only from the last four terms. Then

$$n_+ = \frac{6}{8} + \int_0^\infty\int_0^\infty\int_0^\infty (h_1^2 + h_2^2 + h_3^2 + h_4^2)dxdydz\ ,$$

and

$$n_- = \frac{6}{8} + \int_0^\infty\int_0^\infty\int_0^{-\infty} (h_1^2 + h_2^2 + h_3^2 + h_4^2)dxdydz\ .$$

If the hydrogen atomic orbital is confined only in one of the eight divisions defined above, $n_+ = 0.75 + 1$ and $n_- = 0.75 + 0$. The numbers given by (28a) and (28b) correspond to $n_+ = 0.75 + 0.75$ and $n_- = 0.75 + 0.25$. If we think about the fairly large extension of hydrogen atomic orbital, our results (28a) and (28b) seem to express the electron distribution with fairly large directional dependence.

In conclusion, the authors wish to express their sincere thanks to Professor M. Kotani and the members of his laboratory for their continuous encouragement during the course of this work, and to Mrs. H. Komuro and Mrs. M. Sekiyama for their help in troublesome computations. A part of this work was supported financially by Scientific Expenditure of the Educational Ministry.

References

1) For instance, S. Huzinaga: Progr. Theor. Phys. **15** (1956) 501, and the papers cited there.
2) R. A. Buckingham, H. S. W. Massey and S. R. Tibbs: Proc. Roy. Soc. **A178** (1941) 119.
3) M. J. M. Bernal: Proc. Phys. Soc. **A66** (1953) 514.
4) C. Carter: Proc. Roy. Soc. **A235** (1956) 321.
5) N. H. March: Advances in Phys. **6** (1957) 1.
6) C. C. Torrance: Phys. Rev. **46** (1934) 388.
In course of preparing this manuscript, a review article *"Molecules with almost spherical symmetry"* has been published:
R. A. Buckingham and C. Carter: J. Phys. Chem. **16** (1957) 19.

JOURNAL OF THE PHYSICAL SOCIETY OF JAPAN Vol. 12, No. 9, SEPTEMBER, 1957

On the Radio Wave Propagation in a Stratified Atmosphere II

By Ryozo YAMADA

Faculty of Science and Engineering Meijo University, Nagoya

(Received April 5, 1957)

In this paper a method is developed for determining the electromagnetic field produced by a microwave antenna. The theory is developed for the condition that the index of refraction of the atmosphere varies with height as $A+Bh+Ch^2$, for the flattened earth. From the rigorous solution the geometrical-optical description is derived. The Hertzian vector is split into the geometrical series, each term of which corresponds to the rays reflected 1, 2, 3, $\cdots$ times by the earth, when the "duct" is formed. Among these rays there are the rays whose propagation constants are complex number. The existence of these rays explains the "radio duct phenomena" in the cases when the transmitter and the receiver are located both out of the "duct", and when they are in and out of the "duct", respectively. For the field strength in the vicinity of the cusp of caustic, we use the original integral and calculate by numerical integration. The field strength of the reflected rays at the cusp of caustic is 3.2 times that of free space for $\lambda=2\pi$ cm, $b=5\times10^{-5}$/m, $z_0=100$ m, $z_1=z_2=60$ m, $r=62.8$ km. The interference of this strong field of these reflected rays with the weak field of the diverged direct ray may be the cause of the large fading range when the "duct" is formed.

§ 1. Introduction

In the Part I of this paper[5)] the field from a dipole is expressed in the form of the residue series which converges rapidly when the distance is large. While the convergence is not appropriate for numerical evaluation when the distance is small. In this paper we deal with this problem by ray method starting with the integral (15) of Part I of this paper. The integral (15) is split into two exponential integrals which correspond to the direct ray and the reflected ray by the earth in the case when the "duct" is not formed. In the case when the "duct" is formed, the integral (15) is split into a geometrical series, and each term of this series has the form of an exponential integral and corresponds to the ray reflected 1, 2, 3, $\cdots$ times by the earth. And if a source is located in the "duct", the rays rediated with real angle and once reflected totally by the inhomogeneity of the atmosphere never get out of the "duct". In the cases when the transmitter and the receiver are both located out of the "duct" and when they are in and out of the "duct", respectively, the saddle points of these integrals become complex and these correspond to the rays which start with complex angle and reach the receiver. This explains the "radio duct phenomena" in these cases.

In the case when the "duct" is formed and the source is in the "duct", the ray leaving horizontally has the smallest range between successive reflections at the surfoce of the earth (let this range be $2R$) among the rays leaving the source, as shown in Fig. 1. A ray leaving the source at a negative inclination α has its first reflection at a horizontal distance less than R and its range between successive reflections is $2R+O(\alpha^2)$, hence such rays must form one of a caustic. And the rays leaving the source at positive inclinations may form the second branch of a caustic. The field distribution in the neighbourhood of a caustic can be calculated by Airy's integral, but this treatment does not apply in the neighbourhood of the cusp of caustic. The

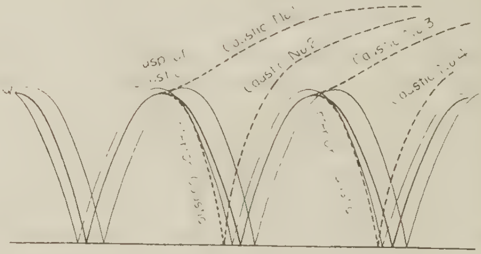

Fig. 1.

field in this neighbourhood was evaluated by D. R. Hartree, Michel and Nicholson[7]. The theory developed here is intrinsically most accurate in this neighbourhood and is less accurate as one recedes from the cusp of caustic. The rays once reflected converge and the field strength at the cusp of caustic due to once reflected rays is large. The interference of this reflected rays with the diverged direct ray in this neighbourhood may be the cause of the large fading range due to the "duct" when the reflection coefficient of the earth is small.

§ 2. Ray Theory

In this section we shall derive from our solution (15) of Part I the geometrical- optical approximation which is valied for short wave length. The procedure has been developed by many writers[1)2)3)4)9)]; we apply this method to our case. By the aid of the asymptotic approximations given in § 3. b), c), d) of Part I for large x, we have the asymptotic expressions for the integrand in (15), and find the value of γ_0 for which the phase of the integrand is stationary, if such point exists, and evaluate the integral around the point of stationary phase. This procedure corresponds to to find the path and the amplitude of the ray.

We rewrite the integral representation (15) of the Hertzian vector in the form

$$\psi=\frac{i}{2H}\int_{\infty}^{-\infty}H_0^{(1)}(k_0r\sqrt{1-4b^2H^2\gamma})v(\gamma)\,d\gamma \qquad (15)$$

$$=\frac{i}{2H}\int_{\infty}^{-\infty}H_0^{(1)}(k_0r\sqrt{1-4b^2H^2\gamma})[U(\gamma)-V(\gamma)]u_2(x_1,\gamma)u_2(x_2,\gamma)\,d\gamma\ , \qquad (2.1)$$

where

$$U(\gamma)=\frac{u_1'(x_0,\gamma)-Hpu_1(x_0,\gamma)}{u_2'(x_0,\gamma)-Hpu_2(x_0,\gamma)} \qquad (2.2)$$

$$V(\gamma)=\frac{u_1(x_1,\gamma)}{u_2(x_1,\gamma)}\quad x_2\geqslant x_1$$

$$V(\gamma)=\frac{u_1(x_2,\gamma)}{u_2(x_1,\gamma)}\quad x_2\leqslant x_1\ . \qquad (2.3)$$

And u_1 and u_2 are expressed in terms of Weber's functions [cf. (9), (10) (I)].

According to the result of Part I of this paper, Weber's functions are expressed as follows: We divide γ-plane into four subdomains corresponding to the four subdomains of w_0-plane (Fig. 1 of Part I), and the corresponding subdomains for the complex $\gamma+i/2=(x_2/4)\sinh^2 w_0$ have the same numbers as shown in Fig. 2. When x is large and positive and γ is large, $D_{-i\gamma-1/2}(e^{i\pi/4}x)$ and $D_{i\gamma-1/2}(e^{-i\pi/4}x)$ are expressed in terms of (w_1), $(w_1+2\pi i)$ and (w_2) in Table I of Part I, and (w_1), $(w_1+2\pi i)$, (w_2) are approximated by their asymptotic expansions as follows,

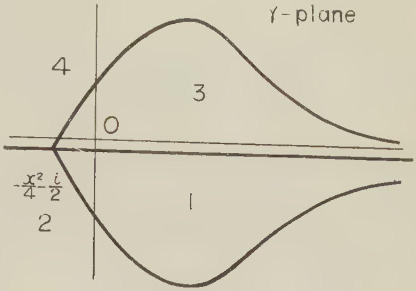

Fig. 2. γ-plane.

$$(w_1)\sim-\sqrt{2\pi}\frac{e^{-5\pi(\gamma-i/2)/4}}{\sqrt[4]{x^2+4(\gamma+i/2)}}\exp i\left\{\frac{\gamma+i/2}{2}+\frac{x}{4}\sqrt{x^2+4(\gamma+i/2)}+\gamma\log\frac{x+\sqrt{x^2+4(\gamma+i/2)}}{2}-\gamma\log(\gamma+i/2)\right\}, \qquad (2.4)$$

$$(w_2)\sim-\sqrt{2\pi}\frac{e^{-\pi(\gamma-i/2)/4}}{\sqrt[4]{x^2+4(\gamma+i/2)}}\exp -i\left\{-\frac{\gamma+i/2}{2}+\frac{x}{4}\sqrt{x^2+4(\gamma+i/2)}+\gamma\log\frac{x+\sqrt{x^2+4(\gamma+i/2)}}{2}\right\}, \qquad (2.5)$$

$$(w_1+2\pi i)\sim-\sqrt{2\pi}\frac{e^{3\pi(\gamma-i/2)/4}}{\sqrt{x^2+4(\gamma+{}^{i}/2)}}\times\exp i\left\{\frac{\gamma+i/2}{2}+\frac{x}{4}\sqrt{x^2+4(\gamma+i/2)}+\gamma\log\frac{x+\sqrt{x^2+4(\gamma+i/2)}}{2}-\gamma\log(\gamma+i/2)\right\}. \qquad (2.6)$$

and $\Gamma(i\gamma+1/2)$, when γ is large, is approximated by

$$\Gamma(i\gamma+1/2)\sim\sqrt{2\pi}\exp\{-i\gamma-1/2+i\gamma\log(\gamma-i/2)-\gamma\pi/2\}\ . \qquad (2.7)$$

When x is large and positive, and γ is small, we use Weber's functions the asymptotic expansions given in § 3. b) of Part I[6)].

For the transitional region, the asymptotic expansions given in § 3. d) are used.

As for negative values of x, $D_{-i\gamma-1/2}$ and $D_{i\gamma-1/2}$ are given by the circuit relations[6];

$$D_n(-e^{i\pi/4}x)=e^{-n\pi i}D_n(e^{i\pi/4}x)+\frac{\sqrt{2\pi}}{\Gamma(-n)}e^{-i(n+1)\pi/2}D_{-n-1}(e^{-\pi/4}x) \tag{2.8}$$

$$D_{-n-1}(-e^{-i\pi/4}x)=\frac{\sqrt{2\pi}}{\Gamma(n+1)}e^{-n\pi i/2}D_n(e^{i\pi/4}x)-e^{-n\pi i}D_{-n-1}(e^{-i\pi/4}x)\,. \tag{2.9}$$

Thus the asymptotic expansions of Weber's functions are different accordings to the sign x and the value of γ in relation to x; the asymptotic expression of (2.1) has the different form according to the signs of x_0, x_1, x_2. We divide this into four cases:

i) $x_0>0,\quad x_1>0,\quad x_1>0.$

ii) $x_0<0,\quad x_1>0,\quad x_2>0.$

iii) $x_0<0,\quad x_1>0,\quad x_2<0,$

or $x_0<0,\quad x_1<0,\quad x_2>0.$

iv) $x_0<0,\quad x_1<0,\quad x_2<0.$

For these four cases the different terms appear in (2.1), and the corresponding ray configurations are different. But as the method of deducing the corresponding rays from these different terms is quite similar, we illustrate this by the example of the case ii) $x_0<0$, $x_1>0$, $x_2>0$, $(x_1>x_2)$ in this section.

To begin with, we divide γ-plane into the sub-subdomains in relation to x_0, x_1, x_2 as follows: We write

$$\gamma+\frac{i}{2}=\frac{x_0^2}{4}\sinh^2 w_{00}=\frac{x_1^2}{4}\sinh^2 w_{01}=\frac{x_2^2}{4}\sinh^2 w_{02}\,,$$

and when w_{00} lies in the subdomain 3, w_{01} in the subdomain 3, w_{02} in subdomain 4, γ lies in the sub-subdomain 3_0, 3_1, 4_2 as shown in Fig. 3. We write the asymptotic expression of (2.1) in these sub-subdomains and evaluate this integral by the method of steepest descents.

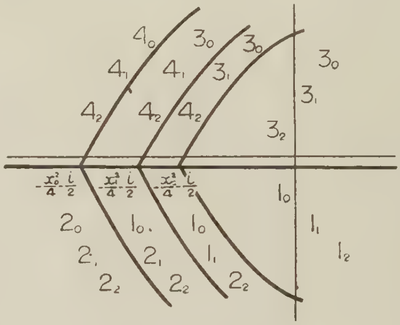

Fig. 3. γ-plane.

In the limit of large r (in comparison with λ) we have

$$H_0^{(1)}(k_0r\sqrt{1-4b^2H^2\gamma}\sim\left(\frac{2}{\pi k_0r\sqrt{1-4b^2H^2\gamma}}\right)^{1/2}\exp(ik_0r\sqrt{1-4b^2H^2\gamma}-i\pi/4)\,.$$

When γ lies in the 3_0, 3_1, 3_2 sub-subdomain, the second term of the right-hand side of (2.1) can be written as

$$-\frac{i}{2H}\int_{\infty}^{-\infty}H_0^{(1)}(k_0r\sqrt{1-4b^2H^2\gamma})\frac{u_1(x_2,\gamma)}{u_2(x_2,\gamma)}u^2(x_2,\gamma)\,u_2(x_1,\gamma)\,d\gamma$$

$$\sim\frac{e^{i\pi/4}}{H\sqrt{2\pi k_0r}}\int_{-\infty}^{\infty}[(1-4b^2H^2\gamma)\{x_1^2+4(\gamma+i/2)\}\{x_2^2+4(\gamma+i/2)\}]^{-1/4}\{\exp iq(\gamma)\}\,d\gamma\,, \tag{2.10}$$

where

$$q(r)=k_0r\sqrt{1-4b^2H^2\gamma}+\frac{x_1}{4}\sqrt{x_1^2+4(\gamma+i/2)}-\frac{x_2}{4}\sqrt{x_2^2+4(\gamma+i/2)}$$
$$+\gamma\log[\{x_1+\sqrt{x_1^2+4(\gamma+i/2)}\}/\{x_2+\sqrt{x_2^2+4(\gamma+i/2)}\}]\,.$$

And when γ and $x_1^2+4\gamma$ are large in comparison with 1/2, we have

$$q(r)=k_0r\sqrt{1-4b^2H^2\gamma}+\frac{x_1}{4}\sqrt{x_1^2+4\gamma}-\frac{x_2}{4}\sqrt{x_2^2+4\gamma}+\gamma\log\frac{x_1+\sqrt{x_1^2+4\gamma}}{x_2+\sqrt{x_2^2+4\gamma}}\,.$$

The point of stationary phase of this integrand is determined from

$$\partial q(r)/\partial\gamma=-(br/\sqrt{1-4b^2H^2\gamma}+\log\{(x_1+\sqrt{x_1^2+4\gamma})/(x_2+\sqrt{x_2^2+4\gamma})\}=0\,. \tag{2.11}$$

The saddle point γ_0 can exist in this sub-subdomain, if $br<(1+b^2H^2x_2^2)^{1/2}\log\{x_1+\sqrt{x_1^2-x_2^2}/x_2\}$, and the value of this γ_0 is real and $\gamma_0>-x_2^2/4$ as shown in Appendix. This saddle point gives a ray which directly reaches the receiver and satisfies the Fermat's principle; a brief calculation gives (2.11) an integral form

$$r=\int_{z_2}^{z_1}\frac{N(z_1)\cos\alpha\,dz}{\sqrt{N^2(z)-N^2(z_1)\cos^2\alpha}}\ ,$$

where α is the inclination with which the ray leaves the source, and $N(z_1)\cos\alpha/N_0=\sqrt{1-4b^2H^2\gamma_0}$. The Hertzian vector due to this ray is calculated by the method of steepest descents, and is given by

$$\begin{aligned}\Psi_{01}\sim\frac{1}{r}\{\exp iq(\gamma_0)\}\Bigg\{&\frac{\sqrt{1-4b^2H^2\gamma_0}}{br}\left(\frac{\sqrt{x_1^2+4\gamma_0}}{x_2+\sqrt{x_2^2+4\gamma_0}}-\frac{\sqrt{x_2^2+4\lambda_0}}{x_1+\sqrt{x_1^2+4\gamma_0}}\right)\\&+\frac{b^2H^2\sqrt{x_1^2+4\gamma_0}\sqrt{x_2^2+4\gamma_0}}{1-4b^2H^2\gamma_0}\Bigg\}^{-1/2}=\alpha_{01}\frac{1}{r}\exp iq(\gamma_0)\ ,\end{aligned}\tag{2.12}$$

where α_{01} is the divergence factor of direct ray due to the inhomogeneity of the atmosphere, and the value of α_{01} is nearly 1 when the distance is small. Further investigation shows that there is no saddle point in the other sub-subdomains, so the contribution of the integral in these sub-subdomains is small.

Next we shall evaluate the Hertzian vector due to $U(\gamma)$. In our case x_0 is negative, we use the circuit relations (2.8), (2.9) and we have

$$\begin{aligned}U(\gamma)&=e^{i\pi/4}\frac{\{(\partial/\partial x)D_{-i\gamma-1/2}(xe^{i\pi/4})\}_{x=x_0}-HpD_{-i\gamma-1/2}(x_0e^{i\pi/4})}{\{(\partial/\partial x)D_{i\gamma-1/2}(xe^{-i\pi/4})\}_{x=x_0}-HpD_{i\gamma-1/2}(x_0e^{i\pi/4})}=e^{i\pi/4}\Bigg[\frac{\Gamma(-i\gamma+1/2)}{\sqrt{2\pi}}e^{-(\gamma-i/2)\pi/2}\\&-\frac{\Gamma(-i\gamma+1/2)}{\sqrt{2\pi}}e^{(\gamma-i/2)\pi/2}\frac{\{(\partial/\partial x)D_{i\gamma-1/2}(xe^{-i\pi/4})\}_{x=|x_0|}+HpD_{i\gamma-1/2}(|x_0|e^{-i\pi/4})}{\{(\partial/\partial x)D_{i\gamma-1/2}(xe^{-i\pi/4})\}_{x=x_0}-HpD_{i\gamma-1/2}(x_0e^{-i\pi/4})}\Bigg].\end{aligned}\tag{2.13}$$

Further the second term of the right-hand side of (2.13) becomes

$$\begin{aligned}&-e^{(\gamma-i/2)\pi/2}\frac{\Gamma(-i\gamma+1/2)}{\sqrt{2\pi}}D_{i\gamma-1/2}(|x_0|e^{-i\pi/4})\left[\left\{\frac{\partial}{\partial x}\log D_{i\gamma-1/2}(xe^{-i\pi/4})\right\}_{x=|x_0|}+Hp\right]\Bigg/\\&\quad-\frac{\sqrt{2\pi}}{\Gamma(-i\gamma+1/2)}e^{-(\gamma-i/2)\pi/2}D_{-i\gamma-1/2}(|x_0|e^{i\pi/4})\left[\left\{\frac{\partial}{\partial x}\log D_{-i\gamma-1/2}(xe^{i\pi/4})\right\}_{x=|x_0|}+Hp\right]\\&\quad+e^{-(\gamma-i/2)\pi}D_{i\gamma-1/2}(|x_0|e^{-i\pi/4})\left[\left\{\frac{\partial}{\partial x}\log D_{i\gamma-1/2}(xe^{-i\pi/4})\right\}_{x=|x_0|}+Hp\right]=e^{\pi(\gamma-i/2)}\left\{\frac{\Gamma(-i\gamma+1/2)}{\sqrt{2\pi}}\right\}^2\\&\quad\times\frac{D_{i\gamma-1/2}(|x_0|e^{-i\pi/4})}{D_{-i\gamma-1/2}(|x_0|e^{i\pi/4})}\left(\frac{B}{C}\right)\left[1-\frac{\Gamma(-i\gamma+1/2)}{\sqrt{2\pi}}e^{-(\gamma-i/2)\pi/2}\frac{D_{i\gamma-1/2}(|x_0|e^{-i\pi/4})}{D_{-i\gamma-1/2}(|x_0|e^{i\pi/4})}\left(\frac{B}{C}\right)\right]^{-1},\end{aligned}\tag{2.14}$$

where

$$B=\left\{\frac{\partial}{\partial x}\log D_{i\gamma-1/2}(xe^{-i\pi/4})\right\}_{x=|x_0|}+Hp\ ,\tag{2.15}$$

$$C=\left\{\frac{\partial}{\partial x}\log D_{-i\gamma-1/2}(xe^{i\pi/4})\right\}_{x=|x_0|}+Hp\ .\tag{2.16}$$

In the domain of γ which satisfies the following relation

$$\left|\frac{\Gamma(-i\gamma+1/2)}{\sqrt{2\pi}}e^{-(\gamma-i/2).\pi/2}\frac{D_{i\gamma-1/2}(|x_0|e^{-i\pi/4})}{D_{-i\gamma-1/2}(|x_0|e^{i\pi/4})}\left(\frac{B}{C}\right)\right|<1\ ,$$

(2.14) can be expanded in the geometrical series. By the similar method that we used when we investigated the residue series in Part I, in the case $Hp=\infty$ this is the domain of γ which satisfies the following relation, if we write $\gamma+i/2=(x_0^2/4)\sinh^2(\alpha_0+i\beta_0)$,

$$\sinh\alpha_0\sin\beta_0-\frac{\sinh 2\alpha_0\sin 2\beta_0}{4}\log\frac{\cosh\alpha_0+\cos\beta_0}{\cosh\alpha_0-\cos\beta_0}-\frac{\cosh 2\alpha_0\sin 2\beta_0-1}{2}\left(\tan^{-1}\frac{\sin\beta_0}{\sinh\alpha_0}-\frac{\pi}{2}\right)>0$$

as is shown in Fig. 4. We write (2.14) in this domain in the form

$$\frac{\Gamma(-i\gamma+1/2)}{\sqrt{2\pi}}e^{3\pi(\gamma-i/2)/2}\sum_{n=1}^{\infty}\left[\frac{\Gamma(-i\gamma+1/2)}{\sqrt{2\pi}}e^{-(\gamma-i/2).\pi/2}\frac{D_{i\gamma-1/2}(|x_0|e^{-i\pi/4})}{D_{-i\gamma-1/2}(|x_0|e^{i\pi/4})}\left(\frac{B}{C}\right)\right]^n . \tag{2.17}$$

Using this result, we write $U(\gamma)$ in (2.2) in the form

$$U(\gamma)=U_0(\gamma)+\sum_{n=1}^{\infty}U_n(\gamma) .$$

At first we consider the Hertzian vector due to $U_0(\gamma)$. When x_0, x_1, x_2, γ are large and γ lies in the 3_0, 3_1, 3_2, sub-subdomain, and γ and $x_1^2+4\gamma$ are large in comparison with 1/2, we have

$$\frac{i}{2H}\int_{-\infty}^{\infty}H_0^{(1)}(k_0r\sqrt{1-4b^2H^2\gamma})U_0(\gamma)u_2(x_1,\gamma)u_2(x_2,\gamma)d\gamma ,$$

$$\sim\frac{e^{-\pi i/4}}{H\sqrt{2\pi k_0r}}\int_{-\infty}^{\infty}\{(1-4b^2H^2\gamma)(x_1^2+4\gamma)(x_2^2+4\gamma)\}^{-1/4}\exp ip_0(\gamma)d\gamma , \tag{2.18}$$

where

$$p_0(\gamma)=k_0r\sqrt{1-4b^2H^2\gamma}+\frac{x_1}{4}\sqrt{x_1^2+4\gamma}+\frac{x_2}{4}\sqrt{x_2^2+4\gamma}+\gamma\log\frac{(x_1+\sqrt{x_1^2+4\gamma})(x_2+\sqrt{x_2^2+4\gamma})}{4\gamma} ,$$
$$+i\pi\gamma , \tag{2.19}$$

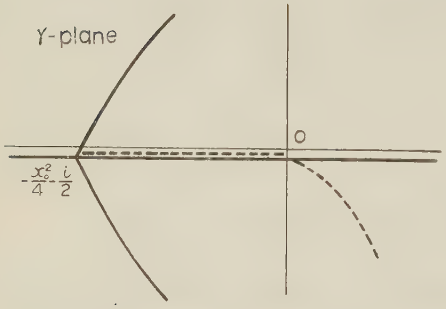

Fig. 4. $\left|e^{-(\gamma-i/2)\pi/2}\frac{\Gamma(-i\gamma+1/2)}{\sqrt{2\pi}}\frac{D_{i\gamma-1/2}}{D_{-i\gamma-1/2}}\right|<1$ in the domain above the dotted line.

and the point of stationary phase of this integrand is determined from

$$\frac{\partial p_0(\gamma)}{\partial\gamma}=-br/\sqrt{1-4b^2H^2\gamma}$$
$$+\log\frac{(x_1+\sqrt{x_1^2+4\gamma})(x_2+\sqrt{x_2^2+4\gamma})}{4\gamma}$$
$$+i\pi=0 . \tag{2.20}$$

The saddle point γ_0 can exist in this sub-subdomain, if

$$br>\sqrt{1+4b^2H^2x_2}\log\{(x_1+\sqrt{x_1^2-x_2^2})/x_2\},$$

and the value of this γ_0 is real and $-x_2^2/4<\gamma_0<0$. This defines the direct ray totally reflected by the inhomogeneity of the atmosphere. The contribution from this ray to the Hertzian vector is evaluated by the saddle point integral, and is given by

$$\Psi_{02}\sim\frac{1}{r}\exp ip_0(\gamma_0)$$
$$\times\left[\frac{\sqrt{1-4b^2H^2\gamma_0}}{br}\left(\frac{\sqrt{x_2^2+4\gamma_0}}{x_1+\sqrt{x_1^2+4\gamma_0}}+\frac{\sqrt{x_1^2+4\gamma_0}}{x^2-\sqrt{x_2^2+4\gamma_0}}\right)-\frac{b_2H^2\sqrt{x_1^2+4\gamma_0}\sqrt{x_2^2+4\gamma_0}}{1-4b^2H^2\gamma_0}\right]$$
$$=\alpha_{02}\frac{1}{r}\exp ip_0(\gamma_0) , \tag{2.21}$$

where α_{02} is the divergence factor of this ray. The point of sationary phase does not exist in the other sub- subdomains of γ. When γ is small in comparison with x_1^2, we use the asymptotic expansions of Weber's function in § 3. b), and we obtain corresponding to (2.21)

$$\Psi_{02}\sim\frac{1}{r}\sqrt{2br}\,\exp\left(-\frac{br}{2}\right)\exp i\left(k_0r+\frac{x_1^2}{4}+\frac{x_2^2}{4}+\gamma_0\right), \tag{2.21'}$$

where

$$-\gamma_0=(x_1x_2)^{1/2}\exp(-br).$$

Next we consider the Hertzian vector due to $U_1(\gamma)$. When x_0, x_1, x_2, γ are large and γ lies in the 3_0, 3_1, 3_2 sub-subdomain, and γ and $x_i^2+4\gamma$ $(i=0, 1, 2)$ are large in comparison with 1/2, we have

$$\frac{i}{2H}\int_{\infty}^{-\infty}H_0^{(1)}\left(k_0r\sqrt{1-4b^2H^2\gamma}\right)U_1(\gamma)u_2(x_1,\gamma)u_2(x_2,\gamma)d\gamma$$
$$\sim\frac{e^{i\pi/4}}{H\sqrt{2\pi k_0r}}\int_{-\infty}^{\infty}\left(\frac{B}{C}\right)\{(1-4b^2H^2\gamma)(x_1^2+4\gamma)(x_2^2+4\gamma\}^{-1/4}\exp ip_1(\gamma)\,d\gamma\,, \tag{2.22}$$

where

$$p_1(\gamma)=k_0r\sqrt{1-4b^2H^2\gamma}+\frac{|x_0|}{2}\sqrt{x_0^2+4\gamma}+\frac{x_1}{4}\sqrt{x_1^2+4\gamma}+\frac{x_2}{4}\sqrt{x_2^2+4\gamma}$$
$$+\gamma\log\frac{(|x_0|+\sqrt{x_0^2+4\gamma})^2(x_1+\sqrt{x_1^2+4\gamma})(x_2+\sqrt{x_2^2+4\gamma})}{16\gamma^2}.$$

And the saddle point is determined by

$$\frac{\partial p_1(\gamma)}{\partial\gamma}=-br/\sqrt{1-4b^2H^2\gamma}+\log\left(\frac{(|x_0|+\sqrt{x_0^2+4\gamma})^2(x_1+\sqrt{x_1^2+4\gamma})(x_2+\sqrt{x_2^2+4\gamma})}{16\gamma^2}\right)=0\,. \tag{2.23}$$

The saddle point lies on the real axis and $\gamma_0>0$. This defines the reflected ray by the earth. And the contribution of this ray to the Hertzian vector is

$$\Psi_1\sim-\left(\frac{B}{C}\right)\frac{1}{r}\{\exp ip_1(\gamma_0)\}\Bigg[\frac{\sqrt{1-4b^2H^2\gamma_0}}{br}\left(\frac{\sqrt{x_2^2+4\gamma_0}}{\sqrt{x_1^2+4\gamma_0}-x_1}+\frac{\sqrt{x_1^2+4\gamma}}{\sqrt{x_2^2+4\gamma_0}-x_2}\right)$$
$$+\left(\frac{b^2H^2}{1-4b^2H^2\gamma_0}-\frac{\sqrt{1-4b^2H^2\gamma_0}}{br\sqrt{x_0^2+4\gamma_0}\,(|x_0|+\sqrt{|x_0|^2+4\gamma_0})}\right)\sqrt{x_1^2+4\gamma_0}\sqrt{x_2^2+4\gamma_0}\Bigg]^{-1/2}. \tag{2.24}$$

By the appropriate approximation, we find

$$-\left(\frac{B}{C}\right)\sim\frac{-(i/2)\sqrt{x_0^2+4\gamma_0}-Hp}{(i/2)\sqrt{x_0^2+4\gamma_0}-Hp}=\frac{(k_2^2/k_0^2)\cos\theta-\sqrt{(k_2^2/k_0^2)-\sin^2\theta}}{(k_2^2/k_0^2)\cos\theta+\sqrt{(k_2^2/k_0^2)-\sin^2\theta}}$$

for a vertical electric dipole

$$=\frac{\cos\theta-\sqrt{(k_2^2/k_0^2)-\sin^2\theta}}{\cos\theta-\sqrt{(k_2^2/k_0^2)-\sin^2\theta}}$$

for a vertical magnetic dipole

where θ is the angle of reflection, and this is the reflection coefficient of the earth. There is no point of stationary phase of this term in the other sub-subdomains. When γ is small in comparison with x_0, x_1, x_2, we obtain corresponding to (2.24)

$$\Psi_1\sim\frac{\sqrt{br}}{r}\sqrt[4]{\frac{|x_0^2|}{x_1x_2}}\exp\left(\frac{-br}{4}\right)\exp i\left(k_0r+\frac{x_0^2}{2}+\frac{x_1^2}{4}+\frac{x_2^2}{4}+2\gamma_0\right), \tag{2.24'}$$

where

$$\gamma_0=|x_0|\sqrt{x_1x_2}\exp\left(\frac{-br}{2}\right)$$

At last we consider the Hertzian vector due to $U_n(\gamma)$. When x_0, x_1, x_2, γ are large and γ lies in the 3_0, 3_1, 3_2 sub-subdomain, and if γ and $x_i^2+4\gamma$ $(i=0, 1, 2)$ are large in comparison with 1/2, we have

$$\frac{i}{2H}\int_{\infty}^{-\infty} H_0^{(1)}\left(k_0 r\sqrt{1-4b^2H^2\gamma}\right)U_n(\gamma)u_2(x_1,\gamma)u_2(x_2,\gamma)d\gamma$$

$$\sim\frac{e^{i\pi/4}}{H\sqrt{2\pi k_0 r}}\int_{-\infty}^{\infty}\left(\frac{B}{C}\right)^n\{(1-4b^2H^2\gamma)(x_1^2+4\gamma)(x_2^2+4\gamma)\}^{-1/4}\exp ip_n(\gamma)\,d\gamma\ , \tag{2.25}$$

where

$$p_n(\gamma)=k_0 r\sqrt{1-4b^2H^2\gamma}+i(n-1)\pi\gamma+\frac{n-1}{2}\pi+\frac{n|x_0|}{2}\sqrt{|x_0|^2+4\gamma}+2n\gamma\log\frac{|x_0|+\sqrt{|x_0|^2+4\gamma}}{2}$$

$$-(n+1)\gamma\log\gamma+\frac{x_1}{4}\sqrt{x_1^2+4\gamma}+\frac{x_2}{4}\sqrt{x_2^2+4\gamma}+\gamma\log\frac{(x_1+\sqrt{x_1^2+4\gamma})(x_2+\sqrt{x_2^2+4\gamma})}{4}=0\,. \tag{2.26}$$

And the saddle point is given by

$$\frac{\partial p_n(\gamma)}{\partial\gamma}=\frac{-br}{\sqrt{1-4b^2H^2\gamma}}+\log\frac{(|x_0|+\sqrt{x_0^2+4\gamma})^{2n}(x_1+\sqrt{x_1^2+4\gamma})(x_2+\sqrt{x_2^2+4\gamma})}{(4\gamma)^{n+1}}+i(n-1)\pi=0\,. \tag{2.27}$$

In this case, the saddle point does not lie on the real axis but γ_0 has the complex value and its imaginary part is positive (as shown in Appendix). This defines the ray which reflects n times from the earth, and is totally reflected and attenuated by the inhomogeneity of the atmosphere. The contribution of this ray to the Hertzian vector is

$$\Psi_n\sim\frac{-1}{r}\left(\frac{B}{C}\right)^n\{\exp ip_n(\gamma_0)\}[(1-4b^2H^2\gamma_0)^{1/2}(x_1^2+4\gamma_0)^{1/2}(x_2^2+4\gamma_0)^{1/2}(1/2br)(-\partial p_n(\gamma_0)/\partial\gamma)]^{-1/2}\,. \tag{2.28}$$

There is no point of stationary phase in the other sub-subdomains of γ. When γ is small in comparison with x_0, x_1, x_2, but is large compared with 1/2, we obtain corresponding to (2.28)

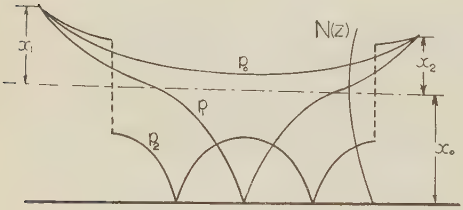

Fig. 5. $x_0<0$, $x_1>x_2>0$.

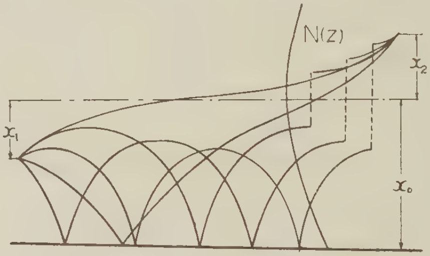

Fig. 7. $x_0<0$, $x_1<0$, $x_2>0$.

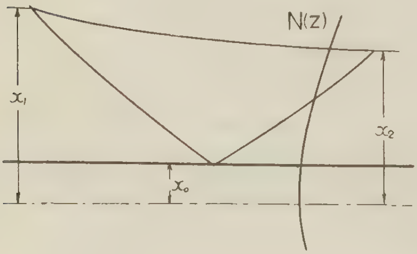

Fig. 6. $x_0>0$, $x_1>0$, $x_2>0$.

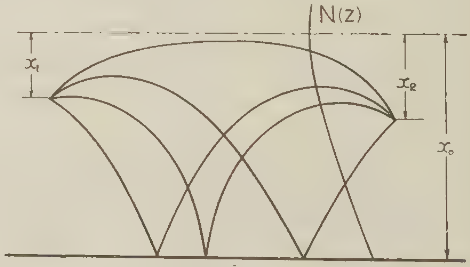

Fig. 8. $x_0<0$, $x_1<0$, $x_2<0$.

$$\Psi_n\sim-\frac{\sqrt{2br}}{r}\left(\frac{B}{C}\right)^n\frac{|x_0|^{n/(n+1)}(x_1x_2)^{-1/2(1-1/(n+1))}}{(n+1)^{1/2}}\exp\frac{-br+i(n-1)\pi}{2(n+1)}\exp i\Big\{k_0r+\gamma_0(n+1)$$

$$+\frac{(n-1)\pi}{2}+\frac{nx_0^2}{2}+\frac{x_1^2}{4}+\frac{x_2^2}{4}\Big\}\,, \tag{2.28'}$$

where

$$\gamma_0=(x_0^{2n}x_1x_2)^{1/(n+1)}\exp\left(\frac{-br}{n+1}+\frac{i(n-1)\pi}{n+1}\right).$$

This shows us that the attenuation of this ray becomes small as n becomes large. The field due to these multi-reflected rays explains the "radio duct phenomena" ray-theoretically in our case. The rays derived above are shown in Fig. 5.

And the rays in the cases i), ii), iv) are shown in Fig. 6, 7, 8, respectively.

§3. The Field in the Vicinity of the Cusp of Caustic

As mentioned in §1, there are the caustic and the cusp of caustic, when the "duct" is formed. The treatment of the field distribution in the neighbourhood of a caustic, away from the cusp, is due to Airy and is classical. This treatment does not apply in the immediate neighbourhood of the cusp of caustic, where three rays of the system pass through each point between the branches which meet in the cusp. The points of the cusp of caustic are, in our case, $x_0<0$, $x_1=x_2<0$ and $br=2n\sqrt{1+b^2H^2x_1^2}\log(|x_0|+\sqrt{x_0^2-x_1^2}/|x_2|)$. In the vicinity of the cusp, the saddle points of the terms in (2,1) corresponding to the reflected rays become nearly to $-x_1^2/4$, and in this transitional region $D_{-i\gamma-1/2}$ and $D_{i\gamma-1/2}$ lose their exponential character, and we can not evaluate the integral by the method of steepest descents. We evaluate the original integral by the numerical integration[10) using the $H_{1/3}$ approximations[8) for $D_{-i\gamma-1/2}$ and $D_{i\gamma-1/2}$, and calculate the field at $x_1=x_1$, $r\sim2\sqrt{1+b^2H^2x_1^2}\log\{(|x_0|+\sqrt{x_0^2-x_1^2})/|x_1|)$, due to the once reflcted rays from the earth.

The Hertzian vector due to the rays reflected once is given

$$\Psi_1\sim\frac{\sqrt{\pi}\,e^{i\pi/12}}{4\sqrt{2}\,H}\int_{-\infty}^{\infty}\frac{Re^{i\phi(\gamma)}\zeta\{H_{1/3}^{(1)}(\zeta e^{-i\pi})\}^2d\gamma}{(k_0r\sqrt{1-4b^2H^2\gamma})\sqrt{x_1^2/4+\gamma}}\,, \tag{2.29}$$

where

$$\phi(\gamma)=k_0r\sqrt{1-4b^2H^2\gamma}+\frac{|x_0|}{2}\sqrt{x_0^2+4\gamma}+2\gamma\log(|x_0|+\sqrt{x_0^2+4\gamma})-\gamma\log(-4\gamma)\,,$$

$$\zeta\equiv\frac{|x_1|}{4}\sqrt{x_1^2+4\gamma}+\gamma\log(|x_1|+\sqrt{x_1^2+4\gamma})-\frac{\gamma}{2}\log(-4\gamma)\,.$$

And we write $\varepsilon\equiv\gamma+x_1^2/4\equiv\gamma-\gamma_0$, then in this transitional region $\zeta\sim4\varepsilon^{3/2}/3x$ for $|4\varepsilon/x_1^2|<1$.

Using these we write (2.29) in the form

$$\psi_1\sim\frac{\sqrt{\pi}\,e^{i\pi/12}}{4\sqrt{2}\,H}\int_{-\infty}^{\infty}\frac{R\exp\{i\phi(\gamma_0)+i\varepsilon\phi'(\gamma_0)+i(\varepsilon^2/2)\phi''(\gamma_0)\}}{(k_0r\sqrt{1-4b^2H^2\gamma})^{1/2}}\left(\frac{4\varepsilon}{3x}\right)\left\{H_{1/3}^{(1)}\left(\frac{4\varepsilon^{3/2}}{3x}e^{-i\pi}\right)\right\}^2d\varepsilon\,. \tag{2.30}$$

Using the relation

$$H_{1/3}^{(1)}(xe^{-i\pi})=H_{1/3}^{(1)}(x)+e^{-i\pi/3}H_{1/3}^{(2)}(x)\,,$$

(2.30) can be written as

$$\begin{aligned}\psi_1\sim&\frac{\sqrt{\pi}\,R\exp i\{\pi/12+\phi(\gamma_0)\}}{4\sqrt{2}\,H(k_0r\sqrt{1-4b^2H^2\gamma_0})^{1/2}}\left[\int_{-\infty}^{\infty}\left\{\exp i\varepsilon\phi'(\gamma_0)+i\frac{\varepsilon^2}{2}\phi''(\gamma_0)\right\}\left(\frac{4\varepsilon}{3x}\right)\left\{H_{1/3}^{(1)}\left(\frac{4\varepsilon^{3/2}}{3x}e^{-i\pi}\right)\right\}^2d\varepsilon\right.\\&+\int_0^{\infty}\left\{\exp i\varepsilon\phi'(\gamma_0)+i\frac{\varepsilon^2}{2}\phi''(\gamma_0)\right\}\left(\frac{4\varepsilon}{3x}\right)\left[\left\{H_{1/3}^{(1)}\left(\frac{4\varepsilon^{3/2}}{3x}\right)\right\}^2+2e^{-i\pi/3}H_{1/3}^{(1)}\left(\frac{4\varepsilon^{3/2}}{3x}\right)H_{1/3}^{(2)}\left(\frac{4\varepsilon^{3/2}}{3x}\right)\right.\\&\left.\left.+e^{-2\pi i/3}\left\{H_{1/3}^{(1)}\left(\frac{4\varepsilon^{3/2}}{3x}\right)\right\}^2\right]d\varepsilon\right]=\frac{\sqrt{\pi}\,R\exp i\{\pi/12+\phi(\gamma_0)\}}{4\sqrt{2}\,H(k_0r\sqrt{1-4b^2H^2\gamma_0})^{1/2}}\int_0^{\infty}\left[\left\{\exp i\varepsilon\phi'(\gamma_0)+i\frac{\varepsilon^2}{2}\phi''(\gamma_0)\right.\right.\\&\left.-i\frac{\pi}{3}\right\}\left(\frac{2}{\pi}\right)^2\left(\frac{4\varepsilon}{3x}\right)\left\{K_{1/3}\left(\frac{4\varepsilon^{3/2}}{3x}\right)\right\}^2+\left\{\exp i\varepsilon e^{i\pi/3}\phi'(\gamma_0)+i\frac{\varepsilon^2}{2}e^{i2\pi/3}\phi''(\gamma_0)-i\frac{2\pi}{3}\right\}\left(\frac{2}{\pi}\right)^2\left(\frac{4\varepsilon}{3x}\right)\\&\times\left\{K_{1/3}\left(\frac{4\varepsilon^{3/2}}{3x}\right)\right\}^2+2\left\{\exp i\varepsilon\phi'(\gamma_0)+i\frac{\varepsilon^2}{2}\phi''(\gamma_0)-i\frac{\pi}{3}\right\}\left(\frac{4\varepsilon}{3x}\right)H_{1/3}^{(1)}\left(\frac{4\varepsilon^{3/2}}{3x}\right)H_{1/3}^{(2)}\left(\frac{4\varepsilon^{3/2}}{3x}\right)\\&\left.+\left\{\exp i\varepsilon e^{-i\pi/3}\phi'(\gamma_0)+i\frac{\varepsilon^2}{2}e^{-2\pi i/3}\phi''(\gamma_0)\right\}\left(\frac{2}{\pi}\right)^2\left(\frac{4\varepsilon}{3x}\right)\left\{K_{1/3}\left(\frac{4\varepsilon^{3/2}}{3x}\right)\right\}^2\right]d\varepsilon\,.\end{aligned} \tag{2.31}$$

Among the terms of this integrand, the term containing $H_{1/3}^{(1)}$ and $H_{1/3}^{(2)}$ gives the largest contribution to the Hertzian vector. And this term corresponds to the rays which form the caustic.

We obtain $\Psi_1=3.2/r$ for the case $\lambda=2\pi\,cm$, $b=5\times10^{-6}/m$, $z_0=z_2=60$ m, $r=62.8km$, the reflection coefficient of the earth -1.

The interference of this converged reflected rays and the diverged direct ray which distance as (2.21′) may be the cause of the large fading range when the " duct " is formed and the refliction coefficient is small.

§ 4. Conclusion

In this paper we developed a method to calculate the field strength when the modified index of refraction varies with height as $A+Bh+Ch^2$. By this method, the electromagnetic field produced by a microwave antenna may be calculated except the cases when x_0, x_1, x_2, γ are small. The field in these regions may be extrapolated from the other region. This method is useful to evaluate the field in the lit region when the " duct " is not formed. But when the distance is large, the calculation of the field due to the rays reflected 1, 2, 3, times becomes tedious in the case when the " duct " is formed, and the calculation by the mode theory may be useful in the lit region.

Appendix. Determination of the Point of Stationary Phase

To determine the point where $\partial p(\gamma)/\partial\gamma=0$, we consider the locus of $\partial p/\partial\gamma$ in the complex plane, when γ lies along the real axis, except it shall include a small semicircular detour in the upper half plane about the singular points on the real axis, and a large semicircular path in the upper half plane as shown in Fig. 10 (we seek the saddle point in the upper half plane). In our case there are no poles in the domain encircled by this contour, if this contour encircles in a positive sense Z zeros, the corresponding contour of $\partial p/\partial\gamma$ encircles the origin Z times in a positive sense. Furthermore from this contour, we are able to determine the point γ, in whose vicinity $\partial p/\partial\gamma=0$ exists. In our case we find the asymptotic expansion of Ψ in certain sub-subdomain, and determine the point of stationary phase of each term by above procedure. If such point exists and this point lies in this sub-subdomain, this is the point of stationary phase of the term of Ψ and this defines the real ray. In our case this is shown for $p_0(\gamma)$ and $p_n(\gamma)$ in Fig. 9, and 10, respectively.

References

1) D. E. Kerr: Propagation of Short Radio Waves (1951).
2) H. Bremmer: Terrestical Radio Waves (1949).
3) C. L. Pekeris: J. Appl. Phys. **18** (1947) 667.
4) Y. Nomura: J. Phys. Soc. Japan **10** (1955) 700.
5) R. Yamada: J. Phys. Soc. Japan **10** (1955) 71.
6) Whittaker and Watson: Modern Analysis 4th ed. 347.
7) D. R. Hartree: Meteorological Factors in Radio Wave Propagation. 127.
8) C. L. Pekeris: J. Appl. Phys. **17** (1946) 1108.
9) B. van d. Pol and H. Bremmer: Phil. Mag. **25** (1938) 817.
10) G. N. Watson: Theory of Bessel Functions (1922) 714-729.

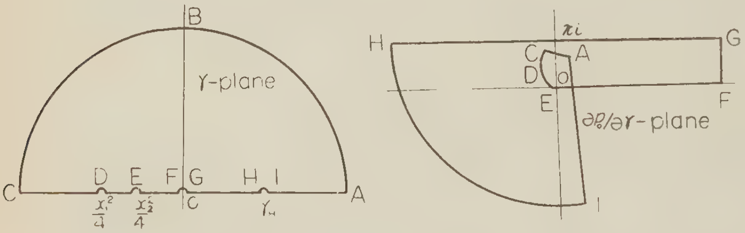

Fig. 9.

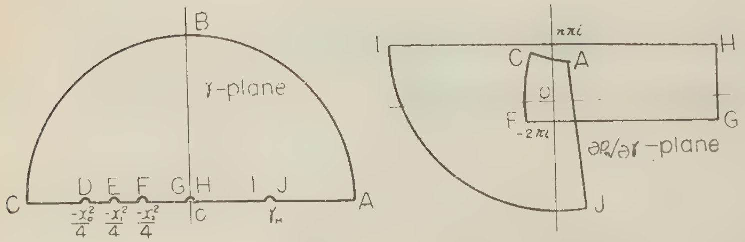

Fig. 10.

JOURNAL OF THE PHYSICAL SOCIETY OF JAPAN Vol. 12, No. 9, SEPTEMBER 1957

On the Two-dimensional Compressible Flow over a Thin Symmetric Obstacle with Sharp Shoulders Placed in an Unbounded Fluid and in a Choked Wind Tunnel

By Ken-ichi KUSUKAWA

Department of Physics, Faculty of Science, Tokyo Metropolitan University

(Received May 11, 1957)

The transonic flow past a two-dimensional symmetric body with sharp shoulders placed in an unbounded compressible fluid and in a choked wind tunnel is studied by the use of the model flow, where the flow is assumed to separate from the surface of the body at the shoulder instead of performing the Prandtl-Meyer expansion. Applying this model flow method to the flow past a finite wedge, and comparing with the more accurate solutions derived by Guderley, Cole, Hida and Marschner, it is found that the accuracy of the predicted values of the pressure distribution over the surface or the head drag coefficient is fairly good, but that as for the choking Mach number this model flow gives a rather different value from that of the real flow. The pressure distributions over the surface of the several symmetric profiles with sharp shoulders are calculated by this model flow method.

§1. Introduction

We shall consider the two-dimensional transonic flow of a compressible fluid past a thin obstacle which is symmetric with repect to the uniform velocity vector and has sharp shoulders at the position of maximum thickness. According to the transonic approximation originally due to von Kármán[1], the fundamental equation can be transformed to Tricomi's differential equation in the hodograph plane. In such a case as a wedge profile, the boundary curve can be explicitly determined in the hodograph plane as well as in the physical plane. The flow can be found by solving Tricomi's equation subject to the given boundary conditions. Thus, Guderley and Yoshihara[2] obtained the solutions for the flow over a wedge at Mach number 1, and Cole[3] and Trilling and walker[4] obtained the solutions at high subsonic speeds. Marschner,[5] Hashimoto[6] and Hida[7] studied the flow past the wedge placed along the center line between the two plane walls. Since the boundary curve in the hodopraph plane cannot be explicitly determined in more general cases, it is not convenient to deal with the problem by the hodograph equation.

On the other hand, the pure subsonic flow can be very easily dealt with by the simplified W. K. B. method,[8],[9] provided the corresponding incompressible flow can be known. In our cases, the surface velocity attains the local sound velocity at the shoulder. If we make use of an appropriate incompressible flow, the velocity of which becomes a corresponding value to the sonic velocity of the compressible flow at the shoulder and on the same curve as the sonic line of the compressible flow, we can find the velocity distribution of the compressible fluid on the surface of the front part of the given body (the region from the nose to the shoulder). In this paper we shall restrict the analysis to find the solution in the forward subsonic region, but the solution in the supersonic region can be given by the method of characteristics, if it is desired.

As the sonic line cannot be known a priori, we must assume it. In this paper we shall use a flow with free streamlines as a model. It is assumed that the flow separates from the surface of the body at the shoulder, and that along the free streamlines the fluid velocity continues to be sonic to the point where the inclination θ of the velocity vector vanishes, and behind this point θ continues to be zero.

This assumption was used by Roshko[10] to estimate the drag of a bluff body in an incompressible fluid. By the use of this model flow, we can study the forward subsonic region in the flow past a thin symmetric obstacle with sharp shoulders by the W.K.B. method.[8),9)]. Especially in the case of the flow past a finite wedge at sonic and high subsonic speeds, the pressure distributions on the surface derived by this model flow method will be compared with the exact solutions due to Guderley and Yoshihara[2)] and Cole[3)]. This model can be modified to treat the flow past the obstacle placed along the centre line between the two parallel plane walls. Also in this case, the pressure distribution past the wedge derived by this model will be compared with that obtained by the more accurate methods due to Marschner[5)] and Hida[7)]. As the numerical examples we evaluate the pressure distributions on the front surface of several thin obstacles with curved walls and sharp shoulders placed in an unbounded fluid and in a choked wind tunnel.

§ 2. Outline of W.K.B. Method

Applying the K.W.B. method derived by Imai[8),9)] to the thin obstacle in the transonic flow, and neglecting the higher order terms of perturbation, we can obtain the following simple relation between the magnitudes q, Q of the velocity of a compressible and an incompressible fluids on the surface of the same obstacle:

$$\varepsilon=(9/8\Gamma)^{1/3}\eta^{2/3}, \qquad (2.1)$$

with

$$\varepsilon=1-q\,, \qquad (2.2)$$

$$\eta=1-Q\,, \qquad (2.3)$$

$$\Gamma=(\gamma+1)/2\,, \qquad (2.4)$$

where the sonic velocity and the corresponding velocity of an incompressible flow are taken to be the units of the velocity of the compressible and the incompressible fluids respectively.

Defining the pressure coefficient C_p by

$$C_p=(p-p_\infty)\Big/\frac{1}{2}\rho_\infty q_\infty^2, \qquad (2.5)$$

where p and ρ denote the pressure and the density respectively, and suffix ∞ refers to the quantity at infinity upstream, the surface pressure coefficient can be given as follows within the accuracy of the approximation considered here:

$$C_p=2(\varepsilon-\varepsilon_\infty)=(9/\Gamma)^{1/3}\{\eta^{2/3}-\eta_\infty^{2/3}\}$$

$$=t^{2/3}\Gamma^{-1/3}[9^{1/3}(\eta/t)^{2/3}-2K_1]\,, \qquad (2.6)$$

in which

$$K_1=(1-M_1)t^{-2/3}\Gamma^{-2/3}\,, \qquad (2.7)$$

and t and M_1 denote the half thickness ratio of the body and the free stream Mach number respectively.

As the non-dimensional perturbation velocity η of an incompressible flow is proportional to the half thickness ratio t in the first approximation of the thin wing expansion theory, the expression (2.6) can satisfy the Kármán's transonic similarity law[1)]. Introducing the usual transonic parameter ξ_0 and the reduced pressure coefficient $\tilde{C}_p$ defined by

$$\xi_0=(1-M_1^2)/t^{2/3}(1+\gamma)^{2/3}=2^{1/3}K_1\,, \qquad (2.8)$$

and

$$\tilde{C}_p=(1+\gamma)^{1/3}t^{-2/3}C_p\,, \qquad (2.9)$$

respectively, Eq. (2.6) is expressed as

$$\tilde{C}_p=18^{1/3}(\eta/t)^{2/3}-2\xi_0\,. \qquad (2.10)$$

When we consider the flow of a compressible fluid past the obstacle placed along the centre line between the two parallel plane walls γ distance $2L$ apart, the corresponding incompressible flow may be taken to be the flow past the same body placed in the similar wind tunnel, but with the corresponding width $2L_0$.

As the flow is almost parallel and uniform at a great distance upstream, the W. K. B. method can be reduced to the usual Prandtl-Glauert's law. Thus there exists the following relation between the distances L and L_0:

$$L/L_0=1/\sqrt{1-M_1^2}\,. \qquad (2.11)$$

§ 3. Flow Past an Obstacle in an Unbounded Fluid

We shall consider the flow with separation of an incompressible fluid past a thin symmetric obstacle with a flat base. We shall introduce the complex coordinate $z=x+iy$, and the complex velocity potential $\omega=\varphi+i\psi$, where x and y denote the Cartesian coordinates of physical plane, and φ and ψ denote the velocity potential and the stream function respectively. Owing to the theory of the incompressible flow, ω should be an analytic function of z. It is convenient to introduce a new analytic function f of z such that

$$f=\log\left(\frac{dz}{d\omega}\right)=r+i\theta\ , \qquad (3.1)$$

where

$$r=\log(1/Q)\ , \qquad (3.2)$$

and Q and θ denote the magnitude and the inclination of the velocity vector of an incompressible fluid. Denoting the half thickness ratio by t, and taking the chord length to be unity, the profile may be expressed as

$$y=\pm tH(x)\ ,\quad 0\leqq x\leqq 1\ . \qquad (3.3)$$

The magnitude of the velocity at the shoulder being taken to be the unit of the velocity, the analytic function f should satisfy the following boundary conditions in the z-plane (cf. Fig. 1(a)):

along $\psi=\pm 0$;

$$\left.\begin{array}{lll} \text{for} & -\infty\leqq x<0, & \theta=0, \\ \text{for} & 0\leqq x<1, & \theta=\pm tH'(x), \\ \text{for} & 1\leqq x<\alpha, & r=0, \\ \text{for} & \alpha\leqq x\leqq\infty, & \theta=0, \end{array}\right\} \qquad (3.4)$$

where α denotes an undermined constant.

These boundary conditions (3.4) are originally given by Roshko[10] as a modified Helmholtz flow for an incompressible fluid.

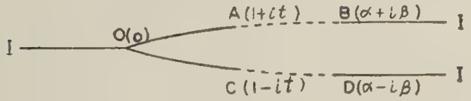

(a) Z − Plane

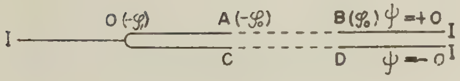

(b) ω−Plane

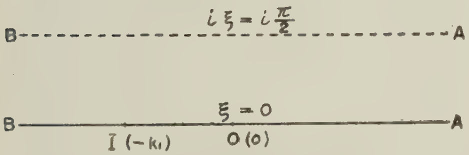

(c) ζ − Plane

Fig. 1. Boundary conditions for the flow past a body in an unbounded fluid.

In the ω-plane the boundary conditions (3.4) are transformed as follows (cf. Fig. 1 (b)):

along $\psi=\pm 0$;

$$\left.\begin{array}{lll} \text{for} & -\infty\leqq\varphi<-\varphi_1, & \theta=0, \\ \text{for} & -\varphi_1\leqq\varphi<-\varphi_0, & \theta=\pm tH'(x), \\ \text{for} & -\varphi^0\leqq\varphi<\varphi_0, & r=0, \\ \text{for} & \varphi_0\leqq\varphi\leqq\infty, & \theta=0, \end{array}\right\} \qquad (3.5)$$

where φ_0 and φ_1 denote undetermined positive constants.

Now, an auxiliary plane $\zeta=\delta+i\xi$ is introduced such that

$$\zeta=\delta+i\xi=\frac{1}{2}\log\left(\frac{\omega-\varphi_0}{\omega+\varphi_0}\right)-k_1\ , \qquad (3.6)$$

with

$$k_1=\frac{1}{2}\log\left(\frac{\varphi_1+\varphi_0}{\varphi_1-\varphi_0}\right). \qquad (3.7)$$

The upper half part of the ω-plane is mapped onto the strip

$$-\infty\leqq\delta\leqq\infty,\quad 0\leqq\xi\leqq\pi/2$$

i.e., the intervals of the bounding streamlines on which θ is known correspond to $\xi=0$, $-\infty\leqq\delta\leqq\infty$: while the remaining interval corresponds to $\xi=\pi/2$, $-\infty\leqq\delta\leqq\infty$. (cf. Fig. 1 (c))

Since $f(\omega)$ is analytic, so also is $f(\zeta)$ and boundary conditions (3.5) can be transformed to the following form in the ζ-plane:

$$\left.\begin{array}{ll} \text{along } \xi=0; & \\ \quad\text{for } -\infty\leqq\delta<0, & \theta=\theta_0=0, \\ \quad\text{for } 0\leqq\delta\leqq\infty, & \theta=\theta_0=tH'(x), \\ \text{along } \xi=\pi/2; & \\ \quad\text{for } -\infty\leqq\delta\leqq\infty, & r=r_0=0, \end{array}\right\} \qquad (3.8)$$

where θ_0 and r_0 are known functions of δ.

Woods[11] found the form of the analytic function $f(\zeta)$ subject to the boundary conditions (3.8) as follows:

$$f(\delta,\ \xi)=\frac{1}{\pi}\int_{-\infty}^{\infty}[\theta_0(\delta^*)\operatorname{cosech}\{\delta^*-(\delta+i\xi)\}$$
$$+r_0(\delta^*)\operatorname{sech}\{\delta^*-(\delta+i\xi)\}]d\delta^*\ . \qquad (3.9)$$

In our case, according to the conditions (3.8), Eq. (3.9) can be reduced to

$$f(\delta,\ \xi)=\frac{1}{\pi}\int_0^{\infty}tH'(x)\operatorname{cosech}\{\delta^*-(\delta+i\xi)\}d\delta^* \qquad (3.10)$$

Putting $\xi=0$ in Eq. (3.10), the value of r on the real axis of the ζ-plane is given by

$$r=\frac{t}{\pi}\int_0^{\infty}H'(x)\operatorname{cosech}(\delta^*-\delta)d\delta^*. \qquad (3.11)$$

As the body is very thin, we can obtain

$$x=(e^{2\delta}-1)/(e^{2\delta}-e^{-2k_1})+O(t). \qquad (3.12)$$

Substituting Eq. (3.12) into Eq. (3.11), and remembering Eq. (2.3), we can obtain

$$\eta=\frac{t}{\pi}\int_0^\infty H'\left(\frac{e^{2\delta^*}-1}{e^{2\delta^*}-e^{-2k_1}}\right)\operatorname{cosech}(\delta^*-\delta)d\delta^* +\mathrm{O}(t^2)\,, \tag{3.13}$$

where H' denotes the derivative of H with respect to the argument x.

Introducing new variables such that

$$u=e^{\delta^*},\quad v=e^{\delta}, \tag{3.14}$$

Eq. (3.13) can be transformed to a more convenient form:

$$\eta=\frac{2tv}{\pi}\int_1^\infty H'\left(\frac{u^2-1}{u^2-e^{-2k_1}}\right)\frac{du}{u^2-v^2}\,, \tag{3.15}$$

with

$$v=\left\{\frac{1-xe^{-2k_1}}{1-x}\right\}^{1/2},\quad -\infty\leqq x\leqq 1. \tag{3.16}$$

For a given profile, Eq. (3.15) with Eq. (3.16) gives the non-dimensional perturbation velocity of an incompressible fluid on the surface of the body.

As

$$x\to-\infty,\quad v\to e^{-k_1}$$

and

$$\eta_\infty=\lim_{v\to e^{-k_1}}\left[\frac{2tv}{\pi}\int_1^\infty H'\left(\frac{u^2-1}{u^2-e^{-2k_1}}\right)\frac{du}{u^2-v^2}\right]. \tag{3.17}$$

Combining Eq. (3.17) with Eq. (2.6), we can obtain the relation between the transonic parameter K_1 and an undetermined constant k_1.

Thus substitutions of Eq. (3.15) into Eqs. (2.6) and (2.10) give pressure- and the reduced pressure coefficients of a compressible fluid on the surface of the given profile for a given transonic parameter K_1.

Especially putting $k_1=\infty$ in Eq. (3.17), the transonic parameter K_1 vanishes, and this is the case for the flow at Mach number 1.

§ 4. The Flow Past an Obstacle in a Choked Wind Tunnel

We shall consider the transonic flow past a thin symmetric obstacle with a flat base placed along the centre line between the two parallel plane walls a distance $2L$ apart under the choking conditions. For the model flow, the choking conditions may be given by putting the magnitude of the velocity along the free streamlines to be sonic. Thus the boundary conditions are given by (cf. Fig. 2 (a))

$$\left.\begin{array}{lll} \text{along } \psi=\pm 0; & & \\ \quad\text{for} & -\infty\leqq x<0, & \theta=0, \\ \quad\text{for} & 0\leqq x<1, & \theta=\pm tH'(x), \\ \quad\text{for} & 1\leqq x\leqq\infty, & r=0, \\ \text{along } y=\pm L_0; & & \\ \quad\text{for} & -\infty\leqq x\leqq\infty, & \theta=0, \end{array}\right\} \tag{4.1}$$

where $2L_0$ and $2t$ denote the corresponding width of tunnel of the incompressible flow and the thickness ratio of the body respectively and the profile is represented by Eq. (3.3).

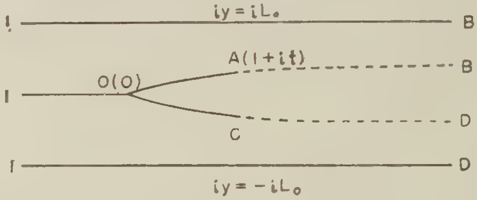

(a) z-plane

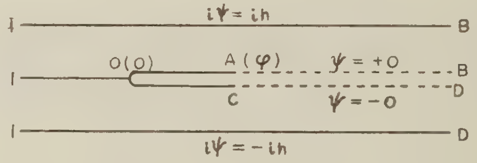

(b) w-plane

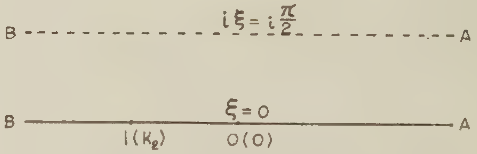

(C) ζ-plane

Fig. 2. Boundary conditions for the flow past a body in a choked wind tunnel.

In the ω-plane, the boundary conditions (4.1) are transformed as follows (cf. Fig. 2 (b))

$$\left.\begin{array}{lll} \text{along } \psi=\pm 0; & & \\ \quad\text{for} & -\infty\leqq \varphi<0, & \theta=0, \\ \quad\text{for} & 0\leqq \varphi<\varphi_2, & \theta=\pm tH'(x), \\ \quad\text{for} & \varphi_2\leqq \varphi\leqq\infty, & r=0, \\ \text{along } \psi=\pm h & & \\ \quad\text{for} & -\infty\leqq \varphi\leqq\infty, & \theta=0, \end{array}\right\} \tag{4.2}$$

where φ_2 and h denote undetermined constants.

Now an auxiliary plane $\zeta=\delta+i\xi$ is introduced such that

$$\exp\left\{2\left(k_2+\frac{\pi}{2}i-\zeta\right)\right\}+1=\exp\{(\pi/h)(\omega-\varphi_2)\}, \tag{4.3}$$

with

$$2k_2=\log\left(1-e^{-\pi\varphi_2/h}\right) \tag{4.4}$$

The strip $-\infty\leqq\varphi\leqq\infty$, $0\leqq\psi\leqq h$ in the ω-plane is mapped onto the strip $-\infty\leqq\delta\leqq\infty$, $0\leqq\xi\leqq\pi/2$ in the ζ-plane, (cf. Fig. 2 (c)). In the ζ-plane, the boundary conditions (4.2) for the function f can be transformed to the form expressed by Eq. (3.8). Thus the problem can be reduced to the same form as that for the case of the flow in an unbounded fluid.

Considering the relation between x and δ along the surface of the body, Eq. (3.11) may be reduced to the following convenient form:

$$\eta=\frac{2tv}{\pi}\int_1^\infty H'\left(1+\frac{h}{\pi}\right.$$

$$\left.\times\log\{1-[1-e^{-\pi/h}]u^{-2}\}\right)\frac{du}{u^2-v^2}, \tag{4.5}$$

where

$$v=(1-e^{-\pi/h})^{1/2}/\{1-e^{(\pi/h)(x-1)}\}^{1/2}. \tag{4.6}$$

Performing the integral (4.5) and putting $x=-\infty$ in Eqs. (4.5) and (4.6), we can obtain the relation between η_∞ and h. Remembering Eq. (2.6), the undetermined constant h can be related to the transonic parameter K_1.

Next, we shall find the relation between the width $2L$ of tunnel, the thickness ratio $2t$ of the body and the transonic parameter K_1 under the choking state. As the flow becomes uniform at infinity upstream, we obtain the relation in the first approximation:

$$\int_0^{L_0}Q_\infty dy=\int_0^h d\psi$$

or

$$h=L_0Q_\infty=L_0(1-\eta_\infty)\doteqdot L_0\,, \tag{4.7}$$

where Q_∞ denotes the magnitude of the velocity of the incompressible flow at infinity upstream. Combining Eq. (4.7) with Eq. (2.11), we obtain

$$h/L=\sqrt{1-M_1{}^2}+\text{higher oder terms.} \tag{4.8}$$

Remembering Eq. (2.7), Eq. (4.8) can be transformed to

$$Lt^{1/3}\Gamma^{1/3}=2^{-1/2}hK_1{}^{-1/2}. \tag{4.9}$$

Since h is a function of K_1, $Lt^{1/3}\Gamma^{1/3}$ can be expressed as a function of the transonic parameter K_1. Hashimoto[6)] studied the flow past a finite wedge placed in the choked wind tunnel by solving Tricomi's equation in the hodograph plane, and assured that $Lt^{1/3}\Gamma^{1/3}$ can be expressed as a function of the transonic parameter K_1 or ξ_0.

§ 5. Examples

We shall first apply the present method of simple model flow to the transonic flow past a finite wedge in an unbounded fluid and in the choked wind tunnel, and examine the accuracy of this method by comparing the results with the more accurate solutions derived by Guderley and Yoshihara[2)], Cole[3)], Marschner[5)] and Hida[7)]. Then we shall apply the present method to the flow past a body with curved walls and a flat base.

(I) Wedge

(A) In an unbounded fluid

As a wedge of unit length is represented by

$$y=\pm tx \qquad 0\leqq x\leqq 1, \tag{5.1}$$

the integrals (3.15) and (3.17) are evaluated as follows:

$$\eta=\frac{t}{\pi}\log\left|\frac{v+1}{v-1}\right|, \tag{5.2}$$

and

$$\eta_\infty=\frac{t}{\pi}\log\left|\frac{1+e^{-k_1}}{1-e^{-k_1}}\right|, \tag{5.3}$$

where v is given by Eq. (3.16). The relation between k_1 and ξ_0 is given by

$$e^{-2k_1}=\tanh^2(\pi\xi_0{}^3/3)\,. \tag{5.4}$$

Substitution of Eq. (5.2) into Eq. (2.10) gives the reduced pressure coefficient $\tilde{C}_p$ on the surface of the body. It is expanded in the power series in ξ_0 such that

$$\tilde{C}_p=\tilde{C}_p{}^*-2\xi_0 \tag{5.5}$$

with

$$\tilde{C}_p{}^*=18^{1/3}(\eta/t)^{2/3}=P(x)+2N(x)\xi_0{}^3\cdots, \tag{5.6}$$

$$P(x)=\left(\frac{18}{\pi^2}\right)^{1/3}\log^{2/3}\left|\frac{1+\sqrt{1-x}}{1-\sqrt{1-x}}\right|, \tag{5.7}$$

$$N(x)=\frac{1}{3}\left(\frac{18}{\pi^2}\right)^{1/3}\left(\frac{\pi}{3}\right)^2(1-x)^{1/2}$$

$$\cdot\log^{-1/3}\left|\frac{1+\sqrt{1-x}}{1-\sqrt{1-x}}\right|, \tag{5.8}$$

where the functions $P(x)$ and $N(x)$ are shown in Figs. 3 and 4.

Within the accuracy of the approximation considered here, the left hand side of Eq. (5.6) denotes the reduced pressure coefficient with respect to the sonic point defined by

$$\tilde{C}_p{}^* = t^{-2/3}(\gamma+1)^{1/3}C_p{}^*, \tag{5.9}$$

with

$$C_p{}^* = (p-p^*)\Big/\frac{1}{2}\rho^* q^{*2}, \tag{5.10}$$

where the asterisk refers to the quantity at the sonic point.

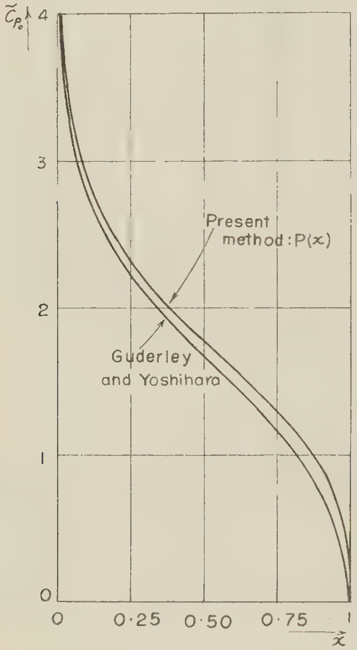

Fig. 3. The reduced pressure distribution on the surface of a wedge of unit length at $M_1=1$.

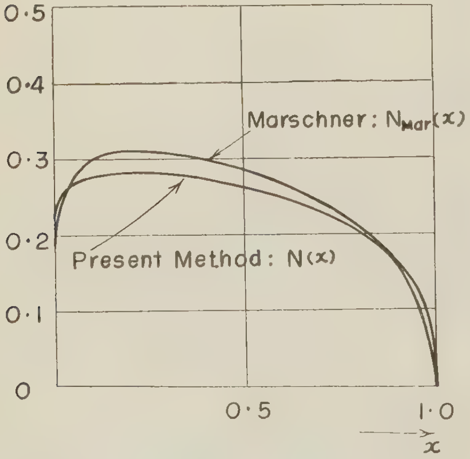

Fig. 4. The perturbation function $N(x)$.

The function $P(x)$ represented by Eq. (5.7) should be compared with the exact solution derived by Guderley and Yoshihara[2], which is also shown in Fig. 3.

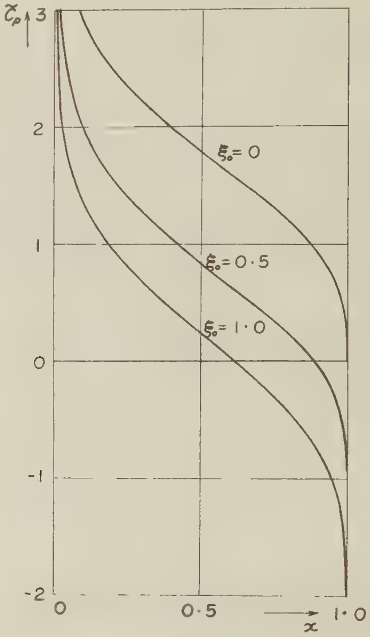

Fig. 5. The distributions of $\tilde{C}_p$ on the surface of a finite wedge in an unbounded fluid.

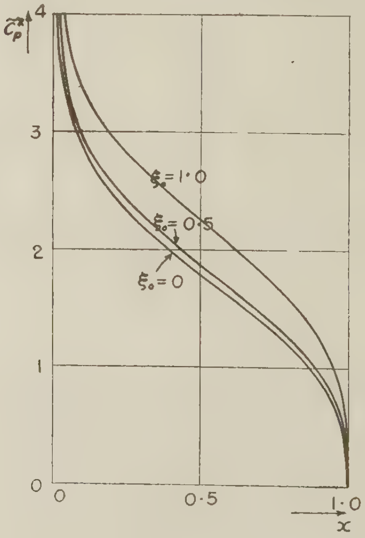

Fig. 6. The distributions of $\tilde{C}_p{}^*$ on the surface of a finite wedge in an unbounded fluid.

For several values of ξ_0, the surface distributions of $\tilde{C}_p$ and $\tilde{C}_p{}^*$ past the wedge are calculated by the present method, and they are shown in Figs. 5 and 6 respectively.

The head drag coefficient is obtained by integrating the horizontal component of the pressure coefficient on the front surfaces of the body or

$$C_d = t\int_0^1 C_p H'(x)dx\,. \tag{5.11}$$

Defining the reduced head drag coefficients $\tilde{C}_d$, $\tilde{C}_d^*$ with respect to the uniform- and the sonic velocities respectively by

$$\tilde{C}_d = t^{-5/3}(\gamma+1)^{1/3}C_d\,, \tag{5.12}$$

$$\tilde{C}_d^* = t^{-5/3}(\gamma+1)^{1/3}C_d^*\,, \tag{5.13}$$

and integrating Eqs. (5.5) and (5.6), we obtain

$$\tilde{C}_d = \tilde{C}_d^* - 2\xi_0\,, \tag{5.14}$$

$$\tilde{C}_d^* = \tilde{C}_{d_0} + B_{fr}\xi_0^3 + \cdots, \tag{5.15}$$

where

$$\tilde{C}_{d_0} = \int_0^1 P(x)dx\,, \tag{5.16}$$

$$B_{fr} = 2\int_0^1 N(x)dx\,. \tag{5.17}$$

Cole[3)] and Hida[7)] studied the flow past a wedge at high subsonic speeds by solving Tricomi's equation subject to the somewhat approximated boundary conditions in the hodograph plane. Their results, together with the exact values of $\tilde{C}_{d_0}$ derived by Guderley and Yoshihara[2)], are given and compared with the values obtained by the present method in Table I. (Hida[7)] estimated the value of $\tilde{C}_{d_0}$ by the same method as Cole's[3)] and revised it.)

Table I.

Author	$\tilde{C}_{do}$	B_{fr}	B_{ch}
Guderley and Yoshihara[2)]	1.75	—	—
Cole[3)]	1.67	0.6809	—
Hida[7)]	1.627	0.6809	0.2723
Marschner[5)]	(1.75)	—	0.2528
Present Method	1.837	0.4746	0.2373

(B) In the choked wind tunnel

Integrating Eq. (4.5), η is evaluated and we can obtain the pressure coefficient by the use of Eq. (2.6) or Eq. (2.10). The relation between h and ξ_0 is obtained as

$$\pi/h = 2\log\cosh\left(\frac{\pi}{3}\xi_0^{3/2}\right). \tag{5.18}$$

By the use of Eq. (5.18), the reduced pressure coefficient $\tilde{C}_p^*$ with respect to the sonic point can be expressed as follows:

$$C_p^* = P(x) + N(x)\xi_0^3 + \cdots \tag{5.19}$$

where the functions $P(x)$ and $N(x)$ are given by Eqs. (5.7) and (5.8).

Marschner[5)] studied the flow past a double wedge in a choked wind tunnel by the perturbation method applied to the Guderley's[2)] solution at Mach number 1. After him the reduced pressure coefficient is

$$\tilde{C}_p^* = \tilde{C}_{p_0} + N_{Mar}(x)\xi_0^3, \tag{5.20}$$

$$N_{Mar}(x) = 2(2/3)^{4/3}\frac{0.611}{0.586}F(x) \tag{5.21}$$

where $\tilde{C}_{p_0}$ was given by Guderley and Yoshihara and $F(x)$ was shown in Fig. 10 of reference [5]. The function $N_{Mar}(x)$ is also shown in Fig. 4.

For several values of ξ_0, the distributions of $\tilde{C}_p$ and $\tilde{C}_p^*$ over the surface of the wedge are obtained by the present method and they are shown in Figs. 7 and 8 respectively.

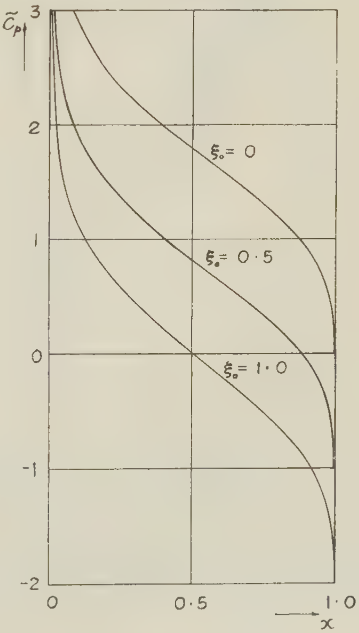

Fig. 7. The distributions of $\tilde{C}_p$ on the surface of a finite wedge in a choked wind tunnel.

The reduced head drag coefficient with respect to the sonic point is given by integrating Eq. (5.19) or (5.20) as follows:

$$\tilde{C}_d^* = \tilde{C}_{d_0} + B_{ch}\xi_0^3 + \cdots \tag{5.22}$$

where the coefficient B_{ch} is gigen by integrating $N(x)$ or $N_{Mar}(x)$. Hida[7)] also estimated the head drag coefficient of the finite wedge in the choked wind tunnel by an approximate treatment, and obtained the reduced head drag coefficient expressed in the same form as Eq. (5.22). The values of the coefficient B_{ch} evaluated by these authors are given in Table I.

Table I and Figs. 3 and 4 show that this simple model flow method gives a fairly good approximation for the pressure coefficient and the head drag coefficient of the finite wedge in the choked wind tunnel as well as in an unbounded fluid. Especially in the case of choked wind tunnel the present method seems to be very reliable.

Next, we shall consider the relation under the choking state. Substituting Eq. (5.18) into Eq. (4.9), and remembering Eq. (2.8), we obtain the relation:

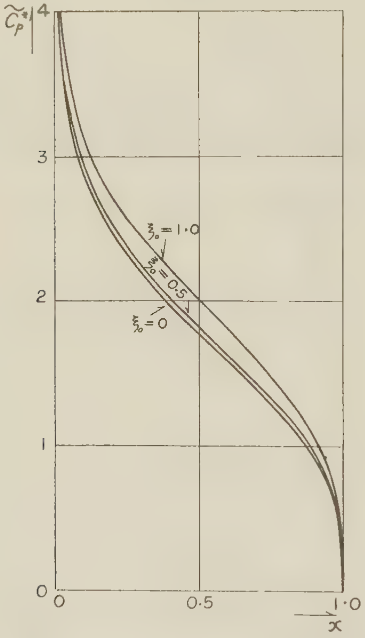

Fig. 8. The distributions of $\tilde{C}_p^*$ on the surface of a finite wedge in a choked wind tunnel.

$$L^{-1}(\gamma+1)^{-1/3}t^{-1/3}$$
$$=\left(\frac{2}{\pi}\right)\xi_0{}^{1/2}\log\cosh\left(\frac{\pi}{3}\xi_0{}^{3/2}\right). \quad (5.23)$$

For the small value of ξ_0, Eq. (5.23) is reduced to

$$L^{-1}(\gamma+1)^{-1/3}t^{-1/3}=(\pi/9)\xi_0{}^{7/2} \quad (5.24)$$

This result should be compared with the exact relation derived by Marschner⁵⁾:

$$L^{-1}(\gamma+1)^{-1/3}t^{-1/3}$$
$$=(1.235\times0.586)\times\left(\frac{2}{3}\right)^{4/3}\xi_0{}^{5/2} \quad (5.25)$$

Thus, it seems to the author that the present method of the model flow is useful to obtain the pressure distribution and the head drag coefficient, but the reliable relation among L, t and ξ_0 under the choking state cannot be obtained by this method.

We shall proceed to apply this method to the flow past a thin symmetric profile with curved walls and a flat base.

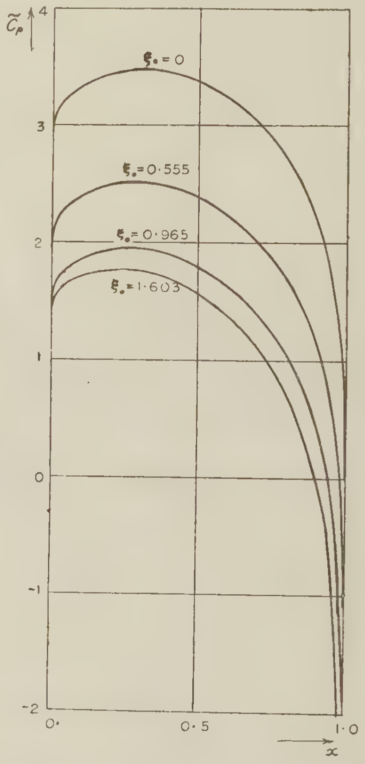

Fig. 9. The distributions of $\tilde{C}_p$ on the surface of a profile $y=\pm tx^2$ in an unbounded fluid.

(II) Profile $y=\pm tx^2$

(A) In an unbounded fluid

By the use of Eq. (3.15), we obtain

$$\eta=\frac{2t}{\pi}\left[x\log\left|\frac{v+1}{v-1}\right|\right.$$
$$\left.-e^{k_1}\sqrt{(1-x)(1-xe^{-2k_1})}\log\left(1-\frac{2e^{-k_1}}{1+e^{-k_1}}\right)\right], \quad (5.26)$$

where v is given by Eq. (3.16). For several values of ξ_0 the distributions of $\tilde{C}_p$ and C_p^* over the surface of the profile are calculated and they are shown in Figs. 9 and 10.

For small values of ξ_0, $\tilde{C}_p{}^*$ is expanded in power series in ξ_0 as

$$\tilde{C}_p{}^* = \tilde{C}_{p_0} + 2R(x)\xi_0{}^3 + \cdots \tag{5.27}$$

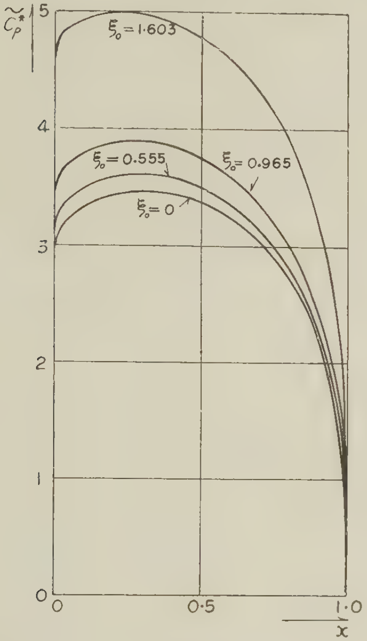

Fig. 10. The distributions of $\tilde{C}_p{}^*$ on the surface of a profile $y = \pm tx^2$ in an unbounded fluid.

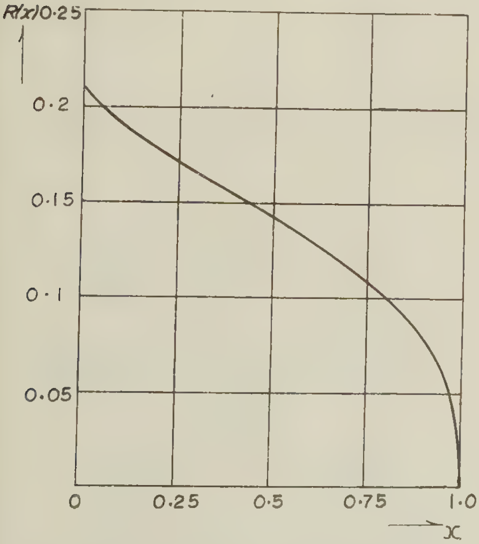

Fig. 11. The perturbation function $R(x)$.

with

$$\tilde{C}_{p_0} = \left(\frac{18}{\pi^2}\right)^{1/3}\left[2x \log\left|\frac{1+\sqrt{1-x}}{1-\sqrt{1-x}}\right| + 4\sqrt{1-x}\right]^{2/3}. \tag{5.28}$$

and

$$R(x) = \frac{(18)^{1/3}}{36}\pi^{4/3}(1-x)^{1/2} \times\left[2x \log\left|\frac{1+\sqrt{1-x}}{1-\sqrt{1-x}}\right| + 4\sqrt{1-x}\right]^{-1/3}. \tag{5.29}$$

The value of $R(x)$ is shown in Fig. 11.

Integrating Eq. (5.11) graphically, the reduced head drag coefficient $\tilde{C}_d$ is obtained and is shown in Fig. 12.

(B) In the choked wind tunnel

In this case Eq. (4.5) becomes

$$\eta = \frac{4tv}{\pi}\int_1^\infty \left\{1 + \frac{h}{\pi}\log(1-[1-e^{-\pi/h}]u^{-2})\right\}\frac{du}{u^2-v^2}, \tag{5.30}$$

where v is given by Eq. (4.6). When the width L of tunnel is very large, the value of h may also be large. Then, the integral of Eq. (5.30) may be evaluated in the form of series in (π/h). Thus we can obtain the distribution of $\tilde{C}_p{}^*$ in the following form:

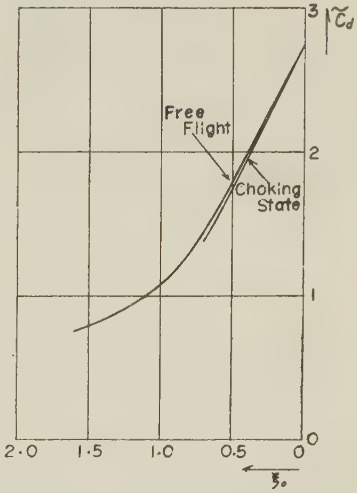

Fig. 12. The variation with the transonic parameter ξ_0 of the reduced head drag coefficient $\tilde{C}_d$ of a profile $y = \pm tx^2$ in an unbounded fluid and in a choked wind tunnel.

$$\tilde{C}_p{}^* = \tilde{C}_{p_0} + R(x)\xi_0{}^3 + \cdots, \tag{5.31}$$

with

$$\xi_0 = (4/\pi)^{2/3}(\pi/h)^{1/2} + \cdots, \tag{5.32}$$

where $\tilde{C}_{p_0}$ hnd $R(x)$ are given by Eqs. (5.28) and (5.29).

The values of $\tilde{C}_p$ and $\tilde{C}_p{}^*$ calculated for several values of the transonic parameter ξ_0 are shown in Figs. 13 and 14 respectively.

The variation of the reduced head drag coefficient $\tilde{C}_d$ is also shown in Fig. 12 in comparison with the case in an unbounded fluid.

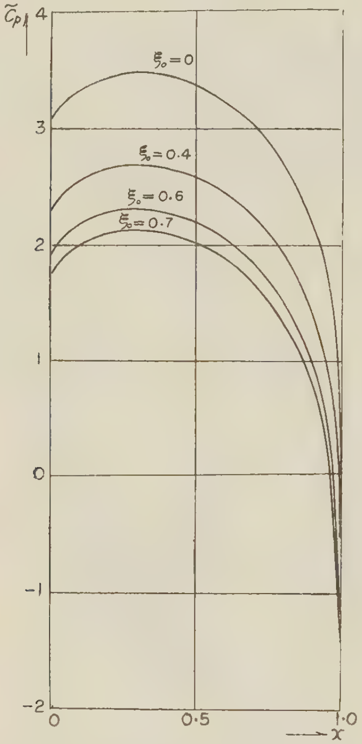

Fig. 13. The distributions of $\tilde{C}_p$ on the surface of a profile $y=\pm tx^2$ in a choked wind tunnel.

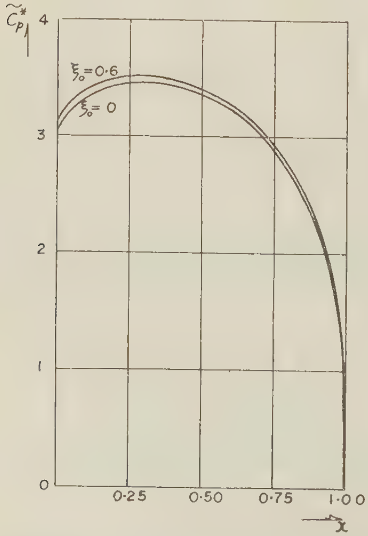

Fig. 14. The distributions of $\tilde{C}_p$* on the surface of a profile $y=\pm tx^2$ in a choked wind tunnel.

(III) Profile: $y=\pm tx^4$

Now we shall calculate the reduced pressure coefficient a Mach number 1.

Substituting $e^{-k_1}=0$, $H(x)=x^4$ into Eq. (3.15), and performing the integral we obtain

$$\eta=\frac{4t}{\pi}\left[\left\{1-\frac{3}{v^2}+\frac{3}{v^4}-\frac{1}{v^6}\right\}\log\left|\frac{v+1}{v-1}\right|\right]$$
$$+\frac{4tv}{\pi}\left[\frac{11}{5}\left(\frac{1}{v^2}\right)-\frac{8}{3}\left(\frac{1}{v^4}\right)+\frac{1}{v^6}\right], \tag{5.33}$$

where

$$v=1/\sqrt{1-x}\,. \tag{5.34}$$

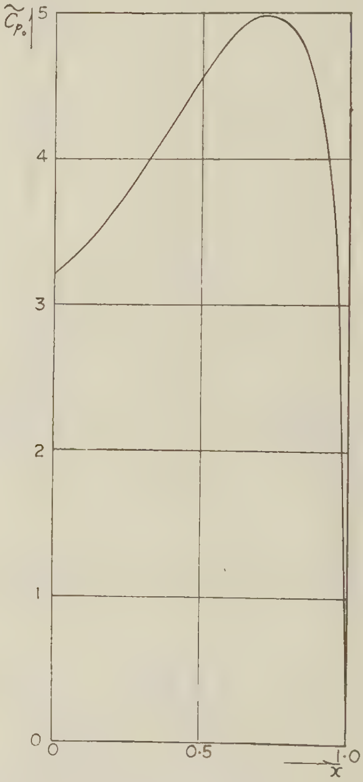

Fig. 15. The distribution of $\tilde{C}_p$ on the surface of a profile $y=\pm tx^4$ at sonic speed.

Table II.

Profile	$\tilde{C}_{d0}$
$y=tx$	1.837
$y=tx^2$	2.749
$y=tx^4$	4.103

Combining Eq. (5.33) with Eq. (2.10), we obtain the reduced pressure coefficient $\tilde{C}_p$ and it is shown in Fig. 15.

Finally the values of the reduced head drag coefficient $\tilde{C}_{a_0}$ of the profiles considered above at Mach number 1 compared in Table II.

§ 6. Conclusion

It has been ascertained that the simple method of the model flow gives a fairly good approximation for the pressure distribution over the surface of a finite wedge placed in an unbounded fluid as well as in a choked wind tunnel at sonic and high subsonic speeds. This simple method was applied to the flows past some profiles with curved surface and sharp shoulders, and several numerical informations were obtained.

Inspecting Figs. 5–10 and 13–14, it is found that the value of $\tilde{C}_p{}^*$ increases as ξ_0 increases, while the value of $\tilde{C}_p$ decreases. Owing to this fact, the value of $\tilde{C}_d{}^*$ also increases as ξ_0 increases, while the value of $\tilde{C}_d$ decreases. (cf. Fig. 12) This model flow method cannot be applied to the flow past a body placed in a sonic free jet, which was studied by Marschner$^{5)}$, because in this case the right-hand side of Eq. (2.11) becomes infinite, and no incompressible flow can be transformed to the compressible sonic free jet of finite width.

In conclusion, the author would like to express his heartiest gratitude to Professor I. Imai for his kind suggestion and valuable discussions during the course of the present investigations.

References

1) Th. von Kármán: Journ. Math. and Phys. **26** (1947) 182.
2) G. Guderley and H. Yoshihara: Journ. Aero. Sci. **17** (1950) 723.
3) J. D. Cole: Journ. Math. and Phys. **30** (1951) 79.
4) L. Trilling and K. Walker, Jr.: Journ. Math. and Phys. **32** (1953) 72.
5) B. W. Marschner: Journ. Aero. Sci. **23** (1956) 368.
6) J. Hashimoto: unpublished
7) K. Hida: unpublished
8) I. Imai: Journ. Phys. Soc. Japan **3** (1948) 352.
9) I. Imai: Journ. Math. and Phys. **28** (1949) 173.
10) A. Roshko: Journ. Aero. Sci. **22** (1955) 73).
11) L. C. Woods: Quart. J. Mech. Appl. Math. **7** (1954) 263.

Journal of the Physical Society of Japan Vol. 12, No. 9, September, 1957

On the Compressible Flow over a Slender Body of Revolution with a Flat Base Placed in an Unbounded Fluid and in a Choked Wind Tunnel

By Ken-ichi KUSUKAWA

Department of Physics, Faculty of Science, Tokyo Metropolitan University

(Received May 11, 1957)

The flows past a slender body of revolution with a sharp shoulder placed in an unbounded compressible fluid and along the axis of a choked circular wind tunnel have been studied by the method of the correspondence between the axisymmetric and the two-dimensional flows, which was derived by the present author³⁾. The corresponding two-dimensional flow, which is necessary for evaluating the axisymmetric flow, is given by the model flow method in the previous paper⁴⁾. By comparing the pressure coefficient on the surface of a cone at sonic speed calculated by this method with Yoshihara's result²⁾ obtained by the relaxation method, the accuracy of this method has been ascertained. Then we have applied this method to the several flows past a body of revolution of finite length with a curved surface.

§ 1. Introduction

The flow past a body of revolution with a sharp shoulder at high subsonic and sonic speeds cannot be dealt with by the so-called linearized theory, because a Prandtl-Meyer expansion occurs at the shoulder, and the flow has a typical transonic character. In this case it is necessary to consider the fundamental equation of the transonic approximation originally due to von Kármán¹⁾.

While the fundamental equation of the two-dimensional flow can be reduced to a linear equation by the hodograph transformation, that of the axisymmetric flow remains nonlinear in the hodograph space as well as in the physical space. Owing to this reason it is very difficult to obtain the solution of the transonic equation of the axisymmetric flow subject to the given boundary conditions. Yoshihara²⁾ obtained the flow past a slender cone-cylinder at Mach number 1 by the relaxation method. Except this, no solution has been given for the axisymmetric transonic equation subject to given boundary conditions as far as the author is aware. In the previous paper³⁾, the present writer treated this transonic eqpation with some approximation, and found the relation between the axisymmetric flow and a corresponding two-dimensional transonic flow. In that paper, starting from the flow past a finite wedge at Mach number 1, the author obtained the flow past a paraboloid of revolution at Mach number 1.

If the flow past an two-dimensional symmetric obstacle with sharp shoulders in an unbounded fluid (in a choked wind tunnel) is known, we can obtain the flow past a corresponding axisymmetric body in the unbounded fluid (in a choked circular wind tunnel).

In another paper⁴⁾, the present writer utilized the flow separating from the surface of the body at the shoulder as a model flow of the two-dimensional transonic flow with a Prandtl-Meyer expansion at the shoulder, and obtained the pressure distribution and the head drag coefficient by the simplified W.K.B. method⁵⁾ with fairly high accuracy. As examples the flows past a finite wedge, and some symmetric profiles were studied, and the pressure distributions over the surface of these bodies were obtained. In this paper, starting from these two-dimensional flows, we shall find the solutions for the flow past a finite cone and a finite body of revolution with a curved surface.

§ 2. Correspondence between the Axisymmetric and the Two-dimensional Flows

For convenience a brief account will be given of the method of correspondence between the axisymmetric and the two-dimensional transonic flows³⁾.

We shall consider the flow past a slender body of revolution placed along the axis of a circular wind tunnel and that past a two-dimensional symmetric obstacle placed along the centre line between the two parallel plane walls at zero incidence.

The two-dimensional symmetric obstacle with sharp shoulders is represented by

$$\eta=\pm\tau H(\xi) \qquad 0\leqq\xi\leqq 1, \tag{2.1}$$

where τ denotes the half thickness ratio, and the chord length is taken to be unity. If the width $2L_1$ of tunnel can be expressed as a function λ_1 of the transonic parameter K_1 such that

$$L_1\tau^{1/3}\Gamma_1{}^{1/3}=\lambda_1(K_1)\,, \tag{2.2}$$

the pressure coefficient on the surface C_{p_1} is given in the following form:

$$C_{p_1}\Gamma^{1/3}\tau^{-2/3}=F(\xi,\,K_1)-2K_1\,, \tag{2.3}$$

where

$$C_{p_1}=(p-p_\infty)\,/\,\tfrac{1}{2}\rho_\infty U_1{}^2 \tag{2.4}$$

$$K_1=(1-M_1)(\tau\Gamma_1)^{-2/3},\quad \Gamma_1=(\gamma_1+1)/2\,, \tag{2.5}$$

and γ_1 denotes the ratio of specific heats, p the surface pressure, and p_∞, ρ_∞ and M_1 denote the pressure, density and the Mach number at infinity upstream.

If we find the pressure distribution (2.3) or the functional form $F(\xi,\,K_1)$ for a given value of K_1, we can obtain the pressure distribution over the surface of an axisymmetric body placed along the axis of a circular wind tunnel of radius L, the meridian curve of which is represented by

$$y=tH^{1/2}(x)\,,\qquad 0\leqq x\leqq 1\,, \tag{2.6}$$

where t denotes the half-thickness ratio.

We shall define the pressure coefficient C_p and the transonic parameter K in the axisymmetrical case respectively by

$$C_p=(p-p_\infty)\,/\,\tfrac{1}{2}\rho_\infty U^2 \tag{2.7}$$

and

$$K=(1-M)t^{-2}\Gamma^{-1},\quad \Gamma=(\gamma+1)/2, \tag{2.8}$$

where U and M denote the uniform velocity and the Mach number at infinity upstream, and γ denotes the ratio of specific heats in the axisymmetric case.

If the radius L of the wind tunnel can be expressed as a function λ of the transonic parameter K such that

$$Lt\Gamma^{1/2}=\lambda(K)\,, \tag{2.9}$$

the pressure coefficient C_p on the surface of the body of revolution is represented by

$$\begin{aligned}C_pt^{-2}=\tfrac{3}{4}F(x,\,K)\,H^{-1/3}(x)-\tfrac{3}{2}H''(x)\{1-H^{2/3}(x)\}&\\+2H''(x)\log\{2(27\Gamma)^{-1/4}\,t^{-1}\}-2K\,,&\end{aligned} \tag{2.10}$$

where

$$K=(3/4)K_1\,, \tag{2.11}$$

and

$$\lambda(K)=4(3)^{-3/2}\,\lambda_1{}^{3/2}(K_1)\,. \tag{2.12}$$

In the extreme case where $1/L$ vanishes, we can obtain the correspondence between the flows past the two-dimensional and the axisymmetric bodies placed in an unbounded fluid. In the case of the flow in a choked wind tunnel, Eqs. (2.2) and (2.9) determine the relations among the width (radius) of tunnel, the thickness ratio of the body and the transonic parameter under the choking state of the two-dimensional and the circular wind tunnels respectively.

The head drag coefficient C_d of a body of revolution is obtained by

$$\begin{aligned}C_d\,t^{-2}=&\int_0^1\left\{\frac{3}{4}F(x,\,K)H^{-1/3}+\frac{3}{2}\,H''H^{2/3}\right\}H'\,dx\\&-\left[\log\{(27)^{1/4}/2\}+\frac{3}{4}\right]\{H'(1)^2-H'(0)^2\}\\&+\{\log(1/\Gamma^{1/4}\,t)\}\{H'(1)^2-H'(0)^2\}-2K\,.\end{aligned} \tag{2.13}$$

Eq. (2.13) should be compared with Miles's result[6):

$$\begin{aligned}C_d\,t^{-2}=&\left(\frac{H'(1)^2}{4}\right)\left[\log\left\{\frac{1.786\left[\int_0^1 H\,dx\right]^3}{H'(1)}\right\}+\frac{7}{2}\right]\\&+\{\log(1/\Gamma^{1/4}\,t)\}H'(1)^2-2K\,.\end{aligned} \tag{2.14}$$

Eq. (2.14) was deduced by matching the linearized theory with the asymptotic solution of Guderley and Yoshihara along the sonic line, and it is worthy to note that Eq. (2.14) cannot be probably applied to a body with a blunt nose.

Under certain circumstances we may use the pressure coefficients $C_{p_1}{}^*$ and $C_p{}^*$ with respect to the sonic point instead of C_{p_1} and C_p respectively, which are defined as

$$C_{p_1}{}^*=(p-p^*)/\tfrac{1}{2}\rho^*U_1{}^{*2}\,, \tag{2.15}$$

$$C_p{}^*=(p-p^*)/\tfrac{1}{2}\rho^*U^{*2}\,, \tag{2.16}$$

where the asterisk refers to the quantities at the sonic point.

Remembering Eqs. (2.4), (2.5), (2.7) and (2.8), we obtain the following relations within the accuracy of the approximation considered here:

$$C_{p_1}\Gamma_1^{1/3}\tau^{-2/3}=C_{p_1}{}^*\Gamma_1^{1/3}\tau^{-2/3}-2K_1\,, \tag{2.17}$$

$$C_p t^{-2} = C_p{}^* t^{-2}-2K\,. \tag{2.18}$$

Comparing Eqs. (2.17) and (2.18) with Eqs. (2.3) and (2.10) respectively, we obtain the following relations:

$$C_{p_1}{}^*\Gamma_1^{1/3}\tau^{-2/3}=F(\xi,\,K_1), \tag{2.19}$$

$$C_p{}^*t^{-2}=\tfrac{3}{4}F(x,\,K)H^{-1/3}(x)-\tfrac{3}{2}H''(x)\{1-H^{2/3}(x)\}$$
$$+2H''(x)\log\{2(27\Gamma)^{-1/4}t^{-1}\}. \tag{2.20}$$

In Reference [4], we introduced the reduced pressure coefficient $\tilde{C}_{p_1}{}^*$ and the transonic parameter ξ_0 in the two-dimensional case, which were respectively defined as

$$\tilde{C}_{p_1}{}^*=C_{p_1}{}^*(1+\gamma_1)^{1/3}\tau^{-2/3}\,, \tag{2.21}$$

$$\xi_0=(1-M_1^2)\tau^{-2/3}(1+\gamma_1)^{-2/3}\,. \tag{2.22}$$

Comparing Eqs. (2.21) and (2.22) with Eqs. (2.19) and (2.5) respectively, we obtain

$$\tilde{C}_{p_1}{}^*=2^{1/3}F(\xi,\,K_1)\,, \tag{2.23}$$

$$\xi_0 = 2^{1/3}K_1\,. \tag{2.24}$$

In the paper [4], the several examples of the transonic flow past a two-dimensional symmetric body of unit length placed in an unbounded fluid and in a choked wind tunnel were studied. Starting from the distribution of $\tilde{C}_{p_1}{}^*$, and utilizing Eqs. (2.10), (2.11), (2.23) and (2.24), we can obtain the pressure distribution over the surface of a corresponding body of revolution. We shall study the several examples in the following section.

§ 3. Examples

(A) *Paraboloid of Revolution*

As the meridian curve of a paraboloid revolution of unit length is represented by

$$y=tx^{1/2}\,, \qquad 0\leqq x\leqq 1\,, \tag{3.1}$$

the corresponding two-dimensional profile is a finite wedge. The pressure distributions on the surface of a finite wedge placed in an unbounded fluid for $\xi_0=0$, 0.5 and 1.0 are shown in Fig. 6 of the reference [4]. Starting from these distributions, we can calculate the pressure distributions on the surface of the paraboloid of revolution of unit length placed in an unbounded fluid. The second and the third terms in the right hand side of Eqs. (2.10) and (2.20) vanish, as the second derivative of $H(x)=x$ vanishes. Thus $C_p t^{-2}$ or $C_p{}^* t^{-2}$ can be represented as a function of x and the transonic parameter K. The surface distributions of $C_p t^{-2}$ and $C_p{}^* t^{-2}$ for $K=0$, 0.298 and 0.595 are shown in Figs. 1 and 2 respectively. It is found that the value of $C_p{}^* t^{-2}$ increases with increasing value of K, while the value of $C_p t^{-2}$ decreases.

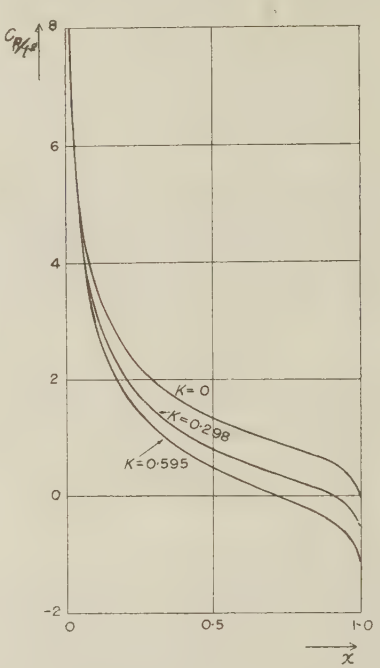

Fig. 1. The distributions of C_p/t^2 over the surface of a paraboloid of revolution in an unbounded fluid.

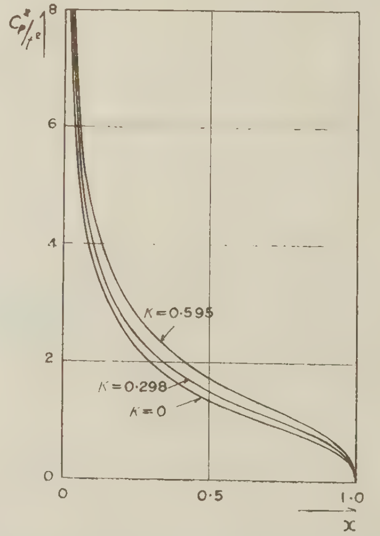

Fig. 2. The distributions of $C_p{}^*/t^2$ over the surface of a paraboloid of revolution in an unbounded fluid.

If we desire to study the flow past the

paraboloid of revolution placed along the axis of a choked circular wind tunnel, we must start from the flow past the wedge placed along the centre line between the two parallel plane walls under the choking state. By the use of the pressure distributions for the two-dimensional case (cf. Fig. 8 of Reference [4]), the distributions of $C_p t^{-2}$ and $C_p^* t^{-2}$ on the surface of the paraboloid of revolution in the choked wind tunnel are obtained, and they are shown in Figs. 3 and 4 respectively.

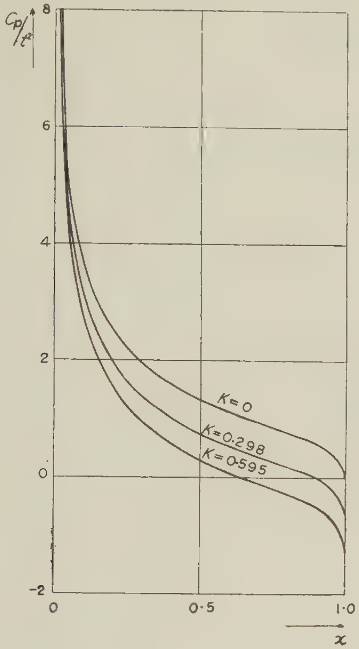

Fig. 3. The distributions of C_p/t^2 over the surface of a paraboloid of revolution of unit length in a choked wind tunnel.

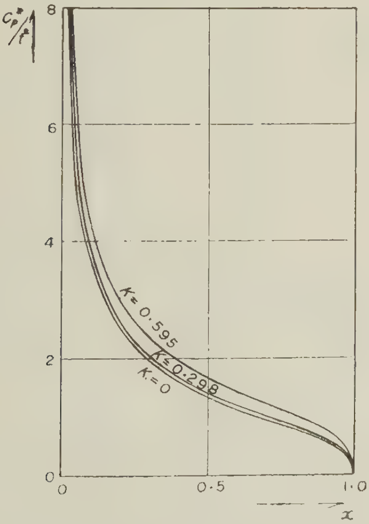

Fig. 4. The distributions of C_p^*/t^2 over the surface of a paraboloid of revolution of unit length in a choked wind tunnel.

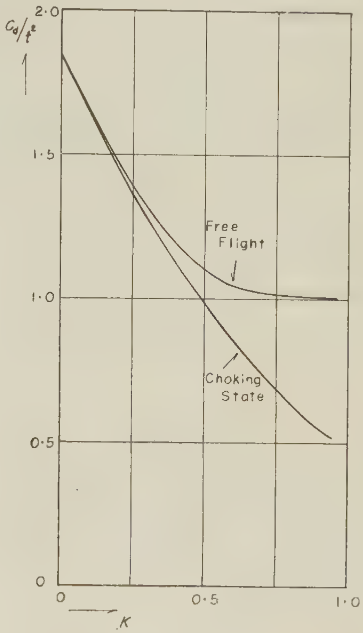

Fig. 5. The variation with the transonic parameter K of the head drag coefficient of a paraboloid of revolution.

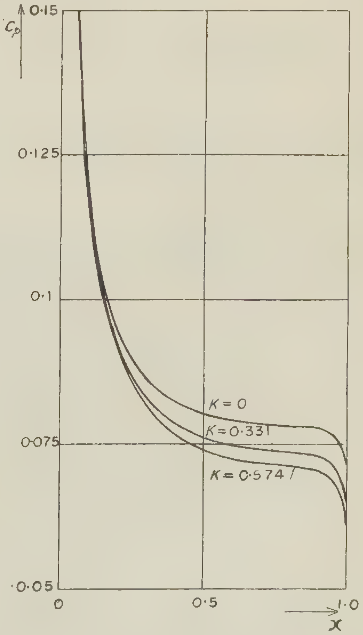

Fig. 6. The distributions of C_p over the surface of a cone of the half vertex angle 5° in an unbounded fluid.

The drag coefficient C_d is evaluated by integrating the curve in Figs. 1 and 3 graphically, and is shown in Fig. 5. In this case we cannot utilize Miles's equation (2.14) because the nose of the paraboloid is blunt.

In a previous paper [3], it has been shown that as for the choking Mach number the model flow method cannot give a good approximation, though we can obtain the pressure distribution with good accuracy by the method. Marschner[7] gave the choking Mach number of the wedge in the wind tunnel by the perturbation method applied to the Guderley's solution[8]. For the small value of the transonic parameter ξ_0, his result can be transformed into the following form[4]:

$$L_1^{-1}(\gamma_1+1)^{-1/3}\tau^{-1/3}=1.235\times 0.586\times(2/3)^{4/3}\xi_0^{5/2}, \tag{3.2}$$

where $2L_1$ denotes the width of tunnel. Comparing Eq. (3.2) with Eq. (2.2), and remembering Eqs. (2.9), (2.11), (2.12) and (2.24), we find the choking relation for the flow past a paraboloid of revolution placed along the axis of a circular wind tunnel such that:

$$\begin{aligned}&(Lt\sqrt{\Gamma})^{-1}\\ &=\frac{3\sqrt{3}}{4}\Big\{1.235\times 0.586\times(2/3)^{4/3}\\ &\qquad\times 2^{5/6}\times(4/3)^{5/2}\Big\}^{3/2}K^{15/4}.\end{aligned} \tag{3.3}$$

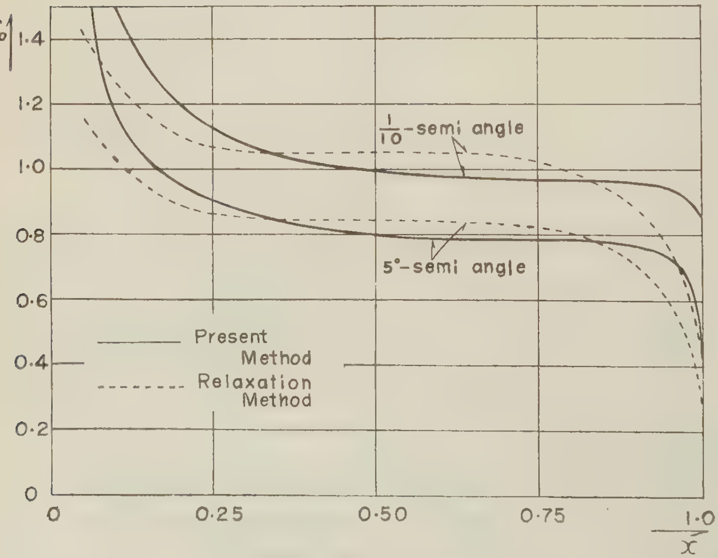

Fig. 7. The pressure distributions over the surface of a finite cone at sonic speed.

(B) *Cone*

The meridian curve of a cone of unit length is represented by

$$y=tx \qquad 0\leq x\leq 1\,. \tag{3.4}$$

The corresponding two-dimensional profile is represented by

$$\eta=\pm\tau\xi^2\,, \qquad 0\leq\xi\leq 1\,. \tag{3.5}$$

The pressure distributions on the surface of this two-dimensional profile placed in an unbounded fluid are shown in Fig. 10 of Reference [4].

Starting from these distributions we calculate the pressure distributions on the surface of a cone of the half vertex angle 5° (or $t=\tan 5°=0.08716$) for several values of K. The results are shown in Fig. 6.

Yoshihara[2] obtained the pressure distributions over the surface of a cone of the half vertex angle 5° and 1/10 radian at sonic speed by the relaxation method. Our results are compared with those of Yoshihara in Fig. 7.

The coincidence seems to be fairly good except the vicinities of the shoulder and the nose. As was shown in the paper [3], the correspondence between the pressure distributions over the surfaces of a two-dimensional and of an axisymmetric bodies was derived on the assumptions that the fluid velocity is almost sonic and that there exists the general transonic similarity law of the axisymmetric flow originally due to Oswatitsch and Berndt.[9] Then the departure of the present result from Yoshihara's exact solution may be anticipated because the fluid velocity vanishes at the nose and because the general similarity law does not completely consistent with the Prandtl-Meyer expansion at the shoulder. The variation of the head drag coefficient of the cone with the transonic parameter K is shown in Fig. 8.

When the cone is placed in the circular wind tunnel, and the flow is choked, we must start from the flow past the correponding two-dimensional profile placed along the centre line between the two parallel plane walls under the choking state. The surface distributions of $C_{p_1}{}^*$ for this two-dimensional flow are shown in Fig. 14 of the reference [4]. Starting from these distributions, we calculate the distributions of C_p on the surface of the cone in the choked circular wind tunnel, and they are shown in Fig. 9.

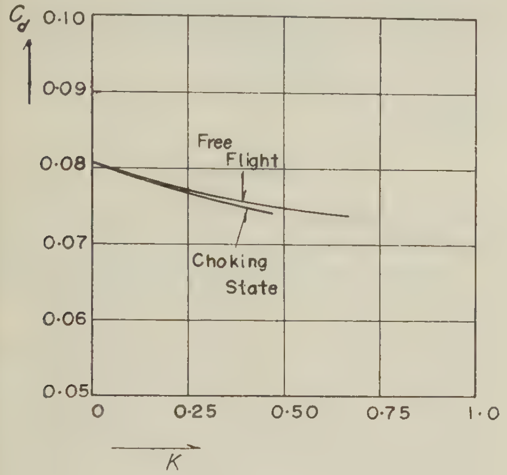

Fig. 8. The variation with the transonic parameter K of the head drag coefficient of a cone of the half vertex angle 5°.

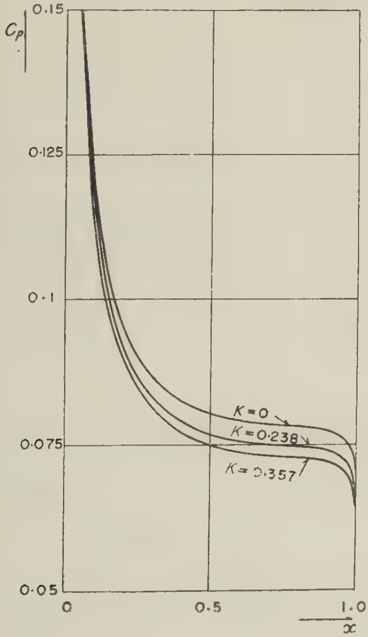

Fig. 9. The distributions of C_p over the surface of a cone of the half vertex angle 5° in a choked wind tunnel.

From Figs. 6 and 9, it is found that C_p decreases with increasing value of K. Evaluating $C_p{}^*$ defined by Eq. (2.16) for these values of K, the $C_p{}^*$-distribution slightly increases with ikcreasing value of K. But the differences are so small that these $C_p{}^*$-curves are almost the same curve as C_{p_0}-curve for $K=0$ in Figs. 6 and 9. The head drag coefficient of the cone placed in the choked wind tunnel is obtained by graphical integration, and is also shown in Fig. 8.

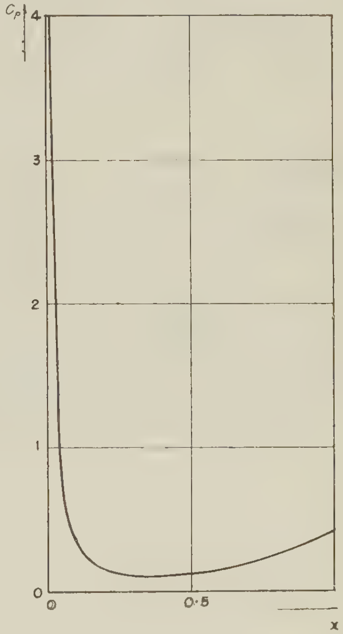

Fig. 10. The pressure distribution over the surface of a body of revolution $y=0.0872x^2$ at sonic speed.

(C) *Profile*: $y=tx^2$, *for* $0\leq x\leq 1$

The corresponding two-dimensional body is represented by

$$\eta=\pm\tau\xi^4\,,\qquad 0\leq\xi\leq1\,. \tag{3.6}$$

The pressure distribution on the surface of the two-dimensional body at sonic speed is shown in Fig. 15 of Reference [4]. Starting from this distribution, we calculate the pressure distribuiton on the surface of the body of revolution of the same thickness as the cone of the half vertex angle 5°. Since the velocity at the shoulder is sonic and the meridian curve has a cusp at the nose of the body, the pressure coefficient should vanish and take a finite value at the shoulder and the nose respectively. The result shown in Fig. 10

does not satisfy these conditions because the assumption in the present method does not hold at the shoulder and near the nose. (cf. (b) case of cone).

The head drag coefficient of the body is given in Table I together with those of other profiles at sonic speed.

Table I. The head drag coefficient of several bodies of revolution of half thickness ratio $t=0.08716$ at sonic speed for $\gamma=1.4$.

Profile	Present	Yoshihara	Miles
$y=t\sqrt{x}$ (paraboloid)	0.014	—	—
$y=tx$ (cone)	0.080	0.076	0.073
$y=tx^2$	0.281	—	0.226

§ 4. Conclusion

Combining the correspondent relations between the axisymmetric and the two-dimensional flows with the simple model flow method, we have obtained the pressure distributions on the surface of several bodies of revolution with sharp shoulder in an unbounded fluid and in a choked circular wind tunnel. In the case of wedge, we compared the present result with the exact solution derived by the relaxation method. Considering that the flow assumed in the present method is very simple, the result may be regarded as satisfactory.

In conclusion, the author would like to express his heartiest gratitude to Professor I. Imai for his kind suggestion and valuable discussions during the course of the present investigations.

References

1) Th. von Kármán: Journ. Math. and Phys. **26** (1947) 182.
2) H. Yoshihara: WADC Tech. Rep. 52-295 (1952).
3) K. Kusukawa: Journ. Phys. Soc. Japan **12** (1957) 401.
4) K. Kusukawa: Journ. Phys. Soc. Japan **12** (1957) 1031.
5) I. Imai: Journ. Phys. Soc. Japan **3** (1948) 352.
6) J. W. Miles: Journ. Aero. Sci. **23** (1956) 146.
7) B. W. Marschner: Journ. Aero. Sci. **23** (1956) 368.
8) G. Guderley and H. Yoshihara: Journ. Aero. Sci. **17** (1950) 723.
9) K. Oswatitsch and S. B. Berndt: KTH-AERO TN **15** (1950).

Short Notes

This section is intended to secure prompt publication of important discoveries in physics. The reports should not exceed 800 words in length. A figure of size 7 cm × 7 cm will be counted as 150 words.

J. PHYS. SOC. JAPAN **12** (1957) 1049

Dynamic Programming and the Variational Solution of the Thomas-Fermi Equation

By Richard BELLMAN

The RAND Corporation Santa Monica, California

(Received April 24, 1957)

1. *Introduction.* In a recent paper, Ikebe and Kato, [8], considered the problem of the numerical integration of the nonlinear equation

$$u''-u^{3/2}x^{-1/2}=0\ ,\quad u(0)=1\ ,\quad u(\infty)=0 \qquad (1)$$

which arises in connection with the Thomas-Fermi statistical model of a free neutral atom. Equations of this type arose a number of years before in connection with astrophysical questions, Emden, [4], Fowler, [5], [6], [7], Bellman, [3], Sansone, [9].

In their paper, Ikebe and Kato treat the problem of determining $u'(0)$ by means of the associated variational problem: Minimize

$$J(u)=\int_0^\infty\left(u'^2+\frac{4}{5}u^{5/2}x^{-1/2}\right)dx \qquad (2)$$

over all functions u for which the integral exists and which satisfy the constraints $u(0)=1$, $u(\infty)=0$.

In this note we wish to indicate a new approach to problems of this type based upon the functional equation technique of the theory of dynamic programming, [1], [2]. Detailed computational results will be presented subsequently.

2. *Functional Equations.* Define the new functional

$$J(u)=\int_a^\infty(u'^2+u^m x^{-n})dx\ ,\quad u(a)=c\ ,\quad u(\infty)=0\ , \qquad (1)$$

where $a>0$, $-\infty<c<\infty$. Define the function $f(a, c)=\operatorname*{Min}_u J(u)$. Then as in [1] and [2], we have the nonlinear partial differential equation.

$$\frac{\partial f}{\partial a}=\frac{1}{4}\left(\frac{\partial f}{\partial c}\right)^2-c^m a^{-n}\ . \qquad (2)$$

As pointed out by a referee, this is the Hamilton-Jacobi equation associated with the variational problem.

Making the transformations, $x=ay$, $w(y)=u(ay)a^{-k}$, we see that

$$f(a, c)=a^{(2+m-2n)/(2-m)}f(1, c/a^{(2-n)/(2-m)})\ . \qquad (3)$$

Thus $f(a,c)=a^{(2+m-2n)/(2-m)}\phi(c/a^{(2-n)/(2-m)})$, where $\phi(x)=f(1, x)$.

Substituting in (2), we obtain the ordinary differential equation

$$\left(\frac{2+m-2n}{2-m}\right)\phi(x)-\left(\frac{2-n}{2-m}\right)x\phi'(x)=\frac{\phi'(x)^2}{4}-x^m \qquad (4)$$

Since $\phi(x)=f(1, x)$, we see that $\phi(0)=0$.

The original second order differential equation with a two-point boundary value problem has been replaced by the above first order equation. The numerical integration, however, requires some care since the equation is singular at $x=0$. We have

$$f(0, 1)=\lim_{x\to\infty}x^{2n-m-2/2-n}\phi(x)\ . \qquad (5)$$

The equation $u''-(m+1/2)e^{\lambda x}u^m=0$ gives rise to the problem of minimizing $J(u)=\int_a^\infty(u'^2+e^{\lambda x}u^m du)$, over all functions u satisfying the constraints $u(a)=c$, $u(\infty)=0$. It may be treated in a similar fashion.

References

1) R. Bellman: *The Theory of Dynamic Programming*, Bull. Amer. Math. Soc. **60** (1954) 503–516.

2) ――――: *Dynamic Programming*, Princeton University Press, June, 1957.

3) ――――: *Stability Theory of Differential Equations*, McGraw-Hill, 1954.

4) R. Emden: *Gaskugeln, Anwendungen der Mechanischen Warmentheorie Auf Kosmologie und Meteorologische Probleme*, Chap. XII, B. G. Teubner, Leipzig, 1907.

5) R. H. Fowler: *The Form near Infinity of Real, Continuous Solutions of a Certain Differential Equation of the Second Order*, Quart. J. Math. **45** (1914) 289–350.

6) ――――: *The Solution of Emden's and Similar Differential Equations*, Monthly Notices of the Royal Astr. Soc. **91** (1920) 63–91.

7) ――――: *Further Studies of Emden's and Similar Differential Equations*, Quart. J. Math. **2** (1931) 259–288.

8) T. Ikebe and T. Kato: *Application of Variational Method to the Thomas-Fermi Equation*, Jour. Phys. Soc. Japan **12** (1957) 201–204.

9) G. Sansone: *Sulle Soluzioni di Emden della Equazione di Fowler*, Univ. Roma e. 1st Naz. Alta. Mat. Rend. Mat. e Appl., Ser. 5, **1** (1940) 163-176.

J. PHYS. SOC. JAPAN **12** (1957) 1050

Effect of Iron Group Ions on the Dielectric Properties of $BaTiO_3$ Ceramics

By Tunetaro SAKUDO

Electrotechnical Laboratory, Nagatacho, Tokyo

(Received June 5, 1957)

In the investigation of $BaTiO_3$ single crystal grown by the method of Remeika, it was observed that the Curie point of the crystals was lowered very remarkably when a small amount of Fe_2O_3 was introduced[1].

To examine the effect in the case of other iron group ions, ceramic samples containing several atomic percent of the ions were prepared. The change in the Curie point with the content of the ions is shown in Fig. 1, determined by the measurement of ε-T curve (permittivity vs. temperature) at 70 Kc.

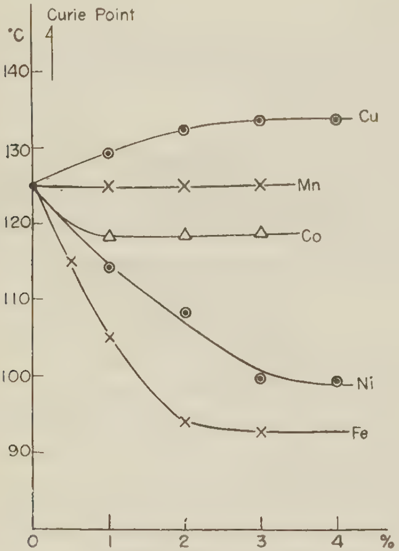

Fig. 1.

In the cases of Fe and Ni ions, the Curie point drops linearly up to 2～3 atomic percent content, whereas it remains almost constant while the content is further increased. For Mn and Co ions, only small change in the Curie point is observed, almost independent of the added amount.

These tendencies can be explained as the results of different solubility-limit of the ions in the $BaTiO_3$ lattice. These solubility-limit seem to be unaffected by sintering conditions, i.e. firing temperature, sintering atmosphere and cooling rate. In the case of Cu ion, however, the Curie point rises unexpectedly with the content of the ions. Fig. 2. shows the change in the Curie point with added Cu ion up to 30 atomic percent, with indicated composition of starting materials. Fig. 3 shows the examples of ε-T curves in these cases. As can be seen from the figure, the peak value of ε decreases with increasing amount of added ions. The dielectric measurement becomes very hard for Cu amount of more than 40 percent, as the d.c. conductivity of the samples increases with the added amount.

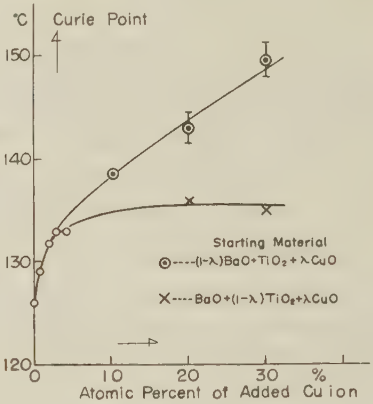

Fig. 2.

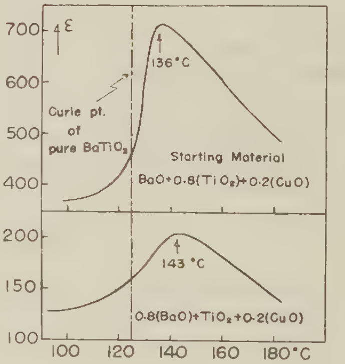

Fig. 3.

In the X-ray diffraction pattern of the samples containing Cu ion of the concentration of 10～50 percent, there were observed other lines than those corresponding to perovskite structure. Extra lines resemble the diffraction pattern of the samples made by sintering BaO and CuO, but not yet identified. The latter samples show ordinary paraelectric properties.

This effect might be attributed to some apparent phenomena arising from d.c. donductivity and dielectric loss.

But the change in the Curie point was ascertained to be frequency independent by measurement of the ε-T curves of the above samples again at 6 Mc.

Studies are going on to find the mechanism of the effect.

This work was supported by the Scientific Research Expenditure of the Ministry of Education.

Reference

1) A. Nishioka and K. Sekikawa: J. Phys. Soc. Japan **11** (1956) 180.

J. PHYS. SOC. JAPAN **12** (1957) 1051

Paramagnetic Susceptibility of $CoCl_2 \cdot 6H_2O$ between 290°K–1.52°K

By Taiichiro HASEDA and Eizo KANDA
The Research Institute for Iron, Steel and Other Metals, Tohoku University, Sendai, Japan

(Received June 14, 1957)

We have measured the paramagnetic molar susceptibility, χ_m, of $CoCl_2 \cdot 6H_2O$ in the temperature range between 290°K and 1.52°K by the usual a.c. bridge method. The results are shown in Figs. 1 and 2. The broad hump located at about 3.0°K in Fig. 2 may be considered as due to antiferromagnetic transition. However, this transition temperature is higher than that expected from the usual picture that each Co^{+2} ion is surrounded by six water molecules octahedrally.

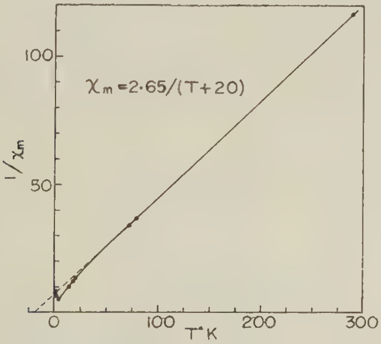

Fig. 1. Inverse molar susceptibility, $1/\chi_m$ of $CoCl_2 \cdot 6H_2O$ in the temperature range below the room temperature.

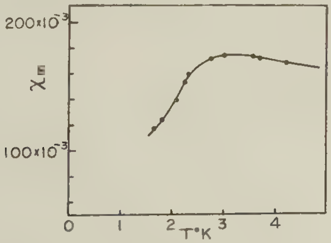

Fig. 2. Molar susceptibility, χ_m, of $CoCl_2 \cdot 6H_2O$ near the liquid helium temperature.

Some of the hydrated halides of iron group metals which have two or four water molecules were studied down to the liquid helium temperature[1]. Among these, for instance, $CuCl_2 \cdot 2H_2O$ shows antiferromagnetic transition at 4.31°K. It is well known that, in $CuCl_2 \cdot 2H_2O$, each Cu^{+2} ion is surrounded by two water molecules and two chlorine atoms. Along the a axis, two Cu^{+2} ions are adjacent to each other, locating one chlorine atom between them. In general, in most of the hydrated halides so far investigated, magnetic ions are separated from each other at least along one direction by only *one* diamagnetic atom.

In halides which have more than six hydrated water molecules, metallic ions are surrounded, in general, by six water molecules octahedrally, as in alums or Tutton salts. In these cases, magnetic ions are separated by at least *two* of the diamagnetic atoms or molecules. Then it may be expected that the magnetic transition temperatures of these salts are lower than those of the former salts. In alums or Tutton salts, the octahedron formed by the surrounding six water molecules are separated further by sulphate ions or monovalent anions. It may be considered, in these cases, that exchange or superexchange interaction between magnetic ions passes over *several* atoms or molecules, so that any magnetic transition, say, antiferromagnetic one occurs below 1°K as is actually the case.

On the other hand, in anhydrous halides and sulphates, distance between magnetic ions is considerably short. For instance, in $CoCl_2$ which has the layer structure, ($CdCl_2$ structure) magnetic ions interact each other directly in a layer and through two chlorine atoms between layers. In such halides and sulphates the antiferromagnetic transition or some anomalous behaviour has been observed at rather high temperatures such as the liquid hydrogen and liquid nitrogen temperatures.

Thus, it may be inferred, from the above stated consideration that in $CoCl_2 \cdot 6H_2O$ one or two chlorine atoms will take positions of octahedral coordination in the place of water molecules and these octahedrons are adjacent to each other without inserting any atom or molecule.

The determination of crystal structure of $CoCl_2 \cdot 6H_2O$ by J. Mizuno, K. Ukei and T. Sugawara in our Institute[2] is now in progress. The most probable structure inferred at present from their results is such that each Co^{+2} ion is surrounded by four water molecules forming a square and by two chlorine atoms on an axis normal to the square. This picture is quite consistent with the magnetic behaviour observed.

H. J. Gerritzen failed to detect paramagnetic resonance in this salt at liquid hydrogen temperatures[3] Antiferromagnetic resonance measurement made, using 9800 Mc, by M. Date in our Institute has also yielded negative result[4].

The sample used was that from Kanto Chem. Co. Japan and analysed to be exactly $CoCl_2 \cdot 6H_2O$.

References

1) For instance, T. Nagamiya. K. Yoshida and R. Kubo: Adv. in Phys. **4** (1955) 1.
2) J. Mizuno, K. Ukei and T. Sugawara, to be published soon.
3) H. J. Gerritzen, Thesis 1955.
4) M. Date: unpublished.

J. PHYS. SOC. JAPAN **12** (1957) 1052

Convex Molecules in Non-Uniform Gases,— Supplement

By Taro KIHARA and Akiji ŌUCHI

Department of Physics, Faculty of Science, University of Tokyo

(Received July 3, 1957)

In "Geometrical Theory of Convex Molecules in Non-Uniform Gases" by T. Kihara (J. Phys. Soc. Japan **12** (1957) 564) a geometrical theorem on convex bodies was applied to transport phenomena in gases, molecules being represented by rigid convex bodies without attraction. Collisions between heavy convex molecules and light spherical molecules were treated; shape and size of molecules of nitrogen, carbon dioxide, carbon tetrachloride, sulfur hexafluoride, and benzene were determined from the coefficients of diffusion in hydrogen. This note is a supplement, in which results for several other molecules are added. Tables Ia through IVa and Fig. 2a are continuations of the corresponding tables and Fig. 2.

Table Ia. Interatomic distance.

Molecule		Bond	Distance in A
Carbon disulfide	CS_2	C–F	1.54

Table IIa. The cores of molecules.

Mole-cules	Cores	V_0 (A^3)	S_0 (A^2)	M_0 (A)
CS_2	thin rod joining 2S's	0	0	9.68
CH_4	tetrahedron joining 4H's	0.67	5.52	10.23
C_2H_4	rectangle joining mid-points of C–H	0	3.48	8.95
$C_{10}H_8$	octagon joining mid-points of C–H	0	44.74	25.75
$C_{14}H_{10}$	octagon joining mid-points of C–H	0	70.13	33.32

Table IIIa. Coefficients of diffusion D at 0°C, 1 atm. and the effective cross sections Q in Eq. (13).

Gases	D (cm^2/sec)	Q (A^2)	$S_A+S_B+\frac{1}{2\pi}M_AM_B$ (A^2)
H_2-CS_2	0.369	204	
H_2-CH_4	0.625	126	
H_2-C_2H_4	0.486	158	
CO_2-CS_2	0.063	316	292
CS_2-Air	0.0892	258	253
CO_2-CH_4	0.153	201	196
$C_{10}H_8$-Air	0.0513	502	
$C_{14}H_{10}$-Air	0.0421	423	

The values of D are also taken from *International Critical Tables* vol. V (McGraw-Hill, New York, 1929).

Table IVa, Constants of rigid convex-body model of molecules determined from coefficients of diffusion at 0°C.

Molecules	a (A)	S (A^2)	A (A)
CS_2	2.06	92.9	35.5
CH_4	1.11	43.8	24.2
C_2H_4	1.59	63.8	28.9
$C_{10}H_8$	2.08	206	51.8
$C_{14}H_{10}$	2.06	260	59.1

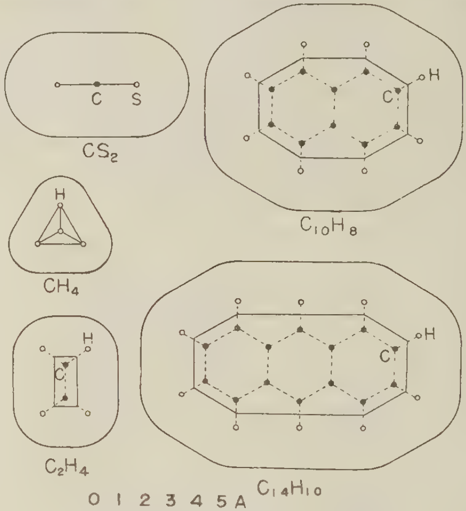

Fig. 2a. Shape and size of molecules according to the rigid convex-body model determined from diffusion coefficients at 0°C.

Carbon disulfide CS_2 can be treated just as carbon dioxide. Diffusion of naphthalene $C_{10}H_8$ and anthracene $C_{14}H_{10}$ in air can be approximately treated as a collision phenomenon between a light spherical molecule and a heavy convex molecule with a large moment of inertia. As regards the radius of the sphere representing an "air molecule" we have $b=1.73$ A, which is effective for diffusion at 0°C. Diffusion of methane CH_4 and ethylene C_2H_4 in hydrogen can be treated within the accuracy of the "geometrical approximation" mentioned in the main article.

Erratum: in Eq. (4) change $\boldsymbol{r}\cdot(\cdots)$ to $\boldsymbol{u}\cdot(\cdots)$.

J. Phys. Soc. Japan **12** (1957) 1053

Proposal for a Solid State Radio-Frequency Maser

By Junkichi Itoh
Department of Physics, Osaka University

(Received July 4, 1957)

Bloembergen[1] has proposed a solid state maser in microwave frequency range by the use of double resonance among fine structure levels of paramagnetic ion in crystal, and this method has been applied by Scovil, Feher, and Seidel[2] to a gadolinium salt with great success.

By a similar double resonance method, it seems possible to construct a radio-frequency solid state maser, using Zeeman levels of pure quadrupole spectrum.

Consider nuclei with spin 3/2 in a single crystal and assume that there exists large axially symmetric nuclear quadrupole interaction for these nuclei. When this single crystal is inserted in a magnetic field, H_0, two pure quadrupole levels, $\pm 3/2$ and $\pm 1/2$, split into four levels as shown in Fig. 1[3].

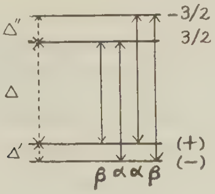

Fig. 1.

Two levels split from $\pm 1/2$ level are mixed states which will be denoted as (+) and (−) levels, respectively. By the assumption of large e^2qQ, energy differences $\varDelta'$ and $\varDelta''$ indicated in the figure are very much smaller than $\varDelta$. By some thermal motions in the crystal, spin-lattice relaxation processes take place, and assuming that main contribution comes from electric quadrupole interaction, the probabilities of thermal transitions between these levels are denoted as α and β, respectively, as shown in the figure.

When a sufficiently strong r.f. field is applied on the crystal, with the frequency equal to $(\varDelta+\varDelta'')/h$, the states $-3/2$ and (+) will saturate and the population difference between these two levels will disappear. At the same time, the population difference between (+) and (−) levels. $N_- - N_+$, becomes

$$N_- - N_+ \fallingdotseq (n/4)(\varDelta/kT)(\alpha+\beta)/(2\alpha+\beta) \tag*{(1)*}$$

where n is total number of nuclei in the crystal, and T is the temperature of the crystal. Therefore, $N_- - N_+$ which is proportional to $\varDelta'/kT$ when there is no r.f. field becomes to be proportional to $\varDelta/kT$ when the transition between $-3/2$ and (+) levels saturates. Since $\varDelta \gg \varDelta'$, the population difference increases enormously by this procedure.

When a sufficiently strong r.f. field with the frequency $(\varDelta+\varDelta')/h$ is applied on the crystal, the population difference, $N_- - N_+$ becomes negative, with the absolute magnitude equal to that given by (1)**. In this case, emission spectrum by the transition between (+) and (−) levels will be expected. When another weak r.f. field with the frequency $\varDelta'/h$, which lies generally in r.f. frequency range for the value of the static field of few thousand oersteds, is applied with the amplitude $2H_2$, the power of induced emission by this radiation field, P, can be calculated easily to be

$$P=(1/2)(\varDelta/kT)\varDelta' n\gamma^2 H_2{}^2 T_2(\alpha+\beta)/(2\alpha+\beta) \tag{2}$$

where T_2 is the spin-spin relaxation time and γ is the gyromagnetic ratio, and this r.f. field is assumed to have a direction to give maximum transition probability. In the case where $\gamma=10^4\,\mathrm{sec}^{-1}\,\mathrm{gauss}^{-1}$, $T_2=10^{-4}\,\mathrm{sec}$, $H_2=3\times10^{-2}$ oersted, $H_0=10^4$ oersted, $n=0.1$ mole, and $\alpha \ll \beta$***, P becomes to be about $3(\varDelta/kT)\cdot 10^{-3}$ watt, or, if $\varDelta/kT \sim 10^{-2}$, the power obtainable will be about 30 microwatts.

When $Q(\text{loaded})^{-1} > P/\omega \times (\text{storage energy}) > Q(\text{unloaded})^{-1}$, cw amplification will be possible, and when $P/\omega \times (\text{storage energy}) > Q(\text{loaded})^{-1}$, self-sustained oscillation will be realized. With the same values of γ, T_2 and H_0 given above, and assuming $Q(\text{loaded})=100$ and the volume occupied by a nucleus $=6\times10^{-23}$ cc, the condition for self-sustained oscillation is $(e^2qQ/kT) > 0.01$, or, if we take $T=1$°K, e^2qQ/h should be larger than 460 Mc/sec.

Thus, in favorable cases, it will be possible to construct an r.f. maser by this principle, though it might be less important in actual applications as compared with microwave maser.

References

1) N. Bloembergen: Phys. Rev. **104** (1956) 324.
2) Scovil, Feher and Seidel: Phys. Rev. **105** (1957) 762.
3) R. V. Pound: Phys. Rev. **79** (1950) 675.

---

* When a strong r.f. field with the frequency $\varDelta/h$ is applied, a similar expression for $N_- - N_+$ is obtained in which α and β are mutually interchanged.

** When a strong r.f. field with the frequency $(\varDelta+\varDelta'+\varDelta'')/h$ is applied, $N_+ - N_-$ becomes equal to $N_- - N_+$ of the case with the frequency $\varDelta/h$.

*** This condition is not always necessary. For arbitrary values of α and β, the power obtainable differes only within a factor of two.

J. PHYS. SOC. JAPAN **12** (1957) 1054

Free Bonds on the Clean Surfaces of Germanium Single Crystals

By Akio KOBAYASHI and Shinji KAWAJI
The Research Institute for Catalysis, Hokkaido University, Sapporo, Japan

(Received June 22, 1957)

There is good evidence that two types of surface states, fast and slow states, exist on germanium surfaces[1)2)]. According to the latest investigations of several workers, the density of fast states is about 10^{11}/cm^2 ev. If the fast states are Tamm levels, their density should be about 10^{15}/cm^2. Field effect experiments on germanium surface cleaned by ion bombardment were carried out by Handler and others[3)] lately. But they could not observe the minimum of conductance by field effect, therefore, their estimation might include some ambiguity in the density of fast states. We have observed field effect patterns of clean germanium surface and their change with introduction of oxygen. In all cases we could observe the minimum of conductance so that we have obtained the density of the fast states.

The sample used was an etched slice of 40 ohmcm p-type germanium single crystal, $0.5 \times 2.5 \times 15$ mm^3, which was mounted on the sample holder shown in Fig. 1. Field effect was measured using a 50 cps voltages from peak to peak 4×10^5 volts/cm applied to a field probe. The circuit used was similar to Montgomery and Brown's. After the sample stood in hydrogen gas at pressure about 5 cmHg at 500°C for 24 hours in order to reduce the germanium surface, the system was evacuated to 10^{-8} mmHg. The sample was then heated upto about 800°C for ten minutes by passing an ac current through itself and, then allowed to cool to room temperature at the free radiation rate. After measurements for this clean surface were carried out, oxygen gas was introduced into the vacuum system. The measured field-effect patterns for clean and oxidized surfaces are shown in Fig. 2.

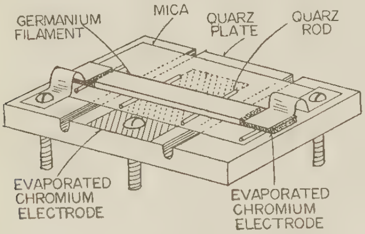

Fig. 1. The sample holder.

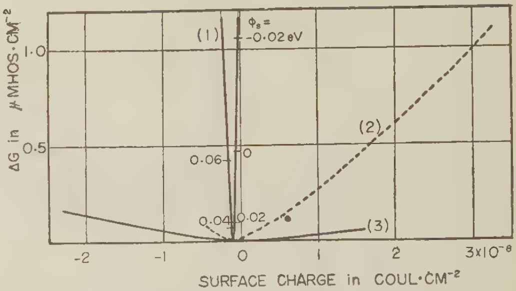

Fig. 2. Curve (1): theoretical conductance changes. ϕ_s is the position of the Fermi level at the surface measured with respect to the Fermi level in intrinsic material. Curve (2): conductance changes for clean surface and, Curve (3): that for oxidized surface.

In this figure the minimum points of experimental patterns are shifted at the same point of theoretical one.

From this figure the density of fast states is estimated at 1.7×10^{13}/cm^2 ev for clean surface and at 2.4×10^{12}/cm^2 ev for oxidized surface. The surface potential, defined as the difference of the electrostatic potential at the surface from its bulk value, decreased by 0.03 volts with the introduction of oxygen. The decrease in the density of fast states with introduction of oxygen shows that the fast states are dangling bonds at the surface of the germanium proper. But the observed density of fast states is still much lower than expected as Tamm states. This discrepancy may be attributed to the contamination of the surface by residual gases during experiments.

References

1) H. C. Montgomery and W. L. Brown: Phys. Rev. **103** (1956) 865.
2) J. Bardeen et al: Phys. Rev. **104** (1956) 47.
3) P. Handler; "Semiconductor surface physics", Univ. Pennsylvania Press, 1957, p 23.
4) C. G. B. Garrett and W. H. Brattain: Phys. Rev. **99** (1955) 376.

PROGRESS OF THEORETICAL PHYSICS

(*Founded by H. Yukawa in 1946*)

Published for the

Research Institute for Fundamental Physics

The Physical Society of Japan

Progress of Theoretical Physics Vol. 17, No. 4, April 1957

On the Vibration of Disordered Linear Lattice ....J. HORI and T. ASAHI..523

Cluster Development Method in the Quantum Mechanics of Many Particle System, I ....F. IWAMOTO and M. YAMADA..543

On the Elastic Scattering of Charged Particles by Nuclei in the Intermediate Energy Region ....S. N. GHOSHAL and B. B. BALIGA..556

Saturation of Nuclear Forces—Neutron Proton Scattering ....A. B. BHATIA and S. M. SHAH..561

The l-Forbidden Magnetic Dipole Transitions....A. ARIMA, H. HORIE and M. SANO..567

Pion-Nucleon Scattering and Structure of Fourth-Order Matrix Elements in Ps(Ps) Meson Theory ....K. NAKABAYASI and K. HASEGAWA..581

Mathematical Formulation of the Gell-Mann-Nishijima Scheme for New Particles ....Sigeo HANAWA..592

Letters to the Editor:

On the Air Shower Core ....S. HASEGAWA..603

A Kinematical Test for the Relation between the Coupling Constants in Meson Theory ....K. HIIDA..605

Electron-Neutron Interaction ....F. ANDO and H. MIYAZAWA..607

Viscosity and Heat Conductivity of Liquid He^3 ....S. K. TRIKHA..609

On the Annihilation Cross Section of the Antinucleon and the Nucleon ....Y. YAMAGUCHI..612

Interaction with the Sound Quanta in a System Consisting of Two Kinds of Charged Particles—*The Method of Supplementary Variables*— ....Z. GALASIEWICZ..613

The Catalysis of Nuclear Fusion Reactions by μ-Mesons .... C. HAYASHI, T. NAKANO, M. NISHIDA, S. SUEKANE and Y. YAMAGUCHI..615

Errata 618

Progress of Theoretical Physics Vol. 7, No. 5, May 1957

Quantum-Electrodynamical Corrections to Energy-Levels of Helium ....Huzihiro ARAKI..619

The Penetration of the Diffuse Nuclear Potential Barrier ....Ken KIKUCHI..643

The Photon-Nucleon Scattering ....S. MINAMI and Y. YAMAGUCHI..651

Note on the Ferromagnetic Resonance Absorption ....Takehiko OGUCHI..659

On Solutions of He^3 and He^4 ....S. K. TRIKHA and V. S. NANDA..679

On Collective and Internal Motions in a Bose System ....Toshiyuki NISHIYAMA..711

Letters to the Editor:

On the Systematization of the Strongly Interacting Particles ......M. IDA..733

Errata 734

Contents of Journ. of Phys. Soc. of Japan, Vol. 12, No. 3, 4 735

Progress of Theoretical Physics Vo. 17, No. 6, June 1957

Giant Stars with Shell Source of C-N and p-p Reactions................C. HAYASHI..737
Selection Rule Imposed by Mass Reversal................................T. OUCHI..743
Investigation of the Chew-Low Equation by Iteration......H. FUJINO and J. OSADA..751
On the Asymptotic Conditions in Quantum Field Theory..............K. NISHIJIMA..765
Mass Difference of Σ^+, Σ^- and Σ^0 Hyperons.......................H. KATSUMORI..803
A Remark on High Energy Phenomena......S. AMAI, T. MUROTA and M. NISHIDA..807

Letters to the Editor:

Effect of Long-Range Correlations on Free Electron Diamagnetism .. ..B. DONOVAN, H. KANAZAWA and N. H. MARCH..813
Acceleration of Cosmic Rays by Hydromagnetic Wave............. .... Y. TERASHIMA, K. KITAO and K. OGAWA..814
Interpretation on the Ratio of the Emission Probabilities for Protons and Neutrons..........................R. NAKASIMA and K. KIKUCHI..816
Some Remarks on the Charged Mesic Decay of $^3H_\Lambda$................ .... T. OGIMOTO and Y. YAMAGUCHI..817
An Attempt of Generalizing the Invariance of the Theory under the Charge Conjugation ....O. HARA, Y. FUJII and Y. OHNUKI. 819
Pion-Nucleon Interaction according to the Previous Theory ....O. HARA, Y. FUJII and Y. OHNUKI..820
The Annihilation of Antinucleon according to the Previous Theory.. ....O. HARA, Y. FUJII and Y. OHNUKI..822
The Production Ratio of K^+ to K^- Mesons...................... ....Y. KAKUDO and K. KOBAYAKAWA..823

Errata...825

Contents of Phys. Soc. of Japan, Vol. 12, No. 5 826

Contents and Authors Index to Vol. 17..829

Price $ 1.25 per copy
$ 15.00 per year (postage inclusive)
Annual dues for foreign members (individual subscribers)
$ 12.00 (postage inclusive)
〃 for foreign members of the Physical Society of Japan
$ 10.00 (postage inclusive)

Application for members, subscriptions and orders for back numbers should be sent, directly or through book-dealers, to

The Publication Office
in
Yukawa Hall, Kyoto University, Kyoto, Japan

JOURNAL OF THE PHYSICAL SOCIETY OF JAPAN Vol. 12, No. 10, OCTOBER, 1957

Angular Distributions of the Si^{28} (d, p) Si^{29} Reaction

Shigeo TAKEMOTO, Tsunekichi DAZAI and Shinji SUGANOMATA

Department of Physics, Faculty of Science,
Tohoku University, Sendai, Japan

(Received July 3, 1957)

The angular distributions of five proton groups from the Si^{28} (d, p) Si^{29} reaction have been measured in energy range 0.77- to 1.30-Mev. In our energy region complicated compound nucleus effect was observed.

§ 1. Introduction

Holt and Marsham[1)] investigated the Si^{28} (d, p) Si^{29} reaction at 8-Mev deuteron energy. Their results showed pronounced stripping effect in the angular distribution of various proton groups. Recently, the experiments of Cox and Williamson[2)] have shown many resonance structures in the Si^{28} (d, p) Si^{29} excitation curve at 50° to the beam direction, but no such structures at 0°. We have studied whether stripping effect is present or not in our low energy region (0.77- to 1.30-Mev).

§ 2. Experimental Procedure

In order to measure the angular distribution, a multiple plate camera was used. Nuclear emulsion plates used to detect protons were the Sakura 100 μ nuclear plates.* Their properties are believed not to differ appreciably from those of the Ilford C2 emulsions. Aluminium foils, inserted in front of them, were 70 to 100 microns thick. Apparatus and procedure were described in detail in the previous report[3)].

The homogeneous deuteron beam from the Tohoku Van de Graaff generator was used to bombard a thin silicon target. The deuteron energy spread was about 1% and the calibration of the energy scale was made at the known $Li^7(p, \gamma)Be^8$ 441-kev resonance using a diatomic beam.

A thin silicon target, few tenths of a micron thick, was prepared by vacuum evaporation of natural metallic silicon onto a silver backing, about 1 mg/cm² thick. As the target thickness and the beam current were not measured precisely, the absolute cross sections could not be obtained.

§ 3. Results and Discussions

A typical range spectrum of Si^{28} (d, p) Si^{29} protons is shown in Fig. 1. A number of proton groups is clearly resolved, and assignment to known levels in Si^{29} was carried out with the aid of the range-energy relation of the Sakura nuclear emulsion and known reaction Q-values.[4)] Groups P_0, P_1, P_2, P_3 and P_4 correspond to the ground state, 1st. (1.28-Mev), 2nd. (2.03-Mev), 3rd. (2.43-Mev). and 4th. (3.07-Mev) excited state in Si^{29}, respectively. C group is protons from C^{12} (d, p) C^{13}

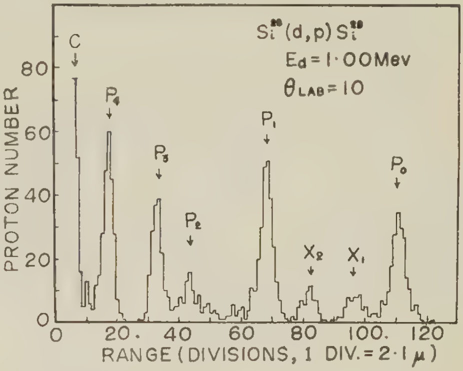

Fig. 1. Range spectrum of protons at $\theta_{lab}=10°$ from the Si^{28}(d, p) Si^{29} reaction (Q=6.25 Mev, E_d=1.00 Mev.)

Table I. Intensity ratio of proton groups from the reaction Si^{28} (d, p) Si^{29} (Q=6.25 Mev) at $\theta_{lab}=90°$.

Proton group	Ex in Si^{29} (Mev)	Deuteron energy (Mev, in Lab. system)			
		0.77	1.00	1.30	1.80*
P_0	0.00	1.0	1.0	1.0	1.0
P_1	1.28	3.6	1.7	1.4	1.4
P_2	2.03	2.0	1.0	1.8	1.2
P_3	2.43	2.5	0.7	1.3	0.8
P_4	3.07	3.4	1.2	2.3	0.5

* reference 5.

---

* Sakura 100 microns nuclear plates were supplied by the Chemical Research Laboratory of Konishi-Roku Photographic Industry.

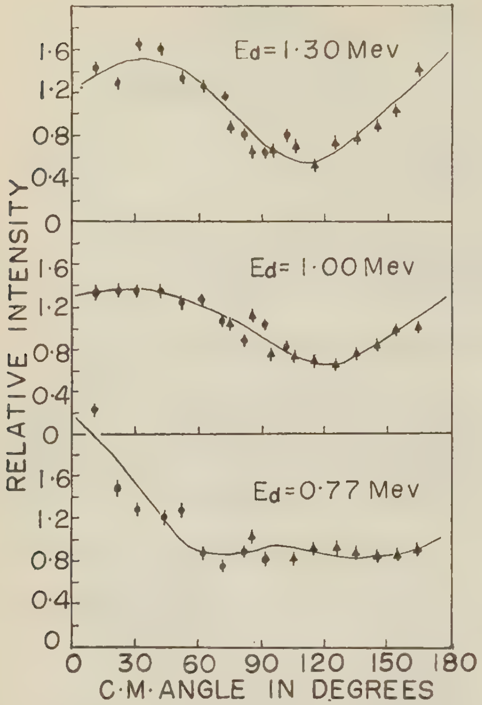

Fig. 2. Angular distributions of P_0 group from the reaction Si^{28} (d, p) Si^{29} at three bombarding energies (0.77-, 1.00- and 1.30-Mev). Solid curves are the expansion in terms of Legendre polynomials up to $P_4(\theta)$.

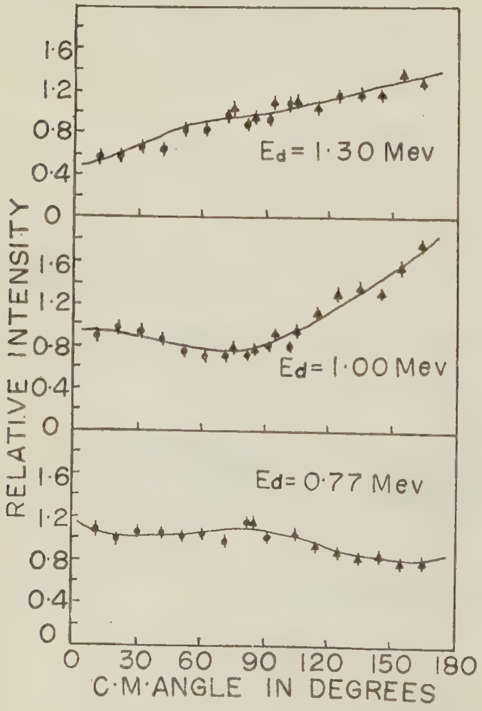

Fig. 3. Angular distributions of the P_1 group.

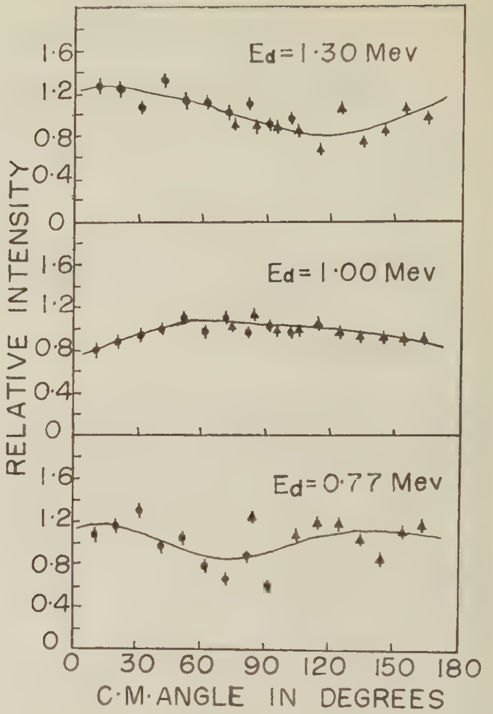

Fig. 4. Angular distributions of the P_2 group.

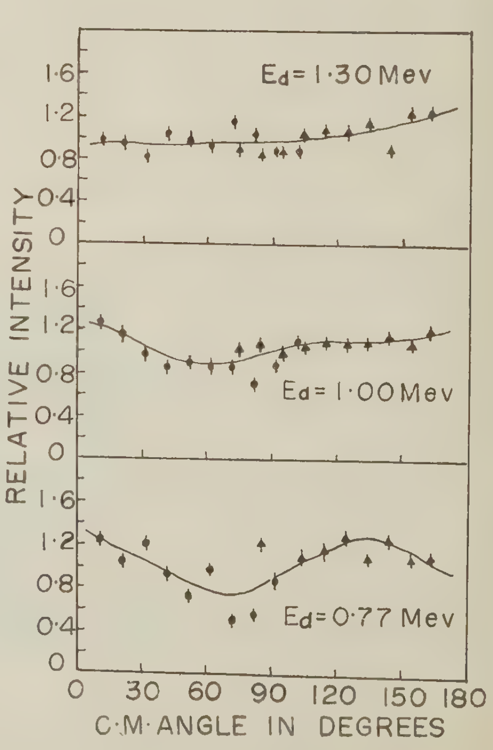

Fig. 5. Angular distributions of the P_3 group.

(Q=2.72 Mev) for carbon contamination deposited during the target preparation process and the running time. Although groups X_1 and X_2 is not undoubtedly assigned to any excited state in Si^{29}, one of them may be due to C^{13} (d, p) C^{14} (Q=5.94 Mev) and the other due to other contamination. Relative intensities of five assigned groups at $\theta_{lab}=90°$ are given in Table I, together with those reported by Van Patter and Buechner[5)].

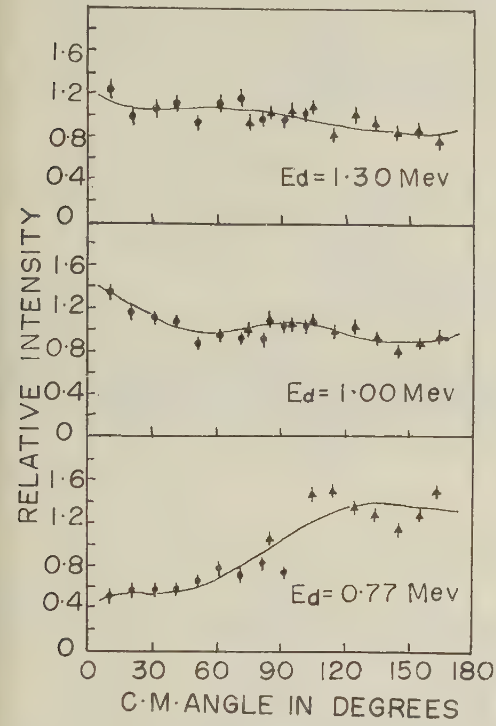

Fig. 6. Angular distributions of the P_4 group.

The angular distributions for each group are shown in Figs. 2, 3, 4, 5 and 6, for deuteron energies at 0.77-, 1.00- and 1.30-Mev. Distributions of all groups vary appreciably with deuteron energy, and the strong stripping effect in forward direction, which was revealed in the work of Holt and Marsham[1)] at $E_d=8$ Mev, is not observed in the present investigation at low bombarding energies. However, the distribution for P_3 is isotropic even at 8-Mev, and present results for that group is also nearly isotropic (Fig. 5). Cox and Williamson[2)] stated that, in energy region 1.3- to 3.0-Mev, although interference effects between stripping and compound nucleus formation process is present in the Si^{28} (d, p) Si^{29} excitation curve for P_0 group at $\theta_p=50°$, such effects in not seen at all at 0°. In our work excitation curves were not measured, but strong resonance effect is surely present not only for P_0, as seen from rapid variations of distribution patterns with deuteron energy.

All angular distributions were expanded

Table II. Coefficients in the expansion,

$$\sigma(E_d,\ \theta_{c.M.})1 \propto +\sum_{i=1}^{4} a_i(E_d)P_i(\theta_{c.M.}).$$

Proton group	Deuteron energy (Mev)	a_1	a_2	a_3	a_4
P_0	0.77	+0.27±0.05	+0.31±0.07	+0.28±0.08	+0.19±0.09
	1.00	+0.35±0.01	+0.19±0.02	−0.23±0.02	+0.04±0.02
	1.30	+0.39±0.03	+0.47±0.05	−0.37±0.05	−0.09±0.06
P_1	0.77	+0.12±0.01	−0.11±0.02	−0.01±0.02	+0.07±0.03
	1.00	−0.35±0.02	+0.34±0.03	−0.02±0.03	−0.01±0.04
	1.30	−0.31±0.02	−0.03±0.02	−0.08±0.03	−0.05±0.04
P_2	0.77	−0.05±0.04	+0.17±0.06	+0.13±0.07	−0.05±0.08
	1.00	+0.02±0.01	−0.12±0.02	−0.04±0.02	−0.05±0.02
	1.30	+0.21±0.03	+0.16±0.04	−0.13±0.05	+0.04±0.05
P_3	0.77	−0.16±0.04	+0.20±0.05	+0.30±0.06	−0.09±0.06
	1.00	−0.08±0.02	+0.11±0.02	+0.12±0.03	+0.07±0.03
	1.30	−0.11±0.03	+0.09±0.04	−0.04±0.04	+0.01±0.05
P_4	0.77	−0.53±0.05	−0.07±0.07	+0.17±0.07	+0.01±0.09
	1.00	+0.09±0.02	−0.01±0.02	+0.12±0.03	+0.15±0.03
	1.30	+0.12±0.03	−0.03±0.03	−0.01±0.04	+0.04±0.04

into series of Legendre polynomials of the C.M. angle, as

$$\sigma(\mathrm{E}_d,\ \theta_{C.M.})1 \propto + \sum_{i=1}^{4} a_i(\mathrm{E}_d)\mathrm{P}_i(\theta_{C.M.})\ ,$$

by means of the least square method. The expansion coefficients, a_i, are given in Table II. The presence of large odd terms exhibits strong interference effects between levels of opposite parity at excitation energy of about 12-Mev in the compound nucleus P^{30*}.

We have made the same experiments with Mg^{24}, and similar figures to those obtained in the present investigation have been obtained in this case also.

§ 4. Acknowledgment

To the authors' great regret, Mr. S. Ito, one of the collaborators, died in October, 1956, after having been transferred to the Institute for Nuclear Study, University of Tokyo.

It is pleasant to thank Prof. M. Kimura fo his helpful discussions and encouragements The authors wish also to thank Mr. Y. Wakabayashi of the Chemical Research Laborator of Konishi-Roku Photographic Industry fo his kind preparation of nuclear plates.

We are indebted to Miss N. Komatsu fo her co-operation in calculation.

References

1) J. R. Holt and T. M. Marsham; Proc. Phys Soc. (London) **A66** (1953) 467.
2) S. A. Cox and R. M. Williamson; Phys. Rev **105** (1957) 1799.
3) S. Takemoto et al; J. Phys. Soc. Japan **9** (1954 447.
4) P. M. Endt and J. C. Kluyver; Rev. Mod. Phys **26** (1954) 95, and see also reference 5.
5) D. M. Van Patter and W. W. Buechner; Phys Rev. **87** (1952) 51.

JOURNAL OF THE PHYSICAL SOCIETY OF JAPAN Vol. 12, No. 10, OCTOBER, 1957

Cluster Variation Method of Cooperative Phenomena and its Generalization II. Quantum Statistics

By Tohru MORITA

Physics Department, Tokyo Institute of Technology

(Received June 12, 1957)

The formulation of the cluster variation method of approximation for cooperative phenomena is generalized to the cases where the quantum statistics is to be taken into account. In this generalization, the nature of approximation becomes more obscure, but the quantum counterparts of the various approximations introduced in classical statistics are easily found.

The method in its lowest approximation—the point approximation—is applied to the lattice model of liquid helium proposed by Matsubara and Matsuda and found to lead to the same results as they obtained under the consideration of the analogy to an anisotropic spin system.

The formulation proposed by the present author in I[1] is translated word for word to the quantum statistical case. The equations in this paper are numbered with the same numbers as the corresponding classical equations in I[*].

The system to be considered in this pape is one which is characterized by the followin three conditions: 1) The configuration of th system is described by the configurations o L fixed points in it. 2) The possible configurations x_i for i-th point (i=1, 2,..., L) ar denoted by $\alpha_i, \beta_i, \ldots, \nu_i$. 3) The Hamiltonia of the system $\boldsymbol{H}$ is given by

---

[*] No quantum counterparts of classical equations (8) and (9′) in I, were found; so equations with these numbers will not appear in this paper.

$$\boldsymbol{H}=\sum_{i=1} H_i^{(1)}+\frac{1}{2}\sum_{\substack{i=1\\(i\neq j)}}^{L}\sum_{j=1}^{L} H_{ij}^{(2)}$$

$$+\frac{1}{3!}\sum_i\sum_j\sum_k H_{ijk}^{(3)}+\dots \tag{1}$$

which is explicitly expressed as

$$\boldsymbol{H}(x_1,\dots,x_L;\,x_1',\dots,x_L')=\sum_{i=1}^{L} H_i^{(1)}(x_i;\,x_i')$$

$$+\frac{1}{2}\sum_i\sum_j H_{ij}^{(2)}(x_i,\,x_j;\,x_i',\,x_j')$$

$$+\frac{1}{3!}\sum_i\sum_j\sum_k H_{ijk}^{(3)}(x_i,\,x_j,x_k;\,x_i',\,x_j',\,x_k')$$

$$+\dots \tag{1'}$$

in the representation where the configurations of the L points are diagonal*.

The problem in this paper is to calculate the free energy of the system abovementioned. The free energy is given by the minimum value of

$$F\equiv\mathrm{Tr}\,[\rho^{(L)}\cdot\boldsymbol{H}+kT\,\rho^{(L)}\cdot\ln\rho^{(L)}] \tag{2}$$

under the variation of the density matrix $\rho^{(L)}$ (elements of which are $\rho^{(L)}(x_1,\dots,x_L;\,x_1',\dots x_L')$), the variation being restricted by the normalization condition

$$\mathrm{Tr}\rho^{(L)}=\sum_{x_1=\alpha_1}^{\nu_1}\dots\sum_{x_L=\alpha_L}^{\nu_L}\rho^{(L)}(x_1,\dots,x_L;\,x_1,\dots,x_L)=1. \tag{3}$$

Likewise as in I, we introduce 2^L-1 clusters, a "cluster" meaning any set of points selected from the L fixed points. Then, we introduce two kinds of matrices and two kinds of functions connected with a cluster $(i_1,\dots,i_n)$: the reduced density matrix $\rho_{i_1,\dots,i_n}^{(n)}$ defined by

$$\rho_{i_1,\dots,i_n}^{(n)}(x_{i_1},\dots,x_{i_n};\,x_{i_1}',\dots,x_{i_n}')$$

$$=\sum_{x_1''=\alpha_1}^{\nu_1}\dots\sum_{x_L''=\alpha_L}^{\nu_L}\;\sum_{x_1'''=\alpha_1}^{\nu_1}\dots\sum_{x_L'''=\alpha_L}^{\nu_L}\;\prod_{s=1}^{n}\delta_{x_{i_s},\,x_{i_s}''}\;\delta_{x_{i_s}',\,x_{i_s}'''}\prod_{\substack{i=1\\(i\neq i_1,\dots,\,i_s)}}^{L}\delta_{x_i'',\,x_i'''}\;\rho^{(L)}(x_1'',\dots,x_L'';\,x_1''',\dots x_L'''), \tag{4}$$

the correlation matrix $g_{i_1,\dots,i_n}^{(n)}$ by

$$\rho_{ij}^{(2)}(x_i,\,x_j;\,x_i',\,x_j')=\rho_i^{(1)}(x_i;\,x_i')\rho_j^{(1)}(x_j;\,x_j')g_{ij}^{(2)}(x_i,\,x_j;\,x_i',\,x_j') \tag{5''}$$

$$\rho_{ijk}^{(3)}(x_i,\,x_j,\,x_k;\,x_i',\,x_j',\,x_k')=\rho_i^{(1)}(x_i;\,x_i')\,\rho_j^{(1)}(x_j;\,x_j')\,\rho_k^{(1)}(x_k;\,x_k')\,g_{ij}^{(2)}(x_i,\,x_j;\,x_i',\,x_j')$$

$$\times g_{jk}^{(2)}(x_j,\,x_k;\,x_j',\,x_k')\,g_{ik}^{(2)}(x_k,\,x_i;\,x_k',\,x_i')\,g_{ijk}^{(3)}(x_i,\,x_j,\,x_k;\,x_i',\,x_j',\,x_k') \tag{5'''}$$

. . . .

$$\rho_{1,\dots,L}^{(L)}(x_1,\dots,x_L;\,x_1',\dots x_L')=\prod_{i=1}^{L}\rho_i^{(1)}(x_i;\,x_i')\prod_{i>j}g_{ij}^{(2)}(x_i,\,x_j;\,x_i',\,x_j')$$

$$\times\prod g_{ijk}^{(3)}(x_i,\,x_j,\,x_k;\,x_i',\,x_j',\,x_k')\dots g_{1,\dots,L}^{(L)}(x_1,\dots,x_L;\,x_1',\dots,x_L'), \tag{5^L}$$

the function $G^{(n)}(i_1,\dots,i_n)$ defined by

$$\ln G^{(n)}(i_1,\dots,i_n)=-\mathrm{Tr}\,[\rho_{i_1,\dots,i_n}^{(n)}\ln\rho_{i_1,\dots,i_n}^{(n)}], \tag{6}$$

and the correlation function $F^{(n)}(i_1,\dots,i_n)$ by

$$G^{(2)}(i,\,j)=G^{(1)}(i)G^{(1)}(j)F^{(2)}(i,\,j) \tag{7''}$$

$$G^{(3)}(i,\,j,\,k)=G^{(1)}(i)G^{(1)}(j)G^{(1)}(k)F^{(2)}(i,\,j)F^{(2)}(j,\,k)F^{(2)}(k,\,i)F^{(3)}(i,\,j,\,k) \tag{7'''}$$

. . . .

$$G^{(L)}(1,\dots,L)=\prod_{i=1}^{L}G^{(1)}(i)\prod_{i>j}F^{(2)}(i,\,j)\prod F^{(3)}(i,\,j,\,k)\dots F^{(L)}(1,\dots,L). \tag{7^L}$$

By means of these functions, we rewrite Eq. (2) as

$$F=\sum_{i=1}^{L}\mathrm{Tr}\,[\rho_i^{(1)}\cdot H_i^{(1)}]+\frac{1}{2}\sum_{\substack{i=1\\(i\neq j)}}^{L}\sum_{j=1}^{L}\mathrm{Tr}\,[\rho_{ij}^{(2)}\cdot H_{ij}^{(2)}]+\frac{1}{3!}\sum_i\sum_j\sum_k\mathrm{Tr}\,[\rho_{ijk}^{(3)}\cdot H_{ijk}^{(3)}]+\dots$$

$$+kT\,[\sum_{i=1}^{L}\ln G^{(1)}(i)+\sum_{i>j}\ln F^{(2)}(i,\,j)+\sum\ln F^{(3)}(i,\,j,\,k)+\dots+\ln F^{(L)}(1,\dots,L)]. \tag{9}$$

The cluster variation method of approximation is as follows: We divide 2^L-1 clusters into two groups, “preserved clusters” and “not-preserved clusters”. We rewrite the right-hand side of Eq. (9) and express the first row in terms of the preserved $\rho^{(n)*}$ and the not-preserved $g^{(n)}$ with no preserved $g^{(n)}$ or not-preserved $\rho^{(n)}$ and the second row in terms of the preserved $G^{(n)}$ and the not-preserved $F^{(n)}$ with no preserved $F^{(n)}$ or not-preserved $G^{(n)}$. In the expression for F thus obtained, we equate $F^{(n)}$ and $g^{(n)}$ to 1, and substitute from (6) into preserved $G^{(n)}$. Then the function F is obtained in terms of the preserved $\rho^{(n)}$'s. Now we let this approximate expression for F take the minimum value with respect to the preserved $\rho^{(n)}$'s. In doing so we have to notice that there exist the recurrence relations

---

* In the following, this representation will be always used to express any matrix in explicit form.

$$\rho^{(s-1)}_{i_1,\ldots,i_{s-1}}(x_{i_1},\ldots,x_{i_{s-1}};x'_{i_1},\ldots,x'_{i_{s-1}})$$
$$=\sum_{x_{i_s}=\alpha_{i_s}}^{\nu_{i_s}}\cdots\sum_{x_{i_n}=\alpha_{i_n}}^{\nu_{i_n}}\rho^{(n)}_{i_1,\ldots,i_n}(x_{i_1},\ldots,x_{i_{s-1}},x_{i_s},\ldots,x_{i_n};x'_{i_1},\ldots,x'_{i_{s-1}},x_{i_s},\ldots,x_{i_n}) \qquad (10)$$

between two preserved $\rho^{(s-1)}$ and $\rho^{(n)}$ and the normalization conditions

$$\mathrm{Tr}\,\rho^{(n)}_{i_1,\ldots,i_n}=\sum_{x_{i_1}=\alpha_{i_1}}^{\nu_{i_1}}\cdots\sum_{x_{i_n}=\alpha_{i_n}}^{\nu_{i_n}}\rho^{(n)}_{i_1,\ldots,i_n}(x_{i_1},\ldots,x_{i_n};x_{i_1},\ldots,x_{i_n})=1 \qquad (11)$$

for the preserved $\rho^{(n)}$'s. The minimum value obtained can be considered to be an approximate value to the exact free energy.

Which clusters are to be preserved must be decided from physical considerations. The approximation will generally be improved as larger and more clusters are preserved. The lowest approximation of the method is “the point approximation”, where L clusters of one point are preserved. This corresponds to the Bragg-Williams approximation in classical statistics. To the Bethe-Fowler approximation corresponds “the point pair approximation”, where $L(L-1)/2$ clusters of pair of points are preserved. And so on.

Application to a Lattice Model of Liquid Helium

In the following, the method in the point approximation is applied to the lattice model of liquid helium proposed by Matsubara and Matsuda[2)].

The system they took up as the model for liquid helium is characterized by that: 1) The configuration of the system is described by the configurations of L fixed points, which constitute a simple cubic lattice with lattice constant d in the coordinate space of the system. 2) The possible configurations of any point are “a particle is present at the point—present” and “no particle is at the point—absent”. 3) The Hamiltonian of the system is

$$\boldsymbol{H}=\frac{\hbar^2}{2md^2}\sum_{\langle ij\rangle}(a_i^*-a_j^*)(a_i-a_j)$$
$$-v_0\sum_{\langle ij\rangle}a_i^*a_ia_j^*a_j \qquad (\mathrm{A1})^*$$

where the summations are taken over nearest neighbor lattice site pairs, and a_i^* and a_i are

$$a_i^*=\begin{array}{c|cc} & \text{p. at i} & \text{a. at i}\\ \hline \text{p. at i} & 0 & 1\\ \text{a. at i} & 0 & 0\end{array},$$
$$a_i=\begin{array}{c|cc} & \text{p. at i} & \text{a. at i}\\ \hline \text{p. at i} & 0 & 0\\ \text{a. at i} & 1 & 0\end{array} \qquad (\mathrm{A2})$$

in the representation where the configurations of the L points are diagonal; either of a_i^* and a_i and either of a_j^* and a_j being commutative when $i\neq j$.

We apply the point approximation to this system, then the function F is to be written in terms of $\rho_i^{(1)}$. In the fluid, the point reduced density matrices $\rho_i^{(1)}$'s are equal for all of the lattice points, i's, which we write as

$$\rho^{(1)}=\begin{array}{c|cc} & \mathrm{p} & \mathrm{a}\\ \hline \mathrm{p} & \rho & \xi\\ \mathrm{a} & \xi & 1-\rho\end{array}, \qquad (\mathrm{A3})$$

where $\rho=N/L$, N being the number of particles in the system, and ξ is the parameter which is determined by minimizing F. (This ξ is found to be identified to ξ introduced in the theory of Matsubara and Matsuda.) To find the entropy term in F, we need the eigenvalues of $\rho^{(1)}$ which are

---

* The terminology, preserved $\rho^{(n)}$, not-preserved $g^{(n)}$, etc., follows that introduced in I.

* $\hbar^2/m$ and v_0 are constants characteristic to the system under consideration.

$$\frac{1}{2}(1\pm\sqrt{(1-2\rho)^2+4\xi^2})\ . \tag{A4}$$

In the point approximation,

$$\begin{aligned}\frac{F}{LkT}=&\frac{6\hbar^2}{4md^2kT}(2\rho-2\xi^2)-\frac{\rho^2}{2kT}\cdot 6v_0\\&+\frac{1}{2}(1+\sqrt{(1-2\rho)^2+4\xi^2})\\&\times\ln\frac{1}{2}(1+\sqrt{(1-2\rho)^2+4\xi^2})\\&+\frac{1}{2}(1-\sqrt{(1-2\rho)^2+4\xi^2})\\&\times\ln\frac{1}{2}(1-\sqrt{(1-2\rho)^2+4\xi^2})\ .\end{aligned}\tag{A5}$$

The condition determining ξ is $0=\partial/\partial\xi^2\cdot F/LkT$ which reduces to

$$\begin{aligned}\frac{3\hbar^2}{md^2kT}=&\frac{1}{\sqrt{(1-2\rho)^2+4\xi^2}}\\&\times\Big[\ln\frac{1}{2}(1+\sqrt{(1-2\rho)^2+4\xi^2})\\&-\ln\frac{1}{2}(1-\sqrt{(1-2\rho)^2+4\xi^2})\Big]\end{aligned}\tag{A6}$$

which can be rewritten as

$$\begin{aligned}\tanh&\left[\frac{T_0}{T}\sqrt{(1-2\rho)^2+4\xi^2}\right]\\&=\sqrt{(1-2\rho)^2+4\xi^2}\end{aligned}\tag{A6$'$}$$

where $kT_0=3\hbar^2/2md^2$. The last is the equation (28) with (30) and (18) in Matsubara and Matsuda's paper. When T is large, this equation has no solution, where the minimum of F corresponds to $\xi^2=0$. The transition line, T_c—ρ_c, between these regions is given by

$$\tanh\left[\frac{T_0}{T_c}|1-2\rho_c|\right]=|1-2\rho_c|\ . \tag{A7}$$

The free energy of the system is given by Eq. (A 5), when ξ^2 is determined by Eq. (A 6) at lower temperature than T_c and equated to zero at higher temperature. The thermodynamical quantities will be obtained from this free energy.

The identity of the results of this calculation to those of Matsubara and Matsuda, is convinced by confirming from their results that their

$$f_L+\rho\mu=\left(f-\frac{1}{N\beta}\ln C\right)+\rho\mu \tag{A8}$$

is coincident to our free energy, F/L from Eq. (A 5) with (A 6) or $\xi^2=0$ (cf. Eq. (16) of ref. 2).

The author wishes to express his cordial thanks to Prof. A. Harasima and Dr. K. Hiroike for the former's continual guidance and the latter's suggestive discussions and also for their kind inspection of the manuscript.

References

1) T. Morita: J. Phys. Soc. Japan **12** (1957) 753. This paper will be referred to as **I**.
2) T. Matsubara and H. Matsuda: Prog. Theor. Phys. **16** (1956) 569.

JOURNAL OF THE PHYSICAL SOCIETY OF JAPAN Vol. 12, No. 10, OCTOBER, 1957

The Input Power Limit of the Cylindrical Rotating Anode of a X-ray Tube

By Tsutomu ISHIMURA, Toshio SHIRAIWA and Masao SAWADA

Department of Physics, Faculty of Science, Osaka University

(Received March 18, 1957)

The permissible maximum input power of the cylindrical anode of a continuous operating X-ray tube was calculated. Calculation was done for the cyclic dynamical steady state which was realized after sufficiently long continuous operation. This thermal problem was treated by DuMond as a one-dimensional problem in which heat flow was normal to the surface of the target. In our case a focus of an electron beam was a line focus and the width was small compared with the thickness of the target and the problem was treated as a two-dimensional problem containing transversal thermal flow.

§ 1. Introduction

The temperature of a rotating anode or a mobile focal spot on stationary target of an X-ray tube was calculated by many authors, who treated mainly the problem in which the input power was applied for a very brief time. In the case of a continuously operated mobile focal spot, a rough estimation has been done by Oosterkamp[1] and a exact theoretical analysis by the dynamically steady cyclic thermal state has been made by DuMond.[2] He treated this thermal problem as a one-dimensional problem. His assumption was that the flow of heat was straight back normally from the target surface to the inner surface cooled by water without any lateral spreading of the heat. This is the approximation in the case of the larger dimensions of a focal spot compared with the thickness of the target. For a small focal spot compared with the thickness of the target, the deviation from his calculation increases. In the case of a rotating anode X-ray tube which planned in our laboratory, the thickness of the target was the order of 1 mm and the width of a focal line was the order of 1/10 mm, so that we had to consider the transversal flow of heat. This paper is the result of our calculation for a rotating cylindrical target, in which DuMond's treatment is extended into the two-dimensional problem.

§ 2. Statement of Thermal Problem

The target has a cylindrical form of the constant thickness, d, and it is rotated around the axis of the cylinder of which radius, k, is large compared with the thickness. The inner surface of the target is cooled by water and the temperature on the inner surface is assumed as constant T_0 (Fig. 1). A focus of an electron beam on the target is a line shape focus along the generatrix of the cylinder. The length of the focal line is sufficiently large compared with the width, b, and we can treat the thermal problem as a two-dimensional problem, in which we consider the longitudinal flow normal to the surface and the transversal flow normal to the generatrix.

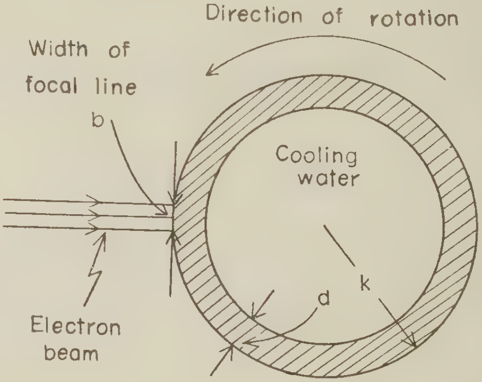

Fig. 1. Diagram of a target.

Instead of the rotating anode and the stationary electron beam, we suppose that the anode is fixed and the focal line moves on the surface of the anode. As the thickness of the target is sufficiently small compared with to the radius, we can assume that the surface of the target is a plane normal to the electron beam. We shall further assume that the input power per unit area, value, w, is uniform over the focal area, that is, the small area of the target surface will receive heat at the surface rate, w, for τ_1 seconds and will be left for τ_2 seconds. τ_1 and τ_2 is (Fig. 2)

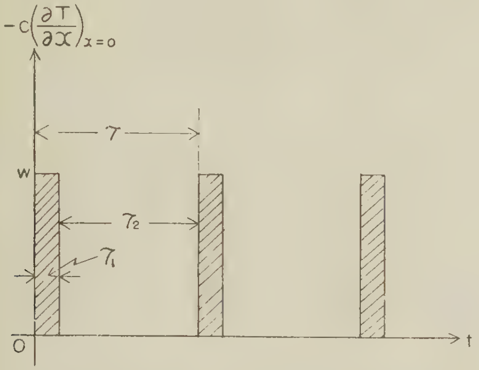

Fig. 2. Illustrating heat input on an element of the target surface as a function of time.

$$\tau_1=\frac{1}{n}\times\frac{b}{2\pi k},\quad \tau_2=\tau-\tau_1,\quad \tau=\frac{1}{n},$$

where n is the number of rotations of the target per second. In the present paper the same nomenclature used by DuMond are adopted for the convenience of reference. (Table I)

Table I. Nomenclature.

ρ	mass density of target material
c	heat conductivity of target material
σ	heat capacity of target material per unit mass
w	watts input per unit area in the focal area
d	thickness of target from face to cooling water
b	width of the focal line
k	radius of target
n	the number of rotations per second of target
τ	period of a rotation
τ_1	heating time in a rotation
r	τ_1/τ
v	velocity of a point on target surface

§ 3. Thermal Equation and Solution

Thermal equation: We take the x-axis along the normal of the surface of the target and y-axis along the normal of the generatrix on the surface of the target that indicated in Fig. 3.

The equation of the thermal flow is

$$\frac{\partial^2 T}{\partial x^2}+\frac{\partial^2 T}{\partial y^2}=\frac{\rho\sigma}{c}\frac{\partial T}{\partial t} \tag{1}$$

where ρ is the density, c is the heat conductivity and σ is the heat capacity per unit mass of the target material.

We shall confine the problem to the stationary state in which the temperature is a periodic function of τ. This dynamically steady cyclic thermal state will be established after a sufficiently long time in the continuous operation. An input beam moves along the y-axis with the constant speed, v, where $v=2\pi kn$ and we can put

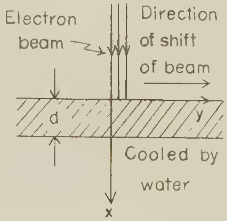

Fig. 3. A part of the target is represented by shaded area and instead of a rotating target and stationary electron beam we assume the focal area moves on the stationary target surface.

$$T(x,\,y,\,t)=T(x,\,o,\,t-y/v).$$

Let

$$t-\frac{y}{v}=u\,,$$

then equation (1) becomes

$$\frac{\partial^2 T}{\partial x^2}+\frac{1}{v^2}\frac{\partial^2 T}{\partial u^2}=\frac{\rho\sigma}{c}\frac{\partial T}{\partial u} \tag{2}$$

Boundary condition: For boundary conditions we obtain

$$T=T_0 \qquad \text{at} \qquad x=d \tag{3}$$

$$-c\left(\frac{\partial T}{\partial x}\right)_{x=0}=\begin{cases} w \text{ for interval } \tau_1 \\ 0 \text{ for interval } \tau_2 \end{cases} \text{at } x=0. \tag{4}$$

Solution of the equation: The particular solutions of eq. (2) are

$$T=T_c-gx$$
$$\left.\begin{aligned} T&=e^{-\alpha x}\sin(2\pi nu-\beta x)\\ T&=e^{-\alpha x}\cos(2\pi nu-\beta x)\end{aligned}\right\}$$
$$\text{or } T=e^{-(\alpha+i\beta)}\,xe^{i2\pi nu}$$

where

$$\alpha=a\alpha',\quad \beta=a\beta',\quad a=\pm(\pi n\rho\sigma/c)^{1/2},$$

$$\alpha'=\left\{\sqrt{1+\frac{4\pi^2c^2n^2}{v^4\rho^2\sigma^2}}+\frac{2\pi cn}{v^2\rho\sigma}\right\}^{1/2},$$

$$\beta'=\left\{\sqrt{1+\frac{4\pi^2c^2n^2}{v^4\rho^2\sigma^2}}-\frac{2\pi cn}{v^2\rho\sigma}\right\}^{1/2}.$$

The most general solution for the state of steady thermal oscillation is the sum of the particular solutions multiplied by constant coefficients, then

$$\begin{aligned} T = T_c - gx &+ \sum_{s=1}^{\infty} A_s \exp(-\alpha_s x)\sin(2\pi n_s u - \beta_s x) \\ &+ \sum_{s=1}^{\infty} B_s \exp(-\alpha_s x)\cos(2\pi n_s u - \beta_s x) \\ &+ \sum_{s=1}^{\infty} C_s \exp(\alpha_s x)\sin(2\pi n_s u + \beta_s x) \\ &+ \sum_{s=1}^{\infty} D_s \exp(\alpha_s x)\cos(2\pi n_s u + \beta_s x). \end{aligned} \tag{5}$$

In this solution s takes only integer values from 1 to infinity and expressed as $n_s = ns$ from periodicity.

Our problem consists in evaluating A_s, B_s, C_s, D_s and g so as to fit the expression (5) to the boundary conditions (3) and (4). From condition (4) we obtain

$$g = wr/c\ , \tag{6}$$

$$\alpha_s' A_s - \beta_s' B_s - \alpha_s' C_s + \beta_s' D_s = \frac{w}{\pi c s a_s}\{1 - \cos(2\pi s r)\}\ , \tag{7}$$

$$\beta_s' A_s + \alpha_s' B_s - \beta_s' C_s - \alpha_s' D_s = \frac{w}{\pi c s a_s}\sin(2\pi s r)\ , \tag{8}$$

and from condition (3)

$$T_c = T_0 + \frac{wr}{c}d\ , \tag{9}$$

$$\begin{aligned} A_s \exp.(-\alpha_s d)\cos\beta_s d &+ B_s \exp(-\alpha_s d)\sin\beta_s d \\ &+ C_s \exp(\alpha_s d)\cos\beta_s d \\ &- D_s \exp(\alpha_s d)\sin\beta_s d = 0\ , \end{aligned} \tag{10}$$

$$\begin{aligned} -A_s \exp(-\alpha_s d)\sin\beta_s d &+ B_s \exp(-\alpha_s d)\cos\beta_s d \\ &+ C_s \exp(\alpha_s d)\sin\beta_s d \\ &+ D_s \exp(\alpha_s d)\cos\beta_s d = 0\ . \end{aligned} \tag{11}$$

From eq. (7) and (8)

$$A_s - C_s = \frac{w}{2\pi c s a_s} \times \left\{ \frac{2\alpha_s'}{\alpha_s'^2 + \beta_s'^2}(1 - \cos 2\pi s r) + \frac{2\beta_s'}{\alpha_s'^2 + \beta_s'^2}\sin 2\pi s r \right\} \equiv P_s'\ , \tag{12}$$

$$D_s - B_s = \frac{w}{2\pi c s a_s} \times \left\{ \frac{2\beta_s'}{\alpha_s'^2 + \beta_s'^2}(1 - \cos 2\pi s r) - \frac{2\alpha_s'}{\alpha_s'^2 + \beta_s'^2}\sin 2\pi s r \right\} \equiv Q_s'\ , \tag{13}$$

and from eq. (10), (11), (12) and (13), we obtain

$$A_s + C_s = \frac{P_s' \sinh\alpha_s d \cosh\alpha_s d + Q_s' \sin\beta_s d \cos\beta_s d}{\cos^2\beta_s d + \sinh^2\alpha_s d}\ , \tag{14}$$

$$D_s + B_s = \frac{P_s' \sin\beta_s d \cos\beta_s d - Q_s' \sinh\alpha_s d \cosh\alpha_s d}{\cos^2\beta_s d + \sinh^2\alpha_s d}\ , \tag{15}$$

where

$$\begin{aligned} &\alpha_s = a_s\alpha_s', \quad \beta_s = a_s\beta_s', \quad a_s = (\pi\rho\sigma/c)^{1/2}(sn)^{1/2}, \\ &\alpha_s' = \left\{ \sqrt{1 + \frac{4\pi^2 c^2 n^2 s^2}{v^4\rho^2\sigma^2}} + \frac{2\pi c n s}{v^2\rho\sigma} \right\}^{1/2} \\ &\beta_s' = \left\{ \sqrt{1 + \frac{4\pi^2 c^2 n^2 s^2}{v^4\rho^2\sigma^2}} - \frac{2\pi c n s}{v^2\rho\sigma} \right\}^{1/2} \end{aligned} \tag{16}$$

The calculation of the temperature at every point and every time from above solution is very complicated, then we choose the point of the surface at $x=0$ and at the time of the end of a heating period, that is at $u = \tau_1$, of which temperature T_m is considered nearly the maximum temperature of the target. T_m is expressed as follows

$$\begin{aligned} T_m &= T_c + \sum_{s=1}^{\infty}(A_s + C_s)\sin 2\pi s r + \sum_{s=1}^{\infty}(D_s + B_s)\cos 2\pi s r \\ &= T_0 + \frac{wr}{c}d + \frac{w}{2\pi c}\sum_{s=1}^{\infty}\frac{1}{s a_s}\,\frac{p_s' \sinh\alpha_s d \cosh\alpha_s d - q_s' \sin\beta_s d \cos\beta_s d}{\cos^2\beta_s d + \sinh^2\alpha_s d}\ , \end{aligned} \tag{17}$$

where

$$\begin{aligned} p_s' &= \left[\frac{2\alpha_s'}{\alpha_s'^2 + \beta_s'^2}(1 - \cos 2\pi s r) + \frac{2\beta_s'}{\alpha_s'^2 + \beta_s'^2}\sin 2\pi s r \right]\sin 2\pi s r \\ &\quad - \left[\frac{2\beta_s'}{\alpha_s'^2 + \beta_s'^2}(1 - \cos 2\pi s r) - \frac{2\alpha_s'}{\alpha_s'^2 + \beta_s'^2}\sin 2\pi s r \right]\cos 2\pi s r \\ &= \frac{2\alpha_s'}{\alpha_s'^2 + \beta_s'^2}\sin 2\pi s r + \frac{2\beta_s'}{\alpha_s'^2 + \beta_s'^2}(1 - \cos 2\pi s r)\ , \end{aligned}$$

$$q_s'=-\left[\frac{2\beta_s'}{\alpha_s'^2+\beta_s'^2}(1-\cos 2\pi sr)-\frac{2\alpha_s'}{\alpha_s'^2+\beta_s'^2}\sin 2\pi sr\right]\sin 2\pi sr$$

$$-\left[\frac{2\alpha_s'}{\alpha_s'^2+\beta_s'^2}(1-\cos 2\pi sr)+\frac{2\beta_s'}{\alpha_s'^2+\beta_s'^2}\sin 2\pi sr\right]\cos 2\pi sr$$

$$=\frac{2\alpha_s'}{\alpha_s'^2+\beta_s'^2}(1-\cos 2\pi sr)-\frac{2\beta_s'}{\alpha_s'^2+\beta_s'^2}\sin 2\pi sr\ .$$

We put

$$\theta=d(\pi\rho\sigma/c)^{1/2}n^{1/2}\ ,\qquad \theta_s=\theta\cdot s^{1/2}$$

$$a_s d=\theta_s=\frac{\theta_s'}{2}\ ,\qquad \alpha_s d=\alpha_s'\theta_s=\varphi_s=\frac{\varphi_s'}{2}\ ,\qquad \beta_s d=\beta_s'\theta_s=\psi_s=\frac{\psi_s'}{2}\ ,$$

then we get

$$T_m=T_0+\frac{wr}{c}d+\frac{wd}{\pi c}\sum_{s=1}^{\infty}\frac{1}{s\theta_s'}\frac{p_s'\sinh\varphi_s'-q_s'\sin\psi_s'}{\cosh\varphi_s'+\cos\psi_s'}\ . \tag{18}$$

Now let

$$X=\sum_{s=1}^{\infty}\frac{1}{s\theta_s'}\frac{p_s'\sinh\varphi_s'-q'_s\sin\psi_s'}{\cosh\varphi_s'+\cos\psi_s'}$$

$$=\sum_{s=1}^{\infty}\frac{F_-}{s\theta_s'}-\sum_{s=1}^{\infty}\frac{F_-}{s\theta_s'}\cos 2\pi sr+\sum_{s=1}^{\infty}\frac{F_+}{s\theta_s'}\sin 2\pi sr\ , \tag{19}$$

where

$$F_+=\frac{m_1\sinh\varphi_s'+m_2\sin\psi_s'}{\cosh\varphi_s'+\cos\psi_s'}\ ,$$

$$F_-=\frac{m_2\sinh\varphi_s'-m_1\sin\psi_s'}{\cosh\varphi_s'+\cos\psi_s'}\ , \tag{20}$$

$$m_1=\frac{2\alpha_s'}{\alpha_s'^2+\beta_s'^2}\quad\text{and}\quad m_2=\frac{2\beta_s'}{\alpha_s'^2+\beta_s'^2}$$

we obtain

$$T_m=T_0+\frac{wr}{c}d+\frac{wd}{\pi c}X \tag{21}$$

If the number of rotations, n, is infinite, that is, the input energy is distributed uniformly over the target surface,

$$T_m=T_0+\frac{w}{c}rd$$

so wdX/c is the temperature increase due to the finite shape of the focus or finite number of rotations.

Now, we proceed to the calculation of X-function (19). For this purpose we explain the properties of functions which are included in X-function.

α_s', β_s', m_1, and m_2 functions: These are functions of s and we put

$$\xi_s=\frac{2\pi cn}{v^2\rho\sigma}s=\frac{1}{2\pi nk^2}\frac{c}{\rho\sigma}s\ , \tag{22}$$

then

$$\alpha_s'=\sqrt{\sqrt{1+\xi_s^2}+\xi_s}\ ,\qquad \beta_s'=\sqrt{\sqrt{1+\xi_s^2}-\xi_s}\ ,$$

$$m_1=\frac{\sqrt{\sqrt{1+\xi_s^2}+\xi_s}}{\sqrt{1+\xi_s^2}}\quad\text{and}\quad m_2=\frac{\sqrt{\sqrt{1+\xi_s^2}-\xi_s}}{\sqrt{1+\xi_s^2}}\ .$$

When ξ_s tends to 0, α_s', β_s', m_1, and m_2 converge to 1. More precisely when $\xi_s\leq 0.002$, α_s', β_s', m_1, and m_2 are between $1-0.01$ and $1+0.01$. When ξ_s tends to $+\infty$, α_s' diverges to $+\infty$, and β_s', m_1 and m_2 converge to 0. Especially for m_1 and m_2, we obtain following expression,

$$m_1=\frac{1}{\sqrt{\xi_s}}\sqrt{\frac{\sqrt{1+1/\xi_s^2}+1}{1+1/\xi_s^2}}$$

$$\to\sqrt{\frac{2}{\xi_s}}\qquad(\text{for }\xi_s\to+\infty)\ ,$$

and if $\xi_s>5$, the error which is caused by substituting $\sqrt{2/\xi_s}$ for m_1 is smaller than 0.01. And

$$m_2=\frac{1}{\sqrt{\xi_s}}\sqrt{\frac{\sqrt{1+1/\xi_s^2}-1}{1+1/\xi_s^2}}$$

$$\to\frac{1}{\sqrt{2\xi_s^3}}\qquad(\text{for }\xi_s\to+\infty)$$

and if $\xi_s>3.5$, the error which is caused by substituting $1/\sqrt{2\xi_s^3}$ for m_2 is smaller than 0.01. These approximation formulae are utilized to calculate F-functions. The graphical forms of α_s', β_s', m_1 and m_2 functions are given in Fig. 4.

F-functions (20): For convenience, we put $\mu=8\pi^2d^2k^2\rho^2\sigma^2/c^2$, for example, in the case of a copper anode, whose radius 5 cm, the thickness 0.3 cm and number of rotations is 20 sec^{-1}, the value of μ is 7.1×10^4. As $\xi_s=\theta_s'^2/\mu$, if $\mu \gtrsim 10^4$, the value of α_s', β_s', m_1 and m_2 are approximately 1 within errors of 1% for the value $\xi_s \leq 0.02$. In this region,

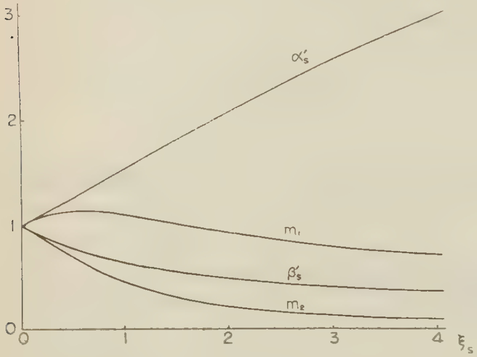

Fig. 4. Illustrating the behavior of functions α_s', β_s', m_1 and m_2 as functions of ξ_s.

$$F_+(\theta_s')=\frac{\sinh\theta_s'+\sin\theta_s'}{\cosh\theta_s'+\cos\theta_s'},$$

$$F_-(\theta_s')=\frac{\sinh\theta_s'-\sin\theta_s'}{\cosh\theta_s'+\cos\theta_s'},$$

and these are coincident with DuMond's formulae. Furthermore, when $\theta_s'>2\pi$, each function is approximated with 1, because in this region hyperbolic functions are larger than circular functions and two hyperbolic functions are almost equal.

In the case of $\xi_s>0.02$, they have following expressions,

$$F_+=m_1(\xi_s) \qquad \text{and} \qquad F_-=m_2(\xi_s)$$

and from the properties of m_1 and m_2, each F_+ and F_- has two appoximation formulae corresponding to the two regions of ξ_s, i.e. $0.02<\xi_s\leq5$ and $\xi_s>5$.

Conclusively, we obtain four expressions of F-functions corresponding to the four regions of ξ_s for $\mu \gtrsim 10000$.

(i) $$F_+^{(1)}(\theta_s')=\frac{\sinh\theta_s'+\sin\theta_s'}{\cosh\theta_s'+\cos\theta_s'},$$

$$F_-^{(1)}(\theta_s')=\frac{\sinh\theta_s'-\sin\theta_s'}{\cosh\theta_s'+\cos\theta_s'},$$

$$\left(\text{for } \theta_s'^2\leq4\pi^2 \text{ or } s\leq\frac{\pi^2}{\theta^2}\right) \tag{23}$$

(ii) $$F_+^{(2)}=F_-^{(2)}=1,$$

$$\left(\text{for } 4\pi^2<\theta_s'^2\leq0.02\,\mu \text{ or } \frac{\pi^2}{\theta^2}<s\leq\frac{0.005}{\theta^2}\,\mu\right) \tag{24}$$

(iii) $$F_+^{(3)}=\frac{\sqrt{\sqrt{1+\xi_s^2}+\xi_s}}{\sqrt{1+\xi_s^2}},$$

$$F_-^{(3)}=\frac{\sqrt{\sqrt{1+\xi_s^2}-\xi_s}}{\sqrt{1+\xi_s^2}},$$

$$\left(\text{for } 0.02<\xi_s\leq5 \text{ or } \frac{0.005}{\theta^2}\,\mu<s\leq\frac{5}{4\theta^2}\,\mu\right) \tag{25}$$

(iv) $$F_+^{(4)}=\sqrt{\frac{2}{\xi_s}},$$

$$F_-^{(4)}=\frac{1}{\sqrt{2\xi_s^3}}.$$

$$\left(\text{for } \xi_s>5 \text{ or } s>\frac{5}{4\theta^2}\,\mu\right) \tag{26}$$

We calculated numerically the functions $F_+^{(1)}$, $F_-^{(1)}$, $F_+^{(3)}$ and $F_-^{(3)}$ and the graphical forms of F-functions are given in fig. 5 (a), (b) and (c).

X-function: When the condition $\mu \geq 10000$ is fulfiled, X-function can be expressed with

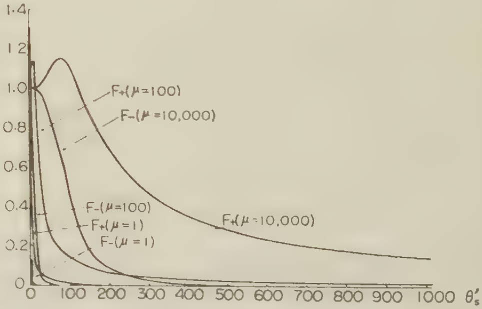

Fig. 5 (*a*). Illustrating the behavior of functions F_+ and F_- for several μ values and range of θ_s' from 0 to 1000.

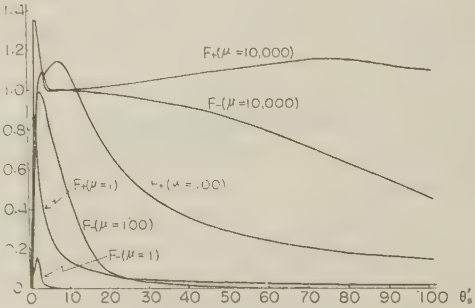

Fig. 5 (*b*). Illustrating the behavior of functions F_+ and F_- for several μ values and range of θ_s' from 0 to 100.

the next form from the properties of F-functions,

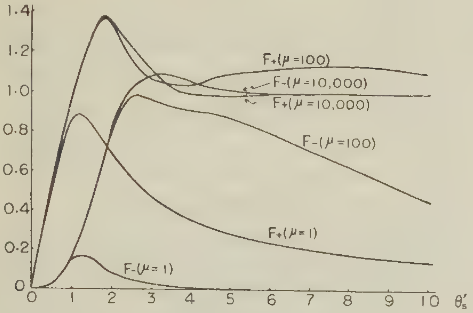

Fig. 5 (*c*). Illustrating the behavior of functions F_+ and F_- for several μ values and range of θ'_s from 0 to 10.

$$
\begin{aligned}
X=&\left\{\Sigma\frac{F_+{}^{(1)}}{s\theta_s'}\sin 2\pi sr+\Sigma\frac{F_-{}^{(1)}}{s\theta_s'}(1-\cos 2\pi sr)\right\}\\
&+\left\{\Sigma\frac{F_+{}^{(2)}}{s\theta_s'}\sin 2\pi sr+\Sigma\frac{F_-{}^{(2)}}{s\theta_s'}(1-\cos 2\pi sr)\right\}\\
&+\left\{\Sigma\frac{F_+{}^{(3)}}{s\theta_s'}\sin 2\pi sr+\Sigma\frac{F_-{}^{(3)}}{s\theta_s'}(1-\cos 2\pi sr)\right\}\\
&+\left\{\Sigma\frac{F_+{}^{(4)}}{s\theta_s'}\sin 2\pi sr+\Sigma\frac{F_-{}^{(4)}}{s\theta_s'}(1-\cos 2\pi sr)\right\}.
\end{aligned}
\tag{27}
$$

From this expression, when $r \ll 1$, $\sin 2\pi sr$ and 1–$\cos 2\pi sr$ in the first blacket are so small that the influence of the other terms are comparatively large and X cannot be approximated by the sum of finite terms of the beginning of the series. So we adopt the next method where $r \ll 1$ is assumed, that is, following calculations are allowable under the condition $r=1/1000$ or small.

Except the region where $s \leq \pi^2\theta^2$, F-functions change very slowly with the change of s, and $\sin 2\pi sr$ and 1–$\cos 2\pi sr$ also change very slowly. Regarding $1/s\theta_s'$ it changes rapidly with the change of s in the region of small s, but in the case where s reaches at 50, the change is only a few percent for a unit change of s. So, in the region of $s > 50$, we can substitute an integral for the summation. In the region of $s < 50$, each term is numerically calculated and summed. Usually the latter region include the first, the second and some of the third bracket in the expression (27). The integrals in the former region, usually including the fourth and some of the third bracket are calculated as follows.

For the third term,

$$
\begin{aligned}
&\Sigma\frac{F_+{}^{(3)}}{s\theta_s'}\sin 2\pi sr+\Sigma\frac{F_-{}^{(3)}}{s\theta_s'}(1-\cos 2\pi sr)\\
&=\frac{1}{\sqrt{\mu}}\int_a^5\frac{1}{\xi_s\sqrt{\xi_s}}\left\{F_+{}^{(3)}(\xi_s)\sin 2\pi\frac{\mu r}{4\theta^2}\xi_s\right.\\
&\qquad\left.+F_-{}^{(3)}(\xi_s)\left(1-\cos 2\pi\frac{\mu r}{4\theta^2}\xi_s\right)\right\}d\xi_s\,,
\end{aligned}
\tag{28}
$$

where a is the value of ξ_s corresponding to the value of $s=51$. For the fourth term

$$
\begin{aligned}
&\Sigma\frac{F_+{}^{(4)}}{s\theta_s'}\sin 2\pi sr+\Sigma\frac{F_-{}^{(4)}}{s\theta_s'}(1-\cos 2\pi sr)\\
&=\sqrt{\frac{2}{\mu}}\int_5^\infty\frac{1}{\xi_s{}^2}\sin 2\pi\frac{\mu r}{4\theta^2}\xi_s\cdot d\xi_s\\
&\qquad+\frac{1}{\sqrt{2\mu}}\int_5^\infty\frac{1}{\xi_s{}^3}\left(1-\cos 2\pi\frac{\mu r}{4\theta^2}\xi_s\right)d\xi_s
\end{aligned}
\tag{29}
$$

Above method of calculation is restricted only in the region where $\mu \gtrsim 10000$ and $r \leq 1/1000$.

§ 4. Application to Actual Problems

In § 3 we have given the method of calculation of X-function. In this paragraph we describe a few examples of calculations, which are limited to the tube which has a copper anode and dimensions given in Table II.

Table II. Dimensions of the target and other conditions ofa X-ray tube to which calculation was applied.

No.	k(cm)	d(cm)	n(sec⁻)	b(cm)	r
1	2	0.3	20	0.013	1/1000
2	5	0.3	20	0.031	1/1000

Table III. Numerical values of parameters.

No.	θ	θ^2	$\sqrt{\mu}$	μ	π^2/θ^2	$4\theta^2/\mu(\times 10^3)$	$4\theta^2$
1	2.38	5.66	106.6	11370	1.75	1.99	22.6
2	2.38	5.66	266.6	71062	1.75	0.318	22.6

From these numerical values, we calculated necessary parameters which are given in Table III. From these values the summations from $s=1$ to $s=50$ are 0.01795 and 0.01831, each of which corresponds to example 1 and 2. The integrals corresponding (28) are difficult to calculate because of frequently oscillating terms of $\sin 2\pi\mu r\xi_s/4\theta^2$ and $1-\cos 2\pi\mu r\xi_s/4\theta^2$, but the upper limits of these integrals are easily calculated from the following formulae,

$$
\begin{aligned}
&\int_a^5\frac{1}{\xi_s\sqrt{\xi_s}}F_+{}^{(3)}(\xi_s)\sin 2\pi\frac{\mu r}{4\theta^2}\xi_s\cdot d\xi_s\\
&\qquad<\int_a^5\frac{1}{\xi_s\sqrt{\xi_s}}F_+{}^{(3)}(\xi_s)\cdot d\xi_s\,,
\end{aligned}
$$

$$\int_a^5 \frac{1}{\xi_s\sqrt{\xi_s}} F_-^{(3)}(\xi_s)\left(1-\cos 2\pi\frac{\mu r}{4\theta^2}\xi_s\right)d\xi_s$$

$$<2\int_a^5 \frac{1}{\xi_s\sqrt{\xi_s}} F_-^{(3)}(\xi_s)d\xi_s\,, \tag{30}$$

and right hand integrals are evaluated by Simpson's method. Calculating these values, we obtained the upper limits of values of (28), 0.0144 and 0.0251 for example 1 and 2. Similarly for the upper limit of (29) we obtained next formulae,

$$\int_5^\infty \frac{1}{\xi_s^2}\sin 2\pi\frac{\mu r}{4\theta^2}\xi_s\cdot d\xi_s < \int_5^\infty \frac{1}{\xi_s^2}d\xi_s = \frac{1}{5}\,,$$

$$\int_5^\infty \frac{1}{\xi_s^3}\left(1-\cos 2\pi\frac{\mu r}{4\theta^2}\xi_s\right)\cdot d\xi_s$$

$$<2\int_5^\infty \frac{1}{\xi_s^3}d\xi_s = \frac{1}{25}\,, \tag{31}$$

and obtained values 0.00279 and 0.00111 respectively for example 1 and 2.

From above numerical values we obtained following X values

for example 1, $X<0.03514$, $X/\pi<0.01119$ and $r+X/\pi<0.01219$,

for example 2, $X<0.04452$, $X/\pi<0.01417$ and $r+X/\pi<0.01517$.

If the anode is stationary and the transversal thermal flow is negligible the temperature T_m is expressed by

$$T_m = T_0 + \frac{w}{c}d$$

and from eq. (21) it is shown that the value of $r+X/\pi$ gives the efficiency of heat divergency due to the rotation and the transversal flow. For example 1 the ratio of temperature rise is smaller than 1.2%, and for example 2 the ratio is smaller than 1.5%, or the permissible input power per unit area is more than 82 times of the stationary anode with the large focus for example 1, and for example 2 it is more than 66 times.

The heat conductivity of copper is 0.8 cal. cm.$^{-1}$ sec.$^{-1}$ deg.$^{-1}$ or 3.4 joule cm.$^{-1}$ sec.$^{-1}$ deg.$^{-1}$ at 1000°C and the value below 1000°C is larger than this value, and the melting point of copper is 1083°C. For the conditions T_m=melting point and $T_0=100$°C the boiling point of water, we obtain

$$w = \frac{(T_m-T_0)c}{(r+X/\pi)d} = \frac{3.34\times10^3}{(r+X/\pi)d}\ \text{watts/cm}^2\,.$$

The values for both examples are

$w=9.13\times10^5$ watts/cm² for example 1,

and

$w=7.33\times10^5$ watts/cm² for example 2.

Each permissible input power per unit length of the focal line is calculated as follows,

$W=1.19\times10^4$ watts/cm for example 1,

and $W=2.30\times10^4$ watts/cm for example 2.

§ 5. Conclusion and Discussion

In paragraphs from 2 to 4 we have described the method of calculation and have given a few examples of numerical calculation. These calculations are unfortunately so complicated that we cannot give a general formula of the input limit as a function of r, n, μ, etc. Furthermore when more accurate estimation is wanted, we must remark such questions that the point of maximum temperature is closely near to the end of the heating period, the temperature of the internal surface cooled by water is the same of the cooling water and the input power distributes uniformly upon the focal area.

If the number of rotations increases the temperature approaches asymptotically to the T_0+wrd/c which corresponds infinite number of rotations, for instance in DuMonds calculation, $r=2/10$, the permissible input power at 20 r.p.s. is 57% of that for infinite number of rotations and the effect of further increasing the number of rotations is very small. But in our case $r\leq 1/1000$ the power limit is sufficiently small compared with the case of infinite rotations and input power can be increased by increasing the number of rotations.

Regarding the comparison with the one-dimensional procedure, the third and the fourth terms of formula (27) is different, as the functions F are different for both procedures, and for $r\ll 1$ i.e. for small width of the focal line, the difference of both procedures are prominent, because the first and the second terms of formula (27) are very small and the other terms have significant influence to X.

References

1) W. J. Oosterkamp: Philips Res. Rep. **3** (1948) 303.

2) J. W. M. DuMond, B. B. Watson and B. Hicks: Rev. Sci. Inst. **6** (1935) 183.

JOURNAL OF THE PHYSICAL SOCIETY OF JAPAN Vol. 12, No. 10, OCTOBER, 1957

Determination of Dislocation Densities Through Nuclear Resonance Studies

By Eizo OTSUKA and Hazimu KAWAMURA

Institute of Polytechnics, Osaka City University, Osaka

(Received May 14, 1957)

Studies of quadrupolar effects of mixed alkali halide on nuclear resonance previously reported for Na in NaCl–NaBr have been extended to Br in KBr–NaBr. Amplification factor for eQq is thus derived and making use of this factor densities of dislocation are determined for a series of plastically deformed crystals of KBr. Although the effects of the screw and edge dislocations are additive for the broadening of the spectral line, their contributions to the net shift of the center of gravity of the line are in the opposite directions for $H_0//[100]$. Hence the two kinds of dislocation are separable in density through the measurement of the breadth and asymmetry of the spectral line. Extrapolation to zero strain shows that for an undeformed crystal screw and edge dislocations are nearly balanced in number and their total density lies around $4\times10^8\,\mathrm{cm}^{-2}$. Linear Compression more favors the production of screw dislocations than that of edge dislocations and the density of each type dislocation increases quite linearly with strain up to fourty percent deformation. For the heaviest deformed sample the total dislocation density achieved was about $3\times10^9\,\mathrm{cm}^{-2}$.

§ 1. Introduction

Recently the authors investigated the quadrupolar effect on the nuclear magnetic resonance line of sodium in the mixed alkali halide crystal NaCl–NaBr¹⁾, which arises from the electric field gradients due to the local strains produced by halogen ion substitution, and succeeded in giving a similar analysis to that made by Bloembergen and Rowland for the case of alloys²⁾. Differing from the negative ions in KBr and KI, the sodium nuclei in pure NaCl retain in its absorption line not only the central line component corresponding to $m=1/2\rightarrow m=-1/2$ transition, but also the satellite components arising from $m=3/2\rightarrow m=1/2$ and $m=-1/2\rightarrow m=-3/2$ transitions, and these are little affected by the internal crystalline defects such as dislocation or vacancies, indicating that the eQq at the sodium site is relatively small in a pure specimen. On the other hand, once a small amount of NaBr is dissolved into the NaCl crystal, intensity of the satellites promptly diminishes and even the central line undergoes the second order broadening upon heavier doping of NaBr. This latter effect, i.e., the second order broadening of the central line, is observable only when the minority halogen comes next to the sodium nucleus and hence has a remarkable directional asymmetry characteristic depending upon the relative directions of the crystalline axes and the applied magnetic field, offering a striking contrast to the case of powdered alloys.

The work on a metallic ion in alkali halide required a sister work on a halogen ion of a mixed crystal, having a common negative but different positive ions. Two convenient candidates lying at hand are KBr–NaBr and KI–NaI, in which the bromine and iodine nuclei are to be checked on account of their finite nuclear electric quadrupole moments. However, such trial on these elements ought to be accompanied by much difficulty not seen in the NaCl–NaBr case. Apart from the technical difficulty in growing a mixed alkali halide crystal bearing different alkalis, we have to be encountered with the fact that because of the large eQq at the sites of bromine and iodine nuclei, even in pure KBr and KI the satellite components of these resonance lines have been almost perfectly smeared out, and the central lines only can be observed³⁾. Hence if we further introduce NaBr or NaI into them and make mixed crystals, there arises a possibility that even a little bit addition of such minority component might cause a fatal second order broadening so that no signal could be picked out from the noise level. This is the barrier, though not insurmountable, in the mixed crystal experiment for bromine and iodine. Nevertheless, the large *eQq*, which produces the cause of difficulty on one hand, brings a convenient means to study the internal defects in pure crystals on the other, chiefly the effect of dislocations. Effects of this sort could not be easily seen in pure NaCl, but now in pure KBr or KI, situation is quite different and dislocation effect is an object of easy detection. In fact, Watkins[3] has brought it to light that quadrupolar interaction with these dislocations is responsible for the disappearance of the satellites and further that increased dislocation density upon cold working could even bring about the second order broadening of the central line itself; in other words, the nuclear magnetic resonance signals of these elements are very sensitive to the presence of dislocations. Unfortunately, however, no sufficient information is available as to the quantitative nature of the quadrupolar interaction with dislocations. Total density of dislocations and the way in which they are divided into edge- and screw-type ones are not clear at present. Moreover, the amplification factor for *eQq* due to the ion core distortion is out of our knowledge and this makes the problem entangled all the more. For the first time Watkins led experimentally the value ten for the amplification factor, β in his notation. Although his way of derivation is quite consistent, yet he puts a little too much confidence upon Seitz's estimation of dislocation density, that the determination of the amplification factor had to be rather subordinate. The value ten seems to be a little too small in the light of today's konwledge, since now Kranendonk[4] predicts much larger value from his point charge model, and even for free polar molecules, such calculations as made by Sternheimer et al.[5] suggest larger values for these heavy elements. One way of determining this amplification factor, we shall henceforth denote it by λ, is to investigate the resonance signal of mixed crystals. The dividend paid for performing a difficult mixed crystal experiment is that λ can be determined through an experiment independent of dislocation analysis. This consideration drove us to grow KBr–NaBr mixtures. In the following paragraphs the quadrupolar interaction due to the introduction of minority alkali is described as well as the dislocation studies pursued at the same time, using a number of plastically deformed crystals. Their analyses are intimately connected with each other. For the specimens containing iodine, similar experiments will be reported in a later paper.

§ 2. Experimental Techniques

The measuring equipments are essentially the same as those described in the previous paper. However, the object in this time is bromine which contains two isotopes of nearly equal abundance in nature. Moreover, the disappearance of the satellites further reduces the signal strength to one-fifth of that for sodium even at pure KBr. With a mixed crystal, the signal observed will still be much weaker. Thus the sensitivity required for the measuring equipment becomes very high. A handiest way to get a larger signal to noise ratio is to raise the resonance observation frequency. This must be accompanied by a higher applied magnetic field strength. Unfortunately, however, the small capacity of our electromagnet could not control its too fast a heating-up under a heavier current supply with all cooling water velocity. Hence we rather kept the magnetic field strength around 3,600 oersted just as in the previous work, but altered the magnetic field modulation frequency from 30 to 320 cps. By this we meant to reduce the flicker noise in order to get a higher signal to noise ratio. In absence of any established theory of flicker noise, we are not sure to what an extent this method is effective. However, it seems to be true that the higher the frequency, the less the flicker noise. In fact, thanks to this raised modulation frequency, the noise level has been much reduced and we could throughout operate the phase-sensitive amplifier with a time constant of about one second for chart-recording. This shorter time constant responds quickly the incoming true signal, yet much more insensitive to the unfavorable noise signal than in the case of 30 cps modulation. One disadvantage in using a high frequency modulation is the need of a compensator as a preventive against the pick-up from the modulation coil system to r-f. This was achieved by winding a pair of Helmholtz coils, some fifty turns in total, on the outer surface of the cylindrical shielding copper wall around the r-f coil.

Every specimen used in the present work has been grown in our laboratory from the melt within a platinum crucible by the Kyropoulos method. When dealing with NaCl-NaBr mixture, even growing an extremum of 50–50 crystal was a relatively easy task. This time, however, we were met with an extremely slow rate of growing for a crystal containing only a few percent minority. And the actually dissolved amount of the minority within a grown crystal could not be the same as that added while the reagents had been still in powder form, but would somewhat be less in quantity on account of the segregation effect during crystallization. Real quantities of the minority were later determined at the Department of Chemistry of Osaka University with a Beckman flame spectrometer, by analyzing the alkali flame intensities. In Table I is shown the actually dissolved amounts of the minority, together with its added amounts before crystal-growth. The maximum degree of doping is 1.87 percent. In view of the fast decay of the signal, any heavier doping than this would not be a sensible one. The pure KBr specimen as the intensity standard was selected in respect of its perfect singleness and growing and annealing conditions. Its size was cylindrical in form with 1.2 cm in diameter and 2 cm in height, and just fit the r-f coil. The standard was changed three times in the course of experiment, and it was confirmed that all the characteristics of the resonance line were common to each one; neither asymmetry of the line nor intensity change being noticeable. It must be noted in passing, however, that for a crystal bearing a slight trace of small angle boundaries and even a crystal quenched in mineral oil from a temperature just below the melting point showed no remarkable reduction in its signal strength. At least, there was not the faintest indication of a second order broadening so long as the crystal was pure and undeformed, and hence we had not to get too nervous in selecting the standard.

Table I. The relative concentrations of the minority in the specimens used.

Sample	Added amount	Actually dissolved
1	0.01	0.0061
2	0.03	0.0147
3	0.05	0.0187

In performing plastic deformation, two different methods were conducted. In the first place, the specimens were cleaved in rectangular shapes and linearly compressed between the plates of an oil compressor capable of producing the weights ranging from zero to one ton over the plates. As buffer, a pair of tin foils were placed on the upper and lower surfaces of the specimen. The creep rate for plastic flow was accelerated by irradiating the metallic plates with an infrared lamp, thus somewhat elevating the temperature of the crystal indirectly. In this way we were able to get a series of deformed crystals, ranging from 4.7 percent to 40.9 percent in the produced strains.

Another way of plastic deformation was first to cut a cleaved crystal into several thin slices and each of them be put within a hollow cylindrical brass tube with its inner radius of curvature 1.4 cm. Then, while warming up the tube with a burner, one presses the slice with a thick cylindrical iron rod placed on it. In this manner many arc-shaped slices having the equal radius of curvature 1.4 cm were produced. The aim of this device was to get many edge-type dislocations having a uniform direction. The effect of the deformation process of this type will be discussed in later sections.

All the measurements were carried out at room temperature.

§ 3. Experimental Results and Their Analyses

3.1) Doped Crystals

The intensity measurements were made both for Br^{79} and for Br^{81}. Since both of these nuclei in pure KBr give only 0.4 times the total absorption signal, we are bound to ascribe any change observed in a doped crystal to the second order broadening. In Fig. 1 are plotted the changes in maximum meter deflections against the relative concentration of the minority. One can see how quickly the line broadens on a little bit addition of the minority. Since the quadrupole moment of Br^{79} is $0.335 \times 10^{-24}\,\text{cm}^{-2}$ and that of Br^{81} is $0.280 \times 10^{-24}\,\text{cm}^{-2}$, the effect is more striking for the former. In Fig. 2 are shown the integrated absorption curves for Br^{81}. For doped crystals, the lines have an asymmetry characteristic of having a somewhat longer tail on the higher magnetic field side. This asymmetry is a little more noticeable at derivative curves, and has little dependence on the direction of the magnetic field, in contrast with NaCl–NaBr mixtures. That is to say, in the latter case the second order broadening occurs for only so heavy a doping that the probability of the minority halogen coming next to sodium becomes appreciable, and therefore, the number of halogen sites around the sodium nucleus responsible for the effect is limited to six. Under this situation, a simple analysis shows that for $[100]//H_0$ the line should have a tail on the lower magnetic field side, while for $[110]//H_0$ tails should appear on the both sides. In the case of KBr, however, the second order broadening comes into existence even if the location of the sodium ion is pretty far. Hence the radius vectors connecting the bromine nucleus and the sodium responsible for the broadening have a considerable angular spread with respect to the direction of the applied magnetic field for a given r. According to the second order perturbation theory, the energy difference corresponding to $m=1/2 \rightarrow m=-1/2$ transition perturbed by a quadrupolar interaction with an axially symmetric electric field gradient is given by

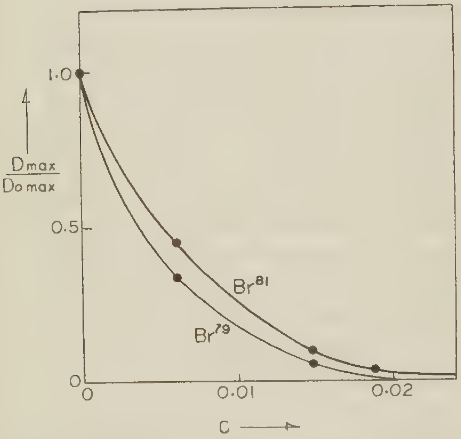

Fig. 1. Normalized signal strengths of both Br^{79} and Br^{81} in $(1-c)$KBr-cNaBr plotted against the relative concentration c of the minority.

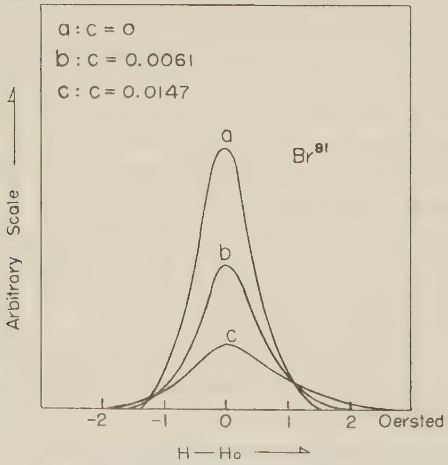

Fig. 2. Integrated absorption curves for Br^{81} in a series of mixed crystals $(1-c)$KBr-cNaBr.

$$\Delta E_{1/2\rightarrow -1/2}=h\nu_0+\frac{9}{64}\frac{2I+3}{4I^2(2I-1)}\frac{e^4Q^2q^2}{h\nu_0}\times(1-9\cos^2\theta)(1-\cos^2\theta)\ . \qquad (1)$$

Or writing the deviation from the Zeeman frequency as $\Delta\nu$

$$h\Delta\nu=A(1-9\cos^2\theta)(1-\cos^2\theta)\ , \qquad (2)$$

where

$$A=\frac{9}{64}\frac{2I+3}{4I^2(2I-1)}\frac{e^4Q^2q^2}{h\nu_0}\ . \qquad (3)$$

The minority ion placed at a distance r from the nucleus concerned will produce a field gradient:

$$eq=6\lambda e(a_i-a_0)/ar^3\ , \qquad (4)$$

where a_i and a_0 are the ionic radii of the minority and majority alkalis, respectively, a the lattice constant of KBr and λ the amplification factor including the Sternheimer correction. Putting this into (3), and (3) into (2), we get the shift of the Zeeman frequency due to the ionic substitution with a given radial distance r from the nucleus concerned. Since θ, the angle between the direction of the magnetic field and the axis of the electric field gradient, varies as the minority ion moves on the sphere of radius r around the nucleus, the frequency shift will take a series of values corresponding to the possible locations of the minority ion on this spherical surface. If there correspond many such possible orientations for a given r, we shall have a broad frequency spectrum having two peaks whose separation is given by

$$\Delta\nu_Q=\frac{25}{9}\frac{A}{h}$$

$$=\frac{225}{16}\frac{2I+3}{4I^2(2I-1)}\frac{e^4Q^2}{h\nu_0 r^6}\left(\frac{a_i-a_0}{a}\right)^2\lambda^2\ . \qquad (5)$$

This gives the order of the second order quadrupolar broadening due to the minority ion on the sphere of the radius r. We shall then be able to assume that, if the minority ion comes within a certain critical sphere, the line is so much shifted that it contributes almost nothing to the peak intensity. This assumption can easily be accepted, since $\Delta\nu_Q$ given by (5) varies in the inverse sixth power of r.

Thus the peak intensity of the integrated absorption curve will be proportional to the probability that the minority ion does not come within this critical sphere. If there are n sites for the positive ion and the mean concentration of the minority ion is c, this probability is given by

$$I_c/I_0=(1-c)^n\ , \qquad (6)$$

where I_0 is the peak intensity for pure KBr. Since $c<0.02$, we may safely put

$$\ln(I_c/I_0)=-nc\ , \qquad (7)$$

and the semilogarithmic plot will give the value of n. In Fig. 3 are shown the plots of this kind. The intensity measurements were carried out both for $[100]//H_0$ and $[110]//H_0$ and the averages of the two are given there, though no significant difference in slope for the two directions occurs. The heaviest doped sample gives no point for Br^{79} and even for Br^{81} the point is written with a white circle, indicating that the determination is not so certain. The remaining three points for each isotope, however, assure the linearity. The values of n calculated from these slopes are 105 and 92 for Br^{79} and Br^{81}, respectively. The latter corresponds to the number of alkalis just as far as the fifth ones, while the former lies between the fifth and sixth. The distance from a bromine to its fifth alkali neighbor is $\sqrt{11}a$ and to sixth $\sqrt{13}a$, where a is the lattice constant as before and 3.29 A for KBr. Then, we may be justified by equating the critical radius r_i to $\sim\sqrt{11}a$ for Br^{81} and $\sim\sqrt{12}a$ for Br^{79}. Using this critical radius, we can deduce the amplification factor by equating (5) to a definite broadening of reasonable magnitude, say the dipolar width for each nucleus. Theoretical values for dipolar broadening obtained by applying the Van Vleck's formula[6)] are $\Delta\nu_{79}=0.73$ kcps and $\Delta\nu_{81}=0.79$ kcps with $H_0//[100]$. On the other hand, experimental values are 1.07 kcps and 1.20 kcps for each. These discrepancies may partly arise from the invalidity of the Van Vleck's formula for a resonance line split and partly from the inhomogeneity broadening due to the finite dimension of the specimen as well as the slight saturation broadening; yet the second order broadening by virtue of the inner defects such as dislocations or impurities should be ruled out, since no asymmetry feature, characteristic of the second order broadening, does not turn up. The assumption that a broadening of this order occurs as the minority comes at the distance of the critical radius may be justified by the fact that the observed wings of the doped crystals extend over the range nearly of this width. The minorities nearer to the bromine would contribute the wings too far to be observed. Thus we may find the value of λ by equating the left-hand side of (5) tentatively to the theoretical dipolar widths, at the same time putting the critical radii determined above, for Br^{79} and Br^{81}. In this way the amplification factor is determined separately for each isotope as

$$\lambda=35 \text{ for } Br^{79}\ ,$$
$$\lambda=39 \text{ for } Br^{81}\ .$$

Considering the not so strictly sharp a nature of the way of derivation for these values, we had better put $\lambda\sim40$ for both isotopes.

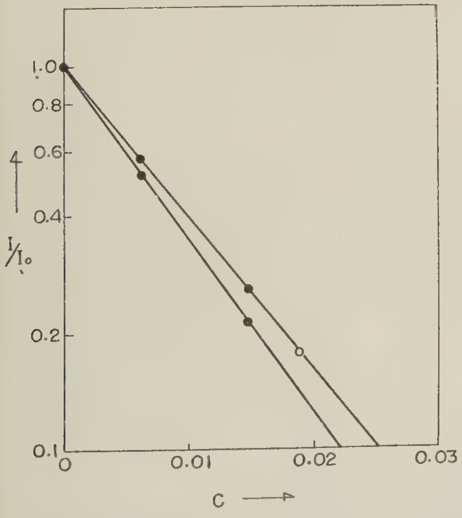

Fig. 3. Semilogarithmic plot of the relative peak intensities of both Br^{79} and Br^{31} resonance lines against the relative concentration c of the minority.

3.2) Linearly Compressed Crystals

In Fig. 4, the relative signal strengths $D_{\max}/D_{0\max}$ are plotted against the degree of strain for a number of deformed crystals. Since only the data of Br^{79} were used for dislocation analysis, those of Br^{81} are not shown in the figure, but suffice it to note that the effect of plastic deformation is again greater for Br^{79} than for Br^{81}. In the same figure is given a similar plot for $\sqrt{D_{\max}/D_{0\max}}$ which is very nearly equal to the ratio of the peak intensities I/I_0. The measurement was made thoroughly with $[100]//H_0$. The cross in the figure is the value of I/I_0 obtained by Watkins using a higher magnetic field of 6380 gauss[3]. In Fig. 5, a couple of absorption curves for deformed crystals are shown for illustration. Every absorption curve has a common feature of having a longer tail on the higher magnetic field side. Apparently this is quite analogous to the case of polycrystalline alloys under the second order broadening; however, the inner situation is rather different, since the strains which are responsible for the effect would not be caused by point defects such as impurities or vacancies, but mostly by dislocations which bear a line character. This will be checked a little more quantitatively in the next section. For the present, we shall implicitly assume that dislocations play a dominant role and proceed along this line.

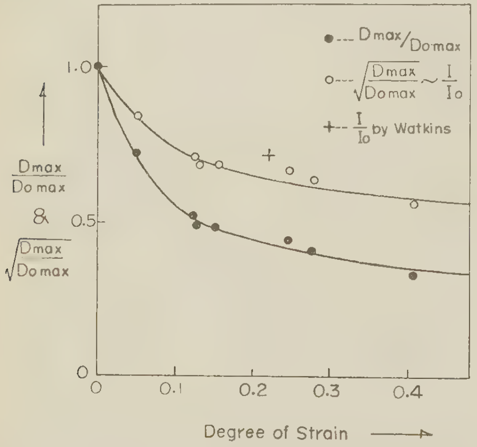

Fig. 4. Normalized signal strengths for Br^{79} in pure KBr and their square roots which are very nearly equal to the relative peak intensities plotted against the degree of strain. The cross indicates I/I_0 previously reported by Watkins.

It is expected that the result of linear compression will be that the produced dislocations are such that edge- and screw-types being mixed-up. So we have to consider two types of field gradients: one is that due to edge-type dislocations and the other due to screw-type ones. In alkali halides, a slip occurs always on a (110) sheet, the Burgers vector being parallel to the [110] direction with magnitude $|\boldsymbol{b}|=\sqrt{2}a$. The screw dislocation line lies along the slip direction and accordingly parallel to the [110] direction, while the edge dislocation line is perpendicular to this, lying along the [100] direction. The stress field of the former is cylindrically symmetric and described solely with the shear stress $\sigma_{\theta z}$ in the cylindrical coordinates. On the other hand, the latter is more complicated and three components of the stress tensor appear; namely, σ_{xx}, σ_{yy} and σ_{xy}. However, the compliance constants are $s_{11}=3.0$, $s_{12}=-0.43$ and $s_{44}=20.00$ for KBr[7] and hence the largest component is shear. Thus, for an approximate treatment we may be justified by neglecting all other components than shear in dealing with edge dislocation. This has been done also by Watkins. Justification for this approximation will be all right also for KI, for which $s_{11}=3.9$, $s_{12}=-0.53$ and $s_{44}=23.8$[7].

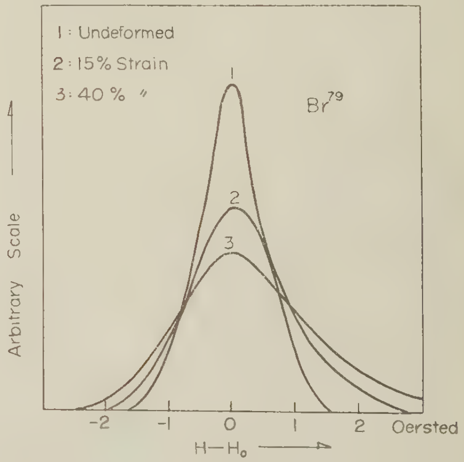

Fig. 5. Absorption curves of Br^{79} for a series of deformed pure KBr crystals.

Moreover, we shall approximate that the field gradients produced by the squeeze corresponding to a dislocation is axially symmetric around the squeeze direction and hence described by the following familiar expressions[8]:

$$\left.\begin{aligned}(\nabla E)_0&=\frac{1}{4}\,eq(3\cos^2\theta-1)\,,\\(\nabla E)_{\pm1}&=\pm\frac{1}{4}6^{1/2}eq\sin\theta\cos\theta e^{\pm i\varphi}\,,\\(\nabla E)_{\pm2}&=\frac{1}{8}6^{1/2}eq\sin^2\theta e^{\pm2i\varphi}\,.\end{aligned}\right\}\quad(8)$$

Now with H_0 being parallel to [100] and considering only the electric field due to the six nearest neighbors, Watkins shows for a squeeze in an arbitrary direction

$$(\nabla E)_0=3\eta\frac{e}{a^3}(3\cos^2\theta-1)\,,\qquad(9)$$

where η is the fractional compression, or strain. Comparing this with the first expression of (8) we see that we are dealing with an axially symmetric field with $eq=12\eta\frac{e}{a^3}$. Any squeeze in an arbitrary direction should be accompanied by another one with opposite sign in the perpendicular direction to it; in other words, the strain is composed by tension and compression. Hence we must add two terms of ∇E components having two θ's corresponding to tension and compression, in order to calculate the frequency shift due to the quadrupolar interaction. Detailed accounts of such calculations will be given in the appendix and suffice it to say here that θ varies only for a screw dislocation and hence averaging process is unnecessary for edge dislocations in order to get the first and second moments of the frequency deviation.

If there are screw and edge dislocations with the densities of c_S and c_E, the first moment, or the center of gravity of the absorption curve, becomes

$$\langle\nu-\nu_0\rangle=-\frac{36}{\pi^2}\lambda^2\frac{e^4Q^2}{h^2a^6\nu_0}\times\left(\frac{363}{4096}\pi a^2c_S\ln\frac{1}{9\pi a^2c_S}-\frac{49}{1016}\pi a^2c_E\ln\frac{1}{9\pi a^2c_E}\right).\qquad(10)$$

It is worthwhile to note here that the directions of the shift are opposite to each other for screw and edge dislocations. This enables us to separate the effects of the two type dislocations as shown later. For the time being, however, we might as well tentatively put $c_S=c_E$, since this assumption is not unreasonable so long as an order of magnitude discussion is concerned. Then we are able to deduce the dislocation density by experimentally determining the first moment for a deformed crystal which shows a second order broadening. The observed first moments and the corresponding dislocation densities are given in the Table II for four representative deformed crystals. The large probable error for the heaviest deformed crystal is caused by the small sample size and too much broadened tails at the far wings. For the crystals not shown here, errors are even greater than this on account of their smallness in size and hence not used for a quantitative analysis.

Table II. The observed first moments together with their corresponding dislocation densities for representative deformed crystals with the assumption $c_S=c_E$.

Degree of Strain	$-\langle\nu-\nu_0\rangle$ in cps.	c in cm^{-2}
4.7%	104 ± 6	$(8.0\pm0.5)\times10^8$
15.4%	239 ± 11	(19.7 ± 0.9) 〃
27.5%	361 ± 4	(31.2 ± 0.4) 〃
40.9%	496 ± 59	(44.0 ± 5.2) 〃

As mentioned above, the assumption that $c_S=c_E$ will not cause a serious error so long as the order of magnitude estimation is concerned. However, this may not be true in reality, and we are tempted to find a way by which the ratio c_S/c_E can be determined. This is qualitatively achieved through second moment analysis. For the quadrupolar second moment the effects of screw and edge dislocations are additive, and the expression becomes

$$\langle\delta\nu^2\rangle=\frac{729}{128}\left(\frac{e^4Q^2}{h^2a^6\nu_0}\right)^2\frac{\lambda^4}{\pi^3}\left(\frac{a}{r_i}\right)^2\times\left(\frac{81011}{16384}c_Sa^2+\frac{2401}{2304}c_Ea^2\right).\qquad(11)$$

Here r_i is the inner cut-off radius in the course of integration. This quantity is so defined that the signal from the nuclei nearer to the dislocation line than r_i escapes observation on account of the fatal frequency shift. The corresponding frequency spread will be expressed in terms of r_i as

$$\Delta\nu_{Q,\,\mathrm{disl}}=\frac{75}{8\pi^2}\frac{e^4Q^2}{h^2a^6\nu_0}\left(\frac{a}{r_i}\right)^2\lambda^2\,.\qquad(12)$$

Insertion of (12) into (11) will eliminate r_i. Writing $\sqrt{\langle\delta\nu^2\rangle}=\delta\nu_Q$ and $\Delta\nu_{Q,\,\mathrm{disl}}/\delta\nu_Q=\alpha$, we have

$$\delta\nu_Q=0.193\alpha\frac{e^4Q^2}{h^2a^6\nu_0}\lambda^2\left(\frac{81011}{16384}c_Sa^2+\frac{2401}{2304}c_Ea^2\right).\qquad(13)$$

The parameter α in this equation can be determined experimentally and its order of magnitude can be inferred to be 3~10 as seen just from the line shapes illustrated in Fig. 5. Combining (10) and (13), we can construct a set of simultaneous equations for c_S and c_E. $\delta\nu_Q$ is determined by subtracting the dipolar second moment, or half the line width of the undeformed crystal, thus picking up the broadening having purely quadrupolar nature. Before solving the simultaneous equations, we might as well again tentatively put $c_S=c_E$ in (13). In Table III, $\delta\nu_Q$'s and the corresponding dislocation densities times α thus derived are shown.

Table III. The quadrupolar broadenings together with the corresponding dislocation densities times α.

Degree of Strain	$\delta\nu_Q$ in cps.	αc in cm^{-2}
4.7%	165.0 ± 19.1	$(6.0\pm0.7)\times10^9$
15.4%	366.5 ± 40.3	(13.4 ± 1.5) 〃
27.5%	485.5 ± 41.1	(17.8 ± 1.5) 〃
40.9%	637.5 ± 76.1	(23.3 ± 2.8) 〃

Comparing Table II and Table III, the parameter α can be determined. This parameter, however, can also be found otherwise by directly measuring $\Delta\nu_{Q,\,\mathrm{disl}}$ for each absorption curve. Since $\Delta\nu_{Q,\,\mathrm{disl}}$ is by definition the separation of the frequencies where the signal intensity just escapes observation, it can be determined experimentally, although the determination itself cannot be said so definite. At any rate, two sets of α values are derived in this manner and in Table IV are listed these two kinds of α for each deformed crystal. Their coincidence is fairly good, so that one may expect the solution to lie near at hand around $c_S=c_E$. This situation facilitates the actual solution of the simultaneous equations. That is, the logarithmic factors in the first moment expression may safely be put equal and expressed by κ. Thus the final expressions for c_S and c_E are written as

Table IV. The parameter $\Delta\nu_{Q,\mathrm{disl}}/\delta\nu_Q=\alpha$ with two different ways of derivation, one with the assumption $c_S=c_E$, the other just through direct observation.

Degree of Strain	$\alpha_{c_S=c_E}$	α_{exp}
4.7%	7.55	8.5
15.4%	6.80	8.3
27.5%	5.70	7.6
40.9%	5.27	7.0

$$\left.\begin{aligned}c_S&=\left[-0.580\frac{\langle\nu-\nu_0\rangle}{\kappa}+1.60\frac{\delta\nu_Q}{\alpha}\right]\times10^7\,\mathrm{cm}^{-2},\\ c_E&=\left[2.76\frac{\langle\nu-\nu_0\rangle}{\kappa}+2.94\frac{\delta\nu_Q}{\alpha}\right]\times10^7\,\mathrm{cm}^{-2}.\end{aligned}\right\}\tag{14}$$

Thus combining the shift $\langle\nu-\nu_0\rangle$ and broadening $\delta\nu_Q$, we are able to separate c_S and c_E, where the experimentally determined values are to be used for α. The obtained c values are plotted in Fig. 6 for each stage of deformation. It is seen that each kind of dislocation increases quite linearly with degree of strain, and the screw dislocation outnumbers the edge dislocation in the deformed crystals. Extrapolation to the zero strain shows that for an undeformed crystal, the densities of the screw and edge dislocation are nearly balanced in number and the total density lies around $4\times10^8\,\mathrm{cm}^{-2}$.

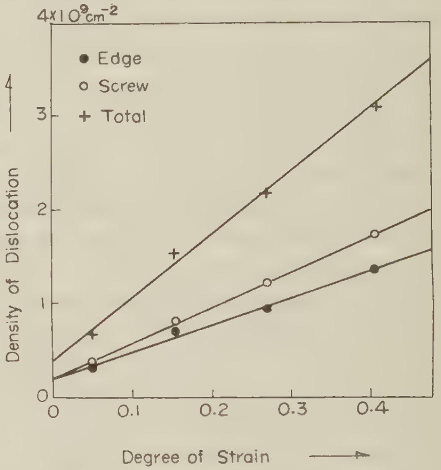

Fig. 6. Edge, screw and their total dislocation densities plotted against the degree of strain.

3.3) Circularly Bent Crystals

In contrast with the linearly compressed crystals, in which we could observe remarkable second order broadenings, neither broadening nor asymmetry characteristic was found for the circularly bent crystals. Of this negative result we shall discuss in the next section.

§4. Discussions

It is already accepted as an established fact that even with a pure and undeformed

KBr, the resonance lines of both Br^{79} and Br^{81} are perfectly split, the satellites being so widely spread out under the noise level. It is believed that this first order broadening is caused not by point defects such as impurities or vacancies but by dislocations. Indeed if we try to have the satellites spread over a range of 10 kcps by adding an impurity of the same valence, say Na, to the perfect KBr crystal, a simple first order perturbation calculation will show that a lower limit of impurity concentration needed for that spread of satellites is $\sim 10^{19}\,\mathrm{cm}^{-3}$. In usual reagents such a high impurity concentration is not allowed. Also an impurity of different valence ordinarily does not exceed $10^{16}\,\mathrm{cm}^{-3}$ in concentration. Accordingly, apart from an artificially added one, a quadrupolar effect due to impurity can be said entirely negligible.

Then how about the vacancies? The eQq due to a vacancy is similar to that due to a divalent ion, and may be assumed by not more than an order of magnitude greater than that due to Na. Their concentration, however, scarcely exceeds 10^{17} per unit volume even for $T=1{,}000°\mathrm{K}$, if calculated from the thermal equilibrium condition $n=N\exp(-W/2kT)$, putting $N=10^{22}\,\mathrm{cm}^{-3}$ and $\frac{1}{2}W=0.96$ ev. for KBr; hence for a crystal quenched at very high temperature, we might as well ascribe the satellite reduction only in part to these vacancies. Yet it is far from the second order broadening, and as stated in § **2**, the signal intensity for a quenched crystal showed no observable change compared with a good one.

Now for the plastic deformation: Although the quadrupolar effect is highly sensitive to a linear compression, practically no effect is observable for a circularly bent crystal. The aim of this bending technique was to get a certain regularity of the field gradient by producing many edge-type dislocations pointing the same direction. If this had been done for a sufficient degree, we should have been able to observe an asymmetry characteristic of the absorption curve dependent on the magnetic field direction. The possibility of a directional effect for asymmetry characteristic will be discussed in more detail in a later paper, and for the present we discuss simply the reason why this trial ended in a negative result for KBr. A simple theory⁹⁾ predicts that when we bend a thin slice of the crystal, the order of magnitude density of the dislocations produced by bending will be given by

$$c=1/rb\,, \tag{15}$$

where b is the magnitude of the Burgers vector and r the radius of curvature. By putting $r=1.4\,\mathrm{cm}$ and $b=4.65\times10^{-8}\,\mathrm{cm}$, we obtain $c\sim2\times10^{7}\,\mathrm{cm}^{-2}$. On the other hand, from the analysis for the linear compression we see that a density of more than $10^{8}\,\mathrm{cm}^{-2}$ is needed to cause an observable second order broadening. This may be the possible reason for the negative result. The value of c obtained from (15), however, is not necessarily the maximum density attainable through this technique. For example, by repeating the bending back and forth several times, we might be able to get more than 10^{8} unidirectional edge dislocations per unit area. This repitition of bending indeed was put on trial, but with no avail. An observable effect might be expected for an element with larger eQq. Potassium iodide is one with such a possibility. An experiment on this object is now under preparation.

It is not so certain why linear compression does introduce much more dislocations than bending. However, some clue might be obtained if one considers the fact that the most important increases of dislocations occur when those belonging to different slip systems intersect each other. In the case of bending the specimen surfaces are free over most of their area and the strain may be brought about by only one slip system in any one region. In linear compression, on the contrary, there is constraint from the pressure plates over a large part of the surface area, which will usually compel intersecting slip systems to operate. The conclusion that liner compression introduces much more dislocations is therefore quite an acceptable one, but the situation is rather complicated for one to have been able to predict this with certainty.

It is of interest to compare the two kinds of frequency spread (5) and (12). Since λ is common to both the formulae, the critical radii responsible for broadening comparable with dipolar one are connected by the relation

$$\frac{\sqrt{2}}{\pi}\,\frac{a}{r_d}=\frac{a^3}{r_i^3}\,\frac{a_i-a_0}{a}\,, \tag{16}$$

where r_d is the critical radius for the dislocation. For Br^{79} we may put $r_i \sim \sqrt{12}a$, and get $r_d/a \sim 200$. If the dislocation density c exceeds $(\pi r_d^2)^{-1} \sim 7\times10^9\,\mathrm{cm}^{-2}$, each nucleus undergoes a broadening at least comparable with the dipolar broadening; in other words, the central line itself will practically be smeared out. However, even for the fourty percent deformed crystal the signa does not vanish, thus proving that its dislocation density has not yet exceeded this limit. In fact, we see from Fig. 5 that c still lies around $3\times10^9\,\mathrm{cm}^{-2}$ for this crystal and hence well below the above-mentioned limit.

The undeformed crystal has a perfectly symmetrical absorption curve and thus for this sample $c \ll 7\times10^9\,\mathrm{cm}^{-2}$. Or, a little more strictly, we may safely assume that for this crystal less than ten percent of the total nuclei are closer to the dislocation line than r_d. Thus $c < 7\times10^8\,\mathrm{cm}^{-2}$ would be a pretty reasonable value as an upper limit of dislocation density for an undeformed crystal.

On the other hand, the lower limit of the dislocation density for an undeformed crystal can be deduced from the requirement that the satellites be smeared out by the strains due to dislocations. The first order perturbation calculation gives for the frequency shift due to a dislocation as

$$h\Delta\nu = (2m-1)(3\cos^2\theta-1)\frac{3e^2Q\lambda}{8I(2I-1)}\,\frac{12}{\sqrt{2}\,\pi}\cdot\frac{1}{a^2r}\,. \tag{17}$$

If we replace $3\cos^2\theta-1$ by 3, we get a measure of the spreading range of the satellites for a given r. The signal would become unobservable for sufficient spread, say 10 kcps, and the value of r corresponding to this spread gives the above-mentioned lower limit for the dislocation density. Calculation shows that this limit is $5\times10^7\,\mathrm{cm}^{-2}$. The allowable range for the dislocation density for an undeformed crystal therefore becomes

$$5\times10^7 < c < 7\times10^8\,\mathrm{cm}^{-2}\,. \tag{18}$$

The extrapolation made in Fig. 6 drops just within the range prescribed by this condition and $c = 4\times10^8\,\mathrm{cm}^{-2}$ would be a reasonable result consistent with all these analyses.

§ 5. Conclusion

The absence of the knowledge of the correction factor λ in the quadrupolar interaction has often been an obstacle for the study of lattice imperfections. Through an experiment of mixed crystals we have found this value to be ~ 40 for bromine in KBr. Using this value thus derived, we have been able to determine the dislocation density for plastically deformed crystals and thence further estimate the density for an undeformed crystal. It is concluded that the dislocation density for a usual pure and undeformed potassium bromide lies in the stage of $10^8\,\mathrm{cm}^{-2}$, the edge and screw dislocations being nearly balanced in quantity. The linear compression, however, more favors the production of screw dislocations rather than that of edge dislocations and for the heaviest deformed crystal, 40.9 percent strain, the total dislocation density achieved is $3\times10^9\,\mathrm{cm}^{-2}$. Up to this high stage of plastic deformation, the dislocation density seems to increase quite linearly with strain.

§ 6. Acknowledgement

We should like to express our profoundest gratitude to Prof. F. C. Frank for his deep interest shown to our work and also for many valuable discussions. We are also very much indebted to Mr. T. Honda for his technical assistance during the course of experiment. Discussions with Mr. M. Tomura and Mr. H. Okura on dislocation topics were most welcome.

Appendix

The frequency shift due to the second order quadrupolar interaction for nuclei with $I=3/2$ is given by

$$\nu-\nu_0 = -\frac{e^2Q^2}{h^2\nu_0}\left\{|\nabla E_{-1}|^2 - \frac{1}{2}|\nabla E_{+2}|^2\right\}. \tag{A1}$$

where ∇E_{-1} and ∇E_{+2} are those in (8) in the text. In order to calculate the field gradients due to dislocations, we must refer to the stress equations of a dislocation.

1) Screw Dislocation

In rectangular coördinates, the stress has only two nonvanishing components:

$$\left.\begin{aligned} \sigma_{xz} &= -\frac{Gb}{2\pi}\frac{y}{x^2+y^2}\,, \\ \sigma_{yz} &= \frac{Gb}{2\pi}\frac{x}{x^2+y^2}\,, \end{aligned}\right\} \tag{A2}$$

where G is the shear modulus and the direction of the screw dislocation line is taken as the z-axis, which is parallel to [110]. The plane perpendicular to this is shown in Fig. 7. In cylindrical coördinates, the stress tensor yields only one nonvanishing component:

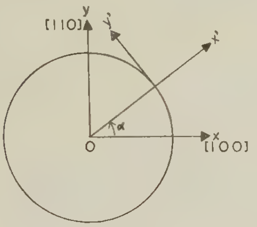

Fig. 7. A diagram indicating the cylindrical symmetry of a screw dislocation, with yz plane being the slip plane and Oz the dislocation line which is parallel to a [110] type direction.

$$\sigma_{\theta z}=\frac{Gb}{2\pi r}\,. \tag{A3}$$

Thus the stress field is in the form of cylindrical symmetry. By deriving the direction cosines of both the magnetic field direction and the axis of the field gradient with respect to the x, y and z axes of the dislocation, we can find the angle θ appearing in (8). Since the magnetic field has been applied throughly along the [100] direction, its direction cosines are either $(\pm1, 0, 0)$ or $(0, \pm1/\sqrt{2}, \pm1/\sqrt{2})$. In other words, there are two kinds of equivalent (110) sheets on which a slip occurs with regard to the magnetic field direction. We shall next introduce a new coördinate system $(x'y'z')$, which is rotating on the surface of a cylinder of radius r coaxial with the dislocation as shown in Fig. 7. The z' axis is fixed and identical with the z axis of the dislocation. Then the axes of the field gradients lie in the $y'z'$ plane and along the lines $y'=\pm z'$; one is for compression and the other for tension, whose magnitudes being given by

$$\left.\begin{aligned}(eq)_1&=+12\lambda\frac{e}{a^3}\frac{\sigma_{\theta z}}{G}\,,\\(eq)_2&=-12\lambda\frac{e}{a^3}\frac{\sigma_{\theta z}}{G}\,.\end{aligned}\right\} \tag{A4}$$

Now that their direction cosines with respect to the rotating coördinates are $(0, \pm1/\sqrt{2}, \pm1/\sqrt{2})$, those with respect to the axes of the fixed coördinate system can now be expressed in terms of the rotation angle α of the $(x'y'z')$ system and thus written as $(-1/\sqrt{2}\sin\alpha,\ 1/\sqrt{2}\cos\alpha,\ \pm1/\sqrt{2})$.

Hence the angle θ between the direction of the magnetic field and the axis of the field gradient is found to be either

$$\left.\begin{aligned}&\text{a)}\qquad \cos\theta=\pm\frac{1}{\sqrt{2}}\sin\alpha\,,\\&\text{or}\\&\text{b)}\qquad \cos\theta=\frac{1}{2}\cos\alpha\pm\frac{1}{2}\,.\end{aligned}\right\} \tag{A5}$$

This set of cosine values should properly be associated with corresponding tension and compression. Introducing (A5) into (A1) and averaging over the angle α and radial distance r, we get the contribution of screw dislocations to (A1). It becomes

$$\begin{aligned}\langle\nu-\nu_0\rangle_{\text{Screw}}&=-\frac{363}{4096}\cdot\frac{72}{\pi^2}\lambda^2\left(\frac{e^2Q}{ha^3}\right)^2\frac{1}{\nu_0}\int_{3a}^{(\pi c_S')^{-1/2}}\frac{1}{r^2}r\,dr\Big/\int_0^{(\pi c_S')^{-1/2}}r\,dr\\&=-\frac{363}{4096}\cdot\frac{72}{\pi^2}\lambda^2\left(\frac{e^2Q}{hd^3}\right)^2\frac{1}{\nu_0}(\pi a^2c_S')\ln\frac{1}{9\pi a^2c_S'}\,,\end{aligned} \tag{A6}$$

where c_S' is half the screw dislocation density, or the density on an equivalent set of the two of the (110) sheets with regard to the magnetic field direction. The lower limit of the radial integration has been rather arbitrarily chosen $3a$ as by other authors, within which one may expect that Hooke's law would fail to be valid. This arbitrariness will be allowed if one considers the logarithmic nature of the result.

2) Edge Dislocation

As stated in the text, we shall only consider the shear component in dealing with an edge dislocation. This greatly simplifies the problem and all we have to do is to consider the two squeezes which always lie along [100] type directions (See Fig. 8). Hence $\cos\theta$ in this case is either 0 or 1, and there is no need of averaging process. There are again two kinds of equivalent (110) sheets on which a slip occurs: one for which $(eq)_1$ satisfies $\cos\theta=1$ and $(eq)_2$ $\cos\theta=0$, the other for which both $(eq)_1$ and $(eq)_2$ satisfy $\cos\theta=0$. For $\cos\theta=1$, there is no frequency shift corresponding to

(A1). For $\cos\theta=0$, we have

$$|\nabla E_{-1}|^2-\frac{1}{2}|\nabla E_{+2}|^2=-\frac{3}{64}e^2q^2\,, \tag{A7}$$

with

$$\left.\begin{aligned}(eq)_1&=+12\lambda\frac{e}{a^3}\frac{\sigma_{xy}}{G}\,,\\ \text{and}\quad (eq)_2&=-12\lambda\frac{e}{a^3}\frac{\sigma_{xy}}{G}\,,\end{aligned}\right\} \tag{A8}$$

where

$$\sigma_{xy}=\frac{Gb}{2\pi(1-\nu)}\cdot\frac{x(x^2-y^2)}{(x^2+y^2)^2} \tag{A9}$$

$$=\frac{Gb}{2\pi(1-\nu)}\cdot\frac{\cos\alpha\cos 2\alpha}{r}\,. \tag{A10}$$

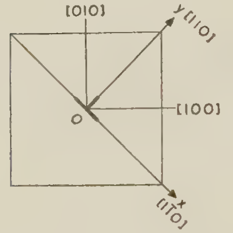

Fig. 8. The coördinate system for an edge dislocation, with xz plane being the slip plane and Oz the dislocation line which is parallel to [001].

Averaging q^2 over a cylinder of radius r coaxial with the dislocation, and then again integrating with respect to r, we obtain

$$\langle\nu-\nu_0\rangle_{\text{Edge}}=\frac{49}{1016}\frac{72}{\pi^2}\lambda^2\left(\frac{e^2Q}{ha^3}\right)^2\frac{1}{\nu_0}\times(\pi a^2c_E')\ln\frac{1}{9\pi a^2c_E'}\,; \tag{A11}$$

here the value 1/7 has been inserted for the Poisson's ratio, and c_E' has the same nature as c_S'. One should note that (A10) gives a contribution having only positive value. This arises from the absence of averaging process over θ. Changing the direction of the magnetic field, contributions having negative values may also be derived for edge dislocations. In any case, with H_0//[100] we get the first moment expression just combining (A6) and (A11), thus yielding (10) in the text.

Squaring (A1) and averaging in a similar way we can find the quadrupolar second moment given as (11) in the text.

References

1) H. Kawamura, E. Otsuka and K. Ishiwatari: Jour. Phys. Soc. Japan **11** (1956) 1064.
2) N. Bloembergen and T. J. Rowland: Acta Metallurgica **1** (1953) 731.
T. J. Rowland: Acta Metallurgica **3** (1955) 74.
N. Bloembergen: "Nuclear Magnetic Resonance in Imperfect Crystals" (Report at the Bristol Conference, 1954).
3) G. D. Watkins: Thesis, Harvard University 1952.
G. D. Watkins and R. V. Pound: Phys. Rev. **89** (1953) 658.
4) J. van Kranendonk: Physica **20** (1954) 781.
5) R. M. Sternheimer and H. M. Foley: Phys. Rev. **92** (1953) 1460.
6) J. H. Van Vleck: Phys. Rev. **74** (1948) 1168.
7) C. Kittel: *Introduction to Solid State Physics*; Second Edition, 1956, p. 93 (New York: John Wiley and Sons).
8) R. V. Pound: Phys. Rev. **79** (1950) 685.
9) A. H. Cottrell: *Dislocat ons and Plastic Flow in Crystals*, 1953, p. 29 (Oxford: University Press).

JOURNAL OF THE PHYSICAL SOCIETY OF JAPAN Vol. 12, No. 10, OCTOBER, 1957

Magnetic Properties of the $FeTiO_3$-Fe_2O_3 Solid Solution Series

By Yoshikazu ISHIKAWA
Institute of Science and Technology, Tokyo University

and Syun-iti AKIMOTO
Geophysical Institute, Tokyo University

(Received June 25, 1957)

Magnetic properties of the synthesized solid solution $x\,FeTiO_3\cdot(1-x)Fe_2O_3$ of ilmenite ($FeTiO_3$) and hematite (Fe_2O_3) were investigated in detail for the whole range of $0 \leqq x \leqq 1$. On the experimental side of the study, the most suitable method for preparing the specimen with the largest intensity of magnetization was found. Changes of the Curie point, the estimated intensity of magnetization at 0°K, the Curie constant and the asymptotic paramagnetic Curie point with the composition were presented. It was found that the magnetic properties of the solid solution, $xFeTiO_3\cdot(1-x)Fe_2O_3$, could be divided into three parts, (i) $x=1$, (ii) $1>x\gtrsim 0.5$ and (iii) $0.5>x\geqq 0$: Pure ilmenite ($FeTiO_3$) is antiferromagnetic below 55°K and the specimens for $1>x\gtrsim 0.5$ are very strongly ferromagnetic and for $0.5>x\geqq 0$ they are again antiferromagnetics on which feeble parasitic ferromagnetism is superimposed.

On the theoretical side of the study, these magnetic properties were discussed by using the approximation of molecular field. It was shown that we could explain an outline of the magnetic properties of the solid solution if we assume that the tetravalent Ti ions always occupy one of the two sublattices in the specimens for $1\geqq x\gtrsim 0.5$, while such an ordering of Ti ions and Fe ions is disturbed for $0.5>x\geqq 0$.

§ 1. Introduction

Both hematite (α-Fe_2O_3) and ilmenite ($FeTiO_3$) which are of rhombohedral crystal structure have been considered as antiferromagnetic substances1),2). Below its Néel point of about 950°K, hematite shows a parasitic ferromagnetism with a transition temperature of magnetic susceptibility around 260°K3). Néel proposed an idea that this parasitic ferromagnetism is due to an imperfect compensation of two antiferromagnetic sublattices4). Although many experiments have been carried out on this substance5),6),7), no decisive explanation of the magnetic properties of hematite has not yet been attained. On the other hand, very little work has been done8),9) with respect to the detailed magnetic properties of ilmenite which has recently been found to be antiferromagnetic below 68°K by Bizette and Tsai2). Practically nothing has been known about the spin orientation or its interaction in the antiferromagnetic state.

A systematic investigation of the solid solution of hematite and ilmenite, $xFeTiO_3\cdot(1-x)Fe_2O_3$, was first carried out by Pouillard10), who found hematite and ilmenite form solid solution only for two limited ranges of composition ($1\geqq x\geqq 0.66$ and $0.33\geqq x\geqq 0$), when the specimens are prepared by sintering at 950°C for two hours. Nicholls proposed a phase diagram of hematite and ilmenite by making use of this result11). We have found that, when the specimens are quenched from the sintering temperature higher than 1100°C, it is possible to make the solid solution in the whole range of the composition12).

On the magnetic properties of this solid solution series, Nagata, Akimoto and Uyeda found that certain minerals composed of the solid solution of hematite and ilmenite have very strong ferromagnetism13), sometimes playing a very important role in the magnetic properties of the rocks, especially in the characteristics of the thermoremanent magnetism. For example, the existence of the ilmenite-hematite solid solutions results in the self-reversal of thermoremanent magnetism of some rocks14). Since the ferromagnetism of the ilmenite-hematite solid solution series was discovered, experimental studies on this solid solution series have been rather systematically continued by ourselves and many other investigators for both natural minerals and synthesized specimens[12),15),16)]. But any comprehensive experiments and plausible explanation of the experimental results have not yet been presented up to now.

The characteristics of the magnetic properties of this solid solution series can be summarized into the following three parts, which must be explained consistently when we try to discuss the magnetic properties completely.

a) The ferromagnetism of this ilmenite-solid solution series appears only in the limited region of the composition; that is, the solid solution of $x\mathrm{FeTiO_3}\cdot(1-x)\mathrm{Fe_2O_3}$ is ferromagnetic only for $0.95 \geqq x \gtrsim 0.5$.

b) As for the strong ferromagnetic specimens, the intensity of magnetization increases almost linearly with temperature from near the Curie temperature down to the liquid nitrogen temperature. It has been reported that some compounds of the spinels show the same thermomagnetic characteristics for the very restricted conditions[17),18)].

c) The intensity of magnetization of the ferromagnetic specimen is remarkably affected by heat treatments[19)], indicating that the magnetization of this series has a great correlation with the ordering of cations.

In the experimental part of the present study, the authors will investigate these magnetic properties of the solid solution synthesized with special care of the ordering of cations in the whole range of the composition, and in the theoretical part they will discuss the experimental results as consistently as possible by using the molecular field theory.

Part I. Experimental Studies

§ 2. Preparation of Specimens

The specimens dealt with in the present study were prepared by the usual ceramic method. Pure hematite and ilmenite were prepared in advance by the method described in the previous paper[9)]. Both were ground in an agate mortar to pass a 200 mesh sieve and were mixed in the desired proportion. Then the mixture of pure hematite and ilmenite, sealed in a quartz tube evacuated approximately to 10^{-3} mm mercury, was sintered at high temperatures for a long time.

It is, however, necessary to find the most suitable heat treatment for preparing the specimens perfectly ordered or having the largest intensity of magnetization. Thermomagnetic curves of the specimens prepared by various heat treatments are shown in Fig. 1.

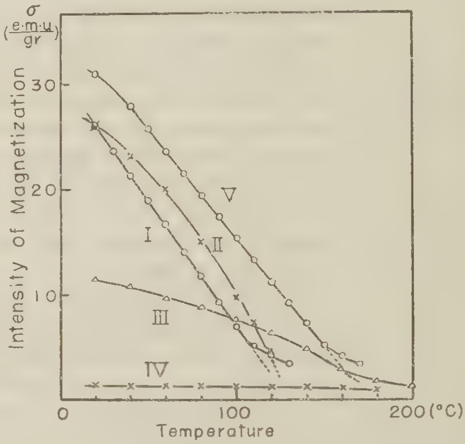

Fig. 1. Intensity of magnetization in a field strength of 8500 Oe vs. temperature of the specimens prepared by various heat treatments.

I. a specimen prepared by quenching from 1200°C after being maintained at this temperature for more than 12 hours.

II. a specimen prepared by quenching from 1200°C after being maintained at this temperature for 6 hours.

III. a specimen prepared by quenching from 1300°C.

IV. a specimen prepared by quenching from 1370°C.

V. a specimen prepared by slow-cooling from 1200°C.

Before heat treatment each specimen had the same original composition of about $0.7\,\mathrm{FeTiO_3}\cdot 0.3\,\mathrm{Fe_2O_3}$. It was found from this experiment that we could obtain the specimen having the largest intensity of magnetization at 80°K when it was quenched from 1200°C after being maintained at this temperature for more than 12 hours. The thermomagnetic curve of this specimen is almost linear down to 80°K. This method of preparation is denoted in the present paper as I hereafter. When, on the other hand, the specimen was quenched from

1200°C after being kept at this temperature for less than six hours, the thermomagnetic curve is convex, the intensity of magnetization at 80°K being fairly smaller than that of the specimen prepared by the method I. Of course, the solid reaction proceeded enough even in this case, the prepared specimen having the same composition and the crystal parameters as that prepared by the method I. This method is denoted as II. The specimen prepared by this method seems to be in the partially ordered state. When the temperature of sintering is higher than 1200°C, the ordering seems to be disturbed by the thermal agitation, intensity of magnetization getting smaller with the elevation of the sintering temperature. It is further remarked that when the sintering temperature was higher than 1300°C some amounts of oxygen might flow into the quartz tube through its wall so that the composition of the specimen deviated from the expected value towards the hematite and some Fe_2TiO_5-$FeTi_2O_5$ solid solution series was also produced[20]. It was also found that we could obtain the homogeneous specimen even when it was prepared by cooling slowly in the furnace from 1200°C. Its thermomagnetic characteristic is, however, not better than that prepared by the method I.

§ 3. X-ray Analysis and Chemical Analysis

X-ray analysis of this ilmenite-hematite solid solution series has already been carried out by one of the authors for both synthesized specimens and natural minerals in the whole range of the solid solution[12]. Those results are reproduced in Fig. 2 and 3, in which the results obtained thereafter are also plotted. The chemical analysis was carried out by Katsura, Dept. of Geochemistry, Tokyo Institute of Technology, for the three main components, FeO, Fe_2O_3 and TiO_2 and the details were described in the previous paper[12].

It was confirmed from the X-ray analysis carried out by a *"Norelco"* X-ray diffractometer that the specimens dealt with here were of sufficiently pure single phase of the rhombohedral crystal structure. Some specimens contained a trace of $FeTi_2O_5$-Fe_2TiO_5 solid solution series, but it was acertained that they had negligible influence on the magnetic properties of the specimens[20]. No other trace such as titanomagnetite, ($y Fe_2TiO_4 \cdot (1-y) Fe_3O_4$) of the cubic structure could be observed at all.

In Fig. 2, the chemical composition of the specimens is plotted on a FeO-Fe_2O_3-TiO_2 ternary diagram and in Fig. 3 the volume V, of the unit cell of the crystal, calculated from the two crystal parameters a_{rh} and α_{rh} of the rhombohedral structure, is plotted against the mol. per cent of $FeTiO_3$. This figure shows that the volume of the unit cell varies linearly with the composition from 100.43Å^3 of α-Fe_2O_3 to 105.22Å^3 of $FeTiO_3$. Hence, the chemical composition of the specimens were determined in the present study from their volume of unit cell determined by X-ray analysis on the assumption that the above empirical linear relation always hold true. Such a method of determination of the composition seems to be more plausible than chemical analysis when the specimen involves

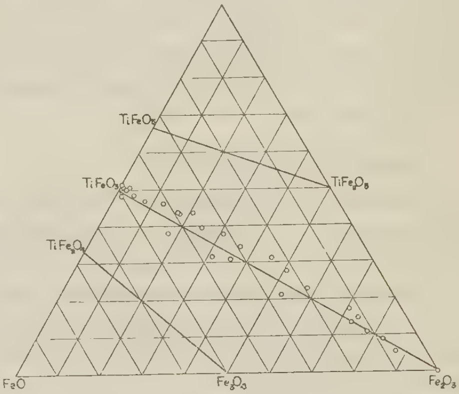

Fig. 2. Chemical composition of the $FeTiO_3$-Fe_2O_3 series specimens represented on a FeO-Fe_2O_3-TiO_2 ternary diagram in mol. per cent.

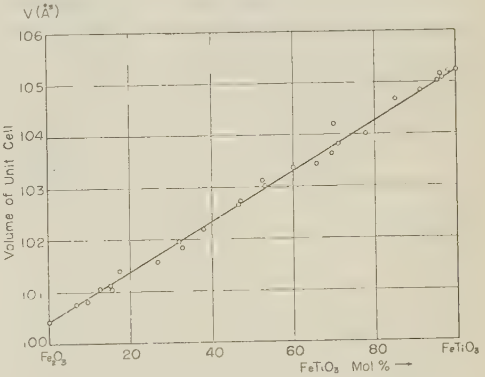

Fig. 3. Volume of unit cell vs. composition of the $FeTiO_3$-Fe_2O_3 solid solution series.

some other impurities of oxides such as $FeTi_2O_5$-Fe_2TiO_5 solid solution series. For some specimens used in this paper, the chemical analysis was also performed and the compositions determined by both methods were found to accord well with each other.

§ 4. Thermomagnetic Measurement

The magnetic properties of ilmenite-hematite solid solution series, $x\mathrm{FeTiO_3}\cdot(1-x)\mathrm{Fe_2O_3}$ can be classified into three groups; that is, i) $x=1$, ii) $1>x\gtrsim 0.5$ and iii) $0.5>x\geqq 0$. Therefore they are discussed separately in the following.

4. 1. *Intensity of Magnetization*

The intensity of magnetization was measured by means of the magnetic balance described elsewhere[9]. The amounts of the specimens used for this measurement were a few milligrams as for the strong ferromagnetic ones. Consequently the largest error is caused from the weighing of specimen, it is, however, estimated to be less than four per cent.

i) $x=1$

Pure ilmenite, being found to be antiferromagnetic at very low temperatures, will be dealt with in the next section (4. 2).

ii) $1>x\gtrsim 0.5$

In Fig. 4 several examples of the thermomagnetic curve down to the liquid nitrogen temperature in a field strength of 8500 Oe are shown. The specimens used are the ones either prepared by the method I described in § 2 or of which magnetization were intensified by an appropriate heat treatment after they were prepared by the method II[19]. The latter is denoted as **h** in the figure. A few specimens of which thermomagnetic curve were extended to the liquid helium temperature in the figure were measured at Research Institute for Iron, Steel and Other Metals, Tôhoku University, for the field strength of 5000 Oe. The field dependence of magnetization of the specimens at 80°K are given in Fig. 5. It is seen in this figure that the magnetization is almost saturated by the field strength of 8500 Oe for the specimens of $x<0.8$, while it is far from saturation at the same field strength for the specimens of $x>0.8$.

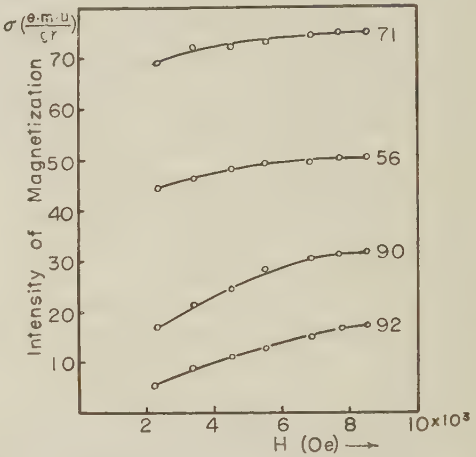

Fig. 5. Intensity of magnetization vs. magnetic field strength at 80°K. Numerals attached to each curve indicate the $FeTiO_3$ mol. per cent.

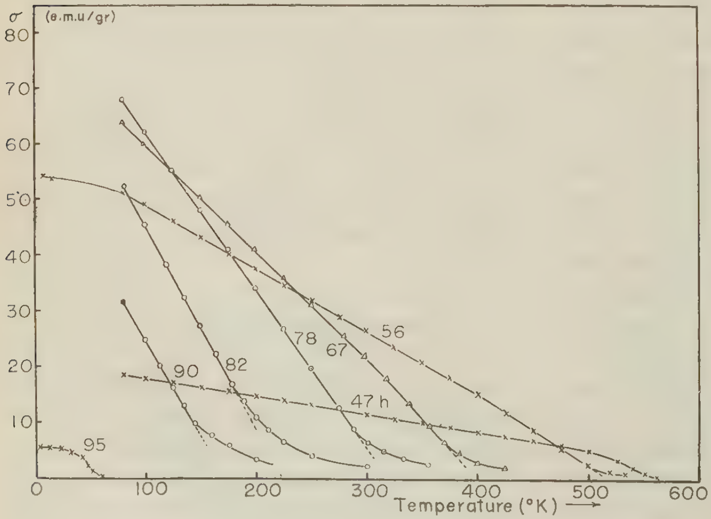

Fig. 4. Intensity of magnetization in a field strength of 8500 Oe vs. temperature for the specimens of $0.95\geqq x\geqq 0.47$. Numerals attached to each curve indicate the $FeTiO_3$ mol. per cent.

As was shown in Fig. 4, it is a remarkable characteristic for the thermomagnetic curve of this solid solution series that magnetization changes almost linearly with temperature to the liquid nitrogen temperature and then approaches to the final value of 0°K with the decreasing slope.

Hence we can not extrapolate the thermomagnetic curve linearly to 0°K in the estimation of the saturation value of magnetization at that temperature. Then, the following procedure was tentatively adopted to obtain the approximate value of the magnetization at 0°K, $\boldsymbol{J}(0)$.

$$\boldsymbol{J}(0)=\frac{\boldsymbol{J}_0+\boldsymbol{J}(80)}{2},$$

where $\boldsymbol{J}(80)$ and $\boldsymbol{J}_0$ indicate respectively the observed value of magnetization at 80°K and the one calculated by assuming that the linear character of thermomagnetic curve can be extrapolated to 0°K without any modification.

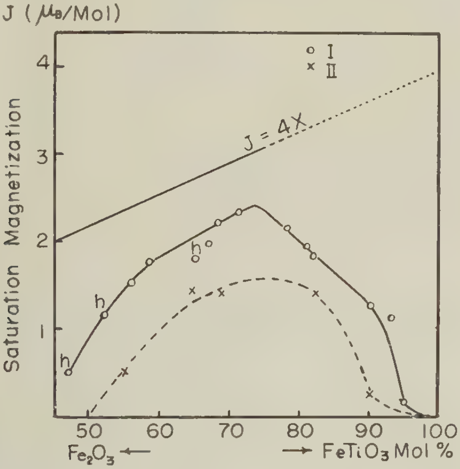

Fig. 6. Estimated saturation magnetization at 0°K vs. composition for the specimens of $1>x\geqq 0.47$. The solid straight line indicates the theoretical value.
○ : the specimens prepared by the method I.
× : the specimens prepared by the method II.
h : the specimen of which magnetization was intensified by heat treatment after being prepared by the method II.

Fig. 6 shows the dependence of the estimated value of the saturation magnetization at 0°K upon the composition of the solid solution series. In this figure the intensity of magnetization is expressed by the Bohr magneton number per one molecule of $x\mathrm{FeTiO_3}\cdot(1-x)\mathrm{Fe_2O_3}$. Although such an estimation as mentioned above includes a fairly large error for the specimens of $1>x>0.8$, the general tendency that the magnetization attains to the largest value around $x=0.75$ and decreases on both sides of the composition seems to be true. In the figure the magetization of the specimens prepared by the method II is also plotted for comparison. The above-mentioned general tendency remains unchanged even in this case.

iii) $0.5>x\geqq 0$

All specimens in this region are feeble ferromagnetics when they are quenched from any temperature higher than 1100°C. The thermomagnetic curve down to the liquid nitrogen temperature are given in Fig. 7 and the intensity of magnetization at 80°K for a field strength of 9350 Oe is plotted in Fig. 8 against the composition of the specimen. It is clearly seen in these figures that the

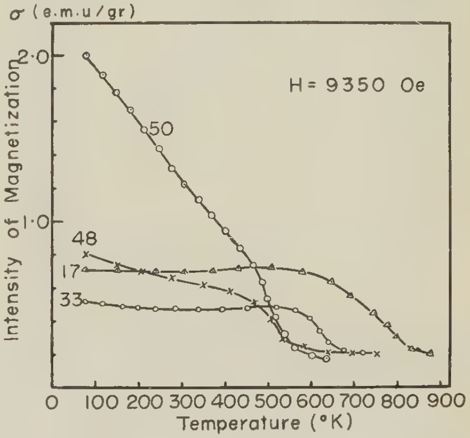

Fig. 7. Intensity of magnetization in a field strength of 9350 Oe vs. temperature for the specimens of $0.5>x>0$. Numerals attached to each curve indicate the FeTiO₃ mol. per cent.

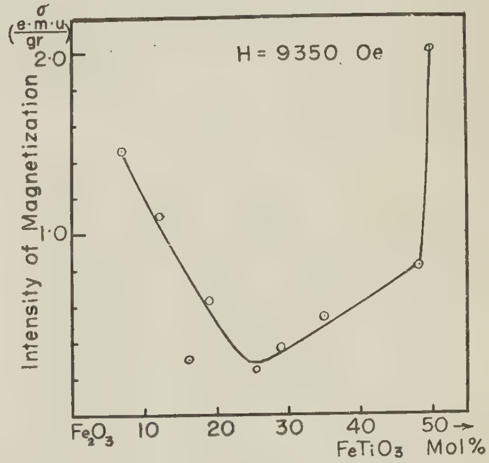

Fig. 8. Intensity of magnetization in a field strength of 9350 Oe at 80°K vs. composition for the specimens of $0.5>x>0$.

magnetic properties of the solid solution series change with their composition very abruptly when x approaches to 0.5. It must be noticed in Fig. 7 that the thermomagnetic curves of the specimen for $x=0.50$ and $x=0.48$ differ one another remarkably in their general modes; the thermomagnetic curve of the specimen of $x=0.50$ is distinguished in a large temperature coefficient, $\partial J/\partial T$, from that of $x=0.48$. It must be further noted that, as to the specimens of x greater than 0.07, a discontinuous change in magnetization at the lower temperatures as Morin found in α-Fe_2O_3[3] was not observed.

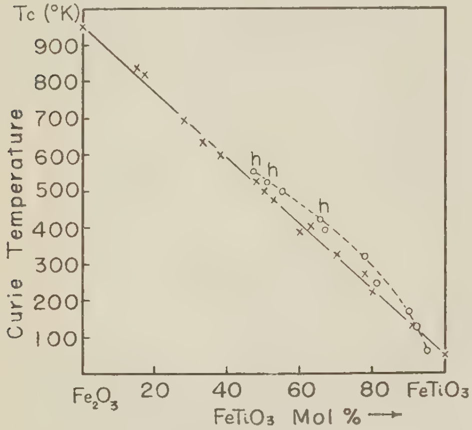

Fig. 9. Variation of Curie temperature with composition in the $FeTiO_3$-Fe_2O_3 series.

×: the specimens prepared by the method II.

○: the specimens prepared by the method I or of which magnetization was intensified by heat treatment after being prepared by the method II.

We plotted the Curie point of the specimens against their compositions in Fig. 9, where it was found that the Curie point of the specimens with the weak magnetization (those for $x<0.5$ or those prepared by the method II) changes almost linearly from 950°K of α-Fe_2O_3 to 55°K of $FeTiO_3$, but as for the specimens of which magnetization was intensified the Curie point deviated distinctly from this line towards the higher temperature side. These facts will be discussed in detail in the theoretical considerations of the second part of this paper.

4. 2. *Magnetic Susceptibilities*

Change in the magnetic susceptibility with temperature was also measured by the magnetic balance. The specimens of 100~200 milligram in their weight were used in this case. The specimens for $0.5>x\geq 0$ were measured in the atmospheric pressure, while for $1.0\geq x\geq 0.5$ in the state sealed into a quartz tube evacuated below 10^{-3} mm mercury.

In Fig. 10, the change in the reciprocal magnetic susceptibility with temperature is given. In this figure it must be noted first of all that pure ilmenite is antiferromagnetic below 55°K as has been reported by Bizette and Tsai[2], but its Néel point is lower than that of their specimen. The pure ilmenite specimen used in the present study has the very high electrical resistivity ($10^6\,\Omega$-cm at the room temperature) and is expected to have no trace of Fe^{3+}. This was also confirmed by the chemical analysis. This measurement at the very low temperatures was also carried out at Research Institute for Iron, Steel and Other Metals, Tôhoku University.

The reciprocal magnetic susceptibility versus temperature curve ($1/\chi-T$ curve) of the specimens for $x<0.5$ shows a particular mode which can be interpreted as the simple superposition of the parasitic ferromagnetism upon the antiferromagnetism proper to this sub-

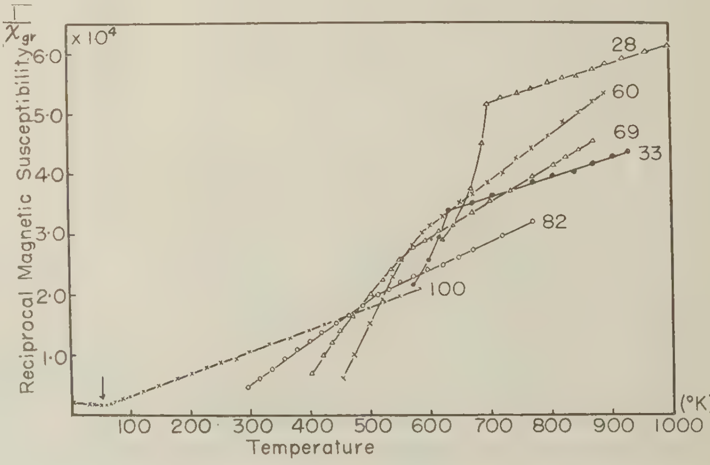

Fig. 10. Reciprocal magnetic susceptibility vs. temperature. Numerals attached to each curve indicate the $FeTiO_3$ mol. per cent.

stance. On the other hand the $1/\chi-T$ curve for the specimen around $x=0.5$ shows a mode unique to the ferrimagnetic substances: a concavity towards the temperature axis is clearly seen in the curve. It must be further noted that when x approaches 1, the $1/\chi-T$ curve approaches to the straight line which is distinguished from that of the ordinary ferrimagnetics.

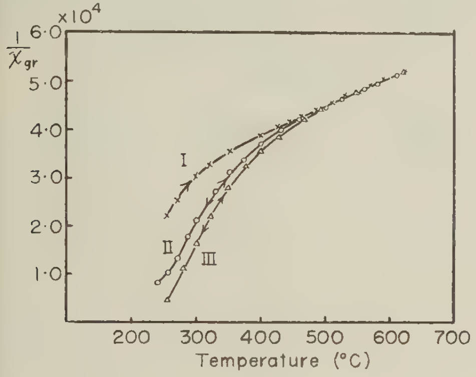

Fig. 11. Reciprocal magnetic susceptibility vs. temperature for the specimen of $x=0.5$.

We showed in Fig. 11 the change in the reciprocal magnetic susceptibility with temperature of the specimen for $x=0.5$ in detail. The specimen originally prepared by the method I has the very weak magnetization. When it is heated up above its Curie point, the reciprocal magnetic susceptibility follows the curve I, but in the cooling process it follows the curve II. This shows the magetization was intensified appreciably by cooling under the magnetic field. The $1/\chi-T$ curve of the specimen in re-heating and re-cooling process coincides well with the initial cooling curve. Furthermore, we could make this specimen strongly ferromagnetic by the heat treatment described in another paper[19]. The $1/\chi-T$ curve of the specimen of which magnetization was intensified in this way follows the curve III. It may be worthwhile to note that in any cases the magnetic susceptibilities coincide well at high temperatures within the experimental errors. Hence, we may need not pay too much attention in the measurement of magnetic susceptibility by what method the specimens were prepared.

We could find that the $1/\chi-T$ curve for all the specimens obeys the Curie-Weiss' law, $\chi=C_M/T-\Theta$, quite well at high temperatures. The values of C_M and Θ were determined by means of the method of least squares, their variations with composition of the solid solution series being given in Fig. 12 and Fig. 13. The cross marks in these figures are the

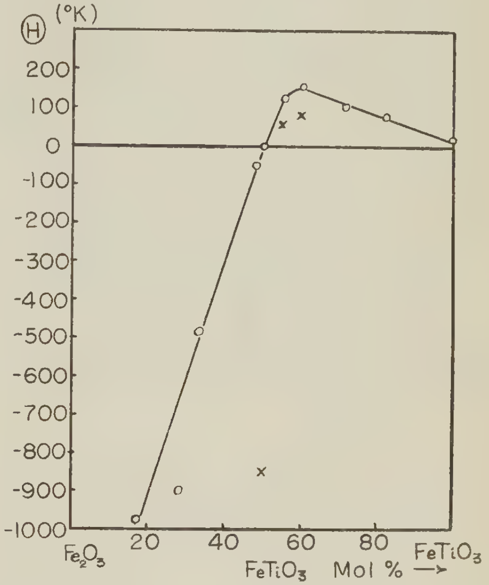

Fig. 12. Variation of the asymptotic paramagnetic Curie temperature with composition in the $FeTiO_3$-Fe_2O_3 series.

○ : calculated from $1/\chi=(T-\Theta)/C$

× : calculated from $1/\chi=(T-\Theta)/C-\sigma/(T-\theta)$

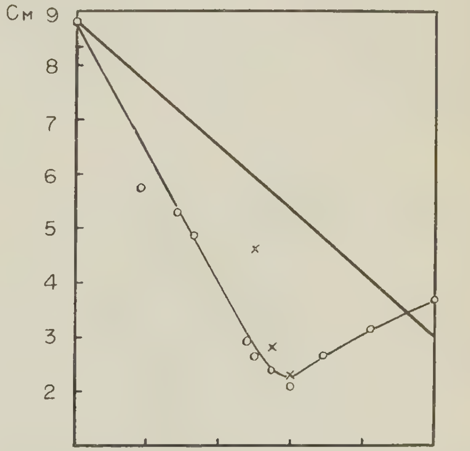

Fig. 13. Variation of Curie const. per mol. with composition in the $FeTiO_3$-Fe_2O_3 series.

○ : calculated from $1/\chi_M=(T-\Theta)/C_M$

× : calculated from $1/\chi_M=(T-\Theta)/C_M-\sigma/(T-\theta)$

Straight line represents the theoretical value obtained from the assumption that only spins contribute to magnetic susceptibility.

values determined by using the following equation,

$$\frac{1}{\chi}=\frac{T-\Theta}{C_M}-\frac{\sigma}{T-\theta}\,.$$

It is suggested in Fig. 12, by taking the sign of Θ into consideration, that there are ferromagnetic coupling in the specimens for $1>x>0.55$ and when the composition approaches to 0.5 antiferromagnetic coupling comes to predominate. The latter result is very consistent with other experimental results. However, we can also find that the value of C_M decreases and the value of Θ increases in holding its positive sign as the composition change from $x=1$ to $x=0.5$. This fact can not be explained by such a simple theory as will be stated in the second part of the present paper.

Part II. Theoretical Considerations

§ 5. Super Exchange Interactions in the Rhombohedral Structure

Before we discuss the magnetic properties of the solid solution series, it is necessary to understand fully the configuration of cations and the exchange interaction between them in the rhombohedral sesquioxide. This has been recently discussed by Li[21] and Iida[22].

In the rhombohedral sesquioxide the cations form a hexagonal lattices but they deviates slightly from the hexagonal lattice points towards the direction of arrows illustrated in Fig. 14. As we can see in the figure the cation sites can be divided into four sublattices; A_1, A_2, B_1 and B_2. Such cation pairs along C axis as A_1-B_2 or B_1-A_2 form the pseudo-molecules.

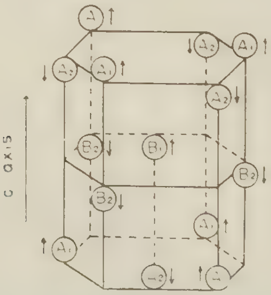

Fig. 14. Cation lattice in a rhombohedral sesquioxide. The cations deviate from the hexagonal sites towards the direction of arrows.

Then the exchange interaction between these cations can be classified as is given in Table I. In the third column of the table, the number of the nearest neighbour having the same kind of interaction is given. The angles between metal-oxygen-metal tabulated in the last column were calculated by Iida for α-Fe$_2$O$_3$. As this angles show, Γ_a and Γ_b; the interactions between the cations on different layers are expected to be stronger than Γ_c, i.e. those between the cations on the same layer. This is because the overlapping of electrons of cations and oxygen is larger for Γ_a and Γ_b than for Γ_c. Hence, the magnetic lattice might be chiefly determined by these interactions. It must be further noticed that Γ_a and Γ_b have the same sign for α-Fe$_2$O$_3$ but different for Cr$_2$O$_3$. Li proposed that Γ_d, the interaction between cations of the pseudo-molecule plays also an important role on the construction of magnetic lattice, while Iida has omitted it as the secondary effect. We also disregard this interaction in the present paper.

Table I. The configurations of Me–O–Me with close contacts between Me and O. The angle ∠Me O Me is calculated for αFe$_2$O$_3$. n is the number of the nearest neighbour having the same kind of interaction.

Exchange interaction	Cation sites	n	∠Me O Me
Γ_a	$A_i\ B_i$	6	132°41′
Γ_b	$A_i\ B_j (i\neq j)$	3	116°59′
Γ_c	$A_i\ A_j$ $B_i\ B_j$	3	94°20′
Γ_d	$A_j\ B_i$ (pseudo molecule)	1	88°23′

§ 6. Cation Distribution in Hexagonal Lattice

In order to understand the magnetic properties of the solid solution series, we must know how the cations distribute among four sublattices described in § 5. It has recently been confirmed by both X-ray* and neutron analysis* that the crystal structure of the ferromagnetic specimen in the solid solution series keeps the same space group $R\overline{3}$ as pure ilmenite[23]. In other words we could detect a kind of super structure of Ti ions and Fe ions, where the layers involving Ti ions selectively alternate along *C*-axis with the layers involving only Fe ions. Accordingly we can assume with sufficient plausibility that Ti ions occupy only two sublattices B_1 and B_2 in our rhombohedral structure for the ferromagnetic specimen which we denote hereafter as the ordered specimen. Generally speaking, there are four possible configurations of Fe^{2+}, Fe^{3+} and Ti^{4+} ions among four sublattices and the number of occupation of these ions on each sublattice is given in Table II for the solid solution of $x FeTiO_3 \cdot (1-x) Fe_2O_3$.

---

* The results of the X-ray analysis for a single crystal of the ferromagnetic specimen of the FeTiO$_3$-Fe$_2$O$_3$ solid solution series will be published separately in near future.

In this table, the configuration I and II correspond to the cases when each Fe^{2+} and Ti^{4+} ions occupy the one of the four sublattices preferentially; that is, A_1 and B_1 for configuration I and A_1 and B_2 for configuration II. But in the configuration III, Fe^{2+} and Fe^{3+} distribute at random among A_1 and A_2 sublattices and Ti^{4+} and Fe^{3+} among B_1 and B_2 sublattices. Configuration IV is the case when all ions distribute at random among the cation sites, corresponding to the disordered state.

Table II. Possible distributions of Fe^{2+}, Fe^{3+} and Ti^{4+} ions among four sublattices and the number of the occupation of these ions on each sublattice in $x TiFeO_3 \cdot (1-x) Fe_2O_3$ solid solution series.

	I	II	III	IV
A_1	$Fe^{2+}\ \frac{1}{2}$	$Fe^{2+}\ \frac{1}{2}$	$Fe^{2+}\frac{x}{2}\ Fe^{3+}\frac{(1-x)}{2}$	$Fe^{2+}\frac{x}{4}\ Ti^{4+}\frac{x}{4}\ Fe^{3+}\frac{(1-x)}{2}$
A_2	$Fe^{2+}\left(x-\frac{1}{2}\right)Fe^{3+}(1-x)$	$Fe^{2+}\left(x-\frac{1}{2}\right)Fe^{3+}(1-x)$	〃	〃
B_1	$Ti^{4+}\ \frac{1}{2}$	$Ti^{4+}\left(x-\frac{1}{2}\right)Fe^{3+}(1-x)$	$Ti^{4+}\frac{x}{2}\ Fe^{3+}\frac{(1-x)}{2}$	〃
B_2	$Ti^{4+}\left(x-\frac{1}{2}\right)Fe^{3+}(1-x)$	$Ti^{4+}\ \frac{1}{2}$	〃	〃

In pure ilmenite Fe^{2+} ions always occupy the A sublattice, so the configuration such as Fe^{2+} ions enter into the B sublattice seems to be unnatural for the ordered specimens. Besides, the simple consideration of the magnetic properties excludes this configuration as will be stated in the next paragraph. Consequently such a configuration was omitted for the ordered structure from the outset.

It is very difficult to know which of these three configurations I, II and III is the most stable and is realized in the ordered specimens, because it can be determined only by the careful X-ray or neutron diffraction studies. In the present stage, we know nothing about it, so we calculated the electrostatic energy of these three configurations to see which is the more stable. The calculation was carried out for the specimen of $x=0.5$ where the superstructure within the layer as well as along *C*-axis can be established.

In Fig. 15, the super lattices established for the configuration I and II are shown, and in the bottom of the figure, the calculated gains of the electrostatic energy by forming the superstructure are presented. $E^{(1)}$ is the value calculated by considering only the nearest neighbour interaction, while in the case of $E^{(2)}$ the interaction is considered up to the second nearest neighbour. In these calculations the energy for the disordered state is taken null and the unit is arbitrary. As the Coulomb force is very slow to converge, we must consider the interaction between the more remote neighbour to obtain the more accurate value of the energy. We can see, however, from these two calculations that the energy difference between these two configurations is getting less when we consider the interaction more completely. In other words it is expected that the configuration I and II are realized with an almost equal probability. Consequently, the configuration III seems to be the most probable for the ordered specimens so long as we consider the electrostatic energy alone, since the configuration III may be regarded as the average state of the configuration I and II. Hence, in the following discussions we always assume this configuration for the ordered state.

---

* Private Communication from Dr. G. Shirane.

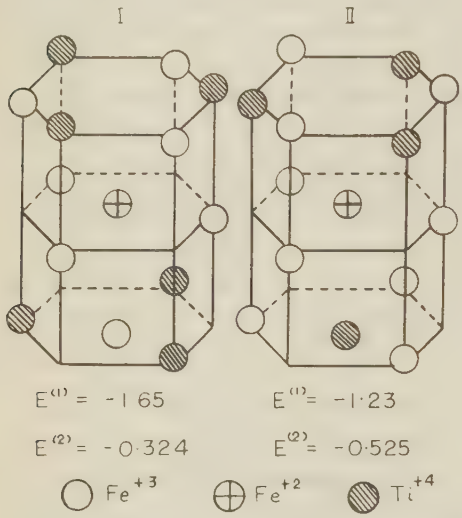

Fig. 15. Superstructure of the cations in the specimen of $x=0.5$. Numerical values at the bottom of the figure indicate the gain of electrostatic energy by forming the superstructure. (in arbitrary unit)

§ 7. Simple Explanation of the Magnetic Properties of the $FeTiO_3$-Fe_2O_3 Solid Solution Series

In this paragraph, we will discuss briefly an outline of the magnetic properties of the solid solution series. The more detailed discussion is stated in the next paragraph.

i) *Antiferromagnetism of ilmenite* ($FeTiO_3$)

We have already confirmed in § 4 that ilmenite is antiferromagnetic below 55°K. This temperature is a little lower than that of ilmenite measured by Bizette and Tsai. Considering that their specimen is a natural mineral, this discrepancy may be due to the presence of an impurity in their specimen. Shomate reported a marked hump on the heat capacity versus temperature curve at 58°K for synthesized ilmenite[24]. If we suppose this temperature corresponds to the Néel point, our Néel temperature agrees well with it.

In order to understand the magnetic structure of antiferromagnetic ilmenite, it is very important to know the valency of Ti ions. We have found through the study of the electrical conduction of the $FeTiO_3$-Fe_2O_3 solid solution series it is more plausible to assume that Ti ions is always tetravalent in the solid solution[25]. So we assumed in the following discussion Ti^{4+} ions play no part on the magnetic coupling.

Accordingly, we can consider the two different magnetic structures for the antiferromagnetic ilmenite which are given in Fig. 16 schematically.

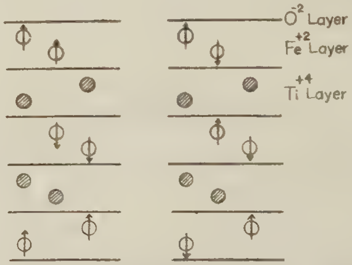

Fig. 16. Schematic illustrations of two possible antiferromagnetic structure in ilmenite.

We can explain the outline of the magnetic properties of the solid solution by using either of these models.

ii) $1>x\gtrsim 0.5$: *ferromagnetic region*

In this region, the ordering of Fe and Ti ions established for pure ilmenite is retained. So, the cation configuration is assumed to be the case III. If we put another assumption for the specimens of $0.75>x>0.5$ that the interaction Γ_a and Γ_b are negative and their strengthes are fairly large compared with Γ_c, the magnetic moment on each layer is orientated in the same direction, coupling antiferromagnetically between neighbouring layer. Consequently, the saturation magnetization of the solid solution, $x FeTiO_3\cdot(1-x) Fe_2O_3$ at 0°K can be given for this region of x by

$$J=x\cdot J_{Fe^{2+}}=4x$$

where J is the magnetization per one molecule of the solid solution expressed by the number of Bohr magnetons. In Fig. 6 this value is drawn by a solid line. Though the experimental values are deviated from this line, this configuration may be the most plausible, because the discrepancy becomes larger when we assume the other configurations.

The decrease in the magnetization for $x>0.75$ may be attributed to the following reason. So long as the magnetic ions in B layers are few and the interaction between A and B layer is weak, the magnetic moments on the A layer are orientated antiparallel with each other by the interaction within the layer and they can not align in the same direction as is assumed in the above consideration. Consequently, the total magnetization decreases with the increase of the number of ions coupled antiferromagnetically on the A layer, tending to zero for pure ilmenite.

It may be very probable to suppose that the specimens are not completely ordered* since they were prepared by quenching from high temperatures. The theoretical value of the magnetization for $0.75>x>0.5$ can be approached more closely the experimental value when we consider this imperfect ordering.

iii) $0.5>x\geqq 0$: *antiferromagnetic region*

When the concentration of $FeTiO_3$ is less than 50 mol. per cent, the state that Fe^{2+} and Ti^{4+} distribute at random between A and B lattices is assumed to be more stable. Consequently these two sublattices become equivalent, the magnetic structure being antiferromagnetic as a whole. The reciprocal magnetic susceptibility versus temperature curve which was given in Fig. 10 clearly shows this character at high temperatures. It is, however, impossible that these two sublattices become completely equivalent, so the parasitic ferromagnetism appears owing to an uncompensation of magnetization between two sublattices. When the composition approaches to $x=0.5$, the tendency that Fe^{2+} ions concentrate on A layers and Ti^{4+} ions B layers begins to appear, resulting in the abrupt increase of the parasitic ferromagnetism around $x=0.5$.

It has already been shown in the experimental part of the present paper and in another paper[19)] that such an ordering of Ti^{4+} and Fe^{2+} ions could be either established or disturbed by the appropriate heat treatments especially for the specimen of x around 0.5. The mechanism of the order-disorder transformation of this substance, however, is so complicated that it will be discussed elsewhere in near future.

§ 8. Detailed Discussion

In the above paragraph we have proposed a model which can explain the outline of the magnetic properties of the solid solution series. In this paragraph we shall discuss them more in detail by using the molecular field theory and examine whether such an approximation can be applied successfully to the interpretation of the magnetic properties of this rhombohedral solid solution series in the same manner as has been done for many ferrites[26)].

Since we have assumed in the previous paragraph that the cations distribute at random within each layer, the molecular field coefficient in the structure is reduced to α and γ which correspond respectively to the interaction within a layer and between layers, being expressed by the following equations,

$$\begin{aligned}\alpha&=2(3\Gamma_c)/Ng^2\mu_B^2\\ \gamma&=2(6\Gamma_a+3\Gamma_b)/Ng^2\mu_B^2\,.\end{aligned}\qquad(8.1)$$

Then, the molecular field acting on each magnetic ion on different layer becomes

$$\begin{aligned}\vec{h}_{IA}&=(1-x)\gamma_{I\,II}\vec{J}_{IIB}+x\alpha_{I\,I}\vec{J}_{IA}+(1-x)\alpha_{I\,II}\vec{J}_{IIA}\\ \vec{h}_{IIA}&=(1-x)\gamma_{II\,II}\vec{J}_{IIB}+x\alpha_{II\,I}\vec{J}_{IA}+(1-x)\alpha_{II\,II}\vec{J}_{IIA}\\ \vec{h}_{IIB}&=(1-x)\alpha_{II\,II}\vec{J}_{IIB}+x\gamma_{II\,I}\vec{J}_{IA}+(1-x)\gamma_{II\,II}\vec{J}_{IIA},\end{aligned}\qquad(8.2)$$

where $\vec{h}_{IA}$, $\vec{h}_{IIA}$ and $\vec{h}_{IIB}$ indicate the molecular field acting on a Fe^{2+} ion on the A sublattice, that on Fe^{3+} ion on the A sublattice and that on Fe^{3+} ion the B sublattice respectively. $\gamma_{I\,II}$, $\alpha_{I\,I}\cdots$ indicate the molecular field coefficient between Fe^{2+} (I) and Fe^{3+} (II) ions, Fe^{2+} (I) and Fe^{2+} (I) ions$\cdots$. $\vec{J}_{IA}$ and $\vec{J}_{IIA}$ are the magnetic moment per gram ion of Fe^{2+} and Fe^{3+} on the A sublattice, and $\vec{J}_{\mathrm{IIB}}$ is that of Fe^{3+} on the B sublattice. The magnetic moment J at any temperature T is given by

---

* This was also expected from the neutron diffraction analysis. (Private Communication from Dr. G. Shirane)

$$\vec{J}_{\mathrm{IA}}(T)=\vec{J}_{\mathrm{IA}}(0)\,B_J(\vec{H}+\vec{h}_{\mathrm{IA}}/kT)\,. \tag{8.3}$$

i) *The Curie point*

We have found in § 4 that the Curie points of the series vary almost linearly from the Curie point of α-$\mathrm{Fe_2O_3}$ to that of $\mathrm{FeTiO_3}$ when the magnetization is weak or the ordering is not complete, whereas some deviation from this straight line was seen when the magnetization becomes large. In this section we show that such a characteristics can be derived from the above theory.

The Curie temperature of the solid solution is determined from the following equation

$$\begin{vmatrix} x\alpha_{\mathrm{I\,I}}-T/C(x) & (1-x)\alpha_{\mathrm{I\,II}} & (1-x)\gamma_{\mathrm{I\,II}} \\ x\alpha_{\mathrm{I\,II}} & (1-x)\alpha_{\mathrm{II\,II}}-T/C(x) & (1-x)\gamma_{\mathrm{II\,II}} \\ x\gamma_{\mathrm{I\,II}} & (1-x)\gamma_{\mathrm{II\,II}} & (1-x)\alpha_{\mathrm{II\,II}}-T/C(x) \end{vmatrix}=0, \tag{8.4}$$

where $C(x)$ is the Curie constant per gram ion of the solid solution of $x\mathrm{FeTiO_3}\cdot(1-x)\ \mathrm{Fe_2O_3}$. In special cases for $x=1(\mathrm{FeTiO_3})$, and $x=0(\mathrm{Fe_2O_3})$, the Curie temperatures are reduced from eq. (8.4) as follows,

$$\begin{aligned} T_{\mathrm{FeTiO_3}}&=C(1)\,\alpha_{\mathrm{I\,I}} \\ T_{\mathrm{Fe_2O_3}}&=C(0)\,(\alpha_{\mathrm{II\,II}}+\gamma_{\mathrm{II\,II}})\,. \end{aligned} \tag{8.5}$$

In order to solve the eq. (8.4) for general case, we neglect the quadratic terms of α because α is very small compared with γ. The Curie point of the specimen for any x is given by a root of the following equation.

$$\begin{aligned} \left(\frac{T}{C(x)}\right)^3-\left(\frac{T}{C(x)}\right)^2[\alpha_{\mathrm{I\,I}}x+2(1-x)\alpha_{\mathrm{II\,II}}]-\left(\frac{T}{C(x)}\right)[(1-x)\,x\gamma^2_{\mathrm{I\,II}}+(1-x)^2\,\gamma^2_{\mathrm{II\,II}}] \\ -x(1-x)^2[2\alpha_{\mathrm{I\,II}}\,\gamma_{\mathrm{I\,II}}\,\gamma_{\mathrm{II\,II}}-\alpha_{\mathrm{II\,II}}\,\gamma^2_{\mathrm{I\,II}}-\alpha_{\mathrm{I\,I}}\,\gamma^2_{\mathrm{II\,II}}]=0\,. \end{aligned} \tag{8.6}$$

The last term of the equation is expected to be very small and is also neglected. Then T/C is given by

$$\begin{aligned} \frac{T}{C(x)}&=\frac{1}{2}\,[\alpha_{\mathrm{I\,I}}x+2(1-x)\,\alpha_{\mathrm{II\,II}}]+\sqrt{(1-x)x\,\gamma^2_{\mathrm{I\,II}}+(1-x)^2\,\gamma^2_{\mathrm{II\,II}}} \\ &\therefore\ \frac{1}{2}\,T_{\mathrm{TiFeO_3}}/C(1)\times x+T_{\mathrm{Fe_2O_3}}/C(0)\times(1-x)+\bar{\gamma}[\sqrt{1-x}-(1-x)]\,. \end{aligned} \tag{8.7}$$

On the other hand, in the disordered state, A and B sublattices becomes equivalent and the molecular fields $\vec{h}_{\mathrm{I}}$ and $\vec{h}_{\mathrm{II}}$ are reduced as follows by ignoring the distinction of A and B in eq. (8.2).

$$\begin{aligned} \vec{h}_{\mathrm{I}}&=\frac{x}{2}\,(\alpha_{\mathrm{I\,I}}+\gamma_{\mathrm{I\,I}})\,\vec{J}_{\mathrm{I}}+(1-x)(\alpha_{\mathrm{I\,II}}+\gamma_{\mathrm{I\,II}})\,\vec{J}_{\mathrm{II}}\,, \\ \vec{h}_{\mathrm{II}}&=\frac{x}{2}\,(\alpha_{\mathrm{I\,II}}+\gamma_{\mathrm{I\,II}}\vec{J}_{\mathrm{I}}+(1-x)(\alpha_{\mathrm{II\,II}}+\gamma_{\mathrm{II\,II}})\vec{J}_{\mathrm{II}}\,. \end{aligned} \tag{8.8}$$

Then the Curie temperature is determined from the following equation

$$\begin{aligned} \left(\frac{T}{C(x)}\right)^2-\left(\frac{T}{C(x)}\right)\left[\frac{x}{2}\,(\alpha_{\mathrm{I\,I}}+\gamma_{\mathrm{I\,I}})+(1-x)\,(\alpha_{\mathrm{II\,II}}+\gamma_{\mathrm{II\,II}})\right] \\ +\left[(\alpha_{\mathrm{I\,II}}+\gamma_{\mathrm{I\,II}})^2-(\alpha_{\mathrm{I\,I}}+\gamma_{\mathrm{I\,I}})\,(\alpha_{\mathrm{II\,II}}+\gamma_{\mathrm{II\,II}})\right]\frac{x(1-x)}{2}=0\,. \end{aligned} \tag{8.9}$$

The last term is also neglected in the same reason as in eq. (8.6), since it is expected that $(\alpha_{\mathrm{I\,II}}+\gamma_{\mathrm{I\,II}})$ may be the mean value of $\alpha_{\mathrm{I\,I}}+\gamma_{\mathrm{I\,I}}$ and $\alpha_{\mathrm{II\,II}}+\gamma_{\mathrm{II\,II}}$. Thus, the Curie temperature for the disordered state is finally expressed by

$$T/C(x)=\frac{x}{2}(T_{\mathrm{FeTiO_3}}/C(1)+\gamma_{\mathrm{II}})+(1-x)\,T_{\mathrm{Fe_2O_3}}/C(0). \tag{8.10}$$

The difference of the Curie temperature for the ordered and disordered state of the same composition is

$$(T/C)_{\mathrm{order}}-(T/C)_{\mathrm{disorder}}=\sqrt{(1-x)\,x\,\gamma^2_{\mathrm{I\,II}}+(1-x)^2\gamma^2_{\mathrm{II\,II}}}-\left[\frac{x}{2}\gamma_{\mathrm{I\,I}}+(1-x)\gamma_{\mathrm{II\,II}}\right]. \tag{8.11}$$

In order to compare this theory with the experimental results, we plotted in Fig. 17 the value of the Curie temperature divided by the Curie constant $C(x)$, $T_c/C(x)$ against the composition. As for $C(x)$ we used rather theoretical value obtained from $C(x)=xC(1)+(1-x)C(0)$, where $C(0)$ and $C(1)$ are the atomic Curie constant for Fe^{2+} and Fe^{3+} ions, being 3.00 and 4.38 respectively. These values are calculated from the assumption that the spin for Fe^{2+} ions is $j=4/2$ and for Fe^{3+} ions is $j=5/2$.

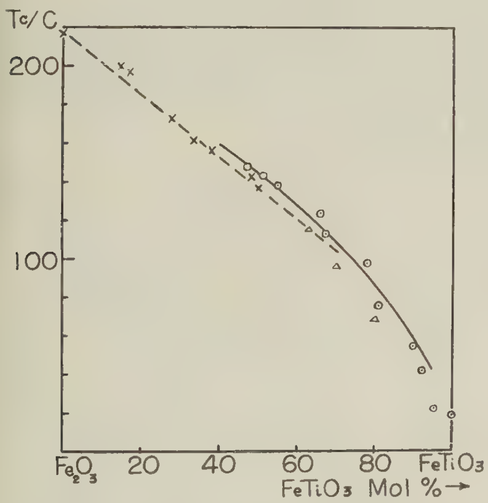

Fig. 17. Variation of the reduced Curie temperature $T_c/C(x)$ with composition in the $FeTiO_3$-Fe_2O_3 series.

⊙: ordered specimen.

△: partially ordered specimen.

×: disordered specimen.

—: theoretical value for the ordered case.

---: theoretical value for the disordered case.

In the figure cross marks indicate the Curie temperature of the disordered specimens, while triangle marks and circles show that of partially or nearly completely ordered specimens. On the other hand, the solid line represents the theoretical curve calculated from eq. (8.7) by estimating $\bar{\gamma}=150$ and the broken line was calculated from eq. (8.10) by estimating $\gamma_{\mathrm{II}}=98$. These estimated values seem not to be unreasonable, because it can be inferred from eq. (8.5) that $\gamma_{\mathrm{II\,II}}+\alpha_{\mathrm{II\,II}}=216$ and furthermore $\gamma_{\mathrm{I\,II}}$ or $\gamma_{\mathrm{I\,I}}$ are expected to be smaller than $\gamma_{\mathrm{II\,II}}$. As we can see in the figure, the agreement is fairly well. The linear decrease of the Curie temperature of the specimens prepared by the method II with composition from that of hematite to ilmenite may be only apparent, since we can not expect any linear relation between the Curie temperature and the composition from the present theory.

Besides we may expect from these considerations that the magnitude of superexchange interactions in this rhombohedral structure is given by the following order,

$$\mathrm{Fe^{3+}{-}O{-}Fe^{3+}>Fe^{3+}{-}O{-}Fe^{2+}>Fe^{2+}{-}O{-}Fe^{2+}}.$$

This is also expected from the mechanism of the superexchange interaction theoretically.

It may safely be said that the number of the interaction between Fe^{2+} and Fe^{3+} increases and that between Fe^{2+} and Fe^{2+} decreases as the cation configuration changes from disordered state to ordered state. Accordingly as was shown in the figure, it was expected that the Curie temperature of the ordered specimen is higher than that of the disordered specimen only for $x<0.75$ provided that we adopt the above-estimated values for $\bar{\gamma}$ and $\gamma_{\mathrm{I\,I}}$. But it was found from the experimental results which was shown in Fig. 9 that the increase of the Curie temperature attains to the largest value around $x=0.75$. This discrepancy may become smaller if we take the configuration I or II for the ordered state in place of III and adopt the experimental value for $C(x)$.

ii) *Magnetization*

In this section we try to explain the general mode of the thermomagnetic curve and the magnetization at 0°K by the present theory.

For this purpose, we simplify the expression of eq. (8.2) a little more by assuming that the magnetization of all ions on the same sublattice changes with the same temperature coefficient; that is, $\vec{J}_{IA}=n\vec{J}_{IIA}$ for any temperature, where $n=4/5$ in our case.

Then eq. (8.2) can be reduced to

$$\begin{aligned}\vec{h}_A&=[xn\alpha_{I\,I}+(1-x)\alpha_{I\,II}]\vec{J}_A+(1-x)\gamma_{I\,II}\vec{J}_B\\&=\alpha'\vec{J}_A+(1-x)\gamma\vec{J}_B\,,\qquad(8.12)\\\vec{h}_B&=[xn\gamma_{I\,II}+(1-x)\gamma_{II\,II}]\vec{J}_A+(1-x)\alpha_{II\,II}\vec{J}_B\\&=\gamma'\vec{J}_A+(1-x)\alpha\vec{J}_B\,.\end{aligned}$$

This equation corresponds to that for the case when one kind of magnetic ions distribute on A and B sublattices with the ratio of $1:(1-x)$. This was treated by Néel in detail[26]. So we can adopt his results if the assumption made above is permitted. According to his theory, the thermomagnetic curve takes very different modes as the values of α, α', γ and γ' change relatively. When they are in some restricted range which he denoted as **R**, the thermomagnetic curve becomes linear as is found in our specimens. The type **R** corresponds to the case when the interaction within the A layer α, α' is not so weak compared with that of ions between the neighbouring layer and they are all negative. In this case the magnetization on the A layer does not saturate even at 0°K, while that on the B layer saturates, total magnetization changing linearly with temperature.

This model seems to be able to be applied to our case, because the interaction between the layer is diluted by concentration of non magnetic ions only on the B sublattice. Then the magnetization on the A sublattice is expected not to be saturated, while that of B sublattice is saturated. Consequently the total magnetization of the specimens must take the smaller values than in the case when the magnetization is saturated on both the sublattices. The deviation of the observed value of magnetization from the theoretical curve which was seen in Fig. 6 for the specimens of $0.75>x>0.5$ may be partially attributed to this effect.

When we calculate the total magnetic moment J at 0°K mathematically by following Néel's procedure, it becomes for **R** type

$$J=(1-x)\left(\frac{|\gamma|+|\gamma'|-2|\alpha|}{2|\alpha|}\right)J_{AII}\,.\qquad(8.13)$$

This value can not be fitted to the observed value for $0.75>x>0.5$ even though we choose any proper value for γ, γ' and α, indicating that the magnetization on the A sublattice seems to be more saturated than is expected from the theory. This fact suggests that, though we assumed in the above consideration that the superexchange interaction within the layer was negative, there exists some force to align the magnetic moment parallel. Existence of such a force is also expected from the measurement of magnetic susceptibility.

iii) *Magnetic Susceptibility*

If the above molecular field approximation can be applied to the magnetic susceptibility above the Curie temperature, it must obey the following equation rather than the simple Curie-Weiss' law

$$\frac{1}{\chi}=\frac{T-\Theta}{C}-\frac{\sigma}{T-\theta}\,.\qquad(8.14)$$

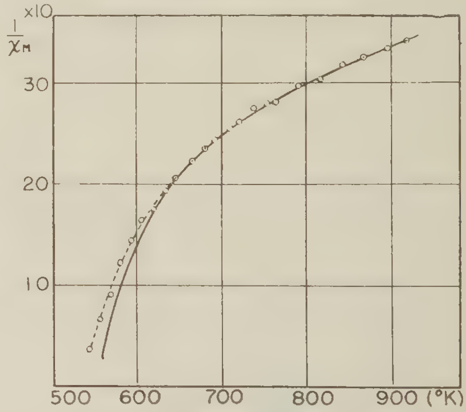

Fig. 18. Theoretical curve for $1/\chi_M=(T+854)/4.61-17733/(T-496)$ and the experimental values for the specimen of $x=0.5$. (the case III in Fig. 11)

We showed in Fig. 18 that this equation can be fitted well to the observed values for the specimen of $x=0.5$. The values of Θ and C determined from this equation are also plotted in Fig. 12 and Fig. 13. When x becomes larger than 0.7, however, it is found that this equation can not be adapted to the observed curve. Therefore, it is clear that the above model is still unsatisfactory for explaining the magnetic properties of the solid solutions $x\text{FeTiO}_3\cdot(1-x)\text{Fe}_2\text{O}_3$ over the whole range of x.

Furthermore, the positive value of Θ (that is the positive interaction) for the specimens of $1>x>0.5$ can not be expected from the above model where we assumed all interactions to be negative. The decrease of the Curie constant or the atomic moment with the decrease of x, which was shown in Fig. 13, is much more unexplainable. Such a deviation of C from the theoretical value is generally attributed to the decrease of the ionic character of ions as has been done for some cobaltite[27]. But such a situation can not be expected for the present solid solution series, because we could not find any extraordinary change of the lattice parameters and the electrical conductivity for the specimen of $1>x>0.5$, which would be expected if the covalent character should appear only in this region.

It must be noticed that in the case of the solid solution of $NiTiO_3$ and Fe_2O_3, which is also ferromagnetic and has the same characteristics of the thermomagnetic curve and the magnetization at 0°K as that of the present solid solution series[28], we have not observed any anomalous change for Θ and C. Hence, such an anomalous character as was stated above may be, if really exists, due partially to the instability of the compound or the presence of Fe^{2+} ions whose orbital moment is not quenched. Because in case of the $NiTiO_3$–Fe_2O_3 solid solution series, the compound is stable and orbital moment seems to be quenched.

§ 9. Conclusion

Magnetic properties of the synthesized solid solution of $x\mathrm{FeTiO_3}\cdot(1-x)\mathrm{Fe_2O_3}$ have been examined in detail both experimentally and theoretically for the whole range of $0\geqq x\geqq 1$. The general conclusions obtained may be summarized as follows:

1). We have found that the specimens having the largest intensity of magnetization (or perfectly ordered) can be prepared by quenching the mixture of ilmenite and hematite in a given ratio from 1200°C after being maintained at this temperature for more than 12 hours. The magnetic properties of ilmenite–hematite solid solution series $x\mathrm{FeTiO_3}\cdot(1-x)\mathrm{Fe_2O_3}$ can be classified into three groups; i) $x=1$, ii) $1>x\gtrsim 0.5$, and iii) $0.5>x\geqq 0$. As for the pure ilmenite, we have found that it is antiferromagnetic below 55°K. The specimens for $1>x\gtrsim 0.5$ are strongly ferromagnetic. Estimated intensity of magnetization at 0°K increases as the composition x becomes large from 0.5 to 0.75 and reaches maximum around $x=0.75$, then decreasing towards pure ilmenite. The specimens for $0.5>x\geqq 0$ are again antiferromagnetic on which feeble parasitic ferromagnetism is superimposed. Curie temperature of the specimens with a weak magnetization (the specimens of $x<0.5$ and those imperfectly ordered for $1>x\gtrsim 0.5$) changes almost linearly from 950°K of α-Fe_2O_3 to 55°K of $FeTiO_3$. But, as for the specimens having a large intensity of magnetization, the Curie temperature deviated distinctly from this straight line towards the higher temperature side. Dependence of the Curie constant C_M and the asymptotic paramagnetic Curie temperature Θ, which were determined from the reciprocal magnetic susceptibility versus temperature curve, upon the composition has also been examined. We have found, for the specimens of $1>x>0.5$, the anomalous decrease and increase on the value of C_M and Θ respectively.

2) These experimental results were discussed by using the approximation of molecular field. It was shown that we could explain an outline of the magnetic properties of the soild solution provided that the tetravalent Ti ions always occupy preferentially one of the two sublattices in the specimen for $1\geqq x\gtrsim 0.5$, while such an ordering of Ti and Fe ions is disturbed for $0.5>x\geqq 0$. However, we have also found in detailed study that the simple molecular field theory can not explain all the magnetic properties consistently.

Since the present theory stands on many assumptions, they must be verified by the further precise experiments.

Acknowledgement

The authors wish to express their hearty thanks to Profs. T. Nagata and S. Sawada for their kind encouragement throughout the course of the present study. Their sincere thanks are also due to Dr. T. Katsura for his chemical analysis, to Drs. S. Maeda and I. Tsubokawa for their kindness of measuring the magnetization at the liquid helium temperature, to Drs. S. Iida and S. Uyeda for their fruitful discussions and comments and especially to Mr. Kondho for his analysis of the magnetic susceptibility versus temperature curve and other useful suggestions.

References

1) L. Néel and R. Pauthenet: C. R. Acad. Sci. **234** (1952) 2172.
2) H. Bizette and B. Tsai: C. R. Acad. Sci. **242** (1956) 2124.
3) F. J. Morin: Phys. Rev. **78** (1950) 819.
4) L. Néel: Rev. Mod. Phys. **25** (1953) 58.
5) P. W. Anderson, F. R. Merritt, J. P. Remeika and W. A. Yager: Phys. Rev. **93** (1954) 717.
6) H. Kumagai, H. Abe, K. Ôno, I. Hayashi, J. Shimada and K. Iwanaga: Phys. Rev. **99** (1955) 1116.
7) H. M. A. Urquhart and J. E. Goldman: Phys. Rev. **101** (1956) 1443.
8) R. Chevallier: Bull. Soc. Chim. France **20** (1953) 973.
9) Y. Ishikawa and S. Sawada: J. Phys. Soc. Japan **11** (1956) 496.
10) E. Pouillard: Ann. de Chimie **5** (1950) 164.
11) G. D. Nicholls: Advances in Phys. **4** (1955) 139.
12) T. Nagata and S. Akimoto: Geofisica Pura e Applic. Milano **34** (1956) 36.
13) T. Nagata, S. Akimoto and S. Uyeda: J. Geomag. Geoelec. **5** (1953) 168.
14) S. Uyeda: J. Geomag. Geoelec. **7** (1955) 9.
15) S. Kume: Proc. Japan, Acad. **31** (1955) 709.
16) R. Chevallier, J. Bolfa and S. Mathieu: Bull. Soc. France. Min. Crist. **78** (1955) 307, 365.
17) C. Guillaud: J. de Phys. Rad. **12** (1951) 239.
18) L. R. Maxwell and S. J. Pickart: Phys. Rev. **92** (1953) 1120.
19) Y. Ishikawa and S. Akimoto: J. Phys. Soc. Japan. **12** (1957) 834.
20) S. Akimoto, T. Nagata and T. Katsura: Nature **179** (1957) 37.
21) Y. Y. Li: Phys. Rev. **102** (1956) 1015.
22) S. Iida: J. Phys. Soc. Japan **11** (1956) 1300.
23) F. W. Barth and E. Posnjak: Zeits. für Krist. **88** (1934) 265.
24) C. Howard Shomate: J. Amer. Chem. Soc. **68** (1946) 964.
25) Y. Ishikawa: J. Phys. Soc. Japan, in the press.
26) L. Néel: Ann. de Phys. **12** (1948) 137.
27) F. K. Lotgering: Philips Res. Rep. **11** (1956) 337.
28) Y. Ishikawa: J. Phys. Soc. Japan **12** (1957) 1165.

JOURNAL OF THE PHYSICAL SOCIETY OF JAPAN Vol. 12, No. 10, OCTOBER, 1957

Radiative Collisions between Molecular and Electron Beams
III. Angular Momentum Distribution of OH* Radicals Liberated from Alcohol Molecules

By Tadao HORIE, Masamoto OTSUKA
Faculty of Science, Osaka University
and Takayuki NAGURA
Institute of Physics, South College, Osaka University

(Received June 29, 1957)

The light induced when a homogeneous electron beam (500–700 eV) intersects normally a localized jet of methyl, ethyl, or n-propyl alcohol vapor in a vacuum of 10^{-4} mmHg has been found to be almost entirely due to the emissions from the fragments H*, CH* and, OH*. The angular momentum distributions of the OH* radicals split from alcohol molecules of the respective species have been measured by the molecular spectrophotometric method. They all differ notably from that previously found for OH* from H_2O, that is, the first maximum appears near the rotational quantum number 7 and the second maximum is entirely absent except for OH* from CH_3OH. Qualitative discussions are also given to the multiple fragmentation by electron impact of these alcohol molecules.

§ 1. Introduction

Molecular dissociation due to electron impact is usually a consequence of excitation or ionization of some electronic state of the molecule. Transitions from the ground state of the neutral molecule to some excited or ionized state are governed by the Franck-Condon principle. The energy involved in the dissociation is related to the relative situation of the upper-state potential energy surface to the ground state one. Let E_V be the vertical excitation or ionization potential to raise the molecule from the neutral ground state to a certain unstable state without changing the internuclear distances in the interior of the molecule, and let E_D be the energy of the dissociation limit of the upper state above the ground state of the neutral molecule. Then the total excess energy, E_V-E_D, will be partitioned among various degrees of freedom of the fragments formed by dissociation, being in part converted into the mutual kinetic energy with which the fragments separate from one another.

When the parent molecule is diatomic, the dissociation process is usually treated as follows. For instance, let us consider the reaction $XY+e\rightarrow X^{+}+Y+2e$. Then the kinetic energy possessed by the ion, $E(X^+)$, can be expressed by the following equation, for the conservation laws of energy and momentum,

$$E_V-E_D=E(X^+)M_{XY}/M_Y\ ,$$

where M_{XY} and M_Y are the masses of the parent molecule and the neutral atom formed along with the ion, respectively. On the other hand, as far as the translational energy of fragment ions is concerned, there has been a well established method of observation[1)2)]. The energy, $E(X^+)$, can be measured by employing a plane parallel retardation field in front of the ion-collector plate in a mass spectrometer and recording the ion current as a function of retarding potential. The first derivative of this curve with respect to the voltage scale gives the distribution of translational energies among the fragment ions produced in the dissociation process.

When the parent molecule is polyatomic, however, no satisfactory method can be used to determine how the total excess energy will be distributed among the fragments, especially when multiple fragmentation takes place. In general, it will be transformed not only into translational energies but also into rotational and vibrational energies of the fragment atoms, ions, and radicals according to the conservation laws of energy, linear momentum, and angular momentum. A measurement of the angular momentum distribution of fragment radicals would be a valuable addition to the knowledge of the kinetics of fragmentation by electron impact of polyatomic molecule.

Molecular spectro-photometric studies of the angular momentum distribution of diatomic free radicals split from polyatomic molecules by a single electron collision have been in progress at our laboratory for more than ten years. The program was initiated with the intention of investigating the fundamental processes involved in the so-called abnormal rotation of OH which was first observed in 1934 by O. Oldenberg[3] in an electrical discharge through H_2O. In the preceding papers[4][5][6], studies of the OH^* radicals split by electron impact from water and hydrogen peroxide have been reported in detail. In the case of H_2O the angular momentum distribution curve has double maxima near the rotational quantum numbers 5 and 17, while in the case of H_2O_2 it has a single maximum near the rotational quantum number 20. Putting it in other terms, electron impact of H_2O molecules leads to a swarm of OH^* radicals with rotational energies corresponding to the rotational temperature of 14,000°K, while electron bombardment of H_2O_2 molecules results in a swarm of OH^* radicals with a little higher energies of rotation corresponding to the rotational temperature of 20,100°K. With the view of having a further insight into the manner in which the angular momentum distribution for OH^* depends upon the structure of the parent molecule, the present experiment has been carried out with CH_3OH, C_2H_5OH and $n-C_3H_7OH$.

§ 2. Experimental Procedure

The light induced when a beam of electrons intersects normally a localized jet of vapor of methyl, ethyl, and n-propyl alcohol was observed. The beam of electrons was supplied from an electron gun provided with a focusing solenoid producing a coaxial magnetic field. The electron gun, which was specially designed to suit our own purpose of making molecular collision experiments, produces in a horizontal direction a collimated electron beam with nearly homogeneous velocities for electrons of energies ranging from 20 to 1,000 eV. Under the optimum condition of operation, it is possible to raise the beam intensity up to 50 mA or more, but in the present experiment the gun was operated within the limits of the beam intensity from 20 to 30 mA and of the electron energy from 500 to 700 eV. After vacuum distillations of each of the alcohol samples had been repeated several times at the dry ice temperature, the vapor was allowed to enter a source chamber and then to jet into a vacuum chamber through an image and a source slit of a molecular beam projector.

The vacuum chamber was beforehand evacuated down to a pressure of 10^{-5} mmHg or less, and then a beam of alcohol molecules of the respective species was projected into it through the image slit, and at the same time a homogeneous electron beam was fired across the localized jet of vapor. Immediately after having traversed a short distance of 10 mm or so, the molecular beam was condensed on a surface of a liquid air trap to prevent the background pressure within the chamber from being deteriorated. However, the hydrogen gas produced by decomposition of alcohol molecules at the intersection of the two beams and the stray beams from the image slit caused the background pressure to rise up to 10^{-4} mmHg.

The light from the glow appearing at the intersection of the two beams was inspected with the help of an ordinary quartz prism spectrograph with a small dispersion which covers the whole range of wave-lengths from λλ 2,000 to 8,000 within a span of 77 mm on a photographic plate. In order to make photographic photometry measurements for the OH (0,0) band near λ 3064, a Littrow-type quartz prism spectrograph with one 60° and one 30° prism (dispersion, 5.5 Å/mm near λ 3000) was used together with a recording microphotometer provided with a phototube and a string electrometer.

The light excited by the passage of electrons with energies of 500 eV or more across a jet of vapor of any species of alcohol is almost entirely due to the hydrogen Balmer series, the OH band near λ 3064, and the CH bands near λλ 3900 and 4300 as shown in Fig. 1, the C_I line at λ 2478 being too faint to be shown in the same figure. Especially when exposures of long duration were made, the negative system of N_2^+ was also detected, whereas any band of N_2 did not appear at

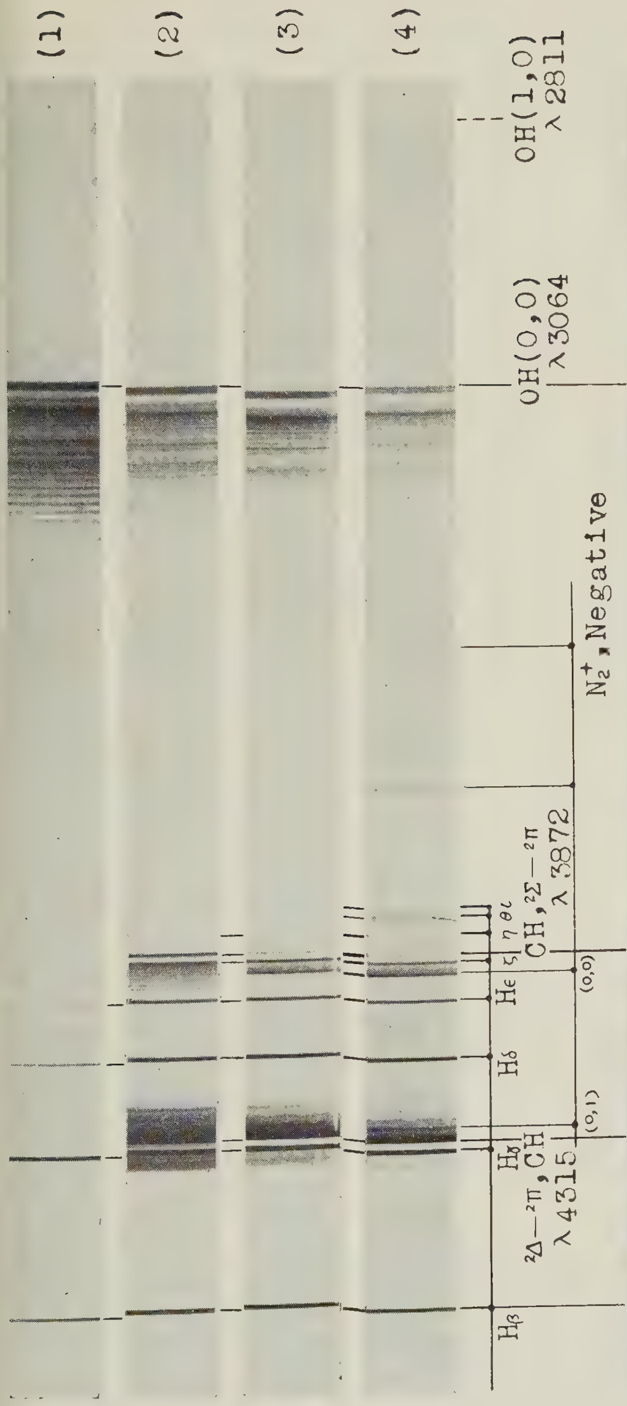

Fig. 1. Electron-impact spectra; (1) H_2O, (2) CH_3OH, (3) C_2H_5OH, and (4) n-C_3H_7OH.

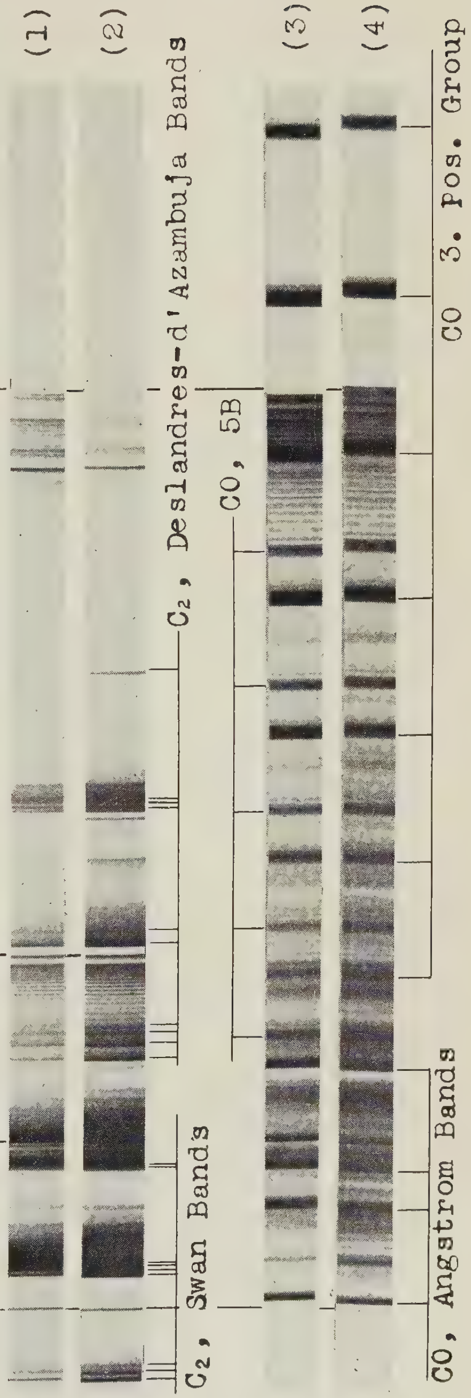

Fig. 2. Discharge spectra; condensed discharge through (1) CH_3OH and (2) n-C_3H_7OH, uncondesed discharge through (3) CH_3OH and (4) n-C_3H_7OH.

all. The (0,0) and (0,1) bands of this system near λλ 3914 and 4278 are in appearance more intensive than would be expected from weak intensities of the other bands of the same system, since they are much enhanced by their superpositions with the CH bands near λλ 3900 and 4300, respectively.

As a result of several tests on the purification procedure of the samples and on the background pressure in the collision chamber, it looks likely that these bands of the N_2^+ negative system are not due to impurities contained in the samples, but entirely due to the residual air in the observation chamber. Such a presumption is in good accordance with the recent experiment performed by C. Y. Fan[7] on the optical emission induced by the passage of a monoenergetic beam of particles through an observation chamber containing a rarefied air sample ($10^{-7}-10^{-5}$ mmHg), in which it has been shown that the first and the second positive systems of N_2 are practically the only emissions in the spectrum excited by 23 eV electrons, but their intensity is negligible compared with the negative system of N_2^+ in the spectra excited by 500 eV electrons and 20 keV protons.

In order to show how simple are the electron-impact spectra for these alcohol molecules, some examples of complicated spectra for the same molecules excited in electrical discharges are presented in Fig. 2. In a condensed discharge through CH_3OH or n-C_3H_7OH vapor, the Swan and the Deslandres-d'Azambuja bands system of C_2 are much stronger than the line of H_β and the bands of CH and OH. In an uncondensed discharge through the same vapor, the spectra are almost entirely due to the Ångstrom, the 3 Pos. Group and the 5 B bands of CO. Furthermore, the C_I line at λ 2478 appears very strongly in a condensed discharge, but does not at all in an uncondensed discharge. On comparison with the electron-impact spectra it is seen that various kinds of secondary processes must be considered to take place in electrical discharges. For instance, the fact that the C_2 bands come out with strong intensities even in a condensed discharge through CH_3OH may be accounted for only by some recombination reactions among fragment carbon atoms which may occur in the interior of the gas or at the side wall of the discharge tube.

§3. Experimental Results and Discussion

In Fig. 1 are compared the electron-impact spectra for CH_3OH, C_2H_5OH, and n-C_3H_7OH with that for H_2O. In the case of H_2O, the light is entirely due to the hydrogen Balmer series and the OH band near λ 3064. In the other cases, it contains the bands of CH near λλ 3900 and 4300 into the bargain. In the former the Balmer series extends only up to the member H_ε at λ 3970, while in the latter even the higher member H_η at λ 3835 can be easily recognized, and further the line of H_ι at λ 3770 is also detectable especially on the original plates taken with C_2H_5OH and n-C_3H_7OH. Furthermore, it looks likely that the tail of the OH band extends towards longer wavelength with decreasing number of hydrogen atoms contained in the parent molecule varying from C_2H_5OH to H_2O. The line C_I at λ 2478 could not be observed unless exposures of exceedingly long duration were made.

When bombarded by an incident electron with such an energy as high as 500 eV or so, if an alcohol molecule were split directly into fragments of different species of H, CH, and OH at a single stroke, the abundance ratio among these fragments would be 2:1:1 for CH_3OH, 3:2:1 for C_2H_5OH and 4:3:1 for n-C_3H_7OH, respectively. If so, when the intensity of the OH band is taken as a standard, the intensity of the CH bands would be expected to increase with increasing number of carbon atoms within the parent molecule. Actually, however, a lowering in intensity is found, e.g., for the band near λ 3900 on going from CH_3OH to C_2H_5OH. Such a discrepancy between the prediction from the simple rupture of the bonds and the observed intensity of the CH bands must be attributed to much more complicated processes of dissociation of the alcohol molecules.

Mass spectrometric investigations have already been made of the products of ionization resulting from electron collisions in several of the simpler alcohols. Methyl and ethyl alcohols were studied by C. S. Cummings, II and W. Bleakney[8], n- and iso-propyl alcohols by T. Kambara[9]. According to the observed relative abundances for electron energy of 70 volts, the greater number of the fragment ions from, for example, CH_3OH are of the species of CH_3OH^+, CH_2OH^+, HCO^+, and CH_3^+, their approximate percentages being estimated as 19.1, 33.6, 25.7, and 12.3, respectively. The formation of these ions except the first must result in the liberation of the neutral fragments H and OH. If any of these fragments have electronic excitational energies, the following processes can be considered to take place,

$$CH_3OH + e \rightarrow CH_2OH^+ + H^* + 2e\,, \qquad (1)$$

$$CH_3OH + e \rightarrow HCO^+ + H_2 + H^* + 2e\,, \quad (2)$$

and

$$CH_3OH + e \rightarrow CH_3^+ + OH^* + 2e\,, \qquad (3)$$

where the asterisk means the excitation of electronic state. The strong emission from the CH* radical, however, must be attributed to another kind of dissociation process of CH_3OH, which will be discussed as follows.

In order to account for the double maxima in the angular momentum distribution curve for OH* from H_2O, the following two processes were proposed in the previous paper[5)],

$$H_2O + e \rightarrow OH^* + H + e\,,$$

and

$$H_2O + e \rightarrow OH^* + H^* + e\,.$$

The former involves only the excitation of the O (2*p*) electron, while the latter the simultaneous excitation of both the O (2p) and the H (1*s*) electrons making a pair bond with each other before dissociation. The former process contributes to the second maximum, and the latter not only to the first maximum but also to the emission of the Balmer lines. In the case of CH_3OH also, let us make a proposal which is in line with that made in H_2O, namely —

$$CH_3OH + e \rightarrow OH^* + CH_3 + e \qquad (4)$$

and

$$CH_3OH + e \rightarrow OH^* + CH_3^* + e\,. \qquad (5)$$

The free methyl radical in its ground state has been proved theoretically by J. W. Linnett and A. J. Poë[10)] to be nonplanar and further by T. Itoh, K. Ohno and M. Kotani[11)] to have the most stable configuration of a pyramidal structure with the angle of 80° between the line C—H and the axis of symmetry. An attempt to obtain the absorption spectrum of the free CH_3 radical has recently been made by G. Herzberg and J. Shoosmith[12)] by means of the flash photolysis technique using $Hg(CH_3)_2$ as the parent compound. They have succeeded in finding diffuse absorption bands of the Rydberg type in the vacuum ultraviolet region and shown that these bands are unambiguously due to the free methyl radical. The former of the two processes newly proposed here, (4), results in a free methyl radical in its stable ground state. However, when a methyl radical is excited up to some unstable electronic state in the latter, (5), it may spontaneously decompose into a CH* radical and hydrogen atoms as, for instance,

$$CH_3OH + e \rightarrow OH^* + CH^* + H^* + H + e. \quad (5')$$

The observed strong bands of CH are likely due to the CH* radicals produced in reaction processes of this kind.

On the other hand, the OH* radicals are liberated in the processes (3), (4), and (5′). In (3) and (4), the parent molecule dissociates into two pieces with nearly equal masses and with a variety of internal degrees of freedom. In these processes as well as in the multiple fragmentation, (5′), only a small fraction of the total excess energy, $E_V - E_D$, will be converted into the rotational energy of the OH* radical. According to the mass spectrometric investigations cited above of the fragment ions from methyl, ethyl, and propyl alcohol, the more complicated the parent molecule is, the more different kinds of processes of dissociation into pieces must be considered to take place.

In Fig. 3 there are presented the results of photographic photometry measurements for the rotational lines of the Q_1 branch in the (0,0) band emitted from the OH* radicals split from methyl, ethyl, and n-propyl alcohol molecules, respectively. The previous result for H_2O and the Maxwell-Boltzmann distribution for 2,800°K are also shown in the same figure for the sake of comparison. In every one of these alcohol molecules the first maximum shifts towards a little higher rotational quantum number near 7, as compared with the case of H_2O, and moreover the second maximum is quite flat in CH_3OH and entirely absent in both C_2H_5OH and n-C_3H_7OH. The distribution of rotational energies among OH* radicals is in all cases quite similar to the distribution calculated for the rotational temperature of 2,800°K. It is true some traces of the second maximum is still retained in the simplest molecule of alcohols, CH_3OH, but in C_2H_5OH and n-C_3H_7OH the number of degrees of freedom among which the total excess energy will be partitioned is so great that any energy of abnormal rotation is not likely given to the OH* radicals splitting from these molecules.

In 1938 a study was made by H. Wakeshima[13] of intensity distributions in the OH (0,0) band excited in an electrical discharge through H_2O, CH_3OH, and C_2H_5OH, in which no appreciable variation was pointed out. Now that a great difference has been found to exist between the electron-impact and the discharge spectra, even for the same alcohol, it goes without saying that his result must not be considered as contradictory to ours that reveals a remarkable difference between the angular momentum distribution for OH* from H_2O and that for OH* from several of the simpler alcohols, in the most fundamental process of excitation by electron impact.

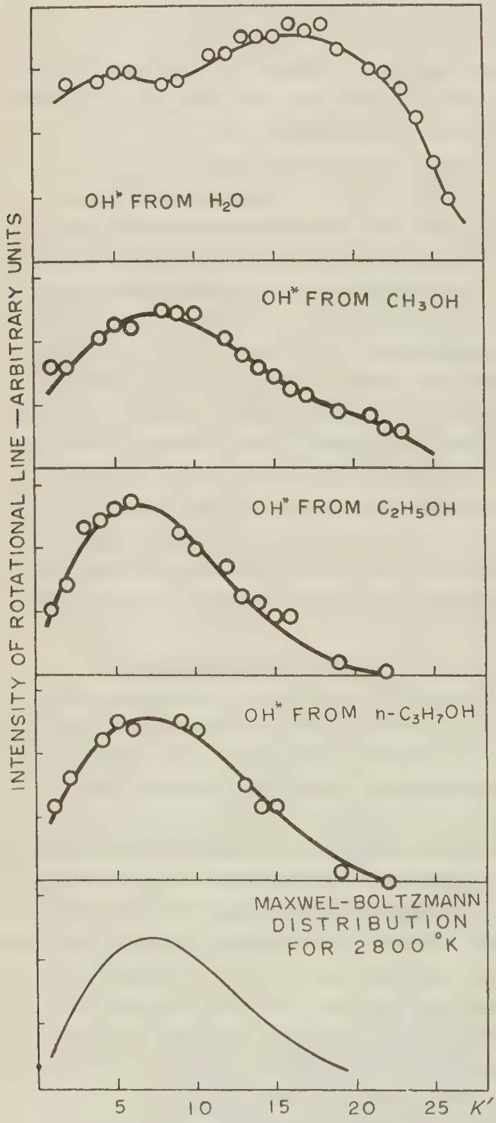

Fig. 3. The rotational intensity distributions for OH* from CH_3OH, C_2H_5OH and n-C_3H_7OH in comparison with that for OH* from H_2O and with the Maxwell-Boltzmann distribution for 2,800°K.

§ 4. Acknowledgments

The authors wish to express their sincere thanks to Dr. Herbert P. Broida of the National Bureau of Standards for his interest in the preceding papers and for his kind encouragements throughout the course of this series of works. The authors are also obliged to Prof. C. A. Coulson of the University of Oxford and Prof. K. Niira of the Tokyo Institute of Technology for valuable suggestions on the structure of water type molecules containing OH within themselves. They also would like to express their hearty thanks to Prof. T. Asada for placing various experimental facilities at their disposal.

References

1) H. D. Hagstrum: Rev. Mod. Phys. **23** (1951) 185.
2) J. D. Morrison: Rev. Pure. Appl. Chem. **5** (1955) 22.
3) O. Oldenberg: Phys. Rev. **46** (1934) 210.
4) T. Horie, T. Nagura and M. Otsuka: Phys. Rev. **104** (1956) 547.
5) T. Horie, T. Nagura and M. Otsuka: J. Phys. Soc. Japan **11** (1956) 1157.
6) T. Horie, T. Nagura and M. Otsuka: J. Phys. Soc. Japan **12** (1957) 500.
7) C. Y. Fan: Phys. Rev. **103** (1956) 1740.
8) C. S. Cummings: II and W. Bleakney, Phys. Rev. **58** (1940) 787.
9) T. Kambara: J. Phys. Soc. Japan **5** (1950) 31; 36.
10) J. W. Linnett and A. J. Poë: Trans. Faraday Soc. **47** (1951) 1033.
11) T. Itoh, K. Ohno and M. Kotani: J. Phys. Soc. Japan **8** (1953) 41.
12) G. Herzberg and J. Shoosmith: Can. J. Phys. **34** (1956) 523.
13) H. Wakeshima: Proc. Phys. Math. Soc. Japan **20** (1938) 374.

JOURNAL OF THE PHYSICAL SOCIETY OF JAPAN Vol. 12, No. 10, OCTOBER, 1957

Nuclear Quadrupole Resonance of Antimony Isotopes in Solids

By Shizuko OGAWA*

Department of Physics, Faculty of Science, Ochanomizu University, Tokyo

(Received July 5, 1957)

Measurements of nuclear quadrupole resonances of antimony isotopes in solids have been made at a relative accuracy of about one part in 10^6. Detectors are superregenerative oscillators. Relative accuracy was achieved by measurement of two or three resonance frequencies in a very short time. For antimony trichloride the results were almost in agreement with Wang's data, but the resonant frequency ν_3 of the Sb^{123} isotope, was higher about 2.5 kc. This implies that the cedecipole coupling constant might not have an order of magnitude which leads to a definitely measurable amount. In antimony oxide the simultaneous measurement was more easy, since it has a small asymmetry parameter. In this case, the deviation of resonance frequencies from a multiple relation is very small. These results are discussed in terms of cedecipole interaction and thermal vibration.

§ 1. Introduction

The first indication of the existence of nuclear electric cedecipole interaction was given by Wang through the experiment of nuclear quadrupole resonances of antimony isotopes[1]. Antimony consists of two isotopes, Sb^{121} and Sb^{123}, with relative abundances of 57.2% and 42.7%, respectively. The isotope Sb^{123}, having a spin of 7/2, gives rise three nuclear quadrupole resonances, whereas the isotope Sb^{121}, having a spin of 5/2, has two resonances. The frequencies of each resonances depend upon two quantities, i.e., nuclear quadrupole coupling constant eQq and asymmetry parameter of field gradient tensor η. Wang measured three resonance frequencies of Sb^{123} in $SbBr_3$ with a great deal of care at 0.4°C, and found that the frequency of the third resonance, calculated from eQq and η, which were obtained from the measured frequencies of the first and the second resonances, showed a small disagreement with the measured one. He attributed this small discrepancy to nuclear cedecipole interaction. In his experiment the amount of the discrepancy was only 2 kc, but the width of the resonance line was about 12 kc and the temperature dependence of the line was about 7~17 kc/degree. He also measured $SbCl_3$ and Sb_2S_3 in single crystals. Descrepancies of measured and calculated ν_3 frequencies range from nearly zero to 4 kc. The present work aims at a similar measurement of nuclear quadrupole resonances of antimony isotopes in Sb_2O_3, where the resonance line is more sharp and the dependency of the frequency upon temperature is smaller. The resonances of antimony isotopes in $SbCl_3$ studied by Wang were also measured for comparison.

§ 2. Experimental Procedure and Apparatus

In order to compare the frequencies of nuclear quadrupole resonances to an accuracy of about 0.001 percent, it is necessary that the center of the resonance line be determined accurately and that the temperature of the sample be kept constant during a series of measurements.

a) Apparatus

Two types of superregenerative oscillator were used. The first oscillator was a push pull feed back type with *LC* tuning circuit. It is responsible to a frequency range between 20 and 90 Mc, with two similar circuits cover the lower and higher range. The circuit diagram is shown in Fig. 1. The second oscillator had a transmission line tuned circuit similar to one reported by Kojima et al.[2] The frequency range was between 90 and 200 Mc. In order to measure three resonance frequencies of Sb^{123} three oscillators were used corresponding to their resonance frequencies. By use of a long sample three oscillator coils could be arranged linearly as shown in Fig. 2. If the coils have been coupled more closely, the oscillators would interacted with each other. Exact simultaneous operations were avoided on account of pulling phenomena of oscillations. Therefore, the three oscillators were operated in turn. A block diagram of the complete system is given in the same figure. Thus three frequencies were measured in a time of about a few minutes.

---

* This experiment was done at the laboratory of the Physics Department, Tokyo University of Education.

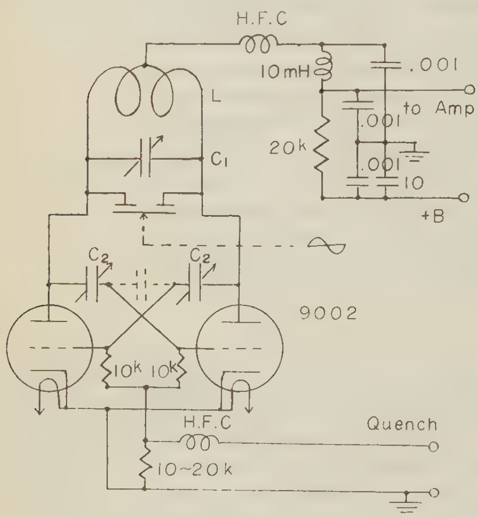

Fig. 1. Circuit of *LC* tuning oscillator.

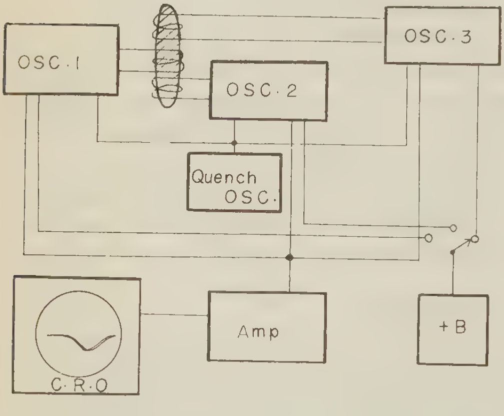

Fig. 2. Block diagram of system.

b) Method to Determine the Center of the Line

Generally simple regenerative spectrometers are adequate for studying line shapes. Such spectrometers were tested at the beginning of this experiment. However, because of the high sensitivity, superregenerative spectrometer were used for all measurements. The superregenenerative spectrometer gives many signals resulting from the side bands separated by the quenching frequency. These signals have various shapes owing to their different phases which depend on the frequency and amplitude of the quenching oscillator[3]. Moreover the resonance shape displayed on the cathod ray oscilloscope is asymmetric to the direction of sweep, since it receives some distortion from the finite pass band of the amplifier. The center of the resonance line was determined by superposing the two patterns at sinusoidal sweep as shown in Fig. 3. The phase of sweep was adjusted by receiving a sharp marker signal from a test oscillator. When the frequency of a line was measured, the signal from the test oscillator was superimposed on the resonance line.

Preliminary adjustment of marker frequency of test oscillator to the center of the line was carried out to be consistent for all the shapes of three or four side bands of superregenerative oscillator.

c) Method to measure the three frequencies at the same temperature

It is often experienced that the temperature of a sample rises during a measurement by its absorption of radio frequency power. Therefore, to keep a sample at a constant temperature, it is not sufficient even if a thermostat is used. To avoid the rise of temperature the oscillation level must be kept low and the necessary measurements must be carried out in a very short time at the beginning of operation. Indeed, the third resonance frequency of Sb^{123} in $SbCl_3$ was observed to change 0.01 percent during five minutes from the time of switch on of oscillator operation at some condition. Thus two or three frequencies are measured almost simultaneously by a suitable arrangement of the apparatus. Accurate measurements were obtained by changing the switch of supply voltage, and by varying the quenching power as shown in Fig. 2. Measurements were repeated many times.

d) Measurement of Frequencies

The test oscillator used had a frequency range between 10 and 15 Mc. Its frequency

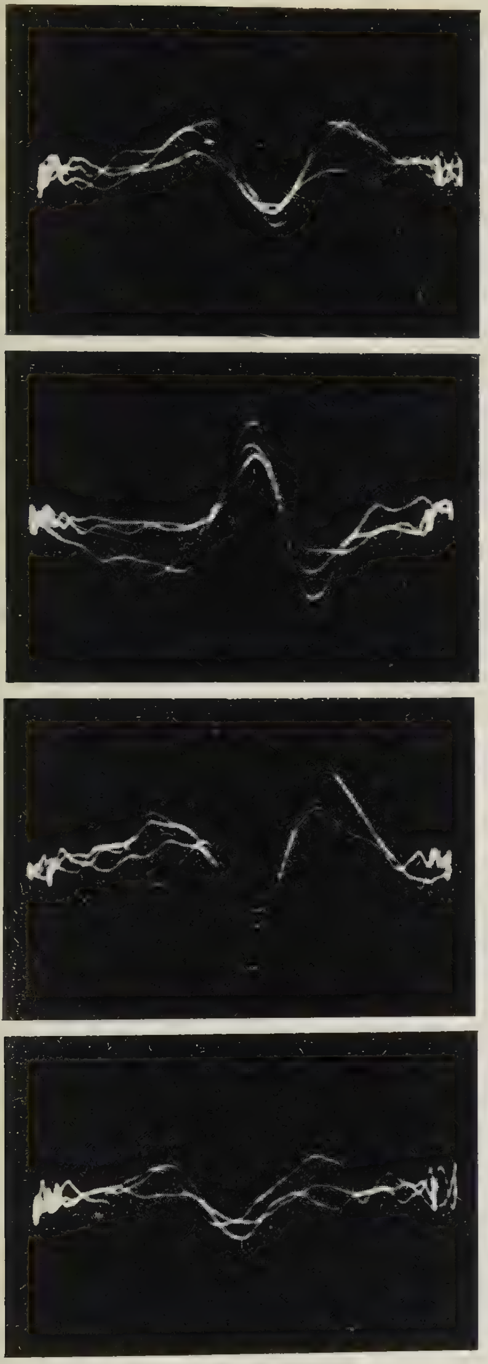

(a)

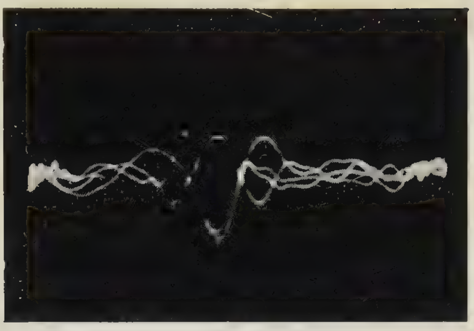

(b)

Fig. 3. A series of resonance absorptions of side bands (a) and marker signal (b) viewed on oscilloscope.

was stabilized to about one part in 10^5. Soon after adjustment to the center of resonance lines its frequency was measured accurately beating with the higher harmonics of a precission frequency meter, having a working range between 1 and 2 Mc and an accuracy of one cycle. The frequency meter was always calibrated against the standard frequency of 4 Mc from *JJY*. Thus measured frequency has a accuracy of about 0.0001 percent of resonance frequency.

§ 3. Results and Discussion

a) Sb_2O_3

The resonance frequencies of Sb^{121} and Sb^{123} of Sb_2O_3 were measured by Barnes and Bray at room temperature and liquid air temperature[4]. We also measured these frequencies at room temperature. The temperature dependency is about -3×10^{-5} Mc/deg. at all frequencies which are very small compared to $SbCl_3$ and its other compounds. This small temperature variation of resonance frequencies increases the accuracy of the measurement. Signal to noise ratio was five to ten for all the resonances, which is better signal to noise ratio than other Sb compounds. The line widths were about 8 kc on oscilloscope measurements. The asymmetry parameter was almost equal to zero. A signal of one frequency from test oscillator could be used to measure all resonance frequencies of one isotope. Therefore it is very convenient to measure resonance frequencies relative to one another. Plots of ν_1 and ν_3 relative to ν_2 are expected almost to coinside with the line inclined 45°. Resonance frequencies are shown in Table I.

Table I. The resonance frequencies of Sb in Sb_2O_3.

Isotope	T°C	ν_1	ν_2	ν_3 (Mc/sec.)
Sb^{123}	16.8±0.5	50.20608	100.41144	150.61572
Sb^{121}	〃	82.70832	165.41928	—

The averaged values of frequency differences from multiple relation are obtained over all measured values supposing that they do not depend upon temperature in this small region. Errors are weighted mean of mean square deviation in every measurement at each temperature. The deviation from multiple ratio was obtained which was comparable to the experimental error of measured frequencies.

From resonance frequencies of Sb^{123}, the asymmetry parameter η and the cedecipole coupling constant eMm was calculated. For $I=3/2$, the energy level has an exact solution but for $I=5/2$ the energy level are obtained from an expansion in powers of η^2. In Sb_2O_3 the asymmetry factor is very small, therefore it is sufficient to use terms of the order of η^2. The nuclear cedecipole term which is the next term to be considered in the electric interaction of nucleus with surrounding electrons will be zero unless nuclear spin $I \geqq 2$ and the electron configuration has an angular momentum, such as, d or f orbitals. For $I=7/2$, and 5/2 the resonance frequencies will be deduced from the equation of the energy levels[1].

$$I=7/2 \quad \nu_1=\frac{1}{14}eQq\left(1+\frac{109}{30}\eta^2\right)-\frac{1}{32}eMm\,,$$

$$\nu_2=\frac{2}{14}eQq\left(1+\frac{17}{30}\eta^2\right)-\frac{5}{224}eMm\,,$$

$$\nu_3=\frac{3}{14}eQq\left(1-\frac{1}{10}\eta^2\right)+\frac{5}{112}eMm\,.$$

$$I=5/2 \quad \nu_1=\frac{3}{20}eQq\left(1-\frac{59}{54}\eta^2\right)-\frac{5}{64}eMm\,,$$

$$\nu_2=\frac{3}{10}eQq\left(1-\frac{11}{54}\eta^2\right)+\frac{1}{16}eMm\,.$$

With the values of the asymmetry parameter of Sb^{123} the cedecipole coupling constant and quadrupole coupling constant of Sb^{121} were calculated. Table II indicates these calculate values and the frequency differences in kc/sec

b) **$SbCl_3$**

Sb^{123} in $SbCl_3$ has three frequencies ν_1, ν_2 and ν_3 of about 37 Mc, 68Mc and 103 Mc respectively. Simultaneous measurement were carried out for the three frequencie ν_1, ν_2, and ν_3 in a temperature range betwee 17 and 20°C. The observed frequencies ν and ν_3 are plotted against ν_2, which has th smallest temperature dependence in these

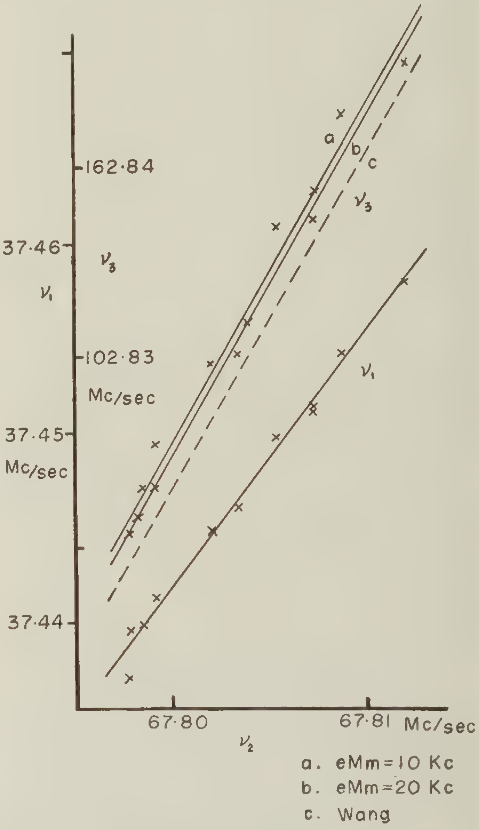

Fig. 4. Resonance frequencies ν_1 and ν_3 vs. ν_2 in $SbCl_3$.

Table II.

Isotope	$\nu_1-\nu_2/2$ (kc/sec.)	$\nu_1-\nu_3/3$ (kc/sec)	η	$\|eQq\|$ (kc/sec.)	$\|eMm\|$ (kc/sec.)
Sb^{123}	0.36±0.74	0.84±0.84	0.0006±0.001	702877.3±0.5	18±10
Sb^{121}	1.36±0.92	—	〃	551382.2±0.5	12±5

Table III. The resonance frequencies of Sb in $SbCl_3$.

Isotope	T°C	ν_1	ν_2	ν_3	ν_3 cal (Mc/sec.)
Sb^{123}	19.4±0.5	37.4449	67.8022	102.8283	102.8285
Sb^{121}	〃	58.1925	112.6443	—	

three frequencies, as shown in Fig. 4. Wang has measured these frequencies at the two temperatures of 0.8 and 30.07°C. The results which were extrapolated from Wang's data to our temperature range are shown in Fig. 4 with a broken line. On the resonance ν_1, the present result agrees well with Wang's data. On the other hand for the resonance ν_3, however, the present values are higher than his value by about 2.5 kc. The frequencies at 18°C, estimated from the points on the figure, are summarized in Table III. The temperature was measured with a thermocouple. Since the frequencies ν_1 and ν_3 were measured relative to ν_2, the error of temperature did not affect the discussion. The resonance frequencies of Sb^{121} was also measured. In this case the measured values agree with Wang's data. The resonance lines of Sb^{121} have better signal to noise ratio than those of Sb^{123}. $\nu_{3\mathrm{cal.}}$ is calculated from measured frequencies of ν_1 and ν_2 under the assumption that the resonance frequencies are depend upon the quadrupole coupling constant and the field asymmetry parameter. In this calculation the energy level equations which were described with the terms of eQq and η to the order of η^8 1) were used. Indicated lines in Fig. 4 are calculated under assumption that $SbCl_3$ has a cedecipole coupling constant of the order of about 10 kc and 20 kc and has sign opposite to the electric quadrupole interaction.

c) Discussion

The valence electrons of the antimony isotopes are in *5p* orbitals which may be hybridized with *5d* orbitals. The hybridization factor of configuration will depend upon their bonding angles. In $SbCl_3$ bond length and angles have been investigated by microwave experiment and $Sb-Cl=2.325\pm0.005$ Å, $Cl-Sb-Cl=99.5\pm0.5°$.5) In Sb_2O_3 these values are also obtained which is about 2.22 Å and $O-Sb-O\sim100°$, respectively6). In this respect, they seemed to be hybridized with similar configurations. By Wang's data $SbCl_3$ has a cedecipole interaction to be many times larger than our results, which lead the value of 10 kc at the most. It seems very difficult to deduce an accurate value of cedecipole interaction factor in this experimental accuracy.

The atoms Sb and O in crystal of Sb_2O_3 are arranged as shown in Fig. 5.6) Sb atom has three bonds to the three oxygen atoms with the same bond length and lies on one of the body diagonals of cubic lattice, thus the asymmetry parameter will vanish.

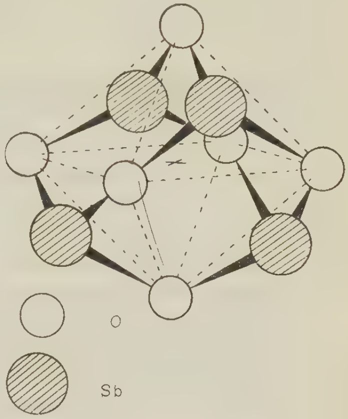

Fig. 5. Molecular structure of antimony oxide.

In consideration for cedecipole interaction, calculated results introduce small asymmetry factor of about 0.0006, which could not be distinguish from zero within the limits of experimental error. It is consistent with the consideration of crystal structure. This small value of η, if it exists, would be ascribed to the thermal vibration of molecule. The effect of the thermal vibraiton of molecule on asymmetry parameter has been studied by H. Bayer.7) Accurate measurements at the different temperatures would be favourable, but at other temperature differing from the room temperature, it would be very difficult.

Acknowledgements

The author wishes to thank to Professor Shoji Kojima, University of Education, for the encouragement and the guidance through this experiment. She also indebted to Miss Kiyoe Kato for cooperation in measurements. The present work was supported by the Scientific Research Expenditure of the Ministry of Education.

References

1) T. C. Wang: Phys. Rev. **99** (1955) 566.
2) S. Kojima, K. Tsukada, A. Shimauchi and Y. Hinaga: J. Phys. Soc. Japan **9** (1954) 795.
3) K. Tsukada: J. Phys. Soc. Japan **11** (1956) 956.

4) R. G. Barnes and P. J. Bray: J. Chem. Phys. **23** (1955) 1177.
5) P. Kisliuk: J. Chem. Phys. **22** (1954) 86.
6) R. W. G. wyckoff, *Crystal Structure* Interscience Publishers, Inc., New York (1948).
7) H. Bayer: Z. Physik **130** (1951) 227.

JOURNAL OF THE PHYSICAL SOCIETY OF JAPAN Vol. 12, No. 10, OCTOBER, 1957

Oscillations of Electron Cloud in External Fields

By Masao SUMI
Electrical Communication Laboratory, Tokyo

(Received May 10, 1957)

The collective behavior of density fluctuations in a purely electronic cloud which is not neutralized by positive ions is analysed under the influence of external electromagnetic fields. In an equilibrium state the electrostatic space charge force is counter-balanced by the external fields and it gives rise to the mean drift flow of electronic cloud accompanying with the oscillations similar to those in the usual plasma. The classical description lead to the dispersion relation, which involves additional terms due to the drift velocity of electron flow. The effect of this drift velocity on the frequency shift is briefly discussed.

§ 1. Introduction

The collective behavior of the electrons in an electron gas has since been analyzed and developed in a number of papers[1)2)], where the "electron gas" is usually assumed to be neutralized by the positive charge of ions distributed over the volume considered. There are sometimes the cases that the positive ions are eliminated or of absence in the electron clouds or beams*. Even in such a purely electronic cloud there have been observed plasma-like oscillations when external fields confine the assembly of electrons appropriately[3)]. These plasma-like oscillations may be qualitatively illustrated as follows: let us consider a simple case where external electric and magnetic fields counter-balance the electrostatic space-charge forces of electron clouds. Then it will give rise to the steady drift flow in this clouds. When we observe on a sliding frame of reference with the velocity of the drift flow, the external and space-charge forces vanish in the clouds and there remains the density fluctuations of electrons, bringing about the plasma-like collective oscillations as usual. Back to the laboratory frame of reference the drift flow of electrons will reappear which affects these plasma-like oscillations, resulting in the shift of oscillating frequency. We shall deal with these situations first in the classical theory of density fluctuations and next in the quantum-mechanical theory of collective descriptions.

In the simple classical treatment of section 2, the velocity of individual electron will be devided into the steady component of drift flow and the fluctuating component. Then we shall find by the method of the Fourier decomposition of density fluctuations[1)] that the latter component brings about the plasma-like oscillations and the former the corresponding shift of frequency.

In section 3, we shall give a more precise dispersion relation by the quantum-mechanical description, which is equivalent to the general method by Bohm and Pines[2)], and by Tomonaga[4)]. The center-of-mass coordinate and momentum conjugate to each other for the electron assembly will be introduced, while internal coordinates and momenta will simply be obtained for the system with a sufficiently large number of electrons. The Hamiltonian for the system will be decomposed into a part representing the center-of-mass motion and an internal part describing an internal motion of electron assembly, the latter of which leads to the plasma-like oscillations and accordingly to the dispersion relation by the method of usual collective descriptions[2)4)5)].

---

* For instance, in the interaction space of magnetrons or in an electron beam of vacuum tubes, there remains almost purely electronic cloud or beams.

The effect of drift flow on the dispersion relation will be considered in section 4, but for the present we shall have to restrict ourselves to give rather formal discussions.

§ 2. Classical Treatment of Oscillatory Behavior

We shall first treat classically an aggregate of electrons under the influence of external electric and magnetic fields. Coulomb repulsive forces between electrons will provide an electrostatic space-charge force, as an average, and a fluctuating force caused by the density fluctuation. It will be shown that a macroscopically steady state is attained, when the repulsive space-charge force is counterbalanced by the external electromagnetic forces. Then the assembly of electrons will exhibit a flow with a steady drift velocity.

If we ride on a frame of reference which moves with the same velocity as that of drift flow, we might no more observe the drift flow of electron gas, since net forces acting on the electrons vanish on the average in this frame of reference. This means that the external electromagnetic fields play as similar an effective role to cancel out the repulsive space-charge forces in this case as positive ions do in the case of usual neutralized plasma.

Then it would be seen that the density fluctuation causes the collective oscillations as if the electron cloud would be the usual plasma. If we go back to the frame of reference fixed on the laboratory, the frequency shift of oscillations would be expected to appear due to the drift flow of electron cloud. These situations will be clarified in the following analysis.

The particle density of point electrons in a box of unit volume is expressed as:

$$\rho(\boldsymbol{x})=\sum_{j=1}^{N}\delta(\boldsymbol{x}-\boldsymbol{x}_j) \tag{2.1}$$

where N is the number density: $N=\int\rho(\boldsymbol{x})d\boldsymbol{x}$.

Splitting $\rho(\boldsymbol{x})$ into Fourier components,

$$\rho(\boldsymbol{x})=\sum_{j,k}e^{i\boldsymbol{k}(\boldsymbol{x}-\boldsymbol{x}_j)}=\sum_{k}\rho_k e^{i\boldsymbol{k}\boldsymbol{x}}\,, \tag{2.2}$$

$$\rho_k=\sum_j e^{-i\boldsymbol{k}\boldsymbol{x}_j}\,. \tag{2.3}$$

Note that ρ_0 represents the mean electron density N and the ρ_k with $k\neq 0$ the density fluctuations.

The equation of motion of the j-th electron is described by

$$\ddot{\boldsymbol{x}}_j=\dot{\boldsymbol{v}}_j=-\frac{e}{m}[\boldsymbol{E}(\boldsymbol{x}_j)+\boldsymbol{v}_j\times\boldsymbol{B}(\boldsymbol{x}_j)]\,, \tag{2.4}$$

the dot denoting the time derivative. MKS rationalized unit is used throughout this paper. $\boldsymbol{E}$ is devided into static and fluctuating parts: static part consists of two parts, i. e., one due to the mean charge distribution of electrons $\boldsymbol{E}_0$ and the other due to the external agency $\boldsymbol{E}_{ext}$; the fluctuating part $\boldsymbol{E}_1$ is due to the density fluctuations of electron charge. Hence the total electric field becomes

$$\boldsymbol{E}=\boldsymbol{E}_{ext}+\boldsymbol{E}_0+\boldsymbol{E}_1\,. \tag{2.5}$$

Denoting the electric potential by $\varphi(\boldsymbol{x})$,

$$\begin{aligned}\nabla^2\varphi(\boldsymbol{x})&=\frac{e}{\varepsilon_0}\rho(\boldsymbol{x})\\&=\frac{e}{\varepsilon_0}\Big(\rho_0+\sum_{k\neq0}\rho_k e^{i\boldsymbol{k}\boldsymbol{x}}\Big)\,.\end{aligned} \tag{2.6}$$

Hereafter the summation over k implies not to include the term of $k=0$. Also splitting $\varphi(\boldsymbol{x})$ into two parts

$$\nabla^2\varphi_0(\boldsymbol{x})=\frac{e}{\varepsilon_0}\rho_0\,, \tag{2.7}$$

$$\nabla^2\varphi_1(\boldsymbol{x})=\frac{e}{\varepsilon_0}\sum_k\rho_k e^{i\boldsymbol{k}\boldsymbol{x}}\,, \tag{2.8}$$

then we get

$$\varphi_1(\boldsymbol{x})=-\frac{e}{\varepsilon_0}\sum_k\frac{\rho_k}{k^2}e^{i\boldsymbol{k}\boldsymbol{x}}\,, \tag{2.9}$$

and

$$\boldsymbol{E}_0(\boldsymbol{x})=-\nabla\varphi_0(\boldsymbol{x})\,, \tag{2.10}$$

$$\boldsymbol{E}_1(\boldsymbol{x})=-\nabla\varphi_1(\boldsymbol{x})=\frac{ei}{\varepsilon_0}\sum_k\frac{\boldsymbol{k}}{k^2}\rho_k e^{i\boldsymbol{k}\boldsymbol{x}}. \tag{2.11}$$

We can regard (2.4) as the equation of motion of a specified electron in a small volume element located at $\boldsymbol{x}$. It may be written as

$$\begin{aligned}\dot{\boldsymbol{v}}_j=-\frac{e}{m}\,\boldsymbol{E}_1(\boldsymbol{x}_j)-\frac{e}{m}&\\ \times[\boldsymbol{E}_0(\boldsymbol{x}_j)+\boldsymbol{E}_{ext}(\boldsymbol{x}_j)+\boldsymbol{v}_j\times\boldsymbol{B}(\boldsymbol{x}_j)]\,.&\end{aligned} \tag{2.12}$$

If we take an average of Eq. (2.12) over all particles in the volume element, assuming reasonably $\boldsymbol{B}_0$, $\boldsymbol{E}_{ext}$ and $\boldsymbol{B}$ to be uniform over this volume element, we can drop out the first term in the righthand side and obtain in the following macroscopic equation of motion,

$$\dot{\boldsymbol{v}}_0=-\frac{e}{m}[\boldsymbol{E}_0(\boldsymbol{x})+\boldsymbol{E}_{ext}(\boldsymbol{x})+\boldsymbol{v}_0\times\boldsymbol{B}(\boldsymbol{x})]\ . \qquad (2.13)$$

As a macroscopically steady state is reached, $\dot{\boldsymbol{v}}_0=0$. The relation that the righthand side of Eq. (2.13) is put equal to zero yields a function of $\boldsymbol{x}$, $\boldsymbol{v}_0(\boldsymbol{x})$, which represents the drift velocity of electron cloud.

Putting

$$\boldsymbol{v}_j=\boldsymbol{v}_0+\boldsymbol{v}_{1j}\ ,$$

then

$$\dot{\boldsymbol{v}}_j=\dot{\boldsymbol{v}}_0+\dot{\boldsymbol{v}}_{1j}=\dot{\boldsymbol{v}}_{1j}\ . \qquad (2.14)$$

Hence Eq. (2.12) becomes

$$\dot{\boldsymbol{v}}_{1j}=-\frac{e^2i}{m\varepsilon_0}\sum_{j',k}\frac{\boldsymbol{k}}{k^2}e^{i\boldsymbol{k}(\boldsymbol{x}_j-\boldsymbol{x}_{j'})}-\frac{e}{m}\boldsymbol{v}_{1j}\times\boldsymbol{B}(\boldsymbol{x}_j). \qquad (2.15)$$

Now differentiation of (2.3) gives

$$\dot{\rho}_k=-i\sum_j(\boldsymbol{k}\boldsymbol{v}_j)e^{-i\boldsymbol{k}\boldsymbol{x}_j}\ , \qquad (2.16)$$

$$\ddot{\rho}_k=-\sum_j[(\boldsymbol{k}\boldsymbol{v}_j)^2+i\boldsymbol{k}\dot{\boldsymbol{v}}_j]e^{-i\boldsymbol{k}\boldsymbol{x}_j}\ . \qquad (2.17)$$

By the use of (2.15) and the random phase approximation, (2.17) becomes

$$\ddot{\rho}_k+\sum\left[\left(\frac{Ne^2}{m\varepsilon_0}\right)+(\boldsymbol{k}\boldsymbol{v}_j)^2-\frac{ie}{m}(\boldsymbol{k}\cdot\boldsymbol{v}_{1j}\times\boldsymbol{B})\right]e^{-i\boldsymbol{k}\boldsymbol{x}_j}=0. \qquad (2.18)$$

Furthermore assuming the random distribution of $\boldsymbol{v}_{1j}$ and averaging over all electrons, we see that the third term in the bracket of the last equation is cancelled out, because the magnetic field gives the gyromagnetic motion to the electron but does not alter the magnitude of electron speed. Then we get

$$\ddot{\rho}_k+[\omega_p{}^2+(\boldsymbol{k}\boldsymbol{v}_0)^2+\langle(\boldsymbol{k}\boldsymbol{v}_{1j})^2\rangle]\rho_k=0\ , \qquad (2.19)$$

where $\omega_p{}^2=Ne^2/m\varepsilon_0$ and the bracket $\langle\ \rangle$ means the average concerned. We find this equation indicates the oscillatory behavior of the density fluctuations, the frequency of which is given by the relation

$$\omega^2=\omega_p{}^2+(\boldsymbol{k}\boldsymbol{v}_0)^2+\langle(\boldsymbol{k}\boldsymbol{v}_{1j})^2\rangle. \qquad (2.20)$$

The second term in the right hand side represents the frequency shift due to the drift velocity which confirms the qualitative illustration mentioned previously. The third term is due to the usual thermal agitations.

If we separate the density fluctuations ρ_k into two parts, i. e., the collective and individual components, we shall obtain also in this case the more refined dispersion relation, as was shown by Pines and Bohm. But we shall stop here the classical treatment and in the next section we shall reconfirm the effects of drift flow by means of the quantum-mechanical treatment.

§ 3. Quantum-mechanical Descriptions

In the previous section we have discussed in a classical description the effect of external fields to the density fluctuations of purely electronic cloud. This section will present the more precise description of our problems by quantum-mechanical methods.

We start with a system containing N electrons in a box of unit volume affected by the external electric and magnetic fields, which is represented by the potential φ_e and $\boldsymbol{A}_e$. This system can be described by a Hamiltonian of the form

$$H=\frac{1}{2m}\sum_j[\boldsymbol{p}^{(j)}+e\boldsymbol{A}_e(\boldsymbol{x}^{(j)})]^2$$
$$+\frac{e^2}{2\varepsilon_0}\sum_{\substack{i,j,k\\ i\neq j,k\neq 0}}\frac{e^{i\boldsymbol{k}(\boldsymbol{x}^{(i)}-\boldsymbol{x}^{(j)})}}{k^2}$$
$$-e\sum_j[\varphi_0(\boldsymbol{x}^{(j)})+\varphi_e(\boldsymbol{x}^{(j)})]$$

where φ_0 corresponds to the potential due to the uniform distribution of electronic charge, satisfying the equation $\nabla_j{}^2\varphi_0(\boldsymbol{x}^{(j)})=e/\varepsilon_0$. It is well known this Hamiltonian is equivalently transformed by introducing the longitudinal vector potential $\boldsymbol{A}(\boldsymbol{x})$ and electric field intensity $\boldsymbol{E}(\boldsymbol{x})$, which is expressed by

$$H=\frac{1}{2m}\sum[\boldsymbol{p}^{(j)}+e\boldsymbol{A}_e(\boldsymbol{x}^{(j)})+e\boldsymbol{A}(\boldsymbol{x}^{(j)})]$$
$$+\frac{\varepsilon_0}{2}\int\boldsymbol{E}^2(\boldsymbol{x})d\boldsymbol{x}-e\sum[\varphi_0(\boldsymbol{x}^{(j)})+\varphi_e(\boldsymbol{x}^{(j)})]\ , \qquad (3.1)$$

together with a subsidiary condition restricting allowable state vectors

$$\Omega\Phi\equiv\left[div\boldsymbol{E}(\boldsymbol{x})+e\sum_{j=1}^{N}\delta(\boldsymbol{x}-\boldsymbol{x}^{(k)})\right]\Phi=0\ . \qquad (3.2)$$

Now we consider a motion of a center-of-mass coordinate of this system. Defining a center-of-mass coordinate by

$$\boldsymbol{x}_0=\frac{1}{N}\sum_{j=1}^{N}\boldsymbol{x}^{(j)}\ , \qquad (3.3)$$

a center-of-mass momentum conjugate to this quantity can be introduced by the relation for each component

$$p_{0x}=\frac{iNm}{\hbar}[T, x_0], \text{ etc.}, \tag{3.4}$$

where T is the kinetic energy of this system, $(1/2m)\sum_{j=1}^{N}\boldsymbol{p}^{(j)2}$. Hence we get

$$\boldsymbol{p}_0=\sum_{j=1}^{N}\boldsymbol{p}^{(j)}. \tag{3.5}$$

Clearly in this case

$$[p_{0x}, x_0]=-i\hbar, \text{ etc.}, \tag{3.6}$$

hold.

Internal coordinates $\boldsymbol{x}_j$ must satisfy the relations

$$[p_{0x}, x_j]=0, \text{ etc.},$$

which is fulfiled by putting

$$\boldsymbol{x}_j=\boldsymbol{x}^{(j)}-\boldsymbol{x}_0 . \tag{3.7}$$

As internal momenta conjugate to these we take

$$\boldsymbol{p}_j=\boldsymbol{p}^{(j)}-\frac{1}{N}\boldsymbol{p}_0 . \tag{3.8}$$

Then

$$[p_{jx}, x_j]=-\left(1-\frac{1}{N}\right)i\hbar\approx-i\hbar, \text{ etc.}, \tag{3.9}$$

for $N\gg1$, which shows that the internal momenta defined by (3.8) are sufficient approximations for large N. Clearly we get

$$[p_{jx}, x_0]=0, \text{ etc.}, \tag{3.10}$$

and

$$\sum_{j=1}^{N}\boldsymbol{p}_j=0 . \tag{3.11}$$

Thus we can write for $N\gg1$,

$$\boldsymbol{x}^{(j)}=\boldsymbol{x}_j+\boldsymbol{x}_0 ,$$

$$\boldsymbol{p}^{(j)}=\boldsymbol{p}_j+\frac{1}{N}\boldsymbol{p}_0 . \tag{3.12}$$

Insertion of (3.12) into the Hamiltonian (3.1) leads

$$H=H_c+H_0 , \tag{3.13}$$

$$H_c=\frac{1}{2Nm}[\boldsymbol{p}_0+Ne\boldsymbol{A}_e(\boldsymbol{x}_0)]^2-Ne[\varphi_0(\boldsymbol{x}_0)+\varphi_e(\boldsymbol{x}_0)] , \tag{3.14}$$

$$H_0=\frac{1}{2m}\sum_j\boldsymbol{p}_j^2+\frac{e}{2m}\sum_j\Big[\Big\{\boldsymbol{p}_j+\frac{1}{N}\boldsymbol{p}_0+e\boldsymbol{A}_e(\boldsymbol{x}_0)\Big\}\times\boldsymbol{A}(\boldsymbol{x}_0+\boldsymbol{x}_j)+\boldsymbol{A}(\boldsymbol{x}_0+\boldsymbol{x}_j)\times\Big\{\boldsymbol{p}_j+\frac{1}{N}\boldsymbol{p}_0+eA_e(\boldsymbol{x}_0)\Big\}\Big]+\frac{e^2}{2m}\sum_j\boldsymbol{A}^2(\boldsymbol{x}_0+\boldsymbol{x}_j)+\frac{\varepsilon_0}{2}\int\boldsymbol{E}^2d\boldsymbol{x} , \tag{3.15}$$

here consideration are taken into account that static fields are regarded as uniform in the volume concerned, so that $\boldsymbol{A}_e$, φ_0 and φ_e are functions of $\boldsymbol{x}_0$ only. The Hamiltonian H_c represents the center-of-mass motion in the external fields, while H_0 yields the internal motion of electronic cloud affected by the external fields.

The total Hamiltonian H determines the motion of state vector of the system by the Schroedinger equation

$$H\Phi=i\hbar\frac{\partial}{\partial t}\Phi . \tag{3.16}$$

By making a unitary transformation $\Phi=U_c\Psi$,

$$U_c=\exp\left[-\frac{i}{\hbar}H_ct\right], \tag{3.17}$$

the equation satisfied by the new state vector Ψ becomes

$$U_c^{-1}H_0U_c\Psi\equiv\mathscr{H}_0\Psi=i\hbar\frac{\partial}{\partial t}\Psi . \tag{3.18}$$

The motion of center-of-mass coordinates is represented by

$$i\hbar\frac{d}{dt}x_0^*=[x_0^*, H_c]=e^{(i/\hbar)H_ct}[x_0, H_c]e^{(-i/\hbar)H_ct},$$

and for the other components, so that

$$\boldsymbol{v}_0^*=\dot{\boldsymbol{x}}_0^*=\frac{1}{Nm}(\boldsymbol{p}_0+Ne\boldsymbol{A}_e)^*$$

and

$$i\hbar\dot{v}_{0x}^*=[v_{0x}^*, H_c] , \text{ etc.}$$

Hence a condition for the steady motion of *c-m*-coordinates corresponds to $[v_{0x}, H_c]=0$, etc.; i. e.,

$$[p_{0x}+NeA_{ex}, H_c]=0, \text{ etc.} \tag{3.19}$$

Returning to the original Hamiltonian (3.1) and applying the unitary transformation

$$U=\exp\left[-\frac{1}{\hbar}\sum_{j,k>k_c}\frac{e}{k\sqrt{\varepsilon_0}}q_ke^{i\boldsymbol{kx}^{(j)}}\right]$$

to it, we see that (3.15) is equivalently replaced by H_0' as follows,

$$H_0'=\frac{1}{2m}\sum_j\boldsymbol{p}_j^2+\frac{e}{2m\sqrt{\varepsilon_0}}\sum_{\substack{j\\k<k_c}}\left[\left(\boldsymbol{p}_j+\frac{\boldsymbol{p}_0}{N}+e\boldsymbol{A}_e\right)q_k\varepsilon_ke^{i\boldsymbol{k}(\boldsymbol{x}_0+\boldsymbol{x}_j)}+q_k\varepsilon_ke^{i\boldsymbol{k}(\boldsymbol{x}_0+\boldsymbol{x}_j)}\left(\boldsymbol{p}_j+\frac{\boldsymbol{p}_0}{N}+e\boldsymbol{A}_e\right)\right]$$
$$-\frac{1}{2}\sum_{k<k_c}p_kp_{-k}+\frac{e^2}{2\varepsilon_0}\sum_{\substack{j,j'\\k>k_c}}\frac{e^{i\boldsymbol{k}(\boldsymbol{x}_j-\boldsymbol{x}_{j'})}}{k^2}+\frac{e^2}{2m\varepsilon_0}\sum_{\substack{j\\k,l<k_c}}\varepsilon_k\varepsilon_lq_kq_le^{i(\boldsymbol{k}+\boldsymbol{l})(\boldsymbol{x}_0+\boldsymbol{x}_j)} \tag{3.20}$$

where q_k and p_k are Fourier amplitudes of $\boldsymbol{A}$ and $\boldsymbol{E}$,

$$\boldsymbol{A}(\boldsymbol{x})=\frac{1}{\sqrt{\varepsilon_0}}\sum_k q_k\varepsilon_k e^{i\boldsymbol{kx}}, \tag{3.21}$$

$$\boldsymbol{E}(\boldsymbol{x})=\frac{1}{\sqrt{\varepsilon_0}}\sum_k p_{-k}\varepsilon_k e^{i\boldsymbol{kx}}, \tag{3.22}$$

$$[p_k, q_{k'}]=-i\hbar\delta_{kk'},\ [p_k, p_{k'}]=[q_k, q_{k'}]=0\ . \tag{3.23}$$

Subsidiary conditions becomes

$$\Omega\Psi\equiv\left[p_{-k}-i\left(\frac{e}{k\sqrt{\varepsilon_0}}\right)\sum_j e^{i\boldsymbol{kx}^{(j)}}\right]\Psi=0\ , \tag{3.24}$$

for $k<k_c$, where k_c is the usual maximum wave vector beyond which we cannot expect the collective description of oscillations.

Now the transformed Hamiltonian $\mathscr{H}_0=U_c^{-1}H_0\,U_c$ can be written as

$$\begin{aligned}\mathscr{H}_0=&\frac{1}{2m}\sum_j \boldsymbol{p}_j^2\\&+\frac{e}{m\sqrt{\varepsilon_0}}\sum_{\substack{j\\k<k_c}}\varepsilon_k q_k\left\{\boldsymbol{p}_j-\frac{\hbar\boldsymbol{k}}{2}+\frac{1}{N}\left(\boldsymbol{p}_0+Ne\boldsymbol{A}_e-\frac{\hbar\boldsymbol{k}}{2}\right)\right\}e^{i\boldsymbol{k}\{\boldsymbol{x}_0+(1/Nm)(\boldsymbol{p}_0+N_e\boldsymbol{A}_e+\hbar\boldsymbol{k}/2)t\}}e^{i\boldsymbol{kx}_j}\\&+\frac{e^2}{2m\varepsilon_0}\sum_{\substack{j\\k,l<k_c}}\varepsilon_k\varepsilon_l q_k q_l e^{i(\boldsymbol{k}+\boldsymbol{l})\,[\boldsymbol{x}_0+(1/Nm)\{\boldsymbol{p}_0+Ne\boldsymbol{A}_e+(\hbar/2)(\boldsymbol{k}+\boldsymbol{l})\}t}e^{i(\boldsymbol{k}+\boldsymbol{l})\boldsymbol{x}_j}\\&-\frac{1}{2}\sum_{k<k_c}p_k p_{-k}-\frac{Ne^2}{2m\varepsilon_0}\sum_{k<k_c}q_k q_{-k}+\frac{e^2}{2\varepsilon_0}\sum_{\substack{j,j'\\k>k_c}}\frac{e^{i\boldsymbol{k}(\boldsymbol{x}_j-\boldsymbol{x}_{j'})}}{k^2}\ .\end{aligned} \tag{3.25}$$

Here use has been made of the condition for steady flow (3.19). In (3.25) the third term can be neglected by random phase approximation and the last term which represents the short range screening interaction between electrons may also be dropped out as we are not concerned here with it. Thus it becomes.

$$\mathscr{H}_0=\mathscr{H}_p+\mathscr{H}_f+\mathscr{H}_i \tag{3.26}$$

$$\mathscr{H}_p=\frac{1}{2m}\sum_j \boldsymbol{p}_j^2, \tag{3.27}$$

$$\mathscr{H}_f=-\frac{1}{2}\sum_{k<k_c}(p_k p_{-k}+\omega_p^2 q_k q_{-k}), \tag{3.28}$$

$$\mathscr{H}_i=\frac{e}{m\sqrt{\varepsilon_0}}\sum_{j,k}\varepsilon_k q_k \boldsymbol{P}_j^- e^{i\boldsymbol{k}(\boldsymbol{x}_0+(1/m)\boldsymbol{P}_0^+t)}e^{i\boldsymbol{kx}_j}\ , \tag{3.29}$$

where

$$\boldsymbol{P}_j^\pm=\boldsymbol{p}_j\pm\frac{\hbar\boldsymbol{k}}{2}+\frac{1}{N}\left(\boldsymbol{p}_0+Ne\boldsymbol{A}_e\pm\frac{\hbar\boldsymbol{k}}{2}\right), \tag{3.30}$$

$$\boldsymbol{P}_0^\pm=\frac{1}{N}\left(\boldsymbol{p}_0+Ne\boldsymbol{A}_e\pm\frac{\hbar\boldsymbol{k}}{2}\right). \tag{3.31}$$

We introduce creation and destruction operators a_k^* and a_k,

$$\begin{aligned}q_k&=(\hbar/2\omega)^{1/2}(a_k-a_{-k}^*)\ ,\\p_k&=i(\hbar\omega/2)^{1/2}(a_k^*+a_{-k})\ ,\end{aligned} \tag{3.32}$$

where

$$[a_k, a_{k'}^*]=\delta_{kk'}, \quad \text{other commutaters vanish.}$$

Then we have

$$\begin{aligned}\mathscr{H}_f&=\sum\left(\frac{\hbar\omega}{2}\right)(a_k^*a_k+a_ka_k^*)+\sum\left(\frac{\hbar}{2\omega}\right)(\omega_p^2-\omega^2)(a_k^*a_k+a_ka_k^*-a_ka_{-k}-a_k^*a_{-k}^*)\\&=\mathscr{H}_h+\mathscr{H}_{anh}\,,\end{aligned} \tag{3.33}$$

$$\mathscr{H}_i=\frac{e}{m}\left(\frac{\hbar}{2\omega\varepsilon_0}\right)^{1/2}\sum\left[\varepsilon_k\boldsymbol{P}_j^-a_ke^{i\boldsymbol{k}(\boldsymbol{x}_0+(1/m)P_0^+t)}e^{i\boldsymbol{k}\boldsymbol{x}_j}+e^{-i\boldsymbol{k}(\boldsymbol{x}_0+(1/m)\boldsymbol{P}_0^-t)}e^{-i\boldsymbol{k}\boldsymbol{x}_j}a_k^*\varepsilon_k\boldsymbol{P}_j^-\right]. \tag{3.34}$$

In (3.33) $\mathscr{H}_h$ and $\mathscr{H}_{anh}$ represents harmonic and anharmonic parts of the oscillating field, respectively.

Next we pass to the interaction representation with unperturbed Hamiltonian $\mathscr{H}_p+\mathscr{H}_h$ by means of the U-transformation

$$U_0=\exp\left[-(i/\hbar)(\mathscr{H}_p+\mathscr{H}_h)t\right].$$

Hence

$$\Psi=U_0\psi\,,$$

$$i\hbar\frac{\partial}{\partial t}\psi=U_0^{-1}(\mathscr{H}_i+\mathscr{H}_{anh})U_0\psi=(\mathrm{H}_i+\mathrm{H}_{anh})\psi\,. \tag{3.35}$$

$$\mathrm{H}_i=\frac{\partial}{m}\left(\frac{\hbar}{2\omega\varepsilon_0}\right)\sum_{j,k}\left[\varepsilon_k\boldsymbol{P}_j^-a_ke^{-i\omega t}\cdot e^{i(k/m)\boldsymbol{P}_j^-t}\cdot e^{ik(x_0+x_j)}+e^{-ik(x_0+x_j)}e^{-i(k/m)\boldsymbol{P}_j^-t}a_k^*e^{i\omega t}\varepsilon_k\boldsymbol{P}_j^-\right], \tag{3.36}$$

$$\mathrm{H}_{anh}=\frac{\hbar}{4\omega}(\omega_p^2-\omega^2)\sum\left[a_k^*a_k+a_ka_k^*-a_ka_{-k}e^{-i[\omega(k)+\omega(-k)]t}-a_k^*a_{-k}^*e^{i[\omega(k)+\omega(-k)]t}\right]. \tag{3.37}$$

If we can cancel out the interaction terms by a suitable transformation, the representation corresponds to the system consisting of the bare electrons without interaction and collective oscillations.

If we make the transformation given by

$$\psi=e^{iS/\hbar}\cdot\phi\,,\quad S=-\int_{-\infty}^{t}\mathrm{H}_i(t')dt'\,, \tag{3.38}$$

the wave equation for ϕ becomes

$$i\hbar\frac{\partial}{\partial t}\phi=\left\{\mathrm{H}_{anh}+\frac{i}{2\hbar}[\mathrm{H}_i, S]\right\}\phi\,, \tag{3.39}$$

to the approximation retaining only quadratic terms in the field variables. $i/2\hbar[\mathrm{H}_i, S]$ involves terms respresenting the residual interaction of electrons through virtual collective field, which include the self-action of individual electrons. The remaining terms combined with the H_{anh} provides the anharmonic part of collective oscillations. The residual parts of electron-electron interaction can be written as

$$\mathrm{H}_{r.p.}=-\frac{e^2}{4m^2\omega\varepsilon_0}\sum\left[\frac{(\varepsilon_k\boldsymbol{P}_j^-)(\varepsilon_k\boldsymbol{P}_{j'}^+)}{\omega-(\boldsymbol{k}/m)\boldsymbol{P}_j^+}e^{ik(x_j-x_{j'})}+e^{ik(x_j-x_{j'})}\frac{(\varepsilon_k\boldsymbol{P}_j^-)(\varepsilon_k\boldsymbol{P}_{j'}^+)}{\omega-(\boldsymbol{k}/m)\boldsymbol{P}_j^+}\right]. \tag{3.40}$$

This term may be negligible also in this case in comparison with the screening interaction according to Bohm and Pines.

The elimination of anharmonic collective oscillations leads us to the dispersion relation as follows:

$$\frac{e^2}{m\varepsilon_0}\sum_j \frac{1}{\left(\omega-\frac{\boldsymbol{k}}{m}\boldsymbol{P}_j^-\right)\left(\omega-\frac{\boldsymbol{k}}{m}\boldsymbol{P}_j^+\right)}=1\,, \tag{3.41}$$

which becomes for $N\gg 1$,

$$\frac{e^2}{m\varepsilon_0}\sum_j \frac{1}{\left[\omega-\frac{\boldsymbol{k}}{m}\left\{\boldsymbol{p}_j+\frac{1}{N}(\boldsymbol{p}_0+Ne\boldsymbol{A}_e)\right\}\right]^2-\left(\frac{\hbar k^2}{2m}\right)^2}=1\,. \tag{3.42}$$

While the self-action term becomes

$$H_{\text{self}}=-\frac{e^2}{4m\varepsilon_0\omega^2}\sum_j\left[\frac{(\varepsilon_k\boldsymbol{P}_j^-)^2}{\omega-\frac{\boldsymbol{k}}{m}\boldsymbol{P}_j^-}+\frac{(\varepsilon_k\boldsymbol{P}_j^+)^2}{\omega-\frac{\boldsymbol{k}}{m}\boldsymbol{P}_j^+}\right]. \tag{3.43}$$

Neglecting the terms of $\hbar k$, $\boldsymbol{P}_j^+\approx\boldsymbol{P}_j^-=\boldsymbol{P}_j$ and assuming $|\boldsymbol{k}\boldsymbol{P}_j/m\omega|\ll 1$,

$$H_{\text{self}}\approx-\frac{N'}{3N}\sum_j\frac{\boldsymbol{P}_j^2}{2m}\,, \tag{3.44}$$

where

$$N'=\frac{k_c^3}{6\pi^2}\,. \tag{3.45}$$

This self-action can be reflected into the original kinetic energy which gives the effective mass as usual:

$$\frac{1}{2mN}(\boldsymbol{p}_0+Ne\boldsymbol{A}_e)^2+\frac{1}{2m}\sum\boldsymbol{p}_j^2+H_{\text{self}}\approx\frac{3N-N'}{3N}\sum\frac{\boldsymbol{P}_j^2}{2m}\equiv\sum\frac{\boldsymbol{P}_j^2}{2m^*}\,, \tag{3.46}$$

so that

$$m^*=[3N/(3N-N')]m\,. \tag{3.47}$$

Finally the new subsidiary conditions which is obtained after the transformation reduces to, for $k<k_c$,

$$\left[\sum_j\frac{\omega^2}{\omega^2-\left(\frac{\boldsymbol{k}}{m}\boldsymbol{P}_j^-\right)^2}e^{i\boldsymbol{k}(\boldsymbol{x}_0+\boldsymbol{x}_j)}\right]\phi=0\,, \tag{3.48}$$

where the dispersion relation (3.41) has been taken into account.

§ 5. Discussions

If we donote $\boldsymbol{p}_j/m=\boldsymbol{v}_j$ and $(\boldsymbol{p}_0+Ne\boldsymbol{A}_e)/Nm=\boldsymbol{v}_0$ in the dispersion relation (3.41), the approximation for small k such that $|\boldsymbol{k}\boldsymbol{v}_j/\omega|\ll 1$ and $|\boldsymbol{k}\boldsymbol{v}_0/\omega|\ll 1$ gives the following relation as

$$\omega^2=\omega_p^2\left[1+2\frac{(\boldsymbol{k}\boldsymbol{v}_0)}{\omega}+3\frac{(\boldsymbol{k}\boldsymbol{v}_0)^2}{\omega^2}+3\frac{\langle(\boldsymbol{k}\boldsymbol{v}_j)^2\rangle}{\omega^2}+\left(\frac{\hbar k^2}{2m\omega}\right)^2+\cdots\right], \tag{4.1}$$

where assumption of the isotropic distribution is made for $\boldsymbol{v}_j$.
Hence

$$\omega\approx\omega_p\left[1+\frac{(\boldsymbol{k}\boldsymbol{v}_0)}{\omega_p}+\frac{(\boldsymbol{k}\boldsymbol{v}_0)^2}{\omega_p^2}+\frac{3\langle(\boldsymbol{k}\boldsymbol{v}_j)^2\rangle}{2\omega_p^2}+\frac{1}{2}\left(\frac{\hbar k^2}{2m\omega_p}\right)\right]^2. \tag{4.2}$$

The terms containing $\boldsymbol{v}_0$ represent the effect of drift velocity of the electron cloud. If the magnitude of $\boldsymbol{v}_0$ is much smaller than that for the mean velocity of thermal agitations, the effect of drift velocity would be negligible and (4.2) reduces to the dispersion relation for the usual plasma. In some cases the magnitude of the drift velocity would be expected much greater than that of the mean velocity for thermal electrons*. Then the drift velocity has the main effect on the dispersion for the collective oscillations.

In practical cases, however, it is a rather complicated problem that with what wave vector $\boldsymbol{k}$ the wave would be excited which satisfies given initial and boundary conditions. Accordingly it is difficult to give the quantitative estimation for this effect, but we must content ourselves for the present with the qualitative or formal discussions of the problem.

If the excited wave travels towards one direction, the term $(\boldsymbol{k}\boldsymbol{v}_0)/\omega_p$ contributes to the frequency shift and the sign of this contribution is dependent on whether the direction of the wave vector is the same or opposite to the drift velocity. If the standing wave is excited, the term $(\boldsymbol{k}\boldsymbol{v}_0)/\omega_p$ vanishes and $(\boldsymbol{k}\boldsymbol{v}_0)^2/\omega_p{}^2$ yields the main contribution.

Note that in (4.2) we must replace the effective mass m^* expressed in (3.47) for the electron mass m, except in $\omega_p{}^2=Ne^2/m\varepsilon_0$; hence $\boldsymbol{v}_j$ and $\boldsymbol{v}_0$ should also be replaced by $\boldsymbol{v}_j{}^*=\boldsymbol{p}_j/m^*$ and $\boldsymbol{v}_0{}^*=(\boldsymbol{p}_0+NeA_e)/m^*$ respectively. In the usual electron gas N' would be small compared with N so that the effect of these replacements would not be remarkable.

---

* For example, the drift velocity of electrons in an interaction space of magnetron is nearly expressed as $v_0=E/B$. For typical values of applied voltage 1000 volts over 2 mm and magnetic flux 1000 Gauss, $v_0\sim5\times10^6$ m/sec. This is much greater than the thermal speed of electron, $v_T\sim2\times10^5$ m/sec for the electron temperature of 1000°K or 6×10^5 m/sec for that of 10000°K.

References

1) As the first paper for the collective longitudinal oscillations, D. Pines and D. Bohm: Phys. Rev. **85** (1952) 338.
2) D. Bohm and D. Pines: Phys. Rev. **92** (1953) 22.
3) Y. Yasuoka: Jour. Phys. Soc. Japan **10** (1955) 1102.
4) S. Tomonaga: Prog. Theor. Phys. **13** (1955) 467, 482.
5) S. Hayakawa and N. Hokkyo: Prog. Theor. Phys. **15** (1956) 193.

JOURNAL OF THE PHYSICAL SOCIETY OF JAPAN Vol. 12, No. 10, OCTOBER, 1957

The Scattering of light from Metal Aventurine Surface and Their Statistical Models

By Hirosi HASUNUMA and Jiro NARA

Department of Applied Physics, Faculty of Engineering, University, of Tokyo

(Received June 22, 1957)

The scattered light from Cr-plated aventurine surfaces were measured by a goniophotometer. The results were analysed assuming that the surfaces are covered by randomly distributed small facets and the scattered light consists of ones reflected regularly by the facets. It is concluded that the inclinations of the facets are distributed by Gaussian process, the r.m.s. values of them lying between 4° to 10°. The results were compared with the theoretical one calculated by the equi-inclination model.

§ 1. Introduction

The angular distributions of scattered light $I(\alpha, \varphi)$ from matt surfaces are dependent on the profile of the surfaces, where α and φ indicate the angle of incidence and the angle of view respectively (Fig. 1). The experimental results obtained until now may be summarised as follows:

1) At any setting of α, the relation of log I to $(\varphi-\alpha)$ are nearly linear or quadric as the roughness of the surfaces are small or large respectively.

2) The intensity of specular reflection increases as α increases, the rate of increases being much larger than that expected by the simple application of the Fresnel's formula.

There are two methods for the theoretical treatments of the problem, the one being the approximation based on the geometrical optics and the other based on the wave optics. The former may fit to rougher surfaces and the later to finer surfaces.

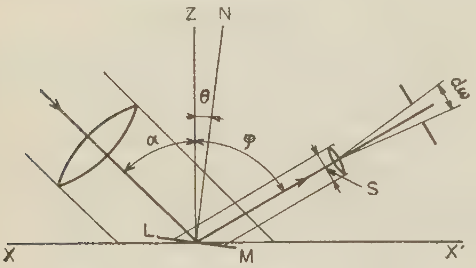

Fig. 1. Reflection by a facet.

We[1] analysed the scattered light from surfaces whose r.m.s. roughness h being smaller than $0.5\,\mu$, by a wave optical method. It was assumed that the height z of any point of the surface is a statistical quantity following the Ornstein-Uhlenbeck process. The surfaces are then represented by two constants h and β. Here $1/\beta$ has the dimention of "length" and indicates the range of the extents of the autocorrelation of z. The critical angle of sheen and curves of diffuse reflection are explained by assuming some adequate values for $1/\beta$, which is about $10\,\mu$ for the surfaces $h=0.2\,\mu$.

The Kirchhoff's diffraction theory tells us that the half-value width of a zeroth order diffraction pattern is inversely proportional to the slit width and is approximately 1° for a slit of $30\,\mu$ width. The geometrical approximation of scattering, then, may be sufficient for the much rougher surfaces than we have treated.

Kappler and Schricker[2] analysed the scattered light from matt glass surfaces by a geometrical approximation. The surfaces are assumed as consisted of small facets which may be set at any angle to mean surface. The intensity of light which is received at any angle is considered to be proportional to the Fresnel's coefficient besides the area of the facets suitably directed. Their analysis reveals that for matt glass surfaces, prepared by lapping with #150 to 500 abressives, the geometrical models are well fitted and the distribution of the inclination of facets is Gaussian. For finer surfaces prepared by #2000 powder, these approximation are insufficient.

Tanaka[3] measured the reflection charactoristics of matt glass surfaces using polarized light and got a result similar to that of Kappler and Schrlicker's.

In the following paper, we have measured the scattering of light from metal aventurine surfaces and analysed them by geometrical approximations which are believed sufficient for our purpose. The mean inclination of the facets obtained by the analysis are compared with the one calculated from profilo-curves by the Katto's[4] methods.

§ 2. The Theory of the Analysis

The intensity of scattered light was measured by a goniophotometer. Figs. 1 and 2 give the schematical arrangement of the apparatus. Sufficiently large area of the test surface is illuminated uniformly by a parallel beam of light, the angle of incidence being α. The light scattered to the direction φ is received by a photomultiplier tube. The solid angular aperture of the receiver $d\omega$ is limited by a diaphragm situated at the focal plane of a lens whose effective area is s_0. The apertures of the optical systems and the area of test pieces are carefully selected so that the reflected flux are always limited by the area s_0 throughout the experiments.

It was assumed that the beam of light is reflected regularly by facets LM whose normal inclining θ, where $\theta=(\alpha+\varphi)/2$. I_0 is the flux density of the incident beam, and $R(\alpha+\theta)$, the coeficient of reflection of the metal. $\Phi(\theta)d\theta$ is the probability density of existence of the facets, i.e., the sum of the projection upon XX' of all facets having the inclination θ, divided by the area of XX'.

The intensity of reflection is given by the following consideration. The intensity of illumination of the surface LM is $I_0\cos(\alpha+\theta)$

The area of the surface which reflects the light to the direction φ passing the aperture s_0 is $\Phi(\theta)s_0 d\theta/\cos\varphi\cos\theta$. The solid angular range of the direction of facets which reflects light flux involved in the cone $d\omega$, is $d\omega/4\cos(\alpha+\theta)$. The distribution of facets is considered constant for small angle of $d\omega$. Multiplying these factors, the intensity of the received light is given by;

$$I(\alpha+2\theta)=\frac{I_0 R(\alpha+\theta)s_0\Phi(\theta)}{4\cos(\alpha+2\theta)\cos\theta}d\omega \qquad (1)$$

If $R(\alpha+\theta)$ is known, we can calculate $\Phi(\theta)$ from the observed intensity $I(\alpha+2\theta)$ by (1). That is the case of transparent materials as reported by Kappler and Schricker or Tanaka. Although the coefficient of reflection of metals are unknown, it can be approximated as constant for small angle of incidence.

If we put

$$R(\alpha-\theta)=\text{const.} \quad \text{for} \quad \alpha-\theta\leqq 20° \qquad (2)$$

assuming

$$\Phi(\theta)=\Phi(-\theta)\ .$$

$$I(\alpha-2\theta)=\frac{I_0 R(\alpha-\theta)\,s_0\Phi(\theta)}{4\cos(\alpha-2\theta)\cos\theta}d\omega \qquad (3)$$

$$R(\alpha+\theta)=\frac{I(\alpha+2\theta)\cos(\alpha+2\theta)}{I(\alpha-2\theta)\cos(\alpha-2\theta)}R(\alpha-\theta) \qquad (4)$$

we can calculate $R(\alpha+\theta)$ successively from the experimental data by (4) and then $\Phi(\theta)$ by (1) numerically.

§ 3. Apparatus and Results of Measurements

a) Goniophotometer. The goniophotometer used is given in Fig. 2. The angular aperture of both the incident and the reflected beam

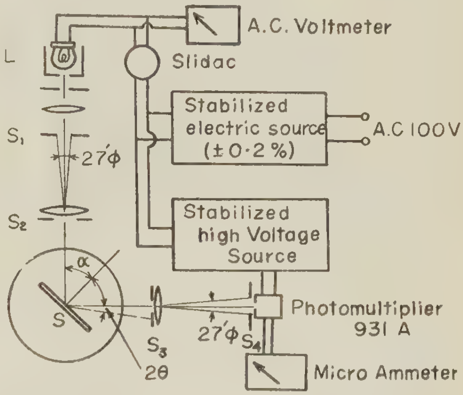

Fig. 2. The apparatus.

Table I. The Results

	Details of the working cond.			Inclinations		r.m.s. roughness	
Test pieces	Abressives of liquid horning	Times electropolish	Times Ni-electroplate	Optical	profil.	Kosth	cal.
				γ	θ_0	h	h
S. 234	A*#180	0 min	15 min	6,9	7,7	1,8	1,79
S. 221	〃	1	〃	5,5	7,6	1,8	1,62
S. 224	〃	3	〃	4,8	6,3	1,5	1,48
S. 67	〃	〃	〃	5,5	7,0	1,5	1,50
S. 226	〃	5	〃	4,2	6,3	1,5	2,20
S. 231	〃	7	〃	3,9	4,8	1,4	1,60
S. 232	〃	9	〃	4,2	6,0	1,6	1,73
S. 75	〃	3	5	7,1	8,5	1,6	1,40
S. 76	〃	〃	〃	6,9	8,8	1,6	1,81
S. 63	〃	〃	10	5,8	6,9	1,5	1,58
S. 64	〃	〃	〃	6,4	8,2	1,4	1,89
S. 27	〃	〃	20	5,6	6,4	1,9	1,41
S. 79	〃	〃	〃	5,3	6,1	1,5	1,62
S. 78	〃	〃	25	5,0	6,8	2,0	1,60
S. 237	S #120	3	15	6,6	10,0	2,3	2,06
S. 242	S #150	〃	〃	4,5	5,8	0,8	0,89
S. 202	S #320	〃	〃	4,0	5,4	0,9	0,81

* The powder marked "A" are alundum and "S", carborandum.

are 27′. The aperture of the incident and the receiving lens are 50 mm and 10 mm respectively.

b) Test pieces. The test pieces were Cr-plated aventurine surfaces. Brass plates were roughened by liquid horning and electro-polished, then electroplated by Ni and finally by Cr. The details of the processes were listed in the 2nd to 4th columns of the Table I.

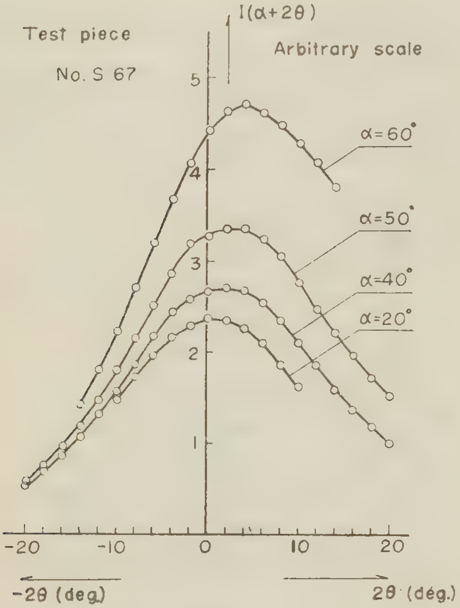

Fig. 3. Distributions of scattered light.

c) Measurments and calculations. A series of reflection curves were obtained on each plates, namely, the intensities of scattered light I against θ were measured, the angle of incidence α being fixed at 20°, 25°, 30°, 40°, 50° and 60° on each plates. Some examples are given in Fig. 3.

$R(\alpha+\theta)$ were calculated successively by the formula (2) and (4), Fig. 4 is a result of calculation, where curves (a) and (b) are the $R(\alpha+\theta)$ taken separately for the reversed directions of the same plate whose distribution of inclination is expected symmetrical. Their differences may be due to the accumulated errors of the calculation which are apt to occur by the successive application of (4). For the calculation of $\Phi(\theta)$ we used the mean of the tw curves. It is shown from Fig. 4 that the as sumption (2) is reasonable. The R-curves fo different test pieces are similar. Fig. 5 the $\Phi(\theta)$ of a sample calculated separatel for each incident angle α using a common R curves. All the curves coincide perfectly wit each other.

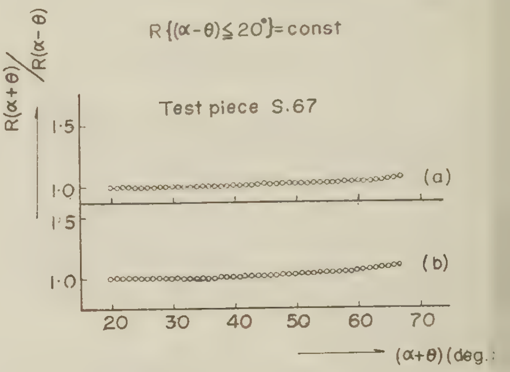

Fig. 4. Reflectivity of a Cr- plated surface (No. S 67).

Examples of the $\Phi(\theta)$ curves of the tes pieces averaged over α are given in Fig. 6 then R-curves being calculated separetely fo each plates.

The distribution of the inclination of facet are then approximated by Gaussian Process i.e.,

$$\Phi(\theta)=\Phi_0 e^{-\theta^2/2\gamma^2} \qquad (5$$

γ being the r.m.s. inclination. The 5th column of the Table I give the values of γ..

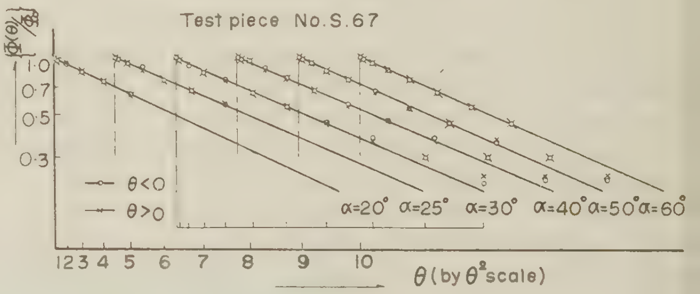

Fig. 5. Distribution of inclinations of facets. (No. S 67)

§ 4. The Analysis of the Profilocurves o the Surfaces

Katto[4] analysed profilocurves of randon surfaces and concluded that they can be re presented by a model named the equi-inclination profile with the Gaussian distribution It is assumed that the boundary of the sur ace consists of straight lines inclined by a onstant angle θ_0 and the height of the vertex f the triangle is a random function of aussian process. (Fig. 7)

If a straight line drawn parallel to the orizon at z, cut the profile at A_1B_1, A_2B_2, $\cdots A_nB_n$, in the unit length of the mean urface, the sum of these length $\sum_{i=1}^{n} A_iB_i$ ivided by unit length is the probability $P(z)$ hat the height of a point on the surface is higher than a definite value of z.

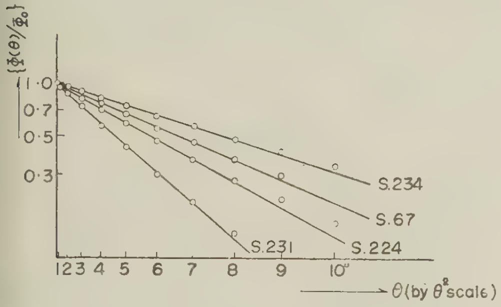

Fig. 6. Distribution of the inclination of facets.

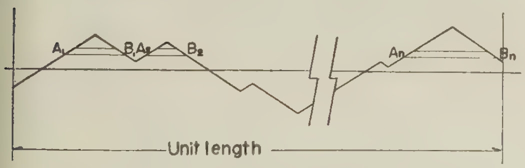

Fig. 7. Katto's equi-inclination profile.

The probability density $\Phi(z)dz$ is the increase of $P(z)$, i.e.,

$$\Phi(z)\Delta z = P(z+\Delta z) - P(z)$$
$$= 2n(z)\cot\theta_0\Delta z \qquad (6)$$

where $n(z)$ is the number of cut in the unit length.

The distribution of z is considered Gaussian

$$\Phi(z) = \frac{1}{\sqrt{2\pi}\,h}\exp\left\{-\frac{1}{2}\left(\frac{z}{h}\right)^2\right\} \qquad (7)$$

h being the r.m.s. roughness of the furface. If n_0 indicate the number of cut by the mean ine ($z=0$),

$$2n_0\cot\theta_0\Delta z = \Phi_0\Delta z = \frac{1}{\sqrt{2\pi}\cdot h}\Delta z$$

or

$$\tan\theta_0 = 2\sqrt{2\pi}\,n_0h \qquad (8)$$

and

$$h = \frac{\Delta z}{\sqrt{2\pi}}\,\frac{\sum_{-\infty}^{\infty} n(z)}{n_0} \qquad (9)$$

We have proceeded the analysis of our profilocurves*, the vertical and the horizontal magnifications being 5000× and 100× respectively. Cares were taken to get a profile as accurate as possible. We had tested several types of profilograph as it was found that some one do not record the detailed structure of surfaces missing small peaks, and selected a optical lever type profilograph designed by Yamamoto.

The main inclination and the r.m.s. roughness, calculated from the record of 600 mm length (corresponding the 6 mm of the real surfaces) by the equation (8) and (9), are given on the 6th and 8th column of the Table I.

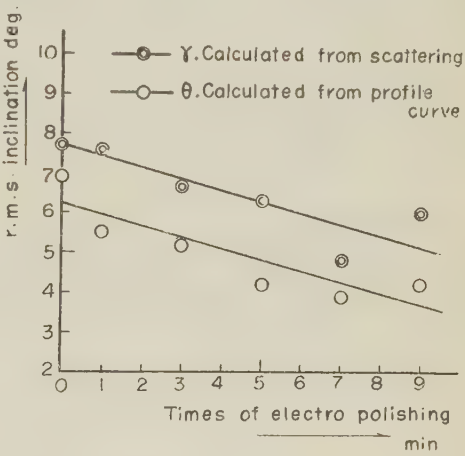

Fig. 8. Decrease of inclination by Electro-polishing.

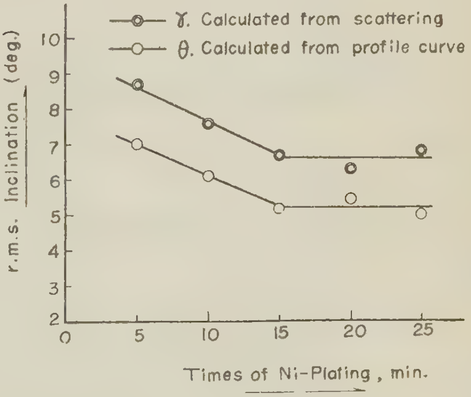

Fig. 9. Decrease of inclination by Ni-plating.

The 7th column of the Table I is the r.m.s. roughness of the surfaces measured by a Kosth's profilometer which measures the r.m.s. value of the roughness directly.

---

* We are indebted to Miss Iwasaki for these curves.

The mean inclination γ and θ_0 plotted against the time of electropolishing and the time of Ni-electroplating are given in Fig. 8 and Fig. 9. It is shown that the mean inclination reduces as the time of electropolishing increases and seems to reduce and saturate as the time of Ni-plating increases. No such relations observed between the times and the roughness heights.

The inclination γ calculated by optical method is always lower than θ_0 obtained by the Katto's method. This discrepancy may be attributed to the approximate nature of the latter model which assumes the sharply pointed vertex whereas that of the real surfaces are rounded.

§ 5. Conclusions

1) The scattering of light by metal aventurine surface whose r.m.s. roughness ranged 1,5 μ to 2 μ may be treated on the bases of the geometrial optics.

2) Both the inclination and the height z of the facts are random functions of Gaussia process. The r.m.s. inclinations are range between 4° to 10°.

Acknowledgments

The authers wish to express our sincer thanks to Mr. K. Yamamoto and Miss G Iwasaki of the Central Inspection Institute o Weight and Measure Tokyo for their kind cooperation. We also wish to express ou thanks to Mr. M. Miyagawa of the Konishirok Photoindustrial Co. for making the test pieces These works has been supported in part b the Scientific Research Fund of the Ministr of Education.

References

1) H. Hasunuma and J. Nara: Journ. Phys. Soc Japan **11** (1956) 69.
2) E. Kappler u. G. Schricker: Glastech. Ber. **23** (1950) 29.
3) S. Tanaka: Journ. Appl. Phys. Japan **26** (1957 85. (In Japanese)
4) Y. Katto: Trans. Jap. Soc. Mech. Eng. **22** (1956) 693. (In Japanese)

JOURNAL OF THE PHYSICAL SOCIETY OF JAPAN Vol. 12, No. 10, OCTOBER, 1957

A Method of Calculating the Solid Angle Subtended by a Circular Aperture

By Minoru NAITŌ
Department of Physics, University of Akita

(Received March 8, 1957)

Practical formulae in terms of elliptic integrals have been obtained which are useful for calculating the solid angle subtended by a circular aperture at a point which is not on the axis of the aperture. Like the familiar formulae in terms of zonal harmonics, these formulae can be used not only to calculate the solid angle with an accuracy of 4 significant figures, but are also applicable to cases in which the former formulae cannot be employed owing to their slow rate of convergence. The results of some preliminary calculations are shown in tables.

§ 1. Introduction

As is well known, the solid angle Ω_P subtended by an aperture at any point P is given by the expression

$$\Omega_P=\iint_S \frac{\cos\gamma}{R^2}\,dS\,, \qquad (1)$$

where S is a surface bounded by the aperture, R is the distance from P to a point Q on the surface, and γ is the angle between the normal to the surface element dS at Q and the line PQ (Fig. 1).

Such a solid angle occurs in various branches of physics, e.g. in the radiation or radioactivity measurements, in the calculation of magnetic potential produced by a current, the mutual inductance, etc. Especially, in radiation physics circular apertures appear very commonly, and the ratio of the solid angle subtended by the aperture Ω_P to 4π is often called the "geometrical factor" G_P of the aperture:

$$G_P=\Omega_P/(4\pi) \tag{2}$$

Even for a simple case of a circular aperture, Ω_P or G_P cannot be expressed in a simple closed form unless the point P lies on the axis of the aperture. Many workers[1)-4)] have already given various approximate and practical formulae for facilitating the calculation of the solid angle, e.g. those in terms of binomial series, zonal harmonics and elliptic integrals, and the formulae in terms of zonal harmonics* seem to have been used most usually.

Recently, Jaffey[2)] and supplementarily Garrett[3)] have presented excellent summary of practical formulae and tables useful for calculating the solid angle. Especially, the latter has pointed out that a formula in terms of elliptic integrals is excellent in its validity in comparison with other formulae. The object of the present work is to investigate the behaviours of such a formula. First, the writer has derived analytically a reasonable formula by carrying out exact calculation of Ω_P in terms of elliptic integrals, and has given a preliminary table as computed by our formulae. Next, he has given supplementarily geometrical interpretations of the parameters appearing in the formulae.

§ 2. Derivation of Exact Solution of Ω_P

Referring to Fig. 1 let ABC be a circular aperture of radius a with its centre at the origin O of the coordinate-axes, and let the cylindrical coordinates of P and Q be $(x, 0, z)$ and $(r, \theta, 0)$ respectively. Then, since

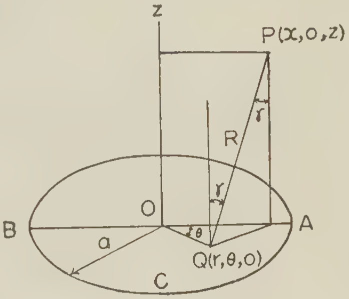

Fig. 1.

$$R^2=z^2+x^2+r^2-2xr\cos\theta\,, \quad \cos\gamma=z/R\,,$$

we have

$$\Omega_P=\int_0^{2\pi}\int_0^a \frac{zrd\theta dr}{(z^2+x^2+r^2-2xr\cos\theta)^{3/2}}\,. \quad (z\neq 0) \tag{3}$$

Carrying out integration with respect to r, we have, after some laborious calculations,

$$\Omega_P=2\pi-\frac{4zK(k)}{[z^2+(a+x)^2]^{1/2}}+2zx\int_0^{\pi}\frac{\cos\theta(a-x\cos\theta)d\theta}{(z^2+x^2\sin^2\theta)[z^2+(a+x)^2-4ax\cos^2\theta/2]^{1/2}}\,, \tag{4}$$

where $K(k)$ represents the complete elliptic integral of the first kind with modulus k given by

$$k^2=4ax/[z^2+(a+x)^2]\,, \tag{5}$$

accordingly its complementary modulus k' being

$$k'^2=1-k^2=[z^2+(a-x)^2]/[z^2+(a+x)^2]\,. \tag{6}$$

Thus, $0\leq k\leq 1$ whenever $x\geq 0$ and $z>0$.

The last integral in (4) can be decomposed into three integrals, one of which gives the same integrals as the second with minus sign and the remaining two are denoted by I_1 and I_2. Changing the integration variable from θ to φ by the relation $\theta=\pi-2\varphi$ we get

---

* The formulae in terms of zonal harmonics are as follows:
When $x<a$

$$\Omega_P=2\pi\left[1-\frac{2}{(z^2+a^2)^{1/2}}+\frac{a^2}{z^2+a^2}\sum_{n=2,4,\dots}^{\infty}\frac{1}{n}P_n(0)P_n'\left(\frac{z}{\sqrt{z^2+a^2}}\right)\left(\frac{x}{\sqrt{z^2+a^2}}\right)^n\right],$$

and when $x>a$

$$\Omega_P=-2\pi\sum_{n=2,4,\dots}^{\infty}P_n(0)P_{n-1}\left(\frac{z}{\sqrt{z^2+x^2}}\right)\left(\frac{a}{\sqrt{z^2+x^2}}\right)^n.$$

$$\Omega_P = 2\pi + I_1 + I_2 \,, \tag{7}$$

where

$$I_1 = \frac{-2z[(z^2+x^2)^{1/2}-a]}{[(z^2+x^2)^{1/2}+x]\,[z^2+(a+x)^2]^{1/2}} \int_0^{\pi/2} \frac{d\varphi}{(1-\lambda_1{}^2\sin^2\varphi)(1-k^2\sin^2\varphi)^{1/2}} \,, \tag{8}$$

$$I_2 = \frac{-2z[(z^2+x^2)^{1/2}+a]}{[(z^2+x^2)^{1/2}-x]\,[z^2+(a+x)^2]^{1/2}} \int_0^{\pi/2} \frac{d\varphi}{(1+\lambda_2{}^2\sin^2\varphi)(1-k^2\sin^2\varphi)^{1/2}} \,, \tag{9}$$

with

$$\lambda_1{}^2 = 2x/[(z^2+x^2)^{1/2}+x] \,, \qquad \lambda_2{}^2 = 2x/[(z^2+x^2)^{1/2}-x] \,. \tag{10}$$

In order to evaluate the above two integrals I_1 and I_2, let us introduce two constant parameters α and β such that

$$k^2 \operatorname{sn}^2\alpha = \lambda_1{}^2 \,, \qquad k^2 \operatorname{sn}^2\beta = -\lambda_2{}^2 . \tag{11}$$

In general α and β will take complex values (see (A.6), (A.7)).

Then both I_1 and I_2 can be reduced to the fundamental complete elliptic integrals of the third kind by the substitution $\sin\varphi = \operatorname{sn}\xi$, and referring to (A.18) in Appendix, we have

$$I_1 = \frac{-2i \operatorname{cn}\alpha \operatorname{dn}\alpha K(k)}{\operatorname{sn}\alpha} - 2i\Pi(K,\, \alpha,\, k) \,, \tag{12}$$

$$I_2 = \frac{-2i \operatorname{cn}\beta \operatorname{dn}\beta K(k)}{\operatorname{sn}\beta} - 2i\Pi(K,\, \beta\ k) \,, \tag{13}$$

where $\Pi(K, \alpha, k)$ and $\Pi(K, \beta, k)$ are the complete elliptic integrals of the third kind with modulus k, amplitude $K(k)$ and parameters α and β respectively, namely:

$$\left.\begin{aligned} \Pi(K,\, \alpha,\, k) &= k^2 \operatorname{sn}\alpha \operatorname{cn}\alpha \operatorname{dn}\alpha \int_0^K \frac{\operatorname{sn}^2\xi\, d\xi}{1-k^2\operatorname{sn}^2\alpha\operatorname{sn}^2\xi} \,, \\ \Pi(K,\, \beta,\, k) &= k^2 \operatorname{sn}\beta \operatorname{cn}\beta \operatorname{dn}\beta \int_0^K \frac{\operatorname{sn}^2\xi\, d\xi}{1-k^2\operatorname{sn}^2\beta\operatorname{sn}^2\xi} \,. \end{aligned}\right\} \tag{14}$$

If we use the well-known relation:

$$\Pi(u,\, a,\, k) - \Pi(a,\, u,\, k) = uE(a,\, k) - aE(u,\, k) \,,$$

where $E(a, k)$ and $E(u, k)$ represent elliptic integrals of the second kind, these integrals can be written in the forms:

$$\Pi(K,\, \alpha,\, k) = K(k)E(\alpha,\, k) - \alpha E(k) \,, \qquad \Pi(K,\, \beta,\, k) = K(k)E(\beta,\, k) - \beta E(k) \,. \tag{15}$$

Thus, (7) becomes

$$\Omega_P = 2\pi - 2i\left[\left(\frac{\operatorname{cn}\alpha\operatorname{dn}\alpha}{\operatorname{sn}\alpha} + \frac{\operatorname{cn}\beta\operatorname{dn}\beta}{\operatorname{sn}\beta}\right)K(k) + \Pi(K,\, \alpha,\, k) + \Pi(K,\, \beta,\, k)\right], \tag{16}$$

which, by the use of the relation[5)]

$$\Pi(K,\, \alpha,\, k) + \Pi(K,\, \beta,\, k) = \Pi(K,\, \alpha+\beta,\, k) + k^2K(k)\operatorname{sn}\alpha\operatorname{sn}\beta\operatorname{sn}(\alpha+\beta) \,,$$

as well as the relation like (15), may be changed into

$$\Omega_P = 2\pi - 2i\left[\frac{\operatorname{sn}(\alpha+\beta)}{\operatorname{sn}\alpha\operatorname{sn}\beta}K(k) + K(k)E(\alpha+\beta,\, k) - (\alpha+\beta)E(k)\right]. \tag{17}$$

Making use of the imaginary transformation[6)] of $E(u)$ and referring to (A.19), (A.20) and (A.21) in Appendix, the second and third terms in the parenthesis of Eq. (17) are written in a more practical form containing real parameters alone, namely:

$$K(k)E(\alpha+\beta,\, k)-(\alpha+\beta)E(k)=i[w\{K(k)-E(k)\}-K(k)E(w,\, k)+k'^2K(k)\,\overline{\mathrm{sn}}\,w\,\overline{\mathrm{cn}}\,w/\overline{\mathrm{dn}}\,w] \tag{18}$$

Here w is a new real constant parameter introduced in place of $\alpha+\beta$ (see Appendix), and $\overline{\mathrm{sn}}\,w$, $\overline{\mathrm{cn}}\,w$ and $\overline{\mathrm{dn}}\,w$ represent Jacobi's elliptic functions with the complementary modulus k'. Thus, we arrive at a final result (the first formula):

$$\begin{aligned}\Omega_{\mathrm{P}}&=2\pi+2[w\{K(k)-E(k)\}-K(k)E(w,\, k')-k'K(k)\,\overline{\mathrm{sn}}\,w]\\&=2\pi+2[F(\phi,\, k')\{K(k)-E(k)\}-K(k)E(\phi,\, k')-k'K(k)\sin\phi]\,,\end{aligned} \tag{19}$$

where, by means of (A.16), the real constant parameter w has been replaced by the elliptic integral of the first kind:

$$w=\int_0^\phi \frac{d\theta}{(1-k'^2\sin^2\theta)^{1/2}}=F(\phi,\, k')\,, \tag{20}$$

or

$$\overline{\mathrm{sn}}\,w=\sin\phi=z/[z^2+(a-x)^2]^{1/2} \qquad \text{(see (A.17))}\,. \tag{21}$$

In the above calculations we have made no restriction to variables except $x\geqq 0$, $z>0$. Therefore, the formula (19) is applicable to any values of x and z such that $x\geqq 0$, $z>0$, so that this is also applicable to the cases of $x=a$ and $(z^2+x^2)^{1/2}=a$, or $(z^2+a^2)^{1/2}=x$, where the usual formula in terms of zonal harmonics is of poor convergence. When $x=a$, with the aid of the well-known formula

$$E(k)K(k')+K(k)E(k')-K(k)K(k')=\pi/2\,, \tag{22}$$

the formula (19) is reduced to a very simple form:

$$\Omega_{\mathrm{P}}=\pi-2k'K(k)\,. \tag{23}$$

Next, we shall derive from the first formula (19) a more interesting and practically applicable formula by applying Landen's transformation[5),6)], by which we have

$$F(\phi,\, k')=2F(\phi_1,\, k_1')/(1+k')\,, \tag{24}$$

$$E(\phi,\, k')=(1+k')\{E(\phi_1,\, k_1')+(1-k')F(\phi_1,\, k_1')/(1+k')\}-k'\sin\phi\,, \tag{25}$$

$$K(k)=2K(k_1)/(1+k')\,, \tag{26}$$

$$E(k)=(1+k')E(k_1)-2k'K(k_1)/(1+k')\,, \tag{27}$$

with

$$k_1=(1-k')/(1+k')\,, \qquad k_1'=2\sqrt{k'}/(1+k')\,, \tag{28}$$

where ϕ_1 represents the amplitude of the elliptic integral with new modulus k_1' and is related with the amplitude ϕ of the elliptic integral (20) by the equation:

$$\tan\phi=\sin 2\phi_1/(k'+\cos 2\phi_1) \qquad \text{or} \qquad \tan(\phi-\phi_1)=k_1\tan\phi_1\,. \tag{29}$$

Putting (24)∼(27) into (19), we have a formula (the second formula):

$$\Omega_{\mathrm{P}}=2\pi+4[F(\phi_1,\, k_1')\{K(k_1)-E(k_1)\}-K(k_1)E(\phi,\, k_1')]\,, \tag{30}$$

with

$$k_1=\frac{1-k'}{1+k'}=\frac{[z^2+(a+x)^2]^{1/2}-[z^2+(a-x)^2]^{1/2}}{[z^2+(a+x)^2]^{1/2}+[z^2+(a-x)^2]^{1/2}}\,, \tag{31}$$

$$k_1'=\frac{2\sqrt{k'}}{1+k'}=\frac{2[z^2+(a+x)^2]^{1/4}[z^2+(a-x)^2]^{1/4}}{[z^2+(a+x)^2]^{1/2}+[z^2+(a-x)^2]^{1/2}}\,, \tag{32}$$

$$\sin^2\phi_1=\frac{z^2+x^2-a^2+[z^2+(a+x)^2]^{1/2}[z^2+(a-x)^2]^{1/2}}{2[z^2+(a+x)^2]^{1/2}[z^2+(a-x)^2]^{1/2}}\,. \tag{33}$$

According to Garrett[3], this result is identical with that by Tallqvist[4]. It will readily b proved that when $x \geqq 0$, $z > 0$ the inequality:

$$F(\phi_1, k_1')\{K(k_1) - E(k_1)\} < K(k_1)E(\phi_1, k_1')$$

always holds so that the second term in (30) is negative.

§ 3. An Asymptotic Formula for Ω_P

By repeating Landen's transformations n—1 times more successively, we have from (30

$$\Omega_P = 2\pi + 2^{n+1}[F(\phi_n, k_n')\{K(k_n) - E(k_n)\} - K(k_n)E(\phi_n, k_n')] \\ +4[k_1'K(k_1)\sin\phi_1 + 2k_2'K(k_2)\sin\phi_2 + \cdots + 2^{n-2}k_{n-1}'K(k_{n-1})\sin\phi_{n-1}] , \qquad (34$$

where $k_1, k_2, \cdots, k_n, k_1', k_2', \cdots, k_n'$ are moduli such that $k_n \to 0$, $k_n' \to 1$ as $n \to \infty$ and ϕ_1, $\cdots, \phi_n$ are parameters such that ϕ_n tends to a definite limit, ϕ_∞ say, as $n \to \infty$.

It will readily be seen that as $k_n \to 0$,

$$K(k_n) - E(k_n) \to 0 ,$$

$$K(k_n)E(\phi_n, k_n') \to \frac{\pi}{2} \sin\phi_n .$$

Thus we obtain finally an asymptotic formula (the third formula) in the form:

$$\Omega_P = 2\pi + 4\left[k_1'K(k_1)\sin\phi_1 + 2k_2'K(k_2)\sin\phi_2 + \cdots + 2^{n-2}k_{n-1}'K(k_{n-1})\sin\phi_{n-1} - 2^{n-1}\frac{\pi}{2}\sin\phi_n \right], \qquad (34$$

and this formula can be conveniently used for calculating Ω_P to 3 or 4 significant figures.

§ 4. Geometrical Meanings of k', k_1, ϕ and ϕ_1

In the first place, it will easily be seen from (6) that referring to Fig. 2 k' is equal to the ratio of the minimum generating line to the maximum one of the cone subtending the solid angle Ω_P with the circular aperture as its base, i.e.

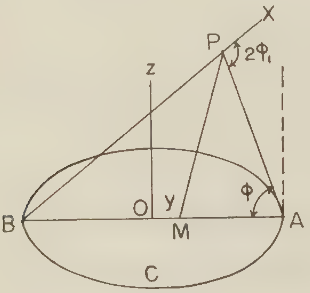

Fig. 2.

$$k' = [z^2 + (a-x)^2]^{1/2} / [z^2 + (a+x)^2]^{1/2} = \mathrm{AP/BP} . \qquad (35)$$

If the point of intersection of the line bisecting the vertex angle $\angle$APB with the diameter AB be denoted by M and let OM$=y$, then we have

$$k_1 = (1-k')/(1+k') = y/a = \mathrm{OM/OA} . \qquad (3$$

Next, it is apparent from (21) that the amplitude ϕ gives the angle between the diamete AB and the minimum generating line AP o the cone. Thus, when $x = a$, ϕ is equal t $\pi/2$ irrespectively of z.

Lastly, we can easily prove by (33) that 2ϕ is the complementary angle of the verte angle $\angle$APB. Thus, it is found that whe $x < a$, $\sin^2\phi_1$ reduces to zero as z decreases whereas when $x > a$, $\sin^2\phi_1$ has a minimu value at $z^2 = x^2 - a^2$ and tends to unity as approaches 0 or ∞.

§ 5. Numerical Computations

Numerical values of the solid angle Ω_P hav been calculated by the third formula (34). Th number of times n of Landen's transformations which should be repeated until k_n' becomes nearly equal to unity within the accuracy of at least 5 figures is different fo different starting values of k'. Table I shows in its second row, such required numbers o times for different starting values of k' a shown in the first row.

The starting values of k and k' can be ob tained by the geometry. Thus, for example, when $x=z=a$, we have, by (5) and (6),

$$k=0.8944272\ ,\quad k'=0.4472136\ .$$

An example of numerical calculations for the case in which $x=z=a$ is shown in Table II.

Table I.

k'	10^{-4}	10^{-2}	0.1	0.2	0.7	0.8	0.95	0.994
n	5	4	4	3	3	2	2	1

Table II.

First stage ($n=0$)	Second stage ($n=1$)	Third stage ($n=2$)	Fourth stage ($n=3$)
$\log k'$ $\bar{1}.6505150$	$\log k_1'$ $\bar{1}.9657549$	$\log k_2'$ $\bar{1}.9996626$	$\log k_3'$ 0
$\log K(k)$ 0.3535710	$\log K(k_1)$ 0.2130736	$\log K(k_2)$ 0.1962885	$\log K(k_3)$ 0.1961198
$\log \sin \phi$ 0	$\log \sin \phi_1$ $\bar{1}.9297513$	$\log \sin \phi_2$ $\bar{1}.9136557$	$\log \sin \phi_3$ $\bar{1}.9134871$
$\log \cos \phi$ $-\infty$	$\log \cos \phi_1$ $\bar{1}.7207637$	$\log \cos \phi_2$ $\bar{1}.7579962$	
$\log(1+k'/2)$ $\bar{1}.8595026$	$\log(1+k_1'/2)$ $\bar{1}.9832149$	$\log(1+k_2'/2)$ $\bar{1}.9998313$	

The values of the complete elliptic integrals $K(k)$, $K(k_1)$, etc. have been calculated conveniently by the formula

$$K(k)=\frac{\pi}{2}\,\frac{2}{1+k_{n-1}'}\cdots\cdots\frac{2}{1+k'}\ ,$$

$$\cdots\cdots$$

$$K(k_{n-1})=\frac{\pi}{2}\,\frac{2}{1+k_{n-1}'}\ .$$

The value of Ω_P in this case when $x=z=a$ has been calculated by an approximate formula:

$$\Omega_P=2\pi-4[k_1'K(k_1)\sin\phi_1 +2k_2'K(k_2)\sin\phi_2-2\pi\sin\phi_3]\ ,$$

and the result is $\Omega_P=1.122689$. This should be compared with the result $\Omega_P=1.122686$ which has been calculated by the use of the formula (23), and also with the result $\Omega_P=1.1225$ as calculated from Jaffey's table[2].

It will be seen that our asymptotic formula (34) can be used with sufficient accuracy for calculating the solid angle Ω_P.

In conclusion, the author wishes to express his hearty thanks to Professor Suekichi Kawata of Konan University for his helpful remarks.

Appendix

Properties of Constant Parameters α, β and Associated Constants

First, let us determine the values of α and β satisfying (11). Among Jacobian elliptic functions of α and β satisfying (11) we may choose the following:

$$\operatorname{sn}\alpha=+\lambda_1/k\ ,\quad \operatorname{sn}\beta=+i\lambda_2/k\ . \tag{A.1}$$

It is apparent from (5) and (10) that the relations $\lambda_1/k\geq 1$ and $\lambda_2/k\geq 1$ hold for any values of x and z except for $z=0$, and therefore $\operatorname{sn}\alpha$ and $\operatorname{sn}\beta$ are restricted respectively to the following ranges, namely:

$$1\leq\operatorname{sn}\alpha<(x+a)/2\sqrt{ax}=[1/k]_{z=0}\ , \tag{A.2}$$

$$1\leq|\operatorname{sn}\beta|<\infty\ . \tag{A.3}$$

Comparing these ranges with the fundamental period-parallelogram of sn functions[5),6)], it will be found that α and β should take the following values:

$$\alpha=K(k)+iu\ ,\quad K(k)+i[K(k')+u]; \tag{A.4}$$

$$\beta=iv\ ,\qquad i[K(k')+v]\ , \tag{A.5}$$

where u and v are both real constant values such that $-K(k')<u<K(k')$, $0<v<K(k')$. Hence, α is a complex constant and β a purely imaginary constant.

As the required values of α and β we may conveniently choose the simplest forms, namely:

$$\alpha=K(k)+iu\ , \tag{A.6}$$

$$\beta=iv\ . \tag{A.7}$$

Thus, we can derive other Jacobian Elliptic functions from the above relations:

$$\left.\begin{aligned}
\operatorname{sn}\alpha&=\operatorname{sn}(K+iu)=\frac{\lambda_1}{k}=\frac{[z^2+(a+x)^2]^{1/2}}{(2a)^{1/2}[(z^2+x^2)^{1/2}+x]^{1/2}}\ ,\\
\operatorname{cn}\alpha&=\operatorname{cn}(K+iu)=\frac{-i(\lambda_1^2-k^2)^{1/2}}{k}=\frac{-i[(z^2+x^2)^{1/2}-a]}{(2a)^{1/2}[(z^2+x^2)^{1/2}+x]^{1/2}}\ ,\\
\operatorname{dn}\alpha&=\operatorname{dn}(K+iu)=(1-\lambda_1^2)^{1/2}=\frac{[(z^2+x^2)^{1/2}-x]^{1/1}}{[(z^2+x^2)^{1/2}+x]^{1/2}}\ ,
\end{aligned}\right\} \tag{A.8}$$

$$\left.\begin{aligned}
\mathrm{sn}\,\beta&=\mathrm{sn}\,iv=\frac{i\lambda_2}{k}=\frac{i[z^2+(a+x)^2]^{1/2}}{(2a)^{1/2}[(z^2+x^2)^{1/2}-x]^{1/2}}\,,\\
\mathrm{cn}\,\beta&=\mathrm{cn}\,iv=\frac{(k^2+\lambda_2{}^2)^{1/2}}{k}=\frac{a+(z^2+x^2)^{1/2}}{(2a)^{1/2}[(z^2+x^2)^{1/2}-x]^{1/2}}\,,\\
\mathrm{dn}\,\beta&=\mathrm{dn}\,iv=(1+\lambda_2{}^2)^{1/2}=\frac{[(z^2+x^2)^{1/2}+x]^{1/2}}{[(z^2+x^2)^{1/2}-x]^{1/2}}\,.
\end{aligned}\right\}\tag{A.9}$$

and from these equations we can easily determine the forms of u and v, namely:

$$\left.\begin{aligned}
\mathrm{sn}\,u(k')&=\overline{\mathrm{sn}}\,u=\frac{(z^2+x^2)^{1/2}-a}{[z^2+(a-x)^2]^{1/2}}\,,\\
\mathrm{cn}\,u(k')&=\overline{\mathrm{cn}}\,u=\frac{(2a)^{1/2}[(z^2+x^2)^{1/2}-x]^{1/2}}{[z^2+(a-x)^2]^{1/2}}\,,\\
\mathrm{dn}\,u(k')&=\overline{\mathrm{dn}}\,u=\frac{(2a)^{1/2}[(z^2+x^2)^{1/2}+x]^{1/2}}{[z^2+(a-x)^2]^{1/2}}\,,
\end{aligned}\right\}\tag{A.10}$$

$$\left.\begin{aligned}
\mathrm{sn}\,v(k')&=\overline{\mathrm{sn}}\,v=\frac{[z^2+(a+x)^2]^{1/2}}{(z^2+x^2)^{1/2}+a}\,,\\
\mathrm{cn}\,v(k')&=\overline{\mathrm{cn}}\,v=\frac{(2a)^{1/2}[(z^2+x^2)^{1/2}-x]^{1/2}}{(z^2+x^2)^{1/2}+a}\,,\\
\mathrm{dn}\,v(k')&=\overline{\mathrm{dn}}\,v=\frac{(2a)^{1/2}[(z^2+x^2)^{1/2}+x]^{1/2}}{(z^2+x^2)^{1/2}+a}\,.
\end{aligned}\right\}\tag{A.11}$$

If we denote the amplitudes of the elliptic integrals of u and v by ψ_1 and ψ_2 respectively we have

$$\left.\begin{aligned}
\sin\psi_1&=\frac{(z^2+x^2)^{1/2}-a}{[z^2+(a-x)^2]^{1/2}}\,,\\
\sin\psi_2&=\frac{[z^2+(a+x)^2]^{1/2}}{(z^2+x^2)^{1/2}+a}\,.
\end{aligned}\right\}\tag{A.12}$$

Next, we consider elliptic functions of $\alpha+\beta$. By means of the addition theorem for the Jacobian functions[5),6)] and Jacobi's imaginary transformation[5),6)], we get

$$\left.\begin{aligned}
\mathrm{sn}\,(\alpha+\beta)&=\mathrm{sn}\,(K+i(u+v))=\mathrm{cn}\,iw/\mathrm{dn}\,iw=1/\overline{\mathrm{dn}}\,w=[z^2+(a+x)^2]^{1/2}/(a+x)\,,\\
\mathrm{cn}\,(\alpha+\beta)&=\mathrm{cn}\,(K+i(u+v))=-k'\,\mathrm{sn}\,iw/\mathrm{dn}\,iw=-ik'\,\overline{\mathrm{sn}}\,w/\overline{\mathrm{dn}}\,w=-iz/(a+x)\,,\\
\mathrm{dn}\,(\alpha+\beta)&=\mathrm{dn}\,(K+i(u+v))=k'/\mathrm{dn}\,iw=k'\,\overline{\mathrm{cn}}\,w/\overline{\mathrm{dn}}\,w=(a-x)/(a+x)\,,
\end{aligned}\right\}\tag{A.13}$$

where $w=u+v$ is given by

$$\alpha+\beta=K(k)+iw\,.\tag{A.14}$$

Thus, we finally obtain

$$\overline{\mathrm{sn}}\,w=\frac{z}{[z^2+(a-x)^2]^{1/2}}\,,\qquad \overline{\mathrm{cn}}\,w=\frac{a-x}{[z^2+(a-x)^2]^{1/2}}\,,\qquad \overline{\mathrm{dn}}\,w=\frac{a+x}{[z^2+(a+x)^2]^{1/2}}\,,\tag{A.15}$$

and consequently, w can be written in the form:

$$w=\int_0^{\phi}\frac{d\theta}{(1-k'^2\sin^2\theta)^{1/2}}=F(\phi,\,k')\,,\tag{A.16}$$

where ϕ is the amplitude of the elliptic integral of w, so that

$$\left.\begin{aligned} \overline{\mathrm{sn}}\, w = \sin\phi &= \frac{z}{[z^2+(a-x)^2]^{1/2}}\,, \\ \overline{\mathrm{cn}}\, w = \cos\phi &= \frac{a-x}{[z^2+(a-x)^2]^{1/2}}\,, \end{aligned}\right\} \tag{A.17}$$

Further, a few results will be given which are useful for the calculation of the solid angle Ω_P in § 2.

(i) By the help of (A.8) and (A.10) the terms in front of the integrals in (8) and (9) may be rewritten in terms of the constant parameters α and β as:

$$\frac{z[(z^2+x^2)^{1/2}-a]}{[(z^2+x^2)^{1/2}+x][z^2+(a+x)^2]^{1/2}} = \frac{i\,\mathrm{cn}\,\alpha\,\mathrm{dn}\,\alpha}{\mathrm{sn}\,\alpha}\,, \quad \frac{z[(z^2+x^2)^{1/2}+a]}{[(z^2+x^2)^{1/2}-x][z^2+(a+x)^2]^{1/2}} = \frac{i\,\mathrm{cn}\,\beta\,\mathrm{dn}\,\beta}{\mathrm{sn}\,\beta}\,. \tag{A.18}$$

(ii) By (A.8), (A.9) and (A.13) we have

$$\frac{\mathrm{sn}\,(\alpha+\beta)}{\mathrm{sn}\,\alpha\;\mathrm{sn}\,\beta} = \frac{k'^2\,\overline{\mathrm{sn}}\,w\,\overline{\mathrm{cn}}\,w + k'\,\overline{\mathrm{sn}}\,w\,\overline{\mathrm{dn}}\,w}{\mathrm{i}\,\overline{\mathrm{dn}}\,w}\,. \tag{A.19}$$

(iii) According to (A.14), $E(iw)$ and $E(\alpha+\beta)$ may be evalualed in terms of the elliptic integrals with real amplitude ϕ. Thus,

$$E(iw) = i[w - E(w,\, k') + \overline{\mathrm{sn}}\,w\,\overline{\mathrm{dn}}\,w/\overline{\mathrm{cn}}\,w]\,, \tag{A.20}$$

$$\begin{aligned} E(\alpha+\beta) &= E(K+iw) = E(iw) + E(k) - ik^2\,\overline{\mathrm{sn}}\,w\,\overline{\mathrm{dn}}\,w/\overline{\mathrm{cn}}\,w \\ &= i[F(\phi,\, k') - E(\phi,\, k') + k'^2\,\overline{\mathrm{sn}}\,w\,\overline{\mathrm{cn}}\,w/\overline{\mathrm{dn}}\,w] + E(k)\,. \end{aligned} \tag{A.21}$$

(iv) With the aid of (A.17) the amplitude relation (29) in Landen's transformation may be rewritten in a convenient form as:

$$\cos 2\phi_1 = -k'\,\overline{\mathrm{sn}}^2\,w + \overline{\mathrm{cn}}\,w\,\overline{\mathrm{dn}}\,w\,, \tag{A.22}$$

$$\begin{aligned} \sin^2\phi_1 &= \frac{1}{2}\left(1 + k'\,\overline{\mathrm{sn}}^2\,w - \overline{\mathrm{cn}}\,w\,\overline{\mathrm{dn}}\,w\right) \\ &= \frac{1}{2}\,(1 + k'\sin^2\phi - \cos\phi\sqrt{1-k'^2\sin^2\phi})\,. \end{aligned} \tag{A.23}$$

References

1) A. F. Kivorik and N. J. Adams: Phys. Rev. **40** (1932) 718.
E. Berne: Rev. Sci. Instr. **22** (1951) 509.
J. H. Smith and M. L. Strom: J. Appl. Phys. **25** (1954) 519.
I. G. Weinberg and F. R. Cohen: Nucleonics **13** (1955) No. 7 25.
A. V. Masket: Rev. Sci. Instr. **28** (1957) 191.
2) A. H. Jaffey: Rev. Sci. Instr. **25** (1954) 349.
3) M. W. Garrett: Rev. Sci. Instr. **25** (1954) 1208.
4) Hj. Tallqvist: Soc. Sci. Fennicae, Commentations Phys.-Math. **5** (1931), N. 24.
5) E. T. Whittaker and G. N. Watson: *Modern Analysis* (1935).
6) T. Takenouchi: *Introduction to the Theory of Elliptic Functions* (in Japanese) (1936).

JOURNAL OF THE PHYSICAL SOCIETY OF JAPAN Vol. 12, No. 10, OCTOBER, 1957

Viscous Flows past a Spheroid

By Shōichi WAKIYA

Faculty of Engineering, Niigata University, Nagaoka

(Received June 24, 1957)

A solution of the Stokes equations of motion of a viscous fluid is given in a form suitable for dealing with the flows past an ellipsoid. When the ellipsoid has rotational symmetry, the solution is expressed in infinite triple integrals.

By utilizing these results, two kinds of steady flows of a viscous fluid past a spheroid are studied when the direction of the main stream is parallel to the axis of symmetry of the spheroid. The first is the flow past a spheroid between two parallel plane walls and the second is the flow past a spheroid in a cylindrical pipe with its axis of revolution along the axis of the pipe.

In particular, the drag and the moment acting on the spheroid as well as the pressure drop in the pipe are discussed in detail. It is worth noticing that the moment of force acting on a spheroid moving uniformly between two parallel walls changes its sign when the rate of roundness of the spheroid exceeds a certain definite value.

§ 1. Introduction

The method by which Faxén has studied the effect of boundary walls upon the steady translation of a sphere in a viscous fluid was recently applied to the investigation of the flow of a viscous fluid past a sphere placed in a cylindrical pipe[2),5)] or between two parallel plane walls[3)]. No discussion on other similar problems in the three-dimensional case seems to have been made yet, however. In this paper, boundary-value problems for a spheroid will be treated.

In the first place, Oberbeck's solution[4)] of Stokes' equations of a viscous flow past an ellipsoid is extended to the case of more general fields of flow and then the infinite integral expression of the solution is given for the special case of an ellipsoid of revolution. Next, by making use of this solution, two kinds of steady flows of a viscous fluid past a spheroid are discussed; the first is the flow past a spheroid between two parallel plane walls and the second is the flow past a spheroid in a cylindrical pipe. The drag and the moment acting on the spheroid as well as the pressure drop in the pipe are discussed with special reference to the cases of a circular plate and a sphere.

§ 2. Solution for the Flows round an Ellipsoid

Referring to the rectangular coordinates (x, y, z), Stokes' equations for the steady motion of an incompressible viscous fluid are expressed as follows:

$$\frac{\partial p}{\partial x}=\mu\nabla^2 u\,,\quad \frac{\partial p}{\partial y}=\mu\nabla^2 v\,,\quad \frac{\partial p}{\partial z}=\mu\nabla^2 w\,, \tag{2.1}$$

where $\nabla^2=\partial^2/\partial x^2+\partial^2/\partial y^2+\partial^2/\partial z^2$, μ is the coefficient of viscosity of the fluid, p is the pressure and u, v, w are the velocity components. The equation of continuity is

$$\frac{\partial u}{\partial x}+\frac{\partial v}{\partial y}+\frac{\partial w}{\partial z}=0\,. \tag{2.2}$$

The coordinate system may be so chosen that the fixed or uniformly moving ellipsoid is given by

$$\frac{x^2}{a^2}+\frac{y^2}{b^2}+\frac{z^2}{c^2}=1\,. \qquad (a,\ b,\ c\text{: constants}) \tag{2.3}$$

Now, we may construct the solutions of (2.1) and (2.2) which are regular outside of the ellipsoid (2.3) and vanish at infinity, by the aid of the harmonic functions defined by

$$\chi_n=\int_\lambda^\infty \frac{1}{2^n}\left(\frac{x^2}{a^2+s}+\frac{y^2}{b^2+s}+\frac{z^2}{c^2+s}-1\right)^n \frac{ds}{\sqrt{(a^2+s)(b^2+s)(c^2+s)}}, \qquad (n=0,\ 1,\ 2,\ \cdots) \tag{2.4}$$

where $\lambda(x, y, z)$ is a positive root of

$$\frac{x^2}{a^2+\lambda}+\frac{y^2}{b^2+\lambda}+\frac{z^2}{c^2+\lambda}=1\,. \tag{2.5}$$

In particular, we shall use here the following solution:

$$\left.\begin{aligned}
u_1=&\frac{\partial}{\partial x}\left\{Ax\chi_0+C\frac{\partial}{\partial z}(x\chi_1)+\frac{1}{2}\left(E\frac{\partial^2}{\partial z^2}+G\frac{\partial^2}{\partial x^2}\right)(x\chi_2)\right\}-2A\chi_0-G\frac{\partial^2\chi_2}{\partial x^2}\\
&-\frac{\partial^2}{\partial x^2}\left\{a^2A\chi_1+\frac{1}{2}\left(F+a^2C\frac{\partial}{\partial z}\right)\chi_2+\frac{a^2}{6}\left(E\frac{\partial^2}{\partial z^2}+G\frac{\partial^2}{\partial x^2}\right)\chi_3\right\}\\
&-\frac{\partial}{\partial z}\left\{(B+C)\chi_1+\frac{1}{2}(D+E)\frac{\partial\chi_2}{\partial z}\right\},\\
v_1=&\frac{\partial}{\partial y}\left\{Ax\chi_0+C\frac{\partial}{\partial z}(x\chi_1)+\frac{1}{2}\left(E\frac{\partial^2}{\partial z^2}+G\frac{\partial^2}{\partial x^2}\right)(x\chi_2)\right\}\\
&-\frac{\partial^2}{\partial x\partial y}\left\{a^2A\chi_1+\frac{1}{2}\left(F+a^2C\frac{\partial}{\partial z}\right)\chi_2+\frac{a^2}{6}\left(E\frac{\partial^2}{\partial z^2}+G\frac{\partial^2}{\partial x^2}\right)\chi_3\right\},\\
w_1=&\frac{\partial}{\partial z}\left\{Ax\chi_0+C\frac{\partial}{\partial z}(x\chi_1)+\frac{1}{2}\left(E\frac{\partial^2}{\partial z^2}+G\frac{\partial^2}{\partial x^2}\right)(x\chi_2)\right\}\\
&-\frac{\partial^2}{\partial x\partial z}\left\{a^2A\chi_1+\frac{1}{2}\left(F+a^2C\frac{\partial}{\partial z}\right)\chi_2+\frac{a^2}{6}\left(E\frac{\partial^2}{\partial z^2}+G\frac{\partial^2}{\partial x^2}\right)\chi_3\right\}\\
&+\frac{\partial}{\partial x}\left\{(B-C)\chi_1+\frac{1}{2}(D-E)\frac{\partial\chi_2}{\partial z}\right\},\\
p_1=&2\mu\frac{\partial}{\partial x}\left\{A\chi_0+C\frac{\partial\chi_1}{\partial z}+\frac{1}{2}\left(E\frac{\partial^2}{\partial z^2}+G\frac{\partial^2}{\partial x^2}\right)\chi_2\right\},
\end{aligned}\right\} \tag{2.6}$$

with arbitrary constants $A,\ B,\ C,\ \cdots$.

Further we assume that there exists an external flow which tends to the form:

$$\left.\begin{aligned}
u_0&=a_0+a_1z+a_2z^2+a_3x^2\,,\\
v_0&=b_2xy\,,\\
w_0&=c_1x+c_2xz\,.
\end{aligned}\right\} \tag{2.7}$$

on the surface of the ellipsoid (2.3), where the constants a_n, b_n, c_n may have some relations with a, b and c. The boundary conditions: $u=v=w=0$ on the ellipsoid can be satisfied by (2.6) and (2.7) with properly chosen constants. Namely, in terms of a_n, b_n, c_n we have

$$A=\frac{1}{K+a^2L_1}\left\{a_0+\frac{1}{3}(c^2a_2+a^2a_3)\right\},\qquad B=\frac{c^2a_1-a^2c_1}{a^2L_1+c^2L_3},\qquad C=\frac{a_1L_1+c_1L_3}{(a^2L_1+c^2L_3)M_3},\ \cdots \tag{2.8}$$

where

$$\left.\begin{aligned}
K&=\int_0^\infty\frac{ds}{\sqrt{(a^2+s)(b^2+s)(c^2+s)}}\,, & L_1&=\int_0^\infty\frac{ds}{(a^2+s)\sqrt{(a^2+s)(b^2+s)(c^2+s)}}\,,\\
L_3&=\int_0^\infty\frac{ds}{(c^2+s)\sqrt{(a^2+s)(b^2+s)(c^2+s)}}\,, & M_3&=\int_0^\infty\frac{ds}{(a^2+s)(c^2+s)\sqrt{(a^2+s)(b^2+s)(c^2+s)}}\,.
\end{aligned}\right\} \tag{2.9}$$

If a_n, b_n, c_n involve A, B, C, $\cdots$, (2.8) may be regarded as a set of infinite simultaneous equations for determining the constants A, B, C, $\cdots$.

We put $a_3=a_3^*+a_3^{**}(c^2-a^2)/a^2$ and assume that a_1, a_2, b_2, c_1, c_2 and a_3^*, a_3^{**} have all definite values for $a\to 0$. The values in (2.8) reduce to

$$\left.\begin{aligned} A&=\frac{c}{\pi}\left\{a_0+\frac{c^2}{3}(a_2+a_3^{**})\right\}, & B&=C=\frac{2}{\pi}c^3a_1\,, \\ D&=E=\frac{8}{3\pi}c^5a_2\,, & F&=2G=\frac{4}{3\pi}c^5(a_2+2a_3^{**})\,, \end{aligned}\right\} \tag{2.8a}$$

for a circular plate ($a=0$, $b=c$), and

$$\left.\begin{aligned} A&=\frac{3}{8}a\left\{a_0+\frac{a^2}{3}(a_2+a_3^*)\right\}, & B&=\frac{3}{4}a^3(a_1-c_1)\,, & C&=\frac{5}{4}a^3(a_1+c_1)\,, \\ D&=\frac{25}{16}a^5\left(\frac{3}{5}a_2+b_2-c_2\right), & E&=\frac{35}{16}a^5(a_2-b_2+c_2)\,, & & \\ F&=\frac{5}{8}a^5(a_2+3a_3^*+c_2)\,, & G&=\frac{35}{16}a^5(a_3^*-b_2)\,, & & \end{aligned}\right\} \tag{2.8b}$$

for a sphere ($a=b=c$).

The total force on the ellipsoid exerted by the flow given by (2.6) is in the direction of the x-axis and becomes

$$W=16\pi\mu A\,, \tag{2.10}$$

and the moment of force about the centre of the ellipsoid has only the y-component, which is given by

$$N=16\,\pi\mu B\,. \tag{2.11}$$

Finally, in case when the ellipsoid has axial symmetry so that $b=c$ (say), we can express χ_n and $x\chi_n$ in the forms of infinite integrals; among those the followings are utilized in the later analysis.

For $a<c$,

$$\left.\begin{aligned} \chi_0&=\frac{1}{\pi^2}\iiint_{-\infty}^{\infty}\frac{\sin(\sigma\sqrt{c^2-a^2})}{\sigma\sqrt{c^2-a^2}}e^{i(\xi x+\eta y+\zeta z)}\frac{d\xi\,d\eta\,d\zeta}{\rho^2}\,, \\ x\chi_0&=-\frac{2i}{\pi^2}\iiint_{-\infty}^{\infty}\frac{\sin(\sigma\sqrt{c^2-a^2})}{\sigma\sqrt{c^2-a^2}}e^{i(\xi x+\eta y+\zeta z)}\frac{\xi\,d\xi\,d\eta\,d\zeta}{\rho^4}\,, \\ \chi_1&=\frac{1}{\pi^2}\iiint_{-\infty}^{\infty}\left[\frac{\cos(\sigma\sqrt{c^2-a^2})}{(\sigma\sqrt{c^2-a^2})^2}-\frac{\sin(\sigma\sqrt{c^2-a^2})}{(\sigma\sqrt{c^2-a^2})^3}\right]e^{i(\xi x+\eta y+\zeta z)}\frac{d\xi\,d\eta\,d\zeta}{\rho^2}\,, \\ x\chi_1&=-\frac{2i}{\pi^2}\iiint_{-\infty}^{\infty}\left[\frac{\cos(\sigma\sqrt{c^2-a^2})}{(\sigma\sqrt{c^2-a^2})^2}-\frac{\sin(\sigma\sqrt{c^2-a^2})}{(\sigma\sqrt{c^2-a^2})^3}\right]e^{i(\xi x+\eta y+\zeta z)}\frac{\xi\,d\xi\,d\eta\,d\zeta}{\rho^4}\,, \end{aligned}\right\} \tag{2.12}$$

and for $a>c$,

$$\chi_0=\frac{1}{\pi^2}\iiint_{-\infty}^{\infty}\frac{\sin(\xi\sqrt{a^2-c^2})}{\xi\sqrt{a^2-c^2}}e^{i(\xi x+\eta y+\zeta z)}\frac{d\xi\,d\eta\,d\zeta}{\rho^2}\,,$$

$$x\chi_0=-\frac{2i}{\pi^2}\iiint_{-\infty}^{\infty}\left\{\frac{\sin(\xi\sqrt{a^2-c^2})}{\xi\sqrt{a^2-c^2}}-\frac{a^2-c^2}{2}\rho^2\left[\frac{\cos(\xi\sqrt{a^2-c^2})}{(\xi\sqrt{a^2-c^2})^2}-\frac{\sin(\xi\sqrt{a^2-c^2})}{(\xi\sqrt{a^2-c^2})^3}\right]\right\}$$
$$\times e^{i(\xi x+\eta y+\zeta z)}\frac{\xi\,d\xi\,d\eta\,d\zeta}{\rho^4}\,,$$

$$\left.\begin{aligned}\chi_1&=\frac{1}{\pi^2}\iiint_{-\infty}^{\infty}\left[\frac{\cos(\xi\sqrt{a^2-c^2})}{(\xi\sqrt{a^2-c^2})^2}-\frac{\sin(\xi\sqrt{a^2-c^2})}{(\xi\sqrt{a^2-c^2})^3}\right]e^{i(\xi x+\eta y+\zeta z)}\frac{d\xi d\eta d\zeta}{\rho^2},\\ x\chi_1&=-\frac{2i}{\pi^2}\iiint_{-\infty}^{\infty}\left\{\left[\frac{\cos(\xi\sqrt{a^2-c^2})}{(\xi\sqrt{a^2-c^2})^2}-\frac{\sin(\xi\sqrt{a^2-c^2})}{(\xi\sqrt{a^2-c^2})^3}\right]\right.\\ &\qquad\left.+\frac{a^2-c^2}{2}\rho^2\left[\left(1-\frac{3}{(\xi\sqrt{a^2-c^2})^2}\right)\frac{\sin(\xi\sqrt{a^2-c^2})}{(\xi\sqrt{a^2-c^2})^3}+3\frac{\cos(\xi\sqrt{a^2-c^2})}{(\xi\sqrt{a^2-c^2})^4}\right]\right\}\\ &\qquad\qquad\times e^{i(\xi x+\eta y+\zeta z)}\frac{\xi d\xi d\eta d\zeta}{\rho^4},\end{aligned}\right\}\quad(2.12a)$$

where $i=\sqrt{-1}$, $\sigma=\sqrt{\eta^2+\zeta^2}$ and $\rho=\sqrt{\xi^2+\eta^2+\zeta^2}$.

FLOWS PAST A SPHEROID BETWEEN TWO PARALLEL WALLS

§ 3.1. General Formulae

Making use of the above solution (2.6), we shall discuss the flow past a spheroid ($b=c$) placed between two plane walls which are parallel to the xy-plane and are given by

$$z=-d_1,\quad z=d_2\qquad (d_1,\ d_2:\ \text{positive constants})\tag{3.1}$$

respectively.

Suppose that, at large distances from the spheroid, the flow is represented by

$$u_\infty=\alpha+\beta z+\gamma z^2,\quad v_\infty=w_\infty=0,\qquad (\alpha,\ \beta,\ \gamma:\ \text{constants})\tag{3.2}$$

which is a solution of (2.1) and (2.2) with

$$p_\infty=2\mu\gamma x+\text{const.}$$

Then the boundary conditions to be satisfied are

$$u=u_\infty,\qquad v=w=0\qquad \text{at infinity,}\tag{3.3}$$

$$u=v=w=0\qquad \text{for } z=-d_1 \text{ and } z=d_2,\tag{3.4}$$

$$u=v=w=0\qquad \text{on the spheroid.}\tag{3.5}$$

Now, on integration of (2.12) or (2.12a) with respect to ζ, we obtain the following formulae which are valid for both oblate and prolate spheroids, when $|z|>|\varepsilon|$,

$$\begin{aligned}\chi_0&=\frac{1}{\pi}\iint_{-\infty}^{\infty}\frac{\sinh(\varepsilon\xi)}{\varepsilon\xi}e^{i(\xi x+\eta y)-k|z|}\frac{d\xi d\eta}{k},\\ x\chi_0&=-\frac{i}{\pi}\iint_{-\infty}^{\infty}\left\{(1+k|z|)\frac{\sinh(\varepsilon\xi)}{\varepsilon\xi}-\varepsilon^2k^2\left[\frac{\cosh(\varepsilon\xi)}{(\varepsilon\xi)^2}-\frac{\sinh(\varepsilon\xi)}{(\varepsilon\xi)^3}\right]\right\}e^{i(\xi x+\eta y)-k|z|}\frac{\xi d\xi d\eta}{k^3},\\ \chi_1&=-\frac{1}{\pi}\iint_{-\infty}^{\infty}\left[\frac{\cosh(\varepsilon\xi)}{(\varepsilon\xi)^2}-\frac{\sinh(\varepsilon\xi)}{(\varepsilon\xi)^3}\right]e^{i(\xi x+\eta y)-k|z|}\frac{d\xi d\eta}{k},\\ x\chi_1&=\frac{i}{\pi}\iint_{-\infty}^{\infty}\left\{(1+k|z|)\left[\frac{\cosh(\varepsilon\xi)}{(\varepsilon\xi)^2}-\frac{\sinh(\varepsilon\xi)}{(\varepsilon\xi)^3}\right]\right.\\ &\qquad\left.-\varepsilon^2k^2\left[\left(1+\frac{3}{(\varepsilon\xi)^2}\right)\frac{\sinh(\varepsilon\xi)}{(\varepsilon\xi)^3}-3\frac{\cosh(\varepsilon\xi)}{(\varepsilon\xi)^4}\right]\right\}e^{i(\xi x+\eta y)-k|z|}\frac{\xi d\xi d\eta}{k^3},\end{aligned}\tag{3.6}$$

where $k=\sqrt{\xi^2+\eta^2}$ and $\varepsilon=\sqrt{c^2-a^2}$ (real or imaginary).

By substituting (3.6) into (2.6), we have when $|z|>|\varepsilon|$

$$\left.\begin{aligned}
u_1&=\frac{1}{\pi}\iint\limits_{-\infty}^{\infty}\left\{f_1+\frac{\xi^2}{k^2}(f_2+k|z|f_3)\right\}e^{i(\xi x+\eta y)-k|z|}\,\frac{d\xi d\eta}{k}\,,\\
v_1&=\frac{1}{\pi}\iint\limits_{-\infty}^{\infty}\frac{\xi\eta}{k^2}(f_2+k|z|f_3)\,e^{i(\xi x+\eta y)-k|z|}\,\frac{d\xi d\eta}{k}\,,\\
w_1&=\frac{1}{\pi}\iint\limits_{-\infty}^{\infty}\frac{z}{|z|}\frac{i\xi}{k}\left\{(f_1+f_3)+(f_2+k|z|f_3)\right\}e^{i(\xi x+\eta y)-k|z|}\,\frac{d\xi d\eta}{k}\,,\\
p_1&=\mu\frac{2}{\pi}\iint\limits_{-\infty}^{\infty}i\xi f_3\,e^{i(\xi x+\eta y)-k|z|}\,\frac{d\xi d\eta}{k}\,,
\end{aligned}\right\}\quad(3.7)$$

where

$$\left.\begin{aligned}
f_1(\xi,\eta)&=-2A\frac{\sinh(\varepsilon\xi)}{\varepsilon\xi}-\frac{z}{|z|}(B+C)\,k\left[\frac{\cosh(\varepsilon\xi)}{(\varepsilon\xi)^2}-\frac{\sinh(\varepsilon\xi)}{(\varepsilon\xi)^3}\right]+\cdots\,,\\
f_2(\xi,\eta)&=A\frac{\sinh(\varepsilon\xi)}{\varepsilon\xi}-Ac^2k^2\left[\frac{\cosh(\varepsilon\xi)}{(\varepsilon\xi)^2}-\frac{\sinh(\varepsilon\xi)}{(\varepsilon\xi)^3}\right]+\cdots\,,\\
f_3(\xi,\eta)&=A\frac{\sinh(\varepsilon\xi)}{\varepsilon\xi}+\frac{z}{|z|}Ck\left[\frac{\cosh(\varepsilon\xi)}{(\varepsilon\xi)^2}-\frac{\sinh(\varepsilon\xi)}{(\varepsilon\xi)^3}\right]+\cdots\,.
\end{aligned}\right\}\quad(3.8)$$

In analogy to (3.7), we can easily verify that another set of solutions of (2.1) and (2.2) is given by

$$\begin{aligned}
u^*&=\frac{1}{\pi}\iint\limits_{-\infty}^{\infty}\left\{g_1+\frac{\xi^2}{k^2}(g_2+kzg_3)\right\}e^{i(\xi x+\eta y)-kz}\,\frac{d\xi d\eta}{k}\,,\\
v^{**}&=\frac{1}{\pi}\iint\limits_{-\infty}^{\infty}\frac{\xi\eta}{k^2}(g_2+kzg_3)\,e^{i(\xi x+\eta y)-kz}\,\frac{d\xi d\eta}{k}\,,\\
w^*&=\frac{1}{\pi}\iint\limits_{-\infty}^{\infty}\frac{i\xi}{k}\left\{(g_1+g_3)+(g_2+kzg_3)\right\}e^{i(\xi x+\eta y)-kz}\,\frac{d\xi d\eta}{k}\,,\\
p^*&=\mu\frac{2}{\pi}\iint\limits_{-\infty}^{\infty}i\xi g_3\,e^{i(\xi x+\eta y)-kz}\,\frac{d\xi d\eta}{k}\,,
\end{aligned}\quad(3.9)$$

and

$$\left.\begin{aligned}
u^{**}&=\frac{1}{\pi}\iint\limits_{-\infty}^{\infty}\left\{h_1+\frac{\xi^2}{k^2}(h_2-kzh_3)\right\}e^{i(\xi x+\eta y)+kz}\,\frac{d\xi d\eta}{k}\,,\\
v^{**}&=\frac{1}{\pi}\iint\limits_{-\infty}^{\infty}\frac{\xi\eta}{k^2}(h_2-kzh_3)\,e^{i(\xi x+\eta y)+kz}\,\frac{d\xi d\eta}{k}\,,\\
w^{**}&=\frac{1}{\pi}\iint\limits_{-\infty}^{\infty}\frac{-i\xi}{k}\left\{(h_1+h_3)+(h_2-kzh_3)\right\}e^{i(\xi x+\eta y)+kz}\,\frac{d\xi d\eta}{k}\,,\\
p^{**}&=\mu\frac{2}{\pi}\iint\limits_{-\infty}^{\infty}i\xi h_3\,e^{i(\xi x+\eta y)+kz}\,\frac{d\xi d\eta}{k}\,.
\end{aligned}\right\}\quad(3.10)$$

If the functions $g_n(\xi,\eta)$ and $h_n(\xi,\eta)$ are determined such that

$$\left.\begin{aligned}
g_1(\xi,\eta)&=-\frac{t_2 f_1^{(-)}-f_1^{(+)}}{t-1}, \qquad h_1(\xi,\eta)=-\frac{t_1 f_1^{(+)}-f_1^{(-)}}{t-1},\\
g_2(\xi,\eta)&=\frac{t_2 f_1^{(-)}+f_2^{(+)}}{t-1}+\frac{t_2 f_3^{(-)}+f_3^{(+)}}{2(t-1)}+\frac{kd_2 f_3^{(+)}}{t-1}+\left\{\frac{2k(td_1+d_2)}{t-1}-1\right\}\frac{g_3}{2},\\
h_2(\xi,\eta)&=\frac{t_1 f_1^{(+)}+f_2^{(-)}}{t-1}+\frac{t_1 f_3^{(+)}+f_3^{(-)}}{2(t-1)}+\frac{kd_1 f_3^{(-)}}{t-1}+\left\{\frac{2k(td_2+d_1)}{t-1}-1\right\}\frac{h_3}{2},\\
g_3(\xi,\eta)&=\frac{2}{(t-1)^2-4tk^2d^2}\Big\{(t-1)t_2(f_1^{(-)}+f_2^{(-)})+2tkd(f_1^{(+)}+f_2^{(+)})\\
&\qquad+\frac{1}{2}(t-1)(t_2 f_3^{(-)}+f_3^{(+)})+tkd(1+2kd_2)f_3^{(+)}+t_2k(td_1+d_2)f_3^{(-)}\Big\},\\
h_3(\xi,\eta)&=\frac{2}{(t-1)^2-4tk^2d^2}\Big\{(t-1)t_1(f_1^{(+)}+f_2^{(+)})+2tkd(f_1^{(-)}+f_2^{(-)})\\
&\qquad+\frac{1}{2}(t-1)(t_1 f_3^{(+)}+f_3^{(-)})+tkd(1+2kd_1)f_3^{(-)}+t_1k(td_2+d_1)f_3^{(+)}\Big\},
\end{aligned}\right\} \tag{3.11}$$

where $t_1=e^{2kd_1}$, $t_2=e^{2kd_2}$, $t=t_1\cdot t_2=e^{2kd}$, $d=d_1+d_2$, and $f_n^{(-)}$, $f_n^{(+)}$ denote the values of f_n for $z=-d_1$ and $z=d_2$ respectively, the integrals in (3.9) and (3.10) converge and the boundary conditions on the walls (3.4) are satisfied by the sum of (3.9), (3.10) and (3.7). Also, considering (3.11), (u^*, v^*, w^*) and (u^{**}, v^{**}, w^{**}) tend to zero at infinity. Thus, we have a solution satisfying the conditions (3.3) and (3.4) as:

$$\left.\begin{aligned}
u&=u_1+u^*+u^{**}+u_\infty,\\
v&=v_1+v^*+v^{**},\\
w&=w_1+w^*+w^{**},\\
p&=p_1+p^*+p^{**}+p_\infty.
\end{aligned}\right\} \tag{3.12}$$

On the spheroid: $x^2/a^2+(y^2+z^2)/c^2=1$, the flow $(u^*+u^{**}, v^*+v^{**}, w^*+w^{**})$ is expanded in the form:

$$\left.\begin{aligned}
u^*+u^{**}&=\frac{1}{\pi}\iint_{-\infty}^{\infty}\left[(g_1+h_1)+(g_2+h_2)\frac{\xi^2}{k^2}\right]\left(1-\frac{c^2}{2}\eta^2+\cdots\right)\frac{d\xi d\eta}{k}\\
&\quad-\frac{z}{\pi}\iint_{-\infty}^{\infty}\left\{(g_1-h_1)+[(g_2-h_2)-(g_3-h_3)]\frac{\xi^2}{k^2}+\cdots\right\}d\xi d\eta\\
&\quad+\frac{z^2}{\pi}\iint_{-\infty}^{\infty}\left\{\left[(g_1+h_1)+(g_2+h_2)\frac{\xi^2}{k^2}\right]\left(1-\frac{\xi^2}{2k^2}\right)-(g_3+h_3)\frac{\xi^2}{k^2}+\cdots\right\}kd\xi d\eta\\
&\quad-\frac{x^2}{\pi}\iint_{-\infty}^{\infty}\left[(g_1+h_1)+(g_2+h_2)\frac{\xi^2}{k^2}\right]\left(\frac{\xi^2}{k^2}-\frac{c^2}{a^2}\frac{\eta^2}{k^2}+\cdots\right)\frac{k}{2}d\xi d\eta+\cdots,\\
v^*+v^{**}&=-\frac{xy}{\pi}\iint_{-\infty}^{\infty}(g_2+h_2)\left(\frac{\xi^2\eta^2}{k^4}+\cdots\right)kd\xi d\eta+\cdots,\\
w^*+w^{**}&=-\frac{x}{\pi}\iint_{-\infty}^{\infty}\left[(g_1-h_1)+(g_2-h_2)+(g_3-h_3)\right]\left(\frac{\xi^2}{k^2}+\cdots\right)d\xi\, d\eta\\
&\quad+\frac{xz}{\pi}\iint_{-\infty}^{\infty}\left\{\left[(g_1+h_1)+(g_2+h_2)\right]\frac{\xi_2}{k^2}+\cdots\right\}kd\xi d\eta+\cdots.
\end{aligned}\right. \tag{3.13}$$

This (3.13) together with u_∞ tends to the flow mentioned in (2.7). Therefore, using the values of A, B, C, $\cdots$ determined from (2.8), we can also make (3.12) satisfy the conditio (3.5) on the spheroid approximately.

The drag acting on the spheroid and the moment about its centre due to the flow (3.12 are given by (2.10) and (2.11), since those due to the flows except (u_1, v_1, w_1) are all equa to zero.

If, in the $\xi\eta$-plane, we introduce the polar coordinates (k, θ) defined as:

$$\xi = k\cos\theta\,, \quad \eta = k\sin\theta\,,$$

the integration of (3.13) with respect to θ can be carried out directly by expanding th hyperbolic functions. For the last integration, we may rely on numerical means¹⁾.

§ 3.2. Numerical Computations

As a numerical example, we have carried out calculations for the case in which $d_1 = d/$ and $d_2 = 3d/4$, and arrived at the following results:

$$\begin{aligned}
&a_0 = \alpha + 6.9613\,A/d - 9.8466\,a^2A/d^3 - 23.405\,c^2A/d^3 + 0.3594\,B/d^2 - 3.4518\,C/d^2 + \cdots\,,\\
&a_1 = \beta - 9.2766\,A/d^2 + \cdots\,, \qquad\qquad a_2 = \gamma + 33.112\,A/d^3 + \cdots\,,\\
&a_3 = -(29.540 - 20.665\,c^2/a^2)\,A/d^3 + \cdots\,, \qquad b_2 = -8.8748\,A/d^3 + \cdots\,,\\
&c_1 = -11.4340\,A/d^2 + \cdots\,, \qquad\qquad c_2 = 67.955\,A/d^3 + \cdots\,. \qquad (3.14
\end{aligned}$$

Substituting these values into (2.8), we have

$$\left.\begin{aligned}
&A\left\{1 - \frac{1}{l(K+a^2L_1)}\left(1.7403 - 0.3077\,\frac{a^2}{l^2} - 0.0856\,\frac{c^2}{l^2}\right)\right\}\\
&\quad = \frac{1}{K+a^2L_1}\left\{\left(\alpha + \frac{c^2}{3}\gamma\right) + 0.0225\,\frac{B}{l^2} - 0.2157\,\frac{C}{l^2}\right\}\,,\\
&B = \frac{2c^2}{l(K+a^2L_1)}\left\{l\beta - \left(0.5798 - 0.7146\,\frac{a^2}{c^2}\right)\frac{A}{l}\right\}\,,\\
&C = \frac{2}{l(K+a^2L_1)}\,\frac{L_1}{M_3}\left\{l\beta - \left(0.5798 + 0.7146\,\frac{L_3}{L_1}\right)\frac{A}{l}\right\}\,,\\
&\quad\cdots\cdots\cdots\cdots\,,
\end{aligned}\right\} \quad (3.15$$

where l denotes the distance from the centre of the spheroid to the nearer wall, i.e. $l = d/4$ and the relation: $a^2L_1 + c^2L_3 = (K + a^2L_1)/2$ has been used. G becomes zero in the case of sphere.

By (3.15), the effect of the boundary walls can be estimated for A up to the order o $(a \text{ (or } c)/l)^4$ and for B up to the order of $(a \text{ (or } c)/l)^3$.

Using the values of A and B determind from (3.15), we can obtain the formulae for th drag and the moment in three cases such as:

Case (A) in which a spheroid is moving with a constant velocity $(-U)$ along the x-axis

Case (B) in which a spheroid is in the Couette flow which may be realized by the stead translstion of one of the two walls in its own plane,

Case (C) in which a fixed spheroid is immersed in the two-dimensional Poiseuille flow, which correspond respectively to three sets of the values of (α, β, γ) in (3.2), namel $(U, 0, 0)$, $(U, U/d_1, 0)$ and $(U, 2U/d_2, -U/(d_1d_2))$. Some values of $W\Big/\dfrac{16\pi\mu U}{K+a^2L_1}$ and $N/\mu c^2U$ are shown in Tables I and II.

It can be seen from (3.15) that the moment due to the additional flow $(u^* + u^{**}, v^* + v^{**}, w^* + w^{**})$ changes its sign when the ratio a/c exceeds a certain definite value. If terms o the order higher than $(a \text{ (or } c)/l)^3$ are neglected, we have

$$(a/c)_{\text{crit}} \doteqdot 0.901 \qquad (3.16$$

Table I. Values of $W\Big/\dfrac{16\pi\mu U}{K+a^2L_1}$

Case (A) in which $u_\infty=U$:

c/l \ a/c	0	0.5	1	2	4
0.05	1.03	1.03	1.03	1.04	1.05
0.1	1.06	1.06	1.07	1.08	1.11
0.2	1.12	1.13	1.15	1.18	1.23
0.3	1.20	1.21	1.24	1.29	1.34
0.4	1.28	1.31	1.34	1.40	
0.5	1.38	1.41	1.46	1.53	
$16\pi/c(K+a^2L_1)$	16	17.06	18.85	22.69	30.12

Case (B) in which $u_\infty=U(1+z/d_1)$:

c/l \ a/c	0	0.5	1	2	3
0.05	1.03	1.03	1.03	1.04	1.05
0.1	1.06	1.06	1.07	1.08	1.11
0.2	1.12	1.13	1.15	1.18	1.23
0.3	1.19	1.21	1.23	1.27	1.31
0.4	1.27	1.29	1.32	1.37	
0.5	1.36	1.38	1.42	1.45	

Case (C) in which $u_\infty=U(1+z/d_1)(1-z/d_2)$:

c/l \ a/c	0	0.5	1	2	4
0.05	1.03	1.03	1.03	1.04	1.05
0.1	1.06	1.06	1.07	1.08	1.11
0.2	1.12	1.13	1.14	1.17	1.22
0.3	1.18	1.20	1.22	1.27	1.30
0.4	1.25	1.27	1.30	1.36	
0.5	1.32	1.35	1.39	1.44	

Table II. Values of $N/\mu c^2U$.

Case (A) in which $u_\infty=U$:

c/l \ a/c	0	0.5	1	2	4
0.01	−0	−0	0	0	0.06
0.05	−0.02	−0.01	0	0.12	1.03
0.1	−0.06	−0.05	0.02	0.54	4.33
0.2	−0.26	−0.21	0.09	2.16	18.9
0.3	−0.62	−0.49	0.21	5.2	

Case (B) in which $u_\infty=U(1+z/d_1)$:

c/l \ a/c	0	0.5	1	2	4
0.01	0.32	0.34	0.38	0.46	0.64
0.05	1.58	1.70	1.89	2.39	4.04
0.1	3.14	3.37	3.79	5.04	10.35
0.2	6.14	6.62	7.63	11.24	31.0
0.3	8.98	9.75	11.51	18.8	

Case (C) in which $u_\infty=U(1+z/d_1)(1-z/d_2)$:

c/l \ a/c	0	0.5	1	2	4
0.01	0.21	0.23	0.25	0.31	0.44
0.05	1.05	1.13	1.26	1.63	3.04
0.1	2.07	2.23	2.53	3.53	8.34
0.2	4.00	4.43	5.11	8.22	27.0
0.3	5.78	6.33	7.74	14.3	

as the critical value at which such an effect just vanishes (cf. Fig. 1).

In particular, the formulae of the drag and the moment for a circular plate perpendicular both to the main stream and to the walls are expressed as follows:

Case (A) in which $u_\infty=U$,

$$W=16\,\mu cU\,/\,(1-0.5540\,c/l+0.0272\,c^3/l^3-0.023\,c^4/l^4)\ ,$$

$$N=-32\,\mu c^2U(c/l)(0.1846\,c/l+0.102\,c^2/l^2)\ .$$

Case (B) in which $u_\infty=U(1+z/l)$,

$$W=16\,\mu cU\,/\,(1-0.5540\,c/l+0.1502\,c^3/l^3-0.023\,c^4/l^4)\ ,$$

$$N=32\,\mu c^2U(c/l)(1-0.1846\,c/l-0.102\,c^2/l^2)\ .$$

Case (C) in which $u_\infty=U(1+z/l)(1-z/3l)$,

$$W=16\,\mu cU(1-c^2/9l^2)\,/\,(1-0.5540\,c/l+0.1092\,c^3/l^3-0.023\,c^4/l^4)\ ,$$

$$N=\frac{16}{3}\,\mu c^2U\,(c/l)(1-0.2769\,c/l-0.153\,c^2/l^2)\ .$$

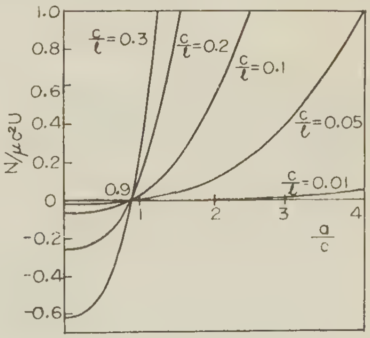

Fig. 1. $N/\mu c^2U$ in the case (A).

On the other hand, the formulae for W and N in the case of a sphere become respectively

Case (A):—

$$W=6\pi\mu aU/(1-0.6526\,a/l+0.1475\,a^3/l^3-0.132\,a^4/l^4)\,,$$
$$N=12\pi\mu a^2U(a/l)(0.0506\,a/l+0.033\,a^2/l^2)\,.$$

Case (B):—

$$W=6\pi\mu aU/(1-0.6526\,a/l+0.4003\,a^3/l^3-0.132\,a^4/l^4)\,,$$
$$N=12\pi\mu a^2U(a/l)(1+0.0506\,a/l+0.033\,a^2/l^2)\,.$$

Case (C):—

$$W=6\pi\mu aU(1-a^2/9l^2)/(1-0.6526\,a/l+0.3160\,a^3/l^3-0.132\,a^4/l^4)\,,$$
$$N=8\pi\mu a^2U(a/l)(1+0.0758\,a/l+0.049\,a^2/l^2)\,.$$

Some of these formulae for a sphere have already been obtained[1),3)] correct to the order of $(a/l)^5$.

FLOWS PAST A SPHEROID IN A CYLINDRICAL PIPE

§ 4.1. General Formulae

Next, utilizing the solution (2.6), we shall consider the flow past a spheroid in an infinitely long straight pipe having a circular cross section, its axis coinciding with the axis of symmetry of the spheroid, i.e. the x-axis.

We assume that the undisturbed flow through the pipe has the form:

$$u_\infty=\alpha+\delta(y^2+z^2)\,,\qquad v_\infty=w_\infty=0\quad(\alpha,\ \delta\text{: constants})\tag{4.1}$$

which together with

$$p_\infty=4\mu\delta x+\text{const.}$$

satisfies (2.1) and (2.2). Then the boundary conditions to be satisfied are

$$u=u_\infty\,,\quad v=w=0\qquad\text{for}\quad x=\pm\infty\,,\tag{4.2}$$
$$u=v=w=0\qquad\text{for}\quad \sqrt{y^2+z^2}=r_0\,,\tag{4.3}$$
$$u=v=w=0\qquad\text{on the spheroid}\,,\tag{4.4}$$

where r_0 is the radius of the pipe.

Integrating (2.12) or (2.12a) with respect to η and ζ, we find that, when $r\ (=\sqrt{y^2+z^2})>|\varepsilon|$,

$$\left.\begin{aligned}\chi_0&=\frac{4}{\pi}\int_0^\infty\frac{\sinh(\varepsilon\xi)}{\varepsilon\xi}K_0(\xi r)\cos(\xi x)d\xi\,,\\ x\chi_0&=\frac{4}{\pi}\int_0^\infty\left.\frac{\sinh(\varepsilon\xi)}{\varepsilon\xi}\xi rK_1(\xi r)-\left[\cosh(\varepsilon\xi)-\frac{\sinh(\varepsilon\xi)}{\varepsilon\xi}\right]K_0(\xi r)\right\}\sin(\xi x)\frac{d\xi}{\xi}\,,\\ \chi_1&=-\frac{4}{\pi}\int_0^\infty\left[\frac{\cosh(\varepsilon\xi)}{(\varepsilon\xi)^2}-\frac{\sinh(\varepsilon\xi)}{(\varepsilon\xi)^3}\right]K_0(\xi r)\cos(\xi x)d\xi\,,\end{aligned}\right\}\tag{4.5}$$

where K_n is the modified Bessel function of the second kind.

In the present case, due to the symmetry of the field we may put

$$B=C=D=E=0\,.$$

Then, using (4.5), general solution (2.6) is expressed for $r>|\varepsilon|$ in the integral forms as:

$$\left.\begin{aligned} u_1 &= \frac{4}{\pi}\int_0^\infty \Big\{ S_1\xi r K_1(\xi r) - (2S_1+T_1)\,K_0(\xi r) \Big\} \cos(\xi x)d\xi\;, \\ q_1 &= \frac{y}{r}\,v_1 + \frac{z}{r}\,w_1 = \frac{4}{\pi}\int_0^\infty \Big\{ T_1 K_1(\xi r) - S_1\xi r K_0(\xi r) \Big\} \sin(\xi x)d\xi\;, \\ p_1 &= -\mu\frac{8}{\pi}\int_0^\infty S_1\xi K_0(\xi r)\sin(\xi x)d\xi\;, \end{aligned}\right\} \tag{4.6}$$

referring to the cylindrical coordinates $(x,\ r,\ \varphi)$, where

$$S_1(\xi) = A\frac{\sinh(\varepsilon\xi)}{\varepsilon\xi} + \cdots, \qquad T_1(\xi) = Ac^2\xi^2\left[\frac{\cosh(\varepsilon\xi)}{(\varepsilon\xi)^2} - \frac{\sinh(\varepsilon\xi)}{(\varepsilon\xi)^3}\right] + \cdots. \tag{4.7}$$

Hence, the second solution may be found as follows:

$$\left.\begin{aligned} u_2 &= \frac{4}{\pi}\int_0^\infty \Big\{ S_2\xi r I_1(\xi r) + (2S_2+T_2)I_0(\xi r) \Big\} \cos(\xi x)d\xi\;, \\ q_2 &= \frac{4}{\pi}\int_0^\infty \Big\{ T_2 I_1(\xi r) + S_2\xi r I_0(\xi r)d\xi \Big\} \sin(\xi x)d\xi\;, \\ p_2 &= \mu\frac{8}{\pi}\int_0^\infty S_2\xi I_0(\xi r)\sin(\xi x)\,d\xi\;, \end{aligned}\right\} \tag{4.8}$$

where I_n is the modified Bessel function of the first kind.

If the functions $S_2(\xi)$ and $T_2(\xi)$ are determined such that

$$\left.\begin{aligned} S_2(\xi) &= S_1(\xi)\frac{K_0(\xi r_0)}{I_0(\xi r_0)} - \frac{1}{\Delta}\left\{ S_1(\xi)\frac{I_1(\xi r_0)}{I_0(\xi r_0)} - \frac{T_1(\xi)}{\xi r_0} \right\}, \\ T_2(\xi) &= T_1(\xi)\frac{K_0(\xi r_0)}{I_0(\xi r_0)} - \frac{1}{\Delta}\left\{ T_1(\xi)\left(\frac{I_1(\xi r_0)}{I_0(\xi r_0)} + \frac{2}{\xi r_0}\right) - S_1(\xi)\xi r_0 \right\}, \end{aligned}\right\} \tag{4.9}$$

with

$$\Delta = 2I_0(\xi r_0)I_1(\xi r_0) - \xi r_0\{[I_0(\xi r_0)]^2 - [I_1(\xi r_0)]^2\}\;,$$

the integrals in (4.8) converge and the boundary conditions on the inner surface of the pipe are satisfied by (4.6) and (4.8). Also, with the value of (4.9), $u_2 = q_2 = 0$ for $x = \mp\infty$ and p_2 at infinity is evaluated as:

$$(p_2)_{x=\mp\infty} = \mp 4\mu[S_2(\xi)\xi^2 I_0(\xi r)]_{\xi=0}\;, \tag{4.10}$$

by applying Dirichlet's integral theorem.

The flow $(u_2,\ q_2)$ is expanded on the spheroid in approximately the same form as (2.7) where $a_1 = a_2 = c_1 = 0$ and $b_2 = c_2$, namely:

$$\left.\begin{aligned} u_2 &= \frac{4}{\pi}\int_0^\infty \Big\{ (2S_2+T_2) + (S_2+T_2/4)c^2\xi^2 + \cdots\cdot \Big\} d\xi \\ &\quad - x^2\frac{4}{\pi}\int_0^\infty \Big\{ [(2S_2+T_2)/2 + (c^2/a^2)(S_2+T_2/4)]\,\xi^2 + \cdots \Big\} d\xi + \cdots\;, \\ q_2 &= xr\frac{4}{\pi}\int_0^\infty \Big\{ (2S_2+T_2)\xi^2/2 + \cdots \Big\} d\xi + \cdots\;. \end{aligned}\right\} \tag{4.11}$$

On the spheroid, the undisturbed flow (4.1) becomes

$$u_\infty = (\alpha + c^2\delta) - (c^2/a^2)\delta x^2\;, \qquad v_\infty = w_\infty = 0\;, \tag{4.12}$$

which may also be regarded as a special case of the flows of type (2.7).

Thus, we can obtain the approximate solution of the problem as follows:

$$\left.\begin{aligned}&u=u_1+u_2+u_\infty\,,\\&q=(y/r)v+(z/r)w=q_1+q_2\,,\\&p=p_1+p_2+p_\infty\,.\end{aligned}\right\}\tag{4.13}$$

Our solution (4.13) satisfies exactly the boundary conditions on the walls as well as at infinity, and also satisfies the ones on the surface of the spheroid approximately with the values of A, B, C, $\cdots$ as determined by (2.8).

The integrals in (4.11) may be evaluated numerically. We have thus obtained, from (4.11) and (4.12),

$$\left.\begin{aligned}&a_1=\alpha+c^2\delta+(5.6112-1.0106\,a^2/r^2_0-4.4289\,c^2/r_0^2)A/r_0+\cdots\,,\\&a_3=-(c^2/a^2)\delta-(3.0316-2.6574\,c^2/a^2)A/r_0^3+\cdots\,,\\&b_2=c_2=3.0316\,A/r_0^3+\cdots\,.\end{aligned}\right\}\tag{4.14}$$

By inserting these values into (2.8), we have, neglecting the terms of the order higher than $(a \text{ (or } c)/l)^4$,

$$A=\frac{1}{K+a^2L_1}\left(\alpha+\frac{2}{3}c^2\delta\right)\Bigg/\left\{1-\frac{1}{r_0(K+a^2L_1)}\left(5.6112-2.0211\frac{a^2}{r_0^2}-3.5431\frac{c^2}{r_0^2}\right)\right\}\,. \tag{4.15}$$

§ 4.2. Drag and Blocking Effect of the Spheroid

When the constants $(\alpha,\ \delta)$ involved in u_∞ take the values $(U,\ 0)$ or $(U,\ -U/r_0^2)$, we have either of the following two cases respectively:

Case (A) in which a spheroid is moving with constant velocity $(-U)$ along the axis of the pipe.

Case (B) in which a fixed spheroid is immersed in the Poiseuille flow through the pipe.

The additional pressure difference between the both ends of the pipe which is required to maintain the same total flux through the pipe as in the case of no spheroid is given by

$$\varDelta p=2(p_2)_{x\to-\infty}=32\,\mu\frac{A}{r_0^2}\left(1-\frac{2}{3}\frac{c^2}{r_0^2}\right)+\cdots\,. \tag{4.16}$$

On the other hand, the drag acting on the spheroid due to the flow (4.13) is given by (2.10) as well. Hence, as far as terms of the order higher than $(a \text{ (or } c)/l)^3$ are neglected, the force P necessary for maintaining the pressure difference as given by (4.16) is connected with the drag of the spheroid by the relation:

$$P=\varDelta p\,\pi r_0^2=2W\left(1-\frac{2}{3}\frac{c^2}{r_0^2}\right), \tag{4.17}$$

which should be compared with the case of the sphere problem[5)].

In particular, the formulae for W and $\varDelta p$ for a circular plate $(a=0)$ are given as follows:

$$W=16\,\mu c\left(\alpha+\frac{2}{3}c^2\delta\right)\Bigg/\left(1-1.786\frac{c}{r_0}+1.128\frac{c^3}{r_0^3}\right), \tag{4.18}$$

$$\varDelta p=\frac{32\,\mu c}{\mu r_0^2}\left\{\alpha+\frac{2}{3}c^2\left(\delta-\frac{\alpha}{r_0^2}\right)\right\}\Bigg/\left(1-1.786\frac{c}{r_0}+1.128\frac{c^3}{r_0^3}\right), \tag{4.19}$$

where $\alpha=U$, $\delta=0$ in the case (A) and $\alpha=U$, $\delta=-U/r_0^2$ in the case (B).

The results for the case of the sphere are in perfect agreement, to our present approximation, with those obtained previously by the present author[2)], namely

$$W=6\,\pi\mu a\left(\alpha+\frac{2}{3}a^2\,\delta\right)\Bigg/\left(1-2.104\frac{a}{r_0}+2.087\frac{a^3}{r_0^3}\right),$$

and so on.

The values of $W\Big/\dfrac{16\pi\mu U}{K+a^2L_1}$ and $P\Big/\dfrac{32\pi\mu U}{K+a^2L_1}$ or some values of a/c and c/l are shown in ables III∼V.

Table III. Values of $W\Big/\dfrac{16\pi\mu U}{K+a^2L_1}$ for $u_\infty=U$.

a/c $/r_0$	0	0.5	1	2	4
0.01	1.02	1.02	1.02	1.03	1.03
0.05	1.10	1.11	1.12	1.14	1.20
0.1	1.22	1.23	1.26	1.33	1.46
0.2	1.53	1.59	1.68	1.87	2.00
0.3	2.02	2.15	2.35	2.62	

Table IV.

Values of $W\Big/\dfrac{16\pi\mu U}{K+a^2L_1}$ for $u_\infty=U(1-r^2/r_0^2)$.

Values of $P\Big/\dfrac{32\pi\mu U}{K+a^2L_1}$ for $u_\infty=U$.

a/c $/r_0$	0	0.5	1	2	4
0.01	1.02	1.02	1.02	1.03	1.03
0.05	1.10	1.10	1.12	1.14	1.20
0.1	1.21	1.22	1.25	1.32	1.45
0.2	1.49	1.55	1.63	1.82	1.95
0.3	1.90	2.02	2.21	2.46	

Table V.

Values of $P\Big/\dfrac{32\pi\mu U}{K+a^2L_1}$ for $u_\infty=U(1-r^2/r_0^2)$.

a/c c/r_0	0	0.5	1	2	4
0.01	1.02	1.02	1.02	1.03	1.03
0.05	1.09	1.10	1.11	1.14	1.19
0.1	1.20	1.22	1.25	1.31	1.44
0.2	1.45	1.50	1.59	1.77	
0.3	1.79	1.90	2.08		

Acknowledgments

The author wishes to express his sincere thanks to Professor I. Imai of the University of Tokyo who suggested the problem and encouraged him, and to Professor S. Asaka and Dr. M. Kawaguti who kindly read the manuscript. The author is greatly indebted to Professor S. Tomotika who has kindly inspected and revised the paper.

References

1) H. Faxén: Ann. d. Phys. **68** (1922) 89.
2) S. Wakiya: J. Phys. Soc. Japan, **8** (1953) 254.
3) S. Wakiya: Res. Rep. Fac. Eng. Niigata Univ. Japan, **5** (1956) 1.
4) A. Oberbeck: Crelles J. **81** (1876).
5) J. Happel and B. J. Byrne: Ind. Eng. Chem. **46** (1954) 1181.

JOURNAL OF THE PHYSICAL SOCIETY OF JAPAN Vol. 12, No. 10, OCTOBER, 1957

Structure of Magnesium Fluoride Films on Amorphous Substrates

By Nobuyoshi MORITA

Scientific Research Institute, Tokyo

(Received April 6, 1957)

Structure of magnesium fluoride films of thickness from 40 Å to 8000 Å evaporated on optical glass and on fused quartz was studied by means of electron microscope and diffraction and its correlation with optical properties and tenacity of the films was examined. Films deposited at room temperature are amorphous, and the grains remain considerably small and tend to grow in height. Effects of residual gas, contamination of substrate surface and rate of deposition were examined. Films deposited in poor vacuum are shown to be porous in structure. Films deposited on substrate kept above 220°C have [301] preferred orientation, and the grains remain thin and grow along the substrate surface. The causes of tenacity of the films deposited at high substrate temperatures are discussed.

§ 1. Introduction

Properties of evaporated magnesium fluoride films depend upon the conditions of preparation. For example, scattering of light from films depends upon substrate material and substrate temperature during deposition.[1] Refractive index depends upon the conditions of evaporation as seen by reported values ranging between 1.35 and 1.41.[1][2][3] Structure of metal films has hitherto been studied extensively by electron microscope,[4][5] but little attention has been given to structure of magnesium fluoride films in spite of the fact that they are widely used in optics. In the previous paper,[1] the film structure was inferred based upon the experimental results about optical properties of magnesium fluoride films. It is the purpose of the present investigation to examine the effects of condition of preparation on the structure by means of electron microscope and diffraction, particularly the effects on the structure due to (1) material and temperature of substrate, (2) film-thickness, (3) deposition rate and pressure of residual gas and to correlate the observed structure with optical properties and tenacity of the films.

§ 2. Experimental Procedures

Magnesium fluoride was evaporated from tungsten basket onto borosilicate crown glass (BK7) or fused quartz placed 22 cm above the basket. To degas adsorbed molecules, the substrate was heated at 350°C for an hour high vacuum before deposition. Film w deposited at the rate between 200 Å/min an 300 Å/min at pressure 5×10^{-5} mmHg. Th measurement of film-thickness was carrie out by multiple-beam interferometry.[6] Th surface structure of film was studied by a electron microscope* using carbon replica.

§ 3. Experimental Results

(1) Change in structure with increasin film-thickness

Films of thickness from 40 Å to 8000 Å we examined. Some of them were deposite simultaneously on an optical glass and a fuse quartz plate in order to study the effect substrate on the film structure. When a fil is deposited on fused quartz at room tempe ature (Fig. 1), it consists of patches of i regular shape at 40 Å thickness. With i creasing thickness, the initially develope patches do not increase in size but interstic between them are filled and the surface film becomes extremely smooth at 280 Å thic ness. With further increase of film-thicknes the grain size increases gradually and becom as large as 300 Å in films of thickness 5000 When a film is deposited on fused quartz 400°C (Fig. 2), the grains are aggregated in nearly spherical granules at 40 Å thicknes With increasing thickness, the grains join ar merge together in large and flat grains.

---

* Akashi Tronscope TRS-5.

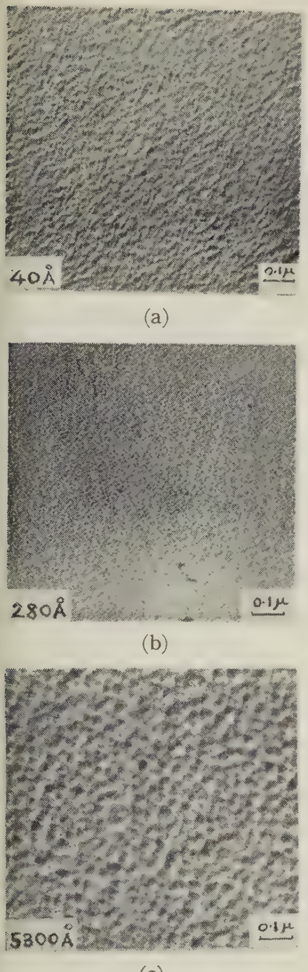

(a)

(b)

(c)

Fig. 1. Electron micrographs of films of the indicated thicknesses, deposited on fused quartz kept at room temperature.

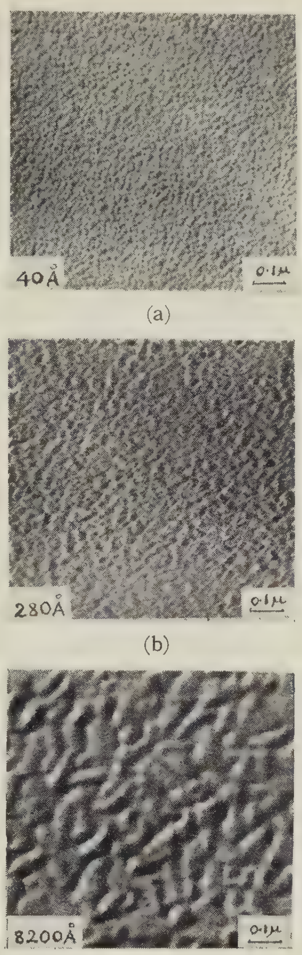

(a)

(b)

(c)

Fig. 2. Electron micrographs of films of the indicated thicknesses, deposited on fused quartz kept at 400°C.

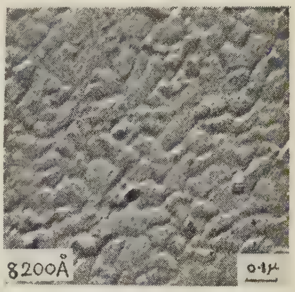

Fig. 3. Electron micrograph of film deposited on optical glass kept at 400°C at the same time with the film shown in Fig. 2 (c).

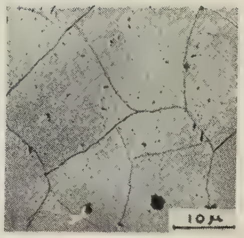

Fig. 4. Electron micrograph of film 8200 Å thick deposited on fused quartz kept at 400°C. The film is the same as that shown in Fig. 2 (c), the magnification of this micrograph being 1/50 of that of Fig. 2 (c).

room temperature, no remarkable difference due to substrate material is detected. At higher temperatures, difference in film structure is distinct. Films on fused quartz show granular surface and those on optical glass show considerably flat appearance (Figs. 2(c) and 3). Moreover, in films of thickness above 6000 Å on fused quartz many cracks are observed which separate the film into blocks of about 10 μ (Fig. 4), while films deposited simultaneously on optical glass show no such cracks. The scattering of light by films on fused quartz which has been reported by the present author1) is found to be caused by the cracks in the film.

(2) Effects of substrate temperature on structure and tenacity of films

The surface structure of films deposited at high temperatures is distinctly different from that deposited at room temperature (Figs. 1 and 2). It is well known that films deposited at high temperatures adhere to glass surface with greater tenacity than those deposited at room temperature.7) In order to find out correlation between tenacity and structure of films, films of thickness about 700 Å were deposited at various temperatures from 30°C to 400°C and both tenacity and structure of the films were examined. Tenacity of film was measured with abrasion test. Film surface was rub-

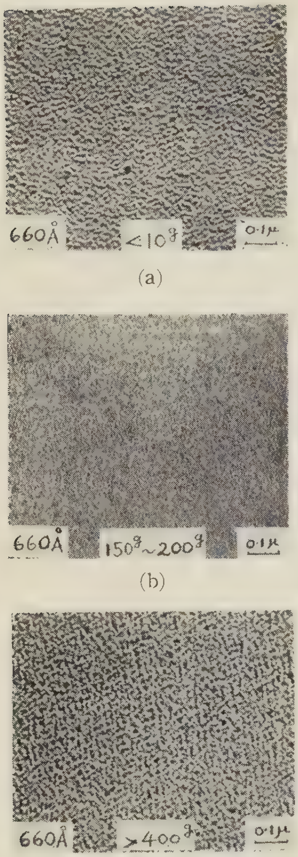

(a)

(b)

(c)

Fig. 6. Electron micrographs of films deposited on optical glass
(a) kept at 30°C,
(b) kept at 90°C,
(c) kept at 230°C.
The tenasity of film is given on each figure.

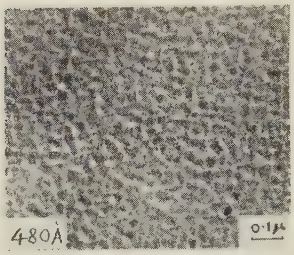

Fig. 7. Electron micrograph of film deposited on fused quartz kept at room temperature at pressure 7×10^{-4} mmHg.

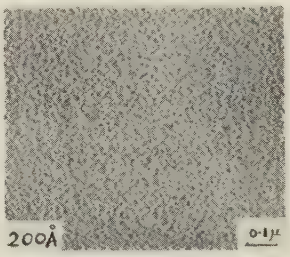

Fig. 8. Electron micrograph of film deposited on contaminated surface of fused quartz kept at room temperature.

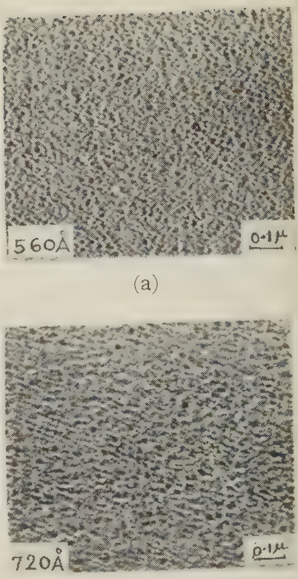

(a)

(b)

Fig. 9. Electron micrographs of films (a) deposited in 1 minutes, (b) deposited in 15 minutes, on optical glass kept at room temperature.

Fig. 10. Electron diffraction pattern of film 900 Å thick deposited on optical glass kept at 220°C.

bed with a piece of glass with spherical surface (radius of curvature 10 mm) which was pressed against the film surface under a given weight. With each weight, the surface was rubbed several times at different places. The heaviest weight which the film could withstand and the lightest with which the film was injured on the average were determined. The value of tenacity of the film was defined to lie within these two values. Tenacity of film increases rapidly as substrate temperature is raised (Fig. 5). The difference in tenacity due to substrate material can scarcely be detected. Films deposited on optical glass at 90°C (Fig. 6(b)) consist of extremely fine grains which are far smaller than those of films deposited at 30°C (Fig. 6(a)). The grains in films deposited at 230°C (Fig. 6(c)) are nearly of the same size as those of films deposited at 30°C but show the tendency to remain thin and to grow along the substrate surface, while the grains in films deposited at 30°C show the tendency to grow more in height, i.e. become thicker before joining together. Heat treatment at 350°C for an hour in vacuum after deposition was found to reduce height of grains in films deposited at room temperature. The effect on flattening of the film surface by heat treatment, however, is smaller than that by depositing at 230°C. The tenacity of films which underwent heat treatment after deposition is between those of films deposited at room temperature and 230°C.

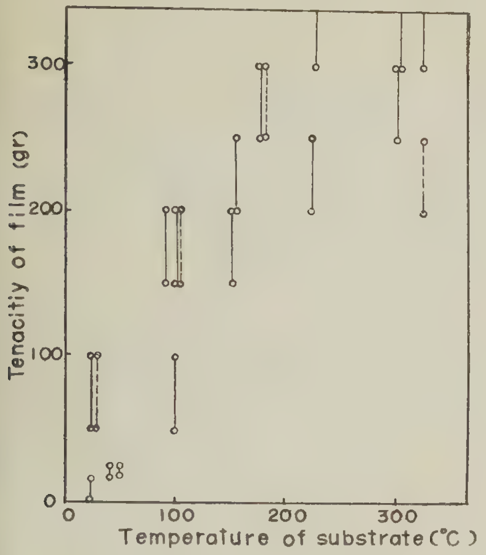

Fig. 5. Experimental value of tenacity of film 700 Å thick as a function of substrate temperature. Full line indicates the value for film depositted on optical glass and dotted line indicates the value for film deposited on fused quartz.

(3) Effect of residual gas on structure of films deposited at room temperature

Films of thickness about 500 Å were deposited on fused quartz at room temperature at various pressures from 5×10^{-5} mmHg to 7×10^{-4} mmHg. Films deposited in poor vacuum (Fig. 7) have more aggregated structure than those deposited in high vacuum.

(4) Effect of contamination of substrate surface on structure of films deposited at room temperature

A fused quartz plate was cleaned by clothes dipped in the mixture of ethyl alcohol and ether and was used as substrate without degasing it in vacuum before deposition. The film of thickness 200 Å deposited on such a substrate (Fig. 8) is more granular than the film of nearly the same thickness deposited on a degased substrate surface (Fig. 1(b)).

(5) Effect of evaporation rate on structure of films deposited at room temperature

Two films of thickness about 600 Å were prepared, one taking 1 minute for deposition and the other 15 minutes. The slowly deposited film has more aggregated structure and larger surface area than the rapidly deposited film (Figs. 9(a) and 9(b)).

(6) Results of electron diffraction study

Electron diffraction by reflection failed to give any distinct pattern for films deposited on optical glass at room temperature. By films of thickness 7000 Å deposited on fused quartz at room temperature, a faint pattern which is likely to indicate [301] orientation can be obtained, though no such patterns are observed for films deposited simultaneously on optical glass.

At substrate temperatures above 220°C, however, [301] orientation can be observed at thickness below 1000 Å (Fig. 10). This reflection continues to dominate the pattern as the film thickness is increased up to 6000 Å. This orientation can also be detected in thin films below 1000 Å deposited at 220°C at high pressures such as 5×10^{-3} mmHg, though diffuseness of the pattern is larger for such films. No remarkable difference in the pattern due to substrate material is detected at high temperatures.

§ 4. Discussion of the Results

(1) Crystallization in films

The growth of magnesium fluoride films deposited at room temperature does not follow the usual sequence which can be seen in metal films such as silver⁵⁾ and gold.⁸⁾ According to Schulz,⁹⁾ films up to thickness 1000Å deposited on slide glass at room temperature produce no reflection pattern, but films of thickness from 2000 Å to 1 μ, a faint broad rings with (301) reflection. In the present experiment, (301) reflection is observed only for films deposited on fused quartz but not on optical glass at room temperature. Grains of size about 300 Å observed in films of thickness 5000 Å (Fig. 1(c)) might not be individual crystallites, for crystallites of this size would have given sharp rings. At room temperature, the kinetic energy of deposited molecules is insufficient to surmount the potential barrier on substrate surface, and crystallization can not develop in the film on account of extremely limited range of migration of the deposited molecules on the substrate surface. At high substrate temperatures, the deposited molecules on substrate surface obtain sufficient energy to surmount the barrier on the surface and crystallize rapidly. The [301] orientation observed in films deposited at high temperatures originates from the tendency of molecules to aggregate first in close packing to form plane sheets of monomolecular thickness on the substrate, as (301) plane is the most densely populated net plane in magnesium fluoride crystal. Though the films deposited at 30°C and at 230°C have similar appearance of surface as shown in Figs. 6(a) and 6(c), respectively, the former is amorphous and the latter is crystalline having distinct orientation.

(2) Coagulation in films due to adsorbed gas molecules

High pressure of residual gas, contamination of substrate surface and slow rate of evaporation are all effective in increasing grain size in thin films deposited at room temperature. As these films are amorphous, grains in the films are formed merely by coagulation and not by crystal growth. These effects seem to be caused mainly by gas molecules adsorbed on substrate and film surface. At pressure 5×10^{-5} mmHg, the rate at which residual gas molecules strike a surface is such as to form five molecular layers in a second. The assumption that some of these residual gas molecules are adsorbed on substrate and film surface kept at room temperature and coagulate the grains in the film will be confirmed from comparison of Fig. 6(a) with Fig. 6(b). As the residual gas molecules impinged upon the surface kept at 90°C would reevaporate from the surface, the deposited magnesium fluoride molecules stick to the place where they hit the substrate under the strong binding force of the substrate. Accordingly, grains in the film remain extremely small without coagulating together. At room temperature, however, adsorbed layers prevent the deposited molecules from coming within the true surface force of the substrate and reduce the binding force of substrate to the deposits. Therefore, the deposited molecules can not stick to the place where they hit the substrate, but coagulate together to form large grains in the film apart from the substrate surface. The flat surface of films deposited at high temperatures compared with that of films deposited at room temperature (Fig. 6(c) and Fig. 6(a) or Fig. 2 and Fig. 1) suggests the reduced effect of residual gas on coagulation of the deposits and the development of crystallization in the films. Such films can be thought to be compact and stable in structure. The fact that films which underwent heat treatment have also flattened surface suggests that residual gas molecules occluded in the films are released from the films and crystallization is stimulated both by removal of the residual gas and increased kinetic energy of the deposited molecules.

The coagulation in films deposited at slow rate of evaporation is not so distinguished as that observed in metal films such as antimony[4] and silver.[5] As the range of migration of magnesium fluoride molecules is extremely small compared with that of the metal atoms, the effect of evaporation rate on the mobility of deposited molecules may be considerably small. Therefore, residual gas molecules adsorbed on the film surface during prolonged deposition would be the main cause for coagulation of the slowly deposited films.

In poor vacuum, residual gas affects the molecular beam by producing collisions between the individual evaporated molecules near the filament, producing thereby large clumps of molecules before they reach the substrate. The film deposited at pressure 7×10^{-4} mmHg* (Fig. 7) is thought to be formed by deposition of these large clumps of molecules and porous in structure having voids within the film.

(3) Correlation between structure and optical properties of films

As films deposited at room temperature in poor vacuum are porous in strucure (Fig. 7), the films can be thought to have lower refractive index than the bulk material from Lorentz-Lorenz formula which relates the refractive index with the density. The variations in refractive indices which are lower than the bulk material[10][11] as reported by some investigators[2][3] for the films deposited at room temperature, can be explained by the different amount of voids in the films. The aging effect observed for such films[2][3] is thought to be caused by sintering of coagulated grains in the porous films with time.

* The mean free path of magnesium fluoride molecules at this pressure is 3 cm.

As the coagulation of grains due to adsorbed gas molecules is observed in films deposited at room temperature at pressure 5×10^{-5}mmHg (Fig. 6(a)), such films may also be considered to be porous in structure and sinter with time. As reported in the previous paper, however, their refractive indices are the same as that of the bulk material within the experimental error of 1 %, and the contractions in film-thickness shown by some of them are only several milli-microns. Therefore, it can not be concluded decidedly that such films are porous and sinter with time. The fact that films deposited at high temperatures show no contraction as reported in the previous paper, indicates the stable structure of the films in accordance with the conclusion obtained by the present experiment.

The fact that grains in films deposited at room temperature remain sufficiently small compared with the wavelength of visible light and those deposited on optical glass at high temperatures remain thin and grow along the substrate surface explains the small scattering of light from such films.[1)]

(4) Correlation between structure and tenacity of films

Tyler[7)] has suggested that the increase in durability and tenacity of magnesium fluoride films might be caused by high concentration of high energy magnesium fluoride molecules. The author[12)] examined the tenacity of cryolite films prepared under various conditions and pointed out that it is essential for obtaining tenacious films to prevent residual gas molecules from depositing within the films. It was found by the present experiment that coagulation of grains in height caused by adsorbed gas molecules has tendency to reduce the tenacity of the films when deposited at room temperature. On the contrary, tenacious films which may be thought to scarcely be affected by gas molecules were found to consist of extremely fine grains. Films deposited at high substrate temperatures also have flat appearance of surface and are extremely tenacious. Accordingly, smoothness of film surface is thought to be a factor which favour the tenacity of the films. The great hardness of films obtained at high deposition temperatures indicates the strong cohesive force within the films and large adhesive force of deposited molecules to the substrate. The fact that films obtained at high deposition temperatures have definite crystal orientation and little tendency to grow in height suggests the compact structure of films and strong cohesive force within the films. The strong adhesive force may be caused by the increased binding force of oxygen atoms of substrate at high temperatures to deposited magnesium fluoride molecules.

(5) Difference in affinity of optical glass and fused quartz to magnesium fluoride molecules

The different behavior of films deposited simultaneously on optical glass and fused quartz as is explained in § 3 (1) and (6), suggests that surface force of optical glass to the deposited magnesium fluoride molecules is larger than that of fused quartz. Optical glass used as substrate contains sodium and potassium ions which are thought loosely bound by surrounding oxygen atoms.[13)] Strong surface force of glass substrate to the deposited magnesium fluoride molecules may be attributed to these ions in the glass.

Summary

Thin films of magnesium fluoride when deposited on optical glass and on fused quartz kept at room temperature consist of extremely fine grains. Distinct reflection patterns can not be obtained for such films by electron diffraction. High pressure of residual gas, surface contamination and slow rate of deposition stimulate the coagulation of grains in height.

The possibility of lower refractive index and sintering with time can be considered for films which are affected by the residual gas molecules.

In films deposited at high substrate temperatures, [301] preferred orientation is found to be distinct. With increasing film-thickness, the grains aggregste rapidly to form large and flat granules.

Scattering of light by films deposited on fused quartz kept at high temperatures is found to be caused by cracks in the films.

The tenacity of films has close correlation with flatness of film surface, compactness of films and surface force of substrate atoms to the deposited magnesium fluoride molecules.

The author is deeply indebted to Miss E. Iguchi of Akashi Manufacturing Co., Ltd. for the preparation of electron micrographs and to Dr. S. Yamaguchi for electron diffraction observation. He expresses his sincere thanks to Professor R. Uyeda for stimulating the investigation by electon microscope with carbon replica and for comments on the manuscript prior to publication, to Professor K. Ishiguro for advices on preparing the paper and to Dr. K. Shinohara for his continued encouragement and guidance.

References

1) N. Morita: J. Phys. Soc. Japan **11** (1956) 975.
2) J. L. Rood: J. Opt. Soc. Am. **39** (1949) 854.
3) J. F. Hall and W. F. C. Ferguson: J. Opt. Soc. Am. **45** (1955) 74.
4) H. Levinstein: J. Appl. Phys. **20** (1949) 306
5) R. S. Sennett and G. D. Scott: J. Opt. Soc Am. **40** (1950) 203.
6) S. Tolansky: Multiple-Beam Interferometr of Surfaces and Films. Clarendon Press Oxford (1948).
7) J. E. Tyler: Rev. Sci. Instr. **18** (1947) 368.
8) R. G. Picard and O. S. Duffendack: J. Appl Phys. **14** (1943) 291.
9) L. G. Schulz: J. Chem. Phys. **17** (1949) 115
10) J. Errera and H. Ketelaar: J. Phys. Rad. (7 **3** (1932) 242.
11) Handbook of Chemistry and Physics (Chemica Rubber Publishing Co., Cleveland, 1947).
12) N. Morita: J. Sci. Res. Inst. **44** (1950) 130.
13) J. E. Stanworth: Physical Properties of Gla Clarendon Press, Oxford (1953).

JOURNAL OF THE PHYSICAL SOCIETY OF JAPAN Vol. 12, No. 10, OCTOBER, 1957

The Visco-elastic Properties of Network Structure

II. Structural Viscosity

By Misazo YAMAMOTO

Department of Chemistry, Faculty of Science, Kyoto University

(Received July 1, 1957)

Viscosity behaviors of concentrated polymer solution are treated by making use of the model of weak Gaussian network. If chain-breakage coefficient, i.e. the probability of breakage of a chain in the network is independent of elongation of the chain, such system shows the Newtonian flow. Proper choice of chain-breakage coefficient, for example, that of square well type, yields a typical rate dependence of viscosity; the larger the rate of shearing flow, λ, the smaller the value of viscosity coefficient, μ. The tensile viscosity, μ^*, is also considered, which in general increases with the rate of stretching, λ^*, for small values of the rate. The so-called Trouton's formula, $\mu^*=3\mu$ is satisfied only in the limit of zero values of rates λ and λ^*.

§ 1. Introduction

The so-called structural viscosity or, in modern terminology, non-Newtonian viscosity is one of the most interesting rheological phenomena on high polymeric systems. In solutions of high polymeric substances, usually the viscosity is very sensitive to rate of shear of the flow; the larger the rate of shear, the smaller the value of viscosity coefficient. It is likely that in such systems there exists some structure which may respond to this particular behavior. When the magnitude of applied deformation or its time rat becomes larger, such structure may progressively be broken down and, as a result the resistance of the system to the deformatio becomes smaller. For extremely dilute solutions of polymers where interactions betwee coiled chain molecules are negligible, a numbe of theoretical studies have been worked ou on their rheological behavior by previous investigators.[1] It appears, however, that n satisfactory theory is yet available for the structural viscosity of concentrated polymer solution.

When the concentration of a given polymer solution is increased, the viscosity coefficient increases rapidly and its shear-rate dependence becomes quite marked. In such solutions the interchain interactions may play a role in their rheological behavior. The chain molecules may entangle each other and form a temporary, weak network structure throughout the solution. In a previous paper[2)] a statistical mechanical theory of such a weak network structure was presented and in terms of it the stress-strain relation for general deformation was derived. One of the purposes of the present paper is to provide the concrete expression of the shearing stress for simple shear deformation. It is shown that, when the probability at which the network "junction" breaks is independent of the state of network deformation, the shearing stress becomes proportional to the rate of shear. This results in the viscosity coefficient, μ, independent of rate of shear. This is actually the particular case investigated by Green and Tobolsky,[3)] and is nothing but an ideal case. In actual systems the probability of chain breakage may increase with increasing tension acting on network junctions. It is shown below that such a system really shows a typical structural viscosity.

The so-called tensile viscosity, μ^*, is also considered for simple elongation. The classical theory of elasticity shows a simple relation to hold between the viscosity coefficients for shearing and stretching deformations, that is

$$\mu^* = 3\mu \tag{1}$$

This relation is sometimes called Trouton's formula. For actual polymeric substances, this in general does not obtain. Nitchmann-Schrade's experimental results[4)] for concentrated solutions of nitrocellulose in diphenyl chloride show that the tensile viscosity coefficient increases with rate of stretching. This behavior should be contrasted with that in simple shearing. It is shown that our network theory yields a qualitative interpretation of these characteristics of viscosity behavior as functions of rate of deformation.

§ 2. General Considerations

From the statistical thermodynamical point of view, viscous flow is considered as one of the dissipative processes. In terms of the energy of dissipation $\Delta\mathcal{E}$ in a simple shearing flow the viscosity coefficient μ is defined by the equation

$$\mu = \Delta\mathcal{E}/\lambda^2 , \tag{2}$$

where λ is the rate of shear or the velocity gradient of the flow. The viscosity coefficient is usually defined in terms of the shearing flow. However, it is possible to extend the concept of viscosity to deformations of other types, if rates of deformation are properly defined in respective cases. For example, let us consider simple elongation. It is shown that the length α^* of the sample must be changed exponentially with time to maintain the deformation steady. Thus

$$\alpha^* = \alpha_0^* e^{\lambda^* t} , \tag{3}$$

where λ^* is considered as a measure for the rate of stretching. We may then apply Eq. (2) and define the "tensile viscosity" or "Trouton viscosity" coefficient μ^*. In terms not of energy of dissipation but of normal stress σ^* and strain α^*, μ^* is then defined such that

$$\mu^* = \sigma^* \Big/ \frac{1}{\alpha^*}\frac{d\alpha^*}{dt} = \sigma^*/\lambda^* . \tag{4}$$

In this paper, for simplicity of calculation, we assume that any chain in polymer network is represented by the Gaussian chain, i.e., its free energy, ϕ, for stretching is proportional to the square of the end-to-end distance $\boldsymbol{h} = (\xi, \eta, \zeta)$, such that

$$\phi(|\boldsymbol{h}|, N, T) = \frac{3kT}{2}\frac{|\boldsymbol{h}|^2}{a^2 N} , \tag{5}$$

where k is Boltzmann constant, T is the absolute temperature, and a and N are the length and the number of statistical segments in a chain, respectively. It has been shown in a previous paper that with this simplification, the stress tensor $\boldsymbol{s}$ corresponding to the strain tensor $\boldsymbol{e}$ is given in terms of the "chain distribution function" $F(\boldsymbol{h}, N, t)$. Thus

$$\boldsymbol{s} = \boldsymbol{s}_n + P\boldsymbol{1} \tag{6}$$

with

$$\boldsymbol{s}_n = \sum_N \iiint \frac{3kT}{a^2 N} (\boldsymbol{hh}) F(\boldsymbol{h}, N, t) d\boldsymbol{h} , \tag{7}$$

where $(\boldsymbol{hh})$ is a tensor defined as

$$(\boldsymbol{hh})=\begin{pmatrix} \xi^2 & \xi\eta & \xi\zeta \\ \eta\xi & \eta^2 & \eta\zeta \\ \zeta\xi & \zeta\eta & \zeta^2 \end{pmatrix}. \qquad (8)$$

It has been shown[2)] that the chain distribution function F must satisfy

$$\frac{\partial F(\boldsymbol{h}, N, t)}{\partial t} = -\nabla F(\boldsymbol{h}, N, t)\frac{d\boldsymbol{e}}{dt}\boldsymbol{e}^{-1}\boldsymbol{h} - \frac{1}{|\boldsymbol{e}|}\frac{d|\boldsymbol{e}|}{dt}F(\boldsymbol{h}, N, t)+G(\boldsymbol{h}, N, t) - \beta(\boldsymbol{h}, N)F(\boldsymbol{h}, N, t)\,, \quad (9)$$

where $\beta(\boldsymbol{h}, N)$, the "chain-breakage coefficient", is the probability of breakage of the chain (junction), and $G(\boldsymbol{h}, N, t)$, the "chain-reformation function", is the instantaneous distribution function of chains reformed at time t.

For actual calculations, however, the following integral form of the chain-distribution function is more convenient than the above differential form:

$$|\boldsymbol{e}(t)|F(\boldsymbol{h}, N, t)=F_0(\boldsymbol{e}^{-1}(t)\boldsymbol{h}, N)\exp\left[-\int_0^t \beta(\boldsymbol{e}(t')\boldsymbol{e}^{-1}(t)\boldsymbol{h}, N)\,dt'\right] + \int_0^t |\boldsymbol{e}(t')|G(\boldsymbol{e}(t')\boldsymbol{e}^{-1}(t)\boldsymbol{h}, N, t')\exp\left[-\int_{t'}^t \beta(\boldsymbol{e}(t'')\boldsymbol{e}^{-1}(t)\boldsymbol{h}, N)\,dt''\right]dt'\,. \quad (10)$$

§ 3. Shearing Stress and Viscosity Coefficient

Let the bulk of a given system flow in the x-direction with a constant velocity gradient λ in the y-direction. The strain tensor for this deformation is

$$\boldsymbol{e}(t)=\begin{pmatrix} 1 & \lambda t & 0 \\ 0 & 1 & 0 \\ 0 & 0 & 1 \end{pmatrix}. \qquad (11)$$

It follows from Eq. (9) that in order to maintain the flow steady, the quantity $(d\boldsymbol{e}/dt)\boldsymbol{e}^{-1}$ must be independent of time. Eq. (11) fulfills this condition. Introduction of this strain tensor into Eq. (10) gives

$$F(\xi, \eta, \zeta;\, N)=F(\xi-\lambda\eta t, \eta, \zeta;\, N)\exp\left[-\int_0^t \beta(\xi-\lambda\eta(t-t'), \eta, \zeta;\, N)\,dt'\right] + \int_0^t G(\xi-\lambda\eta(t-t'), \eta, \zeta;\, N)\exp\left[-\int_{t'}^t \beta(\xi-\lambda\eta(t-t''), \eta, \zeta;\, N)\,dt''\right]dt\,.$$

The time variable t can be eliminated from Eq. (12) by making a transformation

$$\begin{aligned} t' &\longrightarrow \xi' =\xi-\lambda\eta(t-t')\,, \\ t'' &\longrightarrow \xi''=\xi-\lambda\eta(t-t'')\,, \end{aligned} \qquad (13)$$

and letting t to infinity. In this limit,

$$|\xi-\lambda\eta t|\to\infty\,, \qquad F(\xi-\lambda\eta t, \eta, \zeta;\, N)\to 0\,, \qquad (14)$$

so that we have

$$F(\xi, \eta>0, \zeta;\, N)=\frac{1}{\lambda\eta}\int_{-\infty}^{\xi} G(\xi', \eta, \zeta;\, N)\exp\left[-\frac{1}{\lambda\eta}\int_{\xi'}^{\xi} \beta(\xi'', \eta, \zeta;\, N)\,d\xi''\right]d\xi'\,, \qquad (15)_1$$

$$F(\xi, \eta<0, \zeta;\, N)=\frac{1}{\lambda|\eta|}\int_{-\infty}^{-\xi} G(\xi', |\eta|, \zeta;\, N)\exp\left[-\frac{1}{\lambda|\eta|}\int_{\xi'}^{-\xi} \beta(\xi'', \eta, \zeta;\, N)\,d\xi''\right]d\xi'\,, \qquad (15)_2$$

where we have used the relation

$$G(\xi, \eta, \zeta;\, N)=G(-\xi, -\eta, \zeta;\, N)\,. \qquad (16)$$

This holds here because the flow occurs in the plane normal to the z-direction, so that in the symmetry condition $G(\boldsymbol{h}, N)=G(-\boldsymbol{h}, N)$ ζ may be replaced by $-\zeta$. It is readily shown that this condition results in

$$F(\xi, \eta, \zeta; N)=F(-\xi, -\eta, \zeta; N) \tag{17}$$

which, in turn, reduces the integration of Eq. (7) with respect to $\boldsymbol{h}$ to that only in the half-space $\Omega'(\eta>0)$.

Substitution of Eq. (16) into Eq. $(15)_1$, use of Eq. (7) and the definition

$$\mu=\sigma_{12}/\lambda \tag{18}$$

give the viscosity coefficient μ. Exchange of the order of integration, exchange of symbols ξ and ξ', and transformation of the variables such that

$$\begin{aligned} \xi' &\longrightarrow \theta=\xi'/|\xi| , \\ \xi'' &\longrightarrow \theta'=\xi''/|\xi| , \end{aligned} \tag{19}$$

thus provide

$$\begin{aligned} \mu(\lambda)=2\cdot\frac{3kT}{a^2}\sum_N\frac{1}{N}\iiint_{\Omega''}\frac{\xi^2}{\lambda^2}\Big[&G(\xi, \eta, \zeta; N)\int_1^\infty\theta\exp\left\{-\frac{\xi}{\lambda\eta}\int_1^\theta\beta(\xi\theta', \eta, \zeta; N)d\theta'\right\}d\theta \\ &+G(-\xi, \eta, \zeta; N)\int_{-1}^\infty\theta\exp\left\{-\frac{\xi}{\lambda\eta}\int_{-1}^\theta\beta(\xi\theta', \eta, \zeta; N)d\theta'\right\}d\theta\Big]d\boldsymbol{h} , \end{aligned} \tag{20}$$

where Ω'' denotes the quartary space, $\xi>0$ and $\eta>0$. Furthermore, if $G(\boldsymbol{h}, N)$ and $\beta(\boldsymbol{h}, N)$ are spherically symmetric, Eq. (20) may be simplified to

$$\mu(\lambda)=\frac{3kT}{2a^2}\sum_N\frac{1}{N}\iiint_\Omega\xi^2G(\boldsymbol{h}, N)J(\boldsymbol{h}, N, \lambda)d\boldsymbol{h} , \tag{21}$$

where

$$J(\boldsymbol{h}, N, \lambda)=J_+(\boldsymbol{h}, N, \lambda)+J_-(\boldsymbol{h}, N, \lambda) , \tag{22}$$

$$J_\pm(\boldsymbol{h}, N, \lambda)=\frac{1}{\lambda^2}\int_{\pm1}^\infty\theta\exp\left[-\frac{1}{\lambda}\left|\frac{\xi}{\eta}\right|\int_{\pm1}^\theta\beta(\xi\theta', \eta, \zeta; N)d\theta'\right]d\theta . \tag{23}$$

No more reduction of these equations may be made without actual information about $G(\boldsymbol{h}, N)$ and $\beta(\boldsymbol{h}, N)$ for given values of λ. In the vicinity of such limiting λ-values as $\lambda\to0$ and $\lambda\to\infty$, asymptotic forms of the viscosity coefficient are obtained:

i) For sufficiently small value of λ, μ may be expanded in powers of λ to give

$$\mu(\lambda)=\mu_0+\mu_1\lambda+\mu_2\lambda^2+\cdots . \tag{24}$$

Simple but lengthy calculation determines the expansion coefficients $\mu_0, \mu_1, \mu_2, \cdots$ in the form (Appendix A):

$$\begin{aligned} \mu_0&=\frac{3kT}{a^2}\sum_N\frac{1}{N}\iiint_\Omega\eta^2\frac{G(\boldsymbol{h}, N)}{\beta^2(\boldsymbol{h}, N)}\left[1-\frac{\xi}{\beta}\frac{\partial\beta}{\partial\xi}\right]d\boldsymbol{h} \\ &=\frac{3kT}{a^2}\frac{4}{3}\pi\sum_N\frac{1}{N}\int_0^\infty r^4\frac{G(r, N)}{\beta^2(r, N)}\left[1-\frac{1}{5}\frac{r}{\beta(r, N)}\frac{d\beta(r, N)}{dr}\right]dr , \end{aligned} \tag*{$(25)_1$}$$

$$\mu_1=0 , \tag*{$(25)_2$}$$

$$\begin{aligned} \mu_2=-\frac{3kT}{a^2}\sum_N\frac{1}{N}\iiint_\Omega\frac{\eta^4}{\xi^2}\frac{G(\boldsymbol{h}, N)}{\beta^4(\boldsymbol{h}, N)}\Big[&\frac{\xi^3}{\beta}\frac{\partial^3\beta}{\partial\xi^3}+4\frac{\xi^2}{\beta}\frac{\partial^2\beta}{\partial\xi^2} \\ &-10\left(\frac{\xi^2}{\beta}\frac{\partial^2\beta}{\partial\xi^2}\right)\left(\frac{\xi}{\beta}\frac{\partial\beta}{\partial\xi}\right)-15\left(\frac{\xi}{\beta}\frac{\partial\beta}{\partial\xi}\right)^2+15\left(\frac{\xi}{\beta}\frac{\partial\beta}{\partial\xi}\right)^3\Big]d\boldsymbol{h} \end{aligned} \tag*{$(25)_3$}$$

$$=-\frac{3kT}{a^2}\frac{4}{3}\pi\frac{1}{35}\sum_N\frac{1}{N}\int_0^\infty r^4\frac{G(r,N)}{\beta^4(r,N)}\left[\frac{r^3}{\beta}\frac{d^3\beta}{dr^3}+18\frac{r^2}{\beta}\frac{d^2\beta}{dr^2}+66\frac{r}{\beta}\frac{d\beta}{dr}\right.$$
$$\left.-10\frac{r^3}{\beta^2}\frac{d\beta}{dr}\frac{d^2\beta}{dr^2}-65\left(\frac{r}{\beta}\frac{d\beta}{dr}\right)^2+15\left(\frac{r}{\beta}\frac{d\beta}{dr}\right)^3\right]dr\,.$$

ii) To obtain an asymptotic expression of μ for sufficiently large λ it is assumed that for sufficient large r-value $\beta(r, N)$ varies approximately proportional to the nth power of r, that is,

$$\lim_{r\to\infty}\beta(r,N)\longrightarrow Ar^n\,. \tag{26}$$

It follows then that

$$\lim_{\lambda\to\infty}\mu(\lambda)\longrightarrow\begin{cases}\infty\\ \text{finite}\\ 0\end{cases} \tag{27}$$

in accordance with the condition

$$(-1<)n\gtreqless 0\,, \tag{28}$$

respectively. (Appendix. B)

§ 4. Tensile Stress and Tensile Viscosity

Making use of a similar procedure as described above permits calculation of the tensile stress and the tensile viscosity. Let us consider an incompressible sample being stretched in the x-direction. The strain tensor for this deformation is

$$\boldsymbol{e}=\begin{pmatrix}\alpha & 0 & 0\\ 0 & 1/\sqrt{\alpha} & 0\\ 0 & 0 & 1/\sqrt{\alpha}\end{pmatrix} \tag{29}$$

The condition of steady state, $(d\boldsymbol{e}/dt)\boldsymbol{e}^{-1}=\text{const.}$, leads $\alpha(t)$ to the form

$$\alpha(t)=\alpha_0 e^{\lambda^* t}=e^{\lambda^* t}\,, \tag{30}$$

where it has been chosen that $\alpha(0)=1$ at $t=0$.

In that follows, we are interested only in the normal components of the stress, which contain the isotropic hydrodynamic inner pressure P. In the present theory of network structure, P is rather an integration constant to be determined from the boundary condition. The boundary condition is that the side of the sample is free from external force; this gives $\sigma_{22}=\sigma_{33}=0$. Combination of Eqs. (6) and (7) then results in

$$P=-\frac{3kT}{a^2}\sum_N\frac{1}{N}\iiint\begin{pmatrix}\eta^2\\ \text{or}\\ \zeta^2\end{pmatrix}F(\boldsymbol{h},N)d\boldsymbol{h}\,, \tag{31}$$

which readily leads to the tensile stress $\sigma^*=\sigma_{11}$ in the form

$$\sigma^*=\frac{3kT}{2a^2}\sum_N\frac{1}{N}\iiint(2\xi^2-\eta^2-\zeta^2)F(\boldsymbol{h},N)d\boldsymbol{h}\,. \tag{32}$$

We introduce into Eq. (10) the new integral variables $\xi'=e^{\lambda^* t'}\xi_0$ and $\xi''=e^{\lambda^* t''}\xi_0$ in place of t' and t'', respectively, and let t go to infinity, taking into account that

$$\lim_{t\to\infty}\boldsymbol{h}_0=\lim_{t\to\infty}(\xi_0,\eta_0,\zeta_0)=(0,\infty,\infty)\,,$$
$$\lim_{t\to\infty}F(\boldsymbol{h}_0,N)=0\,. \tag{33}$$

Remembering further that $\sqrt{\xi_0}\eta_0=\sqrt{\xi}\,\eta$ and $\sqrt{\xi_0}\zeta_0=\sqrt{\xi}\,\zeta$, the final expression of the steady chain-distribution function reads

$$F(\boldsymbol{h}, N)=\frac{1}{\lambda^*}\int_0^{\xi}\frac{1}{\xi'}G\left(\xi', \sqrt{\frac{\xi}{\xi'}}\eta; \sqrt{\frac{\xi}{\xi'}}\zeta; N\right)\exp\left[-\frac{1}{\lambda^*}\int_{\xi'}^{\xi}\beta\left(\xi'', \sqrt{\frac{\xi}{\xi''}}\eta, \sqrt{\frac{\xi}{\xi''}}\zeta; N\right)d\xi''\right]d\xi' . \tag{34}$$

As in the treatment of shearing flow, Eq. (34) is substituted into Eq. (32), and suitable transformation of the intergral variables and exchange of the order of integration are made. We then obtain

$$\sigma^*=\frac{3kT}{a^2}\frac{1}{\lambda^*}\Sigma_N\frac{1}{N}\iiint_{\Omega'}G(\boldsymbol{h}, N)d\boldsymbol{h}\int_{\xi}^{\infty}\frac{1}{\xi'}\left(2\xi'^2-\frac{\xi}{\xi'}\eta^2-\frac{\xi}{\xi'}\zeta^2\right)$$
$$\times\exp\left[-\frac{1}{\lambda^*}\int_{\xi}^{\xi'}\frac{1}{\xi''}\beta\left(\xi'', \sqrt{\frac{\xi}{\xi''}}\eta, \sqrt{\frac{\xi}{\xi''}}\zeta; N\right)d\xi''\right]d\xi' ,$$

where Ω' is the half-space $\xi>0$.

Because of cylindrical symmetry, it is convenient to use the cylindrical coordinate

$$(\xi, \eta, \zeta)\longrightarrow(\xi, \rho, \varphi) . \tag{36}$$

In terms of the dimensionless variables

$$\theta=\xi'/\xi \qquad \text{and} \qquad \theta'=\xi''/\xi \tag{37}$$

the tensile viscosity coefficient defined by Eq. (4) is then written

$$\mu^*(\lambda^*)=\frac{3kT}{a^2}\Sigma_N\frac{1}{N}L(N, \lambda^*) , \tag{38}$$

where

$$L(N, \lambda^*)=2L_1(N, \lambda^*)-L_2(N, \lambda^*) , \tag{39}$$

$$L_{1,2}(N, \lambda^*)=\frac{2\pi}{\lambda^{*2}}\int_0^{\infty}d\xi\int_0^{\infty}d\rho\begin{pmatrix}\xi^2\\ \rho^2\end{pmatrix}\rho G(\xi, \rho; N)M_{1,2}(\xi, \rho; N; \lambda^*) , \tag{40}$$

and

$$M_{1,2}(\xi, \rho; N; \lambda^*)=\int_1^{\infty}\begin{pmatrix}\theta\\ 1/\theta^2\end{pmatrix}\exp\left[-\frac{1}{\lambda^*}\int_1^{\theta}\frac{1}{\theta'}\beta(\xi\theta', \rho/\sqrt{\theta'}; N)d\theta'\right]d\theta . \tag{41}$$

The double subscripts 1 and 2 refer to the above and below factors in the parenthesis of the integrand, respectively.

For the two limiting cases, $\lambda^*\to0$ and $\lambda^*\to\infty$, the asymptotic forms are derived as follows:

i) For $\lambda^*\to0$,

$$\mu^*(\lambda^*)=\mu_0^*+\mu_1^*\lambda^*+\mu_2^*\lambda^{*2}+\cdots , \tag{42}$$

$$\mu_0^*=\frac{3kT}{a^2}\cdot4\pi\,\Sigma_N\frac{1}{N}\int_0^{\infty}r^4\frac{G(r, N)}{\beta^2(r, N)}\left[1-\frac{1}{5}\frac{r}{\beta}\frac{d\beta}{dr}\right]dr , \tag*{$(43)_1$}$$

$$\mu_1^*=\frac{3kT}{a^2}\cdot4\pi\,\Sigma_N\frac{1}{N}\int_0^{\infty}r^4\frac{G(r, N)}{\beta^3(r, N)}\left[1-\frac{33}{35}\frac{r}{\beta}\frac{d\beta}{dr}-\frac{2}{35}\left\{\frac{r^2}{\beta}\frac{d^2\beta}{dr^2}-3\left(\frac{r}{\beta}\frac{d\beta}{dr}\right)^2\right\}\right]dr , \tag*{$(43)_2$}$$

$$\mu_2^*=\frac{3kT}{a^2}\cdot12\pi\,\Sigma_N\frac{1}{N}\int_0^{\infty}r^4\frac{G(r, N)}{\beta^4(r, N)}\left[1-\frac{311}{105}\frac{r}{\beta}\frac{d\beta}{dr}-\frac{4}{7}\frac{r^2}{\beta}\frac{d^2\beta}{dr^2}+\frac{43}{21}\left(\frac{r}{\beta}\frac{d\beta}{dr}\right)^2\right.$$
$$\left.-\frac{1}{35}\left\{\frac{r^3}{\beta}\frac{d^3\beta}{dr^2}-10\left(\frac{r^2}{\beta}\frac{d^2\beta}{dr^2}\right)\left(\frac{r}{\beta}\frac{d\beta}{dr}\right)+15\left(\frac{r}{\beta}\frac{d\beta}{dr}\right)^3\right\}\right]dr . \tag*{$(43)_3$}$$

ii) For $\lambda^*\to\infty$,
if it is assumed that asymptotically

$$\lim_{r\to\infty}\beta(r, N)\longrightarrow Ar^n\,, \tag{44}$$

there is obtained

$$\lim_{\lambda^*\to\infty}\mu^*(\lambda^*)\longrightarrow\begin{cases}\infty\\ \text{finite}\\ 0\end{cases} \tag{45}$$

in accordance with

$$(0<)n\gtreqless 1\,. \tag{46}$$

§ 5. Chain Breakage Coefficient of the Square-Well Type

Let us consider a chain-breakage coefficient $\beta(r, N)$ of the square-well type

$$\beta(r, N)=\begin{cases}\beta_0 & r<R\\ \infty & r\geq R\,,\end{cases} \tag{47}$$

This type indicates that chains reformed at r larger than R immediately break off. Hence it can be assumed that the chain-reformation function $G(r, N)$ vanishes for $r\geq R$. Application of Eq. (47) brings the shearing viscosity Eq. (21) to the form

$$\mu(\lambda)=\frac{3kT}{a^2}\frac{1}{\beta_0{}^2}\Sigma_N\frac{1}{N}\iiint_\Omega G(\boldsymbol{h}, N)\Big[\eta^2\Big\{1-\exp\Big[-\frac{\beta_0}{\lambda|\eta|}(\xi_0-\xi)\Big]\Big\}$$
$$+\frac{\beta_0}{\lambda}|\eta|\Big\{\xi-\xi_0\exp\Big[-\frac{\beta_0}{\lambda|\eta|}(\xi_0-\xi)\Big]\Big\}\Big]d\boldsymbol{h}\,, \tag{48}$$

where ξ_0 is connected with R, η and ζ by

$$\xi_0{}^2+\eta^2+\zeta^2=R^2\,. \tag{49}$$

Fig. 1 shows schematically the rate-dependence of viscosity as estimated from the integrand of Eq. (48) as a function of λ. The curve horizontally enters the μ-axis, which means the Newtonian flow to appear at the limit of sufficiently small velocity-gradients, in agreement with the finding from Eqs. (24) and (25). Viscosity decreases with increasing rate of flow and appears to approach zero in inverse proportion of the square of λ for sufficiently large values of it.

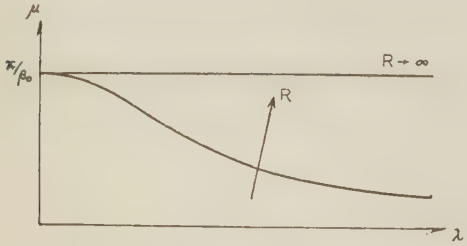

Fig. 1. Structural Viscosity.

If the chain-breakage coefficient is constant, i.e., if $R\to\infty$ in Eq. (47), viscosity is independent of rate of flow, as has been shown by Green-Tobolsky,[3] that is

$$\mu(\lambda)=\frac{3kT}{a^2}\frac{1}{\beta_0{}^2}\Sigma_N\frac{1}{N}\iiint_\Omega\eta^2G(\boldsymbol{h}, N)d\boldsymbol{h}$$
$$=\kappa/\beta_0 \tag{50}$$

where κ denotes the instantaneous elastic modulus for simple shear deformation.

For the simple stretching, the expression of tensile viscosity with the chain-breakage coefficient of the square-well type is so complex that complete rate-dependence of such viscosity is not ready to follow. However, it is shown, taking Eqs. (42)∼(46) into consideration that

i) the tensile viscosity vs. rate of stretching curve enters the μ^*-axis with a finite (positive) slope;

ii) for $\lambda^*\to\infty$, $\mu^*(\lambda^*)\to 0$. (51)

It is also shown that for constant chain-breakage coefficient $\mu^*(\lambda^*)$ goes to infinity if stretching rate λ^* exceeds the value $\beta_0/2$ (the divergent term is M_2 in Eq. (41)). Then the tensile viscosity would vary with rate of stretching as shown in Fig. 2. This curve has a maximum and shows the "inverse structural viscosity" in the range of small λ^*; this behavior may be found in the experimental data of Nitchmann and Schrade.[4]

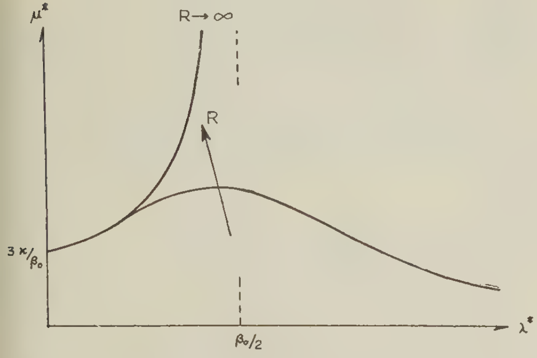

Fig. 2. Tensile Viscosity.

Although the theoretical interpretation of the abnormal viscosity given above appears satisfactory at least qualitatively, it is rather an accident. Use of a different form for the chain-breakage coefficient results in a $\mu-\lambda$ relation of different behavior. There is a type of β in which viscosity increases with velocity gradient even in the shearing flow. This behavior may be compared to that often called "dilatancy". The actual mechanisms of dilatancy may be much more complicated than what we are considering here. For such system the quantities appeared in our theory may have no direct physical meanings even if the theoretical results are consistent with experimental ones.

§ 6. Comparison between Two Viscosities $\mu(\lambda)$ and $\mu^*(\lambda^*)$

As has been shown in the above section, the rate-dependence of the shearing viscosity is entirely different from that of the tensile viscosity. However, there may be a close connection between them because the dissipative mechanism is the same in both deformations. In the introductory section we pointed out that classical phenomenological theory leads to a simple interrelation between the shearing and tensile viscosity coefficients of the ideal, Newtonian fluid, that is, "Trouton's formula" $\mu^*=3\mu$. This relation is in general not valid in our network theory. At the limit of small rate of deformation, however, there obtains

$$\lim_{\lambda^*\to 0}\mu^*(\lambda^*)=3\lim_{\lambda\to 0}\mu(\lambda) \qquad (52)$$

from Eqs. (24), (25), (42) and (43).

The fact that the shearing viscosity curve horizontally intersects the axis comes out of symmetric property in the inversion of the direction of flow. Change of the sign of flow-rate gives the identical flow in the opposite direction, and the viscosity coefficient must therefore be symmetric about the μ-axis. This means that the shearing viscosity intersects the ordinate horizontally when plotted against the rate of shear. This is not the case with simple strectching deformation. A positive value of λ^* corresponds to a simple stretching, and a negative to a simple compressing deformation. Any simple symmetric property does not obtain in this type of deformation.

The rate-dependence may be more pronounced for tensile viscosity than for shearing viscosity. This fact is understood if we consider the relative degree of orientation of network chains in both stationary flows. In shearing flow, the network chains may be oriented in the flow direction in proportion to the time, so far as the chain-breakage does not take place. If the value of β is independent of chain-stretching, the average orientation of chains would be proportional to the rate of flow λ, and thus the system shows the Newtonian flow. On the other hand, the orientation of chains in simple stationary stretching may increase exponentially with time (see Eq. (30)). If λ^* approaches the value $\beta/2$ with constant β, certain numbers of chains may be elongated infinity without breakage. This results in getting the tensile viscosity diversed at $\lambda^*=\beta/2$. In actual systems, however, β may increase with the end-to-end distance of a chain, and chains will break down at finite elongations.

§ 7. Summary

Viscosity coefficients of concentrated polymer solutions are discussed assuming a Gaussian weak network with the chain-breakage (c-b-) coefficient as an arbitrary function of elongation of a chain. The c-b-coefficient of square-well type yields the typical rate-dependent shearing and tensile viscosities. However, some other choices of the form of the c-b-coefficient lead to physically meaningless results. For example, the form that $\beta(r, N)=$

$Ar^n, n>5$ gives a negative viscosity coefficient for small values of velocity gradient. Then, there should exist some physical restrictions on the allowable functional form of the c-b-coefficient. This problem is beyond the scope of the present paper.

The dependence of viscosity on molecular weight is another problem of extreme interest on concentrated solutions of polymers. Recent experiments demonstrate that the viscosity increases with the 3.4th power of molecular weight and that this dependence is practically independent of polymer species if M.W. and concentration of highpolymer are not so low. Unfortunately, introduction of the concept of molecular weight into our network model seems to be so difficult that at present we must await a further development of the theory for the interpretation of such behavior.

Acknowledgments

The author would express his sincere thanks to Professor T. Yamamoto, Dr. E. Teramoto and the members of Research Group of High Polymer in Kyoto for their encouragement and valuable discussions. He is further obliged to Professor H. Fujita for his kindly amendment of the munuscript, Miss F. Iizuka for a trial of lengthy calculation and Misses M. Matsuda and M. Eto for the preparation of the munuscript. The present investigations has been supported partly by the Scientific Research Grant of the Ministry of Education.

Appendix A

Let us consider the viscosity coefficient $\mu(\lambda)$ for sufficiently small value of velocity gradient λ. The exponential factors in the integrands of $J\pm(\boldsymbol{h}, N, \lambda)$ (Eq. (22)) become negligible for θ not extremely close to ±1 except for particular values of ξ, η and β. For sufficiently small λ, there is a small positive number Δ which satisfies the condition

$$\Delta/\lambda \gg 1 \quad \text{and} \quad \Delta^2/\lambda \ll 1 \tag{A.1}$$

(The first condition is more important; so far as $\beta(\boldsymbol{h}, N)$ is not so singular, the second condition may be ignored.) Use of the new integral variables $t=\theta\mp1$ etc. reduces Eq. (23) to

$$J_\pm(\boldsymbol{h}, N, \lambda)=\frac{1}{\lambda^2}\int_0^\Delta (t\pm1)\exp\Bigg[-\frac{1}{\lambda}\left|\frac{\xi}{\eta}\right|$$

$$\times\int_0^t \beta(\xi(t'\pm1), \eta, \zeta; N)dt'\Bigg]dt+\varepsilon_\pm, \tag{A.2}$$

$$\varepsilon_\pm \sim P(\Delta/\lambda)e^{-(\Delta/\lambda)\bar{\beta}}, \tag{A.3}$$

where $P(x)$ is a polynomial of finite order of x and $\bar{\beta}$ is a "representative value" of $\beta(\boldsymbol{h}, N)$. As λ becomes sufficiently small and Δ/λ very large, $\varepsilon_\pm$ may approach zero. It is assumed that $\beta(\xi(t'\pm1), \eta, \zeta; N)$ can be expanded about the point $\boldsymbol{h}=(\xi, \eta, \zeta)$ in powers of t' which is confined to the range $0\sim\Delta$ Thus

$$\beta(\xi(t'\pm1); \eta, \zeta; N)$$
$$=\beta_\pm+\frac{1}{1!}\left[\frac{\partial\beta}{\partial\xi}\right]_\pm \xi t'+\frac{1}{2!}\left[\frac{\partial^2\beta}{\partial\xi^2}\right]_\pm \xi^2 t'^2+\cdots \tag{A.4}$$

where the following abbreviations are used:

$$\left.\begin{aligned}\beta_\pm&=\beta(\pm\xi, \eta, \zeta; N),\\ \left[\frac{\partial^n\beta}{\partial\xi^n}\right]_\pm&=\left[\frac{\partial^n\beta(\boldsymbol{h}, N)}{\partial\xi^n}\right]_{\xi=\pm\xi}.\end{aligned}\right\} \tag{A.5}$$

Substitution of Eq. (A.4) into Eq. (A.2), and carrying out of the integration with respect to t' give the series expansion of the exponential in powers of t $(0<t<\Delta)$ except for the factor of which exponent has the factor $\beta_\pm t$. That is

$$J_\pm(\boldsymbol{h}, N, \lambda)$$
$$=\frac{1}{\lambda^2}\int_0^\Delta (t\pm1)\exp\left(-\frac{1}{\lambda}\left|\frac{\xi}{\eta}\right|\beta_\pm t\right)[\cdots]dt+\varepsilon_\pm, \tag{A.6}$$

where $[\cdots]$ is the abbreviation of the power series of t. Replacement of Δ by ∞, which may give rise to a negligible contribution to the integral, reduces Eq. (A.6) to

$$J_\pm(\boldsymbol{h}, N, \lambda)$$
$$=\frac{1}{\lambda^2}\Bigg[\pm\left|\frac{n}{\xi}\right|\frac{\lambda}{\beta_\pm}+\left(\frac{\eta}{\xi}\right)^2\{1\mp D_\pm\beta\}\frac{\lambda^2}{\beta_\pm{}^2}$$
$$-\left|\frac{\eta}{\xi}\right|^3\{3D_\pm\beta\pm D_\pm{}^2\beta\mp3(D_\pm\beta)^2\}\frac{\lambda^3}{\beta_\pm{}^3}$$
$$-\left(\frac{\eta}{\xi}\right)^4\{4D_\pm{}^2\beta\pm D_\pm{}^3\beta\mp10(D_\pm\beta)(D_\pm{}^2\beta)$$
$$-15(D_\pm\beta)^2\pm15(D_\pm\beta)^3\}\frac{\lambda^4}{\beta_\pm{}^4}+O(\lambda^5)\Bigg], \tag{A.7}$$

where

$$D_\pm{}^n\beta=\frac{\xi^n}{\beta_\pm}\left[\frac{\partial^n\beta}{\partial\xi^n}\right]_{\xi=\pm\xi}. \tag{A.8}$$

If $\beta(\boldsymbol{h}, N)$ is spherically symmetric,

$$D_\pm{}^n\beta\fallingdotseq(-)^n\frac{\xi^n}{\beta}\left[\frac{\partial^n\beta}{\partial\xi^n}\right]\equiv(-)^n D^n\beta. \tag{A.9}$$

The final expression of $J(\boldsymbol{h}, N, \lambda)$ is thus

$$J(\boldsymbol{h}, N, \lambda)=2\left(\frac{\eta}{\xi}\right)^2\frac{1}{\beta^2}[1-D\beta]$$
$$-2\left(\frac{\eta}{\xi}\right)^4\frac{1}{\beta^4}[D^3\beta+4D^2\beta-10(D^2\beta)(D\beta)$$
$$-15(D\beta)^2+15(D\beta)^3]\lambda^2+O(\lambda^4)\ . \quad (A.10)$$

Substitution of Eq. (A.10) into Eq. (21) permits integration of $\mu(\lambda)$ with respect to the angular components of $\boldsymbol{h}$ under the assumption of the spherically symmetric chain-reformation function $G(\boldsymbol{h}, N)$. The final expressions are Eqs. (24) and (25).

The similar calculation can be made for the tensile viscosity to yield Eqs. (42) and (43).

Appendix B

If the spherically symmetric chain-breakage coefficient $\beta(\boldsymbol{h}, N)$ is a smooth function of $\boldsymbol{h}$, it may be assumed that $\beta(\boldsymbol{h}, N)$ varies approximately proportional to the nth power of $|\boldsymbol{h}|=r$ for sufficiently large r. Namely, there is a quantity R for any positive ε such that for $r>R$

$$\left|\frac{\beta(r, N)}{A(N)r^n}-1\right|<\varepsilon \quad (B.1)$$

or

$$A(N)r^n(1-\varepsilon)<\beta(r, N)$$
$$<A(N)r^n(1+\varepsilon)\ . \quad (B.2)$$

When $r\leq R$, on the other hand, we define the quantity $B(R)$ by

$$B(R)=\mathrm{Max}_{(r\leq R)}\{\beta(r, N),\ A(N)(1+\varepsilon)r^n\}\ . \quad (B.3)$$

Let us consider the integral

$$K_\pm(\theta)=\int_{\pm1}^{\theta}\beta(\xi\theta', \eta, \zeta\,;N)d\theta'\ . \quad (B.4)$$

For sufficiently large R, Θ may be chosen such that

$$R^2=\xi^2\Theta^2+\eta^2+\zeta^2\simeq\xi^2\Theta^2\ . \quad (B.5)$$

The correction for the approximation involved may, if necessary, be included in ε. It then follows that

i) For $\theta<\Theta$,

$$0<K_\pm(\theta)<B(\Theta+1)\ , \quad (B.6)$$

ii) For $\theta>\Theta$,

$$\frac{A}{1+n}(1-\varepsilon)\xi^n\Theta^{n+1}-B(\Theta+1)$$
$$<K_\pm(\theta)<\frac{A}{1+n}(1+\varepsilon)\xi^n\theta^{n+1}+B(\Theta+1)\ . \quad (B.7)$$

Use of abbreviations

$$\frac{A}{1+n}\xi^n=a' \quad \text{and} \quad B(\Theta+1)=b' \quad (B.8)$$

and substitution of Eqs. (B.6) and (B.7) into Eq. (23) results in

$$J_\pm(\boldsymbol{h}, N, \lambda)=\frac{1}{\lambda^2}\left[\int_{\pm1}^{\Theta}+\int_{\Theta}^{\infty}\right]>\frac{1}{\lambda^2}\int_{\Theta}^{\infty}$$
$$>\frac{1}{\lambda^2}\left[\int_0^{\infty}\theta\exp\left[-\frac{1}{\lambda}\left|\frac{\xi}{\eta}\right|(a'(1+\varepsilon)\theta^{n+1}+b')\right]d\theta-\int_0^{\Theta}\theta d\theta\right], \quad (B.9)$$
$$J_\pm(\boldsymbol{h}, N, \lambda)<\frac{1}{\lambda^2}\left[\int_0^{\infty}\theta\exp\left[-\frac{1}{\lambda}\left|\frac{\xi}{\eta}\right|(a'(1-\varepsilon)\theta^{n+1}-b')\right]d\theta+\int_0^{\Theta}\theta d\theta\right]. \quad (B.10)$$

These integrations are evaluated under the condition $n>-1$ to give

$$\frac{1}{\lambda^2}\left[e^{-b/\lambda}\frac{1}{n+1}\Gamma\left(\frac{2}{n+1}\right)\left(\frac{\lambda}{a(1+\varepsilon)}\right)^{\frac{2}{1+n}}-\frac{\Theta^2}{2}\right]<J_\pm(\boldsymbol{h}, N, \lambda)$$
$$<\frac{1}{\lambda^2}\left[e^{+\frac{b}{\lambda}}\frac{1}{n+1}\Gamma\left(\frac{2}{n+1}\right)\left(\frac{1}{a(1-\varepsilon)}\right)^{\frac{2}{1+n}}+\frac{\Theta^2}{2}\right]. \quad (B.11)$$

where

$$\left|\frac{\xi}{\eta}\right|a'\equiv a \quad \text{and} \quad \left|\frac{\xi}{\eta}\right|b'\equiv b\ . \quad (B.12)$$

Limiting processes λ and $\Theta\to\infty$ with $\Theta/\lambda\to0$ and $b/\lambda\to0$ give the final expression

$$\lim_{\lambda\to\infty}J_\pm(\boldsymbol{h}, N, \lambda)$$
$$=\frac{1}{n+1}\Gamma\left(\frac{2}{n+1}\right)a^{-2/(n+1)}\lambda^{-2n/(n+1)}\ . \quad (B.13)$$

Use of Eq. (B.13) in Eq. (21) finally leads to the limiting value of the viscosity as appeared in Eq. (27) with Eq. (28).

References

1) A. Peterlin and M. Côpic: J. Appl. Phys. **27** (1956) 434; M. Côpic: J. Chem. Phys. **53** (1956) 440; Y. Ikeda: J. Phys. Soc. Japan **12** (1957) 378; W. Kuhn and H. Kuhn, Helv. chim. acta. **28** (1945) 1533; *ibid.* **29** (1946) 71.
2) M. Yamamoto: J. Phys. Soc. Japan **11** (1956) 413.
3) M. S. Green and A. V. Tobolsky: J. Chem. Phys. (1946) 80.
4) Hs. Nitschmann and J. Schrade: Helv. chim. acta. **31** (1948) 297.

JOURNAL OF THE PHYSICAL SOCIETY OF JAPAN Vol. 12, No. 10, OCTOBER, 1957

On the Piezoelectric Effect of Bone

By Eiichi FUKADA

Kobayasi Institute of Physical Research, Kokubunji, Tokyo

and Iwao YASUDA

Department of Orthopaedic Surgery, Kyoto Prefectural Medical University, Kamikyo-ku, Kyoto

(Received August 15, 1956, Revised July 9, 1957)

The piezoelectric effect of bone has been observed similarly to the case of wood or ramie. The specimens were cut out from the femur of man and ox, and dried completely by heating. The piezoelectric constants were measured by three different experiments, that is, measurements of the static direct effect, the dynamic direct effect and the dynamic converse effect. The piezoelectric effect appears only when the shearing force is applied to the collagen fibres to make them slip past erch other. The magnitude of piezoelectric constant depends on the angle between the applied pressure and the axis of the bone. The maximum value of piezoelectric constant amounts to 6×10^{-9} c.g.s. e.s.u., which is about one-tenth of a piezoelectric constant d_{11} of quarts crystal. The specimens which were boiled in hot water and afterwards dried completely showed little change in the piezoelectric effect, the fact ascertaining that the effect is not of biological origin. The origin to piezoelectricity in bone may be ascribed to the piezoelectric effect of the crystalline micelle of collagen molecules. The consideration of the symmetry of the configulation of collagen fibres in the bone texture shows the existence of effects which are represented by only two piezoelectric constants d_{14} and d_{25}, which are the same in magnitude but opposite in sign.

§ 1. Introduction

In previous papers it has been shown that the piezoelectric effect is observed in wood[1)2)], wool and hair[3)]. Recently Fukada has succeeded in confirming the direct and converse piezoelectric effects in wood[4)] and ramie[5)]. The piezoelectric effect in these materials is due to the crystalline properties of cellulose micelle which are highly orientated in the direction of the fibre axis.

Yasuda has been studying the dynamic properties of bone for some years[6)] and has found that the piezoelectric effect is observed in bone[7)]. The authors have undertaken the quantitative measnrement of the piezoelectric constants of bone by means of both direct and converse piezoelectric effect.

§ 2. Specimens

The bone of femur is comprised of outer hard layers of collagen and inner soft tissues. If one takes out these tissues, the most parts of bone look like a hollow cylinder except both ends which have peculiar shapes. It is mainly composed of highly orientated collagen fibres and inorganic crystals, called apatite, imbedded among collagen fibres. The axis of bone is designated as the direction of length of the cylinder. The large arrow shown in Fig. 1 is the axis of bone thus defined. The collagen fibres make the spiral structure along the axis and the direction of winding of spiral is reversed to right and left by each successive layers which compose the outer cylinder. Thus the properties of bone is assumed to be symmetrical to this axis.

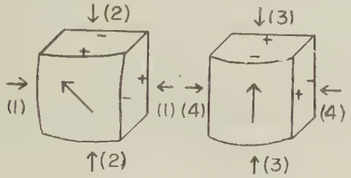

Fig. 1. Specimens of bone. Signs represent those of electric polarization which appear in square planes when pressure is applied on each side plane.

Small square plates of bone as shown in Fig. 1 were cut out from the outer layer of the femur of a man and an ox. The length of the edge of square plates was about 90 to 15 mm. The thickness was about 2 to 3 mm. Specimens obtained from the femus of man had been air-dried for years and were dried for a week or so in a desicater containing calcium chloride before measurements. Specimens obtained from the femur of ox were heated up to about 120°C for about 5 hours for drying. Some specimens were boiled in the hot water for about 2 hours and then dried by the same way.

Very thin silver foils were attached to the square planes by means of alcoholic solution of shellac and those were used as electrodes.

§3. Measuring Apparatus

Measurements of both the direct and converse piezoelectric effect were carried out using the apparatus which was described in the previous paper⁵⁾. The direct effect could be observed easily by the static method. The pressure was applied on the side plane of specimen by a lever mechanism and the electrical charge appeared on the square plane was led to the grid of the UX-54 vacuume tube and the deflection of a galvanometer inserted in the plate circuit was read.

The converse piezoelectric effect could be measured by the dynamical method. The principle of measurement is shown in Fig. 2 schematically. The specimen, an x-cut quartz plate and a completely shielded rochelle salt crystal were clamped together with a metal frame, with polystyrene insulating plates between them. When the electrodes of specimen are earthed and the alternating voltage is applied to the quartz electrodes, the oscillational force is transmitted to the rochelle salt crystal due to the converse piezoelectric effect of quartz. Therefore, the rochelle salt crystal produce the alternating voltage, which can be amplified enough to be read by a voltmeter.

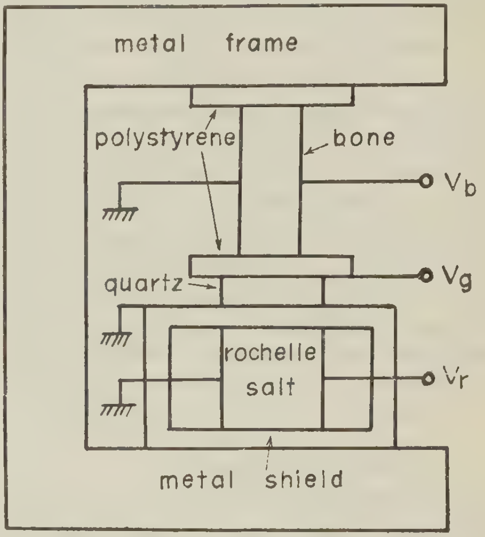

Fig. 2. Schematic diagram of measuring device.

When electrodes of quartz are earthed and a.c. voltage is applied to electrodes of bone specimen, the converse piezoelectric effect of bone can be measured in the same way as in the case of quartz.

If applied voltages V_b and V_q are necessary to cause the same output voltage of rochelle salt crystal in bone and quartz respectively, the piezoelectric constant of bone d_b is given by the following formula:

$$\frac{d_b}{d_q}=\frac{2c}{a}\frac{V_q}{V_b} \qquad (1)$$

where d_q is the piezoelectric constant d_{11} of x-cut quartz crystal and $d_{11}=6.5\times10^{-8}$ c.g.s.

e.s.u., a the height of bone plate, and c the thickness of bone plate.

The frequency of applied voltage is around 2000 c/s. As the size of specimen of bone is very small as described above, the frequency of measurement is sufficiently small compared to the resonance frequency of the specimen. However, a mechanical resonance of the clamped system, presumably due to the outer metal frame, occured by chance around 2000 c/s and the use of this resonance point was very convenient for the measurement. The gain of amplifier was about 100 db. The required voltage applied on the bone specimen was about 100 volts.

The direct piezoelectric effect of bone could be also measured dynamicall by the same apparatus. When electrodes of specimen are earthed and a.c. voltage is applied to the rochelle salt crystal, the oscillating force is transmitted to the quartz and the bone. Then the output voltage of quarts due to the direct piezoelectric effect of quartz plates can be amplified and measured by the voltmeter. On the contrary, when quartz plates are earthed, the bone specimen produces the a.c. output voltage due to the direct piezoelectric effect of bone. The piezoelectric constant of bone can be calculated by the same formula as eq. (1), if we take V_q and V_b to be the necessary applied voltage to rochelle salt crystal in order to obtain the same output voltage of quartz and bone respectively.

§ 4. Experimental Results

Fig. 1 shows the signs of electrical polarization which appear on the square planes when the pressure is applied on each side plane as represented by the small arrows with numbers. The sign and the amount of polarization vary considerably with the direction of pressure. The relation between polarization and applied pressure in the case of direction (1) is represented in Fig. 3. The circles and triangles denote the charge appeared on the bone plate when the pressure is applied and removed respectively. Their signs are, therefore, reverse.

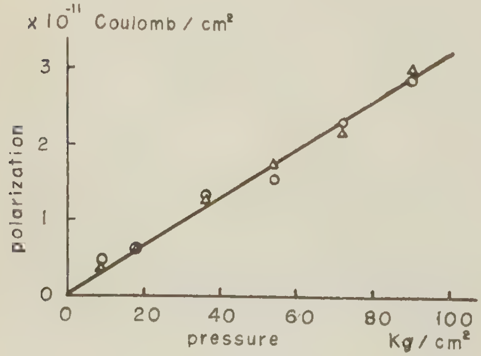

Fig. 3. The direct piezoelectric effect of bone.

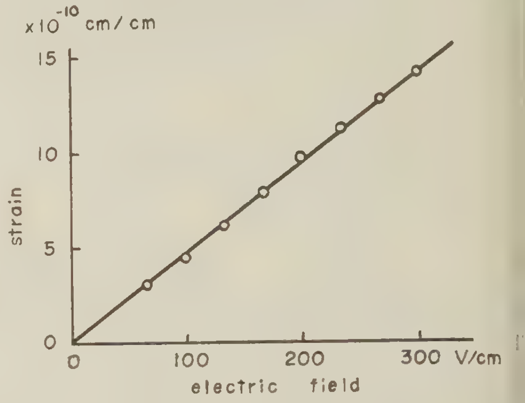

Fig. 4. The converse piezoelectric effect of bone.

The strain vs. applied electric field relationship is protted in Fig. 4 using the results of the converse piezoelectric effect measurement Both figures show that the linear relationship exists between polarization and stress or between strain and electric field. This is an evidence that the effect is truely piezoelectric and not electrostrictive. The electrostriction can be observed in every materials but in this effect the strain is proportional to the square of the applied electric field.

The measured values of piezoelectric constant of bone in the case of (1) and (2) in Fig. 1 are represented in Table I. Lower values in the static piezoelectric measurement may be due to the leakage at the specimen and the measuring apparatus.

Table I. Piezoelectric constant of bone of man. (c.g.s. e.s.u.)

	direct effect		converse effect
	static	dynamic	dynamic
(1)	2.0×10^{-9}	2.9×10^{-9}	2.9×10^{-9}
(2)	2.2×10^{-9}	3.6×10^{-9}	3.5×10^{-9}

The specimens cut as shown in Fig. 1 have been examined in various ways of applying pressure. Silver foils were attached to the side planes as electrodes and the pressure was applied upon the other side planes or the square planes. The piezoelectric effect could not be observed in these cases.

The sign and magnitude of charge appeared on the square plane are very different according to the direction of pressure as shown (1), (2), (3) and (4) in Fig. 1. We take the piezoelectric constant of bone d_b as positive when the front square plane in the specimen in Fig. 1, that is, the outside plane of bone is positively polarized, as in the cases of (2) and (4). If we plot d_b against the angle between the bone axis and the direction of pressure, we obtain Fig. 5. The piezoelectric effect disappears when the direction of pressure makes the angle of about 10 degrees with the bone axis.

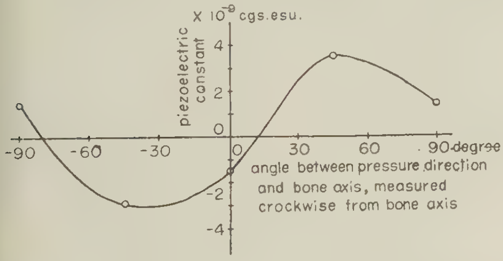

Fig. 5. Dependence of the piezoelectric constant of femur of man upon the angle between the pressure direction and the bone axis.

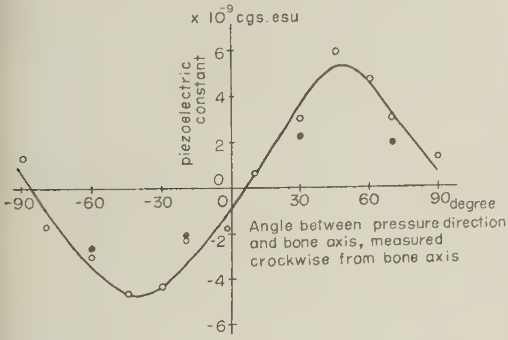

Fig. 6. Dependence of the piezoelectric constant of femur of ox upon the angle between the pressure direction and the bone axis.

The relation of d_b and the angle between the bone axis and the pressure direction were investigated more extensively using the bone of ox. Several pieces of plate were cut out from the femur of ox, which have different angles with the bone axis. The results are given in Fig. 6. The piezoelectric constants were determined by the measurement of the converse effect.

The similar curve as in Fig. 5 was obtained. The piezoelectric constant is zero at the angle of about 10 degrees, too. Black points show data when the specimen was first boiled in hot water for about 2 hours and afterwards dried completely by heating up to 120°C for about 5 hours. Little difference was observed between specimens boiled and unboiled, which ascertains that the effect is not entirely of biological origin.

Formerly Yasuda has observed that the piezoelectric effect still remains after the immersion of human bone specimen in acid for three weeks, so that the apatite crystals lying between the collagen fibres has completely dissolved.

The highest value of piezoelectric constant in the bone of ox is 6×10^{-9} c.g.s. e.s.u., which is about one-tenth of the piezoelectric constant d_{11} of quartz crystal.

§ 5. Discussions

From the above described experimental results we can conclude that the bone manifests the piezoelectric effect similar to that of the crystalline materials. The value of the piezoelectric constant amounts to about one-tenth of that of quartz.

In general the anisotropic crystals have the piezoelectric effect and their piezoelectric constants can be represented by the following matrix[8]:

$$\begin{pmatrix} d_{11} & d_{12} & d_{13} & d_{14} & d_{15} & d_{16} \\ d_{21} & d_{22} & d_{23} & d_{24} & d_{25} & d_{26} \\ d_{31} & d_{32} & d_{33} & d_{34} & d_{35} & d_{36} \end{pmatrix}$$

In the case of bone, the piezoelectricity appears only when the shearing force acts on the orientated collagen fibres so that they slip past one another. Considering the present results of experiments we can deduce the matrix of piezoelectric constant in this case as follows;

$$\begin{pmatrix} 0 & 0 & 0 & d_{14} & 0 & 0 \\ 0 & 0 & 0 & 0 & -d_{14} & 0 \\ 0 & 0 & 0 & 0 & 0 & 0 \end{pmatrix}$$

if the symmetry axis Z is inclined about 10 degrees to the right side from the bone axis. This matrix is quite the same as that of wood and ramie bundle.

The crystalline structure of collagen fibres has been well investigated. For example, Romachandran and Kartha[9] have proposed the hexagonal symmetry in the unit cell of collagen. The matrix of piezoelectric constant of crystal possessing hexagonal symmetry D_6 is represented by the same formula as described obove.

The microscopic structure of bone consists of the thin layers of spirals of collagen fibrils which are alternatively turned to the right and to the left. The crystallites of collagen are highly orientated in the direction of the axis of fibrils. The consideration of the symmetry of this system shows us that the above mentioned matrix of piezoelectric constant holds good, except that the value of d_{14} in the total system is lower than that of single crystal of collagen molecules. Even if the symmetry of the collagen micelle is not hexagonal, for example, monoclinic or rhombic, the matrix of the total system is also represented by the same formula.

It is noticeable that the Z axis assigned in this matrix is inclined about 10 degrees to the long axis of bone of femur. The x-ray diffraction patterns of the specimen has also shown the inclination of symmetry axis to the bone axis. We suppose that it might be caused by the fact that the bone axis of femur is not vertical when man or ox is in the standing position, so that the bone axis is slightly inclined to the direction of gravitational force, in which the resultant axis of collagen fibrils lies. If the bone of leg (tibia), where the bone axis is in the same direction as the gravitational force, is examined, then the Z axis in the piezoelectric matrix might coincide with the bone axis. More extensive studies using specimens which are cut out in various directions and different positions seem to be necessary.

References

1) V. A. Bazhenov and V. P. Konstantinovo: Doklady Akad. Nauk. S.S.S.R. **71** (1950) 283; Chem. Abst. **45** (1951) 2747.
2) V. A. Bazhenov: Doklady Akad. Nauk. S.S.S.R. **90** (1953) 281.
3) A. J. P. Martin: Proc. Phys. Soc. **53** (1941) 186.
4) E. Fukada: J. Phys. Soc. Japan. **10** (1955) 149.
5) E. Fukada: J. Appl. Phys. Japan. **24** (1955) 299. (in Japanese)
6) I. Yasuda: J. Bone Joint Surg. **37**-A No. 6 (1955).
7) I. Yasuda: J. Japan Arthop. Surg. Soc. **28** No. 3, 4 (1954). (in Japanese)
8) W. G. Cady; Piezoelectricity Mcgraw-Hill (1946).
9) G. N. Ramachandran and G. Nartha: Nature **174** (1954) 269.

Short Notes

This section is intended to secure prompt publication of important discoveries in physics. The reports should not exceed 800 words in length. A figure of size 7 cm × 7 cm will be counted as 150 words.

J. PHYS. SOC. JAPAN **12** (1957) 1163

Photoelectric Emission of Oxide Coated Cathodes

By Tadaichi YABUMOTO and Syôzi YAMADA

Institute of Electronic Engineering, Shizuoka University, Hamamatsu, Japan

(Received August 7, 1957)

The spectral sensitivity of photoelectric emission current from barium strontium oxide coated cathodes has been studied at room temperature. Under some conditions a new peak of the sensitivity curve was found at about 4.7 ev in incident photon energy.

This peak was observed on the cathode to which a small amount of oxygen gas was added. Fig. 1 is an example of the cases, where the curves were obtained from the cathode after being exposed to oxygen atmosphere of 10^{-5}–10^{-6} mmHg for about five minutes. This peak disappeared, when the cathode was heated at about 700°K, or was exposed to oxygen atmosphere of 10^{-4}–10^{-5} mmHg as shown in the figure. These phenomena are reproducible provided the chathode is aged in vacuum or electrolytically activated. During both activation processes the gas pressure in the tube was found to increase to 10^{-6}–10^{-7} mmHg, and it may be attributed to the releasing of oxygen from the cathode.

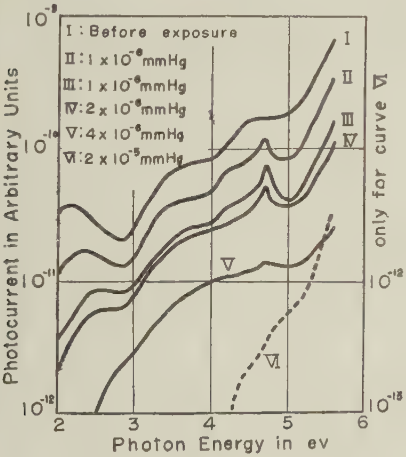

Fig. 1. Spectral sensitivity of photoemission after oxygen exposure.

If batalum getter near the cathode was heated in short duration after an appropriate aging process, it was found that the peak at 4.7 ev initially increased and then gradually diminished. Thereafter no peak appeared by successive heating of the getter. The results are shown in Fig. 2. These facts suggest that the peak is not attributed to barium but to other material initially evaporated from the getter. (probably oxygen).

Accordingly, it seems that the source of this peak is closely connected to oxygen added on the cathode. Since optical activation energy from the top of the filled band to the vacuum level has been known to be about 5.0 ev in BaO[1], the energy level corresponding to the oxygen will be situated at about 0.3 ev above the top of the filled band.

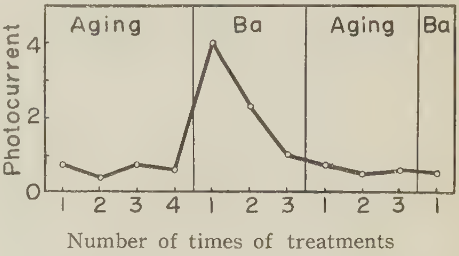

Fig. 2. Variation of photoelectric sensitivity peak at 4.7 ev with aging of the cathode and heating of a batalum getter.

It may be either the surface level due to adsorption of oxygen or the acceptor level. Though it is not clear at present which is the case, the levels are probably localized at the surface region of the oxide from the following reasons: 1) photon absorption coefficient is so large at these high energy region[2] that these photons cannot penetrate into the bulk, 2) the peak easily disappears by heating the cathode (diffusion or evaporation of the centers), 3) at room temperature the peak appears by oxygen exposure and disappears after a long time and 4) the magnitude of this peak is closely connected to the oxygen pressure in the experimental tube before the measurements.

References

1) L. Apker, E. Taft and J. Dickey: Phys. Rev. **84** (1951) 508.

2) W. W. Tylers: Phys. Rev. **76** (1949) 176 and 1887. H. B. Devore and J. W. Dewdney: Phys. Rev. **83** (1951) 805.

J. PHYS. SOC. JAPAN **12** (1957) 1164

The Galvanomagnetic Effects in Single Crystal of PbTe

By Kisaburo SHOGENJI and Susumu UCHIYAMA
Department of Electrical Engineering, Faculty of Engineering, Nagoya University, Nagoya

(Received July 18, 1957)

Measurements of the magnetoresistance of single crystal of semiconductor give an important information of its band structure.[1][2] Here we report measurements of the magnetoresistance effect and also the planar Hall effect[3] in synthetic p-type

Curve	Current	ax. of rot.
1	[100]	[010]
2	[110]	[1̄10]
3	[1̄10]	[110]
4	[110]	[001]

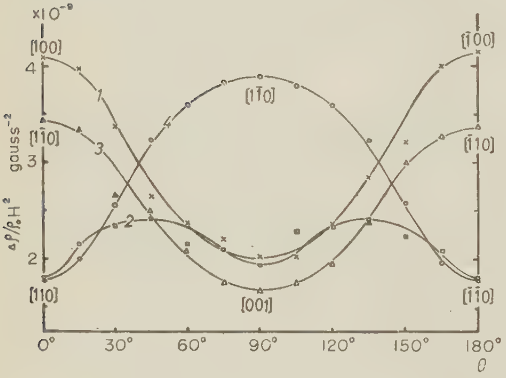

Fig. 1.

single crystal of PbTe. The measurements were made for two specimens, one of which had its long axis in [100] direction and the other in [110] direction; they were cut from the same ingot whose Hall coefficient was $+2.48\, cm^3/coul.$ and resistivity $1.93\times10^{-1}\,\Omega\, cm$ at 90° K, their temperature d pendence being normal.

The measured results at 90°K and with 80 gauss are shown in Figs. 1 and 2. In Fig. 1 vari tion of the magnetoresistance with respect to angle between the electrical current and the magn tic field, is shown with the direction of curren and the axis of rotation as it is measured. T

Curve	Current	ax. of rot.
I	[100]	[001]
II	[110]	[001]

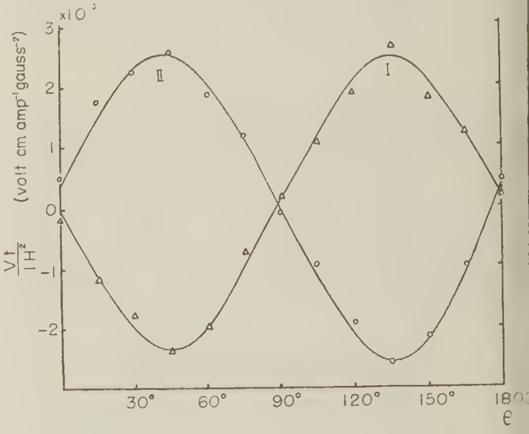

Fig. 2.

planar Hall effect is shown in Fig. 2 and its vari ation with regard to angle is sinusoidal as expecte from the theory.[3] The field dependence of th magnetoresistance and the planar Hall voltage i approximately expressed as the square of the fiel up to 10000 gauss in all cases: exactly speaking however, their exponent with respect to field i a slightly smaller than two. The relation $\Delta\rho/\rho_0 H$ *vs.* θ does not necessarily conform to Seitz' theory.[4] The behaviour of curve *2*, which deviate appreciably from curve expected theoretically, tell us an appearance of terms of higer order i magnetoresistance, *i.e.* terms proportional to H^4.

From magnetoresistance						From planar effect	
$b\times10^9$	$c\times10_6$	$d\times10^9$	$\beta\times10^5$	$\gamma\times10^5$	$\delta\times10^5$	$c\times10^9$	$d\times10^9$
2.00	−2.16	4.20	−9.60	9.68	−2.18	−2.59	5.29

The constants[1] of magnetoresistance obtained are shown in Table, which represent the data plotted in Fig. 1 fairly well except curve *2*. In Table the values of c and d which are obtained from planar Hall effect[3] are also shown; Their values are satisfactorily in accordance with those obtained from the magnetoresistance.

When the results are interpreted according to Shibuya's theory,[2] p-type PbTe may be concluded to have spheroidal energy surfaces with their extrema along [111] and its equivalent axes, since the values of $\beta+\gamma+\delta$ and $\beta+\gamma-\delta$ are far apart fro zero as compared to the value $\beta+\gamma$, and $\delta<0$.

The authors wish to thank Professor Y. Sakak for his kind guidance in carring out this research

References

1) G. L. Person and H. Suhl: Phys. Rev. **8** (1951) 768.
2) M. Shibuya: Phys. Rev. **95** (1954) 1385.
3) C. Goldberg and R. E. Davis: Phys. Rev. **9** (1954) 1121.
4) F. Seitz: Phys. Rev. **79** (1950) 372.

J. Phys. Soc. Japan **12** (1957) 1165

Magnetic Properties of $NiTiO_3$–Fe_2O_3 Solid Solution Series

By Yoshikazu Ishikawa

Institute of Science and Technology,
University of Tokyo, Tokyo

(Received June 18, 1957)

Hitherto, the magnetic properties of solid solu- ions of ilmenite ($FeTiO_3$) and hematite (Fe_2O_3) have been studied in detail.1)2) They are entirely new type of ferromagnetics and other ferromagne- ic compounds which belong to this type have not yet been found. In these studies, it was supposed hat the complicated magnetic properties of these materials would be partially due to unstableness of $FeTiO_3$ at high temperature.

We have reported in the previous paper3) that $NiTiO_3$ is a stable compound having the same crystal structure as $FeTiO_3$. If, therefore, the magnetic properties of the solid solutions of $FeTiO_3$ and Fe_2O_3 has its origin in their crystal structure, we could expect the same situation for the solid solutions between $NiTiO_3$ and Fe_2O_3. To examine this idea, we have prepared the solid solution of $NiTiO_3$ and Fe_2O_3 and investigated their magnetic properties.

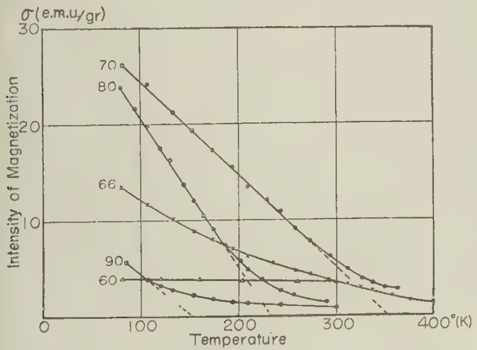

Fig. 1. The intensity of magnetization for a field of 8350 Oe vs. temperature. The numbers in the figure indicate mole percentages of $NiTiO_3$ in the compounds.

In this paper we report the outline of our results. t was found by X-ray analysis that $NiTiO_3$ and Fe_2O_3 can make the solid solutions over the whole range of composition. Their magnetizations were measured down to the liquid nitrogen temperature n a field of 8350 Oe as shown in Fig. 1. The numbers in the figure indicate the mole percentages of $NiTiO_3$ in the solid solutions. As is seen in the igure, the specimens become strongly ferromagne- ic only in a limited region of composition just ike the solid solution of $FeTiO_3$ and Fe_2O_3; that s, x $NiTO_3$—$(1-x)$ Fe_2O_3 seems to be ferromagnetic only for $0.9 \geqq x > 0.6$. The thermomagnetic curves are quite similiar to those of solid solutions of $FeTiO_3$ and Fe_2O_3. Besides, the circumstance that the magnetization is largest for $x \simeq 0.7$ is also same as that for the case of $FeTiO_3$ series.

As all specimens prepared contain a trace of impurities of the ferromagnetic spinels, the Curie temperatures of antiferromagnetic specimens ($x \leqq 0.6$) can not be determined from this experiment. For ferromagnetic specimens ($x > 0.6$), however, we can estimate them from the figure. The changing rate of the Curie temperatures with composition seems to be same as that of $FeTiO_3$ series.

The magnetic susceptibilities of this solid solutions were found to obey the Curie-Weiss law at high temperature. In Fig. 2 C_m and Θ obtained from the formula $\chi_m = C_m/T+\Theta$ are plotted against composition. We find that they vary almost linearly with composition. This is not the case for $FeTiO_3$ series, for which the anomalous dependences of C_m and Θ upon composition are observed for the ferromagnetic specimens.

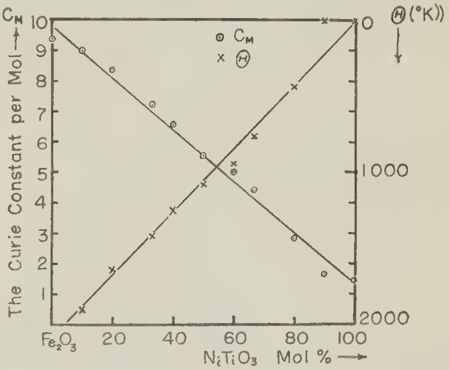

Fig. 2. C_m and Θ obtained from the Curie-Weiss law $\chi_m = C_m/T+\Theta$ vs. the composition.

Another marked difference is as follows: For $NiTiO_3$ series the magnetization of the specimen for $x=0.6$ is very weak, while for $FeTiO_3$ series the specimen of 0.6 $FeTiO_3$–0.4 Fe_2O_3 is strongly ferromagnetic. We may suppose that such differences are to some extent attributed to the following situation. In the case of $FeTiO_3$ series, the conductivity being relatively high, the ordering of Fe^{+2} and Fe^{+3} ions can occur merely by the electron transfer. In the case of $NiTiO_3$ series, on the other hand, Ni^{+2} and Fe^{+3} ions are fixed to lattice sites at the time of preparation of specimen.

The auther withes express his sincere thankes to Prof. Shozo Sawada for his encouragement throughout this investigation.

References

1) T. Nagata and S. Akimoto: Geofisica Pura e Applicata Milano **34** (1956) 36.
2) Y. Ishikawa and S. Akimoto: J. Phys. Soc. Japan **12** (1957) 1083
3) Y. Ishikawa and S. Sawada: J. Phys. Soc. Japan **11** (1956) 496.

J. Phys. Soc. Japan **12** (1957) 1166

Iodine Quadrupole Resonances in ICl_3 and AlI_3

By Shigeo Hagiwara, Kiyoe Kato, Yoshihito Abe and Midori Minematsu

Department of Physics, Tokyo University of Education

(Received July 31, 1957)

Nuclear quadrupole resonances of I^{127} have been measured in solid iodine trichloride and aluminium triiodide with superregenerative spectrometers. A sample of iodine trichloride was produced by adding iodine into liquid chrorine. Aluminium triiodide was produced by direct interaction between aluminium and iodine. The high frequency lines of ICl_3 were detected with the cavity-type spectrometer[1] and other lines with the transmission type spectrometers[2]. The obtained results are listed in Table I.

The frequencies of two resonance lines in Al were measured simultaneously to get rid of th change of temperature of sample[3]. The structu of solid ICl_3 is considered as built up of plan I_2Cl_6 molecules, which consist of ICl_4^- and ICl_2^+ The obtained coupling constant of ICl_3 is very nea the value of ICl, 3008.3 Mc[4] at 20°C. Therefor the observed resonance is probably arisen fro ICl_2^+. Because of filled *p* orbitals the iodine n cleus in ICl_4^- seemes to give rise to no resonance The chlorine resonances in ICl_3 was first studie by Bray[6]. He reported two resonance lines a liquid nitrogen temperatures. We have also mea sured the lines at 31°C and obtained the frequen cies of 34.87 Mc and 33.39 Mc, which agreed we with Bray's value taking into account temperatu effect. If the molecule had a resonance structu as the case of AlI_3 three resonance line should b detected. However, only two resonance were ob served.

Table I. Nuclear Quadrupole Resonance of I^{127}.

sample	T(°C)		ν_1 (Mc)	ν_2 (Mc)	η (%)	eQq (Mc)
ICl_3	20		451.22±0.01	895.76±0.02	7.5	2989.3±0.1
	−15		452.87±0.01	899.70±0.02	7.4	3002.3±0.1
AlI_3	−25	A	111.369±0.005	212.67 ±0.02	19.92	712.20±0.05
		B	129.894±0.005	259.74 ±0.02	1.20	865.62±0.05
		C	130.493±0.005	260.78 ±0.02	2.48	869.36±0.05
	25	A	111.011±0.005	210.88 ±0.02	20.44	708.60±0.05
		B	129.326±0.005	258.57 ±0.02	1.54	861.95±0.05
		C	129.939±0.005	259.59 ±0.02	2.91	865.44±0.05
	24*	A	111.017±0.019	211.052±0.052	18.1	723.38
		B	129.327±0.030	258.972±0.060	0	876.52
		C	127.763±06030	259.961±0.060	0	879.33

* S. L. Segel and R. G. Barnes: J. Chem. Phys. **25** (1956) 578.

The three resonance lines of I^{127} in AlI_3 was already studied by Segel and Barnes[7]. They suggested the indirect spin-spin interaction from their results that the ratio ν_3/ν_1 was slightly greater than two and the lines were broad having line width of about 50 kc. In the present experiment the lower resonance frequencies ν_1's are in agreement with their values. The higher resonance frequencies ν_2's, however, are lower than their values by about 500 kc. As a result the ν_2/ν_1 become smaller than two and yielded real value of asymmetry parameter. The line width of the higher frequency lines was observed as 40 kc. But the lower frequency lines were not so broad and had a line width of about 10 kc∼14 kc. Therefore, large indirect spin-spin interaction as the case of iodine is not expected.

Acknowledgement

The authors wish to express their thanks t Prof. S. Kojima for his guidance throughout thi work.

References

1) S. Kojima, A. Shimauchi, S. Hagiwara and Y Abe: J. Phys. Soc. Japan **10** (1955) 930.
2) S. Kojima, S. Ogara, S. Hagiwara, Y. Abe an M. Minematsu: J. Phys. Soc. Japan **11** (1956 964.
3) S. Ogawa: J. Phys. Soc. Japan **12** (1957) 1105
4) H. G. Dhemelt: Naturwiss **37** (1950) 398.
5) R. Kiriyama: "*Kozomukikagaku*" (in Japa nese). Kyoritsu Co., Ltd., Tokyo.
6) P. J. Bray: J. Chem. Phys. **23** (1955) 703.

J. Phys. Soc. Japan **12** (1957) 1167-1168

On the Dielectric Properties of α-phase n-Higher Alcohols and Associated Electromotive Force

By Mikio Takeyama

Department of Physics, Faculty of Science, Hiroshima, University

(Received April 18, 1957)

The author has measured ε' and ε'' of n-higher alcohols in the frequency-range from several hundreds cycles to kMc (λ=1.2 cm.) and observed that, in α-phase, a dielectric dispersion occurs in microwave region as well as in low frequency region. The frequency dependence of ε' and ε'' of octadecyl alcohol, $C_{18}H_{37}OH$, is given in Fig. 1. A similar curve has been obtained for tetradecyl alcohol, $C_{14}H_{29}OH$. But for cetyl alcohol, $C_{16}H_{33}OH$, two peaks have not been clearly separated, though it is certain that a dielectric dispersion occurs in microwave region.

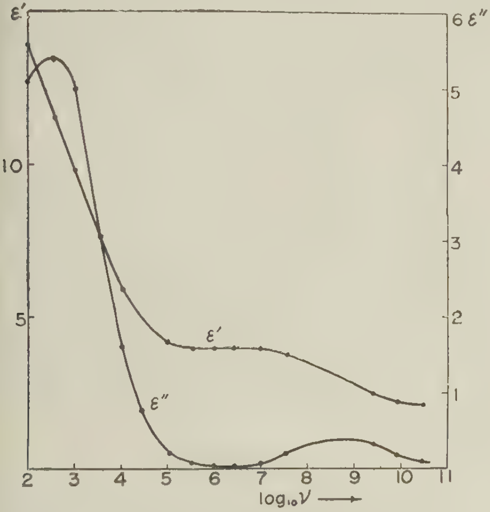

Fig. 1. Frequency dependence of dielectric constant of octadecyl alcohol (in α-phase).

It seems reasonable to consider that such a dispersion in microwave region is due to a certain degree of freedom of OH-radicals of those alcohols.

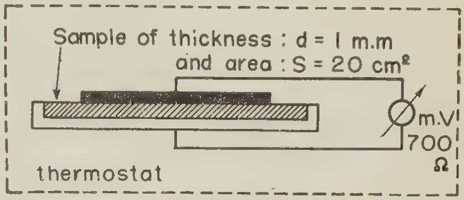

Fig. 2.

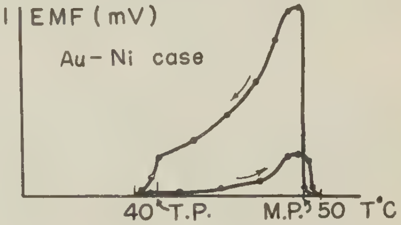

Fig. 3. Temperature dependency of the electromotive force of cetyl alcohol.

On the other hand, sample pieces of α-phase placed, as shown in Fig. 2, between two metallic plates of different kinds (for example, Pt and Ni) give rise to such electromotive forces as given in Table I. The temperature dependence of the electromotive force is represented by the curve given in Fig. 3. Such an electromotive force appears neither in β-phase nor in liquid state. It should be noted that the form of this curve is very much alike with that of the temperature dependence of ε' and ε'' of this sample and the electromotive orce is closely related to the work functions of he two metals, as one can see in Table I.

Table I.

Plates and polarity ⊕	⊖	Work function difference (eV)	Electromotive force (mV) max. value $C_{16}H_{33}OH$	$C_{18}H_{37}OH$
Pt —	Ni	5.3−4.6=0.7	2.1±0.2	
Pt —	Au	5.3−4.9=0.4	1.2±0.2	
Au —	Ni	4.9−4.6=0.3	1.0±0.1	0.3±0.1
Au —	Au	4.9−4.9=0	0	0

One may get a hint from this fact, as to explaining the proton transfer mechanism[1,2,3] of those lcohols which has been discussed by many workers.

The detailed report and discussion on the experimental results is to be published in "Journal of Science of Hiroshima University (Series **A**)". The samples used in this experiment were chemicals of Eastman Kodak Company.

In conclusion, the author wishes to express his sincere thanks to Prof. I. Takahashi of Kyoto University and Prof. H. Takeyama for their encouragement and useful advices.

References

1) J. D. Hoffman and C. P. Smyth: J. A. C. S. **71** (1949) 431.
2) Y. Kakiuchi, T. Sakurai and T. Suzuki: J. Phys. Soc. Japan **5** (1950) 369.
3) K. Asai, E. Yoda and S. Yamanaka: J. Phys. Soc. Japan **10** (1955) 634.

J. PHYS. SOC. JAPAN **12** (1957) 1168

Antiferromagnetic Resonance in $CuCl_2 \cdot 2D_2O$

By Muneyuki DATE

Research Institute for Iron, Steel and Other Metals, Tôhoku University, Sendai, Japan

(Received July 25, 1957)

We have performed the experiments of the antiferromagnetic resonance in $CuCl_2 \cdot 2D_2O$ at 16100 Mc/sec of which the main purpose is to find out any slight difference of the antiferromagnetic properties of $CuCl_2 \cdot 2D_2O$ from that of $CuCl_2 \cdot 2H_2O$ which was previously investigated in detailed by the Leiden group.[1]

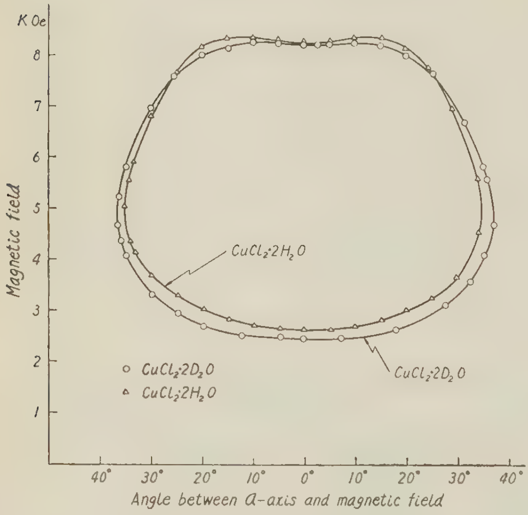

Fig. 1. Antiferromagnetic resonance in $CuCl_2 \cdot 2D_2O$ and $CuCl_2 \cdot 2H_2O$ in the *ab*.plane at 1.4°K.

The single crystal of $CuCl_2 \cdot 2D_2O$ was crystalized from saturated solution which contained 10 gr. D_2O as the solvent. The colour of the crystal is bright blue being slightly lighter than that of $CuCl_2 \cdot 2H_2O$. The size of the crystal used is of about 0.5 mm and the static magnetic field was applied in the *ab*-plane. The microwave circuit is usual one o the transmission type and the second harmonics o 2K25 klystron was used for the experiments. Special care was taken for the precise compariso of the results on $CuCl_2 \cdot 2D_2O$ and $CuCl_2 \cdot 2H_2O$ crystals. To avoid any slight difference in the experimental condition day by day, both crystal were mounted together but with orientations dif fering from each other and experiments were repeated for both crystals.

The experimental result are shown in Fig. 1 and may be summarized as follows :

1) The resonance constant C_1 in Nagamiya' theory[2] of the antiferromagnetic resonance is the same in both crystals within the experimental error

2) The resonance line of the low field branc at $a//H$ in $CuCl_2 \cdot 2D_2O$ is lower than that o $CuCl_2 \cdot 2H_2O$ and this means, according to the present theory of the antiferromagnetic resonance the smaller value of the other resonance constan C_2 of $CuCl_2 \cdot 2D_2O$ compared with that of $CuCl_2 \cdot 2H_2O$.

3) The dip appeared in $CuCl_2 \cdot 2H_2O$ at the top of the circle (Fig. 1) is reduced in $CuCl_2 \cdot 2D_2O$.

4) The total angle range in which the resonance can be observed in the *ab*-plane is 74° in $CuCl_2 \cdot 2D_2O$ whereas it is 70°30′ in the $CuCl_2 \cdot 2H_2O$.

The detailed account of the results and discussions will be published later. Finally the author wishes to express his cordial thanks to Prof. T Fukuroi for the stimulations during the course o the present research.

References

1) N. J. Poulis, Van den Handel, J. Ubbink, J. A Poulis and C. J. Gorter: Phys. Rev. **82** (1951) 552. J. Ubbink, J. A. Poulis, H. J. Gerritser and C. J. Gorter: Physica **18** (1952) 361; **19** (1953) 928. H. J. Gerritsen, R. Okkes, B. Bolger, and C. J. Gorter: Physica **21** (1955) 629 H. J. Gerritsen: Physica **21** (1955) 639. M Garber and H. J. Gerritsen: Physica **21** (1956) 189. H. J. Gerritsen and M. Garber: Physica **21** (1956) 197. H. J. Gerritsen and G. W. J Drewes: Physica **21** (1956) 213.
2) T. Nagamiya: Prog. Theoret. Phys. **4** (1951) 350, ibid. 11, (1954) 369. See also T. Nagamiya K. Yosida, and R. Kubo: Advances in Phys. **4** (1955) 1.

J. PHYS. SOC. JAPAN **12** (1957) 1169

Galvanomagnetic Effects in n-type Indium Antimonide at Very Low Temperatures*

By Yasuo KANAI

Electrical Communication Laboratory, Musashinoshi, Tokyo

and Wataru SASAKI

Electrotechnical Laboratory, Nagatacho, Tokyo

(Received June 25, 1957)

Recently, anomalous (oscillatory) galvanomagnetic effects in n-type Indium Antimonide (InSb) at liquid helium temperatures were found independently in the work done by Frederikse and Hosler[1] and in ours.[2] To obtain the more complete informations about these anomalous effects, we measured the galvanomagnetic effects of the single crystals of tellulium doped n-type InSb, which had the different electron densities and crystal orientations.

In Table I, the values of resistivity (ρ) and Hall coefficient (R) of our samples at various temperatures are listed. The ratio of the Hall coefficient R in the various magnetic field H to the value of R, $R_{10,000}$, in the magnetic field of 10 kG are shown in Fig. 1 as a function of the inverse value of the magnetic field. And it seems to us that these curves in Fig. 1 show the existence of the anomalous (oscillatory) Hall effect in the n-type InSb at very low temperatures.

Table I. The values of resistivity (ρ) and Hall coefficient (R) at various temperatures. In the all cases of Hall measurements, magnetic field was applied in the 001-direction.

Sample No.	3-2-2		8-2-3		8-2-2		12-2-3		12-2-2	
Direction of electric current	110		100		110		100		110	
	$\rho\times10^4$ ohm-cm	R cm^3/coul.	$\rho\times10^4$ ohm-cm	R cm^3/coul.	$\rho\times10^4$ ohm-cm	R cm^3/coul.	$\rho\times10^4$ ohm-cm	R cm^3/coul.	$\rho\times10^4$ ohm-cm	R cm^3/coul.
273°K	6.39	12.0*	10.05	19.6*	8.81	21.1*	21.8	109*	28.8	166*
90	6.17	12.2*	10.7	23.6*	9.12	23.4*	22.1	112*	36.3	170*
4.2			11.2	23.7**		22.6**	17.4	105**		
1.4	6.44	11.1**	11.9	24.4**					40.5	165**

* The value in the magnetic field of 5.7 kG.　** The value in the magnetic field of 10 kG.

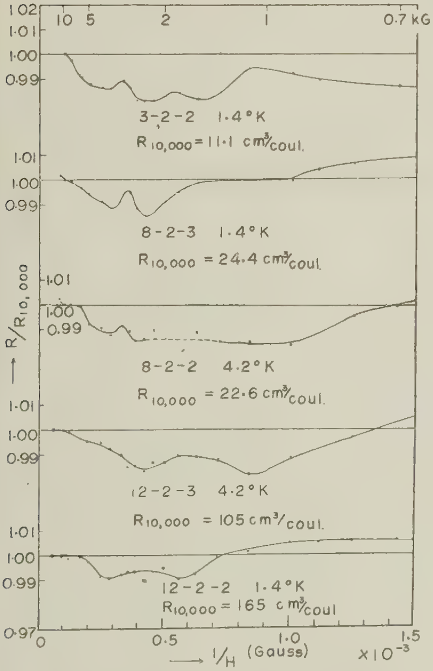

Fig. 1. The ratio of the Hall coefficient R at various magnetic field to the value of R, $R_{10,000}$, in the magnetic field of 10 kG as a function of the inverse magnetic field.

Corresponding to the anomaly in the Hall coefficient, the magnetoresistance of our samples also showed the same anomaly (oscillation) at very low temperatures. Unfortunately, however, it was found that the magnetoresistance of the n-type InSb was usualy depend on the shape of the sample, the absolute value of this effect was quite erroneous.

The authors are grateful to Prof. T. Fukuroi and his corworkers for the hospitality given in using the helium apparatus at the Research Institute for Iron, Steel and Other Metals of Tohoku University, and also to Mr. R. Nii and Miss C. Yamanouchi for their assistances in this work.

References

1) Y. Kanai and W. Sasaki: J. Phys. Soc. Japan **11** (1956) 1017.
2) H. P. R. Frederikse and W. R. Hosler: Bull. Amer. Phys. Soc. Ser. II, **1** (1956) 298 and Canad. Jour. Phys. **34** (1956) 1377.

---

* This work was carried at the Research Institute for Iron, Steel and Other Metals, Tohoku University.

Errata

On the Variational Problem connected with the Thomas Fermi Method

By Yukito TANABE

J. Phys. Soc. Japan **12** (1957) 974

P. 974 right column
line 4 — N should be read Ne.
line 25 — U or ∇V_e should be read ∇U or ∇V_e.

Impedance of Bulk Semiconductor in Junction Diode

By Toshio MISAWA

J. Phys. Soc. Japan **12** (1957) 882

P. 884 right column, line 4; $\bar{I}\exp(i\omega t)$ should be read $\tilde{I}\exp(i\omega t)$.

P. 884 left column; Eq. (16)

$$\delta\tilde{\varphi} = -\int_0^{x_b} \frac{d\tilde{\varphi}_n}{dx}\, dx_n$$

should be read

$$\delta\tilde{\varphi}_n = -\int_0^{x_b} \frac{d\tilde{\varphi}_n}{dx}\, dx\,.$$

In Eq. (18), $\delta\varphi$ should be read $\delta\varphi_n$.

P. 885 right column; in Eq. (29) τ_p should be read τ_n.

P. 886 right column, line 37; $d\varphi_u$ should be read $d\varphi_n$.

P. 887 right column; in Eqs. (45) and (46) μ_n should be read μ_p.

Stress-Strain Relations for Viscoelastic Large Deformation

By Wataru SEGAWA

J. Phys. Soc. Japan **12** (1957) 996–998

The notations $\varepsilon_{xx},\cdots\varepsilon_{yz},\cdots$ must be ammended as $\varepsilon'_{,xx}\cdots\varepsilon'_{yz}\cdots$, respectively, except in § 3.

p. 997, left column, line 11, " According to the Neo-Hookian Theory " must be eliminated.

p. 997, right column, line 6, " but finite " must be eliminated.

p. 997, right column, line 8, "finite strains " must be amended as " $\varepsilon'_{xx},\cdots\varepsilon'_{yz}\cdots$".

JOURNAL OF THE PHYSICAL SOCIETY OF JAPAN Vol. 12, No. 11, NOVEMBER, 1957

Nuclear Interactions in Nucleon-Proton and Nucleon-Carbon Nucleus Collisions above 10 GeV

By Koichi SUGA

Institute for Nuclear Study, University of Tokyo, Tanashimachi, Kitatamagun, Tokyo

(Received May 14, 1957)

Nuclear interactions in hydrogen and carbon by nucleon (a few to several tens of GeV) have been studied using a multiplate cloud chamber which contained paraffin, carbon and lead at mountain altitude. The cross-section for the nuclear interaction by nucleon-proton collision was found to be 60±17 mb, assuming the cross-section for nucleon-carbon nucleus 320 mb. Energy spectra of neutral pions produced in paraffin, graphite and lead were compared. The energy distribution of neutral pions in paraffin-interactions is more steep in low energy region and similar in high energy region compared with that in carbon-interactions, and possible interpretation will be given. Charged secondary particles are emitted isotropically in c.m. system in nucleon-nucleon collision, and in the carbon nucleus some secondary particles undergo secondary collisions in the same nucleus. The azimuthal angle distribution of secondary particles was examined and some comments will be mentioned.

§1. Introduction

Results of an experiment on penetrating showers from hydrogen and carbon will be reported. The experiment was carried out at Mt. Norikura Cosmic-Ray Laboratory, University of Tokyo (2840 m altitude), from summer to winter of 1955. This work is the continuation of previous studies[1] by CH_2–C subtraction method with a counter hodoscope. Main purposes of the present experiment are as follows: (I) To check results of the previous experiment (the cross-section of meson-production in hydrogen) with newly designed experimental arrangement. Ambiguities of the results caused by secondary interactions in the producer and the uncertainty of identifying the penetrating shower with a counter hodoscope were overcome by using a multiplate cloud chamber which contained thin producers of paraffin and carbon. (II) To obtain informations about neutral pions produced in hydrogen and carbon, using lead sheets in a cloud chamber. (III) To study the angular distribution of shower particles in the nuclear interaction.

§2. Experimental Arrangement

A sketch of the apparatus is shown in Fig. 1. The whole apparatus consisted of a hodoscope of G.M. counters and a multiplate cloud chamber which contained paraffin, graphite and lead sheets. The cloud chamber is of rear-illumination and lateral-expansion type, and was filled with 85 cm Hg argon and saturated vapor of ethyl alcohol. The illuminated region is about 50 cm×50 cm×40 cm. The chamber contained four layers of paraffin and graphite and three layers of the lead sheet of 1 cm thickness. Thickness of each layer of paraffin and graphite was made to 3.14 g/cm^2 and 2.68 g/cm^2, respectively, so that the both contained the same number of carbon nuclei. It is perhaps desirable that appearances of paraffin and graphite layers are made indistinguishable from each other, so that the personal bias is prevented which come into the visual inspection of cloud chamber photographs. Each graphite layer was composed of two slices piled up with spacers, and was covered with aluminium-foil of 50 microns thickness same as in the case of paraffin layer. Thus apparent thicknesses (of 3.5 cm) and appearances of paraffin and graphite were made to be very similar with each other. In order to reduce the effect from the difference of the detection-efficiency of nuclear interactions in paraffin and graphite by the counter coincidence system, each layer of paraffin and graphite (23 cm×41 cm) was set as shown in Fig. 1. In the course of the experiment, positions of paraffin and graphite were frequently interchanged.

There were four trays of G. M. counters

called *A*, *S*, *B* and *C*, respectively. Tray *S* consisted of 21 counters of 36 cm length and 2 cm diameter. Tray *A* and *B* contained 14 counters of 40 cm length and 4 cm diameter. Tray *C* was a group of 17 counters of 50 cm length and 4 cm diameter. Tray *B* was separated from Tray *S* by 15 cm of lead and 4 cm of iron. Each counter of this tray was wrapped by a lead sheet of 3 mm in thickness to reduce the effect of knock-on electrons. Tray *C* was separated from *B* by 5 cm lead. All counters of these trays were connected to each corresponding neon lamp through each hodoscope circuit.

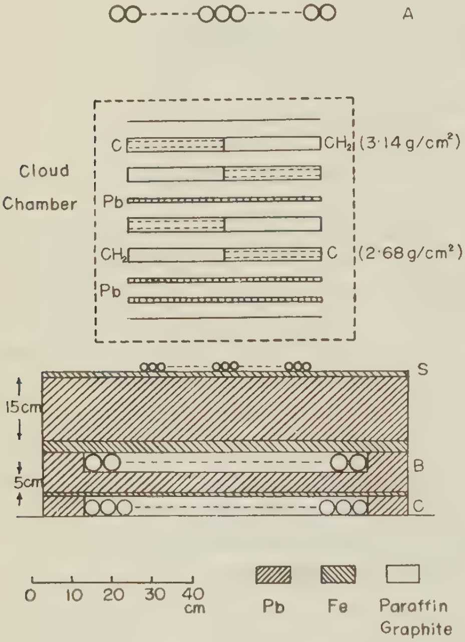

Fig. 1. A Sketch of the experimental arrangement.

The condition for a master pulse was simultaneous discharges of at least two counters of tray *S* and discharges of at least three counters in tray *B* and at least one counter in tray *C*. Photographs of the cloud chamber by two 35 mm cameras and photographs of the hodoscope by 16 mm cine-camera were taken with these master pulses. Experimental conditions of the cloud chamber were tested by visual inspection and electronic circuits were checked a few times per day.

§3. Analysis of Photographs

Cloud chamber photographs were taken with pieces of 35 mm films, each of which contained about 50 pictures. In order to avoid th personal bias in the course of visual inspectio of cloud chamber photographs, numbers o four orders which were obtained from th table of random number were attached t each piece of film before photography. Eac film was represented by these numbers. I the course of analysis, pieces of films wer mixed randomly and then the piece picked u was scanned. Photographs taken with th triggering master mentioned above show pene trating showers produced in paraffin, graphit or lead plate as well as air showers or som other spurious events. For the present study events which were produced in paraffin o graphite layers and were convincingly re garded as nuclear interactions were picke up and analysed stereoscopically. After th analysis, the assignment of events to paraffi (*P*) or graphite (*G*) was done with the aid o the number attached to each piece of film Criterion of the nuclear interaction was a follows: (1) event with one secondary partic which penetrates at least 2 cm of lead withou multiplication (penetrating particle) and one o more heavily ionizing particles and/or one o more cascade showers (2) with two or mor penetrating particles (3) with two or mor penetrating particles and one or more heavil ionizing particles and/or one or more cascad showers (4) with two or more cascade shower and/or heavily ionizing particles. Event which were produced in the region of 1 c from the edge of each producer were excluded because the uncertainty of determination o the position was about ±1 cm in this experiment.

§4. Results and Discussions

(1) Cross-Section for the Nuclear Interaction in Hydrogen

Scanning of all of photographs in this experiment has not yet been completed, 15 *P*-interactions and 120 *G*-interactions (produce in paraffin and graphite, respectively) wer obtained by both charged and neutral primar particles, after scanning and stereoscopic analysis of about a half of photographs along th procedure mentioned above. If the cross-section for nuclear interaction by nucleon-carbo nucleus collision is assumed, the cross-sectio for nucleon-proton collision can be obtaine from above rates of *P*- and *G*-interaction.

In order to inspect whether the ratio of rates of *P*- and *G*-interaction (*P/G*) is free from the personal bias and instrumental defects or not, distribution of *P/G* values was examined from the following points of view: (1) *P/G* values in the case of the different relative position of paraffin and graphite layers in the cloud chamber (2) *P/G* values at different height of producers in the cloud chamber (3) *P/G* values in producers in right and left sides in the chamber (4) *P/G* values in sequence of time in the course of scanning (5) *P/G* values in sequence of time in the course of the operation of the cloud chamber. The distribution of *P/G* values was consistent with that expected from the Poissonian fluctuation.

After the correction of the materials (Al-foil and adhesive material) that covered the producer, ratio $P/G=1.33\pm0.15$ was obtained. The energy of primary particles is considered to be a few to several tens of GeV as described in Section **4** (**3**) [**A**]. The cross-section for nuclear interaction by nucleon-carbon collision in this energy region is known to be about 320 mb by many authors[2)]. Then the cross-section for nucleon-proton collision is 53 ± 24 mb, because *P/G* ratio is equal to the value of (2×cross-section of proton + cross-section of carbon nucleus) divided by cross-section of carbon nucleus. This value is consistent with previously obtained cross-section in same energy region; that is 67 ± 25 mb. Taking weighted average of these two values, one obtains 60 ± 17 mb. This value is almost equal to the geometrical cross-section of 60 mb ($=\pi r_0^2$, $r_0=1.4\times10^{-13}$ cm), but is slightly higher than 42 mb at 2.75 GeV[3)] and 29.5 mb at 5.3 GeV[4)] obtained by the Cosmotron and Bevatron. Recently, E. Brenner and R. W. Williams[5)] obtained $\sigma=21$ mb for effective elementary nucleon-nucleon cross-section at 50 GeV from the cross-section for nucleon-iron nucleus collision; i.e. 615∼605 mb obtained experimentally. In our case, the cross-section for nucleon-proton collision is 49 ± 14 mb, even if we take 260 mb for the cross-section for nucleon-carbon nucleus collision which is the lowest value obtained up to present time in the energy region of a few to several tens of GeV.

As to the difference of the cross-section by proton and neutron primaries, none was observed, just as in the previous experiment.

(2) Production of Neutral Pions from Hydrogen and Carbon

Neutral pions produced in nucleon-proton and nucleon-carbon nucleus collisions were studied with the aid of cascade showers developed by the lead plates in the cloud chamber. In the present analysis, cascade showers which convincingly associate with nuclear interactions were examined, and cascade showers which have only one or two particles in only one space under a lead plate—namely cascade showers of very low energy—were excluded. No noticiable difference in multiplicity distribution and angular distribution between *P*-interactions and *G*-interactions was observed.

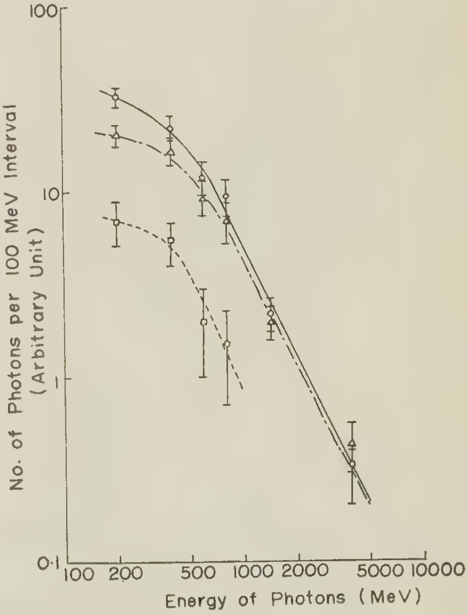

Fig. 2. Energy distribution of cascade showers produced in Paraffin (○), Graphite (△) and lead (□). The abscissa shows the energy of cascade showers in MeV, and the ordinate shows the number of cascade showers per 100 MeV interval in arbitrary unit.

The energy of cascade showers of *P*-interactions and *G*-interactions was estimated from the transition in three lead plates of 1 cm thick each, following the theoretical cascade curve by Snyder[6)7)]. It is preferable to use the correct curve by Monte Carlo Method, but it is not available up to several GeV. The energy distribution of cascade showers produced by the nuclear interaction in paraffin and carbon thus obtained is shown in Fig. 2, as well as one in lead. Because of missing some showers of low energy and of inaccuracy of the refered cascade curve, the absolute energy spectrum of cascade showers can not be shown, but the difference of energy distribution between paraffin and carbon may be discussed based on these results. In Fig. 2, the abscissa shows the energy of photons and the ordinate shows the number of photons observed for the same running time in paraffin and graphite and for rather small amounts of running time in lead in 100 MeV interval in arbitrary unit.

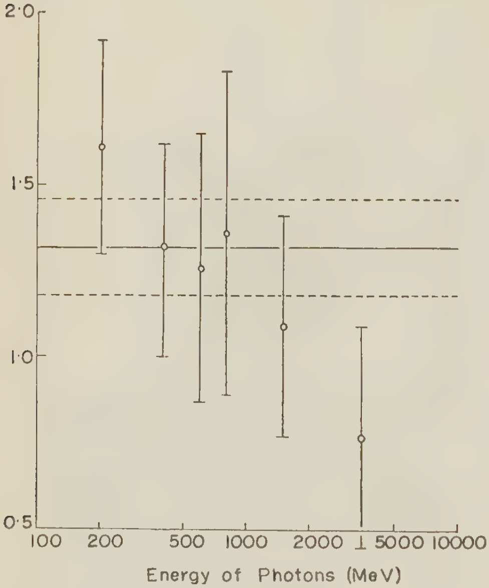

Fig. 3. Ratio of the number of photons produced in *P*- and *G*-interactions for the same running time vs. the energy of photons.

Although experimental errors are rather large, it may be seen that the energy distribution of photons in *P*-interactions is more steep in low energy region and similar in high energy region compared with that in *G*-interactions. And the energy distribution of photons in interactions in lead shows the same tendency as that of *G*-interaction. The ratio of numbers of the cascade shower in *P*- and *G*-interaction is shown in Fig. 3 with respect to the energy of photons. The full line and dotted lines show the ratio of the numbers of *P*-interaction and *G*-interaction and its statistical accuracy. From this figure, it may be seen that the ratio of the cascade shower for both interactions is rather high in low energy and rather low in high energy compared with the ratio of the number of both interactions These behavoirs might be due to the insufficient statistical accuracy, and the hasty conclusion is to be reserved. But those might be tentatively understood by the hypothesis that the production of charged pions of high energy is usual but that of neutral pions of high energy is rather less in the nucleon-nucleon collisions, and/or that neutral pions of low energy are absorbed by the successive collisions with nucleons in the same nucleus in carbon and lead.

(3) Angular Distribution of Charged Secondary Particles

In those interactions which contained cascade showers, charged secondary penetrating particles were often masked by these cascade showers. So, those 46 interactions which showed only charged secondaries and were caused by charged primaries were selected from 276 interactions produced in paraffin and graphite layers and were studied.

[A] *Colatitude-angle distribution of secondary particles*

Angles between the charged primary particle and each secondary penetrating particle were measured in each interaction and are named colatitude angles (θ). The colatitude-

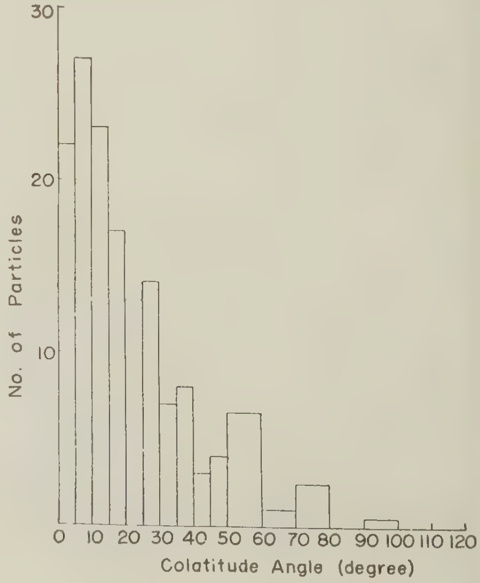

Fig. 4a) Colatitude-angular distribution of charged secondary particles in the laboratory system for total interactions.

angle distribution and the so-called F-plot[8] are shown in Fig. 4, including total events. F-plot is almost linear as is expected from the isotropic distribution and the approximate relation $m=\beta_c/\beta_\pi=1$ in the center-of-mass system in the nucleon-nucleon collision where β_c and β_π is the velocity of incident nucleon and produced pions in unit of the velocity of light, respectively. The tangent of the line, however, is not equal to 2, while it is expected so in the above condition. Further analysis, therefore, seemed to be necessary. Interactions were divided into three groups according to the mean colatitude-angle of each interaction (i.e. the primary energy or the Lorentz factor (γ_c) of primary particle—probably nucleon—in the c.m. system). Fig. 5 shows the distribution of mean colatitude-angle of each interaction and Table I shows the character of each group.

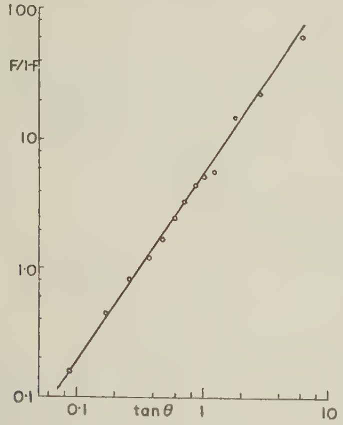

Fig. 4b) F-plot for the same data.

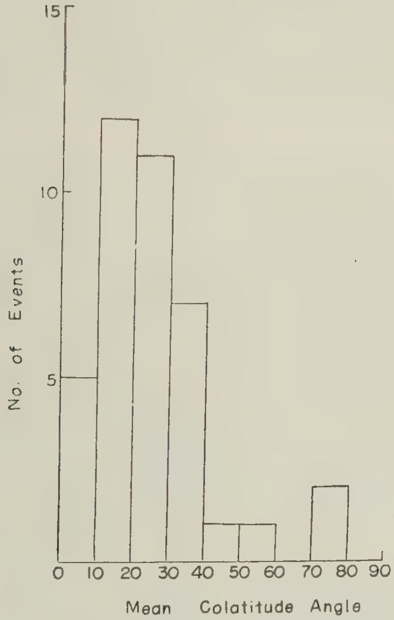

Fig. 5. Distribution of the mean colatitude-angle of each interaction in the laboratory system.

F-plots corresponding to each group are shown in Fig. 6, together with the F-plots corresponding to the case of smaller breadth of γ_c than Group I (Group I′) and to the case with at least 4 secondary particles (Group I″). Though errors are rather large, it may be seen from this figure that lines of Group I, I′ and I″ are almost linear but lines of Group II and III are curved. F-plots corresponding to the isotropic distribution with $m=1$, isotropic distribution with $m=1.03$, $\cos^2\theta$ distribution with $m=1$ and $\cos^2\theta$ distribution with $m=1$ and $\cos^2\theta$ distribution with $m=1.03$, in c.m. system assuming $\gamma_c=4$ are calculated and shown in Fig. 7, in order to examine what meanings those experimental F-plots show. From these curves and Fig. 6, it may be seen that Group I, I′ and I″ show nearly isotropic distribution with $m\approx1$ and Group II and III show rather sharp distribution in the forward and the backward directions with $m>1$ in c.m. system. And, also, Table I shows that the Group II and III have not less multiplicity than Group I irrespective of smaller value of $\bar{\gamma}_c$ than Group I and I′. These tendencies may

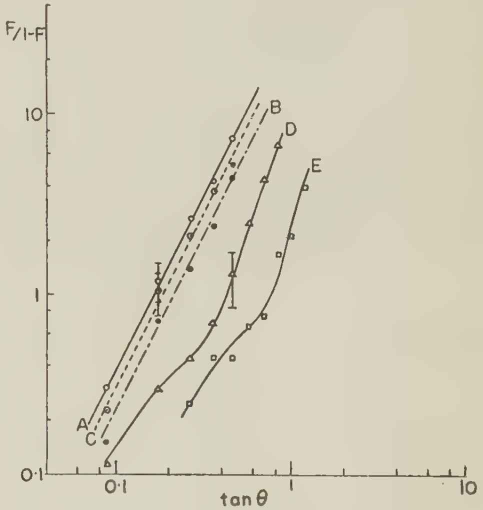

Fig. 6. F-plots for each group as shown in Table I. *A*: Group I, *B*: Group I′, *C*: Group I″, *D*: Group II and *E*: Group III.

Table I.

	Group I	Group II	Group III	Group I′	Group I″ e)
breadth of γ_c a)	10~3	3~2	2~1.5	5~3	10~3
$\bar{\gamma}_c$ b)	5.9	2.3	1.7	4.5	5.6
number of interactions	18	11	7	12	10
mean multiplicity	3.8	3.6	4.5	4.0	4.8
angular distribution in c.m. system c)	nearly isotropic	rather sharp in forward and backward directions	rather sharp in forward and backward directions	nearly isotropic	nearly isotropic
m d)	≈1	>1	>1	≈1	≈1

a) determined from the mean angle of secondary particles; $\gamma_c=1/\bar{\theta}$.
b) determined from F-plot, assuming the nucleon-nucleon collision.
c)d) determined from the shape of line in F-plot assuming the nucleon-nucleon collision.
d) $m=\beta_G/\beta_\pi$ in the center-of-mass system.
e) in this group, interactions with at least 4 secondary particles were selected.

be interpreted by the following hypothesis. The nucleon-nucleon collision and nucleon-nucleus collision without secondary interaction in the same nucleus show the isotropic distribution of secondary particles and have pions of high energy in c.m. system. But the nucleon-nucleus collision with secondary interactions will produce pions of rather low energy and shows rather sharp distribution in the forward and the backward directions, due to the analysis by the assumption of successive nucleon-nucleon collision, though each process of the nucleon-nucleon collision probably has the isotropic distribution. Under the above interpretation, the energy of primary particles may be a few to several tens of GeV from γ_c in Table I.

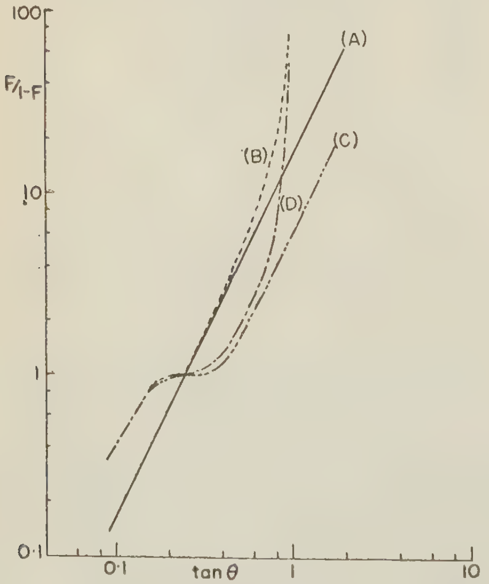

Fig. 7. F-plots for $\gamma_c=4$ calculated theoretically, assuming (*A*) isotropic distribution with $m=1$, (*B*) isotropic distribution with $m=1.03$, (*C*) $\cos^2\theta$ distribution with $m=1$ and (*D*) $\cos^2\theta$ distribution with $m=1.03$.

[B] *Azimuthal angle distribution of charged secondary particles*

Events examined in this section are the same as in the former section. The incoming direction of the primary particle was taken as *Z*-axis in the polar coordinate, and the so-called azimuthal angle (ψ) of the charged secondary particle was studied. The importance of the azimuthal angle distribution of secondary particles in the nucleon-nucleon collisions has been noticed from the view-point of the mechanism of the multiple production of mesons and especially from the possible role of the angular momentum of incoming nucleon to the multiple production of mesons.9) In this analysis, the arbitrary determination of origin in azimuthal angle is difficult and not adequte. So, the separation in the azimuthal angle between each secondary particle and its nearest neighbour was taken.

The separation angle is $\phi=\psi_{i+1}-\psi_i$, and $P(\phi)$ is the frequency of cases with angular separation ϕ. $W(\phi)=\int_{\phi}^{2\pi}P(\phi)d\phi \Big/ \int_{0}^{2\pi}P(\phi)d\phi$ vs. ϕ is shown in Fig. 8 (a) and (b) in interactions with three and six secondary particles respectively, together with same curves obtained by the Monte Carlo Method assuming the random and $\cos^2\psi$ distribution. In interactions with three secondary particles, decision whether the experimental distribution belongs to the random distribution or $\cos^2\psi$ distribution

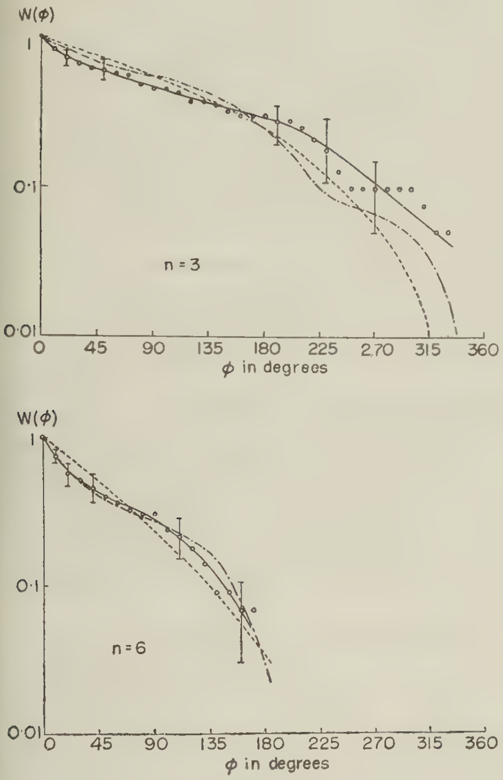

Fig. 8. Curves which shows the relation between

$$W(\phi)=\int_{\phi}^{2\pi}P(\phi)d\phi \Big/ \int_{0}^{2\pi}P(\phi)d\phi \text{ and } \phi.$$

(a): for interactions with 3 secondaries, (b) for interactions with 6 secondaries. Full line shows the experimental curve and dotted and dot-dashed curves show the curves obtained theoretically assuming the random and $\cos^2\psi$ distribution, respectively.

is very difficult, owing partly to the large statistical error and partly to the contribution of neutral secondary particles and effect of the momentum of secondary particles. But in interactions with six secondary particles, the observed curve is close to the curve expected from the $\cos^2\psi$ distribution. Any decisive conclusion is to be reserved in the present state of analysis. But considering the interpretation described in the preceding section that interactions with many secondary particles may undergo some secondary interactions, the $\cos^2\psi$ distribution may be due to the fact that a special secondary particle as a case of fluctuation collides with a nucleon in the same nucleus and produces some tertiary particles so that such particle may make some small angular separations ϕ in a special direction and the azimuthal angle distribution looks like $\cos^2\psi$ distribution as the result of the statistical accumulation of these cases along the present procedure of analysis. Nothing is concluded in the cases of nucleon-nucleon collisions, but these lines of analysis, perhaps, may be effective if data will be accumulated more.

Acknowledgment

The author wishes to express his sincere appreciation to Professor Yuzuru Watase for his very helpful discussions and advices. And he is also indebted to Mr. Y. Tanaka and Mr. S. Mitani for their skill and effort in construction of the equipment and co-operation in the course of the observation. Without their valuable assistances, this work could not be achieved. Also, the author is greatly indebted to Prof. I. Miura and Mr. G. Tanahashi who have informed their results before publication and gave valuable advices to the author, and to Prof. M. Oda who has read this article and given valuable criticism. This work was done when the author had been at Department of Physics, Faculty of Sience, Osaka University. And this work was partly financed by the Ministry of Education in Japan under the Fundamental Scientific Research Expenditure.

References

1) Y. Watase, K. Suga, Y. Tanaka and S. Mitani: Nuovo Cimento **II** (1955) 1183.
2) See the references of (1), R. W. Williams: Phys. Rev. **98** (1955) 1393.
3) M. M. Block et al: Phys. Rev. **103** (1956) 1484.
4) R. W. Wright, G. Saphir and W. M. Powell: B. A. P. S. **30**, No. 8 (1955) 18.
5) E. Brenner and R. W. Williams: B. A. P. S. **2** (1957) 53.
6) H. S. Snyder: Phys. Rev. **76** (1949) 1563.
7) K. Hinotani, K. Suga and Y. Tanaka: Jour. Phys. Soc. Japan **9** (1954) 883.
8) N. M. Dullar and W. D. Walker: Phys. Rev. **93** (1954) 215.
9) for example: W. L. Kraushaar and L. J. Marks: Phys. Rev. **93** (1954) 326.

JOURNAL OF THE PHYSICAL SOCIETY OF JAPAN Vol. 12, No. 11, NOVEMBER, 1957

Gamma Rays from the Excited States of ^{16}O

By Tetsuo WAKATSUKI, Yasuo HIRAO, Eiji OKADA
and Iwao MIURA

Department of Physics and the Laboratory of Nuclear Studies,
Faculty of Science, Osaka University, Osaka

(Received July 30, 1957)

By bombarding fluorine target with 5.7 MeV protons, a new gamma radiation of energy 3.86±0.02 MeV was observed with a three crystal pair spectrometer. This gamma radiation was proved to be emitted from 10.98 MeV (or 10.77 MeV) state in ^{16}O in the transition to 7.12 MeV (or 6.91 MeV) state by gamma-gamma coincidence experiments. No gamma radiation corresponding to the transitions from this state to other lower states in ^{16}O was observed. 0^- (or 3^+) was assigned to this state.

An 8.87 MeV gamma radiation corresponding to the direct transition to the ground state from the 2^- excited state in ^{16}O was observed.

A hard gamma radiation of about 11 MeV energy was found at proton energies between 4.8 and 5.7 MeV and was ascribed to the capture radiation in ^{19}F$(p\gamma)^{20}$Ne reaction.

A weak gamma radiation of about 4.9 MeV energy was also observed.

§ 1. Introduction

Excited states of ^{16}O have been the objects of many experimental and theoretical investigations. Experimentally, the excited states of ^{16}O were observed chiefly in ^{19}F$(p, \alpha)^{16}$O*1)2)3)7), ^{16}O$(p, p')^{16}$O*1)4), ^{16}O$(n, n')^{16}$O*5) and ^{15}N$(d, n)^{16}$O*1)6)7) reactions or observed as the compound nucleus levels in ^{12}C$(\alpha, \alpha)^{12}$C8), ^{15}N$(p, \alpha)^{12}$C1)9) and ^{15}N$(p, n)^{15}$O1)10) reactions.

Dennison11) and Kamney12) have calculated the excited states of ^{16}O using alpha particle model and showed good correspondence between the theory and experiments. According to Kamney, of the first nineteen excited states which are experimentally observed (0–12.95 MeV), fourteen are definitely predicted, two levels (11.10 and 12.95 MeV) are observed but not predicted and three levels (8.87, 11.08 and 12.02 MeV) are tentatively predicted but await experimental determination of spins and parities. (Identification (a) of reference (12)).

To the first of these three excited states (8.87 MeV), 2^- was assigned in accordance with theoretical prediction by Wilkinson, Toppel and Alburger2) in the investigation of the gamma rays from ^{19}F$(p, \alpha)^{16}$O* reaction at proton energy of 3.7 MeV.

The spins and parities for 11.08 and 12.02 MeV states predicted by Kamney's theory are 3^+ and 1^+ respectively. But there are no experimental evidences for such assignments.

As the protons of energy up to 5.7 MeV are obtainable with our newly built cyclotron13), we undertook an examination of the higher excited states of ^{16}O using the same reaction ^{19}F$(p, \alpha)^{16}$O* as the above experiment

§ 2. Experimental Methods

Molecular ion beam of hydrogen accelerated by Osaka University 44 inch cyclotron was focussed onto a target located at about meters from the cyclotron by a wedge type focussing magnet through concrete shield wal of 1.5 meter thickness. The energy of the proton was estimated to be 5.7±0.1 MeV from the measurements of the range in air and in nuclear emulsion. To vary the energy of the incident proton, aluminium absorbers of different thicknesses were imposed at about one meter in front of the target. The beam defining slit was made of a gold plate with a circular hole two millimeters in diameter in gamma-gamma cascade experiment, but the diameter was increased to one centimeter in most other cases. The proton current was varied with the problem in hand from a few thousandths of a microampere up to about 0.5 microampere.

Teflon or BaF$_2$ targets of a few mg/cm thickness were bombarded by protons and the gamma rays were observed with scintillatio spectrometers.

We have used single crystal spectrometers with Harshaw NaI(Tl) crystal 1½ inch in diameter and 1½ inch in length. In a later work, a larger crystal 3 inches in diameter and 3 inches in length was emplyed. We have also used a three crystal pair spectrometer[14] with center crystal 1 inch in diameter and 2 inches in length. The energy resolution of the three crystal spectrometer for 4.43 MeV gamma ray was about 6%.

The time resolution of the coincidence circuit in the three crystal pair spectrometer and in gamma-gamma coincidence work was 0.1 microsecond. In gamma-gamma coincidence work, the "fast-slow coincidence" technique was used. The pulses from one crystal which were in coincidence with selectively chosen gamma rays detected by the other crystal were analysed.

To avoid the back ground gamma rays, scintillation spectrometers were surrounded by lead blocks ten centimeters in thickness.

For the measurements of pulse height distribution, Atomic Instrument Company 20-channel pulse height analyzer was used. The calibrations of the energies were performed by 2.75 and 6.13 MeV gamma rays produced in $^{19}F(p, \alpha\gamma)^{16}O$ reaction[2] and 4.43 MeV gamma rays produced in $^{12}C(pp'\gamma)^{12}C$ reaction[1]. As the monochromatic 4.43 MeV gamma ray is produced with high intensity when polyethylene is bombarded by protons, this gamma ray was used frequently as the reference line in the determination of gamma ray energies.

§ 3. Results and Discussions

Fig. 1 and Fig. 2 show the gamma ray spectrums observed with the three crystal spectrometer placed at right angle to the proton beam when BaF_2 and teflon were bombarded by 5.7 MeV protons. In addition to the well known gamma rays of 6.13, 6.91 and 7.12 MeV energy from the excited states of ^{16}O[1], 1.76, 1.96, 2.75, 3.86 and 4.9 MeV gamma rays are observed. The first three of them were shown by Wilkinson et al.[2] to come from the 8.87 MeV excited states of ^{16}O. In Fig. 2, the deexcitation gamma rays from the first excited state of ^{12}C (4.43 MeV) are also observed.

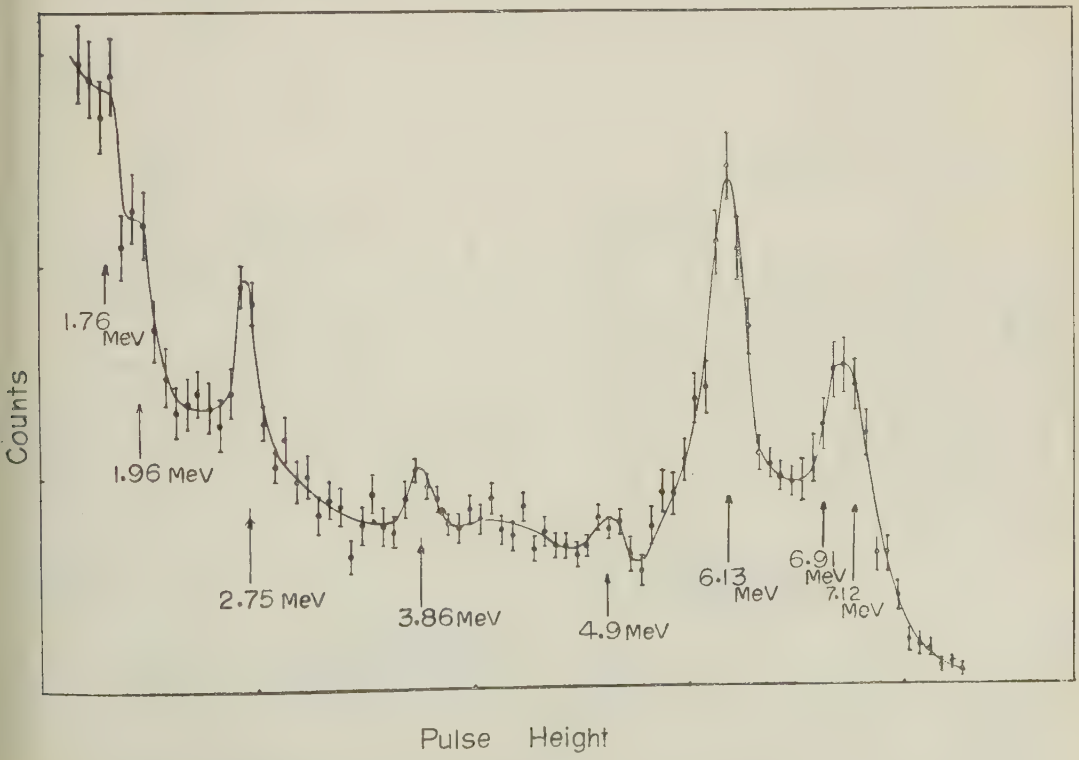

Fig. 1. Three-crystal pair spectrum; BaF_2+p at 5.7 MeV and 90° with respect to the proton beam.

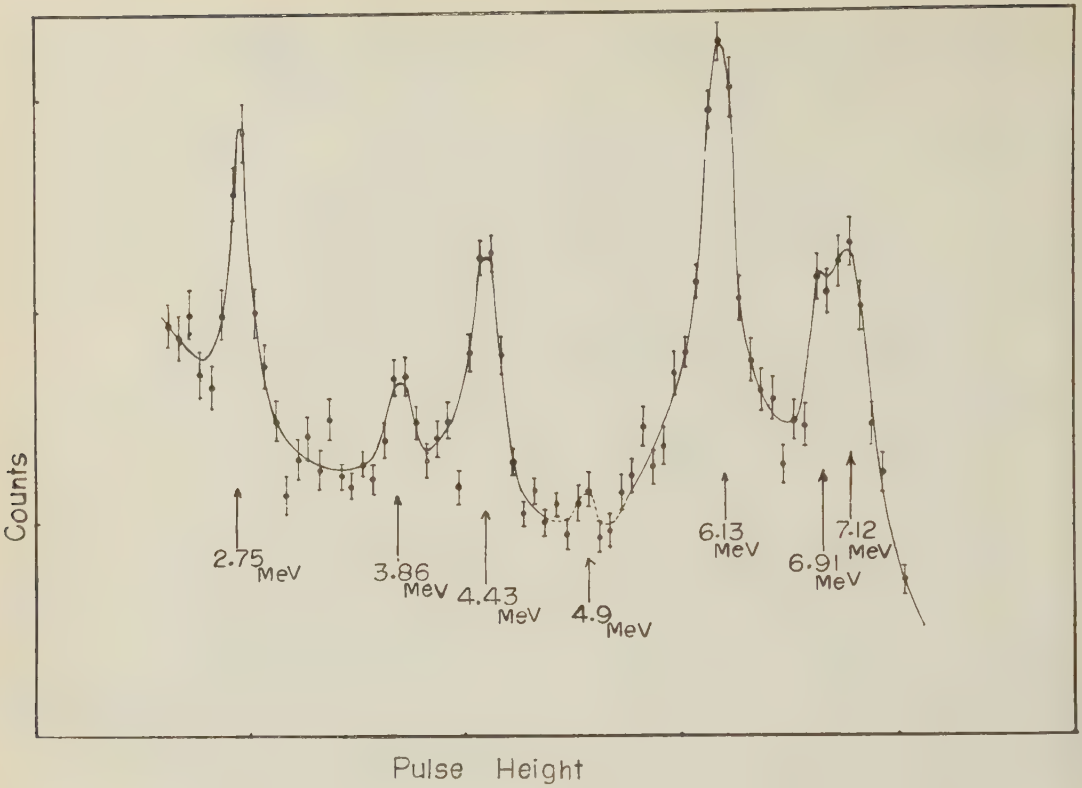

Fig. 2. Three-crystal pair spectrum; Teflon+p at 5.7 MeV and 90° with respect to the proton beam.

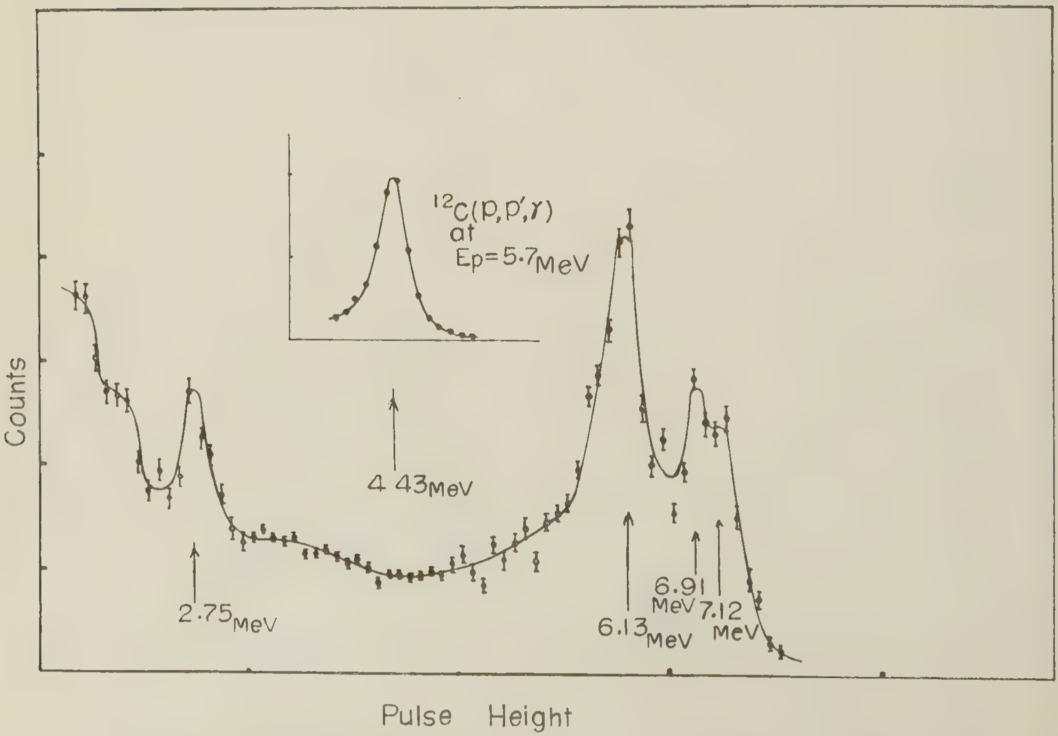

Fig. 3. Three crystal pair spectrum; Teflon+p at 4.8 MeV and 90° with respect to the proton beam.

Fig. 3 shows the gamma ray spectrum when he incident proton energy was lowered to .8 Mev. It is evident from Fig. 3 that new amma rays of 3.86 and 4.9 MeV disappeared t this energy while all the gamma rays of ther energies are still observed.

While the 4.9 MeV gamma ray was too veak to be investigated further, the intensity f 3.68 MeV gamma ray was enough for urther work.

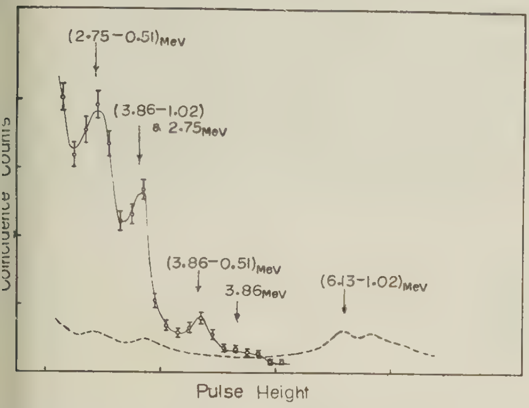

Fig. 4. Gamma ray spectrum in coincidence with gamma rays of energy larger than 4 MeV; BaF_2+p at 5.7 MeV and 90° with respect to the proton beam.

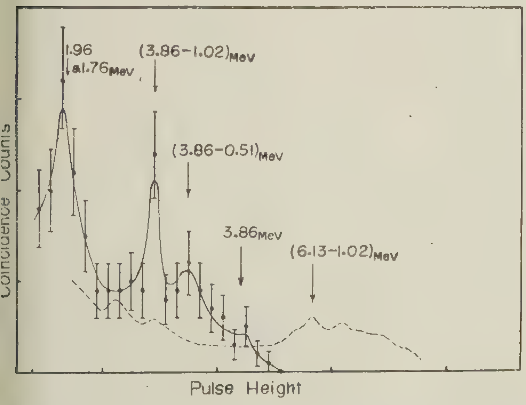

Fig. 5. Gamma ray spectrum in coincidence with gamma rays of energy larger than 6.3 MeV; BaF_2+p at 5.7 MeV and 90° with respect to the proton beam.

The energy measurement was made with he three crystal spectrometer and the value .86±0.02 MeV was obtained after the careful heck of the linearity between pulse heights nd gamma ray energies.

To investigate the origin of 3.86 MeV amma radiation, gamma-gamma coincidence experiments were performed with two NaI (T1) crystals each at 90° to the beam on each side of the target.

Fig. 4 and Fig. 5 are the gamma ray spectra in coincidence with gamma rays whose energies are greater than 4.0 MeV and 6.3 MeV respectively. The dotted line represents the upper limit of background counts calculated from surplus counts in the 20 channel analyser and the pulse height distribution in each single crystal spectrometer.

In identifying the energies to the peaks in Fig. 4 and Fig. 5, the knowledge of the pulse height distribution for monochromatic gamma ray for the same crystal is necessary. The pulse height distribution shown in Fig. 6 was obtained for the 4.43 MeV gamma ray under the same experimental conditions (1½ inch dia., 1½ inch length, NaI(T1)).

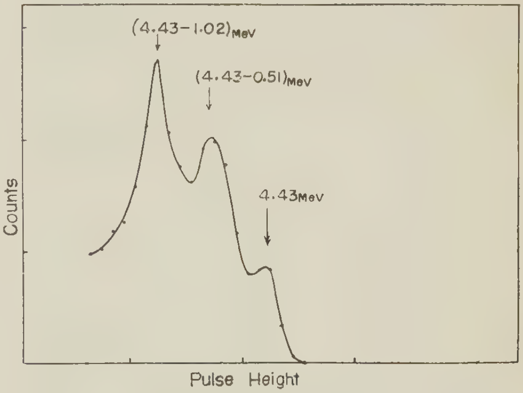

Fig. 6. Singles spectrum of 4.43 MeV gamma radiation.

From these results it is concluded that the 3.86 MeV gamma ray is emitted in cascade with the 7 MeV gamma ray (6.91 or 7.12 MeV) while the 2.75 MeV gamma ray is in cascade with the 6.13 MeV gamma ray. Therefore both of them are the deexcitation gamma rays from the excited states of ^{16}O at about 11 MeV (10.77 or 10.98 MeV) and 8.87 MeV respectively. The latter result with the 2.75 MeV gamma ray is in agreement with the work of Wilkinson et al.

If we assume that the 3.86 MeV gamma radiation originates from the 10.77 MeV state, transition to the 6.13 or 6.06 MeV state from this state will produce a gamma radiation of 4.64 or 4.71 MeV respectively. The gamma radiation corresponding to those energies was not observed and the intensity was estimated to be less than 1/10 of the 3.86 MeV radiation.

If we assume that the 3.86 MeV gamma radiation comes from the 10.98 MeV state, the energy of gamma radiation corresponding to the transition to 6.13 or 6.06 MeV will be 4.85 or 4.92 MeV respectively. The observed 4.9 MeV radiation just coincides with those energy and the intensity is about 1/4 of the 3.86 MeV radiation.

Next, a search for hard gamma radiations due to direct transitions from the 11 and 8.87 MeV states to the ground state was made using both single crystal and three crystal spectrometers.

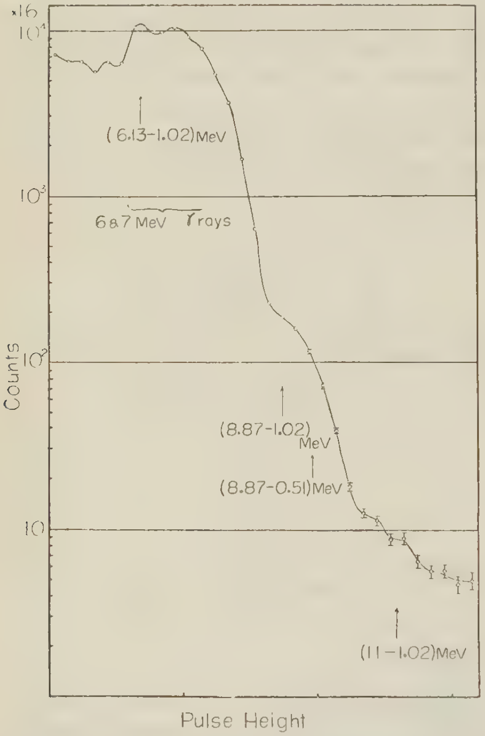

Fig. 7. Singles spectrum in search for hard gamma ray; F+*p* at 5.7 MeV and 90° with respect to the proton beam.

From the single crystal spectrum shown in Fig. 7, it is apparent that the 8.87 and 11 MeV gamma rays are emitted at E_p=5.7 MeV. The intensity of the 8.87 MeV radiation relative to the 2.75 MeV radiation was about 1/160 while that of the 11 MeV radiation relative to the 3.86 MeV radiation was found to be about 10^{-3} correcting for the efficiencies of scintillater for each gamma ray energies. At proton energy of 4.8 MeV (Fig. 8) both gamma rays are observed bu the intensity of the 11 MeV radiation relativ to the 6 and 7 MeV (joint intensity) gamm radiation increased considerably compared t the case of E_p=5.7 MeV.

Fig. 9 shows the excitation curves for th 6 and 7 MeV gamma radiations and the 1 MeV gamma radiation respectively in th proton energy region between 4.8 and 5. MeV.

The intensity of the 11 MeV radiation re lative to the 6 and 7 MeV radiations increase by a factor of 3.7 when the proton energy i lowered from 5.7 MeV to 4.8 MeV. If th 11 MeV radiation is the direct transitio gamma ray to the ground state, the 3.8 MeV peak in pulse height distribution shoul increase by the above ratio at proton energ of 4.8 MeV. As is evident from Fig. 3, th 3.86 MeV peak does not increase but disappears.

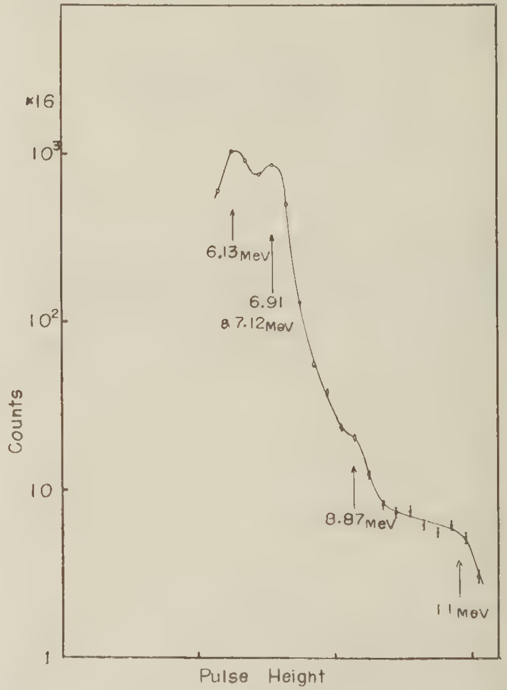

Fig. 8. Three crystal pair spectrum; F+*p* at 4.8 MeV and 90° with respect to the proto beam.

From this fact, it is concluded that th origin of the observed 11 MeV gamma radiation is different from that of the 3.86 Me radiation. Perhaps it is emitted from ^{20}N formed by the capture of proton by ^{19} nucles.

As to the 8.87 MeV radiation, its strength (M2) relative to the 2.75 MeV (M1) radiation would be predicted to be 1/90 by the use of Weisskopf's formula based on the single particle model if 2^- is assigned to the 8.87 MeV state[2]. The value obtained by our observation (1/160) does not conflict with the experimental upper limit 0.15 given by Wilkinson et al.[2], and is in good agreement with theoretical prediction, justifying the 2^- assignment to 8.87 MeV state.

We then tried to estimate the spin and parity of the 11 MeV state from the observed branching ratios of gamma radiations from this state.

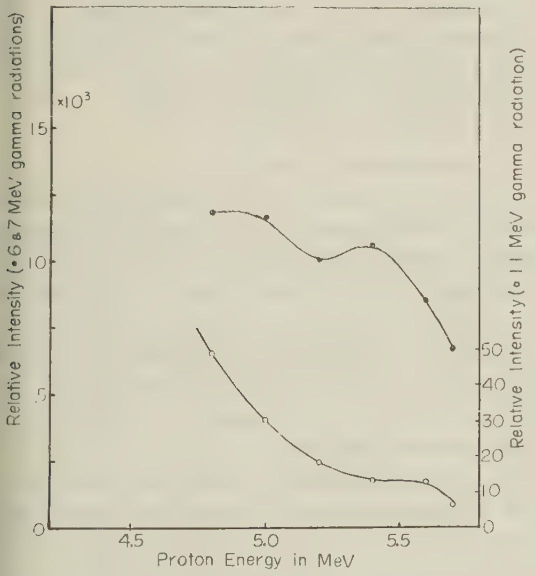

Fig. 9. Excitation curve for 6 and 7 MeV gamma radiations (upper curve) and 11 MeV gamma radiation (lower curve).

Since ^{16}O above an excitation of 7.15 MeV is energetically unstable against break up into ^{12}C in its O^+ ground state and an alpha particle, we have restricted ourselves to the examination of 0^-, 1^+, 2^-, 3^+ only.

We shall discuss exclusively by the use of the single particle formula as the calculation on transition probabilities based on the alpha particle model is not available for indivisual cases.

As the E1 transition is forbidden in ^{16}O by the isotopic spin selection rule and its inhibition factor amounts to a factor of 100 to 1000,[2] an inhibition factor 500 was assumed for E1 radiations.

We shall examine the indivisual case in the following: O^-: Assignment of O^- to the 11 MeV state results in ascribing the 3.86 MeV radiation as a M1 transition from the 10.98 MeV state to the 7.12 MeV (1^-) state. The ground state transition is forbidden, in accordance with experimental result. The intensity of the 4.85 MeV gamma radiation corresponding to the transition from the 10.98 MeV to 6.13 MeV (3^-) state is estimated to be 2×10^{-8} of the 3.86 MeV radiation. Therefore, though the observed gamma radiation of about 4.9 MeV is close to 4.84 MeV in energy, it must find another explanation on intensity consideration.

1^+: In this case the energy of the 11 MeV state must be 10.77 MeV as the transition probability from this state to the 6.91 MeV (2^+) state is estimated to be about 20 times larger than that to the 7.12 MeV (1^-) state. The direct transition to the ground state has larger probability than the transition to the 6.91 MeV state by a factor of 20, contrary to the experiment. Therefore 1^+ assignment is abandoned.

2^-: The transition probability from the 2^- 11 MeV state to the 7.12 MeV state is estimated to be 15 times larger than that to the 6.91 MeV state. The transition from the 10.98 MeV state to the 6.13 MeV (3^-) state is estimated to yield a 4.85 MeV gamma radiation with probability about 1/2 of the 3.86 MeV radiation. In this way the observed 4.9 MeV radiation can be explained. The intensity ratio of 10.98 MeV gamma radiation to 3.86 MeV radiation is calculated to be about 1/180. This is very large compared to the experimental upper limit of about 10^{-4}. Thus 2^- is also abandoned.

3^+: The 3.86 MeV gamma radiation is interpreted as a M1 radiation from the 10.77 MeV (3^+) state to the 6.91 MeV (2^-) state. The intensity of the 10.77 MeV radiation relative to the 3.86 MeV radiation is estimated to be about 10^{-5}, which is consistent with the experiment. The transition from the 10.77 MeV state to the 6.13 MeV (3^-) state will produce a 4.64 MeV radiation about 1/10 of the 3.86 MeV radiation in intensity. This value is not in contradiction with our observation. The transition probabilities from the 10.77 MeV (3^+) state were also calculated on the alpha particle model by R. Nakajima in our laboratory. His results show that the intensity ratio of 10.77 MeV radiation and 3.86 MeV radiation is about 1/70.

After all, the spin and parity for 11 MeV state deduced from the single particle model is either 0^- or 3^+. For the latter assignment, the calculation by the alpha particle model, however, gives too large probability for the transition from the 11 MeV state to the ground state as compared with the experiment.

Next we shall compare the energy for the excited state deduced from this experiment (10.98 MeV (0^-) or 10.77 MeV (3^+)) with the values obtained in other experiments.

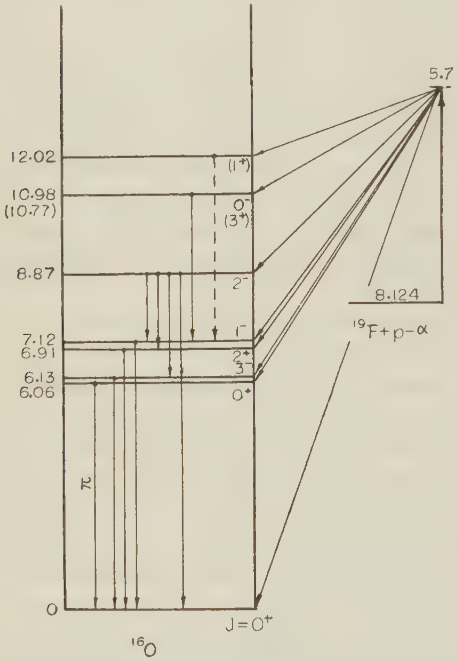

Fig. 10. Energy level diagram of ^{16}O up to 12.08 MeV.

Hornyak and Sherr[4)] observed an excited state of ^{16}O at 11.08 MeV by the analysis of protons inelastically scattered from ^{16}O. They have also confirmed that a gamma radiation is emitted from this state.

Squires, Bockelman and Bruechner[3)] obtained the value 11.085±0.0014 MeV corresponding to this state by precise magnetic analysis of alpha particles emitted in ^{19}F($p\alpha$)^{16}O reaction.

Of the two values 10.98 and 10.77 MeV, the former is more close to the above value, which is in favor of the assignment 0^-.

Recently Bent et al.[7)] in Columbia University report a 3.86 MeV gamma radiatio emitted in ^{19}F($p\alpha$)^{16}O* reaction as in our ex periment. The Columbia group[6)] also foun excited states of ^{16}O at 10.937±0.010 Me and 11.063±0.015 MeV from the study o ^{15}N(d, n)^{16}O reactions. The former value i more close to the value 10.98 MeV obtaine from the gamma ray experiment.

The excited states of ^{16}O relating to th present experiment are shown in Fig. 10.

Considering the above results, it is con cluded that the level at about 11 MeV is pro bably the 10.98 MeV 0^- state.

This conclusion, however, is not very ob jectionable to the alpha particle model, as th assignment 3^+ is in identification (a) i Kamney's article, and in identification (b) th the assignment of 0^- is suggested for th level at about 11.5 MeV.

§ 4. Conclusion

An excited state at 10.98 MeV (or 10.7 MeV) in ^{16}O emits a gamma radiation o 3.86±0.02 MeV energy in transition to th 7.12 MeV (or 6.91 MeV) state. No gamm radiation corresponding to the transition t other lower states was observed. The spi and parity for this state are probably 0^- (o 3^+). Of these two values, 0^- assignmen seems more probable.

A direct transition gamma radiation fro the 8.87 MeV state (2^-) in ^{16}O was observed Its intensity is consistent with single partic considerations.

A capture gamma ray of about 11 Me energy emitted from ^{20}Ne formed by th capture of proton by ^{19}F was observed in th proton energy interval between 4.8 and 5. MeV.

A weak gamma radiation about 4.9 MeV i energy was found and was tentatively as signed to the transition from 12.02 MeV t 7.12 MeV state in ^{16}O.

§ 5. Acknowledgments

The authors wish to thank Prof. S. Kiku chi for his kind interest in this work, an Prof. T. Toyoda, Mr. K. Sugimoto and Mr R. Nakajima for their discussions.

This work was supported by the Grant fo Scientific Research of the Ministry of Educa tion.

References

1) F. Ajzenberg and T. Lauritsen: Rev. Mod. Phys. **27** (1955) 134.
2) D. H. Wilkinson, B. J. Toppel and D. E. Alburger: Phys. Rev. **101** (1956) 673.
3) G. L. Squires, C. K. Bockelman and W. W. Bruechner: Phys. Rev. **104** (1956) 413.
4) W. F. Hornyak and R. Sherr: Phys. Rev. **100** (1955) 1409.
5) L. C. Thompson and J. R. Risser: Phys. Rev. **94** (1954) 941.
6) J. Weil, K. W. Jones, L. J. Lidofsky, H. Smotrich and J. Baicker: Bull. Am. Phys. Soc. II. **2** (1957) 52.
7) R. D. Bent, T. H. Kruse, L. J. Lidofsky and K. E. Eklund: Bull. Am. Phys. Soc. II. **2** (1957) 52.
8) J. W. Bittner and R. D. Moffat: Phys. Rev. **96** (1954) 374.
9) S. Bashkin and R. R. Carlson: Phys. Rev. **106** (1957) 261.
10) K. W. Jones, L. J. Lidofsky and J. Weil: Bull. Am. Phys. Soc. II. **2** (1957) 52.
11) D. M. Dennison: Phys. Rev. **57** (1940) 454, **96** (1954) 378.
12) S. L. Kamney: Phys. Rev. **103** (1956) 358.
13) S. Kikuchi et al.: Ann. Rep. Scient. Works, Fac. Sci. Osaka Univ. **3** (1955) 1.
14) I. Miura, Y. Hirao, E. Okada and T. Wakatsuki: Genshikaku-Kenkyu (in Japanese) **3** (1957) 76.

JOURNAL OF THE PHYSICAL SOCIETY OF JAPAN Vol. 12, No. 11, NOVEMBER, 1957

Theory of Excitations in Liquid Helium 4

By Fumihiko TAKANO

Physics Department, Tokyo University of Education, Tokyo

(Received June 1, 1957)

A modified "phonon-roton" model for liquid Helium II is proposed and is shown to be connected smoothly with the theory of Bose condensation. The method used is the direct extension of the method of "auxiliary variables" used by Bogolyubov and Zubarev, and is equivalent to that used by Bohm and Pines in the theory of the electron gas in metals. The phonon excitation is described in terms of the density operator, and the roton part by the so-called individual coordinates. The elimination of the kinematical interaction leads to the following model: The excitations for long wave length are described by phonons, and for short wave length by rotons, and the total number of excitations cannot exceed the total number of the particles. The thermal properties of this model is seen to agree with the experimental fact qualitatively.

§ 1. Introduction

The peculiar properties of liquid He^4 at very low temperatures have been one of the most interesting subjects in low temperature physics since their discovery. The phenomenological theory, usually called two fluid theory, has been very successful to explain these properties. In this theory, the liquid helium is assumed to be composed of two interpenetrating components. One has the properties which are same in all respects as those of the usual liquids and is called the normal fluid part. The other is called the superfluid part and has quite different properties from the normal part.

The derivation of this two-fluid model from the first principle and the explanation of the λ-transition are very interesting subjects for theoretical physicists. The first proposal was due to London$^{1)}$, who noted that the He^4 atoms obeyed Bose statistics and the ideal He^4 gas with the density of the liquid underwent the Bose condensation at the temperature very near to the λ-point of real liquid He^4. Then, Tisza$^{2)}$, proposed the idea that, below this Bose condensation temperature, the particles in the lowest energy level were the superfluid part of the liquid helium and the remainder were the normal fluid part. Although these theories are based upon the ideal gas model, the explanation of λ-transition in terms of Bose condensation is supposed to be true and supported by the fact that the isotope He^3 obeying Fermi statistics does not exhibit any such transition. Recently, Penrose and Onsager[3] showed that "there exists Bose condensation" in liquid He^4 at 0°K by only assuming the absence of the long range order, and at finite temperatures using the Feynman's expression[4] for the partition function.

On the other hand, Landau[5] proposed a quite different point of view. His idea is that the excitations in liquid He^4 are essentially different from those in the ideal gas, and consist of the so-called "phonons" and "rotons" with the following spectrum,

$$\mathcal{E}(k)=\begin{cases}\hbar ck\,, & \text{for phonons,}\\ \Delta+\dfrac{\hbar^2}{2\mu}(k-k_0)^2\,, & \text{for rotons.}\end{cases} \tag{1.1}$$

By choosing appropriate values of the adjusting parameters Δ, μ and k_0, he succeeded to explain various properties of liquid helium. In this theory, the normal fluid density ρ_n is calculated from the inertia of the excitations and the superfluid density ρ_s is equated to $\rho_0-\rho_n$ (ρ_0 is the density of the liquid helium). The λ-point is defined as the temperature at which $\rho_n=\rho_0$, $\rho_s=0$. But nothing can be said about the transition.

Since then, many authors have tried to derive this "phonon-roton" model from the first principle or to revise the Landau's idea by quantizing the classical hydrodynamics in a similar way as in the case of the quantum electrodynamics (quantum hydrodynamics[6]). Although these authors succeeded in some respects, it does not seem that any of them succeeded to explain the presence of the phase transition.

As mentioned above, it is perhaps certain that the transition is due to the Bose statistics. Brenig[7] proposed the model in which the number of rotons was restricted and the Bose condensation could occur. However, his model does not seem to have a concrete basis. It is one of the purposes of this paper to connect the phonon-roton model with the Bose condensation theory more smoothly.

The other purpose of this paper is to write down the interactions among excitations explicitly. This is necessary, for example, for the calculation of the viscosity coefficient This is done by Usui and Matsudaira[8], wh adopted the procedure used by Dyson[9] in hi theory of spin wave interactions in ferromagnets, and took $b_k^+=\frac{1}{\sqrt{N}}c_k^+c_0$ as the creation operator of the excitation with wave numbe k, where c_k, c_k^+ are usual operators whic annihilate and creat the particle with momentum $\hbar k$, respectively. However, their Hamiltonian, although rigorous, contains interactio terms up to sixth power of b_k or b_k^+, and s is very inconvenient to deal with. This show that their choice of b_k^+ was inadequate.

Many authors took the density operator

$$\rho_k=\frac{1}{\sqrt{N}}\sum_{j=1}^{N}e^{ikx_j}=\frac{1}{\sqrt{N}}\sum_{K}c_{K+k}^{+}c_K \qquad (1\,2$$

as the variables describing phonons. For rotons, however, it is not clear what coordinat is to be taken. For Bose systems, it is no impossible to describe all the excitations i terms of ρ_k's only. But it seems that ρ_k' are variables not so appropriate to short wav length excitations (rotons) as they are to lon wave length excitations (phonons). We consider the roton excitations as particle-like Then the problem reduces to one of the collective descriptions in which the collectiv coordinate corresponds to phonons and th individual one to rotons. Nishiyama[10] an Brenig[7] attempted to derive the phonon-roto spectrum (1.1) using the method of Tomonaga[11]. However, since the Hamiltonian cannot be written in a closed form by the metho of Tomonaga, we resort to a different method which is a direct extension of the method o the "auxiliary variables" used by Bogolyubo and Zubarev[12]. The Hamiltonian obtained i equivalent to the one which Bohm and Pines[13] used in the case of the electron gas in metals

The elimination of what Dyson calls th "kinematical interaction" leads to the following model: The excitations are composed o two parts. For long wave length the excitations are described by ρ_k's (phonons) and fo short wave length the excitations are particle-like (rotons). Moreover, the total number o the excitations cannot exceed the total numbe of particles, leading to the Bose condensatio of second order. Thus the two purposes mentioned above can be achieved.

§ 2. Hamiltonian

As was mentioned in § 1, we take $\rho_{\boldsymbol{k}}$'s, Eq. (1.2), as the variables describing the phonon excitations and the individual coordinates $\boldsymbol{x}_j$'s as the roton excitations. The Hamiltonian which describes the motions of these $\rho_{\boldsymbol{k}}$'s as well as $\boldsymbol{x}_j$'s is constructed in the following way. The method is an extension of that used by Bogolyubov and Zubarev[12], and is applicable for the variables other than $\rho_{\boldsymbol{k}}$'s, but here, for simplicity, we treat only the case of $\rho_{\boldsymbol{k}}$'s. As was mentioned in § 1, $\rho_{\boldsymbol{k}}$'s are good variables for small k, but for large k they are no longer supposed to be good. So we restrict $\rho_{\boldsymbol{k}}$'s only for $|\boldsymbol{k}| \leq k_c$, k_c being determined later.

The Hamiltonian for the system of N identical particles with the mass m is written as

$$H = -\frac{\hbar^2}{2m}\sum_{j=1}^{N}\Delta_j + \frac{1}{2}\sum_{i \neq j}\sum G(r_{ij}) = T + G\ , \tag{2.1}$$

where Δ_j is the Laplacian operator for the j-h particle, and $G(r)$ is the interaction energy between two particles with mutual distance r. f we expand $G(r)$ in Fourier series*

$$G(r) = \frac{1}{V}\sum_{\boldsymbol{k}} G(k) e^{i\boldsymbol{k}\boldsymbol{r}}\ , \quad G(k) = \int G(r)\, e^{-i\boldsymbol{k}\boldsymbol{r}} d\boldsymbol{r}\ , \tag{2.2}$$

then the interaction part G of Eq. (2.1) becomes

$$\begin{aligned} G = {} & \frac{N}{2V}\sum_{0<|\boldsymbol{k}|\leq k_c} G(k)\rho_{\boldsymbol{k}}\rho_{-\boldsymbol{k}} - \frac{N}{2V}\sum_{0<|\boldsymbol{k}|\leq k_c} G(k) \\ & + \frac{1}{2V}\sum_{i \neq j}\sum_{k_c<|\boldsymbol{k}|} G(k)\, e^{i\boldsymbol{k}(\boldsymbol{x}_i-\boldsymbol{x}_j)} + \frac{N^2}{2V} G(0)\ . \end{aligned} \tag{2.3}$$

The kinetic energy T of Eq. (2.1) is written down as follows. We consider that the wave unction Ψ includes $\rho_{\boldsymbol{k}}$'s as well as the particle coordinates $\boldsymbol{x}_j$'s. Then the differential operator in T is written as

$$\begin{aligned} \frac{\partial\Psi}{\partial\boldsymbol{x}_j} & = \left(\frac{\partial\Psi}{\partial\boldsymbol{x}_j}\right)_\rho + \sum_{0<|\boldsymbol{k}|\leq k_c}\frac{\partial\rho_{\boldsymbol{k}}}{\partial\boldsymbol{x}_j}\left(\frac{\partial\Psi}{\partial\rho_{\boldsymbol{k}}}\right)_x \\ & = \left(\frac{\partial\Psi}{\partial\boldsymbol{x}_j}\right)_\rho + \frac{1}{\sqrt{N}}\sum_{0<|\boldsymbol{k}|\leq k_c} i\boldsymbol{k}\, e^{i\boldsymbol{k}\boldsymbol{x}_j}\left(\frac{\partial\Psi}{\partial\rho_{\boldsymbol{k}}}\right)_x \end{aligned} \tag{2.4}$$

$$\begin{aligned} \frac{\partial^2\Psi}{\partial\boldsymbol{x}_j^2} = {} & \left(\frac{\partial^2\Psi}{\partial\boldsymbol{x}_j^2}\right)_\rho + \frac{2}{\sqrt{N}}\sum_{0<|\boldsymbol{k}|\leq k_c} i\boldsymbol{k}\, e^{i\boldsymbol{k}\boldsymbol{x}_j}\frac{\partial^2\Psi}{\partial\boldsymbol{x}_j\partial\rho_{\boldsymbol{k}}} \\ & - \frac{1}{\sqrt{N}}\sum_{0<|\boldsymbol{k}|\leq k_c}\boldsymbol{k}^2\, e^{i\boldsymbol{k}\boldsymbol{x}_j}\frac{\partial\Psi}{\partial\rho_{\boldsymbol{k}}} \\ & - \frac{1}{\sqrt{N}}\sum_{0<|\boldsymbol{k}|,\,|\boldsymbol{k}|\leq k_c}\sum (\boldsymbol{k}\cdot\boldsymbol{k}')\, e^{i(\boldsymbol{k}+\boldsymbol{k})\boldsymbol{x}_j}\frac{\partial^2\Psi}{\partial\rho_{\boldsymbol{k}}\partial\rho_{\boldsymbol{k}'}}\ . \end{aligned} \tag{2.5}$$

Summing both sides of Eq. (2.5) over j, and considering $\rho_{\boldsymbol{k}}$'s as independent variables, the kinetic energy T can be written as

$$\begin{aligned} T = {} & \frac{1}{2m}\sum_{j=1}^{N}\boldsymbol{p}_j^2 \\ & + \frac{1}{\sqrt{N}}\sum_{j=1}^{N}\sum_{0<|\boldsymbol{k}|\leq k_c} e^{i\boldsymbol{k}\boldsymbol{x}_j}\frac{\hbar\boldsymbol{k}}{2m}\cdot\boldsymbol{p}_j\frac{\partial}{\partial\rho_{\boldsymbol{k}}} \\ & + \sum_{0<|\boldsymbol{k}|\leq k_c}\frac{\hbar^2 k^2}{2m}\rho_{\boldsymbol{k}}\frac{\partial}{\partial\rho_{\boldsymbol{k}}} \\ & + \frac{1}{\sqrt{N}}\sum_{\substack{0<|\boldsymbol{k}|,\,|\boldsymbol{k}'|\leq k_c \\ 0<|\boldsymbol{k}+\boldsymbol{k}'|\leq k_c}}\sum\frac{\hbar^2(\boldsymbol{k}\cdot\boldsymbol{k}')}{2m}\rho_{\boldsymbol{k}+\boldsymbol{k}'}\frac{\partial^2}{\partial\rho_{\boldsymbol{k}}\partial\rho_{\boldsymbol{k}'}} \\ & - \sum_{0<|\boldsymbol{k}|\leq k_c}\frac{\hbar^2 k^2}{2m}\frac{\partial^2}{\partial\rho_{\boldsymbol{k}}\partial\rho_{-\boldsymbol{k}}} \\ & + \frac{1}{N}\sum_{j=1}^{N}\sum_{\substack{0<|\boldsymbol{k}|,\,|\boldsymbol{k}'|\leq k_c \\ k_c<|\boldsymbol{k}+\boldsymbol{k}'|}}\sum\frac{\hbar^2(\boldsymbol{k}\cdot\boldsymbol{k}')}{2m}e^{i(\boldsymbol{k}+\boldsymbol{k}')\boldsymbol{x}_j}\frac{\partial^2}{\partial\rho_{\boldsymbol{k}}\partial\rho_{\boldsymbol{k}'}}\ . \end{aligned} \tag{2.6}$$

Thus, the total Hamiltonian can be written as

$$\mathscr{H} = \mathscr{H}_{\text{col.}} + \mathscr{H}_{\text{ind.}} + \mathscr{H}_{\text{int.}}\ , \tag{2.7}$$

where the collective part $\mathscr{H}_{\text{col.}}$ is

$$\begin{aligned} \mathscr{H}_{\text{col.}} = {} & \sum_{0<|\boldsymbol{k}|\leq k_c}\left\{-\frac{\hbar^2 k^2}{2m}\frac{\partial^2}{\partial\rho_{\boldsymbol{k}}\partial\rho_{-\boldsymbol{k}}} + \frac{N}{2V}G(k)\rho_{\boldsymbol{k}}\rho_{-\boldsymbol{k}}\right\} \\ & + \frac{1}{\sqrt{N}}\sum_{\substack{0<|\boldsymbol{k}|,\,|\boldsymbol{k}'|\leq k_c \\ 0<|\boldsymbol{k}+\boldsymbol{k}'|\leq k_c}}\sum\frac{\hbar^2(\boldsymbol{k}\cdot\boldsymbol{k}')}{2m}\rho_{\boldsymbol{k}+\boldsymbol{k}'}\frac{\partial^2}{\partial\rho_{\boldsymbol{k}}\partial\rho_{\boldsymbol{k}'}} \\ & - \frac{N}{2V}\sum_{0<|\boldsymbol{k}|\leq k_c} G(k) + \frac{N^2}{2V}G(0)\ , \end{aligned} \tag{2.7a}$$

and the individual part $\mathscr{H}_{\text{ind.}}$ is

$$\begin{aligned} \mathscr{H}_{\text{ind.}} = {} & \frac{1}{2m}\sum_{j=1}^{N}\boldsymbol{p}_j^2 \\ & + \frac{1}{2V}\sum_{i \neq j}\sum\sum_{k_c<|\boldsymbol{k}|} G(k)\, e^{i\boldsymbol{k}(\boldsymbol{x}_i-\boldsymbol{x}_j)}\ , \end{aligned} \tag{2.7b}$$

and the interaction part $\mathscr{H}_{\text{int.}}$ is

$$\begin{aligned} \mathscr{H}_{\text{int.}} = {} & \frac{1}{\sqrt{N}}\sum_{j=1}^{N}\sum_{0<|\boldsymbol{k}|\leq k_c}\frac{\hbar\boldsymbol{k}}{2m}(e^{i\boldsymbol{k}\boldsymbol{x}_j}\boldsymbol{p}_j + \boldsymbol{p}_j e^{i\boldsymbol{k}\boldsymbol{x}_j})\frac{\partial}{\partial\rho_{\boldsymbol{k}}} \\ & + \frac{1}{N}\sum_{j=1}^{N}\sum_{\substack{0<|\boldsymbol{k}|,\,|\boldsymbol{k}'|\leq k_c \\ k_c<|\boldsymbol{k}+\boldsymbol{k}'|}}\sum\frac{\hbar^2(\boldsymbol{k}\cdot\boldsymbol{k}')}{2m}e^{i(\boldsymbol{k}+\boldsymbol{k}')\boldsymbol{x}_j}\frac{\partial^2}{\partial\rho_{\boldsymbol{k}}\partial\rho_{\boldsymbol{k}'}}\ . \end{aligned} \tag{2.7c}$$

---

* Actually, this Fourier expansion is not pos-ible due to the presence of the strong repulsive nteraction of short range between Helium atoms. Here, we neglect this fact temporarily, and shall iscuss this problem in § 6.

If we set $\boldsymbol{p}_j=0$ for all j, that is, if the wave function does not contain $\boldsymbol{x}_j$'s explicitly (this is allowed only for Bose systems), and put $k_c\to\infty$, then the Hamiltonian $\mathscr{H}$ is reduced to that used by Bogolyubov and Zubarev[12], who attempted to describe the motion of the system only in terms of the density $\rho_{\boldsymbol{k}}$. In this case, $\mathscr{H}_{\text{ind.}}=0$, and the second term in $\mathscr{H}_{\text{int.}}$ vanishes and the first term reduces to the form $\sum_{\boldsymbol{k}}\dfrac{\hbar^2k^2}{2m}\rho_k\dfrac{\partial}{\partial\rho_k}$, which makes the Hamiltonian of Bogolyubov and Zubarev non-Hermitian*. Here, we adopt the form of Eq. (2.7c) in order to keep the Hermitian property of our Hamiltonian.

Moreover, the Hamiltonian (2.7) is equivalent to that used by Bohm and Pines[13], as is easily seen when we set

$$\rho_k=\frac{-ik}{\sqrt{4\pi Ne}}p_k\,,\qquad \frac{\partial}{\partial\rho_k}=\frac{\sqrt{4\pi N}}{\hbar k}eq_k\,.$$

That is to say, the method of Bogolyubov and Zubarev is a special case of Bohm and Pines.

The second term of Eq. (2.7a) is considered to be small by Bohm and Pines[13] by the random phase approximation, and is completely neglected by Brenig[7], who assumes the orthogonality of $\rho_{\boldsymbol{k}}$'s. But since the number of the modes considered is very large, this term cannot completely be neglected. For, even if the error resulting from this assumption is of the order of $1/\sqrt{N}$ for each mode, the total error for all modes is very large. In fact, this term represents the interactions among phonons, and is necessary for the calculation of the viscosity coefficient.

The Hamiltonian $\mathscr{H}$, Eq. (2.7), contains excess number of independent variables. Usually, this is avoided by setting the subsidiary conditions

$$\rho_k-\frac{1}{\sqrt{N}}\sum_{j=1}^{N}e^{i\boldsymbol{k}\boldsymbol{x}_j}=0\,,\qquad 0<|\boldsymbol{k}|\leqslant k_c\,. \tag{2.8}$$

However, this method is too formal and inconvenient to deal with. It is very difficul to find the wave functions satisfying thes conditions (2.8), and, in fact, such wave func tions have never been found in literatures The problem how to avoid this excess of th independent variables corresponds to wha Dyson[9] calls the "kinematical interactions. To eliminate this kinematical interactions w do not use the subsidiary conditions (2.8), bu use a quite different method, which will b discussed in § 4.

§ 3. Energy Spectrum

To obtain the energy spectrum of the ex citation, we must diagonalize the Hamiltonian First, we consider the collective part $\mathscr{H}_{\text{col.}}$ (2.7a), which is separated into two parts,

$$\mathscr{H}_{\text{col.}}=\mathscr{H}_{\text{phon.}}+\mathscr{H}'\,, \qquad (3.$$

where

$$\begin{aligned}\mathscr{H}_{\text{phon.}}=\sum_{0<|\boldsymbol{k}|\leq k_c}&\left\{-\frac{\hbar^2k^2}{2m}\frac{\partial^2}{\partial\rho_k\partial\rho_{-k}}\right.\\&\left.+\frac{N}{2V}G(k)\rho_k\rho_{-k}\right\}\\&-\frac{N}{2V}\sum_{0<|\boldsymbol{k}|\leq k_c}G(k)+\frac{N^2}{2V}G(0)\end{aligned} \qquad (3.1$$

is the phonon energy, and

$$\mathscr{H}'=\frac{1}{\sqrt{N}}\sum_{\substack{0<|\boldsymbol{k}|,|\boldsymbol{k}'|\leq k_c\\0<|\boldsymbol{k}+\boldsymbol{k}'|<k_c}}\sum\frac{\hbar^2(\boldsymbol{k}\cdot\boldsymbol{k}')}{2m}\rho_{\boldsymbol{k}+\boldsymbol{k}'}\frac{\partial^2}{\partial\rho_k\partial\rho_{k'}} \qquad (3.1$$

is the interaction energy among phonons, was mentioned above. Now, we introduce th annihibilation and creation operator b_k, b_k^+ phonons as follows

$$\left.\begin{aligned}\rho_k&=\sqrt{\frac{T(k)}{E(k)}}(b_k^{\,+}+b_{-k})\,,\\\frac{\partial}{\partial\rho_k}&=\frac{1}{2}\sqrt{\frac{E(k)}{T(k)}}(b_k-b^+_{-k})\,,\end{aligned}\right\} \qquad (3.$$

where b_k, b_k^+ satisfy the commutation relati

$$[b_k,b^+_{k'}]=\delta_{k,k'}\,, \qquad (3.$$

and

$$\left.\begin{aligned}T(k)&=\frac{\hbar^2k^2}{2m}\,,\\E(k)&=2\left[T(k)\frac{N}{2V}G(k)\right]^{1/2}.\end{aligned}\right\} \qquad (3.$$

Then, $\mathscr{H}_{\text{phon.}}$, (3.1a) becomes immediately

---

* When we set $\boldsymbol{p}_j=0$ and the number of ρ_k's is equal to $3N$, our transformation of the Hamiltonian can be considered as the transformation of variables from $\boldsymbol{x}_j$'s to ρ_k's. Then, if we take into consideration the Jacobian of this transformation, the transformed Hamiltonian must remain Hermitian. But since ρ_k's are treated as independent variables, the Hamiltonian of Bogolyubov and Zubarev seems to be non-Hermitian.

$$\mathscr{H}_{\text{phon.}} = \sum_{0<|\boldsymbol{k}|\leq k_c} \left\{ \frac{1}{2} E(k)(b_{\boldsymbol{k}}^{+}b_{\boldsymbol{k}} + b_{\boldsymbol{k}}b_{\boldsymbol{k}}^{+}) - \frac{N}{2V} G(k) \right\} + \frac{N^2}{2V} G(0) . \tag{3.5}$$

Thus, the phonon energy is given by $E(k)$, Eq. (3.4). For small values of k, $E(k)$ is proportional to k,

$$E(k) \simeq \hbar \sqrt{\frac{NG(0)}{mV}}\, k , \qquad \text{for small } k, \tag{3.6}$$

as can be expected. For finite k, strictly speaking, $E(k)$ deviates from linearity to k and show the dispersion.

Using the transformation (3.2), the interaction term $\mathscr{H}'$ can be written as

$$\mathscr{H}' = \frac{1}{\sqrt{N}} \sum_{\substack{0<|\boldsymbol{k}|,|\boldsymbol{k}'|\leq k_c \\ 0<|\boldsymbol{k}+\boldsymbol{k}'|\leq k_c}} \sum \frac{\hbar^2(\boldsymbol{k}\cdot\boldsymbol{k}')}{2m} \frac{\lambda_{|\boldsymbol{k}+\boldsymbol{k}'|}}{\lambda_k \lambda_{k'}} \times \{ b_{\boldsymbol{k}+\boldsymbol{k}'}^{+} b_{-\boldsymbol{k}}^{+} b_{-\boldsymbol{k}'}^{+} + b_{\boldsymbol{k}+\boldsymbol{k}'}^{+} b_{\boldsymbol{k}} b_{\boldsymbol{k}'} - 2 b_{\boldsymbol{k}+\boldsymbol{k}'}^{+} b_{-\boldsymbol{k}}^{+} b_{\boldsymbol{k}'} + \text{c.c.} \} , \tag{3.7}$$

where

$$\lambda_k = [T(k)/E(k)]^{1/2} ,$$

and c.c. represents the operators conjugate to the preceding ones.

On the other hand, $\mathscr{H}_{\text{ind.}}$ has the form

(kinetic energy)+(short range interactions).

As was suggested by Feynman⁴⁾, the excited states of such a system have a wave function of the form

(the permanent of the plane waves)
×(the ground state wave function),

and the excitation energy can be given approximately as

$$\mathcal{E}(k) = \frac{\hbar^2 k^2}{2m^*} , \tag{3.8}$$

where m^* is the effective mass.

Substitution Eq. (3.2) into Eq. (2.7c), leads to

$$\mathscr{H}_{\text{int.}} = \frac{1}{\sqrt{N}} \sum_{j=1}^{N} \sum_{0<|\boldsymbol{k}|\leq k_c} \frac{\hbar \boldsymbol{k}}{2m} \cdot (e^{i\boldsymbol{k}\boldsymbol{x}_j} \boldsymbol{p}_j + \boldsymbol{p}_j e^{i\boldsymbol{k}\boldsymbol{x}_j}) \frac{1}{2\lambda_{\boldsymbol{k}}} (b_{\boldsymbol{k}} - b_{-\boldsymbol{k}}^{+}) + \frac{1}{N} \sum_{j=1}^{N} \sum_{\substack{0<|\boldsymbol{k}|,|\boldsymbol{k}'|\leq k_c \\ k_c<|\boldsymbol{k}+\boldsymbol{k}'|}} \sum \frac{\hbar^2(\boldsymbol{k}\cdot\boldsymbol{k}')}{2m} e^{i(\boldsymbol{k}+\boldsymbol{k}')\boldsymbol{x}_j} \frac{1}{4\lambda_k \lambda_{k'}} \times (b_{-\boldsymbol{k}}^{+} b_{-\boldsymbol{k}'}^{+} - 2 b_{-\boldsymbol{k}}^{+} b_{\boldsymbol{k}'} + b_{\boldsymbol{k}} b_{\boldsymbol{k}'}) . \tag{3.9}$$

Thus, the interactions among various excitations can be written down explicitly. Eq. (3.7) represents the interaction between phonons, and Eq. (3.9) between phonons and rotons. The interactions between rotons are included in $\mathscr{H}_{\text{ind.}}$.

§ 4. Kinematical Interactions

As was mentioned in § 2, our Hamiltonian $\mathscr{H}$ involves excess degrees of freedom. Usually, this excess freedom is avoided by the subsidiary conditions (2.8), which is too formal and inconvenient. Here we use another procedure which is generally applicable to Bose systems.

The basic idea is the following: We consider the Hilbert space which consists of the wave functions which contain $\boldsymbol{x}_j$'s and ρ_k's as independent variables and call this space U. An element of this U-space will be denoted as $|\alpha)$. The Hamiltonian $\mathscr{H}$, Eq. (2.7), is an operator in this U-space. On the other hand, let the Hilbert space which consists of the wave functions which contain $\boldsymbol{x}_j$'s only as independent variables be V, an element of which will be written as $|\alpha\rangle$. The original Hamiltonian H, Eq. (2.1), is an operator in this V-space.

Then we can define an operator P which operates on $|\alpha)$ in U-space and puts it into a state $|\alpha\rangle$ in V-space

$$P|\alpha) = |\alpha\rangle . \tag{4.1}$$

To write down this operation explicitly, we may proceed as follows,

$$P\varphi(\boldsymbol{x}_j;\ \rho_k) = \varphi(\boldsymbol{x}_j;\ \rho_k(\boldsymbol{x}_j)) . \tag{4.2}$$

The meaning of this equation is as follows: When we operate P on any function φ which contains ρ_k's as independent variables, then ρ_k's in $P\varphi$ are no longer regarded as independent variables, and so $P\varphi$ depends on $\boldsymbol{x}_j$'s through ρ_k's as well as explicitly.

Now we take the sub-space U_1 of U-space which has the following property: From complete orthonormal set of functions $|\alpha_1)$, $|\alpha_2)$, $\cdots$ in this sub-space U_1 we can get the set of the functions in V-space, $P|\alpha_1) \equiv |\alpha_1\rangle$, $P|\alpha_2) \equiv |\alpha_2\rangle \cdots$. If we choose U_1 properly, then $|\alpha_1\rangle, |\alpha_2\rangle, \cdots$ can be made linearly independent of each other and, moreover, form a complete set in V-space. That is, any function $|\,\rangle$ in V-space can be expanced in terms of these $|\alpha_j\rangle$'s,

$$|\,\rangle = \sum_j |\alpha_j\rangle c_j \tag{4.3}$$

the coefficients c_j's being determined uniquely.

These $|\alpha_j\rangle$'s are not always normalized and orthogonal to each other, since $\langle\alpha_i|\alpha_j\rangle=(\alpha_i|P|\alpha_j)$ is not always equal to δ_{ij}.

Now let us consider the eigenvalue problem and also the calculation of the trace in V-space in terms of this non-orthogonal set. The result is very simple as shown in the following: For any operator A in V-space, we can write

$$A|\alpha_i\rangle=\sum_j|\alpha_j\rangle A_{ji}\,. \tag{4.4}$$

This is possible because of the completeness of the set $|\alpha_j\rangle$. We can not, however, set $A_{ji}=\langle\alpha_i|A|\alpha_i\rangle$, because $|\alpha_i\rangle$'s are not orthonormal.

Using the coefficients A_{ji}'s in Eq. (4.4), we can write down the secular equation determining eigenvalue a of A as follows,

$$|A_{ji}-a\delta_{ji}|=0\,, \tag{4.5}$$

and the trace of A can be calculated

$$\mathrm{Tr}\,A=\sum_i A_{ii}\,. \tag{4.6}$$

Eqs. (4.5) and (4.6) are obvious because A_{ji} can be considered as a matrix representation of the operator A.

Next let us define the operator $\mathfrak{A}$ in U-space corresponding to the physical observable A in V-space in the following way

$$P\mathfrak{A}=AP\,. \tag{4.7}$$

This procedure is equivalent to that used by Dyson[9)] to construct the operator in the "ideal" space from that in the original space.

That our Hamiltonian $\mathscr{H}$, Eq. (2.7), satisfies the relation (4.7) is seen as follows: The operator A is a function of the particle coordinates $\boldsymbol{x}_j$'s and momenta $\boldsymbol{p}_j$'s. From the relation (4.7) we get

$$P\mathfrak{A}\mathfrak{B}=ABP\,,$$

meaning that if $\mathfrak{A}$ corresponds to A, and $\mathfrak{B}$ to B, then the operator corresponding to AB is $\mathfrak{A}\mathfrak{B}$. Thus it is sufficient to construct the operator in U-space which corresponds to the operators $\boldsymbol{x}_j$'s and $\boldsymbol{p}_j$'s in V-space.

Now we can write for $\boldsymbol{x}_j$:

$$\boldsymbol{x}_jP\varphi(\boldsymbol{x}_j;\ \rho_k)=\boldsymbol{x}_j\varphi(\boldsymbol{x}_j;\ \rho_k(\boldsymbol{x}_j))=P\{\boldsymbol{x}_j\varphi(\boldsymbol{x}_j;\ \rho_k)\}\,.$$

Thus, $\boldsymbol{x}_j$'s need not be rewritten. But when the form $\sum_{j=1}^{N}e^{i\boldsymbol{k}\boldsymbol{x}_j}$ appears, we may write it either as ρ_k or as $\sum_{j=1}^{N}e^{i\boldsymbol{k}\boldsymbol{x}_j}$. Therefore, the arbitrariness of this sort remains in the definition (4.7), showing that Eq. (4.7) is necessary but not sufficient to define $\mathfrak{A}$. We take the form (2.3) for the interaction energy G.

Next, for $\boldsymbol{p}_j$'s we can write

$$\begin{aligned}\frac{\partial}{\partial\boldsymbol{x}_j}P\varphi(\boldsymbol{x}_j;\ \rho_k)&=\frac{\partial}{\partial\boldsymbol{x}_j}\varphi(\boldsymbol{x}_j;\ \rho_k(\boldsymbol{x}_j))\\&=P\left\{\left(\frac{\partial\varphi}{\partial\boldsymbol{x}_j}\right)_\rho+\sum_k\frac{\partial\rho_k}{\partial\boldsymbol{x}_j}\left(\frac{\partial\varphi}{\partial\rho_k}\right)_k\right\}.\end{aligned}$$

This is just the transformation used in Eq. (2.4). Thus, it is proved that our Hamitonian (2.7) satisfies the relation (4.7).

Now, Eq. (4.4) is written in terms of the operator $\mathfrak{A}$ defined by Eq. (4.7),

$$P\mathfrak{A}|\alpha_i)=P\sum_j|\alpha_j)A_{ji}\,. \tag{4.8}$$

In general, $\mathfrak{A}|\alpha_i)$ has components $|\beta_k)$'s orthogonal to U_1,

$$\mathfrak{A}|\alpha_i)=\sum_j|\alpha_j)A_{ji}+\sum_k|\beta_k)A'_{ki}\,. \tag{4.9}$$

From the orthonormal property of $|\alpha_j)$'s in U-space, we can calculate the matrix element A_{ji} in a usually way

$$A_{ji}=(\alpha_j|\mathfrak{A}|\alpha_i)\,. \tag{4.10}$$

Thus the secular equation (4.5) and the trace (4.6) in V-space can be written as

$$|\,(\alpha_j|\mathfrak{A}|\alpha_i)-a\delta_{ji}\,|=0\,, \tag{4.11}$$

and

$$\mathrm{Tr}\,A=\sum_i(\alpha_i|\mathfrak{A}|\alpha_i)\,. \tag{4.12}$$

It is to be noted that in Eqs. (4.11) and (4.12) $|\alpha_j)$'s should not be taken as the complete set of the entire U-space, and A'_{ki} in Eq. (4.9) has no physical meaning. Thus, for example, we must not take $|\beta_k)$'s into consideration even in the intermediate virtual states in the perturbation calculation. It is necessary and sufficient to consider the sub-space U_1 only.

In our case the above-mentioned sub-space U_1 can be constructed easily. According to the arguments in § 3 the wave function of the excited state, in which the phonons with wave numbers $\boldsymbol{k}_1,\cdots,\boldsymbol{k}_m$ and the rotons with wave numbers $\boldsymbol{K}_1,\cdots,\boldsymbol{K}_n$ are excited, has the form in our approximation

$$\begin{aligned}\Phi_i&\equiv\Phi_{\{\boldsymbol{k}_1\cdots\boldsymbol{k}_m;\boldsymbol{K}_1\cdots\boldsymbol{K}_n\}}\\&=\rho_{\boldsymbol{k}_1}\cdots\rho_{\boldsymbol{k}_m}\Psi_{\{\boldsymbol{K}_1\cdots\boldsymbol{K}_m\}}\Phi_0\,,\end{aligned} \tag{4.13}$$

where Φ_0 is the ground state wave function, and $\Psi_{\{\boldsymbol{K}_1\cdots\boldsymbol{K}_n\}}$ is a permanent of plane waves,

$$\Psi_{\{\boldsymbol{K}_1\cdots\boldsymbol{K}_n\}}=\sum_P P\exp\left[i(\boldsymbol{K}_1\boldsymbol{x}_1+\cdots+\boldsymbol{K}_n\boldsymbol{x}_n)\right]\,,$$

where the summation is over all permutations

P of N particles. On the other hand, the functions

$$\begin{aligned}\Psi_i&=\Psi_{\{\boldsymbol{k}_1\cdots\boldsymbol{k}_m,\boldsymbol{K}_1\cdots\boldsymbol{K}_n\}}\\&=\sum_P P\exp[i(\boldsymbol{k}_1\boldsymbol{x}_1+\cdots+\boldsymbol{k}_m\boldsymbol{x}_m+\boldsymbol{K}_1\boldsymbol{x}_{m+1}\\&\qquad+\cdots+\boldsymbol{K}_n\boldsymbol{x}_{n+m})]\,,\quad m+n\leq N\,,\qquad(4.14)\end{aligned}$$

form a complete orthogonal set in V-space. Thus, if we impose the restrictions $|\boldsymbol{k}_i|\leq k_c$, $|\boldsymbol{K}_i|>k_c$ and $m+n\leq N$ on the wave functions (4.13), we can make one-to-one correspondence between the set Φ_i and Ψ_i. Therefore, when such restrictions are imposed on the wave functions (4.13), they form a sub-space U_1 which has the same property as those mentioned above.

In other words, we can say that the roton excitations with wave numbers smaller than k_c are inhibited and the excitations for $|\boldsymbol{k}|\leq k_c$ are described only in terms of phonons, and that the total number of these excitations cannot exceed the total number N of the particles*.

The above argument applies only to Bose systems. In Fermi systems, it is not possible to describe the excitations only in terms of ρ_k's even for small $|\boldsymbol{k}|$. This is possibly the reason why liquid He^3 obeying Fermi statistics exhibits quite different behaviors from those of liquid He^4.

In the case of the electron gas in metals, treated by Bohm and Pines[13)], the collective oscillations, usually called plasma oscillations, have very high frequencies compared with the individual excitation energies. Hence if the temperature is not so high, the plasma excitations may be neglected, and we need consider only the individual oscillations. In this case, the sub-space U_1 consists of the individual excitations only. Thus, the usual procedure in which we neglect the presence of the subsidiary conditions is justified. However, in the case when the plasma excitations play an important role, it is necessary to consider this problem more carefully.

§ 5. The Bose Condensation

From the arguments in § 3 and § 4, we can derive the following model for the liquid helium 4: The total energy can be written as

$$E=E_0+\sum_{\boldsymbol{k}} n(\boldsymbol{k})\mathcal{E}(\boldsymbol{k})\,,\qquad(5.1)$$

where E_0 is the ground state energy, and $\mathcal{E}(\boldsymbol{k})$ is given by

$$\mathcal{E}(\boldsymbol{k})=\begin{cases}E(k)=2\left[T(k)\dfrac{N}{2V}G(k)\right]^{1/2}, & \text{for } |\boldsymbol{k}|\leq k_c\,,\\[2ex] \dfrac{\hbar^2k^2}{2m^*}\,, & \text{for } |\boldsymbol{k}|>k_c\,,\end{cases}\qquad(5.2)$$

and $n(\boldsymbol{k})$ is subjected the following restriction

$$\sum_{|\boldsymbol{k}|\neq 0} n(\boldsymbol{k})\leq N\,,\qquad(5.3)$$

where N is the total number of particles. It is remarked here that Eq. (5.3) is the results of the kinematical interactions as was shown in § 4. There remain only "dynamical interactions," i.e., the non-diagonal term in the Hamiltonian. We cannot show that these interactions are very small and can be neglected, and, in fact, these interactions is supposed to modify the energy spectrum (5.2) to approach the Landau spectrum (1.1). Since, however, calculation is very complicated, we do not carry out the calculation here, but proceed the arguments based upon Eq. (5.2). Furthermore, the phonon spectrum (5.2) for $|\boldsymbol{k}|\leq k_c$, may be replaced by $\hbar ck$, if the dispersion can be neglected. Therefore, only the qualitative conclusions can be drawn.

First of all, it is evident that the above model exhibits the Bose condensation because of the restriction (5.3). Furthermore, the transition due to Bose condensation is of the second order. This is due to the form of the spectrum (5.2) which is linear for small k. To prove this, we consider the relation between the energy spectrum and the order of

---

* It might seem to be strange that the number of phonons is restricted. In fact, in the solid state, no restriction is imposed on the number of phonons, although the number of the modes of phonons must be equal to $3N$. But in solids, the coordinates describing phonons are different from ours, Eq. (1.2), and are defined as

$$u_k=\frac{1}{\sqrt{N}}\sum_{j=1}^{N}e^{ikx_j^0}(\boldsymbol{x}_j-\boldsymbol{x}_j^0)\,,$$

where $\boldsymbol{x}_j^0$ is the equilibrium position of j-th atom in the crystal. This is a linear transformation from $\boldsymbol{x}_j$ to $\boldsymbol{u}_k$, and the inverse transformation is possible if and only if the number of the modes is $3N$. If this is the case, no kinematical interactions enter, and the whole system can be described by u_k's. In our case, the inverse transformation of Eq. (1.2) is difficult to find, and it is more convenient to restrict the number of phonons. Moreover, it is due to this difference between above equation and Eq. (1.2) that our phonons can carry the momentum although the phonons in solids do not.

the Bose condensation. In general, let us consider the N particles which have the energy spectrum $\mathcal{E}(k)$ and obey the Bose statistics*.

To investigate the Bose condensation, we may only construct the grand partition function, from which we can get the equation determining the chemical potential μ as a function of the temperature T, the volume V and the number of the particles N. If we get the solution for fixed V and N, in which μ becomes zero below a certain temperature T_c, the Bose condensation occurs at $T=T_c$. The order of the transition is determined by the value of $(\partial\mu/\partial T)_{+T_c}$ and $(\partial^2\mu/\partial T^2)_{+T_c}$, etc. That is, if $(\partial\mu/\partial T)_{+T_c}\neq 0$, the transition is of the second order, and if $(\partial\mu/\partial T)_{+T_c}=0$ and $(\partial^2\mu/\partial T^2)_{+T_c}\neq 0$, then the order becomes third.

Now the equation for μ is given by

$$N=\frac{1}{e^{\alpha}-1}+\frac{V}{8\pi^3}\int_0^\infty 4\pi k^2 dk\frac{1}{e^{\alpha+\beta\mathcal{E}(k)}-1}\,, \qquad (5.4)$$

where $\alpha=-\mu/kT$, and $\beta=1/kT$. In Eq. (5.4), we assume that there is no gap in the excitation energy, that is, $\mathcal{E}(0)=0$ and that $\mathcal{E}(k)$ is a positive function of $|\boldsymbol{k}|=k$ only. The second term of Eq. (5.4) can be written as

$$N_{\text{exc.}}=\frac{V}{2\pi^2}\sum_{n=1}^{\infty}e^{-n\alpha}\int_0^\infty e^{-n\beta\mathcal{E}(k)}k^2dk\,. \qquad (5.5)$$

Here we expand $\mathcal{E}(k)$ in powers of k,

$$\mathcal{E}(k)=a_0k^l(1+a_1k+\cdots)\,, \qquad l>0\,. \qquad (5.6)$$

Substituting Eq. (5.6) into (5.5) and putting $a_0n\beta k^l=y$, we obtain

$$\begin{aligned}N_{\text{exc.}}&=\frac{V}{2\pi^2}\sum_{n=1}^{\infty}\frac{e^{-n\alpha}}{l(n\beta a_0)^{3/l}}\\&\quad\times\int_0^\infty e^{-y(1+a_1(y/n\beta a_0)^{1/l}+\cdots)}y^{(2/l)-1}dy\\&=\frac{V}{2\pi^2}\frac{1}{l}\frac{1}{(\beta a_0)^{3/l}}\sum_{n=1}^{\infty}\frac{e^{-n\alpha}}{n^{3/l}}\\&\quad\times\int_0^\infty e^{-y}y^{(2/l)-1}\left(1+O\left(\frac{y}{n}\right)^{1/l}\right)dy\,.\end{aligned}$$

The integral over y converges because $l>0$. Thus we obtain the equation

$$N_{\text{exc.}}=A_1(T)F_{3/l}(\alpha)+A_2(T)F_{4/l}(\alpha)+\cdots\,, \qquad (5.7)$$

where

$$F_p(\alpha)=\sum_{n=1}^{\infty}\frac{e^{-n\alpha}}{n^p}\,. \qquad (5.8)$$

Now as $\alpha\to 0$, $F_p(\alpha)$ becomes infinite if $p\leq 1$, but remains finite if $p>1$. As is well known, if $N_{\text{exc.}}$, Eq. (5.7), can become infinite, then we always obtain the solution $\alpha>0$, and the Bose condensation does not occur. But, if $N_{\text{exc.}}$ can not become infinite, as $\alpha\to 0$, we obtain the solution in which $\alpha>0$ for $T>T_c$ and $\alpha=0$ for $T\leq T_c$, leading to the Bose condensation. Thus, the condition for Bose condensation to occur is determined by the first term of (5.7) and becomes

$$\frac{3}{l}>1\,, \quad \text{i.e.,} \quad l<3\,. \qquad (5.9)$$

Of course, to determine the condensation temperature T_c all the terms in Eq. (5.7) must be considered.

The order of the transition is determined by the values of the derivatives of α with respect to T when $T\to +T_c$. For $T\geq T_c$, in the equation (5.4) for α, the first term representing the number of the ground state particles can be ignored, and the right hand side of Eq. (5.7) is equal to N. Thus, differentiating Eq. (5.7) with respect to T, and putting $T\to T_c$ and $\alpha\to 0$, we obtain

$$\begin{aligned}0=&\left(\frac{dA_1}{dT}\right)_{T_c}F_{3/l}(0)\\&-A_1(T_c)F_{(3/l)-1}(0)\left(\frac{d\alpha}{dT}\right)_{+T_c}\,,\end{aligned} \qquad (5.10)$$

here we neglect all terms except the first. From Eq. (5.10), we see that if $(3/l)-1\leq 1$, then $(d\alpha/dT)_{+T_c}=0$, and $d\alpha/dT$ is continuous at $T=T_c$ and the transition is of more than third order, and that if $(3/l)-1>1$, then $(d\alpha/dT)_{+T_c}\neq 0$, and $d\alpha/dT$ shows discontinuity at $T=T_c$, the transition being of second order. Thus, we obtain the following relation;

$$\begin{array}{ll}3\leq l & :\ \text{no Bose condensation}\\(3/2)\leq l<3: & \text{Bose condensation, transition}\\ & \text{of third order or more}\\0<l<(3/2): & \text{Bose condensation transition}\\ & \text{of second order}\end{array} \qquad (5.11)$$

In our case, $l=1$ and we obtain the second order transition, while, in the ideal gas, $l=2$ and the transition is of the third order. Thus, our model agrees with the experiment qualitatively.

---

* In our case, the total number of the excitations is not always equal to N. But this does not contradict with the usual statistics of N particles. The right hand side $\sum_{|\boldsymbol{k}|\neq 0}n(\boldsymbol{k})$ of Eq. (5.3) represents the number of excited particles, and the remaining $N-\sum_{|\boldsymbol{k}|\neq 0}n(\boldsymbol{k})$ represents the number of the particles in the ground state.

As was mentioned above the quantitative results are not supposed to have any physical meaning. But we suppose that by adjusting the values of m^* and k_c we can obtain the value of T_c and the specific heat curve which agree with the experimental data.

The temperature dependence of the viscosity coefficient will be investigated in another paper, using the interaction term given in this paper.

§ 6. Conclusions

The two purposes of this paper mentioned in § 1, that is, to connect the excitation theory with the Bose condensation theory, and to write down the interactions among various excitations explicitly, can be achieved by a simple method. The Hamiltonian, derived in § 2 and § 3, is rigorous, and the interactions between phonons are given by $\mathscr{H}'$, Eq. (3.7), and those between phonons and rotons by $\mathscr{H}_{\text{int.}}$, Eq. (3.9), and the roton-roton interactions are included in $\mathscr{H}_{\text{ind.}}$, Eq. (2.7c). The energy spectrum of the excitations has the form, Eq. (5.2), so that our model exhibits the second order transition due to Bose condensation as was shown in § 5. It is noted that this is the result of the elimination of the kinematical interactions. The method of this elimination is very simple and convenient compared with the method of the subsidiary conditions.

As was mentioned in § 2, the interaction energy $G(r)$ between two Helium atoms contains the strong repulsion term of short range, and this makes the Fourier expansion of $G(r)$ impossible. This is completely neglected in the above discussion, and the velocity of sound is determined only by $G(0)=\int G(r)d\boldsymbol{r}$, but does not contain the zero-point energy of Helium atoms. In order to avoid this difficulty about the Fourier expansion of $G(r)$, Bogolyubov[14] proposed that $G(k)$ may be replaced by the matrix element of scattering, and Kanazawa[15] showed that such a procedure was really possible in the method of Bogolyubov. In our case, however, this seems to be impossible. Instead, the following procedure may be employed: We divide the interaction potential $G(r)$ into two parts at the distance r_0,

$$G(r)=G_1(r)+G_2(r)\,,$$

$$G_1(r)=\begin{cases}0 & \text{for} \quad r\leq r_0\,,\\ G(r) & \text{for} \quad r>r_0\,,\end{cases}$$

$$G_2(r)=\begin{cases}G(r) & \text{for} \quad r\leq r_0\,,\\ 0 & \text{for} \quad r>r_0\,.\end{cases}$$

We expand only the first part $G_1(r)$ into Fourier siries and use this to obtain the phonon spectrum and the second part $G_2(r)$ is included in $\mathscr{H}_{\text{ind.}}$, (2.7b). The cut-off length r_0 may be determined from the condition of minimum energy, although this procedure has not such a precise meaning as the usual variation method. Then, the zero-point energy of rotons will affect the phonon spectrum through the value of r_0.

In any way, our model emphasizes the fact the excitation theory can be connected with the Bose condensation theory smoothly, but is not concerned with another characteristic properties of liquid Helium, i.e., the superfluidity below the λ-point, and the reason why the liquid Helium does not solidify under the normal pressure, etc. These are the problems about the ground state of an assembly of Helium atoms.

Nothing is said about the dynamical interactions. One of the effects of these interactions would be the modification of the energy spectrum (5.2) which will probably approach the spectrum Eq. (1.1), proposed by Landau. The other important effect of the interactions will be the scattering of the excitations by each other. The calculation of the cross sections for these scatterings and of the viscosity coefficient of liquid helium will be carried out in another paper.

There remain some ambiguities in our model, for example, about the energy and the wave function of the roton part, and about the smallness of the dynamical interactions. We believe, however, that our model represents the essential properties of liquid helium at least qualitatively.

Finally the value of k_c, introduced in § 2, is determined from the minimization of the ground state energy. In our approximation, the ground state energy of phonon is given by

$$E^0_{\text{phon.}}=\sum_{|k|\leq k_c}\left[\frac{1}{2}E(k)-\frac{N}{2V}G(k)\right]+\frac{N^2}{2V}G(0)\,. \tag{6.1}$$

We do not know about the roton part, but, since the roton energy is supposed to be almost independent of k_c, we may neglect this in the qualitative determination of k_c. In Eq. (6.1), the summand is negative for small k, because there $E(k)\propto k$ and $G(k)\sim G(0)>0$. For large k, $G(k)\to 0$ and the summand is positive, so that the minimum value of $E^0_{\text{phon.}}$ can be obtained by taking as the value of k_c,

$$\frac{1}{2}E(k_c)=\frac{N}{2V}G(k_c)\,. \tag{6.2}$$

Substituting Eq. (3.4) into the above equation, we obtain

$$T(k_c)=\frac{N}{2V}G(k_c)\,. \tag{6.3}$$

We cannot solve this equation exactly because of the lack of the knowledge about $G(k)$, but in the approximation in which the dispersion of sound velocity is neglected, we can set

$$\frac{N}{2V}G(k)\sim\frac{N}{2V}G(0)=\frac{1}{2}mc^2\,.$$

Therefore, from Eq. (6.2) we obtain the value of k_c,

$$\frac{1}{2}\hbar ck_c\approx\frac{1}{2}mc^2\,,\quad k_c\sim 10^8cm^{-1}\,.$$

This gives the right order of magnitude.

The author wishes to express his sincere thanks to Professor A. Harashima and to Professor R. Kubo for their valuable discussions.

References

1) F. London: Nature **141** (1938) 643, Phys. Rev. **54** (1938) 947.
2) L. Tisza: Nature **141** (1938) 913, Phys. Rev. **72** (1947) 838.
3) O. Penrose and L. Onsager: Phys. Rev. **104** (1956) 576.
4) R. P. Feynman: Phys. Rev. **91** (1953) 1291.
5) L. E. Landau: J. Phys. U.S.S.R. **5** (1941) 71.
6) see, for example: A. Thelling, Helv. Phys. Acta. **29** (1956) 103.
7) W. Brenig: Zeits. f. Physik **144** (1956) 488.
8) T. Usui and N. Matsudaira: Busseironkenkyu **100** (1956) 76, in Japanese.
9) F. J. Dyson: Phys. Rev. **102** (1956) 1217.
10) T. Nishiyama: Busseironkenkyu **86** (1955) 44, **93** (1956) 185, **103** (1957) 114, in Japanese.
11) S. Tomonaga: Prog. Theor. Phys. **13** (1955) 467, 482.
12) N. N. Bogolyubov and D. N. Zubarev: J. Exp. Theor. Phys. U.S.S.R. **28** (1955) 129.
13) D. Bohm and D. Pines: Phys. Rev. **92** (1953) 609.
14) N. N. Bogolyubov: J. Phys. **11** (1947) 23.
15) H. Kanazawa: Busseironkenkyu **81** (1955) 1, in Japanese.

JOURNAL OF THE PHYSICAL SOCIETY OF JAPAN Vol. 12, No. 11, NOVEMBER, 1957

Cell Theory of Classical Liquid. Phase Transition between Gas, Liquid and Solid.
Parts I and II.

By Tohru MORITA

Physics Department, Tokyo Institute of Technology

(Received July 4, 1957)

The cell theories of liquid in the past have assumed that the molecules are localized near the centers of cells. In this respect, they may be considered as the theories for solid. In this article, the correlations between the occupations in neighboring cells are taken into account in the degree of Bethe approximation. This improvement of the cell theory is shown to be followed by the transitions between gas, liquid and solid; the liquid and gas states corresponding to the states where the distribution function $\rho^{(1)}(\boldsymbol{r})$ is constant throughout the volume of the system, and the solid state to the state where the distribution function $\rho^{(1)}(\boldsymbol{r})$ is localized near the centers of cells.

The development of the theory is based on the cluster variation method for cooperative phenomena in the cell pair approximation. For the illustrative purpose, the method is first applied to a system of square lattice gas.

The numerical calculations are performed for the oritical point, phase diagram and second Virial coefficient in a very rough approximation, where the intermolecular potential of Lennard-Jones (6–12) type is used.

Part I. Square Lattice Gas

The phase transitions of two-dimensional lattice gases composed of molecules with both hard core and attractive interaction were discussed by Kikuchi[1] and Shimose[2]. Applying the cluster variation method, Kikuchi treated a triangular lattice gas composed of molecules whose potential energy of interaction is infinity between nearest neighbor lattice sites, negative constants between 2nd and 3rd neighbor lattices sites and zero thereafter. Grouping all the lattice sites into three sublattices as shown in Fig. I-1, and assuming that the solid state corresponds to the state where the molecules are more populated in one of sublattices (e.g. ● in Fig. I-1) than the others (○ and ×), he obtained the result that, in order that the stable liquid state exists, it is necessary that the depth of the potential energy of interaction is greater between 3rd neighbor lattice sites than between 2nd neighbor lattice sites. In another approximation, Shimose calculated the equation of state for a square lattice gas composed of molecules whose potential due to a molecule is infinity at the nearest and second neighbor lattice sites, a negative constant at the 3rd and 4th neighbor lattice sites and zero thereafter. Grouping all the lattice sites into four sublattices as shown in Fig. I-2, and assuming that the solid state corresponds to the state where the molecules are more populated in one of sublattices (e.g. ●) than the others (○, × and △), he obtained the result that the stable liquid region would appear.

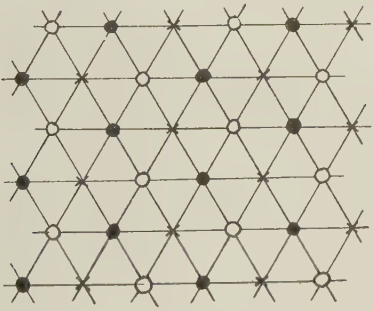

Fig. I-1.

In the following in part I, the square lattice gas, whose constituent molecules have the potential of the type (1′), will be treated by the cluster variation method of approximation[3]. It will then be shown that, if the same premise for the solid state and the same potential as those used by Shimose[2] are adopted, the stable liquid region will not be expected to appear. This problem is, of course, of quite academic nature*. This part may be considered to have the meaning only as the preliminary calculation to part II.

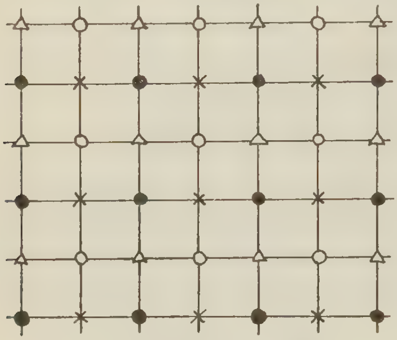

Fig. I–2.

In this part, the part from "Phase Transition of Lattice Gas I" published by the present author in Busseiron Kenkyu No. 106 (March 1957) 30–38 (in Japanese) is translated, which seems to be useful for the development of the following part. Three dimensional lattice gas composed of molecules with both hard core and attractive potential was also discussed by the present author in Busseiron Kenkyu No. 106 (March 1957) 39–50 (in Japanese).

§ 1. Application of the Cluster Variation Method

Let us consider a square lattice with lattice constant $a/2$. Let N indistinguishable particles be on $4L$ lattice sites. Let the potential energy of the system be the sum of contributions from pairs of molecules and the potential energy between two particles, one at $\boldsymbol{r}_s$ and another at $\boldsymbol{r}_t$, be of the form

$$V^{(2)}(\boldsymbol{r}_s, \boldsymbol{r}_t)=V^{(2)}(|\boldsymbol{r}_s-\boldsymbol{r}_t|)\ , \tag{1}$$

$$V^{(2)}(r)\begin{cases}=\infty\ , & r=0,\ a/2,\ \sqrt{2}\,a/2\\ \leqq 0\ , & r\leqq a\\ =0\ , & r\to\infty\ ;\end{cases} \tag{1'}$$

the particles have cores of diameter $\sqrt{2}\,a/2$.

This system may be characterized by the following three conditions: 1) The configuration of the system is described by the configurations of $4L$ lattice sites. 2) The possible configurations x_s for s-th lattice site ($s=1, \cdots, 4L$) are "a particle is present at the site s——$x_s=$p. at s" and "no particle is at the site s——$x_s=$a. at s". 3) The potential energy of the system is, for the configuration $(x_1, \cdots, x_{4L})$,

$$\Phi(x_1, \cdots, x_{4L})=\frac{1}{2}\sum_{s=1}^{4L}\sum_{\substack{t=1\\(s\neq t)}}^{4L} V^{(2)}(x_s, x_t) \tag{2.}$$

$$V^{(2)}(x_s, x_t)=V^{(2)}(\boldsymbol{r}_s, \boldsymbol{r}_t)$$

if both $x_s=$p. at s and $x_t=p$. at t,

$$V^{(2)}(x_s, x_t)=0 \quad \text{if otherwise.} \tag{2'}$$

These conditions allows us to apply directly the formulation of the cluster variation method proposed in CVM to this system.

At first, we have to decide the preserved clusters and the not-preserved clusters. We introduce cells in the lattice as shown in Fig. I-3; a cell consisting of 4 lattice sites. μ-th lattice site in i-th cell will be denoted as $i\mu$ ($i=1, \cdots, L$; $\mu=1, 2, 3, 4$). We divide the clusters, clusters whose constituent lattice sites are conceived either in one or two cells and clusters whose constituent lattice sites are over three or more cells. We adopt the former ones as the preserved and the latter ones as the not-preserved. We will call this way of decision "the cell and cell pair approximation". In this approximation, the function F, whose minimum value is to be taken as the free energy, is written as, according to (CVM-9 and 7)**,

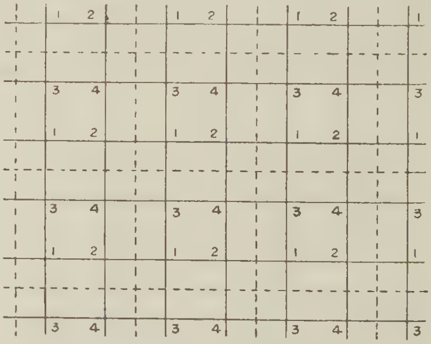

Fig. I–3. The numbers attached to lattice points denote the values of μ.

---

* A possible example of the system, for which the argument of part I will be applied, is the adsorbed monolayer on a crystal surface, when the diameter of the adsorbed molecule is about twice as large as the lattice constant of the crystal surface.

** (CVM–9) means Eq. (9) in CVM[3].

$$
\begin{aligned}
=\sum_{i<j}\sum_{\mu=1}^{4}\sum_{\nu=1}^{4}\rho^{(2)}(x_{i\mu}=\text{p.},x_{j\nu}=\text{p.})V^{(2)}(|\boldsymbol{r}_{i\mu}-\boldsymbol{r}_{j\nu}|)\\
+kT\Bigl[\sum_{i=1}^{L}\ln G^{(4)}(i1,i2,i3,i4)\\
+\sum_{i<j}\ln\frac{G^{(8)}(i1,\cdots,i4,j1,\cdots,j4)}{G^{(4)}(i1,\cdots,i4)G^{(4)}(j1,\cdots,j4)}\Bigr].
\end{aligned}
\tag{3}
$$

The approximate equation (3) can be obtained rom another point of view, where the cell is aken as the unit. Then, the system can be haracterized by that: 1) The configuration of he system is described by the configurations f the L cells. 2) The possible configurations x_i of i-th cell are "a particle is present at attice site $i\mu$——p. at $i\mu$", $(\mu=1,2,3,4)$, and "no particle is in the cell i —a. in i". 3) The potential energy of the system is, for he configuration $(x_1,\cdots,x_L)$,

$$
\Phi(x_1,\cdots,x_L)=\frac{1}{2}\sum_{\substack{i=1\\(i\neq j)}}^{L}\sum_{j=1}^{L}V^{(2)}(x_i,x_j)
\tag{4}
$$

$V^{(2)}(x_i,x_j)=V^{(2)}(|\boldsymbol{r}_{i\mu}-\boldsymbol{r}_{j\nu}|)$

if both $x_i=$p. at $i\mu$ and $x_j=$p. at $j\nu$,

$=0$ if otherwise. (4′)

In this point of view, if we take all cells and all pairs of cells as the preserved clusters and the others as the not-preserved, then we obtain Eq. (3) for F.

Now, we introduce $\rho^{(\text{cell})}$ (or $\rho^{(4)}$) and $\rho^{(\text{cell pair})}$ (or $\rho^{(8)}$) taking into account of (CVM-10 and 11) as in Tables I and II.

Table I.

configuration of cell i	its probability
present at $i\mu$	$\rho^{(1)}(\mu)$, $(\mu=1,2,3,4)$
absent in i	$1-\rho$, $\rho=\sum_{\mu=1}^{4}\rho^{(1)}(\mu)=\frac{N}{L}$

Table II.

configuration of cell pair (i,j)	its probability
p. at $i\mu$ and p. at $j\nu$	$\rho^{(2)}(i\mu,j\nu)$ $=\rho^{(1)}(\mu)\rho^{(1)}(\nu)g'^{(2)}(i\mu,j\nu)$
p. at $i\mu$ and a. in j	$\rho^{(1)}(\mu)-\sum_{\nu=1}^{4}\rho^{(2)}(i\mu,j\nu)$
a. in i and p. at $j\nu$	$\rho^{(1)}(\nu)-\sum_{\mu=1}^{4}\rho^{(2)}(i\mu,j\nu)$
a. in i and a. in j	$1-2\rho+\sum_{\mu=1}^{4}\sum_{\mu=1}^{4}\rho^{(2)}(i\mu,j\nu)$

$g'^{(2)}(i\mu,j\nu)=g^{(2)}(\mu,\nu;\boldsymbol{r}_{i1}-\boldsymbol{r}_{j1})$

By using these tables with (CVM-6), (3) becomes

$$
\begin{aligned}
\frac{F}{LkT}=&\frac{1}{2kT}\sum_{\substack{j=1\\(j\neq i)}}^{L}\sum_{\mu=1}^{4}\sum_{\nu=1}^{4}\rho^{(1)}(\mu)\rho^{(1)}(\nu)g^{(2)}(i\mu,j\nu)V^{(2)}(|\boldsymbol{r}_{i\mu}-\boldsymbol{r}_{j\nu}|)\\
&+\sum_{\mu=1}^{4}\rho^{(1)}(\mu)\ln\rho^{(1)}(\mu)+(1-\rho)\ln(1-\rho)\\
&+\frac{1}{2}\sum_{\substack{j=1\\(j\neq i)}}^{L}\Bigl\{\sum_{\mu=1}^{4}\sum_{\nu=1}^{4}\rho^{(1)}(\mu)\rho^{(1)}(\nu)g^{(2)}(i\mu,j\nu)\ln g^{(2)}(i\mu,j\nu)\\
&+\sum_{\mu=1}^{4}\rho^{(1)}(\mu)\Bigl[1-\sum_{\nu=1}^{4}\rho^{(1)}(\nu)g^{(2)}(i\mu,j\nu)\Bigr]\ln\frac{1-\sum_{\nu=1}^{4}\rho^{(1)}(\nu)g^{(2)}(i\mu,j\nu)}{1-\rho}\\
&+\sum_{\nu=1}^{4}\rho^{(1)}(\nu)\Bigl[1-\sum_{\mu=1}^{4}\rho^{(1)}(\mu)g^{(2)}(i\mu,j\nu)\Bigr]\ln\frac{1-\sum_{\mu=1}^{4}\rho^{(1)}(\mu)g^{(2)}(i\mu,j\nu)}{1-\rho}\\
&+\Bigl[1-2\rho+\sum_{\mu=1}^{4}\sum_{\nu=1}^{4}\rho^{(1)}(\mu)\rho^{(1)}(\nu)g^{(2)}(i\mu,j\nu)\Bigr]\ln\frac{1-2\rho+\sum_{\mu=1}^{4}\sum_{\nu=1}^{4}\rho^{(1)}(\mu)\rho^{(1)}(\nu)g^{(2)}(i\mu,j\nu)}{(1-\rho)^2}\Bigr\}.
\end{aligned}
\tag{5}
$$

$\rho^{(1)}(\mu)$ and $g^{(2)}(i\mu,j\nu)$ are to be determined so as to minimize this equation (5). It is easily seen that $g^{(2)}(i\mu,j\nu)$ is zero when $V^{(2)}(|\boldsymbol{r}_{i\mu}-\boldsymbol{r}_{j\nu}|)=\infty$ and unity when between two cells i and j $V^{(2)}(|\boldsymbol{r}_{i\mu}-\boldsymbol{r}_{j\nu}|)=0$ for any of $\mu=1,\cdots,4$ and any of $\nu=1,\cdots,4$.

In the next section, we restrict the variational functions $\rho^{(1)}$ and $g^{(2)}$ and proceed the approximate calculation.

§ 2. Approximate Calculation

In a quite rough approximation, we restrict the variational functions in the form

$$g^{(2)}(i\mu, j\nu)=\begin{cases} 0 & \text{if } V^{(2)}(|\boldsymbol{r}_{i\mu}-\boldsymbol{r}_{j\nu}|)=\infty \\ 1 & \text{if otherwise}\,, \end{cases} \tag{6}$$

$$\rho^{(1)}(1)=\frac{\rho}{4\cosh^2\beta}e^{2\beta},\quad \rho^{(1)}(2)=\rho^{(1)}(3)=\frac{\rho}{4\cosh^2\beta},$$

$$\rho^{(1)}(4)=\frac{\rho}{4\cosh^2\beta}e^{-2\beta}; \tag{7}$$

the only parameter β is to be determined so as to minimize F. Substituting these into (5), we obtain $\beta=0$ as one of roots for $\partial F/\partial\beta=0$, and calculating $(\partial^2F/\partial\beta^2)_{\beta=0}$, we find that $\beta=0$ corresponds to the minimum at higher temperatures than T_1 given by

$$\begin{aligned}-\frac{1}{kT_1}(4\varphi_a-8\varphi_c)=&\frac{4}{\rho_1}-5-\frac{1}{3}\\ &+\frac{1}{3}\frac{1}{1-\frac{3}{4}\rho_1}+\frac{2}{1-\frac{1}{2}\rho_1}\\ &-2\ln\left(1-\frac{1}{2}\rho_1\right)+2\ln\left(1-\frac{3}{2}\rho_1\right)\\ &-\ln\left(1-\frac{3}{4}\rho_1\right)+\ln\left(1-\frac{5}{4}\rho_1\right)\end{aligned} \tag{8}$$

and to the maximum at the lower temperatures; where

$$4\varphi_a\equiv\sum_{j=1}^{L}{}^{*}\,V^{(2)}(|\boldsymbol{r}_{i1}-\boldsymbol{r}_{j1}|)\,, \tag{9a}$$

$$8\varphi_b\equiv\sum_{j=1}^{L}{}^{*}\,[V^{(2)}(|\boldsymbol{r}_{i1}-\boldsymbol{r}_{j2}|)+V^{(2)}(|\boldsymbol{r}_{i1}-\boldsymbol{r}_{j3}|)]\,, \tag{9b}$$

$$8\varphi_c\equiv\sum_{j=1}^{L}{}^{*}\,V^{(2)}(|\boldsymbol{r}_{i1}-\boldsymbol{r}_{j4}|)\,, \tag{9c}$$

where * on the summations means that in the summations j for which $V^{(2)}(|\boldsymbol{r}_{i\mu}-\boldsymbol{r}_{j\nu}|)=\infty$ should be omitted.

When $\beta\neq0$, one of sublattices (e.g. $\mu=1$) is more populated than the others ($\mu=2, 3, 4$) and the state may be considered as the solid state. On the contrary, if $\beta=0$, then $\rho^{(1)}(1)=\rho^{(2)}(2)=\rho^{(1)}(3)=\rho^{(1)}(4)$ and this state may be considered as the fluid state. The transition between these states is given by Eq. (8), which is drawn in Fig. I-4. The quantities for fluid state can easily be calculated; for instance the critical point is given by

$$\rho_c=0.332\,,\qquad 1/\rho_c=3.01\,,$$

$$\frac{kT_c}{-(\varphi_a+2\varphi_b+2\varphi_c)}=0.1380\,. \tag{10}$$

The potential used by Shimose is $\varphi_a=\varphi_b=-$ $\varphi_c=0$; for these values $kT_c=0.414$, this crit cal value is also plotted in Fig. I-4.

This figure I-4 shows that from our ap proximate calculation we cannot expect th appearance of the stable liquid region.

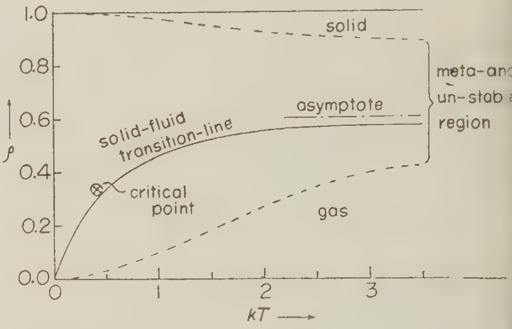

Fig. I-4. Phase Diagram. ($\varphi_a=\varphi_b=-1$, $\varphi_c=0$; th dotted lines are schematically drawn.)

Part II. Classical Liquid

In this part, we translate the calculation c the previous part to the case where the num ber of the lattice sites in a cell is very large and then we make this number tend t infinity.

§ 1. Application of the Cluster Variatio Method

The system considered in this part is suc that N particles are interacting with eac other by Lennard-Jones (6–12) potential in volume V.

At first, we consider the case where th particles constituting the system have har cores of diameter σ. Let us divide the volum V of the system into L cells in such a wa that the diameter of any of the L cells doe not exceed σ. Moreover, let each cell b divided into s volume elements. Then, thi system may be characterized by that: 1) Th configuration of the eystem is described b the configurations of sL volume elements. 2 The possible configuration for a volume ele ment is either "a particle is present in it or "no particle is in it". 3) The potentia energy of the system is the sum of potential between pairs of volume elements, and th potential between a pair of volume element is $V^{(2)}(r)$, r being the distance between th volume elements, when the configurations c both volume elements are "a particle is pre sent in it" and is zero otherwise. In thi ase, we need an additive term (CVM-12) for ne function F, whose minimum is to be aken as the free energy of the system: This erm is calculated by putting $n(x_i=$" a particle s present in i "$)=u_i$, u_i being the volume of ne volume element i, $(i=1, \cdots, sL)$, and $(x_i=$" no particle is in i "$)=1$. Applying the luster variation method in the cell and cellair approximation, we obtain an expression or F analogous to (I-3)*. This equation is btained form another point of view where he cell is taken as the unit, just as is done n part I. In this point of view, the system s characterized by that: 1) The configuration f the system is described by the configuraions of L cells. 2) The possible configurations f cell i are " a particle is present in volume lement $i\mu$——p. in $i\mu$ " $(\mu=1, \cdots, s)$ and " no article is in the cell i -a. in i ". 3) The otential energy of the system is, for the coniguration $(x_1, \cdots, x_L)$,

$$\Phi(x_1, \cdots, x_L)=\frac{1}{2}\sum_{\substack{i=1\\(i\neq j)}}^{L}\sum_{j=1}^{L} V^{(2)}(x_i, x_j) \qquad (1)$$

$$V^{(2)}(x_i, \cdots x_j)=V^{(2)}(|\boldsymbol{r}_{i\mu}-\boldsymbol{r}_{j\nu}-\boldsymbol{R}_{ij}|)$$
$$\text{if both } x_i=\text{p. in } i\mu \text{ and } x_j=\text{p. in } i\nu\,,$$
$$=0 \qquad \text{if otherwise}\,, \qquad (1')$$

where $\boldsymbol{r}_{i\mu}$ is the vector from the center of cell i to that of the volume element $i\mu$ and $\boldsymbol{R}_{ij}$ is the vector from the center of cell i to that of cell j. The additive term to F is calculated by taking $n(x_i=\text{p. in } i\mu)=u_{i\mu}$ and $n(x_i=\text{a. in } i)=1$.

We take as L cells decahedrons of equal volume $u=V/L$, then the centers of cells constitute a face centered cubic lattice, the distance between nearest neighbor lattice sites being $(u/\sqrt{2})^{1/3}$. Denoting a volume element by $d\boldsymbol{r}$, where $\boldsymbol{r}$ is the vector drawn from the cell center, we take the probabilities for the configurations of cell and cell pair as in Tables I and II.

Table I.

configuration of cell	its probability
present in $d\boldsymbol{r}$ at $\boldsymbol{r}$	$\rho^{(1)}(\boldsymbol{r})d\boldsymbol{r}$, $(\boldsymbol{r}$ in $u)$
absent in the cell	$1-\rho$, $\rho\equiv\int^{u}\rho^{(1)}(\boldsymbol{r})d\boldsymbol{r}$

Table II.

configuration of cell pair (i, j)	its probability
p. in $d\boldsymbol{r}_i$ at $\boldsymbol{r}_i$ and p. in $d\boldsymbol{r}_j$ at $\boldsymbol{r}_j$	$\rho^{(2)}(\boldsymbol{r}_i, \boldsymbol{r}_j; \boldsymbol{R}_{ij})d\boldsymbol{r}_i d\boldsymbol{r}_j=\rho^{(1)}(\boldsymbol{r}_i)\rho^{(1)}(\boldsymbol{r}_j)g^{(2)}(\boldsymbol{r}_i, \boldsymbol{r}_j; \boldsymbol{R}_{ij})d\boldsymbol{r}_i d\boldsymbol{r}_j$
p. in $d\boldsymbol{r}_i$ at $\boldsymbol{r}_i$ and a. in j	$\left[\rho^{(1)}(\boldsymbol{r}_i)-\int^{uj}\rho^{(2)}(\boldsymbol{r}_i, \boldsymbol{r}_j; \boldsymbol{R}_{ij})d\boldsymbol{r}_j\right]d\boldsymbol{r}_i$
a. in i and p. in $d\boldsymbol{r}_j$ at $\boldsymbol{r}_j$	$\left[\rho^{(1)}(\boldsymbol{r}_j)-\int^{ui}\rho^{(2)}(\boldsymbol{r}_i, \boldsymbol{r}_j; \boldsymbol{R}_{ij})d\boldsymbol{r}_i\right]d\boldsymbol{r}_j$
a. in i and a. in j	$1-2\rho+\int^{ui}\int^{uj}\rho^{(2)}(\boldsymbol{r}_i, \boldsymbol{r}_j; \boldsymbol{R}_{ij})d\boldsymbol{r}_i d\boldsymbol{r}_j$

Using these tables, we make the function F. In the limit of $s\rightarrow\infty$, the function F becomes

$$\begin{aligned}\frac{F}{LkT}=&\frac{1}{2kT}\sum_{\substack{j=1\\(j\neq i)}}^{L}\int^{ui}\int^{uj}d\boldsymbol{r}_i d\boldsymbol{r}_j V^{(2)}(\boldsymbol{r}_i, \boldsymbol{r}_j; \boldsymbol{R}_{ij})\rho^{(2)}(\boldsymbol{r}_i, \boldsymbol{r}_j; \boldsymbol{R}_{ij})\\&+\int^{u}d\boldsymbol{r}\rho^{(1)}(\boldsymbol{r})\ln\rho^{(1)}(\boldsymbol{r})+(1-\rho)\ln(1-\rho)\\&+\frac{1}{2}\sum_{\substack{j=1\\(j\neq i)}}^{L}\Bigg[\int^{ui}\int^{uj}d\boldsymbol{r}_i d\boldsymbol{r}_j\rho^{(2)}(\boldsymbol{r}_i, \boldsymbol{r}_j; \boldsymbol{R}_{ij})\ln g^{(2)}(\boldsymbol{r}_i, \boldsymbol{r}_j; \boldsymbol{R}_{ij})\\&+\int^{ui}d\boldsymbol{r}_i\left(\rho^{(1)}(\boldsymbol{r}_i)-\int^{uj}d\boldsymbol{r}_j\rho^{(2)}(\boldsymbol{r}_i, \boldsymbol{r}_j; \boldsymbol{R}_{ij})\right)\ln\frac{1-\int^{uj}d\boldsymbol{r}_j\rho^{(1)}(\boldsymbol{r}_j)g^{(2)}(\boldsymbol{r}_i, \boldsymbol{r}_j; \boldsymbol{R}_{ij})}{1-\rho}\\&+\int^{uj}d\boldsymbol{r}_j\left(\rho^{(1)}(\boldsymbol{r}_j)-\int^{ui}d\boldsymbol{r}_i\rho^{(2)}(\boldsymbol{r}_{\cdot i}\ \boldsymbol{r}_j; \boldsymbol{R}_{ij})\right)\ln\frac{1-\int^{ui}d\boldsymbol{r}_i\rho^{(1)}(\boldsymbol{r}_i)g^{(2)}(\boldsymbol{r}_i, \boldsymbol{r}_j; \boldsymbol{R}_{ij})}{1-\rho}\\&+\left(1-2\rho+\int^{ui}\int^{uj}d\boldsymbol{r}_i d\boldsymbol{r}_j\rho^{(2)}(\boldsymbol{r}_i, \boldsymbol{r}_j; \boldsymbol{R}_{ij})\right)\ln\frac{1-2\rho+\int^{ui}\int^{uj}d\boldsymbol{r}_i d\boldsymbol{r}_j\rho^{(2)}(\boldsymbol{r}_i, \boldsymbol{r}_j: \boldsymbol{R}_{ij})}{1-\rho}\Bigg], \quad (2)\end{aligned}$$

---

* (I-3) means Eq. (3) of part I.

[illegible] and [illegible] and $L=V/u$ are determined so as to make this function F a minimum. As t $g^{(2)}$, the statement under Eq. (I-5) is valid. The variation by $g^{(2)}$ gives

$$e^{-V^{(2)}(\boldsymbol{r}_i,\boldsymbol{r}_j;\,\boldsymbol{R}_{ij})/kT}=\frac{\rho^{(2)}(\boldsymbol{r}_i,\boldsymbol{r}_j;\,\boldsymbol{R}_{ij})\left(1-2\rho+\int^{ui}\int^{uj}d\boldsymbol{r}_i\,d\boldsymbol{r}_j\rho^{(2)}(\boldsymbol{r}_i,\boldsymbol{r}_j;\,\boldsymbol{R}_{ij})\right)}{\left(\rho^{(1)}(\boldsymbol{r}_i)-\int^{uj}d\boldsymbol{r}_j\rho^{(2)}(\boldsymbol{r}_i,\boldsymbol{r}_j;\,\boldsymbol{R}_{ij})\right)\left(\rho^{(1)}(\boldsymbol{r}_j)-\int^{ui}d\boldsymbol{r}_i\rho^{(2)}(\boldsymbol{r}_i,\boldsymbol{r}_j;\,\boldsymbol{R}_{ij})\right)},\quad (3$$

This is the generalization of the approximate formula which is the basis of the Bethe or quasi-chemical approximation[4].

In the above arguments, we have proceeded the discussion under the restriction that the diameter of a cell does not exceed σ. When the diameter of a cell is allowed to exceed σ, we have to take into account the probability that two particles are present in a cell in addition. However, if the probabilities of such configurations are negligible, we may consider these probabilities to be zero before the variation is taken; which will affect the result very little. And with this procedure, the function F to be minimized becomes the form of Eq. (2) again. In conclusion, if the cell size is not very large compared with the diameter of a particle, we may calculate the free energy of the system using Eq. (2) for F. Analogously, when, even if the particles do not have the hard cores, the interparticle potential is rather singular and the probability that two or more particles are present in a cell is negligible, we may calculate the free energy by using (2).

We will apply Eq. (2) to the case of Lennard-Jones (6–12) potential

$$V^{(2)}(r)=4\left(\frac{1}{r^{12}}-\frac{1}{r^{6}}\right). \qquad (4)$$

In equation (2), if we put $g^{(2)}=1$, then only the first three terms are retained, which is just the form from which Mayer and Careri[5] started their variational calculation. This approximation may be called "the cell approximation" in our scheme of development. Moreover, if $\rho=1$, it reduces to the equation introduced by Kirkwood[6]. In our scheme, the hole theory of liquid[7], in its features, may be considered as the approximation where $g^{(2)}(\boldsymbol{r}_i,\boldsymbol{r}_j;\,\boldsymbol{R}_{ij})$ is taken in the form $g^*(\boldsymbol{r}_i)g^*(\boldsymbol{r}_j)$, $g^*(\boldsymbol{r})=\alpha\{\rho^{(1)}(\boldsymbol{r})\}^{\beta}$, α and β being constants, when i and j are neighboring cells and taken unity otherwise. When we take $g^*(\boldsymbol{r})=c^{1/2}$, c: constant to be determined so as to minimize F, the obtained form of F is also obtained i in the theory of Levine, Mayer and Aroeste[8] the rigorous grand partition function ψ_0 to a lattice gas is replaced by the function whic is obtained by applying Bethe-Fowler approx mation. It is my opinion that with the ap proximation of the form $g^{(2)}(\boldsymbol{r}_i,\boldsymbol{r}_j;\,\boldsymbol{R}_{ij})=$ $g^*(\boldsymbol{r}_i)g^*(\boldsymbol{r}_j)$ the localization of $\rho^{(1)}(\boldsymbol{r})$ near th centers of cells is inevitable, and as the co sequence we cannot expect the transition be tween solid and liquid or gas. It is to b noted that when we start with "the cell an point pair approximation" then the last thre terms in the sum of the fourth term of drop, and when we start with "the point an point pair approximation", then the third term drops in addition.

In our approximation, as u is taken to b smaller, the number of the preserved cluster is reduced and the evaluation of entropy term will be worse. So, we will restrict the valu of u so as not to become too small and deter mine $\rho^{(1)}$, $g^{(2)}$ and u so as to minimize th function F.

As to the result of the variation, it i expected from the calcuations for lattic gases*, that two regions will appear: th "fluid" region where $\rho^{(1)}(\boldsymbol{r})=1/v$ (constan independent of $\boldsymbol{r}$) at large specific volume and high temperature kT and the "solid region where $\rho^{(1)}(\boldsymbol{r})$ is localized near the cente of cell at small v and low kT. We will henc take up two sets of variational functions wit one parameter, each corresponding to one o these two regions, and adopt the smaller o the two minimum values for F as the ap proximate value of the free energy.

§ 2. Approximate Calculations

2a. Fluid Region. The variational func tions corresponding to the fluid state ar chosen to be

$$\rho^{(1)}(\boldsymbol{r})=1/v\,,\quad v=V/N=u/\rho \qquad (5$$

---

* Part I and several papers cited there.

$$g^{(2)}(\boldsymbol{r}_i, \boldsymbol{r}_j; \boldsymbol{R}_{ij}) = g^{(2)}(|\boldsymbol{r}_i - \boldsymbol{r}_j - \boldsymbol{R}_{ij}|) \qquad (6)$$

$$g^{(2)}(\boldsymbol{r}) = 0 \quad r < a\,, \qquad = 1 \quad r > a \qquad (6')$$

in the same degree of approximation as used in Part I. Substituting these into the right-hand side of Eq. (2), retaining the contributions between nearest neighbor cells only in the sum of the fourth term and estimating the integrals in the last three terms in the sum of the fourth term in an approximate way, we obtain, for $f \equiv F/N$,

$$\begin{aligned} \frac{f}{kT} &= \frac{1}{2}\,\frac{\rho}{ukT}\int_a^\infty V^{(2)}(r)\,4r^2 g\left(\frac{r}{a}, \xi\right)dr \\ &\quad + \ln\frac{\rho}{u} + \frac{1}{\rho}(1-\rho)\ln(1-\rho) \\ &\quad + 12(1-\gamma\rho)\ln\frac{1-\gamma\rho}{1-\rho} \\ &\quad + \frac{6}{\rho}(1-2\rho+\gamma\rho^2)\ln\frac{1-2\rho+\gamma\rho^2}{(1-\rho)^2} \end{aligned} \qquad (7)$$

where

$$\gamma u \equiv \int^{u_j} g^{(2)}(\boldsymbol{r}_i = 0, \boldsymbol{r}_j; |\boldsymbol{R}_{ij}| = (u/\sqrt{2})^{1/3})\,d\boldsymbol{r}_j \qquad (8)$$

and $\xi \equiv a^3/u$; γ being the function of ξ only. $g(r/a, \xi)$ is the factor due to the fact that there cannot be two particles in a single cell at a time. Substituting (4) into (7), assuming ξ to be constant and approximating that $g(r/a, \xi) \equiv 1$, we find that the value of u which minimize f/kT is given by

$$\begin{aligned} \frac{2}{\xi^2 u^2} &= 1 + \left\{1 - \frac{6kT}{4\sqrt{2}\,\pi}\left[\frac{1}{\rho} - \frac{11}{\rho^2}\ln(1-\rho)\right.\right. \\ &\quad + 12\gamma\ln(1-\gamma\rho) \\ &\quad \left.\left. + \left(\frac{6}{\rho^2} - 6\gamma\right)\ln(1-2\rho+\gamma\rho^2)\right]\right\}^{1/2}. \end{aligned} \qquad (9)$$

The equation of state is obtained from (7) and (9) to be

$$\frac{pv}{kT} = \frac{1}{vkT}\,\frac{16\pi}{9\xi u}\left(\frac{2}{\xi^2 u^2} - 3\right) + 1\,. \qquad (10)$$

In these equations, on the one hand, we have retained the correlations between nearest neighbor cells only, which is justified if ξ is small, and, on the other hand, we have put $g(r/a; \xi) \equiv 1$, which is justified if ξ is large. As the point of compromise, we may estimate that $\xi \fallingdotseq \sqrt{2}$ from intuition; when $\xi = \sqrt{2}$, a is equal to the distance between centers of neighboring cells. In the following, we use for numerical calculations

$$\xi = \sqrt{2} \quad \text{and} \quad \gamma = 0.594\,. \qquad (11)$$

The critical values obtained are

$kT_c = 1.31$, $v_c = 2.77$, $p_c = 0.168$, $p_c v_c / kT_c = 0.354$,

which are to be compared with the experimental values for argon:

$kT_c = 1.26$, $v_c = 3.14$, $p_c = 0.117$, $p_c v_c / kT_c = 0.291$.

In Figs. II-1 and II-2, the pressure and density under liquid-gas equilibrium calculated by using (9) and (10) are drawn.

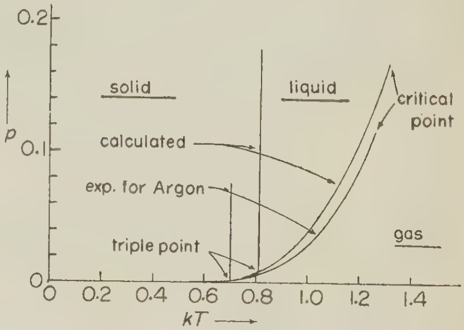

Fig. II-1. Phase Diagram (p-kT).

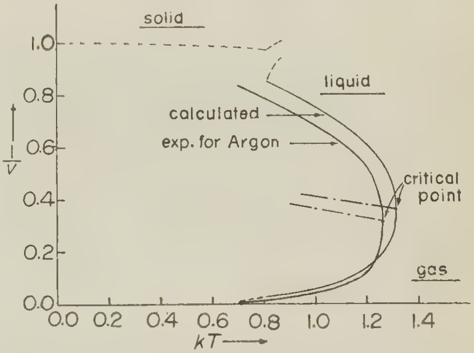

Fig. II-2. Phase Diagram ($1/v$-kT).

In the limit of $v \to \infty$, (10) and (9) reduce to

$$\frac{pv}{kT} = 1 + \frac{B}{v} \qquad (12)$$

$$B = \frac{1}{kT}\,\frac{16\pi}{9u\xi}\left(\frac{2}{\xi^2 u^2} - 3\right) \qquad (13)$$

$$\frac{2}{\xi^2 u^2} = 1 + \sqrt{1 + \frac{3\sqrt{2}}{4\pi}(6.5 - 6\gamma)kT}\,. \qquad (14)$$

The second Virial coefficient B calculated with $\gamma = 0.594$ is compared with the rigorous value in Fig. II-3*.

---

* If we determine the value of γ so that the value of B at high temperature ($kT = 400$) may fit with the rigorous value, we obtain $\gamma = 0.639$. The curve of B with this γ is also drawn in Fig. II-3. Using $\gamma = 0.639$ and $\xi = 1.3042$, we obtain for the critical values

$kT_c = 1.38$, $v_c = 2.95$, $p_c = 0.179$, $p_c v_c / kT_c = 0.382$.

2b. Solid Region. The variational functions corresponding to the solid state are chosen to be

$$\rho^{(1)}(\boldsymbol{r})=\left(\frac{6}{2^{1/3}\pi y}\right)^{3/2} e^{-6r^2/2^{1/3}y}\ , \qquad (15)$$

$$g^{(2)}(\boldsymbol{r}_i,\ \boldsymbol{r}_j;\ \boldsymbol{R}_{ij})=1\ , \qquad (16)$$

$$u=v\equiv x^3 \quad \text{or} \quad L=N\ . \qquad (17)$$

Of course, it might seem to be desirable to choose the variational functions with more parameters, e.g. those used by Mayer and Careri[5] or those analogous to Levine, Mayer and Aroeste's[8]. However, at the density of solid these reduce to the one we have chosen, which is seen from the Table I in Mayer and Careri's paper, so it is satisfactory to calculate with our variational functions.

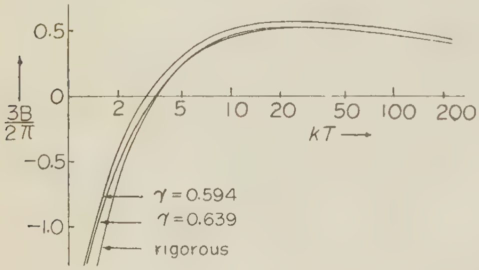

Fig. II-3. Second Virial Coefficient.

Substituting (15)–(17) into (2) and adopting such approximations in the first term that the potential energy is replaced by Morse type

$$V^{(2)}(r)=e^{-12[(r/2^{1/6})-1]}-2e^{-6[(r/2^{(1/6)})-1]} \qquad (4')$$

when the contributions from nearest neighbor cells are calculated and by the values for the distance between the centers of cells when the contributions of the further apart cells are calculated, we obtain

$$\frac{f}{kT}=\frac{f_1}{kT}+\frac{1}{kT}\left(\frac{0.06594}{v^4}-\frac{2.45392}{v^2}\right) \qquad (18)$$

$$\frac{f_1}{kT}=\frac{6}{kT}[(1-2xy)e^{12x^2y-12x+12}-2(1-xy)e^{3x^2y-6x+6}]$$

$$-\frac{3}{2}\ln y+\frac{3}{2}\ln\frac{6}{2^{1/3}\pi e}-3\ln x \qquad (18')$$

where y is determined by

$$\frac{kT}{8xy}=-[1-6x(1-2xy)]e^{12x^2y-12x+12}$$

$$+[1-3x(1-xy)]e^{3x^2y-6x+6}\ , \qquad (19)$$

which has been obtained from (18) by taking $\partial(f/kT)/\partial y=0$.

f/kT from (7) and (9) and from (18) and (19) are drawn in Fig. II-4 for $kT=0.7$, 0.8 and 0.85. The lower of these two is taken to give the approximate value for the free energy. From this figure, the values for solid and liquid equilibrium with $p=0$ are read to be

$$kT_{\text{tr.}}=0.81\ ,\quad v_{\text{tr. solid}}=1.03\ ,\quad v_{\text{tr. liquid}}=1.17$$

which may be compared with the values for melting point of argon ($p=0.0024$)

$$kT_{\text{m.}}=0.699\ ,\quad v_{\text{m. solid}}=1.07\ ,\quad v_{\text{m. liquid}}=1.17\ .$$

The equilibrium curves between solid and liquid and also between solid and gas are drawn in Fig. II-1 and II-2, in a very rough approximation; the values being taken from Fig. II-4.

Though the calculations have been very rough, our cell theory may be said to be the theory for gas, liquid and solid, while the cell theories of liquid in the past to be rather theories for solid and unstable solid. Considering the roughness of the approximations used, numerical values obtained may well be said to be generally in good agreement with the experimental values.

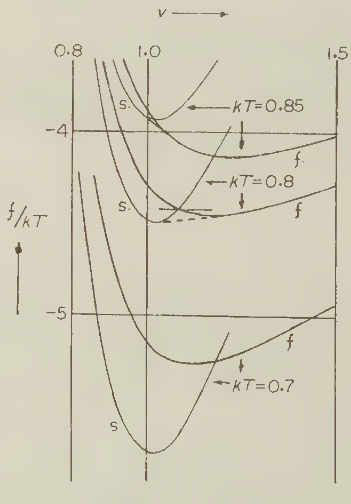

Fig. II-4.

The author wishes to express his cordial thanks to Prof. A. Harasima for his continual guidance and kind inspection of the manuscript and to Dr. K. Hiroike of this Institute and Dr. T. Usui of Tokyo University for their helpful discussions and criticisms.

References

1) R. Kikuchi: J. Chem. Phys. **19** (1951) 1230.
2) I. Shimose: J. Phys. Soc. Japan **10** (1955) 860.

3) T. Morita: J. Phys. Soc. Japan **12** (1957) 753. This paper will be referred to as CVM in the following.
4) e.g. R. H. Fowler and E. A. Guggenheim: *Statistical Thermodynamics*, Cambridge (1952), § 1323, Eq. (1323.1).
5) J. E. Mayer and G. Careri: J. Chem. Phys. **20** (1952) 1001.
6) J. G. Kirkwood: J. Chem. Phys. **18** (1950) 380.
7) J. S. Rowlinson and C. F. Curtiss: J. Chem. Phys. **19** (1951) 61, and several papers cited in it.
8) H. B. Levine, J. E. Mayer and H. Aroeste: J. Chem. Phys. **26** (1957) 207.

JOURNAL OF THE PHYSICAL SOCIETY OF JAPAN Vol. 12, No. 11, NOVEMBER, 1957

Statistical-Mechanical Theory of Irreversible Processes. II. Response to Thermal Disturbance

By Ryogo KUBO, Mario YOKOTA*
Department of Physics, University of Tokyo
and Sadao NAKAJIMA
Physical Institute, Nagoya University.

(Received August 3, 1957)

The possibility is examined to give rigorous expressions for kinetic coefficients such as heat conductivity, diffusion constant, thermoelectric power and so on which relate the flow of a certain kind to the generalized forces of thermal nature. We take here as the fundamental assumption Onsager's assumption that the average regression of spontaneous fluctuation of macroscopic variables follows the macroscopic physical laws. The kinetic coefficient G_{jl} appearing in the phenomenological equation, $\dot{\alpha}_j=\sum G_{jl}\,(\partial S/\partial\alpha_l)$ is shown then to be expressed as

$$G_{jl}=(k\beta)^{-1}\int_0^\infty d\tau\int_0^\beta <\dot{\alpha}_l(-i\hbar\lambda)\,\dot{\alpha}_j\,(\tau)>d\lambda$$

where k is the Boltzmann constant and $\beta=1/kT$. This is the same type of formula as we have for kinetic coefficients for mechanical disturbances (Kubo, J. Phys. Soc. **12** (1957) 570). The theory is illustrated for the example of electronic transport phenomena.

§ 1. Introduction

In the preceding paper by one of the present authors[1] a general theory has been developed for the calculation of kinetic coefficients such as electric conductivity and complex susceptibility in periodic field. It was shown that these kinetic coefficients are expressed in terms of time fluctuation of appropriate internal variables of the system. This conclusion was obtained by a perturbational calculation of linear response of the system to the external disturbance which is explicitly involved in the Hamiltonian of the system. We shall call in the following such disturbance as *mechanical*.

The mechanical disturbance is controlled by the observer in a mechanical way and the interaction of the system with the outer body which is directly controlled can be expressed by an additional perturbation energy which perturbs the natural motion of the system. There exists another kind of outer disturbances which will be called *thermal* disturbances. We are dealing with this kind of disturbance when we observe a non-equilibrium system in which temperature, pressure or concentration of particles is changing spacially or temporally. Thermal disturbances can not be expressed by definite perturbation energy in an unambiguous way.

---

* Now at the Research Institute for Fundamental Physics, University of Kyoto, Kyoto.

Now the question arises if it is possible to give similar expressions of the kinetic coefficients for thermal disturbances as those obtained for the mechanical disturbances. The answer should be yes, as we anticipate from the fact that the whole theory developed in I is a sort of generalization of the Einstein relation which means the conductivity is related to the diffusion constant. The aim of the present paper is to give a physical argument to justify this anticipation.[2] We shall do this by following the line of logics used by Onsager[3] in his monumental work on the reciprocity theorem. The general idea will be discussed in the first two sections. This will be further illustrated in the last section by the example of electron transport phenomena. The exact expressions are given for the kinetic coefficients appearing in the linear relations connecting electric and heat currents with the gradient of electrochemical potential and temperature.

§ 2. Application of Onsager's Assumption. Classical Case

In order to derive the generalized reciprocity law, Onsager[3] made the fundamental assumption;

(*A*) *The average behavior of fluctuation of a physical quantity in an aged system is governed by the macroscopic physical law which governs the macroscopic change of the corresponding macroscopic variable.*

This assumption is easily understood by a simple example. We may have local and temporal fluctuation of the temperature distribution in a system in thermal equilibrium. This fluctuation will decay in time on the average, following the Fourier law of heat conduction. We shall call this *Onsager's assumption.*

This will be expressed mathematically in the following way. Let $\alpha_j (j=1, 2, \cdots n)$ be a set of macroscopic variables of a system which we observe. These variables are considered as stochastic variables. We further introduce the variable,

$$\alpha_j(t+\Delta t|\alpha')\,,$$

which is defined as the stochastic variable α_j at the time point $t+\Delta t$ when the observed values of $(\alpha_1, \cdots, \alpha_n)$ at the time t are specified to $(\alpha_1', \cdots, \alpha_n')$. Now the assumption asserts that the relation,

$$\overline{\alpha_j(t+\Delta t|\alpha')}-\alpha'_j=\sum_k G_{jk}\frac{\partial S}{\partial \alpha'_k}\Delta t\,, \qquad (2.1$$

holds for a time interval Δt which is short i macroscopic sense but is sufficiently long o microscopic scale. In Eq. (2.1) $\overline{\alpha_j(t+\Delta t|\alpha')}$ i the average of $\alpha_j(t+\Delta t|\alpha')$ for all possibl initial states at the time t, which are com patible with the prescribed values α' at t On the right hand side of the equation, S i the entropy which is considered as the func tion of the variables α_1', α_2', $\cdots$ α_n', so tha $\partial S/\partial\alpha'_j$ multiplied by the temperature T i the generalized force which drives th variables α_1', $\cdots$ α_n' to change in macroscopi way. The constants G_{jk} are the macroscopic coefficients which correlate the motion of α to the driving forces. As far as we confin ourselves to those cases where the deviatio from equilibrium is small enough, we general ly expect the existence of linear relation between the average velocity of regression o α_j' and the driving forces.[3][4] In such case G_{jk}'s are simply constants in which we ar now interested.

Onsager obtained his celebrated law of re ciprocity from this assumption and the prin ciple of microscopic reversibility by showin that

$$\langle\alpha_j(t+\Delta t)\alpha_l(t)\rangle-\langle\alpha_j(t)\alpha_l(t)\rangle=-kG_{jl}\Delta t \qquad (2.2$$

where k is the Boltzmann constant and $\langle$ means the average over the equilibrium en semble.

Now we see that Onsager's assumptio provides us, besides the general proof of re ciprocity, a method of calculating G_{jl} in term of the time correlation of fluctuating variable α if the correlation can be calculated.

This is essentially the way of our reason ing employed in the present paper. In th preceding paper[1] we pursued the dynamica response of the system to a mechanical oute disturbance to derive the admittance i general, which is expressed as the Fourie component of time fluctuation of correspond ing physical quantities (fluctuation-dissipatio theorem).[1][5] Onsager's assumption is rathe a consequence of that argument. But, no we reverse our standpont, and start fro Eq. (2.1), that is the assumption (A).

In order to obtain a concrete expression o the coefficient G_{jl}, we rewrite Eq. (2.2) as follows.

$$
\begin{aligned}
G_{jl} &= -\frac{1}{k\Delta t}\langle \alpha_j(t+\Delta t)\alpha_l(t)-\alpha_j(t)\alpha_l(t)\rangle \\
&= +\frac{1}{k\Delta t}\int_0^{\Delta t} dt' \int_0^{t'} \langle \dot\alpha_j(t+\tau)\dot\alpha_l(t)\rangle\, d\tau \\
&= \frac{1}{k}\int_0^{\Delta t}\left(1-\frac{\tau}{\Delta t}\right)\langle \dot\alpha_j(t+\tau)\dot\alpha_l(t)\rangle\, d\tau \qquad (2.3)
\end{aligned}
$$

In this transformation we used the relation,

$$\frac{d^2}{d\tau^2}\langle \alpha_j(t+\tau)\alpha_l(t)\rangle = -\langle \dot\alpha_j(t+\tau)\dot\alpha(t)\rangle\,, \qquad (2.4)$$

which follows from the condition of stationary process,

$$
\begin{aligned}
\langle \alpha_j(t)\alpha_l(t')\rangle &= \langle \alpha_j(t+t_0)\alpha_l(t'+t_0)\rangle \\
&= \langle \alpha_j(t-t')\alpha_l(0)\rangle \\
&= \langle \alpha_j(0)\alpha_l(t'-t)\rangle\,, \qquad (2.5)
\end{aligned}
$$

and the assumption* that

$$\langle \dot\alpha_j\alpha_l\rangle = -\langle \alpha_j\dot\alpha_l\rangle = 0\,. \qquad (2.6)$$

Eq. (2.3) can further be written as

$$
\begin{aligned}
G_{jl} &\simeq \frac{1}{k}\int_0^\infty \langle \dot\alpha_j(t+\tau)\dot\alpha_l(t)\rangle\, d\tau \\
&= \frac{1}{k}\int_0^\infty \langle \dot\alpha_j(t)\dot\alpha_l(0)\rangle\, dt\,, \qquad (2.7)^{**}
\end{aligned}
$$

provided that the correlation time of $\dot\alpha_j$ and $\dot\alpha_l$ is short enough compared with that of α_j and α_l which is governed by the macroscopic law and is measured by

$$\tau_{\text{macro}} = \langle \alpha_j\alpha_l\rangle / kG_{jl}\,. \qquad (2.8)$$

As we see from Eq. (2.2), Eq. (2.7) is just the type of expression which we want to discuss in the following.

We shall examine more in detail in later sections the reasoning which leads to Eq. (2.7). We only note here that the argument made here is legitimate only in *classical* mechanics so that a certain revision is required to apply it to quantum-mechanical cases. The revised form is rather easily anticipated from the results of the previous paper. We shall discuss this in the next section.

Before doing that, we shall briefly describe here the classical derivation of (2.2) from (2.1) for the convenience of later reference. We multiply the both sides of Eq. (2.1) by α_l' and average them with the probability distribution density $W(\alpha_1', \cdots \alpha_n')$, which is the stationary probability for the realization of the values $(\alpha_1', \cdots \alpha_n')$ in the aged system. The left-hand side becomes evidently the correlation functions which appear in Eq. (2.2). The right-hand side is now transformed as

$$
\begin{aligned}
&\sum_m G_{jm}\Delta t\int\cdot\cdot\int \alpha_l'\left\{\frac{\partial}{\partial\alpha_m'}S(\alpha_1'\cdots\alpha_n')\right\}\cdot W(\alpha_1'\cdots\alpha_n')d\alpha_1'\cdots d\alpha_n' \\
&= k\sum_m G_{jm}\Delta t\int\cdot\cdot\int \alpha_l'\frac{\partial}{\partial\alpha_m'}W(\alpha_1'\cdots\alpha_n')d\alpha_1'\cdots d\alpha_n' \\
&= -kG_{jl}\Delta t
\end{aligned}
$$

which coincides with the right-hand side of Eq. (2.2). We made here use of the assumption

$$W(\alpha_1'\cdots\alpha_n') = C\exp\left\{\frac{1}{k}S(\alpha_1\cdots\alpha_n')\right\} \qquad (2.9)$$

where C is the normalization constant.

§ 3. Application of Onsager's Assumption

For quantum-mechanical systems, it is not always possible to define a simultaneous distribution of the observed values of α_1, α_2, $\cdots$ and α_n. Or more specifically, we may not be able to prepare a statistical ensemble like that defined classically by (2.9). This is so because such variable are not necessarily commutable with each other or with the Hamiltonian itself. It is true that they are nearly commutable if they are really macroscopic quantities. But still caution is requir-

---

* If the condition (2.6) is not fulfilled, Eqs. (2.3) and (2.7) must be corrected by the additional term.

$$-\frac{1}{k}\langle \dot\alpha_j\alpha_l\rangle = \frac{1}{k}\langle \alpha_j\dot\alpha_l\rangle\,.$$

** The infinite integral here is rather the Cesaro limit as one sees at once from the last form of Eq. (2.3). The Cesaro limit may be replaced by the Abel limit,

$$\lim_{\varepsilon\to+0}\int e^{-\varepsilon t}\langle \dot\alpha_j(t)\dot\alpha_l(0)\rangle\, dt\,.$$

We omitted here more rigorous mathematical statement because physicists are rather accustomed to use improper integrals which are summarable in some way or another.

ed for the effect which may enter as a consequence of non-commutability.

Considering this circumstance, we propose here to interprete Onsager's assumption in a little less stringent way than what Eq. (2.1) literally implies. Namely, we now regard $\overline{\alpha_j(t+\Delta t|\alpha')}$ as the expectation of the variable α_j at the time $t+\Delta t$ for a statistical ensemble for which the variables $(\alpha_1, \cdots \alpha_n)$ have the expectation values $(\alpha_1', \cdots, \alpha_n')$ at the time t. This ensemble is represented by the statistical operator $\rho(t+\Delta t|\alpha')$ which, by definition, has the properties,

$$\mathrm{Tr}\,\rho(t+0|\alpha')\alpha_j=\alpha_j' , \tag{3.1}$$

$$\mathrm{Tr}\,\rho(t+\Delta t|\alpha')\alpha_j=\overline{\alpha_j(t+\Delta t|\alpha')} . \tag{3.2}$$

According to our new interpretation, Eq. (2.1) is now read as

$$\mathrm{Tr}\,\rho(t+\Delta t|\alpha')\alpha_j-\alpha_j'=\sum_k G_{jk}\frac{\partial S}{\partial \alpha_k'}\Delta t . \tag{3.3}$$

Now the question is what will be this density matrix $\rho(t+0|\alpha')$. This is the most subtle point of the whole argument. It seems to us that the most natural answer for the form of $\rho(t+0|\alpha')$ is

$$\rho(t+\Delta t(\alpha')=\exp[\beta(\Omega-\mathscr{H})-\beta\sum A_j\alpha_j] , \tag{3.4}$$

which is a sort of canonical distribution. Here Ω is a free energy and A_j's $(j=1, 2, \cdots, n)$ are scalar quantities which are defined by the conditions (3.1) and correspond to the forces associated with the coordinates α_j's. The density operator (3.4) is the solution of maximization problem of the entropy

$$S=-k\,\mathrm{Tr}\,\rho\log\rho , \tag{3.5}$$

with the supplementary conditions (3.2) and other well known conditions. The parameters A_j's enter here as the undetermined multipliers. We see at once that

$$\beta\frac{\partial\Omega}{\partial A_j}=\bar{\alpha}_j-\alpha_j' , \tag{3.6}$$

$$S=-k\beta\Omega+k\beta\mathscr{H}+\sum_j kA_j\bar{\alpha}_j , \tag{3.7}$$

where $\mathscr{H}$ and $\bar{\alpha}_j$ are the everage values for the ensemble represented by (3.4), and

$$\frac{\partial S}{\partial \alpha_j'}=k\beta A_j . \tag{3.8}$$

Therefore Eq. (3.3) now becomes

$$\mathrm{Tr}\exp[\beta(\Omega-\mathscr{H})-\beta\sum_l A_l\alpha_l]\{\alpha_j(\Delta t)-\alpha_j(0)\}$$
$$=k\beta\sum_l G_{jl}A_l\Delta t . \tag{3.9}$$

where $\alpha_j(\tau)$ means the Heisenberg representation of the variable α_j. Namely they are defined by

$$\dot{\alpha}_j(\tau)=\frac{1}{i\hbar}[\alpha_j(\tau), \mathscr{H}] ,$$
$$\alpha_j(\tau)=\exp(i\mathscr{H}\tau/\hbar)\,d\exp(-i\mathscr{H}\tau/\hbar) .$$
(3.10

We now assume the linear dissipative systems, so that the deviation from the equilibrium is small. This means that the forces A_j's are really small. Thus we expand the left-hand side of Eq. (3.9) and leave only the linear term. Using the formula

$$\exp[-\beta\mathscr{H}-\beta\sum_l A_l\alpha_l]$$
$$=\exp(-\beta\mathscr{H})$$
$$-\int_0^\beta \exp(-\beta\mathscr{H})\sum_l A_l\,\alpha_l(-i\hbar\lambda)d\lambda+o(A) ,$$
(3.11

we obtain at once

$$\overline{\alpha_j(t+\Delta t|\alpha')}=\langle\alpha_j\rangle$$
$$-\sum A_l\int_0^\beta\langle\alpha_l(-i\hbar\lambda)\alpha_j(\Delta t)\rangle d\lambda$$
$$+o(A) .$$
(3.12

where $\langle\ \rangle$ means the average over the equilibrium distribution $\exp\beta(\Omega^0-\mathscr{H})$ so that $\langle\alpha_j\rangle$ is the equilibrium value of α_j. Eq. (3.12) reduces, in particular for $\Delta t=0$, to

$$\overline{\alpha_j(t|\alpha')}\equiv\alpha_j'$$
$$=\langle\alpha_j\rangle-\sum_l A_l\int_0^\beta\langle\alpha_l(-i\hbar\lambda)\alpha_j\rangle d\lambda$$
$$+o(A) ,$$
(3.13

which is the condition to determine the forces A in terms of the deviation $\alpha_j'-\langle\alpha_j\rangle$ from the equilibrium. The set of Eq. (3.13) is equivalent to Eq. (3.6).

Inserting Eq. (3.11) into (3.9) we get easil

$$\frac{1}{\beta}\int_0^\beta\langle\alpha_l(i\hbar\lambda)\{\alpha_j(\Delta t)-\alpha_j(0)\}\rangle d\lambda$$
$$=-kG_{jl}\Delta t ,$$
(3.14

which corresponds to Eq. (2.2), as we see from the fact that the left-hand side of Eq. (3.14) becomes the correlation function appearing in Eq. (2.2) in the classical lim $\hbar\to 0$.

Like Eq. (2.4) for the classical correlatio function, we evidently have the relation

$$\frac{d^2}{d\tau^2}\int_0^\beta\langle\alpha_l(-i\hbar\lambda)\alpha_j\rangle d\lambda$$
$$=-\int_0^\beta\langle\dot{\alpha}_l(-i\hbar\lambda)\dot{\alpha}_j(\tau)\rangle d\lambda .$$
(3.1

Thus, if the condition

$$\int_0^\beta \langle \dot{\alpha}_l(-i\hbar\lambda)\alpha_j \rangle \, d\lambda$$
$$= -\int_0^\beta \langle \alpha_l(-i\hbar\lambda)\dot{\alpha}_j \rangle \, d\lambda = 0 \,, \tag{3.16}$$

is satisfied, Eq. (3.14) can be transformed into

$$G_{jl} = \frac{1}{k\beta}\int_0^{\Delta t}\left(1-\frac{\tau}{\Delta t}\right)d\tau$$
$$\times \int_0^\beta \langle \dot{\alpha}_l(-i\hbar\lambda)\dot{\alpha}_j(\tau) \rangle \, d\lambda \,. \tag{3.17}$$

just in the same way as we did in Eq. (2.3). If, furthermore, the characteristic time of decay of the integrand of (3.17) is small enough compared with that which corresponds to (2.8), Eq. (3.17) gives

$$G_{jl} = \frac{1}{k\beta}\int_0^\infty d\tau \int_0^\beta \langle \dot{\alpha}_l(-i\hbar\lambda)\dot{\alpha}_j(\tau) \rangle \, d\lambda \,. \tag{3.18}$$

as the wanted expression for the kinetic coefficient G_{jl}. The infinite integral may be regarded as the Cesaro limit or the Abel limit. We note finally that the condition (3.16) is satisfied if

$$\frac{1}{i\hbar}\langle [\alpha_l, \alpha_j] \rangle = 0 \,, \tag{3.19}$$

that is, if α_l and α_j are commutable on the average. The equivalence of (3.19) to (3.16) is seen from the identity, Eq. (3.7) of I, i.e.,

$$[\exp(-\beta\mathscr{H}), A]$$
$$= i\hbar \int_0^\beta \exp(-\beta\mathscr{H})\dot{A}(-i\hbar\lambda)\, d\lambda \,. \tag{3.20}$$

Therefore we have

$$\int_0^\beta \langle \dot{\alpha}_l(-i\hbar\lambda)\alpha_j \rangle \, d\lambda$$
$$= (i\hbar)^{-1}\,\mathrm{Tr}\,[\exp\beta(\Omega^0-\mathscr{H}), \alpha_l]\alpha_j$$
$$= (i\hbar)^{-1}\,\mathrm{Tr}\exp\beta(\Omega^0-\mathscr{H})[\alpha_l, \alpha_j] \,.$$

It should be remembered that the expression (3.18) becomes rigorous only when the choice of infinitely large Δt is proved to be possible for the particular choice of the variables α. Otherwise, it remains only a certain approximation.

This should be particularly emphasized, because we see in literatures certain confusion about this point.[6)][7)] Some of formulae of the type (2.17) or (3.18) given in literatures are by no means rigorous since the above-mentioned choice of $\Delta t \to \infty$ is simply impossible. These approximate formulae, though we should not underestimate their usefulness, must be discriminated from such rigorous formulae as we are concerned with in the present work.

For instance, the expression of conductivity, $S_{\mu\nu}{}^{(1)}$ in Eq. (4.6) of the present paper, which was derived in the preceding paper I, is rigorous. We may write this as

$$\sigma = \int_0^\infty \int_0^\beta \langle J_x J_x(t+i\hbar\lambda) \rangle \, d\lambda dt = \frac{ne}{m^*}\tau \,, \tag{3.21}$$

where we defined the effective mass m^* by

$$\frac{ne}{m^*} = \int_0^\beta \langle J_x J_x(i\hbar\lambda) \rangle \, d\lambda \,,$$

(see Eq. (8.12), I) and the average relaxation time τ by

$$\tau = \int_0^\infty \phi(t)dt \,, \tag{3.22}$$

with

$$\phi(t) = \int_0^\beta \langle J_x J_x(t+i\hbar\lambda) \rangle \, d\lambda \Big/ \int_0^\beta \langle J_x J_x(i\hbar\lambda) \rangle \, d\lambda \,. \tag{3.23}$$

Now an approximation for this relaxation time is given by

$$\frac{1}{\tau} \sim -\int_0^{\tau_c} \ddot{\phi}(t)dt$$
$$= \int_0^{\tau_c} dt \int_0^\beta \langle \dot{J}_x \dot{J}_x(t+i\hbar\lambda) \rangle \Big/ \int_0^\beta \langle J_x J_x(i\hbar\lambda) \rangle d\lambda \,, \tag{3.24}$$

which may be used as good approximation under certain restricted conditions. Namely it may be used when the function $\phi(t)$ behaves like $\exp(-t/\tau)$, or in other words, when the spectrum of relaxation time of $\phi(t)$ is nearly degenerate. It is easy to show that Eq. (3.24) gives the Grüneisen formula when applied to electrons scattered by phonons.[8)] One of the present authors proved many years ago that the Grüneisen formula is derived from the Bloch equation by calculating the average of the relaxation frequencies and equating this to the reciprocal of the average relaxation time τ in Eq. (3.21).[9)]

We may see the approximation (3.24) roughly by applying the same transformation technique as used for Eqs. (2.3) and (3.17) to the function $\phi(t)$, that is,

$$\phi(t) = 1 + \int_0^t (t-\tau)\ddot{\phi}(\tau)d\tau \sim 1 + t\int_0^{\tau_c}\ddot{\phi}(\tau)d\tau \,. \tag{3.25}$$

The last form may be used for t which is much longer than the characteristic time τ_d

of $\ddot{\phi}(\tau)$ and shorter than the relaxation time τ of $\phi(t)$ provided that such a choice of t is possible.* For such t, $\phi(t)$ is decreasing as $1-t/\tau$, τ being that defined by Eq. (3.24). Note that here the assumption is introduced for the existence of a plateau value of the integral, i.e.,

$$\int_0^t \ddot{\phi}(\tau)d\tau \sim \int_0^{\tau_c} \ddot{\phi}(\tau)\,d\tau\ ,$$

for $\tau_d \ll t \ll \tau$.

It is essential in the expression (3.24) to stop the integration at a finite upper limit, because we ought to have

$$\int_0^\infty dt \int_0^\beta \langle\, \dot{j}_x \dot{j}_x(t+i\hbar\lambda)\,\rangle\, d\lambda = 0\ , \tag{3.26}$$

if the integral (3.21) does exist.

It should be also noticed that the Kirkwood formula[6]

$$\zeta = m/\tau = \beta \int_0^{\tau_c} \langle\, \dot{P}_x \dot{P}_x(t)\, dt\ , \tag{3.27}$$

for the friction constant ζ of a Brownian particle is simply a special case of Eq. (3.24).

Thus the Kirkwood formula (3.27) and the similar formula (3.24) rely upon rather restricted assumptions about the nature of $\phi(t)$, which can by no means be proved to be generally valid. On the other hand, Eq. (3.21) itself is rigorous and fundamental as was proved in I and also in § 4 of the present paper. We should discriminate between these two classes of expressions for kinetic coefficients.

§ 4. Electron Transport Phenomena

Let us now consider, as an illuminating example of the argument made in the preceding sections, the electronic transport phenomena in metals or semi-conductors. According to the phenomenological theory,[10] the electric current density $\boldsymbol{j}$ and the heat flow density $\boldsymbol{q}$ are linear functions of the gradients of the electrochemical potential

$$\mu = \zeta - e\varphi\ , \tag{4.1}$$

of the electrons and the gradient of temperature. The charge of electron is taken here as $-e$. Namely we have

$$\boldsymbol{j} = \mathfrak{S}^{(1)}\left(\boldsymbol{E} + \frac{T}{e}\nabla\xi\right) + \mathfrak{S}^{(2)}\frac{1}{T}\nabla T$$

$$\boldsymbol{q} = -\mathfrak{S}^{(3)}\left(\boldsymbol{E} + \frac{1}{e}\nabla\xi\right) - \mathfrak{S}^{(4)}\frac{1}{T}\nabla T\ , \tag{4.2}$$

where $\boldsymbol{E}$ is the electric field and ξ is defined by

$$\xi = \zeta / T\ . \tag{4.3}$$

Eq. (4.2) can be written as

$$\boldsymbol{E} = \rho\,\boldsymbol{j} - \frac{1}{e}\mathfrak{S}\nabla T - \frac{1}{e}\nabla\zeta$$

$$\boldsymbol{q} = \pi\boldsymbol{j} - \kappa\nabla T - \frac{1}{e}\zeta\boldsymbol{j}\ , \tag{4.4}$$

where the constants are

$$\begin{aligned} \rho &= \mathfrak{S}^{(1)-1} = \sigma^{-1}\ , \\ \mathfrak{S} &= (e\rho\mathfrak{S}^{(2)} - \zeta)\,/\,T\ , \\ \pi &= -\mathfrak{S}^{(3)}\rho - \zeta/T\ . \\ \kappa &= (\mathfrak{S}^{(4)} - \mathfrak{S}^{(3)}\rho\mathfrak{S}^{(2)})\,/\,T\ . \end{aligned} \tag{4.5}$$

Here ρ is the electric resistance, κ the heat conductivity, $-\mathfrak{S}/e$ the absolute thermoelectric power per unit temperature difference, and π is the Peltier constant. All of $\mathfrak{S}^{(r)}$ $(r=1,\cdots 4)$ and other coefficients are tensors of the second rank. Our problem is now to find exact expressions for these coefficients in Eqs. (4.2) or (4.4).

The answer is easily anticipated, because we know already the exact expression of $\mathfrak{S}^{(1)}$, that is the conductivity tensor. Thus we want to show that the equations,

$$\begin{aligned} S^{(1)}_{\mu\nu} &= \int_0^\infty \int_0^\beta \langle\, j_\nu j_\mu(t+i\hbar\lambda)\,\rangle\, d\lambda dt \\ S^{(2)}_{\mu\nu} &= \int_0^\infty \int_0^\beta \langle\, q_\nu j_\mu(t+i\hbar\lambda)\,\rangle\, d\lambda dt \\ S^{(3)}_{\mu\nu} &= \int_0^\infty \int_0^\beta \langle\, j_\nu q_\mu(t+i\hbar\lambda)\,\rangle\, d\lambda dt \\ S^{(4)}_{\mu\nu} &= \int_0^\infty \int_0^\beta \langle q_\nu q_\mu(t+i\hbar\lambda)\,\rangle\, d\lambda dt\ , \end{aligned} \tag{4.6}$$

hold as rigorous expressions for these kinetic coefficients. Expressions similar to Eqs. (4.6) have been given indepently by Mori[7]. His formulae, however, differ from (4.6) in the upper limit of the time integral which he put as finite. This reflects the difference of the ways of reasoning. We shall show that it can be extended to infinity and that Eqs. (4.6) are rigorous in their nature. We follow the line of reasoning described in the foregoing sections in order to arrive at these results.

---

* Physically, the function $\ddot{\phi}(t)$ corresponds to the time correlation of forces acting on the electrons. The characteristic time τ_d of this will be the duration time of collision if the electrons are scattered by phonons or other perturbers only with rare chances and short duration of collision.

It is most convenient to consider the electron number density $n(\boldsymbol{r})$ and the energy density $\mathcal{E}(\boldsymbol{r})$. We regard an electron gas system with the volume V as an isolated system and define the total entropy as the sum of entropy density under the assumption of local equilibrium. The local entropy density is a function of $n(\boldsymbol{r})$ and $\mathcal{E}(\boldsymbol{r})$. Thus the entropy S can be expanded in terms of fluctuations $\Delta n(\boldsymbol{r})$ and $\Delta\mathcal{E}(\boldsymbol{r})$ of $n(\boldsymbol{r})$ and $\mathcal{E}(\boldsymbol{r})$ as

$$\begin{aligned} S &= \int s(\boldsymbol{r})d\boldsymbol{r} \\ &= \int\left[s_0 + \frac{\partial s}{\partial\mathcal{E}}\Delta\mathcal{E} + \frac{\partial s}{\partial n}\Delta n + \frac{1}{2}\left\{\frac{\partial^2 s}{\partial\mathcal{E}^2}(\Delta\mathcal{E})^2 + 2\frac{\partial^2 s}{\partial\mathcal{E}\partial n}(\Delta\mathcal{E}\,\Delta n) + \frac{\partial^2 s}{\partial n^2}(\Delta n)^2\right\}\right]d\boldsymbol{r} + \cdots \\ &= S_0 + \frac{1}{2}\left(\frac{\partial}{\partial\mathcal{E}}\frac{1}{T}\right)\int(\Delta\mathcal{E})^2 d\boldsymbol{r} + \left(\frac{\partial}{\partial n}\frac{1}{T}\right)\int\Delta\mathcal{E}\Delta n d\boldsymbol{r} - \frac{1}{2}\left(\frac{\partial}{\partial n}\right)\int(\Delta n)^2 d\boldsymbol{r} + \cdots, \end{aligned} \tag{4.7}$$

where S_0 is the equilibrium entropy of whole system so that the linear terms in $\Delta\mathcal{E}$ and Δn must vanish. We made in Eq. (4.7) use of the relations,

$$\frac{\partial s}{\partial\mathcal{E}} = \frac{1}{T}, \quad \text{and} \quad \frac{\partial s}{\partial n} = -\frac{\zeta}{T}.$$

Now the fluctuations $\Delta\mathcal{E}(\boldsymbol{r})$ and $\Delta n(\boldsymbol{r})$ are developed in the Fourier components. Eq. (4.7) is rewritten as

$$S = S - \frac{1}{2}\frac{1}{T^2}\left(\frac{\partial T}{\partial\mathcal{E}}\right)_n V\sum_{\boldsymbol{k}}\mathcal{E}_{\boldsymbol{k}}\mathcal{E}_{-\boldsymbol{k}} - \frac{1}{T^2}\left(\frac{\partial T}{\partial n}\right)_{\mathcal{E}} V\sum_{\boldsymbol{k}}\mathcal{E}_{\boldsymbol{k}}n_{-\boldsymbol{k}} - \frac{1}{2}\left(\frac{\partial\xi}{\partial n}\right)_{\mathcal{E}} V\sum_{\boldsymbol{k}} n_{\boldsymbol{k}}n_{-\boldsymbol{k}} + \cdots, \tag{4.8}$$

where $n_{\boldsymbol{k}}$ and $\mathcal{E}_{\boldsymbol{k}}$ are the Fourier components of $n(\boldsymbol{r})$ and $\mathcal{E}(\boldsymbol{r})$ respectively.

The general thermodynamics of irreversible processes here asserts that the flows $\dot{\mathcal{E}}_{\boldsymbol{k}}$ and $\dot{n}_{\boldsymbol{k}}$, when they are present as macroscopic observables and hence their fluctuation is neglected, are linearly related to the driving forces, $\partial S/\partial n_{\boldsymbol{k}}$ and $\partial S/\partial\mathcal{E}_{\boldsymbol{k}}$. Namely the phenomenological equations are

$$\dot{n}_{\boldsymbol{k}} = \sum_{\boldsymbol{k}'} G^{(1)}_{\boldsymbol{k}\boldsymbol{k}'}\frac{\partial S}{\partial n_{\boldsymbol{k}'}} + \sum_{\boldsymbol{k}'} G^{(2)}_{\boldsymbol{k}\boldsymbol{k}'}\frac{\partial S}{\partial\mathcal{E}_{\boldsymbol{k}'}}, \qquad \dot{\mathcal{E}}_{\boldsymbol{k}} = \sum_{\boldsymbol{k}'} G^{(3)}_{\boldsymbol{k}\boldsymbol{k}'}\frac{\partial S}{\partial n_{\boldsymbol{k}'}} + \sum_{\boldsymbol{k}'} G^{(4)}_{\boldsymbol{k}\boldsymbol{k}'}\frac{\partial S}{\partial\mathcal{E}_{\boldsymbol{k}'}}, \tag{4.9}$$

which, with the aid of Eq. (4.8), are written as

$$\begin{aligned} \dot{n}_{\boldsymbol{k}} &= -V\sum_{\boldsymbol{k}'} G^{(1)}_{\boldsymbol{k}\boldsymbol{k}'}\left\{\left(\frac{\partial\xi}{\partial n}\right)_{\mathcal{E}} n_{-\boldsymbol{k}'} + \frac{1}{T^2}\left(\frac{\partial T}{\partial n}\right)_{\mathcal{E}}\mathcal{E}_{-\boldsymbol{k}'}\right\} \\ &\quad - V\sum_{\boldsymbol{k}'} G^{(2)}_{\boldsymbol{k}\boldsymbol{k}'}\left\{\frac{1}{T^2}\left(\frac{\partial T}{\partial n}\right)_{\mathcal{E}} n_{-\boldsymbol{k}'} + \frac{1}{T^2}\left(\frac{\partial T}{\partial\mathcal{E}}\right)_n\mathcal{E}_{-\boldsymbol{k}'}\right\} \\ \dot{\mathcal{E}}_{\boldsymbol{k}} &= -V\sum_{\boldsymbol{k}'} G^{(3)}_{\boldsymbol{k}\boldsymbol{k}'}\left\{\left(\frac{\partial\xi}{\partial n}\right)_{\mathcal{E}} n_{-\boldsymbol{k}'} + \frac{1}{T^2}\left(\frac{\partial T}{\partial n}\right)_{\mathcal{E}}\mathcal{E}_{-\boldsymbol{k}'}\right\} \\ &\quad - V\sum_{\boldsymbol{k}'} G^{(4)}_{\boldsymbol{k}\boldsymbol{k}'}\left\{\frac{1}{T^2}\left(\frac{\partial T}{\partial n}\right)_{\mathcal{E}} n_{-\boldsymbol{k}'} + \frac{1}{T^2}\left(\frac{\partial T}{\partial\mathcal{E}}\right)_n\mathcal{E}_{-\boldsymbol{k}'}\right\}. \end{aligned} \tag{4.10}$$

The flows $\boldsymbol{j}(\boldsymbol{r})$ and $\boldsymbol{q}(\boldsymbol{r})$ are related to the densities $n(\boldsymbol{r})$ and $\mathcal{E}(\boldsymbol{r})$ by the phenomenological equations,*

---

* These equations leave an ambiguity for the current components which are derived from the antisymmetric part of the tensors $\mathfrak{S}^{(r)}$, which vanish automatically in the divergence.[1] Thus the following argument is, strictly speaking, incompetent as the proof of the antisymmetric parts of Eqs. (4.6). This point will be considered in a forthcoming paper.

$$\dot{n}(\boldsymbol{r})=\frac{1}{e}\operatorname{div}\boldsymbol{j}(\boldsymbol{r}) ,$$

$$\dot{\varepsilon}(\boldsymbol{r})=-\operatorname{div}\boldsymbol{q}(\boldsymbol{r}) , \tag{4.11}$$

so that we have

$$\dot{n}_{\boldsymbol{k}}=\frac{1}{e}i(\boldsymbol{k}\boldsymbol{j}_{k}) ,$$

$$\dot{\varepsilon}_{\boldsymbol{k}}=-i(\boldsymbol{k}\boldsymbol{q}_{k}) , \tag{4.12}$$

where $\boldsymbol{j}_{\boldsymbol{k}}$ and $\boldsymbol{q}_{\boldsymbol{k}}$ are the Fourier components of the flow densities. Inserting the Fourier components of Eq. (4.2) into Eq. (4.12) and making use of the equations,

$$\nabla T=\frac{\partial T}{\partial\varepsilon}\nabla\varepsilon+\frac{\partial T}{\partial n}\nabla n ,$$

$$\nabla\xi=\frac{\partial\xi}{\partial\varepsilon}\nabla\varepsilon+\frac{\partial\xi}{\partial n}\nabla n .$$

we obtain

$$e\dot{n}_{\boldsymbol{k}}=-\left(\frac{T}{e}\frac{\partial\xi}{\partial\varepsilon}\boldsymbol{k}\mathfrak{S}^{(1)}\boldsymbol{k}+\frac{1}{T}\frac{\partial T}{\partial\varepsilon}\boldsymbol{k}\mathfrak{S}^{(2)}\boldsymbol{k}\right)\varepsilon_{\boldsymbol{k}}$$
$$-\left(\frac{T}{e}\frac{\partial\xi}{\partial n}\boldsymbol{k}\mathfrak{S}^{(1)}\boldsymbol{k}+\frac{1}{T}\frac{\partial T}{\partial n}\boldsymbol{k}\mathfrak{S}^{(2)}\boldsymbol{k}\right)n_{\boldsymbol{k}}$$

$$\dot{\varepsilon}_{\boldsymbol{k}}=-\left(\frac{T}{e}\frac{\partial\xi}{\partial\varepsilon}\boldsymbol{k}\mathfrak{S}^{(3)}\boldsymbol{k}+\frac{1}{T}\frac{\partial T}{\partial\varepsilon}\boldsymbol{k}\mathfrak{S}^{(4)}\boldsymbol{k}\right)\varepsilon_{\boldsymbol{k}}$$
$$-\left(\frac{T}{e}\frac{\partial\xi}{\partial n}\boldsymbol{k}\mathfrak{S}^{(3)}\boldsymbol{k}+\frac{1}{T}\frac{\partial T}{\partial n}\boldsymbol{k}\mathfrak{S}^{(4)}\boldsymbol{k}\right)n_{\boldsymbol{k}} . \tag{4.13}$$

Comparing Eq. (4.10) with Eq. (4.13) we find that

$$eVG^{(r)}_{\boldsymbol{k},-\boldsymbol{k}}=\frac{T}{e}\boldsymbol{k}\mathfrak{S}^{(r)}\boldsymbol{k} , \qquad r=1,\cdots 4, \tag{4.14}$$

and that

$$G^{(r)}_{\boldsymbol{k},\boldsymbol{k}'}=0 , \qquad \text{if} \quad \boldsymbol{k}+\boldsymbol{k}'\neq 0 .$$

These relations must hold in order that the "thermodynamic" relations, (4.9), are consistent with the phenomenological equations (4.2).

Now we are in position to apply our logics of previous section to obtain rigorous expressions for $G^{(r)}_{k,-k}$. Eq. (3.14) is now read as

$$\frac{1}{\beta}\int_0^\beta\langle n_{-\boldsymbol{k}}(t-i\hbar\lambda)\{n_{\boldsymbol{k}}(t+\Delta t)-n_{\boldsymbol{k}}(t)\}\rangle d\lambda=-kG^{(1)}_{\boldsymbol{k},-\boldsymbol{k}}\Delta t ,$$
$$\frac{1}{\beta}\int_0^\beta\langle \varepsilon_{-\boldsymbol{k}}(t-i\hbar\lambda)\{n_{\boldsymbol{k}}(t+\Delta t)-n_{\boldsymbol{k}}(t)\}\rangle d\lambda=-kG^{(2)}_{\boldsymbol{k},-\boldsymbol{k}}\Delta t .$$
$$\frac{1}{\beta}\int_0^\beta\langle n_{-\boldsymbol{k}}(t-i\hbar\lambda)\{n_{\boldsymbol{k}}(t+\Delta t)-\varepsilon_{\boldsymbol{k}}(t)\}\rangle d\lambda=-kG^{(3)}_{\boldsymbol{k},-\boldsymbol{k}}\Delta t ,$$
$$\frac{1}{\beta}\int_0^\beta\langle \varepsilon^{-}{}_{\boldsymbol{k}}(t-i\hbar\lambda)\{\varepsilon_{\boldsymbol{k}}(t+\Delta t)-\varepsilon_{\boldsymbol{k}}(t)\}\rangle d\lambda=-kG^{(4)}_{\boldsymbol{k},-\boldsymbol{k}}\Delta t . \tag{4.15}$$

By the remark made at the end of § 3, it is evident that we have

$$\int_0^\beta\langle n_{-\boldsymbol{k}}(t-i\hbar\lambda)\,\dot{n}_{\boldsymbol{k}}(t)\rangle d\lambda=0 ,$$

and

$$\int_0^\beta\langle \varepsilon_{-\boldsymbol{k}}(t-i\hbar\lambda)\,\dot{\varepsilon}_{\boldsymbol{k}}(t)\rangle d\lambda=0 .$$

Corresponding expressions containing $n_{\boldsymbol{k}}$ and $\varepsilon_{\boldsymbol{k}}$ are also zero, because we have by virtue of Eq. (3.20)

$$\int_0^\beta\langle \dot{n}_{-\boldsymbol{k}}(t-i\hbar\lambda)\,\varepsilon_{\boldsymbol{k}}(t)\rangle d\lambda=\frac{1}{i\hbar}\langle[n_{-\boldsymbol{k}},\varepsilon_{\boldsymbol{k}}]\rangle=-i(\boldsymbol{k}\boldsymbol{j})/e .$$

The last expression is obtained by explicit calculation of the commutator $[n_{-\boldsymbol{k}},\varepsilon_{\boldsymbol{k}}]$ in terms of quantized wave functions. The average of current in equilibrium is equal to zero, so that we may put

$$\int_0^\beta\langle n_{-\boldsymbol{k}}(t-i\hbar\lambda)\,\dot{\varepsilon}_{\boldsymbol{k}}(t)\rangle d\lambda=\int_0^\beta\langle \varepsilon_{-\boldsymbol{k}}(t-i\hbar\lambda)\dot{n}_{\boldsymbol{k}}(t)\rangle d\lambda=0 .$$

Therefore we can safely rewrite Eqs. (4.14) in the form of Eq. (3.17).

Furthermore, Eq. (4.14) shows that the decay of the functions on the left-hand sides of Eq. (4.15) becomes infinitely slow if the wave number k approaches to zero. Speaking in classical language, the time of the decay of the fluctuation of n and $\mathcal{E}$ becomes infinitely slow as the wave length of the spacial fluctuation becomes infinitely large. This is physically evident. This provides a sound basis for the transformation of Eq. (4.15) into the expressions of the type Eq. (3.18) in the limit of $k\to 0$. Thus we arrive at the equations

$$\begin{aligned}
\lim_{k\to 0} G^{(1)}_{k,-k} &= \lim \frac{1}{k}\int_0^\infty\int_0^\beta \langle \dot{n}_{-k}(-i\hbar\lambda)\, \dot{n}_k(t)\rangle\, d\lambda dt\,, \\
\lim_{k\to 0} G^{(2)}_{k,-k} &= \lim \frac{1}{k}\int_0^\infty\int_0^\beta \langle \dot{\mathcal{E}}_{-k}(-i\hbar\lambda)\, \dot{n}_k(t)\rangle\, d\lambda dt\,, \\
\lim_{k\to 0} G^{(3)}_{k,-k} &= \lim \frac{1}{k}\int_0^\infty\int_0^\beta \langle \dot{n}_{-k}(-i\hbar\lambda)\, \dot{\mathcal{E}}_k(t)\rangle\, d\lambda dt\,, \\
\lim_{k\to 0} G^{(4)}_{k,-k} &= \lim \frac{1}{k}\int_0^\infty\int_0^\beta \langle \dot{\mathcal{E}}_{-k}(-i\hbar\lambda)\, \dot{\mathcal{E}}_k(t)\rangle\, d\lambda dt\,. \qquad (4.16)
\end{aligned}$$

Now Eq. (4.12) is used to rewrite the expressions on the right-hand sides of these equations and the resulting expressions are compared with Eq. (4.14). Thus we find that Eq. (4.6) are obtained rigorously from Onsager's assumption.

Acknowledgements

The authors wish to express their thank to our colleagues at the Department of Physics, University of Tokyo, and the Physical Institute, Nagoya University, for illuminating discussions. The present study was partially financed by the Scientitic Research Fund of the Ministry of Education.

References

1) R. Kubo: J. Phys. Soc. Japan **12** (1957) 570.
2) The material of this paper was preliminarily reported in; R. Kubo and M. Yokota: Busseiron-Kenkyu, **89** (1955) 99 and S. kakajima: ibid **102** (1956) 24, **104** (1957) 6.
3) L. Onsager: Phys. Rev. **37** (1931) 405; **38** (1931) 2265.
4) See for instance, S. R. de Groot: Thermodynamics of Irreversible Processes.
5) H. B. Callen and T. A. Welton: Phys. Rev. **83** (1951) 34. H. Takahasi: J. Phys. Soc. Japan **7** (1952) 439.
6) J. G. Kirkwood: J. Chem. Phys. **14** (1946) 180.
7) H. Mori: J. Phys. Soc. Japan **11** (1956) 1029.
8) H. Nakano: Prog. Theor. Phys. **15** (1956) 77; Busseiron Kenku **84** (1955) 25. S. Nakajima: Busseiron-Kenkyu **88** (1955) 45.
9) R. Kubo: Nippon Sugaku-Butsuri-Gakkaishi **16** (1942) 243; Busseiron-Kenkyu **89** (1955) 72.
10) M. Kohler: Ann. Phys. (5) **40** (1941) 601.
A. H. Wilson: Theory of Metals, 2nd ed. p. 194.

JOURNAL OF THE PHYSICAL SOCIETY OF JAPAN Vol. 12, No. 11, NOVEMBER, 1957

Growth of Oxide Whiskers on Metals at High Temperature

By Riitsu TAKAGI

Government Mechanical Laboratory, Sumiyoshi-cho, Suginami-ku, Tokyo

(Received July 15, 1957)

Growths of α-Fe_2O_3 whiskers formed on pure iron in oxygen at 400~850°C were studied by electron microscopy and diffraction using specimens cut off successively from a uniformly oxidized wire which was heated consecutively to avoid ill effect of contamination condensed during electron-microscopic observation. Whisker grows at the tip by surface diffusion of molecules from base to tip. Axial growth at a fixed temperature is approximately given by: $l=kt^{0.3}$, where k, a constant, depends on temperature and has a maximum at 700~750°C. Initial diameter corresponds to that which gives the minimum strength necessary to keep whisker shape at the growth temperature. A whisker has an axis parallel to $<110>_{\text{hex}}$, becoming thereafter blade-shaped crystal parallel to (001). Further growth at the tip of a blade-shaped crystal occurs at those sites which are in a plane parallel to (001), and similar growth happens on a fracture surface of a mechanically truncated crystal, too.

§ 1. Introduction

Whisker growths on the surfaces of metals and alloys oxidized at high temperatures were recently investigated by Pfefferkorn[1], Takagi[2], Cowley[3], Morita et al.[4], and Arnold & Koonce[5] either with electron microscope or with a combination of electron microscope and diffraction. Since current theory of oxidation of metals fails to account for this phenomenon,[6] interest was aroused in their growth behavior. Pfefferkorn pointed out, after tracing the growth of a particular needle crystal on phosphor bronze or iron by alternating oxidation and observation, that these oxide needles grow at their tips by means of surface diffusion of constituent elements, and Cowley, from the fine structure of electron diffraction spots obtained with his high resolution apparatus, explained the characteristic structure of CuO needles as resulting from growth about one or more screw dislocations.

In course of our electron-microscopic study of the growth of oxide whiskers subsequent to the previous paper[2] we found it impossible to trace the natural growth of a particular oxide whisker by observing successively in electron microscope. Then we devised a new method of observation avoiding the ill effect of electron irradiation on the natural growth. The object of the present paper is primarily to report the results obtained by this method and in consequence to clarify the growth processes of oxide whiskers in conformity with the facts known from the conventiona oxidation theory.

§ 2. Experimental

It was found that most conspicuous whiske growths are seen in Fe_2O_3 on iron and steel CuO on copper and phosphor bronze, and Zn on zinc and brass. Among them iron appear to be the most suitable material for stud since wide temperature range of the whiske formation exists below melting point of th metal and the structure of the oxide, $\alpha-Fe_2O_3$ is fairly simple (rhombohedral)*. Hence w used pure iron in most of the experiments Results with other metals are reported fo supplementary purposes in this paper.

Iron specimens were of purest materia available. Electrolytic iron was subjected t re-electrolysis, and then vacuum cast an drawn into a wire of diameter 0.3 mm, whic was kindly given by Mr. T. Nagashima o Electrotechnical Laboratory. Drawn wire wa annealed for three hours at 850°C in flowin purified hydrogen. Surfaces of the iro specimen were electropolished in a fresh bat of a mixture of H_3PO_4 90% and H_2SO_4 10 using lead cathode.

Heating furnace was a tube of 2 cm i diameter and 30 cm in length wound externa ly with nichrome wire. Both ends of th tube were equipped with rubber stoppers through which tank oxygen dried by passage over $CaCl_2$ and P_2O_5 was kept flowing at an approximate rate of 50 cc/min. Temperature of the specimen was measured by a thermocouple placed in the furnace and automatically kept constant.

---

*) For convenience hexagonal indices will b used throughout.

For successive observation of growth behavior of a particular whisker, a piece of wire, 3 mm in length, was passed across an electron microscope specimen supporter and was placed in the central region of the furnace, to be repeatedly heated and observed (*Method A*). But since this direct way of studying growth with an electron microscope was regrettably found to be accompanied with a serious drawback, following alternative method (*Method B*) was adopted. An iron wire, 5 cm in length, was fixed to a frame of nichrome wire at one end and uniformly oxidized in the furnace. A 3 mm-long piece was cut off from the free end of the wire, and it was observed under electron microscope. The rest of the wire was preserved and used for further oxidation. The process of heating the remaining wire and cutting off a specimen can be continued again and again as long as the wire is long enough for the next specimen. Accelerating voltage of electron beam was 50 kV for microscopy and 70 kV for diffraction.

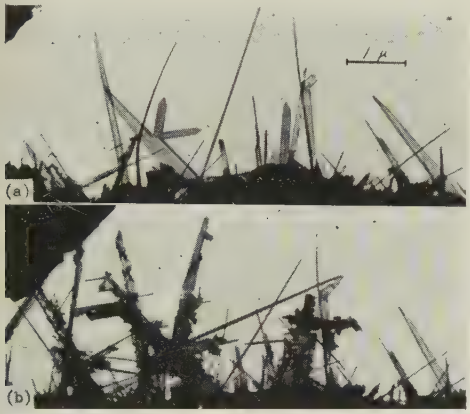

Photo. 1. Successive observation of the same ZnO whiskers on zinc formed at 450°C in: (a) 6 and (b) 6+12 min.

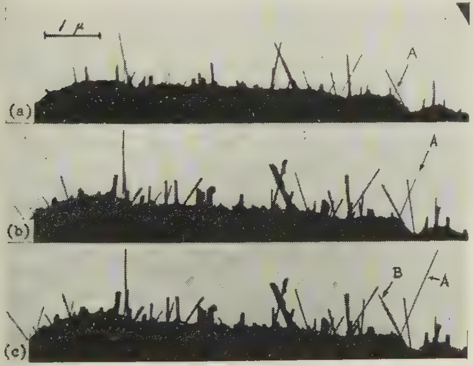

Photo. 2. Successive observation of the same CuO whiskers on copper formed at 470°C in: (a) 3, (b) 3+10 and (c) 3+10+10 min.

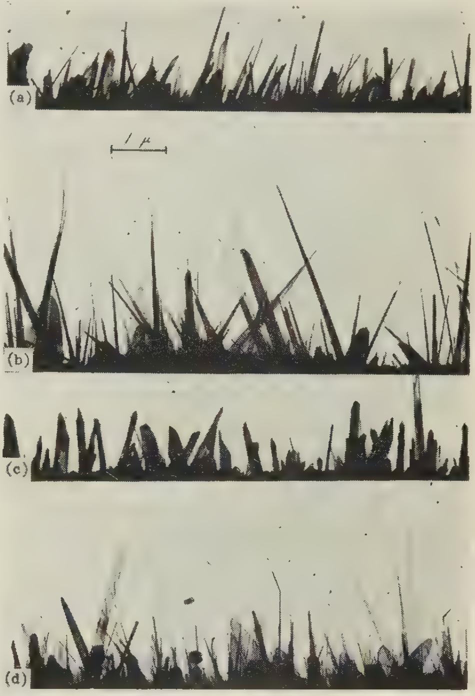

Photo. 3. Fe_2O_3 whiskers on iron formed at: (a) 700°C 1 min., (b) 700°C 1 min. + 500°C 13 min., (c) 700°C 1 min. + 500°C 70 min. + 700°C 1 min. and (d) 700°C 1 min. + 500°C 70 min. + 700°C 1 min. + 500°C 5 min.

Photo. 4. Initition of further growth at 500°C in 3 min. on the tip of a blade-shaped Fe_2O_3 crystal formed at 750°C in 100 min.

§ 3 Results

(1) *Factors influencing upon the formation and growth of whiskers*

Atmosphere: Densities of whiskers formed in air were compared with those formed i oxygen. Whiskers on iron and copper had large preference for oxygen, while those o zinc and brass showed little difference between the two atmospheres.

Temperature: Temperature ranges withi

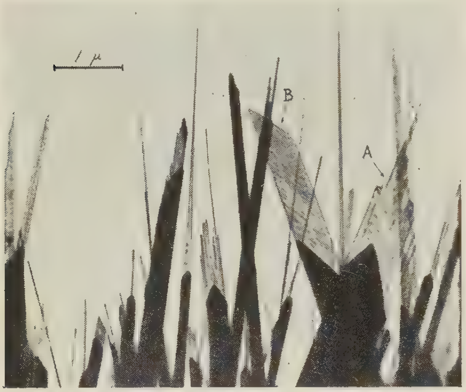

Photo. 5. Further growth at 500°C in 100 min. on the tips of Fe_2O_3 crystals formed at 750°C in 100 min.

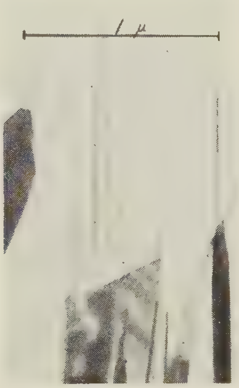

Photo. 6. Further growth at 500 C in 20 min. on a fracture surface of an Fe_2O_3 crystal formed at 725°C in 40 min.

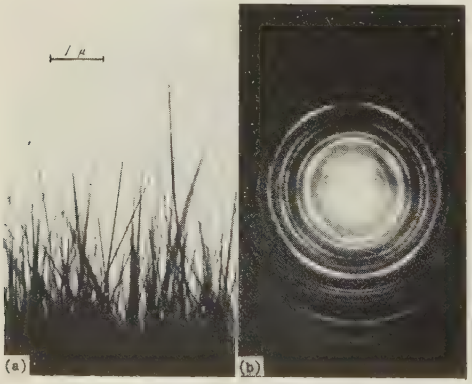

Photo. 7. (a) Fe_2O_3 whiskers formed at 650°C in 30 min. (b) Electron diffraction pattern of the specimen shown in (a).

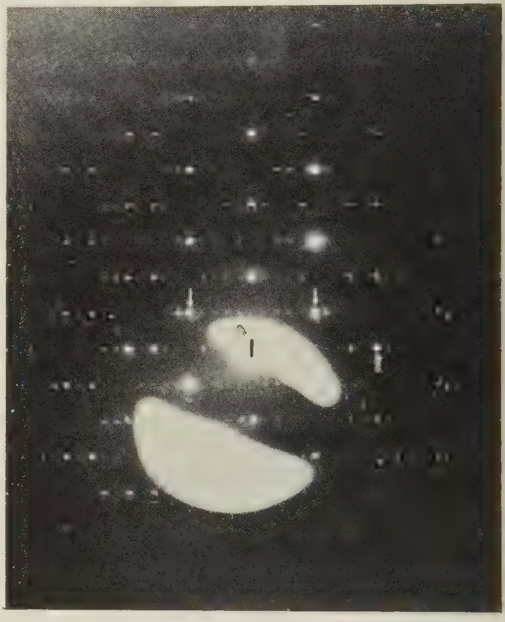

Photo. 8. Electron diffraction pattern of an Fe_2O_3 crystal formed at 700°C in 2 h. The beam coming through a hole in Al film is parallel to [001]. Bright area of Al around the hole due to partial transmission of electron beam casts diffuse shadow of specimen, which facilitates correct movement of the specimen. Probable position of the crystal in the shadow image is indicated by a black line. Note a line of 9 anomalous spots between 2 normal spots indicated, e.g., by 2 downward white arrows. $(\bar{3}30)$ spot is indicated by an upward arrow.

Photo. 9. Coagulation after electron irradiation of Fe_2O_3 crystals formed at 700°C in 20 min.

which whiskers readily grow in oxygen are listed in the following table.

Iron and steel	400∼850°C
Copper and phosphor bronze	400∼550 〃
Zinc and brass	300∼850 〃

Surface impurity: A remarkable property found for iron is that the attachment of a small amount of moist substance or slight touch of finger tip on electropolished clean surface accelerates the whisker formation.*

Electron irradiation: Most of the whiskers once observed by an elcetron microscope do not grow in a natural way, but those located just outside the field of view and received little electron beam irradiation grow quite naturally on heating them afterwards in an oxygen atmosphere. The cessation of normal axial growth due to electron beam irradiation is presumably caused by the condensation of carbonaceous contamination on the growth site at the tip of the whiskers.

(2) *Successive observation of whisker growth*

(*a*) *Growth of a particular whisker* (*Method A*). Photo. 1 shows the growth of ZnO on oxidized zinc. Whiskers in Photo. 1 grow either at the tip or at the branchings directed to an angle of 60 or 120° from the tip direction. Photo. 2 shows CuO on copper, where some grow normally (such as A) while the other stop their axial growth and increase in thickness. Thinner oxide is seen growing at the tip of a thickened crystal (B).

(*b*) *Growth of whiskers in general* (*Method B*). When one and the same heating temperature was used throughout several repeated cycles of heating the wire, cutting off a specimen and observation, whiskers did not show any sign of discontinuity in thickness along their length. General trend of axial growth was estimated from experiments specially designed for that purpose: A series of several electron micrographs were successively taken for different heating times at a fixed heating temperature. The length of the longest whisker on each electron micrograph was measured and plotted against time as shown in Fig. 1. Though scattering of individual points is considerable as might have been expected from the method of measurement, yet a straight line may be drawn for each heating temperature, which is approximated by the general equation

$$l = kt^{0\cdot 3},$$

where l is whisker length, t is time and k is a constant. k depends on temperature and attains a maximum value at 700∼750°C.

Whisker thickness increased as the heating temperature was raised, and Fig. 2 shows the minimum thickness estimated from an electron micrograph of the specimen heated for one minute at each temperature. By utilizing the fact that whisker thickness changes remarkably with heating temperature, next experiments were carried out: An iron specimen was heated in the first place at 500°C and, after ascertaining the growth of thin whiskers, then heated at 700°C. It was found electron-microscopically that thin whiskers which had grown at 500°C disappeared entirely on heating at 700°C, so that solely thicker whiskers grown at 700°C remained there. On the contrary, when thicker whiskers

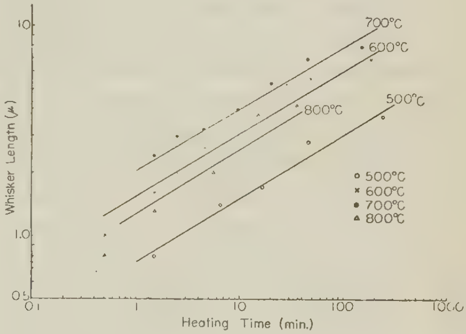

Fig. 1.

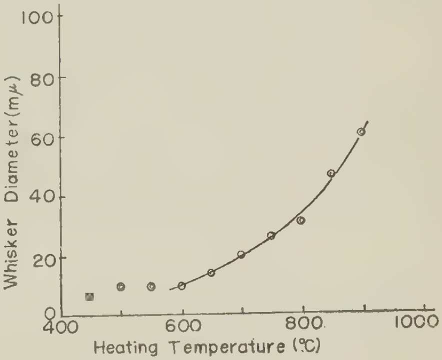

Fig. 2. Minimum whisker thickness. Lowest three points are near the resolution limit and uncertain.

---

*) In this connection Fricke et al.7) obtained Fe_2O_3 needles by heating γ-FeOOH in air.

grown in the first place at 700°C (*P*) were heated subsequently at 500°C, thin whiskers (*S*) grew at the tips of the original thicker whiskers (Photo. 3 (a) and (b)). When this specimen was again heated at 700°C, *S* parts disappeared completely while *P* parts remained with increase in thickness (Photo. 3 (c)). When these remaining *P* parts were heated again at 500°C, thin whiskers grew at the tips of the thicker whiskers as before (Photo. 3 (d)). The usually observed behavior of initial formation of *S* whisker is shown in Photo. 4, where many tiny crystallites are formed apparently independently of each other on the advancing edge of a blade-shaped crystal, gradually growing together into a sheet of single crystal as they grow further afterwards (Photo. 5, A). There are, however, some crystals showing exceptionally parallel growth, such as B in Photo. 5. It seems in both cases that the place where a plane passing through the axis of the crystal and parallel to the flat blade surfaces meets the advancing edge of the original crystal has a particular ability of providing *S* crystal with growth site on subsequent heating. When a *P* crystal broken mechanically by rolling the oxidized straight wire between two parallel glass plates kept at an appropriate distance was further heated at 500°C, *S* crystal grew on the fracture surface likewise (Photo. 6), but nothing grew from the broken pieces.

(3) *Electron diffraction observation*

Photo. 7 (b) is an electron diffraction pattern of densely grown α-Fe_2O_3 whiskers, and from the fiber diagram which is the direction of whisker axis can be determined to be <110>. The direction is in accord with the result of Miyake[8)], who reported the fiber orientation of Fe_2O_3 on oxidized iron surface though he did not refer it to whisker growth. Single crystal electron diffraction pattern of a relatively thick crystal produced at 600∼800°C could be obtained by a three-stage electron microscope or, more accurately, by placing an aluminum film with a hole of about 5 $\mu\phi$ in front of the specimen and sliding the specimen relative to the hole in search of an appropriately oriented crystal (e.g. Photo. 8). Photo. 8 shows a pattern of α-Fe_2O_3 always obtained when the crystal is placed so that its (001) plane, which is parallel to flat blad surfaces, is normal to the electron beam where lines of anomalous spots correspondin to a period equal to ten times the spacing o ($3\bar{3}0$) plane can be seen besides normal cross grating spots. This period, 14.35 Å, is equa to a length of a line of five contiguous oxyge ions when α-Fe_2O_3 is supposed to consist o close-packed oxygen ions. In cases of Zr and CuO, no regular row of anomalous spot was observed except for extraordinary elongation of diffraction spots reported earlier[2)3)

§ 4. **Discussion**

(1) *Tip growth*

From the results described in § **3** (2) (*b*), i is known that *S* crystal grows at the tip o *P* crystal. In principle we cannot find an discontinuity in the growth mechanism at th boundary of *P* and *S*, which are two differen parts of the same crystal, and the apparen departure at the boundary from the norma growth is merely the discontinuous change i thickness due to abrupt fall of temperatur in the course of its growth. Hence it ma be generally concluded that crystals grow a their tips even when there are no observabl thickness changes. Results of Photos. 1 an 2 also indicate the tip growth. But there th situation is rather complicated and it is supposed as follows: Contaminant film attache on to the growth site at the tip during observation stops the axial growth temporarily and thickening takes place; the latter seem less sensitive to contamination. When th contaminant film on the tip is broken, axia growth is resumed by a thin whisker.

(2) *Material supply*

There are three possible processes of supplying materials for growing oxide whiskers (i) Evaporation followed by condensation, (ii surface diffusion, and (iii) internal diffusion The process (i) occurs partly in ZnO in th form of zinc atoms since the vapor pressur of zinc at the temperature employed is, as i well-known, quite high. Actually ZnO whiskers were often observed growing at place separated from zinc or zinc oxide. But Fe_2O or CuO whiskers were found only on the respective metal or oxide showing that th process (i) is negligible. Internal diffusion o material which usually requires higher activa ion energy than surface diffusion is unlikely n Fe_2O_3 whiskers from the following considerations: It is known that during oxidation of iron the main diffusing component in the outermost Fe_2O_3 layer is the oxygen advancing from O_2/Fe_2O_3 interface through Fe_2O_3 phase up to Fe_2O_3/Fe_3O_4 interface, in the form of oxygen ion vacancy and electron diffusing in the reverse direction.[9] If Fe_2O_3 whiskers grow by this mechanism, they should grow at their base instead of the experimentally found tip of whiskers. Since other possible processes of internal diffusion are less likely to occur, it may be supposed that Fe_2O_3 whiskers, and most of the other oxide whiskers, too, grow by surface diffusion, provided that evaporation is negligible. High mobility of the constituent elements on the surface is indicated by the meniscus-shaped accumulation of material at the contact places of two crystals described by Pfefferkorn,[1] and also by the spherical coagulation generated when Fe_2O_3 whiskers are irradiated with intense electron beam giving rise to extraordinary local thinnings without still any bending or breaking of whiskers (Photo. 9).

Oxidation theory of iron described in the preceding paragraph further reveals that Fe_2O_3 whiskers are not buried in the bulk oxide from the base during later oxidation, since Fe_2O_3 layer grows in thickness at the inner interface Fe_2O_3/Fe_3O_4, so that the measured whisker length in Fig. 1 contains no error arising from this source.

If we assume that (i) the increase in whisker length is effected solely through surface diffusion of oxide molecules adsorbed on the whisker surface from base to tip, (ii) the evaporation of adsorbed molecules is negligible, and (iii) surface concentration of adsorbed molecules at a given time during growth varies simply linearly along the length of the whisker just like the variation of concentration of ratedetermining diffusing component along the oxide layer thickness in conventional parabolic oxidation theory, axial growth would be expressed by $l \propto t^{0 \cdot 5}$ under constant temperature and radius. The difference in rate from the experimentally found axial growth may be ascribed to the radial growth which is actually observed.

(3) *Thickness of whiskers*

It was known that thickness of whiskers increases as they are heated at heigher temperatures and for longer periods. But we may suppose that thickness of whiskers, at the outset of their growth at a given temperature i.e. nearly the value given by Fig. 2, corresponds to the diameter of a crystal having the minimum shear strength necessary to maintain the whisker shape against surface tension force at that temperature. The observation shown in Photo. 3 can then be explained in such a way that the crystal parts grown at 500°C collapsed at 700°C because they do not have enough strength at 700°C. Actually, however, whiskers formed grow slowly in radial direction, particularly in directions parallel to (001) plane which is approximately close-packed with larger oxygen ions, so that most of the observed whiskers have considerably larger thickness than that indicated in Fig. 2.

(4) *Formation and growth of whiskers*

We have treated the problem by surface diffusion of oxide molecules without regard to how oxidation really takes place. In this respect present problem is not much diffferent from the growth of needle crystals on tungsten when oxidized tungsten is heated in vacuum where evaporation and condensation of tungsten oxide takes place considerably besides surface diffusion.[10] In order to make it clearer that an oxide whisker forms in some way and grows by surface diffusion it would be convenient to assume the existence of perpetual step at the tip provided by screw dislocation with Burgers vector parallel to the whisker axis as Cowley[3] has done. These dislocations will be produced, for instance, by slip in Fe_2O_3 crystals due to stress generated during the formation and growth of Fe_2O_3 layer. Once a screw dislocation is produced in an appropriate direction of a crystallite, molecules adsorbed on the surface migrate toward the step until the crystal grows to a diameter large enough for preserving whisker shape. After that the axial growth commences.

It seems from the observations shown in Photos. 4 and 5 that on the advancing edge of a whisker numerous growth steps are distributed in a line on a plane parallel to the basal plane. Though we cannot satisfactorily explain how such a particular plane occurs in a crystal, it appears that the particular plane persists within crystal even after the crystal has fully grown, as shown by Photo.

6. We cannot find the relation, if any, between the assumed dislocations and the periodic imperfections found by electron diffraction as shown in Photo. 8.

In conclusion, the author wishes to express his sincere thanks to Professor Ryozi Uyeda for suggestion of this problem and continude interest during this work. He is also indebted to Dr. T. Kawada for encouragement and advice.

References

1) G. Pfefferkorn: Naturwiss. **40** (1953) 551; Z. Wiss. Mikroskopie **62** (1954) 109; Z. Metallk. **46** (1955) 204.
2) R. Takagi: J. Phys. Soc. Japan **9** (1954) 162; cf. Proc. 1st Reg. Conf. E. M. in Asia and Cceania, Tokyo, 1956.
3) J. M. Cowley: J. Electrochem. Soc. **101** (1954) 277.
4) T. Morita, S. Usio and T. Seiyama: J. Appl Phys. Japan **25** (1956) 70. (In Japanese).
5) S. M. Arnold and S. E. Koonce: J. Appl. Phys. **27** (1956) 964.
6) cf. Th. Heumann: Passivierende Filme un Deckschichten, ed. by H. Fischer et al. Springer, 1956, p. 204.
7) R. Fricke, Th. Schoon and W. Schröder: Z physik. Chem. **B 50** (1941) 13.
8) S. Miyake: Sci. Pap. I. P. C. R. **31** (1937 161.
9) M. H. Davies, M. T. Simnad and C. E. Birchenall: J. Metals **3** (1951) 889; ibid. (1953) 1250.
10) R. Takagi: J. Electronmicroscopy **3** (195 18.

JOURNAL OF THE PHYSICAL SOCIETY OF JAPAN Vol. 12, No. 11, NOVEMBER 1957

Theory of Viscoelasticity of Amorphous Polymers

II. A Note on the Time-Temperature Reducibility of the Relaxation and Retardation Spectra

By Osamu NAKADA*

Kobayasi Institute of Physical Research, Kokubunji, Tokyo

(Received June 8, 1957)

Equivalence of temperature change and shift of log-time scale is usually assumed empirically in obtaining a master curve of relaxation and retardation spectra in polymers.

In this paper the molecular theoretical basis of this assumption—which we call here the *time-temperature reducibility*—is elucidated by an examination of the generalized diffusion equation in the configuration space of a polymer chain.

Several criterions for the reducibility are deduced as the results of the analysis which in fact give a gurantee to the reducibility in the case of simple intra-chain relaxation phenomena in amorphous polymers. Critical examinations of some other cases are also made.

§ 1. Introduction

Extensive progress has been made recently in measuring the dynamic response of various polymers in very wide frequency ranges, and thus characteristic features of relaxation phenomena in polymers have been elucidated progressively.[1]

But in actual experiments a single run of the measurement can cover in most cases only a limited range of frequency which is usually rather narrow compared with the required range of the relaxation spectrum. Thus, in order to get a complete relaxation spectrum, we usually make resort to the assumption that a change of temperature in observations of relaxation phenomena is equivalent to a proper shift of log-time scale.[2),3),4),5)] This assumption enables us to constract a " master

---

* Present address: Hitachi Central Research Laboratory, Kokubunji, Tokyo.

curve" of the relaxation spectrum at reference temperature by shifting and joining successively a number of segmental curves obtained at different temperatures. We will call here the assumption mentioned in the above the *time-temperature reducibility.* (Cf. § 2) It is indeed probable that such an assumption of reducibility is satisfied at least approximately in a narrow range of frequency and temperature in the case of amorphous polymers. But it is open to question whether it really holds over the whole range of the spectrum required. Unless the physical ground for validity of the assumption is clarified, we may not be able to rely upon the obtained master curves of the relaxation spectrum based on the assumption.

In the following we will try to elucidate the applicability of the time-temperature reducibility from a molecular theoretical aspect.*)

§ 2. The Time-Temperature Reducibility of the Relaxation Spectrum and of the Retardation Spectrum

The dynamic elastic modulus, e.g. the shear modulus G, can be expressed in general as a function of angular frequency ω and of temperature T in the following integral form:

$$G(\omega, T)=G_0(T)+\int_{-\infty}^{\infty}\frac{i\omega\tau H(\tau, T)}{1+i\omega\tau}d(\ln\tau)\,, \quad (1)$$

where G_e is the static elastic modulus (i.e. the modulus for zero frequency). The function $H(\tau, T)$ in the integrand is called the distribution function of relaxation times or simply the relaxation spectrum, and the variable τ is called the relaxation time.

According to Ferry et. al.,[4] the effect of temperature on the relaxation spectrum is assumed as follows: First, the integral of the equation (1) is interpreted as representing an ensemble of rubberlike elastic elements. Then $H(\tau, T)$ should be proportional to the absolute temperature. Next, *all* relaxation times τ's of elastic elements are assumed to be multiplied by the *same* shift factor a_T when temperature is changed from T_0 to T. Thus

$$H(\tau, T)=(T/T_0)H(\tau/a_T, T_0) \quad (2)$$

$$a_T=1 \quad \text{at} \quad T=T_0\,. \quad (3)$$

Since, however, the introduction of the factor T/T_0 in the above equation in analogy with the rubber elasticity is without ground,**) we here define the *time-temperature reducibility* of the relaxation spectrum by the following equations:

$$H(\tau, T)=\beta_G(T)H(\alpha_G(T)\tau, T_0) \quad (4)$$

$$\alpha_G(T_0)=1\,. \quad (5)$$

These relations are visualized in Fig. 1. If the relaxation spectrum $H(\tau, T)$ is time-temperature reducible, the log (modulus) *vs.* log (frequency) curves at diverse temperatures can be superposed on a single master curve at a reduced temperature by proper shifts of original curves along both axes.

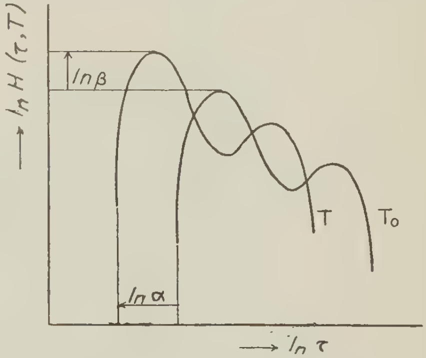

Fig. 1. A schematic diagram of a time-temperature reducible relaxation spectrum $H(\tau, T)$.

The reducibility of the retardation spectrum is defined in a similar manner. The dynamic elastic compliance $J(\omega, T)$ is expressed with the aid of the retardation spectrum $L(\tau, T)$ as

$$J(\omega, T)=J_\infty(T)+\int_{-\infty}^{\infty}\frac{L(\tau, T)}{1+i\omega\tau}d(\ln\tau)\,, \quad (6)$$

where J_∞ denotes the compliance in high frequency limit.

---

* Recently Onogi and Ui made an experimental confirmation of the time-temperature reducibility for polyvinylidene-vinyl chloride fibre and PVC-DMT gel. (S. Onogi, K. Ui: J. Colloid Sci. **11** (1956) 214.) On the other hand, Okano discussed the reducibility from the viewpoint of thermodynamics of irreversible processes. (K. Okano: Reps. of the Sci. Res. Inst. **32** (1956) 197.)

** The relaxation spectrum $H(\tau, T)$ may be considered to be a product of the factor $\lambda(\tau, T)$ representing the intensity of each relaxing element and the factor $\mu(\tau, T)$ representing the density of elements in the range $d\tau$. Indeed the intensity factor λ will be proportional to the absolute temperature if we assume the each element to be rubberlike, but the density factor μ will also depend on temperature in general. Accordingly the relaxation spectrum H will not necessarily be proportional to the absolute temperature. (Cf. reference (6))

Then we define the reducibility of the retardation spectrum $L(\tau, T)$ by

$$L(\tau, T)=\beta_J(T)L(\alpha_J(T)\tau, T_0) \tag{7}$$

$$\alpha_J(T_0)=1\ . \tag{8}$$

Real and imaginary parts of $G(\omega, T)$ and $J(\omega, T)$, $H(\tau, T)$, and $L(\tau, T)$ are not independent of each other, and if one of them is given in the whole range of the variable, others are derivable from it.[7] Hence the relations (3) and (4) can not be independent of relations (7) and (8). According to Gross,[7] the relaxation spectrum $H(\tau)$ is derived from the retardation spectrum $L(\tau)$ by the following formula.

$$H(\tau)=\frac{L(\tau)}{[\Omega(\tau)]^2+[\pi L(\tau)]^2} \tag{9}$$

$$\Omega(\tau)=J_\infty(\tau)+\Omega'(\tau) \tag{10}$$

$$\Omega'(\tau)=\int_{-\infty}^{\infty}\frac{\tau L(u)}{\tau-u}d(\ln u)\ . \tag{11}$$

Substituting Eq. (7) into Eqs. (10) and (11), we get

$$\left.\begin{aligned}\Omega(\tau, T)&=J_\infty(T)+\beta_J\int_{-\infty}^{\infty}\frac{\alpha_J\tau L(u, T_0)}{\alpha_J\tau-u}d(\ln u)\\&=\frac{J_\infty(T)}{J_\infty(T_0)}J_\infty(T_0)+\beta_J\Omega'(\alpha_J\tau, T_0)\ .\end{aligned}\right\} \tag{12}$$

Thus we see from Eqs. (9), (10) and (12) that the reducibility of the retardation spectrum leads to the reducibility of relaxation spectrum if J_∞ is negligible compared to Ω', or if

$$\frac{J_\infty(T)}{J_\infty(T_0)}=\beta_J=(T)\ . \tag{13}$$

Also it will be seen from Eq. (9) that when the reducibilities of the relaxation and retardation spectra are compatible with each other shift factors of the two spectra are related by

$$\beta_G=1/\beta_J(T)\ , \qquad \alpha_G=\alpha_J\ . \tag{14}$$

Since the fulfilment of the condition (13) will be rather fortuitous, it will be necessary that J_∞ is negligible compared to Ω' in order that the reducibility of the retardation spectrum is compatible with the reducibility of the relaxation spectrum. These circumstances will be discussed again in the later section (§5). In the following we confine our discussion in the reducibility of the retardation spectrum in the convenience of a molecular theoretical treatment.

§3. Phenomenological Meaning of the Reducibility

When the step function-like stress,

$$\sigma=\begin{cases}0\ , & t<0\\ \sigma_0\ , & t\geq 0\end{cases} \qquad (15$$

is applied to the system which has the dynami compliance given by Eq. (6), the retarde strain γ of the system increases with tim according to the following equation as it i well known in the phenomenological theor of linear viscoelasticity,[8]

$$\gamma(t)=\left\{\int_{-\infty}^{\infty}L_J(\tau)[1-e^{-t/\tau}]d(\ln\tau)\right\}\sigma\ . \qquad (1$$

The function in the curly bracket in the abov equation is usually called the creep function

The retarded response of the system unde δ-functionlike stress,

$$\sigma=\sigma_0\delta(t) \qquad (17$$

is given by the derivative of Eq. (16)[8]

$$\gamma'(t)=\left\{\int_{-\infty}^{\infty}\frac{1}{\tau}L_J(\tau)e^{-t/\tau}d(\ln\tau)\right\}\sigma\ . \qquad (18$$

Substituting Eqs. (7) and (8) into Eqs. (16 and (18), we get

$$\gamma(t, T)=\beta_J(T)\gamma(t^*, T_0) \qquad (19$$

$$\gamma'(t, T)=\alpha_J(T)\beta_J(T)\gamma'(t^*, T_0) \qquad (20$$

$$t^*=\alpha_J(T)t\ . \qquad (21$$

These equations derived in the above wil tell us the phenomenological meaning of the time-temperature reducibility: *When the system has the reducible retardation spectrum the intensity and the rate of the response o the system against external excitations are in creased or reduced along with a temperature change only by constant factors which depen only on temperature.*

§4. The Molecular Theoretical Basis of the Reducibility

Now we proceed to the molecular theoretica consideration of the physical meaning of the time-temperature reducibility.

The system is assumed to be uniform and to be composed of microscopic structural units such as molecules, chain segments, network chains etc. We denote by q's a set of generalized coordinates which are sufficient to describe the configuration of the structural unit, and we define a probability distribution function $f(q)$ in such a way that the probability of a unit to be in small range dq equals $f(q)dq$. We consider a *simple* macroscopic quantity X which is determined directly by the distri-

ution function of the unit $f(q)$ in the follow-
ng way:

$$X(t, T)-X_0(T)=c\int x(q)[f(q, t, T)-f_0(q, T)]dq \tag{22}$$

Iere suffix zero means a value in equiliblium;
(q) is a microscopic physical quantity cor-
esponding to X; and c is a constant deter-
ined by an arrangement of units.

In amorphous cross-linked polymers we may
hoose as a structural unit a network chain
etween adjacent cross-links, and simple
acroscopic quantities such as polarization,
hear strain, refractive index, etc. are deter-
ined directly by corresponding microscopic
uantities, i.e. dipole moment, end-to-end
istance, polarizability, etc. of a network chain.

Now in order that the strain γ satisfies the
ondition of the reducibility, Eq. (19) to Eq.
0), it is sufficient, so far as we assume γ to
e one of simple macro-quantities, that the
eviation of the distribution function $f-f_0$ is
educible in a similar way:

$$f_1\equiv f-f_0=\lambda(T)g(q, t^*, T_0) \tag{23}$$

$$t^*=\alpha(T)t \tag{24}$$

he relations, (23) and (24), are obviously more
eneral than the relations (19) or (20) and (21),
volving that all first order deviations of
mple macro-quantities should be reducible in
me and temperature. So we will distinguish
e two by calling the latter the *macroscopic*
educibility and the formers the *microscopic*
educibility. We have, however, some evi-
ences in relaxation in polymers for that the
acroscopic reducibility is originated from the
icroscopic reducibility, as we shall see later.
f. § 5) So hereafter we will seek for con-
itions of the microscopic reducibility.

Under the influence of thermal agitation
ructural units of the system are changing
eir configrations incessantly in the medium.*)
herefore, the change of configurations of
nits with time is described properly by a
eneralized diffusion equation which can be
t up in the following way.9)

The distribution function of the structural
nit satisfies the equation of continuity in the
onfiguration space,

$$\operatorname{div} j+\frac{\partial f}{\partial t}=0 \tag{25}$$

Here j is the flux of the probability density in the configuration space, which is composed of four components:

$$j=j_d+j_m+j_i+j_e \tag{26}$$

where

$$j_d=-\left(\frac{kT}{\zeta}\right)\operatorname{grad} f \tag{27}$$

$$j_m=v_m f \tag{28}$$

$$j_i=\frac{1}{\zeta}F_i f \tag{29}$$

$$j_e=\frac{1}{\zeta}F_e f, \qquad \text{or} \quad =v_e f \tag{30}$$

Here ζ means the friction tensor of the structural unit in the medium, v_m the flow velocity of the medium, v_e the additional excitation flow of the medium. F_i the force exerted internally to the unit, and F_e the additional excitation force exerted externally to the unit. The first component j_d means the diffusion flow which obeys Fick's law. The second component j_m is the flow along with a motion given to the medium. The third component j_i is due to forces exerted internally to the unit. The last component j_e means the flow corresponding to a small excitation exerted to the unit by an external force F_e or by an additional excitation flow v_e of the medium. Substituting Eqs. (26), (27), (28), (29) and (30) into Eq. (25) we get the required generalized diffusion equation for the structural unit in the configuration space $\{q\}$.

Now assuming that the external excitation is given by the force F_e which is sufficiently small we expand the distribution function f in power series of the external excitation force F_e:

$$f=f_0+f_1+O(F_e^2) \tag{31}$$

Substituting Eq. (31) into Eq. (25) and taking account of Eqs. (26) to (30), we get the following equation for f_1.

$$\mathrm{L}f_1+\frac{\partial f_1}{\partial t}=-\operatorname{div}\left(\frac{1}{\zeta}F_e f_0\right) \tag{32}$$

Here L is an operator given by

$$\mathrm{L}=\mathrm{L}_d+\mathrm{L}_m+\mathrm{L}_i \tag{33}$$

$$\mathrm{L}_d=-kT\operatorname{div}\frac{1}{\zeta}\operatorname{grad}\cdot \tag{34}$$

$$\mathrm{L}_m=\operatorname{div} v_m\cdot \tag{35}$$

---

* By the term “medium” we mean any homo-
enious surrounding of a representative unit, which
ay be either a foreign solvent or structural units
emselves.

$$\mathrm{L}_i = \mathrm{div}\ \frac{1}{\zeta} F_i . \qquad (36)$$

In the case where the excitation is given by a flow of the medium v_e we need only replace F_e/ζ in the above equations by v_e.

For the purpose to examine the reducibility, it is sufficient to consider the response of the system to the δ-function-like excitation. If δ-function-like force F_e is applied to the system, the right hand side of Eq. (32) becomes also a δ-function, so that

$$\mathrm{L} f_1 + \frac{\partial f_1}{\partial t} = 0 , \qquad \text{for} \quad t > 0 . \qquad (37)$$

First we assume that the microscopic reducibility, i.e. Eqs. (23) and (24), holds for the system. Then substituting Eq. (23) into Eq. (37), we get

$$\mathrm{L} g + \frac{\partial g}{\partial t} = 0 , \qquad t > 0 . \qquad (38)$$

Or, taking account of Eq. (24),

$$\frac{1}{\alpha(T)} \mathrm{L} g = -\frac{\partial g}{\partial t^*} , \qquad t^* > 0 . \qquad (39)$$

Since the function g defined in Eq. (23) is assumed not to depend on temperature explicitly, the righthand side of the Eq. (39) does not depend on the variable T, so that $\mathrm{L}/\alpha(T)$ on the lefthand side of the equation also should not contain T explicitly. The reverse statement of the above deduction can be easily verified by retracing the equations. Therefore the necessary and sufficient condition for the microscopic reducibility is that the operator L in Eq. (32) can be writen in a form,

$$\mathrm{L} = \alpha(T) \mathrm{L}_0 \qquad (40)$$

where α is a shift factor which is function of T, and L_0 is an operator which does not depend on T explicitly.

According to Eqs. (34) to (36), three components of the operator L, i.e. L_d, L_m and L_i depend on temperature in mutually different manners so that Eq. (40) does not hold generally when more than one components coexist in L. Therefore the microscopic reducibility should hold only in the following three cases:

$$\left.\begin{array}{lll} \text{i)} & \mathrm{L}_d \neq 0, & \mathrm{L}_m = \mathrm{L}_i = 0 \\ \text{ii)} & \mathrm{L}_m \neq 0, & \mathrm{L}_d = \mathrm{L}_i = 0 \\ \text{iii)} & \mathrm{L}_i \neq 0, & \mathrm{L}_d = \mathrm{L}_m = 0 \end{array}\right\} \qquad (41)$$

Moreover, in order that the operator L can be expressed in the form of Eq. (40) the friction tensor ζ should be written in a form,

$$\zeta = \phi(T) \zeta_0 \qquad (42)$$

where $\phi(T)$ is a scalar constant which depen only on temperature and ζ_0 is a tensor whic is independent of temperature. Then the shi factor $\alpha(T)$ in each of three cases in Eq. (4 is given by

$$\alpha(T) = \left\{ \begin{array}{ll} kT/\phi(T) & \text{for case (i)} \\ 1 & \text{for case (ii)} \\ 1/\phi(T) & \text{for case (iii) .} \end{array} \right\} \qquad (4$$

As far as we consider the irreversible flo phenomena along the line developed here, can not eliminate essentially the diffusion fl operator L_d, so that cases (ii) and (iii) can be realized in a strict sense. It might however, realized in an approximate sense a low temperature where $\mathrm{L}_d \ll \mathrm{L}_m$ or $\mathrm{L}_d \ll$

An approximate reducbibility also holds we see in the following, when the activati energy of the elementary process of the fl is sufficiently large. If we assume convenient the Andrade's equation for the temperatu dependence of the friction constant i.e., if assume

$$\phi(T) = A T^n e^{E/kT} , \qquad (4$$

relative changes of magnitudes of the operato L_d and L_i can be written as

$$\left.\begin{array}{l} \dfrac{\Delta|\mathrm{L}_d|}{|\mathrm{L}_d|} = \left(\dfrac{\partial}{\partial T} \ln |\mathrm{L}_d| \right) \Delta T \\ \qquad = \{(E/kT) - (n-1)\}(\Delta T/T) \end{array}\right\} \qquad (4$$

$$\frac{\Delta|\mathrm{L}_i|}{|\mathrm{L}_i|} = \{(E/kT) - n\}(\Delta T/T) . \qquad ($$

Accordingly in the case where

iv) $E/kT \gg n$ and 1, $\mathrm{L}_m = 0$,

the temperature dependence of L_d and L_i comes almost the same, and

$$\Delta \mathrm{L} = \Delta \alpha(T) \mathrm{L}_0 , \qquad ($$

so that the microscopic reducibility holds proximately at least in a comparatively sm temperature range.

§ 5 Applications to the Relaxation of Po mers

Now we will apply the criterions for reducibility of the retardation spectrum tained in the above to actual cases. T reducibility of the spectrum has been us most effectively in determing master curv of shear relaxation spectra of amorphous po mers such as polyisobutylene in very w frequency ranges.[10] It is well establis both experimentally and theoretically that shear relaxation spectrum of linear amorphous polymers consist mainly of two parts, the *wedge* type part in a shorter relaxation time range and the *box* type part in a longer relaxation time region.[11] The former originates from the configurational relaxation of each of chains between junctions,[6][12][13] and the latter implies the relaxation of the junctions themselves which are either temporary entanglements or secondary bonds between chains.[14][15][16] So cross-linked polymers such as vulcanized rubber which are considered to have permanent chemical junctions between chains naturally lack the box type spectrum. Besides the wedge and box spectra, there often appears a third relaxation region in high frequency in certain polymers, which can be usually attributed to rotation of a side group. In the following, we will examine these cases in turn, as well as some other cases.

a) The wedge type spectrum. As a structural unit in this case we may choose a network chain between adjacent junction points. The macroscopic shear strain may be assumed to be proportional to the microscopic strain of network chains. It should be emphasized that in homogeneous amorphous polymers the internal energy does not change effectively with the change of configurations of the network chain, so that the internal force F_i acting on a chain can be neglected. Hence the operator L is made up of only one component L_d when the flow of the medium is zero. While, the friction tensor ζ can be expressed in the form of Eq. (42), since the underlying elementary processes are the same for all internal freedoms of the chain. Thus it turns out that the configurational relaxation of a chain in amorphous polymers belongs to the case (i) in Eq. (41) which together with Eq. (42), guarantees the microscopic reducibility and hence also the macroscopic reducibility of the retardation spectrum.

In order to prove the reducibility of the relaxation spectrum, it is necessary to verify the compatibility of the reducibility of the relaxation and retardation spectra. Ω' in Eq. (11) can be evaluated approximately as follows:

$$\Omega'(\tau)=\int_{-\infty}^{\infty}\frac{\tau \mathrm{L}(u)}{\tau-u}d(\ln u)\simeq\int_{-\infty}^{\ln\tau}\mathrm{L}(u)d(\ln u)$$

$$-\int_{\ln\tau}^{\infty}\frac{\tau}{u}\mathrm{L}(u)d(\ln u)\simeq\int_{-\infty}^{\ln\tau}\mathrm{L}(u)d(\ln u) \quad (48)$$

Now from Eq. (6) it is seen, with the use of Alfrey's approximation, that

$$J(\omega, T)\simeq J_\infty+\int_{-\infty}^{\ln(1/\omega)}\mathrm{L}(\tau, T)d(\ln\tau) \quad (49)$$

With the aid of Eq. (49), Eq. (48) can be rewritten as

$$\Omega'(\tau)\simeq J(1/\tau)-J_\infty \quad (50)$$

Except when τ takes a value quite near to the shortest retardation time, the relation

$$J(1/\tau)-J_\infty\gg J_\infty \quad (51)$$

holds experimentally in amorphous polymers. From Eqs. (50), (51) and (11), it is seen that

$$\Omega'\gg J_\infty \quad (52)$$

for the major range of the retardation spectrum, which is sufficient for the compatibility of the two spectra.

Thus we see the time temperature reducibility is valid in the wedge type relaxation spectrum.

b) The box type spectrum. In this case we can not take a network chain as the structural unit, because here the relaxation phenomena concern with the inter-chain interaction of rater complex nature—i.e. breaking and reforming of entanglements or secondary bonds among chains. Nevertheless, we should be able to formulate the problem, at least in principle, in the formalism developed in § 3, if we can choose a proper structural unit. The structural unit in this case should contain an internal freedom concerning to breaking and reformation of junctions.

Thus, in the problem of the box type spectrum, the essential point consists in the nature of temporary junctions. If they would be of energetic nature, e.g. caused by hydrogen bonds or dipolar interactions, the intervention of a L_i term should prevent the time-temperature reducibility to hold in rigorous sense. If, on the countary, junctions would be merely caused by entanglements without any special interaction between chains, the reducibility should hold favourably in the box type region as well as in the wedge type region. Non-polar linear polymer like polyisobutylene $[CH_2CH(CH_3)_n$ may belong to the favourable case.

c) The side group relaxation. The typical example of the relaxation of this type is found in polymethylmethacrylate $[CH_2C(CH_3)COOCH_3]_n$, in which rotational relaxation of $(COOCH_3)$

group is considered to take place in a higher frequency.[14]

Apart from the wedge and box spectra, the spectrum of the side group relaxation alone may be time-temperature reducible. But it can not be reducible simultaneously with the wedge and box spectra, since the relaxing unit in this case will be quite different from that of the wedge-box parts. In terms of our formulation it should imply the inadequacy of Eq. (42); instead, the friction tensor will be written in a form

$$\zeta=\left[\begin{array}{c|c} \phi_1(T)\zeta_1 & 0 \\ 0 & \phi_2(T)\zeta_2 \end{array}\right] \qquad (53)$$

where $\phi_1\zeta_1$ corresponds to the side group relaxation, and $\phi_2\zeta_2$ to the wedge-box relaxation. Thus the two relaxation processes may be treated seperately, so far as the two relaxation region does not overlap. In these cases the shift factor α depends not only on temperature as usually assumed, but also on the kind of relaxing unit, and may be better expressed by

$$\alpha_k(T)\,, \qquad k=1, 2, \cdots, \qquad (54)$$

where k denotes the kind of the relaxing unit.

d) Relaxations in crystalline polymers. Crystalline polymers are usually imagined to be made up of fine crystalline phases embedded in the amorphous phase, each chain molecule penetrating several crystalline and amorphous regions. If we can assume that the both phases are perfect and that the elasticity and relating relaxation phenomena are exclusively attributed to that of the amorphous phase, then the reducibility of the crystalline polymers will be reduced to that of the purely amorphous polymers. But we should remember that the two phase description of crystalline polymers is only a convention, and that there should be at least intermediate regions between the two limiting phases. In other words, if we consider a representative chain in amorphous region the friction force suffered by segments of the chain will change along with chain length so that the friction tensor ζ in this case also will not be expressed in the simple form of Eq. (42).

e) The relaxation spectrum of dynamic bulk modulus. The linear amorphous polymers are shown to exhibit the dispersion in the bulk modulus as well as in the shear modulus.[15] This is attributable to the cor figurational relaxation of a chain just as i the shear relaxation.[16] It should be re membered, however, that there is an apprec able change of internal energy accompanie by the volume change, so that the operat L_i (Eqs. (33), (36)) can not be neglected. More over the bulk modulus is not expressed in simple form of Eq. (22). These circumstance together will interfere with the reducibilit of the spectrum of the bulk modulus.

§ 6. Discussions

In the above treatments we have ascribe the molecular basis of the time-temperatur reducibility defined macroscopically by Eq (7) and (8) (i.e. the macroscopic reducibilit to the reducibility of the distribution functio of the structural unit, Eqs. (23) and (24) (i. the microscopic reducibility). It is obviou that the latter yields a sufficient but not neces sary condition for the former, except whe all macroscopic quantities of the system whic can be expressed in the simple form of Ec (22) would satisfy the reducibility. Thoug comparative experimental investigations c various relaxation phenomena have not bee made thoroughly, Ferry et. al[17] found tha shift factors $\alpha(T)$'s, of the dynamic and d electric relaxations in many polymers coincid with fairly good precision. This fact seem to give us a resonable, though not sufficien evidence to presume that the macroscopi reducibility is originated from the microscopi reducibility.

We can imagine in Eq. (35) or (36) the cas where $v_m \neq 0$ with div $v_m f=0$, or $F_i \neq 0$ wit div $F_i f_1=0$. But these odd cases mean phys cally that the occurrence of the flow v_m c the force F_i does not give any effective in fluence on the dynamical behavior of th system, so that they will belong to trivia cases, and we shall not go into further detai of them.*)

Acknowledgments

Thanks are due to Prof. S. Oka, Prof. A Ookawa, Prof. N. Saito, Mr. Y. Ikeda an

---

* A similar case have appeared, in fact, in ou previous treatment of the wedge type spectrum, where imposing of a static tensile force on the re presentative chain did not give any effect on th resulting spectrum.

Mr. Y. Chikahisa for their kind encouragenent and valuable discussions. The author vould also express his hearty gratitude, at he occasion of leaving the Kobayashi Institute of Physical Research, to all his colleagues in nis pleasant days in the institute. The present work was supported partly by the Scientific Research Grant of the Ministry of Education. 1957, May 4)

References

1) H. A. Stuart: Die Physik der Hochpolymeren Bd. **4**.
2) H. Leaderman: "Elastic and Creep Properties of Filamentous Materials" (1943) 175.
3) F. Schwarzl, A. J. Staverman: J. Appl. Phys. **23** (1952) 838.
4) J. D. Ferry: J. Amer. Chem. Soc. **72** (1950) 3746; J. D. Ferry, E. R. Fitzgerald, L. D. Grandine, M. L. Williams: Ind. Engng. Chem. **44** (1952) 703.
5) A. V. Tobolsky, R. D. Andrews: J. Chem. Phys. **13** (1945) 3; R. D. Andrews, N. Hofman-Bang, A. V. Tobolsky: J. Polymer Sci. **3**(1948) 669.
6) O. Nakada: J. Phys. Soc. Japan **10** (1955) 804.
7) B. Gross: "Mathematical Structure of the Theories of Viscoelasticity" (1953) 42.
8) H. A. Stuart: Die Physik der Hochpolymeren Bd. **4** (1956) 11.
9) J. G. Kirkwood: Rec. Trav. chim. **68** (1949) 649.
10) V. G. W. Harrison: Proc. 2nd. Intern. Congr. Rheology (1954) 140, 156.
11) A. V. Tobolsky, J. R. McLoughlin: J. Polymer Sci. **8** (1953) 543.
12) F. Bueche: J. Chem. Phys. **21** (1953) 603.
13) J. D. Ferry, R. F. Landel, M. L. Williams: J. Appl. Phys. **26** (1955) 359.
14) S. Iwayanagi, T. Hideshima: J. Phys. Soc. Japan **8** (1953) 368.
15) R. S. Marvin, R. Aldrich, H. S. Sack: J. Appl. Phys. **25** (1954) 1213.
16) O. Nakada: Bul. Kobayasi Inst. Phys. Res. **6** (1956) 193.
17) J. D. Ferry, E. R. Fitzgerald: J. Colloid Sci. **8** (1953) 224; J. D. Ferry, M. L. Williams, E. R. Fitzgerald: J. Phys. Chem. **59** (1955) 403.

JOURNAL OF THE PHYSICAL SOCIETY OF JAPAN Vol. 12, No. 11, NOVEMBER, 1957

Structure of Nuclear Quadrupole Resonance Line

II. Solid Bromine

By Shoji KOJIMA, Yoshihito ABE, Midori MINEMATSU, Kineo TSUKADA* and Akira SHIMAUCHI**

Department of Physics, Tokyo University of Education Otsuka, Tokyo

(Received June 26, 1957)

Broad resonance lines of Br^{79} and Br^{81} in a single crystal of bromine have been studied. If the theory of indirect spin-spin coupling is applied, ten components are expected for each lines even when asymmetry of the field gradient tensor is neglected. The observed derivative curves of the lines could not be resolved into more than three lines. Provided that the each components have a finite line width a rough agreement was obtained with the interaction constant of 3 kc. This value is resonable if the s-character of Br–Br bond is 18%. The ratio between overall line width of Br^{79} and Br^{81} accorded approximately with the ratio of the square of nuclear magnetic moment.

§1. Introduction

In a earlier report it was shown that nuclear quadrupole resonance lines in solid iodine, bromine and iodine monochloride have a fine structure which was probably arisen from electron-coupled spin-spin interaction¹⁾. The preceding paper, **I** of this series, has dealt with a detailed measurements of the splitting of the resonance line of solid iodine²⁾. The present paper contains an extension of that measurement to solid bromine, whose crystal structure is the same as iodine. Solid bromine contains two isotopes, Br^{79} and Br^{81}, with nearly equal abundances and the spin numbers of both isotopes are 3/2, whereas iodine consists of single isotope having spin of 5/2. An investigation of bromine seems to be interesting in the fact that splittings due to the indirect spin-spin interaction are simpler than iodine owing to smallness of the spins. Moreover, comparison between the splittings of both isotopes will be valuable to verify the origin of the splitting.

---

* Now at Japan Atomic Energy Research Institute, Minato-ku Tokyo.

** Now at Institute for Optical Research, Tokyo University of Education, Shinjuku-ku Tokyo.

Sometimes spurious complex patterns of resonance lines were observed for a number of compounds when the samples were locally heated by radio-frequency field. Such cases are described in the Appendix. Iodine monochloride is also discussed there.

§ 2. Experimental Procedures

Bromine used was purified by means of dehydration and distillation from a commercial sample. The purified sample was kept from moisture, otherwise it showed no fine structure of the resonance line. A single crystal of bromine was produced by the method of pointed-bottom crucible, which was used in the previous experiment on the Zeeman effect of bromine[3)].

The detector was a super-regenerative detector with a transmission line tuned circuit as previously[3)]. The transmission line, however, was extended to about one wave length, so that the sample was located far from the vacuum tubes. The recording system was the same as discribed in **I**.

The crystallographic axes of bromine were determined through the method of Zeeman effect of nuclear quadrupole resonance with larger Helmholz coil than that of the previous experiment. The Helmholz coils consisted of air cooled coils with separation of 11 cm. Each coil had inner diameter of 25 cm, outer diameter of 35 cm and thickness of 4.3 cm with 5000 turnes of No. 24 enamelled copper wire. These coils were mounted in a goniometer.

§ 3. Result of Experiments

The absorption curve of Br^{81} was observed by an oscilloscope with large modulation of frequency. The observed pattern is reproduced in Fig. 1. In order to keep the sample at constant temperature this observation was made at the melting point of bromine of −7.9°C, while a small part of sample was melting. Although the large modulation of frequency gave rise to distortion of pattern, the observed curve showed a complex structure. By using small modulation a derivative curve was recorded which showed complex structure more decidedly (Fig. 2). The obtained pattern could be resolved into three lines.

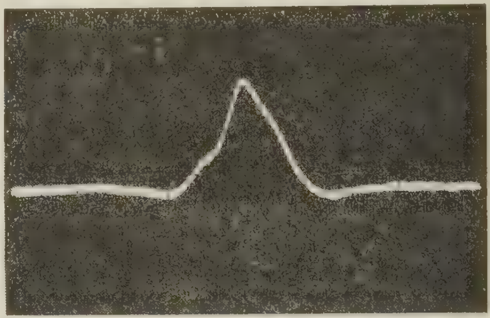
Fig. 1. Absorption curve of Br^{81} at −7.9°C.

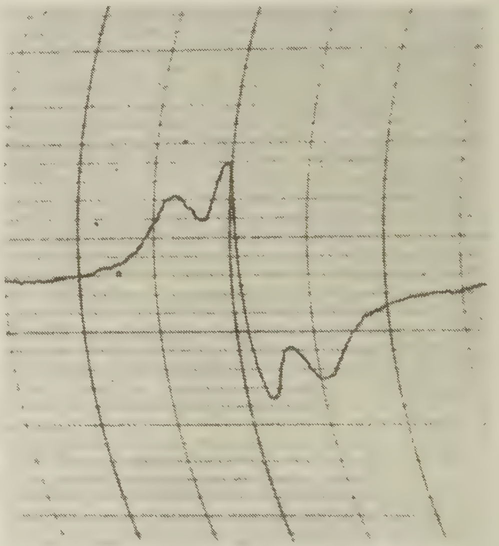
Fig. 2. Derivative curve of Br^{81} at −7.9°C. Frequency increases from the left to the right.

Since the previous experiment on the single crystal of iodine revealed that the pattern of the absorption line depended on the orientation of the applied radio-frequency field. The pattern had to be studied at various orientatio of the rf field with a single crystal whose crystallographic axes were determined. In order to carry out many measurements with one single crystal the experiment at the melting point of the sample is unfavourable. Then the following experiments were carried out at

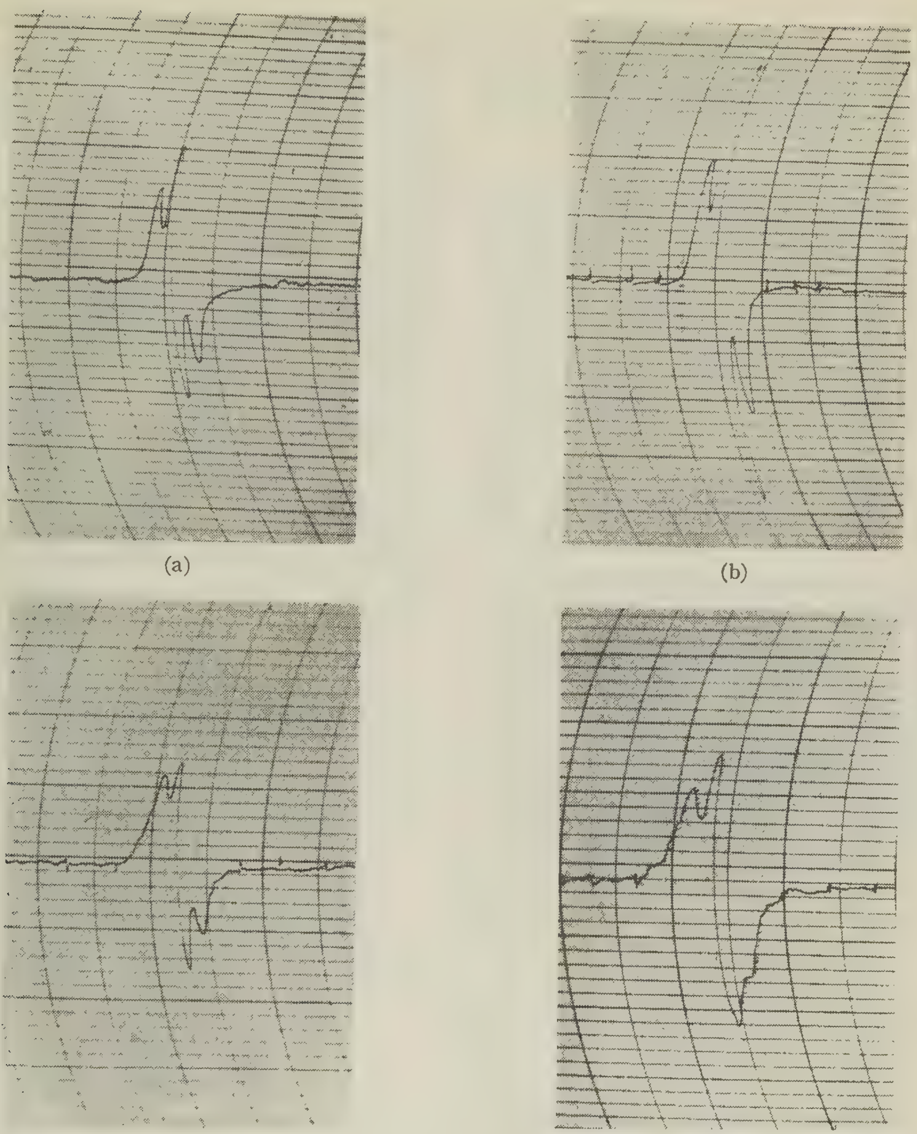

(a)　(b)

(c)　(d)

Fig. 3. Derivative curves at −23°C.

(a) Br^{81}. The rf field parallel to the *a* axis.
(b) Br^{81}. The rf field parallel to the *b* axis.
(c) Br^{81}. The rf field parallel to the *c* axis.
(d) Br^{79}. The rf field parallel to the *a* axis.

−23°C which was the melting point of carbon-etra-chloride.

Derivative curves of the resonance line of r^{79} and Br^{81} were recorded at various orienta-ions of the rf magnetic field. Their frequ-encies were about 378 Mc and 315 Mc respec-ively. Some of the recordings are reproduced n Fig. 3. The curve Fig. 3 (a) agreed well ith the curve of Fig. 2. The over-all split-ings of the patterns of Br^{79} and Br^{81} are 21.0 ±0.5 kc and 24.0±0.5 kc respectively. These were determined as the spreading between two outer peaks of the derivative curves.

Shapes of absorption curves can be obtained by integrating the derivative curves. As an example, a curve which was obtained by graphical integration is shown in Fig. 4.

§ 4. Calculation of the Splitting

Theory of the electron coupled spin-spin interaction in solid iodine was recently given by Itoh and Kambe[4]. By their theory the Hamiltonian of the interaction is expressed by*,

$$\mathscr{H}_{\text{int}}=J\boldsymbol{I}_{1z}\boldsymbol{I}_{2z}+K(\boldsymbol{I}_{1x}\boldsymbol{I}_{2x}+\boldsymbol{I}_{1y}\boldsymbol{I}_{2y})\,, \tag{1}$$

where $\boldsymbol{I}_1$ and $\boldsymbol{I}_2$ are spins of a pair of nuclei in a molecule. The interaction constants J and K are,

$$J=\frac{2\hbar^2}{\Delta E}\left[\beta\gamma\left\{\frac{8\pi}{3}\alpha|\psi(0)|^2+\frac{4}{5}(1-\alpha)\left\langle\frac{1}{r^3}\right\rangle\right\}\right]^2,$$
$$K=\frac{2\hbar^2}{\Delta E}\left[\beta\gamma\left\{\frac{8\pi}{3}\alpha|\psi(0)|^2-\frac{2}{5}(1-\alpha)\left\langle\frac{1}{r^3}\right\rangle\right\}\right]^2, \tag{2}$$

In this expression α is the s-character of the chemical bond, β the Bohr magneton, γ the gyro-magnetic ratio of the nucleus and ΔE is the mean energy difference of excited states from the ground state. $|\psi(0)|^2$ is approximately expressed by $Z\delta^2/\pi n' a_0^3$ where Z is the atomic number, δ Slater's orbital exponent, n' the effective principal quantum number and a_0 is the Bohr radius. For bromines Z, δ and n' are 35, 1.65 and 3.7 respectively. $\langle 1/r^3\rangle$ can be obtained from the coupling factor of hyperfine structure of $^2P_{3/2}$ term. By King and Jaccarino[5] the factor, $\frac{16}{15}\beta\gamma\frac{1}{2\pi}\left\langle\frac{1}{r^3}\right\rangle$, of Br^{79} and Br^{81} are given as 884.810 Mc and 953.770 Mc respectively.

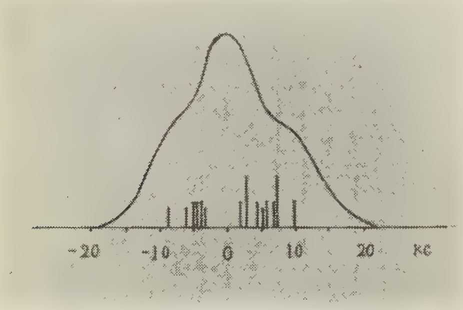

Fig. 4. Integrated curve obtained from the curve (a) in Fig. 3. The line spectrum is calculated from the theory assuming that $J\approx K=3$ kc.

Splitting of the nuclear quadrupole energy levels were calculated by perturbation theory started from the eigenstates $\psi_{m_1}\psi_{m_2}$, where m_1 and m_2 refer to the magnetic quantum numbers of the two spins. The splittings are different between homonuclear molecules, Br^{79} Br^{79} and $\text{Br}^{81}\text{Br}^{81}$, and heteronuclear molecule $\text{Br}^{79}\text{Br}^{81}$, on account of mixing and nonmixin of the states $\psi_{3/2}\psi_{1/2}$ and $\psi_{1/2}\psi_{3/2}$. The resu of calculation by the first order perturbatio theory is shown schematically in Fig. 5, wher asymmetry of field gradient tensor is neglect ed for simplicity. Transitions are allowed i $\Delta m_1=\pm 1$, $\Delta m_2=0$ and if the character of sym metry for exchange of nuclei is conserve As shown in Fig. 5, five resonance lines ar expected for both types of molecule**. Relative intensities of these five lines a, b, c, and e are 2:2:1:1 and 2 for both types o molecules. The lines are independent o orientations of the rf field at this stage o approximation.

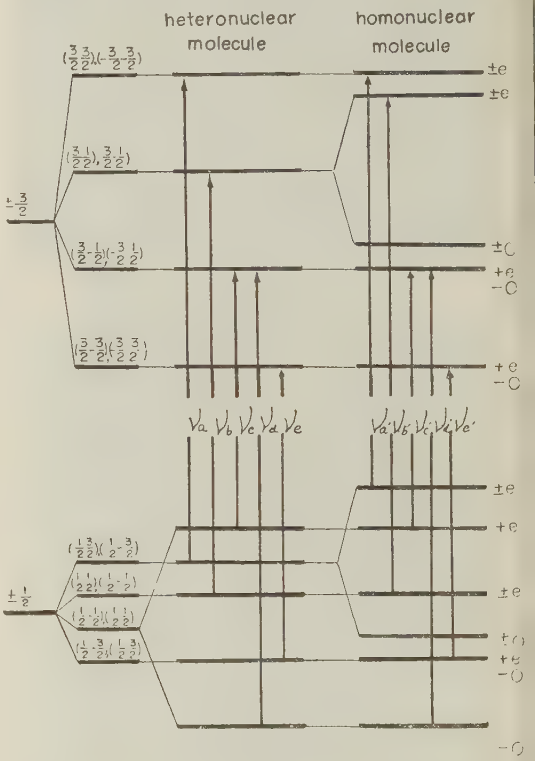
heteronuclear molecule
homonuclear molecule
$\pm\frac{3}{2}$
$(\frac{3}{2}\frac{3}{2}),(-\frac{3}{2}-\frac{3}{2})$
$(\frac{3}{2}\frac{1}{2}),(\frac{3}{2}\frac{1}{2})$
$(\frac{3}{2}-\frac{1}{2}),(-\frac{3}{2}\frac{1}{2})$
$(\frac{3}{2}-\frac{3}{2}),(\frac{3}{2}\frac{3}{2})$
$\pm\frac{1}{2}$
$(\frac{1}{2}\frac{3}{2}),(\frac{1}{2}-\frac{3}{2})$
$(\frac{1}{2}\frac{1}{2}),(\frac{1}{2}-\frac{1}{2})$
$(\frac{1}{2}-\frac{1}{2}),(\frac{1}{2}\frac{1}{2})$
$(\frac{1}{2}-\frac{3}{2}),(\frac{1}{2}\frac{3}{2})$
±e
±e
±o
+e
−o
+e
−o
ν_a ν_b ν_c ν_d ν_e
ν_a' ν_b' ν_c' ν_d' ν_e'
±e
+e
±e
±o
+e
−o
−o

Fig. 5. Energy level diagram.

The quadrupole interaction of solid bromine is known to have a small deviation from axia symmetry. The asymmetry parameter define by $\eta=(q_{xx}-q_{yy})/q_{zz}$ was experimentally deter mined as -0.20[3]. This effect is accounte by the additional Hamiltonian;

$$\mathscr{H}_{\text{asy}}=\eta\left\{\frac{h\nu_1}{6}(\boldsymbol{I}_{1x}{}^2-\boldsymbol{I}_{1y}{}^2)+\frac{h\nu_2}{6}(\boldsymbol{I}_{2x}{}^2-\boldsymbol{I}_{2y}{}^2)\right\}, \tag{3}$$

---

* Eq. (1) in the paper I was misprinted. $AI_1I_2+B(I_{1x}I_{2x}+I_{1y}I_{2y})$ should be read $AI_{1z}I_{2z}+B(I_{1x}I_{2x}+I_{1y}I_{2y})$.

** The resonance frequencies are given in Eqs (4) and (5), by putting $\eta=0$.

where ν_1 and ν_2 are the resonance frequencies of nuclei 1 and 2. Splittings of energy levels were calculated by the second order perturbation theory. In this calculation, however, the small terms containing K^2, J^2 and η^2 were omitted. The result for the heteronuclear molecules shows that the two degenerate states $\psi_{\pm 3/2}\psi_{\mp 1/2}$ and $\psi_{\pm 1/2}\psi_{\mp 3/2}$ split each into a pair of states having additional energy of $\pm\eta K$ and that the states $\psi_{\pm 1/2}\psi_{\pm 1/2}$ into a pair states of $\mp 2\eta K$. The first state of the pairs is represented by a symmetric wave function with respect to the reflection by the *ac*-plane and the second by an antisymmetric one. In the homonuclear molecules the splitting of the states $\psi_{\pm 1/2}\psi_{\pm 1/2}$ is the same as the heteronuclear molecules, but the degenerate state which are represented by four eigen function $\psi_{\pm 3/2}\psi_{\mp 1/2}$ and $\psi_{\pm 1/2}\psi_{\mp 3/2}$, split into three states having the additional energy of $2\eta K$, 0 and $-2\eta K$* with the character of $(+, e)$, $(\pm, o)$ and $(-, e)$ respectively, where e and o indicate the even and odd character of exchange of nuclei and $\pm$ the symmetric character respect to the reflection by the *ac*-plane.

The resonance frequencies expected from these levels are expressed by

$$\left.\begin{aligned}
\nu_a &= \nu_o + (3/2)J\,, \\
\nu_{b_1}, \nu_{b_2} &= \nu_o + (1/2)J \pm 2\eta K\,, \\
\nu_{c_1}, \nu_{c_2} &= \nu_o - (1/2)J + 2K \pm \eta K\,, \\
\nu_{d_1}, \nu_{d_2} &= \nu_o - (1/2)J - 2K \pm \eta K\,, \\
\nu_{e_1}, \nu_{e_2} &= \nu_o - (3/2)J \pm \eta K\,,
\end{aligned}\right\} \qquad (4)$$

for heteronuclear molecules and

$$\begin{aligned}
\nu_{a'} &= \nu_o + (3/2)J - (3/2K)\,, \\
\nu_{b_1'}, \nu_{b_2'} &= \nu_o + (1/2)J + (3/2)K \pm 2\eta K\,, \\
\nu_{c'} &= \nu_o - (1/2)J + 2K\,, \\
\nu_{d_1'}, \nu_{d_2'} &= \nu_o - (1/2)J - 2K \pm 2\eta K\,. \\
\nu_{e_1'} &= \nu_o - (3/2)J\,, \\
\nu_{e_1'}, \nu_{e_3'} &= \nu_o - (3/2)J \pm 2\eta K\,.
\end{aligned} \qquad (5)$$

for homonuclear molecules.

Relative intensities of lines, a, b_1, b_2, c_1, c_2, d_1, d_2, e_1 and e_2 are 2:1:1:Y:X:X:Y:1:1 where $X=\cos^2\theta$ and $Y=\cos^2\phi$ being θ the angles between the rf field and the X axis and ϕ the angle between the rf field and the Y axis of field gradient tensor**. For lines a', b_1', b_2', c', d_1', d_2', e_1', e_2' and e_3', relative intensities are 2:1:1:1:X:Y:1:Y:X.

§ 5. Analysis of the Resuls

The observed spectrum on Br^{81} is the mixing of spectrum of homonuclear molecule $Br^{81}Br^{81}$ and that of heteronuclear molecules $Br^{79}Br^{81}$ with nearly equal intensities. Taking into account the difference between the values of the magnetic moments of Br^{79} and Br^{81}, 18 lines are expected from the calculation. The theoretical spectrum is a function of the ratio of K/J. The line spectrum shown in Fig. 4 is calculated with $J \approx K \approx 3$ kc. On the other hand, the observed spectrum could not be resolved into more than three lines because of a finite width of each lines. Therefore, exact comparison between theory and experiment is impossible. If we assume that *s*-character of the Br–Br bond is 18%***, we can calculate J and K by using Eq. (2). The calculated values of J and K are 2.9 kc and 0.46 kc for Br^{81}. The obtained spectrum, however, shows poor agreement with the observed one. If we assume that $J \approx K \approx 3$ kc as the case of iodine, better agreement is obtained than the previous case, although some discrepancies still remain. In this case, in order to fit the spreading of the observed pattern the width of the each components must be about 15 kc.

The ratio of overall splitting of the resonance of Br^{79} to Br^{81} is about 1.14. This value accords approximately with the ratio of the square of nuclear magnetic moment****, 1.16, and does not with the ratio of the nuclear quadrupole moment. If the splittings were arisen from nonequivalent position of nuclei, the splitting would be proportional to the nuclear quadrupole moment. The dependence of the spectrum in bromine upon the orientation of rf field is less than in the case of iodine. The reason is that the pairs of lines, which have the intensity X and Y, are near each other and cancel the effect.

---

* For homonuclear molecules the energies of levels are also calculable by using the general formula derives by Itoh and Kambe, *i.e.*, Eq. (22) of Ref. (4).

** When the character of asymmetry for the reflection to the *ac*-plane changes, the intensity is proportional to Y and when it does not change, the intensity is proportional to X.

*** R. S. Mulliken (J. Am. Chem. Soc. **77** (1955) 884) estimated theoretically the *s*-characters of the F_2 molecule and the Cl_2 molecule to be 2% and 10% respectively. T. Itoh and K. Kambe[4)] obtained 22% *s*-character for the I_2 molecule from the analysis of indirect spin-spin interaction.

**** Strictly speaking, when the ratio are taken for the homonuclear molecules. $Br^{79}Br^{79}$ and Br^{81}–Br^{81}, the ratio should agree with the square of the magnetic moment. In the practical case where heteronuclear molecules exist the ratio will be reduced somewhat.

The present results on bromine are summerized in Table I. For comparison, the previous results on iodine are also summerized in the Table.

Table I.

	Br^{79}	Br^{81}	I^{127}
Resonance freq. (Mc)	378	315	332
Overall splitting (kc)	21	24	48
Interaction constant (kc)	2.6	3.0	3.0
s-character of the bond (%)	20	20	22

The mechanism of indirect spin-spin coupling seems adequate to account for the observed structure of the absorption line. The agreement between the observed pattern and the calculated pattern, however, is not satisfactory.

Acknowledgement

The authors wish to thank Dr. K. Kambe and Dr. T. Itoh for valuable advice in theoretical considerations. The present work was partially supported by the Scientific Research Expenditure of the Ministry of Education.

Appendix

It was often experienced that a resonance frequency shifted during observation. This effect resulted from a rise of temperature of samples due to heat conduction from vacuum tubes and to dielectric absorption of radiofrequency power. An experiment on paradibromobenzene with a super-regenerative spectrometer which was operated at high power level demonstrated a temperature rise of about 4°C.

If a sample is so large that its ends extend to outside of the rf-coils, the temperature in the sample will be non-uniform. Non-uniform distribution of temperature may given rise to spurious fine structure of the resonance line. Indeed, a sample of dibromobenzene in a suitable condition showed a broad resonance line having a complex structure. This pattern, however, changed with time. Therefore it could be distinguished from the structure du to indirect spin-spin coupling.

In early experiment on iodine monochlorid a complex resonance line was observed almos stably as shown in Fig. 6. Using a mor pure sample we have repeated the experiment In the present experiment* the resonance lin showed an ordinaly pattern having a width o about 25 kc. The oscillograph display is reproduced in Fig. 7.

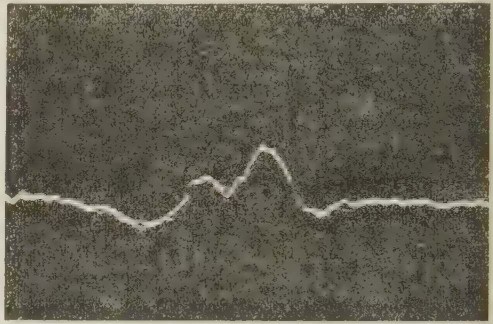

Fig. 6. Complex structure arisen from local heating of sample (ICl).

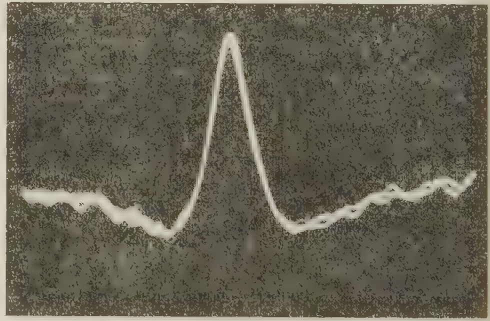

Fig. 7. Absorption curve of I^{127} in iodine monochloride.

Transiently, however, a complex structur Fig. 6 was observed in the present experiment. This pattern was not arisen from th indirect spin-spin interaction, but from th mechanism of local heating. If the crysta used is perfect and in nonstress, the rathe broad width will be accounted from the indirect spin-spin interaction. The coupling however, is much smaller than the cases o bromine and iodine.

References

1) S. Kojima and K. Tsukada: J. Phys. Soc. Japa **10** (1955) 591.

---

* The authors wish to thank to Miss. K. Kat and Mr. S. Hagiwara for their cooperation.

S. Kojima, S. Ogawa, S. Hagiwara, Y. Abe and M. Minematsu: J. Phys. Soc. Japan **11** (1956) 964.

S. Kojima, K. Tsukada, A. Shimauchi and Y. Hinaga: J. Phys. Soc. Japan **9** (1954) 795.

4) T. Itoh and K. Kambe: J. Phys. Soc. Japan **12** (1957) 763.

5) J. King and V. Jaccarino: Phys. Rev. **94** (1954) 1610.

JOURNAL OF THE PHYSICAL SOCIETY OF JAPAN Vol. 12, No. 11, NOVEMBER, 1957

Paramagnetic Resonance Absorption in Chromous Sulphate Pentahydrate

By Kazuo Ôno

Institute for Solid State and Chemical Physics, University of Tokyo

(Received July 23, 1957)

The paramagnetic resonance spectra of Chromous sulphate pentahydrate have been analyzed at room temperature for the wavelengths between 0.54 cm and 1.1 cm. The results show that this crystal has a structure similar that of copper sulphate pentahydrate. The observed data have been analyzed by the so-called spin Hamiltonian and the positions and intensities of the absorption lines are adequately explained by a crystalline electric field of rhombic symmetry. The parameters determined have been found to be quite consistent with the values of the spin-orbit coupling constant and spin-spin interaction constant obtained from spectroscopic data. The line width varies from 1 K oer. to 3 K oer. with the direction of the magnetic field and high frequency field and seems to be broader than that expected from magnetic dipolar interaction alone.

1. Introduction

The method of paramagnetic resonance has een developed for a detailed investigation of ıe lowest energy levels of paramagnetic ions ı crystals. This method is the observation f transitions caused by resonance of a high-requency magnetic field at right angle to ıe magnetic field. The consequence absorp-on of energy therefore shows a series of ıaxima as the static magnetic field is varied. y repeating the experiment for a series of ifferent values of the frequency of the high requency field, it is possible to plot out the nergy levels as a function of the static field. ı particular, one can very accurately estimate ıe splitting of the energy levels in the ab-ence of magnetic fields. Then the resonance ata provide valuable information on the bulk roperties of the crystal e.g. susceptibility and pecific heat at very low temperature.

Amongst the common salts of the first (iron) ansition group, the splitting is small in the ase of Cr^{+++}, V^{++}, Mn^{++}, Fe^{+++}, Co^{++}, and Cu^{++} which have been studied in great detail. In the case of Ni^{++}, Cr^{++}, and Fe^{++}, the splittings are generally larger than the energy of the microwave used usually. So the resonance must be observed with rather high frequencies. That is: $NiSO_4 \cdot 7\,H_2O$1)2) shows a resonance at 0.54 cm and 0.66 cm wavelengths but does not at 1.25 cm because it has zero field splitting of about $2\,cm^{-1}$.

Moreover, the Cr^{++} ion is very unstable and has a strong tendency to oxidize, especially in aqeuous solution. Then it is difficult to obtain a large crystal of divalent chromium salt. So few measurements3)4) have heretofore been made of the magnetic properties of the Cr^{++} ion. Only one salt, $Cr(NH_4)_2(SO_4)_2 \cdot 6H_2O$5), has been studied by the paramagnetic resonance method and it was reported that no resonance was observed at 3 cm wavelength.

The present paper describes the paramagnetic resonance spectra found in chromous sulphate pentahydrate at room temperature for wave-lengths between 0.54 cm and 1.1 cm.

The result shows that the fivehold spin degeneracy is completely lifted by the crystalline electric field of rhombic symmetry and the spacing between the adjacent energy levels are found to be 1.94 cm^{-1}, 0.60 cm^{-1}, 6.42 cm^{-1}, and 0.01 cm^{-1}. A brief account of the measurements on this salt has already been given by Ôno et al.[6)]

§ 2. Crystal Preparation

A solution of Cr^{++} salt is rapidly oxidized by atomospheric air and forms a green one of Cr^{+++}. Hence the solution of Cr^{++} must be prepared and treated in an evacuated vessel. The author obtained fairly large crystals of chromous sulphate as follows (See Fig. 1):

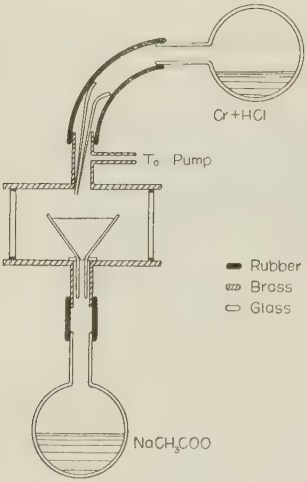

Fig. 1. Apparatus for the preparation of chromous acetate.

A solution of chromous chloride was formed in an evacuated vessel by dissolving chromium metal with hydrochlonic acid. When dissolving was over, the solution was filtered through a paper into a solution of sodium acetate. Chromous acetate, which is sparingly soluble, comes down as red crystals. The chromous acetate was taken out from the vacuum vessel and filtered off in the air because this salt is not oxidized readily.

The chromous acetate was then dissolved in a rather concentrated sulphuric acid in another evacuated vessel and was left overnight. Many crystals were obtained, which have a blue colour, somewhat more violet in tint than that of copper salts. In order that a few well-formed crystals should be obtained it is necessary to ensure that crystal nuclei are not present in too great number. Therefor the filtering of chromous chloride in the evacuated vessel is essential to obtain a goo crystal.

The crystal thus obtained, $CrSO_4 \cdot xH_2O$, i triclinic and the results of resonance absorption show that each unit cell seems to contai two unequivalent ions. The number of wate molecules of crystallization in this crystal wa determined as follows. The weighed crystal were put in a glass tube as shown in Fig. 2 The tube was then evacuated by a mechanica pump, after which the tube was sealed off.

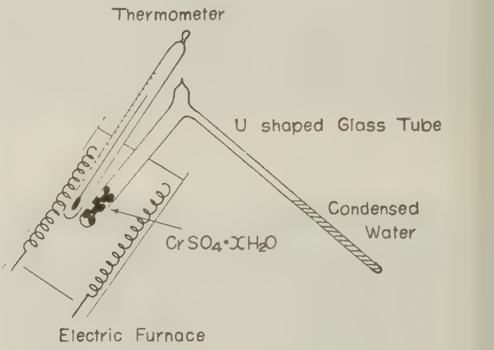

Fig. 2. Apparatus for the determination of the number of water molecules of crystallization i chromous sulphate, $CrSO_4 \cdot xH_2O$.

Then the crystals were heated very slowl keeping the other end of the tube at roo temperature. The hydration water came dow abruptly at about 260°C. The amount o water remained almost constant as the temperature was raised until the unhydrate crystals were decomposed at about 400°C The condensed water of crystallization wa weighed and x was determined to be

$$x = 4.90 \pm 0.50$$

Thus the formula of the crystal becam $CrSO_4 \cdot 5\,H_2O$. It could not be determined readily from the external form of the crysta whether it were isomorphous with coppe sulphate pentahydrate or not.

§ 3. Apparatus and Experimental Procedu

In paramagnetic resonance experiments th advantages of working at shorter wavelength than those used usually ($\lambda = 3$ cm, 1.25 c are;

1) ions with a large zero splitting can investigated;

2) the intensity of absorption goes up as e frequency is raised;
nd 3) measurements can be done by smaller mounts of materials.

Chromous salts has a large initial splitting nd cannot be obtained in a sufficiently large ingle crystal. Then, in the present investiation, it is necessary to use millimeter waveengths.

A crystal multiplier driven by a klystron re frequently used as a source of radiation f the millimeter wave-lengths in micro-wave pectroscopy. But power output from a clytron is quite low, and only second or third armonic is available for physical measureents in solid state spectroscopy, which equires higher power than that in gaseous ne. Since one cannot easily obtain a klytron below the wavelength of 3 cm in Japan, xperiments in millimeter wave region are ifficult.

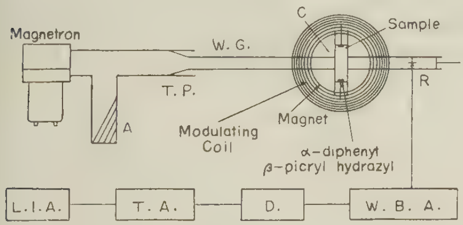

Fig. 3. Schematic diagram of paramagnetic resonance absorption apparatus at millimeter waves employing magnetron harmonics.

It has been reported by Klein et al[7] that nagnetrons emit harmonics of their fundanental frequency of oscillation. Employing he techniques reported by them, harmonics s high as the sixth have been obtained from igh power magnetron. That is: the waveengths used, $\lambda=6.6$ mm and $\lambda=5.4$ mm, were he fifth and the sixth harmonics of the nagnetron of $\lambda=3$ cm.

The main components of the apparatus are hown in Fig. 3. The magnetron is operated vith a pulse length of about one micro-second nd a repetition rate of about 600 per second.

Microwave radiation of the fundamental scillation is reflected back by the tapered iston, T. P., and absorbed by the absorber, . Radiaton of harmonics goes through the vave-guide W. G. The sample crystal is laced at the center of the piston of the ectangular cavity, C. excited in the H_{10n} mode and can be rotated in the plane of the static and micro-wave magnetic field. An external magnet applies a field to the crystal which can be varied from zero to 20 kilogauss. The intensity of the static magnetic field was measured using a fluxmeter and calibrated by the magnetic field for the absorption peak of α-diphenyl β-picryl hydrazyl ($g=2.00$, $\Delta H=$ several gauss) at $\lambda=5.4$ mm. A pair of subsidiary coils wound on the pole-pieces are used to modulate this field to a depth of about 200 gauss at a frequency of 30 c/sec.

The absorption of micro-wave energy by the sample in the cavity reduced the Q-value of the cavity, and was registered as a diminution of the power transmitted. The power is detected by the silicon rectifier, R, which is a demountable one constructed with a silicon wafer and a tungsten cat whisker within the wave-guide. Then the power, modulated with 30 c/sec, is fed through the wide-band amplifier, W.B.A., the detector D, the amplifier, T. A., tuned to the modulation frequency, and the lock-in amplifier, L.I.A. This amplifier output is read on a meter.

The wave-length of $\lambda=11$ mm is obtained by a harmonics multiplier of silicon diode crystal from the fundamental oscillation of a 2K25 klystron. ($\lambda=3$ cm). The measuring method is essentially the same as that of the wavelength of 5.4 mm and 6.6 mm.

The positions of absorption lines vary very rapidly with the direction of the applied magnetic field, and hence with the accuracy of the cutting and mounting of the crystal. The sample used is very small (about 2 mm × 1.5 mm × 0.5 mm) and the accuracy of this process is rather bad.

§ 4. Preliminary Discussion of the Spectrum

Before describing the observed spectrum, it is convenient to consider the theoretical basis for its interpretation.

The free ion Cr^{++} is in a ^5D state but the orbital momentum is strongly quenched by a crystalline electric field. (shown in Fig. 4). The orbital levels are split by a cubic field into a triplet Γ_5 and a doublet Γ_3. The nonmagetic doublet is split by a tetragonal or rhombic field, and paramagnetic resonance is observed for the lower level. The combined effects of the non cubic part of the crystalline field and the spin-orbit coupling then produce a further small splitting of the lowest orbital singlet, which has five fold degeneracy due to the spin ($S=2$).

When static magnetic field is applied this spin quintuplet is approximately descrived by the Hamiltonian

$$\mathscr{H}=\{SD_z^2-1/3\,S(S+1)\}+E(S_x^2-S_y^2)$$
$$-\beta(g_xH_xS_x+g_yH_yS_y+g_zH_zS_z) \qquad (1)$$

The term in D represents the fine structure due to the crystalline field of axial symmetry, while small departures from this due to the rhombic component appear as the term in E. Here g is the spectroscopic splitting factor, β is the Bohr magneton, and $\boldsymbol{H}$ is the applied magnetic field.

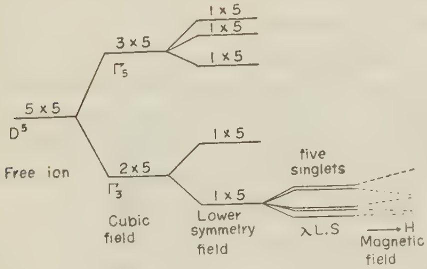

Fig. 4. Schematic energy levels of Cr++ ion in crystalline electric field.

The expressions for the parameters D, E, and g are derived by Koide and Sekiyama;[7)]

$$D=-3(l^2-m^2)\left(\frac{\lambda^2}{\Delta E}+\rho\right) \qquad (2)$$

$$E=-2\sqrt{3}\,lm\left(\frac{\lambda^2}{\Delta E}-\rho\right) \qquad (3)$$

$$\left.\begin{aligned} g_x&=2-2(l-\sqrt{3}\,m)^2\lambda/\Delta E\\ g_y&=2-2(l+\sqrt{3}\,m)^2\lambda/\Delta E\\ g_z&=2-8l^2\lambda/\Delta E \end{aligned}\right\} \qquad (4)$$

where λ is the spin-orbit coupling coefficient, ρ is the spin-spin coupling constant between $3d$ electrons, ΔE is the spacing between Γ_3 and Γ_5, and l and m satisfy the relations

$$\left.\begin{aligned} 2lm/[\sqrt{3}\,(l^2-m^2)]&=E/D\\ l^2+m^2&=1 \end{aligned}\right\} \qquad (5)$$

Spectroscopic data indicated $\lambda=58\,\mathrm{cm}^{-1}$ and $\rho=0.42\,\mathrm{cm}^{-1}$ [8)9)] for the free Cr++ ion. Assuming $E=0$ we have two alternative cases in the above formula, i.e., $l=1$, $m=0$ and $m=1$, $l=0$. Since copper sulphate corresponds to the former, it is resonable to assume that for chromous sulphate it is also the case With the values of $\lambda=58\,\mathrm{cm}^{-1}$, $\rho=0.42$ cm and $\Delta E=10000\,\mathrm{cm}^{-1}$, it is obtained from eq. (and eq. (4) that

$$D=-2\,\mathrm{cm}^{-1} \qquad g_z=1.95 \qquad g_x=g_y=1.99\,.$$

The assumed value of $\Delta E=10000\,\mathrm{cm}^{-1}$ reasonable considering the color of the cryst which is due to transition between Γ_3 and

The levels of the spin quintuplet when $\boldsymbol{H}=$ are seen from (1) to be

$$\left.\begin{aligned} W_1&=-2\sqrt{D^2+(3E)^2}\\ W_2&=-D-3E\\ W_3&=-D+3E\\ W_4&=2D\\ W_5&=2\sqrt{D^2+(3E)^2} \end{aligned}\right\} \qquad (6$$

When $\boldsymbol{H}$ is present, these levels vary wit $\boldsymbol{H}$. In Mn++, Fe+++, and Cr+++, D is sma compared with $g\beta H$ and they can be approx mated by simple formulae, but this is not th case in Cr++.

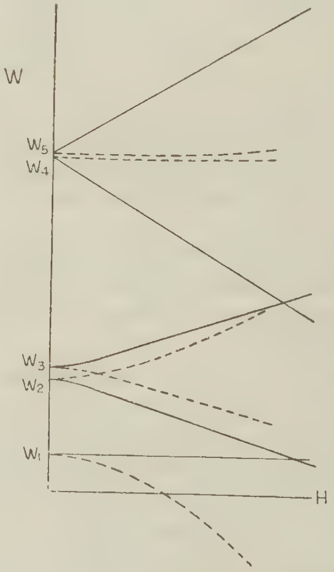

Fig. 5. Relative positions of the lowest energy levels of the Cr++ ion in $CrSO_4\cdot 5H_2O$. The full lines are those for H//z and the dashed lines for H//y.

Fig. 5 shows the calculated values of W using eq. (1) with the values $D=2.24\,\mathrm{cm}^{-}$ $E=0.10\,\mathrm{cm}^{-1}$ and $g_x=g_y=g_z=2.00$. The micro wave transition ($W_2 \leftrightarrow W_1$) can be observe when $\boldsymbol{H}$ is parallel to z and that betwee ($W_2 \leftrightarrow W_3$) when $\boldsymbol{H}$ is applied in the xy plane The transition ($W_2 \leftrightarrow W_3$) is energitically possible in the case of $\boldsymbol{H}//z$, but forbidden b selection rule.

5. Experimental Results

The analysis of the spectrum of chromous ulphate is very complicated with the followng reasons.

1) The value of D is large compared with βH.

2) The structure of this crystal is trinclinic nd magnetic axes bear no relation to the rystalline axes.

3) The spectrum is doubled by the presence of two inequivalent ions in a unit cell.

To determine the constants D, E and g, it requires to be two things.

1) To find directions of the rohmbic axes $x_1y_1z_1)(x_2y_2z_2)$ associated with the dissimilar ons in unit cell.

2) To observe the resonance fields with **H** parallel to any particular rhombic axis for different values of λ, so that the parameters n eq. (1) can be determined.

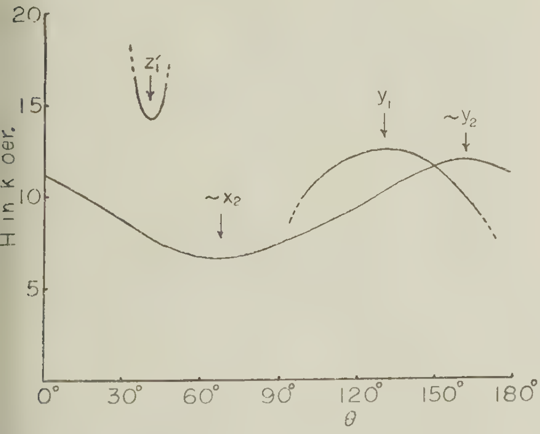

Fig. 6. The angular dependence of the resonance field in the $z_1'y_1$ plane with λ=11 mm. x_1, y_1, z_1 and x_2, y_2, z_2 indicate the rhombic axes of the crystalline fields corresponding to the two kinds of ions, respectively.

It is remembered that the resonance field with **H** parallel to any particular rhombic axis as a maximum or minimum one. For example, one of the rhombic axis, z_1, can be determined precisely as follows.

The crystal is mounted in a cutted plane, say α' plane, which was found to contain z_1' and y_1' nearly parallel to z_1 and y_1, respectively. Fig. 6 shows the resonance field against the direction of **H** in this plane with λ=11 mm. The direction of the minimum value of resonance field **H** corresponds to z_1'. Then the crystal is remounted in a α'' plane which is rotated by about 2 degree about an axis perpendicular to z_1' in the α' plane. The resonance fields near z_1' against **H** were also observed and z_1'' axis was obtained corresponding to the minimum value of **H**. A series of the values of **H** corresponding to z_1', $z_1''\cdots$ thus obtained are plotted against the angle of rotation in Fig. 7. The minimum value of **H** in Fig. 7 corresponds to the true z_1 axis.

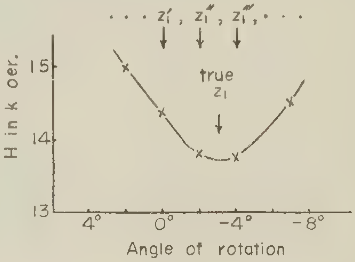

Fig. 7. A series of the values of H corresponding to z_1', z_1'', $\cdots$

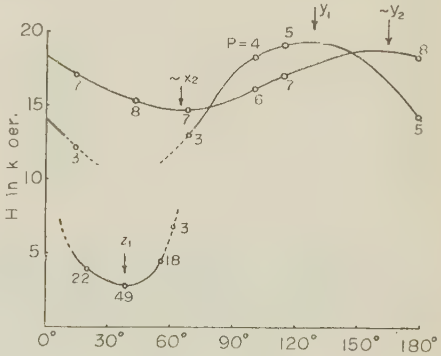

Fig. 8. The angular dependence of the resonance field in the z_1y_1 plane with λ=5.4 mm. Here P is the intensity of the absorption, the product of the muximum absorption and the width of the absorption line.

Thus the positions of absorption lines with **H** parallel to any particular rhombic axis were precisely determined, although the sample used was so small that the accuracy of the cutting and mounting was not sufficient.

Fig. 8 shows the angular dependence of the resonance field in the z_1x_1 plane with λ=5.4 mm and Fig. 9 and Fig. 10 shows that in the z_1x_1 plane and the z_1z_2 plane with λ=6.6mm respectively. We can see in Fig. 10 that the angle between z_1 and z_2 is 86°. This angle is the same as that obtained by the author for copper sulphate pentahydrate. In the figures, the positions where the intensity is low are written with the dashed curves. They disappear with $\boldsymbol{H}$ parallel to z_1 where the transition ($W_2 \longleftrightarrow W_3$) is forbidden by selection rule.

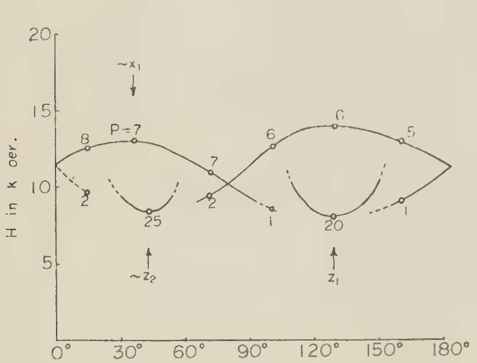

Fig. 9. The angular dependence of the resonance in the z_1x_1 plane with $\lambda=6.6$ mm. Here P is the intensity of the absorption.

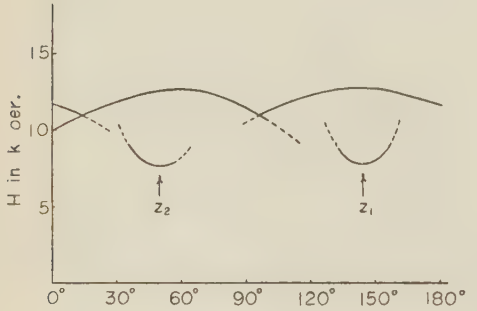

Fig. 10. The angular dependence of the resonance field in the z_1z_2 plane with $\lambda=6.6$ mm.

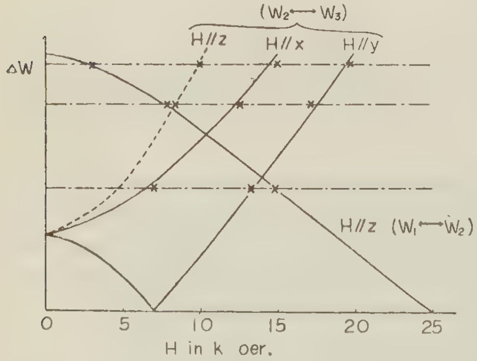

Fig. 11. ΔW as a function of H. The full line indicate the theoretical values and the crosses the experimental ones.

Assuming $g_x=g_y=2.00$, the best fit of the experimental transitions is obtained with $D=2.24\,\mathrm{cm}^{-1}$, $E=0.10\,\mathrm{cm}^{-1}$ and $g_z=1.96$. Fig. 11 shows the calculated values of ΔW (full lines) using these values from eq. (1), and th crosses are the experimental points. Thes values of D and g_z are quite consistent wit those calculated from the eq. (4) using spectro scopic data. With $D=2.24\,\mathrm{cm}^{-1}$ and $E=0.1$ cm^{-1}, it is also obtained from eq. (5) that

$$m=0.035 \quad \text{and} \quad l=1.00\,.$$

For a splitting of the type shown to exist Cr^{++}, the principal susceptibilities for an io with axial symmetry are

$$\left.\begin{aligned} \chi_{\parallel} &= 2Ng_{\parallel}{}^2\beta^2/kT(1-7D/5kT) \\ \chi_{\perp} &= 2Ng_{\perp}{}^2\beta^2/kT(1-7D/10kT) \end{aligned}\right\} \qquad (7)$$

Then, the sign of D may be determined by observing the anisotropy. The contribution to the specific heat from these splittings o the energy levels is given by;

$$CT^2/R=\left(\frac{hc^2}{k}\right)\frac{14}{5}(D^2+3E^2) \qquad (8)$$

The susceptibility of chromous sulphate hexahydrate, $CrSO_4 \cdot 6H_2O$, in a powdered form has been studied by Lips[3]. Over the temperature range 54°K to 400°K he found the Weiss law to be obeyed with an effective Bohr number of 4.82, in agreement with the value of eq. (7) neglecting the D term. Unfortunately, for the lack of data on susceptibility and specific heat at very low temperature, comparison between measured and calculated ones cannot be made.

§ 6. Line Widths

Because of the rather closer spacing of the Cr^{++} ions in the crystal, there may be exchange interaction between identical and non-identical ions as can be seen in the case of $CuSO_4 \cdot 5\,H_2O$(1) which contributes fairly to line widtns. Moreover, the experimental magnetic field is never really large compared with the Stark splitting of the energy levels. So the observed magnetic width is not in general linearly related to the frequency width, and this can have the effect of broadening the observed line, especially in the transition ($W_1 \longleftrightarrow W_2$). Van Vleck has calculated the line width from magnetic dipolar interaction alone. In the crystal, the calculated dipolar width is about 1.3 K oer., but the calculation can not be applied to the case in details from the reasons mentioned above.

The observed widths of absorption lines varied with the orientation of the crystal, rom 1 K oer. to 1.5 K oer. in the transition $W_2 \leftrightarrow W_3$) and from 1.3 K oer. to 3.0 K oer. ı the transition ($W_1 \leftrightarrow W_2$). Fig. 12 shows ıe absorption curves in the z_1x_1 plane with $=5.4$ mm. The error of the broadest line ridth is estimated at 30%～40% on account f low signal to noise ratio, while that of the arrower one is correct within 10%. Line idth does not vary remarkably with wave-ngth and that multiplied by $d(\Delta W)/dH$, erived from Fig. 11, gives almost a constant ith the same orientation of the crystal. The ıape of every absorption line is near to ıussian.

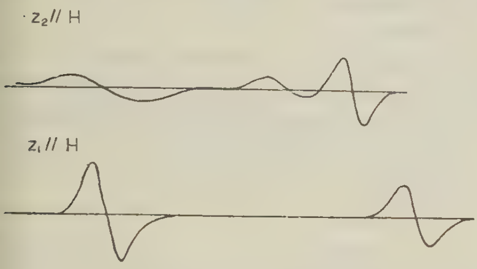

ig. 12. Paramagnetic resonance spectrum of Cr^{++} ion (1) and ion (2) in the z_1z_2 plane with $\lambda=5.4$ mm.

7. The Intensity of the Absorption Lines

The intensity of the absorption lines varied ith the direction of the external field $\boldsymbol{H}$, ith the direction of the oscillating field h, ıd with the wavelengths λ. Fig. 8 and Fig. show relative intensities of absorption in ıe z_1y_1 plane with $\lambda=5.4$ mm and in the z_1x_1 ane with $\lambda=6.6$ mm. In the figures, inten-ty, P, are normalized by an absorption of diphenyl β-picryl hydrazyl mounted in the me measuring cavity containing the crystal. he intensity of the absorption is nearly otropic both with the direction of the exter-ıl field $\boldsymbol{H}$, and the oscillating field h in the plane, while the intensity varies remarkably ith $\boldsymbol{H}$ and h in the plane containing the axis.

A comparison is made in Table I between perimental and calculated transition proba-lities. The theoretical values of relative ansition probabilities between two eigen-ates, 1 and 2, for a single system per unit ne with eigenvalues differing the energy $_0$ for x-polarized radiation is

$$P=(2\pi/\hbar)^2|\mu_{12}{}^x|^2 I\,. \qquad (9)$$

Where $\mu_{12}{}^x$ is the matrix element of the magnetic moment operator $\mu^x=g_x\beta S_x$ and I is the total energy in the incident radiation field per unit volume per unit frequency interval. A conversion must be made, however, because the theoretical probabilities are calculated at the constant field as a function of frequency, while the observations were made at the constant frequency. This is accomplished to a first order by the factor $d(\Delta W/dH)$, the slope of the transition energy curve as a function of magnetic field in Fig. 11. In Table I, $P(z,x)$ refers to the transition probability when $\boldsymbol{H}$ is parallel to z and h is parallel to x, $P(z,X)$ in which large letter X is used instead of small one x or y is calculated with $E=0$, and $\widehat{xy}$ indicates the bisector of x and y. Here experimental transition probability means the product of the maximum absorption and the width of the absorption line. The agreement between experimental and calculated values is fairly good.

Table I. Comparison of experimental and theoretical transition probabilities. For the notation used see the text.

transition probabilities observed	λ mm	expt. ratio	theor. ratio.
$\frac{P(z,x)}{P(z,\widehat{xy})}$	6.6	0.7	0.6
$\frac{P(z,\widehat{xy})}{P(x,z)}$	5.4 6.6	6.0 3.0	4.8 3.4
$\frac{P(z,y)}{P(X,Y)}$	5.4 6.6 11.0	5.7 3.5 4.4	7.0 4.8 4.2
$\frac{P(y,z)}{P(X,Y)}$	5.4 6.6 11.0	0.7 1.8 1.2	0.7 0.9 1.1
$\frac{P(y,x)}{P(y,z)}$	5.4	1.4	1.7
$\frac{P(x,z)}{P(\widehat{xy},z)}$	6.6	1.2	1.1
$\frac{P(z,x)}{P(X,z)}$	5.4 6.6	2.3 2.5	1.3 2.2

Acknowledgements

The author would like to thank Professor T. Muto and Professor H. Kumagai for valuable discussion and Dr. H. Abe and Miss M. Ohtsuka for their assistance in the experiment. The author is also indebted to Dr. S. Koide an Dr. H. Sekiyama for the help that they have given on the theoretical side. He would also like to thank Mr. H. Osafune of the Nippon Electric Co. Ltd. for supplying a part of silicon wafers, to Mr. Y. Yasuoka and coworkers of Japan Radio Co. Ltd. for supplying the pulse-type magnetrons and to Professor R. D. Myers of the University of Maryland for offering α-diphenyl β-picryl hydrazyl as the marker.

References

1) K. Ôno: J. Phys. Soc. Japan **8** (1953) 802.
2) D. J. E. Ingram: Sectroscopy at Radio and Microwave Frequencies (Butterworths Sci. Pub., London, 1955) p. 144.
3) E. Lips: Helv. Phys. Acta. **7** (1934) 537.
4) D. N. Hume and H. W. Stone: J. Am. Chem Soc. **63** (1941) 1200.
5) A. Abragam and M. H. L. Pryce: Proc. Roy Soc. **A 205** (1951) 142.
6) K. Ôno et al: Phys. Rev. **96** (1954) 38.
7) J. A. Klein et al: Rev. Sci. Inst. **23** (195 78.
8) S. Koide and H. Sekiyama: private commun cation.
9) O. Raporte: z. Physik **47** (1928) 761.
10) M. H. L. Pryce: Phys. Rev. **80** (1950) 1107
11) D. M. S. Bagguley and J. H. E. Griffiths: Proc Roy. Soc. **A 201** (1950) 366; K. Ono and M Ôhtsuka: to be published.

Journal of the Physical Society of Japan Vol. 12, No. 11, November, 1957

A Semi-empirical Theory of the Conjugated Systems

I. General Formulation

By Yuzuru Ooshika

Kobayasi Institute of Physical Research, Kokubunzi, Tokyo

(Received July 23, 1957)

A general semi-empirical theory of conjugated double bond systems, including those with non closed-shell structures and heteroatoms, is developed. The general formulation is similar with that of Pariser and Parr and that of Pople and others, but for non closed-shell structure our equations are somewhat different from those of Pople et al. The necessary parameters for hydrocarbons, which have previously been determined arbitrarily as the case may be, are estimated, in the present paper, by using the experimental data of the ethane and ethylene molecules. The theory is checked by some simple examples and found to be in satisfactory agreement with experiments.

§1. Introduction

One of the most interesting branches in the field of the molecular physics, so-called the π-electron theory of the conjugated double bond systems, has been developed by many investigators and an enormous number of papers have been published in later years. The theoretical basis of such π-electron theory was discussed by Lykos and Parr[1], and we shall limit our discussion in the π-electron approximation. General properties of such conjugated systems were thoroughly discussed by various authors, especially by English school, on the basis of the simple L.C.A.O. molecular orbital theory and many useful methods and definitions are introduced, which may be regarded as a theoretical basis of the "electr nic theory of organic chemistry".

In the simple molecular orbital theory, t electronic interactions are taken account only in terms of a suitable average potenti but their explicit consideration is very impo tant both from the theoretical and the pra tical point of view. Of course, in relative simple systems, calculations can be alwa carried out on the exact non-empirical bas including electronic interactions, but, in co plex systems, non-empirical such approa faces prohibitory difficulty due to the labor computation. Thus, in recent years, attemp have been made to develop semi-empiric methods of calculation including electron

teractions, which are practically applicable
› complex molecules.

Pariser and Parr[2] proposed such a semi-
npirical method, where they neglected dif-
rential overlapping between atomic orbitals
ntered about different nuclei for the calcu-
tion of electronic repulsion integrals com-
etely and, among necessary integrals for the
ediction of energy levels, only $(aa|aa)$ and
$a|bb)$ types of integrals were calculated by
sing a simple model. Thus, their method
as successfuly applied to many condensed
ydrocarbons and heterocyclics, probably due
the large reduction of the configulation
teraction. But, in their treatment, the re-
nance integral, β, still remains an adjus-
ble parameter. On the other hand, Pople,
onguet-Higgins and others developed a semi-
npirical theory in the self-consistent scheme[3],
d discussed a wide range of properties in
njugated systems, i.e., ionization potentials,
sorption energies, inductive and mesomeric
fects, etc. Their method of calculation of
e integrals is more or less similar to that
Pariser and Parr. In the present paper,
e shall develop a general semi-empirical
eatment of the L.C.A.O.M.O. type on π-
ectron systems, which will be easily appli-
ble for any complex molecule at a suitable
ep of approximation and in which all the
rameters that we shall not neglect will be
iquely determined by using the experimen-
l data on the simple molecules, and we shall
ow various applications to discussions on
emically interesting properties of conjuga-
d molecules.

2. Forms of Matrix Elements

Before we derive the general S.C.F. equations for the π-electron systems, we shall formulate the hamiltonian matrix elements, when we take a linear combination of Slater determinants as the electronic wave function, into a favorable form for us, though the general formulation has already been given in many literatures[4].

We take a linear combination of antisymmetrized products of orthonormalized one-electron functions (orbital function × spin function)

$$\Phi = \Sigma a_p \Psi_p ,$$

$$\Psi_p = \frac{1}{\sqrt{N!}} \det|\phi_1{}^p(1)\phi_2{}^p(2)\cdots\phi_N{}^p(N)| , \quad (1)$$

$$\int \phi_i(1)\,\phi_j(1) d\tau_1 = \begin{cases} 1 , & \phi_i \equiv \phi_j , \\ 0 , & \phi_i \not\equiv \phi_j \end{cases}$$

as the approximate electronic wave function. The approximate hamiltonian for an N- electron system is, neglecting the magnetic and the nuclear multipole interactions,

$$\boldsymbol{H} = \sum_{i=1}^{N} H(i) + \sum_{i,j} \frac{e^2}{r_{ij}} + H_0 ,$$

where H_0 is the part independent upon the electronic coordinates. The hamiltonian matrix elements are to be linear combinations of such terms as

$$\int \Psi_p{}^* \boldsymbol{H} \Psi_q d\tau_1 \cdots d\tau_N .$$

We can now rearrange the one-electron functions in Ψ_p and can make the maximum number of $\phi_i{}^p$'s in Ψ_p to coincide with $\phi_i{}^q$'s in Ψ^q. Thus, we may assume that

$$\phi_i{}^p \equiv \phi_i{}^q , \quad 1 \leq i \leq N - N_{pq} ,$$

$$\phi_i{}^p \not\equiv \phi_i{}^q , \quad N - N_{pq} < i \leq N .$$

We, then, obtain by a straightforward calculation

$$\int \Psi_p{}^* \Sigma H(i) \Psi_q d\tau_1 \cdots d\tau_N$$

$$= \frac{(-1)^{P_{pq}}}{(N-1)!} \Big\{ (N-N_{pq}-1)(N-N_{pq}-2)\cdots(1-N_{pq}) \sum_l{}' \int \phi_l{}^{p*} H \phi_l{}^q d\tau$$

$$+ (N-N_{pq})(N-N_{pq}-1)\cdots(2-N_{pq}) \sum_l{}'' \int \phi_l{}^{p*} H \phi_l{}^q d\tau \Big\} , \quad (2)$$

here $\sum_l{}'$ means the sum over l where $\phi_l{}^p \equiv \phi_l{}^q$ and $\sum_l{}''$ means the sum over l where
$^p \not\equiv \phi_l{}^q$,

$$\int \Psi_p{}^* \Big(\sum_{ij} \frac{e^2}{r_{ij}} \Big) \Psi_q d\tau_1 \cdots d\tau_N$$

$$= \frac{(-1)^{P_{pq}}}{2(N-2)!} \Big\{ (N-N_{pq}-2)\cdots(1-N_{pq}) \sum_l{}' \sum_k{}' \Big(\iint \phi_l{}^{p*}(1)\, \phi_k{}^{p*}(2) \frac{e^2}{r_{12}} \phi_l{}^q(1) \phi_k{}^q(2) d\tau_1 d\tau_2$$

$$
\begin{aligned}
&-\iint \phi_l^{p*}(1)\, \phi_k^{p*}(2) \frac{e^2}{r_{12}} \phi_k^q(1)\phi_l^q(2)d\tau_1 d\tau_2 \Big) \\
&+2(N-N_{pq}-1)\cdots(2-N_{pq}) \sum_l{}' \sum_k{}'' \Big(\iint \phi_l^{p*}(1)\phi_k^{p*}(2) \frac{e^2}{r_{12}} \phi_l^q(1)\phi_k^q(2)d\tau_1 d\tau_2 \\
&-\iint \phi_l^{p*}(1)\phi_k^{p*}(2) \frac{e^2}{r_{12}} \phi_k^q(1)\phi_l^q(2)d\tau_1 d\tau_2 \Big) \\
&+(N-N_{pq})\cdots(3-N_{pq}) \sum_l{}'' \sum_k{}'' \Big(\iint \phi_l^{p*}(1)\phi_k^{p*}(2) \frac{e^2}{r_{12}} \phi_l^q(1)\phi_k^q(2)d\tau_1 d\tau_2 \\
&-\iint \phi_l^{p*}(1)\phi_k^{p*}(2) \frac{e^2}{r_{12}} \phi_k^q(1)\phi_l^q(2)d\tau_1 d\tau_2 \Big) \Big\} ,
\end{aligned}
$$

and

$$
\begin{aligned}
&\int \Psi_p^* H_0 \Psi_q d\tau_1 \cdots d\tau_N \\
&= \frac{(-1)^{P_{pq}}}{N!} \{(N-N_{pq}-1)\cdots(1-N_{pq})\rho'^{pq}(1, 1)+(N-N_{pq})\cdots(2-N_{pq})\rho''^{pq}(1, 1\} H_0 ,
\end{aligned}
$$

$$\rho'(1, 2)=\sum_l{}' \phi_l^{p*}(1)\phi_l^q(2) ,$$

$$\rho''(1, 2)=\sum_l{}'' \phi_l^{p*}(1)\phi_l^q(2) ,$$

where P_{pq} is the ordinal number of the permutation for coinciding the maximum number of one-electron functions in Ψ_p with those in Ψ_q.

§ 3. Self-Consistent Field Equations for π-Electron Systems

Roothaan[5)] derived the self-consistent field equations in the L.C.A.O.M.O. scheme for the closed-shell configuration in quite a general way, and we have only to simplify his equations so as to apply to our semi-empirical scheme. For the ground state of neutral non-radical molecules, this procedure is expected to give favorable results because of the uniformity of the electronic density pointed out by Longuet-Higgins[6)]. For the non closed-shell excited or ionized states, we shall construct the electronic wave functions conveniently by assigning the electrons to various real and virtual orbitals obtained from the ground state S.C.F. equations, since, if solving the S.C.F. equations for the particular excited states separately, the problem of the orthogonality between the wave functions would complicate the calculations extremely, and since the results obtained by this troublesome procedure would not be expected to be more favorable than those obtained by the simpler procedure. In this respect, Mulliken[7)] showed that the ionization potential calculated by using the same one-electron orbitals as in the groun state also for the ionized state was in close agreement with the experiment than that ob tained by solving the S.C.F. equations sep rately.

There are some interesting systems tha have non-closed-shell ground states, i.e., rad cals, and, in later parts of this series, w shall intend to construct a larger conjugate system from the smaller ones, of which w assume that we have solved the S.C.F. equa tions already, and some of which are of th free radical character. So, we shall deriv a kind of S.C.F. equations for those non close shell structure as well as for the closed-she structure in the L.C.A.O.M.O. scheme of th π-electron systems. Pople and others[3f,g,h)] pr posed a form of S.C.F. equations for the electron systems with non closed-shell stru ture, but, here, we shall take a somewha different procedure from that of Pople an others.

We take as the molecular orbitals for electrons

$$\psi_l=\sum_a c_{la}\psi_a ,$$

where ψ_a is the normalized real $2p\pi$ atom orbital of the a-th atom. The coefficient c is to be determined by the S.C.F. metho We neglect the differential overlapping ψ_a^* between atomic orbitals centered about diffe ent nuclei except in the resonance integr between neighboring orbitals, ar Pariser an Parr, and Pople did. Thus,

$$\sum_a |c_{la}|^2 = 1\ ,$$

$$\int \psi_a H \psi_b d\tau = \beta_{ab}\ , \quad \text{if } a,\ b \text{ neighbor}\ ,$$

$$= 0\ , \quad \text{if } a,\ b \text{ non-neighbor}\ .$$

ere, $H(i)$ is the effective potential for the th electron from the atomic core skeleton, nd we assume it to be of the form

$$H(i) = \sum_a H_a(i)\ .$$

i. Closed shell structure

In this case, the necessary equations were already given by Pople and we shall only rewrite them in our notations and approximations. Assume that $2n$ electrons occupy the molecular orbitals $\psi_1, \cdots, \psi_n$ doubly. Denote the one-electron spin wave functions α and β. Then the electronic wave function is

$$\Phi = \frac{1}{\sqrt{(2n)!}} \det|\psi_1(1)\alpha(1)\psi_1(2)\beta(2)\cdots\psi_n(2n)\beta(2n)|\ . \tag{5}$$

nergy integral for this configuration is given by

$$\mathscr{E} = \int \Phi^* \boldsymbol{H} \Phi d\tau_1 \cdots d\tau_{2n}$$

$$= 2\sum_{l=1}^{n}\sum_a c_{lu}^* c_{la}\left\{-I_a + \frac{1}{2}\sum_{k=1}^{n} c_{ka}^* c_{ka}(I_a - E_a) - \sum_{b \neq a}\left(\frac{Z_b e^2}{R_{ab}} - \sum_{k=1}^{n} c_{kb}^* c_{kb}\frac{e^2}{R_{ab}}\right)\right\}$$

$$+ 2\sum_{l=1}^{n}\sum_a \sum_{b \neq a} c_{la}^* c_{lb}\left\{\beta_{ab} - \frac{1}{2}\sum_{k=1}^{n} c_{kb}^* c_{ka}\frac{e^2}{R_{ab}}\right\} + H_0\ , \tag{6}$$

here, as we wish to estimate various inte- rals in terms of empirically obtained quan- ty, we used the following approximations:

$$\int \psi_a H_a \psi_a d\tau = -I_a\ , \tag{7}$$

$$\iint \psi_a(1)\psi_a(2)\frac{e^2}{r_{12}}\psi_a(1)\psi_a(2)d\tau_{12} = I_a - E_a\ , \tag{8}$$

$$\int \psi_a H \psi_b d\tau = \beta_{ab} = \beta_{ba}\ , \tag{9}$$

$$\int \psi_a H_b \psi_a d\tau = -\frac{Z_b e^2}{R_{ab}}\ , \tag{10}$$

$$\iint \psi_a(1)\psi_b(2)\frac{e^2}{r_{12}}\psi_a(1)\psi_b(2)d\tau_{12} = \frac{e^2}{R_{ab}}\ . \tag{11}$$

and E_a are the 'ionization potential' and e 'electron affinity' of the atom a in the propriate valence state, respectively, Z_a is e number of the formal positive charges of e atomic core, and $1/R_{ab}$ does not mean the verse interatomic distance, $1/r_{ab}$, but is a itable function of r_{ab}, which will be given a later part of this paper. β_{ab} is assumed be determined by the species of atoms a d b and the interatomic distance, which, in rn, should be determined by the bond order neglecting the effects of the formal charge. us, by the variational method, the S.C.F. equations are

$$c_{la}\left\{-I_a + \sum_{k=1}^{n} c_{ka}^* c_{ka}(I_a - E_a)\right.$$

$$\left. - \sum_{b \neq a}\left(\frac{Z_b e^2}{R_{ab}} - 2\sum_{k=1}^{n} c_{kb}^* c_{kb}\frac{e^2}{R_{ab}}\right)\right\}$$

$$+ \sum_{b \neq a} c_{la}\left\{\beta_{ab} - \sum_{k=1}^{n} c_{kb}^* c_{ka}\frac{e^2}{R_{ab}}\right\} = \varepsilon_l c_{la}\ . \tag{12}$$

Of course, the right-hand sides of these equations should be, in general, of the form of $\sum_k \varepsilon_{lk} c_{ka}$, but the electronic energy is invariant for the orthogonal transformotion between c_{la}'s ($l=1, \cdots, n$; $a=1, 2, \cdots$), we can choose c_{la}'s so that $\varepsilon_{lk}=0$ for $l \neq k$, and the equations above would reduce to a normal eigen-value problem if the c_{la}'s in the bracket would be known.

ii. Closed-shell plus unpaired electrons all with parallel spins

Assume that $2n$ electrons occupy the molecular orbitals $\psi_1, \cdots, \psi_n$ doubly and m electrons occupy the molecular orbitals $\psi_{n+1}, \cdots \psi_{n+m}$ singly all with parallel spins. Pople and others assumed that electrons with different spins occupy two distinct sets of molecular orbitals. We adopt a somewhat different assumption as mentioned above, and take the electronic wave function as follows,

$$\Phi = \frac{1}{\sqrt{(2n+m)!}} \det|\psi_1(1)\alpha(1)\psi_1(2)\beta(2)\cdots\psi_n(2n)\beta(2n)$$

$$\times \psi_{n+1}(2n+1)\alpha(2n+1)\cdots\psi_{n+m}(2n+m)\alpha(2n+m)| \tag{13}$$

The energy integral is

$$\begin{aligned}\mathscr{E}=2\sum_{l=1}^{k}\sum_{a}c_{la}^{*}c_{la}\Big\{-I_a+\frac{1}{4}\sum_{k=1}^{n+m}\sigma_k c_{ka}^{*}c_{ka}(I_a-E_a)-\sum_{b\neq a}\Big(\frac{Z_b e^2}{R_{ab}}-\frac{1}{2}\sum_{k=1}^{n+m}\sigma_k c_{kb}^{*}c_{kb}\frac{e^2}{R_{ab}}\Big)\Big\}\\ +\sum_{l=n+1}^{n+m}\sum_{a}c_{la}^{*}c_{la}\Big\{-I_a+\frac{1}{2}\sum_{k=1}^{n}c_{ka}^{*}c_{ka}(I_a-E_a)-\sum_{b\neq a}\Big(\frac{Z_b e^2}{R_{ab}}-\frac{1}{2}\sum_{k=1}^{n+m}\sigma_k c_{kb}^{*}c_{kb}\frac{e^2}{R_{ab}}\Big)\Big\}\\ +\sum_{l=1}^{n+m}\sum_{a}\sum_{b\neq a}\sigma_l c_{la}^{*}c_{lb}\Big\{\beta_{ab}-\frac{1}{4}\sum_{k=1}^{n+m}\sigma_k c_{kb}^{*}c_{ka}\frac{e^2}{R_{ab}}\Big\}+H_0\,,\end{aligned}$$

where σ is the occupation number. The S.C.F. equations are

$$\begin{aligned}&c_{la}\Big\{-I_a+\frac{1}{2}\sum_{k=1}^{n+m}\sigma_k c_{ka}^{*}c_{ka}(I_a-E_a)-\sum_{b\neq a}\Big(\frac{Z_b e^2}{R_{ab}}-\sum_{k=1}^{n+m}\sigma_k c_{kb}^{*}c_{kb}\frac{e^2}{R_{ab}}\Big)\Big\}\\ &\quad+\sum_{b\neq a}c_{lb}\Big\{\beta_{ab}-\frac{1}{2}\sum_{k=1}^{n+m}\sigma_k c_{kb}^{*}c_{ka}\frac{e^2}{R_{ab}}\Big\}=\varepsilon_l c_{la}+\sum_{k=n+1}^{n+m}\frac{\varepsilon_{lk}}{2}c_{ka}\,,\qquad \text{for}\quad 1\leq l\leq n\,,\\ &c_{la}\Big\{-I_a+\sum_{k=1}^{n}c_{ka}^{*}c_{ka}(I_a-E_a)-\sum_{b\neq a}\Big(\frac{Z_b e^2}{R_{ab}}-\sum_{k=1}^{n+m}\sigma_k c_{kb}^{*}c_{kb}\frac{e^2}{R_{ab}}\Big)\Big\}\\ &\quad+\sum_{b\neq a}c_{la}\Big\{\beta_{ab}-\Big(\sum_{k=1}^{n}c_{kb}^{*}c_{ka}+\sum_{k=n+1}^{n+m}c_{kb}^{*}c_{ka}\Big)\frac{e^2}{R_{ab}}\Big\}=\sum_{k=1}^{n}\varepsilon_{lk}c_{ka}+\varepsilon_l c_{la}\,,\\ &\qquad\qquad\qquad\qquad\qquad\qquad\qquad\qquad \text{for}\quad n+1\leq l\leq n+m\end{aligned}$$

where $\varepsilon_{lk}^{*}=\varepsilon_{kl}$.

It should be noted that, in this case, $\varepsilon_{lk}\neq 0$ if the occupation numbers of ψ_l and ψ_k are not equal, because we cannot perform the orthogonal transformation between the orbitals with different occupation numbers. As mentioned in the earlier part of this section, we do not attempt to construct the S.C.F. wave functions for individual states, and it is desirable to use for any state the orbitals derived by the S.C.F. equations for the appropriate standard state. If the standard state is of a closed-shell structure, we can define a set of virtual orbitals in addition to real orbitals, because the equations would be linear ones associated with a normal secular equation being independent of l, if the c_{la}'s in the bracket at the left-hand side of Eq. (15) would have been determined, and we can construct the wave functions of the excited or ionized states in terms of these virtual orbitals. Unfortunately, this is not the case if the standard state is not of a closed-shell structure, because the equations are different from orbital to orbital depending on the occupation number and coupling of spin, and we cannot define virtual orbitals uniquely. But, in order to discuss the properties related solely with the ground state, the S.C.F. method is still most convenient even for non closed-shell configulation, and, for the phenomena related also with the excited or ionized states, it may necessary to simplify the calculation so th the method is a one which is capable of d fining virtual orbitals as well as real orbita With respect of this point, Hall[8] proposed idea of the standard excited state, i.e., t state where all the electrons have the sam spin. In this case, the S.C.F. equations ar for an m-electron system,

$$\begin{aligned}&c_{la}\Big\{-I_a-\sum_{b\neq a}\Big(\frac{Z_b e^2}{R_{ab}}-\sum_{k=1}^{m}c_{kb}^{*}c_{kb}\frac{e^2}{R_{ab}}\Big)\Big\}\\ &\quad+\sum_{l\neq a}c_{lb}\Big\{\beta_{ab}-\sum_{k=1}^{m}c_{kb}^{*}c_{ka}\frac{e^2}{R_{ab}}\Big\}=\varepsilon_l c_{la}\,.\end{aligned}$$

These would be a normal eigen-value proble if the c_{la}'s in the bracket would have bee known. Hall's idea is convenient for our pr sent purpose and we shall discuss on t problem in a later part of this series from somewhat different point of view.

In the method used by Pople, there are milar difficulties to those mentioned abov and, in addition, it may be more serious th his wave function is not the correct eige function for the total spin operator.

§ 4. Estimation of Parameters for Hydr carbons

In the present procedure, we intend to timate the integrals β and e^2/R in terms mpirical data for smaller molecules. This an be carried out for carbon-carbon pairs as nown in the following.

For the ethylene molecule, the first singlet nd triplet state energies and the ionization nergy are given by

$$E_S=\frac{1}{2}(I_C-E_C)-\frac{1}{2}\frac{e^2}{R}-2\beta\,, \qquad (18)$$

$$E_T=-\frac{1}{2}(I_C-E_C)+\frac{1}{2}\frac{e^2}{R}-2\beta\,, \qquad (19)$$

$$I=\frac{1}{2}(I_C+E_C)+\frac{1}{2}\frac{e^2}{R}-\beta\,, \qquad (20)$$

espectively, neglecting configuration interacons. In the present approximation, the trilet energy is equal to the π-bond energy. is the ionization potential of the valence ate of the carbon atom and concerned with ^{3}(IV) → sp^2(III) and E_C is the electron affiity concerned with sp^3(IV) → sp^4(III). We nall adop the value 11.54 eV and 0.46 eV for and E_C, respectively, estimated by Skinner nd Pritchard9).

We must determine the values of β and $/R$ as functions of the interatomic distance. he precise dependence of these parameters n the interatomic distance is not very imortant at the present stage of approximation nd we may assume rather crudely that

$$\frac{e^2}{R}=\frac{1-\exp(-\kappa r)}{r}\,. \qquad (21)$$

is a parameter, which is determind by

$$\frac{e^2}{R}(r=0)=I_C-E_C=11.08\,.$$

$$\kappa=0.7645/\text{Å}$$

sing this value of κ, the value of β at $r=$ .34 Å is determined by equations (18), (19) nd (20), so that the calculated E_S, E_T and I gree with experiments as well as possible. he value of $\beta=-2.2016$ eV is found to be ost favorble. The calculated and expeiental values of E_S, E_T and I are shown elow.

	calc.	exptl.
E_S	6.48 eV	7.60 eV$^{10a)}$
E_T	2.30 〃	3.30 〃 $^{10b)}$
I	11.67 〃	10.62 〃 $^{11)}$

Ve assume that the double bond energy is ivided into the part due to the σ-bond and at due to the π-bond; the former attains to s maximum value at $r=1.54$ A, i.e., the C—C distance in the ethane moleculue, and the maximum of the whole double bond energy is at $r=1.34$ A, i.e., the C—C distance in the ethylene molecule. The π-bond energy is, therefore, assuming the parabolic variation of bond energies with $r^{12)}$,

$$E_\pi=E_0-f_d(r-r_d)^2+f_s(r-r_s)^2$$
$$=-\frac{1}{2}(I_C-E_C)+\frac{1}{2}\frac{e^2}{R}-2\beta\,, \qquad (22)$$

where E_0 is a constant, and f_d and f_s are half the stretching force constant for the C=C bond of the ethylene and the C—C bond of the ethane molecule, respectively. From the above, we can determine the value of β as a function or r, using$^{13)}$

$$f_s=14.045\ \text{eV/A}^2\,,$$
$$f_d=29.963\ \text{eV/A}^2\,,$$
$$E_\pi(r=1.34\ \text{A})=2.30\ \text{eV}\,.$$

The calculated values of β are shown in the Table below as a function of r.

Table I. Value of β as a function of r.

r	$-\beta$
1.34 A	2.2016 eV
1.35	2.1781
1.36	2.1533
1.37	2.1267
1.38	2.0984
1.39	2.0687
1.40	2.0373
1.41	2.0042
1.42	1.9694
1.43	1.9331
1.44	1.8951
1.45	1.8556
1.46	1.8144
1.47	1.7716
1.48	1.7272
1.49	1.6810
1.50	1.6385
1.51	1.5843
1.52	1.5335
1.53	1.4812
1.54	1.4271

If the configuration interaction can be neglected as above, the concept of bond order is useful for the closed-shell structures, and, if assuming that the bond distance is determined by the bond order of the bond concerned, irrelevant to the remaining part of the molecule, when the steric condition is favorable, it is useful to set down the relation between the π-bond order and the double bond length. The π-bond order p has been defined by

$$p_{ab}=\frac{1}{2}\sum_{l}\sigma_l(c_{lb}{}^*c_{la}+c_{lb}c_{la}{}^*)$$

and, for the closed-shell structure, the part of the total energy due to the bond $a-b$ is

$$E_{ab}=E_s+p_{ab}\left\{2\beta-\frac{p_{ab}}{2}\frac{e^2}{R}\right\} \tag{23}$$

except for the effects of the formal charge and the steric hindrance. E_s is the σ-bond energy which is given by

$$E_s=E_{so}+f_s(r-r_s)^2\ . \tag{24}$$

If the state is not of the closed-shell structure, E_{ab} is not given by equation (23). The interatomic distance is determined by the minimization of E_{ab} with respect to r for a given p, and p, in turn, is determined by the electronic wave function and, hence, by r through the parameters β and e^2/R. Thus, the wave function should be self-consistent for the variation of r, as well as it should be so for equation (23). The relation between p and r is shown in the figure.

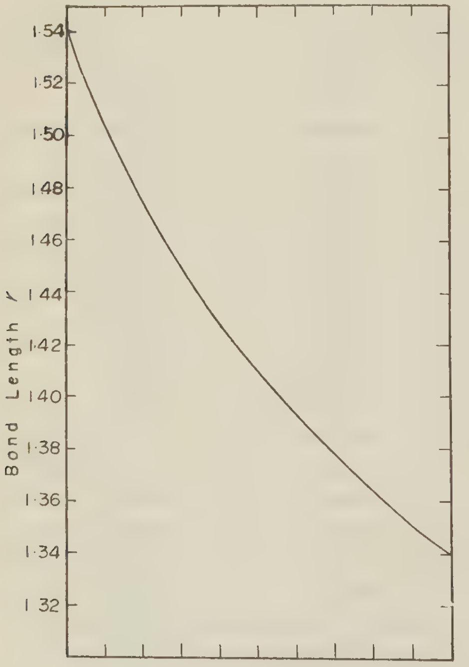

Fig. 1.

§ 5. Some Simple Application to Hydrocarbons

Though the electronic structures of simple alternant hydrocarbonmolecules have been discussed by many investigators, using both semi-empirical and non-empirical method, and their spectra have been explained systematically14), we shall illustrate some typical applications to those molecules in order to show that our method gives quite reasonable result in spite of its simplicity.

It should be noted that, in the previously proposed molecular orbital theories which do or do not include the electronic interaction in the semi-empilical scheme, the parameter β, remains an adjustable constant so as to agree the calculated results with the experiments for the individual cases. It has been thus pointed out that, in order to predict the positions of the energy levels of the linear and the condensed alternant hydrocarbons, we must use different values of β, or, in order to predict the values of the resonance energy and the excitation energies of a hydrocarbon molecule, we cannot do with one value of β15). Our present method gives the way how to determine the value of β for individual bonds as a function of the interatomic distance of the bond, which we can calculate self-consistently, if desired.

In the Table below, we show the results of the calculation for the butadiene and the benzene molecules. For alternant hydrocarbons Hueckel orbitals are self-consistent except the use of the same resonance integral for all the bonds, instead of $\beta-\frac{p}{2}\frac{e^2}{R}$ which are to be different for different bonds in the present approximation, and we have used here Hueckel orbitals instead of the true S.C.F. orbitals for the butadiene molecule. Moreover, we have considered only the configuration interaction between states that have the same energy in the simple Hueckel theory, which Moffitt called the first order configuration interaction. The agreement between the calculated and the observed results is found to be satisfactory.

Butadiene

		calc.	obs.
Bond length (Å)	1–2	1.35	1.35
	2–3	1.42	1.45

Vertical resonance energy (eV)		0.52(trans)	
		0.58(cis)	
Bond compressional energy (〃)		0.21	
Adiabatic resonance energy (〃)		0.31	0.28[a]
		0.37	
Vertical ionization potential (〃)		10.40	9.3[b]
		10.50	8.7[b]
Excitation energies (〃)			
	^1B_u	5.12(trans)	6.0[c]
	$^1B_1$	4.82(cis)	
	^3B_u	1.53(trans)	
	$^3B_1$	1.46(cis)	

a) R. S. Mulliken and R. G. Parr: J. Chem. Phys. **19** (1951) 1271.

b) T. M. Sugden and A. D. Walsh: Trans. Farad. Soc. **41** (1945) 76.

c) J. R. Platt and H. B. Klevens: Rev. Mod. Phys. **16** (1944) 182.

Benzene

		calc.	obs.
Bond length (Å)		1.39	1.39
Vertical resonance energy (eV)		3.80	
Bond compressional energy (〃)		1.16	
Adiabatic resonance energy (〃)		2.6	1.9[a]
Vertical ionization potential (〃)		11.13	9.52[b]
Vertical electron affinity (〃)		0.87	
Excitation energies (〃)			
	$^1B_{2u}$	4.39	4.9
	$^1B_{1u}$	5.02	6.2
	$^1E_{1u}$	6.43	7.0

a) R. S. Mulliken and R. G. Parr: J. Chem. Phys. **19** (1951) 1271.

b) J. D. Morrison and A. J. C. Nicholson: J. Chem. Phys. **20** (1952) 1021.

References

1) P. G. Lykos and R. G. Parr: J. Chem. Phys. **24** (1956) 1166.

2) R. Pariser and R. G. Parr: ibid. **21** (1953) 466, 767.

3) a. J. A. Pople: Trans. Farad. Soc. **49** (1953) 1375.
   b. J. A. Pople: Proc. Phys. Soc. **A68** (1954) 81.
   c. H. C. Longuet-Higgins and J. N. Murrell: ibid. 329.
   d. H. C. Longuet-Higgins and J. A. Pople: ibid. 591.
   e. H. C. Longuet-Higgins and J. N. Murrell: ibid. 601.
   f. A. Brickstock and J. A. Pople: Trans. Farad. Soc. **50** (1954) 901.
   g. N. S. Hush and J. A. Pople: ibid. **51** (1955) 600.
   h. J. A. Pople and R. K. Nesbet: J. Chem. Phys. **22** (1954) 571.

4) e.g., Eyring, Walter and Kimball: *Quantum Chemistry* (Wiley, 1944).

5) C. C. J. Roothaan: Rev. Mod. Phys. **23** (1951) 69.

6) H. C. Longuet-Higgins: J. Chem. Phys. **18** (1950) 265.

7) R. S. Mulliken: J. Chem. Phys. **46** (1949) 497.

8) G. G. Hall: Proc. Roy. Soc. **A213** (1952) 102.

9) H. A. Skinner and H. O. Pritchard: Trans. Farad. Soc. **49** (1953) 1254.

10) a. P. G. Wilkinson and H. L. Johnston: J. Chem. Phys. **18** (1950) 190.
    b. The triplet state energy is uncertain and we adopt the value of 3.30 eV used in the reference 2.

11) R. E. Honig: J. Chem. Phys. **16** (1948) 105.

12) R. S. Mulliken and C. A. Rieke set up the Morse potential curve using the corrected value of the force constant for anharmonicity. Cf., ref. 15 of Mulliken and Parr: J. Chem. Phys. **19** (1951) 1271. Here, we assume a parabolic form for simplicity.

13) G. Herzberg: *Infrared and Raman Spectra of Polyatomic Molecules* (D. Van Nostrand, 1945).

14) M. J. S. Dewer and H. C. Louguet-Higgins: Proc. Phys. Soc. **A67** (1954) 795, W. Moffitt: J. Chem. Phys. **22** (1954) 1820; R. Pariser: J. Chem. Phys. **24** (1956) 250.

15) K. Ruedenberg: J. Chem. Phys. **22** (1954) 1878.

JOURNAL OF THE PHYSICAL SOCIETY OF JAPAN Vol. 12, No. 11, NOVEMBER, 1957

A Semi-empirical Theory of the Conjugated Systems

II. Bond Alternation in Conjugated Chains

By Yuzuru OOSHIKA

Kobayasi Institute of Physical Research, Kokubunzi, Tokyo

(Received July 23, 1957)

The problem of the convergence of the absorption wave-lengths of chain conjugated systems, polyenes, and merocyanines, is discussed, by using the method developed in the previous paper. It is shown that the bond alternation as the cause of the convergence of the absorption wave-lengths, which has been presumed from the view of the resonance theory but cannot be deduced in terms of the ordinary molecular orbital theory, do actually occurs even for an infinite polyene chain, but the calculated limiting wavelength does not agree with the experiment quantitatively, possibly because of the coulomb attraction between the excited electron and the hole.

§1. Introduction

The explanation of the low energy transitions of chain conjugated molecules have long been a subject of many theoretical papers since Herzfeld and Sklar[1] first discussed such molecules in detail on the basis of both the molecular orbital and the resonance method. The most remarkable experimental fact is that, though wave-lengths of absorption maxima of certain types of molecules, e.g., symmetrical cyanines, increase linearly about by 1000 A for every vinylene group in the chain, those of other types of molecules, e.g. unsymmetrical cyanines, merocyanines, and polyenes, deviate more and more towards shorter wave-lengths from those of symmetrical cyanines as the lengths of the chains become larger and larger, and seem to converge to certain limiting wave-lengths. On the details of the experimental results, the reader can refer to many papers referred by J. R. Platt,[2] especially to a series of works by L. G. S. Brooker.

Attempts have been proposed by many investigators to explain the deviations and the convergence of the absorption wave-lengths of the so-called convergent dyes (or molecules). Herzfeld and Sklar[1] showed that, on the basis of the resonance theory, the energy of the first transition converges to a finite value as the length of the chain becomes infinitely large, if the energies of the two lowest extreme resonance structures are different, but that, if we use the ordinary molecular orbital method, the transition energy of the unsymmetrical dye approaches to zero as well as that of the symmetrical dye, though the former deviates from the latter. On the other hand, Kuhn,[3] using the free electron model, showed that, if the potential for the electrons is not uniform but has maxima and minima at the alternate carbon atoms, respectively, the transition energy approaches a finite value with increasing chain length. The polyenes have only one lowest resonance structure, and it may be reasonable to suppose that the potential is of such a form that Kuhn assumed from the point of view of the resonance theory, because of the bond alternation in the lowest resonance structure. The situation is similar in unsymmetrical cyanines and merocyanines. But, from the point of view of the molecular orbital theory, it is not obvious whether the effect Kuhn supposed remains for an infinitely long chain, since the effect is to be considered only an end effect.

From the entirely different point of view, Araki and others,[4] applying the theory of the plasma oscillation, showed that the deviation and the convergence of the absorption wave-length can be successfully explained by taking into account the electronic interaction, which is of primary importance for large systems. Though the predictions of the absorption by their method can be brought into very good agreement with the experiments by using only one parameter for very large number of molecules, and though the electronic interaction is undoubtedly of importance as they suggested, the value of the parameter cannot be considered physically reasonable, and, further, the reason why the absorption wave-lengths of some homologues seem to increase linearly with increasing chain length, while those of others seem to be strongly convergent is not clear.

Recently, Platt[2] published a paper, in which he discussed the problem of the absorption spectra of the conjugated chain molecules in detail, and gave a way how to predict the absorption wave-length for any molecule semi-empirically. He postulated the importance of the "configuration interaction," as he called, and stated that the configuration interaction causes the bond alternation and, hence, the potential is of such a form as Kuhn supposed, and thus the absorption wave-length converges. But he did not formulate actually how the configuration interaction causes the bond alternation.

From all the experimental and theoretical facts mentioned above, it may be almost without doubt that the electronic interaction and the bond alternation resulting from it are the cause of the convergence of the absorption wave-lengths of the convergent molecules. But, if we stand on the basis of the previously proposed treatment in terms of the ordinary molecular orbital theory, even if the bonds near the ends of the chain have single and double bond characters alternately, it is shown that the degree of the alternation becomes smaller and smaller as we go towards the center of the chain, and that, for an infinite chain, the bond alternation gives only an infinitesimal effect on the energy levels and the wave functions.

The purpose of the present paper is to show that the bond alternation can actually exist for an infinite polyene chain by means of the semi-empirical molecular orbital method developed in the preceding paper, and to predict the absorption spectra of the polyene chains.

§ 2. Bond Alternation in Conjugated Hydrocarbon Chains

Consider a polyene molecule composed of $2n$ carbon atoms. If we assume that the interaction integral $\gamma\left(=\beta-\dfrac{p}{2}\dfrac{e^2}{R}\right.$ in our preceding notation) between neighboring carbon atoms is independent upon the position of the bond, and that the other interactions are negligible, the molecular orbitals (Hueckel orbitals) are

$$\psi_l=\sqrt{\frac{2}{2n+1}}\sum_{s=1}^{2n}\sin\frac{ls\pi}{2n+1}\phi_s\,, \tag{1}$$

where ϕ_s's are the normalized $2p\pi$—atomic orbitals, and the orbital energies are

$$\varepsilon_l=\alpha+2\cos\frac{l\pi}{2n+1}\gamma\,. \tag{2}$$

The firist singlet excitation energy is, therefore,

$$\left.\begin{aligned}E(n,n+1)=&-\frac{2}{2n+1}\left(\cos\frac{n+1}{2n+1}\pi-\cos\frac{n}{2n+1}\pi\right)\gamma\\&+\frac{4}{(2n+1)^2}\left\{\sum_s\sin^2\frac{(n+1)s}{2n+1}\pi\sin^2\frac{ns}{2n+1}\pi(I_c-E_c)\right.\\&-\sum_s\sum_{t\neq s}\sin^2\frac{(n+1)s}{2n+1}\pi\sin^2\frac{ns}{2n+1}\pi\cdot\frac{e^2}{R_{st}}\\&\left.+2\sum_s\sum_{t\neq s}\sin\frac{ns}{2n+1}\pi\sin\frac{nt}{2n+1}\pi\sin\frac{(n+1)s}{2n+1}\pi\sin\frac{(n+1)t}{2n+1}\cdot\frac{e^2}{R_{st}}\right\}\end{aligned}\right\} \tag{3}$$

The bond order between the s-th and the t-th carbon atom is

$$P_{st}=\frac{1}{2n+1}\left\{\frac{\sin(s-t)\pi/2}{\sin\dfrac{(s-t)\pi}{2(2n+1)}}-\frac{\sin(s+t)\pi/2}{\sin\dfrac{(s+t)\pi}{2(2n+1)}}\right\} \tag{4}$$

These Hueckel orbitals are, of course, not self-consistent, because of the difference of bond orders for different bonds. But, for an infinitely long polyene chain, the bond order between the s-th and the $s+1$-th atom is

$$\begin{aligned}P_{s,\,s+1}=&\lim_{n\to\infty}\frac{1}{2n+1}\left\{\frac{1}{\sin\pi/2(2n+1)}-\frac{\sin(s+1/2)\pi}{\sin((s+1/2)\pi/(2n+1))}\right\}\\=&\,2/\pi-(-1)^s2/(2s+1)\pi\,.\end{aligned}$$

Thus, the bond alternation occurs near the chain ends, but it is damped as s increases till the bond order becomes $\pi/2$ for bonds far from the ends. The Hueckel orbitals are, therefore, self-consistent for an infinitely long chain except for the bond alternation near the ends of the chain, and, as the end effect may be neglected for a long chain, the results obtained by using the Hueckel orbitals may be correct for a long chain. (The Hueckl orbitals are actually Bloch orbitals for an infinite chain.) Hence, it is shown that the first excitation energy $E(n, n+1)$ tends to zero with $n \to \infty$ from equation (3).

Thus, it is impossible to show by such an ordinary method that the bond alternation still remains for an infinitely long chain and that the wave-length does not increase linearly with the chain length but converges to a certain definite limit. But the self-consistency of the Hueckel orbitals does not mean the minimum of the total energy with respect to any variation of the parameters, but means only the stationary value of the energy, and if we allow the alternate increase and decrease of the interaction integrals between neighboring atomic orbitals, it may be quite possible that the minimum of the energy is at the point where the two interaction integrals mentioned above are different from each other and that the bond alternation occurs actually also near the center of the chain.

Now, for an infinite system, we shall obtain the same result, no matter whether we treat an open chain, or we connect the two end atoms and make a closed ring. So we carry out the calculation for a $2n$-membered ring and consider the limit $n \to \infty$ for the sake of simplicity of the boundary condition. Number the atoms as $1, 2, 3, \cdots, 2n$, and denote $-\gamma_1$ by the interaction intgral for bonds between the $2s-1$-th and the $2s$-th atom and by $-\gamma_2$ that for bonds between the $2s$-th and the $2s+1$-th atom, including the bond between the $2n$-th and the first atoms. γ_1 and γ_2 are assumed to be independent on s, and the interactions between non-neighbors are assumed to be negligible. The latter assumption does not influence the form of the molecular orbitals for a closed ring. The molecular orbitals are expressed as follows,

$$\begin{aligned} \psi_l^1 &= x\psi_{l0} + x'\psi_{le} , \\ \psi_l^2 &= x'\psi_{l0} - x\psi_{le} , \end{aligned} \qquad l=0, 1, 2, \cdots, n-1 \qquad (6)$$

$$\begin{aligned} \psi_{l0} &= \frac{1}{\sqrt{n}} \sum_{s=1}^{n} e^{ik(2s-2)}\psi_{2s-1} , \\ \psi_{le} &= \frac{1}{\sqrt{n}} \sum_{s=1}^{n} e^{ik(2s-1)}\psi_{2s} , \end{aligned} \qquad k=\frac{\pi}{n} l \qquad (7$$

$$\begin{aligned} (\alpha-\mathcal{E})x-(\gamma_1 e^{ik}+\gamma_2 e^{-ik})x' &= 0 , \\ -(\gamma_1 e^{-ik}+\gamma_2 e^{ik})x+(\alpha-\mathcal{E})x' &= 0 , \end{aligned} \qquad (8$$

where $\mathcal{E}$ is the orbital energy. Solving the equations (8) and considering the normalization we obtain

$$x=\frac{1}{\sqrt{2}}e^{i\theta} , \qquad x'=\frac{1}{\sqrt{2}}e^{-i\theta} , \qquad (9$$

$$\tan 2\theta = \frac{\gamma_1-\gamma_2}{\gamma_1+\gamma_2} \tan k , \qquad \pi > 2\theta \geq 0 , \qquad (10$$

$$\alpha-\mathcal{E} = \pm\sqrt{\gamma_1{}^2+\gamma_2{}^2+2\gamma_1\gamma_2 \cos 2k} , \qquad (1$$

Here, we assumed $\gamma_1 \geq \gamma_2 > 0$, and, hence, the plus and minus signs in the equation (11) correspond to $\psi_l{}^1$, $\psi_l{}^2$, respectively. Thus, we can see that the one electron energy levels are split into two bands, as expected, one the bonding and the other the antibonding. Now we shall determine γ_1 and γ_2 by means of the method in the preceding paper, and shall show that the bond alternation remains for an infinite chain.

The partial π-bond order of the $2s-1$—$2s$ bond ("double bond") and the $2s$—$2s+1$ bond ("single bond") due to the bonding orbital k are

$$\left.\begin{aligned} p_d(k) &= \frac{1}{n}(x^*x'e^{ik}+xx'^*e^{-ik}) \\ &= \frac{\gamma_1+\gamma_2 \cos 2k}{n\sqrt{\gamma_1{}^2+\gamma_2{}^2+2\gamma_1\gamma_2 \cos 2k}} , \\ p_s(k) &= \frac{1}{n}(x^*x'e^{-ik}+xx'^*e^{ik}) \\ &= \frac{\gamma_2+\gamma_1 \cos 2k}{n\sqrt{\gamma_1{}^2+\gamma_2{}^2+2\gamma_1\gamma_2 \cos 2k}} , \end{aligned}\right\} \qquad (12)$$

respectively. Thus, for an infinitely large ring, the bond order of the "double" and the "single" bond are

$$\left.\begin{aligned} P_d &= \lim_{n\to\infty} \sum_{\text{bonding}} p_d(k) \\ &= \frac{1+z}{\pi}E\left(\frac{2\sqrt{z}}{1+z}\right)+\frac{1-z}{\pi}K\left(\frac{2\sqrt{z}}{1+z}\right) \end{aligned}\right\} \qquad (13)$$

$$\left.\begin{aligned} P_s &= \lim_{n\to\infty} \sum_{\text{bonding}} p_s(k) \\ &= \frac{1+z}{z\pi}E\left(\frac{2\sqrt{z}}{1+z}\right)-\frac{1-z}{z\pi}K\left(\frac{2\sqrt{z}}{1+z}\right) \end{aligned}\right\} \qquad (14)$$

where $z=\gamma_2/\gamma_1$ and K and E are the perfect elliptic integrals of the first and the second kind, respectively.

From these equations for P_d and P_s, and he relation between the bond order and the nteraction integral $\beta-\frac{p}{2}\frac{e^2}{R}$, we can determine the bond orders, bond lengths, and the values of $\beta-\frac{p}{2}\frac{e^2}{R}$ self-consistently. The results are shown below.

	$z=1$	$z=0.484$ "double bond"	"single bond"
P	$2/\pi$	0.938	0.249
r	1.389 A	1.346 A	1.463 A
γ	4.244 eV	5.437 eV	2.632 eV

The solution $z=1$ corresponds to an ordinary cyclic polyene, and it is easily seen by calculating the adiabatic resonance energy from the values of γ_1 and γ_2 above that $z=0.484$ corresponds to the lower energy. The calculation of the adiabatic resonance energy for $z=1$ and $z=0.484$ is shown below.

total π-electron energy	double bond	single bond
(per two electrons)	−8.040 eV	−8.262 eV
vertical resonance energy (〃)	0.484	0.427
bond compressional energy (〃)	0.392	0.084
adiabatic resonance energy (〃)	0.092	0.343

Thus, we see that the bond alternation lowers the total energy.

In the calculation above, we neglected the effects of the interactions between non-neighboring atoms, but, for benzene, they contribute only 10 % to the resonance energy, and it is not probable that they influence the conclusion reached above.

Our calculation concerns with an infinitely large conjugated ring, the result of which is also applicable to an infinitely long polyene, and, if a position of a "double" and "single" bond is determined at any part of the molecule, its influence extends to the whole molecule. For an infinitely long chain, the bond alternation is to occur at the ends as short—long—short—long— as shown in the earlier part of this section, and the whole bond alternation is determined by the ends of the molecule, i.e., the atoms do know how far they are from the end.

As one-electron energy levels are slipt into two bands as shown above, it is expected that the absorption wave-length does not tend to infinity with increasing chain length. The singlet transition energy is

$$E(n,n+1)=I-E$$
$$-\int\phi_n^*(1)\phi_{n+1}^*(2)\frac{e^2}{r}\phi_n(1)\phi_{n+1}(2)d\tau$$
$$+2\int\phi_n^*(1)\phi_{n+1}^*(2)\frac{e^2}{r}\phi_{n+1}(1)\phi_n(2)d\tau$$

and the calculated limit of the absorption energy equals to the gap between the bands, because the last two terms in the right-hand side of the above equation tend to zero for an infinite system. But, for such an infinite system, it cannot be expected that the excitation energy is correctly calculated by the method above, because of the neglect of the attraction between the hole and the electron. In fact, the energy gap between the filled and the vacant band is 5.6 eV, and the experimental limiting excitation has been estimated to be about 2.5 eV2) i.e., about half the calculated value.

§ 3. Discussion

The conclusion above is to be applied to all chain molecules, and the limiting absorption wave-length of any such molecule is to tend to the same finite value, because the bond alternation is a "bulk" effect and not a "surface" effect. But, actually, the absorption wave-lengths of symmetrical cyanines seem to tend to infinity, while those of unsymmetrical cyanines and merocyanines seem to tend to individual values. Here, we must remember that the experiments on various homologous series which led to the above conclusion have been carried out for molecules with at most about 10 carbon-carbon bonds, and, in such cases, our conclusions for an infinite system are not applied as such. As shown by the resonance theory, it is no wonder that, for cyanines with conjugated systems with odd numbers of atoms, symmetrical ones do not show any convergence of the absorption wave-lengths and the deviations of unsymmetrical ones are different from molecule to molecule for conjugated chains not sufficiently long.

The treatment in the previous section is to be applied to smaller systems, and it may be interesting to examine whether the benzene molecule would be of the configuration with the bond alternation. We shall show that this is not the case, and that the bond alternation does not occur in the benzene molecule. For $n=3$, the total π-bond orders of the "double" and the "single" bond are

$$P_d=\frac{1}{3}+\frac{2-z}{3\sqrt{1-z+z^2}}$$

$$P_s=\frac{1}{3}+\frac{2z-1}{3\sqrt{1-z+z^2}}\,,$$

respectively. By the method similar to that in the previous section, we can obtain the self-consistent solution, but, in this case, $z=1$ is the only solution and, hence the benzene molecule has the hexagonal symmetry.

References

1) K. F. Herzfeld and A. L. Sklar: Rev. Mod. Phys. **14** (1942) 294.
2) J. R. Platt: J. Chem. Phys. **25** (1956) 80.
3) H. Kuhn: J. Chem. Phys. **17** (1949) 1198.
4) G. Araki and T. Murai: J. Chem. Phys. **20** (1952) 1661; **21** (1953) 381; Prog. Theor. Phys. **8** (1952) 639; G. Araki and H. Araki: Prog. Theor. Phys. **11** (1954) 20.

JOURNAL OF THE PHYSICAL SOCIETY OF JAPAN Vol. 12, No. 11, NOVEMBER, 1957

The Lower Excited States and the Phosphorescent State of Diphenyl I.

By Kaoru IGUCHI

Centre de Chimie Théorique de France

(Received July 10, 1957)

We have calculated the lower excited π electronic states of diphenyl, employing Pariser approximation and assuming empirical values for the atomic Coulomb integrals: $(11|11)=10.959$ ev, $(11|22)=6.895$ ev, $(44|55)=6.546$ ev. We have obtained B_{3u} state for the lowest excited singlet, against the B_{2u} state obtained by London where the products of wave functions for benzene molecule were utilized. A method to treat the phenomena of phosphorescence has been suggested and the group theoretical classification of combination by L–S interaction is discussed.

§ 1. Introduction

The electronic energy levels of polyacene have been calculated and discussed by many authors[1)-7)], but the polyphenyl molecules are not yet treated so much. The π electronic energy levels of diphenyl were calculated by London[1)] by utilizing, as an approximation, the product of wave functions computed for benzene molecule by Goeppert-Mayer and Sklar[9)]. The method of London, however, does not take account enough of the ionic structures which seem to be important in view of the remarkable properties of fluorescene and phosphorescence of this molecule[8)]. In this article, the lower excited levels of diphenyl have been calculated by the molecular orbital method, constructing the linear combination of atomic π orbitals for all the molecule, employing the approximation proposed by Pariser. This method will probably overestimate the importance of the ionic structures such as;

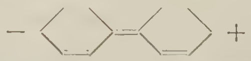

However, a certain number of recent publications have shown that the relative weight of these structures is great even in the ground state when the configuration interaction is taken into account[10)]. We have obtained the results which are a little different from those of London. Probably the actual situation might be between the two types of approximation.

§ 2. Calculation

The geometric structure of the molecule and the axes of coordinates are assumed as hown in Fig. 1. The molecule has the symnetry of V_h and each symmetry orbital beongs to one of the irreducible representations B_{1u}, B_{2g}, B_{3g} and A_{1u} as shown in the Table I.

---

* On leave from the Electrical Commumication Laboratory, Musashino-shi, Tokyo, Japan. (present address)

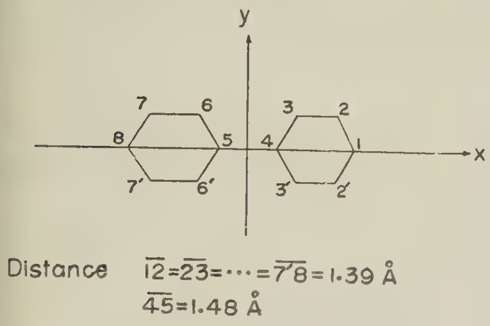
y
x
7
6
3
2
8
5
4
1
7'
6'
3'
2'
Distance $\overline{12}=\overline{23}=\cdots=\overline{78}=1.39$ Å
$\overline{45}=1.48$ Å

Fig. 1. Geometric structure

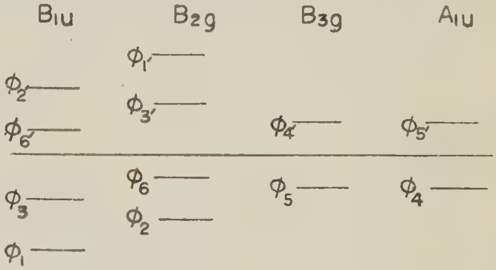

Fig. 2. Energy level scheme of Hückel orbitals.

Table I. Symmetry orbitals

$$B_{1u}:\ \frac{1}{\sqrt{2}}(\chi_1+\chi_8)\,,\quad \frac{1}{\sqrt{2}}(\chi_4+\chi_5)\,,\quad \frac{1}{2}(\chi_2+\chi_{2'}+\chi_7+\chi_{7'})\,,\quad \frac{1}{2}(\chi_3+\chi_{3'}+\chi_6+\chi_{6'})$$

$$B_{2g}:\ \frac{1}{\sqrt{2}}(\chi_1-\chi_8)\,,\quad \frac{1}{\sqrt{2}}(\chi_4-\chi_5)\,,\quad \frac{1}{2}(\chi_2+\chi_{2'}-\chi_7-\chi_{7'})\,,\quad \frac{1}{2}(\chi_3+\chi_{3'}-\chi_6-\chi_{6'})$$

$$B_{3g}:\ \frac{1}{2}(\chi_2-\chi_{2'}+\chi_7-\chi_{7'})\,,\quad \frac{1}{2}(\chi_3-\chi_{3'}+\chi_6-\chi_{6'})$$

$$A_{1u}:\ \frac{1}{2}(\chi_2-\chi_{2'}-\chi_7+\chi_{7'})\,,\quad \frac{1}{2}(\chi_3-\chi_{3'}-\chi_6+\chi_{6'})$$

One can express the symmetry orbital S_l of symmetry Γ in the form:

$$S_l=\sum_A \sigma_A{}^l(\Gamma')\chi_A\,,\quad \Gamma=\Gamma'\times B_{1u}\,, \tag{1}$$

where A numerates the nuclei, and χ_A is the $2p\pi$ atomic orbital of Slater type centred on A and we have taken $Z=3.18$.

In every subspace corresponding to an irreducible representation, we have solved the secular equation of Hückel[11] which gives the energy of each orbital in the form;

$$E=E^0-\alpha+\rho\beta\,. \tag{2}$$

The value of ρ obtained are given in the Table II[12].

Table II. Values of ρ

B_{1u}	B_{2g}	B_{3g}	A_{1u}
$\rho_{2'}$ 1.8909	$\rho_{1'}$ 2.2791	$\rho_{4'}$ 1.0000	$\rho_{5'}$ 1.0000
$\rho_{6'}$ 0.7049	$\rho_{3'}$ 1.3167	ρ_5 −1.0000	ρ_4 −1.0000
ρ_3 −1.3167	ρ_6 −0.7049		
ρ_1 −2.2791	ρ_2 −1.8909		

For every value of ρ, the corresponding molecular orbital of Hückel is constructed in the form of linear combination of symmetry orbitals given in Table I.

With these MO's (molecular orbitals) ϕ_i, we construct the antisymmetrized wave functions for all the molecule as;

$$\left.\begin{array}{ll} \text{ground state} & V_0=|1\bar{1},\,2\bar{2},\,\cdots,\,6\bar{6}|\,, \\ \text{excited states} & \left\{\begin{array}{l} \text{singlets}\ \ V_{ik'}=\dfrac{1}{\sqrt{2}}\{|1\bar{1},\,\cdots,\,i\bar{k}',\cdots,\,6\bar{6}|-|1\bar{1},\,\cdots,\,\bar{i}k',\,\cdots,\,6\bar{6}|\} \\ \text{triplets}\ \ T_{ik'}=\dfrac{1}{\sqrt{2}}\{(1\bar{1},\,\cdots,\,i\bar{k}',\cdots,\,6\bar{6}|+|1\bar{1},\,\cdots,\,\bar{i}k',\,\cdots,\,6\bar{6}|\} \end{array}\right. \end{array}\right\} \tag{3}$$

Here the number without bar means a MO with α spin, and that with bar a MO with β spin.

For the consequence, the lower energy levels of the molecule are, in the Hückel approximation, as follows:

1st $\cdots$ $V_{66'}$, $T_{66'}(B_{3u})$,
2nd $\cdots$ $V_{56'}=V_{65'}$, $T_{56'}=T_{65'}(B_{2u})$, $V_{46'}=V_{64'}$, $T_{46'}=T_{64'}B(_{1g})$,

3rd ··· $V_{55'}$, $V_{44'}$, $T_{55'}$, $T_{44'}(B_{3u})$, $V_{54'}=V_{45'}$, $T_{54'}=T_{45'}(A_{1g})$,
4th ··· $V_{63'}=V_{36'}$, $T_{63'}=T_{36'}(A_{1g})$,
etc. ···

By our approximation the wave functions of molecule are represented as linear combinations of the lower mono-excited functions belonging to the same irreducible representation of the symmetry group of the molecule, for example,

$$\psi_a=A_1V_1+A_2V_2+\cdots \qquad (4$$

The energy E_a and the coefficients A_i are given by the solution of a system of secular equations,

$$\sum_n A_n\{H_{mn}-\delta_{mn}E\}=0\,. \qquad (5$$

In the present case, the elements H_{mn} are denoted for the singlet states

$$H_{mn}=\int V_m H V_n dv=\{V_m|V_n\}\,,$$

and for triplet states

$$H_{mn}=\int T_m H T_n dv=\{T_m|T_n\}\,,$$

with

$$H=H^{\text{core}}+\sum_{p<q}1/r_{pq} \text{ in atomic units.} \qquad (6)$$

However[7],

$$\left.\begin{aligned}
&\begin{matrix}\{V_{ik'}|V_{ik'}\}\\ \{T_{ik'}|T_{ik'}\}\end{matrix}-\{V_0|V_0\}=I_{k'k'}-I_{ii}+[ii|k'k']+[ik'|ik']-[ii|ii]-\sum_{f\neq i}\{2[ff|ii]\\
&\qquad\qquad\qquad -2[ff|k'k']-[fi|fi]+[fk'|fk']\}\,,\\
&\{V_{ik'}|V_{jl'}\}=2[ik'|jl']-[ij|k'l']\,,\\
&\{T_{ik'}|T_{jl'}\}=-[ij|k'l']\,,\qquad \text{etc.},\\
&\text{with}\\
&[ij|kl]=\int\phi_i(1)\,\phi_j(1)\frac{1}{r_{12}}\phi_k(2)\phi_l(2)dv_{12}\,,\\
&I_{ii}=\int\phi_i H^{\text{core}}\phi_i dv\,.
\end{aligned}\right\} \qquad (7)$$

For β, the empirical value 2.371 ev proposed by Pariser[7] has been utilized.

These integrals are given as linear combinations of the integrals over the atomic orbitals. In the Pariser approximation the atomic exchange and hybrid integrals are all negleted. For the atomic Coulomb integrals, we have utilized the formulas by Roothaan[13] except for the large interatomic distance where the approximate formula by Pariser[7] (Eq. 75) has been utilized. On the other hand, when the atoms are very near, the semi-empirical values are adopted for the Coulomb integrals, because the atomic orbital of Slater type can not give good values for the small distance. The semi-empirical values employed are as following;

$$\left.\begin{aligned}
&(11|11)=10.959 \text{ ev}\,,\\
&(11|22)=\ \ 6.895 \quad\ ,\\
&(44|55)=\ \ 6.546 \quad\ ,\\
&\text{where}\\
&(pp|qq)=\int\chi_p(1)\,\chi_p(1)\frac{1}{r_{12}}\chi_q(2)\chi_q(2)dv_{12}\,.
\end{aligned}\right\} \qquad (8)$$

The penetration integrals have been calculated by the method of Parr and Crawford[14]. The results of calculation are shown in Table III. Fig. 3 compares the results with those of London.

Table III. Energy levels of the molecule

Symmetry	Wave functions	Energy
A_{1g}	${}^1\phi_0^-$ (V_0)	0 ev
B_{1g}	${}^1\psi_{46}^+$	6.707
	${}^1\psi_{46}^-$	6.765
	${}^3\psi_{46}^+$	6.009
	${}^3\psi_{46}^-$	6.765
B_{2u}	${}^1\psi_{56}^+$	6.647
	${}^1\psi_{56}^-$	6.402
	${}^3\psi_{56}^+$	5.912
	${}^3\psi_{56}^-$	6.402
B_{3u}	${}^1\psi_1 = 0.5675\,{}^1\psi_{44}^+ + 0.7171\,{}^1\psi_{55}^+ - 0.4046\,{}^1\psi_{66}^+$	5.551
	${}^1\psi_2 = 0.1079\,{}^1\psi_{44}^+ - 0.0529\,{}^1\psi_{55}^+ + 0.9928\,{}^1\psi_{66}^+$	5.730
	${}^1\psi_3 = -0.7332\,{}^1\psi_{44}^+ + 0.6627\,{}^1\psi_{55}^+ + 0.1527\,{}^1\psi_{66}^+$	7.409
	${}^3\psi_1 = 0.6210\,{}^3\psi_{44}^+ + 0.7078\,{}^3\psi_{55}^+ + 0.3368\,{}^3\psi_{66}^+$	3.068
	${}^3\psi_2 = 0.1822\,{}^3\psi_{44}^+ + 0.2825\,{}^3\psi_{55}^+ - 0.9418\,{}^3\psi_{66}^+$	4.425
	${}^3\psi_3 = -0.7615\,{}^3\psi_{44}^+ + 0.6466\,{}_3\psi_{55}^+ + 0.0477\,{}^3\psi_{66}^+$	7.192

$$ {}^1\psi_{ik}^{\pm} = \frac{1}{2}(V_{ik'} \pm V_{ik'})\,, \quad {}^3\psi_{ik'}^{\pm} = \frac{1}{2}(T_{ik'} \pm T_{ki'})\,. $$

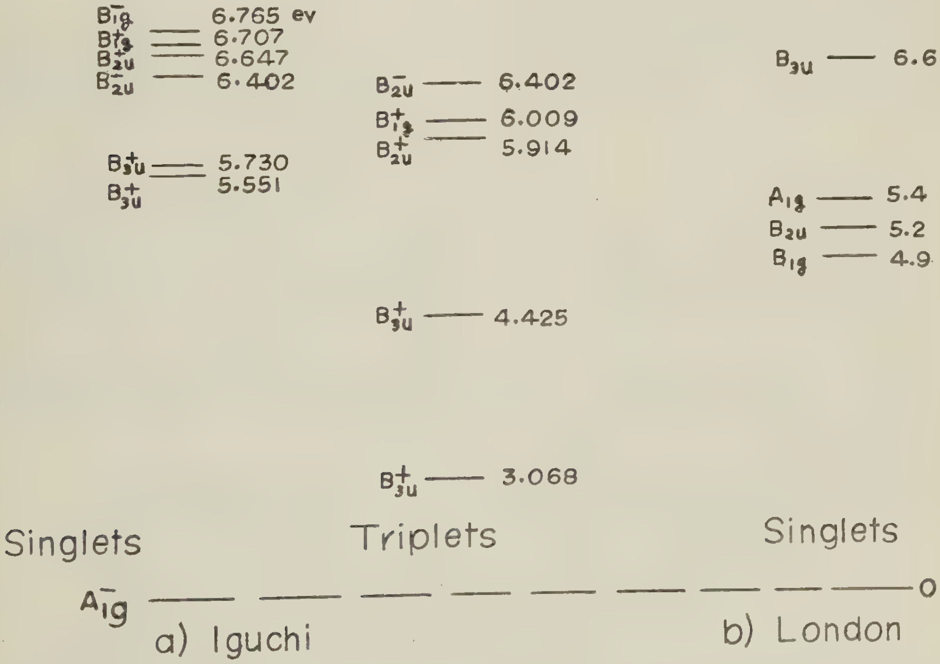

Fig. 3. Energy levels

§ 3. Discussion on the Absorption Spectra

We see that among all the lower excited singlet states B_{3u} state comes to the lowest in our scheme, whereas in the calculation by London B_{2u} comes to the lowest (B_{1g} is neglected because of its optical inactivity). This is the natural result of Hückel approximation. The accordance with the experimental values of absorption spectra is reasonable in both calculations. At present we have no experimental data sufficient to determine the symmetry of the lowest excited singlet state. When higher excited states are taken into account in the configuration interaction, the order of upper states might be changed a little.

§ 4. Treatment of the Phosphorescent State

The phenomenon of the phosphorescence has been studied by many authors[15]. Lewis and Kasha[16] have discussed thoroughly these problems and demonstrated that the phosphorescent level of a molecule is unique, that is, the lowest triplet state. At the low temperature, the lowest triplet state has no vibrational motion, and the fine structure of phosphorescence spectrum shows nothing but the vibrational motions of the ground state.

But the quantitative evaluation of the intensity of the phosphorescence spectrum or the lifetime of the phosphorescent state is difficult, because the matrix elements of the dipole transition are very sensitive to the form of wave functions.

Mizushima and Koide[17] have shown a theoretical method to treat these problems utilizing the theory of group. According to them, the L–S interaction term of a molecule is given, for the jth electron, by:

$$\begin{aligned} H_{LS}(j) &= -\frac{\hbar}{(2mc)^2}\boldsymbol{\sigma}(\mathrm{grad}\ V\times\boldsymbol{p})_j \\ &= \frac{i\hbar^2}{8m^2c^2}\left[2\sigma_z\left(\frac{\partial V}{\partial x}\frac{\partial}{\partial y}-\frac{\partial V}{\partial y}\frac{\partial}{\partial x}\right)\right. \\ &\quad +\frac{\sigma^+ + \sigma^-}{2}\left(\frac{\partial V}{\partial y}\frac{\partial}{\partial z}-\frac{\partial V}{\partial z}\frac{\partial}{\partial y}\right) \\ &\quad \left.+\frac{\sigma^+ - \sigma^-}{2i}\left(\frac{\partial V}{\partial z}\frac{\partial}{\partial x}-\frac{\partial V}{\partial x}\frac{\partial}{\partial z}\right)\right]_j . \end{aligned} \tag{9}$$

For the V_h symmetry, this is written as

$$H_{LS}(j)=\sigma_z B_{1g}+\frac{\sigma^+ + \sigma^-}{2}B_{3g}+\frac{\sigma^+ - \sigma^-}{2i}B_{2g}\ , \tag{10}$$

where $\boldsymbol{\sigma}$ is the spin operator and V is th
potential.

By the H_{LS} term, the triplet states mix wit
the singlet states (intermediate states), an
the dipole transition can take place from thes
intermediate states to the ground state. Ther
are two processes of intercombination:

a) The electron in the excited MO of th
triplet state is transferred, by the H_{LS} term
to the excited MO of the singlet state, an
then drops into the MO of the ground stat
by the dipole radiation. (Fig. 4a)

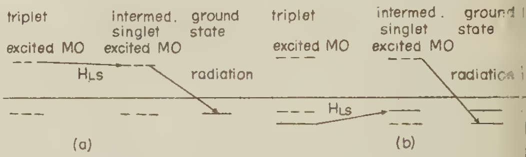

--- show the singly occupied orbital
—— show the doubly occupied orbital

Fig. 4. Scheme of intercombination.

b) An electron in the lower MO of the tripl
state is transferred, by the H_{LS} term, t
the MO of the singlet state which was eve
singly occupied, and then the electron in th
excited MO drops into the MO of the groun
state. (Fig. 4b)

The theory of group shows that only th
B_{1g} term of H_{LS} is effective for the intercom
bination and the result is given in Table IV
The state T_{44} does not participate in th
intercombination.

Now the problem of intercombination
reduced to the evaluation of the followin
integral between two combining MO's ϕ ar
ψ;

$$\int V\left(\frac{\partial\phi}{\partial x}\frac{\partial\psi}{\partial y}-\frac{\partial\phi}{\partial y}\frac{\partial\psi}{\partial x}\right)dv\ . \qquad (1$$

Table IV. Scheme of intercombination

	a				b			
Triplet state	$T_{55'}(B_{3u})$	$T_{65'}(B_{3u})$	$T_{56'}(B_{2u})$	$T_{66'}(B_{3u})$	$T_{55'}(B_{3u})$	$T_{56'}(B_{2u})$	$T_{65'}(B_{2u})$	$T_{66'}(B_{3u}$
MO of the triplet state	$\phi_{5'}(A_{1u})$		$\phi_{6'}(B_{1u})$		$\phi_{5'}(A_{1u})$	$\phi_{6'}(B_{1u})$	$\phi_{5'}(A_{1u})$	$\phi_{6'}(B_{1u})$
MO of the intermed. sing. state	$\phi_{6'}(B_{1u})$		$\phi_{5'}(A_{1u})$		occupied: ϕ_5 doubly ϕ_6 singly		ϕ_6 doubly ϕ_5 singly	
Intermed. sing. state	$V_{56'}(B_{2u})$	$V_{66'}(B_{2u})$	$V_{55'}(B_{3u})$	$V_{65'}(B_{2u})$	$V_{65'}(B_{2u})$	$V_{66'}(B_{3u})$	$V_{55'}(B_{3u})$	$V_{56'}(B_{2u}$

f one takes for ϕ and ψ the ordinary linear ombinations of $2p\pi$ atomic orbital and reduces he integral to the sum of integrals between $p\pi$ atomic orbitals, the integrals always anish because of the symmetry property. Mizushima and Koide have avoided this difficulty by including the σ orbitals (though the enzene molecule they have treated has the ymmetry of D_{6h}). But we suppose the problem might be solved even in the domain of orbitals only. For this surpose some modiications of MO are necessary and we are now roceeding on the calculation of modification f MO by the perturbation method, and the esult will be published later.

Acknowledgement

The author wishes to express his sincere hanks to Prof. R. Daudel, Dr. R. Lefebvre of entre de Chimie Théorique de France, and qually to Prof. M. Kotani of the University f Tokyo for their very kind and useful dvice.

References

1) A. London: J. Chem. Phys. **13** (1945) 396.
2) C. A. Coulson: Proc. Soc. **60** (1948) 257.
3) Dewer and Longuet-Higgins: Proc. Phys. Soc. **67** (1954) 795.
4) Longuet-Higgins and Pople: Proc. Phys. Soc. **68** (1955) 591.
5) C. Moser: J. de Chim. Phys. **52** (1955) 24.
6) R. Lefebvre and C. Moser: J. Chem. Soc. 1557 (1956).
7) R. Pariser: J. Chem. Phys. **24** (1956) 250.
8) R. Sangster and J. W. Irving, Jr.: J. Chem. Phys. **24** (1956) 670.
9) M. G. Mayer and A. L. Sklsr: J. Chem. Phys. **6** (1938) 645.
10) K. Iguchi: J. Chem. Phys. **23** (1955) 1983.
11) E. Hückel: Z. Physik. **76** (1932) 628.
12) The values of ρ for a number of polyacenes and polyphenyles have been calculated recently by C. A. Coulson and R. Daudel; Dictionary of values of molecular constants, vol. II.
13) J. C. C. Roothann: J. Chem. Phys. **19** (1951) 1445.
14) R. G. Parr and B. L. Crawford: J. Chem. Phys. **16** (1948) 1049.
15) For the review, see, for example, M. Kasha and S. P. McGlynn: Ann. Rev. Phys. Soc. **7** (1956).
16) G. N. Lewis and M. Kasha: J. Am. Chem. Soc. **66** (1944) 2100.
17) M. Mizushima and S. Koide: J. Chem. Phys. **20** (1952) 765.

JOURNAL OF THE PHYSICAL SOCIETY OF JAPAN Vol. 12, No. 11, NOVEMBER, 1957

Paramagnetic Resonance in Copper Acetate Monohydrate

By Hidetaro ABE* and Junji SHIMADA

Institute of Science and Technology, University of Tokyo, Tokyo

(Received August 1, 1957)

At four microwave frequency bands (λ=78, 10, 16 and 32 mm), single crystals of copper acetate monohydrate, $Cu(CH_3COO)_2H_2O$, were examined at room temperature by the method of paramagnetic resonance absorption, the results differing somewhat from those of usual copper salts. They can be explained by a spin-Hamiltonian with an effective spin $S=1$ which is considered to be originated from a pair of Cu^{++} ions each in ^2D state, holding a strong interaction between them. This is consistent with the results of X-ray crystallography; this crystal consists of bimolecular units $Cu_2(CH_3COO)_4 \cdot 2H_2O$, in which two copper ions approach as close as 2.64 Å. Exchange energy between these copper ions in the unit was estimated using the parameters determined from the resonance spectra and its temperature dependence is discussed.

1. Introduction

When usual hydrated copper salts are examined by the method of paramagnetic resonance absorption, there appears one resonance peak at the value of applied static field H given by

---

* Member of Physics Department, Ochanomizu niversity, Tokyo.

$$h\nu = g\beta H \qquad (1)$$

where h is the Planck constant, ν the frequncy of microwave used, β the Bohr magneton, and g the spectroscopic splitting factor which ranges from 2.0 to 2.4. In these salts, other than from ions of non-equivalent orientation in unit cell, there appears one peak and its resonance field H varies in proportion to the frequency ν of the *rf*-field. This can be deduced from the fact that the copper ion has $(3d)^9$ electronic configuration, *i.e.*, one electron missing from the complete $3d$ shell. So, under an influence of a crystalline field, it leaves a Kramers' doublet ($S=1/2$) as the lowest ground state. Resonance transition occurs between levels of the doublet, their splitting being in proportion to the applied magnetic field.

On the other hand, copper acetate monohydrate has a quite different appearance its paramagnetic resonance spectra whi resemble somewhat to the spectra of hydrat nickel salts having spin triplet ($S=1$). R sonance peaks observed in copper acetate ca be well fitted to an effective spin Hamiltonia

$$\mathscr{H} = g\beta\vec{H}\vec{S} + D\left\{S_z^2 - \frac{1}{3}S(S+1)\right\} + E(S_x^2 - S_y^2) \qquad (2$$

with two paramagnetic units in unit cell. D tailed resonance measurements were achiev at four different frequency bands to determi parameters appearing in the spin Hamiltoni and directions of three principal axes of cr stalline field (z, x and y).

§ 2. Experimental

Single crystals of copper acetate mon

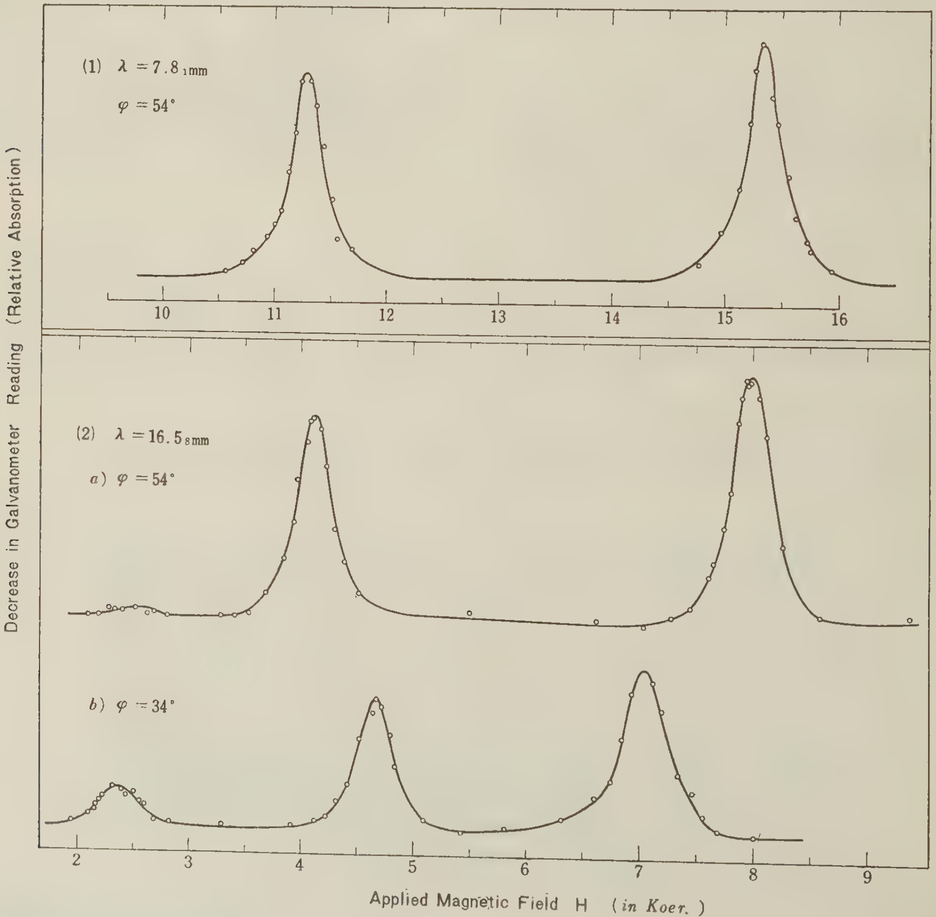

Fig. 1. Paramagnetic resonance spectra in copper acetate monohydrate at wavelengths of 7.8_1 and 16.5_8 mm, the direction of static magnetic field being indicated by the angle φ in the ac-plane.

hydrate were prepared by means of the vaporization method from aqueous solution. They belong to the monoclinic system having parameters[1] of

$$a:b:c=1.5320:1:0.8108, \text{ and } \beta=116°26'$$

and show themselves as twins arround $(20\bar{1})$ plane, the twinning plane. This twinning plane is expressed as $(10\bar{1})$ plane refered to the unit cell determined by X-ray crystallography which was given by Kiriyama *et al*[2] as

$$a=13.10\text{ Å},\quad b=8.56\text{ Å},\quad c=13.88\text{ Å}$$
$$\text{and } \beta=116°26'$$

and by van Niekerk and Schoening[3] as

$$a=13.15\text{ Å},\quad b=8.52\text{ Å},\quad c=13.90\text{ Å}$$
$$\text{and } \beta=117°0'$$

Since the detailed descriptions on our experimental apparatus will be reported elsewhere[4], only a slight glance is given here. By crystal multipliers, higher harmonics were produced from the fundamental 3-cm wave supplied by a 2K25-type klystron. The 2nd, 3rd and 4th order hormonic was separately utilized as our *rf*-power source of $\lambda=16$, 10, and 8 mm wave, respectively.

Microwave power with appropriate frequency goes through attenuators to the silicon diode after transmitting through a cavity resonator containing the sample crystal. The rectified current of the diode is then fed to a sensitive galvanometer. Resonance absorption causes galvanometer deflection decrease as a function of the static magnetic field applied. Some examples are shown in Fig. 1. The magnetic field strength H corresponding to the maximum decrease in galvanometer deflection was determined as a function of the *rf*-frequency and of the direction in which the static field was applied. Between the observed values of resonance peaks and the calculated ones, the best fit is obtained when the parameters appearing in the Hamiltonian (2) are determined as listed in Table I. Experimental results reported in our preliminary works[5][6] were also used to determine the proper values of parameters in the Table. This Table also contains the parameters given by Bleaney and Bowers[7][8] which were determined from their experiments at 90°K. From the spectra of paramagnetic resonance, orientations of three mutually perpendicular (z, x, and y) axes of crystalline field acting on copper ions can be determined refering to the crystallographic axes. Experimental results show the existence of a pair of paramagnetic units in unit cell, where the magnetic unit consists of two copper ions. One of the magnetic units can be derived from the other by an operation of mirror reflection with the *ac*-plane. The results are given in Table II, where angles ψ and α have the following definitions: ψ means the angle between the c-axis and the projection of the two z-axes on the *ac*-plane, measured from the c-axis towards the $+a$-axis whereas α means the angle between the z-axes and the *ac*-plane. This orientation may be considered to be that of a line joining the two copper ions in the

Table I. Parameters in the Hamiltonian (2) determined as giving the best fit.

Authors Temperature	This report 300°K	Bleaney & Bowers 90°K
g_z	$2.34_4\pm0.01$	2.42 ± 0.03
g_x	$2.05_3\pm0.005$	2.08 ± 0.03
g_y	$2.09_3\pm0.005$	2.08 ± 0.03
D (cm^{-1})	$0.34_5\pm0.005$	0.34 ± 0.03
E (cm^{-1})	0.005 ± 0.005	0.01 ± 0.005

Table II. Orientation of the principal axes of crystalline field of copper acetate monohydrate.

Method	P. R. A.	P. R. A.	X-ray	Static χ
Authors	Abe and Shimada	Bleaney et al	van Niekerk et al	Guha
Reference	This report	Refs. 7 & 8	Ref. 3	Ref. 9
ψ(in deg.)	-34.5 ± 1.5	-33	-32.7 (-34.1)[a]	$+23$[b] (-33)[b]
α(in deg.)	33 ± 1	33	34.6	—

Remarks a) Mean value calculated for a twinning crystal.

b) In Guha's report, it is supposed that the $(20\bar{1})$ plane (the twinning plane) was treated as the c-plane.

unit. In Table II, the angles indicating this direction which were obtained by the methods other than the paramagnetic resonance, are also listed: X-ray cristallography and static susceptibility. There comes some complexity from the twinning character of this crystal. Considerations were put on this twinning character to prepare the Table II.

§ 3. Discussions

From the measured spectra of paramagnetic resonance absorption, a conclusion can be deduced that there must be clusters of copper ions having a strong interaction within ions in pair.

The effective spin Hamiltonian (2) can be deduced[8] by combining two Hamiltonians $\mathscr{H}_1$ and $\mathscr{H}_2$ which describe isolated copper ions under cristalline field X and a dot type exchange term $J\vec{S}_1\vec{S}_2$

$$\mathscr{H}=\mathscr{H}_1+\mathscr{H}_2-J\vec{S}_1\vec{S}_2 \qquad (3)$$

where

$$\mathscr{H}_i=X_i+\lambda\vec{L}_i\vec{S}_i+\beta\vec{H}(\vec{L}_i+2\vec{S}_i) \qquad (i=1 \text{ or } 2) \quad (4)$$

The parameter D in the effective Hamiltonian can be derived[8] from these equations as

$$D=-\frac{J}{8}\left[\frac{1}{4}(g_{//}-2)^2-(g_{\perp}-2)^2\right] \qquad (5)$$

Using parameters in Table I, exchange energy J can be estimated. Our results at room temperature give $|J_{300}|=116\,\text{cm}^{-1}$ whereas Bleaney and Bowers' give $|J_{90}|=73\,\text{cm}^{-1}$. Taking account of the range of errors (containing neglection of rhombic part of the crystalline field), J_{300} ranges from 95 to 140 cm^{-1} and J_{90} from 62 to 87 cm^{-1}. These results show the exchange energy between two copper ions increases with temperature. Assumption of isotropic thermal expansion gives the reverse temperature variation in exchange energy. To explain this reverse temperature dependence, anisotropic thermal expansion must be assumed causing a thermal contraction between two copper ions. If the exchange inte

action between two directly interacting copp

ions can be assumed to obey to the Bor

Mayer's relation,

$$J\propto \exp\,(-\varDelta R/0.345) \qquad (6$$

there must be a contraction of order of 4

$=-0.027$ Å in the distance between the cop

ions in pair when the temperature of cryst

changes from 90°K to 300°K. Although t

value itself is not so unreasonable one but

expected order from the view-point of therm

expansion, it is somewhat doubtful wheth

the difference of J has a physical meaning

not.

A survey on the variation of absorpti

intensity of each lines will be reported els

where.[10]

The authors wish to express their since

thanks to Professor H. Kumagai for his co

nuous guidance and to Drs. K. Ôno and I. H

yashi for their helps in measurements at 3

region. They also wish to thank Profs.

Kambe and R. Kiriyama for their valuable d

cusssion and suggestions.

References

1) P. Groth: *Chemsiche Kristallographie* (Le
zig, 1910) Vol. **3**, p. 66.
2) R. Kiriyama *et al.* (unpublished work).
3) J. N. van Niekerk and F. R. L. Schoenin
Acta Cryst. **6** (1953) 227.
4) H. Abe and J. Shimada: to be published
the Natural Sci. Rep. of Ochanomizu Univ
sity Vol. 8, 2 (1957).
5) H. Kumagai, H. Abe, and J. Shimada: Ph
Rev. **87** (1952) 385.
6) H. Abe and J. Shimada: Phys. Rev. **90** (19
316.
7) B. Bleaney and K. D. Bowers: Phil. Mag.
(1952) 372.
8) B. Bleaney and K. D. Bowers: Proc. R
Soc. **A 214** (1952) 451.
9) B. C. Guha: Proc. Roy. Soc. **A 206** (19
353.
10) H. Abe and T. Negishi, and Y. Obata: to
published.

Journal of the Physical Society of Japan Vol. 12, No. 11, November, 1957

Studies on the Magnetic Anisotropy Induced by Cold Rolling of Ferromagnetic Crystal (I) Iron-Nickel Alloys

By Sōshin CHIKAZUMI, Kenzō SUZUKI and Hiroko IWATA

Department of Physics and Chemistry, Gakushuin University, Mejiro, Tokyo, Japan

(Received August 2, 1957)

Investigation was made on the magnetic anisotropy induced by mechanical rolling of ferromagnetic alloys. Experiments were carried out on the single crystals of Ni_3Fe through observation of magnetic domain patterns and torque measurements. Easy magnetizing direction was found to be normal to the roll direction for (110) [001] and (001) [100] rolling, while it changes to parallel to roll direction at about 30% reduction for (001) [110] rolling. The maximum value of uniaxial anisotropy was $2 \sim 3 \times 10^5$ erg/cc. The results were satisfactorily explained by assuming the appearance of directional order by slip deformation. It was shown theoretically that the anisotropies thus induced are classified into long range order (fine slip) type and short range order (coarse slip) type. Relation to the superlattice formation was also discussed.

§ 1. Introduction

It is well known that iron-nickel alloys develop a large magnetic anisotropy when they are plastically deformed by rolling or stretching. Isoperm is a magnetic material treated in this manner. This phenomenon was first found by W. H. Six, J. L. Snoek and W. G. Burgers[1] in 1934. Detailed investigations were reported by H. W. Conradt, O. Dahl and K. Sixtus[2] in 1940 and by G. W. Rathenau and J. L. Snoek[3] in 1941. It was confirmed by these investigators that the magnetic anisotropy induced by rolling (roll anisotropy) is not merely related to a magnetostriction and internal stress nor to a crystal magnetic anisotropy.

Recently L. Néel[4] and independently S. Taniguchi and M. Yamamoto[5] interpreted the mechanism of this anisotropy in terms of the "directional order" or "orientational superlattice" which means an asymmetrical distribution of AA, BB and AB atom pairs in the solid solution of A and B atoms. Their theories are based upon the idea that a directional order would be induced by a strong stress exerted during rolling or stretching, where atom migration during plastic deformation plays an important role in bringing the atoms into their stable positions.

On the other hand, it was confirmed by one of the present authors and T. Oomura[6] that a roll anisotropy reported by Rathenau and Snoek is quite similar to the anisotropy due to magnetic annealing in their dependence on the alloy composition. This fact also confirms us in the view that the origin of roll anisotropy is closely related to the directional order, as is the case for magnetic annealing.[4],[5],[7]

The present investigation was made for the purpose of making out the true mechanism of the appearance of directional order by plastic deformation. Experiments were carried out on several sorts of single crystal and polycrystal through observation of magnetic domain patterns and measurement of magnetic anisotropy energy. The results were satisfactorily explained by assuming that the directional order are induced by slip deformation. It was theoretically expected that the anisotropy thus induced can be classified into two types i.e. long range order (fine slip) type and short range order (coarse slip) type. Calculations along this concept are found to be in good agreement with experimental facts.

§ 2. Specimens and Experimental Procedure

Specimens used in this experiment were prepared by melting electrolytic iron and nickel in a high vacuum induction furnance. Large crystals were obtained by solidifying the alloy slowly in a crucible. This procedure was carried out first in a molybdenum wire resistance furnace, but recently in a high vacuum induction furnace. These crystals were cut into rectiangular plates having desired crystallographic orientation. The size of the specimen was 10 ~ 20 mm in length, 3 ~ 5 mm in width and 1 ~ 2 mm in thickness. In some cases thick pieces of single crystal (2 ~ 3mm in thickness) were used in order to observe the domain pattern on the thin edge.

Specimens were in some cases previously quenched from 700°C to attain the disorder state or annealed for 200 hours at from 490° to 430° to attain the prefect order state. The specimen indicated by "slow cool" is that which was cooled naturally in a cruicible before shaping.

Cold work on the specimen was carried out by a small rolling machine with rollers of 50 mm in diameter, which rotate at 11 r.p.m. A reduction of the thickness by one pass was about 0.03 mm.

Domain patterns were observed by means of the usual powder pattern technique with a light electrolytic polishing of the rolled surfaces.

Measurement of the magnetic anisotropy was carried out in various ways. For (110) [001] rolling, the anisotropy was determined by the measurement of magnetization curve by using long specimens. Since the easy direction in this case is normal to the roll direction, magnetization takes place by rotation and therefore gives rise to a linearly inclined magnetization curve. The anisotropy was obtained from the inclination of the linear part. In the case of the polycrystal, long specimens were cut from the rolled sheet, one in parallel and the other in perpendicular to the roll direction. The anisotropy was determined by the comparison of the magnetization curves for both specimens.

Exact determination of the anisotropy was made by means of the torque measurement. Specimens for this were cut in a shape of circular plate from the rolled single crystal. In some cases successive rolling and shaping were made on a circular specimen for the purpose of measuring the torque as a function of roll reduction. The size of the specimens was 3 ~ 13 mm in diameter.

Composition of the specimens used in the present experiment was restricted to Ni_3Fe where the superlattice formation is most effective, because the dependence of the anisotropy on the composition has been known to be simple as reported by Rathenau an
Snoek.

§ 3. Experimental Results

(1) (110) [001] rolling

Simple and well-defined domain pattern
were observed on the rolled crystal surfac
(110), when the direction of rolling is paralle
to [001]. Pl. 1, 2, 3, 4, 5 and 6 are the serie
of the photographs in the course of rolling
For more than 30% reduction, many domain
divided by 180° walls which are running i
perpendicular to the roll direction appeare
Although the pattern becomes more an
more clear as the reduction increases, th
essential feature does not change until 94
reduction. Even when the roll directio
rotates to the other direction in the sam
plane, the direction of domain magnetizatio
is also parallel to the same crystallographi
direction $[1\bar{1}0]$. The patterns for $[1\bar{1}2]$ an
$[1\bar{1}0]$ roll are shown in Pl. 7 and 8.

The anisotropy energy in this case wa
determined from magnetization curve. Sinc
the magnetization takes place by rotation, th
magnetization curve is linearly inclined on

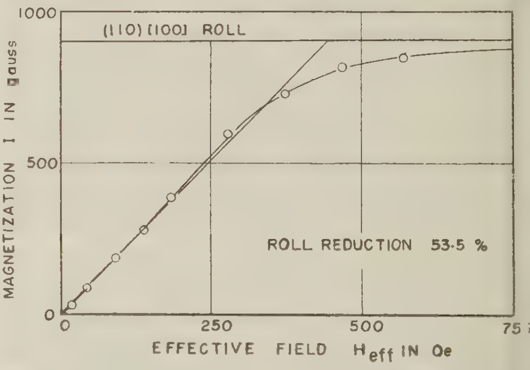

Fig. 1. Magnetization curve for rolled (110) [001
crystal. Specimen was previously cooled slowly. Reduction is 53.5%.

as shown in Fig. 1. The coefficient o
uniaxial anisotropy K_u (cf. Eq. (32)) is cal
culated from the inclination of the linea
part. The results are summarized in Fig.
for variously treated specimens as a functio
of roll reduction. The point marked by dou
ble circle is obtained from torque measure
ment, being in good agreement with tha
obtained from magnetization curve. It i
interesting to note that a curve for slowl

cooled specimen, for annealed for 1 hour at 490°C and a point for quenched from 700°C are in good coincidence with one another, whereas the curve for perfectly ordered specimen shows a very slow development of the anisotropy. The domain patterns for perfect ordered crystal are shown in Pl. 9 and Pl. 10. Zigzag character of the pattern in Pl. 9 may be due to the relatively large crystal anisotropy energy (~ 3×10^4 erg/cc) of the perfect order state. Uniaxial domains similar to Pl. 3~6, however, appeared at the later stage of rolling (Pl. 10).

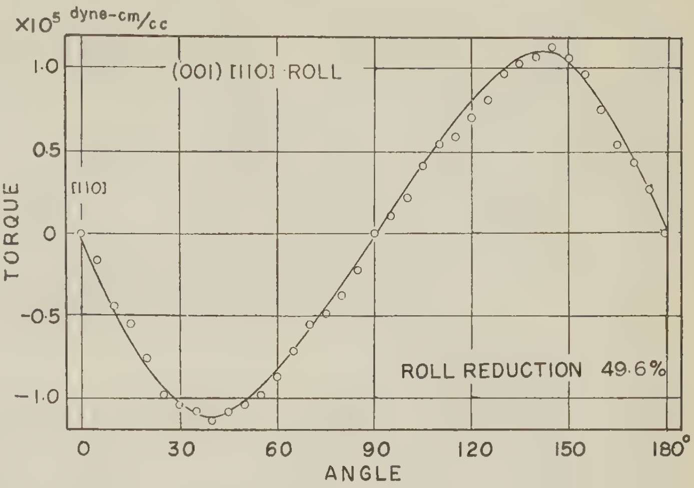

Fig. 3. Torque curve for rolled (001) [110] crystal. Specimen was previously in a perfect order state. Roll reduction is 49.6%.

(2) (001) [110] rolling

The domain patterns appearing on the rolled surface are not so simple as to allow a straightforward interpretation as shown in Pl. 11, 12, 13 and 14. We could observe, however, well-defined domain patterns on the thin edge of the rolled plate as shown in Pl. 15 and 16. It is interesting that the patterns of the upper and lower half of the side surface are symmetrical with respect to the intermediate plane, corresponding to the slip bands which are observed on the same surface as are shown in Pl. 27 and 28. The black and white strips are the uniaxial domains, whose direction rotates gradually to a horizontal direction as the reduction increases. It is concluded that the very small spikes observed on the rolled surface (Pl. 13 and 14) are the reverse domains which are responsible to the reduction of a magnetostatic energy. It is observed that the spikes become longer and longer as the basal domains rotate to make the smaller angle to the surface.

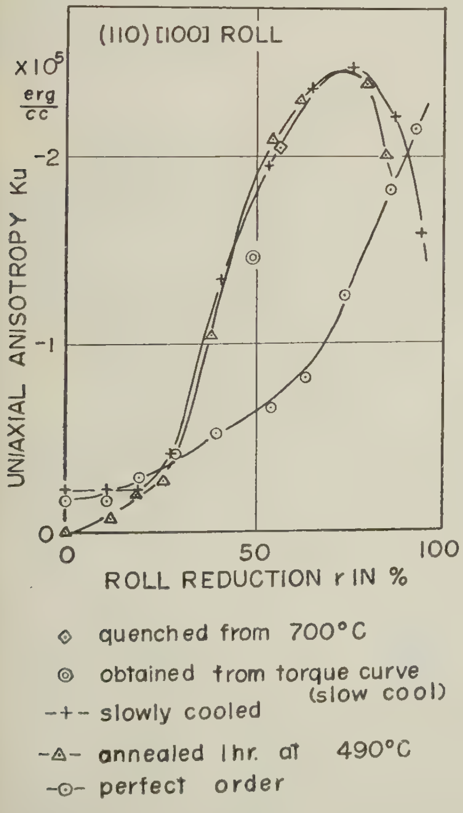

Fig. 2. Coefficient of anisotropy as a function of roll reduction. Specimens are (110) [001] crystals, previously heat-treated as indicated.

Anisotropy energy in the rolled surface was measured by means of torque magnetometer by using a circular plate. One example of the torque curve is shown in Fig. 3. Since this curve includes a small amount of crystal anisotropy K_1 term, the uniaxial term K_u was calculated by eliminating the K_1 term by the Fourier analysis. K_1 was less than 0.02×10^6 erg/cc for slowly cooled specimen and equal to 0.25×10^5 erg/cc for perfectly ordered one.

K_u is graphically shown in Fig. 4 as a function of roll reduction. It is interesting that K_u is at first negative (easy direction being normal to roll direction), while it changes its sign to positive (easy direction being parallel to roll direction) at about $r=20\sim30\%$. Increase of K_u in positive sense for larger reduction corresponds to rotation of uniaxial domain to the roll direction, as is observed in the domain pattern.

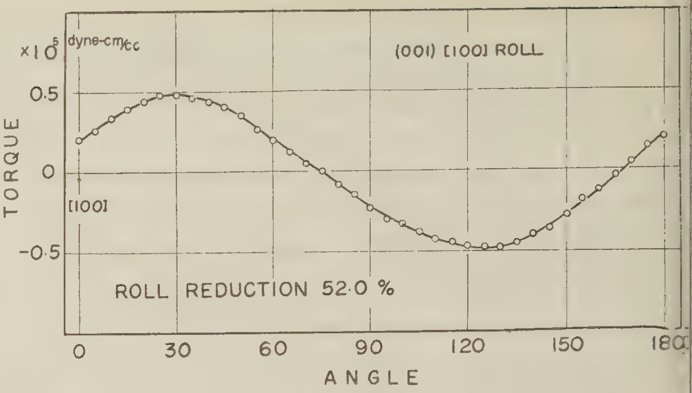

Fig. 5. Torque curve for rolled (001) [100] crystal. Specimen was previously cooled slowly. Roll reduction is 52.0%

(3) (001) [100] rolling

The crystallographic orientation in this case is the same as that of recrystallization texture which is applied to the "isoperm". The torque curve is shown in Fig. 5, which proves that the easy direction is nearly normal to the roll direction as is well known for isoperm. The value of K_u obtained from this curve is -0.48×10^5 erg/cc for $r=52\%$, which is also in good agreement with the value obtained by Rathenau and Snoek. The domain pattern in this case, however, is very complicated as shown in Pl. 17, 18 and 19. The patterns on the thin edge have the character similar to the patterns observed on the basal plane of cobalt (Pl. 20 and 21). The star-like patterns in these plates prove that the domain direction strikes the side surface at a deep glancing angle. Patterns on the rolled surface at latter stage of rolling (Pl. 19) shows a gradual approach of the domain direction to the roll surface (normal to the roll direction.).

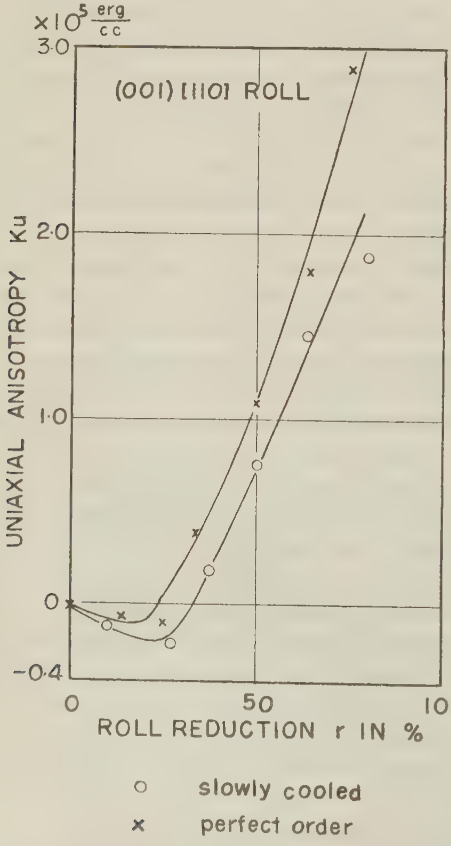

Fig. 4. Coefficient of uniaxial anisotropy as a function of roll reduction for (001) [110] rolling.

(4) Polycrystal

The domain patterns for rolled polycrystal are shown in Pl. 22, 23 and 24, in which numerous uniaxial domains are observed in the individual crystallites. It is recognized that there are statistically many domains which have the magnetization parallel to roll

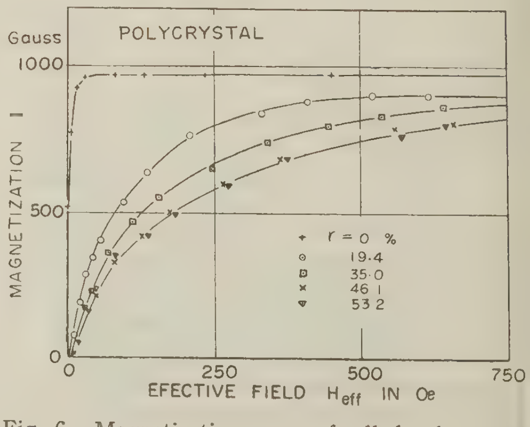

Fig. 6. Magnetization curve of rolled polycrystal measured by applying the filed normal to the roll direction. Specimen was annealed for 100 hours at 490°C.

direction. This is also confirmed by the measurement of magnetization curve. Fig. 6 is a variation of magnetization curve which is measured by applying the field normal to the roll direction.

The work necessary to magnetize to saturation are shown in Fig. 7 as a function of roll reduction for parallel- and perpendicular-cut specimens. The fact that the energy is larger for perpendicular cut than for parallel cut specimen means that the average easy direction is parallel to the roll direction. This fact was also reported by Rathenau and Snoek. It should be noted that the anisotropy energy in this case increases with a progress of order formation, on the contrary to the (110) [001] case. Moreover it should be added that stress hardening increases considerably with a progress of order formation, so that the perfectly ordered specimen was broken at their crystal boundaries by the rolling of only 10% reduction (Cf. Pl. 25). This was not the case for any single crystals.

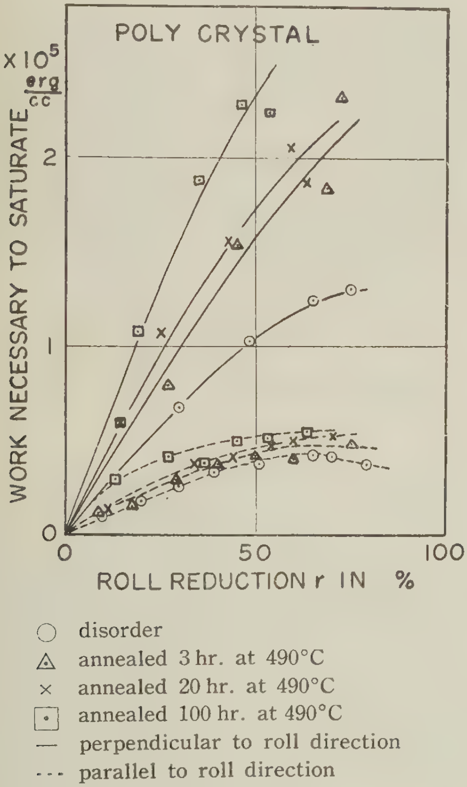

Fig. 7. Comparison of the energy necessary to magnetize to saturation between parallel and perpendicular-cut specimens of rolled polycrystal. Crystal was previously heat-treated as indicated.

§4. The Mechanism of Appearance of Magnetic Anisotropy due to Slip Deformation

In this section we shall deal with the calculation of magnetic anisotropy induced by slip deformation. Now the dipole-dipole interaction between neighboring atomic moments gives rise to the energy

$$w_i = l\cos^2\varphi_i\,, \qquad (1)$$

where φ_i is the angle between magnetization and pair direction. This energy, however, does not give rise to any anisotropy energy as far as the orientational distribution of the atomic pairs is of a cubic symmetry. If, however, the coefficient l takes the different values l_{AA}, l_{BB} and l_{AB} for AA, BB and AB pairs respectively in the solid solution containing A and B atoms, unbalanced distribution of these atomic pairs (directional order) should give rise to the anisotropy energy. Since N_{AAi}, N_{BBi} and N_{ABi}, the numbers of AA, BB and AB pairs per unit volume having i-th bond direction, are related to N_A and N_B, i.e. the numbers of A and B atoms in a unit volume, by

$$\left.\begin{aligned} 2N_{AAi}+N_{ABi}&=2N_A \\ 2N_{BBi}+N_{ABi}&=2N_B \end{aligned}\right\}, \qquad (2)$$

we can express the anisotropy energy by the form which includes only N_{BB}, namely

$$\begin{aligned} E&=\sum_i (N_{AAi}l_{AA}+N_{BBi}l_{BB}+N_{ABi}l_{AB})\cos^2\varphi_i \\ &=\sum_i N_{BBi}(l_{AA}+l_{BB}-2l_{AB})\cos^2\varphi_i+\text{const.} \\ &=l\sum_i N_{BBi}\cos^2\varphi_i+\text{const.}\,, \end{aligned} \qquad (3)$$

where

$$l=l_{AA}+l_{BB}-2l_{AB}\,. \qquad (4)$$

For iron-nickel alloys the numerical value of l has been estimated by Néel[4] from the magnetostriction data as

$$Nl=N(l_{NiNi}+l_{FeFe}-2l_{FeNi})=3\cdot1\times10^8 \text{ erg/cc}, \qquad (5)$$

where N is the total number of atoms in a unit volume.

Next we shall calculate the distribution of BB pairs induced by slip deformation. It was found that the directional order thus induced can be classified into two types according as the travelling of atoms by the slip is confined within an original order domain or extends to another order domain of the opposite side of the slipped plane.

(a) Anisotropy of Long Range Order (Fine Slip) Type

Fig. 8 shows the long range ordered A_3B type lattice (face-centered cubic) which is deformed by one-step slip along (111) plane in the direction of $[01\bar{1}]$. Although no BB pairs are found in the non-deformed part, it is recognized in the figure that many BB pairs which direct to [011] appeared at the slipped part. We shall calculate the number of BB pairs thus induced. It is verified by simple calculation that the number of B atoms occupied at β-sites on a unit area of (111) plane is larger by $S/\sqrt{3}\,a^2$ than that of α-sites, where S is the degree of long range order and a is the lattice constant. The number of BB pairs induced per unit area of (111) plane is thus given by $p_0S^2/2\sqrt{3}\,a^2$ on the average, where the factor 1/2 comes from the fact that a chance of appearance of BB pairs are limited to the case that the slip is made by the displacement of the odd number of dislocations. It is, however, generally accepted that the dislocations tend to move as in pairs in the ordered crystal so as to recover the ordered state.[8] On this reason the probability p_0, that a dislocation does not become in pairs with another one, was introduced in the above expression.

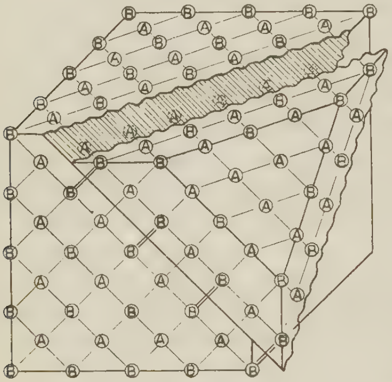

Fig. 8. Appearance of BB pairs by one-step slip along (111) plane in the direction $[01\bar{1}]$ in the long range ordered A_3B type lattice.

Now let us suppose that ns dislocations passed per n atomic planes which belong to the referred slip system. We shall call s as "slip density" hereafter. Then the number of slipped planes is given by $\sqrt{3}\,p'|s|/a$ per unit depth, where p' is the probability for one dislocation to start in a virginal atomic plane. The total number of BB pairs for i-th slip system is given by

$$N_{BBi}=\frac{p_0S^2}{2\sqrt{3}\,a^2}\times\frac{\sqrt{3}\,p'|s_i|}{a}$$
$$=\frac{1}{8}NpS^2|s_i|\,, \tag{6}$$

where

$$p=p_0p'\,. \tag{7}$$

In face-centered crystal the slip plane is known to be {111} and the slip direction is to be ⟨110⟩, so that the total number of slip systems is 4×3=12. The direction cosines of BB pairs induced by the slips of individual slip system i (β_{1i}, β_{2i}, β_{3i}) are given in Tab. I. By using the direction cosines (α_1, α_2, α_3) of the inner magnetization together with (β_{1i}, β_{2i}, β_{3i}) and Eq. (6), Eq. (3) becomes

$$E=\frac{1}{8}NlpS^2\sum|s_i|(\alpha_1\beta_{1i}+\alpha_2\beta_{2i}+\alpha_3\beta_{3i})^2$$
$$=\frac{1}{8}NlpS^2\sum|s_i|f_i(\alpha_1,\ \alpha_2,\ \alpha_3)\,, \tag{8}$$

where

$$f_i(\alpha_1,\alpha_2,\alpha_3)=\beta_{1i}^2\alpha_1^2+\beta_{2i}^2\alpha_2^2+\beta_{3i}^2\alpha_3^2$$
$$+2\beta_{2i}\beta_{3i}\alpha_2\alpha_3+2\beta_{3i}\beta_{1i}\alpha_3\alpha_1$$
$$+2\beta_{1i}\beta_{2i}\alpha_1\alpha_2\,. \tag{9}$$

The coefficient of each term in $f_i(\alpha)$ is also tabulated in Tab. I for every slip systems.

It should be added that this type of anisotropy should be induced irrespective of the degree of order, as far as the slip distance per one atomic plane is less than the diameter of the antiphase order domain (fine slip).

(b) Anisotropy of Short Range Order (Coarse Slip) Type

When many dislocations pass through a definite atomic planes so as to bring the one side of the crystal to the out of phase order domain of the opposite side of the crystal, it is expected that the directions of the induced BB pairs are different from that given in Fig. 8. In the case of $(111)\,[01\bar{1}]$ slip the directions of BB pairs is [011], [101] or [110] or they disappear, depending upon the sorts of antiphase domain and upon the number of dislocations. It is easily verified that the

Table I. Direction cosines of BB pairs and the coefficients of each term in $f_i(\alpha_1, \alpha_2, \alpha_3)$ in the expression of long range order (fine slip) type anisotropy. Cf. Eq. (9).

No. of Slip System	Slip plane	Slip direction	$\beta_1,$	$\beta_2,$	β_3	Coefficients in $f(\alpha_1\alpha_2\alpha_3)$					
						α_1^2	α_2^2	α_3^2	$\alpha_2\alpha_3$	$\alpha_3\alpha_1$	$\alpha_1\alpha_2$
1	(111)	$[01\bar{1}]$	$0,$	$\frac{1}{\sqrt{2}},$	$\frac{1}{\sqrt{2}}$	0	$\frac{1}{2}$	$\frac{1}{2}$	1	0	0
2		$[10\bar{1}]$	$\frac{1}{\sqrt{2}},$	$0,$	$\frac{1}{\sqrt{2}}$	$\frac{1}{2}$	0	$\frac{1}{2}$	0	1	0
3		$[1\bar{1}0]$	$\frac{1}{\sqrt{2}},$	$\frac{1}{\sqrt{2}},$	0	$\frac{1}{2}$	$\frac{1}{2}$	0	0	0	1
4	$(11\bar{1})$	[101]	$\frac{1}{\sqrt{2}},$	$0,$	$-\frac{1}{\sqrt{2}}$	$\frac{1}{2}$	0	$\frac{1}{2}$	0	-1	0
5		[011]	$0,$	$\frac{1}{\sqrt{2}},$	$-\frac{1}{\sqrt{2}}$	0	$\frac{1}{2}$	$\frac{1}{2}$	-1	0	0
6		$[1\bar{1}0]$	$\frac{1}{\sqrt{2}},$	$\frac{1}{\sqrt{2}},$	0	$\frac{1}{2}$	$\frac{1}{2}$	0	0	0	1
7	$(1\bar{1}1)$	[110]	$\frac{1}{\sqrt{2}},$	$-\frac{1}{\sqrt{2}},$	0	$\frac{1}{2}$	$\frac{1}{2}$	0	0	0	-1
8		$[10\bar{1}]$	$\frac{1}{\sqrt{2}},$	$0,$	$\frac{1}{\sqrt{2}}$	$\frac{1}{2}$	0	$\frac{1}{2}$	0	1	0
9		[011]	$0,$	$\frac{1}{\sqrt{2}},$	$-\frac{1}{\sqrt{2}}$	0	$\frac{1}{2}$	$\frac{1}{2}$	-1	0	0
10	$(\bar{1}11)$	$[01\bar{1}]$	$0,$	$\frac{1}{\sqrt{2}},$	$\frac{1}{\sqrt{2}}$	0	$\frac{1}{2}$	$\frac{1}{2}$	1	0	0
11		[101]	$\frac{1}{\sqrt{2}},$	$0,$	$-\frac{1}{\sqrt{2}}$	$\frac{1}{2}$	0	$\frac{1}{2}$	0	-1	0
12		[110]	$\frac{1}{\sqrt{2}},$	$-\frac{1}{\sqrt{2}},$	0	$\frac{1}{2}$	$\frac{1}{2}$	0	0	0	-1

probability of finding one case among these four cases is equally 1/4. Since the probability of finding BB pairs among the atomic pairs which have a certain bond direction is also 1/4 in the disordered state, we can regard the distribution of atomic pairs which connect the both sides of the slipped plane as disordered one. Now let us suppose that the crystal was previously in the partially ordered state, which is characterized by σ the degree of short range order. It is easily verified that the number of BB pairs lying in a unit area of (111) plane is $(1-\sigma)/(4\sqrt{3}a^2)$, which is smaller by $\sigma/(4\sqrt{3}a^2)$ than that of disorder state. Then it follows that the number of BB pairs connecting the both sides of the slipped plane is larger by $\sigma/(4\sqrt{3}a^2)$ per unit area of (111) plane than before the slip takes place. Thus the number of BB pairs induced by the slips in a unit volume is given by

$$N_{BB\,i}=\frac{\sigma}{4\sqrt{3}\,a^2}\times\frac{\sqrt{3}\,p'|s_i|}{a}$$

$$=\frac{1}{16}Np'\sigma|s_i|\,. \tag{10}$$

Since the bond direction of BB pairs thus induced is [011], [101] or [110], the average interaction energy becomes

$$w=\frac{l}{3}(\cos^2\varphi_{[011]}+\cos^2\varphi_{[101]}+\cos^2\varphi_{[110]})$$

$$=\frac{l}{3}\sum_{k=1,2,3}(\beta_{1k}\alpha_1+\beta_{2k}\alpha_2+\beta_{3k}\alpha_3)^2$$

$$=\frac{l}{3}(\alpha_2\alpha_3+\alpha_3\alpha_1+\alpha_1\alpha_2)+\text{const.} \tag{11}$$

This functional form means that the slip plane (111) is an easy magnetizting plane and a normal to it is a hard direction, provided $l>0$. Then the interaction energy for i-th slip system whose slip plane's normal is (n_{1i}, n_{2i}, n_{3i}) becomes

$$w_i=l(n_{2i}n_{3i}\alpha_2\alpha_3+n_{3i}n_{1i}\alpha_3\alpha_1+n_{1i}n_{2i}\alpha_1\alpha_2). \tag{12}$$

The resultant anisotropy is

$$E=\sum_i N_{BB\,i}\,w_i$$

$$=\frac{1}{16}Nlp'\sigma\sum_i|s_i|\,g_i(\alpha_1,\ \alpha_2,\ \alpha_3)\,, \tag{13}$$

Table II. Direction cosines of the normal of slip plane and coefficient of each term in $g_i(\alpha_1, \alpha_2, \alpha_3)$ in the expression of short range order (coarse slip) type anisotropy. Cf. Eq. (14).

No. of Slip System	n_1,	n_2,	n_3	Coefficients in $g(\alpha_1\alpha_2\alpha_3)$		
				$\alpha_2\alpha_3$	$\alpha_3\alpha_1$	$\alpha_1\alpha_2$
1	$\frac{1}{\sqrt{3}}$,	$\frac{1}{\sqrt{3}}$,	$\frac{1}{\sqrt{3}}$	$\frac{1}{3}$	$\frac{1}{3}$	$\frac{1}{3}$
2		〃		$\frac{1}{3}$	$\frac{1}{3}$	$\frac{1}{3}$
3		〃		$\frac{1}{3}$	$\frac{1}{3}$	$\frac{1}{3}$
4	$\frac{1}{\sqrt{3}}$,	$\frac{1}{\sqrt{3}}$,	$-\frac{1}{\sqrt{3}}$	$-\frac{1}{3}$	$-\frac{1}{3}$	$\frac{1}{3}$
5		〃		$-\frac{1}{3}$	$-\frac{1}{3}$	$\frac{1}{3}$
6		〃		$-\frac{1}{3}$	$-\frac{1}{3}$	$\frac{1}{3}$
7	$\frac{1}{\sqrt{3}}$,	$-\frac{1}{\sqrt{3}}$,	$\frac{1}{\sqrt{3}}$	$-\frac{1}{3}$	$\frac{1}{3}$	$-\frac{1}{3}$
8		〃		$-\frac{1}{3}$	$\frac{1}{3}$	$-\frac{1}{3}$
9		〃		$-\frac{1}{3}$	$\frac{1}{3}$	$-\frac{1}{3}$
10	$-\frac{1}{\sqrt{3}}$,	$\frac{1}{\sqrt{3}}$,	$\frac{1}{\sqrt{3}}$	$\frac{1}{3}$	$-\frac{1}{3}$	$-\frac{1}{3}$
11		〃		$\frac{1}{3}$	$-\frac{1}{3}$	$-\frac{1}{3}$
12		〃		$\frac{1}{3}$	$-\frac{1}{3}$	$-\frac{1}{3}$

where

$$g_i(\alpha_1, \alpha_2, \alpha_3) = n_{2i}n_{3i}\alpha_2\alpha_3 + n_{3i}n_{1i}\alpha_3\alpha_1 + n_{1i}n_{2i}\alpha_1\alpha_2. \quad (14)$$

The coefficients of each term in (14) are tabulated in Tab. II for every slip systems.

It should be noted that this type of anisotropy should be induced irrespective of the degree of order as far as the slip distance is larger than the diameter of antiphase order domain.

§ 5. Calculation of Slip Deformation

In order to calculate the magnetic antisotropy for individual rolling cases from Eq. (8) or (13), it is necessary to determine the value of slip density $|s_i|$ for every slip systems. The deformation by (110) [01$\bar{1}$] slip system (No. 1) is shown in Fig. 9. By considering that the distance of atomic plane is $a/\sqrt{3}$ and length of one step of slip (Burger's vector) is $a/\sqrt{2}$, it is easily verified that the components of strain tensor are given by

$$\left.\begin{array}{lll} \gamma_{xx1}=0, & \gamma_{yy1}=s_1, & \gamma_{zz1}=-s_1 \\ \gamma_{yz1}=0, & \gamma_{zx1}=-s_1/2, & \gamma_{xy1}=s_1/2 \end{array}\right\}, \quad (15)$$

where s_1 is the slip density as defined in § 4 (a). The strain tensors for the other slip systems are similarly calculated and tabulated in Tab. III. The resultant deformation is

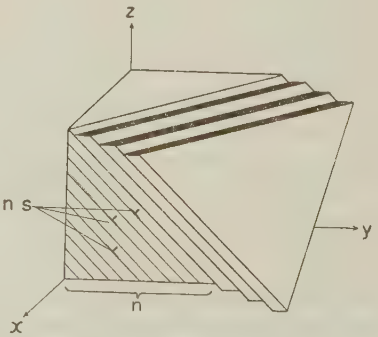

Fig. 9. Deformation by the slips which belong to (110) [01$\bar{1}$] slip system.

Table III. Components of strain tensor for every slip systems.

No. of Slip System	γ_{xx}	γ_{yy}	γ_{zz}	γ_{yz}	γ_{zx}	γ_{xy}
1	0	S_1	$-S_1$	0	$-\frac{1}{2}S_1$	$\frac{1}{2}S_1$
2	$-S_2$	0	S_2	$\frac{1}{2}S_2$	0	$-\frac{1}{2}S_2$
3	S_3	$-S_3$	0	$-\frac{1}{2}S_3$	$\frac{1}{2}S_3$	0
4	S_4	0	$-S_4$	$\frac{1}{2}S_4$	0	$\frac{1}{2}S_4$
5	0	$-S_5$	S_5	0	$-\frac{1}{2}S_5$	$-\frac{1}{2}S_5$
6	S_6	$-S_6$	0	$-\frac{1}{2}S_6$	$-\frac{1}{2}S_6$	0
7	$-S_7$	S_7	0	$-\frac{1}{2}S_7$	$-\frac{1}{2}S_7$	0
8	$-S_8$	0	S_8	$-\frac{1}{2}S_8$	0	$\frac{1}{2}S_8$
9	0	$-S_9$	S_9	0	$\frac{1}{2}S_9$	$-\frac{1}{2}S_9$
10	0	S_{10}	$-S_{10}$	0	$\frac{1}{2}S_{10}$	$-\frac{1}{2}S_{10}$
11	S_{11}	0	$-S_{11}$	$-\frac{1}{2}S_{11}$	0	$-\frac{1}{2}S_{11}$
12	$-S_{12}$	S_{12}	0	$\frac{1}{2}S_{12}$	$\frac{1}{2}S_{12}$	0

given by

$$\left.\begin{array}{lll}\gamma_{xx}=\sum_i \gamma_{xx\,i}, & \gamma_{yy}=\sum_i \gamma_{yy\,i}, & \gamma_{zz}=\sum_i \gamma_{zz\,i} \\ \gamma_{yz}=\sum_i \gamma_{yz\,i}, & \gamma_{zx}=\sum_i \gamma_{zx\,i}, & \gamma_{zy}=\sum_i \gamma_{xy\,i}\end{array}\right\}. \quad (16)$$

(1) (110) [001] rolling

It is assumed that the rolling of the specimen plate results in an elongation in length and a reduction in thickness but no widening of the specimen width. This assumption is exactly reallized in the (110) [001] rolling, although there are some exceptional cases which will be mentioned later. Then the tensor components with respect to the coordinate fixed to the crystal should be given by

$$\left.\begin{array}{lll}\gamma_{xx}=-r, & \gamma_{yy}=-r, & \gamma_{zz}=2r \\ \gamma_{yz}=0, & \gamma_{zy}=0, & \gamma_{xy}=-r\end{array}\right\}, \quad (17)$$

where r is the reduction in thickness.

It should be expected that the slip systems contributing to this deformation are No. 1, 2, 4 and 5 (i.e. that of (111) and (111) slip plane), because the others have the slip planes normal to the roll plane and the slip along them should not contribute in reducing the thickness (Cf. Fig. 10). If it is true, the rolling in any direction for (110) plate might always induce the preferred elongation in the direction [001]. In fact it was observed that the specimen having different crystallographic direction are rolled into the various shapes as shown in Fig. 11, which are found to be caused by the preferred elongation in [001].

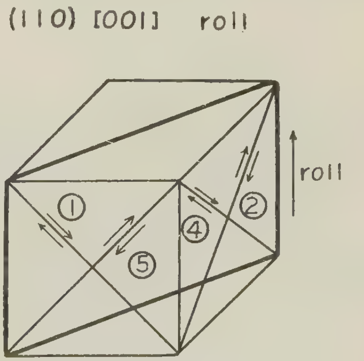

Fig. 10. The slip systems contributing to (110) [001] roll.

Then the strain components are expressed in terms of s_i's by referring Tab. III. Thus we have

$$\left.\begin{aligned}\gamma_{xx}&=-s_2+s_4\,,\\ \gamma_{yy}&=s_1-s_5\,,\\ \gamma_{zz}&=-s_1+s_2-s_4+s_5\,,\\ \gamma_{yz}&=\tfrac{1}{2}(s_2+s_4)\,,\\ \gamma_{zx}&=\tfrac{1}{2}(-s_1-s_5)\,,\\ \gamma_{xy}&=\tfrac{1}{2}(s_1-s_2+s_4-s_5)\end{aligned}\right\}. \tag{18}$$

By assuming the symmetry consideration, i.e.

$$s_1=-s_2=s_4=-s_5\,, \tag{19}$$

we have by the comparison between (17) and (18)

$$s_1=s_4=-r/2,\quad s_2=s_5=r/2\,. \tag{20}$$

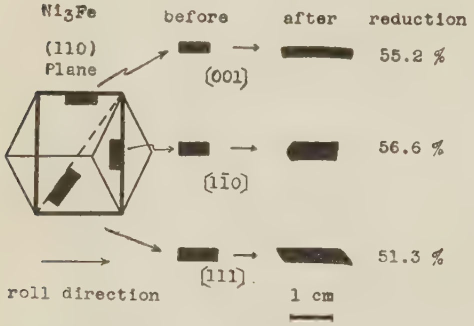

Fig. 11. Change of shapes of the specimens cut from (110) plate by the rolling along various direction.

(2) (001) [110] rolling

The deformation for this case should be given by

$$\left.\begin{matrix}\gamma_{xx}=r, & \gamma_{yy}=r, & \gamma_{zz}=-2r\\ \gamma_{yz}=0, & \gamma_{zx}=0, & \gamma_{xy}=r\end{matrix}\right\}. \tag{21}$$

The slip systems which can contribute for this deformation are also No. 1, 2, 4 and 5, but the real contribution was made only by No. 1 and 2. This is because the slips in this case are made by easy glide. Pl. 27 and 28 are the microphotographs of the slip bands appearing on the thin edge of the specimen. It can be seen in the plates that easy glide takes place in the upper and lower halves of the crystal and the slip bands in each region rotate to the roll direction with a progress of rolling. The reason why easy glide takes place in this case is as follows: In this case the slip plane (111) makes the angle of 54.5° with rolling plane (Fig. 13), and therefore the slip along it causes the rotation of the crystal which results in a decrease of the angle from 54.5°. This chang of orientation results in an increase of th shearing stress component along its slip plan and thus favors the slips along itself. I the case of (110) [001] rolling, however, (11 slip plane makes the angle of 35.5° with ro plane and the slip along it results in a decrerse of angle from 35.5°. This crystal rotation disfavors the original slips and favors the slip along another slip plane (11$\bar{1}$), resulting in the both slips as assumed in §5 (1).

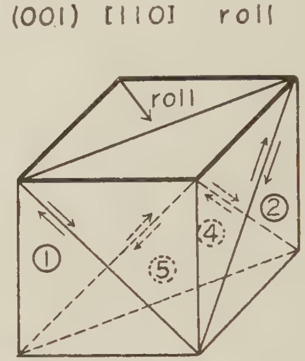

Fig. 12. The slip systems contributing to the (001) [110] rolling.

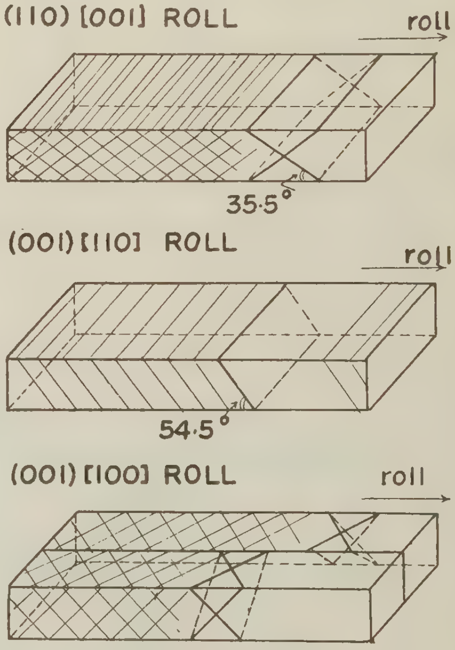

Fig. 13. Actual slips by the rolling in various crystallographic direction.

The deformation is given by

$$\left.\begin{aligned} &\gamma_{xx}=-s_2\,, \\ &\gamma_{yy}=s_1\,, \\ &\gamma_{zz}=-s_1+s_2\,, \\ &\gamma_{yz}=\tfrac{1}{2}s_2\,, \\ &\gamma_{zx}=-\tfrac{1}{2}s_1\,, \\ &\gamma_{xy}=\tfrac{1}{2}(s_1-s_2) \end{aligned}\right\} . \tag{22}$$

By comparing (22) with (21), we have

$$s_1=r\,,\quad s_2=-r\,, \tag{23}$$

although they do not give the right values for γ_{yz} and γ_{zx}.

For the under half of the crystal where effective slip systems are No. 4 and 5, we have

$$s_4=r\,,\quad s_5=-r\,. \tag{24}$$

(3) (001) [100] rolling

The deformation for this case should be

$$\left.\begin{aligned} &\gamma_{xx}=2r, \quad \gamma_{yy}=0, \quad \gamma_{zz}=-2r \\ &\gamma_{yz}=0, \quad \gamma_{zx}=0, \quad \gamma_{xy}=0 \end{aligned}\right\} . \tag{25}$$

The slip systems which contribute to the deformation are No. 2, 4, 8 and 11, because No. 3, 6, 7 and 12 should not contribute in reducing the thickness and No. 1, 5, 9 and 10 should cause the widening of the specimen width. In this case the easy glide is also expected, because the slip by No. 2 causes the crystal rotation which favors No. 2 itself and No. 11 and disfavors No. 4 and No. 8. The calculation is given in Appendix. It is, therefore, probable that the slips by both No. 2 and No. 11 take place in some places and those by both No. 4 and No. 8 in the other places (Cf. Fig. 13). The slip bands in this cases are shown in Pl. 29 and 30.

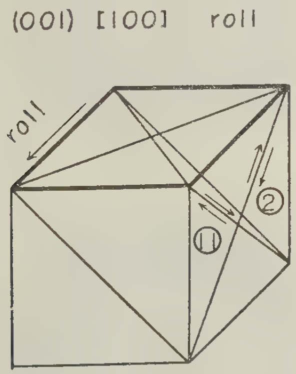

Fig. 14. Slip systems which contribute to the (001)[100] rolling.

The deformation due to No. 2 and No. 11 is given by

$$\left.\begin{aligned} &\gamma_{xx}=-s_2+s_{11}\,, \\ &\gamma_{yy}=0\,, \\ &\gamma_{zz}=s_2-s_{11}\,, \\ &\gamma_{yz}=\tfrac{1}{2}(s_2-s_{11})\,, \\ &\gamma_{zx}=0\,, \\ &\gamma_{xy}=-\tfrac{1}{2}(s_2+s_{11}) \end{aligned}\right\} . \tag{26}$$

By comparing (25) and (26) we have

$$s_2=-r\,,\quad s_{11}=r\,, \tag{27}$$

although they give a finite value for γ_{yz}. For the deformation due to No. 4 and No. 8, it follows

$$s_4=r\,,\quad s_8=-r\,. \tag{28}$$

Although the results (23), (24) or (27), (28) give the finite values for γ_{yz}, γ_{zx} or γ_{yz} which do not conform with (21) or (25), the actual deformation of crystal did support the presence of these strain component.

§ 6. Calculation of Magnetic Anisotropy for Individual Cases and Comparison with Experiments

(1) (110) [001] rolling

By putting the values of s_i given in (20) into (8), we have for the anisotropy of long range order type (L.F. type)

$$E=\frac{1}{16}NlpS^2r(\alpha_1^2+\alpha_2^2+2\alpha_3^2)$$

$$=\frac{1}{16}NlpS^2r\alpha_3^2+\text{const.} \tag{29}$$

Similarly by putting (20) into (13), we have for short range order type (S.C. type)

$$E=\frac{1}{24}Nlp'\sigma r\alpha_1\alpha_2 \tag{30}$$

Eq. (29) (L.F. type) gives the anisotropy which makes x-y plane easy magnetizing *plane*, while (30) (S.C. type) gives the anisotropy which makes $[1\bar{1}0]$ easy magnetizing *direction*. Thus both anisotropies make $[1\bar{1}0]$ as stable direction which is in good agreement with experiments. The resultant anisotropy in (110) plane can be expressed by

$$E=\frac{1}{48}Nlr(3pS^2+p'\sigma)\cos^2\theta\,, \tag{31}$$

where θ is the angle between magnetization and roll direction. Since the coefficient K_u of the uniaxial anisotropy energy is defined by

$$E=-K_u\cos^2\theta\,, \tag{32}$$

we have

$$K_u=-\frac{1}{48}Nlr(3pS^2+p'\sigma)\,. \tag{33}$$

By comparing it with $K_u=-1.9\times10^5$ erg/cc at $r=0.5$ for slow cool specimen (Cf. Fig. 2), we have, by using the numerical value of Nl given in (5),

$$3pS^2+p'\sigma=5.9\%\,. \tag{34}$$

For perfect order specimen, since $K_u=-0.64\times10^5$ at $r=0.5$

$$3pS^2+p'\sigma=2.0\%\,. \tag{35}$$

(2) (001) [110] rolling

By putting (23) into (8), we have for L.F. type

$$E=\frac{1}{16}NlpS^2r(\alpha_1^2+\alpha_2^2+2\alpha_3^2+2\alpha_2\alpha_3+2\alpha_3\alpha_1)$$

$$=\frac{1}{16}NlpS^2r\,\alpha_3(2\alpha_1+2\alpha_2+\alpha_3)+\text{const.}\,, \tag{36}$$

and by putting (23) into (13), we have for S.C. type

$$E=\frac{1}{24}Nlp'\sigma r(\alpha_2\alpha_3+\alpha_3\alpha_1+\alpha_1\alpha_2)\,. \tag{37}$$

If we assume that s_4 and s_5 also take place together with s_1 and s_2 in the same region, the anisotropy becomes

$$E=\frac{1}{16}NlpS^2r\alpha_3^2 \tag{38}$$

for L.F. type and

$$E=\frac{1}{24}Nlp'\sigma r\alpha_1\alpha_2 \tag{39}$$

for S.C. type. Since the roll plane is $\alpha_3=0$, only S.C. type would be effective for this case. In actual case, however s_1 and s_2 take place in the upper half of the crystal as assumed in (23), so we must use (36) and (37) by taking into consideration of the crystal rotation.

As one will easily verify from Eq. (A. 2) in Appendix, the angle of the crystal rotation, ψ (the angle between [001] and normal of the plate), is given by

$$\psi=\sqrt{2}\,r\,. \tag{40}$$

Then the anisotropy in the rotated surface becomes

$$E=-\frac{\sqrt{2}}{8}NlpS^2r\psi\cos^2\theta$$

$$=-\frac{1}{4}NlpS^2r^2\cos^2\theta \tag{41}$$

for L.F. type and

$$E=\frac{1}{24}Nlp'\sigma r(1-\sqrt{2}\,\psi)\cos^2\theta$$

$$=\frac{1}{24}Nlp'\sigma r(1-2r)\cos^2\theta \tag{42}$$

for S.C. type. Thus the coefficient of uniax al anisotropy in the roll plane becomes

$$K_u=\frac{1}{24}Nl\{-p'\sigma r+2(p'\sigma+3pS^2)r^2\} \qquad (4$$

which is a quadratic function of r and ca be well fitted with the experimental curve a shown in Fig. 15. From this comparison w have

$$\left.\begin{aligned}pS^2&=0.36\%\\ p'\sigma&=0.78\%\end{aligned}\right\} \qquad (4$$

for slow cooled and

$$\left.\begin{aligned}pS^2&=0.50\%\\ p'\sigma&=0.54\%\end{aligned}\right\} \qquad ($$

for perfect order specimen.

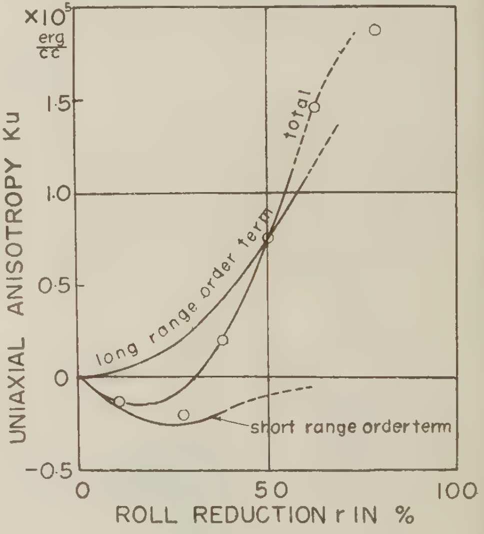

Fig. 15. Comparison of K_u-r curve for (001 [110] rolling between calculation and experiment. The experimental points are that fo previously slow-cooled specimen.

(3) (001) [100] rolling

By putting (27) into (8) we have

$$E=\frac{1}{8}NlpS^2r(\alpha_1^2+\alpha_3^2)$$

$$=-\frac{1}{8}NlpS^2r\alpha_2^2+\text{const.} \qquad (4$$

for L.F. type and by putting (27) into (13) w have

$$E=\frac{1}{24}Nlp'\sigma\alpha_2\alpha_3 \qquad (4$$

Pl. 1

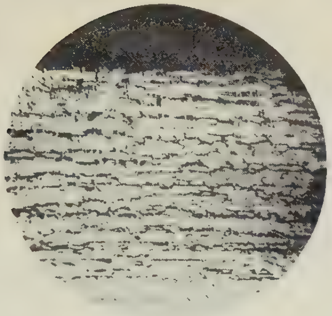

Pl. 2

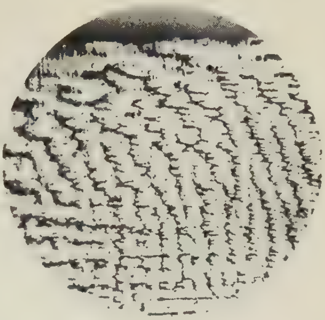

Pl. 3

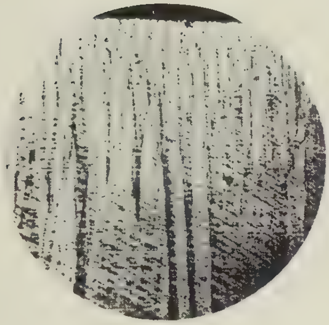

Pl. 4

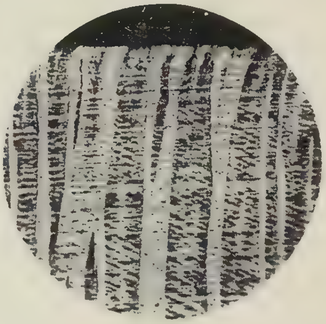

Pl. 5

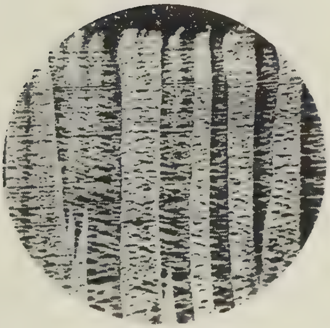

Pl. 6

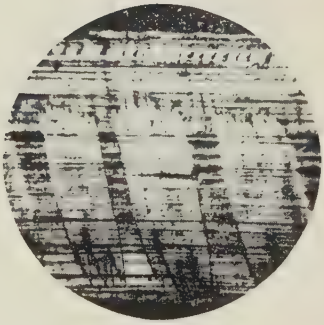

Pl. 7

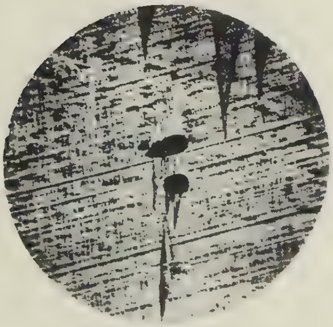

Pl. 8

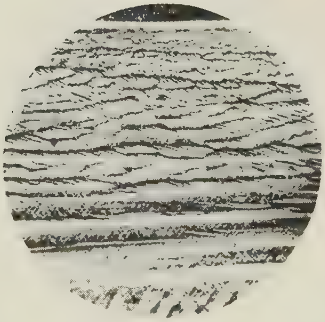

0.5 mm

Illustration of the Plates

Pl. 1. Domain pattern of rolled (110) [001] Ni_3Fe (previously cooled slowly) $r=11\%$.

Pl. 2. ditto, $r=20\%$.

Pl. 3. ditto, $r=30\%$.

Pl. 4. ditto, $r=42\%$.

Pl. 5. ditto, $r=55\%$.

Pl. 6. ditto, $r=94\%$.

Pl. 7. Domain patterns of rolled (110) $[1\bar{1}2]$ Ni_3Fe (previously cooled slowly) $r=44\%$.

Pl. 8. Domain patterns of rolled (110) $[1\bar{1}0]$ Ni_3Fe (previously cooled slowly) $r=57\%$.

Pl. 9

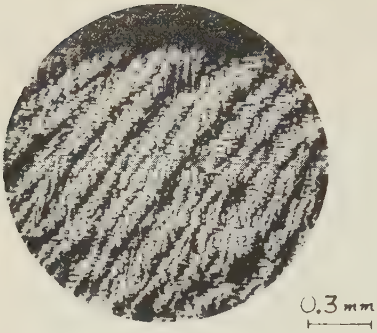

Pl. 10

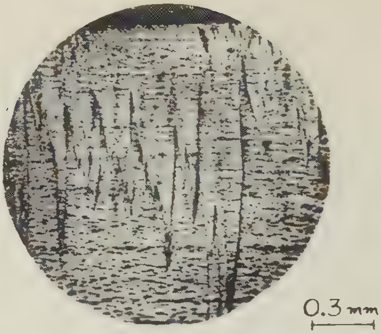

Pl. 11

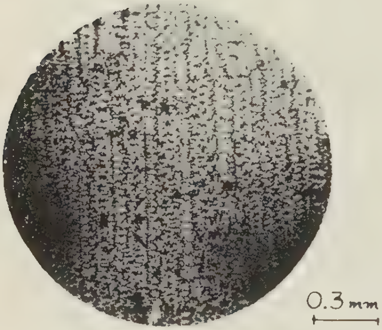

Pl. 12

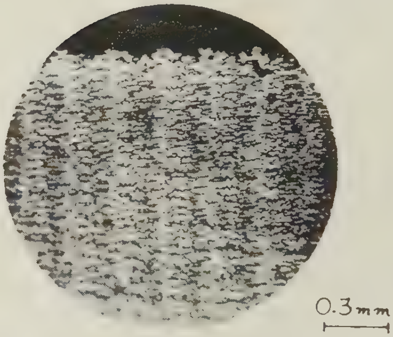

Pl. 13

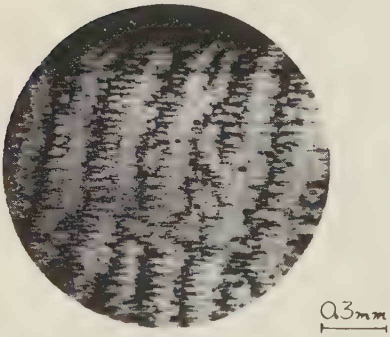

Pl. 14

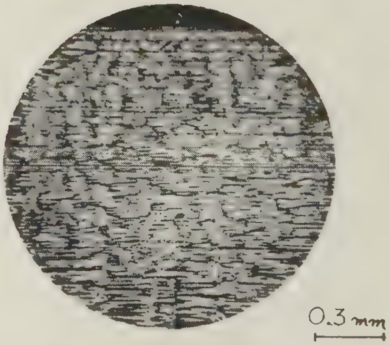

Pl. 15

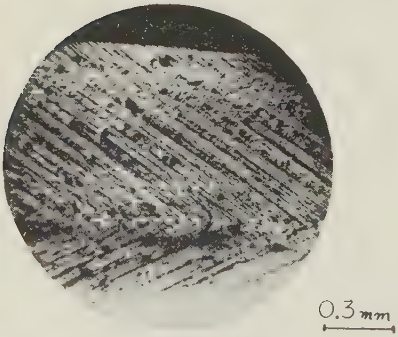

Pl. 16

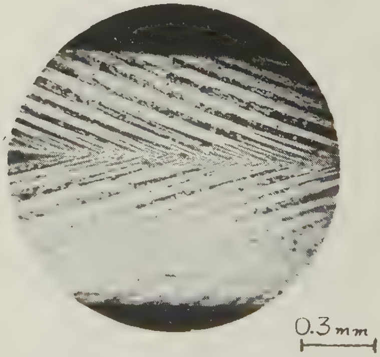

Pl. 9. Domain Patterns of rolled (110) [001] Ni_3Fe (previously in perfect ordered state) $r=29\%$.

Pl. 10. ditto, $r=73\%$.

Pl. 11. Domain pattern of rolled (001) [110] Ni_3Fe crystal (slow cool) $r=42\%$.

Pl. 12. ditto, $r=53\%$.

Pl. 13. ditto, $r=60\%$.

Pl. 14. ditto, $r=68.5\%$.

Pl. 15. ditto, observed on the thin edge. $r=42\%$.

Pl. 16. ditto, observed on the thin edge. $r=60\%$.

Pl. 17

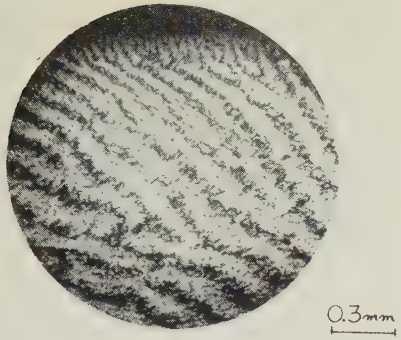

Pl. 18

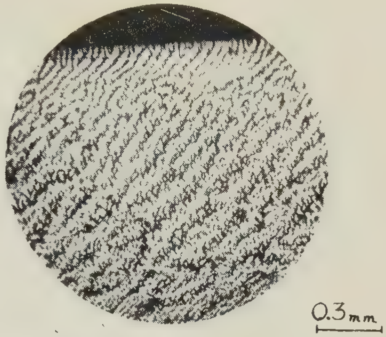

Pl. 19

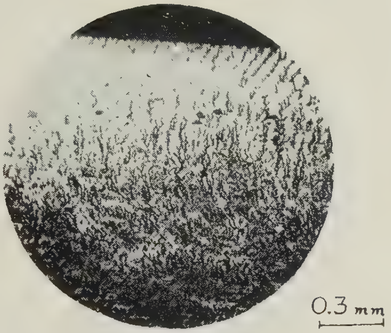

Pl. 20

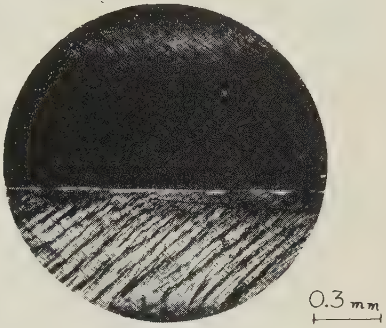

Pl. 21

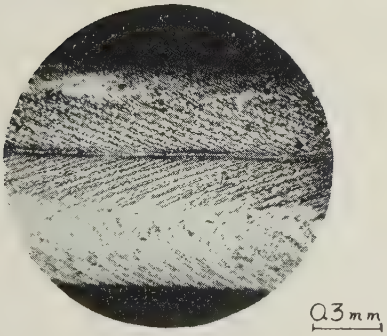

Pl. 22

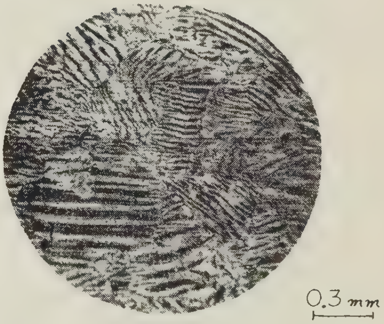

Pl. 23

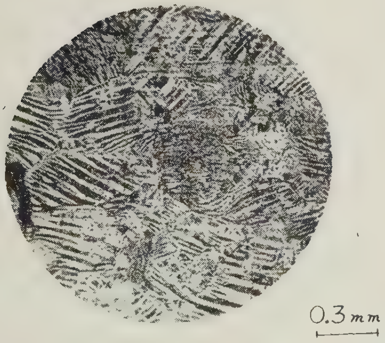

Pl. 24

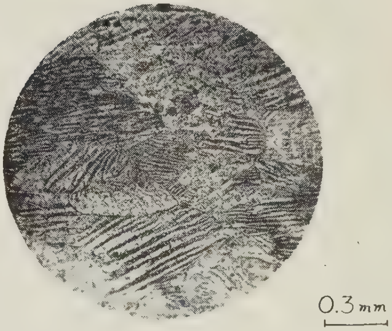

Pl. 17. Domain pattern of rolled (001) [100] Ni_3Fe (slow cool) $r=39\%$.

Pl. 18. ditto, $r=50\%$.

Pl. 19. ditto, $r=60\%$.

Pl. 20. ditto, observed on the thin edge. $r=30\%$.

Pl. 21. ditto, observed on the thin edge. $r=50\%$.

Pl. 22. Domain pattern of rolled polycrystal line Ni_3Fe (previously in disordered state.) $r=20\%$.

Pl. 23. ditto, $r=39\%$.

Pl. 24. ditto, $r=51\%$.

Pl. 25

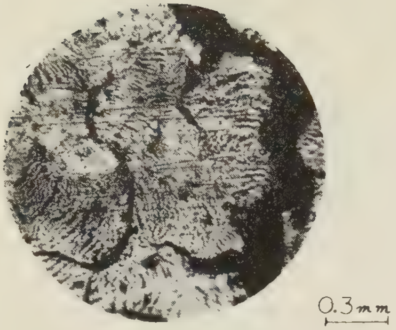

Pl. 26

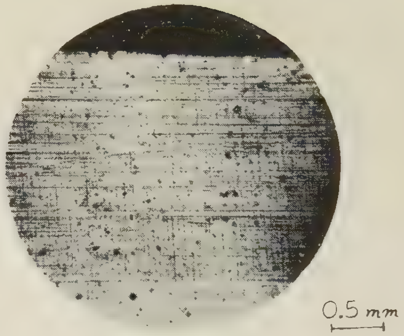

Pl. 27

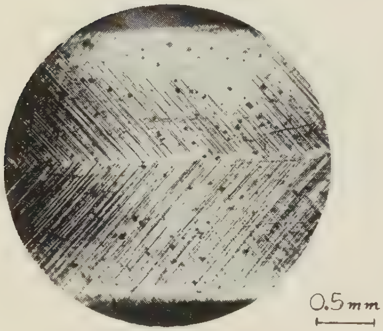

Pl. 28

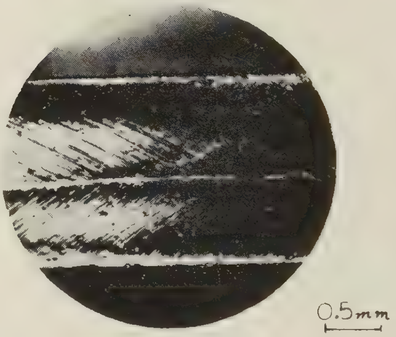

Pl. 29

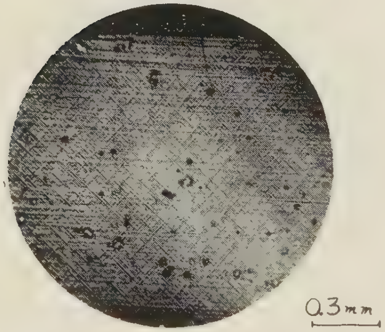

Pl. 30

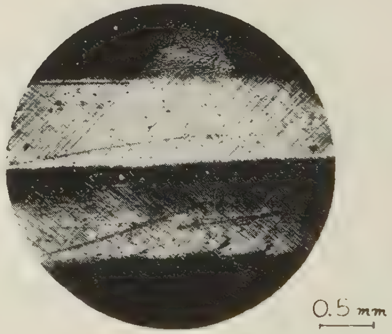

Pl. 25. Domain pattern of rolled polycrystal line Ni_3Fe (previously in perfect order state.) $r=30\%$.

Pl. 26. Slip bands observed on the surface of (001) [110] rolled crystal. $r=9.1\%$.

Pl. 27. Slip bands observed on the thin edge of (001) [110] rolled crystal. $r=9.1\%$.

Pl. 28. ditto, $r=42\%$.

Pl. 29. Slip bands observed on the surface of (001) [100] rolled crystal. $r=10\%$.

Pl. 30. Slip bands observed on the thin edge of (001) [100] rolled crystal. $r=10\%$.

Roll direction is horizontal for all plates

for S.C. type. Since $\alpha_3=0$ in the roll plane (001), S.C. type (47) does not contribute to the torque. The L.F. type (46) makes [010] easy direction, being in good agreement with torque measurement. Since $K_u=-0.48\times10^5$ erg/cc at $r=0.52$, we have from (46)

$$pS^2=0.24\%. \tag{48}$$

Since easy direction of S.C. type anisotropy (47) is $[01\bar{1}]$, it would make the real easy direction to make a glancing angle with roll plane. This would be the reason why no clear domain was observed on the rolled surface. It should be expected that the crystal rotation in this case causes the rotation of $[01\bar{1}]$ towards the roll plane. Actually we can find the distorted uniaxial domains at the latter stage of rolling (Pl. 19).

§ 7. Discussion

As mentioned in § 6, principal points obtained by the experiments are well explained by the present interpretation. The values of pS^2 and $p'\sigma$ calculated for each case are summarized in Tab. IV. The fairly good agreement between different cases indicates the quantitative validity of the formulae. The order of magnitude of pS^2 or $p'\sigma$ may be also plausible, although we cannot make an exact estimation because of lack of informations about p or p'.

Table IV. Values of pS^2 and $p'\sigma$ calculated from the data for each rolling.

	(110) [001]	(001) [110]	(001) [100]
$3pS^2+p'\sigma$	5.9% (2.0)	1.8_6% (2.0_4)	—
pS^2	—	0.36 (0.50)	0.24
$p'\sigma$	—	1.6 (1.1)	—

It is interesting that the values of pS^2 and $p'\sigma$ for perfect order specimen are not so much different from that for slowly cooled specimen.* This is partly because that p_0 mentioned in § 4 (a) should decrease with an increase of S. Moreover it would be related to the fact that the manner of slips depends upon the degree of order[9),10),11)]. The fact that the anisotropy for a quenched specimen exhibits a large value (Cf. Fig. 2) would be also explained along the same line. It is interesting further that the anisotropy for polycrystal increases with a progress of order (Cf. Fig. 7), contrary to the case of single crystal. One possible explanation will be as follows: Since the individual crystallites in a polycrystal are surrounded by other crystallities, easy glide along one slip system should not be permitted. If several slip systems must contribute to the deformation at the same time, pairs of dislocations travelling along one slip system might be separated by another dislocation which belongs to the other slip systems. Then the separated dislocations would become effective in inducing the anisotropy. Thus the anisotropy would increase with a progress of order. If, however, order progresses to too much extent, the pairs of dislocations would become hard to be separated, resulting in an independent deformation for each crystallite which would lead to the break down at the crystal boundaries (Cf. Pl. 25).

Further detailed investigations on the roll anisotropy will offer the valuable informations about slip mechanism.

Acknowledgement

The authors are indebted to Prof. A. Ookawa for his full discussions about the problem of slip mechanism. This research was supported by the research grant of the Ministry of Education.

Appendix

Calculation of Crystal Rotation by Slip

Let us suppose that the face centered cubic crystal having the surface parallel to x-y plane is deformed by the slips which belong to the slip system having slip direction (d_1, d_2, d_3) and the normal of the slip plane (n_1, n_2, n_3). It can be shown by a simple calculation that the crystal surface rotates to the plane whose normal is

$$\left.\begin{aligned} p_1 &= -\sqrt{\frac{3}{2}}\,sn_1d_3 \\ p_2 &= -\sqrt{\frac{3}{2}}\,sn_2d_3 \\ p_3 &\doteqdot 1 \end{aligned}\right\} . \qquad \text{(A1)}$$

The angle of crystal rotation ψ, which is the angle between z axis and the normal (p_1, p_2, p_3), is given by

$$\psi = \sqrt{p_1{}^2+p_2{}^2} = \sqrt{\frac{3}{2}}\,sd_3\sqrt{n_1{}^2+n_2{}^2}\,. \qquad \text{(A2)}$$

The Component of Shearing Stress for Given Slip System

When the crystal is under the stress given by

$$\left.\begin{aligned} \sigma_{xx} &= T \\ \sigma_{yy} &= 0 \\ \sigma_{zz} &= -T \end{aligned}\right\} , \qquad \text{(A3)}$$

the shearing stress for given slip system whose slip direction is (d_1, d_2, d_3) and the normal of slip plane is (n_1, n_2, n_3), becomes

$$\tau = (d_1n_1 - d_3n_3)T\,. \qquad \text{(A4)}$$

Calculation for (001) [100] Rolling

The angle of crystal rotation caused by the slip No. 2 can be calculated by (A3), thus

---

* *Note added in proof*: The extremely slow development of anisotropy for perfect order (110) [001] specimen (Cf. Fig. 2) may be due to occurrence of easy glide.

$$\psi=\frac{|s_2|}{\sqrt{2}}\,. \qquad (A5)$$

By this rotation the component of the shearing stress should be changed by

$$\delta\tau=-\{2d_1n_3+d_2n_3+d_3(2n_1+n_2)\}\frac{\psi}{\sqrt{2}}\,. \qquad (A6)$$

Then it is easily found that

$$\frac{\delta\tau}{\tau}=+\frac{\psi}{2\sqrt{2}}>0 \quad \text{for No. 2 and No. 11}$$
$$=-\frac{\psi}{2\sqrt{2}}<0 \quad \text{for No. 4 and No. 8.} \qquad (A7)$$

References

1) W. Six, J. L. Snoek and W. G. Burgers: De Ingenier **49** E195–200 (1934).
2) H. W. Conradt, O. Dahl and K. J. Sixtus: Z Metallkunde **32** (1940) 231–8.
3) G. W. Rathenau and J. L. Snoek: Physica (1941) 555.
4) L. Néel: Compt. rend **238** (1954) 305, J Phys. Rad. **15** (1954) 225.
5) S. Taniguchi and M. Yamamoto: Sci. Repts Research Inst. Tohoku Univ. **A6** (1954) 330.
6) S. Chikazumi and T. Oomura: J. Phys. Soc Japan. **10** (1955) 842.
7) S. Chikazumi: J. Phys. Soc. Japan **11** (1956 551.
8) J. C. Fisher: Acta Metal. **2** (1954) 9.
9) T. Nagashima and T. Yamamoto: Acta Meta **4** (1956) 94.
10) T. Taoka ond S. Sakata: Acta Metal. (1957) 61.
11) T. Taoka and R. Honda: J. of Electro Microscopy **5** (1957) 19.

JOURNAL OF THE PHYSICAL SOCIETY OF JAPAN Vol. 12, No. 11, NOVEMBER, 1957

Oscillations in Plasma I

By Shoji, KOJIMA, Kiyoe KATO and Shigeo HAGIWARA

Tokyo University of Education, Otsuka, Tokyo

(Received July 31, 1957)

By using super-regenerative detector plasma oscillations have been studied. On similar discharge tubes to Looney-Brown's tube many plasma oscillations were observed without auxiliary electron beams. When a small beam was introduced into main plasma, all the oscillations became stronger but their frequencies remain unchanged. For the excitation of plasma oscillations the existence of thick ion sheaths was not necessary. With usual discharge tubes plasma oscillations were detected from the outside of tubes by a small antenna. Many plasma oscillations having slight different frequencies were always observed. However, details of these oscillations are still obscure.

§ 1. Introduction

Ionized gases at low pressure are known to generate oscillations with frequencies of order of 1000 Mc. These oscillations are interpreted as the plasma-electron oscillation, whose frequency is expressed by

$$f_p=\sqrt{Ne^2/\pi m}\,, \qquad (1)$$

being N the electron concentration, e the charge and m the mass of electron.[1] Since the frequency is independent on the wave length, the group velocity of plasma waves should be zero. Recently Bohm and Gross took into account thermal motions of electrons and gave the following expression for th frequency:

$$f^2=f_p^2+(V_{th}/\lambda)^2 \qquad (2$$

where V_{th} is the mean velocity of electro and λ the wave length.[2] Then the grou velocity becomes $V_{th}^2/\lambda f$. Since λf is ord of the velocity of primary electrons, the grou velocity is usually very small. Therefore th each plasma oscillation is expected to be loca ized in a definite region of space. Such plasm oscillations had been cleary observed by Me rill and Webb[3]. By using a movable prob they showed that the oscillation with lar amplitude was detectable in a narrow region being near the layer where primary electrons received anomalous scattering. Merrill and Webb pointed out that the primary electrons were subject to velocity modulation when they passed throuth the oscillating layer of plasma and bunched subsequently at the region where the oscillations were detectable. Recent experiment by Bailey and Emeleus seems to confirm this interpretation[4]. In these experiments the oscillations were detected with a crystal rectifier.

With a super-heterodyne detecter and a specially designed discharge tube Looney and Brown[5] attempted to test the postulate of Bohm and Gross that plasma oscillations could be excited by a beam of electrons alone. However, they could not observe plasma oscillations except when large ion sheaths were introduced on the electrodes and a standing wave was set up in the region bounded by the sheaths.

The present experiments using more sensitive detecters have been undertaken to study of the effect of probe in Merrill and Webb's experiment and to study of the effect of ion sheaths in Looney and Brown's experiment.

§ 2. Apparatus

The coaxial cavity spectrometer which was discribed in a report on nuclear quadrupole resonances[6] was applied for the detection of plasma oscillations. The main part of the spectrometer is a two-cavity grid separation oscillator with a light-house tube 2C43. The block diagram of the detecting system is shown in Fig. 1. The oscillator works as a super-regenerative receiver when a quenching oscillater is applied or as a simple regenerative receiver without quenching oscillator. Frequency modulation was established by a vibrating metal sheet which was inserted into the plate cavity. The range of modulation could be extended upto 4 Mc, which was broader than the line widths of oscillations.

The super regenerative type has an advantage to be more sensitive than the simple regenerative type, but has a disadvantage that the quenching produces many sidebands spaced by its frequency. The quenching frequency adequate for the operation was about 1 Mc, which was smaller than the line width of oscillations. Therefore the super-regenerative type gave broadened line-shapes owing to the sidebands. The effect of sidebands, however, did not exceed several megacycles.

The frequency was measured by comparing with a overtone of a test oscillater of the frequency range between 30 and 500 Mc/s whose frequency was read acculately with a frequency meter.

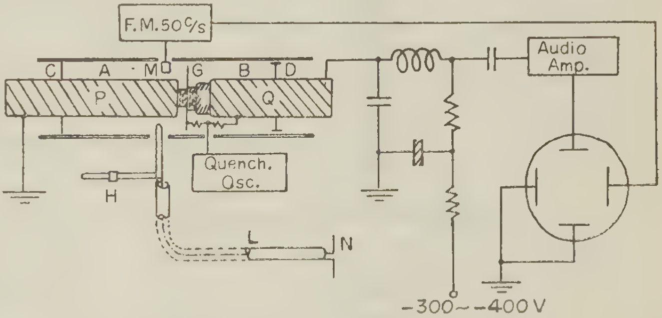

Fig. 1. Block diagram of detecting system.
A: Plate cavity, B: Cathode cavity, C: Plate plunger, D: Cathode plunger, G: Grid disk, H: Quarter wave trap, L: Coaxial cable, M: Modulation stub, N: Antenna, P: Plate cylinder, Q: Cathode cylinder, T: Light house tube (2C43).

Three types of discharge tubes containing mercury drops were employed. The type A was similar to descrived by Merrill and Webb. The type B was same as the type A except having no probes. The type C was simular to that described by Looney and Brown. The discharges were run in mercury vapour at a pressure of order of 10^{-3} mmHg.

§ 3. Results with the Discharge Tubes of the Type A

Diagram of a discharge tube of the type A is shown in Fig. 2. The cathode was a oxide coated type having a diameter of 5 mm and the anode a nickel disk having a diameter of 12 mm. The gap length was 16 mm. Movable double probes were used to pick up the oscillation and to measure the concentration and temperature of electrons, whereas a single probe was used by Merrill and Webb. The double probes consisted of two parallel tungsten wires of diameter 0.06 mm having a separation of 5 mm. Each probes were coated by glass except the both ends. By the courtesy of the double probes rather strong oscillations were picked up. So that the spectrometer was used as a simple regenerative receiver. An observed spectrum at the discharge current 26 mA and the room temperature 11°C is reproduced in Fig. 3. The center frequency of the plasma oscillation was 944.58±0.25 Mc and the half width was about 2 Mc. The center frequency was checked by the method of crystal detector and parallel wires resonator.

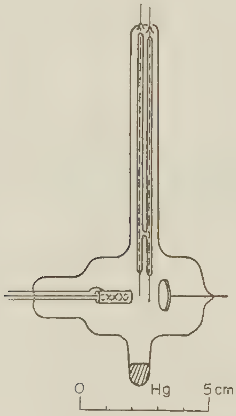

Fig. 2. Discharge tube of type A (Merrill-Webb's type)

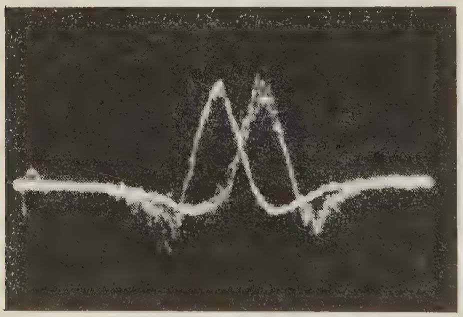

Fig. 3. An oscilloscope display of plasma oscillation with sinusoidal frequency modulation. The pattern is duplicated at increasing and decreasing sweeps of frequency.

The frequency of the oscillation changed linearly with discharge current. When the probes were moved parallel to the axis of tube, a slight change of frequency was observed. The maximum intensity of the oscillation occured in the middle region of discharge. Beside these strong oscillations many weak oscillations having different frequencies were simultaneously observed. Plots of thi observed frequencies against to the discharg currents are shown in Fig. 4. The plotes wer obtained by a series of measurements wher the oscillations were detected at a fixed fre quency of the receiver by changing the dis charge current. The plots were highly repro ducible. In order to determine the concen tration and temperature of eleclrons doubl probe charactors were measured. The squar of frequency of the oscillations were plotte against to the saturation current of the doubl probes which is proportional to the concen trating of electrons. The result is shown i Fig. 5. The linear relation accords qualita

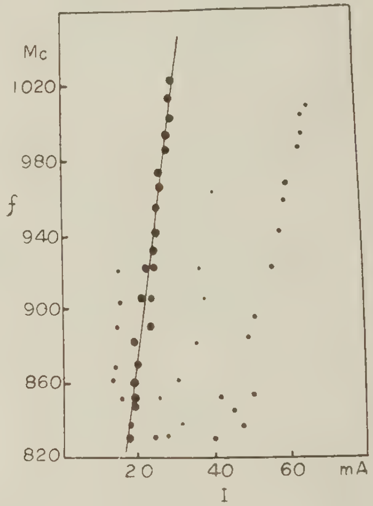

Fig. 4. Plots of frequencies of oscillations *vs* discharge currents on a tube of Merrill-Webb's type. Large circles indicate strong oscillations.

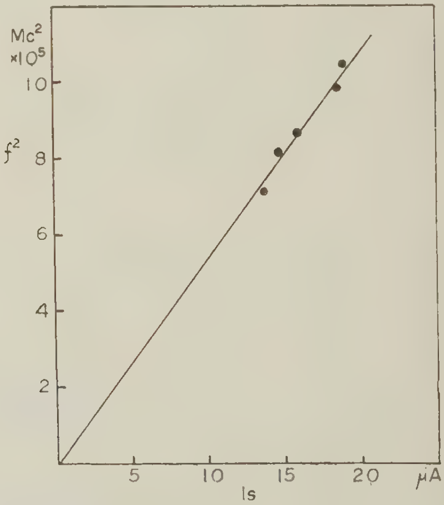

Fig. 5. Square of frequency *vs* saturation current.

tively with Eq. (1). The electron temperature obtained from the double probe measurement was about 18,500°K. Since the ion temperature was not obtained from the double probe measurement, it had to be assumed. Taking the ion temperature as 500°K the concentration of electrons, N, was evaluated as about 6×10^{10}. Eq. (1) gives 2200 Mc which is higher than observed frequency 938 Mc by facter 2.

§ 4. Results with the Tubes of Type B

Diagram of a discharge tube of the type B is shown in Fig. 6. The cathode was an oxide coated type 3 mm in diameter. The gap length and the diameter of the anode were same as the tubes of type A. The diameter of the glass envelope was somewhate larger than that of type A, but the total volume was smaller. The oscillations were detected with the super-regenerative receiver with the aid of a small antenna which was set outside of the discharge tube. Very weak plasma oscillations could be detected, and their frequencies were measured. The plots of frequencies against to the discharge current are reproduced in Fig. 7. In this case too, many oscillations were observed. At the condition that the electrodes were earthed with by-path condensors, the maximum intensity of oscillations was occured at the almost middle region of the gap. Therefore these oscillations did not arise from the anode current. When the antenna was moved away from the wall of the discharge tube, the intensity of oscillation was decreased approximately by the low of inverse square of distance. Since the plasma oscillation does not radiate transverse waves, the antenna would receive electrostatic induction of the oscillation. This experiment shows that for exciting plasma oscillations the existence of probes is not essential. The plots shown in Fig. 7 are qualitatively in accord with the result shown in Fig. 4. A series of oscillations in Fig. 4, however, were made strong by the existence of probes.

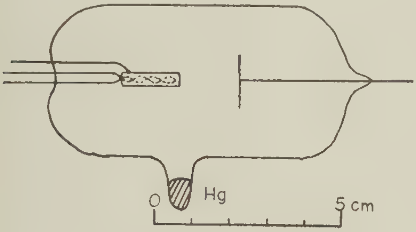

Fig. 6. Discharge tube of type B.

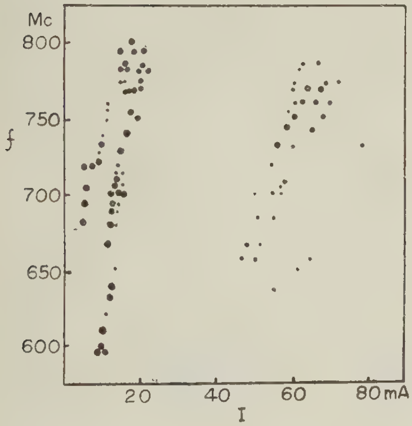

Fig. 7. Plots of frequencies of oscillations *vs* discharge currents on the tube having no probes.

§ 5. Results with the Tubes of Type C

Diagram of a tube of the type C is shown in Fig. 8. A pair of oxcide coated cathodes C_p's and a pair of ring anode W's produced main plasma. A cathod C_b, an accelerating anode A, an anode of the auxiliary discharge G, and an anode disk D formed a electron gun which provided auxiliary electron beams for exciting plasma oscillations. The oscillations were picked up with a movable single probe.

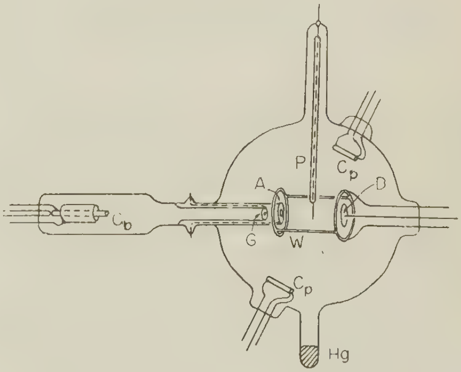

Fig. 8. Discharge tube of type C (Looney-Brown's type).
A: Accelerating electrode, C_p: Cathode for main discharge, C_b: Cathode for auxiliary discharge, D: Anode disk, G: Anode for auxiliary discharge, P: Probe, W: Ringe anode for main discharge.

(i) Without auxiary beams

In the present experiment plasma oscillations could be observed even when no auxiliary beam was introduced. These oscillations were probably excited by primary electrons which maintained the main plasma. The plots of frequencies of the oscillations against to the discharge currents are reproduced in Fig. 9.

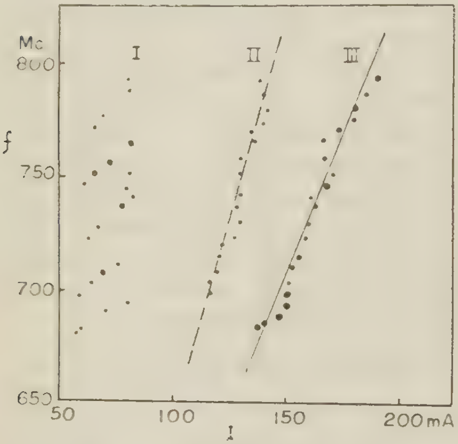

Fig. 9. Plots of frequencies of oscillations *vs* discharge currents on a tube of Looney-Brown's type.

From the plots the oscillations were classified into three groups as indicated in the figure. The first group appeared at discharge currents below 100 mA where the discharge showed visible change. Below this critical discharge current some of low frequency oscillations were often observed. The second and third group appeared above this critical discharge current. When receiver was kept at a fixed frequency, and the discharge current was changed, the second group appeared at lower discharg currents and the third group appeared at higher discharge currents. The oscillations of both groups were stable, whereas those of the first group were unstable.

For the all oscillations the efiect of ion sheaths was examined. The electrodes A and D were biased up to −200 V and thick ion sheaths were produced. However, any change of oscillations were not observed. On the other hand, when a thick ion sheath was produced on the probe, the oscillations belonging to the first and second groups became weaker, but not changed their frequencies. In this case too, the intensities of oscillations of the third group were almost constant.

By changing the position of probe the oscillations were studied. When the probe wa
moved slightly from the center of plasma t
a cathode C_p, the frequencies of oscillation
increased a little and the intensities change
The second group became stronger and th
third group became weaker. When the prob
was moved between the electrodes D and
the first group exhibited intensity maximu
at the central part and those of the secon
and third groups were almost constant throug
the region. The frequencies of the all osci
lations were slightly decreased as the prob
was apart from the center of the gap. B
using the prove and the electrode D as floa
ing double probe system the characteristi
curves were measured. The relation betwee
the square of frequency and the saturatio
current, which is proportional to the concent
ration of electrons, is shown in Fig. 10.

The oscillations of the third group are i
agreement with Eq. (1) qualitatively. There
fore these oscillations seem to correspond t
the oscillations indicated by solid line of Fig
4. The electron temperature determined fro
the double probe measurement was 27800°K
Assuming the ion temperature to be 500°K
the concentration of electrons was evaluate

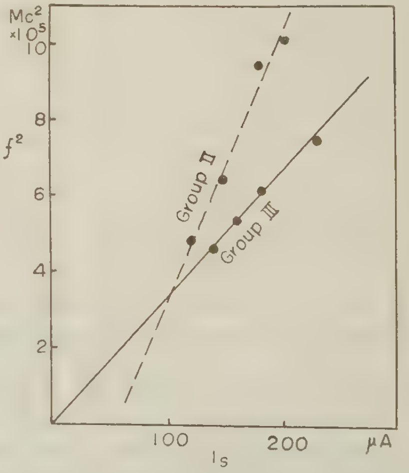

Fig. 10. Square of frequency *vs* saturation current.

as 1.1×10^{11}. With these values Eq. (1) giv
2900 Mc which is higher than observed fre
quency 825 Mc by factor 3. Such descrepanc
ies were recently discussed by Esprester an
Hang[7]. Their interpretation, however, seem
to be not appricable for the localized plasm
oscillations. The present descrepancy probabl

comes from the error of probe measurements.

(ii) With auxiliary beams

An auxiliary electron beam of about 1.5 mA was introduced in the main plasma whose discharge current was between 50 mA and 200 mA. By the auxiliary beam all the oscillations became stronger, but their frequencies did not changed. The auxiliary beam of the present experiment was so small that the main plasma was not disturbed by it and much smaller than the case of Looney and Brown's experiment. Even when ion sheaths on the electrodes A and D were produced by applying a bias potential, oscillations were generally unchanged. When the ion sheaths were appropriate, some of the oscillations exhibited standing waves. Two examples of intensity distributions of the oscillations measured with the movable probe were shown in Fig. 11. One is the case presenting no standing waves and the other case presenting standing waves. For comparisons, the intensity distributions, where the auxiliary beam was absent were also shown by dotted lines in the figure.

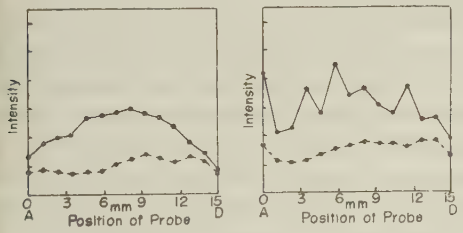

(a) $\begin{cases} f=850\text{ Mc} \\ I=183\text{ mA} \end{cases}$ (b) $\begin{cases} f=740\text{ Mc} \\ I=180\text{ mA} \end{cases}$

Fig. 11. Intensity distribution.

§6. Conclusion

(1) Plasma oscillations were detected from the outside of a discharge tube. It was shown that probes were not essential for the oscillations.

(2) Without the aid of remarkable ion sheaths plasma oscillations were excited.

(3) Frequencies of plasma oscillations were independent to the beam of electrons. Intensities of the oscillations were increased by the beam.

These results suport Bohm and Gross's theory.

(4) Many plasma oscillations having slight different frequencies were detected. However, details of the oscillations are still obscure.

The authors are grateful to Dr. T. Ichimiya of the Electrical Communication Laboratory for continuous interest and for making available to obtain the discharge tubes. The authors are also grateful to Dr. K. Takayama for helpful discussion. This work was financed by the Scientific Research Fund of the Ministry of Education.

References

1) I. Langmuir and L. Tonks: Phys. Rev. **33** (1929) 195.
2) D. Bohm and E. P. Gross: Phys. Rev. **75** (1949) 1851.
3) H. J. Merrill and H. W. Webb: Phys. Rev. **55** (1939) 1191.
4) R. A. Bailey and K. G. Emeleus: Proc. Roy. Irish Acad. **57** (1955) 53.
5) D. H. Looney and S. C. Brown: Phys. Rev. **93** (1954) 965.
6) S. Kojima, A. Shimauchi, S. Hagiwara and Y. Abe: J. Phys. Soc. Japan **10** (1955) 930.
7) A. Esprester and A. Hang: Z. angw. Physik **7** (1955) 180.

JOURNAL OF THE PHYSICAL SOCIETY OF JAPAN Vol. 12, No. 11, NOVEMBER, 1957

On the Phototubes Sensitive to the Wide Spectral Region

By Masao SUGAWARA

Hitachi Central Research Lab. Kokubunji-machi, Kitatamagun, Tokyo

(Received July 20, 1957)

Phototubes sensitive to light in the spectral region from ultraviolet to near infrared were made. It is revealed that these phototubes are suitable for the spectral photometry throughout the spectral region above mentioned.

The light transmission and photoelectric yields of the thin photocathode films such as antimony-caesium, silver-caesiumoxide and bismuth-caesiumoxide were investigated.

§1. Introduction

In, 1938, Goerlich[1] has made a phototube which has a comparatively uniform response to light in the visible spectral region. In this tube, an antimony-caesium or bismuthcaesium film of appropriate thickness is evaporated on a silver-caesiumoxide surface. It is expected that we may have a phototube with the similar character, too, if a half of the inner wall is covered with a semi-transparent antimony-caesium photosurface, and the other half of the wall with an ordinary silver-caesiumoxide photosurface.

If the spectral yields of phototubes prepared in these methodes are comparable to those of the ordinary silver-caesiumoxide phototubes in the reddish spectral region and to those of the antimony-caesium phototubes in the bluish one, they are very useful for spectral photometers, especially for those of self-recording type.

In the phototubes firstly prepared by Goerlich, a certain amount of incident light is absorbed by the upper layer, and the remainder stimulates the underlying photosensitive layer. Photoelectrons generated there have to pass through the upper layer to escape into vacuum.

Thus, it is important to control the thickness and the structure of the upper layer. In this method, however, it is not easy to control them since the interaction between two layers is unavoidable.

In the phototubes prepared in the second method, the photoelectrons can escape into vacuum directly from the photosurface. Of course, the tube characteristics are affected by the thickness of the semi-transparent photosurface. In this second method, however, it can be measured through the optical transmission.

In this point of view, the second method i adopted to prepare a phototube sensitive t the light in a wide spectral region. The co bination of antimony-caesium and silver-caes umoxide photosurfaces (Sb-Ag type), and tha of bismuth-caesiumoxide and silver-caesium oxide (Bi-Ag type) are mainly investigated.

When the semi-transparent photosurface i made of the antimony or bismuth film of th thickness of about 2.0 μg per cm^2, the photo tubes are obtained, which have satisfactoril high responses for spectral photometry in th spectral region from $\lambda 400$ mμ to $\lambda 800$ mμ.

The appropriate thickness of antimony o bismuth film above mentioned was determine by the preliminary experiments in which th light transmission and photoelectric yields o the photosurfaces of various thickness wer measured in the spectral region from $\lambda 400$ m to $\lambda 800$ mμ. Futhermore, from these result some considerations on the structures of photosurfaces and the sources of photoelectric emission are made.

§2. Light Transmissions and Photoelectri Yields of Thin Photosurfaces

(1) *Experimental procedure*

A schematic diagram of the experimenta tube is shown in Fig. 1. A small piece o metal 2 mg in weight are evaporated on th glass plate "b" by resistive heating of tungsten coil "f". The distance between "f and "b" is 10 mm. As a source of caesium a nickel capsule "l" containing a mixture o caesiumchromate and silicon powder is use The tube is sealed onto the pumping syste in such a position that the glass plate lies horizontally, looking down the evaporator. The shield plate "j" slides down on the tube wall to keep clear the portion of the inner wall from metal evaporation. The metal is wholly evaporated in a vacuum of the order of 10^{-7} mm Hg. The average rate of evaporation is estimated at about 0.2 mg per minute. The thickness of the evaporated film is calculated by the geometrical arrangement of the evaporator and the glass plate.

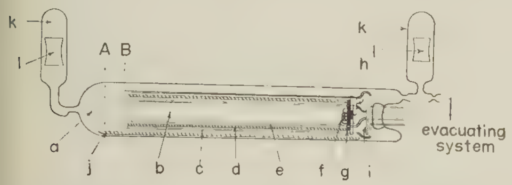

Fig. 1. Schematic diagram of experimental tube a, glass envelope; b, glass plate; c, Ni support; d, Al evaporated; e, anode; f, *W* small helical coil; g, aquadac film; h, cathode lead; i, mica plate; j, movable Ni plate shield; k, side tube; l, caesium source; AB, reference part in transmission measurements.

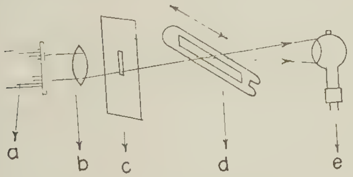

Fig. 2. Arrangements for transmission measurements a, monochrometer; b, lens; c, aperture; d, experimental tube: e, phototube.

In the cases of bismuth and silver, the film formed on the glass plate "b" is oxidized to some extents. Caesium is liberated in the side tubes by eddy current heating. The tube, together with the side tubes, is then sealed off from the vacuum system. The light transmission in this stage is measured. Then the sensitization with caesium is done by heating the whole system of tube at 100°~110°C in a thermostatt. The transmission and photoelectric yields of these tubes are measured in both cases of the light of λ380~λ800 mμ is incident on the glass and photosurface sides of the cathods.

The arrangement of apparatus used in the transmission measurment is diagramatically shown in Fig. 2. The incident light is focused to a rectangle of 8×0.5 mm on the photocathode surface. The transmission is defined as the ratio of the light intensity passed throgh the glass envelope, photosurface and glass plate to that through only the glass envelope, or the light transmitted through the portion of the tube indicated by AB in Fig. 1. The monochrometer and the photocurrent amplifier used in these measurements are the same as described in the previous paper.[2] The photoelectric measurement is also made in the same arrangement, applying the voltage to the experimental tubes. To simplify the process of experiment, the slit of the monochrometer is maintained at a constant width of 0.08 mm. The relative energy distribution in this case of the monochrometer, measured with a thermopile, is shown in Fig. 3.

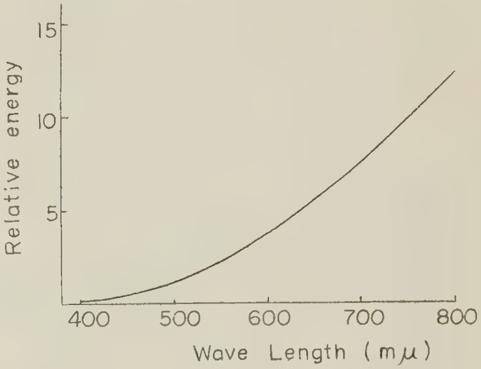

Fig. 3. Energy distribution of light from the monochrometer with a constant slit width.

In this paper, transmission and the photoelectric yields is plotted against the thickness of initially evaporated metal film expressed in the unit of μg per cm², for it is very difficult to measure accurately the thickness of such a photosurface which has a very complicated structure.

(2) *Results of experiments*

In antimony film, a distinct boundary line is observable at the thickness of about 10 μg per cm², the thinner portion being coloured blownish, while the thicker portion greyish.[3] The obtained results of the transmission of the antimony film are shown as dotted curves in Fig. 4. The appearance of the antimony-caesium photosurface is different from that of antimony itself. In the portion thicker than 40 μg per cm², the interference fringes appear, instead of a distinct boundary. In Fig 4, the transmission of the antimony-caesium film for the light of shorter wave length decreases logarithmically with the film thickness, while that for longer wave length varies periodically. Similar results are also obtained by Wallis.[4]

In Figs. 5 and 6, the photoelectric yields of the antimony-caesium photosurfaces are plotted against the film thickness. In case of th light incident on the glass side, the curve ha a peak at about 2 μg per cm² thick. (Fig. 5) In case of light incident on the photosurfac side, the yield is almost constant in the portio thicker than 6~8 μg per cm² (Fig. 6). How ever, in both cases the photoelectric yield falls abruptly at about 1.0 μg per cm² thic as shown by chain lines, and the fluctuatio of the photocurrent is observed. But wher a glass plate covered with a transparent conductive film, neither abrupt change nor fluctuation of the photocurrent is observed.

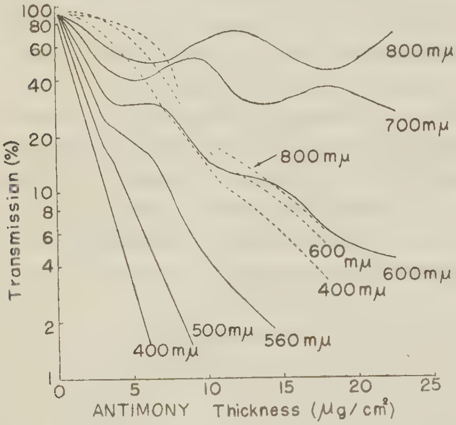

Fig. 4. Transmission of antimony and antimony-caesium films.
···· antimony film, —— antimony-caesium film.

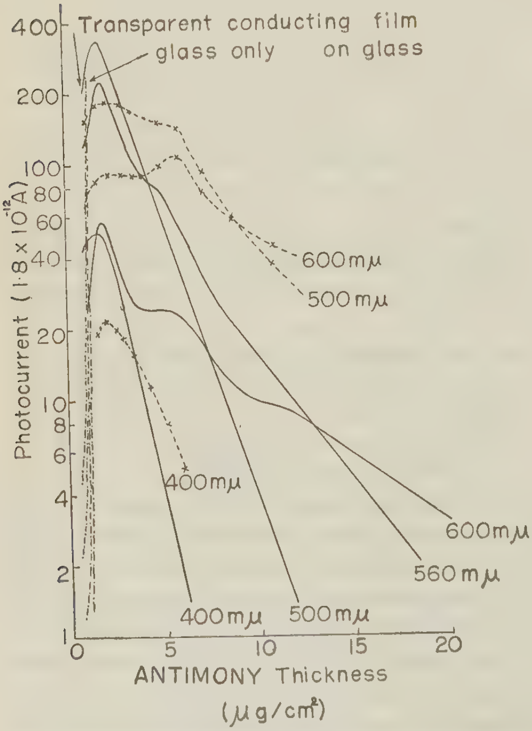

Fig. 5. Photoelectric yields of the antimony-caesium film for the light incident on the glass side.
—— usual case ···· excess caesium case.

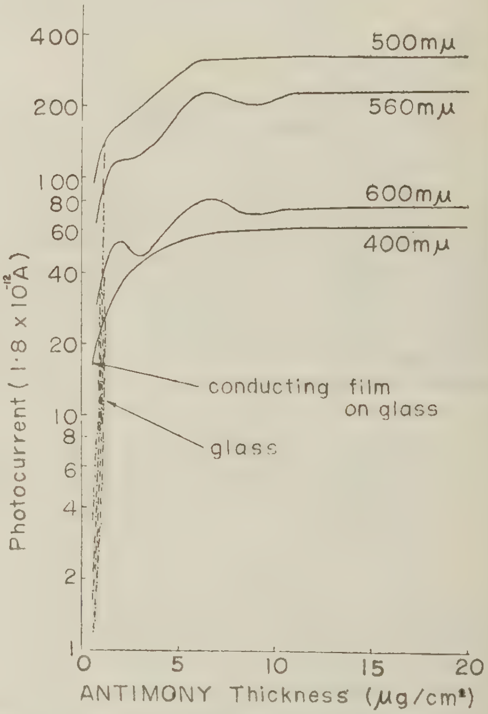

Fig. 6. Photoelectric yields of the antimony-caesium film for the light incident on the photosurface side.

Dotted curves in Fig. 5 are obtained when the caesium more than usual is evoporated into the experimental tube. It is interesting that the curve for λ600 mμ is higher than that obtained in usual case.

In Fig. 7, the transmission of silver film for the light of λ600 mμ is shown. Dotte curves "a" and "b" correspond to that befor and after the oxidation, and the solid curves to the completed silver-caesiumoxide film, re spectively. The transmission increases in ac companying with the progress of oxidatio of silver, and decreases as the silver caesium-oxide film is formed.

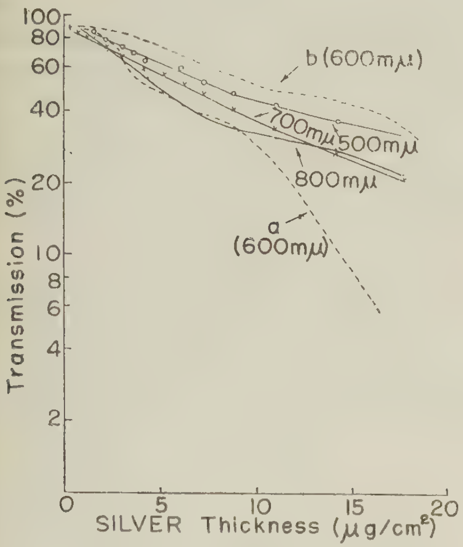

Fig. 7. Transmission of silver and silver-caesium-oxide films.
a, silver film (for λ600 mμ); b, after oxidation (for λ600 mμ); solid curves, silver-caesiumoxide fiilm.

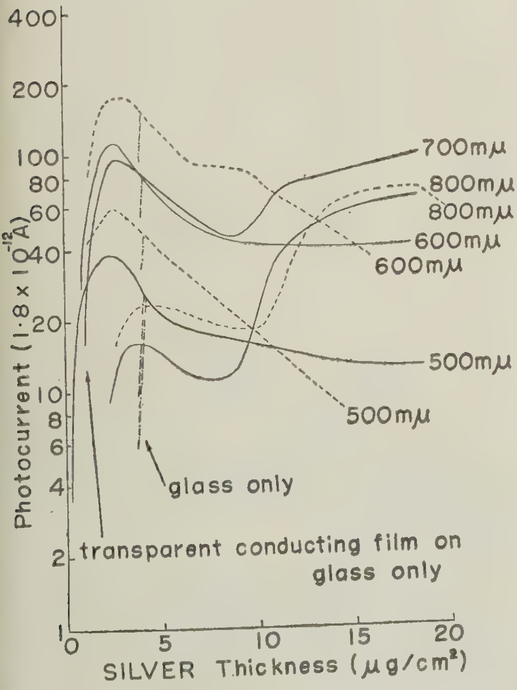

Fig. 8. Photoelectric yields of the silver-caesium-oxide film.
—— light incident on the photosurface side:
.... light incident on the glass side.

In Fig. 8 the photoelectric yields of silver-caesiumoxide film are plotted against the film thickness. The yield decreases abruptly at the thickness of about 4 μg per cm² as shown by chain lines. In the portion thinner than this critical thickness, the photocurrent fluctuate similarly just as in case of antimony-caesium.

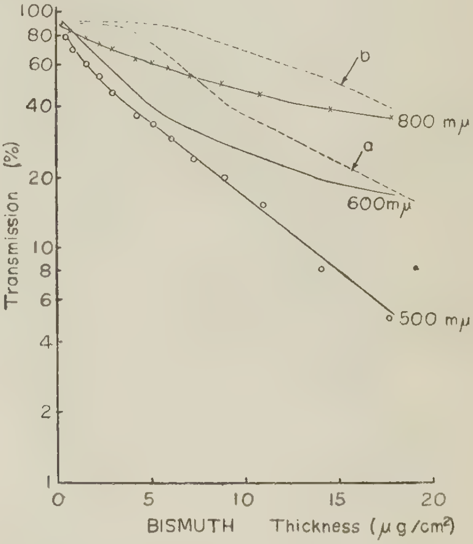

Fig. 9. Transmission of bismuth and bismuth-caesiumoxide films.
a, bismuth film (for λ600 mμ)
b, after oxidation (for λ600 mμ)
solid curves, bismuth-caesiumoxide film.

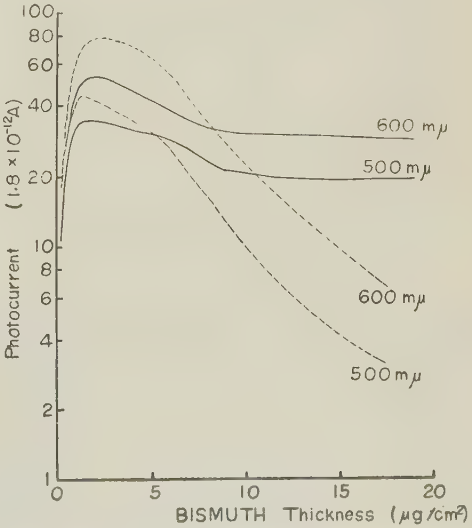

Fig. 10. Photoelectric yields of bismuth-caesium-oxide films.
—— light incident on the photosurface side;
.... light incident on the glass side.

In the thicker portion, the yields decreases with the film thickness for the light of shorter wave length, while for the longer wave length light it begins to increase steeply at the thickness of about 9 μg per cm^2.

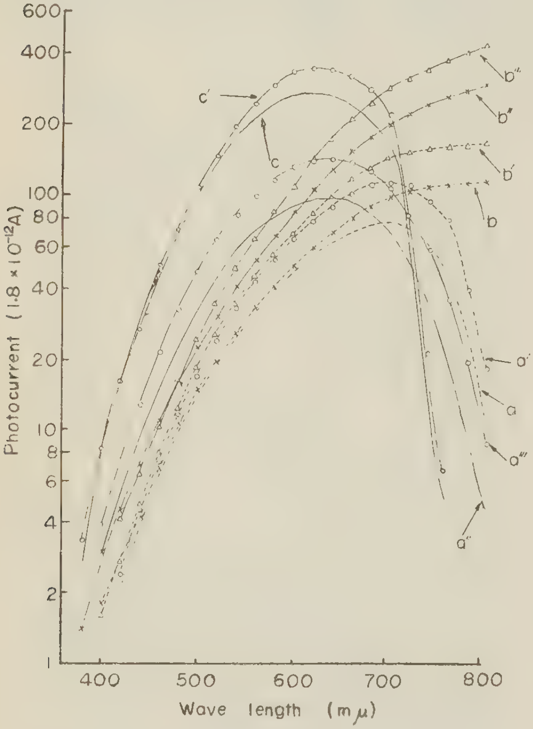

Fig. 11. Spectral responses of semi-transparent photosurfaces.
a, silver-caesiumoxide, 6 μg per cm^2 thick, before silver re-evaporation, light incident on the photosurface side; *a'*, ditto, light incident on the glass side; *a''*, after silver re-evaporation, light incident on the photosurface side; *a'''*, ditto, light incident on the glass side; *b*, *b'*, *b''*, *b'''*; silver-caesiumoxide, 12 μg per cm^2 thick, refering respectively as above; c, bismuth-caesiumoxide, light incident on the photosurface side; c', ditto, light incident on the glass side.

When a transparent conducting film was formed previously on the glass plate, the yield, having a maximum at about 2 μg per cm^2, does not show any abrupt change and fluctuation. In this case also, the yield for the light of λ800 mμ is small in the thinner portion. Dotted curves " a " and " b " in Fig. 9 represent the transmissions of the bismuth film before and after the oxidation, respectively. In Fig. 10, the yields of the bismuth caesiumoxide photosurface are plotted against the film thickness. The variation of the yield with the film thickness is similar to that of th silver-caesiumoxide photosurface.

In Fig. 11, the spectral response of sem transparent silver-caesiumoxide photosurfac and that of semi-transparent bismuth-caesium oxide one are shown. The sensitization b re-evaporation of silver as already Asao[5] ha developed is also made. The yield of a thi ner silver-caesiumoxide photosurface for th red and the infrared region is also small eve after the silver re-evaporation.

§ 3. The Phototubes Responsible for Wid Regions of Spectra

From the results described in the precee ing section, it is infered that antimony-caesium

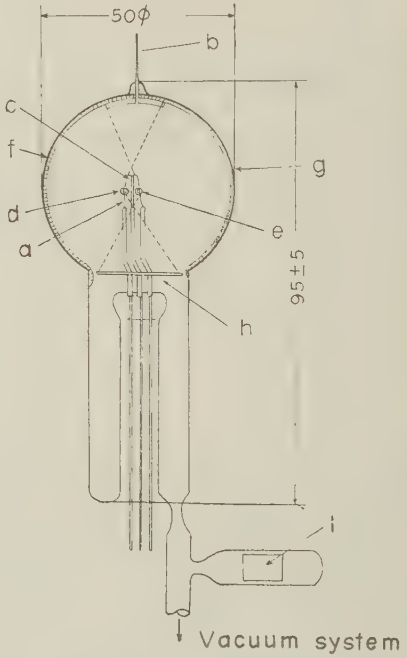

Fig. 12. Schematic view of the tube construction a, anode; b, cathode lead; c, Ni plate; d, silve head; e, antimony bead; f, silver-caesiumoxid photosurface; g, semi-transparent antimony caesium photosurface; h, mica plate; i, caesiur source.

or bismuth-caesiumoxide photosurface, n silver-coesiumoxide one, should be used as semi-transparent photosurface. For, the la is not sensitive to the reddish light in th thinner portion.

The schematic view of the phototube no prepared is shown in Fig. 12. Small amoun of antimony (or bismuth) and of silver a mounted separately in tungsten helical coils situated both sides of nickel circular plate of 8 mm in diameter. An ordinary silver-caesium-oxide photosurface is formed on a nearly half of the inner wall of the globe, while on a remaining half, a semi-transparent antimony-caesium (or bismuth-caesium) film are formed respectively. By measuring the light transmission, the evaporated amount and consequently, the film thickness is controled. The typical examples of the spectral yields of the Sb-Ag type phototubes prepared in this manner and those of ordinary phototubes are shown in Fig. 13, and those of Bi-Ag type phototubes in Fig. 14. It has been confirmed that phototubes having a response such as "a" and "a′" in Fig. 13 are suitable for spectral photometry in the spectral region from λ400 mμ to λ800 mμ. The curve "a′" is more uniform than curve "a", with the high yield in the range between λ600 mμ to λ700 mμ. This is considered to be due to the excess of caesium. But the more excess caesium does not give a better result, lowering the yield over all the spectral region. Curves "b" and "c" in Fig. 13 correspond to the spectral response when the antimony film is too thin and too thick respectively. The response shown in Fig. 14 is superior in its uniformity, but inferior in the yield, especially in the ultraviolet region, to the curves "a" and "a′" in Fig. 13.

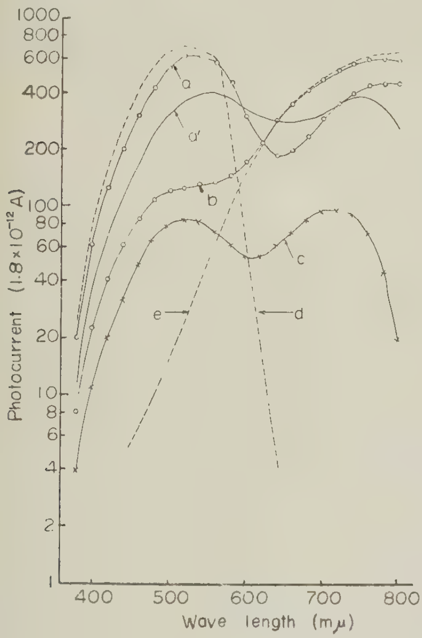

Fig. 13. Spectral yield variation due to the thickness of semi-transparent antimony-caesium photosurface.
a, appropriate thickness and moderate caesium; a′, appropriate thickness and excess caesium; b, thinner thickness; c, thicker thickness; d, antimony-caesium phototube (30 μA/lumen); e, silver-caesiumoxide phototube (30 μA/lumen).

In Fig. 15, the relation between the photocurrent and the flux of incident light are shown in the case of the Sb-Ag type phototubes. In this figure it is noticeable that the proportionality of the photocurrent to the illuminating light flux is well satisfied in the range less than 10^{-9} A. Any abnormal effects such as time lag described in the previous paper[9)] are not observed.

The deviation from proportionality in curves "A" and "B" is due, as Widmaier and Engstrom[6)] have pointed out, to the high resistivity of the semi-stransparent antimony-caesium film. When the inner surface of the glass globe is covered with a transparent conductive film, the proportionality holds in the photocurrent range larger than 10^{-9} A. as shown by "C" and "C′" in Fig. 15.

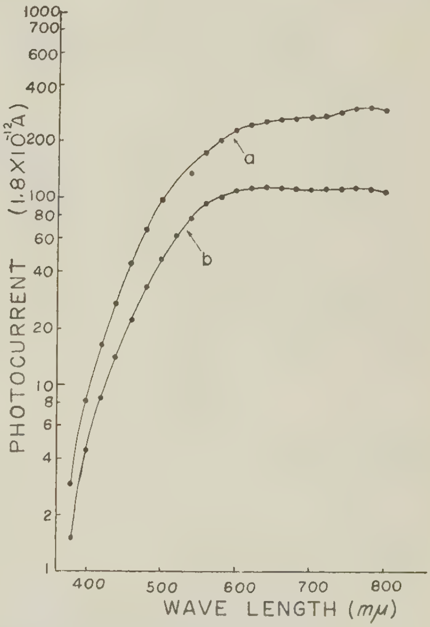

Fig. 14. Spectral yield variation due to the thickness of semi-transparent bismuth-caesiumoxide photosurface.
a, moderate thickness; b, thicker thickness.

In Fig. 16, current-voltage curves for light of various wave length are shown. The hump at about 15 volts is due to the secondary electrons produced by the photoelectrons which return to the cathode. Such discontinuities, as reported by Gordon-Smith[11] and also by Taylor[8] are not observed. The phototubes of Bi-Ag type also have the similar characteristics with those of Sb-Ag type.

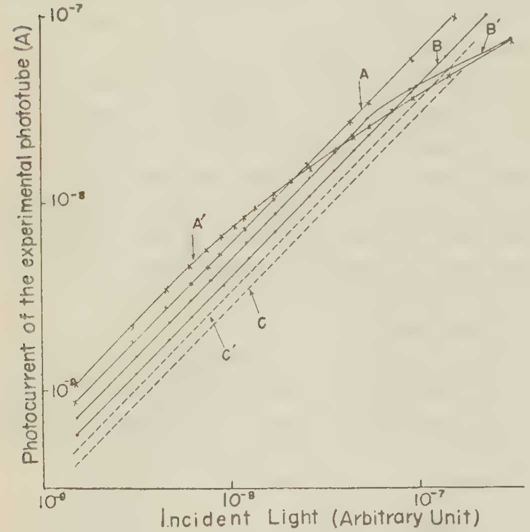

Fig. 15. Current-incident light curves of the Sb-Ag type phototubes.
A, phototube No. 1, for λ720 mμ; A', for λ520 mμ;
B, phototube No. 2, for λ720 mμ; B', for λ520 mμ;
C, phototube No. 3, for λ720 mμ: C', for λ520 mμ.

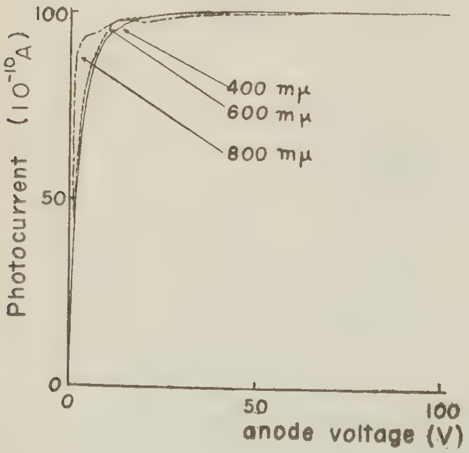

Fig. 16. Current-voltage curves of the Sb-Ag type phototube.

After all it can be concluded that the phototubes now prepared have the characteristics suitabe for spectral photometry in the region from λ400 mμ to λ800 mμ. If the envelope is made of fused silica instead of glass, thes
phototubes are used in the spectral regio
from λ200 mμ to λ1000 mμ.

§ 4. Some Considerations on the Thin Photo cathode

According to Hammer,[9] when the lig
with wave length λ passes through no
absorbing film on a glass plate, transmissio
maxima and minima arise at the thickness
satisfying the following conditions;

$$nd=(2\,\mathrm{m}+1)\,\frac{\lambda}{4}\,,\quad \text{for minima}$$

$$nd=(2\,\mathrm{m}+2)\,\frac{\lambda}{4}\,,\quad \text{for maxima}\quad \mathrm{m}=0,1,2,\cdot\cdot$$

where n is the refractive index of the mediu
and d, the thickness. According to Wallis,
n of antimony-caesium film for the light o
λ800 mμ is 1.8. Considering the antimony
caesium film as a non-absorbing film for th
longer wave length light, the thicknesses co
responding to the maxima and minimum
the upper most curve (for λ800 mμ) in Fig.
are calculated to be $d=110$ and 330 mμ fo
minima, and $d=220$ mμ for maximum, an
these coincide well with those obtained b
Wallis. By comparing these values with th
corresponding thickness of initially evaporate
antimony film of 6.5, 19, 13 μg per cm^2, re
spectively, it is known that the thickness o
antimony film increases to 11 times of th
initial value after it turns into the antimony
caesium film. Using this factor 11, the ab
sorption coefficient of antimony-caesium fo
the light of λ400 mμ is determined as 11×10
cm^{-1} from Fig. 4. This is somewhat large
than Wallis' value 4×10^5 cm^{-1} for the lig
of 404 m, and Burton's[10] 4.7×10^5 cm^{-1} for th
ultraviolet light. But the difference is tole
able as the reflection is not taken into ac
count in our case. It is well known that th
films of silver, antimony and bismuth ar
composed of separate aggregates. As the fil
thickness increases, the separate aggreate
grow in size and merge into together.[3] A
the results, the discontinuous change in th
resistivity, photoemission and other propertie
occurs. In antimony-caesium film this chang
takes place at about 10 μg per cm^2 thic
while in the antimony-caesium film at abou
1 μg per cm^2 thick, the ratio is 10. This
in a good agreement with the value 11 calc

lated from the transmission measurement.

Mayer and Nossek[11)] measured the variation of the photoelectric yield with film thickness for potassium. The yield was independent on the film thickness in the portion thicker than 3∼4 atom layers. From this fact, they concluded that the photoelectric effect of the potassium is the surface effect. In Fig. 6, the yield of the antimony-caesium is almost constant in the portion thicker then 6∼8 μg per cm^2 (90∼120 mμ).

This result seems to show that, for antimony-caesium, the volume photoelectric effect is concerned.

As to the effect of excess caesium for the antimony-caesium yield in Fig. 5 and 13, it is presumed that the atoms of caesium in excess migrate into the Cs_3Sb film and form the emission sources which are rather sensitive for the light of longer wave length.

The variation of curves for the light incident on the photosurface side in Figs. 8 and 11 are explained as follows. In the thinner portion, by oxidation and reaction with caesium, the silver or bismuth aggregates grow in size. The obtained photosurface in this portion is coarse-grained, accompanying with the irregularities of the film lattice which are greatest at some thickness. The photoelectrons are generated chiefly in these irregular portion of lattice and the maximum of the yield appears.

In the thicker portion, the film is composed of a continuous layer and the variation of the photoelectric surface with film thickness is not so large as in the thinner portion. So the photoelectric yield changes more gradually with the film thickness in the portion thicker than about 10 μg per cm^2 in Figs. 8 and 11.

The steep rise of the yield for the longer wave length light at the thickness of 9 μg per cm^2 in Fig. 8 is due to the silver layer underlying the caesimoxide layer. It is presumed that the active centers of photoelectrons for the longer wave length are formed mainly on the intricated boundaries between silver and caesiumoxide.

The large absorption coefficient of antimony-cresium for the shorter wave length light in Fig. 4 is due to lattice absorption.[4)10)] The transmission of the silver-caesium and bismuth-caesiumoxide in Figs. 7 and 9 decreases with film thickness more gradually than those of antimony-caesium above mentioned. This means that the absorption of light in the former two is small and may not be thought as lattice absorption. This is in agreement with above considerations as to the sources of photoelectrons.

The photoelectric yield for the light incident on the glass side is mainly dependent on the depth where the photoelectrons are generated, but in the silver-caesiumoxide and bismuth-caesiumoxide, it seems to be affected also by the film structure.

Summary

The light transmission and the photoelectric yield of the antimony-caesium, bismuth-caesiumoxide and silver-caesiumoxide photosurface of various thickness were measured in the spectral region from λ400 mμ to λ800 mμ. Applying these results, the photoelectric tubes which are highly sensitive to the light in the wide spectral region were prepared. These tubes can be satisfactorily used in the spectral photometry. It is concluded that the yield variation with thickness is caused by the change in film structure.

The writer wishes to express his gratitude to Dr. Hamada, Dr. Tadano, Dr. Nakamura, Messrs Kiuchi and Makino for their kind guidance throughout this work. He also wishes to thank Messrs. Takei, Fukushi, Kobayashi, Miss Kumasaka and Miss Saito for their helpful assistance.

References

1) P. Goerlich: Z. f. Phys. **109** (1938) 374.
2) M. Sugawara: J. Phys. Soc. Japan **11** (1956) 169.
——: J. Phys. Soc. Japan **11** (1956) 271.
3) W. Lotmar: Helv. Phys. Acta **18** (1945) 369.
H. Murman: Z. f. Phys. **54** (1929) 741.
M. Rome: J. appl. Phys. **26** (1955) 166.
H. Levinstein: J. appl. phys. **20** (1949) 306.
4) G. Wallis: Ann. d. Phys. **17** (1956) 401.
5) S. Asao: Proc. Phys. Math. Soc. Japan **22** (1940) 448.
6) W. Widmaier and R. W. Engstrom: RCA Rev. **16** (1955) 109.
7) J. S. Preston and G. W. Gordon Smith: Brit. J. appl. **6** (1955) 329.
8) A. H. Taylor: G. E. Rev. **52** (1949) 43.
9) K. Hammer: Z. Tech. Phys. **24** (1943) 169.
10) J. A. Burton: Phys. Rev. **72** (1947) 531.
11) H. Mayer and R. Nossek: Z. f. Phys. **138** (1954) 33.

12) R. S. Sennett and G. D. Scott: J. O. S. A. **40** (1950) 203.
T. A. McLanchlan, R. S. Sennett and G. D. Scott: Canadian, J. Research **28** (1950) 530

13) C. T. Keogh and A. H. Weber: J. appl. Phy **19** (1948) 1077.

JOURNAL OF THE PHYSICAL SOCIETY OF JAPAN Vol. 12, No. 11, NOVEMBER, 1957

A Study on the Attenuation of Shock Waves due to Obstacles in the Passage

By Ryuma KAWAMURA and Haruo KAWADA

Institute of Science and Technology, University of Tokyo

(Received June 14, 1957)

Results are reported of a shock-tube experiment on the retardation of shock waves due to obstacles in the passage. A one-dimensional analysis is applied on the flow field resulting from the interaction of shocks and obstacles, and a theoretical relation between the attenuation of shocks and the resistance of the passage is derived. The drag coefficients of a series of simple bluff obstacles used in the experiment are estimated. Comparisons with available steady-flow data are made along with some discussions.

§ 1. Introduction

It has been recognized that a plane shock front is highly stable as it propagates through a stagnant gas in a uniform channel. Thus, when it hits an obstacle placed in the passage, the propagating front gets once curved as it is transmitted beyond but restores the plane shape in a short distance of travel downstream which we shall call "the formation distance."

On the other hand, with the advent of the shock front an unsteady flow is induced around the obstacle accompanied by a complicated system of waves produced by multiple reflections and interactions. But these waves decay rapidly and the flow reaches a steady state after a short time interval. In the course of these processes, flow separation (for bluff obstacles) and/or choking (for large-blockage ones) are considered to occur.

The shock front transmitted past the obstacle is weaker than the incident one and is retarded with respect to the latter. The flow field suffers momentum loss due to the resistance of the obstacle in the unsteady and steady stages. Apparently the retardation of the shock must balance with this momentum loss, and especially, the attenuation in the ultimate state with the steady-flow resistance of the obstacle. This condition will be form lated in the next section on the basis of on dimensional wave theory.

It was intended in the present experiment investigate the effect of simple bluff obstacl on the attenuation of weak plane shocks p duced in a shock tube and also to check t analytical theory to be developed in the ne section.

The interaction of a plane shock wave w simple-shaped obstacles has been treated fr a different angle, i.e. as the diffraction p blem, by various authors, experimentally w shock tubes4) as well as theoretically. these studies, attentions are given to t two-dimentional flow field behind the sho wave as it passes over the surface of t body. On the other hand, the interaction a shock with wire screens or porous pla placed normally in the passage has recen been investigated experimentally by seve researchers.1)2)6) This problem is essentia the same with the present one, and the resu obtained are parallel. The present one m be regarded as a microscopic model of t phenomenon. The attenuation of a shock p pagating through an empty channel is a rat old problem and has already been studied every detail. The attenuation is evidently caused by the wave system generated by the growth of wall boundary layers, and must balance with the momentum loss due to the wall friction. Some theories have been presented with reasonable experimental verifications.[3)]

§ 2. Theory

Sufficiently long after the incidence of the shock front on the obstacle, as stated above, a steady flow is established around it. The transmitted shock front is situated far downstream and is plane and uniform. The reflection of the incident shock at the fore surface of the obstacle forms an upstream-propagating shock front. It is then plane and uniform, too. Thus the flow field in the ultimate state is as shown in Fig. 1 (a), where S_R and S_T denote, respectively, the reflected and transmitted shocks, and C the contact layer consisting of the particles passed by the waves during the transient stage. The flow regions (I), (II) and (IV) are those of uniform states behind the incident, transmitted and reflected shocks, respectively, and (0) is the region of rest. (III) is the region downstream of the obstacle and is regarded as uniform.

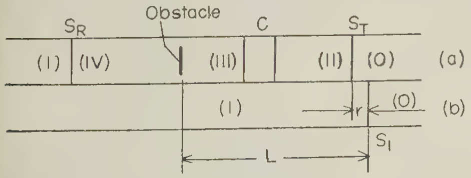

Fig. 1. Idealized model of flow field.
(a) Obstacle present, (b) Obstacle absent.

In the absence of the obstacle, the flow field at the same instant consists, as in Fig. 1 (b), merely of two uniform regions (I) and (0) separated by the undisturbed incident shock S_I.

The regions (IV) and (III) are connected by the steady flow past the obstacle. The obstacle exerts resistance D on the flow. Let us denote density, flow velocity, pressure and specific enthalpy with ρ, u, p and H, respectively. ($H=3.5\,p/\rho$ for air.) Let the physical quantities of the regions (0), (I). (II), (III), and (IV) be designated with subscripts 0, 1, 2, 3 and 4, respectively. The conservation laws of mass, momentum and energy can be expressed as follows:

$$\rho_4 u_4=\rho_3 u_3, \tag{1}$$

$$p_4+\rho_4 u_4^2=p_3+\rho_3 u_3^2+D/A\,, \tag{2}$$

$$u_4^2/2+H_4=u_3^2/2+H_3\,, \tag{3}$$

where A is the cross-sectional area of the channel.

Pressure and velocity are invariant through the contact layer, i.e. $p_3=p_2$ and $u_3=u_2$. So the above equations are transformed into the following forms including only quantities of (IV) and (II):

$$p_4+\rho_4 u_4^2=p_2+\rho_4 u_4 u_2+D/A\,, \tag{4}$$

$$\rho_4 u_4^3+7p_4 u_4=\rho_4 u_4 u_2^2+7p_2 u_2\,. \tag{5}$$

Now let all the physical quantities be made non-dimensional by dividing them with those in the region (0). (For the case of velocity u we make it non-dimensional by dividing with the speed of sound in (0), a_0.) Thus

$$\tilde{p}_i\equiv p_i/p_0,\quad \tilde{\rho}_i\equiv \rho_i/\rho_0,\quad \tilde{u}_i\equiv u_i/a_0\,,\cdots.$$

We get from Eqs. (4) and (5)

$$\tilde{p}_4+1.4\tilde{\rho}_4\tilde{u}_4^2=\tilde{p}_2+1.4\tilde{\rho}_4\tilde{u}_4\tilde{u}_2+1.4\tilde{D}\,, \tag{6}$$

$$\tilde{\rho}_4\tilde{u}_4^3+5\tilde{p}_4\tilde{u}_4=\tilde{\rho}_4\tilde{u}_4\tilde{u}_2^2+5\tilde{p}_2\tilde{u}_2\,, \tag{7}$$

where $\tilde{D}\equiv D/(\rho_0 a_0^2 A)$.

Next, let us denote the pressure ratio across a shock with the shock Mach number M with $P(M)$, the density ratio with $R(M)$, and the velocity behind it divided by the speed of sound ahead of it with $U(M)$. M is the ratio of the propagation speed of the shock to the speed of sound ahead of it, and is a parameter representing the shock strength. Let the shock Mach number of S_I, S_R and S_T be M_I, M_R and M_T. Moreover, abbreviations such as P_R, R_R, P_T, etc. are used here for $P(M_R)$, $R(M_R)$, $P(M_T)$, etc. It follows from the definitions that

$$\tilde{p}_4=P_R P_I,\quad \tilde{\rho}_4=R_R R_I,\quad \tilde{u}_4=U_I-U_R A_I\,,$$
$$\tilde{p}_2=P_D\,,\quad \tilde{u}_2=U_D\,,$$

and Eq. (6) and (7) are rewritten in the following forms:

$$F_1(M_R,M_T;M_I)=\tilde{D}: \tag{8}$$

$$P_R P_I+1.4R_R R_I(U_I-U_R A_I)^2$$
$$=P_D+1.4R_R R_I(U_I-U_R A_I)U_D+1.4\tilde{D}\,,$$

$$F_2(M_R,M_T;M_I)=0: \tag{9}$$

$$R_R R_I(U_I-U_R A_I)^3+5P_R P_I(U_I-U_R A_I)$$
$$=R_R R_I(U_I-U_R A_I)U_D^2+5P_D U_D$$

Eliminating M_R from (8) and (9), we get a relation between M_T and $\tilde{D}$ as

$$F_3(M_T;\, M_I)=D\,, \qquad (10)$$

which, in practice, can only be solved by graphical calculations for fixed values of M_I. Now, define "the attenuation rate" of the shock, m, by

$$m=(M_I-M_T)/M_I\,,$$

and the drag coefficient of the obstacle referred to the cross-sectional area of the tube, C_D, by

$$C_D=D/(1/2\cdot\rho_4 u_4^2 A)\,.$$

Then Eq. (10) can be reduced to the form:

$$F(m, C_D;\, M_I)=0\,. \qquad (11)$$

This relation between m and C_D was calculated for the strengths of the incident shock $\xi=0.6$, 0.5 and 0.4 ($M_I=1.25$, 1.36 and 1.51, respectively), where ξ is the reciprocal of the shock pressure ratio, i.e. the ratio of the pressure ahead of the shock to that behind it. The result of the calculation is shown in Fig. 2.

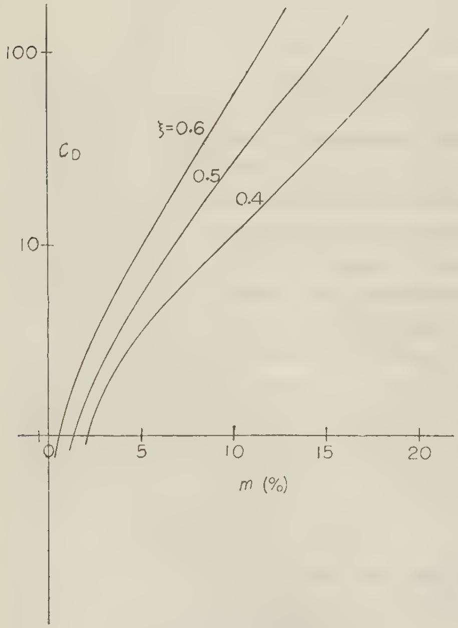

Fig. 2. Relation between m and C_D.

The transcendental equations (8) and (9) are reduced to linear ones in the limiting case where the blockage ratio of the obstacle, $b=B/A$, is either very small or very near to unity, B being the blockage area of the obstacle.

(i) The case $b\ll 1$:

S_R is slightly stronger than a sound wave, and S_T slightly weaker than the incident shock Put

$$M_R=1+\varepsilon_1 \qquad (12)$$

$$M_T=M_I(1-\varepsilon_2)\,. \qquad (13)$$

Further, we may put $C_D=C_{D0}\times b$, wher C_{D0} is the free-stream drag coefficient of th obstacle. Second- and higher-order terms o ε_i being neglected in Eq. (8) and (9), w obtain linear equations for ε_1 and ε_2, and thence, the following numerical results:

ξ	0.6	0.5	0.4
$\varepsilon_1/C_{D0}b$	0.033	0.076	0.182
$\varepsilon_2/C_{D0}b$	0.0125	0.0196	0.0290

(14)

(ii) The case $1-b\ll 1$:

In this case the flow is considered to b always choked. S_R is slightly weaker tha the normal reflection of the incident shock, i.e

$$M_R=M_N-\varepsilon_1\,, \qquad (15)$$

and S_T slightly stronger than a sound wave i.e.

$$M_T=1+\varepsilon_2\,, \qquad (16)$$

where M_N is determined by M_I and is some what smaller than the latter. The flow Mac number in the region (IV), M_4, is decided b assuming the isentropic contraction of th flow from (IV) to the throat section wit a contraction ratio (1–b). Thus

$$(U_I-U_R A_I)/A_R A_I=M_4=M_{cr}(b)$$

Putting the expressions (15) for M into th above equation and neglecting higher-orde terms of ε_i, we obtain the following results

ξ	0.6	0.5	0.4
$\varepsilon_1/(1-b)$	0.45	0.49	0.64

(17)

Then from Eq. (9) ε_2 is calculated as

ξ	0.6	0.5	0.4
$\varepsilon_2/(1-b)$	2.16	3.20	4.96

(17′)

§ 3. Experiment

The experiment was performed by the us of a shock tube with a 5 cm×15 cm cross section.[6] A test chamber of 60 cm in lengt is situated about 3 cm downstream of the dia phragm station. A 50 cm×15 cm glass obser vation window presents a wide field of view convenient for schlieren photography employed in the experiment.

A 5 mm-thick brass plate was inserted horizontally in the test-chamber dividing it into the upper and lower channels, which are 10 cm and 4.5 cm, respectively, in heights. The obstacles were set at the upstream end of the upper channel, while nothing was placed in the lower channel. Thus the disturbed transmitted and undisturbed incident schocks could be observed simultaneously, and the retardation lengths measured directly from the photographs.

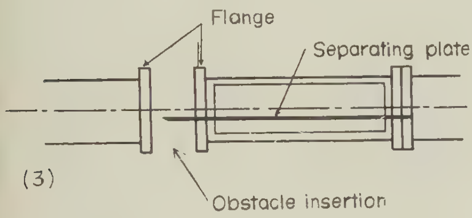

Fig. 3. Test section.

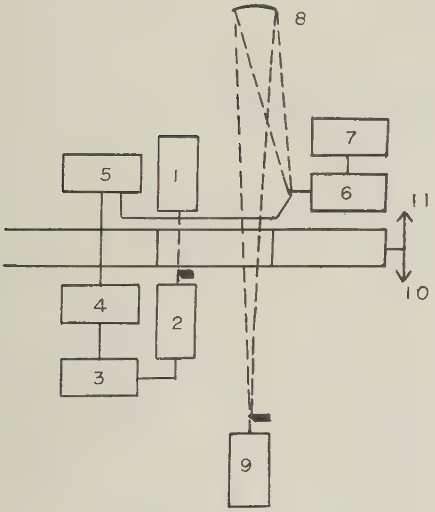

Fig. 4. Experimental arrangement.

1. Photo-screen light source
2. Photo-multiplier
3. Thyratron relay
4. Delay circuit
5. Spark trigger
6. Spark unit
7. High-tension supply
8. Cocave mirror
9. Camera
10. To pressure gauge
11. To vacuum pump

The high-pressure chamber was kept at atmospheric pressure and the low-pressure channel was evacuated with a 1 HP vacuum pump to an appropriate pressure, by which the strength of the incident shock was regulated. The shock strength used in the experiment was between 0.6 and 0.4 in terms of ξ, the reciprocal of pressure ratio.

For schlieren photography use was made of two kinds of spark light sources. The one is an ordinary 15 KV single-shot unit, and the other is a newly-designed 8 KV "multiflash" unit capable of giving several shots at a repetitive frequency of about 5 KC.⁷⁾ A photo-screen was set through the glass window at the upstream end of the lower channel, and the incident shocks were picked up with a photo-multiplier, the output signal of which triggered the spark light source through thyratron relays and a pulse-delay circuit. Wave-speed measurements were not made for individual snapshots, and the shock strengths were calculated from the initial pressure ratios across the diaphragm according to the previous calibrations. The schlieren axis was set in most cases at 40 cm to 45 cm downstream of the obstacle position. The field of view was 15 cm to 25 cm in diameter. Some photographs were also taken in the field 10 cm to 20 cm downstream in order to observe the formation process of plane fronts.

Table I. List of obstacles.

No.	size
	(Circular cylinders)
1	40 mm
2	58 mm
3	25 mm × 3 (row)
	(Normal plates)
4	40 mm
5	58 mm
6	29 mm × 2 (row)
7	14.5 mm × 4 (row)
8	25 mm × 3 (row)
9	30 mm × 3 (row)
	(Semi-circular shells)
10	40 mm
11	58 mm

Normal flat plates, circular cylinders and semi-circular shells of various sizes were adopted as obstacles either singly, or, to diminish the formation distance, in combination into grids. They are tabulated in Table I. Let us denote, for simplicity, the shapes of obstacles with s; $s=1$, 2, and 3 are to correspond, respectively, to circular cylinders, normal flat plates, and semi-circular shells, In order to produce measurable retardations of shocks within the test-chamber length, obstacles with fairly large blockage ratios, amounting at minimum to 40%, had to be used in the experiment.

Table II. Measured values of retardation rates r/L (%).

No.	s	b(%)	L(cm)	0.6	0.5	0.4
1	1	40	50		1.5	
2	1	58	50	3.2	3.7	4.4
3	1	75	45	5.4	7.5	9.5
4	2	40	35–40	2.4	2.9	
5	2	58	40–45	5.8	6.1	7.3
6	2	58	30–45	4.2	5.3	
7	2	58	30–45	3.0	3.8	
8	2	75	45	7.2	10.0	11.0
9	2	90	30–45	10.9	13.9	17.6
10	3	30	30–45		4.0	
11	3	58	30–40		7.9	

(5)

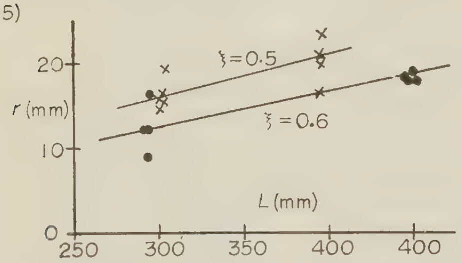

Fig. 5. Example of original data of r. No. 6-obstacle.

(6)

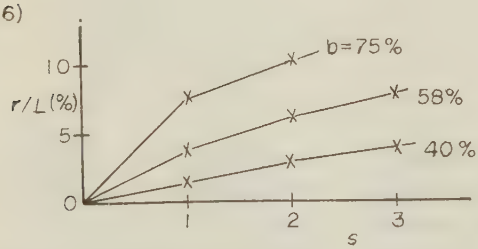

Fig. 6. Experimental result: r/L versus s. $\xi=0.5$.

In the field of view more than 30 cm downstream of the obstacle, where most photographs were taken, transmitted shock fronts were apparently plane and normal in any case. Only when the obstacle was single, were observed a pair of thin oblique wave fronts attached behind the main front. From each schlieren record the streamwise coordinate of the incident shock L measured from the obstacle center and the retardation distance of the transmitted shock with respect to th incident one, r, were obtained. The orde of magnitude of r's was a few to severa centimeters, and they were determined with a accuracy of 0.5 mm which was the thicknes of shock fronts appearing on the photograph The observed values of r's showed a fairl large scatter (see Fig. 5). For every (s, b, ξ combination the average value of r/L w determind. They were surprisingly small to large values of b, and even for $b=90\%$ t transmitted shocks were much stronger th sound waves. (See Table II and Figs. 6 to

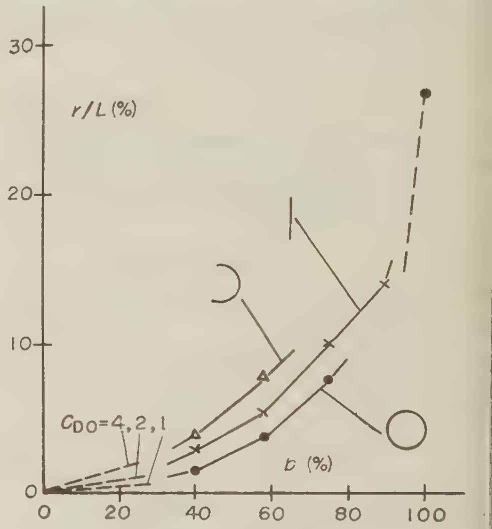

Fig. 7. Experimental result: r/L versus b. ξ=0.5
(Broken lines: theory, (12)~(17))

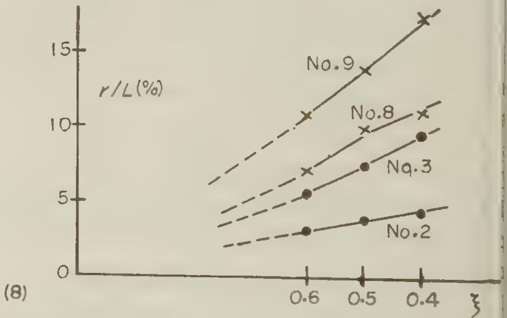

Fig. 8. Experimental result: r/L versus ξ.

At 10 cm to 20 cm downstream of the o stacle the transmitted shock fronts were pe ceptively curved and the accompanying wa systems appeared fairly thick, indicating t transient flattening process in progress ther Let us call the foot of the transmitted fro B and its belly C as in Fig. 9, and denote t retardation distances of B and C with respe to the incident shock with r_1 and r_2. They are plotted versus L in Fig. 10 for a 58%-blockage single normal-plate obstacle. (r_2-r_1), the thickness of the curved front, is also plotted in Fig. 11. In most part of the 10 cm field of view (r_2-r_1) is positive so that the shock front is convex to the up-stream, but it decreases with distance and near $L=200$ cm changes its sign. The thickness (defined as positive when the front is convex towards the upstream) thus appears to undergo a damped oscillation around zero till finally a plane and normal front is established.

Nos. 5, 6, and 7 obstacles have similar shapes and same blockage ratio. If scale effects or wall effects on the flow are absent, the retadation data for them are expected to lie on a single curve when plotted in terms of r/B_1 versus L/B_1, where B_1 denotes the channel height for a single obstacle and the mesh length of the grid for a multiple one. As shown in Fig. 12, No. 5 and No. 6-data appear to continuate smoothly but No. 7 data lie considerably lower than the extension of the other two sets. The reason is not yet clear. Typical schlieren photographs are presented in Plates 1 to 4.

§4. Analysis and Discussions

Sufficiently far downstream of the obstacle, that is for L much larger than the channel height, the retardation rate of the shock, r/L, may be equated with the attenuation rate in shock Mach number, $m=(M_I-M_T)/M_I$. When L is not so large, some correction is necessary, depending on the formation character of the plane front behind the obstacle. The simplest form of the correction may be: $(r-r_0)/L=m$. r_0 in this equation was estimated to be 3 mm or so for the 58%-blockage single normal plate. This quantity will be halved for a double obstacle. The systematic evaluation of the necessary correction is difficult and was not made. It is assumed here to be small, and we put $r/L=m$. Then, from Eq. 11 (Fig. 2) and Table II, C_D can be calculated for various (s, b, ξ)-combinations. C_D may be somewhat overestimated here because of the negligence of the corrections.

It is noticeable that C_D changes only little with ξ in the present experimental range. For example, $C_D=11.0$, 12.0, and 9.8, respectively, for $\xi=0.6$, 0.5, and 0.4 for No. 3-obstacle. A variation of ξ for fixed s and b corresponds to variations of Mach and Reynolds numbers of the incoming flow. The

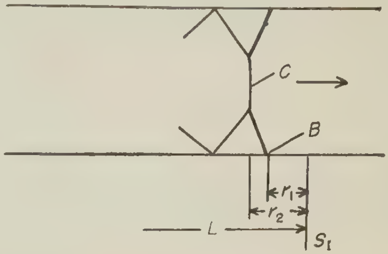

Fig. 9. Transmitted shock front near the obstacle.

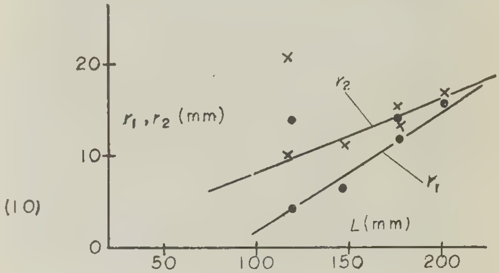

Fig. 10. Experimental result: r_1, r_2 versus L. No. 5-obstacle.

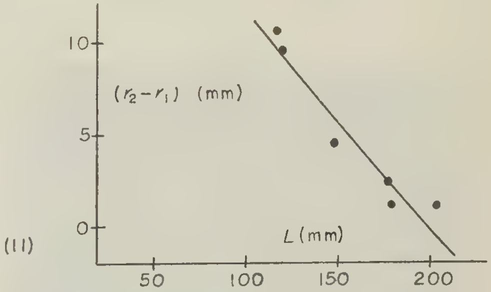

Fig. 11. Experimental result: (r_2-r_1) versus L. No. 5-obstacle.

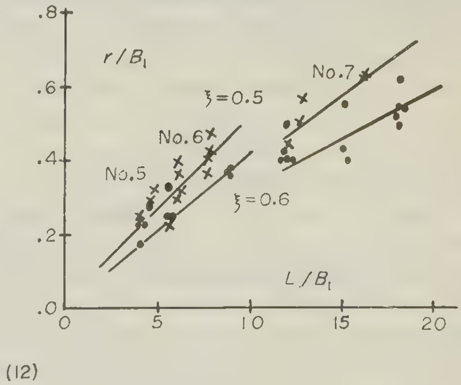

Fig. 12. Experimental result: r/B_1 versus L/B_1. Nos. 5- to 7-obstacles.

above-mentioned result shows that the drag coefficients of the bluff bodies which we adopted as obstacles are insensitive to Mach and Reynolds numbers, and is in accordance with ordinary experimental facts.

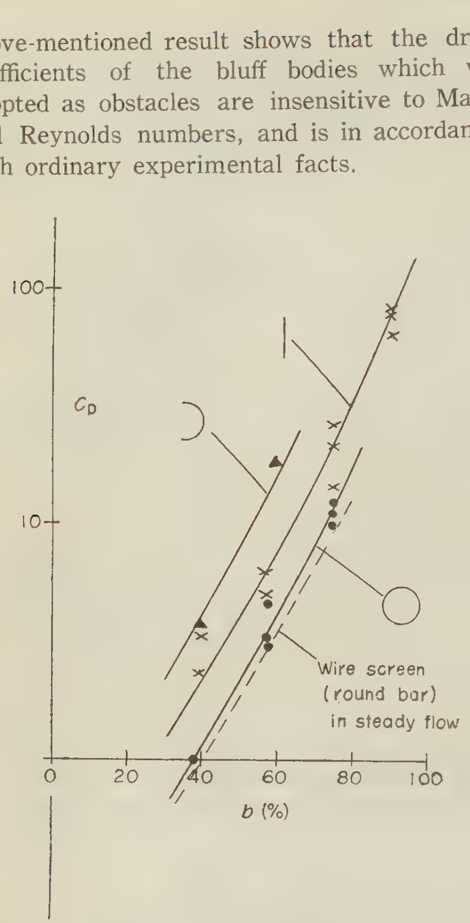

Fig. 13. Relation between estimated C_D and b. (Data for $\xi=0.6$, 0.5 and 0.4 compiled.)

C_D increases with b exponentially (Fig. 13). Steady-flow data of the drag coefficients of such large-blockage obstacles are not available, but the above result may be compared with the low-speed pressure-drop-coefficient data (which are practically equal to C_D) of wire screens. The dependence of C_D on b is similar for both, and the order of magnitude agrees reasonably.

A few critical remarks may be necessary here. In the first place, the presence of the walls and the large blockage ratio of the adopted obstacles modified the steady flow to a considerable extent. For example, the total pressures in front of and behind the obstacle were very different, and in about half of the cases the flow is considered to have been choked. Secondly, the flow field past the obstacle was always limited in the upstream and downstream by the reflected shock front and the contact layer, respectively, contrary to an ordinary steady flow. Lastly, although the obstacles were two-dimensional in shape, their span-to-diameter ratios were not sufficiently large, and some three-dimensional effects may have been caused. However, in the present experiment, the insensitivity of the separation-point locations of the bluff obstacles to the flow character and the smallness of the viscosity effects in the short-duration flow are considered to have prevented such troubles.

Next, a consideration must be given on the mechanism of the retardation and attenuation of the shock. It is diffracted as it passes the obstacle, being retarded and disfigured, and then, by the action of the reflected-wave system catching over it, converges to the original plane shape. If a steady potential flow were to be established around the obstacle in the ultimate state, the shock front would eventually acquire the original strength (attenuation being absent), since there would be no steady resistance. But there would be an amount of retardation corresponding to the momentum loss due to the transient-stage resistance of the obstacle, which is caused by the assymmetric pressure distribution on the fore- and rear-half surface. In the real flow, separation takes place on the surface of the obstacle, giving rise to a certain pressure resistance even in the ultimate state. The separated flow generates a wave system, which catches over and weakens the transmitted front, the ultimate attenuation of which must balance with the steady-state resistance. Such a wave system is superposed on the regular row of the reflected waves, but is not visible contrary to the latter.

The phenomenon treated here is a complicated one which is essentially instationary, and, unlike ordinary shock diffraction phenomena, involves viscosity. There exists no theory to describe the phenomenon completely. For the full understanding of it, the unsteady flow character around the bluff body in the shock tube must be investigated in detail.

In this experiment large scatters of data made the result somewhat unsatisfactory along with the uncertainty in the photographic measurements of small quantities. If stronger shocks are used with similar arrangements, greater retardations will be realized. However, the steady flow will be always choked and the retardation effects of wall friction will not be negligible.

§ 5. Conclusions

The retardations and attenuations of weak shocks due to various simple-shaped obstacles placed in the passage have been measured by use of a shock tube and instantaneous schlieren photography. The formation process of plane shock fronts behind the obstacles have also been investigated in some detail. On the theoretical side, a method of estimating the drag of the obstacle from the attenuation of the shock has been developed on an assumption of a simple quasi-steady flow model. Using the experimental data of the shock retardations, the drag values of a series of obstacles have been calculated. They show reasonable agreements with available steady-flow results.

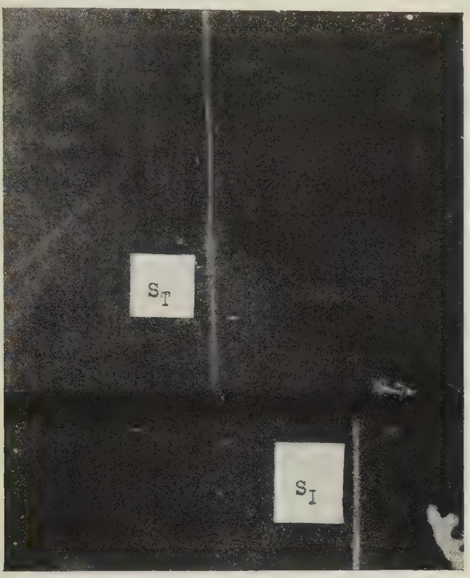

Plate 1. 45 cm downstream of No. 5-obstacle.

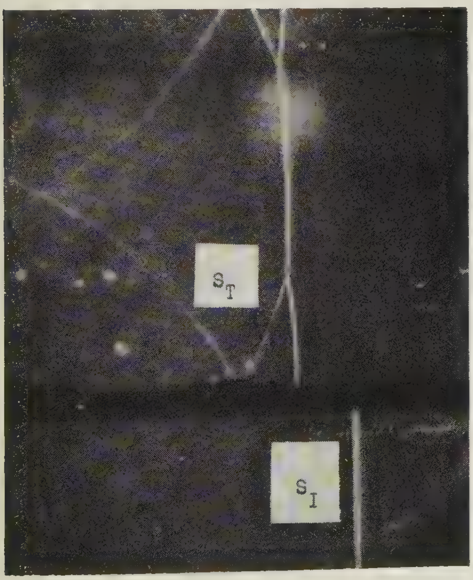

Plate 2. 15 cm downstream of No. 5-obstacle.

The authors wish to express their gratitudes to Professor J. Tamiya and Mr. H. Saito for their kind advices and instructions about devices and measurements. Thanks are also due to Mr. S. Watanabe for his assistance in the experiment.

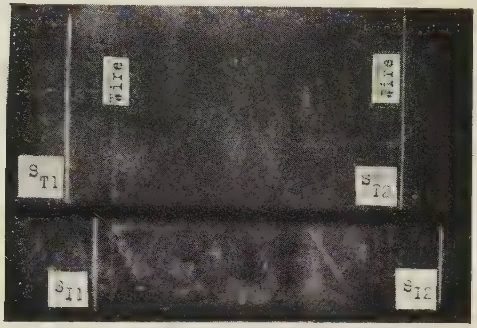

Plate 3. "Multiflash" photograph. 30 cm to 45 cm downstream of No. 6-obstacle. Shot interval: about 400 microseconds.

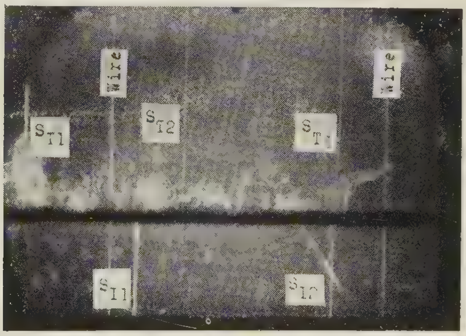

Plate 4. "Multiflash" photograph. 30 cm to 45 cm downstream of No. 9-obstacle. Shot interval: about 200 microseconds.

References

1) I. I. Glass, W. Martin and G. N. Patterson: Inst. Aerophysics, Univ. Toronto (UTIA) Rep. No. 2, Nov. 1953.
2) UTIA Annual Progress Report, 1956.
3) D. W. Boyer: UTIA Technical Note No. 8, May, 1956.
4) C. S. Kim and K. Oshima: Jour. Phys. Soc. Japan **11** (1956) 178.
5) D. S. Dosanjh: NACA Technical Note 3680, Sept. 1956.

6) R. Kawamura and H. Saito: Rept. Inst. Science and Technology, Univ. Tokyo, Vol. 9, No. 4, 1955.

7) J. Tamiya, M. Inaba and A. Saeki: Proc. 6th Japan National Congr. Appl. Mech., 1956, pp. 269–271.

JOURNAL OF THE PHYSICAL SOCIETY OF JAPAN Vol. 12, No. 11, NOVEMBER, 1957

An Approximate Solution of the Hypersonic Laminar Boundary-Layer Equations and its Application

By Tosimitu NAGAKURA and Humio NARUSE

Department of Physics, Faculty of Science,
Tokyo Metropolitan University

(Received July 31, 1957)

Approximate formulae of the displacement thickness and the skin friction of the hypersonic laminar boundary layer are derived by use of von Kármán's integral method, assuming the heat-insulated wall, the Prandtl number of unity and Chapman and Rubesin's formula for the variation of viscosity with temperature. The results obtained are compared with some exact solutions. Because of the good agreement, it seems that these formulae are very useful.

These formulae, together with the tangent-wedge-approximation, are applied to the viscous flow over slender bodies with a sufficiently sharp leading edge. As an example, the pressure distribution over a flat plate is calculated numerically over the entire region of the surface. Comparison with other author's theoretical results as well as experimental values is made.

§ 1. Introduction

In the hypersonic flow the laminar boundary layer is rather thick because of high temperatures in this region, and its thickness increases like M^2 for a given Reynolds number on the assumption of Chapman and Rubesin's formula for the variation of viscosity with temperature. The outward deflection of the streamline induced by this thick boundary layer causes a significant increase of the pressure in the main flow and this induced pressure in turn feeds back into the boundary layer and affects its rate of growth, and thus so-called shock-wave-boundary-layer interaction occurs.

Recently many works concerning this interaction have been published. For instance several theoretical studies on these problems for a flat plate or a wedge with an infinitely sharp leading edge have been made by Bertram⁽¹⁾, Kuo⁽²⁾, Lees⁽³⁾, Lees and Probstein⁽⁴⁾, Li and Nagamatsu⁽⁵⁾, Maslen⁽⁶⁾, Pai and Shen⁽⁷⁾, Shen⁽⁸⁾, and Stewartson⁽⁹⁾, and a few experimental studies by Bertram⁽¹⁰⁾, Hammitt and Bogdonoff⁽¹¹⁾, and Kendall⁽¹²⁾.

From these studies we may expect that the hypersonic viscous flow over slender bodies with a sufficiently sharp leading edge can be separated in two regions, namely the usual boundary layer and the inviscid layer of small disturbance, and that Prandtl's boundary layer equations remain valid even in the presence of interaction as long as $(\delta/x)^2 \ll 1$.

In these interaction problems the displacement thickness of the boundary layer plays a particularly important role, since it represents an effective thickening of the body. Therefore it is desirable to have an approximate formula of the displacement thickness when the pressure distributions on the body surface are prescribed.

In this paper these formulae, together with those of the skin-friction, are derived by approximating the velocity profile by a polynomial of degree four of the Howarth normal distance, as in the usual von Kármán-Pohlhausen approach, and comparison with a few exact solutions is made.

Further these formulae, together with the tangent-wedge-approximation, are applied to the viscous flow over slender bodies with a sufficiently sharp leading edge, and then it is shown that the solution over the entire region of the surface can be obtained numerically and especially the inverse problem can be solved easily. Lastly, the pressure distribution over a flat plate is calculated numerically and comparison with other author's results as well as with Kendall's experimental values is made.

§2. Basic Equations

The equations of the two-dimensional compressible boundary layer are as follows.

$$(\partial/\partial x)(\rho u)+(\partial/\partial y)(\rho v)=0\ , \tag{2.1}$$

$$\rho u(\partial u/\partial x)+\rho v(\partial u/\partial y) = -dp/dx+(\partial/\partial y)\{\mu(\partial u/\partial y)\}\ , \tag{2.2}$$

$$\partial p/\partial y=0\ , \tag{2.3}$$

$$\rho u(\partial/\partial x)(C_pT)+\rho v(\partial/\partial y)(C_pT)=u(dp/dx) +(\partial/\partial y)\{(\mu C_p/\sigma)\partial T/\partial y\}+\mu(\partial u/\partial y)^2\ , \tag{2.4}$$

$$p=R\rho T\ , \tag{2.5}$$

where $(x,\ y)$ are the distances along and normal to the surface, $(u,\ v)$ the velocity components in the $(x,\ y)$ directions, p, ρ, T the pressure, the density, the absolute temperature at $(x,\ y)$ respectively, C_p the specific heat at constant pressure, σ the Prandtl number, and R is the gas constant referred to unit mass.

Integrating (2.1) and (2.2) across the boundary layer and combining the results we have the familiar momentum integral equation, which can be written as

$$\frac{\mu_w}{\rho_\infty u_\infty{}^2}\left(\frac{\partial u}{\partial y}\right)_w=\frac{d}{dx}\left[\frac{\rho_1u_1{}^2}{\rho_\infty u_\infty{}^2}\int_0^\delta\frac{\rho u}{\rho_1u_1}\left(1-\frac{u}{u_1}\right)dy\right] -\frac{p_\infty}{\rho_\infty u_\infty{}^2}\left[\frac{d}{dx}\left(\frac{p_1}{p_\infty}\right)\right]\int_0^\delta\left(1-\frac{\rho u}{\rho_1u_1}\right)dy\ , \tag{2.6}$$

where μ is the coefficient of viscosity, δ the boundary layer thickness, and the suffixes w, 1, ∞, 0 denote respectively the corresponding values at the surface of the body, at the outer edge of the boundary layer, at infinity upstream and at the stagnation point.

If we write

$$\left.\begin{aligned} &y/\delta=\eta\ ,\\ &-(\delta^2/\mu_wu_1)\,dp_1/dx=\Lambda\ ,\\ &\frac{\gamma-1}{2}M_1{}^2\int_0^1\frac{\rho u}{\rho_1u_1}\left(1-\frac{u}{u_1}\right)d\eta=Q(\Lambda)\ ,\\ &\int_0^1\left(1-\frac{\rho u}{\rho_1u_1}\right)d\eta=\delta^*/\delta=1-\lambda(\Lambda)\ , \end{aligned}\right\} \tag{2.7}$$

where δ^* is the displacement thickness of the boundary layer, γ the ratio of specific heats and M the Mach number, and we expand u/u_1 in power series of η as follows:

$$u/u_1=a(\Lambda)\eta+b(\Lambda)\eta^2+O(\eta^3)\ , \tag{2.8}$$

we have from (2.6), (2.7) and (2.8)

$$\frac{d}{dx}\left(\frac{p_1}{p_\infty}Q\delta\right)-\frac{\gamma-1}{2\gamma}\,\delta(1-\lambda)\,\frac{d}{dx}\left(\frac{p_1}{p_\infty}\right) =\mu_wu_1\frac{(\gamma-1)M_\infty{}^2}{2\rho_\infty u_\infty{}^2}\frac{a}{\delta}\ . \tag{2.9}$$

Using (2.7), this can be transformed into

$$\frac{d}{dx}\delta^2+2\frac{p_\infty}{p_1}\frac{d}{dx}\left(\frac{p_1}{p_\infty}\right)\delta^2+\frac{2}{Q}\frac{dQ}{dx}\delta^2 =\mu_wu_1\frac{(\gamma-1)M_\infty{}^2}{\rho_\infty u_\infty{}^2}\frac{p_\infty}{p_1}\left[\frac{a(\Lambda)-\{1-\lambda(\Lambda)\}\Lambda}{Q(\Lambda)}\right]. \tag{2.10}$$

In the next section (Figs. 1, 2) we shall show that the three functions $a(\Lambda)$, $\lambda(\Lambda)$, $Q(\Lambda)$ approximately satisfy the following relations:

$$[a(\Lambda)-\{1-\lambda(\Lambda)\}\Lambda]/Q(\Lambda)=A+B\Lambda\ , \tag{2.11}$$

$$a(\Lambda)=a_1+b_1\Lambda\ , \tag{2.12}$$

where A, B, a_1, b_1 are constants. By using these relations, we can get two different formulae for δ as follows.

Case I. If we substitute (2.11) in (2.10) and put

$$\left.\begin{aligned} &2+(\gamma-1)B/\gamma=\alpha\ ,\\ &(\gamma-1)A\mu_wu_1\,M_\infty{}^2/\rho_\infty u_\infty{}^2=K\ , \end{aligned}\right\} \tag{2.13}$$

then α is constant and we can obtain from (2.10) and (2.7) the relation:

$$\frac{d}{dx}\delta^2+\alpha\frac{p_\infty}{p_1}\frac{d}{dx}\left(\frac{p_1}{p_\infty}\right)\delta^2+\frac{2}{Q}\frac{dQ}{dx}\delta^2=K\frac{p_\infty}{p_1}\ . \tag{2.14}$$

This can be integrated to give

$$\delta^2=\left(\frac{p_1}{p_\infty}\right)^{-\alpha}Q^{-2}\left\{\int_{x_0}^x KQ^2\left(\frac{p_1}{p_\infty}\right)^{\alpha-1}dx+\text{const.}\right\}. \tag{2.15}$$

We shall discuss the functional form of $Q(\Lambda)$ in the next section.

Case II. If we substitute (2.12) in (2.10) and put

$$\left.\begin{aligned} &2-\{(\gamma-1)(1-\lambda-b_1)/\gamma Q\}=\alpha\ , \\ &a_1(\gamma-1)M_\infty{}^2\mu_w u_1/\rho_\infty u_\infty{}^2 Q=K\ , \end{aligned}\right\} \tag{2.16}$$

we can obtain again (2.14) and (2.15) as in Case I. Here α is assumed to be constant and its justification will be given in the next section.

On the other hand the skin-friction at the wall, τ_w, is given by the equation:

$$\tau_w=\mu_w(\partial u/\partial y)_w=u_1\mu_w a(\Lambda)/\delta\ , \tag{2.17}$$

where the relations (2.7) and (2.8) are used.

In either case, introducing (2.12) into (2.17), we get

$$\tau_w=a_1u_1\mu_w/\delta-b_1\delta(dp_1/dx)\ . \tag{2.18}$$

§ 3. Determination of $Q(\Lambda)$ and the Various Constants

In the following analysis, we shall assume (i) $(\partial T/\partial y)_w=0$, (ii) $C_p=$const., (iii) $\sigma=1$, (iv) $\mu/\mu_\infty=C(T/T_\infty)$, where

$$C=(T_w/T_\infty)^{1/2}(T_\infty+S)/(T_w+S)$$

where S is Sutherland's constant.

Then we get from (2.2) and (2.4) the well-known integral form:

$$\rho_1/\rho=T/T_1=1+[(\gamma-1)M_1{}^2/2][1-(u/u_1)^2]\ . \tag{3.1}$$

Further, if we substitute (2.7) and (2.8) in (2.2) and put $y=0$, we get

$$b(\Lambda)=-\Lambda/2\ . \tag{3.2}$$

It is well known that, if the above assumptions (i)~(iv) are satisfied, there exists a virtual incompressible flow corresponding to a real compressible flow and that such an incompressible flow can be obtained by Stewartson's transformation as follows:

$$\left.\begin{aligned} &X=\int g(x)dx\ , \\ &Y=f(x)\int_0^y \frac{\rho}{\rho_1}dy\ , \end{aligned}\right\} \tag{3.3}$$

$$U(X,\ Y)/U_1(X)=u(x,\ y)/u_1(x)\ , \tag{3.4}$$

where X, Y and U, U_1 are the coordinates and the velocity components of the transformed flow, and $g(x)$ and $f(x)$ are given known functions[13]. Assuming Pohlhausen's polynomial of degree four for the velocity distribution in the corresponding incompressible flow, we have

$$\begin{aligned} U/U_1=&(2+\Lambda_i/6)Y/\Delta-(\Lambda_i/2)(Y/\Delta)^2 \\ &-(2-\Lambda_i/2)(Y/\Delta)^3+(1-\Lambda_i/6)(Y/\Delta)^4\ , \end{aligned} \tag{3.5}$$

where

$$\Delta=f(x)\cdot\delta\int_0^1\frac{\rho}{\rho_1}d\eta\ , \tag{3.6}$$

and Λ_i is Pohlhausen's parameter of the transformed incompressible flow. If we substitut (3.1) and (2.8) in (3.3), we have

$$\begin{aligned} Y&=f(x)\int_0^y\frac{dy}{1+[(\gamma-1)M_1{}^2/2][1-(u/u_1)^2]} \\ &=\frac{f(x)\cdot\delta}{1+(\gamma-1)(M_1{}^2/2)}\int_0^\eta\frac{d\eta}{1+O(\eta^2)}\ . \end{aligned}$$

Expanding Y in power series of η and using (3.6), we have

$$Y/\Delta=[1/F(\Lambda_i)][\eta+O(\eta^3)]\ , \tag{3.7}$$

where

$$F(\Lambda_i)=\frac{T_0}{T_1}\int_0^1\frac{\rho}{\rho_1}\ d\eta\ . \tag{3.8}$$

Substituting (3.7) in (3.5), we have

$$\begin{aligned} U/U_1=&(2+\Lambda_i/6)\eta/F(\Lambda_i) \\ &-(\Lambda_i/2)[\eta/F(\Lambda_i)]^2+O(\eta^3)\ . \end{aligned} \tag{3.9}$$

From (2.8) and (3.2) we get

$$u/u_1=a(\Lambda)\eta-(\Lambda/2)\eta^2+O(\eta^3)\ . \tag{3.10}$$

Taking account of $u/u_1=U/U_1$, we get from (3.9) and (3.10)

$$a(\Lambda)=(2+\Lambda_i/6)/F(\Lambda_i)\ , \tag{3.11}$$

$$\Lambda=\Lambda_i/[F(\Lambda_i)]^2\ . \tag{3.12}$$

By substituting (3.5) and (3.8) in the relation:

$$\begin{aligned} \delta&=\int_0^\delta\frac{T}{T_1}\frac{\rho}{\rho_1}dy \\ &=\int_0^\delta\left[1+\frac{\gamma-1}{2}M_1{}^2\left\{1-\left(\frac{u}{u_1}\right)^2\right\}\right]\frac{\rho}{\rho_1}dy \\ &=\delta\int_0^1\frac{\rho}{\rho_1}\ d\eta+\frac{\gamma-1}{2}M_1{}^2\frac{\Delta}{f(x)}\int_0^1\left[1-\left(\frac{U}{U_1}\right)^2\right]d\left(\frac{Y}{\Delta}\right) \end{aligned}$$

and neglecting $O(1/M_1{}^2)$, we have

$$F(\Lambda_i)=1/[1-l(\Lambda_i)]\ , \tag{3.13}$$

where

$$\begin{aligned} l(\Lambda_i)&=\int_0^1\left(\frac{U}{U_1}\right)^2d\left(\frac{Y}{\Delta}\right) \\ &=\frac{367}{630}+\frac{71}{7560}\Lambda_i+\frac{1}{9072}\Lambda_i{}^2\ . \end{aligned} \tag{3.14}$$

By using (2.7), (3.3), (3.4), (3.5), and (3.8) and neglecting $O(1/M_1{}^2)$, we get

$$Q(\Lambda)=F(\Lambda_i)[m(\Lambda_i)-l(\Lambda_i)]\ , \tag{3.15}$$

$$\lambda(\Lambda)=O(1/M_1{}^2)\ , \tag{3.16}$$

where

$$m(\Lambda_i)=\int_0^1\left(\frac{U}{U_1}\right)d\left(\frac{Y}{\Delta}\right)=\frac{7}{10}+\frac{1}{120}\Lambda_i\ . \tag{3.17}$$

From (2.7) δ^*/δ is equal to $1-\lambda(\Lambda)$ and, if we neglect $O(1/M_1^2)$, it can be concluded from (3.16) that[†]

$$\delta^* = \delta \,. \tag{3.18}$$

Now $a(\Lambda)$, $Q(\Lambda)$, $\lambda(\Lambda)$ can be determined from (3.11)~(3.17) as functions of Λ, and $[a(\Lambda)-\{1-\lambda(\Lambda)\}\Lambda]/Q(\Lambda)$ and $a(\Lambda)$ are shown as functions of Λ in Figs. 1, 2. Thus A, B, a_1, b_1 in (2.11) and (2.12) can be determined graphically using Figs. 1, 2.

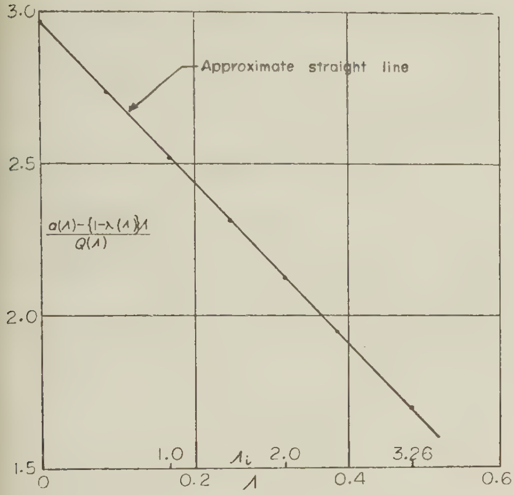

Fig. 1. The value of $[a(\Lambda)-\{1-\lambda(\Lambda)\}\Lambda]/Q(\Lambda)$.

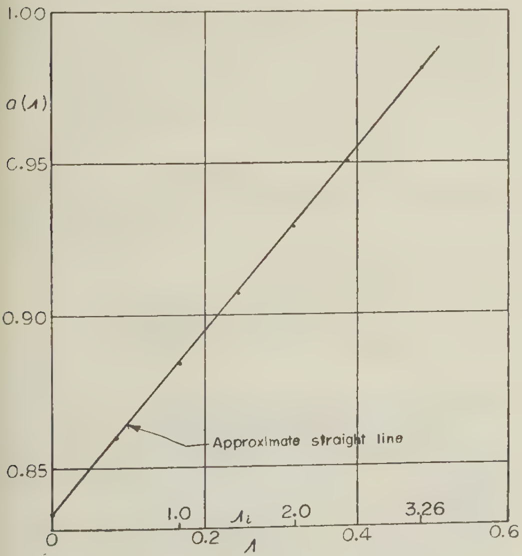

Fig. 2. The value of $a(\Lambda)$.

Stewartson[9)] has shown that, when a flat plate in the hypersonic flow has a sufficiently sharp leading edge, a similar solution exists in the neighbourhood of the leading edge (in the strong interaction region) where $p_1 \propto x^{-1/2}$ and $\Lambda_i = 3.26$. Therefore we may expect that Λ_i will change in general from 3.26 to 0 on the surface of slender bodies with a sufficiently sharp leading edge. Now as shown in Figs. 1 and 2, the curves of $[a(\Lambda)-\{1-\lambda(\Lambda)\}\Lambda]/Q(\Lambda)$ and $a(\Lambda)$ against Λ are almost straight lines in the region $0<\Lambda_i<3.26$. Thus we get the approximate relations (2.11) and (2.12), where

$$A = 2.967\,, \qquad B = -2.65\,, \tag{3.19}$$

$$a_1 = 0.835\,, \qquad b_1 = 0.302\,. \tag{3.20}$$

Further, in the above-mentioned range $Q(\Lambda)$ varies quite slightly and Q in (2.15) and (2.16) can be replaced by the mean value Q_m. ($|Q-Q_m|/Q_m < 0.02$ in this range.)

On the other hand, if $dY/dx \ll 1$ holds, where $Y(x)$ denotes the shape of the shock wave, the hypersonic small disturbance theory can be applied and u_1 can be replaced by u_∞, so that we can treat K as a constant.

§4. Formulae of the Displacement Thickness and the Local Skin-Friction Coefficient, and Comparisons with Exact Solutions

As mentioned above, Q and K in (2.15) can be treated as constants and therefore we get from (2.15)

$$\begin{aligned}\delta^{*2} &= \delta^2 \\ &= K\left(\frac{p_1}{p_\infty}\right)^{-\alpha}\left\{\int_{x_0}^{x}\left(\frac{p_1}{p_\infty}\right)^{\alpha-1}dx + \text{const.}\right\}\,,\end{aligned} \tag{4.1}$$

where the following relation has been used:

$$\begin{aligned}\mu_w &= C\mu_\infty(T_w/T_\infty) \\ &= [(\gamma-1)/2]CM_\infty^2\mu_\infty[1+O(1/M_\infty^2)]\,.\end{aligned} \tag{4.2}$$

The local skin-friction coefficient C_f can be obtained from (2.18) by using (4.2)

$$\begin{aligned}C_f = 2\tau_w/\rho_\infty u_\infty^2 &= [a_1(\gamma-1)C\mu_\infty M_\infty^2/\rho_\infty u_\infty\delta] \\ &\quad -(2b_1\delta/\rho_\infty u_\infty^2)\,dp_1/dx\,.\end{aligned} \tag{4.3}$$

In these formulae, a_1, b_1 are given by (3.20) and K, α are given in Table I.

Here, we can easily calculate (4.1) and (4.3) in the case when the pressure distribution is given by $p_1/p_\infty = p_0 x^{-1/2}$ or $p_1 = p_\infty$, in which the exact boundary layer solutions have been studied under the conditions of §3, (i)~(iv)[9),14)]. In Tables II and III the results obtained

---

[†] This fact has already been noticed by other authors, for example, Reference [9].

Table I

	α	$\alpha(\gamma=1.4)$	$\frac{\rho_\infty u_\infty K}{C\mu_\infty M_\infty^4}\equiv\tilde{K}$	$\tilde{K}(\gamma=1.4)$	Q_m
Case I	$2-2.65(\gamma-1)/\gamma$	1.243	$1.484(\gamma-1)^2$	0.2374	
Case II	$2-2.43(\gamma-1)/\gamma$	1.306	$1.455(\gamma-1)^2$	0.2328	0.2870

Table II. $(p_1/p_\infty=p_0x^{-1/2})$

	$\delta\Big/\sqrt{\frac{C\mu_\infty}{p_0\rho_\infty u_\infty}}M_\infty^2x^{3/4}$	$C_f\Big/\sqrt{\frac{Cp_0\mu_\infty}{\rho_\infty u_\infty}}x^{-3/4}$
Case I	0.520	0.754
Case II	0.524	0.750
exact solution	0.525	0.764

Table III. $(p_1=p_\infty)$

	$\delta\Big/\sqrt{\frac{C\mu_\infty}{\rho_\infty u_\infty}}M_\infty^2x^{1/2}$	$C_f\Big/\sqrt{\frac{C\mu_\infty}{\rho_\infty u_\infty}}x^{-1/2}$
Case I	0.487	0.686
Case II	0.482	0.693
exact solution	0.478	0.664

from the above theory are compared with the exact solutions.

From these tables, it may be concluded that these formulae are very useful in the almost entire region of the surface in view of the good agreement with exact solutions in both the strong interaction region $(p_1\propto x^{-1/2})$ and the weak interaction region $(p_1=p_\infty)$.

§ 5. The Viscous Flow over Slender Bodies

On the basis of the assumption that the hypersonic viscous flow over slender bodies with a sufficiently sharp leading edge is separated into the boundary layer and the inviscid layer, the pressure distributions induced by the boundary layer on a flat plate or a wedge have been studied by many authors, but these works have been mostly limited to the strong or the weak interaction region only.

Now, if we use the formula (4.1) for the boundary layer and the tangent-wedge-approximation for the inviscid layer, we can calculate the pressure distribution and the skin-friction in the entire region of the surface as follows.

In the hypersonic case when $O(1/M_1^2)$ can be neglected, $\delta^*=\delta$ and therefore the oute edge of the boundary layer coincides almos with the streamline. Then, neglecting $O(1/M_1^2$ and $O(\theta^3)$, we get

$$\theta_1=\theta_b+d\delta/dx\ , \tag*{(5.1}$$

where θ_b, θ_1 are respectively the angles o inclination of the surface element and th streamline along the outer edge of the bound-ary layer to the flight direction.

From the tangent-wedge-approximation we have, assuming that $\theta_1\ll1$,

$$\frac{p_1}{p_\infty}=1+\frac{\gamma(\gamma+1)}{4}M_\infty^2\theta_1^2$$
$$+\gamma M_\infty\theta_1\sqrt{1+\left(\frac{\gamma+1}{4}\right)^2M_\infty^2\theta_1^2}\ , \tag*{(5.2}$$

where p_1 is the pressure at the outer edge of the boundary layer. Of course, p_1 can also be regarded as the pressure on the surface of the body. From (5.1), (5.2) and (4.1), we get

$$\theta_1=\frac{1}{M_\infty}\sqrt{\frac{2}{\gamma(\gamma+1)}}\frac{(p_1/p_\infty)-1}{\sqrt{(p_1/p_\infty)+(\gamma-1)/(\gamma+1)}}\ ,$$
$$\theta_b=\theta_1-\frac{d}{dx}\left[K\left(\frac{p_1}{p_\infty}\right)^{-\alpha}\right.$$
$$\left.\times\left\{\int_{x_0}^{x}\left(\frac{p_1}{p_\infty}\right)^{\alpha-1}dx+\text{const.}\right\}\right]^{1/2}. \tag{5.3}$$

If θ_b is given, we can determine p_1, θ_1 from (5.3), and δ from (5.1), and C_f from (4.3). It is noteworthy that Eqs. (5.3) are particularly convenient for the inverse problem in which p_1 is given and θ_b is to be determined.

§ 6. The Viscous Flow over a Flat Plate

The flow over a flat plate can be calculated easily from (5.3), putting $\theta_b=0$ in (5.3). If we put

$$\left.\begin{aligned}&\sqrt{C\mu_\infty/\rho_\infty u_\infty}M_\infty^3x^{-1/2}=s\ ,\\&(\rho_\infty u_\infty/C\mu_\infty M_\infty^5)\delta=\Theta\ ,\end{aligned}\right\} \tag{6.1}$$

we have from (5.1) and (5.3)

$$\left.\begin{aligned}\Theta^2&=\left(\frac{p_1}{p_\infty}\right)^{-\alpha}\Bigg[-\beta(\gamma-1)^2\\&\qquad\times\int_{s_0}^{s}\left(\frac{p_1}{p_\infty}\right)^{\alpha-1}\frac{ds}{s^3}+\text{const.}\Bigg],\\-\frac{s^3}{2}\frac{d\Theta}{ds}&=\sqrt{\frac{2}{\gamma(\gamma+1)}}\frac{(p_1/p_\infty)-1}{\sqrt{(p_1/p_\infty)+(\gamma-1)/(\gamma+1)}}\,.\end{aligned}\right\}\tag{6.2}$$

where β is $A/2$ ($=1.484$) for Case I and $a_1/2Q_m$ ($=1.455$) for Case II. Equation (6.2) have been solved numerically for Case II† and $\gamma=1.4$. The results obtained are shown in Fig. 3, together with other author's results and Kendall's experimental values ($M_\infty=5.8$). It is clear from Fig. 3 that our results agree well witn the experimental values. When $s\gg1$ or $s\ll1$, we have the following series expansions from (6.2).

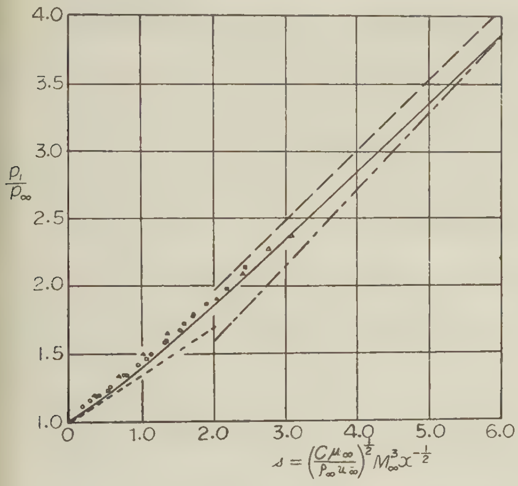

Fig. 3. The pressure distribution over the surface of a flat plate.

present theory,
------- Lees and Probstein, 1st. order weak interaction theory,
— · Lees, 1st. order strong interaction theory,
— - — - — Stewartson, 1st, order strong interaction theory,
○, □, △ Kendall, experimental values ($M_\infty=5.8$).

In the region $s\gg1$,

$$p_1/p_\infty=(3\sqrt{\beta}/4\sqrt{3-\alpha})(\gamma-1)\sqrt{\gamma(\gamma+1)}\,s+(4-\alpha)(3\gamma+1)/(9-\alpha)(\gamma+1)+\cdots\,.\tag{6.4}$$

In the region $s\ll1$,

$$p_1/p_\infty=1+(\sqrt{\beta}/2)\gamma(\gamma-1)s+(\beta/16)\gamma(\gamma+1)(\gamma-1)^2s^2+\cdots\,.\tag{5}$$

In these equations, we put the value of Case II† for α and β, and $\gamma=1.4$. The results thus obtained, as well as other authors' results for $\gamma=1.4$, are as follows.

In the region $s\gg1$, we have from (6.2)

$$p_1/p_\infty=0.510s+0.759+\cdots,$$

from Lees' results[15)]

$$p_1/p_\infty=0.52s+0.92+\cdots,$$

and from Stewartson's result[9)]

$$p_1/p_\infty=0.555s+0.489+\cdots.$$

In the region $s\ll1$, we have from (6.2)

$$p_1/p_\infty=1+0.338s+0.049s^2+\cdots.$$

and from Lees and Probstein's result[15)]

$$p_1/p_\infty=1+0.35s+0.05s^2+\cdots.$$

The agreement is very good except for Stewartson's result. The difference between the Stewartson's result and ours seems to be solely due to our use of tangent-wedge-approximation for the inviscid layer, but not due to our method of treatment of the boundary layer.

§7. Conclusion

The approximate formulae of the displacement thickness, together with those of the skin-friction, are derived by approximating the velocity profile by a polynomial of degree four of the Howarth normal distance. Comparisons with a few exact solutions are made and good agreement is obtained.

When these formulae, together with the tangent-wedge-approximation, are applied to the viscous flow over slender bodies with a sufficiently sharp leading edge, it is shown that the solution over the entire region of the surface can be calculated numerically and that the calculation is especially easily for the inverse problem. Lastly, the pressure distribution over a flat plate is calculated numerically and its result agrees well with experimental values.

References

1) M. H. Bertram: NACA TN 2773, 1953.
2) Y. H. Kuo: J. Aeron. Sci. **23** (1956) 125.

---

† We may expect from Tables II and III that Case II will give more accurate results as far as the pressure distribution is concerned.

3) L. Lees: J. Aeron. Sci. **20** (1953) 143.
4) L. Lees and R. F. Probstein: Princeton Univ. Aero. Engi. Labo. Rep. 195, 1952.
5) Ting-Yi Li and H. Nagamatsu: J. Aeron. Sci. **20** (1953) 345.
6) S. H. Maslen: NACA TN 2818, 1952.
7) S. I. Pai and S. F. Shen: 50 Jahre Grenzschichtforschung (1955) 112.
8) S. F. Shen: J. Math. and Phys. **31** (1952) 192.
9) K. Stewartson: J. Aero. Sci. **22** (1955) 303.
10) M. H. Bertram: NACA TN 2773, 1953.
11) S. M. Bogdonoff and A. G. Hammitt: J. Aer Sci. **23** (1956) 108.
12) J. M. Kendall. J. Aero. Sci. **24** (1957) 47.
13) K. Stewartson: Proc. Roy. Soc. Series A, **200** (1949) 84.
14) Ting-Yi Li and H. Nagamatsu: J. Aero. Sci **22** (1955) 607.
15) Lees: IAS-RAeS Proceedings (1955) 241.

JOURNAL OF THE PHYSICAL SOCIETY OF JAPAN Vol 12, No. 11, NOVEMBER, 1957

Experimental and Theoretical Investigations on the Oscillating Cylinder Viscometer for Non-Elastic Liquids

By Ali Abdel Kerim Ibrahim Ph. D. (Lond.) and
Abdel Monem I. Kabiel Ph. D. (Alexandria)
Physics Department, Faculty of Science, The University, Alexandria, Egypt

(Received June 11, 1957)

A new and exact theory of the oscillating cylinder viscometer is given for non-elastic liquids.

By introducing into the final solution a dimensionless parameter defined by:

$$\sqrt{2Ba}=x$$

where the symbols have their usual significance and x may take any value, the following expression is obtained.

$$\frac{\theta_0}{\dot{\varphi}_0}{}^2=\frac{A'n^4}{B'+C'n^2+D'n^4}$$

where A', B', C' and D' are constants and whose values depend on:—

i—The density of the liquid under study.
ii—The constants of the apparatus used.
iii—The numerical value of x chosen.

The theoretical curve representing the previous expression satisfies the experimental curve in one point (n_s, ψ_s) at which they intersect.

Hence, by substituting the value of x chosen and the value of n_s obtained in the following equation,

$$\eta=\frac{2\pi a^2}{x^2}\cdot\rho n_s$$

the value of η is determined.

Experiments have been carried out on shell motor oil X-100-60, shell motor oil X-100-50, shell motor oil X-100-40, glycerine, caster oil, pump oil, and paraffin oil.

The results obtained confirm the validity of the theory and method.

§1. Introduction

An approximate theory of the oscillating cylinder viscometer has been dealt with by Oldroyd[1], his method is to solve the differential equation in terms of Bessel function and approximated by asymptotic expansion.

Markovitz[2] devised another approximate solution. He solved the differential equation in terms of Bessel function followed by approximation using Taylor expansion.

Abdel-Kerim Ibrahim and A. M. Kabiel[3),4),5)] gave another approximate theory, very different in appearance from either that of Oldroyd or that of Markovitz, they approximate in the original equation of motion and obtain a simple and elementary solution to the problem.

This paper gives an exact theory of the oscillating cylinder viscometer i. e. free from any approximation and offers a convenient method for determining the coefficient of viscosity of non-elastic liquids.

Experimental results were obtained by us to verify the theory and method.

§ 2. The Theory

Consider a cylindrical bob of diameter 2a cms. and moment of inertia I gm. cm^2. about its major axis suspended coaxially, by a delicate torsion wire of torsion constant τ gm. cm^2. sec^{-2}, to a depth L cms. in a cup of diameter $2b$ cms. containing a liquid of density ρ gm. cm^{-3}. and viscosity coefficient η in gm. cm^{-1}. sec^{-1}.

The cup is caused to oscillate, about its vertical axis, through a very small fixed angular amplitude ϕ_0(of the order of approximately one degree) so that the liquid is following the forced oscillations of the cup.

Since the motion is axially symmetric and in two dimensions, therefore the velocity V in cm. sec^{-1}. of the liquid at any radial distance from the central vertical axis is given by:

$$\frac{1}{\nu}\frac{\partial v}{\partial t}=\frac{\partial^2 v}{\partial r^2}+\frac{1}{r}\frac{\partial v}{\partial r}-\frac{V}{r^2} \tag{1}$$

where ν is the kinematic viscosity of the liquid.

The angular displacement of the liquid at any radial distance from the central vertical axis is given by:

$$\theta=\phi\, e^{i\omega t} \tag{2}$$

where ϕ is a function of r only.
and ω is the angular velocity in sec^{-1}. of the outer cylinder.

Therefore equatian (1) may have the form:

$$\frac{\partial^2\phi}{\partial r^2}+\frac{3}{r}\frac{\partial\phi}{\partial r}+\frac{2B^2}{i}\phi=0 \tag{3}$$

where $B=(\pi\rho n/\eta)^{1/2}$
n is the frequency of the outer cylinder.

The solution of equation (3) may be obtained in terms of Bessel function of complex argument, thus,

$$\phi=(1/r)[AJ_1(i\sqrt{i}\sqrt{2}Br) \\ +\mathrm{c}y_1(i\sqrt{i}\sqrt{2}Br)] \tag{4}$$

But since $y_1(i\sqrt{i}\sqrt{2}Br)$ is infinite when Br is finite; which is an undesirable feature in the solution of practical problems, it is more convenient to take the modified Bessel function of the second kind as the second solution since it approaches zero asymptotically as Br tends to infinity and vice versa.
Hence, equation (4) can be replaced by:

$$\phi=(1/r)[A_1J_1\{-B(1-i)r\}+iC_1K_1\{B(1+i)r\}] \tag{5}$$

where A_1 and C_1 are two arbitrary constants to be determined by the boundary conditions.

Thus,

$$\theta=(1/r)[A_1J_1\{-B(1-i)r\} \\ +iC_1K_1\{B(1+i)r\}]e^{i\omega t} \tag{6}$$

and the angular velocity:

$$\dot{\theta}=\frac{iw}{r}[A_1J_1\{-B(1-i)r\}+iC_1K_1\{B(1+i)r\}]e^{i\omega t} \tag{7}$$

and the rate of change of the relative motion of adjacent layers of the liquid.

$$\frac{d\dot{\theta}}{dr}=\frac{\omega B(1+i)}{r}[C_1K_2\{B(1+i)r\} \\ +A_1J_2\{-B(1-i)r\}]e^{i\omega t} \tag{8}$$

and the angular velocity gradient in the neighbourhood of the inner cylinder.

$$\left(\frac{d\dot{\theta}}{dr}\right)_{r=a}=\frac{\omega B(1+i)}{a}[C_1K_2\{B(1+i)a\} \\ +A_1J_2\{-B(1-i)a\}]e^{i\omega t} \tag{9}$$

The Equation of Motion of the inner cylinder.

The suspended bob experiences:

i—The shearing torque C' due to the liquid, where:

$$C'=2\pi La^3\eta\left(\frac{d\dot{\theta}}{dr}\right)_{r=a} \tag{10}$$

ii—The torque C'' due to the suspension wire, where:

$$C''=-\tau\theta_0 \tag{11}$$

and θ_0 is the angular amplitude of the suspended cylinder.

As a result, the eqution of motion of the suspended cylinder is given by the following equation:

$$I(\ddot{\theta})_{r=a}=K\eta\left(\frac{d\dot{\theta}}{dr}\right)_{r=a}-\tau\theta_0 \qquad (12)$$

where $K=2\pi La^3$

Thus,

$$\theta_0=\frac{K\eta}{\tau-I\omega^2}\left(\frac{d\dot{\theta}}{dr}\right)_{r=a} \qquad (13)$$

and,

$$(\dot{\theta})_{r=a}=\frac{-K\eta}{\tau-I\omega^2}\cdot\frac{\omega^2B(1-i)}{a}e^{i\omega t}$$
$$\times[A_1J_2\{-B(1-i)a\}+C_1K_2\{B(1+i)a\}] \qquad (14)$$

where $(\dot{\theta})_{r=a}$ is the angular velocity in $\sec^{-1}$. of the liquid in the neighbourhood of the curved surface of the inner cylinder.

The boundary conditions

The arbitrary constants A_1 and C_1 are determined by the boundary conditions.

The two conditions are:

$$\left.\begin{array}{lll}\text{i—when} & r=a\,, & \theta=i\omega\theta_0 \\ \text{ii—when} & r=b\,, & \dot{\theta}=i\omega\phi_0\end{array}\right\}e^{i\omega t}$$

where ϕ_0 is the amplitude of the outer cylinder. Therefore,

$$\left.\begin{array}{l} C_1=\dfrac{\phi_0bE}{F'E-FE'} \\ \text{and} \\ A_1=\dfrac{-\phi_0bF}{F'E-FE'}\end{array}\right\} \qquad (15)$$

where:

$$E=\gamma J_1\{-B(1-i)a\}-(1+i)J_2\{-B(1-i)a\}$$
$$F=i\gamma K_1\{B(1+i)a\}-(1+i)K_2\{B(1+i)a\}$$
$$E'=J_1\{-B(1-i)b\}$$
$$F'=iK_1\{B(1+i)b\}$$

and

$$\gamma=\frac{\tau-I\omega^2}{k\eta\omega B}$$

therefore:

$$\frac{\dot{\theta}}{\phi_0}=\frac{i\omega be^{i\omega t}}{r[F'E-FE']}$$
$$\times[iEK_1\{B(1+i)r\}-FJ_1\{-B(1-i)r\}] \qquad (16)$$

and

$$\frac{d\dot{\theta}}{dr}=\frac{\omega B\phi_0b(1+i)e^{i\omega t}}{r[F'E-FE']}$$
$$\times[EK_2\{B(1+i)r\}-FJ_2\{-B(1-i)r\}] \qquad (17)$$

It is often quite convenient to consider the modulus or the absolute value, therefore on solving equation (16) we have:

$$\left|\frac{\dot{\theta}}{\phi_0}\right|^2=\frac{\omega^2b^2}{r^2}\cdot\frac{L_1^2+M_1^2}{L^2+M^2} \qquad (18)$$

Now, let:

$$\sqrt{2}\,Ba=P \qquad \sqrt{2}\,Bb=Q$$

and,

$$\sqrt{2}\,Br=S$$

Therefore:

$$L_1=-\begin{vmatrix} \mathrm{ker}_1\,S & \mathrm{kei}_1\,S & 0 & 0 \\ \gamma/2 & -\gamma/2 & 1 & 0 \\ -\mathrm{bei}_2\,P & \mathrm{ber}_2\,P & -\mathrm{bei}_1\,P & \gamma/2 \\ \mathrm{ber}_1\,P & \mathrm{ber}_1\,P & 0 & 1 \end{vmatrix} + \begin{vmatrix} \mathrm{ber}_1\,S & \mathrm{bei}_1\,S & 0 & 0 \\ \gamma/2 & -\gamma/2 & 1 & 0 \\ -\mathrm{kei}_2\,P & \mathrm{ker}_2\,P & -\mathrm{kei}_1\,P & \gamma/2 \\ \mathrm{ker}_1\,P & \mathrm{ker}_1\,P & 0 & 1 \end{vmatrix}$$

$$M_1=-\begin{vmatrix} \mathrm{ker}_1\,S & \mathrm{kei}_1\,S & 0 & 0 \\ \gamma/2 & \gamma/2 & 1 & 0 \\ \mathrm{ber}_2\,P & \mathrm{bei}_2\,P & \mathrm{bei}_1\,P & \gamma/2 \\ \mathrm{ber}_1\,P & -\mathrm{ber}_1\,P & 0 & 1 \end{vmatrix} + \begin{vmatrix} \mathrm{ber}_1\,S & \mathrm{bei}_1\,S & 0 & 0 \\ \gamma/2 & \gamma/2 & 1 & 0 \\ \mathrm{ker}_2\,P & \mathrm{kei}_2\,P & \mathrm{kei}_1\,P & \gamma/2 \\ \mathrm{ker}_1\,P & -\mathrm{ker}_1\,P & 0 & 1 \end{vmatrix}$$

$$L=-\begin{vmatrix} \mathrm{ker}_1\,Q & \mathrm{kei}_1\,Q & 0 & 0 \\ \gamma/2 & -\gamma/2 & 1 & 0 \\ -\mathrm{bei}_2\,P & \mathrm{ber}_2\,P & -\mathrm{bei}_1\,P & \gamma/2 \\ \mathrm{ber}_1\,P & \mathrm{ber}_1\,P & 0 & 1 \end{vmatrix} + \begin{vmatrix} \mathrm{ber}_1\,Q & \mathrm{bei}_1\,Q & 0 & 0 \\ \gamma/2 & -\gamma/2 & 1 & 0 \\ -\mathrm{kei}_2\,P & \mathrm{ker}_2\,P & -\mathrm{kei}_1\,P & \gamma/2 \\ \mathrm{ker}_1\,P & \mathrm{ker}_1\,P & 0 & 1 \end{vmatrix}$$

and,

$$M=-\begin{vmatrix} \mathrm{ker}_1\, Q & \mathrm{kei}_1\, Q & 0 & 0 \\ \gamma/2 & \gamma/2 & 1 & 0 \\ \mathrm{ber}_2\, \mathrm{P} & \mathrm{bei}_2\, \mathrm{P} & \mathrm{bei}_1\, \mathrm{P} & \gamma/2 \\ \mathrm{ber}_1\, \mathrm{P} & -\mathrm{ber}_1\, \mathrm{P} & 0 & 1 \end{vmatrix} + \begin{vmatrix} \mathrm{ber}_1\, Q & \mathrm{bei}_1\, Q & 0 & 0 \\ \gamma/2 & \gamma/2 & 1 & 0 \\ \mathrm{ker}_2\, \mathrm{P} & \mathrm{kei}_2 \mathrm{P} & \mathrm{kei}_1\, \mathrm{P} & \gamma/2 \\ \mathrm{ker}_1\, \mathrm{P} & -\mathrm{ker}_1\, \mathrm{P} & 0 & 1 \end{vmatrix} \tag{19}$$

Equation (18) gives the angular velocity amplitude through the liquid at any distance from the curved surface of the inner cylinder. It is related to linear velocity amplitude (V) (which is actually measured in practice) at some place; where:

$$\left|\frac{V}{\phi_0}\right| = r\left|\frac{\dot\theta}{\phi_0}\right| \tag{20}$$

also,

$$\left|\frac{\dot\theta}{\phi_0}\right|_{r=a} = \frac{\omega^2 b^2}{a^2} \cdot \frac{L_2{}^2+M_2{}^2}{L^2+M^2} \tag{21}$$

where,

$$L_2=-\begin{vmatrix} 1 & 0 & 0 \\ 1 & \mathrm{kei}_1\, \mathrm{P} & \mathrm{ker}_1\, \mathrm{P} \\ 1 & \mathrm{ber}_2\, \mathrm{P} & \mathrm{bei}_2\, \mathrm{P} \end{vmatrix} + \begin{vmatrix} 1 & 0 & 0 \\ 1 & \mathrm{bei}_1\, \mathrm{P} & \mathrm{ber}_1\, \mathrm{P} \\ 1 & \mathrm{ker}_2\, \mathrm{P} & \mathrm{bei}_2\, \mathrm{P} \end{vmatrix} \tag{22}$$

and,

$$M_2=-\begin{vmatrix} 1 & 0 & 0 \\ 1 & -\mathrm{kei}_1\, \mathrm{P} & \mathrm{ker}_1\, \mathrm{P} \\ 1 & \mathrm{bei}_2\, \mathrm{P} & \mathrm{ber}_2\, \mathrm{P} \end{vmatrix} + \begin{vmatrix} 1 & 0 & 0 \\ 1 & -\mathrm{bei}_1\, \mathrm{P} & \mathrm{ber}_1\, \mathrm{P} \\ 1 & \mathrm{kei}_2\, \mathrm{P} & \mathrm{ker}_2\, \mathrm{P} \end{vmatrix} \tag{23}$$

L and M are given by equation (19) and

$$\left|\frac{V}{\phi_0}\right|_{r=a} = a\left|\frac{\dot\theta}{\phi_0}\right|_{r=a} \tag{24}$$

Now, the rate of the relative motion of adjacent layers of the liquid can be expressed by:

$$\left|\frac{d\dot\theta}{dr}\right|^2 = \frac{w^2B^2\phi^2b^2}{r^2} \cdot \frac{L_3{}^2+M_3{}^2}{L^2+M^2} \tag{25}$$

where,

$$L_3=-\begin{vmatrix} \mathrm{ker}_2\, \mathrm{S} & \mathrm{kei}_2\, \mathrm{S} & 0 & 0 \\ -1 & 1 & 0 & 1 \\ \mathrm{bei}_2\, \mathrm{P} & \mathrm{bei}_2\, \mathrm{P} & \gamma & \mathrm{ber}_2\, \mathrm{P} \\ \mathrm{bei}_1\, \mathrm{P} & -\mathrm{ber}_1\, \mathrm{P} & 1 & 0 \end{vmatrix} + \begin{vmatrix} \mathrm{ber}_2\, \mathrm{S} & \mathrm{bei}_2\, \mathrm{S} & 0 & 0 \\ -1 & 1 & 0 & 1 \\ \mathrm{kei}_2\, \mathrm{P} & \mathrm{kei}_2\, \mathrm{P} & \gamma & \mathrm{ker}_2\, \mathrm{P} \\ \mathrm{kei}_1\, \mathrm{P} & -\mathrm{ker}_1\, \mathrm{P} & 1 & 0 \end{vmatrix}$$

and,

$$M_3=-\begin{vmatrix} \mathrm{ker}_2\, \mathrm{S} & \mathrm{kei}_2\, \mathrm{S} & 0 & 0 \\ -1 & 1 & 0 & -1 \\ \mathrm{ber}_2\, \mathrm{P} & \mathrm{ber}_2\, \mathrm{P} & \gamma & \mathrm{bei}_2\, \mathrm{P} \\ \mathrm{ber}_1\, \mathrm{P} & \mathrm{bei}_1\, \mathrm{P} & 1 & 0 \end{vmatrix} + \begin{vmatrix} \mathrm{ber}_2\, \mathrm{S} & \mathrm{bei}_2\, \mathrm{S} & 0 & 0 \\ -1 & 1 & 0 & -1 \\ \mathrm{ker}_2\, \mathrm{P} & \mathrm{ker}_2\, \mathrm{P} & \gamma & \mathrm{kei}_2\, \mathrm{P} \\ \mathrm{ker}_1\, \mathrm{P} & \mathrm{kei}_1\, \mathrm{P} & 1 & 0 \end{vmatrix} \tag{26}$$

L and M have their usual significance. and,

$$\left|\frac{d\dot{\theta}}{dr}\right|^2=\frac{\omega^2B^2\phi^2b^2}{a^2}\cdot\gamma^2\,\frac{L_2^2+M_2^2}{L^2+M^2} \tag{27}$$

Hence the velocity gradient amplitude may be obtained from the relation.

$$\left|\frac{dv}{dr}\right|=r\left|\frac{d\dot{\theta}}{dr}\right|+|\dot{\theta}| \tag{28}$$

and,

$$\left|\frac{dv}{dr}\right|_{r=a}=a\left|\frac{d\dot{\theta}}{dr}\right|_{r=a}+|\dot{\theta}|_{r=a} \tag{29}$$

Also from equations (6) and (7), it follows that,

$$|\dot{\theta}|=\omega|\theta|=\omega|\phi|\left|\frac{\theta}{\phi}\right| \tag{30}$$

Therefore, from equation (18), we have,

$$|\psi^2|=\left|\frac{\theta}{\phi_0}\right|^2=\frac{1}{\omega^2}\left|\frac{\dot{\theta}}{\phi_0}\right|^2$$

$$=\left(\frac{b}{r}\right)^2\cdot\frac{L_1^2+M_1^2}{L^2+M^2} \tag{31}$$

This gives the angular amplitude of oscillation in the liquid at any radial distance from the curved surface of the inner cylinder to that of the outer.

Also, from equation (21), we have,

$$|\psi|^2_{r=a}=\left|\frac{\theta_0}{\phi_0}\right|^2=\frac{b^2}{a^2}\cdot\frac{L_2^2+M_2^2}{L^2+M^2} \tag{32}$$

the exact relationship between the measured quantity $|\psi|_{r=a}$ and the desired quantity η.

Also equation (32) can be obtained by comparing equation (13) and (27).

Viscosity Determination

Although equation (32) represents the exact relationship between the measured quantity $|\psi|_{r=a}$ and the desired quantity η yet it is not a direct relation since the Bessel function involves η.

However, by introducing in equation (32), a dimensionless parameter defined by:

$$\sqrt{2}\,Ba=x$$

where the symbols have their usual significance and x may take any positive value, the following expression is obtained.

$$\left|\frac{\theta_0}{\phi_0}\right|^2=|\psi|^2_{r=a}=\frac{A'n^4}{B'+C'n^2+D'n^4} \tag{32}$$

where A', B', C' are constants and whose values depend on:

i—the density of the liquid.
ii—the constants of the apparatus.

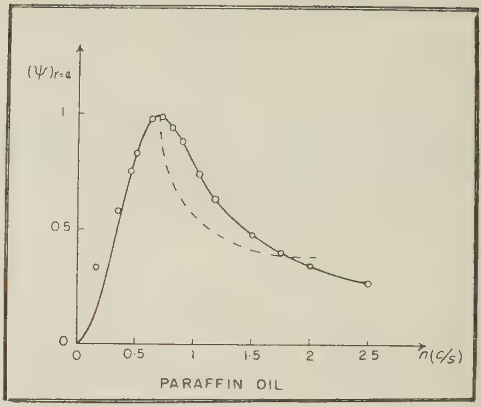

Fig. 1.

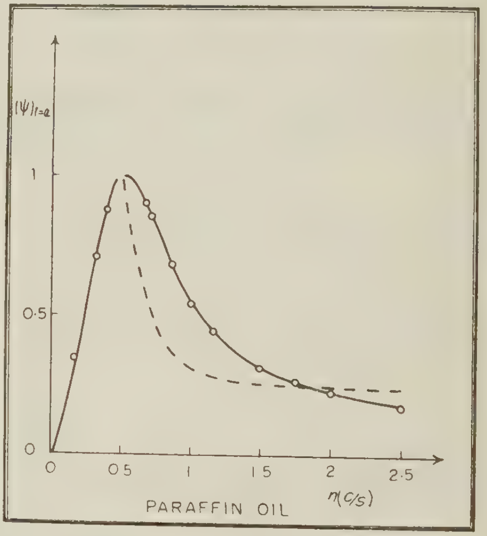

Fig. 2.

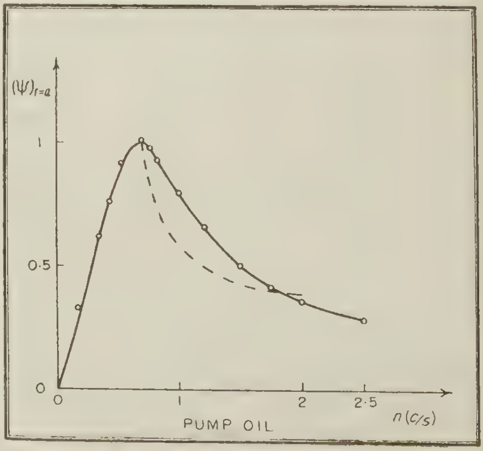

Fig. 3.

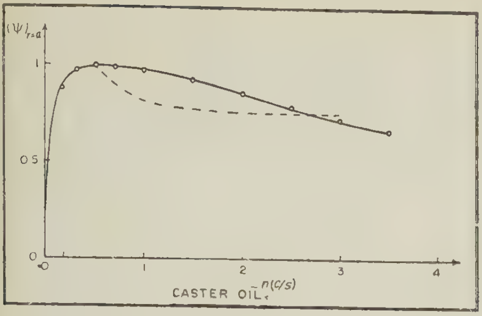

Fig. 4.

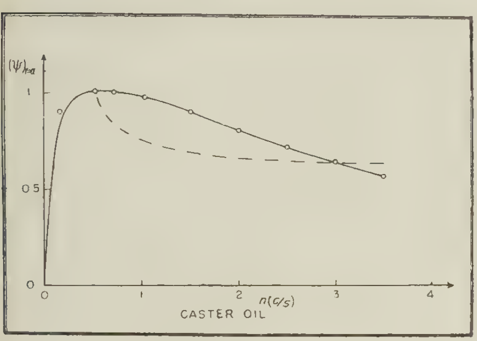

Fig. 5.

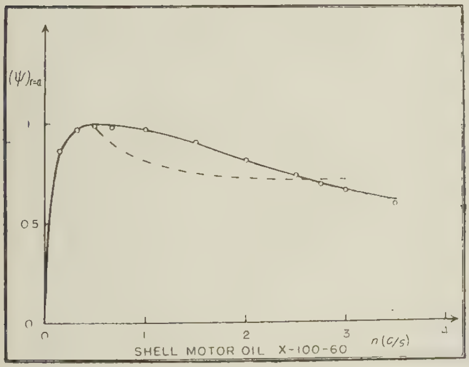

Fig. 6.

iii—the numerical value of x chosen.

The theoretical curve derived from equation (32) and the experimental curve coincide only at the point (n_s, ψ_s).

Hence, by substituting the value of x chosen and the value of n_s obtained, in the following relation:

$$\eta = \frac{2\pi \rho a^2 n_s}{x^2}$$

the value of η is determined.

In our experimental work, the values of x has been chosen:—

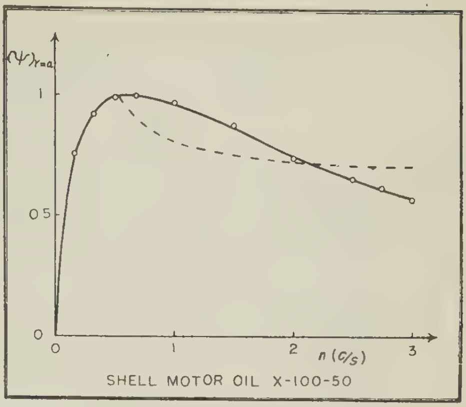

Fig. 7.

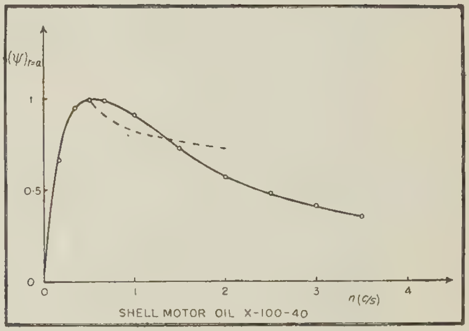

Fig. 8.

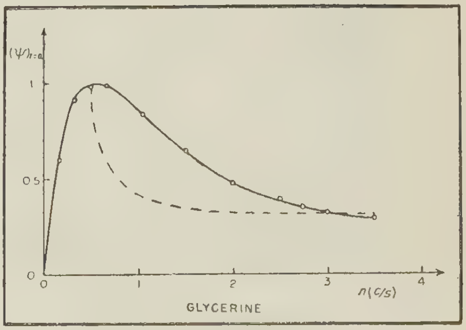

Fig. 9.

i— $\sqrt{2}\,Ba = x = 0.5$

therefore,

$$\sqrt{2}\,Bb = x\frac{b}{a} = 0.7$$

hence,

$$|\psi^2|_{r=a} = \frac{7.84}{7.846 - \frac{\gamma}{2}(0.024) + \frac{\gamma^2}{4}(0.235)}$$

where,

Table I.

$2a=0.9$ cm., $b=0.63$ cm., $\tau=459.6$ gm. cm^2. sec^{-2}.

Liquid	temp. °C.	ρ density gm. cm^{-3}.	η in Poise Stokes	η in Poise Dimensionless Parameter
Paraffin oil $I=24.5$ $L=9.9$	20	0.875	—	1.95
Paraffin oil $I=39.48$ $L=10.6$	19	0.875	—	1.96
Pump oil $I=24.5$ $L=10.3$	18.8	0.88	—	2.01
Caster oil $I=39.48$ $L=10.8$	18.7	0.972	13.1	13.27
Caster oil $I=39.48$ $L=7.8$	18.7	0.972	13.1	14.6
Shell motor oil X-100-60 $I=39.48$ $L=10.3$	19.2	0.888	11.8	11.83
Shell motor oil X-100-50 $I=39.48$ $L=10.3$	19.2	0.886	9.46	9.56
Shell motor oil X-100-40 $I=39.48$ $L=10.4$	19.3	0.884	—	6.03
Glycerine $I=39.48$ $L=10.2$	20.2	1.245	4.649	4.86

L is the length of immersion of the inner cylinder.
I is the moment of inertia of the inner cylinder.

$$\frac{\gamma}{2}=\frac{459.6-4\pi^2In^2}{28.72\rho Ln^2}$$

ii—

$$\sqrt{2}\,Ba=1$$

therefore,

$$\sqrt{2}\,Bb=1.4$$

hence,

$$|\psi|^2_{r=a}=\frac{1.96}{1.963-\frac{\gamma}{2}(0.0441)+\frac{\gamma^2}{4}(0.235)}$$

where,

$$\frac{\gamma}{2}=\frac{459.6-4\pi^2In^2}{14.35\rho Ln^2}.$$

§ 3. Results

Experiments have been carried out on paraffin oil, pump oil, caster oil, shell motor oil X-100-60 shell motor oil X-100-50, shell motor oil X-100-40 and glycerine.

Figs. (1–9) represent the variation of $(\psi)_{r=a}$ with n for the respective liquids.

The dotted line in each fig. shows the dimensionless parameter curve while the full line represents the experimental curve.

Table I provides the final results which confirm the validity of the theory and method.

§ 4. Conclusion

Considering our results in general, it appears that resonance occurs between the liquid and the inner cylinder at a certain frequency almost exactly equal to the frequency of free oscillation of the inner cylinder and the torsion wire, figs. (1–9).

Therefore copper rings were made which could be fastened on the top of the inner cylinder to change its moment of inertia and the resonant frequency of the instrument, figs. (1–2). These rings enable measurements to be made over a wide range of viscosity.

From the frequencies of the outer cylinder less than 25 c./m. and liquids of viscosity less than 5 poise nearly, the motion of the inner cylinder is not perfectly simple harmonic motion and that is probably why the observed readings in this region are subject to experimental error and inconvenient.

Also the end effect has been investigated. Since viscous forces are proportional to area,

$$F_1/F_2 = 2\pi aL/\pi a^2$$

where F_1 is the tangential viscous force at the surface of the cylinder and F_2 is the viscous force on the base or,

$$F_1/F_2 = 2L/a$$

hence, the end corrections are negligible and the effective depth of immersion is the actual length, if $a/2L$ is very small, if not the neglect of end effect will affect our results, figs. (4 and 5).

In addition, since a free surface is present at the top of the annular gap, we expect a departure from two dimensional motion, this can be made negligible by sufficiently reducing the annular gap and the amplitude of oscillation of the outer cylinder. In practice the amplitude is 1°.

Also the results are compared with that of the falling sphere method.

The results obtained in Table I confirm the validity of the theory and method discussed and indicate the sensitivity of the apparatus for slight change of temperature.

References

1) J. G. Oldroyd: Quart. J. Mech. and Appl. Math. Vol. IV, Pr. 3P. **271** (1951).
2) H. Markovitz: J. Appl. Phys. **23, 1070** (1952).
3) Alin A. K. Ibrahim and A. M. Kabiel: J. Appl. Phys. **23, 7** (754–756) (1952).
4) Ali A. K. Ibrahim and A. M. Kabiel: ZAMP, Fasc 5, Vol. V. (1954).
5) Ali A. K. Ibrahim and A. M. Kabiel: ZAMP, Fasc 5, Vol. VI; (1955).

This section is intended to secure prompt publication of important discoveries in physics. The reports should not exceed 800 words in length. A figure of size 7 cm × 7 cm will be counted as 150 words.

J. Phys. Soc. Japan **12** (1957) 1312

Technique of Obtaining a Minute Pinhole in a Metal Plate. II

By Tadasi Numata

Nagasaki University, Ohasi-Machi, Nagasaki

(Received July 14, 1957)

In the previous paper1) (to be refered to here as I), the author has reported a method of obtaining a minute pinhole in a metal plate having comparatively low melting point by using a needle of a glass fibre.

In order to obtain a straight minute pinhole in the metal plate whose thickness is l, it is necessary to put the needle (its length$>l$) into the molten metal against resisting force due to the surface tension of the molten metal without bending of the needle. But if l is longer than a critical length l_0, the needle can unable to be put into the molten metal without bending. One may, therefore, suppose that the maximum thickness of the metal plate having the pinhole with a diameter R is equal to the critical length l_0 corresponding to the upper limit for the stability of the undeflected equilibrium position of the needle. It is also equal to the length associated with the first mode of the bent needle when the needle originally in a vertical position is acted upon and bent by compressive forces P at the ends of the needle.

This critical length l_0 can be easily obtained by solving the Euler's equation2) for bending momen of a light needle under plausible boundary conditions. The equation is

$$\frac{d^2y}{dx^2}+k^2y=0\,, \qquad \text{(1}$$

where

$$k^2=\frac{P}{B}\,, \quad B=\frac{\pi E R^4}{64}\,,$$

B and E being the flexural rigidity and the Young's modulus, respectively. The quantity y is the deflection from the equilibrium position of the centra axis of the needle at any point whose distance from one end is x. By imposing on Eq. (1) the boundary conditions that $y=0$ when $x=0$ and $x=l$, the length of the needle corresponding to the first mode o its bending is given by $l_0k=\pi$. The corresponding load is given by $P=B\pi^2/l_0^2$. On the other hand the value of P is approximately equal to πRH, as one end of the needle is supported on the surface of the molten metal by its surface tension H. The corresponding critical length l_0 is, then, given by

$$l_0=\frac{\pi}{8}\left(\frac{ER^3}{H}\right)^{1/2}. \qquad \text{(2}$$

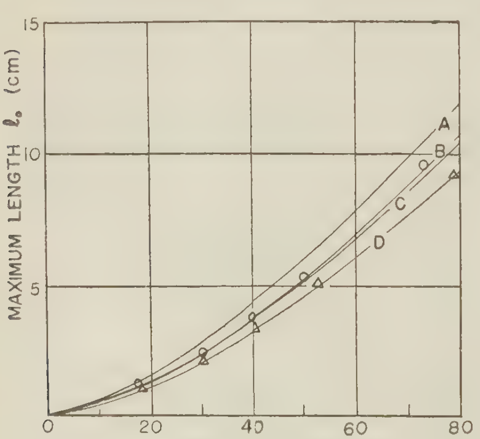

Fig. 1. Relation between the maximum length l_0 and the diameter of pinholes. Experimental: ○ (Wood's metal), △ (lead).

Fig. 1 shows the examples of the calculation by Eq. (2). The curves A and C are, respectively the calculated ones for Wood's metal and lead using fused quartz needles. The curves B and D are respectively, for Wood's metal and lead using glass needless. In the above calculations, $H=338$ dynes cm^{-1} for Wood's metal3), $H=450$ dynes cm^{-1} for lead3), $E=5\times10^{11}$ dynes cm^{-2} for glass needles, and $E=(27/R+5.9)\times10^{11}$ dynes cm^{-2} for fused quart needles5) are assumed, and the temperature dependences of H and E are not taken into account. The observed values of l_0 for Wood's metal and lead using glass needles are also shown in Fig. 1.

Finally, the author expresses his sincere thanks to Professor A. Okazaki of the Kyushu University for his encouragements.

References

1) T. Numata: J. Phys. Soc. Japan **12** (1957) 559
2) H. Bateman: Partial Differential Equations o Mathematical Physics.
3) K. Shiba: Physical Constant Tables (in Japanese).
4) K. Hisano and M. Munakata: Glass Fibres and Its Applications (in Japanese).
5) J. Strong: Procedures in Experimental Physics

J. PHYS. SOC. JAPAN **12** (1957) 1313-1314

Oscillator Strength of *M*-center of KCl

By Hiroshi OKURA

Institute of Polytechnics, Osaka City University, Osaka

(Received August 22, 1957)

Conversion of *F*-center to *M*-center and vice versa by irradiation with *F*-light and suitable heat treatment, allows us to determine the oscillator strength of *M*-center. In this report we shall describe the way and the result for KCl.

Single crystals of KCl were grown within a platinum crucible by the Kyropoulos method, using the melted reagent containing less than 0.001% divalent impurities. The crystals thus prepared were then colored additively, keeping them at 500°C for nearly eighty hours in the vapour of potassium or sodium. These colored crystals, however, naturally contain subsidiary centers other than *F*-center. In order to rule them out, the specimens were put into the furnace and kept at 500°C for one minute, after being cleaved into a thin rectangular slice as to fit the optical measurement, and then cooled down on the massive copper block at room temperature very rapidly. Care was taken that this quenching process be done in the dim light.

Every specimen subject to this treatment did show little trace of the unwanted subsidiary bands. The optical absorption measurements were carried out with a Beckman Model DU spectrophotometer at room temperature. After the absorption of such a quenched colored crystal was measured, the same specimen was exposed to the *D*-line of a sodium lamp (λ=5,890 A) for two minutes and subsequently the optical measurement was repeated, a typical results of which is shown in Fig. 1.

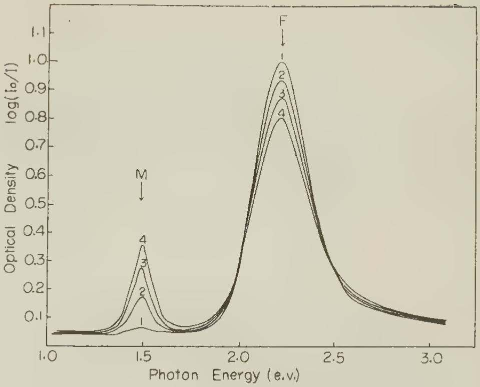

Fig. 1. Changes of the absorption curves upon successive irradiations by *F*-light (λ=5,890 A). From 1 to 4, the two-minute-exposure was repeated. The concentration of initial *F*-centers is 2.0×10^{17} 1/c.c. Measurements were done at room temperature (20°C).

Comparing the two absorption spectra with different conditions, it was confirmed that no appreciable change was observable in the region from 2,100 A to 15,000 A, except for the *F* and *M* bands. Moreover, by quenching again the irradiated specimen with the same technique described above, the original unirradiated state was quite perfectly recovered. So we safely assume that, during these short exposures, the total number of electrons is unchanged and the conversion occurs in the form of $F \rightleftarrows M$. With this assumption the increased number of electrons at *M*-center will be equal to the decreased one at *F*-centers, and this leads us to the determination of the oscillator strength for the *M*-center.

Namely, let $\Delta\alpha_F$ and $\Delta\alpha_M$ be the changes of the peak intensities of the *F* and *M* bands, respectively; then the ratio of the oscillator strengths for these two centers, using the Smakula's formula, is

Table

Specimen	Concentration of *F*-centers (c.m.$^{-3}$)	Time of Exposure (min.)	$\Delta\alpha_F$ (c.m.$^{-1}$)	$\Delta\alpha_M$ (c.m.$^{-1}$)	f_F/f_M
1*	2.0×10^{17}	2	1.22	2.24	0.58
		2	1.47	2.24	0.49
		2	1.30	1.53	0.40
2	4.8×10^{17}	2	5.30	4.70	0.30
		2	4.20	3.64	0.26
3	4.5×10^{16}	10	0.60	0.75	0.42
4	4.6×10^{16}	10	0.74	0.92	0.41

$f_F/f_M=0.41\pm0.01$.

*: Data for this specimen are shown in Fig. 1.

given by

$$\frac{f_M}{f_F}=-\frac{\Delta\alpha_M\cdot W_M}{\Delta\alpha_F\cdot W_F}$$

where W_F, W_M are the half breadths for F and M bands, their observed values being 0.36 e.v. and 0.12 e.v., respectively.

From the measured values of $\Delta\alpha$'s, we obtai f_M/f_F. These values are tabulated in the Tabl for the specimens with various *F*-center concentra tions. Taking $f_F=0.83$, we find $f_M=0.34\pm0.01$.

The author wishes to express his gratitude t Professor H. Kawamura for his helpful discussion and advices.

J. Phys. Soc. Japan **12** (1957) 1314

Anomalous Magnetic Properties of $Cu(NH_3)_4SO_4\cdot H_2O$ and $MnSO_4\cdot H_2O$

By Muneyuki DATE

Research Institute for Iron, Steel and Other Metals, Tōhoku University, Sendai

(Received October 3, 1957)

During the course of the studies on antiferromagnetism at low temperatures, we have found some anomalies in the magnetic properties of $Cu(NH_3)_4SO_4\cdot H_2O$ and of $MnSO_4\cdot H_2O$ from the measurements of paramagnetic resonance and susceptibilities. Paramagnetic resonances at 9800 and 18000 Mc/sec were observed with both substances. $Cu(NH_3)_4SO_4\cdot H_2O$ showed the anomalous broadening of the resonance lines which was reported previously by the present author[1], while $MnSO_4\cdot H_2O$ showed no resonance absorption in the liquid helium temperature region but showed a strong paramagnetic resonance above the liquid nitrogen temperatures. On the other hand, among the hydrates of $MnSO_4$, the mono-hydrate has the strongest exchange interaction, as may be seen from the narrowness of the paramagnetic resonance lines observed by Kumagai et al.[2] at room temperature. It may, then, easily be inferred that the antiferromagnetic transition may occur in the liquid helium temperature region. To clarify more precisely the magnetic anomalies of these substances, the magnetic susceptibility, specific heat measurements etc. are desired. So, we performed experiments of powder susceptibilities by the usual a.c. bridge method. The specimen of $Cu(NH_3)_4SO_4\cdot H_2O$ was obtained from the saturated ammoniac solution and that of $MnSO_4\cdot H_2O$ was obtained by heating $MnSO_4\cdot 4H_2O$ at 80°C for 5 hours. The latter specimen was carefully weighed before and after the heating and a check for the water constituent was done. More than 98% of mono-hydrate was guaranteed in our sample. The experimental results are shown in Fig. 1. χ_{curie} shows the curve that must be followed if the two salts obey the Curie law. It ma be clear that the most remarkable results are th flatness of the susceptibilities in both substance at low temperatures. One of the cause of such temperature independent susceptibility at low temperature was analyzed recently by Haseda and th present author[3] to be the non-existence of Kramer doublet for the case of Ni^{++} ion. But, as is we known, Cu^{++} and Mn^{++} have Kramers' doubl and so this cause does not apply. It may be i teresting to investigate these anomalies below 1°

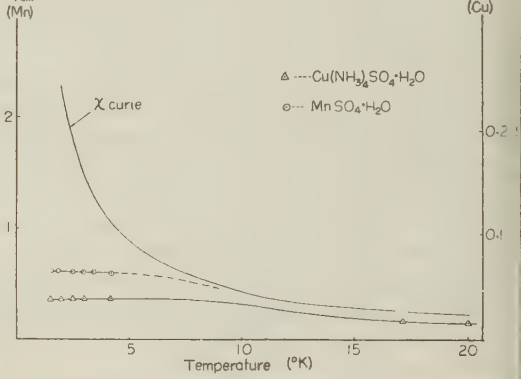

Fig. 1. Temperature dependency of magneti susceptibilities in powdered $Cu(NH_3)_4SO_4\cdot H_2$ and $Mn\ SO_4\cdot H_2O$.

The author wishes to express his cordial than to Mr. T. Haseda for the measurements of t susceptibilities and also to Prof. T. Fukuroi f encouragement given to him during the course this research. The present research was subsidize by a Research Grant form the Ministry of Educatio

References

1) M. Date: J. Phys. Soc. Japan **11** (1956) 101
2) H. Kumagai, K. Ōno, I. Hayashi, H. Abe, Shimada, H. Shōno and H. Ibamoto: Phy Rev. **83** (1951) 1077.
3) T. Haseda and M. Date: to be published short in this journal.

J. Phys. Soc. Japan 12 (1957) 1315

Diffusion of Activator of Cathode Sleeve

By Hiroyuki Mizuno
Matsushita Electronics Corporation Takatsuki

(Received July 31, 1957)

It is pointed out by several authors that there is an affection of a diffusion coefficient of an element in an alloy from the other additional elements included in the alloy[1]. We have performed some measurements of the affection of the diffusion of magnesium activator in a cathode sleeve from the other activator elements contained in the sleeve. The test pieces were made by pressing nickel strips usually used as cathode sleeve in rolling dies till 0.005 cm thickness and shaped to a rectangular form of $0.6\times3.4\,\mathrm{cm}^2$. The rectangular filaments were cleaned completely and mounted into a vacuum equipment which was evacuated till 10^{-6} mmHg. These filaments were heated and the measurement of the magnesium left in the filament was carried out on a small group of filaments after different periods of heating life test. The results are given in Fig. 1*.

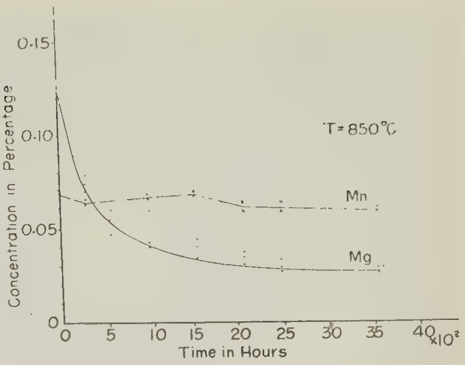

Fig. 1. The decrease of magnesium content in the sleeve with time.

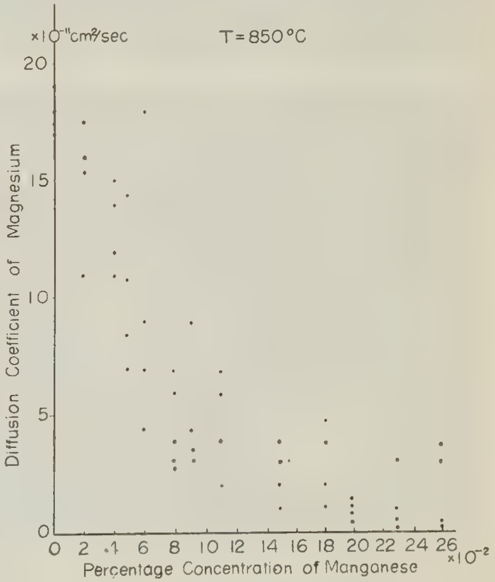

Fig. 2. The decrease of D of magnesium with increase of manganese.

Let initially the activator concentration be uniformly distributed with the constant density C_0 and it be always zero at the surface. This is a well known problem[2] with the following solution for the total amount of evolved activators Q for the time $t>0$.

$$Q=2aC_0S\left[1-\frac{8}{\pi^2}\exp\left(-D\frac{\pi^2}{4a^2}t\right)\right] \qquad (1)$$

Where D, $2a$, and S are the diffusion coefficient, filament thickness and filament surface area respectively. Then the diffusion coefficient D is given by

$$D=\frac{4a^2}{\pi^2 t}\log\frac{\pi^2}{8}\left(1+\frac{Q}{2aSC_0}\right) \qquad (2)$$

From Eq. (2), we can get the diffusion coefficient D referring to Fig. 1. In Fig. 2, we show the result of the affection of magnesium diffusion from the change of manganese contents keeping the quantity of the other elements in nickel sleeve constant as shown in Table I. From Fig. 2, we can see that the increase of manganese content may result the decrease of the diffusion coefficient of magnesium. The affections from the other elements are left for future work.

Table I. Components of Nickel.

Ni	Co	Mg	Mn	Si	Fe	S	Al	Cu
Residue	0.01	0.12	To be changed	Trace	Trace	0.001	Trace	Trace

(Weight percentage).

---

* In the Fig. 1, the decreasing curve of manganese is also given. The manganese decrease during life is negligibly small compared with magnesium, therefore the following result is given without serious error.

References

1) For example; W. Seith: Diffusion in Metallen 1939, pp. 70–80.
2) H. S. Carslaw and J. C. Jaeger: Conduction of Heat in Solids. (Oxford University press, London 1948).

J. PHYS. SOC. JAPAN **12** (1957) 1316

LCAO-MO Treatment of Phthalocyanine

By Asa CHIKAYAMA, Yuzuru OOSHIKA,
Reikiti ITOH and Isao OSHIDA.
Kobayasi Institute of Physical Research,
Kokubunji, Tokyo, Japan

(Received August 19, 1957)

The electronic energy levels of phthalocyanine are worth studying, for the dye is considered an imitation of porphyrins, which are biologically important pigments. We have calculated the electronic energy levels of metal-free phthalocyanine by simple LCAO-MO approximation, in which only the π-electrons are taken into account. As for the precise position of the two central hydrogen atoms, some ambiguity is left at present; we assume a planer structure with D_{2h} symmetry as shown in Fig. 1, according to Erdman and Corwin[1]).

There are thirty-eight centers, namely, thirty-two carbon atoms and the six nitrogen atoms without hydrogen. The number of the electrons are also thirty-eight; the lone pairs on the two nitrogen atoms linked with hydrogens are omitted from the conjugated system, because they are almost fixed on the nitrogen atoms. For the sake of simplicity, the overlap integrals are ignored, the coulombic integrals α for the carbon and the nitrogen atoms are assumed to be all equal, and the resonance integrals between adjacent atoms are regarded as β, being common to all; while the resonance integrals between non-adjacent atoms are neglected.

The secular equation that determines the energy levels, being of the thirty-eighth order, can be separated into four, the two of the tenth order and the two of the nineth order, according to the irreducible representations b_{1u}, b_{2g}, and b_{3g} and a_{1u} respectively.

The results are shown in Fig. 2, in which the value of β is taken as 23000 cm^{-1}. The transitions a_{1u}—b_{2g}, b_{2g}—b_{1u}, a_{1u}—b_{3g} and b_{3g}—b_{1u} are allowed, while others are forbidden. The calculated absorption wavelengths are compared with the experimental values of Estigneev and Kraonovskii[2]) as shown in Fig. 3. Both of them have six absorption bands in the visible region, but the spacings are so different that the identification of each band is not possible. The calculation gives two more absorption bands situated in the near infrared, which have not been found experimentally.

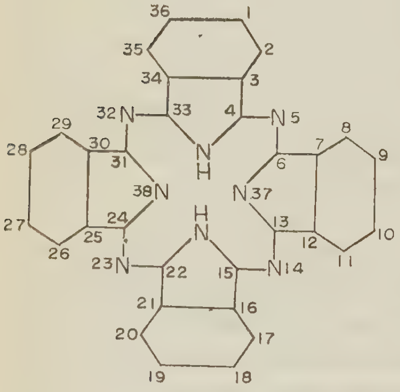

Fig. 1.

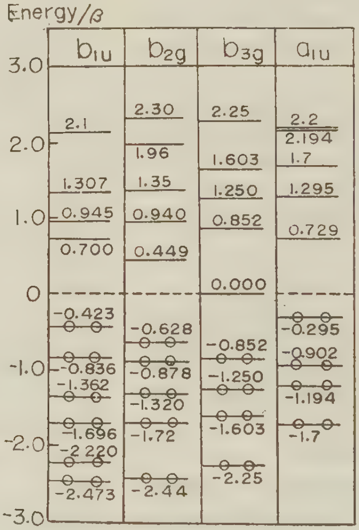

Fig. 2.

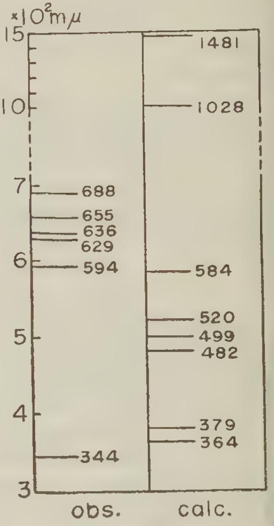

Fig. 3.

The change of the numerical value of β, and the closer approximation might give better results, but the disagreement seems to come from more basic reason, for instance, inadequate assumption concerning with the position of the hydrogen atoms at the center. The similar treatment of metal phthalocyanine is expected to throw light on this point.

The details, with similar study of porphyrins, will be published elsewhere.

References

1) F. G. Erdman and A. H. Corwin: J. Am. Chem. Soc. **68** (1946) 1885.
2) V. B. Estigneev and A. A. Kraonovskii, Doklady Akad. Nauk. SSSR. **58** (1947) 1399. cf. A. Stern and F. Pruckner: Z. phsik. Chem. **A178** (1937) 420.

J. PHYS. SOC. JAPAN **12** (1957) 1317

Elongated Lichtenberg Figure

By Yoshimi KAMADA* and Kwai UMEDA
Department of Physics, Okayama University

(Received September 18, 1957)

With an initial aim to study the primary Lichtenberg figure in nonstationary conditions (for instance, with moving electrode or in turbulent air layer), we rotated in customary experimental arrangements the photographic plate about an axis perpendicular to the plane of itself, the needle-electrode being placed at some distance from the rotation axis, thus lightly scratching a circular track on the plate.

By this procedure the negative figure happened to be elongated along the circular track symmetrically in both directions, while the positive one didn't vary at all, as shown in Fig. 1. The lack of the expected effect of the sense of rotation may be because the formation velocity of the Lichtenberg figure is extremely high (about 10 cm/sec) in comparison with the motion of our plate, and suggests further that for the elongation it would be neither essential nor necessary to carry out the discharge in the midst of rotation. In fact, similar figures can be obtained even when the discharge takes place after stopping the rotation. Thus, the elongation seems to be caused by the metal streak rubbed on the plate glass by the sliding needle-electrode. This point of view is in favor with the fact that the amount of elongation is affected by the nature of the electrode metal and the method of rubbing the electrode on the plate (for another instance, reciprocating rubbing by hand). The distinctly different effects of the metal streak on positive and negative figures respectively may be consistent with the current theory on the Lichtenberg figure that the electron flow alone plays significant role in their formation.

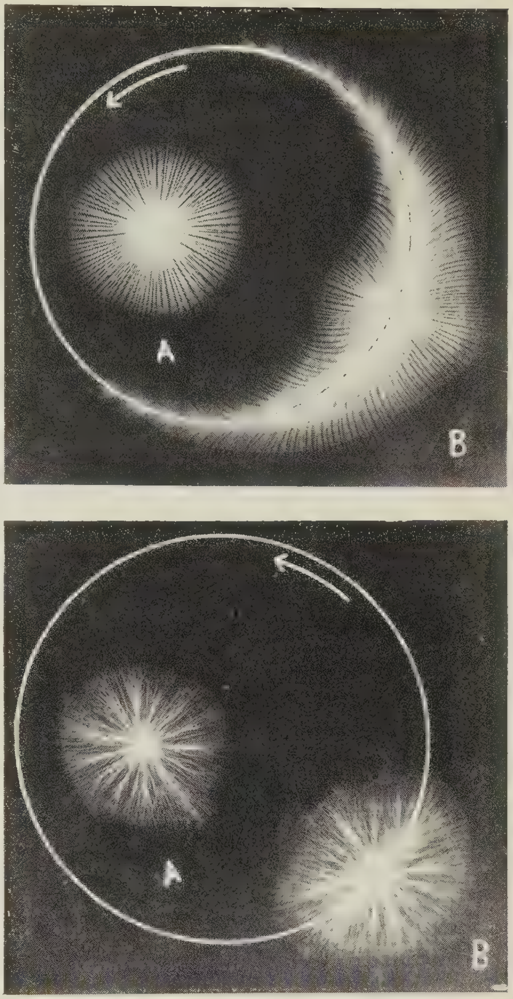

Fig. 1. Upper: negative figure; lower: positive figure. *A*: plate at rest (ordinary figure): *B*: rotating plate. Discharge voltage=about 31 kV. Rotation=about 1800 rpm. Arrow shows the sense of rotation.

---

* On leave from the Kōchi University.

Errata

Free Bonds on the Clean Surfaces Germanium Single Crystals

By Akio KOBAYASHI and Shinji KAWAJI

J. Phys. Soc. Japan **12** (1957) 1054

Fig. 2. Curve (2) and curve (3) should be exchange with each other.

Viscous Flows past a Spheroid

By Shōichi WAKIYA

J. Phys. Soc. Japan **12** (1957) 1130

P. 1137. Case (B)

$$W=16\mu cU/(1-0.5540\,c/l+0.1502\,c^3/l^3-0.023\,c^4/l^4)$$

should be read

$$\cdots(\cdots+0.1502\,c^3/l^3-0.091\,c^4/l^4)$$

P. 1137. Case (C)

$$W=16\mu cU/(1-c^2/9l^2)/(1-0.5540\,c/l+0.1092\,c^3/l^3-0.023\,c^4/l^4)$$

should be read

$$\cdots(\cdots+0.1092\,c^3/l^3-0.068\,c^4/l^4)$$

P. 1138. Case (B)

$$W=6\pi\mu aU/(1-0.6526\,a/l+0.4003\,a^3/l^3-0.132\,a^4/l^4)$$

should be read

$$\cdots(\cdots+0.4003\,a^3/l^3-0.297\,a^4/l^4)$$

P. 1138. Case (C)

$$W=6\pi\mu aU(1-a^2/9l^2)/(1-0.6526\,a/l+0.3160\,a^3/l^3-0.132\,a^4/l^4)$$

should be read

$$\cdots(\cdots+0.3160\,a^3/l^3-0.242\,a^4/l^4)$$

Conical Spiral Structure and Laminar Cleavage of Graphite

By Takuro TSUZUKU

J. Phys. Soc. Japan **12** (1957) 778–788.

Page	Column	Line		(should be read)
779	right	9	For Photo. 2......	For Photo. 1......
781	right	bottom	Photo. 5. Remarkable gliding a conical crystal.	Photo. 5. Remarkable gliding of a conical crystal.
784	left	25	Furthermore, can see......	Furthermore, one can see......
784	right	6	A_0D_0, C_0D_0, E_0F_0......	A_0B_0, C_0D_0, E_0F_0......
785	left	23	multiple layeas......	multiple layers......

PROGRESS OF THEORETICAL PHYSICS

(*Founded by H. Yukawa in 1946*)
Published for the
Research Institute for Fundamental Physics
The Physical Society of Japan

Progress of Theoretical Physics Vol. 18, No. 1, July 1957

Theory of Liquid He^3 .... S. K. TRIKHA.. 1
On the Electron-Lattice Interaction in Non-Polar Semiconductors.. Shigeharu KOSHINO.. 23
Remarks on Mayer's Reduced Density Matrix Method .... Yukio MIZUNO and Takeo IZUYAMA.. 33
Parity Nonconservation and Decay of Hyperon .... Shigeo MINAMI and Yoshio YAMAGUCHI.. 39
Criticism on the Assumptions in the Formal Scattering Theory .... Tsutomu IMAMURA.. 51
Cloudy Crystal Ball Model for Neutron Reactions at Higher Energies .... Mitsuji KAWAI, Masayuki NAGASAKI, Michitoshi SOGA, Tokuo TERASAWA, Haruo UI and Yasushi WADA.. 66
Charge Distribution of Pions produced in High Energy Nuclear Collisions .... Yoshihiro YAMAMOTO.. 81

Letters to the Editor:

E2+M1 Mixed Transitions in Heavy Odd A Nuclei ...... M. KAWAMURA.. 87
On the Effective Coupling Strength in the Static Pion Theory .... T. KOBAYASHI, J. OSADA and S. TANI.. 89
Numerical Discussions on P-Wave Meson-Nucleon Scattering .... T. SAWAGURI and J. OSADA.. 91
Stationary Fusion Reactions at Low Temperatures .... T. NISHIYAMA, T. SEKIYA and Y. WATANABE.. 93
Some Remarks on the Goldhaber Model for Strange Particles.. R. KAWABE.. 96
The Indirect (p, d) Process .... H. HAGIWARA and M. TANIFUJI.. 97
Magnetic Dipole Sum Rules for Photodisintegration of the Deuteron .... M. L. RUSTGI and J. S. LEVINGER.. 100
Addenda and Errata 101
Contents of Journ. of Phys. Soc. of Japan 102

Progress of Theoretical Physics Vol. 18, No. 2, August 1957

Inelastic Scattering of Nucleons by Light Nuclei .... Ryoichi KAJIKAWA and Wataro WATARI.. 103
Covariant Solutions of the Bethe-Salpeter Equation .... H. S. GREEN and S. N. BISWAS.. 121
The Repulsive Potential between Two Normal Helium Atoms .... Sigeru HUJINAGA.. 139
On Einstein's Relativistic Theory of the Non-Symmetric Field........ Mineo IKEDA.. 154
Inelastic Scattering of Neutrons and Surface Direct Precesses .... Haruo UI.. 163
Nuclear Magnetic Relaxation in Solid Hydrogen .... Tôru MORIYA and Kazuko MOTIZUKI.. 183
On the Theory of the Unstable Particle in Lee's Model .... Kunio NAITO.. 200

Letters to the Editor:

Ratio of Hyperons produced by Cosmic Rays .... S. H. HSIEH.. 209

On the Observability of a New Hyperon .... S. H. HSIEH..211
On the Heavy Meson Production in the π^--Proton Reaction .... T. OGIMOTO and T. SHIMIZU..213
Contribution Rules and Means of Proofreading .... i–iv
Contents of Journ. of Phys. Soc. of Japan, Vol. 12, No. 7 v
Announcement on "Supplement" of Prog. Theor. Phys., No. 4 vi

Progress of Theoretical Physics Vo. 18, No. 3 September 1957

On the Magnetic Properties of Cubic Cerium .... Tsuyoshi MURAO and Takeo MATSUBARA..215
The Electric-Octupole Transitions of Nuclei .... Mitsuo SANO..223
A Theory of Elementary Particles .... Takao TATI..235
Theory of Collective Oscillation of Electrons in Solids .... Yoshi H. ICHIKAWA..247
π^--P Interaction in High Energy Region .... Daisuke ITO, Tetsuro KOBAYASHI, Miwae YAMAZAKI and Shigeo MIMAMI..264
On the Structure of Extensive Air Showers ...... Akira UEDA and Naofumi OGITA..269
On the Subsidiary Conditions in the Bohm-Pines Theory of Electron Plasma .. .. Hideo KANAZAWA..287
The Parity Conservation and the Strength of the Interaction of Elementary Particles .... Sho TANAKA..295

Letters to the Editor:

On the Production of Mesons in Hydrogen and Carbon above 10 Gev, II .... Y. WATASE, S. MITANI, K. SUGA and Y. TANAKA..314
On the Pressure Shift of the Inversion Frequency of Ammonia .... K. TOMITA..316
Pion Production in Nucleon-Nucleon Collisions in Bev Range .... T. KOBAYASHI..318
On the Cut-off Theory in Quantum Field Theory .... S. ARAMAKI..320
Preliminary Note on the Indirect (p, t) Process .... H. HAGIWARA and M. TANIEUJI..322
On the Many-Body Pseudopotential for a System of Hard-Spheres. R. ABE..324
Ferromagnetism of a Gas of Hard Sphere Fermions with Spin 1/2 .. .. T. MORITA, R. ABE and S. MISAWA..326
Dispersion Relations in Nucleon-Nucleon Scattering .... S. MATSUYAMA and H. MIYAZAWA..329
Contents of Journ. of Phys. Soc. of Japan, Vol. 12, No. 8 330

Price	$ 1.25 per copy
	$ 15.00 per year (postage inclusive)
Annual dues for foreign members (individual subscribers)	
	$ 12.00 (postage inclusive)
〃 for foreign members of the Physical Society of Japan	
	$ 10.00 (postage inclusive)

Application for members, subscriptions and orders for back numbers should be sent, directly or through book-dealers, to

The Publication Office
in
Yukawa Hall, Kyoto University, Kyoto, Japan

JOURNAL OF THE PHYSICAL SOCIETY OF JAPAN Vol. 12, No. 12, DECEMBER, 1957

Irreversible Processes and Fluctuations

By Nobuhiko SAITÔ
Department of Applied Physics
Waseda University, Tokyo

(Received September 6, 1957)

Introduction of fluctuating forces into the phenomenological equations of irreversible processes allows us to treat the irreversible processes as Brownian motions. Along this method Fokker-Planck's equation describing the probability of occurrence of a set of events is obtained and Onsager's reciprocal relations and the principle of the least dissipation of energy are derived. An interpretation of irreversible production of entropy is proposed. Finally a critique of Popov and Karanikolov's theory is given.

§1. Introduction

Since Nyquist[1)] it has been established that the irreversible process is accompanied by fluctuation and *vice versa*. Professor Takahasi[2)] of Tokyo University expressed this in the word "fluctuation is Nature's own experiment."

A method of realizing this view may be to introduce fluctuating forces in macroscopic equations of irreversible processes such as Fick's law of diffusion or Fourier's law of heat conduction.* Then the fluctuating forces should be intimately connected with the kinetic coefficients of the irreversible processes. These macroscopic equations complemented with fluctuating forces are nothing but Langevin's equations of Brownian motions. From this point of view we give a derivation of Onsager's reciprocal relation, and propose an interpretation of the irreversible production of entropy. Finally we want to criticize the theory of Popov on the derivation of reciprocal relations.

§2. Fokker-Planck Equation

As Wigner[3)] pointed out clearly, there are two ways of the demonstration of Onsager's reciprocal relations, i.e., the one is based on the assumption that the irreversible process is equivalent to the regression of fluctuation in thermal equilibrium, and the other is a natural out come from a statistical mechanical theory of irreversible processes. There are numerous theories from both points of view for the derivation of reciprocical relations. In this paper we give a derivation from the first standpoint as an application of the theory of the Brownian motion.

Consider a system with constant energy and let α_i, $i=1, 2, \cdots, N$, be a complete set of thermodynamical quantities assumed $\alpha_i=0$ in equilibrium state. The entropy is assumed to be a function of these quantities. The deviation of the entropy $\varDelta S$ from the equilibrium state is expressed in quadratic form of α_i's as follows,

$$\varDelta S=-\frac{1}{2}\sum_{i,k=1}^{N} g_{ik}\alpha_i\alpha_k \qquad (1)$$

where we have evidently

$$g_{ik}=g_{ki} \qquad (2)$$

and these coefficients form a positive definite matrix. As we confine ourselves to the linear irreversible processes, the development of $\varDelta S$ up to second order of α_i's as is expressed in (1) suffices to our consideration.

The rate of change of α_i's is assumed to obey the following phenomenological equations

$$\dot{\alpha}_i=\sum_{k=1}^{N} L_{ik}F_k \qquad (i=1, \cdots, N) \qquad (3)$$

$$F_k=\partial\varDelta S/\partial\alpha_k=-\sum_{i=1}^{N} g_{ik}\alpha_i \qquad (4)$$

where F_k's are the thermodynamical forces giving rise to the regression of the fluctuations α_q's, and L_{ik}'s are kinetic coefficients characteristic of the irreversible processes concerned. The relation to be demonstrated is the symmetric property of the kinetic coefficients, $L_{ik}=L_{ki}$. Denoting the inverse matrix of the matrix L^* by R, we have

---

* Introduction of fluctuating forces into macroscopic equations was first proposed by Hashitsume,[6)] whose theory is based on Onsager's principle of least dissipation of energy. In this paper we go backwards to lead to Onsager's principle and reciprocity of kinetic coefficients.

$$\sum_k R_{ik}L_{kj}=\delta_{ij} \tag{5}$$

$$\sum_j L_{ij}R_{jk}=\delta_{ik} \tag{6}$$

and from (3)

$$\sum_k R_{ik}\dot{\alpha}_k=F_i\ .$$

We now introduce fluctuating forces into these equations and interprete the phenomenological equations as the averaged ones of these fluctuations,

$$\sum_{k=1}^{N} R_{ik}\dot{\alpha}_k=F_i+X_i\ . \tag{6}$$

The fluctuating forces are assumed to have the following properties

i) $$\langle X_i\rangle=0 \tag{7}$$

ii) $$\langle X_i(t)X_j(t+\tau)\rangle=b_{ij}\delta(\tau) \tag*{(8)**}$$

$$b_{ij}=b_{ji} \tag{9}$$

where b is a positive definite matrix, and further

iii) the distribution $X_1, X_2, \cdots, X_N$ is N-dimensional Gaussian distribution with averages and dispersions given by (7) and (8),

$$P(X_1, X_2, \cdots, X_N)$$
$$=\frac{1}{(2\pi)^{N/2}\sqrt{\|b\|}}\exp\left\{-\frac{1}{2}\sum_{i,k}\frac{B_{ik}}{\|b\|}X_iX_k\right\} \tag{10}$$

where $\|b\|$ is the determinant of matrix b and B_{ik} is the cofactor of its *ik* element, and $B_{ik}/\|b\|$ is, therefore, *ik* element of the inverse matrix of b, which will be denoted by a_{ik}.

$$a=b^{-1}\ , \qquad a_{ik}=a_{ki}=B_{ik}/\|b\|$$

In these assumptions it is noted that the assumption (ii) implies that the correlation $\langle X_i(t)X_j(t+\tau)\rangle$ is an even function of τ, which is never realized in a system described by so-called β-variable.[4] This case will be treated in § 4.

Define

$$B_i(\Delta t, t)=\int_t^{t+\Delta t}X_i(t)dt\cong X_i(t)\Delta t$$

for small Δt, then we obtain

$$\langle B_i(\Delta t, t)B_k(\Delta t, t)\rangle=\iint_t^{t+\Delta t}\langle X_i(s_k)X(s')\rangle dsds'$$
$$=b_{ik}\Delta t\ , \tag{11}$$

which yields for the probability of a path in $\alpha\sim t$ diagram,[5]

$$\Psi\,(\text{path})\propto\exp\left\{-\frac{1}{2}\sum_{i,k}a_{ik}\int_{t_1}^{t_2}X_iX_kdt\right\}\ . \tag{12}$$

Following the method developed by Saitô and Namiki,[5] the Fokker-Planck equation for a set of Langevin equations (6) can be immediately written down by defining Lagrangian $\mathscr{L}$, momentum π_i and Hamiltonian $\mathscr{H}$ in the following way by making use of (6) and (12)

$$\mathscr{L}=\frac{1}{2}\sum_{i,k}a_{ik}X_iX_k$$
$$=\frac{1}{2}\sum_{i,k}a_{ik}(\sum_j R_{ij}\dot{\alpha}_j-F_i)(\sum_t R_{kt}\dot{\alpha}_t-F_k)\ , \tag*{(13}$$

$$\pi_i=\frac{\partial\mathscr{L}}{\partial\dot{\alpha}_i}=\frac{1}{2}\sum_{j,k}a_{jk}R_{ji}(\sum_t R_{kt}\dot{\alpha}_t-F_k)$$
$$+\frac{1}{2}\sum_{j,k}a_{jk}(\sum_t R_{jt}\dot{\alpha}_t-F_j)R_{ki}$$
$$=\sum_k(aR)_{ki}(\sum_t R_{kt}\dot{\alpha}_t-F_k) \tag*{(14}$$

and

$$\mathscr{H}=\sum\pi_i\dot{\alpha}_i-\mathscr{L}$$
$$=\frac{1}{2}\sum_{k,j}a_{kj}\{\sum_i R_{ji}\dot{\alpha}_i-F_j\}\{\sum_t R_{kt}\dot{\alpha}_t+F_k\}\ , \tag*{(15}$$

which should be rewritten as a function of and α. From (14) we have

$$\sum_i \pi_i(R^{-1}a^{-1})_{ik}=\sum_t R_{kt}\dot{\alpha}_t-F_k$$

which is substituted into (15), to obtain

$$\mathscr{H}(\pi,\alpha)=\frac{1}{2}\sum_{k,j}a_{kj}\sum_i\pi_i(R^{-1}a^{-1})_{ik}$$
$$\times\{\sum_t\pi_t(R^{-1}a^{-1})_{tj}+2F_j\}\ . \tag*{(1}$$

The Fokker-Planck equation is obtained b "quantization" $\pi_i\rightarrow-\frac{\partial}{\partial\alpha_i}$, with the result

$$\frac{\partial W}{\partial t}=\mathscr{H}\left(-\frac{\partial}{\partial\alpha}, \alpha\right)W$$
$$=-\frac{1}{2}\sum_{k,j}a_{kj}\sum_i\frac{\partial}{\partial\alpha_i}(R^{-1}a^{-1})_{ik}$$
$$\times\left\{-\sum_t\frac{\partial}{\partial\alpha_t}(R^{-1}a^{-1})_{tj}+2F_j\right\}W$$

---

* In the following we denote by A without indices the matrix whose components are defined by A_{ik}.

** Introduction of δ-function is of course a mathematical trick of the physical requirement that for small τ_0,

$$\langle X_i(t)X_j(t+\tau)\rangle=b_{ij} \qquad \tau\leq\tau_0$$
$$=0 \qquad \tau>\tau_0\ .$$

This consideration is also necessary in (33) and (34) in later section (§ 4).

$$=-\sum_i \frac{\partial}{\partial\alpha_i}\sum_j \frac{1}{2}R^{-1}_{ij}$$
$$\times\left\{-\sum_t \frac{\partial}{\partial\alpha_t}(R^{-1}a^{-1})_{tj}+2F_j\right\}W. \quad (17)$$

In this connection, it should be mentioned of the order of the factors in (16), because different order of π gives different forms of the resulting Fokker-Planck equation. This order is so chosen as to conserve the normalization of the probability[5]; i.e.,

$$\int W\prod_{i=1}^{N} d\alpha_i=1$$

and

$$\int\frac{\partial W}{\partial t}\prod_{i=1}^{N} d\alpha_i=\int\mathscr{H}W\prod_{i=1}^{N} d\alpha_i=0 .$$

§ 3. Derivation of Reciprocal Relations

The Fokker-Planck equation derived in the preceding section is not complete in respect that the constants b_{ik} or a_{ik} are merely introduced as parameters describing the fluctuations and are not connected with the kinetic coefficients. This connection is achieved by considering the equilibrium state.

In Fokker-Planck equation (17) we put

$$\frac{\partial W}{\partial t}=-\sum_i \frac{\partial}{\partial\alpha_i}(j_iW)$$

$$j_iW=\sum_j \frac{1}{2}R^{-1}_{ij}\left\{-\sum_t \frac{\partial}{\partial\alpha_t}(R^{-1}a^{-1})_{tj}+2F_j\right\}W . \quad (18)$$

This is i-th component of the current of the probability density in α-space and must vanish in equilibrium state. The conditions for vanishing j_i for $i=1, 2, \cdots, N$ require

$$\left\{-\sum_t \frac{\partial}{\partial\alpha_t}(R^{-1}a^{-1})_{tj}+2F_j\right\}W=0 . \quad (19)$$

On the other hand in equilibrium state the probability density W is given by

$$W\propto \exp(\Delta S/k)=\exp\left(-\frac{1}{2k}\sum_{i,k} g_{ik}\alpha_i\alpha_k\right). \quad (20)$$

In our treatment the existence of fluctuations is essential and in general $\alpha_i\neq 0$, though $\langle\alpha_i\rangle=0$, in equilibrium state, contrary to the statement of § 2 that $\alpha_i=0$ in equilibrium. Substitution of (20) and (4) into (19) yields

$$\left[\sum_t (R^{-1}a^{-1})_{tj}\left\{\frac{1}{k}\sum_i g_{it}\alpha_i\right\}-2\sum_i g_{ij}\alpha_i\right]W=0 . \quad (21)$$

In order for (21) to vanish identically, we have

$$\frac{1}{k}\sum_t (R^{-1}a^{-1})_{tj}g_{it}-2g_{ij}=0$$

or

$$\sum_t g_{it}(R^{-1}a^{-1})_{tj}=2kg_{ij} , \quad (22)$$

which leads immediately to

$$(R^{-1}a^{-1})_{tj}=2k\delta_{tj} \quad (23)$$

or

$$L^{-1}=R=\frac{1}{2k}a^{-1}=\frac{1}{2k}b . \quad (24)$$

Thus the correlation (8) is written as

$$\langle X_i(t)X_j(t+\tau)\rangle=2kR_{ij}\delta(\tau)$$
$$=2kL^{-1}_{ij}\delta(\tau) , \quad (25)$$

which is equivalent to the Nyquist's relation.

The symmetry property of L and R follows from the symmetry property of b as is seen in (24).

In concluding this section we rewrite Lagrangian and Fokker-Planck equation given by (13) and (18) respectively by making use of (24),

$$\mathscr{L}=\frac{1}{4k}\sum_{i,j}(\sum_t R_{it}\dot{\alpha}_t-F_i)L_{ij}(\sum_k R_{jk}\dot{\alpha}_k-F_j) \quad (26)$$

$$=\frac{1}{4k}[2\Phi(\dot{\alpha}, \dot{\alpha})+2\Psi(F, F)-2\dot{S}(\alpha)] , \quad (26')$$

where

$$\Phi(\dot{\alpha}, \dot{\alpha})=\frac{1}{2}\sum_{i,j} R_{ij}\dot{\alpha}_i\dot{\alpha}_j ,$$

$$\Psi(F, F)=\frac{1}{2}\sum_{i,j} L_{ij}F_iF_j ,$$

from which follows immediately the principle of the least dissipation of energy,[9] and

$$\frac{\partial W}{\partial t}=-\sum_i \frac{\partial}{\partial\alpha_i}j_iW$$

$$j_i=\sum_j L_{ij}\left\{-\frac{k}{W}\frac{\partial W}{\partial\alpha_j}+F_j\right\} \quad (27)$$

which is already obtained by Hashitsume.[6]

§ 4. Systems with β-variables

As is seen in relation (24), the reciprocal relation $L_{ik}=L_{ki}$ is the immediate consequence of the reciprocity of b, $b_{ik}=b_{ki}$, which, on the other hand, is equivalent to the assumption that the correlation functions of the fluctuating forces are even functions of time. This point requires further consideration. After Casimir, we divide the thermodynamical variables into two groups, α's and β's, according to the parity of time reversal, i.e., α-variables are even and β-variables are odd for time reversal. Then the development (1) of entropy ΔS must be in general separated into two groups,

$$\Delta S=-\frac{1}{2}\sum_{i,k} g_{ik}\alpha_i\alpha_k-\frac{1}{2}\sum_{\lambda,\mu} g_{\lambda\mu}\beta_\mu\beta_\lambda \qquad (28)$$

in which cross terms of α and β do not appear because the entropy is even for time reversal. Thus we have two kinds of thermodynamical forces, even and odd,

$$F_i=-\sum_k g_{ik}\alpha_k\ , \qquad (29)$$

$$F_\lambda=-\sum_\mu g_{\lambda\mu}\beta_\mu\ . \qquad (30)$$

Therefore the fluctuating forces to be introduced in phenomenological equations are even or odd, according to the parity of thermodynamical forces to be combined. That is, X_i's are even, and X_λ's are odd. Consequently, $\langle X_i(t)X_j(t+\tau)\rangle$ and $\langle X_\lambda(t)X_\mu(t+\tau)\rangle$ are even functions of τ, but $\langle X_i(t)X_\lambda(t+\tau)\rangle$ is regarded as an odd function of τ. In effect,

$$\begin{aligned}\langle X_i(t)X_\lambda(t-\tau)\rangle&=-\langle X_i(-t)X_\lambda(-t+\tau)\rangle\\&=-\langle X_i(t)X_\lambda(t+\tau)\rangle\ . \qquad (31)\end{aligned}$$

Further the relation

$$\langle X_i(t)X_\lambda(t-\tau)\rangle=\langle X_i(t+\tau)X_\lambda(t)\rangle \qquad (32)$$

leads at once to the assumption

$$\langle X_i(t)X_\lambda(t+\tau)\rangle=b_{i\lambda}\delta(\tau) \qquad (33)$$

$$\langle X_\lambda(t)X_i(t+\tau)\rangle=b_{\lambda i}\delta(\tau) \qquad (34)$$

for $\tau\geq 0$ with

$$b_{i\lambda}=-b_{\lambda i}\ . \qquad (35)$$

Then following the same procedure as in (11) and (12)*, we have

$$\langle B_i(\Delta t,t)B_\lambda(\Delta t,t)\rangle=0 \qquad (36)$$

and the probability for a path is given by

$$\Psi(\text{path})\propto\exp\left\{-\frac{1}{2}\sum_{i,k} a_{ik}\int_{t_1}^{t_2} X_iX_k dt-\frac{1}{2}\sum_{\lambda,\mu} a_{\lambda\mu}\int_{t_1}^{t_2} X_\lambda X_\mu dt\right\}\ , \qquad (37)$$

which does not contain the coefficients $a_{i\lambda}$ or $a_{\lambda i}$. However, because $a_{i\lambda}=-a_{\lambda i}$ we may write instead of (37)

$$\Psi(\text{path})\propto\exp\left\{-\frac{1}{2}\sum_{l,m} a_{lm}\int_{t_1}^{t_2} X_lX_m dt\right\} \qquad (38)$$

where l and m run for all i and λ. In what follows l,m and n stand for both i and λ. The Lagrangian $\mathscr{L}$ is

$$\begin{aligned}\mathscr{L}&=\frac{1}{2}\sum_{l,m} a_{lm}X_lX_m\\&=\frac{1}{2}\sum_{l,m} a_{lm}\Big(\sum_n R_{ln}\dot{\alpha}_n-F_l\Big)\Big(\sum_{n'} R_{mn'}\dot{\alpha}_{n'}-F_m\Big)\end{aligned} \qquad (39)$$

and defining a^* by $a^*=(a+\tilde{a})/2$, $\tilde{a}$ being the transposed matrix of a, we have for momentum π_l

$$\pi_l=\sum_m (a^*R)_{ml}\Big(\sum_{n'} R_{mn'}\dot{\alpha}_{n'}-F_m\Big) \qquad (40)$$

and for Hamiltonian $\mathscr{H}$

$$\mathscr{H}=\frac{1}{2}\sum_l \pi_l\times\sum_m\{(R^{-1}a^{*-1}aa^{*-1}\tilde{R}^{-1})_{lm}\pi_m+2(R^{-1})_{lm}F_m\}\ . \qquad (41)$$

Making use of the differential representation for momentum, we obtain for the condition of vanishing current in equilibrium

$$(R^{-1}a^{*-1}aa^{*-1}\tilde{R}^{-1})_{lm}=2k(R^{-1})_{lm} \qquad (42)$$

corresponding to (23).

Thus we have

$$a^{*-1}aa^{*-1}\tilde{R}^{-1}=2k\times\text{unit matrix}$$

or

$$\tilde{R}^{-1}=2ka^*a^{-1}a^*=2ka^*ba^*\ .$$

The matrix a^* has a form of $\left(\begin{array}{c|c} /// & 0 \\ 0 & /// \end{array}\right)$ separated into parts of α-variables and β-variables, we finally obtain

$$\left.\begin{aligned}L_{ij}&=L_{ji}=2ka_{ij}=2ka_{ji}\\L_{\lambda\mu}&=L_{\mu\lambda}=2ka_{\lambda\mu}=2ka_{\mu\lambda}\\L_{i\lambda}&=-L_{\lambda i}=2k\sum_{\mu,j} a_{\lambda\mu}{}^*b_{\mu j}a_{ji}{}^*\\&=-2k\sum_{\mu,j} a_{ij}{}^*b_{j\mu}a_{\mu\lambda}{}^*\end{aligned}\right\}\ . \qquad (44)$$

Needless to say, in the presence of magnetic field or Coriolis force, (24) and (44) still hold on inversing these external forces.

§ 5. Entropy

Consider an ensemble of N loosely coupled identical systems each of which can be treated in the above sections. The entropy of this ensemble may be defined as

---

* As is stated in the foot-note to (8), (33) and (34) mean that the correlations of the left-sides vanish for $\tau>\tau_0$, τ_0 being a small quantity. Thus in the present case the probability P of finding X_i's and X_λ's at the same time may be written as a similar form as (10), but X_iX_λ is to be regarded as $X_i(t)X_\lambda(t+\tau)$, $\tau_0>\tau>0$ and $X_\lambda X_i$ as $X_\lambda(t)X_i(t+\tau)$ with $\tau_0>\tau>0$. In this way (36) and (37) follow, with a defined as the inverse of b whose elements are b_{ij}, $b_{i\lambda}$, $b_{\mu j}$ and $b_{\lambda\mu}$.

$$S=N\int W\Delta S\prod_i d\alpha_i-kN\int W\log W\prod_i d\alpha_i\,. \tag{45}$$

The first term of (45) means the sum of the entropies of each systems, when they were isolated and were regarded as in states of thermal fluctuations, and the second is the "mixing" entropy or entropy arising form weak coupling. In equilibrium state W is equal to $W_0=e^{(-\Omega+\Delta S)/k}$, which reduces (45) to

$$S=kN\Omega-kN\int W\log(W/W_0)\prod_i d\alpha_i \tag{46}$$

S/N is considered to be an average entropy of the system. Then we have

$$\frac{dS}{dt}=N\int\frac{\partial W}{\partial t}\Delta S\prod_i d\alpha_i-kN\int\frac{\partial W}{\partial t}\log W\prod_i d\alpha_i \tag{47}$$

The first and the second terms of this equation are rewritten by making use of (27), (4) and partial integration, as follows

$$\begin{aligned}N\int&\frac{\partial W}{\partial t}\Delta S\prod_j d\alpha_j\\&=-N\int\sum_i\frac{\partial}{\partial\alpha_i}(j_iW)\Delta S\prod_j d\alpha_j\\&=N\int\sum_i j_iW\frac{\partial\Delta S}{\partial\alpha_i}\prod_j d\alpha_j\\&=N\int\sum_i j_iF_iW\prod_j d\alpha_i\end{aligned} \tag{48}$$

and

$$\begin{aligned}-kN\int&\frac{\partial W}{\partial t}\log W\prod_j d\alpha_j\\&=kN\int\sum_i\frac{\partial}{\partial\alpha_i}(j_iW)\log W\prod_j d\alpha_j\\&=-kN\int\sum_i j_i\frac{\partial W}{\partial\alpha_i}\prod_j d\alpha_j\\&=N\int[\sum_{ij}R_{ij}j_ij_j-\sum_i j_iF_i]W\prod_k d\alpha_k\end{aligned} \tag{49}$$

Thus we have

$$\frac{dS}{dt}=N\int\sum_{i,j}R_{ij}j_ij_jW\prod_k d\alpha_k \tag{50}$$

which is non negative as is to be expected. The entropy of the system increases in the average.

§6. A Critique of Popov's Theory

Recently, Popov[7] presented a theory that the phenomenological equation (3) is the first integral which has the properties $\alpha_i\to0$ at $t\to\infty$ (in equilibrium state) of the following differential equations of second order

$$\ddot{\alpha}_i=-F_i\qquad(i=1,2,\cdots,N) \tag{51}$$

and further he showed that the reciprocal relations are derived from this mathematical condition. However it seems strange to observe that equations (51) are defined only through thermodynamical quantities (4) and yet are derived from these the phenomenological equations (3) which contain kinetic coefficients of entirely different character from thermodynamical quantities. In his theory, Popov showed merely that if one write the first integrals of (51) consistent with the above condition there exist reciprocal relations between the coefficients. Popov demonstrated this in the case of two variables and Karanikolov[8] extended Popov's theory to the case of three variables.

However their calculation is easily generalized to any number of variables. Substitution of (4) into (51) gives

$$\ddot{\alpha}_i=\sum_j g_{ij}\alpha_j\qquad i=1,2,\cdots,N \tag{52}$$

which can be transformed into diagonal form

$$\ddot{x}_i=h_{ii}x_i\,,\qquad i=1,2,\cdots,N \tag{53}$$

by an orthogonal transformation T which transforms g into diagonal matrix h

$$h=TgT^{-1}\,,\qquad x=T\alpha \tag{54}$$

and then $h_{ii}>0$, because g is a positive definite matrix. Thus the solution of (53) which vanishes for $t\to\infty$ is

$$x_i=x_i(0)\exp(-\sqrt{h_{ii}}t)\,, \tag{55}$$

which yields for the first integral of (52)

$$\begin{aligned}\dot{\alpha}_i&=\sum_j T_{ij}^{-1}\dot{x}_j=-\sum_j T_{ij}^{-1}\sqrt{h_{jj}}x_j\\&=-\sum_{j,k}T_{ij}^{-1}\sqrt{h_{jj}}T_{jk}\alpha_k\\&=\sum_{j,k}T_{ij}^{-1}\sqrt{h_{jj}}T_{jk}g_{kt}^{-1}F_t\\&=\sum_{j,k}T_{ij}^{-1}\sqrt{h_{jj}}h_{jj}^{-1}T_{jk}F_k\\&=\sum_k M_{ik}F_k\end{aligned} \tag{56}$$

where the fourth line follows from the third by noting $g^{-1}=T^{-1}h^{-1}T$ and M_{ik} is defined by

$$\begin{aligned}M_{ik}&=\sum_j T_{ij}^{-1}h_{jj}^{-1/2}T_{jk}\\&=\sum_j h_{jj}^{-1/2}T_{ji}T_{jk}\end{aligned} \tag{57}$$

because T is an orthogonal transformation,

$T^{-1}_{ij}=T_{ji}$. From (57) we get immediately

$$M_{ik}=M_{ki} \tag{58}$$

which is the reciprocal relation Popov and Karanikolov want to prove. They did not show any physical meanings of the equations (51) and the coefficients M_{ik} in the first integrals. In effect the coefficients M_{ik} have nothing to do with the kinetic coefficients.

What, then, should take the place of equation (51)? Euler's equation of our system is

$$\frac{d}{dt}\frac{\partial \mathscr{L}}{\partial \dot{\alpha}_i}-\frac{\partial \mathscr{L}}{\partial \alpha_i}=0 \tag{59}$$

where Lagragian $\mathscr{L}$ is given by (26). This equation is written, making use of the reciprocal relation of L_{ik}, as

$$\sum_j R_{ij}\ddot{\alpha}_j+\sum_j (gL)_{ij}F_j=0$$

or

$$\begin{aligned}\ddot{\alpha}_i&=-\sum_j (LgL)_{ij}F_j\\&=\sum_j(LgLg)_{ij}\alpha_j\end{aligned} \tag{60}$$

This should be used instead of (51). Following the same procedure as from (51) to (56), we define a diagonal matrix S by means of an orthogonal transformation T,

$$S=T(Lg)T^{-1}, \qquad g=L^{-1}T^{-1}ST, \tag{61}$$

then we have

$$\dot{\alpha}_i=\sum_j K_{ij}F_j \tag{62}$$

and

$$\begin{aligned}K_{ij}&=\sum T^{-1}_{ik}S_{kk}T_{kt}g^{-1}_{tj}\\&=\sum T^{-1}_{ik}S_{kk}T_{kt}(T^{-1}S^{-1}TL)_{tj}\\&=L_{ij}\end{aligned} \tag{63}$$

The above consideration is nothing but a conclusion of the Onsager and Machlup's variational principle.[9]

Note added on Oct. 12.

After submitting this manuscript to the Physical Society of Japan a paper of Tisza and Mannig (Phys. Rev. **105** (1957) 1695) came to the author's attention, which is closely related to this paper. Their theory is based on the property of the Lagrangian of Onsager-Machlup's theory (which they call OM function) as is done by Hashitsume, and is developed for one variable. Nothing is said about reciprocity relation, but mention is made of the spectral representation.

References

1) H. Nyquist: Phys. Rev. **32** (1928) 110.
2) H. Takahashi: J. Phys. Soc. Japan. **7** (195
439.
3) E. Wigner: J. Chem. Phys. **22** (1954) 1912.
4) H. B. G. Casimir: Rev. Modern Phys. **17** (1945
343.
5) N. Saitô, M. Namiki: Prog. Theor. Phys. **16**
(1956) 71.
6) N. Hashitsume: Prog. Theor. Phys. **8** (1952
461; *ibid*. **15** (1956) 369.
7) K. Popov: J. Exp. Theor. Phys. (USSR) **2**
(1955) 257; C. R. (Paris) **235** (1952) 648; *ibid*
236 (1953) 785, 1640; *ibid*. **238** (1954) 331
Ann. de phys. **9** (1954) 261.
8) Ch. Karanikolov: J. Exp. Theor. Phys. (USSR
28 (1955) 283.
9) L. Onsager, S. Machlup: Phys. Rev. **91** (1953
1505.

JOURNAL OF THE PHYSICAL SOCIETY OF JAPAN Vol. 12, No. 12, DECEMBER, 1957

The Measurements of the Galvanomagnetic Tensors of Bismuth

By Toshihiro OKADA

Department of Physics, Faculty of Science, Kyushu University

(Received October 19, 1956)

The anisotoropy of the galvanomagnetic effects in the single crystals of pure bismuth was investigated at the temperatures between −160° and 45°C. The results were analysed by the phenomenological theory of the galvanomagnetic effects. Two components of the resistivity tensor, two components of the Hall tensor, eight components of the magnetoresistance tensor and six components of the third order galvanomagnetic tensor were determined as the functions of temperature.

§ 1. Introduction

The galvanomagnetic effects of bismuth are very remarkable even in weak magnetic field, and the anisotrioy of these effects of single crystals have been studied extensively.[1)-8)] When we intend to carry out the complete measurements, it seems to be necessary to consider these effects phenomenologically by means of tensor analysis from the view-points of Onsager's reciprocal relation and rotatory symmetry of crystals.[9)-12)] The results obtained by these considerations were employed for the design of the experimental apparatus and for the preparation of specimens. In this work, the eighteen components of the galvanomagnetic tensors were determined as the functions of the temperature between −160°∼45°C, and the preliminary report has been published already.[13)] Recently Abeles and Meiboom[14)] performed the similar measurements and determined some components of the galvanomagnetic tensors. Their values are nearly concordant with this work in general cases, but in some components the discrepancy of about factor 2 were found between two measurements.

§ 2. Tensor Consideration

According to the phenomenological theory the galvanomagnetic effects of a single crystal can be expressed by the following tensor-equation[11),12)] if the electric field is not too strong:

$$E_i=\rho_{ij}(\boldsymbol{H})I_j+\varepsilon_{ijk}I_jR_k(\boldsymbol{H})\,, \qquad (1)$$

where

$$\rho_{ij}(\boldsymbol{H})=\rho_{ji}(\boldsymbol{H})\,.$$

In Eq. (1), $E_i(i=1,2,3)$ is the component of the electric field which is applied to the crystal, $I_j(j=1,2,3)$ the component of the current density flowing through the crystal, $\rho_{ij}(\boldsymbol{H})$ is the even function with respect to $\boldsymbol{H}$, and $R_k(\boldsymbol{H})$ is the odd function. ε_{ijk} is Eddington's tensor of the third rank.*

When the magnetic field is weak, we can expand $\rho_{ij}(\boldsymbol{H})$ and $R_k(\boldsymbol{H})$ in the power series near zero field as follows:

$$\left.\begin{aligned}\rho_{ij}(\boldsymbol{H})&=\rho_{ij}+\rho_{ij,mn}H_mH_n+\cdots\,,\\ R_k(\boldsymbol{H})&=R_{k,m}H_m+R_{k,mno}H_mH_nH_o+\cdots\end{aligned}\right\}\qquad(2)$$

ρ_{ij} is the resistivity tensor of the second rank, whose subscripts can be interchangeable; $\rho_{ij,mn}$ is the magnetoresistance tensor of the fourth rank, which has the interchangeability with respects to pairs of subscripts before or after the comma; $R_{k,m}$ is the Hall tensor of the second rank; $R_{k,mno}$ is the third order galvanomagnetic tensor of the fourth rank, whose subscripts *mno* can be interchanged with each other[12)].

A bismuth crystal has the ratotory symmetry D_{3d} which is galvanomagnetically equivalent to D_3 having one trigonal axis and three binary axes. If we assume the trigonal axis as the third axis of the cartesian coordinate (x_3), and one of binary axes as the first (x_1), and the axis which is perpendicular to both x_1 and x_3 as the second (x_2), the components of the galvanomagnetic tensors can be expressed as follows[12)]:

$$\rho_{ij}=\begin{pmatrix}\rho_{11} & 0 & 0\\ 0 & \rho_{11} & 0\\ 0 & 0 & \rho_{33}\end{pmatrix}, \qquad (3)$$

---

* ε_{ijk} is zero if $i=j$ or k, or $k=j$, but equal to $+1$ if $ijk=123$, 231 or 312, and equal to -1 if $ijk=213$, 321 or 132.

$$\rho_{ij,mn}=\begin{pmatrix} \rho_{11,11} & \rho_{11,22} & \rho_{11,33} & \rho_{11,23} & 0 & 0 \\ \rho_{11,22} & \rho_{11,11} & \rho_{11,33} & -\rho_{11,23} & 0 & 0 \\ \rho_{33,11} & \rho_{33,11} & \rho_{33,33} & 0 & 0 & 0 \\ \rho_{23,11} & -\rho_{23,11} & 0 & \rho_{23,23} & 0 & 0 \\ 0 & 0 & 0 & 0 & \rho_{23,23} & \rho_{23,11} \\ 0 & 0 & 0 & 0 & \rho_{11,23} & \frac{1}{2}(\rho_{11,11}-\rho_{11,22}) \end{pmatrix}, \qquad (4$$

$$R_{k,m}=\begin{pmatrix} R_{1,1} & 0 & 0 \\ 0 & R_{1,1} & 0 \\ 0 & 0 & R_{3,3} \end{pmatrix}, \qquad (5$$

$$R_{k,mno}=\begin{pmatrix} R_{1,111} & 0 & \frac{1}{3}R_{1,111} & 0 & 0 & R_{1,123} & 0 & R_{1,133} & 0 & 0 \\ 0 & \frac{1}{3}R_{1,111} & 0 & R_{1,111} & R_{1,123} & 0 & -R_{1,123} & 0 & R_{1,133} & 0 \\ 0 & R_{3,112} & 0 & -R_{3,112} & R_{3,113} & 0 & R_{3,113} & 0 & 0 & R_{3,333} \end{pmatrix}. \qquad (6$$

In the two dimensional representation of the last tensor, the subscript k is arrayed vertically, and the subscripts mno are arrayed horizontally in such a sequence as 111, 112=121=211, 122=212=221, 222, 113=131=311, 123=132=213=231=312=321, 223=232=322, 133=313=331, 233=323=332 and 333.

It can easily seen that there are two independent material constants for ρ_{ij}, eight for $\rho_{ij,mn}$, two for $R_{k,m}$ and six for $R_{k,mno}$, respectively. In order to measure all of the above shown components, it seems to be necessary to perform three sets of measurements about several types of specimens got from one single crystal. The shape of the specimen should be a rectangular parallelepipedon elongated in such a direction that makes the angle θ_2 with the trigonal axis in the x_1-x_3 plane (see Fig. 1(a) and (b)); its cross section should be square or nearly square, and the elongated side faces should be parallel or perpendicular to x_2-axis.

The first set of measurements As shown in Fig. 1(a), under the external magnetic field $\boldsymbol{H}$ in such a direction which makes the angle φ from x_3-axis in x_1-x_3 plane, the electric field E_1' along the long side of the specimen and the Hall field E_2 along x_2-axis should be measured by two pairs of probes when the current I_1' passes through the specimen. The resistivity E_1'/I_1' may b calculated by the following method. As th direction cosine of the current vector $\boldsymbol{I}_1'$, i $(\sin\theta_2,\ 0,\ \cos\theta_2)$, we have

$$\boldsymbol{I}_1'=(I_1'\sin\theta_2,\ 0,\ I_1'\cos\theta_2)\ , \qquad (7$$

then Eq. (1) reduces to

$$\frac{E_1}{I_1'}=\sin\theta_2\rho_{11}(\boldsymbol{H})+\cos\theta_2\rho_{13}(\boldsymbol{H})-\cos\theta_2 R_2(\boldsymbol{H})\ ,$$

$$\frac{E_2}{I_1'}=\sin\theta_2\rho_{12}(\boldsymbol{H})+\cos\theta_2\rho_{23}(\boldsymbol{H})+\cos\theta_2 R_1(\boldsymbol{H})-\sin\theta_2 R_3(\boldsymbol{H})\ ,$$

$$\frac{E_3}{I_1'}=\sin\theta_2\rho_{13}(\boldsymbol{H})+\cos\theta_2\rho_{33}(\boldsymbol{H})+\sin\theta_2 R_2(\boldsymbol{H})\ , \qquad (8$$

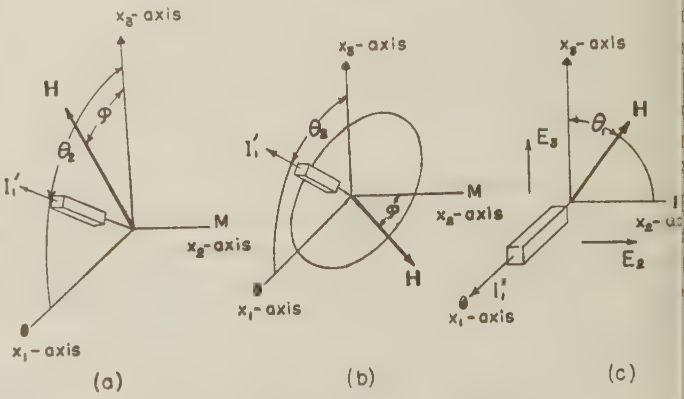

Fig. 1. Geometry of measurements.
(a) For the first set. (b) For the second set.
(c) For the third set.

so the resistivity is given by

$$\frac{E_1'}{I_1'}=(\sin\theta_2 E_1+\cos\theta_2 E_3)/I_1'$$
$$=\sin^2\theta_2\rho_{11}(\boldsymbol{H})+\cos^2\theta_2\rho_{33}(\boldsymbol{H})+2\sin\theta_2\cos\theta_2\rho_{13}(\boldsymbol{H})\,, \tag{9}$$

in which the terms concerning the Hall effect vanish. Expanding as the power series of H_i as shown by Eq. (2), we have

$$\left.\begin{aligned}\rho_{11}(\boldsymbol{H})&=\rho_{11}+\rho_{11,11}H_1^2+\rho_{11,33}H_3^2+\cdots,\\ \rho_{33}(\boldsymbol{H})&=\rho_{33}+\rho_{33,11}H_1^2+\rho_{33,33}H_3^2+\cdots,\\ \rho_{13}(\boldsymbol{H})&=2\rho_{23,23}H_2H_3+\cdots\,.\end{aligned}\right\} \tag{10}$$

From $\boldsymbol{H}=(H\sin\varphi,\ 0,\ H\cos\varphi)$, Eq. (9) reduces to

$$\frac{E_1'}{I_1'}=\rho^{(2)}(\theta_2)+H^2\rho^{(4)}(\theta_2,\varphi)+\cdots, \tag{11}$$

where

$$\rho^{(2)}(\theta_2)=\rho_{11}\sin^2\theta_2+\rho_{33}\cos^2\theta_2\,, \tag{12}$$

$$\begin{aligned}\rho^{(4)}(\theta_2)=&\left\{\frac{\rho_{11,11}+\rho_{11,33}}{2}\sin^2\theta_2+\frac{\rho_{33,11}+\rho_{33,33}}{2}\cos^2\theta_2\right\}\\ &+\left\{\frac{\rho_{11,33}-\rho_{11,11}}{2}\sin^2\theta_2+\frac{\rho_{33,33}-\rho_{33,11}}{2}\cos^2\theta_2\right\}\cos 2\varphi\\ &+\{\rho_{23,23}\sin 2\theta_2\}\sin 2\varphi\,.\end{aligned} \tag{13}$$

By measuring the resistance under the magnetic field, we can determine the value of $\rho^{(2)}(\theta_2)$ as a function of θ_2 and the value of $\rho^{(4)}(\theta_2,\varphi)$ as a function of θ_2 and φ. Eq. (12) shows that $\rho^{(2)}(\theta_2)$ has the period π for θ_2, while Eq. (13) shows that $\rho^{(4)}(\theta_2,\varphi)$ consists of three terms; the first one is independent of φ, and the second and third are proportional to $\cos 2\varphi$ and $\sin 2\varphi$, respectively. From analysis of the experimental results concerning $\rho^{(4)}(\theta_2,\varphi)$, the θ_2-dependency of the factors within the large brackets can be found so as to determine the numerical values of $\rho_{11,11}$, $\rho_{11,33}$, $\rho_{33,11}$, $\rho_{33,33}$ and $\rho_{23,23}$, although the values of the remaining components $\rho_{11,22}$, $\rho_{23,11}$ and $\rho_{11,23}$ cannot be obtained by these measurements. The components of the Hall tensor $R_{k,m}$ may be found from Eq. (8); as the direction cosines of $\boldsymbol{I}_1'$ are $(\sin\theta_2,\ 0,\ \cos\theta_2)$, and those of E_2 $(0, 1, 0)$, the components of the unit vector which is perpendicular to both $\boldsymbol{I}_1'$ and E_2 are $(-\cos\theta_2,\ 0,\ \sin\theta_2)$. Then the odd part[*] of E_2/I_1' becomes $\cos\theta_2 R_1(\boldsymbol{H})-\sin\theta R_3(\boldsymbol{H})$, so we have

$$\begin{aligned}\text{Odd Part of } E_2/I_1'&=R^{(2)}(\theta_2,\varphi)H\\ &=(R_{1,1}\cos\theta_2\sin\varphi-R_{3,3}\sin\theta_2\cos\varphi)H\,,\end{aligned} \tag{14}$$

if the first terms in the power expansion of $R_k(\boldsymbol{H})$ is retained. $R^{(2)}(\theta_2,\varphi)$ has the period 2π with respect to φ, and its amplitude is given by

$$\{(R_{1,1}\cos\theta_2)^2+(R_{3,3}\sin\theta_2)^2\}^{1/2}\,. \tag{15}$$

The second set of measurements The specimens used in these measurements are the same as in the first set; but the magnetic field is applied always in a direction perpendicular to the current $\boldsymbol{I}_1'$ as is shown in Fig. 1(b). As the direction cosines of $\boldsymbol{H}$ are $(\sin\varphi\cos\theta_2,\ \cos\varphi,\ -\sin\varphi\sin\theta_2)$, where φ is measured from x_2-axis clockwise in the plane perpendicular to $\boldsymbol{I}_1'$, the resistivity is calculated by the following equations:

$$\frac{E_1'}{I_1'}=\rho_{11}+H^2\left[\left(\frac{\rho_{11,22}+\rho_{11,33}}{2}\right)+\left(\frac{\rho_{11,22}-\rho_{11,33}}{2}\right)\cos 2\varphi-\rho_{11,23}\sin 2\varphi\right], \qquad (\theta_2=90^\circ)$$

---

[*] The term which is odd with respect to $\boldsymbol{H}$ in the second equation of (8) could be obtained by measuring $\frac{1}{2}\left\{\frac{E_2(\boldsymbol{H})}{I_1'}-\frac{E_2(-\boldsymbol{H})}{I_1'}\right\}$, that is, one half of the difference between E_2/I_1' for a magnetic field $(\boldsymbol{H})$ and that for the reverse one $(-\boldsymbol{H})$.

$$=\frac{\rho_{11}+\rho_{33}}{2}+H^2\Bigg[\left(\frac{\rho_{11,11}+\rho_{11,33}+\rho_{33,11}+\rho_{33,33}}{2}-\rho_{23,23}\right)\sin^2\varphi$$

$$+\frac{\rho_{11,22}+\rho_{33,11}}{2}\cos^2\varphi+\left(\frac{\rho_{23,11}}{\sqrt{2}}-\frac{\rho_{11,23}}{2}\right)\sin 2\varphi\Bigg]\,, \qquad (\theta_2=45^\circ)$$

$$=\rho_{33}+H^2[\rho_{33,11}]\,. \qquad (\theta_2=0^\circ) \qquad (1$$

And from the second equation of (8) we have

$$\text{Odd Part of } E_2/I_1'=(R_{1,1}\cos^2\theta_2+R_{3,3}\sin^2\theta_2)\sin\varphi H\,, \qquad (1$$

which may be used for the determination of $R_{1,1}$ and $R_{3,3}$ in some cases, and

$$\text{Even Part of } E_2/I_1'=-\rho_{23,11}H^2\,, \qquad (\text{if } \theta_2=0) \qquad (1$$

which corresponds to the planar Hall effect. By means of Eqs. (16) and (18) we can find th values of $\rho_{11,22}$, $\rho_{23,11}$, $\rho_{11,33}$ and $\rho_{11,23}$.

The third set of measurements The six components of $R_{k,mno}$ can be determined by th following method. For the specimen with $\theta_2=0$, two pair of probes, which are set perp dicular with each other, are used to measure the electric fields along x_2- and x_3-axes. If th magnetic field is applied in the x_2-x_3 plane as shown in Fig. 1(c), $R_k(\boldsymbol{H})$ may be expande as follows:

$$\left.\begin{aligned}
&R_1(\boldsymbol{H})=0\,,\\
&R_2(\boldsymbol{H})=R_{1,1}H_2+R_{1,111}H_2^3-3R_{1,123}H_2^2H_3+3R_{1,133}H_2H_3^2\,,\\
&R_3(\boldsymbol{H})=R_{3,3}H_3-R_{3,112}H_2^3+3R_{3,113}H_2^2H_3+R_{3,333}H_3^3\,.
\end{aligned}\right\} \qquad (1$$

Let θ_1 be the angle between the magnetic field and x_3-axis, then we have

$$\text{Odd Part of } E_2/I_1'=-R_{3,3}\cos\theta_1 H+R_2^{(4)}(\theta_1)H^3\,, \qquad (2$$

where

$$R_2^{(4)}(\theta_1)=R_{3,112}\sin^3\theta_1-3R_{3,113}\sin^2\theta_1\cos\theta_1-R_{3,333}\cos^3\theta_1\,, \qquad (2$$

$$\text{Odd Part of } E_3/I_1'=R_{1,1}\sin\theta_1 H+R_3^{(4)}(\theta_1)H^3\,, \qquad (2$$

where

$$R_3^{(4)}(\theta_1)=R_{1,111}\sin^3\theta_1-3R_{1,123}\sin^2\theta_1\cos\theta_1+3R_{1,133}\sin\theta_1\cos^2\theta_1\,. \qquad (2$$

From the θ_1-dependencies of $R_2^{(4)}(\theta_1)$ and $R_3^{(4)}(\theta_1)$, six components of $R_{k,mno}$ can be calculate

By means of these sets of measurements described in this section, we can find values all the components of the galvanomagnetic tensors ρ_{ij}, $\rho_{ij,mn}$, $R_{k,m}$ and $R_{k,mno}$.

§ 3. Experimental

An ingot of bismuth, whose length is about 80 mm and diameter is about 8 mm, was made of Merck "extra pure" bismuth. The ingot was zone-refined five times with the zone-width of 10∼15 mm and with the speed of 15 mm/hr, then this became a single crystal. Specimens were cut off from its middle part. The purity was not determined by the quantitative analysis, but supposed to be the order of four-nine.*

As is well known, the cleavage planes of bismuth crystal are (000,1), and on the planes are seen many faint stripes intersectin by the angle 120° with each other. Th direction of the stripes proved to be coincide with binary axes by X-ray photograph. R ferring to the cleavage planes and bina stripes six specimens with the following sha were prepared: the length is 6∼8 mm, t cross section is nearly square (2×2 mm²). S different values are taken for θ_2, namely 0 30°, 45°, 60°, 75° and 90°. The shaping a grinding of specimens are made by means a watch-lathe equipped with the tip of denta grinder.** The dimension of specimens w measured within the accuracy of 0.01 mm by a screw-micrometer or by a comparator. The error of the angle θ_2 may be $\pm(1\sim2)°$.

---

* By spectroscopic qualitative analysis the existence of the following elements was proved: Ag, As, Cu, Fe, Hg, In, Ni, Pb and Sn (in alphabetical arrangement). The author is indebted to Mr. H. Suzuki for this analysis.

** For the preparation of specimen the author indebted to Messrs. K. Hirakawa and A. Okazaki

The resistance and the Hall voltage were measured by means of a D. C. potentiometer and a galvanometer. The magnetic field of 200~1500 gauss was supplied from an electro-magnet, which can be rotated around the vertical axis to vary φ or θ_1. The intensity of the magnetic field was measured by a fluxmeter and a search-coil calibrated by nuclear resonance.

We must take care that large magnetic field should not be applied to specimens, because the galvanomagnetic tensors $\rho_{ij,mn}$ and $R_{k,mno}$ are the coefficients of the power expansions of $\rho_{ij}(\boldsymbol{H})$ and $R_k(\boldsymbol{H})$, respectively, near the zero point of the field.

§4. Results

By the method described in §2, the components of the galvanomagnetic tensors ρ_{ij}, $\rho_{ij,mn}$, and $R_{k,m}$ were obtained for the following four standard temperatures, namely 45°, 0°, −70° and −160°C; but as for $R_{k,mno}$ the measurements were carried out only for the three temperatures 27.₅°, −70° and −167°C.

a) The components ρ_{ij} The resistivity was measured as the function of temperature for the specimens whose θ_2 are 0°, 30°, 45°, 60° and 90°. Results for 0°C and 45°C are shown in Fig. 2; in which $\sin^2\theta_2$ is taken as the abscissa and $\rho^{(2)}(\theta_2)$ as the ordinate. According to Eq. (12), $\rho^{(2)}(\theta_2)$ should be a linear function of $\sin^2\theta_2$. In Fig. 2 the observed values are represented by crosses, which seem to be on straight lines. The probable values of ρ_{11} and ρ_{33} can be easily obtained from such lines, and their temperature-dependency is shown in Fig. 3, and their numerical values are tabulated in Table I with their estimated errors.

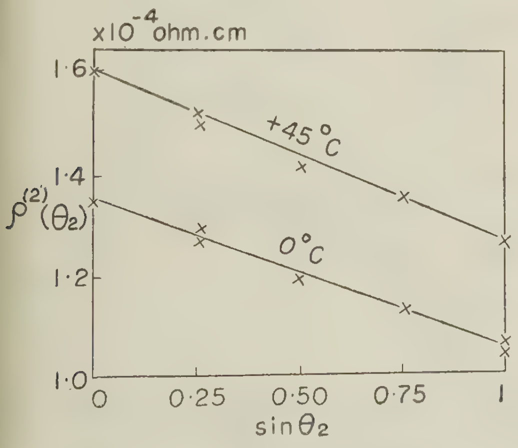

Fig. 2. θ_2-dependencies of $\rho^{(2)}$.

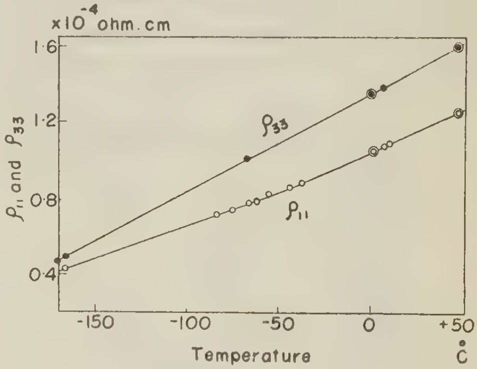

Fig. 3. Temperature dependencies of ρ_{11} and ρ_{33}. The values shown by ⊙ and ◎ are obtained from the lines drawn in Fig. 2. The values shown by ● and ○ are obtained by measuring the resistivities of specimens whose θ_2 are 0° and 90° respectively.

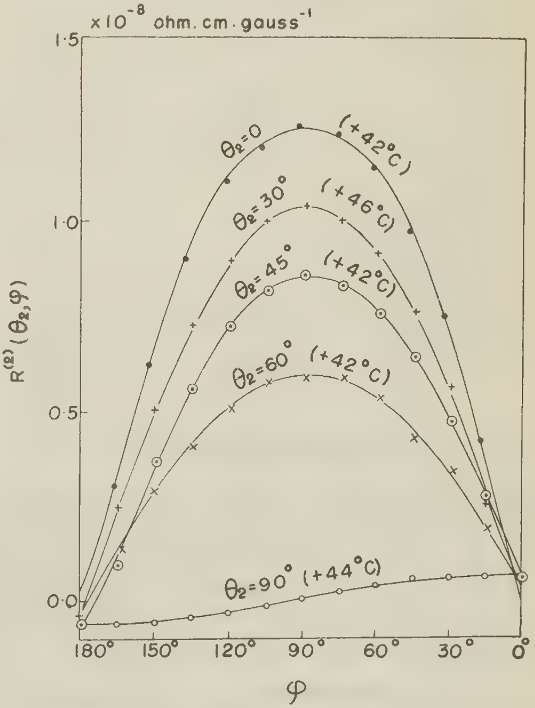

Fig. 4. φ-dependencies of $R^{(2)}$.

b) The components $R_{k,m}$ According to the method described in §2, the φ-dependency of $R^{(2)}(\theta_2,\varphi)$ given by Eq. (14) was measured and some of the results are shown in Fig. 4. It is evident that the square of the amplitude of the curves in Fig. 4 is given by $R_{1,1}^2\cos^2\theta_2+R_{3.3}^2\sin^2\theta_2$, which is the linear function of $\sin^2\theta_2$. This relation is shown in Fig. 5, from which the most probable value of $R_{1,1}^2$ may be found; on the other hand, the value of $R_{3.3}^2$ could not be found because the absolute value of $R_{3,3}$ is very small. But by inspecting the curves in Fig. 4 we can find that the sign of $R_{3,3}$ is probably opposite to that of $R_{1,1}$ and the absolute-value of the former seems to be as small as 1/20~1/30 of $|R_{1,1}|$. In Fig. 6 and Table I the temperature dependencies of $R_{1,1}$ and $R_{3,3}$ are shown.

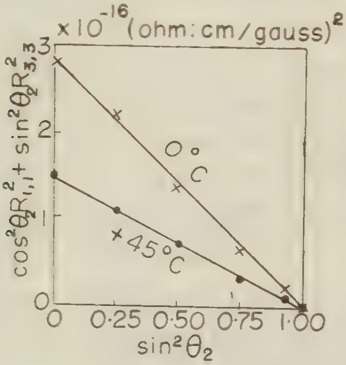

Fig. 5. Linear relation between the square of amplitude of $R^{(2)}$ and θ_2.

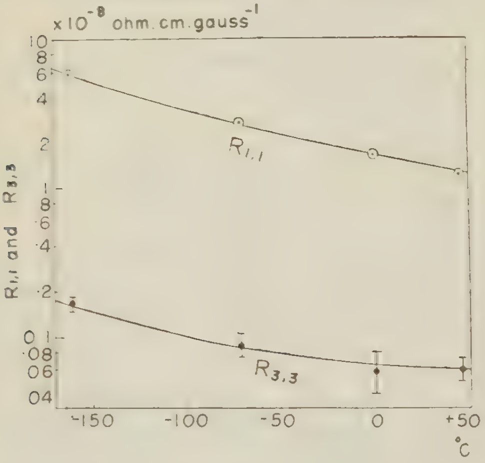

Fig. 6. Temperature-dependencies of $R_{1,1}$ and $R_{3,3}$.

c) **The components** $\rho_{ij,mn}$ By means of the first set of measurments, the values of $\rho_{11,11}$, $\rho_{11,33}$, $\rho_{33,11}$, $\rho_{33,33}$ and $\rho_{23,23}$ were found. The resistivity under various magnetic field strengths (H) and the directions (φ) of the magnetic fields were measured, and in Fi 7(a) is shown one of these results which r present the linear relation between the r sistance and H^2 at 45°C, and from this curv the value of $\rho^{(4)}(\theta_2,\varphi)$ for $\theta_2=0°$, $\varphi=90°$ obtained. As the temperature decreases, th range of the magnetic field where the linearli between the resistance and H^2 exists becom narrower, so at the liquid air temperature th measurements were performed for $H=0\sim2$

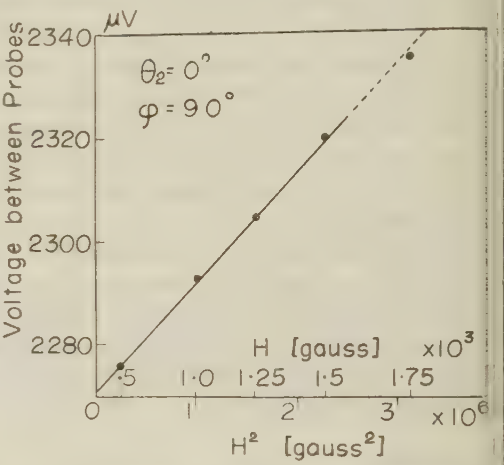

Fig. 7(a). Observed values of E_1'/I_1' as functio of H^2.

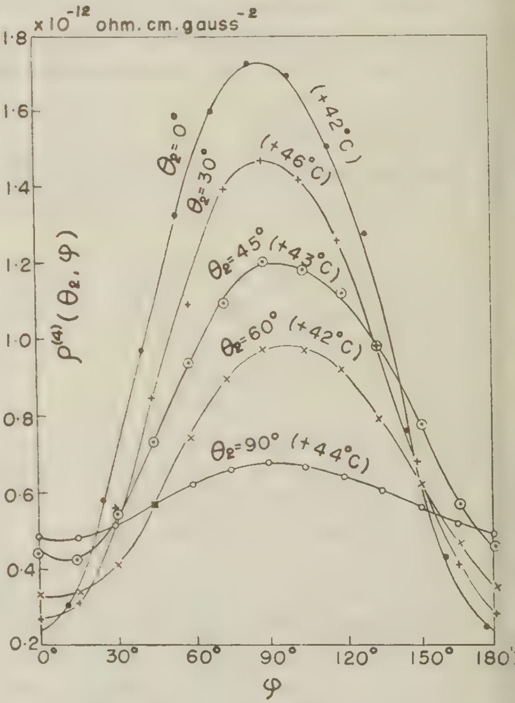

Fig. 7(b). φ-dependencies of $\rho^{(4)}$.

Table I. The values of components of galvanomagnetic tensors.

Tensor	The Present Author				Abeles-Meiboom[14)		Vergler, Stierstadt etc.
	45°C	0°C	−70°C	−160°C	+23°C	−193°C	+21°C
	$\times 10^{-4}$	$\times 10^{-4}$	$\times 10^{-4}$	$\times 10^{-4}$	$\times 10^{-4}$	$\times 10^{-4}$	$\times 10^{-4}$
ρ_{11}	1.26 ±0.01	1.055±0.01	0.76 ±0.02	0.445±0.02	1.2	0.36	1.06 1)
ρ_{33}	1.595±0.01	1.35 ±0.01	0.995±0.02	0.52 ±0.02	1.5	0.37_5	1.28 1)
	$\times 10^{-8}$	$\times 10^{-8}$	$\times 10^{-8}$	$\times 10^{-8}$	$\times 10^{-8}$	$\times 10^{-8}$	$\times 10^{-8}$
$R_{1,1}$	1.21 ±0.02	1.69 ±0.02	2.74 ±0.04	5.9 ±0.2	1.35	8.4	1.0_2 4)
$R_{3,3}$	−0.06 ±0.01	−0.06 ±0.02	−0.09 ±0.02	−0.17 ±0.02	−0.05	—	0.1_3 4)
	$\times 10^{-12}$	$\times 10^{-12}$	$\times 10^{-12}$	$\times 10^{-12}$	$\times 10^{-12}$	$\times 10^{-12}$	$\times 10^{-12}$
$\rho_{11,11}$	0.67 ±0.04	1.64 ±0.10	5.65 ±0.3	42.0±2.5	0.94	105	0.5_8 5)
$\rho_{11,33}$	0.45 ±0.03	0.95 ±0.06	3.5 ±0.2	20.4±1.5	0.32	29	0.2_2 5)
$\rho_{33,11}$	1.79 ±0.04	3.81 ±0.06	15.25 ±0.2	78.2±2.5	1.9_5	125	0.8_3 5)
$\rho_{33,33}$	0.24 ±0.04	0.53 ±0.06	2.35 ±0.2	11.2±2.5	0.1_5	11	0.0_7 5)
$\rho_{11,22}$	1.02 ±0.03	2.28 ±0.06	8.74 ±0.2	59.2±1.5	1.5_6	162	0.8_3 5)
$\rho_{11,23}$	0.18 ±0.03	0.43 ±0.07	1.47 ±0.3	13.2±3 :	—	—	0.1_5 5)
$\rho_{23,11}$	0.06 ±0.03:	0.12 ±0.06:	0.90 ±0.2	6.4±2	—	—	—
$\rho_{23,23}$	−0.12 ±0.02	−0.25 ±0.05	−0.80 ±0.2	−5.1±2	—	—	-0.0_2 5)
	$\times 10^{-16}$		$\times 10^{-16}$	$\times 10^{-15}$			
$R_{1,111}$	$-2._8$*		−28	$-10._5$:**	—	—	—
$3R_{1,123}$	$-3._1$*		$-23._5$	$-13._7$:**	—	—	—
$R_{1,133}$	−0.5:*		−13	$-9._0$:**	—	—	—
$R_{3,112}$	-0.1_5*		$-1._0$	$-1._3$:**	—	—	—
$3R_{3,113}$	-0.6_3*		$-7._9$	$-4._8$:**	—	—	—
$R_{3,333}$	-0.2_9*		$-2._9$	$-0._5$:**	—	—	—

The unit: ρ_{ij} in ohm. cm.; $R_{k,m}$ in ohm. cm. gauss^{-1}; $\rho_{ij,mn}$ in ohm. cm. gauss^{-2}, $R_{k,mno}$ in ohm. cm. gauss^{-3}.

* at $+27._5$°C ** at −167°C : less accurate values

gauss. The φ-dependencies of $\rho^{(4)}(\theta_2, \varphi)$ were shown in Fig. 7(b), and may be expressed by the following equation:

$$\rho^{(4)}(\theta_2, \varphi) = A_0(\theta_2) + A_1(\theta_2)\cos 2\varphi + B(\theta_2)\sin 2\varphi \,. \tag{13'}$$

The accurate values of A_0, A_1 and B_1 may be found by means of numerical Fourier analysis*, and we have, for example,

$$\left.\begin{aligned} &A_0 = 1.8_1 \times 10^{-12}\ \text{ohm. cm/gauss}^2\,, \\ &A_1 = -0.9_7 \times 10^{-12}\ \text{ohm. cm/gauss}^2\,, \\ &B_1 = -0.22_5 \times 10^{-12}\ \text{ohm. cm/gauss}^2\,, \\ &(A_2 = -0.01 \times 10^{-12}\ \text{ohm. cm/gauss}^2\,, \\ &B_2 = -0.00_5 \times 10^{-12}\ \text{ohm. cm/gauss}^2.)^* \end{aligned}\right\} \tag{24}$$

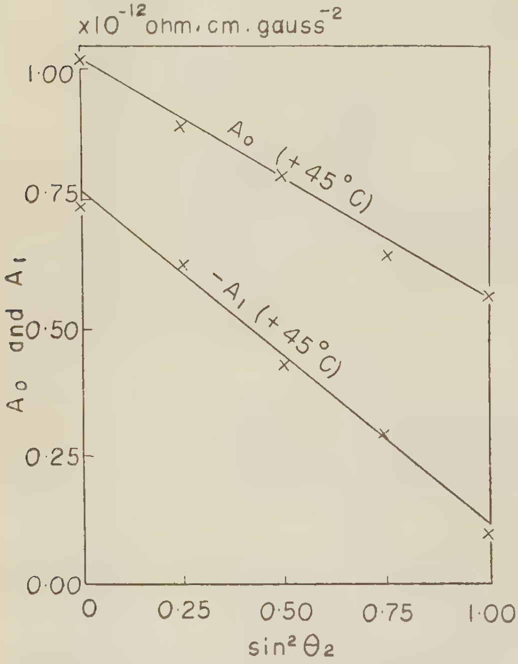

Fig. 8. Linear relation between θ_2 and A_0 or A_1.

for the specimen with $\theta_2=45°$ at 0°C. Therefore, if the θ_2-dependencies of A_0, A_1 and B_1 were found, it is easy to obtain the values of $\rho_{11,11}$, $\rho_{11,33}$, $\rho_{33,11}$, $\rho_{33,33}$ and $\rho_{23,23}$ from comparision of Eq. (13) and Eq. (13′) (see Fig. 8). Similarly, according to the second set of measurements for specimen whose θ_2 is 90°, one can easily find the values of $\rho_{11,23}$, $\rho_{11,22}$ and $\rho_{11,33}$; the last of which proves to agr with the value of $\rho_{11,33}$ obtained in the fir set of measurements within the experiment error. The only remaining component of t galvanomagnetic tensor is $\rho_{23,11}$, which determined by means of Eq. (18). All t values of $\rho_{ij,mn}$ and their temperature pendencies are shown in Fig. 9 and in Table

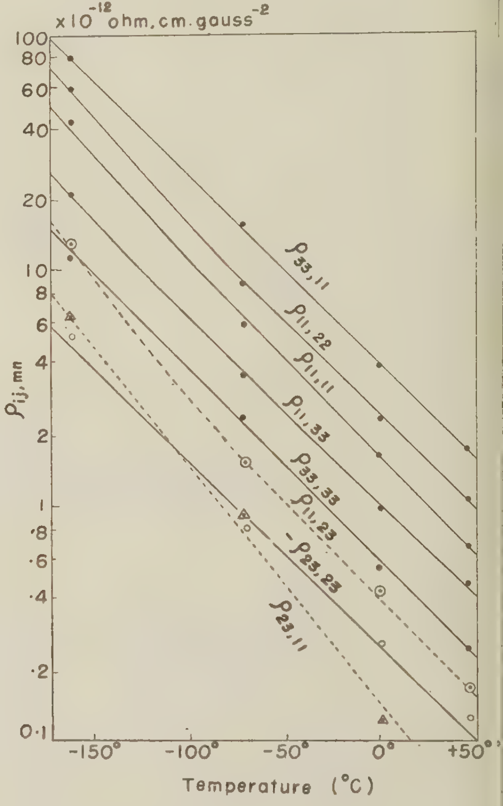

Fig. 9. Temperature-dependencies of $\rho_{ij,mn}$.

d) The components $R_{k,mno}$ According the third set of measurements, the odd pa of E_2/I_1' and E_3/I_1' were measured as functio of H, and by plotting $E_2/I_1'|H|\,vs H^2$ a $E_3/I_1'|H|\,vs H^2$ we can find the values $R_2^{(4)}(\theta_1)$ and $R_2^{(4)}(\theta_1)$ in Eq. (21) for vario values of θ_2. The results the three differe temperatures are shown in Fig. 10(a) and (b

---

* The terms A_n and B_n ($n \geq 2$) in Fourier expansion

$$\rho^{(4)}(\theta_2, \varphi) = A_0 + \sum_n A_n \cos 2n\varphi + \sum_n B_n \sin 2n\varphi$$

proved to be as small as one percent of A_1 in most cases, so that we can assume that $\rho^{(4)}(\theta_2, \varphi)$ is represented by Eq. (13′).

* The applied magnetic field must be so sm that the curves $E_2/I_1'|H|\,vs H^2$ or $E_2/I_1'|H|\,vs$ remain linear; on the contrary if the field is t large these curves should bend, and then some e perimental errors would be introduced into $R_2^{(4)}($ or $R_3^{(4)}(\theta_1)$. In this work, we were obliged to app the magnetic field of 200~1500 gauss for specimen and this seems to be too strong at liquid air temp ature, so that the final results for this temperatu are considered to be less accurate than others.

By the analyses of these curves by means of Eqs. (21) and (23), six components of $R_{k,mno}$ are found and tabulated in Table I. Using these values of $R_{k,mno}$, $R_2^{(4)}(\theta_1)$ and $R_3^{(4)}(\theta_1)$ are recalculated and shown in Fig. 10(a) and (b) by solid curves. The dotted curves in the lower part of Fig. 10(a) are $-\cos^3\theta_1 R_{3,333}$, $-3\sin^2\theta_1\cos\theta_1 R_{3,113}$ and $\sin^3\theta R_{3,112}$, respectively, and the sum of them should be equal to $R_2^{(4)}(\theta_1)$ according to Eq. (21).

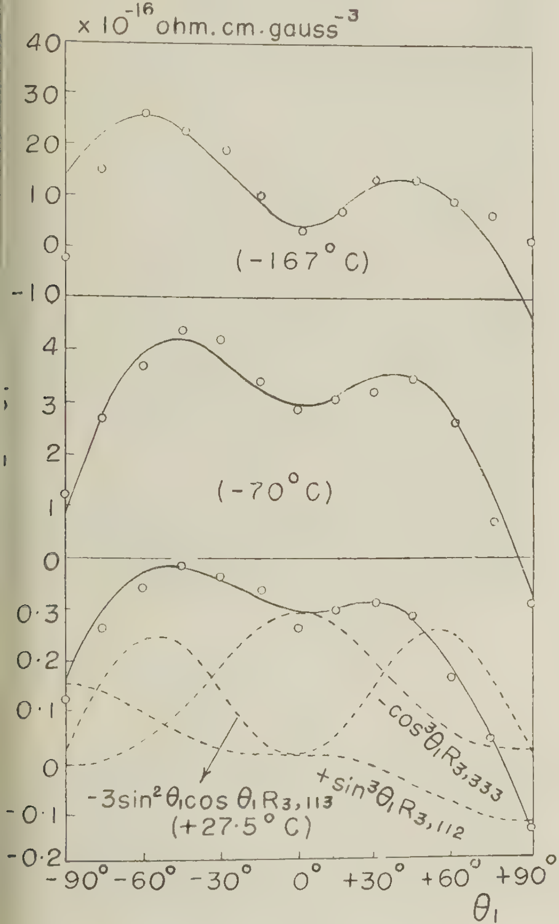

(a)

Fig. 10(a). Values of $R_2^{(4)}$ as function of θ_1. The calculated values are shown by solid and dotted curves, the observed ones are shown by small circles.

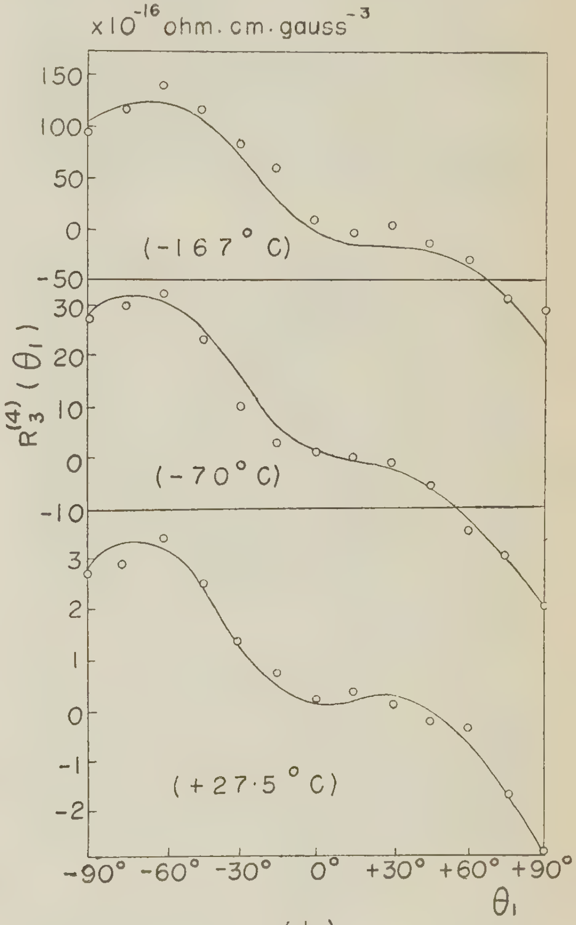

(b)

Fig. 10(b). Values of $R_3^{(4)}$ as function of θ_1. The calculated values are shown by solid curves, and the observed are shown by small circles.

§ 5. Discussion

Some components of the galvanomagnetic tensors were already measured by several investigators; and in Table I values measured by Abeles-Meiboom,[14] Vergler[4] and Stierstadt[5] are also listed. Values of components of the resistivity tensor and Hall tensor obtained by Abeles-Meiboom coincide with those of this work. As for the magnetoresistance tensor, their values of $\rho_{11,11}$, $\rho_{33,11}$ and $\rho_{11,22}$ are consistent with ours;* whereas our values of $\rho_{11,33}$ and $\rho_{33,33}$ are about two times larger than theirs.*,** The quantitative concordance between our values and Vergler's or Stierstadt's are not remarkable as shown in Table I.

Both components of the resistivity tensors

---

* From Fig. 9, values of components of the magnetoresistance tensor for 23°C are interpolated as follows:

$\rho_{11,11}=1.0_1\times10^{-12}$, $\rho_{11,33}=0.66\times10^{-12}$,
$\rho_{33,11}=1.9_6\times10^{-12}$, $\rho_{33,33}=0.37\times10^{-12}$
$\rho_{11,22}=1.5_2\times10^{-12}$.

** Values of $\rho_{11,23}$, $\rho_{23,11}$ and $\rho_{23,23}$ were not measured by Abeles-Meiboom.

ρ_{ij} increase linearly with the increasing temperature as shown in Fig. 3, and if the curve for ρ_{33} is extrapolated to lower temperatures it will intersect the abscissa at −256°C or 17°K. Therefore, roughly speaking, the resistance is proportional to the temperature except for the very low temperature region, and this temperature dependency has already been observed for pure bismuth by several authors.[15)] The order of magnitude of the resistivity is 10∼100 times greater than that of normal metals, because of very small concentration of the free carriers. The degree of anisotropy is not so large, as ρ_{33}/ρ_{11} is 1.2_7 at 45°C, 1.2_8 at 0°C, 1.3_1 at −60°C and 1.2 at −160°C.

Whereas the anisotropy of the Hall effect is very remarkable. The component $R_{1,1}$ which can be measured when the weak magnetic field is applied along x_1-(or x_2-) axis of the crystal, is positive* and amounts to 1.21×10^{-8} ohm. cm. gauss^{-1} at 45°C and becomes nearly five times greater at −160°C (cf. Fig. 6). But the absolute value of $R_{3,3}$, which is the Hall coefficient measured when the weak magnetic field is applied along x_3-axis, is very small (less than 5% of $R_{1,1}$), and its sign may be negative as described in the preceding section.

The transverse magneto-resistance effect for weak magnetic field relates to the components $\rho_{ij,mn}$, where the subscripts before the comma mean the direction of current, and the subscripts after the comma the direction of magnetic field. Among these components the following relation was observed:

$$\rho_{33,11} > \rho_{22,11} > \rho_{11,33} ,$$

and $\rho_{33,11}$ is about four times larger than $\rho_{11,33}$.**

The change of resistance in the longitudinal magnetic field will be estimated by $\rho_{11,11}$ and $\rho_{33,33}$, and the former is about three times larger than the latter; and it is noteworthy that "$\rho_{11,11}$ is larger than $\rho_{11,33}$", or the longitudinal effect is more remarkable than the transverse one in this case. On the whole, it can be said that the change of resistance is most striking when the field is applied along x_1-axis. The magnitude of the remaining components $\rho_{11,23}$, $\rho_{23,11}$ and $\rho_{23,23}$ are smalle than the others, and any intuitive interpretation can not be given for these components The temperature-dependency of $\rho_{ij,mn}$ is very noticeable, as is shown in Fig. 9; the value of $\rho_{ij,mn}$ at −160°C is about one hundred times larger than that at 45°C.

The galvanomagnetic tensor $R_{k,mno}$ is concerned with the field-dependency of the Hal coefficient. The components $R_{1,111}$ and $R_{3,33}$ are defined by the following equations:

$$\left.\begin{aligned} \frac{E_3}{I_1'H}&=R_{1,1}+R_{1,111}H^2 , \qquad (H//x_2\text{-axis}) \\ -\frac{E_2}{I_1'H}&=R_{3,3}+R_{3,333}H^2 , \qquad (H//x_3\text{-axis}) \end{aligned}\right\} \quad (25$$

where E_2 or E_3 is the electric field produced along x_3- (or x_2-) axis when the magnetic fiel is applied along x_2- (or x_3-) axis, and the current I_1' flow in the direction of x_1-axis. As shown in Table I, $R_{1,1}$ is positive, whereas $R_{1,111}$ is negative, so that the magnitude o $E_3/I_1'H$ becomes smaller as H increases. $R_{3,33}$ is also negative, but it is very small as compared with $R_{1,111}$.

From Table I, it is easy to see that the order of magnitude of various galvanomagnetic tensors at 45°C are given as follows:

$$\left.\begin{aligned} \rho_{ij}&\simeq10^{-4}\ \text{ohm. cm} , \\ R_{k,m}&\simeq10^{-8}\ \text{ohm. cm. gauss}^{-1} , \\ \rho_{ij,mn}&\simeq10^{-12}\ \text{ohm. cm. gauss}^{-2} , \\ R_{k,mno}&\simeq10^{-16}\ \text{ohm. cm. gauss}^{-3} , \end{aligned}\right\} \quad (26$$

neglecting the anisotropies of the each galvanomagnetic tensors. On the other hand, according to the formal theory of electronic conductors, the order of magnitude can be evaluated such as, if the anisotropy is neglected

$$\rho_{ij}\simeq\frac{m^*}{e^2}\frac{1}{n\tau}=\frac{1}{nec}\left(\frac{m^*c\omega_c}{e}\right) , \quad (27$$

where m^* is the effective mass of electron $\tau=1/\omega_c$ the collision time, and n the concentration of the free electrons. If one defines that

$$R=\frac{1}{nec} , \qquad H_c=\frac{m^*c\omega_c}{e} , \quad (28$$

Eq. (27) reduces to

$$\rho_{ij}\simeq RH_c . \quad (29$$

Similarly the order of magnitude for othe tensors can be estimated as follows[16)]:

$$R_{k,m}\simeq R , \quad \rho_{ij,mn}\simeq R/H_c , \quad R_{k,mno}\simeq R/H_c^2 . \quad (29$$

---

* The sign of $R_{i,i}$ is defined as positive for n-type conductor in this paper.

** Cf. Eqs. (28) of 16).

Comparing (26), (29) and (29′), we have

$$\left.\begin{aligned} R &\simeq 10^{-8}\ \text{ohm. cm. gauss}^{-1}, \\ H &\simeq 10^{4}\ \text{gauss}, \end{aligned}\right\}\ (\text{at } 45°\text{C}), \qquad (30)$$

from which the free electron concentration and the mobility are estimated as

$$\left.\begin{aligned} n &\simeq 6\times10^{19}\ \text{cm}^{-3} = 2\times10^{-4}\ \text{per atom}, \\ \mu &= \frac{e}{m^*}\frac{1}{\omega_c} \simeq 10^{4}\ .^* \end{aligned}\right\} \qquad (31)$$

In the actual bismuth, it may be necessary to consider electrons and positive holes simultaneously as discussed by Jones[17] and Abeles and Meiboom.[14] The results obtained in this work are now being analysed by applying the multi-ellipsoid theory of the galvanomagnetic tensors.[16]

The author wishes to express his sincere thanks to Prof. A. Okazaki for his kind encouragement and interest in this work. He is also indebted to Prof. Z. Miduno for his helpful advice about numerical Fourier analysis, and also to Messrs. K. Hirakawa, K. Hashimoto, S. Asanabe, A. Okazaki and H. Suzuki for their assistance in the measurements and for the preparation of specimens. This work was supported by the Scientific Research Expenditure of the Ministry of Education.

---

* At $-160°$C, $\mu \simeq 10^5$.

References

1) A. B. Focke and J. R. Hill: Phys. Rev. **50** (1936) 179.
2) H. H. Craig: Phys. Rev. **27** (1926) 772.
3) C. W. Heaps: Phys. Rev. **30** (1927) 61.
4) H. Verleger: Z. f. Phys. **76** (1932) 760.
5) O. Stierstadt: Z. f. Phys. **80** (1933) 636; **85** (1933) 310 and 697; **87** (1934) 687; **93** (1935) 676; **95** (1935) 355.
6) M. Kohler: Z. f. Phys. **95** (1935) 365.
7) P. Kapitza: Proc. Roy. Soc. **119** (1928) 358; **123** (1929) 292 and 342.
8) E. Grüneisen and J. Gielessen: Ann. d. Phys. **26** (1936) 449; **27** (1936) 243; **28** (1937) 225.
9) M. Kohler: Ann. d. Phys. **20** (1934) 878 and 891.
10) D. Shoenberg: Proc. Camb. Phil. Soc. **31** (1935) 265 and 271.
11) W. P. Mason, W. H. Hewitt and R. F. Wick: J. Appl. Phys. **24** (1953) 166.
12) T. Okada: Memoirs Faculty Sci. Kyushu Univ. B Vol. 1, No. 5 (1955) 157.
13) T. Okada: J. Phys. Soc. Japan **11** (1956) 89.
14) B. Abeles and S. Meiboom: Phys. Rev. **101** (1956) 544.
15) For example, N. Thompson: Proc. Roy. Soc. **155** (1936) 111.
16) T. Okada: Memoirs Faculty Sci. Kyushu Univ. B Vol. 1, No. 5 (1955) 168.
17) H. Jones: Proc. Roy. Soc. **155** (1936) 653.

JOURNAL OF THE PHYSICAL SOCIETY OF JAPAN Vol. 12, No. 12, DECEMBER, 1957

Recombination of Excess Carriers in Semiconductors

By Jun'ichi OKADA

Matsuda Research Laboratory, Tokyo Shibaura Electric Co.,
Kawasaki-city, Japan

(Received August 22, 1957)

The recombination of excess carriers in semiconductors is discussed on the basis of a model in which the recombination occurs through multiple-levels. The theory is extended to apply to germanium. The dependence of carrier lifetime on temperature in most of pure n-type germanium samples can be explained by introducing two sets of traps, recombination centers ($E_C-E_r=0.30$eV) and hole trapping centers ($E_t-E_V=0.30$eV), in our temperature range. However, the minority carrier lifetime of samples containing comparatively high dislocation density (10^4-10^5/cm^2) is shown to vary with the dislocation density, and the results is expressed in terms of two lifetimes: τ_d, that associated with random dislocations, and τ_b, that due to the recombination centers of an undetermined origin. It is also shown that anomalous temperature dependence of the steady-state photoconductivity of high-resistivity p-type nickel doped germanium can be interpreted by assuming that two acceptor levels of nickel atom are effective at the same time, but different in the effect on the recombination process.

§ 1. Introduction

It is well known that in usual semiconductors the recombination of excess carriers is enhanced by lattice imperfections. These imperfections may introduce localized energy levels in the forbidden gap, which provide an intermediate step for recombination. We may call these localized levels as carrier traps. Shockley and Read[1] have discussed the hole-electron recombination rate resulting from the presence of only one set of such traps. However, in general there may be several different types of imperfections and an imperfection of each type may give several discrete energy levels[2]. Therefore it is necessary to consider the case where various sets of traps are effective. In the following we shall discuss the recombination through these multiple levels. The extension of simple theory to the case of multiple levels will first considered and then the experimental results for germanium will be compared with the extended theory.

§ 2. Theory

With the multiple-levels model we shall consider the rates of electron or hole transition between the traps and the conduction and valence bands owing to the processes which establish thermal equilibrium. Quantities which refer to localized levels or tra are given subscripts j, where different valu of j denote different levels.

Let R_{nj} and R_{pj} be the net rates of captu of free electrons and holes respectively by level. We can write

$$\left.\begin{aligned} R_{nj}&=\gamma_{nj}nN_j^+-g_{nj}N_j^-,\\ R_{pj}&=\gamma_{pj}pN_j^--g_{pj}N_j^+, \end{aligned}\right\}\qquad ($$

where γ_{nj} and γ_{pj} are the rates of capturi an electron and hole by a single j-trap, g and g_{pj} are the rates for converse processe n is the concentration of electrons in condu tion band, p is the concentration of holes valence band, and N_j^- and N_j^+ are the co centrations of j-traps occupied by electro and holes respectively. Here the relati between N_j^- and N_j^+ is given by

$$N_j^-+N_j^+=N_j\,,\qquad ($$

where N_j is the concentration of j-traps.

According to the principle of detail balance, $R_{nj}=R_{pj}=0$ in equilibrium. Ther fore,

$$\left.\begin{aligned} \gamma_{nj}n_0N_{j0}^+&=g_{nj}N_{j0}^-,\\ \gamma_{pj}p_0N_{j0}^-&=g_{pj}N_{j0}^+, \end{aligned}\right\}\qquad ($$

subscript 0 referring to the thermal equi brium condition. For nondegenerate sem conductors,

$$\left.\begin{aligned} n_0&=N_C\exp\{(F_0-E_C)/kT\}\ ,\\ p_0&=N_V\exp\{(E_V-F_0)/kT\}\ ,\end{aligned}\right\}\qquad(4)$$

and

$$\left.\begin{aligned} N_{j0}^-&=N_j(1+n_j/n_0)^{-1}=N_j(1+p_0/p_j)^{-1},\\ N_{j0}^+&=N_j(1+n_0/n_j)^{-1}=N_j(1+p_j/p_0)^{-1},\end{aligned}\right\}\qquad(5)$$

where N_C and N_V are the effective densities of states for conduction band and valence band respectively, F_0 is the Fermi level, E_C is the bottom energy of conduction band, E_V is the top energy of valence band, and n_j and p_j are the concentrations of free electrons and holes, respectively, when the Fermi level equals to the effective energy, E_j, of j-level. Thus, from (3), (4) and (5), we obtain

$$\left.\begin{aligned} g_{nj}/\gamma_{nj}&=n_j\ ,\\ g_{pj}/\gamma_{pj}&=p_j\ .\end{aligned}\right\}\qquad(6)$$

For small changes of carrier concentrations, denoted by Δn and Δp, lifetimes of electrons and holes are defined[*] by

$$\left.\begin{aligned} \tau_n&=\Delta n/\Delta R_n\ ,\\ \tau_p&=\Delta p/\Delta R_p\ ,\end{aligned}\right\}\qquad(7)$$

where $R_n=\sum_j R_{nj}$ and $R_p=\sum_j R_{pj}$.

Suppose that the disturbances in carrier concentrations are small enough that only first-order terms in Δn and Δp need be considered. From (1), (2) and (6), we get

$$\left.\begin{aligned} \Delta R_{nj}&=\gamma_{nj}\{N_{j0}^+\Delta n-(n_0+n_j)\Delta N_j^-\}\ ,\\ \Delta R_{pj}&=\gamma_{pj}\{N_{j0}^-\Delta p-(p_0+p_0)\Delta N_j^+\}\ .\end{aligned}\right\}\qquad(8)$$

Condition of electrical neutrality requires

$$\Delta n=\Delta p+\sum_j\Delta N_j^+=\Delta p-\sum_j\Delta N_j^-\ .\qquad(9)$$

As a further simplification, we shall limit ourselves here to steady-state condition,

$$\Delta R_{nj}=\Delta R_{pj}\ .\qquad(10)$$

In this case we have

$$\tau_p/\tau_n=\Delta p/\Delta n\ ,\qquad(11)$$

and Eqs. (8) and (10) give

$$\Delta N_j^+=-\Delta N_j^-=(\gamma_{pj}N_{j0}^-\Delta p-\gamma_{ni}N_{j0}^+\Delta n)/B_j\ ,\qquad(12)$$

where

$$B_j=\gamma_{nj}(n_0+n_j)+\gamma_{pj}(p_0+p_j)\ .$$

Substitution (12) into (9), we get

$$\Delta p/\Delta n=(1+H_p)/(1+H_n)\ ,\qquad(13)$$

where

$$\left.\begin{aligned} H_n&=\sum_j(\gamma_{pj}N_{j0}^-/B_j)\ ,\\ H_p&=\sum_j(\gamma_{nj}N_{j0}^+/B_j)\ .\end{aligned}\right\}$$

Hence, using (7), (8), (12) and (13), it is found that steady-state lifetimes are given by

$$\left.\begin{aligned} \tau_n&=(1+H_n)\,/\,\{n_0(1+H_p)+p_0(1+H_n)\}H\ ,\\ \tau_p&=(1+H_p)\,/\,\{n_0(1+H_p)+p_0(1+H_n)\}H\ ,\end{aligned}\right\}\qquad(14)$$

where

$$H=\sum_j(\gamma_{nj}\gamma_{pj}N_j/B_j)\ .$$

§ 3. Applications to Germanium

A. *Control Germanium Single Crystals*

In the case of control germanium samples known (from resistivity and lifetime measurements) to be high purity, it may be considered that

$$H_n \text{ and } H_p\ll 1\ .$$

Thus, from (14), we have single lifetime τ given by

$$1/\tau=1/\tau_n=1/\tau_p=\sum_j(1/\tau_j)\ ,\qquad(15)$$

where

$$\tau_j=\{\tau_{pj}(n_0+n_j)+\tau_{nj}(p_0+p_j)\}\,/\,(n_0+p_0)\ .\qquad(16)$$

Here τ_{nj} and τ_{pj} are the lifetimes defined by the equations

$$\tau_{nj}=1/(\gamma_{nj}N_j)\ ,$$

and

$$\tau_{pj}=1/(\gamma_{pj}N_j)\ .$$

Let us now consider the temperature dependence of τ.

Considering n-type samples ($n_0\gg p_0$), and assuming that the recombination centers lie in upper half of the energy gap ($n_j\gg p_j$), Eq. (16) reduces to

$$\tau_j=\tau_{pj}(1+n_j/n_0)\ .\qquad(17)$$

Thus, in the extrinsic region, at lower temperatures ($n_j\ll n_0$)

$$\tau_j\simeq\tau_{pj}\ ,$$

while at higher temperatures ($n_j\gg n_0$)

$$\tau_j\propto\exp\{(E_j-E_C)/kT\}\ .$$

This implies that, with decreasing temperature, τ_j decreases with the slope corresponding to (E_C-E_j) and reaches a plateau at lower temperatures. Temperature dependence of τ is given by substituting (17) to (15). In Fig. 1 we show in a qualitative fashion the dependence of τ_j and τ on temperature.

In order to test these results, we have measured the carrier lifetimes of control germanium samples as a function of temperature. Measurements were made by using experiment similar to that of Navon *et al.*[3)], wherein the time-decay of excess carriers injected electrically by a pulse is observed. Typical results on *n*-type germanium are shown in Fig. 2. In this figure, τ_R indicates the time constant of fast decay and τ_S is that of slow decay which follows the fast one These results are similar to that of Fan e *al.*[4)] Therefore we may conclude that τ_R and τ_S are accounted for by recombination and hole trapping centers respectively.

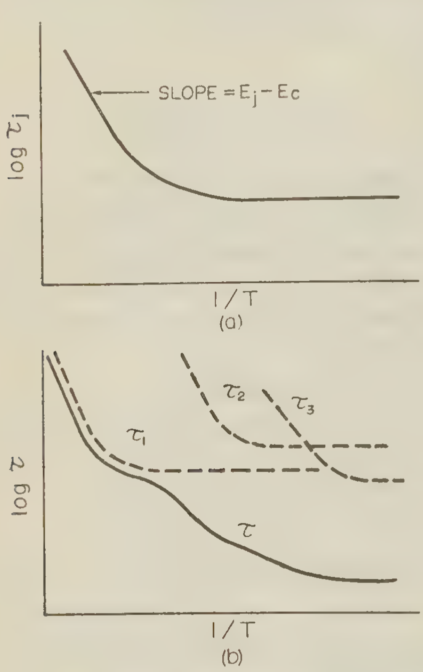

Fig. 1. The temperature dependence of lifetimes of control samples (qualitative only).
(a) τ_j *vs* $1/T$; (b) τ *vs* $1/T$.

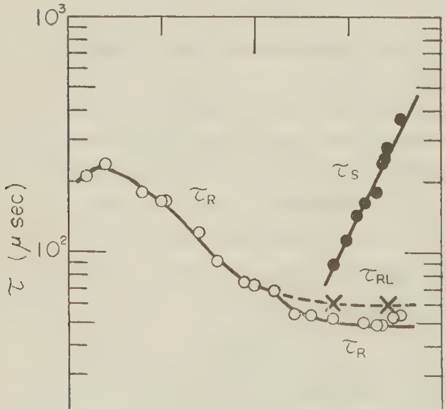

Fig. 2. Time constants τ_R and τ_S in 21 ohm-cm *n*-type germanium *vs* $10^3/T$.

We shall first consider τ_R. In this case we have two plateaus. This seems to mean that there exist at least two sets of recombination centers. However, as shown as dashed curve denoted by τ_{RL} in the figure, one of them can be removed by bias light. This is characteristics of trapping centers. Thus we can conclude that only one set of recombina tion centers is effective in our temperatu range and that the experimental curve ca be fitted by Eq. (17). Taking $\tau_{pr}=60\,\mu$ se and plotting $\log\{(\tau_R/\tau_{pr})-1\}$ *vs* $10^3/T$ give points shown in Fig. 3. Assuming E_C-E_r 0.30 eV, the calculated values of n_r/n_0 is als plotted in the figure, and is in good agre ment with the experimental data.

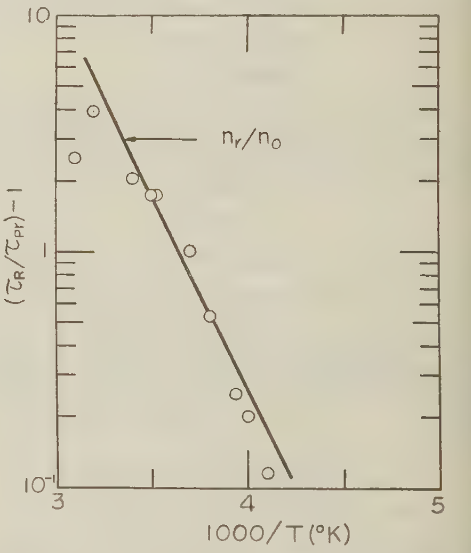

Fig. 3. $(\tau_R/\tau_{pr})-1$ *vs* $10^3/T$. The open circles ar experimental points and the solid line is plo of n_r/n_0.

We shall next consider the case where on one set of hole trapping centers is effectiv In this case, using the theory of trappin under transient conditions similar to that Fan[5)], we get

$$\tau_S \simeq 1/(\gamma_{pt}\,p_t)\,,$$

or

$$\tau_S \propto \exp\{(E_t-E_V)/kT\}\,,$$

and

$$1/\tau_R - 1/\tau_{RL} = N_t \gamma_{pt} ,$$

where suffix t denotes a trapping level. Using these relations, experimental data give $E_t - E_V = 0.30$ eV, $N_t = 8.4 \times 10^{11}/\text{cm}^3$ and $\gamma_{pt} = 3.4 \times 10^{-9}$ cm^3/sec.

On the other hand, when one set of recombination centers ($\gamma_{nr} \simeq \gamma_{pr}$) and one set of hole trapping centers ($\gamma_{nt} \ll \gamma_{pt}$; $B_r \ll B_t$) are effective, Eq. (14) gives two steady-state lifetimes,

$$\tau_n = \tau_{pr}\{1 + (N_t/p_t)\} ,$$

and

$$\tau_n = \tau_{pr} .$$

From these expressions, it follows that appreciable trapping effect occurs only when $N_t/p_t \geq 1$. Thus, using the experimental values of $E_t - E_V$ and N_t, we can calculate the critical temperature for hole trapping being the order of 200°K. This is in agreement with experiment. However, we cannot determine at this time what causes recombination or trapping centers.

B. *Recombination at Dislocations*

It has been shown that dislocations in and near the edge orientation act like rows of closely spaced acceptor centers with energies of about 0.2 eV below the bottom of conduction band in germanium[6]. Furthermore, unlike other imperfections, we have some methods to determine the dislocation density. Thus it is interesting to investigate the effect of dislocations on carrier lifetimes ingermanium. However, as mentioned above, in most of control samples the effect of other unknown imperfections predominates. Therefore, in order to distinguish the effect of dislocations, we must found a correlation between the lifetime and the dislocation density. When the dislocation density is not so high, this is done by using Eq. (15), and lifetime is given by

$$1/\tau = 1/\tau_d + 1/\tau_b ,$$

where τ_d is the lifetime due to dislocations and τ_b is the bulk lifetime due to the recombination centers of an undetermined origin. Let N_d is the density of randomly distributed dislocations per unit area and let ν is the number of traps per unit length of each dislocation. The concentration of dislocation traps is given by νN_d. For n-type samples,

$$\tau_d = (1/\gamma_{pd} \nu N_d)(1 + n_d/n_0) ,$$

because the level of dislocation traps lies in upper half of the energy gap. Then, if τ_b remains constant independent of dislocation density, plot of the inverse lifetime $1/\tau$ *vs* N_d should give a straight line.

We confirmed this relation in the following way.

Specimens for this investigation were selected from the single crystals of Sb-doped n-type germanium in 2.5 ohm-cm resistivity range. The dislocation density was determined by counting the etch pits[7]. Carrier lifetimes were obtained by the travelling light spot or Morton-Haynes method wherein the diffusion length of the minority carriers is measured[8].

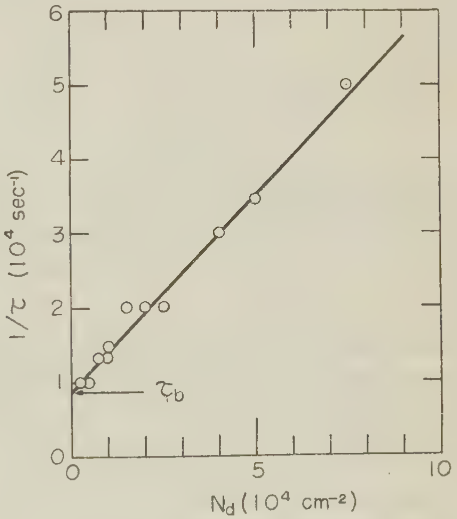

Fig. 4. Inverse lifetime as a function of dislocation density for 2.5 ohm-cm n-type germanium.

Experimental data are shown in Fig. 4, and the resulting straight line appears to prove our simple theory. The slope corresponds to $\gamma_{pd}\nu/(1 + n_d/n_0) = 5.5 \times 10^{-1}$ cm^2/sec, or $\gamma_{pd}\nu = 11$ cm^2/sec, if we take $E_C - E_d = 0.20$ eV. This is in good agreement with the value obtained from the measurements of the recombination velocity of minority carriers at the lineage boundary[9]. On the other hand, in order to obtain the values of γ_{pd} and ν separately, we must have the detailed knowledge of the electronic structure at a dislocation. Kurtz *et al.*[10] have discussed possible models by which the effect of dislocations on the recombination process might be explained. However, this is rather qualitative. Hence we do not know at this time by what means further analysis can be done.

C. *Nickel Doped Germanium*

Recently it has been found that some kinds of impurities each introduces several energy levels in germanium. Therefore such impurities can be expected to give the examples of the recombination through multiple-levels.

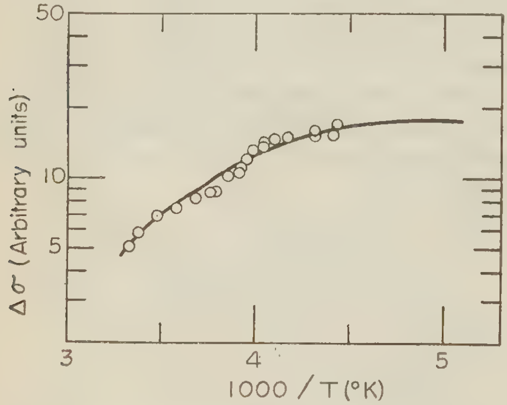

Fig. 5. Photoconductivity as a function of temperature for a high-resistivity *p*-type Ni-doped germanium. The open circles are experimental points and the solid line is calculated from Eq. (18).

However, the number of levels of each kind is not constant, but depends on the average degree of ionization of the impurities. Hence, in order to test the validity of our theory, it is necessary to use particular samples.

Experimentally we studied nickel as recombination center. Pure nickel was electroplated on originally *n*-type germanium samples. Then the samples were holded in nitrogen atmosphere at an appropriate temperature for such a time as to closely approximate the solubility limit of nickel in germanium throughout the sample[11]. This process permits us to control the concentration of nickel and the position of Fermi level. However, for reasons to be given below, among these samples, only the high-resistivity *p*-type samples were studied. Typical measurements of steady-state photoconductivity $\Delta\sigma$ are shown in Fig. 5. Results indicate that $\Delta\sigma$ increases with decreasing temperature but saturates gradually. Such a behavior of $\Delta\sigma$ is in contrast with that of control samples as shown in Fig. 6. This anomalous effect may be explained qualitatively by assuming that the capture cross-sections for free carriers are affected by charge distribution in nickel atom[12]. However, more quantitative explanation can be given in terms of multiple-levels model as follows.

It has been shown that nickel introduces two acceptor levels in germanium: one (upper level) at 0.30 eV below the bottom of the conduction band, the other (lower level) at 0.22 eV above the top of the valence band[13]. These levels are not always independent. The lower acceptor level is defined by placing an electron upon a neutral nickel atom, while the upper level is defined by placing an electron upon a singly charged (Ni⁻) ion. Thus the upper level when filled destroys the lower level. However, in the case of high-resistivity *p*-type nickel doped germanium, it is possible to assume that both levels are effective at the same time, because the Fermi level is so close to the lower level.

For our samples, the resistivity data shown in Fig. 7 indicate that

$$E_1 > (E_C + E_V)/2 > (E_1 + E_2)/2 > F_0 > E_2 \,,$$

and

$$N_1 = N_2 = N_t \,,$$

where subscripts 1 and 2 denote upper and lower levels respectively, and N_t is the concentration of nickel atoms. In this case, if $\gamma_{n1} \simeq \gamma_{p1}$ and $\gamma_{n2} \simeq \gamma_{p2}$, Eq. (14) gives

$$\tau_n = \tau_{n1} \,,$$

$$\tau_p = \{\tau_{n1} + \tau_{p1}(N_t/p_0)\} / \{1 + (N_t/p_2)\} \,.$$

Then the steady-state photoconductivity of these samples is

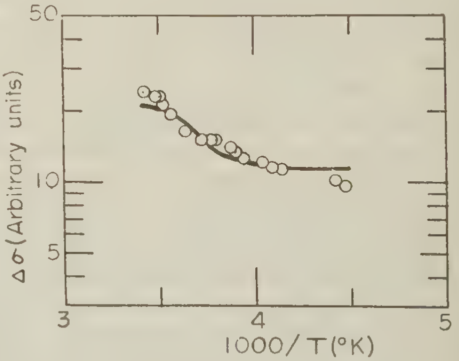

Fig. 6. Photoconductivity as a function of temperature for control *n*-type germanium (21 ohm-cm). The open circles are experimental points and the solid line is calculated from $\Delta\sigma = L\tau(\mu_n + \mu_p)$.

$$\begin{aligned}\Delta\sigma &= L(\tau_n\mu_n+\tau_p\mu_p)\\ &= L\tau_{n1}\,[\mu_n+\mu_p\{1+(\gamma_{n1}/\gamma_{p1})(N_t/p_0)\}\\ &\quad \div\{1+(N_t/p_2)\}]\,,\end{aligned} \tag{18}$$

where L is the rate of excitation and μ_n and μ_p are the mobilities of electrons and holes respectively. This implies that, at higher temperatures where $p_0<N_t<p_2$, $\Delta\sigma\simeq L\tau_{p1}\mu_p\times(N_t/p_0)$ or $\Delta\sigma\propto\exp\{(F_0-E_V)/kT\}$, and that, at lower temperatures where $p_0<p_2<N_t$, $\Delta\sigma\simeq L\tau_{p1}\mu_p(p_2/p_0)$ or $\Delta\sigma\propto\exp\{(F_0-E_2)/kT\}$. Since $F_0\simeq E_2$, Eq. (18), therefore, shows the expected temperature dependence. Quantitatively, it is necessary to know the values of parameters involved in Eq. (18). The values for N_t and p_0 are obtained from resistivity data, p_2 is calculated from Eq. (4) with $F_0-E_V=0.22$ eV, and the values of γ_{n1} and γ_{p1} can be estimated experimentally by comparing the effective lifetimes, defined by $\Delta\sigma/L(\mu_n+\mu_p)$, for two p-type nickel doped samples, where the value of L is determined by separate measurements at room temperature on a sample of known carrier lifetime. The solid curve in Fig. 5 is computed from Eq. (18) using the following parameters: $\gamma_{n1}=0.9\times10^{-9}$ cm^3/sec, $\gamma_{p1}=1.8\times10^{-9}$ cm^3/sec and $N_t=7\times10^{14}$/cm^3. The good agreement between the computed curve and the experimental data suggests that the model is valid, and shows that two acceptor levels of nickel are entirely different in the effect on the recombination process[14]. In the case of high resistivity p-type samples, most of excess holes are free at high temperatures and are trapped in the lower level at low temperatures, whereas most of excess electrons are trapped in the upper level and then recombine with free holes for all temperatures.

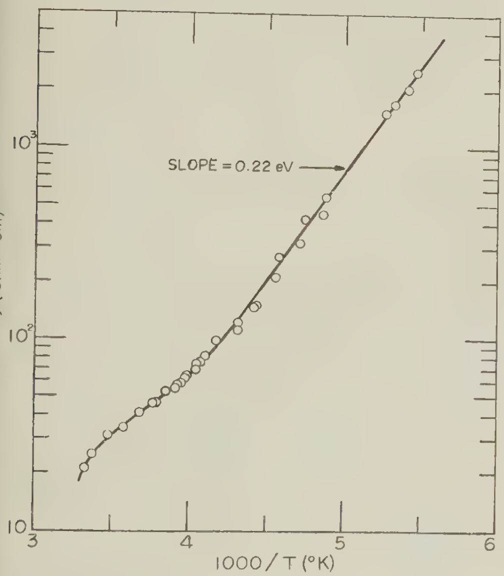

Fig. 7. Resistivity as a function of temperature for the sample of Fig. 5.

Furthermore, from the formula for Hall coefficient,

$$R=e(-C_n n\mu_n^2+C_p p\mu_p^2)/\sigma^2\,,$$

it follows that

$$\Delta p/\Delta n=[(C_n\mu_n+\delta)\,/\,(C_p\mu_p-\delta)]\,(\mu_n/\mu_p)\,,$$

$$\delta\equiv(R_L\sigma_L^2-R_0\sigma_0^2)\,/\,(\sigma_L-\sigma_0)\,,$$

where C_n and C_p are constants (Hall mobility/drift mobility) and subscripts 0 and L refer to dark and illuminated states respectively. This equation gives additional evidence for our interpretation. Experimentally we observed Hall coefficients and conductivities of our samples with and without a steady illumination. Taking $C_n=1.05$ and $C_p=1.85$[15], measurements for above sample give $\Delta p/\Delta n\simeq 3$. This is in good agreement with calculated value of 2.9. (Measurements for control samples give $\Delta p/\Delta n\simeq1$.)

Battey and Baum[16] have observed the similar temperature dependence of carrier lifetimes in nickel doped germanium. These results have been interpreted qualitatively in terms of variable cross-section model. However, even in this case, our theory may give another possible explanation.

Acknowledgement

The author would like to express his indebtness to the members of the Semiconductor Research groups of Matsuda Research Laboratory for their aid in this work.

References

1) W. Shockley and W. T. Read, Jr.: Phys. Rev. **87** (1952) 835; see also F. W. G. Rose and D. J. Sandiford: Proc. Phys. Soc. (London) **B68** (1955) 894.
2) P. T. Landsberg: Proc. Phys. Soc. (London) **A69** (1956) 1056.
3) D. Navon, R. Bray and H. Y. Fan: Proc. I. R. E. **40** (1952) 1342; see also J. P. McKelvey and R. L. Longini: J. Appl. Phys. **25** (1954) 634.
4) H. Y. Fan, D. Navon and H. A. Gebbie: Physica **20** (1954) 855.

5) H. Y. Fan: Phys. Rev. **92** (1953) 1424.
6) G. L. Pearson, W. T. Read, Jr. and F. J. Morin: Phys. Rev. **93** (1954) 666.
7) J. Okada: J. Phys. Soc. Japan **10** (1955) 1018.
8) L. B. Valdes: Proc. I. R. E. **40** (1952) 1420.
9) J. Okada: J. Phys. Soc. Japan **10** (1955) 1110.
10) A. D. Kurtz, S. A. Kulin and B. L. Averbach: Phys. Rev. **101** (1956) 1285.
11) F. van der Maessen and J. A. Brenkman: Phillips Research Repts. **9** (1954) 225.
12) W. W. Tyler and H. H. Woodbury: Phys. Rev. **96** (1954) 874; see also W. W. Tyler and R. Newman: Phys. Rev. **98** (1955) 961.
13) W. W. Tyler, R. Newman and H. H. Woodbury: Phys. Rev. **98** (1955) 461.
14) J. Okada: J. Phys. Soc. Japan **12** (1957) 741
15) F. J. Morin: Phys. Rev. **93** (1954) 62.
16) J. F. Battey and R. M. Baum: Phys. Rev. **100** (1955) 1634.

JOURNAL OF THE PHYSICAL SOCIETY OF JAPAN Vol. 12, No. 12, DECEMBER, 1957

An Electrical Resistance Study of the System $(Cr_xMn_{1-x})Sb$*

By Toshiro SUZUOKA

The Research Institute for Iron, Steel and Other Metals,
Tohoku University, Sendai

(Received August 22, 1957)

The temperature dependence of electrical resistance in the system $(Cr_xMn_{1-x})Sb$ was studied, which forms a homogeneous nickel-arsenide type solid solution of ferromagnetic MnSb and antiferromagnetic CrSb over the whole concentration range. It has been found that the resistance increases with rising temperature until it reaches a maximum at the Curie or the Néel point, and then it decreases. For the compounds with chromium concentration of $0.7 \leqq x \leqq 0.8$, another type of anomaly, that is, a small discontinuity of the resistance curve was observed at low temperatures. It is concluded that this anomaly may be attributed to the magnetic transition between ferrimagnetic and antiferromagnetic states, which was previously proposed to exist in this range of x.

§ 1. Introduction

The compound MnSb is a ferromagnetic substance with the Curie point at 310°C, while the compound CrSb is an antiferromagnetic one with the Néel point at 440°C. These two compounds, having the same crystal structure of the nickel-arsenide type, form a system of homogeneous solid solutions $(Cr_xMn_{1-x})Sb$ over the whole range of chromium concentration x. This system is known to show interesting magnetic behaviors[1]: if we substitute manganese atoms in the ferromagnetic compound MnSb with chromium atoms, the saturation moment decreases at first slowly ($x \leqq 0.1$) then falls rapidly with further substitution, and finally disappears at about $x=0.8$. Ferrimagnetism is expected, from the reciprocal susceptibility *vs* temperature curves, to prevail in the ranges of $0.1 \leqq x \leqq 0.8$. Also the Curie point lowers in a manner similar to the saturation moment (cf. Fig. 3). For the compound with $x=0.8$ (probably also with $x=0.9$), however, a type of antiferromagnetism appears in a temperature range above its ferrimagnetic Curie point. If we further increase the chromium concentration, this type of antiferromagnetism seems to become the typical one of CrSb, corresponding to $x=1$.

Such complicated magnetic behaviors may be explicable on the basis of the concept of triangular spin arrangement proposed by Yafet and Kittel[2]: a theoretical expectation[3] on a few reliable assumptions for the system showed good agreement with the experimental results concerning the relationship between the saturation moment and the concentration as well as that between the Curie point and the concentration. The theory further predicts that the magnetic transformation from ferrimagnetic to antiferromagnetic state would not be of the first order, hence it is expected that with such a transformation no appreciable anomaly would be observed in any physical properties, for instance, in electrical resistance, specific heat, etc. or it would be small if any. The primary purpose of the present investigation is to test this prediction through the measurement of the electrical resistance, which might also be of value in comprehending other physical proporties of these substances.

---

* This investigation was carried out at Prof. Hirone's laboratory in the Research Institute for Iron, Steel and Other Metals, Tohoku University, and was supported in part by the Grant-in-Aid of Fundamental Scientific Research of Ministry of Education.

§2. Experimental Results

The compounds to be measured were prepared by means of the ceramic method as described previously[1]. Namely, the mixtures of desired proportions of manganese, chromium and antimony powders below 100 mesh were sealed in evacuated silica tubes and were heated at temperatures somewhat below the melting points or the solidus line of the system for about 24 hours and slowly cooled down in the furnace. Reaction products thus obtained were powdered to 200 mesh or less and pressed into brickets of about 2×5×30 mm in size under the pressure of about 5 tons/cm^2, and then they were heated again by the same procedure as before.

These sintered samples were conductive enough to be measured by the potentiometric method; the resistivity at room temperatures was about 1×10^{-4} ohm-cm for MnSb and 3×10^{-4} ohm-cm for CrSb, while those for the intermediate compositions roughly lay between the terminal values. Connection of specimens with electrical leads, which were platinum wires of 0.15 mm in diameter, was made by welding with electric discharge from a condenser of 60 μF. The temperature range in which the measurements were made was that from the liquid nitrogen temperature to about 500°C, the maximum temperature being limited by the softening of the vacuum case made of S.B. glass.

The temperature dependence of the electrical resistance of the compounds $(Cr_xMn_{1-x})Sb$ is shown in Fig. 1, in which the magnitude of the resistance is represented by the ratio r/r_0, r_0 being that at 0°C. The sesistance of each compounds increases at first with increasing temperature, reaches a maximum at a certain temperature, and then decreases above it. Those critical temperatures, shown by downward arrows in the figure, accord with the magnetic Curie points observed previously[1]. Moreover, in the chromium-rich side we have found another type of anomaly or a small discontinuity which locates at 40°C for $x=0.7$, at 20°C for $x=0.75$ and at -60°C for $x=0.8$, as shown by upward arrows in the figure. This kind of anomaly is very small, say below 1%, as seen from an enlarged figure (Fig. 2). They are probably ascribed to the abovementioned transition between ferrimagnetic and antiferromagnetic states.

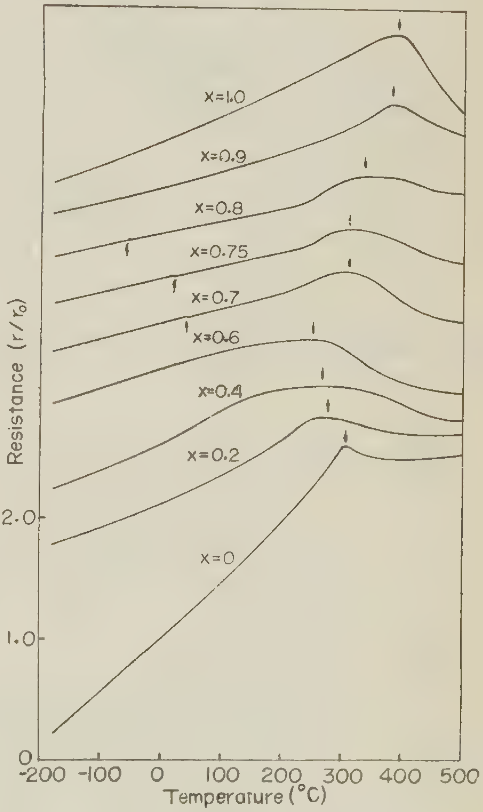

Fig. 1. Temperature dependence of the electrical resistance of $(Cr_xMn_{1-x})Sb$ system. The magnitude of resistance is represented by the ratio r/r_0, r_0 being that at 0°C. Resistance scale is indicated only for MnSb with $x=0$.

In Fig. 3, the temperatures of the anomalies (open circles) obtained from the resistance measurements are plotted against the chromium concentration x, and compared with the Curie points (full circles) found by the magnetic measurements referred to before[1]. The agreement between these temperatures is very good for low concentrations. As for CrSb as well as for compounds in the chromium-rich region, however, the agreement is not so good. The disagreement seems to be inherent in CrSb, since we have ascertained the difference between the Néel point (440°C*) as determined by the magnetic measurement conducted newly by the present author and the temperature (390°C) of anomaly found in the electrical measurement mentioned above.

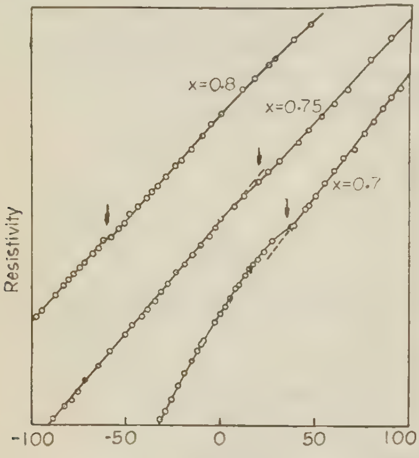

Fig. 2. Resistivity of the compounds with x from 0.7 to 0.8.

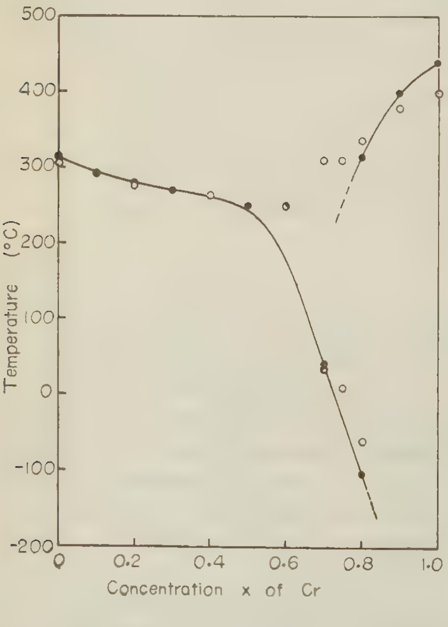

Fig. 3. Magnetic phase diagram of $(Cr_xMn_{1-x})Sb$ system. Full circles represent Curie points obtained from the magnetic studies[1], open circles those from the resistance measurements.

§ 3. Discussion

As mentioned above, the magnetic properties of this system may be explained on the basis of the idea of triangular spin arrangement that the resultant spin moments of different kinds of cations form an angular coupling due to the presence of various kinds of exchange interactions, which may be expected to exist in such a substitutional type of compounds with off-stoichiometric concentrations[3]. The angle between spin directions depends on the concentration since spin moments are affected by such exchange interactions; in the present case these interactions may be assumed to be ferromagnetic for a pair of Mn-ions as well as for a Mn–Cr pair while it may be antiferromagnetic for a pair of Cr-ions. Thus the ferromagnetism observed in the intermediate range of x is considered to be a special type of ferrimagnetism, in which the moments of cations partially compensate each other by the angular arrangement. It may also be pointed out that this tendency will be put forward with increasing temperature and at the ferrimagnetic Curie point the moments of cations wholly compensate each other. If it is the case here, in the compounds with $x=0.7\sim0.8$, the magnitude of the total spin moment of each sublattice will not change at the ferrimagnetic Curie point but only the interrelation between the directions of spins on different sublattices leads to the disappearance of the resultant moment. It will therefore be expected that on passing through the transition from one type of spin angular arrangement to another, appreciable energy change of the system will not occur. Thus at the transition temperature the specific heat will exhibit no anomaly, also the resistance as well. Of course the above picture is very crude one, and so the occurrence of a extremely small anomaly is not precluded. On the contrary, at the Curie points of the compounds on the manganese-rich side or at the Néel points of those on the chromium-rich side these physical properties will display large anomalous changes due to the disordering of spins. The result of our resistance measurements supports the above expectation.

---

* This temperature is in accord with that given in reference (1).

Finally, according to the present measurements of electrical resistance it seems that the antiferromagnetic region on the chromium-rich side extends towards somewhat more manganese-rich side than deduced from the magnetic measurements¹⁾, since at least for $x=0.7$ the antiferromagnetic region exists. In the previous measurement of magnetic susceptibility of the compound with $x=0.7$, the minimum in the reciprocal susceptibility *vs* temperature curve, which should be expected to appear for an antiferromagnetic, was not found, but instead there appeared only an inflexion point. The present measurement, however, demonstrates clearly that the substance has surely an antiferromagnetic state by the appearance of two anomalies in the electrical resistance, since these two anomalies should be of the same nature as those found in the specimens with larger chromium content.

In closing the author wishes to express his sincere thanks to Mr. S. Maeda and Dr. H. Watanabe for their encouragement and valuable discussions.

References

1) T. Hirone, S. Maeda, I. Tsubokawa and N. Tsuya: J. Phys. Soc. Japan **11** (1956) 1083.
2) Y. Yafet and C. Kittel: Phys. Rev. **87** (1952) 290.
3) T. Hirone and K. Adachi: J. Phys. Soc. Japan **12** (1957) 156.

JOURNAL OF THE PHYSICAL SOCIETY OF JAPAN Vol. 12, No. 12, DECEMBER, 1957

Lifetime Measurements of Minority Carriers Across and Along a Dislocation Wall in a Germanium Crystal

By Ryukiti R. HASIGUTI and Etsuyuki MATSUURA

Department of Metallurgy, University of Tokyo

(Received August 26, 1957)

Lifetime of minority carriers were measured across and along a dislocation wall in a *n*-type germanium crystal. The spacing of dislocations in the wall is about 2×10^{-4} cm. Recombination diameter of a dislocation in the dislocation wall is 2.2×10^{-8} cm. The lifetime is unusually large (about 210μ sec.), when it is measured along the wall. The usual value of lifetime is about 70μ sec. in this specimen. It is suggested that the dislocation wall forms a *p*-type thin layer in a *n*-type crystal.

§1. Introduction

Vogel et al.¹⁾²⁾ found a beautiful dislocation wall by means of etch pits technique in a small angle grain boundary in a germanium crystal. This kind of wall is precisely what the dislocation theory predicts. On the other hand it is known that the lifetime of minority carriers decreases when dislocations exist in germanium crystal.³⁾ It is expected, therefore, that the lifetime will be decreased, if the measurements are made across the wall which is made of dislocation array.

This was actually confirmed by several authors⁴⁾⁵⁾⁶⁾, but it is desirable at present to have more data in different conditions.

Experiments were carried out to obtain more data on this effect of dislocation wall. We also measured the lifetime along a dislocation wall, and obtained a very interesting and unexpected result.

§2. Observation of Dislocation Walls

Fig. 1 shows a dislocation wall, which was revealed by etching a germanium crystal by CP4 solution²⁾. The top and back faces of this crystal are {100} planes, and four side faces are {110} planes. The trace of dislocation wall on the top face (001) runs in [110] direction (Fig. 2). It was found by careful observations on top and back faces of the specimen that this wall penetrates through the whole thickness of the specimen (4 mm) from top face to back face, and it was also found that the wall is perpendicular to the top and back faces. This was also confirmed by the fact that the continuous etching of top face did not change the position and external appearence of the array of etch pits in the wall. Irregular network figure which is observed on both sides of the wall becomes faint and often disappears by changing the etching solution. For instance Fig. 3 shows the etch figure revealed by a modified CP4 solution and network figure is vanishingly faint. Incidentally the photograph in Fig. 3 suggests the structure of bottom of etch pits. It seems that the bottom has such a structure as shown in Fig. 4, when the direction of shadow is considered.

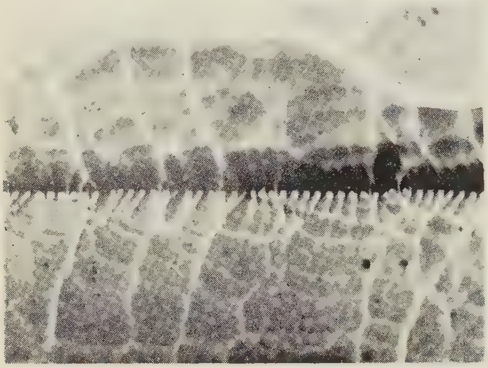
Fig. 1. A dislocation wall in a germanium crystal. Etched by CP4. Magnification: ×640.

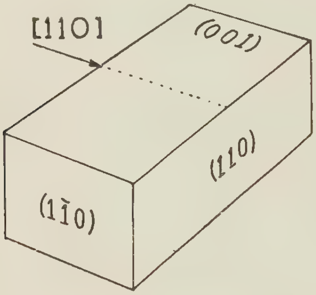

Fig. 2. Germanium crystal used.

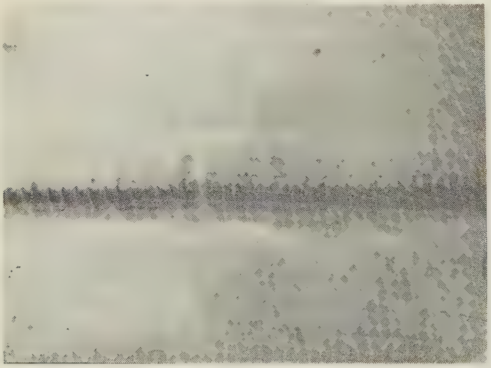
Fig. 3. The same dislocation wall as in Fig. 1. Etched by modified CP4. Magnification: ×900.

The next problem is to consider the direction of dislocation line. Vogel considers that the direction of dislocation lines is [001] in his specimen[2]. Although we did not use the X-ray measurement as Vogel did, we can conclude from the above mentioned surface observations and some other additional indirect evidences that the dislocation lines in our specimen may have one of the following two directions. These alternatives are:

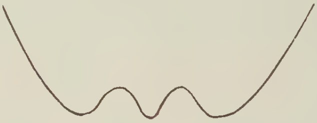
Fig. 4. Structure of the bottom of an etch pit. (Schematic).

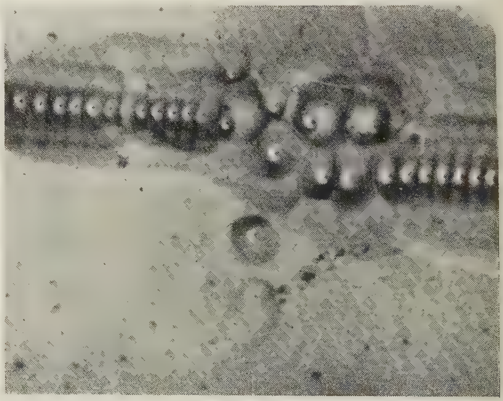
Fig. 5. A complex array of dislocations including doublets and triplets. Magnification: ×950.

(i) [001] edge dislocations with Burgers vector $a/2$ [$\bar{1}$10] in a slip plane {110}, and

(ii) [$\bar{1}\bar{1}$2] edge dislocations with Burgers vector $a/2$ [$\bar{1}$10] in a slip plane {111}.

In germanium, however, only {111} planes are known at present as slip planes from the experiments of plastic deformation, but {110} planes are not yet known as slip planes.

On the other hand a complex dislocation array was found in the extreme end portion of our dislocation wall as shown in the microphotograph of Fig. 5. This is an assembly of dislocation doublets and triplets as shown schematically in Fig. 6. Such stable arrangements of dislocations in doublets or triplets were calculated in simple cases by means of elastic theory of dislocation by Uemura[7)].

In our opinion dislocations have actually moved in the direction perpendicular to the dislocation wall in the formation process at high temperatures of such doublets and triplets. This means that our dislocations in the wall should be glissile (or glidable) dislocations. Therefore, if the slips in germanium are limited on {111} planes, our dislocations should be the $[\bar{1}\bar{1}2]$ dislocations. But if it is possible that {110} planes become slip planes, for instance at high temperatures near the melting point, it is also possible that our dislocations are [001].

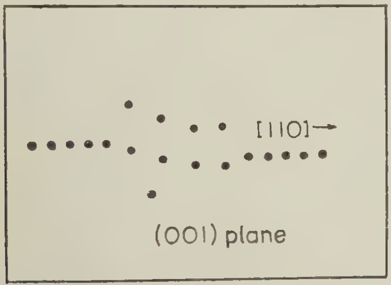

Fig. 6. A schematic representation of Fig. 5.

If we consider [001] dislocation lines, the spacing of our dislocation array is about 2.1×10^{-4} cm., and if we take $[\bar{1}\bar{1}2]$ dislocation lines, the spacing will be about 1.5×10^{-4} cm.

§3. Lifetime Across a Dislocation Wall

We obtained the recombination velocity v and the diameter g of the cylindrical recombination region associated with a dislocation (i.e., recombination diameter of a dislocation) from signals of Morton-Haynes' photo-injection method[8)] on both sides of the dislocation wall which was described in the preceding section. This is n-type germanium and its electrical resistivity is 2.5 Ωcm.

The results of measurements are shown in Fig. 7. The abscissa represents the distance between the photo-injection line and the collector probe, and the ordinate the collector voltage in arbitrary unit. From these measurements the recombination velocity was calculated by Vogel-Read-Lovell method[4)] to be

$$v=1.43\times10^3\ \text{cm/sec}.$$

From this value of v, the recombination diameter g is calculated[9)] as

$$g=2.2\times10^{-8}\ \text{cm}.$$

On the other hand it is admitted that the minority carrier lifetime τ in a germanium crystal with randomly distributed dislocations is correlated with the dislocation density N_d as follows:

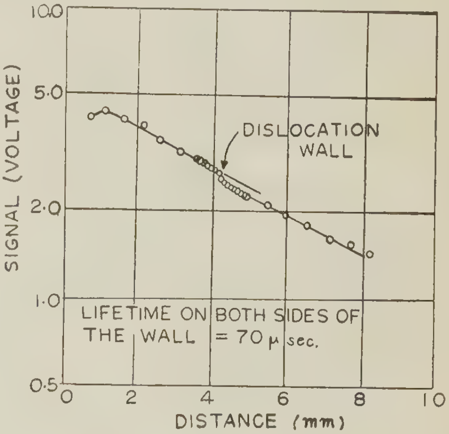

Fig. 7. Collector voltage vs light-probe distance. Measurement across the dislocation wall.

$$\tau=1/(N_d g\bar{c})\ ,$$

where $\bar{c}$ is the thermal velocity of minority carriers. Using the above value of g and 2.101×10^7 cm for $\bar{c}$[6)], we obtain

$$\tau=2.16/N_d.$$

This relation is plotted as a line (e) in Fig. 8.

In Fig. 8 data from different authors were plotted for comparison. The line (a) represents data from 4 Ωcm n-type crystal with uniformly distributed dislocations (Kurtz et al.[3)]); the line (b) shows the results from a dislocation wall in n-type germanium (McKelvey[6)]); the line (c) was plotted from the data of plastically deformed n-type crystals (Wertheim and Pearson[10)]); the line (d) represents the results from n-type crystals with randomly distributed dislocations (Okada[5)]). Okada's results from dislocation wall with

$g=2.3\times10^{-8}$ cm agree completely with our results (e).

Results obtained in our laboratory from 3~7 Ωcm n-type germanium with randomly distributed dislocations were also shown as open circles and crosses in Fig. 8. Here the dislocation densities were measured in two ways. Firstly only large etch pits with figures of concentric circles around the respective centers of etch pits were counted. These are expressed by open circles. Secondly all etch pits including small ones without concentric circles around them were counted. These are shown as crosses. The latter value seem to be closer to the real values of density. These measurements on τ and N_d were made on (100) planes of crystals.

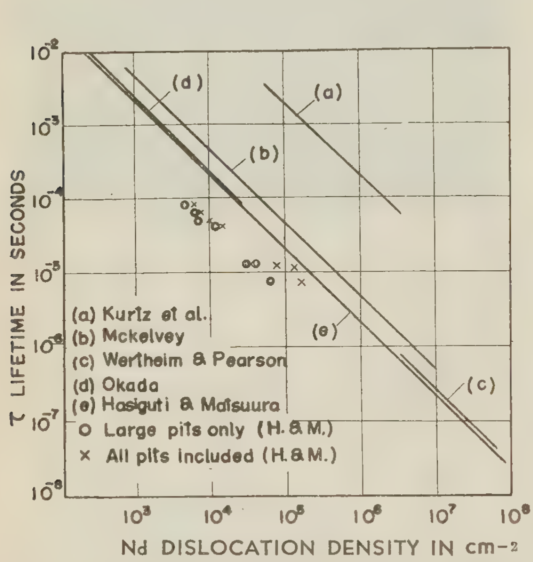

Fig. 8. Lifetime in n-type germanium vs dislocation densities.

It is considered that

$$\frac{1}{\tau}=\frac{1}{\tau_b}+\frac{1}{\tau_d},$$

where τ_b is the body lifetime due to recombination centers other than dislocations and τ_d is the lifetime due to randomly distributed dislocations. Using the data shown as crosses in Fig. 8, τ_b is calculated by Okada's method[5] to be

$$\tau_b=153\ \mu\text{sec}.$$

Using this value of τ_b, we obtain values of τ_d from the values (crosses) in Fig. 8. These τ_d's as a function of N_d's agree quite well with our plot from dislocation wall (the line (e) in Fig. 8).

§ 4. Lifetime Along a Dislocation Wall

A very interesting result was obtaine when the measurements were made puttin the collector probe on the dislocation wall As shown in Fig. 9 A, we found a very lon lifetime, which is 210 μsec., when photo injection site is moved along the dislocatio wall. In Fig. 9 B, the results are show when photo-injection line was moved perpendicularly to the wall. The lifetime is 70 μ sec which is the same as was found on bo sides of the wall in the preceding sectio (Fig. 7).

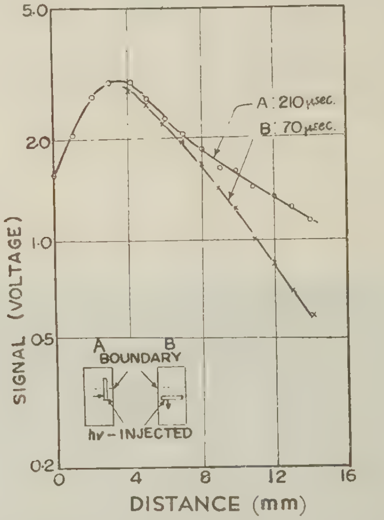

Fig. 9. Collector voltage vs light-probe distance.
(A) Measurement along the dislocation wall.
(B) Measurement perpendicular to the dislocation wall.

It is interesting and important that a ver long lifetime is found when the measurements are made along the dislocation wall It is supposed that this phenomenon is du to the same mechanism which gives rise t the fictitious long lifetime in a germaniu crystal with alloy junction on the surface[11].

In our experiment the dislocation wall i considered to form a p-type thin layer whic results in a p-n junction. Thus it is conceivable that our dislocation junction gives ris to a long lifetime just as the alloy junctio does. In another paper[12], we shall repor the effect of deuteron irradiation on th surface of germanium crystal. Again fictitious long lifetimes were found. It is interesting to note that the lattice defects produce by deuteron irradiation also form a p-type thin layer in an n-type crystal.

§ 5. Summary

1. Observations were made on a dislocation wall in a germanium crystal.

2. Recombination diameter of a dislocation in a dislocation wall was measured in n-type germanium. It is 2.2×10^{-8} cm. From this value a relation between lifetimes and densities of randomly distributed dislocations was obtained which agrees fairly well with experimental results of other authors.

3. Minority carrier lifetime is unusually long (fictitiously long), when it is measured along a dislocation wall. This seems to show that the wall forms a p-type layer.

Acknowledgement

The authors' thanks are due to Prof. Y. Uemura for his valuable discussions and to Tokyo Tsushin Kogyo, Ltd. for supplying them with germanium specimens. The expense for this research has been partly defrayed by the Scientific Research Grant from the Ministry of Education.

References

1) F. L. Vogel, W. G. Pfann, H. E. Corey and E. E. Thomas: Phys. Rev. **90** (1953) 489.
2) F. L. Vogel: Acta Metallurgica **3** (1955) 245.
3) A. D. Kurtz, S. A. Kulin and B. L. Averbach: Phys. Rev. **101** (1956) 1285.
4) F. L. Vogel, W. T. Read and L. C. Lovell: Phys. Rev. **94** (1954) 1791.
5) J. Okada: J. Phys. Soc. Japan **10** (1955) 1110.
6) J. P. McKelvey: Phys. Rev. **106** (1957) 910.
7) Y. Uemura: J. Phys. Soc. Japan **11** (1956) 479.
8) L. B. Valdes: Proc. Inst. Radio Engng. **40** (1952) 1420.
9) J. P. McKelvey and R. L. Longini: Phys. Rev. **99** (1955) 1227.
10) G. K. Wertheim and G. L. Pearson: Phys. Rev. **107** (1957) 694.
11) A. R. Moore and W. M. Webster: Physica **11** (1954) 1046.
12) R. R. Hasiguti, E. Matsuura and S. Ishino: J. Phys. Soc. Japan **12** (1957) 1351.

JOURNAL OF THE PHYSICAL SOCIETY OF JAPAN Vol. 12, No. 12, DECEMBER, 1957

Lifetime Measurements of Minority Carriers in Deuteron Irradiated Germanium Crystals

By Ryukiti R. HASIGUTI, Etsuyuki MATSUURA
and Shiori ISHINO
Department of Metallurgy, University of Tokyo

(Received August 26, 1957)

Minority carrier lifetimes were measured on the deuteron irradiated surfaces of n-type germanium crystals. Fictitiously long lifetimes were obtained which suggest the formation of a p-type thin layer by the deuteron irradiation. Etch figures were observed on the irradiated surfaces.

§ 1. Introduction

Studies of radiation damage in germanium crystals have been carried out by K. Lark-Horovitz and his coworkers[1] and many others in recent years. It has been recognized that the irradiation of germanium crystals by high energy particles produces lattice defects which act as acceptors in n-type germanium, and that n-type germanium is converted into p-type by prolonged irradiation.

Fast neutron irradiation may produce a homogeneous distribution of lattice defects, which may be relatively easy to analyse. In the case of charged particle irradiation, however, the analysis of results may be very difficult, because the distribution of produced defects must be heterogeneous on account of short range of charged particles in germanium crystals. Nevertheless we can expect some kinds of interesting phenomena in the case of charged particle bombardment. For instance a number of lattice defects may concentratively be produced around the place where bombarding particles come to standstill and, therefore, a thin *p*-type layer may be formed in a *n*-type germanium crystal. The aim of this study is to explore such kinds of problems.

§ 2. Experimental Procedure and Results Obtained

Specimens used were *n*-type germanium crystals with more than 30Ω cm resistivity, cut into slabs with dimensions of about 1.5 ×4×10 mm, polished and etched by CP4 solution[2]. They were irradiated by deuterons from a cyclotron at Scientific Research Institute (Tokyo). After irradiation, lifetimes of minority carriers were measured on the irradiated surface by photo-injection method developed by Morton-Haynes[3]. Then the irradiated surface was etched off little by little by modified CP4 solution (CH_3COOH increased), and lifetimes were determined on every stages of etching. Depths from the initial surface were measured by means of a microscope and a micrometer.

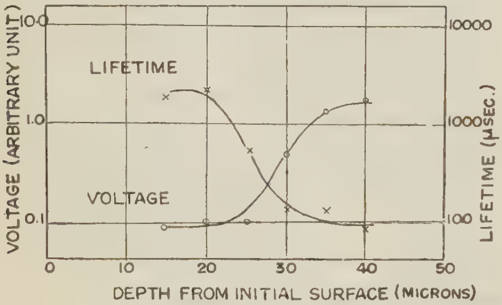

Fig. 1. Lifetime and maximum collector voltage as a function of depths from the initial surface in a deuteron irradiated n-type germanium. Irradiated at room temperature. Measurements 830 hr. after irradiation.

Fig. 1 shows the results obtained as a function of depths from the initial surface. In this case the specimen was placed outside the cyclotron window in the atmosphere at room temperature, and was irradiated by 2 MeV deuterons. The irradiation dose was 1.1×10^{16} deuterons/cm². Measurements of lifetimes were started 830 hours after the irradiation.

As shown in Fig. 1 the lifetime is unusually long at the initial surface after irradiatio It is sometimes larger than 2000 μsec. A the surface layer is etched off, the lifetim decreases gradually and restores its origina value (before irradiation), when about 40 μ the surface layer were removed. This valu of depth is about the same as the range deuteron in germanium.

When the photo-injection line falls on th same position as the collector probe, the co lector voltage comes to a maximum, of whic the plot is given also in Fig. 1 as a functio of the depths from the initial surface. Th maximum voltage is proportional to the phot current collected at the negative probe. I is very small (i.e. only 2 ∼ 3 times as larg as the noise level) at the initial surface an increases as the surface layer is etched off The maximum voltage seems to show a pea just before it restores the original value (Fig 2).

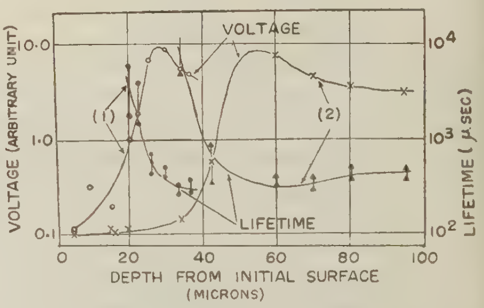

Fig. 2. Lifetime and maximum collector voltage as a function of depths from the initial surface in a deuteron irradiated n-type germanium. Irradiated at liquid oxygen temperature. (1) Measurements 26 hr. after irradiation. (2) Measurements 190 hr. after irradiation.

In the case of Fig. 2 germanium specimen were placed in vacuum inside the cyclotron and were irradiated by 3 MeV deuterons while being cooled by liquid oxygen. Irradiation dose was 5.8×10^{15} deuterons/cm². Lifetime measurements were carried out at room temperature. Two sets of curves correspon to different specimens. Curves (1) show set of observed results, of which the measurements were started 26 hours after the irradiation. Another set of measurement (curves (2)) were started 190 hours after th irradiation. Curves in Fig. 2 are much th same as those in Fig. 1 in their general ten dencies, but the peaks of maximum voltages appear clearly in Fig. 2.

A schematic representation of the collector voltage in an irradiated *n*-type specimen as a function of light-probe distance is shown in Fig. 3. Both ends of the specimen were covered by lead to make them free from radiation damage, thus corresponding maxima of collector voltage are found. Our model of the deuteron irradiated crystal which contains a *p*-type thin larger is shown in the lower part of Fig. 3.

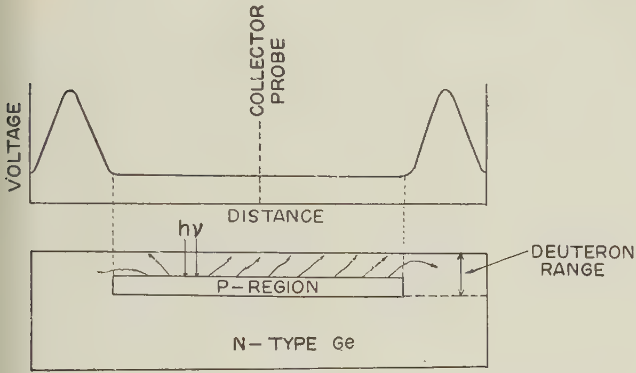

Fig. 3. Upper figure: a schematic representation of the collector voltage in a deuteron irradiated n-type germanium as a function of light-probe distance. The collector probe is at the center of the specimen. Lower figure: our model of irradiated specimen.

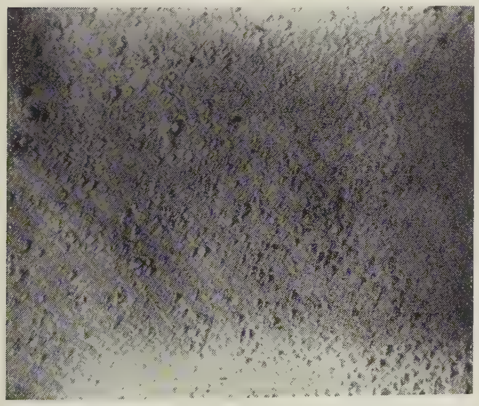

Fig. 4. Etching figure on {110} surface of germanium two days after irradiation. Etched by CP4 solution. Magnification: ×560.

The chemical etching figures of deuteron irradiated specimens were also observed. Although etching by CP4 solution does not usually exhibit any dislocation pit on {110} surfaces of germanium crystals, a great number of pit-like patterns were found on {110} surfaces of deuteron irradiated crystals. Irradiation dose used were about $10^{15} \sim 10^{16}$ deuterons/cm^2. Figs. 4 and 5 show these patterns. They are likely to be pyramidal etch hillocks rather than etch pits as they look. The microphotograph of Fig. 4 was taken two days after irradiation and Fig. 5 nine months after irradiation. Hillocks in Fig. 5 have grown to the size much greater than those in Fig. 4. These hillocks disappear, when the radiation damaged layer is etched off.

§ 3. Discussion of the Results

It is well known that a number of acceptors are formed in a germanium crystal, when it is irradiated by high energy particles, and a *n*-type crystal is converted into a *p*-type, if the irradiation is continued. It is expected, therefore, that a thin *p*-type layer will be formed within the range of deuteron in our *n*-type germanium.

Moore and Webster[4] measured the lifetimes in a germanium bar with alloy junction on back surface, and obtained fictitiously long lifetime. Our radiation-damaged specimen has a *p*-type thin layer under the irradiated surface, which acts just in the same way as Moore-Webster's alloy junction. The fictitious lifetime effect of irradiated surface decreases, when the surface is etched off gradually, as shown in Figs. 1 and 2. The effect disappears completely, when the surface layer is removed to the depth of about 40∼50 μ which is the same order of magnitude as the deuteron range in

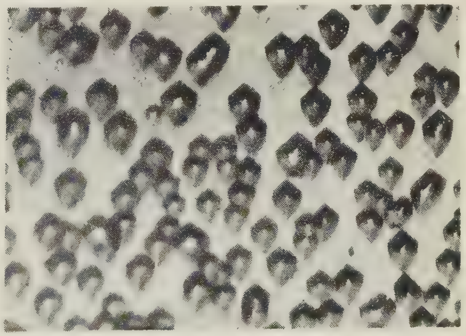

Fig. 5. Etching figure on {110} surface of germanium nine months after irradiation. Etched by CP4 solution. Magnification: ×320.

germanium. The peak of maximum voltage which appears just before it restores its initial value (Fig. 2) seems to correspond to intrinsic region of semiconductor.

The distribution of acceptors in the irradiated layer is not yet known. It is supposed that the density of acceptors will increase towards the end of deuteron range, because the cross section of displacement collision increases as the deuteron energy decreases.

A shift of curves is found between the two sets of curves in Fig. 2. This shift may be due to the difference in annealing time at room temperature after irradiation at liquid oxygen temperature. The difference in irradiation temperature seems also to affect the shape and position of the depth curve. Further investigations on these problems are being continued in our laboratory.

In another paper⁵⁾, we have reported that a dislocation wall forms a *p*-type thin layer, and unusually long lifetimes are obtained, when measurements are made along the dislocation wall. This phenomenon seems to be similar to the fictitious lifetime effect on the deuteron irradiated germanium surfaces which was reported in this paper.

§ 4. Summary

1. Minority carrier lifetimes were measured on the deuteron irradiated surfaces of *n*-type germanium crystals as a function of etched off depths from the initial surfaces.

2. Fictitiously long lifetimes were obtained which suggest the formation of a *p*-type thin layer in a *n*-type crystal by deuteron irradiation.

3. Etch figures were observed on the deuteron irradiated surfaces.

Acknowledgement

The authors wish to express their sincere thanks to Dr. A. Sugimoto for his kind guidance in using the cyclotron and to Tokyo Tsushin Kogyo, Ltd. for supplying them with germanium specimens. The expense of this research has been partly defrayed by the Government Atomic Energy Development Expenditure granted through the Japan Society for the Promotion of Scientific Research.

References

1. See, for example, H. Y. Fan and K. Lark-Horovitz: Defects in Crystalline Solids (Bristol Conference) 1955, p. 232.
2. F. L. Vogel: Acta Metallurgica **3** (1955) 245.
3. L. B. Valdes: Proc. Inst. Radio Engng. **40** (1952) 1420.
4. A. R. Moore and W. M. Webster: Physica **11** (1954) 1046.
5. R. R. Hasiguti and E. Matsuura: J. Phys. Soc. Japan **12** (1957) 1347.

JOURNAL OF THE PHYSICAL SOCIETY OF JAPAN Vol. 12, No. 12, DECEMBER, 1957

Electronic Structure of Simple Homonuclear Diatomic Molecules
II. Lithium Molecule

By Eiichi ISHIGURO,
Department of Physics, Ochanomizu University
Kunihusa KAYAMA, Masao KOTANI, and Yukio MIZUNO
Department of Physics, University of Tokyo

(Received August 3, 1957)

Based on LCAO MO CI method, the wave functions of Li_2 in the ground state $^1\Sigma_g{}^+$ and three lower excited states $^3\Sigma_u{}^+$, $^1\Sigma_u{}^+$, and $^1\Pi_u$ are calculated non-empirically. Calculation is performed at internuclear distances of 4.5, 5.0 and 5.5 a.u. by use of $1s$, $2s$, and $2p$ atomic orbitals of Stater type. Further, for the ground state, various approximations are investigated. Among other results, it is to be noted that HL method gives a lower total energy than MO method, and that in CI wave function a configuration corresponding to π-bond appears with an unexpectedly large coefficient. By using these wave functions depth of adiabatic potentials, dissociation energy, and vertical excitation energies are calculated and compared with the observed values. Further, molecular quadrupole moment, gradient of the electric field at each nucleus, and oscillator strengths are calculated. It is found that, in general, CI improves appreciably the values of these quantities calculated by the single configuration. Some of our wave functions are analysed by the population analysis method developed by Mulliken. Finally, we have examined to what extent the virial theorem is satisfied by the present wave functions and the reason for the disagreement is discussed.

§ 1. Introduction

The present paper constitutes the second part of our series, and is devoted to the investigation of the lithium molecule, Li_2. The reason why this particular molecule was chosen as subject for study was already explained in part I$^{1)}$; we note here that the lithium molecule is the simplest molecule for which the effect of inner shell electrons can be studied and for which s-p hybridization, mixing of configurations involving π orbitals, etc., become important.

Many years ago, Bartlett-Furry$^{2)}$ and Rosen-Ikehara$^{3)}$ already treated this molecule by completely shrinking the $1s$ electrons into the respective nuclei and using Slater's nodeless AO, $2s$, for valence electrons, and they obtained satisfactory results for the dissociation energy. Later, however, James$^{4)}$ carried out an elaborate calculation using a variational wave function, taking inner shell electrons into account, and he showed that the shrinking method can hardly be justified.

In this paper we investigate this molecule from the standpoint somewhat different from James', that is, by LCAO MO CI method. Configurations involving π orbitals, which were not taken into account in James' calculation, are included in our calculation. Further, we carry out similar calculations for the lower excited states $^3\Sigma_u{}^+$, $^1\Sigma_u{}^+$, and $^1\Pi_u$ of this molecule, and various physical quantities are evaluated.

§ 2. Parameters used and Method of Calculation

Calculation has been performed with three sets of parameters (α, β), where $\alpha=\delta_1 R$ and $\beta=\delta_2 R$, δ_1 and δ_2 being orbital exponents of Slater AO's (I, (1)) and R being the internuclear distance. These sets of (α, β) are denoted by I, II, and III, and the values of

Table I. Sets of parameters.

Set / α, β	I	II	III
α	14.00	13.25	14.00
β	3.00	3.25	3.50

Table II. Values of orbital exponents δ_1 and δ_2.

Set	I		II		III	
R \ δ	δ_1	δ_2	δ_1	δ_2	δ_1	δ_2
4.5	3.11111 11	0.66666 67	2.94444 44	0.72222 22	3.11111 11	0.77777 78
5.0	2.80000 00	0.60000 00	2.65000 00	0.65000 00	2.80000 00	0.70000 00
5.5	2.54545 45	0.54545 45	2.40909 09	0.59090 91	2.54545 45	0.63636 36

them are shown in Table I. For each set, further, R is chosen, as 4.5, 5.0, and 5.5. a.u., on the by consideration that the equilibrium internuclear distance of the ground state ${}^1\Sigma_g{}^+$ is 5.05 a.u. The values of δ_1 and δ_2 corresponding to these values of α, β, and R are shown in Table II. These values are to be compared with 2.70 and 0.65 a.u., respectively, given by Slater's rule.[5)]

Tacle III. Values of coefficients α_{ij}, β_{ij}, γ_g and γ_u in Schmidt-OMO.[a)]

α,β,γ \ Set	I	II	III
α_{11}	0.70708 32	0.70706 15	0.70708 32
α_{21}	−0.11365 46	−0.13810 93	−0.13813 95
α_{22}	0.55971 03	0.57121 90	0.57966 24
α_{31}	−0.03735 83	−0.03024 54	−0.01969 30
α_{32}	−0.12526 31	−0.21145 83	−0.20806 00
α_{33}	0.70763 78	0.68684 09	0.67083 84
γ_g	0.96945 70	0.92636 11	0.89099 07
β_{11}	0.70713 04	0.70715 21	0.70713 04
β_{21}	−0.08020 21	−0.11373 86	−0.12386 42
β_{22}	1.18160 28	1.11965 41	1.06407 36
β_{31}	0.03898 60	−0.01013 22	−0.03304 84
β_{32}	2.77957 82	2.10767 48	1.63550 15
β_{33}	1.98685 46	1.72124 92	1.52334 76
γ_u	0.58360 93	0.59394 58	0.60408 47

a) See Eq. (I, (3)).

As in the case of O_2, Schmidt-OMO's (I, (3)) are constructed from symmetry orbitals (I, (2)) expressed in terms of AO's. The values of coefficients α_{ij}, β_{ij}, γ_g, and γ_u of symmetry orbitals in Schmidt-OMO's depend on α and β but not on R. These values are shown in Table III.

The values of molecular integrals involving Slater type AO's [6)7)] and also Schmidt-OMO's[8)] were calculated rigorously and were already published.

Among ten Schmidt-OMO's, σ_{1g} and σ_{1u} orbitals, which are constructed from AO's $(1s)_a$ and $(1s)_b$ only, have much lower orbital energies than the others. Therefore, four electrons out of all the six are assumed here to occupy these orbitals and to form the ion cores. The remaining two electrons may be considered valence electrons. Next to σ_{1g} and σ_{1u}, σ_{2g} and σ_{2u} are supposed to have lower energies. With the use of these two orbitals besides the core orbitals, we can obtain the ground state ${}^1\Sigma_g{}^+$ and two lower excited states, ${}^1\Sigma_u{}^+$ and ${}^3\Sigma_u{}^+$. Among them two singlet states are observed spectroscopically, together with ${}^1\Pi_u$ state. In this paper we shall study these four states.

Tablel. IV. Configurations[a)] used in CI calculation for ground state ${}^1\Sigma_g{}^+$.

i	σ_{1g}	σ_{2g}	σ_{3g}	$\pi_g{}^+$	$\pi_g{}^-$	σ_{1u}	σ_{2u}	σ_{3u}	$\pi_u{}^+$	$\pi_u{}^-$
A	2	2				2				
B	2		2			2				
C	2					2	2			
D	2					2		2		
E	2	1	1			2				
F	2					2	1	1		
G	2			1	1	2				
H	2					2			1	1

a) See the footnote a) of (I, Table IV).

Following the procedures explained in I, primitive functions for each state are constructed from products of Schmidt-OMO's and then configurational wave functions are set up by antisymmetrizing products of these primitive functions and spin functions. In primitive functions unpaired orbitals are written first, followed by paired ones (for example, (I, (8)).

For each type of symmetry, the configurations are denoted, by A, B, C, ...*, in which

---

* A, B, C, ... are denoted by 1′ 2′ 3′ ... in references (8) and (9).

Table V. Coefficients c_i's[a] of configurations in normalized wave functions and energies E's obtained by using eight configurations, together with energies E_0's obtained by single configurations A's and with energy depressions $|\Delta E| = |E - E_0|$ for $^1\Sigma_g^+$ state.

Set	I			II			III		
i \ R	4.5	5.0	5.5	4.5	5.0	5.5	4.5	5.0	5.5
A	0.9307	0.9226	0.9135	0.9336	0.9303	0.9257	0.9379	0.9367	0.9343
B	−0.0666	−0.0545	−0.0406	−0.0747	−0.0664	−0.0572	−0.0814	−0.0764	−0.0714
C	−0.1197	−0.1099	−0.1020	−0.1259	−0.1239	−0.1230	−0.1349	−0.1388	−0.1437
D	−0.0070	−0.0093	−0.0121	−0.0069	−0.0089	−0.0114	−0.0060	−0.0085	−0.0102
E	0.2023	0.2527	0.2950	0.1813	0.2193	0.2513	0.1622	0.1885	0.2104
F	−0.0258	−0.0357	−0.0446	−0.0223	−0.0339	−0.0449	−0.0180	−0.0294	−0.0409
G	−0.0051	−0.0054	−0.0056	−0.0029	−0.0039	−0.0044	−0.0030	−0.0038	−0.0040
H	−0.2708	−0.2617	−0.2537	−0.2713	−0.2558	−0.2436	−0.2625	−0.2471	−0.2350
E_0(a.u.)[b]	−14.4657	−14.8010	−14.7808	−14.6844	−14.8268	−14.6771	−14.4453	−14.7999	−14.7927
E(a.u.)[b]	−14.5013	−14.8359	−14.8152	−14.7208	−14.8614	−14.7103	−14.4826	−14.8347	−14.8254
$\|\Delta E\|$ (e.v.)	0.968	0.949	0.936	0.992	0.941	0.903	1.016	0.946	0.892

a) See Eq. (I, (12)).

b) These energies include the nuclear repulsion energy, $9/R$ a.u. We note that $9/R$ is omitted in references (8) and (9).

Table VI. Coefficients of structures in normalized wave functions which are obtained by transformation from MO scheme for $^1\Sigma_g^+$ state.

Set	I			II			III		
R	4.5	5.0	5.5	4.5	5.0	5.5	4.5	5.0	5.5
$\overset{\circ}{s}-\overset{\circ}{s}$[a]	0.9725	1.0375	1.1069	0.8445	0.9042	0.9680	0.7716	0.8249	0.8782
$\overset{\circ}{s}-\sigma$[a]	0.3382	0.4332	0.5245	0.2667	0.3404	0.4130	0.2099	0.2687	0.3211
$\sigma-\sigma$[a]	−0.0083	0.0132	0.0386	−0.0211	−0.0072	0.0098	−0.0328	−0.0213	−0.0122
$\pi-\pi$[a]	−0.1365	−0.1312	−0.1267	−0.1428	−0.1332	−0.1260	−0.1408	−0.1314	−0.1246
$\overset{\circ}{s}\overset{\circ}{s}-$[b]	−0.1415	−0.2410	−0.3413	0.0115	−0.0709	−0.1555	0.1099	0.0420	−0.0246
$\overset{\circ}{s}\sigma-$[b]	−0.0328	−0.0718	−0.1186	0.0130	−0.0181	−0.0563	0.0465	0.0177	−0.0104
$\sigma\sigma-$[b]	−0.0859	−0.0903	−0.0961	−0.0795	−0.0823	−0.0869	−0.0733	−0.0783	−0.0809
$\pi\pi-$[b]	−0.1515	−0.1471	−0.1431	−0.1505	−0.1434	−0.1375	−0.1481	−0.1406	−0.1341

a) Covalent structure.

b) Ionic structure.

A may be taken as the configuration with the lowest energy.

Formulae[9] and numerical values[8] of all the required matrix elements for these configurations were derived following the method explained in I and were already published elsewhere.

§ 3. Calculation of Energy of the Ground State $^1\Sigma_g^+$.

We can construct eight configurations with $^1\Sigma_g^+$ symmetry from ten kinds of Schmidt-OMO's on the assumption that 1*s* electrons form closed shells. These configurations are listed in Table IV.

The single configuration A corresponds to the usual antisymmetrized orthogonalized molecular orbital wave function (ASOMO) built from linear combinations of atomic orbitals (LCAO). The total energies obtained by this approximation are shown in Table V as E_o for each values of α, β, and R.

Further, taking all the eight configurations into accounts, we have performed variational calculations for each set and each R. The resulting coefficients c_A, c_B, ... in the normalized wave function and the total energy E are given in Table V. The energy depression due to CI, $|\Delta E|=|E-E_0|$, is also listed in the same table.

Now these wave functions can be written also in terms of various structures in HL scheme, and the results are shown in Table VI. For convenience, we denote the normalized covalent and ionic structures built from two AO's x and w of valence electrons, as x–w and xw–, respectively. Thus, for example, $\mathring{s}$–σ and $\mathring{s}\sigma$– mean the normalized wave functions built from the primitive functions, (normalization constant) $\times\{(2\mathring{s}_a)(2p\sigma_b)+(2\mathring{s}_b)(2p\sigma_a)\}\times(1s_a)^2(1s_b)^2$ and (normalization constant) $\times\{(2\mathring{s}_a)\times(2p\sigma_a)+(2\mathring{s}_b)(2p\sigma_b)\}(1s_a)^2(1s_b)^2$, respectively. Interpretation of the coefficients in Table VI, however, is to be given with special caution because the structural wave functions form an *oblique* coordinate system. The relative instability of the coefficients with respect to the change of R and δ, as compared with the case of expansions in MO scheme, is also due to this obliqueness of the coordinate system. (See Tables V and VI.)

From Table V, we see that the total energy E obtained for Set II and R=5.0 a.u. is the best of all. Accordingly for this set and

Table VII. Expressions of various wave functions obtained for Set II and R=5.0 in terms of configurations, and their total energies.

i \ Case	1 A	2 A+C	3 A+E	4 $(g)^2$	5 $g'g''$
A	1	0.9644	0.9594	0.9691	0.9638
B				0.0309	−0.1069
C		−0.2645			
D					
E			0.2820	0.2446	0.2441
F					
G					
H					
E	−14.8268	−14.8401	−14.8388	−14.8369	−14.8410

i \ Case	6 LCAO−SCF	7 σ−electron CI	8 A+H	9 A+C+H	10 A+C+E+H
A		0.9592	0.9556	0.9455	0.9276
B		−0.0903			
C		−0.1784		−0.2078	−0.1395
D		−0.0105			
E		0.1952			0.2239
F		−0.0409			
G					
H			−0.2948	−0.2507	−0.2647
E	−14.8376	−14.8479	−14.8442	−14.8524	−14.8600

Table VII. (continued)

Case i	11 8 dim. CI	12 Pure HL	13 Ionic structure	14 HL with $s-p$ hybrid.	15 Semiloc. and $s-p$ hybrid.
A	0.9303	0.9678	0.9678	0.9733	0.9596
B	−0.0664			0.0149	0.0186
C	−0.1239	−0.2519	0.2519	−0.1510	−0.2052
D	−0.0089			−0.0024	−0.0025
E	0.2193			0.1702	0.1889
F	−0.0339			−0.0268	−0.0321
G	−0.0039				
H	−0.2558				
E	−14.8614	−14.8401	−14.7929	−14.8445	−14.8453

Case i	16 $(\overset{\circ}{s}-\overset{\circ}{s})+(\pi-\pi)$	17 $A'(S(1s_a, 2\overset{\circ}{s}_b)=0)$	18 $HL'(S(1s_a, 2\overset{\circ}{s}_b)=0)$	19 A (shrunk core)	20 8 dim. CI (shrunk core)
A	0.9439			1	0.7832
B					−0.0977
C	−0.2457				−0.0528
D					0.0004
E					0.2217
F					−0.0291
G	0.0839				0.0699
H	−0.2041				−0.5651
E	−14.8487	−14.8490	−14.8635	−0.2411	−0.2940

we have investigated 22 different approximations, Case 1—Case 22, similar to those considered in I, § 4. Each of these 22 "cases" corresponds to a more or less restricted CI, and the resulting wave function (characterized by expansion coefficients in terms of normalized wave functions for configurations given in Table IV) and the corresponding total energy for each of the first 20 cases are shown in Table VII. In the followings are given explanations and comments to each individual case.

Case 1. *Configuration* A (*single configuration*)

Case 2. A+C (*semilocalization*)

Mixing of these two configurations is equivalent to HL type description with the use of "semilocalized" orbitals for valence electrons:

$$2s_a^{sl}=2\overset{\circ}{s}_a+\mu(2\overset{\circ}{s}_b) \text{ and } 2s_b^{sl}=2\overset{\circ}{s}_b+\mu(2\overset{\circ}{s}_a) \qquad (1)$$

Thus this improvement can be ascribed to the semilocalization of valence electrons. The total energy obtained is lower than that of Case 1 by 0.361 e.v., The value of μ in (1) is found to be negative, −0.0131.

Case 3. A+E (*s–p* hybridization)

Mixing of configuration E to configuration A means *s–p* hybridization. This gives the total energy lower than that of Case 1 by 0.325 e.v.

Case 4. $(g)^2$ *approximation*

In the single configuration approximation of Case 1 we adopted Schmidt-OMO's for molecular orbitals of valence electrons as well as core electrons, partly for the sake of mathematical simplicity. This result can be improved by using as orbitals for valence electrons a linear combination of Schmidt-OMO's σ_{2g} and σ_{3g}. The total energy thus obtained is lower than that of Case 1 by 0.275 e.v. The resulting normalized MO is here called g orbital, and the coefficients for expansions in terms of Schmidt-OMO's and of the unnormalized symmetry orbitals (I, (2) and I, (30)) are shown in Table VIII. We note here that this approximation is a counterpart of $(u)^2$ approximation in I (§ 4, Case 4).

Case 5. A+C+E *or* $g'g''$ *approximation*

The result of Case 1 can further be improved by using for two valence electrons two different MO's both of which are still linear combinations of Schmidt-OMO's σ_{2g} and σ_{3g}. Variational calculation has given the total energy lower than that of Case 1 by 0.386 e.v. or lower than that of Case 4 by 0.111 e.v. The resulting normalized MO's are here denoted by g' and g'', and the coefficients for expansions in terms of Schmidt-OMO's and of the unnormalized symmetry orbitals are shown in Table VIII.

Table VIII. Coefficients of Schmidt-OMO's[a] and unnormalized symmetry orbitals[b] in g, g', and g'' orbitals.

	Schmidt-OMO		Symmetry orbital		
	σ_{2g}	σ_{3g}	$(\sigma 1s)_g$	$(\sigma \overset{\circ}{2s})_g$	$(\sigma 2p)_g$
g	0.9844	0.1757	−0.0511	0.5174	0.1207
g'	0.8735	0.4868	−0.0674	0.3902	0.3343
g''	0.9808	−0.1952	−0.0263	0.5926	−0.1341

a) See Eq. (I, (3)).
b) See Eqs. (I, (2)) and (I, (30).

This approximation is a counterpart of $u'u''$ approximation in I (§ 4, Case 5) having a nature of the so-called (longitudinal) in-out effect.

Case 6. *The* LCAO SCF *method*

Roothaan's procedure[10] can be applied straightforwardly to our problem. SCF MO's (I, (23)) can be expressed in the form of linear combinations of Schmidt-OMO's as well as of those of the symmetry orbitals. These expansion coefficients of SCF MO's are given in Table IX.

For σ SCF MO's the orbital energies can be calculated directly by means of Roothaan's procedure. For π SCF MO's, however, it is not applicable, so that we use the following formulae

$$\varepsilon_a=h(a)+\sum_k\{2J(k,a)-K(k,a)\}$$ (2

($k=1\sigma_g$, $1\sigma_u$, and $2\sigma_g$; $a=1\pi_g{}^+$, $1\pi_g{}^-$, $1\pi_u{}^+$, or $1\pi_u{}^-$),

where $h(a)$ is one electron energy of φ_a orbital and $J(k, a)$ and $K(k, a)$ are Coulomb and Exchange integrals between φ_k and φ_a orbitals. The orbital energies thus calculated are also given in Table IX.

The total energy obtained is lower than that of Case 1 by 0.294 e.v. (Table VII). The wave function of Case 6 is superior to that of Case 4, because, in the former the form of the core orbitals is also improved. This improvement reduces the total energy by 0.019 e.v., which is fairly small.

Case 7. *σ-electron configurational interaction*

As long as two valence electrons are prescibed to occupy $2s_{a,b}$ and/or $2p\sigma_{a,b}$ AO's, the possible configurations are the first six, A to F in Table V. Taking into consideration these six configurations, we have performed the CI calculation. The total energy obtained is lower than that of Case 1 by 0.573 e.v.

Table IX. Coefficients of Schmidt-OMO's[a] and unnormalized symmetry orbitals[b] in SCF MO's,[c] and orbital energies.

	Schmidt-OMO				Symmetry orbital				orbital energy (a.u.)
SCF MO	$\sigma_{1g,\,u}$	$\sigma_{2g,\,u}$	$\sigma_{3g,\,u}$	$\pi_g{}^{\pm}{}_{,\,u}$	$(\sigma 1s)_{g,\,u}$	$(\sigma \overset{\circ}{2s})_{g,\,u}$	$(\sigma 2p)_{g,\,u}$	$(\pi^{\pm}2p)_{g,\,u}$	
$1\sigma_g$	0.9999	0.0123	0.0003		0.7065	0.0069	0.0002		−2.4403
$2\sigma_g$	−0.0122	0.9843	0.1759		−0.0598	0.5173	0.1208		−0.1802
$3\sigma_g$	0.0019	−0.1759	0.9844		−0.0571	−0.3041	0.6761		0.0917
$1\pi_g{}^{\pm}$				1.0000				0.9264	0.1603
$1\sigma_u$	0.9999	0.0114	0.0039		0.7094	0.0206	0.0067		−2.4401
$2\sigma_u$	−0.0106	0.9860	−0.1667		0.0113	0.7414	−0.2869		0.0290
$3\sigma_u$	−0.0057	0.1666	0.9860		0.3558	2.2311	−1.6972		0.3615
$1\pi_u{}^{\pm}$				1.0000				0.5939	0.0641

a) See Eq. (I, (3)). b) See Eq. (I, (2)). c) See Eq. (I, (23)).

Case 8. A+H (*transverse correlation*)

From Table V, it is found that besides A the contribution of configuration H is most important. Therefore, we have here considered only CI between A and H. The energy depression from the energy of Case 1 amounts to 0.473 e.v.

The wave function here obtained can be generated from the following primitive function:

$$\text{(normalization constant)}\times\{(\sigma_{2g}+\mu\pi_u{}^x)(\sigma_{2g}-\mu\pi_u{}^x)+(\sigma_{2g}+\mu\pi_u{}^y)(\sigma_{2g}-\mu\pi_u{}^y)\}\ \sigma_{1u}{}^2\ \sigma_{1g}{}^2, \tag{3}$$

where

$$\pi_u{}^x=\frac{1}{\sqrt{2}}(\pi_u{}^+ + \pi_u{}^-),$$

$$\pi_u{}^y=\frac{1}{\sqrt{2}\,i}(\pi_u{}^+ - \pi_u{}^-), \tag{4}$$

and

$$\mu=0.6605 \tag{5}$$

Thus, in this approximation, valence electrons are considered as occupying two orbitals, $\sigma_{2g}+\mu\pi_u{}^x$ and $\sigma_{2g}-\mu\pi_u{}^x$, or $\sigma_{2g}+\mu\pi_u{}^y$ and $\sigma_{2g}-\mu\pi_u{}^y$, and so the correlation between two valence electrons is to some extent taken into account, since these two orbitals are hybridized to opposite directions perpendicular to the molecular axis.

Case 9. A+C+H (*semilocalization and transverse correlation*)

In Case 2 some longitudinal correlation between two valence electrons has been taken into account by mixing configuration C, whereas in Case 8 some transverse correlation has been considered by mixing configuration H. Here both correlations are taken into consideration. Actually CI calculation has been performed with these three configurations, A, C, and H. The total energy obtained is lower than that of Case 1 by 0.696 e.v. From Table VII, it is found that the coefficient of H is large and is even larger than that of C. This fact can be understood as follows. In the ground state of the Be atom, it is expected that configurational mixing of $(1s)^2(2p)^2\sim(1s)^2\times\{(2p\sigma)^2+(2p\pi^x)^2+(2p\pi^y)^2\}$ to $(1s)^2(2s)^2$ is fairly important. Now $2p\sigma$, $2p\pi^x$, and $2p\pi^y$ orbitals in Be have a character resembling σ_{2u}, $\pi_u{}^x$, and $\pi_u{}^y$ orbitals of our Li_2 case, respectively, if, in the Li_2 ground state, charge distribution of valence electrons is approximately spherical. If the charge distribution were completely spherical, however, the amount of mixing of configuration $H\sim(\pi_u{}^x)^2+(\pi_u{}^y)^2$ would be twice as large as that of $C\sim\sigma_{2u}{}^2$.

Case 10. A+C+E+H (*semilocalization, hybridization, and transverse correlation*)

In Case 9 the effect of *s–p* hybiridization has not been considered, which also was found to be important from the result of Case 3. Configuration E is here added to those considered in Case 9. The energy depression from Case 1 is found to be 0.902 e.v.

Case 11. *Eight dimensional* CI

The results for this approximation were already given in Table V. The depression of the total energy from that of Case 1 is 0.941 e.v. By comparing these results with those of the previous case, we can see that four configurations considered in Case 10 are most important and the contribution of the remaining configurations is very small.

Case 12. *Pure* HL *approximation*

In the Heitler-London (HL) approximation, the structural wave function $\overset{\circ}{s}$-$\overset{\circ}{s}$ is adopted. This wave function is expressed in the form of a linear combination of A and C. The energy depression from Case 1 is 0.360 e.v., which shows that the HL approximation is, in our Li_2 case, better energetically than the MO approximation. This result is contrary to the situation found for the oxygen molecule (See I), and the reason for this difference will be discussed in paper III.

Case 13. *Ionic structure*

To see the feature of the ionic structure, we here employ the wave function of a simple ionic structure, $\overset{\circ\circ}{ss}-$. The total energy is higher than that of the pure HL approximation (Case 12) by 1.284 e.v.

From the results of Cases 2 and 12, it is found that

(i) the improvement of the pure HL approximation by semilocalization is fairly small, and that

(ii) the value of μ in Eq. (1) is small and negative, which shows the charge density between two nuclei, decreases slightly through semilocalization, contrary to the H_2 case.

Further the amount of ionic character can be seen by reexpressing the normalized wave function obtained in Case 2 as

$$\Phi\mathrm{so}=\frac{1}{d}\ \{(\overset{\circ}{s}-\overset{\circ}{s})+c(\overset{\circ\circ}{ss}-)\}\,, \tag{6}$$

where

$$d=0.9772, \text{ and } c=-0.0262.$$

Case 14. HL *with s–p hybridization*

Here the pure HL approximation (Case 12) has been improved by introducing *s–p* hybridization. The wave function for this purpose is constructed from the primitive function:

$$\Phi=(\text{normalization constant})$$
$$\times\{\phi_a\,\phi_b+\phi_b\,\phi_a\}\ (1s_a)^2\,(1s_b)^2\,,$$

with

$$\phi_a=2\overset{\circ}{s}_a+\lambda(2p\,\sigma_a)\,,$$
$$\phi_b=2\overset{\circ}{s}_b+\lambda(2p\,\sigma_b)\,. \tag{7}$$

Parameter λ has been determined by variational treatment and turned out to be 0.1558. Then the degree of *s–p* hybridization becomes 0.0237, if it is defined by $\lambda^2/(1+\lambda^2)$. The energy depression from the energy of the pure HL approximation (Case 12) is 0.120 e.v.

Case 15. HL *with semilocalization and s–p hybridization*

Both semilocalization and *s–p* hybridization can be taken into account by adopting the primitive function:

$$\Phi=(\text{normalization constant})$$
$$\times\{\phi_1\,\phi_2+\phi_2\,\phi_1\}(1s_a)^2\,(1s_b)^2\,, \tag{8}$$

where orbitals ϕ_1 and ϕ_2 have the form:

$$\phi_1\ \propto\ \{2\overset{\circ}{s}_a+\nu_1(2p\sigma_a)+\nu_2(2\overset{\circ}{s}_b)+\nu_3(2p\sigma_b)\}$$
$$\propto\ \{\sigma_{2g}+\kappa_1(\sigma_{3g})+\kappa_2(\sigma_{2u})+\kappa_3(\sigma_{3u})\}$$
$$+(\text{a linear combination of } \sigma_{1g} \text{ and } \sigma_{1u}),$$
$$\phi_2\ \propto\ \{2\overset{\circ}{s}_b+\nu_1(2p\sigma_b)+\nu_2(2\overset{\circ}{s}_a)+\nu_3(2p\sigma_a)\}$$
$$\propto\ \{\sigma_{2g}+\kappa_1(\sigma_{3g})-\kappa_2(\sigma_{2u})-\kappa_3(\sigma_{3u})\}$$
$$+(\text{a linear combination of } \sigma_{1g} \text{ and } \sigma_{1u}). \tag{9}$$

By variational calculation these parameters are found to be

$$\begin{aligned} \nu_1&=0.1597\,, & \kappa_1&=0.4625\,,\\ \nu_2&=0.0717\,, & \kappa_2&=0.1392\,,\\ \nu_3&=0.0066\,, & \kappa_3&=0.0511\,. \end{aligned} \tag{10}$$

The energy depression from the energy of the pure HL approximation (Case 12) is 0.141 e.v.

Case 16. $(\overset{\circ}{s}-\overset{\circ}{s})+(\pi-\pi)$ (HL *with transverse correlation*)

From the result of Case 8, the effect of perpendicular correlation in MO scheme turns out to be very remarkable. Here this effect has been reexamined with HL scheme by considering the resonance between two structures $(\overset{\circ}{s}-\overset{\circ}{s})$ and $(\pi-\pi)$. In this case, the wave function has the form:

$$\Phi=(\text{normalization constant})$$
$$\times\{(\overset{\circ}{s}-\overset{\circ}{s})+c(\pi-\pi)\}\,, \tag{11}$$

which can be constructed from the following primitive function:

$$\Phi=(\text{normalization constant})\times\{\Phi_{a,b}+\Phi_{b,a}\}\,,$$
$$\Phi_{a,b}=\{(2\overset{\circ}{s}_a+\tau\pi_a{}^x)(2\overset{\circ}{s}_b-\tau\pi_b{}^x)+(2\overset{\circ}{s}_a+\tau\pi_a{}^y)$$
$$\times(2\overset{\circ}{s}_b-\tau\pi_b{}^y)\}\times(1s_a)^2\,(1s_b)^2 \tag{12}$$

By variational calculation we have found that $c=--0.2262$ and $\tau=0.5836$, respectively. The energy depression from the energy of the pure HL approximation (Case 12) is 0.23[illegible] e.v.

Case 17. A′ (*assuming* S $(1s_a,\ 2\overset{\circ}{s}_b)=0$)

Here we have tried a calculation using the wave function obtained by replacing σ_{2g} in A′ by the normalized symmetry orbital $(\sigma 2\overset{\circ}{s})_g$ and assuming the overlap integral between 1*s* AO of one atom and $2\overset{\circ}{s}$ AO of the other atom to be zero. This approximation is similar to that adopted by Greenhow and Smith[11] and in Case 16 of I. The depression of energy from Case 1 is 0.603 e.v.

Case 18. HL′ (*assuming* S $(1s_a,\ 2\overset{\circ}{s}_b)=0$)

Here we have attempted a calculation similar to the preceding case (Case 17), by assuming S $(1s_a,\ 2\overset{\circ}{s}_b)=0$ in the calculation of Case 12. The depression of energy from Case 12 (pure HL) amounts to 1.329 e.v.

In the following cases, we shall examine the approximation of shrinking the (1*s*) core electrons into the nuclei (shrunk core model). The Hamiltonian is written as

$$H=-\tfrac{1}{2}\sum_{i=1}^{2}\Delta_i-\sum_{i=1}^{2}\left(\frac{1}{r_{ai}}+\frac{1}{r_{bi}}\right)$$
$$+\frac{1}{r_{12}}+\frac{1}{R}\,, \tag{13}$$

and the electron configurations can be obtained by omitting the orbitals of the core electrons in configurations A, B, ... of Table IV, and they will be designated by the same notation A, B, ... for the sake of convenience.

Case 19. A (*shrunk core*)

We have here employed the configuration in which the two valence electrons occupy Schmidt-OMO σ_{2g}, namely configuration A.

Case 20. Eight dimensional configurational interaction (*shrunk core*)

On the assumption of shunk core model, eight dimensional CI calculation similar to Case 11 is here performed. The depression of the total energy from the preceding case is 1.439 e.v. In this case, the mixing of configuration H is much more pronounced than in the case of the complete treatment (Case 11). This may be understood as follows. In the shrunk core model, the incompleteness of the screening effect due to (1*s*) electrons is perfectly neglected. Therefore the energy of (2*s*) orbital, of which the penetration into (1*s*) core is appreciable, is overestimated. Thus the energy difference between A and H has a smaller value than in the case of the complete treatment (Case 11).

Case 21. $\mathring{s}$–$\mathring{s}$ (*pure* HL *on shrunk core model*)

Here we have taken the wave function to be obtained by shrinking the core electrons in Case 12 (pure HL). The total energy is found to be −0.33526 a.u. and to be lower than that of the preceding case by 1.122 e.v. This is not surprizing since orbital (2$\mathring{s}$) is not orthogonal to the core orbital of the neighbouring atom, contrary to Schmidt-OMO σ_{2g}.

Case 22. *s*–*s* (*Rosen-Ikehara's treatment*)

Here we have used the nodeless Slater AO, 2*s*, in place of 2$\mathring{s}$ in the wave function of the preceding case. This approximation is nothing but that adopted already by Rosen-Ikehara[3]. The total energy is found to be −0.53743 a.u.

§ 4. Calculation of Energy of Excited States

In this section, we investigate the three lower excited states, $^1\Sigma_u^+$, $^3\Sigma_u^+$, and $^1\Pi_u$ explained in § 2. All the configurations within our framework for each of these states are listed in Tables X and XI.

Table X. Configurations[a] used in CI calculation for $^3\Sigma_u^+$ and $^1\Sigma_u^+$ states.

i	σ_{1g}	σ_{2g}	σ_{3g}	π_g^+	π_g^-	σ_{1u}	σ_{2u}	σ_{3u}	π_u^+	π_u^-
A	2	1				2	1			
B	2	1				2		1		
C	2		1			2	1			
D	2		1			2		1		
E	2			1		2				1

a) See the footnote a) of (I, Table IV).

Table XI. Configurations[a] used in CI calculation for $^1\Pi_u$ state.

i	σ_{1g}	σ_{2g}	σ_{3g}	π_g^+	π_g^-	σ_{1u}	σ_{2u}	σ_{3u}	π_u^+	π_u^-
A	2	1				2			1	
B	2		1			2			1	
C	2			1		2	1			
D	2			1		2		1		

a) See the footnote a) of (I, Table IV).

For each set of parameters (α, β) and each value of R stated in § 2, the total energies E_0 for configuration A are calculated. Further, the improved calculation is carried out by taking all the configurations into account. The energies, and the coefficients of configurations in the resulting wave function are listed in Tables XII, XIII, and XIV.

Table XII. Results[a] of CI calculation for $^3\Sigma_u^+$ state.

Set	I			II			III		
i \ R	4.5	5.0	5.5	4.5	5.0	5.5	4.5	5.0	5.5
A	0.9719	0.9606	0.9493	0.9712	0.9658	0.9603	0.9697	0.9687	0.9674
B	−0.0707	−0.0550	−0.0391	−0.1147	−0.0859	−0.0561	−0.1493	−0.1165	−0.0817
C	0.1842	0.2358	0.2775	0.1635	0.2037	0.2355	0.1462	0.1750	0.1983
D	−0.0581	−0.0673	−0.0741	−0.0687	−0.0755	−0.0784	−0.0742	−0.0798	−0.0818
E	0.1142	0.1184	0.1215	0.1101	0.1124	0.1142	0.1027	0.1051	0.1066
E_0 (a.u.)	−14.4392	−14.7788	−14.7619	−14.6544	−14.8040	−14.6594	−14.4113	−14.7762	−14.7761
E (a.u.)	−14.4486	−14.7890	−14.7730	−14.6666	−14.8145	−14.6692	−14.4271	−14.7878	−14.7854
$\|\varDelta E\|$ (e.v.)	0.256	0.279	0.303	0.331	0.285	0.265	0.429	0.316	0.253

a) See the caption of Table V.

Table XIII. Results[a)] of CI calculation for $^1\Sigma_u{}^+$ state.

Set	I			II			III		
i \ R	4.5	5.0	5.5	4.5	5.0	5.5	4.5	5.0	5.5
A	0.8336	0.8203	0.8090	0.8220	0.8146	0.8084	0.8123	0.8077	0.8038
B	−0.1668	−0.1720	−0.1773	−0.2137	−0.2088	−0.2039	−0.2484	−0.2406	−0.2326
C	0.4891	0.5115	0.5292	0.4917	0.5080	0.5214	0.4919	0.5052	0.5165
D	−0.0471	−0.0446	−0.0418	−0.0646	−0.0575	−0.0497	−0.0800	−0.0711	−0.0617
E	−0.1893	−0.1842	−0.1796	−0.1808	−0.1774	−0.1747	−0.1734	−0.1720	−0.1710
E_0 (a.u.)	−14.3413	−14.6907	−14.6818	−14.5468	−14.7072	−14.5714	−14.2928	−14.6694	−14.6791
E (a.u.)	−14.4221	−14.7684	−14.7562	−14.6390	−14.7912	−14.6487	−14.3971	−14.7613	−14.7614
$\lvert\Delta E\rvert$ (e.v.)	2.200	2.113	2.025	2.507	2.285	2.103	2.838	2.500	2.237

a) See the caption of Table V.

Table XIV. Results[a)] of CI calculation for $^1\Pi_u$ state.

Set	I			II			III		
i \ R	4.5	5.0	5.5	4.5	5.0	5.5	4.5	5.0	5.5
A	0.9501	0.9386	0.9250	0.9495	0.9400	0.9297	0.9480	0.9393	0.9302
B	0.1093	0.1808	0.2415	0.0889	0.1421	0.1846	0.0825	0.1147	0.1405
C	−0.2912	−0.2910	−0.2879	−0.3007	−0.3085	−0.3151	−0.3073	−0.3228	−0.3371
D	−0.0251	−0.0403	−0.0562	−0.0151	−0.0313	−0.0481	−0.0067	−0.0208	−0.0360
E_0 (a.u.)	−14.3501	−14.6939	−14.6812	−14.5660	−14.7148	−14.5711	−14.3211	−14.6825	−14.6817
E (a.u.)	−14.3736	−14.7179	−14.7058	−14.5920	−14.7409	−14.5975	−14.3501	−14.7114	−14.7105
$\lvert\Delta E\rvert$ (e.v.)	0.640	0.654	0.669	0.706	0.711	0.717	0.788	0.786	0.783

a) See the caption of Table V.

Table XV. Results[a)] of CI obtained by shrinking inner shells for Set II and $R=5.0$ a.u.

i \ state	$^1\Sigma_g{}^+$	$^3\Sigma_u{}^+$	$^1\Sigma_u{}^+$	$^1\Pi_u$
A	0.7832	0.8937	0.7353	0.7952
B	−0.0977	−0.1718	−0.2809	−0.4386
C	−0.0528	0.2841	0.5708	−0.4090
D	0.0004	−0.1381	−0.0980	0.0901
E	0.2217	0.2683	−0.2123	
F	−0.0291			
G	0.0699			
H	−0.5651			
E_0 (a.u.)	−0.2411	−0.2254	−0.1286	−0.1948[b)]
E (a.u.)	−0.2940	−0.2481	−0.2414	−0.2212
$\lvert\Delta E\rvert$ (e.v.)	1.439	0.617	3.069	0.720

a) See the caption of Table V.

b) The energy of the configuration $(\sigma_{3g}\pi_u{}^+)$ is −0.1994 a.u., which is lower than −0.1948 a.u. of A.

Next, we shall apply some of the approximations, considred in § 3, to the excited states for $R=5.0$ a.u. using parameter Set II.

a) *Pure* HL *approximation*

The HL wave functions, Φ_{HL}, are constructed from the following primitive functions:

$$(\text{normalization constant})\times(2\mathring{s}_a\,2\mathring{s}_b-2\mathring{s}_b\,2\mathring{s}_a)\,(1s_a)^2\,(1s_b)^2 \text{ for } {}^3\Sigma_u{}^+,$$

$$(\text{normalization constant})\times(2\mathring{s}_a\,2\mathring{s}_a-2\mathring{s}_b\,2\mathring{s}_b)\,(1s_a)^2\,(1s_b)^2 \text{ for } {}^1\Sigma_u{}^+,$$

and

$$(\text{normalization constant})\times(2\mathring{s}_a\,\pi_b{}^+-2\mathring{s}_b\,\pi_a{}^+)\,(1s_a)^2\,(1s_b)^2 \text{ for } {}^1\Pi_u\,. \quad (14)$$

By using the configurations of Tables X and XI, Φ_{HL} are expressed as

$$\Phi_{\mathrm{HL}}({}^3\Sigma_u{}^+)=\mathrm{A}\,,\qquad \Phi_{\mathrm{HL}}({}^1\Sigma_u{}^+)=\mathrm{A}\,,$$
$$\Phi_{\mathrm{HL}}({}^1\Pi_u)=0.9504\ \mathrm{A}-0.3109\ \mathrm{C}\,. \quad (15)$$

Namely, for both $^3\Sigma_u{}^+$ and $^1\Sigma_u{}^+$ states, the pure HL approach coincides with the single configuration A. For $^1\Pi_u$ state, the total energy obtained is −14.7392 a.u., and so the depression of energy from that calculated by

Table XVI. Vertical excitation energies in e.v. obtained by taking differences of calculated total energies.

Set	Method \ R	$^3\Sigma_u{}^+ - {}^1\Sigma_g{}^+$ 4.5	5.0	5.5	$^1\Sigma_u{}^+ - {}^1\Sigma_g{}^+$ 4.5	5.0	5.5	$^1\Pi_u - {}^1\Sigma_g{}^+$ 4.5	5.0	5.5
I	A	0.72	0.60	0.52	3.39	3.00	2.69	3.14	2.91	2.71
	CI	1.43	1.27	1.15	2.15	1.84	1.61	3.47	3.21	2.98
II	A	0.82	0.62	0.48	3.74	3.26	2.88	3.22	3.05	2.88
	CI	1.48	1.28	1.12	2.23	1.91	1.68	3.51	3.28	3.07
III	A	0.92	0.65	0.45	4.15	3.55	3.09	3.38	3.19	3.02
	CI	1.51	1.28	1.09	2.33	1.99	1.74	3.61	3.35	3.13
	Obs.				2.01	1.86	1.73	2.73	2.59	2.50

Table XVII.

(A) Parameters T_e, D_e and R_e in Morse potentials.[a)]

State	$^1\Sigma_g{}^+$	$^1\Sigma_u{}^+$	$^1\Pi_u$
T_e (e.v.)	0	1.744	2.533
D_e (e.v.)	1.052	1.155	0.366
R_e (a.u.)	5.050	5.873	5.549
β (a.u.)	0.4605	0.3194	0.5994

(B) Morse Potentials $U(R)$[a)] in e.v.

R \ State	$^1\Sigma_g{}^+$	$^1\Sigma_u{}^+$	$^1\Pi_u$
4.5	0.087	2.092	2.813
5.0	0.000	1.862	2.589
5.5	0.037	1.762	2.534

a) See Eq. (16) and reference (12).

Table XVIII. Vertical excitation energies in e.v. obtained by several approximations for Set II and R=5.0 a.u.

Method \ State	$^3\Sigma_u{}^+ - {}^1\Sigma_g{}^+$	$^1\Sigma_u{}^+ - {}^1\Sigma_g{}^+$	$^1\Pi_u - {}^1\Sigma_g{}^+$
A	0.62	3.26	3.05
HL	0.98	3.62	2.74
CI	1.28	1.91	3.28
A (shrunk core)	0.43	3.06	1.26
CI (shrunk core)	1.25	1.43	1.98
Obs.		1.86	2.59

he corresponding single configuration is found o be 0.665 e.v.

) A (*shunk core*)

A calculation similar to Case 19 of the round state is made by omitting the core rbitals in each configuration A of the excited states. The obtained total energies E_0 are given in Table XV.

We notice here that, in this shrunk core model, A is the lowest configuration for $^1\Sigma_g{}^+$, $^3\Sigma_u{}^+$, and $^1\Sigma_u{}^+$ states, whereas for $^1\Pi_u$ state B is the lowest one.

c) *Full configurational interaction* (*shrunk core*)

Here we have investigated, for each state, the treatment similar to Case 20 of § 3, where all the configurations derived from configuration A, B,... by dropping the core orbitals are taken into account. For convenience the latter configurations are also denoted by the same notation A, B,... The coefficients of configurations in the wave function here obtained and the energies are listed in Table XV.

The vertical excitation energies from the ground state to each of the excited states are obtained by taking the differences of the respective total energies calculated for each set of parameters and each R, (i) by the single configuration A, (ii) by considering all the configurations in Tables IV, X, and XI. The results are given in Table XVI, together with the observed ones obtained by using Morse potentials:

$$U(R) = T_e + D_e[1 - \exp\{-\beta(R - R_e)\}]^2 . \quad (16)$$

In this formula, the values of parameters T_e, D_e, R_e, and β are determined by using the spectroscopic data[12)] and are given in Table XVII. Further, the vertical excitation energies are calculated by using the results of approximations (a), (b), and (c) for Set II and R=5.0 and are shown in Table XVIII. All the results obtained for Set II and R=5.0 are also compared with the observed ones in Fig.

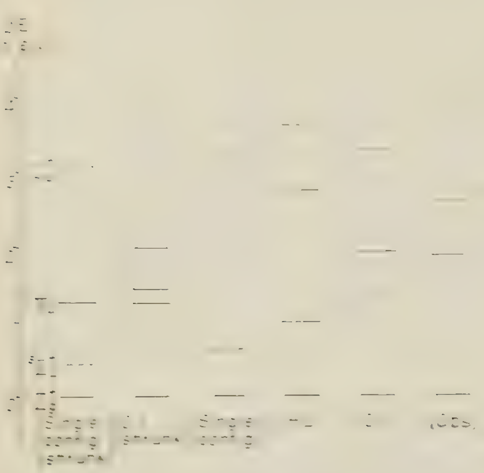

Fig. 1. Comparison of energy levels calculated by various approximations with experiment.

From Tables XVI, XVIII and Fig. 1, w can see that the order of the levels for ${}^1\Sigma_u$ and ${}^1\Pi_u$ states changes by introducing CI t agree with the experiment. Further the valu of the vertical excitation energy for ${}^1\Sigma_u^+$ fairly improved due to CI, though for ${}^1\Pi$ state CI makes the result a little worse. Th defect may be removed by using a better orbital.

Moreover, from Table XVIII and Fig. 1 w can see that, in case the inner shells a neglected, the results are improved for bot ${}^1\Sigma_u^+$ and ${}^1\Pi_u$ states by taking CI into accoun although the coefficients of the configuratio are very different from those obtained by in cluding the inner shells.

§ 5. Molecular Quantities

By using the wave functions obtained in § and § 4. (1) the depth of adiabatic potenti

Table XIX. Term values of Li(${}^2S$) and Li(${}^2P$) in a.u. calculated by using Slater AO's with the orbital exponents given in Table II.

R \ Set	${}^2S$ I	${}^2S$ II	${}^2S$ III	${}^2P$ I	${}^2P$ II	${}^2P$ III
4.5	−7.23936 05	−7.34703 93	−7.22570 22	−7.15940 26	−7.26503 16	−7.13881 19
5.0	−7.40457 22	−7.41654 90	−7.40247 39	−7.33457 36	−7.34227 84	−7.32326 41
5.5	−7.39277 86	−7.34049 26	−7.39845 36	−7.33060 41	−7.27262 91	−7.32569 47

The observed values of them are −7.47792 and −7.4100 a.u. for Li(${}^2S$) and Li(${}^2P$) states, respe tively, from reference (15).

Table XX. Depth of adiabatic potential, $D(R)$[a], in e.v. for each state.

State	R \ Set	Single Configuration I	Single Configuration II	Single Configuration III	CI I	CI II	CI III	Obs.
${}^1\Sigma_g^+$	4.5	−0.354	−0.264	−0.166	0.614	0.728	0.850	0.97
	5.0	−0.222	−0.170	−0.137	0.727	0.770	0.809	1.05
	5.5	−0.129	−0.105	−0.116	0.807	0.799	0.776	1.02
${}^3\Sigma_u^+$	4.5	−1.076	−1.079	−1.090	−0.820	−0.748	−0.661	
	5.0	−0.826	−0.792	−0.783	−0.547	−0.507	−0.467	
	5.5	−0.644	−0.586	−0.565	−0.342	−0.321	−0.313	
${}^1\Sigma_u^+$	4.5	−1.565	−1.775	−1.951	0.635	0.732	0.887	0.81
	5.0	−1.318	−1.405	−1.532	0.795	0.880	0.969	1.04
	5.5	−1.132	−1.135	−1.225	0.894	0.968	1.012	1.14
${}^1\Pi_u$	4.5	−1.323	−1.252	−1.180	−0.683	−0.547	−0.393	0.09
	5.0	−1.231	−1.198	−1.176	−0.577	−0.487	−0.390	0.31
	5.5	−1.149	−1.142	−1.154	−0.479	−0.425	−0.371	0.37

a) See Eq. (17).

Table XXI. Depth of adiabatic potential $D(R)$[a] in e.v. which is calculated for Set II and $R=5.0$ a.u. by several approximations for three excited states.

	A	HL	CI	(shrunk core)	CI(shrunk core)	Obs.
$^3\Sigma_u{}^+$	-0.792	-0.431	-0.507	-1.111	-0.493	
$^1\Sigma_u{}^+$	-1.405	-1.045	0.880	-3.218	-0.148	1.04
$^1\Pi_u$	-1.198	-0.533	-0.487	-1.418	-0.698	0.31

a) See Eq. (17)

$D(R)$ for each state, (2) the molecular quadrupole moment Q, (3) the oscillator strength f_{lk}, and (4) the gradient of the electric field at the nucleus q, are calculated. These values serve for discussing the features of the various approximations employed in this paper, though, unfortunately the observed values are not available for them except $D(R)$.

(*1*) *Adiabatic potential* $U(R)$

The depth of adiabatic potential $D(R)$ is given by

$$D(R)=E(R_\infty)-E(R)\,, \tag{17}$$

where $E(R)$ and $E(R_\infty)$ are the energies of the molecule in the state under consideration at a finite internuclear distance R and at the infinite nuclear separation R_∞, respectively.

In our case, it is easily shown that

$$E(R_\infty)=E(^2S)+E(^2S) \text{ for } {}^1\Sigma_g{}^+ \text{ and } {}^3\Sigma_u{}^+$$

and

$$E(R_\infty)=E(^2S)+E(^2P) \text{ for } {}^1\Sigma_u{}^+ \text{ and } {}^1\Pi_u\,, \tag{18}$$

where $E(^2S)$ and $E(^2P)$ are the energies of the free Li atom in the ^2S and ^2P states, respectively. These $E(^2S)$ and $E(^2P)$ are calculated by using the wave functions constructed from primitive functions $(1s)^2$ $(2\mathring{s})$ and $(1s)^2$ $(2p)$, respectively, both of which are built from Slater AO's (I, (1)) with the orbital exponents δ_1 and δ_2 shown in Table II. The results of the calculation are given in Table XIX. From this table we can see the values of $E(R_\infty)$ easily. By subtracting the value of $E(R)$ from that of $E(R_\infty)$ for each fixed parameters δ_1, δ_2, and R, we have obtained $D(R)$ associated with the two kinds of approximations (single configuration and CI) for each state. The results are given in Table XX. The observed values of $D(R)$ have been derived by using the Morse potentials constructed in § 4, and these are given in the same table.

From this table, we can see that (i) the effect of CI is very important, (ii) the results

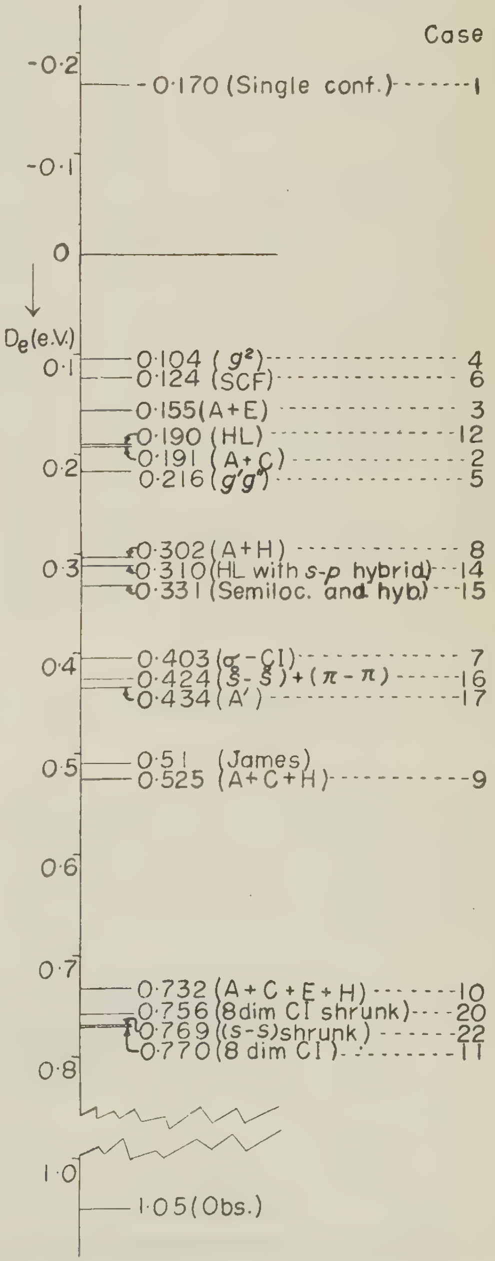

Fig. 2. Comparison of dissociation energies in e.v.

Table XXII. Molecular quantities calculated for Set II and $R=5.0$ a.u.

Case	D_e (e.v.)	$R^{-2}\langle x^2+y^2\rangle^{a)}$	$R^{-2}\langle z^2\rangle^{a)}$	Q (a.u.)$^{a)}$	$2R^2\langle q_a'\rangle^{b)}$	q' (a.u.)$^{b)}$
1 A (single configuration)	−0.170	1.041	1.846	8.72	5.110	0.0036
2 A+C	0.191	1.034	1.902	5.75	5.065	0.0037
3 A+E	0.155	0.998	1.529	23.48	6.212	−0.0008
4 $(g)^2$	0.104	1.005	1.556	22.29	6.047	−0.0002
5 A+C+E $(g'g'')$	0.216	1.003	1.608	19.65	6.084	−0.0003
6 LCAO-SCF	0.124	1.005	1.556	22.31	6.009	−0.0000
7 σ-electron CI	0.403	1.011	1.666	16.96	5.782	0.0009
8 A+H	0.302	1.060	1.833	9.82	4.745	0.0050
9 A+C+H	0.525	1.050	1.871	7.69	4.818	0.0047
10 A+C+E+H	0.732	1.024	1.605	20.36	5.585	0.0017
11 8 dim. CI	0.770	1.024	1.623	19.46	5.591	0.0016
12 Pure HL	0.190	1.035	1.897	6.03	5.069	0.0037
13 Ionic structure	−1.094	1.035	1.897	6.03	5.069	0.0037
14 HL with $s-p$ bybrid.	0.310	1.018	1.656	17.63	5.648	0.0014
15 Semiloc. and $s-p$ hybrid.	0.331	1.013	1.650	17.82	5.704	0.0012
16 $(\overset{\circ}{s}-\overset{\circ}{s})+(\pi-\pi)$	0.424	1.044	1.890	6.60	4.847	0.0046
17 A$'(S(1s_a, 2\overset{\circ}{s}_b)=0)$	0.434	1.043	1.847	8.72	5.150	0.0034
18 HL$'(S(1s_a, 2\overset{\circ}{s}_b)=0)$	1.519	1.032	1.896	6.02	5.116	0.0035
19 A (shrunk core)	−0.683	0.996	0.824	8.72	1.110	0.0036
20 8 dim. CI (shrunk core)	0.756	1.033	0.608	20.42	2.522	−0.0021
21 $(\overset{\circ}{s}-\overset{\circ}{s})$ (shrunk core)	1.878	0.987	0.873	6.02	1.116	0.0035
22 $(s-s)$ (shrunk core)	0.769	0.960	0.862	5.92	1.206	0.0032
James$^{c)}$	0.51					−0.0030
Obs.	1.05					

a) See Eq. (21).
b) See Eq. (22).
c) James' calculation was made at $R=5.63$ a.u. and so the q' value in this table is also the one at $R=5.63$ a.u.[13)]

of CI calculation are fairly good for ${}^1\Sigma_g{}^+$ and ${}^1\Sigma_u{}^+$, but not so for ${}^1\Pi_u$, and (iii) the observed value of $D(R)$ is larger than the calculated ones except the one case, that is for ${}^1\Sigma_u{}^+$ state, $R=4.5$, and Set III.

Now, since for $R=5.0$ and Set II $E(R)$ was calculated by using various approximations in §§3 and 4, we can obtain the corresponding $D(R)$'s easily. As the values $E({}^2\mathrm{S})$ and $E({}^2\mathrm{P})$, we have adopted the same ones as were used in calculating $D(R=5.0)$ for Set II in Table XX, except the cases of shrinking the inner shells. In the latter cases we use, as those, the energy of a system composed of one electron and a proton, which is calculated by using the same Slater AO, $2\overset{\circ}{s}$, $2s$, or $2p$ as was used in calculating the respective $E(R)$. These values are

$$\begin{aligned} E({}^2\mathrm{S}) &= -0.13311\,64 \text{ a.u. for } 2\overset{\circ}{s}\,, \\ &= -0.25458\,33 \text{ a.u. for } 2s\,, \\ E({}^2\mathrm{P}) &= -0.11375\,00 \text{ a.u.}\,. \end{aligned} \tag{19}$$

The values of $D(R=5.0)$ thus obtained are given in Table XXI for the excited states. Those for the gound state are given in Table XXII as the dissociation energy D_e, since the observed equilibrium internuclear distance differs little from 5.0 a.u. In Fig. 2, all the results of D_e obtained for Set II are compared with the experiment.

Table XXI shows that the result is disappointing for ${}^1\Pi_u$ state. In addition, in the approximation of shrunk core model in MO scheme, even if CI is taken into account, the result is poor also for $^1\Sigma_u{}^+$ state.

Next, from Table XXII and Fig. 2, we can see the following points:

(a) The dissociation energy D_e given by our best approximation (Case 11) amounts to 0.77 e.v., which is about 73% of the observed one. This value is a little better than the result of the most elaborate calculation hitherto performed by James[4)] and Harris-Melkanoff[13)] (0.51 e.v.), though the latter authors employed, as the energy of the Li atom $E(^2S)$, the one obtained by using Wilson's four parameter function[14)], which is lower than ours by 0.072 e.v.

(b) D_e by the pure HL approximation (Case 12) is 0.19 e.v. James [4)] also made a similar calculation to ours assuming $\delta_1=2.68$, $\delta_2=0.670$, and $R=3.18$ Å, and obtained $D_e=0.265$ e.v. The reason of the discrepancy of our result from James' one lies in the different choice of the parameters δ_1, δ_2, and R.

(c) D_e obtained by assuming $S(1s_a, 2\overset{\circ}{s}_b)=0$ in the single configuration A (Case 17) is rather good, whereas the one obtained by the same assumption in the pure HL approximation (Case 18) turns out to be much larger than the observed value.

(d) In the shrunk core model in MO type, the result of the single configuration A (Case 19) is not so good, but this is improved appreciably by introducing CI (Case 20). The result obtained in the latter case almost coincides with our best result (Case 11).

(e) In a shrunk core model of HL type, D_e given by the structure ($\overset{\circ}{s}$-$\overset{\circ}{s}$) (Case 21) is found to be 1.878 e.v., which shows that this simplified approximation can not be safely applied to obtain a reasonable value of D_e.

(f) If we use nodeless Slater AO's $2s$ (Case 22) in place of $2\overset{\circ}{s}$ in the above approximation, however, we can obtain $D_e=0.769$ e.v., which is almost as good as our best calculated value (Case 11). Rosen and Ikehara[3)] already performed the similar calculation assuming somewhat diffferent values for parameters, namely, $\delta_2=0.65$ and $R=2.28$,Å and obtained D_e of 1.11 e.v. Since the reason of their good result was criticized in detail by James [4)], we do not discuss further on this point.

Finally, we remark the fact that, as to the result of CI calculation based on the shrunk core model for $^1\Sigma_u{}^+$ and $^1\Pi_u$ states, the agreement of the calculated to observed value is disappointing for $D(R)$ but it is not so wrong for $\Delta E(R)$. (See Tables XVIII and XXI.) This situation suggests that the calculated value of $\Delta E(R_\infty)$ is inaccurate, because

$$D_{\text{excited}}(R)-D_{\text{normal}}(R)=\Delta E(R_\infty)-\Delta E(R). \quad (20)$$

For the sake of comparison, we give in Table XXIII $E(^2P)-E(^2S)$ values calculated by each approximation using Slater orbitals of Set II and $R=5.0$ a.u. The fact that the value of $E(^2P)-E(^2S)$ obtained by using nodeless Slater AO ($2s$) in a shrunk core model is very large compared with the experiment[15)] was already pointed out by Rahman [16)].

(2) *Molecular Quadrupole Moment Q*

The molecular quadrupole moment Q is given by

$$Q=\int r^2(3\cos^2\theta\ -1)\,\rho\,dv=ZR_2$$
$$-2\langle z^2\rangle+\langle x^2+y^2\rangle, \quad (21)$$

where Z is the nuclear charge and is equal to 1 or 3 according as the inner core electrons are shrunk or not. ρ is the charge density of the nuclei and electrons. The meanings of θ, $\langle z^2\rangle$, and $\langle x^2+y^2\rangle$ are the same as

Table XXIII. Values of $E(^2P)-E(^2S)$[a)] (in a.u.) obtained by using Slater orbitals of Set II and $R=5.0$ a.u.

	Including inner shells	Shrinking inner shells		Obs.
		$^2S(2\overset{\circ}{s})$	$^2S(2s)$	
$E(^2P)$	−7.34227 84	−0.11375 00	−0.11375 00	−7.41000
$E(^2S)$	−7.41654 90	−0.13311 64	−0.25458 33	−7.47792
$E(^2P)-E(^2S)$	0.07427 06	0.01936 64	0.14083 33	0.06792

a) See Eqs. (18) and (20).

those of I, § 6. We have calculated $<x^2+y^2>/R^2$, $<z^2>/R^2$, and Q, using the single configuration and CI wave function for each parameters α, β, and R. The result is given in Table XXIV. From this table we can see the following facts.

(a) For a fixed R, Q increases as the orbital exponent δ_2 decreases. This can be understood by considering that the charge density of the valence electrons in the neighbourhood of the molecular axis decreases as δ_2 decreases.

(b) For a fixed set, the value of Q calculated by the single configuration increases in proportion to R^2. This increasing tendency of Q with R is seen even in CI calculation though its dependency on R^2 no longer holds, and is too large to be ascribed to the fact mentioned in (a). Thus, we can expect that the calculated Q value increases with R in the neighbourhood of the equilibrium internuclear distance, even if the same values of the orbital exponents δ_1 and δ_2 are used.

Table XXIV. Values of $Q^{a)}$ and $q'^{b)}$ (in a.u.) for each set and R.

(A)

Set	Method	R	$R^{-2}\langle x^2+y^2\rangle^{a)}$	$R^{-2}\langle z^2\rangle^{a)}$	$2R^3\langle q_a'\rangle^{b)}$
I	A		1.197	1.917	4.899
	CI	4.5	1.181	1.687	5.228
		5.0	1.169	1.631	5.432
		5.5	1.158	1.584	5.626
II	A		1.041	1.846	5.110
	CI	4.5	1.031	1.662	5.404
		5.0	1.024	1.623	5.591
		5.5	1.017	1.590	5.761
III	A		0.901	1.785	5.366
	CI	4.5	0.894	1.637	5.628
		5.0	0.889	1.612	5.781
		5.5	0.885	1.605	5.913

(B)

	Set	Method R	4.5	5.0	5.5
$Q^{a)}$	I	A	7.36	9.09	11.00
		CI	16.33	22.70	29.98
	II	A	7.06	8.72	10.55
		CI	14.33	19.46	25.33
	III	A	6.70	8.72	10.01
		CI	12.57	16.65	20.41
$q'^{b)}$	I	A	0.0060	0.0044	0.0033
		CI	0.0042	0.0023	0.0011
	II	A	0.0049	0.0036	0.0027
		CI	0.0033	0.0016	0.0007
	III	A	0.0035	0.0025	0.0019
		CI	0.0020	0.0009	0.0003

(C)

	Set	Method R	4.5	5.0	5.5
$\langle Q\rangle_{val}{}^{c)}$	I	A	12.888	15.911	19.252
		CI	3.925	2.296	0.270
	II	A	13.186	16.279	19.698
		CI	5.919	5.544	4.924
	III	A	13.551	16.730	20.243
		CI	7.681	8.355	9.844
$\langle q_a'\rangle_{val}{}^{d)}$	I	A	0.00493	0.00359	0.00270
		CI	0.00674	0.00573	0.00489
	II	A	0.00609	0.00444	0.00334
		CI	0.00770	0.00636	0.00529
	III	A	0.00750	0.00547	0.00411
		CI	0.00894	0.00713	0.00575

a) See Eq. (21).
b) See Eq. (24).
c) See Eqs. (22) and (23).
d) See Eqs. (25) and (26).

We note here that Q for $R=0$ is negative, since, in this limiting case, the ground state of Li_2 becomes ^1D state of a carbon atom and the corresponding Q is -2.2722 a.u. if calculated by using Slater AO's with the orbital exponent $\delta_2=1.625$, whereas Q for the infinite nuclear distance is of course zero. Considering that the calculated values of Q are positive in the neighbourhood of the equilibrium internuclear distance, we can expect that the value of Q increases from a negative value at $R=0$ to a positive one and tends to zero at the infinite nuclear separation.

Further, in Table XXII, $<z^2>/R^2$, $<x^2+y^2>/R^2$, and Q calculated by using the various wave functions for Set II and $R=5.0$ a.u. obtained in § 3 are given. From this table we can see the following situation.

(a) The calculated values of Q can be classified, as a whole, into two groups, namely, the one around 20 a.u. and the other smaller than 10 a.u., depending on whether s–p hybridization is taken into account or not. This difference comes mainly from that of $\langle z^2\rangle$. The fact that $\langle z^2\rangle$ decreases by introducing s–p hybridization is reasonable, since we can expect that the charge density in the region between two nuclei increases by s–p hybridization. In the O_2 molecule, we encountered a similar situation, though the effect of s–p hybridization on the charge density in that case is of the opposite direction.

(b) Values of Q of Case 2 (semilocalization) and Case 12 (pure HL approximation) are smaller than that of Case 1 (single configuration) mainly due to the fact that the values of $\langle z^2\rangle$ of the former cases are larger than that of the latter. This result is reasonable since the charge density of σ_{2u} orbital is larger than that of σ_{2g} in the outer region of the molecule.

(c) The Q value of Case 2 is even smaller than that obtained byt he pure HL approximation (Case 12). This fact can be expected since μ in Eq. (1) is negative. (See the discussion in the end of Case 13, § 3.)

(d) The effect of mixing the configurations involving π orbitals increases the value of $\langle x^2+y^2\rangle$ and accordingly increases that of Q. (Compare Cases 1 and 8, and Cases 12 and 16.)

(e) Q obtained by the pure ionic structure (Case 13) coincides with that obtained by the pure HL approximation (Case 12), since the charge density is identical for these two approximations.

(f) Contrary to the case of D_e, Q value does not change appreciably by assuming $S\,(1s_a, 2s_b)=0$. (Compare the Q values of Cases 1 and 17. and Cases 12 and 18.)

(g) Q values obtained by the various approximations in the shrunk core model are not so different from those obtained by the corresponding ones including the inner shells. (Compare Q values of Cases 1 and 19, Cases 12, 21, and 22, and also Cases 11 and 20.)

Now we have undertaken to see the variation of Q due to the use of different approximations for the valence electrons. For this purpose, we have defined $\langle Q\rangle_{val}$, which is considered to be the contribution of the charge density of valence electrons by the following equation:

$$Q=R^2-\langle Q\rangle_{val}\,, \tag{22}$$

that is

$$\langle Q\rangle_{val}=\{2\langle z^2\rangle-\langle x^2+y^2\rangle\}-2R^2\,, \tag{23}$$

since, in the approximations considered in this paper except SCF, Q can be expressed as

$$Q=3R^2-\langle Q\rangle_{val}-\langle Q\rangle_{core}\,,$$

where $-\langle Q\rangle_{core}$ is the contribution of the core electrons to Q, and is closely equal to $-2R^2$. The numerical values of $\langle Q\rangle_{val}$ are shown in (C) of Table XXIV. Since, in the actual electron distribution, $\langle Q\rangle_{val}$ is expected to be negative, the upper limit of Q will be R^2. The results given in Tables XXII and XXIV are contradictory to this fact. The fact that the value of $\langle Q\rangle_{val}$ in CI calculation is very small means that the charge distribution of the valence electrons is nearly spherical around the center of the molecule.

(3) *Gradient of Electric Field at a Nucleus, q.*

The gradient of the electric field at one nucleus, q, is defined by

$$\left.\begin{aligned} q&=2eq' \\ q'&=\int\frac{3\cos^2\theta_a-1}{2r_a{}^3}\,\rho dv \\ &=\frac{Z}{R^3}-\langle q_a'\rangle, \\ \langle q_a'\rangle&=\int\frac{3\cos^2\theta_a-1}{2r_a{}^3}\,\rho_{el}dv\,, \end{aligned}\right\} \tag{24}$$

where ρ_{el} is the number density of electrons, and the meanings of r_a, and θ_a are explained in § 6, (2) and (3) of I. Since q' is zero in the ground state of a Li atom, it becomes zero at the infinite internuclear distance for the Li_2 ground state. Even in the neighbourhood of the equilibrium internuclear distance, q' is expected to be close to zero, and so it is difficult to assess the accurate value for q'.

In order to study the dependence of $\langle q_a'\rangle$ and q' on R and the parameter value δ_2, we have calculated the values of these quantities for three values of R with the use of the single configurational wave function (A) as well as CI wave function, for three different sets of (α, β). From Table XXIV, in which our results are given, we note that Z/R^3 and $-\langle q_a'\rangle$ almost cancel with each other, yielding very small values for q'. This makes the reliable estimate of q' very difficult: we note, however, that all values obtained in this way are positive. Further from this table we can see the following facts.

(a) For a fixed value of R, q' increases (or $\langle q_a'\rangle$ decreases) with decreasing δ_2. This is reasonable since the charge distribution of the valence electrons in the neighbourhood of the molecular axis decreases with decreasing δ_2, whereas that near the nucleus A is roughly spherically symmetric around that nucleus, irrespectively of δ_2.

(b) For a fixed set, q' decreases with increasing R (or decreasing δ_2). This can be easily seen as follows: $R^3 <q_a'>$, which is independent of R on the single configurational wave function, is found to be a increasing function of R when CI wave function is employed. Hence $R^3\ q'$ which is equal to $Z-R^3 \times <q_a'>$, is a decreasing function of R, and q' decreases with R more rapidly than R^{-3}, provided that q' is positive.

From (a) and (b) we can conclude that, for a constant δ_2, q' decreases with increasing R, at least in the neighbourhood of the equilibrium internuclear distance R_e.

As to the dependence of q' on R over the whole range $(0, \infty)$, the following discussions might be of some interest. In the limit of the united atom, that is, in ^{1}D of the carbon atom, the value of $<q_a'>$ calculated by using Slater AO with $\delta_2=1.625$ is 0.57124 a.u., which in the limit of the infinite nuclear separation is of course zero. Further, for any finite value of R, $<q_a'>$ is expected to have a positive value. Accordingly, q' is infinitely large at $R=0$ and becomes zero at $R=\infty$ and its upper limit is $3/R^3$ for any R. The situation mentioned in (b) suggests that in the neighbourhood of the equilibrium internuclear separation, q' is positive and a decreasing function of R. It may be quite possible, however, that q' becomes negative at a certain value of R larger than the equilibrium internuclear distance R_e.

Further, the values of q' calculated by using the various approximations for Set II and $R=5.0$ a.u. obtained in § 3 are given in Table XXII. From this table, we can see the following points.

(a) Similarly to the case of Q, the calculated q values can be divided into two groups. Namely, if s–p hybridization is not considered q' is larger than 30×10^{-4} a.u., whereas it is smaller than 16×10^{-4} a.u. if s–p hybridization is taken into account. This variation of q' is reasonable, since s–p hybridization increases the charge density in the neighbourhood of the molecular axis.

(b) Contrary to the case of Q, the effect of semilocalization is not so important. (Compare Case 1 with Cases 2 and 12.)

(c) By mixing the configurations which involve π orbitals, q' value becomes fairly large (Compare Cases 1 and 8, Cases 12 and 16.)

(d) The pure ionic structure (Case 13) an the pure HL approximation yield the same q value, similarly to the case of Q.

(e) No appreciable difference is found betwee Cases 1 and 17, and Cases 12 and 18. Tha is, contrary to the Q value of O_2, the assumption of $S(1s_a, 2\mathring{s}_b)=0$ does not appreciably affect the q' value of Li_2.

(f) The q' values for the various approximations in the shrunk core model are close t those for the corresponding approximation involving the inner shells. (Compare Cases and 19, and Cases 12, 21, and 22.) The onl one exception exists between Cases 11 an 20. This is easily understood, however, b considering that the amounts of mixing o each configuration are quite different for thes two cases.

Now to investigate the contribution to q' o only the valence electrons, we have define $<q_a'>_{val}$ by the relations similar to Eqs. (22 and (23) mutatis mutandis, namely.

$$q'=\frac{1}{R^3}-<q_a'>_{val}\ , \qquad (25$$

or

$$<q_a'>_{val}=<q_a'>-\frac{2}{R^3}\ , \qquad (26$$

The values of $<q_a'>_{val}$ obtained by usin the single configuration and CI wave functio for each parameter set and R are given i (C) of Table XXIV. From this table we ca see that, as Harris and Melkanoff predicted[13] $<q_a'>_{val}$ is not very sensitive to the chang of R.

Accordingly, assuming $<q_a'>_{val}$ to be constant with respect to R, we have estimate q', for the equilibrium internnclear distanc $R_e=5.05$ a.u. using Eq. (25). The results fo the single configuration, pure HL approximation, and eight dimengional CI considered i § 3 for Set II and $R=5.0$ a.u., together wit the ones obtained by Harris-Melkanoff an also Sternheimer[17] by using the pure HL wav function and the James variational wave function, are shown in Table XXV.

The difference of their result obtained b using the James variational function from our mainly comes from the following features of the James wave function.

(a) Charge density of valence electrons increases in the neighbourhood of the molecular axis by mixing more basic functions of σ type than ours.

(b) In his function, transverse correlation of π type which will decrease the charge density near the molecular axis is not considered. Further, their assumption is somewhat doubtful, that $\langle q_a'\rangle_{val}$ is almost constant over the wide region of R around R_e.

Now, we note that, in order to obtain the value of q' in fair accuracy, we may have to consider the effect of departure from spherical symmetry of the core electrons, that is, Sternheimer correction17). The results of this correction calculated by Sternheimer and Foley17), using the pure HL and the James variational function, are given in Table XXV. Then, assuming that the corrections for our single configuration and pure HL is equal to his correction for his pure HL, and that the correction for our CI wave function are equal to his for the James variational wave function, we have made a rough estimate of this correction and the result is added in Table XXV with parentheses. From this table we can expect that q' still remains positive though it is reduced appreciably by this correction.

Finally we have averaged the value of q' over the zero point vibration by assuming $\langle q_a'\rangle_{val}$ to be constant with respect to R. Then the averaged value $\langle q_a'\rangle_{00}$ is

$$\langle q'\rangle_{00}=\langle \frac{1}{R^3}\rangle_{00}-\langle q'_a\rangle_{val}\,,$$

where $\langle 1/R^3\rangle_{00}$ is the average of $1/R^3$ over the zero point vibration. Inserting $\langle 1/R^3\rangle_{00}$ calculated by using Morse potential (Table XVII) and the formulae given by E. Ishiguro and others18), we have

$$\langle q'\rangle_{00}=\frac{1}{R_e^3}-\langle q_a'\rangle_{val}-0.00007(\text{in a.u.})\,.$$

Thus the departure of $\langle q'\rangle_{00}$ from $q'(R_e)$ is very small.

By using the value of $\langle q'\rangle_{00}$ obtained by our best wave function, and by neglecting or including Sternheimer correction, the nuclear quadrupole moment of Li^7, $Q(\mathrm{Li}^7)$, is estimated as $+9.6\times10^{-26}\,\mathrm{cm}^2$ or $+10.8\times10^{-26}\,\mathrm{cm}^2$, respectively, from the observed value of eqQ (Li): +0.060 MC/sec19). This positive signe of Q(Li) is contrary to the result obtained by using the James function and also to the prediction from the side of a simple application of the nuclear shell model. This prediction, however, does not seem to be so conclusive, because configurational interaction, inclusion of tensor force etc. may alter the situation.20)

(*4*) *Oscillator Strengths f_{lk}*

As explained in I, §6, subsection (4), the oscillator strength f_{lk} for transition from a state l to another state k ($E_k>E_l$) can be calculated by either the dipole length or the dipole velocity method, that is

$$f_{lk}=\frac{2}{3}\;|(\sum_i \boldsymbol{r}_i)_{lk}|^2\;(\Delta E)_{lk} \qquad (27)$$

Table XXV. Estimated values of q' for R=5.05 a.u. obtained by including or neglecting Sternheimer correction (in a.u.).

Wave function	$\langle q_a'\rangle_{val}$a)	q'	Sternheimerb) correction	q' including Sternheimer correction
Ac)	0.00444	0.00332	(−0.00088)f)	(0.00244)
Pure HLc)	0.00428	0.00349	(−0.00088)	(0.00261)
CIc)	0.00636	0.00140	(−0.00015)	(0.00125)
Pure HLd)	0.00422	0.00354	−0.00088	0.00026
Variationald)e)	0.00867	−0.00091	−0.00015	−0.00106

a) See Eqs. (24) and (26).
b) From reference (17).
c) Our wave functions for Set II and R=5.0 a.u.
d) See references (17) and (13). q' values in two references are somewhat different with each other. The values listed here are the ones in reference (17).
e) James variational wave function obtained for R=5.63 a.u.
f) Values within parentheses are the estismated ones.

Table XXVI. $R^{-1}\langle z\rangle_{lk}$ a), $R\langle\zeta\rangle_{lk}$ b), $R^{-1}\left\langle\frac{1}{\sqrt{2}}(x-iy)\right\rangle_{lk}$ a) and $R\left\langle\frac{1}{\sqrt{2}}(\xi-i\eta)\right\rangle_{lk}$ b).

A) $^1\Sigma_g{}^+-{}^1\Sigma_u{}^+$

l	k	Method	Set	I		II		III	
			R	$R^{-1}\langle z\rangle_{lk}$	$R\langle\zeta\rangle_{lk}$	$R^{-1}\langle z\rangle_{lk}$	$R\langle\zeta\rangle_{lk}$	$R^{-1}\langle z\rangle_{lk}$	$R\langle\zeta\rangle_{lk}$
$^1\Sigma_g{}^+$	$^1\Sigma_u{}^+$	A		−0.9218	−0.9862	−0.8814	−1.0116	−0.8475	−1.0354
		CI	4.5	−0.7017	−1.1254	−0.6786	−1.0756	−0.6599	−1.0765
			5.0	−0.6726	−1.1520	−0.6577	−1.1145	−0.6449	−1.1172
			5.5	−0.6446	−1.1757	−0.6381	−1.1531	−0.6310	−1.1586

B) $^1\Sigma_g{}^+-{}^1\Pi_u$

l	k	Method	Set	I		II		III	
			R	$R^{-1}\left\langle\frac{1}{\sqrt{2}}(x-iy)\right\rangle_{lk}$	$R\left\langle\frac{1}{\sqrt{2}}(\xi-i\eta)\right\rangle_{lk}$	$R^{-1}\left\langle\frac{1}{\sqrt{2}}(x-iy)\right\rangle_{lk}$	$R\left\langle\frac{1}{\sqrt{2}}(\xi-i\eta)\right\rangle_{lk}$	$R^{-1}\left\langle\frac{1}{\sqrt{2}}(x-iy)\right\rangle_{lk}$	$R\left\langle\frac{1}{\sqrt{2}}(\xi-i\eta)\right\rangle_{lk}$
$^1\Sigma_g{}^+$	$^1\Pi_u$	A		0.7044	1.0433	0.6521	1.0483	0.6055	1.1194
		CI	4.5	0.5298	1.1831	0.4898	1.1844	0.4606	1.2587
			5.0	0.5336	1.1764	0.4980	1.1742	0.4681	1.2467
			5.5	0.5363	1.1682	0.5037	1.1640	0.4736	1.2354

a) See Eq. (27).
b) See Eq. (28).

or

$$f_{lk}=\frac{2}{3}\,|(\sum_i \nabla_i)_{lk}|^2/(\Delta E)_{lk}\,, \tag{28}$$

respectively.

Now among the four states considered in this paper, it is easily seen that the possible transitions are only ${}^1\Sigma_g^+-{}^1\Sigma_u^+$ and ${}^1\Sigma_g^+-{}^1\Pi_u$. The former corresponds to the one electron jump $\sigma_{2g}-\sigma_{2u}$ and is induced by z components of the dipole length and velocity. The latter corresponds to the one electron jump $\sigma_{2u}-\pi_u^{\pm}$ and is induced by x and y components of them.

The matrix elements of the dipole length and velocity corresponding to these two transitions are calculated by using the same wave functions as were used in calculating $(\Delta E)_{lk}$ of Table XVI and the result is shown in Table XXVI. By using these values of matrix elements together with the respective $(\Delta E)_{lk}$'s given in Table XVI, f_{lk}'s are calculated and the result is given in Table XXVII.

From this table we can see that

(a) when CI is taken into account, the results obtained by these two methods agree fairly well for each set and R, and further the difference of f_{lk}'s due to the different choice of parameter sets and R is reduced appreciably,

(b) in general, the f_{lk} value obtained by the length method is larger than that by the velocity method, except the one, namely f_{lk} for ${}^1\Sigma_g^+-{}^1\Pi_u$ obtained by using Set III and $R=4.5$ a.u., and that

(c) contrary to the case of ${}^3\Sigma_g^- - {}^3\Sigma_u^-$ transition in the O_2 case, f_{lk} calculated by the velocity method increases by introducing CI.

Further we have carried out a calculation using the various wave functions obtained for Set II and $R=5.0$ a.u. The necessary matrix elements of the coordinate and velocity are shown in Table XXVIII, while $(\Delta E)_{lk}$ can be taken from Table XVIII. The resulting values of f_{lk} are listed in Table XXIX.

From this table, we can see that, similarly to the case of D_e, the results of the pure HL approximation are somewhat better than those of the single configuration.

Further, as to the transition probability for ${}^1\Sigma_g^+-{}^1\Pi_u$, the results obtained by the shrunk core model are very different from those by including the inner shells. This fact is one

Table XXVII. Oscillator strength f_{lk}[a)] for each set and R.

A) ${}^1\Sigma_g^+-{}^1\Sigma_u^+$

l	k	Method	Set / R	I Length	I Velocity	II Length	II Velocity	III Length	III Velocity
${}^1\Sigma_g^+$	${}^1\Sigma_u^+$	A	4.5	1.428	0.257	1.443	0.245	1.479	0.231
			5.0	1.562	0.235	1.549	0.228	1.562	0.219
			5.5	1.697	0.216	1.656	0.213	1.645	0.208
		CI	4.5	0.526	0.527	0.509	0.465	0.503	0.446
			5.0	0.509	0.524	0.506	0.472	0.508	0.454
			5.5	0.494	0.516	0.506	0.475	0.514	0.462

B) ${}^1\Sigma_g^+-{}^1\Pi_u$

l	k	Method	Set / R	I Length	I Velocity	II Length	II Velocity	III Length	III Velocity
${}^1\Sigma_g^+$	${}^1\Pi_u$	A	4.5	0.774	0.310	0.679	0.306	0.615	0.332
			5.0	0.886	0.271	0.794	0.262	0.717	0.285
			5.5	0.997	0.241	0.909	0.228	0.820	0.249
		CI	4.5	0.484	0.361	0.417	0.358	0.380	0.393
			5.0	0.560	0.313	0.498	0.305	0.450	0.336
			5.5	0.635	0.275	0.577	0.265	0.520	0.293

a) See Eqs. (27) and (28).

Table XXVIII. $R^{-1}\langle z\rangle_{lk}{}^{a)}$, $R\langle\zeta\rangle_{lk}{}^{b)}$, $R^{-1}\left\langle\frac{1}{\sqrt{2}}(x-iy)\right\rangle_{lk}{}^{a)}$ and $R\left\langle\frac{1}{\sqrt{2}}(\xi-i\eta)\right\rangle_{lk}{}^{b)}$.

A) ${}^1\Sigma_g^+ - {}^1\Sigma_u^+$

l	k	Method	$R^{-1}\langle z\rangle_{lk}$	$R\langle\zeta\rangle_{lk}$
${}^1\Sigma_g^+$	${}^1\Sigma_u^+$	A	−0.8814	−1.0116
		HL	−0.6310	−1.2338
		CI	−0.6577	−1.1145
		A (shrunk core)	−0.8814	−1.0116
		CI (shrunk core)	−0.6067	−0.8306

B) ${}^1\Sigma_g^+ - {}^1\Pi_u$

l	k	Method	$R^{-1}\left\langle\frac{1}{\sqrt{2}}(x-iy)\right\rangle_{lk}$	$R\left\langle\frac{1}{\sqrt{2}}(\xi-i\eta)\right\rangle_{lk}$
${}^1\Sigma_g^+$	${}^1\Pi_u$	A	0.6521	1.0483
		HL	0.6458	1.0369
		CI	0.4980	1.1742
		A (shrunk core)	0.6521	1.0483
		CI (shrunk core)	0.1546	0.9479

a) See Eq. (27).
b) See Eq. (28).

Table XXIX. Oscillator strength $f_{lk}{}^{a)}$ for Set II and $R=5.0$ a.u.

A) ${}^1\Sigma_g^+ - {}^1\Sigma_u^+$

l	k	Method	Length	Velocity
${}^1\Sigma_g^+$	${}^1\Sigma_u^+$	A	1.549	0.228
		HL	0.882	0.305
		CI	0.506	0.472
		A (shrunk core)	1.457	0.242
		CI (shrunk core)	0.323	0.350

B) ${}^1\Sigma_g^+ - {}^1\Pi_u$

l	k	Method	Length	Velocity
${}^1\Sigma_g^+$	${}^1\Pi_u$	A	0.794	0.262
		HL	0.701	0.284
		CI	0.498	0.305
		A (shrunk core)	0.329	0.632
		CI (shrunk core)	0.029	0.329

a) See Eqs. (27) and (28).

Table XXX. Vertical excitation energies (in e.v.) calculated by Eq. (29).

A) Results for each set and each R.

		${}^1\Sigma_u^+ - {}^1\Sigma_g^+$			${}^1\Pi_u - {}^1\Sigma_g^+$		
Set	Method $\diagdown$ R	4.5	5.0	5.5	4.5	5.0	5.5
I	A	1.44	1.16	0.96	1.99	1.61	1.33
	CI	2.15	1.86	1.64	3.00	2.40	1.96
II	A	1.54	1.25	1.03	2.16	1.75	1.45
	CI	2.13	1.84	1.63	3.25	2.57	2.08
III	A	1.64	1.33	1.10	2.48	2.01	1.66
	CI	2.19	1.88	1.65	3.67	2.90	2.35
	Obs.	2.01	1.86	1.73	2.73	2.59	2.50

B) Results obtained by using several approximations for Set II and $R=5.0$ a.u.

Method	${}^1\Sigma_u^+ - {}^1\Sigma_g^+$	${}^1\Pi_u - {}_1\Sigma_g^+$
A	1.25	1.75
HL	2.13	1.75
CI	1.84	2.57
A (shrunk core)	1.25	1.75
CI (shrunk core)	1.49	6.67
Obs.	1.86	2.59

of the most conspicuous shortcoming of the shrunk core model.

Finally, the values of $(\Delta E)_{lk}$ are calculated by the following formula:

$$\langle \Delta E\rangle_{lk} = \frac{\langle \sum_i \partial/\partial u_i \rangle_{lk}}{\langle \sum_i u_i \rangle_{lk}}, \quad v=x, y, \text{ or } z\,. \tag{29}$$

Here we have used the values of the matri elements of the dipole length and the corresponding ones of the dipole velocity shown in Tables XXVI and XXVIII. The results are given in Table XXX.

As can be seen from this table, the very good agreement with the observation is obtained by taking CI into account. The only one exception exists, namely $<\Delta E>_{lk}$ of ${}^1\Sigma_g^+ - {}^1\Pi_u$ obtained for Set III and $R=4.5$ a.u. Further, we can see that the situation similar to the case of the f_{lk} values holds also for the $<\Delta E>_{lk}$ values obtained by using the HL approximation and the shrunk core model. (See (B) of this table.)

§ 6. Population Analysis

As introduced in Part I, various specific overlap and specific AO populations in orthonormalized MO

$$\varphi=\sum_i c_{i,\,rk}\,\chi_{rk}\ (r=a,b;\ k=1s,\,2\overset{\circ}{s},\,2p\sigma,\,2p\pi^{\pm}) \tag{30}$$

have the following forms:

$$n'(i;\,k,\,l)=\begin{cases} 2c_{i,\,ak}\,c_{l,\,bk}\,S_{ak,\,bk} & \text{for } k=l \\ 4c_{i,\,ak}\,c_{i,\,bl}\,S_{ak,\,bl} & \text{for } k\neq l\,, \end{cases} \tag{31.1}$$

$$n'(i)=\sum_{k\geqq l} n'(i;\ k,\ l)\,, \tag{31.2}$$

$$N'(i;\,k)=c_{i,\,ak}^2+c_{i,\,bk}^2+2\sum_l c_{i,\,ak}\,c_{i,\,bl}\,S_{ak,\,bl}\,, \tag{31.3}$$

where $S_{rk,\,sl}=\int \chi_{rk}\,\chi_{sl}\,dv$. Then the overlap population $n(i)$, gross AO population $N(i;\,k)$, and total overlap population n. defined by Mulliken[21] can be expressed as

Table XXXI. Coefficients $c_{i,rk}$[a)] in MO φ_i.

	$(\sigma 1s)_{g,u}$[b)]	$(\sigma 2\overset{\circ}{s})_{g,u}$[b)c)]	$(\sigma 2p)_{g,u}$[b)]
σ_{1g}	0.70706	0	0
σ_{2g}	−0.04004	0.56274	0
σ_{3g}	−0.06655	−0.20832	0.68684
σ_{1u}	0.70715	0	0
σ_{2u}	0.07850	1.10303	0
σ_{3u}	0.35174	2.07638	1.72125
σ_{2g}'[d)]	−0.04959	0.52505	0.10321
σ_{3g}'[d)]	−0.05978	−0.29051	0.67904
σ_{2u}'[d)]	0.14602	1.48920	0.33792
σ_{3u}'[d)]	0.32948	1.81942	1.68775

a) See Eq. (30).
b) See Eq. (I, (2)).
c) See Eq. (I, (30)).
d) See Eq. (I, (60)).

Table XXXII. Specific overlap populations $n'(i;k,\,l)$[a)].

i	$n'(i;1s,\,1s)$	$n'(i;1s,\,2\overset{\circ}{s})$	$n'(i;1s,\,2p\sigma)$	$n'(i;2\overset{\circ}{s},\,2\overset{\circ}{s})$	$n'(i;2\overset{\circ}{s},\,2p\sigma)$	$n'(i;2p\sigma,\,2p\sigma)$	$n'(i;2p\pi^{\pm},\,2p\pi^{\pm})$
σ_{1g}	0.0001	0	0	0	0	0	
σ_{2g}	0.0000	−0.0064	0	0.3699	0	0	
σ_{3g}	0.0000	0.0040	−0.0217	0.0507	−0.2789	0.2068	
σ_{1u}	−0.0001	0	0	0	0	0	
σ_{2u}	0.0000	−0.0246	0	−1.4210	0	0	
σ_{3u}	0.0000	−0.2079	−0.2869	−5.0355	−6.9666	−1.2986	
$1\sigma_g$	0.0001	0.0014	0.0001	0.0001	0.0000	0.0000	
$2\sigma_g$	0.0000	−0.0088	−0.0034	0.3125	0.1218	0.0064	
$3\sigma_g$	0.0000	0.0049	−0.0183	0.1080	−0.4007	0.2004	
$1\sigma_u$	−0.0001	−0.0042	−0.0023	−0.0005	−0.0003	0.0000	
$2\sigma_u$	0.0000	−0.0024	0.0015	−0.6420	0.4147	−0.0361	
$3\sigma_u$	0.0000	−0.2260	−0.2862	−5.8140	−7.3810	−1.2625	
g	0.0000	−0.0075	−0.0029	0.3126	0.1217	0.0064	
σ_{2g}'	0.0000	−0.0074	−0.0024	0.3220	0.1056	0.0047	
σ_{3g}'	0.0000	0.0049	−0.0192	0.0986	−0.3845	0.2021	
σ_{2u}'	0.0000	−0.0619	−0.0234	−2.5902	−0.9809	−0.0501	
σ_{3u}'	0.0000	−0.1706	−0.2636	−3.8663	−5.9856	−1.2486	
$\pi_g^{\pm}$							−0.7163
$\pi_u^{\pm}$							0.2945

a) See Eq. (31.1).

Table XXXIII. Specific gross AO populations $N'(i;k)$[a] and specific overlap populations $n'(i)$[b] in each orbital.

i	$N'(i;1s)$	$N'(i,2\mathring{s})$	$N'(i;2p\sigma)$	$n'(i)$
σ_{1g}	1	0	0	0.0001
σ_{2g}	0	1	0	0.3635
σ_{3g}	0	0	1	−000391
σ_{1u}	1	0	0	−0.0001
σ_{2u}	0	1	0	−1.4457
σ_{3u}	0	0	1	−13.7955
$1\sigma_g$	0.9991	0.0009	0.0000	0.0016
$2\sigma_g$	0.0010	0.9042	0.0948	0.4285
$3\sigma_g$	−0.0002	0.0950	0.9052	−0.1057
$1\sigma_u$	1.0031	−0.0019	−0.0012	−0.0073
$2\sigma_u$	−0.0002	0.6635	0.3367	−0.2643
$3\sigma_u$	−0.0029	0.3384	0.6645	−14.9697
g	0	0.9051	0.0940	0.4303
σ_{2g}'	0	0.9224	0.0776	0.4224
σ_{3g}'	0	0.0776	0.9224	−0.0982
σ_{2u}'	0	1.3238	−0.3238	−3.7065
σ_{3u}'	0	−0.3238	1.3238	−11.5347
$\pi_g^{\pm}$				−0.7163
$\pi_u^{\pm}$				0.2945

a) See Eq. (31.3).
b) See Eq. (31.2).

$$n(i)=N(i)n'(i)\,, \qquad (32.1)$$

$$N(i;\,k)=N(i)N'(i;\,k)\,, \qquad (32.2)$$

and

$$n=\sum_i n(i)\,, \qquad (32.3)$$

respectively, where $N(i)$ is the number of electrons in MO φ_i. Mulliken[21] proposed that

Table XXXIV. Occupation numbers $N(i)$, overlap populations $n(i)$[a] in each orbital, and $n'(i)/n$[b].

(A) Single configuration A (Case 1)

i	$N(i)$	$n(i)$	$n'(i)/n$
σ_{1g}	2	0.0003	0.0002
σ_{2g}	2	0.7269	0.5000
σ_{3g}	0	0	−0.0538
σ_{1u}	2	−0.0003	−0.0002
σ_{2u}	0	0	−1.9888
σ_{3u}	0	0	−18.9786
$\pi_g^{\pm}$	0	0	0.9854
$\pi_u^{\pm}$	0	0	0.4051

(B) g^2 approximation (Case 4)

i	$N(i)$	$n(i)$	$n'(i)/n$
σ_{1g}	2	0.0003	0.0002
σ_{1u}	2	−0.0003	−0.0002
g	2	0.8606	0.5000

(C) LCAO SCF (Case 6)

i	$N(i)$	$n(i)$	$n'(i)/n$
$1\sigma_g$	2	0.0033	0.0019
$2\sigma_g$	2	0.8570	0.5067
$3\sigma_g$	0	0	−0.1250
$1\sigma_u$	2	−0.0147	−0.0087
$2\sigma_u$	0	0	−0.3125
$3\sigma_u$	0	0	−17.7022
$1\pi_g^{\pm}$	0	0	−0.8470
$1\pi_u^{\pm}$	0	0	0.3482

a) See Eq. (32.1).
b) See Eq. (33).

Table XXXV. Occupation numbers $N(i)$[a], gross AO populations $N(i,k)$[b], and overlap populations $n(i)$[c] in each orbital, for the case of eight dimensional configurational interaction (Case 11).

i	$N(i)$	$N(i;1s)$	$N(i;2\mathring{s})$	$N(i;2p\sigma)$	$N(i;2p\pi^{\pm})$	$n(i)$
σ_{1g}	2	2	0	0	0	0.0002
σ_{2g}'[a]	1.81971	0	1.6786	0.1412	0	0.7687
σ_{3g}'[a]	0.01619	0	0.0013	0.0149	0	−0.0016
σ_{1u}	2	2	0	0	0	−0.0002
σ_{2u}'[a]	0.03311	0	0.0438	−0.0107	0	−0.1227
σ_{3u}'[a]	0.00004	0	0.0000	0.0000	0	−0.0005
$\pi_g^{\pm}$	0.00003	0	0	0	0.0000	0.0000
$\pi_u^{\pm}$	0.13092	0	0	0	0.1309	0.0386
Sum	6	4	1.7237	0.1454	0.1309	0.6825

a) See Eq. (I, (60)). b) See Eq. (32.2). c) See Eq. (32.1).

Table XXXVI. Total overlap populations $n^{a)}$ and $s-p$ promotion in percent.

Method	Single configuration	g^2	SCF	8 dim. CI
n	0.7269	0.8606	0.8456	0.6825
$s-p$	0	9.49	9.36	13.82

a) See Eq. (32.3).

overlap populations $n(i)$ and n can be taken as a measure of "bonding power".

To investigate the features of the three wave functions, (A) the single configuration (Case 1), (B) g^2 (Case 4), and (C) SCF MO (Case 6), obtained for the ground state and for Set II and $R=5.0$. a.u., we have calculated the various populations by the above formulae. The coefficients in Eq. (30) for the wave functions (B) and (C) were already given in Tables VIII and IX, respectively. Those for (A) are given in Table XXXI. The obtained results of the various populations are summarized in Tables XXXII, XXXIII, and XXXIV.

Further, as explained in I, we can also analyze the eight dimensional configurational wave function (Case 11) using the above formulae, if MO φ_i and the occupation number $N(i)$ in the above formulae are replaced by the natural orbital[22)] φ_i' and the effective number of electrons N(i). (See Eq. (I, (60).) The coefficients $c_{i,\ rk}$ in the natural orbital φ_i' are given in Table XXXI. The obtained results of the various populations are given in Table XXXV.

Table XXXVII. Comparison between values of $(n_0-n_k)/n_0{}^{a)}$ calculated by (SCF)′ rnd CI, together with experimental values of $2(R_k-R_0)/R_0{}^{a)}$.

k	$(n_0-n_k)/n_0$	$2(R_k-R_0)/R_0$	Remarks
$Li_2(^1\Pi_u)$	0.1585 (0.5045)[b)]	0.1975	One electron in $Li_2(^1\Sigma_g{}^+)$ being excited from $2\sigma_g$ to $1\pi_u{}^\pm$
$Li_2(^1\Sigma_u{}^+)$	0.8192 (0.5648)[b)]	0.3257	One electron in $Li_2(^1\Sigma_g{}^+)$ being excited from $2\sigma_g$ to $2\sigma_u$

a) See Eq. (33).

b) The values within parentheses are those calculated by using CI wave functions.

Table XXXVIII. Values of kinetic energy T in a.u. for wave function for each set and each R.

Set	R	Method	$^1\Sigma_g{}^+$	$^3\Sigma_u{}^+$	$^1\Sigma_u{}^+$	$^1\Pi_u$
I	4.5	A	19.7985	19.8172	19.8172	19.7643
		CI	19.8259	19.8329	19.8703	19.7912
	5.0	A	16.0368	16.0520	16.0520	16.0091
		CI	16.0663	16.0711	16.0974	16.0389
	5.5	A	13.2535	13.2661	13.2661	13.2306
		CI	13.2834	13.2865	13.3053	13.2612
II	4.5	A	17.8989	17.9447	17.9447	17.8373
		CI	17.9154	17.9351	17.9554	17.8645
	5.0	A	14.4981	14.5352	14.5352	14.4482
		CI	14.5171	14.5345	14.5457	14.4766
	5.5	A	11.9819	12.0125	12.0125	11.9407
		CI	12.0017	12.0178	12.0227	11.9690
III	4.5	A	19.9903	20.0660	20.0660	19.9276
		CI	20.0008	20.0333	20.0427	19.9559
	5.0	A	16.1922	16.2534	16.2534	16.1414
		CI	16.2046	16.2343	16.2366	16.1695
	5.5	A	13.3819	13.4326	13.4326	13.3400
		CI	13.3952	13.4235	13.4204	13.3675

The amounts of s–p promotion and the total overlap population n, obtained by the population analysis method for the above four wave functions, are given in Table XXXVI. From this table we can see the following points.

(a) The charge distribution is nearly the same for SCF and g^2 wave functions.

(b) The values of n for SCF and g^2 wave functions are larger than that for the single configurational wave function. This tendency is, however, not so remarkable as that encountered in the case of O_2, though the amount of s–p promotion is comparable. (cf. Table XIX of Part I.)

(c) The value of n for eight dimensional configurational wave function is even smaller than that of the single configurational wave function due to the electron correlation (cf. remarks below Table XX of I.).

(d) The amount of s–p promotion increases considerably if configurations involving π orbitals are taken into account.

Finally, we have examined the relation suggested by Mulliken[21])

$$\frac{n_0-n_k}{n_0}=2\frac{R_k-R_0}{R_0} \tag{33}$$

where n_0 and R_0 are the total overlap population and the equilibrium internuclear distance in the ground state, respectively, and n_k and R_k are those in the excited state. n_0 and n_k are calculated by using SCF MO's obtained for the ground state. In Table XXXVII the experimental values[12]) of $2(R_k-R_0)/R_0$ are compared with the calculated values of $(n_0-n_k)/n_0$. From this table, we can see that, contrary to the O_2 case, the relation (33) does not hold satisfactorily especially for the transition from ${}^1\Sigma_g{}^+$ to ${}^1\Sigma_u{}^+$. In O_2 case, all the SCF MO's used to calculate n_k were the occupied orbitals, while in Li_2 case, an unoccupied SCF MO such as $2\sigma_u$, which is considered unsuitable for describing excited states, enters in this calculation. In this connection we have calculated $(n_0-n_k)/n_0$ by using CI wave functions for both the ground and excited states (Table XXXVII). The result, however, becomes worse for ${}^1\Pi_u$ state, though it is improved for ${}^1\Sigma_u{}^+$ state.

§ 7. Virial Theorem

The virial theorem for a diatomic molecule can be expressed as[23])

$$T(R)=-\left\{E(R)+R\frac{\partial E(R)}{\partial R}\right\}, \tag{34}$$

where $T(R)$ is the kinetic energy of all the electrons and $E(R)$ is the adiabatic potential of the molecule. We have here intended to examine to what extent this relation is satis-

Table XXXIX. Kinetic energy T in a.u. together with ratios of computed to observed values of total energy E and dissociation energy D_e, for various approximations of Set II and $R=5.0$ a.u.

	Case	T	E	D_e
1	A (single configuration)	14.4981	0.9888	−0.16
2	A+C	14.5033	0.9897	0.18
3	A+E	14.5301	0.9896	0.15
4	$(g)^2$	14.5268	0.9895	0.10
5	A+C+E $(g'g'')$	14.5233	0.9898	0.21
6	LCAO SCF	14.4866	0.9895	0.12
7	σ-electron CI	14.5238	0.9902	0.38
8	A+H	14.4894	0.9900	0.29
9	A+C+H	14.4950	0.9905	0.50
10	A+C+E+H	14.5168	0.9910	0.70
11	8 dim. CI	14.5171	0.9911	0.73
12	Pure HL	14.5028	0.9897	0.18
13	Ionic structure	14.5028	0.9865	−1.04
14	HL with $s-p$ hybrid.	14.5208	0.9900	0.30
15	Semiloc. and $s-p$ hybrid.	14.5251	0.9901	0.32
16	$(\mathring{s}-\mathring{s})+(\pi-\pi)$	14.4994	0.9903	0.40
17	$A'(S(1s_a, 2\mathring{s}_b)=0)$	14.3458	0.9903	0.41
18	$HL'(S(1s_a, 2\mathring{s}_b)=0)$	14.3861	0.9913	1.45
19	A (shrunk core)	0.4531	0.5543[a])	−0.65
20	8 dim. CI (shrunk core)	0.4415	0.6760[a])	0.72
21	$(\mathring{s}-\mathring{s})$ (shrunk core)	0.3411	0.7709[a])	1.79
22	$(s-s)$ (shrunk core)	0.1241	1.2356[a])	0.73

a) Experimental value of E' considered in § 7 is adopted as that of $E(Li_2)$ in shrunk core model ($E'(R=5.0)=-0.43494$ a.u.).

fied by the approximations considered in this paper.

For this purpose, $T(R)$ is separated from $E(R)$ given already and the result is shown in Tables XXXVIII and XXXIX.

Table XL. Values of $R\{\partial E(R)/\partial R\}^{a)}$ obtained by using Morse potential $U(R)$ (in a.u.).

State / R	$^1\Sigma_g{}^+$	$^1\Sigma_u{}^+$	$^1\Pi_u$
4.5	-0.0594_1	-0.1039_5	-0.1190_8
5.0	-0.0042_4	-0.0576_3	-0.0436_1
5.5	0.0297_7	-0.0212_2	-0.0026_8

a) See Eq. (34).

Further, the values of $R\{\partial E(R)/\partial R\}$, which are calculated by using the Morse function with the parameters in Table XVII, are given in Table XL.

From this table and the tables of E and T given before, we can see that the relation (34) is not satisfied well by any of all our approximations. This large disagreement seems to be originated mainly in the errors of $T(R)$ due to the unsuitableness of the adopted orbital exponent of 1s, δ_1. In order to examine this point, we have estimated the change of $T(R)$ arising from the replacement by a more suitable value of δ_1, that is $\delta_{1,\text{ best}}$. This change may essentially be approximated by that of the kinetic energy of 1s cores, which is given by $2(\delta_1{}^2{}_{,\text{ best}}-\delta_1{}^2)$. In Table XLI, this value is written, which is found by assuming $\delta_{1,\text{ best}}=2.688$ determined by Zener's rule[24]. By comparing this result with the discrepancy of relation (34), $T+E+R\{\partial E/\partial R\}$ shown in the same table, we can see that our expectation is essentially correct.

Table XLI. Correction of kinetic energy of core electrons for $^1\Sigma_g{}^+$ state.

Set	Method	Energy / R	4.5	5.0	5.5
I	A	T	19.7985	16.0368	13.2535
		E	−14.4657	−14.8010	−14.7808
		$T+E+R(\partial E/\partial R)^{a)}$	5.2734	1.2315	− 1.4975
		$2(\delta_{1,\text{best}}{}^2-\delta_1{}^2)^{b)}$	− 4.9073	− 1.2293	1.4920
	CI	T	19.8259	16.0663	13.2834
		E	−14.5013	−14.8359	−14.8152
		$T+E+R(\partial E/\partial R)$	5.2652	1.2262	− 1.5021
		$2(\delta_{1,\text{best}}{}^2-\delta_1{}^2)$	− 4.9073	− 1.2293	1.4920
II	A	T	17.8989	14.4981	11.9819
		E	−14.6844	−14.8268	−14.6771
		$T+E+R(\partial E/\partial R)$	3.1551	− 0.3330	− 2.6655
		$2(\delta_{1,\text{best}}{}^2-\delta_1{}^2)$	− 2.8888	0.4057	2.8433
	CI	T	17.9154	14.5171	12.0017
		E	−14.7208	−14.8614	−14.7104
		$T+E+R(\partial E/\partial R)$	3.1351	− 0.3486	− 2.6789
		$2(\delta_{1,\text{best}}{}^2-\delta_1{}^2)$	− 2.8888	0.4057	2.8433
III	A	T	19.9903	16.1922	13.3819
		E	−14.4453	−14.7999	−14.7927
		$T+E+R(\partial E/\partial R)$	5.4856	1.3880	− 1.3810
		$2(\delta_{1,\text{best}}{}^2-\delta_1{}^2)$	− 4.9073	− 1.2293	1.4920
	CI	T	20.0008	16.2046	13.3952
		E	−14.4826	−14.8347	−14.8254
		$T+E+R(\partial E/\partial R)$	5.4587	1.3657	− 1.4004
		$2(\delta_{1,\text{best}}{}^2-\delta_1{}^2)$	− 4.9073	− 1.2293	1.4920

a) See Eq. (34).

b) $\delta_{1,\text{best}}=2.688$ given by Guillemin and Zener[24]. See also reference (14).

Table XLII. Values of $E'(R)$[a] and $T'(R)$[a] in a.u.

(A) $E'(R)$

Set	R	Method	$^1\Sigma_g^+$	$^3\Sigma_u^+$	$^1\Sigma_u^+$	$^1\Pi_u$
I	4.5	A	−0.3793	−0.3527	−0.2548	−0.2637
		CI	−0.4149	−0.3622	−0.3357	−0.2872
	5.0	A	−0.3810	−0.3588	−0.2707	−0.2739
		CI	−0.4159	−0.3690	−0.3484	−0.2979
	5.5	A	−0.3759	−0.3569	−0.2768	−0.2762
		CI	−0.4103	−0.3680	−0.3513	−0.3008
II	4.5	A	−0.3711	−0.3412	−0.2336	−0.2528
		CI	−0.4076	−0.3533	−0.3257	−0.2787
	5.0	A	−0.3843	−0.3615	−0.2647	−0.2723
		CI	−0.4189	−0.3720	−0.3487	−0.2984
	5.5	A	−0.3869	−0.3691	−0.2811	−0.2809
		CI	−0.4201	−0.3789	−0.3584	−0.3072
III	4.5	A	−0.3589	−0.3249	−0.2064	−0.2347
		CI	−0.3962	−0.3407	−0.3107	−0.2637
	5.0	A	−0.3799	−0.3562	−0.2494	−0.2625
		CI	−0.4147	−0.3678	−0.3414	−0.2914
	5.5	A	−0.3877	−0.3712	−0.2742	−0.2768
		CI	−0.4205	−0.3805	−0.3564	−0.3056
Obs.	4.5		−0.4317		−0.3581	−0.3316
	5.0		−0.4349		−0.3665	−0.3398
	5.5		−0.4336		−0.3702	−0.3418

(B) $T'(R)$

Set	R	Method	$^1\Sigma_g^+$	$^3\Sigma_u^+$	$^1\Sigma_u^+$	$^1\Pi_u$
I	4.5	A	0.4405	0.4592	0.4592	0.4063
		CI	0.4679	0.4749	0.5123	0.4332
	5.0	A	0.3568	0.3720	0.3720	0.3291
		CI	0.3863	0.3911	0.4174	0.3589
	5.5	A	0.2949	0.3074	0.3074	0.2720
		CI	0.3247	0.3278	0.3466	0.3025
II	4.5	A	0.5594	0.6052	0.6052	0.4978
		CI	0.5759	0.5956	0.6159	0.5250
	5.0	A	0.4531	0.4902	0.4902	0.4032
		CI	0.4721	0.4895	0.5007	0.4316
	5.5	A	0.3744	0.4051	0.4051	0.3332
		CI	0.3943	0.4104	0.4153	0.3616
III	4.5	A	0.6323	0.7080	0.7080	0.5696
		CI	0.6428	0.6752	0.6847	0.5979
	5.0	A	0.5122	0.5734	0.5734	0.4614
		CI	0.5246	0.5543	0.5566	0.4895
	5.5	A	0.4233	0.4739	0.4739	0.3813
		CI	0.4366	0.4648	0.4617	0.4088

[a] See below Eq. (35).

Table XLIII. Values of $\Delta T^{a)}$ and $-\left\{\Delta E^{b)}+\Delta\left(R\frac{\partial E(R)^{c)}}{\partial R}\right)\right\}$ in a.u.

Set	R	Method	${}^1\Sigma_u{}^+-{}^1\Sigma_g{}^+$		${}^1\Pi_u-{}^1\Sigma_g{}^+$	
			ΔT	$-\left\{\Delta E+\Delta\left(R\frac{\partial E(R)}{\partial R}\right)\right\}$	ΔT	$-\left\{\Delta E+\Delta\left(R\frac{\partial E(R)}{\partial R}\right)\right\}$
I	4.5	A	0.0187	−0.0799	−0.0342	−0.0559
		CI	0.0444	−0.0346	−0.0347	−0.0680
	5.0	A	0.0152	−0.0569	−0.0277	−0.0677
		CI	0.0311	−0.0141	−0.0274	−0.0786
	5.5	A	0.0126	−0.0481	−0.0229	−0.1268
		CI	0.0219	−0.0080	−0.0222	−0.1366
II	4.5	A	0.0458	−0.0930	−0.0616	−0.0587
		CI	0.0400	−0.0373	−0.0509	−0.0692
	5.0	A	0.0371	−0.0662	−0.0499	−0.0727
		CI	0.0286	−0.0168	−0.0404	−0.0811
	5.5	A	0.0307	−0.0547	−0.0412	−0.1331
		CI	0.0210	−0.0107	−0.0327	−0.1399
III	4.5	A	0.0757	−0.1080	−0.0627	−0.0645
		CI	0.0419	−0.0410	−0.0449	−0.0729
	5.0	A	0.0613	−0.0770	−0.0508	−0.0780
		CI	0.0320	−0.0199	−0.0351	−0.0839
	5.5	A	0.0507	−0.0626	−0.0420	−0.1380
		CI	0.0251	−0.0131	−0.0277	−0.1420

a) See Eq. (36).
b) ΔE's are the calculated values in Table XVI.
c) From Table XL.

To study this situation, further, we have subtracted from $E(R)$ the core energy

$$2\{(\sigma_{1g}|\mathrm{h}|\sigma_{1g})+(\sigma_{1u}|\mathrm{h}|\sigma_{1u})\}+J(\sigma_{1g},\sigma_{1g})+J(\sigma_{1u},\sigma_{1u})$$
$$4J(\sigma_{1g},\sigma_{1u})-2K(\sigma_{1g},\sigma_{1u})+8/R\,, \qquad (35)$$

and from $T(R)$ the corresponding quantity. The resulting quantities are denoted by $E'(R)$ and $T'(R)$ respectively. The calculated values of $E'(R)$ and $T'(R)$ are shown in Table XLII.

From this table we can see that $T'(R)$ varies reasonably with respect to δ_2 as compared with $T(R)$, and $E'(R)$ is fairly stationary with δ_2.

As to the alternative way of eliminating the errors connected with the core electrons, we take the difference of the corresponding quantities of two states. Then the virial theorem can be expressed as

$$\Delta T=-\left\{\Delta E+\Delta\left(R\frac{\partial E(R)}{\partial R}\right)\right\}, \qquad (36)$$

where ΔT means the difference of the kinetic energy of the two states, and so on. The values of ΔT and $\Delta E+\Delta\left(R\frac{\partial E(R)}{\partial R}\right)$ for each set and R are given in Table XLIII. From this table we can see that our wave functions do not satisfy the virial theorem. We can expect, however, that if we use δ_2's for ${}^1\Sigma_u{}^+$ and ${}^1\Pi_u$ somewhat smaller than that of ${}^1\Sigma_g{}^+$, the relation (36) might be improved. This has been not important for the case of vertical excitation energies because of the nearly stationary character of $E'(R)$.

Finally we note that we could not determine the best δ_2 and R by using $E'(R)$ in Table XLII. This fact means that the subtraction of the core energy by Eq. (35) is not so accurate as to make this possible.

§ 8. Summary

In order to see the accuracy of the various approximations considered in this paper, we have calculated the ratios of the calculated values to the observed ones of the total energy E, dissociation energy D_e, and vertical excitation energy ΔE. These ratios are given in Tables XXXIX and XLIV.

Table XLIV. Ratio of computed to observed value of vertical excitation energy.

(A) From difference of energies

(i) Result for each set and R.

Set	Method \ R	$^1\Sigma_u^+ - ^1\Sigma_g^+$ 4.5	5.0	5.5	$^1\Pi_u - ^1\Sigma_g^+$ 4.5	5.0	5.0
I	A	1.69	1.61	1.55	1.15	1.12	1.08
	CI	1.07	0.99	0.93	1.27	1.24	1.19
II	A	1.86	1.75	1.66	1.18	1.18	1.15
	CI	1.11	1.03	0.97	1.29	1.27	1.23
III	A	2.06	1.91	1.79	1.24	1.23	1.21
	CI	1.16	1.07	1.01	1.32	1.29	1.25

(ii) Result for Set II and R=5.0 a.u.

Method	$^1\Sigma_u^+ - ^1\Sigma_g^+$	$^1\Pi_u - ^1\Sigma_g^+$
A	1.75	1.18
HL	1.95	1.06
CI	1.03	1.27
A (shrunk core)	1.65	0.49
CI (shrunk core)	0.77	0.76

(B) From Eq. (29)

(i) Result for each set and R.

Set	Method \ R	$^1\Sigma_u^+ - ^1\Sigma_g^+$ 4.5	5.0	5.5	$^1\Pi_u - ^1\Sigma_g^+$ 4.5	5.0	5.5
I	A	0.72	0.62	0.55	0.73	0.62	0.53
	CI	1.07	1.00	0.95	1.10	0.93	0.78
II	A	0.77	0.67	0.60	0.79	0.68	0.58
	CI	1.06	0.99	0.94	1.19	0.99	0.83
III	A	0.82	0.72	0.64	0.91	0.78	0.66
	CI	1.09	1.01	0.95	1.34	1.12	0.94

(ii) Result for Set II and R=5.0 a.u.

Method	$^1\Sigma_u^+ - ^1\Sigma_g^+$	$^1\Pi_u - ^1\Sigma_g^+$
A	0.67	0.68
HL	1.15	0.68
CI	0.99	0.99
A (shrunk core)	0.67	0.68
CI (shrunk core)	0.80	2.58

From these tables, we can see that the results are improved appreciably by taking CI into account. Above all, ΔE calculated by the relation (29) is improved excellently.

Contrary to the O_2 case, the HL approach yields a better result than the MO one, in so far as the total energy is concerned. (Compare Case 1 with Case 12.) Further, it seems clear that the effect of taking into account s–p hybridization, mixing the configurations involving π orbitals, and also semilocalization is significant.

Finally, it is shown that the relation (34) concerning the virial theorem is not satisfied well by using the wave functions here considered. This discrepancy, however, can be removed considerably by improving the orbital exponent δ_1 of the core orbital. The results obtained here will be discussed in Part III of this series of papers.

Acknowledgments

The authors have the pleasure to express their sincere thanks to Dr. T. Arai for his valuable discussions, and to Miss M. Sakamoto and Dr. T. Nakamura for informing us their unpublished results. They further appreciate the help of Dr. K. Takayanagi and Miss M. Aoyagi in the early stage of this work. They are also indebted to the Ministry of Education and to the members of Kotani Laboratory for their financial aids. Finally, they would like to thank Misses N. Mizushima, N. Sugawara, S. Noguchi, and Mrs. H. Komuro for their valuable assistance in the numerical work, and moreover, to Mrs. Y. Yuminami for her secretary service.

References

1) M. Kotani, Y. Mizuno, K. Kayama, and E. Ishiguro: J. Phys. Soc. Japan **12** (1957) 707. This paper will be referred to as, I, throughout the present paper.
2) J. H. Bartlett and W. H. Furry: Phys. Rev. **38** (1931) 1615.
3) N. Rosen and S. Ikehara: Phys. Rev. **43** (1933) 5.
4) H. M. James: J. Chem. Phys. **2** (1934) 794.
5) J. C. Slater: Phys. Rev. **36** (1930) 57.
6) M. Kotani, A. Amemiya, E. Ishiguro, and T. Kimura: Table of Molecular Integrals, Maruzen Co., Ltd., Tokyo, 1955.
7) E. Ishiguro, T. Arai, and M. Sakamoto: Nat. Sci. Rep. Ocha. Univ. **6** (1956) 204.
8) E. Ishiguro, Y, Mizuno, K. Kayama, T. Arai

and M. Sakamoto: Nat. Sci. Rep. Ocha. Univ. **7** (1956) 63.

9) E. Ishiguro, Y. Mizuno, and K. Kayama: Nat. Sci. Rep. Ocha. Univ. **8** (1957)

10) C. C. Roothaan: Rev. Mod. Phys. **23** (1951) 69.

11) C. G. Greenhow and W. V. Smith: J. Chem. Phys. **19** (1951) 1298.

12) G. Herzberg: Molecular Spectra and Molecular Structure, I. Spectra of Diatomic Molecules, D. Van Nostrand Comp. Inc. New York, 1950.

13) E. G. Harris and M. A. Melkanoff: Phys. Rev. **90** (1953) 585.

14) E. B. Wilson: J. Chem. Phys. **1** (1933) 210.

15) C. E. Moore, Atomic Energy Levels, Nat. Bur. Stand. (U. S.) Circ. 467, Vol. I, 1949.

16) A. Rahman: Physica, XX (1954) 623.

17) R. M. Sternheimer and H. M. Foley: Phys. Rev. **92** (1953) 1460.

18) E. Ishiguro, T. Arai, M. Mizushima, and M. Kotani: Proc. Phys. Soc. (London) **A65** (1952) 178.

19) R. M. Logan, R. E. Coté, and P. Kusch: Phys. Rev. **86** (1952) 280.

20) R. Avery and C. H. Blanchard: Phys. Rev. **78** (1950) 704. R. D. Present: Phys. Rev. **80** (1950) 43.

21) R. S. Mulliken: J. Chem. Phys. **23** (1955) 1833, 1841, 2338, 2343.

22) P. O. Löwdin: Phys. Rev. **97** (1955) 1474.

23) H. Eyring, J. Walter, and G. E. Kimball: Quantum Chemistry, New York: John Wiley and Sons, Inc., 1944.

24) V. Guillemin and C. Zener: Zeits. f. Physik, **61** (1930) 199.

Errata of Part I

Page		
707	between authors' names and abstract	(Received March 15, 1957) should be inserted
707	in the last line	hybridization
709	in Eq. (1)	$\cdots\frac{1}{\sqrt{2}}\sin\theta_{a1}e^{+i\varphi_1}, \cdots\frac{1}{\sqrt{2}}\sin\theta_{a1}e^{-i\varphi_1}$
712	in Eq. (11)	$P\Psi^{\Lambda}_{\Omega}\Theta_{S,M}$ should be replaced by $P\Psi^{\Lambda}_{\Omega}\cdot\Theta_{S,M,h}$
713	in footnote a) of Table IV	The following remarks should be added; spins associated with two orbitals with the same superbar are coupled to form a triplet, while spins associated with two orbitals with the same subber are coupled to form a singlet.
715	in Table V	$1\pi_u^{\pm}$ in Line 5 and Column 1 should be replaced by $1\pi_g^{\pm}$
721	Eq. (42)	$\rho=\rho_n-\rho_{el}$.
722	under Table XI	ρ_{el} should be the number density of electrons
724	in Table XII	0.00006 in Line 15 and Column 4 should be replaced by -0.00006
726	in the beginning of § 4	···transition from a state l to an energetically higher level k is expressed as···
726	in Table XIII	l and k in the first and second columns should be exchanged.
727	in Eq. (48)	See Eq. (29) of the present paper.
729	in Eq. (57.3)	See Eq. (31.3) of the present paper.
729	in Table XVI, Column 6	$n'(i;2\overset{\circ}{s}_a, 2p\sigma_b)+(a\longleftrightarrow b)$
730–731	in Eq. (59), Table XX, and the sentence above this table.	$\frac{n_k-n_0}{n_0}$ should be replaced by $-\frac{n_k-n_0}{n_0}$. See also Eq. (33) of the present paper.
731	in Line 7	matrix
734	Line 30	$J(k, l)=(\varphi_k\varphi_k\|\varphi_l\varphi_l)$.
736	reference 13)	Van Nostrand Comp.

JOURNAL OF THE PHYSICAL SOCIETY OF JAPAN Vol. 12, No. 12, DECEMBER, 1957

Structural Investigation by Means of Nuclear Quadrupole Resonance III

(Arsenic Tribromide)

By Kenji SHIMOMURA

Minami Branch, Hiroshima University, Hiroshima

(Received August 8, 1957)

The structure of $AsBr_3$ is investigated by means of nuclear quadrupole resonance at about 10°C, and is compared with Braekken's results of X-ray analysis. $AsBr_3$ has the orthorhombic symmetry, and the Br–As–Br bond angles are $99°38'\pm16'$, $99°14'\pm18'$ and $102°51'\pm13'$. The polar angles specifing the directions of the As-Br bonds with respect to the crystal axes are $(62°4'\pm13', 56°9'\pm8')$, $(64°7'\pm15', -61°46'\pm11')$, and $(61°54'\pm8', 180°50'\pm20\ )$. The bond angles are larger than those of Braekken by about 1°. The asymmetry parameter of field gradient at the bromine nucleus is about 0.04 ± 0.02. Single, double, and ionic character of As–Br bond are 61.4%, 1.2% and 37.4%, respectively, and the bond length is deduced to be 3.20 A. These results are consistent with those of X-ray analysis except the slight disagreement in the bond angles.

§ 1. Introduction

A brief preliminary report on the X-ray analysis of crystal structure of $AsBr_3$ has been published by Braekken[1]. The structure is orthorhombic with four molecules unit with the dimensions:

$$a=10.15\,kX,\ b=12.07\,kX,\ c=4.31\,kX\,.$$

Atoms are in the following special positions of $V^4\,(P2_12_12_1)$:

4 As: $x=0.300$, $y=0.215$, $z=0$,
12 Br: $x_1=-0.193$, $y_1=0.123$, $z_1=0.262$,
$x_2=0.133$, $y_2=0.123$, $z_2=-0.262$,
$x_3=0.482$, $y_3=0.123$, $z_3=-0.250$.

The structure consists of pyramidal $AsBr_3$ molecules. This report, however, is not listed in Wyckoff's Crystal Structures[2] and in the Strukturbericht[3].

On the other hand, the molecule of gaseous state has been found to have trigonal pyramidal form by the electron diffraction method; A. H. Gregg et al[4] obtained the values $100°\pm2°$, 2.36 ± 0.02 A; O. Hassel et al[5] 101°30′, 2.31 A; while M. W. Lister et al[6] $100°\pm2°$, 2.36 ± 0.04 A for the bond angle ∠Br–As–Br and As–Br bond distance, respectively.

The quadrupole spectrum of this substance has been studied by some workers[7][8] and the single line at about 60 Mc and a pair of triplets at about 170 Mc and 200 Mc have been ascribed to the As^{75}, Br^{81}, and Br^{79}, respectively, but the Zeeman and the detailed quadrupole spectrum analyses have not yet been made.

In the present experiment, the structure of $AsBr_3$ has been studied by means of NQR and the results have been compared with those of Braekken.

§ 2. Experimental Procedure

Dry powdered arsenic was introduced in small portions at a time into a flask containing bromine, and then the product was distilled from an excess of arsenic. $AsBr_3$ thus prepared was sealed in a glass cylinder with a bottom tapered to a capillary tube[9]. The single crystal which was obtained by descending the glass container slowly into water through a vertical furnace (at about 50°C) was set on a rotational axis of the crystal analyzer, which was described in some detail in a previous paper[9], so that the axis of the glass container might be approximately coincident with the rotational axis and was rotated in the hf coil of the superregenerative detector. Four different magnitudes of Zeeman fields were used, in order to avoid the misreading of the spurious signal which was built accidentally at the zero-field absorption frequency on a persistent screen of a cathode-ray oscilloscope, by the concurrence of Zeeman-splitting lines of the two sidebands on both sides of the central absorption line. Zeeman analysis was carried out on each Br^{81} line of the triplet individually at about 10°C. In order to locate two closely spaced *N. E. D.*[9], magnetic field of 350 gauss was used.

§ 3. Experimental Results

Let the triplet lines of Br^{81} be designated as ***A***, ***B*** and ***C*** from the high to the low frequency ends. The analysis shows that ***A*** and ***B*** lines are contributed by the atoms Br_{A1}, Br_{A2}, Br_{A3}, Br_{A4} and Br_{B1}, Br_{B2}, Br_{B3}, Br_{B4}, respectively. On the other hand, in any magnetic field of less than about 160 gauss ***C***-line has been found to consist of two *N. E. D.* making an angle of about 56° with each other, while the Zeeman analysis in the field of 350 gauss has revealed that each of these *N. E. D.* consists of two closely spaced *N. E. D.* The results of Zeeman analysis are shown in Fig. 1. The orientation of all *N. E. D.* are plotted on a globe on which the axis of the globe is taken to be coincident with the rotational axis of the sample (Plate 1), and the symmetry axes of the crystal are easily found from the symmetrical distributions of *N. E. D.*

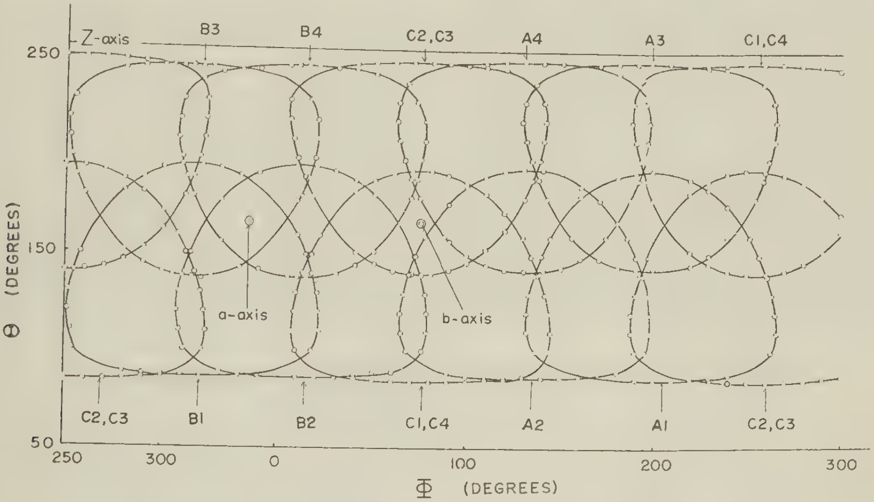

Fig. 1. Zerosplitting-direction patterns of Zeeman lines of $AsBr_3$. Θ, Φ are polar angle specifing zerosplitting-direction with respect to the orthogonal coordinate axes *XYZ* fixed to the sample. A1, A2, etc., represent the zerosplitting-directions of Zeeman lines at the nuclei Br_{A1}, Br_{A2}, etc., respectively. The closed contours which are labeled as C1, C4; and C2, C3 represent the mean directions of zerosplitting at the nuclei Br_{C1}, Br_{C4}; and Br_{C2}, Br_{C3} respectively.

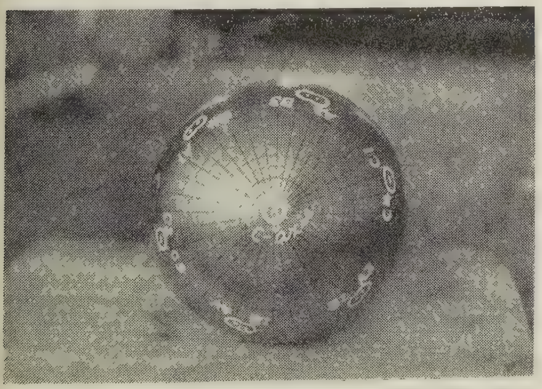

Plate 1. Plotting of directions of z-axes of field gradients on a globe. A1, A2, etc., represent the directions of the z-axes at the nuclei Br_{A1}, Br_{A2}, etc., respectively.

The magnitudes of polar angles (Θ, Φ) specifing the bond directions of As–Br_A, As–Br_B, and As–Br_C with respect to the crystal axes are (62°4′±13′, 56° 9′±8′), (64° 7′±15′, 61°46′±11′), and (61°54′±8′, 180°50′±20′), respectively. The bond angles between all *N. E. D.* are listed in Tabe I where the angle in parenthesis is supplementary angle of the other one. This duality of the choice of the bond angle is ascribed to the fact that the Zeeman analysis cannot distinguish between positive and negative directions of the z-axes of field gradient, therefore, we may assign either of two cases, i.e., α and $180°-\alpha$, to the bond angle.

Table I. The angles between all As–Br bonds in the crystal.

As–	Br$_{C1}$	Br$_{C2}$	Br$_{C3}$	Br$_{C4}$	Br$_{B1}$	Br$_{B2}$	Br$_{B3}$	Br$_{B4}$	Br$_{A1}$	Br$_{A2}$	Br$_{A3}$
Br$_{C2}$	123°55′ (56° 5′)										
Br$_{C3}$	56° 9′ (123°51′)	178°39′ (1°21′)									
Br$_{C4}$	178°37′ (1°23′)	56°15′ (123°45′)	123°39′ (56°21′)								
Br$_{B1}$	**100°46′** (79°14′)	55°13′ (124°47′)	126° 7′ (53°53′)	80°28′ (**99°32′**)							
Br$_{B2}$	55°44′ (124°16′)	**100°33′** (79°27′)	80°36′ (**99°24′**)	125°40′ (54°20′)	50°24′ (129°36′)						
Br$_{B3}$	127°16′ (52°44′)	80°21′ (**99°39′**)	**100°40′** (79°20′)	54° 3′ (125°57′)	51°52′ (128° 8′)	75°30′ (104°30′)					
Br$_{B4}$	81°40′ (**98°20′**)	125°46′ (54°14′)	55°32′ (124°28′)	**99°20′** (80°40′)	74°50′ (105°10′)	51°42′ (128°18′)	50°23′ (129°37′)				
Br$_{A1}$	**101°32′** (78°28′)	48°31′ (131°29′)	130°12′ (49°48′)	77°33′ (**102°27′**)	**99°49′** (80°11′)	126°19′ (53°41′)	124°42′ (55°18′)	174°19′ (5°41′)			
Br$_{A2}$	48° 8′ (131°52′)	**102°28′** (77°32′)	76°34′ (**103°26′**)	130°33′ (49°27′)	126°50′ (53°10′)	**100°19′** (79°41′)	175°24′ (4°36′)	125°30′ (54°30′)	59°16′ (120°44′)		
Br$_{A3}$	129°37′ (50°23′)	77°18′ (**102°42′**)	**101°37′** (78°23′)	49° 0′ (131° 0′)	125°25′ (54°35′)	174°34′ (5°26′)	**99°10′** (80°50′)	125°32′ (54°28′)	55°52′ (124° 8′)	85° 4′ (94°56′)	
Br$_{A4}$	77°12′ (**102°48′**)	130°35′ (49°25′)	48° 4′ (131°56′)	**101°39′** (78°21′)	174° 1′ (5°59′)	125° 9′ (54°51′)	124°57′ (55° 3′)	**99°15′** (80°45′)	86° 8′ (93°52′)	55°51′ (124° 9′)	58°41′ (121°19′)

α
(180°$-\alpha$)

Table II. Possible arrangements of As and Br atoms which satisfy Eqs. (1) and (3) of the previous paper*.

Nucleus	As^{75}		Br^{81}			
Number of resonance lines	1		3			
N	n_1	p_{ij}	n'_1	n'_2	n'_3	p'_{ij}
1	1	$p_{11}=1$	3	0	0	$p'_{11}=p'_{12}=p'_{13}=1$
2	impossible		2	1	0	$p'_{11}=2,\ p'_{12}=1,\ p'_{21}=3$
3	impossible		1	1	1	$p'_{11}=p'_{21}=p'_{31}=3$

* See reference 10.

The value of η obtained from the zero-splitting angles[9] for all directions is estimated 0.04 ± 0.02. The x-axis of field gradient tensor at the Br$_C$ nucleus has been found to lie in a plane containing both the z-axis and c-axis.

§ 4. Discussions

The number of resonance lines of As^{75} and Br^{81} is 1 and 3, respectively, hence the possible atomic arrangements are given in Table II from the pure quadrupole spectrum analysis[10][11], where n_i is the number of non-equivalent positions resonant atoms in a molecule belonging to the ith group, one of N sorts of groups of crystallographically non-

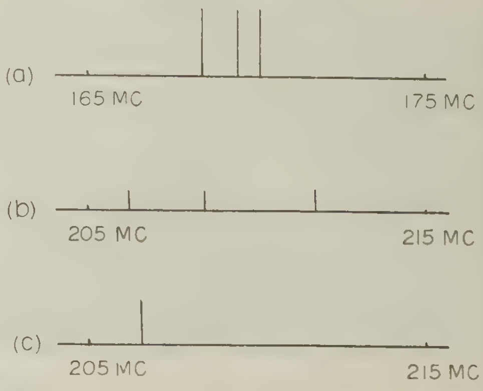

Fig. 2. Pure quadrupole spectra of Br^{81} and I^{127} of AsBr$_3$ and AsI$_3$.
(a) AsBr$_3$ (b) AsI$_3$ (at 383°K) (c) AsI$_3$ (at 300°K).

equivalent molecules in a unit-cell, and p_{ij} is the number of atoms belonging to the jth positions, i.e., one of the n_i nonequivalent ones, in that molecule.

Since the cases $N=2$ and $N=3$ are impossible for As^{75}, the possible case is $N=1$, $p_{11}(As)=1=p'_{11}(Br)=p'_{12}(Br)=p'_{13}(Br)$; each atom in $AsBr_3$ molecule has the same number of equivalent positions in a unit-cell, and the triplet line of Br^{81} are ascribed to the three bromine atoms in one molecule.

As Fig. 2 shows, the resonance spectrum for each bromine isotope is composed of three closely spaced lines and the spacing parameter⁹⁾ Δu^* for these lines is 2.7×10^{-3}, so the existence of predominantly interacting partner molecule is not very obvious in this case. In other words, we may safely conclude that the three bromine atoms in one molecule have nearly the same bond character.

While, through the Zeeman analysis we may assign the crystal to the orthorhombic symmetry class since four *N. E. D.*¹²⁾ are possible only in the orthorhombic, tetragonal or cubic symmetry class, and moreover, the fourfold symmetrical arrangements of *N. E. D.* do not exist in this case. This symmetry is consistent with that of the exterior of the crystal.

On the other hand, Kojima et al⁷⁾ have found that the pure quadrupole spectrum of of AsI_3 above 90°C has triplet lines and suggested that the crystal has the similar structure to that of $AsBr_3$ which shows a triplet spectrum, but taking the following facts into account we may deduce that their structures are somewhat different from each other: (1) their spectra have somewhat different features (Fig. 2); (2) in AsI_3 the value of η is of the order of 0.12, while that of $AsBr_3$ is smaller (0.04); (3) since the values for η and the resonance frequencies of iodine nuclei of high-temperature phase AsI_3 are almost equal to those of low-temperature one, the bond character of iodine atom may be almost the same in the two phases, so the resonance frequency of As atom, though it is not yet known, is perhaps equal to that observed in low-temperature phase (about 110 Mc⁸⁾),** whereas that of $AsBr_3$ is 62 Mc⁷⁾⁸⁾ and is appreciably different from that of AsI_3.

However, we must examine if such strong intermolecular covalent bonding as suggested by Kojima et al⁷⁾ in the case of AsI_3 in which the z-axis of field gradient at the iodine nucleus is perpendicular to the two As-I bond axes may be possible in our case. As Plate 1 shows, the z-axes of Br_A, Br_B, and Br_C nuclei are distributed about one of the crystal axis almost exactly with threefold symmetry character. Therefore, in order to interpret this fact in terms of the model in which, as Fig. 3 shows, the bromine atom is equally bonded to the two neighbouring As atoms, taking into consideration of similarity of bonding character of three bromine atoms in the molecule, we must have the three nonequivalent bromine atoms and nearest neighbouring three equivalent As atoms nearly at threefold symmetrical positions around the central As atom. However, since the

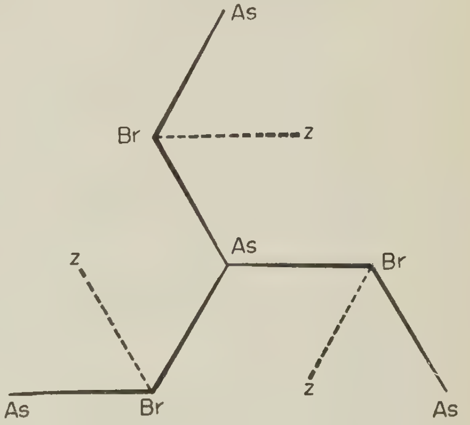

Fig. 3. The configuration of As and Br atoms which satisfies the distribution of the z-axes of field gradient which is shown in Plate 1 when the Br atom is assumed to be equally bonded to the two neighbouring As atoms.

---

* Δu for $SbBr_3$ and $AlBr_3$ are 2.20×10^{-2} and 4.34×10^{-2}, respectively. $AlBr_3$** has been known to consist of dimeric molecules. $SbBr_3$ at 77°K may have some predominantly interacting partner molecule. Distinct, moderate, and indistinct existence of such partner molecule can be infered from the values of Δu of the order of 10^{-2}, 10^{-3} and 10^{-4}, respectively in AB_n type molecule, where A and B denote the nonresonant and resonant atoms, respectively.

** See reference 2.

** Note added in proof: Recently S. Ogawa observed the As quadrupole spectrum at about 32 Mc at room temperature.

crystal has the orthorhombic symmetry, we cannot expect the threefold symmetrical configuration of equivalent points about an axis which is nearly parallel to one of the crystal axis, therefore, the bonding which is found in the case of AsI_3 does not exist in this case.

On the other hand, the possibility of deviation of the direction of z-axis of field gradient from the bond axis due to moderate intermolecular covalent bonding[13] such as in I_2 is practically neglected, because in such case the value of η is expected to be large (in I_2 the deviation angle[14] is about 30′ and $\eta=0.16$).

From these considerations we may safely assume that the direction of the z-axis of field gradient is coincident with the bond axis as is the case with common substances in which the nuclear quadrupole spectra have been observed. Since the free molecule of $AsBr_3$ has been found to consist of an trigonal pyramid, one may expect that this molecule has the similar form in the solid state also. Therefore, if we take account of the fact that the bond angle of the gaseous molecule is about 100°, it may be concluded that Br_{A1}, Br_{B1}; Br_{A2}, Br_{B2}; etc., belong to each molecule, in which $\angle Br_A\text{–}As\text{–}Br_B$ are equal to 99°38′±16′, since, as has been shown in the above discussion, the three bromine atoms forming the molecule must be made up of three atoms, each of which is picked up from the Br_A, Br_B and Br_C groups in Table I, respectively.

Unfortunately, in this case it is difficult for us to determine which group of $Br_{A1}Br_{B1}$ and $Br_{A4}Br_{B4}$ should contain the Br_{C1} atom on the basis of the criterion of similarity of molecular structure in both states of solid and gas, since Br_{C1}–As makes nearly equal angles 101°32′ and 102°48′ with As–Br_{A1} and As–Br_{A4}, respectively (it will be shown in § 5 that Br_{A1}, Br_{B1}, Br_{C4}; Br_{A2}, Br_{B2}, Br_{C3}; etc., construct their own molecules). But in any case the applicable bond angles ∠Br–As–Br, which are shown in Gothic type in Table I, are nearly equal to that of the gaseous molecule, and the above-mentioned threefold symmetrical arrangement of z-axes of the field gradient is shown to be due to this pyramidal molecule. But these bond angles are larger than the value 87° or 93° which was suggested by Kojima et al.[7]

The slight asymmetry of the trigonal pyramid indicates the existence of intermolecular interaction, but the facts that the bond angles in the solid state are nearly equal to that of the gaseous molecule and that the value of η is small suggest that the intermolecular interaction is weak.

If we assume that the origin of η is due to the double bond character of As–Br bond, the fractional importance of ionic, single, and double bond character; β, $1-\beta-\gamma$, and γ, respectively, can be obtained from the following equations[15]:

$$U_p=(1-\beta-\gamma)(1-\alpha)+\left(\frac{1}{2}-\alpha\right)(1+\mathcal{E})\gamma$$

$$\eta=\frac{3\gamma(1+\mathcal{E})}{2U_p}\,, \qquad (1)$$

where α is the amount of s-hybridization[16] of the p_σ-bond, $\mathcal{E}$ is a correction[16] for the change in screening caused by the charge and U_p is the number of unbalanced p-electron[17] of the resonant atom (which is obtained from the observed resonance frequency, the value of η, and the atomic beam measurement). Introducing the value $\alpha=0.15$[16], $\mathcal{E}=0.15$[16], $\eta=0.04$, and $U_p=405.4/769.6=0.527$, one obtains 61.4%, 1.2% and 37.4% for the amount of single, double, and ionic bond character, respectively. Therefore we may conclude that the most predominant resonant structure is written as

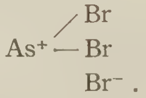

Introducing the single and double covalent radii for Br and As with Schomaker-Stevenson correction for ionic character into Pauling's formula[17], one obtains 2.30 A for As–Br bond distance.

§ 5. Comparison with the Results of X-ray Analysis

Comparing the values of (Θ, Φ) specifing the directions of As–Br′, As–Br″, and As–Br‴ obtained from the X-ray analysis (Fig. 4) with those for As–Br_A, As–Br_B, and As–Br_C which have been studied by the Zeeman analysis, we may conclude that Br_A, Br_B, and Br_C, correspond to Br′, Br″, and Br‴, respectively (Table III), and the bond angles which are obtained from the Zeeman and

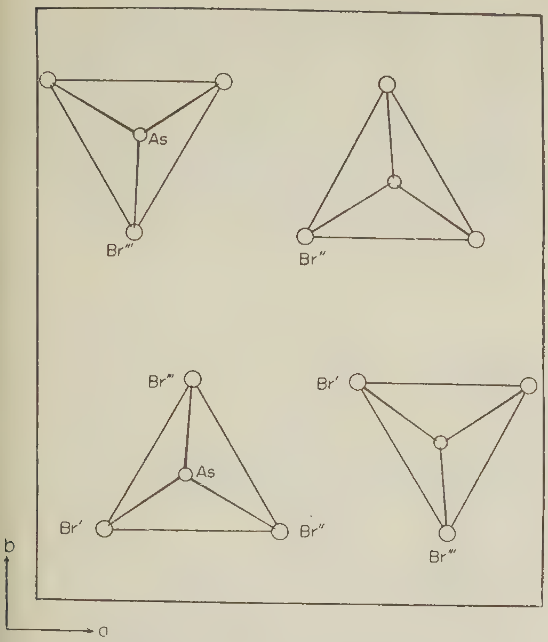

Fig. 4. The arrangement of AsBr$_3$ molecules (after Braekken[1]).

X-ray analyses are listed in Table IV. The directions of As–Br bonds with respect to the crystal axes which have been studied in this experiment are shown in Fig. 5. The bond angles obtained from Braekken's data are smaller than our values by about 1°. This discrepancy exceeds our experimental errors. However, except the slight disagreement of the bond angles, all other data including the bond distances and the directions of the principal axes of field gradient at the bromine nucleus seem to be nearly consistent with the results of the X-ray analysis. So we may conclude that the crystal analysis by Braekken is considerably exact.

In our case, we found that the c-axis of the crystal was almost coincident with the rotation axis of the sample (Plate 1), that is, with the axis of the glass container of the sample. This means that the crystal grows up most easily along the direction of the c-axis.

Acknowledgements

The author wishes to express his sincere thanks to Professor R. Kiriyama of Ōsaka University for his helpful discussions. A part of this work was supported by the Scientific Research Expenditure of the Ministry of Education.

Table III. The orientation of As–Br bond with respect to the crystal axes.

Zeeman analysis	As–Br$_A$	As–Br$_B$	As–Br$_C$
(θ, ϕ)	(62° 4′±13′, 56° 9′±8′)	(64° 7′±15′, −61°46′±11′)	(61°54′±8′, 180°50′±20′)
X-ray analysis	As–Br′	As–Br″	As–Br‴
(θ, ϕ)	(60°52′, 56°48′)	(63°25′, −59° 1′)	(60° 0′, 182° 5′)

Table IV. The Br–As–Br bond angles which were obtained from the Zeeman and X-ray analyses.

Zeeman analysis	∠Br$_A$–As–Br$_B$	∠Br$_B$–As–Br$_C$	∠Br$_C$–As–Br$_A$
Bond angle	99°38′±16′	99°14′±18′	102°51′±13′
X-ray analysis	∠Br′–As–Br″	∠Br″–As–Br‴	∠Br‴–As–Br′
Bond angle	97°0′	98°41′	101°11′

Appendix

Resolving Power in the Zeeman Analysis

When two *N. E. D.* make small angle with each other, their zerosplitting cones also come so close together that we cannot identify these directions using a weak magnetic field.

Now for simplicity, let us consider the case of an axially symmetric electric field. When one of the z-axes of field gradients satisfies the zerosplitting condition, the resonance frequencies of Zeeman lines corresponding to the other nonequivalent direction ν_{I}, ν_{II}, ν_{III} and

ν_{IV} between the levels $m=\pm 3/2$ and $m'=\pm 1/2$ are given in the following formulas[10]:

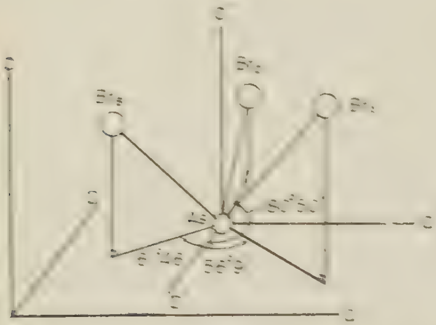

Fig. 5. The orientation of $AsBr_3$ molecule with respect to the crystal axes which has been studied through the Zeeman analysis. $As\text{-}Br_A$, $As\text{-}Br_B$, $As\text{-}Br_C$ orient at the angles 62°4', 64°7', 61°54', respectively, to the c-axis.

$$\nu_{I,II}=\nu_Q\pm\frac{3}{2}\frac{\mu_I H}{Ih}\cos\theta \pm\frac{1}{2}\frac{\mu_I H}{Ih}\sqrt{\left(I+\frac{1}{2}\right)^2\sin^2\theta+\cos^2\theta}$$

$$\nu_{III,IV}=\nu_Q\pm\frac{3}{2}\frac{\mu_I H}{Ih}\cos\theta \mp\frac{\mu_I H}{2Ih}\sqrt{\left(I+\frac{1}{2}\right)^2\sin^2\theta+\cos^2\theta} \tag{2}$$

where ν_Q is the resonance frequency in the absence of external magnetic field, μ_I and I are the magnetic moment and spin of the resonant nucleus, respectively, h is Planck's constant, and θ is the angle between the z-axis of field gradient and the external magnetic field H.

Since the resonance line has finite half maximum width $\Delta\nu$, the frequency difference between the inner component of Zeeman lines and zerosplitting one must be larger than $\Delta\nu$ in order to clearly locate the zerosplitting line. Consequently, the resolving power $\Delta\theta$ for Br^{81} can be defined as the difference between the zerosplitting angle 54°44' and θ which satisfies the following equations:

$$\left.\begin{aligned}\Delta\nu&=\frac{\xi H}{2}\left(3\cos\theta-\sqrt{4-3\cos^2\theta}\right)\\ \xi&=\frac{2\mu_I}{3h}\end{aligned}\right\} \tag{3}$$

The minimum value of magnetic field required in order to locate the two $N.E.D.$ of Br^{81} which make the angle $\Delta\theta$ with each other is given in Fig. 6. Eqs. (3) can also be applied to the study of zerosplitting near the overlapping area of nonequivalent zerosplitting cones. The above estimation has been found to be valid in our case through the study of zerosplitting in such region which is most convenient for testing the relation.

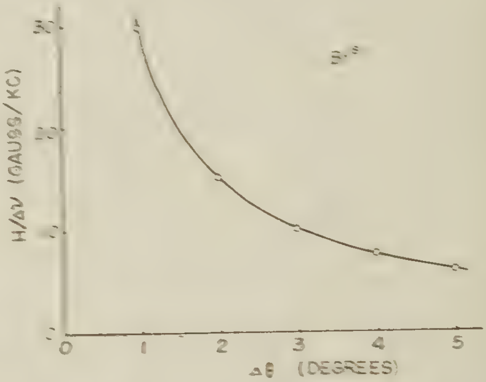

Fig. 6. The relation between resolving power $\Delta\theta$ and magnetic field which is required to discriminate two $N.E.D$.

Of course, we may locate the zerosplitting direction exactly in the area in which the zerosplitting cone situates far from the other one, since the orientation of maximum intensity of zerosplitting line can be observed without the disturbance of Zeeman lines corresponding to the other $N.E.D$.

References

1) H. Braekken: Kong. Norsk. Vidensk. Selsk. Forhand. **8** (1935) 1.
2) R. W. G. Wyckoff: ***Crystal Structure***, Interscience Publishers, Inc. New York (1948).
3) Strukturbericht: Akademische Verlagsgesellschaft, Leipzig, 1913–1939.
4) Gregg, Hampson, Jenkins, Jones and Sutton: Trans. Faraday Soc. **33** (1937) 852, 868.
5) O. Hassel and A. Sandbo: Z. Phys. Chem. B **41** (1938) 75.
6) M. W. Lister and L. E. Sutton: Trans. Faraday Soc. **37** (1941) 393, 406.
7) Kojima, Tsukada, Ogawa, Shimauchi and Abe: J. Phys. Soc. Japan **9** (1954) 805.
8) R. G. Barnes and P. J. Bray: J. Chem. Phys **23** (1955) 407, 1178.
9) K. Shimomura: J. Phys. Soc. Japan **12** (1957) 657.
10) K. Shimomura: J. Chem. Phys **25** (1956) 1298
11) K. Shimomura: to be published.

12) K. Shimomura: J. Phys. Soc. Japan **12** (1957) 652.
13) C. H. Townes and B. P. Dailey: J. Chem. Phys. **20** (1952) 35.
14) K. Tsukada: J. Phys. Soc. Japan **11** (1956) 956.
15) Kojima, Tsukada and Hinaga: J. Phys. Soc. Japan **10** (1955) 498.; S. Sekino and T. Nishikawa: J. Phys. Soc. Japan **12** (1957) 43.
16) C. H. Townes and A. L. Schawlow: *Microwave Spectroscopy*, McGraw-Hill Book Co., New York (1955) Chap. 9.
17) Gordy, Smith and Trambarulo: *Microwave Spectroscopy*, John Wiley and Sons, Inc., New York, (1953) pp. 313, 310.
18) H. Krüger and U. Meyer-Berkhout: Z. Phys. **132** (1952) 221.

JOURNAL OF THE PHYSICAL SOCIETY OF JAPAN Vol. 12, No. 12, DECEMBER, 1957

On the Viscoelasticity and Complex Dielectric Constant in the Presence of an Electric Field and a Shearing Laminar Flow in Solution of Macromolecules

By Nobuhiko SAITÔ and Tomokazu KATO

Department of Applied Physics, Waseda University, Tokyo

(Received September 6, 1957)

The effect of an electric field on the intrinsic viscoelasticity and the effect of shearing laminar flow on the dielectric properties of dilute solutions are calculated, based on the model of a spheroidal macromolecule with dipole moment along its symmetry axis. It is shown that the intrinsic viscosity increases proportionally to the square of the applied electric field and the dielectric constant increases proportionally to the square of the velocity gradient. Simple thermodynamical considerations are given.

§ 1. Introduction

In recent years some attentions have been directed to the cross phenomena in solution of macromolecules. Of course, the most familiar cross phenomenon may be flow birefringence or Maxwell effect. Usually no birefringence can be observed without laminar flow, however, the phenomenon is rather simple because the light or the electromagnetic field can be considered not to interact with the movement of particles in the flow field. We may cite as similar instances the effect of an electric field[1] or a streaming flow[2] on the light scattering. In this paper we discuss the cross phenomena between electric field and streaming laminar flow in solution of polar macromolecules, i.e., the effect of the electric field on the intrinsic viscosity and the effect of the velocity gradient of flow on the dielectric properties of solution of polar molecules. From the outset we can surmise that each field of the two can never interact in the first order of another field from the Curie's law[3] on cross phenomena, because the electric field is of vector (first order tensor) character, while the velocity gradient is of the second order tensor character. We can, however, expect that the interactions are to be found in the second order of the strengths of the fields. In effect, Andrade et al[4],[5],[6] showed that the viscosity of liquids of polar molecules increases proportionally to the square of the applied electric field.

Onsager[7] demonstrated the so-called reciprocal relations between the coefficients of first order interaction, but we have nothing general between the coefficients of the second order interaction. We tried to find in vain any simple relation between these coefficients of the second order interaction.

On almost finishing this study, we are informed by Dr. E. Wada of Scientific Research Institute that a similar investigation was carried out by Peterlin[8]. His model is very similar to ours, but the detailed calculation is limited to the intrinsic viscosity of dumbbell molecules in two-dimensional case and nothing is said about the cross phenomenon of irreversible processes.

§ 2. Model and Applied External Forces

It may be most natural to adopt as a model of macromolecules the necklace of pearls connected by bonds of definite length or by Hookian springs. The former was adopted by Kirkwood[9] and his theory is considered to be the most rigorous statistical mechanical theory of irreversible process in solutions of macromolecules. However, the detailed calculations are very tedious and no definite conclusions can be drawn without rather drastic simplifications. The latter, Hookian spring model, proposed first by Rouse[10], was extended with success by Nakada[11] and Zimm[12] to the discussions of the mechanical and electrical relaxation phenomena in solutions or amorphous solids. This model may be seen as the most tractable and preferable, however, as Zimm pointed out, the nonlinearity can not be obtained in simple treatment. For this reason, we take up a spheroidal model of macromolecules, the intrinsic viscosity of which was treated by one of the authors[13] several years ago. Thus our model of polar macromolecules is a spheroidal rigid particle with principal axes of length $2a_1$, $2a_2=2a_1$ and $2a_3$, and has a permament dipole moment μ along the symmetry axis a_3. Let (x, y, z) and (ξ, η, ζ) be rectangular coordinate systems referred to the axes fixed in space and in the particle, respectively, with common origin taken at the center of the particle. The two coordinate systems are connected by an orthogonal transformation matrix A whose components are expressed in terms of the Eulerian angles (θ, ϕ, ψ) as follows

$$A=(a_{ij})=\begin{pmatrix} \cos\phi\cos\theta\cos\psi-\sin\phi\sin\psi & -\cos\phi\cos\theta\sin\psi-\sin\phi\cos\psi & \cos\phi\sin\theta \\ \sin\phi\cos\theta\cos\psi+\cos\phi\sin\psi & -\sin\phi\cos\theta\sin\psi+\cos\phi\cos\psi & \sin\phi\sin\theta \\ -\sin\theta\cos\psi & \sin\theta\sin\psi & \cos\theta \end{pmatrix} \tag{2.1}$$

Then we have

$$\boldsymbol{r}=A\boldsymbol{s} \quad \text{or} \quad \boldsymbol{s}=A^{-1}\boldsymbol{r}. \tag{2.2}$$

where

$$\boldsymbol{r}=\begin{pmatrix} x \\ y \\ z \end{pmatrix} \quad \text{and} \quad \boldsymbol{s}=\begin{pmatrix} \xi \\ \eta \\ \zeta \end{pmatrix}.$$

The solution of macromolecules under consideration is assumed to be so dilute that particles suspended in it behave independently, i.e., dipolar, hydrodynamical and other interactions among particles are neglected. The solution is assumed to be exerted simultaneously by a shearing force and an electric field. The former makes the fluid in motion in the direction of positive y-axis with velocity gradient g along x-axis, and the latter is applied in the direction parallel to x-axis. Then the original velocity of flow $\boldsymbol{v}^0$ in the absence of particles and the intensity of the electric field $\boldsymbol{E}$ are given in (x, y, z)-system, respectively, as follows

$$\boldsymbol{v}^0=G\boldsymbol{r}, \quad G=\begin{pmatrix} 0 & 0 & 0 \\ g & 0 & 0 \\ 0 & 0 & 0 \end{pmatrix}, \tag{2.3}$$

$$\boldsymbol{E}=(E,\ 0,\ 0), \tag{2.4}$$

while in (ξ, η, ζ)-system they are given by

$$\boldsymbol{u}^0=(A^{-1}GA)\boldsymbol{s}, \tag{2.3'}$$

$$\boldsymbol{E}=(a_{11}E,\ a_{12}E,\ a_{13}E). \tag{2.4'}$$

The shearing rate in (2.3′) is divided into symmetric or pure shearing-rate part and antisymmetic or rotational part, which are denoted by $H=(h_{ij})$ and $O=(o_{ij})$, respectively,

$$\boldsymbol{u}^0=H\boldsymbol{s}+O\boldsymbol{s},$$

$$\left.\begin{aligned} H=(h_{ij})&=\frac{1}{2}(A^{-1}GA)+\frac{1}{2}(A^{-1}GA)', \\ O=(o_{ij})&=\frac{1}{2}(A^{-1}GA)-\frac{1}{2}(A^{-1}GA)', \end{aligned}\right\} \tag{2.5}$$

where the primed matrices are transposed ones.

The equation of motion for the rotatory motion of particles under these fields is

$$\frac{d\boldsymbol{M}}{dt}=\boldsymbol{L}+\boldsymbol{\mu}\times\boldsymbol{E}, \tag{2.6}$$

where $\boldsymbol{M}$ is the angular momentum of the particle and the two terms of the right-hand side $\boldsymbol{L}$ and $\boldsymbol{\mu}\times\boldsymbol{E}$ are respectively the moments of forces exerted by the flowing fluid and by the electric field upon the particle.

The components of $\boldsymbol{L}$ are given in (ξ, η, ζ)-system by Jeffery,[14]

$$\begin{aligned}
L_\xi &= c_1\{-ph_{23}+(o_{32}-\omega_\xi)\}\,, \\
L_\eta &= c_1\{ph_{13}+(o_{13}-\omega_\eta)\}\,, \\
L_\zeta &= c_3(o_{21}-\omega_\zeta)\,, \\
c_1 &= \frac{16\pi\eta(a_1^2+a_3^2)}{3(a_1^2\alpha_0+a_3^2\gamma_0)}\,, \\
c_3 &= \frac{16\pi\eta}{3\alpha_0}\,, \\
p &= \frac{a_3^2-a_1^2}{a_3^2+a_1^2}\,,
\end{aligned} \tag{2.7}$$

where c_1 and c_3 are the friction constants of rotatory motion of an ellipsoid about its principal axes and η is the coefficient of viscosity of the solvent. α_0 and γ_0 are the constants whose numerical values can be evaluated when a_1 and a_3 are given. Generally, we must add a fluctuation force due to thermal agitation of the liquid, but we disregard it here because we can take this effect into consideration through diffusion equation. Ignoring the inertia effect, we put (2.6) equal to zero, then we can immediately determine the angular velocity of particle, substituting (2.7) into (2.6), with the result

$$\begin{aligned}
\omega_\xi &= o_{32}-ph_{32}+\frac{\mu E}{c_1}a_{12}\,, \\
\omega_\eta &= o_{13}+ph_{13}+\frac{\mu E}{c_1}a_{11}\,, \\
\omega_\zeta &= o_{21}\,,
\end{aligned}$$

or

$$\begin{aligned}
\dot\theta &= \frac{pg}{2}\sin 2\phi\sin\theta\cos\theta+\frac{\mu E}{c_1}\cos\phi\cos\theta\,, \\
\dot\phi &= \frac{pg}{2}\cos 2\phi+\frac{g}{2}-\frac{\mu E}{c_1}\frac{\sin\phi}{\sin\theta}\,, \\
\dot\psi &= -\frac{pg}{2}\cos\theta\cos 2\phi+\frac{\mu E}{c_1}\frac{\cos\theta\sin\phi}{\sin\theta}\,.
\end{aligned} \tag{2.8}$$

§ 3. Diffusion Equation

The diffusion equation which determines the time evolution of distribution function of the orientation of the particles under the external forces can be written down at once following the general theory of Brownian motion[9], as follows

$$\frac{\partial\rho}{\partial t} = -\frac{D}{\sin\theta}\left\{\frac{\partial}{\partial\theta}(j_\theta\rho\sin\theta)+\frac{\partial}{\partial\phi}(j_\phi\rho\sin\theta)\right\}, \tag{3.1}$$

$$\begin{aligned}
j_\theta &= \dot\theta - D\frac{\partial}{\partial\theta}\log\rho\,, \\
j_\phi &= \dot\phi - \frac{D}{\sin^2\theta}\frac{\partial}{\partial\phi}\log\rho\,, \\
j_\psi &= \dot\psi + \frac{D\cos\theta}{\sin^2\theta}\frac{\partial}{\partial\phi}\log\rho\,,
\end{aligned} \tag{3.2}$$

where $D=kT/c_1$ is rotatory diffusion constant. The flux j_ψ vanishes in (3.1) since our model is symmetric about its third axis.

Suppose that the external driving forces vary sinusoidally with time,

$$g=g_0\cos\omega_g t\,, \quad E=E_0\cos\omega_e t\,, \tag{3.3}$$

and the influences of these forces upon the orientation of molecules are small enough to be considered as the perturbations upon the equilibrium distribution $1/4\pi$. Hence we expand the solution of (3.1) in powers of $(\mu E_0/kT)$ and $(g_0c_1/2kT)$,

$$\begin{aligned}
\rho &= \frac{1}{4\pi}\left[1+\sum_{i,j,l,m}\left(\frac{\mu E_0}{kT}\right)^i\left(\frac{g_0c_1}{2kT}\right)^j {}_{ij}f_l^{(m)}(t)P_l^{(m)}(\cos\theta)\begin{matrix}\cos m\phi\\ \sin m\phi\end{matrix}\right] \\
&= \frac{1}{4\pi}\Big[1+\left(\frac{\mu E_0}{kT}\right)_{10}f_1^{(1)}(t)P_1^{(1)}(\cos\theta)\cos\phi+\left(\frac{g_0c_1}{2kT}\right)_{01}f_2^{(2)}(t)\,P_2^{(2)}\sin 2\phi \\
&\quad +\left(\frac{\mu E_0}{kT}\right)^2\{{}_{20}f_2^{(2)}(t)P_2^{(2)}(\cos\theta)\cos 2\phi+{}_{20}f_2^{(0)}(t)P_2(\cos\theta)\} \\
&\quad +\left(\frac{g_0c_1}{2kT}\right)^2\{{}_{02}f_2^{(0)}(t)P_2(\cos\theta)+{}_{02}f_4^{(0)}(t)P_4(\cos\theta)+{}_{02}f_2^{(2)}(t)P_2^{(2)}(\cos\theta)\cos 2\phi \\
&\quad +{}_{02}f_4^{(4)}(t)P_4^{(4)}(\cos\theta)\cos 4\phi)\} \\
&\quad +\left(\frac{\mu E_0}{kT}\right)\left(\frac{g_0c_1}{2kT}\right)\{{}_{11}f_1^{(1)}(t)P_1^{(1)}(\cos\theta)\sin\phi+{}_{11}f_3^{(1)}(t)P_3^{(1)}(\cos\theta)\sin\phi \\
&\quad +{}_{11}f_3^{(3)}(t)P_3^{(3)}(\cos\theta)\sin 3\phi\}+\cdots\Big]\,,
\end{aligned} \tag{3.4}$$

where $P_l^{(m)}(\cos\theta)$ denotes Legendre's associated function. The coefficients ${}_{ij}f_l^{(m)}(t)$'s are given as the real part of the following formulae,

$$ {}_{10}f_1^{(1)};\quad \frac{\exp(i\omega_e t)}{1+i\omega_e/2D} \qquad\qquad {}_{01}f_2^{(2)};\quad \frac{p}{6}\,\frac{\exp(i\omega_g t)}{1+i\omega_g/6D} $$

$$ {}_{20}f_2^{(0)};\quad -\left[\frac{1}{6}+\frac{\exp(2i\omega_e t)}{12\left(1+\dfrac{i\omega_e}{3D}\right)\left(1+\dfrac{i\omega_e}{D}\right)}\right] $$

$$ {}_{20}f_2^{(2)};\quad \left[\frac{1}{12}+\frac{\exp(2i\omega_e t)}{24\left(1+\dfrac{i\omega_e}{3D}\right)\left(1+\dfrac{i\omega_e}{D}\right)}\right] $$

$$ {}_{02}f_2^{(0)};\quad -p^2\left[\frac{1}{21}+\frac{\exp(2i\omega_g t)}{42\left(1+\dfrac{i\omega_g}{3D}\right)^2}\right] $$

$$ {}_{02}f_4^{(0)};\quad p^2\left[\frac{1}{70}+\frac{\exp(2i\omega_g t)}{140\left(1+\dfrac{i\omega_g}{3D}\right)\left(1+\dfrac{i\omega_g}{10D}\right)}\right] $$

$$ {}_{02}f_2^{(2)};\quad -p\left[\frac{1}{36}+\frac{\exp(2i\omega_g t)}{\left(1+\dfrac{i\omega_g}{3D}\right)^2}\right] $$

$$ {}_{02}f_4^{(4)};\quad -p^2\left[\frac{1}{1680}+\frac{\exp(2i\omega_g t)}{3360\left(1+\dfrac{i\omega_g}{3D}\right)\left(1+\dfrac{i\omega_g}{10D}\right)}\right] $$

$$ \begin{aligned} {}_{11}f_1^{(1)};\quad & \frac{p}{20}\left[\frac{\exp\{i(\omega_g+\omega_e)t\}}{\left\{1+\dfrac{i(\omega_g+\omega_e)}{2D}\right\}\left\{1+\dfrac{i(\omega_g+\omega_e)}{6D}\right\}}+\frac{\exp\{i(\omega_g-\omega_e)t\}}{\left\{1+\dfrac{i(\omega_g-\omega_e)}{2D}\right\}\left\{1+\dfrac{i(\omega_g-\omega_e)}{6D}\right\}}\right] \\ & +\frac{3p}{20}\left[\frac{\exp\{i(\omega_g+\omega_e)t\}}{\left\{1+\dfrac{i(\omega_g+\omega_e)}{2D}\right\}^2}+\frac{\exp\{i(\omega_g-\omega_c)\,t\}}{\left\{1+\dfrac{i(\omega_g-\omega_e)}{2D}\right\}}\right] \end{aligned} $$

$$ \begin{aligned} {}_{11}f_3^{(1)};\quad & \frac{p}{360}\left[\frac{\exp\{i(\omega_g+\omega_e)t\}}{\left\{1+\dfrac{i(\omega_g+\omega_e)}{6D}\right\}\left\{1+\dfrac{i(\omega_g+\omega_e)}{12D}\right\}}+\frac{\exp\{i(\omega_g-\omega_e)t\}}{\left\{1+\dfrac{i(\omega_g-\omega_e)}{6D}\right\}\left\{1+\dfrac{i(\omega_g-\omega_e)}{2D}\right\}}\right] \\ & -\frac{p}{90}\left[\frac{\exp\{i(\omega_g+\omega_e)t\}}{\left\{1+\dfrac{i(\omega_g+\omega_e)}{12D}\right\}\left\{1+\dfrac{i(\omega_g+\omega_e)}{2D}\right\}}+\frac{\exp\{i(\omega_g-\omega_e)t\}}{\left\{1+\dfrac{i(\omega_g-\omega_e)}{12D}\right\}\left\{1+\dfrac{i(\omega_g-\omega_e)}{2D}\right\}}\right] \end{aligned} $$

$$ \begin{aligned} {}_{11}f_3^{(3)};\quad & \frac{p}{360}\left[\frac{\exp\{i(\omega_g+\omega_e)t\}}{\left\{1+\dfrac{i(\omega_g+\omega_e)}{12D}\right\}\left\{1+\dfrac{i(\omega_g+\omega_e)}{6D}\right\}}+\frac{\exp\{i(\omega_g-\omega_e)t\}}{\left\{1+\dfrac{i(\omega_g-\omega_e)}{12D}\right\}\left\{1+\dfrac{i(\omega_g-\omega_e)}{6D}\right\}}\right] \\ & +\frac{p}{180}\left[\frac{\exp\{i(\omega_g+\omega_e)t\}}{\left\{1+\dfrac{i(\omega_g+\omega_e)}{2D}\right\}\left\{1+\dfrac{i(\omega_g+\omega_e)}{12D}\right\}}+\frac{\exp\{i(\omega_g-\omega_e)t\}}{\left\{1+\dfrac{i(\omega_g-\omega_e)}{2D}\right\}\left\{1+\dfrac{i(\omega_g-\omega_e)}{12D}\right\}}\right] \end{aligned} $$

$$ {}_{30}f_1^{(1)};\quad \frac{p}{240}\left[\frac{6\exp(i\omega_e t)}{1+\dfrac{i\omega_e}{2D}}+\frac{\exp(3i\omega_e t)}{\left(1+\dfrac{i\omega_e}{D}\right)\left(1+\dfrac{3i\omega_e}{D}\right)\left(1+\dfrac{3i\omega_e}{2D}\right)}\right] $$

$$ {}_{12}f_1^{(1)};\quad \frac{137p^2}{1760}\left[\frac{\exp\{i(\omega_e+2\omega_g)t\}}{\left\{1+\dfrac{i(\omega_e+2\omega_g)}{12D}\right\}\left\{1+\dfrac{i(\omega_e+2\omega_g)}{2D}\right\}\left\{1+\dfrac{i(\omega_e+2\omega_g)}{6D}\right\}}\right. $$

$$+\frac{\exp\{i(\omega_e-2\omega_g)t\}}{\left\{1+\frac{i(\omega_e-2\omega_g)}{12D}\right\}\left\{1+\frac{i(\omega_e-2\omega_g)}{2D}\right\}\left\{1+\frac{i(\omega_e-2\omega_g)}{6D}\right\}}$$

$$\left.+\frac{2\exp(i\omega_e t)}{\left(1+\frac{i\omega_e}{12D}\right)\left(1+\frac{i\omega_e}{2D}\right)\left(1+\frac{i\omega_e}{6D}\right)}\right]+\frac{11p^2}{527}\left[\frac{\exp\{i(\omega_e+2\omega_g)t\}}{\left\{1+\frac{i(\omega_e+2\omega_g)}{2D}\right\}^2\left\{1+\frac{i(\omega_g+2\omega_g)}{12D}\right\}}\right.$$

$$\left.+\frac{\exp\{i(\omega_e-2\omega_g)t\}}{\left\{1+\frac{i(\omega_e-2\omega_g)}{2D}\right\}^2\left\{1+\frac{i(\omega_e-2\omega_g)}{12D}\right\}}+\frac{2\exp(i\omega_e t)}{\left(1+\frac{i\omega_e}{2D}\right)^2\left(1+\frac{i\omega_e}{12D}\right)}\right]$$

$$-\frac{p^2}{120}\left(\frac{1}{7}+\frac{1}{p}\right)\left[\frac{\exp\{i(\omega_e+2\omega_g)t\}}{\left\{1+\frac{i(\omega_e+2\omega_g)}{6D}\right\}^2\left\{1+\frac{i(\omega_e+2\omega_g)}{2D}\right\}}\right.$$

$$\left.+\frac{\exp\{i(\omega_e-2\omega_g)t\}}{\left\{1+\frac{i(\omega_e-2\omega_g)}{6D}\right\}^2\left\{1+\frac{i(\omega_e-2\omega_g)}{2D}\right\}}+\frac{2\exp(i\omega_e t)}{\left(1+\frac{i\omega_e}{6D}\right)^2\left(1+\frac{i\omega_e}{2D}\right)}\right]$$

$$+\left(\frac{3}{200}p^2+\frac{3}{160}p-\frac{1}{96}\right)\left[\frac{\exp\{i(\omega_e+2\omega_g)t\}}{\left\{1+\frac{i(\omega_e+2\omega_g)}{2D}\right\}^2\left\{1+\frac{i(\omega_e+2\omega_g)}{6D}\right\}}\right.$$

$$\left.+\frac{\exp\{i(\omega_e-2\omega_g)t\}}{\left\{1+\frac{i(\omega_e-2\omega_g)}{2D}\right\}^2\left\{1+\frac{i(\omega_e-2\omega_g)}{6D}\right\}}+\frac{2\exp(i\omega_e t)}{\left(1+\frac{i\omega_e}{2D}\right)^2\left(1+\frac{i\omega_e}{6D}\right)}\right]$$

$$+\left(\frac{9}{200}p^2+\frac{9}{160}p-\frac{1}{32}\right)\left[\frac{\exp\{i(\omega_e+2\omega_g)t\}}{\left\{1+\frac{i(\omega_e+2\omega_g)}{2D}\right\}^3}+\frac{\exp\{i(\omega_e-2\omega_g)t\}}{\left\{1+\frac{i(\omega_e-2\omega_g)}{2D}\right\}^3}\right.$$

$$\left.+\frac{2\exp(i\omega_e t)}{\left(1+\frac{i\omega_e}{2D}\right)^3}\right]$$

$${}_{21}f_2^{(2)};\quad\left(\frac{31}{4032}p-\frac{1}{576}\right)\left[\frac{2\exp(i\omega_g t)}{\left(1+\frac{i\omega_g}{6D}\right)^2\left(1+\frac{i\omega_g}{2D}\right)}+\frac{\exp\{i(2\omega_e-\omega_g)t\}}{\left\{1+\frac{i(2\omega_e-\omega_g)}{6D}\right\}^2\left\{1+\frac{i(2\omega_e-\omega_g)}{2D}\right\}}\right.$$

$$\left.+\frac{\exp\{i(2\omega_e+\omega_g)t\}}{\left\{1+\frac{i(2\omega_e+\omega_g)}{6D}\right\}^2\left\{1+\frac{i(2\omega_e+\omega_g)}{2D}\right\}}\right]+\frac{1}{640}\left(p+\frac{5}{3}\right)\left[\frac{2\exp(i\omega_g t)}{\left(1+\frac{i\omega_g}{6D}\right)\left(1+\frac{i\omega_g}{2D}\right)^2}\right.$$

$$\left.+\frac{\exp\{i(2\omega_e+\omega_g)t\}}{\left\{1+\frac{i(2\omega_e+\omega_g)}{6D}\right\}\left\{1+\frac{i(2\omega_e+\omega_g)}{2D}\right\}^2}+\frac{\exp\{i(2\omega_e-\omega_g)t\}}{\left\{1+\frac{i(2\omega_e-\omega_g)}{6D}\right\}\left\{1+\frac{i(2\omega_e-\omega_g)}{2D}\right\}^2}\right]$$

$$-\frac{11p}{30240}\left[\frac{2\exp(i\omega_g t)}{\left(1+\frac{i\omega_g}{6D}\right)^2\left(1+\frac{i\omega_g}{12D}\right)}+\frac{\exp\{i(2\omega_e+\omega_g)t\}}{\left\{1+\frac{i(2\omega_e+\omega_g)}{6D}\right\}^2\left\{1+\frac{i(2\omega_e+\omega_g)}{12D}\right\}}\right.$$

$$\left.+\frac{\exp\{i(2\omega_e-\omega_g)t\}}{\left\{1+\frac{i(2\omega_e-\omega_g)}{6D}\right\}^2\left\{1+\frac{i(2\omega_e-\omega_g)}{12D}\right\}}\right]+\frac{361p}{30240}\left[\frac{2\exp(i\omega_g t)}{\left(1+\frac{i\omega_g}{2D}\right)\left(1+\frac{i\omega_g}{6D}\right)\left(1+\frac{i\omega_g}{12D}\right)}\right.$$

$$+\frac{\exp\{i(2\omega_e+\omega_g)t\}}{\left\{1+\frac{i(2\omega_e+\omega_g)}{2D}\right\}\left\{1+\frac{i(2\omega_e+\omega_g)}{6D}\right\}\left\{1+\frac{i(2\omega_e+\omega_g)}{12D}\right\}}$$

$$\left.+\frac{\exp\{i(2\omega_e-\omega_g)t\}}{\left\{1+\frac{i(2\omega_e-\omega_g)}{2D}\right\}\left\{1+\frac{i(2\omega_e-\omega_g)}{6D}\right\}\left\{1+\frac{i(2\omega_e-\omega_g)}{12D}\right\}}\right]$$

$${}_{21}f_4^{(2)};\quad-\frac{p}{268800}\left[\frac{2\exp(i\omega_g t)}{\left(1+\frac{i\omega_g}{6D}\right)\left(1+\frac{i\omega_g}{12D}\right)\left(1+\frac{i\omega_g}{20D}\right)}\right.$$

$$+\frac{\exp\{i(2\omega_e+\omega_g)t\}}{\left\{1+\frac{i(2\omega_e+\omega_g)}{6D}\right\}\left\{1+\frac{i(2\omega_e+\omega_g)}{12D}\right\}\left\{1+\frac{i(2\omega_e+\omega_g)}{20D}\right\}}$$

$$+\frac{\exp\{i(2\omega_e-\omega_g)t}{\left\{1+\frac{i(2\omega_e-\omega_g)}{6D}\right\}\left\{1+\frac{i(2\omega_e-\omega_g)}{12D}\right\}\left\{1+\frac{i(2\omega_e-\omega_g)}{20D}\right\}}\Bigg]$$

$$-\frac{p}{22400}\Bigg[\frac{2\exp(i\omega_g t)}{\left(1+\frac{i\omega_g}{2D}\right)\left(1+\frac{i\omega_g}{12D}\right)\left(1+\frac{i\omega_g}{20D}\right)}$$

$$+\frac{\exp\{i(2\omega_e+\omega_g)t}{\left\{1+\frac{i(2\omega_e+\omega_g)}{2D}\right\}\left\{1+\frac{i(2\omega_e+\omega_g)}{12D}\right\}\left\{1+\frac{i(2\omega_e+\omega_g)}{20D}\right\}}$$

$$+\frac{\exp i(2\omega_e-\omega_g)t\}}{\left\{1+\frac{i(2\omega_e-\omega_g)}{2D}\right\}\left\{1+\frac{i(2\omega_e-\omega_g)}{12D}\right\}\left\{1+\frac{i(2\omega_e-\omega_g)}{20D}\right\}}\Bigg]$$

$$-\frac{p}{1344}\Bigg[\frac{2\exp(i\omega_g t)}{\left(1+\frac{i\omega_g}{2D}\right)\left(1+\frac{i\omega_g}{6D}\right)\left(1+\frac{i\omega_g}{20D}\right)}$$

$$+\frac{\exp\{i(2\omega_e+\omega_g)\}}{\left\{1+\frac{i(2\omega_e+\omega_g)}{2D}\right\}\left\{1+\frac{i(2\omega_e+\omega_g)}{6D}\right\}\left\{1+\frac{i(2\omega_e+\omega_g)}{20D}\right\}}$$

$$+\frac{\exp\{i(2\omega_e-\omega_g)\}}{\left\{1+\frac{i(2\omega_e-\omega_g)}{2D}\right\}\left\{1+\frac{i(2\omega_e-\omega_g)}{6D}\right\}\left\{1+\frac{i(2\omega_e-\omega_g)}{20D}\right\}}\Bigg]$$

$$_{03}f_2{}^{(2)};\quad \frac{1}{8}\left(\frac{p^3}{1764}-\frac{p}{18}\right)\left[\frac{\exp(3i\omega_g t)}{\left(1+\frac{i\omega_g}{2D}\right)^3}+\frac{3\exp(i\omega_g t)}{\left(1+\frac{i\omega_g}{6D}\right)^3}\right]-\frac{p^3}{160}\Bigg[\frac{\exp(3i\omega_g t)}{\left(1+\frac{i\omega_g}{6D}\right)^2\left(1+\frac{3i\omega_g}{20D}\right)}$$

$$+\frac{3\exp(i\omega_g t)}{\left(1+\frac{i\omega_g}{6D}\right)^2\left(1+\frac{i\omega_g}{20D}\right)}\Bigg]$$

$$_{03}f_4{}^{(2)};\quad \frac{-p^3}{25870}\left[\frac{\exp(3i\omega_g t)}{\left(1+\frac{i\omega_g}{2D}\right)\left(1+\frac{3i\omega_g}{20D}\right)^2}+\frac{3\exp(i\omega_g t)}{\left(1+\frac{i\omega_g}{6D}\right)\left(1+\frac{i\omega_g}{20D}\right)^2}\right]$$

$$-\frac{p^2}{20160}\left[\frac{\exp(3i\omega_g t)}{\left(1+\frac{i\omega_g}{2D}\right)^2\left(1+\frac{3i\omega_g}{20D}\right)}+\frac{3\exp(i\omega_g t)}{\left(1+\frac{i\omega_g}{6D}\right)^2\left(1+\frac{i\omega_g}{20D}\right)}\right]$$

$$_{03}f_6{}^{(2)};\quad \frac{13}{4656960}\left[\frac{\exp(3i\omega_g t)}{\left(1+\frac{i\omega_g}{2D}\right)\left(1+\frac{3i\omega_g}{20D}\right)\left(1+\frac{i\omega_g}{14D}\right)}+\frac{3\exp(i\omega_g t)}{\left(1+\frac{i\omega_g}{6D}\right)\left(1+\frac{i\omega_g}{20D}\right)\left(1+\frac{i\omega_g}{42D}\right)}\right]. \tag{3.5}$$

§ 4. Viscoelasticity of the Solution

The viscoelasticity of the solution is calculated along the same procedure as adopted by one of the present authors in the previous paper.[13]

Suppose two plates, parallel to yz-plane and separated at a distance $2h$ in the fluid, by means of which we can apply the shearing force and electric field simultaneously upon the fluid. The decrease of effective velocity gradient $g-g_{eff}$ upon adding macromolecules into the pure solvent is given by[13]

$$g-g_{eff}=\frac{16\pi N}{3g}\int\rho\biggl\{\frac{\alpha_0''h_{11}^2+\beta_0''h_{22}^2+\gamma_0''h_{33}^2}{\beta_0''\gamma_0''+\gamma_0''\alpha_0''+\alpha_0''\beta_0''}+\frac{h_{12}^2}{a_1^2\gamma_0'}+\frac{(\alpha_0+\gamma_0)(h_{13}^2+h_{23}^2)}{\alpha_0'(a_1^2\alpha_0+a_3^2\gamma_0)}$$
$$+\frac{(a_3^2-a_1^2)\alpha_0'+(\alpha_0-\gamma_0)}{\alpha_0'(a_1^2\alpha_0+a_3^2\gamma_0)}(h_{13}o_{13}-h_{23}o_{32})+\frac{a_1^2+a_3^2}{a_1^2\alpha_0+a_3^2\gamma_0}(o_{32}^2+o_{13}^2)+\frac{o_{21}^2}{\alpha_0}$$
$$-\frac{(a_3^2-a_1^2)h_{23}-(a_1^2+a_3^2)o_{32}}{a_1^2\alpha_0+a_3^2\gamma_0}j_\xi+\frac{(a_3^2-a_1^2)h_{13}+(a_1^2+a_3^2)}{a_1^2\alpha_0+a_3^2\gamma_0}j_\eta-\frac{o_{21}}{\alpha_0}j_\zeta\biggr\}d\Omega\,, \tag{4.1}$$

where N is number of particles per unit volume of the solution and j_ξ, j_η, j_ζ denote the fluxes with respect to the principal axes of ellipsoid connected with j_θ, j_ϕ, j_ψ by the following relation

$$\begin{pmatrix} j_\xi \\ j_\eta \\ j_\zeta \end{pmatrix}=\begin{pmatrix} \sin\psi & -\sin\theta\cos\psi & 0 \\ \cos\psi & \sin\theta\sin\psi & 0 \\ 0 & \cos\theta & 1 \end{pmatrix}\begin{pmatrix} j_\theta \\ j_\phi \\ j_\psi \end{pmatrix}. \tag{4.2}$$

Substitution of (4.3) into (4.1) making use of (2.8), (3.2) and (3.4) yields

$$g-g_{eff}$$
$$=\frac{16\pi N}{3}\int\rho\biggl[\frac{g}{4\gamma_0'a_1^2}\cos^2\theta+\biggl\{\frac{\alpha_0''+\gamma_0''}{2\alpha_0''\gamma_0'a_1^2}-\frac{2}{\alpha_0'(a_1^2+a_3^2)}\biggr\}g\sin^4\theta\sin^2\phi\cos^2\phi+\frac{g\sin^2\theta}{2\alpha_0'(a_1^2+a_3^2)}$$
$$+\frac{3\mu Ep}{4\pi kT\eta}(\sin 3\phi\sin^3\theta+\sin\phi\sin^3\theta-2\sin\theta\sin\phi)$$
$$+\frac{D(a_1^2+a_3^2)}{4(a_1^2\alpha_0+a_3^2\gamma_0)}\biggl\{(a_3^2-a_1^2)\biggl(\sin 2\theta\sin 2\phi\frac{\partial}{\partial\theta}\log\rho+2\cos 2\phi\frac{\partial}{\partial\phi}\log\rho\biggr)+2\frac{\partial}{\partial\phi}\log\rho\biggr\}\biggr]d\Omega\,, \tag{4.3}$$

where the integration must be performed over all possible orientations of particles. The first line of this equation is the term due to hydrodynamical effect calculated by Jeffery, the second is the contribution from the electric field and the last is due to the rotatoryd iffusion. The specific viscosity η_{sp} is given by

$$\eta_{sp}=(g-g_{eff})/g_{eff}\simeq(g-g_{eff})/g$$
$$=\frac{4\pi N}{9\gamma_0'a_1^2}+\frac{16\pi N}{9\alpha_0'(a_1^2+a_3^2)}-\frac{112\pi N}{45}\biggl\{\frac{\alpha_0''+\gamma_0''}{2\alpha_0''\gamma_0'a_1^2}-\frac{2}{\alpha_0'(a_1^2+a_3^2)}\biggr\}$$
$$+\biggl(\frac{\mu E_0}{kT}\biggr)^2\biggl[\frac{8\pi N}{45\gamma_0'a_1^2}-\frac{16\pi N}{45\alpha_0'(a_1^2+a_3^2)}-\frac{256\pi N}{315}\biggl\{\frac{\alpha_0''+\gamma_0''}{2\alpha_0''\gamma_0'a_1^2}-\frac{2}{\alpha_0'(a_1^2+a_3^2)}\biggr\}\biggr]{}_{20}f_2^{(0)}$$
$$+\biggl(\frac{g_0c_1}{2kT}\biggr)^2\biggl[\biggl\{\frac{8\pi N}{45\gamma_0'a_1^2}-\frac{16\pi N}{45\alpha_0'(a_1^2+a_3^2)}-\frac{256\pi N}{315}\biggl(\frac{\alpha_0''+\gamma_0''}{2\alpha_0''\gamma_0'a_1^2}-\frac{2}{\alpha_0'(a_1^2+a_3^2)}\biggr)\biggr\}{}_{02}f_2^{(0)}$$
$$+\biggl\{\frac{\alpha_0''+\gamma_0''}{2\alpha_0''\gamma_0'a_1^2}-\frac{2}{\alpha_0'(a_1^2+a_3^2)}\biggr\}\biggl(\frac{16\pi N}{945}{}_{02}f_4^{(0)}-\frac{128\pi N}{9}{}_{02}f_4^{(4)}\biggr)\biggr]$$
$$+\frac{Nc_1}{2\eta}\biggl[\biggl(\frac{\mu E_0}{kT}\biggr)^2\biggl\{\biggl(\frac{6}{7}{}_{11}f_3^{(3)}-\frac{1}{30}{}_{11}f_1^{(1)}-\frac{1}{35}{}_{11}f_3^{(1)}\biggr)+p\biggl(-\frac{4}{5}{}_{21}f_2^{(2)}+4\,{}_{21}f_4^{(2)}\biggr)\biggr\}$$
$$+\biggl(\frac{g_0c_1}{2kT}\biggr)^2\biggl(-\frac{4}{5}{}_{03}f_2^{(2)}+4\,{}_{03}f_4^{(2)}+4\,{}_{03}f_6^{(2)}\biggr)\biggr]. \tag{4.4}$$

The complex intrinsic viscosity $[\eta]$ is given by $\lim\eta_{sp}/c$, where c is the concentration of the macromolecules in grams per 100 cc of solvent. The deviation of intrinsic viscosity from non-Newtonian part in the absence of external forces depends on the square of the velocity gradient. The value of intrinsic viscosity at the extreme case of spherical model is

$$[\eta]=2.5\biggl(\frac{4\pi a^3}{3}\biggr)\bigg/100\,M\,, \tag{4.5}$$

where M is molecular weight of the macromolecule. This result does not depend on the electric field, and coincides with that of Einstein.

Recently Kirkwood and Plock[16] calculated non-Newtonian viscoelasticity in the absence of electric field.

§ 5. Polarization

We now discuss the dielectric properties of the solution. The interaction between particles and the influence of dielectric character of solvent are not taken into consideration. Then we use the same notation for the applied field and for internal field. Electric displacement $\boldsymbol{D}$ can be written as the sum of two terms, electronic part and dipolar part

$$\boldsymbol{D}=\varepsilon_\infty \boldsymbol{E}+4\pi N\langle\boldsymbol{\mu}\rangle \tag{5.1}$$

where ε_∞ denotes the dielectric constant for the applied field of the frequency of optical range, and $\langle\boldsymbol{\mu}\rangle$ is mean value of the component of dipole moment along the direction of electric field. The mean value is calculated with the distribution function $\rho(\theta, \phi, t)$. The component of dipole moment along the field is given by

$$\mu\cos(\boldsymbol{E}_\wedge\boldsymbol{\mu})=\mu\sin\theta\cos\phi\ . \tag{5.2}$$

Taking the average with respect to the orientation by means of (3.4), we obtain

$$\langle\mu\rangle=\int\mu\sin\theta\cos\phi\ \rho(\theta, \phi, t)\,d\Omega=\frac{\mu^2E_0}{3kT}\left\{{}_{10}f_1^{(1)}(t)+\left(\frac{\mu E_0}{kT}\right)^2{}_{30}f_1^{(1)}(t)+\left(\frac{gc_1}{2kT}\right)^2{}_{12}f_1^{(1)}(t)+\cdots\right\} \tag{5.3}$$

up to the third order terms of small quantities. In case of a vanishing velocity gradient g and negligible third order terms with respect to $(\mu E/kT)$, the average value (5.3) coincides with Debye's formula. The effect of the shear gradient on the polarization is not the first order of g but the second.

For the spherical model, the mean value of polarization is obtained from (5.3).

$$\begin{aligned}\langle\mu\rangle=\frac{\mu^2E_0}{3kT}\Bigg[&{}_{10}f_1^{(1)}(t)+\left(\frac{\mu E_0}{kT}\right)^2{}_{30}f_1^{(1)}(t)-\frac{1}{96}\left(\frac{gc_1}{2kT}\right)^2\Bigg\{\frac{\exp\{i(\omega_e+2\omega_g)t\}}{\left\{1+\dfrac{i(\omega_e+2\omega_g)}{2D}\right\}^2\left\{1+\dfrac{i(\omega_e+2\omega_g)}{6D}\right\}}\\&+\frac{\exp\{i(\omega_e-2\omega_g)t\}}{\left\{1+\dfrac{i(\omega_e-2\omega_g)}{2D}\right\}^2\left\{1+\dfrac{i(\omega_e-2\omega_g)}{6D}\right\}}+\frac{2\exp(i\omega_e t)}{\left(1+\dfrac{i\omega_e}{2D}\right)^2\left(1+\dfrac{i\omega_e}{6D}\right)}\\&+\frac{3\exp\{i(\omega_e+2\omega_g)t\}}{\left\{1+\dfrac{i(\omega_e+2\omega_g)}{2D}\right\}^3}+\frac{3\exp\{i(\omega_e-2\omega_g)t\}}{\left\{1+\dfrac{i(\omega_e-2\omega_g)}{2D}\right\}^3}+\frac{6\exp(i\omega_e t)}{\left(1+\dfrac{i\omega_e}{2D}\right)^3}\Bigg\}\Bigg]\ .\end{aligned} \tag{5.4}$$

The third term of this equation expresses the effect of shearing force on the polarization.

§ 6. Entropy Balance

In this section a simple thermodynamical consideration is given on the cross phenomena above discussed between electric vector force and hydrodynamical tensor force. As the system under consideration we take the solution of unit volume, making the laminar motion. Increment of energy due to the motion of viscous liquid in time dt is expressed in the form

$$du=d'Q+\boldsymbol{E}d\boldsymbol{D}/4\pi+\eta_{eff}\,g^2_{eff}\,dt\,,\qquad \eta_{eff}g_{eff}=\eta g\ . \tag{6.1}$$

Each terms of the right-hand side represent heat flow, works done by electric field and by hydrodynamical force, respectively. The second law of thermodynamics is written as

$$Tds=d'Q+T(ds)_{irr}\ .\qquad (ds)_{irr}\geq 0 \tag{6.2}$$

where $(ds)_{irr}$ means irreversible production of entropy. (6.2) and (6.1) give immediately for entropy production

$$\left(\frac{\partial s}{\partial t}\right)_{irr}=\left(\frac{\partial s}{\partial t}\right)+\frac{\boldsymbol{E}}{4\pi}\frac{\partial \boldsymbol{D}}{\partial t}+\eta_{eff}g^2_{eff}-\frac{\partial u}{\partial t}\,. \tag{6.3}$$

On the other hand we have

$$s=-Nk\int\rho\log\rho d\Omega+s'\,, \tag{6.4}$$

for the entropy from the well-known Gibbs formula, where s' means the entropy other than the orientation of macromolecules, and for the electric work from (5.1)

$$\frac{1}{4\pi}\boldsymbol{E}\frac{\partial \boldsymbol{D}}{\partial t}=\frac{\partial}{\partial t}\left(\frac{\varepsilon_\infty}{4\pi}E^2\right)+NE\int\mu\sin\theta\cos\phi\frac{\partial\rho}{\partial t}d\Omega\,, \tag{6.5}$$

and for the hydrodynamical work from (4.3) with the aid of (3.2) and (2.8) ηg multiplied by

$$\begin{aligned}g_{eff}=g-\frac{16\pi N}{3}\int\Bigg[&\left(\frac{g}{4\gamma_0'a_1^2}+\frac{g}{4\alpha_0}\right)\cos^2\theta+\left\{\frac{g(\alpha_0''+\gamma_0'')}{2\alpha_0''\gamma_0'a_1^2}-\frac{g(\alpha_0+\gamma_0)}{\alpha_0'(a_1^2\alpha_0+a_3^2\gamma_0)}\right\}\sin^4\theta\sin^2\phi\cos^2\phi\\&+\frac{g\sin^2\theta}{2\alpha_0'(a_1^2\alpha_0+a_3^2\gamma_0)}(\alpha_0\cos^2\phi+\gamma_0\sin^2\phi)+\frac{g(a_3^2-a_1^2)}{4(a_1^2\alpha_0+a_3^2\gamma_0)}\sin^2\theta\cos^2\phi\\&+\frac{(a_3^2+a_1^2)g}{4(a_1^2\alpha_0+a_3^2\gamma_0)}\sin^2\theta\Bigg]\rho\,d\Omega+\frac{16\pi N}{3}\int\frac{a_3^2+a_1^2}{4(a_1^2\alpha_0+a_3^2\gamma_0)}\\&\{p(j_\theta\sin 2\theta\sin 2\phi+2j_\phi\sin^2\theta\cos 2\phi)+2j_\phi\sin^2\theta\}+\frac{1}{2\alpha_0}(j_\phi\cos^2\theta+j_\psi\cos\theta)\Bigg]\rho\,d\Omega\,.\end{aligned} \tag{6.6}$$

The work done by hydrodynamical force is divided into three parts, the work dissipated even in the absence of macromolecules in order to maintain the velocity gradient in the solvent ηg^2, the excess work necessary after introducing macromolecules at rest in the solvent and the work required when particles are in motion expressed by the first integral in (6.6). Because our main interest is concerned with the orientation of macromolecules and the irreversible production of entropy arising from this $(\partial s/\partial t)_{irr.\ orient.}$, the last part should be retained in evaluating $(\partial s/\partial t)_{irr.\ orient.}$ by means of (6.3). Thus we put as the work done by electric force with the help of diffusion equation (3.1)

$$NE\mu\int\cos\phi\left\{\frac{\partial}{\partial\theta}(j_\theta\rho\sin\theta)+\frac{\partial}{\partial\phi}(j_\phi\rho\sin\theta)\right\}d\Omega\,, \tag{6.7}$$

and as the work done by hydrodynamical force

$$\begin{aligned}&Nc_1\int\left\{\frac{gp}{2}\left(\frac{1}{2}j_\theta\sin 2\theta\sin 2\phi+j_\phi\sin^2\theta\cos 2\phi\right)+\frac{g}{2}j_\phi\sin^2\theta\right\}\rho\,d\Omega\\&\qquad+Nc_3\int\frac{g}{2}\cos\theta(j_\phi\cos\theta+j_\psi)\rho\,d\Omega\,,\end{aligned} \tag{6.8}$$

and also we have from (6.4)

$$\left(\frac{\partial s}{\partial t}\right)_{orient.}=N\int\left\{j_\theta\left(-kT\frac{\partial\rho}{\partial\theta}\right)+j_\phi\left(-kT\frac{\partial\rho}{\partial\phi}\right)\right\}d\Omega\,, \tag{6.9}$$

making use of the diffusion equation and partial integration. Substituting these results into (6.3), we have

$$\begin{aligned}\left(\frac{\partial s}{\partial t}\right)_{irr.\ orient.}=\frac{N}{T}\int\Bigg[&j_\theta\left\{-kT\frac{\partial}{\partial\theta}\log\rho+\mu E\cos\phi\cos\theta+\frac{gp}{2}\sin 2\theta\sin 2\phi\right\}\\&+j_\phi\left\{-kT\frac{\partial}{\partial\phi}\log\rho-\mu E\sin\phi\sin\theta+\frac{gp}{2}c_1\sin^2\theta\cos\phi+\frac{g}{2}\sin^2\theta+\frac{gc_3}{2}\cos^2\theta\right\}\end{aligned}$$

$$+ j_\psi \frac{gc_3}{2}\cos\theta \Big]\rho\, d\Omega\,. \tag{6.10}$$

The coefficients of j_θ, j_ϕ and j_ψ multiplied by ρ correspond to general affinities defined in irreversible thermodynamics. When one reminds of (3.2) and (4.2) we have

$$\left(\frac{\partial s}{\partial t}\right)_{irr.} = \frac{N}{T}\int\{c_1(j_\xi^2+j_\eta^2)+c_3 j_\zeta^2\}\rho\, d\Omega \tag{6.11}$$

where c_1, c_2 $(=c_1)$ and c_3 are rotatory friction coefficients around three principal axes. This result is consistent with that of Saitô and Sugita,[15] based on simple rigid pearl necklace model, and is a complement of their discussion to spheroidal macromolecules.

§ 7. Discussions

Unfortunately we have not found any experimental report on polymer solution which is to be compared with our results. From the measurements on the viscosity of polar and non-polar liquids such as monochlorobenzene, chloroform and amyl acetate, Andrade et al[4),5),6)] observed following characteristics in liquids; the viscosities of non-polar liquids are not influenced by the presence of electric field but the viscosities of polar liquids increase proportionally with the square of the intensity of an applied electric field and the increments are proportional to the square of the frequency of the electric field. All these behaviors are in qualitative agreement with our results. Because our model can not be considered to fit for the polar liquids whose viscosities were measured by Andrade et al, we will not undertake any numerical comparison with their experiments. Peterlin[8)] treated a quite similar problem with similar model. His calculation, however, is restricted only to the effect of electric field on the viscosity of dumb-bell molecules and the detailed calculation is carried out in two-dimensional case.

In the above treatment, the interactions of the electric current and momentum flow are considered, forces generating these currents being electric field of vector character and shearing stress of tensor character. The interactions of both forces in the first order are evidently denied by Curie's law but on higher order terms with regards to the magnitude of these forces nothing can be mentioned and the interactions of higher order may take place, as is shown in our calculation. Vectors j's are axial vectors. Thus they are coupled with $\boldsymbol{\mu}\times\boldsymbol{E}$ and terms containing $g/2$ of the same tensor character as is seen in (3.2) and (2.8).

This work is supported by Scientiffc Research Grant for the Research Group of Macromolecular Physics from the Ministry of Education.

References

1) A. Isihara, R. Koyama, N. Yamada and A. Nishioka: J. Polymer Sci. **17** (1955) 341.
C. Wippler: J. Polymer Sci. **23** (1957) 199.
2) A. Peterlin: J. Polymer Sci. **23** (1957) 189.
3) S. R. de Groot: *Thermodynamics of Irreversible Processes. Amsterdam* (1952).
4) E. N. Andrade and C. Dodd: Proc. Roy. Soc. **A187** (1946) 296.
5) E. N. Andrade and C. Dodd: Proc. Roy. Soc. **A204** (1951) 449.
6) E. N. Andrade and J. Hart: Proc. Roy. Soc. **A225** (1954) 463.
7) L. Onsager: Phys. Rev. **37** (1931) 405. **38** (1931) 2265.
H. B. G. Casimir: Rev. Mod. Phys. **17** (1945) 343.
8) A. Peterlin: Razprave (Dissertatione) **7/1** Solvenska Akademija Znanosti in Umetnosti. Ljubljana (1956).
9) J. G. Kirkwood: Rec. trav. chim. **68** (1949) 649.
10) P. E. Rouse Jr.: J. Chem. Phys. **21** (1953) 1272.
11) O. Nakada: J. Phys. Soc. Japan. **10** (1955) 804.
12) B. H. Zimm: J. Chem. Phys. **24** (1956) 270.
13) N. Saitô: J. Phys. Soc. Japan. **6** (1951) 297, 302.
14) G. B. Jeffery: Proc. Roy. Soc. **A102** (1923) 161.
15) N. Saitô and M. Sugita: J. Phys. Soc. Japan. **7** (1952) 554.
16) J. G. Kirkwood, R. J. Plock: J. Chem. Phys. **24** (1956) 665.

JOURNAL OF THE PHYSICAL SOCIETY OF JAPAN Vol. 12, No. 12, DECEMBER, 1957

On the Properties of Long-Gap Streamers

By Kanji HONDA

Department of Physics, University of Tokyo, Tokyo

(Received August 19, 1957)

The paper is a trial of systematic explanation of long-gap streamers including step-leaders of lightning discharge. The paper gives various quantities concerning streamer properties as functions of "unbroken length", and satisfactorily explains the well-known facts about streamers, that is, that stepping occurs in lightning leaders, that the mean spark gradient becomes 5 kV/cm for long gaps and so on. The theory also points out that streamer can not cause any sensible temperature rise by itself, or in other words that they can only be cold streamers.

Introduction

In the atmospheric air, long-gap sparks are initiated by filamentary, ionized paths called "streamers". They have been studied by many authors since the discovery of Lichtenberg's figure, but their nature can not be said to have been perfectly understood. On the other hand, Schonland[1)] has explored the structure of lightning discharge through his rotating-camera observation extending over a long time. One of the most interesting properties is the stepping of its initial leader which corresponds to a long-gap streamer followed by spark discharge.

Meek[2)], and then Schonland[3)] published a paper treating this step-phenomenon theoretically. Schonland's theory especially stresses that the lightning leader is nothing but a special case of ordinary long-gap streamers, and pays keen reference to the data of laboratory streamers.

According to his theory a pilot treamer, the head part of the leader, with ionizing tip field cuts its way through air with drift velocity about 10^7 cm/s and for every $10 \sim 80$ m advance of the pilot the rear part of the leader called "channel" overtakes the pilot tip with far larger velocity ($\sim 10^9$ cm/s) and then stays there until the next new step is traced by the pilot. The large channel velocity is caused by the breakdown occurring at the channel head due to the space charge of the pilot.

The present author was stimulated by Schonland's theory and tried to obtain more generalized theory as to cover any streamer breakdown of ordinary long gaps. The following paper will show that his theory, though unrefined yet, is enough to explain some well-known empirical facts about streamers as summarized ahead.

THEORY

I. General

§ 1. General View

The streamer means a filamentary, conductive path stretching from one or both of the electrodes in gas and provides a preparatory path for a spark in a long gap or in lightning discharge.

The remarkable property of the streamer is that it extends with velocity v_0 of about 10^7 cm/s in the atmospheric air carrying at its tip an ionizing field X_0 due to its own space charge, where v_0 and X_0 must have a close relation of course.

The filamentary body of the streamer is considered to contain plenty of electrons and positive ions and to be in a state of conductive plasma with weak axial field. Then there must be a charge layer of the same polarity as the streamer surrounding the plasma in order to protect it from the external field, and charge must continuously be supplied for this purpose to the freshly producing portion at the tip. Accordingly the charge q per unit length of the streamer relates to the streamer current I as

$$I = q v_0 . \qquad (1)$$

According to Schonland's observation, the initial lightning stremer called "stepped leader" remains in space longer than 0.01 second. The largest part of such a streamer must therefore be in quasi-steady state and be distinguished from the freshly produced transient part of the streamer tip. Let us call this quasi-steady long part "channel" and the transient part "pilot" hereafter in accordance with Schonland's nomenclature.

To make conditions clear, the author treats the case where a streamer of one polarity, either positive or negative, spreads toward a wide plane electrode in the air of 1 atm pressure. A lightning leader spreading toward the earth surface may be considered to be an example of such a case.

§ 2. Pilot Model

Let us first assume that the pilot has a spherical seat of ionizing field X_0 at its head and a cylindrical stem part of radius r as shown in Fig. 1 though the idea "cylindrical" must be corrected later on.

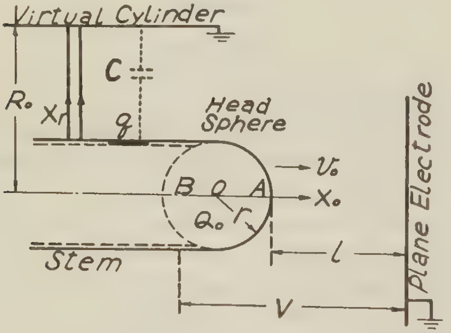

Fig. 1. Pilot model.

The velocity v_0 and the tip field X_0 are considered to be most essential for streamer progression. According to various observations v_0 does not differ much from case to case and always of the order of $(10^6 \sim 10^7)$ cm/s. So let us consider that v_0 is constant during progression and that X_0 remains constant as well.

About the stem part of the pilot we shall assume the external field X_r to be radial, or in other words that the pilot forms a cylindrical condenser with a concentric virtual cylinder of zero potential. This assumption may be allowed approximately so far as we discuss the streamer extended midway in a long gap. Then the capacity per unit length C can be expressed by

$$C = \frac{1}{2 \ln (R_0/r)}, \qquad (2)$$

where R_0 is the radius of the virtual outer cylinder. R_0 is unknown but r will after be shown to be proportional to the "unbroken length" l, that is, the distance which lies between the pilot head and the opposite electrode; and what is more, we may imagine the field configuration around the streamer to be approximately similar for different l, that is, R_0 also nearly proportional to l. Therefore we can expect that the capacity C may not be so much affected by l, and thus we shall assume it as a constant.

Let the potential of the pilot be V, then the charge per unit length q is given by

$$q = CV. \qquad (3)$$

Now we are considering the streamer which will subsequently grow to a spark, so V means the spark voltage for the unbroken length l. Then we may write V as

$$V = Kl \qquad (4)$$

in first approximation. This relation holds for the electrode voltage which is required to produce spark in a large gap, and not for the instantaneous voltage which exists between the streamer tip and the opposite electrode at spark occurrence. But if the internal gradient of the streamer be nearly equal to K of Eq. (4) as we shall discuss in § 5, the above relation can also be applicable for streamer tip voltage.

The constant K may be called the mean spark gradient for a long air gap and for 1 atm is nearly

$$K = 5 \text{ kV/cm}$$
$$= 16.7 \text{ esu/cm}. \qquad (5)$$

By the way, the introduction of C and l into equations is the most essential point of this paper. From (3) and (4) we get the relation

$$q = CKl. \qquad (6)$$

In our theory the stem part can not keep its original form, but tends to assume the final state by lateral expansion. Therefore C and q are affected by stem radius in themselves, but the effect will be shown to be so small that the above values of C and q may be used also for expanding pilot stem and the channel with an error of about 1%.

Eq. (6) shows that q varies proportional to the unbroken length l and so takes forwardly decreasing distribution along the streamer.

For an electrode-distance L the total charge

Q demanded by the bridging streamer is therefore

$$Q=\int_{l=0}^{L} q dl=\frac{1}{2}CKL^2 .$$

This expression enables us to estimate the value of C by means of Schonland's data about lightning leaders. According to him the mean values of Q and L are as follows:

$$Q=4 \text{ coul}=1.2\times10^{10} \text{ esu}$$

and

$$L=5 \text{ km}=5\times10^{5} \text{ cm} .$$

Inserting these values in the above equation we get

$$C=0.00575 \text{ esu/cm} , \tag{7}$$

and (6) can therefore be written as

$$q=0.096\, l . \tag{8}$$

§ 3. Pilot Radius

Here pilot radius r originally means that of the head-sphere, and not the radius of the pilot stem. The stem has of course the same radius at first, but subsequently expands due to its own surface field. The head-sphere must also expand outward, but for the present the author neglects its expansion and gives the following hypothetical structure to the head-sphere:

i) the radius r is not affected by the expansion of the stem.

ii) the sphere is electrically insulated from the stem, but one half of its surface is perfectly shielded by the stem plasma. (B-side in Fig. 1)

Let us assume that the charge Q_0 producing the tip field distributes uniformly on the surface of the head-sphere. Then

$$X_0=\frac{Q_0}{r^2} .$$

Now the power input IV is consumed in the work done by the hemisphere $(Q_0^2/8r^2)v_0$ and the energy storage of the freshly producing stem part $(CV^2/2)v_0$. Here V is the potential of the pilot stem referred to the opposite electrode and does not contain the drop in the channel. Then

$$IV=\frac{CV^2}{2}v_0+\frac{Q_0^2}{8r^2}v_0 ,$$

but since IV can be transformed by (1) and (3) as follows:

$$IV=qv_0V=CV^2v_0 ,$$

we get the relation

$$r=\frac{2\sqrt{C}V}{X_0}=\frac{2.53\, l}{X_0} . \tag{9}*$$

If we put $rX_0=V$ in (9), that is, if we assume the stem and the head-sphere to be euipotential, C would take a definite value 1/4, and is far larger than the value of (7). This is why the assumption (ii) is necessary.

§ 4. Channel Radius

As already mentioned, the channel is a final quasi-steady state that the pilot stem assumes after lateral expansion. Therefore the channel radius R must be larger than the pilot radius given by (9).

The condition that determines R is that outside R-cylinder the rate of electron loss is greater than the rate of electron production. Since in normal air the loss due to attachment is far greater than that due to recombination for an electron, we here consider the former only.

If Z_S is the ionizing collision frequency and β the attachment coefficient of an electron, R is determined from the condition

$$\beta=Z_S , \tag{10}$$

where Z_S implies ionization by single collision, because at the R-surface electrons would be exposed to the strong external field.

In Fig. 2 point A satisfies the condition (10) and so gives the external field intensity X_R at the surface of the channel, and consequently its radius R is determined according to the expression

$$X_R=\frac{2q}{R} . \tag{11}$$

The charge per unit length of the channel q should originally be distinguished from that of the pilot given by (3) since $R \not\fallingdotseq r$. However their difference being neglisibly small as may be inferred from the form of (2), we need not discriminate them from each other.**

In Fig. 2 β-curve was taken from Loeb's book[4] and Z_S-value from Sanders' α/p-

---

* According to (9) the charge of the head-sphere Q_0 $(=X_0r^2)$ varies with l, that is, as the sphere advances; and therefore produces another component of current. But $|dQ_0/dt|$ being 10^{-4} times as large as qv_0, we may leave Eq. (1) unchanged.

** $(q_R-q_r)/q_r$ is 1.54% for positive streamers and 0.28% for negative streamers.

values.[5] We also made a reference to von Engel and Steenbeck's formula[6] of ionizing collision frequency. From Fig. 2 we get

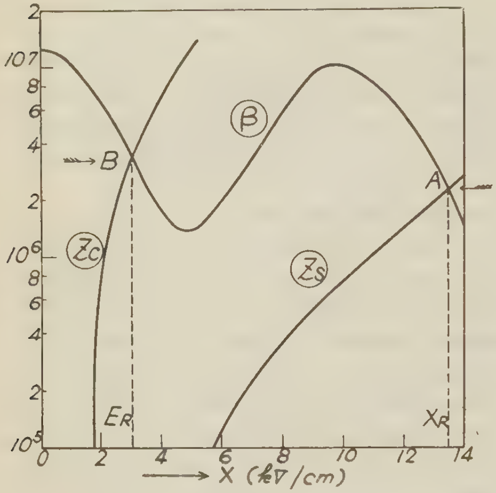

Fig. 2.

$$X_R = 13500 \text{ V/cm}$$
$$= 45 \text{ esu/cm} \qquad (11a)$$

and

$$R = 4.27 \times 10^{-3}\, l\,. \qquad (12)$$

§ 5. Internal Condition of Channel

Eq. (10) must equally hold in channel plasma because here also the balance of loss and generation of electrons is the only one probable governing condition. (Refer to B) § 14)

The channel plasma is perfectly shielded from the external field, hence in first approximation there can be only an axial field E_R required for maintenance of streamer current. However as the densities of electrons and ions are very large, E_R must be very small compared with the surface field X_R and so the point A of Fig. 2 cannot express the internal field condition by itself.

On the other hand, the existence of the relation (4) strongly suggests that K must mean some value near the internal field of the streamer channel E_R. Then, however, Z-curve will have to intersect β-curve somewhere near the minimum which occurs at 5 kV/cm as shown in Fig. 2. We can answer as follows.

Since the electron density is large and the field intensity E_R rather small in the channel, cumulative ionization must play an important role. Then Z-curve will shift toward the left in Fig. 2. As a trial if we put the metastable potential of N_2 in place of its ionization potential in Z-equation, the calculated Z-curve shown by Z_C in the figure crosses β-curve at point B near the minimum. Let us take the field of point B as E_R for the present, then from the figure

$$E_R = 3.0 \text{ kV/cm} = 10 \text{ esu/cm}\,. \qquad (13)$$

Here it is worth notice that points A and B are attained by the expanding pilot simultaneously but from opposite directions as shown by arrows in Fig. 2. Because when the pilot is expanding its surface field is decreasing while the internal field is increasing due to the decrease of the densities of electrons and ions.

Furthermore there is another point of remark. Since we are treating the case of static breakdown, voltage KL exists between the electrodes, where L denotes the electrode distance. When the streamer spreads out x cm long along the field from one electrode, the potential drop in it becomes $E_R x$. So the remaining unbroken space bears a part of voltage $(KL - E_R x)$, or nearly Kl if K and E_R have somewhat similar values. Then whatever position the streamer tip arrives at, there appears no large over- or under-voltage state and the relations (4) and (6) hold for any value of x.

However if x occurs athwart the field, under-voltage state will appear and the streamer can not help stopping unless some other circumstance energizes it, because $(KL - E_R x)$ becomes less than Kl in such a case. This explains why many branches of streamers are apt to disappear midway on their way.

II. Negative Streamer

§ 6. Negative Streamer Velocity

So far we have discussed general properties of the streamer that are common for both positive and negative polarities. We know however that positive ions can not move so swiftly as electrons; and we must take this polarity effect into account to explain the details of streamer properties.

As to the negative streamer, there is little ambiguity about the relation between X_0 and v_0, because v_0 is nothing but the drift velocity of the pilot head electrons. In this case however, electrons move in their own field, so the expression

$$v_0=\frac{1}{2}\mu X_0 \tag{14}$$

must be used instead of μX_0, where μ expresses the mobility of an electron.

The velocity v_0 may be considered to be common to all streamers of the same polarity and Schonland's value for lightning leader

$$v_0=4\times10^7\ \text{cm/s} \tag{15}$$

will be used in our calculation. Then X_0 is obtained from (14) as

$$\begin{aligned}X_0&=2.30\times10^5\ \text{V/cm}\\&=760\ \text{esu/cm}\,,\end{aligned} \tag{15a}$$

where the following value of μ is employed:

$$\begin{aligned}\mu&=350\ \text{(cm/s)/(V/cm)}\\&=1.05\times10^5\ \text{(cm/s)/(esu/cm)}.\end{aligned} \tag{15b}$$

Introducing (15a) in (9) we get

$$r=3.34\times10^{-3}\,l\,. \tag{16}$$

§7. Transition from Pilot to Channel —Stepping—of Negative Streamer

The channel has a radius larger than the pilot as obvious from comparison of (12) and (16). The pilot stem, once produced, expands laterally on account of the radial surface field. Then how much time will it take to assume the final state "channel"?

This time $\Delta\tau$ can easily be calculated as follows:

$$\Delta\tau=\int_{\rho=r}^{R}\frac{d\rho}{v_\rho}=\int_{\rho=r}^{R}\frac{d\rho}{\frac{1}{2}\mu X_\rho}\,, \tag{17}$$

where X_ρ is the surface field when the pilot stem reaches any radius ρ and given by $2q/\rho$. Whence

$$\Delta\tau=\frac{1}{2\mu q}(R^2-r^2)\,, \tag{18}$$

where q is regarded as a constant.* (Refer to §2) While the pilot expands laterally, its head advances forward, so it takes a form as shown in Fig. 3. If any abrupt change does not follow, the streamer will keep this form throughout its advance. It is more likely, however, that such steady advance is rather difficult for the streamer. The reason is as follows.

The internal space of the expanding pilot is filled with plasma, but it can hardly be neutral, because in accordance with the advance of the pilot head, continuous supply of charge is demanded by the freshly producing surface. This surface charge is of course supplied by the streamer current (1) after all, but the plasma must be its momentary source.

Moreover, electrons produce new ones on their expansion, then some of the latter must join the former. From these reasons it is most probable that the plasma of the pilot is deficient in electrons and hence has some content of positive space charge.

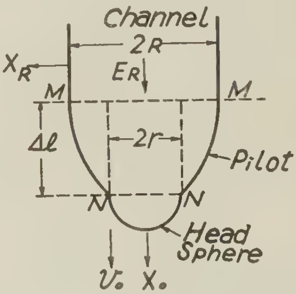

Fig. 3. Steady form of streamer tip.

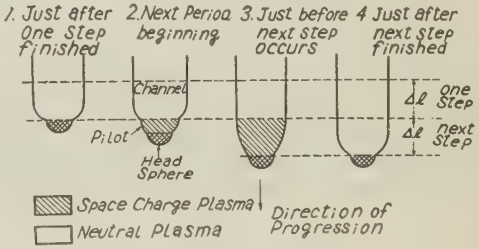

Fig. 4. Stepwise progression.

Since the channel plasma is considered to be nearly neutral, this space charge produces the strongest field at the bottom of pilot M M of Fig. 3. If this field be sufficient for enough ionization, this field disturbance must propagate through the whole pilot plasma like a moving striation and its velocity of propagation may be larger than that of pilot advance by a similar reason as for the positive streamer. (See §8)

In such a case the pilot can not keep the steady form of Fig. 3, but repeats a periodic change of form in accordance with its advance as shown in Fig. 4. This explains the stepping of the lightning initial leader and (18) gives its period. However q therein must be larger than the normal value given by (8) on account of the above mentioned reason. We assume twice the normal value as a rough estimation.

---

* The erorr due to treating q as a constant is 0.575%.

The advance of the pilot during $\Delta\tau$, that gives the step length, is given by

$$\Delta l = v_0 \Delta\tau . \tag{19}$$

III. Positive Streamer

§ 8. X_0 and r of Head-Sphere

In the case of positive streamer v_0 can not be explained by the drift motion of positive ions; because measured v_0 of the positive streamer is even greater than that of the negative streamer.

In this case electrons flow into the pilot head from the adjacent space ionizing air along their paths. The pilot head will then be surrounded by plasma and a new space charge laryer appearing at the tip of this plasma will take over the tip field X_0. Therefore the velocity of a positive streamer means the phase velocity of the ionizing seat and not the drift velocity of ions.

We shall assume a value

$$v_0 = 8 \times 10^7 \text{ cm/s} \tag{20}$$

for our calculation.

Imagine a stationary head-sphere whose center locates at O on x-axis and assume that its ionizing field reaches as far as N-sphere distant by s ahead the head center O in Fig. 5. Then the electrons which enter N-sphere will ionize M N space and a positive ion layer of some thickness Δ will appear in contact with N-surface. Midway between M and N no such a layer can appear since the space will be filled by plasma.

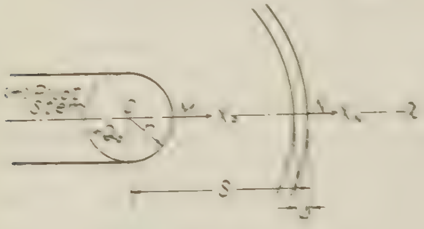

Fig. 5. Positive pilot.

If the space charge field X_N due to this ion layer becomes equal to the head-sphere field X_0, this means nothing but the advance of the pilot head M up to N. X_N takes the minimum ionizing field X_m at first and the head-sphere field X_0 at last. Then from its initial condition

$$X_m s^2 = X_0 r^2 , \tag{21}$$

and together with the relation (9) we get

$$\frac{r}{l} = \frac{X_m}{2\sqrt{CK}} \left(\frac{s}{l}\right)^2 \tag{21a}$$

and

$$X_0 = \frac{4CK^2}{X_m} \left(\frac{s}{l}\right)^{-2} . \tag{21b}$$

As X_m we shall use the value

$$X_m = 23 \text{ kV/cm} = 77 \text{ esu/cm} , \tag{22}$$

then (21a) and (21b) can be written as

$$\frac{r}{l} = 30.3 \left(\frac{s}{l}\right)^2 \tag{23a}$$

and

$$X_0 = 8.34 \times 10^{-2} \left(\frac{s}{l}\right)^{-2} . \tag{23b}$$

Since we are assuming X_0 to be independent of l as for the negative streamer, s/l must also be independent of l by (23b). Then r becomes proportional to l by (23a).

Next we shall consider about the time required by X_N for building up from X_m to X_0. If we denote it by t_0, it relates to the streamer velocity v_0 as follows:

$$v_0 t_0 = s - r . \tag{24}$$

The time t_0 is obtained in the following manner.

The field increment dX_N at N during dt is given by

$$dX_N = 4\pi e n_0 \mu X_N A dt , \tag{25}$$

where n_0 is the electron density at N before ionization; A is amplification due to ionization in Δ-space and is given by

$$A = \varepsilon^{-\int_s^{s-\Delta} \alpha dx} - 1 \sim \varepsilon^{-\int_s^{s-\Delta} \alpha dx} . \tag{26}$$

A is a function of X_N, but since Δ is expected to decrease with increasing X_N, A should change rather moderately with X_N. As a preferable form let us assume that

$$A = aX_N^{3/2} = 0.12 X_N^{3/2} . \tag{26a}$$

which gives $\Delta = 1.6$ cm for 30 kV/cm for instance.

The electron density n_0 at N-surface is conveniently assumed to decrease with increasing X_N. Put

$$n_0 = \frac{b}{X_N} . \tag{27}$$

where the constant b will be given later by (31). By virtue of (26a) and (27) we can get t_0 from (25), that is,

$$t_0=\int_{X_m}^{X_0}\frac{dX_N}{4\pi e\mu n_0 A X_N}$$

$$=\frac{1}{2\pi e\mu ab}\left(\frac{1}{X_m{}^{1/2}}-\frac{1}{X_0{}^{1/2}}\right). \qquad (28)$$

Next consider the total electron charge q_0 which enters N-hemisphere during t_0; it is given by

$$q_0=\int_0^{t_0} en_0 2\pi s^2\mu X_N dt=2\pi s^2 e\mu b t_0. \qquad (29)$$

Since, however, the charge of the head-sphere must decrease by the same amount,

$$q_0=-\frac{dQ_0}{dt}t_0=\frac{dQ_0}{dl}v_0 t_0.$$

From the relation $s/l=$constant

$$\frac{ds}{dl}=\frac{s}{l},$$

and also

$$Q_0=s^2X_m,$$

so

$$q_0=\frac{v_0X_m 2s^2}{l}t_0. \qquad (30)$$

Equating (29) and (30), we get

$$b=\frac{v_0X_m}{\pi e\mu l}. \qquad (31)$$

Put t_0 into (24) and further substitute r and X_0 therein by (23a) and (23b), then s/l will be obtained as one of the roots of the following equation:

$$x^2-3.94\times10^{-2}x+2.04\times10^{-4}=0.$$

Taking the smaller x, we get

$$\frac{s}{l}=6.1\times10^{-3}. \qquad (32)$$

From this result we can derive various quantities as follows:

$$X_0=2200\ \text{esu/cm}=660\ \text{kV/cm}, \qquad (32a)$$

$$\frac{r}{l}=1.13\times10^{-3}, \qquad (32b)$$

and

$$bl=4.87\times10^5 v_0. \qquad (32c)$$

§ 9. Transition from Pilot to Channel —Stepping—of Positive Streamer

We shall next discuss about the stepping of the positive streamer. Here also the similar calculation principle as for the head-sphere must be applied. This case is however far simpler, because the position of the limit surface, which corresponds to N-surface of Fig. 5, remains constant ($=X_m$) during expansion. So we can estimate $\Delta\tau$ by the following equation directly:

$$4\pi en_0\mu X_m\cdot\Delta\tau\cdot A=X_m.$$

This is further transformed by virtue of (26a) and (31) as

$$\Delta\tau=\frac{l}{4aX_m{}^{3/2}v_0}. \qquad (33)$$

The above estimated $\Delta\tau$ means the duration of expansion up to radius ρ_1, where the minimum ionizing field exists. We denote the $\Delta\tau$ of (33) by $\Delta\tau_1$, and putting the numerical values of X_m and a in it, we get

$$\Delta\tau_1=3.09\times10^{-3}\frac{l}{v_0}. \qquad (33a)$$

Also the limit radius ρ_1 is given by

$$\rho_1=\frac{2q}{X_m}=2.5\times10^{-3}l. \qquad (34)$$

From ρ_1 up to the final channel radius R, on the other hand, the surface continues to expand with ionic velocity $(1/2)\mu_i X$ as in the case of the negative streamer, where μ_i means ion mobility. The time required for this expansion becomes

$$\Delta\tau_2=\int_{\rho_1}^{R}\frac{d\rho}{\frac{1}{2}\mu_i X_\rho}=\frac{1}{2\mu_i q}(R^2-\rho_1{}^2). \qquad (35)$$

Assuming the value

$$\mu_i=1.5\ \text{(cm/s)/(V/cm)}=450\ \text{(cm/s)/(esu/cm)}, \qquad (36)$$

$\Delta\tau_2$ becomes as follows:

$$\Delta\tau_2=13.8\times10^{-8}l. \qquad (37)$$

For lightning leaders, $\Delta\tau_2$ becomes milliseconds or more while $\Delta\tau_1$ is of the order of microseconds. This means that a positive streamer expands rapidly up to the radius of ionization limit, but then expands very slowly. Then step period of the positive lightning leader must therefore be decided by $\Delta\tau_1$.

On the contrary, for gaps of meter length $\Delta\tau_1$ becomes negligibly small and $\Delta\tau_2$ becomes measurable order. Therefore if stepping be observed for such gaps $\Delta\tau_2$ should be taken into account.

IV. Numerical Calculation and Discussion

§ 10. Systematizing the Theory

So far we have succeeded in obtaining

various important quantities concerning the structure of the streamer. The mutual interconnections among them are shown in the following diagram Fig. 6 for the convenience of calculation.

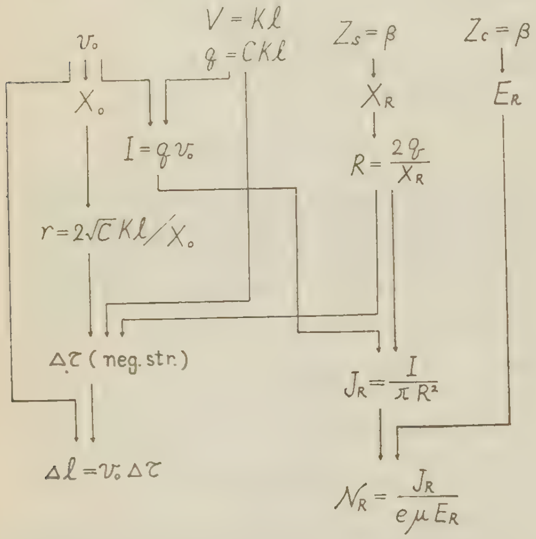

Fig. 6. Diagram showing the procedure of calculation.

In the diagram $\varDelta\tau$ is shown for the negative streamer; for $\varDelta\tau_1$ and $\varDelta\tau_2$ of the positive streamer (33) and (35) should be referred to.

By virtue of the above diagram we can derive various quantities as the functions of l. The result is summarized in Table I for positive and negative streamers whose velocities are 8×10^7 and 4×10^7 cm/s respectively.

§ 11. Stepped Leader of Lightning

According to the above table we can evaluate the step period $\varDelta\tau$ and step length $\varDelta l$ of a lightning leader if we put an appropriate l value in those expressions of a negative streamer; that is, for $l=3.0$ km* we get

$$\varDelta\tau=53.4\ \mu\text{s} \quad \text{and} \quad \varDelta l=21.4\ \text{m}.$$

These values show good coincidence with Schonland's data:

$$\varDelta\tau=50\ \mu\text{s} \quad \text{and} \quad \varDelta l=20\ \text{m}.$$

As to the positive lightning leader, the author knows only the data obtained at Empire State Building in New York. According to Hagenguth and Anderson's report[7], regular stepping with 25 μs period began to appear when a positive leader advanced 300 ft high above the building and continued up to 500 ft. The velocity was 3×10^7 cm/s.

Table I. Summary of Calculation Formulas
(Unbroken length l in cm)

Quantity	Negative Streamer ($v_0=4\times10^7$ cm/s)	positive Streamer ($v_0=8\times10^7$ cm/s)
spark voltage V (kV)	$5l$	$5l$
charge/length q (coul/cm)	$3.2\times10^{-11}l$	$3.2\times10^{-11}l$
tip field X_0 (kV/cm)	230	660
pilot radius r (cm)	$3.34\times10^{-3}l$	$1.13\times10^{-3}l$
channel radius R (cm)	$4.27\times10^{-3}l$	$4.27\times10^{-3}l$ ($\rho_1=2.5\times10^{-3}l$)
streamer current I (A)	$1.28\times10^{-3}l$	$2.56\times10^{-3}l$
channel current density J (A/cm²)	$22.4/l$	$44.8/l$ ($130/l$)
channel internal field E_R (kV/cm)	3.0	3.0
channel electron density N_R (cm⁻³)	$1.11\times10^{14}/l$	$2.22\times10^{14}/l$ ($6.43\times10^{14}/l$)
step period $\varDelta\tau$ (μs)	$1.78\times10^{-4}l$	$\varDelta\tau_1=3.86\times10^{-5}l$ $\varDelta\tau_2=0.138l$
step length $\varDelta l$ (cm)	$7.12\times10^{-3}l$	$\varDelta l_1=3.08\times10^{-4}l$ $\varDelta l_2=11l$

(Parenthesized values of the last column are for ρ_1.)

The position 300 ft above the building corresponds to 480 m above the earth surface. If we assume the negative cloud as 3.5 km high above the earth, l between the leader tip and cloud amounts 3 km long. Inserting this l-value into $\varDelta\tau_1$-expression, we get

$$\varDelta\tau_1=26.5\ \mu\text{s},$$

which is quite satisfactory provided that the $\varDelta\tau_1$-formula of Table I is corrected to the measured v_0.

§ 12. Streamers of Ordinary Gaps

Table I tells us that for 1 m gap length the radius of channel is equal to 0.427 cm and it decreases with its advance toward the opposite plane electrode. The current is several tenths of ampere and the current density reaches hundreds mA/cm^2.

---

* This implies a streamer which has spreaded 500 m long from the negative cloud 3.5 km above the earth surface.

The radius of the channel is equal for positive and negative streamers, but we have already noticed that the positive streamer has a tendency to take the semifinal radius ρ_1 determined by ionization limit, which becomes 0.25 cm for $l=1$ m. Therefore the positive steamer radius is equal to or rather less than the negative one, that seems quite cooperative with our understanding about streamers.

As to the stepping of ordinary gap streamers the thory suggests following remarks.

For negative streamers the step period becomes hundredth of microsecond, which can hardly be observed by a rotating camera.

For positive streamers, the step period becomes several microseconds if $\Delta\tau_2$ determines it and therefore observable. However as the step length Δl_2 becomes almost equal to or rather larger than the electrode distance, it may be hard to observe regularly stepped streamers.

§ 13. Temperature Rise of Streamer

We have so far left this problem untouched, but here we show that no sensible rise of temperature can occur in any streamer.

The energy input W per 1 g of air at any part of the streamer is given by the following expression:

$$W=J_R E_R \tau \frac{n_1}{N}, \tag{38}$$

where τ is the duration of that portion up to spark occurrence and given by l/v_0, n_1 the number of gas molecules per 1 g of air and N that per unit volume.

A part of this energy is lost by thermal conduction and radiation, but we leave these losses out of consideration for a while and assume that the total energy is spent exclusively on raising the streamer temperature. Then the final temperature rise ΔT is given by W/c_p, where c_p is the specific heat of air under constant pressure. Since

$$n_1=2.08\times10^{22}, \quad N=2.7\times10^{19},$$

$$c_p=0.24 \text{ cal/g deg} \quad \text{and} \quad E_R=3.0 \text{ kV/cm},$$

we get

$$\Delta T=1.4 \text{ deg}. \tag{39}$$

Even the optimum value is thus extremely small. Actual ΔT must be smaller than this limit value and so we need not consider the temperature effect at all. We can therefore safely conclude that streamers can not have arc property by itself so far as our theory is not wrong.

The above temperature rise occurs uniformly along the streamer and also is independent of v_0 and polarity of the streamer.

§ 14. Remarks

A) We determined the channel radius R from the self-maintaining condition (10) for electrons. Outside the surface of R-cylinder electrons are estimated to be able to move only $3\sim4$ cm along the field before they attach upon gas molecules. Owing to this reason there must exist an ion-layer immediately outside the channel. The charge q which is required to protect the plasma from the external field is due to the difference between positive and negative ions per unit length of this layer. The densities of positive and negative ions in this layer are calculated to be of the order of $10^{14}/l$, provided that the layer thickness is assumed to be $10^{-3}\,l$.

B) The proof that the condition (10) also exists in the channel may be given as follows. If we consider the balance of loss and generation of electrons in volume element $2\pi\rho d\rho$ around the axis the following equation is obtained:

$$-D_a\frac{dN}{d\rho}2\pi\rho+D_a\frac{d}{d\rho}\left(N+\frac{dN}{d\rho}d\rho\right)2\pi(\rho+d\rho)$$
$$+Z_G N d\rho 2\pi\rho-\beta N d\rho 2\pi\rho=0,$$

where N is electron density, D_a ambipolar diffusion coefficient and Z_G, β the same as in § 5.

Putting

$$x=\rho\sqrt{\frac{Z_G-\beta}{D_a}},$$

the above equation is transformed into the form

$$\frac{d^2N}{dx^2}+\frac{1}{x}\frac{dN}{dx}+N=0,$$

therefore

$$N=J_0(x).$$

If we assume that $N=0$ at $\rho=R$ as in the theory of positive column of glow discharge,

$$Z_C-\beta=D_a\left(\frac{2.45}{R}\right)^2 .$$

Inserting the known values of R and D_a (=1.16 for E_R)

$$Z_C-\beta=\frac{3.83\times10^5}{l^2} .$$

Since Z_C and β are of the order of 10^6 as shown in Fig. 2, we get

$$Z_C-\beta\sim0 ,$$

that is, the same result as (10).

C) As to the pilot model applied in this theory, there still remains a doubt about its appropriateness. To avoid an unconceivably large value of stem capacity, the author assumed that the head-sphere is electrically insulated from the stem as explained in § 3.

However this assumption causes another difficulty that the potential difference between the stem and the head-sphere $(Kl-X_0r)$ takes unreasonably large value. This is quite the question left for future study.

About the model of head-sphere structure we may probably suggest that the head-sphere has some intimate relation to the phenomenon " ball-lightning " as it is called, whose structure remains still mysterious. When a lightning leader runs athwart the vertical field of thunder-storm, under-voltage state will appear at the leader tip (refer to § 5), and the freshly producing stem part will not be able to maintain enough potential difference against the head-sphere and thus has a liability to let it free. The origin of the ball-lightning may then be explained by such a detached head-sphere.

Acknowledgement

The author wishes to express his cordial thanks to the research group on gaseous discharge in his laboratory and also to the members of lightning study in Meteorological Laboratory for their helpful discussions. His appreciation is also due to the financial aid granted by the Ministry of Education.

References

1) Schonland, B. F. G. and others: Proc. Roy. Soc. A **143** (1934)–**191** (1947).
2) Meek, J. M.: Phys. Rev. **55** (1939) 972.
3) Schonland, B. F. G.: Proc. Roy. Soc. A **220** (1953) 25.
4) Loeb, L. B.: " Electrical Discharge in Gases ", p. 279, Fig. 121.
5) Ditto: p. 345, Table 22.
6) von Engel, A. und Steenbeck, M.: " Elektrische Gasentladungen ", Bd. 1, S. 89.
7) Hagenguth, J. H. and Anderson, J. G.: AIEE Tech. Paper (1952) 52–175.

JOURNAL OF THE PHYSICAL SOCIETY OF JAPAN Vol. 12, No. 12, DECEMBER, 1957

On a Theory of Shock Waves in Locally Supersonic Zone and a New Boundary-value Problem for Tricomi's Equation

By Shun-ichi TSUGÉ

Department of Aeronautics, Faculty of Engineering, University of Tokyo, Tokyo

(Received September 5, 1957)

The hodograph behavior of the shock wave in transonic flow with non-uniform initial state is discussed. Besides the shock polar, two conditions are derived which, as a special case, comprise Busemann's spine and serve to eliminate the indeterminateness which constitutes specific difficulty for the treatment of high subsonic flow with shock waves. Applying these three equations to the transonic flow over an airfoil, a new boundary-value problem is proposed. The problem still involves indeterminateness, but in a special case when the airfoil has a ridge it can be simplified so as to develop further analysis.

§ 1. Introduction

The early stage of the investigation of the transonic flow was exclusively confined to the discovery of the possibility of smooth deceleration through the speed of sound. Though the contributions of S. Tomotika & K. Tamada1), M. J. Lighthill2) and T. M. Cherry3) gave the affirmative conclusion for this problem, the real phenomena or the results of experiments could hardly be in accord with these theoretical predictions. Thus the second stage to be proposed for the theory of transonic flow should be to revise the existing theory so as to allow the occurrence of shock waves. In this case, however, there occurs a mathematical indeterminateness (in the hodograph plane); one shock polar is not sufficient as in the treatment of the detached shocks and a *series* of them are necessary whose initial state distributes along a curve which itself is unknown. Thus we encounter with the boundary-value problem in which neither the boundary nor the boundary condition is prescribed. Though it seems impossible at the present stage to find out all of the lacking conditions, it is found that some of them can be derived as an immediate result of the shock relation, which in a special case has led A. Busemann4) to the discovery of the "spine". We shall show how these relations are found out and we shall also give some criticism for their ability to construct complete flow pictures.

§ 2. The Fundamental Equations

Since whole procedure is carried out in the hodograph plane, we must, from the outset, assume the two-dimensional character of the flow problem. Furthermore, the neglect of the vorticity induced by the presence of the shock should be postulated. This approximation seems doubly beneficial, since the main object of the present investigation, i.e. non-uniform state before the shock, is a phenomenon only proper to the transonic flow ($M \lesssim 1$). This is accomplished by assuming the flow to be in the transonic range:

$$q=a^*\{1+(\gamma+1)^{-1/3}w\}\ , \qquad w \ll 1 \qquad (1)$$

where q is the magnitude of the velocity vector, a^* critical speed of sound and γ the adiabatic index (=1.4 for air).

Under the assumption (1) the gasdynamic equation is simplified to the degree that it gives the well-known Tricomi's equation:

$$\Psi_{ww}-w\Psi_{\theta\theta}=0\ , \qquad (2)$$

where Ψ is the stream function and θ is the inclination of the velocity vector measured counterclockwise from the direction of undisturbed stream. In supersonic region ($w>0$) Eq. (2) is associated with the family of characteristic curves:

$$d\theta/dw=\pm w^{1/2} \text{ or } \theta\mp(2/3)w^{3/2}=\text{const.} \qquad (3)$$

In gasdynamics the boundary conditions are made up of two factors, namely, the condition on the surface of the obstacle and the condition on the shock wave. If we lay aside the details concerning the first, the second condition is expressed as follows:

$$\theta-\tilde{\theta}=\pm(\tilde{w}-w)\sqrt{(w+\tilde{w})}/2\ , \qquad (4)$$

and

$$dy/dx=(\gamma+1)^{-1/3}(\tilde{w}-w)/(\theta-\tilde{\theta})\ , \qquad (5)$$

where the quantities with and without the tilde (~) refer respectively to those measured immediately before and after the shock wave. Eq. (4) which is the equation for shock polar to transonic approximation shows the locus of the possible shock transition from any point in supersonic domain of the hodograph plane, and Eq. (5) gives the direction of the shock wave in the physical plane. These are the immediate consequences of the rotation of the axis of reference of the ordinary shock relations ($\tilde{\theta}=0$), but we should remark that this rotation brings essential feature of non-uniformity before shocks in which we are interested.

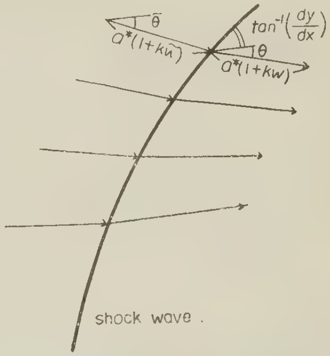

Fig. 1. Shock wave with non-uniform initial state ($k=(\gamma+1)^{-1/3}$).

§ 3. Relation between the Limiting Line and the Shock Wave

In 1941, von Kármán5) predicted that the location of the shock wave on the airfoil with embedded supersonic zone concides with the line of break-down of the mapping from the hodograph to the physical plane. Analytically

$$\partial(x, y)/\partial(q, \theta)=0\ , \tag{6}$$

which, by use of the relations:

$$\left.\begin{aligned} x_w&=(\gamma+1)^{1/3}w\Psi_\theta\ ,\\ x_\theta&=(\gamma+1)^{1/3}\Psi_w\ ,\\ y_w&=\Psi_w\ ,\\ y_\theta&=\Psi_\theta\ , \end{aligned}\right\} \tag{7}$$

is written as:

$$\Psi_w^2-w\Psi_\theta^2=0\ , \tag{6a}$$

while, along the streamline, we have

$$0=d\Psi=\Psi_w dw+\Psi_\theta d\theta\ ,$$

or

$$(d\theta/dw)_\Psi=-\Psi_w/\Psi_\theta\ . \tag{8}$$

Then the condition (6a) results in

$$(d\theta/dw)_\Psi=\pm w^{1/2}\ , \tag{6b}$$

where the subscript Ψ denotes the differentiation along the streamline. The left-hand side of (6b) specifies the direction of the spine in Busemann's sense. By Eq. (3) this condition (6b) may be written in an alternative form:

$$(d\theta/dw)_\Psi=(d\theta/dw)_{\text{characteristic}}\ . \tag{6c}$$

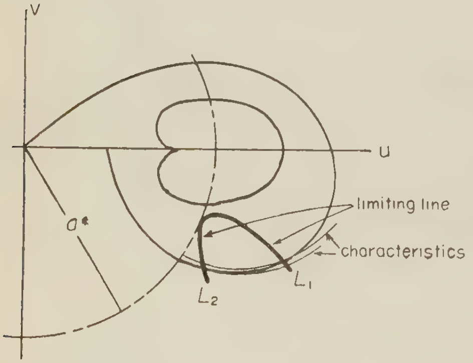

Fig. 2(a). Flow with a limiting line (hodograph plane).

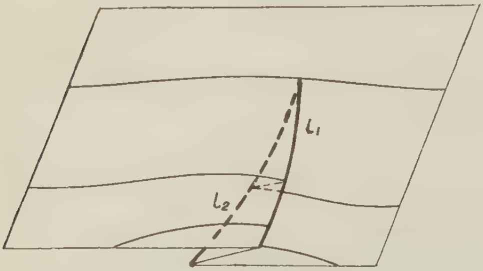

Fig. 2(b). Flow with a limiting line (physical plane).

This is an important property of the limiting line. Its conspicuous feature in the physical plane is the reflection of the streamline along it. Then, in general, the physical plane is composed of three sheets, which is physically impossible (Fig. 2b).

To correct the situation, we must give up the premise "irrotationality" or we must admit the presence of the shock wave between l_1 and l_2[6] (Fig. 3b). But if the physical plane is revised so as to be made up of a single sheet, the corresponding hodograph plane must have a *crevice* limited by S^+ and S^- between which L_1 and L_2 locate. Then the question arises: "How can the shock wave S^+ and S^- be predicted (in the hodograph plane)?" We cannot, however, content ourselves with

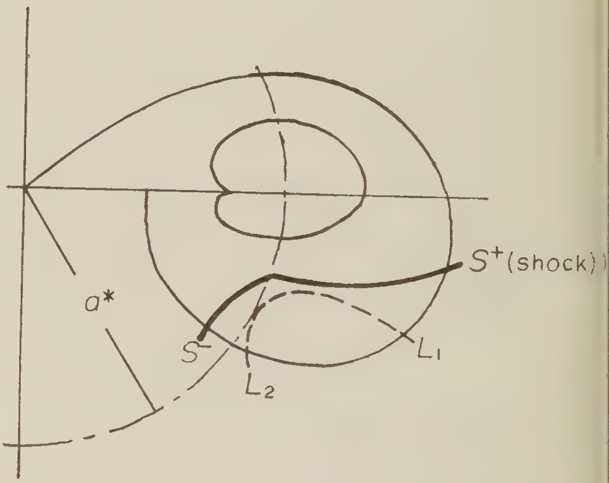

Fig. 3(a). Flow with a shock wave (hodograph plane).

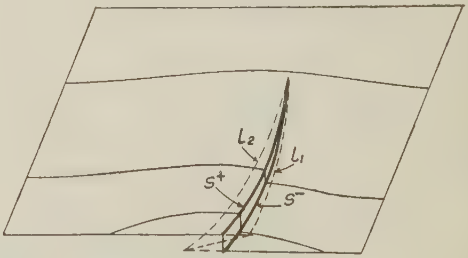

Fig. 3(b). Flow with a shock wave (physical plane).

knowing its shape only, but we have to inquire further after the boundary condition held along it. Then the second question asks "How is the specified condition on S^+ and S^- instead of the condition (6b) on L?" These two questions have to be discussed and to be answered in the following sections.

§ 4. Hodograph Behavior of the Shock Wave with Non-uniform Initial State

There is an asymmetry in the expression (5) of the shock wave, since the left-hand side involves the quantities of the physical plane, while the right-hand side is exclusively composed of the hodograph variables. We shall now express the left-hand side in terms of the hodograph variables. Differentiating x and y along the shock wave and making use of (7), we have

$$dx = x_w dw + x_\theta d\theta = (\gamma+1)^{1/3}(w\Psi_\theta dw + \Psi_w d\theta) ,$$

$$dy = y_w dw + y_\theta d\theta = \Psi_w dw + \Psi_\theta d\theta .$$

Then Eq. (5) becomes

$$\frac{(d\theta/dw)_S + \Psi_w/\Psi_\theta}{w + (\Psi_w/\Psi_\theta)(d\theta/dw)_S} = \frac{\tilde{w}-w}{\theta-\tilde{\theta}} ,$$

or, by Eq. (8),

$$\frac{(d\theta/dw)_S - (d\theta/dw)_\Psi}{w - (d\theta/dw)_S (d\theta/dw)_\Psi} = \frac{\tilde{w}-w}{\theta-\tilde{\theta}} , \tag{9}$$

where the subscript S denotes the derivative "along the shock wave", while Ψ denotes the derivative "along the streamline".

As we have seen in the preceding section, a single curves of the shock wave in the physical plane is splitted up into *two* branches S^+, S^- in the hodograph plane. Thus we must apply the condition (9) to each of them, and therefore *single equation* (5) *produces two conditions* of the following form:

$$\frac{(d\tilde{\theta}/d\tilde{w})_S - (d\tilde{\theta}/d\tilde{w})_\Psi}{\tilde{w} - (d\tilde{\theta}/d\tilde{w})_S (d\tilde{\theta}/d\tilde{w})_\Psi} = \frac{\tilde{w}-w}{\theta-\tilde{\theta}} \quad (\text{along } S^+) , \tag{10}$$

and

$$\frac{(d\theta/dw)_S - (d\theta/dw)_\Psi}{w - (d\theta/dw)_S (d\theta/dw)_\Psi} = \frac{\tilde{w}-w}{\theta-\tilde{\theta}} \quad (\text{along } S^-) . \tag{11}$$

These two equations, in conjunction with Eq. (4) give information about the flow just before and after the shock wave. It is of some interest to remark here that if we formally regard the tilde as the operator for producing the complex conjugate, the operation of it over Eq. (10) gives Eq. (11) and *visa versa*, while Eq. (4) remains unchanged. Thus the set of equations (4), (10) and (11) are *symmetrical* with respect to the quantities with and without the tilde (dynamical reversibility), and the only asymmetry arises from the second law of thermodynamics:

$$\tilde{w} > w .$$

In case when we deal with a flow with a head wave ($\tilde{w} = w_\infty =$ const. and $\tilde{\theta} = 0$) as a special case, the curve S^+ shrinks into a point. In such a case Eq. (10) proves to be meaningless and Eq. (11) together with Eq. (4) gives the shock polar and Busemann's spine.

§ 5. Correspondence between the Initial and Final State of Shock Transition

Let P$^+$ be a point just ahead of the shock wave in the velocity plane and P$^-$ the corresponding point after the shock transition. The terminology "corresponding" means that they have the same value for the stream function. In the case of non-uniform initial state, they have one-to-one correspondence, which we may denote

$$\tilde{w} = f(w) . \tag{12}$$

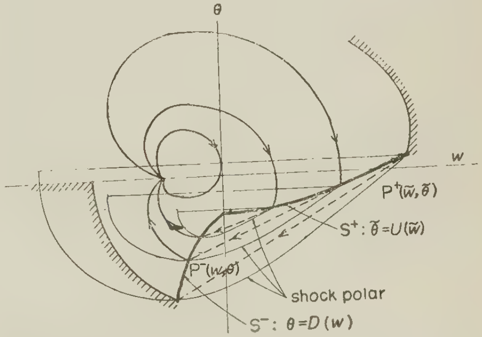

Fig. 4. Schematic figure in the vicinity of the shock wave.

Now we propose a problem: Given a initial curve:

$$S^+: \quad \tilde{\theta} = U(\tilde{w}) , \tag{13}$$

and the "spine" along it:

$$\tilde{\mu} = \tilde{\mu}(\tilde{w}) = (d\tilde{\theta}/d\tilde{w})_\Psi \tag{14}$$

what can be said about

1) the transforming function f,

2) the curve S^- of the final state $\theta = D(w)$, and

3) the spine towards downstream

$$\mu=\mu(w)=(d\theta/dw)_\Psi ?$$

The first question can immediately be answerd by Eqs. (4) and (10). Thus,

$$U'(f)\tilde{\mu}(f)\pm\sqrt{(w+f)/2}\{U'(f)-\tilde{\mu}(f)\}-f=0\,, \tag{15}$$

in which only $f(w)$ stands as the unkown. Once the transforming function $\tilde{w}=f(w)$ is found by the algebraic relation (15), the knowledge of the distribution of values of Ψ on S^+ can readily be shifted to that on S^- as stated at the beginning of this section. The function $f(w)$, thus specified, further contributes to answer the second question when we substitute it into Eq. (4),

$$\theta=D(w)=U(f)\pm(f-w)\sqrt{(w+f)/2}\,. \tag{16}$$

Finally the direction of the spine on S^- towards downstream is found from Eq. (11) by noticing Eqs. (15) and (16)

$$\mu(w)=\left(\frac{d\theta}{dw}\right)_\Psi=\frac{f\mp\sqrt{(w+f)/2}D'(w)}{D'(w)\mp\sqrt{(w+f)/2}}\,. \tag{17}$$

Thus Eqs. (15), (16) and (17) fix the physical state after the shock transition in terms of the initial state.

Hence, we must proceed to the second stage, viz. the state of affairs governing the initial state itself. Though the complete construction of the problem is the subject of the next section, it will be useful, as a stepping stone to go further, to remark the following fact. Though, as the matter of definition, the characteristic curve (Eq. (3)) is such that the discontinuity of the higher derivatives than the second order of the dependent variable can propagate along it, which, under some condition, can also be a carrier of the discontinuity of the first order derivative (shock wave!)[7]. So it stirs up our curiosity whether the curve S^+ coincides with one of the characteristic curves (plus family of Eq(3)) or not. If S^+ is a characteristic,

$$\tilde{\theta}=U(f)=\frac{2}{3}f^{3/2}\,.$$

When it is applied to Eq. (15), we have

$$(\sqrt{f}\mp\sqrt{(w+f)/2})(\tilde{\mu}(f)-\sqrt{f})=0$$

$$\text{i.e. } w=f \text{ or } \tilde{\mu}=f^{1/2}\,.$$

The demand for $w=f$ allows no discontinuity, so that it is reduced to an ordinary Mach wave. The second requirement $\tilde{\mu}=\sqrt{f}$ is identical with the limiting line condition (6). Thus we can summarize this fact as follows: Unless the limiting line is identified with a characteristic curve, the discontinuity due to the shock wave runs along a curve different from one of the characteristics. This fact, though seemingly trivial, brings inner importance when it provides us with a critical difference between Tricomi's problem and the one to be proposed in the next section.

In the same way, the possibility for the limiting line L_1 to coincide with the initial shock curve S^+ is discussed by the use of the limiting line condition (6b):

$$\tilde{\mu}(f)=f^{1/2}\,.$$

Substitution of it into Eq. (15) gives

$$(\sqrt{f}\pm\sqrt{(w+f)/2})(U'(f)-\sqrt{f})=0\,,$$

$$\text{i.e. } w=f \text{ or } U=\frac{2}{3}f^{3/2}\,.$$

Thus, the requirement is either that the transition is continuous, or that the initial line is a characteristic curve. Consequently, L must locate somewhere *between* S_1^+ and S_2^- (see again Fig. 3.a) since the extreme case is prohibited.

§ 6. A New Boundary-value Problem

Let us devote our attention to the state of affairs only about the initial curve of the shock wave S^+ (Fig. 5). By the preceding discussion the possibility that the initial curve S^+ coincides with a characteristic curve Γ_o is excluded. Furthermore, it can be generally concluded that S^+ lies inside the curvilinear triangle ACE. For, if the opposite situation stood, S^+ would be steeper than Γ_o, so that

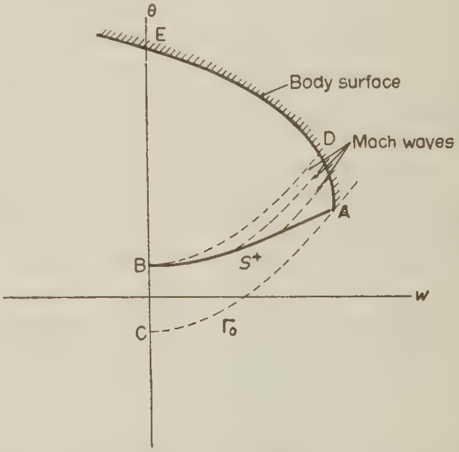

Fig. 5. Initial state of the shock wave and Mach waves from the body surface.

compression Mach wave originating from any part of the body surface could not reach it. This prediction is in accord with the experiment carried out by F. Tamaki[8] (Fig. 6).

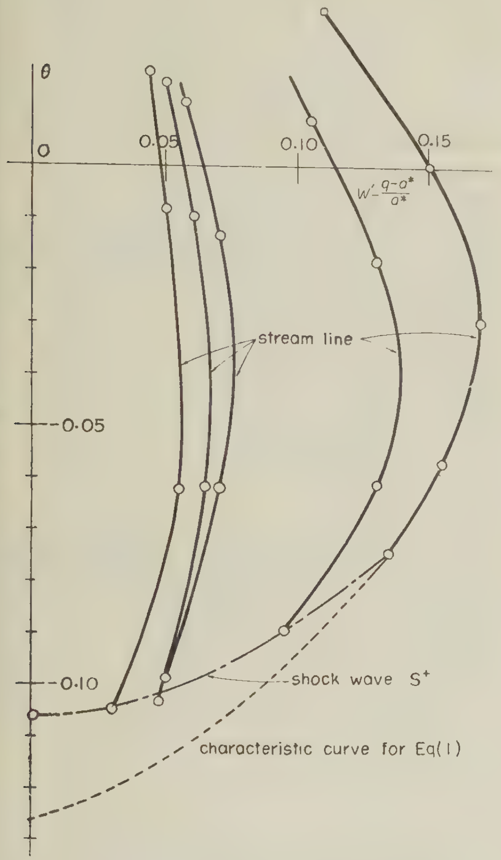

Fig. 6. Transonic flow over a Tomotika-Tamada airfoil at $M_\infty=0.763$ (Tamaki's experiment[8]).

Thus we come to the following problem: (New boundary-value problem) *Search for the solution of the equation*

$$\Psi_{ww}-w\Psi_{\theta\theta}=0\ ,$$

which satisfies the following boundary conditions: (see Fig. 7)

I. $\Psi=0$ on CDEA ,

where A *lies outside the curvilinear triangle* EFB, *where* EF *and* BF *are characteristic curves of the opposite family expressed by Eq. (3).*

II. *Along* S^+ (*or* AB) *and* S^- (*or* BC), *three conditions (15), (16) and (17) are prescribed.*

Our problem becomes much involved by the presence of the shaded part of Fig. 7 due to which the indeterminateness will occur in general. If the troublesome area vanishes, viz. if A situates on characteristic curve BF, we have Frankl's problem and as a special case if A is identified with F, our problem is reduced to Tricomi's one so long as one is concerned with the configuration in the hyperbolic domain. The second and no less important difference between the present and Tricomi's or Frankl's problem is the condition II, that is, the boundary value (according to Eq. (15)) and the derivatives (according to Eq. (17) and Eq. (8)) are prescribed *simultaneously* on S^-. Thus we encounter the overdetermined boundary-value problem in subsonic range, while, as we have seen, the supersonic domain involves underdetermination. In the present stage, we have no knowledge how to relate these under- and over-determinations, but we shall see that difficulties are reduced to some extent in the following special case.

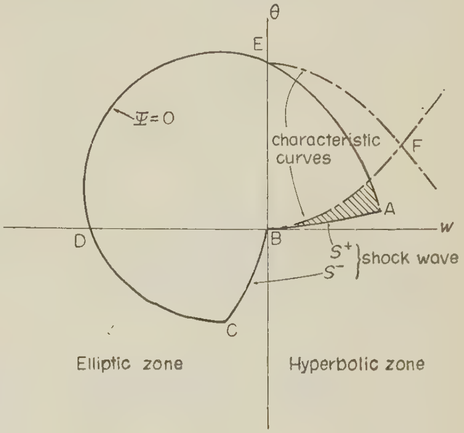

Fig. 7. New boundary-value problem.

§ 7. Flow round a Finite Wedge

In order to allow a simple hodograph configuration, let us choose, as a special model, a finite wedge immersed in gas flow, the free-stream Mach number of which is not much less than unity (Fig. 8). This problem was already solved by J. D. Cole[9] in the form of a singular (fundamental) solution which satisfies the boundary condition along CD and DE and is *opened free* for the remaining parts of the boundary. The exact setup of the problem on the standpoint of the present theory is shown in Fig. 8. viz.

I. $\Psi=0$ for $\theta=0,\ \theta=\theta_0$ $(w<0)$,

$\theta+(2/3)w^{3/2}=\theta_0$ $(w>0)$, where θ_0 is the half-wedge angle,

II. Along S^- the following two conditions are prescribed:

$$U'(f)\tilde{\mu}(f) \pm \sqrt{(w+f)/2}\{U'(f)-\tilde{\mu}(f)\}-f=0\,, \tag{15}$$

where, as before,

$$\tilde{w}=f(w)\,,$$

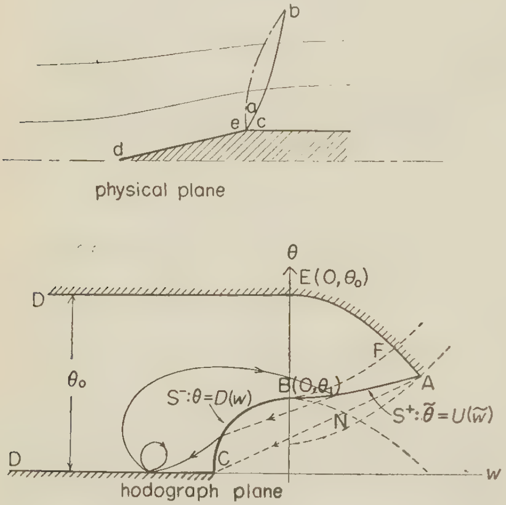

Fig. 8. Transonic flow round a wedge.

and

$$\mu(w)=\frac{f \mp D'(w)\sqrt{(w+f)/2}}{D'(w) \mp \sqrt{(w+f)/2}}\,. \tag{17}$$

III. S^- is specified by

$$\theta=D(w)=U(f) \pm (f-w)\sqrt{(f+w)/2}\,. \tag{16}$$

We should remark here that $U(f)$, or the curve AB is not given by the initial data, but belongs to *some* curve connecting the sonic line and the characteristic curve originating from E. So is also the curve BC or $D(w)$, since it depends on the behavior of $U(f)$ by Eq. (16) (Boundary-value problem with floating boundary curve).

But the present flow problem includes a special profit, viz. the coincidence of the boundary EA with a characteristic curve (Prandtl-Meyer expansion wave), which allows a remarkable simplification. For, then, the area ABF can be determined unlike the general problem stated in the preceding section. This can be verified by use of the special technique of analysis known as *the characteristic initial-value problem* in the following way.

As stated before, we are to treat Tricomi's problem if we replace the curvilinear triangle EBA by EBF in the configuration in hyperbolic domain. Then through the use of the initial data on the sonic line EB

$$\left.\begin{aligned}\Psi(0,\theta)&=\tau(\theta)\,,\\ \Psi_w(0,\theta)&=\nu(\theta)\,,\end{aligned}\right\}\quad \text{for} \quad \theta_1 \leqq \theta \leqq \theta_0 \text{ or EB}$$

Cauchy's problem is solved inside EBF[10]:

$$\begin{aligned}\Psi(w,\theta)=&-\frac{\Gamma(5/3)}{\{\Gamma(5/6)\}^2}\,w\int_0^1 \nu\left(\theta+\frac{2}{3}w^{3/2}(2t-1)\right)t^{-1/6}(1-t)^{-1/6}dt\\ &+\frac{\Gamma(1/3)}{\{\Gamma(1/6)\}^2}\int_0^1 \tau\left(\theta+\frac{2}{3}w^{3/2}(2t-1)\right)t^{-5/6}(1-t)^{-5/6}dt\,.\end{aligned} \tag{20}$$

Then we have the boundary value on BF,

$$\begin{aligned}\Psi=G(w_s,\theta_s)=&-\frac{\Gamma(5/3)}{\{\Gamma(5/6)\}^2}\,w_s\int_0^1 \nu\left(\theta_1+\frac{4}{3}w_s^{3/2}(t-1)\right)t^{-1/6}(1-t)^{-1/6}dt\\ &+\frac{\Gamma(1/3)}{\{\Gamma(5/6)\}^2}\int_0^1 \tau\left(\theta_1+\frac{4}{3}w_s^{3/2}(t-1)\right)t^{-5/6}(1-t)^{-5/6}dt\,.\end{aligned} \tag{21}$$

Since BF and FA are characteristics, only the value of Ψ (and not that of its derivatives) on BF and FA is necessary and *sufficient* for our purpose of determining the flow field FANB. We meet just the corresponding situation, viz.

$$\left.\begin{aligned}&\Psi=0 &&\text{on FA}\,,\\ &\text{Eq. (21)} &&\text{on BF}\,.\end{aligned}\right\} \tag{22}$$

It is not difficult to obtain the explicit expression for Ψ, since we have known Riemann's function for Tricomi's equation[10];

$$\left.\begin{aligned} &Z(\xi,\eta;\xi_s,\eta_s)\\ &\quad=\frac{(\xi-\eta)^{1/3}}{(\eta-\xi_s)^{1/6}(\eta_s-\xi)^{1/6}}F\left(\frac{1}{6},\frac{1}{6};1;\sigma\right),\\ &\text{and}\\ &\sigma=\frac{(\xi-\xi_s)(\eta_s-\eta)}{(\eta_s-\xi)(\eta-\xi_s)},\end{aligned}\right\} \tag{23}$$

where ξ, η are the characteristic coordinates of Eq. (1),

$$\left.\begin{aligned}\xi&=\theta-(2/3)w^{3/2},\\ \eta&=\theta+(2/3)w^{3/2}.\end{aligned}\right\} \tag{24}$$

Using Z thus defined, we have the complete solution valid inside the rectangle BNAF (Fig. 9)[11],

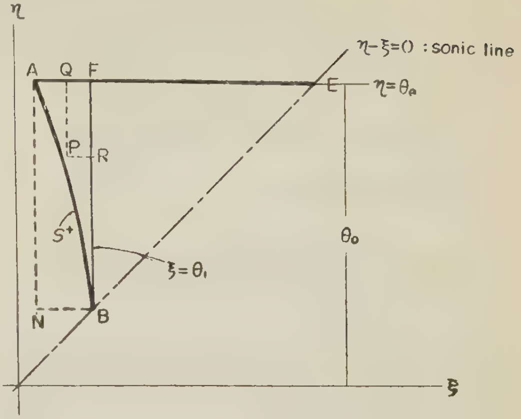

Fig. 9. Characteristic initial value problem.

$$\begin{aligned}(\Psi(\xi,\eta))_P&=(\Psi Z)_F+\int_F^R\left(\frac{\partial\Psi}{\partial\eta_s}-\frac{\Psi}{6(\theta_1-\eta_s)}\right)Zd\eta_s+\int_F^Q\left(\frac{\partial\Psi}{\partial\xi_s}+\frac{\Psi}{6(\xi_s-\theta_0)}\right)Zd\xi_s\\ &=(\Psi Z)_R-\int_F^R\left(\frac{Z}{6(\theta_1-\eta_s)}+\frac{\partial Z}{\partial\eta_s}\right)\Psi d\eta_s,\end{aligned} \tag{25}$$

by taking the condition (22) into consideration. This can be calculated by Eqs. (21), (22) and (23) to give a more intimate form

$$\Psi(\xi,\eta)=G(\theta_1,\eta)\frac{(\eta-\xi)^{1/6}}{(\theta_1-\eta)^{1/6}}-\int_{\theta_0}^{\eta}A(\xi,\eta;\theta_1,\eta_s)G(\theta_1,\eta_s)d\eta_s,$$

where

$$\begin{aligned}A(\xi,\eta;\xi_s,\eta_s)=\frac{1}{36}\frac{(\xi-\eta)^{1/3}}{(\eta-\xi_s)^{1/6}(\eta_s-\xi)^{1/6}}&\left\{6\left[\frac{1}{\xi_s-\eta_s}+\frac{1}{\xi-\eta_s}\right]F\left(\frac{1}{6},\frac{1}{6};1;\sigma\right)\right.\\ &\left.+\frac{(\xi-\xi_s)(\eta-\xi)}{(\eta-\xi_s)(\eta_s-\xi)^2}F\left(\frac{7}{6},\frac{7}{6};2;\sigma\right)\right\}.\end{aligned} \tag{26}$$

Thus the physical state is determined. Provided that the initial curve S^+: $\tilde{\theta}=U(\tilde{w})$ is assumed to be given, we can find the value of the spine

$$\tilde{\mu}(\tilde{w})=-\left(\frac{\Psi_w}{\Psi_\theta}\right)_{\substack{\theta=\tilde{\theta}\\ w=\tilde{w}}}=\tilde{w}^{1/2}\cdot\frac{\Psi_{\tilde{\xi}}-\Psi_{\tilde{\eta}}}{\Psi_{\tilde{\xi}}+\Psi_{\tilde{\eta}}},$$

the right-hand side of which being calculated by Eq. (26).

Summarizing, in virtue of the reduction to the characteristic initial-value problem, we have reduced the number of unknowns to a single quantity i.e. the shape of the initial state of the shock or S^+: $\tilde{\theta}=U(\tilde{w})$. How this unknown is connected with the compatibility of the simultaneous conditions (Eqs. (16) and (17)) on the final curve S^- is still too involved to allow a straightfoward analysis. Further investigation would be necessary to meet the complete physical pictures.

References

1) S. Tomotika & K. Tamada: Quart. Appl. Math. **9** (1951) 129.
2) M. J. Lighthill: Proc. Roy. Soc. A. **191** (1947) 352.
3) T. M. Cherry: Proc. Roy. Soc. A. **192** (1947) 45.
4) A. Busemann: N.A.C.A. T.N. 1858 (1949).
5) Th. von Kármán: J. Aero. Sci. **8** (1941) 337.
6) G. Guderley: Z.A.M.M. **22** (1942) 121.
7) R. Courant und D. Hilbert: *Methoden der Mathematischen Physik*, Bd. 2, (Julius Springer, Berlin (1937)) p. 297.
8) F. Tamaki: J. Phys. Soc. Japan **12** (1957) 544.
9) J. D. Cole: J. Math. Phys. 30 (1951) 79.
10) F. Tricomi: Brown Univ. Trans. A9-T-26.
11) R. Courant und D. Hilbert: loc. cit. p. 316.

Short Notes

This section is intended to secure prompt publication of important discoveries in physics. The reports should not exceed 800 words in length. A figure of size 7 cm × 7 cm will be counted as 150 words.

J. Phys. Soc. Japan **12** (1957) 1420

Phosphorescence of Acetic Acid

By Kikusaburo Osada

Faculty of Engineering, Nagoya University

(Received September 19, 1957)

It was reported in the previous paper¹⁾ that sodium- and potassium-acetates phosphoresce emitting a green light, when excited in vacuum with the ultraviolet radiation. In order to investigated the mechanism of this phenomenon, experiments on acetic acid were carried out at low temperatures.

Acetic acid (commercial reagent of the special grade) does not phosphoresce, when it is cooled near to −60°C with the mixture of dry ice and amyl acetate in apparatus as shown in Fig. 1 and is excited with the radiation. However, acetic acid solutions which are dissolved a little amount of $Na(C_2H_3O_2)$, KCl, or $NaHCO_3$, phosphoresce weakly emitting a green light at lower temperature than −30°C. We measured the decay curves of afterglow of them at several temperatures between −30°C and −60°C by a photo-multiplier tube with a d.c. amplifier and an oscilloscope¹⁾, and estimated the initial intensity by the extrapolation of the curve. The relations between the intensity and temperature are shown in Fig. 2. It was observed by using the two filters (Matsuda V–C1B and V–Y1A) that these spectra composed of a green band and a blue one, but the intensity of them was too weak to record separately the decay curve of each band. When lead acetate is used as solute, we can not observe the emission down to −60°C.

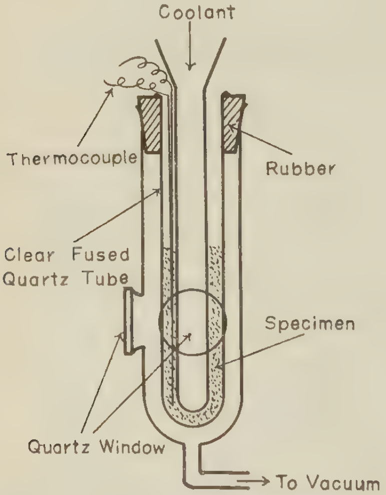

Fig. 1. Apparatus for observation of phosphorescence.

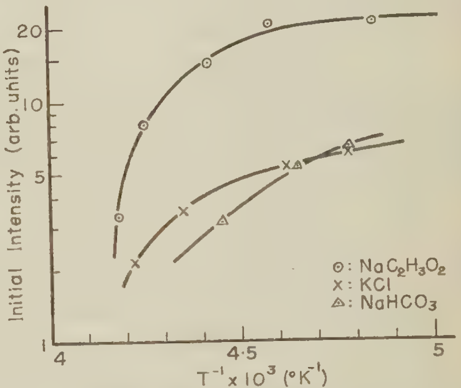

Fig. 2. Temperature dependence of phosphorescence of acetic acid contained a salt.

Here, we shall consider the origin of phosphorescence from these results. When the acetic acid solutions are cooled down, they solidify at lower temperature than that of melting point of acetic acid. We can not measure the state and amount of salts which are contained in the solidified acetic acid, but the salts seem to be slightly contained in ionic state as impurities in the solid. The salts do not phosphoresce by themselves with the exception of sodium- and potassium-acetates, after excited in vacuum with the ultraviolet radiation, and acetic acid contained lead acetate does not, too. Therefore, we may conclude that the phosphorescence is due to sodium- and potassium-ions which are contained as impurities in the solidified acetic acid and interact with the acetic ions.

Reference

1) K. Osada: J. Phys. Soc. Japan **11** (1956) 425.

J. PHYS. SOC. JAPAN **12** (1957) 1421

Experiments on the Cylindrical Blast Waves

By Kōichi ŌSHIMA

Institute of Science and Technology, University of Tokyo, Tokyo

(Received November 11, 1957)

Since a century ago, a number of investigators[1] have studied the phenomena of electrically "exploding wires" observed when a bank of large capacitors is discharged through a very fine wire. The author observed the internal structure, the propagation and the reflection of disturbance waves produced by these explosions in the surrounding medium.

The mild copper wires with diameters ranging from 0.1 to 0.16 millimeter were stretched perpendicularly to two parallel flat walls 5 centimeter apart, and exploded by the discharge current of condensers with capacity of 2–10 microfarads charged by 4–10 kilovolts source. The disturbances created by this method were observed through the glass windows attached on the walls using the instantaneous photographs of schlieren method and Mach-Zehnder interferometer. These disturbances are typical cylindrical blast waves preceded by a shock wave. The two-dimensional character of the blast wave was verified by the photographs taken parallel to the two walls.

The ratio of the air density inside the blast wave, ρ, to the one of the outer still air, ρ_0, are presented in Fig. 1, where D is the diameter of the exploded wire, C is the capacity of the condenser bank, V is the charging voltage, r is the distance from the exploded wire and R is the distance from the wire to the shock front. These curves were measured from the interferograms taken at 250 microseconds after the explosion, and agreed qualitatively with the theoretical predictions.[2] By these curves and shock relations, the strength of the shock wave, p/p_0, was calculated and plotted in Fig. 2. As the charging voltage increases or the diameter of the wire increases, the shock wave becomes stronger. At the very low charging voltage, however, the explosion of the thick wire becomes incomplete.

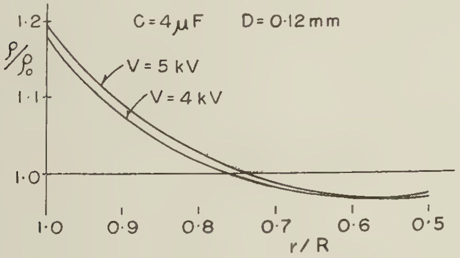

Fig. 1. Density Distribution.

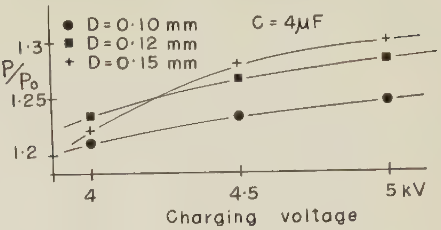

Fig. 2. Shock Strength.

Figs. 3 and 4 show the interferograms of the Mach and regular reflections of the cylindrical blast waves produced by this method on the flat surface. These interferograms were taken by the zero fringe method, so that the fringes appearing in the fields are the contours of constant density in the air. The so-called slip flow in the case of Mach reflection cannot be recognized on the interferograms, and the transition angle from regular to Mach reflection is greater than the one in the case of plane uniform shock wave with the same strength.

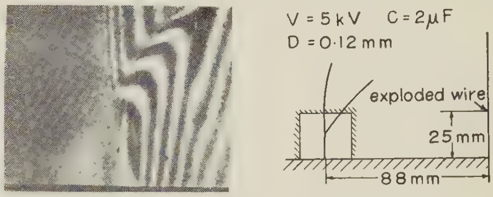

Fig. 3. Mach Reflection.

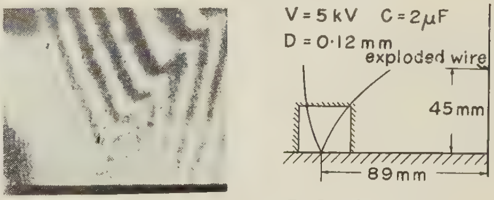

Fig. 4. Regular Reflection.

Similar experiments were carried out in water. The Mach and the regular reflection on the flat plate and the reflection on the free surface of the water were observed on schlieren photographs.

These experiments were carried out at the Institute of Science and Technology. The author wishes to express his sincere thanks to the members of the Institute for their encouragements and useful advice.

References

1) G. J. Singer and A. Croses: Phil. Mag. **46** (1815) 161.
H. Nagaoka and T. Futagami: Sci. Papers Inst. Phys. Chem. Res. Tokyo **8** (1928) 269.
2) A. Sakurai: J. Phys. Soc. Japan **8** (1953) 662, **8** (1954) 256 and **10** (1955) 1018.
G. B. Whitham: Proc. Roy. Soc. London A **203** (1950) 571.

J. PHYS. SOC. JAPAN **12** (1957) 1422

Effect of Electron Bombardment on Sodium Chloride

By Shigetomo YOSHIDA and Toshio IKEDA

Research Institute for Scientific Measurements, Tôhoku University, Sendai

(Received Septemper 12, 1957)

We have hitherto investigated the effect of electron bombardment on sodium chloride by electrical and optical methods.[1] This note concerns the formation of colloidal sodium in sodium chloride by electron bombardment.

Sodium chloride single crystals (5×5×1 mm) cleaved out from rock salt (Halle Co., Germany) were used as specimens after annealing. The bombarding voltage employed ranged from 7 to 20 KV while the current density and bombarding time were fixed at 40 μA/cm² and 60 minutes, respectively. The specimens were colored yellowish for the bombarding voltage below 13 KV and their absorption spectra showed distinct F and M absorption bands. At the voltage higher than 16 KV, blue-colored parts developed apperciably among yellowish ones. Under 20 KV bombardment the specimens acquired deep blue color. In the last case the strong absorption band with a peak at about 590 mμ was always accompanied by the weak one at 390 mμ, as shown in Fig. 1(a).

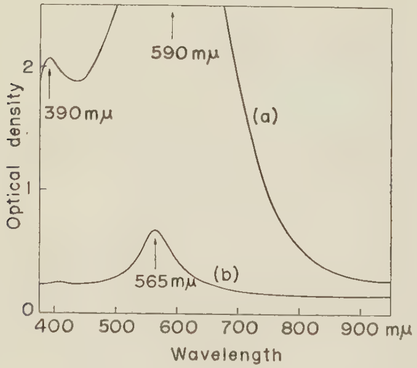

Fig. 1.

The same phenomenon was observed at 13 KV with the increase of current density from 40 μA/cm² to 70 μA/cm². When the specimens were kept at 150°C during bombardment, they also became blue in color even at the bombarding condition of 7 KV and 40 μA/cm².

Although this blue color was very stable at room temperature, the position of peak shifted to shorter wavelength side by annealing and reached to 565 mμ after the heating to 390°C at the rate of 0.7°C per minute, as shown in Fig. 1(b). This band, however, bleached entirely at 450°C and any other band was not observed at all.

On the other hand, when the specimens were maintained at high temperatures during bombardment, the position of peak shifted to longer wavelength side and the shape of band became less sharp. One example of this effect is shown in Fig. 2. Finally at about 300°C the specimens did not show any coloration and became cloudy.

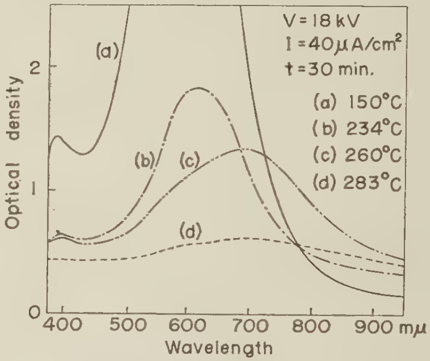

Fig. 2.

With specimens kept at high temperatures during bombardment, we observed also the scattering of dull red light from the crystal surface. This behaviour will be related to the scattering of light by colloidal particles, because their diameter, according to Savostianova's observation on natural blue rock salt, decides the position of peak of the absorption band and the rate of scattering. Thus, the strong absorption band with a peak at 590 mμ or thereabout may be identified as the colloidal band. Moreover, the before-mentioned weak peak at about 390 mμ may correspond to the peak of the photoconducing current curve plotted against the wavelength in blue or violet rock salt containing colloidal sodium[3].

From these results it may be concluded that the formation of colloidal sodium under electron bombardment is influenced greatly by the temperature of specimens which is also related to the bombarding wattage.

We are indebted to Prof. T. Hibi for the stimulating discussions and to the Electrical Communication Laboratory for the grant-in-aid.

References

1) S. Yoshida and T. Ikeda: Read at the meeting of Phys. Soc. Japan (Tokyo, 1956).
2) M. Sabostianova: Zeit. f. Phys. **64** (1930) 262.
3) Z. Gyulai: Zeit. f. Phys. **35** (1926) 411.

J. Phys. Soc. Japan **12** (1957) 1423

Electrical Properties of SnTe, SnSe and InBi at Low Temperatures

By Kimio Hashimoto

Department of Physics, Faculty of Science, Kyusyu University, Hukuoka

(Received September 30, 1957)

The electrical resistivity ρ and the Hall coefficient R of SnTe, SnSe and InBi have been measured in the temperature range between about 2° and 100°K.

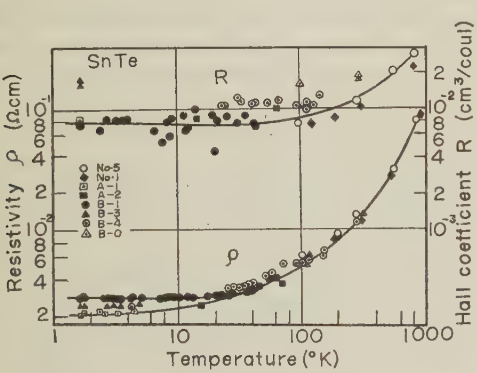

Fig. 1. Resistivity and Hall coefficient of SnTe as functions of temperature.

a) *SnTe.* R and ρ are shown in Fig. 1 as functions of the temperature. Both R and ρ increase with increasing temperature in the higher temperature range, but in the range below 30°K they seem to be independent of the temperature. The electrical properties of specimens No. 1 and No. 5 above liquid air temperature were reported in the previous letter.[1] A detailed discussion for the electrical properties of SnTe will be done elsewhere.

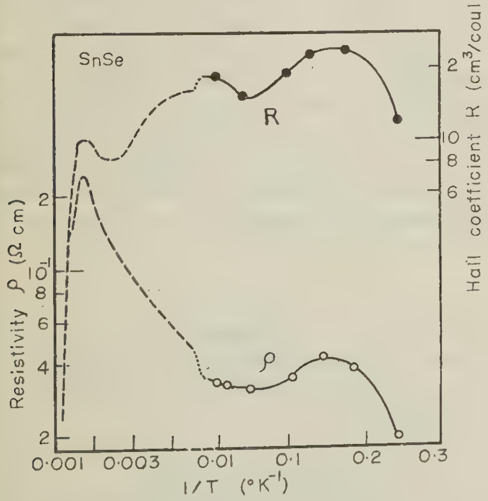

Fig. 2. Resistivity and Hall coefficient of SnSe as functions of temperature. Dotted curves show the values obtained by A. Okazaki and S. Asanabe[3].

b) *SnSe.* The temperature dependencies of R and ρ are shown in Fig. 2. Both R and ρ reach maximum values at about 6°K and then decrease with decreasing temperature.

c) *InBi.* The measured samples were the single crystal specimens used by S. Asanabe[2] for the investigation of anisotropy in resistivity above 100°K. The temperature dependency of ρ_{11}, the component of resistivity tensor, for specimen 503 is shown in Fig. 3 (see reference 2 for the definition of ρ_{11}). The linearity in the curve of ρ_{11} *versus* temperature is still maintained down to liquid helium temperature (see Fig. 2 in reference 2), but ρ_{11} decreases rapidly below liquid helium temperature. The Hall coefficient of specimen 503 could not be measured in the low temperature range. The transversal magnetoresistance effect of about 2% was observed for specimen 505A in the magnetic field of 20 000 Oe.

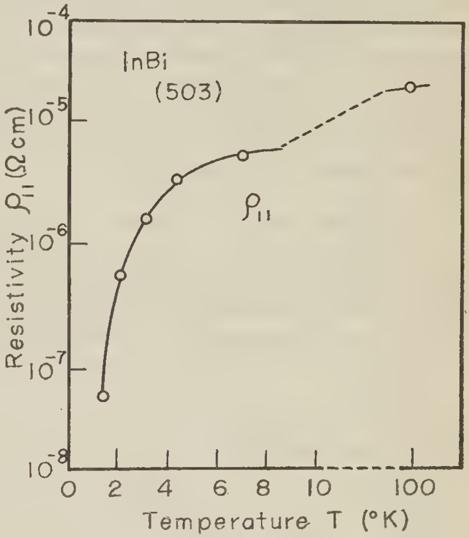

Fig. 3. Resistivity of InBi as a function of temperature.

I should like to express my hearty thanks to Professor T. Fukuroi, Professor Y. Shibuya and Professor S. Tanuma of the Research Institute for Iron, Steel and Other Metals, Tohoku University, for their guidance and for placing research facilities at my disposal.

References

1) K. Hashimoto and K. Hirakawa: J. Phys. Soc. Japan **11** (1956) 716.
2) S. Asanabe: Mem. Fac. Sci. Kyusyu Univ., **B2** (1956) 82.
3) A. Okazaki and S. Asanabe: to be published.

J. PHYS. SOC. JAPAN **12** (1957) 1424

On the Formation of Small Guinier-Preston (1) Aggregates During the Plastic Deformation of an Al-Cu Alloy

Keisuke MATSUURA
Hokkaido Gakugei Univ.
Yoshikazu HAMAGUCHI*
and
Shigeyasu KODA
Hokkaido Univ.

(Received September 9, 1957)

As previously reported[1], an abnormal increase of the electrical resistivity was observed during the plastic deformation of a supersaturated solid solution of an Al-Cu 4% alloy in room temperature, but the increase was of an ordinary order in an alloy of over-aged state. This abnormal increase of the supersaturated solid solution may be associated with the formation of small Guinier-Preston (1) aggregates that occurs during the plastic deformation. This interpretation presented by the authors is consistent with the results of X-ray investigation by Graf and Guinier[2] and of the tensile testing of single crystals by Carlsen and Honeycombe[3]. In this short note, a fuather information of such an abnormal change of the electriclal resistivity during the plastic deformation will be given.

Polycrystalline wires of 0.95 mm. in diameter were solution-treated for 30 minutes at 530°C. One group of them was air-quenched in order to obtain a state of supersaturated solid solution and the other was furnace-cooled so that a state of over-ageing was attained. The resistivity of these specimens was measured during the deformation of pure extension in room temperature and at −196°C, respectively.

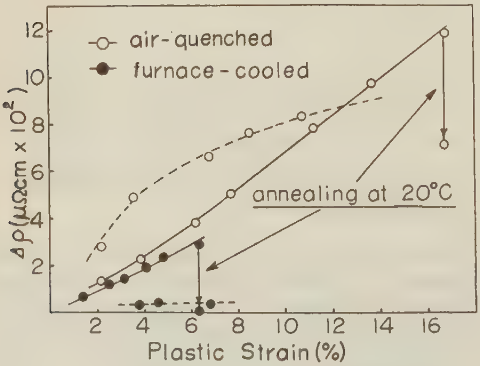

---- deformed at room temperature.
—— 〃 at −196°C.

Fig. 1. Increaces in specific resistivity by the plastic deformation.

The figure shows a typical example of the results. In an air-quenched specimen, the magnitude of resistivity change $\Delta\rho$ at room temperature showed a remarkably rapid increase in the range of small plastic strain ε. So, the $\Delta\rho-\varepsilon$ curve is convex. However, the resistivity of the furnace-cooled specimen scarecely increases at room temperature. Therefore, such an increase of the air-quenched specimen may be associated with the formation of small G.P. (1) aggregates that occurs during the plastic deformation, for such an effect was not observed in the case when the specimen was furnace-cooled. On the other hand, at −196°C in the air-quenched specimen, the rapid increase of resistivity continues to the range of large strain. The relation between $\Delta\rho$ and ε can be approximately expressed by $\Delta\rho=k\varepsilon^{1.1\sim1.2}$, where k is a constants. The results of the furnace-cooled specimen also showed a similar trend to increase. The diffusion of solute atoms which form G.P. (1) aggregates is appreciably suppressed at −196°C. So, in the case of −196°C, the most part of increase of $\Delta\rho$ in both specimens may be ascribed to the point imperfections, i.e. vacancies or interstitials created during the plastic deformation, because the point imperfections can hardly recover at such a low temperature. This fact may also be confirmed from the following two reasons. (1) A similar relation between $\Delta\rho$ and ε has been found in pure metals, such as copper, experimentally and theoretically.[4,5] In this case, the $\Delta\rho$ is attributed to the vacancies formed during the plastic deformation. However, it must be mentioned that the $\Delta\rho$ of the present investigation is appreciably larger than that of pure metals. (2) When the specimens tested at −196°C held at 20°C for a few minutes at the last stage of the deformation, the resistivity decreases to or below the $\Delta\rho$-ε curve for room temperature, as shown in the figure. This decrease may be understood to the caused by understood to be caused by the recovery of the point imperfections.

References

1) K. Matsuura, R. Nagasaki and S. Koda: Nippon Kinzoku Gakkaishi, to be published.
2) R. Graf et A. Guiner: Compt. rend. **238** (1954) 2175.
3) K. M. Carlsen and R. W. K. Honeycombe: J. Inst. Metals **83** (1954–55) 449.
4) H. G. van Bueren: Z. Metallkd. **46** (1955) 272.
5) H. G. van Bueren: Acta Met. **3** (1955) 519.

---

* Now Japan Atomic Energy Research Institute.

J. Phys. Soc. Japan **12** (1957) 1425

On Some Singular Solutions of the Tricomi Equation Relating to Transonic Flow

By J. B. Diaz

Institute for Fluid Dynamics and Applied Mathematics, University of Maryland, College Park, Maryland

(Received November 11, 1957)

In his interesting paper with the same title, Professor Kinzo Hida (Journal of the Physical Society of Japan, Vol. 10, No. 10, October 1955, 869–881) employs on page 871, equation (2.11), what he calls Cole's solution

$$\Gamma_{-}(z, v, z_1) = \tfrac{1}{4}(\tfrac{2}{3}zz_1)^{1/3}\int_0^\infty e^{-\alpha v}J_{-1/3}(\alpha z)J_{-1/3}(\alpha z_1)d\alpha\,. \tag{1}$$

Professor Hida has probably overlooked that Cole himself, in his paper (Journal of Mathematics and Physics, Vol. 30, No. 2, July 1951, 79–93), in a footnote on page 85, attributes this solution to A. Weinstein. Incidentally, Cole's footnote contains a misprint, he means Weinstein's formula (19), *not* (24). Moreover, Cole refers also to another paper of Weinstein (Proceedings Naval Ordnance Laboratory Aeroballistic Research Symposia, 1950, 73–81) in which Weinstein applies his formula and other more general formulas to the problem of the flow around a wedge.

In view of these facts it may be of interest to mention some additional literature on the same subject, part of which appeared in purely mathematical journals:

A. Weinstein, (Proceedings of the Fourth Symposium in Applied Mathematics of the American Mathematical Society, held June 1951 at the University of Maryland, published 1953, pages 167–178);

L. Trilling and K. Walker, Jr., (Journal Math. Phys., Vol. 32, 1953, 72–79, specially page 74);

P. Germain and R. Bader, (Bulletin Société Mathématique de France, Vol. 81, 1953, 145–174, specially page 161);

P. Germain, (Communications on Pure and Applied Mathematics, Vol. 7, 1954, 117–144);

A. G. Mackie and D. C. Pack, (Journal of Rational Mechanics and Analysis, Vol. 4, 1955, 177–199).

Several other expressions can be given for such singular solutions, see, for instance J. B. Diaz and A. Weinstein, (Studies in Mathematics and Mechanics presented to Richard von Mises, Academic Press, New York, 1954, 97–102).

Erratum

Elongated Lichtenberg Figure

By Yoshimi Kamada and Kwai Umeda

J. Phys. Soc. Japan **12** (1957) 1317

Left column, line 20 (about 10 cm/sec) should be read (about 10^7 cm/sec)

PROGRESS OF THEORETICAL PHYSICS

CONTENTS

Progress of Theoretical Physics Vol. 18, No. 4, October 1957

Nuclear Matrix Element Relations in the Fermi Theory of Beta Decay ...... Tino AHREN.. 331
Cluster Development Method in the Quantum Mechanics of Many Particle System, II—Saturation of Nuclear Forces— ...... Fumiaki IWAMOTO and Masami YAMADA.. 345
A Lattice Model of Liquid Helium, III—Equilibrium Properties of Liquid He^4 and Mixtures of He^4 and He^3— ...... Hirotsugu MATSUDA.. 357
On the Vibration of Disordered Linear Lattice, II ...... Jun-ichi HORI.. 367
Anomalous Magnetic Moments of Hyperons and Mirror Theorem ...... Hiroshi KATSUMORI.. 375
Static Model in the Meson Theory ...... Masao SUGAWARA.. 383
A Remark on the Moments of Inertia of Rotating Nuclei ...... Satio HAYAKAWA and Toshio MARUMORI.. 396
On the Ground Level Splitting of Mn^{++} and Fe^{+++} in Nearly Cubic Crystalline Field ...... Hiroshi WATANABE.. 405
On the Exciton Problem in Insulating Crystals ...... Yosihisa TAKEUCHI.. 421
Ionization Loss near the Origin of an Electron Pair of Very High Energy ...... Iwao MITO and Hiroshi EZAWA.. 437
Letters to the Editor: On the Line Width in Ferromagnetic Resonance ...... S. TAKENO.. 448
Errata: $E2+M1$ Mixed Transitions in Heavy Odd A Nuclei, 18 (1957), 87(L) ...... M. KAWAMURA.. 450

Price $ 1.25 per copy
$ 15.00 per year (postage inclusive)
Annual dues for foreign members (individual subscribers)
$ 12.00 (postage inclusive)
〃 for foreign members of the Physical Society of Japan
$ 10.00 (postage inclusive)

Application for members, subscriptions and orders for back numbers should be sent, directly or through book-dealers, to

The Publication Office
in
Yukawa Hall, Kyoto University, Kyoto, Japan

Contents

(Vol. 12)

No. 1

Masatoshi YAMAZAKI: Group-Theoretical Treatment of the Energy Bands in Metal Borides MeB$_6$ 1
Kunio FUJIWARA: On the Period of Out-of-step of Ordered Alloys with Anti-phase Domain Structure 7
Kyozaburo KAMBE: Study of Simultaneous Reflexion in Electron Diffraction by Crystals I. Theoretical Treatment 13
Kyozaburo KAMBE: The Phase Effect in Simultaneous Reflexion in Electron Diffractions II. Experimental Confirmation 25
Akira ISIHARA and Ryuzo KOYAMA: Intermolecular Potential between Large Molecules 32
Takeshi OKA, Hiromasa HIRAKAWA and Akira MIYAHARA: Dependence of Quadrupole Coupling Constant on the Vibrational State in ICN Molecule 39
Shōzō SEKINO and Tetsuji NISHIKAWA: Microwave Spectrum of Vinylidene Chloride .. 43
Yoshitaka KÔI: Line Width of the Pure Quadrupole Resonance of Bromine in NaBrO$_3$ 49
Jien NISHIWAKI: Gloss of Machine Glazed Papers 53
Isao IMAI: Application of the M^2-Expansion Method to Compressible Flow past Isolated and Lattice Aerofoils 58
Hidenori HASIMOTO: Boundary Layer Growth on a Flat Plate with Suction or Injection 68
Yaso'o MATUNOBU: Application of the Thin-Wing-Expansion Method to the Compressible Flow past an Elliptic Cylinder, with Special Reference to its Fourth Approximation 72
Otohiko NOMOTO: Phenomenological Theory of the Molecular Absorption and Dispersion of Sound in Fluids and the Relation between the Relaxation Time of the Internal Energy and the Relaxation Time of the Internal Specific Heat 85

No. 2

J. MUTO, E. TAKEKOSHI, T. NAKAMURA, A. IMAMURA and Y. TSUNEOKA: The Multipolarity of γ-ray Absorption in ^{12}C(γ, 3α) Reaction produced by (Li, p) γ-rays. 109
Saburo MIYAKE, Kensaku HINOTANI and Kan-ichi NUNOGAKI: Intensity and Energy Spectrum of Fast Neutrons in Cosmic Radiation 113
Masahiro KODAMA, Kazuaki MURAKAMI and Yataro SEKIDO: Observation of Cosmic-Ray Neutron Intensity at Geomagnetic Latitude 25°N, Part I. Atomospheric Effects 122
Yasuo KANAI and Riro NII: Electrical Properties of Nickel Doped Germanium at Low Temperatures 125
Makoto KIKUCHI: Peripheral Inhomogeneties of the Alloyed Germanium $p-n$ Junction 133
Einosuke FUKUSHIMA and Akiya OOKAWA: Observation of the Grain Boundary in Soap Bubble Raft. Part III. The Grain Boundary in Vibrating State 139
Shozo SAWADA, Ine TAKOO and Shin'ichi FUJII: An X-ray Tube with a Rotating Anode and an Earthed Cathode 147
Masao KURIYAMA, Kazutake KOHARA and Satio TAKAGI: Electron Diffraction Study on Polish Layers of Gold, I 151
Tokutaro HIRONE and Kengo ADACHI: On the Magnetic Properties of Nickel Arsenide Type Crystals 156
Kazuko MOTIZUKI: Theory of the Para-Ortho Conversion in Solid Deuterium 163
Kazuo HORIUCHI: Electromagnetic Fields due to Current Flowing Parallel to Interface of Two Different Media 170
Michiru YASUHARA: On the Hypersonic Viscous Flow past a Flat Plate with Suction or Injection 177
Yutaka SHIGEMITSU: Experimental Studies on Laminar Sub-layer in Turbulent Boundary Layer involving Separation 183

Yûkichi NOMURA and Shigetoshi KATSURA: Diffraction of Electromagnetic Waves by Ribbon and Slit, I 190
Teruo IKEBE and Tosio KATO: Application of Variational Method to the Thomas-Fermi Equation 201
Tasaburô YAMAGUTI: A New Method of Electro-Machining of Hard Metals 204
Tikao HUJITA: On the Ricochet Motion of a Projectile Striking a Water Surface 208

No. 3

Senzo TOKUNAGA, Kiyoshi NISHIKAWA and Taka ISHII: A Cascade Shower in Nuclear Emulsion 219
Shûichi IIDA: Layer Structures of Magnetic Oxides 222
Masakazu MARUTAKE and Takuro IKEDA: Anisotropy in Polarized Barium Titanate Ceramics 233
Maurice L. HUGGINS and Yosio SAKAMOTO: Lattice Energies and Other Properties of Crystals of Alkaline Earth Chalcogenides 241
Kisaburo SHOGENJI and Susumu UCHIYAMA: On Electrical Resistivity and Hall Coefficient of PbTe Crystals 252
Makoto HIRABAYASHI and Shiro OGAWA: On the Superstructure of the Ordered Alloy Cu_3Pb II. X-ray Diffraction Study 259
Akira ODAJIMA, Junkichi SOHMA and Mitsuru KOIKE: Proton Magnetic Resonance in Chain Polymers 272
Atsuo NISHIOKA, Hachiro KOMATSU and Yoshinobu KAKIUCHI: Nuclear Magnetic Resonance in Some Crystalline Polymers 283
Masataka ARIYAMA, Kunihusa KAYAMA and Masayoshi SUGIMOTO: Self-consistent Field without Exchange for Doubly Ionized Cobalt 285
Shinji KUWABARA: The Forces Experienced by Two Circular Cylinders in a Uniform Flow at Small Raynolds Numbers 291
Otohiko NOMOTO: Theory of the Ultrasonic Absorption in Aqueous Solutions (II) Aqueous Solutions of Some Alcohols 300

No. 4

Sadao HOSHINO: Crystal Structure and Phase Transition of Some Metallic Halides IV 315
Kazuo HIROIKE: Radial Distribution Function of Fluids I 326
Takao SATO and Seiichiro NOGUCHI: Note on Some Properties of Gamma Brass 335
Tatsumi KUROSAWA: On the Melting of Ionic Crystal 338
Sumitada ASANO and Yasuo TOMISHIMA: Rotational Lattice Vibration in Complex Crystals Part 1. Vibrational Modes and Special Heat 346
Yoshihiko MIZUSHIMA, Zenjiro ODA and Osamu OCHI: The Structure of Evaporated Barium Films 355
Shintaro SUGAI and Jiro FURUICHI: Studies of High Polymers by Radioactive Method II Self-diffusion of Polystyrene in Its Dilute Solution 369
Keiji YAMAMOTO and Yasaku WADA: An Investigation of the Dynamic Mechanical Properties of Glassy Polymers by the Composite Oscillator Method 374
Yuichi IKEDA: On the Effective Diffusion Tensor of a Segment in a Chain Molecule and its Application to the Non-Newtonian Viscosity of Polymer Solutions 378
Motoyoshi YUZURI, Tokutaro HIRONE, Hiroshi WATANABE, Seizo NAGASAKI and Seijiro MAEDA: On the Magnetic Properties of Chromium Sulfides 385
Jun OKANO: Preliminary Report on an Electromagnetic Isotope Separator 390
Ken-ichi KUSUKAWA: On the Transonic Flow of a Compressible Fluid past an Axisymmetic Slender Body at Zero Incidence 401
Ken-ichi KUSUKAWA: On the Transonic Flow of a Compressible Fluid past a nearly Axisymmetric Slender Body 411
Sadatoshi TANEDA: Experimental Studies of the Life on Two Equal Circular Cylinders placed side by side in a Uniform Stream at Low Reynolds Numbers 419
Hiroomi FUJIKAWA: Expansion Formulae for the Forces acting on Two Equal Circular Cylinders placed in a Uniform Stream at Low Values of Reynolds Number 423

No. 5

Shinjirō YASUMI: Nuclear Reactions induced by the 14 MeV Neutrons ... 443
Senzo TOKUNAGA: Meson Showers by Heavy Primary Particles ... 454
Umejiro YOSHIDA and Akira SUZUKI: The Surface Potential of Selenium and its Relation to the Rectification and the Photovoltaic Effects ... 459
Wataru KINASE and Hidetosi TAKAHASI: On the 180°-type Domain Wall of $BaTiO_3$ Grystal ... 464
Terutaro NAKAMURA: After Effect of the Domain Motion in Rochelle Salt Crystal ... 477
Sigemaro NAGAKURA: Study of Metallic Carbides by Electron Diffraction Part I. Formation and Decomposition of Nickel Carbide ... 482
Tadashi INO: Studies on the Radial distribution Analysis in Diffraction Methods I. Errors due to the Approximation of Integration by Summation ... 495
Tadao HORIE, Takayuki NAGURA and Masamoto OTSUKA: Radiative Collisions between Electron and Molecular Beams II. Angular Momentum Distribution of OH* Radicals Splitting from H_2O_2 Molecules ... 500
Teruo YUKITOSHI, Hirosi SUGA, Syûzô SEKI and Junkichi ITOH: Nuclear Magnetic Resonance Experiment on Solid Hexamethyldisilane ... 506
Hiroshi WATANABE: Magnetic Properties of Perovskites Containing Strontium I. Strontium-Rich Ferrites and Cobaltites ... 515
Yoshika MASUDA: Nuclear Magnetic Resonance Experiment on Metal Cadmium ... 523
Yoshio SHIBAOKA: On the Buckling of an Elliptic Plate with Clamped Edge II ... 529
Yasujiro KOBASHI: Measurements of Pressure Fluctuation in the Wake of Cylinder ... 533
Fumio TAMAKI: Experimental Studies on the Stability of the Transonic Flow past Airfoils ... 544
Fumio TAMAKI and KIM, Chul-Soo: Studies on the Hypersonic Flow Using a Double-Diaphragm Shock Tube ... 550

No. 6

Minoru TAKEDA, Michiya KONDO, Syohei KATO, Chuin HU, Ryuzo NAKASIMA and Shotaro YAMABE: Elastic Scattering of 5.7 Mev Protons from Ni and Cu ... 561
Taro KIHARA: Geometrical Theory of Convex Molecules in Non-Uniform Gases ... 564
Ryogo KUBO: Statistical-Mechanical Theory of Irreversible Processes I. General Theory and Simple Applications to Magnetic and Condition Problems ... 570
Ziro MIKURA: Electron-Electron Interaction and Superconductivity. I ... 587
Sigeo YOMOSA and Takeo NAGAMIYA: Diffuse Scattering of X-rays by a Point-Imperfection in Diamond Lattice ... 610
Hide YOSHIOKA: Effect of Inelastic Waves on Electron Diffraction ... 618
Masao SAWADA, Kenjiro TSUTSUMI and Akira HAYASE: Fine Structures of X-ray Absorption Spectra of Cobalt in the Face Centered Cubic Lattice and Close-packed Hexagonal Lattice ... 628
Shigeya KUWABARA: Variation of Electron Diffraction Intensity with Crystal Size ... 637
Reikiti ITOH: Effect of the Basic Strength of Attached Groups on Light Absorption Spectra I. Light Absorption of Triphenylmethane Dyes ... 644
Kenji SHIMOMURA: Structural Investigation by Means of Nuclear Quardrupole Resonance I. Determination of Crystal Symmetry ... 652
Kenji SHIMOMURA: Structural Investigation by Means of Nuclear Quardrupole Resonance II. Tin Tetrabromide ... 657
Tetsuji NISHIKAWA: Microwave Studies on the Internal Motion and the Structure of Methyl-Amine ... 668
Takeshi KOJIMA and Tetsuji NISHIKAWA: Potential Barrier and Molecular Structure of Methyl Mercaptan from its Microwave Spectra ... 680
Koichi SHIMODA, Hidetosi TAKAHASI and Charles H. TOWNES: Fluctuations in Amplification of Quanta with Application to Maser Amplifiers ... 686
Yasuaki NAKAGAWA: Magnetic Susceptibility of Iron-Nickel Alloys in Liquid and Solid States ... 700
Masao KOTANI, Yukio MIZUNO, Kunifusa KAYAMA and Eiichi ISHIGURO: Electronic Structure of Simple Homonuclear Diatomic Molecules I. Oxygen Molecule ... 707

No. 7

Sigeo NAKAGAWA, Eiji TAMAI, Humiaki HUZITA and Kiyoaki OKUDAIRA: On the Analysis of the Slow Particles Emitted from Cosmic-Ray Stars (II) 747
Thoru MORITA: Cluster Variation Method of Cooperative Phenomena and its Generalization I 753
Makoto KIKUCHI: Some Experiments on the Surface Field Effects in Germanium Single Crystals 756
Takashi ITOH and Kenjiro KAMBE: Electron Coupled Interaction in Solid Iodine 763
Masaki HIRASHIMA and Shoichi MIYASHIRO: Some Factors Affecting the Decay of Secondary Electron Emission of Silver-Magnesium Alloys 770
Takuro TSUZUKU: Conical Spiral Structure and Laminar Cleavage of Graphite 778
Toshio SHIRAIWA, Tsutomu ISHIMURA and Masao SAWADA: Fine Structures of X-ray Absorption Spectra of Crystalline and Amorphous Germanium 788
Kenjiro TSUTSUMI, Akira HAYASE and Masao SAWADA: Fine Structures of X-ray *K* Absorption Spectra of Copper in Various Copper Compounds 793
Itaru TATSUZAKI and Yasaburo YOKOZAWA: Influence of Temperature on the Pure Nuclear Quadrupole Resonance in Hexachloroethane 802
Reikiti ITOH: Effect of the Basic Strength of Attached Groups on Light Absorption Spectra II. Near Ultraviolet Absorption Spectra of Para-substituted Aniline Derivatives 809
T. GHOSE, S. K. GHOSH and D. K. ROY: A Study on the Effects of Off-Resonance on the Spin-Echo Signals 816
Takeshi OKA and Hiromasa HIRAKAWA: Microwave Spectrum of BrCN and Dependence of Quadrupole Coupling Constant on the Vibrational State 820

No. 8

Itaru NONAKA, Susumu MORITA, Nawoyuki KAWAI, Toshiyuki ISHIMATSU, Kenji TAKESHITA, Yutaka NAKAJIMA and Nawoyuki TAKANO: On the Neutrons from the $N^{14}(d, n)O^{15}$ Reaction-II 841
Saburo MIYAKE, Kensaku HINOTANI, Itsuo KATSUMATA and Tatsunosuke KANEKO: Cosmic Ray Nuclear Interaction in Nitrogen Gas 845
Shūji FUKUI, Takashi KITAMURA and Yōjirō MURATA: On the Range Spectrum of μ-Mesons at Sea-Level at Geomagnetic Latitude 24°N 854
Kazuo HIROIKE: Radial Distribution Function of Fluids II 864
Masaru WATANABE: Submicroscopic Topography of Oxidized Surface of Stibnite and Etched Surface of Zincblende 874
Toshio MISAWA: Impedance of Bulk Semiconductor in Junction Diode 882
Sumitada ASANO and Yasuo TOMISHIMA: Rotational Lattice Vibration in Complex Crystals Part II. Vibrational Modes in Optical Branches and Interaction with a Conduction Electron 890
Sumitada ASANO and Yasuo TOMISHIMA: Rotational Lattice Vibration in Complex Crystals Part III. Vibrational Frequencies in Cubic $NaClO_4$ Crystals 900
Tadanobu KOJIMA: Electronic States of the *F*-Center in Lithium Fluoride. I 908
Tadanobu KOJIMA: Electronic States of the *F*-Center in Lithium Fluoride. II 918
Kinshiro HIRAKAWA: The Magnetic Properties of Iron Selenide Single Crystals 929
Kimio OHNO: On the Electronic Structure of the BH Molecule 938
Teruko SOEYA and Ryusuke KŌNO: On Some Transition Phenomena in Aqueous Solution of Polyvinylalcohol 950
Mitsuru ASANUMA and Shinji OGAWA: On the Magnetic Aging of Commercial Pure Iron 955
Humio NARUSE: Application of the Thin-Wing-Expansion Method to the Compressible Flow past Profiles of Arbitrary Shape 959
Hiroshi FUJITA: Notes on the Calculation of Electrophoresis of Polyelectrolytes with Partial Free-Drainage 968

No. 9

Mitsuo SAKAI, Haruko OHMURA and Teruo MOMOTA: Multichannel Angular Correlation Measurement of Gamma Rays from the Disintegration of Ag^{110m} and Spin

Assignment of Excited Levels of Cd^{110} 985
Taro KIHARA and Shobu KANEKO: Temperature Variation of Mayer's Cluster Integral 994
Wataru SEGAWA: Stress-Strain Relations for Viscoelastic Large Deformation 996
Shiro OGAWA, Joji MIZUNO, Denjiro WATANABE and F. Eiichi FUJITA: On the Twin Structure of Nickel Films Electrodeposited on Single Crystals of Copper 999
Kōichi SHIMODA: Characteristics of the Beam Type Maser I 1006
Shoichiro KOIDE, Hisao SEKIYAMA and Toshio NAGASHIMA: One-Center Molecular Orbital Wave Function for Methane 1019
Ryozo YAMADA: On the Radio Wave Propagation in a Stratified Atmosphere II 1022
Ken-ichi KUSUKAWA: On the Two-dimensional Compressible Flow over a Thin Symmetric Obstacle with Sharp Shoulders Placed in an Unbounded Fluid and in a Choked Wind Tunnel 1031
Ken-ichi KUSUKAWA: On the Compressible Flow over a Slender Body of Revolution with a Flat Base Placed in an Unbounded Fluid and in a Choked Wind Tunnel. 1042

No. 10

Shigeo TAKEMOTO, Tsunekichi DAZAI and Shinji SUGANOMATA: Angular Distributions of the $Si^{28}(d, p) Si^{29}$ Reaction 1057
Tohru MORITA: Cluster Variation Method of Cooperative Phenomena and its Generalization II. Quantum Statistics 1060
Tsutomu ISHIMURA, Toshio SHIRAIWA and Masao SAWADA: The Input Power Limit of the Cylindrical Rotating Anode of a X-ray Tube 1064
Eizo OTSUKA and Hazimu KAWAMURA: Determination of Dislocation Densities Through Nuclear Resonance Studies 1071
Yoshikazu ISHIKAWA and Syun-iti AKIMOTO: Magnetic Properties of the $FeTiO_3$-Fe_2O_3 Solid Solution Series 1083
Tadao HORIE, Masamoto OTSUKA and Takayuki NAGURA: Radiative Collisions between Molecular and Electron Beams III. Angular Momentum Distribution of OH* Radicals Liberated from Alcohol Molecules 1099
Shizuko OGAWA: Nuclear Quadrupole Resonance of Antimony Isotopes in Solids 1105
Masao SUMI: Oscillations of Electron Cloud in External Fields 1110
Hirosi HASUNUMA and Jiro NARA: The Scattering of Light from Metal Aventurine Surface and Their Statistical Models 1117
Minoru NAITŌ: A Method of Calculating the Solid Angle subtended by a Circular Aperture 1122
Shōichi WAKIYA: Viscous Flows past a Spheroid 1130
Nobuyoshi MORITA: Structure of Magnesium Fluoride Films on Amorphous Substrates. 1142
Misazo YAMAMOTO: The Visco-elastic Properties of Network Structure II. Structural Viscosity 1148
Eiichi FUKUDA and Iwao YASUDA: On the Piezoelectric Effect of Bone 1158

No. 11

Koichi SUGA: Nuclear Interaction in Nucleon-Proton and Nucleon-Carbon Nucleus Collisions above 10 GeV 1171
Tetsuo WAKATSUKI, Yasuo HIRAO, Eiji OKADA and Iwao MIURA: Gamma Rays from the Excited States of ^{10}O 1178
Fumihiko TAKANO: Theory of Excitations in Liquid Helium 4 1185
Tohru MORITA: Cell Theory of Classical Liquid. Phase Transition between Gas, Liquid and Solid. Parts I and II 1195
Ryogo KUBO, Mario YOKOTA and Sadao NAKAJIMA: Statistical-Mechanical Theory of Irreversible Processes. II. Response to Thermal Disturbance 1203
Riitsu TAKAGI: Growth of Oxide Whiskers on Metals at High Temperatures 1212
Osamu NAKADA: Theory of Viscoelasticity of Amorphous Polymers. II. A Note on the Time-Temperature Reducibility of the Relaxation and Retardation Spectra 1218
Soji KOJIMA, Yoshihito ABE, Midori MINEMATSU, Kineo TSUKADA and Akira SHIMAUCHI: Structure of Nuclear Quardrupole Resonance Line. II. Solid Bromine 1225
Kazuo ONO: Paramagnetic Resonance Absorption in Chromous Sulphate Pentahydrate. . 1231

Yuzuru OOSHIKA: A Semi-empirical Theory of the Conjugated Systems. I. General Formulation 1238

Yuzuru OOSHIKA: A Semi-empirical Theory of the Conjugated Systems. II. Bond Alternation in Conjugated Chains 1246

Kaoru IGUCHI: The Lower Excited States and the Phosphorescent State of Diphenyl. I. . 1250

Hidetaro ABE and Junji SHIMADA: Paramagnetic Resonance in Copper Acetate Monohydrate 1255

Sōshin CHIKAZUMI, Kenzō SUZUKI and Hiroko IWATA: Studies on the Magnetic Anisotropy Induced by Cold Rolling of Ferromagnetic Crystal (I). Iron-Nickel Alloys 1259

Shoji KOJIMA, Kiyoe KATO and Shigeo HAGIWARA: Oscillations in Plasma. I 1276

Masao SUGAWARA: On the Phototubes Sensitive to the Wide Spectral Region 1282

Ryuma KAWAMURA and Haruo KAWADA: A Study on the Attenuation of Shock Waves due to Obstacles in the Passage 1290

Tosimitu NAGAKURA and Humio NARUSE: An Approximate Solution of the Hypersonic Laminar Boundary-Layer Equations and its Application 1298

Ali Abdel Kerim IBRAHIM and Abdel Monem I. KABIEL: Experimental and Theoretical Investigations on the Oscillating Cylinder Viscometer for Non-Elastic Liquids. . 1304

No. 12

Nobuhiko SAITŌ: Irreversible Processes and Fluctuations 1321

Toshihiro OKADA: The Measurements of the Galvanomagnetic Tensors of Bismuth . . 1327

Jun'ichi OKADA: Recombination of Excess Carriers in Semiconductors 1338

Toshiro SUZUOKA: An Electrical Resistance Study of the System $(\mathrm{Cr}_x\mathrm{Mn}_{1-x})\mathrm{Sb}$* 1344

Ryukiti R. HASIGUTI and Etsuyuki MATSUURA: Lifetime Measurements of Minority Carriers Across and Along a Dislocation Wall in a Germanium Crystal 1347

Ryukiti R. HASIGUTI, Etsuyuki MATSUURA and Shiori ISHINO: Lifetime Measurements of Minority Carriers in Deuteron Irradiated Germanium Crystal 1351

Masao KOTANI, Yukio MIZUNO, Kunihusa KAYAMA and Eiichi ISHIGURO: Electronic Structure of Simple Homonuclear Diatomic Molecules II. Lithium Molecule 1355

Kenji SHIMOMURA: Structural Investigation by Means of Nuclear Quadrupole Resonance III (Arsenic Tribromide) 1386

Nobuhiko SAITŌ and Tomokazu KATO: On the Viscoelasticity and Complex-dielectric Constant in the Presence of Electric Field and Shearing Laminar Flow in Solution of Macromolecules 1393

Kanji HONDA: On the Properties of Long-Gap Streamers 1403

Shun-ichi TSUGÉ: On a Theory of Shock Waves in Locally Supersonic Zone and a New Boundary-value Problem for the Tricomi's Equation 1412

SHORT NOTES

No. 1

Yoshiro MORIGUCHI and Yutaka KOGA: Electrical Properties of GeTe 100

Toshinosuke MUTO and Sei-ichi OYAMA: Electronic Structure of a Moving Exciton in Alkali Halides 101

Michiru YASUHARA: Asymptotic Behaviour of the Laminar Compressible Boundary Layer over a Circular Cylinder with Uniform Suction 102

Yasuo MATUKURA: Carrier Concentration Changes in p-Si Induced by Heat Treatment 103

Hirosi, HASEGAWA, Sigeru NAKANO and Natsuki HASHITSUME: On the Hall Effect in Bismuth at Low Temperature 104

Makoto KIKUCHI and Seiichi DENDA: Spiral Etch Pits on Germanium Surface 105

Tetsuji IMAI and Isao MITSUFUJI: On the Release of Alkaline Earth Metals by the Electron Dissociation of Oxide Films Evaporated from the Oxide Coated Cathodes 106

Yasaburo YOKOZAWA and Isao MIYASHITA: Temperature Dependence of Electron Spin Resonance Absorption of Thiophenol in Sulfuric Acid 107
Toshinosuke MUTO and Hiroshi OKUNO: On the Electronic Structure of Localized Exciton in Alkali Chlorides 108

No. 2

Noriaki ITO and Tokuo SUITA: Effect of Plastic Deformation on the Dielectric Breakdown of Silver Chloride Crystals 214
Y. TANAKA, K. SUGA and S. MITANI: The Energy Spectrum of Nucleons in the Air Shower 215
Shigeo NAGAO: Effects of Shock Wave upon Gaseous Discharge 216
Eijirô HAGA: On the Electrical Properties of Degenerate Semiconductors 217
Kazuo KAWABE and Shozo SAWADA: Preparation of $BaTiO_3$ Single Crystals in Coal Gas Atmosphere 218

No. 3

Takeshi MIYAUCHI: An Empirical Regularity of Energy Gap in Semiconductors...... 308
Tadashi SUGAWARA: Nuclear Magnetic Resonance is Solid Solutions of Transition Metals in Copper and Aluminum 309
Chiyoe YAMANAKA and Tokuo SUITA: Multiplication of Charge Carriers and Breakdown in Ge p-n Junction I 310
Otohiko NOMOTO and Tadashi KISHIMOTO: Molecular Sound Velocity of Aqueous Sugar Solutions 311
Hisao MIYAZAWA and Suezo SUGAIKE: Phase Transition of In_2Se_3.................. 312
Kiyoshi AZUMA and Hiroshi KAMETANI: The Generation of EMF During Melting and Freezing of Ionic Crystalline Substances..................................... 313
Kiyokata MATSUURA, Yoshikazu SUGIURA and G. M. HATOYAMA: Frequency Shift in Ammonia Absorption due to Self-broadening.................................. 314

No. 4

Susumu UCHIYAMA and Kisaburo SHOGENJI: Anomalies of Electrical Properties of Lead Telluride Crystal 431
Zeniti KIYASU, Kazuo FUSIMI and Keisuke KATAOKA: Quasi-static Hysteresis in Barium-titanate Single Crystals 432
Hideo FUTAMA and Hidejirō TANAKA: The Thermal Decomposition of Polyvinyl-Alcohol Using Mass Spectrometer... 433
Kisaburo SHOGENJI and Susumu UCHIYAMA: Resistivity and Hall Coefficient of Semiconductors 434
Hidetaro ABE: Manganese Impurities in Silver Halides Studied by the Paramagnetic Resonance Absorption 435
Makoto KIKUCHI: Observation of the Drift of Germanium Surface by Field Effect Experiment.. 436
Kenji MITANI and Hiroshi KUBO: Randomness of Microwave Gas Breakdown Voltage.. 437
Goro MIYAMOTO, Giiti IWATA, Sigeru MORI and Kenji INOUE: A Possible Fusion Reactor 438
Yoshio INUISHI: Noise from Ge PN Junction and γ-ray Irradiation Effect 439
Ali Abdel Kerim IBRAHIM: A Graphical Method for Determining the Coefficient of Viscosity of Newtonian Liquids using an Oscillating Cylinder Viscometer III.... 440
Yasuo KANAI and Riro NII: Anomalous Electrical Properties of Lead Telluride 441
Takeshi MORIMOTO: Cross Section for Displacement of Atoms by Heavy Particle Irradiation 442

No. 5

Yukito TANABE and Satoru SUGANO: The Absorption Spectra of Ruby 556
Masakazu MURAKAMI and Toshiro MAEDA: The Absolute Intensities of Cosmic Rays at 2840 Meters and Geomagnetic Latitude 25°N 557
Koichi SHIMODA: Precise Frequency of the 3,3 Inversion Line of Ammonia.......... 558
Tadasi NUMATA: Technique of Obtaining a Minute Pinhole in a Metal Plate 559

No. 6

Shigehiro KOBAYASHI: Hartree-Fock Values of Diamagnetic Susceptibilities of Neon-like Ions 737
Toshio KATOH, Masao NOZAWA, Yasukazu YOSHIZAWA and Yujiro KOH: Beta Interaction in the Decay of Cs^{137} 738
Otohiko NOMOTO: Intermolecular Free Length in Liquids in Relation to Sound Velocity 739
Hiroyuki MIZUNO: On the Conducting Mechanism of Oxide Coated Cathode........ 740
Jun'ichi OKADA: On the Carrier Recombination through Nickel Impurities in Germanium 741
Yoshimichi AIYAMA, Hisashi SEKIZAWA and Shûichi IIDA: Magnetic Annealing Effect in Iron-Nickel Ferrites 742
Tadamiki HIHARA, Miyuki MURAKAMI and Eiji HIRAHARA: Magnetic and Electrical Anisotropies of the Iron Sulfide Single Crystal 743
Jumpei TSUJIUCHI: A Density Filter Improving Aberrant Optical Image 744
Kazuo ÔNO, Junji SHIMADA, Keiichi KURODA and Shigeya TANAKA: Angular Distribution of Proton Groups from the Reaction F^{19} (d, p) F^{20} 745

No. 7

Makoto KIKUCHI and Shigeru IIZIMA: A Simpler Method for Removing Copper from Germanium........ 824
Akiya OOKAWA: On the Mechanism of Deformation Twin in fcc Crystal 825
Hazime KUSUMOTO: Nuclear Magnetic Resonance in Irradiated Teflon 826
Tetuo OHOYAMA: Some Comments on the Theory of Coercive Force of Fine Particles. 827
Mikio TSUJI: Electron Transport in Metals 828
Reikiti ITOH: A Method of Evaluating the Dissociation Constant in the Excited State of a Molecule 829
Makoto HIRABAYASHI and Yoshio MUTO: Electrical Resistance of $CuAu_3$ and Cu_3Au at Low Temperatures........ 830
Tetsuji IMAI: Barium Supplied Oxide coated Cathodes 831
Takao SATO: Note on Collective Energy Losses in Metals 832
Ryosuke YOKOTA and Kazuo SHIMIZU: Absorption Band due to Colloidal Silver 833
Yoshikazu ISHIKAWA and Syun-iti AKIMOTO: Effect of Heat Treatments on the Magnetic Properties of the $FeTiO_3$-Fe_2O_3 Solid Solution Series........ 834
Kiyokata MATSUURA, Yoshikazu SUGIURA and G. M. HATOYAMA: Frequency Shift in Ammonia Absorption due to Foreign Gases 835
Terutaro NAKAMURA, Wataru KINASE and Yoshinori KATŌ: Some Aspects of Wedge-Shaped Domains in $BaTiO_3$ Crystal 836
Yoshikazu SUGIURA and Georege Mitio HATOYAMA: Paramagnetic Resonance of Silicocarbon 837

No. 8

Yukito TANABE: On the Variational Problem connected with the Thomas Fermi Method........ 974
Tadayoshi YAMASHITA and Eiji TATSUMOTO: Magnetic Anisotropy in Connection with Rolling in the Course of Producing Single Crystals of Silicon Steel 975
Yasuo MATSUKURA and Takeaki SUZUKI: Etch Pits in Silicon Single Crystals........ 976
Hideo TAKAMI and Humio NARUSE: A Characteristic of Tomotika-Tamada's Gas as Affecting the Velocity Distribution Around a Profile........ 977
Ojiro NAGAI: Notes on the Ground State of Antiferromagnetism 978
Wataru SASAKI and Eiichi YOSHIDA: Acoustoelectric Effect in n-type Germanium 679
Minori TAKEDA, Michiya KONDO, Ryuzo, NAKASIMA, Chuin HU, Atsutomo TOI, Takashi YAMAZAKI and Shotaro YAMABE: Elastic Scattering of 5.7 Mev Protons 979
Shigehiro KOBAYASHI: Series Expansion of the Fermi Part η_0 of the TF Function.... 980
Ken-ichi KUSUKAWA: Supplementary Note to "On the Transonic Flow past a Nearly Axisymmetric Slender Body"........ 981
Mikio YAMAMOTO: Theory of the Wiedemann Effect 981

No. 9

Richard BELLMAN: Dynamic Programming and the Variational Solution of the Thomas-Fermi Equation 1049
Tunetaro SAKUDO: Effect of Iron Group Ions on the Dielectric Properties of $BaTiO_3$ Ceramics 1050
Taiichiro HASEDA and Eizo KANDA: Paramagnetic Susceptibility of $CoCl_2 \cdot 6H_2O$ between 290°K–1.52°K 1051
Taro KIHARA and Akiji ŌUCHI: Convex Molecules in Non-Uniform Gases,—Supplement 1052
Junkichi ITOH: Proposal for a Solid State Radio-Frequency Maser 1053
Akio KOBAYASHI and Shinji KAWAJI: Free Bonds on the Clean Surfaces of Germanium Single Crystals 1054

No. 10

Tadaichi YABUMOTO and Syôzi YAMADA: Photoelectric Emission of Oxide Coated Cathods 1163
Kisaburo SHOGENJI and Susumu UCHIYAMA: The Galvanomagnetic Effects in Single Crystal of PbTe 1164
Yoshikazu ISHIKAWA: Magnetic Properties of $NiTiO_3 \cdot Fe_2O_3$ Solid Solution Series 1165
Shigeo HAGIWARA, Kiyoe KATO, Yoshihito ABE and Midori MINEMATSU: Iodine Quadrupole Resonance in ICl_3 and AlI_3 1166
Mikio TAKEYAMA: On the Dielectric Properties of α-phase n-Higher Alcohols and Associated Electromotive Force 1167
Muneyuki DATE: Antiferromagnetic Resonance in $CuCl_2 \cdot 2D_2O$ 1168
Yasuo KANAI and Wataru SASAKI: Galvanomagnetic Effects in n-type Indium Antimonide at Very Low Temperatures 1169

No. 11

Tadasi NUMATA: Technique of Obtaining a Minute Pinhole in a Metal Plate. II 1312
Hiroshi OKURA: Oscillator Strength of M-center of KCl 1313
Muneyuki DATE: Anomalous Magnetic Properties of $Cu(NH_3)_4SO_4 \cdot H_2O$ and $MnSO_4 \cdot H_2O$ 1314
Hiroyuki MIZUNO: Diffusion of Activator of Cathode Sleeve 1315
Asa CHIKAYAMA, Yuzuru OOSHIKA, Reikiti ITOH and Isao OSHIDA: LCAO-MO Treatment of Phthalocyanine 1316
Yoshimi KAMADA and Kwai UMEDA: Elongated Lichtenberg Figure 1317

No. 12

Kikusaburo OSADA: Phosphorescence of Acetic Acid 1420
Kōichi ŌSHIMA: Experiments on the Cylindrical Blast Waves 1421
Shigetomo YOSHIDA and Toshio IKEDA: Effect of Electron Bombardment on Sodium Chloride 1422
Kimio HASHIMOTO: Electrical Properties of SnTe, SnSe and InBi at Low Temperatures 1423
Keisuke MATSUURA, Yoshikazu HAMAGUCHI and Shigeyasu KODA: On the Formation of Small Guinier-Preston (1) Aggregates During the Plastic Deformation of an Al–Cu Alloy 1424
J. B. DIAZ: On Some Singular Solutions of the Tricomi Equation Relating to Transonic Flow 1425

Errata

No. 4

Makoto HIRABAYASHI and Shiro OGAWA: On the Superstructure of the Ordered Alloy Cu_3Pd. II. X-ray Diffraction Study 442
Noriaki ITOH and Tokuo SUITA: Effect of Plastic Deformation on the Dielectric Breakdown of Silver Chloride Crystals 442

No. 7

Sadao HOSHINO: Crystal Structure and Phase Transition of Some Metalic Halides (IV) On the Anomalous Structure of α-Ag I 838
Takeshi MORIMOTO: Cross Section for Displacement of Atoms by Heavy Particle Irradiation 838

No. 8

Makoto KIKUCHI and Sigeru IIZIMA: A Simpler Method for Removing Copper from Germanium 982

No. 9

Hiroshi FUJITA: Notes on the Calculation of Electrophoresis of Polyelectrolytes with Partial Free Drainage 998

No. 10

Yukito TANABE: On the Variational Problem connected with the Thomas Fermi Method 1170
Toshio MISAWA: Impedance of Bulk Semiconductor in Junction Diode 1170
Wataru SEGAWA: Stress-Strain Relations for Viscoelastic Large Deformations 1170

No. 11

Akio KOBAYASHI and Shinji KAWAJI: Free Bonds on the Clean Surfaces Germanium Single Crystals 1318
Shōichi WAKIYA: Viscous Flows past a Spheroid 1318
Takuro TSUZUKU: Conical Spiral Structure and Laminar Cleavage of Graphite 1318

No. 12

Yoshimi KAMADA and Kwai UMEDA: Elongated Lichtenberg Figure 1425

AUTHOR INDEX TO Vol. 12

ABE Hidetaro;

———: Manganese Impurities in Silver Halides Studied by the Paramagnetic Resonance Absorption 435

——— and J. SHIMADA: Paramagnetic Resonance in Copper Acetate Monohydrate........ 1255

ABE Yoshihito;

S. HAGIWARA, K. KATO, ——— and M. MINEMATSU: Iodine Quadrupole Resonance in IC_3 and AlI_3 1166

S. KOJIMA, ———, M. MINEMATSU, K. TSUKADA and A. SHIMAUCHI: Structure of Nuclear Quadrupole Resonance Line. II. Solid Bromine 1225

ADACHI Kengo;

T. HIRONE and ———: On the Magnetic Properties of Nickel Arsenide Type Crystals 156

AIYAMA Yoshimichi;

———, H. SEKIZAWA and S. IIDA: Magnetic Annealing Effect in Iron-Nickel Ferrites 742

AKIMOTO Syun-iti;

Y. ISHIKAWA and ———: Effect of Heat Treatments on the Magnetic Properties of the $FeTiO_3$–Fe_2O_3 Solid Solution Series........ 834

Y. ISHIKAWA and ———: Magnetics Properties of the $FeTiO_3$–Fe_2O_3 Solid Solution Series 1083

ARIYAMA Masataka;

———, K. KAYAMA and M. SUGIMOTO: Self-consistent Field without Exchange for Doubly Ionized Cobalt........ 285

ASANO Sumitada;

——— and Y. TOMISHIMA: Rotational Lattice Vibration in Complex Crystals Part I. Vibrational Modes and Special Heat 346

——— and Y. TOMISHIMA: Rotational Lattice Vibration in Complex Crystals Part II. Vibrational Modes in Optical Branches and Interaction with a Conduction Electron 890

——— and Y. TOMISHIMA: Rotational Lattice Vibration in Complex Crystals Part III. Vibrational Frequencies in Cubic $NaClO_4$ Crystals........ 900

ASANUMA Mitsuru;

——— and S. OGAWA: On the Magnetic Aging of Commercial Pure Iron 955

AZUMA Kiyoshi;

——— and H. KAMETANI: The Generation of EMF During Melting and Freezing of Ionic Crystalline Substances 313

BELLMAN Richard: Dynamic Programming and the Variational Solution of the Thomas-Fermi Equation........ 1049

CHIKAYAMA Asa;

———, Y. OOSHIKA, R. ITOH and I. OSHIDA: LCAO-MO Treatment of Phthalocyanine........ 1316

CHIKAZUMI Sōshin;

———, K. SUZUKI and H. IWATA: Studies on the Magnetic Anisotropy Induced by Cold Rolling of Ferromagnetic Crystai (I). Iron-Nickel Alloys.... 1259

DATE Muneyuki: Antiferromagnetic Resonance in $CuCl_2 \cdot 2D_2O$ 1168

———: Anomalous Magnetic Properties of $Cu(NH_3)_4SO_4 \cdot H_2O$ and $MnSO_4 \cdot H_2O$. 1314

DENDA Seiichi;

M. KIKUCHI and ———: Spiral Etch Pits on Germanium Surface........ 105

DAZAI Tsunekichi;

S. TAKEMOTO, ——— and S. SUGANOMATA: Angular Distributions of the $Si^{28}(d, p)Si^{29}$ Reaction........ 1057

DIAZ, J. B.: On Some Singular Solutions of the Tricomi Equation Relating to Transonic Flow 1425

FUJII Shin'ichi;

S. SAWADA, I. TAKOO and ———: An X-Ray Tube with a Rotating Anode and an Earthed Cathode 147

FUJIKAWA Hiroomi: Expansion Formulae for the Forces acting on Two Equal Circular Cylinders placed in a Uniform Stream at Low Values of Reynolds Number . 423
FUJITA Hiroshi: Notes on the Calculation of Electrophoresis of Polyelectrolytes with Partial Free-Drainage... 968
———: (Errata) Notes on the Calculation of Electrophresis of Polyelectrolytes with Partial Free-Drainage 998
FUJITA F. Eiichi;
S. OGAWA, J. MIZUNO, D. WATANABE and ———: On the Twin Structure of Nickel Films Electrodeposited on Single Crystals of Copper 999
FUJIWARA Kunio: On the Period of Out-of-step of Ordered Alloys with Anti-phase Domain Structure... 7
FUKUDA Eiichi;
——— and I. YASUDA: On the Piezoelectric Effect of Bone.................1158
FUKUI Shūji;
———, T. KITAMURA and Y. MURATA: On the Range Spectrum of μ-Mesons at Geomagnetic Latitude 24°N 854
FUKUSHIMA Einosuke;
——— and A. OOKAWA: Observation of the Grain Boundary in Soap Bubble Raft. Part III. The Grain Boundary in Vibrating State 139
FURUICHI Jiro;
S. SUGAI and ———: Studies of High Polymers by Radioactive Method II Self-diffusion of Polystyrene in Its Dilute Solution....................... 369
FUSIMI Kazuo;
Z. KIYASU, ——— and K. TAKAOKA: Quasi-static Hysteresis in Barium-titanate Single Crystals 432
FUTAMA Hideo;
——— and H. TANAKA: The Thermal Decomposition of Polyvinyl-Alcohol Using Mass Spectrometer... 433

GHOSE, T.;
———, S. K. GHOSH and D. K. ROY: A Study on the Effects of Off-Resonance on the Spin-Echo Signals 816
GHOSH S. K.;
T. GHOSE, ——— and D. K. ROY: A Study on the Effects of Off-Resonance on the Spin-Echo Signals 816
HAGA Eijirô: On the Electrical Properties of Degenerate Semiconductors 217
HAGIWARA Shigeo;
———, K. KATO, Y. ABE and M. MINEMATSU: Iodine Quadrupole Resonance in ICl$_3$ AlI$_3$ 1166
S. KOJIMA, K. KATO and ———: Oscillations in Plasma. 1..................1276
HAMAGUCHI Yoshikazu;
K. MATSUURA, ——— and S. KODA: On the Formation of Small Guinier Preston (1) Aggregated During the Plastic Deformation of an Al–Cu Alloy 1424
HASEDA Taiichiro;
——— and E. KANDA: Paramagnetic Susceptibility of CoCl$_2$·6H$_2$O between 290°K–1.52°K...1051
HASEGAWA Hirosi;
———, S. NAKANO and N. HASHITSUME: On the Hall Effect in Bismuth at Low Temperature 104
HASHIMOTO Kimio: Electrical Properties of SnTe, SnSe and InBi at Low Temperatures...1423
HASHITSUME Natsuki;
H. HASEGAWA, S. NAKANO and ———: On the Hall Effect in Bismuth at Low Temperature 104
HASIGUTI Ryukiti R.;
——— and E. MATSUURA: Lifetime Measurements of Minority Carriers across along a Dislocation Wall in a Germanium Crystal 1347
———, E. MATSUURA and S. ISHINO: Lifetime Measurements of Minority

Carriers in Deuteron Irradiated Germanium Crystals........................1351

HASIMOTO Hidenori: Boundary Layer Growth on a Flat Plate with Suction or Injection 68

HASUNUMA Hiroshi;

——— and J. NARA: The Scattering of Light from Metal Aventurine Surface and Their Statistical Models 1117

HATOYAMA George Mitio;

K. MATSUURA, Y. SUGIURA and ———: Frequency Shift in Ammonia Absorption due to Self-broadening 314

K. MATSUURA, Y. SUGIURA and ———: Frequency Shift in Ammonia Absorption due to Foreign Gases 835

Y. SUGIURA and ———: Paramagnetic Resonance of Sillicocarbon 837

HAYASE Akira;

M. SAWADA, K. TSUTSUMI and ———: Fine Structures of X-ray Absorption Spectra of Cobalt in the Face Centered Cubic Lattice and Closepacked Hexagonal Lattice 628

K. TSUTSUMI, ——— and M. SAWADA: Fine Structures of X-ray *K* Absorption Spectra of Copper in Various Copper Compounds 793

HIHARA Tadamiki;

, M. MURAKAMI and E. HIRAHARA: Magnetic and Electrical Anisotropies of the Iron Sulfide Crystal 743

HINOTANI Kensaku;

S. MIYAKE, ——— and K. NUNOGAKI: Intensity and Energy Spectrum of Fast Neutrons in Cosmic Radiation 113

S. MITAKE, ———, I. KATSUMATA and T. KANEKO: Cosmic Ray Nuclear Interactions in Nitrogen Gas 845

HIRABAYASHI Makoto;

——— and S. OGAWA: On the Superstructure of the Ordered Alloy Cu_3Pd II. X-ray Diffraction Study........................ 259

——— and S. OGAWA: (Errata) On the Superstructure of the Ordered Alloy Cu_3Pd II. X-ray Diffraction Study 442

——— and Y. MUTO: Electrical Resistance of $CuAu_3$ and Cu_3Au at Low Temperatures 830

HIRAHARA Eiji;

T. HIHARA, M. MURAKAMI and ———: Magnetic and Electrical Anisotropies of the Iron Sulfide Single Crystal 743

HIRAKAWA Hiromasa;

T. OKA, ——— and A. MIYAHARA: Dependence of Quadrupole Coupling Constant on the Vibrational State in ICN Molecule 39

T. OKA and ———: Microwave Spectrum of BrCN and Dependence of Quadrupole Coupling Constant on the Vibrational State........................ 820

HIRAKAWA Kinshiro: The Magnetic Properties of Iron Selenide Single Crystals...... 929

HIRAO Yasuo;

T. WAKATSUKI, ———, E. OKADA and I. MIURA: Gamma Rays from the Excited States of ^{16}O 1178

HIRASHIMA Masaki;

——— and S. MIYASHIRO: Some Factors Affecting the Decay of Secondary Electron Emission of Silver-Magnesium Alloys 770

HIROIKE Kazuo: Radial Distribution of Fluids I 326

———: Rad.al Distribution of Fluids II 864

HIRONE Tokutaro;

——— and K. ADACHI: On the Magnetic Properties of Nickel Arsenide Type Crystals 156

M. YUZURI, ———, H. WATANABE, S. NAGASAKI and S. MAEDA: On the Magnetic Properties of Chromium Sulfides 385

HONDA Kanji: On the Properties of Long-Gap Streamers 1403

HORIE Tadao;

, T. NAGURA and M. OTSUKA: Radiative Collisions between Electron and Molecular Beams II. Angular Momentum Distribution of OH* Radicals Splitting from H_2O_2 Molecules 500

———, M. OTSUKA and T. NAGURA: Radiative Collisions between Molecular and Electron Beams III. Angular Momentum Distribution of OH* Radicals Liberated from Alcohol Moleules 1099

HORIUCHI Kazuo: Electromagnetic Fields due to Current Flowing Parallel to Interface of Two Different Media 170

HOSHINO Sadao: Crystal Structure and Phase Transition of Some Metallic Halides IV 315

———: (Errata) Crystal Structure and Phase Transition of Some Metalic Halides (IV) On the Anomalous Structure of α-Ag I 838

HU Chuin;

M. TAKEDA, M. KONDO, S. KATO, ———, R. NAKASIMA and S. YAMABE: Elastic Scattering of 5.7 Mev Protons from Ni and Cu 561

M. TAKEDA, M. KONDO, R. NAKASIMA, ———, A. TOI, T. YAMAZAKI and S. YAMABE: Elastic Scattering of 5.7 Mev Protons 979

HUGGINS Maurice L.;

——— and Y. SAKAMOTO: Lattice Energies and Other Properties of Crystals of Alkaline Earth Chalcogenides 241

HUZITA Humiaki;

———: On the Ricochet Motion of a Projectile Striking a Water Surface.... 208

S. NAKAGAWA, E. TAMAI, ——— and K. OKUDAIRA: On the Analysis of the Slow Particles Emitted from Cosmic-Ray Stars (II) 747

IBRAHIM Ali Abdel Kerim;

———: A Graphical Method for Determining the Coefficient of Viscosity of Newtonian Liquids using an Oscillating Cylinder Viscometer III 440

and A. M. I. KABIEL: Experimental and Theoretical Investigations on the Oscillating Cylinder Viscometer for Non-Elastic Liquids 1304

IGUCHI Kaoru: The Lower Excited States and the Phosphorescent State of Diphenyl. I 1250

IIDA Shūichi: Layer Structures of Magnetic Oxides 222

Y. AIYAMA, H. SEKIZAWA and ———: Magnetic Annealing Effect in Iron-Nickel Ferrites 742

IIZIMA Shigeru;

M. KIKUCHI and ———: A Simpler Method for Removing Copper from Germanium 824

M. KIKUCHI and : (Errata) A Simpler Method for Removing Copper from Germanium 982

IKEBE Teruo;

——— and T. KATO: Application of Variational Method to the Thomas Fermi Equation 201

IKEDA Takuro;

M. MARUTAKE and ———: Anisotropy in Polarized Barium Titanate Ceramics. 233

IKEDA Toshio;

S. YOSHIDA and : Effect of Electron Bombadment on Sodium Chloride .1422

IKEDA Yuichi: On the Effective Diffusion Tensor of a Segment in a Chain Molecule and its Application to the Non-Newtonian Viscosity of Polymer Solutions .. 378

IMAI Isao: Application of the M^2-Expansion Method to Compressible Flow past Isolated and Lattice Aerofoils 58

IMAI Tetsuji;

——— and I. MITSUFUJI: On the Release of Alkaline Earth Metals by the Electron Dissociation of Oxide Films Evaporated from the Oxide Coated Cathodes 106

———: Barium Supplied Oxide coated Cathodes 831

IMAMURA Akira;

J. MUTO, E. TAKEKOSHI, T. NAKAMURA, ——— and Y. TSUNEOKA: The Multipolarity of γ-ray Absorption in $^{12}C(\gamma, 3\alpha)$ Reaction produced by (Li, p) γ-rays 109

INO Tadashi: Studies on the Radial Distribution Analysis in Diffraction Methods I. Errors due to the Approximation of Integration by Summation 495

INOUE Kenji;
G. MIYAMOTO, G. IWATA, S. MORI and ———: A Possible Fusion Reactor .. 438

INUISHI Yoshio: Noise from Ge PN Junction and γ-ray Irradiation Effect 439

ISHIGURO Eiichi;
M. KOTANI, Y. MIZUNO, K. KAYAMA and ———: Electronic Structure of Simple Homonuclear Diatomic Molecules I. Oxygen Molecule 707
, K. KAYAMA, M. KOTANI and Y. MIZUNO: Electronic Structure of Simple Homonuclear Diatomic Molecules II. Lithium Molecule 1355

ISHIHARA Akira;
——— and R. KOYAMA: Intermolecular Potential between Large Molecules .. 32

ISHIKAWA Yoshikazu;
——— and S. AKIMOTO: Effect of Heat Treatments on the Magnetic Properties of the $FeTiO_3$–Fe_2O_3 Solid Solution Series.............................. 834
——— and S. AKIMOTO: Magnetic Properties of the $FeTiO_3$–Fe_2O_3 Solid Solution Series 1083
———: Magnetic Properties of $NiTiO_2$–Fe_2O_3 Solid Solution Series 1165

ISHIMATSU Toshiyuki;
I. NONAKA, S. MORITA, N. KAWAI, ———, K. TAKESHITA, Y. NAKAJIMA and N. TAKANO: On the Neutrons from the $N^{14}(d, n)O^{15}$ Reaction–II 841

ISHIMURA Tsutomu;
T. SHIRAIWA, ——— and M. SAWADA: Fine Structures of X-ray Absorption Spectra of Crystalline and Amorphous Germanium 788

ISHINO Shiori;
R. R. HASIGUTI, E. MATSUURA and ———: Lifetime Measurements of Minority Carriers in Deuteron Irradiated Germanium Crystals 1351

ISHII Taka;
S. TOKUNAGA, K. NISHIKAWA and ———: A Cascade Shower in Nuclear Emulsion 219

ISHIMURA Tsutom;
———, T. SHIRAIWA and M. SAWADA: The Input Power Limit of the Cylindrical Rotating Anode of a X-ray Tube 1064

ITO Noriaki;
——— and T. SUITA: Effect of Plastic Deformation of the Dielectric Breakdown of Silver Chloride Crystals 214

ITOH Junkichi;
T. YUKITOSHI, H. SUGA, S. SEKI and ———: Nuclear Magnetic Resonance Experiment on Solid Hexamethyldisilane 506
: Proposal for a Solid State Radio-Frequency Maser 1053

ITOH Takashi;
——— and K. KAMBE: Electron Coupled Interaction in Solid Iodine 763

ITOH Noriaki;
——— and T. SUITA: (Errata) Effect of Plastic Deformation on the Dielectric Breakdown of Silver Chloride Crystals 442

ITOH Reikiti;
: Effect of the Basic Strength of Attached Groups on Light Absorption Spectra I. Light Absorption of Triphenylmethane Dyes.................... 644
———: Effect of the Basic Strength of Attached Groups on Light Absorption Spectra II. Near Ultraviolet Absorption Spectra of Para-substituted Aniline Derivatives... 809
———: A Method of Evaluating the Dissociation Constant in the Excited State of a Molecule.. 829
A. CHIKAYAMA, Y. OOSHIKA, ——— and I. OSHIDA: LCAO-MO Treatment of Phthalocyanine 1316

IWATA Giiti;
G. MIYAMOTO, ———, S. MORI and K. INOUE: A Possible Fusion Reactor.. 438

IWATA Hiroko;
S. CHIKAZUMI, K. SUZUKI and ———: Studies on the Magnetic Anisotropy Induced by Cold Rolling of Ferromagnetic Crystal (I). Iron-Nickel Alloys..1259

KABIEL Abdel Monem I.;
  A. A. K. IBRAHIM and ———: Experimental and Theoretical Investigations on the Oscillating Cylinder Viscometer for Non-Elastic Liquids 1304
KAKIUCHI Yoshinobu;
  A. NISHIOKA, H. KOMATSU and ———: Nuclear Magnetic Resonance in Some Crystalline Polymers 283
KAMADA Yoshimi;
  ——— and K. UMEDA: Elongated Lichtenberg Figure 1317
  ——— and K. UMEDA: (Erratum) Elongated Lichtenberg Figure 1425
KAMBE Kenjiro;
  T. ITOH and ———: Electron Coupled Interaction in Solid Iodine 763
KAMBE Kyozaburo;
  ———: Sutdy of Simultaneous Reflexion in Electron Diffraction by Crystals I. Theoretical Treatment 13
  ———: The Phase Effect in Simultaneous Reflexion in Electron Diffractions II. Experimental Confirmation 25
KAMETANI Hiroshi;
  K. AZUMA and ———: The Generation of EMF During Melting and Freezing of Ionic Crystalline Substances 313
KANAI Yasuo;
  ——— and R. NII: Electrical Properties of Nickel Doped Grmanium at Low Temperatures 125
  ——— and R. NII: Anomalous Electrical Properties of Lead Telluride 441
  ——— and W. SASAKI: Galvanomagnetic Effects in n-type Indium Antimonide at Very Low Temperatures 1169
KANDA Eizo;
  T. HASEDA and ———: Paramagnetic Susceptibility of $CoCl_2 \cdot 6H_2O$ between 290°K–1.52°K..1051
KANEKO Shobu;
  T. KIHARA and ———: Temperature Variation of Mayer's Cluster Integrals. 994
KANEKO Tatsunosuke;
  S. MIYAKE, K. HINOTANI, I. KATSUMATA and ———: Cosmic Ray Nuclear Interactions in Nitrogen Gas 845
KATAOKA Keisuke;
  Z. KIYASU, K. FUSIMI and ———: Quasi-static Hysteresis in Barium-titanate Single Crystals 432
KATO Kiyoe;
  S. HAGIWARA, ———, Y. ABE and M. MINEMATSU: Iodine Quadrupole Resonance in ICl_3 and AlI_3 1166
  S. KOJIMA, ——— and S. HAGIWARA: Oscillations in Plasma. I. 1276
KATO Shohei;
  M. TAKEDA, M. KONDO, ———, C. HU, R. NAKASIMA and S. YAMABE: Elastic Scattering of 5.7 Mev Protons from Ni and Cu 561
KATO Tomokazu;
  N. NAITŌ and ———: On the Viscoelasticity and Complex-dielectric Constant in the Presence of Electric Field and Shearing Laminar Flow in Solution of Macromolecules 1393
KATO Tosio;
  T. IKEBE and ———: Application of Variational Method to the Thomas-Fermi Equation.. 201
KATŌ Yoshinori;
  T. NAKAMURA, W. KANSE and ———: Some Aspects of Wedge-Shaped Domains in $BaTiO_3$ Crystal 836
KATOH Toshio;
  ———, M. NOZAWA, K. YOSHIZAWA and Y. KOH: Beta Interaction in the Decay of Cs^{137} 738

KATSUMATA Itsuo;
S. MIYAKE, K. HINOTANI, ——— and T. KANEKO: Cosmic Ray Nuclear Interactions in Nitrogen Gas 845
KATSURA Shigetoshi;
Y. NOMURA and ———: Diffraction of Electromagnetic Waves by Ribbon and Slit, I 190
KAWABE Kazuo;
——— and S. SAWADA: Preparation of $BaTiO_3$ Single Crystals in Coal Gas Atmosphere 218
KAWADA Haruo;
R. KAWAMURA and ———: A Study on the Attenuation of Shock Waves due to Obstacles in the Passage........1290
KAWAI Nawoyuki;
I. NONAKA, S. MORITA, ———, T. ISHIMATSU, K. TAKESHITA, Y. NAKAJIMA and N. TAKANO: On the Neutrons from the $N^{14}(d, n)O^{15}$ Reaction-II........ 841
KAWAJI Shinji;
A. KOBAYASHI and ———: Free Bonds on the Clean Surfaces of Germanium Single Crystals 1054
A. KOBAYASHI and ———: (Errata) Free Bonds on the Clean Surfaces of Germanium Single Crystals 1318
KAWAMURA Ryuma;
——— and H. KAWADA: A Study on the Attenuation of Shock Waves due to Obstacles in the Passage 1290
KAWAMURA Hazimu;
E. OTSUKA and ———: Determination of Dislocation Densities Through Nuclear Resonance Studies 1071
KAYAMA Kunihusa;
M. KOTANI, Y. MIZUNO, ——— and E. ISHIGURO: Electronic Structure of Simple Homonuclear Diatomic Molecules I. Oxygen Molecule........ 707
M. ARIYAMA, ——— and M. SUGIMOTO: Self-consistent Field without Exchange for Doubly Ionized Cobalt 285
E. ISHIGURO, ———, M. KOTANI and Y. MIZUNO: Electronic Structure of Simple Homonuclear Diatomic Molecules II. Lithium Molecule 1355
KIHARA Taro;
———: Geometrical Theory of Convex Molecules in Non-Uniform Gases 564
——— and S. KANEKO: Temperature Variation of Mayer's Cluster Integrals. 994
——— and A. ŌUCHI: Convex Molecules in Non-Uniform Gases-Supplement .1052
KIKUCHI Makoto;
——— and S. DENDA: Spiral Etch Pits on Germanium Surface 105
———: Peripheral Inhomogeneties of the Alloyed Germanium p–n Junction.. 133
———: Observation of the Drift of Germanium Surface by Field Effect Experiment 436
———: Some Experiments on the Surface Field Effects in Germanium Single Crystals 756
——— and S. IIZIMA: A Simpler Method for Removing Copper from Germanium 824
——— and S. IIZIMA: (Errata) A Simpler Method for Removing Copper from Germanium........ 982
KIM, Chul-Soo;
F. TAMAKI and ———: Studies on the Hypersonic Flow Using a Double-Diaphragm Shock Tube........ 550
KINASE Wataru;
——— and H. TAKAHASHI: On the 180°-type Domain Wall of $BaTiO_3$ Crystal. 464
T. NAKAMURA, ——— and Y. KATŌ: Some Aspects of Wedge-Shaped Domains $BaTiO_3$ Crystal 836
KISHIMOTO Tadashi;
O. NOMOTO and ———: Molecular Sound Velocity of Aqueous Sugar Solutions. 311
KITAMURA Takashi;
S. FUKUI, ——— and Y. MURATA: On the Range Spectrum of μ-Mesons at Sea-Level at Geomagnetic Latitude 24°N 854

KIYASU Zeniti;

, K. FUSIMI and K. TAKAOKA: Quasi-static Hysteresis in Barium-titanate Single Crystals 432

KOBASHI Yasujiro: Measurements of Pressure Fluctuation in the Wake of Cylinder .. 533

KOBAYASHI Akio;

and S. KAWAJI: Free Bonds on the Clean Surfaces of Germanium Single Crystals 1054

and S. KAWAJI: (Errata) Free Bonds on the Clean Surfaces of Germanium Single Crystals 1318

KOBAYASHI Shigehiro: Series Expansion of the Fermi Part η_0 of the TF Function .. 980

: Hartree-Fock Values of Diamagnetic Susceptibilities of Neon-like Ions 737

KODA Shigeyasu;

K. MATSUURA, Y. HAMAGUCHI and ——: On the Formation of Small G.P. (1) Aggregated During the Plastic Deformation of an Al–Cu Alloy 1424

KODAMA Masahiro;

——, K. MURAKAMI and Y. SEKIDO: Observation of Cosmi-Ray Neutron Intensity at Geomagnetic Latitude 25°N, Part I. Atomospheric Effects 122

KOGA Yutaka;

Y. MORIGUCHI and ——: Electrical Properties of GeTe........ 100

KŌI Yoshitaka: Line Width of the Pure Quadrupole Resonance of Bromine in $NaBrO_3$ 49

KOIDE Shoichiro;

, H. SEKIYAMA and T. NAGASHIMA: One-Center Molecular Orbital Wave Function for Methane 1019

KOH Yujiro;

T. KATOH, M. NOZAWA, Y. YOSHIZAWA and — . Beta Interaction in the Decay of Cs^{137} 738

KOHRA Kazutake;

M. KURIYAMA, —— and S. TAKAGI: Electron Diffraction Study on Polish Layers of Gold, I........ 151

KOIKE Mitsuru;

A. ODAJIMA, J. SOHMA and — —: Proton Magnetic Resonance in Chain Polymers........ 272

KOJIMA Shoji;

, Y. ABE, M. MINEMATSU, K. TSUKADA and A. SHIMAUCHI: Structure of Nuclear Quadrupole Resonance Line. II. Solid Bromine 1225

, K. KATO and S. HAGIWARA: Oscillations in Plasma. I........ 1276

KOJIMA Tadanobu: Electronic States of the F-Center in Lithium Fluoride, I 908

: Electronic States of the F-Center in Lithium Fluoride, II 918

KOJIMA Takeshi;

and T. NISHIKAWA: Potential Barrier and Molecular Structure of Methyl Mercaptan from its Microwave Spectra 680

KOMATSU Hachiro;

A. NISHIOKA, —— and Y. KAKIUCHI: Nuclear Magnetic Resonance in Some Crystalline Polymers 283

KONDO Michiya;

M. TAKEDA, —, S. KATO, C. HU, R. NAKASIMA and S. YAMABE: Elastic Scattering of 5.7 Mev Protons from Ni and Cu 561

M. TAKEDA, , R. NAKASIMO, C. HU, A. TOI, T. YAMAZAKI and S. YAMABE: Elastic Scattering of Mev Protons 979

KŌNO Ryusuke;

T. SOEYA and ——: On Some Transition Phenomena in Aqueous Solution of Polyvinylalcohol 950

KOTANI Masao;

——, Y. MIZUNO, K. KAYAMA and E. ISHIGURO: Electronic Structure of Simple Homonuclear Diatomic Molecules I. Oxygen Molecule........ 707

E. ISHIGURO, K. KAYAMA, —— and Y. MIZUNO: Electronic Structure of Simple Homonuclear Diatomic Molecules II. Lithium Molecule 1355

KOYAMA Ryuzo;
A. ISHIHARA and ———: Intermolecular Potential between Large Molecules . 32
KUBO Hiroshi;
K. MITANI and ———: Randomness of Microwave Gas Breakdown Voltage .. 437
KUBO Ryogo;
———: Statistical-Mechanical Theory of Irreversible Processes, I. General Theory and Simple Applications to Magnetic and Conduction Problems 570
———, M. YOKOTA and S. NAKAJIMA: Statistical-Mechanical Theory of Irreversible Processes. II. Response to Thermal Disturbance 1203
KURODA Keiichi;
K. ONO, J. SHIMADA, ——— and S. TANAKA: Angular Distribution of Proton Groups from the Reaction F^{19} (d, p) F^{20}.................................. 745
KURIYAMA Masao;
———, K. KOHRA and S. TAKAGI: Electron Dffraction Study on Polish Layers of Gold, I 151
KUROSAWA Tatsumi: On the Melting of Ionic Crystals 338
KUSUKAWA Ken-ichi;
———: On the Transonic Flow of a Compressible Fluid past an Axisymmetric Slender Body at Zero Incidence 401
———: On the Transonic Flow of a Compressible Fluid past a nearly Axisymmetric Slender Body 411
———: Supplementary Note to "On the Transonic Flow past a Nearly Axisymmetric Slender Body".. 981
———: On the Two-dimensional Compressible Flow over a Thin Symmetric Obstacle with Sharp Shoulders Placed in an Unbounded Fluid and in a Choked Wind Tunnel...1031
———: On the Compressible Flow over a Slender Body of Revolution with a Flat Base Placed in an Unbounded Fluid and in a Choked Wind Tunnel....1042
KUSUMOTO Hazime: Nuclear Magnetic Resonance in Irradiated Teflon 826
KUWABARA Shigeya: Variation of Electron Diffraction Intensity with Crystal Size.... 637
KUWABARA Shinji: The Forces Experienced by Two Circular Cylinders in a Uniform Flow at Small Raynolds Numbers.. 291

MAEDA Seijiro;
M. YUZURI, T. HIRONE, H. WATANABE, S. NAGASAKI and ———: On the Magnetic Properties of Chromium Sulfides 385
MAEDA Toshiro;
M. MURAKAMI and ———: The Absolute Intensities of Cosmic Rays at 2840 Meters and Ceomagnetic Latitude 25°N 557
MARUTAKE Masakazu;
——— and T. IKEDA: Anisotropy in Polarized Barium Titanate Ceramics .. 233
MASUDA Yoshika: Nuclear Magnetic Resonance Experiment on Metal Cadmium 523
MATSUKURA Yasuo;
——— and T. SUZUKI: Etch Pits in Silicon Single Crystals.................. 976
MATSUURA Keisuke;
———, Y. HAMAGUCHI and S. KODA: On the Formation of Small Guinier Preston (1) Aggregated During the Plastic Deformation of an Al-Cu Alloy..1424
MATSUURA Etsuyuki;
R. R. HASIGUTI and ———: Lifetime Measurements of Minority Carriers across and along a Dislocation Wall in a Germanium Crystal 1347
R. R. HASIGUTI, ——— and S. ISHINO: Lifetime Measurements of Minority Carriers in Deuteron Irradiated Germanium Crystals.......................1351
MATSUURA Kiyotaka;
———, Y. SUGIURA and G. M. HATOYAMA: Frequency Shift in Ammonia Absorption due to Self-broadening 314
———, Y. SUGIURA and G. M. HATOYAMA: Frequency Shift in Ammonia Absorption due to Foreign Gases 835
MATUKURA Yasuo: Carrier Concentration Changes in p-Si Induced by Heat Treatment 103

MATUNOBU Yaso'o: Application of the Thin-Wing-Expansion Method to the Compressible Flow past an Elliptic Cylinder, with Special Reference to its Fourth Approximation 72

MIKURA Ziro: Electron-Electron Interaction and Superconductivity. I 587

MIMNEMATRU Midori;

S. HAGIWARA, K. KATO, Y. ABE and ———: Iodine Quadrupole Resonance in ICl_3 and AlI_3 1166

S. KOJIMA, Y. ABE, ———, K. TSUKADA and A. SHIMAUCHI: Structure of Nuclear Quadruple Resonance Line. II. Solid Bromine 1225

MISAWA Toshio: Impedance of Bulk Semiconductor in Junction Diode 882

: (Errata) Impedance of Bulk Semiconductor in Junction Diode 1170

MITANI Kenji;

——— and H. KUBO: Randomness of Microwave Gas Breakdown Voltage.... 437

MITANI S.;

Y. TANAKA, K. SUGA and ———: The Energy Spectrum of Nucleons in the Air Shower 215

MITSUFUJI Isao;

T. IMAI and ———: On the Release of Alkaline Earth Metals by the Electron Dissociation of Oxide Film Evaporated from the Oxide Coated Cathodes 106

MIURA Iwao;

T. WAKATSUKI, Y. HIRAO, E. OKADA and ———: Gamma Rays from the Excited States of ^{16}O 1178

MIYAHARA Akira;

T. OKA, H. HIRAKAWA and ———: Dependence of Quadrupole Coupling Constant on the Vibrational State in ICN Molecule 39

MIYAKE Saburo;

———, K. HINOTANI and K. NUNOGAKI: Intensity and Energy Spectrum of Fast Neutrons in Cosmic Radiation 113

, K. HINOTANI, I. KATSUMATA and T. KANEKO: Cosmic Ray Nuclear Interactions in Nitrogen Gas 845

MIYAMOTO Goro;

, G. IWATA, S. MORI and K. INOUE: A Possible Fusion Reactor 438

MIYASHIRO Shoichi;

M. RIRASHIMA and ———: Some Factors Affecting the Decay of Secondary Electron Emission of Silver-Magnesium Alloys 770

MIYASHITA Isao;

Y. YOKOZAWA and ———: Temperature Dependence of Electron Spin Resonance Absorption of Thiophenol in Sulfuric Acid 107

MIYAUCHI Takeshi: An Empirical Regularity of Energy Gap in Semiconductors 308

MIYAZAWA Hisao;

——— and S. SUGAIKE: Phase Transition of In_2Se_3 312

MIZUNO Hiroyuki;

: On the Conducting Mechanism of Oxide Coated Cathode 740

: Diffusion of Activator of Cathode Sleeve 1315

MIZUNO Joji;

S. OGAWA, ———, D. WATANABE and F. E. FUJITA: On the Twin Structure of Nickel Films Electrodeposited on Single Crystals of Copper 999

MIZUNO Yukio;

M. KOTANI, ———, K. KAYAMA and E. ISHIGURO: Electronic Structure of Simple Homonuclear Diatomic Molecules I. Oxygen Molecule 707

E. ISHIGURO, K. KAYAMA, M. KOTANI and ———: Electronic Structure of Simple Homonuclear Diatomic Molecules II. Lithium Molecule 1355

MIZUSHIMA Yoshihiko;

, Z. ODA and O. OCHI: The Structure of Evaporated Barium Films.... 355

MOMOTA Teruo;

M. SAKAI, H. OHMURA and ———: Multichannel Angular Correlation Measurement of Gamma Rays from the Disintegration of Ag^{110m} and Spin Assignment of Excited Levels of Cd^{110} 985

MORI Sigeru;
G. MIYAMOTO, G. IWATA, —— and K. INOUE: A Possible Fusion Reactor.. 438
MORIGUCHI Yoshiro;
—— and Y. KOGA: Electrical Properties of GeTe 100
MORIMOTO Takeshi;
: Cross Section for Displacement of Atoms by Heavy Particle Irradiation 442
: (Errata) Cross Section for Displacement of Atoms by Heavy Particle Irradiation 838
MORITA Nobuyoshi: Structure of Magnesium Fluoride Films on Amorphous Substrates. 1142
MORITA Susumu;
I. NONAKA, ——, N. KAWAI, T. ISHIMATSU, K. TAKESHITA, Y. NAKAJIMA and N. TAKENO: On the Neutrons from $N^{14}(d, n)O^{15}$ Reaction–II 841
MORITA Tohru;
——: Cluster Variation Method of Cooperative Phenomena and its Generalization I. 753
——: Cluster Variation Method of Cooperative Phenomena and its Generalization II. Quantum Statistics 1060
——: Cell Theory of Classical Liquid. Phase Transition between Gas, Liquid and Solid. Part I and II. 1195
MOTIZUKI Kazuko: Theory of the Para-Ortho Conversion in Solid Deuterium 163
MURAKAMI Kazuaki;
M. KODAMA, —— and Y. SEKIDO: Observation of Cosmic-Ray Neutron Intensity at Geomagnetic Latitude 25°N, Part 1. Atomospheric Effects 122
MURAKAMI Masakazu;
—— and T. MAEDA: The Absolute Intensities of Cosmic Rays at 2840 Meters and Geomagnetic Latitude 25°N 557
MURAKAMI Miyuki;
T. HIHARA, —— and E. HIRAHARA: Magnetic and Electrical Anisotropies of the Iron Sulfide Single Crystal 743
MURATA Yōjirō;
S. FUKUI, T. KITAMURA and —— : On the Range Spectrum of μ-Mesons at Sea-Level at Geomagnetic Latitude 24°N 854
MUTO Jiro;
——, E. TAKEKOSHI, T. NANAMURA, A. IMAMURA and Y. TSUNEOKA: The Multipolarity of γ-ray Absorption in $^{12}C(\gamma, 3\alpha)$ Reaction produced by (Li, p) γ-rays 109
MUTO Toshinosuke;
and S. OYAMA: Electronic Structure of a Moving Exciton in Alkali Halides 101
and H. OKUNO: On the Electronic Structure of Localized Exciton in Alkali Chlorides 108
MUTO Yoshio;
M. HIRABAYASHI and —— : Electrical Resistance of $CuAu_3$ and Cu_3Au at Low Temperatures 830

NAGAI Ojiro: Notes on the Ground State of Antiferromagnetism 978
NAGAKURA Sigemaro: Study of Metallic Carbides by Electron Diffraction Part I. Formation and Decomposition of Nickel Carbide 482
NAGAKURA Tosimitu;
and H. NARUSE: An Approximate Solution of the Hypersonic Laminar Boundary-Layer Equations and its Application 1298
NAGAMIYA Takeo;
S. YOMOSA and ——: Diffuse Scattering of X-rays by a Point-Imperfection in Diamond Lattice 610
NAGAO Shigeo: Effect of Shock Wave upon Gaseous Discharge 216
NAGASAKI Seizo;
M. YUZURI, T. HIRONE, H. WATANABE, —— and S. MAEDA: On the Magnetic Properties of Chromium Sulfides 385

NAGASHIMA Toshio;
  S. KOIDE, H. SEKIYAMA and ———: One-Center Molecular Orbital Wave Function for Methane 1016
NAGURA Takayuki;
  T. HORIE, ——— and M. OTSUKA: Radiative Collisions between Electron and Molecular Beams II. Angular Momentum Distribution of OH* Radicals Splitting from H_2O_2 Molecules 500
  T. HORIE, M. OTSUKA and ———: Radiative Collisions between Molecular and Electron Beams III. Angular Momentum Distribution of OH* Radicals Liberated from Alcohol Molecules 1099
NAITŌ Minoru: A Method of Calculating the Solid Angle subtended by a Circular Aperture 1122
NAKADA Osamu: Theory of Viscoelasticity of Amorphous Polymers. II. A Note on the Time-Temperature Reducibility of the Relaxation and Retardation Spectra.1218
NAKAGAWA Shigeo;
  ———, E. TAMAI, H. HUZITA and K. OKUDAIRA: On the Analysis of the Slow Particles Emitted from Cosmic-Ray Stars (II) 747
NAKAGAWA Yasuaki: Magnetic Susceptibility of Iron-Nickel Alloys in Liquid and Solid States 700
NAKAJIMA Sadao:
  R. KUBO, M. YOKOTA and ———: Statistical-Mechanical Theory of Irreversible Processes. II. Response to Thermal Disturbance 1203
NAKAJIMA Yutaka;
  I. NONAKA, S. MORITA, N. KAWAI, T. ISHIMATSU, K. TAKESHITA, ——— and N. TAKANO: On the Newtrons from the $N^{14}(d, n)O^{15}$ Reaction II 841
NAKAMURA Teruo;
  J. MUTO, E. TAKEKOSHI, ———, A. IMAMURA and Y. TSUNEOKA: The Multipolarity of γ-ray Absorption in $^{12}C(\gamma, 3\alpha)$ Reaction produced by (Li, p) γ-rays 109
NAKAMURA Terutaro:
  ———: After Effect of the Domain Motion in Rochelle Salt Crystal 477
  ———, W. KINASE and Y. KATO: Some Aspects of Wedge-Shaped Domains in $BaTiO_3$ Crystal 836
NAKANO Sigeru;
  H. HASEGAWA, ——— and N. HASHITUME: On the Hall Effect in Bismuth at Low Temperature 104
NAKASIMA Ryuzo;
  M. TAKEDA, M. KONDO, S. KATO, C. HU, ——— and S. YAMABE: Elastic Scattering of 5.7 Mev Protons from Ni and Cu 561
NAKASHIMA Ryuzo;
  M. TAKEDA, M. KONDO, ———, C. HU, A. TOI, T. YAMAZAKI and S. YAMABE: Elastic Scattering of 5.7 Mev Protons 979
NARA Jiro;
  H. HASUNUMA and ———: The Scattering of Light from Metal Aventurine Surface and Their Statistical Models 1117
NARUSE Humio: Application of the Thin-Wing-Expansion Method to the Compressible Flow past Profiles of Arbitrary Shape 959
  H. TAKAMI and ———: A Characteristic of Tomotika-Tamada's Gas as Affecting the Velocity Distribution Around a Profile 977
  T. NAGAKURA and ———: An Approximate Solution of the Hypersonic Laminar Boundary-Layer Equations and its Application 1298
NII Riro;
  Y. KANAI and ———: Electrical Properties of Nickel Doped Germanium at Low Temperatures 125
  Y. KANAI and ———: Anomalous Electrical Properties of Lead Telluride.... 441
NISHIKAWA Kiyoshi;
  S. TOKUNAGA, ——— and T. ISHII: A Cascade Shower in Nuclear Emulsion 219
NISHIKAWA Tetsuji;
  S. SEKINO and ———: Microwave Spectrum of Vinylidene Chloride.... 43

——— : Microwave Studies of the Internal Motion and the Structure of Methyl-Amine 668

T. KOJIMA and ——— : Potential Barrier and Molecular Structure of Methyl Mercaptan from its Microwave Spectra 680

NISHIOKA Atsuo;

———, H. KOMATSU and Y. KAKIUCHI: Nuclear Magnetic Resonance in Some Crystalline Polymers 283

NISHIWAKI Jien: Gloss of Machine Glazed Papers...... 53

NOGUCHI Seiichiro;

T. SATO and : Note on Some Properties of Gamma Brass 335

NOMOTO Otohiko: Phenomenological Theory of the Molecular Absorption and Dispersion of Sound in Fluids and the Relation between the Relaxation Time of the Internal Energy and the Relaxation Time of the Internal Specific Heat.. 85

: Theory of the Ultrasonic Absorption in Aqueous Solutions (II) Aqueous Solutions of Some Alcohols 300

and T. KISHIMOTO: Molecular Sound Velocity of Aqueous Sugar Solutions 311

: Intermolecular Free Length in Liquids in Relation to Sound Velocity.. 739

NOMURA Yûkichi;

——— and S. KATSURA: Diffraction of Electromagnetic Waves by Ribbon and Slit, I 190

NONAKA Itaru;

———, S. MORITA, N. KAWAI, T. ISHIMATSU, K. TAKESHITA, Y. NAKAJIMA and N. TAKANO: On the Neutrons from the N^{14}(d, n)O^{15} Reaction—II 841

NOZAWA Masao;

T. KATOH, ———, Y. YOSHIZAWA and Y. KOH: Beta Interaction in the Decay of Cs^{137}...... 738

NUMATA Tadasi: Technique of Obtaining a Minute Pinhole in a Metal Plate 559

——— : Technique of Obtaining a Minute Pinhole in a Metal Plate II 1312

NUNOGAKI Kan-ichi;

S. MIYAKE, K. HINOTANI and ———: Intensity and Energy Spectrum of Fast Neutrons in Cosmic Radiation...... 113

OCHI Osamu;

Y. MIZUSHIMA, Z. ODA and ——— : The Structure of Evaporated Barium Films 355

ODA Zenjiro;

Y. MIZUSHIMA, ——— and O. OCHI: The Structure of Evaporated Barium Films 355

ODAJIMA Akira;

, J. SOHMA and M. KOIKE: Proton Magnetic Resonance in Chain Polymers 272

OGAWA Shinji;

M. ASANUMA and ——— : On the Magnetic Aging of Commercial Pure Iron.. 955

OGAWA Shiro;

M. HIRABAYASHI and ——— : On the Superstructure of the Ordered Alloy Cu$_3$Pd II. X-ray Diffraction Study 259

M. HIRABAYASHI and ——— : (Errata) On the Superstructure of the Ordered Alloy Cu$_3$Pd II. X-ray Diffraction Study 442

———, J. MIZUNO, D. WATANABE and F. E. FUJITA: On the Twin Structure of Nickel Films Electrodeposited on Single Crystals of Copper...... 999

OGAWA Shizuko: Nuclear Quadrupole Resonance of Antimony Isotopes in Solids......1105

OHMURA Haruko;

M. SAKAI, ——— and T. MOMOTA: Multichannel Angular Correlation Measurement of Gamma Rays from the Disintegration of Ag^{110m} and Spin Assignment of Excited Levels of Cd^{110}...... 985

OHNO Kimio: On the Electronic Structure of the BH Molecule 938

OHOYAMA Tetuo: Some Comments on the Theory of Coercive Force of Fine Particles 827

OKA Takeshi;

———, H. HIRAKAWA and A. MIYAHARA: Dependence of Quadrupole Coupling Constant on the Vibrational State in ICN Molecule 39

—— and H. HIRAKAWA: Microwave Spectrum of BrCN and Dependence of Quadrupole Coupling Constant on the Vibrational State 820

OKADA Eiji;
T. WAKATSUKI, Y. HIRAO, ——— and I. MIURA: Gamma Rays from the Excited States of ^{10}O 1178

OKADA Jun'ichi: On the Carrier Recombination through Nickel Impurities in Germanium 741
———: Recombination of Excess Carriers in Semiconductors.. 1338

OKADA Toshihiro: The Measurements of the Galvanomagnetic Tensors of Bismuth ..1327

OKANO Jun: Preliminary Report on an Electromagnetic Isotope Separator........... 390

OKUDAIRA Kiyoaki;
S. NAKAGAWA, E. TAMAI, H. HUJITA and ———: On the Analysis of the Slow Particles Emitted from Cosmic-Ray Stars (II) 747

OKUNO Hiroshi;
T. MUTO and ———: On the Electronic Structure of Localized Exciton in Alkali Chlorides 108

OKURA Hiroshi: Oscillator Strength of *M*-center of KCl 1313

ONO Kazuo;
——— J. SHIMADA, K. KURODA and S. TANAKA: Angular Distribution of Proton Groups from the Reaction F^{19} (d, p) F^{20}.................................. 745
———: Paramagnetic Resonance Absorption in Chromous Sulphate Pentahydrate.1231

OOKAWA Akiya;
E. FUKUSHIMA and ———: Observation of the Grain Boundary in Soap Bubble Raft. Part III. The grain Boundary in Vibrating State 139
———: On the Mechanism of Deformation Twin in fcc Crystal............. 825

OOSHIKA Yuzuru: A Semi-empirical Theory of the Conjugated Systems. I. General Formulation 1238
———: A Semi-empirical Theory of the Conjugated Systems. II. Bond Alternation in Conjugated Chains 1246
A. CHIKAYAMA, ———, R. ITOH and I. OSHIDA: LCAO-MO Treatment of Phthalocyanine 1316

OSADA Kikusaburo: Phosphorescence of Acetic Acid 1420

OSHIDA Isao;
A. CHIKAYAMA, Y. OOSHIKA, R. ITOH and ———: LCAO-MO Treatment of Phthalocyanine 1316

ŌSHIMA Kōichi: Experiments on the Cylindrical Blast Waves.......................1423

OTSUKA Eizo;
— and H. KAWAMURA: Determination of Dislocation Densities Through Nuclear Resonance Studies 1071

OTSUKA Masamoto;
T. HORIE, T. NAGURA and ———: Radiative Collisions between Electron and Molecular Beams II. Angular Momentum Distribution of OH* Radicals Splitting from H_2O_2 Molecules 500
T. HORIE, and T. NAGURA: Radiative Collisions between Molecular and Electron Beams III. Angular Momentum Distribution of OH* Radicals Liberated from Alcohol Molecules..1099

OUCHI Akiji;
T. KIHARA and ———: Convex Molecules in Non-Uniform Gases—Supplement.1052

OYAMA Sei-ichi;
T. MUTO and ———: Electronic Structure of a Moving Exciton in Alkali Halides.. 101

D. K. ROY;
T. GHOSE, S. K. GHOSH and ———: A Study on the Effects of Off-Resonance on the Spin-Echo Signals 816

SAITŌ Nobuhiko: Irreversible Processes and Fluctuations...........................1321
and T. KATO: On the Viscoelasticity and Complex-dielectric Constant in the Presence of Electric Field and Shearing Laminar Flow in Solution of Macromolecules 1393

SAKAI Mitsuo;

, H. OHMURA and T. MOMOTA: Multichannel Angular Correlation Measurement of Gamma Rays from the Disintegration of Ag^{110m} and Spin Assignment of Excited Levels of Cd^{110}........ 985

SAKAMOTO Yosio;
M. L. HUGGINS and : Lattice Energies and Other Properties of Crystals of Alkaline Earth Chalcogenides........ 241

SAKUDA Tunetaro: Effect of Iron Group Ions on the Dielectric Properties of $BaTiO_3$ Ceramics........1050

SASAKI Wataru;
— and E. YOSHIDA: Acoustoelectric Effect in *n*-type Germaium........ 979
Y. KANAI and ——: Galvanomagnetic Effects in *n*-typ Indium Antimonide at Very Low Temperatures........1169

SATO Takao;
——— and S. NOGUCHI: Note on Some Properties of Gamma Brass........ 335

SATO Takao: Note on Collective Energy Losses in Metals........ 832

SAWADA Masao;
K. TSUTSUMI, A. HAYASE and ———: Fine Structures of X-ray *K* Absorption Spectra of Copper in Various Copper Compounds........ 793
T. ISHIMURA, T. SHIRAIWA and ———: The Input Power Limit of the Cylindrical Rotating Anode of a X-ray Tube........1064
—, K. TSUTSUMI and A. HAYASE: Fine Structure of X-ray Absorption Spectra of Cobalt in the Face Centered Cubic Lattice and Closepacked Hexagonal Lattice........ 628
T. SHIRAIWA, T. ISHIMURA and ———: Fine Structures of X-ray Absorption Spectra of Crystalline and Amorphous Germanium........ 788

SAWADA Shozo;
———, I. TAKOO and S. FUJII: An X-Ray Tube with a Rotating Anode and an Earthed Cathode........ 147
K. KAWABE and ———: Preparation of $BaTiO_3$ Single Crystals in Coal Gas Atmosphere........ 218

SEGAWA Wataru: Stress-Strain Relations for Viscoelastic Large Deformation........ 996
———, (Errata) Stress-Strain Relations for Viscoelastic Large Deformation....1170

SEKI Syôzô;
T. YUKITOSHI, H. SUGA, ——— and J. ITOH: Nuclear Magnetic Resonance Experiment on Solid Hexamethyldisilane........ 506

SEKIDO Yataro;
M. KODAMA, K. MURAKAMI and ———: Observation of Cosmic-Ray Neutron Intensity at Geomagnetic Latitude 25°N, Part I. Atmospheric Effects........ 122

SEKINO Shōzō;
——— and T. NISHIKAWA: Microwave Spectrum of Vinylidene Chloride.... 43

SEKIYAMA Hisao;
S. KOIDE, ——— and T. NAGASHIMA: One-Center Molecular Orbital Wave Function for Methane........1019

SEKIZAWA Hisashi;
Y. AIYAMA, ——— and S. IIDA: Magnetic Annealing Effect in Iron-Nickel Ferrites........ 742

SHIBAOKA Yoshio: On the Buckling of an Elliptic Plate with Clamped Edge II...... 529

SHIGEMITSU Yutaka;
Experimental Studies on Laminar Sub-layer in Turbulent Boundary Layer involving Separation........ 183

SHIMADA Junji;
K. Ôno, ———, K. KURODA and S. TANAKA: Angular Distribution of Proton Groups from the Reaction $F^{19}\ (d, p)\ F^{20}$........ 745
H. ABE and ———: Paramagnetic Resonance in Copper Acetate Monohydrate.1255

SHIMODA Koichi: Precise Frequency of the 3,3 Inversion Line of Ammonia........ 558
, H. TAKAHASHI and C. H. TOWNES: Fluctuations in Amplification of Quanta with Application to Maser Amplifiers........ 686

———: Characteristics of the Beam Type Maser I 1006

Shimauchi Akira;

S. **Kojima**, Y. **Abe**, M. **Minematsu**, K. **Tsukada** and ———: Structure of Nuclear Quadrupole Resonance Line. II. Solid Bromine 1225

Shimizu Kazuo;

R. **Yokota** and ———: Absorption Band due to Colloidal Silver 833

Shimomura Kenji;

———: Structural Investigation by Means of Nuclear Quardrupole Resonance I. Determination of Crystal Symmetry 652

———: Structural Investigation by Means of Nuclear Quardrupole Resonance II. Tin Tetrabromide 657

———: Structural Investigation by Means of Nuclear Quadrupole Resonance III. (Arsenic Tribromide) 1386

Shiraiwa Toshio;

———, T. **Ishimura** and M. **Sawada**: Fine Structure of X-ray Absorption Spectra of Crystalline and Amorphous Germanium 788

T. **Ishimura**, ——— and M. **Sawada**: The Input Power Limit of the Cylindrical Rotating Anode of a X-ray Tube 1064

Shogenji Kisaburo;

——— and S. **Uchiyama**: On Electrical Resistivity and Hall Coefficient of PbTe Crystals 252

S. **Uchiyama** and ———: Anomalies of Electrical Properties of Lead Telluride Crystal 431

——— and S. **Uchiyama**: Resistivity and Hall Coefficient of Semiconductor.. 434

——— and S. **Uchiyama**: The Galvanomagnetic Effects in Single Crystal of PbTe..1164

Soeya Teruko;

——— and R. **Kōno**: On Some Transition Phenomena in Aqueous Solution of Polyvinylalcohol 950

Sohma Junkichi;

A. **Odajima**, ——— and M. **Koike**: Proton Magnetic Resonance in Chain Polymers 272

Suga Hiroshi;

T. **Yukitoshi**, ———, S. **Seki** and J. **Itoh**: Nuclear Magnetic Resonance Experiment on Solid Hexamethyldisilane 506

Suga Koihi;

Y. **Tanaka**, ——— and S. **Mitani**: The Energy Spectrum of Nucleons in the Air Shower 215

Suga Koichi: Nuclear Interactions in Nucleon-Proton and Nucleon-Carbon Nucleus Collisions above 10 GeV..1171

Sugai Shintaro;

——— and J. **Furuichi**: Studies of High Polymers by Radioactive Method II Self-diffusion of Polystyrene in Its Dilute Solution......................... 369

Sugaike Suezo;

H. **Miyazawa** and ———: Phase Transition of In_2Se_3 312

Sugano Satoru;

Y. **Tanabe** and ———: The Absorption Spectra of Ruby 556

Suganomata Shinji;

S. **Takemoto**, T. **Dazai** and ———: Angular Distributions of Si^{28} (d, p) Si^{29} Reaction 1057

Sugawara Masao: On the Phototubes Sensitive to the Wide Spectral Region 1282

Sugawara Tadashi: Nuclear Magnetic Resonance in Solid Solutions of Transition Metals in Copper and Alminum.. 309

Sugimoto Masayoshi;

M. **Ariyama**, K. **Kayama** and ———: Self-Consistent Field without Exchange for Doubly Ionized Cobalt...................................... 285

Sugiura Yoshikazu;

K. **Matsuura**, ——— and G. M. **Hatoyama**: Frequency Shift in Ammonia

Absorption due to Foreign Gases 835
——— and G. M. HATOYAMA: Paramagnetic Resonance of Sillicocarbon...... 837

SUITA Tokuo;
N. ITOH and ———: Effect of Plastic Deformation on the Dielectric Breakdown of Silver Chloride Crystals 214
N. ITOH and ———: (Errata) Effect of Plastic Deformation on the Dielectric Breakdown of Silver Chloride Crystals 442
C. YAMANAKA and ———: Multiplication of Charge Carriers and Breakdown in Ge p–n Junction I 310

SUMI Masao: Oscillations of Electron Cloud in External Fields 1110

SUZUKI Akira;
U. YOSHIDA and ———: The Surface Potential of Selenium and its Relation to the Rectification and the Photovoltaic Effects 459

SUZUKI Kenzo;
S. CHIKAZUMI, ——— and H. IWATA: Studies on the Magnetic Anisotropy Induced by Cold Rolling of Ferromagnetic Crystal (I). Iron-Nickel Alloys 1259

SUZUKI Takeaki;
Y. MATSUKURA and ———: Etch Pits in Silicon Single Crystals 976

SUZUOKA Toshiro; An Electrical Resistance Study of the System (Cr_xMn_{1-x}) Sb* 1344

TAKAHASI Hidetosi;
W. KINASE and ———: On the 180°C-type Domain Wall of $BaTiO_3$ Crystal.. 464
K. SHIMODA, ——— and C. H. TOWNES: Fluctuations in Amplification of Quanta with Application to Maser Amplifiers 686

TAKAGI Satio;
M. KURIYAMA, K. KOHRA and ———: Electron Diffraction Study on Polish Layers of Gold, I.. 151

TAKAGI Riitsu: Growth of Oxide Whiskers on Metals at High Temperatures 1212

TAKAMI Hideo;
——— and H. NARUSE: A Characteristic of Tomotika-Tamada's Gas as Affecting the Velocity Distribution Around a Profile 977

TAKANO Fumihiko: Theory of Excitations in Liquid Helium 4 1185

TAKANO Nawoyuki;
I. NOAKA, S. MORITA, N. KAWAI, T. ISHIMATSU, K. TAKESHITA, Y. NAKAJIMA and ———: On the Neutrons from the N^{14} (d, n) O^{15} Reaction II 841

TAKEDA Minoru;
———, M. KONDO, S. KATO, C. HU, R. NAKASHIMA and S. YAMABE: Elastic Scattering of 5.7 Mev Protons from Ni and Cu 561
———, M. KONDO, R. NAKASHIMA, C. HU, A. TOI, T. YAMAZAKI and S. YAMABE: Elastic Scattering of 5.7 MeV Protons.. 979

TAKEKOSHI Eiko:
J. MUTO, ———, T. NAKAMURA, A. IMAMURA and Y. TSUNEOKA: The Multipolarity of γ-ray Absorption in ^{12}C $(\gamma, 3\alpha)$ Reaction produced by (Li, p) γ-ray 109

TAKEMOTO Shigeru;
———, T. DAZAI and S. SUGANOMATA: Angular Distributions of the Si^{28} (d, p) Si^{29} Reaction 1057

TAKESHITA Kenji;
I. NONAKA, S. MORITA, N. KAWAI, T. ISHIMATSU, ———, Y. NAKAJIMA and N. TAKANO: On the Neutrons from the N^{14} (d, n) O^{15} Reaction–II 841

TAKEYAMA Mikio: On the Dielectric Properties of α-phase n-Higher Alcohols and Associated Electromotive Force 1167

TAKOO Ine;
———, S. SAWADA and S. FUJII: An X-Ray Tube with a Rotating Anode and an Earthed Cathode.. 147

TAMAI Eiji;
S. NAKAGAWA, ———, H. FUJITA and K. OKUDAIRA: On the Analysis of the Slow Particles Emitted from Cosmic-Ray Stars (II) 747

TAMAKI Fumio;
———: Experimental Studies on the Stability of the Transonic Flow past

Airfoils 544
and KIM, C. S: Studies on the Hypersonic Flow Using a Double-Diaphragm Shock Tube 550

TANABE Yukito;
——— and S. SUGANO: The Absorption Spectra of Ruby 556
———: On the Variational Problem connected with the Thomas Fermi Method 974
———: (Errata) On the Variational Problem connected with the Thomas Fermi Method 1170

TANAKA Hidejirō;
H. FUTAMA and ———: The Thermal Decomposition of Polyvinyl-Alcohol Using Mass Spectrometer 433

TANAKA Shigeya;
K. ÔNO, J. SHIMADA, K. KURODA and ———: Angular Distribution of Proton Groups from the Reaction F^{19} (d, p) F^{20} 745

TANAKA Yasuo;
———, K. SUGA and S. MITANI: The Energy Spectrum of Nucleons in the Air Shower 215

TANEDA Sadatoshi: Experimental Studies of the Lift on Two Equal Circular Cylinders placed side by side in a Uniform Stream at Low Reynolds Numbers 419

TATSUMOTO Eiji;
T. YAMASHITA and ———: Magnetic Anisotropy in Connection with Rolling in the Course of Producing Single Crystals of Silicon Steel 975

TATSUZAKI Itaru;
——— and Y. YOKOZAWA: Influence of Temperature on the Pure Nuclear Quadrupole Resonance in Hexachloroethane 802

TOI Atsutomo;
M. TAKEDA, M. KONDO, R. NAKASHIMA, C. HU, ———, T. YAMAZAKI and S. YAMABE: Elastic Scattering of 5.7 Mev Protons 979

TOKUNAGA Senzo;
———, K. NISHIKAWA and T. ISHII: A Cascade Shower in Nuclear Emulsion 219
———: Meson Showers by Heavy Primary Particles 454

TOMISHIMA Yasuo;
S. ASANO and ———: Rotational Lattice Vibration in Complex Crystals Part I. Vibrational Modes and Special Heat 346
S. ASANO and ———: Rotational Lattice Vibration in Complex Crystals Part II. Vibration Modes in Optical Branches and Interaction with a Conduction Electron 890
S. ASANO and ———: Rotational Lattice Vibration in Complex Crystals Part III. Vibrational Frequencies in Cubic $NaClO_4$ Crystals 900

Charles H. TOWNES
K. SHIMODA, H. TAKAHASI and ———: Fluctuations in Amplification of Quanta with Application to Maser Amplifiers 686

TSUGÉ Shun-ichi: On a Theory of Shock Waves in Locally Supersonic Zone and a New Boundary-value Problem for the Tricomi's Equation......................1412

TSUJI Mikio: Electron Transport in Metals 828

TSUJIUCHI Jumpei: A Density Filter Improving Aberrant Optical Image 744

TSUKADA Kineo;
S. KOJIMA, Y. ABE, M. MINEMATSU, ——— and A. SHIMAUCHI: Structure of Nuclear Quadrupole Resonance Line II. Solid Bromine 1225

TSUNEOKA ;
J. MUTO, E. TAKEKOSHI, A. IMAMURA and ———: The Multipolarity of γ-ray Absorption in ^{12}C $(\gamma, 3\alpha)$ Reaction Produced by (Li, p) γ-rays 109

TSUTSUMI Kenjiro;
M. SAWADA, ——— and A. HAYASE: Fine Structures of X-ray Absorption Spectra of Cobalt in the Face Centered Cubic Lattice and Close-packed Hexagonal Lattice 628
———, A. HAYASE and M. SAWADA: Fine Structures of X-ray K Absorption Spectra of Copper in Various Copper Compounds 793

TSUZUKU Takuro: Conical Spiral Structure and Laminar Cleavage of Graphite 778
———: (Errata) Conical Spiral Structure and Laminar Cleavage of Graphite..1318
UCHIYAMA Susumu;
K. SHOGENJI and ———: On Electrical Resistivity and Hall Coefficient of PbTe Crystals 252
——— and K. SHOGENJI: Anomalies of Electrical Properties of Lead Telluride Crystal 431
——— and K. SHOGENJI: Resistivity and Hall Coefficient of Semiconductors 434
——— and K. SHOGENJI: The Galvanomagnetic Effects in Single Crystal of PbTe..1164
UMEDA Kwai;
Y. KAMADA and ———: Elongated Lichtenberg Figure 1317
Y. KAMADA and ———: (Erratum) Elongated Lichtenberg Figure 1425
WADA Yasaku;
K. YAMAMOTO and ———: An Investigation of the Dynamic Mechanical Properties of Glassy Polymers by the Composite Oscillator Method 374
WAKATSUKI Tetsuo;
———, Y. HIRAO, E. OKADA and I. MIURA: Gamma Rays from the Excited States of ^{16}O 1178
WAKIYA Shōichi;
———: Viscous Flows past a Spheroid 1130
———: (Errata) Viscous Flows past a Spheroid 1318
WATANABE Hiroshi;
M. YUZURI, T. HIROSE, ———, S. NAGASAKI and S. MAEDA: On the Magnetic Properties of Chromium Sulfides 385
———: Magnetic Properties of Perovskites Containing Strontium I. Strontium-Rich Ferrites and Cobaltites 515
WATANABE Masaru: Submicroscopic Topography of Oxidized Surface of Stibnite and Etched Surface of Zincblende 874
WATANABE Denjiro;
S. OGAWA, J. MIZUNO, ——— and F. E. FUJITA: On the Twin Structure of Nickel Films Electrodeposited on Single Crystals of Copper 999
YABUMOTO Tadaichi;
——— and S. YAMADA: Photoelectric Emission of Oxide Coated Cathods 1163
YAMABE Shotaro;
M. TAKEDA, M. KONDO, S. KATO, C. HU, R. NAKASIMA and ———: Elastic Scattering of 5.7 Mev Protons from Ni and Cu 561
M. TAKEDA, M. KONDO, R. NAKASIMA, C. HU, A. TOI, T. YAMAZAKI and ———: Elastic Scattering of 5.7 Mev Protons 979
YAMADA Ryozo: On the Radio Wave Propagation in a Stratified Atmosphere II......1022
YAMADA Syôzi;
T. YABUMOTO and ———: Photoelectric Emission of Oxide Coated Cathods ..1163
YAMAGUTI Tasaburô: A New Method of Electro-Machining of Hard Metals.......... 204
YAMAMOTO Keiji;
——— and Y. WADA: An Investigation of the Dynamic Mechanical Properties of Glassy Polymers by the Composite Oscillator Method.................... 374
YAMAMOTO Mikio: Theory of the Wiedemann Effect 981
YAMAMOTO Misazo: The Visco-elastic Properties of Network Structure II. Structural Viscosity 1148
YAMANAKA Chiyoe;
——— and T. SUITA: Multiplication of Charge Carriers and Breakdown in Ge *p–n* Junction I 310
YAMASHITA Tadayoshi;
——— and E. TATSUMOTO: Magnetic Anisotropy in Connection with Rolling in the Course of Producing Single Crystals of Silicon Steel 975
YAMAZAKI Masatoshi: Group-Theoretical Treatment of the Energy Bands in Metal Borides MeB$_6$.. 1
YAMAZAKI Takashi;

M. TAKEDA, M. KONDO, R. NAKASIMA, C. HU, A. TOI, ——— and S. YAMABE: Elastic Scattering of 5.7 Mev Protons 979

YASUDA Iwao;

E. FUKUDA and ———: On the Piezoelectric Effect of Bone 1158

YASUHARA Michiru;

———: Asymptotic Behaviour of the Laminar Compressible Boundary Layer over a Circular Cylinder with Uniform Suction 102

———: On the Hypersonic Viscous Flow past a Flat Plate with Suction or Injection 177

YASUMI Shinjiro: Nuclear Reaction induced by the 14 MeV Neutrons 443

YOKOTA Ryosuke;

——— and K. SHIMIZU: Absorption Band due to Colloidal Silver 833

YOKOTA Mario;

R. KUBO, ——— and S. NAKAJIMA: Statistical-Mechanical Theory of Irreversible Processes II. Responce to Thermal Disturbance 1203

YOKOZAWA Yasaburo;

——— and I. MIYASHITA: Temperature Dependence of Electron Spin Resonance Absorption of Thiophenol in Sulfuric Acid 107

I. TATSUZAKI and ———: Influence of Temperature on the Pure Nuclear Quadrupole Resonance in Hexachloroethane 802

YOMOSA Sigeo;

——— and T. NAGAMIYA: Diffuse Scattering of X-rays by a Point-Imperfection in Diamond Lattice 610

YOSHIDA Eiichi;

W. SASAKI and ———: Acoustoelectric Effect in *n*-type Germanium 979

YOSHIDA Hide: Effect of Inelastic Waves on Electron Diffraction 618

YOSHIDA Shigetomo;

——— and T. IKEDA: Effect of Electron Bombardment on Sodium Chloride 1421

YOSHIDA Umejiro;

——— and A. SUZUKI: The Surface Potential of Selenium and its Relation to the Rectification and the Photovoltaic Effects 459

YOSHIZAWA Yasukazu;

T. KATOH, M. NOZAWA, ——— and Y. KOH: Beta Interaction in the Decay of Cs^{137} 738

YUKITOSHI Teruo;

———, H. SUGA, S. SEKI and J. ITOH: Nuclear Magnetic Resonance Experiment on Solid Hexamethyldisilane 506

YUZURI Motoyoshi;

———, T. HIRONE, H. WATANABE, S. NAGASAKI and S. MAEDA: On the Magnetic Properties of Chromium Sulfides 385